Silicon Carbide and Related Materials

ECSCRM2000

Proceedings of the 3rd European Conference on Silicon Carbide and Related Materials, Kloster Banz, Germany, September 2000

Editors:

G. Pensl, D. Stephani and M. Hundhausen

20010502 133

TRANS TECH PUBLICATIONS LTD
Switzerland Germany UK USA

ECSCRM2000 SPONSORS:

Deutsche Forschungsgemeinschaft
European Commission, High-Level Scientific Conferences Contract No. HPCF-CT-1999-00181
US-ARL-European Research Office
US-Office of Naval Research International Field Office

CORPORATE SPONSORS:

Cree
Aixtron
DaimlerChrysler
Emcore
Epigress
H. C. Starck
Infineon Technologies
Leybold
NovaSiC
Omicron
Phys Tech
Saes Getters
SiCrystal
Siemens
Specs
Steag RTP Systems
Sterling Semiconductors
TDI
Triple-O Microscopy
II-VI Incorporated
Varian
Wacker Siltronic

Silicon Carbide and Related Materials

Copyright © 2001 Trans Tech Publications Ltd, Switzerland
ISBN 0-87849-873-7

Volumes 353-356 of
Materials Science Forum
ISSN 0255-5476

***Distributed** in the Americas by*

Trans Tech Publications Inc
PO Box 699, May Street
Enfield, New Hampshire 03748
USA
Phone: (603) 632-7377
Fax: (603) 632-5611
e-mail: ttp@ttp.net
Web: http://www.ttp.net

and worldwide by

Trans Tech Publications Ltd
Brandrain 6
CH-8707 Uetikon-Zuerich
Switzerland
Fax: +41 (1) 922 10 33
e-mail: ttp@ttp.net
Web: http://www.ttp.net

Printed in the United Kingdom
by Hobbs the Printers Ltd,
Totton, Hampshire SO40 3WX

ECSCRM2000 CHAIRPERSONS:

G. Pensl	University of Erlangen-Nürnberg, Germany
D. Stephani	SiCED, Erlangen, Germany

ECSCRM2000 LOCAL COMMITTEE:

M. Bockstedte	University of Erlangen-Nürnberg
R. Eckstein	SiCrystal AG
T. Frank	University of Erlangen-Nürnberg
D. Hofmann	University of Erlangen-Nürnberg
M. Hundhausen	University of Erlangen-Nürnberg
O. Klettke	University of Erlangen-Nürnberg
M. Krieger	University of Erlangen-Nürnberg
M. Laube	University of Erlangen-Nürnberg
G. Loy	University of Erlangen-Nürnberg
N. Schulze	University of Erlangen-Nürnberg
A. Seubert	University of Erlangen-Nürnberg
U. Starke	University of Erlangen-Nürnberg
M. Weidner	University of Erlangen-Nürnberg

ECSCRM2000 STEERING COMMITTEE:

C. Brylinski	Thomson CSF/LCR, France
W. J. Choyke	University of Pittsburgh, USA
V. Dmitriev	TDI/Ioffe Institute, St.Petersburg, Russia
C. Harris	ACREO, Sweden
R. Helbig	University of Erlangen-Nürnberg, Germany
E. Janzen	University of Linköping, Sweden
H. Matsunami	Kyoto University, Japan
B. Monemar	University of Linköping, Sweden
J. Robert	University of Montpellier II, France
D. Siche	Institute of Crystal Growth, Berlin, Germany
J. Stoemenos	Aristotle University of Thessaloniki, Greece
A. Winnacker	University of Erlangen-Nürnberg, Germany

ECSCRM2000 PROGRAM COMMITTEE:

F. Bechstedt	University of Jena, Germany
J. Camassel	University of Montpellier II, France
E. Janzen	University of Linköping, Sweden
R. Madar	LMGP/UMR 5628 INPG/CNRS/ENSPG, France
H. Mitlehner	SiCED, Erlangen, Germany
B. Monemar	University of Linöping, Sweden
R. Nieminen	Helsinki University of Technology, Finland
J. Stoemenos	Aristotle University of Thessaloniki, Greece
M. Stutzmann	Walter-Schottky-Institute, TU München, Germany
B. Svensson	KTH, Stockholm, Sweden

Preface

The Third European Conference on Silicon Carbide and Related Materials (ECSCRM2000), held September 3-7, 2000 in Kloster Banz, Germany, developed into a truly important forum in the field of wide bandgap semiconductors. All continents – some 320 participants from 21 different countries - were represented and 15 exhibitors maintained booths and demonstrated the increasingly industrial interest in and the economic impact of the wide bandgap semiconductors. Scientists from Universities and Industry discussed the exciting progress in the fields of SiC and III-Nitrides. Many young scientists have been among the participants; they are regarded as the guarantee to successfully solve the forthcoming tasks.

These proceedings reveal the present experimental and theoretical knowledge on the growth of bulk crystals and epitaxial layers, the mechanical, thermal and electronic properties of the grown material, the development of suitable processes and electronic devices, which will have a profound effect on society's ability to better utilize its strategic resources in the future.

Contained in these proceedings are 184 contributed and 10 invited papers. The Program Committee recommended to avoiding parallel sessions, to put emphasis on plenary sessions and to make the poster sessions as comfortable as possible. Based on these recommendations, three plenary sessions and two extended poster sessions, which attracted intensive discussions, were organized. In addition, emphasis on the strengthening of the interaction between scientists from Universities and Industry has been facilitated by organizing events like the "Defect Forum" and the session on "Special Industrial Contributions". Social events (the Opening and Get-Together, the Conference Banquet in the wine cellar of the Staatliche Hofkellerei in Würzburg and the Barbecue Party) provided good opportunities to trigger and to stengthen personal ties amongst this international group of researchers.

The success of ECSCRM2000 was due to a smooth team work by many committed people. The Steering Committee made many valuable proposals regarding the scientific content of the conference, the Program Committee has carefully reviewed and selected the scientific contributions and put together the technical program. The session chairmen took care that the oral presentations ran smoothly and on time. All the reviewers deserve great appreciation for carefully reading the manuscripts during the conference to guarantee a high scientific standard of the proceedings.

An outstanding portion of the success was due to the careful assistance and the enthusiasm of the members of the local Organizing Team; we wish to thank Michel Bockstedte, Kai Christiansen, Florin Ciobanu, Thomas Frank, Jürgen Gajowski, Hans Heißenstein, Oliver Klettke, Michael Krieger, Michael Laube, Gabi Loy, Alrun Pensl, Horst Sadowski, Konrad Schneider, Norbert Schulze, Kurt Semmelroth, Achim Seubert, Ulrich Starke and Michael Weidner. We would especially like to express to Gabi Loy our deepest appreciation for her expert leadership in all the financial affairs and in organizing the registration and accomodation for the participants. In many hopeless situations, Gabi never lost track of things and always discovered an optimal solution. We are very grateful to Michael Krieger, who developed the computer program for the complete organization of the conference, to Michael Laube, who designed and took care of the outstanding home page on the internet, to Thomas Frank, Oliver Klettke and Michael Weidner for their dedicated help in preparing the manuscripts for the Conference Proceedings. Last but not least we would like to thank Michael Möslein and Lucia Gieß of the Hanns-Seidel-Stiftung for their professional

commitment to creating an elevating atmosphere and for taking care of all the organizational matters at Kloster Banz.

The generous support of the many industrial and government sponsors enabled the organizers to provide funding for young scientists and for participants from Eastern European countries and to keep the conference fee at an affordable level.

The next conference in this series will move to the nothern part of Europe. It will be held in Linköping, Sweden in 2002. General Chairman will be Prof. Erik Janzén. We wish the organizers of the next conference much success.

Erlangen, November 2000

Gerhard Pensl
Dietrich Stephani
Martin Hundhausen

Overview

Chapter 1: SiC Bulk Growth 1

Chapter 2: SiC Epitaxy and Thin Film Growth 89
2.1 Homoepitaxial Growth 91
2.2 Heteroepitaxial Growth 151
2.3 Thin Film Growth 191

Chapter 3: Physical Properties of SiC 203
3.1 Surfaces and Interfaces 205
3.2 Structure and Diffusion 259
3.3 Optical Properties 335
3.4 Electrical Properties 421
3.5 Magnetic Resonance Properties 499
3.6 Positron Annihilation 533

Chapter 4: Processing of SiC 541
4.1 Surveys 543
4.2 Doping and Implantation 555
4.3 Contacts and Etching 603
4.4 Dielectrics 627

Chapter 5: SiC Devices 667
5.1 Unipolar Devices 669
5.2 Bipolar Devices 727
5.3 Sensors 747

Chapter 6: III-Nitrides and Related Materials 767
6.1 Growth and Physical Properties 769
6.2 Devices 807

Author Index 819

Keyword Index 827

Table of Contents

Chapter 1: SiC Bulk Growth

Large Diameter, Low Defect Silicon Carbide Boule Growth
C.H. Carter Jr., R. Glass, M. Brady, D. Malta, D. Henshall, S. Müller, V. Tsvetkov, D. Hobgood and A. Powell 3

SiC Single Crystal Growth by Sublimation: Experimental and Numerical Results
C. Moulin, M. Pons, A. Pisch, P. Grosse, C. Faure, A. Basset, G. Basset, A. Passero, T. Billon, B. Pelissier, M. Anikin, E. Pernot, P. Pernot-Rejmánková and R. Madar 7

Impact of SiC Source Material on Temperature Field and Vapor Transport During SiC PVT Crystal Growth Process
P.J. Wellmann, D. Hofmann, L. Kadinski, M. Selder, T.L. Straubinger and A. Winnacker 11

Defect Reduction in Sublimation Grown Silicon Carbide Crystals by Adjustment of Thermal Boundary Conditions
E. Schmitt, M. Rasp, A.-D. Weber, M. Kölbl, R. Eckstein, L. Kadinski and M. Selder 15

Progress in 4H-SiC Bulk Growth
M. Anikin, E. Pernot, B. Pelissier, M. Pons, A. Pisch, C. Bernard, T. Billon, C. Faure, C. Moulin and R. Madar 21

Stability Criteria for 4H-SiC Bulk Growth
T.L. Straubinger, M. Bickermann, D. Hofmann, R. Weingärtner, P.J. Wellmann and A. Winnacker 25

Growth Related Distribution of Secondary Phase Inclusions in 6H-SiC Single Crystals
H.-J. Rost, J. Dolle, J. Doerschel, D. Siche, D. Schulz and J. Wollweber 29

Investigation of a PVT SiC-Growth Set-up Modified by an Additional Gas Flow
T.L. Straubinger, P.J. Wellmann and A. Winnacker 33

Mass Transport and Powder Source Evolution in Sublimation Growth of SiC Bulk Crystals
D.S. Karpov, O.V. Bord, S.Yu. Karpov, A.I. Zhmakin, M.S. Ramm and Yu.N. Makarov 37

Some Aspects of Sublimation Growth of SiC Ingots
S.F. Avramenko, V.S. Kiselev, M.Ya. Valakh and V.A. Yukhimchuk 41

Growth of Highly Aluminum-Doped p-type 6H-SiC Single Crystals by the Modified Lely Method
N. Schulze, J. Gajowski, K. Semmelroth, M. Laube and G. Pensl 45

Study of Boron Incorporation During PVT Growth of p-type SiC Crystals
M. Bickermann, D. Hofmann, M. Rasp, T.L. Straubinger, R. Weingärtner, P.J. Wellmann and A. Winnacker 49

Features of Semi-Insulating SiC Single-Crystal Growth by Physical Vapor Transport
S.A. Reshanov, V.P. Rastegaev and Yu.M. Tairov 53

Virtual Reactor: A New Tool for SiC Bulk Crystal Growth Study and Optimization
M.V. Bogdanov, O.V. Bord, A.O. Galyukov, S.Yu. Karpov, A.V. Kulik, S.K. Kochuguev, A.E. Komissarov, D.K. Ofengeim, A.M. Serkov, A.V. Tsiryulnikov, I.A. Zhmakin, M.S. Ramm, A.I. Zhmakin and Yu.N. Makarov 57

Coupled Thermodynamic - Mass Transfer Modeling of the SiC Boule Growth by the PVT Method
A. Pisch, E. Blanquet, M. Pons, C. Bernard, J.M. Dedulle and R. Madar 61

Numerical Simulation of Thermal Stress Formation During PVT-Growth of SiC Bulk Crystals
M. Selder, L. Kadinski, F. Durst, T.L. Straubinger, P.J. Wellmann and D. Hofmann 65

Crystal Growth of 15R-SiC and Various Polytype Substrates
T. Nishiguchi, T. Shimizu, M. Sasaki, S. Ohshima and S. Nishino 69

Micropipe Filling by the Sublimation Close Space Technique
T. Furusho, S. Ohshima and S. Nishino 73

Mechanism for Damage Healing of Cracked 6H-SiC Substrates by the Sublimation Method
T. Shimizu, T. Nishiguchi, M. Sasaki, S. Ohshima and S. Nishino 77

Chemical Vapor Deposition of SiC by the Temperature Oscillation Method
Yutaka Abe 81

Aluminium-Silicon as a Melt for the Low Temperature Growth of SiC Crystals
D. Chaussende, C. Jacquier, G. Ferro, J.C. Viala, F. Cauwet and Y. Monteil 85

Chapter 2: SiC Epitaxy and Thin Film Growth

2.1 Homoepitaxial Growth

Epitaxial Growth of 4H-SiC in a Vertical Hot-Wall CVD Reactor: Comparison between Up- and Down-Flow Orientations
J. Zhang, A. Ellison, Ö. Danielsson, A. Henry and E. Janzén 91

Influence of the Growth Conditions on the Layer Parameters of 4H-SiC Epilayers Grown in a Hot-Wall Reactor
G. Wagner and K. Irmscher 95

Enlarging the Usable Growth Area in a Hot-Wall Silicon Carbide CVD Reactor by Using Simulation
Ö. Danielsson, U. Forsberg, A. Henry and E. Janzén 99

Modeling Analysis of SiC CVD in a Planetary Reactor
A.N. Vorob'ev, A.K. Semennikov, A.I. Zhmakin, Yu.N. Makarov, M. Dauelsberg, F. Wischmeyer, M. Heuken and H. Jürgensen 103

Influence of Silicon Gas-to-Particle Conversion on SiC CVD in a Cold-Wall Rotating-Disc Reactor
A.N. Vorob'ev, M.V. Bogdanov, A.E. Komissarov, S.Yu. Karpov, O.V. Bord, A.A. Lovtsus and Yu.N. Makarov 107

Ab Initio Study of Silicon Carbide: Bulk and Surface Structures
C. Raffy, L. Magaud, E. Blanquet, M. Pons and A. Pasturel 111

SiC Defect Density Reduction by Epitaxy on Porous Surfaces
S.E. Saddow, M. Mynbaeva, W.J. Choyke, R.P. Devaty, S. Bai, G. Melnychuck, Y. Koshka, V. Dmitriev and C.E.C. Wood 115

Effect of Sublimation Growth on the Structure of Porous Silicon Carbide: SEM and X-Ray Diffraction Investigations
N.S. Savkina, V.V. Ratnikov, V.B. Shuman and A.A. Lebedev 119

Gaseous Etching Effects on Homoepitaxial Growth of SiC on Hemispherical Substrates Using CVD
S. Nishino, Y. Masuda, S. Ohshima and C. Jacob 123

Low Temperature Selective and Lateral Epitaxial Growth of Silicon Carbide on Patterned Silicon Substrates
C. Jacob, P. Pirouz and S. Nishino 127

Characterization of 4H-SiC Epilayers Grown at a High Deposition Rate
H. Tsuchida, T. Tsuji, I. Kamata, T. Jikimoto, H. Fujisawa, S. Ogino and K. Izumi 131

Control of Surface Morphologies for Epitaxial Growth on Low Off-Angle 4H-SiC (0001) Substrates
K. Masahara, M. Kushibe, H. Ohno, K. Kojima, T. Takahashi, Yu. Ishida, T. Suzuki, T. Tanaka, S. Yoshida and K. Arai 135

Surface Morphology of 4H-SiC Inclined towards <1 $\bar{1}$ 00> and <11 $\bar{2}$ 0> Grown by APCVD Using the $Si_2Cl_6+C_3H_8$ System
Y. Masuda, S. Ohshima, C. Jacob and S. Nishino 139

Growth of 3C-SiC Using Off-Oriented 6H-SiC Substrates
M. Syväjärvi, R. Yakimova, H. Jacobsson and E. Janzén 143

SiC Polytype Transformation on the Growth Surface
E.N. Mokhov, S.K. Obyden, A.D. Roenkov, G.V. Saparin and Yu.A. Vodakov 147

2.2 Heteroepitaxial Growth

Improvement of the 3C-SiC/Si Interface by Flash Lamp Annealing
D. Panknin, J. Stoemenos, M. Eickhoff, V. Heera, N. Vouroutzis, G. Krötz and W. Skorupa 151

How to Grow Unstrained 3C-SiC Heteroepitaxial Layers on Si (100) Substrates
T. Chassagne, G. Ferro, C. Gourbeyre, M. Le Berre, D. Barbier and Y. Monteil 155

Growth of 3C-SiC on Si by Low Temperature CVD
T. Cloitre, N. Moreaud, P. Vicente, M.L. Sadowski and R.L. Aulombard 159

Growth of SiC on Si(100) by Low-Pressure MOVPE
A.S. Bakin, A.A. Ivanov, D. Piester, T. Riedl, F. Hitzel, H.-H. Wehmann and A. Schlachetzki 163

The Microstructure and Surface Morphology of Thin 3C-SiC Films Grown on (100) Si Substrates Using an APCVD-Based Carbonization Process
C.H. Wu, J. Chung, M.H. Hong, C.A. Zorman, P. Pirouz and M. Mehregany 167

A Comparison of SiO_2 and Si_3N_4 Masks for Selective Epitaxial Growth of 3C-SiC Films on Si
C.H. Wu, J. Chung, M.H. Hong, C.A. Zorman, P. Pirouz and M. Mehregany 171

Selective Deposition of 3C-SiC Epitaxially Grown on SOI Subtrates
M. Eickhoff, S. Zappe, A. Nielsen, G. Krötz, E. Obermeier, N. Vouroutzis and J. Stoemenos 175

Carbonization Induced Change of Polarity for MBE Grown 3C-SiC/Si(111)
J. Pezoldt, B. Schröter, V. Cimalla, T. Stauden, R. Goldhahn, H. Romanus and L. Spieß 179

The Influence of Ge on the SiC Nucleation on (111)Si Surfaces
J. Pezoldt, T. Wöhner, T. Stauden, J.A. Schaefer and P. Masri 183

In Situ RHEED Studies on the Influence of Ge on the Early Stages of SiC on Si(111) and (100) Surfaces
V. Cimalla, K. Zekentes, K. Tsagaraki, T. Stauden, F. Scharmann and J. Pezoldt 187

2.3 Thin Film Growth

Structural and Optical Properties of SiC Films Deposited on Si by DC Magnetron Sputtering
Y.M. Lei, Y.H. Yu, L.L. Cheng, L. Lin, B. Sundaraval, E.Z. Luo, S. Lin, C.X. Ren, W.Y. Cheung, S.P. Wong, J.B. Xu, S.C. Zou and I.H. Wilson 191

Laser Crystallization of Amorphous SiC Thin Films on Glass
S. Urban and F. Falk 195

TEM Investigation of Si Implanted Natural Diamond
B. Pécz, Á. Barna, V. Heera, F. Fontaine and W. Skorupa 199

Chapter 3: Physical Properties of SiC

3.1 Surfaces and Interfaces

Surface Reconstruction on SiC(0001) and SiC(000$\bar{1}$): Atomic Structure and Potential Application for Oxidation, Stacking and Growth
U. Starke 205

Interplay of Surface Structure, Bond Stacking and Heteropolytypic Growth of SiC
U. Grossner, A. Fissel, J. Furthmüller, W. Richter and F. Bechstedt 211

Room Temperature Initial Oxidation of 6H- and 4H-SiC(0001) 3x3
F. Amy, Y.-K. Hwu, C. Brylinski and P. Soukiassian 215

Comparison of HF and Ozone Treated SiC Surfaces
R.P. Mikalo, P. Hoffmann, D.R. Batchelor, A. Lloyd-Spetz, I. Lundström and D. Schmeißer 219

Preparation and Characterization of Hydrogen Terminated 6H-SiC
N. Sieber, T. Seyller, B.F. Mantel, J. Ristein and L. Ley 223

Polytype and Polarity of Silicon Carbide and Aluminium Nitride Films Growing by MBE: A Nondestructive Identification
B. Schröter, A. Winkelmann, A. Fissel, V. Lebedev and W. Richter 227

Surface Abstraction Reactions at Experimental Temperatures; A Theoretical Study of 4H-SiC(0001)
J. Olander and K. Larsson 231

Combined Scanning Tunneling Microscopy and Photoemission Studies of the β-SiC(100) c(4x2) Surface Reconstruction
V. Derycke, P. Fonteneau, V.Yu. Aristov, H. Enriquez and P. Soukiassian 235

Investigation of the SiC Surface after Nitrogen Plasma Treatment
L.A. Bereznjakova, A.V. Shchukarev and V.I. Ivanov-Omskii 239

Morphology of Sublimation Grown 6H-SiC(000$\bar{1}$) Surfaces
D. Schulz, J. Dolle, H.-J. Rost, D. Siche and J. Wollweber 243

Germanium on SiC(0001): Surface Structure and Nanocrystals
B. Schröter, K. Komlev, U. Kaiser, G. Heß, G. Kipshidze and W. Richter 247

Origin of the Excellent Thermal Stability of Al/Si-Based Ohmic Contacts to p-Type LPE 4H-SiC
L. Kassamakova, R. Kakanakov, I. Kassamakov, K. Zekentes, K. Tsagaraki and G. Atanasova 251

Ion-Irradiation Effect on the Ni/SiC Interface Reaction
F. Roccaforte, L. Calcagno, P. Musumeci and F. La Via 255

3.2 Structure and Diffusion

Analysis of Strain and Defect Formation in Low-Dimensional Structures in SiC
U. Kaiser, K. Saitoh and A. Chuvilin 259

Source Material Related Distribution of Defects in 6H-SiC Single Crystals
H.-J. Rost, D. Siche, J. Dolle, D. Schulz and J. Wollweber 263

Characterization of 2 Inch SiC Wafers Made by the Sublimation Method
M. Sasaki, H. Shiomi and S. Nishino 267

Ion Bombardment Induced Damage in Silicon Carbide Studied by Ion Beam Analytical Methods
E. Szilágyi, N.Q. Khánh, Z.E. Horváth, T. Lohner, G. Battistig, Z. Zolnai, E. Kótai and J. Gyulai 271

Effects of Hydrogen Implantation and Annealing on the Vibrational Properties of 6H-SiC
H.W. Kunert, T.P. Maurice, T. Hauser, J.B. Malherbe, L.C. Prinsloo, D.J. Brink, L.A. Falkovsky and J. Camassel 275

4H- and 6H-SiC Rutherford Back Scattering-Channeling Spectrometry: Polytype Finger Printing
R. Nipoti and A. Carnera 279

X-ray Diffraction, Micro-Raman and Birefringence Imaging of Silicon Carbide
E. Pernot, M. Mermoux, J. Kreisel, O. Chaix-Pluchery, P. Pernot-Rejmánková, M. Anikin, B. Pelissier, A.M. Glazer and R. Madar 283

X-Ray Diffraction Line Profile Analysis of Neutron Irradiated 6H-SiC
C. Seitz, A. Magerl, H. Heissenstein and R. Helbig 287

High-Resolution XRD Evaluation of Thick 4H-SiC Epitaxial Layers
H. Jacobsson, R. Yakimova, M. Syväjärvi, J. Birch, T. Tuomi and E. Janzén 291

Defect Analysis of SiC Sublimation Growth by the *in-situ* X-Ray Topography
T. Kato, N. Oyanagi, H. Yamaguchi, S.i. Nishizawa and K. Arai 295

Crystal Defects as Source of Anomalous Forward Voltage Increase of 4H-SiC Diodes
J.P. Bergman, H. Lendenmann, P.Å. Nilsson, U. Lindefelt and P. Skytt 299

A Simple Non-Destructive Technique to Detect Micropipes in Silicon Carbide
D.J. Morrison, A. Keir, I.H. Preston, K.P. Hilton, M.J. Uren and C.M. Johnson 303

Micropipe and Macrodefect Healing in SiC Crystals during Liquid Phase Processing
B.M. Epelbaum, D. Hofmann, U. Hecht and A. Winnacker 307

Micropipe Closing via Thick 4H-SiC Epitaxial Growth Involving Structural Transformation of Screw Dislocations
I. Kamata, H. Tsuchida, T. Jikimoto and K. Izumi 311

Growth Evolution of Dislocation Loops in Ion Implanted 4H-SiC
P.O.Å. Persson and L. Hultman 315

Lattice Parameter Measurements of 3C-SiC Thin Films Grown on 6H-SiC(0001) Substrate Crystals
J. Kräußlich, A. Bauer, B. Wunderlich and K. Goetz 319

Self Diffusion in SiC: the Role of Intrinsic Point Defects
A. Mattausch, M. Bockstedte and O. Pankratov 323

Modeling of Boron Diffusion in Silicon Carbide
H. Bracht, N.A. Stolwijk, M. Laube and G. Pensl 327

Quantitative Modeling of Hydrogen Diffusion and Reactivation of H-Passivated Al-Acceptors in SiC
C. Hülsen, N. Achtziger, J. Herold and W. Witthuhn 331

3.3 Optical Properties

Optical Characterization of SiC Materials: Bulk and Implanted Layers
J. Camassel, P. Vicente and L. Falkovski 335

Line Broadening of Phonons in the Raman Spectra of Isotopically Disordered SiC
S. Rohmfeld, M. Hundhausen, L. Ley, N. Schulze and G. Pensl 341

Micro-Raman and Photoluminescence Study on n-type 6H-SiC
Z.C. Feng, S.J. Chua, G.A. Evans, J.W. Steeds, K.P.J. Williams and G.D. Pitt 345

Low-Frequency Vibrational Spectroscopy in SiC Polytypes
B. Pajot, C.J. Fall, J.L. Cantin, H.J. von Bardeleben, R. Jones, P.R. Briddon and F. Gendron 349

Free Carrier Diffusion in 4H-SiC
P. Grivickas, A. Martinez, I. Mikulskas, V. Grivickas, R. Tomašiunas, J. Linnros and U. Lindefelt 353

Valence Band Splittings of 15R-SiC Measured using Wavelength Modulated Absorption Spectroscopy
R.P. Devaty, S. Bai, W.J. Choyke, D. Hobgood and D.J. Larkin 357

Zeeman Effect of D_1 Bound Exciton in 4H-SiC
C.Q. Chen, R. Helbig, R. Winkler, A. Wysmolek and M. Potemski 361

As-Grown and Process-Induced Intrinsic Deep-Level Luminescence in 4H-SiC
B. Magnusson, A. Ellison, F.H.C. Carlsson, N.T. Son and E. Janzén 365

Characterization of SiC:P Prepared by Nuclear Transmutation Due to Neutrons
H. Heissenstein and R. Helbig 369

Presence of Hydrogen in SiC
A. Henry, B. Magnusson, M.K. Linnarsson, A. Ellison, M. Syväjärvi, R. Yakimova and E. Janzén 373

Investigation of an Ion-Implantation Induced High Temperature Persistent Intrinsic Defect in SiC
S.G. Sridhara, F.H.C. Carlsson, J.P. Bergman, A. Henry and E. Janzén 377

Differentiation between C and Si Related Damage Centres in 4H- and 6H-SiC by the Use of 90-300 kV Electron Irradiation Followed by Low Temperature Photoluminescence Microscopy
J.W. Steeds, F. Carosella, G.A. Evans, M.M. Ismail, L.R. Danks and W. Voegeli 381

Infrared Investigation of Implantation Damage and Implantation Damage Annealing in 4H-SiC
J. Pernot, J.M. Bluet, J. Camassel and L. Di Cioccio 385

Investigation of Electroluminescence across 4H-SiC $p^+/n^-/n^+$ Structures Using Optical Emission Microscopy
A. Galeckas, J. Linnros, B. Breitholtz and H. Bleichner 389

Defects Characterization in SiC by Scanning Photoluminescence Spectroscopy
L. Masarotto, J.M. Bluet, M. Berenguer, P. Girard and G. Guillot 393

Absorption Measurements and Doping Level Evaluation in n-Type and p-Type 4H-SiC and 6H-SiC
R. Weingärtner, M. Bickermann, D. Hofmann, M. Rasp, T.L. Straubinger, P.J. Wellmann and A. Winnacker 397

Low Temperature Photoluminescence Processes of ^{13}C Enriched 6H- and 15R-SiC Crystals Grown by the Modified Lely Method
H. Sadowski, N. Schulze, T. Frank, M. Laube, G. Pensl and R. Helbig 401

Intrinsic Photoconductivity of 6H-SiC and the Free-Exciton Binding Energy
I.G. Ivanov, T. Egilsson, J. Zhang, A. Ellison and E. Janzén 405

Epitaxial Growth and Properties of SiC Layers Grown on α-SiC(0001) by Solid-Source MBE: A Photoluminescence Study
A. Fissel and W. Richter 409

Prediction of Optical Properties of Si and Ge Dots in SiC
H.-C. Weissker, J. Furthmüller and F. Bechstedt 413

Investigation of Variable Incidence Angle Spectroscopic Ellipsometry for Determination of Below Band Gap Uniaxial Dielectric Function
M. Kildemo and O. Hunderi 417

3.4 Electrical Properties

Theory of Hydrogen in Silicon Carbide
P. Deák, A. Gali and B. Aradi 421

Dissociation Energy of the Passivating Hydrogen-Aluminum Complex in 4H-SiC
M.S. Janson, A. Hallén, M.K. Linnarsson, N. Nordell, S. Karlsson and B.G. Svensson 427

Proton Irradiation Induced Defects in 4H-SiC
L. Storasta, F.H.C. Carlsson, S.G. Sridhara, D. Åberg, J.P. Bergman, A. Hallén and E. Janzén 431

Intrinsic Defect Complexes in α-SiC: the Formation of Antisite Pairs
E. Rauls, Z. Hajnal, A. Gali, P. Deák and T. Frauenheim 435

Generation and Annihilation of Intrinsic-Related Defect Centers in 4H/6H-SiC
T. Frank, M. Weidner, H. Itoh and G. Pensl 439

Implantation Temperature Dependent Deep Level Defects in 4H-SiC
D. Åberg, L. Storasta, A. Hallén and B.G. Svensson 443

Boron in SiC: Structure and Kinetics
M. Bockstedte, A. Mattausch and O. Pankratov 447

Deep Level Investigation of pn-Junctions formed by MeV Aluminum and Boron Implantation into 4H-SiC
A. Schöner, N. Miyamoto, T. Kimoto and H. Matsunami 451

Boron Centers in 4H-SiC
B. Aradi, A. Gali, P. Deák, E. Rauls, T. Frauenheim and N.T. Son 455

Oxygen-Related Defect Centers Observed in 4H/6H-SiC Epitaxial Layers Grown under CO_2 Ambient
O. Klettke, G. Pensl, T. Kimoto and H. Matsunami 459

Electrical Activity of Isolated Oxygen Defects in SiC
A. Gali, D. Heringer, P. Deák, Z. Hajnal, T. Frauenheim and W.J. Choyke 463

Beryllium-Related Defect Centers in 4H-SiC
M. Krieger, M. Laube, M. Weidner and G. Pensl 467

Band Gap States of Cr in the Lower Part of the SiC Band Gap
G. Pasold, N. Achtziger, J. Grillenberger and W. Witthuhn 471

Tantalum and Tungsten in Silicon Carbide: Identification and Polytype Dependence of Deep Levels
J. Grillenberger, N. Achtziger, G. Pasold, R. Sielemann and W. Witthuhn 475

Shallow Dopant and Surface Levels in 6H-SiC MOS Structures Studied by Thermally Stimulated Current Technique
V.S. Lysenko, I.P. Osiyuk, T.E. Rudenko, I.P. Tyagulski, E.Ö. Sveinbjörnsson and H.Ö. Ólafsson 479

Intrinsic Mobility of Conduction Electrons in 4H-SiC
J. Pernot, S. Contreras, E. Neyret, L. Di Cioccio, W. Zawadzki and J.L. Robert 483

A Study of Band to Band Tunneling with Application to High-Field Transport in Hexagonal SiC Polytypes
A. Martinez, H.-E. Nilsson and U. Lindefelt 487

Thermopower Measurements in 4H-SiC and Theoretical Calculations Considering the Phonon Drag Effect
V. Grivickas, M. Stölzer, E. Velmre, A. Udal, P. Grivickas, M. Syväjärvi, R. Yakimova and V. Bikbajevas 491

Donor Densities and Donor Energy Levels in 3C-SiC Determined by a New Method Based on Hall-Effect Measurements
H. Matsuura, Y. Masuda, Y. Chen and S. Nishino 495

3.5 Magnetic Resonance Properties

Intrinsic Defects in Silicon Carbide Polytypes
N.T. Son, P.N. Hai and E. Janzén 499

Radiation-Induced Pair Defects in 6H-SiC Studied by Optically Detected Magnetic Resonance
T. Lingner, S. Greulich-Weber and J.-M. Spaeth 505

Intrinsic Defects in 6H-SiC Generated by Electron Irradiation at the Silicon Displacement Threshold
H.J. von Bardeleben, J.L. Cantin, P.G. Baranov and E.N. Mokhov 509

EPR Study of Proton Implantation Induced Intrinsic Defects in 6H- and 4H-SiC
H.J. von Bardeleben and J.L. Cantin 513

EPR Study of Carbon Vacancy-Related Defects in Electron-Irradiated 6H-SiC
V.Ya. Bratus', I.N. Makeeva, S.M. Okulov, T.L. Petrenko, T.T. Petrenko and H.J. von Bardeleben 517

EPR of Deep Al and Deep B in Heavily Al-doped as Grown 4H-SiC
I.V. Ilyin, E.N. Mokhov and P.G. Baranov 521

The Electronic Structure of the N Donor Center in 4H-SiC and 6H-SiC
A. van Duijn-Arnold, R. Zondervan, P.G. Baranov, E.N. Mokhov and J. Schmidt 525

Identification of Iron and Nickel in 6H-SiC by Electron Paramagnetic Resonance
P.G. Baranov, I.V. Ilyin, E.N. Mokhov and V.A. Khramtsov 529

3.6 Positron Annihilation

Calculated Positron Annihilation Parameters for Defects in SiC
T.E.M. Staab, L.M. Torpo, M.J. Puska and R.M. Nieminen 533

Annealing Process of Defects in Epitaxial SiC Induced by He and Electron Irradiation: Positron Annihilation Study
A. Kawasuso, F. Redmann, R. Krause-Rehberg, P. Sperr, T. Frank, M. Weidner, G. Pensl and H. Itoh 537

Chapter 4: Processing of SiC

4.1 Surveys

Recent Progress in SiC Epitaxial Growth and Device Processing Technology
T. Kimoto, H. Yano, S. Tamura, N. Miyamoto, K. Fujihira, Y. Negoro and H. Matsunami 543

Doping of Silicon Carbide by Ion Implantation
B.G. Svensson, A. Hallén, M.K. Linnarsson, A.Yu. Kuznetsov, M.S. Janson, D. Åberg, J. Österman, P.O.Å. Persson, L. Hultman, L. Storasta, F.H.C. Carlsson, J.P. Bergman, C. Jagadish and E. Morvan 549

4.2 Doping and Implantation

Neutron Irradiation of 4H SiC
F.H.C. Carlsson, L. Storasta, B. Magnusson, J.P. Bergman, K. Sköld and E. Janzén 555

Techniques for Depth Profiling of Dopants in 4H-SiC
J. Österman, A. Hallén, S. Anand, M.K. Linnarsson, H. Andersson, D. Åberg, D. Panknin and W. Skorupa 559

Growth of δ-Doped SiC Epitaxial Layers
S. Karlsson, C. Adås, A. Konstantinov and M.K. Linnarsson 563

Effect of Residual Damage on Carrier Transport Properties in a 4H-SiC Double Implanted Bipolar Junction Transistor
S. Ortolland, N.G. Wright, C.M. Johnson, A.P. Knights, P.G. Coleman, C.P. Burrows and A.J. Pidduck 567

High Electrical Activation of Aluminium and Nitrogen Implanted in 6H-SiC at Room Temperature by RF Annealing
M. Lazar, L. Ottaviani, M.L. Locatelli, C. Raynaud, D. Planson, E. Morvan, P. Godignon, W. Skorupa and J.P. Chante 571

Enhancement of Electrical Activation of Aluminum Acceptors in 6H-SiC by Co-Implantation of Carbon Ions
T. Ohshima, H. Itoh and M. Yoshikawa 575

High Dose Implantation in 6H-SiC
V. Heera, W. Skorupa, J. Stoemenos and B. Pécz 579

Precipitate Formation in Heavily Al-Doped 4H-SiC Layers
M.K. Linnarsson, P.O.Å. Persson, H. Bleichner, M.S. Janson, U. Zimmermann, H. Andersson, S. Karlsson, R. Yakimova, L. Hultman and B.G. Svensson 583

Flash Lamp Annealing of Implantation Doped p- and n-Type 6H-SiC
D. Panknin, T. Gebel and W. Skorupa 587

Structural and Electrical Characterization of Ion Beam Synthesized and n-Doped SiC Layers
C. Serre, D. Panknin, A. Pérez-Rodríguez, A. Romano-Rodríguez, J.R. Morante, R. Kögler, W. Skorupa, J. Esteve and M.C. Acero 591

Channeling Measurements of Ion Implantation Damage in 4H-SiC
A.Yu. Kuznetsov, M.S. Janson, A. Hallén, B.G. Svensson, C. Jagadish, H. Grünleitner and G. Pensl 595

The Monte Carlo Binary Collision Approximation Applied to the Simulation of the Ion Implantation Process in Single Crystal SiC: High Dose Effects
G. Lulli, E. Albertazzi, R. Nipoti, M. Bianconi and A. Carnera 599

4.3 Contacts and Etching

Formation of Large Area Al Contacts on 6H- and 4H-SiC Substrates
O. Korolkov and T. Rang 603

Ru Schottky Barrier Contacts to n- and p-type 6H-SiC
M.E. Samiji, E. van Wyk, L. Wu, A. Venter and A.W.R. Leitch 607

Stability of Molybdenum Schottky Contact to Silicon Carbide
K. Nishikawa, M. Shimizu, B. Foster and H. Iwakuro 611

Effects of Thermal Annealing on Cu/6H-SiC Schottky Properties
T. Hatayama, T. Suezaki, K. Kawahito, Yu. Uraoka and T. Fuyuki 615

Electrochemical Characterization of p-Type Hexagonal SiC
M. Kayambaki, K. Zekentes, K. Tsagaraki, E. Pernot and R. Yakimova 619

A Novel Technique for Shallow Angle Beveling of SiC to Prevent Surface Breakdown in Power Devices
J.N. Merrett, D.C. Sheridan, J.R. Williams, C.C. Tin and John D. Cressler 623

4.4 Dielectrics

Interface States of SiO_2/SiC on $(11\bar{2}0)$ and (0001) Si Faces
H. Yano, T. Kimoto and H. Matsunami 627

Interface Properties of MOS Structures Formed on 4H-SiC C$(000\bar{1})$ Face
K. Fukuda, S. Suzuki, J. Senzaki, W.J. Cho, T. Tanaka and K. Arai 631

Steam Annealing Effects on CV Characteristics of MOS Structures on $(11\bar{2}0)$ Face of 4H-SiC
M. Yoshikawa, T. Ohshima, H. Itoh, K. Takahashi and M. Kitabatake 635

Role of H_2 in Low Temperature Post-Oxidation Anneal for Gate Oxide on 6H-SiC
V. Raineri, S. Lombardo, P. Musumeci, A.M. Maktari and L. Calcagno 639

Influence of the Post-Oxidation Process on the MOS Interface and MOSFETs Properties
S. Suzuki, W.J. Cho, R. Kosugi, J. Senzaki, S. Harada and K. Fukuda 643

Observation of SiO_2/SiC Interface with Different Off-Angle from Si(0001) Face Using Transmission Electron Microscopy
K. Fukuda, S. Suzuki, J. Senzaki, R. Kosugi, T. Tanaka and K. Arai 647

Remote PECVD Oxide Utilized in U-MOS Structures and Different MOSFETs on SiC
S. Scharnholz, O. Hellmund, J. Stein, B. Spangenberg and H. Kurz 651

Indications for Nitrogen-Assisted Removal of Carbon from SiO_2-SiC Interface
P. Jamet, S. Dimitrijev and P. Tanner 655

Dissolution Mechanism of the Carbon Islands at the SiO_2/SiC Interface
O.H. Krafcsik, K.V. Josepovits and P. Deák 659

Dependence of Wet Oxidation on the Defect Density in 3C-SiC
M. Eickhoff, N. Vouroutzis, A. Nielsen, G. Krötz and J. Stoemenos 663

Chapter 5: SiC Devices

5.1 Unipolar Devices

SiC Microwave Power Devices
E. Morvan, O. Noblanc, C. Dua and C. Brylinski 669

1700 V SiC Schottky Diodes Scaled to 25 A
D. Peters, K.O. Dohnke, C. Hecht and D. Stephani 675

Temperature Dependence of Forward and Reverse Characteristics of Ti, W, Ta and Ni Schottky Diodes on 4H-SiC
M. Treu, R. Rupp, H. Kapels and W. Bartsch 679

A High Performance JBS Rectifier - Design Considerations
F. Dahlquist, H. Lendenmann and M. Östling 683

Design and Characterization of 2.5kV 4H-SiC JBS Rectifiers with Self-Aligned Guard Ring Termination
D.C. Sheridan, J.N. Merrett, J.D. Cressler, S.E. Saddow, J.R. Williams, C. Ellis and G. Niu 687

Improvements in the Electrical Performance of High Voltage 4H-SiC Schottky Diodes by Hydrogen Annealing
Q.u. Wahab, E.B. Macák, J. Zhang, L.D. Madsen and E. Janzén 691

Influence of the Buried p-Layer on the Blocking behavior of Vertical JFETs in 4H-SiC
P. Friedrichs, H. Mitlehner, R. Schörner, R. Kaltschmidt, K.O. Dohnke and D. Stephani 695

A Comparison between Physical Simulations and Experimental Results in 4H-SiC MESFETs with Non-Constant Doping in the Channel and Buffer Layers
J. Eriksson, N. Rorsman, H. Zirath, R. Jonsson, Q.u. Wahab and S. Rudner 699

Noise Behavior of 4H-SiC MESFETs at Low Drain Voltage
C. Banc, A.S. Royet, T. Ouisse, E. Bano, O. Noblanc and C. Brylinski 703

Double Implanted Power MESFET Technology in 4H-SiC
A.B. Horsfall, S. Ortolland, N.G. Wright, C.M. Johnson and A.P. Knights 707

Source Resistance Analysis of SiC-MESFET
M. Arai, M. Ogata, H. Honda, H. Sawazaki, A. Nakagawa and M. Kitamura 711

Design and Implementation of RESURF MOSFETs in 4H-SiC
S. Banerjee, K. Chatty, T.P. Chow and R.J. Gutmann 715

Comparison of Super-Junction Structures in 4H-SiC and Si for High Voltage Applications
K. Adachi, C.M. Johnson, H. Ohashi, T. Shinohe, K. Kinoshita and K. Arai 719

SiC Junction Control, an Alternative to MOS Control High Voltage Switching Devices
A. Mihaila, F. Udrea, G. Brezeanu, R. Azar and G. Amaratunga 723

5.2 Bipolar Devices

Long Term Operation of 4.5kV PiN and 2.5kV JBS Diodes
H. Lendenmann, F. Dahlquist, N. Johansson, R. Söderholm, P.Å. Nilsson, J.P. Bergman and P. Skytt 727

Planar p-n Diodes Fabricated by MeV-Energy and High-Temperature Selective Implantation of Aluminum to 4H-SiC
H. Sugimoto, S. Kinouchi, Y. Tarui, M. Imaizumi, K. Ohtsuka, T. Takami and T. Ozeki 731

Silicon Carbide Zener Diodes
K. Vassilevski, K. Zekentes, E.V. Bogdanova, M. Lagadas and A. Zorenko 735

Characteristics of Epitaxial and Implanted N-Base 4H-SiC GTO Thyristors
J.B. Fedison and T.P. Chow 739

Turn-off Performance of a 2.6 kV 4H-SiC Asymmetrical GTO Thyristor
A.K. Agarwal, P.A. Ivanov, M.E. Levinshtein, J.W. Palmour, S.L. Rumyantsev, S.H. Ryu and M.S. Shur 743

5.3 Sensors

SiC Based Gas Sensors and their Applications
S.M. Savage, H. Svenningstorp, L. Unéus, A. Kroutchinine, P. Tobias, L.G. Ekedahl, I. Lundström, C.I. Harris and A. Lloyd Spetz 747

High Temperature 10 Bar Pressure Sensor Based on 3C-SiC/SOI for Turbine Control Applications
S. Zappe, J. Franklin, E. Obermeier, M. Eickhoff, H. Möller, G. Krötz, C. Rougeot, O. Lefort and J. Stoemenos 753

Charged Particle Detection Properties of Epitaxial 4H-SiC Schottky Diodes
F. Nava, P. Vanni, G. Verzellesi, A. Castaldini, A. Cavallini, L. Polenta, R. Nipoti and C. Donolato 757

Thin Heavily Compensated 6H-SiC Epilayers as Nuclear Particle Detectors
A.A. Lebedev, N.B. Strokan, A.M. Ivanov, D.V. Davydov and V.V. Kozlovskii 763

Chapter 6: III-Nitrides and Related Materials

6.1 Growth and Physical Properties

The Role of Threading Dislocations in the Physical Properties of GaN and its Alloys
J.S. Speck 769

AlN Crystal Growth by Sublimation Technique
S.Yu. Karpov, A.V. Kulik, M.S. Ramm, E.N. Mokhov, A.D. Roenkov, Yu.A. Vodakov and Yu.N. Makarov 779

Investigation of the Structure of 2H-AlN Films on Si(001) Substrates
J. Jinschek, U. Kaiser, V. Lebedev and W. Richter 783

Formation and Electronic Transport of 2D Electron and Hole Gases in AlGaN/GaN Heterostructures
A. Link, O. Ambacher, I.P. Smorchkova, U.K. Mishra, J.S. Speck and M. Stutzmann 787

Luminescence of InGaN/GaN Multiple Quantum Wells Grown by Mass-Transport
G. Pozina, J.P. Bergman, B. Monemar, M. Iwaya, S. Nitta, H. Amano and I. Akasaki 791

From Relaxed to Highly Tensily Strained GaN Grown on 6H-SiC and Si(111): Optical Characterization
M. Leroux, H. Lahrèche, F. Semond, M. Laügt, E. Feltin, N. Schnell, B. Beaumont, P. Gibart and J. Massies 795

Electron Traps in Undoped GaN Layers Subjected to Gamma-Irradiation and Annealing
D.V. Davydov, V.V. Emtsev, A.A. Lebedev, W.V. Lundin, D.S. Poloskin, N.M. Shmidt, A.S. Usikov and E.E. Zavarin 799

Characterization of GaAlN/GaN Superlattice Heterostructures
Z. Makkai, B. Pécz, M.A. di Forte-Poisson and F. Huet 803

6.2 Devices

III-Nitride Power Devices - Good Results and Great Expectations
M.S. Shur, R. Gaska and A. Khan 807

High-Performance Surface-Channel Diamond Field-Effect Transistors
H. Umezawa, H. Taniuchi, T. Arima, M. Tachiki, H. Okushi and H. Kawarada 815

Author Index 819

Keyword Index 827

AD NUMBER	DATE	DTIC ACCESSION NOTICE
1. REPORT IDENTIFYING INFORMATION		REQ 1. Put on r 2. Comp 3. Attac mail 4. Use u infor 5. Do not for 6 t
A. ORIGINATING AGENCY Univ. Erlangen-Nürnberg, Germany		
B. REPORT TITLE AND/OR NUMBER 3rd European Conference on Silicon Carbide + Related Materials		
C. MONITOR REPORT NUMBER KD 9028-EE-02		
D. PREPARED UNDER CONTRACT NUMBER		
2. DISTRIBUTION STATEMENT APPROVED FOR PUBLIC RELEASE DISTRIBUTION UNLIMITED PROCEEDINGS		DTIC: 1. Assign 2. Return

20010502 133

DTI... OCT 95 ...EDITIONS ARE OBSOLETE

Chapter 1:

SiC Bulk Growth

Materials Science Forum Vols. 353-356 (2001) pp. 3-6
© 2001 Trans Tech Publications, Switzerland

Large Diameter, Low Defect Silicon Carbide Boule Growth

C.H. Carter Jr., R. Glass, M. Brady, D. Malta, D. Henshall, S. Müller, V. Tsvetkov, D. Hobgood and A. Powell

Cree, Inc., 4600 Silicon Drive, Durham NC 27703, USA

Keywords: Etch Pits, Micropipe, Moissanite, Physical Vapor Transport, Sublimation

Abstract. Realization of the full potential of semiconductor SiC for electronic and optical applications is critically dependent on the production of large diameter SiC single-crystals of high crystalline quality and controlled impurity content. In this paper, recent empirical results reflecting the current state of the art of SiC bulk growth are presented. Recent progress in monocrystalline SiC bulk crystal growth is characterized by the attainment of: substrate diameters up to 100-mm; residual impurities in the 10^{15} cm^{-3} range; thermal conductivity approaching 5.0 W/cmK; near colorless 6H-SiC at crystal diameters up to 75-mm; and micropipe densities as low as 1.1 cm^{-2} over an entire 50-mm diameter 4H-SiC wafer and 8 cm^{-2} for 75-mm diameter 6H-SiC. Additionally, the recent interest in SiC for the production of a unique near colorless gemstone material, moissanite, increases the demand for high quality SiC bulk material.

Introduction

Within the last several years SiC semiconductor device technology for electronic and optoelectronic applications has made tremendous progress resulting primarily from the commercial availability of SiC substrates of ever increasing diameter and quality. Examples of current state of the art devices exploiting the unique electrical and thermophysical properties of silicon carbide include [1]: high brightness blue and green InGaN-based LEDs which take full advantage of the electrical conductivity of the SiC substrate by employing a conductive AlGaN buffer layer; microwave MESFETs on semi-insulating 4H-SiC substrates with power densities as high as 4.6 W/mm at 3.5 GHz and total CW output power of 80 W at 3.1 GHz from a single chip; 12.3 kV p-i-n diodes fabricated on high quality SiC epitaxial layers; thyristors conducting 12 A at 6.5 V with 2600 V blocking voltage; and GaN/AlGaN HEMTs fabricated on semi-insulating SiC substrates with power density of 6.9 W/mm at 10 GHz. Throughout the technical evolution of semiconductor SiC, the fabrication of SiC crystals exhibiting the desired electrical and crystalline properties has played a central role in the realization of the full potential of this important semiconductor material. This paper gives an overview of the current state of the art of bulk SiC growth at Cree, Inc. by highlighting recent advances in the fabrication of large diameter SiC crystals of improved quality.

Diameter Enlargement

6H and 4H-SiC single crystals are grown using the technique of physical vapor transport (PVT) via seeded sublimation. This technique has been recently reviewed [2] and is currently the preferred method for the bulk growth of monocrystalline SiC. Production volumes of 6H and 4H-polytypes are now available at diameters up to 75-mm. Increasing the wafer diameter is crucial for reducing the cost of SiC devices through economies of scale and the use of Si or GaAs device fab equipment. SiC substrate development has been characterized by the continuous increase in crystal diameter from less than 25-mm in the early part of this decade to crystals with diameters up to 100-mm, first

announced in 1999 [3]. Figure 1 illustrates the increase in wafer diameter for 4H-SiC R&D wafers grown at Cree, Inc. since 1992. Early R&D prototype 75-mm diameter wafers suffered from excessive low-angle grain boundaries, near the wafer periphery. This problem was later circumvented allowing extension of the PVT technique to the fabrication of fully single-crystal substrates with diameters up to 100-mm, as shown in Figure 2. Crack-free growth of large diameter SiC crystals requires increased attention to system design and optimization of the thermal distribution in the growth environment to minimize excessive mechanical and thermoelastic stresses [2]. This significant development in wafer enlargement represents a major step toward bringing SiC to parity with III-V compound semiconductors, such as GaAs, in available wafer area for device fabrication.

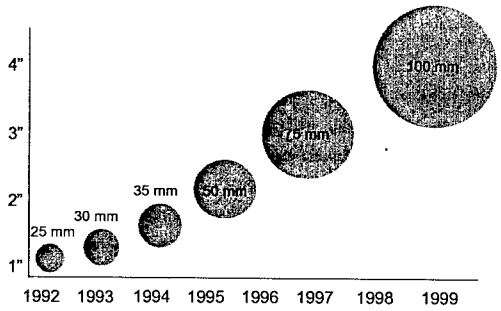


Figure 1. Increase in R&D 4H-SiC wafer diameter vs. year at Cree, Inc.

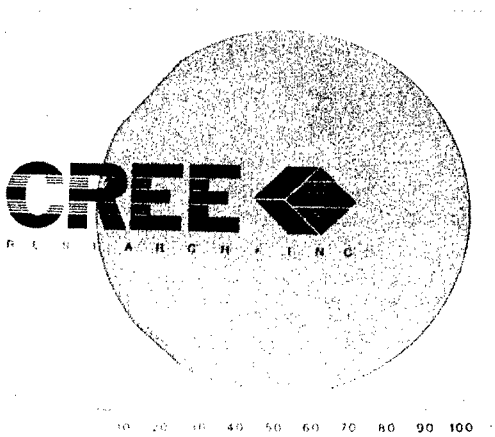
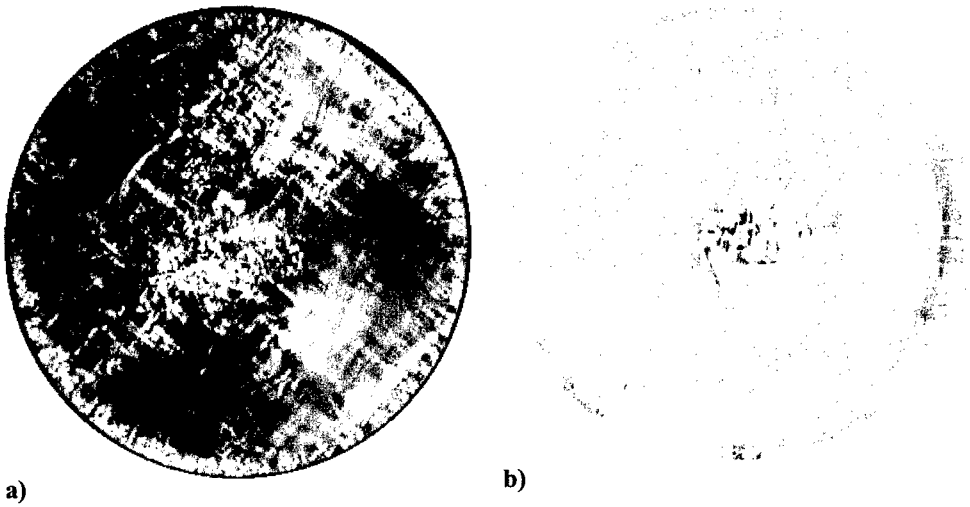


Figure 2. 100 mm 6H SiC wafer

Defects

In parallel with efforts to enlarge crystal diameter, efforts have been directed toward improvement in overall crystal perfection. These improvements have focussed on reduction of stress, reduction in micropipe density, and the elimination of low angle boundaries. The significant overall quality improvement of 75-mm diameter 4H- and 6H-SiC wafers is illustrated in Figure 3 where the reduction of stress birefringence in recent wafers is compared to earlier 75-mm wafers. Micropipe defects occurring to varying extent in all SiC wafers produced to date are seen by many as preventing the commercialization of many types of SiC devices, especially high current power devices. The dislocation content of micropipes is indicated by the existence of growth spirals originating from micropipes, characteristic stress patterns around micropipes visible in stress birefringence [4] and by the results of synchrotron white beam X-ray topography (SWBXT) experiments [5] and their interpretation based on kinematical diffraction theory [6]. Mounting evidence supports the Frank-model of hollow dislocation cores which allows a quantitative correlation of the micropipe radius with the Burgers vector of a screw dislocation associated with the pipe [7]. Regardless of the various fundamental and technological reasons for micropipe formation, we have identified empirically several mechanisms or combination of mechanisms causing micropipes in SiC boules grown by the seeded sublimation method. Our investigations have resulted in a steady decrease in the micropipe density over the past several years indicating that micropipes may be totally eliminated in the next few years. The analysis of KOH etched 4H-SiC wafers from low micropipe density 4H-SiC boules has determined micropipe free material at a diameter of 25-mm and densities as low as 1.1 cm^{-2} for an entire 50-mm diameter wafer, suitable for



a) b)

Figure 3. Quality improvement of 75-mm 4H-SiC substrates as indicated by stress birefringence: a) early R&D wafer, b) recent wafer.

the production of large area devices. In addition, we have recently produced 75-mm diameter 6H-SiC wafers with micropipe densities as low as 8 cm^{-2} over the entire 75-mm diameter (Figure 4).

Even more important than the "best" wafer results are trends in production averages for micropipe densities. Figure 5 shows the rapid improvement in micropipe density for Cree's production 4H-SiC wafers during the time period when production was being transitioned from 35-mm to 50-mm diameter wafers.



Figure 4. 75-mm diameter KOH-etched 6H-SiC wafer with micropipe density of 8 cm^{-2}.

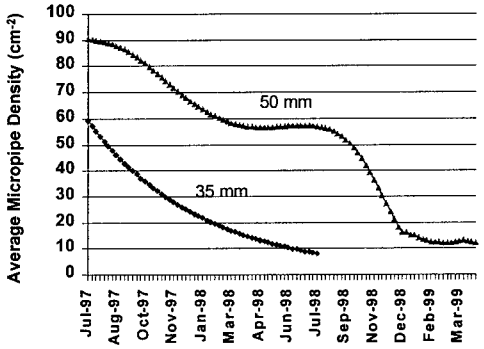


Figure 5. Trend in average MPD for production 4H-SiC wafers during transition from 35-mm diameter to 50-mm.

Concomitant with the growth of large diameter crystals is the tendency of the crystal to form low angle boundaries near the crystal periphery which occur under non-optimized process conditions. In SiC substrates, low angle boundaries are visible as linear crystallographic features extending radially inward from the wafer edge and generally following low-index crystal planes.

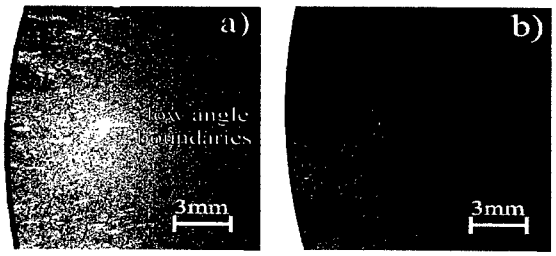


Figure 6. Elimination of low angle boundaries in large diameter SiC substrates: a) early wafer, b) current wafer.

They may sometimes extend through the entire thickness of the wafer. Recent work has resulted in a dramatic reduction in these defects to < 3 with a length of < 3 mm each for production 50-mm wafers (Figure 6), while they are totally eliminated in our current R&D wafers up to diameters of 100-mm. Superimposed on the micropipe distribution in etched wafers is an additional distribution of shallow etch pits at densities typically in the 10^4 cm^{-2} range, associated with the general dislocation background in the wafer. The radial distribution of etch pits across the crystal diameter exhibits a characteristic W-pattern (Figure 7). This spatial variation is consistent with predictions of the radial dependence in resolved shear stress stemming from excess thermoelastic stresses during growth [2]. These results suggest that thermal stresses play a key role in the generation of dislocations during SiC growth.

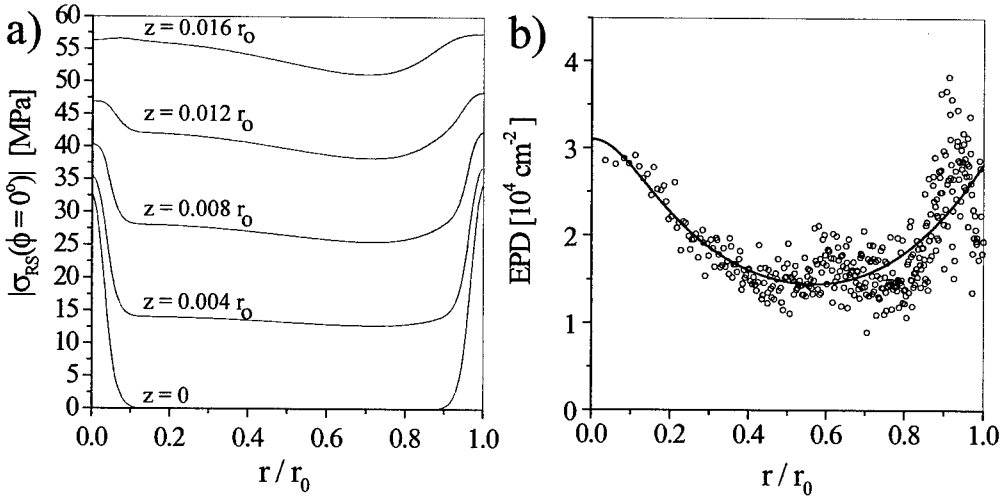


Figure 7. a) Radial dependence of the resolved shear stress in the (0001)<11$\bar{2}$0> glide direction as a function of distance from the growth interface (z=0); b) Radial variation of the local etch pit density within areas of 949 μm x 714 μm on a 6H-SiC wafer.

References

[1] C.H. Carter, Jr., V.F. Tsvetkov, R.C. Glass, D. Henshall, M. Brady, St. G. Müller, O. Kordina, K. Irvine, J.A. Edmond, H.-S. Kong, R. Singh, S.T. Allen, and J. W. Palmour, Mat. Sci. and Eng. **B61-62** (1999) p. 1

[2] St. G. Müller, R.C. Glass, H.M. Hobgood, V.F. Tsvetkov, M. Brady, D. Henshall, J.R. Jenny, D. Malta, and C.H. Carter, Jr., J. Crystal Growth **211** (2000) p. 325

[3] D. Hobgood, M. Brady, W. Brixius, G. Fechko, R. Glass , D. Henshall, J. Jenny, R. Leonard, D. Malta, St. G. Müller, V. Tsvetkov, and C. Carter, Jr., Mat. Sci. Forum **338-342** (2000) p. 3

[4] St. G. Müller, R. Eckstein, W. Hartung, D. Hofmann, M. Kolbl, G. Pensl, E. Schmitt, E.J. Schmitt, A.-D. Weber, and A. Winnacker, Mat. Sci. Forum **264-268** (1998) p. 33

[5] W. Si, M. Dudley, R. Glass, V. Tsvetkov, C. Carter, Jr., J. Elect. Mat. , **26** (1997) p. 128

[6] X.R. Huang, M. Dudley, W.M. Vetter, W. Huang, W. Si, and C.H. Carter, Jr., J. Appl. Crystallography, **32** (1999) p. 516

[7] F.C. Frank, Acta Cryst., 4 (1950) p. 497

Materials Science Forum Vols. 353-356 (2001) pp. 7-10
© 2001 Trans Tech Publications, Switzerland

SiC Single Crystal Growth by Sublimation: Experimental and Numerical Results

Cécile Moulin[1], Michel Pons[2], Alexander Pisch[2], Philippe Grosse[1], Christian Faure[1], Alain Basset[1], Gérard Basset[1], Antoine Passero[1], Thierry Billon[1], Bernard Pelissier[3], Michail Anikin[3], Etienne Pernot[3], Petra Pernot-Rejmánková[3] and Roland Madar[3]

[1] CEA-LETI Grenoble, 17 rue des Martyrs, FR-38054 Grenoble Cedex 9, France

[2] LTPCM-UMR 5614 (CNRS/INPG/UJF), Domaine Universitaire, BP 75, FR-38402 Saint Martin d'Hères Cedex, France

[3] LMGP-UMR 5628 (CNRS/INPG), Domaine Universitaire, BP 46, FR-38402 St. Martin d'Hères Cedex, France

Keywords: Defects, Heat Transfer Simulation, SiC Sublimation Growth

Abstract : 4H-SiC ingots with diameter up to 30mm were grown by the Modified Lely Method. A combined approach of this sublimation technique, involving heat transfer modeling and experimental results is presented. Different geometric modifications of the reactor and process parameter are studied. Their relation with defect occurrence and polytype change are discussed. Calculations show that the modifications have an influence on the radial and axial temperature differences inside the growth cavity. It results from a combination of experiments and calculations that the material characteristics are sensitive to small parameter variations, and that they can be deteriorated by minor variations compared to the working temperatures.

1. Introduction

Significant improvements in both SiC wafer size and quality are still necessary to achieve its full potential for high power, high frequency and high temperature applications. A better understanding of the SiC sublimation growth technique has to be pursued to improve the material quality. The purpose of this study is to propose some correlations between the ingots features and the process parameters by combining fabrication, characterization and process modeling. In a first part, the experimental set-up and modeling of the sublimation growth process will be briefly described. In a second part, different geometric modifications of the reactor and process parameters will be studied. Their relations with defect occurrence and polytype change are presented. Combining process modeling, fabrication and characterization allows to quantify the impact of these design and parameters modifications on the material quality.

2. Experimental set-up and modeling

4H-SiC ingots with diameter up to 30mm have been grown by the Modified Lely method [1]. The experimental configuration of the reactor has previously been described in [2]. The crucible is heated by electromagnetic induction. It is surrounded by a thermal insulating graphite foam which is fitted with holes at the top and the bottom, thus allowing pyrometric measurements. The growth occurs by transport of SiC vapour species from the powder surface to the seed surface. Values of the temperatures measured by a pyrometer at the top of the crucible vary from 2273 to 2473K in our experiments. The growth takes place in an inert atmosphere of argon with pressure ranging from 2 to 10 Torr depending on the experiment. The modeling of the SiC sublimation growth has been undertaken on the basis of this experimental configuration. The temperature distributions inside the crucible are calculated by heat transfer simulation [3,4]. Heat transfer simulation includes conduction, convection, radiation and induction heating as well as the heats of crystallization and sublimation at the crystal-vapour and source-vapour interfaces. Some correlations between the ingots features and calculated temperature gradients inside the deposition cavity are proposed.

3. Results and discussion

3.1. Influence of the radial temperature difference

A graphite foam is always used around the crucible to ensure a good thermal insulation. Some experiments have been conducted with two different insulating foam thicknesses. The other parameters for both kinds of experiments were kept the same. Processes that have been carried out with a reduced foam thickness (reduction of about 30% compared to the stabilised process) have led to crystals displaying the same characteristics : the single crystal initially grows with the 4H polytype and then switches to the 6H polytype. The vertical slice of such a crystal is presented in Fig.1:



Figure 1: Vertical slice of a single crystal displaying 4H to 6H polytype switching

By only increasing the insulating material thickness by about 40%, the 4H polytype has been stabilised again. The effect of the insulating material thickness has been simulated. The results are presented in Fig.2. By increasing the thickness of about 40%, the heat transfer simulation predicts a decrease of the radial temperature difference along the seed (25mm in diameter) of about 30%. It drops from 60 K with a poor insulation to 40 K in the second case. These results indicate that a small increase of the radial temperature difference (in comparison with the working temperature) is sufficient to change the growth mode and strongly deteriorate the material.

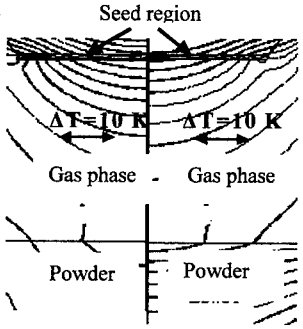


Figure 2: Heat transfer modeling showing the influence of an increase of the thermal insulation thickness (right part)

Some hypothesis can be given to explain why the growth has switched from a 4H polytype to a 6H polytype. One of them may be that the increase of the radial temperature difference gives rise to an increase of the lateral growth rate component. The 6H polytype is always present around the growing 4H-single-crystal in our configuration. It can reach the edge of the seed, and finally continue to grow by the step flow growth mechanism. The occurrence of the 6H polytype and its reproduction by step flow growth, lead to the formation of a 0°/(0001) interface between the 4H and 6H polytype, as seen in Fig. 1 and as explained in Fig. 3. Another explanation could be the following: the increase of the lateral growth rate component can give rise to a strong "step bunching" mechanism, leading to the formation of a large terrace corresponding to the basal plane. The original misorientation being lost, the process of 4H polytype reproduction by step flow growth becomes strongly limited. In this case, and if the growth conditions (pressure, temperature, Si/C ratio..) near the surface are propitious, nucleation of 6H polytype can take place on the basal plane [5].

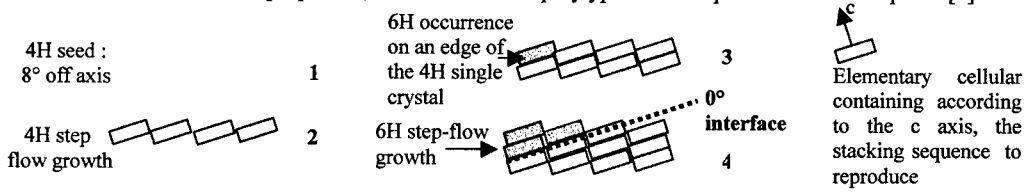


Figure 3 : Formation of the 6H polytype and 0° interface

3.2. Influence of the axial temperature difference

The hole in the graphite foam at the top of the crucible is known to have a strong influence on the axial temperature difference [4]. A relationship between the hole's modification and the defect occurrence in terms of secondary inclusions has been established. The SiC boules generally contain two kind of inclusions: graphite inclusions, and inclusions which looks like droplets, usually associated in the publications with silicon droplets. Their density is characterized by image analysis techniques. Numerous experiments show that the inclusion density (graphite particles and droplets) is about ten times higher when both the hole diameter in the insulating material at the top of the crucible is increased by about 15%, and the growth temperature is decreased by 100 K (measured by pyrometers at the top of the system). Simulations have been carried out in order to quantify the differences resulting from these modifications, the other parameters being

the same. The results are presented in Fig. 4 for different diameter of the pyrometer hole. Simulation predicts that the axial temperature difference is increased by 40% (90 K to 130 K between the seed and the powder surface separated from 20mm) with this experimental modification. Once again, one can notice that a small temperature variation inside the cavity (in comparison with the working temperature) can strongly influence the defect density.

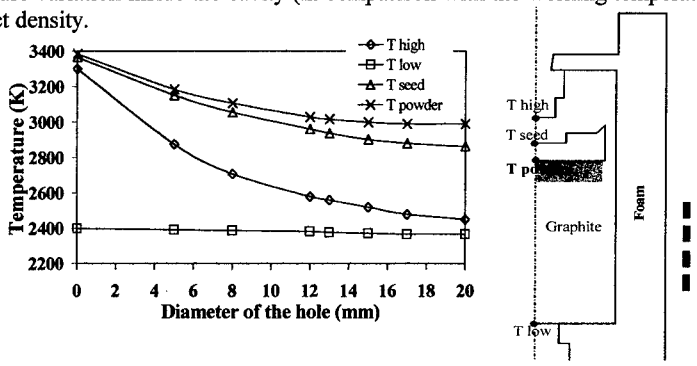


Figure 4 : Influence of the diameter of the hole used for pyrometric measurements on the temperature of the different part of the reactor along the symmetry axis

Graphite particles and silicon droplets probably come from two different mechanisms: graphite particles occurrence is most likely related to a "mechanical effect", whereas silicon droplets occurrence is most likely related to physico-chemical phenomena. The inertia force corresponding to the interfacial fluxes (Stefan flow) can be exerted on fine graphite particles coming from the crucible and from the source. It can be sufficient to overcome the gravity. By this way, they can be incorporated into the growing crystal. The magnitude of this flow is directly proportional to the growth rate which is in its turn linked to the axial temperature difference. This "mechanical effect" can explain the increase of the graphite particle density when the axial temperature difference is increased. Equilibrium thermodynamic calculations have shown that a temperature difference can cause the formation of silicon droplets[3]. It shows that condensation of silicon droplets is possible and that it is favoured by a high axial temperature difference. An investigation on graphite and silicon inclusions occurrence is also presented by Hofmann et al. in Ref [6]. According to the authors, unstable growth conditions (i.e. with inclusions) can be predicted for a temperature gradient of $\Delta T/\Delta Z=30K.cm^{-1}$, with a process temperature of 2500 K. A concept of constitutional supersaturation is considered (CS) for silicon droplets occurrence [6].

3.3. Evolution during a growth run

Crystal growth is mainly controlled by the temperature distribution inside the cavity. As previously discussed, the material quality is strongly dependant on the temperature gradients. The thermal field changes during the sublimation growth of the crystal : the distance between the source and the crystal surface changes and the properties of the SiC powder are also modified. An experiment has been carried out in order to get information on these evolutions. The crystal has been marked by nitrogen injections every 10 hours during a growth run of 62 hours. The growth rate calculated from the doping marks changes from 0.30 mm/h to 0.18 mm/h between the beginning and the end of the process. The decrease of the growth rate with increasing the growth duration is also reported in the literature [7]. One can also observe from the doping marks, the evolution of the growth front shape during time. Based on this result, the simulation gives a quantification of the evolution of the axial temperature difference inside the cavity and inside the crystal (see Fig.5).

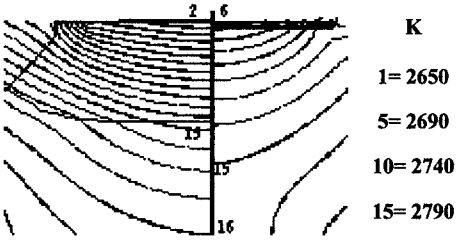


Figure 5: temperature distribution at the end of the growth (on the left) and at the beginning (on the right)

Inside the cavity, the simulation shows that the axial temperature difference decreases from 80K to 40K between the beginning and the end of the growth. This decrease of the axial temperature difference inside the cavity, and therefore the decrease of the growth rate, involves a gradual decrease of the inclusions density.

This may be the result of the lowering of the Stefan flow for graphite particles and of the Si/C ratio for silicon inclusions. Fig. 6 presents the inclusions density calculated by image analysis, versus the substrate position along the crystal. The inclusions density are calculated from the centre of each substrates corresponding to different positions along the crystal, from the seed region to the crystal surface. Results are presented for four crystals fabricated in different experimental conditions.

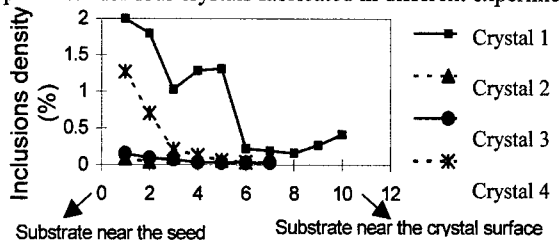


Figure 6 : Inclusions density versus the crystal length

As shown in Fig. 6, the material quality is gradually improving during growth in terms of inclusions density. The decrease of the growth rate should also involve a gradual improvement of the material quality in terms of crystalline quality. Stresses linked to the growth itself are expected to be weaker for lower growth rate. But one must also take into account the thermo-elastic component of the stresses. The increase of the temperature gradient inside the growing crystal leads to more and more important thermo-elastic stresses [7]. We have undertaken topographic analysis at the ESRF to gain information on the stress pattern along entire ingots. Many ingots have been observed by X-Ray topography in transmission with vertical and horizontal slices. Most of the time, we have noticed a better crystalline quality in the centre of the boules (lighter regions in Fig.7). The darker regions are essentially observable at the edge of the boule and at the beginning of the growth (Fig.7). However it is very difficult to conclude on the evolution of the crystalline quality during growth as many reasons can explain the formation of stress and misoriented areas (reproduction from the substrate, instabilities at the initials steps of the growth, crystal enlargement...).



Figure 7 : as-grown ingot observed by X-ray topography in transmission; vertical slice. (seed region at the top of the image; crystal's surface at the bottom).

4. Conclusion

By combining experimental and simulation results, we have given examples of correlation between material quality and macroscopic fields simulated inside the cavity. These first results show how the material characteristics are sensitive to small parameters variations, and how it can be deteriorated (polytype switching, droplets..) by minor variations of temperature compared to the working temperatures. This paper also show a constant compromise between growth rate and material quality. Concerning graphite inclusions, silicon droplets, or even polytype stability, better results are obtained when decreasing the axial and radial temperature gradients, in detriment of the growth rate.

References

[1] Tairov, Y.M., Tsvetkov, V.F., J. Crystal Growth, 43 (1978), p. 209.
[2] P. Grosse, G. Basset, C. Calvat, M. Couchaud, C. Faure, B. Ferrand, Y. Grange, M. Anikin, J. M. Bluet, K. Chourou, R. Madar, Material Science and Engineering, B61-62 (1999), p.58.
[3] M.Pons, E.Blanquet, J.M.Dedulle, I.Garcon, R.Madar, C.Bernard, J.Electrochem.Soc, vol.143, N°11 (1996) p.3727.
[4] M.Pons, M.Anikin, K.Chourou, J.M. Dedulle, R. Madar, E. Blanquet, A.Pisch, C. Bernard, P.Grosse, C. Faure, G. Basset, Y. Grange, Materials science and Engineering B61-62 (1999), P.18.
[5] Yu.M.Tairov, V.F.Tsvetkov, M.A.Chernov, V.A.Taranets, Phys.stat.sol. (a) 43 (1977), p.363.
[6] D.Hofmann, E.Schmitt, M.Bickermann, M.Kolbl, P.J.Wellmann, A.Winnacker, Materials Science and engineering B61-62 (1999), p.48.
[7] S. Yu.Karpov, A.V.Kulik, I.A.Zhamakin, Yu.N.Marakov, E.N.Mokhov, M.G.Ramm, M.S.Ramm, A.D.Roenkov, Yu.A.Vodakov, Journal of Crystal Growth 211 (2000), p.347.

Materials Science Forum Vols. 353-356 (2001) pp. 11-14
© 2001 Trans Tech Publications, Switzerland

Impact of SiC Source Material on Temperature Field and Vapor Transport During SiC PVT Crystal Growth Process

P.J. Wellmann[1], D. Hofmann[1], L. Kadinski[2], M. Selder[2], T.L. Straubinger[1] and A. Winnacker[1]

[1] Department of Materials Science 6, University of Erlangen-Nürnberg, Martensstr. 7, DE-91058 Erlangen, Germany

[2] Institute of Fluid Mechanics, University of Erlangen-Nürnberg, Cauerstr. 4, DE-91058 Erlangen, Germany

Keywords: Numerical Modeling, Physical Vapor Transport, Source Material, X-Ray Imaging

Abstract

We have investigated the impact of morphological changes of the source material during physical vapor transport growth of silicon carbide on the crystal growth process, i.e. global temperature field and vapor transport between source material and crystal, has been studied. Digital x-ray imaging was performed for monitoring of the ongoing processes inside the SiC source material. Numerical modeling was carried out to study the effect on the crystal growth process. Three different SiC sources with varying grain size were investigated. While the SiC source material undergoes fundamental transitions during growth (i.e. evolution from powder to compressed SiC block) it is found that the global growth process is more stable than one would expect. A key role is played by a condensed disk like structure on top of the source material which is present for all SiC sources.

Introduction

Physical vapor transport (PVT) growth is currently the most feasible technique for the preparation of silicon carbide (SiC) bulk crystals and wafers for commercial applications. Usually the growth is carried out in an inductively heated graphite crucible at elevated temperatures (T=2200°C...2400°C) [1-4]. The crystal quality (i.e. low defect density, homogenous doping, etc.) is known to depend sensitively on the temperature field inside the growth cell. In this paper we will investigate the impact of the SiC source material and its morphological changes during growth on the temperature field and vapor transport. The analysis is based on an interchange of experimental monitoring of the morphological changes during growth time and numerical modeling of the corresponding heat transfer processes and the mass transfer between source and crystal seed. For this reason different SiC sources with varying grain size have been studied. Finally, the impact of the temporal evolution of the SiC source material on the global growth process is discussed.

Experiments

We have grown 6H SiC single crystals using the PVT method at about T=2200°C...2400°C. The typical single crystal diameter was 35mm...40mm and the micropipe density was below 200cm^{-2}. We have studied three different SiC sources. Source A was a fine SiC powder with a grain size <5µm and source B contained SiC powder with grains of 10µm...50µm in size. Source C was built out of macroscopic SiC pieces with a size in the range of 5mm...20mm. All sources were synthesized from elemental high purity Si and C in our lab. The evolution of the SiC source material, i.e. its consumption and morphological changes (density, grain size, etc.) during growth time, was monitored using the digital x-ray imaging technique which has been described in detail in [5,6]. From the x-ray image contrast it is possible to determine the average density of the source material [6]. The x-ray image pattern is a measure of the granular structure and allows the

estimation of the SiC powder grain size. Both, the average density and the grain size, determine the porosity of the source material. The porosity is one of the fundamental parameters of the effective heat conductivity in a porous media and serves as input parameter for numerical modeling of the heat transfer in the SiC source material.

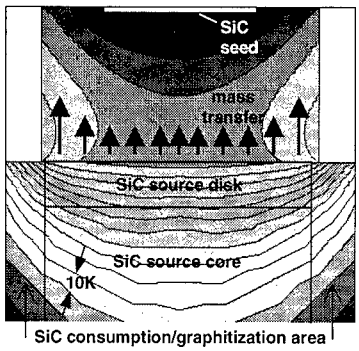


Fig. 1: Calculated temperature field inside PVT growth cell. The SiC source has been divided into 3 blocks: SiC source disk, SiC source core and SiC consumption/ graphitization area.

Numerical modeling

Numerical modeling of the global temperature field was carried out taking into account heat transfer by conduction, radiation and convection [7]. To account for its morphological changes the SiC source was divided into three blocks: (i) disk like structure on top of the source, (ii) core part and (iii) graphitization area close to the crucible walls (Fig. 1). Data from Kitanin et al. [8] and Müller et al. [9] were used to correlate the various morphological in the distinct source areas (determined in the experiment) with an effective thermal conductivity which acts as input parameter for the numerical model. The calculation of the SiC vapor flow between SiC source and seed were carried out using a model which included mass transfer and surface chemistry of the Si- and C containing gas species (i.e. Si, Si_2C, SiC_2) [7].

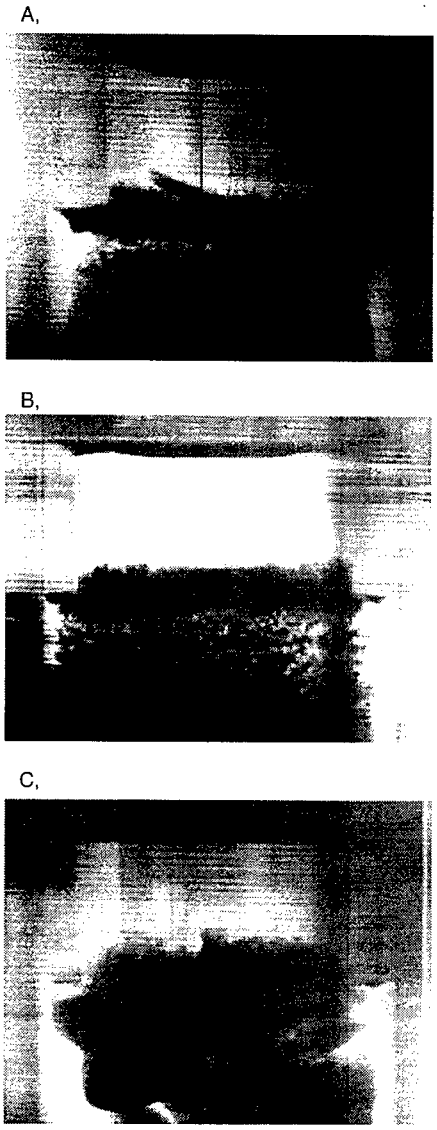


Fig. 2: Comparison of SiC source morphology of source A(<5μm SiC powder), source B (10μm...50μm SiC powder) and source C (5mm...20mm SiC pieces) after 8 hours of growth visualized by x-ray imaging.

Results and discussion

Fig. 2 illustrates the morphology of the three SiC sources (source A - <5μm SiC powder, source B - 10μm...50μm SiC powder, source C - 5mm...20mm SiC pieces) after 8 hours of growth using the digital x-ray imaging technique. In all three cases the formation of a needle like disk is observed on top of the source. An analysis of the x-ray image contrast indicated a compression of the disk of source A and B (both powder sources with large porosity) by a factor of about 2 in comparison to the initial source density. The average density of the core part of source A and B remained almost constant during growth (increase of about 20%), however, the SiC grain size rose. Independent of the initial grain size (source A - <5μm and source B - 10μm...50μm) of the two powder sources, a value of 100μm...250μm is observed after 8 hours of growth. The average density and grain size determine the effective thermal conductivity in porous

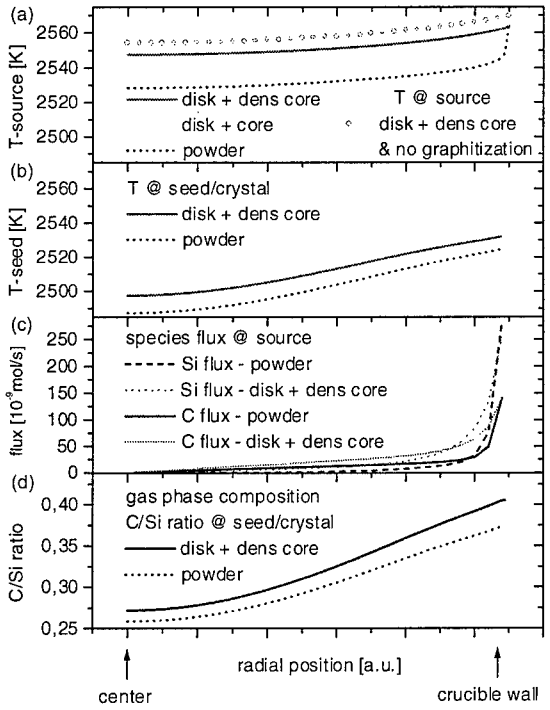


Fig. 3: (a,b) Temperature field on top of the SiC source at different morphological stages. (c) Si and C flow on top of the SiC source for two morphological stages. (d) Composition of gas phase in front of SiC crystal growth interface for two morphological stages of the source.

media. Recently Kitanin et al. [8] and our group [9] have presented heat transfer analysis in porous SiC. We have used these data in order to correlate the experimentally determined evolution of the SiC source morphology with an effective thermal conductivity which itself is used as input parameter for the calculation of the heat transfer and hence temperature field inside the growth cell. The effective heat conductivity of the SiC disk and core was varied in the range of 10W/(K·m)...18W/(K·m) and 2W/(K·m)...8W/(K·m), respectively. The formation of the disk like structure of compressed SiC powder (increased thermal conductivity) causes an increase of the temperature on top of the source of 15K...20K and a significant reduction of the lateral temperature gradient in the vicinity of the crucible walls (solid and dashed line in Fig 3a). Morphological changes in the core part lead to a further increase of the absolute temperature value (5K...10K) but without impact on the temperature gradient (dashed and dotted lines in Fig. 3a). The formation of a disk and dens core in the SiC powder source also increase the temperature in front of the SiC crystal (about 10K), however, no significant changes of the temperature gradient were observed (Fig. 3b).

The evolution of the powder source into a compressed SiC block has a significant impact on the sublimation process. Especially in the vicinity of the crucible walls the Si flux drops and leads to a more homogeneous lateral evaporation (Fig. 3c). The C/Si ratio of the gas phase composition in front of the entire growing SiC crystal rises by about 10%. This could be a growth stabilizing factor in the case of 4H SiC. Due to Tairov and Tsvetkov [10] the growth of "hexagonal rich" SiC polytypes (4H SiC versus 6H SiC) is favored for large C/Si ratios (=lower Si content).

However, in general it should be pointed out that the morphological changes of the SiC powder source described above occur mainly in the initial growth stage (first 3 to 8 hours) and could be interpreted as "short time" instabilities of the growth process. From the experimental point of view it is basically impossible to compensate the mentioned temperature (and related sublimation) changes by a control of growth parameters like RF heating power.

The average density of source C with macroscopic SiC pieces remained over the whole growth time constant at the value of a SiC crystal. Only minor morphological changes were observed in the source core part; the macroscopic SiC pieces sintered together. To account for this observation, the effective thermal conductivity for numerical modeling was chosen as constant over growth time and its value was set to 20W/(K·m) which is below 25W/(K·m), the value of a SiC single crystal.

In all three cases (source A, B and C) the formation a SiC consumption area close to the hot crucible walls is observed (Fig. 2). In this area residual graphite is found. However, it is of such a low density that it does not show up as a image contrast. Weighting of this residual graphite confirms the x-ray image analysis that the total amount is less than 5% of the initial graphite content

in the SiC powder or SiC pieces. This graphitization area acts as a heat transfer insulation (low effective thermal conductivity) between the hot crucible walls and the SiC source core. The latter is confirmed by numerical calculations which showed that the temperature field on top of the SiC source dropped by about 5K...10K if graphitization was considered in the model (Fig. 3a).

Conclusions

In the case of the SiC powder source A (grain size <5μm) and source B (grain size 10μm...50μm) the growth process is improved by the fundamental morphological changes like formation of disk structure, compression, etc. due to a homogenization of the temperature field and SiC sublimation process. Although the growth regime improves, the initial growth time during which most of the morphological changes occur can be interpreted as instability for the seeding process. From this point of view source C with macroscopic SiC pieces would be advantageous. For the latter the effect of SiC consumption and graphitization dominates the evolution of the temperature field (T drops). This "long term" effect could be compensated by a control of growth process parameter control, i.e. increase of rf heating power.

Acknowledgments

This work has been supported by the Deutsche Forschungsgemeinschaft (project Wi393/9 and Du101/47) and the Bayerische Forschungsstiftung (project 176/96).

References

[1] Y.M. Tairov and V.F. Tsvetkov, J.Cryst.Growth **43** (1978), p.209.
[2] G. Ziegler, P. Lanig, D. Theis and C. Weyerich, IEEE Trans. Electron. Devices **30** (1983), p.277.
[3] D. Hofmann, R. Eckstein, M. Kölbl, Y. Makarov, St.G. Müller, E. Schmitt, A. Winnacker, R. Rupp, R. Stein and J. Völkl, J.Cryst.Growth **174** (1997), p.669.
[4] C.H. Carter, Jr., V.F. Tsvetkov, R.C. Glass, D. Henshall, M. Brady, St.G. Müller, O. Kordina, K. Irvine, J.A. Edmund, H.-S. Kong, R. Singh, S.T. Allen and J.W. Palmour, Mat.Sci.Eng. **B61-62** (1999), p.1.
[5] P.J. Wellmann, M. Bickermann, M. Grau, D. Hofmann, T.L. Straubinger and A. Winnacker, Mat. Res. Soc. Symp. Proc., **572** (1999), p.259.
[6] P.J. Wellmann, M. Bickermann, D. Hofmann, L. Kadinski, M. Selder, T.L. Straubinger and A. Winnacker, J.Cryst.Growth **216** (2000), p.263.
[7] M. Selder, L. Kadinski, F. Durst, P. Wellmann, T. Straubinger, D. Hofmann, S. Karpov, M. Ramm, J.Cryst.Growth **211** (2000), p.333.
[8] E.L. Kitanin, M.S. Ramm, V.V. Ris, A.A. Schmidt, Mat.Sci.Engr. **B55** (1998), p.174.
[9] St.G. Müller, J. Fricke, D. Hofmann, R. Horn, O. Nilsson and B. Rexer, Materials Science Forum **Vols. 338-342**, (2000), p.43.
[10] Yu.M. Tairov and V.F. Tsvetkov, Prog.Cryst.Growth Character. **7** (1983), p.111.

Materials Science Forum Vols. 353-356 (2001) pp. 15-20
© 2001 Trans Tech Publications, Switzerland

Defect Reduction in Sublimation Grown Silicon Carbide Crystals by Adjustment of Thermal Boundary Conditions

E. Schmitt[1], M. Rasp[1], A.-D. Weber[1], M. Kölbl[1], R. Eckstein[1], L. Kadinski[2] and M. Selder[2]

[1] SiCrystal AG, Paul-Gossen-Str. 100, DE-91052 Erlangen, Germany

[2] Institute of Fluid Mechanics, University of Erlangen-Nürnberg, Cauerstr. 4, DE-91058 Erlangen, Germany

Keywords: Defects, Numerical Simulation, Supersaturation, Thermal Gradients

Abstract The influence of changes to the crystal growth system was examined by an experimental verification of results from numerical simulation. From elementary tests correlation between growth defects and thermal boundary conditions was established. A significant improvement of crystal quality was achieved by a conversion of the results to the standard growth process.

Introduction The outstanding material properties of silicon carbide make it attractive as substrate material for electronic and optoelectronic semiconductor devices. Despite the continuous improvements of the growth technique [1–4], that lead to an increase in crystal size and quality, some restrictions hinder a faster development. An indispensable prerequisite for the growth of high quality silicon carbide is the precise control of substantial process parameters like temperature and temperature gradients. This aim is not easily achieved, however, because the commonly used interior parts of the growth container are opaque and therefore inaccessible for temperature measurement by optical pyrometry. A recently published X-ray-imaging technique [5], which is sensitive to the absorption of the parts of the container, allows in-situ imaging of the growth process, but there is still a lack of information about temperature and temperature distribution inside the crucible. Without imposing severe changes to the system, the only possibility to know more about the thermal conditions is calculation by numerical modelling.

Simulation Numerical calculations were carried out by using the code FASTEST-CVD [6,7], which is based on a finite volume method, that works on a block-structured, non-orthogonal grid. By solving the Maxwell-Equations, the Joule heat sources are calculated in dependence of the electric field and the electrical resistance of the materials. The temperature distribution inside a reactor is obtained by the numerical calculation of heat transfer by conduction, convection and radiation in an axis symmetrical configuration. For this work emphasis was laid on the calculation of heat transfer, whereas species mass transport, growth rates and stress distribution inside the crystals were not taken into account and remain topics for our further investigations.

Due to the fact that the thermophysical data for the interior materials of the reactor are insufficiently known at temperatures greater than 2000 °C, we carried out a comprehensive study of measured and calculated temperatures at two fixed spots of a test-geometry. With the information from these experiments, the thermophysical data for the used materials were adjusted. After that calculations for a simplified crystal growth setup were carried out. The setup was not designed for the growth of large crystals at high growth rates, but enabled a plain comparison between experiment and simulation, especially when significant changes were made to the system. In two series the influence of the relative position of crucible to induction coil and the cooling of the crystal were investigated separately. All other process parameters were kept constant. For the silicon carbide crystal a flat

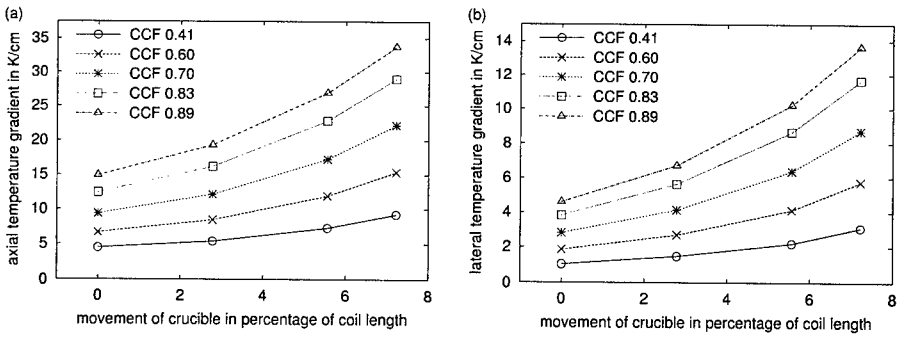


Figure 1: Variation of (a) axial and (b) lateral temperature gradients with crucible position and crystal cooling.

phase boundary and a constant crystal length was assumed. The distance between source and crystal was approximately an order of magnitude larger than the crystal length.

The cooling of the crystal was altered by changes in the heat losses due to radiation and conduction at the backside of the crystal. This is expressed by the so-called crystal-cooling factor (CCF), which is determined by the geometry of the reactor/crucible and can vary between 0 and 1. An increasing CCF corresponds to an increased heat loss at the backside of the crystal, especially in the central region.

For evaluation of effects caused by the above discussed changes, the temperature gradients at the phase boundary crystal/gas were analysed. The axial gradient was determined at the symmetry axis and the lateral gradient at half of the crystal radius. In Fig. 1 the calculated axial and lateral temperature gradients are shown. As can be seen, the temperature distribution inside the crystal can be changed significantly by these alterations. The calculations also show that with both changes the increase in the lateral gradients is higher than in the axial direction.

Experiments Several growth experiments (polytype 6H) were conducted under different thermal gradients, as expected from the calculations. Although it is clear that a precise separation of the temperature field in axial and lateral temperature gradients is not possible, it is appropriate to address specific phenomenons of crystal growth to them.

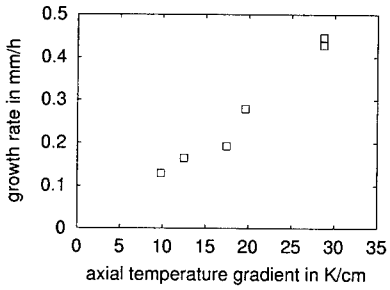


Figure 2: Dependence of experimental growth rate on axial temperature gradient.

Influence of axial temperature gradients The driving force for mass transfer between source and crystal material is their temperature difference. The estimation of the axial thermal gradient from temperature measurements at the bottom and top of the crucible is not accurate, because the powder source has a much lower thermal conductivity than other parts of the crucible [8]. To get better accuracy we took the calculated thermal gradient between the crystal surface in the gaseous spacing. In Fig. 2 a linear dependence of the experimental growth rate on axial temperature gradient is illustrated. Choosing process conditions that caused an increase of the axial temperature gradient by the factor of three resulted in the growth of crystals at a three times higher average growth rate. The linear dependence would represent conditions of diffusion limited crystal growth. For the rising of the growth rate a high axial temperature gradient is desired, but also severe consequences to the crystal-quality have to be expected, which are discussed in the following.

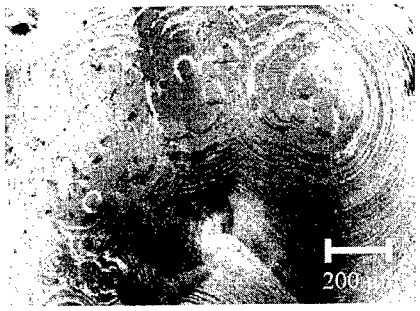


Figure 3: Growth islands on an as-grown (0001)-surface at early stage of growth.

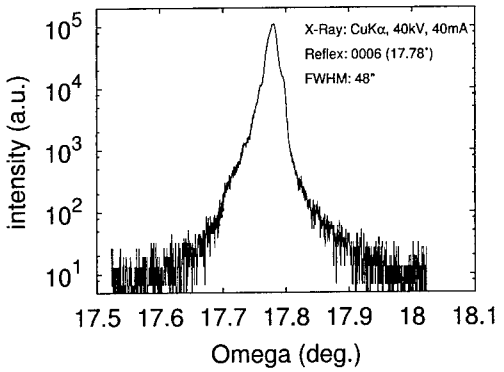


Figure 4: Rocking curve of crystal from Fig. 3.

Under certain circumstances kinetic limitations were observed. Fig. 3 shows the as-grown surface of a crystal at the initiating stages of the growth process, where two-dimensional growth of separated islands prevails. We assume, that at the beginning of the growth the system is not in equilibrium and supersaturation is high. One reason for this enhanced supersaturation could be the higher axial temperature gradient, which was applied to this growth run. From [9, 10] it is known, that at the beginning of the growth the conditions with the highest axial gradient are found, whereas later on a decrease of the thermal gradient is expected. In addition the formation of a crystal facet has a stabilising effect on growth. In Fig. 4 the rocking-curve of the X-ray-diffraction measurement of the as-grown surface shows multiple peaks, that indicate a slight misorientation of the separated islands [11], known as mosaic structure.

A further increase of thermal gradients and supersaturation leads to 3D-nucleation, which is the most unfavourable growth mechanism and distorts the entire crystalline structure (see Fig. 5) of the bulk. In principle two mechanism could explain the 3D-nucleation: Exceeding a critical supersaturation for 2D-growth on the growing crystal surface or constitutional supersaturation ahead of the phase boundary.

Influence of lateral temperature gradients The lateral temperature gradient at one spot is only a reduced testimony of its thermal status of the crystal, thus in our investigations the value for the lateral gradient is used as approximation for the curvature of the temperature field, that gives rise to thermal stress and successive the generation of dislocations. The effect of the lateral gradient is easily observed at crystal boules. The higher the lateral gradient the more convex the crystal shape. Inspection of the surface morphology by the optical microscope showed that numerous disturbances on the surface hindered the lateral movement of the surface steps on the crystal shoulder (Fig. 6). With KOH-etching we found out that large disturbances correspond to screw dislocations or micropipes and the small disturbances correspond to dislocations. The density of the dislocations varies with the crystallographic orientation and has a maximum in the $[11\bar{2}0]$-directions, which suggests a crystallographic glide mechanism. An overview of dislocations in SiC is given in [12, 13]. The etch pit density (EPD) can vary significantly from excellent values of $1 \ldots 5 \cdot 10^3\,\mathrm{cm}^{-2}$ in good areas to $1 \ldots 5 \cdot 10^5\,\mathrm{cm}^{-2}$ in the worse outer regions. If dislocations are screw dislocations with a

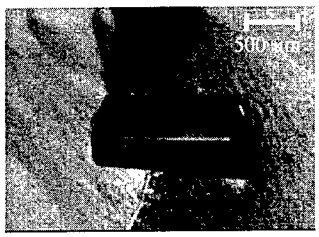


Figure 5: 3-dimensional growth.

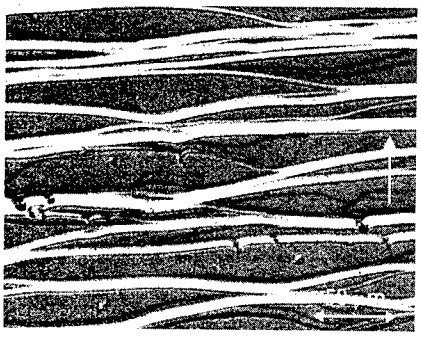


Figure 6: Pinning of surface steps by obstacles (micropipes; dislocations). Lateral growth direction marked by arrow.

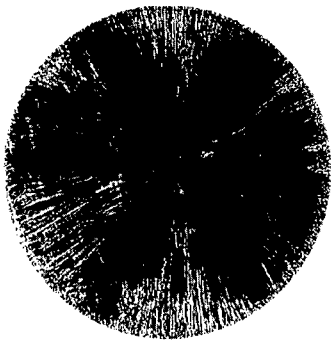


Figure 7: Stress birefringence image of a 35 mm 6H wafer grown under high lateral gradients (test geometry).

large burgers vector, additional micropipes could be generated [14]. The results from the microscopic inspection are underlined by stress birefringence images of wafers from this crystal (Fig. 7), where a six-fold symmetry of high stress contrast is seen. The maximum of stress contrast in the periphery of the crystal, where the calculations predict a high lateral gradient. Crystals grown under conditions with reduced lateral temperature gradients showed to a more flat phase boundary an almost perfect movement of the surface steps (Fig. 8).

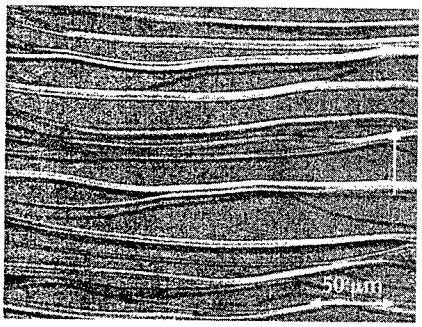
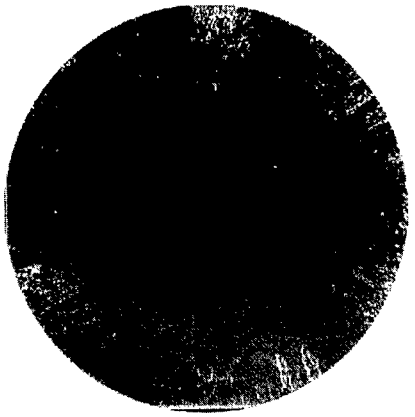


Figure 8: Free movement of surface steps. Lateral growth direction marked by arrow.

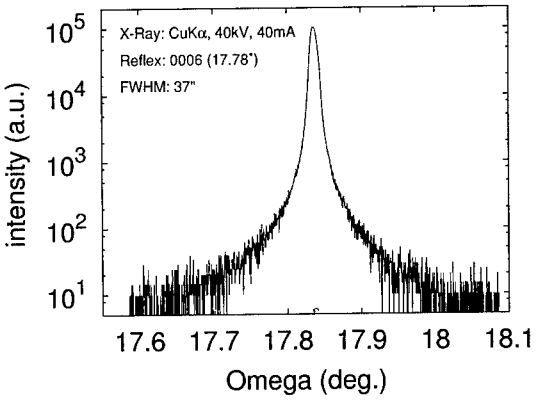
Besides the negative effect of high lateral temperature gradients on crystalline quality, they are still needed in the case of enlargement of the crystal area. The overgrowth of non-monocrystalline material is only satisfactory, when the lateral growth velocity is fast.

Discussion Our experiments showed that – even in a simplified geometry – a precise control of the growth determining parameters is indispensable, especially at the seeding period of the growth, where generation of additional defects has to be avoided. We found out that defects caused during the seeding procedure and the early stages of growth, determine the crystalline perfection of the subsequent grown crystal volume. Later on these defects could not be eliminated completely. The axial and lateral temperature gradients that are imposed on the crystal and its surroundings are of major impact on the defect generation. The above described results show that for different stages and aims of crystal growth different thermal boundary conditions are convenient. This demands a growth system, that is capable of establishing varying thermal boundary conditions (as shown in Fig. 1) in different stages of growth.

With an experimental verification of results from numerical modelling, we were able to establish growth conditions that support defect-reduced growth. The results we achieved by using a test geometry could be transferred to the more sophisticated crucible geometry, that is used to grow crystals with diameters of 2″ and larger. For R&D 2″ 6H wafers values for the average micropipe-density below $20\,cm^{-2}$ are reached. From this elementary improvement an positive reflection on production has been noticed. Fig. 9 shows the stress birefringence image of a stress-reduced 2″ 6H wafer and its rocking curve that has a symmetrical shape and a FWHM of 37 arcseconds.



(a) Stress birefringence image of a 2″ 6H wafer grown under stress-reduced conditions.



(b) Rocking curve of a wafer from Fig. 9(a).

Figure 9: Defect reduction in wafers, achieved by improved thermal field.

Acknowledgements This work is supported by the Bavarian Research Foundation under contract No. 176/96.

References

[1] Yu.M. Tairov, V.F. Tsvetkov, J. Cryst. Growth 43 (1978), p. 209.

[2] G. Ziegler, P. Lanig, D. Theis, C. Weyrich, IEEE TRANSACTIONS ON ELECTRON DEVICES; VOL. ED-30 No. 4 (1983), p. 277.

[3] D.L. Barret, J.P. McHugh, H.M. Hobgood, R.H. Hopkins, P.G. McMullin, R.C. Clarke, J. Cryst. Growth 128 (1993), p. 358.

[4] T. Tsvetkov, R. Glass, D. Henshall, D. Asbury, C.H. Carter, Jr., Mater. Sci. Forum 264-268 (1998), p. 3.

[5] P.J. Wellmann, M. Bickermann, M. Grau, D. Hofmann, T.L. Straubinger and A. Winnacker, Mater. Res. Soc. Symp. Proc. 572 (1999), p. 259.

[6] D. Hofmann, M. Heinze, A. Winnacker, F. Durst, L. Kadinski, P. Kaufmann, Y. Makarov, M. Schäfer, J. Crystal Growth 146 (1995), p. 214.

[7] M. Selder, L. Kadinski, F. Durst, T. Straubinger, D. Hofmann, Mater. Sci. Eng. B61-62 (1999), p. 93.

[8] B. Rexer, Diploma-Thesis, University Erlangen-Nürnberg (1996)

[9] M. Selder, L. Kadinski, F. Durst, T. Straubinger, D. Hofmann, P. Wellmann, Mater. Res. Soc. Symp. Proc., Vol.572 (1999), p. 31.

[10] E. Schmitt, R. Eckstein, M. Kölbl, A.-D. Weber, K. Mizota, Bulletin of Solid State Physics and Applications (Japan Society of Applied Physics) (1999), p. 185.

[11] M. Tuominen, R. Yakimova, R.C. Glass, T. Tuomi, E. Janzen, J. Cryst. Growth 144 (1994), p. 267.

[12] S. Amelinckx, G. Strumane, W.W. Webb, J. Appl. Phys. 41 (1960), p. 1359.

[13] P. Pirouz, Mater. Sci. Forum 264-268 (1998), p. 399.

[14] F.C. Frank, Acta Cryst. 4 (1951), p. 497.

Materials Science Forum Vols. 353-356 (2001) pp. 21-24
© 2001 Trans Tech Publications, Switzerland

Progress in 4H-SiC Bulk Growth

Michail Anikin[1], Etienne Pernot[1], Bernard Pelissier[1], Michel Pons[2], Alexander Pisch[2], Claude Bernard[2], Thierry Billon[3], Christian Faure[3], Cécile Moulin[3] and Roland Madar[1]

[1] LMGP, UMR 5628 CNRS/INPG, Domaine Universitaire, BP 46, FR-38402 St. Martin d'Hères, France

[2] LTPCM, UMR 5614 CNRS/INPG/UJF, Domaine Universitaire, BP 75, FR-38402 Saint Martin d'Hères Cedex, France

[3] LETI-CEA Grenoble, 17 rue des Martyrs, FR-38054 Grenoble Cedex 9, France

Keywords: 4H-SiC Sublimation Growth, Cracking, Crystal Shape, Defects

Abstract 4H-SiC ingots with diameter up to 35 mm have been grown by the Modified Lely Method with « in situ » etching. The influence of the crystal shape on the cracking of SiC crystals has been investigated. The original source design allowed to maintain an excess of Si above the growing crystal to decrease defect density.

Introduction Growth of large ingots with a low defect density is the most important problem of SiC technology. An important factor affecting defect formation is the ingot shape which depends on the design of the crucible assembly and on the growth conditions. A change of design allows to grow the crystals with a convex, concave or flat « as grown » surface. It is important to notice that a change of the ingot shape during growth can cause additional defects.

Enlargement of SiC crystal diameter takes place if the crystal grows in conjunction with poly-SiC due to radial temperature gradient. In this paper the problem of SiC crystal enlargement without cracking is discussed. The problem of defect density reduction is presented.

Experimental details 4H crystals with diameters up to 35 mm have been grown by the Modified Lely Method with « in situ » sublimation etching [1-3, 5]. An experimental setup with RF heating and graphite crucible was used. The crucible was wrapped in graphite felt for thermal insulation, and the whole assembly was placed inside a water cooled quartz reactor. The growth temperature (measured on the top of graphite lid) was about 2200°C and the argon pressure was about 2 Torr. Under these experimental conditions we obtained 4H single crystals with a thickness of approximately 10 mm. The growth rate was between 1.1 and 1.3 mm/h.

The SiC source powder was loaded both between a dense graphite crucible and a thin-walled inner graphite cylinder (as in the design of the Lely Method) and inside of the inner cylinder. This allowed to reduce the influence of the leakage of Si and the reaction of Si from the main central source with the walls to maintain excess of Si over the seed.
The seed was fixed at the top of the crucible. The distance between source and seed was 15-20 mm. The temperature gradient within the growth cell was changed during the growth process [1, 2]. The inversion of the temperature gradient resulted in a etching of the seed. The temperatures of the top and the bottom of the crucible were measured by pyrometers.

Results and discussion

«In situ» etching Under a positive temperature gradient, even at high argon pressure of 650 Torr, growth was observed at temperature as low as 1900°C. To suppress nucleation at a low temperature, which would result in undesirable crystal growth, we started the growth process with a reverse temperature gradient. At temperature of about 1800°C sublimation etching of the seed was observed when the Si vapor pressure over the substrate was maintained close to the equilibrium

vapor pressure over SiC. To obtain SiC surfaces with a regular step structure it was necessary to eliminate the loss of Si vapor from the seed surface which can result in carbon-rich and low-quality surface. The material supply from the source at the periphery of the crucible allowed to reduce the influence of the leakage of Si vapor from the growth cell. The control of temperature gradient and argon pressure became important factors to obtain a high quality SiC surface. A higher reversed temperature gradient and a higher than 1800°C temperature increased the etch rate, but also increased the probability of the seed carbonization. At an argon pressure of less than 10 Torr the step bunching on the seed surface increased drastically. Sometimes, even a carbonization of the seed surface was observed. After etching the sign of temperature gradient was changed, and the pressure was increased to start the growth at a slow rate.

The influence of «in situ» etching conditions and the initial stage of the growth on the defect formation have been investigated. A system of pyramidal holes [1, 2] was found at the interface. The size and the shape of the holes depended on the etching conditions and were greatly affected by the seed orientation. The optimization of etching and the initial stage of the growth allowed to reduce both the number and the size of holes. Defects were usually found at the periphery of the seed only (Fig.1).

The interface morphology of material grown on on- and off-axis substrates was different. Interfaces of the seed-crystal grown on on-axis seeds were continuous on the SEM photo as distinct from the crystal grown on off-axis seeds. (Fig.2). It is important to notice that the ingots without pyramidal holes at the seed-boule interface contained pinholes.

Cracking of SiC crystal Excessive mechanical and thermoelastic stresses results in cracking of the crystals. To reduce these stresses it is necessary to optimize the shape of the growth surface. The shape depends on the flux of SiC vapor and the temperature distribution in the growing crystal. Both vapor flux and the temperature distribution can be changed during the growth process resulting in a change of the shape of the growth surface during the growth. Depending on the design of the crucible and the thermal isolation the shape of the « as grown » surface can be convex, concave or flat. Optimal shape of the surface is flat because it allows to grow the crystal with uniform doping. But with an increase in diameter up to 30 mm the crystals trend to crack (Fig.3). In our case the cracking of the crystal with flat « as grown » surface can be explained by excessive mechanical stresses from poly-SiC growing in conjunction with the boule. The surface of poly-SiC was above the growing crystal. With increase in diameter of the crystal the stresses from poly -SiC increased too due to an enlargement of the crystal.
On-axis and 8° off-axis substrates were used as seeds. In the case of a flat « as grown » surface grown on off-axis seed the facet was located at the periphery, close to poly-SiC, under an angle of 8°, to the surface. An increase of the diameter of the crystal resulted in the formation many facets which occupied the surface from the periphery of the crystal towards the center. In the case of an on-axis seed the crystal was symmetrical and the facet was located in the center.
Due to the low thermal conductivity of the SiC source powder the flux of SiC species at the periphery of the growth cell was higher than in the center, especially at low temperature and pressure. In order to grow the crystal with a convex shape, it was necessary to increase the cooling in the center of the crystal. This can be done by increasing the diameter of the hole for the pyrometer measurements. The variation of the size of this hole allowed to change the shape of the crystal. The crystals with a convex shape had cracks only at the periphery, close to the poly-SiC where the conditions for the growth were not optimal due to a high radial gradient.
Other reasons formation cracks and microcracks is the growth of different domains which can not coalesce. To prevent the formation of cracks it is necessary to facilitate growth from one island in the middle of the seed. The surface of poly-SiC has to be under the growing crystal surface to avoid excessive mechanical stresses.

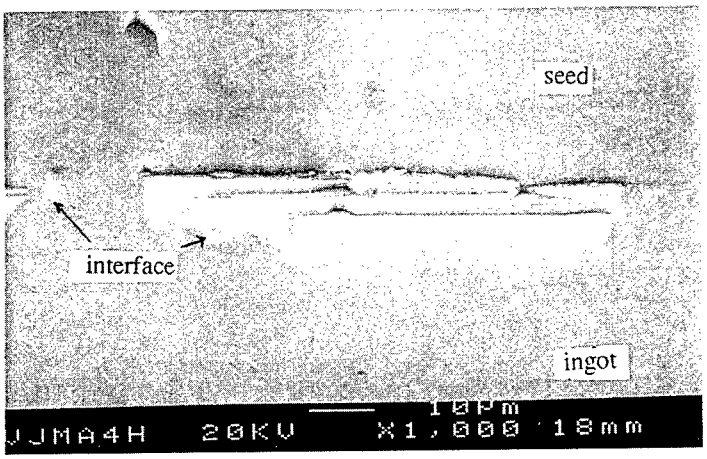


Fig.2 SEM photo of the interface of 4H-SiC ingot grown on off-axis seed.

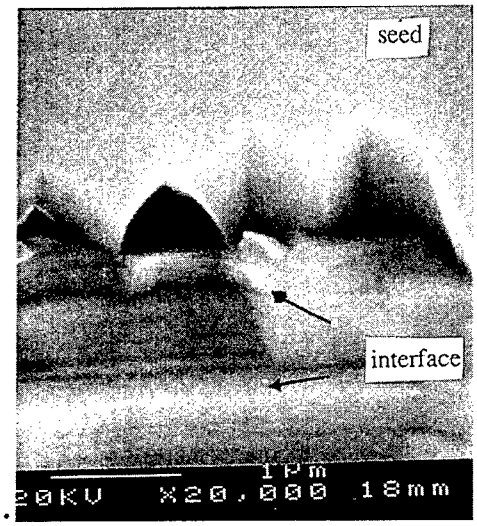


Fig.1. SEM photo of the interface (growth on off-axis seed)

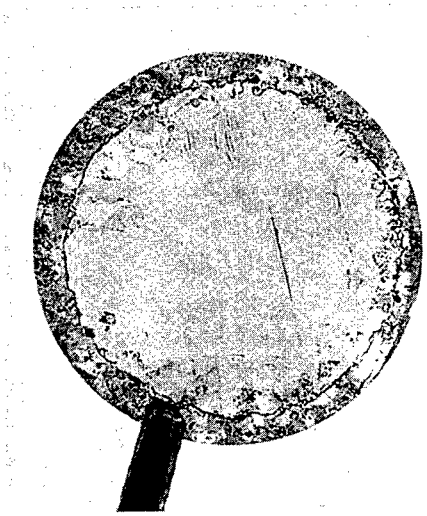


Fig.3. Photo of the wafer with the cracks (30 mm diameter).

6H-SiC inclusions Inclusions of 6H-SiC in the crystals grown on on-axis substrates were often found near the interface between the crystal and the seed. Double transformations of the polytype (4H-6H-4H) was observed in the first millimeter of the crystal. To avoid this effect it was necessary to increase the time of the pressure ramp from 40 min to several hours. In the crystals grown on off-axis substrates double transformations of the polytype existed too, but were observed under 8° to the growing surface. This can be explained, like in the case of CVD epitaxial growth, by the formation of terraces with on-axis orientation.

Morphology Examining the ingot morphology was a useful way of assessing the crystal quality. The morphology of the ingots is greatly affected by the C/Si ratio in vapor phase. Crystals with low defect density exhibited specular, smooth "as-grown" surfaces. Such crystals were grown at a low C/Si ratio which was achieved by a special design of the source and by the use of a tight crucible. The material supply from the source at the periphery allowed to suppress the reaction of Si from the central main source with the graphite walls and the loss of Si, which would have increased the C/Si ratio. The vapor transport is controlled by the main source in the center. Graphitization of the source at the periphery resulted in fast degradation of the main source and consecutively to a degradation of the morphology and quality of the growing crystals. In this case microinclusions were observed in the grown crystals.

Macrodefects Macrodefects were often present in the crystals grown at a temperature higher then 2300°C [4,1-3]. These are holes with an enlargement at the end, which start at the interface between seed holder-seed and which can penetrate deep into the growing crystal. The formation of these defects is explained by a local sublimation of the seed and then of the growing ingot [4]. This is due to the temperature gradient created in the crystal during the growth. Lower growth temperature and lower temperature gradient with optimization of the seed attachment technique allow to achieve the growth of ingots without macrodefects.

Acknowledgements The authors gratefully acknowledge the support of the of the French Ministry of Industry and the European Brite Euram Program (Contract BRPR-CT98-0812-JESICA).

References

[1] M.M.Anikin, R.Madar, A.Rouault, I.Garcon, L. Di Cioccio, J.L.Robert, J.Camassel and J.M.Bluet, Inst. Phys. Conf. Ser. 142 (1996), p.33
[2] M.Anikin, R.Madar, Mat.Sci.and Eng.B46 (1997), p.278.
[3] R.Madar, M.Anikin, K.Chourou, M.Labeau, M.Pons, E.Blanquet, J.M.Dedulle, C.Bernard, S.Milita. J.Baruchel, Diam. Rel. Mat. 6 (1997), p.1249.
[4] R.A.Stein, Physica B 185(1993)211
[5] M.Anikin, K.Chourou, R.Madar et al., Mat. Sci. Eng. B61-62 (1999), p.73.

Materials Science Forum Vols. 353-356 (2001) pp. 25-28
© 2001 Trans Tech Publications, Switzerland

Stability Criteria for 4H-SiC Bulk Growth

T.L. Straubinger, M. Bickermann, D. Hofmann, R. Weingärtner, P.J. Wellmann and A. Winnacker

Department of Materials Science 6, University of Erlangen-Nürnberg, Martensstr. 7, DE-91058 Erlangen, Germany

Keywords: 4H-SiC, Polytypism, PVT Growth

Abstract In this work 4H-SiC bulk growth experiments have been performed to study the generation of three types of polytype instabilities during 4H crystallization from the vapor phase: Island growth of other polytypes during the initial stage, circular ring sector inclusions generated at the edge of the facet and complete conversion from 4H to 6H growth generated on the facet.
The dependence of these instabilities on the process parameters seed surface temperature, inert gas pressure and axial temperature gradient have been investigated.
Types i and ii of polytype instabilities (6H/15R) were observed to be not stable and overgrown by 4H. Furthermore type i could be avoided by a seeding procedure with low supersaturation. No dependence on pressure or axial temperature gradient was noticed for the type ii polytype generation mechanism. Concerning the complete conversion to 6H, 4H stability showed no correlation with the argon pressure but we found a critical temperature for conversion, which depends on the axial temperature gradient. For low axial T-gradients the critical temperature decreased.

Introduction Currently 4H- and 6H-SiC are both commercially available in high crystal quality. However, while the growth of the 6H-polytype is known to be stable for a wide range of process conditions, 4H crystallization is stable only in a narrow range of growth parameters. Therefore it is of particular interest to better understand the origin of 4H to 6H/15R polytype transformations in order to improve the stability of the 4H-SiC crystal growth process.
About the complete conversion to 6H it is stated in literature [1, 2] that an upper critical temperature value for stable 4H region exists. In our experiments we investigated the dependence of this temperature on other process parameters. Additionally we examined the occurrence of other polytype instabilities in 4H crystals and possible correlations with growth conditions.

Experiments More than 20 4H-SiC crystal growth experiments in a conventional PVT reactor [3, 4] with different global temperatures, system pressures and axial temperature gradients were performed. For all runs we used 4H C-face and on-axis orientated seed wafers with a micropipe density of about $200cm^{-2}$ and a diameter of 35mm. The temperature on top of the crucible (seed position) was set to a constant value T>2100°C and a system pressure in the range of p<100mbar was applied. The axial temperature gradient was changed by modifications of the cooling channel on top of the crucible.

Since the thermal conditions inside the growth chamber are not accessible by direct measurement we used a 2-DIM heat transfer program [5] to calculate the axial temperature gradient and the temperature on the seed surface based on the experimental set-points (temperature on top of crucible, power).
After growth the crystals were prepared either as vertical cut or wafers and the polytype distribution was detected by optical microscopy and absorption measurements.

The temporal and local formation of polytype instabilities could be determined through the intentionally introduced doping striations [6] (see Fig. 1), which mark the phase boundary at defined periodic time steps.

Results and Discussion In the grown crystals we were able to distinguish three types of disturbances of the 4H growth. In the beginning of growth several polytype inclusions with isle like geometry were observed in the outer parts of the crystal. These inclusions are pushed out of the crystal during further growth (4H region increases with number of doping striations, Fig. 1). As the surface of the seed is flat containing facetted and quasi-rough crystal faces and does not correspond to an isotherm according to simulations of heat and mass transfer [5] a wide range of crystallization conditions with different supersaturations are present along the radius and therefore the nucleation of parasitic polytypes is possible. In addition non-stationary process conditions might still be present due to the seeding procedure (lowering of system pressure). Two factors explain the disappearance of these polytype instabilities during further growth (see Fig. 2i and 3i):

- The considerable faster lateral growth on the facetted 4H-regions.
- The increased mass transport towards the central facetted area as evident from the shape of the doping striations in Fig. 1.

During the whole growth process an other type of polytype instability, mainly 15R and only sometimes 6H, can be present. The transformation always starts at the edge of the facet (see Fig. 1, Fig. 2ii, Fig. 3ii) and develops into a circular ring sector geometry if viewed upright to the c-axis (see Fig. 2ii). After their nucleation these seeds are able to transmit their polytype information mainly laterally while transmission in growth direction is suppressed. Therefore they are overgrown again by lateral growth from the facet (see Fig. 3ii).

If the growth conditions allow the generation of a 6H seed on the 4H facet this seed will transmit its polytype information laterally and axially and overgrow the 4H part completely perpendicular to the c-axis (see Fig. 1, Fig. 2iii, Fig. 3iii).

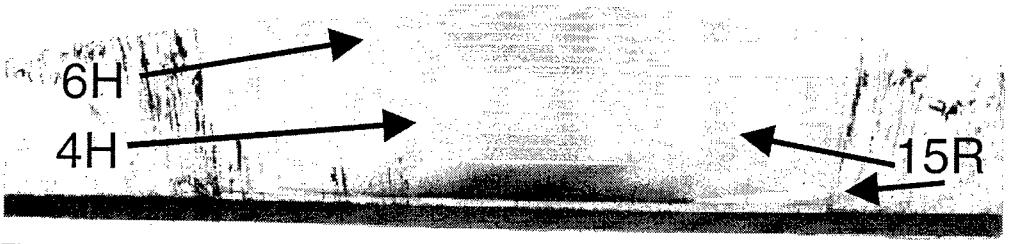


Fig. 1: Axial cut (bottom: seed; top: growth surface) through a SiC bulk crystal with complete conversion of 4H to 6H and polytype inclusions (growth islands: 15R parts on the edge of the seed; circular ring sectors: 15R parts on the right hand). The bright convex lines mark the phase boundary at defined equal time steps. Changes of growth rate in the central area during the first hours are due to an adjustment of the phase boundary to its equilibrium growth shape. The integral mass flux to the crystal surface remains constant.

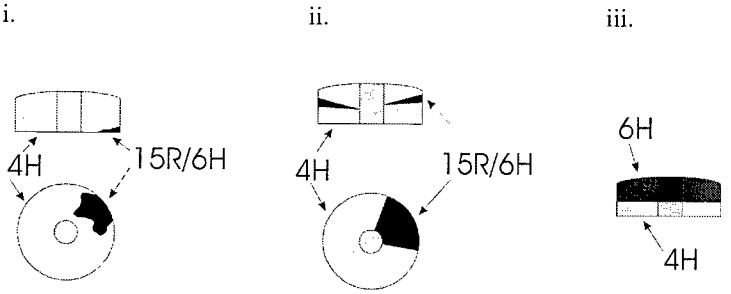


Fig. 2: Scheme of polytype instabilities observed during the 4H-SiC PVT process: i. Island growth of other polytypes and ii. Circular ring sector regions (both axial cut and wafer) iii. Complete conversion (axial cut)

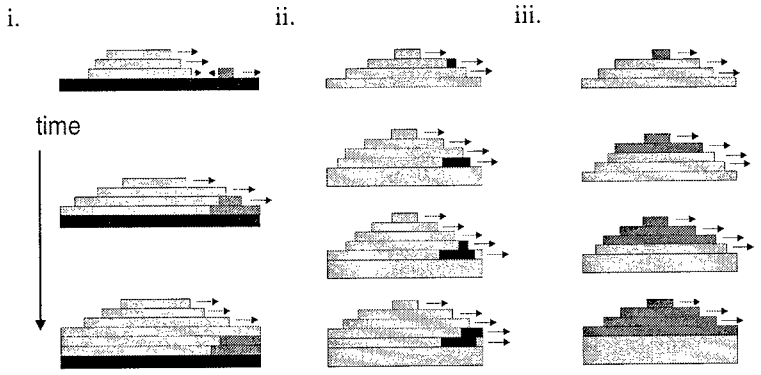


Fig. 3: Models of the generation and elimination for three types of polytype instabilities (time steps indicated by arrow on the left) observed during the 4H-SiC PVT process: i. Island growth (dark) on the seed (black) and overgrowth by the central growth spiral (bright). ii. Circular ring sector inclusion (black) generated on the edge of the facet (bright) and overgrowth. iii. Complete conversion of growing 4H-polytype by 6H nucleation on the facet and lateral overgrowth.

The inclusions in the initial stage are not critical for the main part of the 4H crystal because they are overgrown by the central 4H-growth after approximately 1mm. Furthermore they can be avoided through an initial growth phase with low supersaturation, which is also desirable due to defect formation (micropipes, dislocations) generated at the polytype transformations.

Concerning the circular ring sector polytypes we found no correlation with the process parameters T and p. This phenomenon might be correlated with the local concentration field near the edge between facet and quasi-rough interface (Variation of supersaturation due to the "Berg" effect [7]) and is under investigation.

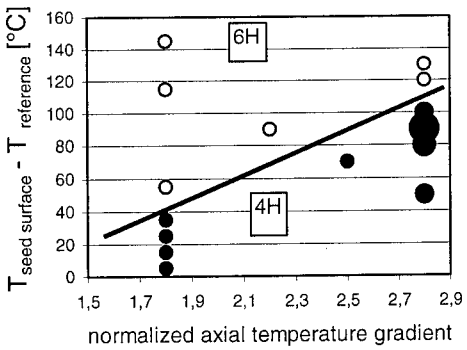


Fig. 4: Influence of seed temperature and temperature gradient on 4H- and 6H polytype formation (complete conversion). The circle area indicates the number of experiments with same process conditions (T, axial gradient, p is not constant).

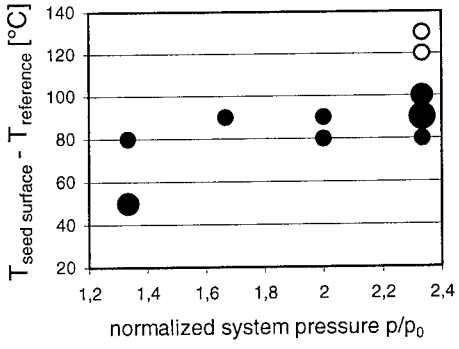


Fig. 5: Influence of seed temperature and system pressure on the 4H- and 6H polytype formation (complete conversion) at a constant axial temperature gradient. The circle area indicates the number of experiment with same process conditions (T, p, axial T-gradient).

Fig. 4/Fig. 5: The filled circles show 4H growth. The open circles stand for complete transformation to 6H.

For the transformation to 6H on the facet we found a critical process temperature, which depends on the axial temperature gradient (see Fig. 4). The critical temperature is decreasing with lower axial temperature gradients. Therefore one has to deal with two problems if lower axial gradients should be applied. The growth rate is decreasing for both reduced axial gradients and a lower 4H-growth temperature. As we can see in Fig. 5 we observe no decrease of the critical temperature with falling system pressure for a constant axial temperature gradient. This fact opens the possibility to reach acceptable growth rates for 4H-SiC through a decrease in pressure without approaching the critical temperatures for 6H- instabilities.
Finally the following comments are made concerning the interpretation of results on 4H growth instability with complete conversion to 6H:

a. The existence of a critical temperature for polytype transition is a fact which has been discussed by several groups [1, 2]. It should reflect the effect that the thermodynamic preference of the 6H polytype at increased process temperatures overrules promotion of 4H crystallization due to growth kinetics.
b. The observation that a reduction of system pressure (increase of growth rate) did not cause a decrease of critical temperature was unexpected as an impact of growth rate on polytype stability is discussed in literature [8, 9].
c. The evident correlation of critical temperature with the axial temperature gradient is, according to the knowledge of the authors, reported for the first time. Analysis of this topic are under work. But one might speculate that a decrease of the temperature gradient has a negative effect on stable growth considering the classical criterion of constitutional supersaturation/supercooling [10].

Conclusions We have shown that the 4H-SiC growth can be disturbed by different kinds of polytype instabilities. In the beginning of growth the nucleation of parasitic polytype inclusions on the outer parts of the seed surface could be excluded by applying lower supersaturations. The generation of polytype transformations on the edge of the facet resulting in circular ring sectors was not affected by variation of growth parameters. The complete transformation to 6H growth generated on the 4H-facet is depending on process temperature and axial temperature gradient but not on the system pressure. Therefore the process parameters should be set to values under the critical temperature while a lower system pressure can adjust the growth rate.

Acknowledgements This work has been supported by the Bavarian Research Foundation (contract No.176/96) and the German Research Foundation (contract No.W:393/9).

References

[1] W.F. Knippenberg, Philips Res. Repts. 18 (1963), p. 161.
[2] G. Augustine, H.McD.Hobgood, V.Balakrishna, G.Dunne and R.H.Hopkins, phys. Stat. Sol. (b) 202 (1997), p. 137.
[3] D. Hofmann, R. Eckstein, M. Kölbl, Y. Makarov, St.G. Müller, E. Schmitt, A. Winnacker, R. Rupp, R. Stein and J. Völkl, J. Crystal Growth 174 (1997), p. 669.
[4] Yu.M. Tairov and V.F. Tsvetkov, J. Crystal Growth 52 (1981), p. 146.
[5] M. Selder, L. Kadinski, Yu. Makarov, F. Durst, P. Wellmann, T. Straubinger, D. Hofmann, S. Karpov and M. Ramm, J. Crystal Growth 211 (2000), p. 333.
[6] E. Biedermann, Sol. State Com. 3 (1965), p. 343.
[7] A. Seeger, Phil. Mag. 44 (1953), p. 1.
[8] M. Anikin, M. Pons, K. Chorou, O. Chaix, J.M. Bluet, V. Lauer and R. Madar, Mater. Sci. Forum 264-268 (1998), p. 45.
[9] M. Tairov and Yu.M. Tsvetkov, Prog. Crystal Growth and Characterisation (1983), p. 111.
[10] "Elementary Crystal Growth", edit. K. Sangwal, saan Puplishers, Lublin, Poland (1994), p. 36.

Materials Science Forum Vols. 353-356 (2001) pp. 29-32
© 2001 Trans Tech Publications, Switzerland

Growth Related Distribution of Secondary Phase Inclusions in 6H-SiC Single Crystals

H.-J. Rost, J. Dolle, J. Doerschel, D. Siche, D. Schulz and J. Wollweber

Institute of Crystal Growth, Max-Born-Str. 2, DE-12489 Berlin, Germany

Keywords: Carbon Particles, Distribution of Carbon Inclusions, Growth Parameter, Inclusion, SiC Bulk Growth

Abstract

To understand and control the mechanism of defect generation is a fundamental aspect of crystal growth. The formation of grown in defects like misoriented regions respectively micropipes may be correlated with second phase inclusions such as silicon droplets or carbon particles. Inclusions could be identified as carbon particles by SEM and EELS. Their distribution along the growth direction and at the phase boundary were investigated by Optical Microscopy. It was found that their density varies in axial as well as radial direction. The dependence of the carbon particle concentration on growth parameters such as temperature stability, time and the distance between source and seed is shown. A concentration model will be discussed. Therefore any change of the vapour phase composition, characterised by the loss of silicon and caused by changing of a growth parameter, may result in a drastic local increase of the carbon particle concentration. The lattice information of the substrate is lost and defects may be formed if a critical value is exceeded.

Introduction

The quality of large diameter 6H-SiC single crystals is strongly influenced by the composition of the vapour phase and the thermal conditions inside the growth chamber. Beside the seed quality the grown in defects like misoriented regions and micropipes determine the yield [1]. Their formation is often correlated with second phase inclusions, such as silicon droplets or carbon particles [2]-[4]. The origin of the inclusions and their role regarding the generation of defects, especially microdefects, is controversially discussed. The appearance and distribution of the inclusions in the crystal in dependence on selected growth parameter are not well understood and were investigated in this paper. A model was proposed to explain the effect and methods were discussed to avoid them.

Experimental

Using an inductively heated furnace 6H-SiC-crystals up to 35mm diameter have been grown by the Modified Lely Method on the (0001)silicon face of a seed in a temperature range between 2100°C-2400°C and an Ar-pressure from 5-50 hPa. The distribution of inclusions was investigated in dependence on the seed temperature, the growth time, the system pressure and the distance between source and seed. The influence of nitrogen doping striations on the inclusions was also analysed using a marking technique [5]. Crystals were cut and polished parallel to the <0001> growth direction. Density and distribution of the inclusions along axial and lateral direction were investigated by Optical Microscopy. To identify the nature of the inclusions Scanning Electron Microscopy (SEM) with BSE-contrast and with EDX-mode was used. Investigations were done on polished wafers and at cleaved surfaces. Measured intensities were related to particle free areas. Additionally, Electron Energy Loss Spectroscopy (EELS) as a TEM-mode was used.

Results and discussion

In dependence on the growth parameters inclusions of different size were found in the volume of a grown crystal under a facet close to the surface (Fig.1a) as well as in a cut parallel to the growth direction (Fig.1b) using Optical Transmission Microscopy. These inclusions could be identified as particles consisting of carbon (Fig.2a). Measurements on polished wafers using Scanning Electron Microscopy (SEM) with BSE-contrast and with EDX-mode showed that the C/Si-ratio was increased up to seven times regarded to a particle free reference area (Fig.2b).

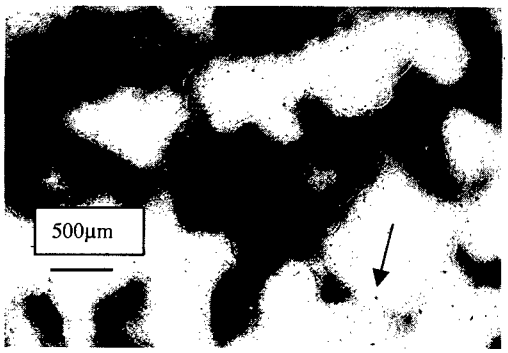


Fig.1a Inclusions from the top view (large black areas are graphite residues on the rear of the seed)

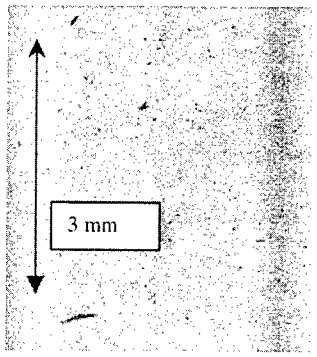


Fig.1b Inclusions parallel to <0001>

Different penetration depths by variation of the exciting energy and investigations at cleaved surfaces could exclude the detection of residual diamond grains from the polishing process. Additionally, Electron Energy Loss Spectroscopy (EELS) was used to identify the consistence of the particles. Fig 2c shows the spectra with the near edge fine structure of the C-K-edge with a distinct sp^2- hybrid structure caused by graphite and in the surrounding matrix.

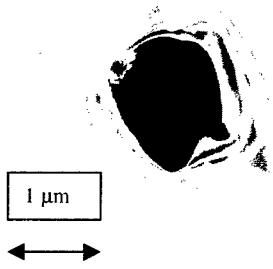


Fig.2a C-particle in BSE-contrast

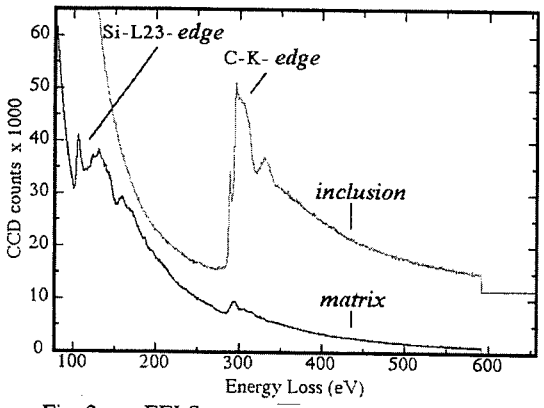
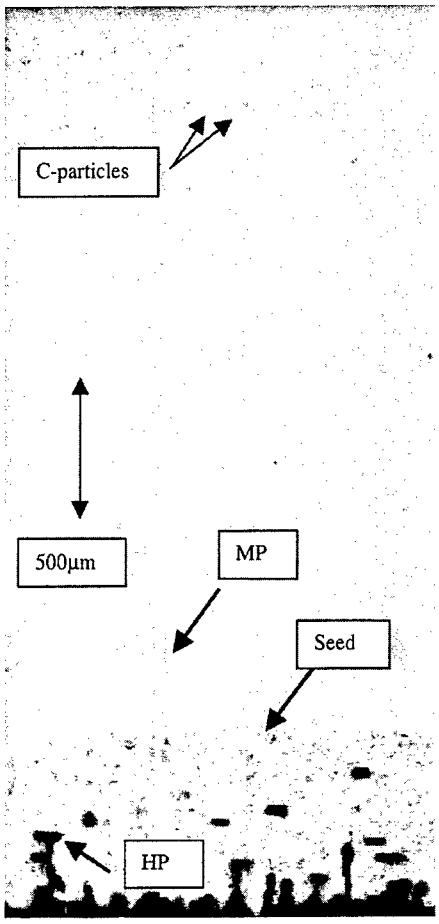


Fig. 2c EELS-spectra

No indication for silicon droplets was found. It can be explained by the surplus of carbon species in the atmosphere and the loss of silicon vapour from the growth system. Inclusions of graphite are formed during the near equilibrium growth and have a size between 1–50 micrometers.
They are usually irregular shaped and can be classified by 3 types (statistical distributed, layer-or stripe shaped, inclusions which are decorating defects).



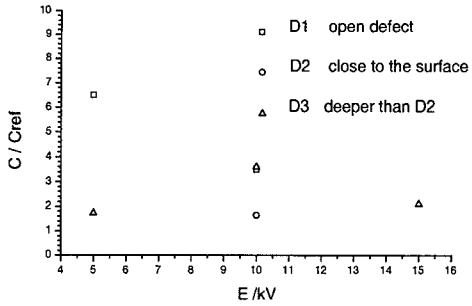


Fig.2b relative concentration of carbon inclusions at different exciting energies (EDX-mode in SEM)

Fig. 3 axial and radial distribution of inclusions (cut parallel to <0001>) MP-Micropipes HP - Hollowpipes

Furthermore, an inhomogeneous distribution of the particle density in radial as well as axial direction was found. The density is increased under the facet close to the centre of the crystal. The edges are nearly particle free although there are higher temperatures and therefore the Si/C-ratio in the vapour phase should be more shifted to the C-side than in the centre part. Otherwise, a stronger supersaturation in the central part because of the stronger cooling (higher axial gradient) was estimated by thermal modelling. In axial direction (Fig.3) the crystal growth starts nearly particle free independent of their concentration in the seed. With advancing process time the particle concentration increases mostly funnel-shaped following the facet. This can be explained by the change of the vapour phase composition, mainly by the loss of silicon and a decrease of axial and radial gradients with increased crystal length. Additionally, a strong dependence of the particle density on the growth temperature and the distance between source and seed was revealed. With increasing temperature the content of the carbon species in the vapour increases in relation to the silicon species [6] and the silicon loss will be enhanced. If for a given axial temperature gradient, which is decisively defined by the geometry of the growth chamber, the supersaturation of the vapour species at the phase boundary at a given temperature exceeds a critical value, the appearance of particles is promoted. The supersaturation itself is defined mainly by the temperature difference between source and seed which can be influenced by changing the coil position and the heat loss conditions. The number of inclusions could be reduced or avoided under comparable growth conditions if a proper ratio between temperature gradient and supersaturation is given. In the same context the stability of the growth conditions is important. Fluctuations of growth conditions (e.g. temperature, system pressure, doping etc.) may initiate the formation of inclusions (Fig 4a, 4b). Grain boundaries and polytype changes (Fig.4c) are favoured for the generation of inclusions. Local fluctuations of the particle density can support the formation of grown in defects like misoriented regions (Fig.4d) and micropipes. Otherwise, the presence of inclusions of any kind does not inevitable generate micropipes in accordance with the literature [4].

To explain the occurrence of C-particles different models are discussed. In our opinion the so called " convection model ", which favours the transport of C-particles by convection from the source or the chamber walls, can be neglected because of the low pressure range used and the small Stephan flux. The arrangement of shields in the growth chamber could not avoid the generation of particles. The so called " diffusion model ", which prefers the generation of precipitates behind the phase boundary during the cooling of the crystal, cannot explain the inhomogeneous distribution (e.g. striation-shaped). We postulate the so called " concentration model " where any change of the species ratio in the vapour phase may result in inclusions like C-particles. This is strongly coupled to the change of growth parameters including the crucible geometry. Furthermore, any change of composition of the vapour phase results in a change of the particle density. It can be found in a long term range by permanent silicon loss and increasing graphitisation with the process time as well as in a short term range by fluctuations of temperature, system pressure or during doping. The absence of inclusions in the first growth period can be explained by a relative constant composition of the vapour phase caused by additionally silicon added to the source to compensate the silicon loss and the absence of a graphitisation layer at the top of the source.
Another way to reduce or avoid the silicon loss at the growth phase boundary is to use a tantalum container [7]. To lower the growth temperature is also a suitable measure to avoid inclusions.

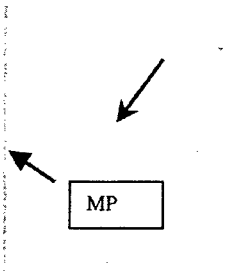


Fig. 4a layer or stripe-shaped arrangement



Fig. 4b inclusions on doping striations

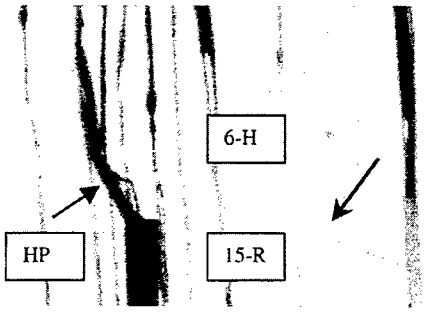


Fig. 4c decoration of polytype changes

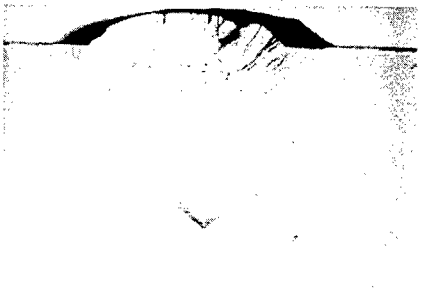


Fig. 4d generation of misoriented regions from stripe-arranged inclusions

Acknowledgements
The authors would like to thank Dr. Schneider from the Humboldt-University for EELS-measurements and acknowledge the support by Siemens AG and by the BMBF under the project number 01M2952B

References

[1] R.C.Glass, D.Henshall, V.F.Tsvetkov, C.H.Carter,Jr., Phys. Stat. Sol. (b) 202 (1997) p.149
[2] M.Dudley et al., A.Powell and S.Wang, P.Neudeck, M.Skowronski, Appl. Phys. Lett., Vol.75, 784 (1999)
[3] M.Tuominen, R.Yakimova, A.Vehanen, E.Janzen, Mater. Sci. Engng. B57 (1999) p.228
[4] D.Hofmann et al., J. Crystal Growth, 198/199 (1999) p.1005
[5] S.G.Müller et al., Mater. Sci. Engng. B44 (1997) p.392
[6] S.K.Lilov, Diamond and Related Materials 4 (1995) p.1331
[7] Y.u.A.Vodakov, A.D.Roenkov, M.G.Ramm, E.N. Mokhov, Y.u.N.Makarov, Phys. Stat. Sol. 202 (1997) p.177

Materials Science Forum Vols. 353-356 (2001) pp. 33-36
© 2001 Trans Tech Publications, Switzerland

Investigation of a PVT SiC-Growth Set-up Modified by an Additional Gas Flow

T.L. Straubinger, P.J. Wellmann and A. Winnacker

Department of Materials Science 6, University of Erlangen-Nürnberg,
Martensstr. 7, DE-91058 Erlangen, Germany

Keywords: Doping, Inclusions, Micropipe Closing, Modified-PVT

Abstract: We have investigated a new type of a so called "modified PVT setup" with an additional gas flow into the growth cell. The motivation was an improvement of the parameter control for doping of SiC using gas sources, i.e. homogenization of doping levels. Since an additional gas flow inside the growth cell could cause severe distortions of the vapor flow we have performed basic investigations of the influence of an inner argon gas stream on thermal field and structural properties of the growing crystal. We have studied the impact of the extern gas flow towards the surface of the growing crystal. Strong evidence for micropipe closing in the initial growth stage and reduction of second phase inclusions was found.

Introduction

As the doping of PVT grown SiC crystals is often inhomogeneous because of varying crystal surface temperature or source depletion during growth time it would be advantageous to supply doping gases directly to the crystal growth interface for better incorporation control [1]. However, the implementation of an additional gas stream into the PVT setup ("modified PVT" or "M-PVT") as indicated in Fig. 1 causes severe distortions of the crystal growth process; i.e. modification of temperature field, etc. In this paper we will introduce the experimental realization of a modified PVT setup with an additional gas stream. We will discuss the necessary steps to optimize the growth conditions and the potential for high n-type of SiC doping with nitrogen. In addition we will present first results on an improvement of the crystal growth process in the modified PVT regime, i.e. strong evidence for micropipe overgrowth in the initial stage of growth and reduction of second phase inclusions (i.e. graphite particles).

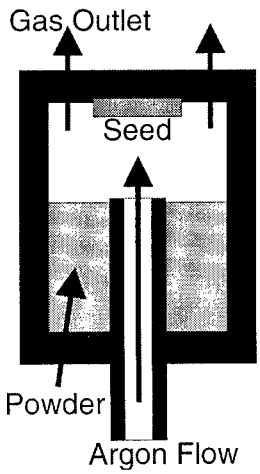


Fig. 1: Schematic M-PVT setup with graphite crucible (black), SiC powder source and SiC seed crystal (both gray) and graphite tube inside the powder.

Experiments

For introduction of the gas flow into the growth cell we modified the conventional PVT setup [2,3] by a second gas source according to Fig. 1. A tube running through both the isolation and the SiC powder source supplied inert gas (argon or helium) and/or the doping gas (e.g. nitrogen) directly in front of the growth boundary. In additional an outlet for the gases was realized by a partly permeable diffusion barrier indicated by two arrows on top of the growth cell in Fig. 1.

After we obtained a suitable thermal field inside the growth cell by adjusting the crucible geometry and the inner gas flow we were able to grow crystals comparable in shape and growth rate to those grown

by conventional PVT process (d>35mm; L>10mm), while no blocking of the gas outlet was observed. The growing polytype was mainly 6H for both carbon and silicon side experiments. The ambient gas for pressure control was pure argon like it is common in the conventional PVT growth regime. In the following we will call it the "outer gas flow" in order clearly distinguish it from the additional and new "inner (doping) gas flow" of the modified PVT setup.

The microstructure was analyzed by optical microscopy and the doping concentrations were determined by absorption spectroscopy [4,5].

Results and Discussion

Establishment of proper growth conditions:

We used a computer program for 2-dim heat transfer calculations [6] to minimize the impact of the geometrical modifications (gas supplying pipe) on the thermal field [Fig. 2, left] inside the growth cell. The main problem was the suppression of concave isotherms over the powder surface [Fig. 2, middle] caused by radiation heating out of the tube that is running through the hot powder core. By using a suitable tube shape this effect could be limited to a small area while the isotherms in the part of the growing crystal remained convex.

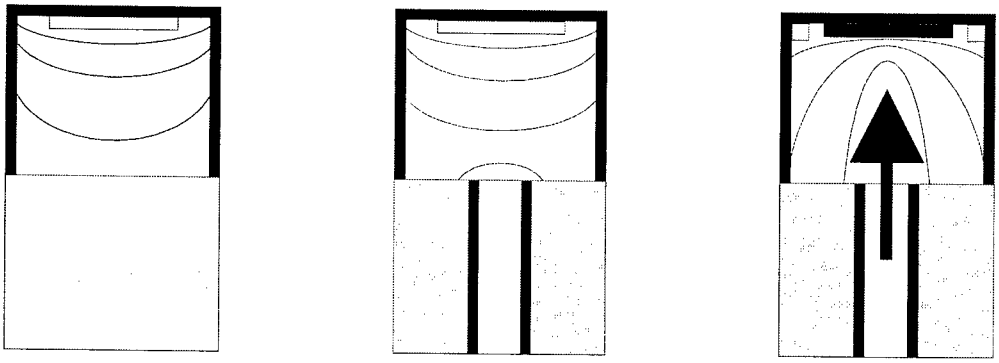


Fig. 2: Schematic set-up with SiC powder source (gray, bottom), SiC seed (gray, top), crucible (black, top) tube (black, bottom), gas flow (arrow) and isothermals (lines).
Left: conventional T-field; middle: T-field with tube and without gas flow; right: T-field with high gas flow carbonized seed and polycrystalline growth in the corners.

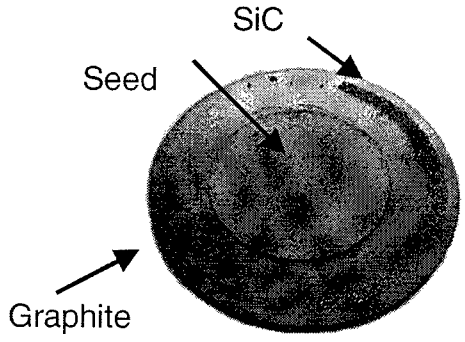


Fig. 3: Graphite seed holder with carbonized seed and polycrystalline SiC in the outer parts.

In additional to geometrical influences the T-field was also disturbed by the inner gas flow itself. The gas species are heated up while flowing through the hot core area of the crucible and enter into the growth cell as hot stream. As a consequence the central parts and especially the seed are heated up. The thermal field [Fig. 2, right] changes dramatically and the "cold" points in the seed area migrate to the edges. Therefore the seed sublimes and polycrystalline SiC growth is observed in the outer parts [Fig. 2, right; Fig. 3]. If the value of the inner gas flow is lowered the shape of the T-field is maintained according to Fig. 2 (middle) and crystal growth is possible.

Furthermore one has to take into account that the inner gas flow also has a significant influence

on the global temperature. The gas entering the reactor at room temperature has to be heated up to around 2000°C and therefore more power (about 1kW for typical flow values) is necessary to reach the growth temperature. Especially if the inner gas flow is varied during the experiment this energy loss must be compensated by a variation of the external power input.

Doping:

If only inert gas without doping atoms was introduced into the growth cell the doping concentration was lower than during the conventional PVT process. In the best case doping levels as low as $n=6*10^{16}/cm^3$ nitrogen atoms were incorporated into the SiC crystal although no extra efforts were made to minimize residual impurities in the isolation, crucible material and SiC source powder. A strong correlation between residual nitrogen doping and growth rate was observed: a factor two higher growth rate of 700µm/h showed a low doping concentration of $n=6*10^{16}/cm^3$ while an experiment at a growth rate of 350µm/h exhibited a doping level of $n=1*10^{17}/cm^3$. If nitrogen gas was supplied through the inner gas tube (same amount as in conventional PVT experiments through the "outer gas flow") a high doping concentration of $n>1*10^{20}/cm^3$ was observed (conventional PVT counterpart: $n=6*10^{17}$-$1*10^{19}/cm^3$). The difference is monitored in Fig. 4 where one can compare the difference in optical transmission between a conventional PVT (lower part; seed) and a M-PVT crystal. This demonstrates that M-PVT is a suitable and efficient method to supply doping atoms in front of the crystal growth interface.

Micro pipe reduction:

On the interface between seed and crystal (Fig. 4), clearly determined by the change in doping concentration we observed a tendency of micropipe closing. This effect is significant (30%), reproducible in several crystals and applies for both micro and macro pipes. Up to now several reasons are under discussion. A reasonable explanation could be a "smoothing" effect of the inner gas flow on the temperature field in front of the seed surface. Low lateral temperature gradients (may also be achieved in PVT) would cause step growth in a large seed areas with lateral crystal overgrowth of the pipes.

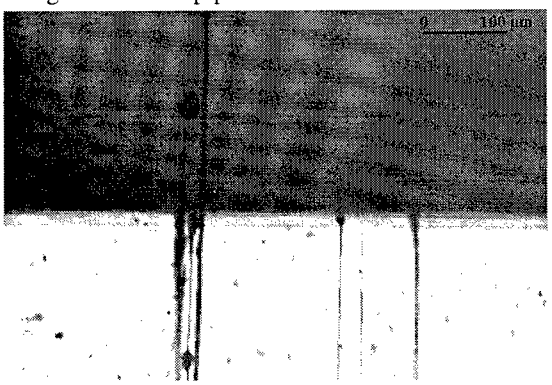


Fig. 4: Transmission Light Microscopy picture of the interface between seed and crystal.
Crystal (top): M-PVT; no carbon inclusions and fewer pipes. More Absorption according to higher nitrogen content.
Seed (bottom): grown by conventional PVT with carbon inclusions and micro/macro pipes; less Absorption according to lower doping concentration.

Inclusions:

In M-PVT experiments carried out at process conditions comparable to conventional PVT (without additional gas flow but equal temperature, pressure and temperature-gradients) we observed no carbon inclusions (Fig. 4, crystal) in the central crystal parts for both low and high n-doped crystals. At normal growth rates (350µm/h) the inclusion free area (Fig. 5a) extended over the whole seed (d=36mm) and only in the outer parts (36mm<d<41mm) inclusions were present. It is believed that this kind of inclusions are carbon particles [7, 8], which migrate from the powder source to the crystal surface, driven by the pressure difference of the gaseous silicon and carbide species along the temperature gradient. It seems that the particles which are homogeneously distributed over the entire crystal diameter in conventional PVT are pushed out of the mono crystalline part by the inner gas flow (M-PVT). As the growth rate was increased up to 700µm/h also the mass transport increased; the particles obtained more kinetic energy and prevailed against

the inert gas flow. Thus the inclusion free area decreased and inclusions appeared inside the seed diameter (d<36mm, Fig. 5b).

As a result the powder source can be determined as one origin of carbon inclusions.

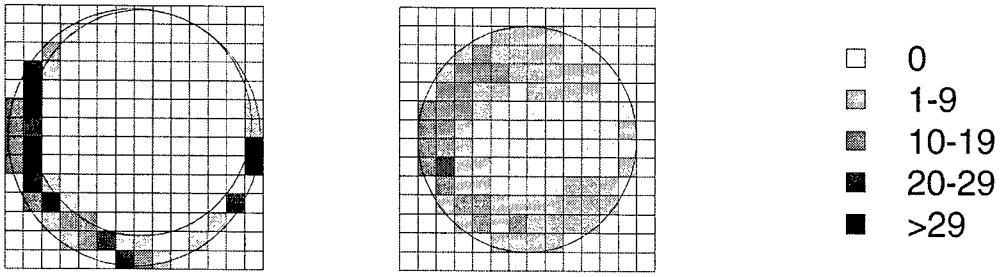


Fig.5: Inclusion density of low doped SiC-Wafers grown by M-PVT in $1*10^6 cm^{-3}$.
a. Growth rate 350µm/h; d=41mm: Inclusions only at the edge.
b. Growth rate 700µm/h; d=36mm: Inner part without inclusions is decreasing.

Conclusions/Summary

We have developed a modified PVT process setup in which we were able to grow crystal at the presence of a gas flow introduced directly into the growth cell. We demonstrated the possibility to control the doping concentration inside the crystal with the additional gas flow. We observed micro pipe healing at the seed to crystal interface in the initial M-PVT growth stage and we have shown that carbon inclusions which originate from the SiC powder source could be avoided through extrusion by the gas flow.

Acknowledgements

This work has been supported by the Bavarian Research Foundation (contract No.176/96) and the German Research Foundation (contract No.W:393/9).

References

[1] A. Ellison, Silicon carbide growth by high temperature CVD techniques, Dissertation, Linköping, 1999.
[2] Yu.M. Tairov and V.F. Tsvetkov, J. Crystal Growth 52 (1981), p. 146.
[3] D. Hofmann, R. Eckstein, M. Kölbl, Y. Makarov, St.G. Müller, E. Schmitt, A. Winnacker, R. Rupp, R. Stein and J. Völkl, J. Crystal Growth 174 (1997), p. 669.
[4] R. Weingärtner, M. Bickermann, S. Bushevoy, D. Hofmann, M. Rasp, T.L. Straubinger, P.J. Wellmann and A. Winnacker, to be published in Mat. Sci. Eng. B (2000).
[5] P.J. Wellmann, S. Bushevoy and R. Weingärtner, to be published in Mat. Sci. Eng. B (2000).
[6] M. Selder, L. Kadinski, Yu. Makarov, F. Durst, P. Wellmann, T. Straubinger, D. Hofmann, S. Karpov and M. Ramm, J. Crystal Growth 211 (1-4) (2000), p. 333.
[7] V. Tsvetkov, R. Glass, D. Henshall, D. Asbury, C.H. Carter, Mater. Sci. Forum 3 (1998), p. 264.
[8] D. Hofmann, M. Bickermann, R. Eckstein, M. Kölbl, St.G. Müller, E. Schmitt, A. Weber and A. Winnacker, J. Crystal Growth 198/199 (1999), p. 1005.

Materials Science Forum Vols. 353-356 (2001) pp. 37-40
© 2001 Trans Tech Publications, Switzerland

Mass Transport and Powder Source Evolution in Sublimation Growth of SiC Bulk Crystals

D.S. Karpov[1], O.V. Bord[1], S.Yu. Karpov[1], A.I. Zhmakin[2], M.S. Ramm[2] and Yu.N. Makarov[3]

[1] Soft-Impact, Ltd., PO Box 33, RU-194156 St.Petersburg, Russia

[2] A.F.Ioffe Physico-Technical Institute, Russian Academy of Sciences, Polytechnicheskaya 26, RU-194021 St.Petersburg, Russia

[3] Institute of Fluid Mechanics, University of Erlangen-Nürnberg, Cauerstr. 4, DE-91058 Erlangen, Germany

Keywords: Evolution, Graphitization, Growth Rate, Porosity, Powder Charge

Abstract. In this paper we study mass transport in SiC powder charge, employed as a source of reactive species in SiC bulk crystal growth, coupled with the species transport in the clearance between the powder and the seed. The study is aimed at finding correlation between growth conditions and powder evolution during a long-term growth process. We also examine how the growth conditions and the powder properties (porosity and mean size of SiC granule) influence SiC growth rate at the seed. The theoretical results are compared with available experimental data.

Introduction

Growth of high-quality SiC bulk crystals suitable for substrate fabrication is a challenge for modern high-temperature and high-power electronics. To grow SiC bulk crystals the sublimation method is found to be most suitable. This technique requires an accurate control of a thermal field in the crucible during the long-term growth process, which is influenced by changes in the crystal shape, deposit formation, SiC powder source degradation with time, etc. The latter factor is still little understood because of difficult *in situ* powder examination. Only limited information on the powder evolution is available at the moment [1-3]. In these publications the following processes occurring in the powder during SiC growth are distinguished:

- Graphitization of SiC granules resulting in formation of a low-density graphite foam in the hot zones of the powder charge;
- Densification of the powder in the cold zones, related to secondary SiC crystallization from the supersaturated vapor species;
- Directional gas flowing through the powder charge. In particular, it results in a shape modification of SiC granules due to their sublimation and secondary crystallization of the reactive species.

However, effects of growth conditions on the processes and the influence of the powder properties on the species transport and SiC growth on the seed are still open questions requiring further examination. Due to evident difficulties in experimental monitoring of SiC powder evolution, modeling can be a powerful tool to find correlation between the growth conditions, temporal changes in powder properties and SiC growth rate on the seed.

In this paper we suggest for the first time a model of species transport through a SiC powder charge coupled with an analysis of sublimation and graphitization of individual granules. Using the model we investigate how growth conditions and powder properties influence SiC growth rate on the seed. We also show that the processes occurring in the powder can be effectively controlled by adjustment of the temperature distribution in the crucible.

Model

Here we employ a simplified one-dimensional approach for modeling of transport of the reactive species (Si, Si_2C and SiC_2) in the powder charge, their transfer in the clearance between the powder and the seed, and SiC growth on the seed. Porosity ε and mean granule diameter δ are chosen to be the basic properties of the powder. The mean granule diameter is assumed to be comparable to the mean size of an individual pore in the powder. Both diffusive and convective mechanisms of species transport in the pore space are taken into account. The Hertz-Knudsen relations modified to take into account the diffusive resistance of the pore are used to describe the mass exchange between the granule surface and the pore space. The phase state of the granule surface is analyzed in every point of the powder charge and the corresponding type of heterogeneous equilibrium [4-5] is assumed to calculate the granule sublimation rate R. We distinguish between two types of the granule phase states and, accordingly, between two types of heterogeneous equilibria: (i) stoichiometric SiC surface (SiC–vapor equilibrium), and (ii) the surface of SiC granule covered with the porous graphite foam (SiC–C–vapor equilibrium). The local granule evaporation rate was then related to the local rate of the porosity change assuming the granule concentration in the powder to be constant: $d\varepsilon/dt = 3R(1-\varepsilon)/\delta$. In more detail the model will be published elsewhere.

Results and discussion

The computations have been carried out with the parameters close to those experimentally used: gas pressure of 25 mbar, initial mean granule diameter of 1 mm, initial porosity of 0.9, powder charge height of 2 cm, clearance between the powder and the seed of 2 cm. First, we assigned a constant axial temperature gradient in the clearance and a parabolic temperature profile inside the charge as shown in Fig.1.

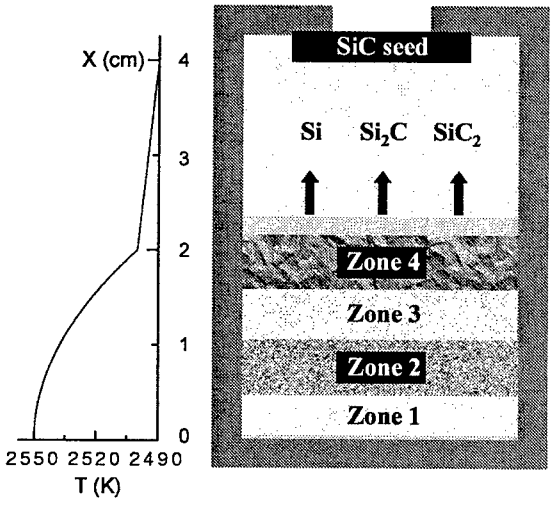


Fig.1. Schematic view of the crucible. Different zones in the powder charge are indicated: (1) empty cavity filled by low-density graphite foam; (2) zone of intensive sublimation; (3) quasi-equilibrium zone; (4) zone of secondary SiC crystallization (see text for details).

The computations predict appearance of several zones in the powder source with very different character of chemical interaction between the gas mixture and the granule surfaces (see Fig.2). Intensive granule sublimation occurs in the hot region near the bottom of the powder charge. Here the granule size and the porosity decrease with time and eventually an empty cavity is formed with $\varepsilon \approx 1$ filled by low-density graphite foam (zone 1). The transition zone where the porosity gradually varies from unity down to about initial value is indicated in Fig.1 as zone 2. The phase state analysis predicts here graphitization of the granule surface. So, the major part of gaseous species produced by the source is formed just in the region where SiC and graphite coexist in the powder. SiC sublimation in zone 2 results in a gas flow acceleration along the axis of the crucible. A heterogeneous equilibrium between the granule and the reactive vapor in the pore space is nearly reached in zone 3. The porosity and the granule diameter practically do not vary here with time and are close to the initial values. Finally, secondary SiC crystallization is predicted in the cold zone of

the source near the top of the charge (zone 4). In this zone the porosity decreases with time and then vanishes. This leads to blocking of the gas flow pathways in the powder and, as a result, to drastic SiC growth rate reduction on the seed.

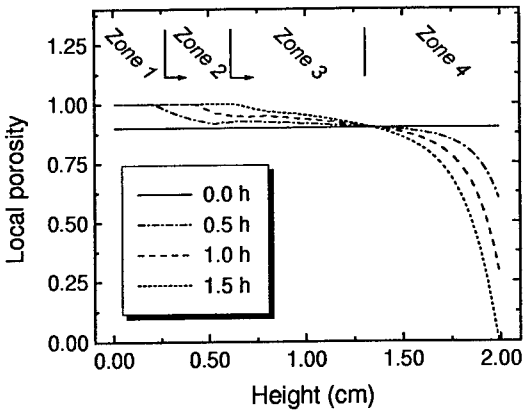


Fig.2. Evolution of the powder porosity computed for the parabolic temperature profile in the powder charge.

In Fig.3 we show by solid circles the temporal evolution of SiC growth rate on the seed predicted by our model. Notice that the growth rate reduction occurs despite a lot of material in the powder charge is still available for sublimation. This result allows better understanding the processes occurring in the growth system with a realistic two-dimensional temperature distribution in the crucible. In such a system, hot zones are located not only at the crucible bottom, but also near its side walls. So, additional empty cavities filled by low-density graphite foam are expected to appear along the crucible walls. A secondary crystallization zone formed at the top of the charge must result in blocking of the gas flow pathways in the powder bulk but the gas transport through the empty cavities near the crucible walls is still possible. Thus, we expect the blocking effect to result (i) in a considerable enhancement of mass transport at the periphery of the growing crystal, (ii) in a remarkable reduction of the growth rate after the secondary crystallization zone is formed, and (iii) in a lower utilization efficiency of the powder charge due to dominating periphery sublimation.

Evolution of SiC powder during sublimation growth has been recently studied experimentally by P.Wellmann et al [3]. The authors of the paper reported on a dense disk formation at the top of the charge after several hours of growth and on considerable powder consumption and graphitization near the hot walls and the bottom of the graphite crucible. In addition, a drastic reduction of the growth rate after about 2 hours of growth was observed in [3]. All these observations agree well with the theoretical predictions.

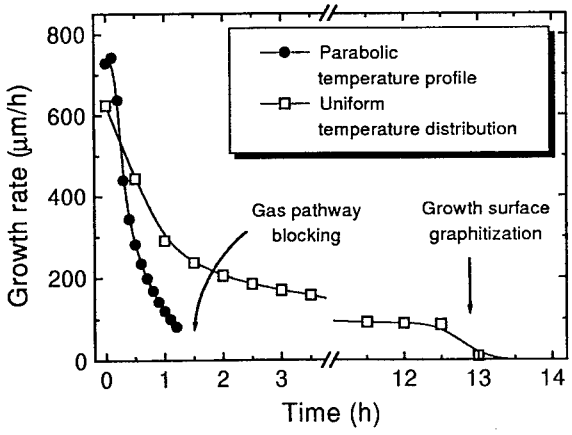


Fig.3. Growth rate evolution computed for different temperature distributions in the powder charge.

To optimize utilization efficiency of the source we examine the effect of the temperature profile on the processes occurring inside the powder and on SiC growth on the seed. The computations carried out for a uniform temperature distribution in the charge (with 50 K difference between the source and the seed) show that use of the uniformly heated SiC powder avoids its densification. The granules sublime in this case both at the bottom and at the top of the charge (see Fig.4), and the reactive species flow easily through the pores in the powder bulk. Almost complete sublimation of the granules occurs over the whole charge. It results in a higher powder utilization

efficiency for the uniform temperature distribution due to prolonged growth (see Fig.3, squares). Vanishing of the growth rate after 13 hours of growth seen in Fig.3 is caused by surface graphitization of SiC crystal. The latter is related to the changes in the vapor composition due to gradual depletion of the powder material. As previously, the SiC growth rate reduces significantly during the first ~1.5 hours although the variation range is much more narrow compared to the case of the parabolic temperature profile. The variation of the growth rate is directly related to stratification occurring in the SiC powder at the initial stage of growth. For two-dimensional temperature distribution in the crucible we expect more uniform growth rate distribution over the seed as compared to the axial parabolic temperature profile discussed above.

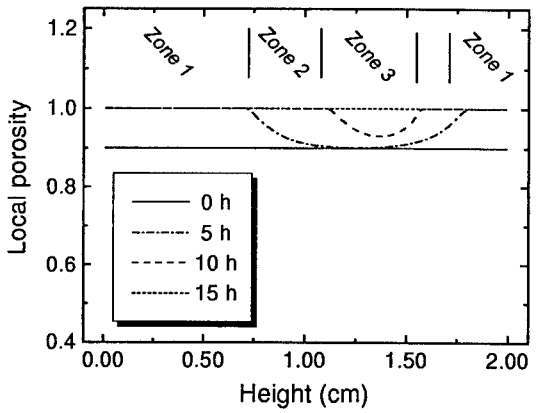


Fig.4. Evolution of the powder porosity distribution computed for uniform temperature distribution in the charge.

Conclusions

In this paper a model of species transport inside SiC powder source is suggested taking into account chemical interaction of the reactive species with SiC granules. Within one-dimensional approach the model has been applied to analyze correlation between the growth conditions, the processes occurring in the powder charge and SiC growth on the seed. Predicted stratification in the powder and significant reduction of the growth rate are in good agreement with the experimental observations.

Two regimes of SiC powder source operation are found theoretically – with and without appearance of a zone where secondary crystallization results in blocking of the gas flow pathways in the powder bulk. The blocking effect should lead to a lower powder charge utilization efficiency, to enhancement of the reactive species transport at the periphery of the seed and to a poorer growth rate temporal stability. This effect can be suppressed by a proper adjustment of the temperature distribution inside the powder charge.

References

[1] St.Müller: PhD thesis, University Erlangen-Nürnberg, 1998.

[2] K.Chourou, M.Anikin, J.M.Bluet, J.M.Dedulle, R.Madar, M.Pons, E.Blanquet, C.Bernard, P.Grosse, C.Faure, G.Basset, Y.Grange: Mat.Sci.Engin.B 61–62 (1999), p. 82.

[3] P.J.Wellmann, M.Bickermann, D.Hofmann, L.Kadinski, M.Selder, T.L.Straubinger, A.Winnacker: J.Cryst.Growth 216 (2000), p. 263.

[4] M.S.Ramm, A.V.Kulik, I.A.Zhmakin, S.Yu.Karpov, O.V.Bord, S.E.Demina, Yu.N.Makarov: MRS Spring Meeting, San-Francisco 2000, Accepted for publication in Symposium Proceedings.

[5] O.V.Bord, S.Yu.Karpov, M.S.Ramm, Yu.N.Makarov: ISSCRM-III, Book of abstracts, Novgorod the Great, Russia (2000), p. 24.

Materials Science Forum Vols. 353-356 (2001) pp. 41-44
© 2001 Trans Tech Publications, Switzerland

Some Aspects of Sublimation Growth of SiC Ingots

S.F. Avramenko[1], V.S. Kiselev[1], M.Ya. Valakh[2] and V.A. Yukhimchuk[2]

[1] Special Design-&-Engineering Bureau with a Pilot Production of the Inst. of Semiconductor Physics, National Academy of Sciences of Ukraine, Lisogorskaya St. 4, Kyiv 03028, Ukraine

[2] Institute of Semiconductor Physics, National Academy of Science of Ukraine, 45 Prospekt Nauki, 03028 Kyiv, Ukraine

Keywords: Crystal Shape, PVT Growth, Residual Stress

Abstract

The aim of the present work is to analyze some parameters of SiC crystals: shape, surface morphology and residual stresses. The shape of the crystals depends on the construction of growth cavity. The change of geometry allowed to grow crystals with convex, concave or flat growth front. It is shown that a flat growth front should be used for excluding radial non-homogenity of doping impurities. The presence of considerable temperature gradients in the bulk crystals during their growing leads to arising mechanical stresses after cooling these crystals. By means of Raman scattering we estimated respective strain values that reach approximately 0.3 Gpa at the centre of the crystal.

Introduction

Silicon carbide is promising material for power high-temperature and microwave electronics. However, the main factor limiting development of SiC device technology is deficiency of high-quality substrates of large diameter with low concentration of structural defects. Growing bulk crystals of silicon carbide by the modified Lely method or Physical vapour transport (PVT) method was offered more than 20 years ago, nevertheless, despite a plethora of works performed along this direction, several aspects of the method remain undeveloped. This work was focused on investigations of effects of a growth front shape and conditions on crystal parameters, namely: ingot shape, homogeneity of doping impurity distribution and presence of residual strains.

Methods of growing crystals and discussion of results

To grow bulk crystals, we used the PVT method. Applied was the industrial furnace REDMET-30 with a resistive graphite heater [1]. As seeds, crystals 6H-SiC with n-type conductivity, grown by the Lely method, or PVT crystals, were used. The seeds had a form of plane-parallel plates orientated along the plane {0001}. These were etched in KOH melt (T=600°C, t=3 - 5 min.). It enabled us to determine orientations of (0001)Si and (0001)C planes. As a vapour source (charge) we used polycrystalline silicon carbide of *n*- or *p*-type conductivity. To synthesize charge, we used graphite and silicon powders of semiconductor purity grade. The synthesis was carried out in argon at the temperature 2000°C.

Crystals were grown at charge temperatures 2350-2550°C in Ar atmosphere and pressures from 2 to 15 mbar. The average growth rate along the *c*-axis was changed from 0.3 to 1.5 mm per hour. To study growth peculiarities, the crystals were cut into plates according to different crystallographic directions that were parallel and perpendicular to the *c*-axis. Thickness of the plates varied within the range of 0.5-1.5 mm. The plates were polished by diamond pastes and etched in molten KOH.

The shape of crystals prepared by the PVT method is mainly determined by a growing cell design. Its change enables to control a growth front and, accordingly, a crystal shape. We used several variants of growing cell designs, which enable us to prepare crystals with convex, concave or flat

growth fronts. Application of a heat field with symmetry close to the spherical one enables to carry out growing crystals along *a*- and *c*-directions simultaneously [2]. Fig.1 shows a schematically crystal structure with a convex growth front and a photo of a typical ingot. The ingot consist of several parts: the monocrystalline one having a conical shape (1), the seed (2) and the polycrystalline outgrowth (3).

The diameter of an ingot monocrystalline part was as large as 25 mm when using the seed diameter up to 10 mm and growth duration about 10 hours. Increasing the seed diameter up to 20 mm we were able to produce the monocrystalline part with 35 mm diameter.

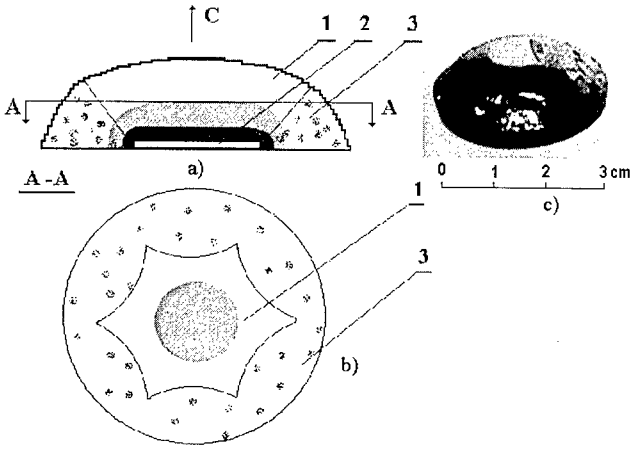


Fig.1.The crystal with a convex growth front: a) crystal cross-section with a plane parallel to *c*-axis, where cipher 1 denotes monocrystalline part, 2-seed crystal, 3 - polycrystalline outgrowth; b) a crystal cross-section with a plane perpendicular to *c*-axis; c) an ingot picture.

Studying cuts perpendicular to *c*-axis showed that growth in a heat field of a quasi-spherical form leads to radial distribution of impurities in the ingot due to vapour composition change in the course of growing. It is obvious that at presence of different impurities in the vapour source, more volatilizing components are continuously driven off during the growth process. It causes non-homogeneous doping substrates owing to the change of the concentration of impurities in vapour during the whole growing process. Fig.1b shows in ingot section. As seen, the plate has non-uniform colour caused by non-homogeneous distribution of doping impurities. The plate colour depends on the type of outgrowing plane (0001)C or (0001)Si and impurities incorporated into the source (aluminum, boron or nitrogen).

Fig.2 shows pictures and crystal structures obtained in a case of concave and quasi-flat growth fronts. When using a flat growth front, outgrowing is insignificant, but it enables to grow crystals with a form close to the cylinrical one and practically excludes any radial nonhomogenity of growing crystals. Thus, from a commercial viewpoint, usage of a flat growth front is preferable [3]. A concave growth front leads to a decrease in diameter of the monocrystalline part, and therefore is not effective.

The crystal surface morphology was investigated using an optical microscope coupled with a videocamera. It was ascertained that crystals with convex growth front can be characterized by the presence of growth macrosteps disposed in the form of concentric circles (Fig.3a). Heights of these steps decrease from the periphery to the crystal centre. In pictures one can see outlets of micropipes on the crystal surface. Causes of these defect formation are connected with inclusions of small carbon particles.

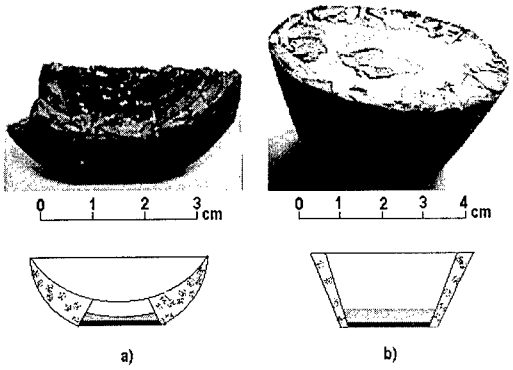


Fig.2. Pictures of crystals with concave and flat growth fronts and their structure.

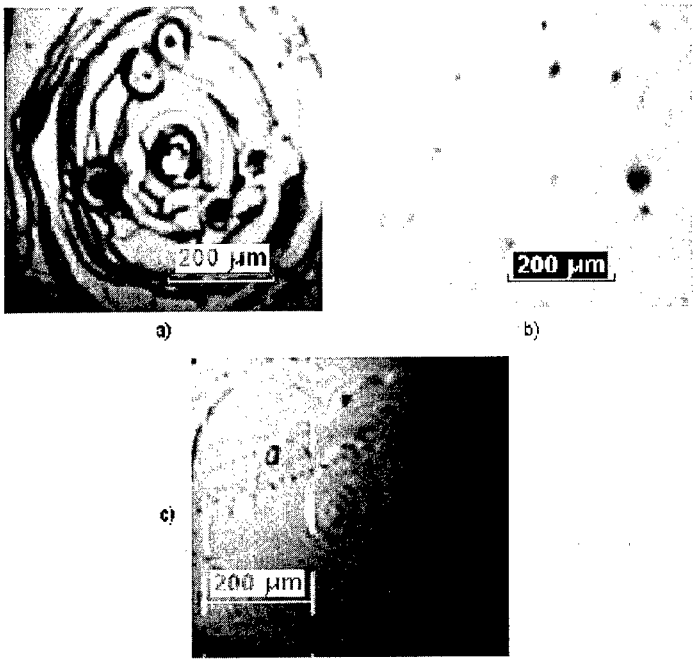


Fig.3. Pictures of central part of the crystals with concave (a) and flat (b,c) growth fronts and their structure.

With a flat growth front, the central part of the crystal has a rather smooth surface (Fig.3b), and, only when using the (0001)Si plane, in some cases we observed spiral structres (Fig.3c).
Side outgrowing provides increasing crystal dimensions, however, in this case radial and axial gradients cause considerable strain. In [4] was reported a frequency change of TO and LO phonons in 6H-SiC, observed by the Raman spectroscopy when applying hydrostatic pressure. The authors ascertained that a frequency difference of TO-bands for compressed and free crystals is in proportion to applied pressure value:

$$\nu_{TO}-\nu^{o}_{TO} = 3.53 см^{-1} \times P(GPa) \qquad (1)$$

where P is the pressure value expressd in GPa units. Fig.4 represent Raman spectra, measured by us in a crystal prepared by the Lely method and in two parts of a bulk crystal with convex growth front.

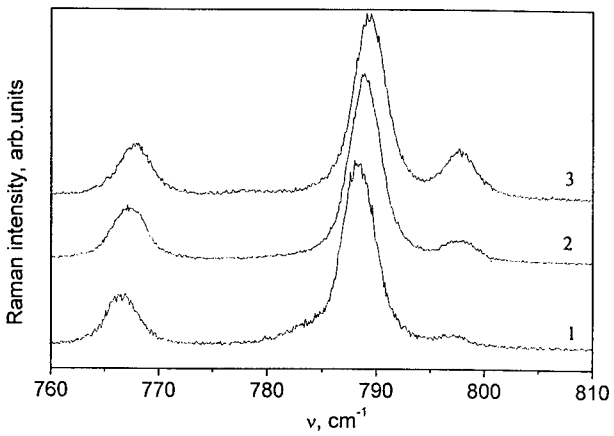


Fig.4. The Raman spectra of 6H-SiC crystals: 1 -Lely crystal, 2 - periphery part, 3 - central part of the bulk crystal.

It was assumed that any mechanical strain was absent in the Lely crystals. The spectra show that the maxima of Raman bands for the bulk crystal are shifted into high-frequency side as compared to the Lely one. This fact indicates that there is compression strain in the bulk crystal, which has a tendency to increase from periphery to centre. Using the formula (1) we estimated respective strain values that reach approximately 0.3 Gpa at the centre of the crystal.

Conclusions

The investigation is focused on ascertaining the influence of a growth shape on the structure of 6H-SiC bulk crystals grown by the PVT method. It is shown that a flat growth front should be used for excluding radial nonhomogenity of doping impurities. The presence of considerable temperature gradients in the bulk crystals during their growing and high curvature of the temperature field [5] leads to arising mechanical strain after cooling these crystals.

Aknowlegments

This work has been supported by INTAS Project No.97-30834.

References.

[1] S.F. Avramenko, V.S. Kiselev, M.Ya. Valakh, V.G. Visotski, Semiconductors Physics, Quantum Electronics & Optoelectronics **2** (1999), p. 76.

[2] S.F. Avramenko, M.Ya. Valakh, V.S. Kiselev, M.Ya. Skorokhod, Met. Phys. Adv. Tech. **18** (1999), p. 29.

[3] M. Anikin, M. Pons, K. Chourou, O. Chaix, J.M. Bluet, V. Lauer, and R. Madar, Materials Sci. Forum **45** (1998), p. 264.

[4] J.F. DiGregorio, T.E. Furtak, J. Am. Ceramic Soc. **75** (1992), p. 1854.

[5] St. G. Muller, R.C. Glass, H.M. Hobgood, V.F. Tsvetkov, M. Brady, D. Henshall, J.R. Jenny, D. Malta, C.H. Carter Jr., J. Crystal Growth **211** (2000), p. 325.

Materials Science Forum Vols. 353-356 (2001) pp. 45-48
© 2001 Trans Tech Publications, Switzerland

Growth of Highly Aluminum-Doped p-type 6H-SiC Single Crystals by the Modified Lely Method

Norbert Schulze, Jürgen Gajowski, Kurt Semmelroth,
Michael Laube and Gerhard Pensl

Institute of Applied Physics, University of Erlangen-Nürnberg,
Staudtstr. 7/A3, DE-91058 Erlangen, Germany

Keywords: Acceptor, Aluminum, C-V Characteristics, Hall Effect, Hall Scattering Factor, p-Type 6H-SiC, SIMS, Sublimation Growth

Abstract. Aluminum- (Al-) doped 6H-SiC crystals have been grown by the modified Lely method. Al_4C_3 is used as Al source during the growth and was put into a separate container which was kept at temperatures about 250 K lower than the SiC source material. Highly aluminum doped p-type 6H-SiC crystals (Al-concentration ca. $1 \cdot 10^{19}$ cm^{-3}) could be grown showing no microscopic aluminum-containing precipitates. The resistivity (at room temperature) is 1.4 Ωcm measured on a wafer, which is prepared from a region close to the seed crystal. The Hall scattering factor for holes $r_{H(p)}$ at temperatures T > 250 K is estimated to be smaller than one; its value at 700 K is determined to be about 0.5.

Introduction

High conductivity p-type SiC substrate material is required for the production of vertical electronic power devices [1]. Since Al is the acceptor with the lowest ionization energy which is known at the present [2], it is desirable to grow highly Al-doped SiC single crystals. The simple attempt to mix Al containing compounds among the SiC source powder fails because of the high partial pressure of Al [3] for all the suitable Al-compounds. Frequently, a considerable incorporation of Al during the initial growth stages forms Al containing precipitates [4]. Furthermore, the crystals show a strong axial decrease of the Al content with continuing growth duration; in some cases, the conductivity type even switches from p- to n-type due to the overcompensation by residual nitrogen (N) donors. In our growth experiments, we put the Al source (Al_4C_3) in a separate container and kept it at lower temperature than the SiC source material resulting in precipitate-free p-type SiC crystals. The comparison of secondary ion mass spectroscopy (SIMS), capacitance-voltage (C-V) and Hall effect results enabled us to give an estimate for the unknown Hall scattering factor for holes in 6H-SiC.

Experimental

6H-SiC bulk single crystals have been grown by sublimation physical vapor transport (PVT) (or so-called modified Lely method). The growth system used as well as the preparation of the graphite parts, the source material, and the seed prior to the growth run are described in [5]. The hot zone of the growth system has been altered in such a manner that the Al source (Al_4C_3 powder) was kept in a separate graphite container providing diffusion channels (drilled holes) for the Al into the growth crucible. Fig.1 shows a detailed drawing of the hot zone of the PVT-system used for the growth of Al-doped SiC crystals. The separate container was kept at temperatures significantly below the temperature of the SiC source (T_{Al} = 1850°C-1930°C). Its temperature distribution has been measured with an arrangement of several W/Re-thermocouples. The determined temperatures are indicated in Fig.1 (full dots). The growth experiments reported in this paper have been conducted according to

the near-thermal-equilibrium process [6]. The source temperature, the seed temperature and the argon pressure inside the growth cell have been established to be T_{source} = 2150°C -2180°C, T_{seed} = 2150°C and p_{Argon} = 1 mbar - 820 mbar, respectively. The exact course of the growth process is described elsewhere [6]. The seed faces have been prepared with on-axis orientation relative to the c-axis.

The incorporation of Al and N has been investigated by secondary ion mass spectroscopy (SIMS), capacitance-voltage (C-V), and Hall effect measurements.

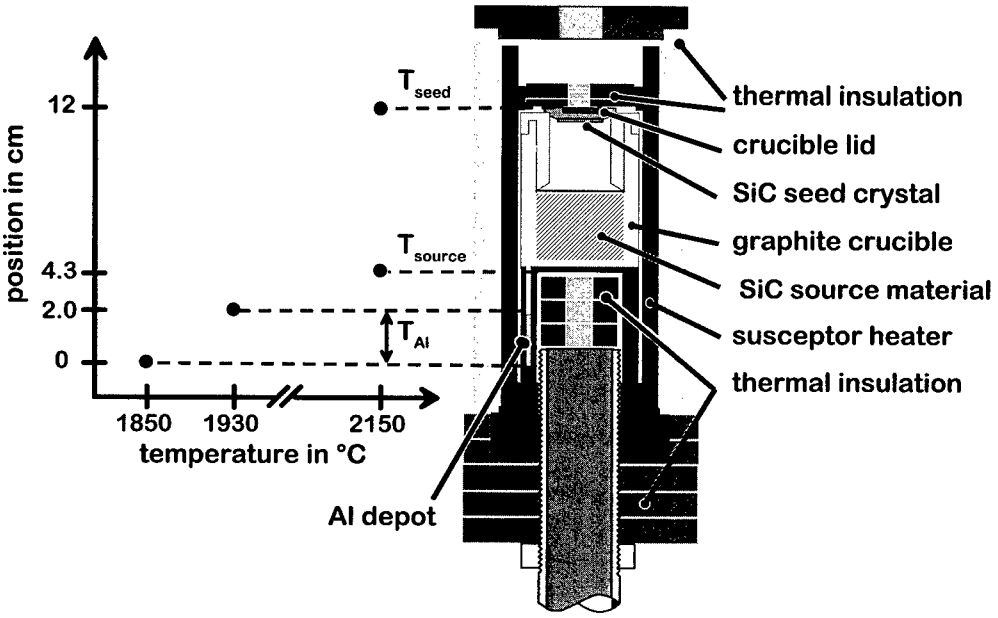


Fig.1. Hot zone of the PVT-system used for the growth of Al-doped SiC single crystals. The parts are made of solid graphite or graphite felt (thermal insulation). The temperature range T_{Al} along the Al depot was determined by an arrangement of W/Re-thermocouples; it is indicated in the figure (full dots). The temperature at the lid and bottom of the growth crucible T_{seed} and T_{source}, respectively, was measured by two-color pyrometers.

Results and Discussion

6H-SiC growth (p-type). We succeeded in growing p-type 6H-SiC boules on the Si-face of an n-type 6H-SiC seed crystal up to a length of about 1 cm. In contrast, the conductivity type of crystals grown on the C-face always switched from p-type to n-type with ongoing crystal growth. This observation can be understood with the polarity dependence of the incorporation of Al and N. While N is incorporated about twice as much on the C-face as on the Si-face, Al (and boron (B)) behaves vice versa (see e.g. [7]). SIMS analyses taken on 6H-SiC crystals grown on the Si-face revealed a decrease of the Al concentration in the axial direction from initially $1 \cdot 10^{19}$ cm^{-3} to $2 \cdot 10^{17}$ cm^{-3} at the tail. However, the conduction type did not switch to n-type as examined before. We could not observe any Al-inclusions or Al-precipitates by Nomarski interference contrast microscopy as has been reported in [4]. The growth rate has not been influenced by Al doping; it is about 0.2 mm/h as has been observed for the near-thermal-equilibrium process [6] in former experiments without Al-doping.

Electrical characterization. The grown 6H-SiC p-type crystals were electrically characterized by Hall effect measurements. Fig.2 shows the temperature dependence of the free hole concen-

tration p (circles) taken on a sample from a region close to the seed crystal. The Hall scattering factor for holes $r_{H(p)}$ is so far not known; for the Hall effect analysis it has been assumed to be $r_{H(p)} = 1$. A least-squares-fit of the neutrality equation to the experimental data (solid line) results in an acceptor concentration, an ionization energy of the acceptors, and a concentration of the compensation of $N(Al) = 5.0 \cdot 10^{19}$ cm^{-3}, $\Delta E(Al) = 177$ meV, and $N(Comp) = 1.1 \cdot 10^{19}$ cm^{-3}, respectively. The density of states (DOS) effective mass of holes used for the fit is taken from [8]. The maximum value of the hole Hall mobility has been measured to be $\mu_{H(p)} = 25 cm^2/Vs$ (at T = 265 K).

SIMS (see Table 1) and C-V measurements conducted on the same sample lead to about $1.0 \cdot 10^{19}$ cm^{-3} for the Al concentration and the net doping concentration, respectively.

The Al-concentration determined by SIMS and C-V is smaller by a factor of five compared to the corresponding value obtained from the Hall effect analysis. We attribute this contradiction to an incorrect assumption for the value of $r_{H(p)}$ used for the Hall effect analysis. It is known for silicon that $r_{H(p)}$ is temperature dependent and significantly smaller than one at high temperatures [9]. Due to the similarity of the valence band structure of silicon and silicon carbide we expect that the value of $r_{H(p)}$ significantly deviates at high temperatures from one for SiC.

Table 1. *Al-acceptor parameters and concentration of the compensation determined by Hall effect and SIMS (identical p-type 6H-SiC sample as investigated in Fig.2). ΔE(Al), N(Al) and N(Comp) denote the Al-ionization energy, the total Al-acceptor concentration and the concentration of the compensation, respectively. With respect to the SIMS data, we have assumed that the chemically determined Al- and N-concentration is completely electrically active.*

	ΔE(Al) [meV]	N(Al) [cm^{-3}]	N(Comp) [cm^{-3}]
Hall	177±10	$(5.0\pm1.0)\cdot10^{19}$	$(1.1\pm0.5)\cdot10^{19}$
SIMS	-	$(1.0\pm0.2)\cdot10^{19}$	$(2.0\pm0.5)\cdot10^{18}$

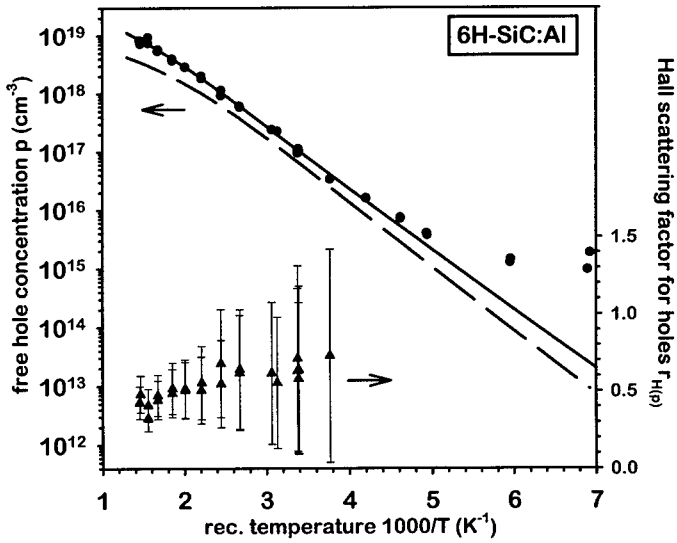


Fig.2. *Free hole concentration p as a function of the reciprocal temperature. The experimental data (dots) are obtained from a Hall effect measurement. The solid line corresponds to a least-squares-fit of the neutrality equation to the experimental data. The fit parameters are given in Table 1.*
The dashed line is the solution of the neutrality equation based on the SIMS data listed in Table 1 and ΔE(Al) = 190 meV for the Al-ionization energy [10]. The ratio of p-values taken from the dashed line and the experimental values (dots) determines the Hall scattering factor for holes $r_{H(p)}$ (triangles); see right y-axis.

Hall scattering factor for holes. In order to estimate the Hall scattering factor for holes, we used the experimental results obtained from SIMS and Hall effect. The temperature dependence of free holes has been calculated by setting the acceptor concentration and compensation equal to the

Al-concentration and N-concentration, respectively, as determined by SIMS. In addition, the Al-ionization energy $\Delta E(Al)$ was taken to be equal to (190±20) meV [10] and the DOS effective mass according to [8]. This estimate is based on the assumption that the chemically determined Al- and N-concentration (SIMS) are completely electrically active. We know from former investigations of n-type SiC crystals that the chemically detected nitrogen atoms are all electrically active as donors; we propose that this observation is also valid for Al-atoms, which act as acceptors since no Al-containing precipitates could be detected. Our assumption is confirmed by C-V investigations which result in almost identical concentrations as those determined by SIMS. The dashed curve in Fig. 2 reveals the calculated temperature dependence of the free hole concentration based on the parameters given above. The ratio of calculated and experimentally determined values of the free hole concentration at corresponding temperatures provides an estimate of the Hall scattering factor for holes $r_{H(p)}$ in 6H-SiC. The calculated $r_{H(p)}$-values are displayed in Fig.2 (triangles) in the temperature range where the measured free hole concentration is not significantly affected by impurity conduction (T > 250 K).

Within the considered temperature range the Hall scattering factor for holes $r_{H(p)}$ ranges from 0.5 to 0.8 similar to the case of silicon [9].

Summary

We have grown p-type 6H-SiC substrate material with low resistivity ($\rho = 1.4\ \Omega$cm at room temperature) in a Lely furnace providing a separate container for the Al-dopant. We did not detect any Al-containing inclusions or precipitates in the grown crystals. SIMS and C-V investigations revealed an aluminum concentration of $N(A) = (1.0\pm0.5)\cdot10^{19}$ and a net doping concentration of $N(A)-N(D) = (1.0\pm0.5)\cdot10^{19}$, respectively. We determined empirically the Hall scattering factor for holes $r_{H(p)}$. The values of $r_{H(p)}$ for temperatures from 250 K to 700 K are in the range of 0.5 to 0.8.

Acknowledgment. The authors would like to thank H. Sadowski for the LTPL measurements, M. Linnarsson (ACREO, Sweden) for the SIMS analysis, and M. Baßler for the thermal oxidation of the seed crystals. The support of this work by the German Science Foundation (Sonderforschungsbereich 292) is gratefully acknowledged.

References

[1] V.F. Tsvetkov, S.T. Allen, H.S. Kong, and C.H. Carter, Inst. Phys. Conf. Ser. **142** (1996), p.17.
[2] T. Troffer, M. Schadt, T. Frank, H. Itoh, G. Pensl, J. Heindl, H.P. Strunk, and M. Maier, phys. stat. sol. (a) **162** (1997), p.277.
[3] C. Qiu, R. Metselaar, J. Alloys and Compounds **216** (1994), p.55.
[4] Y. Kitou, W. Bahng, S. Nishizawa, S. Nishino, and K. Arai, Mater. Sci. Forum **338-342** (2000), p.83.
[5] V.D. Heydemann, N. Schulze, D.L. Barrett, and G. Pensl, Appl. Phys. Lett. **69** (1996), p. 3728.
[6] N. Schulze, D.L. Barrett, and G. Pensl, Appl. Phys. Lett. **72** (1998), p. 1632.
[7] N. Schulze, D. Barrett, M. Weidner, and G. Pensl, Mater. Sci. Forum **338-342** (2000), p.111.
[8] G. Wellenhofer and U. Rössler, phys. stat. sol. (b) **202** (1997), p.107.
[9] F. Szmulowicz, Phys. Rev. B **28** (1983), p.5943.
[10] A. Schöner, Dissertation, Erlangen (1994), p.151

Materials Science Forum Vols. 353-356 (2001) pp. 49-52
© 2001 Trans Tech Publications, Switzerland

Study of Boron Incorporation during PVT Growth of p-Type SiC Crystals

M. Bickermann, D. Hofmann, M. Rasp, T.L. Straubinger, R. Weingärtner, P.J. Wellmann and A. Winnacker

Department of Materials Science 6, University of Erlangen-Nürnberg, Martensstr. 7, DE-91058 Erlangen, Germany

Keywords: Aluminum Doping, Boron Doping, Bulk Growth, Dopant Homogeneity

Abstract. The incorporation of the acceptor boron during vapor growth (PVT) of 6H-SiC bulk crystals has been studied. The chemical segregation coefficient of boron (ratio between B content of the grown crystal and of the source) has been determined to be 0.4±0.1 for a wide range of B concentrations in the starting material (0.3–300 ppm wt). For reference purposes the impurity concentrations in nominally undoped SiC crystals have been analyzed. Whereas both source and SiC crystals exhibit a high purity in regard to p-type (Al, B) and deep level (V, Ti) impurities, a considerable amount of residual nitrogen was detected resulting in carrier concentrations n = 1×10^{16} to 1.5×10^{17} cm^{-3}. Carrier concentrations in the p-type B doped crystals were found to range from 2×10^{14} to 2×10^{16} cm^{-3} for starting B concentrations between 3 to 300 ppm wt. Axial non-uniformities, i.e. carrier concentration in SiC:B increases with crystal length, depend on the compensation ratio. At higher B content the homogeneity improves. Compared with segregation in Al doped SiC, results indicate that SiC:B powder acts as infinite, SiC:Al powder as finite dopant source. The lateral distribution of carrier concentration in SiC:B crystals (wafer mapping) has been measured showing a good homogeneity of electrical properties.

Introduction. The preparation of p-type SiC bulk crystals with low defect densities is an important issue for the future development of SiC-based power and high frequency electronics. Defined p-doping is a prerequisite for both the growth of highly conductive and semi-insulating (s.i.) SiC crystals where deep donor levels like vanadium compensate the residual acceptors. P-conduction is commonly realized by Al or B doping. Difficulties in p-type doping arise from the lack of a suited gas source which will provide homogeneously doped crystals, as can be seen in n-type doping with nitrogen. Furthermore, the knowledge of the amount of incorporated vapor species and related electrical activity of p-dopants under PVT conditions as well as the understanding of dopant non-uniformities in the grown crystal is deficient.

In this paper we focus on the dopant incorporation of boron during PVT growth of SiC crystals. Whereas several groups reported on Al doping during SiC bulk growth [1,2] B doping was not studied in detail up to now. Several aspects are addressed in the present work. First the impurity content of nominally undoped SiC has been investigated for reference purposes. Then the B related chemical segregation behavior between source and grown crystal has been measured. Central topic is the determination of the lateral and longitudinal non-uniformities of electrical properties in B doped SiC with a comparison to the situation in Al doped SiC.

Experiments. 1.4" 6H SiC bulk crystals have been prepared from the vapor phase (PVT technique) in the temperature range of 2200°C–2300°C [3]. Growth was conducted on on-axis seeds using different polarity (Si or C side). Boron and aluminum have been added in different amounts to the SiC powder source. Nominally undoped crystals have been grown for reference purposes. Special care was applied to establish process conditions with reduced impurity content in the growth system

(preheating of the growth set-up at high temperature and low pressure over long durations, use of pure starting materials, etc.). For material analysis wafers and axial cuts were prepared from the boules. Electrical and optical properties were determined by Hall effect and absorption measurements. Chemical analysis of SiC source material and as-grown crystals were performed by glow discharge mass spectrometry (Shiva Technologies, France).

Results and Discussion.

Nominally undoped SiC

Table 1 shows the chemical analysis by GDMS of the most relevant impurities in synthesized SiC powder, the starting material for our growth experiments, and in an as-grown nominally undoped 6H SiC crystal. P-type (Al, B) and deep impurities (V, Ti) are found at rather low concentration levels. These levels decrease considerably in the grown crystal showing a pronounced purification effect during vapor transport. In comparison to recent studies [4,5] on the impurity content of SiC-powder/CVD sources the purity of our starting material seems superior even to CVD sources. The by far highest impurity level in the crystal was measured for nitrogen with 2–8 ppm wt. As the quantitative determination of nitrogen by GDMS in powder material is restricted to values > 500 ppm wt we have presently no information about the nitrogen content of our source material. With regard to the other impurities in the crystal we see no need for measures reducing these levels, also considering the preparation of semi-insulating SiC.

	B	N	Al	S	Ti	V	Cr	Co	Ni
source [ppm wt]	0.28	—	0.5	1.5	0.13	0.02	0.5	< 0.05	0.62
crystal [ppm wt]	0.08	2...8	0.02	0.11	0.015	< 0.005	0.5	< 0.005	0.04

Table 1: Chemical analysis (GDMS) of impurities in SiC powder (sublimation source) and as-grown nominally undoped 6H SiC crystals.

For receiving additional information about the origin of nitrogen contamination during our PVT growth process we investigated the variation of carrier concentration n with the crystallized volume fraction. An exponential decrease of n along the boule in the order of one magnitude ($1{,}5\times10^{17}$ cm^{-3} to 1×10^{16} cm^{-3}) was detected. Recent measurements confirmed that under the chosen process parameters the crystallization rate is essentially constant during the whole growth run [6]. The carrier concentration varies exponentially with process time. This result indicates that the nitrogen is provided by a finite source which may be correlated to desorbed nitrogen in the source or in the graphite environment. Further analysis on the nitrogen-related contamination is presently under work.

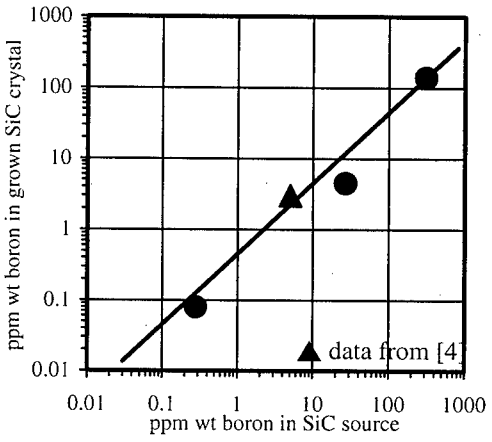


Fig. 1: Measured correlation between boron content in the source material and in the as-grown 6H SiC crystal (detected by GDMS).

Boron doped SiC

Boron was added in different amounts to the source material. Concerning the generation of doping-related imperfections during growth an upper limit of approx. 300 ppm wt in the source was found under the established process conditions to degradate the crystalline properties (formation of inclusions, polycrystalline growth). The incorporation of boron in the grown 6H crystals in dependence of the B content of the source material have been determined. Fig. 1 shows the correlation between

the B concentration in the initial powder and the respective chemical amount in the crystal. In addition measurements of Hobgood et al. [4] are included. The results reveal that the boron segregation coefficient k_B (B content in the crystal/initial B content in the source) does not depend significantly on the B concentration of the starting material and amounts to 0.4±0.1.

As a next step we investigated the uniformity of B incorporation during PVT growth. For a fast, non-destructive determination of the axial and radial B distribution in the grown boules and wafers optical absorption mapping [7] was applied. A calibration curve has been created which gives a linear correlation of the B related absorption peak at λ=730 nm with the carrier concentration p evaluated by Hall effect measurements (Fig. 2).

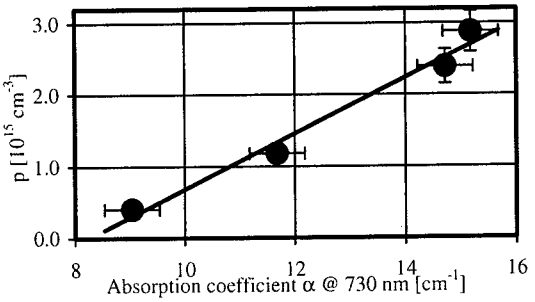


Fig. 2: Calibration curve for the correlation of optical absorption (λ=730 nm) and carrier concentration p at 300 K measured by Hall effect in B doped 6H SiC crystals.

The carrier concentration p versus the crystallized volume fraction for SiC crystals with different boron content of the source and grown with different seed polarity (Si/C side) is shown in Fig. 3. For comparison, the axial distribution of p in an Al-doped SiC crystal is inserted. The plots reflect the B variations in the source material although the absolute magnitude of dopant variation in the source is not reproduced by the electrical properties in the grown crystals. The low p concentration in comparison to the original B content of the source (5×10^{17}–5×10^{18} cm^{-3}) is related to the small amount of ionized B acceptors due to the relatively deep position of the B level in the energy gap. The reduced p concentration in the crystal grown on the C-side seed agrees with the observations of Ohtani et al. [8] reporting that the boron content decreases and the nitrogen incorporation increases if growth in the $(000\bar{1})$ orientation is performed.

The hole concentration in the boron doped samples exhibits axial non-uniformities, p increases with crystal length. This effect is less pronounced in the crystal with higher B content. As we proceed from the assumption that boron is incorporated more or less uniformly, the increase of the hole concentration is attributed to the decrease of the nitrogen contamination with crystallized volume fraction. This has a stronger influence in crystals with lower boron content as they are more compensated (decrease of N_A–N_D).

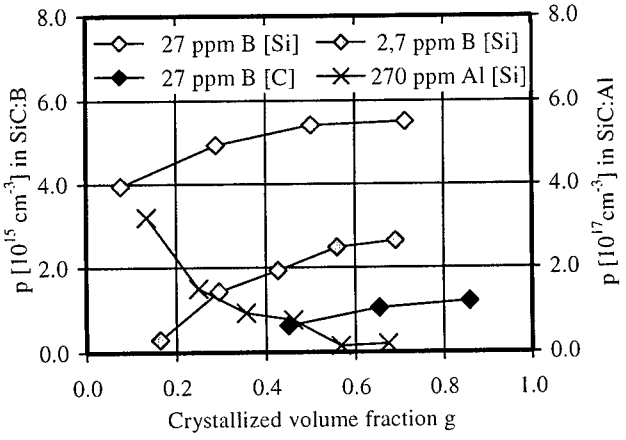


Fig. 3: Carrier concentration p (determined by optical absorption) versus crystallized volume fraction in B doped 6H SiC crystals with different doping level and seed polarity and in an Al doped 6H SiC crystal.

Al doped SiC exhibits a fundamentally different behavior in regard to axial segregation. In that case the carrier concentration p decreases considerably with process time. A comparison of the electrical non-uniformities in Al and B doped SiC indicates that the SiC:B powder acts as an infinite dopant source whereas the Al supply from the SiC powder is exhausted. This behavior is most likely due to the higher vapor pressure of Al at growth conditions.

For the reduction of axial electrical inhomogeneities in SiC:Al studies are presently being conducted in our group to introduce Al in alternative ways, (i) from a SiC:Al source which is kept at a lower temperature and (ii) via a gaseous source.

Fig. 4 shows the lateral distribution of the carrier concentration p in two B-doped 6H-SiC wafers. Whereas the non-uniformity of the carrier concentration in the main area of the wafers is as low as $\Delta p/p \approx 10$–20%, considerable inhomogeneities can occur in the central part (Fig. 4a). The increased B incorporation is due the presence of the (0001) growth facet, which did not form in all of our growth experiments. The reason for the reduced concentration at the periphery of the facet is still under discussion.

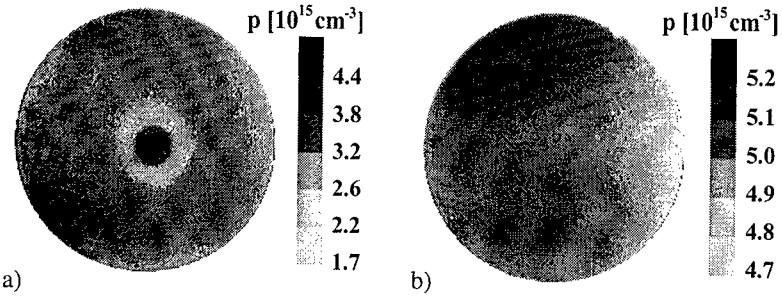


Fig. 4: Mapping of the radial distribution of carrier concentration p (determined by optical absorption at 730 nm) in boron doped 1.4" 6H-SiC wafers, grown on the Si face.

Conclusions. The incorporation of boron and aluminum during PVT growth of SiC crystals has been studied. Chemical analysis reveals that the segregation coefficient of B between source and crystal is relatively constant over a wide range of starting concentrations (0.3 – 300 ppm wt) and amounts to 0.4±0.1. B incorporation was found to be much higher during growth on the Si face than on the C face. Axial non-uniformities of the carrier concentration in SiC:B crystals depend on the compensation ratio, i.e. at higher B content the homogeneity improves. A comparison of SiC:B and SiC:Al crystals indicates that SiC:B powder acts as an infinite, SiC:Al powder as a finite dopant source. Results on wafer mapping of the carrier concentration p in SiC:B have been presented showing a good homogeneity of electrical properties.

Acknowledgement. This work is supported by the Bayerische Forschungsstiftung and SiCrystal AG under contract Nr. 362/99.

References.

[1] V.F. Tsvetkov, S.T. Allen, H.S. Kong, C.H. Carter Jr., Inst. Phys. Conf. Ser. 142 (1996), p. 17.
[2] V.P. Rastagaev, D.D. Avrov, S.A. Reshanov, A.O. Lebedev, Mat. Sci. Eng. B61-62 (1999), p. 77.
[3] D. Hofmann, M. Bickermann, R. Eckstein, M. Kölbl, S. Müller, E. Schmitt, A. Weber, A. Winnacker, J. Cryst. Growth 198/199 (1999), p. 1005.
[4] H.McD. Hobgood, R.C. Glass, G. Augustine, R.H. Hopkins, J. Jenny, M. Skrowonski, W.C. Mitchel, M. Roth, Appl. Phys. Lett. 66 (1995), p. 1364.
[5] V. Balakrishna, G. Augustine, R.H. Hopkins, Mat. Res. Soc. Symp. Proc. 572 (1999), p. 245.
[6] T.L. Straubinger, M. Bickermann, M. Grau, D. Hofmann, L. Kadinski, S.G. Müller, M. Selder, P.J. Wellmann, A. Winnacker, Mater. Sci. Forum 338-342 (2000), p. 39.
[7] R. Weingärtner, M. Bickermann, S. Bushevoy, D. Hofmann, M. Rasp, T.L. Straubinger, P.J. Wellmann, A. Winnacker, Mat. Sci. Eng. B in press.
[8] N. Ohtani, M. Katsuno, J. Takahashi, H. Yashiro, M. Kanaya, S. Shinoyama, Mater. Sci. Forum 264-268 (1998), p. 49.

Materials Science Forum Vols. 353-356 (2001) pp. 53-56
© 2001 Trans Tech Publications, Switzerland

Features of Semi-Insulating SiC Single-Crystal Growth by Physical Vapor Transport

S.A. Reshanov, V.P. Rastegaev and Yu.M. Tairov

Department of Microelectronics, St.Petersburg State Electrotechnical University 'LETI', Prof. Popov 5, RU-197376 St.Petersburg, Russia

Keywords: Aluminium, Doping, Electrical Properties, Growth, LETI-Method, Photoconductivity, Semi-Insulating SiC, Vanadium

Abstract. The problems of obtaining of insulating properties in the bulk single-crystal silicon carbide by vanadium and aluminium doping under the LETI method growth process are considered. It was defined that the solubility limit of vanadium in SiC makes 10^{19} cm^{-3}. The resistivity of obtained SiC:V,Al material exceeds 10^7 Ohm·cm at 20 °C. It can be applied as a semi-insulating substrate material for extreme electronics based on silicon carbide or nitrides. The grown crystals exhibit visual spectrum photoconductivity with long-time relaxation.

1. Introduction

The semi-insulating silicon carbide is required as a basic substrate material for the next-generation extreme electronics devices and sensors, based on large bandgap semiconductors (SiC, GaN, AlN).

Today the basic method of bulk silicon carbide single-crystals preparation is the LETI method, based on physical vapor transport (PVT) growth on seeds [1,2].

In the present study the growth of semi-insulating bulk single-crystal silicon carbide by the LETI method in vacuum from vanadium and aluminium-containing source is considered. Experimental data on the electrical resistivity and photoconductivity of the grown crystals are also presented.

2. Features of semi-insulating crystal growth

The obtaining of semi-insulating properties of a SiC material depends on two issues:
1) obtaining a high-resistivity material by lowering the impurity concentration and compensation;
2) overcompensation of the residual impurities by deep impurity centres.

The problem of high-resistivity material obtaining is mainly determined by the control of residual nitrogen donors and shallow acceptors (B and Al). The aluminium alternative is more preferable since it exhibits significant anisotropy effect of doping (i.e. influence of crystallographic orientation of growth front onto a concentration level), that allows effectively to control the doping.

The physico-chemical features of polytypes impose certain requirements on growth conditions, which in turn determines the level of doping and overcompensation. As we have shown [3] the growth in vacuum (10^{-3}...10^{-5} Torr) under the LETI method of 4H-SiC single-crystals on the (0001)C facet from aluminium containing source allows to obtain high-resistivity crystals with the lowest difference concentration of residual impurities (< 10^{17} cm^{-3}). It should be marked that Al doping requires usage of previously doped by aluminium silicon carbide powder as a growth source instead of introduction metallic Al into the growth cell.

The analysis of parameters of known impurity centres in silicon carbide [4] has shown that the most appropriate of them for obtaining insulating properties is vanadium. Being an electrically amphoteric impurity, vanadium forms both deep donor D^0/D^+ ($V_{Si}^{4+}(3d^1)/V_{Si}^{5+}(3d^0)$) and acceptor levels A^0/A^- ($V_{Si}^{3+}(3d^2)/V_{Si}^{4+}(3d^1)$) located accordingly at 1.35...1.47 and 0.68...0.97 eV below the conduction band bottom in 6H and 4H (Fig. 1). The usage of vanadium donor levels is the most

preferable, especially in 4H polytype. Therefore, initial relevant conditions of growth and Al doping should ensure obtaining of *p*-type 4H material at the absence of vanadium dopant in the growth cell.

Doping of such crystals by vanadium at growth allows to compensate the dominant residual impurities (aluminium and nitrogen) completely and to obtain a semi-insulating material [5]. Its electrical properties in a wide temperature range would only be determined by activation energy of vanadium.

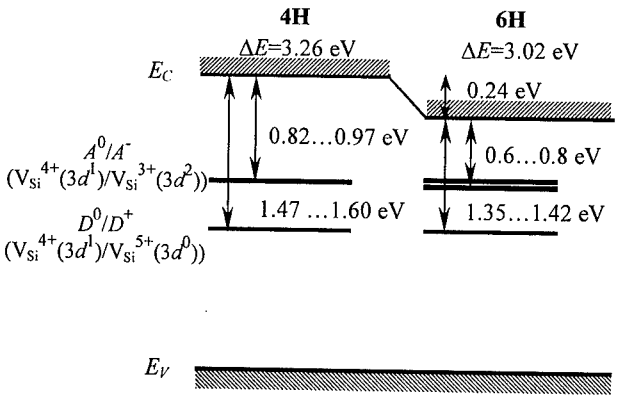


Fig. 1. Bandgap states of vanadium in 4H and 6H SiC

The solubility limit of vanadium in silicon carbide was not previously set, but should be close to the solubility limit of titanium and chromium, which according to [6] makes ~$3 \cdot 10^{17}$ cm^{-3}. However, basing on thermodynamic properties of SiC and VC phases it is possible to assume that it is much higher. The theoretical studies on vanadium impurity in silicon carbide practically miss.

A thermodynamic analysis of the SiC-Al system was explicitly considered in [3]. The SiC-C-V system displays an opportunity of formation of an additional condensed phase VC in the growing crystal at substantial concentrations of vanadium in the vapor phase. Vanadium silicides are not taken in consideration since they do not exist in the presence of C and at temperatures > 2010 °C. Fig.2 is a consideration of a cut phase diagram at a given temperature for the vapor phase. As against aluminium, the partial pressure of vanadium vapors is much smaller than for silicon, and thus it should not be observed exhausting on vanadium in the crystallizing cell at sublimation growth and, accordingly, inhomogeneity of vanadium doping by the length of ingots.

As we have previously set dense graphite (15% porosity) growth cell is the most preferable for the growth of Al-doped SiC in vacuum by the LETI method. Since vanadium transfers only by elementary vapors, its presence should not influence Si, C and Al mass-transfer process and thus the graphite material requirements remains invariable.

It is possible to control the concentration level by variation of growth temperature and composition of growth source mixture. In the present study metallic vanadium was directly introduced into the growth cell in the limits from 0.01 up to 1 mass.% of the growth source contents. However, vanadium as well as aluminium should, apparently, be inlet as a previously doped SiC powder (synthesis of vanadium doped powders described elsewhere [7]), since there was observed a deterioration of crystals quality at the incipient stage of growth. It is necessary to mark, that the transport coefficient of vanadium makes 0.3...0.8, that exceeds a similar one for aluminium [2].

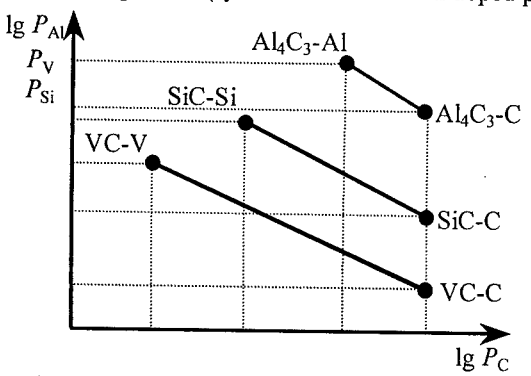


Fig. 2. Pressure of Si, C, Al and V in the Si-C-Al-V system.

As it was supposed, the experimental investigations on the influence of growth plane orientation on obtaining of semi-insulating properties of silicon carbide at vacuum sublimation growth from vanadium (0.01 mass.%) and aluminium containing source has shown, that only growth on (0001)C facet allows to ensure a semi-insulating material on the whole length of ingots. The usage of

(0001)Si growth plane leads to a *p*-type conductivity 6H material. The growth on a lateral face (1010) ensures obtaining semi-insulating SiC only to the end of ingot due to the crystallizing cell exhausting on aluminium.

3. Crystal characterization

All the samples were fabricated by cutting into wafers of the grown bulk *c*-axis 4H and 6H-SiC single-crystals, which possess semi-insulating properties ($\rho > 10^7$ Ohm·cm at 20 °C). The polytype structure of the grown crystals was investigated by X-ray diffraction methods. The presence of vanadium and its concentration in the samples were defined by a X-ray spectral microanalysis (XSMA). The solubility of vanadium has appeared on two order above expected and has made ~10^{19} cm^{-3} at 2500 K. The presence of vanadium was also confirmed (without values definition of concentration) by SIMS. The presence of other transition metals (e.g. Ti, Cr) was less than 10^{17} cm^{-3} and therefore these impurities were electrically insignificant At high temperatures all the obtained samples demonstrated a weak *n*-type conductivity, that was defined by the sign of the thermopower effect. It verifies the donor state of vanadium centres in the grown crystals.

The electrical resistivity of the obtained SiC:V samples was investigated in the open air by means of lateral MSM structures with 0.8 mm gap and rectangular Pt contacts. The pulsed electric field was applied up to 10 kV/cm, depending on the ambient temperature and the maximum current density. The obtained *I-V* characteristics were fairly linear, indicating the ohmic character of the electrical response.

To determine the activation energies from the resistivity data the last squares fits for resistivity versus temperature were performed on the basis of the electrical conductivity equation and the complete electrical neutrality equation for several types of centres in a compensated semiconductor. The data on band structure parameters were taken from [8]. The mobility temperature dependence was assumed to be identical for vanadium undoped initial single-crystals [3] and was approximated by the following expression: $\mu=(1/280+T^{2.5}/3.5\cdot10^8)^{-1}$.

Experimental data on electrical resistivity versus inverse temperature for SiC:V,Al samples are presented in Fig. 3. In the result of the performed temperature investigations of resistivity of the grown SiC:V,Al samples in the range 20…800 °C the activation energy was determined at the level of 1.4...1.6 eV for 4H and 1.2…1.3 for 4H/6H (Table 1), which could be attributed to the ionization energy of vanadium donor state. Besides for a part of the samples (No 4–6) the region with an activation energy ~0.6…0.9 eV was observed.

Table 1. Properties of grown semi-insulating SiC:V,Al single crystals

Sample No.	Crystal polytype	Activation energy (eV)	Vanadium concentration (cm^{-3})	
			$\rho(T)$ fit	XSMA
1	4H	1.4	$9\cdot10^{18}$	$1\cdot10^{19}$
2	4H	1.4	$1\cdot10^{18}$	$1\cdot10^{18}$
3	4H	1.5	$2\cdot10^{19}$	$1\cdot10^{19}$
4	4H	1.6; 0.9	$3\cdot10^{17}$	$< 10^{18}$
5	4H/6H	1.2; 0.6	$1\cdot10^{17}$	$< 10^{18}$
6	4H/6H	1.3; 0.7	$5\cdot10^{17}$	$< 10^{18}$

Irradiation of the specimen during a specific resistance measuring with light (10 mW/cm^2) of a visual spectrum area 200…1200 nm (1…5 eV) has revealed the presence of the photoconductivity effect. The obtained photoconductivity spectrums for the different investigated samples are represented in Fig. 4. The essential distinction of spectrums is stipulated first of all by the presence of a peak at 2 eV. As the Fermi level is pinned near to the middle of the bandgap at vanadium donor level, the defect responsible for these peaks should be completed with electrons, which under activity of light transfer into the conduction band. It means, that the viewed defects are the donors with ionization energy about 2 eV, or acceptors with ionization energy about 1.1eV. Nevertheless

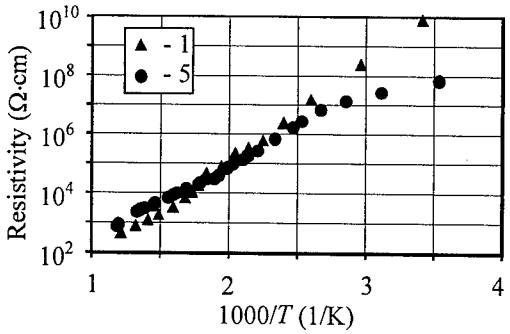


Fig. 3. Resistivity versus inverse temperature for SiC:V,Al grown by the LETI method.

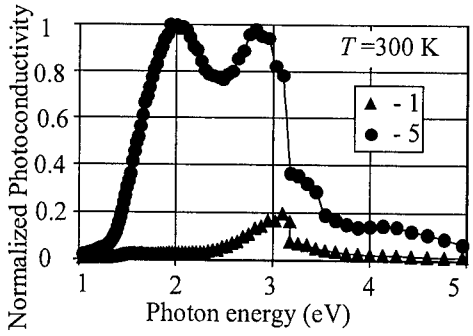


Fig. 4. Photoconductivity spectrum for SiC:V,Al grown by the LETI method.

nature of the observed defects yet does not set. The common double peak located at 2.9 eV is apparently stipulated by participation of residual aluminum and nitrogen impurities. As it is visible from electrical resistivity data versus inverse temperature, the difference between the samples consists in the presence of the region with smaller activation energy at low temperatures for the samples No 4–6, where vanadium concentration is less than 10^{18} cm^{-3}.

It is necessary also to mark the considerable quantity of the photoconduction response time: $10^{2}...10^{3}$ s at 300 K. As it was recently shown [9,10] such abnormal increase by several orders of magnitude in the lifetimes, the photoconduction and specific dark resistance are common effects for semiconductors, intensively compensated by deep recombination impurities.

4. Conclusion

The single-crystals of silicon carbide possessing semi-insulating properties can be grown by physical vapor transport (the LETI method) under the following conditions:

1) growth environment – vacuum (pressure range $10^{-3}...10^{-5}$ Torr);
2) growth cell material – dense graphite (15% porosity);
3) growth source composition – previously sintered silicon carbide powder doped specially by vanadium and aluminium;
4) growth plane orientation – (0001) C

The solubility of vanadium makes up to $1 \cdot 10^{19} cm^{-3}$ at growth under 2500 K.

Semi-insulating SiC:V,Al could possess significant photoconductivity effect in visible spectrum with long-time relaxation, that should necessarily be taken into account and can render negative influence on properties of semi-insulating SiC as a substrate material for high temperature power microwave integrated circuits based on large bandgap semiconductors.

Nevertheless the obtained results prove the viability of application of semi-insulating 4H-SiC:V as a substrate material.

References

[1] Yu.M. Tairov, V.F. Tsvetkov, J. Crystal Growth, 52 (1981), p. 146.
[2] S.I. Dorozhkin, D.D. Avrov, V.P. Rastegaev, Yu.M. Tairov, Mater. Sci. Eng. B 46 (1997), p. 296.
[3] V.P. Rastegaev, D.D. Avrov, S.A. Reshanov, A.O. Lebedev, Mater. Sci. Eng. B 61-62 (1999), p. 77.
[4] A.A. Lebedev, Semiconductors 33 (1999), p. 107.
[5] S.A. Reshanov. Diamond and Relat. Mater. 9 (2000), p. 480.
[6] Yu.A. Vodakov, E.N. Mokhov, M.G. Ramm, A.D. Roenkov, Springer Proceed. in Phys. 56 (1992), p. 329.
[7] W. Hartung, M. Rasp, D. Hofmann, A. Winnacker, Mater. Sci. Eng. B 61-62 (1999), p. 102.
[8] F. Bechstedt. Mater. Sci. Forum. 264-268 (1998), p. 265.
[9] V.A. Kholodnov, P.S. Serebrennikov. Technical Phys. Lett. 23 (1997), p. 268.
[10] S. Zh. Karazhanov, Semiconductors 34 (2000), p. 872.

Materials Science Forum Vols. 353-356 (2001) pp. 57-60
© 2001 Trans Tech Publications, Switzerland

Virtual Reactor: A New Tool for SiC Bulk Crystal Growth Study and Optimization

M.V. Bogdanov[1], O.V. Bord[1], A.O. Galyukov[1], S.Yu. Karpov[1], A.V. Kulik[1], S.K. Kochuguev[1], A.E. Komissarov[1], D.Kh. Ofengeim[1], A.M. Serkov[1], A.V. Tsiryulnikov[1], I.A. Zhmakin[1], M.S. Ramm[2], A.I. Zhmakin[2] and Yu.N. Makarov[3]

[1] Soft-Impact, Ltd., PO Box 33, RU-194156 St.Petersburg, Russia

[2] A.F.Ioffe Physico-Technical Institute, Russian Academy of Sciences, Polytechnicheskaya 26, RU-194021 St.Petersburg, Russia

[3] Institute of Fluid Mechanics, University of Erlangen-Nürnberg, Cauerstr. 4, DE-91058 Erlangen, Germany

Keywords: Deposits, Sublimation, Virtual Reactor

Abstract. In the recent years modeling was found to be beneficial for growth system design and optimization of SiC bulk crystal growth by sublimation technique. In this paper we describe a special software tool called "Virtual Reactor" (VR), which can be operated by user of the code as an actual crystal growth system. VR accounts for major specific features of sublimation growth and includes advanced models for the most important physical processes occurring in the growth system as well as the database for properties of SiC crystal and powder, graphites and thermal insulation. The software simulates global heat transfer in the whole system and inside the crucible, coupled with reactive species mass transport. Virtual characterization of the growing crystal at various stages of growth, in particular, analysis of thermo-elastic stress and dislocation density distribution is provided by VR. In this paper, we discuss basic principles of the VR operation and demonstrate some results of SiC crystal growth simulation using this software.

Introduction

Sublimation growth of SiC bulk crystals is the primary method to obtain high quality large-size SiC single crystals. The quality of the grown material is controlled by a particular temperature distribution in the growth system, which affects simultaneously many factors like crystal shape, powder source graphitization, parasitic deposition on the crucible walls, etc. Experimental optimization of the growth process takes normally much effort and is time-consuming. Thus, modeling can be quite beneficial for growth system design and finding optimal growth condition if the models used allow for important features of the process.

Many studies of the recent years were aimed at the development of a comprehensive model of SiC sublimation growth. Most of the approaches consider SiC sublimation growth to be a steady-state process. However, non-stationarity is evidently an inherent feature of this growth technique, since several factors result in a gradual change of SiC growth rate and properties of the powder charge. Temporal evolution in the sublimation growth was the subject of the recent studies [1-4]. An extensive experimental analysis made in [1] was focused on the powder source degradation. The crystal evolution during sublimation growth was first modeled in [2,3]. We should mention that important feature of sublimation growth – poly-SiC deposition on the reactive crucible walls – was ignored in these theoretical studies. Self-consistent prediction of deposit formation during the growth was reported in [4].

To date only separate aspects of sublimation growth like heat or mass transfer have been modeled systematically. However, to be important for practice, all factors should be considered in

combination and allowed to interact with each other. In this paper, we discuss general concept of a software tool – "Virtual Reactor" – specially developed for simulation of SiC bulk crystal growth using sublimation technique. The VR serves for simplifying and accelerating optimization of both growth system design and process conditions and is intended to be exploited by the growth engineers for R&D and production.

Concept of the "Virtual Reactor"

A key feature of the VR is that it can be operated by the user of the code like an actual growth system. Fig.1 summarizes the stages of the virtual growth process included into the software tool. At the first stage, geometry of a growth system considered is generated. It can be done either manually or by using CAD files containing detailed information on the growth system design. At the second stage, the user should program the growth process by prescribing inductive heating of the system (temporal changes in power supply and inductor coil position) and variation of gas pressure during the whole growth process. This stage is followed by automatic generation of the initial computational grid. Material properties necessary for the following computations are automatically transferred into the code from the database.

At the third stage, heat transfer coupled with the reactive species (Si, Si_2C, SiC_2) transport in the crucible is simulated. The heat transfer is modeled accounting for both conductive and radiative mechanisms. Transport equations are solved using a finite-volume technique and unstructured grids. The homogeneous chemical reactions are neglected, whereas the heterogeneous ones are considered to proceed under near-equilibrium conditions. An advanced model of heterogeneous processes on the growth surface and reactive crucible walls is implemented based on the Hertz-Knudsen approach extended to multi-component vapor. This model allows one to account for possible kinetics of heterogeneous chemical reactions, especially important for low pressures. A special phase analysis is then performed in every point of all reactive surfaces to predict parasitic poly-SiC deposition on the crucible walls [4]. Corresponding boundary conditions are chosen accounting for the deposition or for thermal etching of the graphite wall (considering the etching effects has been shown to be important for adequate prediction of SiC growth rate [2,3]). The boundary conditions are analyzed and properly modified until self-consistency with the species concentration fields in the crucible is achieved. As a result of mass transport modeling, growth rate distribution over the vapor-crystal interface is obtained.

VR is based on a quasi-steady-state approach to simulation of a long-term growth process. Since growth duration is much larger than the transient time of heat and mass-transfer processes, the SiC growth can be considered within a quasi-steady-state approximation. To model the growth, we actually replace an original process with slow parameter variation by a number of coupled steady-state steps with constant parameters. In particular, changes in SiC crystal shape at the next step is calculated through the growth rate obtained at the previous step.

All temporal changes in the system are made by VR automatically including re-generation of the computational grid accounting for geometry modification. The VR-software allows also continuous "virtual characterization" of the growing crystal by calculating thermo-elastic stress, dislocation density distribution, predicting graphite inclusion formation in the crystal during growth, etc. The software is PC-compatible with computing time lying in the range of a few hours.

Example of application

To illustrate VR capabilities, we have chosen a growth system similar to that reported in [5]. The system is shown schematically in the left side of Fig.2. The right side of Fig.2 displays typical unstructured computational grid generated by VR for simulation of the initial growth. The inset in Fig.2 demonstrates the grid near the seed. We focus on the interplay between growth of the main

SiC crystal and deposition of parasitic poly-SiC on the lid near the seed. The latter factor is recognized to affect significantly the shape of the grown crystal.

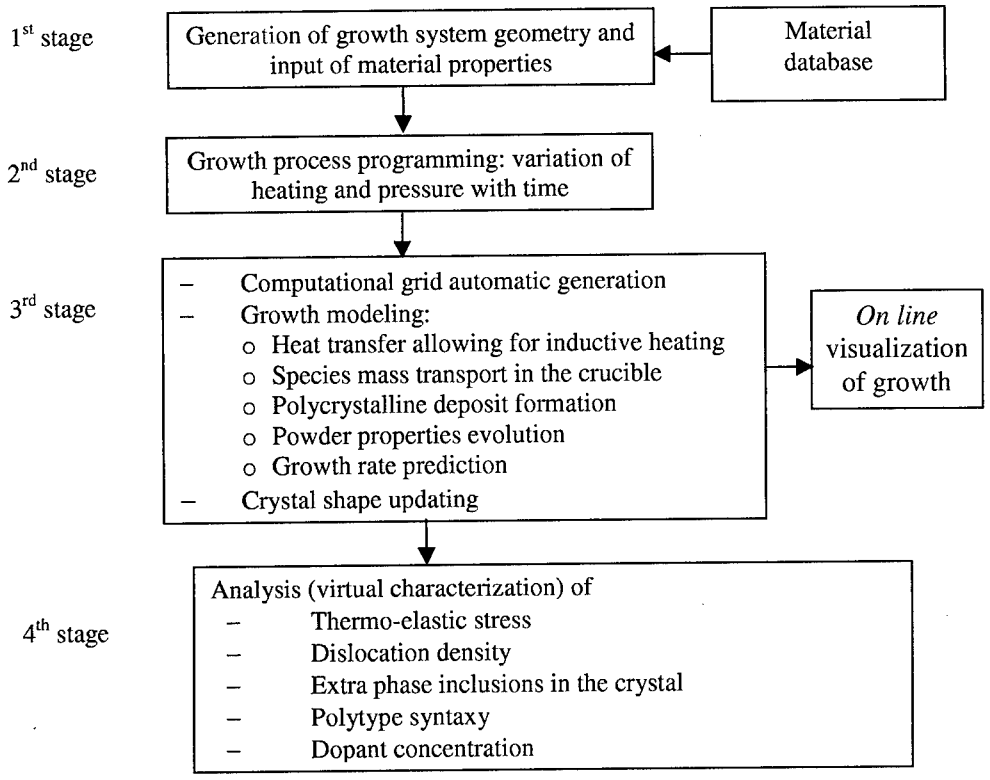


Fig.1. Stages of SiC crystal growth by "Virtual Reactor".

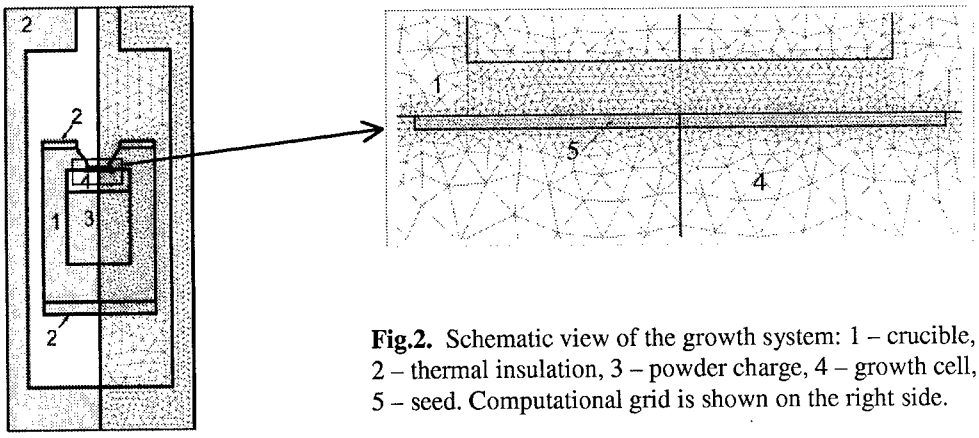


Fig.2. Schematic view of the growth system: 1 – crucible, 2 – thermal insulation, 3 – powder charge, 4 – growth cell, 5 – seed. Computational grid is shown on the right side.

Fig.3 shows computed crystal profiles obtained with account of the poly-SiC deposition on the graphite lid. The profiles correspond to 2 hours (left) and 10 hours (right) of growth. One can see that the main SiC crystal and poly-SiC deposit merge with each after approximately 3 hours of growth. The boundary between them tends to move at the periphery of the crystal. This is advantageous for getting high-quality SiC boule.

To understand possible ways for avoiding parasitic deposition we carried out a parametric study. It has been found that the deposit formation is practically independent of the seed temperature and gas pressure in the crucible. However, poly-SiC deposition can be considerably reduced by optimization of the inductor coil position, which controls the temperature gradients in the growth crucible.

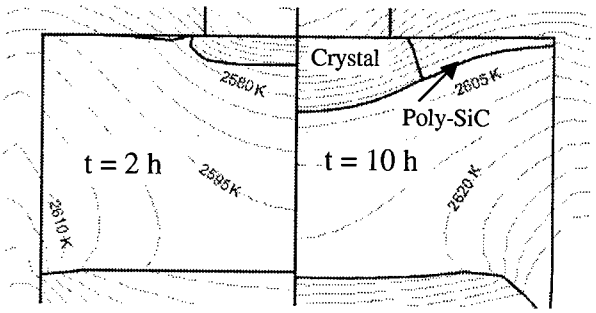


Fig.3. Evolution of crystal shape and powder surface profile, and poly-SiC deposition simulated for two instants of the long-term growth. Isotherms are indicated by contours.

Conclusions

A special software tool called "Virtual Reactor" has been developed for simulation of a long-term SiC bulk crystal growth by sublimation technique. It includes advanced physical models for heat and mass transport in the crucible, for analysis of parasitic deposition on the crucible walls, as well as for prediction thermo-elastic stress in the crystal, gliding dislocation density, etc. VR can be easy supplemented by additional models to be developed in the future. The software tool is expected to be useful for growth engineers involved in R&D and production.

References

[1] P.J. Wellmann, M. Bickermann, D. Hoffmann, L. Kadinsky, M. Selder, T.L. Straubinger, A. Winnacker, J.Cryst.Growth 216 (2000), p. 263.

[2] M. Selder, L. Kadinski, Yu. Makarov, F. Durst, P. Wellman, T. Straubinger, D. Hofmann, S. Karpov, M. Ramm, J.Cryst.Growth 211 (2000) p.333.

[3] S.Yu. Karpov, A.V. Kulik, I.A. Zhmakin, Yu.N. Makarov, E.N. Mokhov, M.G. Ramm, M.S. Ramm, A.D. Roenkov, Yu.A. Vodakov, J.Cryst. Growth. 211 (2000), p. 347.

[4] M.S. Ramm, A.V. Kulik, I.A. Zhmakin, S.Yu. Karpov, O.V. Bord, S.E. Demina, Yu.N. Makarov, to be published in Mat.Res.Soc.Symp.Proc. (2000).

[5] Yu.A. Vodakov, A.D. Roenkov, M.G. Ramm, E.N. Mokhov, Yu.N. Makarov, Phys.Stat.Sol. 202 (1997), p. 177.

Materials Science Forum Vols. 353-356 (2001) pp. 61-64
© 2001 Trans Tech Publications, Switzerland

Coupled Thermodynamic - Mass Transfer Modeling of the SiC Boule Growth by the PVT Method

A. Pisch[1], E. Blanquet[1], M. Pons[1], C. Bernard[1], J.M. Dedulle[2] and R. Madar[2]

[1] LTPCM-UMR 5614 (CNRS/INPG/UJF), Domaine Universitaire, BP 75, FR-38402 Saint Martin d'Hères Cedex, France

[2] LMGP - UMR 5628 (CNRS/INPG), Domaine Universitaire, BP 46, FR-38402 St. Martin d'Hères Cedex, France

Keywords: Bulk Growth, Coupled Thermodynamics-Mass Transfer Modeling, Evaporation Coefficient

Abstract. Evaporation coefficients of SiC have been introduced in the simulation of SiC growth by the Physical Vapor Transport (PVT) method. The total pressure of the reactive species in the gas phase over solid SiC changes compared to previous calculations, where equilibrium conditions were considered at the source powder surface. With these new boundary conditions we simulated the growth of SiC single crystals for two different total pressures (4 mbar and 13 mbar). The shape of the growing crystal is flat at higher pressure and convex at low pressure. This behavior as well as a growth rate of 0.6 to 2.0 mm/h are comparable to the experimental observations, indicating the potential of this approach.

Introduction

Silicon carbide SiC has several properties which makes it an interesting semiconductor material for high temperature, high frequency and high power electronic devices. However, the lack of large area substrates with low defect densities has been the major drawback until now for a further development.

SiC single crystals are classically obtained by the physical vapor transport (PVT) process by the modified Lely method [1]. Pure polycrystalline SiC powder is evaporated under argon atmosphere in a semi-closed inductively heated graphite crucible. The resulting gas species travel through transport phenomena to the cooler seed where crystallization takes place. The temperature at the powder surface ranges in our configuration typically from 2700K to 2900K with an axially gradient of 5K/mm towards the seed surface. Direct measurement or control of the process conditions is difficult due to the high temperature conditions. Numerical modeling of the process is therefore an important way to provide additional information to the experimental knowledge. During the last years, significant progress has been made in the field, as summed up in a review by Pons et al. [2] and by the recent work of Selder et al. [3] and Ramm et al. [4]. This modeling effort is primarily motivated by the need of a better control of the local temperature field inside the crucible. The computed temperature distribution can help to quantitatively obtain the growth history related to the process parameters and the geometry. The global heat transfer generation mechanisms include conduction, convection, radiation and induction heating as well as the heats of crystallization and evaporation at the crystal-vapor and the source-vapor interface.

The determination of the growth rate and the shape of the growing crystal can only be achieved by combining mass transfer to local thermodynamic equilibrium or kinetic calculations for a given temperature distribution inside the growth cavity. In order to obtain a good quantitative information,

the precision of the underlying material properties, especially the thermal conductivity of all reactor material parts and the vaporization and condensation behavior of the SiC source powder is crucial.

The vaporization of SiC possesses several peculiarities. The thermodynamic data of the Si-C solid and gaseous species have been critically assessed recently by Rocabois et al. [5]. The gas phase over solid SiC is mainly constituted of $Si_1(g)$, $Si_2C(g)$, $SiC_2(g)$, $Si_2(g)$ and $C_3(g)$ at high temperature. The vaporization of SiC is not congruent for temperatures lower than 3000K leading to a slow graphitization of the source powder [6]. The other interesting point is the fact that equilibrium partial pressures given by thermodynamic calculations are not reached. The vaporization is retarded due to kinetic barriers and this phenomenon can be modeled by introducing evaporation and condensation coefficients to describe the Hertz-Knudsen flows from the SiC surface. We have determined recently the evaporation coefficients of $Si_1(g)$, $Si_2C(g)$ and $SiC_2(g)$ by high temperature mass spectrometry as a function of temperature [7].

The purpose of this contribution is to show the influence of the introduction of evaporation coefficients in the modeling of the SiC boule growth.

Coupled thermodynamics - mass transfer simulation

The introduction of evaporation coefficients α changes the gas phase composition over solid SiC during evaporation. The values for α used in this study are : 0.07 for $Si_1(g)$ and $SiC_2(g)$ and 0.02 for $Si_2C(g)$, $Si_2(g)$, $Si_3(g)$ and C_3 (g) (the last three ones are only estimated, because their respective partial pressure is too small for a reasonable measurement [7]). As a consequence, the total pressure of all reactive species lowers by an order of magnitude from 4 mbar to 0.3 mbar at 2600K and from 170 mbar to 10.5 mbar at 3000K (Fig 1.). The imposed argon pressure inside the growth chamber, typically between 3 mbar and 20 mbar is therefore mainly diluting the system. The second change is the relative mass fraction of the reactive gas species, because the evaporation coefficients are not identical for the different molecules.

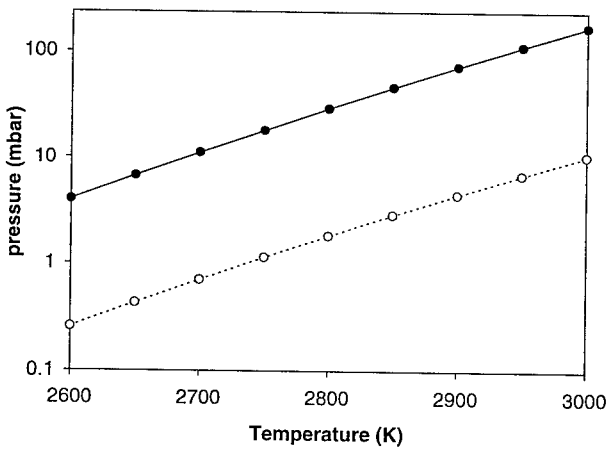


Fig. 1: Total pressure of reactive gas species over solid SiC as a function of temperature with (o) and without (•) evaporation coefficients.

The mass fractions for the three major species $Si_1(g)$, $SiC_2(g)$ and $Si_2C(g)$ are reproduced in Fig.2 with and without evaporation coefficient as a function of temperature. The overall behavior remains the same for all the species, but $SiC_2(g)$ becomes more dominant and the relative amount of $Si_2C(g)$ falls to a value of around 10% only. Therefore, the molar ratio Si/C in the gas phase over solid SiC also changes from 3.3 to 3.17 at 2600K and from 1.8 to 1.5 at 3000K.

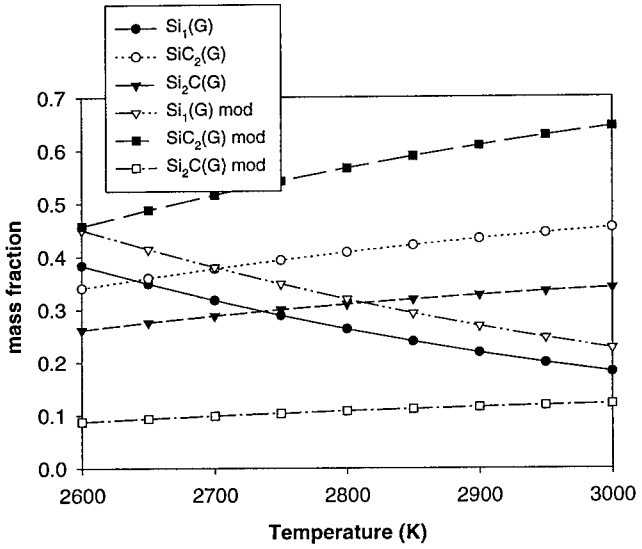


Fig. 2: Calculated mass fraction of the reactive gas species $Si_1(g)$, $SiC_2(g)$ and $Si_2C(g)$ over solid SiC+C as a function of temperature, with and without evaporation coefficients (it should be noted that the total pressure is not constant, but increasing considerably with temperature)

The growth rate and the shape of the growing crystal for the initial steps of the growth have been modeled by a coupled thermodynamic - mass transport simulation which is described elsewhere [8]. The calculations have been performed for a fixed growth geometry and temperature profile. Two total pressures have been simulated (4 mbar and 13 mbar) corresponding to the sum of the reactive species partial pressures plus the corresponding partial pressure of argon gas. The growth rate is determined by the total carbon flux normal to the surface. This carbon flux is drawn for an axis-symmetric configuration in Fig.3. On the left side of the schematic drawing, the total pressure in the chamber is 13 mbar and on the right side it is adjusted to 4 mbar. The carbon flux profile for the higher pressure is almost flat at the early stage of single crystal growth. Almost all the arrows are normal to the surface. The growth rate is around 0.6 mm/h which is also observed experimentally. The profile changes for the lower growth pressure. It is much more convex, especially close to the edge of the seed surface, where the flux is directed under a 45° angle relative to the seed surface. The growth rate is 3 to 4 times higher. This behavior of an increased growth rate has been confirmed experimentally. Because the crucible geometry and the temperature profile are identical in both cases, the diffusion of the reactive species towards the seed surface is the main the origin of this different behavior.

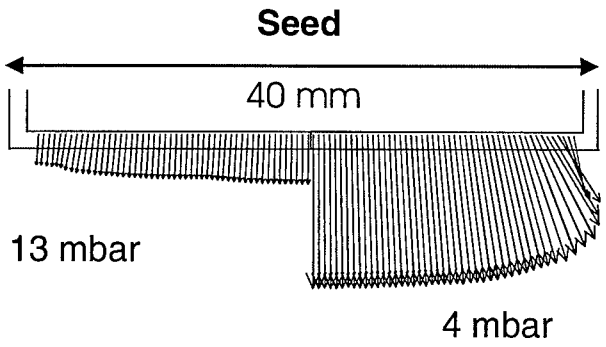


Fig. 3: Carbon flux on the seed surface for two different total pressures: left side 13 mbar, right side 4 mbar. The normal component of the arrows is identical to the shape of the growing crystal.

Conclusion

We have simulated the growth of single crystalline SiC by the PVT method introducing evaporation coefficients measured by high temperature mass spectrometry. For a given crucible geometry and temperature profile, the initial growth of the single crystal has been calculated for two different total pressures by a coupled thermodynamic-mass transfer approach. The growth rate of a few mm/h as well as the calculated crystals shapes are in good agreement with the ones observed experimentally.

Acknowledgements

The authors gratefully acknowledge the support of the French Ministry of Education and Research, the French Ministry of Industry and the European Brite Euram Program (Contract BRPR-CT98-0815- JESICA)

References

[1] Yu.M. Tairov and V.F. Tsvetkov, J. Cryst. Growth **43** (1978) p. 209

[2] M.Pons, M Anikin, K. Chourou, J.M. Dedulle, R. Madar, E. Blanquet, A. Pisch, C. Bernard, P. Grosse, C. Faure, G. Basset, and Y. Grange Mater. Science & Engineering **B56** (1999) p. 18

[3] M. Selder, L. Kandinsky, Yu. Makarov, F. Durst; P. Wellmann, T. Straubinger, D. Hofmann, S. Karpov and M. Ramm, J. Cryst. Growth **211** (2000) p. 333

[4] M.S. Ramm, E.N. Mokhov, S.E. Demina, M.G. Ramm, A.D. Roenkov, Yu.N. Vodakov, A.N. Vorob'ev, S.Yu. Karpov, A.V. Kulik, Yu.N. Makarov, Mat.Sci. Eng **B61-62** (2000) p. 107

[5] P. Rocabois, C. Chatillon, C. Bernard, F. Genet , High Temp. High Press., **27-28** (1995/96) p. 25

[6] R.G. Behrens, G.H. Rinehart in "Characterization of High Temperature Vapors and Gases" Ed. J. Hastie, NBS Special Publication, Gaithersburg FL, (1979) p. 125

[7] A. Pisch, A.M. Ferraria, C. Chatillon, E. Blanquet, M. Pons, C. Bernard, M. Anikin and R. Madar, Mater. Sci. Forum **338-342** (2000) p. 91

[8] M. Pons, E. Blanquet, J.M. Dedulle, I. Garcon, R. Madar and C. Bernard, J. Electrochem. Soc. **143** (1996) p. 3727.

Materials Science Forum Vols. 353-356 (2001) pp. 65-68
© 2001 Trans Tech Publications, Switzerland

Numerical Simulation of Thermal Stress Formation during PVT-Growth of SiC Bulk Crystals

M. Selder[1], L. Kadinski[1], F. Durst[1], T.L. Straubinger[2], P.J. Wellmann[2] and D. Hofmann[2]

[1] Institute of Fluid Mechanics, University of Erlangen-Nürnberg, Cauerstr. 4, DE-91058 Erlangen, Germany

[2] Department of Materials Science 6, University of Erlangen-Nürnberg, Martensstr. 7, DE-91058 Erlangen, Germany

Keywords: Bulk Growth, Global Heat and Mass Transfer, Numerical Modeling, Physical Vapor Transport, Thermoelastic Stress Distribution

Abstract. The thermal stress distribution in growing SiC bulk single crystals is analyzed by a Finite Volume solution approach using anisotropic elasticity theory. The stress calculations are based on a global simulation of heat and mass transfer during the SiC bulk growth process. The temporal evolution of the thermal stress distribution inside the growing crystal is studied. It is found that the conditions for thermal stress formation at fixed positions in the crystal vary significantly during growth. The impact of the stress boundary conditions (free/fixed surfaces) on this behaviour is investigated. The calculated stresses exceed considerably the critical resolved shear stress in SiC which indicates that the observed dislocation formation under the established growth conditions should be caused at least partly by thermal stresses.

1 Introduction

To use SiC wafers as substrate material for electronic and optoelectronic devices in industrial scale, the production of high quality large diameter SiC single crystals at low cost has to be realized. At the moment, the standard technique to prepare SiC bulk single crystals is physical vapour transport (PVT) growth in inductively heated growth reactors by the modified Lely method. The quality of the crystals depends sensitively on the thermal field inside the growth cell. This is at least partly due to the fact that temperature inhomogeneities inside the crystal cause thermal stresses. Stress, in turn, is considered to be a main reason for a variety of crystal defects (e.g. micropipes, dislocations) [1, 2].

While the numerical simulation of heat and mass transfer problems related to SiC bulk crystal growth has been discussed in a variety of publications during the last years (e.g. [3, 4]), only few studies on the numerical modeling of thermal stress formation during growth have been published so far. First investigations in this field have been performed in [5, 6].

In this work, we analyze the thermal stress formation in the growing SiC single crystal. The stress calculations are based on a global simulation of the SiC bulk crystal growth process. Analyzing the main heat and mass transfer processes, we determine the thermal field inside the growth cell and the temporal evolution of the growing crystal. The stress distribution in the crystal at different stages of the growth process is studied.

2 Experiment and Numerical Procedure

6H-SiC crystals were grown in an inductively heated PVT growth reactor. The growth process was controlled experimentally by optical pyrometers. Some details concerning the experimental

set-up are reported in [7]. After growth, the crystals were analyzed by stress birefringency [2].

The simulation of the SiC bulk growth process is based on a Finite Volume solution algorithm for the governing equations of the main heat and mass transfer mechanisms. The modeling approach has been introduced partly in [8]. To calculate the thermal stress distribution in the growing crystal, our simulation code has been added by the basic equations of anisotropic elasticity theory. Details of the approach will be the subject of a forthcoming publication [9].

As there are no studies on the elastic constants of 6H-SiC at high temperatures available, the room temperature values given in [10] were used for the calculations presented in this work. We assumed that the crystal is fixed at the seed holder. The growth surface moves freely. The influence of the boundary condition at the side wall (fixed or free) is analyzed.

3 Results and Discussion

Fig. 1 and 2 show exemplarily results on the stress status in a SiC-crystal obtained using experimental and numerical methods, respectively: The variations of the residual stress within a 6H-SiC wafer visualized by stress birefringency are given in Fig. 1, the calculated distribution of temperature and stress component σ_{rz} in a plane containing the symmetry axis of the crystal are presented in Fig. 2. In the experimental stress pattern, bright contrast indicates regions with higher stress levels. Both experiment and calculations point to increased stress levels at the crystal periphery. (On the correlation of residual stress in crystals and thermal stress at higher temperatures during growth, see e.g. [11].)

Experimental investigations of stress in wafers cut at different axial locations revealed that the stress variations mainly appeared at the periphery of the wafers with the trend to increase with increasing distance from the seed. Performing calculations for identical growth conditions, we found a similar axial and radial dependence for the stress component σ_{rz} (Fig. 3). The component σ_{rz} is considered to be of importance for dislocation formation due to glide in the basal (0001) plane [5].

The assumption that the crystal is fixed at the side wall might be questionable as an interaction of the growing crystal with the crucible wall depends strongly on the established growth conditions. We compared results obtained using this boundary condition to calculations

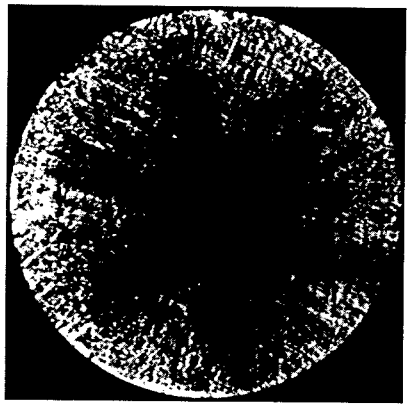


Fig. 1. Stress variation in a SiC-wafer visualized by stress birefringency (bright contrast: high stress level).

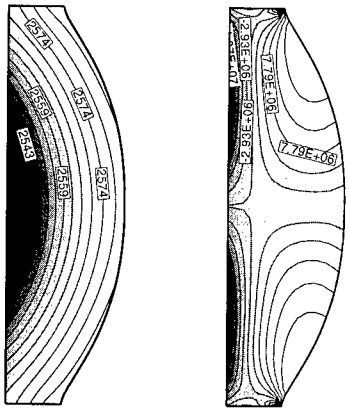


Fig. 2. Calculated distribution of temperature (left) and stress component σ_{rz} in a SiC crystal after 60 hours of growth. The difference between two neighboring isolines is 4 K and 2.7 MPa, respectively.

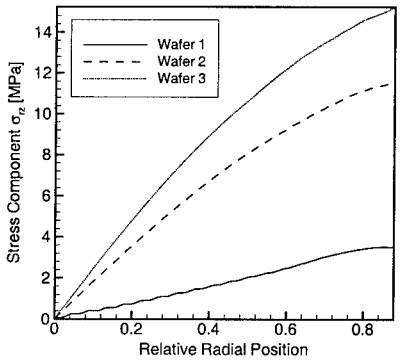


Fig. 3. Calculated radial variation of the stress component σ_{rz} taken at increasing distances from the seed.

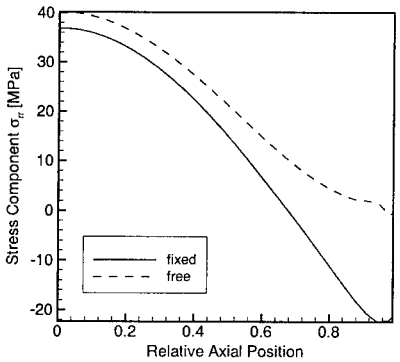


Fig. 4. Calculated radial variation of the stress component σ_{rr} for different boundary conditions at the side wall.

for a free surface at the side wall. The radial profiles of the normal stress component σ_{rr} for these two cases are given in Fig. 4. Using the free surface boundary condition, the absolute stress level is significantly lower near the side wall, while in the inner part of the crystal, the general behaviour and the absolute values are only slightly influenced. A similar trend is found for the components σ_{zz} and σ_{rz}.

To analyze the temporal evolution of stress formation during growth, we have investigated the distributions of temperature and stress in a plane perpendicular to the growth direction at different points in time (distance plane – seed holder: 4 mm). The radial temperature profiles and the radial profiles of the axial temperature gradient given in Fig. 5 show that the thermal conditions in this crystal plane approximately remain unchanged during growth. The different heat transfer mechanisms (radiation and conduction) obviously balance in a manner that realizes a nearly stationary temperature field within the crystal during the major part of growth. In contrast, the distribution of stress in the same plane undergoes remarkable changes (Fig. 6). At a first glance, this temporal variation of stress distribution at constant thermal conditions seems to be contradictory, but this behaviour may be explained by the varying influence of the stress-relevant boundary conditions: The distance of the considered plane to the seed holder (fixed boundary) remains constant, while the distance to the free surface is increasing during growth.

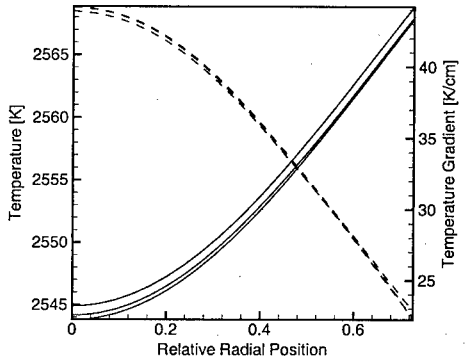


Fig. 5. Radial profiles of temperature (solid lines) and axial temperature gradient (dashed lines) at the same position for three different points in time.

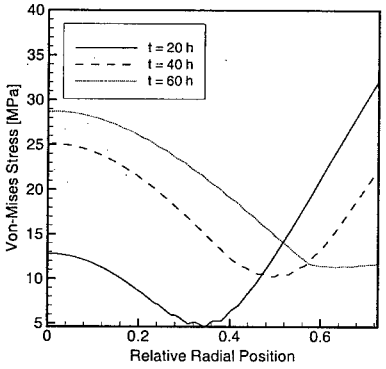


Fig. 6. Radial von-Mises stress profiles at the same position for three different points in time.

Our calculations of both the shear stress σ_{rz} and the von-Mises stress reveal high stress levels up to 30 MPa during growth. These values exceed considerably the stress level of 1 MPa which is discussed to be the critical resolved shear stress σ_{CRS} at T = 2200°C – 2300°C [12] in SiC. σ_{CRS} represents an indicator for the start of plastic deformation, i.e. formation of dislocations. Therefore the dislocation density in our crystals ($> 1000\,cm^{-2}$) should be at least partly due to the thermal stresses. For a quantitative determination of dislocation densities from stress calculations, advanced models [11] have to be used including generation and multiplication of dislocations according to the Alexander/Haasen theory. The application of this approach is presently limited because relevant material data for SiC are not available up to now.

4 Conclusion

We have analyzed the thermal stress distribution in growing SiC bulk single crystals using anisotropic elasticity theory. The temporal evolution of the stress distribution was analyzed. It was shown that the stress depends significantly on the stress-related boundary conditions at the transition crystal/crucible. The assumption of a free surface leads to a reduced magnitude of stresses compared to the fixed condition at the crystal periphery. It was demonstrated that the conditions for stress formation at a position in the crystal vary significantly during growth although the thermal field remains relatively unchanged. The predicted stress levels at the established process conditions are considerably higher than the critical resolved shear stress of approximately 1 MPa which is considered as the critical magnitude for formation of dislocations.

Acknowledgement

Financial support by the Deutsche Forschungsgemeinschaft (contracts Du 101/47 and Wi 393/9) and by the Bayerische Forschungsstiftung (contract 176/96) is gratefully acknowledged.

References

[1] M. Pons, M. Anikin, J.M. Dedulle, R. Madar, K. Chourou, E. Blanquet, C. Bernard, Surf. Coat. Technology 94–95 (1997), p. 279.

[2] D. Hofmann, M. Bickermann, R. Eckstein, M. Kölbl, S.G. Müller, E. Schmitt, A. Weber, A. Winnacker, J. Crystal Growth 198/199 (1999), p. 1005.

[3] M. Pons, M. Anikin, K. Chourou, J.M. Dedulle, R. Madar, E. Blanquet, A. Pisch, C. Bernard, P. Grosse, C. Faure, G. Basset, Y. Grange, Mat. Sci. Eng. B61–62 (1999), p. 18.

[4] M. Selder, L. Kadinski, F. Durst, T. Straubinger, D. Hofmann, P. Wellmannn, Mater. Sci. Forum 338–342 (2000), p. 31.

[5] S.Y. Karpov, A.V. Kulik, I.A. Zhmakin, Y.N. Makarov, E.N. Mokhov, M.G. Ramm, M.S. Ramm, A.D. Roenkov, Y.A. Vodakov, J. Crystal Growth 211 (2000), p. 347.

[6] S.G. Müller, R.C. Glass, H.M. Hobgood, V.F. Tsvetkov, M. Brady, D. Henshall, J.R. Jenny, D. Malta, C.H. Carter jr., J. Crystal Growth 211 (2000), p. 325.

[7] P.J. Wellmann, M. Bickermann, D. Hofmann, L. Kadinski, M. Selder, T.L. Straubinger, A. Winnacker, J. Crystal Growth 216 (2000), p. 263.

[8] M. Selder, L. Kadinski, Y. Makarov, F. Durst, P. Wellmannn, T. Straubinger, D. Hofmann, S. Karpov, M. Ramm, J. Crystal Growth 211 (2000), p. 333.

[9] M. Selder, L. Kadinski, F. Durst, P. Wellmannn, T. Straubinger, D. Hofmann, J. Crystal Growth, to be submitted.

[10] K. Kamitani, M. Grimsditch, J.C. Nipko, C.K. Loong, M. Okada, I. Kimura, J. Appl. Phys. 82(6) (1997), p. 3152.

[11] J. Völkl, Handbook of Crystal Growth, Vol. 2 (edit. D.T.J. Hurle), Elsevier Science (1994), p. 821.

[12] A.V. Samant, P. Pirouz, Int. J. Ref. Metals and Hard Materials 16 (1998), p. 277.

Materials Science Forum Vols. 353-356 (2001) pp. 69-72
© 2001 Trans Tech Publications, Switzerland

Crystal Growth of 15R-SiC and Various Polytype Substrates

T. Nishiguchi, T. Shimizu, M. Sasaki, S. Ohshima and S. Nishino

Kyoto Institute of Technology, Matsugasaki, Sakyo-ku, Kyoto 606-8585, Japan

Keywords: (11$\bar{2}$0) Plane, 15R-SiC, Annealing, Crystal Growth, Stacking Fault, Sublimation Method, Substrate Type

Abstract. Though 15R-SiC has a large mobility for MOSFET devices, 15R-SiC wafers are difficult to obtain. In addition, a 15R-SiC substrate is said to be essential for the 15R-SiC growth. In this paper, crystal growth of 15R-SiC on the more common 4H-SiC and 6H-SiC substrates is discussed. 15R-SiC could be grown on the C-face of 4H-SiC and the Si-face of 6H-SiC. In the case of 15R-SiC and 6H-SiC substrate, growth temperatures lower than 2000°C are important. However, in the case of 4H-SiC, still lower temperature (1700~1800°C) were needed. To examine the thermal stability of 15R-SiC, the grown crystal was annealed at Tb=2300~2650°C. However, definite polymorphic transformation was not observed. Stacking faults in the crystal grown on the (11$\bar{2}$0) plane were investigated by molten KOH etching. Stacking faults in the 15R-SiC were less than in 6H-SiC. Several stacking faults in the 15R-SiC terminated inside the crystal.

1. Introduction

One of the most serious problems in SiC MOSFET devices is the low channel mobility. 15R-SiC is said to have a larger channel mobility than 6H-SiC or 4H-SiC [1]. There are few reports about crystal growth of 15R-SiC, and the use of a 15R-SiC substrate is said to be essential for growing 15R-SiC. However, large 15R-SiC substrates are difficult to obtain. In order to grow large 15R-SiC crystals, it is therefore necessary to establish stable growth conditions for 15R-SiC on 4H-SiC or 6H-SiC substrates. In this paper, crystal growth of 15R-SiC on 4H-SiC and 6H-SiC substrates is discussed. We also focus on the stacking faults in the 15R-SiC grown on the (11$\bar{2}$0) plane.

2. Experiment

Sublimation growth was achieved using a quartz tube reactor with a water-cooled jacket under argon atmosphere at a reduced pressure of 50~200 Torr. Substrates used were 15R-SiC, 4H-SiC and 6H-SiC made by the sublimation method. (11$\bar{2}$0) plane of 15R-SiC and 6H-SiC were also used to investigate the difference between the growth on the (0001) plane and (11$\bar{2}$0) plane. The source material was abrasive SiC powder. The crucible was heated externally by RF induction with a frequency of 300 kHz. The temperatures at the top (Ts) and the bottom (Tb) of the crucible were approximately 1700~2150°C and 2300~2400°C, respectively. The boules were grown several times after recharging the source material. Grown crystals were characterized by optical microscopy, molten KOH etching (500°C, 5 min.) and Raman spectroscopy.

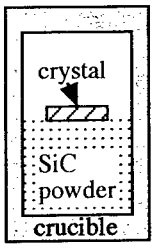


Fig.1 The schematic of the annealing experiment

A 15R-SiC crystal was annealed to investigate its thermal stability. If 15R-SiC is unstable at higher temperatures, it is expected that it would change to a

more stable polytype by solid phase transformation. For the annealing experiment, same set up as that for crystal growth was used. The schematic of the annealing experiment is shown in Fig.1. 15R-SiC crystals were prepared by cutting the boule grown by the sublimation method. It was cut parallel to the c-axis to avoid the growth of another polytype on this crystal. Annealing conditions are summarized in Table 1. The Ar-pressure in the reaction tube was kept at atmospheric pressure to prevent the evaporation of SiC powder.

Table 1. Annealing conditions

2300°C 1h
2300°C 10h
2400°C 10h
2600°C 1h
2600°C 2h
2650°C 1h

3. Results and Discussion

3.1. Crystal growth of 15R-SiC on 4H-SiC and 6H-SiC substrate

The optimum growth conditions for 15R-SiC on 15R-SiC substrates by the modified Lely method have been established [2, 3]. By using a 15R-SiC substrate, the probability of 15R-SiC growth increases. Particularly, 15R-SiC always growth on the (1120) plane of 15R-SiC substrates. It is very important to keep the growth temperature below 2000°C in the case of 15R-SiC substrates.

On the 6H-SiC substrate, the growth experiments were carried out at Ts=1830~2160°C. 15R-SiC did not grow on the C-face of 6H-SiC even though the temperature was changed. On the Si face of 6H-SiC, 15R-SiC occasionally grew at lower temperatures. However, 15R-SiC never grew if the substrate temperature was higher than 2000°C.

On the 4H-SiC substrate, growth experiments were carried out at Ts=1700~2000°C. It was difficult to grow 15R-SiC on the Si-face of 4H-SiC. 15R-SiC grew on the C-face of 4H-SiC with a higher probability than in the case of Si-face of 6H-SiC. However, using the 15R-SiC substrate was still better for growing 15R-SiC. The substrate temperature was also important. If the 15R-SiC substrate is used, 15R-SiC grows well when Ts is lower than 2000°C. However, on the 4H-SiC substrate, still lower temperatures were needed. If Ts was approximately 1700~1800°C, 15R-SiC grew well on the C-face of 4H-SiC. However, in the temperature range around 2000°C, only 4H-SiC grew on the 4H-SiC substrate. This result is clearly seen in Fig.2. During the first three growth runs at temperatures around 2000°C, only 4H-SiC grew. Then the growth temperature was reduced to approximately 1700°C. 6H-SiC grew at the initial stage of the growth, and after growing several hundred μm, 6H-SiC turned to 15R-SiC till the end of the growth. After recharging the source material, the growth was restarted. And again, 15R-SiC grew after 6H-SiC. So in this case, alternative growth of 15R-SiC and 6H-SiC was seen.

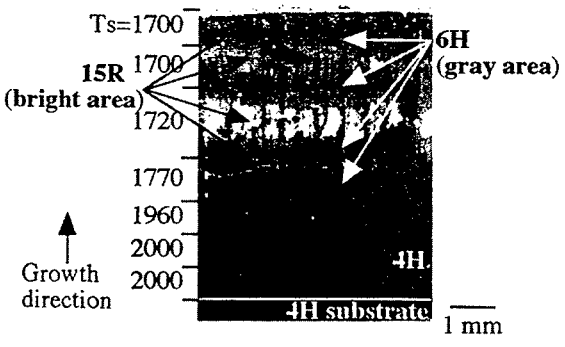


Fig. 2 Optical microscope image of the crystal growth on the C-face of 4H-SiC. Growth was carried out 7 times at corresponding temperatures as shown on the left side. 15R-SiC is bright area, 6H-SiC is gray area and 4H-SiC is dark area.

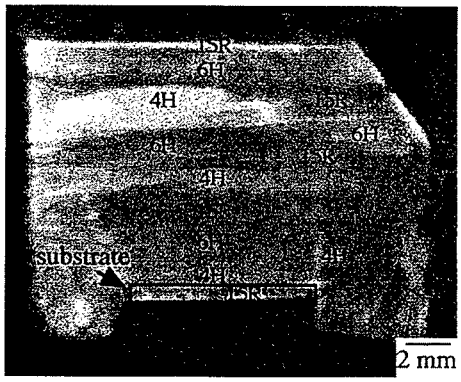


Fig.3 PL image at liquid nitrogen temperature of the crystal grown on the C-face of 15R-SiC. Crystal was grown at Ts=2140°C for 13 hours.

3.2. Crystal annealing

Sometimes 15R-SiC, 4H-SiC and 6H-SiC grew alternately along the growth direction as shown in Fig.2 and 3. Particularly, in the case of Fig.3, grown polytypes along the growth direction are (4H-6H-15R)-(4H-6H-15R)-(4H-6H-15R). Though this alternative growth might be caused by instability of growth conditions, it is also possible that the grown 15R-SiC crystal was transformed to relatively more stable polytype at higher temperatures during the growth as demonstrated by Bootsma et al. [4]. To investigate the thermal stability of 15R-SiC, annealing experiments were carried out at several temperatures as shown in Table 1. Even after 10 hours annealing, polytype remains untransformed at Tb=2300 and 2400°C. At Tb=2600~2650°C, 15R-SiC did not change neither. A definite polymorphic transformation was not observed at these temperatures and time durations. Previous work [4] was carried out with the powdered samples with a diameter of 20~100 μm. In our experiment, sublimation grown crystals of 3x5x7 mm size were used. Using relatively large crystals, polymorphic transformation probability decreased. So, the alternate polytype growth seen in Fig.3 may be caused at the surface during the growth.

3.3. 15R-SiC grown on the (11$\bar{2}$0) plane

In order to improve the MOSFET performance, work has been focused on SiC (11$\bar{2}$0) plane due to the high channel mobility of MOSFETsreported on this plane [1]. The crystals were grown on the (11$\bar{2}$0) plane of 15R-SiC and 6H-SiC. It is well known that there is a large number of stacking faults in the crystal grown on the a-plane [5]. Due to the high density of stacking faults, many macro defects called planar defects are introduced into the crystal, grown on the (11$\bar{2}$0) plane. Fig.4 is the cross sectional transmitted light microscope image of the crystal grown on the (11$\bar{2}$0) plane, 6H-SiC (a and b) and 15R-SiC (c and d). Black dots represent the planar defects. The length of the planar defect changes with the polytype. In 15R-SiC, it is several times longer in the growth direction than in of 6H-SiC. It shows a more rounded shape in 6H-SiC. In the slices close to the substrate (b and d), there is a number of planar defects. Better crystallinity was obtained towards the top of the boule, and planar defects were reduced as crystal became thicker. Particularly, in the case of 15R-SiC, planar defects are decreased dramatically as seen in Fig.4 (c). It might be related to the reduction of stacking faults. KOH etching was carried out in order to investigate the stacking fault density and distribution. In Fig.5, the etched surface of 15R-SiC and 6H-SiC grown on the (11$\bar{2}$0) plane is shown. Linear etch pits directed towards <11$\bar{2}$0> correspond to the stacking faults. It is clearly seen from Fig.5 that the stacking fault density of 15R-SiC is less than that of 6H-SiC. Stacking fault density of 15R-SiC was approximately 2000 cm^{-1}. It is about half that of 6H-SiC, which is approximately 4000 cm^{-1}. Once the stacking faults are generated, they do not terminate up to the end of the growth in the case of 6H-SiC [5]. However, in the case of 15R-SiC,

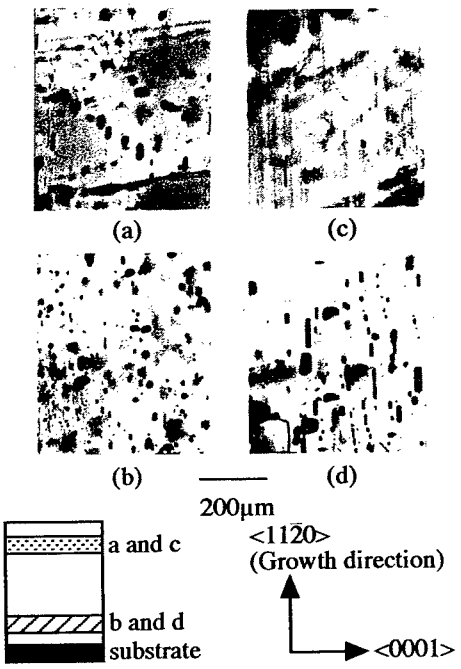


Fig.4 Transmitted light microscope image of the crystal grown on the 6H-SiC(a, b) and 15R-SiC(c, d) substrate. Black dots represent the planar defects.
(a), (c): upper side of the grown crystal
(b), (d): grown crystal close to the substrate

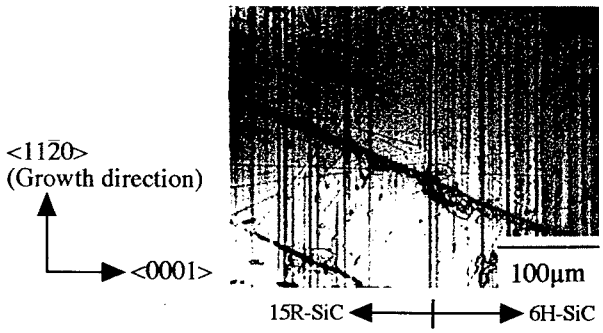


Fig.5 Etched surface of 15R-SiC (left side) and 6H-SiC (right side) grown on the (11$\bar{2}$0) plane.

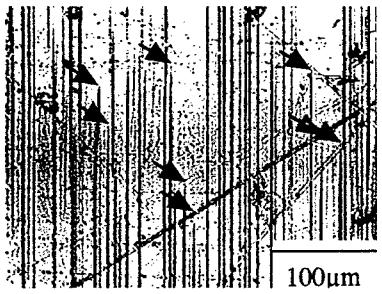


Fig.6 Etched surface of 15R-SiC grown on the (11$\bar{2}$0) plane. Some linear etch pits are terminated during the growth as indicated by arrows.

several stacking faults terminated inside the crystal as indicated by arrows in Fig.6. Actually, in some regions of 15R-SiC, the stacking fault density decreases as the crystal becames thicker, which never occurred in the case of 6H-SiC.

4. Conclusions

The results of 15R-SiC growth vs. substrate type are summarized in Fig.7. 15R-SiC grew on the C-face of 4H-SiC and Si-face of 6H-SiC. As in the case of 15R-SiC substrates, the growth temperature was very important. In the case of 15R-SiC and 6H-SiC substrate, growth temperatures lower than 2000°C are important. However, in the case of 4H-SiC, still lower temperatures (1700~1800°C) were needed. To investigate the thermal stability of these polytypes, annealing experiments were carried out. However, a definite polymorphic transformation was not observed. The stacking fault density of 15R-SiC grown on the (11$\bar{2}$0) plane was less than that of 6H-SiC. Several stacking faults terminated during the growth in the case of 15R-SiC.

a

polarity / polytype	(0001)Si	(000$\bar{1}$)C	(11$\bar{2}$0)
15R-SiC	○	○	○
4H-SiC	×	○	×
6H-SiC	○	×	×

Fig. 7 15R-SiC growth vs. substrate type.
○ useful for growing 15R-SiC
× 15R-SiC never grew

Acknowledgement

This work was partially supported by FED, NEDO Japan, and Ion Engineering Institute (Osaka, Japan).

References:

[1] H.Yano, T.Hirao, T.Kimoto and H.Matsunami, Jpn. J. Appl. Phys., **39** (2000) p.2008
[2] T.Nishiguchi, S.Okada, M.Sasaki, H.Harima and S.Nishino, Materials Science Forum, **338-342** (2000) p.115
[3] N.Schulze, D.Barrett, G.Pensl, phys. stat. sol. (a), **178** (2000), p.645
[4] G.A.Bootsma, W.F.Knippenberg and G.Verspui, J. Crystal Growth, **8** (1971), p.341
[5] J.Takahashi and N.Ohtani, phys. stat. sol. (b), **202** (1997), p.163

Materials Science Forum Vols. 353-356 (2001) pp. 73-76
© 2001 Trans Tech Publications, Switzerland

Micropipe Filling by the Sublimation Close Space Technique

T. Furusho, S. Ohshima and S. Nishino

Department of Electronics and Information Science, Kyoto Institute of Technology,
Matsugasaki, Sakyo-ku, Kyoto 606-8585, Japan

Keywords: Micropipe Filling, Sublimation Close Space Technique, Sublimation Epitaxy, Sublimation Method

Abstract

In this study, micropipe filling by sublimation Close Space Technique is reported. The relationship between the off-axis angle from the (0001) and (000$\bar{1}$) basal planes of 6H-SiC substrates toward <11$\bar{2}$0> direction and the probability of micropipe filling has been investigated. It was established that the probability increased with increasing off-axis angle. At that, the (000$\bar{1}$) face showed better characteristic for micropipe filling than the (0001) face. The micropipe filling could not be observed in the case of epitaxial growth on on-axis substrates. On the basis of the obtained results, it is concluded that substrates with off-axis angle toward <11$\bar{2}$0> direction were important for micropipe filling as the crystal growth proceeded in the step-flow process.

Introduction

Epitaxial growth of SiC was carried out by sublimation Close Space Technique. (CST)[1-3]. This technique is also called sublimation epitaxy [4] and sublimation sandwich method [5]. This method is almost the same as the conventional sublimation method. The difference is the distance between the substrate and the source. It is very small in CST. As a result of this, epitaxial growth proceeds under low supersaturation and therefore high quality epitaxial layers are obtained. For high power devices, thick and high quality SiC films are needed. The growth rate of this technique is 10 times higher than that of CVD method and the operation for crystal growth is fairly simple. Therefore, thick and high quality epitaxial layers are easily obtained in a short time.

If there are micropipes in epitaxial layers, they cause leakage currents in devices and the performance of devices deteriorate. Therefore, many efforts have been made to eliminate micropipes from SiC. Recently micropipe filling was observed in epitaxial layers prepared by LPE [6]. We tried to close micropipes by CST. In this paper, epitaxial growth of SiC and micropipe filling by CST is reported. The results of this investigation could be applied to the conventional sublimation method and bulk crystals of low micropipe density could be obtained.

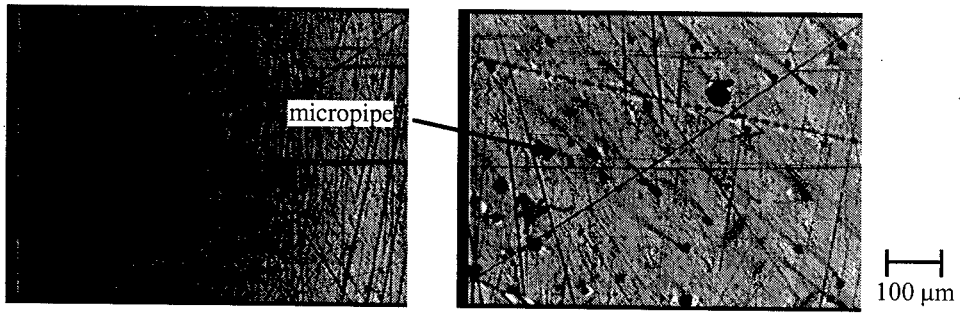
Experiment

3C-SiC polycrystalline plates were used as the SiC source material. 6H-SiC wafers, cut from a bulk crystal grown in our laboratory, were used for preparing the substrates. The wafers were polished by a series of slurries including diamond powder. The diameter of diamond powder was 30, 5 and 0.5 μm, respectively. After polishing, wafers were cut to the size of 6.0 mm x 6.0 mm. The growth temperature was 2060 K measured at the substrate. The temperature gradient was 1.6 K/mm and this value was obtained by the linear approximation of the temperature distribution in the crucible. The crucible was heated by an RF-generator at a frequency of 60 kHz. The growth

pressure was 1.0 ~ 3.0 x 10^{-3} Torr. The distance between the substrate and the source was 1.0 mm. Additionally, there were small pieces of Ta plate in the crucible to suppress carbonization. The growth rate was 20 ~ 50 μm/h under these conditions. Epitaxial layers were characterized by the Nomarsky optical microscope.

Results and discussion

In Figs. 1(a) and (b), the surface image of the epitaxial layer and the image in transmitted light are shown, respectively. These images were taken at the same focus point. The substrate of this epitaxial layer had many micropipes and was used to investigate the relationship between micropipes in the substrate and the epitaxial layer. Many micropipes are observed in Fig. 1(b), but they are reduced in Fig. 1(a). This shows that the epitaxial layer reduces micropipes presence in the substrate. However, small micropipes remain in the epitaxial layer.



(a) Reflected light (b) Transmitted light

Fig. 1 Optical microscope images of the epitaxial layer

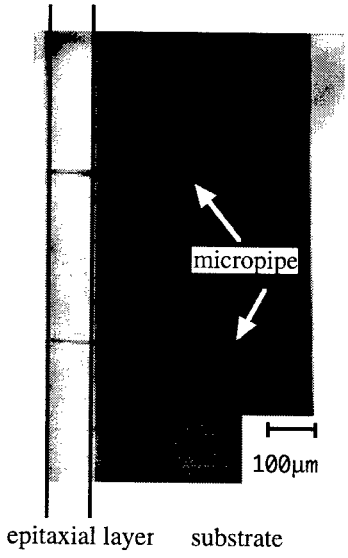


Fig. 2 Cross section image

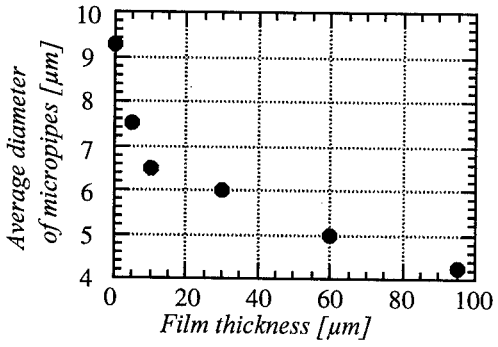


Fig. 3 The relationship between the film thickness and the average diameter of micropipes

In Fig. 2, the cross section image of the substrate and the epitaxial layers shown. It is observed that micropipes continue from the substrate to the epitaxial layer and they do not originate in the epitaxial layer. The diameter of micropipes gradually decreases as the film thickness increases. The relationship between the film thickness and the average diameter of micropipes is show in Fig. 3. Although the diameter of micropipes becomes small, micropipes remains in the epitaxial layer. This was possibly due to the fact that the substrate was not tilted toward <11$\bar{2}$0> direction.

In Fig. 4 is shown the relationship between the off-axis angle and the probability of micropipe filling. All epitaxial layers were grown under the same conditions. The growth temperature was 2060 K and the growth pressure was 1.0 Torr. The epitaxial growth was performed on both (0001) and (000$\bar{1}$) faces. On (000$\bar{1}$) face , the probability of micropipe filling becomes large, as the off-axis angle increases. But on (0001) face, the probability is almost the same at different off-axis angles. This polarity dependence of micropipe filling can be explained as follows [7].

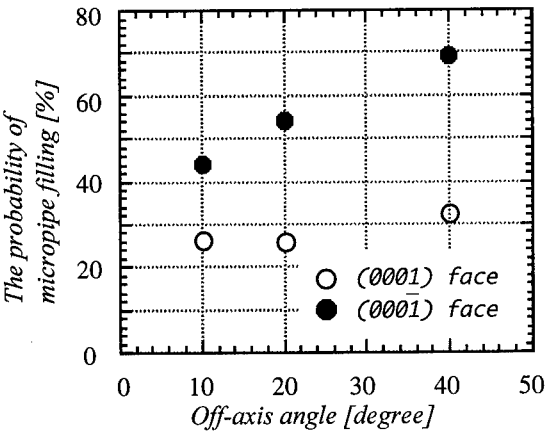


Fig. 4 The relationship between the off angle and the micropipe filling rate

The reaction species more easily bind to the carbon dangling bond than to the silicon dangling bond and the surface free energy of (000$\bar{1}$) face is lower than that of (0001) face. If the substrate is tilted toward <11$\bar{2}$0> direction, two planes, namely (0001) silicon face or (000$\bar{1}$) carbon face and (11$\bar{2}$0) plane, can be present on this substrate. Moreover, on such substrates, the direction of micropipe propagation differs from the direction of crystal growth. These have no relationship each other. In other words, crystal growth on such substrates proceeds according to the step-flow model [8]. Fig. 5 shows the bonding configuration of 6H-SiC along the <11$\bar{2}$0> and the <000$\bar{1}$> directions. On a (11$\bar{2}$0) plane, the number of silicon dangling bonds is the same as that of carbon dangling bonds. There are only silicon dangling bonds on the (0001) face only carbon dangling bonds on the (000$\bar{1}$) face. Therefore in the growth on (0001) face, on substrates which are tilted toward <11$\bar{2}$0> direction, the growth rate along <0001> direction is larger

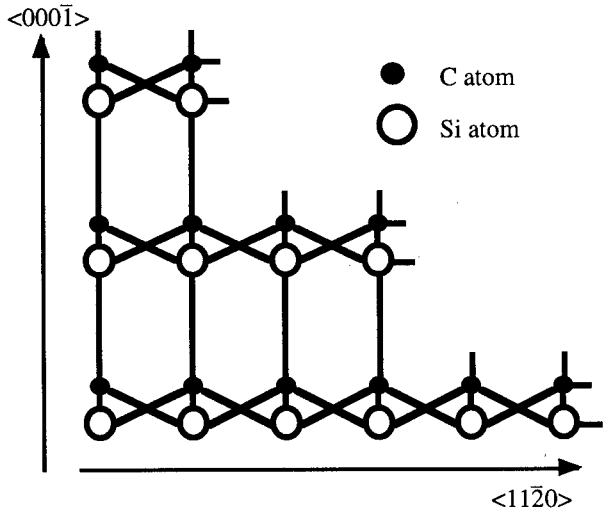


Fig.5 The bonding configration along <11$\bar{2}$0> and <000$\bar{1}$> direction

than toward <11$\bar{2}$0> direction. The growth rate along <11$\bar{2}$0> direction is larger than along <000$\bar{1}$> direction on (000$\bar{1}$) face substrates. From this, it may be concluded that, for micropipe filling, it is necessary that the growth direction is different from the direction of micropipe growth. On (000$\bar{1}$) face, the direction of crystal growth, that is <11$\bar{2}$0> direction, is different from the micropipe propagation, that is <000$\bar{1}$> direction. Besides, as the off-axis angle becomes larger, the number of steps becomes larger and the crystal growth toward <11$\bar{2}$0> direction increases. Therefore, the characteristic shown in Fig. 4 was obtained.

Conclusion

We tried to close micropipes by CST. When the substrate was not tilted toward <11$\bar{2}$0> direction, micropipe filling could not be observed. If the substrate was tilted, micropipe filling could be observed. In order to close micropipes, substrates tilted toward <11$\bar{2}$0> direction are needed and the direction of the crystal growth must differ from the direction of micropipe propagation. In other words, the crystal growth must be carried out under step-flow condition. The (000$\bar{1}$) face shows a better characteristic for micropipe filling than the (0001) face.

Acknowledgment

Thanks are to Mr. Yusuichi Masuda for helping the author and Prof. S.K.Lilov for giving much advice. This work was partially supported by a Grant-in-Aid for Science Research No. 0945001 from the Ministry of Education, Science and Culture, Japan and FED, NEDO Japan and Ion Engineering Institute (Osaka Japan).

References

[1] Yu. M. Tairov, V.F. Tsvetkov, S.K. Lilov and G.K. Safaraliev, Journal of Crystal Growth **36**, (1976), p. 147.

[2] S. Nishino, K. Matsumoto, T. Yoshida, Y. Chen and S.K. Lilov, Materials Science and Engineering **B61-62**, (1999), p. 121.

[3] T. Furusho, K. Matsumoto, H. Harima and S. Nishino, Mater. Sci. Forum **338-342**, (2000), p. 217.

[4] M. Tuominen, R. Yakimova, M. Syväjärvi and E. Janzén, Materials Science and Engineering **B61-62**, (1999), p. 168.

[5] A.S. Segal, A.N. Vorob'ev, S.Yu. Karpov, E.N. Mokhov, M.G. Ramm, M.S. Ramm, A.D. Roenkov, Yu.A. Vodakov and Yu.N. Makarov, Journal of Crystal Growth **208**, (2000), p. 431.

[6] M. Müller, M. Bickermann, D. Hofmann, A.D. Weber and A. Winnacker, Mater. Sci. Forum **264-268**, (1998), p. 69.

[7] S. Nishino, Y. Nishino, Y. Masuda, Y. Chen and C. Jacob, Mater. Sci. Forum **338-342**, (2000), p. 197.

[8] T. Kimoto, Doctoral thesis: *Step-controlled Epitaxy Growth of α-SiC and Device Applications*, Kyoto University, Japan, (1995).

Materials Science Forum Vols. 353-356 (2001) pp. 77-80
© 2001 Trans Tech Publications, Switzerland

Mechanism for Damage Healing of Cracked 6H-SiC Substrates by the Sublimation Method

T. Shimizu, T. Nishiguchi, M. Sasaki, S. Ohshima and S. Nishino

Department of Electronics and Information Science, Kyoto Institute of Technology, Matsugasaki, Sakyo-ku, Kyoto 606-8585, Japan

Keywords: Crack Healing, Multi-Substrate Arrangement, Multi-Substrates, Sublimation Growth

Abstract Recently, the realization of making high-quality and large diameter bulk SiC crystal is required for the device application. In generally, the size of the bulk crystal is gradually enlarged by repeating the growth from small size substrate. It takes a long time to obtain a large size wafer. In stead of this conventional method, we made a new approach to realize a large diameter crystal by arranging the several substrates on the cap. In this method, we grew up bulk on putting two substrates , proved mechanism for groove narrowing and confirmed transition from bi-crystal to mono-crystal.

Introduction

Large diameter of the SiC wafer is needed for the device application. Most of the bulk SiC is made by sublimation method, modified Lely method [1-7]. In generally, enlargement of the bulk SiC is carried out by repeating the growth run starting from small size substrate. It take a time to get large diameter of the bulk. We already studied many strange phenomena on crack healing in the bulk growth and defect formation mechanism [5-7]. In our previous experiment, even though the substrate was intentionally damaged, cracked, the crack was disappeared on the surface after growth. Based on this result, we propose a new method to enlarge the bulk SiC by starting multi-substrate arrangement. The grooves between the substrates will shrink and finally coalesce each other into one single crystal. Namely, by this method, a transition from bi-crystal to mono-crystal is possible. In this report, a mechanism of groove narrowing is discussed.

Experiment

As a substrate, we used homemade 1-inch 6H-SiC wafer polished both side by 0.5 μm diamond slurry. The wafer was divided into two or four pieces, and then these divided wafer were put on the cap of the crucible. Crucible was single wall graphite cylinder. The source material was abrasive SiC powder and put on the bottom of the crucible. The distance between the source and the substrate was 15mm. Crystal growth was achieved using a quartz tube reactor with a water-cooled jacket under argon atmosphere at 50 Torr. The configuration of the system is shown in Fig.1. The crucible was heated externally by RF induction with a frequency of 300 kHz. The temperatures at the top (Ts) and the bottom (Tb) of the crucible were measured by an optical pyrometer. Ts and Tb were approximately 2050~2150 ℃ and 2250~2350 ℃ , respectively. We grew bulk for three or four times by recharging the source material (total 11-20 hours). The growth thickness was approximately 4.4 mm-15mm. Grown bulk was characterized by optical microscope.

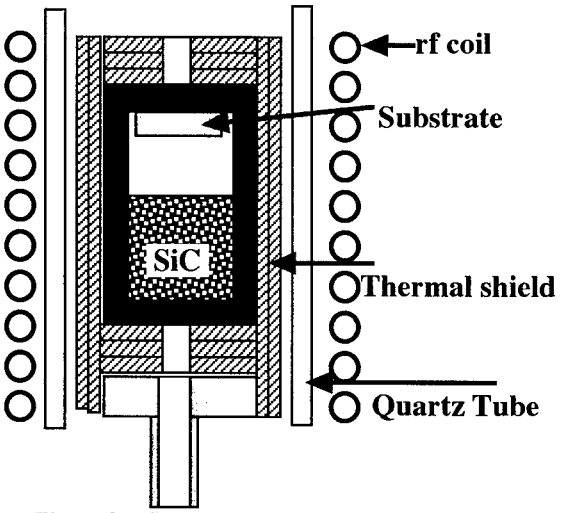


Fig.1 Configuration of the crucible

Result and Discussion

One large substrate was cut into two pieces and put together on the graphite cap as the starting substrate as shown in Fig.2(a) . Small groove between two pieces were about 100 μm. After the first run with 1 mm above the substrate, the facet appeared at the edge of grown surface over the groove. In this figure, the groove still lingers on the facet (indicated by arrow in the figure). However, after the third run with the thickness of about 5 mm, the groove is completely disappeared as shown in Fig.2(c). To investigate propagation of groove, this part was etched by molten KOH, however, groove was almost filled by newly grown layer. This result gave us an idea that groove between two substrates was coalesced, and then the substrates became to single crystal.

The contact areas of the grown surfaces are enlarged as shown in Fig.3. Arrows indicate the same position in each runs in Fig.(a),(b),(c). After the 1st run, groove is clearly seen between faceted areas as indicated by arrow in the Fig.3(a), however, at 2nd run, large groove shrank into small line as shown in Fig.3(b). After 3rd run., the groove was completely disappeared as shown in Fig.3(c). However, a large groove still remained on the off-axis area as black lines as seen in the In this lower side of the Fig.3(c). In this experiment, the two substrates arranged side by side

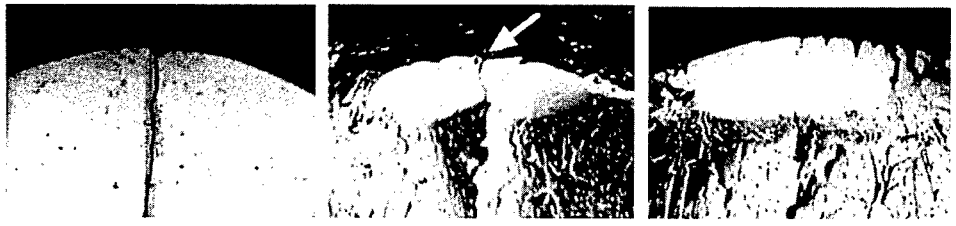


Fig.2 (a) Original substrate, (b) 1st run, (c) 3rd run .

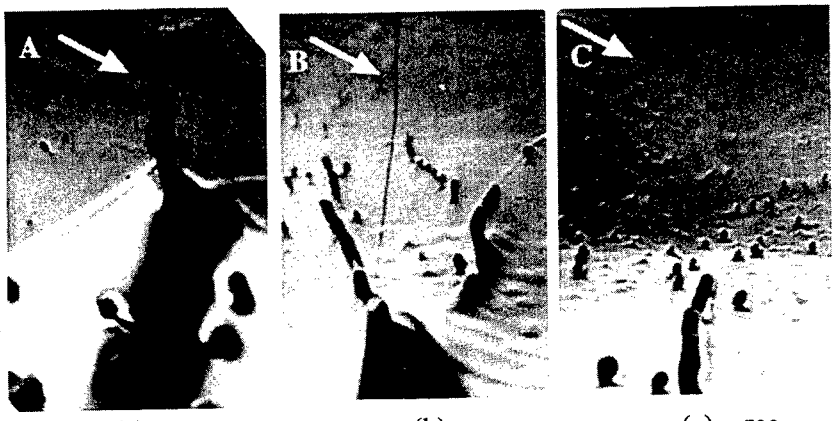
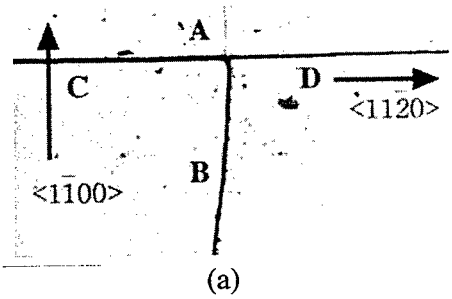
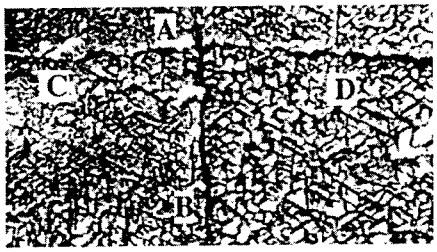


Fig.3 (a) 1 st run, (b) 2nd run, (c) 3rd run.
Arrows indicate the position of the groove existed on the substrate.





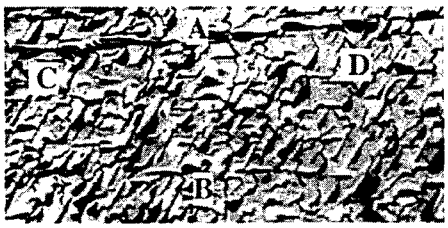


Fig.4 (a) substrates, (b) 2nd growth, (c) 4th growth

were unintentionally off-axis. The facet region appeared at the edge of the substrate at first as seen in Fig.2 (b). Lateral growth rate perpendicular to (0001) which is called on-axis substrate is faster than one on off-axis substrate. By continuing the long growth run, the groove on the off-axis region will shrink.

To observe the orientation dependence of the coalescence of the substrate, one wafer was cut into four pieces as shown in Fig.4(a). The width of the grooves between each pieces of the substrates were different. The width of the groove along <1$\bar{1}$00> direction marked A in Fig.4(a) was narrow about 50 μm. The width of the groove at B was about 200 μm . Growth condition was the same as before. After 2nd run with the thickness of 2 mm, the groove at A shrank, however, groove at B still remained. After 4th runs, the grooves at A and B were almost disappeared. But, large trace of the grooves marked C and D remained along <11$\bar{2}$0> direction as shown in Fig.4(c). It is known that the lateral growth rate along <11$\bar{2}$0> is higher than one along <1$\bar{1}$00> [8]. Consequently, the grooves at A and B were completely burred by newly grown layer. The width of the grooves at C and D were almost same size as the groove B, however, those were not coalesced well. This is because those grooves directed along <11$\bar{2}$0> direction , and the width of the groove is perpendicular to it. The lateral growth direction along <1$\bar{1}$00> is not higher than the <11$\bar{2}$0>. In this experiment, we learned that alignment of the substrate is an important factor to coalesce the two substrates into one. Even though the width of the groove was more than 100 μm, the groove was buried

if the groove was along the <1$\bar{1}$00> which mean edge aligning perpendicular to that direction.

Polytypes of the grown bulk was the same as that of the substrate which was characterized by photoluminescence image at liquid nitrogen temperature. The wafers sliced from those bulk SiC crystal did not contain noticeable groove line, which was confirmed by optical microscope with transmission mode. Level of the surface should be the same and the crystallographic direction of each edge of the substrate should be the same. In our experiment, those parameters were not well fixed, however, better crystallinity of the bulk SiC was obtained. These result show a crew to the large bulk production from the several small pieces of the substrate. Detailed study of small angle grain boundary, misorientation of the substrates and defects density on the junction area should be examined by X-ray diffraction to proceed further progress.

Conclusions

We demonstrated a possibility of producing the large bulk SiC from the multi-wafer arrangement in plane. Once the edges of the substrates are well aligned to each other, large scale bulk is obtained by repeating the growth run. To obtain good crystal, the grooves between the small wafer to wafer should align to <1$\bar{1}$00> direction and the width of the groove should be minimized as possible as we can. Bi-crystal changes into single crystal was achieved.

Acknowledgement

This work was partially supported by FED, NEDO Japan.

References

[1] D. Hobgood, M. Brady, W.Brixius, G. Fechko, R. Glass, D. Henshall, J. Jenny, R. Leonard, D. Malta, St. G. Müller, V. Tsvetkov and C. Carter Jr., Mat. Sci. Forum Vols. 338-342 (2000), p. 3.

[2] M. Anikin, M. Pons, K. Chourou, O. Chaix, J. M. Bluet, V. Lauer and R. Madar, Mat. Sci. Forum Vols. 264-268 (1998), p. 45.

[3] V. F. Tsvetkov, S. T. Allen, H. S. Kong and C. H. Carter Jr., Inst. Phys. Conf. Ser. 142 (1996), p. 17.

[4] M. Sasaki, Y. Nishio, S. Nishino, S. Nakashima and H. Harima, Mat. Sci. Forum Vols. 264-268 (1998), p. 41.

[5] S. Okada, T. Nishiguchi, T. Shimizu, M. Sasaki, S. Ohshima and S. Nishino, Mat. Sci. Forum Vols. 338-342 (2000), p.51.

[6] T. Nishiguchi, S. Okada, M. Sasaki, H. Harima and S. Nishino, Mat. Sci. Forum Vols. 338-342 (2000), p. 115.

[7] N. Sasaki, H. Shiomi, H. Harima and S. Nishino, Mat. Sci. Forum Vols. 338-342 (2000), p. 485.

[8] T. Kimoto and H. Matsunami, Inst. Phys. Conf. Ser. 137 (1994), p.55.

Materials Science Forum Vols. 353-356 (2001) pp. 81-84
© 2001 Trans Tech Publications, Switzerland

Chemical Vapor Deposition of SiC by the Temperature Oscillation Method

Yutaka Abe

Hokkaido Automotive Engineering College, Toyohira-Ku,
Nakanoshima 2-6, Sapporo 062-0922, Japan

Keywords: Selective Method for a Vapor Growth of Crystals, Temperature Oscillation Method

Abstract The applicability of the temperature oscillation method (TOM) for SiC was investigated experimentally using a prototype furnace which consists of two sections. It was experimentally shown that the selection of single nucleation of SiC was possible using TOM. In the present experiment, only β-SiC with relatively large size could be grown. The micropipe density over an area of 5 x 5mm^2 of the grown crystals was less than 20 cm^{-2}.

1. Introduction

In the present paper, a new type of vapor growth method of SiC is described. The source material was placed in a carbon crucible and heated in a furnace with two independent sections (see Fig. 1). The temperatures of the each section could be controlled independently. A temperature oscillation method (TOM) was used in the present experiment. TOM has initially been developed by Scholz and coworkers [1] and was successfully used to grow various single crystals such as GaP, γ-Fe_2O_3, and $NiFe_2O_4$. In the TOM, the temperature gradient is periodically reversed, and the interval of crystal growth alternates with the interval of etching. This periodical processes make the crystal growth highly selective.

The detailed mechanism of micropipe defects (MPD) in SiC has not been cleared yet, it was suggested that the MPD formation is closely correlated with multiple nucleation in the surface region during the initial stage of the crystal growth [2]. TOM allows a selection of single nucleation within the growth section, provided that suitable re-evaporation conditions are used. In this paper, the growing processes without using a previously prepared seed crystal are investigated, because we are more interested in exploring the various possibilities and applicability of the TOM for SiC.

2. Experimental Set-Up

A prototype of furnace with two independent sections was used and the structure of this furnaces is schematically shown in Fig. 1. One of the two sections contains the source material and the other one is for establishing a temperature gradient for the crystal growth. A tantalum strip heater is located between the two sections; it is used for the modification of an actual temperature profile in order to realize a smooth temperature gradient along the growth section. The heater elements of both the sections are 2.4 kW carbon-fiber composite heaters manufactured by Nihon Carbon Co., which can be used up to 1900°C with less degradation. For thermal insulation, a zirconium-based

fire-block is used. A carbon crucible was used as reactive cell. Pt(40)-Rh(20) thermocouples and an optical pyroelectric meter were used for monitoring the temperatures of the furnace. Programmable temperature controllers using mechanical gears were used to control both of the sections. Two types of reactive CVD systems were used in the present experiments:

1) An open system with CH_4 transport gas; the source material consists of a mixture of SiO_2 and C powder, (referred to as experiment I.)

2) A closed system with CI_4 transport gas; the source material is a mixture of SiO_2 and C powder. (referred to as experiment II.)

Here, the open system means that the transport gas is diluted by H_2 which flows out contiguously from the reactor system, whereas the closed system means that an extra gas chamber is connected to the front of the source section and a gas condenser is attached to the end of the growth section. In this case, the flow rate of CI_4 is roughly controlled by the heater attached to the gas chamber.

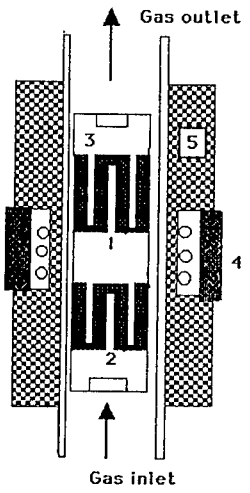


Fig. 1 Prototype electric furnace. 1: heater for the growth section, 2: heater for the source material, 3: carbon crucible, 4: extra tantalum heater, 5: ziluconium-based fire-block.

3. Results and Discussion

Firstly various interval settings for growth period and etching period under the specified source temperatures and the growth temperatures were carried out in order to search an optimal growth condition. Typical results are indicated in the table I.

CI_4 has been synthesized by Dr. T. Mizuno of Department of Engineering Chemistry at Hokkaido University, using the chemical reaction of CaI_2 with CCl_4. Principally, direct use of CCl_4 is possible, but this gas is strongly poisonous. The growth rate of SiC in experiment II was much larger than the one in experiment I. The reason for this difference is not clear at present, because we did not investigate the actual chemical reactions in the growth section in detail. This problem remains to be solved. In general, the etching or re-evaporation rate is very small when the temperatures of the growth region are lower than 1600°C; this feature is strongly in contrast with the crystal growth by TOM reported in the past. Much higher temperature setting was necessary in order to avoid the multiple nucleation in the growth section, as shown in Table 1.

The actual etching rate as a function of temperature is roughly determined by measuring the weight of the growth section before and after the etching process. Fig. 2. indicates the temperature dependence of the growth rate and the etching rate. Most of the grown crystals involved many grain boundaries and a mixture of β-SiC and α-SiC was observed. It is rather difficult to obtain a single

Table 1. Typical results of the experiment I and the experiment II.

No. RUN Total Process time (h)	Growth Conditions		Etching Conditions		Crystal Growth
Experiment I.	T_S / T_G	Interval (min.)	T_G /T_S	Interval (min.)	
I - 1 (80)	1400 / 1300	30	1400 /1300	14	No etching was observed.
I - 2 (90)	1600 / 1500	30	1750 /1500	10	Etching rate was slow. no selection of single nucleation observed.
I - 3 (90)	1600 /1500	initial stage: 20 steady state: 30	1850 /1500	initial stage:20 steady state: 30	A few single nucleations were observed on the surface of the growth section. Occasionally,a relatively large size crystal was obtained.
Experiment II					
II - 1 (40)	1400/1300	30	1400/1300	10	Etching rate is very small.
II - 2 (45)	1600/1500	20	1750/1500	10	Etching rate was still very small. A large number of small- size crystals were observed
II - 3 (45)	1600/1500	initial stage: 15 steady state: 20	1850/1500	initial stage: 15 steady sate: 20	A few single nucleatiobs were observed. Occasionally, relatively large-size crystals of single-phase were obtained.

flow rate of the gas: 300ml/min. Ts: source temperature. TG: growth temperature.

phase of a single SiC crystal. This is considered to be due to the fact that the present crystal deposition depends on spontaneous nucleation. Occasionally, it was possible to obtain crystals of uniform phase with a very small amount of defects. Fig. 3 shows a typical photograph of a relatively large-size single crystal of β-SiC grown in the present TOM. The crystals shown in Fig. 3 were mechanically cut into wafers with thickness of about 0.2 mm (⊥ to <111> axis).

X-ray diffraction patterns of these wafers indicated that the whole crystal consisted of uniform β-phase. The surfaces of these wafers were etched by KOH and the etched surfaces were observed by an optical microscope. Typical area of the cross section of these wafers was 5x5 mm^2. The micropipe density of these specimens was ≈0-20/cm^2, which indicated

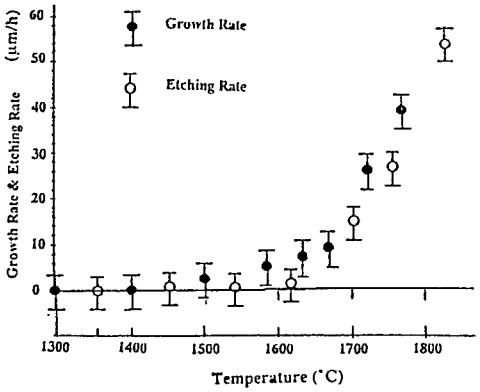


Fig.2 Growth rate and etching rate as a function of temperature.

that the grown crystal involved a very small amount of defects. The most important part of the present growth process was the initial stage of the nucleation. The quality of the grown crystals strongly depends on the re-evaporation process at the initial stage of the crystal growth.

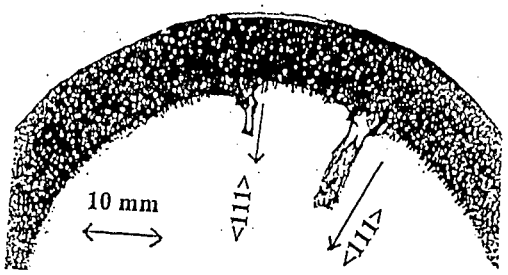


Fig 3 TOM growth of 3C-SiC .

Acknowledgements

The author greatly acknowledges Dr. T. Mizuno of the Department of Engineering Chemistry at Hokkaido University for synthesizing CI_4 and for his valuable suggestions. The author also would like to appreciate Mr. I. Matui, Mr. S. Hara of the Department of Electrical Engineering at Hokkaido University for their supports to the present experiments. This work was partially supported by Hokkaido Foundation for Promotion of Science and Industry Technology, contract number you-020.

References:

[1] H. Scholz, Philips Technical Review, 28 (1967), p.316, H. Scholz and Kluckow, in Crystal Growth, Ed. H. S. Peiser (Pergamon Oxford, 1967), p. 475, L. Van Den Berg, et al., J. Crystal Growth 42 (1977) p.166.

[2] M. M. Anikin et al, Silicon Carbide and Related Materials 1955, Inst. Phys. Conf. Ser. No 42, p.33, A. Okamoto, et al, Silicon Carbide and Related Material 1999, Mater. Sci. Forum 338-342, p. 440.

Materials Science Forum Vols. 353-356 (2001) pp. 85-88
© 2001 Trans Tech Publications, Switzerland

Aluminium-Silicon as a Melt for the Low Temperature Growth of SiC Crystals

D. Chaussende, C. Jacquier, G. Ferro, J.C. Viala, F. Cauwet and Y. Monteil

Laboratoire des Multimatériaux et Interfaces, Université Claude Bernard Lyon 1,
43 Boulevard du 11 Novembre 1918, FR-69622 Villeurbanne Cedex, France

Keywords: Aluminium Melt, Liquid Phase Epitaxy, Low Temperature, Spontaneous Growth

ABSTRACT

An experimental investigation was carried out on the spontaneous growth of β-SiC crystals in the Al-C-Si ternary system under atmospheric pressure. Isothermal experiments were performed at temperatures ranging from 730 to 1200 °C and with Al-Si melts containing 10 to 40 at% of silicon. The size and shape of the crystals spontaneously grown from these melts strongly depended on the temperature and Si content. Well faceted crystals up to 100 μm were obtained under optimal conditions. Results are discussed for further transposition toward epitaxy experiments.

INTRODUCTION

It is many decades since Liquid Phase Epitaxy (LPE) has been tentatively studied as an alternative for growing low cost SiC layers at a fast rate. Recently, it has proven to be the only technique which can "heal" the macro-defects of the commercially available hexagonal substrates [1]. However, LPE is difficult to operate because of the elevated temperatures required (higher than 1600°C) and the high reactivity and vapour pressure of silicon at these temperatures. Baumann has observed the precipitation of β-SiC crystals from a Al-Si-Zn solution at temperatures as low as 525°C [2]. The feasibility of SiC growth by LPE at low temperature has already been demonstrated in Al-Si based liquids to which Ga or Sn were added [3]. Growth rates of 0.1 to 1 μm/h were reported. However, such a procedure requires to master the quaternary systems Al-Si-Ga-C and Al-Si-Sn-C which are far to be well known. We report here the low temperature growth of SiC crystals in the simpler Al-Si-C ternary system for which detailed data on phase relations and phase equilibria are available [4, 5]. According to the Al-Si-C ternary phase diagram, two solid carbides can form at temperatures lower than 1400°C : SiC and Al_4C_3. This diagram also shows that silicon rich alloys are needed to avoid the formation of aluminium carbide. As a preliminary study, we carried out isothermal experiments to determine the best conditions under which SiC could grow from the Al-Si melts located within the liquidus surface of SiC in the Al-C-Si phase diagram.

EXPERIMENTAL SET UP

The Al-Si-C samples were prepared by cold-pressing pure Al, Si and C powders. Carbon was added in small quantity so that the initial Si content of the Al-Si alloy was not drastically changed by the formation of SiC. The temperature and the Si content were varied from 730 to 1200°C and from 10 to 40 at%, respectively. The experiment time was set to 48 hours to ensure a quasi-complete conversion of carbon into carbides. The samples were heated under a static argon pressure of 1 atm to limit aluminium loss by evaporation. To investigate the morphology, size and structure of the crystals produced, two types of material analysis were applied. On the one hand, samples were observed in cross section by optical microscopy and Micro-Raman spectroscopy. On the other hand, the Al-Si melt was removed by chemical dissolution and crystals thus recovered were examined by X-Ray Diffraction (XRD) and Scanning Electron Microscopy (SEM).

RESULTS

It has been found that SiC is the only carbide to form in a wide range of experimental conditions. However, one can distinguish two types of SiC crystals : random shaped aggregates (Fig.1a) and well faceted crystals (Fig.1b). By XRD, the cubic polytype has been identified as the only SiC phase forming whatever the type of crystals. By Raman spectroscopy however, only the second type of crystals exhibits the diffusion lines characteristic for β-SiC single crystals. We will mainly focus on that latter type of crystals, the morphology and size of which have been investigated as a function of temperature and Si content in the melt.

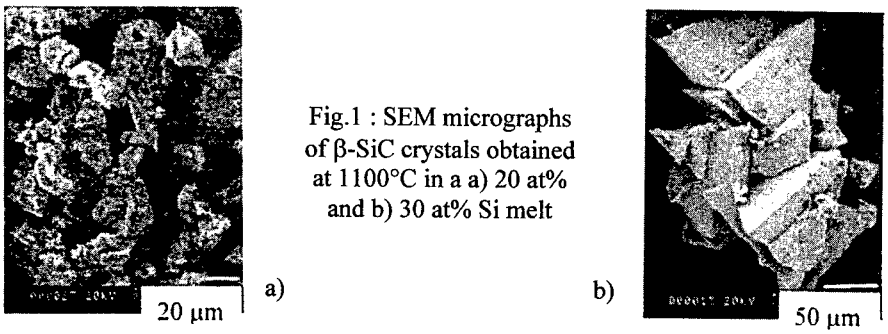


Fig.1 : SEM micrographs of β-SiC crystals obtained at 1100°C in a a) 20 at% and b) 30 at% Si melt

Fig.2 shows the variations with the Si content of the melt of the mean size of the SiC crystals spontaneously grown at three different reaction temperatures (730, 900 and 1100°C). It clearly appears that at each temperature, the mean size goes through a maximum at a well defined value of the Si content in the melt. It can also be seen that this maximum shifts toward higher Si contents with increasing temperature : accordingly, the biggest SiC crystals are obtained from melts with 18 at% at 730 °C, 25 at% at 900 °C and 30 at% at 1100°C.

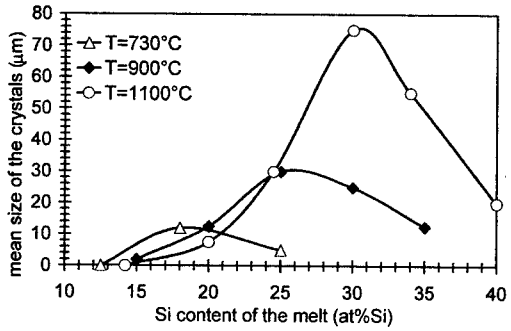


Fig.2 : Mean size of the β-SiC crystals spontaneously grown in the Al-Si melt versus Si content for different reaction temperatures.

As a general trend, it has moreover been observed that SiC crystals grown from melts with a Si content lower than the value corresponding to the maximum crystal size formed random shaped aggregates of the first type whereas crystals grown from melts with Si contents equal to or higher than that value belonged to the second faceted type. At 1100°C for example, SiC crystals grown from a melt with a Si content of 20 at% formed the aggregates of micro-crystallites less than 10 µm in diameter shown in fig.1a; no well shaped crystal was obtained under these conditions. On the other hand, the well faceted crystals up to 100 µm shown in fig.1b were obtained at the same temperature from a melt with a Si content of 30 at%. At Si contents of the melt higher than 30 at%, the SiC crystals grown at 1100 °C had the same morphology as those presented in fig.1b, i.e. faceted, but their mean size decreased rapidly to 55 and 20 µm at 35 and 40 at%Si, respectively. It is worth noting that all these faceted crystals were characterised by triangular faces, as in fig.1b. It is then logical to consider the (111) crystallographic orientation as a preferential growth direction.

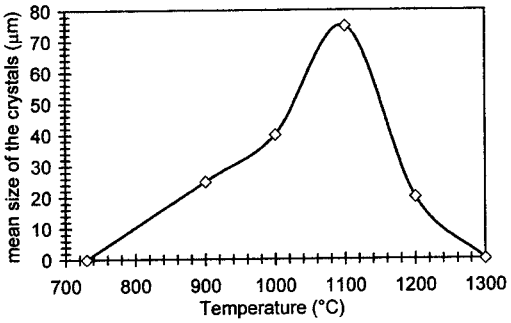


Fig.3 : Mean size of the β-SiC crystals spontaneously grown in a 30 at%Si Al-Si melt versus temperature. The point at 1300°C was taken from Kocherginsky et al. [5].

The evolution with the temperature of the mean size of the β-SiC crystals grown from a 30 at%Si melt are reported in fig.3. This figure clearly shows that there is a particular temperature for which the size of crystals is maximum. It must be added that well faceted crystals developed only at temperatures lower than 1100 °C. Above that temperature, the number and size of the faceted crystals decreased rapidly and at 1300 °C, faceted crystals were no more formed, as reported in the literature [6].

DISCUSSION

From the position of the maximum of the three curves drawn in fig.2, it is possible to define the best conditions of temperature and melt composition under which the largest faceted SiC crystals can be obtained. In the temperature-composition graph presented in fig.4, these optimum conditions are represented by a grey line. In the same graph, we have also drawn a dark curve representing the boundary between the liquidus surfaces of the two carbides Al_4C_3 and SiC in the Al-C-Si phase diagram under a constant pressure of 1 atm [4]. The meaning of the dark curve is simple : under it, the melt is in equilibrium with Al_4C_3 and above, the liquid is conjugated with SiC.

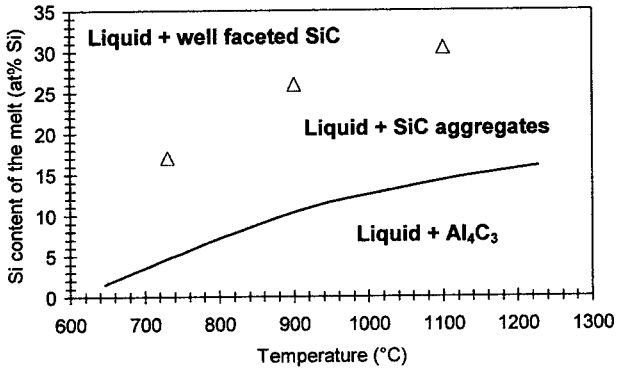


Fig.4: Deviation from the Liquid-Al_4C_3-SiC equilibrium required for the spontaneous growth of β-SiC crystals (Δ). The low Si content curve corresponds to the monovariant line along which the liquid is in equilibrium with Al_4C_3 and SiC, after Viala et al. [4].

From a thermodynamic viewpoint, SiC crystals can only be grown from a liquid having a composition located within the liquidus surface of this compound, i.e. above the dark curve in fig.4. This necessary condition has been verified in the present experiments, even if "out-of-equilibrium" Al_4C_3 crystals were sometimes observed to form in place of SiC at low temperature. But to obtain well shaped SiC crystals with large facets, other requirements have to be met. For example at 1100°C, the minimum Si content in the melt to form SiC is of 14 at% (dark curve) whereas the best shaped crystals with the largest facets are obtained at a Si content in the melt of 30 at% (grey line); above 30 at%Si, SiC crystals remain faceted but are smaller in size. Considering the relative positions of the dark curve and the grey line drawn in fig.4, these requirements could be expressed as follows : to grow well shaped SiC crystals with large facets, there must exist a deviation to the

monovariant equilibrium Al_4C_3-SiC-L in the temperature and Si content of the melt, but that deviation must be neither too small nor too large :

1) too small, i.e. for temperatures and melt compositions located between the dark curve and the grey line, only micro-crystalline aggregates of SiC will be obtained;
2) too large, SiC crystals will be faceted but of small size.

Another requirement which does not appear in fig.4 but which is obvious for such a refractory carbide as SiC is a sufficiently high growth temperature. To sum up, the thick grey line drawn in fig.4 can be seen as the "operating window" for growing β-SiC crystals of good quality from a Al-Si base melt.

To support this model, it is interesting to correlate figures 3 and 4. Indeed, as results reported in fig.3 were obtained at a fixed Si content of 30 at%, they correspond to a horizontal iso-content line at 30 at%Si in fig.4. One can see in that figure that below 1100°C, the deviation from equilibrium is larger than the minimum required, so well faceted crystals are observed. Above this temperature, the deviation from equilibrium is too low to ensure the growth of well shaped crystals. In order to validate these trends at higher temperatures, a complementary experiment was performed at 1200°C for a 40 at%Si melt. It will be recalled that for 30 at%Si, only a few small SiC crystals were obtained at that temperature (fig.3) and micro-crystalline aggregates widely prevailed. In the new experiment at 40 at%Si, all the crystals were well shaped and had an average size close to 40 μm. As a matter of fact, these two points at 30 and 40 at%Si are located on both sides of the grey line in fig.4. So, an extrapolation of our model towards higher temperatures seems to be possible and could explain the observations of Kocherginsky et al. [6]. These authors reported that by reacting carbon with a Al-Si 30 at% alloy at 1300°C, a mass of small crystals formed by the movement of a reaction front from the surface to the centre of the carbon particles. In other words, there was no well faceted crystals but only aggregates of micro-crystals. This result is in agreement with our model which shows that the deviation from equilibrium was not sufficient under that conditions to form faceted crystals. Finally, the optimal deviation from equilibrium pointed out in fig.4 (grey line) would correspond to the minimum driving force required to form SiC crystals via a dissolution and growth mechanism. Only such a mechanism is suitable for further epitaxy experiments as it involves carbon transport through the melt leading to the well facetted crystals previously discussed.

CONCLUSION

We have carried out an experimental investigation on the isothermal growth of β-SiC crystals in the Al-C-Si ternary system under atmospheric pressure. We have proposed a model to explain the growth conditions of well faceted crystals taking into account the temperature and the Si content of the melt. Optimal conditions are realised for a temperature of about 1100°C and a Si content in the melt of 30 at%. Such conditions under which crystals up to 100 μm have been observed to grow will be particularly interesting to use at the deposition zone in a LPE apparatus operating under a thermal gradient.

REFERENCES

[1] R. Yakimova, M. Syväjärvi, E. Janzén, Mater. Sci. Forum 264-268 (1998), p.159.
[2] H.M.Baumann, J. Electrochem. Soc. 99 (1952), p.109.
[3] S. Rendakova, V. Ivantsov, V. Dmitriev, Mater. Sci. Forum 264-268 (1998), p.163.
[4] J.C. Viala, P. Fortier and J. Bouix, J. Mater. Sci. 25 (1990), p.1842.
[5] LL. Oden and R.A. McCune, Metal. Trans. 18A (1987), p.2005.
[6] D.M. Kocherginsky, R.G. Reddy, In Situ React. Synth. Compos., Ceram., Intermet., Proc. Symp. (1995), p.159.

Chapter 2:

SiC Epitaxy

Materials Science Forum Vols. 353-356 (2001) pp. 91-94
© 2001 Trans Tech Publications, Switzerland

Epitaxial Growth of 4H-SiC in a Vertical Hot-Wall CVD Reactor: Comparison between Up- and Down-Flow Orientations

J. Zhang[1], A. Ellison[2], Ö. Danielsson[1], A. Henry[1] and E. Janzén[1]

[1] Department of Physics and Measurement Technology, Linköping University, SE-581 83 Linköping, Sweden

[2] Okmetic AB, Hans Meijers väg 2, SE-583 30 Linköping, Sweden

Keywords: CVD, Flow Orientation, Growth Process, Hot-Wall Reactor

Abstract The effect of reactor orientation on the CVD growth of 4H SiC is investigated. Compared with the up-flow orientation (the chimney reactor), the down-flow orientation (the inverted chimney) shows similar growth rate dependencies on C/Si ratio and pressure. The activation energy of the growth rate in the inverted chimney is lower than that in the chimney. The inverted chimney also produces epilayers with high growth rates (10 – 30 μm/h) and low residual doping (low 10^{16} down to mid 10^{13} cm^{-3}). The epilayer morphology is comparable with that of the chimney samples. A qualitative analysis is performed on the heat transfer mechanisms in these two reactor orientations in terms of dimensionless flow numbers.

1. Introduction

Epitaxial growth of 4H SiC with high growth rates and low residual doping has been reported in a vertical, hot-wall CVD reactor with the up-flow orientation (the chimney reactor) [1]. In the present study, growth experiments were performed in the same reactor operated in the down-flow orientation (inverted chimney) with the purpose to obtain a better understanding of the hot-wall process. The similar geometry of the inverted chimney with that of a hot-wall barrel reactor and the simple substrate mounting provide practical motivation for this investigation [2]. The comparison of the two vertical orientations will also, to a certain extent, give insight into the growth behaviour in a hot-wall horizontal reactor.

2. Experimental

The growth experiments were performed in the inverted chimney reactor with the precursor gases SiH_4 and C_2H_4 diluted in Pd purified H_2 carrier gas flowing from the top inlet downwards through the hot-wall susceptor. The growth parameters were chosen to be comparable with those used in the chimney process. The process temperature ranged from 1750 to 1900 °C and the total pressure varied between 100 and 350 mbar. Highly N-doped epilayers with stair-case structure produced by varying only one growth parameter during the run were grown for the SIMS measurements to determine both the growth rate and the N-doping. In addition, low N-doped epilayers with thickness of 20 – 40 μm were also grown for the systematic study. The thickness of the low doped epilayers was measured with a Fourier Transform Infrared spectrometer.

3. Aspects from the fluid dynamics: comparison of dimensionless flow numbers

The heat transfer mechanism in the gas can be classified as forced convection (no buoyancy effect), free convection (convection caused only by buoyancy) and mixed convection [3]. In purely forced convection, the velocity and temperature distributions are independent on the flow orientation, whereas in free or mixed convection they are distorted by the buoyancy force and the flow orientation relative to the gravity force plays an important role. In the vertical reactor orientation, the relative importance of free and forced convection can be represented by the ratio of Grashof (Gr) to Reynolds (Re) numbers [4]. A high Gr/Re ratio indicates a strong effect of free convection, in which the up-flow is accelerated along the hot surface and decelerated in the centre of the bulk gas, whereas the down-flow is decelerated along the hot surface and accelerated in the centre. These velocity profiles give rise to a more extended cold finger in the middle of the gas flow in the down-flow than in the up-flow orientation.

In a hot-wall reactor, the radial temperature gradients in the hot growth zone are very small. The buoyancy force mainly acts in the entrance region, where the cold bulk gas flows into the heated inlet. The critical

gas phase processes during the CVD growth are the precursor cracking and the gas phase nucleation [1, 5], which are, in turn, influenced by the upstream velocity profile and temperature distribution. As a guide to interpret the experimental results, it is of interest to study the flow characteristics in the entrance region in terms of the dimensionless numbers: Gr and Re. In Table 1, the values of Gr/Re for both the up- and the down-flow orientations are calculated for a cylindrical inlet geometry under several process conditions. The notations are used as follows :

$$\mathrm{Re} = u * D * \rho / \mu$$

$$Gr = g\rho^2 D^3 \left(\frac{T_{wall} - T_0}{T_m} \right) / \mu^2$$

u (m/s): the linear gas velocity, scales as T/P;

D (m): the diameter. D = 0.04 m in this case;

g (m/s^2): the acceleration of gravity;

μ (kg/s · m): the absolute viscosity, temperature dependent;

T_0 (K): the temperature of the cold gas at the entrance. T_0 = 323 K in this case;

T_{wall} (K): the temperature of the hot surface;

T_m (K): the average temperature = $(T_{wall} + T_0)/2$;

ρ (kg/m^3): the density, both pressure and temperature dependent.

Case description	T_{wall} *(K)*	*Pressure (mbar)*	*Flow rate (slm)*	*u (m/s)*	*Gr/Re*
Base case	773	100	4	1	4.3
H_2 flow decreased	773	100	2	0.5	8.6
Pressure increased	773	300	4	0.33	39
Pressure increased further	773	1000	4	0.1	1288
Temperature increased	1623	100	4	1.7	1.6

Table 1: The values of Gr/Re calculated for several process conditions. The temperature dependent ρ and μ values are taken from [6]. The first set of parameters is considered as the base case, upon which one of the above parameters is changed in the cases thereafter.

If the criteria in [7] is followed, i.e. Gr/Re < 1 is the condition for forced convection, all the above cases are shown to be in the mixed or purely free convection regime. However, the free convection effect becomes stronger with decreased flow rate or increased pressure. Under these conditions, the gas velocity in the down-flow is lower along the hot surface, but becomes higher in the centre of the bulk gas. This is expected to lead to more favourable precursor cracking and re-evaporation of growth species from the nucleated clusters in the gas along the hot surface, but also a cold finger in the centre penetrating a longer distance downstream in the down-flow than in the up-flow orientation.

4. Experimental results

As shown in Fig. 1, in both the up- and the down-flow configurations, the growth rate follows the same dependence on C/Si ratio. Below the C/Si ratio of 0.4, the growth is limited by the feed-rate of hydrocarbon and above 0.4, the growth becomes limited by the supply of Si-vapour. The effect of the hydrocarbon flow on the growth rate is therefore shown to be the same despite the different reactor orientations.

The growth rate dependence on the process temperature is expected to give more insight into the dominating growth mechanisms. As shown in Fig. 2, the growth rate in the inverted chimney increases with increasing temperature displaying an activation energy of 27 kcal/mol, whereas the activation energy in the chimney is 44 kcal/mol, where the growth rate starts to drop with still higher temperatures. The lower activation energy in the inverted chimney may reflect the more favourable condition for re-evaporation of the Si from the nucleated clusters in the gas phase. The growth rate falling-off in the

chimney in the higher temperature range has been attributed to the increased hydrogen etching effect at these temperatures [1]. This etching effect is not as pronounced in the inverted chimney even in the high temperature range. This may be related to the more effective preservation of growth species due to gas phase nucleation in the cold finger in the inverted chimney. The subsequent decomposition of the nucleated clusters in the growth zone leads to sufficient supply of the growth species and thereby reduces the etching effect.

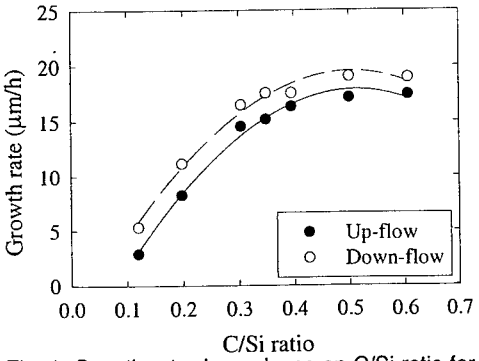


Fig. 1, Growth rate dependence on C/Si ratio for both orientations. T = 1725 °C, P = 210 mbar, H_2 flow: 3.2 *l*/min. The hydrocarbon flow rate was varied during the run.

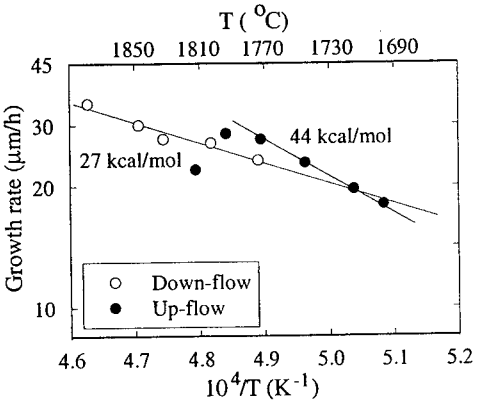


Fig. 2, Growth rate dependence on temperature for both orientations. P = 180 mbar, H_2 flow: 3.2 *l*/min, C/Si = 0.4.

As the Gr number scales as the square of the pressure, the effect of the pressure on the growth rate is expected to differ for the two orientations in the mixed or purely free convection regime. However, Fig. 3 shows a surprisingly similar growth rate dependence on pressure in both of the orientations within the investigated pressure range. The growth rate uniformity is measured as the ratio of standard deviation to mean value in percentage from the thickness data along the height of the epilayer. Fig. 4 shows the growth rate uniformity dependence on pressure in both of the orientations. In the chimney, the growth rate depletion (positive uniformity) shifts to an increase in growth rate along the flow direction (negative uniformity) when the pressure goes below 180 mbar, whereas in the inverted chimney, good uniformity with only minor depletion is obtained at a pressure as low as 120 mbar.

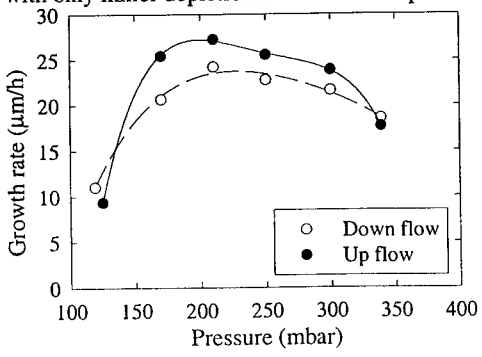


Fig. 3, Growth rate dependence on pressure for both up- and down-flow orientations. T = 1770 °C, H_2 flow: 3.2 *l*/min, C/Si = 0.4.

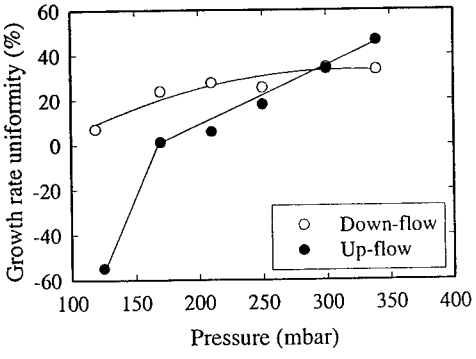


Fig. 4, Growth rate uniformity dependence on pressure. T = 1770 °C, H_2 flow: 3.2 *l*/min, C/Si = 0.4.

The carrier gas flow is another important parameter influencing the growth rate and its uniformity. In the inverted chimney, the growth rate increases with carrier gas flow up to a certain value, and then starts to decrease with further increased carrier flow (Fig. 5). Within the lower flow rate region, the increased hydrogen flow facilitates the precursor cracking and also dilutes the precursor concentration in the gas phase, thereby suppressing the gas phase nucleation, leading to higher growth rates and reduced depletion.

With further increased hydrogen flow rate, hydrogen etching becomes more significant, resulting in decreased net growth rate [1].

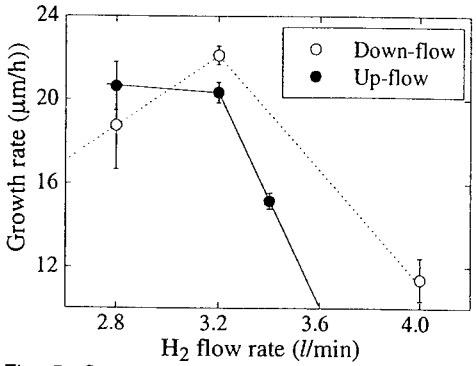


Fig. 5, Growth rate dependence on hydrogen carrier flow for both up- and down-flow orientations. T = 1700 °C, P = 210 mbar, C/Si: 0.4.

5. Summary

In both the chimney and the inverted chimney, the growth rate shows similar dependence on C/Si ratio as well as pressure within the low operating pressure range (100 – 350 mbar). The activation energy is lower in the inverted chimney, where higher growth rates can be achieved at higher temperatures with much reduced hydrogen etching effect. This difference is presumably related to the more persistent cold finger in the inverted chimney, resulting in efficient preservation of growth species in the nucleated clusters until further downstream. More Si-vapour is therefore available in the high temperature growth zone through the subsequent decomposition of the nucleated clusters in the gas phase.

Acknowledgement: The authors would like to thank the SSF Programme in Sweden: SiCEP and ABB Corporate Research for their support in this study.

References

[1] A. Ellison, Doctoral thesis, *Silicon carbide growth by high temperature CVD technique.* Dissertation No. 599, Linköping University, (1999).
[2] E. Fujii, H. Nakamura and Y. Koga, *J. Electrochem. Soc.* **119** (1972), p. 1106.
[3] E. M. Sparrow and J. L. Gregg, *The Physics of Fluids* **2**, (1959), p. 319.
[4] W. L. Holstein and J. L. Fitzjohn, *J. Cryst. Growth* **94** (1989), p. 145.
[5] A. N. Vorob´ev, S. Yu. Karpov, A. I. Zhmakin, A. A. Lovtsus, Yu. N. Makarov and A. Krishnan, *J. Cryst. Growth* **211** (2000), p. 343.
[6] P. M. Lofgren, W. Ji, C. Hallin and C.-Y. Gu, *J. Electrochem. Soc.* **147** (2000), p. 164.
[7] L. S. Yao, *Int. J. Heat Mass Transfer* **26 (1)** (1983), p. 65.

Materials Science Forum Vols. 353-356 (2001) pp. 95-98
© 2001 Trans Tech Publications, Switzerland

Influence of the Growth Conditions on the Layer Parameters of 4H-SiC Epilayers Grown in a Hot-Wall Reactor

G. Wagner and K. Irmscher

Institut für Kristallzüchtung, Max-Born-Str. 2, DE-12489 Berlin, Germany

Keywords: C-V Characteristics, CVD, Hot-Wall Reactor, SIMS, Thickness Mapping

Abstract:
This paper focuses on the growth of epitaxial SiC layers using the hot-wall Chemical Vapour Deposition (CVD) technique. The relation between growth parameters as total flow, system pressure and C/Si ratio and the characteristics of unintentionally doped epitaxial layers such as thickness uniformity and background doping concentration have been investigated. Epitaxial layers with growth rates up to 11 μm/h with a thickness uniformity of about ±4 % were grown on misoriented (0001) Si faces. The electrical conductivity of the layers changed from n- to p-type at a net doping level below 2×10^{14} cm^{-3}, in accordance with the residual impurity concentration of the B and Al acceptors.

1. Introduction

The success of silicon carbide (SiC) for high temperature and high power electronic applications is dependent upon the ability to reproducibly attain high quality SiC epitaxial layers. The growth of high power device material requires thick layers of low, homogenous doping and good morphology. It is furthermore desirable that the epilayers can be grown at high rates. Presently, CVD is the technique which best meets these demands. It was substantially improved by the introduction of the hot-wall reactor concept by Kordina et al. [1].
In this study we investigate the technologies of SiC layer deposition using a commercial hot-wall system. In particular we concentrate our work on the dependence between growth parameters as total flow, system pressure and C/Si ratio and the growth rate, the thickness uniformity and the background doping concentration of the layers.

2. Experimental

The horizontal hot-wall CVD-system used for the investigations was built by EPIGRESS AB (Sweden). The susceptor and the substrate holder were made of high purity graphite with SiC-coating. Silane and propane are used as process gases. 4H-SiC (0001) substrates off-oriented 8° towards $[11\bar{2}0]$ with diameters of 50 mm (Cree Res. Inc.) and 35 mm (SiCrystal Erlangen) were used. Before layer deposition the substrates were etched in hydrogen atmosphere at 1500 °C adding a small quantity of propane to reduce the surface roughness and to remove a residual surface damage layer. Typical ranges of the most important parameters for the CVD-experiments are given in Table 1.

Table 1: Typical growth parameters

silane flow, 2% diluted in H_2	propane flow, 5% diluted in H_2	C/Si ratio	temperature	system pressure	hydrogen main flow
600 sccm	120 to 160 sccm	1.5 to 2	1550 to 1600 °C	150 to 250 mbar	20 to 50 slm

The thickness of the epitaxial layers was determined by means of a Fourier transform infrared spectrometer and a software package (both obtained from BRUKER) evaluating the interference fringes which occurs in the reflectance spectrum [2]. The chemical concentration of residual impurities and their electrical activity were obtained from secondary ion mass spectroscopy (SIMS) and capacitance-voltage (*C-V*) measurements, respectively.

3. Results

3.1 Epitaxial Growth

The growth rate was investigated in dependence on the silane partial pressure (p_{silane}), the growth temperature (T_g) and the system pressure (p_{sys}) for a fixed position of the substrates in the susceptor. It was mainly influenced by changing the silane partial pressure as shown in Fig. 1. The growth rate increases linearly with SiH_4 partial pressure in the investigated range until 0.1 mbar.

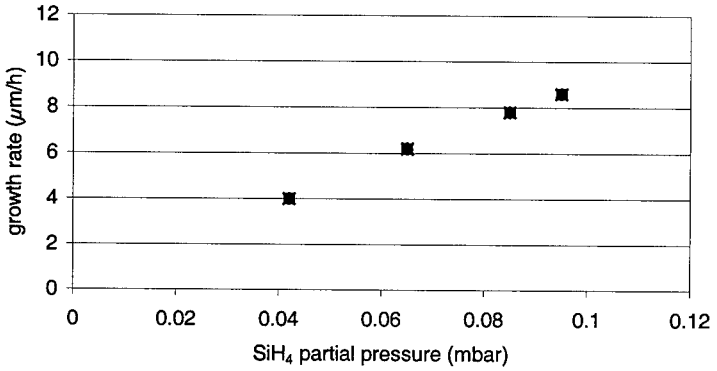


Fig. 1: Growth rate dependence on the silane partial pressure (T_g = 1600 °C, p_{sys} = 250 mbar, C/Si = 1.5).

Only minor effects of the system pressure and the growth temperature on the growth rate were observed (see Fig. 2). A reduction of the system pressure from 250 mbar to 150 mbar increases the growth rate by about 4 % whereas its change between both growth temperatures (1550 °C and 1600 °C) can be neglected.

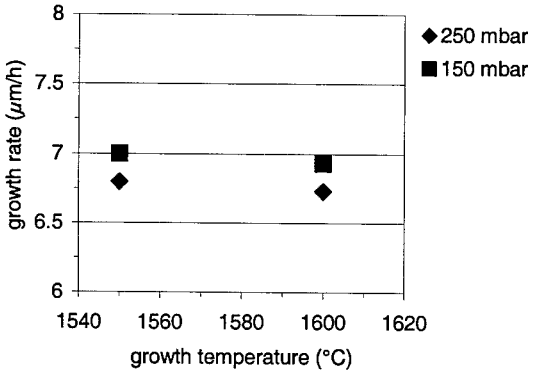


Fig. 2: Growth rate dependence on the growth temperature and system pressure.

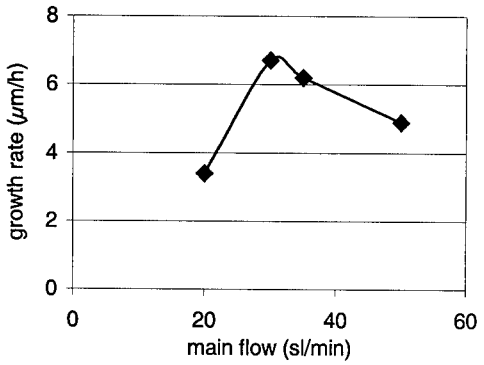


Fig. 3: Growth rate variation with the carrier gas flow (T_g = 1550 °C, p_{sys} = 250 mbar, p_{silane} = 0.06 mbar).

The growth rate as well as the layer thickness distribution were strongly influenced by the main flow of the carrier gas. The corresponding variations are shown in Fig. 3 and 4. During these growth runs the parameters T_g, p_{sys} and p_{silane} were kept constant.

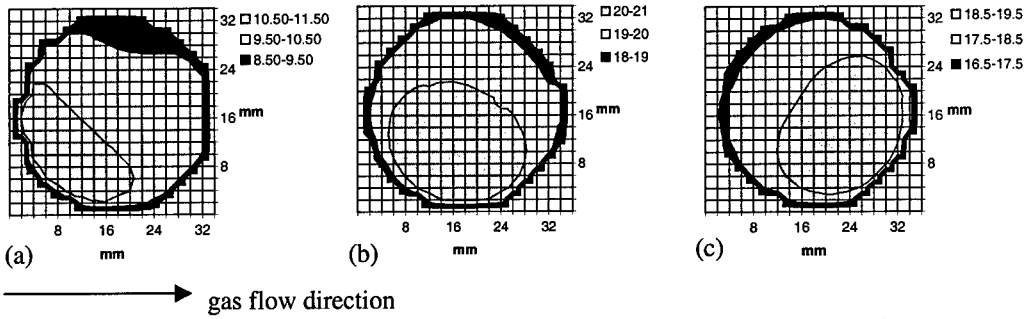


Fig.4: Layer thickness (given in μm) distribution in dependence on the carrier gas flow, (a) 20 sl/min, (b) 30 sl/min, (c) 35 sl/min.

The dependence on the carrier gas flow shows that the position of the maximum layer thickness is shifted from left to right in flow direction (Fig. 4 a-c). The reason for this behaviour is that at high H_2 flow rates the majority of the dissociated gas molecules are deposited on the reaction cell behind the susceptor. On the other hand at low H_2 flow rate the deposition takes place in the front of the susceptor. By optimisation of the carrier gas flow it is possible to shift the area of highest deposition efficiency to the position of the substrate. With optimal values for carrier gas flow and system pressure we got an maximum growth rate of 11 μmh^{-1} at a SiH_4 partial pressure of 0.095 mbar and a thickness uniformity of about ±4 % .

3.2 Residual doping

The main impurities of the epitaxial layers are nitrogen, aluminium and boron. Since the first one is a shallow donor and the other two are acceptors their balance determines the type and height of the residual conductivity. Sources of the unintentional N doping may be the susceptor, the thermal insulation and the reaction cell which all can absorb N during sample loading.

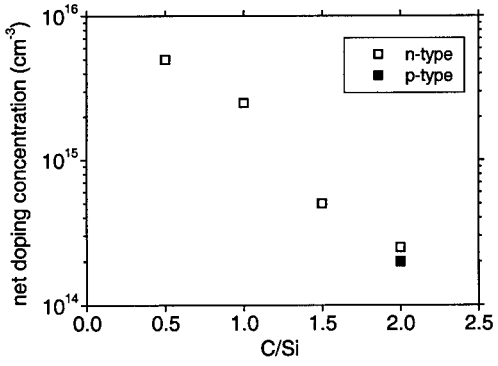


Fig. 5: Dependence of the net doping concentration on C/Si ratio for unintentionally doped 4H-SiC epilayers (Si face).

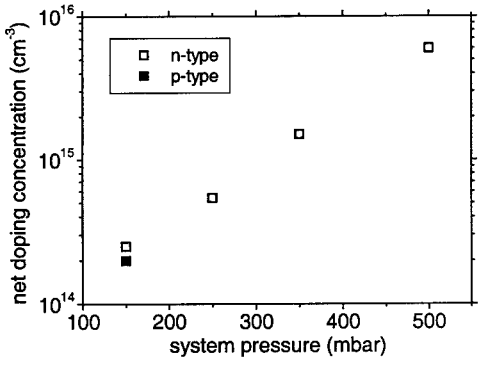


Fig. 6: Dependence of the net doping concentration on system pressure for unintentionally doped 4H-SiC epilayers (Si face).

In accordance with the site competition mechanism the N incorporation can be controlled by the C/Si ratio [3]. This ratio was varied from 0.5 to 2 by keeping all growth parameters constant except the propane flow. The expected suppression of the N incorporation with increasing C/Si ratio was detected by the decreasing average net donor concentration determined by *C-V* measurements as shown in Fig. 5. For a C/Si ratio of 2 the N concentration is already lowered down to that of unintentional acceptor impurities and we have frequently observed *C-V* data indicating nearly completely compensated epilayers or their conversion to p-type conduction. A similar behaviour was observed for the dependence of the net doping concentration on the system pressure presented in Fig. 6. It shows that the N incorporation is also reduced by a decreasing system pressure.

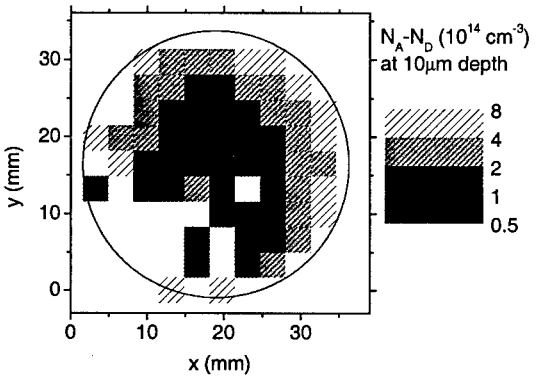


Fig. 7: Mapping of the net doping concentration at a depth of 10 μm of an epilayer which is converted to p-type at a C/Si ratio of 2 and a system pressure of 150 mbar.

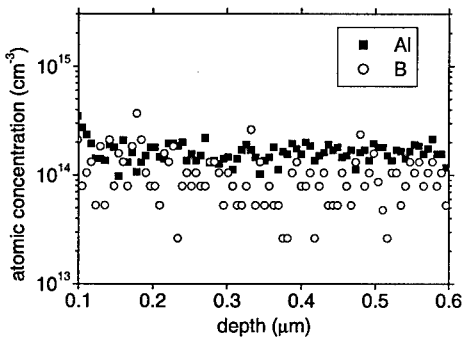


Fig. 8: SIMS profiles of Al and B in the centre of an unintentionally doped 4H-SiC epilayer (same layer as in Fig. 7).

In Fig. 7 a *C-V* map of the net doping concentration of an epilayer already converted to p-type is shown. In the central area the net acceptor concentration amounts to 1 to 2×10^{14} cm^{-3} whereas it is higher at the rim. SIMS measurements near the centre of the epilayers determined Al and B also in the concentration range of 1 to 2×10^{14} cm^{-3} which is well above the detection limit of 2×10^{13} cm^{-3} and 6×10^{13} cm^{-3}, respectively, supporting our interpretation of the *C-V* measurements (see Fig. 8). A source of these impurities can be their leakage out of the graphite of the susceptor which is normally coated by SiC. However, after several growth runs, this coating is partly etched away making possible the evaporation of B and Al at high temperatures.

Acknowledgement
This work was supported by the German Ministry of Education and Research under grant number 01BM070.

References

[1] O. Kordina, C. Hallin, A. Henry, J.P. Bergman, I. Ivanov, A. Ellison, N.T. Son and E. Janzén, phys. stat. sol. (b) 202 (1997), p. 321.
[2] M.F. MacMillan, P.O. Narfgren, A. Henry and E. Janzén, Mater. Sci. Forum 264-268 (1998), p. 645.
[3] D.J. Larkin, phys. stat. sol. (b) 202 (1997), p. 305.

Materials Science Forum Vols. 353-356 (2001) pp. 99-102
© 2001 Trans Tech Publications, Switzerland

Enlarging the Usable Growth Area in a Hot-Wall Silicon Carbide CVD Reactor by Using Simulation

Ö. Danielsson, U. Forsberg, A. Henry and E. Janzén

Department of Physics and Measurement Technology,
Linköping University, SE-581 83 Linköping, Sweden

Keywords: CVD, Epitaxial Growth, Simulation, Temperature Distribution

Abstract

The chemical vapor deposition (CVD) growth of large area silicon carbide epitaxial layers with homogeneous properties requires a large area with homogeneous temperature in the CVD reactor. In the present work we show that by changing the design of the CVD reactor, but keeping the overall dimension the same, this area can be enlarged by at least a factor of three. By using a simulation tool new designs can be tried out and optimized in the computer before testing them in practice. The simulation is set up as a 2D axisymmetric problem and validation is made in a 2D horizontal hot-wall CVD reactor. Very good agreements between simulated and measured results are obtained. The zone with a temperature variation of less than 5 degrees at an operating temperature of 1650°C increased to 64% of the whole susceptor length. In addition, the power input needed to reach the operating temperature decreased by 15%.

1. Introduction

The CVD technique is widely used to grow epitaxial layers of silicon carbide (SiC). The demands for high quality layers with good morphology and uniform doping and thickness require a good knowledge of the CVD process. For the growth of epitaxial layers in a CVD reactor, it is important to have as large area as possible with homogeneous temperature distribution. This improves not only the uniformity of the layers, but also makes it possible to grow on several wafers at the same time. So far the CVD technique for silicon carbide purposes has more or less been developed on a trial-and-error basis and the progress has been expensive and time consuming. Recently it has become possible to use simulation tools to calculate various physical phenomena. These possibilities can be used to gain more understanding of the SiC CVD process. The reactor design can be developed "virtually" before it is manufactured. Improvements of SiC CVD reactors can thus be made faster and less expensive.

The main subject of the present investigation is the understanding and improvement of the temperature distribution in a hot-wall CVD reactor. An improved reactor design, which gives a larger area of homogeneous temperature at less power input, is suggested and tested.

2. Experimental

The reactor used in the experiments is a horizontal hot-wall CVD reactor as previously described by Kordina et al. [1] – an inductively heated hollow graphite susceptor surrounded by insulation, inside an air cooled quartz tube. A special "2D" graphite susceptor (Fig. 1) is used to make it possible to compare simulations with measurements. The susceptor is "2D" because it is axisymmetric, i.e. it consists of a cylindrical graphite tube where the thickness of the wall is constant. Thus, one can make a cut through the reactor and set up the simulation as a 2D axisymmetric problem (Fig. 1). The temperature inside the reactor is measured by a pyrometer, which is focussed in a drilled hole with a depth of 40% of the total susceptor length (approximately black body radiating) from the

back of the susceptor. The influence of the hole (0.6% mass reduction; changed heat generation) is not accounted for in the simulations. The temperature measurements were calibrated by melting silicon pieces.

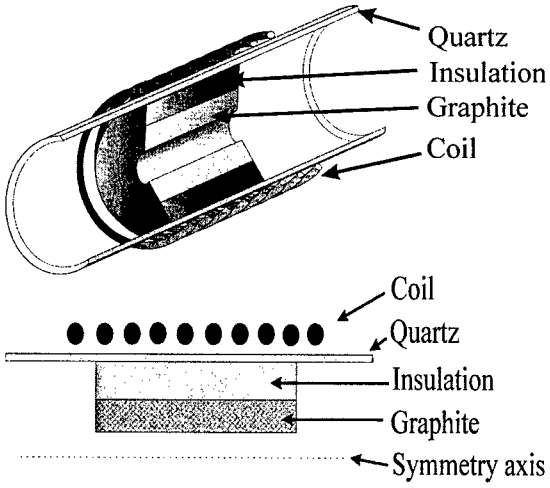


Fig. 1 Experimental "2D" reactor and a cut through image – an image of the simulation domain.

3. Modeling

Induction heating is due to eddy currents induced in electrically conductive materials by a time varying magnetic field. When modeling such a system it is convenient to divide the problem into two parts – induction and heat transfer. The induction part solves the magnetic field and calculates a heat source distribution in the materials. The heat transfer part calculates a temperature distribution from the heat sources. As the electrical conductivity is a temperature dependent parameter the solutions have to be iterated a few times to reach the desired accuracy. The commercially available simulation tool CFD-ACE+ [2] was used in the present investigations. This software package allows the use of specially written subroutines implemented by the user [3], a feature which was used for dividing the simulation problem into the two parts.

The model setup uses the Navier-Stokes equations for flow and heat transfer and Maxwell's equations, using the magnetic vector potential, for solving the magnetic fields produced by the coil. A radiation model based on the discrete ordinate method (S_4 approximation) [4] which is included in the software package is also used. Although the gas flow is not the main scope of this investigation, the gas has a cooling effect and must be included to give a good accuracy of the temperature profile. The gas flow is simulated together with the heat transfer.

The simulations were set up as 2D axisymmetric problems. Although the real growth reactor is a true 3D problem, this approximation is used to obtain some guidelines. This investigation focuses mainly on induction heating and heat transfer in solid parts, which are independent of gravity. The gas flow velocity is chosen so that the velocity at the entrance of the susceptor is close to that of the real growth system. As boundary conditions a zero magnetic field is imposed far from the reactor together with a constant temperature. On the symmetry axis a zero magnetic vector potential is imposed because of the axisymmetric approach. The thermal conductivity of graphite is taken from [5]. The temperature dependent electrical conductivity of graphite and the thermal conductivity of the insulation are estimated from data provided by the suppliers.

4. Results and discussion

Silicon melts at 1410°C [6] and the normal growth temperature for SiC CVD is around 1600°C. As the power in the coil increases, the temperature in the susceptor also increases, but not equally over the whole length of the susceptor. The increase in temperature is larger in the middle than at both ends. The temperature measurements were therefore carried out in the following way. First silicon pieces were distributed along the susceptor. The pyrometer was focussed at the hottest spot in the drilled hole in the susceptor, and the power input to the coil was slowly increased. The temperature readings when the individual Si pieces melted were noted. When all pieces had melted, the temperature was adjusted back to the same value as for the first melted silicon piece by adjusting the power input. Then the pyrometer was re-focussed to read 1410°C, i.e. the melting point for silicon. Thereby the temperature reading would show the temperature of the point where the specific silicon

piece was placed. The power input was then increased to the same value as for the usual growth conditions and the temperature reading of the pyrometer was noted. This temperature would thus indicate the temperature in the susceptor, at normal growth conditions, at the point where the corresponding silicon piece was placed. The temperature was measured at ten different points, resulting in a temperature distribution plot along the susceptor.

Original design

The original reactor design consists of a graphite tube, wrapped in an insulating foam of porous graphite, inside an air cooled quartz tube. A copper coil with equally spaced turns of equal diameter is surrounding the susceptor outside the quartz tube (Fig. 1).

Working conditions similar to the ones used for growth were used, i.e. atmospheric pressure, hydrogen carrier gas flow and a temperature at the deposition zone of 1600 – 1650°C. The temperature profile in the reactor was first simulated and then measured. The result showed a parabolic shaped distribution, with the highest temperature approximately in the middle of the susceptor. The simulated temperature profile agrees very well with the measured one.

New design

The goal when changing the reactor design was to optimize it towards a large area with a homogeneous temperature. The first step was to change the heat source distribution inside the graphite by changing the coil design and thereby changing the magnetic field. This was done in several steps optimizing the temperature distribution on the susceptor wall. The best new coil design was selected for the experiments. Because of the straight coil shape in the original design, the power loss is rather homogeneous (Fig. 2a), resulting in a temperature highest in the middle and dropping fast towards the ends. By changing the coil so that it gives less power loss in the middle part of the graphite and more power loss closer to the ends (Fig. 2b), the temperature distribution is changed towards a more homogeneous one. This can be done in several ways, e.g. by having different distances between the different turns of the coil. At the ends the graphite radiates away heat. To avoid this, extra insulation at both susceptor ends, covering the graphite, was introduced. The simulations show that the thickness of the insulation "lids" should be at least 15 mm to maintain a sufficiently high temperature of the graphite ends. A comparison between the temperature distributions along the graphite wall of the original reactor and the best new design is shown in Fig. 3. The new reactor design increases the zone in which the temperature variation is less than 5 degrees from 14% to over 64% of the total length of the susceptor. The variation of maximum 20 degrees is extended to 78%. The original design had the same variation over 25% of the total length. Löfgren et al. [7] measured a variation of more than 10% of the process temperature over 50% of the susceptor for the same type of reactor in 3D, which is close to our results for 2D. The maximum variation for the new design is less than 100 degrees over the

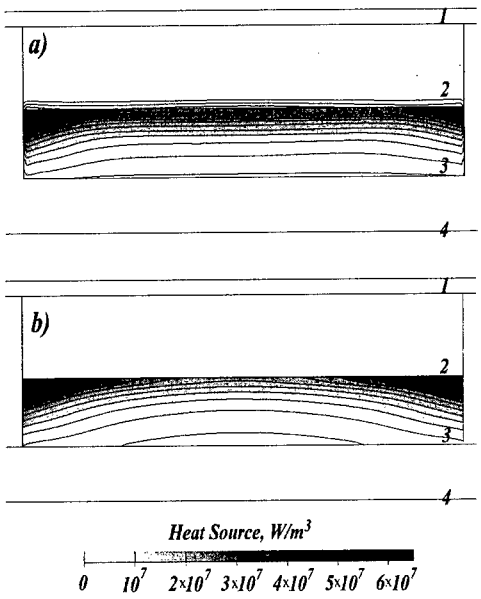


Fig. 2 Calculated heat source distribution for a) the original reactor and b) the new design. (1 – quartz, 2 – insulation, 3 – graphite, 4 – symmetry axis)

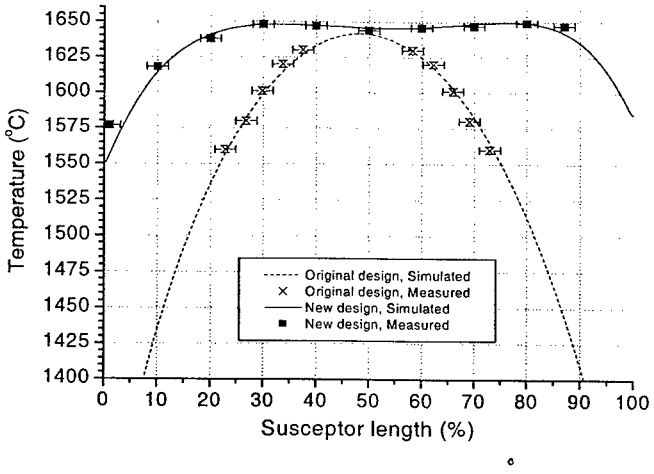


Fig. 3 Temperature distribution along the susceptor wall. Measured and simulated values.

whole susceptor. The new reactor also needs less power input than the original one to reach the same maximum temperature. A decrease of about 15% is obtained, most of it is due to the lower heat loss at the susceptor ends. Although this investigation has been made for a 2D system, we believe that similar changes will improve the real 3D reactor towards a more homogeneous temperature profile and thereby enlarging the usable growth area in the CVD reactor.

5. Summary

The suggested new design of the CVD reactor has a much larger area of homogeneous temperature distribution. An increase of the zone with a temperature variation of less than 5 degrees from 14% to 64% of the whole susceptor length has been obtained. The new design was developed using a simulation tool and the temperature profile was verified by measurements. Very good agreements between simulations and measurements were obtained. The zone with a variation in temperature of not more than 20 degrees was increased by a factor of three. Also the power input needed to reach the desired temperature was decreased.

We have shown that the simulation tool is very reliable in calculating temperature profiles in CVD reactors. By using a simulation tool when designing new CVD reactors one can not only increase the yield of good material, but also decrease the energy cost for running the reactor.

Acknowledgements

Dr. Yuri Makarov and Dr. Andrei Vorob'ev of CompuSoft International are gratefully acknowledged. The support from the Swedish foundation for strategic research (SSF) program SiCEP is gratefully acknowledged.

References

[1] O. Kordina, C. Hallin, A. Henry, J.P. Bergman, I. Ivanov, A. Ellison, N.T. Son and E. Janzén Phys. Stat. Sol. B. **202**, (1997), p. 321

[2] CFD-ACE+ is a software for simulation of fluid dynamics and associated physics by CFD Research Corporation, 215 Wynn Drive, Huntsville, AL 35805, USA.

[3] The user subroutines used with CFD-ACE+ have been developed in cooperation with CompuSoft International, Ravikuja 5C 23, 57710 Savonlinna, Finland.

[4] W.A. Fiveland, J. Heat Transfer, **106**, (1984) p. 699

[5] P.M. Löfgren, W. Ji, C. Hallin and C.-Y. Gu, J. Electrochem. Soc. **147**, (2000), p. 164

[6] Handbook of Chemistry and Physics, R.C. Weast ed. CRC Press, Inc. Boca Raton, Florida, (1985)

[7] P.M. Löfgren, C. Hallin, C.-Y. Gu and W. Ji, Mat. Sci. Forum **338-342** (2000) p. 153

Materials Science Forum Vols. 353-356 (2001) pp. 103-106
© 2001 Trans Tech Publications, Switzerland

Modeling Analysis of SiC CVD in a Planetary Reactor

A.N. Vorob'ev[1], A.K. Semennikov[1], A.I. Zhmakin[2], Yu.N. Makarov[3], M. Dauelsberg[4], F. Wischmeyer[4,5], M. Heuken[4] and H. Jürgensen[4]

[1] Soft-Impact, Ltd., PO Box 33, RU-194156 St.Petersburg, Russia

[2] A.F.Ioffe Physico-Technical Institute, Russian Academy of Sciences, Polytechnicheskaya 26, RU-194021 St.Petersburg, Russia

[3] University of Erlangen-Nürnberg, Cauerstr. 4, DE-91058 Erlangen, Germany

[4] AIXTRON AG, Kackertstr. 15-17, DE-52072 Aachen, Germany

[5] Epigress AB, Ideon Science and Technology Park, SE-2370 Lund, Sweden

Keywords: Epitaxial Growth, Gas Phase Nucleation, Multi-Wafer Hot-Wall Reactor

Abstract. The present paper focuses on the modeling analysis of the SiC CVD in the 5x3" Planetary Reactor® using silane and propane as precursors. The reactor design includes true hot wall conditions and an actively cooled inlet zone with an abrupt transition to the hot reactor environment. For getting a better insight into the SiC growth, we simulated the CVD process, varying the operating parameters in a wide range. The capability to achieve reasonably high growth rates with this reactor design is evaluated by the modeling study. CVD of SiC occurs without significant Si clustering under most growth conditions, even at high silane flow rates and wall temperatures lower than susceptor temperatures.

Introduction

Noticeable progress has been made in the understanding and practical implementation of the SiC chemical vapor deposition (CVD) during the last few years. Currently there is an ongoing competition of different epitaxial setups satisfying specific industry requirements. In particular, high-voltage bipolar devices require thick epitaxial layers with low doping concentration and, hence, a high carrier lifetime. For getting a reasonable yield of these devices, it is necessary to increase the growth rate of epitaxial layers, to achieve a good surface morphology and to provide a high uniformity and controllability of dopant incorporation. Two latter factors are found to depend significantly on the Si/C ratio in the gas mixture supplied onto the growth surface. A new multi-wafer SiC CVD reactor developed by AIXTRON AG is one of the most promising machines for industrial production of SiC based structures. The reactor, based on the design suggested by Frijlink and coworkers [1], features full planetary motion and is capable to grow simultaneously high quality layers on seven two-inch diameter substrates. On the Planetary Reactor® the realization of stringent production performance criteria for SiC epitaxial layers has been successfully demonstrated by Burk [2], Nordby [3] and coworkers. An important improvement of the reactor presented here is the true hot wall concept with independently heated susceptor and reactor top wall, and an actively cooled gas entrance zone. Furthermore, the reactor capacity is increased to grow on five three-inch diameter wafers at a time.

In this paper, the CVD of SiC in the Planetary Reactor® is simulated to understand basic features of the epitaxial process and to demonstrate the capability of the Planetary hot wall concept. The results to be presented here serve to illustrate the effect of operating parameter variation on the growth rate distribution along the wafer. Of special interest is the influence of the silicon gas-phase nucleation on the SiC CVD in this work.

Model

For simulating the CVD of SiC, the heat and mass transport model extended to cover silicon clustering in the gas phase is employed [4]. The cluster formation and their evolution are modeled

by using a moment-type approach. Clusters are considered as a collisionless pseudo-gas of heavy particles with growth rate independent of their size. The nucleation rate is given by the Becker-Döring theory, and the Hertz-Knudsen equation accounts for mass exchange between the clusters and the gas phase. The nucleation model is coupled to the heat and mass transport equations.

Silane (SiH_4) and propane (C_3H_8) are used as the Si- and C-containing precursors, respectively, and hydrogen (H_2) as the carrier gas. The extended set of gas-phase chemical reactions and species involved in the CVD of SiC is presented in [5]. A special sensitivity analysis allows us to reduce the set and to find species responsible for accurate prediction of the growth rate in the temperature range of interest (300-1900 K): H_2, H, C_3H_8, C_2H_5, CH_4, CH_3, SiH_4, SiH_2, and Si. For describing chemical interaction between the reactive gas species and susceptor surface, the near-equilibrium approach [6] is employed which is valid at temperatures used in practice.

Results and Discussion

Velocity vector and temperature distribution inside the reactor are shown in Figs.1 and 2 for typical operating parameters: total pressure of 100 mbar, total H_2 flow rate of 50 slm, SiH_4 and C_3H_8 flow rates of 5 sccm and 3.33 sccm, respectively. Note that, unlike the carrier gas supplied via both inlets, the precursors enter the reactor only through the upper nozzle. As it follows from the figures, the reactor design provides for non-circulating flow pattern and the uniform temperature distribution

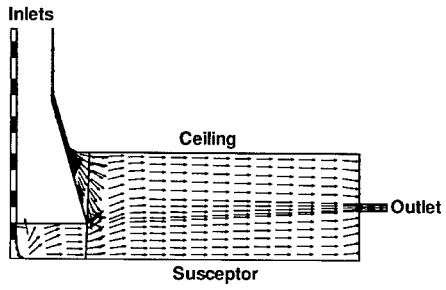


Fig.1 Velocity vector distribution. Total pressure is 100 mbar, total flow is 50 slm.

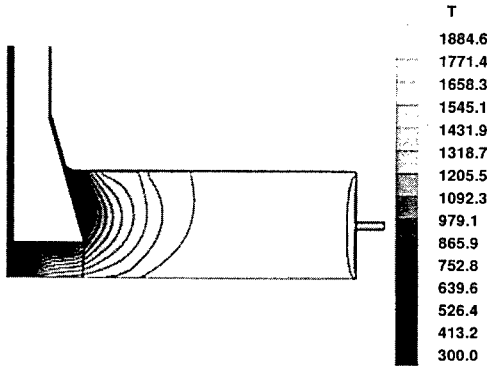


Fig.2 Temperature distribution. Total pressure is 100 mbar, total flow is 50 slm.

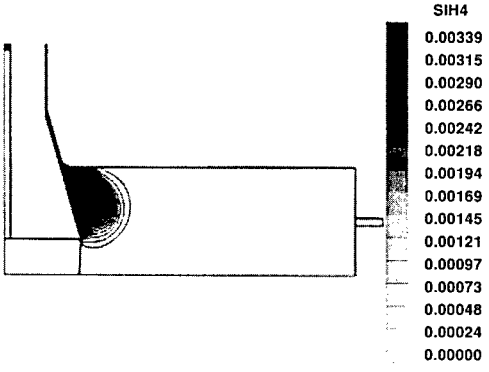


Fig.3 SiH_4 concentration distribution. Total pressure is 100 mbar, total flow is 50 slm.

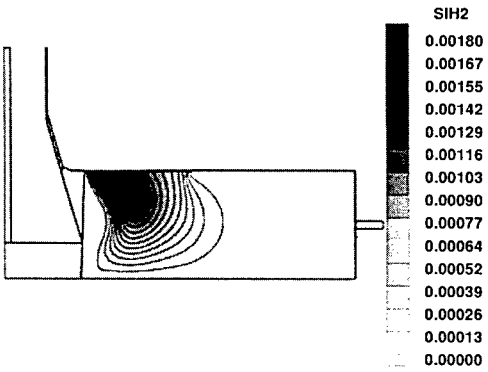


Fig.4 SiH_2 concentration distribution. Total pressure is 100 mbar, total flow is 50 slm.

near the wafer located in the middle of the reactor bottom. The temperature of the ceiling here is 20-30K lower than that of the substrate.

Distributions of precursor and major species concentrations are presented in Figs.3-7. It is well seen that both silane and propane completely decompose producing SiH_2, Si and CH_4. These species have the maximum concentration in comparison with others and primarily control the SiC growth on the wafer. In the considered range of growth temperature between 1500°C to 1650°C CVD of SiC is mass transport limited and growth rates dependent only weakly on growth, mainly related to the temperature dependence of species diffusion properties. The concentration of Si is then considerably lower than that of SiH_2 since the high gas mixture flow prevents complete decomposition of SiH_2 and formation of clusters due to dilution effects and low residence times. No

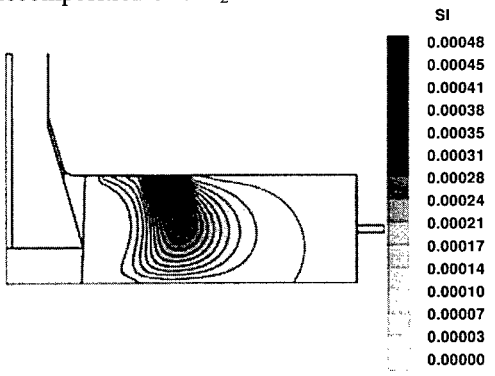


Fig.5 Si concentration distribution. Total pressure is 100 mbar, total flow is 50 slm.

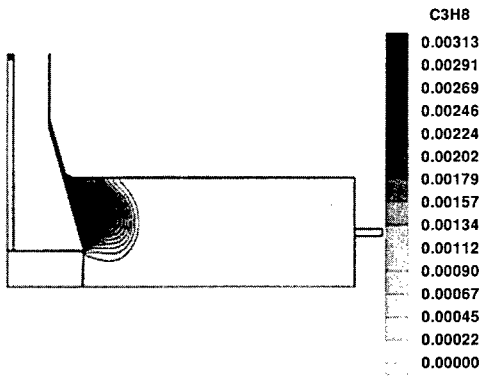


Fig.6 C_3H_8 concentration distribution. Total pressure is 100 mbar, total flow is 50 slm.

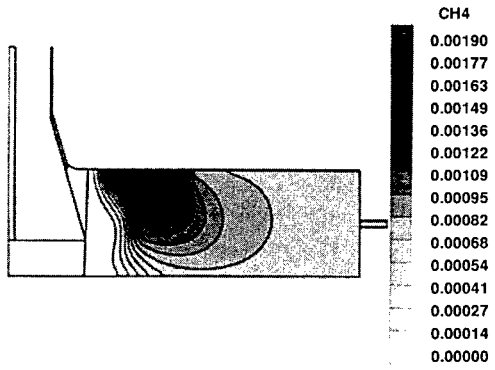


Fig.7 CH_4 concentration distribution. Total pressure is 100 mbar, total flow is 50 slm.

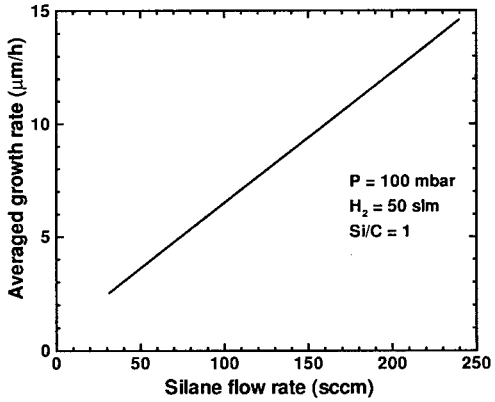


Fig.8 Averaged growth rate vs. silane flow rate.

silicon nucleation is predicted at SiH_4 flow rate of 5 sccm. The absence of any return flow in the gas entrance zone that might transport decomposition products of silane back to the cold inlet is recognized as crucial for controlling the nucleation behavior.

Even at lower temperatures at the ceiling, the silicon gas-to-particle conversion is predicted to be insignificant. Moreover, elevated silane flow rates do not lead to a drastic depletion of the gas mixture in Si-containing species and, hence, to a noticeable decrease in the growth rate as it occurs in a vertical cold-wall rotating-disc reactor [7]. As illustrated in Fig. 8 growth rates of up to 10 μm/h and higher can be achieved with virtually linear dependence of growth rates on silane

supply indicating that the high gas mixture flow effectively prevents the homogeneous nucleation of silicon. This behavior is also demonstrated in Fig. 9 showing that the growth rate of SiC saturates at silane flow rates higher than 10 sccm at fixed propane flow rates corresponding to input Si/C ratios > 1. Note that the thickness uniformity becomes better at higher silane flow rate. In particular, the averaged growth rate and the thickness deviation are predicted to be 4.03 μm/h and 0.56%, respectively, at the silane flow rate of 15 sccm.

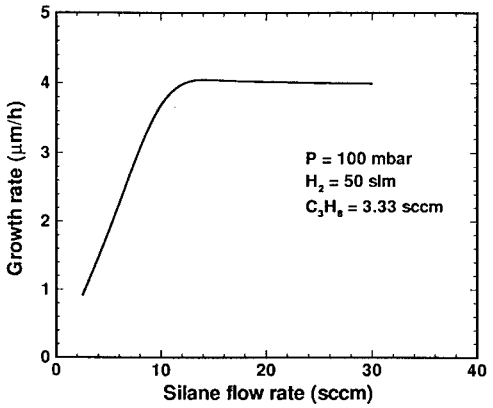


Fig.9 Averaged growth rate vs. silicon-carbon input ratio.

Summary

To get a better insight into the growth mechanisms, we have simulated CVD of SiC in the Planetary Reactor®. Depletion of the gas mixture in silicon-containing species due to the silicon gas-phase nucleation is predicted to be negligibly low under a wide range of operating conditions. The gas-phase nucleation is suppressed because of the high total flow practically used in the reactor. Modeling results suggest that growth rates of up to 10 μm/h can be achieved without onset of Si cluster formation, which in turn would limit growth rates.

References

[1] P.M.Frijlink, J.Crystal Growth, 93, (1988), p. 207.

[2] A.A. Burk, Jr., M.J. O'Loughlin, H.D. Nordby, Jr., J. Crystal Growth, 200, (1999), p. 458.

[3] H.D. Nordby, Jr., M.J. O'Loughlin, M.F. MacMillan, A.A. Burk, Jr., J.D. Oliver, Jr., Materials Science Forum Vols. 338-342 (2000), p. 173.

[4] A.N.Vorob'ev, A.E.Komissarov, A.S.Segal, Yu.N.Makarov, S.Yu.Karpov, A.I.Zhmakin, R.Rupp, Materials Science and Engineering, B61-62 (1999), p. 176.

[5] M.D.Allendorf, R.J.Kee, J.Electrochem.Soc., v.138, No 3, (1991), p. 841.

[6] A.N.Vorob'ev, A.E.Komissarov, M.V.Bogdanov, S.Yu.Karpov, A.A.Lovtsus, Yu.N. Makarov, S.A. Lowry, Proceedings Papers CVD-XV, Toronto, (2000), (to be published).

[7] A.N.Vorob'ev, Yu.E.Egorov, Yu.N.Makarov, A.I.Zhmakin, A.O.Galyukov, R.Rupp, Materials Science and Engineering, B61-62 (1999), p. 172.

Materials Science Forum Vols. 353-356 (2001) pp. 107-110
© 2001 Trans Tech Publications, Switzerland

Influence of Silicon Gas-to-Particle Conversion on SiC CVD in a Cold-Wall Rotating-Disc Reactor

A.N. Vorob'ev[1], M.V. Bogdanov[1], A.E. Komissarov[1], S.Yu. Karpov[1], O.V. Bord[1], A.A. Lovtsus[1] and Yu.N. Makarov[2]

[1] Soft-Impact, Ltd., PO Box 33, RU-194156 St.Petersburg, Russia

[2] Institute of Fluid Mechanics, University of Erlangen-Nürnberg, Cauerstr. 4, DE-91058 Erlangen, Germany

Keywords: C/Si Ratio, Gas Phase Nucleation, Growth Rate, Secondary Phase Formation

Abstract. Chemical Vapor Deposition (CVD) of SiC in a vertical cold-wall rotating-disk reactor is modeled in a wide range of precursor (silane and propane) flow rate variation. It is found that SiC growth rate is limited by the gas mixture depletion in silicon atoms due to gas-phase nucleation. The secondary phase (graphite and silicon) formation on the growing surface is analyzed. The SiC growth window depending on the precursor flow rates is calculated, and a significant influence of the gas-phase nucleation on the window is demonstrated.

Introduction

Significant progress has been achieved by silicon carbide technology in the last few years, with a variety of encouraging device and integrated circuit demonstrations [1]. Nevertheless, there are a number of problems to be resolved before SiC devices become of any substantial commercial value. In particular, high-voltage bipolar devices require thick epitaxial layers with low doping concentration and, hence, a high carrier lifetime. For getting a reasonable yield of these devices, it is necessary to increase the growth rate of epitaxial layers, to achieve a good surface morphology and to provide a high uniformity and controllability of the doping level. Two latter factors are found to depend significantly on the C/Si ratio in the gas mixture supplied onto the growth surface. Control of the Si/C ratio at the growth surface is still a crucial factor for CVD widely used to produce SiC epitaxial films.

Additional problems arise in CVD of SiC due to gas-phase nucleation of silicon clusters. The generated clusters act as a sink for atomic silicon and result in a considerable decrease in the growth rate. Besides, the gas-to-particle conversion of silicon influences the Si/C ratio and, hence, affects the properties of the growing SiC epilayer.

The aim of this paper is to get an insight into a complex mechanism of SiC growth in a vertical cold-wall reactor [2]. Important mechanisms of the process are discussed. Particular attention is given to the growth rate dependence on precursor flow rates and to the effect of silicon vapor condensation in the gas. CVD phase diagram is calculated to estimate growth window for this epitaxial technique.

Results and discussion

The heat and mass transport of the reacting flow coupled with gas-phase nucleation of silicon in the reactor is simulated in terms of the model developed in [3]. The model was verified by comparing the computations with the available experimental data on SiC growth rate as a function of the input propane flow rate. We carried out two sets of computations corresponding to the precursor supply through the whole inlet area and through the central hole, considered as actual designs of the inlet flange. In both cases, the whole inlet area was used for the carrier gas supply. Therewith, the inlet velocity was assumed to be constant over the whole inlet area, and densities of the carrier gas and of the species were chosen in such a way as to keep their flow rates for different inlet flanges. Velocity

vectors and temperature distribution for the precursor supply through the whole inlet area are shown in Fig.1 for typical operating parameters: total pressure of 50 Torr, hydrogen carrier gas flow rate of 15 slm, susceptor temperature of 1450°C, susceptor-inlet distance of 20 cm.

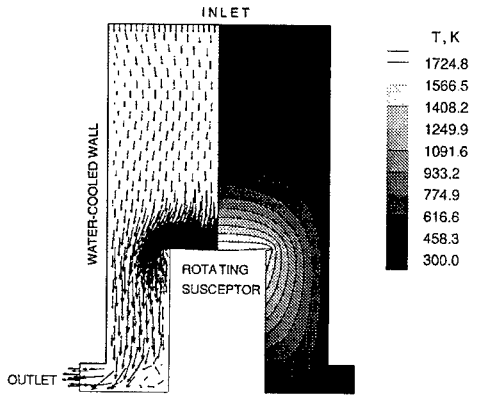


Fig.1 Velocity vectors and temperature distribution.

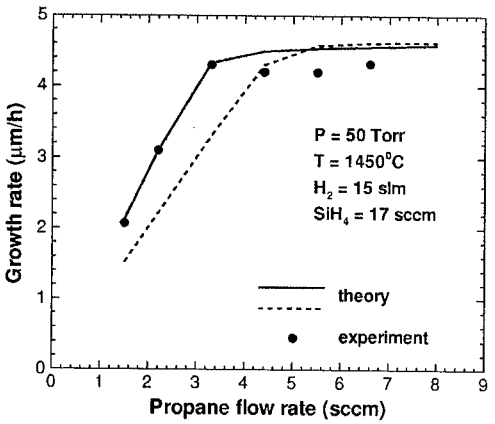


Fig.2 Growth rate vs. propane flow rate.

The growth rate variation with the propane flow rate is plotted in Fig.2 for the silane flow rate of 17 sccm. Other process parameters are equal to their typical values listed above. Solid and dashed lines in the figure correspond to the precursors supply through the central hole of a radius four times smaller than that of the reactor inlet and through the whole inlet area, respectively. As seen from the figure, the computations (solid line) fit well the experiment. The sloping portion of the curve is related to conditions where silane is in excess and the growth rate is controlled by the propane flow rate. The growth rate saturates at the input carbon-to-silicon ratio C/Si ≈ 0.6 and can no longer be raised by elevating the propane flow rate. Usually, the saturation is due to the transition from the propane- to the silane-limited growth conditions and is observed at C/Si ≈ 1. We attribute the earlier saturation of the growth rate seen in Fig.2 to homogeneous nucleation of Si clusters in the gas. The silicon gas-to-particle conversion depletes the vapor in the reactive species needed for SiC film growth. Support for this comes from the irradiating layer observed through the reactor viewport and associated with the black-body radiation scattering by silicon clusters [2]. The result obtained suggests the following mechanism of the gas phase depletion. The clusters affected by the thermophoretic force are accumulated in a thin layer located over the susceptor and can not reach the growing surface. The gas flow takes the clusters away in the radial direction, and, hence, some of the Si atoms stored in the clusters are lost to the SiC growth on the wafer. Note that the model neglecting silicon vapor condensation predicts saturation at C/Si ≥ 1.0 and significantly higher growth rates [4].

A similar growth rate dependence corresponding to the use of the whole inlet section for supplying the precursors is also presented in Fig.2 by dashed line. A comparison shows that a higher propane flow rate of ≈ 5 sccm (C/Si ≈ 0.8) is required to get the maximum growth rate in the latter case. Comparison of the curves plotted in Fig.2 shows that the inlet flange design is an important factor of SiC CVD.

For getting a better insight into growth mechanisms, we carried out computations for the supply of precursors through the whole inlet section, varying their flow rate in the following ranges: C_3H_8 = 1.5-8.0 sccm, SiH_4 = 4.0-60.0 sccm. Other operating parameters were equal to their typical values mentioned above. The computed growth rate is plotted in Fig.3 as a function of C_3H_8 and SiH_4 flow rates. It follows from the figure that the growth rate can not exceed a definite value. The limitation

is caused by a drastic silicon condensation in the vapor at high silane flow rates. This effect provides difficulties for the further increase in the growth rate via the precursor flow rate variation. Thus, the higher flow rates of silane result in a greater loss of silicon atoms involved in SiC growth, and despite the inlet Si/C ratio being much more than unity, the growth rate is then controlled by SiH_4 supply.

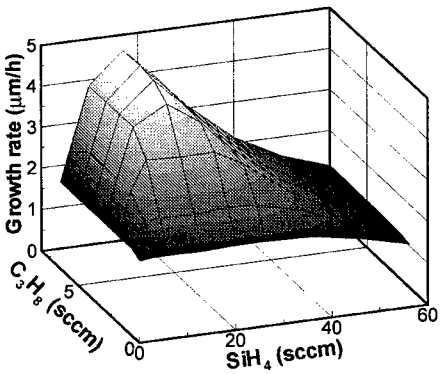


Fig.3 Growth rate vs. propane and silane flow rates.

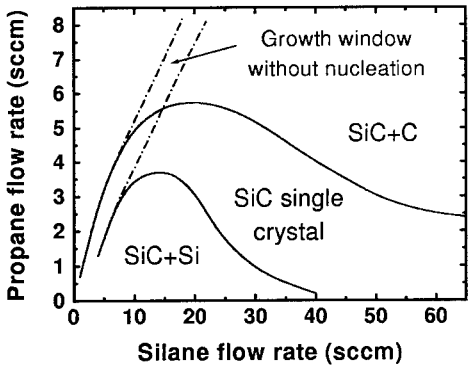


Fig.4 Secondary phase diagram for CVD of SiC.

Formation of parasitic (secondary) phases on SiC surface (solid graphite and either liquid or solid silicon) is an undesirable effect leading to degradation of the material properties. Here we apply a special criterion to predict whether a condensed phase is formed on the growth surface. The analysis of the secondary phase formation was made for the same variation of precursor flow rates. Fig.4 shows by solid lines the boundaries between the zones where the secondary phase formation and/or growth of the SiC single crystal are predicted. For comparison, the similar boundaries computed with neglecting the silicon condensation in the gas are shown by dashed lines. It is seen that the silicon nucleation alters the Si/C ratio over the substrate and, hence, broadens the window for single-crystal SiC growth significantly. It should be noted that the growth window exhibits a rather complex dependence on SiH_4 flow rate and is controlled totally by the silicon clustering. On the other hand, the growth rate is predicted to peak at $SiH_4 \approx 17$ sccm (see Fig.3). So, according to Fig.4, the propane flow rate is allowed to vary in the range $\approx$ 3.3-5.5 sccm to avoid the parasitic phase formation on the growing surface.

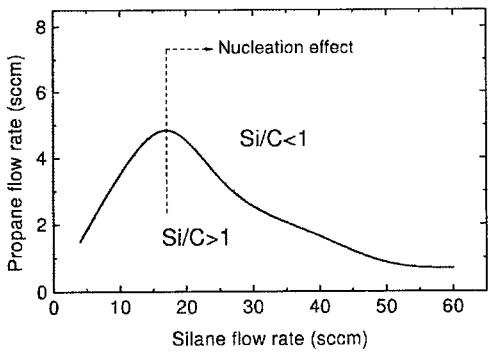


Fig.5 Si/C ratio behavior near the growth surface vs. precursor flow rates.

It is well known that Si/C ratio plays a crucial role for many properties of SiC crystals. In particular, the doping by various impurities, the concentration of carbon vacancies, surface morphology including step bunching, etc. are affected by the surface Si/C ratio which may differ significantly from the Si/C ratio at the reactor inlet.

To get a general pattern of the Si/C ratio near the growth surface, we made computations varying the precursor flow rates in the wide ranges. The Si/C behavior is illustrated in Fig.5. The curve for Si/C = 1 delimits the C- and Si-rich growth regimes. The linear portion of the curve corresponds to the conditions where the silane flow rate is insufficiently high for initiating the nucleation. The Si/C ratio is then controlled by that at the inlet. The silicon gas-to-particle conversion manifests itself as the curve slope. The zone of Si/C < 1 becomes larger than the zone of Si/C > 1 due to the drastic depletion of the vapor in silicon near the growth surface. For this reason, a higher silane flow rate is unable to raise the Si/C ratio at SiH_4 > 17 sccm.

Summary

An advanced model of heat and mass transport coupled with spontaneous condensation of silicon in the gas is employed to simulate SiC CVD in a cold-wall rotating-disc vertical reactor. The comparison of computed growth rates with available experimental data shows a reasonable agreement under typical growth conditions. It is found that gas-phase nucleation of Si clusters considerably influences the CVD process. The simulations predict that the growth rate can not exceed some maximum value at the precursor flow rates varying in a wide range. This is due to a drastic silicon gas phase condensation at high silane flow rates. The analysis shows that the silicon-to-carbon ratio near the growth surface can radically differ from that at the reactor inlet. In turn, this changes the proportion between the silicon and carbon atoms on the wafer and enlarges the range of silane and propane variation where the SiC single epilayer is expected to grow without secondary phase formation resulting in morphology degradation. The model allows us to predict the optimal precursor flow rates, ensuring the maximum growth rate within relatively broad growth window.

References

[1] A.Itoh and H.Matsunami, IEEE Electron Device Lett. 16, (1995), p. 280.

[2] R.Rupp, Yu.N. Makarov, H.Behner, A.Wiedenhofer, Phys. Stat. Sol. (b) 202, (1997), p. 281.

[3] A.N.Vorob'ev, A.E.Komissarov, A.S.Segal, Yu.N.Makarov, S.Yu.Karpov, A.I.Zhmakin, R.Rupp, Materials Science and Engineering, B61-62 (1999), p. 176.

[4] A.N.Vorob'ev, Yu.E.Egorov, Yu.N.Makarov, A.I.Zhmakin, A.O.Galyukov, R.Rupp, Materials Science and Engineering, B61-62 (1999), p. 172.

Materials Science Forum Vols. 353-356 (2001) pp. 111-114
© 2001 Trans Tech Publications, Switzerland

Ab Initio Study of Silicon Carbide: Bulk and Surface Structures

C. Raffy[1,2], L. Magaud[1], E. Blanquet[2], M. Pons[2] and A. Pasturel[3]

[1] LEPES (Lab. d'Etudes des Propriétés Electroniques des Solides),
25 rue des Martyrs, BP 166, FR-38042 Grenoble Cedex 9, France

[2] LTPCM (Lab. de Thermodynamique et Physico-Chimie Métallurgiques),
FR-38402 Saint Martin d'Hères Cedex, France

[3] LPMMC (Lab. de Physique et Modélisation des Milieux Condensés),
FR-38054 Grenoble, France

Keywords: Crystal Growth, Density Functional Theory, Polytypism, Stability, Step Structure

Abstract. The aim of this paper is to improve our understanding of the SiC growth mechanisms from the vapor phase (bulk material or thin film). Detailed studies of bulk and surface structures are therefore needed. The geometries of hexagonal (2H, 4H, 6H) and cubic (3C) polytypes have been optimized thanks to calculations based on density-functional theory (DFT). It appears that 6H and 4H are the most stable phases, which is in agreement with other calculations, but not with experiments that indicate a preference for the growth of the cubic form on flat terraces. Thus, to analyse further the growth processes, we began an investigation of the surface of 4H SiC, which is the most interesting polytype regarding the electronic properties. Since the substrate used during the experiments is an off-oriented hexagonal SiC single crystal, we studied the morphology of the steps along the $[1\bar{1}00]$ direction for C- and Si-terminated surfaces. In these particular cases, the total energy calculations show that the most stable steps are one bilayer high.

1. Introduction

A good control of the cristalline quality of silicon carbide elaborated as bulk material [1] or thin film [2] requires to know the atomic structure in details. It includes a study of the bulk and surface properties.

The structures and energies of the four simplest polytypes (2H, 3C, 4H and 6H) have been investigated using first-principle calculations. The computational method employed is based on the determination of the total energy from the density-functional theory, using the local density approximation (including generalized gradient corrections) for the exchange-correlation potential [3, 4]. We used the code VASP [5] which expands the wave functions in terms of plane waves, and describes the electron-ion interaction by ultrasoft Vanderbilt pseudopotentials [6].

In paragraph 2, we show that the geometries of the hexagonal polytypes are non ideal and that the energy differences of polytypes are very small. Actually, we think that the formation of polytypes is controlled by growth conditions related to epitaxy on on-axis material rather than thermodynamical considerations. It is thus important to know the morphology of the surfaces. This is discussed in paragraph 3. As most experiments use an off-oriented hexagonal SiC single crystal as the substrate [2, 7], we have focused our study on the step structures of the 4H polytype.

2. Bulk properties

2.1. *Structures*

The optimized parameters a and c of the hexagonal cells of the four polytypes investigated are presented in table 1. The calculated values are in good agreement with the experimental data, sligthly larger as a consequence of the GGA technique [8]. Particularly, both confirm the well known tendency that a decreases and c/n increases with the degree of hexagonality h [9]. Moreover, we observe that the hexagonal structures are not ideal, as $c/na \neq \sqrt{2/3}$. The detailed analysis of the intern relaxations shows that the Si-C bond parallel to the c-axis is stretched in comparison with the three other equivalent bonds of the tetrahedron [9]. Some authors think that these distorsions are the driving force of polytypism [10].

Table 1. Lattice parameters of the polytypes 3C and nH (n=2, 4, 6). n is the number of bilayers in the hexagonal cell. The numbers in parentheses are measured values : for 2H, see [11] ; for 3C, see [12] ; for 4H and 6H, see [13].

Polytype	h (%)	a (Å)	c/n (Å)	$c/(na)$
3C *hexag.*	0	3.087 (3.083)	2.520 (2.517)	0.8165 (0.8165)
6H	33	3.084 (3.081)	2.523 (2.520)	0.8181 (0.8178)
4H	50	3.084 (3.080)	2.523 (2.521)	0.8183 (0.8184)
2H	100	3.081 (3.076)	2.530 (2.524)	0.8211 (0.8205)

2.2. *Total energies*

For the relaxed geometries given in table 1, we have calculated the total energies of each polytype. The figure 1 indicates the relative energies of the hexagonal structures with respect to the cubic polytype. They are compared to other LDA calculation results [9, 14-16].
First, our calculations have shown that for either ideal (*i.e.* ideal c/a ratio and a equal to the calculated value of the parameter for the cubic phase) or relaxed structures, the energetical ordering is the same between polytypes. The 2H form is much less stable than 3C which is less stable than 4H and 6H. Actually, the energy difference between 4H and 6H is smaller than 0.5 meV/atom and approaches the accuracy of the calculations, so it is not possible to conclude.
Our results are in agreement with the ones obtained by most authors [14-16]. The slight discrepancies are due to different calculation parameters and different geometries. However, a strong disagreement exists with Käckell *et al* [9] who find different relative stabilities whether the relaxations are considered or not. For ideal structures, they find that the stability decreases with the degree of hexagonality. They report a very high energy for 2H and are the only ones to mention 3C as the most stable structure. In contrast, when they take the relaxations into account, they find 2H to be only 1 meV/atom above 3C, and 4H to be the most stable polytype.

Except for Käckell *et al* when considering ideal structures, the energy calculations are not in agreement with experiments, which indicate a preference for the cubic form [17, 18]. We think that metastability effects are strong in SiC [15, 19] and that the morphology of the surface influences much the growing polytype.

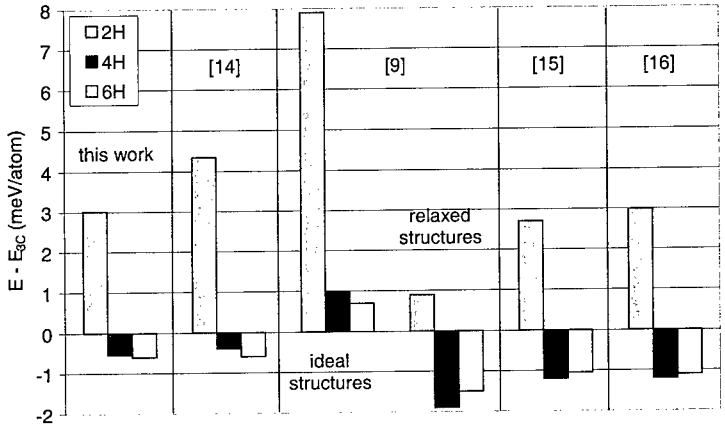


Fig. 1. Relative stabilities of the hexagonal polytypes with respect to 3C (in meV/atom).

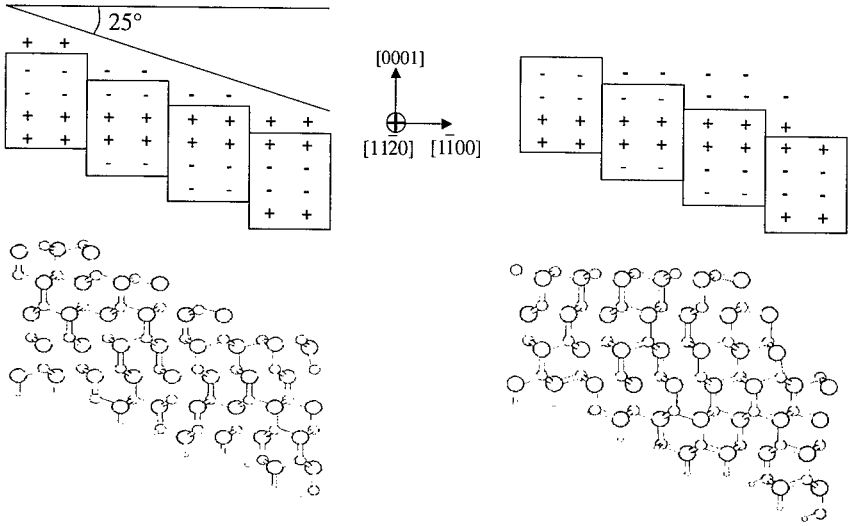
3. Surface

On off-oriented SiC substrate, growth proceeds through a step-flow mode [7]. Our aim is to determine the preferred step height as a function of the direction and the polarity. We present here our first results on steps along the $[1\bar{1}00]$ direction. Experimentally, the substrates are off-oriented by less than 8°. But, because of the numerical constraints, we only considered supercells containing 92 atoms, which corresponds to an angle of 25°. The slabs used contain five Si-C bilayers and three bilayers of vacuum. The dangling bonds of the atoms belonging to the bottom surface were saturated by H atoms. Relaxations were allowed on all the atoms.

For each polarity (C- and Si-terminated surfaces), we considered surfaces constituted by single steps (height = 1 bilayer), and surfaces constituted by multiple-height steps (step bunching phenomenon). We then compared the energy difference between the two configurations to determine the most stable structure. Figure 2 shows the result of the calculated geometries, whereas table 2 gives the values of the energies taking the single step configuration as the reference. We can see that for both polarities, the single step configuration is more stable. The step bunching is less favoured on the Si face compared to the C face, which is in disagreement with experimental observations [7]. This difference may be due to the unrealistic tilt angle used in this first approach. Calculations on 13° off-oriented surfaces are in progress, as well as calculations on steps along the $[11\bar{2}0]$ direction. They should provide with more information on the step structure and their role in polytype growth.

Table 2 : Energy of step bunching vs. single step configuration.

Polarity	step bunching
C-terminated	+ 1.290 eV
Si-terminated	+ 2.294 eV



-a- single steps -b- step bunching

Fig. 2 : Calculated structures for single steps and step bunching C-terminated configurations.

Acknowledgement: The authors wish to thank Prof. J. Hafner and Dr. G.Kresse who provided them with the code VASP.

References

[1] I. Garçon, A. Rouault, M. Anikin, C. Jaussaud, R. Madar, Mater. Sci. Eng. B29 (1995), p. 90.
[2] N. Kuroda, K. Shibahara, W.S. Yoo, S. Nishin, H. Matsunami, Extended abstracts of the 19th conference on solid state devices and materials, Tokyo (1987), p. 227.
[3] P. Hohenberg, W. Kohn, Phys. Rev. 136 (1964), p. 864B.
[4] W. Kohn, L.J. Sham, Phys. Rev. 140 (1965), p. 1133A.
[5] G. Kresse, J. Hafner, Phys. Rev. B 47 (1993), p. 558.
[6] D. Vanderbilt, Phys. Rev. B 32 (1985), p. 8412.
[7] T. Kimoto, A. Itoh, H. Matsunami, T. Okano, J. Appl. Phys. 81 (1997), p. 3494.
[8] J.P. Perdew, J.A. Chevary, S.H. Vosko, K.A. Jackson, M.R. Pederson, D.J.Singh, C. Fiolhais, Phys. Rev. B 46 (1992) p 6681.
[9] P. Käckell, B. Wenzien, F. Bechstedt, Phys. Rev. B 50 (1994), p. 17037.
[10] G.L. Vignoles, J. Cryst. Growth 118 (1992), p. 430.
[11] R.F. Adamsky, K.M. Merz, Z. Krist. 111 (1959), p. 350.
[12] Landolt-Börnstein : Numerical Data and Functional Relationships in Science and Technology, Vol. 17a, new series, Ed. K.H. Hellwege and O. Madelung, Springer-Verlag, Berlin (1982).
[13] A. Bauer, J. Kräusslich, L. Dressler, P. Kuschnerus, J. Wolf, K. Goetz, P. Käckell, J. Furthmüller, F. Bechstedt, Phys. Rev. B 57 (1998), p. 2647.
[14] C. Cheng, R.J. Needs, V. Heine, J. Phys. C 21 (1988), p. 1049.
[15] S. Limpijumnong, W.R.L. Lambrecht, Phys. Rev. B 57 (1998), p. 12017.
[16] M.J. Rutter, V. Heine, J. Phys. : Condens. Matter 9 (1997), p. 8213.
[17] N.W. Jepps, T.F. Page, Prog. Cryst. Growth Charact. 7 (1983), p. 259.
[18] J.N. Ness, T.F. Page, Bull. Mineral. 109 (1986), p. 151.
[19] J. Yeomans, in Solid State Physics, Academic press, Vol. 41 (1988), p.151.

Materials Science Forum Vols. 353-356 (2001) pp. 115-118
© 2001 Trans Tech Publications, Switzerland

SiC Defect Density Reduction by Epitaxy on Porous Surfaces

S.E. Saddow[1], M. Mynbaeva[2], W.J. Choyke[3], R.P. Devaty[3], Song Bai[3], G. Melnychuck[1], Y. Koshka[1], V. Dmitriev[4] and C.E.C. Wood[5]

[1] Department of Electrical & Computer Engineering, Emerging Materials Research Lab., Mississippi State University, Box 9571, Mississippi State MS 39762, USA

[2] A.F.Ioffe Physico-Technical Institute, Russian Academy of Sciences, Polytechnicheskaya, RU-194021 St.Petersburg, Russia

[3] Department of Physics and Astronomy, University of Pittsburgh, Pittsburgh PA 15260, USA

[4] TDI, Inc., 8660 Dakota Drive, Gaithersburg MD 20877, USA

[5] Office of Naval Research, 800 N. Quincy St., Arlington VA 22217, USA

Keywords: Buffer Layers, Epitaxial Growth, Photoluminescence, Porous SiC

Abstract The presence of micropipes and dislocations in SiC wafers used as substrates for SiC epitaxial growth may cause formation of lattice defects in the epi-layers. In this research a chemical vapor deposition (CVD) process on porous SiC (PSC) buffer layers was developed to reduce structural defect concentrations in SiC epi-layers. One possible mechanism for defect reduction is nano-scale lateral epitaxial overgrowth whereby the pores serve as regions to relieve stress at the growth surface. Previous X-ray diffraction, RHEED, SEM and AFM characterization has demonstrated good surface quality of these films grown on PSC substrates compared with conventional (control) substrates. For this study, the porous substrate surface was fabricated by surface anodization on half of a commercial 4H-SiC (0001) Si-face off-axis wafer. The other half of each wafer was protected by wax during this process and served as a control substrate. 4H-SiC epitaxial layers of thickness ranging from 4 to 10 μm were then grown on the processed substrates by atmospheric pressure CVD. LTPL data taken at 2K shows virtually no evidence of the L_1 line for the film grown on PSC while the line is clearly evident in the spectra from films grown on the control substrate. The L_1 line appears in rapid CVD growth and is related to intrinsic defects in films grown too quickly. It appears from this preliminary work that epitaxial films grown on porous SiC buffer layers have a lower density of defects than identical epitaxial films grown on commercially available SiC substrates.

Introduction The presence of micropipes and dislocations in SiC wafers used as substrates for SiC epitaxial growth may cause formation of lattice defects in the epilayers. The objective of this research was to characterize epitaxial layers grown by chemical vapor deposition (CVD) on porous SiC (PSC) buffer layers [1] in order to determine the quality of these epitaxial layers. PSC has been developed for numerous applications, such as power device passivation [2], and as buffer layers for GaN epitaxial growth [3]. PSC buffer layers were formed on one half of the surface of conventional 4H-SiC substrates via the anodization of the substrate in an aqueous HF solution [2]. The PSC layer was observed to extend approximately 5 μm into the SiC substrate thus forming a PSC buffer layer for subsequent epitaxial layer growth [4].

Using a horizontal cold-wall chemical vapor deposition (CVD) system, 4-10 μm thick SiC epitaxial layers were grown simultaneously on both PSC and standard (i.e., 'control') substrates using a standard dual-precursor CVD growth technique described elsewhere [5]. The substrates were 4H-

SiC with an 8° off-axis orientation from the (0001) Si face with an n-type doping density of 5-7 × 10^{18} cm^{-3}. The ratio of silicon to carbon was 0.3 and the growth temperature 1580°C. The epitaxial layers were n-type with a net doping density in the CVD layers of approximately 2-10 × 10^{15} cm^{-3} as measured with deposited Schottky barrier contacts using the Capacitance-Voltage (C-V) technique. After CVD growth, the samples were cleaved and the epitaxial layer morphology observed using cross-section SEM. It was noted that the pores abruptly end at the interface with a high-quality epitaxial layer having been formed on top [4]. Surface characterization was performed on these samples and it was observed that the surface was essentially featureless. To quantify the epi layer surface finish, AFM measurements were conducted on the CVD layers grown on PSC substrates and showed that the rms surface roughness was typically on the order of 5 nm.

Optical Characterization The epitaxial layers were studied using two different optical methods. First luminescence studies were conducted with the sample immersed in liquid nitrogen (approx. sample temperature 77K) using a mercury arc lamp were conducted to observe the optical luminescence over the entire wafer. The excitation wavelength was broad band from the visible to UV with a lamp power of 250 W. Using this technique, it was observed that the luminescence from the epitaxial layer grown on the PSC buffer portion of the substrate (i.e., PSC in Fig. 1a) exhibited a blue luminescence while luminescence from the same epitaxial layer grown on the non-porous portion of the substrate (i.e., STD in Fig. 1a) was dominated by yellow luminescence . For reference an SEM micrograph of the sample is also shown in Fig. 1b.

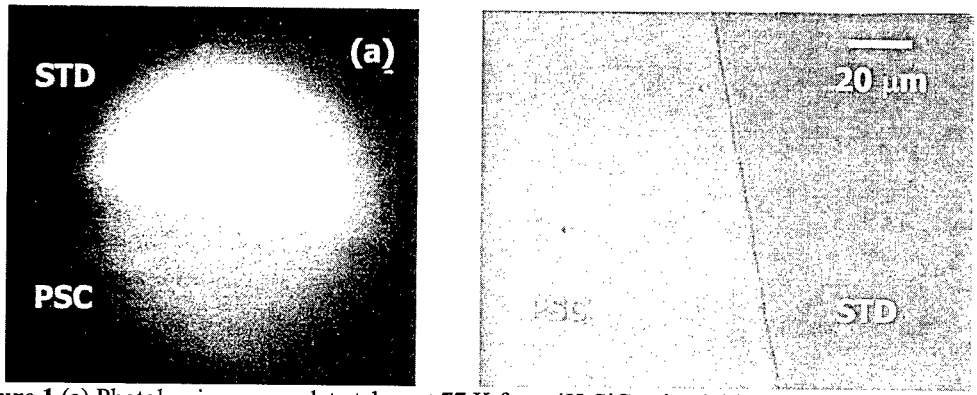


Figure 1 (a) Photoluminescence data taken at 77 K for a 4H-SiC epitaxial layer on standard (top) and PSC buffer layer (bottom). (b) Optical micrograph of structure showing PSC and standard regions after epitaxial growth.

Low-temperature photoluminescence (LTPL) experiments were performed. We show results on a single 4H SiC sample that was processed in part to have a 5 μm porous surface on half the sample. It was then put into a CVD reactor and a 4H SiC single crystal film, less than 10 μm thick, was grown on the whole surface. The sample was excited with 2440 Å radiation from a frequency doubled argon ion laser while immersed in pumped liquid He at 2 K. Figures 2, 3 and 4 show the resulting LTPL spectra. Fig. 2 shows the band edge nitrogen bound exciton peaks P_0 and Q_0, and the broad continuum peaking at roughly 5200Å for the epi film grown on the porous substrate. The ratio of the magnitude of the Q_0 bound exciton to the maximum height of the broad peak is 2.68. For the epi layer grown on the normal boule substrate (STD) of the same sample (Fig. 3) we obtain a ratio of 0.47. By combining the two results one gets a height ratio of the Broad Peak (PSC)/Broad Peak (STD) of 0.175. If the broad band is an indication of defects in the sample then the epitaxial film on the PSC buffer is reduced in defect density by a factor of 0.175 as compared to the STD epi.

More telling is Fig 4. Here we concentrate on the region just beyond the two-phonon replicas of the nitrogen four particle complex. The L_1 line at 4271.9Å is normally an indication of too rapid growth and intrinsic defects [6]. In the case of the STD part, L_1 is quite strong, whereas in the case of the PSC part, L_1 is just barely visible. This is a meaningful comparison and an indication that epitaxial layer on the porous part of the sample has a considerably reduced intrinsic defect density.

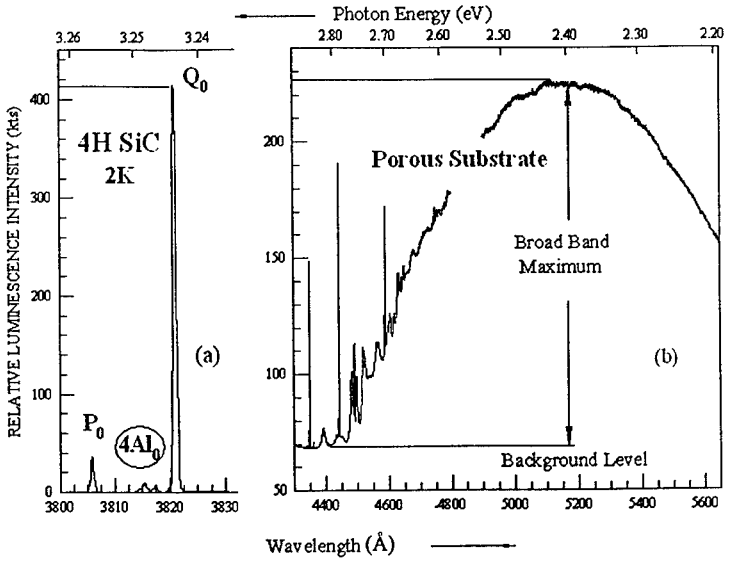


Figure 2: LTPL spectrum of a 4H SiC epitaxial layer grown on a porous 4H SiC substrate. (a) near band edge region showing the nitrogen bound exciton no phonon lines P_0 and Q_0. (b) broad continuum attributed to defects. Note the different scales in (a) and (b).

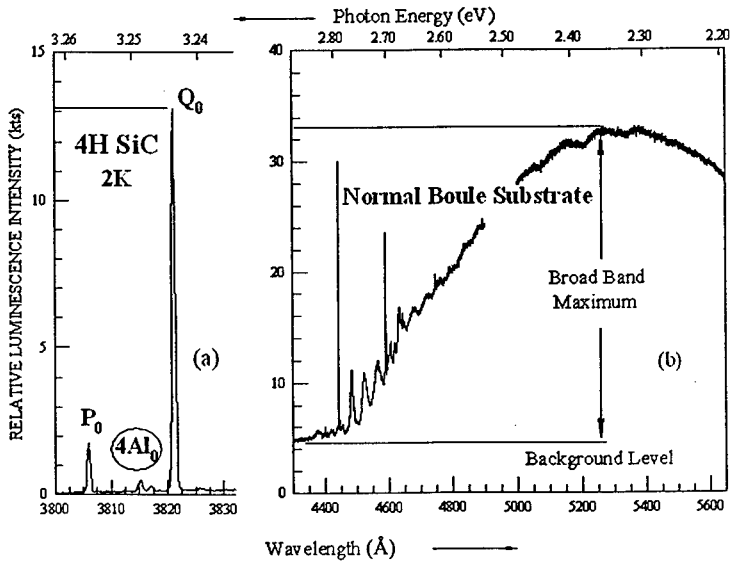


Figure 3: LTPL spectrum of a 4H SiC epilayer grown by CVD on a normal boule substrate (same wafer and same epi growth run as the epilayer shown in Fig. 2, but on the non-anodized region). (a) nitrogen bound exciton no phonon lines; (b) broad band emission attributed to defects.

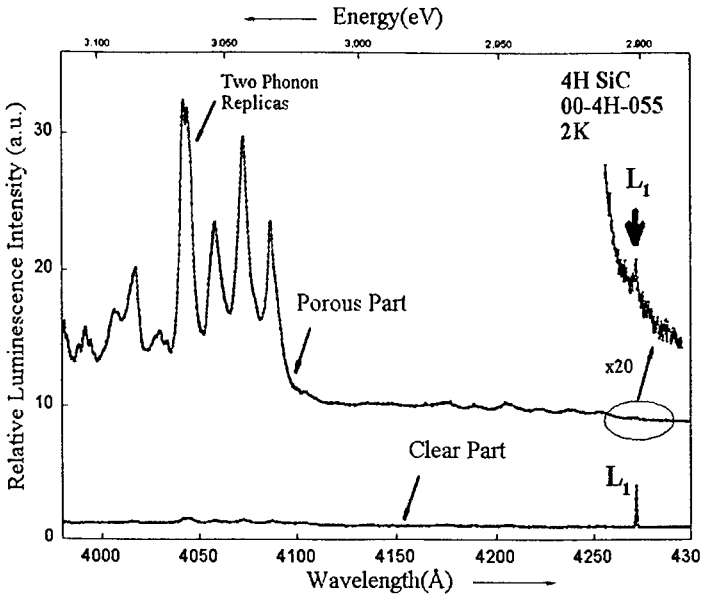


Figure 4 LTPL (2K) data comparing epi grown on PSC (top curve) to that on standard substrate (bottom curve). Note reduction in L_1 and enhanced two-phonon replicas present in epi grown on PSC, indicating a substantially altered epi quality.

Summary Epitaxial layers grown on porous 4H-SiC buffer layers have been characterized using photoluminescence. These layers, grown on substrates that contained porous buffer layers on one half of the surface proved to have a quite different photoluminescence response in comparison with the same epitaxial layers grown on the non-porous portions of the same substrates. Based on the improvement in defect structure indicated by this work, it is believed that epitaxial layers grown on porous SiC buffer layers have a lower defect density than epitaxial layers grown on conventional substrates. Extensive structural characterization is needed to support this assertion, although preliminary TEM data indicate that the epitaxial layers grown on porous buffer layers have very low defect density [7]. X-ray topography and more extensive TEM studies are currently being conducted to further ascertain the structural quality of epitaxial layers grown on porous SiC.

Acknowledgements The authors acknowledge the assistance of I. Nikitina, A. Zubrilov, N. Kuznetsov, Ioffe Institute, and I. Kotousova, N. Seredova, Crystal Growth Research Center for material characterization.

References

[1] J.S. Shor, I. Grimberg, B. Weiss, and A.D. Kurtz, Appl. Phys. Lett. **62** (1993), p. 2836.
[2] C. I. Harris, A. O. Konstantinov, C. Hallin and E. Janzen, Appl. Phys. Lett. **66** (1995), p. 1501.
[3] M. Mynbaeva, N. Savkina, A. Tregubova, M. Scheglov, A. Lebedev, A. Zubrilov, A. Titkov, A. Kryganovskii, K. Mynbaev, D. Tsvetkov, S. Stepanov, A. Cherenkov, I. Kotousova and V. Dmitriev, Proc. of the MRS 1999 Fall Meeting, Boston, MS (1999) (in press).
[4] G. Melnychuk, S.E. Saddow, M. Mynbaeva, S. Rendakova, and V. Dmitriev, Proc. of the MRS Spring 2000 Meeting, (in press) (2000).
[5] S. E. Saddow, M.S. Mazzola, S. V. Rendakova, and V. A. Dmitriev, Mat. Science & Engr. B **61-62** (1999), p. 158.
[6] T. Frank, G. Pensl, S. Bai, R. P. Devaty, and W. J. Choyke, Mater. Sci. Forum 338 – 342(2000), p. 753.
[7] M. Mynbaeva, S.E. Saddow, G. Melnychuk, I. Nikitina, M. Scheglov, A. Sitnikova, N. Kuznetsov, A. Zubrilov, K. Mynbaev, N. Seredova, and V. Dmitriev, Submitted to *Appl. Phys. Lett.*, July 2000.

Materials Science Forum Vols. 353-356 (2001) pp. 119-122
© 2001 Trans Tech Publications, Switzerland

Effect of Sublimation Growth on the Structure of Porous Silicon Carbide: SEM and X-Ray Diffraction Investigations

N.S. Savkina, V.V. Ratnikov, V.B. Shuman and A.A. Lebedev

A.F.Ioffe Physico-Technical Institute, Russian Academy of Sciences,
Polytechnicheskaya, RU-194021 St.-Petersburg, Russia

Keywords: Effective Pore Diameter, Epitaxy, Macrostrains, Porosity, Stresses

Abstract. We have studied porous SiC layers before and after high temperature growth of epitaxial SiC layers by vacuum sublimation. The performed investigations (X-ray measurements, SEM and calculations) demonstrated that heating of porous silicon carbide to 2000°C and the subsequent growth of an epitaxial layer on it lead to a transformation of the initial PSC structure, accompanied by merging of separate pores and decreasing in their number.

Introduction. Among porous materials, silicon carbide (SiC) attracts particular attention owing to its thermal, electrical, and mechanical properties. Although porous silicon carbide (PSC) has long been known, mainly its photoluminescence has been studied so far [1-3]. However, structural studies are necessary [4, 5] in order to understand the promising perspective of this material. Previously, the possibility of obtaining high quality 6H-SiC epilayer on PSC by vacuum sublimation epitaxy has been demonstrated.
The aim of this work was to perform a comparative study of PSC before and after high temperature growth of thin (0.5 - 3μm) epitaxial 6H-SiC layers by X-ray diffraction analysis and scanning electron microscopy (SEM).

Experimental. PSC is obtained similarly to porous silicon by electrochemical anodization [1, 7]. A commercial (CREE) 6H-SiC wafer ($3x10^{18}$ cm^{-3}) with 3.5° off - oriented polished (0001)Si face was used for the experiments. The anodizing was done in a HF : H_2O : C_2H_5OH = 1 : 1 : 2 electrolyte under illumination of the sample surface with UV light at three current densities j : 20, 60 and 100 mA/cm^2. The etching time was chosen on condition that the passage of the same charge through the substrates and was 15, 5, or 3 min, respectively.
Thin epitaxial 6H-SiC layers were grown on PSC in a vertical water-cooled quartz reactor by vacuum sublimation at a temperature of 2000°C. This growth technique was described in [8].
The thickness and morphology of PSC were determined on cleaved substrates by SEM.
X-ray measurements were performed on double- and triple-crystal diffractometers (DCD and TCD) in $CuK\alpha_1$ radiation. The porosity of the samples was evaluated from X-ray absorption porometry [9] (measurement accuracy ±5%) and gravimetry. Stresses were estimated on the basis of the sample curvature radii R measured on DCD [10] and using the Stoney formula [11]. The structural perfection of the layers was monitored by the behavior of the full width at half-maximum (FWHM) of a diffraction peak for the symmetric Bragg's reflection (0006). θ- and (θ-2θ)-scanning modes were used for TCD measurements.

Results and discussions.
Scanning electron microscopy. The thickness' of the PSC samples were measured on the cleaved surfaces before and after high temperature growth of epitaxial layers. Figure 1 presents a cross-sectional SEM image of PSC on the substrate immediately after electrochemical anodization. It can

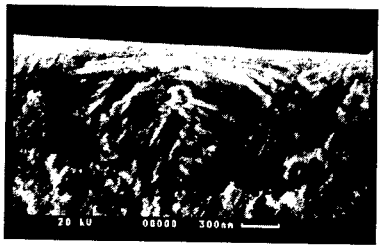


Fig.1. SEM image of the PSC cross section after electrochemical anodizing.

be seen that not all pores reach the sample surface, as described in [4, 5]. The pores start from surface defects, deep inside the volume and line up in a direction perpendicular to the surface.

The existence of a clear boundary between the substrate and the porous layer allows the porous layer thickness to be determined rather accurately. For the given samples the initial PSC thickness at current densities of 20, 60, and 100 mA /cm^2 was 26, 18, and 16 μm, respectively.

Heating in a vacuum to 2000°C changed the PSC structure for all the three samples (Fig. 2), especially at the PSC - substrate interface. The PSC prepared at a current density of 100 mA/cm^2 underwent the most pronounced changes at the bottom interface.

X-ray diffractometry. (a) Curvature and stresses in the samples. The curvature radii R and the biaxial stresses σ_a calculated from them, strain ε_z along the normal to the sample surface, and FWHMs taken on DCD and TCD are presented in Table 1.

During the growth of a PSC layer on SiC substrate, the sign of the substrate curvature changes (an initially concave sample becomes convex). However, the sample curvature radii remain practically unchanged with increasing current density. The biaxial tangential stresses in PSC, determined using the Stoney formula [11], are compressive, and the strain along the normal to the sample surface, calculated from these stresses, $\varepsilon_{z'} = \delta d/d$, is positive.

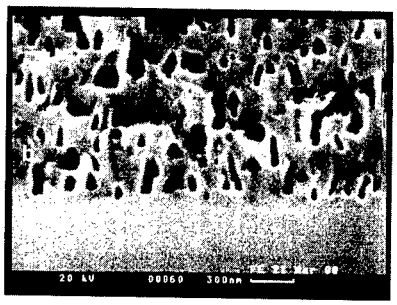


Fig.2. SEM image of the PSC cross section after sublimation growth of the epilayer at 2000°C (a-substrate, b-PSC layer).

Such a behavior of the sample curvature in growth of thin epitaxial SiC layers on PSC may be associated with a structural transformation in the initially grown PSC. This is probably also a reason for a certain enhancement of biaxial stresses in an epitaxial layer grown on a PSC (100 mA/cm^2) with the highest porosity.

Table 1. Curvature radii, biaxial stresses, strains, FWHMs of rocing curves in the structures stadied.

sample	R (m)	σ_a (GPa)	ε_z, 10^{-3}	ω / ω_{ds} (DCD) (arcsec)	ω_θ (TCD) (arcsec)	$\omega_{\theta\text{-}2\theta}$ (TCD) (arcsec)
initial substrate	-3.40	-1.34	+2.70	22 / -	20	6.8
subst.+epi.SiC	+4.07	—	—	22 / -	18	5.5
PSC(20 mA/cm^2)	+2.03	-0.21	+0.41	35 / 2144	34	7.9
PSC+epi.SiC	+2.28	-0.20	+0.40	28 / 1010	25	7.6
PSC(60 mA/cm^2)	+1.82	-0.33	+0.66	37 / 2059	34	7.5
PSC+epi.SiC	+2.14	-0.30	+0.60	30 / 811	24	6.5
PSC(100 mA/cm^2)	+1.90	-0.36	+0.72	38 / 1856	37	7.4
PSC+epi.SiC	+2.28	-0.42	+0.84	46 / 683	40	5.9

The biaxial compressive stresses are 4 - 6 times weaker in the epitaxial layers on PSC than in the layer grown on the initial SiC substrate.

b) Diffraction curves. Table 1 lists FWHMs for the DCD and TCD diffraction pattern recording schemes. The FWHM values are corrected for the sample curvature.

DCD rocking curves have the same shape for all PSC samples on SiC substrates (Fig. 3), each containing a narrow peak on a broad diffuse "hump". The FWHMs ω_θ of the narrow (dynamic) peak in PSC are more than 1.5 times that of the initial substrate and increase only slightly with increasing current density. At the same time, (θ-2θ) curves have the shape of a narrow symmetric peak, which indicates that the lattice constants of PSC and substrate match for all current densities.

The broad low-intensity part of the DCD rocking curve is related to diffuse scattering on the porous structure [12]. The width ω_{ds} of the diffuse peak yields the effective pore diameter. The decrease in ω_{ds} with increasing current density reflects the fact that the pore diameter increases (from 22nm at 20 mA/cm^2 to 28nm at 100 mA/cm^2). The shape of the diffuse peak with a flat maximum is associated with the interference of X-rays scattered by neighboring pores [13].

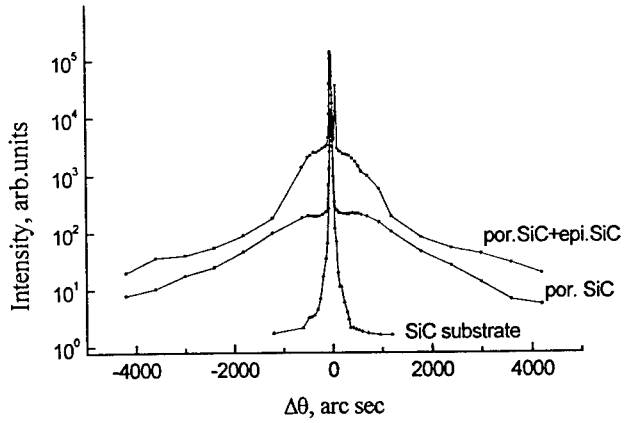


Fig.3. DCD rocking curves. CuKα_1 radiation, Bragg's reflection (0006).

The subsequent growth of an epitaxial layer on PSC is results in a narrowing of both the narrow and the diffuse peak. Since the epitaxial layers are thin (0.5-3 μm), the diffraction curve is mainly determined by the PSC below. The dramatic (2-3 times) decrease in ω_{ds} indicates a transformation of the PSC structure. Estimates give pore diameters of 52nm at 20 mA/cm^2 and 77nm at 100 mA/cm^2.

The characterization of the epilayer by X-ray diffraction analysis is difficult since the PSC thickness exceeds that of the epitaxial layer and their peaks overlap in the diffraction pattern. However, the half width of the dynamic peak suggests that the structural characteristics of this layer compare well with those of the initial substrate. But, in contrast to the latter, the epitaxial layer exhibits good uniformity over the entire sample area.

Sample porosity. X-ray measurements yield porosity values close to those obtained by gravimetry and the effective pore diameters obtained under the same assumptions are similar to those in [12]: (1) the pores have a cylindrical shape and (2) pore openings on the surface are arranged in the form of a square lattice. Knowing these values, the volume and surface area of a single pore can be determined together with the number of pores N per cm^2 of surface (Table 2). The calculation accounted for the fact that the volume of removed SiC is the same for all the three samples since the charge passed through the substrates during anodization was maintained constant. This is confirmed by the fact that Ph ≈ const, where P is the porosity of a layer and h is its thickness. Apparently, Ph = NV, where N is the number of pores per cm^2 of surface and V is the volume of a pore. It can be seen from the table that the pores do not increase in volume with increasing current density and, consequently, the number of pores also remains constant in this range of current densities, N ≈ 3x10^{10} cm^{-2}. Hence follows that the porosity increases with increasing anode current density because of the increasing effective pore diameter. The pore surface area decreases with increasing current density since the porous layer thickness decreases with simultaneously increasing pore diameter.

It was found from X-ray data that, within the measurement accuracy, the porosity remains unchanged after annealing a porous sample prior to deposition of epitaxial SiC layer. At the same time (Table 2), the number of pores decreases, and the surface and the volume of a single pore increases. This fact can be accounted for by a structural transformation in the PSC upon high temperature annealing of the samples, leading to merging of pores and a simultaneous increase of their diameter, which can be seen in Fig.2. It may be assumed that this structural transformation is caused by sublimation transport inside the pores and mechanical stresses in the pores.

Tabl.2. Characterization of the porous silicon carbide layers before and after high temperature growth of the epilayers: h-thickness of a PSC; P-porosity of a layer; d-pore diameter; V-volume of a pore; N-the number of pores per cm^2 ; S-pore surface area.

	j=20 mA/cm^2		j=100 mA/cm^2	
	before	after	before	after
h, μm	26	22	16	12
P, %	11.3	—	20	—
Ph, %μm	295	—	330	—
d, μm	22×10^{-3}	52×10^{-3}	28×10^{-3}	77×10^{-3}
V, μm^3	0.986×10^{-2}	4.67×10^{-2}	0.986×10^{-2}	5.6×10^{-2}
N, cm^{-2}	3×10^{10}	0.53×10^{10}	3.25×10^{10}	0.43×10^{10}
S, μm^2	1.8	3.59	1.41	2.9

Conclusion. The performed investigations demonstrated that heating of porous silicon carbide to 2000°C and the subsequent growth of an epitaxial layer on it lead to a transformation of the initial PSC structure, accompanied by merging of separate pores and a decrease of their number. At the same time, a reduction of the biaxial compressive stresses in an epitaxial layer on PSC by a factor of 4 to 6, structural integrity of the samples improved with the treatment, and the previously observed decrease of the dislocation density by an order of magnitude in the thick layer give reason to suppose that layers of this kind can find application as buffers. However, it should be noted that further investigations are necessary for determining the optimal regimes of PSC fabrication and subsequent annealing.

Acknowledgements.
The authors would like to thank V.Busov for SEM characterization.

References.

[1] T.Matsumoto et al. Appl. Phys. Lett. 64, (1994), p. 226.
[2] A.O.Konstantinov, A.Henry, C.I.Harris, E.Janzén. Appl. Phys.Lett. **66** (17), 24, (1995), p. 2250.
[3] A.M.Danishevskiĭ et al. Semiconductors **31**(4) (1997), p. 354.
[4] A.M.Danishevskiĭ et al, Semicond.Sci.Technol., **3**, (1998), p. 1111.
[5] S.Zangooie, H.Arvin. Extended Abstr. 2-nd Intern. Conf. (Madrid, 12-17 March, 2000) p. 117.
[6] M.Mynbaeva et al. Mat.Res.Soc.Symp.Vol. 587 (C); 2000 Materials Research Society, p.08.6.1
[7] J.S.Shor, I.Grimberg, B.-Z.Weiss, A.D.Kurtz. Appl. Phys.Lett., 62, (1993), p. 2836.
[8] N.S.Savkina et al. Mater. Sci. and Eng., **B 61-62**, (1999), p. 165.
[9] V.V.Ratnikov. Phys.of Sol.State, 39(5) (1997), p. 856.
[10] G.Rozgonyi, P.Petroff, M.Panish. J.Cryst. Growth, 27, (1974), p. 106.
[11] G.Stoney. Proc.R.Soc.London, Ser.A, 82, (1925), p. 172
[12] D.Bellet, G.Dolino, M.Ligeon, P.Blanc, M.Krisch. J.Appl.Phys., 71, (1992), p. 145.

Materials Science Forum Vols. 353-356 (2001) pp. 123-126
© 2001 Trans Tech Publications, Switzerland

Gaseous Etching Effects on Homoepitaxial Growth of SiC on Hemispherical Substrates Using CVD

S. Nishino, Y. Masuda, S. Ohshima and C. Jacob

Faculty of Engineering & Design, Kyoto Institute of Technology,
Matsugasaki, Sakyo, Kyoto 606-8585, Japan

Keywords: C_3H_8 Etching, HCl Etching, Hemispherical Substrate, Homoepitaxial Growth, Off-Orientation, Surface Morphology

Abstract In this study, homoepitaxial growth was carried out by atmospheric pressure CVD using Si_2Cl_6+C_3H_8 gas system. To obtain further information about crystal orientation effects, hemispherically polished substrates of 6H-, 4H- and 15R-SiC were used. The effects of two types gaseous etching (H_2+HCl and H_2+C_3H_8) on grown epitaxial layers were studied. For C-face, 3D-nucleation of 3C-SiC along <1$\bar{1}$20> was observed on the grown epilayers after the H_2+HCl etching. In contrast, 3D nucleation did not extend along <1$\bar{1}$20> of the grown epilayers after the H_2+C_3H_8 etching. This reason is attributed to the anisotropy of the H_2+HCl etching and the difference of dangling bond energy at the step edge. For Si-face, characteristic features for each polytype were observed.

Introduction

Substrate crystalline orientation is a key factor in determining the quality of SiC epitaxial layers formed using CVD [1,2]. Recent work has demonstrated that 4H-SiC epilayers with smooth morphologies and high quality could be grown on (11$\bar{2}$0) faces, and on substrates inclined 8° off from (0001) Si-face toward <1$\bar{1}$00> [3-5]. The surface morphology and the growth mechanism need to be studied in detail for various substrate crystalline orientations. To obtain further information about morphological stability on the tilted substrate, hemispherically polished substrates were used. The orientation dependencies of surface morphology for homoepitaxial layers using 6H-SiC hemispherical substrate have been previously reported [6]. Also, the orientation effects of gaseous etching before growth is important. This work investigates the surface morphology of the grown epitaxial layer from a preparation of gaseous etching (H_2+HCl and H_2+C_3H_8) using 6H-, 4H- and 15R-SiC hemispherical substrates. We show how the growth surface develops after the different etch procedures. Growth mechanisms for each direction are discussed.

Experimental

The hemispherical substrates were prepared on commercial 6H-, 4H- and 15R-SiC substrates inclined 3.5°, 8° off from (0001) Si-face or (000$\bar{1}$) C-face toward <11$\bar{2}$0>, and Lely substrates (on-axis). The diameter of the hemispheres was 15 mm, and off angle was obtatined at least 0° to 15° off from the basal plane, (0001) Si-face and (000$\bar{1}$) C-face. By using those substrates, morphological stability of the epilayer in various directions, <hkil>, could be investigated. The etching flow rate of carrier H_2 gas, HCl and C_3H_8 were 1-3 slm, 3-9 sccm and 0.2-1.2 sccm, respectively. The etching temperatures were 1300°C for the H_2+HCl etch, and 1500°C for the H_2+C_3H_8 etch. The etching time

was between 5 and 30 minutes. The SiC epilayers were grown by atmospheric CVD using Si_2Cl_6 (hexachlorodisilane) as Si source and C_3H_8 as C source [7]. Growth temperature was 1500°C, and the growth time was 60 and 660 minutes. The growth rate on conventional flat substrates was 1.5 μm/h. These growth parameters were optimized to obtain smooth surface of epilayers using 6H-SiC substrate inclined 3.5° off from (0001) Si-face toward <11$\bar{2}$0>. The surface morphologies of the epilayers were observed by optical microscopy with Nomarski mode, and Scanning Electron Microscope (SEM). The polytype of the epilayers was characterized by low temperature photoluminescence measurements and Raman spectroscopy.

Results and Discussion

Clear differences in surface morphology of the grown epitaxial layer after preparation of gaseous etching (H_2+HCl and H_2+C_3H_8) on C-face hemispherical substrates were observed. Fig. 1 shows the surface morphology grown after H_2+HCl etching on C-face of 6H-SiC observed by optical microscopy. We obtained a sixfold symmetry on the hemisphere. The dark and rough regions, where 3D nucleation of 3C-SiC occurred, extended along <11$\bar{2}$0>. In contrast, smooth surface was

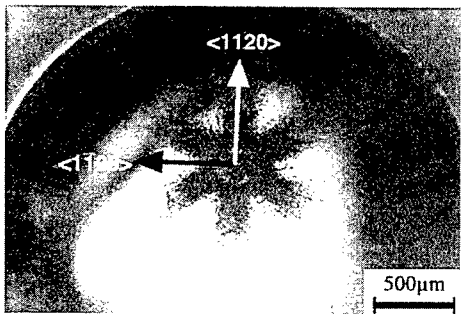


Fig. 1 Optical microscopy image of the surface morphology grown after H_2+HCl etching on C-face of 6H-SiC.

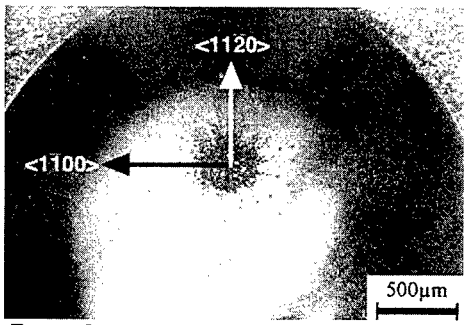


Fig. 2 Optical microscopy image of the surface morphology grown after H_2+C_3H_8 etching on C-face of 6H-SiC.

observed along <1$\bar{1}$00> [6]. Fig. 2 shows the surface morphology of the hemispherical epilayer grown after H_2+C_3H_8 etching on C-face of 6H-SiC. In this case, no 3D nucleation of 3C-SiC occurred along <11$\bar{2}$0>, and slightly rough regions was observed at the boundary between <11$\bar{2}$0> and <1$\bar{1}$00>. On the Si-face, the surface morphology was not significantly dependent on the different etch procedures. We was observable no transformation of surface morphologies after each

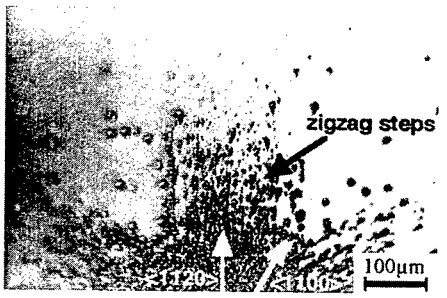


Fig. 3 Optical microscopy image of the surface morphology grown after H_2+HCl etching on C-face of 4H-SiC.

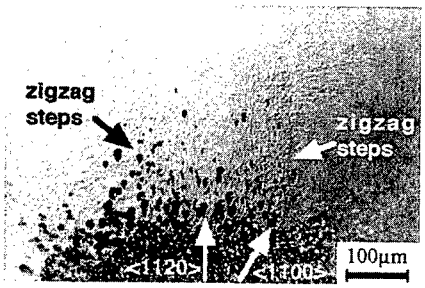


Fig. 4 Optical microscopy image of the surface morphology grown after H_2+C_3H_8 etching on C-face of 4H-SiC.

etching procedures using optical microscopy and SEM. Consequently, it is believed that conceive gaseous etching has an effect on a micro-scale on Si-face substrates.

Figs. 3 and 4 show the surface morphology of epilayers of 4H-SiC after each etching using optical microscopy. In the case of H_2+HCl etching, microsteps with triangular depressions at step edges on 6H-SiC (0001)-vicinal faces were observed toward only <11$\bar{2}$0> [8]. The H_2+HCl etching produced the zigzag steps along <11$\bar{2}$0> as shown in Fig. 5. The growth steps are supposed to align parallel to crystal facets of the substrates. These zigzag steps produced grooves and hillocks aligned along the <11$\bar{2}$0> as shown in Fig. 3. In addition, the surface free energy of <11$\bar{2}$0> is considered to be lower than that of <1$\bar{1}$00> for C-face. Because the surface free energy of C-face is lower than that of Si-face [9]. For the step edge of <11$\bar{2}$0>, which has more C-dangling bonds than that of the <1$\bar{1}$00> for C-face, the surface free energy of <11$\bar{2}$0> is lower than that of <1$\bar{1}$00> for C-face. This indicates nucleation occurs much more frequently along the <11$\bar{2}$0> on C-face under same condition. But, for Si-face, the surface free energy of <11$\bar{2}$0> is higher than that of <1$\bar{1}$00>. And, the nucleation occurs much more frequently along the <1$\bar{1}$00> on Si-face.

In contrast, we propose that the H_2+C_3H_8 etching is isotropic for producing microsteps [5]. The H_2+C_3H_8 etching produced microsteps perpendicular to each off-direction for both <11$\bar{2}$0> and <1$\bar{1}$00>. This produces facets which have the corner of twelvefold symmetry as shown in Fig. 6. In Fig. 4, at the boundary between

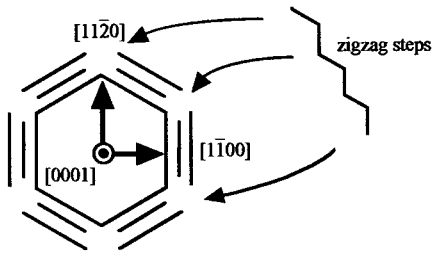


Fig. 5 Schematic representation of step configurations after the H_2 + HCl etching.

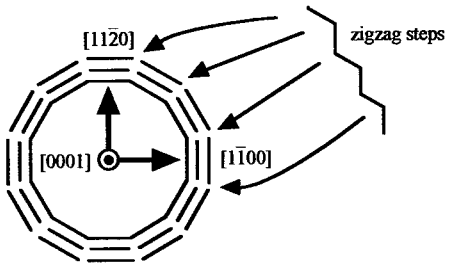


Fig. 6 Schematic representation of step configurations after the H_2 + C_3H_8 etching.

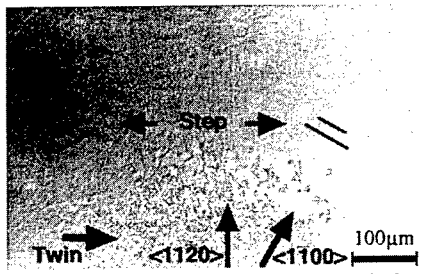


Fig. 7 Optical microscopy image of the surface morphology grown on Si-face of 6H-SiC.

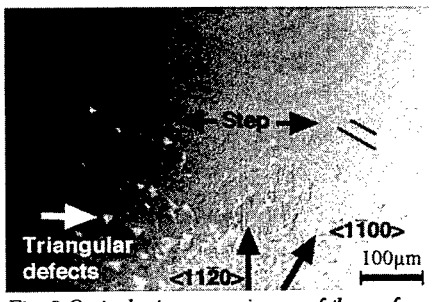


Fig. 8 Optical microscopy image of the surface morphology grown on Si-face of 4H-SiC.

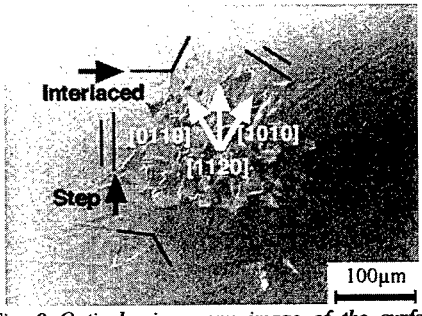


Fig. 9 Optical microscopy image of the surface morphology grown on Si-face of 15R-SiC.

<$11\bar{2}0$> and <$1\bar{1}00$>, the slightly rough regions indicate the presence of the zigzag steps at each corner of the twelvefold symmetry. Using the H_2+C_3H_8 etching, it is difficult to produce zigzag steps for <$11\bar{2}0$>. Consequently, at the initial stage of growth, the rough surface morphology is not obtained along <$11\bar{2}0$> on C-face.

Different epitaxial surface morphologies were obtained for Si-face of each polytype. For 6H-SiC (0001)-vicinal surface, a mosaic pattern of twinned crystalline 3C-SiC was observed as shown in Fig. 7. For 4H-SiC (0001)-vicinal surface, many triangular defects, commonly observed in 4H-SiC growth on low off-axis (0001) flat substrate, and a mosaic pattern were observed as shown in Fig. 8. The triangular defects were observed up until 2° off-axis for all directions. The occurrence of the triangular defects was isotropic. For 15R-SiC (0001)-vicinal surface, a mosaic pattern was observed such as on 6H-, 4H-SiC as shown in Fig. 9. The triangular defect density was between that of 6H and 4H. It was suggested that the high percent of hexagonality in a polytype enhanced the triangular 3C-SiC inclusions [10]. The percent of hexagonality of the 15R structure (40%) is between 4H (50%) and 6H (33%). The observations are consistent with this model. And, for 6H- and 4H-SiC, the step like pattern perpendicular to <$1\bar{1}00$> family was observed. But, for only 15R-SiC, interlaced shape and step like pattern was observed alternately along [$01\bar{1}0$] and [$10\bar{1}0$] as shown in Fig. 9. This growth mechanism is not clear yet, but is probably due to the presence of facets of 15R-SiC. The rhombohedral 15R structure may be the cause of the difference in the surface morphology.

Conclusions

The surface morphologies of epilayers grown on 6H-, 4H- and 15R-SiC hemispherical substrates after the H_2+HCl and H_2+C_3H_8 etching were investigated. For C-face, CVD growth after the H_2+HCl etch produced anisotropy, with 3D nucleation occurred along <$11\bar{2}0$>, whereas CVD growth after the H_2+C_3H_8 etch produced isotropic 3D nucleation. This growth mechanism is caused by the anisotropy of microstep formation of the H_2+HCl etch and the difference of dangling bond energy for the step edge. For Si-face, each polytype produced a characteristic surface morphology. The triangular 3C-SiC inclusions for 4H-SiC were observed up until 2° off for all directions. Alternately interlaced shape and step like pattern along [$01\bar{1}0$] and [$10\bar{1}0$] was observed for 15R-SiC.

Reference

[1] T.Ueda, H.Nishino, and H.Matsunami, J. Crystal Growth **104** (1990), p. 695.
[2] H.S.Kong, J.T.Glass, and R.F.Davis, J. Appl. Phys. **64** (1988), p. 2672.
[3] T.Kimoto, T.Yamamoto, Z.Y.Chen, H.Yano, and H.Matsunami, Mat. Sci. Forum **338-342** (2000), p. 189.
[4] B.E.Landini and G.R.Brandes, Appl. Phys. Lett. **74** (1999), p. 2632.
[5] Y.Masuda, S.Ohshima, C.Jacob, and S.Nishino, *presented in this conference.*
[6] S.Nishino, Y.Nishio, Y.Masuda, Y.Chen, and C.Jacob, Mat. Sci. Forum **338-342** (2000), p. 197.
[7] S.Nishino, T.Miyanagi, Y.Nishio, Mat. Sci. Forum **264-268** (1998), p. 139.
[8] S.Nakamura, T.Kimoto, H.Matsunami, S.Tanaka, N.Teraguchi, and A.Suzuki, Appl. Phys. Lett. **76** (2000), p. 3412.
[9] R.Yakimova, M.Syvajarvi, and E.Janzen, Mat. Sci. Forum **264-268** (1998), p. 159.
[10] J.A.Powell, D.J.Larkin, and A.J.Trunek, Mat. Sci. Forum **264-268** (1998), p. 421.

Materials Science Forum Vols. 353-356 (2001) pp. 127-130
© 2001 Trans Tech Publications, Switzerland

Low Temperature Selective and Lateral Epitaxial Growth of Silicon Carbide on Patterned Silicon Substrates

Chacko Jacob[1], Pirouz Pirouz[2] and Shigehiro Nishino[1]

[1] Department of Electronics & Information Science, Kyoto Institute of Technology, Matsugasaki, Sakyo-ku, Kyoto 606-8585, Japan

[2] Department of Materials Science and Engineering, Case Western Reserve University, 10900 Euclid Ave., Cleveland OH 44106, USA

Keywords: HCDS, HMDS, Lateral Overgrowth, Propane, Selective Epitaxy

Abstract The development of a low temperature selective epitaxial process for the growth of 3C-SiC on patterned Si substrates is reported. Due to the damage caused to the oxide mask at the conventional growth temperatures of ~1350°C, temperatures lower than 1250°C are needed. In order to lower the temperature for epitaxial growth, trimethylaluminium (TMA) was used and epitaxial films successfully grown at 1250°C. However, this approach resulted in the formation of an unidentified phase at the 3C-SiC/Si interface as well as gas phase nucleation. Using HMDS as the single-source precursor, films were grown at 1150°C using a low growth rate. Finally, experiments were performed using HCDS and propane at 1150°C. Long time growth (up to 3 hours) reveals good films with no damage to the oxide. Coalescence has been demonstrated.

Introduction: The absence of high-quality 3C-SiC bulk substrates has hindered the development of this SiC polytype. While homoepitaxial growth of 3C-SiC has not been developed, heteroepitaxial growth of 3C-SiC on Si [1] and other substrates has indicated the promise of high mobility devices, etc. However, the high density of interfacial defects (misfit dislocations, voids) as well as other defects (threading dislocations, twins, stacking faults) result in the growth of lower quality material. A suitable approach towards solving this problem is the use of selective epitaxial growth on patterned silicon substrates followed by epitaxial lateral overgrowth. The successful demonstration of this technique recently in GaN growth [2] has spurred interest in this technique.

The main factors affecting selective epitaxy are temperature of growth, choice of mask material, orientation of windows, mask to window ratio, influence of an etchant (e.g. HCl), quality of the mask material, etc. [3]. In applying this technique to SiC growth, Edgar *et al* [4] report that a limiting factor is the oxide mask as well as the duration of growth. For long growth times, it was difficult to suppress the unwanted nucleation on the oxide. Nishino et al [5] also reported that the use of HCl aided the process of selective epitaxy. In a recent report, Saddow et al [6] reported some preliminary work on the selective epitaxy of SiC on Si using silicon nitride and aluminum nitride as masks. However, there was no evidence of selectivity using either mask. Our earlier work [7] reported the use of hexachlorodisilane (HCDS) and propane as the source materials and an oxide mask to demonstrate selective epitaxy and lateral overgrowth. Unfortunately, the oxide mask was damaged at temperatures above 1250°C. The limitations of using the oxide as a mask were demonstrated and attempts were made to lower the epitaxial growth temperature by adding trimethylaluminium (TMA). While this helped to reduce the epitaxial growth temperature and thus minimized damage to the oxide mask, the reaction tube became very dirty (possibly due to some homogeneous nucleation) and other problems were evident. An unidentified phase was formed at the 3C-SiC/Si interface. This may be a glassy phase formed due to the reaction of the mask with the aluminium in the TMA. Therefore, alternative methods for lower temperature selective epitaxy have

been studied. We report the use of hexamethyldisilane (HMDS) to achieve low temperature selective epitaxy as well as some recent results using HCDS and propane.

Experimental procedures: The substrates used were patterned silicon (001) substrates prepared by depositing a SiO_2 layer (~0.7 μm) as the mask, followed by conventional lithographic techniques to create the pattern. The features ranged in size from a few μm to 100 μm. The windows are of different shapes mostly oriented along the <110> directions. The substrates were cleaned by blowing with dry nitrogen. No additional ex-situ cleaning was performed, as it appeared to increase damage on the mask surface, thereby reducing the selectivity.

A horizontal atmospheric pressure chemical vapor deposition reactor was used. Source gases were hexachlorodisilane (HCDS) and propane. Hydrogen (typically 3 slm) was used as the carrier gas. Hydrogen chloride gas was used as an etchant to suppress the unwanted nucleation on the mask as well as for in-situ cleaning of the substrate. Further details of the CVD growth process have been published earlier [7].

A single source precursor, Hexamethyldisilane (HMDS) was also used. This compound contains both silicon and carbon in a ratio of 1:3 and is thus carbon-rich. Propane was used during the carbonization process and hydrogen (typically 3 slm) as the carrier gas. The HMDS bubbler was maintained at a temperature of 20°C. At this temperature, HMDS has a vapor pressure of 22 Torr. The flow rate of HMDS was in the range of 0.05 sccm – 0.5 sccm.

Results and Discussion: Selective growth was previously demonstrated in films grown at 1350°C and below (Fig.1). This was done utilizing HCDS and propane. However, the damage to the mask at temperatures above 1250°C prompted the use of the alternative precursor, HMDS. In single source precursors, Si-C bonding is already present. Thus, the reaction is one of decomposition of the source followed by the reaction of the various species with the substrate (Si) to form SiC. However, it is rather difficult to get epitaxially oriented nuclei on Si(001). Therefore, the common practice has been to use propane for the carbonization step and then continue growth with HMDS. The carbonization step, using propane, was limited to 1250°C to limit damage to the mask.

The selectivity was a function of temperature and improved at lower temperatures (~1150°C). An additional factor influencing selectivity was the concentration of the precursor (HMDS). At high concentrations, the selectivity was poorer. As the source concentration increased, the morphology of the nuclei deposited on the mask also changed.

The temperature of growth influences the crystallinity. At lower temperatures (1100-1200°C) and normal growth rates, polycrystalline films are obtained. At high temperatures (~1300-1350°C), single crystalline films are formed, as in the case for growth using HCDS [7]. However, the oxide is severely damaged at these temperatures, as mentioned above. Using a lower growth rate could enhance the formation of epitaxial nuclei at lower temperatures. By using a lower concentration of HMDS for growth, we expected to get single crystalline films at lower temperatures, while maintaining mask integrity.

Using the above results, an additional set of experiments was performed using the following conditions. The flow rate of HMDS was 0.10 sccm and the flow rate of HCl was 1.0 sccm. The hydrogen carrier gas flow rate was increased from 3 slm to 5 slm. The film quality improved tremendously and clear spot patterns were obtained by RHEED. The early stages of lateral overgrowth were observed in these films. Nominal growth rate on an unpatterned substrate was

about 0.3-0.4 μm per hour. It is believed that the growth rate is higher in the windows of the patterned substrate due to the higher concentration of growth species in the window area [8].

Since low temperature epitaxial growth was obtained using HMDS by utilizing a slow growth rate, the same approach was then adopted for the HCDS and propane system. Highly selective growth was demonstrated at 1150°C. Clear evidence for lateral overgrowth was also obtained at this temperature (Fig. 1). Lateral to vertical (L/V) growth rates of up to 2 have been observed. The L/V rate depends on the pattern size and shape.

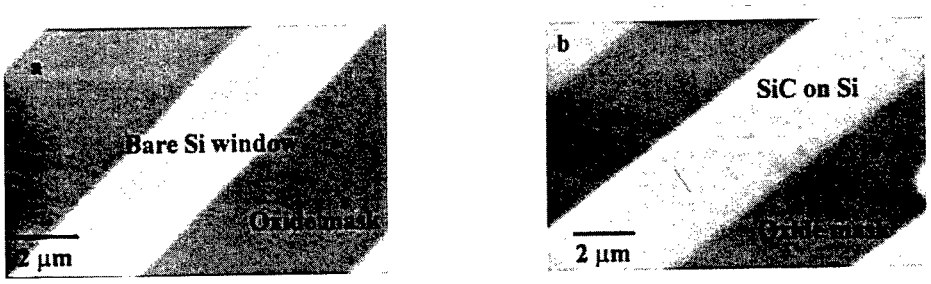


Figure 1 Epitaxial Lateral Overgrowth of SiC on Si (001) substrate a) before growth; b) after growth at 1150°C using HCDS and propane.

Long growth experiments (up to 3 hours) was performed at 1150°C using HCDS and propane. The growth rate was determined to be about 0.6 μm/hour. The films demonstrated good selectivity and the oxide mask remained undamaged even after three hours. Fig. 2a shows the highly selective deposit of stripes. Parts of the mask that were very large in area (> 10 microns in width) showed the formation of unwanted nuclei (Fig. 2b).

Coalescence of laterally overgrown films was achieved and is shown in Fig. 3. The stripes are 1 μm wide. The high level of selectivity can be clearly observed in this figure. Fig. 4 also shows a series of stripes with various widths and spacings. Towards the top of the figure, a series of wide stripes are visible. They have not yet coalesced. However, the stripes towards the bottom of the figure have already coalesced. An additional feature that may be observed in this figure is that the stripes are faceted. Fig. 5 is a schematic of the faceted growth on the stripes.

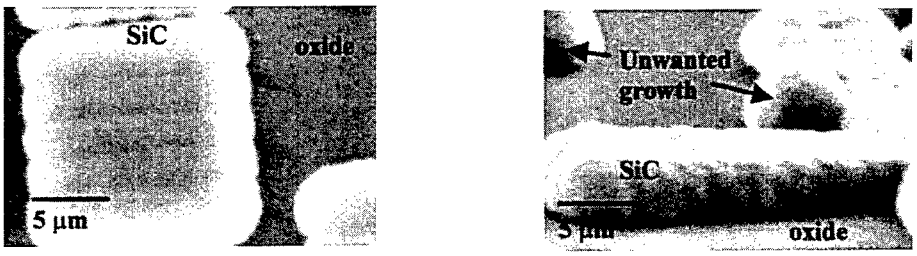


Figure 2a) Highly selective growth of SiC and b) Undesirable nucleation of SiC on wide areas of oxide mask



Figure 3 Coalesced stripes (original width 1 μm)

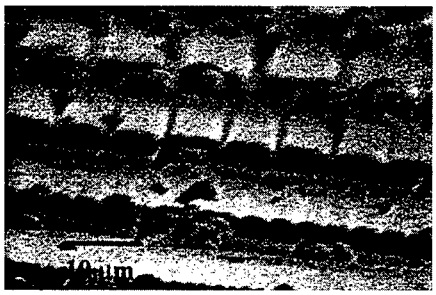


Figure 4 Stripes of varying width showing facet formation and coalescence

In closely spaced stripes, there is almost no unwanted nucleation on the oxide mask. However, the L/V ratio is lower than in more widely spaced stripes. This seems to be related to the availability of laterally diffusing species on the exposed mask.

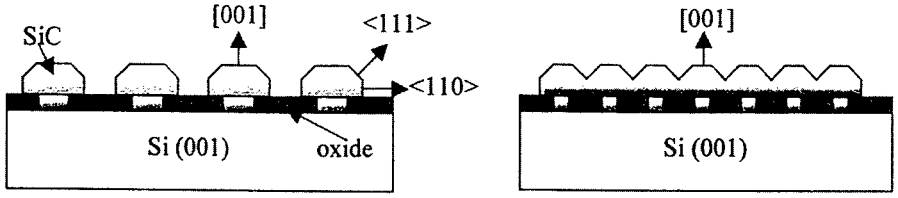


Figure 5 Schematic of faceted lateral overgrowth of stripes of different widths of 3C-SiC on Si

Conclusions: Low temperature selective epitaxial growth has been demonstrated using HMDS as a single source precursor. Low growth rates were necessary to obtain single crystalline films. Using the same approach, highly selective low temperature epitaxy was obtained using HCDS and propane. Lateral overgrowth was observable. Coalescence of the laterally growing film was obtained for closely spaced stripes.

Acknowledgment: CJ was supported by a JSPS Fellowship.

References

[1] S. Nishino, J. A. Powell, and H. A. Will, Appl. Phys. Lett. 42 (1983), p. 460.
[2] T.S. Zheleva, O-H Nam, M. D. Bremser and R. F. Davis, Appl. Phys. Lett. 71 (17) (1997), p. 2472.
[3] L. Jastrzebski, J. Cryst. Growth 63 (1983), p. 493.
[4] J. H. Edgar, Y. Gao, J. Chaudhari, S. Cheema, S. A Casalnuovo, P. W. Yip and M. V. Sidorov, J. Appl. Phys. 84 (1) (1998), p. 201.
[5] S. Nishino, H. Tanaka, K. Takahashi and J. Saraie, Amorphous and Crystalline Silicon Carbide IV, Eds. C. Y. Yang, M. M Rahman and G. L. Harris, (Springer Verlag: Berlin, 1992), p. 411.
[6] S. E. Saddow, G. E. Carter, B. Geil, T. Zheleva, G. Melnychuck, M. E. Okhyusen, M. S. Mazzola, R. D. Vispute, M. Derenge, M. Ervin and K. A. Jones, Proceedings of ICSCRM '99, Edited by C. H. Carter, Jr., R. Devaty and G. Rohrer, Mater. Sci. Forum, Vols. 338-342 (2000), p.245.
[7] C. Jacob, M-H. Hong, J. Chung, P. Pirouz and S. Nishino, Proceedings of ICSCRM '99, Edited by C. H. Carter, Jr., R. Devaty and G. Rohrer, Mater. Sci. Forum, Vols. 338-342 (2000), p. 249.
[8] C. Jacob, J. Chung, M. H. Hong, P. Pirouz and S. Nishino, Mat. Res. Soc. Symp. Proc. Vol. 622, (MRS: Pittsburgh) (2000).

Materials Science Forum Vols. 353-356 (2001) pp. 131-134
© 2001 Trans Tech Publications, Switzerland

Characterization of 4H-SiC Epilayers Grown at a High Deposition Rate

H. Tsuchida[1], T. Tsuji[2], I. Kamata[1], T. Jikimoto[1],
H. Fujisawa[2], S. Ogino[2] and K. Izumi[1]

[1] Central Research Institute of Electric Power Industry,
2-6-1 Nagasaka, Yokosuka, Kanagawa 240-0196, Japan

[2] Fuji Electric Corporate Research & Development, Ltd.,
2-2-1 Nagasaka, Yokosuka, Kanagawa 240-0194, Japan

Keywords: DLTS, Epitaxial Growth, Photoluminescence, Schottky Diodes

Abstract Epitaxial 4H-SiC layers grown at 10-18 μm/h in a vertical radiant-heating reactor have been characterized in terms of their morphology, purity and device performance. Through optimizations of pre-growth hydrogen etching and growth parameters, a good morphology is reproducibly obtained even for thick layers. Photoluminescence and DLTS measurements have been performed for epitaxial layers to determine impurity levels and the intrinsic defect density, and the growth parameters required to obtain a low background doping and smooth surface are discussed. Edge-terminated Ni/4H-SiC Schottky barrier diodes have been fabricated, and electrical performance of the devices is demonstrated.

1. Introduction

Power electronics is a key technology for current and future power transmission and distribution systems, and recent progress in SiC crystal quality and device performance is making the electric power industry the focus of considerable attention. Electric power applications require high-power devices that can handle over several kV and over 100 A (or even over a few kA). Because high-voltage SiC devices need a thick active layer, techniques in SiC epitaxy to obtain a higher growth rate have been studied intensively. It has been reported that growth rates around 10 μm/h are available in a horizontal hot-wall reactor with uniform doping and thickness [1]. A vertical hot-wall reactor has achieved high growth rates of up to 30 μm/h with a specular surface [2]. High-voltage bipolar devices require a long minority carrier lifetime to realize a low on-state forward voltage-drop (V_{on}), and crystallographic defects and impurity levels must be minimized. High power devices with a large active area also require minimizing of defects induced during epitaxial growth, as well as defects in the substrate. From this point of view, improving crystal quality while achieving a high growth rate with a sufficient wafer capacity is a challenge for current SiC epitaxy. In this paper, we report on the quality of epitaxial layers obtained at a high growth rate in a vertical radiant-heating reactor.

2. Experiments

Epitaxial growth was performed on commercial 8° off 4H-SiC(0001) substrates in a vertical radiant-heating reactor. Substrates and a susceptor were placed inside a cylindrical hot-wall, so that the substrates and the susceptor were heated by radiation from the hot-wall [3]. We used SiH_4 and C_3H_8 as precursors with upward H_2 carrier gas flow. Typical growth temperature was 1530-1600°C at the susceptor top, although the hot-wall temperature was considerably higher than the susceptor temperature. Thick 4H-SiC epitaxial layers were grown at 10-18 μm/h under a reduced pressure of as low as around 50 Torr.

Nomarski optical microscopy and atomic force microscopy (AFM) were used to examine the morphology of epitaxial layers. Low temperature photoluminescence (PL) measurements were performed at 8K using a He-Cd laser (λ =325 nm). The Z_1 trap concentration was determined by deep level transient spectroscopy (DLTS) through fabricating Ni-Schottky electrodes. For the DLTS measurements, we applied the reverse bias of -10 V and pulse bias of 0 V for 100 μs.

High-voltage 4H-SiC Schottky barrier diodes (SBD) were fabricated employing Ni as a Schottky metal. Edge termination for Schottky electrodes was achieved by a guard ring structure produced via B^+ implantation. Post-implantation annealing was carried out at 1050°C and 90 min

for the first lot and 1700°C and 30 min for the second lot. After the guard ring formation, Ni-Schottky electrodes were deposited on epitaxial layers through sputtering. Backside Ni ohmic contacts were made by annealing in Ar at 1050°C for 2 min.

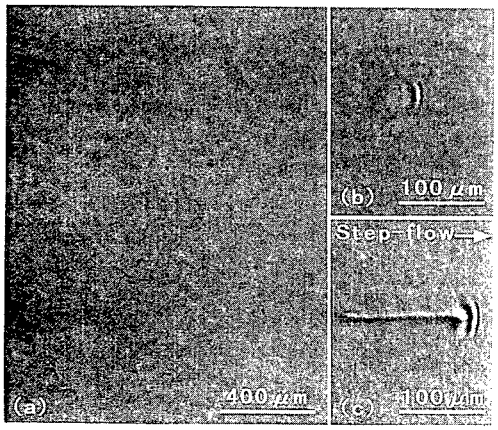


Fig. 1. Nomarski interference contrasts of a 90 μm-thick 4H-SiC epitaxial layer grown at 18 μm/h.

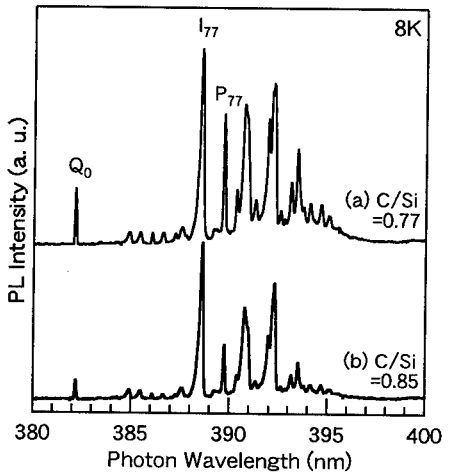


Fig. 2. Near band edge photoluminescence from epitaxial layers grown at (a) C/Si=0.77 and (b) C/Si=0.85 without intentional doping.

3. Results and discussions

3.1 Morphology and purity

First we examined growth pits on epitaxial layers. Figure 1 shows Nomarski contrasts of a 90 μm-thick epitaxial layer grown at 18 μm/h after hydrogen etching at 1400°C (measured for the susceptor top) for 45 min. After the hydrogen etching, epitaxial growth was performed at 1550°C under 50 Torr. A large defect free area without observable growth pits is shown in Fig. 1(a). A good morphology with low density of growth pits was obtained reproducibly by applying pre-growth hydrogen etching at 30 Torr, whereas applying hydrogen etching at 50-760 Torr tended to result in high density (typically 10^3-10^4 cm^{-3}) of growth pits, visible in Nomarski contrast at a low magnification. As this result, the pressure during hydrogen etching is a promising parameter to control growth pit density. An increase in the Si evaporation rate by reducing pressure, leading to inhibit Si enrichment or droplets on the etched surface [4], may be helping the reduction of growth pit density when applying hydrogen etching at 30 Torr. In addition, as shown in Fig. 1(a), traces of polishing-induced scratches are efficiently eliminated from layer surfaces. The most common growth pits remaining on epitaxial layers are wavy-pits [Fig.1 (b)], as classified in Ref. [5], and line-shaped pits [Fig. 1(c)]. Appearance and distribution of wavy-pits were not uniform throughout a sample. The typical density of wavy-pits is 10^1 cm^{-2}, although the density reaches 10^2 cm^{-2} range in some low-grade wafers. Line-shaped growth pits have a straight long depression parallel to the step-flow direction. Our KOH etching analysis revealed that most of the line-shape pits have screw type dislocations (1*C* screw dislocations and/or a micropipe) at the upstream end of the step-flow as described in detail in Ref. [6]. The both types of pits are presenting independently in most cases, whereas some of line-shaped pits accompany with a wavy pit at the downstream end as shown in Fig. 1(c). This implies that a disturbance of the step-flow is a possible origin of the wavy pit.

The purity of epitaxial layers was checked using PL measurements. Figure 2 shows near band edge spectra for epitaxial layers grown at C/Si=0.77 [spectrum (a)] and C/Si=0.85 [spectrum (b)] without intentional doping. The thickness of each layer was 54 μm and 63 μm, respectively. The PL spectra were recorded at a resolution of ~1 Å. Weak nitrogen bound excitons (Q_0, P_{77}) compared to free excitons (I_{77}) suggest that the nitrogen incorporation levels are very low. Aluminum bound excitons and boron bound excitons are also very weak. Reduction of nitrogen incorporation levels as a result of the increasing C/Si ratio from 0.77 to 0.85 is confirmed by the

weakening of the nitrogen bound excitons in Fig. 2. Both layers were identified as n-type, and the net carrier densities (N_d-N_a) were determined as ~8×10^{13} cm^{-3} for C/Si=0.77 and ~2×10^{13} cm^{-3} for C/Si=0.85 at the center of the samples by C-V measurements. The capacitance of the Schottky diodes near the sample edge was not determined for the layer grown at C/Si=0.85, possibly due to an influence of wafer holder that was touching on the sample edge (growth face) along the gas flow [3]. On the other hand, our AFM measurements (not shown) revealed that the layer grown at C/Si=0.77 had a smooth surface without macro step bunching, whereas the layer grown at C/Si=0.85 exhibited deep grooves (stripe type defects) on the surface. To obtain a low background doping and a smooth surface at the same time, we adjust C/Si ratios from 0.77 to 0.80. Although the window for C/Si ratios is very narrow in this reactor, intentional n-type doping from low 10^{15} to low 10^{19} cm^{-3} has been achieved under a constant C/Si ratio of 0.77.

Figure 3 shows a wide-range PL spectrum for a layer doped intentionally to 1.5×10^{15} cm^{-3}. The layer was grown at 15 μm/h under a C/Si ratio of 0.77, and the thickness was 120 μm. Aluminum- or boron-related donor-acceptor pair (DAP) and titanium lines are very weak, however, a defect related L_1 line (427.2 nm) is clearly seen. We also performed DLTS measurements, and the Z_1 trap concentration of a layer grown at C/Si=0.77 (growth rate: 14 μm/h, N_d-N_a: 7×10^{15} cm^{-3}) was determined as ~3×10^{13} cm^{-3}. This Z_1 trap concentration is somewhat higher than the successful result in a conventional horizontal cold-wall reactor [7]. We suppose that reduction of the intrinsic defects while achieving a high growth rate is an additional technical issue with this reactor. The Z_1 trap concentration determined for the intentionally doped layer is comparable to the background N_d-N_a values for the layers appeared in Fig. 2. Since the Z_1 center acts in an acceptor-like manner, compensation by the Z_1 center must be taken into account to the layers without intentional doping.

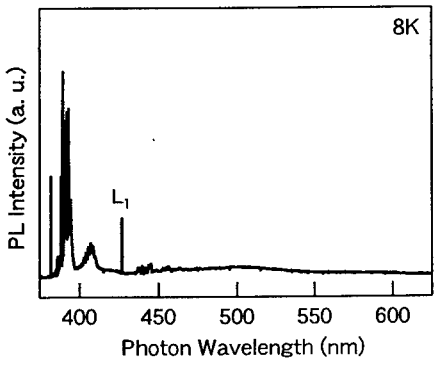


Fig. 3. Photoluminescence from an intentionally doped layer grown at C/Si raio=0.77 (120 μm-thick, 1.5×10^{15} cm^{-3}).

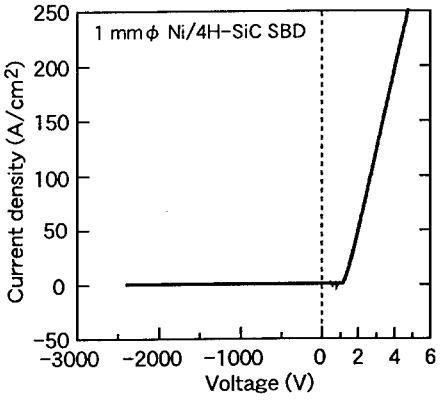


Fig. 4. I-V characteristic of a 1 mmϕ Ni/4H-SiC SBD fabricated on an epitaxial layer (27 μm-thick, 3×10^{15} cm^{-3}).

3.2 Device performance

Electrical performance of epitaxial layers was examined by testing Ni/4H-SiC SBD. A 10 μm-thick epitaxial layer doped intentionally to ~7×10^{15} cm^{-3} was used in the first lot, and a 27 μm-thick epitaxial layer doped intentionally to ~3×10^{15} cm^{-3} in the second lot. These layers were grown at 14-16 μm/h. The best breakdown voltage for 0.2 mmϕ SBD using the 10 μm layer was 1.3 kV, even though the layer was grown in only 40 min. In use of the 27 μm layer, a breakdown voltage of 2.4 kV was achieved for 1 mmϕ SBD as shown in Fig. 4. The on-resistance of the 2.4 kV SBD was 13.8 mΩcm^2 (V_{on}=2.7 V at 100 A/cm^2). Figure 5(a) shows a histogram of leakage current levels at -600 V for 1 mmϕ SBD. The corresponding electric field for -600 V is ~1.2 MV/cm for the 10 μm layer and ~0.79 MV/cm for the 27 μm layer. Some of the 1 mmϕ SBD fabricated using the 27 μm layer was able to block -600 V with a small leakage current density in the order of 10^{-7} A/cm^2, although the average leakage current density was rather high, probably due to fewer optimizations of process parameters and defect issues. The percentage of tolerable ones, that could block -600 V within a critical leakage current less than 1 mA, was over 85% for

1 mm ϕ SBD. The percentage for 2 mm ϕ SBD remained at a reasonable level of 75% as shown in Fig. 5(b). We confirmed large defect-free areas over 10 mm^2, where no observable defects existed except wavy-pits, in microscope observation. This may be attributed to the high yield of 1-2 mm ϕ SBD. In use of both the layers, we succeeded in obtaining 4 mm ϕ SBD capable of blocking -600 V with a leakage current density in the order of 10^{-3} A/cm^2, however, about 80% of 4 mm ϕ SBD resulted in failure within a very small reverse voltage [Fig. 5(C)]. To understand the poor yield of 4 mm ϕ SBD, a density of 10^1 cm^{-2} range for destructive defects is reasonable. This estimated density is close to the density of micropipes.

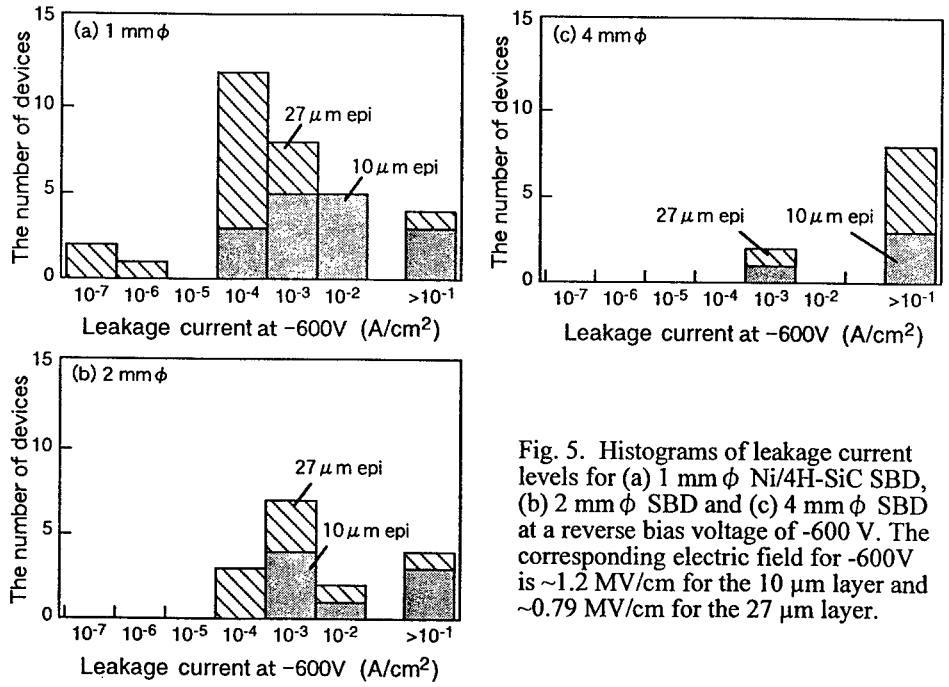


Fig. 5. Histograms of leakage current levels for (a) 1 mm ϕ Ni/4H-SiC SBD, (b) 2 mm ϕ SBD and (c) 4 mm ϕ SBD at a reverse bias voltage of -600 V. The corresponding electric field for -600V is ~1.2 MV/cm for the 10 μm layer and ~0.79 MV/cm for the 27 μm layer.

Conclusions

We identified the characteristics of 4H-SiC epitaxial layers grown at 10-18 μm/h in a vertical radiant-heating reactor. Reduction of epi-induced growth pits was achieved by applying pre-growth hydrogen etching under a reduced pressure as low as 30 Torr. Careful adjustment of the C/Si ratio is needed to obtain a low background doping and a smooth surface at the same time. Photoluminescence measurements showed low impurity levels for the layers. In use of a 27 μm epitaxial layer, a breakdown voltage of 2.4 kV was achieved for 1 mm ϕ Ni/4H-SiC SBD with an on-resistance of 13.8 mΩcm^2 (V_{on}=2.7 V at 100 A/cm^2). Some 1 mm ϕ SBD showed a small leakage current density in the order of 10^{-7} A/cm^2 at -600 V.

References

[1] K.G. Irvine, R. Singh, M.J. Paisley, J.W. Palmour, O. Kordina, and C.H. Carter Jr., Mater. Res. Soc. Symp. **512** (1998), p. 119.
[2] A. Ellison, J. Zhang, W. Magnusson, A. Henry, Q. Wahab, JP. Bergman, C. Hemmingsson, N.T. Son, and E. Janzén, Mater. Sci. Forum **338-342** (2000) p. 131.
[3] H. Tsuchida, I. Kamata, T. Jikimoto, and K. Izumi, Mater. Sci. Forum **338-342** (2000) p.145.
[4] A.A. Burk Jr., L.B. Rowland, J. Cryst. Growth **167** (1996) p. 586.
[5] A. Ellison, Doctoral thesis: Silicon Carbide Growth by high temperature CVD techniques, Dissertation No. 599, Linköping University, Sweden (1999).
[6] I. Kamata, H. Tsuchida, T. Jikimoto, and K. Izumi, this proceeding.
[7] T. Kimoto, A. Itoh, and H. Matsunami, Phys. stat. Sol. (b) **202** (1997) p. 247.

Materials Science Forum Vols. 353-356 (2001) pp. 135-138
© 2001 Trans Tech Publications, Switzerland

Control of Surface Morphologies for Epitaxial Growth on Low Off-Angle 4H-SiC (0001) Substrates

K. Masahara[1], M. Kushibe[1], H. Ohno[1], K. Kojima[1], T. Takahashi[2], Y. Ishida[2], T. Suzuki[1], T. Tanaka[1], S. Yoshida[2] and K. Arai[2]

[1] Ultra-Low-Loss Power Device Technology Research Body (UPR), R&D Association for Future Electron Devices (FED), 1-1-4 Umezono, Tsukuba, Ibaraki 305-8568, Japan

[2] Ultra-Low-Loss Power Device Technology Research Body (UPR), Electrotechnical Laboratory 1-1-4 Umezono, Tsukuba, Ibaraki 305-8568, Japan

Keywords: Low Off-Angled Substrate, Pre-Growth Etching, Surface Morphology

ABSTRACT

The surface morphology of epitaxial layers grown on low off-angle 4H-SiC (0001) substrates is investigated. The epitaxial growth is carried out using a horizontal, hot-wall type CVD reactor. The temperature range and pressure of both H_2 pre-growth etching and epitaxial growth are 1400 – 1600 °C and 188 Torr, respectively. Two kinds of surface features are observed. One is a stripe feature along the direction of $<1\bar{1}00>$ observed after pre-growth etching. The other is a triangular shaped feature observed after epitaxial growth. The stripe features are decreased by lowering the temperature and shortening the time of pre-growth etching. The triangular shaped features are decreased by adding C_3H_8 during pre-growth etching.

INTRODUCTION

8° off-angle 4H-SiC (0001) substrates are usually used for epitaxial growth of 4H-SiC. Recently, lower off-angle substrates are attracting notice from the point of the interface state density of MOS structures [1]. The influence of off-angle on the surface morphology of the epitaxial growth using 6H-SiC (0001) substrates has been already investigated in detail [2]. However, the influence of lower off-angle on the surface morphology after pre-growth etching and epitaxial growth using 4H-SiC (0001) substrates has received less attention. In this work, surface morphologies both after pre-growth etching and after epitaxial growth on lower off-angle 4H-SiC (0001) substrates are observed. Based on the observed results, appropriate conditions of etching and growth to obtain an epitaxial layer with smooth surface are determined.

EXPERIMENTAL

Epitaxial growth was carried out with a horizontal, hot-wall type CVD reactor. The hot-wall susceptor and the substrate loading plate are made of high purity graphite coated with SiC. 4H-SiC (0001) substrates misoriented 0°, 3.5°, and 8° towards $<11\bar{2}0>$ were used. The off-angles have the error within $\pm$ 5 %. Before loading into the reactor, the substrates were cut into 8x8 mm samples and sequentially cleaned with acetone, dipped in 5 % HF, and rinsed in deionised water. SiH_4 (3.3 cc/min.) and C_3H_8 (0.89 cc/min.) were used as source gases with H_2 carrier gas (40 l/min.). Temperature range and pressure of both H_2 pre-growth etching and epitaxial growth were 1400 - 1600 °C and 188 Torr, respectively. Etching time is defined as the time from the time reaching the growth temperature to the time starting the growth. In other words, etching for 0 min. means etching during temperature rising from room temperature to growth temperature. Surface morphologies were observed by Nomarski differential interference contrast microscopy (NDIC).

RESULTS AND DISCUSSION

Figure 1 shows the NDIC images of surface morphologies after epitaxial growth when 0°,

3.5°, and 8° off-angle 4H-SiC (0001) substrates were used. Both pre-growth etching and growth were carried out at 1600 °C. Smooth surface morphology was observed in the case of the epitaxial layer grown on 8° off-angle substrates. On the contrary, stripe features along the <1$\bar{1}$00> direction were observed in the case of the epitaxial layer grown on 3.5° off-angle substrates.

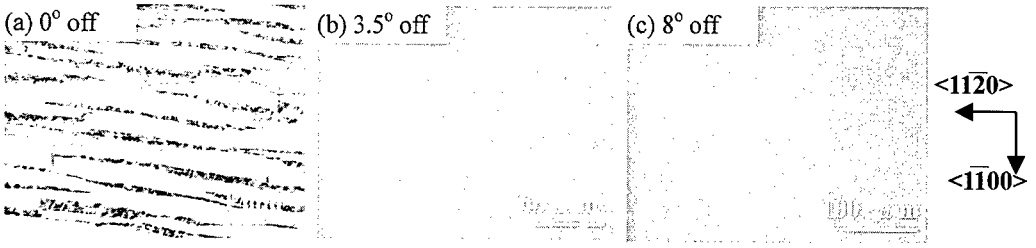


Fig. 1. Effect of off-angle on the morphology of epitaxial films (NDIC images). Epitaxial layer thickness a) 1.8 μm, b) 2.2 μm, c) 2.2 μm.

To clarify when the stripe features occurred on the 3.5° off-angle substrate surface, morphologies after only pre-growth etching were examined. Fig. 2 shows the NDIC images after pre-growth etching. The pre-growth etching was carried out in H_2 for 0, 30, and 60 min. at 1400, 1500, and 1600 °C. The stripe features along the direction of <1$\bar{1}$00> are already observed after pre-growth etching at higher temperature and longer time of pre-growth etching.

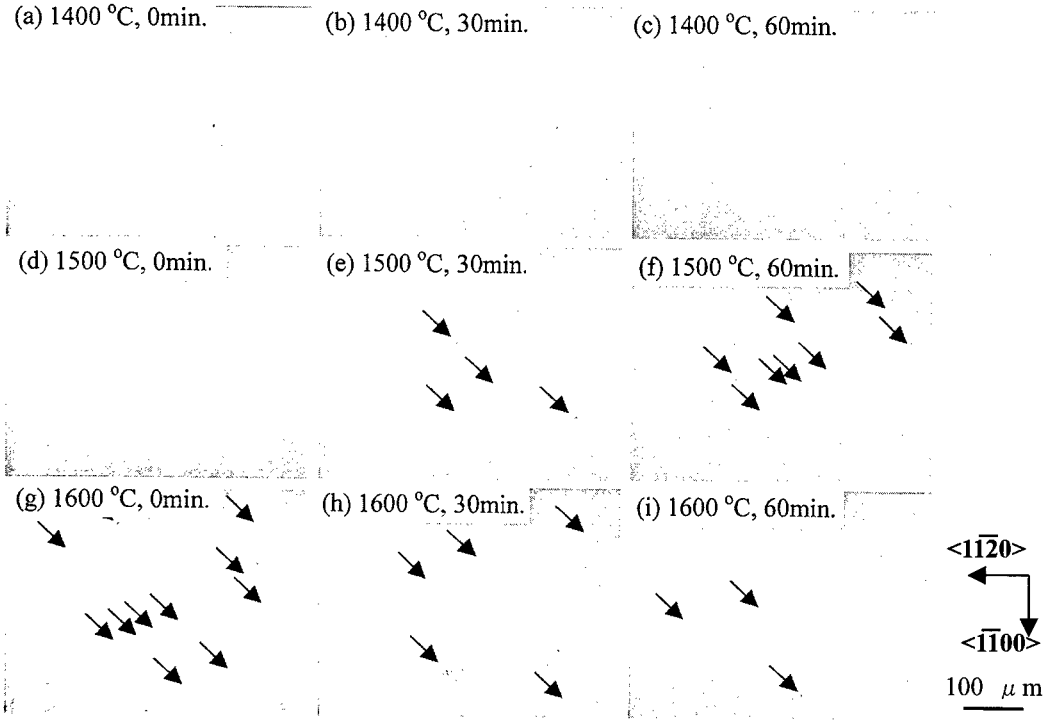


Fig. 2. Surface mophologies after H_2 pre-growth etching of 3.5° off-angle substrates.

Figure 3 shows the NDIC images of surface morphology after pre-growth etching (a) and after epitaxial growth (b) when 3.5° off-axis substrates were used. The pre-growth etching was

carried out in H_2 for 30 min. at 1600 °C. The epitaxial growth was carried out at 1500 °C to avoid the occurrence of stripe features. The stripe features which appeared during pre-growth etching can be also seen after epitaxial growth. This result indicates that the stripe features observed after pre-growth etching are inherited to the surface morphology after epitaxial growth.

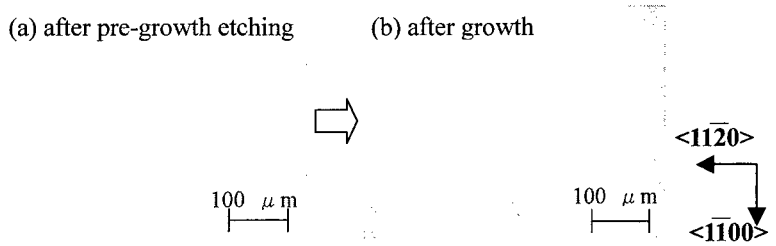


Fig. 3. Surface morphology inheritance on the 3.5° off-axis substrate. a) Pre-growth etching: 1600 °C, 30 min., b) Growth: 1500 °C, 80 min., 3.2 μm (layer thickness)

Figure 4 shows the NDIC images of surface morphology after pre-growth etching (a) and after epitaxial growth (b) when both the pre-growth etching and growth were carried out at 1500 °C to prevent the occurrence of the stripe features. Stripe features were not observed on the surface after pre-growth etching. Triangular shaped features are, however, observed on the surface after epitaxial growth. These triangular features can be eliminated by increasing the epitaxial growth temperature. On the other hand, stripe features increase with increasing H_2 etching temperature as shown in Fig. 2. Therefore, it is very difficult to eliminate both triangular features and stripe features at the same time, as the H_2 etching temperature is inevitably also increased when the growth temperature is raised to eliminate the triangular features.

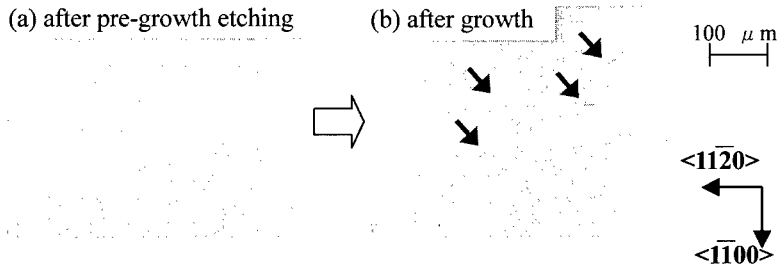


Fig. 4. Triangular shaped feature after growth on the 3.5° off-axis substrate. Epitaxial layer thickness b) 2.0 μm.

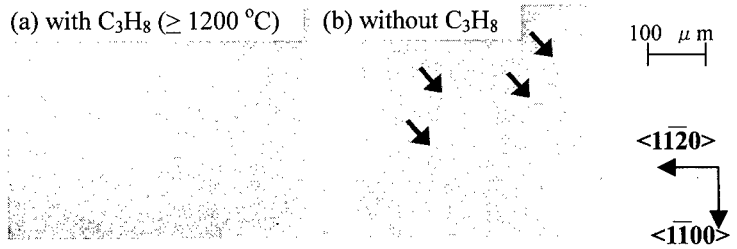


Fig. 5. Effect of adding C_3H_8 during pre-growth etching on the 3.5° off-axis substrate. Epitaxial layer thickness a) 2.2 μm, b) 2.0 μm.

The effect of adding C_3H_8 during the pre-growth etching [3] was examined in order to prevent the occurrence of both triangular features and stripe features after epitaxial growth. Fig. 5

shows the effect of adding C_3H_8 to the H_2 ambience during a pre-growth etching at 1500 °C for 3 min. on the surface morphology after epitaxial growth. C_3H_8 was added to H_2 from the time when the temperature reached 1200 °C during the temperature rising process. It is expected that the stripe feature do not appear at this H_2 etching temperature (1500 °C) from the results of Fig. 2. The conditions of the epitaxial growth were the same as that of Fig. 4. As can be seen in Fig. 5 (a), both stripe and triangular features did not appear after epitaxial growth.

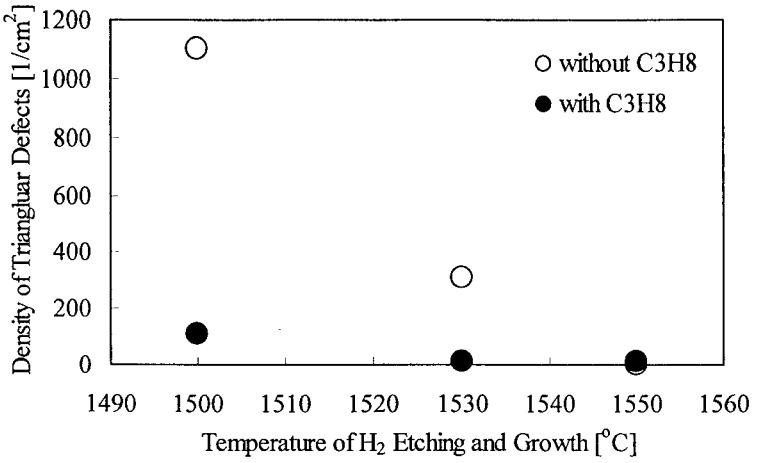


Fig. 6. Effect of adding C_3H_8 during pre-growth etching on the density of triangular shaped features on the 3.5° off-axis substrate.

Figure 6 shows the effect of adding C_3H_8 to the H_2 ambience during pre-growth etching on the density of the triangular shaped features after epitaxial growth. X-axis is the temperature of H_2 etching and epitaxial growth. It can be seen that the addition of C_3H_8 to the H_2 ambience during pre-growth etching is very effective to suppress the occurrence of triangular defects, especially at lower epitaxial growth temperature.

SUMMARY

The surface morphology of epitaxial layers grown on low off-angle 4H-SiC (0001) substrates has been investigated using a horizontal, hot-wall type CVD reactor. Two kinds of surface morphologies are observed. One is a stripe feature along the <1$\bar{1}$00> direction and is already observed after pre-growth etching. The other one is a triangular shaped feature observed after epitaxial growth. The stripe features are decreased by lowering the temperature and shortening the time of pre-growth etching. The triangular shaped features are decreased by adding C_3H_8 during pre-growth etching. It has been demonstrated that epitaxial layers with smooth surface can be achieved on 3.5° off-angle substrates by choosing appropriate conditions for both pre-growth etching and epitaxial growth, as well as adding C_3H_8 to H_2 during pre-growth etching.

Acknowledgement This work was performed under the management of FED as a part of the MITI NSS Program (R&D of Ultra-Low-Loss Power Device Technologies) supported by NEDO.

References

[1] K. Fukuda et al., Materials Science Forum Vols. 338-342 (2000) p. 1283.
[2] T. Kimoto et al., J. Appl. Phys. Vol.75 (2), No.15 (1994) p. 850.
[3] C. Hallin et al., J. Cryst. Growth 181 (1997) p. 241

Materials Science Forum Vols. 353-356 (2001) pp. 139-142
© 2001 Trans Tech Publications, Switzerland

Surface Morphology of 4H-SiC Inclined towards <1$\bar{1}$00> and <11$\bar{2}$0> Grown by APCVD Using the Si_2Cl_6+C_3H_8 System

Y. Masuda, S. Ohshima, C. Jacob and S. Nishino

Faculty of Engineering & Design, Kyoto Institute of Technology,
Matsugasaki, Sakyo, Kyoto 606-8585, Japan

Keywords: AFM, C_3H_8 Etching, HCl Etching, Homoepitaxial Growth, Off-Orientation, Step Height, Surface Morphology, Surface Roughness

Abstract Two types of in situ etching (H_2+HCl and H_2+C_3H_8) and epitaxial growth were performed on 4H-SiC substrates inclined 8° off from (0001) towards <1$\bar{1}$00> and <11$\bar{2}$0>. The H_2+HCl etch produced larger microstep heights on the <1$\bar{1}$00>-off direction compared to the microsteps on the <11$\bar{2}$0>-off direction. The H_2+C_3H_8 etch produced similar microstep structures with the height of 1-2 bilayers on both off-orientations. Even though the films were up to 19 μm thick, high quality epilayers without incorporation of 3C-SiC, large-scale step bunching, and rough 3D nucleation were obtained on 4H-SiC substrates inclined towards both <1$\bar{1}$00> and <11$\bar{2}$0> by APCVD using Si_2Cl_6+C_3H_8 system.

Introduction

In homoepitaxial growth of SiC, step-controlled epitaxy, in which a substrate cut several degrees from the (0001) face toward <11$\bar{2}$0> promotes high quality homoepitaxial growth, has been widely used [1]. Most of the work in SiC epitaxy has focused on substrates inclined toward <11$\bar{2}$0>. On the (0001) substrates inclined toward <1$\bar{1}$00>, stripe-like morphology appears and the incorporation of 3C-SiC polytype defects occurs for long-time growth on 6H-SiC [2,3]. However, epitaxial growth on 4H-SiC (0001) inclined toward <1$\bar{1}$00> has been studied less. Recent work has demonstrated that 4H-SiC epilayers with smooth morphologies can be grown on substrates inclined toward <1$\bar{1}$00> in a low pressure epitaxial growth system [4]. This work investigates the surface morphology by Atomic Force Microscopy (AFM), using two types of in situ etches (H_2+HCl and H_2+C_3H_8), for 4H-SiC substrates inclined 8° off from (0001) towards each <1$\bar{1}$00> and <11$\bar{2}$0> crystalline orientations. We also show how the homoepitaxial growth surfaces develop after the different etching procedures for 4H-SiC substrates inclined towards <1$\bar{1}$00> and <11$\bar{2}$0>.

Experimental

Surface etching and epitaxial growth were carried out on 4H-SiC substrates inclined 8°±1° off from (0001) Si-face towards either <1$\bar{1}$00> or <11$\bar{2}$0>. A horizontal cold-wall CVD reactor [5] was used for the etching and growth. H_2, HCl, C_3H_8 gas flows during etching were 1-3 slm, 3-9 sccm and 0.2-1.2 sccm, respectively. Etching temperatures were 1300°C for the H_2+HCl etch, 1500°C for the H_2+C_3H_8 etch. The etch was performed for 10 minutes in each case. 4H-SiC films were grown by atmospheric pressure CVD using Si_2Cl_6 (hexachlorodisilane) as Si source and C_3H_8 (5 % in H_2) as C source with H_2 as carrier gas. Growth temperature was 1500°C and period of the growth was 60 and 600 minutes. The specific growth parameters chosen for this work were those identified as optimal for growth on 4H-SiC (0001) inclined 8° off toward <11$\bar{2}$0>. No effort was made to optimize the growth parameters for epitaxial growth on 4H-SiC (0001) inclined 8° off toward <1$\bar{1}$00>. AFM

characterization of the samples was done before etching, after etching and after the growth. Surface morphology was characterized using an optical microscopy in the Nomarski mode, and film thickness was measured by cross section using a scanning electron microscope. The AFM analysis was done using a Nanoscope IIIa system running in tapping mode (Digital Instruments).

Results and Discussion

Fig. 1 shows a 1x1 μm^2 AFM image of a 4H as-received substrate. The substrates inclined toward both off-orientations have randomly-oriented polishing scratches, with no observable step structure on either substrate orientation. In Fig. 2a, the substrates inclined toward $<1\bar{1}00>$ has been etched with the H_2+HCl. We observed a pattern of microsteps on both off-orientations. The microsteps are perpendicular to each off-orientation. However, the microsteps on the substrates inclined toward $<1\bar{1}00>$ were more regular than the microsteps on the substrates inclined toward $<11\bar{2}0>$. The microstep heights on the substrates inclined toward $<11\bar{2}0>$ were about 0.25-0.5 nm, corresponding to the height of 1-2 Si-C bilayers. In contrast, the steps on the $<1\bar{1}00>$-off surface were about 1-2 nm in height, which is much larger than 1-2 bilayers.

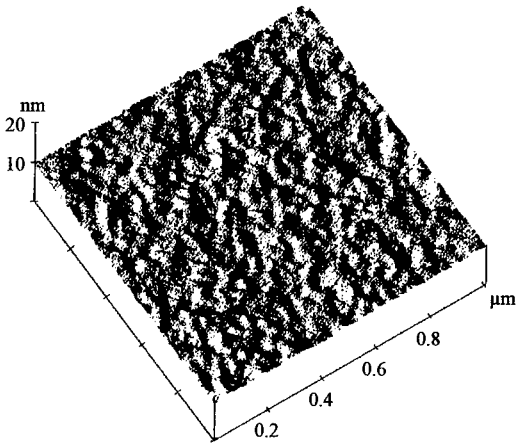


Fig. 1 AFM image of an as-received 4H-SiC substrate inclined toward $<1\bar{1}00>$. Image shows 1x1 μm^2 area and 20 nm/div height scale.

Fig. 2b shows the result for the off-orientation toward $<1\bar{1}00>$ which has been etched with H_2+C_3H_8. A smoother surface was obtained compared to the H_2+HCl etch, and the microsteps were observed on both off-orientations in the small scale image areas (1x1 μm^2). The microstep heights were 1-2 bilayers, and not significantly different for both off-orientations. On some samples, in the large scale image areas (10x10 μm^2) we observed hillocks having a large height of more than 1 nm. The appearance of hillocks with the H_2+C_3H_8 etch is consistent with other reports [6,7].

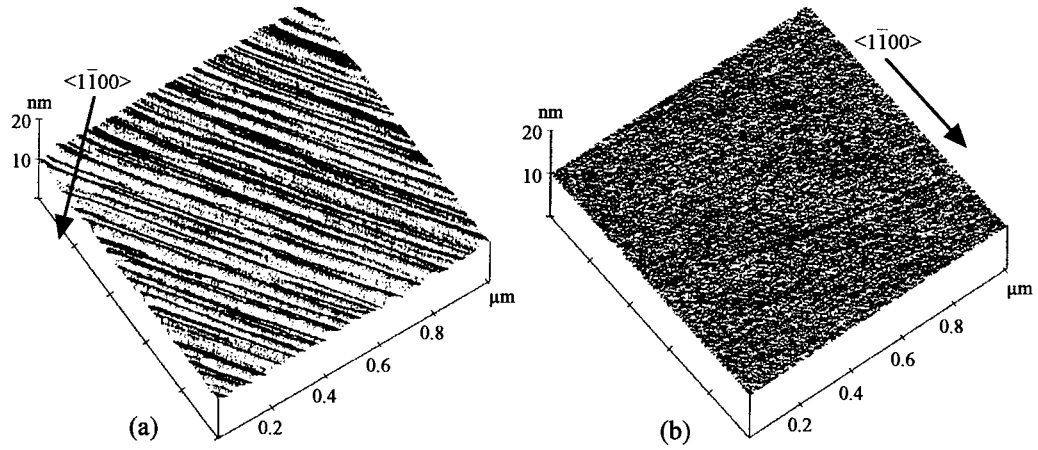


Fig. 2 AFM image of the etched surfaces with off direction toward $<1\bar{1}00>$. (a) H_2 + HCl etch, (b) H_2 + C_3H_8 etch. Images show 1x1 μm^2 areas and 20 nm/div height scales.

These results show that the H_2+HCl etch demonstrates anisotropy, and the H_2+C_3H_8 etch is isotropic for producing microsteps. Etching by H_2 alone has been reported to produce step heights of typically 1-2 bilayers on both off-orientations [8]. The reason for this difference of microsteps for the H_2+HCl etch is not clear yet, but it is clear that only the H_2+HCl etch demonstrates anisotropy. Consequently, we consider that the presence of Cl adatoms affects the microstep formation for each orientation.

Different step structures were obtained by using variable etch conditions. However, after 60 minutes of growth using substrates which had different etch-step structures, we observed no major difference in surface roughness. Table 1 shows the typical average surface roughness after growth for etched substrates (H_2+HCl and H_2+C_3H_8). If we neglect the polishing damage of the substrate, surface morphology of the epitaxial layer was not affected by both etching conditions.

Table 1 The surface roughness value of the AFM images after growth on pre-growth etching substrates.

Substrate	Condition	RMS (nm)	Ra (nm)	Rmax (nm)
		1x1 μm² (10x10 μm²)		
4H-SiC <1$\bar{1}$00> 8° off	as received	0.193 (0.211)	0.158 (0.164)	0.863 (1.101)
	HCl etch +CVD(1h)	0.122 (0.437)	0.092 (0.335)	0.675 (2.05)
	C_3H_8 etch +CVD(1h)	0.083 (0.166)	0.061 (0.116)	0.452 (0.89)
	C_3H_8 etch+ CVD(15μm)	0.15 (0.366)	0.117 (0.294)	0.819 (1.873)
4H-SiC <11$\bar{2}$0> 8° off	as received	0.221 (0.344)	0.169 (0.259)	1.161 (2.529)
	HCl etch +CVD(1h)	0.130 (0.38)	0.098 (0.322)	0.806 (1.445)
	C_3H_8 etch +CVD(1h)	0.114 (0.198)	0.087 (0.139)	0.618 (1.064)
	C_3H_8 etch+ CVD(15μm)	0.109 (0.598)	0.085 (0.49)	0.571 (2.68)

In addition, very smooth epitaxial surface morphologies were obtained on both off-orientations for films up to 19 μm thick. Fig. 3 shows the surface morphology for epilayer thickness of 15 μm grown on the 4H-SiC inclined 8° off toward <1$\bar{1}$00> as observed by optical microscopy. The growth rate of epitaxial films for both off-orientations was equal within experimental error, and was 1.5 μm/h using typical growth conditions. Using Raman scattering and photoluminescence, only the peaks characteristic of 4H-SiC were observed in each spectrum for 19 μm films on both off-orientations. Even though the film thickness was increased, the incorporation of 3C-SiC, large-scale step bunching, and rough 3D nucleation were not observed on both off-orientations by optical microscopy. Consequently, the 4H-SiC epilayers inclined toward <1$\bar{1}$00> exhibited very good epitaxial morphology similar to the epilayers inclined toward <11$\bar{2}$0>. The growth surface obtained in this work was different from the growth surface reported for 6H-SiC substrates inclined toward <1$\bar{1}$00> [2,3]. Further, AFM analysis revealed smooth surfaces for epilayers on both off-orientations, and no evidence of large scale step bunching could be seen when the AFM scan areas were increased (see Table 1). For 15 μm thick films, the microsteps were observed more clearly in the <1$\bar{1}$00>-off epilayers than in the <11$\bar{2}$0>-off epilayers as shown in Fig. 4. This orientation dependence was explained by alignment parallel to the crystal facets [2]. Parallel steps appear on the substrates inclined toward <1$\bar{1}$00>, whereas zigzag steps appear on the substrates inclined toward <11$\bar{2}$0>. The most common step height of these microsteps is about 0.5 nm (2 bilayers) on both off-orientations. But a more detailed transmission electron microscopy (TEM) analysis is needed.

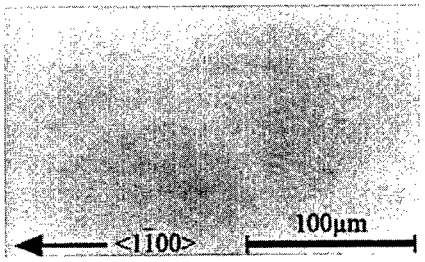


Fig. 3 The surface morphology for epilayer thickness of 15 μm grown on the 4H-SiC inclined 8° off toward <1$\bar{1}$00>.

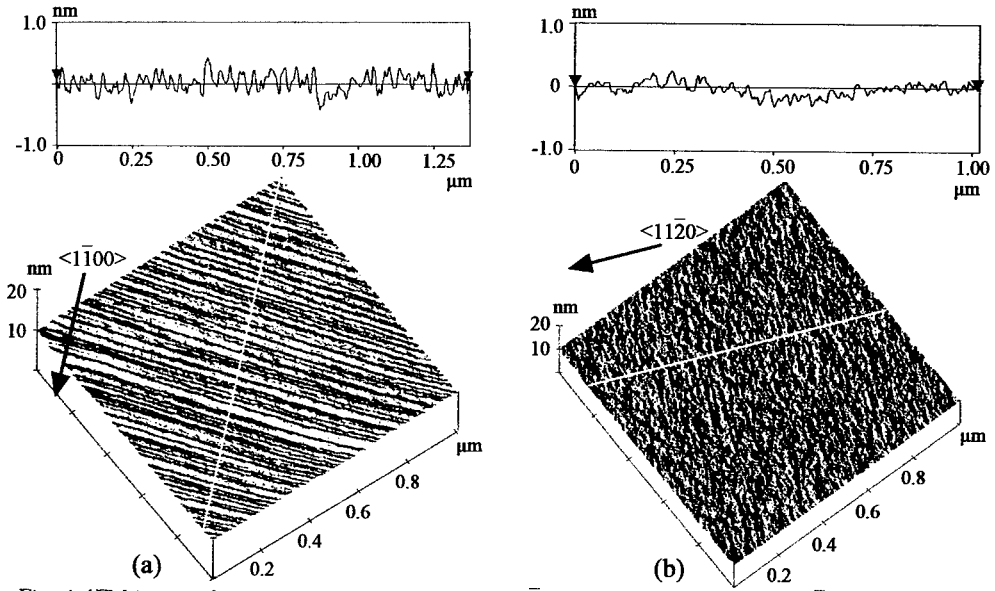


Fig. 4 AFM image of 15 μm epilayers grown on (a) <1$\bar{1}$00>-off substrate and (b) <11$\bar{2}$0>-off substrate. Images show 1x1 μm² areas and 1.0 nm/div height scales.

The 4H-SiC substrates inclined toward <1$\bar{1}$00> also demonstrated high quality epilayers grown by APCVD as compared with the work on 6H-SiC. But, in this study, Si_2Cl_6 was used as the Si source. Adding Cl adatoms to the CVD source gases influence the suppression of gas phase nucleation, the change of the reactant species from hydrides to chlorides, and the etching of SiC. The cause of the smooth epilayer may be attributed to the presence of Cl adatoms.

Finally, Au/4H-SiC Schottky barrier diodes were fabricated on both off-oriented epilayers. The donor concentration of 15-19 μm-thick drift layers was determined to be 4-5x$10^{15}$$cm^{-3}$ by C-V, the breakdown voltage was 500~600 V. The donor concentration and the breakdown voltage showed no significant difference for each epilayer grown under the same growth conditions.

Conclusions

The surface structure of the H_2+HCl and H_2+C_3H_8 etched surfaces and epilayers grown on 4H-SiC substrates inclined 8° off from (0001) Si-face towards <1$\bar{1}$00> and <11$\bar{2}$0> were investigated. The H_2+HCl etch demonstrated anisotropy, whereas H_2+C_3H_8 etch resulted an isotropic microsteps formation. Microsteps were observed more clearly on the <1$\bar{1}$00>-off surface than on the <11$\bar{2}$0>-off surface after growth. The 4H-SiC epilayers up to 19 μm thickness with very smooth surfaces were obtained on both off-orientations grown by APCVD using Si_2Cl_6+C_3H_8 system.

References

[1] N.Kuroda, K.Shibahara, W.S.Yoo, S.Nishino, and H.Matsunami, Extended Abstracts of the 19th Conf. on Solid State Devices and Materials, Tokyo (1987), p. 227.
[2] T.Ueda, H.Nishino, and H.Matsunami, J. Crystal Growth **104** (1990), p. 695.
[3] H.S.Kong, J.T.Glass, and R.F.Davis, J. Appl. Phys. **64** (1988), p. 2672.
[4] B.E.Landini and G.R.Brandes, Appl. Phys. Lett. **74** (1999), p. 2632.
[5] S.Nishino, T.Miyanagi, and Y.Nishio, Mat. Sci. Forum **264-268** (1998), p. 139.
[6] S.Karlsson and N.Nordell, Mat Sci. Forum **264-268** (1998), p. 363.
[7] J.A.Powell, D.J.Larkin, and A.J.Trunek, Mat. Sci. Forum **264-268** (1998), p. 421.
[8] B.E.Landini and G.R.Brandes, Mat. Sci. Forum **338-342** (2000), p. 185.

Materials Science Forum Vols. 353-356 (2001) pp. 143-146
© 2001 Trans Tech Publications, Switzerland

Growth of 3C-SiC Using Off-Oriented 6H-SiC Substrates

M. Syväjärvi, R. Yakimova, H. Jacobsson and E. Janzén

Department of Physics and Measurement Technology,
Linköping University, SE-581 83 Linköping, Sweden

Keywords: 3C-SiC, Bulk Growth, Sublimation Growth

Abstract

Large area growth of 3C-SiC on off-oriented 6H-SiC substrates is demonstrated and the growth evolution is investigated. The structural quality assessed from high-resolution x-ray diffraction ω-rocking curve measurements shows a symmetric peak with a full width at half maximum of 36 arcsec and 2θ/θ measurements show that the lattice in the grown 3C-SiC is not distorted by using 6H-SiC as a substrate.

Introduction

Development in epitaxial growth of the cubic polytype 3C-SiC has been held back due to the lack of 3C-SiC substrates. When homoepitaxial growth is applied on off-oriented α-SiC substrates the substrate polytype is replicated by the epilayer. In this case, it has been demonstrated that the structural quality in the epilayers improves compared to the starting material, mainly due to domain enlargement [1]. Growth conditions for avoiding inclusions of 3C-SiC within 6H and 4H-SiC epilayers have been investigated extensively. Intentional growth of 3C-SiC epitaxial layers has been mostly studied using Si as a substrate. However, the use of α-SiC substrates reduces difficulties which arise due to differences in lattice mismatch, thermal expansion and chemical incompability. In case of using 6H-SiC(0001) substrates, i.e. on-axis growth, defects such as double positioning boundaries (DPBs) [2] are difficult to avoid. We have investigated formation of 3C-SiC grown on 6H-SiC substrates off-oriented 2.8° and 3.5° from (0001) in the $[11\bar{2}0]$ direction. Once 3C-SiC has been formed, a similar effect for improvement of the structural quality as in homoepitaxial growth may be expected. Our earlier studies of sublimation grown 3C-SiC on off-oriented 6H-SiC substrates have shown good quality material by low-temperature photo-luminescence studies and well-ordered 3C-SiC(111) surfaces by low energy electron diffraction and Laue measurements [3]. In this study we present development in the growth of 3C-SiC on off-oriented α-SiC substrates for further understanding of necessary growth conditions for the polytype formation and growth mechanism as well as evaluation of the structural quality from high-resolution X-ray diffraction (HRXRD) measurements.

Experimental

The growth technique used is sublimation epitaxy [4] and the growth rate was about 0.1 mm/h at 1800°C. The substrates were 6H-SiC wafers with diameter 35 mm and the surfaces were off-oriented 2.8° and 3.5° from (0001) in the $[11\bar{2}0]$ direction. No difference in the results when using these off-orientations have been observed. The (0001) face of 6H-SiC is suitable as a substrate for growth of 3C-SiC since the surface atomic structure of the (0001) face is similar to the atomic structure of the 3C-SiC(111) surface [5]. The thicknesses of the 3C-SiC crystals grown in our study reach hundreds of μm or in some cases more than 1 mm. These crystals were grown in several runs

and growth duration varied between 1 and 3 hours. The grown 3C-SiC material has been characterized using optical microscopy, crossed-polarizers, and HRXRD measurements.

Results and discussion

At the first growth run of the crystals (i.e. at the initial growth on the 6H-SiC substrate) we have applied a fast growth rate ramp-up which we have found to be beneficial for the formation of 3C-SiC. By growth rate ramp-up we mean an increase of the growth rate with time up to the 0.1 mm/h growth rate. In subsequent growth runs, i.e. when 3C-SiC is present on the crystal surfaces, the ramp-up of the growth rate was slower since this provides better control of the crystal growth [1]. The fast growth rate ramp-up was 3-5 times the normal one which is 5-15 (μm/h)/min.

It has been reported [6,7] that 3C-SiC can be formed by using a high growth rate (>180-240 μm/h). However, higher growth rates lead to smaller twinning regions, i.e. higher concentration of DPBs [6,7]. Therefore we have used a lower growth rate but still reasonable for growth of thick crystals, and initiated growth of 3C-SiC by applying a fast growth rate ramp-up.

Nucleation of 3C-SiC on the 6H-SiC substrates may occur at the edge of the wafer opposite to the direction of the off-orientation or at edges of domains present within the 6H-SiC wafer. Fig. 1 demonstrates an image taken with crossed-polarizers of 3C-SiC grown on an off-oriented 6H-SiC substrate and where the 3C-SiC growth has started at a domain boundary. The 3C-SiC appears at the domain edge opposite to the off-orientation and at this location the first nucleation takes place. It is easy to discern between the different polytypes by using transmission light microscopy. In this mode the 3C-SiC and 6H-SiC have different colours.

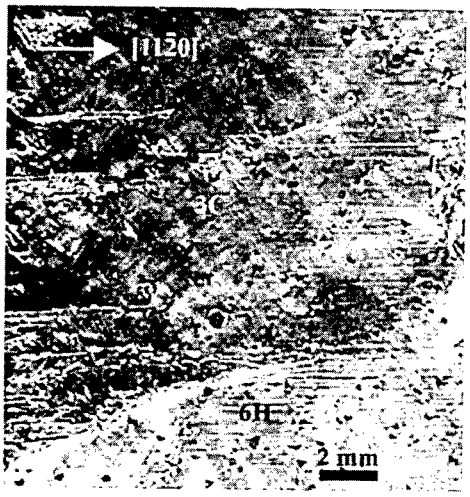


Fig. 1. Crossed-polarizer image of grown 3C-SiC on a 2.8° off-oriented 6H-SiC substrate.

Fig. 2 shows a more detailed picture of the 3C-SiC growth at the domain boundary. At the edge opposite to the off-orientation an on-axis region has appeared and steps are visible in the direction of the off-orientation. The on-axis region is created at the edge of the wafer or at the domain boundary. On-axis surfaces are favorable for appearance of 3C-SiC. Once the initial 3C-SiC has

formed at the on-axis area, the 3C-SiC extends along the off-orientation and overgrows the substrate polytype.

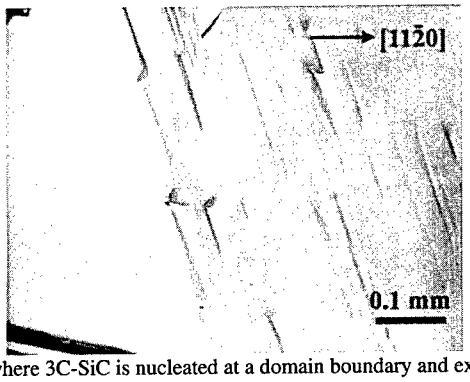


Fig. 2. Closer picture of the area where 3C-SiC is nucleated at a domain boundary and extended by step flow growth.

It is clear that the substructure of the 6H-SiC substrate affects the growth of 3C-SiC. Domains are locations where 3C-SiC can grow and as the number of domains is large, many different areas with 3C-SiC will be present. Also micropipes from the substrate affect the extension of the 3C-SiC in a similar way as in homoepitaxial growth on off-oriented substrates.

Fig. 3 shows how the 3C-SiC can overgrow the 6H-SiC substrate as growth proceeds. The substrate contained several domains and in this case 3C-SiC has been formed at the domain boundaries. Finally, the 3C-SiC has overgrown completely the 6H-SiC material in the down-step direction.

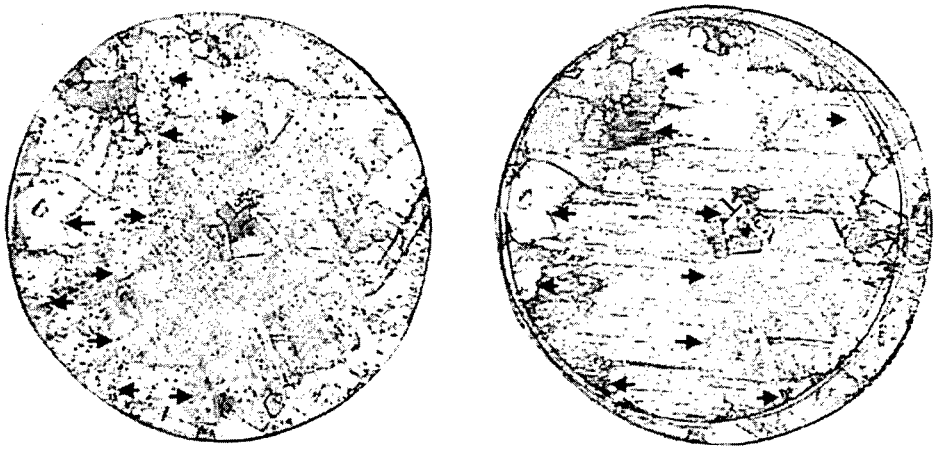


Fig. 3. Overall view of the extension of 3C-SiC grown on off-oriented 6H-SiC substrate using transmission light microscopy; left picture: after initial growth; right picture: after subsequent growth. Arrows mark the borders of 3C-SiC.

HRXRD measurements were performed along the $<11\bar{2}0>$ direction. The lattice matching is demonstrated by $2\theta/\theta$ measurements. The full width at half maximum (FWHM) is locally less than 20 arcsec (using a spot size of 1x1 mm^2) which shows that the 3C crystal grown on 6H-SiC has not

resulted in severe crystal deformation of the 3C-SiC lattice. The ω-rocking curve measurements show a symmetric peak and the FWHM value is 36 arcsec (spot size 2x2 mm^2). This is in the expected range for crystals grown with a moderate growth rate [8] such as used for our results. The value of the FWHM increases at highly distorted areas.

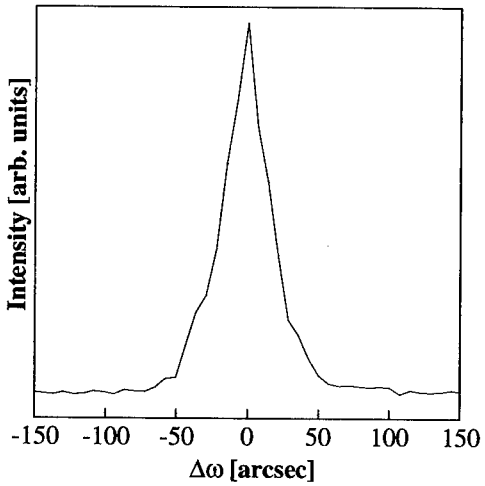


Fig. 4. HRXRD ω-rocking curve of 3C-SiC grown on an off-oriented 6H-SiC substrate, the FWHM is 36 arcsec.

Summary

We have shown that thick 3C-SiC crystals can be grown on off-oriented 6H-SiC wafers acting as substrates. Long-term growth may provide 3C-SiC wafers but the substructure of the 6H-SiC substrates (e.g. domains) makes crystal growth of 3C-SiC bulk material difficult to control. The 6H-SiC is suitable as a substrate for growth of 3C-SiC as shown from investigating the structural quality using HRXRD measurements.

Acknowledgement

This work was supported by the SSF program SiCEP, Wenner-Gren Foundations and Holmbergs Foundation.

References

[1] M. Syväjärvi, R. Yakimova, H. Jacobsson, and E. Janzén: J. Appl. Phys. 88 (2000), p. 1407.

[2] H.S. Kong, J.T. Glass, and R.F. Davis: J. Appl. Phys. 65 (1988), p. 2672.

[3] M. Syväjärvi, R. Yakimova, P.-A. Glans, A. Henry, M.F. MacMillan, L.I. Johansson, and E. Janzén: J. Crystal Growth 198/199 (1999), p. 1019.

[4] M. Syväjärvi, R. Yakimova, M. Tuominen, A. Kakanakova-Georgieva, M.F. MacMillan, A. Henry, Q. Wahab, and E. Janzén: J. Crystal Growth 197 (1999), p. 155.

[5] J.E. Northrup and J. Neugebauer: Phys. Rev. B52 (1995), p. 17001.

[6] A.N. Andreev, N.Yu. Smirnova, A.S. Tregubova, M.P. Scheglov, and V.E. Chelnokov: Semiconductors 31 (1997), p. 232.

[7] A.N. Andreev, A.S. Tregubova, M.P. Scheglov, A.L. Syrkin, and V.E. Chelnokov: Mat. Sci. Eng. B46 (1997), p. 141.

[8] A.N. Andreev, N.Yu. Smirnova, M.P. Scheglov, A.S. Tregubova, V.P. Rastagaev, and V.E. Chelnokov: Inst. Phys. Conf. Ser. 142 (1996), p. 105.

Materials Science Forum Vols. 353-356 (2001) pp. 147-150
© 2001 Trans Tech Publications, Switzerland

SiC Polytype Transformation on the Growth Surface

E.N. Mokhov[1], S.K. Obyden[2], A.D. Roenkov[1],
G.V. Saparin[2] and Yu.A. Vodakov[1]

[1] A.F.Ioffe Physico-Technical Institute, Russian Academy of Sciences,
Polytechnicheskaya, RU-194021 St.Petersburg, Russia

[2] Moscow State University, RU-119899 Moscow, Russia

Keywords: Polytype Transformation, Singular Surface, Sublimation Growth

Abstract. The effect of the growth conditions on the polytype formation in epitaxial SiC layers grown on vicinal and singular surfaces by the sublimation method has been studied by a real color cathodoluminescence SEM technique. A polytype growth instability is observed on a singular surface. The clusters of native defects, spontaneously appearing on the growth surface are proposed to be the nucleation centers for new polytypes.

Introduction

The growth conditions as well as crystallographic orientation of the seed surface are known [1-3] to influence considerably SiC polytype formation. The stable growth of a definite polytype is found to occur on a the surface misoriented of the (0001) plane. This is due to a higher step density on such a surface [1]. In contrast, the character of the polytype transformation on the {0001} faces is poorly understood. According to [4], the polytype transformation is more probable on the (0001)C face rather than on the (0001)Si one. However, the 4H-SiC polytype dominates on the (0001)C face, while the 6H-SiC polytype is found to grow on the (0001)Si plane [5].

The goal of this work was a study of SiC polytype transformation in the sublimation growth with the focus on the type of the growth surface and on the structural defects available on the surface. The results obtained show the polytype transformation to occur on the singular portions of the surface and the structural and morphological defects to be factors stabilizing the polytype growth.

Experiment

SiC epitaxial layers grown by the sublimation sandwich method (SSM) [6] at 1800-2400°C in vacuum (10^{-3}-10^{-4} Torr) or in an atmosphere of inert gas (Ar) have been studied. The supersaturation in the growth zone controlled by the temperature difference between a source and the substrate was varied in a wide range. SiC powder or high-purity SiC single crystal was used as the source. Single-crystalline 4H -, 6H -, 8H-, 15R- and 21R-SiC on axis wafers were used as the substrates. In addition, profiled substrates having some prominent platforms with singular type of surface were used in experiments.. The epitaxial layers were grown both on (0001)C and (0001)Si faces.

A polytype distribution over the wafer was studied by a real color cathodoluminescence scanning electron microscopy (CCL-SEM) technique [7]. To get efficient luminescence in the visible wavelength range the samples were doped by nitrogen and gallium. The electron beam energy was varied between 2 and 20 keV to provide the electron penetration length from 0,5 to 2,6 μm. The use of different electron energies enabled one to estimate the polytype distribution across the grown epilayer [8].

Results

The study has revealed the significant dependence of the polytype transformation probability on the growth mechanism and on the state of the growth surface. Our experiments have shown the

polytype stability to be quite high for the vacuum condensation of SiC where a normal growth is dominating [9]. In this case the seed polytype can be reproduced even at high supersaturation and growth rate. For instance, thick (more than 1 mm thickness) layers of 4H, 15R, 21R or 8H-polytype can be grown at the growth rate of ~1 mm/h. The polytype inclusions on the vicinal surface appears mainly at the initial stage of growth. The appearance of morphological defects, for instance, negative growth pyramids, normally results in the higher density of polytype inclusions.

A step-flow growth mode can be typically obtained when SiC layer is growing in an inert gas atmosphere under mass transport limited conditions. The growth surface is then basically vicinal, i.e. it is covered by steps, whose height is frequently of a macroscopic size. The density of the steps depends on the seed orientation, temperature and crystallization rate. Normally, the density of the growth steps is higher on the (0001)Si plane compared to that on the (0001)C plane under the same growth conditions. This fact accounts for a higher stability of the polytype growing on the (0001)Si plane [4].

A polytype stability is quite high on the substrate surface under a step-flow mode, though the probability of polytype transformation is still higher than that under normal growth conditions. Unlike the vacuum condensation, polytype transformation normally occurs in the bulk of the epitaxial layer rather than at the seed surface.

The structure of the polytype generally depends on the growth conditions: temperature, vapor composition and seed orientation. The impurities and deviation from stoichiometry usually favor the polytype transformation. A controlled polytype transformation can be often achieved by the impurity introduction. For instance, 4H-SiC polytype can be grown on 6H-SiC substrate by the supply of a isovalent impurity into vapor [2]. There is a positive experience of other polytype (3C, 15R) controlled growth. Of interest is the fact that the polytype transformation occurs predominantly on the local singular areas of the surface under a step-flow growth, therefore deterioration of morphological perfection of the growing surface results in the polytype syntaxy of epilayer.

A polytype stability increases with the density of steps. This fact evidently speaks in support of the polytype transformation via nucleation. Indeed, the growth steps serve as sinks for adatoms. The increase of the distance between the steps leads to a higher supersaturation and, as a result, to a higher probability of a new polytype nucleus formation.

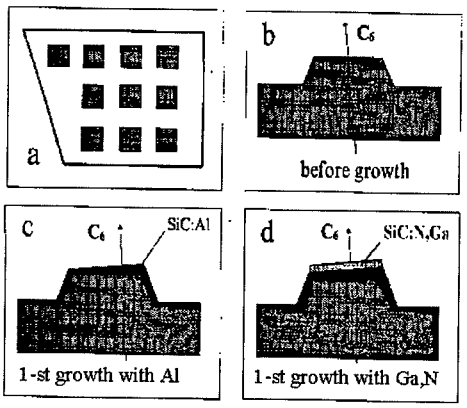


Fig.1. The realization of artificial local surface singularization method. a – the view of profiled substrate surface; b, c, d - the cross section of the sample before and after growth stages.

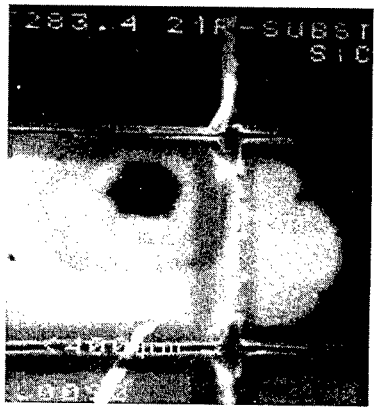


Fig.2. The real CCL-SEM image of 4H-SiC epilayer grown on 21R profiled substrate. Tangential motion of 4H-SiC layer is seen. Polytype 21R (more dark region) is retained only around the screw dislocation exit.

A sharp decrease in the step density is possible only in the particular separated areas of a small size, with no steady-state centers of a normal growth. Our study [10] have shown that the surface of some prominent platforms on the profiled wafers (with the areas less than ~1 mm^2) becomes singular under a high-temperature annealing (Fig.1). The singularity is normally kept during the further sublimation growth. This is chiefly due to the low density of centers generating a normal growth, since the growing layer covers the whole platform before a new nucleus appears. The low density of the crystallization centers is the reason for the fact that the growth rate on the singular surface of the platform is noticeably lower than that on the vicinal surface [10]. Note that the high rate of a lateral growth (10^4 times higher than that of a normal growth) promotes to the surface singularization.

The comparison of the polytype transformation on a vicinal and singular surface has revealed significant differences between them.

An abrupt increase of the polytype transformation at the platforms with the singular surfaces proves to be the main feature of the growth on the profiled wafers. The cathodoluminescence with a noticeable color nonuniformity is an evidence for this fact. The color of the light emitted from the layers grown on different platforms may vary from red to violet. The polytype syntaxy in the layer grown on the vicinal surface is much less pronounced under the same conditions [11]. The further study has revealed the polytype non-uniformity across the grown epilayer [8]. Frequently, SiC epitaxial layer turns out to be a multipolytype composition consisting of polytype interlayers of different thicknesses. The used technique provides visualization of the polytype interlayers with the thickness as thin as 0.1 mm. Still, there may be more thin interlayers of different polytypes.

The polytype transformation probability is high on (0001)-substrates with both Si- and C-faces. A cubic polytype (3C-SiC) forms predominantly on (0001)Si-faces, but more hexagonal polytypes (4H- and 27R-SiC) prevail on C-ones.

The structural perfection of the seed is also a factor significantly affecting the polytype transformation. Contrary to [12], polytype transformation occurs most readily on the high-quality seeds. The initial polytype is principally reproduced on the seeds having high structural defect density (for example, dislocation). These features can be traced most clearly at the profiled substrates (Fig. 2). Fig. 2 shows that the initial seed polytype is kept around the screw dislocation exit.

The used method allows also to visualize the particular nuclei of new polytypes (Fig.3).

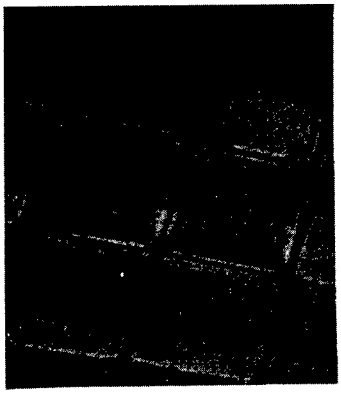


Fig.3. The real CCL-SEM image of SiC samples with epilayer grown on the 6H profiled substrate. A nucleous of new polytype is seen on one of the prominent platform.

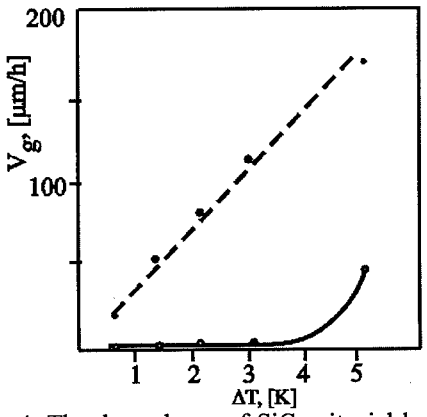


Fig. 4. The dependence of SiC epitaxial layers growth rate on the surface temperature drop for singular (solid line) and vicinal (dotted line) surfaces.

Note that the polytype syntaxy of the epilayers grown on the prominent platforms with singular surfaces are typical only for the growth in a quasi-equilibrium system. The variation of the Si/C ratio in vapor phase or an impurity introduction results in more controllable growth of a definite polytype. Under these conditions, the controlled polytype transformation proves to be more probable in singular areas compared to the rest seed surface. Consequently, 3C and 4H polytypes predominantly grow on the prominent platforms with the singular surfaces [13]. For example, the growth of cubic SiC prevailed in Si-excess system and 4H-SiC dominated in C-excess system.

The growth rate on the singular surface is expected to decrease sharply at a low supersaturation because the formation of a new layer nucleus is needed for the growth on such a surface. Our data contradicts this speculation. It was experimentally found that SiC epitaxial growth on the singular surface occurs even at a very low supersaturation (Fig.4) and the epilayers consist of different polytype interlayers.

This observation may be the evidence of supposition that the various non-stoichiometric clusters including native defects, spontaneously generated on the growth surface, serve as the nuclei of new polytypes. The high thermal stability (up to growth temperatures) of vacancy and interstitial clusters both in irradiated and non-stoichiometric SiC crystals[14] supports the above assumption.

Summary

SiC polytype transformation occurs predominantly by the formation of a new polytype nucleus on the singular surface, followed by its lateral growth. The high probability of different polytype formation on the singular surface leads to polytypical instability of a growing layer. As a result, the layers of different polytypes are successively grown on the substrate. The structural and morphological defects of the substrate stabilize the growing polytype. The clusters of various stoichiometric compositions, including spontaneously appearing on the growth surface native defects, are likely to be nucleation centers of a new polytype at a low supersaturation.

References

[1] V.M.Tairov, V.F.Tsvetkov, In: Progress in crystal growth and characterization. 7 (1983), p.111.
[2] Yu.A.Vodakov, G.A.Lomakina, E.N.Mokhov, Sov. Phys. Sol. St. 24 (1982), p.1377.
[3] A.Fissel. J. Cryst. Growth 212, (2000), p.438.
[4] Yu.A.Vodakov, E.N.Mokhov, A.D.Roenkov, A.D.Saidbekov, Phys. St. Sol. 51 (1979), p.209.
[5] R.A.Stein, P.Lanig, S.Leibenzeder. Mat.Sci.Eng. B11 (1992), p. 69.
[6] Yu.A.Vodakov, E.N.Mokhov, G.Ramm, A.D.Roenkov, Krist und Techn. 14 (1979), p.729.
[7] G.V.Saparin, E.N.Mokhov, S.K.Obyden, A.D.Roenkov, Scanning 18 (1996), p.25.
[8] G.V.Saparin, S.K.Obyden, P.V.Ivannikov, E.N.Mokhov, A.D.Roenkov, Scanning 19 (1997), p.269.
[9] E.N.Mokhov, I.L.Shulpina, A.S.Tregubova, Yu.A.Vodakov, Krist. und Techn. 16 (1981), p.879.
[10] Yu.A.Vodakov, E.N.Mokhov, M.G.Ramm, A.D.Roenkov, Springer Proceed. in Phys. 56 (1992), p.323.
[11] G.V.Saparin, S.K.Obyden, E.N.Mokhov, A.D.Roenkov, B.A.Akhmedov, Scanning 16 (1994), p.21.
[12] A.Powell, J.B.Petit, J.H.Edgar, I.G.Jenkins, L.S.Matus, J.W.Yeng, P.Pirous, W.J.Choyke, L.Clemen, M.Yoganathan, Appl.Phys.Lett. 59 (1991), p.333.
[13] E.N.Mokhov, A.D.Roenkov, G.V.Saparin, S.K.Obyden, Scanning 18 (1996), p.67.
[14] Yu.A.Vodakov, E.N.Mokhov, Inst. Phys. Conf. Ser. N 137 (1994), p.197.

Materials Science Forum Vols. 353-356 (2001) pp. 151-154
© 2001 Trans Tech Publications, Switzerland

Improvement of the 3C-SiC/Si Interface by Flash Lamp Annealing

D. Panknin[1], J. Stoemenos[2], M. Eickhoff[3], V. Heera[1],
N. Vouroutzis[2], G. Krötz[3] and W. Skorupa[1]

[1] Forschungszentrum Rossendorf, PO Box 510119, DE-01314 Dresden, Germany

[2] Physics Department, Aristotle University of Thessaloniki, GR-54006 Thessaloniki, Greece

[3] Daimler-Chrysler AG, Department FT2/M, Postfach 800465, DE-81663 München, Germany

Keywords: 3C-SiC/Si Interface, Flash Lamp Annealing, TEM

Abstract The benefits of irradiation by flash lamps of 3C-SiC films epitaxially grown on Si are discussed. The irradiated energy density is mainly absorbed at the 3C-SiC/Si interface. When the energy density is sufficiently high to melt the Si at the interface a process resembling liquid phase epitaxy (LPE) of SiC occurs resulting to substantial improvement of the SiC film, eliminating also the cavities and the stress at the interface. Energy densities in the range 100 to 150 Jcm^{-2} were used. The method is applicable only for very thin SiC films (20-40nm), which can be used as seeds for subsequent deposition of thicker films.

Introduction

In epitaxially grown films the film quality is strongly depending on the quality of the film, which is formed in the very early stage of the growth. The epitaxial growth of 3C-SiC on silicon substrate is possible in spite of the 21% misfit between the Si and 3C-SiC system [1,2]. Due to the large misfit and the limitation imposed by the melting temperature of silicon, the density of the defects in the early stage of the growth is very high, in the order of 10^{12} cm^{-2}. Part of these defects is annihilated as the film grows. The remaining density of defects at the uppermost part of the 3C-SiC film are in the order of $10^{9}cm^{-2}$ [3,4], which are responsible for the poor electrical characteristics of 3C-SiC films.

In this paper we present results of a short time annealing by xenon flash lamps, which permits annealing of the 3C-SiC several hundred degrees above the melting point of silicon. Annealing by flash lamp was already applied to 6H-SiC in order to activate implanted Al dopant [5]. The structural characteristics of the 3C-SiC films epitaxially grown on Si and irradiated by flash lamps were studied by Transmission Electron Microscopy (TEM).

Experimental procedure

The specimens were irradiated in Argon ambient from an array of xenon lamps with a flash duration in the range of 3 to 20ms. The flash lamp energy densities were in the range of 100 - 150Jcm^{-2}. The specimens were heated from the backside at 700°C. The nominal temperature during irradiation was estimated by the reflected light from a Si reference. Above the Si melting point light reflection is strongly increased and the actual temperatures can be significantly higher than the nominal values.

3C-SiC/Si specimens were deposited in a cold wall CVD reactor under low pressure and lateral gas flow conditions. The substrates were heated directly with a graphite meander. Methylsilane (MeSi, $H_3C\text{-}SiH_3$) was used as precursor gas [6]. Carbonization occurs at 1220°C in ethylene diluted in argon under a total pressure of 0.2mbar. After carbonization, the deposition of SiC starts at 1200°C and 0.5mbar total pressure with methylsilane diluted in hydrogen.

Results and discussion

The results of irradiation by flash lamps on thin 3C-SiC/Si specimens are presented. The specimens were characterized by TEM before and after irradiation.

A) *As deposited 3C-SiC film 44nm thick*

The SiC/Si interface is in general smooth, as shown in the cross-section TEM (XTEM) micrograph in Fig.1a. Large cavities, orders of magnitude larger than the thickness of the SiC film are shown in the inset in Fig.1a [7]. A high defect density in the order of $10^{12}cm^{-2}$ is estimated at the 3C-SiC interface. The SiC film exhibits a granular structure as shown in the Plane View TEM (PVTEM) micrograph in Fig.1b. This is attributed to the slightly misoriented grains, which have a mean diameter of 50nm, resulting to a mosaic structure, as reveal the small arcs in the diffraction pattern in the inset in Fig.1b. A high density of Stacking Faults (SFs), about $6x10^{11}cm^{-2}$, is shown in the Dark Field (DF) micrograph in Fig.1c. Very faint extra 111 spots along the <110> directions are observed in the diffraction pattern in the inset of Fig.1d, revealing a second preferred epitaxial orientation of the type <110>Si//<111>SiC. This is evident in the DF micrograph taken from the 111 spot, which shows small grains in Fig.1d. Probably these are responsible for the larger polycrystalline islands observed in the uppermost part of thick 3C-SiC films.

B) *Same specimen irradiated at 1550°C for 3x20ms*

The specimen was irradiated three times, 20ms each, between the flash intervals the temperature was kept at 700°C. The results of the flash annealing are clearly evident in the XTEM micrograph in Fig.2a. The defect density was reduced at least one order of magnitude, compared with the non-irradiated specimen in Fig.1a. Thickness variations of the 3C-SiC film, up to 80% are observed at the 3C-SiC/Si interface, denoted by arrows in Fig.2a. It is estimated that about 10nm of the 3C-SiC film was dissolved in the melted Si-substrate. The large 3C-SiC steps in the Si-substrate exhibit well developed (111) facets. No cavities are observed in the Si near the interface. The uppermost part of the 3C-SiC film remains smooth revealing that the redistribution of the SiC occurs at the SiC/Si interface. The Si at the interface was melted up to a depth of 150nm as is evident from the formation of twins in this zone. The absence of strain at the interface reveals that the system was relaxed after solidification. The improvement of the SiC film is also evident in the PVTEM micrograph in Fig.2b, the SFs density was significantly reduced as shown in Fig.2b. The related diffraction patterns are now spots and not arcs, as shown in the inset in Fig.2b. No faint extra 111 spots along the <110> directions were observed, revealing that after annealing the small (111) type grains were eliminated.

C) Flash annealed at 1200°C, 20ms.

Low temperature irradiation has no effect on the quality of the SiC film. In contrast enhancement of strain was observed at the interface, as shown in Fig.3, resulting to the rupture at the interface. This behavior can be explained by considering that the irradiation was not sufficient to melt the substrate. Moreover strain was suddenly developed due to the difference in the thermal expansion coefficient at the interface. Therefore the melting of the Si at the interface is substantial in order to prevent rupture during irradiation by flash lamps.

From these experiments it was evident that due to the transparency of the 3C-SiC, the irradiated energy is selectively absorbed at the SiC/Si interface where the most defective and consequently absorbing part of the 3C-SiC film is. The Si absorbs the remaining intensity at the interface. The uppermost part of the SiC film is not affected directly by the flash irradiation, it is annealed by the heat dissipation from the SiC/Si interface. Therefore only very thin films can take the advantages of the flash lamp annealing. This was confirmed by flash irradiation of 1μm thick 3C-SiC film. In this case only the zone near SiC/Si interface was improved. However the uppermost

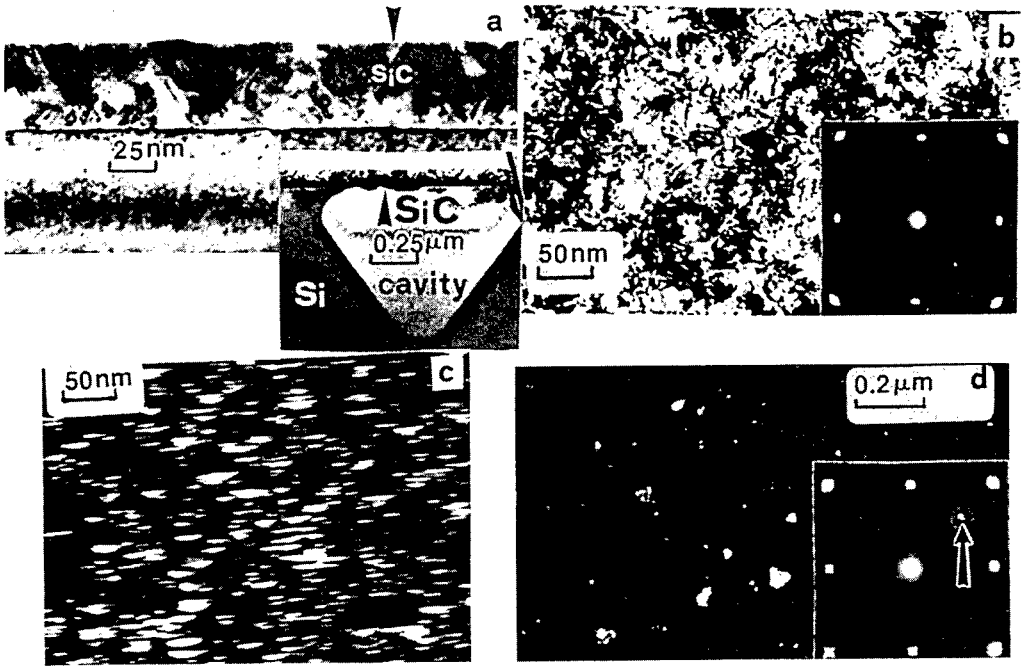


Fig.1 As deposited specimen a) XTEM micrograph from the 44nm thick 3C-SiC film, the film is highly defected, very large cavities were formed in the Si during deposition as shown in the inset b) PVTEM from this film. The corresponding diffraction pattern is shown in the inset. c) DF micrograph from the 3C-SiC taken from the 111 reflection after tilting the specimen in order to have the (110) section. A high density of Stacking faults and microtwins is evident. d) DF micrograph from the 111 diffraction spot shown in the inset of Fig.1b. Small grains having the <110>Si//<111>SiC epitaxial relation.

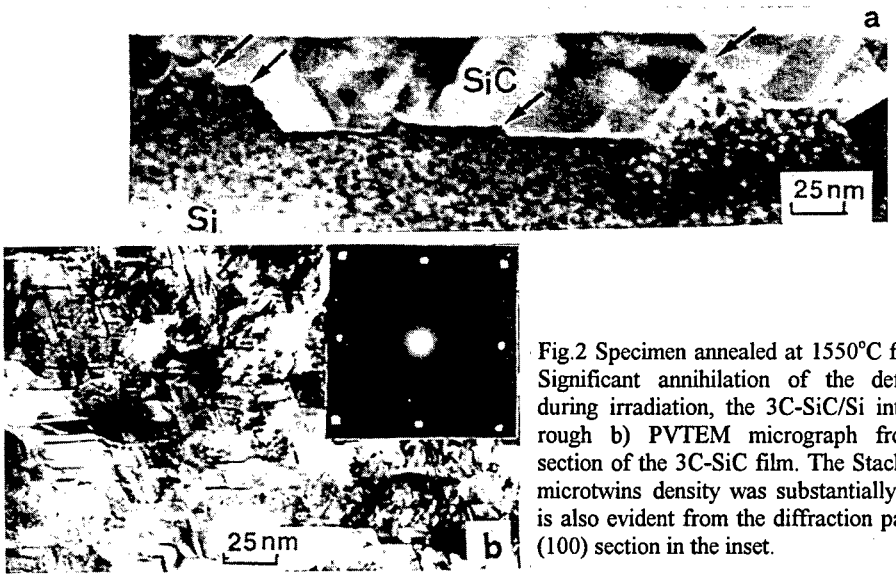


Fig.2 Specimen annealed at 1550°C for 3X20 ms a) Significant annihilation of the defects occurred during irradiation, the 3C-SiC/Si interface is very rough b) PVTEM micrograph from the (110) section of the 3C-SiC film. The Stacking faults and microtwins density was substantially reduced. This is also evident from the diffraction pattern from the (100) section in the inset.

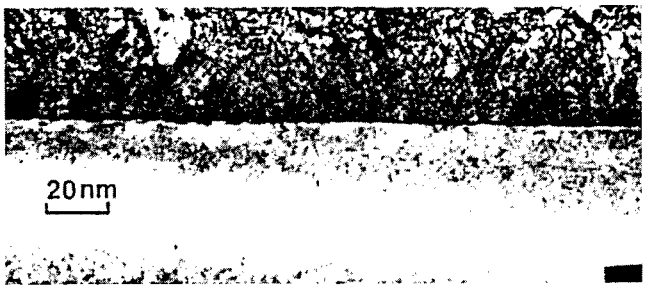


Fig.3 Specimen annealed at 1200°C for 20 ms, the irradiated energy density was not sufficient to melt the Si at the 3C-SiC/Si interface, and strain was accumulated at the interface.

part of the film was not affected. Therefore this method can improve the quality of thin 3C-SiC films, which subsequently can be used as the seed for the growth of thicker 3C-SiC films.

Irradiation by flash lamps of 3C-SiC films on Si is a combination of a high temperature annealing at the uppermost part of the 3C-SiC and LPE [8] at the lower part of the film, according to the following mechanism.

a) The energy due to flash lamp irradiation is mainly absorbed at the SiC/Si interface.
b) The Si near the interface is melted. The process is adiabatic resulting to a significant increase of the temperature at the interface, well above the melting point of Si.
c) The molten silicon dissolves the 3C-SiC layer near the interface.
d) The non melted 3C-SiC at the uppermost part of the film is annealed at a temperature above the melting point of Si and part of the existing defects are annihilated.
e) During solidification phase separation occurs and the dissolved in the silicon SiC is epitaxially deposited on the already annealed uppermost 3C-SiC film, which acts as a seed.

Due to stress relieve the film was buckled in macroscopic scale, experiment are in progress for buckling minimization .

Conclusions

The flash lamp annealing substantially improves the microstructure of thin 3C-SiC films due to the high temperature process. The process resembles LPE, which is extensively applied in SiC epitaxial growth. Elimination of the cavities and stress relaxation occurs at the interface, as soon as the irradiation flux is sufficient to melt the Si at the SiC/Si interface. Thus, solving one of the most serious problems of 3C-SiC deposition on Si. After melting of the Si at the interface the SiC film is buckled due to the stress relieve. Conditions to avoid buckling are under investigation.

References

[1] S. Nishino, J. A. Powell, H. A. Will, Appl. Phys. Lett. 42 (1983), p. 460
[2] F. Bonzso, J.T. Yates, W.J. Choyke, L. Muehlhoff, J. Appl. Phys. 57 (1985), p. 2771
[3] C.H. Carter, Jr. and R.F. Davis, S.R. Nutt, J Mater. Res.1 (1986), p. 811.
[4] J. Stoemenos, C. Dezauzier, G. Arnaud, J. Camassel, J. Pascual, J.L. Robert Mat. Scien. Eng. B29 (1995), p. 160.
[5] H. Wirth, D. Panknin, W. Skorupa, E. Niemann, App. Phys. Lett. 74 (1999), p. 979
[6] H. Möller, M Eickhoff, M.Rapp, H.W. Grueninger and G. Krötz, Appl. Phys. A68, (1999), p. 461.
[7] K. Zekendes, V. Papaioannou, B. Pecz and J. Stoemenos, J. Crys. Growth 157 (1995), p. 392
[8] V. Dmitriev and A. Cherenkov, J. Crys. Growth 128 (1993), p. 343

Materials Science Forum Vols. 353-356 (2001) pp. 155-158
© 2001 Trans Tech Publications, Switzerland

How to Grow Unstrained 3C-SiC Heteroepitaxial Layers on Si (100) Substrates

T. Chassagne[1], G. Ferro[1], C. Gourbeyre[2], M. Le Berre[2], D. Barbier[2] and Y. Monteil[1]

[1] Laboratoire des Multimatériaux et Interfaces, Université Claude Bernard Lyon 1, 43 Boulevard du 11 Novembre 1918, Bât 731, FR-69622 Villeurbanne Cedex, France

[2] Laboratoire de Physique de la Matière, Institut National des Sciences Appliquées Lyon 1, 20 avenue A. Einstein, Bât. 502, FR-69621 Villeurbanne Cedex, France

Keywords: CVD, Heteroepitaxy, Stress

Keywords: Heteroepitaxy, Chemical Vapor Deposition, Stress

Abstract: We report here the achievement of compressive strained 3C-SiC heteroepitaxial layers on Si (100) by APCVD. Substrate curvature was used to measure the residual stress in the β-SiC films. Experimental measurements showed the dependence of the stress value with the conditions of the carburization. We demonstrate the possibility to achieve 3C-SiC layers with compressive or tensile stress by controlling the early stage of the growth.

Introduction

There are mainly two reasons which prevent the development of SiC large scale integration on silicon substrates : (i) the rather poor crystallinity of the 3C-SiC heteroepitaxial layers and (ii) the important strain in the layers which bends the substrate or even makes cracks in the layers. For some applications such as pressure, temperature or gas sensors in which a high crystalline quality is not required, the latter problem becomes of main importance. The strain measured after cooling down of the sample is mainly due to the thermal expansion coefficient mismatch between SiC and Si. Simple calculations taking only into account the thermal expansion coefficients show that SiC should be in tensile stress at room temperature after the usual high temperature growth [1]. Although this tensile stress has been experimentally measured by many researchers [2,3], we report here the achievement of compression strained 3C-SiC heteroepitaxial layers on Si (100) substrates.

Experiments

The experiments were carried out by APCVD in a cold wall vertical reactor. Silane (1% in H_2) and propane (5% in H_2) were used as sources and H_2, purified by a Pd-diffusion cell, as carrier gas. The substrates were heated via a RF coupled graphite susceptor on which the temperature was measured by an optical pyrometer.

Before loading in the reactor, the silicon (100) wafers were degreased and dipped in HF. Prior to the growth, substrates were hydrogen etched in-situ at 1000°C for 5 min. The growth procedure involved two steps as explained in our earlier work [4]. First, the substrate is carbonized at 1150°C under a mixture of H_2 (10 slm) and C_3H_8 (10 sccm) for 10 min. The propane is introduced in the reactor before the heating ramp of 8°C/s at a temperature of about 300°C. Then the growth is carried out at 1350°C under a C/Si ratio of 3.3 and a growth rate of 3 μm/h.

The epilayers were characterized by X-ray diffraction (XRD), atomic force microscopy (AFM) and Hall measurements for structural, morphological and electrical properties respectively. The SiC thickness was obtained with a 0.1 μm accuracy by FTIR spectroscopy method.

Stress measurements

The substrate bends elastically due to the biaxial stress in the epilayer. The amount of the bending depends on the thickness and biaxial elastic modulus of the substrate. As the biaxial elastic modulus is isotropic in the plane of the substrate in the case of Si (100), the film/substrate composite adopts the shape of a spherical shell. Stress of 3C-SiC epilayer was calculated from substrate curvature measurements at room temperature using the bending plates method and the Stoney's equation:

$$\sigma = \frac{E_{Si}}{1-\upsilon_{Si}} \frac{h_{Si}^2}{6h_{SiC}} \left(\frac{1}{R} - \frac{1}{R_0} \right) \quad (1)$$

where E_{Si}, ν_{Si} and h_{Si} are respectively the Young's modulus, the Poisson's ratio and the thickness of the Si substrate. For Si (100), the biaxial modulus $E_{Si}/(1-\nu_{Si})$ calculated to be 180.2 GPa [5]. h_{SiC} is the film thickness, R_0 and R are the substrate radius of curvature before and after deposition respectively. The radius of curvature was measured along different directions by means on a UBM optical profilometer (60 nm depth resolution with 400 pts/mm).

Results and discussion

Fig. 1 shows the XRD diffraction pattern of a 3C-SiC 3 μm thick grown by using the standard procedure. The full width at half maximum (FWHM) of the β-SiC (200) peak was about 140 arcsec without apparatus correction. This value is quite similar to those reported by other authors [2,6].

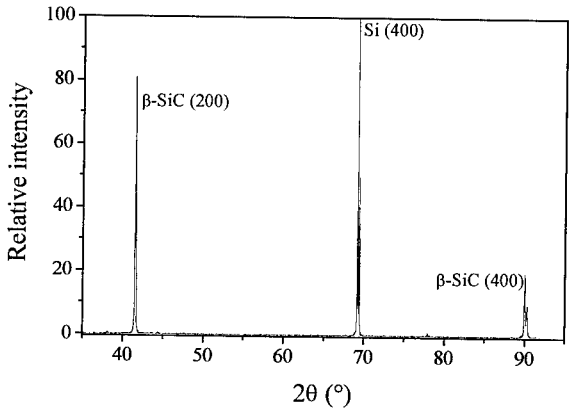


Figure 1: X-ray diffraction pattern of a β-SiC 3 μm thick

AFM characterization shows that the root mean square surface roughness (rms) of a 3 μm film was about 4 nm for a 5*5 μm^2 scan. The mobility and the resistivity were 209 $cm^2/V.s$ and 70 mΩ.cm respectively for 9 μm thick 3C-SiC epilayers. All those results are comparable to the state of art in terms of crystalline quality, morphology and electrical properties for 3C-SiC epitaxial layers.

Unexpectedly, the 3C-SiC films were not tensile but compressive stressed. Typically, a compressive stress of about -500 MPa was measured on the 3 μm thick epilayer. As the tensile strain is most commonly found in 3C-SiC heteroepitaxial films on Si, we should be able to obtain tensile strained layers. Since the strain in the layers originates from the thermal expansion coefficients mismatch with the substrate, we believe that the early stage of growth is very important as it sets the way it is hitched to the substrate. To confirm that hypothesis, we changed the conditions of carburization and measured the resulting strain after standard epitaxial growth.

Fig. 2 shows the residual stress in the film with a constant thickness of 3 μm versus the temperature of introduction of propane (T_{car}) during the heating ramp of the carburization step. One can see that the residual stress changes drastically with the increase of T_{car}. By increasing T_{car} from 300 to 1000°C the residual compressive stress of the 3C-SiC epilayers varied from -579 to -258 MPa. Nevertheless, the more interesting result is the change of the total film stress from compressive to tensile at an average temperature T_{car} of 1050°C. The total variation of strain in the β-SiC is higher than 1 GPa when T_{car} varies from 300 to 1350°C.

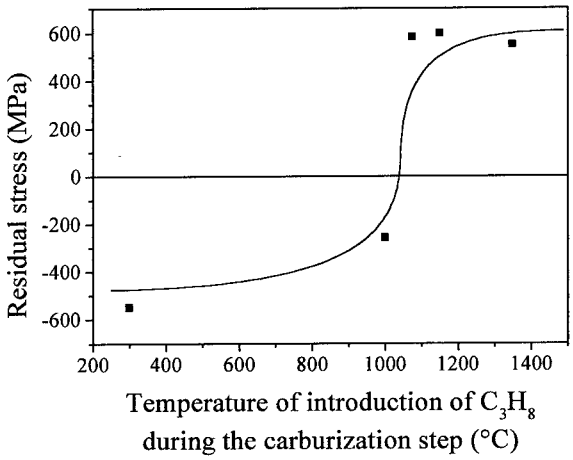


Figure 2: Residual stress versus conditions of carburization. The line is added as a guide.

Table 1 indicates the crystalline quality of the different samples obtained with different T_{car}. One can see that the FWHM increases with the increase of T_{car}. Indeed, for T_{car} higher than 1075°C the crystallinity of the sample decreases drastically. When the propane was introduced at these temperatures, the carburization layer became very rough which altered the quality of epitaxial layers [4]. AFM 5*5 μm^2 scan shows that the surface roughness varied from 0.25 to 2.5 nm when T_{car} varied from 300 to 1150°C.

The change in sign of the residual stress cannot be only attributed to the decrease of the crystallinity at high T_{car}. Indeed, the layer grown with T_{car} = 1075°C shows a tensile stress with a rather comparable FWHM of the β-SiC (200) peak with the one grown with lower T_{car} and compressive stress. However, we believe that the origin of the change of the strain sign could be the change of the mosaicity in the β-SiC layers. Works is under progress to clarify that point mainly by means of double XRD, but also with electrical and optical characterizations.

Sample	T_{car} (°C)	Thickness (μm)	FWHM β-SiC (200) (arcsec)	σ (MPa)
M 46	300	3.20	135	-578
M 76	1000	2.80	132	-259
M 107	1075	3.30	144	580
M 47	1150	3.15	258	596
M 49	1350	3.59	241	549

Table 1: Stress and crystalline quality of the sample

One can notice that the range of T_{car} giving good crystallinity tensile strained layers is very narrow compared to the one giving good quality compressive strained layers. This is due to the lower reactivity of the silicon surface at lower temperature allowing to progressively seal the surface by few SiC monolayers. In the zone of T_{car} where tensile strain is achieved, the reactivity of the silicon surface is high and a little increase in T_{car} involves a dramatic worsening of the buffer layer.

It has to be noted that the possibility to grow either tensile or compressive stressed monocrystalline β-SiC layers has never been reported yet. And if T_{car} is not higher than 1075°C, the tensile and compressive strained layers have equivalent crystallinity. This is a very important point as it demonstrates the possibility to grow state of the art β-SiC unstrained layers by tuning T_{car}, i. e. by controlling carefully the early stage of growth. On the point of view of large scale integration on Si wafers, this a decisive step.

Conclusion

We demonstrated for the first time not only the possibility to grow compressive strained β-SiC layers on Si (100) but also the capability to tune the sign of the strain by controlling the early stage of growth. The tensile strained layers can be grown with identical crystallinity than the compressive strained ones with state of the art quality. Work is under progress to achieve totally unstrained β-SiC layers and to fully understand the origin of the sign change of the strain with T_{car}.

References

[1] H.P. Liaw and R.F. Davis, J. Electrochem. Soc., **131** (1984), p. 3014.
[2] S. Veprek, Th. Kunstman, D. Volm and B.K. Meyer, J. Vac. Sci. Technol. **A 15**, (1997), p. 10.
[3] C. Jacob and P. Pirouz, proceeding of the 10th conference on semiconducting and insulating materials, IEEE (1998), p. 275.
[4] G. Ferro, Y. Monteil, V. Thevenot, H. Vincent, F. Cauwet, Tran Min Duc and J. Bouix, J. Appl. Phys. **80** (1996), p. 4691.
[5] C. Malhaire, PhD thesis, INSA LYON, 1998.
[6] O. Kordina, L.O. Bjôrketun, A. Henry, C. Hallin, R.C. Glaas, L. Hultman, J.E. Sundgren and E. Janzèn, J. Crystal Growth **154**, (1995), p. 303.

Materials Science Forum Vols. 353-356 (2001) pp. 159-162
© 2001 Trans Tech Publications, Switzerland

Growth of 3C-SiC on Si by Low Temperature CVD

T. Cloitre[1], N. Moreaud[1], P. Vicente[1,2], M.L. Sadowski[1] and R.L. Aulombard[1]

[1] Groupe d'Etude des Semiconducteurs, Université Montpellier 2,
Place E. Bataillon, FR-34095 Montpellier Cedex 5, France

[2] Present address: NOVASIC, Pomblière, FR-73600 Moutiers, France

Keywords: CVD, Heteroepitaxy

Abstract. We report on the growth of 3C-SiC/Si using propane and silane as precursor gases. All layers were deposited on exactly <100> oriented Si substrates. The growth temperature ranged from 1200°C to 1350°C and the carbonization temperature from 1150°C to 1350°C. We focused our study on the optimization of the surface morphology and the suppression of interfacial voids at low growth temperature. All layers were characterized by X-ray diffraction (both single diffraction and ω-scan), micro-Raman on cleaved edges, AFM, optical microscopy,2K photoluminescence and IR reflectivity. We have developed a 1150°C carbonization step which, combined with a growth temperature of 1250°C results in good quality material.

Introduction

Optimized, low temperature growth of 3C-SiC on Si is a perquisite for sensor applications [1]. Usually the layer quality decreases as the deposition temperature decreases and some (best) compromise has to be found. The main problem associated with the heteroepitaxy of 3C-SiC on Si is the large differences in lattice constants (20%) and thermal expansion coefficients (8%). This leads to numerous defects in the SiC layers. In order to partially compensate the lattice mismatch effects, a carbonization process is used to build a buffer layer, before the SiC epilayer growth. The quality of the SiC layers is usually improved using high growth temperature (up to 1360°C). However, in this case, the silicon substrate suffers important degradations, resulting in interfacial voids formation at the substrate side of the heterointerface. These defects are formed via atomic Si outdiffusion through the SiC layer. The Si outdiffusion is thermally activated and occurs if diffusion paths, such as grain boundaries, are present in the carbonization and the SiC layers. This interfacial voids formation is reduced when using low growth temperature (1150°C) [2]. A compromise has to be found in order to grow good quality SiC layers without degradation of the substrate surface. In this work, we have optimized the quality of SiC layers by varying independently the carbonization temperature and the growth temperature.

Experimental details

The layers were grown using a home made, cold wall, vertical reactor operated at atmospheric pressure. The precursors used for the growth of SiC were propane (5 % in hydrogen) and silane (10 % in hydrogen). The precursors were additionally diluted by palladium purified hydrogen carrier gas when entering the reactor. All layers were deposited on on-axis Si (100) substrates. The substrates were prepared by using degreasing steps, DI water rinses, and a final dip in a diluted HF solution to obtain a hydrogen terminated surface. After the chemical preparation, the substrates were immediately loaded in the reactor which was then submitted to pumping and H_2 purging cycles. For all samples investigated in this study the common growth procedures were the following : The

carrier gas flow was maintained at 3.15 slm during all the growth steps. The growth process started with a hydrogen etch at 1150°C for 5 min. The temperature was thereafter lowered down to 200°C and the propane flow (50 sccm) was introduced into the hydrogen flow for 5 min. The temperature was then raised to the carbonization temperature (Tc) using a 300°C min^{-1} controlled ramping. The carbonization temperature was varied from 1150°C to 1350°C and held for 1 min to 15 min. After the carbonization step, the temperature was adjusted to the growth temperature (T_G), comprised between 1200°C and 1350°C, and the propane flow was simultaneously lowered to 7.5 sccm. After temperature stabilization (1 min), silane (2 sccm) was introduced, and the growth started for 90 min. A series of samples were grown using various carbonization and growth temperature combinations in order to optimize the SiC layer quality. We report in this paper the most typical results of this study. The relevant growth parameters are presented in table 1. We have paid a particular attention on the susceptor condition by regularly reconditioning its surface, using an outgassing process and in-situ SiC coating. The accumulation of polycrystalline SiC on the graphite susceptor is known to induce a regular degradation of the epitaxial layers from run to run [3].

	Tc [°C]	Carb. Time	Tg [°C]
sample 1	1300	1 min	1300
sample 2	1150	5 min	1350
sample 3	1150	15 mn	1250

Table 1 : Growth parameters

Characterizations

The crystalline quality of the layers was first evaluated by X-ray diffraction. Except for samples grown at 1200°C, all the layers were single crystalline, as demonstrated by single diffraction spectrum (Fig. 1). The layers were further studied by examining the FWMH of the SiC-(400) reflection peak obtained by double crystal X-ray diffraction in the ω-scan configuration (Fig. 2). The FWMH of the reflection line increases as the sample thickness decreases and when the growth temperature decreases. The thicknesses of samples 1, 2 and 3 are $e_1 = 3.3$ μm, $e_2 = 2.7$ μm and $e_3 = 2$ μm. The measured FWMH are 950 arc.sec., 850 arc.sec and 1050 arc.sec. for samples 1, 2 and 3, respectively. The FWMH obtained for sample 3 grown at the lowest temperature indicates a fairly good crystalline quality if we take into account its thickness. As an example, for a 5 μm thick sample grown in the conditions of sample 1, the FWMH of the (400) SiC reflection decreased down to 600 arc.sec. This thickness effect is well known since the defect density decreases gradually in the SiC layer as the distance from the perturbed Si/SiC interface increases.

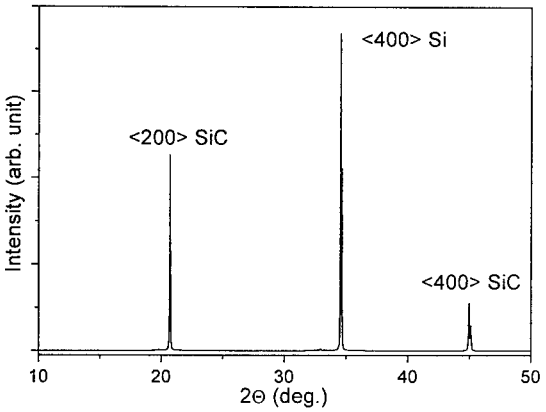


Figure 1 : Diffraction spectrum of sample 3

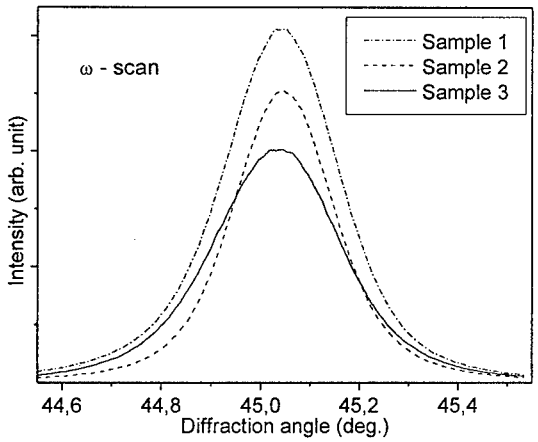


Figure 2 : Double crystal X-ray diffraction

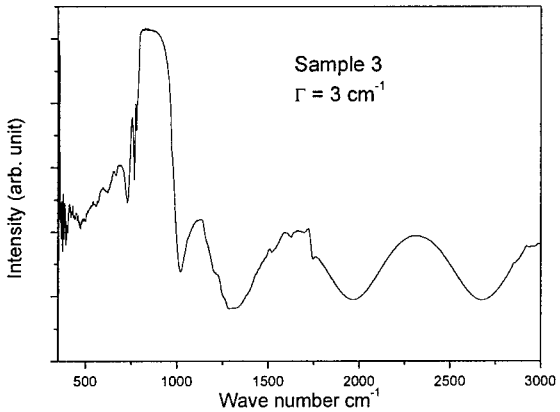


Figure 3 : IR reflectivity of sample 3

A typical IR reflectivity spectrum is reported in Fig. 3. The spectra obtained were fitted with a standard transfer-matrix model [4] in order to deduce the damping parameter and the thickness of the layers. We do not observe any damping or deviation of the line base of the interference fringes when the excitation wave number increases to 6000 cm^{-1}. This indicates a good surface and interface quality with low roughness. More importantly, the calculated damping parameter decreases from samples 1 to 3 indicating the improvement of the sample quality. We calculate $\Gamma = 5\ cm^{-1}$, $\Gamma = 4\ cm^{-1}$ and $\Gamma = 3\ cm^{-1}$ for samples 1, 2 and 3, respectively. Those results indicate a good structural quality for the samples and particularly for the SiC layer grown at 1250°C. Micro-Raman characterization on a cleaved edge of sample 3 is reported in Fig. 5. We do not notice any detectable shift of the Raman lines related to the Si substrate or the SiC layer with the position of the laser spot. Moreover, the positions of the Raman back scattering lines correspond to fully relaxed materials. The FWMH of both the TO and LO modes related lines is around 3 cm^{-1}. This confirms the good quality of sample 3.

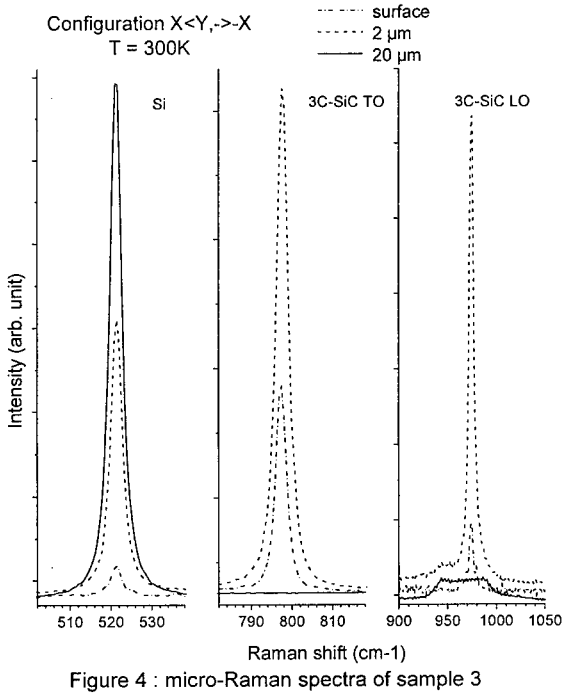


Figure 4 : micro-Raman spectra of sample 3

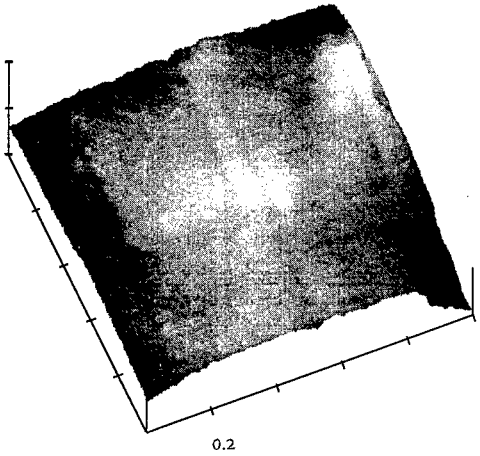


Figure 5 : AFM image of sample 3

The morphology of the epilayers was examined by a Nomarsky microscope and AFM imaging (Fig. 5). For sample 3 we observe a structured surface indicating a 3-D mode growth resulting in islands of few μm^2. The observation of the silicon surface near the cleaved edges revealed that no void was formed in sample 3. Voids were only detected in samples grown at temperatures higher than 1250°C. The

main roughness is due to boundaries between islands while locally the Rms roughness deduced from AFM images is very low (Rms (Rq) = 0.28 nm).
Finally, the optical properties of the SiC layers were examined using 2K photoluminescence. The

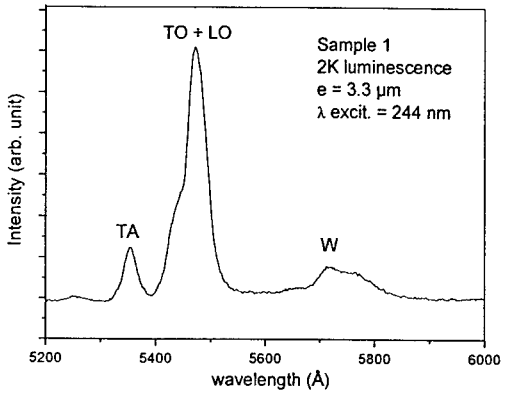


Figure 6 : Photoluminescence of sample 1

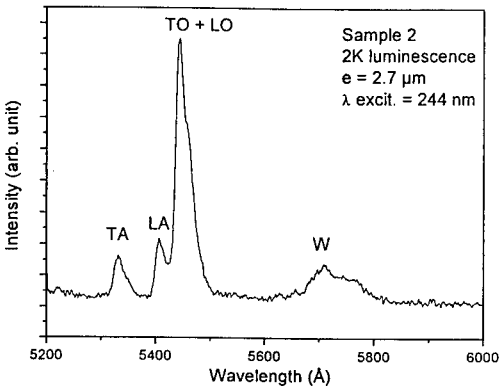


Figure 7 : Photoluminescence of sample 2

spectra presented in Figs. 6-8 for samples 1-3 are very similar and exhibit the classical nitrogen bound exciton (N-BE) related lines. The so-called W band centered at around 5700 Å is generally attributed to plastical deformations in the SiC layer near the interface. Due to its origin, this band is enhanced for thinner SiC layers as exemplified in Fig. 8. The most interesting result is the observation of the N-BE lines for a low thickness of 2 µm and a low growth temperature in the case of sample 3. Such observation is indicative of the good overall quality of this layer and was not reported before to the best of our knowledge.

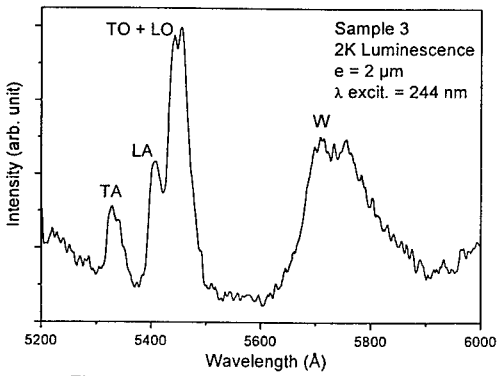


Figure 8 : Photoluminescence of sample 3

Summary

We have developed a 1150°C carbonization process combined with a low growth temperature of 1250°C. This process allowed us to grow good quality 3C-SiC layers from both the optical and the structural point of view.

References

[1] J. Camassel, J. Vac. Science and technology B16 (1998), 1648.

[2] L.-O. Björkentun, L. Hultman, I.P. Ivanov, Q. Wahab andJ.-E Sundgren, J. Cryst. Growth 182 (1997), 379.

[3] J.A. Powell, L.G. Matus and M.A. Kuczmarski, J. Electrochem. Soc. 134 (1987), 1558.

[4] M.L. Sadowski, M. Grynberg, A.M. Witowski, S. Huant and G. Martinez, Phys. Rev. B 60 (1999), 10908.

Materials Science Forum Vols. 353-356 (2001) pp. 163-166
© 2001 Trans Tech Publications, Switzerland

Growth of SiC on Si(100) by Low-Pressure MOVPE

A.S. Bakin[1], A.A. Ivanov[1], D. Piester[1], T. Riedl[2],
F. Hitzel[2], H.-H. Wehmann[1] and A. Schlachetzki[1]

[1] Institute of Semiconductor Technology IHT, Technical University Braunschweig,
Hans-Sommer-Str. 66, DE-38106 Braunschweig, Germany

[2] Institute of Technical Physics, Technical University Braunschweig,
Mendelssohn-Str. 2, DE-38106 Braunschweig, Germany

Keywords: CVD, MOVPE, SiC Growth, SiC on Si

Abstract 3C-SiC was grown on Si(100) using a metal-organic vapour phase epitaxy set-up at temperatures well below 1000°C (mostly at 940°C). A UV-source has been added to the set-up. Carbon tetrabromide (CBr_4) was used as the carbon source. The implementation of UV stimulation during the growth process leads to a higher uniformity of the grown surfaces and in most cases to a lower roughness compared to the growth under the same conditions but without UV stimulation. An additional effect is an increased density of self-organized nano-islands. The results of our recent investigations concerning the growth as well as the growth of initial nano-scale islands are described and discussed in the present paper.

Introduction

Cubic silicon carbide (3C-SiC) is at present a topic of considerable interest due to its potential in electronic device applications, micromechanical systems, etc. [1-7]. Semiconductor materials grown directly on silicon can profit directly from the availability of low-cost large area substrates, their superior thermal conductivity and the possibility to realize a new generation of optoelectronic devices monolithically integrated with silicon microelectronics. An example is lateral epitaxial growth of SiC on Si [7]. It is also important to employ lower growth temperatures. Monocrystalline layers have been grown at temperatures as low as 750°C [8] or 1000°C [5]. In order to obtain such low growth temperature methylsilane was used as a source of both Si and C. In [5] Ge was employed as a surfactant to promote two-dimensional SiC growth at 1000°C by MOCVD. Both 3C-SiC and 6H-SiC were obtained on Si(111). The aim of the present paper is to investigate low temperature growth of SiC on Si(100) using low-pressure metal-organic vapor phase epitaxy (MOVPE) offering the possibility to control the Si/C ratio in the gas phase.

Experimental

The growth was performed in a horizontal infrared-heated MOVPE machine designed by AIXTRON and operated at low pressure (20 to 100 hPa) utilizing the precursors carbon tetrabromide (CBr_4) and monosilane (SiH_4, 2% in H_2) as sources of C and Si, respectively. For more stable operation at high temperatures a modification of the heating system has been made

(compressed air cooling system, Au-coatings of the reflectors and for some cases Au-coated shields over the reactor). A mercury-xenon lamp as a UV-source has been added to the set-up (upper structure in Fig. 1). The growth temperature for most experiments was 940°C. Exactly oriented Si (100) substrates were employed. Our samples were grown with or without UV stimulation. Experiments with varied CBr_4/SiH_4 flow ratios were carried out. A short Si substrate-carbonisation step [1] was added in the experiments at the beginning of the SiC growth process.

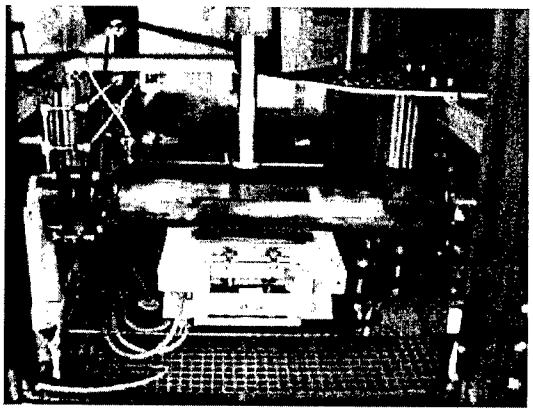
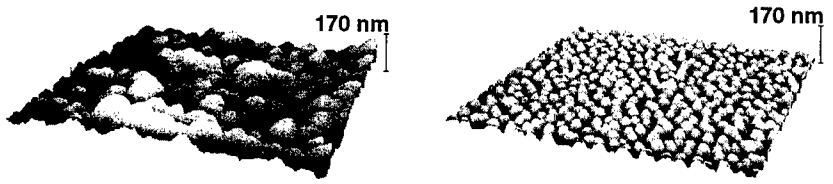


Fig. 1. AIX 200 reactor with the additional source of UV radiation

Results and discussion

The samples obtained were investigated by atomic-force microscopy (AFM), scanning electron microscopy (SEM), photoluminescence (PL), optical microscopy, and transmission electron microscopy (TEM). In this work we concentrated our attention to the initial stages of the SiC growth. The UV stimulation increased the uniformity of the grown surfaces and in most cases decreased their. An example of the UV influence on the initial stage of SiC growth is shown in Fig. 2. AFM revealed the formation of three-dimensional islands with densities up to 10^{10} cm^{-2} (Fig. 2 b) for the growth with UV stimulation.

SEM images of the corresponding surfaces after further SiC growth on Si (100) substrates for the same growth conditions as in Fig. 2 are shown in Fig. 3.



a b

Fig. 2. AFM images ($2\times2\mu m^2$) of the surfaces after SiC growth on Si (100) substrates for the same growth conditions (in particular duration 5 min): a – without UV stimulation; b – with UV stimulation.

AFM images of the surfaces after SiC growth on Si (100) substrates with UV stimulation for the same duration (5 minutes) and different CBr_4/SiH_4 flow ratios (with CBr_4 flow constant for all experiments) are shown in Fig. 4. TEM investigations of these samples revealed the transition from amorphous to fine polycrystalline and then to textured 3C-SiC films with the ratio variation.

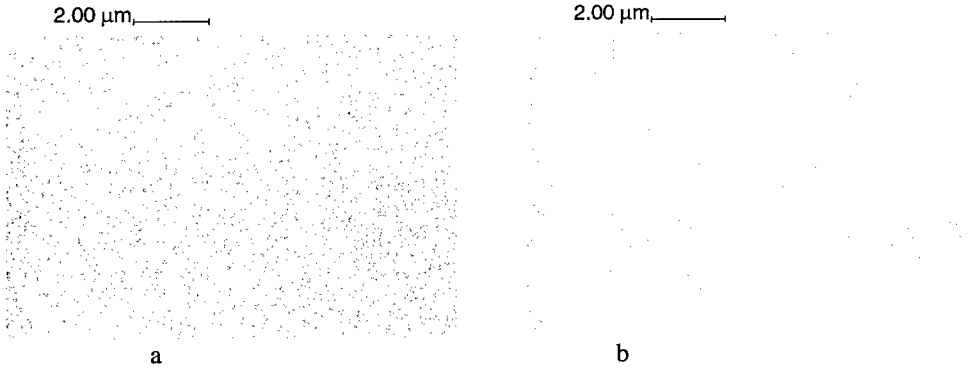


Fig. 3. SEM images of the surfaces after SiC growth on Si (100) substrates for the same growth conditions as in Fig. 2, but with a duration of 30 min: a – without UV stimulation; b – with UV

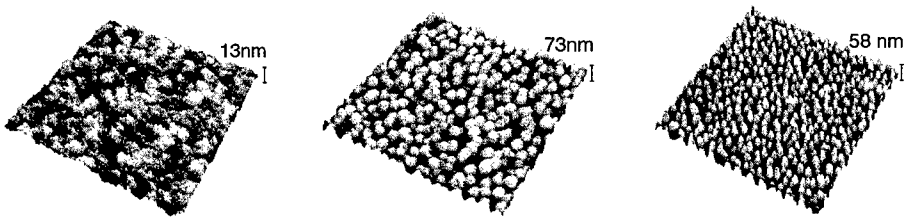


Fig. 4. AFM images ($2\times2\mu m^2$) of the surfaces after SiC initial growth on (001) Si substrates with UV stimulation for the same growth duration, but different CBr_4/SiH_4 flow ratios: a- 3; b- 0.9; c- 0.4.

PL investigations of the samples were carried out at temperatures from 15 to 300 K. An example of the PL spectra measured at 150 K is shown in Fig. 5. A broad PL peak around 2.4 eV was observed. Its FWHM is about 0.44 eV. The PL spectrum is similar to that reported in [9] for 3C-SiC grown by rapid thermal chemical vapor deposition at 1100 or 1200°C.

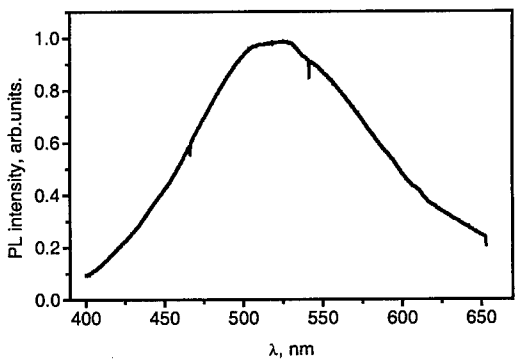


Fig. 5. PL of a SiC sample grown on Si (100) substrate.

Summary

In summary, UV stimulation has been developed as a technique for the low-temperature growth of SiC on Si. The samples obtained were investigated using SEM, AFM, TEM and PL. UV stimulation of

the SiC growth process allows to improve the uniformity of the growth surface, i.e. a lower roughness of the surface, and to increase the density of the self-organized nano-islands at the initial stage of the growth. Investigations regarding the optimisation of growth conditions are ongoing. A further improvement of the quality of the films can be obtained by use of foreign atoms incorporation in the SiC/Si interface or surfactants. The implementation of UV stimulation is possible also for high temperature SiC on SiC growth, as well as for wet and dry SiC etching.

Acknowledgements

The authors should like to thank D. Rümmler, M. Karsten, G. Schulze, and C. Grusewski for technical assistance. Financial support by the Deutsche Forschungsgemeinschaft (DFG) is gratefully acknowledged.

References

[1] S. Nishino, J. A. Powell, and H. A. Will, Appl. Phys. Lett. 42 (1983), p. 460
[2] S. Nishino, S. Suhara, H. Ono, and H. Matsunami, Appl. Phys. 61 (1987), p. 4889
[3] S. Stefanescu, A.A. Yasseen, C.A. Zorman, and M. Mehregany, in Technical Digest, The 10th Int. Conf. Solid-State Sensors and Actuators (Sendai, Japan, June 1999), p. 194
[4] G. H. Krötz, M. H. Eickhoff, H. Möller, Sensors and Actuators 74 (1999), p. 182
[5] W. L. Sarney, L. Salamanca-Riba, P. Zhou, M. G. Spencer, C. Taylor, R. P. Sharma, and K. A. Jones, J. Electron. Mater. 29 (2000), p. 359
[6] J. Pezoldt, P. Masri, M. Rouhani Laridjani, M. Averous, T. Wöhner, J. A. Schaefer, Th. Stauden, G. Ecke, R. Pieterwas, L. Spieß, International Conference of SiC and Related Materials 1999, to be published.
[7] C. Jacob, J. Chung, M.-H. Hong, P. Pirouz, and S. Nishino, Mat. Res. Soc. Symp. 622 (2000), p. T4.1.1-6
[8] I. Golecki, F. Reidinger, and J. Marti, Appl. Phys. Lett. 60 (1992), p. 1703
[9] H. W. Shim, K. C. Kim, Y. H. Seo, K. S. Nahm, E.-K. Suh, H. J. Lee. And Y. G. Wang, Appl. Phys. Lett. 70 (1997), p. 1757

Materials Science Forum Vols. 353-356 (2001) pp. 167-170
© 2001 Trans Tech Publications, Switzerland

The Microstructure and Surface Morphology of Thin 3C-SiC Films Grown on (100) Si Substrates Using an APCVD-Based Carbonization Process

C.-H. Wu[1], J. Chung[1], M.H. Hong[1], C.A. Zorman[2], P. Pirouz[1] and M.Mehregany[2]

[1] Department of Materials Science and Engineering, Case Western Reserve University, 10900 Euclid Ave., Cleveland OH 44106, USA

[2] Department of Electrical Engineering and Computer Science, Case Western Reserve University, Cleveland OH 44106, USA

Keywords: 3C-SiC, APCVD, Carbonization, Si Substrates

Abstract. The carbonization of the Si (100) surface in an APCVD reactor using propane as the carbon source gas and hydrogen as the carrier gas was studied. The layer thickness as a function of carbonization time exhibits a parabolic behavior indicative of a self-limiting process. Voids are produced in the carbonization layer when hydrogen is used during the cool-down step, but not when hydrogen is replaced by argon. Other than the presence of voids, the surface morphology of the carbonization layer is relatively smooth, suggesting that the carbonization layer forms via quasi-two dimensional growth.

Introduction

CVD-based, heteroepitaxial growth of a 3C-SiC film on a Si (100) substrates often requires that the Si surface be converted to 3C-SiC prior to single crystal film growth. The conversion process, commonly called carbonization, is often performed during the temperature ramp-up step in a hydrocarbon ambient and produces a thin crystalline template on which 3C-SiC film growth can occur. Recently, carbonization has been used to produce thin (100) 3C-SiC transition layers suitable for growth of cubic GaN on (100) Si wafers [1]. In both cases, the quality of the epitaxial film is critically dependent on the quality of the carbonization layer. The purpose of this study was to find a proper set of processing conditions for production of high quality carbonization layers on large area (100) Si substrates.

Experimental

For this study, the carbonization of 100 mm-diameter, on-axis, Si (100) wafers was performed in an APCVD reactor using propane as the carbon source gas and hydrogen as the carrier gas. Prior to carbonization, each wafer was subjected to an *in-situ* etch in hydrogen for 5 min at 1000°C to remove the native oxide on the Si surface, after which the temperature was lowered to below 500°C. The carbonization process was initiated by injecting propane (15% in H_2) into the hydrogen gas stream and increasing the temperature to 1280°C. In this study, the flow rates of hydrogen and propane were held at 25 slm and 84 sccm, respectively. At these flow rates, the concentration of propane was 0.049 % of the total gas volume. A large susceptor was required to hold the Si wafers, therefore the ramp-up and the cool-down times exceeded 5 minutes, which translates to a ramp-up rate of about 4 K/s. Upon reaching 1280°C, the temperature and gas flows were held constant for a predetermined period. In this study, carbonization periods ranged from 30 s to 30 minutes. After carbonization, the propane gas flow was turned off and the susceptor temperature was held at 1280°C for 1 minute in the hydrogen gas flow to exhaust any remaining hydrocarbons in the reactor. Finally the wafer was cooled down to room temperature. Atmospheres of hydrogen and argon were used in the cool-down step to see the effect of hydrogen etching on the surface morphology of the SiC layers. SEM and TEM were used to characterize the surface morphology, microstructure and film/substrate interface of the carbonized layers.

Results and Discussion

The thickness of each carbonization layer was determined using cross-sectional TEM. Fig. 1 shows a plot of the carbonization layer thickness versus carbonization period. For the shortest carbonization period (30 s), the carbonization layer thickness was about 2.5 nm. A maximum carbonization layer thickness of 7.3 nm was measured for the 30 min period. The growth rate seems to be highest at the beginning of the carbonization period and decreases with increasing the carbonization time. The shape of the growth curve is similar to the growth curves reported by Cimalla *et al.* [2], but the growth rate is much lower and the saturation thickness (~7.3 nm) is thinner in our work. It should be noted that Cimalla *et al.*, performed carbonization experiments in a RTCVD system using a temperature ramp-up rate of 50 K/s, which is nearly 12 times faster than the rate we used.

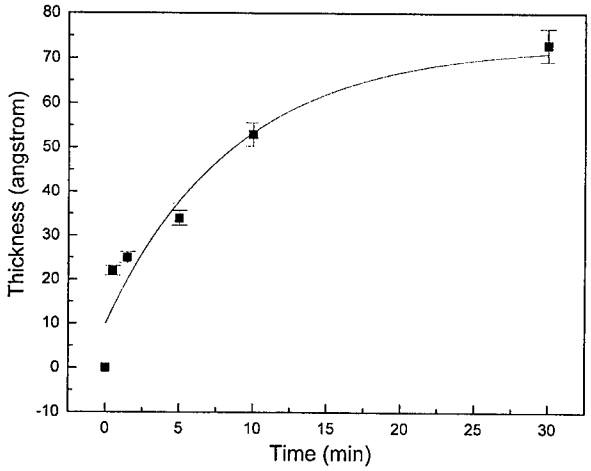


Fig.1. Carbonization layer thickness vs. carbonization time.

The surface morphology of as-grown carbonization layers was characterized using SEM. In general, voids are found in the carbonization layers prepared using the hydrogen-based cool-down step. Fig. 2(a) shows voids in a carbonization layer prepared for 1.5 minutes.

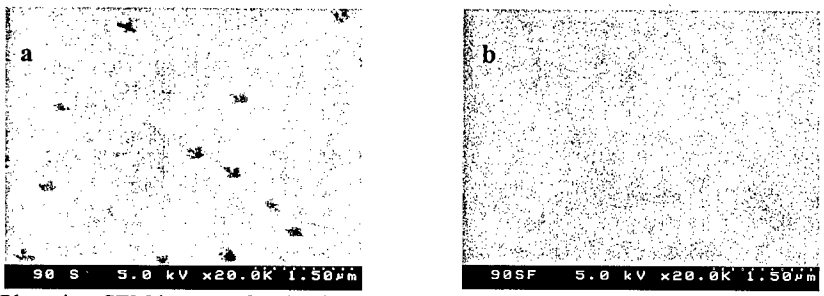


Fig. 2. Plan-view SEM images of carbonized layers prepared using: (a) the hydrogen cool-down step; and (b) the argon cool-down step.

The density of voids on the surface of all films grown using the hydrogen-based cool-down step was about 2 x$10^{11}$$m^{-2}$. Except for voids, no other defects or features were found on the carbonization layer surfaces. Experiments performed using two different susceptors to see if a mechanism other than hydrogen etching could be responsible for the formation of voids showed that void formation was not related to the condition of the susceptor.

In contrast to Fig. 2(a), Fig 2(b) shows that the surface quality of carbonization layers is greatly improved by using the argon-base cool-down step. Note the absence of voids on the surface of the layer.

The microstructure of each carbonization layer and interface was characterized using cross-sectional TEM and SAD. The [011] zone-axis diffraction pattern from the film/substrate interface indicates that the carbonization layer is single-crystalline 3C-SiC. In the SAD pattern, the SiC diffraction spots show a discernible crescent shape, which indicates an azimuthal misorientation of up to 5° relative to the silicon lattice. In some areas, voids can be found in the TEM micrographs of carbonization samples prepared using the hydrogen-based cool-down step, as shown by the arrows in Fig. 3(a). By comparison, no voids were observed in the TEM micrographs of the carbonization samples prepared using the argon-based cool-down step, as shown in Fig. 3(b). As a result, the carbonization layers prepared with the argon cool-down step have better thickness uniformity across the observed area. As with the samples prepared using the hydrogen cool-down step, SAD analysis showed the films be single-crystalline 3C-SiC.

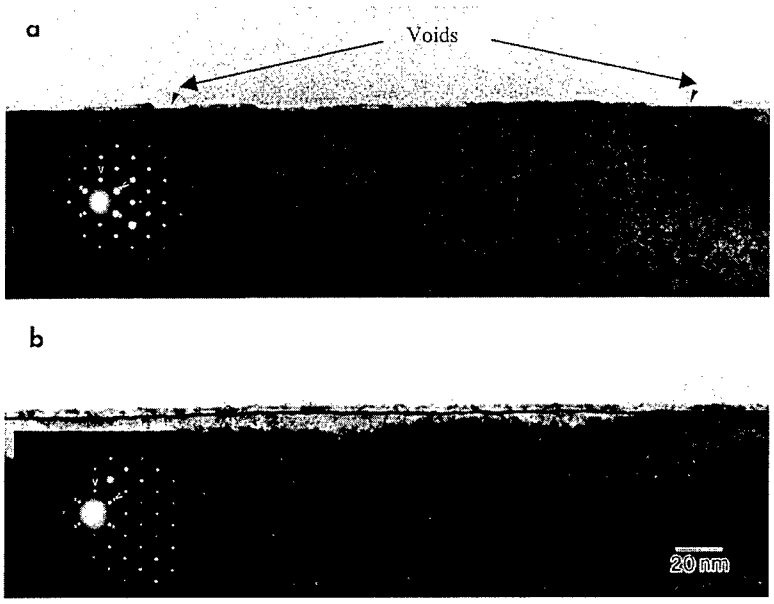


Fig.3. Bright-field TEM micrographs of the 1.5 minute carbonization layer: (a) cooled down in hydrogen; (b) cooled down in argon. The arrows denote the position of voids.

The experimental results clearly show that the hydrogen-based cool-down step causes the formation of the voids in the carbonization layers. The high temperature etching of SiC by hydrogen has long been recognized [3]. During the carbonization step, however, the etching of SiC by hydrogen is suppressed by the existence of a sufficiently high hydrocarbon partial pressure due to the flow of propane. As a result, the growth process dominates and SiC carbonization layers are grown on the Si substrates. However, if the carbonization process is ceased by terminating the supply of propane and cooling the Si substrates in a hydrogen ambient, SiC etching may resume. The etching may be severe if the cool-down period is lengthy, as is the case with large induction-heated susceptors. Since monocrystalline 3C-SiC films grown by the carbonization of Si have inherent crystalline defects, non-uniform preferential etching along these defects is expected, resulting in roughened surfaces. In some areas, hydrogen may completely etch away the carbonization layer and attack the underlyng silicon substrate, creating the voids observed in this study. Our study shows that by simply substituting the hydrogen carrier gas with an inert gas like argon upon terminating the flow

of propane, etching of the carbonization layer and subsequent formation of voids in the Si substrate can be prevented.

It has been proposed that the growth of SiC films by carbonization of Si occurs by out diffusing Si atoms from the substrate reacting with hydrocarbons absorbed at the substrate surface. Hence the growth by carbonization is considered to be a self-limited process due to the very slow diffusion rate of Si in SiC. Usually, the growth rate decreases with increasing film thickness until a saturation thickness is reached, after which, the thickness of the film will not increase with increasing carbonization time due to lack of silicon on the surface. The saturation thickness, as well as the structure and morphology of the carbonized layers, is dependent on the processing parameters such as the hydrocarbon concentration, the substrate temperature, the reaction pressure, and the heating ramp rate [2,4,5]. The formation of voids at the SiC/Si interface has been attributed to non-uniform diffusion of Si from the substrate during the carbonization step [6], not hydrogen etching. As we suggested in an earlier report [7], a relatively slow temperature ramp-up rate may be responsible for preventing the formation of voids during the carbonization step in our APCVD reactor. More recently, Cimalla, *et al.,* studied the dependence of SiC nucleation and growth on propane concentration and temperature ramp-up rate [5]. They found out that for high propane concentrations (>0.1%) and slow ramp-up rates (50K/s), the SiC growth mode is quasi-two dimensional growth, which leads to smooth carbonization surfaces without any morphological defects (voids). Even though our carbonization conditions are not exactly the same as was used by Cimalla, *et al.*, the carbonization layers in our work have characteristics similar to layers undergoing quasi-two dimensional growth. Extremely smooth and saturated void-free SiC layers were formed on the Si surface, resulting in films that seal off diffusion paths for Si atoms from the substrate. Hence, if the carbonization step is immediately followed with an epitaxial film growth step (i.e, the conventional two-step heterepitaxial process) voids will not form at the SiC/Si interface.

Conclusions

APCVD-based carbonization of Si (100) substrates was studied using a relatively low ramp-up rate and high propane concentration. Voids are found on the surface of the carbonization layers when a hydrogen cool-down step is used, while the formation of voids can be prevented if an argon cool-down step is employed. Other than voids, the surface morphology of the as-grown carbonized layers is relatively smooth using both cool-down techniques. The data suggests that the formation of the carbonized layers follow a quasi-two dimensional growth mode, which leads to the flat surfaces without any morphological defects.

The authors acknowledge the support of ARO MURI (Grant # DAAH04-95-10097) and DARPA (Grant # DABT63-98-1-0010).

References

[1] C.J. As, T. Frey, D. Schikora, K. Lischka, V. Cimalla, J. Pezoldt, and R. Goldhahn, Appl. Phys. Lett. 76 (2000), p. 1686.
[2] V.Cimalla, K.V. Karagodina, J. Pezoldt, and G. Eichhorn, Mater Sci. Eng. B29 (1995), p. 170.
[3] J.M. Harris, H.C. Gatos, and A.F. Witt, J. Electrochem. Soc. 116 (1969), p. 380.
[4] R. Scholz, U. Gösele, F. Wischmeyer, and E. Niemann, Mater. Sci. Forum, 264-268 (1998), p. 219.
[5] V.Cimalla, W. Attenberger, J.K.N. Lindner, B. Stritzker, and J. Pezoldt, Mater. Sci. Forum, 338-342 (2000), p. 285.
[6] J. P. Li and A. J. Steckl, J. Electrochem. Soc., 142 (1995), p. 634.
[7] C.A. Zorman, A.J. Fleischmann, A.S. Dewa, M. Mehregany, C. Jacob, S. Nishino, and P. Pirouz, J. Appl. Phys., 78 (1995), p. 5136.

Materials Science Forum Vols. 353-356 (2001) pp. 171-174
© 2001 Trans Tech Publications, Switzerland

A Comparison of SiO_2 and Si_3N_4 Masks for Selective Epitaxial Growth of 3C-SiC Films on Si

C.-H. Wu[1], J. Chung[1], M.H. Hong[1], C.A. Zorman[2], P. Pirouz[1] and M. Mehregany[2]

[1] Department of Materials Science and Engineering, Case Western Reserve University, 10900 Euclid Ave., Cleveland OH 44106, USA

[2] Department of Electrical Engineering and Computer Science, Case Western Reserve University, Cleveland OH 44106, USA

Keywords: 3C-SiC, APCVD, Selective Epitaxy, Si_3N_4, SiO_2

Abstract. A study comparing SiO_2 and Si_3N_4 masks for selective epitaxial growth of 3C-SiC films on Si wafers using a HCl-free APCVD process is reported. Selective growth of SiC films using SiO_2 masks can be achieved, but the microstructure of the SiC films in the unmasked Si areas is polycrystalline. In addition, delamination of the SiO_2 mask was often observed. For dry-etched Si_3N_4 masks, heteroepitaxial growth of 3C-SiC can be achieved inside the unmasked regions, but deposition of polycrystalline SiC on the mask was also observed. Selective epitaxial growth of 3C-SiC films was obtained using wet-etched Si_3N_4 masks. No delamination was found on these masks; however, holes and polycrystalline structures were found in regions where lateral overgrowth fronts converge.

Introduction

For electronic device applications, the use of 3C-SiC films on Si substrates is hampered by the high defect densities in the 3C-SiC films, which not only compromise the electronic behavior of the films, but also lead to unacceptably high leakage currents between the film and substrate. One method currently under development to improve the quality of 3C-SiC films and reduce substrate leakage is selective epitaxial growth in conjunction with lateral overgrowth. Selective epitaxial growth of SiC requires that the masking material must adhere well to the Si substrate, be mechanically stable at high-temperatures (~1300°C), be able to suppress nucleation and growth of polycrystalline SiC, and be chemically stable in a hydrogen atmosphere. In most cases, SiO_2 is used as a masking material. To improve selectivity, HCl is sometimes added to the carrier gas [1], but relatively thick SiO_2 masks are required (500 nm) to compensate for etching of the oxide masking layer. Si_3N_4 has also been used as a masking material for SiC selective epitaxial growth, but a thick, planar 3C-SiC seed layer was first grown on the Si substrate before the Si_3N_4 masks were deposited and patterned [2]. This paper presents the results of an investigation that related the mask material and geometry to the microstructure of 3C-SiC films selectively grown on Si wafers using a two-step, HCl-free growth process.

Experimental

The masks used for selective epitaxial growth were fabricated from 200 nm-thick, thermally-grown SiO_2 and 100 nm-thick, LPCVD Si_3N_4 films deposited on 100 mm-diameter Si (100) wafers. The SiO_2 masks were fabricated by conventional photolithography followed by wet chemical etching in a buffered HF solution, while the Si_3N_4 masks were defined by photolithography and patterned either by RIE using a SF_6-based plasma or by wet etching in hot phosphoric acid. The masks consisted of 2 to 20 μm-wide lines spaced 2 to 20 μm apart. 3C-SiC films were grown on the patterned substrates in an APCVD reactor using a two-step heteroepitaxial process that has been described in detail elsewhere [3]. In this process, silane and propane were used as source gases, and hydrogen was used as the carrier gas. The exposed Si surfaces were carbonized by first heating the

substrates from below 500°C to 1280°C, then holding the temperature constant for 90 s in a propane/hydrogen ambient. Film growth was performed at 1280°C in a silane/propane/hydrogen ambient for growth periods of 3, 10, and 60 min. SEM and TEM were used to characterize the as-grown films deposited on the unmasked regions as well as on top of the masks.

Results and Discussion

The SiO_2 masks and the unmasked Si areas examined by SEM prior to film growth showed smooth sidewalls and featureless surfaces. Following SiC film growth, the thickness of the 3C-SiC film in the unmasked regions was about 0.15 μm and 0.46 μm for the 3 min. and the 10 min. growth, respectively, yielding an estimated growth rate of more than 2.75 μm/hr. For both growth periods, selective SiC growth can be achieved using the 2 μm-wide masks. For the 3 min. growth period, good selectivity is observed for all the mask widths, while selective growth only occurred for linewidths up to 10 μm for the 10 min growth period. The SiC films grew vertically inside the unmasked regions, and did not exhibit observable lateral expansion. For a 60 min growth period, the SEM micrograph in Fig.1(a), shows that SiC grows vertically in the unmasked regions and laterally over the SiO_2 mask surface. The SiC film was 1.28 μm in thickness and grew laterally about 0.83 μm from each side of the mask. The growth rate appeared to decrease once the vertical growth front reached the top surface of the mask. Good selectivity for the 60 min growth period was only achieved using the 2 μm-wide lines. Nucleation and deposition occurred on lines wider than 2 microns, resulting in the formation of large, spherical polycrystalline SiC particles. These polycrystalline particles have poor adhesion and easily detach from the mask leaving numerous etch pits in the SiO_2 surface [4].

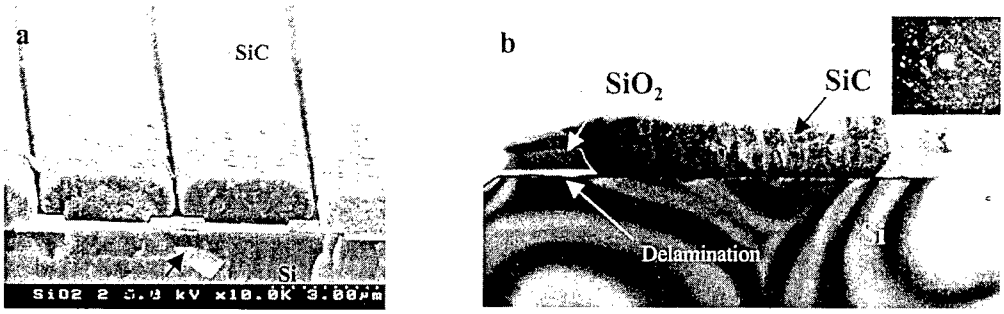


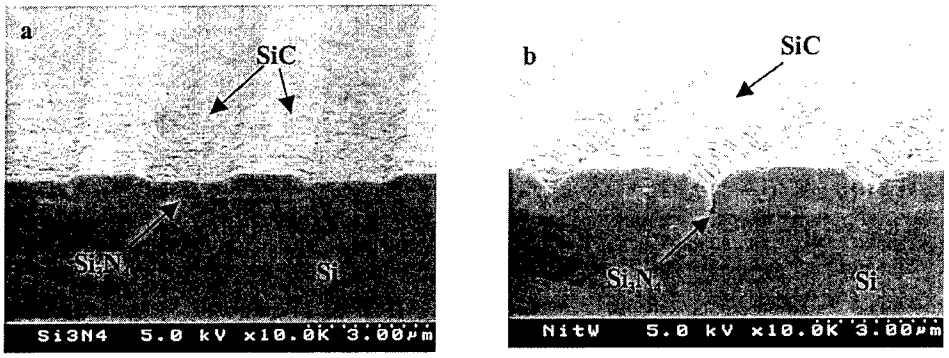
Fig. 1(a). SEM micrograph of selective growth of SiC films on the SiO_2 mask; and (b) XTEM micrograph of SiC films on the SiO_2 mask and the associated SAD pattern.

Cross-sectional TEM samples were prepared to characterize the microstructures of the SiC films and interfaces. A bright-field TEM image and the associated diffraction pattern of a SiC film are shown in Fig. 1(b). The SAD pattern clearly shows that the SiC film inside the unmasked regions was polycrystalline. In general, the SiC films had good adhesion to the unmasked Si and interfacial voids were not seen; however, the SiO_2 masks delaminated from the Si substrate in certain locations, as evidenced in Fig 1(b). Delamination of SiO_2 masks used for selective epitaxial growth of SiC has also been observed by Jacob *et al.* [5] and was attributed to residual stresses in the SiO_2 and SiC films.

As with the SiO_2 masks, SEM was used to verify that surfaces of the Si_3N_4 masks and the unmasked Si areas were smooth before SiC film growth. Since silicon is readily etched by the SF_6-based plasma used to pattern the Si_3N_4 masks, the unmasked Si regions were deeper than the thickness of the Si_3N_4 masking film. The SiC film thickness on the Si_3N_4 masks was about 0.14, 0.24, and 1.2

μm for the 3, 10, and 60 min growth runs, respectively. Using Si_3N_4 masks, good selectivity can only be achieved for a growth period of 3 min, regardless of line widths. Deposition of SiC on the Si_3N_4 mask occurred for all longer growth periods, regardless of line width. Polycrystalline SiC films form on the mask surface, but are thinner than films on the unmasked Si regions. The thickness of the films on the mask was about 0.56 μm, as compared to 1.2 μm in the unmasked Si regions (Fig. 2a). Since the deposition of polycrystalline SiC on the masks occurred before the films grew vertically over the top of the mask, single crystal film growth could not continue laterally over the Si_3N_4 mask. Despite the poor selectivity of the Si_3N_4 mask, 3C-SiC films on the unmasked Si have much smoother surface morphologies and faceted growth fronts than for 3C-SiC growth using SiO_2 masks.

To understand the effects of the Si_3N_4 mask fabrication process on selective epitaxial growth, a hot phosphoric acid solution (~ 130°C) was used as an alternative to dry etching during the patterning process. Fig. 2(b) shows an SEM micrograph of the 3C-SiC films grown on the wet-etched Si_3N_4 masks for a period of 60 minutes. The image shows better selective growth on the wet-etched Si_3N_4 mask, and no evidence of mask delamination. The surface morphology of the films is not as smooth as films using the dry-etched Si_3N_4 mask, but the faceted growth on both sides can still be observed.



page 173

Fig. 2. SEM micrographs of selective growth of 3C-SiC using: (a) the dry-etched Si_3N_4 masks; and (b) the wet-etched Si_3N_4 masks.

The microstructure of the SiC films on the Si_3N_4 masks was further characterized by TEM. A bright-field TEM image and SAD patterns from SiC films on the unmasked Si and on the top of the dry-etch Si_3N_4 mask are shown in Fig. 3. The SAD patterns prove that heteroepitaxial growth of SiC occurs on the unmasked Si, while polycrystalline films grow over the masks. Good adhesion between the SiC/Si and Si_3N_4/Si interfaces was found. However, in some areas of the SiC/Si interface, interfacial voids were observed. Single crystalline films were constrained to grow on the unmasked Si, with very little lateral growth due to the formation of polycrystalline SiC on top of the mask. SiC films grown on wet-etched Si_3N_4 masks were also characterized by cross-sectional TEM, as shown in Fig. 4. Heteroepitaxial growth of 3C-SiC is observed on the unmasked Si, but polycrystalline SiC structures can be found near the growth fronts. In the regions where the growth fronts converge over the Si_3N_4 masking lines, the SiC film is clearly polycrystalline. Even though the mask does not show evidence of delamination, etching of the mask may take place during film growth. Fig. 4 clearly shows that the Si_3N_4 mask is thinner at the center, presumably because this region is the last to be covered with SiC.

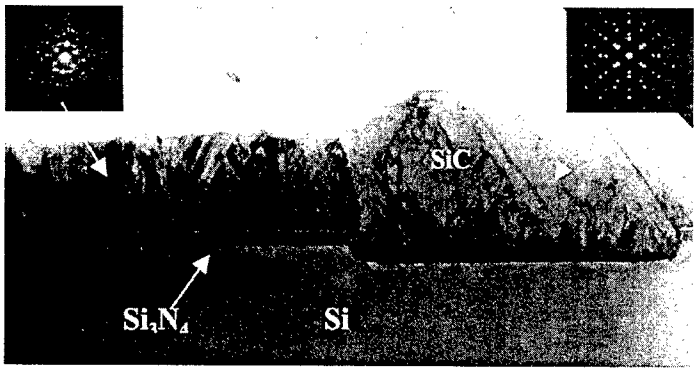


Fig. 3. An XTEM micrograph and SAD pattern of a SiC film grown using a dry-etched Si_3N_4 mask.

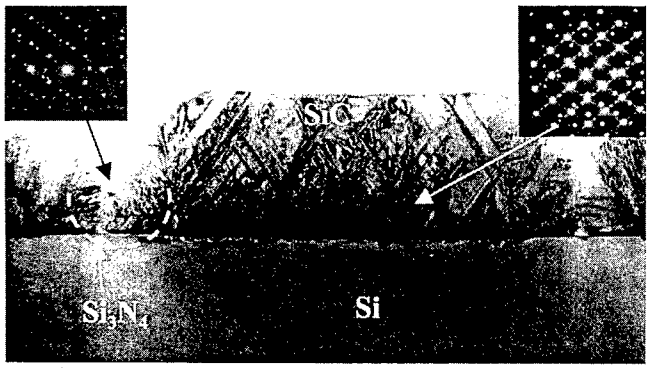


Fig. 4. An XTEM micrograph and SAD pattern of a SiC film grown using a wet-etched Si_3N_4 mask.

Conclusion

In an attempt to achieve selective epitaxial growth without using HCl, growth of 3C-SiC films using SiO_2- and Si_3N_4-masked Si wafers was conducted in an APCVD reactor. Selective growth of SiC films can be achieved using a SiO_2 mask, although the films are polycrystalline. Using Si_3N_4 masks, heteroepitaxial growth of 3C-SiC can be obtained inside the unmasked Si regions. Deposition of SiC on the surfaces of dry-etched Si_3N_4 masks was observed, but not on the wet-etched Si_3N_4 masks. Problems related to delamination and mask geometries were observed.

This work was supported by ARO MURI (Grant # DAAH04-95-10097) and DARPA (Grant # DABT63-98-1-0010).

References

[1] S. Nishino, H. Tanaka, K. Takahashi, and J. Saraie, Amorphous and Crystalline Silicon Carbide IV, (1992) p. 411.
[2] S.E. Saddow, G. Carter, G. Melnychuck, M.E. Okhuysen, M.S. Mazzola, Haibin Su, Li Jin, M. Dudley, B. Geil, T. Zheleva, K. Jones, Mater. Sci. Forum, 338-342, (2000) p. 245.
[3] C.A. Zorman, A.J. Fleischman, A.S. Dewa, M. Mehregany, C. Jacob, S. Nishino, and P.Pirouz, J. Appl. Phys., 78, (1995) p. 5136.
[4] C. H. Wu, C. A. Zorman, and M. Mehregany, Mater. Sci. Forum, 338-342, (2000) p. 541.
[5] C. Jacob, M-H. Hong, J. Chung, P. Pirouz and S. Nishino, Mater. Sci. Forum, 338-342 (2000) p. 249.

Materials Science Forum Vols. 353-356 (2001) pp. 175-178
© 2001 Trans Tech Publications, Switzerland

Selective Deposition of 3C-SiC Epitaxially Grown on SOI Subtrates

M. Eickhoff[1], S. Zappe[2], A. Nielsen[1], G. Krötz[1], E. Obermeier[2], N. Vouroutzis[3] and J. Stoemenos[3]

[1] Daimler Chrysler AG Research and Technology, PO Box 800465, DE-81663 München, Germany

[2] Technical University of Berlin, Secr. TIB 3.1, Gustav-Meyer-Allee 25, DE-13355 Berlin, Germany

[3] Physics Department, Aristotle University of Thessaloniki, GR-54006 Thessaloniki, Greece

Keywords: Selective Epitaxy, TEM

Abstract: The structural characteristics of 3C-SiC mesastructures, realized by selective epitaxy on prestructured Silicon-On-Insulator (SOI) substrates using methylsilane, are studied by Transmission Electron Microscopy (TEM). It is shown that the quality of the film is comparable with the material grown under the standard conditions. The occurance of lateral growth at the edges of the 3C–SiC structures is limited by the layer-thickness. Loss of the oxide mask during the SiC deposition is observed and attributed to the decomposition of SiO_2.

Introduction

Epitaxial growth of 3C-SiC on Si-substrates by chemical vapor deposition (CVD) permits the development of sensors working at high temperatures and in harsh environments having also the advantage of using standard silicon micro-machining processing and large wafer size capability. Despite these advantages, at temperatures greater than 200°C, the SiC/Si heterojunction becomes leaky, short-circuiting the SiC sensing elements through the Si substrate [1]. Epitaxially grown 3C-SiC on SOI structure eliminates the leakage problem as the Buried Oxide (BOX) layer isolates the overgrown SiC from the Si-substrate [2,3]. Moreover the BOX acts as a mechanical buffer, partially absorbing the strain developed due to the significant difference in the thermal expansion coefficients of SiC and Si [3,4]. The strain increases with the thickness of the overgrown 3C–SiC resulting in the bending of the substrate or ruptures the 3C-SiC film at the interface. However for the realization of microsensors most of the deposited 3C-SiC is etched off, demonstrating that deposition of 3C-SiC on the complete wafer surface leads to an unnecessary shrink in applicability. Therefore selective deposition on prestructured Si-substrates has two main advantages in comparison to the standard deposition processes [5,6]: Reduction of the area covered by the 3C-SiC, decreasing the mean strain imposed to the substrate and also simplification of device fabrication by avoiding etching processes of 3C-SiC. In this paper the structural characteristics of selectively deposited 3C-SiC mesastructures on prestructured SOI substrates, applied for microsensor development, is investigated using TEM.

Experimental procedure

Commercially available SOI wafers from SOITEC with 200nm thick Si-overlayer (SOL) were used for the 3C-SiC deposition. At first a 40 nm thick LPCVD silicon nitride layer was deposited at 780°C, subsequently 300nm thick PECVD silicon oxide layer was deposited at 350°C. The oxide was patterned by a photoresist mask layer and by etching in buffered HF for 4 min. After removal of the photoresist the silicon nitride film was structured by wet chemical etching in phosphoric acid

at 160°C for 30min with the PECVD-oxide as a mask layer. Subsequently the latter one was removed by a dip in diluted HF (12%) for 4min.
To define the final mask layer for the 3C-SiC deposition the SOL was selectively oxidized in a wet oxidation step at 1000°C for 100 min. On top of the silicon nitride islands, a thin film of oxinitride was formed during oxidation, which was removed by a dip in ammonia fluoride for 15sec. The silicon nitride islands were removed by wet chemical etching in phosphoric acid at 160°C for 30min. The samples were cleaned in H_2SO_4/H_2O_2 at 120°C for 5min and finally dipped in ammonia fluoride directly before SiC-deposition to ensure oxide-free silicon surfaces.
On the prestructured SOI substrates 3C-SiC was deposited in a cold wall, low pressure CVD reactor at 1200°C, using methylsilane (MeSi) $H_3C\text{-}SiH_3$ diluted in hydrogen [7].

Results and discussion

Three prestructurated specimens (2138, 2217 and 2140) having 3C-SiC overlayer 1.3, 2.0 and 2.8μm, respectively, were characterized by cross-section TEM (XTEM) and the results are the followings:
A) *Specimen 2138:* The resulting quality of the 3C-SiC is comparable to SiC-layers grown under the same growth conditions on standard SOI wafers [2], as shown in the high magnification micrograph in Fig.1a. After deposition the sequence of layers was 410nm BOX, 185nm SOL, 795nm thermal mask-oxide and 1.3μm overgrown 3C-SiC, as shown in Fig1b. Cavities are observed in the SOL without distraction of the BOX, denoted by the letter C in Fig.1b.The structure at the edges of the SiC is shown in Fig.1c. Lateral growth at the edge of the 3C-SiC film is observed, which is comparable to the thickness of the SiC film denoted by the letter LG in Fig.1c. No islands of SiC were observed on the oxide surface out of the edges. The 3C-SiC quality is good even at the lateral growth region as shown in the inset in Fig.1c.
B) *Specimen 2217:* The layer sequence after 3C-SiC deposition is, 400nm BOX, 195nm SOL, 785nm thermal mask-oxide and 2.0μm overgrown 3C-SiC, respectively. The structure at the edges of the SiC is shown in Fig.2a and 2b. Lateral growth of the SiC at the edge of the windows, comparable with the thickness of the SiC film is observed. No rupture at the SiC/Si interface was observed, even in this thicker 3C-SiC film. At the edges of the windows for the SiC epitaxial growth the SOL were overetched, denoted by the letter E in Fig.2a and 2b. The overetched area is extended inside the BOX without touching the Si substrate, excluding short-circuit of the SiC mesa-structure. The overetching occured during structuring of the mask layer and is not related with the instability of the SOI during SiC deposition [8,9]. This was confirmed by using a prestructured (100) Si wafer for the deposition of a 1.8μm thick 3C-SiC layer under the same conditions. Overetching of the Si-substrate at the edge as well as lateral growth of the SiC is evident in Fig.2c. The 3C-SiC quality is good even at those region where lateral growth occurs, as is shown in the inset in Fig.2c.
C) *Specimen 2140:* The general view at the edge of the window after the deposition of a 2.8μm thick 3C-SiC film, is shown in Fig.3. In this case the layer thicknesses are, 410nm BOX and 180nm SOL, respectively. The mask-SiO_2 is about 625nm thick, as shown in Fig.3. This is thinner than expected, because after oxidation of the SOL the total oxide thickness including the BOX should be close to 806nm, revealing a 181nm loss of SiO_2 during SiC deposition. The loss of oxide was already observed during selective growth of 3C-SiC on Si wafers; the reported rate of oxide loss was 400nm/hour [5]. In the present case this value agrees quite well for the deposition of thick 3C-SiC films, however, it is significantly lower for SiC film thinner than 2μm.
The loss of the mask-oxide is attributed to the decomposition of the SiO_2 during the SiC deposition for two reasons:
A) Due to the very low oxygen partial pressure.
Under low oxygen partial pressure SiO_2 decomposition at the Si/SiO_2 interface occurs according to the reaction [10].

$$Si + SiO_2 \rightarrow 2SiO_{(g)} \qquad (1)$$

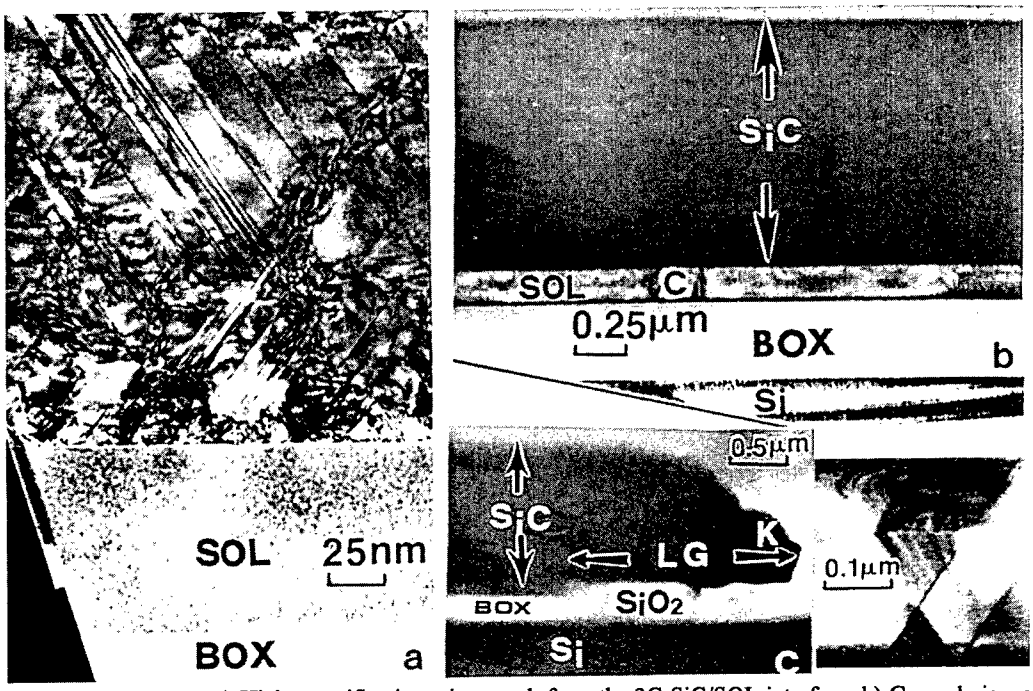


Fig.1: Specimen 2138 a) High magnification micrograph from the 3C-SiC/SOL interface. b) General view of the structure. c) Micrograph from the edge of the oxide mask, the lateral growth of the 3C-SiC is denoted by the letter LG. The laterally grown 3C-SiC, from the region denoted by the letter K, is shown in the inset.

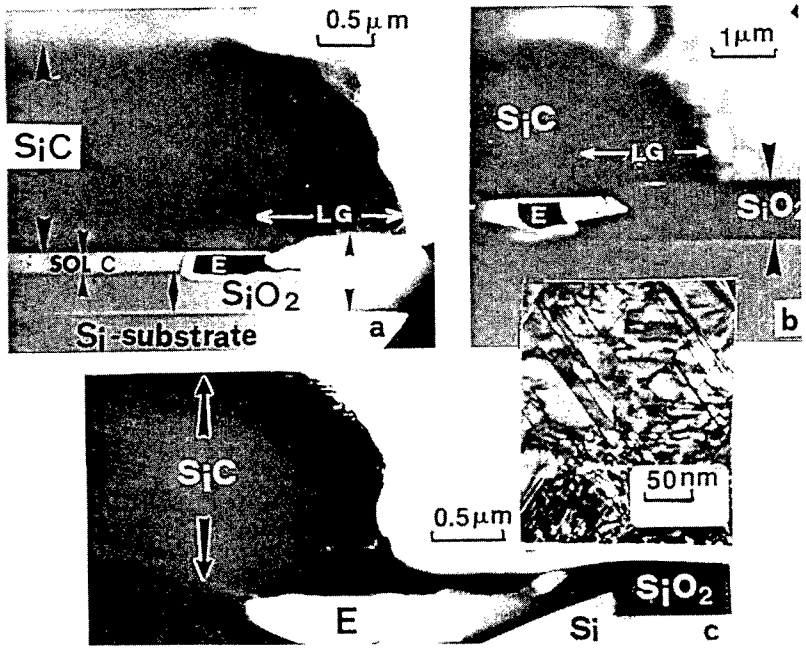


Fig. 2: Specimen 2217 a) and b) The morphology of the 3C-SiC at the edges of the oxide mask. Over-etching at the edges is denoted by the letter E. c) 3C-SiC deposition on prestructured Si wafer. Over-etching is evident at the edge. The quality of the laterally grown 3C-SiC on SiO_2 is shown in the inset.

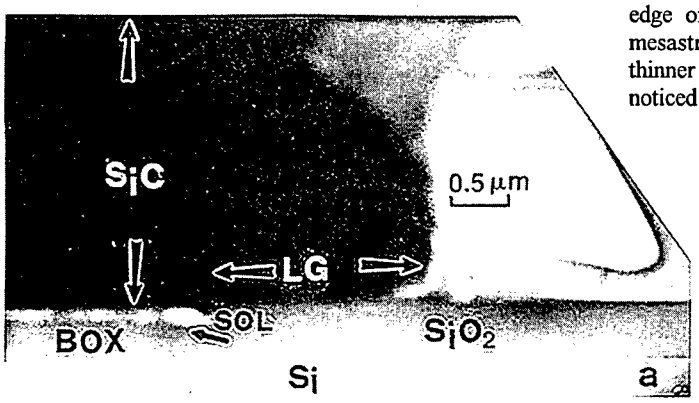


Fig.3. XTEM micrograph from the edge of the 2.8μm thick 3C-SiC-mesastructure.The significantly thinner mask-SiO_2 should be noticed.

The decomposition is enhanced at higher temperatures and lower partial oxygen pressures. For the same reasons the reaction (1) also retards under high SiO partial pressures [11].

B) Due to the presence of hydrogen

During 3C-SiC deposition hydrogen is used as carrier gas, which reacts with the oxide according to the reaction (2) [9].

$$H_2 + SiO_2 \rightarrow H_2O_{(g)} + SiO_{(g)} \qquad (2)$$

The selective epitaxy can not be attributed solely to the difference of the SiC sticking coefficient on Si and SiO_2, but rather to the instability of the oxide layer under the 3C-SiC deposition conditions.

Conclusions

Selective deposition of 3C-SiC at 1200°C using methylsilane is shown to result in a good material quality films even at the edges where lateral growth occurs. This deposition process significantly reduces the area covered by the 3C-SiC and therefore allows a strong decrease of the mean strain imposed to the substrate. The oxide decomposition rate at the process temperature is low and does not cerate process difficulties due to the byproducts SiO and H_2O.

Acknowledgments: This work was supported by the EU, BRITE-EURAM project CT96-0261

References

[1] W. Reichert, E. Obermaier and J. Stoemenos, Diam. Related Mat. 6, (1997) p.1448
[2] G. Krötz, H. Möller, M. Eickhoff, S. Zappe, R. Ziermann, E. Obermeier, J. Stoemenos, Mat. Sc. Eng.B61-62, (1999) p. 516
[3] C. Dezauzier, J.M. Bluet,S. Contreras, J. Camassel, J. Pascual, J.L. Robert, L.DiCioccio, J. Stoemenos. (ICSRM) Kyoto, Eds. S. Nakashima, H. Matsunami, S. Yoshida and H. Harima. Inst. Phys. Con. Ser. Vol.142, (1995) p. 455
[4] F. Namavar, P. Colter, A. Cremins-Costa, C-H. Wu, E. Gagnon, D. Perry and P. Pirouz. Mat. Res. Soc. Symp. Proc. Vol. 423, (1996) p. 409
[5] M. Eickhoff, H. Möller, M.Rapp, G. Krötz, Thin Solid Films 345, (1999) p. 197
[6] S. Nishino, H. Tanoka, K. Takahashi, J. Saraie, R.M. Osgood, Springer Proc. Phys. 71, (1992) p. 411
[7] H. Möller, M Eickhoff, M.Rapp, H.W. Grueninger and G. Krötz, Appl. Phys. A68, (1999) p. 461
[8] H. Möller, S. Zappe, V Papaioannou, G. Krötz, W. Skorupa, E. Obermeier, J. Stoemenos, "Silicon-On-Insulator Technology and Devices" Electrochem. Soc. Proc. Ed P.L. Hemment, Vol.99-3, (1999) p. 31
[9] G. Ferro, N. Planes, D. Chaussende, Y. Monteil, J. Stoemenos, J. Camassel, Mat.Sci. Eng. B61- 62 (1999) p. 586
[10] F.W Smith. and G. J.Ghidim, Electroch. Soc. 129, (1982) p. 1300
[11] S.I Raider., S.R Herd., and R.E Walkup., Appl. Phys. Lett. 59, (1991) p. 2424

Materials Science Forum Vols. 353-356 (2001) pp. 179-182
© 2001 Trans Tech Publications, Switzerland

Carbonization Induced Change of Polarity for MBE Grown 3C-SiC/Si(111)

J. Pezoldt[1], B. Schröter[2], V. Cimalla[3], Th. Stauden[1], R. Goldhahn[4], H. Romanus[5] and L. Spieß[5]

[1] Institut für Festkörperelektronik, TU Ilmenau, Postfach 100 565, DE-98684 Ilmenau, Germany

[2] Inst. Festkörperphys., Friedrich-Schiller-Univ. Jena, Max-Wien-Platz 1, DE-07743 Jena, Germany

[3] Foundation for Research and Technology Hellas, Microelectronic Research Group, PO Box 1527, GR-71110 Heraklion/Crete, Greece

[4] Institut für Physik, TU Ilmenau, Postfach 100 565, DE-98684 Ilmenau, Germany

[5] Institut für Werkstofftechnik, TU Ilmenau, Postfach 100 565, DE-98684 Ilmenau, Germany

Keywords: Carbonization, Heteroepitaxy, Molecular Beam Epitaxy (MBE), RHEED, Surface Polarity, x-Ray Photoelectron Diffraction

Abstract The carbonization and subsequent growth of 3C-SiC layers of both polarities on nonpolar Si(111) substrates were investigated. It is shown that the carbonization environment is the critical parameter for controlling the surface polarity on Si(111). The SiC layers of both polarities were characterized by x-ray photoelectron diffraction, atomic force microscopy, x-ray diffraction and spectroscopic ellipsometry.

Introduction

The lack of large, high-quality 3C-SiC bulk crystals has stimulated several groups to investigate systematically thin film growth on Si substrates. Beside the fundamental aspects of heteroepitaxy in a material system with large lattice mismatch, 3C-SiC/Si layered structures offer some attractive applications. The first is in the field of robust sensors operating at high temperatures and in harsh environments. At second, they can be successfully used as pseudo-substrates for the cubic nitride epitaxy [1]. The common technique to grow SiC on Si is a two step process consisting of a carbonization process, e.g. under CVD or MBE conditions, followed by an epitaxial growth. The influence of the carbonized layer on the subsequent epitaxial process was studied mostly in the context of the structural perfection of the film and how this quantity influences the structural perfection of the grown active layer. However, in most studies, only one method was applied for the conversion of the Si surface into SiC. In this work we present a comparative study of the crystalline quality, surface morphology, and polarity for solid source MBE grown single domain 3C-SiC active layers if different carbonization processes are applied.

Experimental

The Si(111) substrates were carbonized by using two different methods. The first method (RTCVD) is based on the carbonization process in a propane hydrogen atmosphere in a rapid thermal processing reactor described in detail in [2]. The C_3H_8 concentration in H_2 was chosen to obtain a conversion of the Si surface into single domain 3C-SiC. The second one is a MBE based process consisting of the following process steps: (1) deposition of C on a (7x7) reconstructed Si surface at 325 °C, (2) heating up the Si wafer to 660 °C within 3 min, (3) gradually increase of the substrate temperature in steps of 50 degree up to the final growth temperature for SiC epitaxy. On both carbonized substrate types, 120 nm thick 3C-SiC epitaxial layers were grown at 1000 °C with a rate of 1 nm/min under Si rich conditions and continuously operating Si and C sources. The stability of the deposition conditions was controlled by reflection high energy electron diffraction (RHEED) monitoring the silicon related surface reconstruction streaks on the SiC(111) surface. In addition, the growth process was monitored by *in situ* real time spectroscopic ellipsometry (SE). *Ex situ* characterization of the films was per-

formed by atomic force microscopy (AFM), X-ray diffraction (XRD), X-ray photoelectron diffraction (XPD), and SE. The XPD patterns of Si 2p and C 1s core-level intensities have been measured using Mg Kα (1253.6 eV) or Al Kα (1486.6 eV) radiation for photoelectron excitation and a stepper-motor controlled manipulator. The angular resolution of the SPECS hemispherical electron analyzer was 4°. The angle between the X-ray source and the electron analyzer was fixed to 54° and the polar angle between the direction of the analyzer entrance and the normal of the sample surface was varied by rotating the sample holder.

Results and Discussion



Fig.1 3C-SiC RHEED pattern taken after SSMBE carbonization. Azimuth <110>.

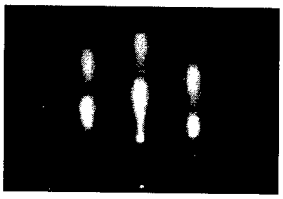


Fig.2 3C-SiC RHEED pattern taken after RTCVD carbonization. Azimuth <110>.

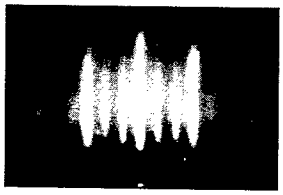


Fig.3 3C-SiC RHEED recorded at room temperature after the growth of 120 nm SiC on a SSMBE carbonized Si(111). Azimuth <110>.

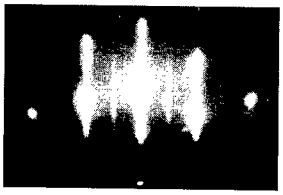


Fig.4 3C-SiC RHEED recorded at room temperature after the growth of 120 nm SiC on a RTCVD carbonized Si(111). Azimuth <110>.

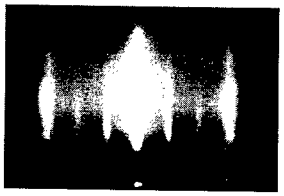


Fig.5 3C-SiC RHEED recorded at room temperature after the growth of 120 nm SiC on a SSMBE carbonized Si(111). Azimuth <112>.

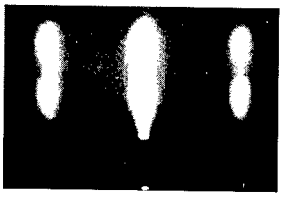


Fig.6 3C-SiC RHEED recorded at room temperature after the growth of 120 nm SiC on a RTCVD carbonized Si(111). Azimuth <112>.

The carried out carbonization process lead in both cases to a single domain 3C-SiC layer as confirmed by RHEED (Figs.1, 2) and XPD measurements. The thickness of the carbonized layer was between 2 and 3 nm. The root mean square surface roughness (*rms*) measured by AFM was in the range between 0.2 and 0.4 nm in the case of RTCVD carbonized layers, whereas in the case of SSMBE carbonization slightly higher *rms* values within the range of 0.4...0.6 nm were obtained.

During the epitaxial growth on these substrates a different growth behaviour was observed. On SSMBE substrates after a thickness of 10 to 50 nm a clear (3×3) surface reconstruction appeared, whereas in the case of RTCVD carbonized substrates this surface reconstruction could not be observed. On these substrates during epitaxial growth only very week half order streaks in the <110> and <112> azimuth were detected. The growth process was interrupted at thicknesses of 120 and 300 nm and the samples were cooled down to room temperature. The RHEED pattern obtained are shown in Figs. 3 and 5 for the SSMBE and in Figs. 4 and 6 for the RTCVD case. The diffraction pattern taken from the SiC layers grown on the SSMBE carbonized Si substrates shows strong third order diffraction streaks indicating on a (3×3)-Si surface reconstruction, which is characteristic for silicon rich Si face α-SiC(0001) and β-SiC(111) surfaces. Furthermore, the mixed 2D - 3D 3C-SiC diffraction behaviour is an evidence for a relatively smooth SiC surface. In the case of the SiC layer grown on the RTCVD carbonized Si substrates only half order streaks in both azimuthal directions and a strong 3D diffraction behaviour was observed. The more pronounced 3D diffraction is due to a higher surface roughness compared to the SSMBE case. The half order streaks can be related to a (2×2)-Si surface reconstruction. This surface reconstruction is not characteristic for SiC(0001) surfaces and was observed only on SiC(000$\bar{1}$) surfaces [3,4]. To confirm the hint of different surface polarity of the grown layers detailed XPD measurements were carried out. This method has been proven capable for determining the

polarity of compound semiconductor surfaces, e.g., of GaN [5], ZnO [6], 6H-SiC [7] and AlN [8]. The XPD pattern is obtained by angular-resolved detection of Si2p and C1s photoelectron intensities. Due to the strong forward focussing nature of the electron scattering in the energy range near 1 keV, the diffraction pattern is dominated by forward scattering (FS) peaks pointing along the low-index directions of nearest-neighbour high-density atomic rows [9]. Thus, information on the atomic structure in real space can be obtained. The situation may be more complicated than in this simple FS picture because of energy-dependent interference and multiple-scattering effects. Thus, more complex XPD patterns are usually observed. The polarity of 3C-SiC can be determined by measuring the Si2p/C1s photoelectron intensity ratio along {111} direction, i.e., normal to the surface. Figs.7, 8 and Figs.9, 10 show subsequently the polar scans of the Si2p and C1s intensities as well as the Si2p/C1s intensity ratios measured in $(2\bar{1}\bar{1})$ plane of our cubic SiC films. Similar to the results obtained by Bischoff on 6H SiC, the polar scans differ for the Si and C faces of 3C-SiC [10]. The main difference of both polar faces is evident from the Si2p/C1s intensity ratios near normal emission (0°).

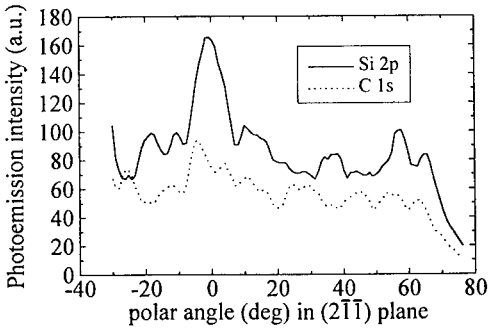


Fig.7 Experimental polar angle scans of Si 2p and C 1s obtained on SiC epitaxial layer grown on SSMBE carbonized (111)Si

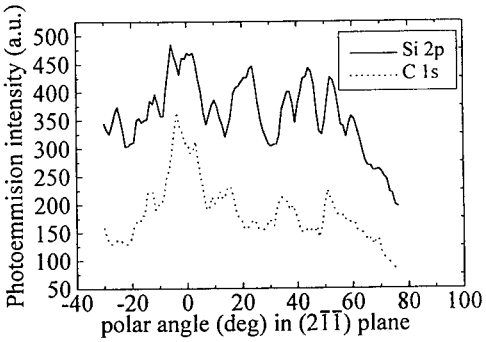


Fig.8 Experimental polar angle scans of Si 2p and C 1s obtained on SiC epitaxial layer grown on RTCVD carbonized (111)Si

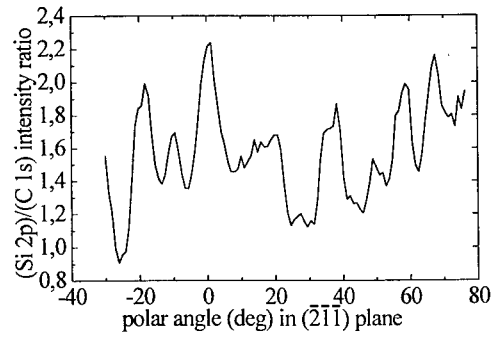


Fig.9 Photoemission intensity ratio of the SSMBE sample.

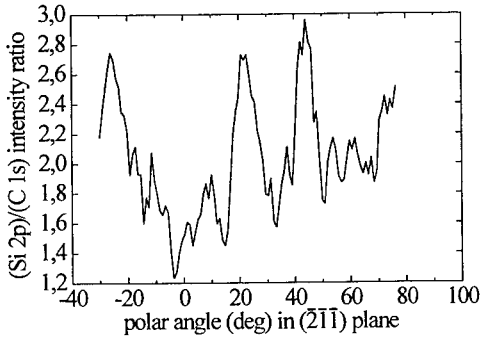


Fig.10 Photoemission intensity ratio of the RTCVD sample.

As forward scattering is strong for short emitter-scatterer distances, one can recognize from the atomic arrangement that in normal direction a C atom has the next neighbour Si in $(\bar{1}\bar{1}\bar{1})$ direction and a Si atom has the next neighbour C in (111) direction. This asymmetry results in strong FS intensity of Si2p photoelectrons and weak FS intensity of C1s photoelectrons in (111) direction, i.e., Si face. The contrary is valid for the C face. Thus, the Si2p/C1s intensity ratio shows a maximum near normal emission on Si face and a minimum on C face. The layers grown on the SSMBE carbonized Si exhibit a Si side polarity and the layers grown on RTCVD carbonized Si have a C side polarity. XPD mea-

surements carried out on layers after the carbonization procedure show the same polarity behaviour. Thus the polarity of the epitaxial film is a replica of the polarity of the carbonized Si surface.

To characterize the surface and interface roughness AFM and SE measurements were carried out. These results and the full width at the half maximum (FWHM) of the (111)SiC peak measured by XRD in the θ-2θ scan are summarized in Table 1. The SSMBE samples are characterized by a smoother surface and a rougher interface compared to the RTCVD samples. The larger roughness on layers with C-faces might be an evidence on a different incorporation mechanism of the deposited atoms and a smaller surface diffusion length compared to the Si-face. The smaller interface width of RTCVD samples indicates a better diffusion barrier behaviour of these samples against Si outdiffusion. Furthermore, the RTCVD samples exhibit lower strain than the SSMBE samples.

Table 1 Surface, interface and crystallographic characteristics

Sample, thickness	*rms* , nm	Interface width, nm	FWHM, °
SSMBE, 120 nm	0.9	6.5	0.238
RTCVD, 120 nm	1.8	1.9	0.205
SSMBE, 300 nm	1.3	12.0	0.241
RTCVD, 300 nm	2.8	6.8	0.211

Conclusion

The results emphasize that both substrate types lead to epitaxial layers characterized by a single domain 3C-SiC structure. The films grown on RTCVD carbonized substrates exhibit a smoother interface between SiC and Si, but a larger surface roughness compared to the layers grown on MBE carbonized wafers. Furthermore, the full width at the half maximum of the (111)SiC XRD peak is found smaller in case of RTCVD material indicating a lower residual stress. Detailed XPD measurement revealed that the epitaxial layer grown on RTCVD material, i.e. in hydrogen rich environments, shows C-face surface polarity, whereas the material grown on SSMBE material, i.e. in hydrogen poor environment, is characterized by a Si-face polarity.

Acknowledgments

This work was supported by DFG under contract number Pe 624/2-1,2-2 and by the SFB196.

References

[1] D.J. As, T. Frey, D. Schikora, K. Lischka, V. Cimalla, J. Pezoldt, R. Goldhahn, S. Kaiser, W. Gebhardt, Appl. Phys. Lett. 76 (2000), p.1686.
[2] V. Cimalla, K.V. Karagodina, J. Pezoldt, G. Eichhorn, Mater. Sci. Eng., B29 (1995), p.170.
[3] J. Bernhardt, A. Seubert, M. Nerding, U. Starke, K. Heinz, Mater. Sci. Forum 338-342 (2000), p.345.
[4] T. Hatayama, T. Fuyuki, S. Nakamura, K. Kurobe, T. Kimoto, H. Matsunami, Mater. Sci. Forum 338-342 (2000), p.361.
[5] M. Seelmann-Eggebert, J. L. Weyher, H. Obloh, H. Zimmermann, A. Rar, S. Porowski, Appl. Phys. Lett. 71 (1997), p.2635.
[6] M. Sambi, G. Granozzi, G. A. Rizzi, M. Casarin, E. Tondello, Surf. Sci. 319 (1994), p.149.
[7] J.L. Bischoff, D. Dentel, L. Kubler, Surf. Sci. 415 (1998), p.392.
[8] V. Lebedev, B. Schröter, G. Kipshidze, W. Richter, J. Cryst. Growth 207 (1999), p. 266.
[9] S. Fadley, in Synchrotron Radiation Research: Advances in Surface Science, edited by R. Z. Bachrach, Plenum, New York, 1992.
[10] B. Schröter, A. Winkelmann, A. Fissel, V. Lebedev, W. Richter, Mater. Sci. Forum (2001), p. 227.

Materials Science Forum Vols. 353-356 (2001) pp. 183-186
© 2001 Trans Tech Publications, Switzerland

The Influence of Ge on the SiC Nucleation on (111)Si Surfaces

J. Pezoldt[1], T. Wöhner[1,2], Th. Stauden[1], J.A. Schaefer[2] and P. Masri[3]

[1] Institut für Festkörperelektronik, TU Ilmenau, Postfach 100 565, DE-98684 Ilmenau, Germany

[2] Institut für Physik, TU Ilmenau, Postfach 100 565, DE-98684 Ilmenau, Germany

[3] Groupe d'Etude des Semiconducteurs, Université Montpellier,
12 Place Eugene Bataillon, FR-34095 Montpellier Cedex 5, France

Keywords: Ellipsometry, Germanium, Heteroepitaxy, Molecular Beam Epitaxy (MBE), RHEED

Abstract The influence of germanium on the carbonization of silicon was studied by comparing different methods of introducing Ge into the conversion process. Independent on the method used Ge leads to an increase of the grain size and reduces the SiC growth rate. If a Ge incorporation into the SiC/Si interface is desired the Ge predeposition at low temperature is preferable.

Introduction

The common technique in the heteroepitaxy of SiC on Si is the formation of a so called buffer layer by using a carbonization procedure. These layers act as a pseudo substrate and a diffusion barrier but are not able to compensate the large lattice mismatch, and especially the difference in thermal expansion. To improve the situation different methods were developed: (1) deposition on SOI substrates, (2) deposition on porous or nanostructured silicon, (3) the incorporation of Ge in the heterointerface between SiC and Si. All this methods lead to an improvement of the growth and a reduction of the residual stress in the heteroepitaxial system. For the last case, namely Ge addition into the growth process, a two fold influence of this element onto the epitaxial growth is expected. On the one hand Ge incorporation may improve the lattice matching between Si and SiC. On the other hand Ge can act as a surfactant during the growth process. The aim of this work is to give an initial insight into the influence of Ge on the SiC nucleation process on (111)Si in dependence on the method applied.

Experimental

The carbonization process was performed with and without additional Ge during the carbonization by depositing evaporated elemental C at high and low substrate temperatures in a solid source molecular beam epitaxy equipment (SSMBE) on (111)Si surfaces. The high temperature process was carried out at 750°C on clean (7×7) (111)Si surfaces. Three samples were prepared differing in the methods of Ge deposition during the carbonization. For comparison one sample was carbonized without Ge (Sample 1). On the second sample prior to the C deposition three monolayers (ML) Ge were deposited on the (111)Si surface at 750°C (ML : With respect to the (111)Si surface). After a subsequent annealing step of 200 s at 750°C the Si surface was converted into SiC (Sample 2). The third sample was carbonized by applying a Ge and C flux simultaneously. After depositing 3 ML Ge the carbonization was continued without Ge (Sample 3). The low temperature regime was chosen in such a way that the SiC nucleation during the carbon deposition was suppressed. The procedure consists of the following steps: (1) 0 ... 4 Monolayer Ge deposition on the (7x7) reconstructed Si surface at 325°C, (2) 6 ML C deposition on the Si substrate, (3) heating up the Si wafer to 660°C for 3 minutes, (4) gradually increase of the substrate temperature in periods of 2 minutes by 50°C up to 950°C. The Ge deposition time was calibrated by reflection high energy electron diffraction (RHEED) oscillations. The calibration of the C flux (2×10^{13} $cm^{-2}s^{-1}$) was carried out by using the deposition time necessary to establish the intensity

maximum of the RHEED streaks of the (√3×√3)R30°-C surface reconstruction on (111)Si.

The process was monitored by *in situ* RHEED and by *in situ* spectroscopic ellipsometry (SE) in real time. The rotating analyser ellipsometer has a wavelength range between 250 ... 850 nm. The angle of incidence was set to 72.6°. Spectra of Ψ and Δ as a function of wavelength were successively measured in parallel mode using a photodiode array (spectral resolution: 0.61nm). The time interval of one measured spectra was about 10s to get a satisfactory signal to noise ratio. The final sample surfaces were investigated *ex situ* by atomic force microscopy (AFM) and X-ray photoelectron spectroscopy (XPS). The AFM images were obtained in contact mode with a $1x1\mu m^2$ scan area. XPS spectra of the Si2p, C1s, O1s, Ge2p and Ge3d core levels were taken using Mg and AlK_α X-ray sources.

High temperature case

Under the chosen experimental conditions the Ge predeposition onto the (111)Si surface did not led to a change of the surface reconstruction. Fig. 1 shows the time dependent RHEED intensities behaviour recorded during different carbonization processes for the three dimensional (3D) (111)SiC diffraction spot, the (11)Si and (1/3,1/3) (√3×√3)R30°-C diffraction streaks. As can be seen Ge predeposition suppresses the formation of the (√3×√3)R30°-C surface reconstruction, which is formed at these substrate temperatures during the early stages of C deposition [1]. Only a (1×1) surface structure was observed until SiC nucleates. The simultaneous deposition of Ge and C led to a similar effect. In this case the diffraction streaks corresponding to the (√3×√3)R30°-C surface reconstruction were very faintly visible. The suppression of the formation of the C induced surface reconstruction might be caused by the low affinity of Ge and C to form Ge-C bonds. Thus only surface areas which are not covered with Ge are able to change their reconstruction into the C induced one. Furthermore the intensity increase of the (111)SiC 3D diffraction spot was faster and exhibited a maximum of intensity if Ge was not used during the carbonization process. Additionally the Si related streaks decreased more rapidly. These is an indication for a faster coverage of the Si surface with SiC if Ge is not used. The slowest coverage rate of the Si surface with SiC was observed for the parallel deposition case of Ge and C. AFM investigations revealed that the grain size increased for the samples carbonized with addition of Ge, i.e. the nucleation density decreases. The final structure of the SiC layers showed twins and misorientations. The structural characteristics of the carbonized layers are summarized in Table 1.

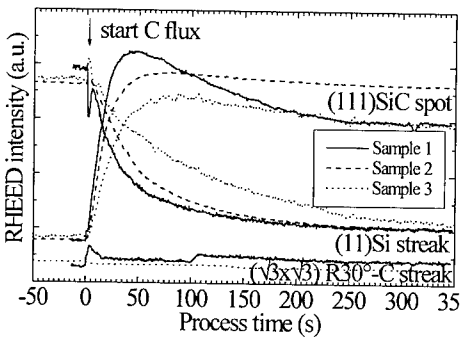


Fig.1 RHEED intensity of the (111)SiC spot and the (11)Si and (√3×√3)R30°-C streaks

Table 1 Carbonization layer characteristics

Measured value	Sample		
	1	2	3
Roughness *rms* (nm)	1.8	2.5	1.8
Thickness d_{SiC} (nm)	2.6	1.95	1.6
Interface width d_{int} (nm)	0.79	0.6	0.54
Grain size D (nm)	30-40	50-60	50-60

The increased SiC grain size led to an increase of the surface roughness in the early stages of the SiC growth and shifts the phase diagram in [2] to lower substrate temperatures and higher carbon fluxes.

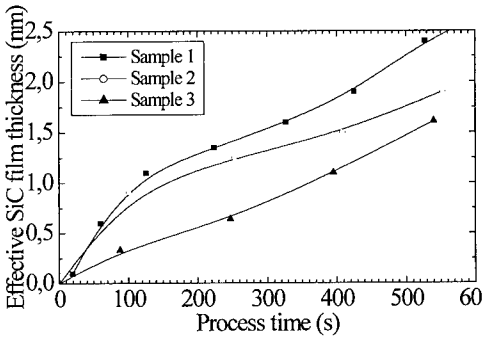


Fig.2 Effective SiC film thickness versus process time

The influence of the Ge on the growth kinetics was studied by SE. The obtained data were fitted by using the Bruggeman effective medium approximation [3]. In this model the different layers used to describe the heteroepitaxial system are approximated by a host material with inclusions. To analyse our system we used the following multilayer models: (a) two layer model (1: SiC/void mixture, 2: c-Si/void mixture) for deposition on (111)Si without Ge; (b) three layer model (1: SiC/Ge/void mixture, 2: Si_xGe_{1-x}/void mixture, 3: c-Si/void mixture) for deposition on (111)Si with Ge. Fig.2 shows calculated effective SiC film thickness d_{SiC} versus process time. The effective SiC film thickness is defined as the product of the layer thickness and the SiC fraction of the upper layer of both introduced models [4]. From Fig.2 it is evident that Ge lowers the SiC growth rate in the initial state. This can be caused by a partial coverage of the surface with Ge and the formation of a $Si_{1-x}Ge_x$ solid solution which was deduced from the ellipsometric and XPS measurements reducing the reaction probability. The reduced growth rate above 100 s for the Sample 2 can be due to the $Si_{1-x}Ge_x$ formation at the SiC/Si interface and the Ge coverage on the surface observed by XPS. This might reduce the Si transport to the growing surface by diffusion leading to a smaller SiC thickness increase.

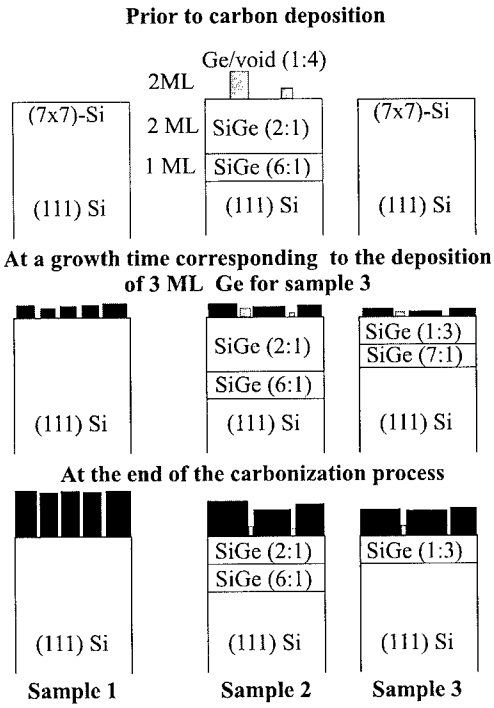


Fig.3 Schematical illustration of the structural and compositional evolution for the high temperature case: sample 1 - carbonization without Ge; sample 2 - Ge predeposition, sample 3 - parallel deposition of Ge and C.

Fig. 3 and Table 1 summarizes the structural evolution and the characteristics of the final state of the carbonized layers extracted from ellipsometric, XPS and AFM measurements. Ge addition (samples 2 and 3) lowers the nucleation density compared to the reference sample 1. A $Si_{1-x}Ge_x$ layer was detected beneath the SiC layer. In the case of sample 3 this layer possessed a higher Ge concentration and a smaller thickness. Furthermore we observed a smaller Ge concentration at the surface indicating on a weaker Ge segregation. We speculate that the Ge concentration at the surface is connected with the concentration of voids within the SiC layer which was higher for sample 2 compared to sample 3. Furthermore with progressing process time the Ge content in Si decreases due to outdiffusion and segregates at the SiC/Si interface. Because of the complicated structure of the samples it was not possible to make conclusions about a $Si_{1-x-y}Ge_xC_y$ the formation near the SiC/Si interface.

Low temperature case

Depending on the deposited amount of Ge onto the (111)Si surface the following surface reconstructions were observed at 325°C: (a) up to 1 ML Ge the (7×7)-Ge surface reconstruction, (b) between

1 ML and 2 ML Ge a mixture of (7×7)-Ge and (5×5)-Ge surface reconstructions and (c) above 2 ML Ge the (5×5)-Ge surface reconstruction. This is in agreement with the phase diagram published in [5]. During the deposition of C on Si surfaces modified and non-modified with Ge the diffraction pattern changed from a streaky into a diffuse diffraction pattern having (1×1) symmetry. The following step by step heating-up phase transformed the near surface layers of the Si substrate into SiC. In dependence on the deposited amount of Ge we observed a reduction of the 3C-SiC formation temperature from 900°C (0 ML GE) to 750°C (2ML Ge). The formed carbonized layer showed only a week evidence of rotational twins (Fig.4). The roughness measured by AFM was in the range of 0.2 ... 0.4 nm which is lower than for the high temperature case (see Table 1). Furthermore an increase of the mean grain size from 60 nm to 90 nm was observed. The XPS, AES and SE investigations revealed a Ge incorporation into the SiC/Si interface. Within the detection limit of the applied methods no Ge was observed at the SiC surface indicating a suppressed outdiffusion of Ge. The final structure formed by applying this method is shown in Fig.5. If the Ge was deposited onto the carbon layer before the step by step heating-up, the intensity of the twin reflection increases. This is an evidence of a deterioration of the crystalline structure compared to the Ge predeposition case (Fig.6), where a strong rotational twin reflection is visible. This might be caused by the weaker Ge incorporation into the SiC/Si heterointerface.

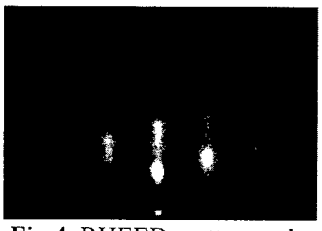


Fig.4 RHEED pattern taken from the sample with 2 ML Ge predeposition after annealing. Azimuth <011>.

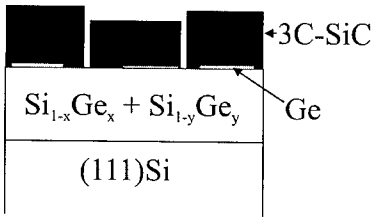


Fig.5 Schematical illustration of the structure of the carbonized layer for the low temperature case.



Fig.6 RHEED pattern taken from the sample with 2 ML Ge deposition on 6 ML C after annealing. Azimuth <011>.

Conclusion

In all considered cases the Ge led to an increase of the SiC grain size. This can be attributed to a higher mobility of the C atoms on the partly Ge covered surface. In the case of high temperatures we observed a reduced SiC growth rate if Ge was added. This might be due to the fact that surface sites, where Ge is located, do not form carbidic bonds, i.e. Ge leads to surface passivation against SiC formation. If Ge incorporation into the SiC-Si heterointerface is desired the Ge predeposition at low temperatures is preferable.

References

[1] V. Cimalla, Th. Stauden, G. Ecke, F. Scharmann, G. Eichhorn, S. Sloboshanin, J.A. Schaefer, J. Pezoldt, Appl. Phys. Lett. 73 (1998), p. 3542.

[2] W. Attenberger, J.K.N. Lindner, B. Stritzker, V. Cimalla, Th. Stauden, G. Ecke, G. Eichhorn, J. Pezoldt, 43. IWK, Vortragsreihen: Mikroelektronische Schaltungen und Systeme, Festkörperelektronik, Innovative Werkstoffe und Oberflächentechnik, Bd.2 (1998), p. 476.

[3] D.A.G. Bruggeman, Ann. Phys. 24 (1935), p.636.

[4] V. Cimalla, J. Scheiner, G. Ecke, M. Friedrich, R. Goldhahn, D.R.T. Zahn, J. Pezoldt, Mat. Sci. Forum, 264-268 (1998), p.641.

[5] K. Kajiyama, Y. Tanishiro, K. Takayanagi, Surf. Sci. 222 (1989), p.38.

Materials Science Forum Vols. 353-356 (2001) pp. 187-190
© 2001 Trans Tech Publications, Switzerland

In Situ RHEED Studies on the Influence of Ge on the Early Stages of SiC on Si(111) and (100) Surfaces

V. Cimalla[1], K. Zekentes[1], K. Tsagaraki[1], Th. Stauden[2], F. Scharmann[2] and J. Pezoldt[2]

[1] Foundation for Research and Technology Hellas, PO Box 1524, GR-71110 Heraklion/Crete, Greece

[2] Institut für Festkörperelektronik, TU Ilmenau, Postfach 100 565, DE-98684 Ilmenau, Germany

Keywords: Carbonization, Germanium, Heteroepitaxy, Molecular Beam Epitaxy (MBE), RHEED

Abstract. The influence of Ge on the initial growth of SiC by low temperature solid-source molecular-beam epitaxy (SSMBE) on (111) and (100)Si was investigated by reflection high energy electron diffraction (RHEED). On both orientations Ge is passivating partially the surface, reducing the growth rate and increasing the grain size. However, according to the results by Auger electron spectroscopy (AES) Ge is not floating on the surface during proceeding carbonization.

Introduction

In the heteroepitaxial growth of SiC on Si substrates the lowering of the growth temperature is still an important issue due to the large thermal mismatch between layer and substrate. The well developed CVD techniques generally require temperatures above 1000°C. The growth of SiC at the lowest temperatures is achievable by SSMBE due to the high reactivity of elemental sources [1,2]. However, this causes several problems like the formation of a distinct grain structure and the deposition of additional phases. As for the CVD case, the nucleation is the most critical step and the initial layer should be closed and block Si out-diffusion to the growing surface [3]. Several approaches have been already presented to improve the initial growth, like nucleation during a defined heating cycle [3] or the supply of Ge during or prior to the nucleation of SiC [4-7]. It is still under discussion whether this element acts as a surfactant for SiC or forms an alloyed buffer layer at the Si-SiC interface resulting eventually in a better lattice matching. In a previous study of SSMBE on (111)Si it was demonstrated that Ge is increasing the mean grain size, decreasing the growth rate [8] and is mainly incorporated at the Si-SiC interface [7]. In this report we compare these results by real time RHEED observations to the initial growth by SSMBE of SiC on (100)Si.

Experimental

The experiments were accomplished in different SSMBE configurations with electron beam evaporators for Si and C. The growth on (111)Si was investigated in an UMS 500 Balzers system, where a Ge electron gun evaporator and a low energy hydrogen plasma with subsequent annealing was used for substrate cleaning [7]. For the growth on (100)Si a VG80S system with Ge effusion cells was used, and the substrates were cleaned chemically with a subsequent *in situ* removing of a protective oxide [5]. The reproducibility of the processes was checked by performing experiments with representative conditions in both growth chambers. The influence of Ge on the initial stages was investigated by depositing a thin 2D Ge layer up to 2 monolayers (ML) on Si immediately prior to the exposure to C. The growth processes were monitored in real time by RHEED in both SSMBE chambers, and additionally by ellipsometry in the case of (111)Si. The grown layers were further analyzed by atomic force microscopy (AFM), scanning electron microscopy (SEM) and AES.

Results and discussion

Without the pre-deposition of Ge the nucleation proceeds through the formation of the known C-induced reconstructions, namely (4x4) and (2x2) for (001)Si and $\sqrt{3}x\sqrt{3}$ for (111)Si, which are only weakly dependent on the temperature with activation energies around 0.1-0.2 eV (Fig. 1 [9]). The nucleation of SiC sets in either parallel to or after the disappearance of the C-induced reconstructions at high or low temperatures, respectively, with a cross-over temperature around 650°C. During the parallel nucleation the islands remain separated for a longer time resulting in a strong erosion of the Si substrate and the growth of polycrystalline SiC. On such initial layers the deposition of single crystalline SiC is impossible [10].

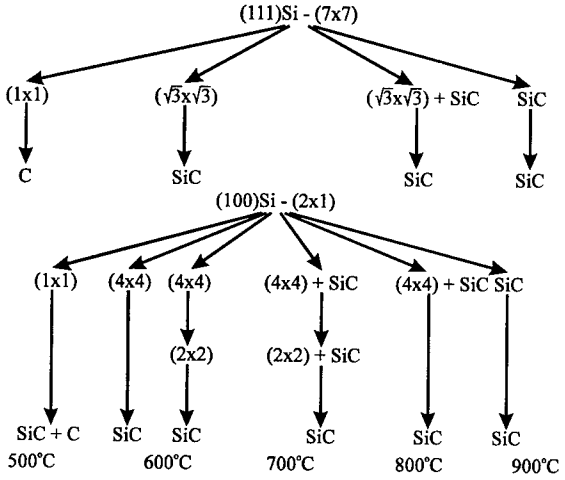


Fig. 1 Carbon induced Si surface reconstructions.
Arrows indicate the reconstruction transformation by continuos carbon supply, "SiC" corresponds to the appearance of SiC transmission spots and "C" corresponds to a diffused RHEED pattern indicating graphitic carbon.

C-induced reconstructions were only weakly present if less than one ML Ge was pre-deposited. For 1 ML and more during the nucleation of SiC the initial reconstructions transform to a disordered (1x1) due to the high aversion between C and Ge atoms (Fig. 2).

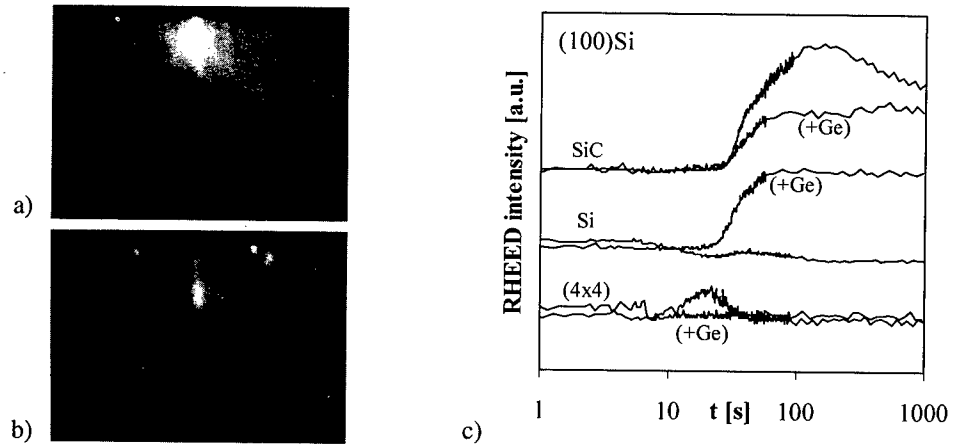
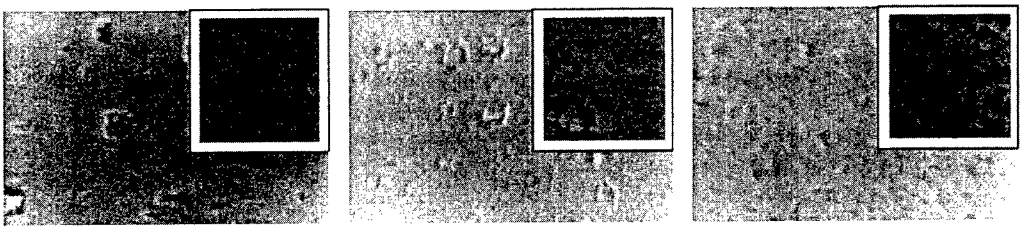


Fig. 2 RHEED images during the nucleation of SiC on (100)Si at 750°C without (a) and with (b) pre-deposition of 1 ML Ge ([001] azimuth). (c) RHEED intensity course for the 1/4 order streak, the SiC and the Si/Ge transmission spots. The corresponding pictures for (111)Si can be found in Ref.[8].

The incubation time until the onset of the SiC nucleation is not affected by the Ge pre-deposition. A noticeable difference is the appearance of clear Si or Ge transmission spots during the SiC

nucleation on the Ge covered Si substrate which evidences an increased surface roughening. Without Ge the SiC spot intensity is increasing very fast and runs through a maximum value, while in the case of Ge pre-deposition it saturates after a slower increasing (Fig.2c). This can be explained by a lateral grain growth. The pre-deposition of Ge is decreasing the grain density and therefore increasing the grain size (Fig.3, [8]). Thus, a very high density of small islands without Ge gives this high increase of the RHEED intensity until the size is comparable or exceeding the free mean path of the electrons. The final structure after carbonization is comparable for the different cases, however, due to the generally larger grains the surface is rougher in the case of Ge pre-deposition. Thus, the process conditions for obtaining a closed initial layer are more critical. For example, on the samples corresponding to the morphology shown in Fig. 3, AES revealed an increased Si:C ratio at the surface for Ge pre-deposition, i.e., parts of the surface are uncovered. On the other hand it was not possible to detect Ge, which in a previous study has been shown to be located mainly at the interface [7]. Finally ellipsometric investigations on (111)Si have demonstrated the decrease of the SiC growth rate by Ge [8], i.e, a decreasing of the reactivity of the Si substrate with carbon.



a) b) c)

Fig. 3 SEM (4x6 μm^2) and AFM (inlet, 1x1 μm^2)images after carbonization of (100)Si at 750°C, 5 min (a) without Ge and with pre-deposition of (b) 1 ML Ge and (c) 2 ML Ge.

There exist mainly two opinions about a possible positive role of Ge in the SiC-on-Si system. First, it can act as a surfactant. In this case Ge should float on the growing surface and modify thermodynamic and/or kinetic properties of it. Regarding the kinetic effects, the surfactant should increase the diffusion length of the adatoms by passivating the surface. This passivation is dependent on the epitaxial system: In homoepitaxy, normally the promotion of the growth at steps is the wanted case in order to stimulate layer-by-layer growth. Thus the steps should remain reactive. In contrast, the misfit in heteroepitaxial systems requires a high density of islands on the terraces for a two-dimensional growth and therefore the steps should be passivated [11]. In analogy to the Monte Carlo simulations for the effects of different surfactants on Si [11], the Ge is expected to passivate terraces on the surfaces but not the steps. Therefore it enhances a preferred nucleation along steps or step bands. From the observed increase of the grain size, it is evident that the Ge mainly affects the initial growth of the SiC nuclei by lowering the reactivity between the carbon atoms and the terraces on the Si surface, but not to the steps. Under these conditions Ge is not an optimal candidate as a surfactant for the heteroepitaxy of SiC on Si. However, this situation may be changed for the growth of "bulk" SiC layers on Si as demonstrated by Mitchell, et al [6].

On the other hand Ge could result in the formation of a Si-Ge-C alloy at the SiC-Si interface for an improved lattice matching. Indeed, on (111)Si the incorporation of Ge during formation of an the initial layer by carbonization has shown a positive effect for epitaxial growth of thicker SiC layers above 100 nm [7]. This improvement of the crystal quality was explained in terms of the S-correlated theory of interface optimization [12] and in fact the observed Ge accumulation at the SiC-Si interface supports this theory.

Since these effects on the initial growth are contradictory on the crystal quality, the initial growth has to be optimized, namely the formation of the large initial nuclei has to be suppressed. Previous studies have shown a crucial improvement depositing carbon during [3] or prior to heating [13] to

the growth temperature in order to stimulate an intermixing of C and Si to an alloy around 600°C prior to the SiC nucleation. While during isothermal carbonization after Ge pre-deposition, twinned and partially polycrystalline material was always grown, the application of defined heating cycles could improve the crystal quality drastically on both (111)Si [7] and (100)Si (Fig. 4).

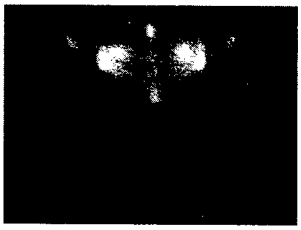
a)  b) 

Fig. 4 RHEED images after 15 min carbonization with pre-deposition of 1 ML Ge on (100)Si: ([011] azimuth): (a) isothermal at 750°C, (b) carbonization during a heating ramp (10 K/min).

Summary

It was shown that the Ge introduced into the system prevent the formation of the carbon induced reconstructions on both (111) and (100)Si. During the growth of SiC on Si, it has a contradictory effect by increasing the grain size and surface roughness of the initial layer but improving the crystal quality of thicker SiC films. For the initial growth, Ge acts as a surfactant by partial passivation of the surface. The improvement for thicker layers can be explained in terms of the S-correlated theory of interface optimization with Si-C-Ge alloy layers. Applying well defined heating cycles during the nucleation the advantages of both effects can be used to grow single crystalline material.

References

[1] G.L. Zhou, Z. Ma, M.E. Lin, T.C Shen, L.H. Allen and H. Morkoc, J. Cryst. Growth 134 (1993), p. 167.

[2] K. Zekentes, V. Papaioannou, B. Pecz and J. Stoemenos, J. Cryst. Growth 157 (1995), p. 392.

[3] V. Cimalla, Th. Stauden, G. Eichhorn, and J. Pezoldt, Mater. Sci. Eng. B61–62 (1999), p. 553.

[4] T. Hatayama, N. Tanaka, T. Fuyuki and H. Matsunami, Appl. Phys. Lett. 70 (1997), p. 1411

[5] K. Zekentes and K. Tsagaraki, Mater. Sci.Eng. B61-62 (1999), p. 559.

[6] S. Mitchel, M.G. Spencer and K. Wongchotigul, Mater. Sci. For. 264-268 (1998), p. 231.

[7] J. Pezoldt, P. Masri, M. Rouhani Laridjani, M. Averous, T. Wöhner, J.A. Schaefer, Th. Stauden, G. Ecke, R. Pieterwas and L. Spieß, Mater. Sci. For. 338-342 (2000), p. 289.

[8] T. Wöhner, Th. Stauden and J.A. Schaefer, J. Pezoldt, Mater. Sci. For. 338-342 (2000), p. 281.

[9] F. Scharmann, P. Maslarski, W. Attenberger, J.K.N. Lindner, B. Stritzker, Th. Stauden and J. Pezoldt, Thin Solid Films, will be published.

[10] W. Attenberger, J.K.N. Lindner, V. Cimalla and J. Pezoldt, Mater. Sci. Eng. B61-62 (1999), p. 544.

[11] D. Kandel and E. Kaxiras, Phys. Rev. Lett. 75 (1995), p. 2742.

[12] P. Masri, Phys. Rev. B52 (1995), p. 16627.

[13] A. Fissel, K. Pfennighaus, U. Kaiser, J. Kräußlich, H. Hobert, B. Schröter and W. Richter, Mater. Sci. For. 264-268 (1998), p. 225.

Materials Science Forum Vols. 353-356 (2001) pp. 191-194
© 2001 Trans Tech Publications, Switzerland

Structural and Optical Properties of SiC Films Deposited on Si by DC Magnetron Sputtering

Y.M. Lei[1], Y.H. Yu[1], L.L. Cheng[1], L. Lin[1], B. Sundaraval[2], E.Z. Luo[2], S. Lin[2], C.X. Ren[1], W.Y. Cheung[2], S.P. Wong[2], J.B. Xu[2], S.C. Zou[1] and I.H. Wilson[2]

[1] Ion Beam Laboratory, Shanghai Institute of Metallurgy, Chinese Academy of Sciences, 865 Changning Road, Shanghai 200050, China P.R.

[2] Department of Electronic Engineering, Chinese University of Hong Kong, Shatin, NT, Hong Kong

Keywords: AES, EMT, GA-XRD, IR Reflectance, Reactive DC Sputtering

Abstract Silicon carbide films were deposited on Si by reactively sputtering of a silicon target in the CH_4 atmosphere of a DC sputtering system. Structural investigation of the stoichiometric SiC films showed that they were composed of microcrystalline and amorphous SiC. The optical behavior of the SiC film was studied by IR reflectance in the range of 400cm^{-1} to 4000cm^{-1}. The experimental IR reflectance in this range was fitted by calculating the complex dielectric function of the films based on effective medium theory (EMT), in which the SiC films were assumed to consist of homogeneously distributed SiC (amorphous and crystalline). The experimental spectra can be best fitted by adjusting the structural parameters and the volume fraction of crystalline phases. The results show that IRRS is a suitable method for detection of the quality of SiC films deposited on Si.

Introduction

Silicon Carbide has attracted intensive research efforts since its excellent physical properties for application in high temperature, high power, high frequency, high erosive, and high irradiative conditions [1]. In this paper, we studied the SiC films deposited on silicon substrates by reactive DC magnetron sputtering. A four-inch silicon target was reactively sputtered in an Ar/CH_4 mixed atmosphere to deposit SiC films onto a silicon substrate of two inches heated to temperatures up to 900°C. The samples were prepared at substrate temperature of 900°C, a total pressure of 0.4Pa and the partial pressure of methane ranging from 0.04Pa to 0.073Pa. The DC power was kept at 120W. The details of the deposition process have been described elsewhere [2].

Experiments

Compositional and structural studies of the deposited SiC films were carried out using Auger electron spectroscopy and non-Rutherford elastic scattering. Structural investigation of the film was performed using grazing-angle X-ray Diffraction (GAXRD) and cross-sectional TEM (on a JEOL JEM-200CX). Atomic Force Microscopy was used to evaluate the surface morphology of the SiC thin films. The infrared reflectance spectra were obtained by a Perkin-Elmer 983 double beam spectrometer for the range of 400cm^{-1} to 4000cm^{-1} using near-normal incidence to the film surface. The quoted accuracy of the Perkin-Elmer instruments is ±1% in absolute reflection. To obtain the

absolute reflection R from the film, the energy reflected from the film was compared with that reflected from the high quality front surface of an Al mirror. The backside of the silicon substrate was coarsened before IR measurement to meet the requirements for semi-infinite substrate assumption.

Results and Discussion

Previously reported AES studies show that under appropriate conditions, the prepared SiC films are stoichiometric with uniform compositional distribution throughout the film thickness [2]. Magnified AES peaks of C KVV and Si LVV also show similar peak shapes as those of SiC reported in literature, indicating the formation of Si-C bond [3, 4]. The results of Non-Rutherford Backscattering NBS were quite close to those of AES studies, agreeing on that the films were uniform in composition and that stoichiometric SiC films were successfully prepared.

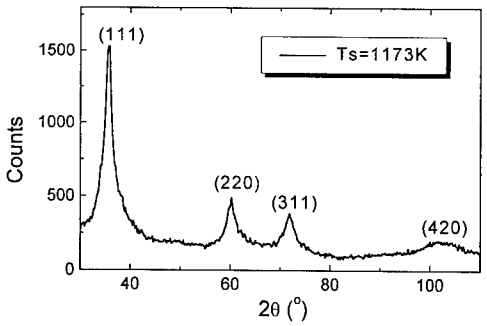


Fig.1 GA-XRD of SiC film deposited at 900°C

The crystalline structure of the deposited films was characterized using XRD, GA-XRD, cross sectional TEM, and planar TEM. XRD patterns show only one SiC peak near 35.6°, corresponding to 3C-SiC(111) crystalline plane diffraction. Glancing angle XRD shown in Figure 1 revealed more 3C-SiC peaks in the diffraction patterns. In this pattern one can find 3C-SiC (111) (220) (311) peaks, indicating the crystalline phase in the films were composed of 3C-SiC, not any other polytypes of SiC. XRD studies also lead to the conclusion that higher temperature (900°C vs. 850°C) could result in better crystalline qualities (larger crystallites) [2].

Figure 2 shows the Hi-Resolution TEM image of the DC sputtered SiC film. From this photograph, it can be concluded that microcrystalline phases exist in the film prepared. As the film is mainly composed of Si-C bonds, it can be inferred that the film consists of mainly SiC microcrystallites and amorphous SiC.

Atomic Force Microscopy is frequently used to evaluate the surface morphology of thin films. Shown in Fig. 3 is the AFM image taken for the stoichiometric sample. The characteristic size of the surface structures is about 20nm to the surface normal, and 100nm lateral. It can be seen that the surface is composed of regular tops of almost similar sizes. No irregular protruding has been

observed. In conclusion, stoichiometric SiC films have been prepared with relatively smooth surfaces.

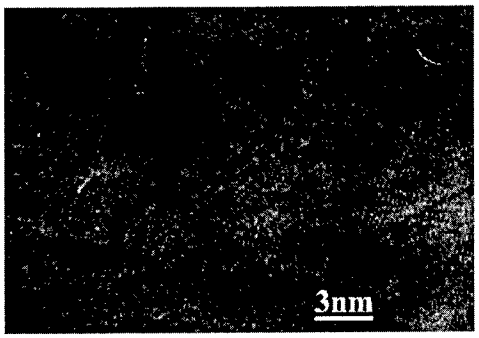


Fig. 2 Hi Resolution TEM of DC sputtered SiC films

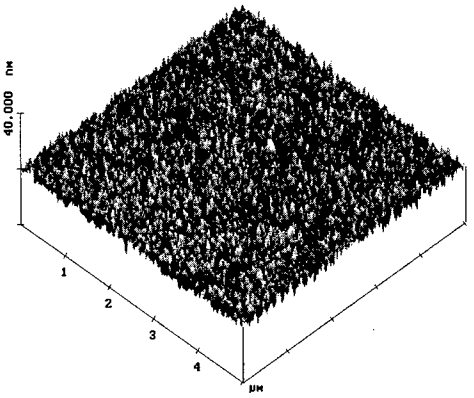


Fig. 3 Surface morphology of stoichiometric SiC films deposited on Si

Infrared reflectance spectra in the range of 400cm^{-1}~4000cm^{-1} were employed to investigate the crystalline structure, structural dimension, structural defects of the SiC/Si and SiCOI structures, with the help of effective medium approaches and routine transfer matrix method. The IRRS of SiC were featured by a restsrahlen peak around 800cm^{-1}~1000cm^{-1}.

The reflectance spectrum was fitted using a classical oscillator model combined with effective medium theory. The system was assumed to include a top SiC film and a semi-infinite silicon substrate (rational as the backside is coarse enough). In the model the complex dielectric function $\varepsilon(\omega)$ of a semiconductor is expressed as,

$$\varepsilon(\omega) = \varepsilon_1 + i\varepsilon_2 = (n - ik)^2$$
$$= \varepsilon_\infty (1 - \omega_p^2 / (\omega^2 + i\gamma\omega)) + \sum_j \rho_j^2 \omega_{Tj}^2 / (\omega_{Tj}^2 - \omega^2 - i\Gamma_j \omega) \quad (1)$$

where ε_∞ is the high frequency dielectric constant, ρ_j, ω_{Tj} and Γ_j are the strength, and resonance frequency and damping constant of the jth transverse optic-phonon, respectively, ω_p is the bulk plasma frequency due to free carriers in the film and γ is the free carrier damping constant.

For the crystals the following parameters[5] were used in the calculation: transverse optical phonon frequency ω_T=794cm^{-1}, longitudinal optical phonon frequency ρ=3.38, Γ=8.5cm^{-1}, and ε_∞=6.7. No free carrier effect is considered in this calculation. Since the transverse optical phonon frequency and the phonon-damping constant for Si-C bond stretching mode is about 780cm^{-1} and 200cm^{-1}, respectively, for a-SiC$_x$:H films [6,7], the phonon-damping constant of the amorphous component was assumed to be Γ'=200cm^{-1}, much larger than that of crystalline 3C-SiC. The ω_T' for the amorphous component is assumed to be 780cm^{-1}, and ρ'=3.2, ε_∞'=7.3. The method used to calculate the effective complex dielectric function was Maxwell-Garnet approach, which can be expressed as following,

$$(\varepsilon_e - \varepsilon_m)/[\varepsilon_m + A_\alpha(\varepsilon_e - \varepsilon_m)] = p(\varepsilon_i - \varepsilon_m)/[\varepsilon_m + A_\alpha(\varepsilon_i - \varepsilon_m)] \quad (2)$$

Shown in Fig. 4 is the experimental and simulated IR reflectance of SiC on Si. The solid line represents experimental data and the dotted line represents the calculated reflectivity. The reststrahlen peak in the region of 800cm^{-1} to 1000cm^{-1} that is the characteristic of the SiC transverse optic-phonon resonance is observed. The peak position 820cm^{-1} is near 3C-SiC's transverse optical phonon frequency (794cm^{-1}). Fig. 5 shows the calculated refractive index of SiC films and those of 3C-SiC and amorphous SiC. The experimental spectra can be best fitted by adjusting the structural parameters and the volume fraction of crystalline phases. The results show that IRRS is a suitable method for detection of the quality of the SiC/Si systems.

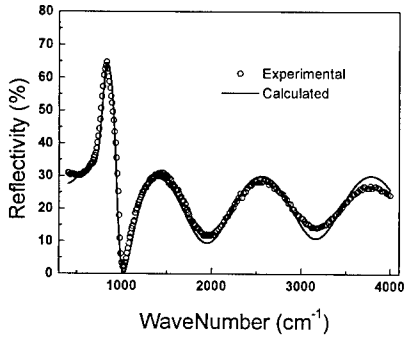


Fig. 4 IRRS of SiC/Si

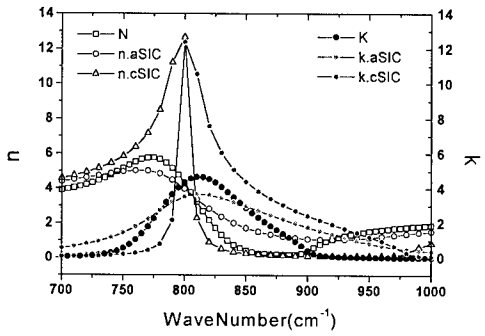


Fig. 5 n & k of DC deposited SiC

Conclusion

To conclude, SiC films were reactively deposited on Si. Structural studies show that the films were composed of 3C-SiC crystallites and amorphous SiC phase. IR reflectance combined with EMT was successfully employed to simulate the IR spectra.

This work is supported by Shanghai Municipal Board of Sciences and Technology under Grant No. 98QME1403

References

1. R.C. Glass, MRS Bulletin **22** (1997), p. 30
2. Y.M. Lei, Y.H. Yu, C.X. Ren, S.C. Zou, D.H. Chen, S.P. Wong, I.H. Wilson, Thin Solid Films, **365** (2000), p. 53
3. Y.M. Lei, Y.H. Yu, L.L. Cheng, C.X. Ren, S.C. Zou, Vacuum (2000), accepted.
4. M. De Seta, S. L. Wang, F. Fumi, and F. Evangelisti, Phys. Rev. B **47** (1993), p.7041
5. D. Olego, M. Cardona, P. Vogl, Phys. Rev. B **25** (1982), p.3878.
6. Y.H. Yu, S.P. Wong, I.H. Wilson, Mater. Sci. Engin. B **52** (1998), p.55.
7. J. Bullot, M.P. Schmidt, Phys. Status Solidi B **143** (1987), p.345.

Materials Science Forum Vols. 353-356 (2001) pp. 195-198
© 2001 Trans Tech Publications, Switzerland

Laser Crystallization of Amorphous SiC Thin Films on Glass

S. Urban and F. Falk

Institut für Physikalische Hochtechnologie, Winzerlaer Str. 10, DE-07743 Jena, Germany

Keywords: Laser Crystallization, Melting, Time Resolved Reflectivity (TRR)

Abstract

Amorphous silicon carbide thin films deposited by laser ablation were crystallized by an excimer laser. Crystallites in the 40 nm range were observed by TEM. From time resolved reflectivity measurements a melt mediated crystallization process is postulated in contradiction to the equilibrium phase diagram.

Introduction

Crystalline silicon carbide (c-SiC) thin films are an ideal material for high-power, high-frequency, and high-temperature electronic devices. Conventional methods for preparing c-SiC thin films are CVD or laser ablation at substrate temperatures above 1000°C [1-3]. Alternatively, amorphous films (a-SiC) were deposited and subsequently crystallized by solid phase crystallization above 800 °C [4]. In both cases a high temperature substrate is required. For economic reasons, however, c-SiC films on glass are of major interest. For this purpose laser crystallization seems to be an attractive method which already is well established for crystallizing amorphous silicon films.

However, up to now laser crystallization of a-SiC has found only little attention. Nearly stochiometric a-SiC:H films deposited by PECVD were crystallized by irradiation with the 20 to 30 ns pulses of excimer lasers [5-7]. Alternatively a-SiC was crystallized by 10 to 250 ms pulses of an argon ion laser (514 nm wavelength) [8,9]. The mechanisms of the crystallization was not studied in these papers. Baeri [10] used a ruby laser (25 ns pulse duration, 694 nm wavelength) to irradiate an SiC wafer amorphized at the surface by ion implantation. Crystal grains below 100 nm in diameter were generated. From time resolved reflectivity measurements melt mediated crystallization was proposed as the underlying mechanism. However, in the phase diagram of SiC no liquid phase occurs at ambient pressure [11]. Liquid SiC (l-SiC) was postulated to exist only at pressures above 100 atm [12]. So a melt mediated crystallization mechanism is in contradiction to the equilibrium phase diagram of SiC.

In the present paper the excimer laser induced crystallization of hydrogen free a-SiC thin films on glass deposited by laser ablation is studied by time resolved reflectivity measurements and by TEM.

Experimental

Hydrogen free a-SiC thin films were deposited by laser ablation from a stochiometric polycrystalline SiC target. A KrF laser (248 nm wavelength, 30 ns pulse duration, 50 Hz repetition rate, 250 mJ pulse energy) was used at a fluence of 2 J/cm^2. During deposition the glass (Corning 7059) or fused silica substrates were heated to 400 °C. At a deposition rate of 0.3 nm/s 120 nm thick films were produced. The amorphous nature of the deposited films was confirmed by TEM.

For crystallization the a-SiC films were irradiated by a single shot of a KrF laser (30 ns pulse duration) in air at ambient pressure. A fluence in the range of 0.1 to 1 J/cm^2 was applied on a 5x2 mm^2 area of the amorphous film.

The crystallization was observed by time resolved reflectivity (TRR) measurements. To this end the beam of a 10 mW cw HeNe laser (633 nm wavelength) was focused onto the spot irradiated by the crystallization laser. The reflected beam intensity was measured by a fast photo diode (2 ns time resolution) and observed on an oscilloscope.
The resulting films were investigated by optical microscopy and by transmission electron microscopy (Phillips CM 30 operated at 300 kV). For the TEM investigations the SiC films were removed from the glass substrate by HF etching. Plan view images and diffraction patterns were recorded.
The composition of the amorphous and laser treated films was determined by RBS (1.4 MeV He^+).

Results

Optical microscopy of films irradiated by a fluence above 250 mJ/cm^2 shows a brownish color in contrast to films irradiated by a lower fluence indicating some film modification.
Plan view TEM images as well as diffraction patterns of the films irradiated by a fluence below 250 mJ/cm^2 show no modification of the amorphous structure. In films irradiated above the threshold of 250 mJ/cm^2 crystallites with a diameter in the 40 nm range were observed (Fig. 1). This is confirmed by the diffraction pattern (insert in Fig. 1). A residual amorphous part in the film can not be excluded. From a high resolution image a distance between atomic planes of 0.256 nm follows which corresponds to c-SiC.
Further TEM investigations are necessary to determine the polytype of the SiC crystallites.

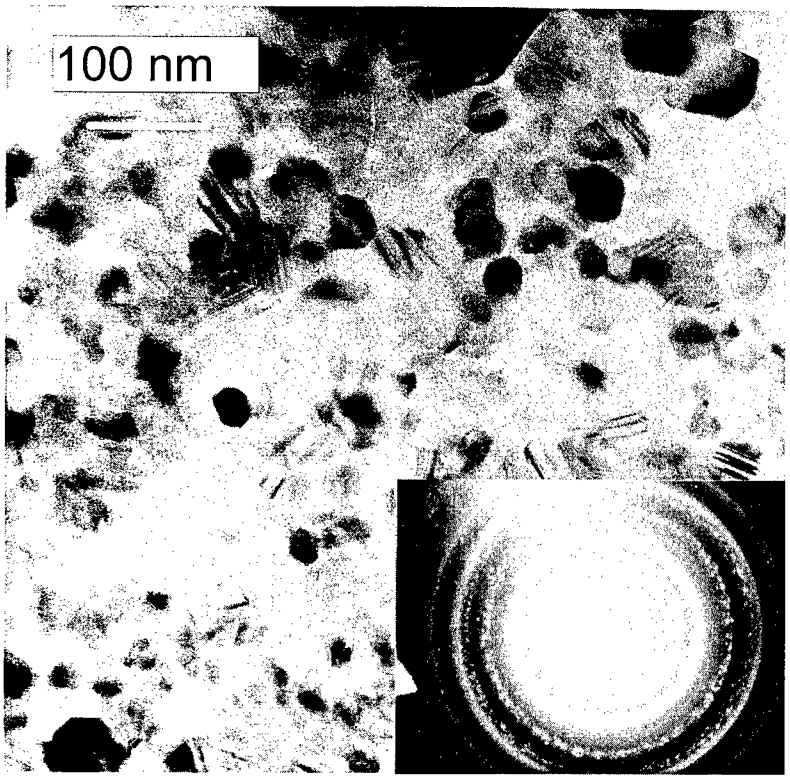


Fig. 1: TEM plan view image and diffraction pattern of a SiC film laser crystallized at a fluence of 300 mJ/cm^2

RBS measurements confirmed a nearly stochiometric composition of 50±5 at % Si in the amorphous as well as in the crystallized films.

Fig. 2 shows TRR curves during irradiation with 140 mJ/cm^2 and 300 mJ/cm^2. Note that the absolute values are influenced by interference. In the low fluence irradiation curve the reflectivity increases weakly which is interpreted as resulting from the film heating. After the irradiation the reflectivity recovers to the previous value so that no permanent modification of the film was detected. For the high fluence irradiation the reflectivity increases to 0.6. A high reflectivity value remains for about 50 ns, which is longer than the irradiation pulse. After 120 ns the reflectivity reaches a permanent value lower than before the pulse corresponding to the permanent modification of the film.

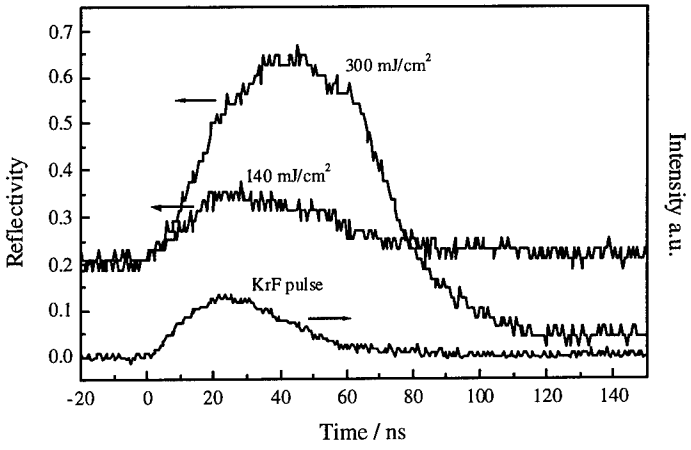


Fig.2: TRR curves together with crystallization pulse

Discussion and Conclusions

Excimer laser irradiation with a fluence of 300 mJ/cm^2 leads to crystallization of hydrogen free a-SiC films with grain sizes in the 40 nm range. The TRR measurements indicate that a transient modification occurs in the films leading to an increased reflectivity which remains longer than the irradiation pulse. Later on the reflectivity attains a value different from that of the a-SiC starting material. We conclude that the laser pulse leads to a melting of the a-SiC film which lasts for approximately 50 ns followed by crystallization. The high reflectivity of the melt indicates metal like properties of l-SiC similar to liquid silicon. However, the postulated existence of the melt is in contradiction to the equilibrium phase diagram of SiC [11]. This states that at ambient pressure there exists no temperature at which a fluid phase is in equilibrium with the crystal. Moreover, there is no temperature range in which a fluid has a lower free energy than the crystal. The phase diagram, however, does say nothing about the relative stability of a-SiC as compared to l-SiC. It is therefore not in contradiction to the phase diagram if the free energy of l-SiC is lower than that of a-SiC above some temperature T_{ma}, the melting point of a-SiC. However, in the temperature range above T_{ma} the liquid is unstable with respect to c-SiC. Therefore a high enough laser fluence may heat a-SiC to a temperature above T_{ma} followed by melting. After less than 100 ns nucleation and growth of c-SiC occurs in the unstable melt.
For a better quantitative understanding a numerical simulation of the process was performed. To this end the equation of heat conduction including the latent heat of melting was numerically solved by the enthalpy method [13]. The material parameters used in the calculation are compiled in Table 1. ρ, c, λ, and T_{la} for a-SiC were taken from [10]. α for a-SiC is taken from [5] whereas R is the value of c-SiC (3C) at 248 nm wavelength taken from [14]. No data were available for l-SiC so that we decided to take for ρ and c the same values as for a-SiC which seems to be no large mistake. R and α for l-SiC as well as H_{la} are the values for liquid silicon. The values for the substrate are those for fused silica.

Table 1: Material parameters used for calculations

	density ρ/gcm^{-3}	specific heat c/Jg^{-1}K^{-1}	heat conductivity λ/Wcm^{-1}K^{-1}	absorption coefficient α/cm^{-1}	reflectivity R	melting point T_{la}/K	latent heat H_{la}/Jg^{-1}
a-SiC	3.2	1.3	0.011	$1.0 \cdot 10^5$	0.3	2445	1300
l-SiC	3.2	1.3	0.7	$1.5 \cdot 10^6$	0.6		
Substrate	2.2	0.71	0.0136	10			

According to the calculations the fluence at which the surface starts to melt at the end of the pulse is 0.21 J/cm^2 whereas the threshold for complete melting is 0.44 J/cm^2. The observed crystallization threshold is in between these values. So the values of Table 1 give a set of data consistent with our experiments.

Acknowledgment

This work was funded by DFG in the program Sonderforschungsbereich 196. We would like to thank Dr. S. Christiansen and M. Nerding (Central Facility for High Resolution Electron Microscopy, University Erlangen-Nürnberg) for TEM investigations and C. Schubert and W. Wesch (University of Jena) for RBS measurements.

References

[1] A.J. Steckl, C. Yuan, J.P. Li, M.J. Loboda, Appl. Phys. Lett. 63 (1993), p. 3347.
[2] L. Rimai, R. Ager, W.H. Weber, E.M. Logothetis, A.-A. Nayef, M. Aslam, J. Appl. Phys. 73 (1993), p. 8242.
[3] M. Diegel, F. Falk, R. Hergt, H. Hobert, H. Stafast, Appl. Phys. A 66 (1998), p. 183.
[4] P. Musumeki, R. Reitano, L. Calcagno, F. Roccaforte, A. Makhtari, M.G. Grimaldi, Phil. Mag. B 76 (1997), p. 323.
[5] S. Wickramanayaka, K. Katimura, Y. Nakanishi, Y. Hatanaka, Mater. Res. Soc. Symp. Proc. 397 (1996), p. 429.
[6] G. De Cesare, S.L. Monica, G. Maiello, G. Masini, E. Proverbio, A. Ferrari, N. Chitica, M. Dinescu, R. Alexandrescu, I. Morjan, E. Rotiu, Appl. Surf. Sci. 106 (1996), p. 193.
[7] S.P. Lau, J.M. Marshall, T.E. Dyer, Phil. Mag. B 72 (1995), p. 323.
[8] C. Palma, M.C. Rossi, C. Sapia, Electr. Lett. 34 (1998), p. 1430.
[9] C. Palma, M.C. Rossi, C. Sapia, E. Bemporad, Appl. Surf. Sci. 139 (1999), p. 24.
[10] P. Baeri, C. Spinella, R. Reitano, Int. J. Thermophys. 20 (1999), p. 1211.
[11] R.I. Scace, G.A. Slack, J. Chem. Phys. 30 (1959), p. 1551.
[12] L.Y. Sadler, M. Shamsuzzoha, J. Mater. Res. 12 (1997), p. 147.
[13] V. Voller, M. Cross, Int. J. Heat Mass Transfer 26 (1983), p. 147.
[14] Landolt-Börnstein, Numerical Data and Functional Relationships in Science and Technology, New Series, Vol. 17a, Heidelberg: Springer 1982, p. 448.

Materials Science Forum Vols. 353-356 (2001) pp. 199-202
© 2001 Trans Tech Publications, Switzerland

TEM Investigation of Si Implanted Natural Diamond

B. Pécz[1], Á. Barna[1], V. Heera[2], F. Fontaine[2] and W. Skorupa[2]

[1] Research Institute for Technical Physics and Materials Science,
PO Box 49, HU-1525 Budapest, Hungary

[2] Forschungszentrum Rossendorf, PO Box 510119, DE-01314 Dresden, Germany

Keywords: Diamond, Electron Microscopy, Ion Implantation, Phase Formation

Abstract. Natural diamond samples have been implanted by Si ions at 900°C at two different doses ($3*10^{17}$ and $1*10^{18}$ ions/cm^2). Layered structure is formed in the lower dose case, which is composed of thin stripes of epitaxial SiC and diamond. The higher dose implantation results in the formation of large, crystalline SiC grains, but leads to the amorphization of the diamond lattice in the top region.

Introduction

Both, diamond and silicon carbide (SiC) are wide band gap semiconductors with excellent electronic properties [1, 2]. Recent ion implantation efforts of diamond are focussed for the n-type doping [3], while focused Si implantation of diamond was used to print photographic images [4] via transformation of diamond to black carbon.

The heterostructure of diamond and SiC promises new applications. The ion beam synthesis of layered, diamond/SiC structures is a challenging task and is the subject of the present paper. For that purpose natural IIa diamond was implanted by Si at 150 keV at a temperature of 900°C. The structure of the implanted diamond region was investigated by transmission electron microscopy (TEM).

Experimental

(100) oriented IIa natural diamond crystals were implanted at 150 keV with two different doses ($3*10^{17}$ and $1*10^{18}$ ions/cm^2). Ion implantation was carried out at an elevated temperature of 900°C to decrease the ion damage and to avoid graphitization.

Cross sectional samples for TEM analysis have been prepared by cutting the diamond pieces and embedding them in face to face position into a special Ti grid with a diameter of 3 mm [5]. The embedded samples have been ground by diamond paste to the thickness of 100 μm. Then the samples were placed into an Technoorg-Linda IV3/H/L type ion miller for further thinning and were bombarded by Ar^+ ions at 10 keV until the perforation of the TEM sample. Grazing angle of incidence was applied during thinning to get a large transparent region around the perforation. The perforated specimen was bombarded further at 200 eV using a special, low energy ion gun to minimise the ion beam damage of the thinning [6]. Amorphization, what is generally observed at the edges of the TEM samples, and graphitization of diamond [7], what is a characteristic artefact of ion beam thinned diamond specimens, were minimised in this way at low energy bombardment. The cross sectional TEM specimens were investigated in a Philips CM 20 electron microscope operating at 200 kV, while high resolution work was carried out in a JEOL 4000 EX microscope operating at 400 kV.

Results: Lower dose case

The cross section of the natural diamond sample implanted to $3*10^{17}$ ions/cm^2 is shown in Figure 1. The top region of the sample is diamond (marked by the letter A in Fig. 1). That region is about 70 nm thick and slightly damaged.

The formation of SiC in the implanted diamond was indicated by Raman spectroscopy [8]. This occurred in the next, about 150 nm thick region (marked by B in Fig. 1), where 3C-SiC grains and diamond are overlapping.

Selected area diffraction pattern (Fig. 2.) taken in region B confirmed the formation of cubic SiC domains in a weakly damaged diamond matrix. (Reflections of diamond (the outer ones) are marked by *, while reflections of 3C-SiC are marked by small black rectangular dots.) All of the 3C-SiC domains are in epitaxial configuration to diamond. SiC domains are formed in layers (2-3 nm thick) inside the diamond, instead of random distribution.



Fig. 1. Cross section of diamond implanted at low dose.

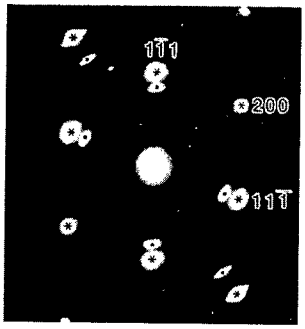


Fig. 2. Selective area diffraction pattern.

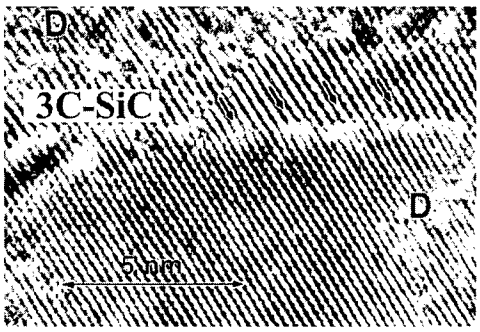


Fig. 3. High resolution image taken from the region marked by a circle in Fig. 1.

One of the 3C-SiC domains is shown inside the diamond matrix in Fig. 3. Diamond regions are marked by letter D, while the misfit dislocations formed between the SiC domain and the diamond matrix are marked by arrows. The two lattices are matched according to the criteria of: 4*(111)SiC=5*(111)diamond=1.0 nm and this results in a periodic array of misfit dislocations. This could be expected when SiC is grown onto diamond and in this case when SiC is produced by ion beam synthesis the above matching also proves the capability of the method. Amorphization and graphitization were completely avoided in this case.

High dose case

The cross section of natural diamond implanted to $1*10^{18}$ ions/cm^2 is shown in Fig. 4. Three different regions are distinguished, although the interfaces are not sharp (threading dislocations are also observed in the deep, unimplanted regions of diamond). The diamond lattice is destroyed in regions 1 and 2 (see Fig. 4). Generally high dose implantation of Si into diamond (at 900°C) leads to the formation of SiC, formed in large grains. However, in the top two regions the diamond lattice is amorphized. This means that in region 1 (about 70-80 nm thick top region) very few crystalline SiC grains can be found in an amorphous matrix, while in region 2 (about 195-200 nm thick) many large, crystalline grains of SiC can be found in amorphous matrix as well. The formed SiC grains are textured according to the selected area diffraction pattern (Fig. 5). SiC grains in region 2 can be as large as 30 nm (see the dark field image of Fig. 6, taken by a 111 type reflection of SiC), while the SiC grains in region 1 are about 10-15 nm large. Fig. 7 is a high resolution image, which shows a small part of two neighbouring SiC grains divided by an amorphous stripe.

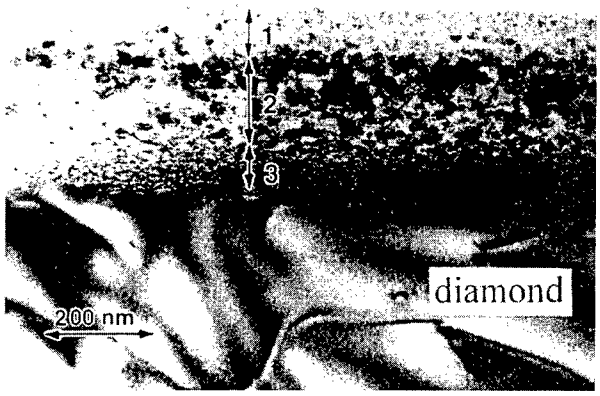


Fig. 4. Cross section of the diamond sample implanted by high dose of Si.

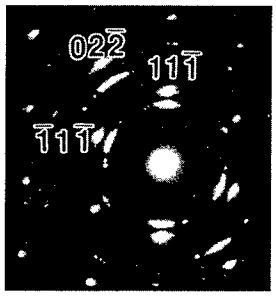


Fig. 5. Selected area diffraction pattern taken on the implanted region of sample shown in Fig. 4.

Region 3 (Fig. 4) of the high dose implanted sample is about 80 nm thick and is similar to the region B in the low dose implanted sample (Fig. 1) as this is composed of stripes of SiC and diamond. The difference to the low dose case is that the SiC stripes are thicker in the high dose case being typically 5-6 nm thick. In this region the formed SiC grains are epitaxially aligned to the preserved diamond lattice. In the upper regions (1 and 2) SiC grains started to be formed inside the diamond lattice, which is destroyed due to the high dose and resulting high amount of energy deposition into nuclear processes. As a result of the dynamic process of SiC growth and diamond amorphization the large SiC grains formed in regions 1 and 2 are slightly misoriented and textured. The explanation of the misorientation is not clear and will be investigated further.

Contrary to the lower dose case, here it is obvious that the applied dose ($1*10^{18}$ ions/cm^2) is too high to avoid the amorphization of diamond.

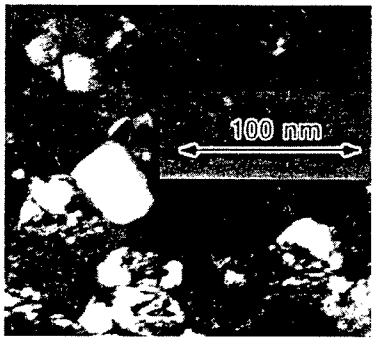


Fig. 6. Dark field image taken by a (111) type reflection of SiC (from region 2).

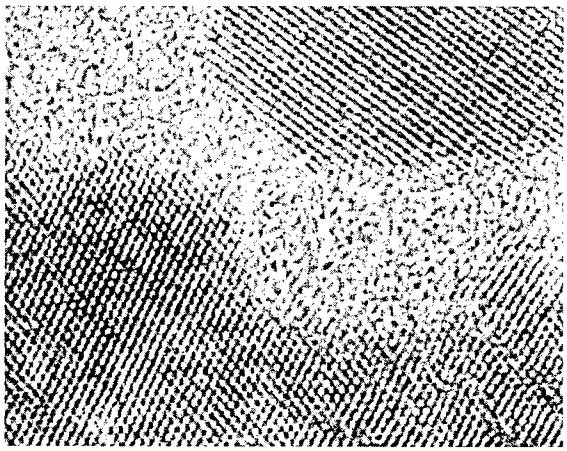


Fig. 7. High resolution image showing a part of two neighbouring SiC grains divided by an amorphous stripe.

Conclusions

High temperature implantation of Si ions into diamond promises an appropriate technology for the formation of SiC/diamond stripes. The formed SiC grains are epitaxial to the matrix of natural diamond. The maximum dose of the implanted silicon ions is limited by the amorphization of the diamond lattice. By a careful selection of the implantation dose and temperature the amorphization can be avoided completely.

Acknowledgement

Financial support of OTKA Contract No. T 030447 is acknowledged. B.P. acknowledges Department of Materials, Oxford University for the access to the JEOL 4000 EX microscope.

References:

[1] "SiC materials and devices" Semiconductors and Semimetals, Vol. 52, (ed. Y.S. Park) (Academic, London, 1998)
[2] J.F. Prins in "The physics of diamond" Proc. of Int. School of Physics "Enrico Fermi" Course CXXXV, (ed. A. Paoletti and A. Tucciarone) (IOS, Amsterdam, 1997) p.411
[3] J.F. Prins: Phys. Rev. B 61 (2000) p.7191
[4] L.E. Erickson, H.G. Champion, J. W. Fraser, R. Hussey, P. Schmuki and C. Porco: J. Vac. Sci. Technol. B 15 (1997) p.2358
[5] Á. Barna, G. Radnóczi and B. Pécz: in Handbook of Microscopy, (eds. S. Amelinckx, D. van Dyck, J. van Landuyt, G. van Tendelo) VCH Verlag, Vol. 3, Chapter II/3, (1997) p.751
[6] A. Barna, B. Pécz and M. Menyhard: Ultramicroscopy 70 (1998) p.161
[7] R. Kalish: Appl. Surf. Sci. 117/118 (1997) p.558
[8] V. Heera, F. Fontaine, W. Skorupa, B. Pécz and Á. Barna: Appl. Phys. Lett. 77 (2000), p.226

Chapter 3:

Physical Properties

Materials Science Forum Vols. 353-356 (2001) pp. 205-210
© 2001 Trans Tech Publications, Switzerland

Surface Reconstruction on SiC(0001) and SiC(000$\bar{1}$): Atomic Structure and Potential Application for Oxidation, Stacking and Growth

U. Starke

Lehrstuhl für Festkörperphysik, Friedrich-Alexander-Universität Erlangen-Nürnberg,
Staudtstr. 7, DE-91058 Erlangen, Germany

Keywords: 3C-SiC, 4H-SiC, 6H-SiC, Auger Electron Spectroscopy, C-Face, Heterostructures, Hexagonal Surfaces, Low-Energy Electron Diffraction, Polytypism, Reconstruction, Scanning Tunneling Microscopy, SiC(0001), SiC(000$\bar{1}$), Si-Face, Stacking Sequence, Surface Structure

Abstract: The atomic arrangement on SiC surfaces appears to have a direct relation to technological applications with respect to oxidation, crystal growth and polytype development. *Ex situ* hydrogen treatment leads to an epitaxially well matching silicon oxide monolayer on both SiC(0001) and (000$\bar{1}$) which promises to allow deposition of low defect density oxide films for MOS devices. The extremely efficient dangling bond saturation on SiC(0001)-(3×3) facilitates step flow growth for monocrystalline homoepitaxial layers. A ($\sqrt{3}\times\sqrt{3}$)R30° phase on SiC(0001) is characterized by a Si adatom in a so-called T4 site. By modifying the preparation condition of this phase the layer stacking in the outermost surface slab can be influenced on hexagonal 4H and 6H samples. This might serve as seed for polytype heterojunctions. A modified stacking can also be obtained below the H3 adatoms of a (2×2) phase on SiC(000$\bar{1}$).

Introduction

A wide selection of electronic devices in areas such as high temperature, high power and high frequencies has become possible due to the specific physical properties of SiC [1]. However, a large scale fabrication of SiC devices is still hampered by material related problems. Growth of high quality crystaline material and the control of the developing polytype as well as the fabrication of oxid layers with low defect state density have to be mentioned in this context. As growth proceeds by attachment of particles to an existing surface it is obvious that the situation on the surface itself has an important impact on the outcoming result of a growth experiment. Growth experiments and device development are mainly carried out on wafers oriented along the basal plane surfaces of SiC, i.e. SiC(0001) and SiC(000$\bar{1}$). Therefore, the structure of these SiC surfaces has raised interest already for several decades. Investigations concerned the preparation of stable surfaces as well as their atomic structures as reviewed recently [2], concentrating mostly on SiC(0001). A simple crystal truncation of SiC along its basal plane would consist of a Si-C bilayer with one unsaturated (dangling) bond per surface atom. In a real, stable surface structure, the number of these dangling bonds is reduced for energetic reasons, e.g. by saturation with foreign adatoms or a compositional change at the surface (Si/C-ratio) usually accompanied by a reconstruction of the outermost surface region. Due to the possible two mutual orientations of adjacent bilayers a crystallographic analysis is not only concerned with adatoms, stoichiometry and reconstruction but also with the stacking sequence of the topmost bilayers at the sample surface. For a detailed discussion see refs. [2, 3].

A structural diagram has been established for both orientations [3, 4] containing a series of stable structures as well as a number of metastable phases. The crystallographic structures of several stable phases have been analysed by a combination of several surface sensitive techniques and show a potential relation to technological problems in the SiC device development [5–8]. Sample morphology and atomic arrangement in the outermost surface layer were investigated using scanning tunneling microscopy (STM) [9]. Auger electron spectroscopy (AES) and X-ray photoelectron spectroscopy (XPS) were used to determine elemental composition and chemical bonding situation on

the surface [10]. For the full crystallographic analysis of the surface structures the low-energy electron diffraction (LEED) intensities were investigated quantitatively [11, 12]. When the necessary requirements were fulfilled, i.e. a prominent adatom is part of the surface structure, a holographic interpretation of the LEED intensities could be used for a coarse model selection [13]. By using bulk and film samples from different sources and of different polytype it could be established that the reconstruction pattern found for different phases is independent of the sample type.

Silicate monolayers on SiC(0001) and SiC(000$\bar{1}$)

To obtain clean and atomically ordered SiC samples requires an initial *ex situ* preparation which typically consists of a thermal oxidation and the removal of the so-called sacrifial oxide by etching in hydrofluoric acid (HF). However, while this results in a (1×1) LEED pattern corresponding to the periodicity of a SiC bilayer [2, 3, 14] the samples are covered by a disordered submonolayer amount of oxygen, hydrogen or hydroxyl groups. Using hydrogen etching or plasma treatment a bright, sharp and background free $(\sqrt{3}\times\sqrt{3})$R30° LEED pattern is observed immediately after transfer of the sample into the UHV chamber corresponding to a well ordered but reconstructed surface. Noteworthy, this kind of well ordered $(\sqrt{3}\times\sqrt{3})$R30° phase can be obtained on surfaces of both polarity. LEED and AES determined a Si_2O_3 monolayer similar to sheet silicates to reside above an otherwise bulk-truncated crystal [6, 15, 16]. This adlayer is formed by a honeycomb-like sublayer of two Si atoms per $(\sqrt{3}\times\sqrt{3})$R30° unit cell connected by two-fold coordinated oxygen atoms in a sublayer 0.47 Å above the Si atoms as shown in Fig. 1. As depicted also in the figure the only significant difference between SiC(0001) and SiC(000$\bar{1}$) is the connection of the silicate layer to the topmost substrate SiC bilayer: On SiC(000$\bar{1}$) the two are directly connected by a Si-C bond (panel b) while on SiC(0001) a linear Si-O-Si bridge mediates the contact (panel c). On both surface orientations the oxygen atoms saturate all bonds of the silicate adlayer, only one of the three Si or C atoms in the topmost substrate bilayer is not saturated having only threefold coordination. This may explain the stability of the structures in UHV and even against exposure to air ambient.

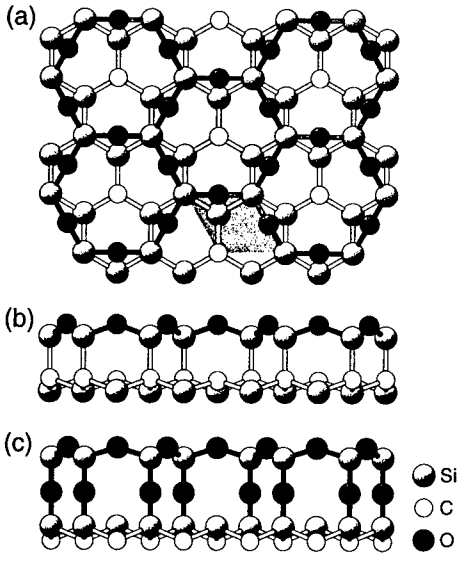


Figure 1: (a) Top view of the oxide structure on SiC(000$\bar{1}$). The silicate adlayer consists of a honeycomb structure with Si–O–Si bonds. In the center of the hexagons one carbon atom of the topmost substrate bilayer is visible (dark shaded area indicates the (1×1)-, light shaded the $(\sqrt{3}\times\sqrt{3})$R30° unit cell). (b) Sideview projection of (a) along the $(11\bar{2}0)$ direction. (c) Sideview projection of the oxide structure on SiC(0001). Linear Si–O–Si bonds connect the silicate layer and the SiC substrate.

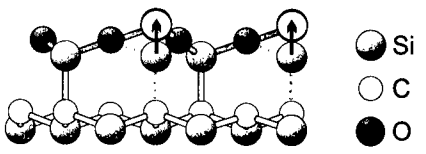


Figure 2: Sketch of the rebonding required to convert the epitaxial silicon oxide layer found on the SiC(0001) surface (one Si sublayer) into a β-tridymite bulk layer with two Si sublayers.

The origin of the silicate adlayer reconstruction found after hydrogen etching and introduction into the UHV chamber remains unresolved from our study. We can only speculate that by the hydrogen

treatment a $(\sqrt{3}\times\sqrt{3})R30°$ periodicity is somehow impressed on the surface which then serves as an ordered seed for the rapid oxidation resulting in the silicate type structure. Oxidation may either take place during sample transfer or even during the H_2 treatment by unavoidable oxygen impurities in the process gas. The ordered seed structure obviously is necessary for the reconstruction to develop, otherwise it should have been also observed in earlier investigations of *ex situ* prepared surfaces. With the initial order absent oxygen adsorption and reaction proceeds statistically on all available sites, i.e., in a (1×1) lattice gas disorder. The lack of such an ordered seed may even be one of the reasons for the high interface state density in thermally oxidized layers on SiC which has been attributed to disordered species [17]. However, the structure of the ordered adlayer being remarkably similar to that of bulk SiO_2 (silicate) certainly is intuitive leading to the speculation that it might serve as seed to deposit thicker oxide films. Indeed, the lateral unit vector of the $(\sqrt{3}\times\sqrt{3})R30°$ periodic lattice matches that of bulk SiO_2 within 95%. The only difference between our silicate monolayer and the bulk structure of a high temperature SiO_2 phase known as β-tridymite is the position of the Si atoms. In the bulk structure a silicate layer consists of three sublayers with the Si atoms alternatingly positioned below and above the oxygen atoms. Hypothetically, the silicate adlayer found on SiC can be transformed to this structure simply by shifting one of the two Si atoms in the unit cell upwards in this upper Si sublayer position. This situation is schematically drawn in Fig. 2 with the arrow depicting the displacement from the monolayer silicate position (full circle) to the bulk silicate position (open circle).

Stable phases prepared by Si deposition and annealing

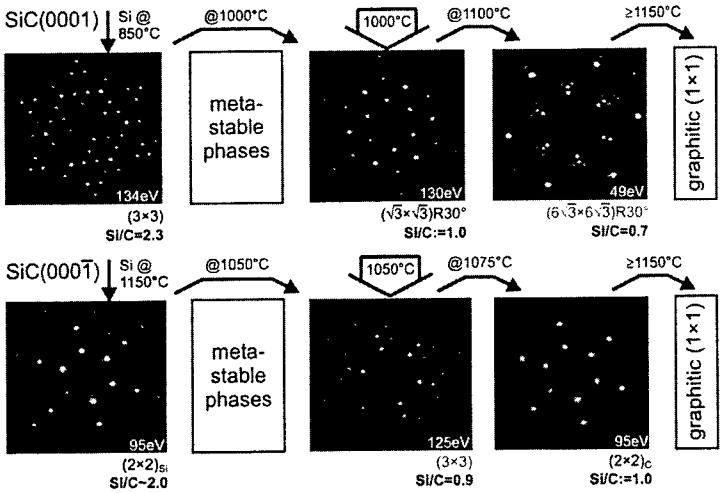


Figure 3: Diagram of stable phases developing on SiC(0001) and SiC(000$\bar{1}$). See text for details.

Annealing of the *ex situ* prepared samples in UHV is used to generate different surface reconstruction phases. Fig. 3 shows a diagram of LEED patterns of stable structures and areas of metastable phases and graphitisation for both SiC(0001) and SiC(000$\bar{1}$). Just annealing of the silicate phase leads to the $(\sqrt{3}\times\sqrt{3})R30°$ phase on SiC(0001) and to the (3×3) phase on SiC(000$\bar{1}$), respectively as indicated by the open arrows. Other Si enriched and depleted phases can be obtained by varying the temperature and simultaneously depositing Si from an electron beam heated evaporator [3, 4]. The surface composition varies from silicon rich for phases shown on the left to carbon rich for those shown on the right side. The Si/C ratio of the AES peak-to-peak intensities are given for each phase normalized with respect to the simple adatom structure independently for each surface orientation (indicated by Si/C := 1). Also indicated in the figure are the annealing temperatures required for each transformation towards a more carbon rich phase. Backward transformations can be carried out by additional deposition of Si. It should be noted that in the region of metastability a variety of structures with different periodicities can exist simultaneously on the surface which in addition assumes a relatively rough morphology [7].

The (3×3) phase on SiC(0001)

Due to its preparation by annealing under simultaneous deposition of Si the (3×3) phase on SiC(0001) is strongly enriched in Si. The original assumption of a (3×3) derivative of the dimer-adatom stacking fault model (DAS) [18] which is well known from the (7×7)-Si(111) was not in line with STM images finding only one prominent (adatom like) structure visible per unit cell [3, 19]. However, this situation allows a holographic interpretation of LEED data [13] which reveals the surrounding geometry of the adatom visible in STM as a T4-type site, i.e. 3 Si atoms forming a hollow and one additional Si atom underneath [20, 21]. Both quantitative LEED [5, 22] and density functional theory (DFT) [5, 23] determined the adatom and the atoms of its hollow site to form an adcluster which sits on top of a planar Si adlayer as displayed in Fig. 4. The adlayer covers the complete surface without cornerholes as in the (7×7)-Si(111). See ref. [22] for details of the LEED structure analysis and the complete geometry.

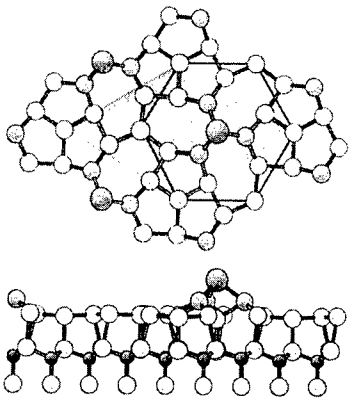


Figure 4: Top and side view of the (3×3)-SiC(0001) phase.

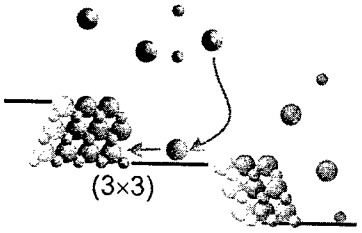


Figure 5: Step flow growth reproducing the polytype stacking.

Due to a rotational displacement within the adlayer (cf. Fig. 4, top view) the interatomic distances can assume values close to the ideal Si-Si bond length. As also visible in Fig. 4 these atoms are situated in a single layer being three-fold coordinated to their Si neighbors with 120° bond angles and one-fold coordinated to the Si atoms of the substrate bilayer. Thus, these Si atoms are effectively sp^2 hybridized and their four bonds fully saturated. The only remaining dangling bond in the unit cell is located at the Si adatom. This provides a very effective passivation of the surface which on the one hand explains the stability of the (3×3) superstructure. On the other hand it can also explain the good homoepitaxial growth possible under Si rich growth conditions. The surface passivation leads to a high mobility of incoming particles such that - on *off-axis* substrates as used in growth experiments - they can diffuse along the terraces until they reach a step. As sketched in Fig. 5 the new material continues the periodic structure of the bilayer at the step and thus reproduces the stacking sequence of the substrate.

The ($\sqrt{3}\times\sqrt{3}$)R30°–SiC(0001): Si adatoms and bilayer reorientation

The next stable structure on SiC(0001) is the ($\sqrt{3}\times\sqrt{3}$)R30° phase. It can be prepared either by annealing the (3×3) or the silicate structure or, starting from any surface phase by annealing at 1000-1100°C under simultaneous Si deposition. LEED structure analyses carried out for all three preparation methods on a 4H-SiC(0001) sample found that the surface is characterized by a single Si adatom in T_4 position on top of a SiC substrate bilayer [7] (see Fig. 6a) in agreement with earlier DFT calculations [24–26] and very recent work using X-ray diffraction (XRD) [27]. This agreement, in fact, can be viewed as confirmation of the theoretical assumption of large electronic correlation effects of the Mott-Hubbard type [28].

However, while in neither DFT nor XRD investigations the surface terminating stacking sequence was considered as a variable parameter the LEED analysis finds significant differences in this respect for the three preparation methods. In fact, for the preparation method of annealing a (3×3) phase the structure cannot be fitted using the two bilayer stacking sequences according to a 4H polytype truncation. (Those are indicated S1 and S2 in Fig. 6b.) A successful analysis requires consideration

of domains with S3 stacking which should not be expected on the 4H-SiC sample (cf. Fig. 6b). In the optimized structure a fraction of 65% of the surface consists of domains with this unusual stacking sequence, i.e. three identically oriented bilayers at the topmost surface which is incompatible with the 4H bulk stacking but is the basic element of 3C- and 6H-SiC polytypes. In contrast, a sample prepared directly by heating in a smaller Si flux contains 35% of the surface covered by S3 terminated areas; when prepared from a silicate phase by heating alone S3 stacking is practically not present. Obviously the stacking sequence depends on the amount of Si present during preparation. (see ref. [7] for details.)

It is important to note that the mechanism of the stacking rearrangement does not preceed via a rotation of a bilayer already present. This would require a large amount of S1 type domains to be present in the initial surface which is not the case. It is rather that an additional bilayer is attached to S2 type domains as a result of a severe roughening of the surface during the (3×3) to $(\sqrt{3}\times\sqrt{3})$R30° transformation. In this transformation stage the sample contains large mesa type structures with different local periodicities on top [7]. In both the initial (3×3) and the final $(\sqrt{3}\times\sqrt{3})$R30° situation the surface shows large flat terraces indicating the rough surface being characteristic for the phase transformation. It should be noted that on 6H-SiC a forth bilayer in "linear" stacking could not be attached (S4 termination). So it is not just cubic growth that is observed. Even more, by adsorption and desorption of oxygen the effect can be reversed and S2 stacking be enhanced on both 4H and 6H samples [29]. So, it appears that it is not primarily the reconstruction geometry that causes the stacking rearrangement. Rather the Si rich conditions present initially when annealing the (3×3) phase or the oxygen provided seem to be the key ingredient. The new stacking structure develops when the surface flattens after the transition. The effects observed may be a key issue for the growth of polytype heterostructures as they demonstrate that one can modify the stacking of newly attached SiC bilayers by variing the growth ambient and generate a polytype heterojunction.

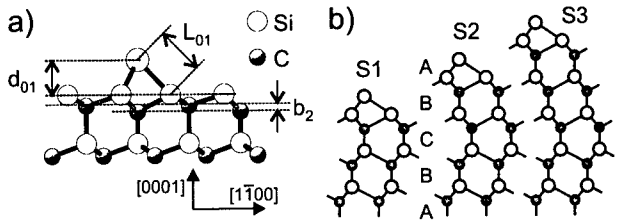


Figure 6: T_4 model for the $(\sqrt{3}\times\sqrt{3})$R30° phase on SiC(0001) displayed in a side view projection along the [11$\bar{2}$0] direction. a) Si adatom fourfold coordinated to three Si and one C atom of the topmost substrate bilayer. See ref. [7] for geometry parameters. b) Different stacking terminations denoted S1, S2 or S3 according to the number of identically oriented bilayers at the surface. Note, that the S3 termination is breaking the 4H bulk stacking sequence.

Hexagonal stacking termination in the $(2\times2)_C$ on SiC(000$\bar{1}$)

On SiC(000$\bar{1}$) also a simple adatom structure exists, namely the $(2\times2)_C$ phase - indicated C for distinction from the more Si rich $(2\times2)_{Si}$ phase (see Fig. 3). By STM, LEED holography and LEED analysis the Si adatom was found in a true threefold hollow, the so-called H3 site [8, 30] - in contrast to the above $(\sqrt{3}\times\sqrt{3})$R30° on SiC(0001). Furthermore the stacking sequence of the topmost surface slab is predominantly S1 which might be interpreted as a preference for hexagonal stacking in this reconstruction or this surface orientation. As in the case of the $(\sqrt{3}\times\sqrt{3})$R30° phase the layer stacking is changed with respect to the original silicate phase. To speculate far one might even think of a seed for a potential 2H film.

Conclusions

The reconstruction geometry of several ordered surface phases on SiC(0001) and SiC(000$\bar{1}$) have been analysed and found to be potentially interesting for a direct impact on different problems of the

SiC device technology. Epitaxial silicate monolayers could serve as seed for a thick oxide layer deposition. The effective surface passivation in the (3×3)-SiC(0001) reconstruction facilitates step flow growth for high quality SiC films. One might speculate that the stacking rearrangement induced during the preparation of the $(\sqrt{3}\times\sqrt{3})R30°$ phase on SiC(0001) can be used as seed for the formation of polytype heterojunction between 4H- and 6H-SiC, a perspective for new types of SiC devices based on polytype heterostructures. The analyses of the simple adatom structures SiC(0001) and SiC(000$\bar{1}$) reveal contrasting adatom sites and different bilayer stacking sequences thus demostrating a strong difference between surfaces of the two polarities.

This work was supported by Deutsche Forschungsgemeinschaft (DFG) through SFB 292.

References

[1] G. L. Harris (ed.), Properties of Silicon Carbide, in: EMIS Datareviews Series, No. 13 (Inspec, London, 1995).
[2] U. Starke, phys. stat. sol. (b) **202** (1997), p. 475.
[3] U. Starke, J. Schardt and M. Franke, Appl. Phys. A **65** (1997), p. 578.
[4] J. Bernhardt, M. Nerding, U. Starke and K. Heinz, Mat. Sci. Eng. B **61-62** (1999), p. 206.
[5] U. Starke, J. Schardt, J. Bernhardt, M. Franke, K. Reuter, H. Wedler, K. Heinz, J. Furthmüller, P. Käckell and F. Bechstedt, Phys. Rev. Lett. **80** (1998), p. 758.
[6] J. Bernhardt, J. Schardt, U. Starke and K. Heinz, Appl. Phys. Lett. **74** (1999), p. 1084.
[7] U. Starke, J. Schardt, J. Bernhardt, M. Franke and K. Heinz, Phys. Rev. Lett. **82** (1999), p. 2107.
[8] A. Seubert, J. Bernhardt, M. Nerding, U. Starke and K. Heinz, Surf. Sci. **454-456** (2000), p. 45.
[9] C. J. Chen, *Scanning Tunneling Microscopy*, Oxford University Press, New York (1993).
[10] H. Ibach (ed.), *Electron Spectroscopy for Surface Analysis*, Topics in Current Physics, Vol. 4, Springer, Berlin (1977).
[11] J. B. Pendry, *Low Energy Electron Diffraction*, Academic Press, London (1974).
[12] K. Heinz, Rep. Prog. Phys. **58** (1995), p. 637.
[13] K. Heinz, U. Starke and J. Bernhardt, Prof. Surf. Sci. *64* (2000), p. 163.
[14] J. Schardt, J. Bernhardt, M. Franke, U. Starke and K. Heinz, Mat. Sci. Forum **264** (1998), p. 343.
[15] U. Starke, J. Schardt, J. Bernhardt and K. Heinz, J. Vac. Sci. Technol. A **17** (1999), p. 1688.
[16] J. Bernhardt, J. Schardt, U. Starke and K. Heinz, Mat. Sci. Forum **338-342** (2000), p. 383.
[17] V. V. Afanasev, M. Bassler, G. Pensl, M. J. Schulz, phys. stat. sol. (a) **162** (1997), p. 321.
[18] R. Kaplan, Surf. Sci. **215** (1989), p. 111.
[19] M.A. Kulakov, G. Henn and B. Bullemer, Surf. Sci. **346** (1996), p. 49.
[20] K. Reuter, J. Bernhardt, H. Wedler, J. Schardt, U. Starke and K. Heinz, Phys. Rev. Lett. **79** (1997), p. 4818.
[21] K. Reuter, J. Schardt, J. Bernhardt, H. Wedler, U. Starke and K. Heinz, Phys. Rev. B **58** (1998), p. 10806.
[22] J. Schardt, J. Bernhardt, U. Starke and K. Heinz, Phys. Rev. B, *accepted.*
[23] J. Furthmüller, P. Käckell, F. Bechstedt, A. Fissel, K. Pfenninghaus, B. Schröter and W. Richter, J. Elec. Mat. **27** (1998), p. 848.
[24] F. Bechstedt, P. Käckell, A. Zywietz, K. Karch, B. Adolph, D. Tenelsen and J. Furthmüller, Phys. stat. sol. (b) **202** (1997), p. 35.
[25] J.E. Northrup and J. Neugebauer, Phys. Rev. B **52** (1995) R17001.
[26] J. Pollmann, P. Krüger and M. Sabisch, Phys. stat. sol. (b) **202** (1997), p. 421.
[27] A. Coati, M. Sauvage-Simkin, Y. Garreau, R. Pinchaux, T. Argunova and K. Aïd, Phys. Rev. B **59** (1999), p. 12224.
[28] J.E. Northrup and J. Neugebauer, Phys. Rev. B **57** (1998) R4230.
[29] J. Bernhardt, A. Seubert, U. Starke and K. Heinz, *to be published.*
[30] J. Bernhardt, A. Seubert, M. Nerding, U. Starke and K. Heinz, Mat. Sci. Forum, **338-342** (2000), p. 345.

Materials Science Forum Vols. 353-356 (2001) pp. 211-214
© 2001 Trans Tech Publications, Switzerland

Interplay of Surface Structure, Bond Stacking and Heteropolytypic Growth of SiC

U. Grossner, A. Fissel, J. Furthmüller, W. Richter and F. Bechstedt

Friedrich-Schiller-Universität Jena, Max-Wien-Platz 1, DE-07743 Jena, Germany

Keywords: Bond Stacking, Heteropolytypic Structure, Homoepitaxial Growth, Polytypism, Surface influence

Abstract A combination of total-energy studies of SiC surface structures with MBE growth experiments monitored by RHEED is used to contribute to an understanding of the interplay of surface geometry and stoichiometry and the resulting bond stacking, i.e. the local SiC polytype. Such an understanding may help to prepare heteropolytypic structures. In particular, the interplay of surface reconstruction, substrate polytype and bond stacking resulting in the subsurface region is studied.

Introduction The growth of heteropolytypic structures makes it possible to build devices from heterostructures consisting of a specific semiconducting material but occurring in different crystal structures [1, 2]. From this point of view SiC is a promising material. More than 200 polytypes with different stackings of the atomic Si-C bilayers in [0001] direction exist. The fundamental energy gap varies by about 1 eV between the cubic zinc-blende (3C) polytype and hexagonal (*n*H) polytypes with a number of *n* Si-C bilayers in a unit cell. The homoepitaxial growth of such heteropolytypic structures is, however, a big challenge. For the polytypes of main interest, 3C, 4H, and 6H, definite nucleation conditions are required. Despite the fact that several effects are discussed regarding their influence on the polytype formation and stabilization, a conclusive theory is still lacking. This holds, in particular, for the identification of special growth conditions under which only one certain polytype occurs.
The solid-source molecular beam epitaxy (MBE) is a suitable method to prepare heteropolytypic structures because the deposition conditions are controlled on an atomic scale and the growth occurs under clean conditions in the ultra high vacuum (UHV). Moreover, the growth process can be monitored *in situ* by reflection high energy electron diffraction (RHEED). Due to the occurrence of surface reconstructions the Si-C ratio may be controlled, and, hence, also the surface conditions [3, 4]. The specific influence of surface reconstructions on the surface energy, the occurrence of a selfsurfactant process and the consequences for polytype growth in the low-temperature epitaxy process ($T < 1300$ K) are suggested [4–7]. There are experimental and theoretical indications that a certain reconstructed free surface supports a transformation between hexagonal and cubic stacking [8, 9]. Heine et al. [10, 11] even predict that a new Si-C bilayer is attached in cubic stacking on a surface during epitaxial growth.

Methods The total-energy (TE) and electronic-structure calculations are based on the *ab initio* pseudopotential-plane-wave code VASP [12]. A supersoftening of the non-normconserving pseudopotentials [13] allows the accurate treatment of slabs with up to 12 Si-C bilayers and about 10 layers of vacuum. The bottom layer is saturated by hydrogen. $\sqrt{3}\times\sqrt{3}$ and 3×3 reconstructions [6, 7, 9] are considered to model different stoichiometries of the Si-terminated surfaces.
The SiC films of different polytypes are grown between 900° and 1350°C in a RIBER-EVA 32 MBE system. The source materials of high-purity Si and C are evaporated separately by means of electron beam guns and controlled by mass-spectrometer based flux meter [3, 4]. High-quality

nominal on-axis 4H- or 6H-SiC(0001) wafers from CREE Inc. are used. The surfaces are prepared by *in situ* sublimation etching in a Si flux to remove surface imperfections [14].

Results In the solid-source MBE growth process at higher temperatures, the graphitization is a serious problem which can only be prevented if a certain excess of Si above the SiC surface is present in the gas phase. In our growth studies the SiC surface exhibits a phase transition from the 1×1 surface superstructure to a ($\sqrt{3}\times\sqrt{3}$)R30°-structure [6] by decreasing the Si flux before the formation of graphite. This indicates a transition from more Si-rich growth conditions to more Si-less ones and can be used to control the growth process. Considering the sticking behaviour of Si atoms, the occurrence of the ($\sqrt{3}\times\sqrt{3}$)R30°-structures is, therefore, a function of temperature as shown in Fig. 1. The corresponding vapor pressures of Si are calculated by the Hertz-Knudsen

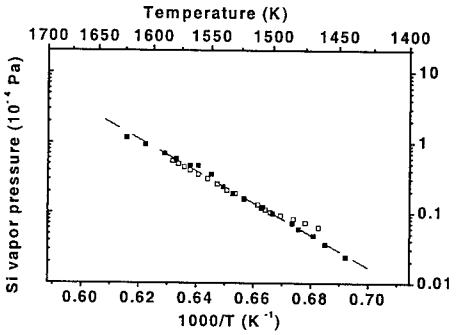


Fig. 1: Arrhenius plot of equilibrium Si vapor pressure to stabilize the $\sqrt{3}\times\sqrt{3}$ surface superstructure. The squares indicate the appearance of the superstructure.

relationship. Recently it has already been demonstrated, that the growth of SiC heterostructures can only be achieved close to equilibrium conditions. These conditions mean that the time for reordering of adatoms or near surface atoms to find the equilibrium positions is shorter than the time to deposit a monolayer. It has been found, that the cubic polytype occurs preferentially under more Si-rich conditions: at lower temperatures (T<1300 K) a Si-rich (3×3)-superstructure occurs [6,15]. The hexagonal polytypes, however, were grown under less Si-rich conditions corresponding to the occurrence of a ($\sqrt{3}\times\sqrt{3}$)R30°-surface superstructure. As an example a resulting heteropolytypic structure is shown in Fig. 2.

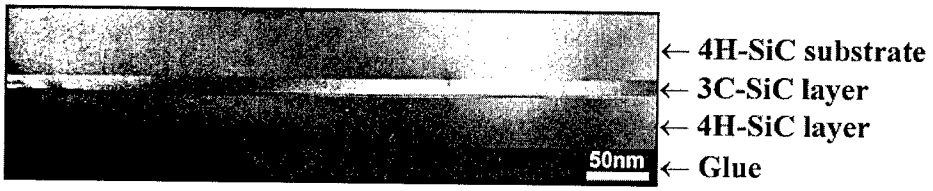


Fig. 2: TEM micrograph of a 4H/3C/4H-SiC(0001) double-heteropolytypic structure. The growth temperatures are 1550 K (3C) and 1600 K (4H). The micrograph was taken by U. Kaiser.

In order to understand the experimental findings we study in Fig. 3 the formation of an intrinsic (extrinsic, triple) stacking fault ISF (ESF, TSF) in a cubic SiC crystal in dependence on its position below the 3×3 or $\sqrt{3}\times\sqrt{3}$ surface. Below the third Si-C bilayer the formation energies are negative in agreement with the fact that in the bulk limit the 4H or 6H polytype is energetically more favorable than the 3C one. The creation of the stacking faults directly underneath the surface is always unfavorable indicating in general a stabilization of the cubic stacking in the uppermost surface layers. Consequently, the results of previous model studies [10, 11] are confirmed by *first-principles* calculations. The absolute values of the negative formation energies are bigger for the

$\sqrt{3}\times\sqrt{3}$ reconstruction. This is in agreement with the observation that the less Si-rich $\sqrt{3}\times\sqrt{3}$ surface stabilizes the growth of the hexagonal polytype. On a first view, the formation energies for the stacking fault generation in the uppermost two Si-C bilayers in Fig. 3 seems to indicate the opposite trend. However, one has to take into consideration that for the 3×3 reconstruction a nominal Si-C bilayer is deeper under the surface as in the $\sqrt{3}\times\sqrt{3}$ case. The 3×3 reconstruction is formed by a Si tetramer on a twisted Si adlayer with clover-like rings [6, 7]. In the $\sqrt{3}\times\sqrt{3}$ case only one adatom

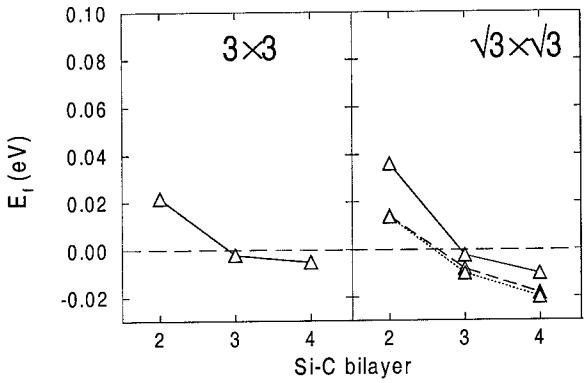


Fig. 3: Formation energy per (1×1) surface unit cell of a stacking fault in a surface region of pure cubic stacking versus location of the Si-C bilayer of creation. ISF: solid line, ESF: dashed line, TSF: dotted line.

occupies the last complete Si-C bilayer [6]. The corresponding difference in the silicon coverage of Θ_{Si} = 13/9 (3×3) and 1/3 ($\sqrt{3}\times\sqrt{3}$) illustrates the influence of surface and subsurface strains on the polytype formation. The silicon adsorbates on top of the SiC substrate tend to increase the bond lengths in the surface region. This gives rise to a tensile strain. The cubic polytype with its larger in-plane lattice constant *a* is therefore more presumable than the hexagonal ones [16]. However, only the larger amount of Si atoms on top of the 3×3 surface gives a net effect with indeed the tendency to stabilize the cubic polytype. In the $\sqrt{3}\times\sqrt{3}$ case the tensile strain virtually vanishes resulting in a tendency for growth of a hexagonal polytype.

In order to give a direct proof of the results concerning the stabilization of cubic stacking at the surface and to discuss the consequences for the growing polytype, we investigate the formation of Si-C bilayers with cubic stacking on top of a 4H-SiC(0001) substrate. As an example the $\sqrt{3}\times\sqrt{3}$ reconstruction is considered within a slab of 12 Si-C bilayers and the respective amount of vacuum layers. The results of the corresponding TE calculations are plotted in Fig. 4. The TE exhibits two pronounced minima. A local minimum appears on the Born-Oppenheimer TE surface after completion of a bulk 4H unit cell in [0001] direction. The global minimum occurs after deposition of two additional, equally (i.e. cubically) stacked bilayers. Experimentally the tendency for completion of unit cells has been found during growth using the step bunching mechanism [17]. Moreover, for ($\sqrt{3}\times\sqrt{3}$)-reconstructed 4H surfaces the coexistence of at least three different surface-stacking terminations has been observed by means of dynamical LEED [9].

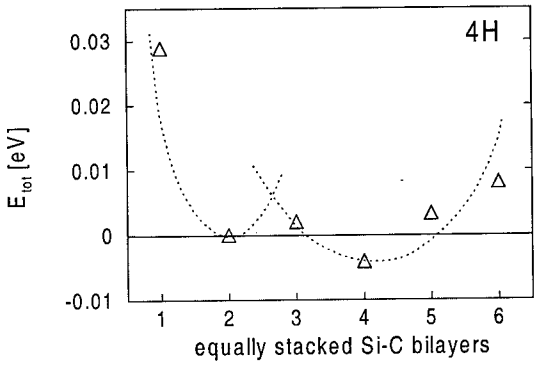


Fig. 4: TE per (1×1) surface unit cell versus number of equally stacked bilayers on 4H-SiC(0001)$\sqrt{3}\times\sqrt{3}$ with a half-bulk-unit-cell termination. The dotted lines indicate the local minima.

Our findings suggest a model for MBE growth of a hexagonal (4H) polytype under more C-rich and surface-stabilized ($\sqrt{3}\times\sqrt{3}$) conditions [5, 6]. After carbonization of a deposited Si layer, a Si-C bilayer with the same stacking direction as the one underneath appears, leading to an overall cubic stacking. This bilayer is slightly strained due to the underlying hexagonal substrate. Consequently, after deposition of a sufficient number of equally stacked (i.e. cubic) bilayers the subsurface system becomes unstable. A solid-phase transition between 3C and 4H [8] occurs in the uppermost two bilayers resulting in a completed layer of hexagonal unit cells. The transformation of the bilayer stacking via a tetrahedron flipping process [18] should be a consequence of a shear stress resulting from the compressive strain due to the substrate and the strain due to the Si adsorbate. Hence, the driving force of the transformation is the strain reduction.

Summary We have performed *first-principles* total-energy calculations for various bilayer stackings and growth experiments under surface-stabilized conditions using solid-source MBE. We show that a surface tends to stabilize a cubic stacking. The strength of this tendency depends on the Si coverage. The near-surface cubic stacking has consequences for a layer-by-layer growth of a hexagonal polytype. We suggest that a solid-phase transition in the uppermost Si-C bilayers is involved in the growth process.

Acknowledgements The authors would like to thank U. Kaiser for the TEM micrograph. This work was supported by the Deutsche Forschungsgemeinschaft (Sonderforschungsbereich 196).

References

[1] M. Ruff, H. Hitlehner and R. Helbig, IEEE Electronic Devices 41 (1994), p. 1040.
[2] F. Bechstedt and P. Käckell, Phys. Rev. Lett. 75 (1995), p. 264,
[3] A. Fissel, B. Schröter and W. Richter, Adv. Sol. State Phys. 38 (1999), p. 87.
[4] A. Fissel, U. Kaiser, E. Ducke, B. Schröter and W. Richter, J. Cryst. Growth 154 (1995), p. 77.
[5] A. Fissel, U. Kaiser, K. Pfennighaus, B. Schröter and W. Richter, Appl. Phys. Lett. 68 (1996), p. 1204.
[6] J. Furthmüller, P. Käckell, F. Bechstedt, A. Fissel, K. Pfennighaus, B. Schröter and W. Richter, J. Electron. Mater. 27 (1998), p. 848.
[7] U. Starke, J. Schadt, J. Bernhardt, M. Franke, K. Reuter, H. Wendler, K. Heinz, J. Furthmüller, P. Käckell and F. Bechstedt, Phys. Rev. Lett. 80 (1998), p. 758.
[8] P. Käckell, J. Furthmüller and F. Bechstedt, Phys. Rev. B60 (1999), p. 13261.
[9] U. Starke, J. Schardt, J. Bernhardt, M. Franke and K. Heinz, Phys. Rev. Lett. 82 (1999), p. 2107.
[10] V. Heine, C. Cheng and R. Needs, J. Am. Soc. Ceram. 74 (1991), p. 2630.
[11] M.J. Rutter and V. Heine, J. Phys.: Condens. Matter 9 (1997), p. 8213.
[12] G. Kresse and J. Furthmüller, Comput. Mater. Sci. 6 (1996), p. 15; Phys. Rev. B54 (1996), p. 11169.
[13] J. Furthmüller, P. Käckell, F. Bechstedt and G. Kresse, Phys. Rev. B61 (2000), p. 4576.
[14] E. Ducke, R. Kriegel, A. Fissel, U. Kaiser, B. Schröter and W. Richter, Inst. Phys. Conf. Ser. 142 (1996), p. 609.
[15] A. Fissel, B. Schröter and W. Richter, Appl. Phys. Lett. 66 (1995), p. 3182.
[16] P. Käckell, B. Wenzien and F. Bechstedt, Phys. Rev. B50 (1994), p. 17280.
[17] T. Kimoto, A. Itoh, H. Matsunami and T. Okano, J. Appl. Phys. 81 (1997), p. 3494.
[18] M.H. Hong, A.V. Samant and P. Pirouz, Phil. Mag. A80 (2000), p. 919.

Materials Science Forum Vols. 353-356 (2001) pp. 215-218
© 2001 Trans Tech Publications, Switzerland

Room Temperature Initial Oxidation of 6H- and 4H-SiC(0001) 3x3

F. Amy[1,2], Y. Hwu[3], C. Brylinski[4] and P. Soukiassian[1,2]

[1] Commissariat à l'Energie Atomique, DSM - DRECAM - SPCSI, Centre d'Etudes de Saclay, Bâtiment 462, FR-91191 Gif-sur-Yvette Cedex, France

[2] Département de Physique, Université de Paris-Sud, FR-91405 Orsay Cedex, France

[3] Institute of Physics, Academia Sinica, Nankang, Taipei 115, Taiwan ROC

[4] Laboratoire Central de Recherches, Thomson-CSF, Domaine de Corbeville, B.P. 10, FR-91401 Orsay Cedex, France

Keywords: 4H-SiC(0001), 6H-SiC(0001), Core Level Photoemission, Interface, Oxidation, SiC Surfaces

Abstract. We investigate the room temperature oxidation of Si-terminated 6H- and 4H -SiC(0001) 3x3 reconstructed surfaces by core level photoemission spectroscopy using synchrotron radiation. On both surfaces, SiO_2 formation for low oxygen exposures suggests very reactive surfaces even at room temperature. Oxygen atoms seem to react below the surface, involving carbon atoms, leading to non abrupt SiO_2/SiC interface formation. The 4H-SiC(0001) 3x3 surface is less reactive to oxygen exposures than the 6H-SiC(0001) 3x3 one with smaller amount of SiO_2 and a less abrupt SiO_2/SiC interface formation.

Introduction

Due to the recent availability of large enough wafers, 6H and 4H hexagonal SiC polytypes are presently the most commonly used in SiC device applications [1,2]. However, silicon carbide surface passivation remains one of the key issues in successful SiC device technology [1-4]. The excellent properties of SiO_2 for insulating gates and the low density of defects of the SiO_2/Si interface are one of the reasons of the success of silicon in microelectronics. In this view, SiC appears to be very promising since its native oxide is also SiO_2. Nevertheless, conventional oxidation process results in formation of a SiO_2/SiC interface with poor electrical properties due to mixed oxide products including carbon, and rough interfaces with a high density of interface states [5-7]. Moreover, recent theoretical calculations suggest that a nonstoichiometric interlayer is required to bond SiC to SiO_2 [8]. The SiO_2/SiC interface states density has been shown to be higher on 4H-SiC as compared to 6H-SiC [9]. However, most of the studies of hexagonal SiC surface oxidation have been performed on non-reconstruction specific surfaces. Interestingly, surface reconstruction and composition have been shown to play a crucial role in SiC initial surface oxidation [3,10-12].

In this work, we perform core level photoemission spectroscopy (CLPS) using synchrotron radiation to study the room temperature initial oxidation of the 4H and 6H-SiC(0001) surfaces. We focus on the 6H- and 4H-SiC(0001) 3x3 reconstructed surfaces which consist of a twisted Si adlayer above the Si-terminated substrate, with Si tetramers on top [13]. The investigation is performed for the initial SiO_2/6H- and 4H-SiC(0001) 3x3 interface formation by direct surface oxidation at 25°C with molecular oxygen exposure ranging from 1 to 1000 L. Our results show that, unlike silicon surfaces, oxidation is already taking place at very low oxygen exposures with SiO_2 formation at room temperature. But, the 4H-SiC(0001) 3x3 surface is less reactive to oxygen exposures than the 6H-SiC(0001) 3x3 surface with less amount of SiO_2. In addition, oxygen goes deep under the surface and reacts with carbon atoms suggesting a non abrupt SiO_2/SiC interface.

Experimental Details

The photoemission experiments were performed at the Synchrotron Radiation Research Center (Hsinchu, Taiwan) using the 6m-HSGM monochromator beamline. The overall (monochromator + analyzer) energy resolution was 180 meV at Si 2p and 360 meV at C 1s. The pressure in the vacuum chamber was in the 10^{-11} Torr range. We used n-doped (nitrogen) 6H- and 4H-SiC(0001) commercial samples from Epitronics. Clean 6H- and 4H-SiC(0001) 3x3 surfaces reconstructions were prepared by a 650°C annealing of the samples under Si flux followed by short annealing at 750°C resulting in sharp low energy electron diffraction (LEED) 3x3 patterns. We have performed O_2 exposures with research grade oxygen at pressure always below 10^{-6} Torr. All other details about the experimental system and high quality 4H- or 6H-SiC(0001) 3x3 surface preparation can be found elsewhere [12,14].

Results and Discussion

We first look at the 25°C oxidation process on both 4H and 6H-SiC(0001) 3x3 surfaces following the evolution of the Si 2p core level for molecular oxygen exposures ranging from 1L to 1000L (1 Langmuir = 1 L = 10^{-6} Torr.sec). Figure 1a (1b) displays 6H-SiC (4H-SiC) corresponding Si 2p spectra recorded at grazing photoelectron emission (θ_e=30° from surface) and using a 150 eV photon energy to maximize surface sensitivity. Under oxygen exposure, Si 2p core levels exhibit core level chemical shifted components on the higher binding energy side that are related to different oxidation states. The relative intensity of these chemical shifted components increases with oxygen exposures. On the 6H-SiC(0001) 3x3 surface (Fig. 1a) a reactive component is clearly observed for an O_2 exposure as low as 1 L. This indicates that the 6H-SiC(0001) 3x3 surface is very reactive upon oxygen exposure when compared to the silicon rich 3C-SiC(100) 3x2 surface [11] or

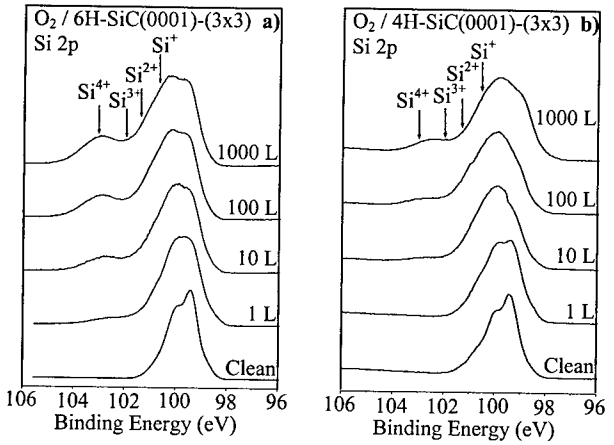


Fig. 1 : Evolution of Si 2p core level spectra recorded in surface sensitive mode (hν = 150 eV and θ_e = 30° from surface) for 1 to 1000 L O_2 exposures.
a) on the 6H-SiC(0001) 3x3 surface.
b) on the 4H-SiC(0001) 3x3 surface.

Si surfaces [15,16] where significantly higher oxygen exposures are necessary to get such a Si 2p reactive component. Oxidation of the 6H-SiC(0001) 3x3 surface generally results into Si^{+}, Si^{2+}, Si^{3+}, Si^{4+} oxidation states with associated core level chemical shifted components located at higher binding energies when compared to silicon surfaces [12]. The presence of the four different oxidation states components is not evident from the raw spectra but their energy positions have been determined by curve fitting and are shown by arrows on Fig. 1. This strongly suggests a non abrupt SiO_2/SiC interface formation. In addition, the comparison between Figs. 1a and 1b clearly indicates that growth of SiO_2 is more efficient on the 6H-SiC(0001) 3x3 surface than on the 4H-SiC(0001) 3x3 one. Indeed, in contrast to what is observed on the 6H-SiC(0001) 3x3 surface, the

intermediate oxides are the very dominant oxidation states on the 4H-SiC(0001) 3x3 surface which clearly indicates an even less abrupt SiO_2/SiC interface with 4H-SiC than with 6H-SiC.
Further insight in the room temperature SiO_2/SiC interface formation on the 6H- and 4H-SiC(0001) 3x3 surfaces could be found by looking at the C 1s core levels. Figures 2a and 2b respectively display the C 1s core level spectra for 6H- and 4H-SiC(0001) 3x3 surfaces exposed at 25°C to 1 up to 1000 L of oxygen. These data have also been taken in a surface sensitive mode using a 330 eV photon energy and grazing emission photoelectron collection (θ_e=30° from surface). On both surfaces C 1s core level peak exhibits a rigid shift to the lower binding energy side for the lower O_2

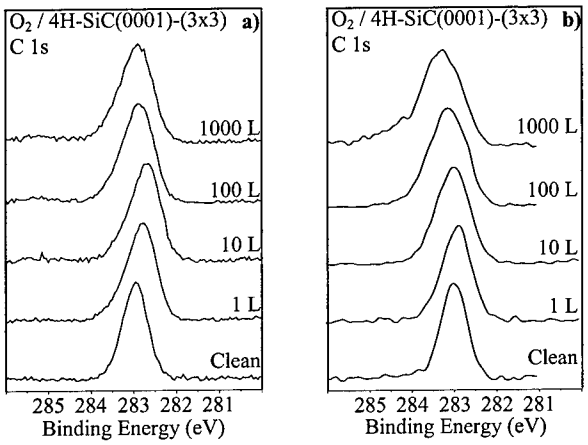


Fig. 2 : Evolution of C 1s core level spectra recorded in surface sensitive mode (hν = 330 eV and θ_e = 30° from surface) for 1 to 1000 L O_2 exposures.
a) on the 6H-SiC(0001) 3x3 surface.
b) on the 4H-SiC(0001) 3x3 surface.

exposure and a shift to the higher binding energy side above 10 L O_2 exposure. This rigid shift is not visible on the Si 2p spectra and thus can hardly be related to band bending modification. It is likely to be due to oxygen interaction with carbon atoms. One can expect that direct oxygen bonding to carbon atoms would result in a C 1s reactive component or a rigid shift to the higher binding energy side. In this view the initial shift of the C 1s core level peak to lower binding energies may be attributed to oxygen interaction with silicon atoms close to the carbon planes. However, for 100 or 1000 L O_2 exposures, the C 1s shift to higher binding energies suggests direct carbon oxygen interaction. Evidence of direct bonding of oxygen to carbon atoms can be found when looking to the C 1s core level spectra of the 4H-SiC(0001) 3x3 surface exposed to 1000 L O_2 (Fig. 2b) which exhibits a large reactive component on the higher binding energy side. For the same oxygen exposure, this reactive component does not exist on the C 1s core level spectra of the 6H-SiC(0001) 3x3 surface which only shows a 30% broadening as compared to the clean surface. These results suggest that oxygen atoms directly react with underneath silicon atoms and then, with further exposures, react with carbon atoms leading to a non abrupt SiO_2/SiC interface involving intermediate (Si^+, Si^{2+}, Si^{3+}) and mixed (Si-O-C) oxides. Additional support for oxygen deep diffusion is brought by LEED patterns that remain 3x3 even for 1000 L O_2 exposures, suggesting that the top surface is not affected. In addition, recent experiments combining CLPS and Infra Red Absorption Spectroscopy (IRAS) show converging evidence that: i) the adatoms and trimers are not affected by initial oxygen adsorption, and ii) oxygen is going well below the surface [17]. Moreover carbon-oxygen bonding related to C 1s core level chemical shifted component only observed on the 4H-SiC, further supports oxygen atoms diffusion and less abrupt SiO_2/SiC interface with 4H-SiC than with 6H-SiC. This finding is especially relevant in view of the higher interface state densities generally observed for oxide/4H-SiC(0001) interfaces [9]. Going from the top surface to the bulk, the 6H- and 4H-SiC(0001) 3x3 structures only start to differ at the third silicon bulk plane encountered, i.e. about 9.6 Å below the top surface atoms. Therefore, the different reactivity to

25°C oxygen exposures observed between 6H- and 4H-SiC(0001) 3x3 surfaces is more likely to be due to different electronic properties than to structural differences.

Conclusion

Using synchrotron radiation core level photoemission spectroscopy, we have investigated the room temperature direct SiO_2/SiC interface formation by low exposition of the 6H- and 4H-SiC(0001) 3x3 surfaces to molecular oxygen. Our results clearly indicate very reactive surfaces even at room temperature with SiO_2 formation for low oxygen exposures. The 4H-SiC(0001) 3x3 surface is less reactive to oxygen exposures than the 6H-SiC(0001) 3x3 surface with smaller amount of SiO_2 and less abrupt SiO_2/SiC interface formation. On both 4H-SiC and 6H-SiC 3x3 reconstructed surfaces, oxygen atoms react below the surface, involving somehow carbon atoms and leading to non abrupt SiO_2/SiC interface formation. These differences are relevant in the present context of better electrical properties of SiO_2/SiC interfaces with 6H polytype than with the 4H one.

This work was supported by the DGA, the Institut Français de Taipei and the National Science Council (NSC, Taipei). It is based upon research conducted at the Synchrotron Radiation Research Center (SRRC), Hsinchu, Taiwan. The authors are especially grateful to the SRRC staff for expert and outstanding assistance and to Dr. Tseng for the use of his experimental system.

References

[1] Silicon Carbide, *A Review of Fundamental Questions and Applications to Current Device Technology*, edited by W.J. Choyke, H.M. Matsunami and G. Pensl, Akademie Verlag, Berlin, Vol. **I & II** (1998); and references therein.

[2] *Silicon Carbide Electronic Devices and Materials*, Materials Research Society Bulletin, Vol. **22** March (1997).

[3] P. Soukiassian, *Fundamental Aspects of Ultrathin Dielectrics on Si-based Devices*, edited by E. Grafunkel, E. Gusev and A. Vul', NATO Science Series **3**, High Technology, Kluwer Academic Press (Dortrecht) (1998), p.257.

[4] G. Lucovsky and H. Niimi, in ref 3, p.447.

[5] V.R. Vathulya, D.N. Wang and M.H. White, Appl. Phys. Lett. **73** (1998), p.2161

[6] V.V. Afanas'ev, A. Stesmans, M. Bassler, G. Pensl, M.J. Schulz, C.I. Harris, Appl. Phys. Lett. **68** (1996), p. 2141.

[7] G.Y. Chung, C.C. Tin, J. R. Williams, K. McDonald, M. Di Ventra, L.C. Feldman, R.A. Weller, Appl. Phys. Lett. **76** (2000), p. 1713.

[8] R. Buczko, S. J. Pennycook and S. Pantalides, Phys. Rev. Lett. **84** (2000), p. 943.

[9] V.V. Afanas'ev, A. Stesmans, M. Bassler, G. Pensl, M.J. Schulz, C.I. Harris J. Appl. Phys. **85** (1999), p. 8292; V.V. Afanas'ev, A. Stesmans, M. Bassler, G. Pensl, M.J. Schulz, Appl. Phys. Lett. **76** (2000), p. 336.

[10] V.M. Bermudez, Appl. Surf. Sci. **84** (1995), p. 45.

[11] F. Semond, L. Douillard, P. Soukiassian, D. Dunham, F. Amy and S. Rivillon, Appl. Phys. Lett. **68** (1996), p. 2144.

[12] F. Amy, P. Soukiassian, Y. Hwu and C. Brylinski, Appl. Phys. Lett. **75** (1999), p. 3360.

[13] U. Starke, J. Schardt, J. Bernhardt, M. Franke, K. Reuter, H. Wedler, K. Heinz, J. Furthmüller, P. Käckell and F. Bechstedt, Phys. Rev. Lett. **80**, (1998), p. 758.

[14] F. Amy, P. Soukiassian, Y.-K. Hwu and C. Brylinski, Surf. Sci. 464 (2000) p. L691.

[15] H.W. Yeom, H. Hamamatsu, T. Ohta, R.I.G. Uhrberg, Phys. Rev. B **59**, (1999), p. R10413.

[16] M. Tabe, T.T. Chiang, I. Lindau, W. E. Spicer Phys. Rev. B **34**, (1986), p. 2706.

[17] F. Amy, H. Enriquez, P. Soukiassian, P. F. Storino, Y. J. Chabal, Y. K. Hwu, C. Brylinski, CLPS and IRAS, recent results.

Materials Science Forum Vols. 353-356 (2001) pp. 219-222
© 2001 Trans Tech Publications, Switzerland

Comparison of HF and Ozone Treated SiC Surfaces

R.P. Mikalo[1], P. Hoffmann[1], D.R. Batchelor[1], A. Lloyd-Spetz[2], I. Lundström[2] and D. Schmeißer[1]

[1] Angewandte Physik-Sensorik, BTU Cottbus, Erich-Weinert-Str. 1, DE-03046 Cottbus, Germany

[2] S-SENCE and Div. of Applied Physics, Linköping University, SE-581 83 Linköping, Sweden

Keywords: Field-Effect Transistor (FET), Gas Sensors, Non-Destructive Depth Profiling, Ozone, Schottky Diodes, Thin Oxide

Abstract

Single crystals of SiC were etched in hydrofluoric acid to remove the native oxide. Ozone exposure at room temperature is shown to give an oxide of about 0.7nm. The differences of interface and bulk oxides regarding their elemental composition and their oxidation states are reported as determined by photoelectron spectroscopy utilizing synchrotron radiation

Introduction

Catalytic metal-insulator-silicon carbide (SiC) devices are utilized as gas sensors for high temperature and corrosive environment [1]. Schottky diode devices have advantages like simple processing and simple electronic circuitry for the measurements, even though today gas sensitive SiC field effect transistor devices have been demonstrated [2]. In the processing of Schottky diodes the native oxide is etched off by hydrofluoric acid (HF) from the SiC surface before deposition of the gas sensitive catalytic gate metal. Ozone cleaning of the SiC surface was introduced as a processing step for Schottky diodes after the HF dip. This showed to give dramatic results in terms of increased long term stability and reproducibility of the gas response of the Schottky diode sensors. The effect of the ozone cleaning was investigated by spectroscopic ellipsometry [3]. Here, we use synchrotron radiation with variable photon energy to obtain information on the oxide thickness and the chemical composition of the oxide in different depth to enable a non-destructive depth profiling.

Experimental

Silicon carbide wafers were cleaned with H_2SO_4 / H_2O_2 (3:1) for 10min and then treated with HF/H_2O (1:1) for 1min to remove the native oxide. Afterwards the samples were oxidized in ozone atmosphere generated by an UV lamp for 10min. After transport to the synchrotron the samples were cleaned from adsorbed hydrocarbons by wiping in methanol and acetone several times prior to introduction into the UHV system. Then they were directly heated for approximately 10min at around 450°C. Our electron spectroscopic experiments have been performed at the undulator beamline U49/2-PGM2 at BESSY-II enabling an energy resolution of better than 200meV [4,5]. As an oxide reference we used a thermally grown silicon oxide on top of a silicon wafer with the thickness determined by ellipsometry and Rutherford back-scattering [6].

Results and Discussion

Fig.1 shows the Si2p emission of the ozone treated SiC surface and the change that occurs after flashing the sample to 1200°C. We notice that the intensity of the oxygen shifted contribution is reduced significantly. There is a shift of the Si2p emission of 0.2eV towards lower binding energies. We also include the contribution of the Si2p(3/2) after an analytical decomposition by subtracting the Si2p(1/2) contribution. The used parameters are the energy separation (0.6eV) and the relative intensities (2:1). This analysis allows a more detailed view on the shift induced by interaction with the oxygen. The energy separation of the oxidic component is 2.6eV. We notice that the shape of the

bulk Si component is rather asymmetric at its high binding energy side. The asymmetry remains after flashing the oxide off. In Fig.1 we have also studied the variations that occur by changing the incident photon energy. For the ozone treated surface we notice the rapid change in the relative intensities of the oxidic and bulk contributions, respectively. For the HF treated surface the emission of the oxidic contribution at -2eV disappears and only a broad tail remains.

In Fig.2 we have displayed the emission in the valence region for the corresponding surface treatments. The spectrum of the ozone treated surface is displayed as well as that after flashing to 1200°C. In the area around the valence band maximum (VBM) we notice a weak emission from defect states which extend up to the Fermi energy. The separation between VBM and E_F is 1.5eV and corresponds to a weak p-type doping. Three oxygen derived valence states show up with a binding energy of 7eV for the most prominent state. The O2s emission peaks at 25eV. In the spectrum of the ozone treated surface there are weak emissions which appear 5.5eV below the O2s an the O2p emissions, respectively. Flashing the sample to 1200°C reduces the oxide emission pattern and causes the valence band states of the SiC to appear with the VBM at 1.75eV. Comparing the valence band spectrum of the HF treated surface we notice that the oxide emission is very similar to that after flashing the ozone treated surface.

In Fig.3 we compare the O1s and C1s emission patterns for the HF treated sample to those of the ozone-oxidized sample after flashing to 1200°C. The O1s main emission is at 531.5eV with a pronounced shoulder at 532.8eV. Before flashing the O1s emission peaks at 532eV (not shown). The oxygen emission is strongly reduced upon flashing. It is observed because of the high surface sensitivity is hardly observable in spectra taken at higher photon energies (omitted for clarity). In the C1s photoemission signal taken at photon energies of 608eV and 1018eV we find an intense signal of the carbidic carbon at 282.4eV and a weaker signal of graphitic carbon at 284eV. For the HF treated surface the contribution of the graphitic carbon is larger.

We first will apply that the thickness of thin oxide layers can be derived from the relative oxidic and bulk Si2p intensities [7] of the Si2p emission pattern by the following description

$$\frac{I_{SiO_2}}{I_{Si}} = \frac{I_\infty}{I_0}\left[\exp\left(d/\lambda_{SiO_2}\right)-1\right] \qquad \text{(Eq.1)}$$

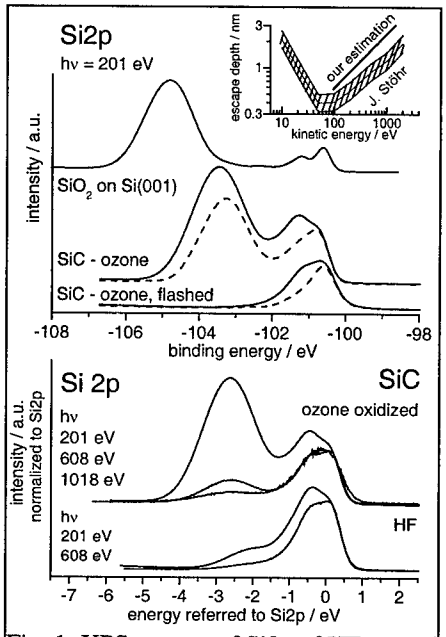


Fig. 1: XPS-spectra of Si2p of HF treated as well as of ozone treated SiC

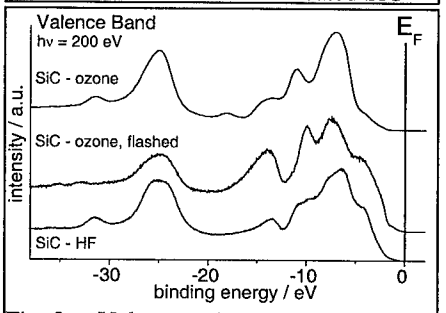


Fig. 2: Valence Band spectra of differently prepared SiC

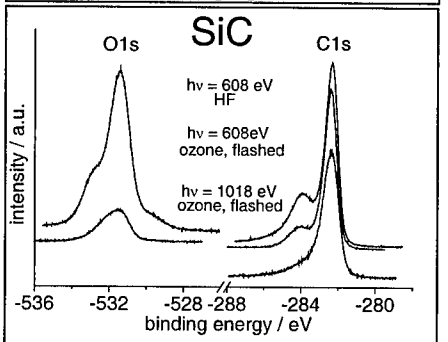


Fig. 3: XPS-spectra of O1s- and C1s-emission of differently prepared SiC

Here I_{SiO_2} is the intensity if the oxidic component of Si2p, I_{Si} is the intensity of the bulk Si2p component, d is the thickness of the oxide layer, and λ_{SiO_2} is the mean electron escape depth. The factor I_∞/I_0 takes into account, that the density of silicon atoms, the photo-ionization cross-section, and the escape depth could be different for silicon in silicon oxide and for silicon in a silicon environment. Analyzing the Si2p emission with its bulk and oxidic components only, we set that factor to unity. Then, the oxide thickness can be derived by Equation 2.

To determine the escape depth λ we used a silicon wafer with a known oxide thickness of d=6nm [6]. Applying Equation 2 we find that λ is 1.57nm and 2.28nm at kinetic energies of 507eV and 910eV, respectively. Furthermore, we applied these values to find consistent values in the photon energy range between 160eV and 800eV by using the native oxide (1.1nm) of an industrial standard wafer. The energy dependence of the as determined electron mean free path is displayed in the inset of Fig.1. Our values are in good agreement with, but slightly above the general accepted electron escape depth curve [8]. In our analysis problems arise when the contributions of the bulk and oxidic components are not well separated but overlap. In that case the analytical decomposition of the (3/2 and 1/2) spin-orbit partners might improve the analysis.

$$d = \lambda \ln\left(1 + \frac{I_{SiO_2}}{I_{Si}}\right) \qquad \text{(Eq.2)}$$

For the SiC analysis we used the spin orbit subtracted curves and integrated the photoelectron peak areas of the Si2p oxidic component up to -1eV below the bulk signal. The values of λ (0.552nm, 1.563nm, and 2.458nm) are chosen for kinetic energies of 101eV, 508ev, and 919eV, respectively. For all photon energies we derive a consistent oxide thickness of 0.65nm for the ozone oxidized SiC surface, in excellent agreement with the ellipsometric value [3]. The thickness of the HF treated surface is much lower (sub-monolayer range below 0.2nm), it is comparable to the thickness of the remaining oxide layer after flashing most of the oxide off.

The chemical shift of the Si2p emission is analysed in detail. In our experiments for the ozone treated SiC sample we find a shift of 2.75eV (Fig. 1). For thermally grown oxide layers on SiC surfaces a shift of 2.5eV is also reported [11]. For silicon surfaces initial shifts of 0.89eV, 1.8eV and 2.7eV are observed of the Si2p emission due to the presence of oxygen [7, 9, 10], which are assigned to the silicon atoms with bonds to one, two, or three oxygen atoms [12]. The behavior is similar for germanium surfaces [10] with a shift of 0.85eV per oxygen bond. For the fully oxidized SiO_2 layer the shift amounts 3.8eV [7]. In excellent agreement we find a value of 4.0eV for a 1.1nm thick SiO_2 layer on a Si(001) surface of industrial wafers. For the SiC surface the value of 2.6eV corresponds to silicon bonded to three oxygen atoms. The electron emission signal indicates that the oxide layer consists of a silicon-rich oxide with quite many defects or Si-Si bonds. This defect rich oxide is the bulk oxide and differs from that right at the surface. The latter can be studied after removing the bulk oxide layer by flashing as well as by the spectra taken at higher photon energies. The increased mean free path allows collection of emission from deeper layers. For both attempts there is evidence of an oxide with a much smaller chemical shift which causes an asymmetric line shape of the bulk Si2p line of SiC. Using the line width recently determined of H-terminated SiC surfaces [13] we can assign a shift of about 1eV for that surface oxide.

The valence band spectra (Fig.2) of the surface oxide of SiC exhibits the typical threefold emission pattern of the O2p derived states. The flashed sample maintains this threefold structure although the total oxide thickness is in the sub-monolayer range. One possible explanation is the formation of oxide clusters, which is rather unlikely. Instead, we conclude the formation of ordered Si-O bonds within that adsorbate layer. An ordered silicate adlayer was recently reported [11].

In the O1s emission signal (Fig.3, $h\nu$= 607eV and 1018eV) of ozone oxidized silicon carbide we still notice oxygen on our samples after flashing the bulk oxide off. Compared to the HF treated silicon carbide we find the main O1s signal at 531.5eV and contributions with about 1.3eV higher

binding energy as well as a shoulder on the lower binding energy side. These additional contributions can be assigned as bulk silicon oxide and as adsorbed surface oxygen, respectively. These correspond to the shifts of the Si2p signal of 2.6eV and of 1eV in Fig.1. Accordingly, there are two oxidation states as at the SiC surface the oxide is different from that in the bulk. The ozone treated samples exhibit a superposition of these different oxygen contributions, resulting in different energetic positions of the oxygen signal at 608eV and 1018eV photon energy.
The C1s emission contains a sharp signal arising from carbidic carbon at 282.4eV and a weaker signal at 284eV. The latter is due to graphitic carbon. The relative contents of both is different for the two investigated samples. While in the HF treated surface the graphitic contribution is about 1/3, the graphitic contribution is about 1/4 for the ozone treated surface. At present this differences can not be assigned to the different surface treatments as we cannot rule out that the used SiC samples do have different qualities. For the ozone treated surface the C1s emission shows only subtle changes upon removing the oxide layer. There is an increase in intensity (x1.5) which indicates that the attenuation by the oxide layer is removed. As the Si2p emission is increased also (x1.3) we can deduce that there is no change in the relative Si and C intensities upon removing the oxide layer. Our data enable us to conclude that the graphitic contribution is located at the surface. As shown in Fig.3 the C1s spectrum of the ozone sample is taken with a photon energy of 1018eV and it has a much weaker graphitic contribution. The same is valid for the HF treated sample.
In conclusion, synchrotron radiation enables the non-destructive characterization of the properties of oxide overlayers. Here we have analyzed the surfaces of an ozone treated SiC surface, which first was subjected to an HF dip. We identify graphitic carbon at the SiC surface as well as different oxidic states right at the SiC surfaces and in the bulk. The thickness of the bulk oxide is about 0.7nm and has a Si-rich composition similar to that in thermally oxidized SiC surfaces. Ozone treatment enables the formation of a dense oxide layer at room temperature to be used in sensor applications.

Acknowledgement
We gratefully acknowledge the excellent support of the BESSY staff as well as the experimental assistance of G. Beuckert. This work is partially supported by the Fonds der Deutschen Chemie and by the Swedish SSF-SiCEP program.

References:

[1] H.Svenningstorp, P.Tobias, P.Salomonsson, B.Häggendal, I.Lundström, L-G.Ekedahl, and A.Lloyd Spetz, Proc.Euros. XIV, Copenhagen, Denmark (2000); L.Unéus, P.Ljung, R.Wigren, P.Mårt-ensson, L.G.Ekedahl, I.Lundström, A.Lloyd Spetz, ISOEN´2000, Brighton, England, July 24-26, 2000, subm.
[2] S.Savage, H.Svenningstorp, L.Unéus, A.Kroutchinine, P.Tobias, L.-G.Ekedahl, I.Lundström, C.Harris, and A.Lloyd Spetz, Conf.Proc.ECSCRM2000, Kloster Banz, Germany, September 3-7, 2000, accepted.
[3] S.Zangooie, H.Arwin, I.Lundström and A.Lloyd Spetz, Proc.of ICSCRM´99, Research Triangle Park, NC, USA, October 10-15, (1999), p. 1085.
[4] D.R.Batchelor, R.Follath, D.Schmeißer, Proceedings SRI2000, Berlin, submitted.
[5] P.Hoffmann, R.P.Mikalo, D.Schmeißer, Solid-State Electronics 44 (2000), p. 837.
[6] J.von Borany, R.Grötzschel, K.H.Heinig, A.Markwitz, B.Schmidt, W.Skorupa, H.J.Thees, Solid-State Electronics 43 (1999), p. 1159.
[7] F.J.Himpsel, F.R.McFeely, A.Taleb-Ibrahimi, J.A.Yarmoff, G.Hollinger, Phys.Rev.B.38 (1988) 6084.
[8] J.Stöhr, NEXAFS Spectroscopy, Springer, 1996.
[9] P.J.Grunthaner, M.H.Hecht, F.J.Grunthaner, J.Appl.Phys. 61 (1987), p. 629.
[10] D.Schmeißer, R.D.Schnell, A.Bogen, F.J.Himpsel, D.Rieger, G.Landgren, J.F.Morar, Surface Sci. 172 (1986), p. 455.
[11] M.Hollering, N.Sieber, J.Ristein, L.Ley, J.D.Riley, R.C.G.Leckey, F.P.Leisenberger, F.P.Netzer, Mater.Sci.Forum 338-342 (2000), p. 387.
[12] G.Hollinger, F.J.Himpsel, J.Vac.Sci.Technol.A1 (1983) 640; G.Hollinger, F.J.Himpsel, Appl.Phys.Lett.44 (1984), p. 93.
[13] N.Sieber, T.Seyller, J.Ristein, L.Ley, T.Heller, D.R.Batchelor, D.Schmeißer, in preparation.

Materials Science Forum Vols. 353-356 (2001) pp. 223-226
© 2001 Trans Tech Publications, Switzerland

Preparation and Characterization of Hydrogen Terminated 6H-SiC

N. Sieber, Th. Seyller, B.F. Mantel, J. Ristein and L. Ley

Institut of Technical Physics, University of Erlangen-Nürnberg,
Erwin-Rommel-Str. 1, DE-91058 Erlangen, Germany

Keywords: Band Bending, Hydrogen Termination, Infrared Spectroscopy, Photoelectron Spectroscopy

Abstract A hydrogen termination of the (0001) and (000$\bar{1}$) 6H-SiC surfaces is achieved by a thermal treatment in ultra pure hydrogen. This results in unreconstructed and quasi-bulk terminated surfaces as demonstrated by a (1x1) LEED patterns which are stable in air. Photoelectron spectra show only bulk related Si 2p and C 1s lines and give no indication of any contamination. Using Fourier transform infrared spectroscopy (FTIR) in the attenuated total reflection (ATR) configuration Si-H stretching modes around 2130 cm^{-1} have been observed in p-polarization but not in s-polarization. This indicates that the Si-H bonds are oriented perpendicular to the surface. Electronically, hydrogenation leads to a complete passivation of the surface with no pinning of the Fermi level. After annealing at 800 °C in UHV the hydrogen completely desorbs and the surface periodicity changes from (1x1) to ($\sqrt{3}$x$\sqrt{3}$)R30°. The photoemission spectra of this ($\sqrt{3}$x$\sqrt{3}$)R30° structure are characteristic for a surface with Si adatoms in T_4 configuration which is formed via a disproportionation of SiC at the surface.

Introduction

On account of its small size and its ability to form strong covalent bonds with most elements hydrogen is perfectly suitable for terminating dangling bonds at semiconductor surfaces. It removes surface reconstructions and clears the gap from surface states. On Si (111) hydrogen terminated surfaces are readily prepared by wet-chemical treatments and the resulting unreconstructed and passivated surfaces exhibit no Fermi level pinning and the lowest surface recombination velocity ever reported for Si. [1,2] Exposure of SiC to atomic hydrogen under ultra high vacuum conditions (UHV) leads to a pronounced reduction in the oxidation rate [3] which indicates hydrogen passivation. The presence of surface Si-H and C-H vibrational modes by IR spectroscopy has been demonstrated in [4]. In this paper we present a detailed analysis of the atomic surface composition and surface geometry of hydrogen terminated 6H-SiC by means of x-ray induced photoelectron spectroscopy (XPS), low energy electron diffraction (LEED), and infrared spectroscopy.

Experiment

Hydrogenation was performed by heating the SiC samples (6H-SiC from CREE Research, p and n doped) for 20 min at 1000 °C in $1 \cdot 10^5$ Pa of ultra pure hydrogen. After the preparation the samples were transferred under UHV conditions to the analysis chamber. The chemical analysis of the surface was carried out with x-ray induced photoelectron spectroscopy using Al K_α radiation (XPS) with an energy resolution of 0.6 eV. The surface periodicity was checked with low energy electron diffraction (LEED). Since hydrogen is detectable neither by XPS nor by LEED the samples were additionally investigated with FTIR. The necessary surface sensitivity was achieved using the ATR mode with a germanium prism as multiple internal reflection element. The resolution was 0.5 cm^{-1}.

Results and Discussion

Photoemission spectra of a Si terminated surface after a wet-chemical treatment and after thermal hydrogenation are displayed in Fig. 1. The survey spectra after the wet-chemical preparation show oxygen and fluorine contamination at the surface. In the Si 2p spectrum we observe a chemically shifted surface component due to Si-O bonds and the corresponding C 1s spectrum has a shoulder due to considerable hydrocarbon contamination. After hydrogenation, the oxygen and fluorine contaminants have effectively been removed from the surface as seen in the survey scan of Fig. 1. Also, the chemically shifted components in the Si 2p and C 1s core level spectra have disappeared. The remaining single lines are due to stoichiometric bulk SiC.

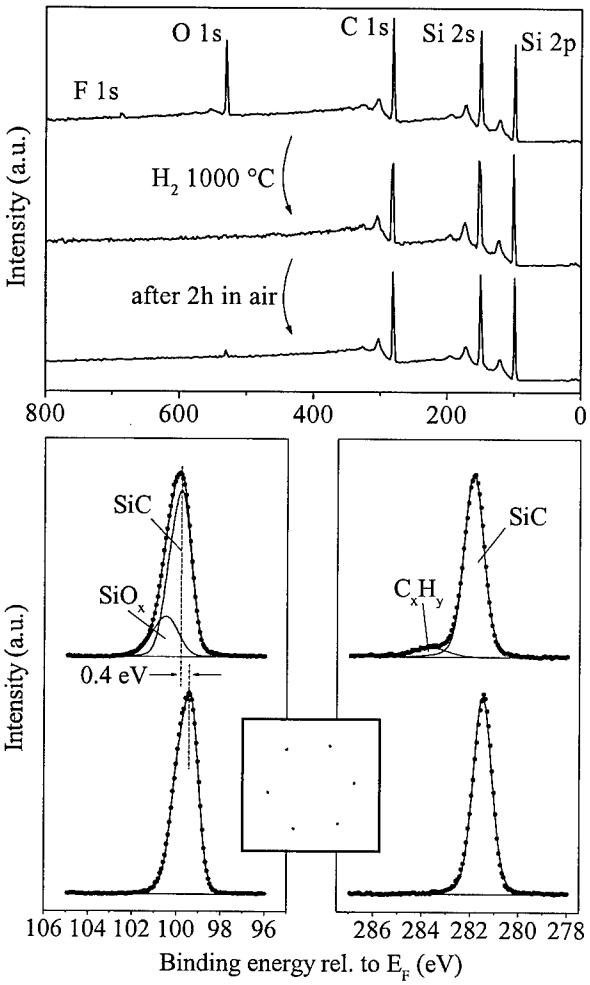


Fig. 1 In the upper viewgraph photoemission survey spectra are depicted after a wet-chemical treatment (upper spectrum), a thermal hydrogen treatment (mid spectrum) and after a 2h exposure to air (lower spectrum). The lower viewgraph shows the Si 2p (left) and C 1s (right) core levels after wet-chemical and thermal hydrogen treatment, and a LEED pattern as seen after hydrogenation is shown in the insert.

After hydrogenation a sharp (1x1) LEED pattern of an unreconstructed surface (see insert in Fig. 1) appears. All these observations point towards a hydrogen saturation of the Si dangling bonds which results in a bulk-like surface termination. The chemical shift in the Si 2p spectra expected on account of the partially ionic Si-H bond is estimated to be 50 meV based on the Pauling electronegativities of the three elements hydrogen, silicon and carbon. This is too small to be resolved by our present resolution. A direct confirmation of hydrogen on the surface is provided by the observation of sharp vibrational modes in the frequency range of Si-H stretching modes by infrared spectroscopy (Fig. 2), which will be discussed later. Hydrogenation also provides an effective passivation of the surface against oxidation. After two hours in air the survey spectrum (compare Fig. 1) shows only a small oxygen contamination, which must be ascribed to adsorbed, oxygen-containing species since no corresponding Si-O component is observed in the Si 2p spectrum. Core level spectra and LEED patterns comparable to the ones just presented have been observed for the C-terminated surface after hydrogenation as well. This surface is, if anything, even more immune against oxidation.

As can be seen from the Si 2p and C 1s core level spectra in Fig. 1 hydrogenation leads to a shift of both core levels to lower binding energies by 0.4 eV. This common shift is due to a change in band bending at the surface such that the Fermi level moves closer to the valence band maximum (VBM)

as expected for an unpinning of E_F upon hydrogenation. As a matter of fact, we measure a difference in surface Fermi level position between p-type and n-type hydrogenated 6H-SiC of 2.7 eV. This is what one expects for the difference in bulk Fermi level positions and it proves that the hydrogen terminated 6H-SiC surfaces are free of any gap states and exhibit flat band conditions.
A typical FTIR-ATR spectrum after hydrogenation of a Si-terminated surface is depicted in Fig. 2 for p- and s-polarization of the incoming IR beam. Two modes in the Si-H stretching region at 2128 cm^{-1} and 2134 cm^{-1} are clearly resolved in p-polarization with a FWHM of about 4 cm^{-1}. The energy separation of 6 cm^{-1} between both peaks is too small to be explained by chemical bond configurations other than C_3Si-H on hydrogen terminated SiC (0001). Thus we ascribe both vibrational modes to monohydride stretching modes. Remarkably no Si-H signal is measured in s-polarization which indicates that the orientation of the Si-H bonds is perfectly perpendicular to the surface. No further contributions in the energy range between 2050 and 2300 cm^{-1} are detectable that might be due to non ideal configurations, e.g. oxygen atoms in back bonds.[4] A weak feature around 2170 cm^{-1} probably originates from residual $CSi-H_3$ at defects.[4] The origin of the splitting of the Si-H stretching modes is still unclear. Tsuchida et al. first observed the existence of different Si-H stretching modes within an energy range of 15 cm^{-1}.[4] They argue that the presence of split Si-H modes as well as $Si-H_2$ and $Si-H_3$ modes are indicative of a microscopically rough surface. However, in our case the intensity ratio of the observed stretching modes is about one. In the case of surface roughness at least one half of the entire surface would have to be rough and disordered. This is in contrast to the sharp and almost background-free LEED patterns, the absence of SiH_2 modes, and the negligibly small SiH_3 contributions in our FTIR spectra. Furthermore, no signal of Si-H modes in s-polarization is detected as it is expected for rough surfaces. Hence, we do not attribute the splitting of the stretching mode to surface roughness.

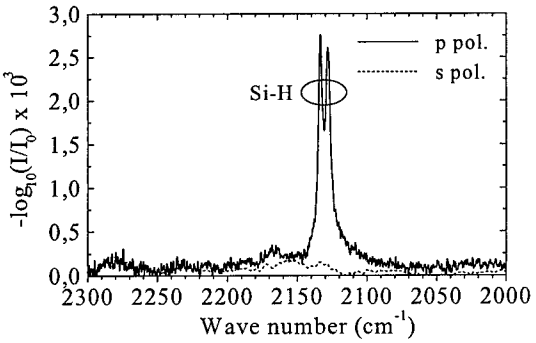


Fig. 2 ATR-FTIR spectra in p and in s polarization after a thermal hydrogen treatment at 1000 °C.

A possible explanation for the splitting would be an induction effect due to different third neighbor environments. In 6H-SiC cubic and hexagonal stacking of the Si-C tetrahedra alternate along the c-axis. Depending on the position where a surface terrace intersects the c-axis the surface silicon atom may be connected to its subsurface third neighbors via a cubic or a hexagonal configuration.[7] That corresponds to different third neighbor distances which could explain the splitting of 6 cm^{-1} of the stretching modes. However, further work is needed to confirm this explanation.
The surface was dehydrogenated after the sample was annealed at 800 °C in UHV. This is accompanied by a transition from the (1x1) LEED pattern to a $(\sqrt{3}x\sqrt{3})R30°$ structure on the Si-terminated surface and noticeable changes in the Si 2p and C 1s core level spectra (see Fig. 3). Additional chemically shifted components are observed at – 0.9 eV and + 1.2 eV binding energy relative to the bulk component in the Si2p and C1s spectra, respectively. By varying the polar angle between sample and analyzer and thus the effective sampling depth it was verified that the shifted components are located at the surface. The additional line in the Si2p spectrum corresponds to a $Si-Si_3$ configuration. In conjunction with the $(\sqrt{3}x\sqrt{3})$ unit mesh this points towards the well known Si-rich reconstruction with Si in T_4 position.[5] The shifted component in the C 1s spectrum has a binding energy that is typical for graphite. Also, both additional components in the Si 2p and C 1s spectra have the same intensities relative to their parent lines. The simultaneous development of two shifted components can be interpreted as a disproportionation of SiC at the surface. In order to reduce the number of dangling bonds at the surface after hydrogen desorption (which was verified

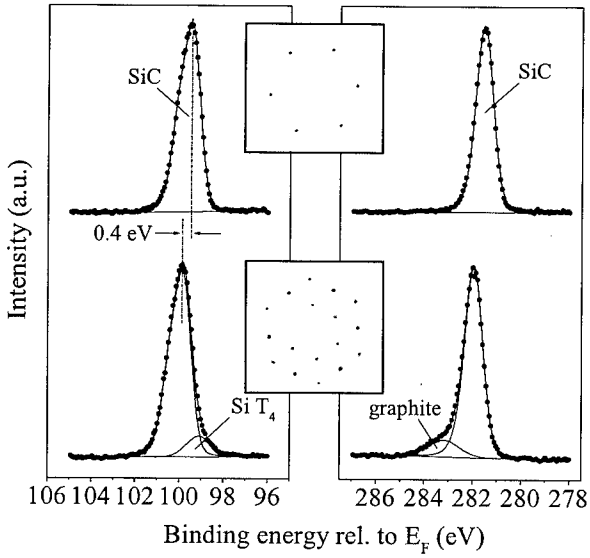


Fig. 3. Si 2p (left) and C 1s (right) core levels of samples after thermal treatment in hydrogen (upper spectra) and after annealing at 800 °C in UHV (lower spectra). The corresponding LEED patterns are given in the inserts.

by FTIR) Si diffuses along the surface to form ($\sqrt{3}$x$\sqrt{3}$)R30° reconstructed Si-rich regions. On the other hand, C-rich regions remain which give rise to the graphitic component in the C 1s spectrum. The ensuing disorder is also reflected in the markedly increased background intensity in the LEED picture of the reconstructed surface (compare Fig. 3). Not unexpected, the desorption of hydrogen and the formation of the ($\sqrt{3}$x$\sqrt{3}$)R30° structure results in a renewed pinning of E_F away from the flat band condition as indicated by a 0.4 eV shift of both core levels towards higher binding energy. The ($\sqrt{3}$x$\sqrt{3}$)R30° structure has one dangling bond per unit mesh which has a lower Hubbard band ~ 0.4 eV above VBM which in turn acts as a pinning level for p-type SiC. [6]

Summary

Annealing 6H-SiC in purified hydrogen at 1000 °C results in unreconstructed surfaces free of any contaminants. Si-H bonds could be directly identified by their vibrational stretching mode in IR spectroscopy on the Si side. A 6 cm^{-1} splitting of this mode is tentatively ascribed to different third neighbor environments of Si encountered on terraces that terminate hexagonal or cubic stacking sequences, respectively. Hydrogenation passivates the surfaces electronically and chemically. The absence of any surface states or defects leads to flat band conditions for p- and n-type doping and a resistance against oxidation even under atmospheric conditions. After annealing at 800 °C hydrogen is completely desorbed and the originally unreconstructed surface turns into a ($\sqrt{3}$x$\sqrt{3}$)R30° reconstructed surface. The reconstruction is the result of a disproportionation of SiC into Si-rich and C-rich regions at the surface.

Acknowledgements

We thank Ralf Graupner for fruitful discussions and gratefully acknowledge financial support by the Deutsche Forschungsgemeinschaft (SFB 292) and the BMBF (grant 05 SE8 WEA 0).

References

[1] S. Miyazaki, J. Schäfer, J. Ristein, L. Ley, Appl. Phys. Lett. 68 (1996), p. 1247.
[2] E. Yablonovitch, D.L. Allara, C.C. Chang, T. Gmitter, T.B. Bright, Phys. Rev. Lett. 57 (1986), p. 249.
[3] V.v. Elsbergen, O. Janzen, W. Mönch, Mater. Sci. Eng. B 46 (1997), p. 366.
[4] H. Tsuchida, I. Kamata, K. Izumi, Mater. Sci. For. 264-268 (1998), p. 351.
[5] U. Starke, J. Schardt, J. Bernhardt, M. Franke, K. Heinz, Phys. Rev. Lett. 82 (1999), p. 2107.
[6] M. Hollering, thesis, Erlangen (2000).
[7] T. Kimoto, A. Itoh, H. Matsunami, T. Okano, J. Appl. Phys. 81 (1997), p. 3494.

Materials Science Forum Vols. 353-356 (2001) pp. 227-230
© 2001 Trans Tech Publications, Switzerland

Polytype and Polarity of Silicon Carbide and Aluminium Nitride Films Growing by MBE: A Nondestructive Identification

B. Schröter, A. Winkelmann, A. Fissel, V. Lebedev and W. Richter

Institut für Festkörperphysik, Friedrich-Schiller-Universität Jena,
Max-Wien-Platz 1, DE-07743 Jena, Germany

Keywords: Electron Channeling, Molecular Beam Epitaxy (MBE), Photoelectron Diffraction, Polarity, Polytypism

Abstract

The polytype, stacking sequence and polarity of SiC and AlN films grown by MBE can be determined by x-ray photoelectron diffraction and electron channeling patterns. The information depth of a diffraction pattern of electrons with medium kinetic energy of one or a few keV is 10 to 20 atomic layers and the pattern is hardly influenced by surface reconstruction and contamination.

Introduction

The growth of heterostructures of SiC polytypes demands definite nucleation and growth conditions for each polytype. Up to now a controlled and reproducible deposition of high-quality heterostructures of various polytypes is an unsolved problem. Using solid-source molecular beam epitaxy, it is possible to control and vary the growth conditions of the cubic 3C and the hexagonal 4H and 6H SiC polytypes [1]. Similarily, aluminium nitride films can exist as a cubic or hexagonal polytype. Wurtzite (2H) AlN films can be grown either with Al face or N face polarity on non-polar Si(111) by varying nucleation conditions [2]. The polarity of III-nitride films is crucial for the growth and the properties of heterostructures.

The determination or monitoring of the growing polytype or of the stacking in a thickness range from a double layer up to a few nanometers, i.e., a few unit cells of the most common polytypes, requires suitable characterization techniques. Surface analysis methods such as LEED or RHEED are sensitive to a few bilayers only. We use these techniques for characterizing the surface structure during growth but an unambiguous determination of the polytype structure is limited due to their high surface sensitivity. Photoluminescence as well as X-ray diffraction and Raman scattering are capable of determining the polytype of thick films. By high-resolution transmission electron microscopy a thin-film polytype identification is possible but it is destructive, expensive and limited to local analyses.

For a nondestructive determination of the polytype and polarity we use the diffraction of electrons with medium kinetic energy of one or a few keV because their interaction length is in the nanometer range appropriate to polytype unit cells [3]. In X-ray photoelectron diffraction (XPD) an angular-resolved detection of *outgoing* photoelectrons in the energy range near 1 keV is performed. The technique of electron channeling pattern (ECP) utilizes the scattering of the *incident* beam in a scanning electron microscope. The electron channeling contrast results from a variation of the backscattering efficiency caused by the change of the incidence angle relative to the crystal lattice during scanning. Both techniques are nondestructive and can be used to study UHV growth processes. In this paper, we like to show the potential of XPD and ECP in investigations on the growth of polytype heterostructures, especially, by MBE.

Experimental

Measurements were done on 4H and 6H SiC bulk crystals from CREE and on MBE films grown ex-situ or in-situ on these substrates in {0001} orientation [1,2]. The 3C SiC(111) films

investigated were grown by solid-source MBE on Si(111) or on SiC{0001} CREE substrates. Most of the ex-situ analysed samples were heated in a silicon flux to prepare clean surfaces with definite reconstruction (3x3, $\sqrt{3}$x$\sqrt{3}$-R30°, 6$\sqrt{3}$ x 6$\sqrt{3}$, 1x1). AlN films were grown ex situ on SiC{0001} or on Si(111) substrates [2]. All samples were characterized by LEED, Auger- and photoelectron spectroscopy. Occasionally, the results of Raman spectroscopy, x-ray diffraction and TEM were compared with XPD and ECP to check unambiguous identification.

The XPD patterns of angular-resolved photoelectron intensities have been measured using Mg Kα (1253.6 eV) and Al Kα (1486.6 eV) radiation for excitation. The angular resolution of the SPECS hemispherical electron analyzer was chosen better than 4°. XPD data are presented as polar scans of the photoemission intensities along a crystallographic direction measured by tilting the sample or as a stereographic projection of a full-scan diffraction pattern.

The electron channeling patterns were obtained at a multi-technique surface analysis system using a 12 keV electron gun or at a Cambridge STEREOSCAN scanning electron microscope.

X-Ray Photoelectron Diffraction

By XPD, chemically resolved diffraction patterns can be measured separately for each element, e.g., Si and C. The information depth varies with energy and emission angle of the photoelectrons between 1 and some 20 monolayers. Thus, XPD is useful to get information on the surface structure as well as on the polytype defined by a unit cell with a few nanometers thickness. Actually, we have found that an XPD pattern of medium-energy photoelectrons near 1 keV at common emission angles up to 70° is hardly influenced by the surface structure or contamination but is sensitive to the polytype structure and the stacking sequence of more than 10 double layers.

Due to the strong forward focusing nature of the electron scattering in that energy range, the diffraction pattern is often dominated by forward scattering (FS) peaks pointing along the low-index directions of nearest-neighbor high-density atomic rows. Thus, information on the atomic structure in real space can be obtained. The situation may be more complicated than in this simple FS picture because of energy-dependent interference and multiple-scattering effects.

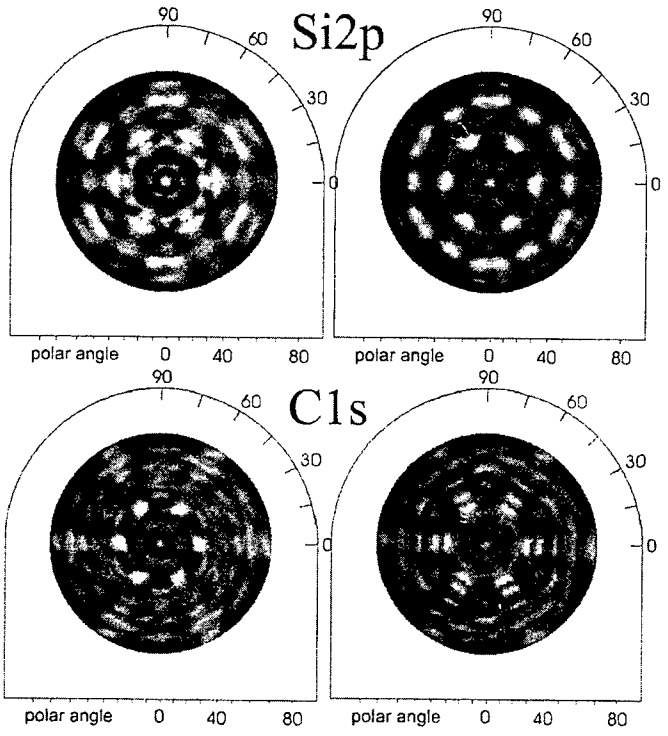


Fig.1
XPD patterns measured on 4H SiC(0001) substrate (left) and on the 3C SiC epitaxial film of 4 Si-C double layers grown in situ by an alternating Si and C supply at 950°C (right).
(Al K excitation,
Si2p: 1386eV, C1s: 1204eV)

We found that the XPD patterns can be well described by a single-scattering cluster (SSC) theory [4]. We measured and calculated the diffraction patterns of the most common polytypes and their polar faces. These patterns can be used as fingerprints for the determination of a thin film's polytype. Furthermore, a simulation of the patterns of other polytypes, of heterostructures or of any stacking sequence is possible by SSC calculations. This is important for monitoring epitaxial growth and has been applied to in situ grown heterostructures of SiC polytypes. In fig. 1 the XPD patterns measured on an on-axis 4H SiC(0001) substrate are shown in comparison with the patterns after in-situ growth of 4 Si-C double layers by an alternating supply of Si and C at 1100 K. The patterns obtained after growth match those measured and calculated on 3C SiC(111). The growth steps of single Si-C layers were monitored by polar scans which display an increase of diffraction features due to cubic stacking. Fig. 2 illustrates this growth of cubic layers in the SSC simulation. Up to three additional Si-C double layers with cubic stacking are considered. One can observe a decreasing intensity of the peak near 31° that is characteristic of the hexagonal stacking and, at the same time, an increasing intensity of the diffraction peaks at polar angles of 22° and 39° which are due to silicon emitters in a cubic stacking sequence.

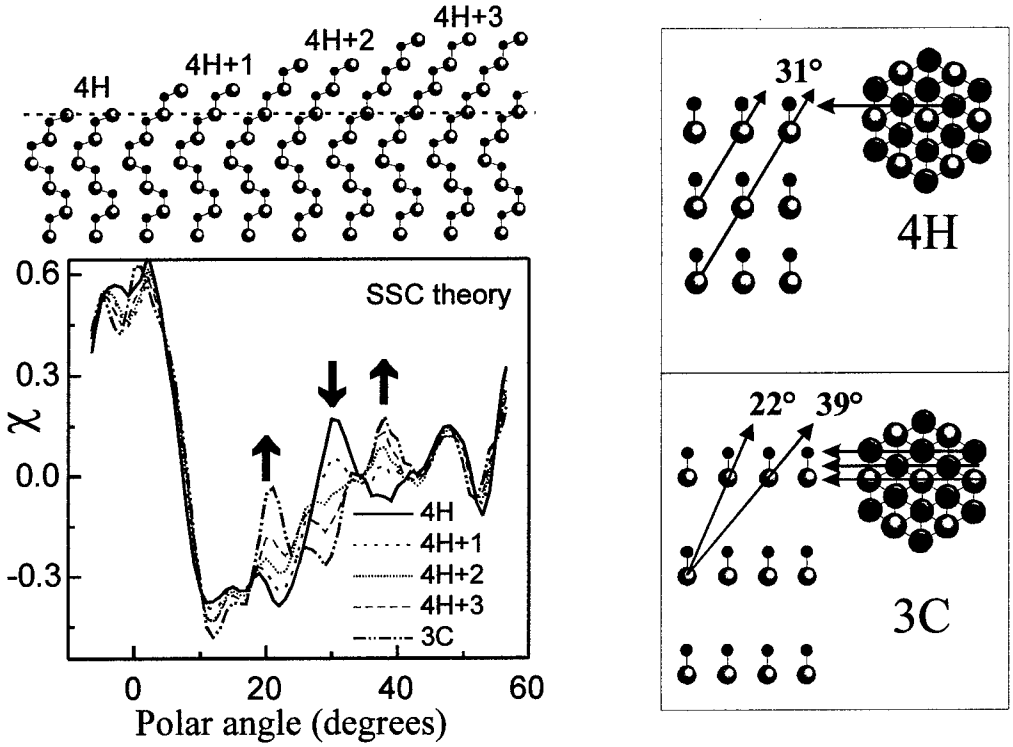


Fig. 2

Left: Calculated Si 2p polar scans in (2-1-1) plane simulating the changes in XPD by growing 1, 2 and 3 Si-C double layers with cubic stacking on 4H SiC(0001). The Si2p photoemission intensity is displayed as $\chi = (I - I_0)/ I_0$ with I_0 being a smooth background fitted to the polar scans and representing isotropic emission.

Right: FS directions in (2-1-1) plane of 3C and equivalent (10-10) plane of 4H SiC characteristic of cubic and hexagonal stacking.

XPD is also useful to identify the polar faces of various polar crystals in a nondestructive way. Especially, the determination of Si and C faces of the common SiC polytypes is easy because

of the very different scattering of the photoelectrons in normal direction to the surface. For wurtzite AlN films, we could show by XPD that depending on the nucleation conditions both polarities can be grown on nonpolar Si(111) [2].

Electron Channeling Pattern

A quick identification of a thin film polytype is also possible in a fingerprint manner by the characteristic electron channeling pattern (ECP) measured for a certain primary electron energy [3]. In contrast to XPD, ECP utilizes the diffraction of the incident beam in a scanning electron microscope and is not element specific. The most interesting part of the pattern can be measured by scanning the electron beam a few degrees around zone axis orientation, e.g., normal incidence on SiC(111) (fig.3a). Locally resolved images of the polytype or of different stacking can be obtained in the micrograph mode by measuring channeling contrast images. The dark and bright regions in fig. 3b are the two domains of cubic films with double-positioning twinning. Fig. 3c shows a nearly single-domain cubic film grown by MBE on 6H(0001). Twinned 3C inclusions occur only at substrate surface imperfections like scratches. Thus, on properly prepared substrates with low defect density, featureless single-domain 3C films could be observed in channeling contrast mode. A weak contrast is observed on hexagonal surfaces with step bunching reflecting the occurence of regions with different surface stacking terminations.

As an electron beam can be scanned on a large range a polytype determination by electron channeling is possible on whole wafers as well as locally resolved in the sub-μm range. The information depth depends on the electron energy and amounts to only few nanometers in the keV energy range.



Fig. 3 (a) (b) (c)
ECP of 3C SiC(111) at E=4200eV (a) and channeling contrast images of the two orientational domains (appearing dark and bright) of a twinned 3C film (b, 40μm x 40μm) and a nearly single-domain 3C film (c, 400μm x 400μm) grown by MBE.

Acknowledgement
This work is supported by the Deutsche Forschungsgemeinschaft (SFB 196).

References

[1] A. Fissel, B. Schröter and W. Richter, Adv. Sol. State Phys. 38 (1999) p. 87;
A. Fissel, K. Pfennighaus, U. Kaiser, B. Schröter, and W. Richter, J. Electron. Mater. 28 (1999) p. 206.
[2] V. Lebedev, B. Schröter, G. Kipshidze, and W. Richter, J. Cryst. Growth 207 (1999) p. 266.
[3] B. Schröter, M. Kreuzberg, A. Fissel, K. Pfennighaus, and W. Richter, Mater. Sci. Forum 264-268 (1998) p. 355.
[4] B. Schröter, A. Winkelmann, W. Richter, J.Electron Spectrosc.Relat.Phenom. (to be published).

Materials Science Forum Vols. 353-356 (2001) pp. 231-234
© 2001 Trans Tech Publications, Switzerland

Surface Abstraction Reactions at Experimental Temperatures; A Theoretical Study of 4H-SiC(0001)

J. Olander and K. Larsson

Department of Inorganic Chemistry, Ångström Laboratory,
Uppsala University, P.O. Box 538, SE-751 21 Uppsala, Sweden

Keywords: Abstraction, Adsorption, Quantum Mechanical Calculations

Abstract

Hydrogen abstraction by gaseous X radicals (X = H, F, Cl, Br) from H-terminated 4H-SiC(0001) surfaces, has been investigated theoretically using Car-Parinello-type molecular dynamics. Experimental temperatures of 1873 and 2573 K were applied. For both the Si(0001) and the C(000-1) surfaces, the hydrogen abstraction reactions were found to be exothermic. As a comparison, the adsorption of H to the corresponding surfaces was studied. The H adsorption energy was found to be more exothermic than the abstraction energy for each of the investigated cases. This indicates that it is more favorable for the surface H atoms to remain bonded to the 4H-SiC surfaces than to become abstracted by any of the gaseous radical atoms H, F, Cl or Br.

1. Introduction

Vapor growth of silicon carbide (SiC) involves various dynamic processes. Experimental as well as theoretical investigations are needed to understand these processes more profoundly. Hydrogen termination is supposed to sustain the surface structure of SiC during growth. Gaseous H radicals are also believed to abstract surface terminating hydrogen atoms from the growing surface. Radical surface sites are then created. Temperatures as high as 2000-2300°C for SiC CVD processes have recently been shown to yield high growth rates [1]. It is questionable whether the surface stays mainly terminated at such temperatures or if the surface-terminating species become abstracted. The abstraction of surface terminating H by gaseous hydrogen radicals has been found to be important for H removal of Si films [2]. The kinetics was then believed to be consistent with a spontaneous Eley-Ridel abstraction process. The same mechanism of abstraction is assumed in the present investigation. Halogens, especially chlorine molecules or radicals, are often present in the atmosphere above the SiC surface during vapor deposition processes. They are supposed to sustain the surface structure by termination in a similar way as H atoms. The purpose of the present study was to investigate whether 4H-SiC surfaces are likely to stay mainly H terminated at the elevated temperatures of 1600°C and 2300°C or not.

2. Method

The calculations have been performed within the framework of Density Functional Theory (DFT) [3,4], using the CASTEP (Cambridge Sequential Total Energy Package) computer program package from Biosym/Molecular Simulation Technologies in San Diego. The abstraction energies were calculated using the extreme total energies obtained. More specifically, the energies corresponding to the most favorable structure of the radical models and the least favorable structure for the completely hydrogen terminated models were used. The abstraction energy, E[abs, H], was then calculated with the following equation:

$$E[abs, H] = E[surf] + E[X\text{-}rad] - (E[surf\text{-}rad] + E[HX]) \quad (1)$$

where E[surf] and E[surf-rad] are the total energies for the 4H-SiC surface without and with a radical surface site, respectively. E[X-rad] and E[HX] denote the total energies for the gaseous X radical and HX molecule, respectively (X = H, F, Cl or Br).

A combined Molecular dynamics (MD)/DFT method, developed by Car and Parinello [5], was used to simulate the abstraction reactions of the 4H-SiC surfaces. A LDA (Local Density Approximation) functional [6] was used for the initial calculations. Subsequently, a GGA (Generalized Gradient Approximation) functional [7] was applied. The atoms were in all calculations represented by nonlocal ultrasoft pseudopotentials in the Kleinman-Bylander separable form [8]. The Si(0001) and C(000-1) surfaces of 4H-SiC were included in the present investigation. Periodically repeated (in three directions) unit cells consisting of 6 atomic layers were used. Each layer contained 6 Si (or C) atoms (see Fig.1) and the distance between the slabs was 7 Å. The uppermost and bottom layers were terminated by H atoms. During the calculations, the 4 uppermost atomic layers and the surface terminating H atoms were allowed to fully relax. The finally relaxed structures of the models were obtained by starting from the bulk structure of 4H-SiC.

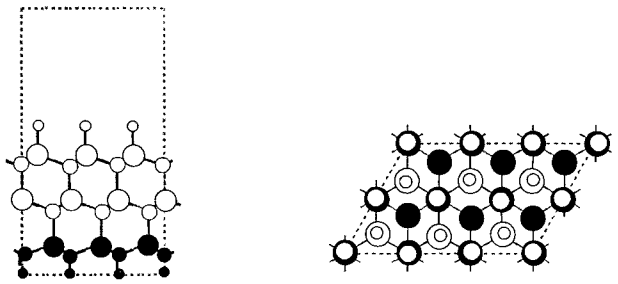


Figure 1. (a) A side view of the model of 4H-SiC(0001) used during the calculations. The black color denotes the atoms that were kept fixed. The large, medium and small circles represent Si, C and H atoms, respectively. (b) A top view of the same model. In this picture, all but the uppermost two layers are colored black.

3. Results and discussion

A. General Among the chemical steps involved in CVD, the adsorption of the gaseous species on the solid surface is frequently a rate-determining step. Either by contributing to the growth rate or by blocking the available surface sites. In order to understand the growth processes it is important to study the prerequisites of adsorption, such as the structure of the surface prior to adsorption. One aspect of the structure is surface saturation, i.e. whether the growing surface is terminated, with e.g., H atoms or not. Hydrogen is assumed to form single bonds with the surface atoms in SiC and thereby sustain their sp^3 configuration. However, it is not certain that H atoms will be chemically bonded to a SiC surface at experimental vapor deposition temperatures. It may, for example, be more favorable for them to desorb, or to become abstracted.

Table I Calculated energies for the abstraction of a surface hydrogen atom from the completely H-terminated Si(0001)- or C(000-1)–plane of 4H-SiC.

	Si-face		C-face	
Temperature (°C)	1600	2300	1600	2300
E(H) (kJ/mol)	**-310**	**-451**	**-401**	**-491**
E(Br) (kJ/mol)	**-353**	**-495**	**-443**	**-534**
E(Cl) (kJ/mol)	**-362**	**-504**	**-452**	**-546**
E(F) (kJ/mol)	**-442**	**-585**	**-533**	**-625**

B. H abstraction with a gaseous H radical The abstraction of a surface H from a completely hydrogen-terminated surface by a gaseous H radical has been studied. Both the Si and the C planes of 4H-SiC were regarded at the temperatures of 1600 and 2300°C. All the obtained abstraction energies were exothermic (see Table I). The investigated H abstraction reactions can therefore thermodynamically be regarded as probable to occur. As expected, the numerical values of the abstraction energies were larger at 2300°C compared to at 1600°C. For the Si(0001) surface, the values obtained are 310 and 450 kJ/mol for 1600 and 2300°C, respectively. The corresponding values for C(000-1) are 350 and 490 kJ/mol. This indicates that the abstraction of a surface H atom is somewhat more favorable from the C surface. A probable explanation for this is the relatively smaller relaxation obtained for the C surface. The radical C atom became lowered by 0.3 Å as a result of the abstraction reaction. This is to be compared with a corresponding lowering of 0.7 Å for the Si surface. The more pronounced relaxation resulted in less favorable abstraction reactions.

Table II Energies calculated for H adsorption to a radical site of an otherwise H-terminated Si(0001) or C(000-1) surface of 4H-SiC.

	Si-face		C-face	
Temperature (°C)	1600	2300	1600	2300
E(H) (kJ/mol)	**-671**	**-804**	**-843**	**-753**

A competing gas phase/solid phase reaction studied was adsorption of a gaseous H radical to each of the surface radical sites described above. The adsorption energies were calculated using:

$$E[ads, H] = E[surf\text{-}rad] + E[H] - E[surf] \quad (2)$$

The energies obtained for H adsorption to the various surface radical sites are presented in Table II. In all the investigated cases, the calculated adsorption energy of H was found to be more exothermic than the corresponding abstraction energy. For the Si plane, the adsorption energy obtained at 1600 (2300) °C is more exothermic by 361 (353) kJ/mol compared to the abstraction energy. The corresponding value for the C-plane is 442 (262) kJ/mol. The surface reactions that take place during vapor deposition are very dynamic and complex. However, adsorption to and abstraction from the surfaces are two major elementary reactions. The present results convey that H adsorption is energetically the most favorable one for the present systems. Hence, this indicates that SiC(0001) surfaces are likely to remain predominantly H terminated even at temperatures as high as 2300 °C.

C. H abstraction by a gaseous halogen radical Chlorine is often a gaseous by-product from the silicon source species obtained during vapor deposition of SiC. The addition of HCl to the gaseous atmosphere during CVD of 3C-SiC has resulted in an improved surface morphology of the growing film [9]. Cl, F and Br have earlier been found efficient in stabilizing the sp^3 hybridization of the surface atoms of diamond (111) surfaces [10]. Because of the structural similarities between diamond and silicon carbide, halogens can be expected to also stabilize SiC surfaces. However, since the gaseous mixture in the CVD reaction chamber commonly contains a great surplus of hydrogen, the growing SiC surfaces are in the present investigation initially assumed to be H-terminated. Sato et al. [11] have calculated the activation energies for H abstraction from SiH_3CH_3 by F to be -22 kJ/mol and +3 kJ/mol from the Si and C atoms, respectively. These activation energies are very small compared to the abstraction energies obtained in the present investigation. This indicates that the activation barriers of the abstraction reactions are not likely to hinder the abstraction reactions.

The capability of abstraction of the surface-bonding H atoms by gaseous halogen radicals has been investigated in the present study. As can be seen in Table I, the exothermic abstraction energy obtained using gaseous F is 442 (585) kJ/mol for the Si surface at 1600 (2300) °C. The corresponding value for the C surface is 533 (625) kJ/mol. As was mentioned in section III.B, the created radical site was more lowered for the Si-plane (0.7 Å) compared to for the C-plane (0.3 Å).

When considering all the gaseous species, the order of exothermic abstraction energies obtained is H < Br < Cl < F for each of the investigated surfaces. The energies of abstraction by fluorine are for all the investigated cases about 130 kJ/mol higher than the ones obtained for abstraction by hydrogen. However, adsorption of H to the SiC surfaces was, in all the cases, found to be energetically more favorable than the corresponding H abstraction using any of the gaseous halogen radicals.

4. Conclusion

Hydrogen abstraction by gaseous X radicals (X = H, F, Cl, Br) from completely H-terminated 4H-SiC(0001) surfaces has been theoretically investigated using Car-Parinello-type molecular dynamics. The Si and C planes of 4H-SiC were then regarded. H as well as the gaseous halogen atoms F, Cl, and Br were all found to perform strong surface H abstraction reactions. For each of the investigated surfaces, the order of the exothermic abstraction energies obtained is H < Br < Cl < F. The values of the abstraction energies were larger at 2300°C than at 1600°C. Furthermore, the abstraction reactions were found to be somewhat more favorable for the C plane than for the Si plane. This can partially be explained by the larger relaxation observed for the radical atom of the Si surface than on the C surface. The adsorption of H to the radical surface sites was also studied. H adsorption to each of the surfaces was then found to be even more favorable than the abstraction reactions studied (including H, F, Cl or Br). Our results show that both the Si- and C-planes of 4H-SiC are likely to stay predominantly H-terminated at high temperatures even in the presence of H, Br, Cl or F.

5. Acknowledgements

This paper was supported by the Swedish Research Council for Engineering Sciences (TFR), and the Ångstrom consortium. The results were generated using the program Cerius^{2} ^{TM}. This program was developed by BIOSYM/Molecular Simulations.

References

[1] A. Ellison et al., Mat. Sci. and Eng. B61-62 (1999), p.113.
[2] E. Srinivasan and G. N. Parsons, Appl.Phys.Lett. 72 (4) (1998), p.456.
[3] P. Hohenberg and W. Kohn, Phys. Rev. B 136 (1964), B864.
[4] W. Kohn and L.J. Sham, Phys. Rev. 140 (1965) A1133.
[5] Car and Parinello, Phys.Rev.Lett. 55 (1985) p.2471.
[6] J.P. Perdew, A.Zunger, Phys. Rev. B 23 (1981), p.5048.
[7] J.P. Perdew, Y.Wang, Phys. Rev. B 45 (1992), p.13244.
[8] L.Kleinman. D.M. Bylander, Phys.Rev.Lett. 48 (1982), p.1425.
[9] Y.Ohshita, Mater. Res. Soc. Symp. Proc. 162, 1990.
[10] K.Larsson, Lunell, S., J.Phys.Chem. A 101, (1997), p.76.
[11] K.Sato. et al., Jpn.J.Appl.Phys. 33 (1994), p.4801.

Materials Science Forum Vols. 353-356 (2001) pp. 235-238
© 2001 Trans Tech Publications, Switzerland

Combined Scanning Tunneling Microscopy and Photoemission Studies of the β-SiC(100) c(4x2) Surface Reconstruction

V. Derycke[1,2], P. Fonteneau[1,2], V.Yu. Aristov[1,2*], H. Enriquez[1,2] and P. Soukiassian[1,2]

[1] Commissariat à l'Energie Atomique, DSM - DRECAM - SPCSI, Centre d'Etudes de Saclay, Bâtiment 462, FR-91191 Gif-sur-Yvette Cedex, France

[2] Département de Physique, Université de Paris-Sud, FR-91405 Orsay Cedex, France

Keywords: Photoemission Spectroscopy, Scanning Tunneling Microscopy, Surface Reconstruction

Abstract. We investigate the β-SiC(100) c(4x2) surface reconstruction by atom resolved scanning tunneling microscopy and Si 2p core level photoemission spectroscopy using synchrotron radiation. The STM data obtained in the filled and empty electronic states allow the identification of both the up and down dimers of the c(4x2) reconstruction. The up dimers are identified when tunneling in the filled states while the down dimers are identified in the empty states. The important electronic difference between the two types of dimers is in very good agreement with core level photoemission results that show two largely shifted surface components associated with both dimers. These combined STM and photoemission experiments further confirm the AUDD model of the β-SiC(100) c(4x2) surface.

I. Introduction

SiC is a wide band gap material that exists in different polytypes [1,2]. The (100) surface of cubic SiC (β) has been widely studied in the past ten years using most of the main surface science techniques and state of the art calculations [3-6]. This β-SiC(100) surface is known to produce up to nine surface reconstructions depending on the atomic composition of the last plane. Indeed, the surface can be silicon rich (3x2, 5x2...), silicon terminated (c(4x2), 2x1), carbon terminated (c(2x2), 1x2) or carbon rich (1x1). Among these surface reconstructions the c(4x2) is of special interest. It corresponds to the surface terminated by one monolayer of silicon atoms [7,8] allowing interesting comparisons with the corresponding Si(100) c(4x2) surface reconstruction.

A previous STM study has established the structural model of the β-SiC(100) c(4x2) surface [9]. It is composed of alternately up and down dimers (AUDD) forming dimer rows. This model is supported by *ab-initio* calculations [10, 11]. The c(4x2) reconstruction is dominated by surface stress that helps the stabilization of the two types of surface dimers. The pioneer STM study has identified the up dimers as the main features observable in the filled electronic states. Intensity profile along and perpendicular to the dimer rows also brought indirect observation of the down dimers. Recently, an alternative model has been proposed on the basis of another *ab-initio* calculation [12]. This MRAD (missing row of asymmetric dimers) model is composed of 1.5 silicon monolayer on top of a complete carbon plane. However, the latter model is so far, not supported by several classes of experimental investigations and by other calculations [14].

In this article, we propose a new STM study of the β-SiC(100) c(4x2) surface [15]. Using the capability of the STM to probe at the same time both filled and empty electronic states, we identify the down dimer as the main feature observable in the empty states images while the up dimers are seen in the filled states images. Combined with the photoemission identification of the Si 2p core level shifted components, this study allows the comparison of the two different structural models : the AUDD and the MRAD models.

* On leave from Institute of Solid State Physics, Russian Academy of Sciences, Chernogolovka, Moscow district 142432, Russia

II. Experimental details

The scanning tunneling microscopy experiments are performed at room temperature using an Omicron STM. We use single domain n-type β-SiC single crystal thin films (0.8 µm thick) that have been grown by C_3H_8 and SiH_4 chemical vapor deposition (CVD) on a 4° Si(100) vicinal surface at LETI (CEA Technologies Avancés, Grenoble). The surface is prepared by initial thermal annealing at 1200°C to remove native oxides leaving a carbon C rich surface. The Si stoichiometry is restored by Si deposition from a heated Si wafer, followed by thermal annealing at 1150°C. The so-prepared surface exhibits sharp c(4x2) low energy electron diffraction (LEED) patterns. The synchrotron radiation photoemission experiments are performed using the soft x-ray light emitted by the Super ACO storage ring at Laboratoire d'Utilisation du Rayonnement Electromagnetique (LURE, Université de Paris-Sud/Orsay) with a total energy resolution better than 150 meV. In order to achieve bulk and surface sensitive conditions, the photoemission measurements are performed at different photon energies. All experiments are performed in a vacuum better than 8.10^{-11} Torr. Other details about high quality β-SiC(100) surface preparation could be found elsewhere [9].

III. Results and discussion

We first look at the β-SiC(100) c(4x2) surface using scanning tunneling microscopy. Figures 1a and 1b display 53 Å x 53 Å STM topographs of the same area of the surface obtained when tunneling in the filled (a) and empty (b) electronic states. Both images exhibit the pseudo-hexagonal pattern characteristic of the β-SiC(100) c(4x2) in which each spot represents a Si-Si dimer. In order to allow further identification of dimer positions, black circles are added around spots of the filled states topograph (a) while small dark spots mark the position of the empty states maximums (b). On figure 1b, the circles from figure 1a have been superimposed. One can immediately notice that the filled electronic states spots are located, along a dimer row, between empty electronic states spots. Such an observation is in excellent agreement with the AUDD model schematically represented in figure 2. It is known that the up-dimers are imaged when tunneling into the filled states [9]. We show here that the down dimers are probed when tunneling into the empty electronic states.

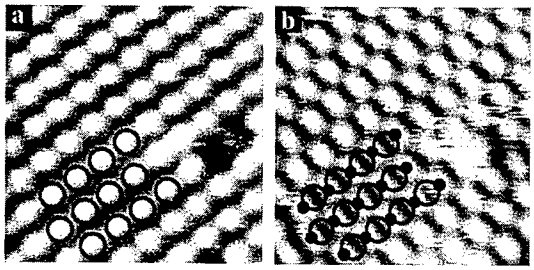
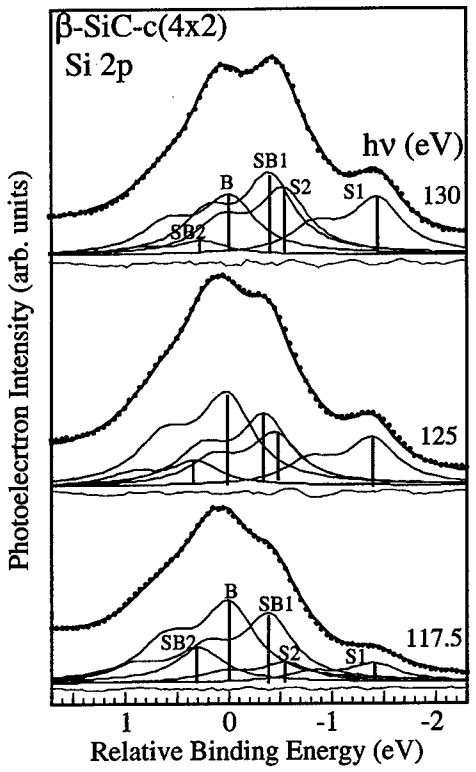


Fig.1 : 53 Å x 53 Å STM topographs of the β-SiC(100) c(4x2) surface obtained by tunneling into the filled (a) and empty electronic states (b). The tip bias are $V_t = 3$ V (a) and -3 V (b) at 0.2 nA tunneling current. Circles indicate maximum of filled states and dark points show maximum of empty states.

Let us emphasize that the empty electronic states STM images of the c(4x2) surface reconstruction are totally inconsistent with the calculated STM images based on the MRAD model [12]. In the latter case, the empty electronic state images have been simulated theoretically to result in two features, corresponding to the two Si atoms forming an asymmetric dimer. Using several different bias in the empty electronic states, we have never observed the splitting of the spots forming the pseudo-hexagonal pattern into smaller spots.

We now look at the Si 2p core level photoemission spectroscopy results which are summarized in figure 3. Using different photon energies and a well established least-squares fitting procedure (in

which a spectrum is decomposed into components consisting of spin-orbit split Voigt functions), we have identified five shifted components [13]. One of them is the dominant feature at low photon energy (117.5 eV). It corresponds to the silicon atoms in the bulk. This bulk component (B) is located at a binding energy of ~101.2 eV. Two other components S1 and S2 have an opposite behavior : both are very intense at higher photon energy (130 eV). Note that S2 has the same intensity as S1 for all photon energies. These two components, separated in energy by 0.9 eV, correspond to the up and down dimers of the AUDD model. The two remaining components (SB1 and SB2) have a bulk character and correspond to subsurface reorganization associated with the reconstruction. If the MRAD model was correct, one should have observed the contribution of the full silicon monolayer which is below the silicon ad-dimers. The precise study of the relative intensity evolution of the different components excludes this possibility. Indeed, the total intensity of SB1+SB2 for the surface sensitive spectra is approximately the same as S1+S2. It would have been twice as intense in the case of the MRAD model.



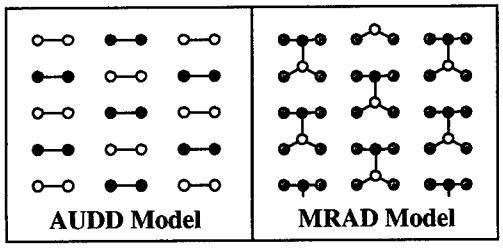


Fig. 2: Schematic of the β-SiC(100) c(4x2) surface structure for the AUDD and MRAD models. All presented atoms are silicon atoms. Up-dimers (AUDD) and up-atoms (MRAD) are represented in black. Down-dimers (AUDD) and down atom (MRAD) are represented in white.

Fig. 3 : Representative decompositions of three Si 2*p* photoelectron spectra. Parameters used for the decompositions are spin-orbit splitting of doublets 0.602 eV, branching ratios: 0.5 eV, Lorentzian : 0.085 eV, Gaussian: 0.6 eV (bulk component) and 0.55 eV (all other components). The Si 2*p* 3/2 energy positions of the four shifted components relative to *B* are : -0.4 eV (SB1), +0.31 eV (SB2), -0.54 eV (S2) and -1.43 eV

IV. Conclusions

The β-SiC(100) c(4x2) surface reconstruction is investigated by atom-resolved scanning tunneling microscopy (filled and empty electronic states) and core level photoemission spectroscopy. STM experiments have unambiguously identified the up and down dimers. This investigation further supports the AUDD (alternately up- and down-dimer) model. The photoemission results also support this model : the large binding energy difference between the S1 and S2 surface core level shifted components is in excellent agreement with the very different electronic status of the two

dimers observed in filled and empty electronic states STM topographs. In strong contrast, the MRAD model is unable to take into account the present experimental results. The MRAD model should indeed show twice as much spots in the empty electronic states topographs in comparison to filled electronic states topographs. Moreover, the ad-dimers of this model lie on a complete silicon plane. The photoemission signature of this complete silicon plane can not be identified. It does not correspond to the SB1 and SB2 components that have a strong bulk character and a too low intensity.

Acknowledgments

The authors are grateful to T. Billon, L. di Cioccio and C. Pudda at LETI (CEA - Technologies Avancées, Grenoble) for providing β-SiC(100) samples.

References

[1] phys. stat. sol. (b) 202, No. 1 (1997), phys. stat. sol. (a) 162, No. 1 (1997), and references therein.
[2] Properties of Silicon Carbide, G. Harris (editor), EMIS Datareview series, INSPEC, London, (1995), Vol. 13.
[3] F. Bechstedt, P. Käckell, A. Zywietz, K. Karch, B. Adolf, K. Tenelsen and J. Furthmüller, Phys. Stat. Sol. b **202** (1997), p. 35 ; and references therein.
[4] V.M. Bermudez, Phys. Stat. Sol. b **202** (1997), p. 447; and references therein.
[5] P. Soukiassian, Mat. Sci. and Engineering B **61** (1999), p. 506; and references therein.
[6] J. Pollman, P. Krüger and M. Sabisch, Phys. Stat. Sol. b **202** (1997), p.421
[7] S. Hara, W.F.J. Slijkerman, J.F. van der Veen, I. Ohdomari, S. Misawa, E. Sakuma and S. Yoshida, Surf. Sci. Lett. **231** (1990), p. L196.
[8] T. Yoshinobu, I. Izumikawa, H. Mitsui, T. Fuyuki and H. Matsunami, Appl. Phys. Lett. **59** (1991), p. 2844.
[9] P. Soukiassian, F. Semond, L. Douillard, A. Mayne, G. Dujardin, L. Pizzagalli and C. Joachim, Phys. Rev. Lett. **78** (1997), p. 907.
[10] A. Catellani, G. Galli, F. Gygi and F. Pellacini, Phys. Rev. B **57** (1998), p. 12255.
[11] L. Douillard, F. Semond, V. Yu. Aristov , P. Soukiassian, B. Delley, A. Mayne and G. Dujardin and E. Wimmer, Materials Science Forum, Trans Tech Publishing Ltd, **264-268** (1998) p. 379.
[12] W. Lu, P. Krüger, J. Pollman, Phys. Rev. Lett. **81** (1998), p. 2292.
[13] V. Yu. Aristov, H. Enriquez, V. Derycke, P. Soukiassian, G. Le Lay, C. Grupp and A. Taleb-Ibrahimi, Phys. Rev. B **60** (1999), p. 16553.
[14] P. Soukiassian, V.Yu. Aristov, L. Douillard, F. Semond, A. Mayne, G. Dujardin, L. Pizzagalli, C. Joachim, B. Delley and E. Wimmer, Phys. Rev. Lett. **82** (1999), p. 3721.
[15] V. Derycke, P. Fonteneau and P. Soukiassian, Phys. Rev. B **62** (2000).

Materials Science Forum Vols. 353-356 (2001) pp. 239-242
© 2001 Trans Tech Publications, Switzerland

Investigation of the SiC Surface after Nitrogen Plasma Treatment

L.A. Bereznjakova[1], A.V. Shchukarev[2] and V.I. Ivanov-Omskii[3]

[1] Department of Microelectronics, St.-Petersburg State Electrotechnical University, Prof. Popov str. 5, RU-197376 St.Petersburg, Russia

[2] Mechanobr-analit

[3] A.F.Ioffe Physico-Technical Institute, Russian Academy of Sciences, Polytechnicheskaya, RU-194021 St.-Petersburg, Russia

Keywords: Chemical Bonding, Etching, Layer-by-Layer Analysis, Nitrogen Plasma, SiC_xN_{1-x}, Surface Morphology, XPS

Abstract

Amorphous thin nitrogen-containing layers, whose stoichiometry is close to SiC_xN_{1-x}, where x is variable in depth, have been obtained by SiC surface treatment with a nitrogen plasma. X-ray photoelectron spectroscopy (XPS) with layer-by-layer analysis was used for the study of the composition and the chemical bonding in depth of nitrogen-containing layers. Both the process of etching in the nitrogen plasma and the process of introducing nitrogen ions in the SiC surface in relation to the time of treatment in the nitrogen plasma were investigated. The surface profile mesurement showed a very smooth surface morphology after the nitrogen plasma treatment.

1.Introduction

The current interest in silicon carbon nitride comes from the recent theoretical prediction about the existence of the superhard phase in the system Si-C-N [1]. Such ternary systems, whose stoichiometry is very close to SiCN, were prepared by using various deposition techniques [2,3]. A wide band gap (Eg=3,26) was observed in this compound [2]. The possibility of silicon carbon nitride formation by a SiC surface treatment with the nitrogen plasma was examined in the present work.

2.Experimental procedure.

The processing was carried out by using a high frequency (HF) sputtering system with a base pressure of 10^{-6}Torr. The samples were placed on the target. The total nitrogen pressure was kept at 5mTorr and the HF power was about 1kW. The ion energy did not exceed 1kV. 6H-SiC Lely substrates with (0001)Si and (0001)C surface orientation and 3C-SiC epitaxial layers grown on a Si-substrate were used as samples. A treatment time between 5min and 5hour was used.

The XPS measurements were performed on a PHI 5400 CI system with a base pressure of 10^{-10} Torr. Layer-by-layer analysis through Ar ions etching with an energy of 2keV and an etching rate of approximately 7 - 7,5A/min was applied for the study of the composition and the chemical bonding in the depth of layers. Quantitative analysis on each element at different chemical states was carried out by the corresponding peak area ratio using the following elemental sensitivity factors: S_{Si}**=0,34;** S_N**=0,48;** S_C**=0.3;** S_O**=0,7.** Curve fitting was carried out using a Gaussian function. A deconvolution of the photoelectron lines of each element was performed for the chemical state determination. In this case the experimental error in the determination of bonding energy and concentration are 0.2eV and 10%, respectively. To consider the surface charge during the process of the photoelectron emission the energy scale was calibrated with C1s E_B=285eV (hydrocarbon line).

3.Results and discussion.

The results of the XPS analysis of the Si-face 6H-SiC after 1hour treatment with nitrogen plasma are shown in the Table. Identical results were received on the C- and Si-face 6H-SiC after 5 min-1hour treatment with nitrogen plasma. Chemical shifts in the bonding energy of the C1s and Si2p photoelectron peaks in the nitrogen-containing layers in relation to the C1s and Si2p bonding energy experimentally determined for SiC (C1s: **E_B=282.5;** Si2p: **E_B=100.3**) are observed with values of at least 1-1.5eV. It occurs when there is a change in the valence state of the bonding atoms and new chemical bonds are forming. The deconvolution results reveal the coexistence of Si-N, Si-C and C-N chemical bonding in the nitrogen-containing layers as shown in the Table.

Table: The change of Binding energy, Concentration, Bonding type with depth of layers.

	Ñ1s				**Si2p**				**N1s**			
sputter. time in Ar, min; depth, A	E_B, eV	[C], àt %	Bond. type	Ref.[3] and experimental data	E_B, eV	[Si], àt%	Bond. type	Ref.[3] and experi-ment. data	$Å_B$, eV	[N], àt%	Bond. type	Ref. [3]
0	283,7 285 286,6	2,7 27,2 4,9	C-Si hydro-carbon Ñ-N	282.5-283,5 285 285,9-288,6	101,8 103,1	20 4	Si-N Si-O	101,5-101,8 in Si_3N_4 102,5-103	397,7 399,5	20 1,4	N-Si N-C	397,1-397,8 398,4-400,3
5 (80-90À)	283,4 285 286,5	16,6 6,1 2,3	C-Si hydro-carbon Ñ-N	282.5-283,5 285 285,9-288,6	101,2 102,2	33,3 5,1	C-Si-N Si-O	101,5-101,8 in Si_3N_4 102,5-103	397,6 399,1	24,5 3,9	N-Si N-C	397,1-397,8 398,4-400,3
15 (160-170À)	283,7 285 286,4	25,7 7,5 2,9	C-Si C-C Ñ-N	282.5-283,5 285 285,9-288,6	101,1 102,3	37 7,5	C-Si-N Si-O	101,5-101,8 in Si_3N_4 102,5-103	398,1 399,5	11,1 2,5	N-Si N-C	397,1-397,8 398,4-400,3
25 (220-230À)	283,3 285	34,8 6,2	C-Si Ñ-Ñ	282.5-283,5 285	100,5 101,6	39,9 8	Si-C Si-N	100,3 101,5-101,8	398,1 399,6	4,2 1,8	N-Si N-C	
40 (330-340À)	283 285	41,1 4,3	C-Si Ñ-Ñ	282,5 285	100,2	48,8	Si-C	100,3	397,5 399,5	1,4 1,2	N-Si N-C	

Careful examination of the binding energy reveals a slight shift in comparison with that one of the binary compound listed as reference in the Table . For example, the binding energy of Si2p bonded with N agrees with that one in the Si_3N_4 compound just on the surface of the nitrogen-containing layers (that is without sputtering in Ar). But after 5min sputtering in Ar, the binding energy of Si2p bonded with N decreased to 0.3-0.5eV. It does not agree with the binding energy of Si2p both for Si_3N_4 and SiC. In addition, the binding energy of Si2p bonded with C was not observed, though the binding energy of C1s bonded with Si exists. These experimental results can be explained supposing that Si is bonded with both N and C whose electronegativity is much less

than that one of N (electronegativities for elements are: **Si-1.8, C-2.5, N-3**). The binding energy of the inner electrons of an element is higher when this element is bonded to an element with high electronegativity, and vice versa. Actually, on the surface of the nitrogen-containing layers the binding energy of Si2p in C-Si-N bonding agrees with that one in Si_3N_4 because the concentration of C in this bonding is low (2,7at%). The binding energy of C1s bonded with Si2p was higher than that one in SiC because of partial replacement of Si in the C-Si bonding by N whose electronegativity is much higher than that one of Si.

This means that a "clear" bonding of Si-N, N-C, Si-C is absent in the nitrogen-containing layers, i.e. each component was bonded to the other two components. Such a ternary system does not contain a mixture of the different phases and it is defined as a solid solution with variable composition in depth. A quantitative analysis resulted in the stoichiometry of these nitrogen-containing layers, which is approximately close to SiC_xN_{1-x}, where x is variable in depth. Using the cut of the ternary phase Si-C-N diagram in approximation of the SiC-Si_3N_4 quasibinary cut, the stoichiometry of this ternary system was refined as $SiC_{x/(3-2x)}N_{(4-4x)/(3-2x)}$. The thickness of SiC_xN_{1-x} films was about 20nm. The Si-C chemical bonds typical for SiC are revealed at greater depth.

The distributions of N concentration with depth of the nitrogen-containing layers are shown in Fig. 1 and Fig. 2.

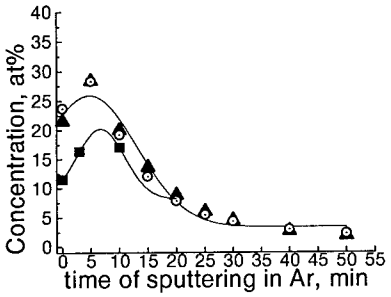


Fig.1. The distribution of N concentration with depth of layers formed on:
▲ C-face of 6H-SiC treated for 1hour
⊙ Si-face of 6H-SiC treated for 1hour
■ C-face of 6H-SiC treated for 5min
Approximation by Gaussian function: ——

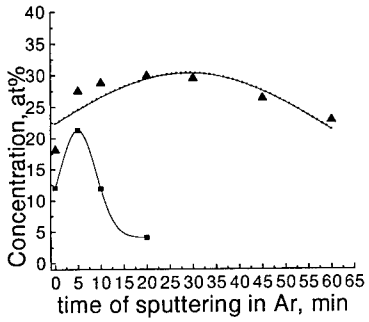


Fig.2.The distribution of N concentration with depth of layers formed on 3C-SiC:
▪ after 20 min treatment in N
▲ after 30 min treatment in N
Approximation by Gaussian function:——

There were no essential differences between the thickness of the nitrogen-containing layers formed on the Si- and C- faces of 6H-SiC substrates as shown in Fig. 1. The thickness did not change with increasing time of treatment from 5min to 1hour (Fig1). The 6H-SiC surface is intensively etched according to our experimental data. The etching rate was about 0.7-0.8 μm/h and 1-1.3 μm/h for the Si- and the C-face of 6H-SiC respectively. It is believed that an equilibrium between the rate of ions introduced in the 6H-SiC surface and the etching rate of 6H-SiC surface was established during no more than 5 min. That determines the constant thickness of the nitrogen-containing layers which does not depend on the time of treatment. The experimental data as shown in Figs. 1 and 2, were approximated by a Gaussian function. It agrees with the theory of

ions passing amorphous targets [4]. However, the thickness of layers formed on the 3C-SiC as shown in Fig. 1 strongly depends on the treatment time (increasing of the nitrogen-containing processing time by a factor of 1.5 enlarges the thickness of SiC_xN_{1-x} layers by a factor of about 5) in contrast to the thickness of layers formed on 6H-SiC. Most likely that is connected with a less perfect structure of 3C-SiC as compared with that one of 6H-SiC. According to our experimental data, the 3C-SiC surface is also intensively etched (1.2 μm/h). It is possible that an equilibrium between the rate of ions introduced in the 3C-SiC surface and the etching rate of 3C SiC surface will be established after a longer treatment time.

Structure and surface morphology were investigated by electron diffraction technique and optical microscopy together with a profile measurement technique. Layers were demonstrated to have amorphous structure.

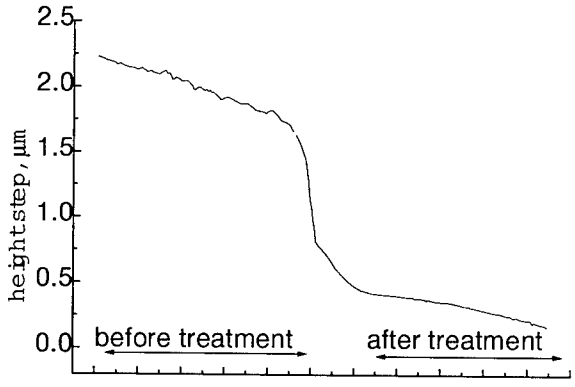


Fig3. The surface profil of the C-face 6H-SiC before and after treatment in nitrogen plasma.

As shown in Fig.3 a smooth surface morphology is formed after the nitrogen plasma treatment where the medium-roughness is less than 0.1μm in comparison to the medium-roughness of about 0.1μm before nitrogen plasma treatment. The same smooth surface was obtained after 5 min and 5 hour treatment with nitrogen plasma.

4.Conclusion.

The XPS-analysis showed that during SiC surface treatment with a nitrogen plasma Si-C bonds were broken and new chemical bonds are formed, where each component was bonded to the other two components. Such a ternary system can be defined as solid solution with variable composition in depth. Quantitative analysis resulted in the stoichiometry of these nitrogen-containing layers, which is approximately close to SiC_xN_{1-x}, where x is variable in depth. The thickness of SiC_xN_{1-x} layers was about 20nm. Layers were demonstrated to have amorphous structure. The surface of nitrogen-containing layers has a smooth morphology, where the medium-roughness is less than 0.1μm.

References.

[1] J.E. Lowther, Superharrd Materials. phys. stat. sol. (b) 217 (2000) p.533
[2] L.C. Chen, C.K. Chen, S.L. Wei., J. Appl. Phys. Lett., 72, (1998) p.2463
[3] X. Xiao, Y.Li, L.Song, Appl. Surf. Sci. 156 (2000) p.155
[4] I.G. Pichugin, Yu. Ì. Tairov. Technology of semiconductors devices. (1984), 215

Materials Science Forum Vols. 353-356 (2001) pp. 243-246
© 2001 Trans Tech Publications, Switzerland

Morphology of Sublimation Grown 6H-SiC(000$\bar{1}$) Surfaces

D. Schulz, J. Dolle, H.-J. Rost, D. Siche and J. Wollweber

Institut für Kristallzüchtung, Max-Born-Str. 2, DE-12489 Berlin, Germany

Keywords: 6H-SiC, C-Terminated Face, Sublimation Growth, Surface Morphology

Abstract Sublimation grown epitaxial layers as well as crystals have been investigated by optical microscopy (NDIC: Nomarski differential interference contrast), atomic force microscopy and photoluminescence. Crystal growth was performed on the C-terminated surface of 6H seeds of 30 mm diameter. In addition seeds with off-orientations a few degrees towards <11$\bar{2}$0> and <1$\bar{1}$00> respectively were used. Even on such seeds step flow growth can only be maintained using source material with Si excess. Step bunching is more pronounced when using a stoichiometric source. In contrast to off-oriented layers the on-axis grown material always exhibited a coalescence of individual islands. Growth spirals could not be observed on (000$\bar{1}$) faces.

Introduction

The surface morphology of crystals reflects the microscopic growth mechanism. This strongly influences not only the incorporation of different species but also the generation and development of defects. Sublimation growth of silicon carbide by the modified Lely method depends on the thermodynamic conditions and on the properties of substrates used. 6H-SiC crystal growth on (000$\bar{1}$) faces has been rarely reported, because of the poor polytype stability. Early studies of Stein et al. claimed, that regardless of the seed polytype the 4H polytype had always been obtained using the C-terminated face during sublimation growth [1].
Therefore surfaces of layers and crystals were studied to reveal the influence of different parameters on the morphology. Growth temperature, supersaturation and seed orientation have been varied.

Experimental

Physical vapour transport experiments have been performed in an inductively heated furnace facility. Different temperatures in the range $2000 \leq T\ (°C) \leq 2100$ and inert gas pressures in the range $100 \leq p\ (Pa) \leq 1000$ were applied. In order to study thin layers the growth process was interrupted by backfilling with inert gas and decreasing the temperature simultaneously. The layer thickness dependent on the growth conditions was in the range from a few microns to several 10 microns. Si was added to the SiC source material, which had been produced from elemental silicon and carbon.
Seed wafers were prepared from 6H boules. The seeds were oxidized in wet atmosphere to remove the surface damage layer induced by mechanical polishing and to identify the C-terminated face.

Results

As has been earlier described for the growth on 6H(0001) seeds, the composition of the source material has a strong impact on the growth mechanism [2]. Homogeneous growth conditions on these on-oriented faces could only be maintained by the addition of Si to the source material.

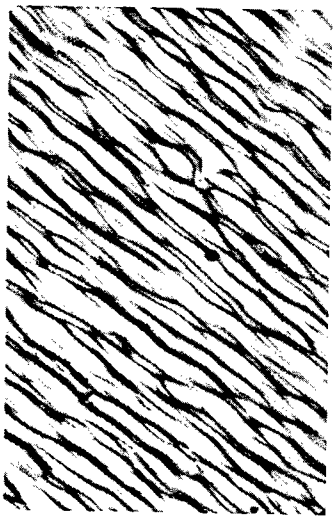


Fig. 1: Optical micrograph of as- grown surface (source with 1% Si excess)

100 µm

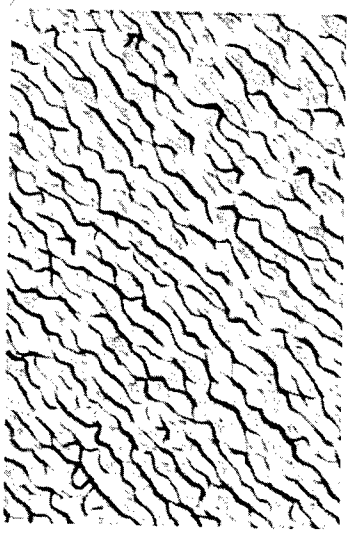


Fig. 2: Optical micrograph of as- grown surface (source without Si excess)

In Figures 1 and 2 the micrographs of layers grown on <11$\bar{2}$0> off-oriented (000$\bar{1}$) substrates are shown. The flow direction is from the lower left to the upper right corner. In the Si excess case the morphology is characterized by step trains with a high degree of bunching. The steps are almost straight with a homogeneous distribution. When using a stoichiometric source the growth morphology deteriorates compared to the case before. Although the steps are of similar height they begin to meander. Nevertheless the surface is macroscopically homogeneous.

A complete change in the morphology is observed when on-oriented seeds are used (Fig. 3a). Large terraces occur separated by high risers. Only occasionally steps can be observed. This growth experiment was performed at 2100 °C and resulted in a layer of about 40 µm in thickness. The terraces turned out to have developed from individual island. This was shown in an experiment carried out at a growth temperature of 2000 °C.

For a more detailed investigation of the influence of the seed orientation on the growth morphology three different growth directions have been examined. In Fig. 3a-c the surfaces of layers grown under identical conditions at a growth temperature of 2100 °C are shown. The observed behaviour of the on-oriented surface indicates that the growth conditions are laterally inhomogeneous and not favourable to crystal growth. The meandering steps in case of <11$\bar{2}$0> off-orientation almost disappear for growth on <1$\bar{1}$00> off-oriented seeds. Only a number of defects and some steps of small height are visible.

The effect of the growth temperature was evaluated in additional experiments at 2000 °C. In Figures 4 and 5 two surfaces can be seen comparable to Fig. 3a and b. As already mentioned the morphology in case of the on-axis growth can be described as 3D growth mode of numerous islands. The top of these islands is flat without any step and between the islands there are deep cavities up to a several microns in depth. It can not be excluded that the cavities reach the original seed surface. Normally the islands exhibit a hexagonal shape.

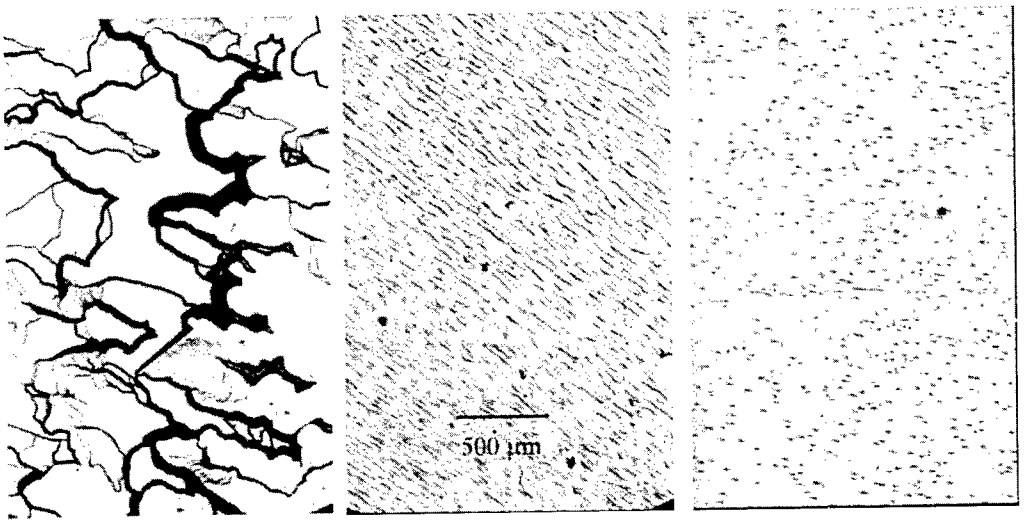


Fig. 3: Micrographs of layers of different seed orientation grown at 2100 °C, from left to right: a) on-axis, b) ≈ 3° off towards <11$\bar{2}$0>, c) ≈ 3° off towards <1$\bar{1}$00>

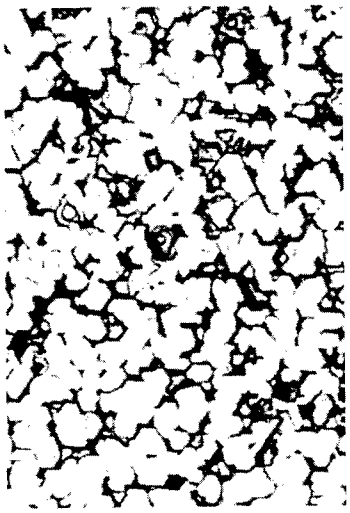


Fig. 4.: Micrograph of layer grown at 2000 °C, on-axis seed

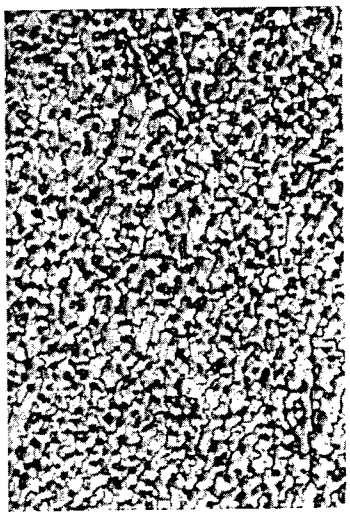


Fig. 5.: Micrograph of layer grown at 2000 °C, off-oriented seed (<11$\bar{2}$0> direction)

The expected step morphology could not be observed on the off-oriented layers grown at 2000 °C. Although there exist steps, they are no longer straight.

Conclusions

The growth morphology of 6H-SiC(000$\bar{1}$) surfaces was studied. The C-terminated face with the lower surface energy leads to a higher nucleation density as compared to the (0001) face [3]. This is reflected by the growth morphology which shows individual islands. These islands coalesce as

crystal growth proceeds and this coalescence may generate defects. Consequently the $(000\bar{1})$ basal plane is not suitable for high quality crystal growth.

The $<11\bar{2}0>$ off-orientation provides conditions for the development of step flow. But at low temperatures (2000 °C) the morphology appears wavy with terraces exhibiting a high degree of step bunching. The macrostep height is up to 10 times the c-axis unit cell parameter. Even at 2100 °C a certain waviness of the step trains remains which is due to anisotropic step bunching [4]. This is a result of different lateral velocities of kinks and steps respectively.

Almost flat surfaces were obtained when growing on seeds with $<1\bar{1}00>$ off-orientation.

Si excess in the source material led to improved layer morphologies. Independent of the used orientation growth spirals have not been observed on $(000\bar{1})$ surfaces of both layers and crystals. In addition, photoluminescence measurements revealed, that under the applied thermodynamic conditions the grown polytype was 6H.

Acknowledgements

The authors would like to acknowledge the support by the Siemens AG Erlangen and by the Bundesministerium für Bildung und Forschung under the project number 01M2952B.

References

[1] R.A. Stein, P. Lanig, S. Leibenzeder, Mater. Sci. Engineer. B**11** (1992) p. 69

[2] D. Schulz, G. Wagner, J. Doerschel, J. Dolle, W. Eiserbeck, T. Müller, H.-J. Rost, D. Siche, J. Wollweber, Mater. Sci. Engineer. B**61-62** (1999) p. 86

[3] H. Matsunami, T. Kimoto, Mater. Sci. Engineer. R**20** (1997) p. 125

[4] M. Syväjärvi, R. Yakimova, T. Iakimov, E. Janzen, Mater. Sci. Forum **338-342** (2000) p. 375

Materials Science Forum Vols. 353-356 (2001) pp. 247-250
© 2001 Trans Tech Publications, Switzerland

Germanium on SiC(0001): Surface Structure and Nanocrystals

B. Schröter[1], K. Komlev[1], U. Kaiser[1], G. Heß[2], G. Kipshidze[3] and W. Richter[1]

[1] Institut für Festkörperphysik, Friedrich-Schiller-Universität Jena, Max-Wien-Platz 1, DE-07743 Jena, Germany

[2] Institut für Optik und Quantenelektronik, Friedrich-Schiller-Universität Jena, Max-Wien-Platz 1, DE-07743 Jena, Germany

[3] A.F.Ioffe Physico-Technical Institute, Russian Academy of Sciences, Polytechnicheskaya, RU-194021 St.Petersburg, Russia

Keywords: Germanium, Molecular Beam Epitaxy (MBE), Nanostructures, Quantum Dots, Scanning Tunneling Microscopy, Surface Structure

Abstract

Germanium nanocrystals as potential candidates for a future optoelectronics in group-IV semiconductors have been grown on SiC(0001). A monoatomic wetting layer is formed in a Stranski-Krastanov growth mode. The surface structure of this wetting layer studied by STM and LEED depends on the SiC surface preparation. 3x3 and 4x4 Ge superstructures are observed by growing on the silicon-rich SiC(0001)-3x3 surface. Surface structures with mainly two-fold periodicity as well as 6x6 are observed after Ge deposition on silicon-deficient SiC(0001)-($\sqrt{3}$x$\sqrt{3}$)-R30° or ($6\sqrt{3}$x$6\sqrt{3}$) surfaces. Two-dimensional Ge islands of lateral dimensions between 2 and 4 nm and a density of $3 * 10^{12}$ cm^{-2} are initially formed on the wetting layer to reduce strain. Further deposition results in the growth of nanocrystals of lateral dimensions between 40nm and 150nm and heights between 5 and 30nm. A maximum density of 10^{10} cm^{-2} and minimum size of these nanocrystals has been obtained for low deposition temperature of 470°C and high rate of 1.5nm/min. The epitaxial orientation of the nanocrystals has been determined as (111) and (220) by TEM and XRD.

Introduction

Low-dimensional semiconductor structures are investigated for their interesting properties for electronic and optical applications [1]. Nanometer scale structures are expected to show electron confinement the stronger the smaller the size. Quantum dots confining the electrons in three dimensions can be grown by Stranski-Krastanov growth mode. Due to the strain induced by a different lattice constant of substrate and deposited material, an initially two-dimensional (2D) epitaxial growth changes to 3D island growth on a thin wetting layer. This formation of self-assembled islands reduces the strain and lowers the total energy of the system.

Germanium nanocrystals embedded in a semiconductor matrix are potential candidates for a future optoelectronics in group-IV semiconductors. Although an indirect semiconductor, high intensity luminescence is expected for germanium quantum dots due to carrier confinement. Many investigations have dealt with Ge on Si(001) or Si(111) [e.g., 2-5]. We have grown Ge on SiC(0001) by solid-source MBE. The wide-band gap semiconductor SiC may give the possibility to arrange quantum dots at a p-n junction for electroluminescent devices. A Stranski-Krastanov-like growth mode is observed due to the huge lattice mismatch of some 30% between silicon carbide and germanium. We investigated the surface structure of Ge on differently prepared SiC(0001) by Scanning Tunneling Microscopy (STM) and Low-Energy Electron Diffraction (LEED). The formation of Ge islands by Stranski-Krastanov growth mode is measured in situ by STM and ex situ by Atomic Force Microscopy (AFM), High-Resolution Transmission Electron Microscopy (TEM), and X-ray diffraction (XRD).

Experimental

The 4H and 6H on-axis and (high miscut) off-axis SiC(0001) surfaces were prepared ex situ either by plasma etching, subsequent oxidation and HF dip or by hydrogen etching and in situ by heating in a Si flux to get definite reconstructions of 3x3, ($\sqrt{3}$x$\sqrt{3}$)-R30° or (6$\sqrt{3}$x6$\sqrt{3}$) observed by electron diffraction (LEED). Germanium was deposited from effusion cells with evaporation rates of 0.1 to 1.5 nm/min at substrate temperatures of 470 and 550°C. Additionally, several samples were deposited with germanium at room temperature and, subsequently, heated to form nanocrystals.
The surface composition before and after Ge evaporation was measured by X-ray Photoelectron Spectroscopy (XPS). Surface structure and morphology as well as size, geometry, density and distribution of nanocrystals were determined in situ by STM and ex situ by AFM, TEM and XRD.

Results and Discussion

A wetting layer was formed by Ge deposition at substrate temperatures of 470 and 550°C. Depending on Ge coverage and surface preparation, different reconstructions were observed in LEED and STM. Most of the samples showed a 1x1 LEED pattern after more than 2ML Ge deposition. In this temperature range the large lattice mismatch causes a transition from 2D to 3D (islands) growth of Ge on SiC at a coverage near 1 monolayer (ML).
After deposition of Ge on a Si-rich SiC(0001)-3x3 surface, 3x3 and 4x4 hexagonal, trigonal and honeycomb structures have been initially observed by STM depending on the coverage in the submonolayer range, annealing temperature and annealing time (fig.1a). A deposition of more than 2ML of Ge at temperatures of 470°C and rates between 0.5 and 1.5nm/min results in nanocrystals of typical dimensions between 50 and 100nm and a Si-Ge alloying as characterized by TEM and XRD [6].
The evaporation of Ge on SiC(0001)-($\sqrt{3}$x$\sqrt{3}$)-R30° or (6$\sqrt{3}$x6$\sqrt{3}$) leads to a wetting layer showing a complex surface structure of mainly two-fold (0.6 nm) periodicity (fig. 1b). Linear „tracks" which may be formed of dimer rows obviously to reduce stress were observed by STM for a higher Ge coverage near 1 ML. Two-dimensional (2D) Ge islands with a high density of some 3 * 10^{12} cm^{-2} and dimensions between 2 and 4 nm are formed on the Ge wetting layer (fig. 2). At step edges of the SiC substrate, two-dimensional Ge islands of up to 50nm lateral dimensions and weak corrugation were observed on top of the first Ge wetting layer (fig. 3). Additionally, small regions of some tens of nm showed a 6x6 surface structure.

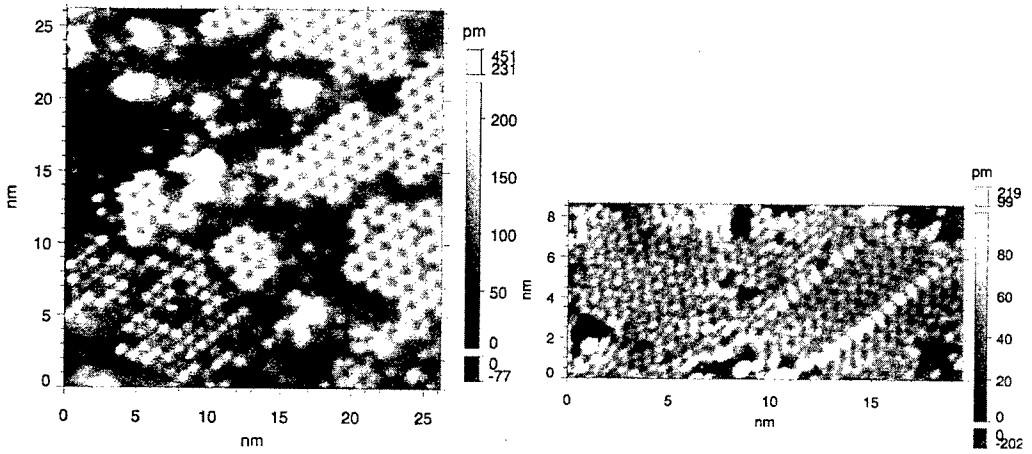


Fig. 1 (a) (b)
STM images of (a) 3x3 and 4x4 reconstructions of Ge on 6H SiC(0001)-3x3 and (b) surface structures observed on 6H SiC-($\sqrt{3}$x$\sqrt{3}$)-R30° showing mainly two-fold periodicity and dimer rows or „tracks".

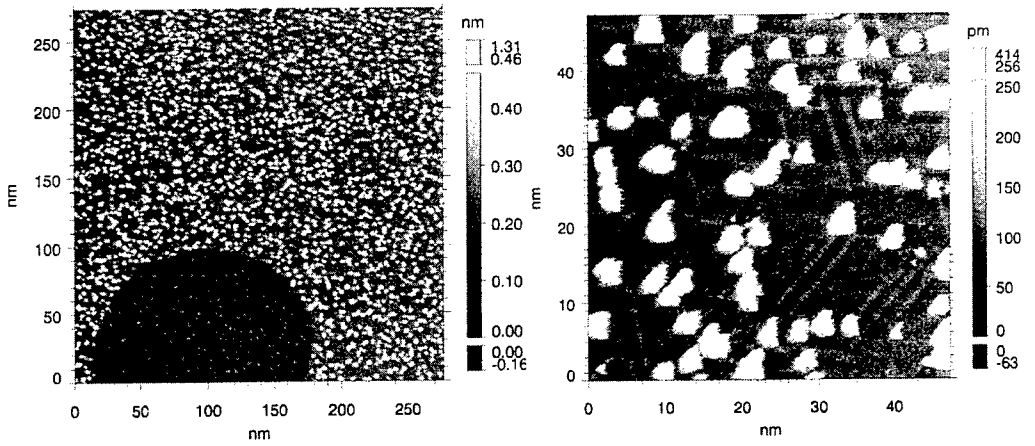


Fig. 2 (a) (b)

STM images of 2D Ge islands grown on 6H SiC(0001)-($\sqrt{3}$x$\sqrt{3}$)-R30° at a deposition rate of 1nm/min at 470°C.

(a) An equal 2D nucleus density is observed on neighboring terraces differing in height of one Si-C layer.

(b) The 2D islands are formed on the Ge wetting layer showing a surface structure with two-fold periodicity and dimer rows.

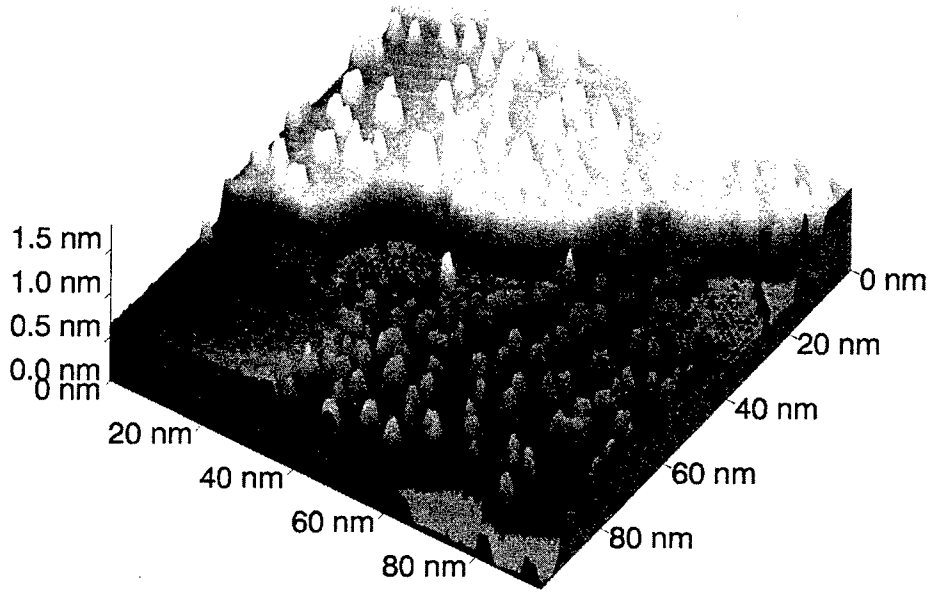


Fig. 3

STM image of approximately 1.5 ML Ge deposited on SiC(0001)-($\sqrt{3}$x$\sqrt{3}$)-R30° showing nanosized 2D Ge islands on a Ge wetting layer. At SiC step edges two-dimensional Ge islands of some 50nm lateral dimensions are observed as well as regions of 6x6 structure.

At a higher Ge coverage between 2 and 8 ML, 3D nanocrystals with average diameters between 40 and 150 nm and heights between 5 and 30 nm were measured on most of the samples. The epitaxial orientation of the nanocrystals has been determined as (111) and (220) by TEM and XRD [6]. Those films grown at lower temperature (470°C) and high rate show a narrow size distribution of the nanocrystals and a maximum density of 10^{10} cm^{-2} (fig. 4). Depending on growth conditions also much smaller nanocrystals of only 2nm in height and a high density in a bimodal distribution of island sizes were observed by AFM. No difference was found for deposition on on-axis and off-axis substrates as well as on 4H and 6H. Especially, large crystals (200 to 800nm) formed at low evaporation rate and high temperature or by annealing a Ge film grown at room temperature showed a regular shape, like pyramides, with facets or with flat top, whereas, no regular shape was observed by AFM for most of the samples.

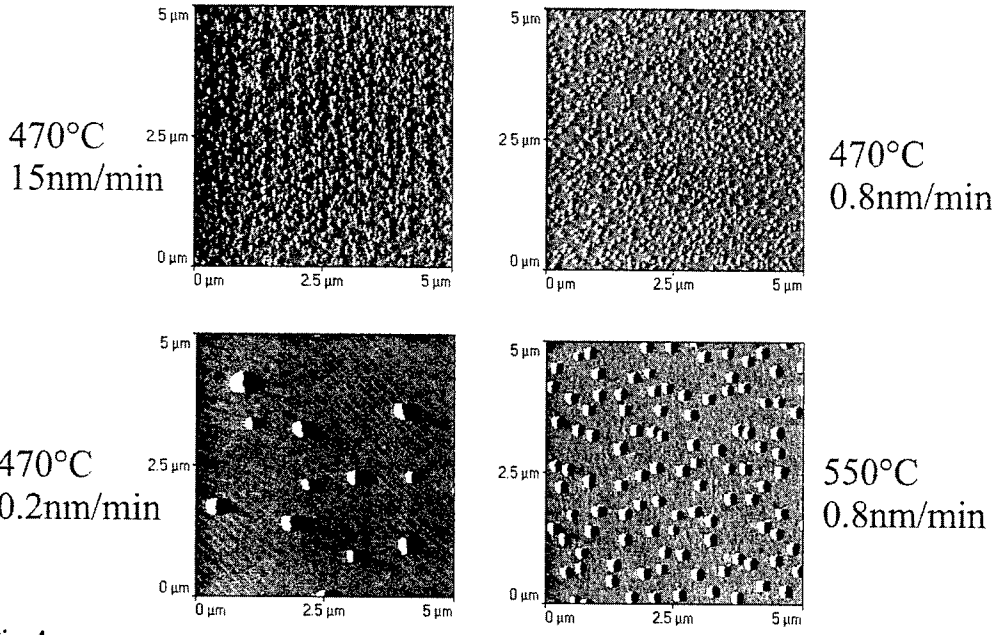


Fig. 4
AFM images of Ge nanocrystals grown on SiC at different deposition rates and temperatures.

Acknowlwdgement
This work is supported by the Deutsche Forschungsgemeinschaft (SFB 196).

References

[1] D. Bimberg, M. Grundmann, N. N. Ledentsov, Quantum Dot Heterostructures, 1999, Wiley, Chichester, England.
[2] F. M. Ross, R. M. Tromp, M. C. Reuter, Science 286 (1999) p.1931.
[3] O. G. Schmidt, C. Lange, K. Eberl, O. Kienzle, F. Ernst, Appl. Phys. Lett. 71 (1997) p.2340.
[4] N. Motta, et al., Surf. Sci. 406 (1998) p. 254.
[5] M. Okada, A. Muto, H. Ikeda, S. Zaima, Y. Yasuda, J. Crystal Growth 188 (1998) p. 119.
[6] G. Heß et al., to be published in Thin Solid Films.

Materials Science Forum Vols. 353-356 (2001) pp. 251-254
© 2001 Trans Tech Publications, Switzerland

Origin of the Excellent Thermal Stability of Al/Si-Based Ohmic Contacts to p-Type LPE 4H-SiC

Liliana Kassamakova[1], Roumen Kakanakov[1], Ivan Kassamakov[1], Konstantinos Zekentes[2], Katerina Tsagaraki[2] and Genoveva Atanasova[3]

[1] Institute of Applied Physics, Bulgarian Academy of Sciences, 59 St. Petersburg Blvd, BG-4000 Plovdiv, Bulgaria

[2] Foundation for Research and Technology Hellas, Institute of Electronic Structure and Laser, Microelectronics Research Group, PO Box 1527, GR-71110 Heraklion/Crete, Greece

[3] Institute of General and Inorganic Chemistry, Bulgarian Academy of Sciences, BG-1113 Sofia, Bulgaria

Keywords: AFM, Ohmic Contacts, Thermal Stability, Transmission Line Model (TLM), XPS

Abstract

Two types of ohmic contacts, namely AlSiTi and Al/Si, have been formed on p-type 4H-SiC grown by LPE. An increase of the optimum annealing temperature was observed for the contacts containing titanium. The lowest resistivity of 9.5×10^{-5} $\Omega.cm^2$ of AlSiTi/SiC contacts was achieved after annealing at 950 °C and a value of 2.5×10^{-4} $\Omega.cm^2$ was measured for Al/SiSiC contacts annealed at 700 °C. It was found that AlSiTi contacts were stable during aging at 600 °C for 100 h while Al/Si contacts deteriorated after 48 h heating. This result can be ascribed to the formation of a stable Al_4C_3 compound in the AlSiTi/SiC contacts annealed at 950 °C.

Introduction

The progress in SiC device processing allows one to fabricate devices operating at higher temperatures. Sensors operating at temperatures above 600 °C have been recently demonstrated [1, 2]. The ohmic contact's thermal stability is one of the main factors that restrict the high temperature application of SiC devices.

The study of Al/Si(2%)/SiC ohmic contacts showed their excellent thermal stability at 500 °C [3]. However, they are not stable at an aging temperature of 600 °C. The experiments with a new contact composition, AlSi(2%)Ti(0.15%), resulted in improved thermal stability of Al/Si-based contacts at 600 °C [4]. In this paper we compare the electrical, thermal and chemical properties of AlSiTi/SiC and Al/Si/SiC contacts. The results of contact composition are discussed in respect to explain the improved thermal stability.

Experiment

Al/Si-based contacts were formed on p-type 4H-SiC layers grown by liquid phase epitaxy (LPE) with a thickness of 0.5 μm and an Al atomic concentration of $(3\text{-}5) \times 10^{19}$ cm^{-3}. The 4H-SiC wafers used for LPE growth were commercially available structures having a top p-type (1×10^{19} cm^{-3}) 1 μm thick epitaxial layer grown on n-type substrates. Two types of metal were deposited by electron beam evaporation: (a) an AlSi(2%)Ti(0.15%) alloy with a thickness of 100 nm, and (b) subsequently deposited Si and Al layers with thickness' of 20 nm and 130 nm respectively. The Si layer thickness was calculated in order to correspond to 2% in the contact film. In the case of the Al/Si/SiC contacts, the annealing of the deposited metals was performed by both resistive heating in a furnace under an Ar flow at a pressure of 760 torr for the temperature range 650-800 °C, and rapid thermal annealing

(RTA) in vacuum at temperatures ranging from 600 °C to 800 °C. The AlSiTi/SiC contacts were annealed in a furnace with resistance heating at temperatures of 700-950 °C.

The contact resistivity was measured using the linear transmission-line-model (TLM) method. The test structure consisted of six pads with a length of 100 μm and a width of 150 μm. The distances between them varied from 7-64 μm. The morphology of the as-deposited and annealed contacts was studied by Atomic Force Microscopy (AFM– Digital Instruments MMAFM-2). The chemical properties of the contacts before and after annealing were studied using an X-ray Photoelectron Spectroscopy (XPS). The XPS analyses were carried out on an ESCALAB MkII (VG Scientific) electron system. In the case of AlSiTi layers AFM and XPS measurements were conducted only in samples annealed at 950 °C i.e. the temperature at which the lowest contact resistivity was achieved. The thermal stability (aging test) of the contacts was investigated by heating for 100 hours at constant temperature of 600 °C in nitrogen ambient. After regular time intervals the samples were cooled down to room temperature for contact resistivity measurements.

Results

The effect of the annealing conditions on the resistivity of Al/Si/SiC contacts was studied at annealing temperatures from 600–800 °C. The experiments showed that after furnace annealing the contact resistivity decreased smoothly up to 700 °C at which temperature a value of 2.5×10^{-4} Ω.cm^2 was measured. This result does not differ significantly from the result (3.8×10^{-4} Ω.cm^2) obtained for the same contact scheme formed at the same temperature on CVD-grown 4H-SiC epilayers with the same doping concentration [3]. Annealing temperature above 700 °C caused an agglomeration of the contact layer and an increase of the resistivity. However, the same agglomeration was observed with the Al/Si/SiC contacts after RTA annealing at 700 °C for 1 min. This difference can be accounted by a discrepancy in the temperature measurement in the two annealing systems. The dependence of the Al/Si/SiC contact resistivity on the annealing temperature is compared in fig.1 with the results obtained for AlSiTi/SiC contacts annealed in the range 700 – 950 °C [4].

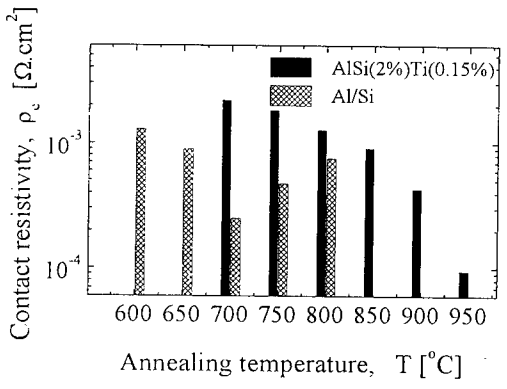


Fig. 1 Dependence of resistivity of Al/Si and Al/Si/Ti contacts on the annealing temperature.

The aging experiments showed the stability of AlSiTi contacts as no change was observed after 100 hours heating at 600 °C while Al/Si contacts became unstable after 48 hours heating at the same temperature [4].

The AFM images showed that the as-deposited and the annealed metal films followed the LPE terraces on the sample surface. In order to not account this surface roughness due to the LPE growth, the ohmic contact roughness analysis has been performed on single terraces. The AFM image of the 2x2 nm area from the as-deposited AlSiTi surface (fig.2a) revealed the granular structure of the metal film. A grain size of ~ 140 nm in diameter was measured. The corresponding surface roughness R_{ms} ~ 9 nm was determined on the area marked by the box. Annealing of the AlSiTi contact at 950 °C caused an increase of R_{ms} to 16 nm (fig.2b). Nevertheless, after the annealing at this temperature no metal agglomerations were observed (fig.2b). The as-deposited Al/Si contact had a smaller granular structure (~60 nm in diameter) in comparison to that of AlSiTi contacts. The contact film covered smoothly the substrate surface and R_{ms} ~ 3 nm was measured (fig. 2c). Annealing at 600 °C did not

change significantly the morphology of the metal layer. However, further increase of the annealing temperature results in larger grain size and more surface roughness. A grain diameter of about 150 nm and R_{ms} ~ 13 nm were measured for Al/Si contacts formed by RTA at 700 °C (fig. 2d). Finally an additional increase of the annealing temperature results in agglomeration of the metal layer.

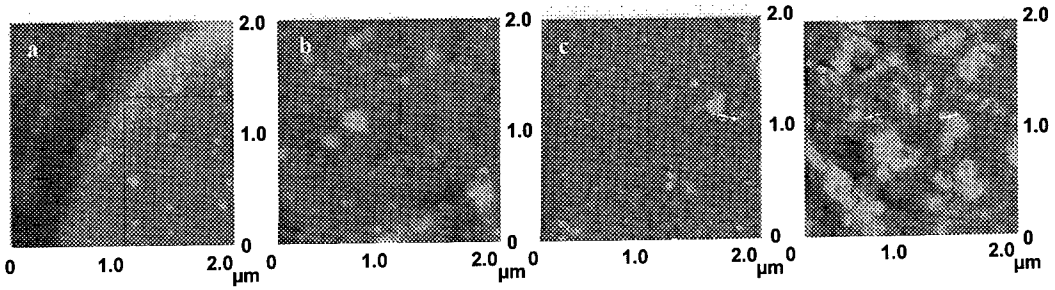


Fig. 2 AFM images of as-deposited (a) and annealed at 950 °C (b) AlSiTi/SiC contacts, and as-deposited (c) and annealed at 700 °C (d) Al/Si/SiC contacts.

Figure 3a shows the in-depth distribution of the elements O, C, Al and Si of the as-deposited AlSiTi contact according to the XPS profile. An abrupt metal/SiC interface, typical of as-deposited samples is revealed. Titanium was registered indirectly by the position of the C1s peak due to its low concentration (0.15%) in the used alloy. Indeed, the position of C1s peak in the sputtering interval 50-110 min indicates carbon in the titanium carbide state (BE 282.5 eV) and in graphite state (BE 284.5 eV). At the surface and subsurface region with sputtering time between 0-10 min hydrocarbons were detected. Aluminum and silicon oxides were also found. The presence of Si in the metal layer is 2-3%, which corresponds to its amount in the used alloy for evaporation. After 50 min sputtering only Al in metal state was observed. The widening of the Al2p peak at the interface with SiC can be considered as a superposition of two peaks determined by the metal and oxide states. We suggest that during the metal deposition Al reduces the native oxide at the SiC surface. The position of Si2p and C1s peaks after 160 min etching indicates that SiC surface is reached.

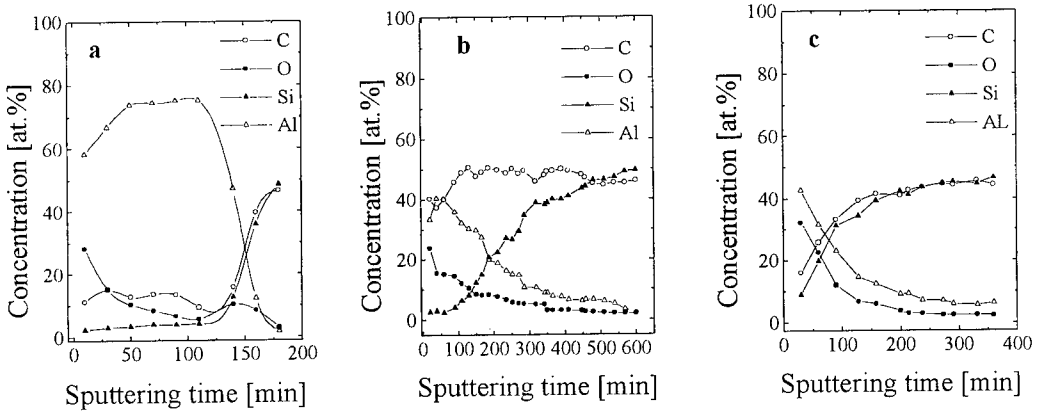


Fig. 3 XPS depth profiles of Al/Si-based contacts: (a) a-deposited AlSiTi/SiC contact, (b) annealed at 950 °C AlSiTi/SiC contact and (c) annealed at 700 °C Al/Si/SiC contact.

The analysis of the photoelectron spectra shows that interdiffusion and chemical reactions during the annealing at 950 °C lead to the transformation of the initial AlSiTi contact layer (fig.

3b). We will consider two characteristic depth regions: contact layer (0-200 min sputtering) and wide interdiffusion region (200-500 min sputtering). At the surface, Al is mainly consumed by forming Al_2O_3. Due to the catalytic effect of Al at elevated temperatures SiC dissociation occurs at the metal/SiC interface [5]. A part of C reacts with Al to form Al_4C_3 (BE 283 eV), while the other part was registered as graphite (BE 284.5 eV) in the contact layer (0-200 min sputtering). The broadened to the lower binding energy C1s peak (BE 283 eV) after 100 min to 150 min sputtering could be assumed as overlapping peaks of C in TiC and Al_4C_3. A weak Si2p peak determined in the contact layer corresponds to the Si-Si bond. After 200 min sputtering aluminum in the metal state only was detected. The intensity of Al2p peak typical for Al in the metal state does not change significantly in the sputtering interval 200-500 min, which suggests diffusion of Al atoms into SiC and formation of a wide interface region.

The deposition of silicon between the Al layer and the SiC substrate as well as the lowering of the annealing temperature decreases the interdiffusion/chemical reaction processes. This effect results in a significantly more abrupt interface of the Al/Si/SiC contact after furnace annealing at 700 °C (fig. 3c). The XPS spectra reveal that the Al is in oxide state at the surface (3 min sputtering) and in metal state in the contact layer and in the interface region with the SiC layer (330 min sputtering).

Conclusion

The investigation carried out on Al/Si-based ohmic contacts established the dependence of their electrical, thermal and chemical properties on the contact structure and composition. The lowest resistivity of 2.5×10^{-4} $\Omega \cdot cm^2$ of Al/Si/SiC contacts was measured after annealing at 700 °C while with AlSiTi/SiC contacts a lowest resistivity of 9.5×10^{-5} $\Omega \cdot cm^2$ was achieved at 950 °C. The higher annealing temperature in the latter case stimulates a higher interdiffusion/chemical reaction of Al with SiC resulting in a dissociation of the SiC surface. The undiffused Al atoms of the contact layer react entirely with the carbon forming a stable compound, Al_4C_3. In contrary, the lowering of the annealing temperature for Al/Si/SiC contacts decreases the interdiffusion/chemical reaction processes. In addition, the Si layer deposited on the substrate surface acts as a barrier for aluminum diffusion. In addition, the dissociation of the SiC surface is poor at 700 °C. As a result, Al in metal state only was established in the XPS spectra of the Al/Si contacts annealed at this temperature. After Aging of Al/Si contacts at 600 °C for 48 hours, areas without a metal film on the contact pads could be seen. This result allows to assume that a part of undiffused Al from the annealed contact layer was evaporated during the long term heating. This process was also observed during the annealing of Al-based contacts at high tmperatures [6]. We suggest that there is a reason for the observed temperature instability of Al/Si ohmic contacts. Indeed, the presence of the chemical stable Al_4C_3 compound and the absence of Al in the metal state are prerequisite for the thermal stability of Al/Si-based contacts as it was demonstrated in the case of AlSiTi contacts which showed an excellent stability at aging temperatures of 600 °C.

Acknowledgements

This work is supported financially by NATO project SfP-971879 for that the authors express their gratitude.

References

[1] S.M. Savage, A. Konstantinov, A. Saroukhan, C. Harris, Mater. Sci. Forum 338-342 (2000), p.1431.
[2] H. Svenningstorp, L. Uneus, P. Tobias, I. Lundstrom, L.-G. Ekedahl, A. Spetz, Mater. Sci. Forum 338-342 (2000), p. 1435.
[3] L. Kassamakova, R. Kakanakov, I. Kassamakov, N. Nordell, S. Savage, E. Svedberg, L. Madsen, Mater. Sci. Forum 338-342 (2000), p. 1009.
[4] R. Kakanakov, L. Kassamakova, I. Kassamakov, K. Zekentes, N. Kuznetsov, Mater. Sci. Eng., in press.
[5] J.R. Waldrop, R.W. Grant, Appl. Phys. Lett. 6 (1993), p. 2685.
[6] J. Crofton, L.M. Porter, J.R. Williams, phys. stat. sol. (b) 202 (1997), p. 581.

Materials Science Forum Vols. 353-356 (2001) pp. 255-258
© 2001 Trans Tech Publications, Switzerland

Ion-Irradiation Effect on the Ni/SiC Interface Reaction

F. Roccaforte[1], L. Calcagno[1], P. Musumeci[1] and F. La Via[2]

[1] Dipartimento di Fisica e Astronomia, Istituto Nazionale per la Fisica della Materia, Corso Italia 57, IT-95129 Catania, Italy

[2] CNR-IMETEM, Stradale Primosole 50, IT-95121 Catania, Italy

Keywords: Interface, Ion Implantation, Nickel Silicide

Abstract The formation of nickel silicide induced by thermal annealing of Ni/SiC samples was studied by means of Rutherford backscattering spectrometry (RBS) and X-Ray diffraction (XRD). Nickel silicide (Ni_2Si) could be observed already after 20 minutes annealing at 600°C, even RBS analysis showed a thin layer of non-reacted Ni on the top of the sample at this temperature. On the other hand, annealing at higher temperature (800°C) led to the complete reaction of the deposited film. Analytical transmission electron microscopy (EDX) showed that carbon was almost uniformly distributed inside the Ni_2Si layer. RBS and Transmission Electron Microscopy (TEM) analysis showed a rough interface between the silicide and the underlying SiC. Ar^+-irradiation of the as-deposited samples and subsequent annealing at 600 and 800°C resulted in the improvement of the silicide/SiC interface with respect to the non-irradiated samples. This effect can be ascribed to the radiation induced damage in the crystalline SiC substrate, which improves the adhesion of the deposited film and enhances the mobility of Ni atoms.

Introduction

Silicon carbide (SiC) is a promising candidate for high temperature and high power electronic devices because of its good thermal conductivity, large band gap, high electric breakdown field, etc. [1]. Metallization is one of the crucial step in the fabrication of electronic devices. Therefore, studying the interaction between metal and silicon carbide substrates during annealing as well as the structural properties of metal silicide-SiC contacts is of primary importance for understanding and controlling electronic devices performances. Several studies have been done in the last decade in order to characterize both the structural and electrical properties of different metallic contacts on SiC, formed with Al, Ti, Co, Pd, Ni, etc. [2,3]. In some of these experimental works, Ni has been proposed as a good candidate for the realization of ohmic and rectifying contacts on n-type crystalline SiC, because of its ease to form silicides even at moderate temperatures [4]. In fact, using Ni for metallization on high doping concentration n^+ 6H-SiC allowed to achieve values of contact resistance as low as $1x10^{-6}$ Ωcm^2 [5]. Recently, high performance 3kV 4H-SiC Schottky barrier diode was realized by using Ni for contacts [6]. However, common to these studies is the difficulty to control the metal contact properties, (e.g. uniformity of the interfacial region, thermal stability, Schottky barrier height), this remaining the biggest limitation for many industrial applications in opto-electronics. In spite of the need to optimize the characteristics of metal-SiC contacts, up to now only few studies on the silicide/substrate interfaces have been reported. Moreover, it still remains controversial the behaviour of carbon during the decomposition of SiC and its redistribution inside the silicide layer [7,8].

In this paper the possibility to improve the silicide/SiC interface by ion-irradiation of the Ni films is pointed out. The redistribution of carbon after formation of nickel silicide is also discussed.

Experimental

Single crystals 6H-SiC, (0001) oriented, purchased by CREE Inc., where used for the experiments. Ni-films were deposited by electron gun evaporation at a rate of 0.5 Å/s. The base pressure in the chamber was $8x10^{-8}$mbar, which increased to $2x10^{-7}$mbar during deposition. An oxide layer 30 nm thick was created on the sample surface by wet oxidation at 1100°C and then removed just before deposition by etching in diluted HF, in order to obtain a fresh surface.
Isochronal (20 minutes) thermal annealing of the samples were carried out in vacuum, at a pressure of $8x10^{-7}$mbar, between 600 and 1000°C. Rutherford backscattering spectrometry (RBS), performed with a 1.6 MeV $^4He^+$ beam, was used to determine the thickness and the stoichiometry of the films. X-ray diffraction (XRD) measurement were performed with a Bruker AXS D5005 diffractometer for identification of the silicide phase and the crystalline structure. Some Ni/SiC samples were irradiated at room temperature with 300 keV Ar^+-ions, at a fluence of $2x10^{15}$ ions/cm^2 before annealing. Cross section Transmission Electron Microscopy (TEM) was used to monitor the quality of the silicide /SiC interface, while analytical transmission electron microscopy (EDX) allowed to determine the depth distribution of all elements after silicide formation.

Results and Discussion

In Fig. 1, the RBS spectra of the as-deposited Ni/SiC samples and those of the samples annealed at 600-800°C are shown. The deposited Ni film is uniform and has a thickness of $1250x10^{15}$ at/cm^2, which corresponds to about 140nm when using a value of $9.1x10^{22}$ g/cm^3 for the Ni density. After annealing in vacuum at 600°C for 20 min, the Ni was almost completely reacted, apart from a thin Ni layer ($80x10^{15}$ at/cm^2 thick) in the near surface region. RBS spectra, simulated by using the computer code RUMP [9], indicated the stoichiometry of the nickel silicide Ni_2Si in the reacted region, whose thickness was $1790x10^{15}$ at/cm^2. The RBS spectra could be fitted with a pure Ni_2Si layer, containing 25 at.% of carbon uniformly distributed through the layer. A similar behaviour was observed after annealing at 800°C, where no unreacted Ni was detected in the surface, and the thickness of the formed silicide was $2000x10^{15}$ at/cm^2. In both the samples, after annealing, the RBS spectra exhibit a broadening of the edge relative to the silicide/SiC interface, indicating the presence of a rough interface and/or surface. No substantial change in the RBS spectra were observed after annealing at 1000°C. Another set of samples was implanted with 300 keV Ar^+-ions after Ni deposition. At this energy, the projected ion range was 136 nm, i.e approximately the depth of the Ni/SiC interface, while the straggling was 60 nm, according to TRIM simulation [10]. After irradiation of the samples no mixing between Ni and Si or Ni and C occurs, as the Ni profile extracted from RBS analysis was the same like the one of the as deposited sample. The RBS spectrum of the implanted sample after annealing at 600 °C is also reported in Fig. 1. In this case complete reaction occurs already at 600°C, with the formation of

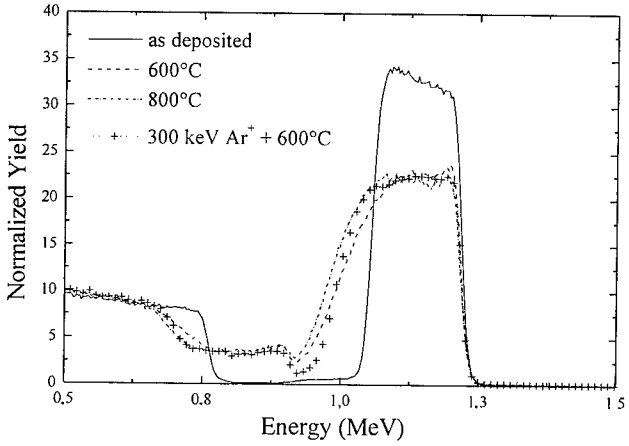


Fig. 1: RBS spectra of the Ni/SiC sample after deposition and annealing at 600 and 800°C. The RBS spectra of the samples after Ar^+-irradiation and annealing at 600 °C is also reported.

pure Ni_2Si, without any residual unreacted Ni surface layer. The main effect of ion-irradiation is evident in the RBS-spectra on the edge corresponding to the silicide/SiC interface, which becomes sharper than the one in the non-irradiated samples.

The silicide phase formation was also monitored by X-ray diffraction. The XRD spectra, shown in Fig. 2, confirm the formation of polycrystalline Ni_2Si already after annealing at 600°C in both the irradiated and non-irradiated sample. The peaks in the XRD spectra can be associated to the formation of Ni_2Si phase. The coexistence with other nickel rich phases like $Ni_{31}Si_{12}$ already reported in Refs. [3,11], which should be the first phase to be formed because of its largest negative enthalpy, was not detected at 600°C. Also after annealing at higher temperatures (800-1000°C) no change in the silicide (Ni_2Si) phase occurred. Moreover, there was no evidence of nickel-carbide formation from the XRD analysis.

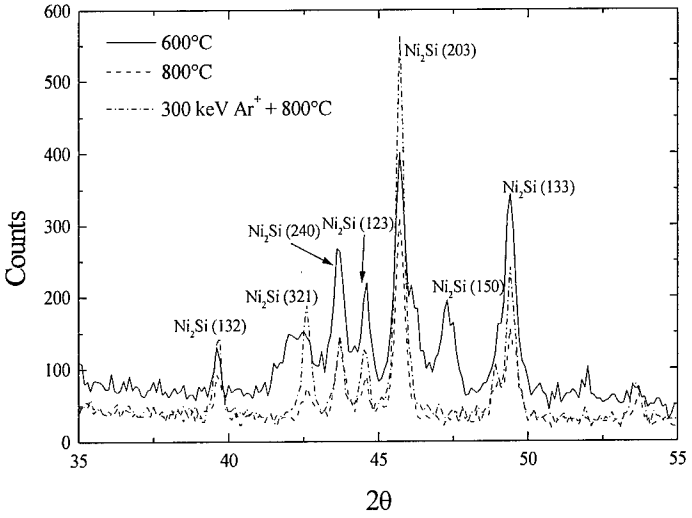


Fig. 2: XRD spectra of the Ni/SiC samples. The Ni_2Si phase forms after annealing at 600°C.

Cross section TEM of the samples was performed in order to monitor the quality of the silicide/substrate interface. From the cross section TEM, reported in Fig. 3, the improvement of the Ni_2Si/SiC interface can be observed, since a very sharp interface is present only in the sample irradiated with Ar^+, after Ni deposition.

On the basis of RBS and TEM results one can try to explain the effect of ion-irradiation on the silicide/SiC interface. After Ar^+-irradiation, at least a thin heavily damaged SiC layer is created in proximity of the Ni interface. Obviously, the thermal diffusivity of Ni atoms increases in the presence of damage. Then a better adhesion of the deposited film and the enhanced diffusivity of Ni into the damaged SiC layer are responsible of the parallel and flat interface. In fact, in the as deposited Ni film a bad adhesion to the SiC substrate leads to a non-uniform growth rate of the reacting silicide front which roughens the interface (see left side of Fig. 3). The absence of unreacted Ni in the irradiated sample annealed at 600°C demonstrates the enhancement of the reaction kinetics, i.e. a higher silicide growth rate, mostly due to the increased diffusivity of Ni atoms in the presence of damage as compared to the crystalline SiC. Independent of ion-

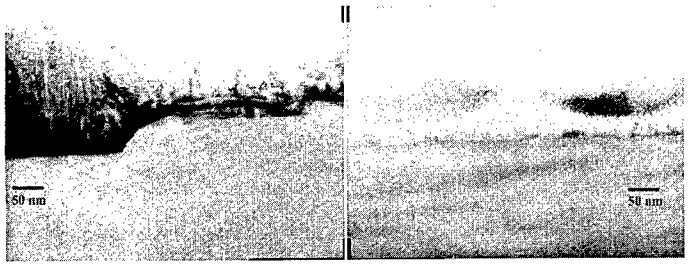


Fig. 3: Cross section TEM of the Ni/SiC samples annealed at 600°C, without irradiation (left) and after irradiation of the deposited Ni film (right).

irradiation, however, the surface of the samples presents a high roughness, which was previously indicated as a consequence of the solid state reaction resulting in the formation of the silicide [12]. In a silicide formation on SiC it is inevitable that carbon atoms are released from the substrate. In order to study the behaviour of carbon during the consumption of the crystalline material in the reaction, elemental microanalysis (EDX) was used. As can be seen from the depth profiles reported in Fig.4, after annealing of the samples the carbon exists as pure phase and is uniformly distributed through the silicide layer. A weak accumulation of carbon at the silicide/SiC interface was observed, both from the peak in the C profile and from the dips present in the Ni and Si profiles at the same depth. It is plausible that, due to the low solubility of C in Ni, the formation of graphite precipitates occurs, which remain trapped at the interfacial sites during reaction.

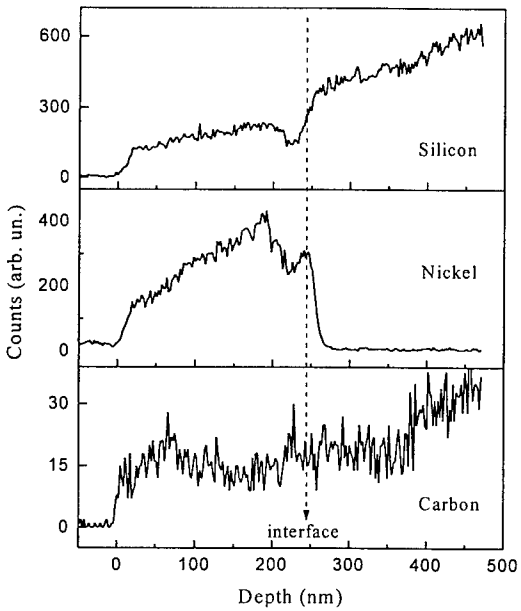


Fig. 4: Depth profiles of carbon, silicon and nickel in the Ni/SiC sample annealed at 600°C, determined by EDX. The position of the silicide/SiC interface is also indicated.

Conclusions

In conclusion, the formation of nickel silicide (Ni_2Si) in Ni/SiC systems was observed at 600°C. After annealing at 800°C the Ni films were completely reacted. It was also demonstrated that ion-irradiation of the deposited Ni films leads to an improvement of the silicide/SiC interface and to an increased reaction kinetics. All these effects were attributed to a better Ni/SiC adhesion after irradiation and to the higher mobility of Ni atoms in the presence of induced radiation damage. Elemental microanalysis showed that the carbon atoms are uniformly distributed through the silicide layer. The weak accumulation of carbon at the silicide/SiC interface, can be due to the formation of graphite precipitates, which remain trapped at the interfacial sites during reaction.

Acknowledgments: The authors thank C. Buongiorno for his help during TEM measurements.

References

[1] H. Morkoç, S. Sitte, G.B. Gao, M.E. Lin, B. Sverdlov, M. Burns, J. Appl. Phys. **76** (1994), p. 1363.
[2] L.M. Porter, R.F. Davies, Mat. Sci. Eng. B **34** (1995), p. 83.
[3] M. Levit, I. Grimberg, B. Z. Weiss, J. Appl. Phys. **80** (1996), p. 167.
[4] J. Crofton, P.G. McMullin, J.R. Williams, M.J. Bozack, J. Appl. Phys. 77 (1995), p. 1317.
[5] T. Uemoto, Jpn. J. Appl. Phys. **34** (1995), p. 7.
[6] Q. Wahab, T. Kimoto, A. Ellison, C. Hallin, M. Tuominen, R. Yakimova, A. Henry, J.P. Bergman, E. Janzén, Appl. Phys. Lett. **72** (1998), p. 445.
[7] I. Ohdomari, S. Sha, H. Aochi, T. Chikyow, S. Suzuki, J. Appl Phys. **62** (1987), p. 3747.
[8] W.F. Slijkerman, A.E.M.J. Fischer, J.F. van der Veen, I. Ohdomari, S. Yoshida, S. Misawa, J. Appl. Phys. **66** (1989), p. 666.
[9] L. R. Doolittle, Nucl. Instrum. Methods B **9**, (1985), p. 344.
[10] J.F. Ziegler, J. P. Biersack, U. Littmark, The stopping and Range of Ions in Solids (Pergamon Press, New York, 1985), Vol. 1.
[11] C.S. Pai, C.M. Hanson, S.S. Lau, J. Appl. Phys. **57** (1985), p. 618.
[12] A.S. Edelstein, D.J. Gillespie, S.F. Cheng, J.H. Perepezko, K. Landry, J. Appl. Phys. **85** (1999), p. 2636.

Materials Science Forum Vols. 353-356 (2001) pp. 259-262
© 2001 Trans Tech Publications, Switzerland

Analysis of Strain and Defect Formation in Low-Dimensional Structures in SiC

U. Kaiser[1], K. Saitoh[2] and A. Chuvilin[3]

[1] Institut für Festkörperphysik, Friedrich-Schiller-Universität Jena, Max-Wien-Platz 1, DE-07743 Jena, Germany

[2] Research Institute for Scientific Measurements, Tohoku University Sendai, Sendai, Japan

[3] Boreskov Institute of Catalysis, SB RAS, av. Lavrentieva 5, RU-630090 Novosibirsk 90, Russia

Keywords: Defect Formation, Ion Implantation, Molecular Beam Epitaxy (MBE), Strain, TEM

Abstract: Advanced transmission electron microscopy techniques have been used to study strain formation in low dimensional structures grown by molecular beam epitaxy (MBE) and after Ge^+- or Si^+-ion implantation and subsequent annealing. Convergent beam electron diffraction patterns (CBED) show that the lattice parameter a of defect-free 3C-SiC MBE quantum films corresponds to that of cubic bulk SiC, however the structure is rhombohedral distorted. A highly defective 3C-SiC layer is formed after room temperature implantation of Ge^+ and annealing. Cracks in the cubic layer have wide strain fields which result in a 6H→3C polytype transformation. In contrast to the thin cubic layers grown by MBE, the resulting cubic stripes are not distorted. ALCHEMI (atom location by channelling enhanced microanalysis) experiments in combination with Bloch wave calculations suggested that for certain implantation conditions the Ge atoms are clustered and located on interstitial positions, straining the SiC matrix. Si nanocrystals formed in the 6H-SiC matrix by Si implantation are unstrained although stacking faults (SFs) parallel to (0001) planes are seen. For Si nanocrystals grown on the surface of cubic SiC, SFs are often seen propagating from the 3C-SiC layer to the dot. Crystals that are 5 to 15nm in size grow in two orientations differing in the misfit to the substrate showing in both orientations only a little strain however larger crystals grow only with the orientation relationship of $(111)_{SiC}$ // $(111)_{Si}$ and $(112)_{SiC}$ // $(112)_{Si}$.

Introduction

SiC is a polytypic material and has the advantage over most other semiconductors that devices can be constructed from the same chemical compound by using a combination of the cubic and hexagonal polytypes. Because of its high thermal conductivity, high break-down electric field strength, high thermal stability and chemical inertness, it has an extremely wide range of possible applications. As the cubic polytype shows a large conduction band discontinuity, a two dimensional electron gas should form when thin cubic quantum films are stacked in a hexagonal matrix, resulting in possible applications in the field of intraband optics. Si or Ge nanocrystals incorporated into the SiC matrix are expected to be strained, and are expected to have a direct transition and an increased band gap [1]. which would be of interest for the development of effective interband optics. In addition, such optical devices could be integrated with the more highly developed Si technology. However the presence of defects on an atomic scale and unstrained nanocrystals can be detrimental to the properties of the devices. Defects such as these are characterized in this paper.

Experimental

Cross-sectional TEM foils were prepared from films of 3C-SiC grown inside hexagonal SiC by MBE [2], from embedded Si nanocrystals and Ge clusters created after Si^+ or Ge^+ ion implantation and subsequent annealing, and from free-standing Si- nanocrystals grown on cubic SiC by MBE [3].

Standard TEM preparation techniques [4], included mechanical polishing, dimpling and low angle Ar-ion milling. The specimens were examined using JEOL-3010 and JEOL-2010 electron microscopes. High-resolution (HR) electron micrographs were obtained at 300kV at the [11-20] zone axis of the 6H-SiC matrix. Image processing was carried out using Gatan Digital Micrograph software. CBED patterns were obtained at 100kV included reflections that are sensitive to small deviations in lattice parameters. Samples are cooled to liquid nitrogen temperature to reduce the contamination.

The site occupancy of Ge atoms in Ge^+ implanted specimens was determined using ALCHEMI [5]. The microscope was operated at 100kV. Bloch state calculations were performed prior to the experiment in order to determine systematic orientations separating Ge interstitial and atom sites into alternating non-equivalent planes and to determine the exact tilt condition for the excitation of single states. The program of Tsuda and Tanaka [6] which is based on full dynamical calculations was used. The characteristic X-ray emission was measured from the elements of interest (Si, C and Ge) at the [12-30] zone axis and at tilts of (1/2g, 1g, 3/2g, 2g and 5/2g) with g=[0006] (parallel to c^*). EDS-measurements were repeated at different places to ensure their reproducibility. Parallel beam conditions were used in thin specimen areas to produce a strong channelling effect.

Results and Discussion

Fig. 1a shows a dark field TEM image of a system of 3C and 4H-SiC thin films grown on 4H-SiC. The substrate-layer-interface can only be identified from strain contrast which may arise from substrate imperfections. The cubic and hexagonal layers were grown far from and near to thermodynamical equilibrium conditions, respectively, as was described more fully elsewhere [7]. For CBED analysis, the [661] 3C-SiC zone axis was chosen. In this orientation, the higher order Laue zone (HOLZ) reflections are symmetrical along the direction indicated by the grey broad perpendicular line in the middle of Fig.1b. The CBED pattern was obtained from a region marked by a circle in Fig. 1a. Distortion from mirror symmetry can be seen at the points marked by arrows. It may be caused by the however small difference in the lattice parameters between the hexagonal and cubic phase. Dynamical simulations were used to match the pattern to lattice parameters of a = 0.4359nm ± 0.0002nm and α = 88.7°±.0.2°. (Details about lattice parameter determination by CBED are given elsewhere [8]).

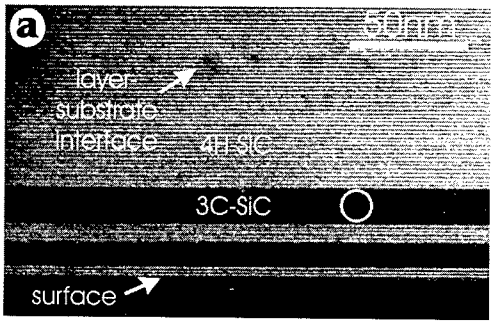


Fig. 1a TEM-DF image of a 4H-3C-SiC layered system grown on 4H-SiC.

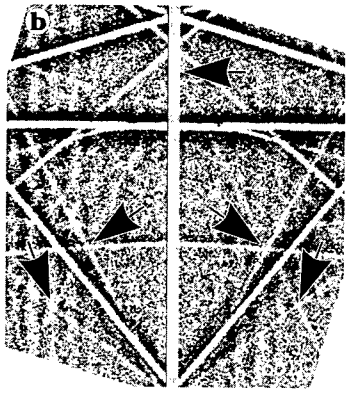


Fig. 1b [661] CBED pattern obtained from the region indicated by a white circle in Fig. 1a.

Fig. 2a shows a highly defective cubic SiC layer produced by room temperature implantation of Ge^+ (dose: 10^{16} cm^{-2}) and annealing at 1200°C. A phase transformation has occurred from the hexagonal to the cubic over the atomically disordered structure. This process is accompanied by a volume decrease, and cracks appear in the cubic layer. These cracks are surrounded by a wide strain field [9], and as a result polytypic transformations take place very deep inside the hexagonal matrix (Fig. 2b). CBED at the [661] zone axis from this cubic stripe shows that cubic symmetry is still present. In conclusion, the thin cubic layers show a small rhombohedral distortion when they grow by MBE, which is not present after the rapid polytype transformation caused by strain.

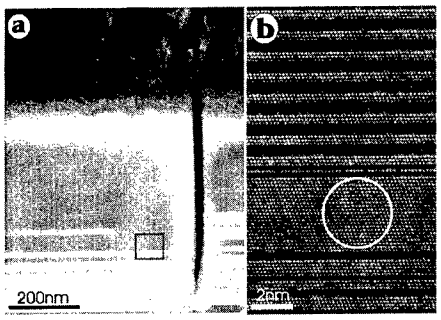


Fig. 2 TEM images of Ge^+ implanted and annealed (1200°C) SiC showing crack-induced polytype changes deep inside the substrate (a) DF-image; (b) HR from the black square shown in a)

The dark-field TEM image in Fig. 3a shows a highly strained crystalline region of the SiC lattice produced after high temperature implantation (700°C) of Ge^+ (dose: 10^{16} cm^{-2}) and annealing at 1200°C, originating from a high density of point defects (interstitials and vacancies), as well as planar and line defects. The Ge EDS signal obtained along the line marked in Fig. 3a is shown in Fig. 3b. It is interesting to note Ge is also present in the less strained region adjacent to the dark region showing strong strain contrast. As no crystalline Ge- containing precipitates formed under these conditions, ALCHEMI [5] was used to determine the preferred site occupancy of Ge in the less strained region. Bloch wave calculations were carried out to enable the determination of optimal tilt conditions for the excitation of atoms on lattice and interstitial sites. Fig. 3c shows that the [12-30] zone axis incidence fulfils the necessary conditions. In Fig. 3d, X-ray emission counts at the [12-30] zone axis incidence for C and Ge are related to the Si counts, which were taken as a reference obtained from exciting the 0003, 0006, 0009, 00012, 00015 reflections, respectively. The area, which was illuminated under parallel beam condition, corresponds to the circle shown in Fig. 3a. The Ge/Si count rate shows an increase with tilt above 3/2 g (g=0006), whereas the C/Si count rate already increases at small deviations from the exact zone axis condition. Ge atoms thus occupy interstitial positions within the SiC lattice, however they do not necessarily only occupy these positions. Molecular dynamic calculations combined with HR-image simulations for different incorporation models are in progress to obtain a fit to the experimental HR image.

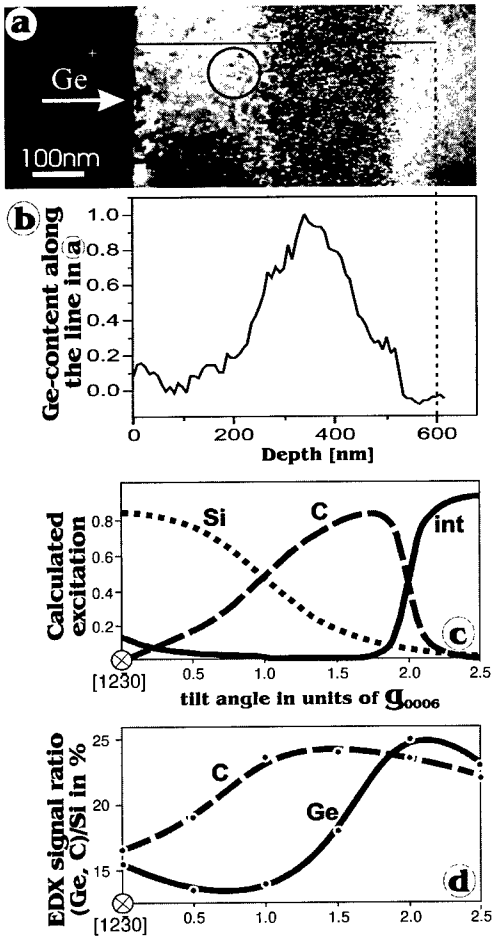


Fig. 3 a) DF TEM image of Ge^+ implanted SiC showing two regions of different strain contrast; b) EDS-Ge content along the line marked in a); c) calculated excitations of Bloch states for Si, C and an interstitial position at the [12-30] zone versus tilt; d) experimental EDS signal versus tilt from [12-30] zone in <0001> direction

Implantation at the same conditions and annealing at higher temperatures led to the formation of Ge- and Si- dots inside the SiC matrix. Fig. 4a shows an overview image, in which the white square corresponds to the Si crystal shown in Fig. 4b. The lattice spacing measured in the FT in Fig. 4c corresponds to the 111 spacing in cubic Si . Stacking faults are present in (111) planes, just as in the hexagonal matrix, and result in a Si nanocrystal with a hexagonality of 40%. In the Fourier filtered image shown in Fig. 4d, the white arrows mark the SFs.

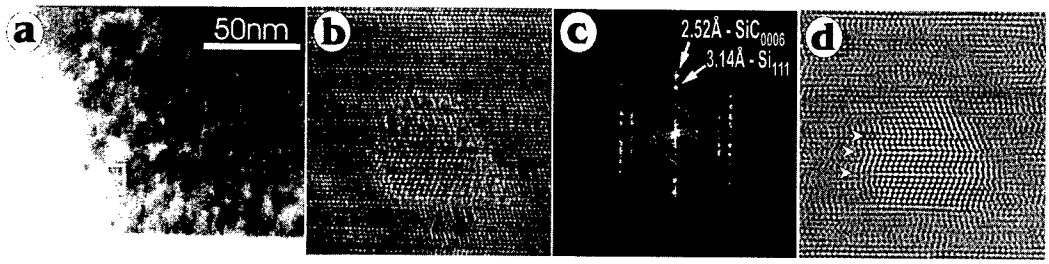


Fig. 4 a) BF TEM image of Si^+ implanted and annealed SiC; b) HRTEM image obtained from the region marked by the white square in a) showing a Si dot in the SiC matrix; c) FT of b); d) Fourier filtered image with arrows marking stacking faults inside Si dot.

Si dots that are 5 to 15nm in size can be grown on the surface of cubic SiC by MBE in two different orientations which have misfits to the substrate of 1.6% and 24.5%. The orientation relationship at [110] zone between the dot and the substrate is $(111)_{SiC}$ // $(220)_{Si}$ and $(11\text{-}2)_{SiC}$ // $(002)_{Si}$ for the low misfit case and is $(111)_{SiC}$ // $(111)_{Si}$ and $(112)_{SiC}$ // $(112)_{Si}$ for the high misfit case. SFs are also often created in these dots as a consequence of a SF propagating through the cubic layer. Although no significant strain could be imaged by CBED it was determined that crystals larger than 20nm grow only with the orientation relationship of $(111)_{SiC}$ // $(111)_{Si}$ and $(112)_{SiC}$ // $(112)_{Si}$.

Conclusions

Thin defect-free cubic MBE layers embedded in 4H-SiC layers are strained and have a rhombohedral distortion. The lattice parameters of the cubic layers were derived from a fit between experimental CBED patterns and fully dynamically simulation. Cubic stripes, which form in the hexagonal SiC matrix as result of strain-induced polytype transformation, are unstrained and it is possible that now the hexagonal matrix becomes strained to relax the however small misfit between the cubic and hexagonal SiC. Implantation causes damage, disorder and strain in a matrix. Here regions of Ge incorporation are not necessarily found to be associated with the presence of greatest lattice damage. ALCHEMI showed that in a region that is less strained, a significant number of Ge atoms are preferentially located at interstitial positions.

Si dots in a SiC matrix and Si dots on the surface of SiC both showed a high probability of SF propagation into the dots. As the crystals are not substantially strained, these SFs may also prevent the dots from becoming strained.

Acknowledgements

We are grateful to Dr. Andreas Fissel and Prof. Wolfgang Richter for providing the MBE layers and to Prof. Werner Wesch and Christian Schubert for providing the implantation material and to all of them for discussions. We would like to thank Prof. M. Tanaka and Dr. K. Tsuda for helpful and stimulating discussions about the ALCHEMI experiments on Ute Kaiser's stay at the RISM, Tohoku University, Japan. The authors acknowledge the support of the Sonderforschungsbereich 196 (No. A03) and the JSPS program (No. RC 29915003).

References

[1] T. Takagahera, K. Takeda, Phys. Rev. B 46 (20) (1992), p. 16678.
[2] A. Fissel, B. Schröter, U. Kaiser, W. Richter, APL Sept. (2000)
[3] A. Fissel, K.Pfennighaus, W. Richter Thin Solid Films 318 (1998), p. 88.
[4] G. Radnoczi, A. Barna, Surf. Coating Techn. 80 (1996), p. 89.
[5] C. J. Rossouw, P.R. Miller, Journal of Electron Microscopy 849-864 (1999), p. 48.
[6] K. Tsuda, M. Tanaka, Acta Crystallogr. A 51 (1995), p. 7.
[7] A. Fissel, J. Cryst. Growth 212 (2000), p. 438.
[8] U. Kaiser, K. Saitoh, K. Tsuda, M. Tanaka, J. Electron Microscopy . 48 (3) (1999), p. 221.
[9] P. Paufler, G. E. R. Schulze, Festkörpereigenschaften II, Akademie Verlag Berlin 1978

Materials Science Forum Vols. 353-356 (2001) pp. 263-266
© 2001 Trans Tech Publications, Switzerland

Source Material Related Distribution of Defects in 6H-SiC Single Crystals

H.-J. Rost, D. Siche, J. Dolle, D. Schulz and J. Wollweber

Institut für Kristallzüchtung , Max-Born-Str. 2, DE-12489 Berlin, Germany

Keywords: Defect Distribution, Inclusions, SiC Bulk Growth, Source Composition

Abstract

The quality of large diameter 6H-SiC single crystals is strongly dependent on the composition of the vapour phase and the thermal conditions inside the growth chamber. Both are also influenced by the composition and structure of the SiC-source and its change during the growth run. To investigate the formation and distribution of defects like micropipes and inclusions, a special series of crystals were grown by the Modified Lely Method on the (0001)silicon face of the seed wafer. The starting composition of the source material was varied while the other growth conditions were kept nearly constant. In the investigated range the number of defects detected at the crystal surface and the average growth velocity showed an inverse behaviour related to the silicon content in the source. Furthermore, the concentration of nitrogen dopants was increased with the silicon content.

Introduction

One of the serious problems in vapour phase growth of 6H-SiC single crystals at high temperatures in porous graphite crucibles is the loss of material, especially silicon, during the growth run. Beside seed quality, the formation of defects and their distribution in the crystal is strongly influenced by the composition of the vapour phase and the thermal conditions inside the growth chamber. They are also dependent on the composition of the SiC-source and its change during the growth process. The role of the powder source is controversially discussed in the literature. The thermal conditions within the powder determine the vapour pressures, the mass fluxes towards the seed, and additional effects like sintering and graphitisation. There exist large radial variations along the powder surface and the temperatures in the powder are highly inhomogeneous [1]. Furthermore, the thermal conductivity of the powder and of the solid (sintered) source are different and so the grain size should have a strong influence, too. On the other hand, for a given set of growth parameters the composition of the source seems to be less important for the crystal quality than the conditions near the growth surface. In this paper the polytype structure and the mechanochemical activation [2] were neglected. The 3C–6H conversion is running in the same way (apart from the sintered source) and the SiC-source powder milling was not applied.

Experimental procedure

To investigate the distribution of defects like micropipes and inclusions, which has been identified as C-particles [3], a special series of crystals with 30 mm diameter were grown by the Modified Lely Method in an inductively heated furnace on the silicon face of a seed. The growth conditions (growth time, crucible geometry, temperature range between 2100°C-2400°C, Ar-pressure between 5-50 hPa) were kept nearly constant. Only the starting composition of the source material was varied. Beginning with a powder source containing 1% silicon excess, in the following runs the sublimated species were replaced by SiC powder from the same charge after removal of the graphite layer. Finally, a growth run was started with the pure sintered solid SiC-source.

The amount of the original charge material was much more than the loss after one growth run. Seeds prepared from the same crystal were used to eliminate the influence of different seed defect

densities. The crystals were cut and polished parallel to the <0001> growth direction. The distribution of the defects along the growth direction and on the crystal surface was investigated by Optical Microscopy.

Results and discussion

The surface of a crystal grown from a powder source (type 1) in Fig.1 and from a sintered one (type 3) in Fig.2 appear different regarding to the number of defects such as micropipes, thermal etch pits or small bubble like scattering centres (voids) which were detected at the surface. The morphology of the facet was also different. A decreased number of defects, especially outside of the facet, with an increased share of SiC- powder was found. While the facets of the type 1 crystals were more smooth with small meander-like growth steps, type 3 crystals showed a more rough structure with many local disturbances caused by step bunching.

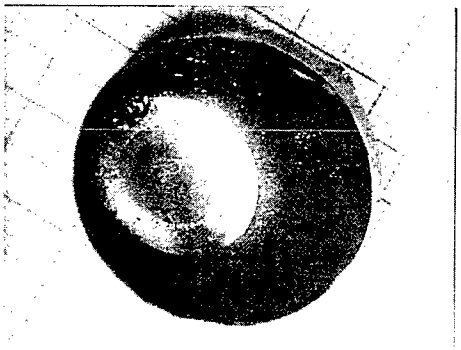


Fig.1 crystal grown from a SiC-powder source (type 1)

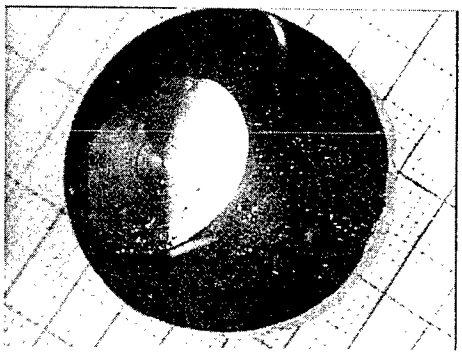


Fig.2 crystal grown from a sintered source (type 3)

This behaviour can be explained by the strong influence of the silicon content on the composition of the vapour phase and the defect generation especially during the first growth steps. The growth parameters were nearly the same except for the different thermal conductivity of the powder and of a sintered solid SiC-source. To deposit stoichiometric solid SiC [4] in a closed system, a non stoichiometric vapour phase composition with a silicon excess in relation to the carbon containing species at the given temperature range is necessary. Caused by silicon loss through the graphite container and the alteration of the source, the silicon deficiency on the carbon side of the phase diagram increases and the system is more shifted away from the stoichiometry. In the case of the new or replaced powder source, we have a noticeable amount of additional silicon which was added to the stoichiometric powder in contrast to the sintered source which consists only of stoichiometric SiC without additional silicon. Therefore, the system will be shifted more towards the equilibrium. The surface of a sintered source was covered by a smaller graphite layer of higher density than the surface of a powder source. The powder density is lower and the incongruently evaporated surface is much larger. So the source efficiency and the silicon excess are increased for a longer time.
Previously we have shown that a composition of the vapour phase closer to the equilibrium creates more favourable conditions for a low defect growth realised by regular step flow without step bunching especially at the beginning of the growth process [5].
The distribution of defects, preferably inclusions, parallel to the growth direction is shown in a type 1 crystal grown from a powder source (Fig.3), a type 2 crystal grown from a source with replacement of the sublimed powder (Fig.5) and a type 3 crystal grown from a sintered source (Fig.4). To compare the inclusion density and distribution, a micropipe-free region close to the centre part of the crystal was chosen. It was revealed that the density of inclusions, carbon particles or voids with inner walls decorated by graphite, was lower by using a sintered source, somewhat higher for the powder source and highest for the source with replacement of the powder. This is in

contradiction to the vapour phase composition model and further investigations are necessary. Furthermore, the inclusions were almost absent at the beginning of the growth process for sources consisting completely or partly of powder (Fig.3+Fig.5). In the case of a sintered source (Fig.4), the concentration of inclusions increased and striation-like arrangements of inclusions occured after half of the growth time. The striation arrangement was stronger at the end of type 2 crystals and has not been seen in crystals of type 1. This can not be related to the excess silicon content of the

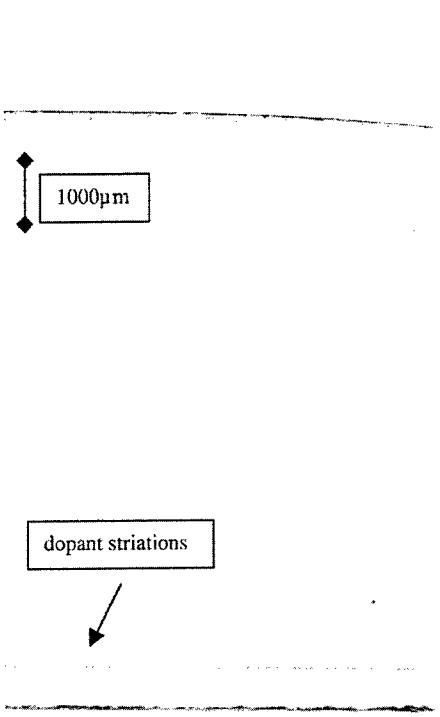


Fig.3 Crystal of type 1
(cut // <0001>)

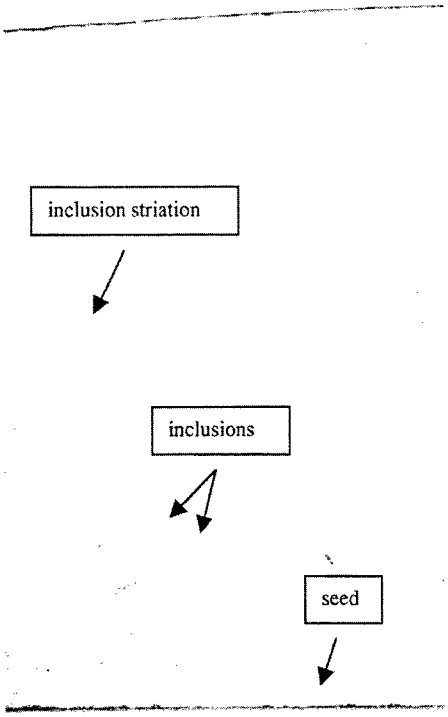


Fig.4 Crystal of type 3
(cut // <0001>)

vapour phase. Although an influence of the silicon content on the inclusion density was revealed, it has to be mentioned, that the main prerequisites for the reduction of the inclusions are a moderate growth temperature and a proper ratio between supersaturation and temperature gradient. Both are defined preferably by the temperature difference between source and seed and the geometry of the system.

With increasing silicon content in the source, an increase of the growth rate was found during the first growth stages [6]. The carbon for these stages comes from the reaction of silicon with the crucible wall [7] and not from the source, located at greater distance. Nevertheless, the average growth rate was reduced for a powder source in comparison to a sintered source. This may result from a higher transport resistance of the thicker graphite layer in relation to the sintered source and transport processes within the source, decreasing the initially higher evaporation efficiency of the source substantially. Additionally, the carbon containing minority species have to diffuse through the silicon majority component.

The increased nitrogen incorporation found in crystals grown from the powder source compared with the sintered source can be explained by a higher content of residual nitrogen and from dopant

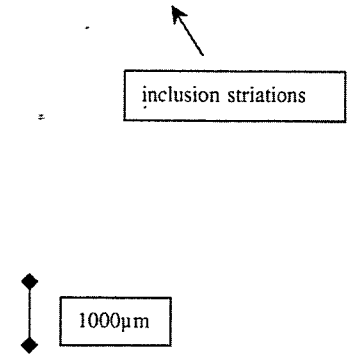


Fig.5 Crystal of type 2
cut // <0001>

marking adhesive to the larger powder surface. On the other hand an axial decrease of nitrogen incorporation was observed. In type 2 crystals an increased nitrogen background concentration of $3x10^{17}$ cm^{-3} has been found because of the large nitrogen contaminated powder surface. During the growth run a sintering and purification process took place lowering the background concentration to $3x10^{16}$ cm^{-3}.

Conclusions

It was found that the number of defects detected at the crystal surface was inversely proportional to the silicon content in the source in the investigated range. The same dependence was registered for the average growth velocity. Furthermore, the growth kinetics, especially the structure of the growth steps at the facet, was improved by silicon excess.

Acknowledgements

The authors would like to thank the Siemens AG Erlangen and the Bundesministerium für Bildung und Forschung (project number 01M2952B) for their support.

References

[1] St.G.Müller, R.Eckstein, D.Hofmann,L.Kadinski, P.Kaufmann, M.Kölbl, E.Schmitt
Mater. Sci. Forum. 264-268 (1998), p.57.
[2] Y.M.Tairov
Mater. Sci. Eng. B 29 (1995) p.83.
[3] H.-J.Rost, J.Dolle, J.Doerschel, D.Siche, D.Schulz, J.Wollweber to be published
[4] Dunbar P.Birnie, W.David Kingery
Journal of Mater. Science 25 (1990) 2827-2834
[5] D.Schulz, G.Wagner, J.Doerschel, J.Dolle, W.Eiserbeck, T.Müller, H.-J.Rost, D.Siche,J.Wollweber
Mater. Sci. Eng. B 61-62 (1999) p.86.
[6] H.-J.Rost, D.Siche, J.Dolle, W.Eiserbeck, T.Müller, D.Schulz, G.Wagner, J.Wollweber
Mater. Sci. Eng. B 61-62 (1999) p.68.
[7] S.Rohmfeld, M.Hundhausen, L.Ley, N.Schulze, G.Pensl
Mater. Sci. Forum. 338-342 (2000), p.579.

Materials Science Forum Vols. 353-356 (2001) pp. 267-270
© 2001 Trans Tech Publications, Switzerland

Characterization of 2 Inch SiC Wafers Made by the Sublimation Method

M. Sasaki, H. Shiomi and S. Nishino

Faculty of Engineering & Design, Kyoto Institute of Technology,
Matsugasaki, Sakyo, Kyoto 606-8585, Japan

Keywords: Cross Polarizer, Sub-Grain Boundary, Sublimation, X-Ray Diffraction (XRD)

Abstract. Two inch 6H-SiC wafers have been studied. Examination of these wafers by cross polarizer showed black and white stripes which corresponded to sub-grain boundaries. The creation of these stripes was influenced by thermal expansion, the shape of bulk surface etc. This phenomena was confirmed by XRD. Two areas were identified by XRD analysis where sub-grain boundaries were easily created or not.

1. Introduction

From the device fabrication point of view, high quality and large size SiC wafers are needed. Recently, the fabrication of monocrystalline SiC bulk wafers with diameters up to 100mm have been reported [1]. However, there are no reports about problems which occur when SiC bulk crystals are enlarged, e.g., the effect of inhomogenity of the substrate temperature. Some defects, especially micropipes and planar defects have been studied [2],[3],[4]. In this report, some problems related to defects and crystallinity were investigated using 2 inch SiC wafers.

2. Experimental Procedure

A 6H-SiC bulk crystal was grown by sublimation method. The growth temperature of the bottom and top of crucible was about 2400 and 2250 °C, respectively. The growth pressure of Ar was about 45 Torr. The graphite crucible was heated by rf induction. The grown 6H-SiC bulk crystal was cut into (0001) wafers.

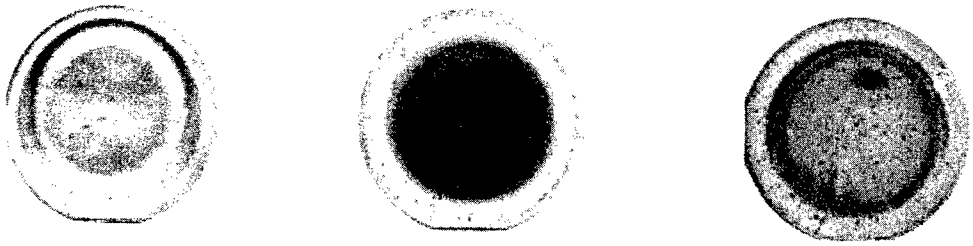
3. Investigation of wafers by some images

Figure.1 shows the optical image of 3 wafers. Figure.1 (a), (b) and (c) were the wafers cut from different positions in the bulk crystal which were about 26.5mm(wafer A), 19mm(wafer B) and 15.5mm(wafer C) from the substrate, respectively. In these wafers, there are some stripes or dark zones which were caused by doping impurities such as N, B, Al etc. Nitrogen which shows green stripes was easily doped in grown layer at early stages of the growth. The black dark areas were identified as p-type by hot probe measurement. These impurities were not intentionally doping.

Figure.2 shows cross polarized images of the same wafers of Figure.1. These wafers were observed under two polarized plates in the dark condition (cross Nicole condition). In this condition, if the wafer is not distorted, the image should be homogeneously dark. However, dark and white regions are mixed together as shown in Figure.2. The existence of the dark and white stripes suggests the existence of distortion. The area near the edge of the wafer has a lot of stripes in all wafers. The origin of the distortion is thought to be due to several reasons. The distortion at the edge area of the wafer is believed to be caused by the difference of thermal expansions between the graphite crucible and SiC bulk crystal. As the size of the

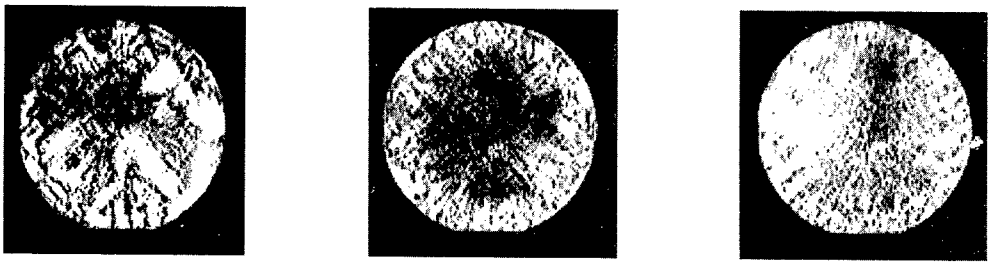
substrate becomes larger, the influence of thermal expansion becomes larger and the crystal is easily distorted. The area of distortion of figure.2 corresponds to the stripes which was made by inclusion doping of figure.1. S.K.Lilov et al reported the strains caused by the heterogeneous distribution of inclusion can enhance the formation of lattice defects and dislocations[5].

In Figure.2 (a), a heavily distorted area is observed compared to other wafers in the center area. This phenomena was influenced by the shape of top surface of grown layer. The bulk surface was convex for every growth run. This phenomena suggests that the growth rate was different between center and edge area of substrate. We believe that this difference in growth rate is related to the temperature gradient on the substrate. Consequently, a thermal stress field was created on the bulk and formed the sub-grain boundaries.



(a) Wafer A (b) Wafer B (c) Wafer C

Fig.1 Photo image of 6H-SiC wafers cut from the same bulk



(a) Wafer A (b) Wafer B (c) Wafer C

Fig.2 Cross polarized image of 6H-SiC wafers

4. Investigation of wafer by XRD

The stripes in the images of Figure.2 correspond to the sub-grain boundaries. They were investigated in more detail by XRD (X-ray diffraction). XRD measurements were carried out using a four-crystal monochromator with CuKα1 radiation. To characterize the crystal quality, the X-ray rocking curve was measured. Two wafers were measured in two configurations as shown in figure.3(a) and 4. In the configurations, FWHM(Full Width at Half Maximum) and the peak angle ω were measured. Type α means that the incident X-ray was along $\langle 11\bar{2}0\rangle$ and measured points were along $\langle 1\bar{1}00\rangle$. Type β means that the incident X-ray was along $\langle 1\bar{1}00\rangle$ and measured points were along $\langle 11\bar{2}0\rangle$. The minimum FWHM was 32.4 sec. These wafers were cut off-axis along $\langle 1\bar{1}00\rangle$. So, in figure.4(b), the peak position of wafer B type β was lower than other data.

The results of Type α of wafer A and B are compared. FWHM became larger and the peak position ω were shifted near the edge of both wafers. But FWHM of wafer A was larger than that of wafer B on left side of figure.4(a) area. This result corresponded to the results of cross polarized image.

The results of Type α and β of wafer B were compared. Type α had a lot of changes both

of FWHM and ω. But Type β results were very flat. It suggested the existence of areas where sub-grain boundaries were easily formed and vice-versa.

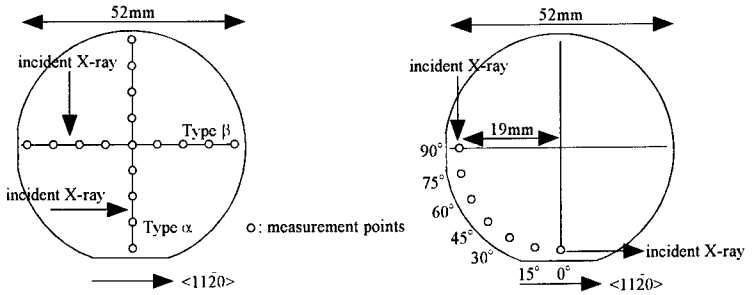
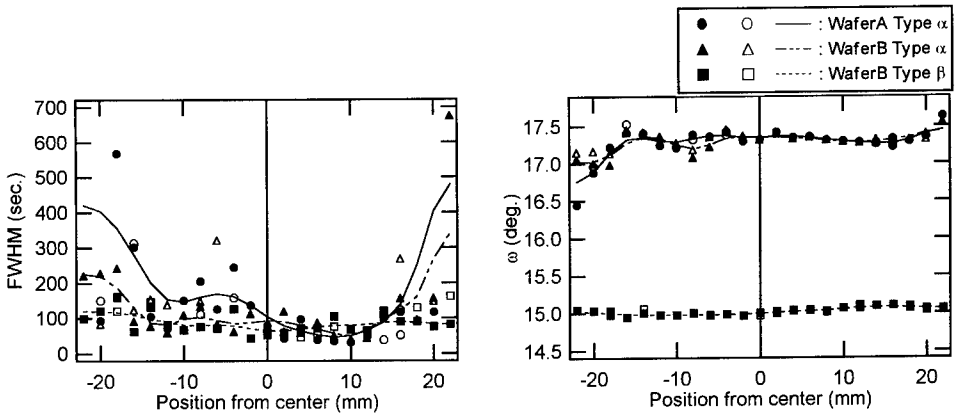


Fig.3 The measurement points and the direction of incident X-ray



(a) FWHM (b) Peak position ω

Fig.4 The results of FWHM and peak position ω at each points by XRD

Areas where the sub-grain boundary is easily formed were studied by measuring some points which were 19 mm distant from the center. The point along $\langle 1\bar{1}00\rangle$ was labeled 0 deg. and the point along $\langle 11\bar{2}0\rangle$ was labeled 90 deg., as shown in figure.3(b). The direction of incident X-ray was perpendicular to the direction connecting the center to each point. Figure.5 shows the results of the analysis. This wafer was tilted along $\langle 1\bar{1}00\rangle$. So the peak point shifted at each measurement point.

There were a lot of peaks at 0 degree. But the number of peaks decreased as also the FWHM at 30 degree. Then the FWHM and the number of peaks increased at 45 deg. and 60 deg. again. At 75 and 90 deg., there were some sub peaks, but the intensity was small. From these results, 0 deg. and 60 deg. were the easiest identified as angles to form sub-grain boundary. The area which was perpendicular to $\langle 11\bar{2}0\rangle$ is more easily susceptible to the formation of sub-grain boundary. Takahashi et al. found the boundaries are edge dislocation walls having $a/3\langle 11\bar{2}0\rangle$ Burgers vectors[6]. The slip vector was $\langle 11\bar{2}0\rangle$. So the stripe of the interface which was a sub-grain boundary appeared on $\langle 1\bar{1}00\rangle$.

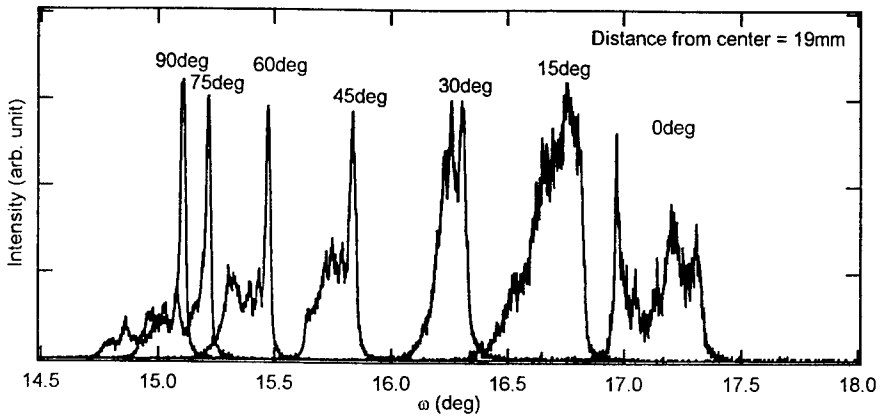


Fig.5 The dependence of the spectrum of XRD at each degree

5. Conclusion

There were a lot of sub-grain boundaries in the 2 inches 6H-SiC wafers examined. At the edge of the wafer, thermal expansion between graphite crucible and SiC bulk crystal and inclusion doping influenced the distortion. The boundaries at the center of the wafer are influenced by the shape of the surface of grown layer. Where there were too many sub-grain boundaries, FWHM of XRD became large and peak angle ω was shifted.

The sub-grain boundary created easily along $\langle 1\bar{1}00 \rangle$ direction.

Acknowledgment

The authors would like to thank Dr.J.Suda for helping with X-ray measurement at Venture Business Laboratory of Kyoto university. This work was partially supported by a Grant-in-Aid for Science Research NO.0945001 from the Ministry of Education, Science and Culture, Japan and FED, NEDO Japan, and Ion Engineering Institute (Osaka, Japan)

References

[1] D. Hobgood, V. Tsvetkov, R. Glass, D. Henshall, M. Brady, J. Jenny, G. Fechko, R. Leonhard, D. Malta, S. Mueller and C. Carter Jr., Mater. Sci. Forum 338-342 (2000), p. 3.
[2] N. Takanaka, S. Nishino and J. Saraie, Inst. Phys. Conf. Ser. 142 (1996), p. 49.
[3] M. Sasaki, Y. Nishino, S. Nishino, S. Nakashima and H. Harima, Mater. Sci. Forum 264-268 (1998), p. 41.
[4] M. Sasaki, S. Shiomi and S. Nishino, Mater. Sci. Forum 338-342 (2000), p. 485.
[5] S.K. Lilov, Yu.M. Tairov, V.F. Tsvetkov and M.A. Chernov, phys. stat. sol. (a) 37 (1976) N1, p. 143.
[6] J. Takahashi, N. Ohtani and M. Kanaya, J. Cryst. Growth 167 (1996), p. 596.

Materials Science Forum Vols. 353-356 (2001) pp. 271-274
© 2001 Trans Tech Publications, Switzerland

Ion Bombardment Induced Damage in Silicon Carbide Studied by Ion Beam Analytical Methods

E. Szilágyi[1], N.Q. Khánh[2], Z.E. Horváth[2], T. Lohner[2], G. Battistig[2], Z. Zolnai[2], E. Kótai[1] and J. Gyulai[2]

[1] Research Institute for Particle and Nuclear Physics, PO Box 49, HU-1525 Budapest, Hungary

[2] Research Institute for Technical Physics and Materials Science, PO Box 49, HU-1525 Budapest, Hungary

Keywords: Carbon Sublattice, Ion Implantation, Nuclear Resonance, Radiation Damage

Abstract. Damage created by implantation of Al^+ ions into 4H-SiC is characterized using Backscattering Spectrometry in combination with channeling. The measurability of the damage profile in the carbon sublattice was demonstrated using the 4260 keV $^{12}C(\alpha,\alpha)^{12}C$ resonance. To create disorder, Al^+ ions with energy of 200 keV and 350 keV were implanted at room temperature. As an independent method, cross-sectional transmission electron microscopy was used to study the damage structure in irradiated 4H-SiC.

Introduction

The only practical method to selectively dope defined regions of SiC is ion implantation. The implantation process is not constrained by thermodynamic limitations and allows species of very low diffusivities to be easily introduced. However, ion beam irradiation damages the crystal lattice of SiC [1–6] and many aspects of the damaging process have not been yet completely clarified. Aluminum has received a great deal of attention as acceptor in SiC due to its low activation energy (0.24 eV).

The overwhelming majority of the ion beam analytical investigations focused on the study of disorder created by ion bombardment only in the silicon sublattice of single crystalline SiC. In the Backscattering Spectrometry in combination with channeling (BS/C) experiments performed in the energy region where the cross section is Rutherford type for the carbon, the small peak originated from the displaced carbon atoms is superimposed on the large background. This fact does not allow evaluation of damage in the carbon sublattice. Nuclear reaction or non-Rutherford elastic scattering methods are used to obtain concentration of low atomic number constituent in a compound sample. Nashiyama et al. applied the $^{12}C(d,p)^{13}C$ nuclear reaction and deuteron BS/C method for investigation both carbon and silicon atom displacements in virgin and proton irradiated 3C-SiC [7]. In our present studies ion implanted SiC samples were investigated by high energy BS/C. Using the 4260 keV $^{12}C(\alpha,\alpha)^{12}C$ resonance, the scattering cross section for carbon enhanced by a factor of hundred as compared to the Rutherford cross section, can be reached. Additionally, cross-sectional transmission electron microscopy (XTEM) was applied to study the buried disorder.

Experimental

Single crystalline 4H-SiC samples (from CREE Res. Inc.) were implanted with 200 keV and 350 keV Al^+ ions at room temperature. In the case of 200 keV the implanted fluences were

$4\times10^{13}/cm^2$ and $8\times10^{13}/cm^2$. For 350 keV implantation the fluence was $4\times10^{13}/cm^2$.
Ion beam studies were performed in a scattering chamber with a two-axis goniometer connected to our 5 MV Van de Graaff accelerator. The He^+ beam was collimated with two sets of four-sector slits to the dimensions of 0.5×0.5 mm^2, while the beam divergence was kept below 0.04 deg. In the scattering chamber the vacuum was better than 1×10^{-4} Pa using liquid N_2 cooled traps along the beam path and around the wall of the chamber. Backscattered He ions were detected using an ORTEC surface barrier detector mounted in Cornell geometry at a scattering angle of 165°. To increase the depth resolution at the surface in some cases a glancing detection angle of 97° was used. To reduce the damage created by the analyzing beam itself [8–9] a low current of 5 nA was used during the measurements and monitored by a transmission Faraday cup [10]. BS spectra were evaluated using the RBX code [11].
The specimen for XTEM was prepared by ion beam milling. The specimen was investigated in a Philips CM20 electron microscope (TWIN configuration).

Results and discussion

The damage distribution created by 200 keV 8×10^{13} Al^+/cm^2 implantation was investigated by BS/C using the 3500 keV He^+ beam and XTEM. Fig. 1 shows the 97° BS channeled and random spectra together with the cross-sectional TEM micrograph of the same sample. In the aligned BS spectrum the broad peak behind the Si surface peak, which reaches the random level, indicates a buried amorphous layer. A slightly damaged region near the surface can also be observed, since the depth resolution for silicon at the surface is about 8 nm [12]. This slightly damaged region is manifested also in the higher yield in the surface peak.

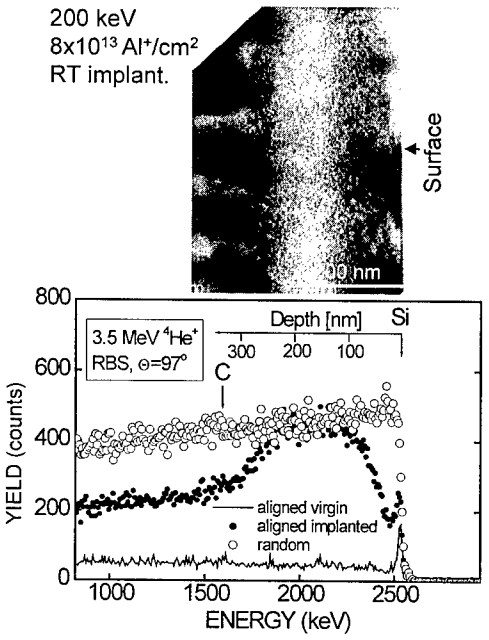


Figure 1. *Backscattering spectra and cross-sectional TEM micrograph of Al^+ implanted 4H-SiC sample. Aligned BS spectra were measured along the <0001> axis. Depth scales for comparison are also shown.*

The same feature can be observed in the XTEM micrograph in Fig. 1. There is a single-crystalline sublayer of about 30 nm thickness at the sample surface, followed by an about 60 nm thick partially amorphized layer. Underneath a 200 nm thick buried amorphous layer was formed. The next zone is partially damaged which is followed by the undamaged single-crystalline bulk material. Results of BS measurements and TEM observation here are easily comparable through the same depth scales shown in Fig. 1. There is a good agreement between results of the two independent methods considering the slightly damaged near surface region and the buried amorphous zone. In this case the scattering cross section is Rutherford type for ^{12}C. Therefore, only a rather small peak is observable at the C edge.
In Figure 2, BS/C spectra of the SiC sample implanted with 200 keV $4\times10^{13}/cm^2$ Al^+ are shown. The scattering angle of 165° was chosen at the beam energy of 3550 keV, taking the advantage that the cross section for carbon is larger by a factor of six than the

Rutherford type one. In contrary to the 97° measurement, where the buried amorphized layer was not visible in the carbon sublattice, here a much smaller damage is well visible in both sublattices. Figure 2 also shows the simulated spectra for implanted aligned 4H-SiC and for the random case. In the simulation of the aligned spectrum the same Gaussian distribution of disorder was assumed for both sublattices. The simulated maximum damage level of 2 % was located at a depth of 160 nm beneath the surface.

The damage in the sample implanted with 350 keV $4\times10^{13}/cm^2$ Al^+ (not shown here) is still visible in both sublattices. However, the damage peak is flatter and spreads deeper comparing to the case for 200 keV implantation that makes the evaluation of the aligned spectrum rather difficult. Let us note that the depth resolution for silicon at the surface is about 34 nm.

Using the 4260 keV resonance for $^{12}C(\alpha,\alpha)^{12}C$ we can enhance the sensitivity of the BS measurement further, however the depth resolution for silicon at the surface is poorer comparing to the previous cases. Figure 3 presents spectra recorded using an analyzing beam energy of 4300 keV, which is above the resonance energy. Aligned spectra taken on virgin and implanted samples are shown.

The area of the resonance peak corresponds to the number of carbon atoms displaced from their lattice sites. Varying the incident beam energy (i.e., determining the excitation curve) the depth distribution of displaced carbon atoms, i.e., damage, can be obtained.

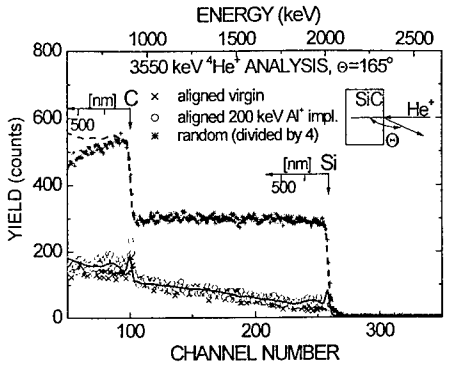


Figure 2. Backscattering spectra of 4H-SiC sample implanted with 200 keV 4×10^{13} Al^+/cm^2. Aligned BS spectra were measured along the <0001> axis. Depth scales for comparison are also shown. The simulated spectra are also shown for implanted aligned 4H-SiC (solid line) and for the random case (dashed line).

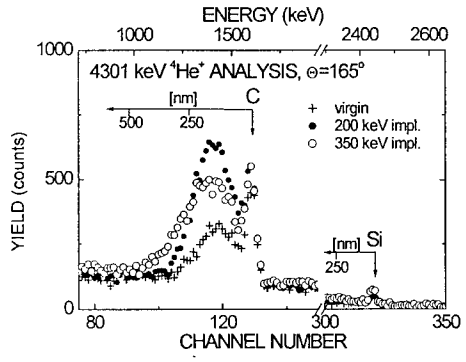


Figure 3. Aligned BS spectra of 4H-SiC samples implanted with 4×10^{13} Al^+/cm^2 of 200 keV and 350 keV energies. For comparison a virgin spectrum is also shown. Aligned BS spectra were measured along the <0001> axis.

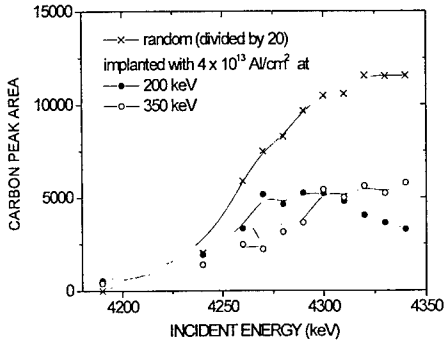


Figure 4. Excitation curves recorded on aligned SiC samples implanted with Al at different energies. The carbon peak areas were determined from similar spectra as shown in Figure 3. Each point was measured with 8 μC/points in fresh spot on the sample to avoid the beam effects,. To eliminate the background the corresponding aligned virgin spectra were subtracted. For comparison the excitation curve for random case is also shown. (Solid lines only for guiding the eyes.)

In Figure 4, excitation curves recorded on the same samples are shown.
The excitation curves roughly follow the damage distributions created by the ion implantation. The excitation curve of 200 keV implanted sample exhibits a maximum around 4300 keV that corresponds to the maximum damage at around 160 nm. The decreasing edge at higher energies shows the decreasing damage at the deeper regions. In the case of 350 keV implantation only the region of increasing damage was exploited due to the fact that the practical maximum energy of the accelerator now was only 4340 keV. The determination of the accurate damage distribution from the excitation curves is in progress.

Conclusion

The combination of Backscattering Spectrometry and channeling with the $^{12}C(\alpha,\alpha)^{12}C$ nuclear resonance at 4260 keV to study radiation damage in the carbon sublattice in 4H-SiC was demonstrated.

Acknowledgments

Partial support from Hungarian Science Research Foundation (OTKA grants No. T025928, No. T030327, No. T030441 and No. T032029) is greatly appreciated. The authors would like to thank P. Deák for supplying the 4H-SiC substrate and J. Waizinger for performing ion implantation.

References

[1] M.G. Grimaldi, L. Calcagno, P. Musumeci, N. Frangis, J. Van Landuyt: Appl. Phys. 81 (1997), p. 7181.
[2] M.V.Rao, P. Griffith, O.W. Holland, G. Kelner, J.A. Freitas, Jr., D.S. Simons, P.H. Chi: J. Appl. Phys. 77 (1995), p. 2479.
[3] T. Troffer, M. Schadt, T. Frank, H. Itoh, G. Pensl, J. Heindl, H.P. Strunk, M. Maier: Phys. Stat. Sol(a) 162 (1997), p. 277.
[4] A. Hallén, A. Henry, P. Pellegrino, B.G. Svensson, D. Aberg: Materials Science and Engineering B 61-62 (1999), p. 378.
[5] A. Heft, E. Wendler, J. Heindl, T. Bachmann, E. Glaser, H.P. Strunk, W. Wesch: Nuclear Instruments and Methods in Physics Research B 113 (1996), p. 239.
[6] E. Valcheva, Paskova, I.G. Ivanov, R. Yakimova, Q. Wahab, S. Savage, N. Nordell, C.I. Harris, J. Vac. Sci. Tech. B: Microelectronics and Nanometer Structures 17 (1999), p. 1040.
[7] I. Nashiyama, T. Nishijima, E. Sakuma, S. Yoshida, Nucl. Instr. Meth. in Phys. Res. B 33 (1988), p. 599.
[8] N.Q. Khánh, Z. Zolnai, T. Lohner, L. Tóth, L. Dobos, J. Gyulai, Nucl. Instr. Meth. in Phys. Res. B 161-163 (2000), p. 424.
[9] W. Fukarek, R.A. Yankov, W. Anwand, V. Heera, Nucl. Instr. Meth. in Phys. Res. B 142 (1998), p. 561.
[10] F. Pászti, A. Manuaba, C. Hajdu, A.A. Melo, M.F. Da Silva, Nucl. Instr. Meth. in Phys. Res. B 47 (1990), p. 187.
[11] E. Kótai, Nucl. Instr. Meth. in Phys. Res. B 85 (1994), p. 588.
[12] E. Szilágyi, F. Pászti, G. Amsel, Nucl. Instr. Meth. in Phys. Res. B 100 (1995), p. 103.

Materials Science Forum Vols. 353-356 (2001) pp. 275-278
© 2001 Trans Tech Publications, Switzerland

Effects of Hydrogen Implantation and Annealing on the Vibrational Properties of 6H-SiC

H.W. Kunert[1], T.P. Maurice[1,2], T. Hauser[1], J.B. Malherbe[1], L.C. Prinsloo[3], D.J. Brink[1], L.A. Falkovsky[2,4] and J. Camassel[2]

[1] Department of Physics, University of Pretoria, 0002 Pretoria, South Africa

[2] Groupe d'Etude des Semiconducteurs, CNRS, Université Montpellier 2, cc074, FR-34095 Montpellier Cedex 5, France

[3] Department of Chemistry, University of Pretoria, 0002 Pretoria, South Africa

[4] Permanent address: Landau Institute, Moscow, Russia

Keywords: 6H-SiC, Annealing, Hydrogen Implantation, Raman Spectroscopy

Abstract : We report 6H-SiC samples implanted with hydrogen at a dose of $1x10^{17}$ H^+ atom/cm^2, using a 1.0 MeV proton beam. Implantation-induced changes in vibration modes were investigated by backscattering Raman spectroscopy. Results have been discussed in the light of the extended zone scheme and some of the forbidden B_1 modes tentatively assigned. After 950°C annealing during 1 hr, incomplete crystal recovery is found.

Introduction

Hydrogen ion implantation in Silicon Carbide (SiC) is a prerequisite to master the SiCOI (SiC On Insulator) formation technology [1]. Because hydrogen is a very light atom, usually, low implantation energies are used (100 to 200 keV). After annealing, delamination occurs at a few thousand angstrom depth [1-3] but a complete recovery of the initial crystal properties is hard to get and implantation damage has been found to affect seriously the final (transferred) SiC layer properties [4]. Even if improved recovery was recently demonstrated to a point where the transfer process can be considered as qualified for electronic device applications [5] nothing is known about the effect of increasing the implantation depth, i.e. splitting away the delaminated zone from the active part of the transferred layer.

In this work, both n-type (nitrogen-doped) and p-type (aluminum doped) 6H-SiC wafers were implanted with hydrogen at a total dose of $1x10^{17}$ H^+ atom/cm^2. A 1 MeV proton beam was used, operated at 90 nA current. TRIM simulation predicts an implantation depth of 15 µm and, to probe the effect of implantation-damage and annealing, changes in the lattice vibration modes were investigated using back-scattering micro-Raman spectroscopy. Using a 100 µm aperture in the confocal mode, and a wavelength of 514.5 nm, a 6 µm deep surface layer was probed [6]. Since the thickness is mainly limited by the 6H-SiC transparency, the measurement are more surface-like for n-type material than p-type.

1 – One-phonon spectrum

1 – a. Background considerations and net implantation effect

Since the pioneering work of Feldman and coworkers [7] the phonon properties of SiC polytypes have been investigated many times. For a review, see Ref.8. There are 33 optical modes in 6H-SiC which, starting from the cubic polytype and taking into account the effect of hexagonal crystal field, can be separated into 4 groups of axial optic (AO), planar optic (PO), axial acoustic (AA) and planar acoustic (PA) frequencies. All originate from the folding of cubic LO, TO, LA and TA branches in such a way that points located at x = 1/3, x = 2/3 and x = 1 of the old (cubic) zone become new zone-center modes.

In our highly doped, as-grown, material ($1x10^{18}$ to 10^{19} cm^{-3}) all series of Raman spectra exhibit all prominent features previously reported [5-8] (see Table 1). The only missing lines are i°) the weak

266 cm^{-1} mode superimposed on our experimental spectra with a strong calibration line, and ii°) the E_1(FPA) doublet at 235/240 cm^{-1} because of our backscattering configuration.

6H-SiC	**First order** (x = 0)	**Folded** (x = 1/3)	**Folded** (x = 2/3)	**Folded** (x = 1)
AO (cm^{-1})	A_1 (**965**)	$2B_1$ (?/?)	$2A_1$ (**888**/?)	B_1 (**833.5***)
PO (cm^{-1})	E_1 (**796**)	$2E_1$ (**788**/?)	$2E_1$ (?/?)	E_1 (**766**)
AA (cm^{-1})	A_1 (acc)	$2B_1$ (?)	$2A_1$ (**504/513**)	B_1 (**615***)
PA (cm^{-1})	E_1 (acc)	$2E_2$ (**144/150**)	$2E_1$ (235/240)	E_1 (266)
Total	6	12	12	6

Table 1: Summary of experimental values obtained in this work (bold) together with a schematic representation of the origin of the 36 vibration modes of 6H-SiC. Only A_1, E_1 and E_2 modes are Raman active; B_1 modes are silent; x denotes the reduced wave vector of phonons. When necessary, our results have been completed by recent literature data [9]. *indicate new modes resolved for the first time.

Despite a low mass of the incident ions, 1 MeV hydrogen implantation changes drastically the first-order spectrum. This is demonstrated in Fig.1 in the experimental range 550-1050 cm^{-1}. The weak A_1(FAO) mode at 888 cm^{-1} disappears and, instead, a broad structure reveals. It extends from the topmost A_1(LO) mode at 965 cm^{-1} (still present but broader and weaker) to about 800 cm^{-1}. This is nothing but clear evidence of the effect of disorder-induced activation of the one-phonon DOS (Density of States) of the AO branch.

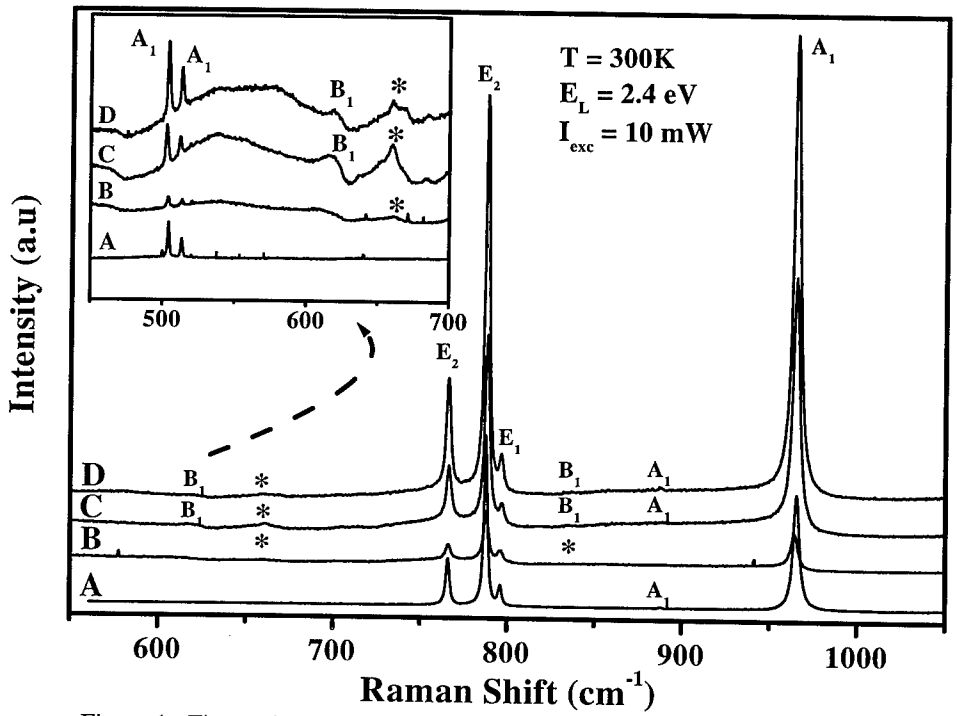


Figure 1 : First-order Raman spectra of (A) as-grown, (B) H^+ implanted, (C) 700C annealed and (D) 950C annealing 6H-SiC samples.

According to Table 1, the AO-DOS should extend from the topmost A_1 mode with x=0 (which is seen) to a forbidden (folded) B_1 mode with x=1 (which is not resolved but, from cubic data [8], should be located around 835 cm^{-1}). Concerning the DOS maximum we notice a broad structure at about 855 cm^{-1} (which is better seen in the n-type material). In agreement with the results of Ref.10, we associate this structure with the maximum DOS of the AO branch. Concerning the PO branch, both the E_1(TO) mode and folded E_2 frequencies at 794.4, 787.3 and 765 cm^{-1}, respectively, are reduced in intensity and shift to lower frequencies. Again to be noticed is that these modes manifest on top of a one-phonon (disorder-activated) DOS which, for the PO branch, is narrow. It occurs between ~800 and 730 cm^{-1} (from Table 1 we expected ~796 to 766 cm^{-1}). Finally, notice that nothing significant appears in the gap of the 1-phonon DOS (800 to 835 cm^{-1}).

This is no longer true when considering the second (larger) gap which, starting from 766 cm^{-1} separates the two optical branches from the top of the folded AA mode (with, again, a forbidden B_1 symmetry). Again, we know from cubic data [8] that this mode should be located around 600 cm^{-1} but, similar to the previous case, nothing is seen. Instead, in both cases of n-type and p-type doped material, a sharp defect mode appears around 658 with additional structures at 704 and 714 cm^{-1}. In the n-type doped sample, a (weak) additional feature also appears around 680 cm^{-1}. In the range of acoustic frequencies (not shown) the implantation shifts and broadens the first-order modes like the FAA and FPA doublets at 504/513 and 144/150 cm^{-1}, respectively. New vibration bands appear also at about 185, 275, 526 and 600 cm^{-1}. Some of them were previously associated with the effect of Si-Si, Si-C and C-C bonds [11-12] but our results suggest a non-negligible contribution from the one-phonon acoustic DOS.

1 - b. Annealing effects

Annealing was done in two steps. First, at 700C for 1 hour and then at 950C for an additional hour. The following has been found:

- annealing for 1 hour at 700C does not reduce significantly the implantation damage. Most features simply become a little bit sharper. The first-order modes still retain a weak intensity compared to the as-grown material, but, in the high energy range this is sufficient to observe i°) a partial recovery of the weak A_1 mode at 888 cm^{-1}, ii°) the DOS maximum at 855 cm^{-1} and iii°) the forbidden B_1 mode at 833 cm^{-1}. The gap modes remain but a new (broad) feature is seen at ~615 cm^{-1}. It corresponds with the onset of the axial acoustic DOS and, in Table 1, has been associated with a second forbidden mode (x=1). The hydrogen-implantation-induced bands at 185, 275, 526, 600, and 658 cm^{-1} are still present but display more fine structure;
- after annealing at 950C for one more hour, most of the disorder-activated DOS disappears and the gap modes reduce drastically. This confirms the H-origin without clarifying the microscopic origin [13]. Remaining are the inverted ratio of intensity between the E_2 mode at 788 cm^{-1} and the A_1(LO) mode at 965 cm^{-1} and weak structures at forbidden B_1 energies.

2 – Two-phonon spectrum

In the two-phonon range, any combination of phonons with opposite wave vectors can be Raman active (and not simply overtones of the one phonon spectrum considered in the Γ-A direction). In other words the unperturbed 2-phonon spectrum is nothing but a combination of points with high DOS in the one-phonon spectrum which satisfy the wave vector selection rule. This is not a very restrictive condition, and the overall spectrum is not very sensitive to the effect of implantation damage. In Fig.2 we compare 4 different spectra which have been collected in the experimental range 1400 – 2000 cm^{-1}. Several structures appear [11,12] which have been labeled "a to h" in agreement with [14] and correspond with overtones or combination of the one-phonon DOS at different points of the Brillouin zone. On the overall, the spectra do not change shape when coming from virgin to implanted and annealed. Modes simply change intensity. Especially the structures labeled "b", "d", "f" and "g" can be easily observed on the 4 spectra.

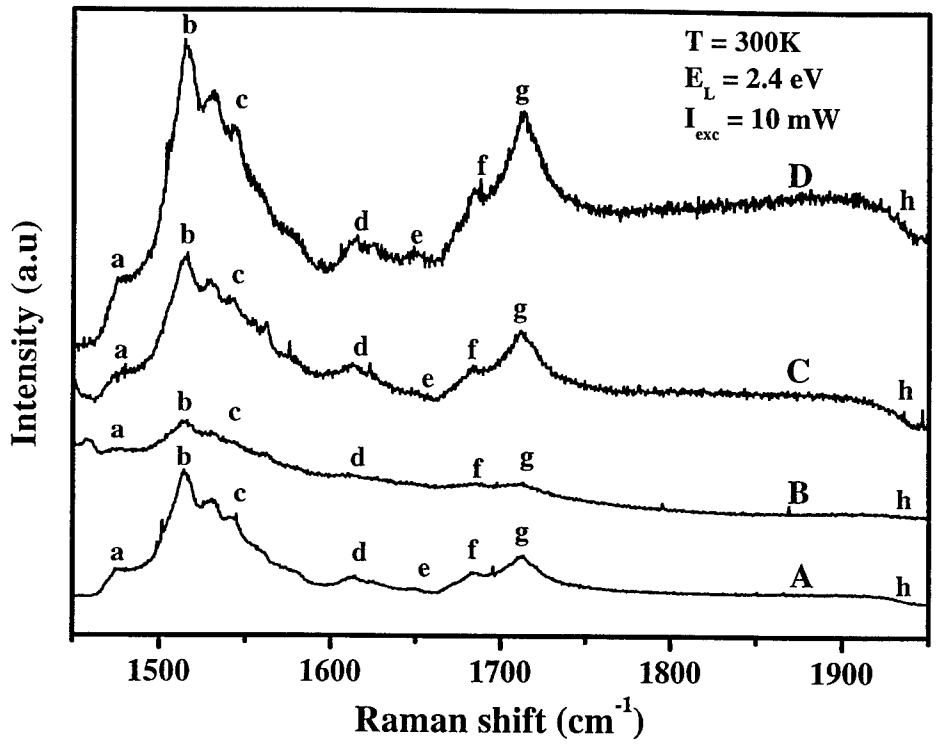


Figure 2: Second-order Raman spectra of A, B, C, and D 6H-SiC samples.

Conclusion

Investigating the effect of 1 MeV H+-ion implantation in 6H-SiC, we have shown incomplete recovery of the topmost part of the implanted layer, even after 1 hour annealing at 950C. Two normally forbidden B_1 modes have been identified and Hydrogen-implantation related gap modes have been found.

References

[1] L.DiCioccio, *et al*, Mat. Science Forum 264-268, (1998), p.765.
[2] T. Hara, *et al*, Materials Science Forum 264-268, (1998), p. 771.
[3] E.A. Chowdhury, *et al*, Materials Science Forum 338-342, (2000), p. 813.
[4] E. Hugonnard-Bruyère, *et al*, Mat. Science and Eng. B61-62, (1999), p. 382.
[5] E. Hugonnard-Bruyère, *et al*, Materials Science Forum 338-342, (2000), p. 715.
[6] F.J. Campos, *et al*, J.A.P. 85, (1999) p. 99.
[7] D.W. Feldman, *et al*, Phys. Rev. 170, (1968), p. 698; ibid., 173, (1968), p. 787.
[8] S. Nakashima and H. Harima, Phys. Stat. Sol. (a), 162, (1997), p. 39.
[9] J.C. Burton, *et al*, J.A.P. 84, (1998), p. 6268.
[10] M. Hofmann, A. Zywietz, K. Karch and F. Bechstedt, Phys. Rev. B50, (1994), p. 13401.
[11] A. Perez-Rodriguez, *et al*, J. Elect. Mat.25, (1996), p. 541.
[12] N. Mestres, *et al*, Mat. Science Forum 338-342, (2000), p. 663.
[13] P. Deak, *et al*, Mat. Science Forum 338-342, (2000), p. 817.
[14] J.C. Burton, L. Sun, F.H. Long, Z.C. Feng and I.T. Ferguson, Phys. Rev. B59 (1999), p. 282.

Materials Science Forum Vols. 353-356 (2001) pp. 279-282
© 2001 Trans Tech Publications, Switzerland

4H- and 6H-SiC Rutherford Back Scattering-Channeling Spectrometry: Polytype Finger Printing

R. Nipoti[1] and A. Carnera[2]

[1] CNR-Istituto LAMEL, via Gobetti 101, IT-40129 Bologna, Italy

[2] Dipartimento di Fisica and INFM, Università degli Studi di Padova, via Marzolo 8, IT-35131 Padova, Italy

Keywords: Channeling, Ion Beam Analysis

Abstract This work compares the 4H- and 6H-SiC Rutherford Back-Scattering channeling spectra and angular dips for low index axes and planes: the spectra and the dip shoulders show features that depend on the polytype, while the dip amplitudes do not. In the light of the theories of the ion scattering within crystals such behaviour shows that the two polytypes have different channeling stopping powers but similar interaction potentials, and, as well known, different long range atomic site simmetry. Some dip shoulders are so peculiar that they can be taken as the polytype finger printing in the RBS spectrometry.

Introduction

This work gives some characteristic figures of the Rutherford Back-Scattering channeling (RBS-C) spectrometry applied to single crystal SiC. The characteristic figures of the RBS-C spectrometry are random and channeling stopping powers, minimum yield values, dechanneling rates, angular dip amplitudes, angular dip shapes and so on. A few are the examples of such studies reported in the literature for SiC [1-3].

This article shows and compares the RBS-C spectra and angular dips of low index axes and planes for 4H- and 6H-SiC. The 4H-SiC data are original while the 6H-SiC ones are those already published in ref. [1]. The analysis of these measurements will bring some conclusions about the parameters that characterise the interaction of energetic ions with different SiC structures.

Experimental

The 4H-SiC samples used for this study were commercial wafers, both bulk and epitaxial [4], and a research wafer epitaxially grown by a hot-wall CVD technique at 1600°C [5]. All of them were <0001> oriented and off-axis. A <0001> Lely crystal was used for the 6H-SiC study [1].

The RBS-C analyses were done in the chamber of the Italian INFM at the LNL in Italy and by using a four axis goniometer: two translation axes with micrometry precision and two orthogonal rotational axes with angular precision equal to $\pm$ 0.01° [6]. The chamber was electrically insulated, and the dose was measured by integrating the beam current at the chamber: in the range 5-200 nA the reproducibility of a given spectrum yield was within the statistical error. The analysis beam was He^+, 2 MeV energy, 0.03° divergence, 0.5 mm diameter and current in the range 40-100 nA. The back-scattered ions were collected at a Si detector placed at 170° from the beam direction. The detector angular acceptance was measured by thin film reference samples or by the amorphous-Si yield [7] and was of the order of 1.5×10^{-3} sr. The energy resolution was in the range 17-19 keV.

Thanks to such an experimental set-up the RBS-C yield can be measured by absolute units, i.e. as "counts/(μC msr keV)". But as usual, a relative unit (%) is used for the dip spectra. The dip normalisation was done with respect to the random spectrum integrated over the same energy

window of the dip. The random spectrum was measured performing a 360° rotation of the <0001> axis around the He^+ beam while keeping the <0001> axis tilted at 3° from the beam direction.
The channeling spectra and dips were averaged on several measurements with the aim to optimise the approximation of a random path in the crystal for the back scattered He ions. In fact, once the SiC crystal is mounted on the goniometer, a given channeling configuration can be obtained by more than one orientation of the SiC crystal with respect to the plane identified by the beam, the detector and the beam impact point at the sample surface. For example a planar channeling spectrum can be measured in six different sample orientation, while a dip trough the <0001> axis and within a (10-10) or (11-20) plane in three ones. Only the axial alignment corresponds to a single crystal orientation. The major dependence of the spectrum yield on the sample orientation was measured for the dip spectra.

Results

Sample homogeneity and crystal stability under beam analysis were tested by the measure of the back scattering yield versus beam impact point and ion fluence value. In general, all the crystals showed a good homogeneity and were more stable for <0001> axial than (11-20) or (10-10) planar alignment. Furthermore, 4H-SiC was much more stable against ion damaging than Lely 6H-SiC. This may be due to the presence of heavy impurities that the authors always detected by RBS in the Lely crystals.

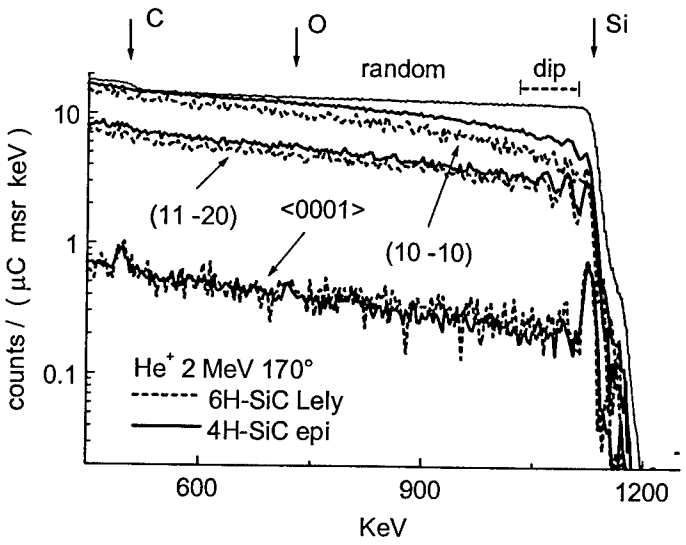


Fig. 1 Low indexes axial and planar RBS-C spectra: comparison between the 4H- and 6H-SiC.

Figure 1 shows the 4H-SiC and 6H-SiC <0001>, (10-10) and (11-20) spectra. The random spectrum is also shown for comparison. The planar spectra were measured with the <0001> axis tilted 3° with respect to the He^+ beam. The arrows show the C, O and Si surface edges. The position of the dip energy window is also shown. The <0001> spectra are equal, while the (11-20) and (10-10) 4H-SiC spectra are higher than the 6H-SiC ones, the difference is wider for the (10-10) plane. The oscillations of the planar spectra, which are more evident for the (11-20) plane, are similar for the two polytypes but those of the 4H-SiC yield at lightly higher energy values.
Figure 2(a-d) shows the 4H- and 6H-SiC angular dips through the <0001> axis within the plane (11-20) or (10-10) (Fig. 2(a,c)) and through the planes (11-20) and (10-10) with the He^+ beam aligned at 3° from the <0001> axis and within a plane orthogonal to (11-20) or to (10-10), respectively (Fig. 2(b,d)). The dip of Fig. 2 correspond to a near surface region less than 100 nm thick and characterised by RBS yield oscillations (Fig. 1), but it was verified that the dip major features were independent on the chosen energy window. The comparison in Fig. 2 shows that 4H- and 6H-SiC have very similar half width dip amplitudes but different shoulder shapes. In particular at the shoulder of the <0001> axis within the (11-20) plane there is a double peak for 4H-SiC and a single peak for 6H-SiC. Among these, one of the first and the latter yield at the same angular value.

Table 1 gives the minimum yields χ and the half-width dip amplitudes $\Psi_{1/2}$ measured from the data of Fig. 1 and Fig. 2. The χ values are the ratio between aligned and random spectra of Fig. 1 integrated over the same energy window. The $\Psi_{1/2}$ data were measured on the spectra of Fig. 2 at the yields $(\chi_{axis} + \chi_{plane})/2$ and $(\chi_{plane} + 1)/2$ for axial and planar dips, respectively.

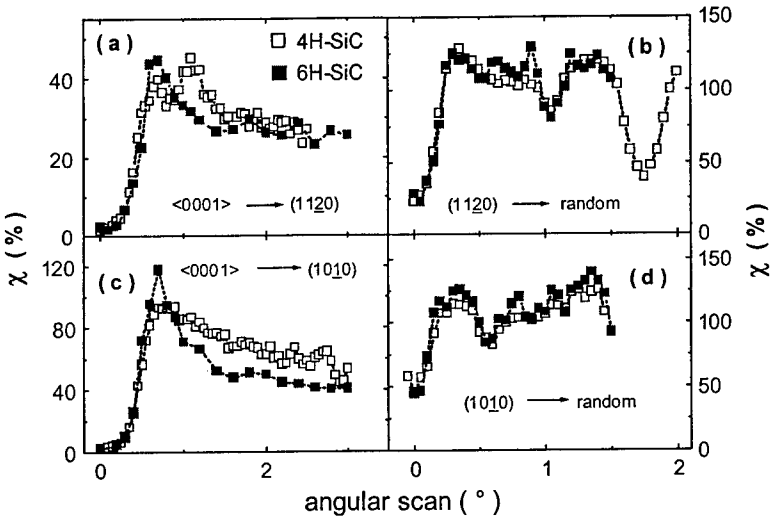


Fig. 2 <0001> axial and (10-10) and (11-20) planar angular dips for the 4H- and 6H-SiC polytypes.

Table 1 Experimental minimum yield χ and angular dip half width amplitude $\Psi_{1/2}$ for 4H- and 6H-SiC.

2 MeV 170°						
spectrum alignment	χ (%)		dip alignment		$\Psi_{1/2}$ (°)	
	6H-SiC 1043÷1105 KeV	4H-SiC 1041÷1105 KeV	from	to	6H-SiC 1023÷1085 keV	4H-SiC 1028÷1085 keV
<0001>	2.1 ± 0.1	2.0 ± 0.1	<0001>	(11-20)	0.39 ± 0.01	0.38 ± 0.01
(11-20)	24.9 ± 0.2	25.2 ± 0.1	<0001>	(10-10)	0.38 ± 0.01	0.40 ± 0.01
(10-10)	40.1 ± 0.6	45.1 ± 0.2	(11-20)	random	0.17 ± 0.01	0.16 ± 0.01
			(10-10)	random	0.10 ± 0.01	0.12 ± 0.01

Discussion

The different stacking sequences in 4H-SiC and 6H-SiC produces crystalline networks that have equal intra plane distances but different point simmetry for the C and Si sites. Because of that energetic He^+ ions channelled within a SiC crystal must interact with polytype dependent distributions of scattering centres, interaction potential and electronic density. The latter mostly influences the channeling stopping power, while the first is responsible for both steering and dechanneling phenomena. The theoretical description of the ion channeling within crystals shows that dip amplitudes are determined by interaction potentials and intra plane distances while the periodicity of spectrum oscillations depends also on the channeling stopping power [8]. Moreover the theory of the RBS spectrometry shows that the count yield is inversely proportional to the He energy loss along the inward and outward paths in the sample [9]. Looking at our experimental data in the light of such theoretical knowledge, the dip amplitude independence of the SiC polytype allows us to hypothesise that axial and planar interaction potentials must be very similar in 4H- and

6H-SiC. While the dependence of the planar oscillations and of the χ values on the SiC polytype allows us to hypothesise that 4H-SiC must have planar channeling stopping powers lower than the 6H-SiC ones.
Preliminary results concerning the simulation of 4H- and 6H-SiC RBS-C spectra under the approximation of binary collisions, as described in [1], account for the spectrum trend from the <0001> axis to the (10-10) plane shown in Fig. 1 even if equal channeling stopping powers were assumed. That allows us to hypothesise that an important contribution to the dechanneling must come also from a different sequence of the nuclear collision in the two polytypes, i.e. from the different atomic site simmetry.
Finally, the shape of the shoulder at the <0001> axial dip within the plane (11-20) (Fig. 2a) is so peculiar for the 4H polytype with respect to the 6H one that it can be considered as the finger printing of the SiC polytype in the RBS-C spectrometry.

Conclusion

Some characteristic RBS-C figures for the 4H- and 6H-SiC polytype are given. They were experimentally obtained. The analysis of such figures allow us to formulate some hypothesis about channeling stopping power, interaction potential and site simmetry of the scattering centres in the two polytypes that would merit a more accurate investigation. In particular, if good quality 4H- and 6H-SiC film on SiO_2/Si substrates would be available, the combination of experimental and simulated RBS-C spectra might be used for a quantitative evaluation of the many effects that contribute to a given RBS-C spectrum as it was already done for Si [10].

Acknowledgments

The authors would like to thanks ABB Corporate Research and the Swedish SICEP program for having supplied a 4H-SiC epi-wafer. Thanks are due also to Dr. G. Lulli for the useful discussion. The Italian Progetto Finalizzato MADESS-II funded this work.

References

[1] M. Bianconi, E. Albertazzi, A. Carnera, G. Lulli, R. Nipoti and A. Sambo, Nucl. Instr. and Meth. In Phys. Res. B 136-138 (1998), p. 1276.
[2] M. Satoh, K. Okamoto, Y. Iwata, K. Kuriyama, M. Kanaya and N. Ohtani, Materials Science Forum Vols. 264-268 (1998), p. 441.
[3] R. Nipoti, G. Lulli, M. Bianconi, E. Albertazzi, A. Carnera and A. Sambo, 9th CIMTEC-World Forum on New Materials, P. Vincenzini, S. Valeri (Editors), Techna srl Vol 19 (1999), p. 107.
[4] CREE Reasearch, Durham, NC, USA
[5] O. Kordina, C. Hallin, A. Henry, J.P. Bergman, I. Ivanov, A. Ellison, N.T. Son, and E. Janzén, Phys. Stat. Sol. B 202 (1997), p. 321.
[6] Carnera and A.V. Drigo, Nucl. Instr. and Meth. In Phys. Res. B 44 (1990), p. 357.
[7] M. Bianconi, F. Abel, J.C. Banks, A. Climent Font, C. Cohen, B.L. Doyle, R. Lotti, G. Lulli, R. Nipoti, I. Vickridge, D. Walsh and E. Wendler, Nucl. Instr. and Meth. In Phys. Res. B 161-163 (2000), p. 293.
[8] L.C. Feldman, J.W. Mayer and S.T. Picraux, "Materials analysis by Ion Channeling", Academic Press Inc. (London) Ltd. (1982), p. 37.
[9] W.K. Chu, J.W. Mayer and M.A. Nicolet, "Backscattering Spectrometry", Accademic Press Inc. (London) Ltd. (1978), p. 68.
[10] G. Lulli, E. Albertazzi, M. Bianconi, G.G. Bentini, R. Nipoti and R. Lotti, Nucl. Instr. and Meth. In Phys. Res. B 170 (2000), p. 1.

Materials Science Forum Vols. 353-356 (2001) pp. 283-286
© 2001 Trans Tech Publications, Switzerland

X-ray Diffraction, Micro-Raman and Birefringence Imaging of Silicon Carbide

E. Pernot[1], M. Mermoux[2], J. Kreisel[3], O. Chaix-Pluchery[1], P. Pernot-Rejmánková[1,4], M. Anikin[1], B. Pelissier[1], A.M. Glazer[3] and R. Madar[1]

[1] LMGP - UMR 5628 CNRS/INPG, BP 46, FR-38402 St. Martin d'Hères, France

[2] LEPMI, UMR 5631 CNRS/INPG, BP 75, FR-38402 St. Martin d'Heres, France

[3] Clarendon Laboratory, University of Oxford, Parks Road, Oxford OX1 3PU, UK

[4] ESRF, BP 220, FR-38043 Grenoble, France

Keywords: Birefringence, Raman Spectroscopy Imaging, X-Ray Topography

Abstract

Transmission and reflection X-ray topography, birefringence imaging and Raman spectroscopy imaging have been performed on a silicon carbide slice. The differences between the images and the information obtained from them are discussed in detail.

Introduction

Despite the significant progress in crystal growth, the industrial applications of silicon carbide crystals have up to now been severely limited by the insufficient quality and size of the commercially available substrates. Typical defects found in SiC are misoriented domains, inclusions, macrodefects, dislocations, micropipes and doping striations [1]. Among the techniques of crystal characterization, X-ray diffraction imaging, polarized light microscopy and Raman spectroscopy imaging have proved of value as powerful tools for studying the defects in SiC.

This paper is devoted to the characterization and comparison of SiC wafers by these three techniques. Stress analysis in SiC crystals can be performed by all of them, however, the physical phenomena involved in the creation of a recorded image are different.

Sample preparation

4H crystals have been grown by the Modified Lely Method. Synthesis details are described in Ref [2]. Ingots were cut 8° off-axis toward [11-20] direction. The obtained slices have been well polished. The diameter of the investigated sample was 30 mm with the 0.4 mm thickness.

X-ray topography

X-ray diffraction imaging (topography) has been performed on the ID19 beam-line at the ESRF. White beam projection topographs in transmission have been recorded to study structural defects within the slice. White beam reflection topography has been performed using a low energy beam in order to observe the defects near the sample surfaces (~ tens of microns). Micropipes and dislocations can be easily observed by this method [3].

The results of diffraction imaging experiment on a part of the crystal are presented on Fig.1a and Fig.1b. The slice has an average structural quality. Some contrasts associate with subgrains and micropipes are visible. The rectangle indicates a high-deformed area. About ten micropipes and high dislocation density have been observed in this region by classical optic measurement and etching in molten KOH. The complex topographic contrast of this group of micropipes is due to the large sample-to-film distance, the small distance between micropipes and, assuming that micropipes are associated with superscrew dislocations, the large magnitudes of their Buergers vector, Ref. [3].

Birefringence imaging

Phenomenon of optical linear birefringence is the result of anisotropy within a sample leading to a

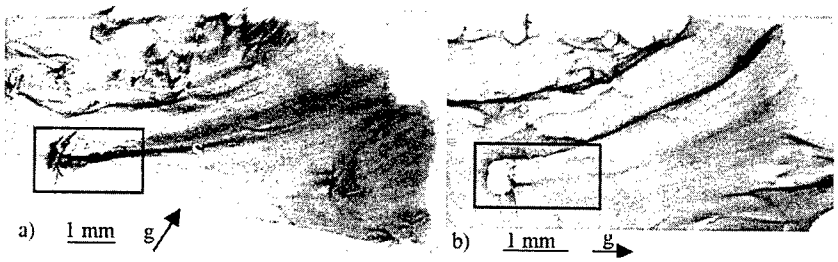


Fig.1: X-ray topography: a) in transmission d = 20cm; b) in reflection, d = 40cm. The rectangle indicates approximately the area studied by Raman spectroscopy and birefringence imaging. The letters **s** and **m** denote a subgrain boundary and a micropipe, respectively.

variation of the refractive index, n, as a function of the polarization of the incoming light. This variation can be represented by an ellipsoid, so-called indicatrix, which is described by three principal refractive indices. The difference in the refractive index Δn implies that two different polarizations will emerge from the sample with a phase difference $\delta = \Delta n L 2\pi/\lambda$, where L is the sample thickness and λ is the wavelength of the light involved. Thus, a beam of linearly polarized light will in general, when passing through the birefringent sample, become elliptically polarized with a phase difference δ. In addition, the amplitude difference depends on the inclination angle φ between the incoming electric field and the ellipse axes.

The birefringence imaging system consists of a polarizing microscope fitted with the computer-controlled rotating polarizer and a circular analyzer [4]. The formula describing the intensity passing through this system is $I = (I_0/2)[1+\sin 2(\alpha-\varphi)\sin\delta]$ where α is the orientation of the polarizer and I_0 is the incident light intensity. Values of the transmittance I, the phase difference δ (or the retardation $|\sin\delta|$) and the orientation φ can be obtained by varying the angle α. A CCD camera is used to record these three quantities for each pixel and grayscale images are then reconstructed to display them.

4H-SiC is an optical birefringence material. Defects in SiC crystals produce locally stresses that modify the orientation and the form of its optical indicatrix. Fig. 2a shows an orientation image of the region of the crystal defined by the rectangle in Fig. 1. When $\varphi = 0°$, the slow direction of light points from the left to the right. The gray level of the background corresponds to $\varphi = 10°$. SiC is hexagonal, consequently in the case of an on-axis sample the cross section of its indicatrix with the basal plane is a circle. Therefore, no orientation can be identified. In the case of an off-axis crystal, the indicatrix is tilted and the cross section is an ellipse with one axis pointing to the direction of the sample disorientation. The angle $\varphi = 10°$ corresponds to the disorientation of the [11-20] direction with respect to the c-axis.

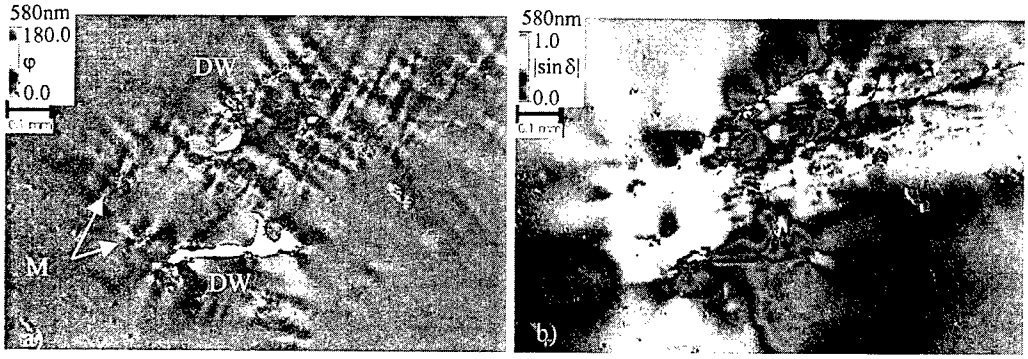


Fig. 2: Birefringence images: a) orientation φ; b) retardation $|\sin\delta|$. area: 1.2 x 0.8 mm^2.

The background of the retardation image is homogeneous ($|\sin\delta| = 0.4$), Fig. 2b. It means that the indicatrix and consequently the stress are homogeneous in this area of the crystal. The orientation and the retardation are modified considerably only in the part of the image where the micropipes are located. The features marked DW on the Fig. 2a correspond probably to some dislocation walls. A complex contrast induced by micropipes, denoted by M, can be distinguished.

Raman imaging

Raman microprobe imaging was performed at room temperature. Raman spectra were recorded using a Dilor XY multichannel spectrometer and a CCD detector. Measurements have been carried out in the backscattering geometry from the (0001) face of the sample using the 514.5 nm line from an argon ion laser for the excitation. The incident laser power was 10 mW at the surface of the sample. The light was focussed to a spot of 2.5 μm in diameter with a penetration depth of 20 μm. Calibration of each Raman spectrum was performed using plasma lines of the laser. Spectra were recorded each 1 μm on a 70x70 μm^2 areas covering several large micropipes, ~ 10 μm in diameter.

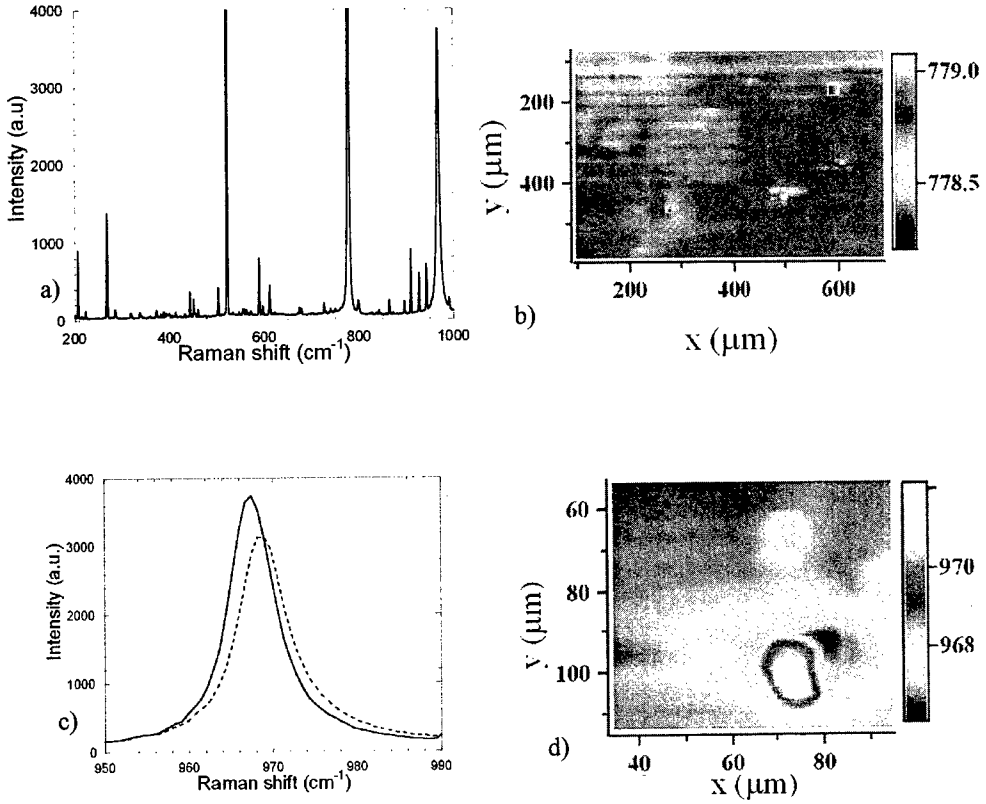


Fig. 3: a) a Raman spectrum of 4H-SiC; b) 776 cm^{-1} TO mode image; c) LO phonon-plasmon coupling mode at 964.5 cm^{-1} close to (continuous line) and far (dotted line) from a micropipe; d) LO phonon-plasmon coupling mode around a micropipe.

MicroRaman spectroscopy is a technique sensitive to the stress and to the doping in SiC. It is also a powerful tool to detect inclusions in the crystals. MicroRaman imaging applied to our sample provides these three kinds of information. Some graphite has been detected inside the micropipes. Moreover, some Raman lines, for example the 776 cm^{-1} TO mode shown in Fig. 3b, are shifted

toward the upper values. But the shift is constant in the observed area even close to the micropipes. It indicates a homogeneous stress in this part of the crystal. Finally, the LO phonon-plasmon coupling mode at 964.5 cm^{-1} is shifted and its shape changes close to the micropipes, as can be seen in Figs.3cd. It has been produced by a modification of the electronics properties of the material. The carrier concentration has been evaluated using the Ref. [4] being 10^{18} cm^{-3} and 7 x 10^{17} cm^{-3} in the bulk and close to the defects, respectively. This suggests a high density of trapping centers in the vicinity of micropipes [5].

Summary

The three imaging techniques, X-ray topography, birefringence and Raman spectrometry imaging give different information. X-ray topography is very sensitive to the strain field. It is impossible in our case to separate the contrast associated with an individual micropipe. Difficulties in the interpretation of a topograph arise from the high density of defects in a crystal with an average structural quality. When using birefringence imaging with a good magnification, it is possible to distinguish the individual defects like micropipes and dislocation walls even in low structural quality regions. Raman spectroscopy revealed the presence of graphite within micropipes and a lower carrier concentration close to them. However surprisingly, no variations of stress have been detected, although X-ray topography and birefringence imaging indicated the presence of highly deformed regions.

Acknowledgements

The authors gratefully acknowledge the support of the French Ministry of Education and Research , the French Ministry of Industry and the European Brite Euram Program (Contract BRPR- CT98-0812-JESICA).

References

[1] R.C. Glass, D. Hensall, V.F. Tsveskov, C.H. Carter Jr; MRS Bull. 22, (1997), p. 30.
[2] M.Anikin, O. Chaix, E. Pernot, B. Pelisier, M. Pons, A. Pish, C. Berard, P. Grosse , C. Faure, Y. Grange, G. Basset, C. Moulin, R.Madar, Mat. Sci. Forum 338-342 (2000), p. 13.
[3] X. R. Huang, M. Dudley, W. M. Vetter, W. Huang, W. Si, C.H. Carter Jr, J. Appl. Cryst 32 (1999), p 516.
[3] M. Geday, J. Kreisel, A.M. Glazer, K. Roleder, J. Appl. Cryst. (2000), in print.
[4] H. Harima, S. Nakashima, T. Uemura, J. Appl. Phys. 78 (3) (1995), p. 1996.
[5] H. Harima, T. Hosoda, S. Nakashima, Mat. Sci. Forum 338-342 (2000), p. 603.

Materials Science Forum Vols. 353-356 (2001) pp. 287-290
© 2001 Trans Tech Publications, Switzerland

X-Ray Diffraction Line Profile Analysis of Neutron Irradiated 6H-SiC

C. Seitz[1], A. Magerl[1], H. Heissenstein[2] and R. Helbig[2]

[1] Lehrstuhl für Kristallographie und Strukturphysik, Universität Erlangen-Nürnberg, Bismarckstr. 10, DE-91054 Erlangen, Germany

[2] Lehrstuhl für Angewandte Physik, Universität Erlangen-Nürnberg, Staudtstr. 7/A3, DE-91058 Erlangen, Germany

Keywords: crystal defects, Neutron Irradiation, Structural Correlation Length, X-Ray Diffraction

Abstract

We have investigated by high resolution X-ray diffraction the change of the structural correlation length in 6H-SiC after neutron irradiation with different fluences and following different annealing procedures. Following a model of Klimanek [1] it is shown, that high fluences lead to a stronger than linear reduction of the correlation length whereas higher annealing temperatures lead to a stronger recovery of the correlation length. In addition, a reorientation of the direction of the defect structure upon annealing is observed.

Applied model

Crystal defects can be divided into two kinds:

1st kind: defects disturbing dominantly the short range order but not the long range order, such as point defects.

2nd kind: defects reducing dominantly the structural correlation length without disturbing the short range order, such as dislocations or stacking faults.

Klimanek [1] and Ungár [2] have developed models to extract quantitative information on defect densities of 2nd kind from X-ray line profile analysis. We used the model of Klimanek [1], assuming that only dislocations being present. Within this description, all defects of 2nd kind lead to a similar broadening of the X-ray diffraction lines of Bragg peaks [3], this model reacts to any defect of 2nd kind. If there were only dislocations, the evaluation in terms of dislocation densities would be quantitatively correct. If, however, other defects like small angle grain boundaries were present, the absolute value is not correct any more. Nevertheless, the model provides a measure of the structural correlation length relating to defects of the 2nd kind. Furthermore, the distribution of the dislocation structures along crystal axis is reproduced by an anisotropicity of the apparent correlation lengths.

Dislocation induced broadening of X-ray diffraction lines

The intensity distribution of an X-ray diffraction peak for a large crystal containing dislocations can be described by the expression [4]

$$I_{\mathbf{H}}(\mathbf{q}) = F_{\mathbf{H}}^2 \sum_{\mathbf{R}} e^{i\mathbf{q}\mathbf{R}} \exp[-T(\mathbf{R}, \mathbf{Q}\mathbf{u}_{\mathbf{R}}, c_{ij})] \qquad (1)$$

H is the reciprocal lattice vector (*hkl*), **Q** is the diffraction vector with **m**=**Q**/Q; **q** is the distance from point **H** in reciprocal space, F_H is the structure factor of the reflection associated with the point **H**, which only serves as a scaling factor. **R** are distance vectors of lattice cell pairs linked by an inversion centre of the position vector in the perfect crystal structure.

All information about the dislocations is contained in the function T, where $\mathbf{u}_\mathbf{R}$ is the dislocation induced displacement vector of the cell pairs at point **R** and c_{ij} are the elastic constants of the material.

The sum in Eq. 1 is a Fourier sum, transforming the Function T from real space expressed by $\mathbf{R}$ to the experimentally accessible reciprocal space expressed by $\mathbf{q}$.
By linearisation of the term $\mathbf{Qu_R}$ and assuming only one type of dislocation the function T can be given by the equation [4]

$$T(\mathbf{R}) = [(\mathbf{Qb})^2/8\pi]\chi(\mathbf{m})\rho\mathbf{R}^2 \ln(R'/R). \quad (2)$$

$\mathbf{b}$ is the Burgers vector of the dislocation, R' is a measure of the extension of the dislocation strain field. ρ is the dislocation density and χ represents the so-called orientation factor. χ considers the effect from an assumed dislocation type on the diffraction line profile of a particular Bragg peak. It depends strongly on the angle between the Burgers vector $\mathbf{b}$ and the diffraction vector $\mathbf{Q}$. The elastic constants c_{ij} account for the anisotropic response of the crystal lattice.
The orientation factors were calculated with the program *HEXAN*, which is described in [5]. In Fig. 1 some orientation factors for 6H-SiC are shown to illustrate the dependence of line broadenings on Bragg reflections and the assumed dislocation type.

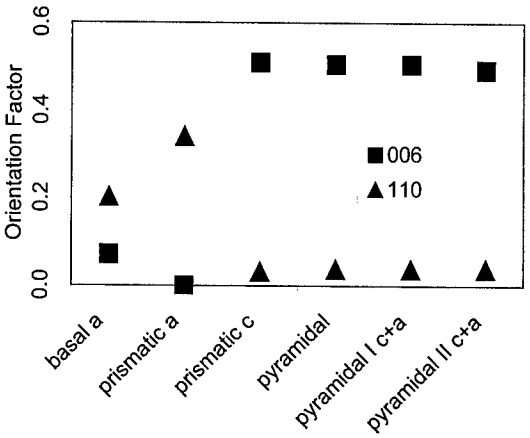


Fig. 1: Orientation factors (6H-SiC) for the reflections 006 and 110. For the reflection 006 the orientation factors are nearly 0 for basal a and prismatic a glide system. For all other types the maximum value is calculated. Opposite behavior is found for the reflection 110.

To extract the dislocation density from the measured line profiles one can look at the Fourier coefficients defined by [4, 6]

$$\ln A_n = -T(nd_{hkl}\mathbf{m}) \quad (3)$$

$$A_n = \exp[-B(\mathbf{m})(nd_{hkl})^2 \ln(R'/nd_{hkl})] \quad (4)$$

$$B(\mathbf{m}) = [(\mathbf{Qb})^2/8\pi]\rho\chi(\mathbf{m}). \quad (5)$$

Eq. 4 shows that the Fourier coefficients A_n have a linear dependence of n^2 with the slope being $B(\mathbf{m})$. Therefore the values for $B(\mathbf{m})$ can be determined from the experimental data and thus by Eq. 5 the dislocation density ρ is obtained. As there is a linear dependence of the values $B(\mathbf{m})$ with Q^2 (respectively $\sin^2\theta$) the distribution of the various types of dislocations can be determined. The orientation factors χ depend on the Bragg reflections and on the type of dislocation. If more than one type occurs, the weighted average over all assumed types of dislocation must be taken. As $B(\mathbf{m})$ versus Q^2 must be a straight line, the fractions of different dislocation types can be determined by minimization of the error of a fitted straight line.
Alternatively the dislocation density can be obtained from the integral breadths β which can be obtained by the formula [4]

$$\beta^{-1} = \int_0^\infty A(nd_{hkl})\, \mathrm{d}nd_{hkl}. \quad (6)$$

With the values for $B(\mathbf{m})$ the equations

$$\beta = [4B(\mathbf{m})\ln P]^{1/2}\left[1 - \frac{\ln(\ln P)}{4\ln P}\right], \quad (7)$$

$$P = R'[B(\mathbf{m})]^{1/2}, \quad (8)$$

show the dependence of the integral breadths β and the values $B(\mathbf{m})$ and thus the dislocation density ρ. The values from the integral breadths are in general more accurate than those from the Fourier

coefficients [5] as they can obtained directly from the measured profile. But for Eq. 8 the value R' must be known. It can't be obtained directly from the profile but it is nearly constant for similar samples.
In conclusion we determined the fractions of the different dislocation types from the integral breadths and the dislocation density from the Fourier coefficients of the profiles.

Experimental
We have studied 6H-SiC samples subjected to different irradiation and annealing procedures (Table 1). The samples had a size of approx. 5x5x0.3 mm^3 and samples M1, M2, M3 and H3 were from the same wafer. They had a p-type epitaxial layer on a p^+-type commercial substrate from CREE [7].
Several Bragg reflections of the samples and on an as-grown reference sample have been measured on a 4-circle X-ray diffractometer with a graphite monochromator and fine slits for high resolution. Particular care was taken to orient all samples identically to eliminate effective geometrical sample size effects on the line profile. As the samples were parts of the same wafer, the angle between the

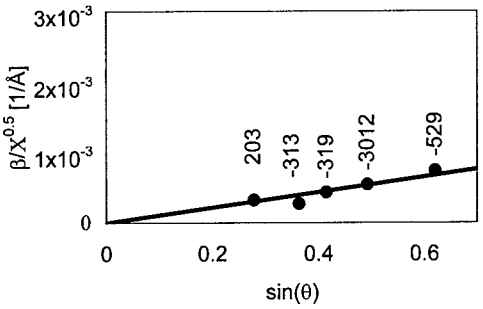


Fig. 2: Sample M1. Dependence of Integral breadth β corrected with orientation factors X on sin(θ).

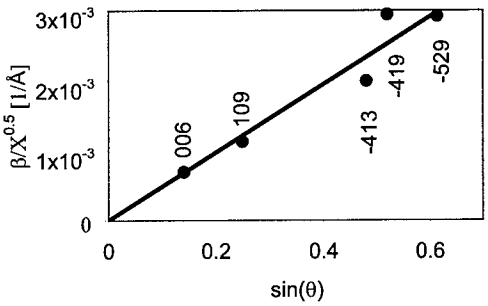


Fig. 3: Sample H3. Dependence of Integral breadth β corrected with orientation factors X on sin(θ).

surface normal and the diffraction vector defines the effective extent of the sample yielding to a broadening of the peak [8].
The profiles of the measured peaks were fitted with a Pseudo-Voigt function and deconvoluted with the profile of the reference sample. The dislocation distribution was determined according to Eq. 7 and the dislocation density according to Eq. 5. Fig. 2 and Fig. 3 show the measured integral breadths corrected for the correct orientation factors against sinθ. Fig. 2 shows the annealed sample M1 and Fig. 3 the highly irradiated and not annealed sample H3. The slope of the lines correspondent to the dislocation densities and thus to the correlation lengths [9]. The results are summarised in Table 1.

Sample	Fluence $x10^{19}cm^{-2}$	Annealing °C	Dislocation density $x10^{13}m^{-2}$	Dislocation fractions
M1	35.3	1850	0.94	96% pyramidal c+a
M2	35.3	1700	1.4	all but pure c
M3	22.7	------	2.2	90% prism a
H3	77.1	------	22	99% prism a
L1	9.4	1600	≈0.2	87% pyramidal c+a

Table 1: Measured samples with irradiation and annealing treatment, dislocation density and fractions.

Results

Samples M3 and H3 show that the dislocation density determined is higher for a higher neutron fluence (see Fig. 4). In accordance with this the correlation length is found reduced. The dislocation densities differ by a factor of 10 while the fluences differ only by a factor of 3-4. This suggests a stronger than linear dependence between fluence and dislocation density. In similar processes (amorphization in zircon due to α-radiation) non-linear relations have been found as well [10].

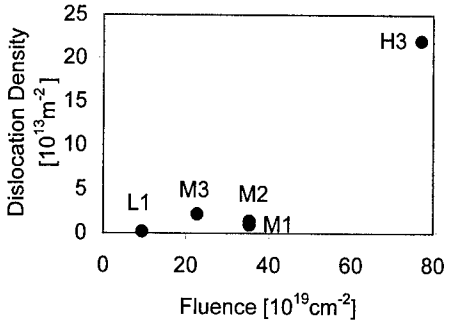


Fig. 4: Dislocation density vs. fluence for measured samples.

The dislocation fractions of nearly pure a-prismatic glide shows that the correlation length after the irradiation is reduced mainly along the a axis.

Inspection of the data for samples M1 and L1 shows that after annealing a reduction of the correlation length can be observed not only along the a axis but also along the c axis.

By comparing samples M1 and M2 the influence of the annealing temperature (1850 and 1700°C, respectively) can be studied. Both samples were irradiated with the same fluences thus having equal dislocation densities before annealing. The dislocation densities determined after the annealing differ clearly by a factor of 1.5 (Table 1). This shows that a higher annealing temperature (1850°C) reduces the dislocation density after neutron irradiation and thus increases the correlation length more strongly than an annealing at a lower temperature (1700°C).

Conclusion

With high resolution X-ray diffraction line profile analysis we have studied the effects of neutron irradiation and annealing on the correlation length of 6H-SiC. Irradiation reduces the correlation length, mainly along the a axis. Higher fluences result in a stronger than linear reduction of the correlation length. By annealing the correlation length can be regained, where higher annealing temperatures also result in longer correlation lengths.

Acknowledgement

We thank reactor centres at GKSS Geesthacht, KFA Jülich and HMI Berlin for the neutron irradiation and we appreciate the financial support by the DFG through the SFB project number 292: Mehrkomponentige Schichtsysteme

References

[1] P. Klimanek, Bergakadamie Freiberg, Habilitation (1992)
[2] T. Ungár, I. Dragomir, Á. Révész, A. Borbély, J. Appl. Cryst. 32 (1999), p. 992.
[3] M. Krivoglaz, X-ray and neutron diffraction in nonideal crystals, Springer (1996)
[4] P. Klimanek, R. Kuzel, J. Appl. Cryst. 21 (1988), p. 59.
[5] R. Kuzel, P. Klimanek, J. Appl. Cryst. 21 (1988), p. 363.
[6] R. Kuzel, P. Klimanek, J. Appl. Cryst. 22 (1989), p. 299.
[7] CREE Research Inc. 2810 Meridian Parkway, Durham, NC 27713, USA
[8] H. King, L. Finger, J. Appl. Cryst. 12 (1979), p. 374.
[9] C. Seitz, Universität Erlangen-Nürnberg, Diplomarbeit (2000)
[10] S. Ríos, E. Salje, M. Zhang, R. Ewing, J. Phys.: Condens. Matter 12 (2000), p. 2401.

Materials Science Forum Vols. 353-356 (2001) pp. 291-294
© 2001 Trans Tech Publications, Switzerland

High-Resolution XRD Evaluation of Thick 4H-SiC Epitaxial Layers

H. Jacobsson[1], R. Yakimova[1], M. Syväjärvi[1], J. Birch[1],
T. Tuomi[2] and E. Janzén[1]

[1] Department of Physics and Measurement Technology,
Linköping University, SE-581 83 Linköping, Sweden

[2] Optoelectronics Laboratory, Helsinki University of Technology,
P.O. Box 3000, FI-02015 TKK, Finland

Keywords: 4H-SiC, Epitaxial Layers, High-Resolution X-Ray Diffraction, Synchrotron Topography

Abstract. 4H-SiC commercial wafers and sublimation grown epitaxial layers with a thickness of 100μm have been studied concerning crystalline structure. The substrate wafers and the epitaxial layers have been separately investigated by high-resolution x-ray diffraction (HRXRD) and synchrotron white beam x-ray topography (SWBXT). The results show that the structural quality was improved in the epitaxial layers in the <11$\bar{2}$0> and <$\bar{1}$100> directions, concerning domain distribution, lattice plane misorientation, mosaicity, and strain, compared with the substrates. Misoriented domains have merged together to form larger domains while the tilt between the domains was reduced, which resulted in non-splitting in diffraction curves. It is also clear that if the misorientation in the substrate gets too large, we can only see a slight decrease in the misorientaion in the layer. At some positions on the substrates there were block structure (mosaicity). ω-rocking curves from epilayers at the same position showed smaller full width at half-maximum (FWHM) values and more uniform and narrow peaks. Curvature was almost the same in grown epilayers compared with the substrates. The shape of the grown epitaxial layers was concave similarly to the substrates.

Introduction

The importance of epitaxial layers with very good crystalline structure is related to the device performance [1]. It is therefore essential in the development phase of a device material to determine the defect distribution. X-ray diffraction and SWBXT methods have been widely employed for characterization of crystalline perfection of crystals. Since most structural features modify the scattering of X-rays, SWBXT is an excellent tool, which yields spatially resolved crystallographic information from studying the interaction of white beam X-rays with the entire crystal. Diffractometry methods facilitate the quantitative measurement of Bragg angles, intensities and diffraction line profiles. Both techniques are non-destructive and need no specimen preparation.
In this paper, detailed studies on commercial substrates and grown epitaxial layers regarding crystalline quality improvements have been conducted. Epilayers of 4H-SiC with a thickness of 100 μm were grown on 4H-SiC substrates by a sublimation technique [2]. Substrates and grown epilayers were separately investigated by HRXRD and SWBXT to reveal crystalline quality, (e.g. domain distribution, curvature, mosaicity, strain) and possible mechanism for structural evolution.

Experimental

Commercially available polished 4H-SiC wafers with C-terminated face were analyzed before and after deposition of layer. The substrates were quarters of a 35mm wafer. The surfaces were off-oriented 8° towards <11$\bar{2}$0> and the layer thickness was 100μm. Triple-axis high-resolution X-ray diffraction measurements were made in the laboratory using a Philips X'pert MRD, with a 3kW Cu

radiation source. The primary beam undergoes four reflections by a Ge(220) crystal monochromator and the resultant beam has an angular divergence of less than 12" in the diffraction plane. Using a triple-bounce Ge (220) collimator crystal on the secondary side, the acceptance of the diffracted beam into the detector is limited to less than 12". Triple-axis measurements were employed to take ω-rocking curves and θ-2θ diffraction curves. The measurement technique and equipment are described in detail elsewhere [3,4]. Diffraction curves were taken with the sample azimuthal orientation such that the incoming X-ray beam was parallel to $<11\bar{2}0>$ and $<\bar{1}100>$ directions. Recorded diffraction reflections were symmetric 004, 008 and 0012. SWBXT measurements were made with the synchrotron radiation from the DORIS III storage ring at the HASYLAB-DESY (Hamburger Synchrotronstrahlungslabor am Deutschen Elektronen-Synchrotron). The positron current was varied between 70-140 mA. For section topography, the beam was limited by a horizontal slit with a width of approximately 12-18 micron. The topographs were recorded on high-resolution VRP-M film.

Results and discussion

Three samples were analyzed before and after deposition of layer. A series of ω-rocking curves and θ-2θ scans were conducted. First, ω-rocking curves were taken with a mapping technique, where the footprint (beam area) on the sample was varied by change of the spot size and incoming beam angle (reflection). The ω-rocking curves provide information about lattice planes tilt. Mosaic structure appears as discrete diffracting blocks, whose different diffraction vectors will give rise to an uneven ω-profile, depending on their mutual misorientations and sizes. Also, the ω-rocking curves are broadened by curvature. The ω-rocking curves recorded from the substrates showed peaks that were broad and also sometimes showed peak splitting and asymmetrical shape. The number of peaks varied from 1-4 peaks depending on the position on the specimen and footprint size. The shape of the diffraction curves with peak splitting suggests that the crystal consist of domains, which are slightly misoriented to each other. To investigate the domain distribution and the misalignment, the footprint on the sample was decreased to 1*2 mm and several ω-scans were made along a 1*10 mm stripe. The result from this decomposition revealed that the broad rocking curve recorded with spotsize of 1*10 mm is a superposition of individual diffraction peaks from small laterally distorted domains, slightly tilted with respect to each other, Fig 1. The separation between

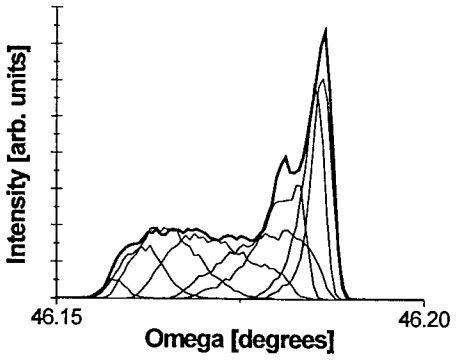


Fig1. Showing superposition of ω-rocking curves with a footprint of 1*2 mm scanned along a 1*10 mm stripe along $<11\bar{2}0>$ direction.

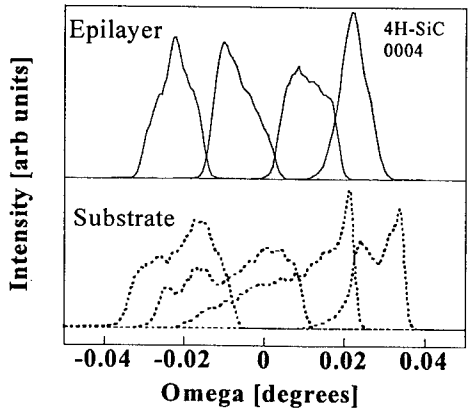


Fig 2. Rocking curves recorded at different positions translated along $<\bar{1}100>$ on substrate and epilayer. Footprint is 1*9 mm.

the peaks corresponds to the misalignment angle between different domains and the domain size seems to vary from approximately 0.5 mm up to several millimeters. Peaks that showed a typical mosaic pattern also had much lower intensity. This low intensity is mainly due to the sensitivity of the technique to crystal defects and grain boundaries, which scatter the intensity into a large angular range. However, at some local areas of the substrates, ω-rocking curves were sharp and narrow with high intensity and a FWHM value of 18-arc sec. The domain distribution showed a random pattern. ω-rocking curves recorded from the epilayer showed a different structure. They had more uniform and narrow shapes. ω-rocking curves recorded from the substrate and the epilayer can be seen in Fig 2. The peaks did not show splitting as much as for the substrates. Also, ω-rocking curves did not show a mosaic pattern. To analyze the domain distribution along the stepped direction, measurements along $<11\bar{2}0>$ were done. The epilayer growth seems to smooth out the small angle boundaries along the direction $<11\bar{2}0>$ and perpendicular along $<\bar{1}100>$. At positions on the specimen where there was strong domain formation, the domain structures of the substrate were replicated into the epilayer. Also, at some local positions on the substrate where the substrate showed a very sharp and narrow ω-rocking curve with a FWHM of 18-22-arc sec, the structure was replicated into the epilayer without evolution.

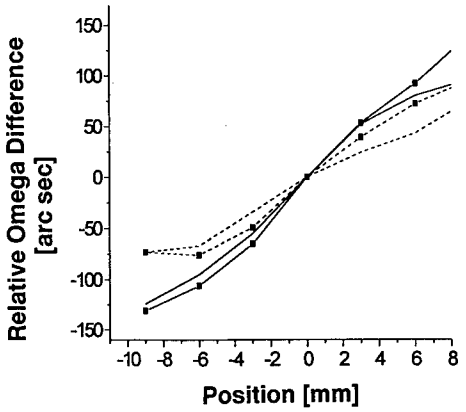


Fig. 3. Relative curvature of substrate and epilayer in the $<\bar{1}100>$ (solid lines) and $<11\bar{2}0>$ (dashed lines). Measurements on the epilayer are marked with black squares.

Curvature was also measured, since this can induce stress in the grown epilayer. Curvature of the atomic planes will induce a systematic shift in the omega-angle along the specimen, which can be observed in Fig. 2, both for the substrate and the epilayer. The curvature was measured along the $<11\bar{2}0>$ direction and perpendicular, along the $<\bar{1}100>$ direction. As shown in Fig.3, curvature is more pronounced along $<\bar{1}100>$ than along step direction $<11\bar{2}0>$. The difference between the curvature of the substrates and the substrates with grown epilayers is small. This shows that the reduced broadening in the epilayers vs. substrates is due to that domains originating at the substrate have merged together to form larger domains. However, the systematic ω-shifts is due to wafer curvature.

When a substrate contains several misoriented domains, step-flow growth will take place over the whole substrate. At the edge opposite to the $<11\bar{2}0>$ direction, domains will increase their size in the $<11\bar{2}0>$ direction by the step-flow growth mechanism. As growth proceeds, these domains will partly or completely overtake domains in the down-step direction. With increasing layer thickness, the domain enlargement will completely overtake domains in the down-step direction (in the ideal situation) [5]. If the angular spread between two domains is large, then each domain replicates into the epilayer. Also, if each domain has high structural quality, then there is no structure evolution, only replication into the epilayer. Fig. 4 is a section transmission topograph showing both the substrate and the epilayer. In this reflection where **g** = 00012, several types of structures are revealed. Screw dislocations are seen as thin black stripes running from the substrate up through the epilayer.

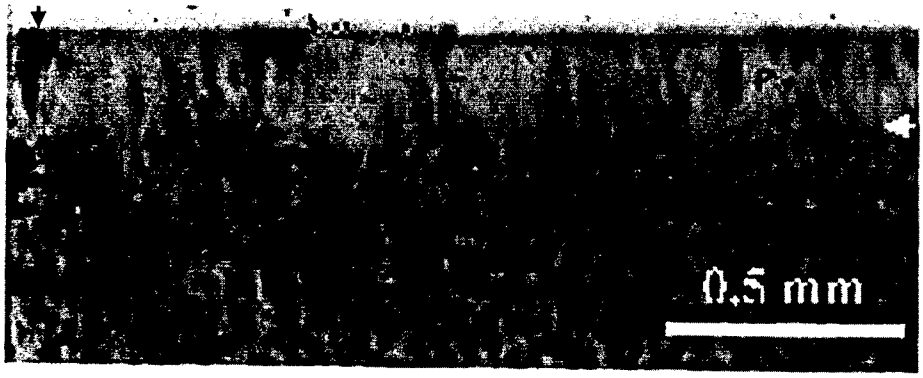


Fig.4 Synchrotron section topograph showing cross-section of the substrate and epilayer. The black arrows show the 100μm grown film. The white arrow marks the interface. **g** = 00012

The screw dislocations are replicated into the epilayer and this is consistent with previous reports showing that screw dislocations are replicated during step-flow epitaxial growth in 4H and 6H polytypes [6]. The dark curved black spots in the substrate are dislocations lying in the basal plane forming a network. These were introduced by surface relaxation during crystal growth [7]. Where the density is high (black regions), individual dislocations cannot be resolved. The dislocation distribution in the epilayer is much more uniform and of a lower densiy, since the basal plane (0001) dislocations in the substrates are mainly parallel to the growing surface of the epilayer, they can not penetrate into the layer during the growth which proceeds in [0001] direction.

Conclusion

To our understanding, the crystalline improvement is related to the fact that almost all dislocations lying in the basal plane in the substrate do not replicate into the epilayer, this can be seen in the section topograph, Fig. 4. Also, when a substrate contains several misoriented domains, step-flow growth will take place over the whole substrate. The domains in the substrate are enlarged by the step-flow growth mechanism, mainly in the $<11\bar{2}0>$ direction. The reduction of the number of domains is enhanced with increasing layer thickness.

Acknowledgement

This work was supported by the SSF-SiCEP programme. We also thank Dr. R. Rantamäki for his qualified help in preparing and guiding the topography measurements at the Hasylab facilities. We thank Dr. P. Bergman for help in carrying out the topographic measurements.

References

[1] P.G. Neudeck, J.A. Powell: IEEE Electron Device Lett. 15 (1995), p. 63.

[2] M. Syväjärvi, R. Yakimova, M. Tuominen, A. Kakanakova, M.F. MacMillan, A. Henry, Q. Wahab and E. Janzén: J. Crystal Growth 197 (1999), p. 155.

[3] P.F. Fewster: J. Appl. Cryst. 24 (1991), p. 178.

[4] R.C. Glass, L.O. Kjellberg, V.F. Tsvetkov, J.E. Sundgren and E. Janzén: J. Crystal Growth 132 (1993), p. 504.

[5] M. Syväjärvi, R. Yakimova, H. Jacobsson, E. Janzén: J. Appl. Phys. 88 (2000), p. 1407.

[6] S. Wang, M. Dudley, C.H. Carter, H.S. Kong: Mat. Res. Symp. Proc. 339 (1994), p. 735.

[7] M. Dudley, S. Wang, W. Huang, C.H. Carter Jr., V.F. Tsvetkov and C. Fazi: J. Appl. Phys. D: Appl. Phys. 28pp (1995), p. A63

Materials Science Forum Vols. 353-356 (2001) pp. 295-298
© 2001 Trans Tech Publications, Switzerland

Defect Analysis of SiC Sublimation Growth by the *in-situ* X-Ray Topography

T. Kato[1], N. Oyanagi[2], H. Yamaguchi[1], S. Nishizawa[1] and K. Arai[1]

[1] Ultra-Low-Loss Power Device Technology Research Body (UPR), Electrotechnical Laboratory, 1-1-4 Umezono, Tsukuba, Ibaraki 305-8568, Japan

[2] Ultra-Low-Loss Power Device Technology Research Body (UPR), R&D Association for Future Electron Devices (FED), 1-1-4 Umezono, Tsukuba, Ibaraki 305-8568, Japan

Keywords: Defect, *in-situ* Observation, Modified Lely Method, X-Ray Topography

Abstract Silicon carbide (SiC) single crystal growth was studied by the *in-situ* observation using x-ray topographic technique. Occurrence and dynamics of defects, dislocations were observed in a real time display and captured as topographic images during sublimation growth (modified Lely method) of SiC crystals. From the analysis of these topographic images, high-density of dislocations and typical large defects, such as micropipes, domain boundaries and macrodefects were investigated. On the basis of our *in-situ* observation and analysis, we argue that dislocation and nucleation control on the seed crystal during initial growth are of prime importance for producing high quality SiC crystals.

1. Introduction

Silicon carbide (SiC) has received a renewed attention as an attractive material for high power, high temperature and high frequency semiconductor devices for the last few years. Generally, SiC bulk single crystals for electronic devices are grown by sublimation (modified Lely method) [1]. However, variety of defects and dislocations still exist in these bulk crystals. The large hollow defects widely known as micropipes are reported as one of the main cause of limiting the quality of SiC-based devices [2,3]. Therefore it is important to find optimum growth conditions for the control of defects and dislocations. *In-situ* observations for crystal growth had been used previously investigating the origin of defects and dislocations formation and for the crystal growth mechanism [4,5]. However, the *in-situ* observation for SiC bulk single crystal growth has been difficult, because the crystal growth is performed in a carbon crucible like a black box and at high temperature over 2000 °C. In a previous paper, we reported on the development of an instrument for real-time observation of SiC bulk single crystal growth by x-ray topography [6,7]. The x-rays can capture defects and strains in the growing crystal as diffraction images through a carbon crucible. Therefore, this *in-situ* x-ray topographic technique is effective to realize a direct analysis for the SiC crystallinity inside the growth crucible. This technique was considered to contribute for optimizing the growth conditions and to interpret the mechanism of defects and dislocations formation. In this paper, we report on the *in-situ* observation SiC crystal growth. Also occurrence and dynamical behavior of the defects during the growth was investigated in a real time display using the x-ray topographic system.

2. Experimental

The experiments for the growth of SiC crystals by the modified Lely method was performed in an rf-induction furnace combined with a x-ray topographic system [6]. The (0001) 6H-SiC crystals grown by Acheson and Lely methods were chosen as seed crystal. The seed was fixed on the lid at the inner side of the crucible, such that its position was at the datum point of the x-ray topography. The crystals were grown at 2000~2200 °C and 10~400 Torr chamber pressure using high purity Ar gas. A molybdenum rotating-anode was used as a source to generate the x-rays with maximum output of 18 kW. The beam irradiates the growing crystal upward through a carbon guide pipe with out interference with the source material in the crucible. A CCD camera was used for direct scanning of topographic images from $g=10\bar{1}1$. The scintillation counter was used for monitoring the thickness of the growing crystal [8]. An optical microscope was also used for the post process observation of these SiC grown crystals. Dislocations and defects in the specimens analyzed by the post processes were compared with the *in-situ* observations.

3. Results and Discussion

Fig. 1 shows the results of *in-situ* x-ray topography for SiC crystal growth. The images were taken from the area close to the seed crystal edge. After the pressure in the chamber was gradually decreased from 700 Torr to 10 Torr (growth pressure) and the growth started, topography revealed some new features as shown in Fig. 1(a). Bright diffuse image appeared dominantly from both right and left sides of the crystal marked as A on the topograph. The image shows generation of new dislocations with high density during the initial growth. Besides this, we also noticed that the crystal edge starts becoming circular attaining the shape of of the carbon lid to which it was attached during the initial growth due to effective sublimation as it was exposed to higher temperature than the center of the crystal [9]. This was observed almost in all of the growth experiments studied by the *in-situ* observation. As the growth proceeds, the bright diffuse images appearing due to the dislocations are elongated towards the inner part of the growing crystal, observed as line images between light and dark spheres and indicated by white arrows in the figure in a real time display. After one-hour growth the topograph recaptured is shown in Fig. 1(b), the line images shown in Fig 1(a) overlapped each other, and newly bright spots appeared marked as B on Fig. 1(b). The growth was analyzed by an optical microscope. We observed that thickness of both right and left sides of the grown crystal is higher than at the center. Several micropipes generated in the center of the crystal. Comparing with *in-situ* topographs, it seems that the

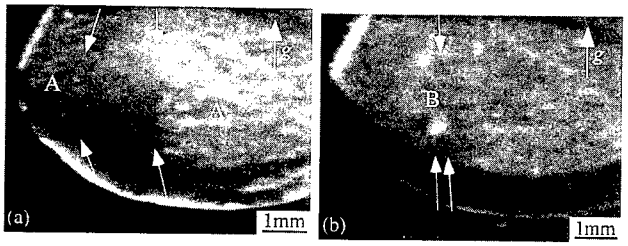


Fig. 1 *In-situ* topographs of SiC growth. (a) Soon after the growth starts, bright diffuse image due to high-density of dislocation in the initialy grown layer appeared from both right and left sides (A). White arrows show the domain edges. (b) Coalescence of the domain edges at the center of the captured image (up and down arrows direction) shows a domain boundary, where several new micropipes (B) are generated as bright spots.

variation in the growth rate on the seed crystal surface forms domain at both right and left sides of the crystal (A's in Fig. 1(a)) in the initial stage of the growth. These domains then progressed toward the center of the crystal as growth proceeds further. When the domain boundaries overlap each other, several new micropipes are generated at the B on Fig. 1(b). The result shows that the domains overlapping cause large screw dislocation of the micropipe. It is reasonable to conclude that stress and/or dislocations due to the overlapping of domains results in large Burgers vector for the screw dislocation.

We also investigated the occurrence of macrodefects [10, 11] by the *in-situ* observation. Macrodefects are composed of tube-like cavities and large void, which are one of the characteristic large defects in SiC bulk crystal. The defects appear in the growing crystal in an ordered generation of tube-like cavities first followed by the large voids from the seed crystal along the growth direction [10, 11]. In the *in-situ* topographs, we have observed many dark spots after the appearance of the bright diffused image due to the high-density of dislocations on the seed crystal surface as shown in Fig. 2(a). The dark spot appearance can be attributed to the imperfect diffraction conditions. As the growth proceeds the topograph gradually changes to image shown in Fig. 2(b). The spots shown in Fig. 2(a) enlarge and connect one another. When these enlarged spots become stable the image gradually changes to uniform light image as shown in Fig. 2(c). Such images were observed many times whenever macrodefect appeared during growth. As we investigate this *in-situ* observation comparing with microscope observation after the growth termination, the small dark spots during the initial growth can be thought as generation of small cavity like tubes. These are followed by the formation of large voids or negative crystals as the small dots connect with one another for the restoration of the degraded crystallinity of the growing crystal, resulting in the formation of macrodefects. In short, we have observed the same ordered generation of macrodefect by the *in-situ* observation as mentioned above in this study as examined by the optical microscope investigations.

The *in-situ* observation of the SiC bulk crystal growth by sublimation method was realized by the x-ray topographic technique. The study shows an advantage of the system that it can be used for the real time analysis for dislocations and defects in the growing crystal. The observation and the analysis of our results show that the high-density of dislocations always



Fig. 2 Macrodefects occurrence captured by the *in-situ* topography. (a) Generation of macrodefects confirmed as dark spot images in the initial growth. (b) As growth proceeds, the dark spot images are enlarged and contact each other. (c) Dark contrast gradually changed to light one after the completion of negative crystal on the top of macrodefect.

appear during the initial stage of SiC crystal growth. We also observed that the irregular growth which starts in parts on the seed crystal surface during the initial growth results in new defects in the grown crystal. Th e results suggest the importance of initial layer growth control to improve the crystallinity of the growing crystal. If initial growth conditions were optimized, there is a possibility that density of defects in the grown crystal can be decrease drastically.

4. Conclusion

SiC single crystal growth was successfully observed by the *in-situ* x-ray topographic system. The system used is a reliable and effective technique for analyzing the SiC growth and the origin of defects and dislocations. The growth behavior in the modified Lely method was clarified in a real time display. Topographs showed that high-density of dislocations appear just above the seed crystal during initial stage of the growth. Occurrence and dynamics of large defects, such as micropipes, macrodefects, were also confirmed clearly as contrast in the topographic images. We argue the importance of dislocation and nucleation control above the SiC seed crystal during the initial growth on the basis of facts and findings observed by the *in-situ* as well as the post process observations of the SiC crystal growth.

Acknowledgements

This study was performed under the support of the Proposal-Based New Industry Creative Type Technology R&D Promotion Program from NEDO of Japan and the management of FED as a part of the MITI NSS (R&D Ultra-Low-Loss Power Device Technologies) supported by NEDO of Japan.

References

[1] Y. M. Tairov and V.F. Tsvetkov, J. Cryst. Growth 43(2) (1978), p. 209.

[2] P.G. Neudeck and J.A. Powell, IEEE Electron Device Lett. 15 (1995), p. 63.

[3] K. Koga, Y. Fujikawa, Y. Ueda and T. Yamaguchi, Springer Proc. in Phys., 71 Amorphous and Crystalline Silicon Carbide IV, Springer-Verlag, Berlin (1992), p. 96.

[4] J. Chikawa, J. Cryst. Growth 24/25 (1974), p. 61.

[5] P.J. Wellmann, M. Bickermann, D. Hofmann, L. Kadinski, M. Selder, T.L. Straubinger and A. Winnacker, J. Cryst. Growth 216 (2000), p. 263.

[6] H. Yamaguchi, S. Nishizawa, T. Kato, N. Oyanagi, W. Bahng, S. Yoshida, K. Arai, Y. Machitani and T. Kikuchi, Rev. Sci. Instru. 71 (2000), p. 2829.

[7] T. Kato, N. Oyanagi, H. Yamaguchi, Y. Takano, S. Nishizawa and K. Arai, Mater. Sci. Forum 338-342 (2000), p. 457.

[8] N. Oyanagi, T. Kato, H. Yamaguchi, S. Nishizawa and K. Arai, Mater. Sci. Forum 338-342 (2000), p. 75.

[9] W. Bahng, Y. Kitou, S. Nishizawa, H. Yamagichi, M. Nasir Khan, N. Oyanagi, S. Nishino, K. Arai, J. Cryst. Growth 209 (2000), p. 767.

[10] R.A. Stein, Physica B185 (1993), p. 211.

[11] M. Anikin, M. Pons, K. Chourou, O. Chaix, J.M. Bluet, V. Lauer and R. Madar, Mater. Sci. Forum 264-268 (1998), p. 45.

Materials Science Forum Vols. 353-356 (2001) pp. 299-302
© 2001 Trans Tech Publications, Switzerland

Crystal Defects as Source of Anomalous Forward Voltage Increase of 4H-SiC Diodes

J.P. Bergman, H. Lendenmann, P.Å. Nilsson, U. Lindefelt and P. Skytt

ABB Corporate Research, SE-721 78 Västerås, Sweden

Keywords: Device Stability, Dislocation, Stacking Fault, Synchrotron Topography

Abstract: We have performed a material study of 4H SiC PN diodes after they have been exposed to long term forward voltage operation. After this operation an increase in forward voltage drop was observed on some of the diodes. Using cathodeluminescence, photoluminescence lifetime mapping and synchrotron white beam X-ray topography we have found that structural defects are created in the epitaxial layers during the operation. The structural defects are interpreted as stacking faults in the 4H SiC basal plane, propagating through the entire n- base layer. The stacking faults, or defects associated with these, are acting as recombination centers reducing the recombination emission intensity and the carrier lifetime in the material.

Introduction

One of the main applications for SiC devices is in high power systems as voltage source converters, in for example motor drives or HVDC transmission systems. These applications have very high demand on the devices regarding high blocking voltage, low switching losses and high current levels. This makes properties such as reliability and long term stability important.

Recently, detailed results regarding performance and reliability of high power SiC diodes have been presented [1,2]. It was reported that some devices exposed to long term operation exhibit an increase of the static forward voltage drop after the testing. In this study we present a material investigation, using cathodeluminescence (CL), photoluminescence (PL) lifetime mapping and synchrotron white beam XRAY topography (SWBXT), of diodes showing this behavior.

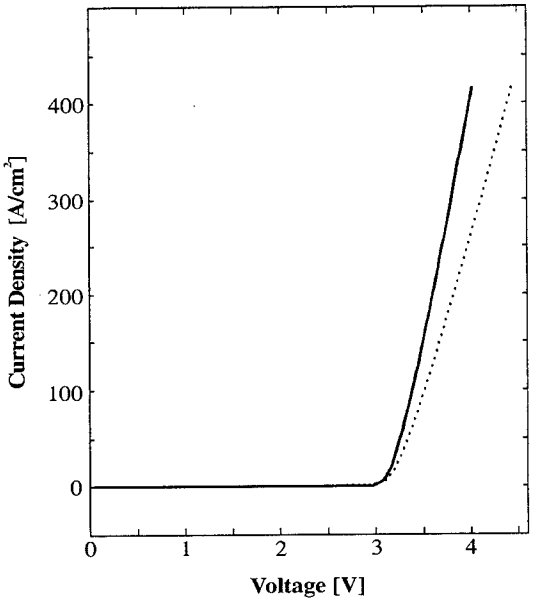


Figure 1. An I-V curve for a typical diode before and after forward voltage stress. A typical increase of the forward voltage drop is in the the range of 50-100 meV.

Experimental Details

The investigated diodes were made on 35 mm 4H SiC wafers from CREE, cut with an 8 degrees off axis angle. An approximately 30μm thick epi-layer was grown using the hot wall CVD technique with a n-type nitrogen doping in the low 3 10^{15} cm^{-3}. Using a standard diodes process [3] devices were fabricated. However, to ease the X-ray characterization in this work, the anode consisted of a simple p-type epilayer. These diodes were then stress tested in a controlled way reflecting continuos converter operation. The forward voltage drop at 100A/cm^2 was originally in the order of 3.4 V. Some of these diodes showed an increased voltage drop in the range of 50-100 mV after testing, as seen in fig. 1. These diodes were further studied and the top metal layer was removed on selected diodes and the remaining epitaxial material was investigated. SWBXT measurement was performed at Desy-lab, Hamburg, Germany.

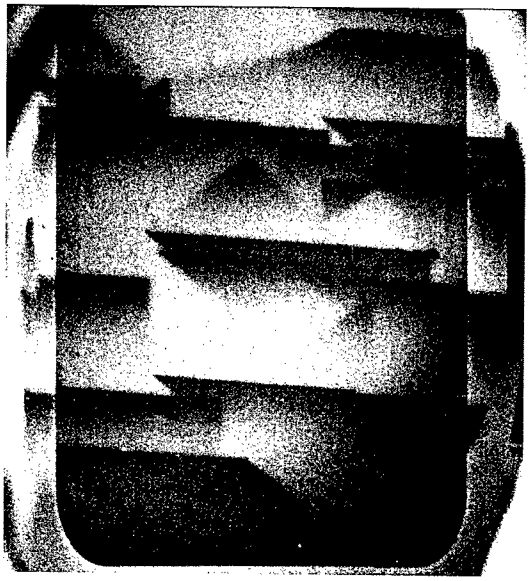


Figure 2. Low temperature panchromatic CL image of a stressed 4H SiC diode. Triangular and rectangular features with reduced emission intensity (darker regions) are observed on stressed diodes.

Experimental Results

CL were performed at low temperatures (<10K) to observe the spatial distribution of the optical emission. An example of a panchromatic CL image is shown in fig 2. The rectangular area is the remaining boundary of one of the stressed diodes. Within this area, regions with reduced emission intensity are observed, corresponding to a darker image. These have triangular, or sometimes rectangular or rhombic shapes, and are gradually reduced towards one direction. These features are only seen on stressed diodes, and extends at maximum approx. 20 μm outside the diode region. The intensity and appearance of these features are changed using different penetration depths, or different sample temperatures. This indicates that the features are extending into the epi-layer.

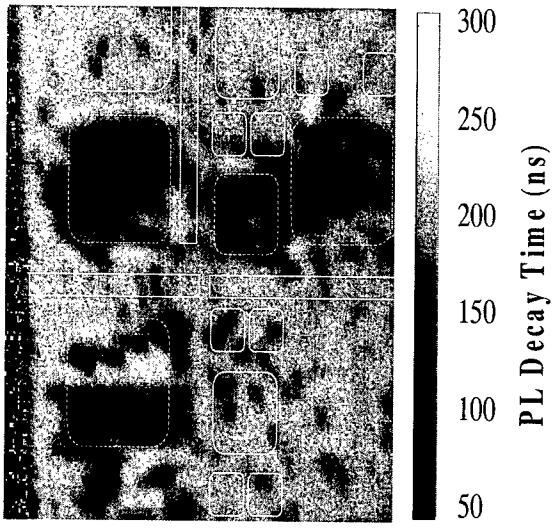


Figure 3. High resolution PL decay mapping of a wafer with stressed and non-stressed diodes. A reduction of the minority carrier lifetime is observed on all 4 stressed diodes.

CL images measured at different detection wavelengths or CL spectral measurements did not show any difference between emission wavelength of darker and brighter areas, or between stressed and non-stressed diodes. Preliminary low temperature PL measurements have also been performed and has not shown any reproducible difference between different regions.

Figure 3 shows a high resolution mapping of the carrier lifetime measured by room temperature PL decay. The mapping covers several diodes, both stressed and non-stressed. A clear reduction of the carrier lifetime is observed on the stressed diodes, marked as dotted rectangles, as compared to the non-stressed diodes. A reduction of the minority carrier lifetime, from about 400ns to below 200ns, was observed in the regions of stressed diodes.

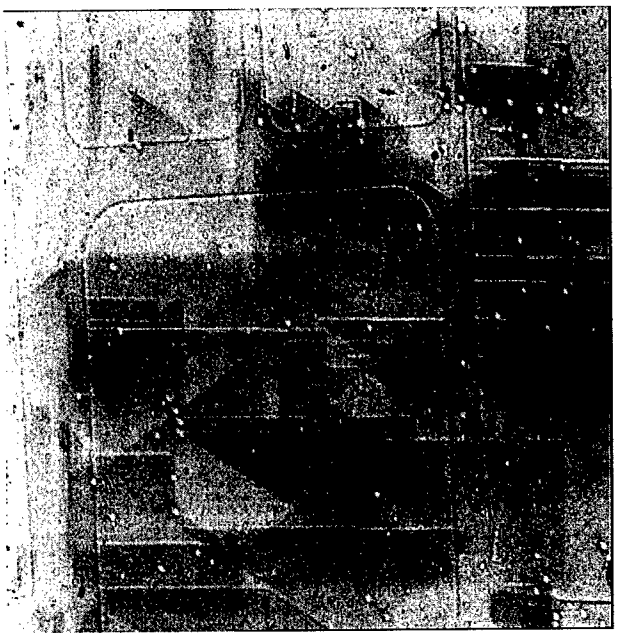


Figure 4. SWBXT image of a forward voltage stressed diode. Bright spots are elementary screw dislocations and the larger rectangles are the diode periphery. The darker triangles are interpreted as stacking faults in the basal plane.

The spatial resolution for this measurement is limited by the carrier diffusion length and the same features as observed in CL shown in fig. 2, cannot be resolved. However, indications of triangular areas with reduced lifetime can be seen in for example the bottom left stressed diode. The diode shown in fig 2, is the smallest of the stressed diodes as seen in fig. 3.

The SWBXT were performed using backscattering geometry, giving a Laue pattern. Each spot consists of a complete image reflection. Figure 4 shows an example of one of these images, measured on the same diode as with CL in fig 2 and with lifetime mapping in fig 3. The boundary of the diodes are clearly seen, probably due to stress introduced between the p+ layer and the n-base layer. White dots in the image is elementary screw dislocations, while no micro-pipes is observed on this image. In addition we observe triangular features often with a stronger bright line along the hypotenuse. The presence and the contrast ratio between the bright lines and the darker regions varies between different reflections, depending on the relative relation between the incoming synchrotron beam, the diffracting plane and the orientation of the crystal defect. In some reflection directions only the boundary of the triangular are seen, and in some direction are no sign of these defects observed. A clear correlation between the structural defects observed with SWBXT and the optical features seen in CL can be seen by comparing fig. 2 and fig. 4.

Discussion and Conclusions

The results from the SWBXT clearly shows that crystal defects are created during electrical stress of the SiC diode. The observed features are observed only on stressed diodes and are restricted to the area of the diode. The fact that dark areas are observed in the SWBXT interference image also shows that the created defect has an at least 2D spatial extension. They also show that these defects have an extension corresponding to the epi-layer thickness along the basal plane.

These defects are interpreted as stacking faults in the (0001) basal plane. The stacking fault are in the case of triangular defects bounded by dislocations in the $<01\bar{1}0>$ and $<10\bar{1}0>$ directions.

The triangular defects are similar to the previously observed 3C inclusions. These are often observed on epitaxial growth on low angle cut substrate, and the formation of the inclusions has previously been explained [4]. However, we have found no evidence, from XRD or optical spectroscopy, of similar 3C inclusion regions in these stressed samples. Neither by XRD or from optical spectroscopy where emission from the lower bandgap 3C polytype would appear in visible range of the spectrum. There is to our knowledge no previous report that similar 3C inclusions are created after growth. The question whether the observed defects are single stacking faults or a larger number of stacking faults in the 4H lattice, requires a further and more detailed study. The results from CL and lifetime mappings shows that these created defects acts as recombination centers which reduces the recombination efficiency and the carrier lifetime. The reduction of the carrier lifetime can also explain the increase in the forward voltage in these diodes.

The formation of crystal defects in devices during operation has previously been observed in many other material systems. This usually influences the device performance and in some cases leads to complete degradation. In early GaAs and II-VI based lasers, rapid degradation was observed induced by pre-existing extended defects, mainly stacking faults, which was formed during epitaxial growth [5]. A more gradual degradation initiated by point defects or local strain has also been observed [5], which seems more similar to the observed behavior in SiC, where the structural defects, interpreted as stacking faults, are not initially present but created during the operation. The formation of stacking faults are most likely induced by local or thermal strain at the PN interface, where dislocation pairs are created initiated by point defects or dislocation loops. These dislocation propagates along the basal plane and terminate at the epilayer substrate interface, leaving a stacking fault in the plane.

The driving force for the dislocation motion is likely enhanced by the energy released by non radiative recombinations in the electron hole plasma. This so called recombination enhanced effect has previously been observed in GaAs and II-VI material systems [6].

The authors acknowledge contributions from the entire ABB SCRIPT team, A. Ellison, H. Jakobsson and T. Tuomi, for help with the SWBXT measurements, and A. Galeckas.

References

[1] H. Lendenmann, F. Dahlquist, N. Johansson, J.P. Bergman, H. Bleichner, and C. Ovren, Invited Talk at 1st int. Workshop on Ultra-low-Loss Power Device technology, Japan, 2000.
[2] H. Lendenmann, F. Dahlquist, N. Johansson, R. Söderholm, P.A. Nilsson, J. P. Bergman, and P. Skytt, This conference.
[3] K.Rottner et al., Mat. Sci. and Eng. B61-62 (1999), p. 330.
[4] W.L. Zhou, P. Pirouz, and J.A. Powell, Mat. Sci. Forum. 264-268 (1998), p. 417.
[5] K. Nakano, Proc. 2nd Int. Symp. on Blue Laser and Light Emitting Diodes (ISBLLED) (1998), p. 395.
[6] L. Sugiura, Appl. Phys. Lett. 70 (1997), p. 1317.

Materials Science Forum Vols. 353-356 (2001) pp. 303-306
© 2001 Trans Tech Publications, Switzerland

A Simple Non-Destructive Technique to Detect Micropipes in Silicon Carbide

D.J. Morrison[1], A. Keir[2], I.H. Preston[2], K.P. Hilton[2], M.J. Uren[2] and C.M. Johnson[1]

[1] Dept. of Electrical and Electronic Engineering, University of Newcastle, Newcastle NE1 7RU, UK

[2] Defence Evaluation and Research Agency, Great Malvern, Worcs. WR14 3PS, UK

Keywords: Crystalline Defects, Electrolysis, Micropipes

Abstract An initial investigation has shown that the electrolysis of water can occur preferentially at macroscopic defects, including micropipes, where a silicon carbide wafer is used as the anode. It is proposed that observing the location of the resulting streams of bubbles, nucleated at the defects, would form the basis for a simple, non-destructive qualification test of SiC wafers.

Introduction

A variety of surface and structural defects exist in SiC but the micropipe is recognised as the most detrimental defect in terms of electrical device operation [1]. Micropipes are hollow core dislocations, ranging from a few nanometers to several micrometers in diameter, that propagate through the wafer [2],[3]. If a micropipe is present in the active device area, the blocking capability of the device will be severely impaired. If larger area (and hence larger current) devices are to be realised the density of micropipes must decrease. Manufacturers such as Cree Inc, are continuing to optimise growth conditions to produce material with lower micropipe densities, but production 50mm diameter wafers still typically have ~10cm^{-2} [3]. Often these micropipes are not evenly distributed across the wafers, but occur in clusters [4]. When developing a fabrication process, it is obviously useful to know which areas and how much of the incoming wafer are relatively micropipe free before fabricating devices.

Micropipe defects can be identified in a number of ways. During device operation to voltage breakdown, micropipes are recognised by the localised appearance of microplasmas. Neudeck et al verify that these plasmas occur at micropipe sites, using optical microscopy [1]. However, mapping an entire wafer before device fabrication using optical transmission microscopy is time consuming and it is often difficult to see smaller micropipes. Synchrotron white beam x-ray topography (SWXT) has also been used to detect micropipes [5, 6]. Whilst this method has proved to be an effective tool in determining the location of micropipes it is an expensive method and therefore not suitable for day to day wafer quality assessment. Etching SiC in molten KOH is commonly used to reveal micropipes but this is a destructive process. Yakimova et al describe a simple wafer mapping method which utilises the electrolytic dissolution of a thin metal layer deposited on the frontside of a SiC wafer [4]. An Al coated wafer is connected to the anode in a sodium carbonate electrolytic cell and a voltage is applied. The electrolyte passes through the micropipe to the metal and results in corrosion of the aluminium at the intersection of the micropipe and the metal, and can easily be observed using an optical microscope. Aluminium may be chemically etched from the surface and the wafer may then be used for device processing. While this method appears to be non-destructive, it seems likely that the electrolyte or the removal of the metallisation will result in contamination. Here we present an alternative electrolytic defect imaging technique, which does not require a metallisation stage.

Experimental Method

A voltage source, an ammeter, a Petri dish of water, an aluminium ring electrode (to ensure equal potential distribution across the wafer) and the SiC wafer were set up to form an electrolytic cell as shown in Fig. 1. In the present configuration, a small amount of silver paste was applied to the backside of the SiC wafer and was connected to the anode (a two cell configuration could easily be used to remove the necessity for this contact). Two wafers were analysed: a low micropipe density n-type 4H-SiC bulk wafer, and a poorer quality p-type 4H-SiC wafer which had a clear line of large defects down the centre of the wafer (visible to the naked eye).

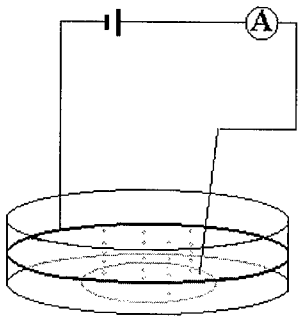


Fig 1:Schematic diagram of electrolytic cell used to detect defects in SiC wafers

The Petri dish containing the wafer was placed under a Reichart Polyvar 2 optical microscope and an increasing voltage was applied until the current was approximately 15mA. Electrolysis of the water led to the formation of hydrogen and oxygen bubbles on the surface of both the ring electrode and the wafer. Defects acted as nucleation sites for bubble formation, resulting in streams of bubbles which rose to the surface of the water. Following electrolysis, the silver paste was removed in acetone and the wafers were thoroughly cleaned in a 1:1 solution of H_2SO_4:H_2O_2, followed by a rinse in de-ionised water. The crystalline quality of the n-type 4H-SiC wafer was also assessed using Cu kα (λ=1.54Å) X-ray topography and was recorded on Fuji Ix 150 film. Bragg angle adjustment was performed at 1mm intervals to compensate for wafer curvature.

Results

An optical micrograph of the p-type wafer during the electrolysis is shown in Fig. 2. A clear line of isolated streams of H_2 and O_2 bubbles can easily be observed right down the centre of the p-type wafer. The position of these streams of bubbles corresponded exactly to the position of large defects.

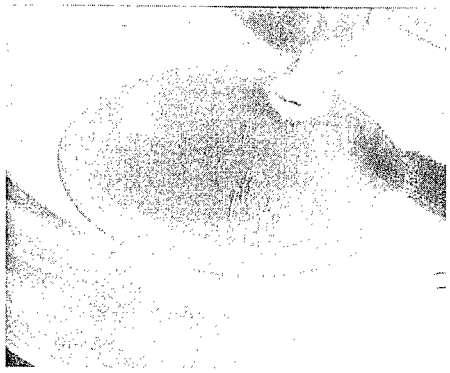


Fig 2: Optical micrograph of p-type 4H-SiC wafer during electrolysis

Fig. 3 depicts an optical micrograph of the n-type 4H-SiC wafer during electrolysis. In contrast to the p-type wafer, the good quality n-type wafer did not have large, discrete defects that could be observed by the unaided eye.

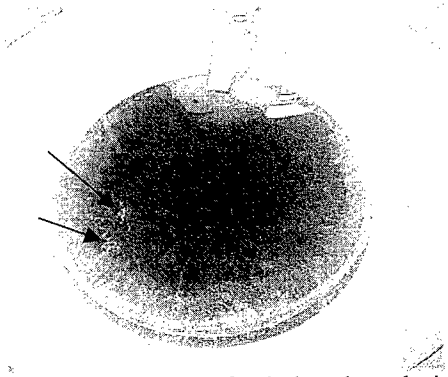


Fig 3: Optical micrograph of n-type 4H-SiC wafer during electrolysis. Particularly large bubble streams from defects are indicated with arrows.

Furious bubbling around the edge of the wafer suggests that there were a large number of defects around the edge of the wafer but the area toward the centre of the wafer was relatively clear of defects. On the left hand side of the wafer two isolated groups of bubbles can be observed.

A negative x-ray topograph image of the n-type 4H-SiC wafer is shown in Fig. 4. Note that the regular vertical banding on this image occurs as a result of the Bragg angle adjustment. On the lower right hand side of the wafer image, it appears that there is some material missing from around the edges of the wafer. However, lattice tilts in the region of 1° (or polycrystalline material) at the edge of the wafer are responsible for this effect. Dark areas on the wafer image correspond to strong x-ray reflections, which in turn are indicative of areas of strain. The size of the area is related to the size of the strain field. Micropipes are revealed as dark dots at the centre of a white annulus. In Fig. 4, these can be observed around the edges of the wafer. The two large dark regions observed on the left hand side of the wafer are areas of high strain associated with clusters of micropipes. A cluster of micropipes, surrounding the dark area on the upper left hand side of the image can be observed in the close up of this region shown in Fig. 5.

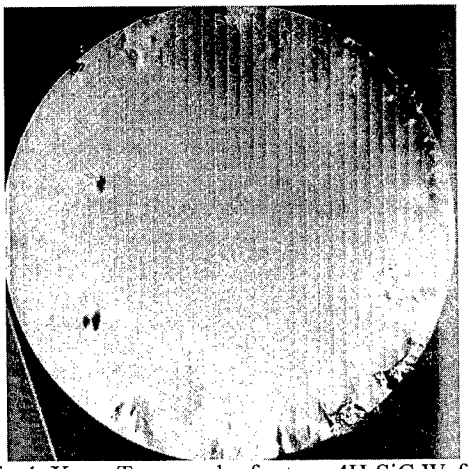


Fig 4: X-ray Topograph of n-type 4H-SiC Wafer

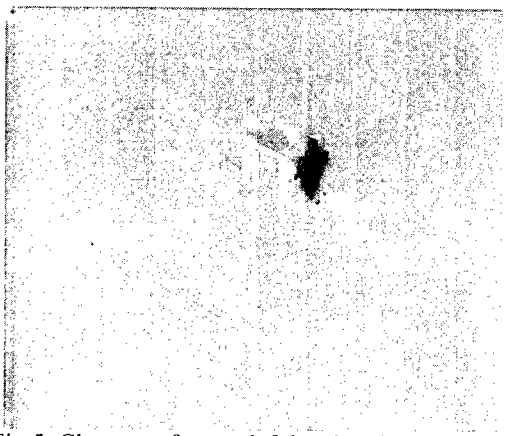


Fig 5: Close up of upper left hand region of Fig. 4.

The XRD topograph shown in Fig. 4 confirms that there is a large number of micropipes around the edge of this wafer, and that the section toward the middle of the wafer has relatively few micropipes. Clusters of micropipes on the upper left hand side of the wafer, observed using electrolysis of water are also observed on the x-ray topograph.

Summary and Conclusions

An initial investigation of a potentially simple, inexpensive and non-destructive technique to image the quantity and the distribution of macroscopic defects such as micropipes in SiC wafers has been described. Defect distribution was verified using optical microscopy and x-ray topography and agreement was achieved with the electrolytic technique.

References

[1] P.G. Neudeck and J.A. Powell, IEEE Electron Device Letters, **15**, (1994) p. 63.
[2] X.R. Huang, M. Dudley, W.M. Vetter, W. Huang, S. Wang, C.H. Carter, Appl. Phys. Lett. **74**, (1999) p. 353.
[3] D. Hobgood, M. Brady, W. Brixius, G. Fechko, R. Glass, D. Henshall, J. Jenny, R. Leonhard, D. Malta, St.G. Müller, V. Tsvetkov, und C. Carter Jr., Mat. Sci. Forum **338-342**, (2000) p 3.
[4] R. Yakimova, T. Yakimov, L. Hitova, E. Janzén, Mat. Sci. and Eng. **B46**, (1997) p. 287.
[5] P.G. Neudeck, Mat. Sci. Forum **338-342**, (2000), p. 1161.
[6] M. Dudley, X.R. Huang, W. Huang, A. Powell, S. Wang, P. Neudeck, M. Skowronski, Appl. Phys. Lett. **75**, (1999) p784.

Materials Science Forum Vols. 353-356 (2001) pp. 307-310
© 2001 Trans Tech Publications, Switzerland

Micropipe and Macrodefect Healing in SiC Crystals during Liquid Phase Processing

B.M. Epelbaum, D. Hofmann, U. Hecht and A. Winnacker

Department of Materials Science 6, University of Erlangen-Nürnberg,
Martensstr. 7, DE-91058 Erlangen, Germany

Keywords: Defect Elimination, Hollow Defects, Liquid Phase Epitaxy, Micropipe

Abstract. Different liquid phase epitaxial (LPE) growth methods, namely dipping and sessile drop techniques have been applied to analyze the evolution of hollow-core defects in PVT SiC crystals during LPE. Experiments were performed on (0001)/(000$\bar{1}$) surfaces of 6H-SiC and 4H-SiC wafers using silicon melt under high pressure of argon. Processing at a low supersaturation allowed us to evaluate the early stage of defects development, and long-time experiments (up to 6 hours) were aimed at the analysis of the stability of defect transformation. Hollow macrodefects 10-50 μm in diameter were found to be very unstable in silicon melt and were overgrown (filled) already at supersaturations close to zero, when growth inside the core occurs due to the Gibbs- Thomson effect. Resulting structures were found to contain a number of dislocations and micropipes. Elimination of screw-dislocation based micropipes requires a higher supersaturation, which can be established by a significant temperature difference between epitaxial surface and carbon source. Micropipes were observed to decompose into individually acting non-hollow core dislocations. After decomposition the activity of growth center based on a micropipe is usually reduced. As a result a new center may dominate the growing surface and make healed micropipes completely invisible.

Introduction. Linear hollow defects in SiC monocrystals usually referred to as screw-dislocation based micropipes (MP) are known to be one of the most critical factors limiting the successful application of this important semiconductor material. For further developments aimed to minimize the density of MP the understanding of the origin of MP and their behavior during the crystal growth process should be improved. One of the fascinating and debatable MP related aspects is the possibility to overgrow MP present in the PVT substrate in the course of subsequent LPE process [1-5]. Several points, however, remain unclear: (i) images of healed MP [1-2] represent objects 20-40 μm in diameter. But in numerous investigations [6 and references therein] of real hollow-core dislocations based on Frank's prediction [7], their diameter was always found to be smaller than 10 μm. Therefore the observed voids should be so-called macrodefects (MD) (it has to be mentioned that there exists still a discussion about the nature of MD [8]). (ii) The resulting MP/MD structures after healing are not studied in detail. Some of hollow defects are claimed to be terminated by a growth spiral on an epitaxial surface, another published example [8] shows a circular pit without any spiral features but with higher macrostep density on a flat bottom.
Our current study presents experimental investigation of LPE growth on PVT substrates containing various hollow-core defects. The specific aspects of our research were (i) the wide range of supersaturation conditions ranging from negative supersaturation (i.e. substrate dissolution in silicon melt) to forced growth achieved under strong temperature gradient in between SiC substrate and graphite source and (ii) both micropipes and macrodefects were included into the study.

Experimental. The scheme of our experimental set-up is shown in Fig.1. In sessile drop (SD) geometry (Fig.1) a PVT grown SiC wafer 30 mm in diameter is placed horizontally on a graphite

pin holder with 0.2-0.3 cm^3 of Si melt on the top. The arrangement is heated to the temperature 1700-2200°C. In SD experiments an external source of carbon is nominally absent. However a limited transport of carbon via gas phase as the result of graphite and SiC evaporation (at temperature>2100°C) and oxidation (transport of carbon in form of CO) could not be totally neglected in our experimental conditions. In all SD experiments a small positive weight change of 0.2-0.3 mg for SiC substrates with covered area of 2-3 cm^2 was found. Consequently, SD processing can be considered as a treatment at nearly equilibrium conditions. During cooling stage dissolved SiC causes limited epitaxial growth. SD treatment resulted in the formation of a recrystallized layer about 1 μm thick on droplet surface and excellent visualization of all hollow defects present in the substrate on its backside because of melt penetration (recrystallized surface on the backside around a defect looks quite different and is always larger than the defect itself making detection very easy, see Fig. 1).

In dipping (D) experiments, Fig. 1, silicon melt is held in a high-purity graphite crucible under thermal gradient conditions. The holder shown in Fig. 1 is designed for bringing the substrate into a 'free-floating' position. The substrate is kept on the melt surface because of surface tension. The holder was fixed inside the heater and the crucible was translated up to the fitting position after the charge was melted. After treatment the substrate was removed from the melt by lowering the crucible unit. In D-experiments supersaturation was produced because of a temperature difference $\Delta T=30\pm15$°C between crucible top and bottom and it was dependent as well on process temperature (solubility of carbon). The sample was brought into contact with the melt heated already up to working temperature, and, after processing, it was removed from the melt at the same temperature, i.e. the conditions for 'freeze-and-look' were completed. The SiC layer growth rate was 1-20 μm/h depending on processing temperature. One experiment was made in reversed temperature gradient in order to evaluate figures of SiC dissolution in silicon melt. All SD and D-experiments were made under argon pressure of 80-120 bar in order to suppress melt evaporation and diminish transport of carbon containing species via gas phase. Treatment time was varied from 1 to 6 hours.

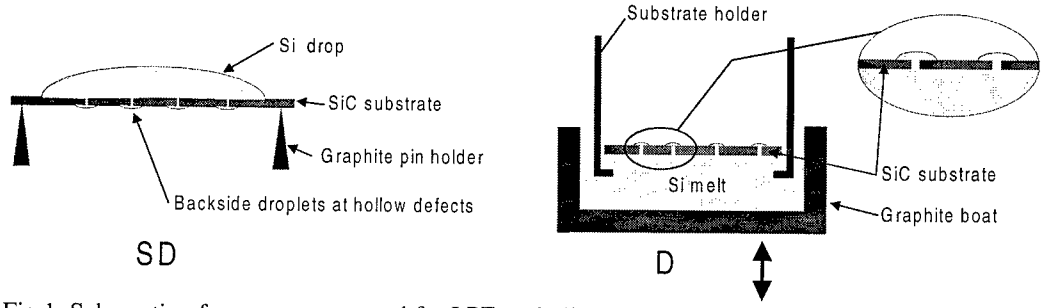


Fig.1. Schematic of arrangements used for LPE on hollow defect containing substrates. SD - sessile drop geometry, D - dipping geometry for 'free-floating' substrate.

After treatment the rest of silicon melt was etched away from the substrate with $HF+HNO_3$. Untreated substrates and growth patterns on both epitaxial and back sides were examined with the use of optical microscopy, SEM and AFM.

Results and discussion. Filamentary voids present in the PVT substrate can be of different configuration and dislocation content. In the further discussion we will refer to as micropipe (MP) *only* nearly cylindrical (often faceted) voids that have diameters < 10 μm and are oriented along (0001) axis. Larger voids up to 100 μm in size with irregular cross-section are termed hollow macrodefects (MD). Our experimental observations of MD and MP behavior in contact with silicon melt can be summarized as follows:

(a) Irregular shaped MD are intrinsically unstable in the silicon melt. Growth inside a defect core occurs even in the absence of external supersaturation due to the Gibbs-Thompson effect. The effect is more pronounced for smaller defects 10-20 μm in diameter. They can be totally overgrown within 2 hours of treatment at a temperature over 1750°C. Closing of large voids 50-100 μm in diameter and elongated splits associated with low angle boundaries on the sample periphery goes in the same manner, but requires sufficient supersaturation produced by temperature difference >30°C between substrate and graphite source and adequate treatment time.

(b) Growth patterns on MD contain generally a number of spirals and mesas pointing on a significant dislocation content of macrodefects. Only very few macrodefects without dislocation patterns were found. Dislocations may have hollow cores, i.e. MD are in fact transformed into groups of micro(nano)pipes, see Fig. 2A.

(c) Micropipe defects independent of their size are stable in silicon melt in the absence of supersaturation and are never healed, but are slightly etched by the melt. They are getting larger in diameter and gain 6-fold symmetry, Fig. 2B.

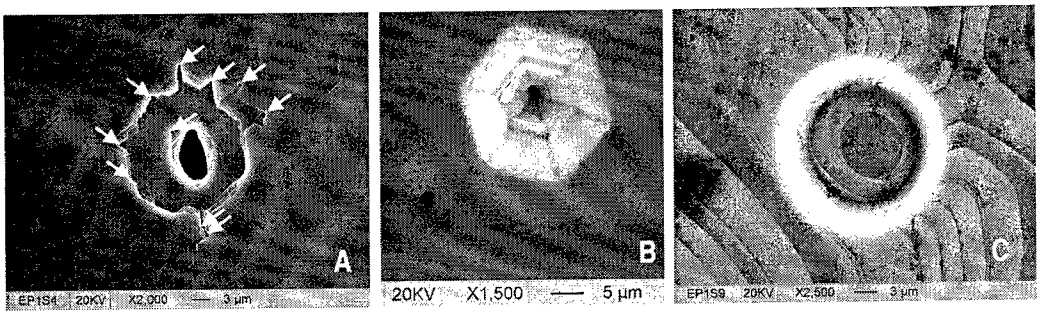


Fig. 2 A - MD appearance after sessile drop experiment, T=1900°C, τ=2h. Initial defect size was about 30 μm. Arrows are pointing on nanopipes; B - single MP etched in silicon melt. T=1800°C, τ=2h, C - circular depression in a epitaxial layer produced by a gas bubble. The area under the depression is defect-free

(d) In the course of epitaxial growth large MP (>1μm in diameter) become unstable and split into a group of prevalently non-hollow-core dislocations with smaller Burgers vectors. Some of produced dislocations were found to have hollow cores, but always less than 400 nm in diameter, Fig. 3A,B and C.

(e) Micropipe decomposition (healing) depends on melt supersaturation and substrate polarity, but no difference was found between growth on 6H and 4H substrates. Healing goes more readily on Si-face than on C-face and increases with supersaturation. Surface roughness however also increases at higher supersaturations. The most homogeneous epitaxial layer growth with effective healing of hollow defects was achieved on (000$\bar{1}$) C-face at 2050-2150°C.

(f) At the beginning of LPE process every MP produces a growth center on growing surface (but not all growth hillocks are necessarily associated with MP). After decomposition the activity of growth center based on MP is reduced. As a result a new center may dominate the growing surface and make the healed micropipe completely invisible.

(g) Circular and hexagonal depressions in epitaxial layers 10-100 μm in diameter are caused by gas bubbles attached to the growing surface and have nothing in common with hollow defects in a substrate. Density of depressions can be sufficiently reduced by using proper substrate positioning and intensive melt stirring, Fig. 2C.

The transformation of MP can be treated in terms of the modified BCF model [10-11]. One important difference between LPE and PVT growth of SiC is the lower supersaturation σ. At sufficiently high σ (PVT growth) small dislocation sources are more active than larger ones [11], but at low σ (LPE growth) MP are observed to act always as growth centers. Crystallization at MP disturbs the concentration field in the MP vicinity. In addition this non-uniformity is more pronounced during LPE due to the much lower diffusion coefficient in Si-melt. These effects can cause growth instabilities peculiar for crystal edges [12] and may promote MP decomposition into a group of dislocations with smaller Burgers vector.

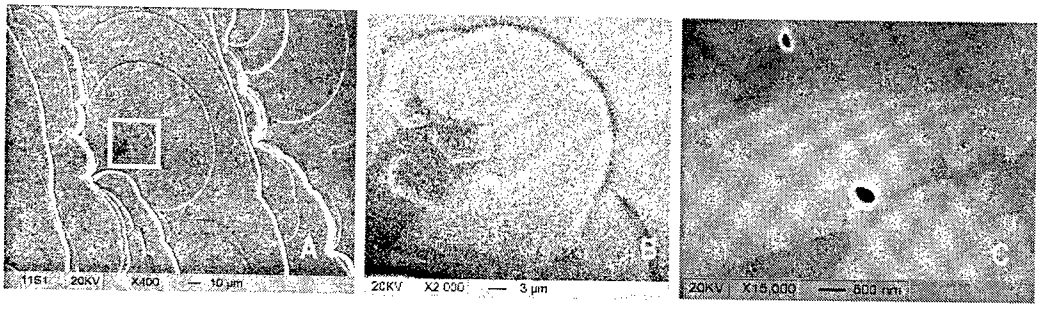


Fig. 3 Decomposition of MP. A and B - decomposition into a group of non-hollow dislocations: A - epitaxy on C-side of 6H wafer at T=2100°C, τ=4h, B - enlarged view on the selected area. C - decomposition into micro/nanopipes and non-hollow core dislocation, same substrate

Summary. Filamentary voids in SiC can be successfully healed in the course of LPE. Macrodefects and micropipes require different conditions to be overgrown, but resulting structures - groups of micro/nanopipes and non-hollow-core dislocations - are very similar. BCF model and theory of morphological stability of Chernov give an explanation for this behavior. Macrodefects in SiC usually have a considerable dislocation content.

Acknowledgments. Authors wish to thank Dr. M. Müller for the realization of growth reactor and P. Olbricht for his excellent technical assistance. This work was supported by the Bavarian Research Foundation under contract 176/96.

References

[1] R. Yakimova, M. Tuominen, A.S. Bakin, J.O. Fornell, A. Vehanen, E. Janzen, Inst. Phys. Conf. Ser. 142 (1996), p. 101.
[2] R. Yakimova, M. Syväjärvi, S. Rendakova, V.A. Dmitriev, A. Henry, E. Janzen, Mater. Sci. Forum 338-342 (2000), p. 237
[3] S. Rendakova, V. Ivantsov, V. Dmitriev, Mater. Sci. Forum 264-268 (1998), p. 163
[4] S.E. Saddow, M.S. Mazzola, S.V. Rendakova, V.A. Dmitriev, Mater. Sci. and Eng. B61-62 (1999), p. 158
[5] D. Hofmann, M. Müller, Mat. Sci. Eng. B 61/62 (1999), p. 29
[6] W. Si, M. Dudley, R. Glass, V. Tsvetkov, C.H. Carter, Jr., Mater. Sci. Forum 264-268 (1998), p. 429
[7] F.C. Frank, Acta Cryst., 4(1951), p. 497
[8] D. Hofmann, M. Bickermann, W. Hartung, A. Winnacker, Mater. Sci. Forum 338-342 (2000), p. 445
[9] TDI, http//tdii.com
[10] W.K. Burton, N. Cabrera, F.C. Frank, Roy. Soc. London Philos. Trans. A 243 (1951), p. 299
[11] J.J. De Yoreo, T.A. Land, L.N. Rashkovich et al., J. Cryst. Growth 182 (1997), p. 442
[12] A.A. Chernov, J. Crystal Growth 24/25 (1974), p. 11

Materials Science Forum Vols. 353-356 (2001) pp. 311-314
© 2001 Trans Tech Publications, Switzerland

Micropipe Closing via Thick 4H-SiC Epitaxial Growth Involving Structural Transformation of Screw Dislocations

I. Kamata, H. Tsuchida, T. Jikimoto and K. Izumi

Yokosuka Research Laboratory, Central Research Institute of Electric Power Industry,
2-6-1 Nagasaka, Yokosuka, Kanagawa 240-0196, Japan

Keywords: 4H-SiC, Elementary Screw Dislocation, Epitaxial Growth, Micropipe, Micropipe Closing, Structural Transformation

Abstract In this paper micropipe closing and structural transformation of screw dislocations were studied using selective defect etching techniques. We confirmed that some micropipes in substrates were closed via gas phase 4H-SiC epitaxial growth, and that micropipe closing involves structural transformation from a hollow core defect to several non hollow core dislocations. Depth analysis revealed that most of the micropipe closings occurred in the initial stage of epitaxial growth.

Introduction

SiC bulk crystals grown by the modified Lely method using {0001} seed crystals contain many micropipe defects and elementary screw dislocations. These defects and dislocations extend along the <0001> growth direction parallel to the crystal *c*-axis. The micropipes are hollow core defects with diameters in the μm range and elementary screw dislocations have no hollow cores. Recent Synchrotron White Beam X-ray Topographic (SWBXT) studies have revealed that a micropipe is a type of screw dislocation with a large Burgers vectors along the <0001> *c*-axis. The Burgers vectors were also estimated from 2*c* to 7*c* in 6H-SiC, and 3*c* to 8*c* in 4H-SiC [1], where *c* is the lattice parameter along the <0001> axis. In recent times, micropipe densities in boule crystals have been achieved less than 1 cm^{-2} on the research level [2], whereas current commercial 4H-SiC (0001) substrates still contain micropipes of density in the order of 10^1 to 10^2 cm^{-2}. If screw dislocations including micropipes exist in the substrate, they will be passed on to the epilayer. This high micropipe density restricts device area enlargement, because the device will suffer destructive damage if a single micropipe is present in the device area.

Micropipe closing through LPE has been reported [3, 4], however it is not yet clearly understood how micropipe closing takes place. In this paper, we report on micropipe closing involving structural transformation of screw dislocations. This structural transformation is similar to the micropipe dissociation process in sublimation growth [5], except that it occurs through gas phase 4H-SiC epitaxial growth in step-flow mode.

Experiment

Molten KOH treatments were carried out on epilayers and substrates for defect etching [6]. The typical temperature and duration of KOH treatments were 480°C and 1 min, respectively. Repetitions of a cycle, abrading of a certain thickness, KOH treatment and pit evaluation were carried out for the purpose of a depth analysis of defects in epilayers. The abraded thickness was accurately determined by measuring at a beveled face of the sample edge.

Commercial 8° off 4H-SiC (0001) substrates were used in this experiment. Thick 4H-SiC epitaxial growth was performed in a radiant-heating reactor. The gas system used for epitaxial growth was SiH_4, C_3H_8 and Pd-cell purified H_2. The doping gas was N_2 for N-doping. Typical growth conditions were as follows: growth temperature 1550 °C, pressure 50 Torr, growth rate 14 - 16 μm/h. Details of the growth are described elsewhere [7]. Layer thickness was measured at a section of beveled surface using an optical microscope or SEM. Carrier concentrations of the samples were determined to be the low 10^{15} cm^{-3} by C-V measurement on Ni-Schottky. The morphology of the as-grown surface was investigated using a Nomarski optical microscope and micropipes in epilayers and substrates were detected using a transmission optical microscope.

Results and Discussion

Figure 1 show micrographs of the epitaxially grown surface. Epitaxial growth was carried out under step-flow growth conditions, and the down step direction [11$\bar{2}$0] is to the left in the micrographs. Thus surface steps moved forward to the left during growth. Growth pits with a line shaped feature along the [11$\bar{2}$0] direction were occasionally observed on the epilayer surface. Here we call these "line-shaped pits". These pits were lying along the step-flow direction and were approximately 160 μm in length on a 90 μm-thick epilayer sample. Micropipes were detected in a substrate at the upstream (right hand) end of the line-shaped pits using a transmission optical microscope. This indicated that micropipes acted as obstacles to moving steps, and a line-shaped pits were configured as shadows of the homogeneous step-flow toward the [11$\bar{2}$0] direction.

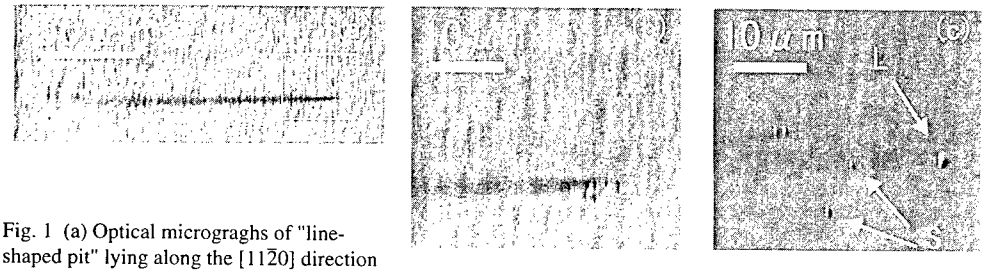


Fig. 1 (a) Optical micrograghs of "line-shaped pit" lying along the [11$\bar{2}$0] direction on epilayer surface, (b) shows highly magnified micrograph of the upstream (right-hand) end of the line-shaped pit. Micrographs (b) and (c) were taken from different pits, [S] and [L] indicate small and large grown pits on the surface.

Figure 1 (b) shows the upstream end of the line-shaped pit highly magnified with seven small pits less than 1 μm in size visible. On the other hand, four small pits and one large pit are visible in the Fig. 1 (c). Micrographs in Fig. 1(b) and (c) were taken from different location. The small pits were the same size as those in the Fig . 1 (b), and the large pit was over 1 μm in size. These small and/or large pits on the as-grown surface were present at the location of a micropipe in the substrate. When many other line-shaped pits were investigated, some of the small pits were aligned along the [11$\bar{2}$0] direction and some were localized randomly in a small area.

Figure 2 (a) shows an upstream end of some line-shaped pit on an epilayer surface after KOH treatment. Seven hexagonal etch pits with round features were roughly aligned along the [11$\bar{2}$0]. We identified these as non hollow core screw dislocations, due to their strong contrast in comparison with the etch pits attributable to edge dislocations.

In our KOH experiments, etch pits associated with non hollow core screw dislocations were observed over the entire surface, distributed in a density of 10^3 cm^{-2}. Neudeck *et. al.* reported that 4H-SiC wafers and epilayers contain 1*c* elementary screw dislocations of density in the order of 10^3 cm^{-2} [8]. Therefore the dominant non hollow core screw dislocations in our 4H-SiC epilayers are also considered as 1*c* elementary screw dislocations. Moreover, when these were compared with the etch pits in Fig. 2 (a), no significant size difference was found, therefore both the etch pits in Fig. 2 (a) and the etch pits distributed over the entire surface were identified as 1c elementary screw dislocations. The non hollow core screw dislocations may exist as two types; one has 1*c* as the Burgers vectors and the other has 2*c* in 4H-SiC, while Si *et. al.* reported that the majority of screw dislocations in 4H-SiC boule crystals have a Burgers vector of 1*c* [1]. Actually, 1c and 2c non hollow core dislocations may appear as different size of etch pits because of different magnitude of their stress, while round etch pits have approximately same size in this experiment.

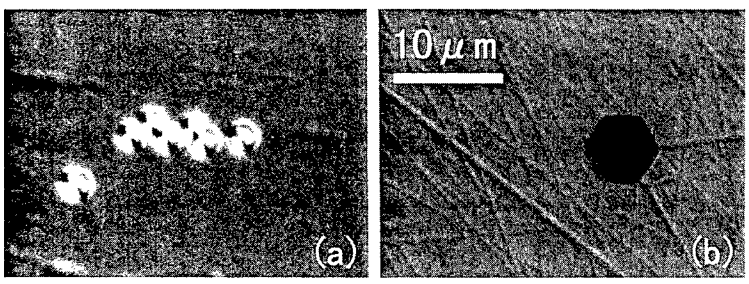


Fig. 2 Optical micrographs on (a) the grown surface, and (b) the abraded surface where all epilayer has been removed. The micrographs were taken from the same place after KOH treatment. A micropipe was closed in the epilayer.

Figure 2 (b) shows the KOH-treated surface after the epilayer has been completely removed by abrading and polishing. The positions of all the micropipes in the samples were recorded using a transmission optical microscope before removing the epilayer, in addition we also use the transmission optical microscope to detect the micropipe positions after the KOH treatment, so that we are sure that Fig. 2 (a) and (b) were taken from exactly the same place. Note that, because the micrograph was taken after polishing, numerous polishing scratches not observed in Fig. 2 (a) appear in Fig. 2 (b). The dark hexagonal etch pit in Fig. 2 (b) indicates that a micropipe existed in the substrate at that location. Following the results of Fig. 2 (a) and (b), the micropipe was closed in the epilayer and seven elementary screw dislocations appeared on the epilayer surface.

The nature of screw dislocations means that the emergent ends of screw dislocations are always appearing on the grown surface during epitaxial growth when (0001) substrates are used, because the Burgers vector aligns along the [0001] axis. Thus the Burgers vectors of each screw dislocation remain the same in magnitude and do not disappear during epitaxial growth, except for the generating or dissolving of a pair of equivalent vectors of opposite directions (+ and -). In addition, the screw component of a micropipe has $|b| \geq 3c$ in 4H-SiC [1] and elementary screw dislocations have $|b|=1c$. From this perspective, our KOH analysis suggested that a micropipe was transformed into several elementary screw dislocations during epitaxial growth. Therefore, the Burgers vector magnitude of the micropipe was divided into several $1c$ of the elementary screw dislocations.

A number of elementary screw dislocations related to the closed micropipes were evaluated on two samples (a 65μm- and a 37μm-epilayer). Approximately one-third of over 150 micropipes closed as a result of epitaxial growth. Elementary screw dislocations originally existing in the substrate surrounding micropipes were excluded from the count. Figure 3 shows a histogram of the relationship between frequency and etch pit numbers on a closed micropipe. The etch pit numbers n should represent the Burgers vectors nc of a closed micropipe. This histogram indicates a deviation of n of the 53 closed micropipes. For example, a micropipe was closed and generated 7 etch pits, and in totally 12 cases of over 150 micropipes, they were dissociated into 7 elementary screw dislocations in this experiment.

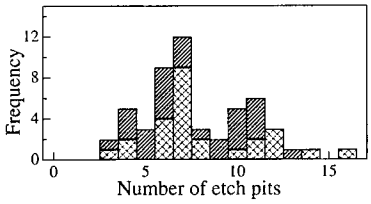


Fig. 3 Deviation of etch pit numbers on a closed micropipe. The striped bar represent the measured data for 65μm-thick sample and the crossed bar represent ones for 37μm-thick sample.

The number of etch pits generated from a closed micropipe varied from three to 16, thus the Burgers vectors of the micropipes were interpreted as $3c$ to $16c$. These numbers seemed too high to be the Burgers vectors for a single micropipe. Recently the dissolving, moving, transformation and recombination of micropipes during boule growth has been reported [2]. Therefore, we believed that many of the micropipes observed were coalescence of two or three micropipes [6].

Some micropipes were not closed. Figure 4 (a) shows one of the penetrated micropipes after the KOH treatment. Two kinds of etch pits appeared, corresponding to the large and small surface pits in the Fig. 1 (c). The dark hexagonal etch pit represents a penetrated micropipe. The side walls of the hexagonal pit were parallel to $<11\bar{2}0>$ directions. Penetration was confirmed by an optical transmission microscope. On the other hand, hexagonal etch pits round in shape represented elementary screw dislocations.

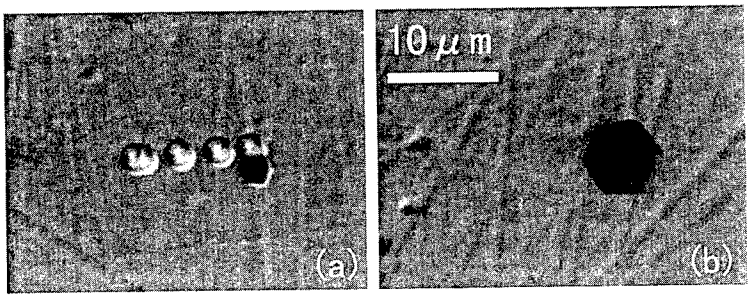


Fig. 4 Optical micrographs on (a) the grown surface and (b) the abraded surface where all epilayer (65μm-thick) has been removed. The micrographs were taken from the same place after KOH treatment. A micropipe was not closed in the epilayer.

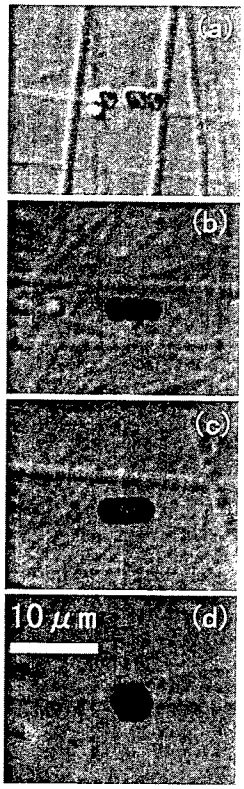


Fig. 5 Micrograph shows the surface of (a) 37μm-thick epilayer (on the grown surface), (b) 17μm-thick epilayer, (c)3μm-thick epilayer, (d) the substrate. All micrographs were taken from the same place after KOH treatment.

To understand when micropipe closing occurs, depth analysis of a 37μm-epilayer was carried out. Figure 5 show optical micrographs taken from the same area in the course of successive polishings and KOH treatments. Four elementary screw dislocations appeared on the grown surface as shown in Fig. 5 (a). Some scratch lines were seen in this micrograph. These lines were hardly observed before KOH treatment on the grown surface and appeared after the KOH treatment. According to successive analyses, Fig. 5 (b) and (c) shows KOH-treated surface of 17 μm- and 3 μm-thick epilayer, respectively. Four elementary screw dislocations were visible in both micrographs. Note that scratch lines visible in the respective micrographs did not remain at the same point even though the micrographs were taken from the same area, because the successive polishing made new scratch lines on their respective polished surfaces. When the abrading reached the substrate, the micropipe appeared as a dark hexagonal etch pit as shown in Fig. 5 (d). This indicates that the micropipe was closed and transformed into four elementary screw dislocations near the interface.

Our investigations of other micropipes confirmed similar tendencies that most of the micropipe closings occurred near the interface. A relationship between the ratio of closed micropipes and the distance from the interface is shown in Fig. 6. The ratio significantly increased near the interface. On the other hand, a further increase in layer thickness shows no marked change and the ratio was saturated to about 30 % in this experiment. Although ratios of closed micropipes varied with different samples, the ratios in some samples exceeded 50 %.

It appears that most of the micropipe closings and the structural transformations occurred at the early stage of epitaxial growth. To understand that the micropipe closings occur near the interface, we suppose that interfacial stress between upper and lower crystals is involved in this phenomenon.

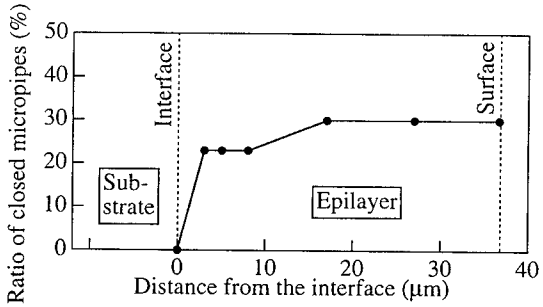


Fig. 6 Ratio of closed micropipes vs distance from the interface.

Conclusion

We confirmed that some micropipes were closed during gas phase epitaxial growth. Our KOH etching analysis suggested that micropipes with Burgers vector *nc* were transformed into *n* elementary screw dislocations of 1*c*. Depth analysis moreover revealed that most of the micropipe closings with structural transformations occurred at the early stage of epitaxial growth.

References

[1] W. Si, M. Dudley, R. Glass, V. Tsvetkov and C.H. Carter, Jr., Mater. Sci. Forum 264-268 (1998), p. 429.
[2] R.C. Glass, D. Henshall, V.F. Tsvetkov and C.H. Carter, Jr., Phys. Stat. Sol. (b) 202 (1997), p. 149.
[3] R. Yakimova, M. Tuominen, A.S. Bakin. J.-O. Fornell, A. Vehanen and E. Janzen, Inst. Phys. Conf. 142 (1996), p. 101.
[4] S. Rendakova, N. Kuznetsov, N. Savkina, M. Rastegaeva, A. Andreev, M. Minbaeva, A. Morozov and V. Dmitriev, *Proc. Mat. Res. Soc. Symp.* 512 (1998), p. 131.
[5] J. Takahashi, N. Ohtani and M. Kanaya, J. Cryst. Growth 167 (1996), p. 596.
[6] I. Kamata, H. Tsuchida, T. Jikimoto and K. Izumi, Jpn. J. Appl. Phys. *in press*
[7] H. Tsuchida, I. Kamata, T. Jikimoto and K. Izumi, *These proceedings*
[8] P.G. Neudeck, W. Huang and M. Dudley, *Proc. Mat. Res. Soc. Symp.* 483 (1998), p. 285.

Materials Science Forum Vols. 353-356 (2001) pp. 315-318
© 2001 Trans Tech Publications, Switzerland

Growth Evolution of Dislocation Loops in Ion Implanted 4H-SiC

P.O.Å. Persson and L. Hultman

Thin Film Physics Division, Linköping University, SE-581 83 Linköping, Sweden

Keywords: Defects, Electron Microscopy, Ion Implantation, Ostwald Ripening, TEM

Abstract
Transmission electron microscopy (TEM) was used to investigate Al ion-implanted 4H-SiC epilayers. A set of annealing experiments were performed to study the evolution of dislocation loops in the implanted region. It was concluded that the dislocation loops evolve according to the extended Ostwald ripening model for small planar precipitates. The activation energy for loop growth was determined to be 2.8 eV.

Introduction
For the purpose of producing SiC planar devices, selective area doping is necessary. Due to negligible diffusion coefficients of candidate dopant elements in SiC, the choice of technique today is mainly ion implantation. This technique has benefits in the sense that it can offer tailored dopant profiles. The implantation process on the other hand damages the crystal by inducing vacancies and interstitials from collisions between the implanted ion and the lattice. By heating the sample during implantation, it has been found that the resulting lattice damage is less pronounced [1]. The as implanted ions predominantly occupy interstitial lattice sites where they are electrically inactive [2]. To electrically activate the implanted ions and to restore the damage induced in the implantation process, the sample is subject to a thermal annealing process. TEM studies show that annealed SiC samples, irradiated by a dose of ions slightly lower than the amorphisation threshold contain extended crystal defects. These have been determined to be interstitial type dislocation loops, typically 1-10 nm wide [3]. It is the intention of this paper to present results on studies of the evolution of these defects after high temperature annealing.

Experimental
In the present study samples were prepared by implanting 4H SiC with Al at 180 keV with a dose of $1.3*10^{14}$ ions cm^{-2}. Samples were subject to annealing studies in which the annealing time and temperature was varied. Annealing experiments were performed in a vertical air cooled quartz reactor with inductively heated graphite crucible. The annealed samples were then studied by electron energy loss spectroscopy (EELS), cross-sectional (XTEM) and plan-view TEM.

Results
Fig. 1 shows an XTEM image of a sample that was implanted at a temperature of 600°C a) before and b) after annealing at 1700°C for 30 min. In the annealed sample a region of dark spots can be seen, representing structural defects in the lattice, that are typical for the present study. The spots are 1-10 nm wide and uniformly distributed around the peak concentration of Al. As determined by SIMS measurements [4] the corresponding defects appear where the Al concentration is ≥

$5*10^{18}cm^{-3}$. It seems that the largest defects are located at a depth where the Al concentration is highest. Higher implantation doses resulted in a higher density of defects.

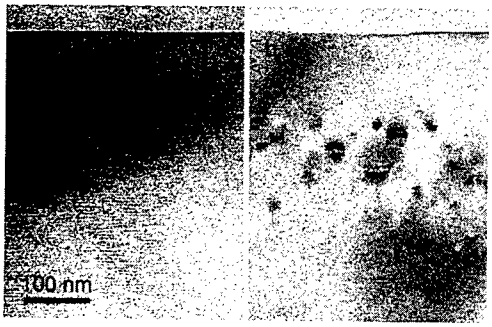


Figure 1. Cross sectional transmission electron microscopy images of a) an as implanted sample and b) annealed sample. The defect rich region of b) corresponds to an Al concentration higher than $5*10^{18}$ cm^{-3}.

Imaging under different tilting and diffraction conditions shows that the defect is of a planar nature such as a Frank loop and this is confirmed by studying the defect at higher magnification as shown in Fig. 2. A dislocation loop, composed of clustered interstitials is inserted on the basal plane causing the surrounding lattice planes to bend.

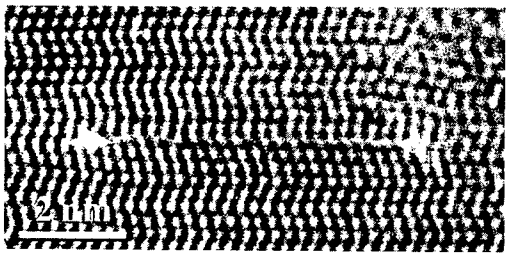


Figure 2. High resolution image in cross section of a 6 nm wide extrinsic dislocation loop from a sample annealed at 1700°C for 30 min. The loop is the row of black dots in between the two arrowheads. Note how the horizontal lattice planes bend to accommodate the loop and generate a corresponding strain field along the c-axis.

EELS analysis has been performed on typical dislocation loops found in the annealed ion implanted samples in the region of the Al peak. No Al was detected in spectra obtained by scanning the beam across the defect and recording the Al K edge at 1560 eV. In Fig. 3 the loop evolution upon annealing at different time steps is shown. The samples were in this case annealed at 1700°C for 10, 30, 60, 120 and 180 min. Fig. 4 shows images of the dislocation loop evolution for samples annealed at 1700°C, 1800°C, 1900°C and 2000°C for 30 min. It is concluded that the area covered by the dislocation loops remain the same throughout the annealing experiments. Assuming a surface density of atoms in the loops similar to that of SiC, enables us to calculate the number of interstitials stored in the loops. This has been estimated to $1*10^{14}$ interstitials cm^{-2} which is slightly below the number of implanted ions, $1.3*10^{14}$ ions cm^{-2}.

Discussion

The presently employed ion implantation doses and thermal annealing yielded a single type of structural defect. The characteristic loop is seen in Fig. 2. The loops did not move or glide when applying local heat to the sample by focussing the e-beam. Apparently, the coarsening behavior of the loops upon annealing (shown in Figs. 3-4) only comes from the ability to store and release the interstitials that they are composed of. To this end the total concentration of interstitials stays constant and the defect containing region acts like a closed box. Such a behavior has also been observed for dislocation loops in ion implanted Si [5].

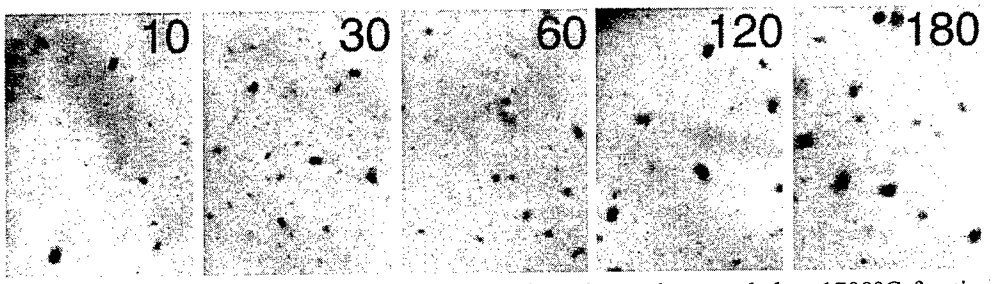


Figure 3. Plan-view micrograph of an Al ion implanted sample annealed at 1700°C for times ranging from10 to 180 min.

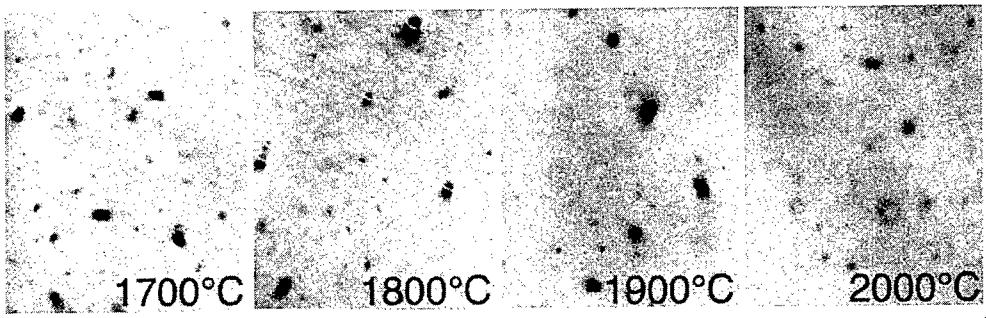


Figure 4. Plan-view micrograph from an Al ion implanted sample annealed at temperatures ranging from 1700° to 2000°C for 30 min. The difference in appearance (open circles or black/black contrast) of the loops arise since the normal two-beam condition does not allow the complete resolution of loops less than 10 nm in diameter.

For finding out the nature of the interstitials stored in the dislocation loops, EELS results gives that there is no elevated concentration of Al in the region of the dislocation loop. This rules out precipitation of the implanted material. Hence it is inferred that the loops are composed of self-interstitials, I_{Si} and/or I_C which are both created during implantation. The type, however, could not be determined by EELS measurements due to the high background intensity of these matrix species. It was concluded that there are almost as many interstitials clustered in loops, as there are implanted Al ions ($1*10^{14}cm^{-2}$ compared to $1.3*10^{14}cm^{-2}$). Such a supersaturation of interstitials strains the lattice and the clustering of interstitials is then a means for reducing the elastic energy. The activation of implanted Al ions after annealing, is very high, between 50%, and 100%, for annealing temperatures higher than 1500°C [6]. Since Al is occupying a Si site in its active state [7], this would generate a high concentration of excess interstitial Si, which would imply that the interstitials clustered in loops would be Si. Such a behavior is known as the "+1" model in which implantation induced vacancies and implanted interstitials recombine during annealing to restore the lattice, leaving one self-interstitial per implanted ion [8]. A coarsening process where large defects grow on the expense of smaller ones can be described by the Ostwald ripening theory [9]. In this theory the driving force for coarsening of defects is differences in chemical potential between the defect and the ambient and the result of growth is a reduction in interfacial and elastic energies. It can be shown that if a loop has a radius less than the mean radius r_m of the population, it shrinks. If the loop is larger than r_m it grows while loops equal to r_m stays the same. After the disappearance of the smaller loops and growth of the larger, r_m increases and the previously stationary loops shrink. For applying the above model on the loop coarsening behavior in the present study, we assume that the dislocation loops exchange self-interstitials in an isolated region. This is consistent with the above observation that no significant change in interstitial concentration could be found in the samples annealed in the investigated cases.

$$K_d = \frac{K_0}{T}\exp\left(\frac{-E_{act}}{kT}\right) \qquad Eq.\ 1$$

By measuring the slope of $r_m^2 exp(-a/r_m)$, where a is a constant, over time, it was possible to determine the coarsening rate K_d from the samples annealed at different timesteps, but at the same temperature. This was done for the temperature of 1700°C. Knowing the coarsening rate it was also possible to calculate the activation energy E_{act} for loop growth through Eq. 1. This was determined from the slope of Fig. 5 and yielded the value of 2.8 eV.

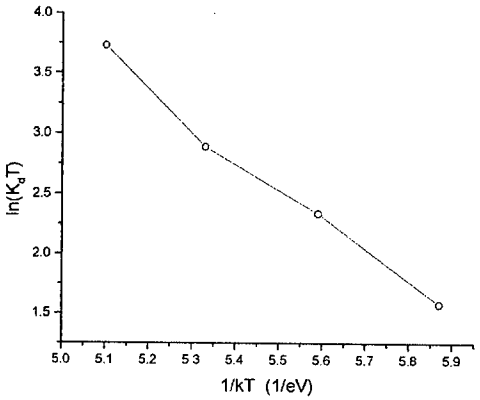


Figure 5. Arrhenius plot for the measurement of activation energy for loop growth.

Conclusions

Defects found in implanted SiC after annealing are interstitial type dislocation loops. They originate from a supersaturation of excess atoms, one per implanted ion according to the +1 model. We show that when an implanted sample is annealed the implantation induced interstitials start to cluster. As soon as equilibrium between point defects and nucleated loops has been established, coarsening of defects occur according to the Ostwald ripening theory. Upon annealing at times or temperatures, above the minimum condition for equilibrium, the number of defects decrease while their mean radius increase, keeping the number of interstitials stored in the loops constant. For steady-state conditions, the activation energy for loop coarsening is 2.8 eV±0.2 eV for 1700°C ≤ T_a ≤2000°C.

Acknowledgements

The Swedish Silicon Carbide Electronics Programme, SiCEP is acknowledged for support. The authors would also like to acknowledge Doc. Rositza Yakimova for the annealing experiments and Dr. Nathalie Brun for EELS analysis.

References

[1] E.Wendler, A.Heft and W.Wesch, Nucl. Instrum. and Methods B 141 (1998), p 105.
[2] M.V.Rao, P.Griffiths, O.W.Holland, G.Kelner, J.A.Freitas, D.S.Simons, P.H.Chi and M.Ghezzo, J. Appl. Phys. 77 (1995), p 2479.
[3] P.O.Å.Persson, Q.Wahab, L.Hultman, N.Nordell, A.Schöner, K.Rottner, E.Olsson and M.K.Linnarson, Mater. Sci. Forum 264-268 (1998), p 413.
[4] P.O.Å.Persson, M. Jansson, A. Hallén and L.Hultman, Unpublished.
[5] G.Z.Pan, K.N.Tu and A.Prussin, J.Appl. Phys. 81 (1997), p 78.
[6] T.Kimoto, A.Itoh, N.Inoue, O.Takemura, T.Yamamoto, T.Nakajima and H.Matsunami, Mater. Sci. Forum 264-268 (1998), p 675.
[7] T.Troffer, M.Schadt, T.Frank, H.Itoh, G.Pensl, J.Heindl, H.P.Strunk and M.Maier Phys. Stat. Sol. 162 (1997), p 277.
[8] N.E.B.Cowern, K.T.F.Janssen and H.F.F.Jos, J. Appl. Phys. 68 (1990), p 6191.
[9] W.Ostwald, Z. Phys. Chem. 34 (1900), p 495.

Materials Science Forum Vols. 353-356 (2001) pp. 319-322
© 2001 Trans Tech Publications, Switzerland

Lattice Parameter Measurements of 3C-SiC Thin Films Grown on 6H-SiC(0001) Substrate Crystals

J. Kräußlich, A. Bauer, B. Wunderlich and K. Goetz

Institut für Optik und Quantenelektronik, Friedrich-Schiller-Universität Jena,
Max-Wien-Platz 1, DE-07743 Jena, Germany

Keywords: Lattice Parameter, Strain and Stress Components, Thin Film, X-Ray Diffraction

Abstract: The lattice parameters of *3C*-SiC thin films epitaxially grown on *6H*-SiC(0001) substrate crystals have been precisely determined by using high resolution x-ray diffraction methods. Reciprocal space maps recorded around symmetrical and asymmetrical x-ray reflections revealed a pseudomorphic growth of the thin film in relation to the substrate lattice, whereas perpendicular to the surface the interplanar spacing of the lattice planes differ slightly $\Delta d/d = 8.7 \cdot 10^{-4}$. This implicates inherent thin film strain (ε) and stress (σ) components. The in-plane components are found to be $\varepsilon_{\parallel} = -4.8 \cdot 10^{-4}$ and $\sigma_{\parallel} = 2.26 \cdot 10^{8}$ N/m^2, whereas perpendicular to the surface the thin film strain component is found to be $\varepsilon_{\perp} = 2.8 \cdot 10^{-4}$.

Introduction

Silicon Carbide (SiC) occurs in many polytypes which differ in their periodic stacking sequences of hexagonal and cubic Si-C bilayers. The SiC lattice parameters differ slightly from polytype to polytype [1]. Using x-ray diffraction methods the lattice parameters of *4H*- and *6H*-SiC single crystal wafers [2] have been determined precisely (Table 1). Unfortunately, large *3C*-SiC single crystals are not available. However, *3C*-SiC thin films can be easily grown and used to derive the lattice parameters of compact *3C*-SiC crystals if one takes the inherent stress, induced by the thin film growth, into account.
The *3C*-SiC thin films (thickness $\approx$ 1.2 µm) were grown by solid-source molecular beam epitaxy on (0001)-oriented on-axis *6H*-SiC crystal wafers at deposition temperatures between 780°C to 950°C and with growth rates between 30 nm/h to 120 nm/h [3].

High resolution x-ray diffraction of *3C*-SiC thin films

Although the lattice parameters of the different SiC polytypes differ only slightly, the x-ray diffraction pattern showed, close to each other but well separated, so-called family reflections of the *3C*-SiC thin film and *6H*-SiC substrate. Using the well known *6H*-SiC bulk crystal values (Table 1) as a reference, we could determine the lattice parameters of the *3C*-SiC thin films with a corresponding accuracy of 10^{-5} for $\Delta a/a$ and 10^{-6} for $\Delta c/c$.
Reciprocal space maps recorded around symmetrical and asymmetrical x-ray reflections (Fig. 1) revealed a pseudomorphous growth of the *3C*-SiC thin films in relation to the substrate lattice (Fig. 2). There is no difference between the lateral interplanar spacing of the lattice planes, but perpendicular to the surface their interplanar spacing differ by $\Delta d/d = 8.7 \cdot 10^{-4}$. The growth direction of the *3C*-SiC thin film was found to be [111] with respect to the surface normal.

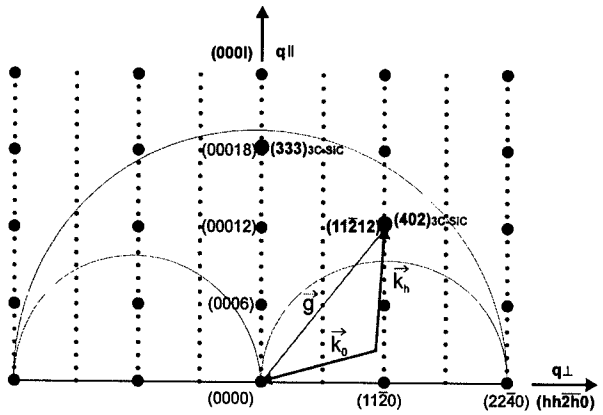


Fig. 1: Vertical section through the reciprocal lattice of (0001)-oriented *6H*-SiC wafer. The surroundings of the symmetrical 00018- and asymmetrical 11$\bar{2}$12-reflection were extensively studied.

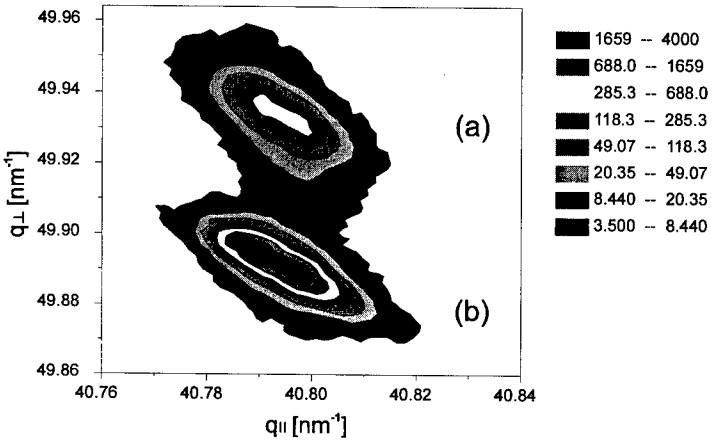
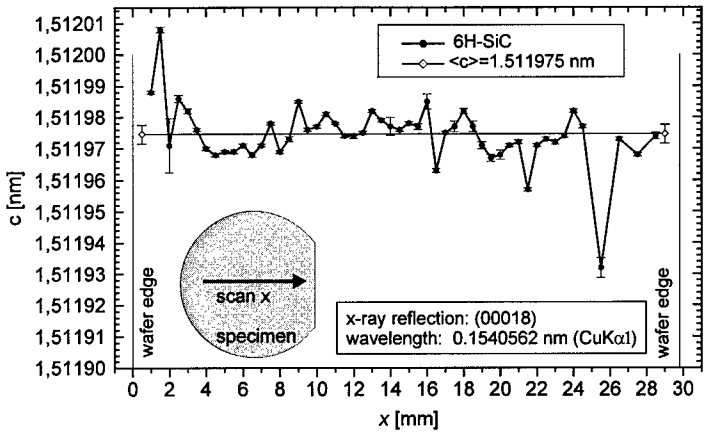


Fig. 2: Reciprocal space mapping of the *3C*-SiC thin film grown on *6H*-SiC(0001) wafer: (a) asymmetrical 403-reflection of *3C*-SiC thin film (b) asymmetrical 11$\bar{2}$12-reflection of *6H*-SiC substrate

High precision lattice parameter measurement of *4H*- and *6C*-SiC single crystals

To answer the question, if there exists a polytype dependence for the SiC bilayer stacking distance c/q and, if so, how strong this dependence is, it is desirable to know the lattice parameters a and c as precisely as possible (q = 4, 6 indicates the number of SiC bilayers per unit cell in stacking direction for 4H- and 6H-polytypes, respectively). This goal was achieved using the x-ray diffraction BOND method [4,5], which allowed the measurement of the lattice parameter with an accuracy of 10^{-6} for $\Delta a/a$ as well as for $\Delta c/c$.

To obtain information about the homogeneity of the commercially available SiC crystal wafers [2] the measurements were carried out by scanning at different lateral positions on the crystal surface.



In regions, which extend over several mm^2, the measured fluctuation of lattice parameters was smaller than $5 \cdot 10^{-6}$.

Fig. 3: Linear scanned lattice parameter c of *6H*-SiC wafer obtained by Bond's x-ray diffration method

Polytype	$cubic/q$ [%]	a [nm]	c [nm]	c/q [nm]	c/qa
4H	50 %	0.308 051 ± 0.000 006	1.008 481 ± 0.000 002	0.252 120 ± 0.000 001	**0.818 436** ± 0.000 017
6H	67 %	0.308 129 ± 0.000 004	1.511 975 ± 0.000 002	0.251 996 ± 0.000 001	**0.817 826** ± 0.000 012
3C	100 %	$\hat{=} a_{cub}/\sqrt{2}$	$\hat{=} \sqrt{3} \cdot a_{cub}$	$\hat{=} \frac{\sqrt{3}}{3} \cdot a_{cub}$	$\sqrt{\frac{2}{3}} =$ **0.816 497** *

Table 1: The hexagonal lattice parameters a and c of *4H*- and *6H*-SiC obtained by x-ray diffraction measurements with large single crystals. q = 4, 6, 3 indicates the number of the SiC bilayers per unit cell in stacking direction for *4H*-, *6H*- and *3C*-SiC, respectively. For the cubic *3C*-SiC the values are here given in adequate hexagonal terms. * Ideal Si-C tetrahedron assumed.

Note that the values of c/qa represent a significant criterion for the hexagonal and cubic ($\hat{=} cubic/q$) proportion of the SiC bilayer stacking sequences inside of the different SiC polytypes.

Results and discussion

3C-SiC thin films, quasi homoepitaxially grown on *6H*-SiC(0001) wafers, were characterized by using high resolution x-ray diffraction methods. From symmetrical $\Theta/2\Theta$-scans we obtained the relative difference $\Delta c/c = 8.7 \cdot 10^{-4}$ of the vertical interplanar spacing of the lattice planes of thin film and substrate. With respect to the meticulously determined $c_{6H\text{-}SiC}/6 = 0.2519960$ nm $\pm 3 \cdot 10^{-7}$ nm of the single crystal *6H*-SiC substrate (Table 1), the interplanar spacing of the SiC bilayers was calculated to be $c^{hex}_{3C-SiC}/3 = 0.251\,78$ nm $\pm 3 \cdot 10^{-5}$ nm, i.e. $c^{hex}_{3C-SiC}/3 < c_{6H-SiC}/6$. (Conveniently, a^{hex}_{3C-SiC} and c^{hex}_{3C-SiC} are here given in adequate hexagonal terms although *3C*-SiC is cubic.)

The reciprocal space map (Fig. 2) recorded with the asymmetric $11\bar{2}12$-reflection of *6H*-SiC revealed pseudomorphous growth of the *3C*-SiC thin films. With respect to the meticulously determined $a_{6H\text{-}SiC} = 0.308129$ nm $\pm 4 \cdot 10^{-6}$ nm of the single crystal *6H*-SiC substrate (Table 1), the lateral interplanar spacing of the *3C*-SiC is equal to the crystal *6H*-SiC, i.e. $a^{hex}_{3C-SiC} = 0.308\,13$ nm $\pm 1 \cdot 10^{-5}$ nm. From these values the normalized ratio c/qa of the *3C*-SiC thin films was calculated to

be $(c^{hex}/(3a^{hex}))_{3C\text{-}SiC} = 0.817\ 116$. This value is larger than $\sqrt{2/3} = 0.816\ 497$ of the corresponding value of the ideal Si-C tetrahedron, i.e. the Si-C tetrahedrons that form the epitaxially grown *3C*-SiC thin films are slightly elongated in the c-direction (parallel to surface normal) and compressed in the lateral a-direction.

Using the above values, it is possible to calculate the inherent stress and strain within the epitaxially grown *3C*-SiC thin films by using the generalized Hook's law $\sigma_m = C_{mn}\,\varepsilon_n$, which is written here in Voigt's subscription (m,n = 1,...,6). The abbreviation C_{mn} denotes the elastic stiffnesses whose values in the succeeding calculation are taken from reference [6], σ_m and ε_n are the stress and strain components, respectively. Assuming the following boundary conditions

$$\begin{array}{lll} \sigma_1 = \sigma_2 \neq 0 & & \sigma_3 = \sigma_4 = \sigma_5 = \sigma_6 = 0 \\ \varepsilon_1 = \varepsilon_2 \neq 0 & \varepsilon_3 \neq 0 & \varepsilon_4 = \varepsilon_5 = \varepsilon_6 = 0 \end{array}$$

we get the stress and strain components

$$\begin{array}{ll} \varepsilon_3 = -0.589 \cdot \varepsilon_1 & \Leftarrow \text{ transverse contraction} \\ \varepsilon_1 = \varepsilon_2 = \Delta a/a = -4.77 \cdot 10^{-4} & \Leftarrow \text{ in-plane strain components } (\varepsilon_{\parallel}) \\ \varepsilon_3 = \Delta c/c = 2.81 \cdot 10^{-4} & \Leftarrow \text{ the normal strain component } (\varepsilon_{\perp}) \\ \sigma_1 = \sigma_2 = 2.26 \cdot 10^{8}\ \mathrm{N/m^2} & \Leftarrow \text{ in-plane stress components } (\sigma_{\parallel}) \end{array}$$

for the 3C-SiC thin films quasi homoepitaxially grown on *6H*-SiC(0001). Using these values, it is possible to derive the stress- and strain-free lattice parameters for entirely relaxed 3C-SiC (Note, that these values are expressed in hexagonal terms.):

$$a^{hex}_{3C\text{-}SiC} = 0.308\ 276\ \mathrm{nm} \pm 4 \cdot 10^{-6}\ \mathrm{nm} \text{ and}$$
$$c^{hex}_{3C\text{-}SiC} = 0.755\ 119\ \mathrm{nm} \pm 9 \cdot 10^{-6}\ \mathrm{nm}.$$

A brief calculation results in

$$a^{cub}_{3C\text{-}SiC} = \sqrt{2}\ a^{hex}_{3C\text{-}SiC} = \frac{1}{\sqrt{3}}\ c^{hex}_{3C\text{-}SiC} = 0.435\ 968\ \mathrm{nm} \pm 6 \cdot 10^{-6}\ \mathrm{nm}$$

the lattice parameter a of the stress- and strain-free *3C*-SiC-polytype in terms of the cubic crystallographic system.

Acknowledgement

This work was supported by the Deutsche Forschungsgemeinschaft (SFB 196, Project A11).

References

[1] A. Bauer, J. Kräußlich, L. Dressler, P. Kuschnerus, J. Wolf, K. Goetz, P. Käckell, J. Furthmüller, F. Bechstedt, Physical Review B **57** (1998), p. 2647.
[2] CREE RESEARCH INC.
[3] A. Fissel, K. Pfennighaus, U. Kaiser, B. Schröter, W. Richter, Diamond and Related Materials **6** (1997), p. 1316.
[4] W.L. Bond, Acta Cryst. **13** (1960), p. 814.
[5] J. Härtwig, St. Großwig, phys stat. sol. (a) **115** (1989), p. 369.
[6] Landolt-Börnstein, New Series III 22a, Springer-Verlag (1987)

Materials Science Forum Vols. 353-356 (2001) pp. 323-326
© 2001 Trans Tech Publications, Switzerland

Self Diffusion in SiC: the Role of Intrinsic Point Defects

Alexander Mattausch, Michel Bockstedte and Oleg Pankratov

Lehrstuhl f. Theor. Festkörperphysik, Universität Erlangen-Nürnberg,
Staudtstr. 7/B2, DE-91058 Erlangen, Germany

Keywords: Ab Initio Defect-Energetics, Defect Complexes, Point Defects, Self-Diffusion

Abstract We apply an *ab initio* method to study the diffusion of intrinsic interstitials and vacancies in 3C-SiC. The structure and the energetics of the relevant transient complexes are calculated. We present possible migration paths and the corresponding barriers and discuss the dominant channels for self-diffusion.

Introduction

Defect formation and diffusion are inevitable processes that accompany ion implantation and subsequent annealing in semiconductors. In boron-doped SiC *transient enhanced diffusion* has been found [1, 2]. This effect destroys the implanted profiles and reduces the active dopant concentration. The enhanced dopant diffusion arises from an excess of mobile intrinsic defects, namely vacancies and interstitials. The same defects also mediate self-diffusion. A microscopic understanding of the role intrinsic defects play in self diffusion in SiC is a key to assess the more complex mechanisms of dopant-diffusion. Yet, the most recent experimental work (c.f. [3] and reference therein) provides only limited insight into such questions.

In a previous paper [4] we have discussed the abundance of intrinsic mobile defects and their complexes. In the present work we focus on their migration. We calculate the migration barriers for interstitials and vacancies and discuss their relative importance for silicon- and carbon-self-diffusion. For simplicity we have restricted our calculations to 3C-SiC. We expect similar results for the other SiC polytypes.

Method

The calculations have been performed using the program package FHI96SPIN [5] within the framework of density functional theory and the local density approximation (LDA) [6]. Supercells with 64 atoms and 216 atoms have been used. Smooth norm conserving pseudopotentials of the Troullier-Martin type [7], a plane wave basis of 30 Ry and special k-point sampling have been employed. In the treatment of charged defects we account for the mandatory charge compensation by using the correction of Makov and Payne [8]. Albeit this correction is approximate, it consistently improves the energetics of defects especially in higher charge states.

In a compound material such as SiC, formation energies of defects depend on the stoichiometry of the crystal. In thermodynamic equilibrium a single parameter—the deviation $\Delta\mu_{\mathrm{Si}}$ of the silicon chemical potential from its value in solid silicon—determines the stoichiometry. $\Delta\mu_{\mathrm{Si}}$ is constrained between 0 (Si-rich condition) and $-\Delta H_{\mathrm{f}}$ (C-rich condition), where ΔH_{f} is the heat of formation of 3C-SiC. For the investigation of migration barriers we have employed two methods. The vacancy migration has been analysed by calculating the potential energy surface using constrained relaxations [9]. The saddle points of the interstitial migration have been obtained by the ridge method [10].

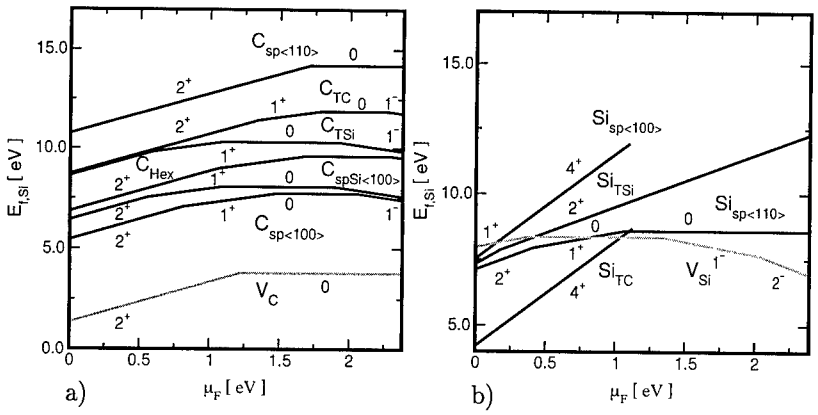


Figure 1: Formation energy $E_{f,Si}$ of mobile intrinsic defects versus the Fermi-level under Si-rich conditions for (a) carbon-related defects and (b) silicon-related defects. Vacancies are denoted by V, interstitials by their species and and their location in the lattice.

Abundance of the mobile intrinsic defects

The activation energy of a defect-mediated diffusion consists of the defect's formation energy and the migration barrier. The former determines the concentration of the defects. In this section we briefly summarise our recent findings for the abundance of intrinsic defects (c.f. [4]) with emphasis on the charge state corrections. The defect migration is described in subsequent sections.

In Fig. 1 we compare the formation energies of vacancies and interstitials as functions of the Fermi-level position under Si-rich conditions. Among the mobile carbon-related defects the carbon vacancy (V_C) has the lowest formation energy outweighing the carbon-interstitials (Fig. 1a), which remains true also in C-rich material. Next favourable are the split-interstitials $C_{sp\langle 100\rangle}$ and $C_{spSi\langle 100\rangle}$, where the additional carbon atom shares a lattice site with a native carbon or silicon atom forming a dumb bell along the $\langle 100\rangle$-direction. The hexagonal carbon interstitial follows in the hierarchy of the most abundant interstitials. The effect of the charge state corrections is to increase the separation of the ionisation levels and to invalidate the charge states 4^+ and 3^+ as possible ground states of $C_{spSi\langle 100\rangle}$ and C_{TC}.

For silicon-related mobile defects the situation is different (Fig. 1b). While in p-type material the tetrahedral carbon-coordinated interstitial (Si_{TC}) is most abundant, in n-type material the silicon vacancy (V_{Si}) is most frequent, followed by the split-interstitial $Si_{sp\langle 110\rangle}$. However, as we described previously [4], the silicon vacancy is metastable with respect to a transformation into a carbon-antisite-vacancy complex at least in p-type and intrinsic material. In this case the energy gain amounts to 4.1 eV. Under n-type conditions both defects have comparable formation energies. We observe the most dramatic effect of the charge state corrections for Si^{4+}_{TC} and $Si^{4+}_{sp\langle 110\rangle}$. The charge correction of the formation energies of both defects amounts to 3.76 eV for the 64-atom cell. Calculations in a 216-atoms supercell have confirmed a correct scaling of the Coulomb correction with the size of the cell. Another consequence of the Coulomb correction is the shift of the ionisation levels of Si_{TC} and $Si_{sp\langle 100\rangle}$ (initially located at the conduction band edge) into the upper half of the band gap. The corresponding defect states have effective-mass-like character. Since a necessary "scissors" correction for the band gap does not allow to precisely determine these ionisation levels we have excluded them in Fig. 1b. Our calculations in the 216-atom cell indicate that $Si_{sp\langle 100\rangle}$ becomes unstable when these orbitals are occupied.

Carbon diffusion

Vacancy migration. For the migration of vacancies we have considered two possible mechanisms based on nearest neighbour and second nearest neighbour hops, respectively. In SiC the migration by second nearest neighbour hops proceeds entirely on the sublattice of the vacancy. Nearest neighbour hops do not directly lead to a defect migration since by each hop atoms simply exchange places between the silicon and carbon sublattices. The net migration appears only due to a more complex ring mechanism which includes a series of hops along a sixfold coordinated ring of crystal sites. However, for the carbon vacancy we have found that the first hop in this series is impossible since the (V_{Si}-Si_C)-complex, which is a product of this hop, is unstable in all possible charge states. Thus the ring-mechanism is not relevant for the migration of carbon vacancies. Consequently we expect a migration by second nearest neighbour hops. The calculated migration barriers are 5.2 eV (V_C^{2+}), 4.2 eV (V_C^{1+}) and 3.5 eV (V_C^0). In the latter cases bonding orbitals are occupied at the transition state resulting in a reduction of the energy.

Interstitial migration. The two split-interstitials $C_{sp\langle 100\rangle}$ and $C_{spSi\langle 100\rangle}$ are the energetically lowest interstitial defects. We expect a relatively small migration barrier between these split-interstitials, as the hexagonal interstitial, a common neighbour of both, has only a slightly higher formation energy. And indeed we find that the transition state lies close to the neighbouring hexagonal interstitial site. Under p-type conditions, i.e. for the charge states 2^+ and 1^+, we find a barrier of 1.68 eV and 0.91 eV rsp. for the process $C_{sp\langle 100\rangle} \rightarrow C_{spSi\langle 100\rangle}$ and barriers of 0.7 eV and 0.22 eV in the following event $C_{spSi\langle 100\rangle} \rightarrow C_{sp\langle 100\rangle}$.

Silicon diffusion

Vacancy migration. As described above, under p-type conditions the silicon-vacancy is metastable and decays into an energetically more favourable (V_C-C_{Si}) complex. Whether or not V_{Si} contributes to silicon self-diffusion depends on the relevant barriers. The migration barrier for the nearest neighbour hop that transforms V_{Si} into a (V_C-C_{Si})-complex ranges from a value of 1.6 eV (V_{Si}^{2+}) to 5 eV (V_{Si}^{2-}). For the reverse process the barrier varies from 6.2 eV ((V_C-C_{Si})$^{2+}$) to 3.3 eV ((V_C-C_{Si})^0). Conversely, the migration barrier for the second nearest neighbour hop is highest (4.2 eV) for V_{Si}^{2+} and lowers down to 2.6 eV for V_{Si}^{2-}. This implies that under n-type conditions a migration of vacancies contributes to the silicon self-diffusion, whereas under p-type conditions the majority of Si-vacancies are converted into (V_C-C_{Si})-complexes. Having only a binding energy of 1.3 eV, the (V_C-C_{Si})-complexes may dissociate and thereby contribute to carbon self-diffusion. From the migration of the carbon vacancy we estimate an energy barrier between 5.2 eV and 6.5 eV for this process. We do not expect a migration of V_{Si} by a ring mechanism as a ring mechanism for the carbon vacancy is impossible.

Interstitial migration We have considered two different processes for the diffusion of the silicon interstitial: a direct migration through the interstice and a kick-in/kick-out process via split-interstitial sites. The former implies a migration of the carbon-coordinated interstitial (Si_{TC}) via the silicon-coordinated site (Si_{TSi}). The transient states for the latter are the stable split-interstitials $Si_{sp\langle 100\rangle}$ and $Si_{sp\langle 110\rangle}$ (under p-type conditions). In the first step Si_{TC} kicks in forming a split interstitial with a lattice site. One of the two atoms then leaves to the interstice and continues the migration (kick-out). For $Si_{sp\langle 110\rangle}$ another competing path exists. After a kick-out the silicon atom can migrate via the energetically higher Si_{TSi} site. Under n-type conditions $Si_{sp\langle 110\rangle}$ is the most favoured interstitial. For this defect a kick-out/kick-in reaction must be considered, which has not been calculated yet.

Under p-type conditions, the barrier for the direct migration of Si_{TC}^{4+} via Si_{TSi}^{4+} is 3.56 eV. The reverse process, though, is more interesting. The barrier for the direct movement of Si_{TSi}^{4+} towards Si_{TC}^{4+} is only 0.3 eV. This barrier allows for a possible electron transfer to the localised defect state, which further reduces the energy needed to leave the site to 0.04 eV for the charge state 3^+ and 0.03 eV for 2^+. The activation energy for the direct migration is comparable to the ones for the kick-in into the split interstitials $Si_{sp\langle 100\rangle}^{4+}$ and $Si_{sp\langle 110\rangle}^{4+}$, which are 3.4 eV and 3.5 eV respectively. For the following kick-out reaction towards Si_{TC}^{4+} the barriers are low (about 50 meV) for both defects with a transition state very close to the split configuration. Indeed, the split-interstitial $Si_{sp\langle 100\rangle}$ even becomes unstable in the lower charge states. The other process implying the kick-out from $Si_{sp\langle 110\rangle}^{2+}$ towards Si_{TSi}^{2+} is possible with a barrier of 0.24 eV. The reverse process costs 0.1 eV.

The migration of the silicon-interstitial through the interstice and the kick-in/kick-out reaction are equally likely under p-type conditions. In the charge state 2^+ this picture changes slightly in favour of the direct migration, since the barrier for leaving Si_{TSi}^{2+} is lower than that for the kick-in into $Si_{sp\langle 110\rangle}^{2+}$. This charge state can be obtained, e.g., by a charge transfer in the Si_{TSi} configuration. Under n-type conditions a kick-out/kick-in interstitial mechanism via $Si_{sp\langle 110\rangle}^{0}$ should exist, which still has to be investigated.

Discussion

We have investigated the migration of vacancies and self-interstitials. Especially for Si-interstitials a variety of migration paths can contribute to migration. A comparison of the formation energies and the migration barriers show that in p-type and intrinsic material the silicon self-diffusion is mediated by interstitials, whereas under n-type conditions a vacancy mechanism becomes viable. In contrast, for carbon self-diffusion the vacancy channel is the dominant mechanism for all doping conditions. Yet the contribution of the interstitial mechanism cannot be neglected, since the corresponding activation energy is close to, but still higher than that for the vacancy mechanism.

Acknowledgement The support of this work by the German Science Foundation (Sonderforschungsbereich 292) is gratefully acknowledged.

References

[1] M. Laube, G. Pensl, and H. Itoh, Appl. Phys. Lett. **74** (1999), p. 2292.

[2] M. S. Janssonet *al.*, Appl. Phys. Lett. **76** (2000), p. 1434.

[3] J. D. Hong, R. F. Davis, and D. E. Newbury, J. Mater. Sci. **16** (1981), p. 2485.

[4] M. Bockstedte and O. Pankratov, Mater. Sci. Forum **338-342** (2000), p. 949.

[5] M. Bockstedte *et al.*, Comput. Phys. Commun. **107** (1997), p. 187.

[6] J. P. Perdew and A. Zunger, Phys. Rev. B **23** (1981), p. 5048; D. M. Ceperley and B. J. Alder, Phys. Rev. Lett. **45** (1980), p. 567.

[7] M. Fuchs and M. Scheffler, Comp. Phys. Commun. **119** (1999), p. 67.

[8] G. Makov and M. C. Payne, Phys. Rev. B, **51** (1995), p. 4041.

[9] M. Bockstedte and M. Scheffler, Z. Phys. Chem. **200** (1997), p. 195.

[10] I. V. Ionova and E. A. Carter, J. Chem. Phys., **98** (1993), p. 6377.
Implementation: E. Pehlke, private communication.

Materials Science Forum Vols. 353-356 (2001) pp. 327-330
© 2001 Trans Tech Publications, Switzerland

Modeling of Boron Diffusion in Silicon Carbide

H. Bracht[1], N.A. Stolwijk[1], M. Laube[2] and G. Pensl[2]

[1] Institut für Materialphysik, University of Münster,
Wilhelm-Klemm-Str. 10, DE-48149 Münster, Germany

[2] Institut für Angewandte Physik, University of Erlangen-Nürnberg,
Staudtstr. 7/A3, DE-91058 Erlangen, Germany

Keywords: Boron, Diffusion, Ion Implantation, Kick-Out Mechanism, SIMS

Abstract. We report modeling of experimental B diffusion profiles in SiC which were measured by means of secondary ion mass spectrometry (SIMS) after B implantation and subsequent diffusion annealing at temperatures between 1700°C and 1800°C. Transient enhanced B diffusion caused by implantation damage was effectively reduced by recovery annealing of the B-implanted samples at 900°C prior to the diffusion anneal. Concentration profiles of B are accurately described on the basis of the kick-out mechanism. Simulations based on this model also accurately reproduce the diffusion from a buried B-doped SiC layer into undoped SiC epitaxial layers. This shows that Si self-interstitials rather than Si vacancies control the diffusion of B in SiC. Moreover, a suppression of B diffusion in SiC coimplanted with C can be explained by taking additionally into account the formation of Si-C pairs.

Introduction

Selective area doping of SiC is generally achieved by implantation of dopant atoms. After ion implantation a subsequent high temperature treatment is usually required to reduce the implantation damage and to electrically activate the dopant. Among the various dopants such as N, Al, Ga, and B, only B is observed to diffuse readily at the applied annealing temperature of typically 1700°C. This temperature treatment causes a rapid diffusion of B towards the surface and a pronounced diffusion of B into the undamaged region of the SiC substrate. This transient-enhanced diffusion (TED) of B is believed to be caused by nonequilibrium concentrations of native point defects which are introduced during the implantation process [1, 2]. Recently it has been demonstrated that TED of B can be effectively suppressed by a coimplantation of C or by a preanneal at 900°C [3, 4]. Samples preannealed in such a way and subjected to temperatures between 1700°C and 1800°C still reveal a diffusion of B into the undamaged SiC substrate. The corresponding profiles as well as B profiles measured after diffusion from a buried B-doped SiC layer in undoped SiC epitaxial layers [5] are considered to reflect B diffusion under near-equilibrium conditions and enable us to determine whether a vacancy or interstitial type mechanism controls the diffusion process.

Experimental

Epitaxial 5 μm thick N-doped (1×10^{17} cm^{-3}) and Al-doped (4×10^{16} cm^{-3}) SiC layers grown on N-doped (4×10^{18} cm^{-3}) and Al-doped (2×10^{18} cm^{-3}) substrates, respectively, were subjected to a five-fold B implantation resulting in a box shaped as-implanted B profile. The as-implanted samples were preannealed at 900°C for 2h and subsequently treated at temperatures between 1700°C and 1800°C. The preanneal at 900°C has been shown to effectively reduce the TED of B [4]. Details about the ion implantation and the temperature treatment have been published elsewhere [3, 4]. Figure 1 (a) illustrates B concentration profiles in ion-implanted Al-doped 6H-SiC before and after the temperature treatments. We observe a pronounced B diffusion into the undamaged region of the epilayer. Similar profiles are observed after B diffusion into N-doped 4H-SiC [4]. A depth profile of B measured with SIMS after annealing an epitaxially grown SiC

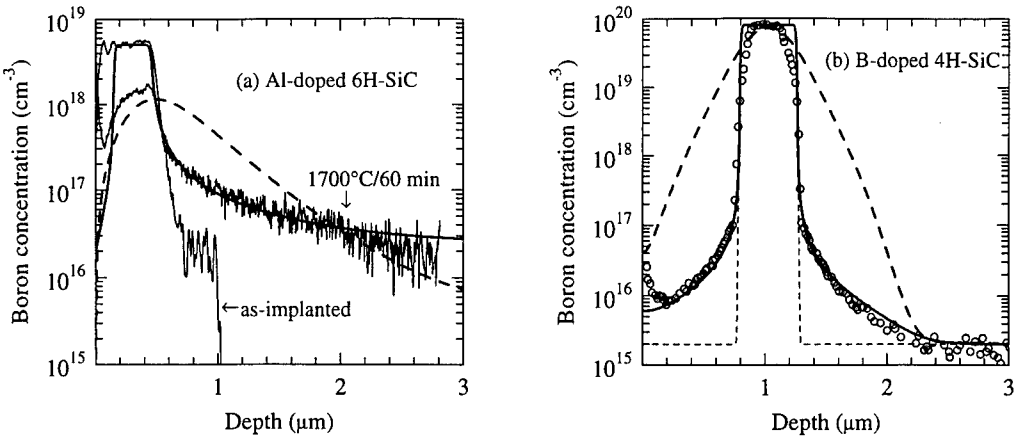


Figure 1: Concentration-depth profiles of B measured by means of SIMS. (a) B profiles (thin solid lines) in Al-doped 6H-SiC epilayers before and after annealing of the B-implanted sample at 900°C (2h) and subsequent diffusion at 1700°C for 60 min. (b) B profiles (o) in 4H-SiC measured after annealing of an epitaxial grown SiC structure with a buried B-doped SiC layer at 1700°C for 60 min. Thick solid lines in (a) and (b) show the best fits obtained on the basis of the kick-out model. The thick dashed lines represent the diffusional broadening in the case that B diffusion proceeds via the dissociative mechanism. The thin dashed line in (b) indicates the initial B distribution taken into account in the simulation.

structure with a buried B-doped SiC layer at 1700°C for 60 min [5] is shown in Fig. 1 (b). In the following section we provide strong evidence that B diffusion in SiC is controlled by Si self-interstitials rather than by Si vacancies.

Modeling of B diffusion

The fast diffusion of B in SiC compared to other dopants and the fact that B prefers the substitutional position of the Si sublattice suggest that an interstitial-substitutional (i-s) mechanism, namely the dissociative and/or the kick-out mechanism, controls the diffusion. These mechanisms have been established for the diffusion of e.g. Au and Zn in Si [6, 7]. For B in SiC the i-s mechanisms are expressed by the reactions

$$B_i + V_{Si} \rightleftharpoons B_{Si} \quad (1)$$

$$B_i \rightleftharpoons B_{Si} + Si_i \quad . \quad (2)$$

Equation (1) represents the dissociative reaction. Mobile interstitial B atoms (B_i) occupy vacancies on the Si sublattice (V_{Si}) and thereby become substitutional defects (B_{Si}). In the kick-out mechanism (see Eq. (2)), the i-s exchange creates a Si self-interstitial Si_i. The mathematical formulation of B diffusion via reactions (1) and (2) is given by a system of four coupled partial differential equations (PDE's). This PDE system together with the proper initial and boundary conditions are given elsewhere [8]. Depending on the defect X ($\in \{B_i, V_{Si}, Si_i\}$) that controls the i-s exchange, the B diffusion coefficient D_B equals $D_X^* = C_X^{eq} D_X / C_{B_{Si}}^{max}$ where C_X^{eq} and D_X are the thermal equilibrium concentration and diffusion coefficient of the respective point defect. For modeling B diffusion the maximum B concentration of the ion-implanted SiC samples (see Fig. 1 (a)) and of the buried B doping layer (see Fig. 1 (b)) are denoted as $C_{B_{Si}}^{max}$.

Figure 1 (a) shows that the experimental B profiles in the undamaged region of an Al-doped 6H-SiC epilayer are accurately reproduced by computer simulations based on the kick-out model

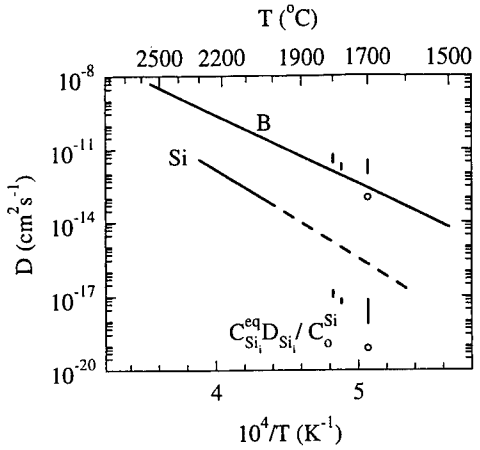


Figure 2: Temperature dependence of the B and Si diffusion coefficients D_B and D_{Si} (solid lines) in 6H-SiC reported in the literature [9, 10] in comparison to our results. D_B for 1700°C indicated by the upper solid bars and the upper symbol (o) were obtained from fitting the experimental B profiles shown in Fig. 1 (a) and 1 (b), respectively. The lower solid bars and symbol (o) represent the Si self-interstitial contribution to Si self-diffusion. D_{Si} (dashed line) extrapolated from high temperature data [10] is shown for comparison.

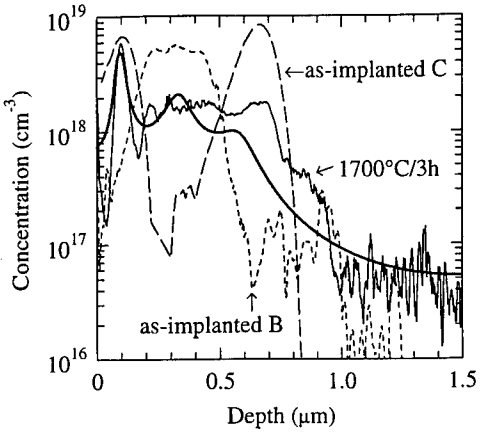


Figure 3: SIMS concentration depth profiles of B in 6H-SiC coimplanted with B and C before (thin short-dashed line) and after annealing (thin solid line) at 1700°C for 3h. The thin long-dashed line indicates the distribution of C calculated with dynamic TRIM. The thick solid line represents the simulation of B diffusion on the basis of the kick-out mechanism (2) and reaction (3) which takes the formation of Si_iC_{Si} pairs into account.

whereas profiles calculated on the basis of the dissociative model do not yield a satisfactory fit. Similar B diffusion profiles in ion-implanted N-doped 4H-SiC are also well described by the kick-out mechanism [8]. Moreover, Fig. 1 (b) demonstrates that the kick-out model reproduces the diffusion-induced broadening of a buried 0.4 μm thick B doping layer into undoped 4H-SiC epitaxial layers [5]. Again the dissociative mechanism fails to describe this process.

Results and discussion

The successful modeling of B diffusion in both ion-implanted SiC and samples with a buried B doping layer provides strong evidence that B diffusion is mediated by Si self-interstitials rather than by Si vacancies. Data deduced for $D^*_{B_i}$ and given in Fig. 2 are in fair agreement with earlier results given by Mokhov et al. [9] which are also considered to represent the B_i-controlled B diffusivity $D^*_{B_i}$. The solid bars in Fig. 2 reflect the error of $D^*_{B_i}$ due to uncertainties in some other parameters entering the diffusion model [8]. The slightly higher $D^*_{B_i}$ values deduced from B diffusion in ion-implanted SiC compared to Ref. [9] may indicate that TED is not completely suppressed by the preanneal at 900°C.

Fitting of the B profiles yields data for $D^*_{Si_i}$. The product $D^*_{Si_i}C^{max}_{BSi}$ reduced by the Si atom density $C^{Si}_o(\approx 2.4\times10^{22}$ cm$^{-3})$ in SiC is equal to the self-interstitial contribution $C^{eq}_{Si_i}D_{Si_i}/C^{Si}_o$ to Si self-diffusion in SiC. Figure 2 shows that this Si_i contribution is about two orders of magnitude lower than the extrapolation of Si self-diffusion in 6H-SiC [10] to lower temperatures. This suggests that Si diffusion is mainly mediated by vacancies on the Si sublattice and not by self-interstitials. In this case the parameter $D^*_{V_{Si}}(=C^{eq}_{V_{Si}}D_{V_{Si}}/C^{max}_{BSi})$ should be about two orders of magnitude higher than $D^*_{Si_i}(=C^{eq}_{Si_i}D_{Si_i}/C^{max}_{BSi})$. However, this conflicts with the fact that the dissociative mechanism does not significantly contribute to B diffusion in SiC. Presumably Si diffusion was determined not accurately enough in order that the extrapolation yields reliable

results. We noticed that the earlier self-diffusion study [10] was performed with ^{30}SiC-^{30}Si-SiC structures leaving some doubt on the accuracy of the data.

Recently it has been reported that C and B coimplantation of SiC strongly suppresses the diffusion of B during a subsequent high-temperature treatment [4]. Figure 3 illustrates the corresponding distribution of B and C after the ion implantation process. The B profile was measured directly with SIMS whereas the C profile was calculated with dynamic TRIM. SIMS analysis of the same structure annealed at 1700°C for 3h reveals that a substantial fraction of B is kept between the two C spikes; no significant diffusion of B into the undamaged region of the SiC epilayer is observed. For modeling of B diffusion in B/C-coimplanted SiC, the kick-out mechanism (2) and the additional reaction

$$Si_i + C_{Si} \rightleftharpoons Si_iC_{Si} \tag{3}$$

are considered. Reaction (3) describes the formation of Si_iC_{Si} pairs via the capture of Si_i by carbon atoms C_{Si} on the Si sublattice. Assuming C_{Si} and Si_iC_{Si} to be immobile and pair formation kinetics with an equilibrium that lies on the right side of reaction (3), the B profile measured after the high-temperature anneal is fairly well described on the basis of reactions (2) and (3) with values for $D^*_{B_i}$ and $D^*_{Si_i}$ which are consistent with the results given in Fig. 2. For simplicity we also assumed that the concentrations of the defects involved in reactions (2) and (3) are in local equilibrium prior to the diffusion at high temperatures, because the distributions of the defects introduced during the implantation process are hardly accessible. Very likely the deviation observed in Fig. 3 between the experimental and calculated B profile is a consequence of inhomogeneously distributed non-equilibrium native point-defect concentrations which were not considered in our calculations.

Conclusions

The analysis of experimental B profiles obtained after annealing of SiC samples, which were either implanted with B or possess a buried B doping layer, provides strong evidence that B diffusion is mediated by a Si_i-mediated kick-out mechanism. Modeling of B diffusion in SiC provides data for the B_i-controlled B diffusion coefficient which are in good agreement with literature data (see Fig. 2). The deduced Si_i-controlled B diffusion coefficient enables us to determine the Si self-interstitial contribution to the Si self-diffusivity in SiC. The suppression of B diffusion in SiC coimplanted with C can be explained on the basis of the kick-out mechanism and an additional reaction which considers the formation of Si_i-C_{Si} pairs. This pair formation eliminates the Si self-interstitials as vehicles for B diffusion.

References

[1] M.V. Rao, J. Gardner, P.H. Chi, O.W. Holland, G. Kelner, J. Kretchmer, and M. Ghezzo, J. Appl. Phys. 81 (1997), p. 6635.

[2] T. Troffer, M. Schadt, T. Frank, H. Itoh, G. Pensl, J. Heindl, H.P. Strunk, and M. Maier, Phys. Status Solidi A 162 (1997), p. 277.

[3] M. Laube and G. Pensl, Mat. Sci. Forum 338-342 (2000), p. 941.

[4] M. Laube, G. Pensl, and H. Itoh, Appl. Phys. Lett. 74 (1999), p. 2292.

[5] M.S. Janson, M.K. Linnarsson, A. Halln, B.G. Svensson, N. Nordell, and H. Bleichner, Appl. Phys. Lett. 76 (2000), p. 1434.

[6] U. Gösele, W. Frank, and A. Seeger, Appl. Phys. 23 (1980), p. 361.

[7] H. Bracht, N.A. Stolwijk, and H. Mehrer, Phys. Rev. B 52 (1995), p. 16542.

[8] H. Bracht, N.A. Stolwijk, M. Laube, and G. Pensl, accepted for publication in Appl. Phys. Lett.

[9] E.N. Mokhov, E.E. Goncharov, and G.G. Ryabova, Sov. Phys. Semicond. 18 (1984), p. 27.

[10] J.D. Hong, R.F. Davis, and D.E. Newbury, J. Mater. Sci. 16 (1981), p. 2485.

Materials Science Forum Vols. 353-356 (2001) pp. 331-334
© 2001 Trans Tech Publications, Switzerland

Quantitative Modeling of Hydrogen Diffusion and Reactivation of H-Passivated Al-Acceptors in SiC

C. Hülsen[1], N. Achtziger[2], J. Herold[1] and W. Witthuhn[1]

[1] Institut für Festkörperphysik, Friedrich-Schiller-Universität Jena, Max-Wien-Platz 1, DE-07743 Jena, Germany

[2] Fraunhofer-Institute for Integrated Circuits IIS-A, Am Weichselgarten 3, DE-91058 Erlangen, Germany

Keywords: Acceptor, Diffusion, Dissociation, Hydrogen, Passivation, Recombination

Abstract: The thermal stability of the hydrogen passivation of aluminum acceptors in p-type silicon carbide is investigated. After passivation by low energy ion implantation, annealing experiments are performed under the influence of an electrical field in a reverse biased Schottky diode. At temperatures around 500K, Al acceptors become reactivated. To study the influence of temperature, p-type doping level, and hydrogen isotope (^{1}H or ^{2}H), a mathematical model is developed and applied to simulate experimental data. Both the diffusion constant of free H as well as the dissociation rate turn out to be thermally activated with activation energies of 2.1 eV and 1.2 eV, respectively.

Introduction

As in many other semiconductors, hydrogen is known to passivate acceptors in p-type silicon carbide. This passivation may exist already after epitaxial growth (Chemical Vapor deposition) [1]. In order to passivate acceptors in SiC intentionally, H-implantation with low ion energy is an established technique. Both boron as well as aluminum acceptors are passivated effectively [2]. Annealing experiments in combination with an electrical field in a reverse biased Schottky diode have demonstrated that passivated aluminum acceptors become reactivated at temperatures around 500 K and that released hydrogen is moving as a positive ion that is able to passivate further free acceptors [3]. This type of experiment has also been done on silicon [4]. Most of our experimental results on SiC and an empirical description of the reactivation rate are already published [5]. In the present work, we now develop and use a mathematical model to achieve a more detailed understanding of the various processes involved. As a result, both the diffusion constant of free hydrogen and the dissociation rate of H-Al complexes are provided.

Experiment

The work was done on commercial p-type epitaxial layers (thickness $\approx 5\mu m$, polytype 4H) on p^+-substrates. The net doping level N_A of the epi-layer is either $6\cdot10^{15}$ cm^{-3} or $2\cdot10^{17}$ cm^{-3}. In addition to the intentional dopant Al, boron is present with a concentration of $2\cdot10^{15}$ cm^{-3}. The effects treated in the present work are due to Al acceptors only as explained in detail in ref. [5].

The passivation is done by implantation of H_2^+ molecular ions with 600eV at 680K as described elsewhere [6]. After implantation, Schottky contacts (titanium, 0.5 mm diameter) were evaporated on the implanted layers. The depth profiles N(x) of electrically active acceptors were measured by Capacitance-Voltage (CV) profiling. During annealing, the Schottky contacts are used to establishe an electrical field by applying a reverse bias U_R at the diode. This procedure is frequently termed 'reverse bias annealing' (RBA).

Results

Experimental results of these RBA experiments are already given in refs. [3,5] and are reviewed here only shortly. The variation of the depth profile of free acceptors during subsequent RBA steps is displayed in Fig. 1: at small depth where the electrical field is strongest and points into the semiconductor, acceptors become reactivated. Released hydrogen is moving deeper where it passivates further acceptors. The main facts are [5]:

(i) The characteristic time constant of the whole reactivation process (involving both dissociation and transport) is found to be thermally activated with an activation energy of about 1.8 eV.

(ii) The reactivation is faster for hydrogen compared to deuterium.

(iii) The reactivation is faster in the heavily doped material than in the lightly doped.

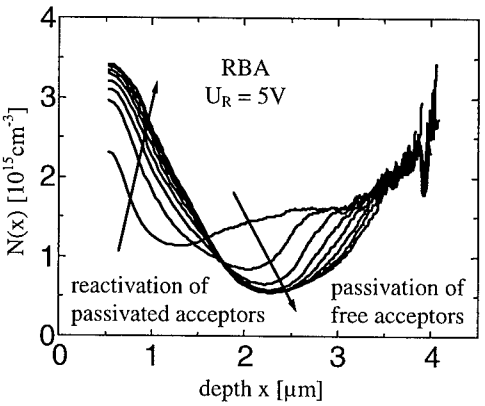


Fig. 1: Depth profiles of electrically active acceptors obtained by CV profiling on ^{2}H-passivated , lightly doped p-type SiC during reverse bias annealing at 530K. The arrows indicate the sequence of measurements. The first profil is unannealed (as implanted). The second was measured after one annealing step of 15 minutes duration, the third after the next anneling step also of 15 minutes duration and so on.

Simulation

In order to analyze the reactivation process quantitatively, a mathematical model is developed. It consists of two coupled partial differential equations which describe four independent single processes: (1) the dissociation of the H-Al complexes, (2) the free diffusion of hydrogen, (3) the drift of positively charged hydrogen ions, and (4) the recombination with free acceptors. For the dissociation and recombination, we suppose that the H-Al complex consists of exactly one hydrogen and one acceptor atom. The concentrations of free acceptors, free hydrogen and of acceptor-hydrogen pairs are denoted by c_A, c_H, and c_{AH}, respectively.

$$\left.\frac{\partial c_H}{\partial t}\right|_{diff} = -\frac{\partial}{\partial x}\left(-D\cdot\frac{\partial c_H}{\partial x} + e\cdot\mu\cdot c_H\cdot\vec{E}\right) \qquad \text{(Eq. 1)}$$

$$\left.\frac{\partial c_H}{\partial t}\right|_{chem} = \left.\frac{\partial c_A}{\partial t}\right|_{chem} = -\left.\frac{\partial c_{AH}}{\partial t}\right|_{chem} = -K\cdot c_A\cdot c_H + \upsilon\cdot c_{AH}\ . \qquad \text{(Eq. 2)}$$

Eq. 1 presents Fick's law for the hydrogen flux consisting of a free diffusion term with a diffusion constant D and a drift term determined by the electrical field E and a mobility µ (e is the elementary charge). µ and D are linked by the Einstein correlation $D=k_BT\mu$ [7] where k_B is the Boltzmann constant and T is the temperature. Eq. 2 describes the pair formation (formation constant K) and the dissociation (dissociation constant ν). The concentration c_{AH} is eliminated by setting $c_{AH}=N_0-c_A$ where the constant N_0 is the total acceptor concentration of the epi-layer. The formation constant K is expressed as $K=4\pi\rho D$, where ρ means the capture radius for recombination [8]. The electric field strength E is calculated from Poisson's equation from the charge density $e(c_H-c_A)$ within the diode's space charge region with the applied reverse bias as a boundary condition. The resulting equations for the two independent functions c_A and c_H are solved numerically by the Euler method. The remaining model parameter D, ρ and ν were adjusted to fit the simulated c_A profiles to measured CV profiles.

Results and discussion

In various cases, the resulting capture radius turned out to be close to the theoretical estimate $\rho=e^2/(4\pi\varepsilon k_B T)$, where ε is the dielectric constant. This expression describes the radius of a sphere around an elementary charge (free acceptor) where the attractive Coulomb energy exceeds the thermal energy $k_B T$, i.e. a re-emission is improbable once a positive H ion is trapped within this sphere. For subsequent simulations, the capture radius was calculated by this equation (about 3nm), leaving only two adjustable model parameters, D and ν.

There are several difficulties that prevent a perfect match of simulated and experimental profiles.

(i) The initial c_A is unknown close to the surface due to a limitation of CV profiling (see Fig. 1). For the simulation, these data are estimated by extrapolation of experimental curves to zero depth.

(ii) The initial concentration of free hydrogen is unknown (assumed to be zero).

(iii) Due to the limited depth resolution of CV profiling, the experimental profiles are not expected to reflect steep slopes in the $c_A(x)$ curves correctly.

(iv) The precise depth of the evolving minimum of $c_A(x)$ sensitively depends on the overall amount of hydrogen available. This number, however, is uncertain due to the extrapolation discussed in (i) and due to the uncertainty concerning boundary conditions (zero flux at the surface is assumed)

(v) Heating and cooling periods of the annealing cycles are ignored in the simulation.

As a consequence, neither the steep slope nor the absolute minimum of the N(x) curves (see Fig. 1) are a reliable criterion for a good simulation. Instead, we focussed on the rate of concentration increase at small depths, on the overall profile shape and on the time dependence in order to judge the quality of simulation. These features are well described by the simulations.

The resulting model parameters D and ν (one set per RBA sequence as shown in Fig.1) will now be discussed. The diffusion constant D as shown in Fig.2 depends exponentially on reciprocal temperature as expected for a thermally activated process with an energy of 2.1 eV and a prefactor $D_0 = 10^7 \ldots 10^9\ cm^2/s$. Compared to the considerable errors, no significant influence of isotopic mass or doping level is obvious.

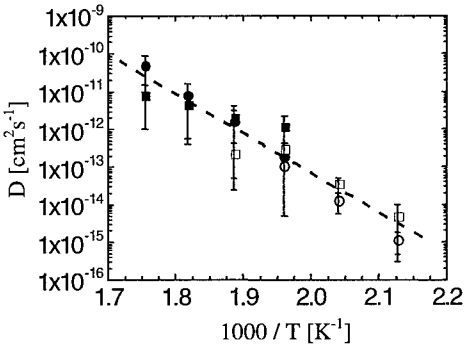


Fig. 2: Diffusion constants of hydrogen in SiC determined from RBA experiments with two different isotopes and acceptor doping levels. Squares stand for deuterium, and circles stand for hydrogen implanted samples. The open symbols indicate the heavily doped, and the closed symbols indicate the lightly doped material. The dashed line indicates a diffusion energy of 2.1 eV.

The dissociation rates ν as determined from the simulations (not shown), however, did surprisingly depend on the samples doping level with the same trend as the empirical reactivation time constant, indicating a faster process at a higher doping level. Since a doping dependence of the ion drift (larger electric field at higher doping level) is already included explicitly in our model, this remaining dependence means, that, in addition to the transport, the dissociation is also faster at the higher doping level. Since we still are in a limit of low concentrations, a direct interaction between adjacent acceptors is not expected. Instead, this dependence also has to be mediated by the electrical field. Thus, we end up with the idea of a field-assisted barrier lowering, accelerating the emission of a hydrogen ion out of an acceptor's Coulomb potential. In the case of electron emission, this is well-know as Poole- Frenkel effect. Since this theory [9] does not depend on masses, we are now using the Pool-Frenkel correction factor to extrapolate the dissociation rates ν, obtained from

the simulation, to zero field strength. The resulting values ν well fit to a straight line in the Arrhenius plot of Fig.3 with a slope corresponding to a dissociation energy of 1.2 eV, i.e. the Poole Frenkel correction successfully removes the apparent doping dependence of the raw data.
Regarding an isotope effect on ν, there is a trend for faster dissociation of ^{1}H compared to deuterium (Fig.3). Due to the considerable errors of the present ν data, this effect is hardly significant. Experimentally, an influence of the isotopic mass on the whole RBA process is definitely significant [5]. From the present simulations, we may state that this effect tends to be dominated by dissociation rather than diffusion, but a clear decision is not possible.

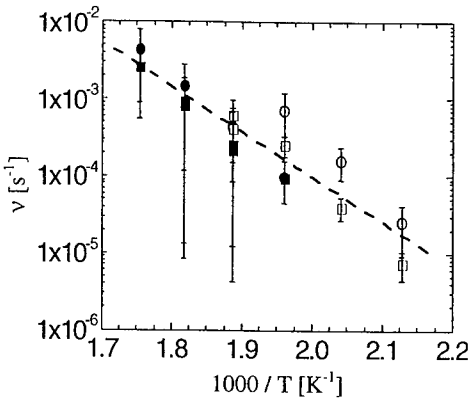


Fig. 3: Dissociation constant of Al-H pairs in SiC, extrapolated to zero field strength. The symbols have the same meaning as in Fig. 2. The dashed line indicates a dissociation energy

Conclusion

The reactivation of hydrogen passivated Al acceptors in SiC is analyzed by a mathematical model of the RBA process treating the dissociation of H-Al complexes, the diffusion and ion drift of free hydrogen, and the recombination with free acceptors as individual processes. The experimentally evident acceleration of the reactivation process with increasing acceptor doping level is successfully explained by the increasing electrical field, which gives rise to a faster ion drift and to a faster, field assisted dissociation.
The dissociation rate of the H-Al complex and, most important, the diffusion constant D of free hydrogen in SiC are determined quantitatively. The activation energies are $E_\nu = 1.2 \pm 0.1$ eV and $E_D = 2.1 \pm 0.1$ eV, respectively.

The work was funded by the German BMBF and DFG.

References

[1] D.J. Larkin, S.G. Sridhara, R.P. Devaty, W.J. Choyke, Jour. of Elec. Mat., Vol. 24, No. 4 (1995), p. 289.
[2] N. Achtziger, J. Grillenberger, W. Witthuhn, M.K. Linnarsson, M. Janson, B.G. Svensson, Appl. Phys. Lett. 73 (1998), p. 945.
[3] N. Achtziger, C. Hülsen, W. Witthuhn, M.K. Linnarsson, M. Janson, B.G. Svensson, phys. stat. sol. (b) 210 (1998), p. 395.
[4] C.H. Seager, R.A. Anderson, D.K. Brice, Jour. Appl. Phys. 68 (1990), p. 3274.
[5] C. Hülsen, N. Achtziger, U. Reislöhner, W. Witthuhn, Mat. Sci. For. Vols. 338-342 (2000), p. 929.
[6] N. Achtziger, C. Hülsen, W. Witthuhn, M. Janson, M.K. Linnarsson, B.G. Svensson, Mat. Sci. For. Vols. 338-342 (2000), p. 933.
[7] T. Zundel, J. Weber, Phys. Rev. B 39 (1989), p. 13549.
[8] M. Janson, M.K. Linnarsson, A. Hallén, B.G. Svensson, Mat. Res. Soc. Symp. Proc., Vol. 513 (1998), p. 439.
[9] J.L. Hartke, communications (1968), p. 4871.

Materials Science Forum Vols. 353-356 (2001) pp. 335-340
© 2001 Trans Tech Publications, Switzerland

Optical Characterization of SiC Materials: Bulk and Implanted Layers

J. Camassel[1], P. Vicente[2] and L.A. Falkovski[1,3]

[1] Groupe d'Etude des Semiconducteurs, Université Montpellier 2 and CNRS, cc074, FR-34095 Montpellier Cedex 5, France

[2] NOVASiC, Pomblières, FR-73600 Moûtiers, France

[3] Permanent address: Landau Institute, Moscow, Russia

Keywords: Implantation Damage, Micro-Raman Spectroscopy, Subsurface Damage, Wafering

Abstract: It is shown that micro-Raman spectroscopy is a sensitive tool to probe the effect of subsurface and implantation damage in SiC. The investigation of subsurface damage is based on the determination of the free carrier density profile in n-type material. The investigation of implantation damage calls for an investigation of the activation of the 1-phonon DOS, combined with a study of the broadening and shift of the first-order Raman modes.

Introduction

Whatever the polytype, there are always a large number of residual defects and inhomogeneity present in SiC material [1]. This constitutes the main limitation to improve the SiC device technology and to achieve a better yield. We have to master this problem. This makes rapid and non destructive optical characterization techniques increasingly popular. In the case of 4H and 6H-SiC wafers, for instance, absorption measurements performed in the visible range have been shown to allow fast, non-contact and non-destructive on-line measurements of the spatial doping homogeneity [2]. Scanning photoluminescence spectroscopy has also been introduced [3] and, similar to the more mature III-V materials, will become rapidly a viable tool for non destructive investigations of the dislocation density in 4H and 6H polytypes. However, in many cases, such simple optical methods suffer from intrinsic limitations due to the wide (indirect) nature of the band gap material [4]. This makes infrared reflectivity [5] and visible light scattering techniques, like micro-Raman spectroscopy, more and more appealing [6].

Provided it is used in a non standard (transverse) configuration, micro-Raman (μR) spectroscopy allows one to probe in-depth perturbation effects. In this case, because the optical phonons are sensitive to strain fluctuations and dislocations, one finds specific (depth-dependant) contributions to the line width and shift [7, 8]. In this work we focus on the effect of slicing and polishing on the interaction of phonons with residual carriers, then we consider the effect of implantation damage and implantation damage annealing.

1. Background considerations

Since the pioneering work of Feldman and coworkers [9] the phonon properties of SiC polytypes have been investigated many times. Because the different polytypes refer simply to different ways of stacking identical bilayers, the changes in lattice dynamics are best understood in the framework of the folded zone scheme. This is nothing but the standard

concept used for a long time in layered materials, like GaS, GaSe or $MoSe_2$ (for additional information see Ref.10). The only difference is that no isolated bilayer exist in the case of SiC and the closest approximation (with two atoms per unit cell) is the cubic form (3C-SiC) considered along the <111> direction.

Given a NH or 3NR polytype, there are 2N atoms per unit cell which give 3 (2N-1) optical branches. Starting from the cubic polytype (3R symmetry) and taking into account the effect of hexagonal crystal field, they split in four groups of axial optic (AO), planar optic (PO), axial acoustic (AA) and planar acoustic (PA) frequencies. They originate from the folding of the old (cubic) LO, TO, LA and TA branches, in such a way that points originally located at reduced wavevector x = k/km = 2m/N of the old (extended) cubic Brillouin zone become new zone-center modes (m is an integer ≤ N/2, for more details see Ref.11).

ROADMAP OF ZONE-CENTER MODES IN SiC POLYTYPES.

3C-SiC	**First order**			
	(x = 0)			
AO (cm^{-1})	LO (972)			
PO (cm^{-1})	TO (796)			
AA	ac.			
PA	ac.			
Total	6			
4H-SiC	**First order**	**Folded**		**Folded**
	(x = 0)	(x = 1/2)		(x = 1)
AO (cm^{-1})	A_1 (964)	$2B_1$ (?/?)		A_1 (838)
PO (cm^{-1})	E_1 (796)	$2E_2$ (776/?)		E_1 (?)
AA (cm^{-1})	ac.	$2B_1$ (?)		A_1 (610)
PA (cm^{-1})	ac.	$2E_2$ (196/204)		E_1 (266)
Total	6	12		6
15R-SiC	**First order**	**Folded**	**Folded**	
	(x = 0)	(x = 2/5)	(x = 4/5)	
AO (cm^{-1})	A_1 (965)	$2A_1$ (932/938)	$2A_1$ (860/?)	
PO (cm^{-1})	E (797)	2E (785/?)	2E (769/?)	
AA (cm^{-1})	ac.	$2A_1$ (331/337)	$2A_1$ (569/577)	
PA (cm^{-1})	ac.	2E (167/173)	2E (255/256)	
Total	6	12	12	
6H-SiC	**First order**	**Folded**	**Folded**	**Folded**
	(x = 0)	(x = 1/3)	(x = 2/3)	(x = 1)
AO (cm^{-1})	A_1 (965)	$2B_1$ (?/?)	$2A_1$ (889/?)	B_1 (?)
PO (cm^{-1})	E_1 (796)	$2E_2$ (789/?)	$2E_1$ (?/?)	E_2 (767)
AA (cm^{-1})	ac.	$2B_1$ (?)	$2A_1$ (504/514)	B_1 (?)
PA (cm^{-1})	ac.	$2E_2$ (145/150)	$2E_1$ (236/241)	E_2 (266)
Total	6	12	12	6

Table 1. Roadmap of zone center modes in usual SiC polytypes. Only A1, E1 and E modes are IR active ; A1, E1, E2 and E modes are Raman active ; B1 modes are silent. Reduced wave vector are denoted by x (see text). All values are "experimental" values after Refs.9 and 11.

A complete roadmap of expected and experimental frequencies for usual SiC polytypes is given in Table 1. Notice that only A1, E1 and E modes are IR active. Both A1, E1, E2 and E modes are Raman active. Finally, B1 modes are silent. Notice also that, depending on the polytype, the same frequency in the extended zone scheme (AO mode for instance with x = 1) can be allowed (4H polytype) or forbidden (6H variety). In both cases, it must be located around 840 cm^{-1}.

2. Investigation of subsurface damage

Due to the intrinsic hardness of SiC polytypes, and because of the high cost of SiC wafer production, achieving a proper optimisation of the wafering technology has long been a critical issue [12]. Basically, since any wafering step (including the cutting one) induces a specific amount of subsurface damage, a next step is necessary to eliminate the previous defects. The process then repeats until a final (acceptable) surface has been achieved. To optimise the process and minimise the material loss, one needs to quantify the damage thickness for different polishing slurries.

Different methods have been used. They range from Transmission Electron Microscopy [13] to Rutherford Backscattering [14] and Photon Backscattering [15]. However, there is not yet a standard answer to the simple question: "How much is the subsurface damage extension in a given wafer?". Depending on the observation method, it has been found to extend from one-half to a few percent of the abrasive slurry size (compare for instance the experimental results reported in Refs. 13 and 14). Recently, this has been investigated using μ-R techniques and valuable results have been found [16].

Used in a transverse configuration, μR scattering allows us to probe the frequency of LO-Phonon–Plasmon coupled modes (LPP modes) at various distance from the surface. Since the subsurface damage influences drastically the carrier concentration, the LPP mode frequency shifts. From a line-shape analysis of the LPP modes, the plasma frequency can be obtained and the change in carrier concentration (damage extension) can be deduced. Typical results obtained in the case of 4H and 6H polytypes (both Si and C faces) are shown in Table 2.

Polytype	6H	6H	4H	6H	4H	4H
Polishing particle size (μm)	40	20	10	5	3	<1
Damaged layer thickness (μm)	>60	23	20	1.5	0.8	<0.1

Table 2. Examples of subsurface damage extension observed for various polishing slurries on n-type doped 4H and 6H-SiC samples.

To perform a quantitative analysis, one has to compute the scattered intensity from the standard expression [11, 16-18] :

$$I(\omega) = S\, A(\omega) \cdot \mathrm{Im}\left[\frac{-1}{\varepsilon(\omega)}\right]$$

in which S is a proportionality constant; the frequency dependent factor A(ω) depends:

i.) on the TO and LO phonon frequencies (ω_T and ω_L), ii.) on the phonon and plasmon broadening parameters (γ and Γ, respectively), iii.) on the plasma frequency (ω_p) and iv.) on the so-called Faust-Henry coefficient C (for more details see Ref.19). For a given LPP mode (with, either, A_1- or E_1-symmetry) this leaves only three unknown parameters : n_R, Γ and γ. Among them the carrier concentration (n_R) is the only one that can adjust the LPP frequency and, provided the starting material is sufficiently doped, the results are i.) non destructive and ii.) reasonably sensitive.

Typical examples are shown in Fig.1 for a series of 4H-SiC wafers polished, respectively, with 10 μm, 3 μm and sub-μm (final) abrasive slurries. Notice that using the final (sub-μm) polishing stage no damage could be detected. This was confirmed by investigation of the surface roughness. Using a 2 μm x 2 μm template, the surface roughness measured by AFM (Atomic Force Microscopy) reduces typically by a factor of 10 (or larger) when the subsurface damage extension varied from ~1.5 μm (1 μm slurry) to negligibly small (sub-μm slurry).

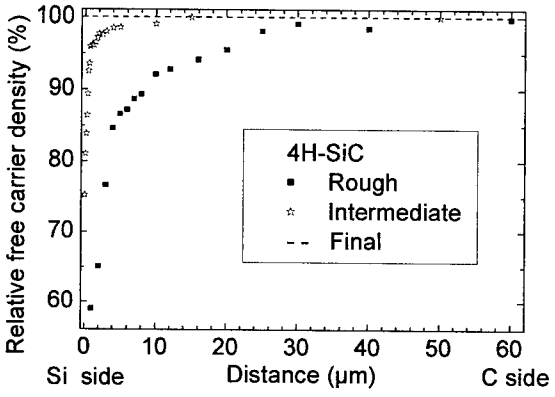


Fig. 1: Change in carrier concentration deduced from the analysis of micro-Raman spectra collected at various distance from the interface. 4H-SiC wafers (Si-face) polished with different slurries (see text).

3. Implantation damage

Ion implantation is the only technique available for selective area doping in SiC. Hydrogen implantation, as well, is necessary for "SiC On Insulator" (SiCOI) formation using the so-called Smart-cut® process [20]. In both cases, a complete recovery of the initial crystal properties is hard to get and implantation damage affects the final (implanted or transferred) SiC layer properties. A proper way to probe the crystal damage (and recovery) is again to look at the change in μR spectra.

In a perfect crystal, group-theory arguments predict only a very limited number of Raman-active modes (see Table 1). Implantation breaks the long-range order and renders (more or less) active, different (previously forbidden) modes. As usual, the activity of the new modes depend on the magnitude of the Fourier transforms of the perturbation potential ($V_{k'}$) which couples a previously Raman active mode with wavevector $U_i(k=0)$ and a "new" (activated) one with wavevector U_j ($k' \neq 0$).

Only the effect of small range perturbations has been considered in the work of Refs.7, 8. It induces a finite broadening and shift of the old Raman modes toward the lower (higher) frequencies, depending on whether the density of states (DOS) is larger at lower (or higher) frequency. A good example is shown in Fig.2.

We consider a series of 6H-SiC wafers implanted with hydrogen at a total dose of $1x10^{17}$ H^+ atom/cm^2 using a 1 MeV proton beam. From TRIM simulation, the projected range (implantation depth) is about 15 μm. This fluence is large enough to probe the crystal damage in the normal backscattering configuration, using a 514.5 nm laser wavelength and a 100 μm aperture in the confocal mode. For more details see Ref.21.

After implantation, all first-order modes shift and broaden. This is evidenced in Fig.2 for the A_1(LO) frequency (AO branch, x=0 in Table 1). Analyzing the data in the light of the theoretical model of Ref.7, we get the results displayed as full lines. Notice the good overall agreement. From the change in broadening parameter, we deduce [22] that upon implantation the density of line defects (mainly dislocations) has increased [22] by typically 20 %.

Not shown in Fig.2 are some discrepancies which are revealed after implantation. This is best seen in Fig.3. Comparing three different samples a) virgin, b) implanted and c) annealed we notice a strong background feature (activation of the 1-phonon DOS) which is manifested in

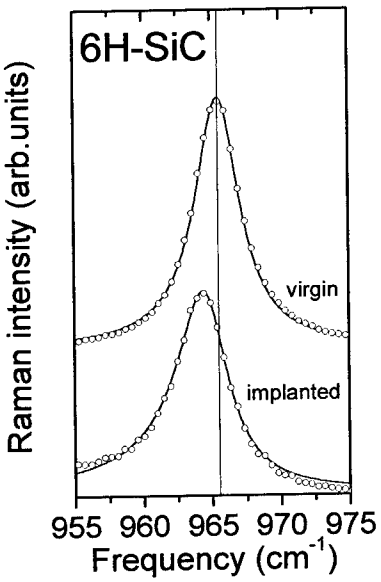


Figure 2: Comparison of experimental line shape (o) with theoretical results (full line) computed for the A_1(LO) mode of 6H-SiC.

Fig.3-b. This comes from the large matrix elements of the Fourier transform of the perturbation. Similar to the effect of isotopic disordering reported in the work of Ref.6, they couple all Raman active and inactive states together.

The 1-phonon DOS of SiC polytypes has been computed in the work of Ref.23. The main features are a large maximum around 860 cm^{-1} for the AO branch and a very strong maximum around 780 for the PO one. Next is a gap and, at lower energy, starting from about 610 cm^{-1} is the rise of the AA-DOS. All these features are revealed in Fig.3-b. The AO-DOS maximum is indicated by a star around 850 cm^{-1}, the PO-DOS maximum revealed as a shoulder superimposed on the base line of the standard lines, the AA-DOS appears below 620cm^{-1}. The original result is the appearance (in the gap of the 1-phonon DOS) of two gap modes. They occur at about 650 and 700 cm^{-1} and, in the work of Ref.24, have been associated with Si-vacancies perturbed by H atoms.

After one hour anneal at 950°C (see Fig.3-c) one local mode disappears, the second one remains. Also seen is a weak activation of the forbidden B_1 mode (AO branch) at 610 cm^{-1} (see Table 1).

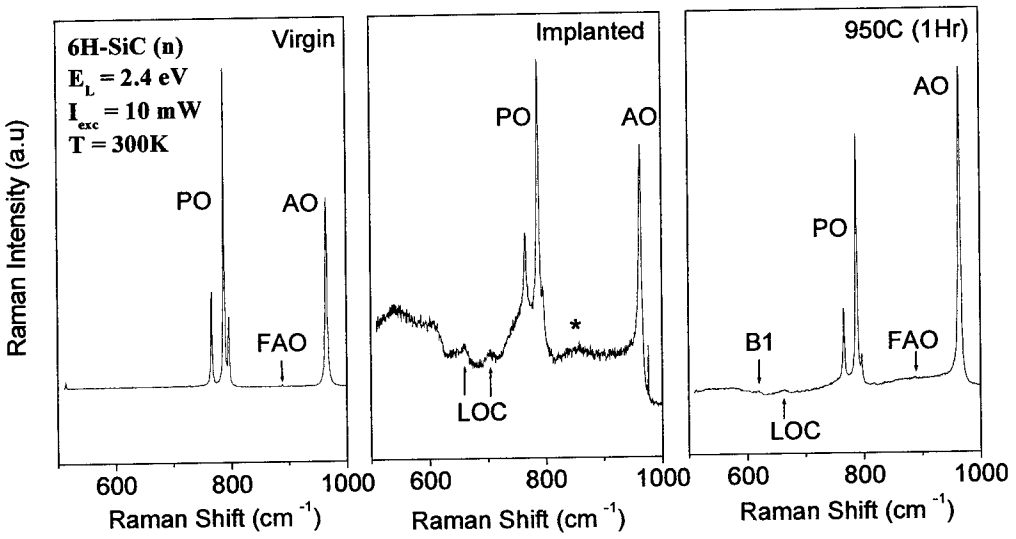


Figure 3: Comparison of virgin, implanted and 950° C annealed for one hour 6H-SiC

Conclusion

Micro-Raman spectroscopy is a sensitive tool to probe the effect of a) subsurface and b) implantation damage in SiC polytypes. The investigation of subsurface damage is based on the determination of the free carrier density profile in n-type material. The investigation of implantation damage calls for an investigation of the activation of the 1-phonon DOS, combined with an investigation of broadening and shift of the first-order Raman modes.

References

[1] O. Noblanc, E. Morvan, C. Dua and C. Brylinski, Mater. Sci. Forum 353-356 (2001) p.669.
[2] R. Weingärtner, M. Bickermann, D. Hofmann, M. Rasp, T.L. Straubinger, P.J. Wellmann and A. Winnacker, Mater. Sci. Forum 353-356 (2001) p.397.
[3] L. Masarotto, J.M. Bluet, M. Berenguer, P Girard and G. Guillot, Mater. Sci. Forum 353-356 (2001) p.393.
[4] A.Henry, I.G.Ivanov, A.Ellison and E.Janzén, Mat. Science and Eng. B 61-62 (1999), p.234.
[5] H.D. Nordby Jr., M.J. O'Loughlin, M.F. MacMillan, A.A. Burk Jr. and J.D. Oliver Jr., Mater. Sci. Forum 338-342 (2000), p. 173.
[6] S. Rohmfeld, M. Hundhausen and L. Ley, Mater. Sci. Forum 353-356 (2001) p.341.
[7] L.A Falkovsky, J.M. Bluet and J. Camassel, Phys. Rev. B 57 (1998), p. 11283; ibid. Phys. Rev. B 55 (1997), p. R14 697.
[8] J. Camassel, L.A Falkovsky and N. Planes, Phys. Rev B (2000), in press.
[9] D.W. Feldman, J.H. Parker Jr., W.J. Choyke and Lyle Patrick, Phys. Rev. 170 (1968), p.698; ibid.,Phys. Rev 173 (1968), p. 787.
[10] "Electrons and phonons in layered crystal structures", T.J. Wieting and M. Schlüter (eds), D. Reidel Publishing Company, Dordrecht, Holland (1979), p. 321.
[11] S. Nakashima and H. Harima, Phys. Stat. Sol. (a) 162 (1997), p. 39.
[12] J.A. Powell and D.J. Larkin, Phys. Stat. Sol. (b) 202 (1997), p. 529.
[13] W. Qian, M. Skowronski, G. Augustine, R.G. Glass, H.M. Hobgood and R.H. Hopkins, J. Electrochem. Soc. 142 (1995), p. 4290.
[14] M. Kanaya, H. Yashiro, N. Othani, M. Katsuno, J. Takahashi and S. Shinoyama, Mater. Sci. Forum 264-268 (1998), p. 359.
[15] W.C. Mitchel, J. Brown, D. Buckman, R. Bertke, K. Malalingham, F. D. Orazio, Pirouz Pirouz, H.J.R. Tseng, U.B. Ramabadran and B. Roughani, Mater. Sci. Forum 338-342 (2000), p. 841.
[16] P. Vicente, D. David and J. Camassel, Proc. EXMATEC, Heraklion (Crete), in press.
[17] M.V. Klein, B.N. Ganguly and P.J. Conwell, Phys. Rev. B 6 (1972), p. 2380.
[18] H. Harima, S. Nakashima and T. Uemura, J. Appl. Phys. 78 (1995), p. 1996.
[19] W.L. Faust and C.H. Henry, Phys. Rev. Lett. 17, (1966) p. 1265.
[20] L. DiCioccio, Y. LeTiec, C. Jaussaud, E. Hugonnard-Bruyère and M. Bruel, Mater. Sci. Forum 264-268, (1998), p. 765.
[21] H.W Kunert, T.P Maurice, T. Hauser, J.B. Malherbe, L.C. Prinsloo, D.J. Brink, L.A. Falkovsky and J. Camassel, Mater. Sci. Forum 353-356 (2001) p.275.
[22] L.A Falkovsky and J. Camassel, Physica B284-288 (2000), p.1145.
[23] M. Hofmann, A. Zywietz, K. Karch and F. Berchstedt, Phys. Rev B50 (1994), p.13401.
[24] Lyle Patrick and W.J. Choyke, Phys. Rev. B8 (1973), p.1660.

Materials Science Forum Vols. 353-356 (2001) pp. 341-344
© 2001 Trans Tech Publications, Switzerland

Line Broadening of Phonons in the Raman Spectra of Isotopically Disordered SiC

S. Rohmfeld[1], M. Hundhausen[1], L. Ley[1], N. Schulze[2] and G. Pensl[2]

[1] Institut für Technische Physik, Universität Erlangen-Nürnberg, Erwin-Rommel-Str. 1, DE-91058 Erlangen, Germany

[2] Institut für Angewandte Physik, Universität Erlangen-Nürnberg, Staudtstr. 7/A3, DE-91058 Erlangen, Germany

Keywords: ^{13}C Isotope, Line Broadening, Raman Spectroscopy

Abstract. We measured Raman spectra of several SiC polytypes (4*H*, 6*H*, 15*R*), which were isotopically enriched by substituting ^{12}C by the ^{13}C isotope. The lines of the different phonon modes of each polytype broaden for the isotopically enriched samples. Moreover, for a given isotope composition, the broadening varies for the different modes. We demonstrate experimentally that the broadening of the zone-center TO phonons due to atomic-mass disorder scales linearly with the phonon density-of-states as predicted in the framework of a mass perturbation theory. From the proportionality factor, we derive the absolute value of the phonon eigenvector of the carbon sublattice as $|e(\mathrm{C})| = 0.83 \pm 0.01$, in good agreement with pertinent *ab-initio* calculations.

1 Introduction

Isotope substitution affects the phonon frequencies that can be measured by Raman spectroscopy. We have used this effect in the past to study the incorporation of carbon from the crucible walls during the growth of silicon carbide (SiC) by the modified Lely technique [1]. In binary compounds such as SiC the isotopic substitution of one element can be used to derive interatomic force constants and phonon eigenvectors [2]. A third application of isotopic substitution is to study the effect of mass disorder on the phonon lifetime and thus on the Raman linewidth. Mass disorder provides an additional scattering mechanism for phonons that has been observed in diamond [3], germanium [4], and ZnSe [5]. Here, we study the effect of mass disorder on the phonon linewidth in SiC by partially replacing the carbon isotope ^{12}C by ^{13}C. The polytypes of SiC are an ideal material for such a study, since there exist a considerable number of Raman active zone-center phonons, which are related to each other via the backfolding concept [6].

2 Experimental details

Three SiC crystals (4*H*, 6*H*, 15*R*) were grown using the modified Lely technique (physical vapor transport method) [7] on corresponding Lely platelets of 6*H*- and 15*R*-SiC with natural carbon isotopic composition ($m_{\mathrm{C}} = 12.01\,\mathrm{u}$) acting as seed crystals. The source material was obtained by sintering a stoichiometric mixture of 99 % pure ^{13}C and silicon powder with natural isotopic composition ($m_{\mathrm{Si}} = 28.09\,\mathrm{u}$) in a graphite crucible. Due to the incorporation of ^{12}C from the crucible the crystals contain ^{13}C with a concentration x varying between 0 and 40 % [1]. Raman spectra were recorded at room temperature in a Raman microprobe setup in backscattering configuration using the 514.5 nm Ar-ion-laser line.

3 Results and Discussion

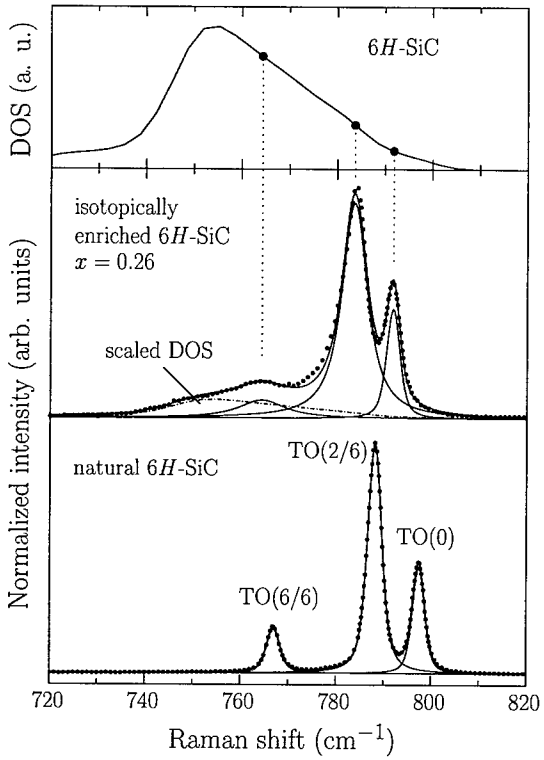


Fig. 1. Raman spectra of the TO modes of natural and isotopically mixed 6*H*-Si^{13}C$_x$ ^{12}C$_{1-x}$. The spectra are normalized to the amplitude of the TO(2/6)-mode. At the top the theoretical phonon density-of-states of 6*H*-SiC from Ref. [10] is shown. The solid circles mark the phonon density-of-states of the TO modes of 6*H*-SiC.

Raman spectra of folded transverse optic (TO) modes of natural and isotopically enriched 6*H*-SiC with a ^{13}C concentration of $x = 0.26$ are shown in Fig. 1. In the spectrum of the natural crystal (bottom) the three characteristic TO modes of 6*H*-SiC appear. The modes are labelled by their wave vector in the extended zone scheme [6]: n/m corresponds to $q = (n/m) \times (\pi/c)$, where c is the distance between two Si-C double layers. For the isotopically enriched sample, the three modes are shifted to lower frequencies. In addition, a broad structure around 750 cm^{-1} appears in the spectrum of the ^{13}C enriched sample. We attribute this structure to an effect of mass disorder, which breaks the translational invariance in the medium and thereby relaxes the (**q**=0)-conservation rule for Raman lines. A similar feature has been reported for isotopically disordered germanium [4]. Such structures roughly coincide with the phonon density-of-states. The most important effect to be discussed now is the broadening of the TO modes to a different degree in the isotopically enriched sample. We assume that additional scattering due to defects and impurities is negligible, since our samples are of good crystalline quality with a low defect density. Thus the additional contribution to the linewidth is ascribed to elastic scattering of phonons via mass fluctuations in isotopically disordered materials.

In the framework of a mass perturbation theory of the harmonic lattice dynamics developed by Tamura [8, 9] the mass-disorder-induced contribution $\Gamma_{\rm iso}$ to the phonon linewidth is given by the elastic scattering rate $\tau_{\rm iso}^{-1}$ which in turn depends on three factors: the relative mass variance g, the phonon density-of-states $\rho(\omega)$ at frequency ω of the Raman mode, and a relevant phonon eigenvector **e**:

$$\Gamma_{\rm iso} = \tau_{\rm iso}^{-1} = \frac{\pi}{6}\omega^2 g\,|\mathbf{e}|^4\,\rho(\omega) \quad . \tag{1}$$

Since the amount of Si isotopic disorder is constant, the relative mass variance for the carbon sublattice is relevant:

$$\begin{aligned} g_{\rm C}(x) &= \sum_i c_i \left(\frac{m_i - \overline{m}}{\overline{m}}\right)^2 \\ &= x\left(\frac{1-x}{12+x}\right)^2 + (1-x)\left(\frac{x}{12+x}\right)^2 \quad , \end{aligned} \tag{2}$$

where c_i is the relative fraction of the isotope with mass m_i and $\overline{m} = x \cdot m_{^{13}C} + (1-x) \cdot m_{^{12}C}$. Eq. (1) has the form of Fermi's Golden Rule in that the scattering rate τ_{iso}^{-1} of a phonon at frequency ω is – for fixed relative mass variance – directly proportional to the density-of-states $\rho(\omega)$ into which the phonon can scatter. The scattering rate is largest for phonons with frequencies where the phonon density-of-states is large. At the top of Fig. 1, the phonon density-of-states of $6H$-SiC is shown and the frequencies of the characteristic TO modes of $6H$-SiC are indicated by solid circles. The density-of-states and hence the scattering induced line broadening is smallest for the TO(0) mode, larger for the TO(2/6) and most obvious for the TO(6/6) mode as expected on the basis of Eq. (1).

In order to quantitatively test the linear dependence between linewidth and phonon density-of-states predicted by Eq. (1) we studied, in addition to $6H$-SiC, the Raman spectra of isotopically disordered $4H$-SiC and $15R$-SiC crystals. In this way, a wider range of phonon density-of-states is covered. All samples have the same ^{13}C concentration of $x = 0.26$ corresponding to a mass variance of $g_C(x = 0.26) = 1.28 \cdot 10^{-3}$ as calculated with Eq. (2). The phonon density-of-states contribution, describing the broad structure around $750\,cm^{-1}$, was calculated from the ^{12}C density-of-states using the relation $\omega^2 \propto \mu^{-1}$, in which the square of the frequency is proportional to the inverse of the reduced mass $\mu = (1/\overline{m}_C + 1/m_{Si})^{-1}$, where $\overline{m}_C$ is the average mass of carbon atoms in a mixture of ^{12}C and ^{13}C ($^{13}C_x\,^{12}C_{1-x}$). The scaling factor of this recalculated phonon density-of-states was used as fit parameter and the result is shown as the dashed-dotted line in Fig. 1. The contribution Γ_{iso} to the linewidth has been obtained by fitting the spectra with Voigt profiles in which the Gaussian width was kept fixed according to the experimental resolution ($1.8\,cm^{-1}$). In order to account for the contribution of line broadening due to anharmonic decay and Si isotopic disorder, respectively, the linewidth Γ_0 obtained for samples with natural composition has been subtracted.

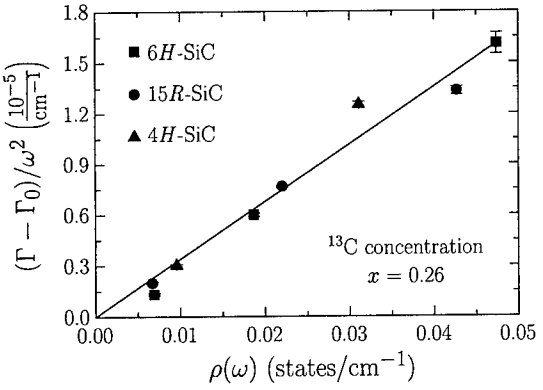


Fig. 2. Linewidths divided by the square of the phonon frequency of the characteristic modes of different SiC polytypes plotted as a function of the phonon density-of-states at the corresponding mode frequencies. The solid line is a linear regression to the experimental data.

In Fig. 2 the values for Γ_{iso}/ω^2 obtained this way are plotted versus the phonon density-of-states as calculated in Ref. [10]. The linear dependence between Γ_{iso} and $\rho(\omega)$ is clearly maintained over one order of magnitude in both quantities as demonstrated by the linear regression to the experimental data indicated by the solid line in Fig. 2. Hence, our data verify the role of the phonon density-of-states $\rho(\omega)$ for the mass-disorder induced contribution to the phonon linewidth as expressed in Eq. (1). Under the assumption that the absolute value of the eigenvectors $|e_C|$ is constant for all TO modes, $|e_C|$ can be calculated from the slope of the linear regression. For the TO branch this assumption is in good conformity with *ab-initio* calculations [11], where the absolute values of the eigenvector do not vary by more than 2 %. We obtain $|e_C| = 0.83 \pm 0.01$, a value which is in good agreement with those of *ab-initio* calculations yielding $|e_C| = 0.84$ at the Γ point and $|e_C| = 0.86$ at the L point. This agreement further supports the theory of Tamura to describe the line broadening in isotopically disordered semiconductors.

4 Conclusion

We have shown that the width of Raman lines of isotopically disordered SiC depends on the phonon frequency. This effect can be quantitatively understood in the framework of a simple scattering theory as formulated by Tamura. In this theory, the elastic scattering by mass fluctuations contributes to the linewidth. The corresponding scattering rate is predicted to be proportional to the density of final phonon states. Our results confirm this proportionality between linewidth and phonon density-of-states. The polytypes of SiC are an ideal testing ground, since the accessible Raman active modes cover a range of phonon density-of-states that is larger than usually found in other materials. Furthermore, the analysis of the line broadening in different polytypes yields an absolute value of the eigenvector of the carbon sublattice which is in agreement with *ab-initio* calculations.

Acknowledgments

We would like to thank A. Zywietz and F. Bechstedt for the digital data of the phonon density-of-states from Ref. [10]. This work was supported by the German Science Foundation in the framework of Sonderforschungsbereich 292 (MEKOS).

References

[1] S. Rohmfeld, M. Hundhausen, L. Ley, N. Schulze, and G. Pensl, Mater. Sci. Forum **338-342** (2000), p. 579.

[2] F. Widulle, T. Ruf, O. Buresch, A. Debernardi, and M. Cardona, Phys. Rev. Lett. **82** (1999), p. 3089.

[3] K. C. Hass, M. A. Tamor, T. R. Anthony, and W. F. Banholzer, Phys. Rev. B **45** (1992), p. 7171.

[4] H. D. Fuchs, P. Etchegoin, M. Cardona, K. Itoh, and E. E. Haller, Phys. Rev. Lett. **70** (1993), p. 1715.

[5] A. Göbel, T. Ruf, J. M. Zhang, R. Lauck, and M. Cardona, Phys. Rev. B **59** (1999), p. 2749.

[6] D. W. Feldman, J. H. Parker, Jr., W. J. Choyke, and L. Patrick, Phys. Rev. **173** (1968), p. 787.

[7] N. Schulze, D. L. Barrett, and G. Pensl, Appl. Phys. Lett. **72** (1998), p. 1632.

[8] S. Tamura, Phys. Rev. B **27** (1983), p. 858.

[9] S. Tamura, Phys. Rev. B **30** (1984), p. 849.

[10] M. Hofmann, A. Zywietz, K. Karch, and F. Bechstedt, Phys. Rev. B **50** (1994), p. 13401.

[11] K. Karch, P. Pavone, W. Windl, O. Schütt, and D. Strauch, Phys. Rev. B **50** (1994), p. 17054.

Materials Science Forum Vols. 353-356 (2001) pp. 345-348
© 2001 Trans Tech Publications, Switzerland

Micro-Raman and Photoluminescence Study on n-type 6H-SiC

Z.C. Feng[1], S.J. Chua[1,2], G.A. Evans[3], J. W. Steeds[3], K.P.J. Williams[4] and G.D. Pitt[4]

[1] Institute of Materials Research & Engineering, 3 Research Link, Singapore 117602, Singapore

[2] Centre for Optoelectronics, Dept. of Electrical & Computer Engineering, National University of Singapore, Singapore 119260, Singapore

[3] H.H. Wills Physics Laboratory, University of Bristol, Bristol BS8 1TL, UK

[4] Renishaw plc, Old Town, Wotton-under-Egde, Gloucestershire, GL12 7DW, UK

Keywords: 6H-SiC, Microscope, n-Type Doping, Photoluminescence, Raman Scattering

Abstract Combined UV Raman and photoluminescence (PL) measurements have been performed on a series of N-doped n-type 6H-SiC bulk wafers. The first order Raman transverse optical (TO) and longitudinal optical (LO) phone modes, the 2.9-eV near edge PL band, and the 2.2-eV defects-related band, can be detected at same runs at room temperature by using a high sensitive microscopic system. Their relative intensity ratios are varied with N-doping levels. Weak folded phonon modes and variations with N-dopings are observed, which might be related to the structural variation near the surface.

Introduction

Research and development of SiC materials, devices and applications have gained much attention in recent years [1-4]. Bulk single crystal wafers of 6H-SiC (since 1991) and 4H-SiC (since 1994) have been commercially available. The demand for good quality SiC wafers is increasing. A convenient technique of characterization is needed to promote these demands, in particular for industrial production. This technique should be non-destructive, performed at room temperature (RT), easily operated, efficient to provide more information, and fast for quality control. Here we present a method to characterize the SiC wafer materials by the combined UV Raman and photoluminescence (PL) measurement via a high sensitivity microscopic system. A series of N-doped n-type 6H-SiC bulk wafers are studied. Interesting results are obtained and discussed.

Experiment

Several commercially purchased 6H-SiC wafers from CREE company were involved in this study. They are nitrogen doped n-type with different values of resistivity and concentration, see Table-I. A piece of un-doped 6H-SiC wafer from II-VI company was also used for comparative measurements.

Table-I Sample information

Sample no.	6H1	6H3	6H5	6H7	6H9
Resistivity (Ω-cm)	0.032	0.057	0.087	0.147	0.33
Doping concentration (x 10^{18} cm^{-3})	6.56	2.28	1.05	0.40	0.11

Two sets of Renishaw Raman microscope systems were used. One is a visible micro-Raman system under a 488 nm excitation from an Ar ion laser, with a resolution ability of ~3 cm^{-1}. Another one is a UV micro-(μ-) Raman-PL system under a 325 nm excitation from a HeCd laser, with a resolution ability of ~8 cm^{-1}. All the measurements in this study were performed at RT.

Experimental Results

UV excited combined PL-Raman spectra

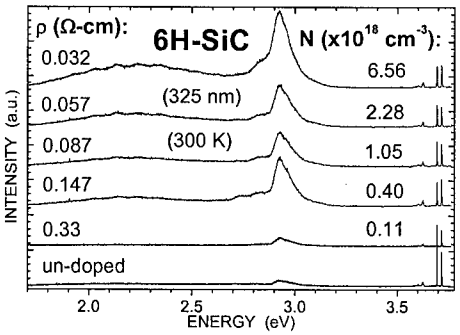


Figure 1. Combined micro-PL-Raman spectra of bulk 6H-SiC, one un-doped and five N-doped with different doping levels or resistivity values, listed in the figure. Spectra were measured at RT and under excitation of 325 nm.

Fig. 1 shows combined UV μ-Raman-PL spectra from a un-doped 6H-SiC, for comparison, and five n-type 6H-SiC wafers with values of resistivity and N-doping concentration listed in Table-I and Fig. 1. Each spectrum consists of sharp lines beyond 3.5 eV which are 6H-SiC characteristic Raman lines [5,6] excited from 325 nm, a band with a peak at 2.93 eV which is the RT band edge luminescence from 6H-SiC and its phonon replica at 2.83 eV as the shoulder in the low energy side [7,8], and a broad band centred at 2.2 eV in the range of 1.7-2.7 eV, which is related to defects in 6H-SiC [8]. Raman and PL features are thus measured at a single run for each SiC sample.

UV excited 1st and 2nd Raman scattering

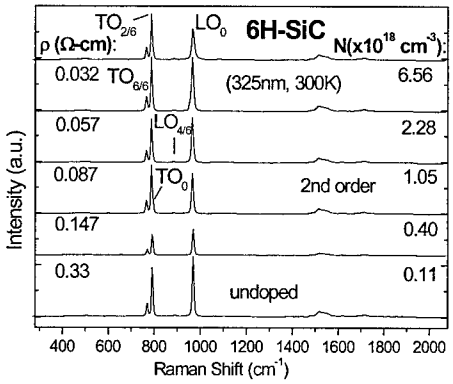


Figure 2. UV 325 nm excited 1st and 2nd order Raman spectra of six 6H-SiC wafers.

Fig. 2 shows Raman spectra of six 6H-SiC wafer, under UV 325 nm excitation, between 300-2000 cm^{-1}. Three strong 1st order Raman modes from 6H-SiC crystal are seen for all samples: LO_0 at ~965 cm^{-1}, $TO_{2/6}$ at ~788 cm^{-1} and $TO_{6/6}$ at ~767 cm^{-1} [5,6,8]. The 2nd order features are spreading over 1400-2000 cm^{-1}.

Visible excited 1st and 2nd Raman scattering

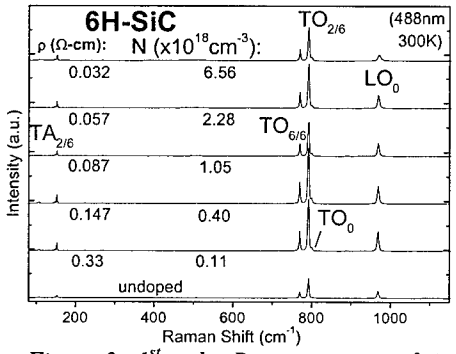


Figure 3. 1st order Raman spectra of six 6H-SiC wafers under visible 488 nm excitation.

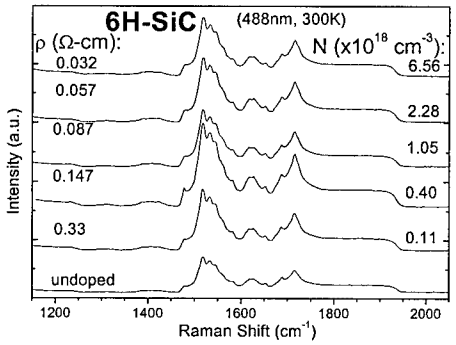


Figure 4. 2nd order Raman spectra of six 6H-SiC wafers under 488 nm excitation.

Figs. 3 and 4 shows the 1st and 2nd order Raman spectra of six 6H-SiC wafers, respectively, under visible 488 nm excitation. Because of higher resolution ability than that in the case of UV excitation in Fig. 2, the 1st order Raman modes of LO_0, $TO_{2/6}$ and $TO_{6/6}$ are seen narrower and better separated. A transverse acoustic mode, $TA_{2/6}$, is also observed at ~150 cm^{-1}. The 2nd order Raman features seem variable little with the doping level.

Discussion

The 2.93 eV band in Fig. 1 is due to the free-to-band (FB) transitions involving nitrogen, FB_N, with a 100 meV phonon side band in its low energy side [7,8]. Its relative intensity with respect to the 1st order Raman features is increasing with an increase of N-doping concentration, accompanying with also an increase of the 2.2 eV defects-related band intensity. But the peak energy of the F_{BN} band is almost unchanged with the variation of N-doping level. Further line shape analyses on the Raman modes and the correlation with the N-doping concentration are in process.

When the spectral data between 100-700 cm^{-1} of Fig. 3 were magnified, some further features can be seen, as shown in Fig. 5. Besides a doublet $TA_{2/6}$ mode which was marked in Fig. 3, another doublet $TA_{4/6}$ at 222 and 242 cm^{-1}, a singlet $TA_{6/6}$ at ~266 cm^{-1} and a doublet $LA_{4/6}$ at 504 and 514 cm^{-1} [5,6] can be observed. A broad feature appears in 470-530 cm^{-1} and is developed with increasing the N-doping level. When UV excited Raman spectra in Fig. 2 are magnified, a similar broad feature is observed also. It is arisen from the amorphous Si-Si vibration, indicating a slight damage of crystalline structure from the heavy N-doping.

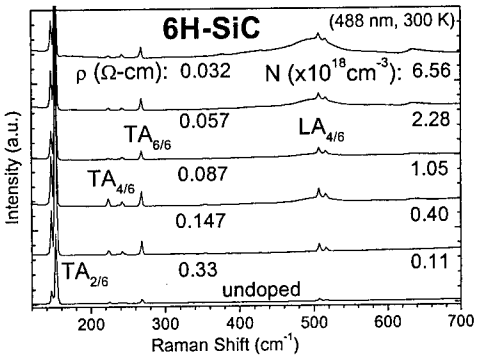
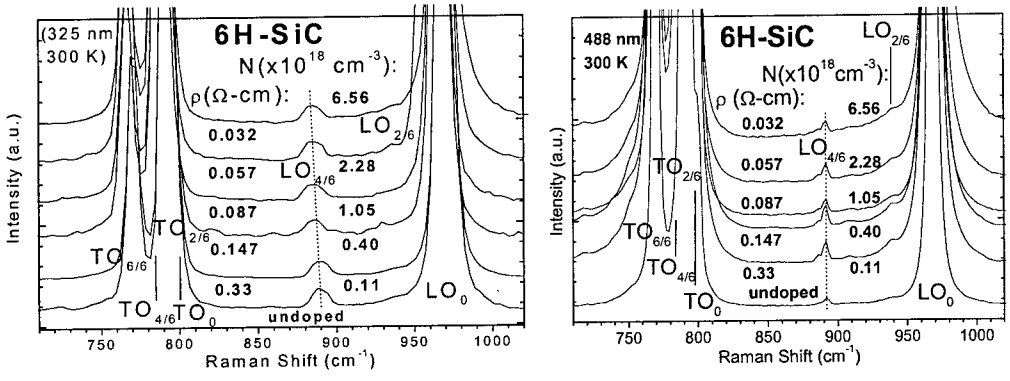


Figure 5. Raman features of folded acoustic modes and amorphous band of six 6H-SiC wafers.



(a) (b)

Figure 6. Observation of the weak $LO_{4/6}$ mode under excitation of (a) 325 nm and (b) 488 nm. Dot lines indicate no shift in (b) and a shift of its central frequency under 325 nm excitation.

When we magnified spectra in Figs. 2 and 3, as shown in Figs. 6 (a) and (b), respectively, weak mode $LO_{4/6}$ at ~890 cm^{-1} is observed clearly, which was observed under a deep UV 266 nm excitation and very weak under 488 nm excitation, previously in the literature [9]. This mode has

been shown with a distinct resonance at deep UV excitation region of 4.25 eV, i.e. 292 nm [10]. Here we have observed this mode under 325 and 488 nm excitation for all samples with different N-dopings, owing to the high sensitivity of the used instruments. It is interesting to find that the $LO_{4/6}$ mode frequency is almost unchanged with different N-dopings under the 488 nm excitation Raman measurements. However, under the UV 325 nm excitation, this mode became very broad, beyond the cause due to the instrument resolution ability. Also, its central frequency moves toward to the low energy side by an amount of about 3 cm^{-1} with an increase of the N-dopings. Because the laser light penetration depth in SiC for the case of UV 325 nm is much shallower than that of visible 488 nm [11], the UV 325 nm light probes mainly the near surface region of the sample. The above shift may predict the structural variations, due to perhaps strains [12], in the near surface region because of impurity doping, or the energy dependent bond-Raman polarizabilities [9,10]. The detailed physical reason of this interesting phenomenon is under investigation.

Conclusion

Visible micro-Raman and combined UV micro-Raman-PL measurements have been performed on a series of N-doped n-type 6H-SiC bulk wafers. The 1st order Raman TO and LO phone modes, the 2.9-eV near edge PL band, and the 2.2-eV defects-related band, can be detected at same runs at RT. Their relative intensity ratios are varied with N-dopings. Weak folded phonon modes and variations with N-dopings are observed, predicting a structural variation near surface. Correlations between the SiC material properties and these Raman-PL spectral features can be established through further spectral analyses and ratio comparisons. These results have primarily shown that combined UV micro-Raman-PL spectroscopy can provides a good way for the convenient characterization of indirect band gap SiC materials. Further work is in process.

Acknowledgement: to Mr. Wenyi Chang for his technical assistance in some graphic preparation.

References

[1] J. A. Powell, P. Pirouz and W. J. Choyke, in *Semiconductor Interfaces, Microstructures and Devices: Properties and Application*, ed. Z. C. FENG, Institute of Physics Pub., Bristol (1993) p. 257.
[2] W. J. Choyke, H. Matsunami and G. Pensl ed., *Fundamental Questions and Applications of SiC*, special issue, Phys. Stat. Sol. (b) 202, No. 1 and (a) 161, No. 1, (1997).
[3] M. M. Anikin, P. A. Ivanov, A. A. Lebedev, S. N. Pytko, A. M. Strel'chuk and A. L. Syrkin, in *Semiconductor Interfaces and Microstructures*, ed. Z. C. FENG, World Scientific Pub., Singapore (1992) p. 280.
[4] Y. S. Park ed., *SiC Materials and Devices*, Volume 52 of *Semiconductors and Semimetals*, ed. R. K. Willardson and R. Weber, Academic, San Diego (1998).
[5] D. W. Feldman, J. H. Parker, Jr., W. J. Choyke and L. Patrick, Phys. Rev. 170 (1968), p. 698; and 173 (1968), p. 787.
[6] S. Nakashima and H. Harima, in [2], Phys. Stat. Sol. (a) 162 (1997), p. 39.
[7] M. Yoganathan, W. J. Choyke, R.P. Devaty and P.G. Neudeck, J. Appl. Phys. 80 (1996), p. 1763.
[8] Z. C. Feng, S. J. Chua, K. Tone and J. H. Zhao, Appl. Phys. Lett. 75 (1999), p. 472.
[9] T. Tomita, S. Saito, M. Baba, M. Hundhausen, T. Suemoto and S. Nakashima, Mat. Sci. Forum 338-342 (2000), p. 587.
[10] R. Püsche, S. Rohmfeld, M. Hundhausen and L. Ley, Mat. Sci. Forum 338-342 (2000), p. 583.
[11] W. J. Choyke, Z. C. Feng and J. A. Powell, J. Appl. Phys. 64 (1988), p. 3163.
[12] Z. C. Feng, W. J. Choyke and J. A. Powell, J. Appl. Phys. 64 (1988), p. 6827.

Materials Science Forum Vols. 353-356 (2001) pp. 349-352
© 2001 Trans Tech Publications, Switzerland

Low-Frequency Vibrational Spectroscopy in SiC Polytypes

B. Pajot[1], C. J. Fall[2], J.L. Cantin[1], H.J. von Bardeleben[1], R. Jones[2], P.R. Briddon[3] and F. Gendron[4]

[1] Groupe de Physique des Solides, UMR 7588 du CNRS, Universités Denis-Diderot, 2 Place Jussieu, FR-75251 Paris Cedex 05, France

[2] School of Physics, University of Exeter, Stocker Road, Exeter EX4 4QL, UK

[3] Department of Physics, University of Newcastle, Newcastle upon Tyne NE1 7RU, UK

[4] LMDH, UMR 7603 du CNRS, UPMC, 4 place Jussieu, FR-75252 Paris Cedex 05, France

Keywords: 15R-SiC, 6H-SiC, Acoustical Phonons, Infrared Absorption, Local Vibrational Modes

Abstract An IR absorption study of p- and n-type SiC samples below the optical phonon bands shows the coexistence of impurities and defect local modes with folded acoustic modes of the SiC polytypes. The local mode results are compared with *ab initio* calculations and the acoustic modes with Raman scattering results.

Introduction

The 6*H* polytype is easily obtained when growing SiC crystals. It is characterised by a *ABCACB* stacking sequence of the atomic layers along the (0001) *c* axis [1]. The symmetry of the second nearest neighbours with respect to a given lattice site of this polytype allows one to distinguish between one hexagonal site (*h*) and two distinct cubic sites, noted k_1 and k_2, differing by the nature of the sites of the first neighbours. Polytypism has consequences on the electronic properties of dopants as the same dopant atom on different sites can display different ionisation energies [2]. In 6*H* SiC, for instance, donor levels at 81, 138 and 142 meV are associated with a N donor atom located on C_h and C_{k1} and C_{k2} sites, respectively [3]. The same is in principle also possible for the local vibrational modes (LVM's) of impurity and dopant atoms.

Experimental information on the LVM's due to impurity and dopant atoms in SiC is scarce and only results on N and Al in 4*H* SiC have so far been reported [4].

As the height of the 6*H* unit cell is about six times that of the 3*C* zinc blende form of SiC, an approximation of the 6*H* phonon dispersion curve is obtained by a 6-folding the dispersion curve of the 3*C* form in the first Brillouin zone. One of the results of this folding is the existence of low-frequency folded acoustical (FA) modes at zero phonon wave vector q_z. These FA modes have been extensively studied by Raman scattering [5,6], but the IR activity of some of them has also allowed absorption measurements [7]. This property is of course not limited to 6*H* SiC and the IR absorption of FA modes has been reported in 4*H*, 8*H* and 15*R* SiC polytypes [8,9] and extended to higher order polytypes [10]. These modes are observed in the same spectral region as some LVMs and it can be of interest to differentiate the two kinds of absorption.

We have investigated the IR absorption of 6*H* and 15*R* SiC samples between room and liquid helium temperatures in the low-frequency transparency range of SiC below about 730 cm^{-1} (~ 90 meV). The experimental results on the LVMs are compared with those obtained from *ab initio* calculations. The results on the TA phonon modes are compared with detailed reports on the Raman investigation of SiC polytypes [5,6]

Results

A Fourier transform spectrometer (BOMEM DA3+) was used for the absorption measurements, with the samples located in the He-gas-filled sample compartment of an Oxford Instrument CF204 continuous flow optical cryostat. The observation conditions were impaired by interference fringes

due to the samples. We tried to remove the fringes without wedging the samples or decreasing the spectral resolution by removing localised data points of the interferogram mainly responsible for the fringes. The latter procedure can however add fringes in initially unfringed regions and it does not gives satisfactory results in spectral regions where the refractive index shows dispersion.
The 15*R* SiC:B sample was grown by the Lely method and the 6*H* SiC samples, obtained from CREE were grown by a modified Lely method. Some of them were bulk Al- or N-doped and others were homoepilayers (p/n and n/p). With the set-up and the samples used, the electric vector ***E*** of the radiation is approximately perpendicular to the *c* axis of the samples.

We present first the results attributed to local modes, followed by those on acoustical phonons.
In almost all the samples, a LVM is observed near 625 cm^{-1} at 6 K, with a full width at half maximum (FWHM) near 5 cm^{-1}. It has also been reported in 4*H* SiC and attributed to N_C [4]. This observation is related to the nearly ubiquitous presence of residual nitrogen in SiC. Frequency differences within 1 cm^{-1} are measured between p-type 15*R* SiC and 6*H* SiC and between p-type 6*H* SiC and n-type 6*H* SiC, but the frequency accuracy for this LVM is about ± 0.5 cm^{-1}. At room temperature, this LVM shifts to 623.5 cm^{-1}, in agreement with the results of [4]. Using the calibration coefficient of this LVM in 4*H* SiC given in [4], the residual N concentration in the SiC samples investigated here is in the 2 - 5 × $10^{17}/cm^3$ range. If truly localised, the frequency of this N mode is expected to depend weakly on the nature of the polytype as the first Si neighbours keep the same symmetry, and also on the charge state of the N atom. Experiments on better samples are needed to say if the differences observed are significant. No equivalent of the mode at 464 cm^{-1} reported in [4] in 4*H* SiC:Al is observed in the 6*H* SiC:Al sample measured in the present study.
In the B-doped 15*R* sample, lines are observed at 704, 711, 718 and 722 cm^{-1} at 6 K with a FWHM near 2 cm^{-1} or less (Fig. 1). They are attributed to LVMs from their frequency shifts at room temperature. The lines at 711 and 722 cm^{-1} are only observed in this B-doped sample. This point and the fact that their relative intensities roughly match the relative isotopic abundance of ^{11}B- and ^{10}B (~ 4/1) lead us to attribute these lines to a B-related centre. Moreover, a simple harmonic model based on the ratio of the modes at 625 (attributed to ^{14}N) and 711 cm^{-1} predicts for the atom responsible of the latter mode a mass near 11 amu. The isotope shift between ^{11}B and ^{10}B is smaller than expected within the crude model used, but similar trends are usually found. A vibrational mode near 700 cm^{-1} has been reported in 6*H* SiC implanted with B and H from a localised phonon replica of a luminescence line [11] and this value is close to the ones reported here.

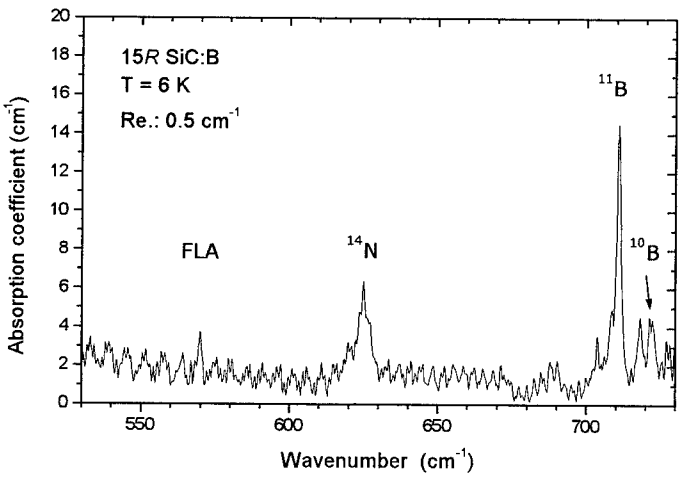


Fig. 1: LVM's due to N and B in 15*R* SiC. The absorption from the TO phonons is subtracted. The small peak noted FLA is due to a folded LA phonon. Other lines above 700 cm^{-1} are left unassigned

Ab initio calculations of the frequencies of the LVMs of N, B and Al substituting for C or Si in 3*C* and 2*H* (the wurtzite form) SiC have been performed within local density functional theory. With the parameters obtained, total energy calculations yield equilibrium lattice constants within 1% of the experimental values. A substitutional impurity atom is placed in a supercell of 64 (72) atoms for 3*C* (respectively 2*H*). Relaxation of the atoms surrounding the impurity is allowed while retaining the T_d (respectively C_{3v}) symmetry and neglecting any possible Jahn-Teller distortion. LVM frequencies are obtained from the second derivatives of the total energy with respect to the atomic displacements of the impurity atoms and its nearest neighbours. Only a summary of the results is given here. $^{14}N^0$ on a C site gives LVM's at 626 (3*C*) and 603 cm^{-1} (2*H*), reasonably close to the experimental value. The predicted frequencies of the LVMs of on centre B on a Si site are in the 600-630 cm^{-1} range, but B modes resonant with the optical phonon DOS are also predicted. The former frequency range is significantly lower than the experimental values reported here and it shows the limits of the simple harmonic model. A relaxation of B_{Si} from the C atom has been evidenced from EPR/ENDOR measurements [12]. The effect of this distortion on the calculated frequencies is presently investigated as it could be an explanation of the differences observed. One can also wonder if the LVMs observed near 700 cm^{-1} are due to isolated B. All the modes of Al on a Si site are predicted to be resonant with the optical phonon DOS and this seems to be consistent with the fact that no Al-related LVM is detected. The frequency changes of the LVM's between the neutral and ionised states of the impurities have been calculated for 2*H* SiC: they are larger in the ionised charge state with differences near 10 and 30 cm^{-1} for B and N, respectively.

Sharp vibrational lines are detected in the samples at lower frequencies. These lines are due to IR-allowed acoustical modes, and their frequencies are characteristic of the folding of the phonon Brillouin zone of the polytype [5,6]. Fig. 2 shows the absorption at 6K of a pair of lines due to FA phonons in 15*R* SiC for a folding $q/q_B = 2/5$ of the Brillouin zone of 3*C* SiC. With a resolution of

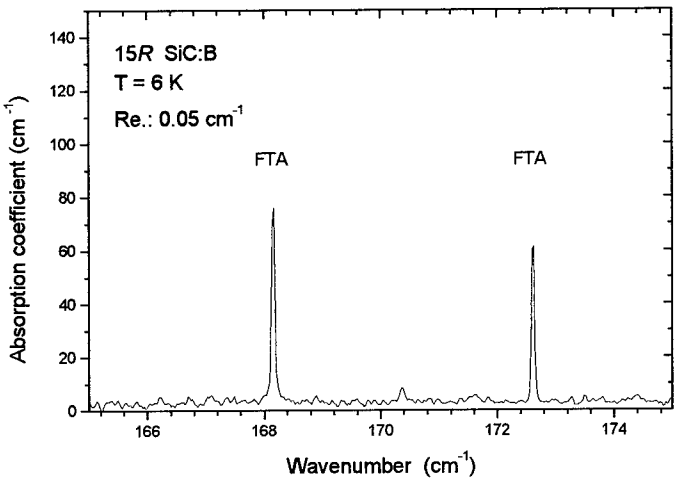


Fig. 2: Absorption of folded TA phonons modes in 15*R* SiC (the atoms vibrate perpendicular to the *c* axis). The peak intensities are resolution-limited. With a higher resolution, the low-energy line saturates. The weak line between the FTA lines is due to residual water vapour.

0.013 cm^{-1}, the FWHM of the high-energy line of Fig. 2 at 172.613 cm^{-1} is 0.028 cm^{-1} while the FWHM of the low-energy line is estimated to be less than 0.03 cm^{-1}.

The characteristics of the FA phonons lines observed in the present study are given in Table 1. The sharpness of the FTA modes has already been pointed out from Raman scattering measurements at 300 K and attributed to a limited number of decay channels for the FTA modes compared to the FTO modes [6]. Here, an increase with frequency of the FWHMs is observed: they are ≤ 0.06 cm^{-1}

Table 1 : Frequencies (cm^{-1}) of the IR-allowed folded transverse (FTA) and longitudinal (FLA) acoustic modes measured at 6 K in the present work , compared with the Raman scattering data (in brackets) at room temperature [6]

Polytype	q/q_B	FTA		FLA
6*H*	4/6	236.08 [236]	240.36 [241]	506.01 [504]
15*R*	2/5	168.15 [167]	172.61 [173]	[331, 337]
	4/5	255.23 [255]	256.82 [256]	569.95 [569, 577]

for the IR active FTAs with the highest frequencies (precise values cannot be given because of saturation in the samples investigated); for the IR active FLAs reported here, they are 0.2 and 0.4 cm^{-1} in 6*H* and 15*R* SiC, respectively. In 4*H* SiC, a FLA mode is observed by Raman scattering at 610 cm^{-1} [5]. It is the origin of the vibrational absorption reported at this frequency in [4] and left unassigned at that time. In this polytype, the IR absorption of a FTA mode has also been reported at 266 cm^{-1} [9]. The Raman scattering of other acoustic modes is observed in 6*H* and 15*R* SiC, but they are either not IR active [5,6] or they could not be observed here under good conditions with the geometry used. Additional lines are also observed here in some 6*H* SiC samples in the vicinity of the FTA mode at 240 cm^{-1} and they could be due to stacking disorder [6].

Summary

In SiC polytypes, N_C gives a LVM near 625 cm^{-1} that depends weakly on the polytype and on the type of the site. This frequency is correctly predicted by *ab initio* calculations. In one SiC:B sample, one LVM near 710 cm^{-1} could be related to boron, but the nature of the related centre is still not clear. Lines due to IR-allowed folded acoustical phonons are reported and some of them are among the sharpest vibrational features observed in a semiconducting material.

References

[1] W. van Haeringen, P. A. Bobbert, and W. H. Backes, phys. stat. sol. (b) 202 (1997), p. 63.
[2] M. Ikeda, H. Matsunami, and T. Tanaka, J. Lumin. 20 (1979), p. 111, and references therein.
[3] W. Suttrop, G. Pensl, W. J. Choyke, R. Stein, and S. Leibenzeder, J. Appl. Phys. 72 (1992), p. 3708.
[4] W. Götz, A. Schöner, W. Suttrop, G. Pensl, W. J. Choyke, R. A. Stein, and S. Leibenzeder, Mater. Sci. Forum 143-147 (1994), p. 69.
[5] D. W. Feldman, J. H. Parker, Jr., W. J. Choyke, and L. Patrick, Phys. Rev. 173 (1968), p. 787.
[6] S. Nakashima and H. Harima, phys. stat. sol; (a) 162 (1997), p. 39, and references therein
[7] L. Patrick, Phys. Rev. 167 (1968), p. 809.
[8] G. B. Dubrovskii and E. I. Radovanova, Sov. Phys. Solid State 14 (1973), p. 2127.
[9] K. Satoh, Y. Harada, H. Nakata, and T. Ohyama, Mater. Sci. Engin. B56 (1998), p. 72.
[10] G. B. Dubrovskii and A. A. Lepneva, Sov. Phys. Sol. State 25 (1983), p. 1330.
[11] C. Peppermuller, A. Schoner, K. Rottner, and R. Helbig, Diam. Relat. Mater. 6 (1997), p. 1321.
[12] T. Matsumoto, O. G. Poluektov, J. Schmidt, E. N. Mokhov, and P. G. Baranov, Phys. Rev. B 55 (1997), p. 39.

Materials Science Forum Vols. 353-356 (2001) pp. 353-356
© 2001 Trans Tech Publications, Switzerland

Free Carrier Diffusion in 4H-SiC

P. Grivickas[1], A. Martinez[1], I. Mikulskas[2], V. Grivickas[2], R. Tomašiunas[2], J. Linnros[1] and U. Lindefelt[1,3]

[1] Department of Solid State Electronics, Royal Institute of Technology, Electrum 229, SE-16440 Kista-Stockholm, Sweden

[2] Institute of Materials Science and Applied Research, Vilnius University, Sauletekio 10, LT-2054 Vilnius, Lithuania

[3] ABB Corporate Research, SE-721 78 Västerås, Sweden

Keywords: Band-Gap Narrowing, Degenerated Statistics, Transient Grating

Abstract. The diffusion coefficient of free carriers in 4H-SiC is experimentally determined over a large injection range. For this purpose two transient gratings techniques are utilized to detect light-induced free-carrier diffusive motion employing the changes in the absorption coefficient or in the refractive index, respectively. At high-injections a smooth reduction of the ambipolar diffusivity is observed with a following sharp increase above $3 \cdot 10^{18}$ cm^{-3}. Theoretical calculations based on dynamic band-gap narrowing in the former case and degenerated statistics in the latter case yields a reasonable agreement with the experimental data.

Introduction. During recent years the quality of silicon carbide (SiC) has gradually increased stimulating successful investigations of both electrical and material properties. The free-carrier diffusion coefficient, however, remains one of the poorest explored ones even though it is a key parameter governing e.g. the collection efficiency of a *p-n* junction and the plasma behavior in power devices. Recently, the injection dependence of the carrier diffusivity has been explored of low-doped, epitaxial 4H-SiC by a Fourier transient grating (FTG) technique, covering the whole transition region from minority-carrier to ambipolar diffusion [1]. At higher injections, $\Delta n = \Delta p = 3 \cdot 10^{16}$ - $3 \cdot 10^{17}$ cm^{-3}, it was experimentally observed that the ambipolar diffusivity D_a gradually reduces. Such behavior, however, is not expected from basic thermodynamic relations which predict a constant ambipolar diffusivity when non-degenerated Boltzmann statistics is applicable. Moreover, at very high injections degenerated Fermi-Dirac statistics take place and the average energy per carrier should sharply increase. Thus, an accelerating $D_a \sim \Delta n^{2/3}$ dependence is anticipated [2].

In the current work, in order to study the carrier diffusivity behavior at high-injections in 4H-SiC, we have extended our measurements up to a level of $5 \cdot 10^{18}$ cm^{-3}. The results were obtained by two light-induced transient grating (TG) techniques based on detection of free-carriers by two different effects: i) a refraction index difference - Holographic TG (HTG) technique [3] and ii) free carrier absorption - previously mentioned FTG technique [1]. In this work we also provide theoretical calculations that can account in appropriate way for the many-body interactions and the change of the carrier statistics that affect the injection dependence of the carrier diffusivity.

Samples and experiment. Measurements have been performed on *n*-type 4H-SiC epilayers grown either by chemical vapor deposition (CVD) or by high temperature CVD (HTCVD) on the heavily doped substrates. Epilayers thickness were 34 and 80 μm, respectively, with extrinsic concentration $n_0 = 6 \cdot 10^{14}$ cm^{-3} and $2 \cdot 10^{15}$ cm^{-3} at room temperature. The high-injection lifetime as measured in the material was τ = 500 ns and 400 ns, respectively. Polishing out the sample substrate attained free standing epilayer films used in the HTG measurements.

The experimental arrangement of the HTG measurement is schematically shown in the top of the Fig. 1. Single mode YAG:Nd^{3+} laser pulses of ~30 ps duration of energy $h\nu$ = 3.5 eV are used for the excitation. The grating is produced by splitting the light into two coherent beams of equal intensity, which are allowed to interfere on the surface of the sample. The absorbed light generates *e-h* pairs in a regular spatial arrangement corresponding to the optical interference pattern. Thus, the grating period inside the sample in the direction defined by the plane of incidence of the two beams is $\Lambda = \lambda_{ex}/2\sin(\Theta/2)$, which can be adjusted by varying the angle Θ between the two excitation beams. The transient grating is monitored with a third probe beam (λ_{pr} = 1064 nm) as it diffracts on the excess carrier grating induced refraction index changes. Probe pulses are delayed by a variable time with respect to the excitation pulse. The time dependence of the first order diffracted pulse $I_{pr}(t)$ is normalized to the initial probe intensity I_{pr0} and provides the decay rate of the diffraction efficiency $\eta(t)$. For the chosen probe wavelength and the sample thickness d = 20 μm, the absorption change in the grating is small and the diffraction is solely due to the change in refractive index $\Delta\mu$. In other words, a *thin phase* grating approximation is valid, i.e. $2\pi\lambda_{ex}d/\Lambda^2\Delta\mu << 1$, so the diffraction appears in the Raman-Nath regime. For such a grating relation entailing the proportionality $\eta \sim I_{ex}^2 = \mu_{eh}\cdot\Delta n^2(t)$ holds with μ_{eh} being the refraction index change per *e-h* pair and $\Delta n(t)$ - density of non-equilibrium charge carriers. We note that for adequate signal to-noise ratio the HTG technique is allowed only a narrow range of excitation. In our measurements a quadratic proportionality has been observed over an order of magnitude varying I_{ex}. We have calibrated the excited carrier concentration in the TG according to the formula:

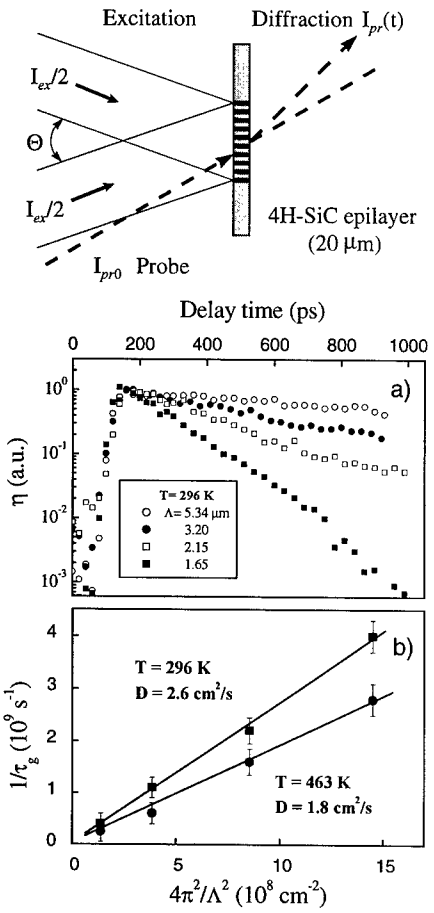


Fig. 1. Schematics of the HTG technique (top) and the data: a) characteristic decays at 296 K and Δn = $1.5\cdot10^{18}$ cm^{-3}; b) diffusion coefficient extraction from the slope of the reciprocal erasure time at two temperatures.

$$\Delta n = \frac{I_{ex}}{d\cdot\pi r^2\cdot\hbar\omega}\left[(1-R)(1-\exp(-\alpha d)) + R(1-R)(\exp(-\alpha d)-\exp(-2\alpha d)+...\right], \qquad (1)$$

where r = 110 ± 20 μm is a well-defined excitation spot radius (in comparison to 50±10 μm for the probe beam), R = 0.25 and α = 200 cm^{-1} are reflection and absorption coefficients at 296 K, respectively. In Eq. 1 the term in the square brackets represents the fraction of the excitation light absorbed accounting for multiple reflections in the sample.

The Fourier transient grating technique using orthogonal scanning has been presented in earlier work [1]. In that measurement the probe beam penetrated the sample along the epilayer for a 1 mm distance (sample width). Such geometry allowed to reach the low-injection case, but lead to early saturation of the induced absorption signal while approaching the high-injection range, because the absorption coefficient change, $\Delta\alpha_{eh}(t)$, is directly proportional to the probe path d. In this work we extend our measurements to very high injection levels by using pure epitaxial layers with both excitation and probe beams entering from the epilayer growth surface. In this collinear configuration the optical absorption path is determined by the small epilayer thickness. We note that

in order to suppress interference effects in such geometry the sample was inclined towards the probe beam close to Brewster angle incidence.

Results. Typical examples of the HTG measurement recorded at room temperature and at an injection level of $1.5 \cdot 10^{18}$ cm^{-3} for four different Λ values are shown in Fig. 1 (a). The data are normalized to the signal peak after the pumping pulse. From the $\eta(t)$ exponential decay slope the erasure time $\tau_g/2$ of the grating is extracted. It has been shown that the erasure time could be expressed using an analytical form $1/\tau_g = 1/\tau_r + 4\pi^2 D/\Lambda^2$, where τ_r describes the carrier recombination lifetime and the second term stands for lateral diffusion decay [3]. This equation predicts that τ_g decreases with decreasing Λ and this behavior is clearly observed (Fig. 1 (a)). The carrier diffusion coefficient D is obtained from the slope of the resulting plots $1/\tau_g$ vs. $4\pi^2/\Lambda^2$, as shown in Fig. 1 (b) at two different temperatures. From the intercept with the vertical axis it is obvious that the recombination rate $1/\tau_r$ is much longer compared with the diffusion erasure time at these grating periods.

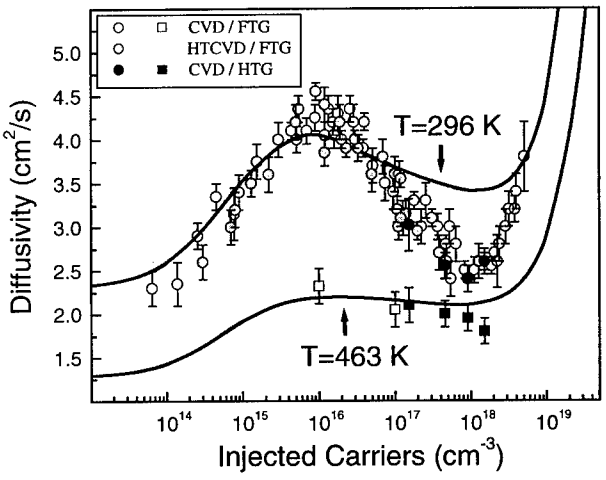


Fig. 2. Free carrier diffusivity versus the injected carrier density at two temperatures. Continuous curves represent theoretical calculations of the diffusion coefficient injection dependence including BGN effect and Fermi-Dirac statistics.

All measured data at two temperatures and for both techniques are summarized in Fig. 2 as a function of injected *e-h* concentration. Different symbols and error bars in the figure stands for two sample types (CVD and HTCVD) and two measurement techniques (FTG and HTG). We get a superb agreement of all the data in all samples and at different experimental conditions and conclude that the obtained injection dependence is a fundamental feature of the carrier diffusion flow. It has been shown that at low injection the rise in the carrier diffusivity is caused by transition from the minority hole diffusion D_p= (2.3±0.3) cm^2/s to the ambipolar diffusion D_a = (4.2±0.4) cm^2/s [1]. In contrary to the predicted saturation of the ambipolar diffusion coefficient at high injections we observe an appreciable D_a reduction by about 40% at 296 K and by 20% at T = 463 K, when the injection level increases from 10^{16} to 10^{18} cm^{-3}. A following sharp increase of D_a at injections above $3 \cdot 10^{18}$ cm^{-3} is clearly observed at room temperature.

Discussion. The observed injection dependencies have been simulated theoretically, while minority carrier diffusion coefficients D_p and D_n have been extended to include effects of band-gap narrowing (BGN) and Fermi-Dirac statistics. Afterwards they were substituted into the formula to calculate the ambipolar diffusivity as a function of the injected excess carrier density in *n*–type material: $D_a = (n_0 + \Delta n + \Delta p)/((n_0 + \Delta n)/D_p + \Delta p/D_n)$. To get the desired expressions we start from the diffusion current density for holes:

$$\vec{J}_p = \mu_p p \nabla \varepsilon_{fp}, \tag{2}$$

where μ_p is the hole mobility, p is their concentration and ε_{fp} is the quasi-Fermi potential. The concentration is stated in the form:

$$p = N_V F_{1/2}(\xi), \tag{3}$$

where N_v is the effective density of states in the valence band, $F_{1/2}$ is the Fermi-Dirac integral and ξ is the normalized chemical potential: $\xi = (\varepsilon_v - q\phi - \varepsilon_{fp})/k_BT$. Here, ε_v is the valence band edge and ϕ is the corresponding electric potential. Combining Eq. 2 and Eq. 3 and assuming that the valence band edge depends on the hole concentration together with the expression $\delta F_{1/2}/\delta\eta = F_{-1/2}$ we get:

$$\vec{J}_p = \mu_p k_B T \left\{ \frac{F_{1/2}}{F_{-1/2}} + \frac{p}{k_B T} \frac{\partial \varepsilon_v}{\partial p} \right\} \nabla p - q\mu_p p \nabla \phi \,. \tag{4}$$

Using the Einstein relation in the generalized form: $\mu = (qD_p/k_BT)\cdot(F_0/F_{1/2})$, we see that the first term in Eq. 4 represents an effective diffusion coefficient:

$$D_p = D_p^0 \frac{F_0}{F_{1/2}} \left\{ \frac{F_{1/2}}{F_{-1/2}} + \frac{p}{k_B T} \frac{\partial \varepsilon_v}{\partial p} \right\}. \tag{5}$$

In the same way an analogous expression for electrons can be obtained. The term $\delta\varepsilon_v/\delta p$ in Eq. 5 represents the BGN and was calculated [4] using the *random phase* approximation [5]. We note that in Ref. 4 it was taken into account the full valence and conduction band structure of 4H-SiC, but calculations were done using a zero-temperature Green's function. Some authors have claimed that Green's function dependence of temperature should not affect the BGN calculations substantially [6,7].

Calculated diffusion dependencies are presented in Fig. 2 by solid curves. Included BGN effects tend to lower the ambipolar diffusion at injections $>10^{16}$ cm^{-3} and is capable to explain half of the observed decrease at 296 K. Calculations are also extended to 463 K with the determined low-injection diffusion versus temperature dependence. The BGN influence is proportionally smaller which agrees with the tendency of experimental data. A qualitative agreement of the sharp diffusivity increase is also seen between the theory and experiment in the region of very high-injection. However, in our calculations we use an effective density of states in the valence band $N_v = 7\cdot10^{18}$ cm^{-3} which is lower than that calculated theoretically [8].

Similar theoretical and experimental discrepancy in diffusion coefficient dependency was also observed in Si. It was proposed that the diffusivity in addition is indirectly affected by *e-h* scattering which may reduce the hole and electron mobilities [9]. Another suggestion is exciton formation in the *e-h* plasma. Excitons may reduce the total experimental diffusivity value if the exciton diffusivity coefficient is lower than the free carrier ambipolar diffusivity [9]. Low temperature diffusivity measurements with corresponding calculations could clarify the importance of these processes.

The authors would like to acknowledge financial support from the Swedish SiCEP and Visby programs and Linköping University for samples.

References

[1] P. Grivickas, J. Linnros and V. Grivickas, Mater. Sci. Forum 338-342 (2000), p. 671.
[2] A. P. Silard and M. J. Duta, J. Appl. Phys. 62 (1987), p. 3809.
[3] H. J. Eichler, P. Gunter and C. W. Pohl, *Laser-induced Dynamic Gratings*, Springer Series in Optical Sciences 50 (1986), Berlin.
[4] C. Persson, U. Lindefelt and B. E. Sernelius, submitted to Sol. State Electron. (1999).
[5] G. D. Mahan, *Many-particle Physics*, Plenum (1990), New York.
[6] B. E. Sernelius, Proc. of the 3rd International Conference on Shallow Impurities in Semiconductors, Ser. No. 95 (1988), p. 137, Linköping.
[7] A. Shenk, J. Appl. Phys. 84 (1998), p. 3684.
[8] C. Persson and U. Lindefelt, Phys. Rev. B 54 (1996), p. 10257.
[9] V. Grivickas, J. Linnros, A. Galeckas and V. Bikbajevas, Proc. ICPS-23, World Scientific, Singapore, Vol. 1 (1996), p. 91.

Materials Science Forum Vols. 353-356 (2001) pp. 357-360
© 2001 Trans Tech Publications, Switzerland

Valence Band Splittings of 15R SiC Measured using Wavelength Modulated Absorption Spectroscopy

R.P. Devaty[1], S. Bai[1], W.J. Choyke[1], D. Hobgood[2] and D.J. Larkin[3]

[1] Department of Physics and Astronomy, University of Pittsburgh, Pittsburgh PA 15260, USA

[2] Cree, Inc., 4600 Silicon Drive, Durham NC 27703, USA

[3] NASA Glenn Research Center, M.S. 77-1, 21000 Brookpark Road, Cleveland OH 44135, USA

Keywords: Absorption, Band Structure, Crystal Field Splitting, Spin Orbit Splitting, Valence Bands

Abstract 15R SiC has significant advantages over 4H and 6H SiC for certain device applications. We have measured the free exciton low temperature photoluminescence (LTPL) spectrum for $\mathbf{E} \perp \hat{c}$ and the wavelength derivative of the absorption coefficient $d\alpha/d\lambda$ of 15R SiC for both polarizations $\mathbf{E} \perp \hat{c}$ and $\mathbf{E} \parallel \hat{c}$ using modulation absorption spectroscopy. We use the $\mathbf{E} \perp \hat{c}$ intrinsic 2 K photoluminescence spectrum to make assignments to features in the $\mathbf{E} \perp \hat{c}$ absorption derivative spectrum. We obtain 7.15±0.25 meV for the spin orbit splitting, in agreement with previous work, but with improved precision. The determination of the crystal field splitting is more challenging. We argue for a value of about 51 meV. This value is in good agreement with recent calculations.

Introduction

As part of our ongoing study of the valence band maxima of the important SiC polytypes [1-3], we turn our attention to 15R SiC. We report measurements of the free exciton low temperature photoluminescence (LTPL) and the wavelength derivative of the absorption coefficient and the analysis to obtain values of the valence band splittings.

The space group of 15R SiC is R3m. It is symmorphic. The point group associated with the point Γ at the center of the Brillouin zone is C_{3v}. With spin included, the irreducible representations [4] labeling the top three valence bands are Γ_{56}, Γ_4 and Γ_4. The energy difference between the top Γ_{56} band and the first Γ_4 band is called the spin orbit splitting Δ_{SO}. The energy difference between the top Γ_{56} band and the second Γ_4 band is called the crystal field splitting Δ_{CF}.

Experiment

High quality 15R SiC boule material was grown at Cree, Inc. Slices of the material were cut into thicknesses of 0.081 cm, 0.19 cm and 0.56 cm and polished. The $\hat{c}$ axis of uniaxial symmetry lies in the plane of the surface, enabling optical measurements for both polarizations $\mathbf{E} \perp \hat{c}$ and $\mathbf{E} \parallel \hat{c}$.

The technique of wavelength modulated absorption spectroscopy and our specially designed apparatus are discussed in earlier publications [1-3]. The measurements were performed with the sample at 2 K using an immersion type liquid He cryostat.

To assist the interpretation of the $\mathbf{E} \perp \hat{c}$ $d\alpha/d\lambda$ spectrum, we measured the low temperature photoluminescence (LTPL) spectrum of a 7-10 μm thick homoepitaxial epilayer of 15R SiC grown at NASA Glenn Research Center by chemical vapor deposition onto the Si face of a polished boule substrate. The sample was excited using the 2440 Å line of a frequency doubled Ar ion laser. The spectrum was acquired using a Fast Fastie spectrometer equipped with an 1800 l/mm grating blazed at 4000 Å and a CCD array. The slits were set at 100 μm.

Results and Discussion

Fig. 1 shows the LTPL spectrum of the 15R SiC epilayer. The intrinsic (free exciton) spectrum dominates the near band edge emission. Each of the eleven most prominent intrinsic lines is labeled

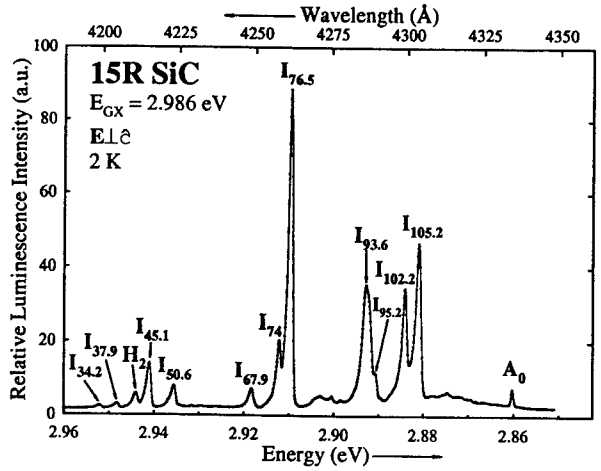


Fig. 1: Low temperature photoluminescence spectrum of a 15R SiC homoepitaxial layer showing strong intrinsic (free exciton) lines. These lines are marked "I" with the subscript specifying the energy of the momentum conserving phonon in meV.

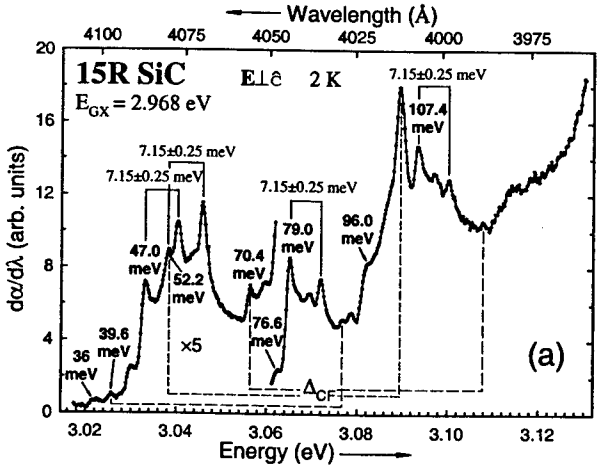
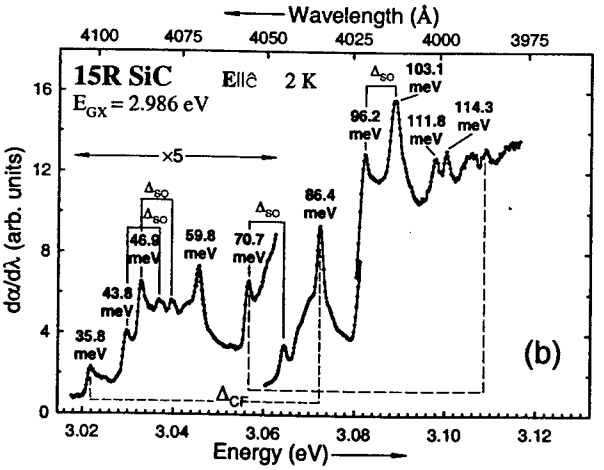


Fig. 2: Wavelength derivative absorption spectra of 15R SiC.

(a) Polarization $\mathbf{E} \perp \hat{c}$. Peaks matching intrinsic photoluminescence lines (Fig. 1) are marked with the energy displacement from the exciton gap E_{GX} = 2.986 eV. Peaks separated by the spin orbit splitting Δ_{SO} = 7.15±0.25 meV are indicated by solid line brackets. Dashed brackets show peaks separated by the proposed value of about 51 meV for the crystal field splitting Δ_{CF}.



(b) Polarization $\mathbf{E} \parallel \hat{c}$. Some of the prominent peaks are labeled with the energy displacement from E_{GX}. Solid brackets and dashed brackets indicate tentatively assigned pairs of peaks to spin orbit splitting and crystal field splitting, respectively.

Table 1: Selection rules for transitions from the initial states $|i\rangle$ (the Γ_3 and Γ_1 valence bands), to the final state $|f\rangle$ (the bottom of the conduction band). The symmetry labels of momentum conserving phonons are listed under Ω. Checks (√) and F's mark allowed and forbidden transitions, respectively.

	$\|i\rangle$	Ω	$\|f\rangle$ X_1	$\|f\rangle$ X_2
$\mathbf{E} \perp \hat{c}$	Γ_3	X_1	√	√
		X_2	√	√
	Γ_1	X_1	√	√
		X_2	√	√
$\mathbf{E} \parallel \hat{c}$	Γ_3	X_1	√	√
		X_2	√	√
	Γ_1	X_1	√	F
		X_2	F	√

"Γ" with a subscript specifying the energy of the associated momentum conserving phonon in meV, based on the value E_{GX} = 2.986 eV [5] for the exciton gap. The labels A_0 and H_2 mark no phonon lines due to Ti [6] and hydrogen [7], respectively.

Figs. 2a and 2b show the wavelength derivative absorption spectrum of the 15R SiC boule material for polarizations $\mathbf{E} \perp \hat{c}$ and $\mathbf{E} \parallel \hat{c}$, respectively. The asymmetric shape of the features with a sharp onset on the low energy side and a high energy tail is in accord with the behavior $d\alpha/dE \propto E^{-1/2}$ predicted by R.J. Elliott's theory for indirect transitions [8]. We use the LTPL intrinsic spectrum (Fig. 1) to assign absorption features associated with the highest valence band in the $\mathbf{E} \perp \hat{c}$ spectrum (Fig. 2a). The $I_{76.5}$ intrinsic line is assigned to the feature marked "79.0 meV" in Fig. 2a. These features are in vertical alignment in the two figures. Since the energy scales in Figs. 1 and 2 are the same, it is then straightforward to make further assignments, most of which are marked on Fig. 2a with the energy of the momentum conserving phonons in meV, assuming E_{GX} = 2.986 eV. Doublets appear in the $d\alpha/d\lambda$ spectrum due to transitions associated with the top two valence bands. Four of the most prominent doublets are connected by solid-line brackets in Fig. 2a. The average value of the separation, 7.15±0.25 meV, is the measured spin orbit splitting of the valence bands. This value agrees with an earlier measurement [9], but with improved accuracy. In the absence of a good LTPL $\mathbf{E} \parallel \hat{c}$ intrinsic spectrum it is a challenge to make assignments to the $\mathbf{E} \parallel \hat{c}$ $d\alpha/d\lambda$ spectrum. We have marked some of the features in Fig. 2b with their energy separations from 2.986 eV, and suggest several pairs of features tentatively assigned to spin orbit splitting.

We use the calculated band structure of 15R SiC and a group theoretical analysis to assist the determination of the crystal field splitting from the $d\alpha/d\lambda$ spectra. It is necessary to neglect spin, and thus the spin orbit interaction, to obtain useful results. According to the calculations of Wellenhofer and Rössler [10], 15R SiC has three equivalent conduction band minima located at the points X in the rhombohedral Brillouin zone. The point group symmetry associated with the X point is C_{1v}. Neglecting electron spin, there are two possible irreducible representations for the conduction band minimum, X_1 and X_2, which are symmetric and antisymmetric, respectively, with respect to reflection in the mirror plane. There are thirty phonons associated with each **k**-space point in the Brillouin zone. At the point X their symmetries are 20 X_1 + 10 X_2. There are no published symmetry assignments for the phonons at X. Neglecting spin, the top valence band is a Γ_3 doublet and the crystal field split off band is labeled Γ_1 in C_{3v}. Table I lists the selection rules for indirect transitions involving all possible phonons for both polarizations. In the case of 4H SiC [3], a similar analysis led to the conclusion that one must use both polarized spectra to determine the crystal field splitting. Due to the low symmetry in the case of 15R SiC, no such restrictions are required. However, Table I indicates that there are fewer allowed transitions from the Γ_1 crystal field split band for $\mathbf{E} \parallel \hat{c}$. With little guidance from theory it is risky to extract a value for Δ_{CF} from the $d\alpha/d\lambda$ spectra. Based on the pairings suggested by dashed brackets shown on Figs. 2a and 2b, we tentatively assign the value Δ_{CF} ≈ 51 meV.

The model of Bir and Pikus [11] provides a framework for interpreting the valence band splittings. Since we are not concerned with **k**-dependence (effective masses) or strain effects, the

version of this model applicable to the hexagonal and rhombohedral polytypes has three parameters, two of which describe the spin orbit interaction, allowing for anisotropy. However, there is no reason to expect that the spin orbit interaction will depend strongly on hexagonality (which may be defined as the fraction of sublattice sites with "hexagonal" local symmetry), or be significantly anisotropic. Neglecting anisotropy, the Pikus and Bir model reduces to Hopfield's quasicubic model [12]. The two parameters are a spin orbit parameter δ_S and a crystal field parameter δ_C. The value δ_S = 10 meV, based on wavelength modulated absorption measurements on 3C SiC [9], is typically used. Lambrecht et al. [13] found a linear dependence between δ_C and hexagonality, based on their band structure calculations for a number of polytypes. Including our new result for 15R SiC, our measured values for the crystal field splitting support this assertion. At least two other calculations of the crystal field splittings for several polytypes have been published [10,14]. Regarding the spin orbit splitting, in the quasicubic model the largest possible value for the splitting of the highest two valence bands is $2\delta_S/3$, which is about 6.7 meV. This splitting increases with increasing δ_C, i.e., hexagonality. This dependence is weak in the interval of hexagonality convered by our measurements on 6H, 4H and 15R SiC. However, our measured values for three polytypes are all larger than 6.7 meV and decrease with increasing hexagonality, although the uncertainties in the measured values are large relative to this weak trend. In this measurement of low temperature absorption we are studying free excitons, and it is possible that the difference in binding energies for excitons made up of holes taken from the two highest valence bands is responsible for these discrepancies. According to Table 6 in Lambrecht et al. [13], the components of the heavy hole (highest valence band) mass tensor are greater than or equal to those of the light hole (spin orbit split valence band). Since binding energy increases with mass, the binding energy of the exciton made up of the hole from the top valence band is larger, based on these calculated masses. This difference will add to the energy separation of an absorption doublet peak for a given momentum conserving phonon.

Conclusion

Our measurements of the wavelength derivative spectrum of high quality 15R SiC boule material lead to values of 7.15±0.25 meV for the spin orbit splitting and about 51 meV for the crystal field splitting. Further details and comparison with results for 4H and 6H SiC will be published.

Acknowledgments

We acknowledge partial support of this research by the Office of Naval Research Grant N00014-96-1-0333 (Colin E.C. Wood) and helpful communications with Walter R.L. Lambrecht.

References

[1] R.P. Devaty, W.J. Choyke, S.G. Sridhara, L.L. Clemen, D.G. Nizhner, D.J. Larkin, T. Troffer, G. Pensl, T. Kimoto and H.S. Kong, Mater. Sci. Forum 264-268 (1998), p. 455.
[2] W.J. Choyke, R.P. Devaty and S.G. Sridhara, Physica Scripta T79 (1999), p. 9.
[3] S.G. Sridhara, S. Bai, O. Shigiltchoff, R.P. Devaty and W.J. Choyke, Mater. Sci. Forum 338-342 (2000), p. 567.
[4] G.F. Koster, J.O. Dimmock, R.G. Wheeler and H. Statz, "Properties of the Thirty-Two Point Groups," (MIT Press, Cambridge, MA, 1963).
[5] L. Patrick, D.R. Hamilton and W.J. Choyke, Phys. Rev. 132 (1963), p. 2023.
[6] L. Patrick and W.J. Choyke, Phys. Rev. B 10 (1974), p. 5091.
[7] L. Patrick and W.J. Choyke, in Silicon Carbide-1973 (Ed. R.C. Marshall, J.W. Faust, Jr. and C.E. Ryan, University of South Carolina Press, SC, 1974), p. 298.
[8] R.J. Elliott, Phys. Rev. 108 (1957), p. 1384.
[9] R.G. Humphreys, D. Bimberg and W.J. Choyke, Solid State Commun. 39 (1981), p. 163.
[10] G. Wellenhofer and U. Rössler, Phys. Stat. Sol. (b) 202 (1997), p. 107.
[11] G.L. Bir and G.E. Pikus, Symmetry and Strain-induced Effects in Semiconductors (John Wiley & Sons, New York, 1974).
[12] J.J. Hopfield, J. Phys. Chem. Solids 15 (1960), p. 97.
[13] W.R.L. Lambrecht, S. Limpijumnong, S.N. Rashkeev and B. Segall, Phys. Stat. Sol. (b) 202 (1997), p. 5.
[14] C. Persson and U. Lindefelt, J. Appl. Phys. 82 (1997), p. 5496.

Materials Science Forum Vols. 353-356 (2001) pp. 361-364
© 2001 Trans Tech Publications, Switzerland

Zeeman Effect of D_1 Bound Exciton in 4H-SiC

C.Q. Chen[1], R. Helbig[1], R. Winkler[2], A. Wysmolek[3] and M. Potemski[3]

[1] Institute of Applied Physics, University of Erlangen-Nürnberg, Staudtstr. 7/A3, DE-91058 Erlangen, Germany

[2] Institute of Technical Physics III, University of Erlangen-Nürnberg, Staudtstr. 7, DE-91058 Erlangen, Germany

[3] CNRS/MPI-FKF, High Magnetic Field Laboratory, BP 166, FR-38042 Grenoble Cedex 9, France

Keywords: 4H-SiC, D_1 Bound Exciton, Zeeman Effect

Abstract. The Zeeman behavior of the D_1 photoluminescence (PL) lines is found to be angular and polarization dependent. From the magnetic splitting, the electronic fine structure of the D_1 bound exciton (BE) is obtained. Besides the L, M and H levels, there exist three other L_H, L_L and N energy levels. Based on thermalization behavior, it is deduced that the Zeeman splitting of the D_1 PL lines originates from the initial states of the luminescence process. This result supports that the D_1 defect is an isoelectronic center. We complement our experimental results by some general considerations concerning the symmetry of the BE.

Introduction

The D_1 defect is expected to be an intrinsic defect since it does not depend on any specific impurities. Its fingerprint is an efficient luminescence of the D_1 bound exciton (BE) which usually dominates the low temperature photoluminescence (PL) spectrum. At low temperature, there is one D_1 no-phonon PL line L (4272.6 Å, 2.9012 eV) in 4H-SiC. Two higher energy no-phonon lines M (4261.3 Å, 2.9087 eV) and H (4257.0 Å, 2.9118 eV) appear at higher temperatures. The large exciton binding energy E_{BX} (the exciton band gap of 4H-SiC is 3.265 eV) and the existence of different forms of D_1 PL lines for low and high temperatures are similar to the behavior of excitons bound to an isoelectronic center observed in other semiconductors. Detailed information on the nature of the defect, to which the exciton is bound, can be obtained from the Zeeman effect. Furthermore, Zeeman spectroscopy reveals the electronic fine structure and the symmetry properties of the BE. In the present paper, we report on the Zeeman effect of the D_1 BE in 4H-SiC.

Experimental

In order to measure the polarization dependence of the D_1 lines, the Zeeman spectra were measured in four configurations as shown in Table I. Two different 4H-SiC samples were used. For Voigt(1) and Faraday (2) configurations with polarization $\mathbf{E} \perp \mathbf{c}$, we used a sample S1 with the **c** axis nearly perpendicular to the surface. To broaden the distribution of the D_1 defects, Al and C ions were implanted with the box profile. Post-implantation annealing was conducted at 1630°C for 30 min in Ar atmosphere. For Faraday (1) and Voigt (2) configurations, a sample S2 was used which was cut from a 4H-SiC boule with the **c** axis parallel to surface. It was implanted by helium ions and subsequently annealed at 1600°C for 30 min. The luminescence was collected with unpolarized light. Thus for sample S2, the electrical field vector of emission includes both polarizations $\mathbf{E} \perp \mathbf{c}$ and $\mathbf{E} \parallel \mathbf{c}$. The measurements were conducted in a resistive magnet with the maximum value of B = 23 T at temperatures from 5 to 35 K. A Kimmon He-Cd laser operating at 325 nm was used as an excitation source. The PL spectra were recorded with a charged-coupled device camera attached to a single grating 0.5m Jobin-Yvon monochromator fitted with a 1800 grooves/mm grating. All PL

Table I. Different configurations for magneto-luminescence measurements in 4H-SiC.

(**B**, **c**)	emission **k**	configurations	emission **E**	sample
B ⊥ **c**	**k** ∥ **B**	Faraday (1)	**E** ∥ **c** and **E** ⊥ **c**	S2
	k ⊥ **B** (**k** ∥ **c**)	Voigt (1)	**E** ⊥ **c**	S1
B ∥ **c**	**k** ∥ **B**	Faraday (2)	**E** ⊥ **c**	S1
	k ⊥ **B**	Voigt (2)	**E** ∥ **c** and **E** ⊥ **c**	S2

measurements were carried out in a near backscattering configuration.

Results and Discussion

The Zeeman effect of the D_1 PL lines in 4H-SiC shows a strong angular dependence. We present the results according to **B** perpendicular and parallel to the **c** axis, respectively.

1. **B** ⊥ **c** (Faraday (1) and Voigt (1))

Figure 1 shows the Zeeman spectra of the D_1 PL lines in Voigt (1) with **B** ⊥ **c** and polarization **E** ⊥ **c** at 30 K. In Fig. 2(a) we present the energy positions of the Zeeman components as a function of the magnetic field *B*. As shown in these figures, two Zeeman components L_a and L_b appear symmetrically around the L line for $B > 0$. At higher fields beyond 15 T, the energy positions of L_a and L_b vary linearly with *B* [Fig. 2(b)]. By making a linear extrapolation to $B = 0$, it is found that the L_a and L_b components can be described by a linear Zeeman splitting of the L line, i.e., the external magnetic field perturbation dominates for large *B*. At lower fields, the energy positions deviate from the linear dependence. The extrapolation leads to two zero-field splitting levels L_H and L_L shifted by about ±0.35 meV with respect to the L level. This indicates that there are other perturbations of the L level which become dominant at low fields. The PL lines intensity ratio I_{Lb}/I_{La} shows a clear thermalization dependence. The energy position of the L and M lines exhibits a very weak diamagnetic shift to higher energies. Around the M line two new components N_a and N_b are observed. The energy positions of the N_b line vary linearly at low field, whereas at high fields they show an anticrossing with the H line. The lower energy N_a line is very weak and can only be resolved at B beyond 16 T. By extrapolating the components N_a and N_b to zero field, an exciton level N about 0.5 meV above the M level is found. This zero field level is consistent with the weak N_1 line in the PLE spectra [1]. The intensity of the N_b line is much lower than that of the N_a line, which cannot be understood based on thermalization. At low fields, the H line shows a small shift to higher energies. At higher fields, this shift becomes larger due to the anticrosssing interaction. For the same configuration **B** ⊥ **c**, we also studied the Zeeman effect of the D_1 lines with polarizations **E** ⊥ **c** and **E** ∥ **c**, in Faraday (1) by using the sample S2. The Zeeman behavior is found to be similar to that in the Voigt (1). Since the energy positions and the intensity distribution of the Zeeman components are very similar in both configurations, we cannot obtain further information about the polarization dependence.

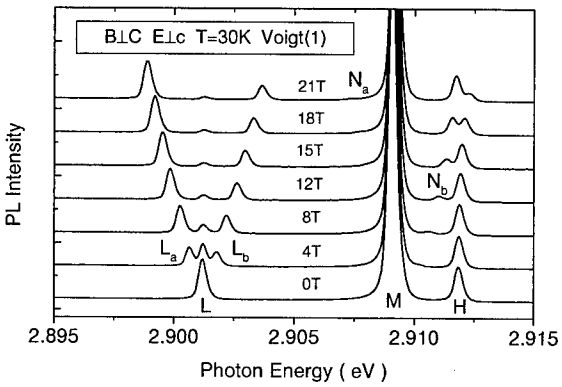


Fig. 1. Zeeman spectra of the D_1 PL lines in the configuration of Voigt(1) with ***B*** ⊥ ***c***.

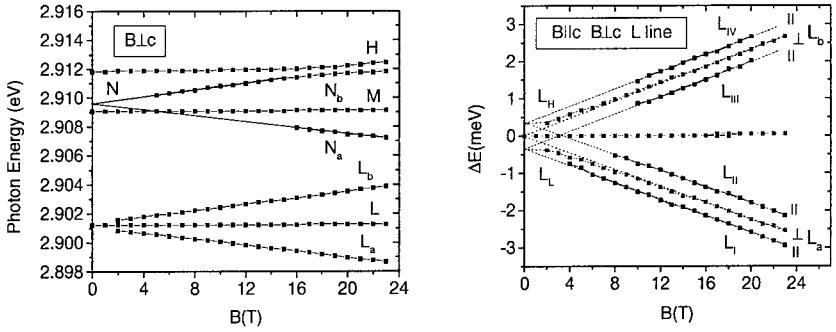


Fig. 2. (a) Fan diagram of the Zeeman behavior of the D_1 PL lines with $\mathbf{B} \perp \mathbf{c}$. *(b) The Zeeman behavior of the L line in configurations with* $\mathbf{B} \perp \mathbf{c}$ *and* $\mathbf{B} \parallel \mathbf{c}$.

2. **B** ‖ **c** (Faraday (2) and Voigt(2))

For **B** ‖ **c** in Faraday (2) with polarization **E** ⊥ **c**, the Zeeman splitting of the L line at 5 K and B = 12 T is shown in Fig. 3. Two Zeeman components L_I and L_{II} appear on the low energy side of the L line. Moreover, two new Zeeman components L_{III} and L_{IV} with higher energies appear at higher temperatures due to the thermalization effect [Fig. 2(b)]. The intensities of these four new components are much weaker as compared with the intensity of the L line at 30 K. The L line shows a small diamagnetic shift. We do not observe any new Zeeman components around the M and H lines. Both lines only show a small diamagnetic shift. The transitions related to the N level cannot be observed in this case. We have confirmed the zero-field splitting of the L level by linearly extrapolating the Zeeman components to B = 0. In Fig. 2(b), one can see that the Zeeman components L_I and L_{III} result from the splitting of the L_H level, while the L_{II} and L_{IV} lines stem from the L_L level. The Zeeman behavior of the L line in 4H-SiC is very similar to that in 6H-SiC [2].

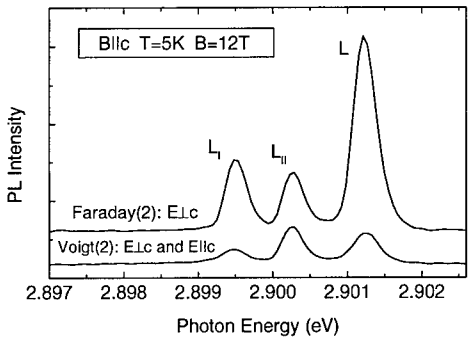


Fig. 3. Zeeman behavior of the L line in two configurations Voigt(2) and Faraday(2) with $\mathbf{B} \parallel \mathbf{c}$.

With the same **B** ‖ **c**, the magnetic behavior of the L line was studied in Voigt (2) for both polarizations (Fig. 3). It can be seen that in Voigt (2) the intensity of the L_{II} line is larger than that of the L_I and L lines, in contrast to the result in Faraday (2) with polarization **E** ⊥ **c**, where $I_{LII} < I_{LI}$. Based on a comparison between the results for Voigt (2) and Faraday (2), we suggest that the L_I, L_{III} and L lines are mainly related to polarization **E** ⊥ **c**, which is similar to the polarization properties of the L, M and H lines at zero field, while the L_{II} and L_{IV} lines are mainly related to polarization **E** ‖ **c** in the configurations with **B** ‖ **c**. As pointed out above, in the configurations with **B** ⊥ **c** and **B** ‖ **c**, the Zeeman effect shows thermalization. Therefore, the Zeeman splitting of the D_1 BE results from the initial states of these luminescence transitions. There is no splitting in the final state in any configuration. This result supports that the D_1 exciton are bound to an isoelectronic center.

We complement our experimental results by some general considerations concerning the symmetry of the BE. The host crystal 4H-SiC has a hexagonal crystal structure (space group C_{6V}^4),

and we will assume that the point group of the D_1 defect is that of a substitutional impurity, i.e., C_{3v}. The topmost valence band in 4H-SiC transforms according to the two-dimensional irreducible representation Γ_5 of C_{6v} (with spin: $\Gamma_7 + \Gamma_9$, Koster's notation [3]). The lowest conduction band has three equivalent minima at the M points. But the C_{3v} crystal field lifts the threefold degeneracy, i.e., we have a valley-orbit splitting of the conduction band states, giving a Γ_1 state and two degenerate Γ_3 states if the conduction band at the M point transforms according to Γ_1 or Γ_2 of C_{2v} ($\Gamma_2 + \Gamma_3$ for a conduction band transforming like Γ_3 or Γ_4). This situation for the BE is completely analogous to donor states in SiC (whereas free excitons in a multivalley semiconductor do not show a valley-orbit splitting). The representation according to which the total exciton wave function transforms is the product of the three representations D_e, D_h and D_x of the electron, the hole and the relative motion, respectively. Obviously, this product representation is rather complicated. Therefore, it is helpful that we have only three distinct single-valued irreducible representations for the point group C_{3v}, which can be contained in this product, namely the two one-dimensional representations Γ_1 and Γ_2 as well as the two-dimensional representation Γ_3. In Table II we have listed the selection rules for optical transitions between exciton states transforming according to these representations and a Γ_1 ground state. Note that we have several nontrivial selection rules for forbidden optical transitions and that these selection rules must be fulfilled by any microscopic model with point group C_{3v} and a ground state transforming according to Γ_1. Unfortunately, we were not able to derive a simple scheme in order to classify our measured spectra based on Table II. We expect that certain peaks in the measured spectra correspond to several almost degenerate states. Forbidden transitions could become allowed due to a distortion of C_{3v}. However, this would imply that the twofold degeneracy of Γ_3 exciton states was lifted, too. We have compared our results with a recent axial model for the D_1 BE due to Egilsson *et al.* which was based on the assumption that the spin-orbit interaction is very small for the D_1 BE [1]. Several excitonic transitions, that are observed experimentally, should be dipole-forbidden according to this model due to its rather high symmetry. Moreover, we would like to note that valley-orbit splitting cannot be taken into account within a model with axial symmetry.

Table II. Selection rules for optical transitions from an exciton state transforming like Γ_i of C_{3v} to a ground state transforming according to Γ_1. 'A' and 'F' denote allowed and forbidden transitions, respectively. Γ_3 splits in the presence of B.

	B = 0		B ⊥ c		B ∥ c	
	E⊥c	E∥c	E⊥c	E∥c	E⊥c	E∥c
Γ_1	F	A	A	A	F	A
Γ_2	F	F	A	F	F	A
Γ_3	A	F	A	A	A	F
			A	F	A	F

Acknowledgments: The authors express their appreciation to H. Sadowski and T. Frank for help. C. Q. Chen acknowledges financial support by VW-Stiftung. A. Wysmolek gratefully acknowledges financial support from the Alexander von Humboldt Foundation. This work was supported by the TMR Programme under contract n° ERBFMGECT950077 and SFB 292.

References:

[1] T. Egilsson, I. G. Ivanov, A. Henry and E. Janzen, Physica B 273 (1999), p. 677.

[2] P. J. Dean, D. Bimberg, and W. J. Choyke, Proceedings of the International Conference on Defects and Radiation Effects in Semiconductors, Nice, France 1978, IOP, London (1979), p. 447.

[3] G. F. Koster et al., Properties of the Thirty-Two Point Groups, MIT, Massachusetts (1963).

Materials Science Forum Vols. 353-356 (2001) pp. 365-368
© 2001 Trans Tech Publications, Switzerland

As-Grown and Process-Induced Intrinsic Deep-Level Luminescence in 4H SiC

B. Magnusson[1], A. Ellison[2], F.H.C. Carlsson[1], N.T. Son[1] and E. Janzén[1]

[1] Department of Physics and Measurement Technology, Linköping University, SE-581 83 Linköping, Sweden

[2] Okmetic AB, Hans Meijers väg 2, SE-583 30 Linköping, Sweden

Keywords: Annealing, Deep Levels, Ion Implantation, Irradiation, Photoluminescence, Zeeman Effect

Abstract: A deep level in 4H SiC is studied by photoluminescence (PL) for different annealing temperatures. The luminescence consists of four no-phonon lines between 1.09 and 1.15 eV and their phonon assisted spectra. No splitting or shifting of the lines could be observed in a magnetic field up to 5T. The defect can be introduced in the material by either ion implantation or irradiation, but may also be present in as-grown samples. The PL intensity increases with annealing up to 1000°C, thereafter decreases and vanishes at 1300°C. We tentatively ascribe this deep level defect to a silicon vacancy related complex.

1 Introduction

In semi-insulating (SI) 4H SiC wafers ($\rho > 10^9$ Ωcm at R.T.) - not intentionally doped with vanadium - grown by high temperature chemical vapour deposition (HTCVD) [1], several deep levels appear [2] which have not been reported before. The activation energy for the defect responsible for the SI properties of the wafers is about 1.15 eV [1] which is close to what has been reported in vanadium-free SI material from another source [3]. In this work we investigate the luminescence from one of these defect levels which we label unknown defect 2 (UD-2). This defect can also be induced during ion implantation or irradiation with electrons, protons or neutrons. A similar defect has earlier been observed in the 6H polytype [4].

In this study we have performed PL and Zeeman measurements. We have made an annealing series which shows the temperatures at which the defect is formed and annealed away. The origin of the center and why it can be found in as-grown material are also discussed. The results are relevant from a device process point of view as they provide a scheme to anneal the material, for instance, after an implantation to remove this particular defect.

2 Experiments

The material used in this study was a hot-wall CVD 4H SiC epitaxial layer [5](thickness ~30 μm and doping 2×10^{14} cm^{-3}). This type of low doped epitaxial layer never shows any luminescence in the infrared region before irradiation. To create the UD-2 defect in high concentration we used neutron irradiation, after which the wafer was cut into 5×5 mm pieces and annealed at different temperatures in the range from 600°C to 1700°C. All annealings besides the one at 1700°C were done in an argon ambient but in the case of the 1700°C anneal a small fraction of silane was added in order not to etch the sample. The annealing times were 90 minutes for temperatures between 600°C and 1200°C, 30 and 10 minutes for the 1300°C and 1700°C anneals, respectively.

The Fourier transformed PL (FTPL) measurements were done either in a continuous flow cryostat at 10 K or in a bath cryostat which allows temperature regulation in the range from

1.6 K to room temperature. The samples were excited using either the ultraviolet lines (351.1-363.8 nm) from an Ar ion laser or the 266 nm line of a frequency-quadrupled Nd:YAG laser. To detect the luminescence a Bomem DA8 Fourier Transform spectrometer equipped with a quartz beamsplitter and a North Coast Ge detector were used.

For Zeeman experiments we used an Oxford split-coil superconducting magnet (0-5 T) with a helium bath cryostat. For the angular dependence studies of the Zeeman splitting rotation of the magnetic field in the $(11\bar{2}0)$ plane can be achieved by rotating the sample holder. The 351.1 nm line from an Ar ion laser with a power of 150 mW was used for excitation. The PL emission was dispersed by a double grating monochromator SPEX-1404, collected at the second order of the 600 grooves/mm gratings and detected with a North Coast Ge detector.

3 Results and Discussion

In figure 1 the FTPL spectrum of the center is shown. It consists of four no phonon-lines at 1.0952, 1.0968, 1.1193 and 1.1495 eV, which are followed by a broad phonon-assisted band. The line width measured with a Fourier transform spectrometer is about 0.4 meV for all lines except the 1.1193 eV line that has a line width of 0.3 meV. It is also worth noting that this PL signal can hardly be observed when one uses below bandgap excitation in contrast to other defects (e.g. the V^{4+} PL center) which give rather strong luminescence in the infrared with both above and below bandgap excitation.

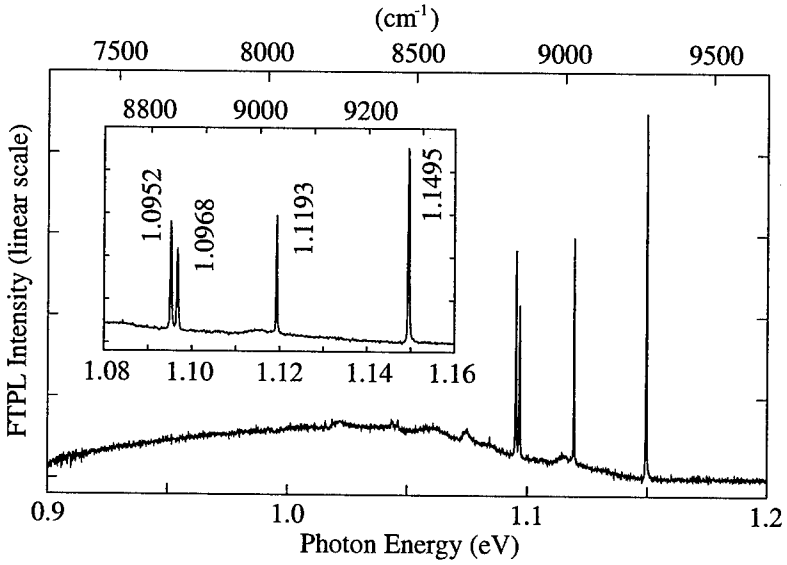


Figure 1: FTPL spectrum observed in a neutron irradiated low-doped 4H SiC epilayer after annealing at 1000°C. The measurement is done at low temperature (2 K), with 266 nm excitation (80 mW).

Zeeman measurements at 5T were done on all four PL lines in figure 1. Even with a line width of typically 0.5 meV or better (in a monochromator system) we could not observe any splitting, broadening or shifting of the lines at any angle between B||c-axis and B⊥c-axis. From this experiment we conclude that both the excited and the ground states of the four emission lines are spin-singlet levels.

The annealing behavior of the defect is presented in figure 2. A weak luminescence is observable in as-irradiated material, which increases slowly in intensity with increasing temperature

up to 600-800°C, then increases much faster until it reaches a maximum at an annealing temperature of 1000°C. Further increase in annealing temperature results in decrease of the FTPL intensity. The spectrum is completely quenched after 1300°C anneal.

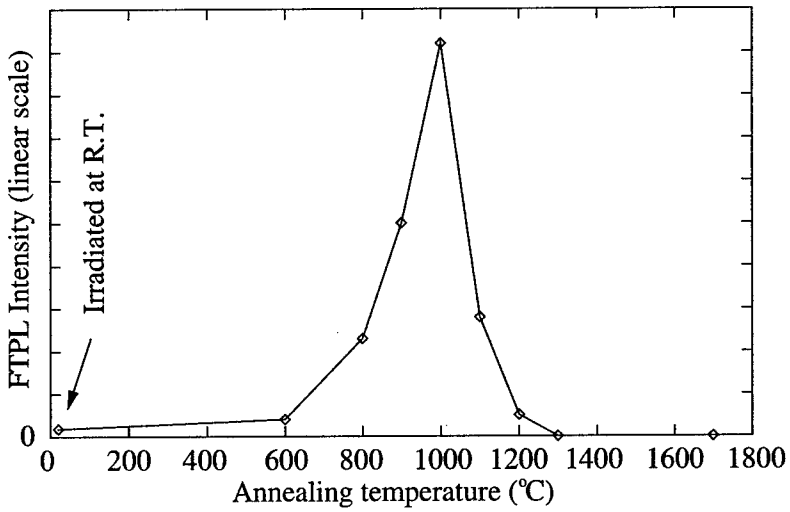


Figure 2: Annealing behavior of the UD-2 defect monitored by the peak hight of the highest energy no-phonon line in figure 1. The measurement is done at low temperature (2 K), with 266 nm excitation (80 mW).

The fact that the defect can be induced by irradiation in both high- and low-doped sample suggests that it is an intrinsic defect. In view of the annealing results, this makes it possible to draw some first conclusions on the composition of the defect. From previous isochronal annealing of electron irradiated 3C SiC one knows that the silicon vacancy anneals out at around 750°C [6]. From the annealing behavior shown in figure 2, it is obvious that at the temperatures where the silicon vacancy gets mobile, the luminescence from the defect increases fast in intensity. The luminescence of the UD-2 defect is therefore attributed to a complex that involves the silicon vacancy. Since the defect can always be detected in irradiated and annealed material independent of the concentration of impurities (both intentional and unintentional doping), such as N, B, Al and other common transition metal impurities, it is likely that the defect complex is entirely intrinsic.

In as-grown HTCVD material we suggest that this defect is introduced during the cooling down phase of the growth since it is not stable at the temperatures where the growth occurs (2100 to 2300°C). Some of the different components in the defect are mobile within the crystal, so when the cooling down process starts they will form the defect center at temperatures below 1300°C. This formation scheme of the defect also gives some insight to why in the as-grown HTCVD material we seldom observe the silicon vacancy related luminescence [7]. This may be due to that some of the silicon vacancies that exist during the growth form the UD-2 defect during the cooling down stage.

It should be noted that the SI properties of SI HTCVD wafers survive after CVD growth at 1600°C - a temperature which is high enough to quench the UD-2 defect spectrum.

4 Conclusion

In summary, we have investigated a deep level defect center (UD-2) which gives luminescence in the infrared region. The PL consists of four no-phonon lines between 1.09 and 1.15 eV which are followed by a broad phonon assisted band. The lines do not split or shift in a magnetic field up to 5T. The defect can be created by ion implantation or irradiation with electrons, protons or neutrons. Annealing at temperatures up to 1000°C increases the luminescence intensity. At higher annealing temperatures the signal decreases and is completely quenched by 1300°C. The defect is also found in semi-insulating wafer demonstrators prepared from HTCVD grown crystals. We conclude that the UD-2 defect is a silicon vacancy related complex and that in the as-grown material it is formed during the post-growth cooling phase.

Acknowledgments

This work was supported by the SSF program SiCEP, the Swedish Research Council for Engineering Sciences (TFR), the Swedish Natural Science Research Council (NFR) and Ångpanneföreningens Forskningsstiftelse.

References

[1] A. Ellison, J. Zhang, W. Magnusson, A. Henry, Q. Wahab, J.P. Bergman, C. Hemmingsson, N.T. Son, and E. Janzén, Mater. Sci. Forum **338-342** (2000), p. 131.

[2] A. Ellison, C. Hemmingsson, B. Magnusson, A. Henry, N.T. Son Q. Wahab, and E. Janzén, UPD2000, Nara, Japan, May 31 - June 2 (2000), Extended Abstracts.

[3] W.C. Mitchel, A. Saxler, R. Perrin, J. Goldstein, S.R. Smith, A.O. Evwaraye, J.S. Solomon, M. Brady, V. Tsvetkov, and C.H. Carter, Jr. Mater. Sci. Forum **338-342** (2000), p. 21.

[4] N.T. Son, E. Sörman, M. Singh, W.M. Chen, C. Hallin, O. Kordina, B. Monemar, J.L. Lindström, and E. Janzén, Diam. Relat. Mater. **6** (1997), p. 1378.

[5] O. Kordina, Doctoral thesis; Growth and Characterisation of Silicon Carbide Power Device Material, Dissertation No. 352, Linköping University, Sweden (1994)

[6] H. Itoh, N. Hayakawa, I. Nashiyama, and E. Sakuma, J. Appl. Phys. **66** (1989), p. 4529.

[7] E. Sörman, N.T. Son, W.M. Chen, O. Kordina, C. Hallin, and E. Janzén, Phys. Rev. B **61** (2000), p. 2613.

Materials Science Forum Vols. 353-356 (2001) pp. 369-372
© 2001 Trans Tech Publications, Switzerland

Characterization of SiC:P Prepared by Nuclear Transmutation Due to Neutrons

H. Heissenstein and R. Helbig

Institute of Applied Physics, University of Erlangen-Nürnberg,
Staudtstr. 7/A3, DE-91058 Erlangen, Germany

Keywords: Defects, FTIR, Hall-Effect, Neutrons, Nitrogen, Phosphorous

Abstract

In order to get phosphorous doped SiC we irradiated 4H SiC samples with several neutron fluences of various energy distributions. After irradiation the samples were sucessively annealed between 1600°C and 1750°C and thereafter characterized by Fourier-Transform-InfraRed spectroscopy (FTIR) and Hall-effect experiments. We compared the ionization energies of 33 meV and 99 meV which we evaluated from Hall-effect with the absorption in the IR-region of 150 cm^{-1} to 5000 cm^{-1}. We observed phosphorous-related and defect-related as well as vibronic and electronic absorptions.

Introduction

Nuclear Transmutation Doping (NTD) is based on the reaction [$^{30}Si(n,\gamma)\ ^{31}Si \xrightarrow{\beta} {}^{31}P$] and thus it is basically useful to produce the P-donor in SiC. The phosphorous doping of SiC was characterized after ion implantation [1] together with the residual doping with nitrogen (Hall-effect after implantation of nitrogen: [1]). The unintentional nitrogen doping of 4H SiC was also characterized with different samples by FTIR and Zeeman-splitting measurements [2]. First attempts applying NTD on SiC were made with respect to the behaviour of SiC in radiative environments [3] and in order to get higher residual doping levels for ESR–investigations [4]. In the last years NTD was introduced in SiC research as a doping technique [5, 6, 7]. The electrical characteristics of irradiated samples are influenced by defects due to fast neutrons which are incorporated inevitably by NTD using reactor spectra [5].

Experimental

We irradiated 4H SiC epitaxial layers grown by Cree on 8.5° off-axis orientated substrates, both p-type and n-type. The samples for Hall-effect measurements were irradiated with a fluence of thermal neutrons of $8.3x10^{19}$ cm^{-2} and a fluence of fast neutrons of $2x10^{18}$ cm^{-2}. In this way we generated n-type epilayers by furnace annealing at 1600°C to 1700°C for half an hour in Ar atmosphere. The original epilayer was p-type with $N_A–N_D \sim 2x10^{15}$ cm^{-3}. With completely activated phosphorous dopants we should get from the applied fluences a net doping of $N_D–N_A \sim 1.25x10^{16}$ cm^{-3} in the layer. The pn-junction generated hereby was used to measure Hall-effect in van der Pauw geometry. By etching the edges of the epilayer we avoided leackage currents over the substrate.
Whereas for FTIR characterization we used samples with applied fluences of thermal neutrons of 3.0; 3.4; $4.0x10^{19}$ cm^{-2} and fluences of fast neutrons of $7.9x10^{16}$ cm^{-2}; $8.8x10^{16}$ cm^{-2} and $4.5x10^{15}$ cm^{-2} respectively. The annealing temperatures of the measured samples were 1600°C and 1750°C. The FTIR measurements were carried out with a Bruker IFS 66 v/S spectrometer. A cold finger cryostat with CsI-windows was used.

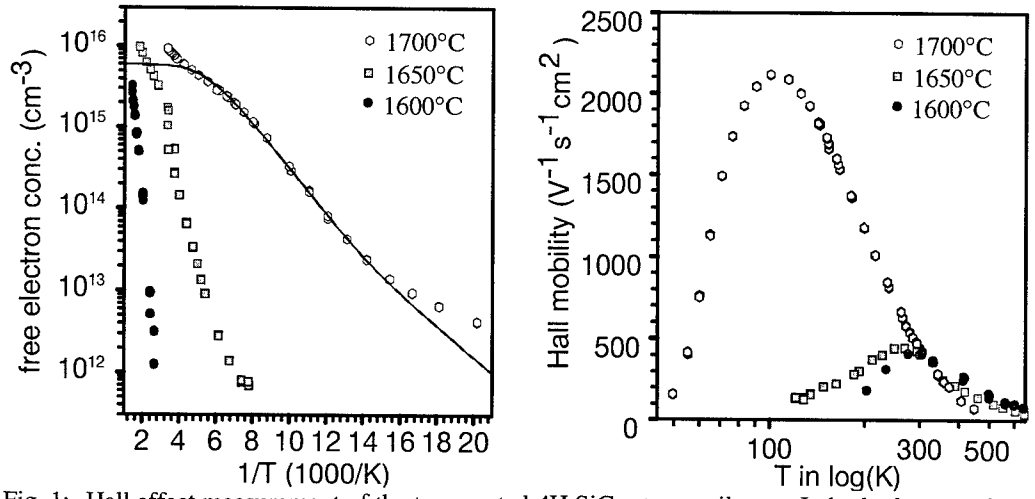


Fig. 1: Hall effect measurement of the transmuted 4H SiC n-type epilayers. In both plots are shown sucessive annealing temperatures applied: a) The analysis of the electron concentration vs. temperature (dots) gives for the donor concentration : 1.2 x 10^{16} cm^{-3}, for the compensation concentration: 5.9 x 10^{15} cm^{-3}; the ionization energies for the hexagonal lattice site (the concentrations of the P-donors on cubic and hexagonal lattice sites were assumed to be equal) is fitted (line) with 33 meV and the cubic lattice site with 99 meV respectively. b) Hall-mobility refering to the measured dots in a).

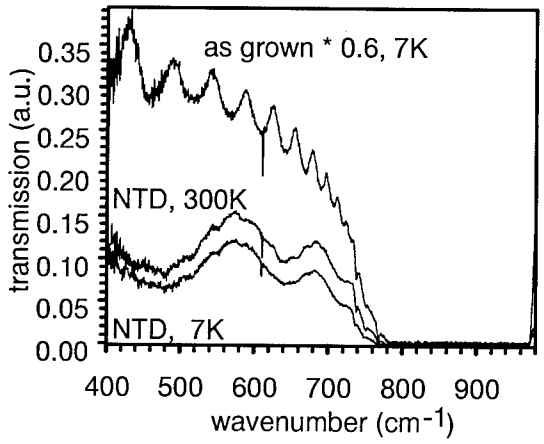


Fig. 2: Transmission up to the "reststrahlenbande" in the mid-IR. An "as grown" and a transmuted sample (annaled at 1700°C) are shown at different temperatures.

For transmission experiments the samples of about 8x8x0.4 mm were thinned stepwise by mechanical polishing and reactive plasma etching to 120 µm, 60 µm, 40 µm, 28µm. In the spectrometer the samples were rotated perpendicular to the beam to get information about lines originating from E⊥C and E∥C with the assumption that the IR-light is elliptic polarized (Fig. 4b).

Results

a) Hall-effect measurements

We measured Hall-effect to get the ionization energies for the P-donors in 4H SiC. We started the series of experiments after annealing the samples at 1600°C and addtionally carried out annealing with steps of 50°C.
After annealing at 1700°C we fitted the concentrations determined by the neutrality equation to the measured dots (Fig. 1a). So we got 33 meV and 99 meV as ionization energies for the P-donors.

b) IR-absorption

With FTIR-spectroscopy we have investigated the above described transmuted 4H SiC samples. For

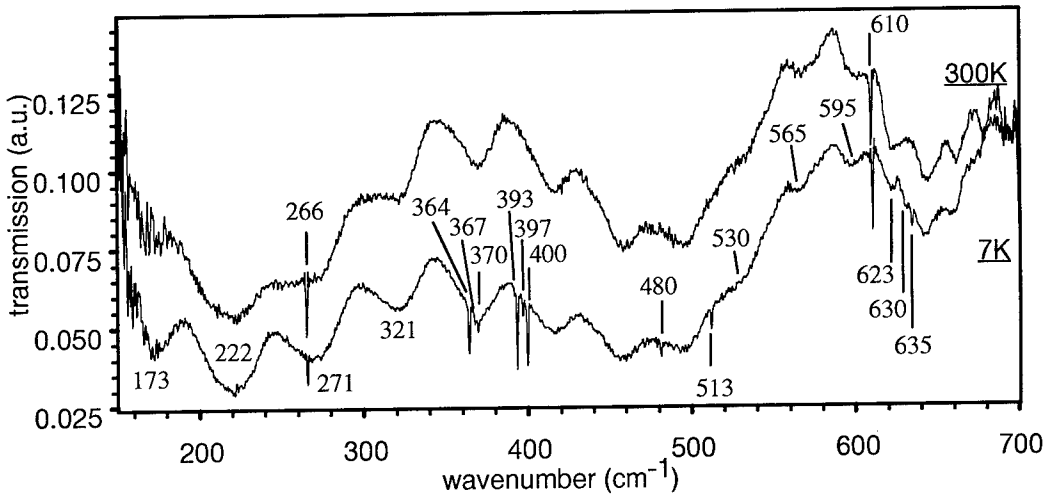


Fig. 3: Transmission over wavenumbers in the far IR of a NTD-sample measured at 300K and at 7K.

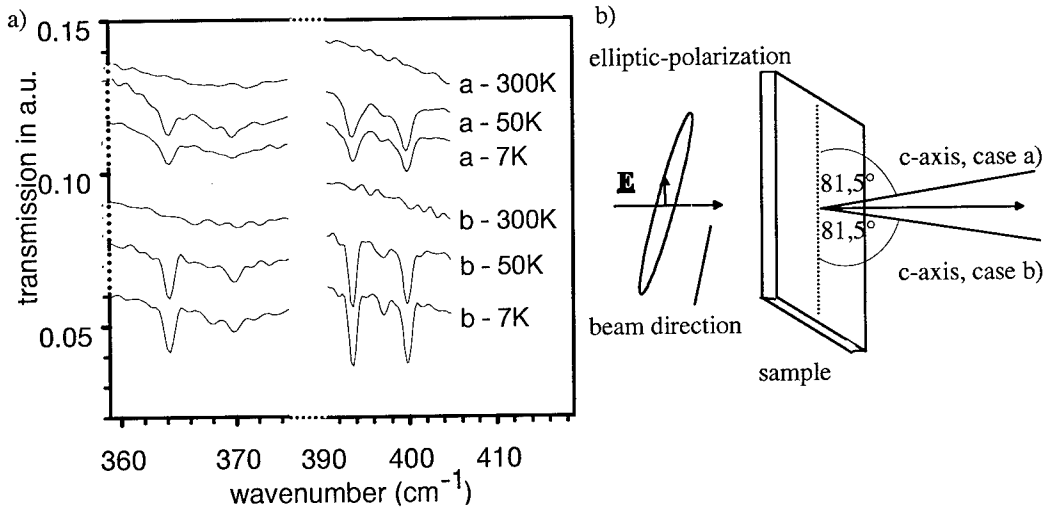


Fig. 4: In a) a detailed extract from the far IR-region with two groups of absorption lines is shown, which grow at low temperatures at about 360-370 cm^{-1} and at 390-400 cm^{-1}. In b) is shown the configuration of measurement of a). The samples are rotated by 180°C (approx. round the a - plane , with 8.5 degree deviation).

comparison a n-type sample with "as grown" epilayer was also measured. The interferences of one and moretimes passed beams in the "as grown" sample (N_D–N_A~$7x10^{14}$ cm^{-3}) prevented an evaluation of the transmission measurements of the "as grown" sample (thickness approx: 20 µm) for less than 800 cm^{-1} (fig. 2). Therefore we compared our results with pubished investigations on nitrogen in 4H SiC [2] in this region. "As transmuted" samples show applicable transmission with a thickness of 120 µm. After annealing at 1600°C the thickness has further to be reduced to 28 µm for further investigations. At energies higher as the „reststrahlenbande" (from 796 to 964 cm^{-1}) there are normally no changes due to NTD expected. But there we observed two broad temperature

independant absorption lines (at 1043 cm^{-1} and 1177 cm^{-1}). In the far IR are broader absorptions ($\approx$25 cm^{-1}) as well as a few narrow lines (1.5 cm^{-1}) appearing at low temperatures (Fig. 3). Two groups of lines between 360 cm^{-1} and 400 cm^{-1} are very conspicious. These are magnified in Fig. 4 where clearly is stated that the intensities vary with rotation of the samples in the beam (Fig. 4b). As well as one can see that both are tripletts. All sharp lines without 266 cm^{-1} and 610 cm^{-1} -which are related to accoustic phonons- develop at low temperatures therefore we assume these lines may be caused by electronic transitions.

Discussion

The high electron mobility evaluated from Hall-effect (fig. 1b) leads to low resistivity of our samples after annealing at 1700°C. This makes plausible that the annealing procedure is sucessful at 1700°C. The fit in fig. 1a shows an activation of phosphorous of 82 %, compared to the phosphorous concentration we expect from the applied neutron fluences. The ionization energy of the deep P-donor (99 meV from our Hall-effect data) is nearly equal to the energy of the optical phonons in 4H SiC ($\approx$95, 104 meV) therefore this ionization process cannot be detected by optical absorption. The observed electronic IR-transition in the 530 cm^{-1} to 650 cm^{-1} area can be attributed to transitions in excited bound states of the deep donor (597 cm^{-1}) in a hydrogenic model.

For the interpretation of electronic transition lines in the 160 cm^{-1} to 500 cm^{-1} region we have taken into account the background doping by nitrogen ($\approx 8x10^{14}$ cm^{-3}). The absorption lines in the 360-400 cm^{-1} region are in excellent agreement with transitions into excited states of the shallow N-donor [2]. We attach the absorption lines at at 173 cm^{-1}, 222 cm^{-1}, 271 cm^{-1}, 321 cm^{-1} to electronic transitions because of the temperature dependent absorption. Therefore 321cm^{-1} is related to the ionization energy of the shallow P-donor, the other lines are absorption lines to transitions in excited states of the shallow P-donor. Thus we evaluate from optical measurements an ionization energy of $\approx$40 meV compared to 33 meV from Hall-effect data. Both measurement techniques show in this respect an excellent agreement. To distinguish $E \perp C$ and $E \parallel C$ correlated absorptions further investigations have to be made.

Acknowledgement

We thank the irradiation groups of the FRG and the FRJ and the BER -reactors at the GKSS, KFA, HMI in Geesthacht, Jülich, Berlin for good cooperation. Special thanks go to the GKSS, where 8 irradiations were done. Further we thank the SFB292 and the BMBF (Kontrakt 01BM701/5) for support.

References:

[1] M.A. Capano, J.A. Cooper, M.R. Melloch, A. Saxler, W.C. Mitchel, J. Appl. Phys. 87, (2000), p.8773
[2] C.Q. Chen, R. Helbig, F. Engelbrecht, J. Zeman, Appl. Phys. A, to be published, (2000)
[3] Il`in, Kosaganova, Solomatin, Barinov, Bulgakov, Sov. Phys. Semicond. 5 (1971), p.506
[4] E.N. Kalabukhova, S.N. Lukin, E.N. Mokhov, Phys. Sol. State 35, (1993), p.361
[5] H. Heissenstein, C. Peppermüller, R. Helbig, J. Appl. Phys. 83, (1998), p.7542
[6] H. Heissenstein, H. Sadowski, C. Peppermüller, R. Helbig, Mat. Sci. For. 338 – 342, (2000) p. 853
[7] S. Tamura, T. Kimoto, H. Matsunami, M. Okada, S.Karazawa, I. Kimura, Mat. Sci. Forum 338 – 342, (2000), p.849

Materials Science Forum Vols. 353-356 (2001) pp. 373-376
© 2001 Trans Tech Publications, Switzerland

Presence of Hydrogen in SiC

A. Henry[1,2], B. Magnusson[1], M.K. Linnarsson[3], A. Ellison[4], M. Syväjärvi[1], R. Yakimova[1] and E. Janzén[1]

[1] Department of Physics and Measurement Technology, Linköping University, SE-581 83 Linköping, Sweden

[2] ABB Corporate Research, SE-721 78 Västerås, Sweden

[3] Solid State Electronics, Royal Institute of Technology, SE-16440 Kista, Sweden

[4] Okmetic AB, Hans Meijers väg 2, SE-583 30 Linköping, Sweden

Keywords: Boron, Hydrogen, Photoluminescence, SIMS

Abstract

An unexpected presence of hydrogen in 4H-SiC was revealed by the observation of hydrogen related lines in the low-temperature photoluminescence (LTPL) spectrum after secondary ion mass spectrometry (SIMS) measurements. The lines were not observed before SIMS. The high-energy ions during SIMS are proposed to break the boron-hydrogen bonds. This phenomenon is observable only for a certain impurity concentration in the material due to the competition of various recombination channels during the LTPL experiment.

Introduction

In the early seventies, Choyke and Patrick [1] reported strong bound exciton (BE) photoluminescence (PL) spectra in silicon carbide (SiC) implanted with the hydrogen isotopes, H (^{1}H) and D (^{2}H). The PL spectra in the case of H and D implantation are very similar apart from the energy positions of some prominent lines in the phonon assisted side-bands. The defect was proposed to consist of an H or D atom bonded to one of the four C atoms neighboring a Si vacancy. From as-grown epitaxial layers the H-related PL spectrum has also been observed when using specific growth conditions [2, 3]. Hydrogen is also known to form stable complexes with e.g. boron in SiC [4].

We will show in this work experimental evidence of the unexpected presence of hydrogen in 4H-SiC. Low-temperature photoluminescence spectra reveal after secondary ion mass spectrometry the presence of both boron and hydrogen related lines, which were not observable before the SIMS measurement.

Experiments

The samples used in this study were grown on a n^+ substrate either by the close space sublimation (CSS) [5] or by the high-temperature chemical vapor deposition (HTCVD) [6] techniques. The CSS technique (or sublimation epitaxy) is referred to as a "hydrogen-free" technique as growth is done generally at a reduced Ar pressure with a solid source material (polycrystalline 3C-SiC plate in our case). In the HTCVD, the transport of the growth species to the seed crystal is directly provided by high purity gas precursors such as SiH_4 and C_2H_4. The transport gas is helium, whereas both precursor gases contain hydrogen.

LTPL experiments were first performed on the as-grown samples. This was done in a bath cryostat (T=2K) with the 244 nm line of a FreD laser as excitation. The laser spot was focussed on the sample with a few mW. The penetration depth of this excitation line is theoretically less than 1 μm, however it has previously reported that the volume under study could reach a few tens of μm

depending of the material purity [7]. The luminescence was dispersed by a single monochromator fitted with a 2400 groves/mm grating blazed at 330 nm and detected by an UV sensitive CCD camera. Then, SIMS measurements were carried out on these samples with a Cameca IMS 4f microanalyse to obtain the depth profiles of impurities such as nitrogen, aluminum or boron. Usually a sputtering beam of 12.5 keV O_2^+ or 13.5keV Cs^+ ions are used depending of the impurity of interest. Finally, LTPL spectra were again recorded on the same samples.

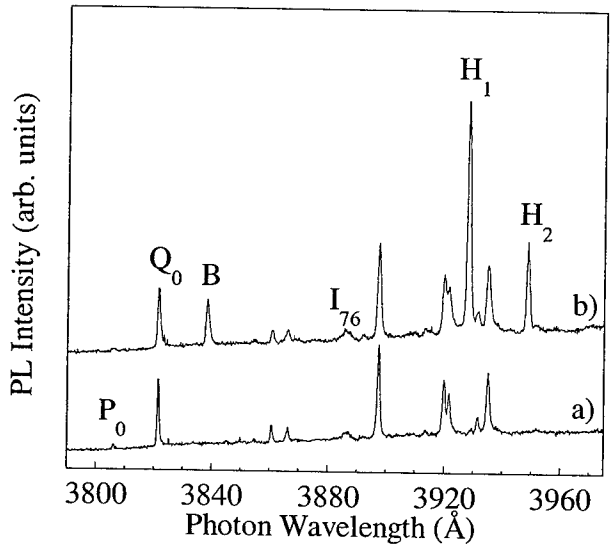


Fig.1: LTPL spectra a) before SIMS and b) after SIMS measurement of a 4H-SiC sample grown with He as carrier gas.

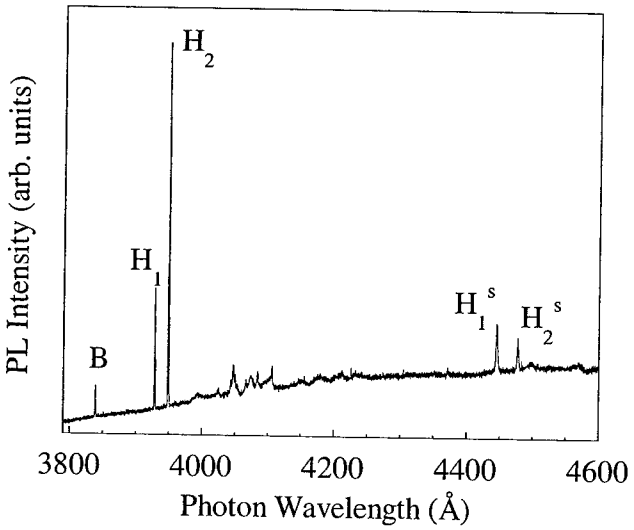


Fig.2: LTPL spectrum of a 4H-SiC sample after SIMS analysis. H_1^s and H_2^s denote the C-H bond-stretching vibrational modes.

The HTCVD samples, also included sliced and polished wafers, which could result in a rather low intensity spectrum when using the 244nm excitation, whereas the CSS samples were as grown material.

Results

A typical LTPL spectrum in the near band gap (NBG) emission of 4H-SiC high resistivity bulk sample grown with HTCVD using helium as carrier gas is shown in Fig.1.a. The spectrum consists of various sharp lines which are identified as the no-phonon lines (P_0 and Q_0) of the N-bound exciton (N-BE), and phonons replicas of the N-BE and weakly of the free exciton (I_{76}) [8]. The PL spectrum was recorded up to 6500 Å but no other emission was observed. After SIMS analysis of this sample, which reveals a boron concentration of ~ $8 \cdot 10^{15}$ cm^{-3}, a change of the NBG emission is observed (Fig.1.b). Firstly, the presence of a line at 3838 Å (labeled B in the figure) which has previously been reported as boron related [9], is detected and secondly, the H-related lines (H_1 and H_2) are clearly observed. These two H-related lines show their typical behavior with a decrease in intensity with

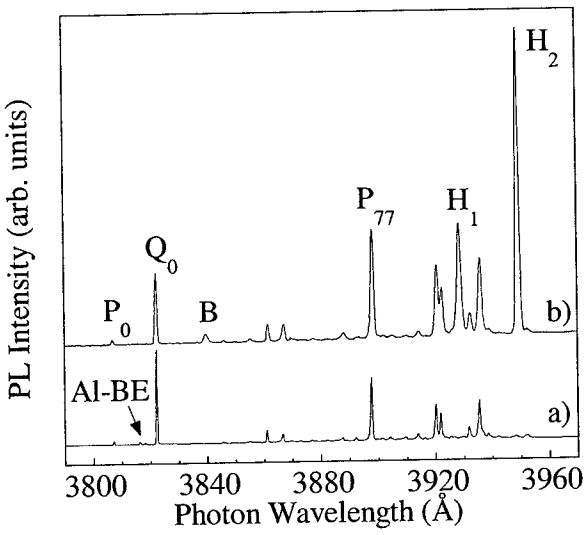


Fig.3: LTPL spectra of a CSS 4H-SiC layer a) before and b) after SIMS analysis.

excitation time at 2K [10], H_2 decreasing faster than H_1. In addition as phonon replicas the C-H bond-stretching vibrational modes at around 369 meV were observed for both H-related lines.

A second sample grown with the same HTCVD technique shows an even more pronounced change of the NBG emission spectrum. Before SIMS analysis, the NBG emission was very weakly observed (not shown here), whereas after SIMS it was dominated by the 3838 Å and H-related lines (Fig.2). The boron concentration of this special sample was particularly high ($2 \cdot 10^{17}$ cm^{-3}).

Fig.3 shows the LTPL spectra recorded from a p-type ($5 \cdot 10^{15}$ cm^{-3}) CSS sample before (a) and after (b) SIMS analysis, respectively. As can be seen, before SIMS (Fig.3.a), the N-BE and the aluminum BE were observed, and after SIMS the H-related lines are well detected together with the 3838 Å line. The Al and B concentrations were $5 \cdot 10^{15}$ cm^{-3} and $4 \cdot 10^{16}$ cm^{-3}, respectively. The Al-BE was very weakly observed after the SIMS analysis. However comparing the spectra before and after SIMS, another behavior is observed here; a change of ratio between the Q_0 and P_{77} line is also observed. The origin of the H incorporation in the CSS growth technique is proposed to be the polycrystalline SiC source, which is grown by a CVD process.

The change of the NBG emission has not been observed for (1) highly doped n-type (n $> 5 \cdot 10^{16}$ cm^{-3}) samples, (2) compensated material showing donor-acceptor N-Al pair emission in the PL spectrum or (3) samples with boron concentration $< 2 \cdot 10^{15}$ cm^{-3}, as determined by SIMS.

Discussion

LTPL spectra reveal after SIMS analysis the presence of both boron and hydrogen related lines, which were not observed before the SIMS measurement. The SIMS experiment conditions that could influence the change of the NBG emission are i) bombardment of high-energy ions, ii) electrons or iii) potential differences between the sample holder and the electron source. However, preliminary results show that the phenomenon of NBG emission change can be observed only when the high-energy ions bombard the sample, however more spectacular change is seen when all conditions to perform SIMS are satisfied. The phenomenon is observed more strongly close to the crater created by the ions, however, it may be also detected a few millimeters from the crater. It is likely that hydrogen is trapped in the material during the growth process or cool-down after the growth as a B-H complex. The high-energy ions used in SIMS analysis break the B-H bonds and release the H atoms. This hydrogen can easily diffuse and be trapped by vacancies to form the known H-vacancy center, giving rise to the PL spectrum. PL lines related to radiation damage, such as observed after electron-irradiation [11], have also been detected after SIMS analysis in low doped epilayers.

The NBG emission change has been observed for material grown with the HTCVD technique where the carrier gas is not hydrogen but helium, however the precursor gases contain hydrogen. Most important is that the SIMS influence on the PL spectrum is also observed for samples grown with a technique such as the close-space sublimation, where hydrogen can be incorporated from the polycrystalline 3C-SiC material used as a source or from water vapor in the residual gas. These growth conditions may suggest that the hydrogen concentration is not very high in these samples, however, it still can be detected by the LTPL technique.
In the case of compensated material, generally very efficient nitrogen-aluminum donor-acceptor pair emission is the dominant feature of the LTPL spectra, which is associated with an efficient recombination channel. This prevent the observation of the H-related lines, however, the H-related defect giving rise to these lines may still be present in the material. The other non-radiative channels should also be considered.

Conclusion

The unexpected presence of hydrogen in SiC can be revealed by the breaking of the B-H bond induced by the ion bombardment during SIMS analysis. Although the H and B-related lines in the PL spectra could only be observed in some samples due to competing recombination channels, the phenomenon probably occurs in all samples, irrespective of doping. Our study shows that hydrogen can exist in SiC trapped to defects.

Acknowledgment

Support for this work was provided by the Swedish Council for Engineering Sciences (TFR), the SSF program SiCEP and the European Union (Brite Euram contract No.BRPR-CT98-0815).

References

[1] W.J. Choyke and L. Patrick, Phys. Rev. B9 (1974) p.3214
[2] D.J. Larkin, phys. stat. sol (b)202 (1997) p.305.
[3] A. Schöner, K. Rottner, N. Nordell, M. Linnarsson, C. Peppermüller and R. Helbig, Diam. Relat. Mater. 6 (1997) p.305.
[4] M.K. Linnarson, M.S. Janson, S. Karlsson, A. Schöner, N. Nordell and B.G. Svensson, Mat. Sc. and Eng. B61-62 (1999), p.275.
[5] M. Syväjärvi, R. Yakimova, A. Kakanakova Georgieva, M. Tuominen, M.F. MacMollan, A. Henry, Q. Wahab, C. Hemmingsson and E. Janzén, J.Cryst. Growth 197 (1999), p.155.
[6] A. Ellison, J. Zhang, W. Magnusson, A. Henry, Q. Wahab, J.P. Bergman, C. Hemmingsson, N.T. Son and E. Janzén, Mater. Sci. Forum 338-342 (2000), p.131.
[7] A. Henry, O. Kordina, C. Hallin, M. Aroyo, T. Egilsson and E. Janzén, Phys. Rev. B 58 (1998), p. 13634.
[8] I.G. Ivanov, U. Lindefelt, A. Henry, O. Kordina, C. Hallin, M. Aroyo, T. Egilsson and E. Janzén, Phys. Rev. B 58 (1998), p13634.
[9] S.G. Sridhara, L.L. Clemen, R.P. Devaty, W.J. Choyke, D.J. Larkin, H.S. Kong, T. Troffer and G. Pensl, J. Appl. Phys. 83 (1998), p.7909.
[10] L.L. Clemen, R.P. Devaty, W.J. Choyke, A.A. Burk, Jr., D.J. Larkin and J.A. Powell, IOP Conf. Proc. No. 137 (IOP Publishing, Bristol, 1994), p.227.
[11] T. Egilsson, A. Henry, I.G. Ivanov, J.L. Lindström and E. Janzén, Phys. Rev. B59 (1999), p8008.

Materials Science Forum Vols. 353-356 (2001) pp. 377-380
© 2001 Trans Tech Publications, Switzerland

Investigation of an Ion-Implantation Induced High Temperature Persistent Intrinsic Defect in SiC

S.G. Sridhara, F.H.C. Carlsson, J.P. Bergman, A. Henry and E. Janzén

Department of Physics and Measurement Technology,
Linköping University, SE-581 83 Linköping, Sweden

Keywords: D_{II}, Persistent Defects, Photoluminescence, Time-Resolved Photoluminescence

Abstract: We report a study of the D_{II} defect spectrum in 6H SiC using different photoluminescence techniques. The spectrum is proposed to be the result of bound exciton recombination at isoelectronic centers.

Introduction

Among the various defect related spectra seen in photoluminescence (PL) of ion-implanted SiC epilayers, only two are known to persist even after a high temperature anneal of 1700°C. These persistent defect spectra have been labeled D_I and D_{II} in the literature. Both the D_I and D_{II} are observed via sharp bound exciton recombinations in the near band-gap spectral region. The D_I has been extensively studied [1,2], however no clear understanding of the actual defect origin has yet been presented. From a device perspective, the persistent nature of these defect spectra makes the defect centers responsible for them important to understand. The D_{II} spectrum has been identified in all the four major polytypes of SiC [3,4,5]. A study of the D_{II} spectrum in 4H SiC with different optical techniques has also been reported [6]. In this paper we report a study of the D_{II} spectrum in 6H SiC using time-resolved, magneto-optical,and variable temperature photoluminescence (PL) techniques.

Experimental

6H SiC epilayers implanted with Ga (implantation energy = 0.1MeV-2MeV, total fluence = $4.5\text{x}10^{13} cm^{-2}$) at 700°C with mean Ga concentration of $4\text{x}10^{17}$ cm^{-3} and subsequently annealed at 1700°C were used for this study. PL measurements were made using an Oxford variable temperature cryostat. A 244nm wavelength, frequency doubled Ar^+-ion laser was used for the excitation source. Time resolved measurements were made using a 355nm, frequency tripled, variable repetition frequency, diode pumped YAG laser. For magneto-optical measurements a He bath cryostat fitted with a 5 Tesla superconducting magnet was used.

Results and Discussion

Fig. 1 shows the no-phonon portion of the D_{II}^{6H} spectrum taken at 2K. The spectrum consists of at least four lines between 73meV to 79meV from the excitonic bandedge, at 3.023eV. They have been labeled d^1 , d^2 , d^3 and d^4 , respectively, in accordance with the labeling in the literature [5]. Vibrational modes of all four no-phonon lines are seen (not shown in figure) with the highest energy mode of 164meV, which is characteristic of this defect spectrum [2,3,4]. The relative intensities of the four lines vary between the epilayers and also between different points on the same epilayer, indicating a sensitivity to stress of the center responsible for these lines. To get a qualitative idea of the response of these lines to stress, we compared the spectrum taken when the sample was glued to a holder, to the spectrum taken when the sample was mounted in a stress-free manner by placing it in a loose pocket. The contraction of the glue at low temperature puts a compressive stress on the back of the sample causing the epilayer to bend. The stress should be in the basal plane in this case. As shown in Fig. 1 there is a clear

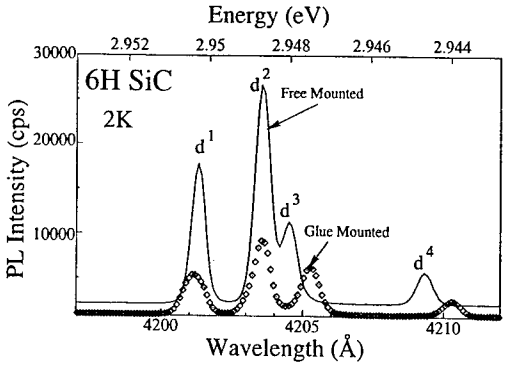


Figure 1: 2K PL spectra illustrating the sensitivity of the D_{II}^{6H} no-phonon lines to stress in the epilayer.

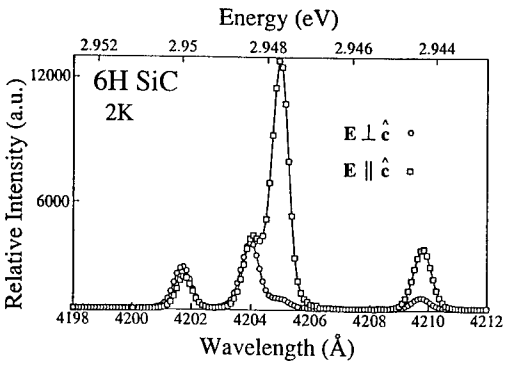


Figure 2: Polarization study of the D_{II}^{6H} no-phonon lines.

difference in the PL intensity of the four lines between the two cases. In addition lines d^3 and d^4 also shift to lower energies by 0.5meV and 0.6meV respectively when the sample is mounted with glue. The absence of splitting of any of the lines under stress might indicate that they are transitions from singlet states as was proposed in the case of nitrogen bound excitons [7]. The shifting of lines with stress was also observed in the case of the nitrogen bound excitons and was suggested to be due to change in bandgap [7]. However since only two out of the four lines in the D_{II}^{6H} spectrum exhibit a shift it is not clear if a change in the bandgap might explain the shift observed here. Nevertheless, such a strong difference between the two cases is still surprising because the implanted layer is estimated to be only 1μm while the stress is being induced from at least 300μm beneath.

The polarization properties of these lines with respect to the crystal c-axis were investigated using a Glan-Taylor prism. The sample was turned so that the c-axis pointed along the direction of the incident laser and the luminescence was collected from the side of the sample. As shown in Fig. 2, lines d^1 and d^2 show no relation to the crystal c-axis but lines d^3 and d^4 are strongly polarized parallel to the c-axis. Both the stress experiment result and the polarization result appear to indicate that the D_{II}^{6H} spectrum might actually comprise two sets of two lines originating from two different defect centers.

Temperature dependence of the no-phonon lines was measured upto 80K. The line d^4 quenches at about 20K while the remaining lines persist up to about 80K when the whole spectrum disappears. This early quenching of the d^4 line despite having the highest binding energy among the four lines suggests that it is a forbidden transition. As shown in Fig. 3, excited states between 4170Å to 4200Å can be seen when the temperature is raised from 2K. These have been labeled from 'a' to 'g'. The origin of these excited states is still under investigation. The total luminescence intensity of the no-phonon lines is plotted as a function of reciprocal temperature and is shown in Fig. 4. The PL intensity of the lines d^1 , d^2 and d^3 can be seen increasing as the temperature is increased which suggests that they may be related to excited states of the bound exciton rather than the ground state. From the quenching of the D_{II}^{6H} no-phonon lines,d^1 , d^2 and d^3 , at high temperatures, the value of the thermal activation energy is calculated to be about 69meV which is about the same value as the binding energies of the four lines. A similar result was reported for the D_{II} spectrum in 4H SiC [6]. The ratios of the areas of d^1 to d^2 and d^3 to d^4 do not fit to the Boltzmann expression, thereby indicating that the lines are not thermalized.

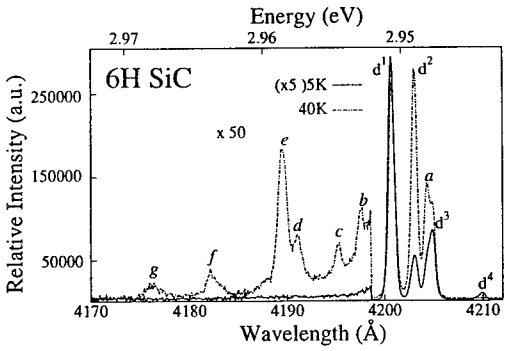


Figure 3: D_{II}^{6H} spectrum at 5K and 40K. Excited states can be seen as the temperature is raised and have been labeled from 'a' to 'g'.

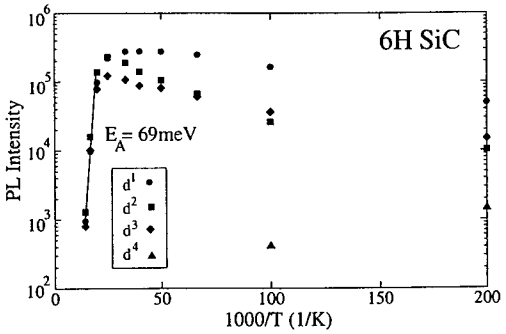


Figure 4: Arrhenius plot of Pl intensity of the D_{II}^{6H} no-phonon lines as a function of temperature. An activation energy of 69meV is obtained from the high temperature portion of the curve.

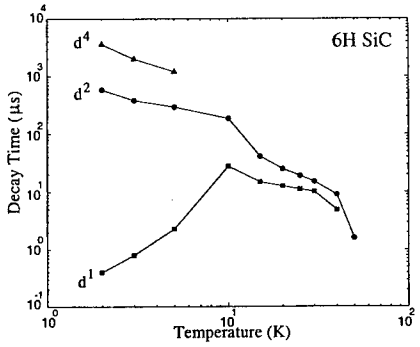


Figure 5: Variation of decay times of the D_{II}^{6H} no-phonon lines with temperature.

The luminescence decay of these lines was studied as a function of temperature and is shown in Fig. 5. Only three lines, d^1 , d^2 and d^4 could be resolved and therefore only the decay times of these lines are shown in the figure. The long decay times of these lines show an absence of competetive Auger recombination processes, which is characteristic of recombination at isoelectronic centers [2]. The very long decay time of the line d^4 indicates that it is a forbidden transition which supports the variable temperature PL data. In the case of the D_I spectrum which has been attributed to recombination at an isoelectronic center [2], a similar result was obtained for the low-temperature 'L-line', associated with the ground state of the bound exciton. On the basis of that, we propose that this line is the transition from the ground state of the bound exciton. The decay times of the two lines, d^1 and d^2 approach each other at higher temperatures indicating thermalization between the two states responsible for the two lines. The increase in the decay time of d^1 and the corresponding decrease in the decay time of d^2 at lower temperatures might then be the result of population changes between the two levels resposible for these lines. It should be remembered however that the decay time of d^2 includes that of d^3 . Based on the lower decay times of these lines and their presence at higher temperatures, we propose that d^1 and d^2 are related to excited states of the bound exciton. The presence of excited states at 2K along with their long decay times suggests a slow relaxation process between the excited states and the ground states of the bound excitons.

Zeeman measurements on the D_{II} spectrum were conducted at 2K in $\mathbf{B} \parallel \hat{\mathbf{c}}$ and $\mathbf{B} \perp \hat{\mathbf{c}}$ configurations. The $\mathbf{B} \parallel \hat{\mathbf{c}}$ measurement was made in back-scattering geometry and therefore the luminescence is polarized perpendicular to the crystal c-axis. As shown in Fig. 6, we see three lines in the spectrum. The intensity of d^3 is expected to be very small in this configuration based on polarization measurements. None of the lines show any splitting even at the highest

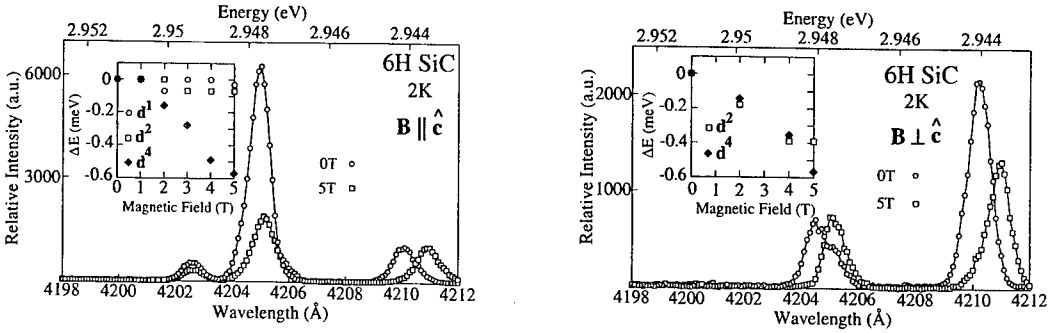


Figure 6: Zeeman measurements on the D_{II}^{6H} no-phonon lines at 2K with $\mathbf{B} \parallel \hat{\mathbf{c}}$ and $\mathbf{B} \perp \hat{\mathbf{c}}$ configurations. Insets show the shifts of the peak positions of the different lines at different magnetic fields, from their respective energy positions at zero magnetic field.

field suggesting that they are transitions from singlet to singlet states, which supports the stress experiment results. The PL intensity of the line d^1 decreases by roughly a factor of two while that of d^2 by a factor of three with increasing field. Line d^4 on the other hand shows no decrease in intensity with increase in field strength but the peak position shifts to lower energy by about 0.6meV as illustrated in the fan diagram (inset). The figure also shows the case of $\mathbf{B} \perp \hat{\mathbf{c}}$. The luminescence, in this case was measured from the side of the epilayer. The luminescence intensity was considerably weaker in this case. Only two lines d^2 and d^4 are observed in this configuration. A shoulder can also be seen in the 0T spectrum which could be the d^3 peak. As the field is increased, both lines shift to lower wavelengths. d^4 also decreases in intensity relative to d^2 as the field is increased. In comparison, no shifts or splittings were seen in the case of the D_{II} spectrum in 4H SiC [6].

Conclusion

The no-phonon lines in the D_{II}^{6H} spectrum are the result of bound exciton recombinations at isoelectronic centers. From the variable temperature CW and pulsed measurements it appears that d^4 is a forbidden transition while the other three lines are related to excited states of the bound exciton. Magneto-optical measurements suggest that these lines are transitions from singlet to singlet states. We do not believe inequivalency to be the reason for the multiple lines in the D_{II} spectrum in 6H as opposed to the single line in 4H SiC [5].

Acknowledgements

Support for this work was provided by the Swedish Council for Engineering Sciences (TFR) and the ABB Corporate Research.

References

[1] Lyle Patrick and W.J. Choyke, Phys. Rev. B **5** (1972), p. 3253.
[2] T. Egilsson, J.P. Bergman, I.G. Ivanov, A. Henry and E. Janzén, Phys. Rev. B **59** (1999), p. 1956.
[3] Lyle Patrick and W.J. Choyke, J. Phys. Chem. Solids **34** (1973), p. 565.
[4] W.J. Choyke and Lyle Patrick, Inst. Phys. Conf. Ser. No. **16** (1972), p. 218.
[5] S.G. Sridhara, D.G. Nizhner, R.P. Devaty, W.J. Choyke, T. Dalibor, G. Pensl and T. Kimoto, Mater. Sci. Forum **264-268** (1998), p. 493.
[6] A. Henry, T. Egilsson, I.G. Ivanov, C.I. Harris, S. Savage and E. Janzén, Mater. Sci. Forum **264-268** (1998), p. 497.
[7] I.G. Ivanov, U. Lindefelt, A. Henry, T. Egilsson, O. Kordina and E. Janzén, Mater. Sci. Forum **264-268** (1998), p. 489.

Materials Science Forum Vols. 353-356 (2001) pp. 381-384
© 2001 Trans Tech Publications, Switzerland

Differentiation between C and Si Related Damage Centres in 4H and 6H SiC by the Use of 90-300 kV Electron Irradiation Followed by Low Temperature Photoluminescence Microscopy

J. W. Steeds, F. Carosella, G.A. Evans, M.M. Ismail,
L. R. Danks and W. Voegeli

Department of Physics, University of Bristol, Bristol BS8 1TL, UK

Keywords: Carbon Displacement Threshold, Diffusion, Displacement Anisotropy, Silicon Displacement Threshold, Two Photon Absorption

Abstract
In this work we have been able to distinguish between silicon and carbon displacements by carrying out near-threshold electron irradiation experiments using a transmission electron microscope. The displacement energies for carbon and silicon are found, respectively, to be about 100 keV and 250 keV. After irradiation the samples have been studied by low-temperature photoluminescence spectroscopy. By carrying out the electron bombardment along (0001) and $(000\bar{1})$ directions significant anisotropy of behaviour is found near the carbon displacement threshold. While the products of silicon displacement are found to be restricted to a region of irradiation those of carbon displacements are found to extend outside this region. Spectral features of higher photon energy than the laser used are explained by a two-photon absorption process.

Experimental Details

The creation of point defects during the irradiation of SiC is of some interest in view of the need to implant the material during device fabrication. In order to study the damage process we have embarked on a study of near-threshold displacement of 4H and 6H SiC using a transmission electron microscope (TEM) with continuously variable accelerating voltage in the range 50-300 kV. After room temperature irradiation we have used low temperature photoluminescence microscopy to investigate the damaged regions; the sample temperature was nominally about 7K but depended somewhat on the laser power. An increase in power of the 325 nm laser by a factor of 100 increased the total sample temperature by about 10K. This technique has the advantage of great sensitivity and relatively high spatial resolution (down to about 1μm) but often leads to a rich variety of results where it can be difficult to distinguish the involvement of intrinsic defects from that of impurities or dopants. We have endeavoured to minimize these complications by studying n (N) and p(Al)-doped samples from a variety of sources (Cree, the Ioffe Institute, Erlangen) both as substrates and epitaxial layers. As compared with elemental semiconductors the photoluminescence spectra of SiC are much more complex. Not only are there two elements but also crystallographically distinct locations, the possibility of new defects (anti-sites) and even regions of unintended polytypes. Nevertheless, recent work from Linköping has identified silicon vacancy-related centres [1] and higher energy centres [2] in high energy electron irradiated SiC. We will compare these results with our own near-threshold observations in what follows.

Results and Discussion

Silicon vacancies
Since the atomic weight of silicon is more than twice that of carbon we carried out a series of irradiations within the voltage range of our TEM. Two clear thresholds were found, one at about 90keV and the other between 225 and 250 keV and we associate the lower threshold with the

displacement of C atoms and the higher one with the displacement of Si atoms. Fig. 1 shows a voltage sequence of spectra obtained for 4H SiC in the wavelength region 770-920 nm. In particular, the spectrum with the zero phonon line doublet at 858.9 and 861.8 nm (1.444 and 1.439 eV) and a vibronic peak with its maximum at 884 nm (1.403 eV) may be associated with the neutral Si vacancy for a number of reasons. First the spectral system is quenched at the

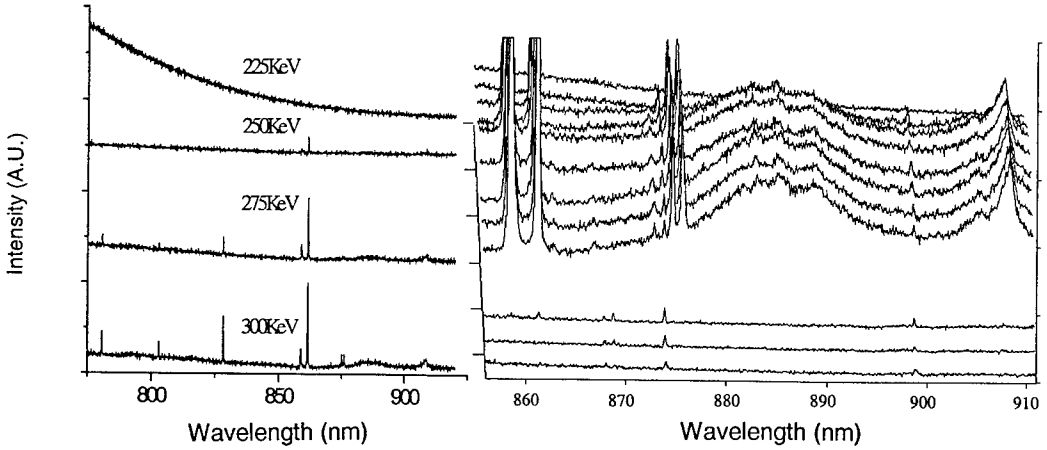


Fig. 1 Spectra obtained at different electron energies to show the onset of silicon displacements in 4H SiC

Fig. 2 Spectra obtained at 20μm spacing across a 300 keV irradiated area of 4H SiC showing the V_{Si} spectrum terminating abruptly (488 nm laser)

anticipated electron energy. Second, one of the zero phonon lines is very close to the PL peak identified by Sörman et al [1] as related to the neutral Si vacancy (1.438 eV). Third, the peak is strictly limited to the irradiated area (Fig. 2) and stops abruptly at its perimeter. This is consistent with the well-established fact that Si vacancies are not mobile below 750°C. Fourth, the spectral system bears a distinct similarity to the GR1 system of the neutral vacancy in diamond although at slightly longer wavelength. This result might have been anticipated since the V_{Si} has four nearest neighbour C atoms just as the vacancy in diamond. Indeed, the energy level calculations for the centre [3,4] give results that resemble the equivalent calculations for the neutral vacancy in diamond [5]. However, there remain several points that do not sit so well alongside these conclusions. First, the 4H SiC centre has a doublet zero-phonon line in all the samples investigated here but Sörman et al [1] only found a singlet with a second line at 1.352 eV that we do not find. Second, we have not found an equivalent centre in 6H SiC, or even a centre with broadly similar spectral properties, that vanishes at accelerating voltage below 250 kV and is restricted to irradiated region. So far our investigation has been limited to a maximum wavelength of about 960 nm. Sörman et al quote three spectral lines for the neutral silicon vacancy in 6H SiC at 1.433, 1.398 and 1.366 eV. We do find three spectral lines of approximately similar energy at 1.434, 1.398 and 1.368 eV but they did not vanish for accelerating voltages below 250 kV (some persisted down to 150 kV) their appearance and relative intensities varied considerably from one sample to another and several other spectral lines in the same wavelength range were also detected. In addition we find a number of other spectral features in 4H SiC, not previously reported, that also vanish at electron energies of less than 250 keV (at 627, 730, 803 and 828 nm). We assume that these correspond to centres created by Si displacements.

Carbon related spectra

These are mostly found in the short wavelength part of the spectrum and broadly correspond to the region described as E_A by Egilsson et al [2] but also include some longer wavelength centres that we will not describe here. Although Egilsson et al [2] have demonstrated that the true situation is very complicated in 4H SiC our results from 4H and 6H SiC are remarkably similar and can be simply described in terms of four apparently independent centres. For 4H SiC these are a complex multiplet at 434 nm (d_1 c_2 c_3 c_4 and d_2 in the notation of [2]) and spectral lines at 437.0 nm, 441.6 nm and 449.5 nm. The equivalent situation in 6H SiC is a complex multiplet at 479 nm (477.7, 478.6, 479.2, 480.5 nm) and spectral lines at 483.8 nm, 490.8 nm and 499.1 nm. In 6H SiC these spectral systems reveal a remarkable asymmetry as the carbon displacement threshold is approached depending on the direction of incidence of the electron beam, (0001) or (000$\bar{1}$). The results are illustrated in Fig. 3. For C above Si during the irradiation the only

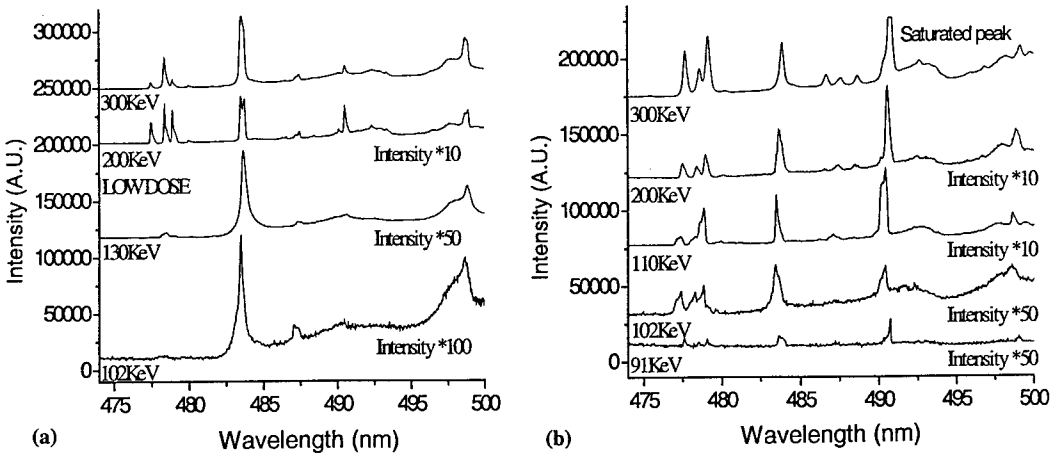


Fig. 3 Electron energy dependence of spectra obtained from (a) carbon above silicon and (b) silicon above carbon during irradiation. (325 nm laser)

spectral systems to survive below 130 keV are those at 483.8 and 499.1 nm while for Si above C all four systems remain right down to the threshold at 91 keV. One very interesting aspect of the spectra related to the C displacements is that, depending on the dose given, certain of the spectral features are found to exist well outside the irradiated region itself. The implied diffusion of C-related defects out of the irradiated zone has previously been reported in electron irradiation of diamond [6]. A simple example of this behaviour is illustrated in Fig. 2. This figure is a small portion of the spectra generated at 20 μm spacings along a line through an electron irradiated area of 4H SiC. The strong peaks are from the silicon vacancy with a sharp zero-phonon doublet and the vibronic band described earlier. On exiting the irradiated area, the V_{Si} system vanishes abruptly and the weak sharp spectral lines that remain are second order lines of the carbon-related luminescence. It is clear that these centres persist at least 40 μm into the unirradiated regions.

Excitation of higher energy systems than the laser

Fig. 4 shows an extended spectrum of 300 kV electron irradiated region of p type 4H SiC. The richness of the spectrum obtained is immediately apparent. However, careful study of the figure (see insert) reveals a more remarkable result. The spectrum evidently continues to shorter

wavelength below the notch filter in which the exciting 488 nm laser line can be seen. Moreover, the spectrum appears to be continuous either side of the notch and the spectral features observed at higher energy than the laser line are exactly what is observed from the same specimen region using a 325 nm laser. In seeking an explanation of this effect, the spectrum was found to behave in an approximately linear fashion with laser power, ruling out second harmonic generation in the SiC or two-photon absorption as a single process. A possible explanation of this effect depends on two centres with rapid energy transfer between them. Suppose centre A has an excited state near the conduction band that transfers its energy very efficiently to a nearby centre B with an excited state

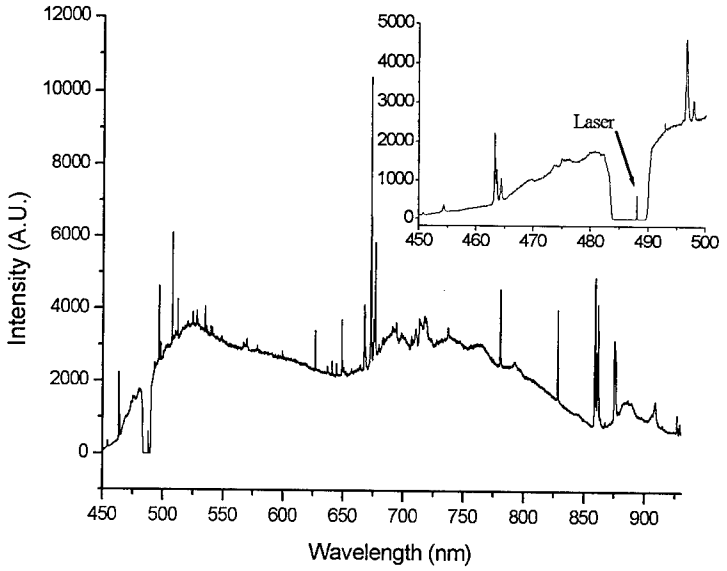


Fig. 4 Extended spectrum of 300 keV electron irradiation region of p type 4H SiC. Inset demonstrates excitation of higher energy level than the exciting 488 nm laser

of similar energy. Suppose that centre B is already excited to a long-lived state near mid-gap and that the electron transferred to the other excited state of B, near the conduction band edge, is easily transferred to the empty ground state. This would give photons of energy greater than those of the laser and also depend linearly on the laser power. The continuity of the spectrum across the notch would seem to imply that such indirect excitation mechanism predominates over direct single centre excitation processes.

The authors wish to acknowledge the supply of SiC specimens from a wide variety of sources, including DERA Malvern (Uren), Case Western University (Pirouz), University of Bath (Wang), Newcastle University (Wright) and the University of Erlangen (Ley).

References

[1] E. Sörman et al, Phys. Rev. B**61** (2000), p.2613.
[2] T. Egilsson et al, Phys. Rev. B**59** (1999), p.8008.
[3] A. Zywietz, J. Furthmüller & F. Bechstedt, Phys. Rev. B**59** (1999), p.15166.
[4] P. Deák, J. Miró, A. Gali, L. Uduardi & H. Overhof, Appl. Phys. Lett. **75** (1999), p.2103.
[5] A. Mainwood & A. M. Stoneham, J. Phys. Condens. Matter **9** (1997), p.2453.
[6] J. W. Steeds et al, Diamond and Relat. Mat. **8** (1999), p.94.

Materials Science Forum Vols. 353-356 (2001) pp. 385-388
© 2001 Trans Tech Publications, Switzerland

Infrared Investigation of Implantation Damage and Implantation Damage Annealing in 4H-SiC

J. Pernot[1], J.M. Bluet[2,3], J. Camassel[1] and L. Di Cioccio[2]

[1] Groupe d'Etude des Semiconducteurs, Université Montpellier 2, CNRS (UMR 5650), cc074, FR-34095 Montpellier Cedex 5, France

[2] CEA/LETI Grenoble, 17 rue des Martyrs, FR-38054 Grenoble Cedex 9, France

[3] Present address: LPM, INSA-Lyon, 20 av. A. Einstein, FR-69621 Villeurbanne Cedex, France

Keywords: 4H-SiC, Aluminium, Annealing, Implantation Damage, Infrared Reflectivity

Abstract

We present an infrared investigation of the effect of Al-implantation and annealing on the reststrahlen band of 4H-SiC crystals. Modeling the IR spectra with a transfer matrix method, we show that the difference corresponds with i) an increased phonon damping parameter in the implanted zones and ii) an activation of silent folded modes. After annealing all differences reduce but, still, weak folded modes manifest with large damping parameters.

Introduction

One problem, common to all SiC polytypes, is to avoid surface deterioration during implantation annealing while still recovering the full crystal properties. Using standard production tools the implantation energy is small ($\sim$ 200 keV or less) and the depth of the implantation damage is limited to a few 1000 Å. In this case, probing the recovery of the crystal properties with non destructive optical techniques is difficult. An interesting approach has been recently introduced by Sands et al. [1] using infrared techniques. In this work, we show that the same technique allows to probe the recovery of 4H-SiC samples implanted with aluminum, using standard implantation and annealing techniques.

Experimental results, analysis and discussion

Most experimental details have been already described [2]. The 4H-SiC samples were 4 μm thick n^- epitaxial layers from Cree Research with a residual doping of about $10^{16}\,cm^{-3}$. The wafer was n^+ doped to about $8 \times 10^{18}\,cm^{-3}$. Multiple-implantation was done with energy ranging from 20 to 200 keV. Four samples were targeted with, a 190 nm square-like profiles and Al concentrations: 1, 2, 4 and $10 \times 10^{20}\,cm^{-3}$ for samples #A, #B,#C and #D, respectively. The implantation temperature was fixed at 650 °C. Post-implantation anneals were done at 1670 °C in a SiC-coated graphite crucible. Short time anneals were chosen with 6 min duration. In order to prevent sample surface sublimation, additional SiC material was introduced into the crucible. After implantation, some of the Al profiles were checked by SIMS. A typical example is shown in Fig.1 (sample #A). The maximum concentration is well achieved (dashed line at 190 nm) but, because of ion channeling, a long tail manifests. This makes the concentration to decrease by one order of magnitude at about 315 nm (second dashed line). In between is a vertical line bar. It represents the average depth of damaged material assumed in this work.

Reflectivity spectra have been collected at room temperature in the range 500 - 4000 cm^{-1}. We used a Bio-Rad FTS 165 spectrophotometer equipped with a MCT detector, operated at near normal incidence. Details of the Reststrahlen band are shown in Fig.2 for the as-implanted (Fig.2-a - open circles) and annealed samples (Fig.2-c - open circles). Similar to the work of

Ref.1 we notice, before annealing, a decrease and broadening of the topmost reflectivity spectrum versus implantation dose. Quantitative values will be discussed later.

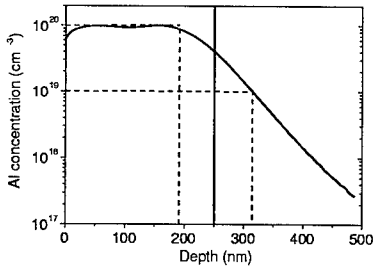


Figure 1: SIMS profile obtained for sample #A (see text).

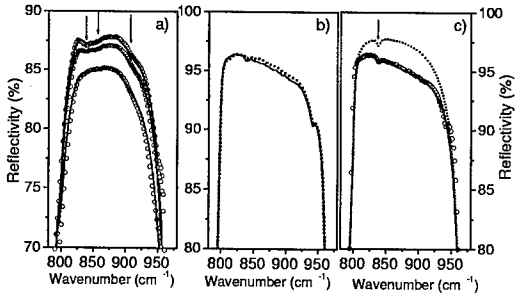


Figure 2: Near normal incidence infrared reflectivity spectra of 4H-SiC: a) samples #A #C #D before annealing (open circles) and calculation (full line), b) sample #A after annealing (full line); typical virgin sample (dotted line), c) sample #A after annealing (open circles); calculation (full line - including B_1 modes; dotted line without B_1 modes).

Table 1: Damping parameters of 4H-SiC modes in Al implanted layers.

			Damping (cm^{-1})		
	E_1(TO)	E_1(LO)	B_{1a}	B_{1b}	A_1
Annealed samples	3.5	3.5	100	120	5
Sample #A - $[Al] = 10^{20}\,cm^{-3}$	20	15	45	70	18
Sample #B - $[Al] = 2 \times 10^{20}\,cm^{-3}$	20.5	15.5	45	70	18
Sample #C - $[Al] = 4 \times 10^{20}\,cm^{-3}$	21.7	16.7	45	70	18
Sample #D - $[Al] = 10^{21}\,cm^{-3}$	26.5	21.5	50	70	25

After annealing, all spectra recover and become identical. We will consider simply the one collected on sample #A. It is shown in Fig. 2-b (full line) and compares well with a typical spectrum collected on a virgin sample (dotted line). Since there is no significant difference, we conclude that most of the cristal structure recovers after annealing. Also shown Fig. 2-c is the result of the theoretical calculation (full line). Between the TO and LO mode frequencies is a small structure at about 838cm^{-1}. This is a weak (folded) A_1-like mode coming from the axial optic branch in the extended zone scheme. It is well known from previous Raman experiments [3] and appears because of finite incidence effects. Similar observations have been made many times for other uniaxial crystals (see, for instance Ref.4 and Refs therein). Notice also that a second (weak) feature appears around 942 cm^{-1}. It is not totaly understood and will be neglected.

To model our infrared reflectivity spectra, we used a transfer matrix method and a factorized form of the dielectric function [5]:

$$\varepsilon(\omega) = \varepsilon_\infty [\prod_n \frac{\omega_{LOn}^2 - \omega^2 + i\omega\Gamma_{LOn}}{\omega_{TOn}^2 - \omega^2 + i\omega\Gamma_{TOn}} - \frac{\omega_{pn}^2}{\omega(\omega + i\gamma_n)}] \quad (1)$$

In this expression, ε_∞ is the dielectric constant at high energy; ω the photon frequency; n runs over all different oscillators considered in the fit. ω_{LO} and ω_{TO} are longitudinal and

transverse phonon frequencies; respectively. Γ_{LO} and Γ_{TO} are the corresponding damping coefficients. Finally, ω_p is the plasmon frequency and γ the plasmon damping parameters.

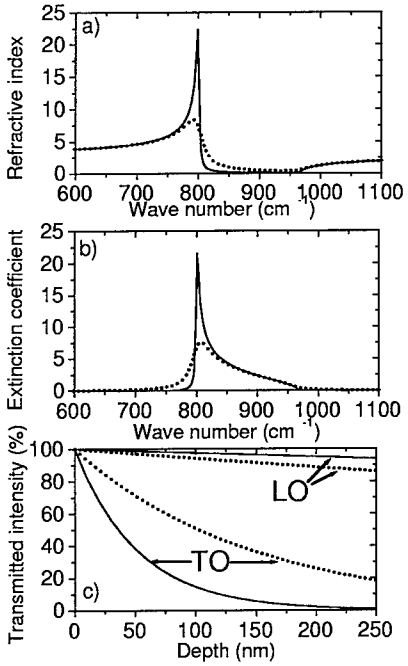


Figure 3: a) Refractive index, b) extinction coefficient and c) calculated percent depth contribution of the implanted layer to the optical response of the Al^+ implanted/ epilayer/ substrate structure. c) Results of calculation at frequencies: $\omega_{TO}(E_1) = 800$ cm^{-1} and $\omega_{LO}(E_1) = 966.4$ cm^{-1}. Full line: sample #D (10^{21} cm^{-3}) annealed. Dashed line: unannealed sample.

We have used the same nominal thickness (4 μm) for all epitaxial layers, allowing only for a small variation of 4% from sample to sample. According to SIMS, we have used an effective thickness of 250 nm for the implanted layer (full bar in Fig.1). Finally, in the three successive layers (implanted, epitaxial and substrate) we used the same phonon

frequencies: $\omega_{TO} = 800$; $\omega_{LO} = 966.4$ cm^{-1} for the main E_1 mode. The values of the epitaxial layer damping parameters were: $\Gamma_{TO} = \Gamma_{LO} = 3.5$ cm^{-1}. In the substrate, the phonon damping is about 7 cm^{-1} for the transverse mode (which is a typical value for bulk 4H-SiC) and 140 cm^{-1} for the longitudinal frequency. This is a very large value, which comes mainly from the fit of oscillations between 1000 and 1500 cm^{-1} (not shown). At the present time, it is not clear whether this comes from the phonon-plasmon interaction or (as suggested in the work of Ref.6 for 6H-SiC) from an extra layer sandwiched between the commercial epilayer and wafer.

index and extinction coefficient of the response of the 4H-SiC: Al^+ implanted/ structure. Full line : sample #D (10^{21} cm^{-3}) Dashed line : annealed sample.

To reproduce the experimental line shape in Fig. 2, it is mandatory to put four oscillators in the implanted layers:

a) E_1 with TO and LO frequencies at 800 cm^{-1} and 966.4 cm^{-1} is the main one;

b) the weak folded mode A_1 with TO and LO frequencies at 838 cm^{-1} and 837.7 cm^{-1} (inverted LO-TO splitting) already discussed;

c) finally, two additional modes with TO frequencies at 855.9 and 906 cm^{-1} and LO frequencies at 854.1 and 903.9 cm^{-1}, respectively. These modes are new.

They manifest clearly (see arrows on Fig.2.a) but have not yet been identified. The folded zone scheme predicts the presence of two B_1 folded modes near 910 cm^{-1} in 4H-SiC but group theory indicates that the B_1modes should be silent. Our results suggest that the implantation-induced disorder in 4H-SiC activates the silent modes, through a coupling with the active A_1-like frequencies, and convert them in two active infrared components. They should not be seen but, similar to the weak A_1 mode, appear through finite incidence effect. Experimental values for the phonons damping parameters of implanted layers have been listed in Table 1. We observe a general increase versus implantation dose which corresponds well with an effect of increasing damage. After annealing, the damping of the two "allowed" (E_1 and A_1) modes decrease and reach reasonably small values. The interesting result is that, on the opposite, after annealing the damping parameters of the two forbidden B_1 modes increase. On the experimental lineshape of Fig.2-c they are still present but (compared with the same sample before annealing)

they have a broadening parameter two times larger. This is because the B_1modes becoming less and less coupled to the allowed ones, the lifetime of the corresponding excitation (phonon-polariton) decreases. To confirm that such modes are indeed present, and do participate in the optical response of the final material, we display a second calculation performed with the same parameters but neglecting the two B_1−like modes (dashed line inFig. 2-c). Obviously, the agreement is much less satisfactory.

To evaluate the extent of implanted layers probed at different wavenumbers, we computed the extinction coefficient k from the standard expression of the dielectric function: $\varepsilon = (n + ik)^2$ where n is the refractive index. Extracting the real and imaginary parts of Eq.1, we have solved this equation to obtain n and k. Results are shown in Fig. 3 for sample #D (full line and dashed line for the annealed and non annealed sample, respectively). In both cases, between the LO and TO frequencies, the strong reflectivity comes from the low value of the refractive index. However, concerning the in-depth interaction, it is clear that the result is very different depending on whether one considers an incident photon frequency close to ω_{TO} or ω_{LO}. At critical value ω_{TO} the interaction is maximum, and the interaction length is minimum. One probes only the surface of the implanted layer. Between LO and TO, the extinction coefficient decreases, first, very rapidly and, then, slows down. Finally, around ω_{LO}, the interaction is weak and one starts probing more and more the total stack of layers and wafer. This is exemplified in Fig. 4. We display for the two limiting frequencies (both as-implanted and annealed samples) the percent (implanted) layer contribution to the optical response. Obviously, since the range of the unexplained structure observed in this work(around 942 cm^{-1}) is close to the region of transparency, it is not clear whether it comes from the initial material (wafer or epitaxial layer) or from some effect of polytype conversion after annealing (a A_1-like mode should be observed at 938.1 cm^{-1} in 15R polytype, see Ref. 7.)Finally, we have found that the high energy dielectric constant ε_∞ varies slightly from medium to medium. It is about 6.56 for the substrate and epitaxial layer and about 10% larger for the implanted layer. This suggests the presence of residuals silicon droplets in the annealed silicon carbide lattice [8].

Conclusion

We have shown that infrared reflectivity constitute a very useful tool to investigate the amount of implantation damage and implantation damage annealing in 4H-SiC. We do not explain all details of the experimental spectra but we have shown that some forbidden B_1 modes certainly contribute.

References

[1] D. Sands, P.H. Key, M. Schlaf, C.D. Walton, C.J. Anthony and M.J. Uren, Mater. Sci. Forum 338-342 (2000), p. 655.
[2] J.M. Bluet, J. Pernot, J. Camassel, S. Contreras, J.L. Robert, J.F. Michaud and T. Billon, J. Appl. Phys. 88 (2000), p. 1971.
[3] D.W. Feldman, J.H. Parker, W.J. Choyke and L. Patrick, Phys. Rev. 173 (1968), p. 787.
[4] A. Goullet, J. Camassel, L. Martin, J. Pascual and E. Philippot, Phys. Rev. B 40 (1989), p. 5750.
[5] F. Gervais and B. Piriou, Phys. Rev. B 10 (1974), p. 1642.
[6] M.F. MacMillan, W.J. Choyke and R.P. Devaty, Springer proceed. Phys. 71 (1992), p. 216.
[7] J.M. Bluet, K. Chourou, M. Anikin and R. Madar, Mater. Sci. Eng. B 61-62 (1999), p. 212.
[8] B.G. Svensson, A. Hallén, M.K. Linnarsson, A.Y. Kuznetsov, M.S. Janson, D. Åberg, P.O. Persson, L. Hultman, L. Storasta, F.C.H. Carlsson, J.P. Bergman, C. Jagadish and E. Morvan, Mater. Sci. Forum 353-356 (2001), p. 549.

Materials Science Forum Vols. 353-356 (2001) pp. 389-392
© 2001 Trans Tech Publications, Switzerland

Investigation of Electroluminescence across 4H-SiC $p^+/n^-/n^+$ Structures Using Optical Emission Microscopy

A. Galeckas[1], J. Linnros[1], B. Breitholtz[1,2] and H. Bleichner[2]

[1] Department of Electronics, Royal Institute of Technology, Electrum 229, SE-16440 Kista-Stockholm, Sweden

[2] ABB Corporate Research, SE-721 78 Västerås, Sweden

Keywords: 4H-SiC, Carrier Recombination, Diffusion Length, Electroluminescence, Imaging Spectroscopy

Abstract. Studies have been conducted on the carrier recombination radiation properties across operating 4H-SiC $p^+/n-/n^+$ structures. Spectral and spatial distributions of the electroluminescence (EL) emitted from the cross-sectional plane of forward biased diodes were investigated by combining optical emission microscopy and imaging spectroscopy techniques. The spectral content of the luminescence across the active region was analyzed as a function of injection in a temperature range of 300-500K. At low currents deep-boron related recombination is dominating within the *p-n* junction region and with rising forward bias is gradually taken over by emission from the injection regions via shallow-dopant transitions. Interestingly, this band-edge EL component is found to extend deep into the substrate, apparently resulting from excess carrier diffusion and recombination. The effective diffusion length of holes was estimated from the profiles of EL penetration into the 4H-SiC substrates. The observed dissimilarity of EL penetration in different diodes is discussed considering carrier trapping and processing-induced effects.

Introduction

Efficient control of SiC material growth and processing properties is a key issue for reliability of electronic applications. Currently, well developed electrical methods (IV, DLTS, CV, etc.) are routinely applied for general device characterization. An increasing concern and interest in device performance-limiting factors, however, calls for a diagnostic technique capable to provide a direct insight into both SiC material properties and dynamic processes taking place in an operative device. Actual distributions of temperature, carrier lifetime, diffusion and injection across the base are highly imperative for optimization of device design. All direct methods to measure carrier diffusion length use a form of excitation, i.e., either an electron beam, a current injecting tip or a light source. The electron-beam induced current (EBIC) technique is well developed and retains high spatial resolution [1]. An alternative way for accurate determination of minority carrier diffusion length could be based on optical emission microscopy method. In this work, we report on a technique capable to analyze spatially and spectrally mechanisms of recombination emission in the active region of forward biased *p-n* devices. In addition, we investigate it's potential to estimate carrier diffusivity parameters from the spatial distribution of injected carriers.

Experimental

We have investigated several different 4H-SiC $p^+/n-/n^+$ and *p-n* diodes with *Al* or *Al/B* co-implanted p^+ anodes. Nominally 25 μm-thick low-doped n^- base layers were epitaxially grown by CVD on commercial n^+ substrates [2]. The utilized technique is based on spectrally resolved imaging of EL emitted from the cross-sectional plane of forward biased diodes. Thus, strip-shaped specimens with centermost located diodes were cut out from the wafers and one of the sidewalls

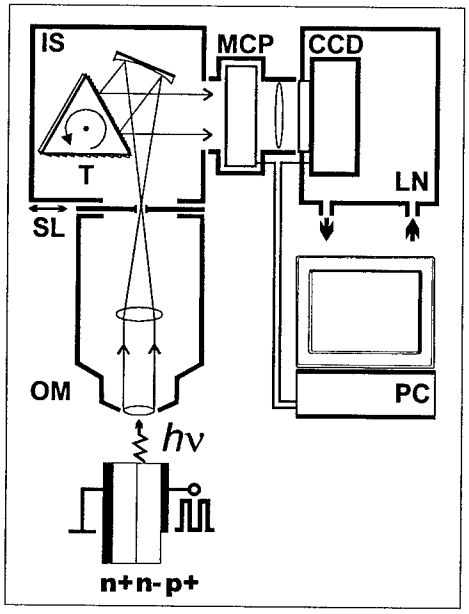


Fig. 1. Schematics of the optical emission microscopy setup: IS - Imaging Spectrometer, T - interchangeable Turret cassette with 2 gratings and mirror, MCP - Micro-Channel Plate image intensifier, CCD - Liquid Nitrogen cooled Charge Couple Device camera, SL - motorized Slit, OM - Optical Microscope, PC - computer controller. *p+/n-/n+* structure is mounted on a thermal chuck in a cross-sectional imaging configuration.

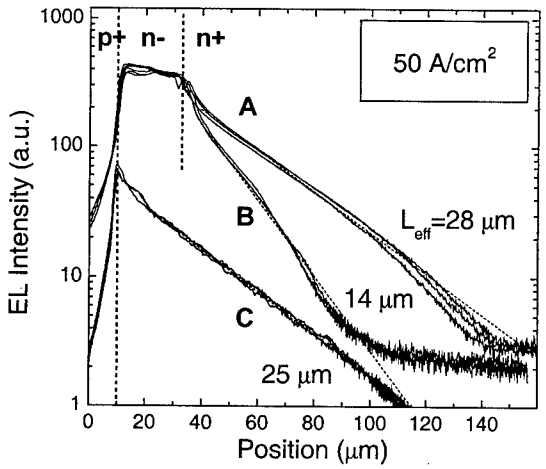


Fig. 2. In-depth variation of the integrated EL emission in different 4H-SiC *p+/n-/n+* structures (A and B) and *p-n* diode (C). Curves within groups represent different measurement positions across diodes.

was then polished straight to the edge of the diodes. An optical emission microscopy setup equipped with a LN-cooled digital CCD camera (*Hamamatsu* C4880-10), gated image intensifier and an imaging spectrometer (*Spex* Triax-190) was employed to obtain the in-depth distributions of EL in a temperature range of 300-500K. Forward biasing was provided in pulsed mode (10 μs duration, 5 kHz repetition rate), yielding current densities in the range 1-200 A/cm^2. The spectral response of the system is in the 200-950 nm wavelength range, whereas the spatial resolution is defined by the 1000×1000 pixels of the CCD sensor. An optical image or a spectral line-scan can be acquired by selecting either a mirror or an optional grating on the interchangeable turret cassette inside the spectrometer. The width of the motorized entrance slit, positioning of the turret, acquisition, amplification and processing of the images were controlled by a computer. A sketch of experimental the setup is shown in Fig. 1.

Results and Discussion

The preliminary imaging of recombination radiation performed in cross-sectional geometry has revealed an extensive propagation of the EL inside the *n+* substrate. Figure 2 summarizes typical in-depth distributions of the integrated (full spectrum) EL emission measured in different diodes. Note an apparent difference in light penetration depth L_{eff} for diodes A and B. To clarify the origin of this phenomenon, EL from the entire active region has been scanned spectrally and analyzed as a function of injection in a temperature range of 300-500K by applying imaging spectrometry technique. A characteristic spectral content of the EL across the *p+/n-/n+* structure is presented in Fig. 3, where the top panel clarifies the layout of spectral imaging. First, the test sample is aligned so that the region of interest appears in the center of the optical image, then the mirror inside the spectrometer is substituted by a grating, and the width of the entrance slit is adjusted for the preferred spectral resolution. It should be emphasized that a single spectral image contains an

immense amount of information. Any horizontal sectioning provides an in-depth EL intensity profile at any selected wavelength, while the vertical one - EL emission spectra at any selected depth. Figure 4 illustrates typical EL spectra from the *p-n* junction region, from the central part of *n-* base and from the *n+* substrate alone. The dominating "blue" peak in the region of 400 nm mainly involves free-to-bound transitions through *N*-donor and *Al*-acceptor levels and also free carrier recombination. A broad "green" peak around 514 nm is attributed to optical transitions of free electrons to neutral deep *B*-acceptor. In addition, intrinsic and post-implantation defects give rise to energetically deep levels in the band gap [3, 4] with the corresponding peaks in the red region of the EL spectrum. Our results show that both with rising temperature and forward bias, the prevailing at low currents deep-*B* related recombination within the *p-n* junction region is gradually taken over by emission from the injection regions via shallow-dopant transitions. Interestingly, this band-edge EL component is found to extend deep into the substrate, apparently resulting from excess carrier diffusion and recombination (see Fig. 3.). The effective diffusion length of holes was estimated from the profiles of EL penetration into the 4H-SiC substrates, for different diodes yielding values in the range from 14 to 28 μm at room temperature. Measurements of both *p+/n-/n+* and *p-n* diodes have revealed a general decrease of characteristic EL penetration depth with temperature. Conversely, no changes in L_{eff} were observed versus forward current density.

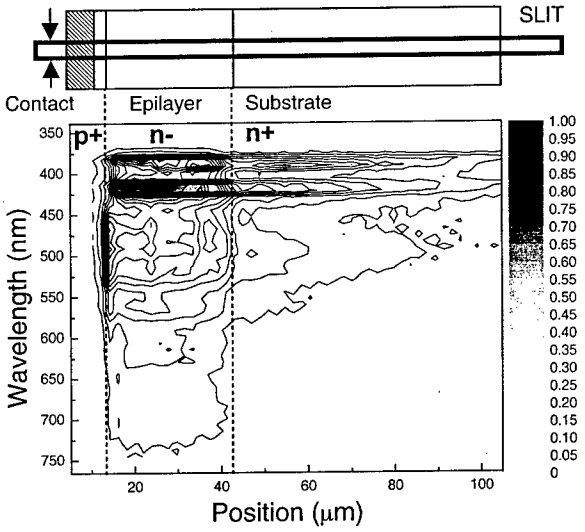


Fig. 3. Spectral content of EL emission across the 4H-SiC p+/n-/n+ structure at T=300K and 100 A/cm^2.

Generally, a probability exists that light generated in the active region might be dispersed by some scattering centers, homogeneously distributed throughout the volume of the substrate material. Considering the light absorption properties of 4H-SiC, the spectral contents of EL emitted from the active region is supposed to go deeply into optically passive areas of the substrate. Specifically, the self-absorption of the shortest wavelength peak in the EL spectrum around 391 nm provides penetration depth α^{-1} of more than 1.1 mm [5]. Clearly, no correlation with the typical EL penetration depths observed in this work can be considered.

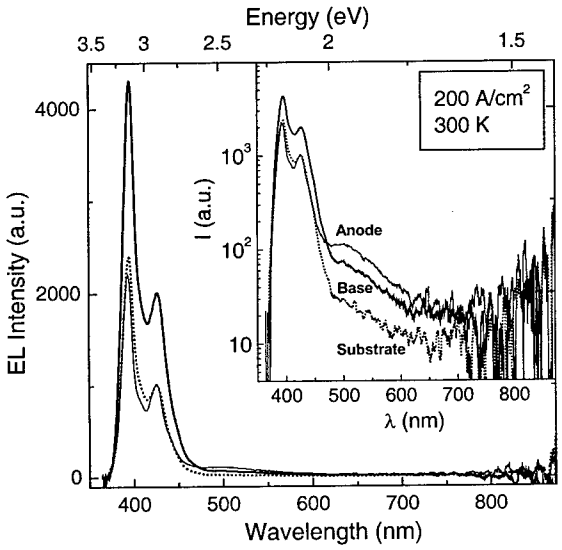


Fig. 4. EL spectra from the *p+/n-* junction region, center of the *n-* base and *n+* substrate, respectively.

The effective lifetime τ is the most critical parameter in determining the effective diffusion length, since $L_{eff} = (D\tau)^{1/2}$. Considering the hole diffusion constant D = 2.6 cm^2/s, the experimentally observed L_{eff} values of about 30 μm insist on unrealistic carrier lifetimes of a few microseconds. Instead, a non-linear carrier relaxation and relatively low τ values in the range of 10-100 ns are commonly observed for the substrate material, mainly as a consequence of inferior crystalline quality. Moreover, the high doping of substrates also implies that higher-order recombination mechanisms, i.e., bimolecular and Auger, are also involved. On the other hand, carrier trapping phenomenon is usually of major concern in wide band-gap semiconductors as 4H-SiC. In contrast to fast processes of trap filling and free-carrier recombination, the relaxation of captured carriers may well take tens of microseconds and more [6]. Generally, an increase of the minority carrier lifetime occurs when recombination traps, which control the lifetime in the substrate, are filled at high concentrations. The holes injected into the substrate may recombine through the trap centers in a radiative way and thus directly contribute to the luminescence yield, while the particular diffusivity and lifetime parameters delineate the in-depth EL distribution. In this way, the experimentally observed extensive L_{eff} is most likely a consequence of the saturation of the dominating recombination channel. The discrepancy in L_{eff} values observed in diodes A and B can therefore be explained taking into account differences in thermal treatment during processing, resulting in different trapping properties of the substrates.

Summary

Our results suggest that emission microscopy in combination with imaging spectrometry is a direct and highly informative technique for localization and analysis of recombination emission in operating devices. We demonstrate its capability to provide carrier diffusivity characteristics along with the spatial distributions of these parameters over the active device area. The estimated extended penetration depth of minority carriers into the highly doped substrate material might be explained considering carrier-trapping effects. The observed dissimilarity of L_{eff} in different devices is attributed to differences in thermal pretreatment.

Acknowledgments

This work was financially supported by the *SiCEP* project of the Swedish Foundation for Strategic research. The ABB Corporate Research SiC Program is gratefully acknowledged for providing test structures used in this study.

References

[1] M. Tabib-Azar, S.M. Hubbard, and C.M. Schnabel, J. Appl. Phys. 84 (1998), p. 3986.

[2] O. Kordina, C. Hallin, A. Henry, J.P. Bergman, I. Ivanov, A. Ellison, N.T. Son, E. Janzen, Phys. Stat. Sol. (b) Vol. 202 (1997), p. 321.

[3] T. Dalibor, G. Pensl, H. Matsunami, T. Kimoto, W. J. Choyke, A. Schöner, and N. Nordel, Phys. Stat. Sol. (a) Vol. 162 (1997), p. 199.

[4] T. Troffer, M. Schad, T. Frank, H. Itoh, G. Pensl, J. Heindl, H.P. Strunk, M. Maier, Phys. Stat. Sol. (a) Vol. 162 (1997), p. 277.

[5] S.G. Sridhara, R.P. Devaty, and W.J. Choyke, J. Appl. Phys. 84 (1998), p. 2963.

[6] A. Galeckas, J. Linnros, M. Frischolz, K. Rottner, N. Nordell, S.Karlsson, V. Grivickas, Mater. Sci. Engineering Vol. B61-62 (1999), p. 239.

Materials Science Forum Vols. 353-356 (2001) pp. 393-396
© 2001 Trans Tech Publications, Switzerland

Defects Characterization in SiC by Scanning Photoluminescence Spectroscopy

L. Masarotto, J.M. Bluet, M. Berenguer, P. Girard and G. Guillot

[1] Laboratoire de Physique de la Matière (UMR CNRS 5511), Institut National des Sciences Appliquées de Lyon, 20 avenue A. Einstein, FR-69621 Villeurbanne Cedex, France

Keywords: Denuded Zones, Dislocation, Gettering, Photoluminescence, Spectral Mapping

Abstract : Integrated and spectrally resolved PL scanning was investigated in 6H-SiC epitaxial layers under a laser excitation with a photon energy of about 5.08 eV. Highly spatial resolved measurements revealed the presence of microscopic pattern (5-20 μm) where the integrated PL intensity increases. We suggest that the gettering effect of dislocations trough their strain field is responsible for these microscopic intensity variations. Spectrally resolved PL mappings shows an enhancement of the near band edge peak intensity and width which confirm the presence of a denuded zone in the neighbourhood of the dislocation.

1. Introduction

During the last several years, tremendous progress in SiC bulk growth and epitaxy has been realised. Nevertheless, the non uniformity of impurity and defect distribution in SiC wafers (particularly in semi-insulating one) and the doping inhomogeneities of the epitaxial layers still act as show-stopper for high performance and high reliability devices development. This is why a spatially resolved, non destructive and few time consuming characterization tool is strongly needed for a tight quality control of the wafers.

Photoluminescence (PL) mapping is a non-destructive and fast method for spatial profiling of impurities and defects in semiconductors. For instance, the method has been successfully utilized for the characterization of the dominant midgap donor EL2 in semi-insulating GaAs wafers [1], for dislocations mapping in InP and GaAs bulks and epitaxial layers [2-4], and for revealing oxygen precipitates [5, 6] and dislocations [7] in Si wafers. The first results related to SiC [8, 9] indicates that PL imaging is a very promising tool for material characterization. This is why we have adapted a integrated PL imaging system from 'SCANTEK' company in order to make integrated and spectrally resolved PL scanning for evaluation of SiC epitaxial layers and bulk wafers. In this study, we evidence, from the PL spatial and spectral profiling, the ability of PL scanning to reveal the screw dislocations in 6H-SiC epitaxy.

2. Experimental procedure

The samples used in the present study are n-type (10^{16} cm-3) 6H SiC epitaxial layers purchased from a commercial source. A block diagram of the PL scanning apparatus is shown in Fig.1. A beam from a doubled Ar ion laser (244 nm) passes through a chopper and a low-pass filter and is then focused to a diameter of about 1 μm on the surface sample using an objective mirror (magnification ×52) of focal length 3.6 mm. The luminescence light is then collected by the objective, dispersed by a monochromator (BENTHAM TM300) and detected by a photomultiplier (HAMAMATSU 5701-50). The electric signal from the PM is amplified by a lock-in (EGG 5209),

and recorded on a computer trough an A-D converter. The sample is placed on a precision x-y stage which can move it by 102 mm in both *x* and *y* directions with a maximal precision and a reproducible adjustment of 1 µm. The *x-y* stage is driven by 3 step by step motors which are controlled by electric pulse from the computer. This one also drives the rotation of monochromator's turret and allows to select a mirror for an integrated PL measurement or a grating for a spectral mapping. We have two grating to cover a spectral range from 0.3 µm to 1.7 µm. One (1200 grooves/mm, blazed at 400 nm, spectral range 0.3-0.9 µm) is associated with the PMT and the other (600 grooves/mm, blazed at 1.1 µm, spectral range 0.8-2.5 µm) disperses the PL collected towards the InGaAs photodetector to make soon measurements in the infrared range. The spectral resolution is 1 nm and our computer program can make a spatial profile of the peak intensity, the peak wavelengths, the Full Width at Half Maximum (F.W.H.M.) and the Half Maximum Positive wavelength (λ_{HMP}).

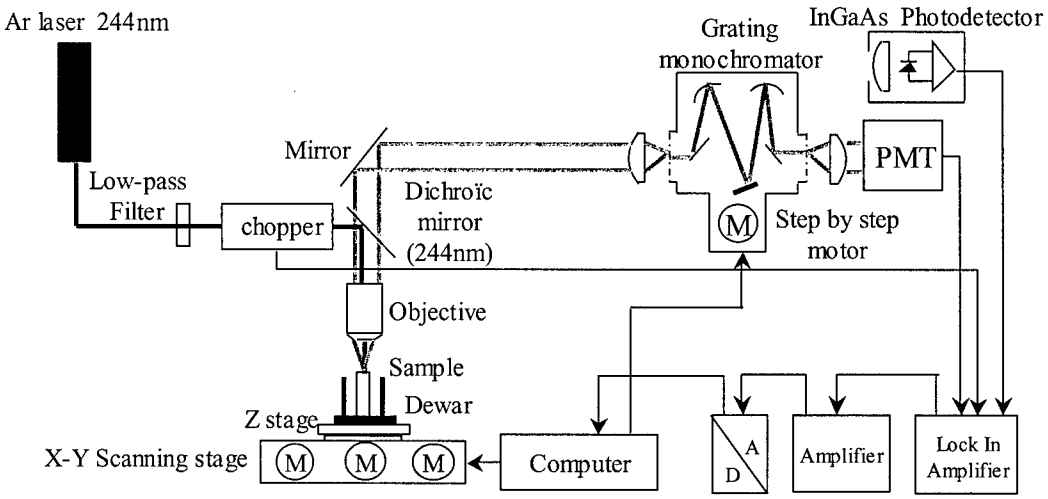


Fig.1 : Block diagram of the experimental setup

3. Results and discussion

Integrated PL images have first been realized. On all the investigated samples, an arbitrary distribution of bright spots (high PL intensity) has been observed. Their density is ranging between 6.10^3 cm^{-2} and $1.2*10^4$ cm^{-2} depending on the sample. On the samples periphery well defined lines formed by closely spaced bright spots were also observed. An example showing 20 of these high PL intensity cells is displayed on fig. 2. Their dimension is ranging between few micrometers to 20 µm. For the three whiter ones, an asymmetric intensity pattern with extension of the bright zone along a preferential direction is clearly observed. For the brightest zones the integrated PL

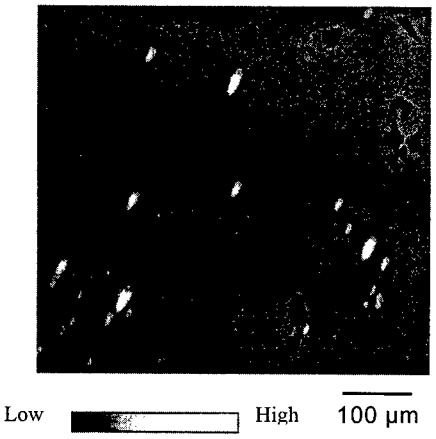


Fig. 2 : Integrated PL intensity mapping of a $0.6*0.6$ mm^2 zone.

intensity is approximately one order of magnitude higher than in the rest of the sample. The density of these bright spots and their distribution imply that they are due to elementary screw dislocations. In order to confirm this hypothesis and to analyse the origin of this localized PL intensity exhausts we have next performed spectral PL mapping in the range 400 – 800 nm with high spatial resolution. Either on the high intensity regions or around them, only near band edge PL signal was found. It consists of a predominant peak at 2.98 eV and a shoulder on the lower energy side at 2.850 eV. This correspond to previously reported values obtained in classical PL measurement [10]. High spatial resolution mapping of the spectral parameters for the predominant near band edge peak are displayed in fig. 3. Fig. 3a) is an integrated PL mapping realized around a bright spot described above. Fig. 3b) and 3c) are respectively the intensity mapping and the FWHM mapping of the 2.98 eV peak in the same spatial zone.

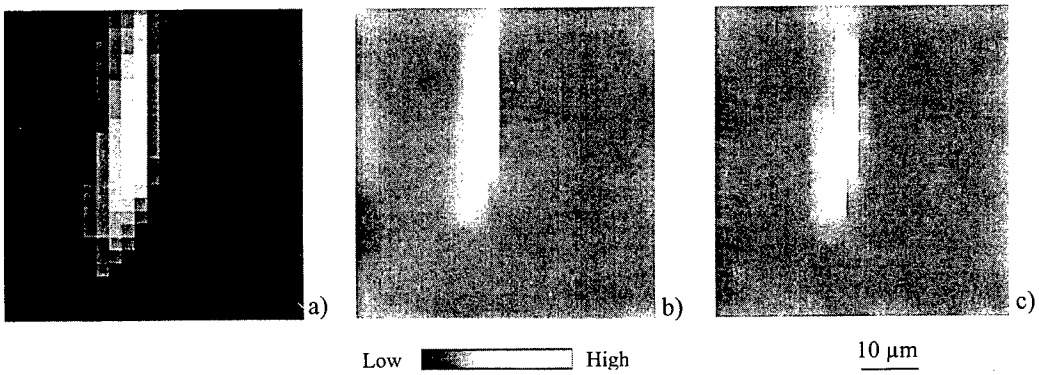


Fig. 3 : Pl mapping of a bright zone with 3 µm spatial resolution. a) Integrated PL intensity, b) 2.98 eV near band edge peak intensity, c) Full Width at Half Maximum for this peak.

We clearly obtain a very good correlation between the integrated PL scanning image and the spectral parameters ones. Classical PL measurement as a function of temperature revealed that N bound exciton lines disappear above 100 K in our samples. In consequence, the peak at 2.98 eV measured at room temperature probably arises from free exciton recombinations. In the case of FE the luminescence intensity is limited by the recombination via non radiative traps acting as lifetime killer centres. Therefore we attribute the local enhancement of the PL to a cleaning of lifetime killer centres in these zones. This phenomenon has been observed in liquid encapsulated Czochralski (LEC) GaAs and attributed to the presence of dislocations [11]. Indeed, impurities and microdefects can be gettered by the strain field existing in the neighbourhood of an extended defects like a dislocation. This result in a local cleaning of a zone around the defect much greater than the defect itself which is known as the denuded zone. In our case, we think that the bright spots we observe, are due to denuded zones in the vicinity of elementary screw dislocations. In this hypothesis, we should observe a small dark point in the centre of the bright cell corresponding to the decorated dislocation core which we have not found even with 1 µm spatial resolution. This can be due either to an insufficient spatial resolution or to a lateral diffusion length of the exciton greater than the spatial resolution. The FWHM observed in fig. 3c is relatively important with a relative variation of 20 %. This peak width enhancement is also consistent with the presence of a dislocation. Indeed, the strain field in the dislocation boundary implies modifications of the band structure resulting in the enlargement of the peak. This phenomenon has been clearly observed for InP and Si doped GaAs [2].

From the previous discussion we so propose that the bright spots observed in our integrated measurements are due the denuded zone around screw dislocations. Nevertheless we cannot

conclude that all the integrated PL intensity come from the near band edge recombination. Indeed some infrared contribution due to gettered metallic impurity like V can also be included in the integrated PL signal. The spectral extension of our equipment in this region, described in section 2, will give us information on this possible effect.

4. Conclusion

A unique PL scanning apparatus, working in the UV range (244 nm for excitation), has been developed with a spatial resolution of 1 μm, a scanned area up to 10*10 cm^2, a spectral resolution of 1 nm and a spectral range cover from 0.3 μm to 1.7 μm. Using this equipment, we have evidenced the gettering effect, due to the strain field, of microdefects acting as lifetime killer centres around the elementary screw dislocations in 6H-SiC epitaxial layers. The understanding of this gettering effect is of crucial importance for the development of SiC devices. For instance, the presence of minority carrier lifetime killers in the screw dislocations vicinity is detrimental for bipolar devices applications.

Acknowledgements
Financial support was received from the Rhône – Alpes region.

References

[1] M. Tajima, Appl. Phys. Lett. 53 (1988), p. 59.
[2] C. Klingelhoffer, PhD Thesis, Ecole Centrale de Lyon, 1995.
[3] M.K. Nuban, PhD Thesis, Ecole Centrale de Lyon, 1996.
[4] P. Bunod, PhD Thesis, University Joseph Fourier of Grenoble, 1989.
[5] M. Tajima, T. Masui and T. Abe: Semiconductor Silicon 1990, eds. H. R. Huff, K.G. Barraclough and J. Chiwaka (Electrochem. Soc., Pennington, 1990), p. 994.
[6] Y. Kitagawara, R. Hoshi and Takenaka, J. Electrochem. Soc. 139 (1992), p. 2277.
[7] J.L. Weyher, P.J. Van der Wel and C. Frigeri, Semicond. Sci. Technol. 7 (1992), p. A294.
[8] M. Tajima, Y. Kumagaya, T. Nakata, M. Inoue and A. Nakamura, Mater. Sci. Forum 264-268 (1998), p. 481.
[9] M. Tajima, Y. Kumagaya, T. Nakata, M. Inoue and A. Nakamura, Jpn. J. Appl. Phys. 36 (1997), p. L1185.
[10] A. Henry, J.P. Bergman, O. Kordina, C. Hallin, I.G. Ivanov and E. Janzen, Inst. Phys. Conf. Ser. N° 142 (1996), p. 357.
[11] S.K. Krawczyk, Encyclopaedia of Advanced Materials, Pergamon Press Oxford, (1994), p. 2318.

Materials Science Forum Vols. 353-356 (2001) pp. 397-400
© 2001 Trans Tech Publications, Switzerland

Absorption Measurements and Doping Level Evaluation in n-Type and p-Type 4H-SiC and 6H-SiC

R. Weingärtner, M. Bickermann, D. Hofmann, M. Rasp,
T.L. Straubinger, P.J. Wellmann and A. Winnacker

[1] Department of Materials Science 6, University of Erlangen-Nürnberg,
Martensstr. 7, DE-91058 Erlangen, Germany

Keywords: Absorption Band, Absorption Mapping, Doping Level Determination, Polytypism

Abstract

An optical characterization method based on the fundamental absorption bands in SiC is presented for determination of the spatial distribution of doping level concentration in n-type 4H- and 6H-SiC and p-type (Al, B) 6H-SiC. Band gap related absorption has been calculated numerically taking into account band filling, band shrinkage and band tailing effects and has been compared with experimental data. In addition, below band gap absorption transitions in n-type 4H-SiC and p-type (B) 6H-SiC at 460nm and 730nm, respectively, have been investigated. Calibration plots correlating these absorption bands with the charge carrier concentration have been determined and the application for mapping of the doping level distribution in SiC wafers will be demonstrated.

1. Introduction

The wide band gap semiconductor silicon carbide (SiC) is of growing interest for industry as a material for high power, high temperature and high frequency device applications. Control of doping level homogeneity and SiC polytype stability are crucial. Optical characterization methods play an important role since they are advantageous in comparison to their electrical counterpart due to their non-contact, non-destructive and non-time-consuming properties.

We will introduce an absorption based measurement method which allows us to determine the doping type and doping level (N_D-N_A). We will discuss the physical origin of the absorption bands of various n-type and p-type doped 4H- and 6H-SiC wafers and investigate their relation to doping level and corresponding charge carrier concentration (section 2). In section 3 calibration plots based on Hall measurements will be presented and we will compare our experimental results with numerical calculation of the band edge related absorption. The presented characterization method is used as a wafer mapping tool, i.e. determination of doping level distribution in SiC wafers.

2. Absorption bands in SiC

The physical origin of absorption bands in SiC are under study since several years [1, 2, 3]. For n-type SiC nitrogen is the common doping material. Typical absorption spectra at room temperature are shown in Fig. 1a for 4H-SiC and in Fig. 1b for 6H-SiC. In Fig. 1c and Fig. 1d we have plotted absorption spectra of aluminum and boron doped p-type 6H-SiC. Each diagram (Fig. 1a to 1d) shows a high doped and a low doped sample; three characteristic absorption bands can be identified. The absorption band (i), the so called band edge related, is caused by the transition of electrons from the valence band into the conduction band (see Fig.2). For an indirect semiconductor like SiC the transition shows a square root dependent behavior of the absorption coefficient (see section 3). The band edge varies strongly with the polytype, i.e. 3.3eV for 4H-SiC and 3.0eV for 6H-SiC. In addition, a variation of the band gap related absorption with charge carrier concentration is observed. Due to charge carrier induced band gap narrowing [7,8] and doping induced band tailing

[4] an increase of the absorption is observed at transition energies close to the fundamental band gap energy E_g of SiC [11].

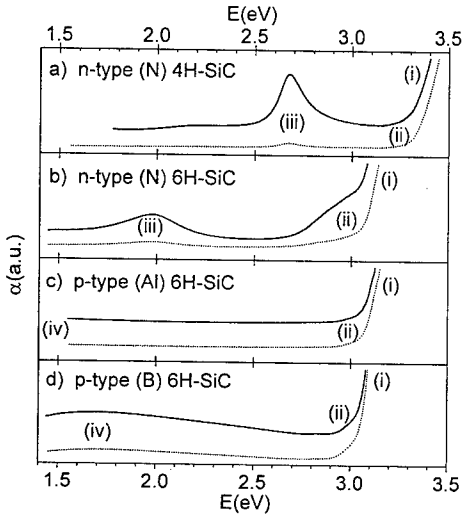


Fig. 1: Typical absorption spectra of a) n-type (N) 4H-SiC, b) n-type (N) 6H-SiC, c) p-type (Al) 6H-SiC and d) p-type (B) 6H-SiC for low (dotted line) and high doped material. The bands (i) to (iv) are defined in Fig. 2.

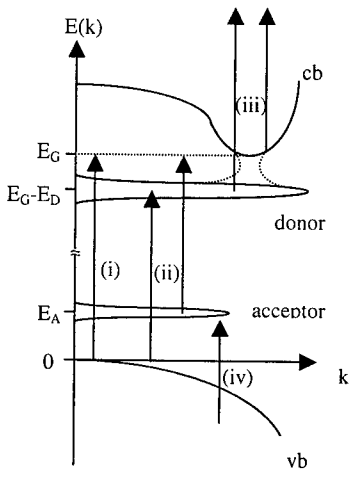


Fig.2: Energy dispersion and doping levels for SiC (schematically). Transitions: (i) valence band (vb) to conduction band (cb), (ii) vb to donor or acceptor to cb, (iii) donor to higher conduction band and (iv) vb to acceptor

The absorption band (ii) is due to a transition from valence band to donor level for n-type material or from acceptor level to conduction band for p-type material and reflects the concentration N_D^+ of positively charged donors and N_A^- of negatively charged acceptors, respectively. The transition (iii) (see Fig. 1a and 1b) is only present in n-type (N) SiC material and shows a strong polarization dependence. In the literature this transition is controversial.

values at 300K	n-type 6H SiC	p-type (Al) 6H-SiC	n-type 4H-SiC	p-type (B) 6H-SiC
band (i)	410nm	410nm	370nm	410nm
band (ii)	430nm	(450nm)	390nm	
band (iii)	630nm	-	460nm	-
band (iv)	-	(>3μm)	-	730nm

Table 1: Fundamental absorption bands and matching wavelengths for wafer mapping.

It is either assumed to be defect related [3,6] or due to intra conduction band transitions [9]. Dubrovskii et al. [3] have shown that there is a linear relationship between the absorption band (iii) and the charge carrier concentration. The presence or absence of this transition can be used to evaluate the doping type (n- or p-type). In the case of p-type doping or low n-type doping ($n<10^{17}cm^{-3}$) this band is not seen (Fig. 1). P-type doped (B) 6H-SiC shows a band (iv) at 730nm (1.7eV) (Fig. 1d) which is believed to be due to a transition from the valence band to the acceptor level (Fig. 2) [5]. For aluminum doped 6H-SiC (Fig.1c) an increase of absorption to higher wavelengths is observed which probably peaks at above 3μm (0.41eV) and may have the same origin as in the boron doped case.

Using monochromatic light which matches band (i), (ii), (iii) or (iv) absorption measurements enabled us to carry out SiC wafer mappings of the doping level distribution based on calibration results with Hall effect described in section 3. The matching wavelengths for the various bands of 4H- and 6H-SiC are listed in table 1.

3. Evaluation of doping levels and wafer mapping

The band edge related absorption can be calculated by taking into account a) the density of initial states D_{vb} and final states D_{cb}, b) the occupation of the initial and final states regulated by the Fermi-function and c) the transition matrix element [11]. The latter is assumed to be constant in the EMA (effective mass) approximation. The transition from the valence band to the conduction band is governed by phonons because of the indirect band structure of SiC. Therefore the optical absorption *Abs(E)* is given by:

$$Abs(E) = const. \cdot \int_0^{E_g - E} dE^* D_{cb}(E^* + E) \cdot (1 - f_{cb}(E^* + E, T)) \cdot D_{vb}(E^*) f_{vb}(E^*, T) \qquad (1)$$

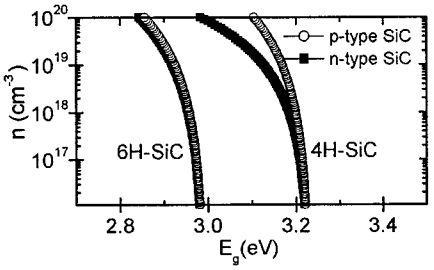


Fig 2: Numerical calculation of the charge carrier concentration dependent band gap

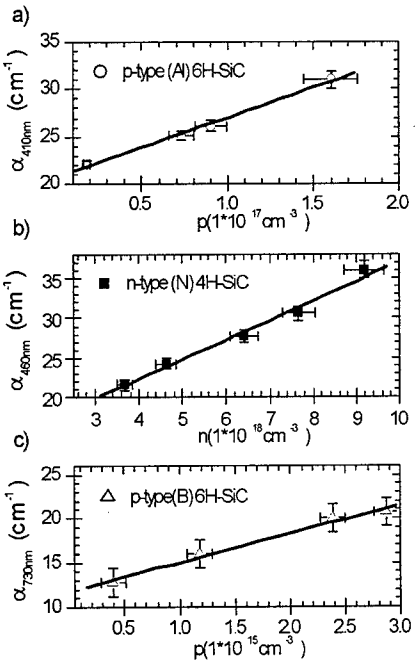


Fig 3: Experimental calibration plots of absorption versus charge carrier concentration for a) p-type(Al) 6H-SiC, b) n-type (N) 4H-SiC and c) p-type(B) 6H-SiC

The integration over E^* in equation (1) takes into account various transitions which are possible at a given energy E. In the case of doped SiC the density of states function has to be modified due to band shrinkage and band tailing using methods derived in [7,8,11]. In the effective mass approximation the band gap related absorption (i) is proportional to E^2 and the $Abs(E)^{1/2}$ plot is linear. Therefore the extrapolation of the $Abs(E)^{1/2}$ to zero value yields the charge carrier concentration dependent band gap $E_g(n)$ which "shrinks" by increasing charge carrier concentration. In Fig. 2 the dependence of the band gap on the doping concentration for n- and p-type 4H- and 6H-SiC is calculated [11]. This allows us to determine the charge carrier concentration from band edge related absorption measurements.

Two methods for wafer mapping i.e. spatial determination of charge carrier concentration are applicable [10,11]:

Method 1

Unlike the above described evaluation of doping concentration the absolute absorption at the band gap $E_g(n=0)$ is used to calculate the charge carrier concentration. Considering band tailing effects as described in [4,11] is obligatory. A calibration plot i.e. absorption coefficient at the matching wavelength versus charge carrier concentration of p-type (Al) 6H-SiC is shown in Fig. 3. An example is shown in Fig. 4a where an axial cut of a p-type (Al) 6H-SiC crystal grown in a so called double seed experiment is shown. A higher doping incorporation is observed in the crystal part grown on the Si-face oriented seed.

Method 2

This method is based on the below band gap absorption bands (iii) in n-type SiC and (iv) for p-type (B) 6H-SiC. Experimental calibration curves were generated by plotting the absorption coefficient at the transition (iii) or (iv) versus the charge carrier

concentration determined by Hall measurements (Fig. 3b, c). A linear relationship between the absorption level and the charge carrier concentration is found. It should be pointed out that for doping levels below about $10^{17}cm^{-3}$ no absorption band (iii) is present in the experimental spectra. Therefore, $n=10^{17}cm^{-3}$ in n-type (N) SiC is the lower limit for doping level determination using method 2. In Fig. 4b and 4c two absorption mappings of low defect wafers of n-type (N) 4H-SiC and p-type (B) 6H-SiC are shown. Note that in both cases a high doped facet is clearly visible. The charge carrier concentration in the 4H-SiC wafer is extremely homogeneous. Whereas the main part of the boron doped wafer show a rather good homogeneity. Non-uniformities are present at the transition to the facetted area.

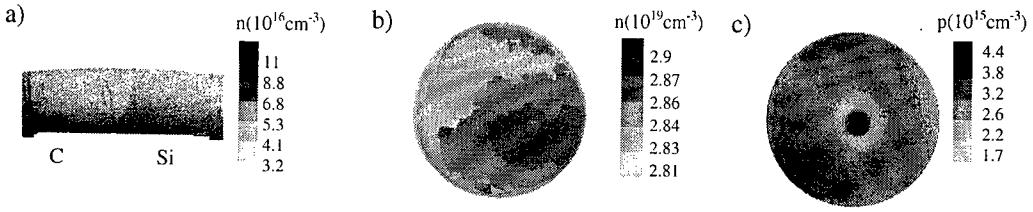


Fig. 4: Absorption Mappings of a) axial cut of p-type (Al) 6H-SiC (double seed) at 410nm, b) n-type (N) 4H-SiC wafer at 460nm, c) p-type (B) 6H-SiC at 730nm

4. Summary

In this paper we investigated the fundamental absorption bands in n-type (N) and p-type (Al, B) 4H- and 6H-SiC. The band gap related absorption was calculated in order to determine the charge carrier concentration. An optical wafer mapping method for the determination of spatial charge carrier concentration distribution was introduced. The method was employed for n-type (N) 4H- and 6H-SiC and p-type (Al and B) 6H-SiC. It is applicable for doping concentrations in the range of $10^{17}cm^{-3}$ up to $10^{20}cm^{-3}$ in both n- and p-type 4H- and 6H- SiC (see also [10,11]). The method can also be used for other polytypes like 3C or 15R if the corresponding dopant correlated absorption bands (not discussed in this paper) are evaluated.

Acknowledgement

This work has been supported by the Deutsche Forschungsgemeinschaft (project Wi393/9) and the Bayerische Forschungsstiftung (project 176/96).

References

[1] E. Biedermann: Sol. St. Comm. **3** (1965), p. 343.
[2] W.J. Choyke and L. Patrick: Phys. Rev. **172** (1968), p. 172.
[3] G.B. Dubrowskii, A.A. Lepneva and E.I. Radovanova: Phys. Stat. Sol. (b) **57** (1973), p. 423.
[4] K.J. Ebeling, Integrierte Optoelektronik, Springer-Berlin (1989), p. 268-274.
[5] W.C. Mitchel, Matthew Roth, A.O. Evwaraye, P.W. Yu, S.R. Smith: J. Elec. Mat. **25** (1996), p.863.
[6] Th. Stiasny and R. Helbig: Phys. Stat. Sol. A **162** (1997), p. 239.
[7] C. Persson and U. Lindefelt: J. Appl. Phys. **83** (1998), p. 266.
[8] U. Lindefelt: J. Appl. Phys. **84** (1998), p. 2628.
[9] Sukit Limpijumnong, Walter R.L. Lambrecht, Sergey N. Rashkeev and Benjamin Segall: Phys. Rev. B **59** (1999), p. 12890.
[10] R. Weingärtner M. Bickermann, S. Bushevoy, D. Hofmann, M. Rasp, T.L. Straubinger, P.J. Wellmann and A. Winnacker: Mat. Sci. Eng. B. in press.
[11] P. J. Wellmann, S. Bushevoy and R. Weingärtner:Mat. Sci. Eng. B. in press.

Materials Science Forum Vols. 353-356 (2001) pp. 401-404
© 2001 Trans Tech Publications, Switzerland

Low Temperature Photoluminescence Processes of ^{13}C Enriched 6H- and 15R-SiC Crystals Grown by the Modified Lely Method

Horst Sadowski, Norbert Schulze, Thomas Frank, Michael Laube, Gerhard Pensl and Reinhard Helbig

Institute of Applied Physics, University of Erlangen-Nürnberg, Staudtstr. 7/A3, DE-91058 Erlangen, Germany

Keywords: ^{13}C Isotope, Low Temperature, Modified Lely, Photoluminescence

Abstract. 6H- and 15R-SiC crystals were enriched by ^{13}C during the sublimation growth in a modified Lely furnace. Furthermore, a ^{13}C enriched 6H-SiC sample was implanted with helium to generate the D_I-defect. The samples have been investigated by low temperature photoluminescence (LTPL). The helium implanted samples were additionally studied by photoluminescence (PL) at temperatures up to 59 K. We report on an isotopic effect in 6H- and 15R-SiC on the momentum-conserving optical phonon lines of the exciton recombination as well as on the zero phonon exciton recombination lines. We estimate a shift to higher energy of the zero-phonon bound exciton lines of a 6H-SiC crystal with pure ^{13}C by 2.19 meV for nitrogen and 0.85 meV for titanium relative to a sample with natural isotopic composition.

Introduction

The atomic isotope composition of crystals strongly influence the electronic and vibrational properties of semiconductors and, therefore, are a subject of current investigations for different semiconductor materials. Most papers are dealing with elemental semiconductors, like germanium (Ge) and diamond [1, 2]. The semiconductor with the largest isotopic mass spread is Ge [^{70}Ge, ^{73}Ge, ^{74}Ge, ^{76}Ge]. Investigations of compound semiconductors, especially SiC, are published by Widulle et al. [3]. SiC is an indirect semiconductor; the optical spectra cover different electronic and vibronic processes and show the influence of the isotopic composition on the different optical transitions [4, 5]. In [3], the isotopic composition of SiC varied between natural Si (92.2% ^{28}Si-atoms) and ^{30}Si. In contrast, we substituted ^{12}C by ^{13}C due to the larger relative mass difference.

We have measured the photoluminescence emission spectra of 6H-and 15R-SiC samples, with different ratios of the ^{13}C to ^{12}C concentration, at low temperature (1.9 K). The emission spectrum correlated to the D_I-defect of a ^{13}C enriched 6H-SiC sample was measured by PL up to 59 K to observe both the zero-phonon low temperature lines (L-lines) and the high temperature lines (H-lines), as reported for 6H-SiC with natural isotopic composition by Patrick et al. [6].

Experimental

The investigated 6H- and 15R-SiC crystals have been grown by the modified Lely method [7] using a mixture of 99% pure ^{13}C powder and natural silicon powder ($m_{Si} = 28.09$ u) as source material in a graphite crucible. The seed crystals showed a natural isotopic composition. Both polytypes were grown simultaneously utilizing the dual-seed-method [8]. Reference samples have been grown under identical conditions using a conventional SiC powder source. The grown samples are nitrogen doped. In order to generate the D_I-defect, 6H-SiC samples were implanted with helium-ions (box-shaped profile of 1 μm in depth) resulting in a mean vacancy concentration of $2x10^{17}$ cm^{-3} (calculated by TRIM_C). The samples were annealed at 1400°C for 30 min.

The LTPL-measurements at 1.9 K are conducted in a bath cryostat containing superfluid helium. For measurements at higher temperature the cryostat is cooled with helium gas. The samples were

excited by a 40 mW He-Cd laser (λ = 325 nm), the helium implanted samples by a 50 mW SHG laser (λ = 257 nm). The luminescence is spectrally resolved by a 0.75 m Czerny–Turner-monochromator (Spex 1700-III) with a 1200/mm grating blazed at 5000 Å and slit widths of 50 µm and 25 µm resulting in a resolution of about 0.4 meV and 0.2 meV, respectively. A S20 photomultiplier tube operating in photon-counting mode is used as detector. To control for an absolute shift of the spectra due to the experimental setup, a reference sample of natural isotopic composition has been measured simultaneously.

Results and Discussion

6H-SiC

We have demonstrated [5] that the optical phonon replica of the nitrogen- (N-) bound exciton emission in the LTPL spectra of ^{13}C enriched samples show a shift to lower energy relative to the corresponding zero phonon lines. In contrast, the acoustic phonon replica don't show that shift.
The ^{13}C concentration x has been determined from the energy of the TO(0) mode in Raman spectroscopy [4] utilizing the indirect proportionality of the energy to the reduced mass μ with:

$$\mu = (1/\overline{m_C} + 1/m_{Si})^{-1} \text{ and } E_{TO(0)}^2 \propto \mu^{-1} \quad (1)$$

where $\overline{m_C}$ is the average mass of carbon atoms in a mixture of ^{12}C and ^{13}C ($^{13}C_x\ ^{12}C_{1-x}$):

$$\overline{m_C} = (12+x)\cdot\text{atomic units} \quad (2)$$

Identically, we calculated the isotopic composition x from the shift of the TO-phonon replica of the N-bound exciton emission lines P_{95}, P_{96}, and $RS_{95/96}$ relative to the zero phonon lines. We obtain a concentration x of ^{13}C up to 0.82 ± 0.16 (see Fig. 1). However, our values are about 0.15 higher as determined by Raman spectroscopy.

As reported in [5], we also observe a shift ΔE_N and ΔE_{Ti} of the zero phonon lines related to the recombination of excitons bound to nitrogen and titanium, respectively. Fig. 1 displays the dependence of the energy shift of the zero phonon lines on the ^{13}C concentration x calculated as stated above. By performing a linear fit we achieve $\Delta E_N = 2.19\ x$ and $\Delta E_{Ti} = 0.85\ x$.

The D_I-defect induced by helium implantation has been investigated at a sample with a mean ^{13}C concentration of about 65%. We measured PL spectra in the temperature range from 1.9 K to 59 K. Fig. 2 shows spectra taken at 37 K of both the ^{13}C enriched sample and a reference sample with natural isotopic composition. The low temperature (L_1 to L_3) and the high temperature (H_1 to H_3) zero phonon lines are visible together with the phonon replica of H_1 (LA, TO, LO). The superscript "loc" denotes replica of the particular lines where a localized mode is involved in the recombination process. The energy shift of the zero phonon lines related to the D_I-defect of the ^{13}C enriched sample is overall 0.8 meV relative to the reference sample (see Fig. 2). This shift is similar to the shift of the titanium related zero phonon lines but significantly smaller than the nitrogen related ones (Fig. 1, [5]). The local modes (energy of about 82.5 meV) of the zero phonon replica of the H- and L-lines

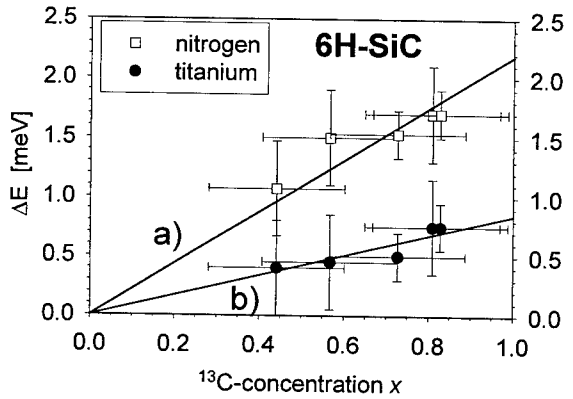


Fig 1: Energy shift ΔE of the zero phonon lines of excitons bound to nitrogen a) and titanium b) as a function of the ^{13}C concentration (calculated from eqs. (1) and (2)).

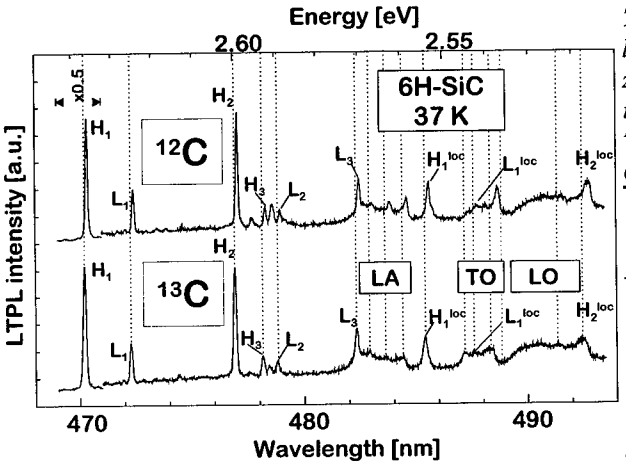


Fig. 2: PL spectra of He-implanted samples (6H-SiC) at a temperature of 37 K (natural reference and the ^{13}C enriched sample). L_1 to L_3 are the low temperature and H_1 to H_3 the high temperature zero phonon lines due to the D_I-defect. LA, TO, and LO denotes the phonon replica of H_1. Replica denoted with the superscript "loc" involve localized vibrational modes in the recombination process.

***Tab. 1:** Energy of the vibrational and localized modes (difference between zero phonon lines and phonon replica) in the D_I-defect related emission of a ^{13}C enriched 6H-SiC sample and a 6H-SiC reference sample.*

Energy [meV]: Mode	^{13}C enriched 6H-SiC	6H-SiC reference sample
Zone edge LA	77.4	77.4
Localized	82.5	82.5
First zone edge TO	91.8	92.8
Last zone edge TO	97.8	98.7

show no energy shift (see Tab. 1) and no splitting, in contrast to the local mode of titanium with an energy of 90 meV (see [5]). An exponential fit of the intensity ratio

$$H_i / L_i = c_i e^{-E_i/kT} \qquad i=1,2,3 \qquad (3)$$

as a function of temperature shows no significant difference between the reference sample and the ^{13}C enriched sample (i.e. activation energy E_i is identical). The acoustic phonons show no energy shift (see Tab. 1: e.g. zone edge LA: ~77 meV) in agreement with the acoustic phonons evaluated from the nitrogen related spectra [5]. However, the optical phonons shift to lower energies by about 1 meV (see Tab. 1), similar to the phonons in the nitrogen related spectra (~ 1.5 meV) [5]. The LO phonon replica of the H_1-line can not be resolved sufficiently due to the interference with replica of further D_I related zero phonon lines. Therefore, a shift of the LO-replica in the ^{13}C enriched sample can only be observed by the broadening of the LO-spectrum relative to the reference sample (Fig. 2). In general, the vibrational replica of the lines due to the D_I-defect of the ^{13}C enriched sample show a lower intensity than the corresponding lines of the reference sample (see peaks at 483.8 nm, 484.6 nm and 488.7 nm in reference spectrum of Fig. 2).

15R-SiC

Fig. 3 shows LTPL spectra of a ^{13}C enriched 15R-SiC sample and the 15R-SiC reference sample. The mean shift of the nitrogen related zero phonon exciton recombination lines (P_0, Q_0, R_0, S_0) of the ^{13}C enriched sample is 1.5 meV (the simultaneously grown 6H-SiC sample showed a shift of 1.7 meV [5]). The titanium related zero phonon lines (e.g. A_0) of the 15R polytype shift to higher energy by 0.9 meV similarly to 6H-SiC (0.8 meV) [5]. The energy of the phonons contributing to the replica of the nitrogen-bound exciton recombination lines of the ^{13}C enriched 15R-SiC sample and the 15R-SiC reference sample is listed in Tab. 2. The acoustic phonons of both samples have an identical energy. However, the energy of the optical phonons differ significantly. The ^{13}C concentration x calculated by Eq. (1) and (2) from the energy shift of the TO-phonons is higher in the 15R-SiC sample ($x_{15R} \sim 0.96$) than in the corresponding 6H-SiC sample ($x_{6H} \sim 0.82$). Nevertheless, the error for the calculation is 0.16.

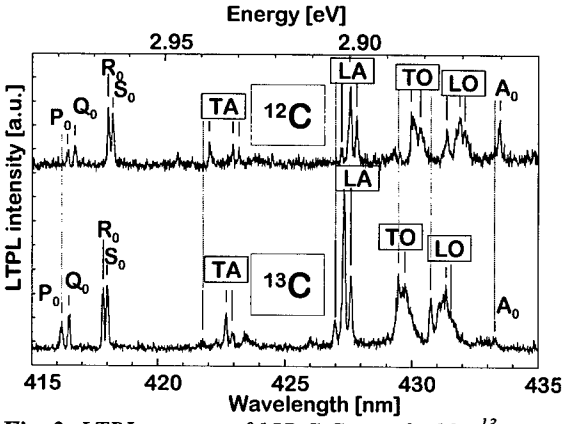


Fig. 3: LTPL spectra of 15R-SiC enriched by ^{13}C and a 15R-SiC reference sample with natural isotopic composition.

Tab. 2: Phonon energy in meV of the ^{13}C enriched 15R-SiC sample (^{13}C) and the 15R-SiC reference sample with natural isotopic composition (^{12}C).

TA		LA		TO		LO	
^{13}C	^{12}C	^{13}C	^{12}C	^{13}C	^{12}C	^{13}C	^{12}C
39.6	39.9	75.3	75.5	92.1	94.6	100.8	103.3
45.7	45.8	77.6	77.4			104.8	106.7

Conclusion

The LTPL spectra of 15R- and 6H-SiC crystals behave similar when substituting ^{12}C-atoms by ^{13}C-atoms. The recombination of bound excitons without phonon contribution could be separated in two different recombination processes. The first type is a radiative recombination at the neutral nitrogen impurity [9, 10] which is determined by the shift of the energy gap due to the isotopic composition [5, 11]. The second type is a strongly localized transition at an impurity like titanium and at the D_I-defect. Latter shows the same energy shift as the titanium related transition (as measured on 6H-SiC). However, the localized mode of the D_I-defect shows no splitting when partially substituting ^{12}C by ^{13}C in contrast to the localized mode of titanium. The D_I-defect related phonon replica behave like the nitrogen related phonon replica, where the optic-phonon replica show a smaller shift than the zero phonon lines. We have evaluated the energy shift of the zero phonon lines of nitrogen and titanium related emission in 6H-SiC as a function of the ^{13}C concentration.

Acknowledgment

We thank Stefan Rohmfeld and Martin Hundhausen for fruitful discussions. This project was supported by the Deutsche Forschungsgemeinschaft (Sonderforschungsbereich 292) and the Bayerische Forschungsstiftung.

References

[1] C. Parks, A. K. Ramdas, S. Rodriguez, K. M. Itoh, and E. E. Haller, Phys. Rev. B **49** (1994), p. 14244.
[2] S. Zollner, M. Cardona, and S. Gopalan, Phys. Rev. B **45** (1992), p. 3376.
[3] F. Widulle, T. Ruf, O. Buresch, A. Debernardi, and M. Cardona, Phys. Rev. Lett. **82** (1999), p. 3089.
[4] S. Rohmfeld, M. Hundhausen, L. Ley, N. Schulze and G. Pensl, Mat. Sci. For. **338-342** (2000), p. 579.
[5] H. Sadowski, Chr. Peppermüller, N. Schulze, M. Laube, G. Pensl, and R. Helbig, Mat. Sci. For. **338-342** (2000), p. 623.
[6] L. Patrick and W.J. Choyke, Phys. Rev. B **5** (1972), p. 3253.
[7] N. Schulze, D.L. Barrett, and G. Pensl, Appl. Phys. Lett. **72,** (1998), p. 1632.
[8] V.D. Heydemann, N. Schulze, D.L. Barrett, and G. Pensl, Appl. Phys. Lett. **69** (1996), p. 3728.
[9] W.J. Choyke, L. Patrick, Phys. Rev. **127** (1962), p. 1868.
[10] L. Patrick, D.R. Hamilton, and W.J. Choyke, Phys. Rev. **132** (1963), p. 2023.
[11] F. Engelbrecht, J. Zeman, G. Wellenhofer, C. Peppermueller, R. Helbig, G. Martinez, and U. Roessler, Phys. Rev. B **56**, 69 (1997), p. 7348.

Materials Science Forum Vols. 353-356 (2001) pp. 405-408
© 2001 Trans Tech Publications, Switzerland

Intrinsic Photoconductivity of 6H-SiC and the Free-Exciton Binding Energy

I.G. Ivanov, T. Egilsson, J. Zhang, A. Ellison and E. Janzén

Department of Physics and Measurement Technology,
Linköping University, SE-581 83 Linköping, Sweden

Keywords: Electronic Bandgap, Exciton Recombination, Excitonic Bandgap, Extrinsic Photocurrent, Intrinsic Photocurrent

Abstract The paper presents a study of the low-temperature photoconductivity of 6H-SiC. The photocurrent at the absorption edge is assigned to Auger recombination of excitons captured to impurities. This is shown to saturate and decrease with increasing the photon energy, so the further increase in the photocurrent, observed in the purest sample, can be attributed to free excitons created in non-bound states in the exciton continuum. Thus, the exciton binding energy can be estimated, $E_{bx} \approx 60 \pm 5$ meV in 6H-SiC.

Introduction The excitonic bandgap E_x, i.e. the lowest energy of the intrinsic free exciton (FE), is known for many SiC polytypes. However, the values reported so far for the binding energy E_{bx} of the FE is not reliable for any of the polytypes (see [1] for a review). Consequently, the energy position of the conduction band $E_g = E_x+E_{bx}$ remains unknown. The main difficulty in determining E_{bx} in indirect semiconductors by optical techniques arises from the fact, that the fundamental absorption edge is due to the onset of phonon-assisted exciton creation. It is continuous versus the incident light energy because phonons of various wavevectors are involved to create excitons of various wavevectors and energy [2]. This absorption creates a huge background which obscures the weak step-like features expected from the absorption into higher excitonic bands. There exist modulation techniques like the electroabsorption [3], or the wavelength modulation spectroscopy [4], which help to get rid of the background absorption to a large extent, yet the assignment of some peaks observed by these methods is rather ambiguous. The electroabsorption technique has been used so far to determine the reported values of E_{bx} for 6H- and 4H-SiC (78 meV and 20 meV, respectively) [3,5].

This study presents the low temperature photoconductivity (PC) spectra of 6H-SiC. The spectra of the purest sample allow us to distinguish the extrinsic photocurrent (due to residual impurities) from the intrinsic (due to free excitons excited in the exciton continuum), and attribute step-like features in the intrinsic photocurrent to phonon-assisted generation of free carriers (non-bound electron-hole pairs, or excitons excited in the exciton continuum). Thus an estimate of E_{bx} for 6H-SiC is obtained. A simple model is presented in order to illustrate the mechanism of saturation of the extrinsic photocurrent.

Theoretical background In a perfect crystal, one would expect that the FEs, being electrically neutral, would not contribute to the photocurrent, unless they are excited into the continuum of non-bound states (above the edge of the conduction band). In this latter case, there exists a probability that the electron and hole excited by light will be separated away in externally applied electric field before they relax to a lower state, or recombine. They will thus contribute to the photocurrent. The conduction band edge (the exciton continuum) would be indicated by a sharp increase in the photocurrent, as soon as the energy of the exciting light minus the lowest energy ($\hbar\Omega$) of a lattice phonon needed to conserve the momentum is enough to reach the bottom of the exciton continuum.

However, in a real crystal, FEs are very efficiently (=rapidly) captured to shallow impurities. The fastest recombination mechanism for a bound exciton (BE) is by Auger process, which produces free carriers (electrons in the case of binding to donors, or holes in the case of acceptors). Thus the FEs contribute to the photocurrent by binding to impurities, and in a real crystal the sharp increase in the photocurrent occurs at the fundamental absorption edge (i.e. $E_x + \hbar\Omega$). Since this photocurrent is due to impurities, we shall call it "extrinsic" in order to distinguish it from the "intrinsic" photocurrent arising from *free* excitons created in the exciton continuum. In the sample with lowest doping ($|N_D-N_A| \approx 10^{13}$ cm^{-3}), we have observed saturation followed by a decrease of the extrinsic photocurrent when increasing the incident light energy. The photocurrent saturation can be viewed as a consequence of the saturation of the mechanism: capturing of FE by impurity => Auger recombination, and the following decrease is due to the decrease of the penetration depth of the incident light.

In order to show that the extrinsic photocurrent saturates and then decreases with increasing absorption when the incident light energy increases, we introduce a simple model. It takes into account the presence of only one capturing impurity (say, shallow nitrogen donors) of homogeneous concentration N_N. The donor can exist in three states, namely, ionized ($N^+(x)$), neutral ($N^0(x)$), and neutral with a bound exciton ($N^{0X}(x)$). The values in brackets denote the concentration of donors in each state in equilibrium at steady illumination and at depth x below the surface of the sample. Obviously, $N^+(x) + N^0(x) + N^{0X}(x) = N_N$. Furthermore, ionized donors are created by Auger recombination of excitons bound to neutral donors, and this also creates free electrons of concentration $e(x) = N^+(x)$, which expresses the electroneutrality condition, as well. The incident light energy is supposed to lie below the excitonic continuum, so only the extrinsic photoconductivity will be investigated, and the photocurrent is assumed to be proportional to the integral $J = \int_0^d e(x)dx$. Here d is the sample thickness. The following system of coupled equations describes the dynamics of the free excitons + donors ensemble (all derivatives vanish in equilibrium):

$$\begin{aligned}
&\frac{dN^0(x)}{dt} = \delta\ N^+(x)e(x) + \beta\ N^{0X}(x) - \kappa\ N^0(x)N_{ex}(x) = 0,\\
&\frac{dN^{0X}(x)}{dt} = \kappa\ N^0(x)N_{ex}(x) - (\beta+\gamma)N^{0X}(x) = 0,\\
&\frac{dN^+(x)}{dt} = \gamma\ N^{0X}(x) - \delta\ N^+(x)e(x) = 0,\\
&N^+(x) + N^0(x) + N^{0X}(x) = N_N, \text{ and } e(x) = N^+(x).
\end{aligned} \qquad (1)$$

Here $N_{ex}(x)$ is the FE-concentration, δ is the rate of capture of electrons by an ionized donor per unit electron concentration, β and γ are the rates of radiative and Auger recombination, respectively, of the BEs, κ is the rate of capture of FEs by a neutral donor per unit FE-concentration. The units for δ and κ are cm^{3}s^{-1}, and for β and γ just s^{-1}. The following equation, describing the generation of FEs by light completes the system:

$$\frac{dN_{ex}(x)}{dt} = A\alpha(E)\exp(-\alpha(E)\cdot x) - \kappa\ N^0(x)N_{ex}(x) - N_{ex}(x)/\tau_0 = 0. \qquad (2)$$

Here τ_0 is the FE radiative lifetime, $\alpha(E)$ is the absorption coefficient dependant on the energy E of the incident light, A is a coefficient proportional to the incident photon flux density, assumed to be a constant. Eqs. 1 and 2 can be solved numerically, and the solutions for various x are then used to calculate the integral J proportional in our approximation to the photocurrent for each fixed value of $\alpha(E)$. Our purpose is to show that the dependence of the integral $J(E)$ has a maximum (saturation followed by decrease), provided the "absorption" function $\alpha(E)$ is

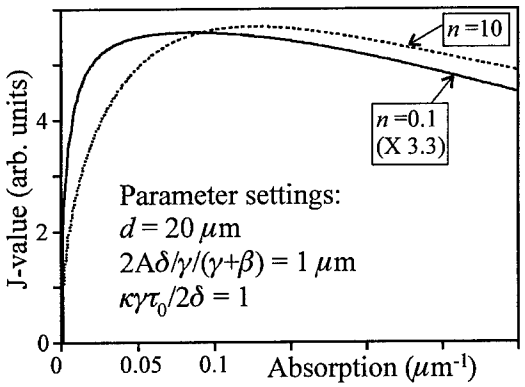


Fig.1. Variation of the photocurent with the "doping" parameter n, according to the model.

monotonically growing with E. In this study, the "absorption" function $\alpha(E)$ is taken simply proportional to E, the other constants are reduced by making the equations dimensionless, and chosen quite arbitrarily (see Fig.1), which however does not affect our qualitative results. Accurate values and more advanced model would be needed if quantitative estimations are to be made.

Fig. 1 shows the result for the numerical solution for the integral J, for two values of the "doping concentration" parameter $n = (2\delta/\gamma)N_N = 0.1$, and $n = 10$. As expected, the integral proportional to the photocurrent saturates, then decreases with the increase of $\alpha(E)$. The figures illustrates also a trend of shift of the maximum to lower energies with decreasing doping concentration (because the saturation occurs at lower value of $\alpha(E)$ when N_N is lower).

Experimental results and discussion The two samples presented here are CVD (or HTCVD) grown 6H epilayers with the substrate etched away. The residual net doping concentrations are in the low 10^{14} cm^{-3} range for sample #1, and low 10^{13} cm^{-3} range for sample #2. The spectra were obtained with a xenon lamp passed through the first half of a double SPEX 1404 monochromator. The samples were cooled down to 2K. Annealed and unannealed Ni contacts were used. Higher doped bulk samples were measured, too, though not presented here because of the overwhelming behavior of the extrinsic photocurrent.

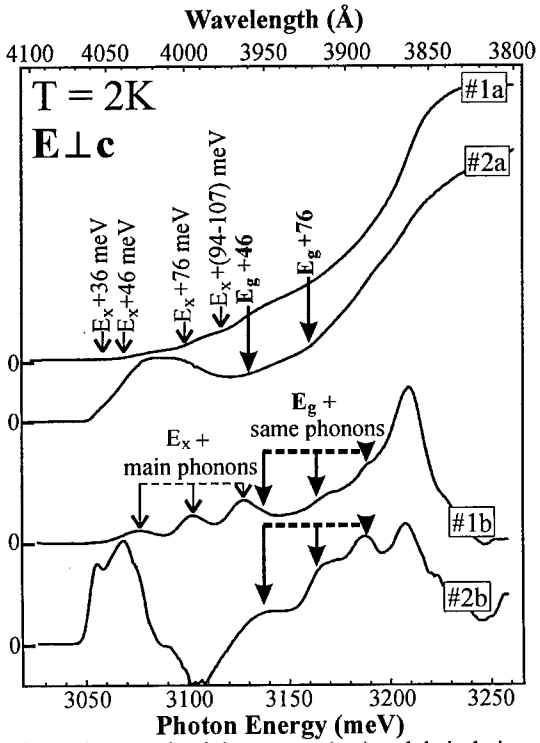


Fig.2. Photoconductivity spectra (top) and their derivatives (bottom) for samples #1 and #2, as denoted on the curves. The Y-axis units are arbitrary linear, the zero is denoted for each curve.

Fig. 2 shows the PC spectra of both samples obtained with nearly constant illumination of ≈50 μW/cm^2, as well as their numerical first derivatives. The spectrum of the higher doped sample (#1a) exhibits a continuously growing photocurrent, with features characteristic for absorption spectrum, i.e. step-like increase of the photocurrent at energies equal to E_x plus the well known (from the photoluminescence and absorption) energies of the main phonons at the edge of the Brillouin zone, where the minima of the conduction and exciton bands occur. The spectrum is therefore dominated by the extrinsic photocurrent, at least in the low-energy part. On the other hand, the spectrum of the low doped sample (#2a)

exhibits saturation of the extrinsic photocurrent at energy ≈3070 meV, followed by decrease, as explained by the above model. A new increase of the photocurrent at higher energies can be anticipated, due to phonon assisted creation of excitons by light in the exciton continuum. This occurs at approximately 3119 ± 5 meV. If we admit that this energy corresponds to E_g + 36 meV (the lowest energy phonon), then further step-like increase will be expected at energies E_g + 46 meV ≈ 3129 ± 5 meV, and E_g + 76 meV ≈ 3159 ± 5 meV, corresponding to the "strongest" assisting phonons. These are pointed out with bold arrows in the spectrum (#2a).

The structure of the spectra is revealed better by considering their first derivatives (curves #1b and #2b). The "main phonons" assisting the light absorption give rise to three peaks in the derivative of the photocurrent of higher doped sample #1 (marked with arrows in fig.2, curve #1b). These are not observed in curve #2b because of the saturation. However, three other peaks with the same separation, and with similar amplitude relations between them are observed at 60 meV above the former peaks. These are marked with bold arrows in curve #2b. It is then natural to assign them to phonon-assisted creation of excitons in the exciton continuum (the conduction band). Moreover, these peaks can also be seen in curve #1b for the higher-doped sample (pointed also with bold arrows), but their overall contribution to the spectrum is much weaker, in agreement with our conclusion that the PC-spectrum of sample #1 is dominated by the extrinsic photocurrent. Thus one can deduce that the features marked with thin arrows in Fig.2, curve #1b are due to the extrinsic photocurrent, whereas the features marked with bold arrows arise from the intrinsic photocurrent, and these two contributions in the total photocurrent can be distinguished by comparing the spectra shown in Fig.2.

Within this picture, the binding energy for the free excitons in 6H-SiC follows to be E_{bx} = 60 ± 5 meV. Thus, the reported value of 78 meV [3] seems to be overestimated. So far, the accuracy of our experiment is limited by the linewidth of the used light source (Xe lamp and monochromator), which is about 5.5 Å with 1 mm slits. It is worth to compare the value $E_{bx} \approx 60$ meV with a value obtained by a simple isotropic hydrogen model. Even though the model is not applicable for anisotropic crystals because of the anisotropy of the electron and hole effective masses, an estimate can be obtained by taking an average effective mass for the electron and hole as $m_e^* = (m_{e\Gamma} \cdot m_{eK} \cdot m_{eL})^{1/3}$ and $m_h^* = (m_{h\parallel c} \cdot m_{h\perp c}^2)^{1/3}$, respectively. Here $m_{e\Gamma}$, m_{eK} and m_{eL} are the main components of the electron effective mass tensor, and $m_{h\parallel c}$, $m_{h\perp c}$ are the two hole effective masses. Since these have been both measured [6] and calculated [7] for 6H-SiC, one obtains for the effective mass of the FE $m_{FE} = (1/m_e^* + 1/m_h^*)^{-1} = 0.4$ electron masses, and $E_{bx} \approx 54$ meV, which is surprisingly close to our experimental value.

Acknowledgements The support from ABB Corporate Research, Okmetic AB, TFR, and the SSF program SiCEP is gratefully acknowledged.

References

[1] R.P. Devaty and W.J. Choyke, phys. stat. sol. (a) 162 (1997), p. 5.
[2] R.Elliott, Phys. Rev. 108 (1957), p. 1384.
[3] V.I. Sankin, Soviet Phys. - Solid State 17 (1975), p. 1191.
[4] R.G. Humphreys, D. Bimberg, W.J. Choyke, Solid State Commun. 39 (1981), p. 163.
[5] G.B. Dubrovskii, V.I. Sankin, Soviet Phys. - Solid State 17 (1975), p. 1847.
[6] N.T. Son, O. Kordina, A.O. Konstantinov, W.M. Chen, E. Sörman, B. Monemar and E. Janzén, Appl. Phys. Lett. 65 (1994), p. 3209.
[7] C. Persson and U. Lindefelt, J. Appl. Phys. 86 (1999), p. 5036.

Materials Science Forum Vols. 353-356 (2001) pp. 409-412
© 2001 Trans Tech Publications, Switzerland

Epitaxial Growth and Properties of SiC Layers Grown on α-SiC(0001) by Solid-Source MBE: A Photoluminescence Study

A. Fissel and W. Richter

Institut für Festkörperphysik, Friedrich-Schiller-Universität Jena,
Max-Wien-Platz 1, DE-07743 Jena, Germany

Keywords: Molecular Beam Epitaxy (MBE), Optical Properties, Photoluminescence

Abstract SiC layers were grown on hexagonal (or α-)SiC(0001) by means of solid-source molecular beam epitaxy. The layers were investigated by photoluminescence at 4.2 K. The dominant emission lines in the spectra for all polytypes were attributed to the recombination of bound excitons at a D_1-center. The intensity of the centre lines was found to increase for layers of higher perfection and doped by boron, resp.. No influence was found regarding a change of the chemical potential from more carbon-rich to Si-rich conditions. A shift of 2 meV to lower energies of the D_1-center lines connected with a decrease in intensity was detected for 3C-SiC layers of high twin-boundaries density. The obtained results support the earlier interpretation of the nature of the D_1-center to be result from a carbon-divacancy. The spectrum of intentionally boron-doped samples exhibits the characteristic signature of the shallow boron-related neutral four particle bound exciton complex.

INTRODUCTION

SiC is a wide-band-gap semiconductor material of great technological interest for devices operating at high temperatures, high power, high frequency and in harsh environments. Especially epitaxial SiC layers; with defined doping level and of high quality; have attracted considerable interest in recent years for application for example in high-power devices. The life time of the devices, however, is strongly depend on the defect level within the material. It is therefore important to study the nature of these defects and the way to influence its appearance. In this field, the analysis of the low temperature photoluminescence (LTPL) is a powerful tool for material characterisation.

Furthermore, despite of the fact that nowadays molecular beam epitaxy (MBE) is widely used for semiconductor epitaxy, it is used only to a small extent for application in SiC technology [1-3] and only some few reports exist regarding the layer properties [1,3]. MBE is advantageous for the preparation of layers with definite properties because of the controlled deposition conditions within an atomic layer range and the clean growth conditions preventing for example the unintentional nitrogen doping. It can be therefore expected that layers grown by MBE exhibit properties somewhat different from those of layers grown by other methods. In this work, we report about photoluminescence investigations of SiC layers grown by solid-source MBE.

EXPERIMENTAL DETAILS

SiC layers were grown on off-axis α-SiC(0001) (Cree Research Inc.) by solid-source MBE (Riber 32). Typical conditions for the growth of the layers as well as experimental details of ex situ and in situ preparation of the substrate surfaces are described extensively elsewhere[4]. Boron was evaporated from an evaporation source at a temperature (T) of 1700 K with a rate of about 10^{19} atoms/s cm^2. After in situ preparation by sublimation etching in a Si flux, the surfaces show a well-developed step structure with steps typically 2-6 monolayers (ML) in height as revealed by atomic force microscopy (AFM). PL measurements were performed at 4.2 K (liquid helium) (LTPL) with excitation with a He-Cd laser operating at a wavelength of 325 nm, with an excitation power of 2 mW and at an angle of incident of the laser beam tilted 85° with respect to the surface normal.

RESULTS

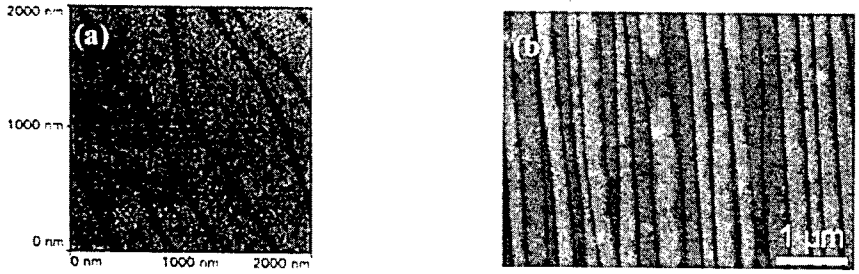


Fig.1: AFM pictures of a 4H-SiC substrate surface after sublimation etching (a) and of 4H-SiC layer grown homoepitaxially on 4H-SiC(0001) (b).

Figure 1 shows the surface morphology of a 4H-SiC substrate after sublimation etching (a) and after growth of a epitaxial layer (b) via step-flow on off-axis 4H-SiC(0001) at 1600 K and growth rate of 30 nm/h. The surface of the layer is very smooth without indications of significant step-bunching. Doping by boron does not influence the surface morphology significantly, where only some needle-like hillocks occur. In the case of heteroepitaxial growth of 3C-SiC on α-SiC double-position boundaries (DPB) occur with domain size up to some hundreds µm.

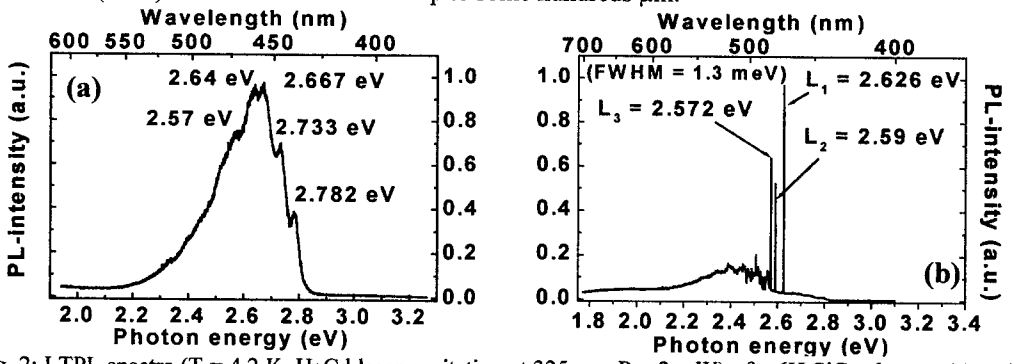


Fig. 2: LTPL spectra (T = 4.2 K, HeCd laser excitation at 325 nm, P = 2 mW) of a 6H-SiC substrate (a) and an undoped 1 µm thick 6H-SiC layer grown by solid-source MBE on 6H-SiC(0001) at 1600 K (b).

A typical LTPL spectrum of a nitrogen-doped 6H-SiC(0001) substrate is shown in Fig.2(a). The spectrum is dominated by a broad band centred at about 2.65 eV due to deeper luminescence related to crystal imperfections. In Fig.2 (b) is shown a spectrum of a undoped 1 µm thick 6H-SiC layer grown on such 6H-SiC(0001) substrate at 1600 K and a growth rate of 40 nm/h. In comparison to the substrate, the spectrum is dominated by three strong lines (L_1-L_3) associated with the so-called D_1-center [5] and its phonon replica. The full width at half maximum (FWHM) of these lines is in the order of 1-2 meV. The strong intensity of the lines indicates a good layer perfection. Because the penetration depth of the laser beam is larger than the layer thickness, even at the angle of incident of 5°, the spectrum is superimposed by the luminescence of the substrate related to defects and the nitrogen bound excitons. To check the influence of the growth conditions to the LTPL spectrum, the chemi-cal potential in the growth process was shifted from more carbon-rich to more Si-rich conditions by an increase in Si-supply by a factor of two. In this case the growth rate was found to increase slightly (about 20 %), however, there was no influence regarding the LTPL spectrum and, especially, the D_1-centre lines intensity.

A LTPL spectrum of 4H-SiC on 4H-SiC(0001) doped by boron is presented in Figure 3. In the high energy region between 3.24 and 3.1 eV, there are seen lines associated with a no-phonon spectrum of the neutral boron acceptor bound excitons, where the recombination can be attributed to a four particle complex ($4B_0$) [6]. At 2.903 eV there occurs a strong line of the zero phonon line of the D_1-

centre with a number of phonon replicas at lower energies. The FWHM is also small with about 1.5 meV. The intensity and the FWHM of the L_1 line are in the same order of magnitude as obtained for 6H-SiC. The LTPL spectrum of undoped 4H-SiC layers also shows such a strong D_I centre peak, however, with a lower intensity.

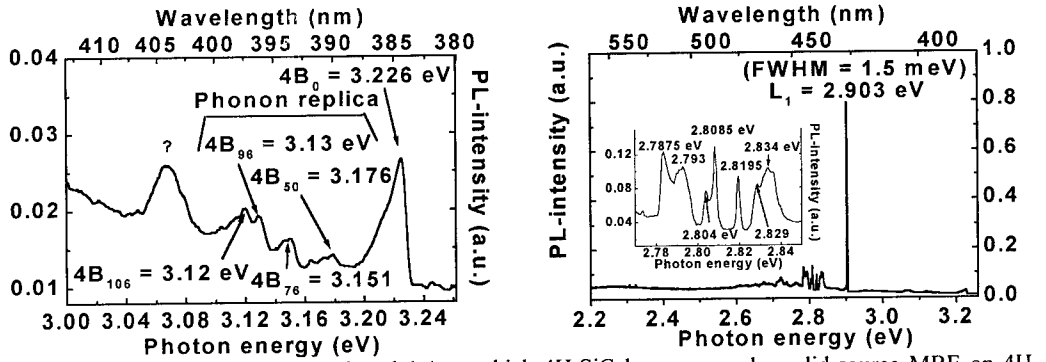


Fig.3: LTPL spectrum of a boron-doped 1.4 μm thick 4H-SiC layer grown by solid-source MBE on 4H-SiC(0001) at 1600 K (T = 4.2 K, HeCd laser excitation at 325 nm, P = 2 mW).

The D_I centre was also observed in case of the heteropolytypic growth of 3C-SiC on α-SiC(0001) as shown in Figure 4c,d. In this case, the D_I centre line appeared at 1.973 eV, however, with a much lower intensity in comparison to 4H- and 6H-SiC. Moreover, in some samples with larger DPB-domain sizes (Fig.4(b)) a blue-shift of the D_I line of about 2 meV was observed connected with an increase in luminescence intensity (Fig.4 (d)). Such blue-shift indicates a high amount of strain in the pseudomorphic grown layer [7]. Indeed, from XRD measurements [8] a stress of about 0.23 GPa has been estimated, for example, for pseudomorphic grown 3C-SiC layers on 6H-SiC(0001). Using the data of Choyke et al. [7], this stress should result in an energy shift in the range of 2 meV, which compares very well to the obtained value within the accuracy of the measurements.

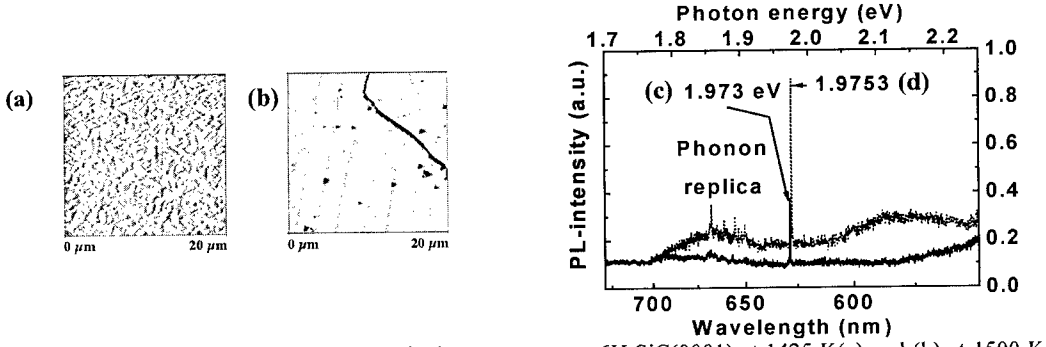


Fig.4: AFM pictures of 1 μm thick 3C-SiC layers grown on 6H-SiC(0001) at 1425 K(a) and (b) at 1500 K showing DPB with different sizes; LTPL spectra of the layer grown at 1425 K (c) and grown at 1500 K (d).

The reduced LTPL intensity of the D_I-centre line intensity of the pseudomorphic grown 3C-layers may be caused on the one hand side by the poorer layer quality due to the formation of double-position boundaries as well as the strain within the layers. However, the influence of the lower growth T of 1425 – 1500 K on the mechanisms related to the D_I centre formation can not be excluded. However, this will be a subject of further investigations.

Generally, no impurity related emission was observed in the spectra of all MBE-grown epilayers.

DISCUSSION

The most dominant figure in the LTPL spectra of SiC layers grown by solid-source MBE is the e-mission from the so-called D_I-centre recombination. This is different from the properties of material

grown by other methods, where only sometimes very small peaks related to the D_I-centre were observed in LTPL measurements of untreated epitaxial layers grown by chemical vapour deposition (CVD) and sublimation [9,10]. First report about these kind of defect was already made thirty years ago [5]. In that investigation, radiation defects were introduced into cubic SiC by He-ion implantation and electron bombardment. After this treatment, the LTPL spectrum obtained at 1.5 K revealed a strong no-phonon line of a new luminescence centre (D_I) at a peak position of 6279.8 A. The D_I-centre was interpreted to be connected with vacancies introduced by the damage. However, the nature of the D_I-centre is still under discussion. In recent years the D_I-related emission was observed in LTPL spectra also for other SiC polytypes after ion implantation and a subsequent annealing, and after high-energy electron bombardment [11-14]. Characteristic features of the corresponding defect are high thermal stability and an unusual temperature dependence of the related emission line in the PL spectrum. Investigations of the D_I-centre emission in 4H-SiC were interpreted by exciton recombination at an isoelectronic centre, where one of the particle of the exciton is weakly bound, whereas the other is more tightly bound [13]. Therefore, the sharpness of the D_I line should be a consequence of such an excitonic effect.

Till now, the investigations presented in literature suggest that the defect will be formed under conditions far from the equilibrium by implantation and a subsequent annealing. These conditions are completely different to those used in the MBE and the question is why this kind of defect preferentially occurs in MBE grown layers. From the point of view of thermodynamics, point defects generally should exist in a certain level dependent on the growth conditions, as for other semiconductor materials. The absence of the D_I-centre luminescence in CVD grown material may be a consequence of the passivation of such kind of point defect, for example, by hydrogen present in a high amount during CVD growth. During implantation the saturating hydrogen will be removed and diffuse out of the sample.

SUMMARY

Summarising the experimental results, it has been found, that in SiC layers grown on SiC under near equilibrium conditions, the D_I-centre generally exist in a high density. The intensity of the centre emission increases by an improvement of the layer quality and by doping with boron. This seems to be in contrast to former results were the D_I-centre was only observed after introducing of defects. Therefore, the discussion about the nature of this defect and especially the question whether this defect appears under thermodynamically equilibrium conditions or not is still open. The results regarding the influence of the B-doping and the change of the growth conditions (chemical potential) can illuminate the discussion.

REFERENCES

[1] S. Kaneda, Y. Sakamoto, C. Nishi, M. Kanaya, S.-I. Hannai, Jap. J. Appl. Phys. 25 (1986), p. 1307.
[2] T. Yoshinobu, H. Mitsui, I. Izumikawa, T. Fuyuki, H. Matsunami, Appl. Phys. Lett. 60 (1992), p. 824.
[3] R.S. Kern, R.F. Davis, Appl. Phys. Lett. 71 (1997), p. 1356.
[4] A. Fissel, B. Schröter, W. Richter, Adv. Sol. State Phys. 38 (1999), p. 87.
[5] W.J. Choyke, L. Patrick, Phys. Rev. B 4 (1971), p. 1843.
[6] S.G. Sridhara, L.L. Clemen, R.D. Devaty, W.J. Choyke, D.J. Larkin, H.S. Kong, T. Troffer, G. Pensl, J. Appl. Phys. 83 (1998), p. 7909.
[7] W.J. Choyke, Z.C. Feng, J.A. Powell, J. Appl. Phys. 64 (1988), p. 3163.
[8] J. Kräußlich, A. Bauer, B. Köcher, K. Goetz, phys. stat. sol. (a) 82, (1998), p. 284.
[9] T.A. Kennedy, J.A. Freitas, S.G. Bishop, J. Appl. Phys. 68 (1990), p. 6170.
[10] K. Nishino, T. Kimoto and H. Matsunami, Jpn. J. Appl. Phys. 34 (1995), p. L1110.
[11] Ch. Haberstroh, R. Helbig, R.A. Stein, J. Appl. Phys. 76 (1994), p. 509.
[12] J. Schneider, K. Maier, Physica B 185 (1993), p. 199.
[13] T. Egilsson, J.P. Bergman, I.G. Ivanov, A. Henry, E. Janzén, Phys. Rev B 59 (1999), p. 1956.
[14] T. Egilsson, A. Henry, I.G. Ivanov, J.L. Lindström, E. Janzén, Phys. Rev. B 59 (1999), p. 8008.
The authors like to acknowledge the support of this work by the Sonderforschungsbereich of the Deutsche Forschungsgemeinschaft 196 (project A03)

Materials Science Forum Vols. 353-356 (2001) pp. 413-416
© 2001 Trans Tech Publications, Switzerland

Prediction of Optical Properties of Si and Ge Dots in SiC

H.-C. Weissker, J. Furthmüller and F. Bechstedt

Friedrich-Schiller-Universität Jena,
Max-Wien-Platz 1, DE-07743 Jena, Germany

Keywords: Dielectric Function, Nanocrystal, Optical Properties, Quantum Dots

Abstract: We present parameter-free calculations of the frequency-dependent dielectric function in order to understand the optical properties of Si and Ge nanoparticles in a SiC matrix. The calculations are based upon a pseudopotential-plane-wave method. The dots are described by clusters up to 239 atoms embedded in cubic SiC or saturated by hydrogen to simulate a polytype with a wider energy gap. The resulting optical spectra are discussed in dependence on the dot size and dot surroundings.

Introduction

Nanometer-sized Si and Ge structures give rise to an efficient photoluminescence in the visible and even blue wavelength region [1, 2, 3]. This observation has prompted many studies, both exploring technological applications and investigating fundamental properties. Such nanostructures have been fabricated by ion implantation in amorphous SiO_2 or Al_2O_3 matrices, by electrochemical etching, or by Stranski-Krastanov growth using molecular beam epitaxy (MBE). Unfortunately, electroluminescence from the nanocrystals is limited by the insulating character or the too small energy gap of the matrix material. To overcome these limitations, embedding the nanoparticles in a wide-gap semiconductor, e.g. hexagonal SiC, seems to be promising. In fact, recent MBE deposition experiments of Si and Ge dots on SiC offer a realistic possibility for the preparation of such embedded dots [4].

Calculational Method

In a first step we calculate the underlying one-electron states from *first-principles* using density-functional theory (DFT) in the local density approximation (LDA). The electron-electron interaction is described within the parametrization of Perdew and Zunger. The interaction of the electrons with the atomic cores is treated by non-normconserving *ab initio* Vanderbilt pseudopotentials [5]. They allow a substantial potential softening even for first-row elements. For instance, in the SiC case the cutoff of the plane-wave expansion of the eigenfunctions has been chosen to be 13.2 Ry. The Vienna ab-initio Simulation Package [6] is used.

The use of a plane-wave expansion requires a supercell approach for the description of the quantum dots. We consider an arrangement of simple-cubic cells with 512 or 216 atoms to describe the case of a tetrahedrally coordinated system. First, we consider cubic SiC and substitute Si or Ge atoms for host atoms such that the T_d symmetry of the initial system is preserved. The resulting nanocrystals of 1, 5, 17, 41, 83, 147, and 239 atoms are highly strained due to the large lattice misfit between Si or Ge and SiC. The strain is homogeneously distributed throughout the dot because we keep to the original atomic positions. The clusters possess different interface bonds in dependence on the choice of a Si or C site as the center of the dot. Second, embedment of Si and Ge in hexagonal SiC leads to a type-I heterostructure, cf. Fig. 2. Hydrogen coverage induces barriers which simulate this

behaviour, although the barrier heigts are overstimated. Hence our calculations considering hydrogenated, unstrained dots model dots within a hexagonal SiC-matrix.
The calculations of the optical properties are performed within the independent-particle picture [7]. We make use of a partial cancellation of self-energy and excitonic effects. The net effect should merely increase the optical transition energies by a size-independent shift [8]. The matrix elements of the optical transition operator are calculated using all-electron wave functions generated by means of the PAW method [9]. The tetrahedron method and a Gaussian-broadening scheme are applied to the k-space integration. The tetrahedron method is combined with k·p perturbation theory in order to circumvent the problem of band allocation at the four tetrahedron vertices and to reduce the minimum number of k points to just one.

Resulting Spectra and Discussion

For Si quantum dots embedded in cubic SiC with Si-C interfaces the imaginary parts of the dielectric functions are plotted in Fig. 1a. One observes a significant change of the spectra from the behaviour of pure cubic SiC [7] with increasing size of the quantum dots. There is a reduction of the high-energy SiC peak located at about 8 eV in the DFT-LDA spectrum with mixed E'_1, E'_0, and E_2 + δ character. The lower-energy peak of the SiC absorption spectrum shows a similar but much more weakened influence of the dot due to its E_0 and E_1 character. On the other hand, a Si-induced shoulder appears at about 5 eV (in the DFT-LDA spectrum). With increasing Si content it becomes more pronounced, increases its intensity and shifts to smaller photon energies. Consequently, an additional peak develops at lower energies at which the SiC crystal is transparent. At much lower photon energies of about 3 eV a further shoulder occurs. Its changes are more significant for the Ge dots embedded in SiC (not shown) than for Si ones.

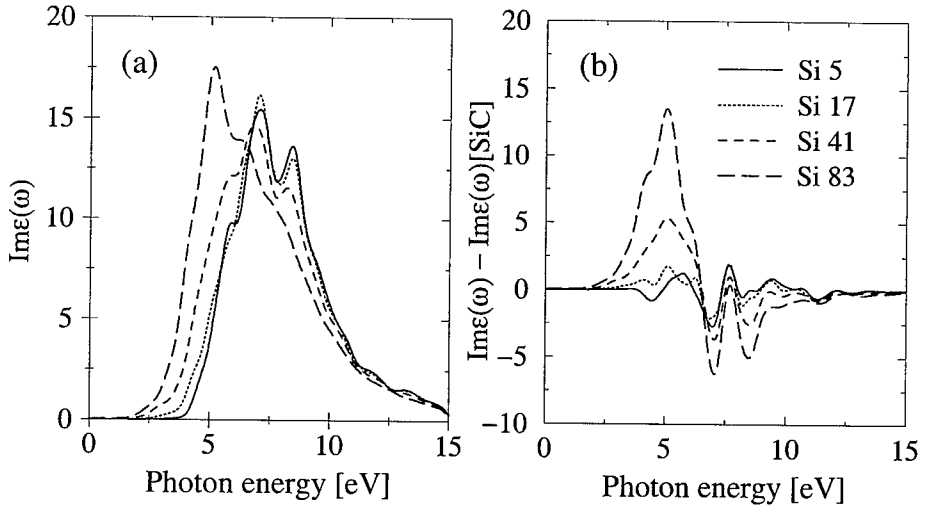


Fig. 1: Dielectric function of spherical Si quantum dots embedded in cubic SiC. (a) Only the imaginary parts Imε(ω) are plotted. The number of dot atoms is indicated. (b) The spectrum of the host material is substracted. A 216-atom supercell is used.

The changes with the number of dot atoms are more obvious in the difference spectra ΔImε(ω) in which the effects of the 3C-SiC host material are substrated (cf. Fig. 1b). In the Si case only one main peak develops slightly to lower energies indicating a weak quantum confinement in the small dots. One may speculate that this peak would develop in unstrained bulk Si into the E_2 absorption structure. A similar situation occurs for Ge. There is an additional strong peak at about 6 eV.

However, this peak does not shift with changing dot size and, hence, is not influenced by any quantum confinement. On the other hand, in the low-energy region of the spectra of both Si and Ge nanocrystals an additional shoulder is visible. Its rapid development is accompanied by a significant red shift. It seems that this shoulder becomes the E_1 structure in unstrained bulk Si and Ge. However, the shifts, in particular of the high-energy peak, do not follow the common rules of spatial quantization. We trace the weakened influence on the dot size back to a type-II heterostructure behaviour. For a 3C-SiC host it is demonstrated in Fig. 2.

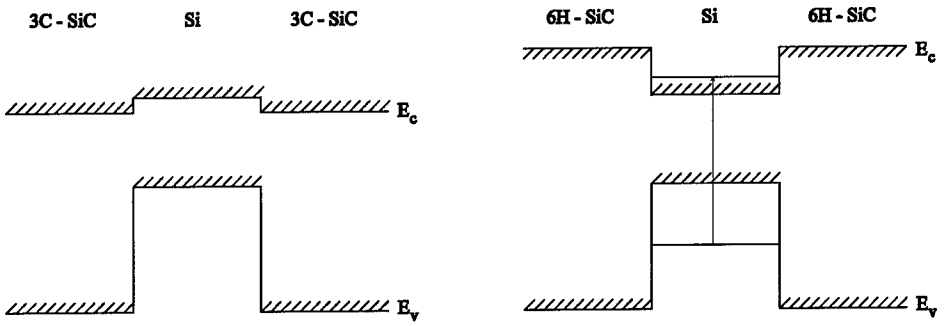


Fig. 2: Band line-up of Si nanostructures embedded in SiC (schematically). The distinct conduction band positions of the cubic (3C) and the hexagonal (6H) polytypes are indicated. The shown band line-up for the valence bands has been calculated using a tight-binding method [10]. The conduction bands followed by adding the experimental energy gaps.

The absorption spectra are plotted in Fig. 3 for unstrained spherical hydrogenated quantum dots. The spectra are substantially influenced by quantum confinement effects. The absorption threshold moves to lower photon energies with increasing dot size. This is clearly indicated by the vertical arrows which represent the respective HOMO-LUMO gap (highest occupied molecular orbital – lowest unoccupied molecular orbital). There is a main peak at photon energies below 5 eV which presumably develops into the bulk E_2 structure. The shoulder at lower energies occurs significantly only in the Ge case. It is stronger influenced by quantum confinement effects. Its energetical shift

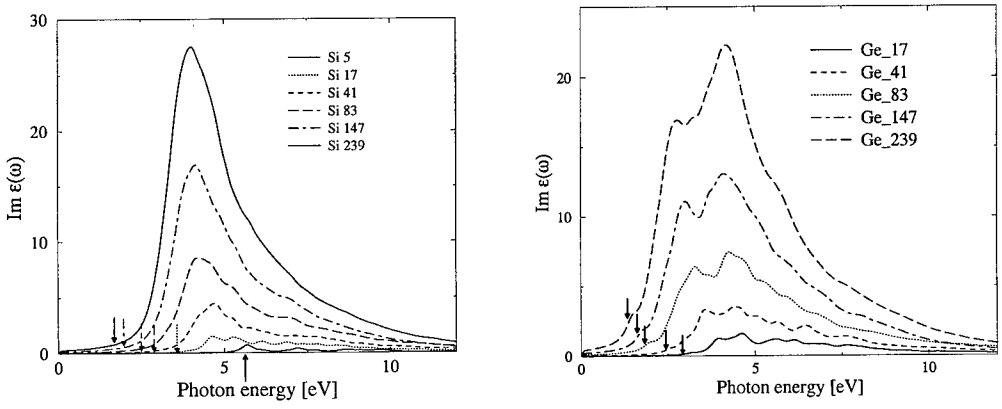


Fig. 3: Imaginary part of dielectric function of Si and Ge nanocrystallites. Their embedment in a wide-gap material is simulated by a hydrogen saturation of the dangling bonds. A Lorentzian broadening is used. The vertical arrows in the absorption spectra indicate the respective HOMO-LUMO gaps. Nominally, a 512-atom cell is used.

towards smaller energies with increasing dot diameter is more drastic. It probably develops into the bulk E_1 absorption structure. However, as a consequence of the absence of excitonic effects it remains a shoulder in correspondence to the DFT-LDA calculations of the optical absorption in bulk crystals [7].

Summary

We have developed a *first-principles* method to calculate the optical properties of embedded quantum dots. This method is based on a supercell approach. Using supersoft non-normconserving pseudopotentials we can fully quantum-mechanically treat 512 atoms in a simple-cubic cell within density-functional theory and a pseudopotential-plane-wave scheme. These supercells allow to study spherical quantum dots of up to 239 atoms but also nanocrystallites of arbitrary shape. Only the size is restricted due to limited computational resources. We found that the absorption behaviour of the quantum dots depends strongly on the embedding matrix material. This is related to the different heterostructure behaviour varying between type II and I. Quantum size effects dramatically change the peak positions and intensities. The development of the spectral character of atomic clusters into bulk spectra of the corresponding crystals has been shown.

Acknowledgements

Financial support from the Deutsche Forschungsgemeinschaft (Sonderforschungsbereich 196, Project No. A8) is acknowledged.

References

[1] Y. Maeda, N. Tsukamoto, Y. Yazawa, Y. Kanemitsu and Y. Masumoto, Appl. Phys. Lett. 59 (1991), p. 3168.
[2] M.D. Mason, G.M. Credo, K.D. Weston and S.K. Buratto, Phys. Rev. Lett. 80 (1998), p. 5405.
[3] C.S. Peng, Y. Huang, W.Q. Cheng, J.M. Zhou, Y.H. Zhang, T.T. Shenf and C.H. Tung, Phys. Rev. B57 (1998), p. 8805.
[4] A. Fissel, K. Pfennighaus and W. Richter, Appl. Phys. Lett. 71 (1997) 2981; Thin Solid Films 318 (1998), p. 88.
[5] J. Furthmüller, P. Käckell, F. Bechstedt and G. Kresse, Phys. Rev. B61 (2000), p. 4576.
[6] G. Kresse and J. Furthmüller, Comput. Mater. Sci. 6 (1996) 15; Phys. Rev. B54 (1996), p. 11169.
[7] B. Adolph, V.I. Gavrilenko, K. Tenelsen, F. Bechstedt and R. Del Sole, Phys. Rev. B53 (1996), p. 9797.
[8] C. Delerue, M. Lannoo and G. Allan, Phys. Rev. Lett. 84 (2000), p. 2457.
[9] B. Adolph, J. Furthmüller and F. Bechstedt, Phys. Rev. B (submitted).
[10] W.A. Harrison, Electronic structure and the properties of solids, Dover Publications, 1989.

Materials Science Forum Vols. 353-356 (2001) pp. 417-420
© 2001 Trans Tech Publications, Switzerland

Investigation of Variable Incidence Angle Spectroscopic Ellipsometry for Determination of Below Band Gap Uniaxial Dielectric Function

M. Kildemo and O. Hunderi

Applied Optics/Surface Physics, Department of Physics,
NTNU, NO-7491 Trondheim, Norway

Keywords: 4H-SiC, Anisotropic Dielectric Function, Birefringence, Brewster Angle, Spectroscopic Ellipsometry (SE), Uniaxial Material

ABSTRACT This paper investigates a novel approach for accurate refinement and direct determination of dielectric properties of uniaxial materials below the gap, available both in form of a thick transparent double side polished wafer, and as a semi-infinite bulk wafer (single side polished). Most of the common hexagonal and trigonal wide band gap materials are uniaxial birefringent. We propose to split the complete accurate characterisation of the optical properties of these materials into several steps, using spectroscopic ellipsometry. The overall goal is thus to determine both the ordinary and extra ordinary components of the dielectric function. The birefringence is determined from a double side polished wafer. A spectroscopic fit is further used to determine the overlayer (oxide) thickness and approximate dielectric functions, while we show that higher sensitivity to the ordinary dielectric function may be obtained through the Brewster angle condition obtained from spectroscopic ellipsometry. The material under investigation in the current paper is 4H-SiC.

INTRODUCTION

Most work related to characterisation of the optical properties of uniaxial semicondutors have focussed on the pseudo-ordinary dielectric function; in case of 4H and 6H-SiC see for example Refs. 1-3. Firstly, because spectroscopic ellipsometry is mainly sensitive to the ordinary component [2,4], secondly, since the extraordinary component is hard to measure accurately, and finally, because the ordinary and extraordinary components are fairly similar below the band gap, it is difficult to measure both accurately.

In a set of recent papers it has been shown that it is indeed possible to enhance the sensitivity to the birefringence substantially by measuring a thick double side polished wafer using spectroscopic ellipsometry [5-7]. Most important, an accurate model was developed that made possible the simultaneous spectroscopic fitting of a Sellmeier type dispersion model for both the ordinary and extraordinary component [5]. Some of these results are directly applicable to SiC wafer characterisation, since the birefringence seem to be a strong function of SiC polytype [8]. In this paper we show a complete set of ellipsometric measurements of double side polished 4H-SiC as a function of energy and as a function of angle of incidence. The aim of the paper is to discuss the use of these measurements, rather to give a compact review of all related theory.

EXPERIMENT AND THEORY

A Phase Modulated Spectroscopic Ellipsometer (PMSE) was used to perform the UV-Visible ellipsometric measurements of

$$I_s = \frac{2\,\mathrm{Im}\langle r_p r_s^* \rangle}{\langle r_s r_s^* \rangle + \langle r_p r_p^* \rangle} \text{ and } I_c = \frac{2\,\mathrm{Re}\langle r_p r_s^* \rangle}{\langle r_s r_s^* \rangle + \langle r_p r_p^* \rangle}, \quad (1)$$

where *Re* and *Im* stand for real and imaginary part respectively. r_p and r_s are the sample reflection coefficients for *p* and *s* polarisations respectively, the asterisk stands for complex conjugate, and the brackets ("<>") denote the ensemble average, introduced to account for the bandwidth, which is necessary when dealing with thick double side polished samples [5]. The resulting averaged products entering into

Eq. 1 in case of a thick double side polished wafer were :

$$\left\langle r_x r_y^* \right\rangle = r_{01x} r_{01y}^* + \frac{(t_{01x} t_{01y}^*)(t_{10x} t_{10y}^*)(r_{12x} r_{12y}^*) e^{2i(\beta_x - \beta_y^*)}}{1 - (r_{10x} r_{10y}^*)(r_{12x} r_{12y}^*) e^{2i(\beta_x - \beta_y^*)}}, \quad (2)$$

where x,y =s in case of s-polarisations, and x,y=p in case of p-polarisation. The $r_{s,p}$ and $t_{12s,p}$ are reflection and transmission coefficients for s and p polarisation respectively [5-7]. The optical phases β_s and β_p are defined by:

$$\beta_s = 2\pi \frac{D}{\lambda} \sqrt{n_o^2 - n^2 \sin^2 \varphi_o} \quad \text{and} \quad \beta_p = 2\pi \frac{D}{\lambda} \frac{n_o}{n_e} \sqrt{n_e^2 - n^2 \sin^2 \varphi_o} \quad (3)$$

where D is the thickness of the layer, n_o and n_e are the ordinary and extraordinary refractive indices of the layer, n is the ambient refractive index, λ is wavelength of light and φ_0 the angle of incidence. The uniaxial dielectric functions are defined as $\varepsilon_{o,e} = n_{o,e}^2$, and the dielectric difference as $\Delta\varepsilon = \varepsilon_e - \varepsilon_o$, where the subscripts o and e denotes the ordinary and extra ordinary components.

RESULTS AND DISCUSSION

Fig. 1 shows the result of the PMSE intensity recorded from a double side polished 4H-SiC wafer. The measurements were recorded as a function of angle of incidence between 35-55 degrees in steps of 0.1 degrees, and as a function of photon energy from 1.5-3.5 eV with a step of 0.025 eV. It is clearly demonstrated that clear interference patterns are observed, both as function of angle of incidence and as a function of photon energy, as a result of the interference in the cross terms $\left\langle r_p r_s^* \right\rangle$ due to the difference in optical path length between the extra-ordinary and the ordinary mode. Fig. 2 shows the same recorded intensity but for the angle of incidence between 65-75 degrees. It is seen that the measured I_c crosses zero at what we now define as the apparent Brewster angle for the uniaxial medium. This observation is very interesting, since in case of a normal Brewster angle measurement, the reflectance goes trough a slow minimum. In the case of ellipsometry, there is a steep line crossing zero, giving a high sensitivity to the ordinary component of the dielectric function. (This is not unique for a double polished material, but is identical for a semi-infinite material, however, in the latter case there are thus no contributions from the backside.)

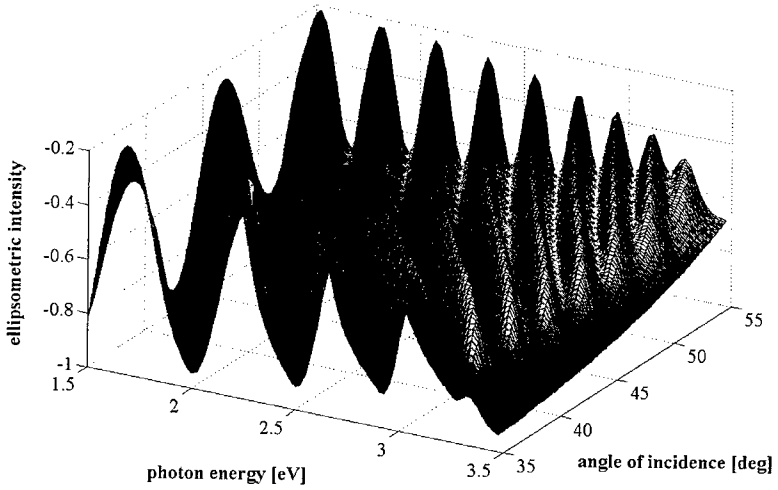


Figure 1. Recorded PMSE intensity I_c from double polished semi-insulating 4H-SiC. The measurements are performed as a function of incidence and as a function of photon energy.

A spectroscopic fit around the apparent Brewster angle was previously presented [5-7] through the use of Sellmeier models for both the ordinary and extra ordinary components . The resulting dispersion models were [7]:

$$n_o^2(E)=1+\frac{5.63*(7.53)^2}{(7.53)^2-E^2} \quad \text{and} \quad n_e^2(E)=1+\frac{5.86*(7.26)^2}{(7.26)^2-E^2}, \tag{4}$$

However, some experimental uncertainty (within 3 %) existed as a function of angle of incidence between 65-75 degrees, and the above results represents an average within this uncertainty. We believe that the best result was obtained at around 68-70 degrees angle of incidence. There are three reasons for this. Firstly, the occurence of the Brewster angle within the measured region, is pinning the ordinary component, which otherwise has a tendency to vary as a function of incidence. Secondly the amplitude of the interference oscillations are reduced, reducing also the errors due to depolarisation by the sample, and finally reduces also errors due to ellipsometer calibrations. However, this uncertainty is the motivation for the investigation of the Brewster angle method.

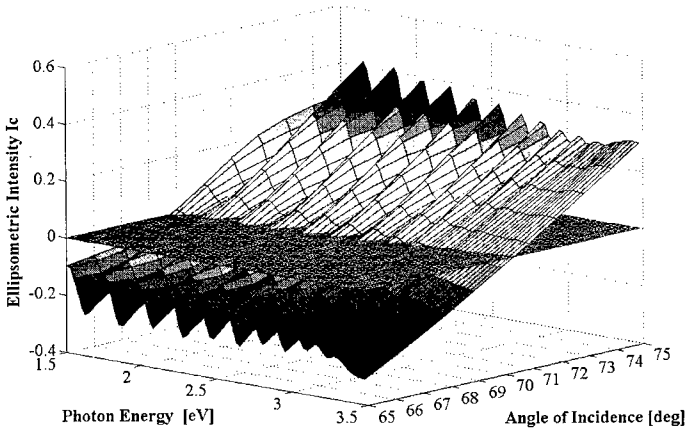


Figure 2. Recorded PMSE intensity I_c from double polished semi-insulating 4H-SiC. The measurements are performed as a function of incidence around the Brewster angle, and as a function of photon energy. The intersection between the flat surface defining I_c=0, and the measured surface we define as the apparent Brewster angle.

From the difference in wavelength or incidence angle of interference-maxima it is possible to calculate the birefringence of the material. Alternatively, they may be used in order to determine the thickness of the wafer [7,9]. In order to measure directly the birefringence of the uniaxial wafer from the maxima as a function of photon energy, the derivatives of the birefringence with respect to wavemumber must be included in order to accurately determine the birefringence or the thickness of the wafer [7,9]. A much more elegant method is to use the interference maxima as a function of angle of incidence (see Fig. 1), and solve numerically for $\Delta\varepsilon$, provided the ordinary dielectric constant ε_o is known. Fig. 3 shows the resulting birefringence from the spectroscopic fit, the spectrocopic half wave method and from the variable incidence half waves. The latter is expected to be the most accurate measurement. We hereby define a new set of parametrized dielectric difference functions from the Sellmeier functions. A fit to the resulting birefringence gives the following parametric model for the dielectric difference in the interval [1.5-3.25] eV : $\Delta\varepsilon(E)=\frac{0.22*(6.3631)^4}{\left((6.3631)^2-E^2\right)^2}$,or using the ordinary component in equation (4) but fitting the ε_e, we get the expression for the extra ordinary component through $\varepsilon_e(E)=1+\frac{5.845*(7.24)^2}{(7.24)^2-E^2}$. It is interesting to note that the dielectric difference function is as representative to the hexagonal uniaxial SiC materials as is the ordinary dielectric function. Furthermore, if 4H and 6H SiC are compared, then in the below band gap region the dielectric difference is 20 %, while the difference in the ordinary dielectric function is less than 5% !

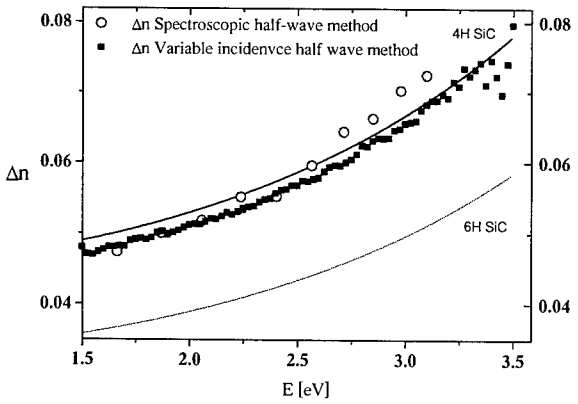


Figure 3. Birefringence of 4H-SiC as determined from Spectroscopic fit using Anisotropic Incoherent Reflection Model [5-7] (full line), spectroscopic half wave method including correction for derivatives [7], and variable incidence half wave method [this work]. The birefringence is compared to 6H-SiC (dotted lines) as extracted from Ref. 10.

BREWSTER METHOD

The determination of absolute birefringence still depends upon the accuracy with which the ordinary component of the dielectric function can be determined. The measured intensity I_c crosses zero (see Fig. 2) when $Re(r_{pp}r_{ss}^*) = 0$, where r_{pp} is the uniaxial anisotropic reflection coefficient for p polarised light. Let φ_B be defined as the apparent Brewster angle for which this crossing appears. If the overlayer (e.g. oxide), the bulk absorption and the backside reflections, are neglected, then the below band gap ordinary dielectric function may be calculated analytically as :

$$\varepsilon_o = \frac{1}{2}\left(\frac{1}{\cos^2\varphi_B} - \Delta\varepsilon\right) + \frac{1}{2}\sqrt{\left(\frac{1}{\cos^2\varphi_B} - \Delta\varepsilon\right)^2 - 4\left(\tan^2\varphi_B - \frac{\Delta\varepsilon}{\cos^2\varphi_B}\right)}. \quad (5)$$

Note that neglecting the birefringence means just letting $\Delta\varepsilon \to 0$ in equation (5). We find in accordance with Ref. 4, only a 0.4 % correction (increase) to the ordinary refractive index, for $\Delta n / n_o \approx 2\ \%$. By also including the overlayer (and eventually absorption determined from, e.g., transmission measurements), a numerical solution of $Re(r_{pp}r_{ss}^*) = 0$, give a further 0.3 % correction to the refractive index (increase) for a 3 nm thick SiO_2 overlayer. It is, however, observed from the measurements in Fig. 1 that one still gets contributions from the back side of the sample (the apparent Brewster angle is an oscillating function of energy, which is surprisingly different from the isotropic case). This means that the complete model including the back-side reflections must be used. This is complicating the analysis, and we plan to perform a new set of measurements on a single side polished wafer. In conclusion, we believe that this approach is extremely powerful in order to accurately completely describe the dielectric function of uniaxial wide band gap semiconductors, and plan to pursue this approach in the near future.

REFERENCES

[1] S. Logothedis and J. Petalas, J. Appl. Phys. **80** (1996), p. 1768.
[2] S. Zollner, J. G. Chen, E. Duda,T. Wetteroth, S.R. Wilson and J. N. Hilfiker, J. Appl. Phys. **85** (1999), p. 8353.
[3] C. Cobet, K. Wilmers, T. Wethkamp, N. V. Edwards, N. Esser, W. Richter, Thin Solid Films **364** (2000), p. 111.
[4] D. E. Aspnes, J. Opt. Soc. Am. **70** (1980), p. 1275.
[5] R. Ossikovski, M. Kildemo, M. Stchakovsky and M. Mooney, Appl. Opt. **39** (2000), p. 2071.
[6] M. Kildemo, M. Mooney, C. Sudre, P. Kelly, G. Crean, Mat. Sci. For. **338-342** (2000) p571.
[7] M. Kildemo, M. Mooney, C. Sudre, P. Kelly, Appl. Opt. **39** (2000), p. 4649.
[8] N. Adolph, K. Tenelsen, V. I. Gavrilenko, and F. Bechstedt, Phys. Rev. B **55** (1997), p. 1422.
[9] M. Kildemo and O. Hunderi, J. Opt. A: Pure Appl. Opt. **2** (2000), p. L33.
[10] J. Choyke and E. D. Palik, in Handbook of Optical Constants of Solids (E.D. Palik ed., Academic Press, Orlando,1985), p. 587.

Materials Science Forum Vols. 353-356 (2001) pp. 421-426
© 2001 Trans Tech Publications, Switzerland

Theory of Hydrogen in Silicon Carbide

Peter Deák, Adam Gali and Bálint Aradi

Department of Atomic Physics, Technical University of Budapest,
Budafoki út 8, HU-1111 Budapest, Hungary

Keywords: Compensation, Hydrogen Concentration, Interstitial H, Passivation, T5 Center, Vacancy-Hydrogen Complex

ABSTRACT. Interaction of hydrogen atoms is considered with the "perfect" lattice and with isolated vacancies (V), by means of ab initio model calculations in 3C- and 4H-SiC. We find that interstitial atomic hydrogen acts as a relatively shallow donor in 3C- and as an amphoteric trap in 4H-SiC. Only two H atoms can be accomodated by V_C and (V_C + nH) complexes are hole traps (n=1,2). V_{Si} can in principle be saturated with H but (V_{Si} + nH) complexes are electron traps for n = 1,2. We predict high concentration of mobile, compensating H_i^+ centers in p-type material. In n-type SiC the stable form of interstitial hydrogen is H_2 (with low solubility) and the dominant hydrogen defects are (V_{Si} + nH) traps. H_i is attracted by shallow acceptors and (V_{Si} + H) but not by shallow donors or (V_C + H). Spectroscopic properties of H-related defects have been calculated. We propose that the T5 center is more likely to arise from $(V_C + 2H)^+$ than from V_C^+.

INTRODUCTION. The use of semiconductors in electronics is based on the tight control of carrier concentration and lifetime. This is jeopardized by the unwanted introduction of defects which starts already with the growth of the crystal. For SiC both bulk and CVD growth are bound to introduce hydrogen which is an inherent contaminant of graphite reactor parts in the former, and intrinsic part of the precursor molecules in the latter. Generally, a defect may diminish the carrier concentration in four different ways: i) deep levels introduced into the gap can act as *traps*, capturing free carriers, ii) shallow levels introduced to the opposite side of the gap with respect to the dopant levels produce free minority carriers, *compensating* the effect of the dopants and pinning the Fermi level, iii) chemical bonds established in a defect-dopant complex *passivate* the dopant, i.e., remove the electrically active level of the dopant from the gap, and iv) the defect may outcompete the dopant in the first place for securing the substitutional sites, thereby *preventing* dopant *activation.* In this paper we will show by means of *ab initio* atomistic model calculations that H in SiC is capable of doing at least two of these evils and can be suspected with the other two as well.

The presence of hydrogen was proven in as grown, B-doped, p-type 6H-SiC epilayers and it was assumed that it had been incorporated as a complex with the B atom [1]. Low temperature H-plasma treatments showed very strong decrease in the hole concentration of p-type samples, which could only be restored after heat treatments at 700 °C [2,3]. Low-energy H-implantation studies have shown that hydrogen is positively charged in p-type material, i.e., it acts as a compensating center, but can also passivate Al acceptors by forming a complex [4a,b]. In contrast, implantation resulted in very low H concentration in n-type material [4a]. The decrease of free carrier concentration after high-dose H-implantation [5] or high density DC plasma treatment [6] was attributed to the intrinsic traps created, and an ECR plasma treatment was ineffective in decreasing the carrier concentration of n-type samples [3]. However, annealing in high temperature, high pressure hydro-

gen gas succeded in doing that not only in p-type but– to a lesser extent – also in n-type material, although no complex formation could be detected in either case [7]. Despite these facts, spectroscopic evidence about the presence of hydrogen in SiC is meager. PL bands arising as phonon replica due to local modes were interpreted as C–H stretch modes due to H in silicon vacancies [8] but vibrations which could be assigned to Si–H stretching modes (~2100 cm^{-1}) have not yet been observed. No new DLTS peaks appeared after deuterium implantion of previously electron-irradiated SiC [9], and no ESR signal has yet been assigned to H either. This general lack of information is intriguing, so *a priori* knowledge about various H-related defects could be helpful — even if the data supplied by model calculations are only approximate.

METHODS. The calculations have been carried out using the FHI98MD [10] and the AIMPRO [11] codes, both utilizing ab initio density functional theory in the local density approximation (LDA). The main parameters of the calculations are given in Table 1, for more details see ref. [12].

Table 1. Main parameters of the calculations.

calculated properties	formation energy, occupancy levels, spin distribution	vibrations
code	FHI98MD	AIMPRO
supercell	32 (128) atoms for 3C, 96 atoms for 4H	64 atoms for 3C
basis	Plane-waves cut-off: 64 (32) Ry	s and p Gaussians Si(4,4), C(4,4), H(3,3), BC(1,1)
k-set	MP 2x2x2	k=0
pseudopot.	Trouiller-Martin	BHS
E_{tot} correction	LDA gap error, dispersion, spin-polarization, zero point energy of H	-
E_{tot} minimization	1st - 2nd neighbors relax	1st - 2nd neighbors relax

Formation energies of the defects in charge state q were calculated as:

$$E^q_{form}(n_{Si},n_C,n_H;\mu_{Si},\mu_C,\mu_H,E_F) = E^q_{tot}(n_{Si},n_C,n_H) - n_{Si}\mu_{Si} - n_C\mu_C - n_H\mu_H + qE_F \qquad /1/$$

where n is the number of constituent atoms, μ is their chemical potential and E_F is that of the electrons. The Fermi-level, E_F was determined as a function of temperature and net carrier concentration from the neutrality condition including the electrically active defects in a self-consistent way.

As a function of the supercell size the calculated formation energies are converged within 0.3 eV [12]. Accuracy of occupation levels (calculated as the difference of total energies) is influenced by the corrections applied in E_{tot}, and are expected to be within 0.15 eV. The estimates for the concentrations are more or less lower bounds but an order of magnitude error is possible. The host atom – hydrogen stretching vibrations are calculated with an estimated accuracy of 40 cm^{-1}.

RESULTS AND DISCUSSION. Atomic interstitial hydrogen has its equilibrium position at an antibonding (AB) site: behind a C atom in the positive and behind a Si atom in the negative charge state (along the axis of the Si–C bond). In the former case a strong covalent three-center bond is formed on the H–C–Si unit, with a H–C distance of 1.14 Å. In the latter, H is 1.74 Å away from Si, close to the T_{Si} site. The C–Si distance is ~ 1.95 Å in both cases (c.f. 1.88 Å in the perfect lattice). The relative stability of the two sites in the neutral charge state depends on the polytype. This can

be understood as follows. Due to the electronegativity difference, C atoms are negatively and Si atoms are positively charged in SiC. Interstitial H introduces a localized (s-like) state which is in a low electron density region if surrounded by Si and a high one if surrounded by C atoms. As a conceqence, the corresponding one-electron energy level lies in the gap and is occupied if H is behind a Si atom. In the other case the level falls into the conduction band (CB), and a delocalized state at the CB edge accomodates the extra electron introduced by hydrogen. Therefore, the energy of H^0 at AB_C depends on the width of the gap (the valence band off-set between the polytypes is small). In case of 3C-SiC the stronger bond between $H_{AB(C)}$ and C compensates the advantage of the lower one-electron energy of $H_{AB(Si)}$, while the latter wins out in 4H-SiC where the gap is wider. The relation of the total energies are shown in Fig. 1. Since the energy of the charged states change very little between the polytypes, position of the (+/-) occupation level is almost the same with respect to the valence band (VB) edge in 3C- and 4H-SiC. The bistability is accompanied with a definite negative U behavior in the latter, while a small stability window for H^0 may exist in the former. Fig. 1 also shows that interstitial atomic H is a relatively shallow donor in 3C-SiC and can compensate p-type doping. It is also attracted to shallow acceptors. In 4H-SiC it is an amphoteric trap. A H_2 molecule is most stable at T_{Si} (in 3C-SiC) but is less more favorable than H_i^+ in p-type material.

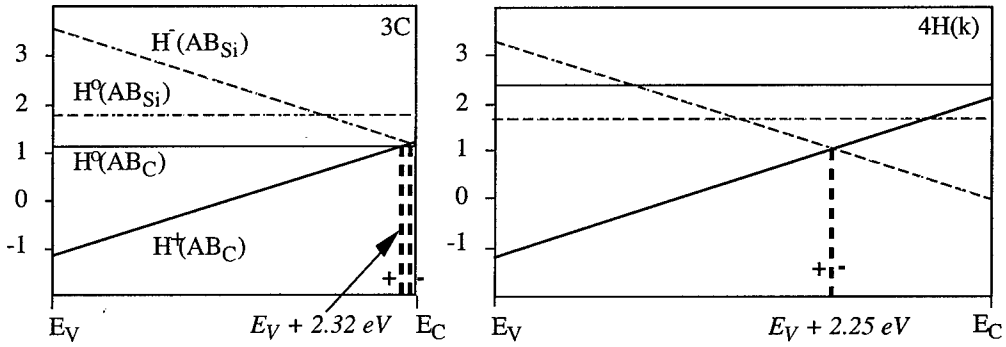


Fig. 1 The energy of the three charge states of H_i with respect to a free H atom in 3C- and 4H-SiC.

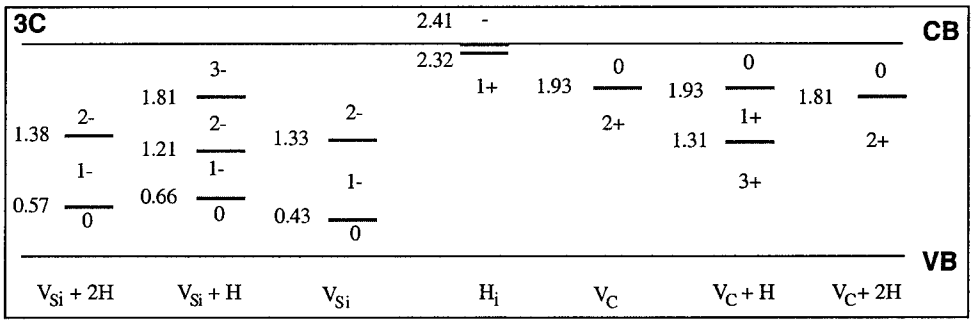


Fig.2 Occupation levels with respect to the VB edge in 3C-SiC. (Positive and higher negative charge states of V_{Si} as well as positive charge states of (V_{Si} + nH) may exist but have not been calculated.)

Within the accuracy of our calculations, the position of the occupation levels with respect to the VB edge of 3C- and 4H-SiC changes also little for the other defects. E.g., the (2+/0) level of (V_C + 2H) is at E_V + 1.81 eV and at E_V + 1.80 eV, while the (0/-) level of (V_{Si} + H) is at E_V + 0.66 eV and at E_V + 0.47 eV, in 3C- and 4H-SiC, respectively. Therefore, we restrict further discussion to 3C-SiC, in

which the occupation levels are shown in Fig.2. The situation is similar with respect to the VB-edge of 4H-SiC, only the CB edge should be shifted up by 0.9 eV.

A hydrogen atom in V_{Si} saturates one dangling bond. Due to the long C–C distances across the vacancy, the interaction of the remaining well localized carbon dangling bonds does not give rise to a significant Jahn-Teller reconstruction, and the symmetry remains close to C_{3v}. The stretching mode vibration frequency of 2961cm^{-1}, calculated in 3C-SiC, agrees well with the values found in 6H- and 4H-SiC [7]. The C dangling bonds give rise to a doubly occupied state in the VB, and a close lying pair of orbitals in the gap, close to the VB edge. These are occupied by only one electron, therefore, $(V_{Si} + H)$ is a multiple electron trap which is negatively charged if the Fermi-level is above $E_V + 0.66$ eV. It may also attract further H_i^+ atoms. In $(V_{Si} + 2H)$ two dangling bonds are still unsaturated, therefore, it is also an electron trap. The energy gain on capturing H atoms in V_{si} (lower bound to the dissociation energy) in n-type material are given by eqs. /2-3/:

$$V_{Si}^{2-} + H^+ + e^- \xrightarrow{-[2.45\ eV+(E_F-E_V)]} (V_{Si} + H)^{2-} \qquad /2/$$

$$(V_{si} + H)^{2-} + H^+ + e^- \xrightarrow{-[2.70\ eV+(E_F-E_V)]} (V_{Si} + 2H)^{2-} \qquad /3/$$

Although the formation energy of V_{Si} is significantly higher than that of V_C, the formation of $(V_{Si} + 2H)$ complexes is already more favorable than that of $(V_C + 2H)$ ones, since the strong C–H bonds compensate the energy needed for creating a vacancy better than the weaker Si–H bonds. Since the stability of the charged states increases as the Fermi-level moves away from the occupation level, $(V_{Si} + nH)$ defects can have rather low formation energies in 4H-SiC.

Hydrogen in a carbon vacancy interacts with two silicon neighbors forming three-center bonds both in 3C- and 4H-SiC [13]. Therefore, only two H atoms can be accomodated. The electrons introduced by H occupy the antibonding combinations of the sp^3 hybrids of the Si neighbors, with one-electron levels in the upper half of the gap. Accordingly, V_C remains a hole trap even after hydrogenation. As can be seen from Fig. 2, interstitial H_i is never attracted to V_C . Also, the binding energy of H in V_C is smaller than in V_{Si}. In p-type material:

$$(V_C + H)^{3+} \xrightarrow{+1.26\,eV} V_C^{2+} + H^+ \qquad /4/$$

$$(V_C + 2H)^{2+} + 2\cdot h^+ \xrightarrow{+[0.03+2(E_F-E_V)]} (V_C + H)^{3+} + H^+ \qquad /5/$$

The calculated stretching mode frequencies for the three-center Si–H–Si bonds are way out of the usual range of Si–H bonds. For $(V_C + H)$ it is 1570 and 991 cm^{-1} in the (0) and 1770 and 1189 cm^{-1} in the (+) charge state (for more details see ref. [13]). The symmetry of $(V_C + H)^0$ in 3C-SiC is C_{2v}, and it has a very similar spin distribution to that of V_C^-. $(V_C + H)^{3+}$ reconstructs to C_{3v}. In case of $(V_C + 2H)$, the (0) and (2+) charge states have D_{2d} symmetry. $(V_C + 2H)^+$ — which is only sligtly unstable with respect to the other charge states — distorts to D_2. This agrees with the symmetry found for the paramagnetic T5 center in 3C-SiC, which was assigned to V_C^+ [14]. (Note, that V_C^+ has D_{2d} symmetry and it is also slightly unstable with respect to V_C^0 and V_C^{2+}.) Apart from the symmetry difference, the spin distribution is very similar on the four silicon neighbors in these two defects, too.

In order to estimate the abundance of hydrogen in as grown CVD layers, we have assumed equlibrium between the H contents of the growing crystal and of the gas phase, at the typical temperature of CVD growth (1400 °C), under atmospheric pressure. Gas phase modeling predicts the pres-

ence of 1 % atomic hydrogen, so we calculated the concentration of hydrogen defects assuming either 1 atm H_2 or 0.01 atm H_a. As can be seen from Fig. 3, H_a in the gas phase is mainly responsible for H incorporation into the crystal during growth. Substantial amounts enter only in p-doped material. If only hydrogen and vacancies are considered, the dominant defect is H_i^+ but the concentration is significantly lower than that of free carriers. If, following ref. [1], we assume that B and H are incorporated together than, even without assuming covalent bonding, the Coulomb attraction between a close B^- and H^+ pair is ~ 0.8 eV. This lowers the formation energy of H_i^+, resulting in equal concentration of H with that of B, as found in ref. [1].

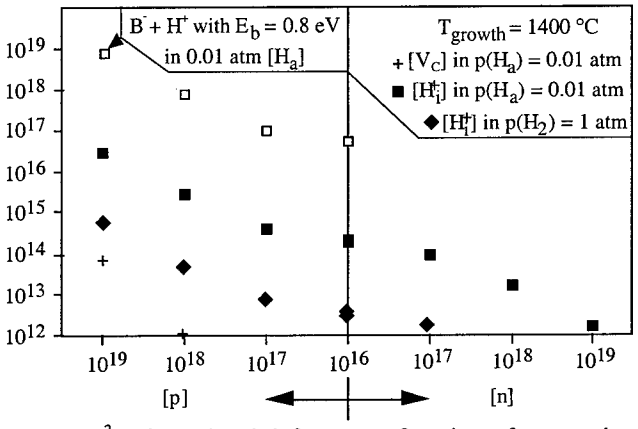


Fig. 3 Concentration [cm^{-3}] of H-related defects as a function of net carrier concentration in 3C-SiC, being in equilibrium with hydrogen gas at 1400 °C. The p(n)-type side was calculated assuming extreme C(Si)-rich conditions. Empty squares represent next neighbor $B^- + H^+$ pairs bonded only by Coulomb-attraction.

[H_i] depends primarily on the Fermi-level position, so higher temperature leads to lower concentrations. Fig. 3 also shows that the detection limit of mobile H_i is reached with the Fermi-level at midgap. This leads us to the suggestion that the T5 center observed in electron-irradiated CVD layers [14] originates from $(V_C + 2H)^+$ rather than V_C^+. The former has the right symmetry (D_2), while V_C^+ is D_{2d}. Both have occupation levels in the upper half of the gap (see Fig. 2), which contradicts the argument of ref. [14] explaining the lack of a T5 signal in even weakly n-type material by assuming an occupation level at midgap. If we assume that electron-irradiation produces a sufficient number of carbon vacancies *and* diffusion of H_i, (V_C + 2H) complexes may arise. Their concentration will be determined by the mobile H_i concentration in the as grown material, which is sufficient for detection in p-type material only!

H-plasma treatment is definitely no equilibrium process but, as a guide, we have calculated the concentration of hydrogen-related defects in stoichiometric 3C-SiC in equilibrium with H_a gas at T = 300 °C and p = 0.03 atm (Fig. 4a). Results for heat treatment in H_2 at 1700 °C and 10 atm are shown in Fig. 4b. There we have assumed that at this temperature ~10 % of the hydrogen is already dissociated.

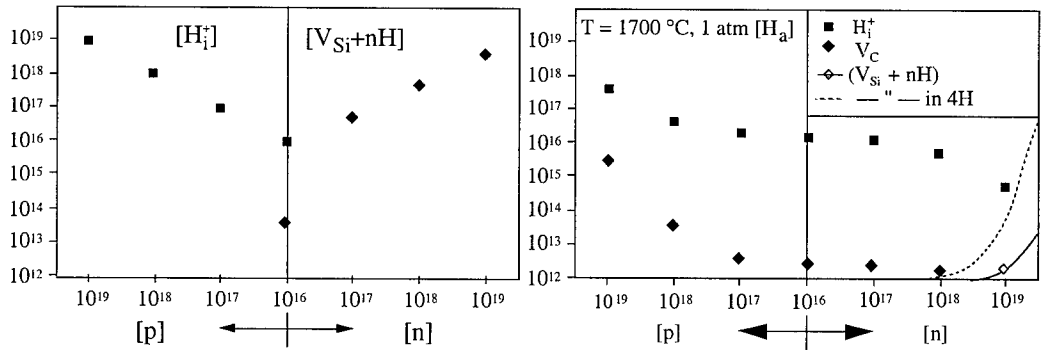


Fig. 4 Concentration [cm^{-3}] of dominant H defects in stoichiometric 3C-SiC being in equilibrium with a) 0.03 atm atomic hydrogen gas at 300 °C, b) 1 atm atomic hydrogen at 1700 °C.

H-plasma treatment in p-type material causes complete compensation, while a considerable amount of electrons will get trapped in (V_{Si} + nH) defects in n-type material. High temperature heat treatment is very effective in introducing hydrogen, but also carbon vacancies. The concentration of (V_{Si} + nH) electron traps becomes substantial in hexagonal polytypes at high level of n-type doping.

SUMMARY. All these findings are in good qualitative agreement with the experimental results described in the introduction. We note that both the paramagnetic properties and the ionization energies are very similar for vacancies and vacancy-hydrogen complexes. Since hydrogen is likely to be present in as grown material, care should be taken in identifying spectroscopic centers. Finally we note that, according to our preliminary results, the reaction $V_{Si} + 4H_i \rightarrow (V_{Si} + 4H)$ may be more exothermic than $V_{Si} + B_i \rightarrow B_{si}$. This may influence the activation rate of implanted B. Further work in this direction is in progress.

References

[1] D. J. Larkin, Phys.Stat.Sol. (b) 202 (1997), p. 305.
[2] G. J. Gerardi, E. H. Pointdexter, D. J. Keeble, Appl. Spectr. 50 (1996), p. 1428.
[3] G. McDaniel et al., J. Vac. Sci. Technol. A 15 (1997), p. 885.
[4] a) N. Achtziger et al., Appl. Phys. Lett. 73 (1998), p. 945; C. Hülsen et al., Mater. Sci. Forum 338-342 (2000), p. 929; b) M. Janson et al., this volume
[5] Th. E. Tiwald et al.. R. Powell, Phys. Rev. B 60 (1999), p. 11464.
[6] A. O. Konstantinov et al., Semiconductors 28 (1994), p. 209.
[7] F. Gendron et al., Appl. Phys. Lett. 67 (1995), p. 1253; B. Clerjaud et al., Sol. State Commun. 93 (1995) p. 463.
[8] W. J. Choyke, L. Patrick, Phys. Rev. B 9 (1974), p. 3214.
[9] M. O. Aboelfotoh and J. P. Doyle, Phys. Rev. B 59 (1999), p. 10823.
[10] M. Bockstedte et al., Comp. Phys. Comm. 107 (1997), p. 18.
[11] P. R. Briddon, R. Jones, Phys. Stat. Sol. (b) 217, (2000), p. 131.
[12] B. Aradi et al., submitted to Phys. Rev. B
[13] A. Gali et al., Phys. Rev. Lett. 84- (2000), p. 4926.
[14] H. Itoh et al., Phys. Stat. Sol. (a) 162 (1997), p. 173.

Materials Science Forum Vols. 353-356 (2001) pp. 427-430
© 2001 Trans Tech Publications, Switzerland

Dissociation Energy of the Passivating Hydrogen-Aluminum Complex in 4H-SiC

M.S. Janson[1], A. Hallén[1], M.K. Linnarsson[1], N. Nordell[2], S. Karlsson[3] and B.G. Svensson[1]

[1] Royal Institute of Technology, Solid State Electronics, Electrum 229, SE-16440 Kista, Sweden

[2] Royal Institute of Technology, Semiconductor Laboratory, Electrum 229, SE-16440 Kista, Sweden

[3] ACREO AB, Electrum 236, Isafjordsgatan 22, SE-164 40 Kista, Sweden

Keywords: Hydrogen, Passivation, SIMS

ABSTRACT The thermal stability of the passivating hydrogen-aluminum complex (^{2}HAl) in 4H-silicon carbide has been studied by determining the effective diffusion constant for hydrogen in an Al-doped epitaxial layer. Assuming a complex comprised of one ^{2}H and one Al acceptor ion, the extracted diffusivities provide the dissociation frequency of the complex. The extracted frequencies cover three orders of magnitude and yield a close to perfect fit to an Arrhenius equation with the extracted dissociation energy for the ^{2}HAl-complex equal to 1.66 (±0.05) eV and a pre-exponential attempt frequency $\nu_0 = 1.7\times10^{13}$ s^{-1} in good agreement with the expected value for a first order dissociation process.

INTRODUCTION

It is a well known fact that hydrogen (H) can electrically passivate doping atoms as well as deeper impurities in silicon and other semiconductors [1]. This feature has recently also been demonstrated in SiC for the acceptors boron (B) [2,3] and aluminum (Al) [3], but no quantitative data has so far been presented. However, since large amounts of H are present in a variety of the SiC processing steps, hydrogen is for example used as a carrier gas in CVD growth of SiC, a more detailed knowledge of the passivation kinetics is needed. In this contribution we focus on the formation and thermal stability of the hydrogen-Al complex in Al-doped epitaxial 4H-SiC.

EXPERIMENT

An epitaxial 4H-SiC film with a buried moderately doped Al-layer was implanted in the low-doped near surface region with 10 keV $^2H^+$ ions to a dose of 1×10^{15} cm^{-2}. The epitaxial layer was grown in a horizontal CVD reactor, described in detail elsewhere [4]. The implanted epi-layer was then annealed at 300 °C for 30 min in a vacuum furnace during which a small amount of the implanted ^{2}H migrated into the buried Al layer. The surface layer, including the implanted ^{2}H, was then etched off using an ICP etch system with a SF_6 plasma. After etching the sample was cut into smaller pieces which were annealed in vacuum at the temperatures 270, 300, 350, and 400°C. Two anneals were performed at each temperature where the longer anneal time was a factor of four greater than the shorter one.

Concentration versus depth profiles for Al, B, and ^{2}H were determined by secondary ion mass spectrometry measurements (SIMS) utilizing a Cameca IMS 4f microanalyser. A primary sputtering beam of 8 keV $(^{16}O)_2^+$ and 13.5 keV $^{133}Cs^+$ ions, for the Al and B, and ^{2}H measurements, respectively, was rastered over an area of 200×200 μm^2. The erosion rate was typically 15 and 25 Å/s in the Cs and O_2 measurements, respectively. Secondary ions of $^{27}Al^+$, $^{11}B^+$, or $^2H^-$ were collected from an area, 60 μm in diameter, in the center of the sputtered crater. The total boron concentration was assumed to be 25% higher than the concentration of ^{11}B in order to account for the ^{10}B isotope. The use of ^{2}H instead of ^{1}H is motivated by the fact that the sensitivity of ^{2}H in the SIMS measurements is three orders of magnitude higher than of ^{1}H. A frequent problem in SIMS analysis of implanted non-annealed, or highly passivated SiC, is sample charging. To minimize this effect a thin gold layer (~20 nm) was deposited on the samples in order to increase the surface conductivity.

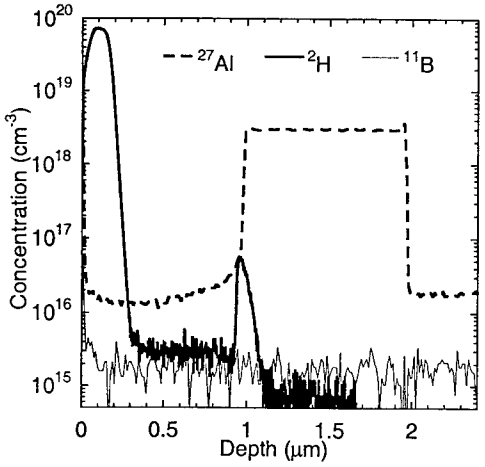


FIG. 1. SIMS profiles of ^{2}H, ^{27}Al, and ^{11}B of a 4H-SiC epitaxial layer with a buried Al-doped region. The sample was implanted with 10 keV $^{2}H^{+}$ ions to a dose of 1×10^{15} cm^{-2} and subsequently annealed at 300 °C for 30 min during which a small amount of the implanted ^{2}H migrated into the buried layer forming a well defined peak of ^{2}H-Al complexes in the buried layer.

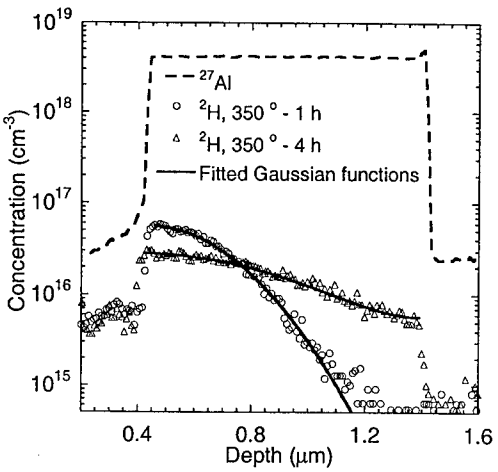


FIG. 2. SIMS profiles of ^{2}H and ^{27}Al of the sample shown in Fig. 1 after a 0.5 μm plasma etch and further annealing at 350 °C for 1 h (circles) and 4 h (triangles), respectively. Least square fits of Eq. (2) (solid lines) to the SIMS profiles provide the effective diffusion constant of the ^{2}H in the Al-layer.

Moreover, electron flooding was employed in the O_2 measurements to further compensate the charging by the primary beam.

RESULTS AND DISCUSSION

Fig. 1 demonstrates the SIMS profiles for the ^{2}H implanted and 300 °C annealed sample. The B content remains homogenous through-out the epitaxial layer at a concentration of 2×10^{15} cm^{-3}. The buried Al-layer starts at a depth of 1 μm and extends at a concentration of 3×10^{18} cm^{-3} to a depth of 2 μm, where the signal falls to the Al-background level in the epitaxial layer equal to 2×10^{16} cm^{-3}. The implanted ^{2}H distribution, reaching a depth of 0.3 μm, exhibits no visible difference compared to the as implanted profile (not shown). This is in agreement with a previous study where implanted ^{1}H remained unaffected by thermal annealing up to temperatures of 650 °C [5]. However, Fig. 1 shows that a small fraction (6×10^{-4}) of the implanted ^{2}H has migrated into the buried Al-layer forming a well defined peak at the edge of the layer. This accumulated ^{2}H peak strongly suggests the formation of ^{2}HAl complexes, an interpretation in accordance with the recent finding of electrical passivation of Al by hydrogen in SiC [3]. Another interpretation suggests that the built-in electric field at the edge of the Al-layer creates the segregation of the mobile positively charged [6,7] hydrogen atoms. However, numerical simulations of a similar structure [7] show that such process could not result in the sharp peak inside the higher doped layer as observed in Fig. 1.

After the initial 300 °C anneal, 0.5 μm of the surface layer is etched off, removing all of the ^{2}H that did not diffuse out of the implanted region. Further annealing will thus not introduce more ^{2}H into that Al-layer but only redistribute the original ^{2}HAl-complex peak. This can be seen in Fig. 2 which shows the ^{2}H SIMS-profiles of two etched samples annealed at 350 °C for 1 and 4 hours, respectively. The redistribution of the ^{2}H indicates that the complexes are not stable at the annealing temperature and the effective diffusion is thus a process of continuous dissociation and formation of ^{2}HAl-complexes. To further analyze the experimental data a kinetic model including diffusion of untrapped ^{2}H as well as the formation and dissociation of immobile ^{2}HAl complexes is taken into

consideration. In the model the complex formation rate is given by the expression [8]: $\partial[^2HAl]/\partial t = 4\pi R_{HAl} D_H [^2H][Al]$, where R_{HAl} is an effective capture radius, D_H is the ^2H diffusion constant, and t is the annealing time. The brackets denote concentration values. The complex dissociation rate is assumed to follow first order kinetics: $-\partial[^2HAl]/\partial t = \nu_{HAl}[^2HAl]$, where ν_{HAl} is the complex dissociation frequency. In the case of a simple dissociation process, ν_{HAl} is expected to follow an Arrhenius temperature dependence: $\nu_{HAl} = \nu_0 \exp(-E_d/k_BT)$, where ν_0 is the so called attempt frequency and E_d is the dissociation energy of the complex. ν_0 should in turn be within the same order of magnitude as the characteristic oscillation frequency of the lattice $\nu_{lattice}$ which can be estimated by weighing each vibration mode ω_k with the energy in that mode: $2\pi\nu_{lattice} = \langle\omega\rangle = \sum \omega_k(\omega_k\hbar\langle n\rangle) / \sum (\omega_k\hbar\langle n\rangle)$, where $\langle n\rangle$ is the quantum number following the Planck distribution. Using the standard Debye approximation with the Debye temperature θ_D = 1120 K for SiC [9], numerical integration of the above expression yields $\nu_{lattice} = 1.6\times10^{13}$ s^{-1} at 350 °C, and is virtually independent on temperature in the investigated temperature range. The capture radius for the ^{2}HB complex in SiC has recently been experimentally determined to R_{HB} = 20 Å at 460 °C [10]. This relatively large value indicates that the driving force in the trapping of ^2H by the acceptor ions is the coulomb attraction between the mobile positively charged ^2H and the ionized acceptor. Since the coulomb attraction from an ionized Al atom should be the same as for B, and since the temperature dependence in R is expected to be weak [10], we use $R_{HAl} = R_{HB}$ = 20 Å.

The diffusion model described above has no general mathematical solution but may be solved analytically for some limiting cases. When the dissociation rate is significant compared to the trapping rate, and the total hydrogen concentration $[^2H_{tot}] = [^2H] + [^2HAl]$ is small compared to the trap concentration, $[^2H_{tot}]$ will diffuse according to standard Fickian diffusion with an effective diffusion constant given by [11]:

$$D_{eff} = \frac{\nu_{HAl}}{4\pi R_{HAl} Al_0}, \tag{1}$$

where Al_0 is the aluminum concentration in the Al-layer. It is interesting to note that D_{eff} is independent on the diffusivity of the mobile H, D_H. Physically, this means that the average time between de-trapping and re-trapping of a ^2H atom is negligible compared to the average lifetime of a complex. The solution to the Fickian diffusion of a thin delta-like profile placed just inside a reflective boundary at $x = x_0$ and with another reflective boundary at $x = x_1$ is given by two Gaussian functions [12]:

$$[^2H_{tot}] = \frac{2Q}{\sqrt{2\pi}\sigma}\left[\exp\left(-\frac{1}{2}\left\{\frac{x-x_0}{\sigma}\right\}^2\right) + \exp\left(-\frac{1}{2}\left\{\frac{x-2x_1+x_0}{\sigma}\right\}^2\right)\right], \tag{2}$$

where Q is the integrated dose of $[^2H_{tot}]$ and σ is the standard deviation of a Gaussian function, related to the diffusivity as $D_{eff} = \sigma^2/2t$. The reflective boundary conditions are motivated by the fact that the trap-limited diffusion mechanism inside the Al-layer enhances the effective transport of ^2H. Least square fits of Eq. (2) to the ^2H SIMS profiles of the etched and annealed samples exhibit excellent agreement for all investigated temperatures and times, illustrated for the 350 °C anneals in Fig. 2. By plotting the extracted σ at each temperature as $\sigma^2/2$ vs. t, D_{eff} is determined independently on the original shape of the ^2H profile. The ^{2}HAl dissociation frequencies are then calculated from the extracted D_{eff} values using Eq. (1). Fig. 3 displays a least square fit of an Arrhenius equation to the extracted ν_{HAl}, showing a close to perfect fit over the three orders of magnitude covered by the extracted frequencies. The Arrhenius fit yields an attempt frequency ν_0 of 1.7×10^{13} s^{-1} and a dissociation energy E_d for the ^{2}HAl-complex of 1.66 (±0.05) eV, which may be compared with the slightly lower value of 1.44 eV for the ^{1}HAl-complex in silicon [13]. The good agreement between ν_0 and $\nu_{lattice}$ supports the validity of the diffusion model with trapping and first order de-trapping of mobile ^2H at Al-trapping centers. However, the spot-on agreement in this

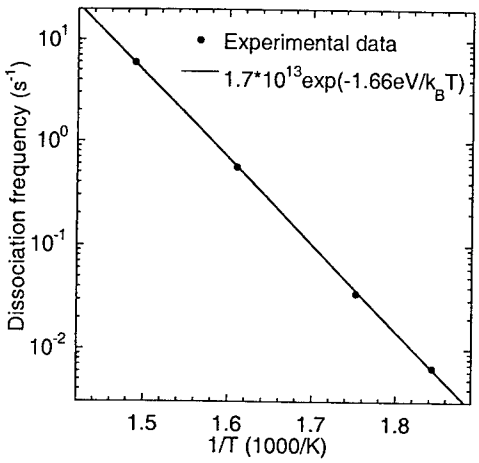


FIG. 3. Arrhenius plot of the experimental dissociation frequencies calculated from the effective ^{2}H diffusion constants by Eq. (1). The fitted Arrhenius equation (solid line) yields a dissociation energy of 1.66 (±0.05) eV for the ^{2}HAl-complex and a pre-exponential attempt frequency $\nu_0 = 1.7\times10^{13}$ s^{-1}.

experiment is most likely coincidental. The small experimental error in E_d alone translates to a factor 2.5 in ν_0. It should also be mentioned that our experiment regards the hydrogen isotope ^{2}H whose diffusion and trapping characteristics may not be identical to that of ^{1}H in SiC. On the other hand, the isotope effect in the H-acceptor dissociation energy is most likely small.

SUMMARY

By measuring the thermal redistribution of a well defined ^{2}H peak in an Al doped epitaxial layer, we have determined the dissociation energy of the passivating ^{2}HAl complex in 4H-SiC to 1.66 (±0.05) eV. The experiment also provides the dissociation attempt frequency $\nu_0 = 1.7\times10^{13}$ s^{-1} which is in excellent agreement with the expected value for a first order dissociation process. The next step in this work is to determine the dissociation kinetics for the ^{2}H-B complex.

ACKNOWLEDGEMENTS

This work was funded by the Swedish Foundation for Strategic Research, within the SiCEP-program. The authors are also grateful to Erik Danielsson for his assistance with the plasma etch.

REFERENCES

[1] J.I. Pankov and N.M. Johnson, *Hydrogen in semiconductors*, (Academic, New York, 1991).
[2] M.K. Linnarsson, M. Janson, A. Schöner, N. Nordell, S. Karlsson, and B.G. Svensson, Mat. Sci. Forum **264-268** (1998), p. 761.
[3] N. Achtziger, J. Grillenberger, W. Witthuhn, M.K. Linnarsson, M. Janson, and B.G. Svensson, Appl. Phys. Lett. **73** (1998), p. 945.
[4] N. Nordell, A. Schöner, and S.G. Andersson, J. Electrochem. Soc. **143** (1996), p. 2910.
[5] M.K. Linnarsson, J.P. Doyle, and B.G. Svensson, Mat. Res. Soc. Symp. **423** (1996), p. 635.
[6] N. Achtziger, C. Hültsen, W. Witthuhn, M.K.Linnarsson, M. Janson, and B.G. Svensson, Phys. Stat. Sol. (b) **210** (1998), p. 395.
[7] M.S. Janson, M.K. Linnarsson, A. Hallén, B.G. Svensson, N. Nordell, and S. Karlsson, Phys. Rev. B. **61** (2000), p. 7195.
[8] T.R. Wait, J. Chem. Phys. **28** (1958), p. 103.
[9] A. Zywietz, K. Karch, and F. Bechstedt, Phys. Rev. B **54** (1995), p. 1791.
[10] M.S. Janson and M.K. Linnarsson, To be published.
[11] T. Zundel and J. Weber, Phys. Rev. B **46** (1992), p. 2071.
[12] J. Philibert, *Atom movements, Diffusion and mass transport in solids* (les éditions de physique, Les Ulis, France, 1991).
[13] T. Zundel and J. Weber, Phys. Rev. B **39** (1989), p. 13549.

Materials Science Forum Vols. 353-356 (2001) pp. 431-434
© 2001 Trans Tech Publications, Switzerland

Proton Irradiation Induced Defects in 4H-SiC

L. Storasta[1], F.H.C. Carlsson[1], S.G. Sridhara[1], D. Åberg[2], J.P. Bergman[1], A. Hallén[2] and E. Janzén[1]

[1] Department of Physics and Measurement Technology, Linköping University, SE-581 83 Linköping, Sweden

[2] Royal Institute of Technology, Department of Electronics, Solid State Electronics, Electrum 229, SE-16440 Kista-Stockholm, Sweden

Keywords: DLTS, Hole Traps, Intrinsic Defects, Minority Carrier Transient Spectroscopy, Proton Irradiation

Abstract: Defects created by proton irradiation of n-type 4H-SiC epilayers with different fluences and six annealing steps were investigated by Deep Level Transient Spectroscopy (DLTS) and Minority Carrier Transient Spectroscopy (MCTS). Three previously unreported hole traps with energy levels of $E_V + 0.35$ eV, $E_V + 0.44$ eV, $E_V + 0.80$ eV and several electron traps were found. Annealing properties and dependence upon irradiation dose of majority and minority carrier traps is presented. High temperature stability of a $E_V + 0.35$ eV trap has been demonstrated.

Introduction:

Irradiation induced defects is a very important issue for all electronic materials, since they are unintentionally created during different device processing steps by ion implantation and are also used for lifetime control in the material. Thus, detailed knowledge about defect dynamics and dependence on irradiation dose and annealing temperatures is needed to control and remove them.

Existing reports about irradiation-induced traps in SiC are often limited to majority carrier traps which are more simple to measure and the results are more easily interpreted. Since n-type 4H-SiC material is more easily available, most deep-level transient spectroscopy (DLTS) studies have been done on electron traps [1-4]. However, knowledge about hole traps is required to complete the picture of the induced defects. Hole traps can be detected by junction-DLTS using p^+n diodes in n-type material [5, 3] or alternatively using standard DLTS on p-type material [6].

In our study we use DLTS to detect electron traps and Minority Carrier Transient Spectroscopy (MCTS) [7] with front illumination for detection of hole traps in n-type material. The latter technique does not require a p^+n junction in order to inject holes into depletion region, but uses above-bandgap illumination to create electron-hole pairs. A Schottky contact can be used for both measurements.

Experimental details:

For these studies we used a 20 μm thick 4H-SiC epilayer grown by hot-wall CVD technique and irradiated by 2.9 MeV protons with fluences $3\cdot10^{11}$, $1\cdot10^{12}$, $3\cdot10^{12}$, $1\cdot10^{13}$ cm^{-2}. The damage profile was flat with a peak located at 60 μm. Therefore vacancies were distributed uniformly in the whole epilayer (20 μm thick). The calculated vacancy concentration (TRIM) in the epilayer ranged from $6\cdot10^{14}$ to $2\cdot10^{16}$ cm^{-3}. Samples were then cut into smaller pieces and annealed for 1 hour at different temperatures: 200 °C, 400 °C, 600 °C, 900 °C, 1100 °C and 1700 °C. Semi-transparent circular 1 mm diameter Schottky barrier contacts were formed by thermally evaporating a 120 Å thick nickel layer. The same contacts were used for both DLTS and MCTS measurements. Backside ohmic contacts to the substrate were created by conducting silver paint. The nitrogen doping, $(3.5\text{-}5)\cdot10^{15}$ cm^{-3}, as measured by C-V, did not change after irradiation for lightly irradiated samples.

The nitrogen donors were partially compensated by the generated intrinsic defects in un-annealed samples, irradiated with doses higher than $3 \cdot 10^{12}$ cm^{-2}, reducing the effective doping and complicating DLTS and MCTS measurements at low temperatures due to carrier freeze-out. Transient capacitance measurements were conducted on the same computer controlled DLTS-MCTS system with full transient acquisition and off-line analysis in the range of 100 – 600 K. The upper temperature limit was restricted by the properties of the contacts. For DLTS measurements, the reverse bias was -5 V, and -0.5 V and 10 ms long filling pulses were applied. Above bandgap excitation for MCTS measurements was provided by 300 ms long Ar laser pulses with a wavelength of 355 nm and an intensity of 20 mW. In order to achieve greater signal to noise ratio, lock-in amplifier simulation with a rate window of 211 ms was used when analyzing capacitance transients. Trap parameters were extracted assuming temperature independent capture cross-section.

Results and discussion

Majority carrier traps. The observed annealing behavior for the sample, irradiated with a fluence of $3 \cdot 10^{12}$ cm^{-2}, is shown in Fig.1. The observed features are similar for all samples irrespective of irradiation doses, while the defect concentration increases with increasing dose. Their general properties are summarized in Table 1, and annealing behavior shown in Fig. 1-2.

Immediately after the irradiation a broad peak at 155 K is observed, probably consisting of two peaks, one of which is annealed out by 200 °C, leaving a single 0.40 eV peak at 168 K, which is annealed out by 400 °C. The properties of this peak are similar to that of the S-level, reported after 300 °C boron implantation [8], but the emission rate is slightly higher.

The Z_1/Z_2 peak is initially hidden by two closely spaced peaks at 263 K and 303 K, with activation energies 0.65 eV and 0.86 eV, respectively. They are very likely the same defects as reported in [4] for electron irradiated 4H-SiC. The higher temperature peak is annealed out at

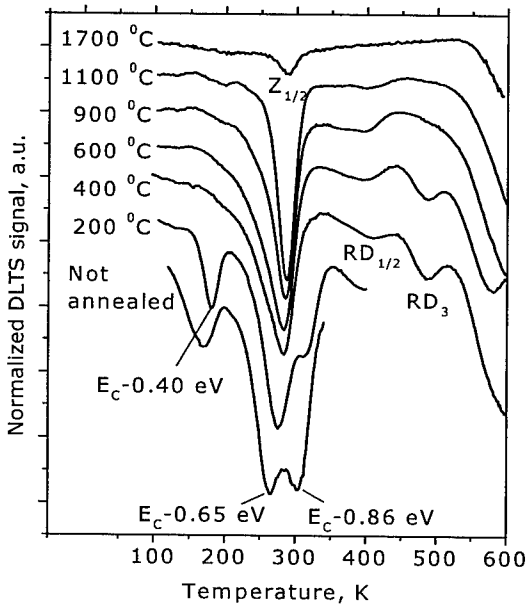


Fig. 1. DLTS spectra obtained for the sample with irradiation dose $3 \cdot 10^{12}$ cm^{-2} after different annealing steps (spectra are shifted vertically for clarity)

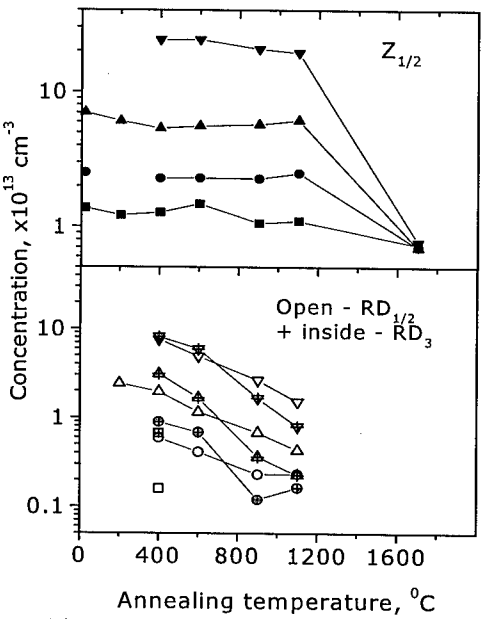


Fig. 2. Defect concentration versus annealing temperature for samples with different irradiation doses: ■ $3 \cdot 10^{11}$, ● $1 \cdot 10^{12}$, ▲ $3 \cdot 10^{12}$, ▼ $1 \cdot 10^{13}$ cm^{-2}.

400 °C, while the lower is stable up to 1100 °C and broadens the low temperature side of the Z_1/Z_2 peak. At irradiation doses higher than $1 \cdot 10^{12}$ cm^{-2} these peaks become stronger than the Z_1/Z_2 peak in un-annealed samples.

The amplitude of the Z_1/Z_2 peak is constant (within ±10%) up to annealing temperatures of 1100 °C (Fig 2). After annealing at 1700 °C the concentration drops to approximately $(7\text{-}8) \cdot 10^{12}$ cm^{-3} for all the irradiation doses, i.e. a factor of 2-30 depending on the irradiation dose (Fig. 2).

Peaks at 395 K ($E_C - 0.87$ eV) and 490 K ($E_C - 0.99$ eV) show good agreement with previously reported $RD_{1/2}$ and RD_3 defects in He^+ irradiated material [1]. Both appear to be quite stable defects, disappearing at temperatures between 1100 °C and 1700 °C. The RD_3 concentration drops somewhat faster than for $RD_{1/2}$ (Fig. 2). A peak emerging at temperatures above 550 K is probably the RD_4 [1] or EH6/EH7 [3] defect, however, it could not be observed completely. But it is still present after 1700 °C annealing. There are possibly several overlapping peaks in this temperature range, as previously noted [3]. A shoulder at 577 K sometimes appeared, but did not show any correlation with implantation dose or annealing temperature and is probably a metastable defect, dependent on measurement and cooling conditions.

Minority carrier traps. Evaluation of MCTS spectra is complicated for two reasons. First, the calculation of concentration, using DLTS formulae is questionable, since many requirements, which are difficult to control, must be fulfilled [9, 10]. Second, MCTS spectra exhibited a finite baseline shift, which can be caused by voltage fluctuations after the end of the light pulse. In order to make the results comparable, contacts on all the samples were prepared at the same time, to ensure the same contact thickness. Further, the same laser power was kept throughout the measurements. Despite this, the MCTS results are only suitable for qualitative comparisons. Defect dynamics for samples irradiated with different doses follow the same profile, but the concentration of the defects is dose dependent. Summary of the detected traps is presented in Table 1.

Un-annealed samples feature a peak labeled HS2 at 170 K with a thermal activation energy of 0.44 eV from the valence band edge. This peak has a small shoulder on the low temperature side which is difficult to resolve by MCTS analysis. This second peak gradually increases with annealing temperature, while the originally present 0.44 eV trap concentration decreases (Fig. 3). The energy level of the second peak is $E_V + 0.35$ eV and is located at 153 K (marked as HS1 in Fig. 3). It can probably be related to the same defect as the HH1 center reported in [3] for electron irradiated and 400 °C annealed 4H-SiC samples, detected by junction-DLTS. After 900 °C anneal the spectra are dominated by the HS1 peak, while the HS2 peak is weaker and completely disappears by 1700 °C. The 0.35 eV level is left with nearly the same (or slightly higher) concentration even after 1700 °C annealing and is the only peak that survives with high concentrations after the final annealing step (estimated $1.4 \cdot 10^{14}$ cm^{-3} for $3 \cdot 10^{13}$ cm^{-2} irradiation dose).

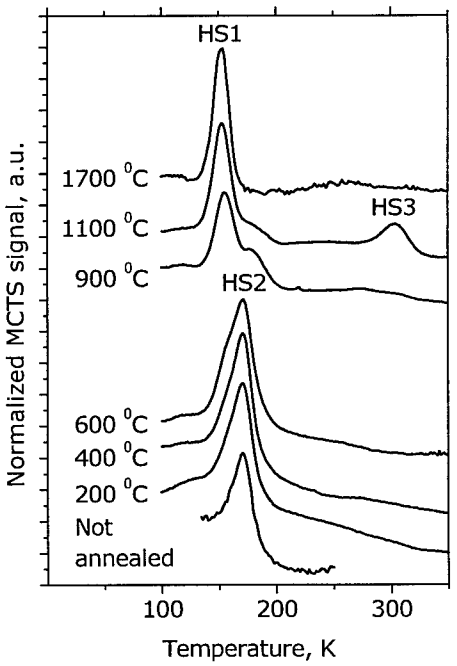


Fig. 3. MCTS spectra obtained for the sample with irradiation dose $3 \cdot 10^{12}$ cm^{-2} after different annealing steps (spectra are shifted vertically for clarity)

Table 1. Properties of electron and hole traps, observed in proton irradiated 4H-SiC. Temperature independent capture cross-section was assumed. Peak temperature T_{peak} corresponds to 211 ms rate window. Capture cross-section σ_{int} is estimated from the intercept of the Arrhenius plot.

T_{peak} [K]	Label	E_A [eV]	σ_{int} [cm^2]	Comments
Electron traps				
168	-	$E_C - 0.40 \pm 0.02$	$7 \cdot 10^{-13}$	Annealed at 400 °C
263	-	$E_C - 0.65 \pm 0.05$	$1 \cdot 10^{-13}$	Annealed at 400 °C
286	$Z_{1/2}$	$E_C - 0.68 \pm 0.02$	$2 \cdot 10^{-14}$	
303	-	$E_C - 0.86 \pm 0.05$	$7 \cdot 10^{-12}$	Stable up to 1100 °C
395	$RD_{1/2}$	$E_C - 0.87 \pm 0.10$	$1 \cdot 10^{-15}$	
490	RD_3	$E_C - 0.99 \pm 0.10$	$2 \cdot 10^{-16}$	
Hole traps				
153	HS1	$E_V + 0.35 \pm 0.02$	$5 \cdot 10^{-14}$	Increases with annealing, thermally stable up to 1700 °C
170	HS2	$E_V + 0.44 \pm 0.02$	$8 \cdot 10^{-13}$	Descreases with annealing, annealed out at 1700 °C
304	HS3	$E_V + 0.79 \pm 0.05$	$4 \cdot 10^{-13}$	Appears after 1100 °C anneal, annealed out at 1700 °C

Another defect level, as observed by MCTS, is the 0.80 eV peak HS3 at 304 K. This peak appears only after the 1100 °C annealing step and it disappears completely after the 1700 °C treatment.

Conclusions:

Proton irradiation creates several electron traps and three hole traps in 4H-SiC. Minority Carrier Transient Spectroscopy was applied on SiC and detected previously unreported hole traps at $E_V + 0.44$ eV and $E_V + 0.80$ eV. A hole trap HS1, located at $E_V + 0.35$ eV was revealed with surprising high temperature stability. It appears to be more stable than the Z_1/Z_2 defect. After the 1700 °C annealing the concentration of the Z_1/Z_2 peak has reduced by a factor of 2 to 30 for lightly and heavily irradiated samples, respectively, while the HS1 amplitude stayed nearly constant. All other defects, created by proton irradiation and detected by DLTS and MCTS, are annealed out after 1700 °C. Further studies to identify the observed defects by comparison with optical techniques have been initiated.

References

[1] T. Dalibor, G. Pensl, T. Kimoto, H. Matsunami, S. Sridhara, R. P. Devaty, and W. J. Choyke, Diamond and Related Materials **6**, (1997), p. 1333.

[2] T. Dalibor, G. Pensl, H. Matsunami, T. Kimoto, W. J. Choyke, A. Schöner, and N. Nordell, Phys. Stat. Sol. **162**, (1997), p. 199.

[3] C. Hemmingsson, N. T. Son, O. Kordina, J. P. Bergman, E. Janzén, J. L. Lindstrom, S. Savage, and N. Nordell, J. Appl. Phys. **81**, (1997), p. 6155.

[4] J. P. Doyle, M. K. Linnarsson, P. Pellegrino, N. Keskitalo, B. G. Svensson, A. Schöner, N. Nordell, and J. L. Lindstrom, J. Appl. Phys. **84**, (1998), p. 1333.

[5] G. C. Rybicki, J. Appl. Phys. **78**, (1995), p. 2996.

[6] M. Gong, S. Fung, C. D. Beling, and You Zhipu, J. Appl. Phys. **85**, (1999), p. 7120.

[7] R. Brunwin, B. Hamilton, P. Jordan, and A. R. Peaker, Electron. Lett. **15**, (1979), p. 349.

[8] D. Åberg, L Storasta, A. Hallén, and B.G. Svensson, these proceedings.

[9] P Blood and J.W. Orton, *The Electrical Characterization of Semiconductors: Majority Carriers and Electron States* (Academic Press Limited, London, 1992).

[10] J. A. Davidson and J. H. Evans, J. Appl. Phys. **81**, (1997), p. 251.

Materials Science Forum Vols. 353-356 (2001) pp. 435-438
© 2001 Trans Tech Publications, Switzerland

Intrinsic Defect Complexes in α-SiC: the Formation of Antisite Pairs

E. Rauls[1], Z. Hajnal[1,2], A. Gali[3], P. Deák[3] and Th. Frauenheim[1]

[1] Fachbereich Physik, Theoretische Physik, Universität-GH Paderborn, Warburgstr. 100, DE-33095 Paderborn, Germany

[2] MTA Research Institute for Technical Physics and Materials Science, PO Box 49, HU-1525 Budapest, Hungary

[3] Dept. of Atomic Physics, Technical University of Budapest, Budafoki út 8, HU-1111 Budapest, Hungary

Keywords: Antisite, Formation, Intrinsic Defects

Abstract: The properties of the Si_C-C_{Si} antisite pair in 4H–SiC as well as its formation mechanism have been investigated. For the formation of an antisite pair in the ideal bulk a high energy barrier has to be overcome. However, in the presence of other defects the formation energy and the barrier are significantly lowered. Here, we present our results concerning formation energies and diffusion barriers for the formation of an antisite pair next to silicon- and carbon-vacancies as well as to the V_C+C_{Si} pair which arises from V_{Si}. Structure and formation energy of the antisite pair have been calculated within *ab initio* density functional theory (DFT) in the local density approximation (LDA). These results are well reproduced by a charge selfconsistent DFT based tight binding method (SCC-DFTB), which was used to calculate the diffusion paths and the activation energies for formation.

Electrically active intrinsic defects may play a critical role in material quality if their formation energy is low. Furthermore, they may segregate during various technological processes forming larger complexes. Isolated antisites in SiC have been theoretically investigated in 3C- and 2H-SiC [1]. They have relatively low formation energies, and the silicon antisite, Si_C, behaves as a hole trap with levels near the valence band. The structure and electronic properties of the antisite pair, Si_C-C_{Si}, in 3C–SiC have recently been reported [2]. It was found that the pair possesses electronic activity similar to Si_C, and the formation energy for the pair (5.8 eV) is lower than the sum of the formation energies of isolated C_{Si} (3.7 eV) and Si_C (4.6 eV). The formation energy of the pair (quoted values refer to stoichiometric 3C material) is still too high to lead to significant concentrations during growth. The question is, however, whether and how such pairs can be formed in existing material. The polytypes of practical interest are 4H and 6H. Regarding the computational costs, we restricted our investigation to stoichiometric 4H-SiC considering only the neutral charge state of the antisite pair at cubic sites.

First we have determined the structure and formation energy of the Si_C-C_{Si} pair at the *ab initio* level using a plane-wave based LDA code (FHI98MD[3]). A 96 atom supercell was used with a $2 \times 2 \times 2$ k-point set [4] and an energy cutoff of 30 Ry. Two shells of neighbors were allowed to relax. Then we have repeated the calculation in a 240 atom supercell using a Γ-point approximation in tight binding framework. (Details of the SCC-DFTB–method are given in Refs. [5, 6, 7].) Based on the good agreement of both geometry and formation energy, we used

the SCC-DFTB method for the very time-consuming investigation of the possible formation mechanisms of the Si_C-C_{Si} pair.

Our *ab initio* calculation for the antisite pair at the cubic site of 4H-SiC gives very similar results to those obtained in 3C-SiC [2]. The bondlengths we obtain differ by less than 0.02 Å and the formation energy, 5.8 eV, is identical. This shows that the defect is of very localized nature. Based on the calculated electronic structure, the hole trap behavior of the antisite pair can be confirmed in 4H-SiC as well.

The SCC-DFTB calculation with Si_C-C_{Si} at cubic sites of the large 4H-SiC supercell reproduces the *ab initio* geometry very well: the differences in bond lengths are again within 0.02 Å. The symmetry is C_{3v}. The bond length between the two antisites is contracted by $\approx 2\%$, the next neigbor C-C–bonds are shortened by 12%, and the Si-Si–bonds are elongated by 15%. All values are respective to the ideal Si-C bulk bond length of 1.88 Å. For the formation energy we find 5.2 eV with the SCC-DFTB scheme which compares well to the 5.8 eV obtained with the *ab initio* method (especially, since the larger supercell allows the lowering of the formation energy). SCC-DFTB calculations for the isolated antisites (on cubic sites) result in 3.6 eV for C_{Si} and 4.1 eV for Si_C, to be compared to 3.7 and 4.6 eV, respectively, obtained in 3C-SiC in Ref. [2] . These results prove that formation energies as well as the geometrical data can be obtained in the SCC-DFTB scheme in good agreement with *ab initio* results.

The relatively low formation energies of the isolated interstitials indicate that they can not be uncommon defects in SiC, especially after irradiation. The high binding energy of the antisite pair predicts a tendency of isolated antisites to conglomerate and form pairs or even larger clusters. To our knowledge, there have not yet been any investigations about how an antisite pair can develop directly. Therefore, we investigated several mechanisms using the SCC-DFTB code. For any given diffusion path we searched for the saddlepoint geometry using an activation-relaxation technique (*ART*) as proposed in Ref. [8]. The saddle point nature of the geometry has been confirmed by the calculated vibrational spectrum showing up exactly one imaginary mode. Starting from the saddle point geometry we let the structure relax without constraints within a steepest descent algorithm and recorded the energy during relaxation.

In the perfect lattice an antisite pair can only be created by the exchange of a Si and a C atom in a rotational movement of a Si-C pair. A simple rotation of a Si-C pair in a $(11\bar{2}0)$ plane of the crystal is energetically very costly. The energetically most favourable mechanism we found is a concerted exchange mechanism as proposed by Pandey [9]. It consists of a simultaneuos movement of the pair with a gradual change of the rotational plane by 60°. Rotation starts in a $(11\bar{2}0)$ plane, then the rotation plane gradually changes. After its rotation by 30°, the saddle point geometry is passed (here the axis of the pair is in a $(10\bar{1}0)$ plane). Finally, after another 30° rotation of the rotation plane the rotation of the pair is finished in the next $(11\bar{2}0)$ plane (60° to the first plane). The movement of the atoms is marked with arrows on the left hand side of Fig. 1 where the minimal energy path is shown on the right hand side. The reaction coordinate r has been constructed by calculating the projection of the actual positions of the diffusing C– and Si–atoms separately onto the connecting vectors from their initial to final positions. In the insert in Fig. 1 these two projections are marked with x for the C-atom and y for the Si-atom. The reaction coordinate is then obtained by summing up these two contributions $r = x + y$ for each geometry during the diffusion process.

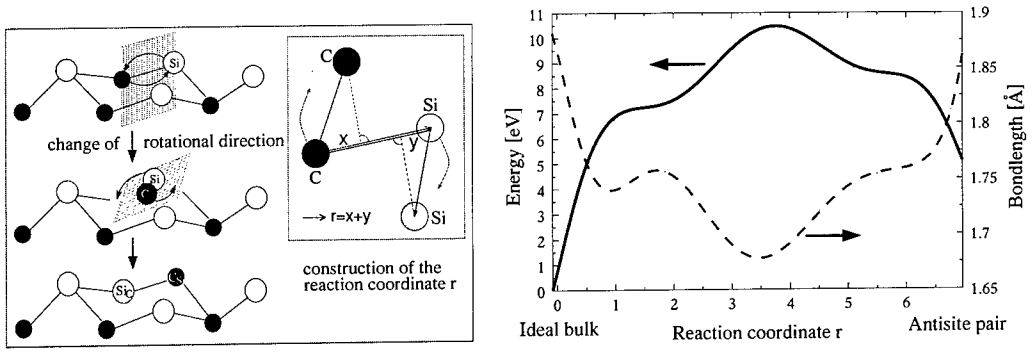


Figure 1: Geometry and movement of the atoms that create the antisite pair (on the left). In the middle the construction of the reaction coordinate is shown (see text for details). On the right the energy difference between the actual geometry and the ideal crystal is shown during the process (*left ordinate*); on the *right ordinate* the bondlength of the rotating Si-C pair is shown.

At the saddle point geometry the distance between the moving C and Si atoms reaches its minimum length with a contraction of 11% compared to the ideal bulk bond length.
The energy barrier between the ideal bulk and the Si_C-C_{Si} defect for this concerted exchange mechanism is found to be 10.5 eV, i.e. $\approx$ 1 eV lower than the barrier for the two atoms rotating in a $(11\bar{2}0)$ plane. This is a very high value, indicating that direct antisite pair formation is unlikely to happen in a perfect lattice.

However, both formation energy and energy barrier for formation can be lowered in the presence of vacancies. We find that the formation energy of an antisite pair next to a carbon vacancy (V_C) is lowered to 3.8 eV. In principle, there are two ways to create the pair next to the vacancy. A simple rotation of a Si-C pair (as in the ideal crystal) has a barrier of 9.0 eV. The second process can be described in two steps. First, one of the Si atoms next to V_C moves into the vacancy, resulting in a Si_C antisite next to a V_{Si}. In the second step one of the carbon atoms moves into V_{Si}. These two steps should happen simultaneously, i.e. the two atoms should move as a pair. The result is V_C+ Si_C-C_{Si}, but the carbon vacancy has moved one site further on the carbon sublattice. The energy barrier for this process is reduced to only 6.0 eV, which is a substantial lowering compared to the value obtained for the ideal lattice.

Investigating the analogue situation for the antisite pair creation next to a silicon vacancy, the V_{Si}+ Si_C-C_{Si} complex turns out to be unstable, since the silicon antisite relaxes directly and without an energy barrier into the V_{Si}, resulting in V_C-C_{Si}. Thus, V_{Si} cannot help the formation of an antisite pair in the same way as V_C.

The pair defect V_C-C_{Si} has a lower formation energy than V_{Si} and can easily develop from an isolated V_{Si} as well with an energy barrier of only 1.8 eV[10]. Therefore, we examined possible mechanisms to create antisite pairs next to V_C-C_{Si}. Since both defects are pair defects, there are several possible relative orientations. The most stable arrangement is to place both defects in a hexagon as shown in Fig. 2. The most favourable mechanism to create the antisite pair consists of the simultaneous movement of a Si and a C atom, in analogy to the process described

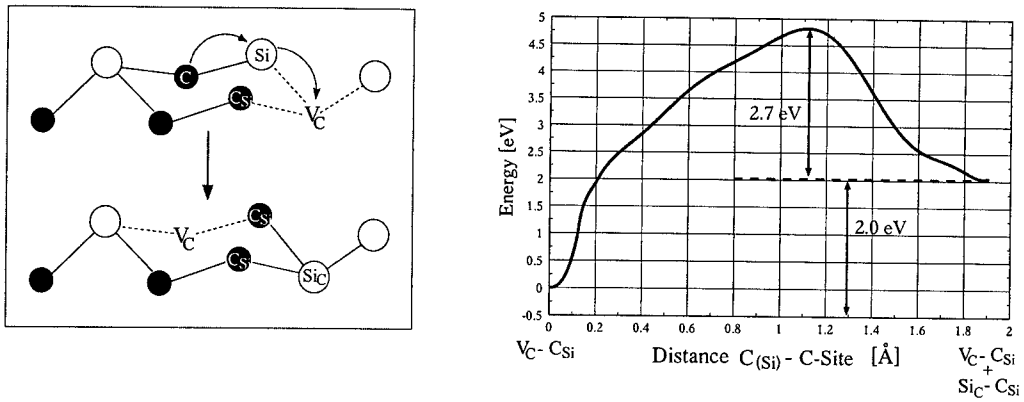


Figure 2: *Left:* Arrangement of the two pair defects in Si_C-C_{Si} +V_C-C_{Si}. Black circles represent C, white circles Si atoms. The movement of the Si-C pair is marked by arrows. *Right:* Energy change during diffusion plotted against the distance the moving C atom has covered from its lattice site to the antisite position.

for the formation next to a single V_C. The motion of the atoms is illustrated schematically in Fig. 2. The formation energy of the antisite pair next to V_C-C_{Si} is only 2.0 eV and the energy barrier is lowered to 4.7 eV!

In conclusion, we find that the Si_C-C_{Si} antisite pair is an electrically active defect in 4H-SiC which has a 2.5 eV binding energy with respect to isolated Si_C and C_{Si}. The formation energy of the antisite pair can be significantly lowered by the presence of other intrinsic defects, becoming as low as 2.0 eV next to a V_C-C_{Si} complex (which developes easily from V_{Si}). In that case the antisite pair can be created even *a posteriori* at the cost of only 4.7 eV.

This work was done in the framework of the bilateral DFG (Nr. 436 UNG113/137/0) - MTA (Nr. 118) project. The authors thank the support of the Hungarian OTKA Nr. T32174 (P.D.) and the German FR889/12-1 (E.R.) projects for support of their work.

References

[1] L. Torpo, S. Pöykkö, R. M. Nieminen, Phys. Rev. B **57** (1998), p. 6243.
[2] L. Torpo, R. M. Nieminen, Mat. Sci. Eng. B **61-62** (1999), p. 593.
[3] M.Bockstedte, A. Kley, J. Neugebauer and M. Scheffler, Comput. Phys. Commun. **107** (1997), p. 187.
[4] H. J. Monkhorst and J. K. Pack, Phys. Rev. B **13**, (1976), p. 5188.
[5] D. Porezag, Th. Frauenheim, T. Köhler, G. Seifert, R. Kaschner, Phys. Rev. B **52**, (1995) p. 11837.
[6] Th. Frauenheim, G. Seifert, M. Elstner, Z. Hajnal, G. Jungnickel, D. Porezag, S. Suhai, R. Scholz, phys. stat. sol. (b), **217** (2000), p. 41.
[7] M. Elstner, D. Porezag, G. Jungnickel, J. Elsner, M. Haugk, Th. Frauenheim, S. Suhai, G. Seifert, Phys. Rev. B **58** (1998) p. 7260.
[8] G. T. Barkema and N. Mousseau, Phys. Rev. Lett. **77**, (1996) p. 4358.
[9] K. C. Pandey, Phys. Rev. Lett. **57** (18) (1986), p. 2287.
[10] E. Rauls, Th. Lingner, Z. Hajnal, S. Greulich–Weber, Th. Frauenheim, J.-M. Spaeth, phys. stat. sol. (b), 217/2 (2000), p. R1.

Materials Science Forum Vols. 353-356 (2001) pp. 439-442
© 2001 Trans Tech Publications, Switzerland

Generation and Annihilation of Intrinsic-Related Defect Centers in 4H/6H-SiC

Th. Frank[1], M. Weidner[1], H. Itoh[2] and G. Pensl[1]

[1] Institute of Applied Physics, University of Erlangen-Nürnberg, Staudtstr. 7/A3, DE-91058 Erlangen, Germany

[2] Japan Atomic Energy Research Institute, 1233 Watanuki, Takasaki, Gunma 370-1292, Japan

Keywords: DLTS, Implantation-Induced Defects, Intrinsic-Related Defects

Abstract. Intrinsic-related defect centers have been generated in n-type 4H/6H-SiC by bombardment with different particles like high-energy electrons (2 MeV), hydrogen (H), helium (He) or ions of heavier masses like neon (Ne) or argon (Ar). The annealing behavior of implantation-induced defects in 6H-SiC has been studied by DLTS investigations after annealing the samples at elevated temperatures. The E_1/E_2-, Z_1/Z_2(6H)- and R-center are the prevailing defect centers observed in DLTS spectra. The activation energy ΔE_A for the annihilation process of the Z_1/Z_2(4H)-center has been determined by isochronal annealing of e^--irradiated 4H-SiC samples.

Introduction

Ion implantation is an important technique to dope silicon carbide (SiC). In order to electrically activate the implanted donor or acceptor species and to largely remove the introduced lattice damage, an annealing step at elevated temperatures is required. As an unintentional side effect electrically active defect centers are generated by the implantation process, which partially survive temperatures up to 1700°C. The chemical composition and microscopic structure of all these defect centers are still unknown. Investigations are partially performed on the formation and thermal stability of implantation-induced defect centers (see e.g. [1-4]).
In this paper, the dependence of generated defect centers in 6H-SiC on the implanted ion mass is studied; in addition, the thermal stability of the Z_1/Z_2-center in 4H-SiC generated by irradiation with high-energy electrons is investigated.

Experimental

For the investigations, samples were cut from n-type 4H-/6H-SiC epilayers (6H-SiC: nitrogen concentration [N] = 5×10^{15} cm^{-3}, thickness d = 5 µm; 4H-SiC: [N] = 9×10^{15} cm^{-3}, d = 5 µm). Defect centers in 6H-SiC were generated by implantation of H^+, He^+, Ne^+ and Ar^+ ions. A box-shaped profile was formed by multiple implantations with different ion energies. The depth of the profile varied between 1.2 µm and 1.6 µm depending on the ion species. The implantation-induced damage is characterized by the total vacancy concentration $[V_{Si}]+[V_C]$ calculated with the TRIM_C Monte-Carlo simulation program after Biersack [5]. The calculated vacancy concentration is just an index and does not correspond to the real vacancy concentration, because the simulation program does not take into account more complicated processes like recombination or clustering. The fluence of the different ion species was adjusted in such a way that a vacancy concentration of 1×10^{18} cm^{-3} was generated. Three sets of 6H-SiC samples were prepared. Set 1 and set 2 samples were identically implanted with different ion species and annealed at 800°C and 1400°C, respectively, for 30 min. Set 3 consisted of 5 samples which were He-implanted ([Vac] = 2×10^{16} cm^{-3}) and annealed at different temperatures (700°C, 800°C, 1000°C, 1400°C and 1700°C) for 30 min. Finally one set of 4H-SiC samples (set 4) was irradiated with high energy electrons (electron energy E_e = 2 MeV, fluence f = 1×10^{15} cm^{-2}, fluence

rate r = 3.2×10^{13} $cm^{-2}s^{-1}$) and annealed at different temperatures between 873 K and 2273 K in a first step for 30 min, followed by a second step for 60 min.
The anneals up to 1000°C were conducted in a rapid isothermal annealing system (RIA) under vacuum. Anneals at higher temperatures were conducted in a graphite furnace; these samples were protected in a SiC crucible and kept in an argon ambient of 1 atm to avoid thermal decomposition of the surface. Prior to the fabrication of contacts, a surface layer of 300 nm thickness was removed by reactive ion etching (RIE) and a standard chemical cleaning process was performed using acetone, aqua regia and hydrofluoric acid. Ni-Schottky contacts with 0.6 mm or 1.0 mm in diameter were evaporated for the DLTS investigations. The DLTS spectra were taken in a temperature range from 100 K to 700 K.

Experimental Results and Discussion

Fig.1(a) and 1(b) display DLTS spectra of 6H samples implanted with H, He, Ne and Ar and annealed at 800°C and 1400°C, respectively. Because of the differing defect concentrations, which are summarized in Tab.1 for the DLTS spectra revealed in Fig.1(a), the scale of the y-axis in both figures is differently selected.

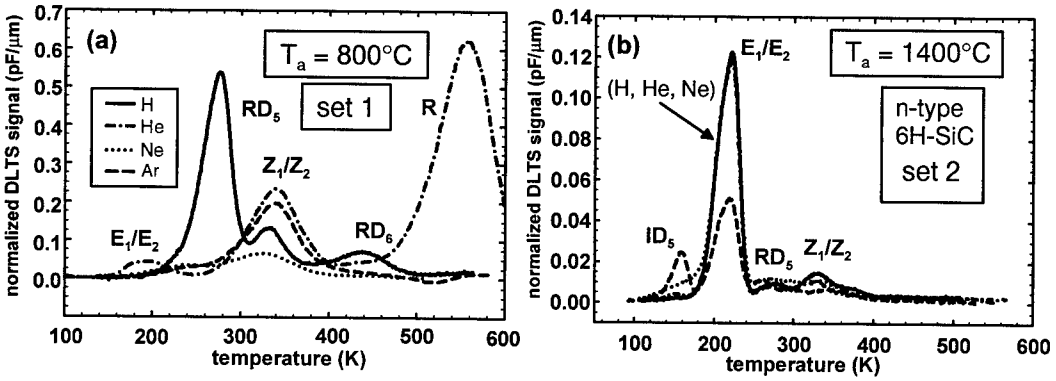


Fig.1: DLTS spectra of H-, He-, Ne- and Ar- implanted n-type 6H-SiC samples annealed at
(a) 800°C for 30 min
(b) 1400°C for 30 min

The peak structure of observed DLTS spectra in Fig.1(a) strongly depends on the implanted ion species. DLTS spectra of Ne- or Ar-implanted samples are similar (dotted, dashed curve): The dominating peak at ≈310 K is caused by the Z_1/Z_2(6H)-center; two further peaks with smaller height (RD_5, RD_6) appear at ≈240 K and ≈440 K, respectively. In the DLTS spectra of the He-implanted sample (chained curve), two large peaks (Z_1/Z_2(6H) and R) are observed; in addition, the E_1/E_2-center is formed at approx. 200 K. In the H-implanted sample (solid curve), three pronounced centers (RD_5, Z_1/Z_2(6H) and RD_6) are generated. All the observed defect centers are described in the literature (for a summary, see e.g. [1]).

Tab.1: Concentration of defect centers in 6H-SiC samples, which have been implanted with H, He, Ne and Ar, respectively, and annealed at 800°C for 30 min (set 1 samples).

	concentration of defect centers (cm^{-3})			
defect center	H	He	Ne	Ar
E_1/E_2	---	$\approx (1 \pm 0.4)\times10^{15}$	---	---
RD_5	$(1 \pm 0.3)\times10^{16}$	---	---	---
Z_1/Z_2(6H)	$\approx (2 \pm 0.6)\times10^{15}$	$(5 \pm 0.2)\times10^{15}$	$(1 \pm 0.5)\times10^{15}$	$(4 \pm 0.2)\times10^{15}$
R	---	$(1.2 \pm 0.4)\times10^{16}$	---	---

Subsequent to the anneal at 1400°C (see Fig. 1(b), set 2 samples), the DLTS spectra of correspondingly implanted 6H-SiC samples look largely similar. The E_1/E_2-center has been formed during the heat treatment and dominates in all the observed DLTS spectra, while the other implantation-induced defect centers are strongly reduced. Only in the Ar-implanted sample (heaviest ion mass), the energetically shallow ID_5-center ($\Delta E(ID_5)$ = (280-320) meV) additionally appears. The defect concentrations obtained from the DLTS peak heights are listed in Tab.2.

Tab.2: Concentration of defect centers in 6H-SiC samples, which have been implanted with H, He, Ne and Ar, respectively, and annealed at 1400°C for 30 min (set 2 samples).

	concentration of defect centers (cm^{-3})			
defect center	H	He	Ne	Ar
ID_5	---	$(3 \pm 0.8) \times 10^{13}$	---	$(5 \pm 0.6) \times 10^{14}$
E_1/E_2	$(2 \pm 0.3) \times 10^{15}$	$(2 \pm 0.3) \times 10^{15}$	$(2 \pm 0.3) \times 10^{15}$	$(1.5 \pm 0.2) \times 10^{15}$
Z_1/Z_2(6H)	$(1.5 \pm 0.2) \times 10^{14}$	$(1 \pm 0.2) \times 10^{14}$	$\approx (1 \pm 0.5) \times 10^{14}$	----
R	not observed after the annealing step			

The formation of implantation-induced defect centers is a complicated process which depends on many parameters like implanted ion species, fluence or generated vacancy concentration, ion current and annealing conditions (temperature, annealing time). Although the generated DLTS peaks (defect centers) are in most cases identical, their concentrations and their abundance depend on the individual experimental conditions. In Fig. 1(a) and 1(b), we have demonstrated the dependence on the implanted ion mass and annealing temperature. The dependence on the generated vacancy concentration and annealing temperature is demonstrated in Fig.2 (set 3 samples). In comparison to set 1/set 2 samples, the generated vacancy concentration in set 3 samples is by approx. two orders of magnitude smaller for corresponding annealing temperatures. As can be seen in Fig.2, the concentration of E_1/E_2 centers dominates subsequent to annealing steps between 700°C and 1700°C in contrast to set 1 samples (Fig.1(a)); maximum concentrations for all the observed defect centers (E_1/E_2, Z_1/Z_2(6H), R) are reached by the anneal at 800°C.

The applied electron irradiation generated a maximum Z_1/Z_2(4H) concentration already without additional annealing step (not shown). For 4H-SiC samples (set 4), the annihilation behavior of the Z_1/Z_2(4H)-center between 873 K and 2273 K is shown in Fig.3. (The Z_1/Z_2(4H)-center in 4H-SiC corresponds to the E_1/E_2(6H)-center in 6H-SiC [7]). Isochronal anneals for 30 min/90 min do not

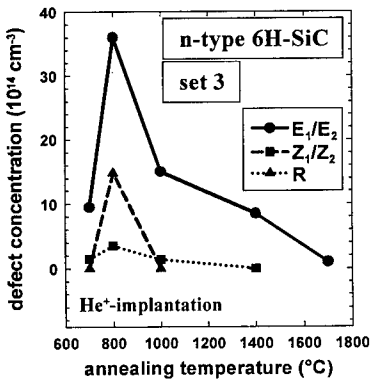


Fig.2: Annealing behavior of the E_1/E_2-, Z_1/Z_2(6H)- and R-center generated in He-implanted 6H-SiC samples.

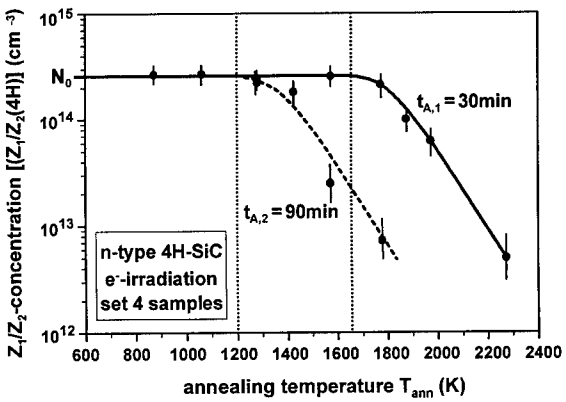


Fig.3: Concentration of Z_1/Z_2(4H)-centers [Z_1/Z_2(4H)] determined in n-type 4H-SiC samples subsequent to isochronal anneals (t_A=30min / 90min).

noticeably reduce the concentration of Z_1/Z_2(4H)-centers up to the annealing temperature $T_{A,2}$ = 1200 K / $T_{A,1}$ = 1700 K; the concentration starts to decrease exponentially at temperatures $T_A > T_{A1}/T_{A2}$.

Assuming first order kinetics, this decrease can be described by

$$\frac{d}{dt}[Z_1/Z_2(4H)] = -K\cdot[Z_1/Z_2(4H)] \quad \text{with the reaction constant} \quad K = K_0\cdot\exp\left\{-\frac{\Delta E_A}{k\cdot T_A}\right\} \qquad (1)$$

Integration over the annealing time t_A leads to

$$\ln\left[\ln\left(\frac{N_0}{[Z_1/Z_2(4H)]}\right)\right] = \ln(K_0\cdot T_A) - \frac{\Delta E_A}{k\cdot T_A} \qquad (2)$$

Eq.(2) is plotted in Fig.4 with the experimental data (dots) taken from Fig.3; the solid and dashed straight lines are least-squares-fits to the experimental data. From the slopes, an activation energy ΔE_A for the annihilation process of 2.1 eV is determined.

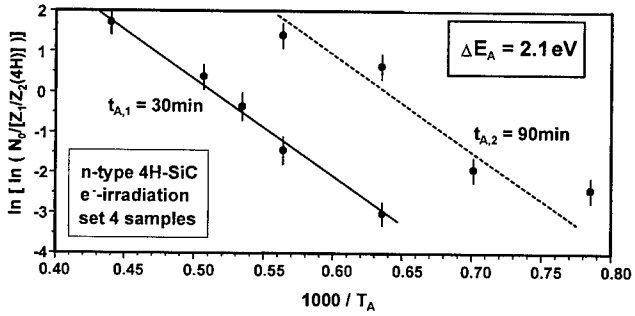


Fig.4: Determination of the activation energy for the annihilation of Z_1/Z_2(4H)-centers; $\ln(N_0/[Z_1/Z_2(4H)])$ is plotted vs. the reciprocal temperature. The activation energy ΔE_A is determined from the slope of the straight lines.

Summary

DLTS investigations were performed on H^+-, He^+-, Ne^+- and Ar^+-implanted 6H-SiC. The formation and annihilation of implantation-induced defects in 6H-SiC was studied as a function of ion mass, fluence (generated [Vac]) and annealing temperature. The Z_1/Z_2(4H)-center was generated in 4H-SiC by irradiation of high-energy electrons. The activation energy ΔE_A for the annihilation process was obtained from isochronal anneals; ΔE_A is equal to 2.1 eV.

Acknowledgement

The support of this work by the German Science Foundation (Sonderforschungsbereich 292) is gratefully acknowledged.

References:

[1] T. Dalibor, C. Peppermüller, G. Pensl, S. Sridhara, R.P. Devaty, W.J. Choyke, A. Itoh, T. Kimoto, H. Matsunami, Inst. Phys. Conf. Ser. 142 (1996), p. 517.

[2] J.P. Doyle, M.O. Aboelfotoh, M.K. Linnarsson, B.G. Svensson, A. Schöner, N. Nordell, C. Harris, J.L. Lindström, E. Janzén, MRS Symp. Proc. Ser. 423 (1996), p. 519.

[3] V.S. Ballandovich, G.N. Violina, Cryst. Latt. Def. and Amorph. Mat. 13 (1987), p. 189.

[4] C.G. Hemmingsson, N.T. Son, E. Janzén, Appl. Phys. Lett. 74 (1999), p. 839.

[5] J.P. Biersack Fortran Monte-Carlo program TRIM Cascade.

[6] H. Ryssel, I. Ruge: Ionenimplantation, B.G. Teubner, S. 58, Stuttgart (1978).

[7] Th. Frank, G. Pensl, Song Bai, R.P. Devaty, W.J. Choyke, Mater. Sci. Forum 338-342 (2000), p. 753.

Materials Science Forum Vols. 353-356 (2001) pp. 443-446
© 2001 Trans Tech Publications, Switzerland

Implantation Temperature Dependent Deep Level Defects in 4H-SiC

D. Åberg[1], L. Storasta[2], A. Hallén[1] and B.G. Svensson[1]

[1] Royal Institute of Technology, Solid State Electronics,
P.O. Box Electrum 229, SE-16440 Kista-Stockholm, Sweden

[2] Department of Physics and Measurement Technology,
Linköping University, SE-581 83 Linköping, Sweden

Keywords: Deep Level, DLTS, Ion Implantation, S-Level, Temperature Stable Defects

Abstract. Deep level transient spectroscopy spectra of the near Z-defect region (150-350K) were investigated for B implanted samples of low doses (10^8-10^9 cm^{-2}). For 300 °C implantation, a level at an energy of 0.41 eV below the conduction band edge was found, referred to as the S-level. The S-center was shown to form in both implanted and electron irradiated 4H-SiC, either after room temperature (R.T.) implantation followed by mild heat treatments or long R.T. storage (several months) or after 200-300 °C implantations/irradiations. The S-center was found to anneal out at temperatures above 250 °C.

1 Introduction

At low doses ($\lesssim 10^{10}$ cm^{-2}) the implantation induced damage in SiC has proven to widely exceed that in Si for the same implantation dose[1] and this poses a major complication for implantation doping in SiC technology. 4H-SiC has a high density with a closest atom distance of ~1.9 Å and a high atomic bonding energy. The high bonding energy manifests itself by a high temperature stability, and likewise high temperatures are needed to anneal out implantation induced damage. Further, as a binary material, there are several different possible substitutional sites for displaced atoms and implanted ions. There exist not only C and Si sites, but the crystal structure also gives rise to both cubic and hexagonal sites. For heavily damaged layers, there is further the possibility of epitaxial re-growth of different polytypes during post-implant annealing.

Electrically active point defects generated by the implantation process affect the doping and carrier lifetimes and very little is yet understood about the identity and formation processes of these defects. For this reason low dose implantation experiments are well suited together with deep level transient spectroscopy(DLTS) for monitoring the evolution of electrically active point defects as a function of implantation parameters and post implantation anneals. Here we concentrate on the region of the DLTS spectra surrounding the most prominent implantation induced defect, the Z-center[2] (150-350 K).

2 Experiment

The material used was epitaxial (10 μm) 4H-SiC layers grown on Cree wafers by chemical vapor deposition (CVD) at Linköping university[3]. The material was nitrogen doped in the range (4 to 8)$\times 10^{15}$ cm^{-3}. The samples were implanted with boron using the Uppsala tandem accelerator facilities at an energy of 2 MeV and doses of 1×10^8 cm^{-2} and 1×10^9 cm^{-2}. This gives rise to a boron distribution with a projected range of 2 μm, according to experimental data[4]. The low dose was selected to produce negligible electrical compensation, thereby eliminating any obfuscating effects during capacitance-voltage analysis and also eliminating the normally necessary post-implantation anneals. The ion implantations were performed at R.T., 300 and 600 °C. One sample was electron

(e^-)-irradiated with 2 MeV electrons at R.T. to a dose of 1×10^{15} cm^{-2}. The samples were cleaned in Aqua Regia, followed by acetone and ethanol rinse and a dip in 10% hydrofluoric acid. Schottky contacts of Ni were grown in an e-beam evaporator at a base pressure of 1×10^{-8} mbar. Capacitance-voltage (CV) measurements were made for doping characterization, followed by temperature scan DLTS and double-pulse DLTS (DDLTS). The measurements were made using a computer controlled setup, consisting of an HP4280A C(t)-meter, an HP8110A dual pulse generator and a Neocera PID temperature controller. The sample was mounted in an adapted Schaefer cryostat, with a temperature range of 77-800 K.

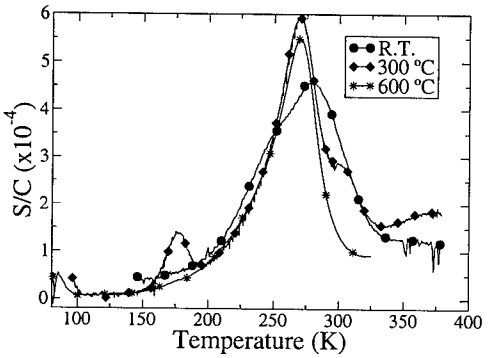


Fig. 1. DLTS spectra (1.6 s rate window) for samples implanted at R.T., 300 °C and 600 °C with a B dose of 1×10^{8} cm^{-2}.

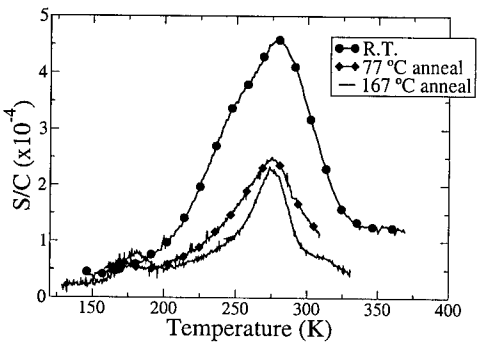


Fig. 2. DLTS spectra (1.6 s rate window) for a R.T. implanted sample directly after implantation and after subsequent isochronal anneals for 15 min.

3 Results and discussion

Different implantation temperatures result in both different defect concentrations and different types of defects, as seen in Fig. 1. All ion implantations give rise to a broad DLTS feature in the range 225-325 K, which has an energy position at 0.7 eV below the conduction band edge (E_C) and is in this contribution, for simplicity referred to as the Z-level. The DLTS spectra after R.T. ion implantation show a broad peak at $\sim$ 280K for 1.6 s rate windows. It is well known that the Z-level DLTS spectrum consists of several different defects[5], of which one type is very temperature stable. The Z-level has been shown to consist of a negative U-center pair[6] in experiments where a light emitting diode (λ=470 nm) was used for emptying traps between filling pulses. For short pulses the Z-level was seen to decrease in amplitude by one half, and the energy shifted towards the conduction band by roughly 0.2 eV. This was attributed to a larger capture cross section for the more shallow energy states, which thus would be filled while the deeper states did not respond until longer pulses were applied.

A level at $\sim$175 K is seen for slightly elevated implantation temperature (here 300 °C, but it is also seen after 200 °C implantation). The level was first detected sporadically in R.T. e^--irradiated samples which had been left at R.T. for several months, and is therefore referred to as the S-level. The S-level is not observed after the 600 °C implantation. DLTS measurements with 19V reverse bias and filling pulse, which cover the implantation region except for the near surface region (0.5 μm), give an energy position of E_C-0.41 eV, and extrapolated capture cross section of 3×10^{-13} cm^2 for the S-level. It is interesting to note that the level has an electronic fingerprint (energy level and capture cross section) close to that of the negative U-centers $Z_{0/+}$[6]. Also, compared to the R.T. implantation, the Z-level is sharpened and increased in concentration at 300 °C implantations and further sharpened at 600 °C implantations.

When the R.T. implanted sample was isochronally annealed for 15 min. the S-level was seen to form above ~100 °C, as shown in Fig. 2 for 1×10^8 cm^{-2} B dose. The maximum concentration was reached for ≈175 °C, and for higher temperatures the signal decreased. The 600 °C sample was likewise annealed, but no change in the DLTS signal was revealed.

The concentration versus depth distribution of the S-level was investigated by DDLTS, using the 300 °C sample and is shown in Fig. 3. Transport of ions in matter code (TRIM)[7] calculations, using SRIM-2000, of the vacancy distribution after implantation is also included; the S-level profile exhibits a very similar half-height width as the vacancy distribution and is clearly an implantation related defect.

Doyle et al. have previously reported[8] a level at $E_C - 0.42$ eV, which was formed after electron irradiation followed by mild heat treatments (216-252 °C for 20 min.). The same level also appeared in samples left at R.T. for 9 months after irradiation. One sample was selected from that study and re-measured with the result given in Fig. 4. It is clear that the S-level is produced in both ion implanted and electron irradiated samples.

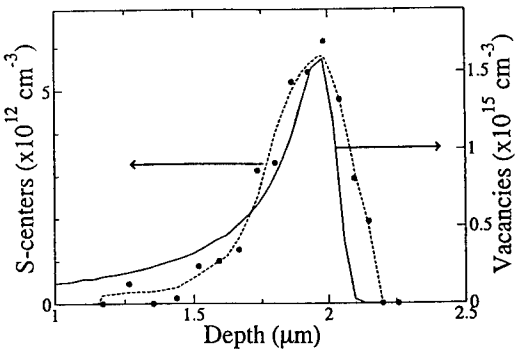


Fig. 3. DLTS depth-profile for the S-level after 300 °C B implantation. Included is also the vacancy distribution for the implantation obtained by TRIM calculation.

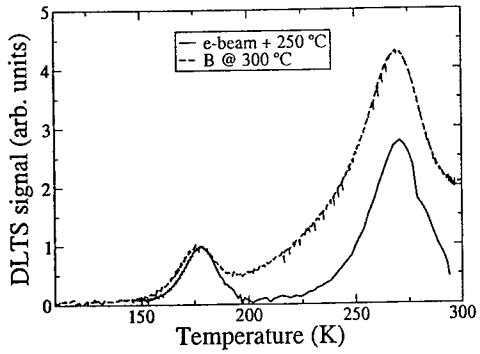


Fig. 4. 4H-SiC sample irradiated with electrons and heat treated at 250 °C for 20 min. displays a concentration of the S-level, comparable to that of the Z-level just as for hot B-implantation.

The energy position of the S-level displays an electric field dependence, ranging from E_C-0.41 eV at a reverse bias of 19V to E_C-0.37 eV at 39 V reverse bias in the B implanted samples. This could be interpreted as a Poole-Frenkel effect, and hence a donor character of the trap as the material is n-type. However, also the electron irradiated sample was measured, using different reverse biases but no shift in the energy position was detected. One major difference between the ion implantation and electron irradiation experiments lies in the damage profile; while for the electron irradiated samples a mostly uniform damage profile is created there is a sharp damage peak for the ion case. This region will have a much higher damage density than the average, and therefore centers in the peak region can be expected to be perturbed by the crystal lattice disorder and stress. Hence, as the different reverse biases were used with a common pulse height (19V), different regions of the damage profile were monitored and this can explain the difference in field dependence for the S-level between the ion implanted and electron irradiated samples. Indeed, one sample was implanted with a higher dose (1×10^9 cm^{-2}) at 200 °C, after which the S-level occurred at E_C-0.35 eV when the surface tail of the implantation profile was measured.

In an attempt to distinguish between the S-level and the $Z_{0/+}$-level short filling pulses (50 ns) were applied and as shown in Fig. 5, both levels were found to exist simultaneously. The sample in Fig. 5 was cooled down under reverse bias after that the Z levels had been thermally emptied. This way, the Z_0 state was available for the short filling pulses, and signals from the $Z_{0/+}$ and $Z_{-/+}$ transitions were both resolved. Not all the states were completely filled as the DLTS-signal was much

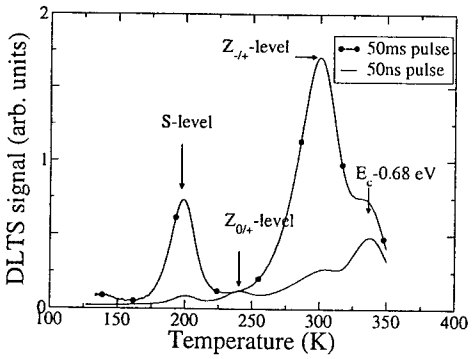


Fig. 5. DLTS scans with different filling pulse lengths. Long pulses give predominantly S-level and $Z_{-/+}$ response, while for short pulses (50 ns) also response from the $Z_{0/+}$ negative U-center charge state can be resolved (providing that all traps have been emptied before cooling down, and reverse bias is maintained during cooling).

weaker than for long pulses.

4 Conclusions

After implantation of boron ions or irradiation of electrons at R.T. there exists an excessive concentration of mobile intrinsic point defects compared to thermal equilibrium in 4H-SiC. After several months storage at R.T., or short time annealing at elevated temperatures a new electronic level forms, here referred to as the S-center level. The S-center is irradiation induced and stable up to temperatures around 250 °C. When samples are implanted at 600 °C, there is no formation of the S-center during post-implantation heat-treatments as for R.T. e^--irradiated samples. The level associated with the S-center has an energy position of $E_C - 0.41$ eV, but shifts to more shallow positions for implanted regions with a high damage density. No correlation with the Z-level is found, and the reported negative U-centers (single ionized form of the Z-center), which has similar electronic fingerprints as the S-level, were shown to co-exist with the S-level. Hence, the S-center is a separate entity relative to the Z-center, an assumption that is further substantiated by its lower temperature stability.

5 Acknowledgement

J. P. Doyle is kindly acknowledged for providing the electron irradiated sample. Financial support from the Swedish Foundation for Strategic Research (SiCEP) is gratefully acknowledged.

References

[1] A. Hallén, A. Henry, P. Pellegrino, B.G. Svensson and D. Åberg, Mat. Sci. Eng., **B61-62** (1999), p. 378.
[2] T. Dalibor, C. Peppermüller, G. Pensl, R.P. Devaty, W.J. Choyke, A. Ito, T. Kimoto and H. Matsunami, Inst. Phys. Conf. Ser. **142** (1996), p. 517.
[3] O. Kordina, C. Hallin, A. Henry, J.P. Bergman, I. Ivanov, A. Ellison, N.T. Son and E. Janzén, phys. stat. sol., **B202** (1997), p. 321.
[4] M.V. Rao, J.A. Gardner, P.H. Chi, O.W, Holland, G. Kelner, J. Kretchmer and M. Ghezzo, J. Appl. Phys., **81** (1997), p. 6635.
[5] D. Åberg, A. Hallén and B.G. Svensson, Phys. B, **273-274** (1999), p. 672.
[6] C. Hemmingsson, N.T. Son, O. Kordina, J.P. Bergman, E. Janzén, J.L. Lindström, S. Savage and N. Nordell, J. Appl. Phys., **81** (1997), p. 6155.
[7] J.P. Biersack and L.G. Haggmark, Nucl. Instrum. Methods, **174** (1980), p. 257.
[8] J. P. Doyle, M.K. Linnarsson, P. Pellgrino, N. Keskitalo and B.G. Svensson, J. Appl. Phys., **84** (1998), p. 1354.

Materials Science Forum Vols. 353-356 (2001) pp. 447-450
© 2001 Trans Tech Publications, Switzerland

Boron in SiC: Structure and Kinetics

Michel Bockstedte, Alexander Mattausch and Oleg Pankratov

Lehrstuhl f. Theor. Festkörperphysik, Universität Erlangen-Nürnberg,
Staudtstr. 7/B2, DE-91058 Erlangen, Germany

Keywords: Ab Initio Defect-Energetics, Boron Migration, Boron-Related Defects, Point Defects

Abstract The structure and kinetics of boron-related defects is investigated by an *ab initio* method. We focus on the stability of the substitutional boron impurities and their migration. We demonstrate that interstitials and carbon vacancies play a prominent role in the migration of substitutional boron.

Introduction

In recent experiments boron-implanted SiC samples were shown to exhibit a transient enhanced diffusion of the dopant [1]. The experiments indicate that silicon interstitials are the driving power of boron diffusion and at the same time affect the electrical activity of boron as a shallow acceptor. Yet, the participation of vacancies in the boron diffusion cannot be excluded. In a previous paper [2] we have presented results for the stable boron defects, mobile intrinsic defects as well as the boron-related complexes. The aim of the present paper is to investigate possible mechanisms of boron diffusion. For simplicity, we have restricted the investigation to cubic 3C-SiC. We expect qualitatively similar results for other polytypes.

Method

Density functional theory has proven to be a reliable and efficient tool for the investigation of defect energetics and migration. The calculations have been performed using the program package FHI96SPIN [3] within the local density approximation (LDA) [4] and including spin-polarisation (LSDA) where indicated. Supercells of 64 atoms and 216 atoms have been employed. The smooth norm-conserving pseudopotentials of the Troullier-Martin type [5] have enabled a plane wave basis of 30 Ry. Special k-point sampling has been employed. The quality of the sampling and basis has been systematically monitored. For charged defects we have applied the approximate technique of Makov and Payne [6] to correct for the mandatory charge compensation under periodic boundary conditions. This technique consistently improves the energetics obtained with a constant background [2], especially for the higher charge states.

In equilibrium the defect concentration is determined by the defect formation energy. The formation energy depends on the stoichiometry, which we express by the Si-chemical potential $\Delta\mu_{\mathrm{Si}}$ and the boron chemical potential μ_{B} as well as on the Fermi-level μ_{F} [2]. $\Delta\mu_{\mathrm{Si}}$ may vary between 0 (Si-rich condition) and $-\Delta H_{\mathrm{f}}$ (C-rich condition), where ΔH_{f} is the heat of formation of 3C-SiC. We have investigated the saddle points of the interstitial migration by the ridge method [7]. For the vacancy-mediated migration and the stability of substitutional boron and boron complexes the potential energy surfaces have been calculated using the constrained relaxations [8].

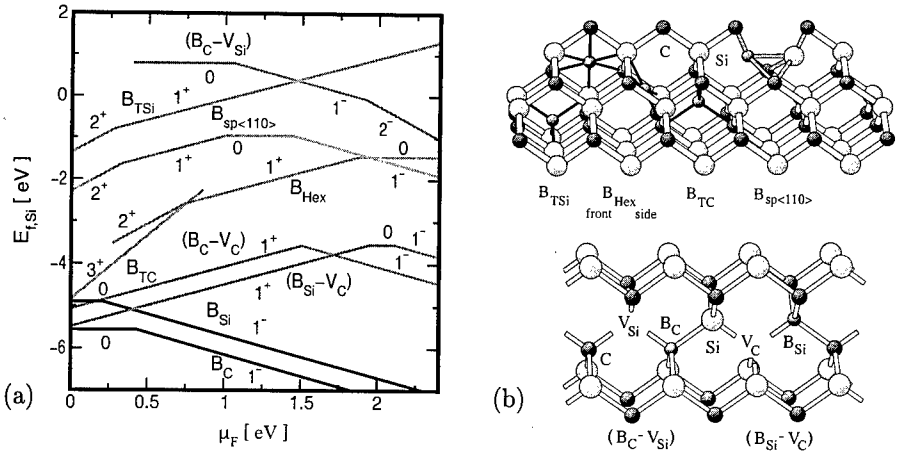


Figure 1: (a) Formation energy $E_{f,Si}$ of boron-related defects versus the Fermi-level position μ_F under Si-rich conditions (c.f. text). (b) Geometry of boron-interstitials (top panel) and the boron-vacancy complexes (bottom panel).

Substitutional boron and boron-related defects

In this section we briefly describe our results on the energetics of substitutional boron and boron-related deep centers, with emphasis on the mobile defects. In Figure 1a we summarise the formation energies of substitutional and mobile defects as a function of the Fermi-level position under Si-rich conditions. Figure 1b displays the geometry of interstitial boron and the boron-vacancy complexes (B_{Si}-V_C) and(B_C-V_{Si}).

Substitutional boron For the substitutional boron, we find, in agreement with earlier calculations [9], that the preferred sublattice is determined by the Si/C ratio: in Si-rich material B_C dominates over B_{Si}, whereas in C-rich material we find the reversed situation. The localised energy levels of B_{Si} and B_C are three-fold degenerate and are located close to the valence band. In the neutral states the boron atom occupies an off-center position as a result of a Jahn-Teller distortion. For B_{Si} and B_C we find ionisation levels $\varepsilon(-|0)$ at 0.2 eV and 0.43 eV as calculated in the 216 atom cell including the charge state corrections and spin polarisation (without charge corrections and spin-polarisation effects we recover the results of the the previous calculation [9]). In order to avoid overcorrection, it is required [6] that the additional electron is well localised within the supercell. For our calculations in the 216-atom cell this is well fulfilled.

Experimentally a boron-related shallow center with an acceptor level in the range 0.22 eV-0.39 eV has been found. The experimentally accepted model is an off-center substitutional boron at a silicon site (c.f. [10] and references therein). A comparison between our results for the acceptor level of B_{Si} and the experimental findings shows a good agreement. For B_C we find our calculated ionisation level close to the position of the deep acceptor level (0.55 eV-0.75 eV, c.f. [10]). Yet, B_C has not been identified experimentally. At first sight, this might be due to a kinetical instability. To verify this, we have tried to move B_C into the interstice, but we have found a large barrier of at least 5 eV (depending on the Fermi level). On the contrary, a direct source of B_C is the recombination of a boron-interstitial and a carbon vacancy, which is accompanied by an energy gain of at least 2 eV (in p-type material). These results suggest that B_C should be present in thermodynamic equilibrium.

Boron-interstitials The boron-interstitials have been described previously without applying charge state corrections [2]. Due to these corrections the formation energy of the boron-interstitials increases. Still the tetrahedral C-coordinated site is the most stable under p-type

conditions. It becomes unstable at a Fermi-level $\sim 1.2\,\mathrm{eV}$, where a weakly localised degenerate orbital gets occupied. The Jahn-Teller-effect drives B_{TC} into B_{Hex}. On the other hand B_{Hex} becomes unstable when this bonding orbital is not occupied. Due to the charge state corrections B_{TSi} and $B_{spSi\langle 110\rangle}$ are at most doubly positive.

Boron-related-complexes Among the boron-vacancy complexes, we have only considered (B_{Si}-V_C) and (B_C-V_{Si}), and the second-nearest-neighbour complex (B_C-V_C), where boron substitutes one of the nearest neighbours (second nearest neighbour rsp.) of the vacancy. Here we note that the (B_{Si}-V_C)-complex and the (B_C-V_C)-complex have a formation energy close to the substitutional defects. However, under Si-rich conditions both are more favourable than the substitutional B_{Si}. For C-rich material only (B_{Si}-V_C) has a lower formation energy. Its formation is insensitive to the Si/C-ratio. The abundance of (B_C-V_{Si}) is negligible due to its high formation energy, furthermore it is unstable in p-type material. We find that (B_{Si}-V_C) and (B_C-V_C) are positively charged in p-type and intrinsic material. Therefore these centers diminish the electrical activation of shallow boron. For both complexes we find ionisation levels in the upper part of the band gap, which we explain in terms of the carbon-vacancy-like character of the center's electronic structure. For both centers it has only a small contribution of the boron-orbitals. Previously (B_{Si}-V_C) has been proposed as a model for the deep acceptor [10, 11]. According to our results for the ionisation levels this is not the case and (B_{Si}-V_C) is not the model for the deep boron-related acceptor. Other recently suggested candidates are boron-antisite complexes [12]. Yet for 3C-SiC we find the acceptor levels of (B_{Si}-Si_C) and (B_C-Si_C) at 1.2 eV and 1.5 eV (0.9 eV and 1.3 eV rsp., without the charge state corrections). Donor levels exist at 0.6 and 0.8 eV (0.8 and 1.1 eV) rsp.. (B_C-C_{Si}) has an acceptor level at 0.7 eV (0.5 eV) and a donor level at 0.2 eV (0.4 eV). Hence only B_C and the latter center have acceptor levels close to or within the range of the deep acceptor. However, since boron-antisite complexes are by 2 eV to 3 eV higher in energy than B_C the kinetic argument has to be invoked [12] to explain the deep acceptor and its experimentally observed large abundance by these complexes.

Boron migration

Boron interstitial migration The interstitial migration of substitutional boron is initiated by a kick-out reaction with intrinsic interstitials. Here we consider a kick-out by a Si-interstitial. The interstitial-boron-complex (Si^{4+}_{TC}-B^{-}_{Si}) is the starting point of the reaction. It has a binding energy of 0.86 eV and is by 3.5 eV higher in energy than the boron interstitial B^{3+}_{TC}. The barrier of this reaction amounts to 1.1 eV. The kick-in reaction has a large barrier of 4.6 eV. This means that once the boron-interstitial has been formed a migration between the most stable interstitial sites is an overwhelmingly likely process. Under p-type conditions these are the B_{TC}-site and the B_{Hex}-site. The latter is preferred under intrinsic conditions. In n-type material also $B_{spSi\langle 110\rangle}$-site becomes important. Here we only consider diffusion in p-type and intrinsic material. The migration barrier between the carbon-coordinated sites for the triply positive charge state amounts to 3.5 eV. The saddle point is located close to the B_{TSi} site. During the migration electrons might be transfered to a localised level that moves down into the band gap. In this case the migration proceeds as for the B_{Hex}-interstitial. For the hexagonal boron-interstitial we distinguish two types of motion. In one type the migration proceeds between B_{Hex}-sites that have the same B_{TC}-site as a nearest neighbour. The barrier amounts to 0.2 eV for B^{2+}_{Hex} and B^{1+}_{Hex}. The other type connects more distant B_{Hex}-sites having a saddle point in the vicinity of the B_{TSi}-site. The barrier amounts to 2.2 eV for B^{2+}_{Hex} and 1.6 eV for B^{1+}_{Hex}. Charge transfer could lower the barrier to at most 1.6 eV for p-type and intrinsic conditions.

Vacancy-mediated boron migration Two mechanisms are considered here: a ring mechanism and migration on the carbon sublattice by second nearest neighbour hops. The ring mechanism is based on nearest neighbour hops: in the first step the neighbouring boron and the vacancy

exchange places, which is followed by a migration of the vacancy around a six-fold ring. The first step transforms (B_{Si}-V_C) into (B_C-V_{Si}). However, we find that $(B_C\text{-}V_{Si})^{1+}$ is unstable. The neutral complex is stable, but the exchange barrier amounts to 5.8 eV contrasted with a small barrier of 0.1 eV for returning to the initial configuration. Since these are the relevant charge states under p-type and intrinsic conditions, we consider a ring mechanisms in this case improbable. In n-type material (B_C-V_{Si}) is stabilised by a larger barrier of 1.0 eV, at the same time the barrier for the initial jump reduces to 3.7 eV. The migration of (B_C-V_C) evolves in three different types of second nearest neighbour hops. The first type is a hop of B_C into the carbon-vacancy. The second and third type correspond to a hop of a carbon atom into the carbon-vacancy which is a second nearest neighbour of boron as well. In the second kind the carbon atom, boron and the vacancy have a common nearest neighbour. Under p-type conditions (B_C-V_C) is singly positive. The barriers are 3.57 eV, 5.57 eV and 5.82 eV rsp. (p-type and intrinsic material). A contribution of (B_{Si}-V_{Si})-complexes to boron diffusion in p-type material is less likely as the Si-vacancy itself is metastable [2].

Discussion

Our investigation of substitutional boron suggests that both B_{Si} and B_C should be present. While we find B_{Si} to be consistent with the model of the shallow acceptor, our results suggest B_C (along with the higher energetic boron-antisite complexes) as a candidate for the deep acceptor. In equilibrium, a high abundance of mobile boron-interstitials and boron-vacancy complexes contributes to electrical deactivation of boron. While the interstitial migration including the kick-out reaction by Si-interstitials have relatively small barriers the kick-in reaction is the bottle-neck of the mechanism. Our results indicate that a vacancy mechanism applies only to boron on the carbon sublattice. Though (B_C-V_C) has a high abundance in equilibrium, the high barrier of the carbon vacancy migration (which is higher than the barrier of the kick-in reaction) is the limiting factor of this mechanism.

Acknowledgement The support of this work by the Deutsche Forschungsgemeinschaft (Sonderforschungsbereich 292) is gratefully acknowledged.

References

[1] M. Laube, G. Pensl, and H. Itoh, Appl. Phys. Lett. **74** (1999), p. 2292.

[2] M. Bockstedte and O. Pankratov, Mater. Sci. Forum **338-342** (2000), p. 949.

[3] M. Bockstedte *et al.*, Comput. Phys. Commun. **107** (1997), p. 187.

[4] J. P. Perdew and A. Zunger, Phys. Rev. B **23** (1981), p. 5048.

[5] M. Fuchs and M. Scheffler, Comput. Phys. Commun. **119** (1999), p. 67.

[6] G. Makov and M. C. Payne, Phys. Rev. B **51** (1995), p. 4041.

[7] I. V. Ionova and E. A. Carter, J. Chem. Phys. **98** (1993), p. 6377.
Implementation: E. Pehlke and P. Kratzer, priv. commun.

[8] M. Bockstedte and M. Scheffler, Z. Phys. Chem. **200** (1997), p. 195.

[9] A. Fukumoto, Phys. Rev. B **53** (1996), p. 4458.

[10] van Duijn-Arnold *et al.* , Phys. Rev. B **57** (1998), p. 1607

[11] A. Gali, P. Deak, R. P. Devaty, and W. J. Choyke, Phys. Rev. B **60** (1999), p. 10620.

[12] B. Aradi *et al.* Mater. Sci. Forum, to be published; P. Deak priv. commun.

Materials Science Forum Vols. 353-356 (2001) pp. 451-454
© 2001 Trans Tech Publications, Switzerland

Deep Level Investigation of pn-Junctions formed by MeV Aluminum and Boron Implantation into 4H-SiC

A. Schöner[1], N. Miyamoto[2], T. Kimoto[2] and H. Matsunami[2]

[1] ACREO AB, Electrum 236, Isafjordsgatan 22, SE-164 40 Kista-Stockholm, Sweden

[2] Department of Electronic Science and Engineering, Kyoto University, Yoshidahonmachi, Sakyo, Kyoto 606-8501, Japan

Keywords: Carbon Co-Implantation, Implantation Induced Defects, Implanted pn-Junction, Isothermal Capacitance Transient Spectroscopy, Post Implantation Anneal

Abstract. ICTS measurements on aluminum, aluminum/carbon, boron, and boron/carbon implanted pn-diodes annealed at 1600°C and 1800°C for 30 min were performed to investigate doping related and implantation induced traps in the vicinity of the pn-junction. An Arrhenius plot analysis was used to determine the trap ionization energies. From this analysis the identified traps can be divided into two groups; one group can be related to the shallow dopants nitrogen and aluminum. The second group consists of deep centers, which can be identified as the implantation induced Z_1-center and the boron related D-center. The concentration of the Z_1-center was reduced by at least 1-2 orders of magnitude in pn-diodes annealed at 1800°C compared with pn-diodes annealed at 1600°C.

Introduction

Electronic devices made from silicon carbide (SiC) are on the edge to be commercialized. To fabricate SiC devices, the formation of pn-junctions has become a critical issue, especially for power devices such as MOSFETs and IGBTs operating at voltages in the kV range. For the fabrication of pn-junctions in SiC, ion implantation is a key technology, because of the possibility to selectively dope through masking techniques. The diffusion process is not applicable due to low diffusion coefficients of commonly used acceptor and donor dopants.
In this study, we investigated pn-junction diodes implanted with MeV acceptor ions using isothermal capacitance transient spectroscopy (ICTS) [1]. ICTS is a variation of deep level transient spectroscopy (DLTS), which is more commonly used for deep level analysis.

Experimental

N-type 4H-SiC epilayers with a donor concentration of $1\text{-}2\cdot10^{15}$ cm^{-3} have been implanted at room temperature with aluminum (Al) and boron (B) ions. A more detailed description of the pn-junction fabrication process can be found in ref. [2]. The total implanted Al and B fluence was adjusted to form a 3 μm box profile with an atomic acceptor concentration of around $1\cdot10^{18}$ cm^{-3}. Post implantation anneal was performed at temperatures of 1600°C and 1800°C for 30 min in argon atmosphere. In addition, the effect of carbon (C) co-implantation as a possible way to enhance the electrical activation of the implanted acceptor species was investigated.
ICTS measurements at temperatures in the range of 120 K to 400 K were performed with various biasing conditions to determine the concentration and ionization energy of deep centers in the depletion region of the implanted pn-diodes. Compared with conventional DLTS, ICTS is not limited by trap concentrations higher or close to the net doping concentration. This allows the acquisition of capacitance transients under forward bias and pulse conditions. Forward biasing the pn-junction limits the extension of the depletion layer close to the vicinity of the actual pn-junction in order to electrically probe the transition area between the layer damaged by the ion implantation and the virgin epilayer.

The analysis of the ICTS spectra was done by a least square fit of the calculated ICTS signal S(t) (Eq. 1) to the measured data.

$$S(t) = t \cdot \frac{dC^2(t)}{dt} = c \cdot \sum_i N_{Ti} \cdot \frac{t}{\tau_{Ti}} \cdot \exp(-t/\tau_{Ti}), \quad c = \frac{q \cdot \varepsilon_s \cdot A^2}{2 \cdot (V_{bi} - V_r)} \qquad \text{Eq. 1}$$

t is the time, N_{Ti} the concentration of trap i, τ_{Ti} the time constant of trap i for capturing or emitting charge carriers, q the electron charge, ε_s the dielectric constant, A the device area, V_{bi} the build-in potential, and V_r the reverse bias voltage during the acquisition of the capacitance transient. The process of a trap changing its charge state by emitting or capturing charge carriers appears as peak or dip in the ICTS spectrum. The peak maximum or dip minimum is correlated with the trap concentration. The time after the filling pulse, where the peak maximum or dip minimum appears, is equal to the time constant τ_T for the changing process of the trap charge state. The ionization energy of the traps can be determined by measuring τ_T at several temperatures and using an Arrhenius plot analysis of the temperature dependent time constant τ_T multiplied with the squared temperature T plotted as function of the reciprocal temperature.

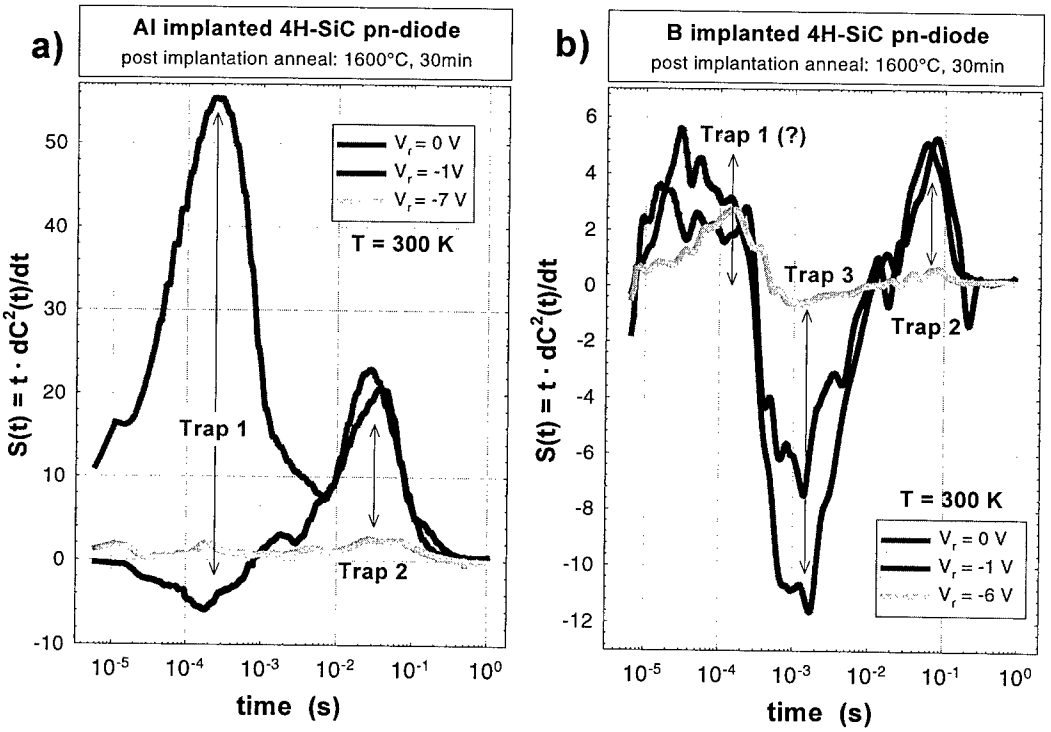


Fig.1 ICTS-spectra at room temperature for an Al implanted (a) and a B implanted (b) pn-diode obtained at different reverse bias voltages V_r with 1V pulse voltage. Observed deep centers are marked with Trap 1 to Trap 3.

Results and Discussion

The ICTS measurements obtained for the different implanted and annealed pn-diodes resulted, depending on the bias conditions during the acquisition of the capacitance transient, in a variety of negative and positive transients corresponding to dips and peaks in the ICTS spectra. Qualitatively the ICTS measurements showed no difference in the spectra for the Al and the Al/C implanted pn-

diodes as well as the B and B/C implanted pn-diodes. Fig. 1 shows for the 1600°C annealed Al and B implanted pn-junctions ICTS spectra at room temperature for 3 different reverse bias voltages and a fixed pulse voltage of 1V. It was found that at a fixed temperature and for different reverse bias voltages some dips and peaks appear at similar time position. The position of these dips and peaks is shifting in the same way with changing the temperature, indicating that they are related to the same trap. An example for that is trap 1 in fig. 1a. The peak analysis revealed that trap 1 consists actually of two traps. The Arrhenius analysis resulted in ionization energies of 55±8 meV and 89±9 meV (fig. 2). These values for the ionization energies are in agreement with the ionization energies of nitrogen sitting on hexagonal and cubic lattice site obtained by Hall effect [3].

In the B implanted pn-diodes a dip can be observed (e.g. T = 300 K, $\tau_{ti} = 1 \cdot 10^{-3}$ s, marked trap 3 in fig. 1b), which is not present in the Al implanted pn-diodes. This dip comes from a single trap and the Arrhenius plot results in an ionization energy of 575±20 meV (fig. 2). Comparing with DLTS results trap 3 can be identified as the boron related D-center [4].

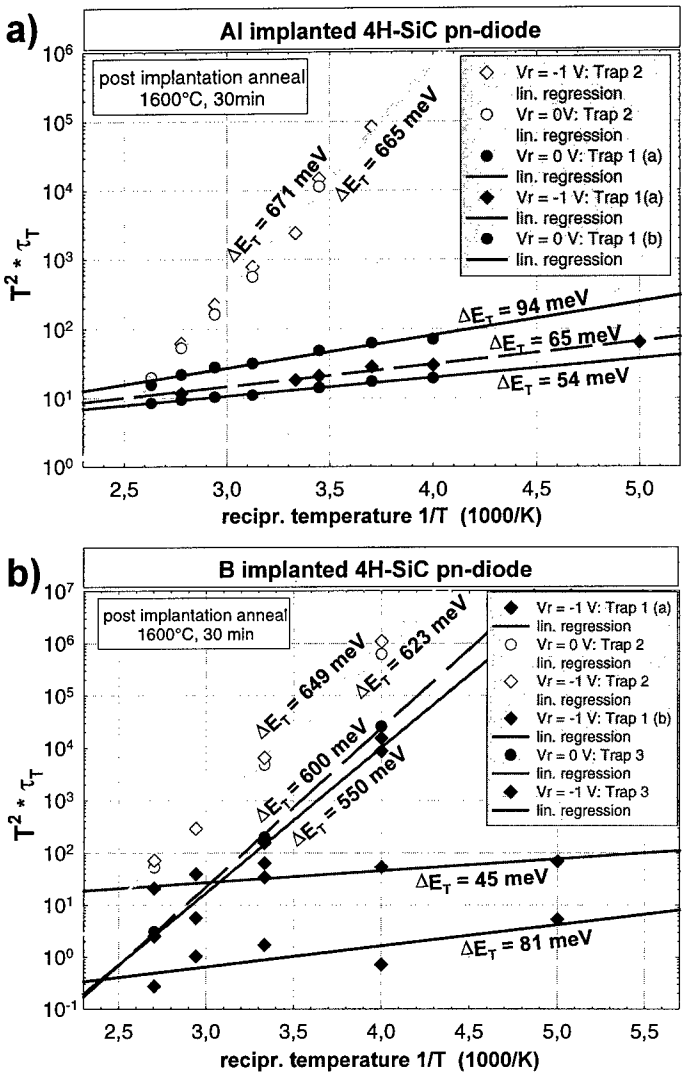


Fig 2 Arrhenius analysis for the traps observed in ICTS measurements of Al (a) and B (b) implanted pn-diodes for reverse bias voltages of –1V and 0V and a pulse voltage of 1V. The slope m of the linear regression lines is correlated to the ionization energy ΔE_T of the traps ($\Delta E_T = k_B$ Ln(10) m, where k_B the Boltzmann constant). The result of the ionization energy calculation for each line is shown in the figure.

Trap 2 is seen in the ICTS spectra of all pn-diodes annealed at 1600°C and appears always as a peak (fig. 1). This peak can be fitted by assuming a single trap and the Arrhenius plot analysis results in an ionization energy of 647±22 meV (fig. 2). This value for the ionization energy of trap 2 corresponds to the ionization energy of the Z_1-center, which is a defect seen in DLTS spectra of implanted layers [5]. Trap 2 is appearing in the Al as well as the B implanted pn-junctions, indicating that it is a defect induced by the implantation. The concentration of trap 2 was observed to be very much dependent on the measurement conditions and increases with increasing measurement temperature. It varies from mid 10^{12} cm^{-3} to mid 10^{13} cm^{-3}.

Fig. 3 shows for two different measurement temperatures a comparison of ICTS spectra for the Al implanted pn-diodes. It can be seen, that trap 2 appears not in the spectra of the diode annealed at 1800°C. Instead a dip (trap 4 in fig. 3) is observed, be identified as aluminum with an ionization energy of 237±7 meV.
In general, trap 2 was not present in the ICTS spectra of the investigated pn-diodes annealed at 1800°C. The lowest concentration observable with ICTS is around 10^{-4} of the net doping concentration. The concentration of trap 2 can be estimated to be less than $2 \cdot 10^{11}$ cm^{-3} after anneal at 1800°C, around 2 orders of magnitude lower than for the diodes annealed at 1600°C.

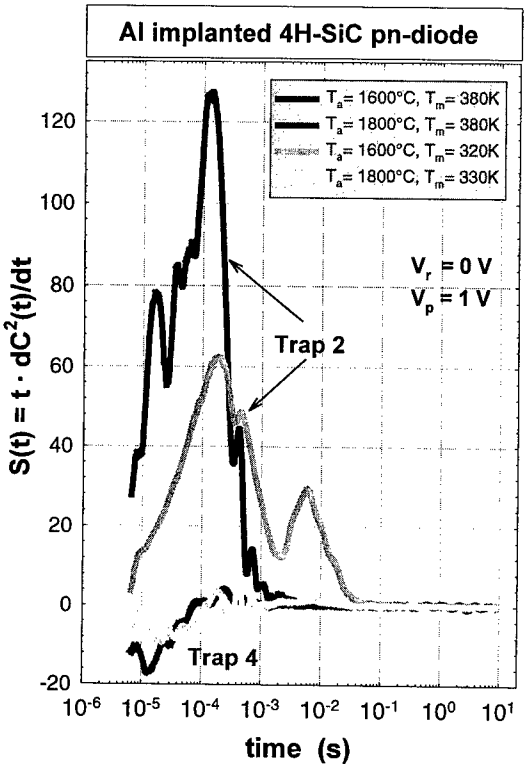


Fig 3 Comparison of the ICTS spectra for Al implanted pn-diodes annealed at T_a=1600°C and T_a=1800°C, taken at two different measurement temperatures T_m.

Summary and Conclusion

In general, we observed two groups of traps in ICTS measurements of Al and B implanted pn-diodes annealed at 1600°C and 1800°C for 30 min. An Arrhenius plot analysis of the trap energies revealed that one group can be related to the shallow dopants nitrogen on hexagonal (trap 1a) and cubic (trap 1b) lattice site and aluminum (trap 4). The second group consists of deep centers with an ionization energy of 575±20 meV identified as the boron related D-center (trap 3) and 647±22 meV, identified as Z_1-center (trap 2). The Z_1-center is a remaining implantation damage. The concentration of the Z_1-center is reduced by at least one order of magnitude through post implantation anneal at 1800°C for 30 min. This reduction in implantation induced defects indicates that higher post implantation anneal temperatures are required for better device performance due to a reduced concentration of possible recombination centers limiting the carrier lifetime.

Acknowledgement

The authors like to thank Prof. I. Kimura and Dr. S. Kanazawa (Dapartment of Nuclear Eng., Kyoto Univ.) for the possibility to use the ICTS equipment and the Kyoto University Venture Business Laboratory for support.

References

[1] H. Okushi, Y. Tokumaru, Jap. J. App. Phys. 19 (1980), p. L335.
[2] N. Miyamoto, A. Saitoh, T. Kimoto, H. Matsunami, Y. Hishida, M. Watanabe, Mater. Sci. Forum 338-342 (2000), p. 1347.
[3] W. Götz, A. Schöner, G. Pensl, W. Suttrop, W.J. Choyke, R. Stein, S. Leibenzeder, J. Appl. Phys. 73 (1993), p. 3332.
[4] M. Ikeda, H. Matsunami, T. Tanaka, Phys. Rev. B 22 (1980), p. 2842.
[5] T. Dalibor, G. Pensl, H. Matsunami, T. Kimoto, W.J. Choyke, A. Schöner, N. Nordell, Phys. Stat. Sol. (a) 162 (1997), p. 199.
[6] A. Schöner, N. Nordell, K. Rottner, R. Helbig, G. Pensl, Inst. Phys. Conf. Ser. 142 (1995), p. 493

Materials Science Forum Vols. 353-356 (2001) pp. 455-458
© 2001 Trans Tech Publications, Switzerland

Boron Centers in 4H-SiC

B. Aradi[1], A. Gali[1], P. Deák[1], E. Rauls[2], Th. Frauenheim[2] and N.T. Son[3]

[1] Department of Atomic Physics, Technical University of Budapest, Budafoki út 8, HU-1111 Budapest, Hungary

[2] Department of Physics, Theoretical Physics, University GH Paderborn, Warburgstr. 100, DE-33095 Paderborn, Germany

[3] Department of Physics and Measurement Technology, Linköping University, SE-581 83 Linköping, Sweden

Keywords: Boron, Intrinsic Defects, Occupancy Level

Abstract. The origin of the "deep boron related acceptor level" in SiC is subject to a lot of controversy. Based on ENDOR investigations, a B_{Si}+V_C model was suggested, while PL studies indicated the acceptor on the carbon sublattice. Our former ab initio LDA *molecular cluster* calculation showed that in the B_{Si}+V_C complex the carbon vacancy acts as the acceptor. Now, ab initio LDA *supercell* calculations have been carried out for boron-related complexes to calculate the occupation levels in 4H-SiC. It has been found that the 0/- level for the B_{Si}+V_C complex lies in the upper half of the gap, therefore it can be disregarded as the origin of the "deep boron-related acceptor level". Investigating other feasible boron-related complexes, B_{Si}+Si_C appears to be the best candidate.

Boron gives rise to a shallow as well as to a deep acceptor level [1] in SiC. The "shallow boron level" was suggested to be an off-center boron substitutional on a Si site (B_{Si}) [2]. Low concentrations (10^{13-14} cm^{-3}) of the center responsible for the "deep boron level" arise in boron doped epilayers grown under C-rich conditions, with higher concentrations in samples grown with high Si/C ratio [3]. From conduction-band-to-neutral-defect photoluminescence (PL) in the latter samples, the position of the one-electron level associated with the negative charge state of this center was estimated to be at $E_v + 0.655$ eV in 4H-SiC [3]. Such a transition implies acceptor character of the center.

In B-implanted p-type 6H-SiC, Deep Level Transient Spectroscopy (DLTS) has revealed a boron related deep level, called D center, [4] which, however, had donor character. B-implantation into n-type material and subsequent annealing produced concentrations in the order of 10^{16} cm^{-3} [5]. It is usually assumed that the D center contains an intrinsic point defect besides B. It is also assumed that the "deep acceptor level" seen in PL experiments and the D center originate from the same amphoteric defect which has close lying +/0 and 0/- occupation levels. The D center was also found in the boron-doped 4H-SiC epilayers mentioned above. DLTS measurements in layers grown with low Si/C ratio put the occupancy level at $E_v + 0.550$ eV [3] (assuming T^{-2} dependence of the capture cross section).

By electron spin resonance (EPR) and electron nuclear double resonance (ENDOR) experiments [6, 7] a boron related complex with a B atom on a Si site next to a C vacancy (B_{Si}+V_C) has been recently identified in 6H material. This complex was suggested [6, 7] as the origin of the "deep boron level".

3C-SiC samples co-doped with N and B have shown a Type I PL spectrum for the deep B acceptors recombining with the shallow nitrogen donors [8], indicating that the ionized donor and acceptor occupy the same sublattice. Since nitrogen sits on a carbon site, the deep B center was associated with a complex containing B at a C site.

Regarding the controversy in the experimental information about the "deep boron level", our paper aims at investigating boron related complexes by means of *ab initio* electronic structure calculations in 4H-SiC. We were looking for a complex

1. with amphoteric electronic activity

2. having a +/0 (donor) occupation level around $E_v + 0.55$ eV
3. having a one-electron level at $E_v + 0.66$ eV in the negative charge state
4. with acceptor activity connected to the carbon site
5. occurring more frequently in silicon-rich material or after implantation

Taking this experimental information into account we studied stable complexes of boron with vacancies and antisites.

Ab initio calculations in the local density approximation of density functional theory [9] (DFT) were performed using the FHI98MD code [10], which applies plane waves to expand the one-electron wave functions. A kinetic energy cut-off of 36 Ry was used in conjunction with Troullier-Martins norm conserving soft-core pseudopotentials [11]. Tests on carbon pseudopotentials have shown the cut-off of 36 Ry to provide convergent results [12]. 4H-SiC was modeled by a 96-atom supercell (SC). Summation over the reduced Brillouin-zone of the supercell was carried out using a 2x2x2 MP scheme [13]. DFT is known to uniformly underestimate the position of the conduction band (CB) states with respect to the valence band maximum (VBM). The band gap in our case was 2.3 eV compared to the experimental 3.3 eV. Defect states are a mixture of states from the CB and VB, therefore defect levels in the band gap have been shifted by $(3.3\text{ eV} - 2.3\text{ eV}) \cdot S$, where S is the overlap of the defect state with the CB states [14]. The total energy was then corrected with this shift, times the occupation number of the defect state. Another correction was made necessary because of the dispersion caused by the interaction of repeated defects in the SC model. An approximate position of the "isolated" defect level was found by a tight binding fit to the energies calculated at different k-points [15]. The total energy was then corrected by the differences between this value and the defect levels calculated at the individual k-points, times the occupation numbers. The dispersion in our calculations were always less than 0.2 eV. For spin half systems the error due to the lack of spin-polarization in the total energy (and in one-electron levels) is estimated to be -0.1 eV, and this value was added as correction. The occupation levels were determined from the difference of the total energies in different charge states.

In an earlier paper we have shown [16] by *ab initio* molecular cluster calculations that the B_{Si}+V_C complex is more stable both in the neutral and in the negatively charged state than the V_{Si}+B_C system (see Fig. 1.a,b). It was also shown that the spin distribution of the B_{Si}+V_C complex corresponds indeed to the EPR/ENDOR signals found in Ref. [7]. In addition, it was pointed out that the acceptor activity is connected to the carbon vacancy. Now, we have calculated the B_{Si}+V_C complex in our supercell to obtain its one-electron and occupation levels with respect to the gap. The calculations were carried out at the cubic site with the complex oriented along the c-axis. After relaxation, the symmetry of this complex is C_{1h} due to a Jahn-Teller distortion from C_{3v}. In the neutral charge state a singly occupied one-electron level was found in the gap at $E_v + 2.3$ eV, associated with the Si neighbors of V_C. The corresponding +/0 and 0/- occupation levels are at $E_v + 1.9$ eV and $E_v + 2.1$ eV, respectively. These values are much too high, so the B_{Si}+V_C complex can be disregarded after all as the origin of the deep boron level! Still, it is a stable amphoteric defect which was detected in EPR and ENDOR. However, this complex is more likely to act as a deep donor.

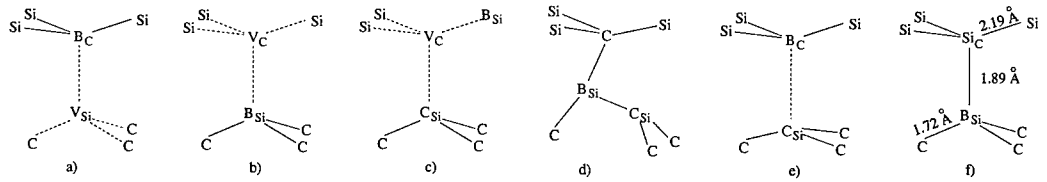


Fig. 1. The investigated complexes: a) V_{Si}+B_C, b) B_{Si}+V_C, c) C_{Si}+V_C+B_{Si}, d) C_{Si}-B_{Si} pair, e) C_{Si}+B_C, f) B_{Si}+Si_C

After excluding boron next to a carbon vacancy, B next to V_{Si} could have been investigated.

However, not only showed the molecular cluster calculation [16] V_{Si}+B_C instable with respect to B_{Si}+V_C by a large margin, V_{Si} itself is metastable with respect to V_C+C_{Si} [17, 18]. Therefore, next we have investigated the latter complex with a Si atom in the neighborhood of V_C substituted by B, forming the C_{Si}+V_C+B_{Si} complex (see Fig. 1.c). This defect turns out to be stable with a singly occupied level in the band gap at $E_v + 1.5$ eV in the neutral charge state. The level can be associated with the dangling bond on C_{Si}. This is a bit surprising, since carbon dangling bonds usually have levels close to the VBM. However, due to the back relaxation of C_{Si} towards the plane of its carbon neighbors, its dangling bond is almost entirely p-like, unlike the usual sp^3 hybrids. The 0/- occupation level is at $E_v + 2.0$ eV. Therefore, this defect can also be discarded as the origin of the "deep boron level".

The lowest energy intrinsic point defects after the vacancies are antisites. First we have investigated boron next to a carbon antisite, both as an interstitial and as a substitutional. The most stable interstitial configuration was the C_{Si}-B_{Si} split-interstitial pair (see Fig. 1.d). It is a stable defect with low formation energy, but it is more a donor than an acceptor. It has a singly occupied level at $E_v + 2.4$ eV in the neutral charge state, associated with a p-like dangling bond on C_{Si}. The position of the level disqualifies this complex as well. Placing boron at a substitutional site next to C_{Si} gives the C_{Si}+B_C structure (see Fig. 1.e). This defect is metastable with respect to B_{Si} (which can be obtained by interchanging the C anti-site and the B atom) by $\sim$ 4 eV. Besides, the acceptor activity of C_{Si}+B_C is connected to C_{Si}, i.e., to the silicon sublattice, so it can also be disregarded as a candidate for the "deep boron level".

Finally, we have investigated substitutional boron next to a silicon antisite at the cubic site, oriented along the c-axis (see Fig. 1.f). The B_{Si}+Si_C complex has C_{3v} symmetry. Similarly to the case of the isolated Si_C [19], we find localized one-electron levels in the gap, relatively close to the VBM. The highest one at $E_v + 0.60$ eV is singly occupied in the neutral charge state. Fig. 1.f) shows the relaxed structure in the neutral charge state. In the negatively charged state the Si-B distance becomes somewhat longer than in the neutral state, but the geometry is essentially the same. The orbital with the unpaired electron in the neutral and accommodating the extra charge in the negative charge state is strongly localized on Si_C. Therefore, the acceptor activity is connected with the carbon sublattice. The 0/- occupation level is at $E_v + 0.64$ eV and the position of the ionized acceptor level is at $E_v + 0.73$. The defect can also be positively ionized. The +/0 occupation level is at $E_v + 0.53$ eV.

Considering the accuracy of our calculations, these energy values, i.e., the +/0 occupation level at $E_v + 0.53$ eV and the one-electron level in the negative charge state at $E_v + 0.73$ eV compare rather nicely with the experimental values of $E_v + 0.55$ eV and $E_v + 0.66$ eV, respectively. Therefore, the B_{Si}+Si_C complex meets the criteria 1–4 mentioned earlier. As for criterion 5, the B_{Si}+Si_C complex implies silicon rich material. It has to be noted, however, that interchanging the boron atom with Si_C in this complex, B_C is obtained, which is significantly lower in energy. As a consequence, the formation of B_{Si}+Si_C complexes in equilibrium is unlikely. However, if created in some non-equilibrium process during growth, it will remain stable. Recent work on antisite pairs [20] has shown that interchanging Si and C atoms in SiC requires an energy barrier of $\sim$ 10 eV. The interchange of B_{Si} and Si_C is expected to have an activation energy in this range as well. The B_{Si}+Si_C complex may well arise in the activation process of implanted boron interstitials. Boron is known to prefer the silicon site [21] but emission of an interstitial Si atom is energetically very costly. Calculations on tetrahedral interstitials in the neutral charge state [22] predict C_i to be $\sim$ 6 eV lower in energy than Si_i. More recent results [23] give smaller differences but for n-type SiC (high Si/C ratio) also predict C_i lower in energy than Si_i. Therefore, the following reaction seems plausible: $B_i \rightarrow B_{Si} + Si_i \rightarrow (B_{Si}+Si_C) + C_i$.

To summarize, several boron-related complexes have been investigated to find the microscopic origin of the deep boron level. We have found that the B_{Si}+V_C complex seen in ENDOR is an amphoteric defect but it is rather a donor than an acceptor. So there ought to be a boron related donor-like level at around $E_v + 1.9$ eV in 4H-SiC! We have found only one boron-related complex with donor

and acceptor occupation levels around $E_v + 0.6$ eV. In agreement with PL results on the "deep boron level", in this B_{Si}+Si_C the final state of the conduction-band-to-neutral-defect photoluminescence is calculated to be at $E_v + 0.73$ eV and is strongly localized on the carbon site. The complex is amphoteric, with a donor-like +/0 occupation level at $E_v + 0.53$ eV, in good agreement with values obtained for the D center in 4H-SiC. The composition of this defect implies higher concentrations in silicon-rich material, and it is likely to be created during B-implantation. It has to be noted, though, that formation of B_C substitutionals is energetically more favorable than the creation of B_{Si}+Si_C complexes. Still, among the investigated complexes, B_{Si}+Si_C fits the experimental information available on the "deep boron level" best.

Acknowledgement The authors are indebted to Prof. J. W. Choyke for many valuable discussions. Support by the Hungarian OTKA T-22139 and FKFP 0289/97 grants as well as the bilateral German-Hungarian (DFG -MTA No. 118) and Swedish-Hungarian (IVA-MTA No. 36) projects are appreciated. This work was also supported by a grant from the National Supercomputing Center (Sweden).

References

[1] J. M. Blank, Mat. Res. Bul. 4 (1969), p. 179.

[2] S. Greulich-Weber, phys. stat. sol. (a) 162 (1997), p. 95.

[3] S. G. Sridhara *et al.*, J. Appl. Phys. 83 (1998), p. 7909.

[4] W. Suttrop, G. Pensl, and P. Lanig, Appl. Phys. A: Solids Surf. 51 (1990), p. 231.

[5] M. Gong *et al.*, Appl. Phys. Lett. 72 (1998), p. 2739.

[6] P. G. Baranov and E. N. Mokhov, Semicond. Sci. Technol. 11 (1996), p. 489.

[7] A. Duijn-Arnold *et al.*, Phys. Rev. B 57 (1998), p. 1607.

[8] H. Kuwâbara and S. Yamada, Phys. Status Solidi A 30 (1975), p. 739.

[9] W. Kohn and L. J. Sham, Phys. Rev. 140 (1965), p. A1133.

[10] M. Bockstedte, A. Kley, J. Neugebauer, and M. Scheffler, Comp. Phys. Comm. **107** (1997), p. 187.

[11] N. Troullier and J. L. Martins, Phys. Rev. B 43 (1991), p. 1993.

[12] M. Bockstedte, private communication.

[13] H. J. Monkhorst and J. K. Pack, Phys. Rev. B 13 (1976), p. 5188.

[14] G. A. Baraff and M. Schlüter, Phys. Rev. B 30 (1984), p. 1853.

[15] S. G. Louie, M. Schlüter, J. R. Chelikowski, and M. L. Cohen, Phys. Rev. B 13 (1976), p. 1654.

[16] A. Gali, P. Deák, R. P. Devaty, and W. J. Choyke, Phys. Rev. B 60 (1999), p. 10620.

[17] E. Rauls *et al.*, phys. stat. sol. (b) 217/2 (2000), p. R1.

[18] M. Bockstedte and O. Pankratov, Mater. Sci. Forum 338-342 (2000), p. 949.

[19] L. Torpo, S. Pöykkö, and R. M. Nieminen, Phys. Rev. B 57 (1998), p. 6243.

[20] E. Rauls *et al.*, Mater. Sci. Forum, this volume (2000).

[21] D. J. Larkin and V. A. Laki, J. Electron. Mater. 24 (1995), p. 289.

[22] C. Wang, J. Bernholc, and R. F. Davies, Phys. Rev. B 38 (1988), p. 12752.

[23] A. Mattausch and V. A. Laki, this volume (2000).

Materials Science Forum Vols. 353-356 (2001) pp. 459-462
© 2001 Trans Tech Publications, Switzerland

Oxygen-Related Defect Centers Observed in 4H/6H-SiC Epitaxial Layers Grown under CO_2 Ambient

Oliver Klettke[1], Gerhard Pensl[1], Tsunenobu Kimoto[2] and Hiroyuki Matsunami[2]

[1] Institute of Applied Physics, University of Erlangen-Nürnberg, Staudtstr. 7/A3, DE-91058 Erlangen, Germany

[2] Department of Electronic Science and Engineering, Kyoto University, Yoshidahonmachi, Sakyo, Kyoto 606-8501, Japan

Keywords: Admittance Spectroscopy, DLTS, Oxygen, SiC Epilayers

Abstract: Nitrogen (N)-doped 4H/6H-SiC epitaxial layers have been grown by the Chemical Vapor Deposition (CVD) technique on SiC substrates of the same polytype under additional CO_2 flow. Deep level transient spectroscopy (DLTS) spectra of these epilayers reveal three energetically deep traps, identical with the defect centers O_{III}, O_{IV} and O_V observed in oxygen (O)-implanted 4H/6H-SiC samples. Admittance spectroscopy (AS) investigations result in the nitrogen donors (N(h), $N(k_1,k_2)$) and a double peak termed O_I/O_{II}. This double peak is caused by two energetically shallow O-related donors. With increasing CO_2 flow, the concentration of O_I/O_{II} donors increases; however, this increase cannot explain the strong increase of the net donor concentration (N_D-N_A) determined by C-V measurements. It is suggested that the incorporation of nitrogen atoms during the CVD growth is enhanced by the presence of oxygen.

Introduction

O-related defect centers in 4H/6H-SiC have mainly been studied in O-implanted and annealed SiC-epilayers [1,2]. AS spectra reveal two energetically shallow, donor-like centers (O_I/O_{II}); three energetically deep, acceptor-like centers ($O_{III}/O_{IV}/O_V$) are observed by DLTS. Positron annihilation experiments result in complexes, which are supposed to be of a vacancy-oxygen-type [3]. In addition, it has been demonstrated that O-related defect centers can occasionally be observed in unimplanted epilayers grown by the CVD technique under standard conditions.

In this paper, we report on experiments with 4H/6H-SiC epilayers grown by the CVD technique with additional CO_2-flow. Electrical analysis methods reveal identical O-related defect centers O_ν (ν=I,...,V) in these epilayers as observed in O-implanted SiC samples. With increasing CO_2 flow rate, the concentration of O-related defect centers increases; however, the striking feature is that, in parallel, a huge increase of the doping level occurs which cannot be created by O-related centers. It seems that the incorporation of N atoms during the CVD growth is strongly enhanced in the presence of CO_2. This paper presents predominantly results taken on the 6H-SiC polytype.

Experimental

Oxygen-doped 4H/6H-SiC epitaxial layers were grown on substrates of the same polytype in a SiH_4-C_3H_8-H_2 CVD system at 1500°C. The substrates were placed side by side on a SiC-coated susceptor. Epilayers of a thickness of 10µm were grown with a typical growth rate of 3µm/h. Growth runs were conducted with three different additional CO_2 flow rates 0.1sccm, 0.5sccm and 1sccm; the other growth parameters were kept constant.

Prior to the preparation of Schottky contacts, a standard chemical cleaning of the sample surface was performed using acetone, aqua regia and hydrofluoric acid. For the DLTS investigations, Schottky contacts with different diameters (0.2mm to 1.0mm) were fabricated by evaporation of

nickel. The DLTS and AS spectra were taken in a temperature range of (100K-700K) and (30K-200K), respectively. The net donor concentration was determined at room temperature (f=1MHz) by the CV method.

Experimental results

In Table 1 the net donor concentration (N_D-N_A) determined by C-V measurements is listed for the investigated 6H/4H-SiC samples (see column 3 and 4). By increasing the CO_2 flow rate by a factor of 10, the net donor concentration (N_D-N_A) determined by CV increases by three to four orders of magnitude. With exception of the CO_2 flow rate, identical growth parameters were used for the three growth runs. It can be excluded that this strong increase of the donor concentration is created by contamination of nitrogen, which may have its origin in the process gases or the graphite susceptor, which was coated with a thick SiC film.

		6H-SiC epilayer/4H-SiC epilayer	
sample	CO_2 flow (sccm)	N_D-N_A (cm^{-3})	N_D-N_A (cm^{-3})
#1a/b	0.1	$1x10^{15}$	$9x10^{14}$
#2a/b	0.5	$2x10^{15}$	$2x10^{15}$
#3a/b	1.0	$4x10^{18}$	$1x10^{19}$

Table 1: Net donor concentration (N_D-N_A) determined by CV; the 4H/6H-SiC epilayers were grown under various CO_2 flow rates.

In order to figure out the chemical nature of the incorporated donor species, which are responsible for this large change of the doping level, AS and secondary ion mass spectroscopy (SIMS) investigations were taken on these samples. Normalized conductance spectra G/ω(T) of the 6H-SiC epilayers #1a and #3a are displayed in Fig.1 and Fig.2, respectively. The dominating peaks in Fig.1 are caused by N-donors residing at hexagonal (h) and cubic (k_1,k_2) lattice sites. The broad peak at T=95K (sample #1a) is attributed to the O-related defect centers O_I/O_{II}.

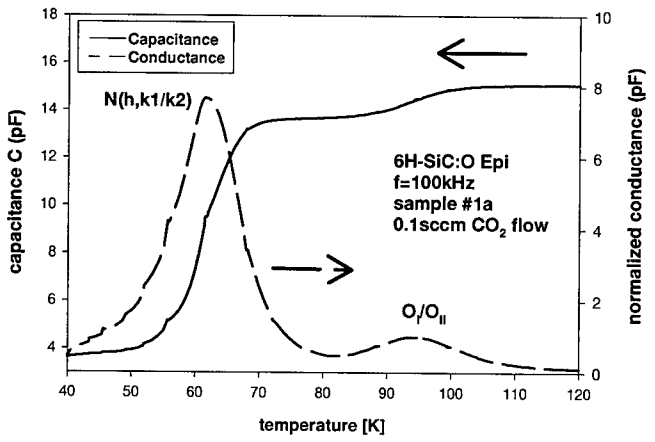


Fig. 1: Normalized conductance G/ω as a function of temperature. The spectra are taken on 6H-SiC epilayer #1a and #2a, respectively.

With increasing CO_2 flow rate (compare Fig.1 and Fig.2) the peak heights and, as a consequence, the defect concentrations of O-related centers and N donors increase. However, the nitrogen donors dominate in both samples. This observation is a strong argument that the doping level in both samples is determined by N donors.

For the 6H-SiC epilayer #3a –grown under the highest applied CO_2 flow rate-, capacitance C and normalized conductance G/ω as a function of the temperature are displayed in Fig.2.

	sample #3a	sample #3b
	concentration (cm^{-3})	concentration (cm^{-3})
O (cm^{-3})	$<5x10^{17}$	$<5x10^{17}$
N (cm^{-3})	$2x10^{18}$	$4x10^{18}$
B (cm^{-3})	$2x10^{16}$	$4x10^{16}$

Table 2: SIMS results of sample #3a and #3b grown under a CO_2 flow rate of 1sccm.

The conductance spectrum shows only one broad peak with a peak height of G/ω=65pF; the individual peaks overlap and can no longer be resolved. From the corresponding capacitance step (see solid curve), a donor concentration of $N_D>3x10^{18}cm^{-3}$ (according to $\Delta C \propto N_D$) is evaluated; this value is in good agreement with the corresponding donor concentration obtained from the CV measurement (see Table 1: $(N_D-N_A)=4x10^{18}cm^{-3}$).

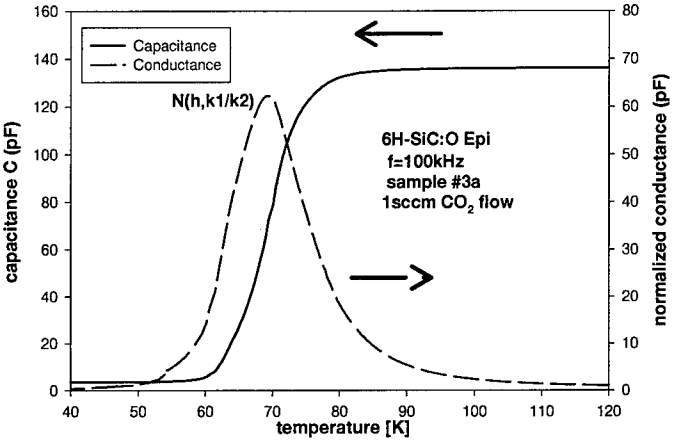


Fig.2: Normalized conductance G/ω and capacitance as a function of temperature. The spectra are taken on 6H-SiC epilayer #3a.

SIMS investigations were conducted to determine the chemical concentrations of O, N and boron (B); the concentration profiles were monitored to a depth of 2μm. The concentration of O, N and B determined in sample #3a are listed in Table 2. The SIMS data (see second column in Table 2) clearly confirm that only the N atoms can account for the high donor concentration of approx. $4x10^{18}cm^{-3}$.

In order to be able to investigate energetically deep centers in epilayers #1 to #3, DLTS spectra of these samples were recorded; they are displayed in Fig. 3. The ionization energies and concentrations of the observed defect centers – determined in epilayer #2a - are summarized in Table 3.

Besides the O-related centers O_{III} and $O_{IV/V}$, two further peaks are observed in the DLTS spectra; peak E_1/E_2 and peak V_1/V_2 are caused by an intrinsic defect and by vanadium, respectively. The O-related peaks O_{III}, $O_{IV/V}$ increase with increasing CO_2 flow (see solid and dashed spectra in Fig.3); the corresponding concentrations in epilayer #2a are seven times as great as in epilayer #1a. In O-implanted SiC samples, it was demonstrated that the formation of O_{III} and $O_{IV/V}$-centers saturates for implanted O concentrations $\geq 10^{17}cm^{-3}$ [2]. The fact that O related centers cannot be observed in the DLTS spectrum of epilayer #3a confirms indirectly the saturation behavior of O_{III} and $O_{IV/V}$ also for the investigated O-doped epilayers. According to the high doping level of epilayer #3a ($N_D \approx 4x10^{18}cm^{-3}$) and the limit of the sensitivity of the DLTS system of $N(defect)/N_D \approx 10^{-5}$, $[O_{III}]$ and $[O_{IV/V}]$ in epilayer #3a are estimated to be equal to or lower than approx. $5x10^{13}cm^{-3}$; this value agrees roughly with the O-related

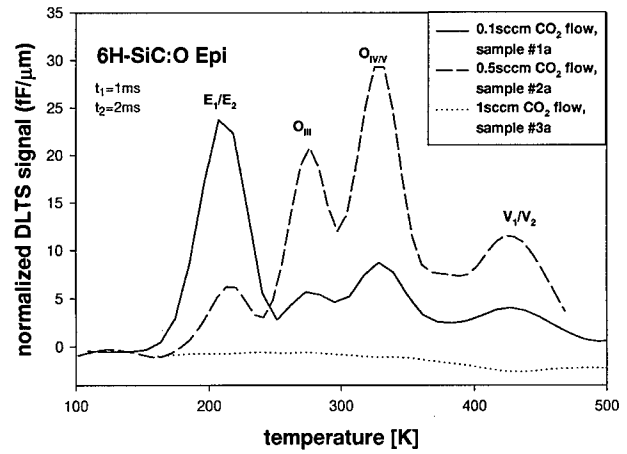


Fig.3: Normalized deep level transient spectroscopy (DLTS) spectra (time window 1ms/2ms) taken on 6H-SiC epilayers #1a, #2a and #3a.

defect concentrations determined in epilayer #2a.
Investigations taken on O-doped 4H-SiC epilayers provide identical results.

	Ionization energy meV	Concentration $x10^{13}cm^{-3}$
O_{III}	508/554	2.1
$O_{IV/V}$	608/661	2.9
V_1/V_2	607/677	0.8

Table 3: DLTS results for epilayer #2a: Ionization energies and concentrations of observed defect centers.

Discussion

4H/6H-SiC epitaxial layers doped with oxygen during the CVD process reveal the same O-related defect centers like O-implanted samples. In addition, the presence of O during the CVD growth of SiC layers strongly enhances the incorporation of N atoms. At the present, the driving force for the enhanced incorporation of N is unknown. Based on the observation that the growth rate of SiC is strongly reduced in the presence of O, we suggest that the growth mechanism is modified. During the CVD growth, "high temperature oxidation" of C and Si occurs. At 1500°C, the equilibrium pressure of CO is higher than that one of SiO leading to a "pronounced" evaporation of C from the growth front. In this way, the probability for the incorporation of N atoms is enhanced. The oxidation process consumes a large portion of oxygen during the CVD growth; as a consequence, the concentration of observed O-related defect centers is smaller (saturation concentration $[O_{III+IV+V} \approx 5x10^{13}cm^{-3}]$) than the corresponding concentration achieved in O-implanted samples ($[O_{III+IV+V} \approx 2x10^{17}cm^{-3}]$). In addition, O atoms could form complexes or precipitates together with C atoms which reside at interstitial lattice sites. In this way, additional C vacancies are provided, which can preferentially be occupied by N atoms. In order to clear up this growth mechanism, further experiments are required.
This doping technique could also be used during the modified Lely growth to fabricate n-type 4H/6H-SiC substrates with extremely low resistivity.

Summary

4H/6H-epilayers could be doped with O during the CVD process by additional CO_2 flow. The incorporated O atoms form identical defect centers as already observed in O-implanted samples. In addition, the presence of O atoms during the CVD process strongly enhances the incorporation of N atoms.

Acknowledgements

This work was partially supported by the Deutsche Forschungsgemeinschaft (SFB 292) and by the Ministry of Education, Science and Culture of Japan.

References:

[1] T. Dalibor, G. Pensl, T. Yamamoto, T. Kimoto, H. Matsunami, S. G. Sridhara, D. G. Nizhner, R. P. Devaty, W.J. Choyke, Mater. Sci. Forum Vols. 264-268 (1998), p.553.
[2] T. Dalibor, H. Trageser, G. Pensl, T. Kimoto, H. Matsunami, D. Nizhner, O. Shigiltchoff, W. J. Choyke, Mater. Sci. & Eng. B 61-62 (1999), p.454.
[3] A. Uedono, S. Tanigawa, T. Ohshima, H. Itoh, Y. Aoki, M. Yoshikawa, I. Nashiyama, J. Appl. Phys. 86 (1999), p.5392.

Materials Science Forum Vols. 353-356 (2001) pp. 463-466
© 2001 Trans Tech Publications, Switzerland

Electrical Activity of Isolated Oxygen Defects in SiC

A. Gali[1], D. Heringer[1], P. Deák[1], Z. Hajnal[2],
Th. Frauenheim[2] and W.J. Choyke[3]

[1] Department of Atomic Physics, Technical University of Budapest,
Budafoki út 8, HU-1111 Budapest, Hungary

[2] Department of Physics, Theoretical Physics, University GH Paderborn,
Warburgstr. 100, DE-33095 Paderborn, Germany

[3] Department of Physics and Astronomy, University of Pittsburgh,
Pittsburgh PA 15260, USA

Keywords: Occupancy Level, Oxygen, Spin Distribution

Abstract. Ab initio LDA calculations have been carried out for the isolated oxygen impurity in 3C(cubic) and 4H(hexagonal) silicon carbide. Cluster models with localized basis functions were used to calculate vibrational frequencies and spin distributions while supercell calculations were used to determine the relative stabilities and occupancy levels.
The substitutional oxygen has been studied in the 2+/+/0/-/2- charge states on both the C and Si site, and compared in stability to interstitial oxygen. It has been found that oxygen at the carbon site (O_C) is the most stable defect and it is an on-center double donor in 3C-SiC. The characteristic vibration frequencies and the spin distributions for the paramagnetic state are given. O_{Si} has a double donor level in the lower half of the band gap. O_i is also electrically active with complicated bonds. The similar behavior of the O_C has been found in 4H-SiC, however O_{Si} is proven to be an amphoteric defect in 4H-SiC.

Introduction MOS devices can be built from SiC because its native oxide is SiO_2. Oxygen may enter the bulk of the SiC crystal as an impurity during processing but it is also a contanimant of the SiC powder used to grow the crystals. It is well-known that oxygen is electrically inactive in its most stable (interstitial) form in silicon, but it can form electrically active defects, like thermal double donors (TDD)[1]. After irradiation and heat treatment of the silicon sample oxygen are trapped into vacancies, form the so-called A-center. In a defect-molecule model, the dangling bonds around the vacancy form quasi-atomic s and p states occupied by four electrons, which interact with the s and the p orbitals of the oxygen atom with six valence electrons. As a result fully occupied a_1 and t_2 bonding orbitals accommodated 8 electrons and the remaining two electrons go to the anti-bonding a_1^* orbital with an empty t_2^* state above that. Due to a dynamic Jahn-Teller effect the oxygen moves out of the on-center position along the [001] direction (C_{2v} symmetry) forming two strong bonds with the Si atoms and leaving two Si dangling bonds behind which create a long bond. The t_2^* states split and they are responsible for the acceptor activity of this center in silicon. It is of interest whether the substitutional or the interstitial oxygen is more stable in SiC and whether oxygen is active. Electrical activity related to oxygen has been reported[2] in O^+ implanted 4H and 6H-SiC. It is found by the deep level transient spectroscopy (DLTS) technique that two shallow donor-like oxygen related centers were created yielding ionization energies at E_v+(2.85-2.87) eV and E_v+(2.80-2.82) eV in 6H, at E_v+(2.99-3.03) eV and E_v+(2.84-2.88) eV in 4H. Three deep acceptor-like oxygen related centers have been found both in 6H and 4H-SiC. These levels are around E_v+2.4 and E_v+2.6 eV. The microscopic origin of these centers are not known. Our paper takes the first step to in this direction by examining the properties of isolated oxygen defects in SiC.

Although at present the technologically important polytypes are the hexagonal 4H and 6H-SiC, cubic 3C-SiC is easier to examine from the theoretical point of view because 3C-SiC has two basis atoms/unit cell comparing to eight and twelve in 4H and 6H-SiC, respectively. Since the calculation

time increases as the third power of the volume size, exploratory calculations were performed in 3C-SiC. Starting from the results obtained on O in 3C-SiC, the most important forms of the isolated oxygen were recalculated in 4H-SiC. The investigation of the site dependencies is not the purpose of this paper, so the oxygen was always placed at the cubic site in 4H-SiC.

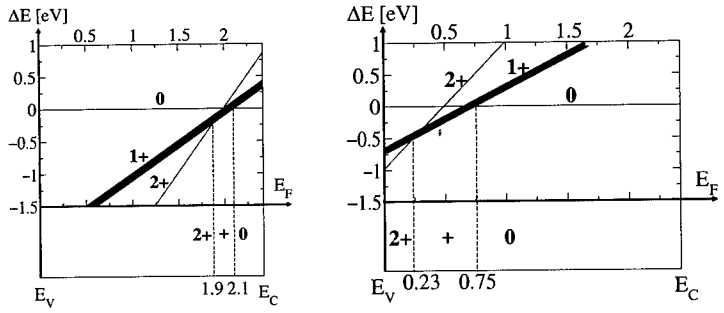
The only theoretical studies we are aware of in SiC considered oxygen solely as interstitials in the neutral charged states, using molecular and supercell models[3, 4]. Ventra *et al.* has found that the oxygen clustering in the (110) plane in 3C-SiC could be energetically feasible which is very similar to the possible core of the thermal double donor in silicon. Relative stabilities with respect to other isolated oxygen impurities has not been investigated in that paper. In an earlier work we calculated interstitial and substitutional oxygen in the neutral state in a molecular cluster modeling 3C-SiC [5] but neither relative stabilities nor occupancy levels were given. Those MCM calculations were recalculated in bigger basis set (for silicon and carbon 8 s-type and 8-type Gaussian-type orbitals (GTO) were used; 3 x s + 3 x p and 8 x s + 8 x p GTOs were taken for hydrogen and oxygen, respectively) in a molecular cluster where the charge oscillations between the Si and C shells around the defect were avoided (for more details see Ref. [6]).

Calculational method This time first principles calculations were carried out in supercells (SC) to determine the relative stabilities and occupancy levels together with molecular cluster calculations to give the spin distributions and local vibration modes. In the SC calculations 3C-SiC was modeled by a 32 atom bcc unit using the FHI98MD code [7]. One electron states were expanded as a plane wave basis with a relatively high kinetic energy cut-off of 64 Ry. Troullier-Martins pseudopotentials were used [8]. Convergence of relative stabilities and localized one-electron levels with SC size were tested on a 128 atom fcc unit. In that case 36 Ry cut-off and the pseudopotential of Ref. [9] were used as well as in the 96 atom hexagonal 4H supercell calculations. Summation over the reduced Brillouin-zone of the supercell were carried out using 2x2x2 and 3x3x3 MP schemes[10] for the all units depending on the nature (localization, dispersion) of the defect states. For the details of applied corrections due to the dispersion and LDA gap, see Ref. [11].

Results on O_C in 3C-SiC We have considered the oxygen substitutional on the carbon site (O_C) in 3C-SiC, first. Neutral O_C was found to remain on-center. The Si-O distances are 2.00 Å. The localized anti-bonding a_1^* one-electron level is lying above the conduction band edge by 0.54 eV, therefore an EMT orbital gets occupied instead. The molecular cluster calculation provided a reconstruction with C_{2v} symmetry because the cluster "gap" was much higher and the localized a_1^* state was coupled. If the gap is reproduced correctly (as in the SC calculation corrected for the LDA gap) then the electrons should occupy the conduction band states, i.e. O_C is a double effective mass like donor in 3C-SiC like sulfur in silicon. (The off-center configuration with C_{2v} symmetry obtained in the molecular cluster calculation is a metastable state with a total energy of about 2.0 eV higher.) The doubly occupied delocalized level splits off from the conduction band to E_c-0.44 eV. In the single and double positively charged states no metastable state have been found and the geometry differs only slightly from the neutral case. The relative energy of the ++/+/0 charge states as a function of the Fermi-energy as well as the occupation levels for the O_C defect in 3C-SiC are shown in Fig. 1(a). (The value of the relative stabilities are convergent within 0.1 eV checked on 128 atom SC.)

Because the O_C^+ is EMT donor, the results in MCM for the spin distribution would not be reliable in this case. However, the charge distribution of the single occupied level projected into (110) plane shows that the electron is sufficiently localized on the oxygen atom to detect it by EPR. The shape of the electron distribution is spherical therefore the Fermi-contact hyperfine interaction must be much bigger than the dipole-dipole one. O_C^{++} is stable for Fermi levels up to E_v+1.9 eV. The characteristic local vibration modes (LVM) are falling into the continuum (around 900 cm^{-1}).

Results on O_{Si} in 3C-SiC We have found that the most stable configuration for the oxygen at the silicon site (O_{Si}) in the neutral state is the on-center position with 1.92 Å C-O distances in the 32 atom unit. A doubly occupied localized a_1^* level appears at E_v+0.33 eV and the empty t_2^* is at



(a) O_C (b) O_{Si}

Fig. 1. The occupation levels of the substitutional oxygen impurities. The thickness of the line represents the uncertainty due to the neglect of spin polarization.

E_c+0.34 eV. However, if the oxygen is placed in the [001] direction with 0.34 Å forming a bridge between two carbon atoms with a distance of 1.61 Å and an angle of 122° then the total energy of this structure is only 0.05 eV higher than of the on-center's one. The barrier energy is very small, 0.13 eV from the on-center to the off-center position. In the 128 atom unit careful test were carried out, three neighbor relaxation were allowed during the geometry optimization. In this case, no metastable state has been found: the structure with T_d symmetry (1.89 Å C-O distances) has the lowest energy. The doubly occupied localized a_1^* level appears at E_v+0.71 eV and the empty t_2^* is at E_c+0.64 eV in this case. The 32 atom calculations provided inadequate results for the occupation levels of O_{Si}. Thus, the occupation levels are determined in the 128 atom unit for O_{Si}. It is clear from the obtained electronic structure that the O_{Si} is a rather deep donor and no acceptor activity takes place in 3C-SiC.

The relative stabilities of the O_{Si} defect in different charge states is shown in Fig. 1(b). The spin distribution of the paramagnetic O_{Si}^+ is 3.1% on the oxygen atom (purely s-like), and 19% on each C neighbor (purely p-like). Because of the localized basis in MCM calculation the localization could be overestimated by a factor of two. The characteristic LVM's are too low to measure.

Results on O_i in 3C-SiC The interstitial oxygen forms complicated bonds between oxygen and carbon (see Fig. 2), and the oxygen with two silicon atom provide two fully occupied levels in the band gap very close to the valence band top (within 0.1 eV). The LVM of 1035 cm^{-1} and 890 cm^{-1} belongs to the C-O, and Si-O stretch mode, respectively. The symmetry of this structure is C_{1h}. (In the earlier paper [5] wrong numbers were given for these stretch modes!)

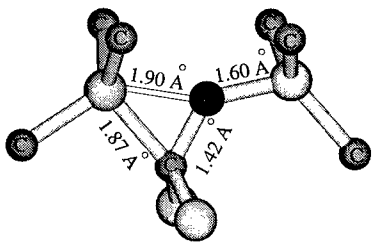


Fig. 2. The relaxed structure of interstitial oxygen in 3C-SiC

Relative stabilities We have investigated the relative stabilities between the isolated oxygen impurities depending on Si/C ratio and the position of the Fermi level. We have found that under any

circumstances O_C is more stable over O_{Si} by more than 5 eV and it is more stable than O_i by at least 3.5 eV! Therefore during growth O_C is the prefered form of the isolated oxygen. In addition, the binding energy of O_{Si} to a Si-vacancy with respect to O_i is 7.3 eV while the binding energy of O_C to a C-vacancy respect to O_i is 10.1 eV. Therefore diffusing O_i prefers the C-vacancy against the Si-vacancy by 2.8 eV if both are present. The difference between the formation energies are so large that the $[O_C] \gg [O_i] \gg [O_{Si}]$ relation may be predicted for all polytypes based on the calculations in 3C-SiC.

Results on O_C in 4H-SiC Based on the results in 3C-SiC, O_C has been first examined in 4H-SiC. O_C is also an on-center in 4H-SiC with C_{3v} symmetry. The doubly occupied a_1^* level corresponding the anti-bonding combination of O and Si atoms is now in the band gap. The ++/+ and +/0 occupation levels are at E_v+2.93 eV and E_v+2.97 eV, respectively, which are very close to the measured occupation levels of the oxygen-related shallow donors in 4H-SiC [2]. Therefore O_C is also a double donor in 4H-SiC, but it is not EMT-like as in 3C-SiC. In this case the spin distribution for O_C^+ can be calculated in MCM. The spin is localized on oxygen with 4.5% (pure s-like) and on the Si neighbors with 61% (pure p-like). Based on this facts we assign the O_C defect to the origin of the shallow donor centers found in 4H and 6H-SiC.

Results on O_{Si} in 4H-SiC The possible acceptor activity of O_{Si}^- is examined in 4H-SiC. In the neutral state the symmetry is C_{1h} (only slightly distorted from C_{3v} with oxygen being 0.12 Å away from the on-center position). The double occupied localized one-electron level is at E_v+0.72 eV (practically same as in 3C-SiC) and the first unoccupied level is at E_v+2.28 eV, therefore acceptor activity can be expected. (The ++/+ and +/0 occupation levels should resided in the same place as in 3C-SiC.) In the negatively charged state the oxygen moves away from the on-center position (0.44 Å) bonding to two C closer than to the other ones (this resembles to C_{2v} symmetry in a cubic cell, as the A-center in silicon). The 0/- level is at E_v+2.0 eV. This value is far from the measured oxygen-related acceptor level at E_v+2.6 eV in 4H-SiC. More work is needed to identify the acceptor centers which are probably related to more complex defects.

Summary To summarize, O_C is far the most stable oxygen impurity in SiC. It is a relatively shallow double donor (EMT in 3C-SiC but not in 4H-SiC). O_{Si} is a deep double donor in 3C-SiC, but it can also act as an acceptor in 4H-SiC. We assign the DLTS donor centers to O_C in 4H-SiC.

Acknowledgement Support by the Hungarian OTKA T-22139, FKFP 0289/97 and AKP 97-92 2,2/27 grants as well as the bilateral US–Hungarian (JFNo. 667), German-Hungarian (DFG -MTA No. 118) and Swedish-Hungarian (IVA-MTA No. 36) projects and the grant PHY970006P from the Pittsburgh Supercomputing Center are appreciated.

References

[1] C. S. Fuller, J. A. Ditzenberger, N. B. Hannay, and E. Buehler, Phys. Rev. B 96, (1954), p. 833.

[2] T. Dalibor *et al.*, Mater. Sci. Forum 264-268, (1998), p. 533.

[3] M. A. Roberson, S. K. Estreicher, and C. H. Chu, J. Phys.: Condens. Matter 5, (1993), p. 8943.

[4] M. D. Ventra and S. T. Pantelides, Phys. Rev. Lett. 83, (1999), p. 1624.

[5] P. Deák *et al.*, Mater. Sci. Forum 264-268, (1998), p. 279.

[6] A. Gali, P. Deák, R. P. Devaty, and W. J. Choyke, Phys. Rev. B 60, (1999), p. 1620.

[7] M. Bockstedte, A. Kley, J. Neugebauer, and M. Scheffler, Comp. Phys. Comm. 107, (1997), p. 187.

[8] N. Troullier and J. L. Martins, Phys. Rev. B 43, (1991), p. 1993.

[9] M. Bockstedte, private communication.

[10] H. J. Monkhorst and J. K. Pack, Phys. Rev. B 13, (1976), p. 5188.

[11] B. Aradi *et al.*, this volume.

Materials Science Forum Vols. 353-356 (2001) pp. 467-470
© 2001 Trans Tech Publications, Switzerland

Beryllium-Related Defect Centers in 4H-SiC

Michael Krieger, Michael Laube, Michael Weidner and Gerhard Pensl

Institute of Applied Physics, University of Erlangen-Nürnberg,
Staudtstr. 7/A3, DE-91058 Erlangen, Germany

Keywords: Acceptor, Beryllium, Diffusion, Doping by Implantation, p-Type 4H-SiC

Abstract It is demonstrated that beryllium (Be) is a strong diffusing species in SiC. Two acceptor-like defect centers are detected in Be-implanted, p-type 4H-SiC epilayers; their ionization energies are: $\Delta E(Be_1)$ = (535/585) meV and $\Delta E(Be_2)$ = (925/1008) meV. Be_1-center is thermally stable up to 620K, while Be_2-center is thermally unstable. In Be-implanted n-type 4H-SiC a series of peaks is observed in the DLTS spectra; among the observed peaks the K_1-center is not yet described in the literature.

Introduction

For vertical electronic power devices, SiC substrates with low resistivity are required. In order to reach this aim, acceptors with small ionization energy ΔE and high solubility are necessary. At the present knowledge, aluminum (Al) providing an ionization energy $\Delta E(Al)$ of approx. 200meV is the acceptor with the smallest ionization energy. Depending on the doping level and compensation the degree of ionization of Al acceptors at room temperature is only a few percent; therefore, an intensive search for acceptors with suitable properties is under way. Beryllium (Be) located in the second column of the periodic table is a possible candidate for a double acceptor in SiC assuming that the Be atoms reside at silicon (Si) or carbon (C) lattice sites [1]. On the other hand, Be atoms which are of small size could also act as donors, if they would occupy an interstitial lattice site. Up to now only a few data are published on the electrical properties of Be-related centers in SiC (see e.g. [2,3]), which do not provide enough information to clarify the problems addressed above.
In this paper, we predominantly report on electrical properties of Be-implanted p-/n-type 4H-SiC epilayers. It turns out that there arise experimental difficulties to achieve p-type conductivity in low-doped, n-type 4H-SiC epilayers by implantation of Be. DLTS spectra taken on Be-implanted p-/n-type 4H-SiC epilayers reveal several energetically deep Be-related defect centers.

Experimental

For the employed electrical analysis methods (Hall effect, deep level transient spectroscopy (DLTS), capacitance-voltage (C-V) technique), n-type 4H-SiC epilayers doped with nitrogen [N] = 9.7×10^{15} cm^{-3} and p-type 4H-SiC epilayers doped with Al ([Al] = 8.5×10^{15} cm^{-3}) were used. Secondary ion mass spectrometry (SIMS) profiles were taken on N-doped 4H-SiC epilayers ([N] = 1.8×10^{15} cm^{-3}). Box-shaped Be profiles were generated to a depth of 1.8μm by eight-fold implantation of Be as shown in Fig. 1. The Be-implanted samples were annealed in two steps: pre-anneal at 900°C for (3 to 10)h followed by a final anneal at (1400 to 1700)°C for 30min.

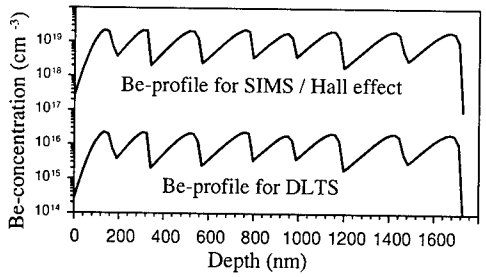


Fig.1. Be box-shaped profiles formed by eight-fold implantation; the Be-profiles are calculated after TRIM-C.

Results and Dicussion

In order to remove the implantation damage and to activate the implanted dopants in SiC, annealing temperatures up to 1700°C are usually required. Based on our experience with boron (B) [4, 5], which is a fast diffusing species in SiC, we also expected a strong diffusion for Be. We have, therefore, in a first step investigated the Be diffusion in the temperature range between 1400°C and 1700°C. SIMS analyses of annealed box-shaped Be profiles (not shown here) resulted in a strong Be diffusion to the bulk and to the surface leading to a considerable out-diffusion of Be atoms (residual Be fluence: 20% / 7% subsequent to an anneal at 1400°C / 1700°C for 30min each). These results compare well with diffusion experiments reported by Henkel et al. [6].

The strong Be diffusion introduced experimental difficulties to achieve p-type films by Be implantation in n-type 4H-SiC epilayers. Hall effect measurements taken on Be-implanted and annealed films indicated p-type conductivity (not shown here). However, the measurement points were affected by a large uncertainity, which made it impossible to determine an ionization energy for the prevailing acceptor; the resistivity at room temperature resulted in $\rho = 3x10^3\,\Omega cm$.

DLTS spectra taken on Be-implanted and subsequently annealed p-type 4H-SiC epilayers are displayed in Fig. 2. The spectra consist of two pronounced peaks termed Be_1 and Be_2; it is assumed that both peaks are Be-related. In order to be able to make a clear chemical assignment to Be, DLTS spectra have to be taken on SiC samples, which are implanted with a radioactive isotope (DLTS-RI) [7], e.g. the radioactive isotope ^7Be, which decays with a lifetime of 53 days into the stable isotope ^7Li. Corresponding DLTS-RI investigations are under way. An Arrhenius evaluation of the DLTS data assuming $\sigma=T^0$ / $\sigma \propto T^{-2}$ results in energy levels at $\Delta E(Be_1) = E_V + (535/585)$ meV and $\Delta E(Be_2) = E_V + (925/1008)$ meV; the corresponding defect concentrations are: $N(Be_1) = 1x10^{14}\,cm^{-3}$, $N(Be_2) = 2x10^{15}\,cm^{-3}$. It turns out that the Be_1-center is stable during the temperature scan of the DLTS measurement, while the Be_2-center strongly decreases with increasing number of DLTS scans that is by repeated exposure to heat treatments up to 620K (see spectra (a), (b) and (c) in Fig. 2).

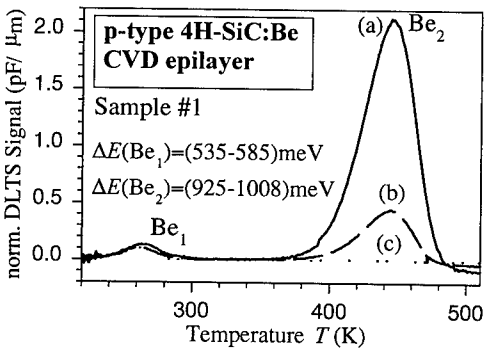


Fig.2. DLTS spectra of Be-implanted and annealed (900°C/3h and 1600°C/30min) Al-doped 4H-SiC samples ([Al] = $8.5x10^{15}\,cm^{-3}$). DLTS spectra are taken: a) directly after implantation and annealing, b)/c) subsequent to 3/6 DLTS temperature scans up to 620 K.

Due to the fact that the Be-implanted samples have been exposed to an annealing step at 1700°C prior to the DLTS measurement, we assume that the Be_2-center is formed during the ramp down of the annealing temperature.

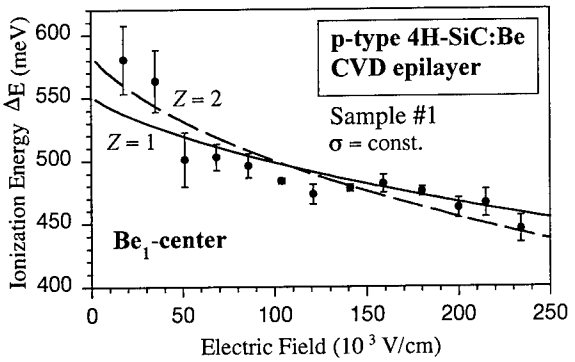


Fig.3. Ionization Energy ΔE(Be_1) as a function of the applied electric field. The full dots are obtained from double-correlated DLTS; the solid/dashed curves are calculated taking into account the Poole-frenkel correction after [8]; Z = 1 and Z = 2 are the assumed charge states of the defect.

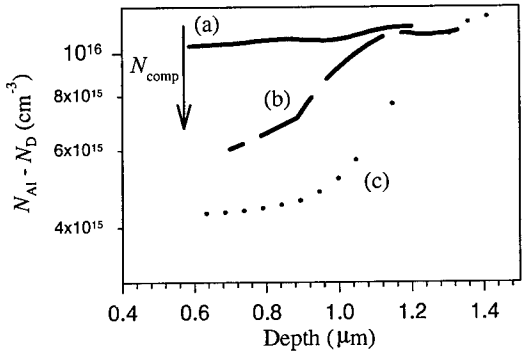


Fig.4. Net Al concentration [N_{Al}-N_D] as a function of the depth determined by C-V; the measurements are taken on the identical samples as described in Fig. 2.

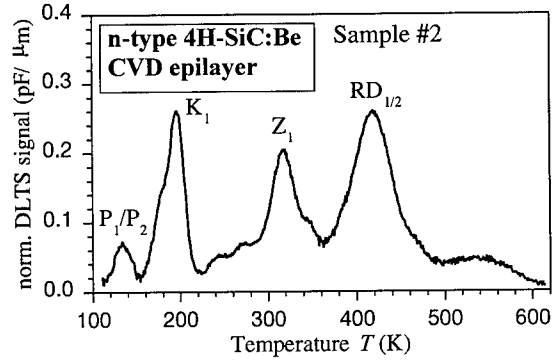


Fig.5. DLTS spectrum taken on a Be-implanted and annealed n-type 4H-SiC sample.

Double correlated DLTS investigations reveal that the ionization energy of both centers depends on the applied electric field; for the Be_1-center, the correponding dependence is shown in Fig. 3. The solid and dashed curve in Fig. 3 are calculated according to the Poole-Frenkel effect [8]. The dependence on the electric field implies that both centers are acceptor-like. Within the measurement uncertainty (see error bars in Fig. 3) there is no clear decision possible whether the final acceptor state (after emission of a hole) is singly (Z=1) or doubly (Z=2) charged. The different peak heights of the Be_1-center and the Be_2-center and their extremely different thermal stability, however, indicate that the two peaks are not caused by a single defect representing the two different charge states of a double acceptor.

In parallel to the DLTS investigations, we have conducted C-V measurements on the identical samples (see Fig. 4). With increasing number of DLTS scans, the net Al acceptor concentration (N_{Al} - N_D) decreased in the surface-near, Be-implanted region (see curves (a), (b) and (c) in Fig. 4). This decrease of the net acceptor concentration can only be caused by an increase of the compensation N_D. A possible mechanism, which could explain the observed phenomena, is the formation of Be donors; the required Be atoms may be released from the Be_2-complexes or precipitates, which are thermally dissolved. The nucleation and growth of such precipitates may originate from a

supersaturation of Be at lower temperatures [6, 9]. DLTS spectra have been taken on Be-implanted n-type 4H-SiC samples; they reveal several peaks (see Fig. 5 and Table 1): peaks P_1/P_2, Z_1 and $RD_{1/2}$ are intrinsic defects [10], defect K_1 is not yet described in the literature. All these peaks, however, are thermally stable; their heights do not increase as a function of the number of DLTS scans. Alternatively, the required donors may energetically be located in the middle of the band gap of 4H-SiC, which is not accessible for standard DLTS. Optical DLTS experiments have to be conducted to clarify this open question.

Defect	Concentration (10^{13} cm^{-3})	Ionization Energy (meV)	
		σ = const.	$\sigma \sim T^{-2}$
P_1/P_2	1.9	221	246
K_1	9.7	367	404
Z_1	5.8	636	696
$RD_{1/2}$	10	826	904

Table 1. Defect parameters obtained from the analysis of DLTS spectra taken on Be-implanted n-type 4H-SiC.

Summary

Implanted Be atoms are a fast diffusing species in SiC at temperatures above 1400°C. No energetically shallow Be-related acceptors in 4H-SiC could be formed by Be implantation. As a consequence, we like to point out that Be is not suited to generate p-type SiC substrates with low resistivity.

Two pronounced defect centers (Be_1, Be_2) are created in Al-doped 4H-SiC by Be implantation; their energy levels are: $\Delta E(Be_1) = E_V + (535/585)$ meV and $\Delta E(Be_2) = E_V + (925/1008)$ meV. Be_1-center is thermally stable during DLTS scans, while Be_2-center thermally dissociates at temperatures up to 620K. Along with the decrease of the Be_2-center, a decrease of the net Al acceptor concentration in the surface-near, Be-implanted region is observed.

Acknowledgement. The support of this work by the German Science Foundation (Sonderforschungsbereich 292) is gratefully acknowledged.

References

[1] P. G. Baranov, Mater. Sci. Forum **264-268** (1998), p. 581.
[2] Yu. P. Maslakovets, E. N. Mokhov, Yu. A. Vodakov, and G. A. Lomakina, Sov. Phys.-Solid State **10** (1968), p.634.
[3] N. Ramungul, V. Khemka, Y. Zheng, R. Patel and T. P. Chow, IEEE Trans. Electron Devices **46** (1999), p. 465.
[4] M. Laube, G. Pensl and H. Itoh, Appl. Phys. Lett. **74** (1999), p. 2292.
[5] M. Laube, G. Pensl, Mater. Sci. Forum **338-342** (2000), p.941.
[6] T. Henkel, Y. Tanaka, N. Kobayashi, S. Nishizawa, and S. Hishita, Mater. Sci. Forum **338-342** (2000), p.953.
[7] M. Lang, G. Pensl, M. Gebhard, N. Achtziger and M. Uhrmacher, Appl. Phys. A **53** (1991), p. 95.
[8] J. L. Hartke, J. Appl. Phys. **39** (1968), p. 4871.
[9] P. W. Voorhees, J. Stat. Phys. **38** (1985), p. 231.
[10] T. Dalibor, G. Pensl, H. Matsunami, T. Kimoto, W. J. Choyke, A. Schöner, N. Nordell, phys. stat. sol. (a) **162** (1997), p. 199.

Materials Science Forum Vols. 353-356 (2001) pp. 471-474
© 2001 Trans Tech Publications, Switzerland

Band Gap States of Cr in the Lower Part of the SiC Band Gap

G. Pasold[1], N. Achtziger[2], J. Grillenberger[1] and W. Witthuhn[1]

[1] Institut für Festkörperphysik, Friedrich-Schiller-Universität Jena,
Max-Wien-Platz 1, DE-07743 Jena, Germany

[2] Fraunhofer-Institut für Integrierte Schaltungen IIS-A,
Am Weichselgarten 3, DE-91058 Erlangen, Germany

Keywords: Chromium, Deep Level, DLTS, Transition Metal, Vanadium

Abstract: Bandgap states of Cr in p-type $4H$-SiC (Silicon Carbide) were investigated by radiotracer-DLTS (Deep Level Transient Spectroscopy). Doping with the radioactive isotope ^{51}Cr was done by recoil implantation followed by annealing ($4h$, $1600K$). Repeated DLTS measurements during the elemental transmutation of the isotope to ^{51}V, reveal the corresponding concentration changes of bandgap states. In the lower part of the band gap accessible by these experiments, we find two Cr-releated levels at $0.53eV$ and $0.63eV$ above the valence band edge, and no level of Vanadium.

1 Introduction

Because of its excellent properties, Silicon Carbide (SiC) will play an important role as a semiconductor for power devices, for high frequency electronics and in high temperature or high radiation environments. Based on magnetic resonance [1], Deep Level Transient Spectroscopy (DLTS) experiments [2, 3, 4, 5, 6] and on theory [7], several transition metals are known to form electrically active band gap states in this material. In the case of chromium, acceptor-like states at about $0.15eV$ and at $0.74eV$ below the conduction band edge of the n-type $4H$-SiC have definitely been identified by radiotracer DLTS [3]. For the first time, the present work provides information on deep levels of chromium and vanadium impurities in the lower part of the band gap by performing DLTS on p-type $4H$-SiC.
The chemical identification of these levels is done by using the radioactive isotope ^{51}Cr. The correspondence of concentration changes of the levels (DLTS spectra depend linearly on concentrations in the present case of low trap concentrations) to the well known elemental transmutation Cr $\rightarrow$ V is used. This technique allows the estimation of the fraction of implanted atoms which are electrically active, too.

2 Experiment

The crystals used in this work were commercial p-type $4H$-SiC CVD-epitaxial layers on heavily p-doped ($5 \times 10^{18} cm^{-3}$) substrates (grown by Cree Inc.). Capacitance-voltage profiling revealed a shallow doping concentration of the epitaxial layer ($|N_A - N_D|$) of $8(2) \times 10^{15} cm^{-3}$. Doping with radioactive ^{51}Cr (decaying to ^{51}V with a nuclear half-life of $T_{1/2} = 27.7d$) was done at the tandem accelerator of the University of Erlangen-Nürnberg by recoil implantation following the (α, n) nuclear reaction with a fluence in the range of $10^{10} cm^{-2}$ [8].
Doping with stable isotopes (^{52}Cr and ^{51}V) was done at the tandetron ion accelerator JULIA of the University of Jena. We used multiple implantations ($1...3MeV$) to achieve fairly homogeneous Cr and V concentrations of about $5 \times 10^{14} cm^{-3}$.

The implantation damage was removed by thermal annealing in sealed quartz ampoules for $4h$ at $1600K$ in oxygen atmosphere. The formed oxygen layer was then removed by etching with hydrofluoric acid before contact preparation (evaporation of $500Å$ Ti $Ø$=$0.5mm$ as Schottky-contacts, $500Å$ Al full area as Ohmic backside) [3].
Before and after the entire sample preparation process, the initial as well as the final number of ^{51}Cr atoms incorporated were determined by γ-ray spectroscopy.
The DLTS measurements were performed with a commercial DLTS system (DL-8000 by Bio-Rad Laboraties). The spectra were taken between 200 and $650K$ (below $200K$ the shallow doping 'freezes out'). The reverse bias U_R was set to $5V$. To fill the traps, the reverse bias was degraded to zero volts ($U_P = 0V$) for $1ms$. The DLTS time constants τ_{ref} were varied from approximately. $1ms$ to $1s$. The spectra shown correspond to $\tau_{ref} = 12.48ms$.

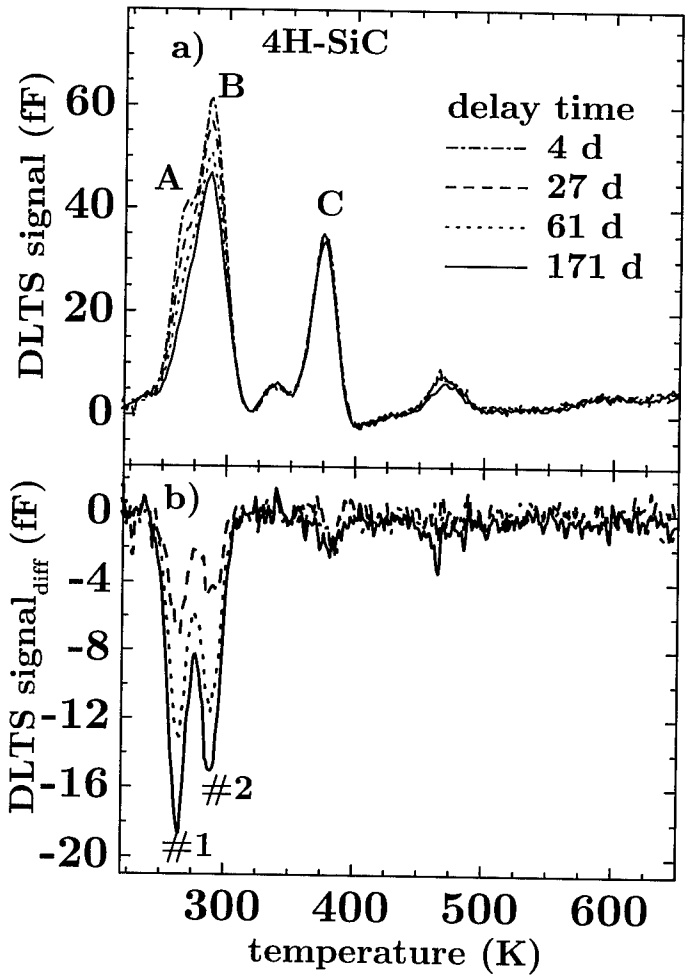


Fig. 1: *a)DLTS-spectra of p-type 4H-SiC, recoil implanted with ^{51}Cr, subsequently measured during the elemental transmutation to ^{51}V. b) DLTS-spectra obtained by subtracting the initial spectrum (measured 4d after annealing) from the subsequently measured spectra.*

3 Results

DLTS spectra of one sample implanted with ^{51}Cr are shown in Fig. 1a. The peaks A and B are diminishing during observation. Fig. 1b shows the difference signals formed by substracting the initially measured spektrum from the others. Thus, time independent signals are eliminated. Negative peaks, labeled ♯1 and ♯2, indicate decreasing concentrations. Fig. 2 shows the heights of the peaks ♯1 and ♯2 from the difference spectra during observation. Exponential curves with the half-life of the nuclear decay ($27.7d$) demonstrate the correspondence with the elemental transmutation and justify the assignment of the peaks to ^{51}Cr.
The level parameters of the Cr-related peaks ♯1 and ♯2 are derived from the difference spec-

tra as usual (assuming σ=const.) [9]. They are summarized in Tab. 1. An increasing signal is not detectable, i.e. a deep level caused by the daughter element vanadium does not exist in the investigated part of the band gap.

In Fig. 3, the initial measurement on a ^{51}Cr doped sample is compared to an unimplanted reference and to samples implanted with stable ^{51}V and ^{52}Cr. The shoulder labeled A is present in the Cr-implanted samples only. It is equivalent to the Cr-level ♯1. Peak B with parameters within the error margins of the Cr-level ♯2 is present in all spectra, i.e. there is an additional defect present that cannot be distinguished from the Cr-level ♯2 by standard DLTS. The existence of this additional defect contributing to peak B is also obvious in the radiotracer experiment. In Fig. 1a, a large peak B finally remains, though ^{51}Cr has vanished. Peak C is an unidentified implantation induced defect with an activation energy of $E_T - E_V = 0.81(2)eV$ and a capture cross section (σ) of $6 \times 10^{-15} cm^2$. It may be equivalent to a level found in similar experiments on p-type $6H$-SiC [10].

An effect of the electriç field strength ($F = 14...140 kV/cm$) on the emission time constant (Poole-Frenkel-Effekt) for the interesting peaks A and B is not detectable in the samples implanted with stable chromium. Though peak B contains an unidentified level in addition to Cr, the absence of any Poole-Frenkel-shift indicates that the chromium-levels ♯1 and ♯2 are donor like.

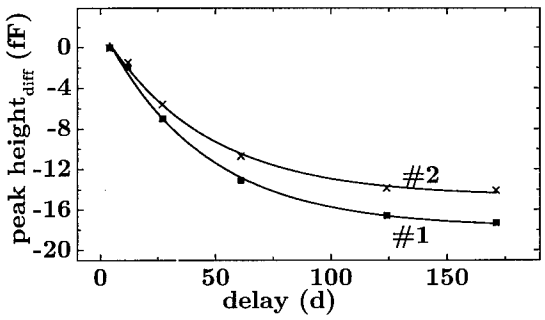


Fig. 2: *Peak height differences of the Cr-related peaks ♯1 and ♯2 versus delay time, measured during the transmutation of ^{51}Cr to ^{51}V. The solid lines are fitted exponential functions with the fixed half-life of the nuclear decay ($T_{1/2} = 27.7d$).*

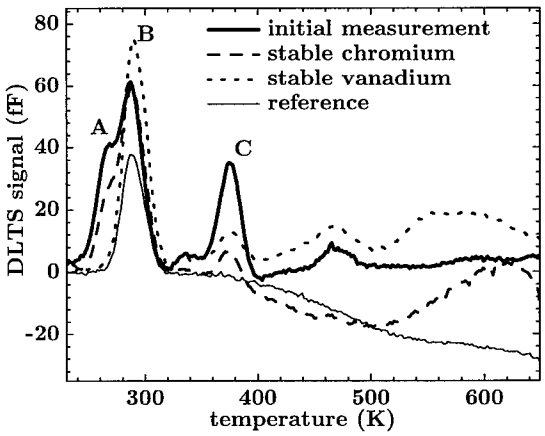


Fig. 3: *DLTS-spectra of p-type 4H-SiC, initial spectrum of a ^{51}Cr doped sample, samples implanted with stable Cr and stable V and a spectrum of an unimplanted part of a sample (reference contact).*

4 Discussion

Performing the tracer experiment, we can definitely assign the peaks ♯1 and ♯2 to chromium. These defects contain one Cr-atom. Peak ♯2 would not have been assigned safely to Cr without the tracer concept due to an underlying additional defect B. This intrinsic defect with the same level parameters as ♯2 probably is the well known D-center described as boron-vacancy-complex [4].

Because of the small energy difference between the two Cr levels, we propose the occupation of inequivalent lattice sites in the $4H$-SiC (quasi-cubic and -hexagonal sites). This interpretation has also been given for the splitting ($0.04eV$) of the Cr double acceptor state (around $E_C - 0.15eV$) [3, 11].

The degree of the electrical activation of the incorporated Cr-isotopes is determined as described in ref. [3]. It is in the order of 75% with an uncertainty of a factor of two. The same degree has been found for Cr in n-type SiC [3].
We shall now compare our data to theoretical results on Cr in $3C$-SiC. To do this, we are assuming that there is no valence band offset between $3C$ and $4H$. This alignement of SiC valence band edges is supported by various experiments [6, 11, 12]. In $3C$, a donor state of Cr in $3C$ at $1.45eV$ above E_V [7] and a double donor state at $E_V + 0.7eV$ is predicted [13]. The first one is too deep to be detected by DLTS, but the second one reasonably well corresponds to the Cr-level around $0.6eV$ (splitting ignored) determined in the present work. Thus, we assign the Cr-levels ♯1 and ♯2 to a (slightly split) double donor level of Cr in $4H$-SiC. The level scheme of Cr in $4H$-SiC is now completely determined, consisting of 4 levels: the double donor reported here, a midgap-donor not detectable by DLTS, but predicted by theory, and the acceptor and double acceptor levels already known [3].

Peak	♯1	♯2
E_T (eV)	E_V+0.54(1)	E_V+0.63(1)
$\sigma(10^{-15}cm^2)$	2	8

Tab. 1: *Energies and capture cross sections of Cr-related levels in 4H-SiC*

5 Conclusion

Based on radiotracer DLTS experiments and on a comparison to theory, a double donor level of Cr is identified in $4H$-SiC. Due to the occupation of inequivalent lattice sites, the level is split, with energies of $0.54eV$ and $0.63eV$ above the valence band edge. Combined with earlier experiments [3], the level scheme of Cr in $4H$ is now completely known. As expected, there is no level of vanadium in the lower part of the band gap.

Acknowledgement
The work was funded partially by the German BMBF and by the Deutsche Forschungsgemeinschaft (SFB196).

References

[1] J.Baur, M.Kunzer and J.Schneider, Phys.Stat.Sol.A **162** (1997), p. 153.
[2] T.Dalibor, G.Pensl, H.Matsunami, T.Kimoto, W.J.Choyke, A.Schöner and N.Nordell, Phys.Stat.Sol.A **162** (1997), p. 199.
[3] N.Achtziger, W.Witthuhn, Phys.Rev.B **57** (1998), p. 12181.
[4] A.A.Lebedev, Semiconductors **33** (1999), p. 107.
[5] J.Grillenberger, N.Achtziger, R.Sielemann and W.Witthuhn, J.Appl.Phys., at press.
[6] N.Achtziger, G.Pasold, R.Sielemann, C.Hülsen, J.Grillenberger and W.Witthuhn, submitted to Phys.Rev.B.
[7] H.Overhof, Mat.Sci.For. **258-263** (1997), p. 677.
[8] N.Achtziger, H.Gottschalk, T.Licht, J.Meier, U.Reislöhner, M.Rüb, W.Witthuhn: Appl.Phys.Lett. **66** (1995), p. 2370.
[9] P.Blood, J.W.Orton: The electrical Characterization of Semiconductors: Majority Carriers and Electron States (Academic Press, London, 1992) p. 407.
[10] J.Grillenberger, N.Achtziger, F.Günther and W.Witthuhn, Appl.Phys.Lett. **73** (1998), p. 3698.
[11] N.Achtziger, J.Grillenberger, W.Witthuhn, Mat.Sci.For. 264-268 (1998), p. 541.
[12] V.V.Afanasev, M.Bassler, G.Pensl, M.J.Schulz and E.Stein von Kamienski, J.Appl.Phys. **79** (1996), p. 3108.
[13] H.Overhof, University of Paderborn, Germany, private communication.

Materials Science Forum Vols. 353-356 (2001) pp. 475-478
© 2001 Trans Tech Publications, Switzerland

Tantalum and Tungsten in Silicon Carbide: Identification and Polytype Dependence of Deep Levels

J. Grillenberger[1], N. Achtziger[2], G. Pasold[1], R. Sielemann[3] and W. Witthuhn[1]

[1] Institut für Festkörperphysik, Friedrich-Schiller-Universität Jena, Max-Wien-Platz 1, DE-07743 Jena, Germany

[2] Fraunhofer-Institut für Integrierte Schaltungen IIS-A, Am Weichselgarten 3, DE-91058 Erlangen, Germany

[3] Hahn-Meitner-Institut Berlin, Glienicker Strasse 100, DE-14109 Berlin, Germany

Keywords: Band Offset, Deep Level, DLTS, Level Splitting, Polytype Dependence, Radiotracer, Tantalum, Tungsten

Abstract:
We characterize band gap states of tantalum and tungsten in n-type SiC (polytpes 4*H*-, 6*H*-, and 15*R*) by means of Deep Level Transient Spectroscopy (DLTS). To establish a definite chemical identification, the radioactive tracer isotopes ^{177}Ta and ^{178}W were used. Both elements have deep band gap states in the investigated polytypes. A comparison of level energies among the three polytypes confirms the validity of the "Rule of Langer-Heinrich".

Introduction

Its excellent material properties make the wide gap semiconductor silicon carbide (SiC) a good candidate to replace Si and/or GaAs in high power or high frequency electronics. The main bottleneck to the application of SiC devices on an industrial scale are the severe problems encountered in the growth of SiC bulk crystals. Several publications about the crystal growth of SiC report the use of tantalum crucibles to avoid graphitization during sublimation growth [1,2,3]. For high voltage devices thicker epitaxial layers are required. To increase the lifetime of the graphite susceptors, tantalum carbide (TaC) is used as a coating material [4].

Due to its thermal stability the transition metal tungsten (W) may play a similar role like Ta in the future. In any case, a transition metal (Ta or W) is present in growth containment and may therefore be a possible contamination in SiC crystals grown in such environments. Transition metals are in general known to give rise to energy levels in the band gap of SiC and may therefore alter the electrical properties of the material. The high technological relevance to electrically characterize the influence of Ta and W on SiC is obvious. Hence, we directed our studies to the investigation of Ta- and W-related deep levels in the band gap of SiC by means of deep level transient spectroscopy (DLTS). This technique is extremely sensitive to minor traces of electrically active impurities (traps). Though, it is difficult to reveal the chemical or structural nature of a trap with DLTS. To provide a definite chemical identification of Ta and W-related band gap states we observe the elemental transmutation of incorporated radioactive tracer isotopes (^{177}Ta and ^{178}W) in 4*H*-SiC: traps corresponding with the parent/daughter isotope will diminish/arise while being observed by means of DLTS (for a comprehensive description of the method see available reviews [5]).Part of the experimental work we present here has already been accepted for publication in reports treating Ta in 4*H*-SiC [6] and W in the three polytypes 4*H*-, 6*H*-, 15*R*-SiC [7]. In this study, we concentrate on the comparison of the level positions of Ta- or W-related traps in the three investigated polytypes. The conduction band offsets between the polytypes we obtain according to the "Langer-Heinrich-Rule" [8] are in good agreement with values already derived in other studies [9].

Experiment

The samples investigated were n-type epitaxial layers grown by Cree Inc. with a net shallow doping level in the range of (1-9)×10^{15} cm^{-3}. Polytype determination was done by Raman spectroscopy. For radiotracer spectroscopy, 4*H*-SiC samples were doped with the radioactive isotopes ^{177}Ta or ^{178}W

by recoil implantation [11] at the Hahn-Meitner-Institute (Berlin). The isotope ^{177}Ta transmutes to stable ^{177}Hf whereas ^{178}W decays to stable ^{178}Hf:

^{177}Ta → ^{177}W, $T_{1/2}$ = 56.6 h and ^{178}W → ^{178}Hf, $T_{1/2}$ = 22 d

$T_{1/2}$ represents the half-life of the respective nuclear decay. The properties of recoil implantation lead to a co-implantation of isotopes with adjacent mass numbers. Hence, we investigated the mixture of implanted isotopes by γ-ray spectroscopy on each implanted sample. We found that isotopes other than the desired have a significantly different half-life or are fewer in number and, therefore, do not influence our experiments. For ^{177}Ta / ^{178}W an implantation fluence of 5×10^{9} cm^{-2} / 1.5×10^{10} cm^{-2} was derived.

Ion implantation of stable Ta and W isotopes was performed at the tandetron accelerator JULIA in Jena at room temperature. To achieve a fairly homogeneous concentration of 2×10^{14} cm^{-3} we performed a sixfold implantation with energies between 1.0 and 6.2 MeV. To remove implantation damage the samples were annealed at 1600 K in oxygen atmosphere and then etched in hydrofluoric acid to remove the resulting oxide layer. DLTS spectra were recorded on Schottky contacts (Ni). Trap parameters were derived from a standard Arrhenius evaluation [12] assuming the capture cross section to be constant.

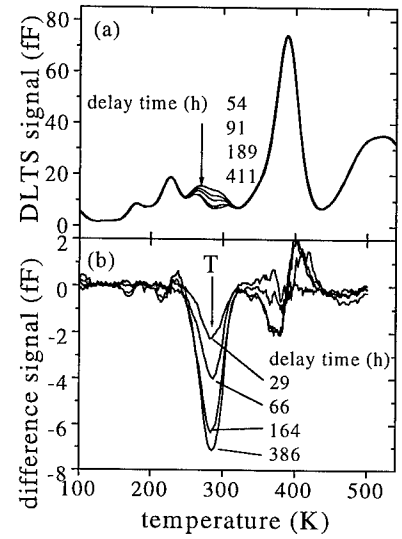


Fig. 1. (a) DLTS spectra of n-type 4H-SiC measured during the elemental transmutation of ^{177}Ta. (b) Difference spectra obtained by subtracting the initial spectrum from subsequently measured spectra.

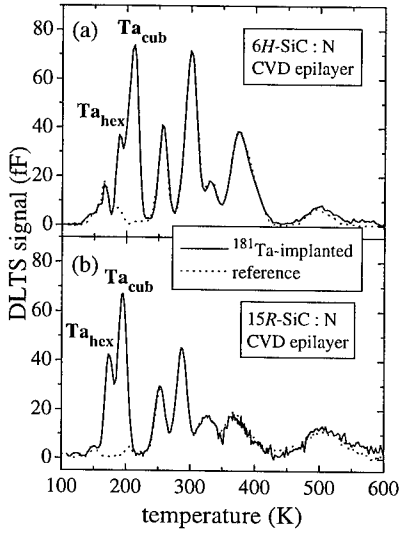


Fig. 2. DLTS spectra of stable ^{181}Ta implanted (a) 6*H*- and (b) 15*R*-SiC. The peak height ratio of the peaks labeled Ta_{hex} and Ta_{cub} reflects the ratio of inequivalent hexagonal and cubic lattice sites in the respective polytype (1 : 2 for 6*H* and 2: 3 for 15*R*).

Results

During the elemental transmutation of the radioisotopes, we subsequently recorded DLTS spectra with delay times adapted to the half-life of the respective radioisotope. The spectra of the 4*H*-SiC samples implanted with ^{177}Ta are highly reproducible except for the temperature range between 280 and 310 K (see Fig. 1a). Within this scope, the DLTS signal is decreasing with delay time. Unfortunately, the signal is superimposed by one ore more stable background peaks. This prevents a standard DLTS-analysis [12]. Taking into account that the DLTS signal is proportional to the trap concentration (the capacitance of the diodes remained unchanged during the experiments), we subtracted the initial spectrum (recorded 25 h after implantation) from the spectra we measured during the nuclear decay of ^{177}Ta and obtain *difference spectra* containing only DLTS peaks related to traps with time dependent concentration (see Fig. 1b). The difference spectra exhibit a broadened peak with a well defined temperature position. The height of peak *T* exponentially decreases with a half-life of 57(±1) h which is in good agreement with the half-life of the nuclear decay of ^{177}Ta. This is a direct proof that level T contains exactly one radioactive parent isotope ^{177}Ta. For the radioisotope ^{178}W in 4*H*-SiC the DLTS spectra

measured at temperatures between 40 and 300 K (Fig. 3a) reveal one peak at 88 K labeled A, that clearly vanishes during the transmutation whereas other peaks remain constant. The height of this peak exponentially decreases with delay time. The DLTS signal in the temperature range measured between 550 and 600 K also decreases with delay time but is a superimposition of two or more background peaks. To isolate time dependent signals from stable ones, we performed the same procedure (see difference spectra in Fig. 3b) as already described for the tantalum related level T. The peak, labeled B, we obtain from the difference spectra exponentially decreases with the same time constant we find for the decrease of peak A. This exponential time-dependence of the peak heights can be well described by a half-life of 21 (±3) d. The close match with the nuclear half-life of ^{178}W immediately demonstrates that the corresponding band gap states are due to defects that involve exactly one W-atom.

After this chemical identification we derive trap parameters and further properties of the Ta- and W-related deep levels from DLTS-measurements carried out on samples implanted with stable isotopes (see Fig. 2 for Ta in 6*H*- and 15*R*-SiC) The trap parameters (Pool-Frenkel corrected in the case of Ta [7]) can be found in Tab. 1. In the case of Ta, we find a split of the corresponding energy levels which we attribute to the occupation of in-equivalent lattice sites in the different SiC polytypes. This split could not fully be resolved in 4*H*-SiC. Double-correlated DLTS (DDLTS) investigations reveal the donor-/acceptor-like character of the Ta-/W-related defect centers [6, 7].

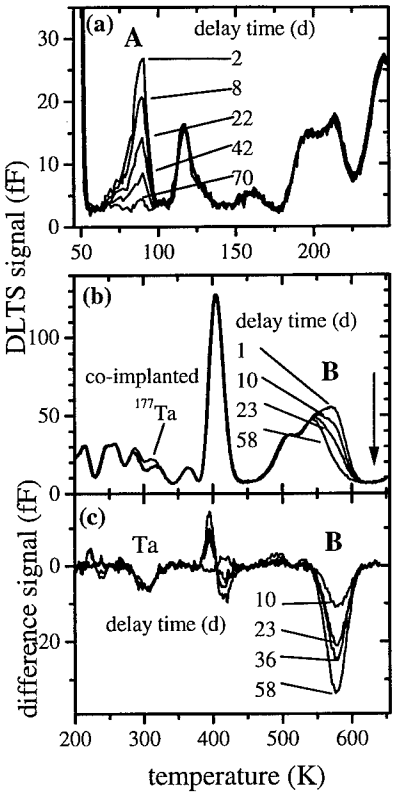


Fig. 3: DLTS spectra of n-type 4*H*-SiC taken sequentially during the transmutation of ^{178}W to Hf: (a, b) Low- and high-temperature part of the spectra. (c) Difference of spectra obtained from Fig. (b).

Tab. 1: Parameters of tantalum- and tungsten-related band gap states: Thermal activation energy of electron emission and electron capture cross section σ (assumed to be independent of temperature). The errors given include all measured samples. The charge states were derived from DDLTS measurements.

Polytype	Level	Energy (eV)	Capture cross section (10^{-13} cm^2)	Interpretation / charge state
4*H*	T	0.68±4	0.1 .. 0.8	Ta / (+ / 0)
	A	0.17±1	0.1 .. 0.6	W / (-- / -)
	B	1.43±4	3 .. 20	W / (- / 0)
6*H*	Ta_{hex} / Ta_{cub}	0.46±2 / 0.43±2	0.1 .. 0.8	Ta / (+ / 0)
	B	1.16±3	4 .. 10	W / (- / 0)
15*R*	Ta_{hex} / Ta_{cub}	0.42±2 / 0.39±2	0.1 .. 0.8	Ta / (+ / 0)
	B	1.14±3	4 .. 10	W / (- / 0)

Conduction band offset and comparison of theory and experiment

According to the empirical "Rule of Langer–Heinrich" deep levels of transition metals are aligned within a group of isovalent compound semiconductors with respect to a common bulk reference level. Obviously, the deep levels of Ta or W exhibit different activation energies in the three

different polytypes investigated. Assuming the Langer-Heinrich-Rule is valid for SiC, this difference can be interpreted as the conduction band offset between the polytypes 4*H*, 6*H*, and 15*R*. In Fig. 4, the alignment of the valence bands of all SiC polytypes is postulated according to Ref. [12]. Obviously, both the statement that the valence bands of all SiC-polytypes are energetically aligned as well as the rule of Langer-Heinrich are valid for SiC. This result agrees with data recently derived by similar means for Cr- and V-related traps in 4*H*- and 6*H*-SiC [9]. Finally we compare our data to theoretical results on Ta and W in the polytype 3*C*-SiC. If we also include conduction band resonances, for each impurity (Ta and W), two states are predicted in 3*C* by theory [13]. For an intelligible comparison in Fig. 4, all energy levels are described by their energetical distance from the valence band in each polytype. Though Fig. 4 suggests a good agreement between theoretical and experimental data concerning level positions, the charge states of W, however, differ from the charge states of the measured levels. We do not have an explanation for this disagreement of the charge states in the case of W. Donor-like states predicted by theory should result in a well detectable Poole-Frenkel-effect. This was not the case in our in DDLTS measurements. Nevertheless, the Ta-related donor state remarkably corresponds to theory.

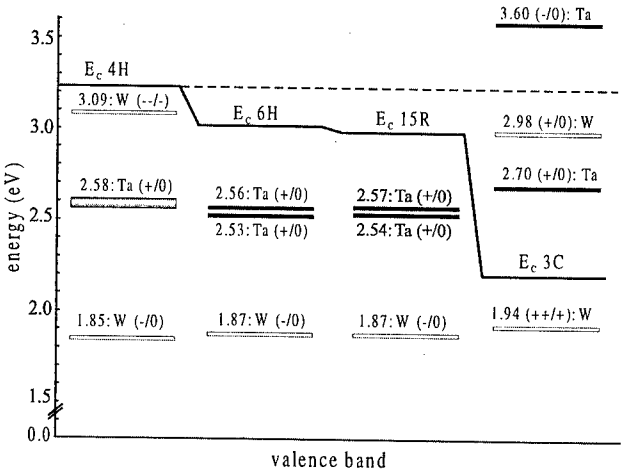


Fig. 4. Energy scheme of the SiC polytypes 3*C*, 4*H*, 6*H*, and 15*R*. It is based on the assumption, that the valence bands of the SiC polytypes are energetically aligned [12].The trap positions in the band gap of the polytypes are given by their energetical distance to the valence bands. The lower part of the gap was not investigated. The values for 3*C*-SiC are theoretical predictions [13].

Acknowledgements

This work was supported by the Deutsche Forschungsgemeinschaft (Sonderforschungsbereich 196).

References

[1]E.N. Mokhov, M.G. Ramm, A.D. Roenkov, Yu.A. Vodakov, J. Cryst. Growth **181** (1997) p.254.
[2]Yu.A. Vodakov, A.D. Roenkov, M.G. Ramm, E.N. Mokhov, Yu.N. Makarov, Phys. Stat. Sol. (b) **202** (1997), p.177.
[3]D. Hoffmann, S.Yu. Karpov, Yu.N. Makarov, E.N. Mokhov, M.G. Ramm, M.S. Ramm, A.D. Roenkov, Yu.A. Vodakov, Inst. Phys. Conf. Ser. **142** (1996), p.29.
[4]L.B. Rowland and G.T. Dunne, Mater. Sci. Forum (2000), p.338.
[5]N.Achtziger, J.Grillenberger, and W.Witthuhn, Hyperfine Interactions 120/121 (1999), p.69.
[6]J.Grillenberger, N.Achtziger, R.Sielemann, and W.Witthuhn, J. Appl. Phys. **80** (2000), at press.
[7]N.Achtziger, G.Pasold, R.Sielemann, C.Hülsen, J.Grillenberger, W.Witthuhn, Phys.Rev.B.
[8]J.M.Langer and H.Heinrich, Phys.Rev.Lett. **55**(13) , (1997), p.1414.
[9]N.Achtziger, J.Grillenberger, W.Witthuhn, Mater. Sci. Forum Vols. 264-268, (1998), p.541.
[10]N.Achtziger, H.Gottschalk, T.Licht, J.Meier,M.Rüb, U.Reislöhner, W.Witthuhn, Appl.Phys.Lett. **66** (1995),p.2370
[11]P.Blood and J.W.Orton, *The electrical characterization of semiconductors: majority carriers and electron states*, (Academic Press, London, 1992), p.344 and p. 426.
[12]V.V.Afanas'ev, M.Bassler, G.Pensl, M.J.Schulz, and E.Stein von Kamienski, J.Appl.Phys. **79**(6) (1996), p3108.
[13]H. Overhof, private communication.

Materials Science Forum Vols. 353-356 (2001) pp. 479-482
© 2001 Trans Tech Publications, Switzerland

Shallow Dopant and Surface Levels in 6H-SiC MOS Structures Studied by Thermally Stimulated Current Technique

V.S. Lysenko[1], I.P. Osiyuk[1], T.E. Rudenko[1], I.P. Tyagulski[1], E.Ö. Sveinbjörnsson[2] and H.Ö. Ólafsson[2]

[1] Institute of Semiconductor Physics, National Academy of Sciences of Ukraine, 45 Prospect Nauki, 03028 Kyiv, Ukraine

[2] Department of Microelectronics ED, Chalmers University of Technology, SE-412 96 Göteborg, Sweden

Keywords: Doping Levels, Interface States, Re-Oxidation, Thermally Stimulated Current Spectroscopy

Abstract. In this work, the shallow majority-carrier traps in 6H-SiC MOS structures are studied using thermally stimulated current (TSC) measurements in the range 6-100 K. In this temperature range, we observe TSC signals from shallow doping levels and from traps at the SiC/SiO_2 interface. The first results of the investigation of very shallow (shallower than doping levels) interface states in differently prepared structures are presented. We find that the re-oxidation anneal, which essentially reduces the density of deep interface states, results in a significant increase (by a factor of 2) in the density of shallow states near the valence band.

Introduction

Silicon carbide MOS structures have a great potential for high-power, high-frequency, and high-temperature electronics. However, the performance of SiC MOS devices is yet limited by the low carrier mobility in the inversion channels at the $SiC-SiO_2$ interface due to interface defects, which can trap or scatter carriers. In this work, we report an investigation of shallow majority-carrier traps in 6H-SiC MOS structures by a thermally stimulated current (TSC) technique [1]. A TSC method, which is based on dc measurements, is not adversely affected by increased series resistance due to the carrier freeze-out. This makes it suitable for the investigation of trap levels located near the band edges. In contrast to conductance spectroscopy, the TSC method is free of uncertainty related to the surface potential fluctuations and thus seems to be well suited for the investigation of shallow surface states at the SiC/SiO_2 interface. The results obtained on differently prepared n- and p-type 6H-SiC MOS structures are presented.

Experimental details

MOS capacitors were fabricated on commercially available Al-doped and N-doped 6H-SiC epitaxial layers grown on the Si-face of SiC substrates. Prior to the oxidation, the samples were cleaned using a modified RCA clean. Thermal oxidation was performed at temperatures 1100^0C and 1150^0C in dry O_2 or in a pyrogenic steam. The loading and deloading of the furnace were carried out at 700^0C. Some of the samples received an additional re-oxidation anneal at 950^0C in a pyrogenic steam. An Al layer was evaporated on the oxidized side of the samples and lithographically patterned to form MOS capacitors. The gate area of the capacitors was 1.25×10^{-3} cm^{-2}. The backside contact was made by rubbing the backside with GaZn eutectic.

TSC measurements were performed with a linear heating rate of 0.2 K/s in the temperature range 6-100 K using a liquid-helium cooling system. The volume and surface components of the TSC spectrum were identified by measurements with various charging (V_0) and discharging (V_d) voltages. In addition to the

TSC measurements, the MOS structures were characterized using the displacement current versus gate voltage measurements with a linear voltage ramp, being directly proportional to the differential capacitance.

Results and discussion

TSC measurements of the n-type samples with various charging voltages shown on Fig. 1(a) reveal two clearly defined peaks and tooth-shaped plateau, which arises from the low-temperature edge of the spectrum as the charging voltage increases. The spectrum reaches "saturation", when the charging voltage corresponds to sufficiently strong accumulation at the surface. When the charging voltage corresponds to flatband or depletion conditions at the surface, only two TSC peaks are observed. (Fig. 1(b)). The behavior of TSC spectra of n-type samples obtained in different oxidation processes was in much the same. We assume that the tooth-shaped plateau in the n-type samples is due to interface states near the conduction band edge, whereas the above peaks are associated with volume traps, that is, with nitrogen in the hexagonal lattice site (h) and cubic (k_1, k_2) sites.

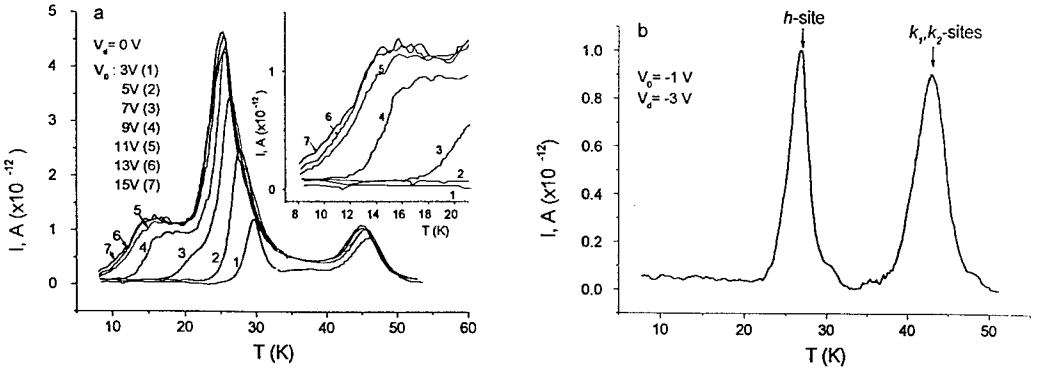


Fig.1. (a) TSC spectra measured on the n-type 6H-SiC MOS structure with a dry oxide grown at T=1100^{0}C for various charging voltages applied to the gate. The insert shows the surface-related part of the spectrum; (b) a TSC spectrum measured on the same sample when the charging voltage corresponds to depletion at the surface (dT/dt=0.2 K/s, d_{ox}=140 nm, d_{epi}=2 μm, N_D=2x10^{15}cm^{-3}).

CV-data derived from the I-V-measurements at different temperatures support the assumption that volume-related TSC peaks result from the doping levels. At temperatures above both peaks, a standard CV-curve is observed with the maximum capacitance value in an accumulation region being equal to the oxide capacitance. At temperatures below both peaks, a C-V plot represents a straight line with the capacitance value corresponding approximately to a series connection of the oxide capacitance and depleted epilayer capacitance indicating that no accumulation layer can be obtained for a reasonable measurement time. This means that the response time of majority carriers dramatically changes in the temperature range corresponding to the above TSC peaks.

The systematic shift of both volume-related peaks to lower temperatures was observed with increasing the discharging (detrapping) voltage indicating that the emission rate from both centers is enhanced by the electric field. In this work, the activation energies of the doping levels were obtained from the slope of the initial rise of the TSC peak measured at low applied voltages and replotted in Arrhenious coordinates. The activation energies obtained with taking into account the Poole-Frenkel effect were 83 meV and 126 meV, that is in a good agreement with reported ionization energies for nitrogen in 6H-SiC in the (h)-site and (k_1k_2)-sites [2, 3].

The tooth-shaped form of the surface-related part of the TSC spectrum in n-type samples suggests the existence of the individual interface traps, which must be separated from one another in energy by the

value exceeding 2kT, so that they could be resolved by TSC measurements. Besides, these traps should be located in the surface space charge region or in the very narrow interfacial layer in the oxide. These results can be considered as evidence of isolated interface traps close to the conduction band edge in the n-type 6H-SiC MOS structures, though bandlike behavior seems to be more natural for interface traps near the band edges.

The measurements of the p-type samples shown in Fig. 2 (a) reveal a TSC peak at around 70 K and a smooth hump at lower temperatures observed only when the SiC surface is in accumulation during cooling. If the SiC surface is depleted during both cooling and measurement, two TSC peaks can be seen, namely, a large peak at 70 K and a small wide peak at 27 K, which appears at high depletion voltages (Fig. 2(b)). This indicates that both peaks are likely caused by volume traps, while the hump in Fig. 2(a) results from the interface traps. The behavior of the C-V characteristics of p-type MOS structures extracted from I-V measurements at temperatures above and below the large volume-related TSC peak is identical to that in n-type samples, as illustrated by the insert in Fig. 2 (b). This strongly suggests that the TSC peak around 70 K is due to the doping level. The doping-related peak shown in Fig. 2(b) has a broader half-width than that expected from a single-level model and depends on the depletion voltage during the measurement. The energy activation obtained from the initial rise of the peak by taking into account of the Poole-Frenkel effect was E≈190 meV, that is in a reasonable agreement with values reported in the literature for Al in 6H-SiC [2, 3]. A small TSC peak at temperature of 27 K observed at high depletion voltages is likely associated with an impurity in the p^+-substrate.

In p-type samples, the surface-related part of the TSC spectrum changes with both charging and discharging voltages, as shown in Fig. 2(a) and Fig. 3(a). This suggests that the hole traps near the valence band are extended from the interface into the bulk of oxide.

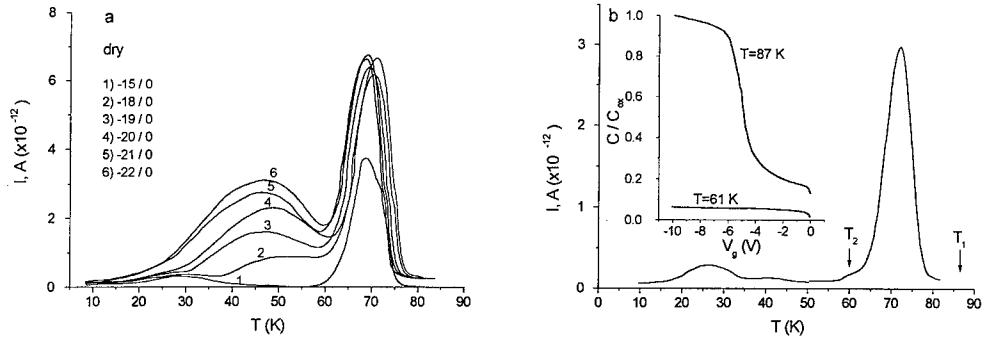


Fig. 2. (a) TSC spectra of the p-type 6H-SiC MOS structure with a dry oxide grown at T=1150^0 C measured for various charging accumulation voltages; (b) a TSC spectrum measured on the same sample when the charging voltage corresponds to depletion at the surface. The insert presents C-V curves measured at temperatures indicated by arrows (d_{ox}=50 nm, d_{epi}=5 μm, N_D=1.3x10^{16} cm^{-3}).

The density of the shallow interface states was found to be very sensitive to the oxide preparation. The lowest value was obtained for the n-type sample with a dry oxide grown at 1100^0 C (2.6x10^{11}cm^{-2}), whereas for the sample with a dry oxide grown at 1150^0 C it was about 1.6x10^{12} cm^{-2}. The absence of significant charge at the SiO_2-SiC interface in the n-type structures at room temperature, as revealed by C-V measurements, suggests that the observed traps are either acceptors, or more likely donors that are neutralized (or compensated) by negatively charged acceptor states located in the lower half of the bandgap. The latter assumption is supported by measurements on the p-type samples prepared in the

same processes, which indicate the presence of almost the same value of the shallow interface state density near the valence band.

Surprisingly the re-oxidation anneal, which essentially (2-3 times) reduces the density of deep interface states [4,5], does not reduce the density of shallow (shallower than doping levels) interface states near the conductance band and significantly (by a factor of 2) increases it near the valence band, as illustrated in Fig. 3. It is quite possible that this is the reason for the appearance of negative effective charge in n-type samples after the re-oxidation treatment [5].

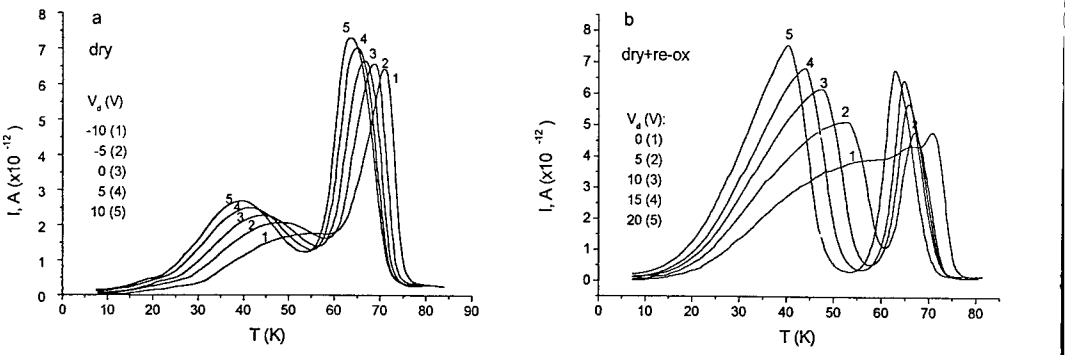


Fig.3. TSC spectra of the p-type 6H-SiC MOS capacitors measured for accumulation charging and various discharging depletion voltages showing the effect of re-oxidation after dry oxidation at T=1150^0 C: (a) a dry oxide without re-oxidation anneal; (b) a dry oxide with re-oxidation anneal.

Conclusion

We have presented the first results of the TSC study of very shallow traps in 6H-SiC MOS structures. We found that two volume-related TSC peaks in n-type samples can be attributed to N in hexagonal site and quasicubic sites. In p-type samples, only one volume-related TSC peak, which can be attributed to Al doping levels, was observed. The measurements of n- and p-type 6H-SiC MOS capacitors prepared in the same dry oxidation process indicate the presence of almost the same value of the shallow interface state density near the conduction and valence band edges. It is shown that re-oxidation anneal, which essentially reduces the density of deep interface states, does not reduce the density of shallow (shallower than doping levels) interface states near the conductance band for n-type and significantly (by a factor of 2) increases it near the valence band for p-type. It is quite possible that this is the reason for the appearance of negative effective charge in n-type samples after the re-oxidation treatment.

Acknowledgements

T.E. Rudenko acknowledges the financial support from the School of Electrical and Computer Engineering of Chalmers University of Technology (Grant N 3150016).

References

1. A.F. Sanders and G.T.Wright, Electronics Lett. **6** (1970), p. 207.
2. W.J.Choyke and G. Pensl, MRS Bull. **22** (1997), p. 25.
3. W. Kaindl, M. Lades, N.Kaminski et.al, J. Electr. Mater. **28** (1999), p. 154.
4. L.A.Lipkin and J.W. Palmour, J. Electr. Mater. **25** (1996), p. 909.
5. E. Ö. Sveinbjörnsson, M.Ahnoff and H. Ö. Ólafsson, Materials Science Forum. **338-342** (2000), p. 1117.

Materials Science Forum Vols. 353-356 (2001) pp. 483-486
© 2001 Trans Tech Publications, Switzerland

Intrinsic Mobility of Conduction Electrons in 4H-SiC

J. Pernot[1], S. Contreras[1], E. Neyret[1,2], L. Di Cioccio[2], W. Zawadzki[1,3] and J.L. Robert[1]

[1] Groupe d'Etude des Semiconducteurs, Université Montpellier 2, CNRS, UMR 5650, cc074, FR-34095 Montpellier Cedex 5, France

[2] CEA/ LETI Grenoble, 17 rue des Martyrs, FR-38054 Grenoble Cedex 9, France

[3] Institute of Physics, Polish Academy of Sciences, PL-02668 Warszawa, Poland

Keywords: 4H-SiC, Hall Concentration, Hall Mobility, Nitrogen Level, Valley Orbit

Abstract

Samples of 4H-SiC grown by cold-wall CVD have been investigated with the use of transport methods in the temperature range 35 K to 850 K. Our best sample had an electron mobility of 12400 cm^2/Vs at 50 K. We describe the temperature dependence of the electron density and mobility and discussed the effects of the two inequivalent lattice sites of the nitrogen levels, including valley-orbit splitting. At room temperature, the density dependence of electron mobility was established, described theoretically, and compared with the results of other authors. The calculated asymptotic value is about 930 cm^2/Vs for weakly doped samples.

Introduction

Because of its wide energy gap, large thermal conductivity and high breakdown electric field, 4H- SiC is a promising material for high power, high frequency and high temperature electronic devices. The purpose of the present contribution is threefold. First report the highest value of electron mobility in 4H-SiC measured by transport methods. Second describe simultaneously the experimental temperature variations of the electron density and mobility taking into account the valley-orbit splitting of nitrogen levels. Third we present our data on the density dependence of mobility at room temperature and compare it with the results of other authors. Ten n-type samples (with carrier concentration ranging from 10^{15} to 10^{20} cm^{-3}) were grown at 1450 K in a cold-wall AP-CVD (Atmospheric Pressure - Chemical Vapor Deposition) reactor already described [1]. Electrical measurements were done using the experimental set-up described in Ref. 2. The temperature dependence of the free electron density n was analyzed using a two inequivalent levels donor $E_{d\,(h,k)}$ model where h and k correspond, respectively, to the hexagonal and cubic C-lattice sites of nitrogen donor in $4H-SiC$. In the effective-mass-approximation (EMA), the multi-valley structure induces a valley-orbit splitting ΔE_{vo} of the ground-state. The optical measurements exhibit a small valley-orbit splitting ($\Delta E_{voh} = 7.6\,meV$) for the hexagonal ($h$) nitrogen level [3,4,5]. Kisielowski et al. measured the splitting of the cubic level (k) ($\Delta E_{vok} = 45.5\,eV$) by EPR [6]. These two excited levels contribute to the thermal ionization of donors [7]. However, due to a large splitting, the cubic split valley-orbit level has a negligible influence. Therefore, we only took into account the valley-orbit splitting of the h-level.

Temperature dependence of the free electron density

We write the neutrality equation for a non degenerate semiconductor as [7]:

$$n+N_a = \frac{N_{dh}}{1+g_h\,n/N_c\,\exp\left(E_{dh}/k_BT\right)+g_{hvo}\,n/N_c\,\exp(E_{dh}/k_BT-\Delta E_{voh}/k_BT)}+\frac{N_{dk}}{1+g_k\,n/N_c\,\exp\left(E_{dk}/k_BT\right)} \quad (1)$$

In this equation, $N_c = 2M_c\,(2\pi\, m^*\, k_B T/h^2)^{3/2}$, M_c is the number of equivalent minima, $m^* = (m_1^* m_2^* m_3^*)^{1/3}$ is the density of states mass, h, k_B and T have their usual meaning. g_h,g_k, and g_{hvo} are the degeneracy factors. In Fig.1 we show the temperature dependence of the electron density (full circles) found for our lowest doped sample ($n = 3 \times 10^{15} cm^{-3}$ at RT). The solid line is calculated from Eq.1 using the parameters listed in Table 1. The anisotropy of the effective mass was introduced using the procedure of Kinoshita et al [8]. The Hall factor was assumed to be unity. The dashed line is calculated with the same parameters except $g_{hvo} = 0$ (in other word, we neglect the valley orbit level). As shown in Fig.1, the valley-orbit level have a sensitive influence at low temperature ($1000/T > 8$) and slows down the exhaustion of the impurity levels. When the thermal energy ($k_B T$) increases and becomes comparable to ΔE_{voh}, impurity electrons are trapped on the *hvo* level. Consequently, the energy of the Fermi level (E_F) progress is slowed down. This is shown in Fig.2, where the temperature dependence of the Fermi levels with and without the valley orbit level are compared with the three energy levels. At very low temperature (T < 20 K), E_F is just above E_{dh} and $k_B T << \Delta E_{voh}$. At very high temperature, almost the totality of impurities are ionized, h, k and hvo are empty. In this two cases the valley orbit level can be neglect. However, if we don't take into account of the valley orbit level in our calculation between (during the ionization of h), we can not fit correctly the experimental results.

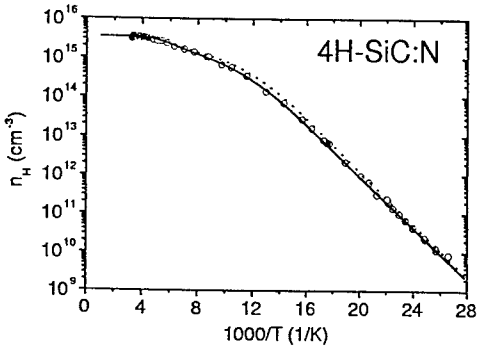


Fig 1: Hall free electron density versus $(1000/T)$, as measured in our best 4H-SiC sample (full circles) and calculated using the two-level donor approximation : solid line - with valley orbit level, dashed line - without valley orbit level.

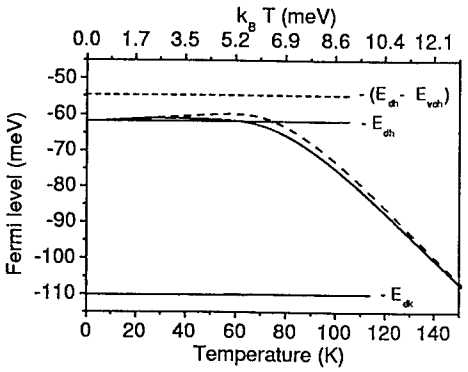


Fig 2: Temperature dependence of Fermi level calculated with (solid line) and without (dashed line) valley orbit level. Energies of cubic (k), hexagonal (h) and hexagonal valley orbit (voh) levels are represented.

Temperature dependence of the Hall mobility

In Fig.3 we show the experimental temperature dependence of the Hall mobility measured in our best sample. Because of the weak compensation and high quality of the epitaxial layer, we could measure a maximum value of 12400 cm^2/Vs at T=50 K. To give quantitative description of the Hall mobility, we have taken into account the scattering of electrons by acoustic and optic phonons (polars and non polars interactions), ionized and neutral impurities. The anisotropy of the effective mass and of the Hall factor were introduced using the procedure of Kinoshita et al [8]. A more detailed description about the calculation of relaxation time can be found in Ref. 2. The result of calculation is shown as solid line in Fig.3 and the fitting parameters listed in Table 1. At low temperatures, the ionized impurity (ii) scattering dominates. At 100 K the mobility becomes controlled by the intervalley acoustic (ia) process. Finally, at

high temperature, the intervalley scattering by high energy phonons (iph) becomes dominant. The important point is that the same deformation potentials describe also the temperature dependences of the mobility in the more strongly doped samples.

Electron density dependence of the mobility at room temperature

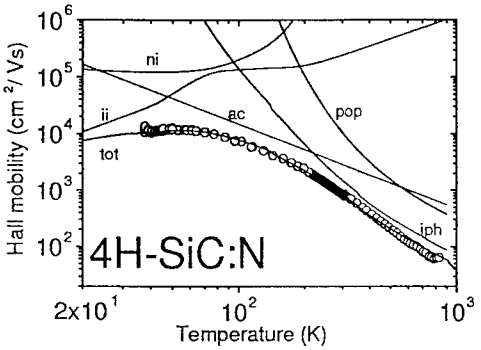


Fig 3: Hall mobility versus temperature, as measured in our best 4H-SiC sample (empty circles) and calculated (solid lines). Scattering modes: ionized (ii) and neutral (ni) impurities, intravalley acoustic (ac), intervalley phonons (iph), polar optic (pop), total mobility (tot).

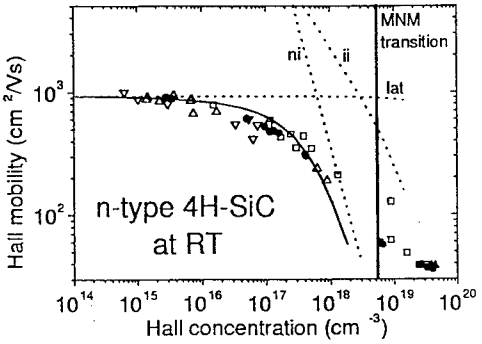


Fig 4: Hall mobility at $292\,K$ versus free electron density. Calculation for zero compensation : (solid line). Experimental data: our results: •, Schaffer et al. [9]: □, Burk et al. [10]: △ and ▽ for single and multi-wafer reactors, respectively. Scattering modes (dotted lines) : ionized (ii) and neutral (ni) impurities and lattice (lat).

The mobility of the ten different samples (corresponding to ten different Hall electron densities) were compared with mobility values quoted in the literature [9,10]. In Fig.4, we plot the room temperature mobility versus Hall concentration : our results (full circles), literature results (open symbols). The solid line corresponds to the theoretical mobility calculated in the ideal case where there is no compensation. We do not introduce broadening effect on the level impurity due to the increase of the doping concentration. We used ionization energies and parameters previously determined. We have plotted using dotted lines mobility due to the intrinsic scattering processes (lattice scattering (lat) which includes (ac), (pop) and (iph) scattering) and mobility due to the extrinsic impurity scattering processes ((ii) and (ni)). Beyond $10^{15}\,cm^{-3}$, only intrinsic scattering controls mobility. The intrinsic 4H-SiC mobility leads to an asymptotic value of about $930\,cm^2/Vs$. The comparison of this asymptotic value with the room temperature mobility of $887\,cm^2/Vs$ measured on our lowest doped layer confirm the high quality of this sample. Increasing the doping concentration, the two impurity modes ((ii), (ni)) start to play a role and become dominant above $10^{17}\,cm^{-3}$. Finally, above few $10^{18}\,cm^{-3}$, our modelization does not account for the experimental mobility. Persson et al [11] predicted at $5.6 \times 10^{18}\,cm^{-3}$ the metal-non-metal (MNM) transition for 4H-SiC and our model becomes invalid.

To summarize, we have investigated high quality 4H-SiC samples and measured the highest mobility reported up to now from transport experiments. We have also successfully described the dependence of $n(T)$ and $\mu(T)$, taking into account the valley-orbit splitting of nitrogen level. Finally, we have investigated the room temperature dependence of the mobility as a function of the free carrier concentration, described it theoretically and compared with literature data. We

conclude that the maximum mobility at room temperature is $\sim 930\,cm^2/Vs$, mainly limited by lattice scattering.

Conduction band[a]				Hexagonal level		Cubic level	
M_c	3			$\mathbf{N_{dh}}$	$\mathbf{1.8 \times 10^{15} cm^{-3}}$	$\mathbf{N_{dk}}$	$\mathbf{1.8 \times 10^{15} cm^{-3}}$
$m_1^*(ML)$	$0.33\,m_0$			$\mathbf{E_{dh}}$	**62 meV**	$\mathbf{E_{dk}}$	**110 meV**
$m_2^*(M\Gamma)$	$0.58\,m_0$			g_h	2	g_k	2
$m_3^*(MK)$	$0.31\,m_0$			ΔE_{voh}	$7.6\,meV$		
				g_{voh}	4		
Lattice scattering				Impurities scattering			
Intravalley	Intervalley[c]			Ionized[d]		Neutral[e]	
11.5 eV[b]	1st phonon	36 meV	**0.7**	$\mathbf{N_a = 4.3 \times 10^{14} cm^{-3}}$		$R_y^* = 54\,meV$	
	2nd phonon	72 meV	**0.5**				
	3rd phonon	94 meV	**5**				

Table 1: Parameters used for the neutrality equation and calculation of the relaxation time. Bold characters correspond to adjustable parameters. [a]Experimental data [12] - [b]Acoustic deformation potential - [c]Phonon energies and coupling constants defined by Herring [13]. - [d]Compensation concentration (plus ionized nitrogen) used in Takimoto model [14] - [e]Effective Rydberg used in neutral impurity model [15].

References

[1] E. Neyret, L. Di Cioccio, J.M. Bluet, J. Pernot, P. Vicente, D. Anglos, M. Lagadas and T. Billon, to be published in Mat. Sci. Eng. B (Proceedings of EXMATEC 2000), (2000).

[2] J. Pernot, S. Contreras, J. Camassel, J.L. Robert, W. Zawadzki, E. Neyret and L. Di Cioccio, Appl. Phys. Lett. (in press).

[3] W. Götz, A. Schöner, G. Pensl, W. Suttrop, W.J. Choyke, R. Stein and S. Leibenzeder, J. Appl. Phys. 73 (1993), p. 3332.

[4] C.Q. Chen, J. Zeman, F. Engelbrecht, C. Peppermüller, R. Helbig, Z.H. Chen and G. Martinez, J. Appl. Phys. 87 (2000), p. 3800.

[5] S. Nakashima and H. Harima, phys. stat. sol. (a) 162 (1997), p. 39.

[6] C. Kisielowski, K. Maier, J. Schneider and V. Oding, Mater. Sci. Forum 83-87 (1992), p. 1171.

[7] J.S. Blakemore, *Semiconductor Statistics*, Pergamon Press Inc., New York (1962).

[8] T. Kinoshita, K.M. Itoh, J. Muto, M. Schadt, G. Pensl and K. Takeda, Mater. Sci. Forum 264-268 (1998), p. 295.

[9] W.J. Schaffer, G.H. Negley, K.G. Irvine and J.W. Palmour, Diamond, SiC and Nitride Wide Bandgap Semiconductors Symposium, 339 (1994), p. 595.

[10] A.A. Burk Jr., M.J. O'Loughlin, R.R. Siergiej, A.K. Agarwal, S. Sriram, R.C. Clarke, M.F. MacMillan, V. Balakrishna and C.D. Brandt, Solid State Electronics 43 (1999), p. 1459.

[11] C. Persson, U. Lindefelt and B.E. Sernelius, Phys. Rev. B 60 (1999), p. 16479.

[12] D. Volm, B.K. Meyer, D.M. Hofmann, W.M. Chen, N.T. Son, C. Persson, U. Lindefelt, O. Kordina, E. Sörman, A.O. Konstantinov, B. Monemar and E. Janzén, Phys. Rev. B 53 (1996), p. 15409.

[13] C. Herring, Bell Syst. Tech. J. 34 (1955), p. 237.

[14] N. Takimoto, J. Phys. Soc. 14 (1959), p. 1142.

[15] J.R. Meyer and F.J. Bartoli, Phys. Rev. B 24 (1981), p. 2089.

Materials Science Forum Vols. 353-356 (2001) pp. 487-490
© 2001 Trans Tech Publications, Switzerland

A Study of Band to Band Tunneling with Application to High-Field Transport in Hexagonal SiC Polytypes

A. Martinez[1], H.-E. Nilsson[2] and U. Lindefelt[1,3]

[1] Solid State Electronics, Dept. of Electronics, Royal Institute of Technology (KTH), Electrum 229, SE-16440 Kista, Sweden

[2] Mid-Sweden University, SE-851 70 Sundsvall, Sweden

[3] ABB Corporate Research, SE-721 78 Västerås, Sweden

Keywords: High Field Transport, k•p Approximation, Monte Carlo Simulation, Tunneling

Abstract. The band structure of hexagonal SiC polytypes has regions in the k-space where two or more energy bands are very close to each other. Tunneling of electrons (or holes) between bands due to a high electric field is one of the processes that may allow the electron to jump between energy bands. It is important to consider this effect in order to understand high-field transport properties in these polytypes. In this work we have used the two-band k•p approximation[1] to calculate the time-dependent tunneling probability for electron transitions between two bands using the approach of Krieger and Iafrate (KI) [2]. Electric field strengths between 0.1-4 MV/cm have been used to study the effect of tunneling. Drift times in the order of 10 fs have been considered, which is representative for the time between scattering events. We have applied the k•p approximation to different points in the Brillouin zone of 4H-SiC and proved that there is considerable tunneling between bands under realistic electric field strengths and scattering times.

Introduction

The importance of having an accurate model for band-to-band tunneling to calculate high-field transport in hexagonal SiC polytypes has been demonstrated in [3]. Here we propose a simple field-dependent two-band model that can be incorporated in the ensemble Monte Carlo (MC) method to describe the tunneling of carriers between bands. We will solve the KI equations [2], using the two-band k•p approximation [1], to describe the motion and tunneling of the electron under the effect of a high electric field in different regions of reciprocal space for 4H-SiC. This simple model can be used in regions where two bands come close to each other and the effect of the other bands on the electron motion can be neglected. First we describe basically the general KI formulation and the two-band k•p approximation. The next section contains some application to 4H-SiC for both valence and conduction bands using this model.

Theory: The Krieger -Iafrate approach and the two band k•p approximation

The equations that describe the tunneling between bands induced by an electric field using the KI approach [2] are:

$$i\hbar\frac{da_n(t)}{dt} = \varepsilon_n(\vec{k}(t))a_n(t) - \sum_{n'} eEX_{nn'}(\vec{k}(t))a_{n'}(t)\,. \qquad (1)$$

Eq. 1 describes the time evolution of the probability amplitude $a_n(t)$ for an electron to be in band n under the influence of the electric field without collisions, and having a wave vector $k(t)$ at a time t, e

is the electron charge and E is the electric field strength (throughout this text we are going to assume that the electric field is in the z-direction), $\varepsilon_n(k(t))$ is the band structure energy, and the expression for $X_{nn'}$ is given by

$$X_{nn'}(\vec{k}) \equiv \frac{1}{i}\int_{cell} U^*_{nk}\frac{\partial}{\partial k_z}U_{n'k}d^3r \ . \tag{2}$$

Here U_{nk} is the periodic part of the Bloch function. The second term in the RHS of eq. 1 allows the electron to change band. In order to solve eq. 1 we need to calculate the coefficients $X_{nn'}$ that represent the interactions between all the bands. We have obtained the coefficients $X_{nn'}$ and solved eq. 1 by using the k•p approximation and by restricting the number of bands to two. However, this approximation is only valid in the neighborhood of those points in k-space where the tunneling between the two chosen bands is supposed to be much larger than the tunneling to the other bands. The general two-band k•p approximation is given by the following Hamiltonian [4]

$$H(\vec{k}) = \begin{bmatrix} \frac{\hbar^2k^2}{2m} + \frac{\hbar(\vec{k}\bullet\vec{p}_{11})}{m} & \frac{\hbar(\vec{k}\bullet\vec{p}_{12})}{m} \\ \frac{\hbar(\vec{k}\bullet\vec{p}_{21})}{m} & E_g + \frac{\hbar^2k^2}{2m} + \frac{\hbar(\vec{k}\bullet\vec{p}_{22})}{m} \end{bmatrix} . \tag{3}$$

Here m is the electron mass, E_g the energy gap between the two bands and the p_{ij} coefficients can be extracted from numerical band structure calculations [5]. The eigenvalue problem can be solved analytically providing simple expressions for the k•p eigenvalues and eigenvectors.
The eigenvalues of eq. 3 can be written

$$\varepsilon^{\pm} = \frac{1}{2}(H_{11}+H_{22}) \pm \frac{1}{2}\left[(H_{11}-H_{22})^2 + 4|H_{12}|^2\right]^{1/2} . \tag{4}$$

where H_{ij} are the matrix elements of the Hamiltonian in eq. 3, and the $\varepsilon^{\pm}$ represent the larger and smaller energy eigenvalue. It is convenient to define the constant

$$c \equiv \frac{H_{11}-H_{22}}{\left[(H_{11}-H_{22})^2 + 4|H_{12}|^2\right]^{1/2}} . \tag{5}$$

which allows us to express the two eigenvectors as

$$\sqrt{2}U_{1k} = \exp(\ i\theta\ )[1+c]^{1/2}\phi_d + [1-c]^{1/2}\phi_u \ . \tag{6a}$$

$$\sqrt{2}U_{2k} = [1-c]^{1/2}\phi_d - \exp(\ -i\theta\ )[1+c]^{1/2}\phi_u \ . \tag{6b}$$

The eigenvectors U_{1k} ,U_{2k} correspond to the upper and lower energy eigenvalues respectively; ϕ_u (ϕ_d) represents the $\varepsilon^+(\varepsilon^-)$ energy wave function at $k = 0$; in our case they stand for the periodic part of the Bloch function at $k = 0$ (or around the critical point). θ is the phase of H_{12}. It should be pointed out that the eigenfunctions given by eq. 6 a, b are valid for both k and $-k$ (unlike Callaway's [4] and Kane's [1] expressions that are only valid for $k > 0$). Note that when $k \to 0$, $c \to$ -1. In the case where p_{11} is equal to p_{22} and k_x, k_y are zero the component X_{12} can be obtained from eq. 2 using the eigenfunctions in eq. 6a, b

$$X_{12} = \frac{2\hbar^2 p_{12}{}^2 k_z}{im^2(1-c^2)c^3E_g^2} \ . \tag{7}$$

Note that eq. 7 is not valid at $k_z = 0$ except as a limit expression. For the general case, the X_{12} component can be obtained from eq. 2 using the eigenfunctions in eq. 6a, b. With all these tools in hand, we can calculate the time dependent probability. The value of X_{ii} is zero in the approximation of this paper.

Results: Tunneling in 4H-SiC

In general, semiconductor materials with a large unit cell have band structures that contain a lot of points where bands are very close to each other. In these materials the band-to-band tunneling is important in order to understand the high field transport properties (i.e. saturation velocity and impact ionization coefficient). In this work we present calculations of the tunneling probabilities at different regions in k-space for 4H-SiC. The pij coefficients appearing in eq. 3 have been deduced by fitting the k•p eigenvalues to the numerical band structure [5]. The first example that we will study is the second and third valence bands of 4H-SiC along the Γ-K direction. In fig. 1 the energy dispersion obtained by the k•p model is compared with the numerical full potential band structure [5]. The corresponding tunneling probabilities are shown in fig. 2 for E=100 kV/cm and in fig. 3 for E=1 MV/cm. The tunneling probability at 100 kV/cm is as high as 65%, which clearly demonstrates the importance of multi-band carrier transport in 4H-SiC. In the next example we will estimate the tunneling probability over the energy gap between the second and third conduction bands along the M-L segment. Full band Monte Carlo simulations of 4H-SiC shows that this energy gap limits the carrier heating for an electric field parallel to the c-axis [6]. Even small band to band tunneling over this barrier may be important to consider in order to study the electron- initiated impact ionization. Fig. 4 compares the conduction band structure from [5] and the k•p model. In this case the fitting is not as good as in the former example, but in essence, the main features as mean energy separation and band curvatures can be reproduced under a certain degree of approximation. The calculated probability for an electric field of 4 MV/cm is 0.02 %.

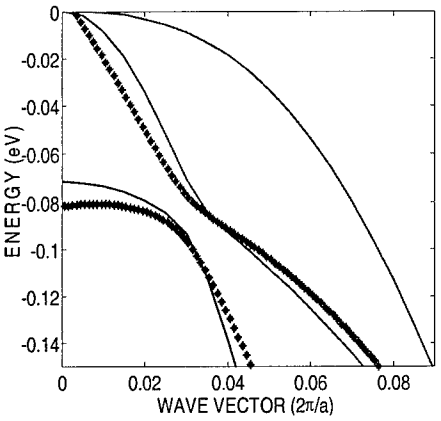


Fig. 1. Dispersion relation for holes in 4H-SiC in the vicinity of the Γ-point. The full thin lines represent the three uppermost valence bands in the Γ-K direction calculated by the full potential method; the thicker lines represent the fitting using the k•p model, and a is the lattice constant equal to 3.0655 Å.

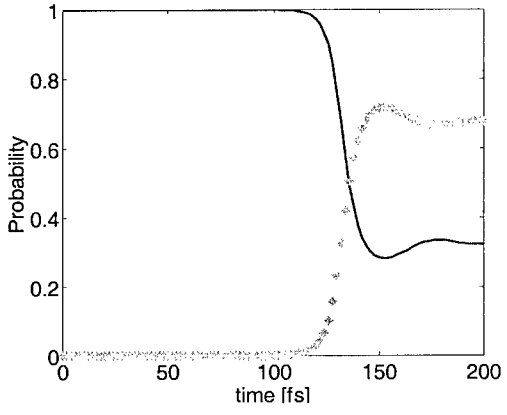


Fig. 2. Probabilities calculated for holes initially in the second band, for an electric field of 100 kV/cm. The full thin line represents the probability for holes to remain in the same band starting from $k = 0$. The thicker line stands for the probability to change band.

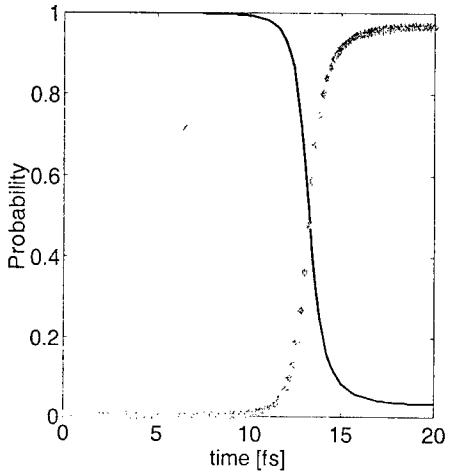


Fig. 3. The same as fig. 2 but for an electric field of 1 MV/cm.

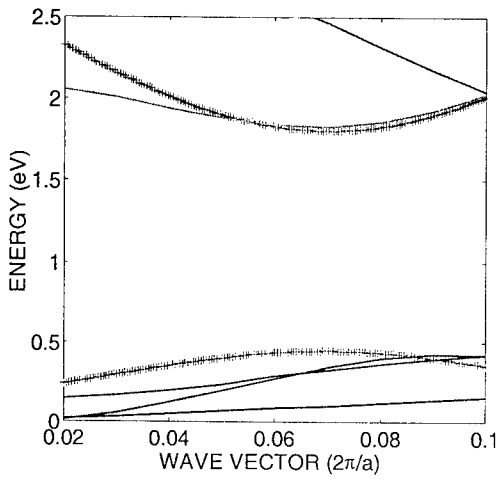


Fig. 4. Full thin lines represent the four lowest conduction bands in M-L direction calculated with the full potential method; the thicker lines represent the fitting using the two-band k•p model.

Conclusions

A simple two-band field-dependent band to band tunneling model has been presented. An inherent feature of the proposed model is that it is time dependent, which makes it suitable for implementation in a Monte Carlo simulation framework. The model has been applied to two different case studies of tunneling in 4H-SiC. The first case study shows that there is a significant tunneling (65%) between valence band two and three along the Γ-K segment at an electric field of 100kV/cm. The minimum energy separation in this case is 10 meV. The 4H-SiC band structure contains large regions where the band separations are below 100 meV. This indicates that band to band tunneling should be considered in accurate modeling of high field carrier transport in 4H-SiC. The second case study addresses tunneling over large energy separations (1.5 eV) in the conduction band. The tunneling probability is only 0.02% in this case. However, the discontinuity at the Brillouin zone boundary of the energy spectra along the c-axis direction for the conduction band in 4H-SiC prevents electrons to reach really high energy levels unless they can tunnel to higher conduction bands [6]. In this case, even a very small tunneling probability may affect the electron initiated impact ionization coefficient significantly.

References

[1] E. O. Kane, J. Phys. Chem. Solids. 12, (1959), p. 181.

[2] J. B. Krieger and G. J. Iafrate, Phys. Rev. B 33, (1986), p. 5494.

[3] E. Bellotti et al., J. App. Phys. 87, (2000), p. 3864.

[4] J. Callaway, "*Quantum Theory of the Solid State*", 2nd ed. Academic Press, (1991).

[5] C. Persson and U. Lindefelt, J. Appl. Phys. 82 , (1997), p. 5496.

[6] H-E. Nilsson et al.: *Silicon Carbide and Related Materials* (Trans Tech Publications, Switzerland 1999), p. 765.

Materials Science Forum Vols. 353-356 (2001) pp. 491-494
© 2001 Trans Tech Publications, Switzerland

Thermopower Measurements in 4H-SiC and Theoretical Calculations Considering the Phonon Drag Effect

V. Grivickas[1], M. Stölzer[2], E. Velmre[3], A. Udal[3], P. Grivickas[4], M. Syväjärvi[5], R. Yakimova[5] and V. Bikbajevas[1]

[1] Institute of Materials Research and Applied Sciences, Vilnius University, Sauletekio 10, LT-2054 Vilnius, Lithuania

[2] FB Physik, Martin-Luther-Universität Halle, DE-06120 Halle, Germany

[3] Institute of Electronics, Tallinn Technical University, Ehitajate tee 5, EE-19086 Tallinn, Estland

[4] Solid State Electronics, Royal Institute of Technology, Electrum 229, SE-16440 Kista-Stockholm, Sweden

[5] Dept. of Physics & Measurement Technology, Linköping Univ., SE-581 83 Linköping, Sweden

Keywords: Phonon-Drag Effect, Seebeck Coefficient, Thermopower

Abstract. The Seebeck coefficient study in a heavily nitrogen-doped *n*-type 4H-SiC epilayer in the direction perpendicular to **c**-axis is presented. The Seebeck coefficient steeply increases from 0.56 mV/K to 1.7 mV/K with decreasing temperature in the range 400-80 K. This behavior is explained by the phonon drag effect. An approach to the theoretical modeling of the phonon drag effect is discussed and simulation of the Seebeck coefficient temperature-dependence is displayed.

Introduction. The thermopower measurement is one of the most sensitive probes of the free carriers charge sign and their energy in semiconductors. One of the thermopower phenomena, the Seebeck effect, refers to a generation of a voltage, U, across two points of the material if a temperature gradient exists between them. The Seebeck coefficient, $S = U/\Delta T$, is in fact a direct measure of the heat per carrier over temperature or the entropy per carrier [1]. In semiconductors charge carriers are transporting energy, which consists of the difference between the Fermi level and the conduction (or valence) band and the kinetic energy of a particle in a classical free electron gas (for Boltzmann statistics $E_{kin} \approx 3/2\ k_B T$) [1]. Thus, S in semiconductors can be of the order of a few mV/K, i.e. about 10^3 times larger than in metals. It is important to note that Seebeck coefficient appears as a factor in the equation term describing any nonisothermal part of actual SiC devices and thus must be included properly during the device modelling.

The Seebeck effect in semiconductors was widely investigated in sixties and seventies. At that time, it was observed that in α-SiC the Seebeck coefficient exceeds the ones in silicon and germanium. It was believed that the reason for that phenomenon is not only in a simple difference in the bandgap energy but also in a stronger phonon-electron coupling – so-called phonon drag effect. The phonon drag effect makes an important contribution to the thermopower in semiconductors at low temperature [2]. It consists in the long wavelength phonons that are carrying heat from the hot to the cold region. Phonons collide with carriers and are swept with them along the temperature gradient. However, in those early investigations the polytype of SiC, the carrier concentration and many transport parameters of the semiconductor were not specified accurately enough. In this work, a Seebeck effect study of a well-defined 4H-SiC crystal is presented.

Experiment. A 300-μm thick epilayer of *n*-type nitrogen doped 4H-SiC was grown on a substrate by sublimation technique [3]. Then the substrate was carefully polished away and Ti contacts were deposited and annealed for 5 min at 950 °C. The measurements of the Hall effect have been performed to determine the electron concentration, n, and their mobility, μ_H, in the temperature range of 80-400 K (Fig. 1). Some data of similarly doped 4H-SiC from literature are also shown in order to illustrate the behavior of the doping influence. The temperature dependence of electron mobility is caused by a mixed ionized impurity and lattice scattering mechanism. The ionized impurity scattering is mainly a limiting factor for mobility at low temperature while lattice scattering causes mobility reduction at high temperature. The carrier concentration increases with

temperature because of the thermal ionization of the donor levels. From electron concentration extrapolation to 1/T = 0 we roughly estimated the total donor concentration in the sample as $6 \cdot 10^{18}$ cm^{-3}. The concentration of compensating acceptors can be evaluated at about 10^{17} cm^{-3}.

The thermoelectric voltage was measured in the direction perpendicular to c-axis of the crystal. Measurements have been produced under nearly steady-state conditions maintaining a small positive or negative temperature drop ΔT between the ends of the sample. Thin copper-constantan (Cu-Con) thermocouples served as voltage probes and temperature sensors at the same time. Some spurious voltages usually appear in the measuring circuit and must be eliminated. An example of measurement at T = 401 K is shown in Fig. 2. Negligibly small spurious voltages (b_1 and b_2) are evident at ΔT = 0. It should be noted that the measured voltages actually depend on the difference in the Seebeck coefficients of the semiconductor sample and the thermocouple wires since they are also experiencing the temperature drop. The double simultaneous measurements using Cu and Con as contact wires provide two slopes (a_1 and a_2) and allow accurate extraction of the Seebeck coefficient of the sample (S = –0.56 mV in particular case shown in Fig. 2). The detail procedure of Seebeck coefficient extracting from the measured parameters can be found in [7].

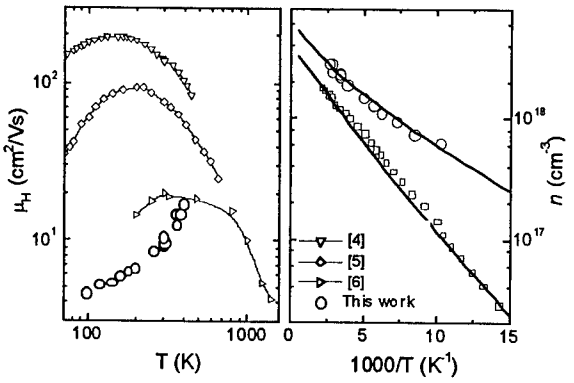


Fig. 1 Temperature dependences of Hall mobility and concentration in 4H-SiC.

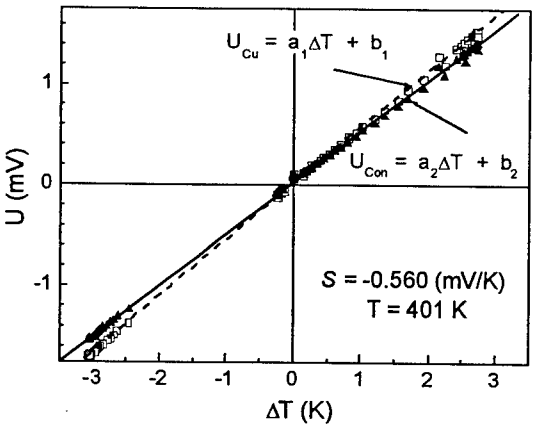


Fig. 2 Example of thermopower voltages versus ΔT. Copper and Constantan is used as contacts to SiC.

Results. The temperature dependence of the Seebeck coefficient is shown in Fig. 3. The Seebeck coefficient increases from 0.56 mV/K up to 1.7 mV/K with decreasing temperature in the range from 400 K to 80 K. The theoretical dependence without taking the electron-phonon coupling into account is also shown in Fig. 3. It is calculated according to the classical expression [2,8]:

$$S_e = -\frac{k_B}{|e|}\left(\frac{5}{2} + \ln\frac{N_c}{n}\right), \quad N_c(\mathrm{T}) = 1.66 \cdot 10^{19}(\mathrm{cm}^{-3}) \cdot \left(\frac{T}{300\mathrm{K}}\right)^{3/2}, \qquad (1)$$

where N_C is the density of the conduction band states. Note that Eq. (1) is valid for nondegenerated statistics; the first term accounts for thermal energy per electron in the band and the second term - for the energy difference between the conduction band edge and the Fermi level [2]. As it is clearly seen in Fig. 1, the conventional Seebeck coefficient obtained from Eq. (1) can describe neither the value nor the temperature dependence of the experimental data.

Phonon-drag effect. Frederikse [8] and Herring [2] have shown that the phonon drag contributes additively to the regular term of the Seebeck coefficient, so $S = S_e + S_{ph}$. The strength of the phonon drag is proportional to the ratio of phonon and electron (or hole) relaxation times

$$S_{ph} = -\frac{k_B}{|e|}\frac{ms_l^2}{k_B T}\frac{<\tau\tau_{ph}/\tau_{ac}>}{<\tau>}, \quad (2)$$

where m is the carrier effective mass, s_l is the average longitudinal sound velocity, τ_{ac} is the electron momentum relaxation time due to acoustic deformation potential scattering, τ is the total relaxation time of mixed carrier scattering. In Eq. (2) τ_{ph} is the low-energy phonon relaxation time, i.e. time averaged over the phonon spectrum in the range from $\mathbf{q}_{min} = 0$ to $\mathbf{q}_{max} = 2\mathbf{k}$ where $\mathbf{k}$ is the electron wave vector. Phonon-drag rises rapidly at low temperatures due to the predominating increase of the phonon mean free path. At very low temperatures (about 10 K), the influence of the phonon drag must saturate due to the sample boundary scattering that will limit the phonon mean free path to the crystal size.

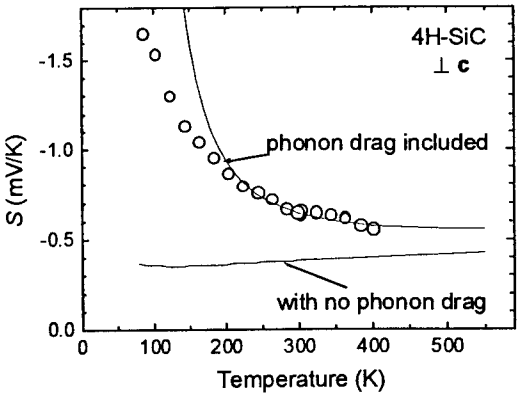


Fig. 3 Experimental and theoretical temperature dependencies of the Seebeck coefficient.

We assume that the main contribution to the mixed carrier scattering is given by the acoustic deformation potential and the ionised impurity scattering mechanisms. In the case of the predominantly ionised impurity scattering ($\tau_{ion} << \tau_{ac}$), the Eq. (2) can be rewritten as

$$S_{ph} = -\frac{k_B}{|e|}\frac{15\sqrt{\pi}}{32}\frac{l_{ph}}{l_{ac}}\sqrt{\frac{4T_c}{T}} \quad (3)$$

where the mean free path of the phonons is $l_{ph} = s_l \cdot <\tau_{ph}>$ and of charge carriers – $l_{ac} = <v_g\tau_{ac}> = 3\sqrt{\pi}/4 \cdot \sqrt{2k_BT/m} < \tau_{ac} >$. The characteristic temperature is defined as $T_c = ms_l^2/2k_B$. Eq. (3) is almost the same as obtained by Frederikse except a slightly different numerical coefficient ($35\sqrt{\pi}/32$ in Eq. (25b) of Ref. [8]). This is resulting from Frederikse's assumption of the energy-independent relaxation time of the phonons. The essential factor in the expression (3) is the ratio of the phonon and electron mean free paths.

The evaluation of l_{ph} is a very complicated theoretical problem. The well-known theory developed by Herring [2] predicts the following dependence of the low-energy phonon-phonon scattering relaxation time

$$\tau_{ph} = \tau_{ph}^* T^{-4} E^{-1} \quad (4)$$

where $\tau_{ph}^* \equiv \hbar^4 \rho s_l^3 / 4k_B m$ and ρ is the density of the material. For pure lattice scattering the temperature dependence of the phonon-drag term might be expected from Eq. (4) as $S_{ph} \sim T^{-7/2}$ [2]. This strong temperature dependence, however, was not confirmed experimentally by comprehensive Seebeck coefficient measurements in high purity silicon and germanium crystals. Instead, the S_{ph} extracted from the experiments is proportional to $T^{-2.3}$ for n- and p-Si, to $T^{-3.2}$ for p-Ge and to $T^{-2.4}$ for n-Ge [9,10]. In the present measurements in 4H-SiC, after subtraction the values of the regular Seebeck coefficient (doted curve in Fig. 3) from the experimental data, we have also deduced a weaker temperature-dependence of S_{ph}, namely $S_{ph} \sim T^{-1.8}$. Actually, the investigated

sample obviously has a large concentration of impurities, which may reduce the phonon mean free path significantly at low temperatures.

Because of the lack of a reliable theoretical model for low-energy phonon-phonon relaxation process we estimated the phonon mean free path using the measured lattice thermal conductance. From Debye's formula for lattice thermal conductance $\kappa_L = 1/3(c_v\, s_l\, l_{ph})$, where c_v is the heat capacity of the unit crystal volume, inserting electron mobility as $\mu_{ac} = e\langle\tau_{ac}\rangle/m$, we obtain from Eq. (3)

$$S_{ph} = -\frac{s_l}{T}\frac{l_{ph}}{\mu_{ac}} = -\frac{3\kappa_L}{c_v T}\frac{1}{\mu_{ac}} \tag{5}$$

This formula agrees with the result obtained by variational solution of the coupled Boltzmann transport equations for electrons and phonons [11]. The final expression used in the present calculations was obtained using substitution of c_v by its expression from Debye's classical theory (see [2]):

$$S_{ph} = -\frac{\kappa_L}{\mu_{ac}}\frac{2\pi^2(s_l\hbar)^3}{(k_B T)^4 J_4(\Theta_D/T)} \tag{6}$$

where $J_4(\Theta_D/T) = \int_0^{\Theta_D/T} \frac{x^4 e^x}{(e^x-1)^2}dx$ and the Θ_D is the Debye temperature. In Eq. (6) the degenerated statistics and incomplete doping ionisation corrections are omitted. To obtain the calculated values of $S(T)$ with phonon-drag effect shown in Fig. 3 the following data were used: $\mu_{ac}(T) = 947\ \mathrm{cm^2/V{\cdot}s}\cdot(T/300\ K)^{-2}$, $\kappa_L(T) = (4.9\ \mathrm{W/cm{\cdot}K})\cdot(T/300\ K)^{-1.7}$, $s_l = 12.6{\cdot}10^5$ cm/s, $\Theta_D = 1200$ K. For the temperature-dependence of the mobility an assumption proposed in Ref. [12] ($\mu \sim T^{-2}$) is used. The temperature-dependence of heat conductivity was obtained by approximating Slack's data [13].

As one can see from Fig. 3, the entering of the S_{ph} sufficiently improves the agreement between experimental points and calculated curve, though the disagreement at low temperatures still exists. For the proper evaluation of this effect, however, we have to conclude that measurements in lower doped samples are needed. These measurements will be performed in a nearest future.

This work was partially financed by the Swedish grants from the SiCEP and Visby programs.

References

[1] P. M. Chaikin, *An Introduction to Thermopower*, In *Organic Superconductors*, ed. by V. Z. Kresin and W. A. Little, Plenum Press, New York, 1990, p. 101.
[2] C. Herring, *The Role of Low-frequency Phonons in Thermoelectricity and Thermal Conduction*, In *Halbleiter und Phosphor*, Academie-Verlag, Berlin, 1958, p. 184.
[3] M. Syväjärvi, R. Yakimova, M. Tuominen, A. Kakanakova-Georgieva, M. F. MacMillan, A. Henry, Q. Wahab, and E. Janzen, J. Crystal Growth 197 (1999), p. 155.
[4] A. Schöner, S. Karlsson, T. Schmitt, N. Nordell, M. Linnarsson and K. Rottner, Mat. Sci. Eng. B61-62 (1999), p. 389.
[5] H. Iwata, K. M. Itoh, and G. Pensl, J. Appl. Phys. 88 (2000), p. 1956.
[6] H. Harima, T. Hosoda, and S. Nakashima, Mater. Sci. Forum 264-268 (1998), p. 449
[7] M. Stölzer, V. Bechstein, and J. Meusel, Thermopower measurement on thin films, Proc. 4th European Workshop on Thermoelectrics, Madrid University, Spain (1998).
[8] H. P. Frederikse, Phys. Rev. 92 (1953), p. 248.
[9] T. H. Geballe and G. W. Hull, Phys. Rev. 98 (1955), p. 940.
[10] T. H. Geballe and G. W. Hull, Phys. Rev. 94 (1954), p. 1134.
[11] D. Dorn, Z. Naturforschung 12a (1957), p. 739.
[12] M. Bakowski, U. Gustafsson, and U. Lindefelt, Phys. Stat. Sol (a) 162 (1997), p. 421.
[13] G. A. Slack, Phys. Rev. 35 (1964), p. 3460.

Materials Science Forum Vols. 353-356 (2001) pp. 495-498
© 2001 Trans Tech Publications, Switzerland

Donor Densities and Donor Energy Levels in 3C-SiC Determined by a New Method Based on Hall-Effect Measurements

H. Matsuura[1], Y. Masuda[2], Y. Chen[2] and S. Nishino[2]

[1] Osaka Electro-Communication University, 18-8 Hatsu-cho, Neyagawa, Osaka 572-8530, Japan

[2] Kyoto Institute of Technology, Matsugasaki, Sakyo, Kyoto 606-8585, Japan

Keywords: Donor Density, Donor Energy Level, Free Carrier Concentration Spectroscopy (FCCS), Graphical Peak Analysis, Hall Effect, Hexamethyldisilane, Temperature Dependence of Majority-Carrier Concentration

Abstract Without any assumption of the number of donor species, the densities and energy levels of donors in undoped 3C-SiC grown from hexamethyldisilane (HMDS; $Si_2(CH_3)_6$) are precisely determined by a graphical peak analysis method proposed here, using the temperature dependence of the majority-carrier concentration obtained from Hall-effect measurements.

1. Introduction

Silicon carbide (SiC) has been regarded as a promising semiconductor for power electronic applications owing to its excellent physical properties. In order to use SiC wafers or epilayers for electronic devices, an accurate evaluation of densities and energy levels of electronically active impurities or defects is essential. Among these impurities and defects, the electronic properties of deep level impurities or defects can be accurately determined by deep level transient spectroscopy (DLTS) or isothermal capacitance transient spectroscopy (ICTS) [1,2].

The temperature dependence of the majority-carrier concentration $n(T)$ obtained from Hall-effect measurements includes important information on shallow level impurities in a semiconductor. However, it has been difficult to determine the energy levels and densities of shallow impurities from the experimentally obtained $n(T)$. A curve-fitting method seems unsuitable because of the uncertainty in the number of impurity species in the semiconductor.

In this article, we introduce a new graphical peak analysis method (free carrier concentration spectroscopy; FCCS) to analyze the free carrier concentration $n(T)$, and apply it to undoped cubic SiC (3C-SiC) grown on silicon (Si) from non-flammable hexamethyldisilane (HMDS). In addition, we investigate the dependence of the donor energy levels on the thickness of the 3C-SiC film.

2. Basic Concept of Free Carrier Concentration Spectroscopy

DLTS or ICTS can uniquely determine the densities and energy levels, because each peak in the signal corresponds one-to-one to an impurity or defect. For example, the ICTS signal is defined as $S(t) \equiv t\mathrm{d}C(T)^2/\mathrm{d}t$, where $C(t)$ is the transient capacitance after a reverse bias is applied. Since $S(t)$ is described as the sum of $N_i e_i t \exp(-e_i t)$, it has a peak value of $N_i e_i t_{\mathrm{peak}i} \exp(-1)$ at a peak time $t_{\mathrm{peak}i} = 1/e_i$. Here, N_i and e_i are the density and emission rate of the i-th energy level. Therefore, $N_i e_i t \exp(-e_i t)$ plays an important role in the analysis.

For the analysis of the free carrier concentration $n(T)$ with respect to impurities, we have introduced a function that is described as the sum of $N_i \exp(-\Delta E_i/kT)/kT$, where N_i and ΔE_i are the density and energy level of the i-th impurity, respectively, T is the measurement

temperature and k is the Boltzmann constant [3,4]. The function $N_i \exp(-\Delta E_i / kT)/kT$ has a peak at $T_{\text{peak}i} = \Delta E_i / k$, which is not for all impurities in the temperature range of the measurement. If we can introduce a function in which the peak appears at $T_{\text{peak}i} = (\Delta E_i - E_{\text{ref}})/k$, we can shift the peak temperature within the measurement temperature range by changing the parameter E_{ref}. This indicates that we can determine N_i and ΔE_i in a wide impurity-energy-level range. Therefore, a function to be evaluated should be described as the sum of $N_i \exp[-(\Delta E_i - E_{\text{ref}})/kT]/kT$, where N_i and ΔE_i determined by this method should be independent of E_{ref} [5,6]. In addition, we have avoided introducing a differential evaluation of $n(T)$, because the differential of experimental data results in an increase of observation errors.

3. Theoretical Consideration of FCCS

For the following theoretical considerations, we assume an n-type semiconductor with n different donor species (density $N_{\text{D}i}$ and energy level $\Delta E_{\text{D}i}$ of the i-th donor for $1 \le i \le n$) and one acceptor density (N_{A}). The donor energy levels $\Delta E_{\text{D}i}$ are measured from the bottom of the conduction band (E_{C}) with $\Delta E_{\text{D}i-1} < \Delta E_{\text{D}i}$. From the charge neutrality condition, the free electron concentration $n(T)$ can be derived as

$$n(T) = \sum_{i=1}^{n} N_{\text{D}i}[1 - f(\Delta E_{\text{D}i})] - N_{\text{A}}, \tag{1}$$

where $f(\Delta E)$ is the Fermi-Dirac distribution function given by

$$f(\Delta E_{\text{D}i}) = \frac{1}{1 + \frac{1}{g_{\text{D}}} \exp\left(\frac{\Delta E_{\text{F}} - \Delta E_{\text{D}i}}{kT}\right)}, \tag{2}$$

ΔE_{F} is the Fermi level measured from E_{C}, and g_{D} is the degeneracy factor of donors.

On the other hand, using the effective density of states $N_{\text{C}}(T)$ in the conduction band, we can describe $n(T)$ as

$$n(T) = N_{\text{C}}(T) \exp\left(-\frac{\Delta E_{\text{F}}}{kT}\right), \tag{3}$$

where $N_{\text{C}}(T) = (kT)^{1.5} N_{\text{C0}}$, $N_{\text{C0}} = 2(2\pi m_{\text{n}}^* / h^2)^{1.5} M_{\text{C}}$, m_{n}^* is the electron effective mass, h is the Planck constant, and M_{C} is the number of equivalent minima in the conduction band.

From Eq. 1 and Eq. 3, we can introduce a favorable function to determine $N_{\text{D}i}$ and $\Delta E_{\text{D}i}$ as follows. We define the function to be evaluated as

$$H(T, E_{\text{ref}}) \equiv \frac{n(T)^2}{(kT)^{2.5}} \exp\left(\frac{E_{\text{ref}}}{kT}\right). \tag{4}$$

Substituting Eq. 1 for one of the $n(T)$ in Eq. 4 and substituting Eq. 3 for the other $n(T)$ in Eq. 4 give

$$H(T, E_{\text{ref}}) = \sum_{i=1}^{n} \frac{N_{\text{D}i}}{kT} \exp\left(-\frac{\Delta E_{\text{D}i} - E_{\text{ref}}}{kT}\right) I(\Delta E_{\text{D}i}) - N_{\text{A}} \frac{N_{\text{C0}}}{kT} \exp\left(\frac{E_{\text{ref}} - \Delta E_{\text{F}}}{kT}\right), \tag{5}$$

where

$$I(\Delta E_{\text{D}i}) = \frac{N_{C0}}{g_{\text{D}} + \exp\left(\frac{\Delta E_{\text{F}} - \Delta E_{\text{D}i}}{kT}\right)}. \tag{6}$$

Finally, using a personal computer, we take the temperature dependence of $I(\Delta E_{\text{D}i})$ into account,

and we can easily determine N_{Di} and ΔE_{Di} for each peak.

4. Experimental

3C-SiC epilayers with thicknesses (8 μ m, 16 μ m and 32 μ m) were grown on (100) Si substrates by atmospheric pressure chemical vapor deposition. HMDS with a flow rate of 0.5 sccm and H_2 with a flow rate of 2.5 slm were introduced at 1350℃. The growth rate was about 4.3 μ m/h.

Each 3C-SiC was cut into pieces of 5x5 mm^2, and Si substrates were removed by chemical etching. The free electron concentration $n(T)$ was measured by the van der Pauw method at temperatures between 85 K and 500 K, at a magnetic field of 5 kG and a current of 1 mA.

5. Results and Discussions

Figure 1 shows the free electron concentration $n(T)$ (open circles) and the function $H(T,E_{ref})$ (solid line) for the 8-μ m-thick 3C-SiC epilayer. $H(T,E_{ref})$ is calculated by interpolating $n(T)$ with a cubic spline function. From the peak, the density (N_{D2}) and energy level (ΔE_{D2}) can be determined to $1.7x10^{17}$ cm^{-3} and 46 meV, respectively.

As is clear from Eqs. 4 and 5, the function that is not influenced by this donor is introduced as

$$H2(T,E_{ref}) \equiv \frac{n(T)^2}{(kT)^{2.5}}\exp\left(\frac{E_{ref}}{kT}\right) - \frac{N_{D2}}{kT}\exp\left(-\frac{\Delta E_{D2}-E_{ref}}{kT}\right)I(\Delta E_{D2}), \quad (7)$$

which is shown by the solid line in Fig. 2. From the lower peak temperature and the lowest measurement temperature, N_{D1}, ΔE_{D1} and N_A are determined to be $1.1x10^{17}$ cm^{-3}, 10 meV and $1.3x10^{16}$ cm^{-3}, respectively.

The function that is not influenced by the first donor, or the second donor, or the acceptor is introduced as

$$H3(T,E_{ref}) \equiv \frac{n(T)^2}{(kT)^{2.5}}\exp\left(\frac{E_{ref}}{kT}\right) - \sum_{i=1}^{2}\frac{N_{Di}}{kT}\exp\left(-\frac{\Delta E_{Di}-E_{ref}}{kT}\right)I(\Delta E_{Di}) + N_A\frac{N_{C0}}{kT}\exp\left(\frac{E_{ref}-\Delta E_F}{kT}\right), \quad (8)$$

which is shown by the broken line in Fig. 2. From the lower peak temperature, N_{D3} and ΔE_{D3} are determined to be $1.1x10^{17}$ cm^{-3} and 107 meV, respectively. In the same matter, N_{D4} and ΔE_{D4} are determined to be $4.6x10^{16}$ cm^{-3} and 156 meV, respectively.

Figure 3 shows the free electron concentration simulated using the values determined here (solid

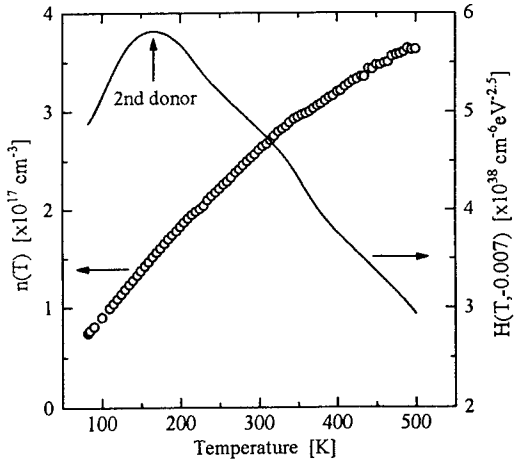


Fig. 1 n(T) and H(T,-0.007) for 8-μm-thick 3C-SiC

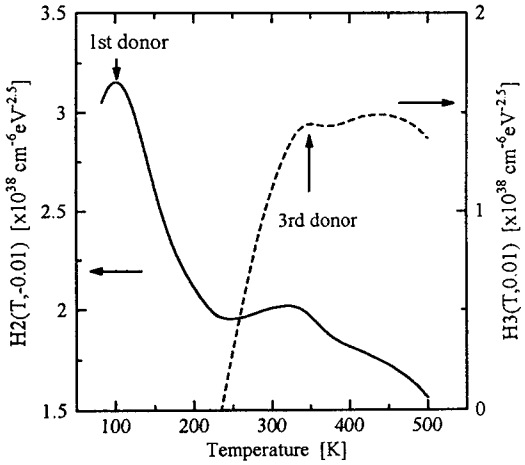


Fig. 2 H2(T,-0.01) and H3(T,0.01) for 8-μm-thick 3C-SiC

line). The open circles represent the experimentally obtained $n(T)$. The simulated free electron concentration is quantitatively in good agreement with the experimentally obtained $n(T)$, indicating that the values determined here are reliable.

In the same way as illustrated for the 8-μ m-thick epilayer, the densities and energy levels of donors in the 16-μ m-thick and 32-μ m-thick 3C-SiC epilayers are determined, and are listed in Table 1.

In undoped 3C-SiC grown from a mixture of SiH_4 and C_3H_8, only the ~15 meV donor with a concentration higher than 10^{18} cm^{-3} was reported with the compensation ratio higher than 0.9 [7]. In high-purity 3C-SiC crystals, on the other hand, a ~50 meV donor was reported [8]. From those reports, Segall *et al.* [7] concluded that both the ~15 meV and ~50 meV donors resulted from substitutional nitrogen (N) atom, and that a high degree of compensation and a large N concentration induced the reduction of the N donor energy level.

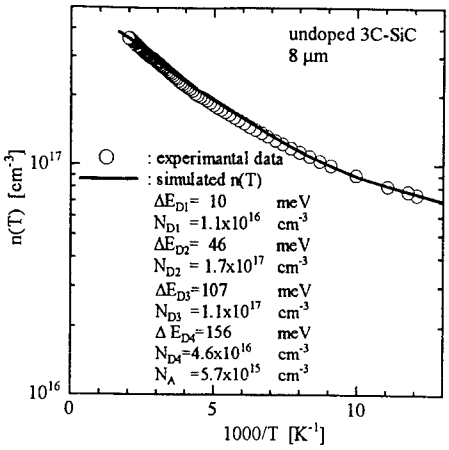


Fig. 3 Experimental and simulated n(T)

Table 1 Values determined by FCCS

Thickness [μ m]	8	16	32
ΔE_{D1} [meV]	10	7	14
N_{D1} [x10^{16} cm^{-3}]	11	8.1	4.7
ΔE_{D2} [meV]	46	46	54
N_{D2} [x10^{16} cm^{-3}]	17	20	8.1
ΔE_{D3} [meV]	107	97	120
N_{D3} [x10^{16} cm^{-3}]	11	13	10
ΔE_{D4} [meV]	156	-----	-----
N_{D4} [x10^{16} cm^{-3}]	4.6	-----	-----
N_A [x10^{16} cm^{-3}]	1.3	0.99	0.57

In the 3C-SiC investigated here, both the ~15 meV and ~50 meV donors coexist. The density of the ~15 meV donor is sensitive to the crystallinity of the epilayer, as shown in Table 1, because the crystallinity of our epilayers was enhanced as the thickness increased. Moreover, the substitutional N donor energy level was reported to be 54 meV from photoluminescence measurements [9]. Therefore, the ~50 meV donor may be ascribed to a substitutional N atom, while the ~15 meV donor may be attributed to some defect-N complex or nonstoichiometric defect, which Freitas *et al.* [9] and Suzuki *et al.* [10] suggested.

6. Conclusion

Even if we do not know the number of impurity species included in a semiconductor, we have found that FCCS can determine the densities and energy levels of shallow impurities accurately. In undoped 3C-SiC grown from HMDS, we detected four types of donors whose energy levels are 7-14 meV, 46-54 meV, 97-120 meV and 156 meV.

References

[1] T. Dalibor, G. Pensl, H. Matsunami, T. Kimoto, W.J. Choyke, A. Schöner and N. Nordell, phys. stat. sol. 162 (1997), p. 199
[2] H. Okusihi, Philos. Mag. B 52 (1985), p. 33.
[3] H. Matsuura, Y. Uchida, T. Hisamatsu and S. Matsuda, Jpn. J. Appl. Phys. 37 (1998), p. 6034.
[4] H. Matsuura , T. Kimoto and H. Matsunami, Jpn. J. Appl. Phys. 38 (1999), p. 4013.
[5] H. Matsuura, Y. Uchida, N. Nagai, T. Hisamatsu, T. Aburaya and S. Matsuda, Appl. Phys. Lett. 76 (2000), p. 2092.
[6] H. Matsuura, Y. Masuda, Y. Chen and S. Nishino, Jpn. J. Appl. Phys. 39 (2000), to be published in September.
[7] B. Segall, S.A. Alterovitz, E.J. Haugland and L.G. Matus, Appl. Phys. Lett. 49 (1987), p. 584.
[8] L.S. Aivazova, S.N. Gorin, V.G. Sidyakin and I.M. Shvarts, Sov. Phys. Semicond. 11 (1977), p. 1067.
[9] J.A. Freitas Jr., S.G. Bishop, P.E.R. Nordquist Jr. and M.L. Gipe, Appl. Phys. Lett. 52 (1988), p. 1695.
[10] A. Suzuki, A. Uemoto, M. Shigeta, K. Furukawa and S. Nakayima, Appl. Phys. Lett. 49 (1986), p. 350.

Materials Science Forum Vols. 353-356 (2001) pp. 499-504
© 2001 Trans Tech Publications, Switzerland

Intrinsic Defects in Silicon Carbide Polytypes

N.T. Son[1], P.N. Hai[1,2] and E. Janzén[1]

[1] Department of Physics and Measurement Technology,
Linköping University, SE-581 83 Linköping, Sweden

[2] Permanent address: Department of Physics, Hanoi University,
90 Nguyen Trai, Dong da, Hanoi, Vietnam

Keywords: Antisite, Electron Irradiation, Electron Paramagnetic Resonance, Vacancies

Abstract Electron paramagnetic resonance (EPR) has been used for investigation of intrinsic defects in 4H and 6H SiC. At W-band frequency (~95 GHz), the detailed structures of most of the EPR spectra in 4H and 6H SiC irradiated with electrons have been observed. We report our observation of two new EPR spectra, labelled EI1' and EI3', which are other configurations of the vacancy-related EI1 and EI3 centers. The transformation from the EI1 and EI3 centers to the EI1' and EI3' configurations, respectively, can be realised by annealing. Two new EPR spectra, labelled EI5 and EI6, with trigonal symmetry and spin S=1/2 were observed in irradiated p-type material. The EI5 and EI6 centers can be identified as the C vacancy and Si antisite in the positive-charge state.

1. Introduction

Intrinsic defects in SiC have been studied for many years but so far only a moderate knowledge on the vacancies and vacancy-related defects has been obtained. The interstitials and antisites in SiC are practically unknown. For antisites only calculations in 3C SiC [1,2] have been reported.

Both the silicon and carbon vacancies are known to be stable at room temperature. The negatively charged silicon vacancy (V_{Si}^-) has been identified by electron paramagnetic resonance (EPR) in the 3C [3], 4H [4] and 6H SiC [5] polytypes. It has a high spin configuration (S=3/2) [4] and is undistorted (T_d symmetry). Such an electronic structure was also supported by theoretical investigations [6,7]. The ground state of the silicon vacancy in the neutral-charge state (V_{Si}^0) in 3C and 2H SiC was theoretically predicted by Torpo et al [6] to be a triplet. This seems to support the assignment of the photoluminescence (PL) centers V1, V2 in 4H and V1, V2 and V3 in 6H SiC (or the P3 and P5 EPR centers, which were previously attributed to long-distance vacancy pairs by Vainer et al [8]) by Sörman et al [9] as originating from the V_{Si}^0 at different inequivalent sites. However, taking into account many-electron interactions, Deák et al [10] found in their calculations that the V_{Si}^0 in 3C SiC has a spin singlet ground state and therefore no EPR signal due to the ground state can be expected.

In the recent calculations [7,11], the carbon vacancy in 3C and 4H SiC was found to be a negative-U system. Therefore, EPR observations of the carbon vacancy in the equilibrium condition can not be expected. This is in contrast to the previous EPR studies by Itoh et al [12], in which they have attributed the T5 center in proton- and electron-irradiated p-type 3C SiC to the positively charged carbon vacancy (V_C^+).

EPR is the most used and important technique for defect identification. However, its use for characterisation of 3C polytype is limited since mainly thin epitaxial films, which are not suitable for the EPR technique, have so far been available. For the hexagonal polytypes, the crystal structure with low symmetry and the existence of different inequivalent lattice sites make EPR studies difficult. It is very common that in irradiated 4H and 6H SiC, many EPR spectra appear together in the region of g-values close to 2, resulting in a severe overlapping between the spectra. As a result,

the hyperfine structure (HFS) due to the interaction with the ^{29}Si or ^{13}C atoms in the nearest neighbour (NN) shell, which can provide the most important information for the defect identification, is often obscured. To overcome the above problems, high frequency EPR is needed.

In this work, we use high frequency EPR to study intrinsic defects in 4H and 6H SiC. At W-band (~95 GHz) frequency, it is possible to separate most of the spectra in 4H and 6H SiC and to obtain detailed structures of several EPR centers. Our results on vacancy-related defects, including the identification and electronic structure of the carbon vacancy and silicon antisite in their positive-charge state are presented.

2. Experimental

The samples used in this work were mainly commercial n- and p-type 4H and 6H SiC substrates but also free-standing, p-type layers grown by high temperature chemical vapor deposition (HTCVD). The p-type substrates were Al-doped (2×10^{17}-1×10^{18} cm^{-3}). The p-type layers were either Al-doped (in the mid 10^{16} cm^{-3} range) or compensated by residual impurities with a concentration below 10^{16} cm^{-3}. The samples were irradiated with 2.5 MeV electrons at room temperature or at 400°C with doses in the range of 1×10^{17}-2×10^{18} cm^{-2}. EPR measurements were performed on Bruker X-band (~9.5 GHz) EPR spectrometers (ER200D-SRC or ELESYS 580) and also on a home made W-band (~95 GHz) EPR setup.

3. Vacancy- and antisite-related defects

3.1. The EI1 and EI3 centers

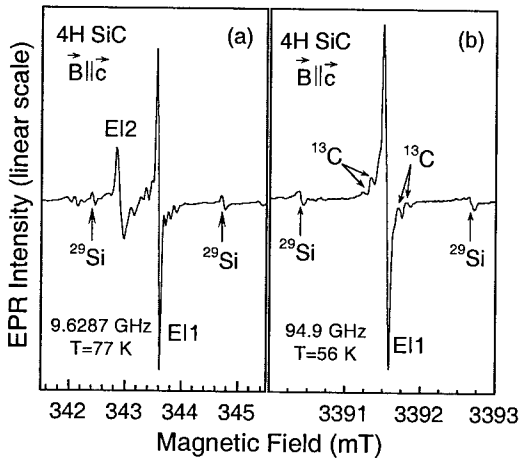


Fig.1: EPR spectra of the EI1 centers in electron-irradiated, p-type 4H SiC at (a) X-band and (b) W-band frequencies.

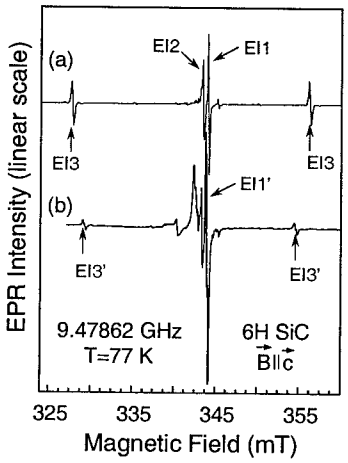


Fig.2: EPR spectra observed in irradiated 6H SiC (a) before and (b) after annealing at 240 °C. At this temperature, the EI1 and EI3 signals completely disappear while the intensities of the two new spectra, EI1' and EI3', reach their maximum.

The EI1 center has previously been observed in electron-irradiated, p-type 4H and 6H SiC [13] at X-band frequency. The EI1 center has C_{1h} symmetry and an effective electron spin S=1/2. It has the HFS due to the interaction with two nearest Si neighbours as can be can seen in Fig.1(a). It is possible that the EI1 center and the PB center in 6H SiC [14] are the same. Based on the similarity in g-values and annealing behaviour compared to the T5 center in 3C SiC [12], the PB center was also suggested to be the V_C^+ [14] despite the difference in the hyperfine (HF) interaction (in the case of the T5 center, the HF interaction is with four nearest Si neighbours). At X-band frequency, the HFS due to the interaction with 12 C atoms in the next nearest neighbour (NNN) shell appears to be confusing with three equidistant satellites on each side of the main line [Fig.1(a)]. At W-band frequency (~95 GHz), the EI1 signal is well separated from the other spectra and the detailed HFS of ^{13}C atoms in the NNN

Table 1: Spin-Hamiltonian parameters that we obtained for some vacancy-related centers and the Si antisite in 4H and 6H SiC. α and β are the angles between the c-axis and the directions of g_z and A_z, respectively. Here the principal g_z and g_x axes are in the $(11\bar{2}0)$ plane and g_y is perpendicular to this plane. The error in the g-values is ±0.0001 for the EI1-EI4 and ±0.00002 for the EI5 and EI6 centers.

Center	Spin and symmetry	Polytype	g	A , D and E [10^{-4} cm^{-1}]	Model
EI1	S=1/2 C_{1h}	4H&6H	g_x =1.9962 g_y =2.0019 g_z =2.0015 $\alpha=41^0$	with 2 Si; two different C_{1h} tensors A_x^1=19, A_y^1=23.4, A_z^1=22.6 A_x^2=23.4, A_y^2=28.6, A_z^2=20.2 $\beta=41^0$	$(V_C+H)^0$ (?)
EI1'	S=1/2 C_{1h}	4H&6H	g_x =1.9954 g_y =2.0013 g_z =2.0014 $\alpha=33^0$	with 2 Si	$(V_C+H)^0$ (?)
EI2	S=1/2 C_{3v}	4H&6H	$g_{\|}$=2.0030 $g_\perp$=2.0049	with 4 C	(?)
EI3	S=1 C_{1h}	4H&6H	g=2.0063 $\alpha=46^0$	with 4 Si 4H: D=552; 6H: D=559	$(V_C+2H)^0$ (?)
EI3'	S=1 C_{1h}	4H&6H	g=2.0063 $\alpha=46^0$	with 4 Si 6H: D=538	$(V_C+2H)^0$ (?)
EI4	S=1 C_{1h}	4H&6H	g_x =2.0051 g_y =2.0038 g_z =2.0029 $\alpha=54^0$	with 4 Si 4H: D=344; E=67 6H: D=328; E=67	$(V_C^+ + V_C^+)$
EI5	S=1/2 C_{3v}	4H 6H 	$g_{\|}$=2.00322 $g_\perp$=2.00484 $g_{\|}$=2.00316 $g_\perp$=2.00461	1 Si: $A_{\|}$= 60.4; $A_\perp$=41.7 3 Si: A_x=46.9, A_y=34.5, A_z=35.6; $\beta=5^0$ 1 Si: $A_{\|}$= 60.6; $A_\perp$=41.1 3 Si: A_x=46.8, A_y=34.5, A_z=35.6; $\beta=5^0$	V_C^+
EI6	S=1/2 C_{3v}	4H 6H 	$g_{\|}$=2.00302, $g_\perp$=2.00473 $g_{\|}$=2.00242, $g_\perp$=2.00489 $g_{\|}$=2.00286, $g_\perp$=2.00478 $g_{\|}$=2.00236, $g_\perp$=2.00487	$A_{\|}$= 123.5, $A_\perp$=84.8 (138 K) $A_{\|}$= 141.0, $A_\perp$=96.2 (23 K) $A_{\|}$= 134.5, $A_\perp$=91.7 (102 K) $A_{\|}$= 146.8, $A_\perp$=100.8 (23 K)	Si_C^+

shell can be detected [Fig.1(b)]. The same spectrum is also observed in 6H polytype. Thus, based on the obtained HFS from the NN and NNN shells it can be unambiguously concluded that the EI1 center is a defect at a C site. The HF interaction with only two of the four Si neighbours is typical for the singly negatively charged vacancy in Si [15], and has also been suggested by calculations for 4H SiC [16]. Therefore, in our previous study [13], the EI1 center was tentatively attributed to either the V_C^- or a complex between the carbon vacancy and an impurity.

The EI3 center has also C_{1h} symmetry, but the spin is S=1 [13]. In irradiated p-type material, this spectrum is always observed together with the EI1 signal. The HF interaction is with four nearest Si neighbours and the EI3 center was attributed to a pair between a carbon vacancy and an impurity [13]. The annealing behaviour of these two centers is very similar to that of the T5 center in 3C SiC [12]. We have performed a careful annealing study and found that the EI1 and EI3 centers are actually transformed to the EI1' and EI3' centers, respectively. In some samples the EI1'is already present together with the EI1 signal, but very weak. The EI3' signal only appears at annealing temperatures around 200°C. At this temperature, the two new centers start increasing in intensity rapidly while the EI1 and EI3 signals decrease and completely vanishes at around 240°C.

The EPR spectra of these centers in 6H SiC before and after annealing at 240°C for 5 minutes are shown in Fig. 2(a) and 2(b), respectively. The EI1' and EI3' centers are very similar to the EI1 and EI3 [13], respectively. The principal g-values of the EI1' center are slightly different from that of the EI1 (see Table 1), but the angle between the principal g_z and the c-axis is 33 ° compared to 41° in the case of the EI1. In both cases, the HF interactions with two nearest Si neighbours are also similar as can be seen in Fig. 2(a) and 2(b). The g-values and the direction of the principal axis of the fine-structure tensor D are the same for both the EI3 and EI3' centers, but the D-value of the EI3' center is smaller (Table 1). Based on the annealing behaviour and the similarity in the spin-Hamiltonian parameters, we assign the EI1 and EI1' centers to two different configurations of the same defect. Similarly, the EI3 and EI3' spectra are suggested to be originated from different configurations of the same center.

The electronic structure of the EI1 and EI1' centers can be explained by either the V_C^- or V_C + impurity model. However, taking into account the link between the EI1 and EI3 centers and the conditions for observation (only in p-type), the latter model appears to be more appropriate. The most probable impurity in this case is hydrogen. The $(V_C+H)^0$ defect with the H making bond with two of the four Si neighbours. The extra electron introduced by the H atom finds places on the antibonding combination of the two Si-H sp^3-hybrid bonds, so that the H atom is at the node of this orbital [17]. Therefore, no HF interaction with the H atom would be expected. Trapping one more H at the other Si-Si bond, this defect becomes $(V_C+2H)^0$, which can explain the electronic structure of the EI3 and EI3' centers. The above models can also explain why these defects could not be detected in n-type material. Recent calculations by Gali et al [17] also predict the stability of these hydrogen-V_C complexes and the similarity in the electronic structures compared to the V_C^-. However, a conclusive identification of these centers requires further investigations.

3.2. The EI5 and EI6 center

In p-type 4H and 6H SiC irradiated at 400°C, several new EPR signals were observed. Fig. 3(a)

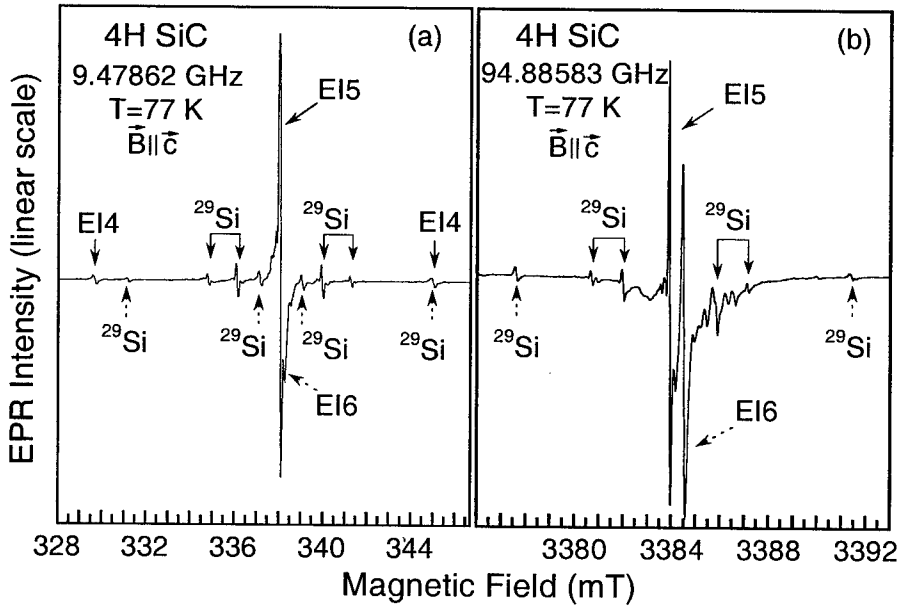


Fig. 3: EPR spectra of the EI4, EI5 and EI6 centers in electron-irradiated, p-type 4H SiC observed for the magnetic field parallel to the c-axis at (a) X-band and (b) W-band frequencies. The solid or dashed arrows indicate the ^{29}Si HF lines related to the EI5 and EI6 centers, respectively. Weak EPR lines at around 3386.5 and 3390 mT in (b) are not related to the EI5 and EI6 spectra.

shows the spectrum observed in 4H SiC at X-band frequency for the magnetic field parallel to the c-axis. The EI4 signal was previously observed and studied [18]. Two strong lines at around 338 mT, labelled EI5 and EI6, could not be resolved at X-band frequency. Each line seems to be accompanied by several satellites as indicated by solid and dashed arrows. The intensity ratio between the satellites and the main line EI5 is about 20 %, which is approximately the natural abundance of four ^{29}Si (I=1/2 and 4.7 % natural abundance) atoms. Therefore, these satellites can be assigned as the HFS due to the interaction between the electron spins and the nuclear spin of ^{29}Si nuclei in the NN shell. Fig. 3(b) shows the spectrum observed in the sample, at the same temperature and the direction of the magnetic field, but at ~95 GHz. As can be seen in the figure, the EI5 and EI6 lines are now well separated. The distances between the satellites corresponding to each center are still the same as at X-band frequency. This confirms that all the satellites are HFSs. The two far-satellites of the EI6 center has the intensity of about 4.5-5% of that of the main line, and therefore, can be attributed to the HFS of one ^{29}Si atom at a C site. A small difference in the intensity of these two satellites is due to a different thermal distribution at I=+1/2 and I=-1/2 HF splitting levels, which becomes pronounced at higher magnetic fields.

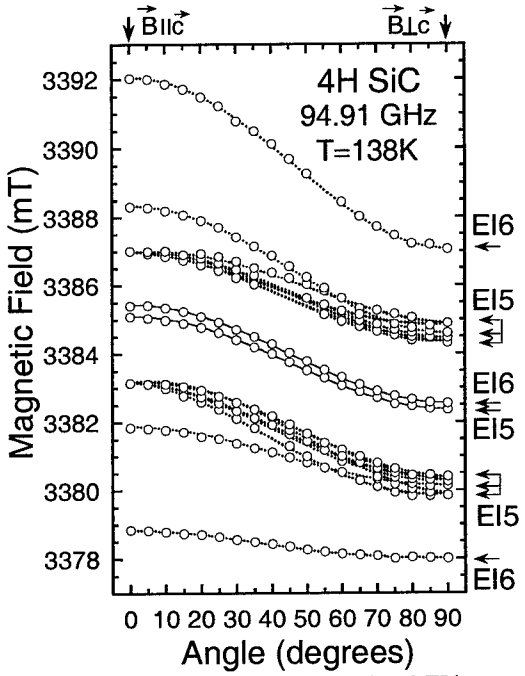


Fig.4: Angular dependencies of the EI5 and EI6 centers in 4H SiC measured at 138 K. Solid and dashed curves are the simulations of the main and HF lines, respectively, using parameters in Table 1.

The angular dependencies of the EI5 and EI6 spectra were studied with the magnetic field rotating in the $(11\bar{2}0)$ plane and at both X-band and W-band frequencies for comparison. As an example, the angular dependencies of these two centers in 4H SiC measured at 138 K and at 94.91 GHz are illustrated in Fig. 4. Both the centers have C_{3v} symmetry and an effective electron spin S=1/2. The g-values obtained from the fit for these centers are given in Table 1. The curves represent the simulation using the spin-Hamiltonian parameters deduced from the fit. The thin and thick dashed curves are the calculated angular dependencies of the ^{29}Si HF lines corresponding to the EI5 and EI6 centers, respectively, using the g-values and HF parameters A given in Table 1. In the case of the EI5 center, the HF interaction with four nearest Si neighbours can be described by two tensors as expected, one with C_{3v} symmetry (for the Si atom on the bond along the c-axis) and the other with C_{1h} symmetry (for three other Si atoms). The g-values of the EI5 in 4H and 6H SiC are very similar. Within experimental errors, the HF tensor of the EI5 center is the same for both polytypes.

The EI5 spectrum is not detectable at temperatures below 25 K or at room temperature, while the EI6 signal can always be observed. The HF interaction with four nearest Si neighbours of the EI5 center clearly indicates that it is a single defect at a C site. This center can only be detected in irradiated materials regardless of the concentration of impurities. We therefore assign the EI5 spectrum as originated from the carbon vacancy. The V_C in either the negative or positive-charge state can have spin S=1/2. Since the EI5 spectrum is detected only in p-type materials, the center the is suggested to be in the positive-charge state. It should be noticed that the A-values of the EI5

center are about two times larger than that of the T5 center, which was attributed to the V_C^+ in 3C SiC [12]. The EI5 center is stable at higher temperatures as compared to the T5 center. Due to overlapping, the annealing study using X-band EPR was not possible.

The observation of the HFS due to a ^{29}Si atom at a C site confirms that the silicon antisite is involved in the EI6 center. The HF interaction with four nearest Si neighbours was also detected. This HFS and the C_{3V} symmetry indicate that the defect is the isolated Si antisite. The observation of the defect in p-type material and its spin S=1/2 suggest that the EI6 center is the silicon antisite in the positive-charge state (Si_C^+). It should be noticed that both the g-values and the HF tensor A of this center change with temperature as can be seen in Table 1 for two different temperatures. Replacing a C atom by a bigger Si leads to an outward relaxation of the defect. However, at low temperatures, the outward relaxation can be difficult. Due to the stress from the surrounding environment the configuration of the defect is changed to a more anisotropic one as can be seen from the g-values. Increasing temperature makes it easier for the defect to relax to the normal configuration, which is less anisotropic. Due to the outward relaxation, the localisation of the wavefunction at the Si_C may reduce, resulting in a decrease of the HF constant.

4. Summary

The EI1 and EI1' centers belong to two different configurations of the same defect, whose electronic structure can be described by the $(V_C+H)^0$ model. The EI3 and EI3' centers are attributed to different configurations of the $(V_C+2H)^0$ complex. Since the V_C^+ and the EI4 spectra are observed in the same sample, the $(V_C^+-V_C^+)$ model is suggested for the EI4 center instead of the $(V_C^-+V_C^-)$, which we previously proposed. Using high frequency EPR, we have identified the EI5 and EI6 centers as the V_C^+ and Si_C^+, respectively. In both 4H and 6H polytypes, no site dependence of the EI5 and EI6 centers has been observed. The outward relaxation of the Si_C^+ is strongly temperature dependence. This center acts as a donor in p-type materials. Therefore, it may be used for compensating acceptors to make semi-insulating SiC.

Acknowledgements: Discussions with Prof. P. Deák and Dr. A. Gali are appreciated. Support for this work was provided by the SSF program SiCEP, the Swedish Research Council for Engineering Sciences (TFR), the Swedish Natural Science Research Council (NFR), ABB Corporate Research, Okmetic AB and the National Defence Research Establishment (FOA).

References

[1] Yuan Li and P. J. Lin-Chung, Phys. Rev. B **36** (1987), p. 1130.
[2] L. Torpo, S. Pöykkö and R.M. Nieminen, Phys. Rev. B **57** (1998), p. 6243.
[3] H. Itoh, M. Yoshikawa, I. Nashiyama, S. Misawa, H. Okumura and S. Yoshida, IEEE Trans. Nucl. Sci. **37** (1990), p. 1732.
[4] T. Wimbauer, B.K. Meyer, A. Hofstaetter, A. Scharmann and H. Overhof, Phys. Rev. B **56** (1997), p. 7384.
[5] J. Schneider and K. Maier, Physica B **185** (1993), p. 199.
[6] L. Torpo, R.M. Nieminen, K.E. Laasonen and S. Pöykkö, Appl. Phys. Lett. **74** (1999), p. 221.
[7] A. Zywietz, J. Furthmüller and F. Bechstedt, Phys. Rev. B **59** (1999), p.15166.
[8] V.S. Vainer and A. Il'in, Sov. Phys. Solid State **23** (1981), p. 2126.
[9] E. Sörman, N.T. Son, W. M. Chen, O. Kordina, C. Hallin and E. Janzén, Phys. Rev. B **61** (2000), p. 2613.
[10] P. Deák, J. Miró, A. Gali, L. Udvardi and H. Overhof, Appl. Phys. Lett. **75** (1999), p. 2103.
[11] F. Bechstedt, A. Zywietz and J. Furthmüller, Europhys. Lett. **44** (1998), p. 311.
[12] H. Itoh, M. Yoshikawa, I. Nashiyama, S. Misawa, H. Okumura and S. Yoshida, J. Electronic Mater. **21** (1992), p. 707.
[13] N.T. Son et al, Mater. Sci. Eng. B**61-62** (1999), p. 202.
[14] D. Cha, H. Itoh, N. Morishita, A. Kawasuso, T. Ohshima, Y. Wantanabe, J. Ko, K. Lee, and Nashiyama, Mater. Sci. Forum **264-268** (1998), p. 615.
[15] G.D. Watkins, in *Radiation Damage in Semiconductors* (Paris, 1965), p. 97.
[16] P. Deák and A. Gali, unpublished.
[17] A. Gali, B. Aradi, P. Deák, W.J. Choyke and N.T. Son, Phys. Rev. Lett. **84** (2000), p. 4926.
[18] N.T. Son et al, Mater. Sci. Forum **338-342** (2000), p. 821.

Materials Science Forum Vols. 353-356 (2001) pp. 505-508
© 2001 Trans Tech Publications, Switzerland

Radiation-Induced Pair Defects in 6H-SiC Studied by Optically Detected Magnetic Resonance

Th. Lingner, S. Greulich-Weber and J.-M. Spaeth

Department of Physics, University of Paderborn,
Warburgstr. 100, DE-33095 Paderborn, Germany

Keywords: Absorption, Annealing, Antisite, Defect Formation, Defects, Electron Paramagnetic Resonance, Luminescence, MCDA, Radiation Defect, Vacancy

Abstract: We used the magnetic circular dichroism of the absorption (MCDA) and MCDA-detected electron paramagnetic resonance (MCDA-EPR) to study a radiation-induced point defect in neutron-irradiated and subsequently annealed 6H-silicon carbide. We found MCDA-lines at photon energies in the 1.0-1.1eV range to be associated with EPR spectra for spin S=1 with positive fine structure constants around $400 \cdot 10^{-4} cm^{-1}$. The analysis of the hyperfine (HF) structure indicates that the defect measured is the excited spin triplet state of the neutral C_{Si}-V_C antisite-vacancy-pair at the three inequivalent lattice sites, which is a possible annealing product of the isolated silicon vacancy.

Introduction

Among the numerous point defects created by irradiation of SiC with high energy particles there are many spin S=1 centers known from EPR experiments. Most of them have tentatively been assigned to vacancy pairs [1]. In most cases their optical transitions have not yet been found, which would allow to identify the defects by photoluminescence (PL). Moreover, differences between the inequivalent lattice sites in hexagonal SiC have not been resolved in most cases. We report on the properties of one of these radiation-induced defects in 6H-SiC. Until now it has been assumed to be a non-radiative recombination center [2], and only two different lattice sites have been resolved [2]. In this study, the identification of its optical transitions, of three different MCDA- and EPR spectra and of the hyperfine (HF) structure is presented. The defect measured is the excited spin triplet state of the neutral C_{Si}-V_C antisite-vacancy pair on the three inequivalent lattice sites in agreement with recent calculations [3].

Experimental

6H-SiC bulk single crystal samples grown by the sublimation sandwich method [4] and irradiated with reactor neutrons were used. For most experiments a sample annealed at 1000°C was used since it provided the highest signal intensities.
The Electron Paramagnetic Resonance (EPR) spectra were detected optically via the magnetic circular dichroism of the absorption (MCDA) which is proportional to the spin polarization of the ground state [5]. The MCDA-EPR measurements were performed in K-band (24GHz) at 1.5K. Some experiments were carried out in a double beam configuration, in which the sample was additionally excited with eiter visible (457.9nm-515.5nm) or UV (351.1nm-363.8nm) light of an Argon ion laser. We will call this briefly "additional excitation". The conventional EPR spectra were measured in an X-band (9.7GHz) spectrometer under illumination of the sample with white light.

Experimental Results

Without additional excitation and with the magnetic field parallel to the $\vec{c}$-axis of the crystal (θ=0°), the MCDA spectrum consists of three lines labelled P6a (1075meV), P6b (1048meV) and P6c (1011meV). With additional excitation and the magnetic field rotated away from the $\vec{c}$-axis, further MCDA signals at 999meV, 1030meV, 1049meV and 1065meV appear (fig. 1). Luminescence lines were observed at the same photon energies as the MCDA lines under excitation of the sample with above band gap light (UV) as well as with below band gap (457.9nm-515.5nm) light.

In the P6a, b and c MCDA lines the MCDA-EPR spectra of Spin S=1 centers with axial symmetry about the c-axis of the crystal were measured (fig. 2). Their parameters are given in table 1, where $g_{\parallel}$ and $g_{\perp}$ have their usual meaning and the fine structure constant D is the zero-field splitting between the m_S=0 and the m_S=±1 levels. It is noted that that the centers with the larger photon energy have the larger fine structure constant. They seem to be proportional to each other.

Without additional excitation, both the high field and the low field MCDA-EPR lines are negative, i. e. the EPR transitions decrease the spin polarization. The spin lattice relaxation time T_1 at 1.5K is of the order of several minutes. Upon additional excitation, the high field MCDA-EPR line becomes inverted, and the relaxation time T_1 is of the order of a few seconds.

To determine the sign of D the relative reduction of the MCDA line intensity upon fully saturating the EPR transitions was measured after the spin system had been left to thermalize. The high field line for $\vec{B}\|\vec{c}$ was the more intense one belonging to the m_S=-1↔m_S=0 transition. Therefore the sign

spectrum	$g_{\parallel}$	$g_{\perp}$	D [$\cdot 10^{-4}$cm^{-1}]	photon energy [meV]
P6a	2.0028(5)	2.003(1)	456(2)	1075(1)
P6b	2.0028(5)	2.003(1)	447(2)	1048(1)
P6c	2.0028(5)	2.003(1)	430(2)	1011(1)

Table 1: Parameters of the P6 center determined by MCDA-EPR at T=1.5K

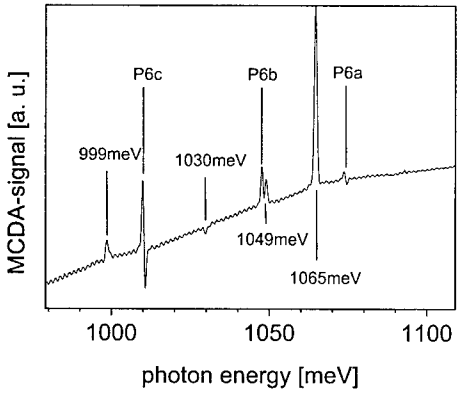


Fig. 1: The MCDA spectrum of neutron-irradiated 6H-SiC annealed at 1000°C. The magnetic field of B=2T was directed θ=25° off the c-axis of the crystal. The sample was additionally excited with visible laser light.

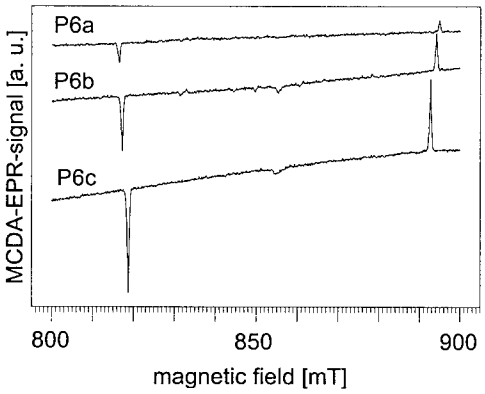


Fig. 2: MCDA-EPR spectra measured in the P6a, b and c MCDA lines under additional excitation at θ=25°. The microwave frequency was 24GHz. The spectra were measured at T=1.5K. They have small differences in their fine structure splitting (table 1).

of D must be positive (fig. 3). The inversion of the high field line under additional excitation indicates an emissive EPR transition due to an enhanced population of the m_S=0 level in the case $\vec{B}\|\vec{c}$.

The 1065meV MCDA line is diamagnetic. In the 999meV, 1030meV and 1049meV MCDA lines MCDA-EPR spectra were measured. Due to a poor signal to noise ratio and a limited angular range in which the signals are detectable, a complete analysis of the angular dependence was very difficult from the MCDA-EPR data. As a preliminary result, we can state that at least the 999meV and the 1049meV spectra seem to correspond to the same type of center as the P6 spectra, but with their fine structure axes directed along the Si-C-bonds which are inclined by 71° relative to the $\vec{c}$-axis.

Taking over the notation by Vainer et al [1], we will call tese the P7 spectra. The P6 and P7 spectra were also found with conventional EPR in the same sample under illumination with hν≥1.eV.

Although no detailled analysis of the annealing behaviour was carried out, it is noted that the P6 MCDA-spectrum is most intense in a sample annealed at 1000°C. In samples annealed at 600°C and 1200°C it is still measurable, but weaker. The intensity ratio between the P6a, b and c spectra varies with irradiation and annealing parameters. The P6 spectrum was neither observed in as-irradiated samples, nor in the unirradiated reference sample of the same batch.

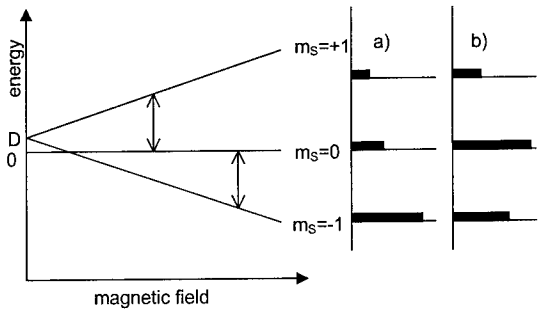


Fig. 3: Illustration of the EPR transitions (left) and relative occupation of the Zeeman levels (right) for the P6 triplet system at $\vec{B}\|\vec{c}$ a) thermalized and b) under additional excitation (see text).

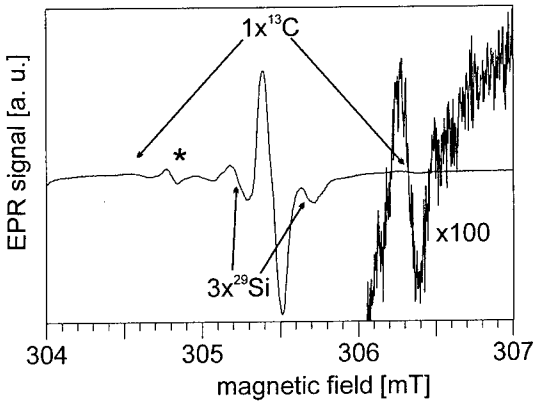


Fig. 4: Hyperfine structure of the P6c low field EPR line at $\vec{B}\|\vec{c}$. The intensity ratio to the central line corresponds to the interaction with three equivalent silicon nuclei and one carbon nucleus. The line marked with an asterisk was not observed in the MCDA-EPR spectra and belongs to a different defect.

The hyperfine (HF) structure was measured with conventional EPR in order to avoid saturation effects which occur in MCDA-EPR. The P6 EPR lines have a symmetric HF splitting of A=12(1)MHz due to the interaction with I=1/2 nuclei (fig. 4). The intensity ratio corresponds to the interaction with three equivalent silicon nuclei (^{29}Si: I=1/2: 4.7% abundance) nuclei. Furthermore, for the P6c line weak hyperfine doublet satellite lines split symmetrically to the central line by 1.7mT (A=48(1)MHz) were observed for $\vec{B}\|\vec{c}$ (fig.4). Their intensity with respect to the central line is 0.7(2)%. This is in good agreement with the expected intensity ratio of 0.55% for one carbon nucleus (1.1% abundance of ^{13}C, I=1/2). The SHF structure of the P7 spectra was not resolved, but their overall linewidth is the same as for the P6 spectra.

Discussion

EPR spectra with similar g-factors and D-values have been found by Pavlov et al [6] in α- and neutron-irradiated SiC (denoted as G6), by Vainer and Il'in [1] in high temperature quenched and

annealed samples (P6 and P7 spectrum) and by Son et al [2] in as-grown and electron irradiated materials. From the sample preparation conditions under which the center has been observed [1,2,6] it is beyond doubt that it is an intrinsic/radiation-induced defect. Among all known radiation-induced spin-1 centers, the P6/P7 centers are the only ones with their axes directed exactly along the Si-C bonds, i. e. they have the symmetry of nearest neighbour pairs.

The question is, what atoms/vacancies are at the neighbouring sites. In principle, there are four possibilities for such a pair defect: The antisite pair (C_{Si}-Si_C), the vacancy pair (V_{Si}-V_C) and antisite-vacancy pairs (C_{Si}-V_C and V_{Si}-Si_C).

For the C_{Si}-Si_C antisite pair and the V_{Si}-Si_C vacancy-antisite pair one would expect a hyperfine interaction with the ^{29}Si antisite. This was not observed. Furthermore, calculations by Rauls et al [7] indicate that V_{Si}-Si_C is not stable at least in the neutral charge state.

The other type of antisite-vacancy pair (C_{Si}-V_C) is stable in the neutral charge state and can be generated from the isolated silicon vacancy by the migration of a neighbouring C-atom into the vacancy [7]. This model can explain that the P6/P7 center appears at temperatures where silicon-vacancy-related centers like V_{Si}^0 [8] are annealed out. As the EPR transitions of the P6/P7 center enhance the efficiency of carrier recombination [2] and are detected in conventional EPR only upon illumination of the sample with $h \cdot \nu \geq 1.1$eV, they are likely to arise from an excited triplet state from which recombination to a (possibly diamagnetic) ground state can occur. While for the vacancy pair (V_{Si}-V_C) both a singulet or a triplet ground state may be possible, the neutral C_{Si}-V_C antisite-vacancy pair can have S=1 only in an excited state with an activation energy of around 1eV over the ground state [3]. The positive sign of the fine structure constant indicates large contributions from spin-orbit interactions exceeding the dipole-dipole interactions and indicates that the electrons are localized in a common orbital. The HF structure of the P6 spectrum indicates a strong interaction with one carbon nucleus and by a factor of three weaker interactions with three equivalent silicon nuclei. From theoretical calculations, the electron and spin density of the neutral C_{Si}-V_C antisite-vacancy pair in its excited triplet state is expected to be localized mainly at the carbon antisite and to a smaller degree at the three silicon neighbours of V_C [3].

Conclusion

The excited triplet state of the annealing product C_{Si}-V_C of the silicon vacancy has been identified. Its optical transitions have been found in the near infrared region. It is noted that the inequivalent sites differ primarily in their zero field splitting D and in the photon energy of the optical transition.

References

[1] V. S. Vainer, V. A. Il'in, Sov. Phys. Solid State 23 (1981), p. 2126.
[2] N. T. Son, P. N. Hai, M. Wagner, W. M. Chen, A. Ellison, C. Hallin, B. Monemar, E. Janzén, Semicond. Sci. Technol. 14 (1999), p. 1141.
[3] H. Overhof, University of Paderborn, Germany, private communication (2000).
[4] Yu. A. Vodakov, E. N. Mokhov, USA Patent no. 4147572.
[5] J.-M. Spaeth, J. R. Niklas, R. H. Bartram, *Structural Analysis of Point Defects in Solids, An Introduction to Multiple Magnetic Resonance Spectroscopy,* Springer Series of Solid State Sciences Vol. 43, Springer-Verlag (Heidelberg) (1992).
[6] N. M. Pavlov, M. I. Iglitsyn, M. G. Kosaganova, V. N. Solomatin, Sov. Phys. Semicond. 9 (1975), p. 845.
[7] E. Rauls, Th. Lingner, Z. Hajnal, S. Greulich-Weber, Th. Frauenheim, J.-M. Spaeth, Phys. Stat. Sol. (b) 217/2 (2000), p. R1.
[8] E. Sörman, N. T. Son, W. M. Chen, O. Kordina, C. Hallin, E. Jantzén, Phys. Rev. B 61 (2000), p.2613.

Materials Science Forum Vols. 353-356 (2001) pp. 509-512
© 2001 Trans Tech Publications, Switzerland

Intrinsic Defects in 6H-SiC Generated by Electron Irradiation at the Silicon Displacement Threshold

H.J. von Bardeleben[1], J.L. Cantin[1], P. Baranov[2] and E.N. Mokhov[2]

[1] Groupe de Physique des Solides, Universités Paris 6 & 7,
2 place Jussieu, FR-75005 Paris, France

[2] A.F.Ioffe Physico-Technical Institute, Russian Academy of Sciences,
Polytechnicheskaya, RU-194021 St.Petersburg, Russia

Keywords: Defects, Electron Irradiation, Frenkel Pairs, Silicon Vacancy

Abstract : The intrinsic defects generated by electron irradiation at energies of the silicon deplacement threshold in p-type and n-type 6H-SiC have been investigated by electron paramagnetic resonance spectroscopy. In p-type Al doped 6H-SiC two main intrinsic defects have been observed. They were attributed to Si-Frenkel pairs V_{Si}^- - Si and carbon monovacancies V_C^+. In n-type material a different defect with spin Hamiltonian parameters electron spin S=1/2 and an axial g-tensor (g//c=2.0026, g⊥c=2.0029) is observed. This spectrum is characterized by an unusual superhyperfine interaction with 6 equivalent Si and (3+1) equivalent carbon neighbours of equal magnitude. The C SHF interaction could only be determined by the use of ^{13}C enriched samples. As a tentative model for this defect the V_{Si}^{3-} - Si pair center is proposed

Introduction

Electron irradiation has been shown in the past to be an excellent tool for the controlled generation of intrinsic defects. It has been applied to 6H-SiC and after high energy electron irradiation (2MeV) various defects have been observed[1-9]. Electron irradiation at variable energies allows also to modify the nature of the defects. A particularly interesting case is irradiation near the threshold for Si or C atom displacements. In this case primary close Frenkel pairs will be generated whereas for high energies spatially separated vacancies and interstitials as well as divacancies will be formed. We have shown recently the interest of such an approach in the case of 6H-SiC :Al for irradiation near the Si displacement threshold [10]. In this paper we will resume the results for p-type 6H-SiC and compare them to the different one's obtained in n-type 6H-SiC.

Experimental

N-type and p-type doped bulk 6H-SiC wafers of 300μm thickness and commercial origin (Cree Research) have been used. Typical doping concentrations were in the $10^{17}cm^{-3}$ to $10^{18}cm^{-3}$ range. One ^{13}C enriched nitrogen doped thick layer has been studied in addition. The samples were irradiated with electrons of energy of 350keV to doses of up to $10^{18}cm^{-2}$. The energy of 350keV is close to the threshold for Si atom displacement in SiC. X-band EPR studies were performed at variable temperatures (4K to 300K). Angular variations of the EPR spectra were measured for rotations of the magnetic field in the (11-20) plane. The g-factors were determined from the microwave frequency and the magnetic field calibrated with a proton NMR probe.

Results and Discussion In p-type Al doped samples we observe (fig.1) two dominant EPR spectra after typical electron doses of $1x10^{18}cm^{-2}$. The first spectrum is an anisotropic spectrum which can

be described by a spin S=1/2 and a g-tensor with principal values of g_1=2.0012,g_2=1.9961,g_3=2.0017 with g_1, g_2 lying in the (11-20) plane and g_2 being oriented 41° from the c-axis. This spectrum, which has been already reported before [7,9], has been attributed

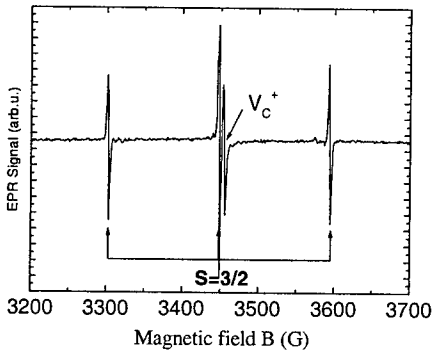


Fig.1 EPR spectra of the V_{Si}^--Si and V_C^+ centers in p-type 6H-SiC; T=300K, B//c

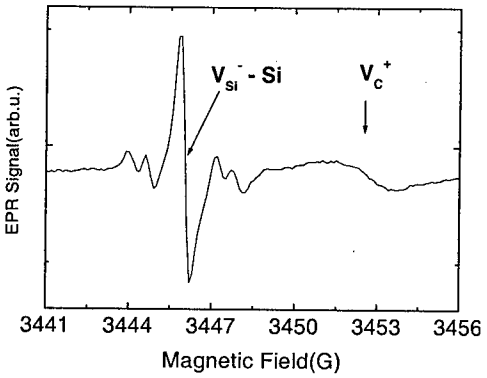


Fig.2 Central part of fig.1

from its spin Hamiltonian parameters to the positively charged carbon vacancy. However, we have shown [11], that this assignment must be reconsidered; similar results have also been obtained by [12]. The second one is an anisotropic three line spectrum of axial symmetry; it is characterized by the following spin Hamiltonian parameters S=3/2, g//c=2.0032, g⊥=2.0028,D=68.7x$10^{-4}$$cm^{-1}$. Its HF parameters are very similar to those of the isolated negatively charged Si vacancy (table 1). At higher resolution (fig.2) the EPR spectrum shows superhyperfine (SHF) interaction with 4 NN carbon and 12 NNN silicon atoms. However, contrary to the case of the isolated V_{Si}^- the 4 C NN as well as the 12 Si NNN are no longer equivalent (table 1). From the spin Hamiltonian parameters and the special irradiation conditions required for its formation we have attributed this center to a negatively charged V_{Si}^--Si Frenkel pair defect oriented parallel to the c axis In the n-type nitrogen doped samples irradiated under the same conditions we do not observe the previous two vacancy defects. Instead we observe at 300K one dominant and different EPR spectrum (fig.3) with axial symmetry, electron spin S=1/2 and g values of $g_{//c}$=2.00026, $g_{\perp c}$=2.0029. The central line shows in addition different SHF spectra in the 2 to 10G range. The SHF doublet with the smallest splitting is isotropic, whereas the lower intensity doublets with

	3C-SiC	**6H- SiC :N**	**6H-SiC :Al**
	e-, n° irradiated	n° irradiated	e- irradiated
Spin	3/2	3/2	3/2
g-tensor D	g_{iso}=2.0029	g_{iso}=2.0015 D=0	g//c=2.0032/g⊥=2.0028 D=68.7x$10^{-4}$$cm^{-1}$
C NN HF Interaction	4 C atoms	4 C atoms	3 C + 1 C atoms
T//c (G)	28.6	28.8	28.6 28.5
T⊥c (G)	11.8	11.6	13.3 17.2
Si NNN HF Interaction	12 Si atoms	12 Si atoms	3 Si + 3 Si + 6 Si
Tiso (G)	2.92	2.98	3.84 3.52 2.53
Model	V_{Si}^-	V_{Si}^-	V_{Si}^--Si
Ref.	[4]	[5]	[10]

Table 1: Spin Hamiltonian parameters for the (1-) negatively charged silicon vacancy defects V_{Si}^-

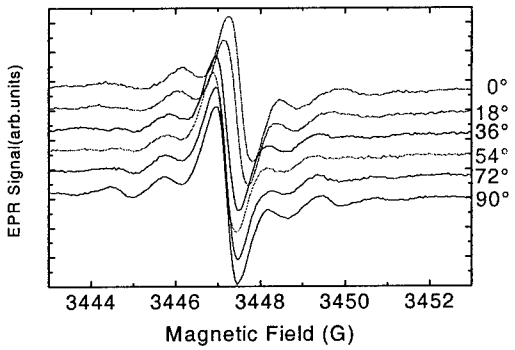


Fig.3 EPR spectra of 6H-SiC:N for a rotation in the (11-20) plane; T=300K

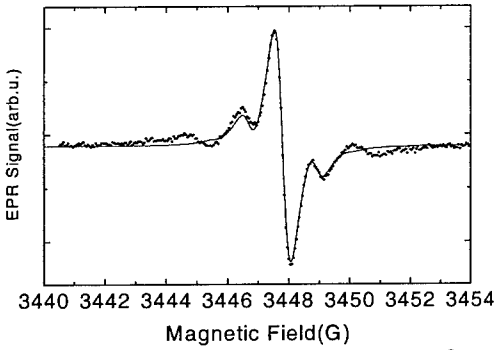


Fig.4 Experimental and simulated spectra for B//c; 6 Si NNN , Tiso= 2.20G

splittings in the 6-10G range are anisotropic. The isotropic SHF doublet can be well simulated by interaction with 6 equivalent Si neighbors and a splitting of 2.20G (fig.4). The angular variation of the anisotropic SHF structure could not be resolved as it is composed of different overlapping components. A search for NN related C and Si SHF lines in the 10 to 40G range have been unsuccessful in spite of in principal sufficient signal to noise ratios for the detection of 4NN. We thus have to conclude that this center does not present any strong SHF interaction, comparable to the cases of the Si vacancy (-/0) or the carbon vacancy(+).In order to further investigate the carbon SHF interactions we have irradiated one free standing thick layer, which had been enriched with ^{13}C to ≈35%. The EPR spectrum observed at 300K is shown in fig.5. The apparent overall linewith

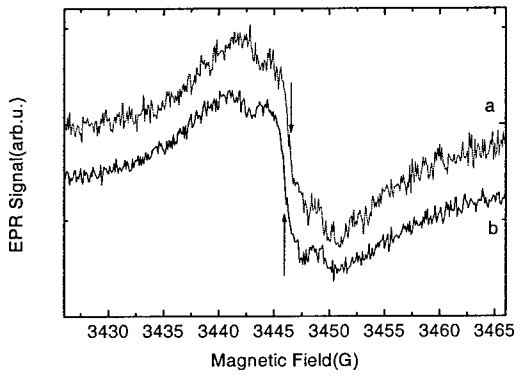


Fig.5 EPR spectra in 6H-Si^{13}C:N for (a) B//c and (b) B⊥c; T=300K

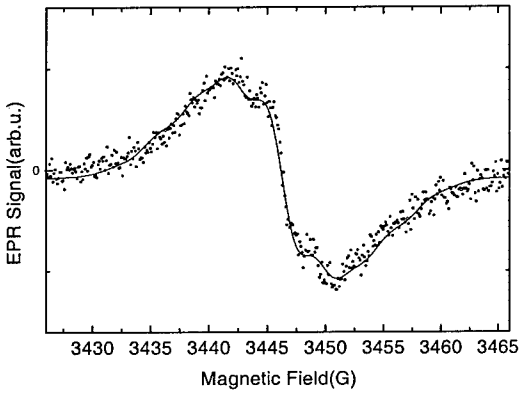


Fig.6 experimental and simulated EPR spectra for B//c; (1+3) C NN 12/6.6G

has dramatically increased from typically 0.5G in unenriched samples to 10G. The spectrum is anisotropic with the same g-values as the one observed in non enriched 6H-SiC. It shows a SHF structure which does not vary with the orientation of the magnetic field. As the effective g-facors are the same as those observed in the non enriched case, we believe that we observe the same defect. This is further confirmed by the simulation of the total lineshape of this spectrum. In fig.6 we present a simulation of the spectrum for a ^{13}C enrichment of 35% and a SHF interaction with 4 non equivalent (1+3) carbon atoms. The SHF splittings used in the simulation are 12.0G (1C) and 6.6G (3C) respectively. The peak to peak linewidth of the individual lines is increased from 0.6G to 3.6G due to inhomogeneous broadening by the 35% ^{13}C atoms. The parameters of this defect are presented in table 2. A simulation of the spectrum in the unenriched case taking into account these

two SHF interactions shows that the anisotropic SHF interaction with splittings in the 6G range must be related to further interaction with Si NNN. As the spin Hamiltonian parameters of this center do not allow an attribution to a simple silicon or carbon vacancy defect only a tentative

spin	g-tensor	Si SHF 6 NNN	C SHF 1+3
S=1/2	g//c=2.0026 g⊥c=2.0029	T_{iso}=2.20G	T_{iso}^{1}=12.0G $T_{iso}^{2,3,4}$=6.6G

Table 2: Spin Hamiltonian parameters for the V_{Si}^{3-} - Si center

model will can be proposed. The irradiation conditions (electron energy/dose) are the same in the p-type and n-type samples and it can be expected that the primary irradiation induced defects are the same: Si Frenkel pairs and separated carbon vacancies and interstitials. It has been observed in many previous studies that the carbon vacancy related defects are only observable in p-type material and are apparently never observed in n-type samples. A probable reason for this might be carbon interstitial / vacancy recombination at room temperature. However, on the contrary the silicon vacancy defects with a high thermal annealing stage at 750°C are stable at 300K. In this case the Fermilevel position –related to the electrical compensation- must be at the origin of the defect transformation. If we assume it to be higher in the n-type doped material, the only more negatively charge state of the silicon vacancy compatible with a spin of S=1/2 is the 3- charge state [13]. The silicon Frenkel pair V_{Si}^{3-} - Si aligned parallel to the c-axis seems thus to be the most probable candidate for the observed defect. Further modeling of the electronic structure of this defect is required to confirm this assignment.

Acknowledgments: this work has been supported by a CNRS / Russian Academy of Science cooperation program (n° 7780)

References

[1] L.A.de S.Balona, J.H.Loubser, J. Phys. C.: Solid St. Phys. 3, (1970), p.2344

[2] N.M.Pavlov,M.I.Iglitsyn,M.G.Kosaganova,V.N.Solomatin, Sov.Phys.Semicond. 9,(1976),p.845

[3] V.S.Vainer, V.A.Il'in, Sov. Phys. Solid State 23, (1982), 2125

[4] H.Itoh, N.Hayakawa, I.Nashiyama, E.Sakuma, J. Appl. Phys. 66, (1989), 4529

[5] T.Wimbauer,B.K.Meyer,A.Hofstätter, A.Scharmann, H.Overhof, Phys. Rev. B 56, (1997), 7384

[6] N.T.Son, W.M.Chen, J.L.Lindström, B.Monemar, E.Janzen, Mat.Science Eng.B61, (1999), 202

[7] N.T.Son, W.M.Chen, J.L.Lindström, B.Monemar, E.Janzen, Materials Science Forum 264-268, (1998), 599.

[8] E.Sörman, N.T.Son,W.M. Chen, O.Kordina, C.Hallin, E.Janzen, Phys.RevB61, (2000), 2613

[9] D.Cha, H.Itoh, N.Morishita, A.Kawasuso, T.Oshshima, Y.Watanabe, J.Ko, K.Lee, I. Nashiyama, Materials Science Forum 264-268, (1998), 615

[10] H. J. von Bardeleben, J. L. Cantin, L. Henry, M. F. Barthe, Phys. Rev. B 61 (Oct 2000).

[11] V. Ya. Bratus, I. N. Makaeeva, S. M. Okulov, T. L. Petrenko, T. T. Petrenko, H. J. von Bardeleben, Mater. Sci. Forum 353-356 (2001), p. 517.

[12] N. T. Son, P. N. Hai, E. Janzén, Mater. Sci. Forum 353-356 (2001), p. 499.

[13] L. Torpo, R. M. Nieminen, K. E. Laason, S. Pöykkö, Appl. Phys. Lett. 74 (1994), p. 221.

Materials Science Forum Vols. 353-356 (2001) pp. 513-516
© 2001 Trans Tech Publications, Switzerland

EPR Study of Proton Implantation Induced Intrinsic Defects in 6H- and 4H-SiC

H.J. von Bardeleben and J.L. Cantin

Groupe de Physique des Solides, Universités Paris 6 & 7, UMR 7588 au CNRS,
2 place Jussieu, FR-75251 Paris Cedex 05, France

Keywords: Defects, Electron Paramagnetic Resonance, Implantation Damage, Vacancy Defect

Abstract. The intrinsic defects generated by high energy (12MeV) proton implantation in the trace region between the surface and the end of range have been studied by electron paramagnetic resonance spectroscopy (EPR). For ion doses in the $10^{16}cm^{-2}$ range we observe in n-type N doped 6H-SiC three paramagnetic defects, attributed to the negatively charged and the neutral silicon monovacancy on hexagonal and quasicubic sites. No carbon vacancy related defect is observed. The total introduction rate is $20cm^{-1}$ and does not vary with dose. The simultaneous observation of the V_{Si} in the - and 0 charge states demonstrate that the Fermilevel is pinned by this defect in the electrically compensated samples. A correlation of the negatively charged V_{Si} on hexagonal and quasicubic sites with the Z1/Z2 centers is proposed.

Introduction. Ion implantation and in particular proton implantation are important issues for the doping of SiC epitaxial layers, electrical isolation and the elaboration of SiC on Insulator structures by the smart cut technique. In addition to the electrical activity of the implanted ion the intrinsic defects generated by the implanted ion have equally to be considered for the electrical compensation of the samples. Previous results for ion implanted n-type SiC have shown strong compensation with the formation of various intrinsic acceptor like deep traps, the most widely studied being the D1 and Z1/Z2 centers [1,2]. The nature of the acceptor like defects has not been established but they are believed to be divacancy defects V_C-V_{Si}.

As the energies transmitted to the lattice atoms in the elastic collisions are different in the trace and end of range (EOR) regions the nature and concentration of the intrinsic defects is expected to be different in these two parts of the sample also. Generally, it is difficult to separate the two regions experimentally and often the distinction between the defect location is not made. However, the understanding of the microscopic structure of the defects and their thermal stability in the two regions is a key parameter for their successful removal by high temperature annealing. In order to simplify the experimental situation we have used high energy proton implantation such that the implanted ions will completely cross the sample. In this case a homogenous defect distribution over the entire sample thickness can be expected and the trace defects can be studied separately without the interaction from the EOR defects.

The concentration, nature and microscopic structure of the radiation damage defects have been studied by the EPR spectroscopy. This technique, which allows to obtain from the spin Hamiltonian parameters of the different defects – in particular the hyperfine interactions- their identification has been already quite successfully applied to SiC. The main intrinsic defects, which have been

attributed previously and which are of importance in this study are the negatively charged Si monovacancy, the neutral Si monovacancy and the positively charged carbon monovacancy [3-6]. First EPR results of the proton implantation related damage have also recently been reported [7].

Experimental details. The samples used in this study were commercially produced (Cree Research) 300μm thick SiC substrates of 6H and 4H polytypes. The samples were n-type Nitrogen doped at $2x10^{17}cm^{-3}$. The samples were irradiated at room temperature with 12MeV protons at doses between 1 and $8x10^{16}cm^{-2}$. The samples were studied by X-band electron paramagnetic resonance spectroscopy. Absolute spin concentrations were determined by comparison with a ruby standard sample.

Experimental Results and Discussion. A first idea of the radiation damage and the projected range of the proton implantation has been obtained by SRIM 2000 [8] simulations. The projected range for 12MeV protons is 700μm, to be compared to the sample thickness of 300μm. Each proton will generate ≈5 primary Carbon vacancies and ≈7 primary Silicon vacancies (Fig.1). As the vacancy profile is rather flat this corresponds at a proton dose of $1x10^{16}cm^{-2}$ to average vacancy concentrations of $[V_C]=1.7x10^{18}cm^{-3}$ and $[V_{Si}]=2.5x10^{18}cm^{-3}$. The simulation program does not account for the formation of multivacancies nor the annihilation of vacancies by interstitial recombination or diffusion to the surface. They represent thus an upper limit only. In the case of Si for example only some percent of the primary vacancy concentrations survive the implantation process.

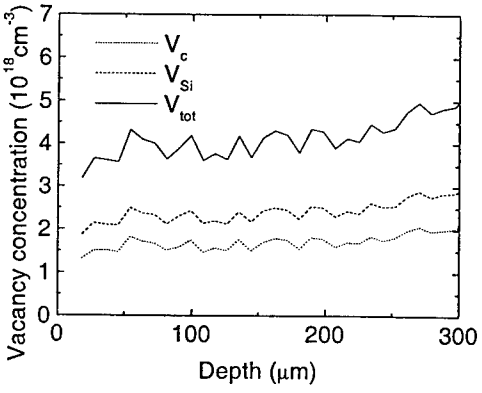


Figure 1: Vacancy concentration after 12MeV $1x10^{16}cm^{-2}$ proton implantation obtained by SRIM 2000 simulations

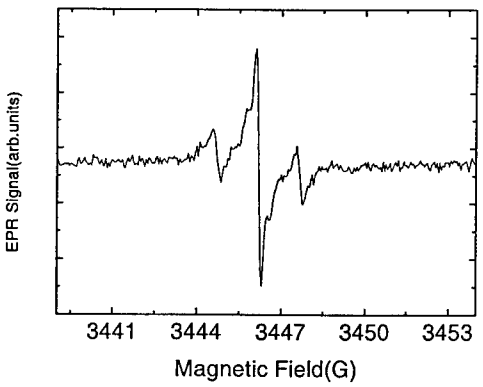


Figure 2: EPR spectrum of 6H-SiC:N after a proton dose of $1x10^{16}cm^{-2}$ B//c, T=300K

The EPR measurements show that for the lowest proton dose of $1x10^{16}cm^{-2}$ the samples are already electrically compensated at room temperature. In 6H samples we observe at 300K three main paramagnetic centers. The EPR spectrum of the first center is shown in fig.2; the spectrum is isotropic with g-factor of $g=(2.0032\pm0.0001)^1$; it shows a central line of width $\Delta Bpp=250mG$ and a hyperfine (HF) doublet with a splitting of $\Delta B=2.94G$ and an intensity ratio (doublet/central line) characteristic for the HF interaction with 12 silicon next nearest neighbours. At higher gain the additional anisotropic HF interaction with 4 equivalent nearest carbon atoms is also observed. This

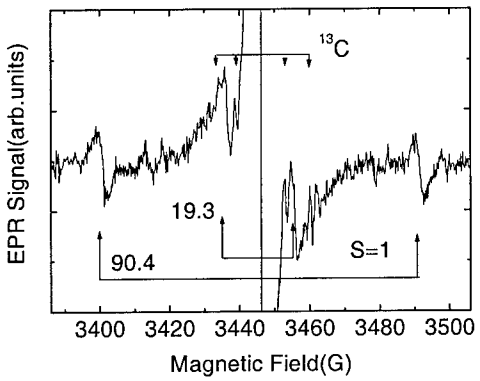


Figure 3: EPR spectrum of 6H-SiC:N after a proton dose of $1x10^{16}cm^{-2}$; B//c, T=300K

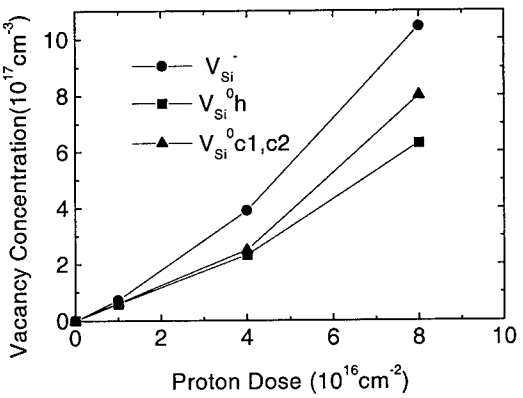


Figure 4: Silicon vacancy concentrations(V_{Si}^0, V_{Si}^0h, $V_{Si}^0c1,c2$) as a function of proton dose

spectrum has been observed before and has been attributed to the negatively charged silicon monovacancy V_{Si}^-[3]. It is a spin S=3/2 center with unresolved zero field splitting. No site dependence has been reported for this center.

For larger field scans two additional anisotropic EPR spectra are observed (fig.3). For B//[0001] they are characterised by doublets with splittings of 90.4G and 19.3G respectively and linewidth of 3G. Their angular variation for a rotation of the magnetic field in the (11-20) plane has been measured and their spin Hamiltonian parameters have been determined to S=1, $g_{//c}$= 2.0032, $g_{\perp c}$=2.0032, $D=42.8x10^{-4}cm^{-1}$ and S=1, $g_{//c}$= 2.0032, $g_{\perp c}$=2.0032, $D=9x10^{-4}cm^{-1}$.

A comparison with previously reported results (table 1) shows that the two defects, which are always simultaneously observed, are identical with the T_V [4]and P [9]centers. The T_V centers were observed in electron irradiated SiC and have been attributed to the neutral silicon vacancy on the two non distinguished quasicubic and the hexagonal sites [4]. The identical zero field splitting parameters D leave no doubt that in the three cases the same defects were observed. The slight differences in the g-factor are attributed to experimental errors and/or T effects. We adopt equally the model proposed in [4] on the basis of the ^{29}Si SHF interaction. The same defects have equally been observed before [9] and were named P3/P5. The defect model proposed at that time was a divacancy pair; however the assignment is believed to be erroneous. In [9] the Si NNN HF

Center Exp.Tech. /T(K)	$g_{//}$	$g_{\perp}$	D ($10^{-4}cm^{-1}$)	Model / reference
EPR / 300K	2.0032	2.0032	9.0	V_{Si}^0 / this work
EPR / 300K	2.0032	2.0032	42.8	V_{Si}^0 / this work
T_{V1a}/ T_{V3a} ODMR / 2	2.0035	2.0037	9.2	V_{Si}^0 (c1,c2)/ [4]
T_{V2a} ODMR / 2	2.0035	2.0038	42.8	V_{Si}^0 (h)/ [4]
P5 EPR / 77K	2.0026	2.0031	9.0	V_{Si}-V_C / [9]
P3 EPR / 77K	2.0026	2.0031	43.0	V_{Si}-V_C / [9]

Table 1: Spin Hamiltonian parameters of the two S=1 centers measured in this work and the S=1 centers reported in previous ODMR and EPR studies; estimated errors $\Delta g= \pm 0.0002$, $\Delta D=\pm 0.2x10^{-4}$ cm^{-1}

interaction as well as the NN HF with 4 NN C atoms was in addition resolved for both P3 and P5; values close to those of V_{Si}^- were found; this can be taken as a further confirmation of the V_{Si}^0 model. Note, that the P3/P5 centers were observed as thermally induced defects in high temperature quenched samples.

In fig.4 we show the variation of the defect concentrations with the proton dose; in the entire dose range these four defects remain the dominant paramagnetic centers. The total V_{Si} concentration is only ≈5% of the one expected from the SRIM simulation. Similar results were equally obtained for n-type 4H-SiC [7].

The simultaneous observation of the V_{Si} monovacancy in two charge states under thermal equilibrium conditions demonstrates that this defect pins the Fermilevel. The nearly constant concentration ratio of the 1- and 0 charge states between proton doses of 1 and $8x10^{16}cm^{-2}$ indicates that the overall electrical compensation (N_D-N_A) is constant. The EPR results can be compared with electrical measurements on proton implanted n-type 6H-SiC. Lebedev et al[10] have reported I(V) and C(V) studies on p+/n junctions implanted with 8MeV protons. They have observed two main implantation induced defects the R center at Ec-1.27eV and Z1/Z2 centers at Ec-0.6/0.7eV. DLTS measurements have equally been reported [11] on n-type samples submitted to 50keV and 120keV proton implantation at 10^{15}-$10^{16}cm^{-2}$ doses. Under these conditions the Z1/Z2 as well as a 'P'center at Ec-0.35eV have been detected. It confirms previous observation that the Z1/Z2 center is a dominant implantation induced acceptor center. Considering our EPR results the association of Z1/Z2 with the silicon monovacancy $V_{Si}^{-/0}$ on quasicubic and hexagonal sites is tempting. As the Z1/Z2 center is thermally stable up to 1500°C this seems to be conflicting with the known annealing stage at 750°C of V_{Si} in electron irradiated material. However, the fact that V_{Si} is also a high temperature thermal defect changes this appreciation. The photoexcitation spectrum of the P3/P5 defects with a threshold at 0.8eV is a further argument for this model; an optical threshold of 0.8eV is in good agreement with the thermal ionisation energy of the Z1/Z2 centers of ≈0.7eV; within this model it corresponds to the photoionisation of the negatively charged silicon vacancy according to $V_{Si}^- \rightarrow V_{Si}^0 + e_{cb}$.

Conclusion: proton implantation in n-type 6H-SiC induces in the trace region one dominant intrinsic defect, the silicon monovacancy. This defect is electrically active and introduces various levels in the gap. The correlation of the Z1/Z2 center with $V_{Si}^{-/0}$ is proposed. No evidence for divacancy defects have been found.

Acknowledgments. We thank M.F.Barthe and L.Henry from the CERI(CNRS/Orleans, France) for the proton implantation and L.DiCioccio and E.Hugonnard-Bruyère (LETI/Grenoble, France) for support of this work

References

[1] T. Dalibor et al., Inst. Phys. Conf. Ser. 142, 517(1995)
[2] W. Skorupa, V. Heera, Y. Pacaud, H. Weishart, Nucl. Instr. Meth. B120, 114(1996)
[3] T. Wimbauer et al., Phys. Rev. B56, 7384(1997)
[4] E. Sörman et al., Phys. Rev. B61, 2613(2000)
[5] D. Cha et al., Mat. Sci. Forum 264-268, 615(1998)
[6] N.T. Son et al., Mat. Science & Engineering B61, 202(1999)
[7] H.J. von Bardeleben, J.L. Cantin, L. Henry and M.F. Barthe, Phys. Rev B62, (2000)
[8] J.J. Ziegler, J.P. Biersack and U. Littmark, http://www.research.ibm.com/ionbeams
[9] V.S. Vainer, V.A. Ily'in, Sov. Phys. Solid State 23, 2126(1981)
[10] A.A. Lebedev et al., Mat. Science & Engineering B61, 450(1999)
[11] E. Hugonnard-Bruyère et al., Mat. Science & Engineering B61, 382(1999)

Materials Science Forum Vols. 353-356 (2001) pp. 517-520
© 2001 Trans Tech Publications, Switzerland

EPR Study of Carbon Vacancy-Related Defects in Electron-Irradiated 6H-SiC

V.Ya. Bratus'[1], I.N. Makeeva[1], S.M. Okulov[1],
T.L. Petrenko[1], T.T. Petrenko[1] and H.J. von Bardeleben[2]

[1] Institute of Semiconductor Physics, National Academy of Sciences of Ukraine,
45 Pr. Nauky, 03028 Kyiv, Ukraine

[2] Groupe de Physique des Solides, Universités Paris 6&7, UMR 75-88 au CNRS,
Tour 23, 2 Place Jussieu, FR-75251 Paris Cedex 05, France

Keywords: Defect, Electron Irradiation, Electron Paramagnetic Resonance

Abstract

The EPR spectra produced in boron-doped 6H-SiC by 2 MeV electron irradiation are described. Three axially symmetric near 77 K spectra Ky1 with $g_{\|1} = 2.0035$ and $g_{\perp 1} = 2.0041$, Ky2 with $g_{\|2} = 2.0028$ and $g_{\perp 2} = 2.0046$, Ky3 with $g_{\|3} = 2.0024$, $g_{\perp 3} = 2.0048$ and with relatively strong hyperfine splittings have been detected. Based on the intensity ratio of HF satellites to the central line these spectra have been assigned to carbon vacancy-related defects. Due to the similarity of HF parameters spectra Ky1 and Ky2 have been tentatively attributed to the same defect in inequivalent crystal sites. The results of preliminary *ab initio* calculations of carbon vacancy in different charge states are briefly discussed.

Introduction

Intrinsic defects in silicon carbide are studied by electron paramagnetic resonance (EPR) over many years [1,2]. A complex situation with numerous spin S=1/2, S=1 and S=3/2 defects has been revealed [3-5]. In spite of highly extensive investigations, structure of most of the defects is still unclear. The tentative models are generally based on the analysis of a hyperfine (HF) interaction with the nearest and next-nearest neighbors, which are well resolved in the EPR spectra. The microscopic structure of an isolated negatively charged Si vacancy (V_{Si}^-) in the high spin state S=3/2 [6] is alone completely understood now in SiC. Certain of the EPR spectra have been assigned to a single positively charged carbon vacancy (V_C^+) and V_C-related defects in 3C-SiC [7] and recently in 4H- and 6H-SiC [8,9]. No site dependence has been observed for both V_{Si}^- and V_C^+ defects in the EPR spectra. The observation of new EPR spectra in electron-irradiated boron-doped 6H-SiC samples is presented in this report. Three spectra with relatively strong HF splittings have been detected. Based on the intensity ratio of HF satellites to the central line the spectra have been assigned to carbon vacancy-related defects. Due to the similarity of HF parameters two spectra have been tentatively attributed to the same defect in inequivalent crystal sites.

Experimental

The samples were high quality Lely-grown 450 μm thick crystals of 6H-SiC with boron content about $4 \cdot 10^{17}$ cm^{-3}. The electron irradiation was performed at 77 K with 2.0 MeV electron beam parallel to the **c**-axis up to the dose of 1×10^{18} cm^{-2}. The X-band EPR studies were done in the 4-300 K temperature range. Most of the K- and Q-band EPR measurements were performed at 77K. The angular variation of the EPR spectra was measured for a rotation of the magnetic field in $(11\bar{2}0)$ and $(1\bar{1}00)$ crystals plane. The g-values of irradiation induced defects were determined with

a precision of $\Delta g = \pm 0.0001$ via a microwave frequency counter and a calibration of the magnetic field by a proton NMR probe (X-band) and relative to the g-values of EPR spectrum of shallow boron observed upon UV illumination (K- and Q-band).

Results and discussion

The EPR spectrum of a shallow boron [10] was found in the initial crystals before irradiation. After irradiation four different EPR spectra are observed near $g \cong 2.0$ over a temperature range 4 - 300 K, a shallow boron resonance is detected only upon UV illumination at $T < 130$ K. Fig. 1 shows the spectra observed at the Q-band at 77 K for two orientation of the magnetic field **B**.

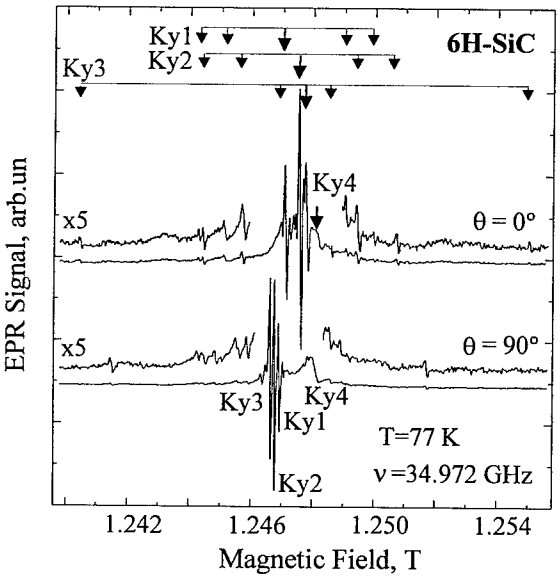


Fig. 1. Q-band EPR spectra of electron irradiated 6H-SiC<B> for orientation of the magnetic field **B** parallel ($\theta = 0^0$) and perpendicular ($\theta = 90^0$) to the **c**-axis. For four spectra and **B** || **c** positions of the central line and corresponding hyperfine doublets are indicated by bold and narrow arrows, respectively.

Each of three spectra labeled Ky1, Ky2 and Ky3 is composed of an intense central line and a group of hyperfine lines. The HF structure of the broader line labeled Ky4 can only be found at a higher gain. Closely spaced central lines of spectra Ky2 and Ky3 superimpose on one another at the X-band. Due to the long relaxation time the central lines of spectra Ky1, Ky2 and Ky3 are readily saturated in the temperature range 4 - 40 K while the hyperfine satellites are saturated at one order of microwave power higher level. It should be noted that the outer HF doublet of spectrum Ky3 is only seen at $T \geq 40$ K. These aspects make the interpretation of experimental data more complicated and the determination of low-temperature symmetry of the defects related to the observed EPR lines is still in progress. Central lines of spectra Ky2, Ky3 and Ky4 at 77 K and spectrum Ky1 at 100 K have axial symmetry around the [0001] axis. They are described by the spin Hamiltonian

$$\mathbf{H} = \mu_B \cdot \mathbf{B} \cdot \mathbf{g} \cdot \mathbf{S},$$

where the effective electron spin $S = 1/2$ and μ_B is the Bohr magneton. The g-values are equal to $g_{\|1} = 2.0035$, $g_{\perp 1} = 2.0041$; $g_{\|2} = 2.0028$, $g_{\perp 2} = 2.0046$; $g_{\|3} = 2.0024$, $g_{\perp 3} = 2.0048$ for spectra Ky1, Ky2 and Ky3, respectively. Slightly anisotropic spectrum Ky4 with $g_{\|4} = 2.0016$ and $g_{\perp 4} = 2.0025$ will no longer be discussed here.

At 4 K the HF structure of each of the spectrum Ky1 and Ky2 involves three doublets with an intensity ratio approximating 1:2:1 (Fig. 2a). At $T > 30$ K a position of closely spaced inner doublets is averaged and at $T = 77$ K the HF structure rearranges to two doublets with intensity ratio of about 1:3. At the later temperature two-doublet HF structure with the same intensity ratio have

been found for spectrum Ky3. For each of these spectra the total intensity of HF lines is about 0.21 ± 0.02 as compared to that of the central line. This ratio is approximately more than ^{29}Si nucleus natural abundance (4.7%, nuclear spin I = 1/2) by a factor of 4. It gives the evidence that the hyperfine structure of spectra Ky1, Ky2 and Ky3 arises from the interaction between the electron spin and the nuclear spins of four nearest-neighbor ^{29}Si atoms.

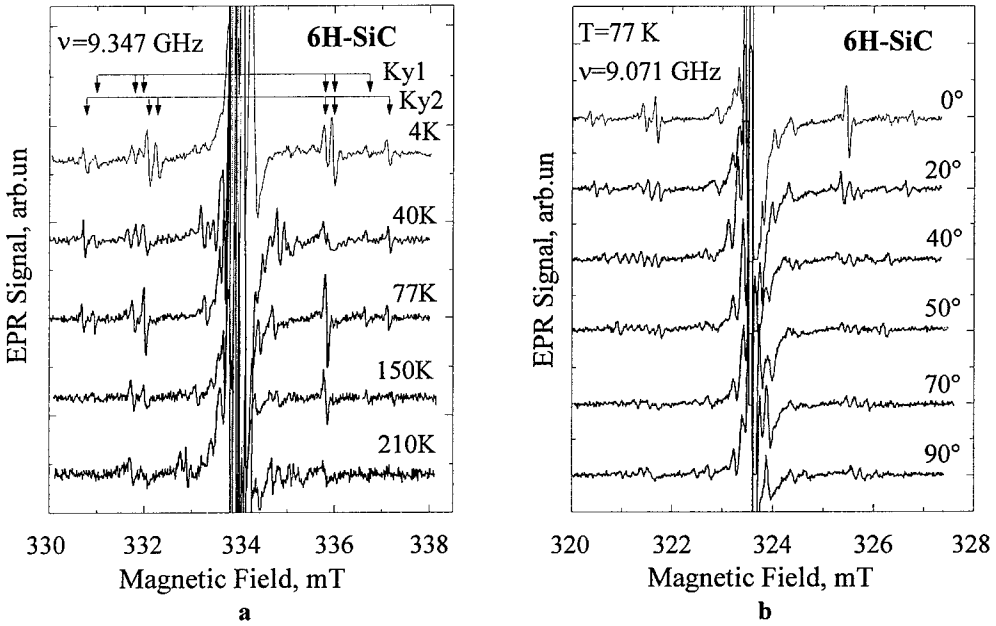


Fig. 2. a – Temperature dependence of the hyperfine structure of spectra Ky1 and Ky2. b – Angular variations of the hyperfine structure of spectra Ky1 and Ky2 in $(11\bar{2}0)$ plane at 77 K. The spectra are shifted keeping the position of spectrum Ky2 central line the same as for $\theta = 0^0$.

The hyperfine interaction for all these spectra has quasi-axial symmetry around the nearest-neighbor directions, the largest value is observed for single ^{29}Si nucleus lying along the **c**-axis (Fig. 1 and Fig. 2b). The numerical values of the Fermi contact isotropic term $a = (A_{\|} + 2A_{\perp})/3$ and anisotropic term $b = (A_{\|} - A_{\perp})/3$ of HF interaction for such nuclei are equal to a_1 = 128.9 MHz, b_1 = 15.6 MHz, a_2 = 140.9 MHz, b_2 = 19.5 MHz, a_3 = 325.6 MHz, b_3 = 43.2 MHz for spectra Ky1, Ky2 and Ky3, respectively. It should be pointed out that HF splittings are temperature independent for spectra Ky1 and Ky2 at T > 77 K (Fig. 2) while a reduction of HF parameters up to 12% is observed for spectrum Ky3 in the temperature range 77-300 K. Spectra Ky1 and Ky2 belong to the defects with identical spin and close values of HF interaction. Their intensity ratio being about of 1:2, so it is reasonable to suggest that these spectra are descended from the same carbon vacancy-related defect in three inequivalent sites of 6H-SiC crystal.

After assignment of spectrum T5 in cubic SiC to isolated carbon vacancy V_C^+ [7] it is generally agreed that HF splitting for this defect is in the range of 1.48 - 2.03 mT [8,9]. Our revealing of the V_C-related defects with higher values of HF splittings have stimulated the calculations of the symmetry, spin state and hyperfine coupling parameters for carbon monovacancy and impurity-carbon vacancy pair. It is not inconceivable that impurity-vacancy complex is relevant in our case since strong hyperfine interaction with a single silicon atom has been found for a group of impurity-vacancy pairs in silicon [11]. Up to now carbon vacancy in the charge states of 1+, 0 and 1– and neutral (B_{Si}–V_C) complex have been examined. Calculations have

been performed for a defect in cubic lattice site using tetrahedral 52- atom clusters $Si_4C_{12}H_{36}$ and $Si_3BC_{12}H_{36}$. The cluster geometry has been fully optimized at UHF/6-31G(d) level of theory [12] with fixed H atoms. Final gradient corrected DFT calculations in the basis of Gaussian functions have been carried out with previously obtained equilibrium structure. Becke's 3-parameter functional including both local and nonlocal terms has been used. Hyperfine interaction with nearest and next-nearest neighbor atoms has been analyzed with the use of the determined spin density matrix.

Geometry optimization leads to the minimum with C_S, C_{3V} and T_d symmetry and spin state of S = 1/2, S = 1 and S = 3/2 for V_C^+, V_C^O and V_C^-, respectively. Calculation of HF parameters for V_C^+ shows a small deviation from the axial symmetry. Close to observed for spectra Ky1 and Ky2 values of $a \approx 159$ MHz and $b \approx 30$ MHz are obtained for a Si atom with the largest HF interaction. For a (B_{Si}–V_C) complex an increase of the spin density on one Si atom ($a \approx 381$ MHz and $b \approx 65$ MHz), much smaller and equal values on two equivalent Si atoms ($a \approx 77$ MHz and $b \approx 11$ MHz), and negligible spin density on boron atom are found. Hence a ratio of 1:2 is expected for the HF doublets opposite to the observed ratio of 1:3 for a spectrum Ky3. Examination of alternative models as well as more precise determination of HF coupling parameters for V_C^+ with the use of 70-atoms cluster and more complete basis set is now in progress. Similar calculations for well-known shallow boron and V_{Si}^- defects in SiC give an excellent agreement with the experimental values.

In summary, four EPR spectra with an effective electron spin S = 1/2 have been observed in electron-irradiated boron-doped 6H-SiC. Based on the analysis of a hyperfine interaction three of them have been attributed to the vacancy-related defects at a carbon site. According to the similarity of HF parameters and their temperature behavior two spectra are assumed to belong to the same defect in three inequivalent sites of 6H-SiC crystal. For all these defects the strongest HF interaction has been found for a single Si atom lying along the hexagonal axis. Preliminary *ab initio* calculations of carbon vacancy in different charge state have revealed that only V_C^+ possesses spin S = 1/2. The calculated HF coupling parameters for V_C^+ have values higher than observed in cubic SiC and close to that of the present study.

This work was partially supported by INTAS 97-2141 grant.

References

[1] L.A.S. Balona, J.H.N. Loubser, J.Phys. C 3 (1970), p. 2344.
[2] J. Schneider, K. Maier, Physica B 185 (1993), p. 199.
[3] N.M. Pavlov, M.I. Iglitsyn, M.G. Kasaganova, V.N. Solomatin, Sov.Phys. Semicond. 9 (1976), p. 845.
[4] V.S. Vainer, V.A.Il'in, Sov. Phys. Solid State 23 (1982), p. 2125.
[5] H. Itoh, A. Kawasuso, T. Ohshima, M. Yoshkawa, I. Nashiyama, S. Tanigawa, S. Misawa, H.Okumura, S. Yoshida, Phys. Stat. Sol. (a) 162 (1997), p. 173.
[6] T. Wimbauer, B.K. Meyer, A. Hofstätter, A. Scharmann, H. Overhoff, Phys. Rev. B 56 (1997), p.7384.
[7] H. Itoh, M. Yoshikawa, I. Nashiyama, S. Misawa, H. Okumura, S. Yoshida, . J. Electr. Mater. 21 (1992),p. 707.
[8] D. Cha, H. Itoh, N. Morishita, A. Kawasuso, T. Ohshima, Y. Watanabe, J. Ko, K. Lee, I.Nasiyama, Mater. Sci. Forum 264-268 (1998), p. 615.
[9] N.T.Son, W.M.Chen, J.L. Lindström, B. Monemar, E. Janzén, Mater. Sci. Engin. B61-62 (1999), p. 202.
[10] T. Matsumoto, O.G. Poluektov, J. Schmidt, E.N. Mokhov, P.G. Baranov, Phys.Rev. B 55 (1997), p.2219.
[11] E.L. Elkin, G.D. Watkins, Phys. Rev. 174 (1968), p.881.
[12] M.J. Frisch et al.: *Gaussian 94, Revision E.1* (Gaussian, Inc., Pittsburgh PA, 1995).

Materials Science Forum Vols. 353-356 (2001) pp. 521-524
© 2001 Trans Tech Publications, Switzerland

EPR of Deep Al and Deep B in Heavily Al-doped as Grown 4H-SiC

I.V. Ilyin, E.N. Mokhov and P.G. Baranov

A.F.Ioffe Physico-Technical Institute, Russian Academy of Sciences,
Polytechnicheskaya 26, RU-194021 St.Petersburg, Russia

Keywords: Aluminium, Boron, Deep Acceptors, Electron Paramagnetic Resonance

Abstract. We report on the electron paramagnetic resonance observation of deep Al in 4H-SiC. EPR spectra due to deep Al acceptors in two positions in the lattice was observed. In both cases symmetry of the center is almost axial along *c*-axis. Deep Al acceptors in 4H-SIC consist of Al atom in Si position next to carbon vacancy along *c*-axis. EPR of deep B in as-grown SiC doped during growth was observed for the first time.

1.Introduction

It is well known that group-III acceptor impurities can form deep and shallow levels in SiC bandgap. Structure of the shallow group-III acceptor centers in SiC is well established by radiospectroscopic investigations [1-4]. In silicon B, Al and Ga form a sequence of energy levels with B being the shallowest. In SiC the situation is quite another:. There is considerable difference in the structures of B on one hand and Al and Ga on the other. All group-III impurities occupy Si sites. Boron, being smaller than Si, moves to off-center position and it's energy level becomes deeper than that of Al [3,4]. Shift of B atom to off-center position leads to change in the electron paramagnetic resonance (EPR) spectra [2-4]. While Al and Ga show effective-mass behavior with very anisotropic *g*-factor, shallow B *g*-factor is nearly isotropic. Besides shallow impurities, deep group-III centers could be observed in SiC. Up to now deep B in 6H-[3,5], 4H- [6] and 3C-SiC [6] as well as deep Al and deep Ga [3] in 6H-SiC were investigated by EPR. Preliminary studies of electron nuclear double resonance (ENDOR) of deep Al in 4H-SiC have been reported [7]. Studies of EPR and ENDOR of deep acceptor centers of boron allowed to establish it's structure: a $B_{Si} - V_C$ pair [3,5]. Complex is oriented along *c*-axis for all non-equivalent positions of the impurity in the lattice. Similarity of the behavior of EPR signals of deep Al and deep Ga with that of deep B in 6H-SiC allowed to suppose that deep Al and Ga acceptors have the same structure as deep B. Up to this work the EPR of deep B could only be observed in SiC after B diffusion and was not observed in as grown SiC crystals.

2. Experimental method

We have investigated *p*-type 4H-SiC crystals heavily doped with Al ($N_{Al} = 10^{20}cm^{-3}$). A bulk 4H-SiC crystal was grown by sublimation sandwich method in vacuum at 2050°C with growth rate 0.8 mm/h. The crystal was Al-doped during growth and contains also trace boron impurity with concentration 10^{17} cm^3. Investigations was carried out on conventional EPR X-band (9.15GHz) spectrometer in the temperature range 3.5 – 300K. The crystal was oriented for rotation in $\{11\bar{2}0\}$ plane.

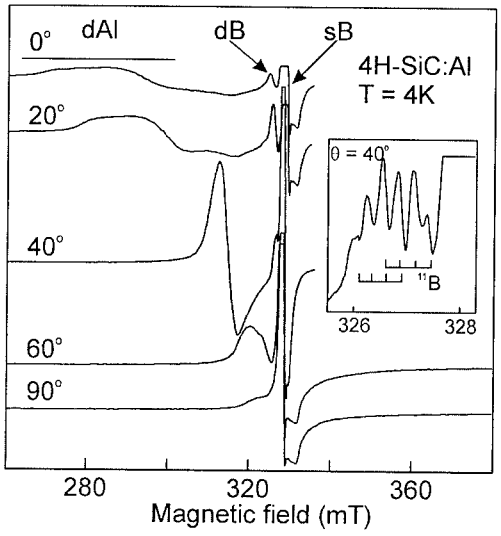


Fig. 1. EPR spectra in 4H-SiC:Al in different orientations of a crystal. Inset shows EPR signal of deep B for θ=40°.

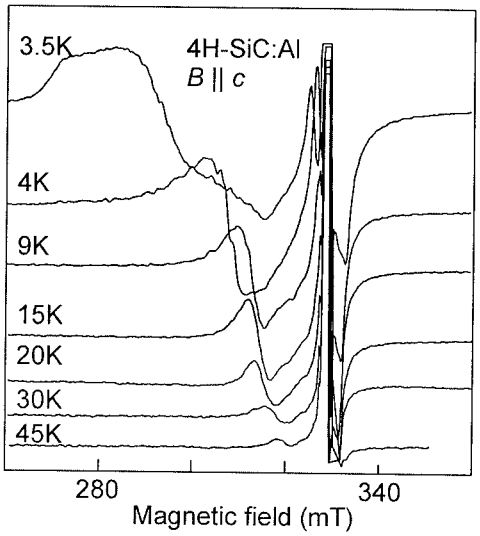


Fig. 2. Temperature dependence of dAl signal for $B \parallel c$.

3. Experimental results.

The Fig. 1 shows the EPR spectra recorded for several orientations in 4H-SiC:Al crystal at 3.5K. In the orientation $B \parallel c$ ($\theta = 0^0$) one can see three distinct EPR signals. One (consisting of two broad lines) is marked as dAl (deep Al). It has angular dependence very close to that observed for deep Al centers in 6H-SIC [3]. Symmetry of this center is almost axial along the c-axis and the signal can be characterized with electron spin $S = 1/2$ and the following g-factors: $g_{\parallel}$=2.35; 2.23. In $B \parallel c$ two lines could be seen for dAl signal at 3.5K. They appear due to the presence of Al impurity in two crystallographically non-equivalent h and k lattice sites. As in the case of deep Al and deep B in 6H-SiC we believe that the low-field line in dAl signal belongs to Al in h-site in the lattice. Contrary to previous observation of deep Al in 6H-SiC [3], in this sample the deep Al EPR signal is not masked by a signal from shallow Al acceptors. EPR intensity of shallow Al signal is at least 200 times of magnitude smaller than that of deep Al and could be hardly observed.

T	$g_{\parallel}$	$g_{\perp}$
3.5	2.24±0.05	1.90±0.1
	2.35±0.05	1.8±0.1
4K	2.14±0.05	2.00±0.1
8K	2.10±0.02	2.00±0.1
15K	2.08±0.02	2.01±0.05
21K	2.07±0.02	2.01±0.05
30K	2.07±0.02	2.02±0.05
45K	2.06±0.02	2.02±0.05

Table 1. The g-factors of deep Al signal for several temperatures.

The dAl EPR signal has strong temperature dependence which is shown in Fig. 2 for $B \parallel c$ orientation. This dependence is qualitatively the same as for deep Al in 6H-SIC: when the temperature is raised, the signal for $B \parallel c$ moves to higher magnetic fields ($g_{\parallel}$ lowers) and it's intensity decreases. But while EPR of deep Al in 6H-SiC almost disappears at 9K, in 4H-SIC it can be observed up to 70K. Since the g-factors, angular and temperature dependence of this signal are very close to that of deep Al in 6H-SIC, we ascribe it to deep Al acceptor centers in 4H-SIC. This

assumption was proved by investigation of ENDOR, which allowed to observe hyperfine and quadruple splitting due to ^{27}Al nuclear spin (I = 5/2) [7].

Angular dependence of dAl g-factors at different temperatures is shown in Fig. 3. The observed values are listed in Table 1. It is difficult to find $g_\perp$ and it could only be estimated from the extrapolation of available experimental data. Lines in Fig. 3 show angular dependence calculated using the g-factors from the Table 1. From Fig. 3 one can see that symmetry of the dAl center is axial for all available temperatures within experimental error. It is evident from Fig. 2 and Fig. 3 that deep Al in h-position (a line with the maximum g-factor) has stronger temperature dependence and is almost undetectable at temperatures higher than 4K. The same behavior was observed for deep Al in 6H-SiC.

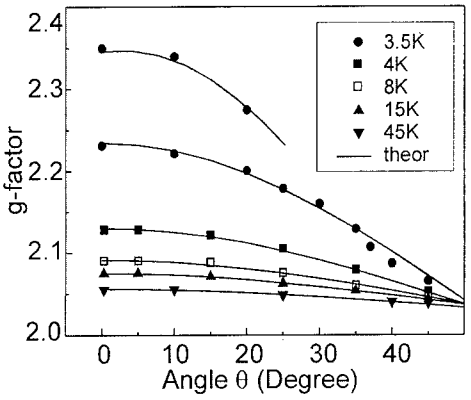


Fig. 3. Angular dependence of dAl g-factors for different temperatures.

Fig.4 shows temperature dependence of the g-factors. It can be seen that dependence of the $g_\parallel$ and $g_\perp$ are different: while $g_\parallel$ lowers when the temperature is raised, $g_\perp$ increases. The rate of changes of $g_\parallel$ and $g_\perp$ are the same within accuracy of the g-factor determination. Both values approach some average value of 2.04.

The line marked as sB in Fig.1 arises due to shallow B centers. Boron is a common trace impurity in p-type SiC. The signal named in Fig. 1 as dB (deep B) has angular and temperature dependence completely the same as that of deep B signals that was found earlier in 4H-SIC after B diffusion [6]. The inset in the figure shows this signal for orientation $\theta = 40^\circ$ in which the characteristic hyperfine structure due to ^{11}B nuclear spin (I = 3/2) is well resolved for two positions of B atom in the lattice. This signal belongs to deep B centers. It is interesting since up to now EPR of deep B could be observed only in the crystals that were doped by diffusion while this sample was doped during growth and boron is a trace impurity.

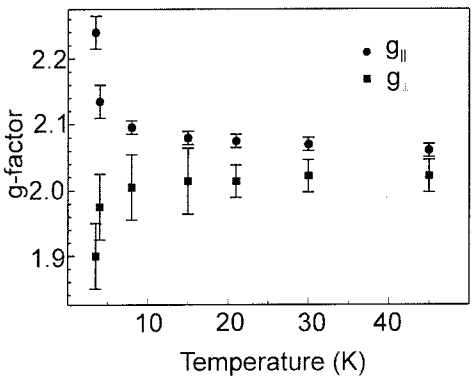


Fig. 4 Temperature dependence of the g-factors of deep Al.

4. Discussion

We believe that deep Al has the same structure as other deep acceptor centers in SiC [3,5]. It is shown in Fig.5: a complex of an impurity in Si site next to carbon vacancy. Investigation of angular dependence shows that the center is oriented along c-axis for all crystallographic positions (see Figs 5a, 5b). This model was proved for deep B centers by first principle calculations which establish B_{Si}-V_C complex as its origin [8].

It could be clearly seen in Fig. 1 that in $B \parallel c$ direction the EPR lines of deep Al are very broad and they become narrower when the crystal is rotated away from $B \parallel c$. This effect was first noticed for deep B, Al and Ga in 6H-SiC and could be explained as influence of random strain in the crystal. This random strain in the crystal arises from a difference in local environments of the individual centers. For $B \parallel c$ this strain leads to spread of the g-factors and thus to line broadening.

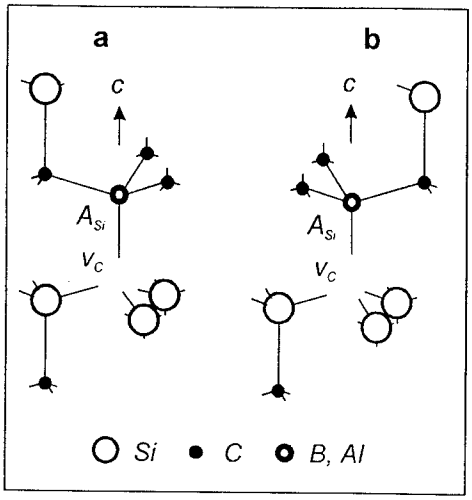


Fig. 5. Structures of deep group-III acceptor centers in 4H-SiC. (a) hexagonal position, (b) quasi-cubic position.

This assumption of influence of *g*-strain on the EPR spectra was proved by EPR measurements on high (95GHz) frequency spectrometer [5].

Deep Al EPR signal has strong temperature dependence. It is also important that anisotropy of the EPR signals decreases when the temperature increases. It can be clearly seen in Figs. 3 and 4: a signal at high temperatures is nearly isotropic. Mechanism of this dependence is not easy to unravel. One can think that both effects of *g*-factor spread and it's dependence on the temperature have the same origin. We believe that distribution of the hole among energy levels of the center plays the main role in both effects. Possible influence of dynamic Jahn-Teller effect on temperature dependence of the *g*-factor should also be considered [5,8].

Important point is nearly complete absence of shallow Al signals and presence of deep B in the studied sample. This implies that growth conditions favor formation of deep centers, i.e., complexes of impurities with V_C. The origin of excess vacancies is deviation from stoicheometry during growth process. At low growth temperatures (2000°C) vapor phase is Si-enriched. Excess Si (and, consequently, V_C), is introduced into the sample. Carbon vacancies act as donors and when concentration of acceptors (Al in our case) is high, their concentration also increases. The third reason is high growth rate (0.8 mm/h) that also lead to great number of V_C. These vacancies form complexes with Al and B atoms which could be detected as deep acceptor centers. Nearly no shallow Al could be found in the sample and all Al atoms formed complexes with V_C. Only small part of B atoms are involved in B-V_C complexes. This is perhaps because Al-V_C complex is more stable than B-V_C one. We have performed a high-temperature annealing of this sample in order to destroy deep Al centers. It was found that they are stable at least up to 2200°C.

Acknowledgments. This work was partially supported by Russian foundation for Basic Research under grant No 00-02-16950

[1] K.M.Lee, L.S.Dang, G.D.Watkins, W.J.Choyke, Phys.Rev.Lett. **45** (1980), p. 390.
[2] S.Greulich-Weber, Phys.Stat.Sol.(a) 162 (1997), p. 95.
[3] P.G. Baranov, I.V. Ilyin and E.N. Mokhov, Solid. St. Comm. **100** (1996), p. 371.
[4] T.Matsumoto, O.G.Poluektov, J.Schmidt, E.N.Mokhov, P.G.Baranov, Phys.Rev.B **55** (1997-II), p. 2219
[5] A.v.Duijn-Arnold, T.Ikoma, O.G.Poluektov, J.Schmidt, E.N.Mokhov, P.G.Baranov, Phys.Rev.B **57** (1998-I), p. 3
[6] P.G. Baranov, I.V. Ilyin and E.N. Mokhov, Phys. Solid State **39** (1997), p. 52.
[7] B.K.Meyer, A.Hofstaetter, P.G.Baranov, Mat.Sci.Forum **264-268** (1998), p. 591
[8] A.Gali, P.Deak, R.P.Devaty, W.J.Choyke, Phys.Rev.B **60** (1999), p. 10620.

Materials Science Forum Vols. 353-356 (2001) pp. 525-528
© 2001 Trans Tech Publications, Switzerland

The Electronic Structure of the N Donor Center in 4H-SiC and 6H-SiC

A. van Duijn-Arnold[1], R. Zondervan[1], P.G. Baranov[2], E.N. Mokhov[2] and J. Schmidt[1]

[1] Huygens Laboratory, Leiden University, PO Box 9504, NL-2300 RA Leiden, The Netherlands

[2] A.F.Ioffe Physico-Technical Institute, Russian Academy of Sciences, Polytechnicheskaya 26, RU-194021 St.Petersburg, Russia

Keywords: Electronic Wave Function, N Donor

Abstract

In this paper we present high-frequency (95 GHz) pulsed electron paramagnetic resonance (EPR) and electron nuclear double resonance (ENDOR) measurements on the nitrogen (N) donor in 4H-SiC (k site) and 6H-SiC (h, k_1 and k_2 sites). From the hyperfine interaction of the unpaired electron spin of the donor with the ^{13}C and ^{29}Si nuclei, the distribution of the electronic wave function of the N donor is determined. The main part of the spin density in 4H-SiC is located on the Si sublattice and the wave function contains a relatively large fraction of Si p-character. For the three sites in 6H-SiC the main part of the spin density is located on the C and the wave function is built mostly of s like C atomic orbitals. Comparing the three sites in 6H-SiC, the h site wave function has the largest delocalization and is most isotropic. The k_2 site wave function is most localised and less isotropic. The difference in behaviour of the wave function in 4H and 6H polytypes seems to find its origin in the difference in their conduction-band structure. Our results indicate that the conduction-band minima in 4H-SiC are mainly Si-like whereas in 6H-SiC the conduction-band minima are most C-like.

Introduction

To further the development of SiC-based semiconducting devices a good understanding of the electronic and geometric properties of the donor and acceptor centers is imperative. An important issue is the spatial delocalisation of the electronic wave function of the donor and acceptor. The method of choice to obtain this information is ENDOR spectroscopy developed by Feher[1], which has been applied to donor impurities in Si by Feher[1], Fletcher et al.[2], Hale, Ivey and Mieher[3] and to acceptor impurities in SiC by A.v.Duijn-Arnold et al[4].

The N donor in SiC has been studied extensively using optical absorption and emission spectroscopy by Choyke, Hamilton and Patrick[5] and using Raman experiments by Colwell and Klein[6]. The first EPR measurements on the N-donor in SiC were done by Woodbury and Ludwig[7] and the first ENDOR measurements by Hardeman and Gerritsen[8,9] both at 9.5 GHz. High-frequency EPR measurements at 142 GHz by Kalabukhova, Kabdin and Lukin[10] allowed to separate overlapping EPR lines, owing to the high spectral resolution, and to assign the various EPR lines to specific sites in the SiC lattice. Additional ENDOR measurements were reported by Greulich-Weber et. al.[11]. An overview of our current knowledge of the electronic properties of the N-donor, obtained by EPR and ENDOR at 9.5 GHz is found in the review papers by Greulich-Weber[12].

In this paper we present the results of an ENDOR study at 95 GHz of the N-donor center in 4H-SiC and 6H-SiC. This high microwave frequency allows to determine the hf interaction of the unpaired electron spin with the surrounding nuclear spins in great detail supplying information from

which the spatial delocalisation of the electronic wave function can be obtained. The measurements were performed on N-doped 4H-SiC and 6H-SiC samples with ^{13}C in natural abundance and with ^{13}C enriched to ~35 %. The samples were free-standing epitaxial layers grown by the sublimation sandwich method.

Results and analysis

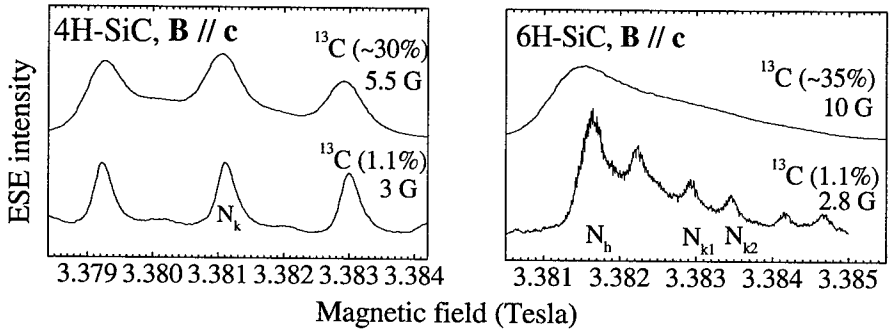


Figure 1: The EPR spectra at 95 GHz of the N donor in 4H-SiC (left) and 6H-SiC (right) with and without ^{13}C enrichment.

Figure 1 shows the EPR spectra of the N donor in non-enriched and ^{13}C-enriched 4H-SiC and 6H-SiC. In 4H-SiC a slight broadening of the EPR line is observed. In 6H-SiC however, the line width is increased more than 3 times. We conclude that in 4H-SiC the main part of the spin density resides on Si atoms, whereas in 6H-SiC it is located on the C atoms. Using the ^{13}C and ^{29}Si ENDOR data a reasonable value for the observed linewidth is calculated[13].

Figure 2a and b show the comparison between the different sites in 4H-SiC and 6H-SiC of the ^{13}C ENDOR and the ^{29}Si ENDOR spectrum for **B // c** respectively. It is clear that the spin density

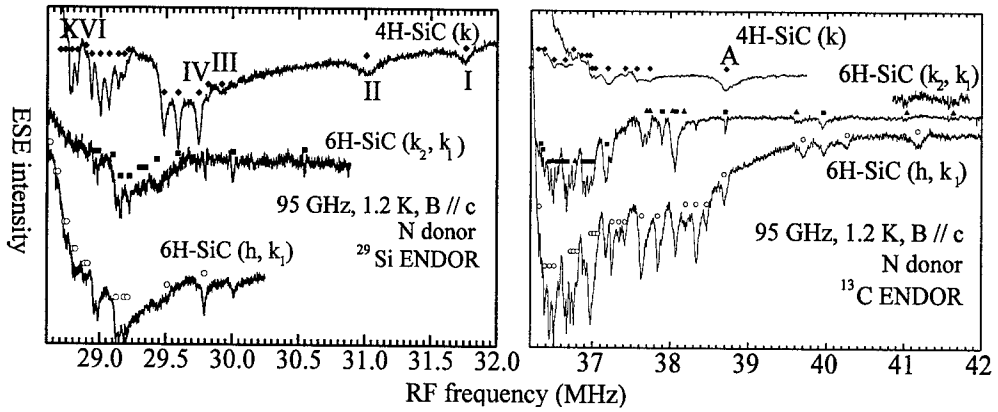


Figure 2: The ^{29}Si (left) and ^{13}C (right) ENDOR spectra of the N donor. The upper spectrum, N_k, belongs to the N donor substituting on a *k* site in 4H-SiC. The middle spectrum was measured on the low-field hf EPR line of the N_{k2} site, which overlaps with the *h* site and the k_1 site hf EPR line. The lower spectrum was measured on the *h* site and low-field N_{k1} site hf EPR lines, which overlap with the k_2 site. By comparing the last two spectra it is possible to make a tentative assignment of ENDOR lines to the different sites in 6H-SiC[13].

distribution of the N-donor electron over the ^{13}C and ^{29}Si nuclei differs between 4H-SiC and 6H-SiC. Whereas the main part of the spin density is localised on the ^{29}Si atoms for the *k* site in 4H-SiC (as expected for a donor electron) it is localised mainly on the ^{13}C atoms in case of the 6H-SiC sites. The roman numbers and letter (I-IV, XVI and A) correspond to the numbers and letter used in fig. 3. Line XVI is very anisotropic (a = 0.47 ± 0.02 MHz and b = 0.40 ± 0.01 MHz) and resembles the anisotorpic behaviour of the shallow donor in Si for the interaction with the Si nucleus in the [111] direction[1]. The resemblance was used as a basis for the assignment of the lines to nuclei.

III. Discussion

The EPR and ENDOR results show that the electronic wave function of the N donor is quite different in the two polytypes. The main part of the spin density in 4H-SiC is located on the Si sublattice and the wave function contains a relatively large portion of Si *p*-character. For each of the three sites in 6H-SiC the main part of the spin density is located on the C sublattice and the wave function is built mostly of *s*-like C atomic orbitals. Comparing the three sites in 6H-SiC, the *h* site wave function has the largest delocalization. The k_2 site wave function is most localised. For the *h*, k_1 and k_2 sites in 6H-SiC the spatial distribution of the wave function of the N donors over the Si and C nuclei is qualitatively the same.

To obtain the distribution of the electronic wave function of the N donor in the SiC crystal, the hf interactions found in the ENDOR spectra have to be assigned to specific (groups of) nuclei in the surrounding of the N donor and then translated to spin densities. The assignment to specific nuclei presents a considerable problem because, due to the of the multi-valley structure of the conduction band, interference effects occur, which make that the overall density of the wave function does not decay monotonically with the distance to the N donor. We use a model

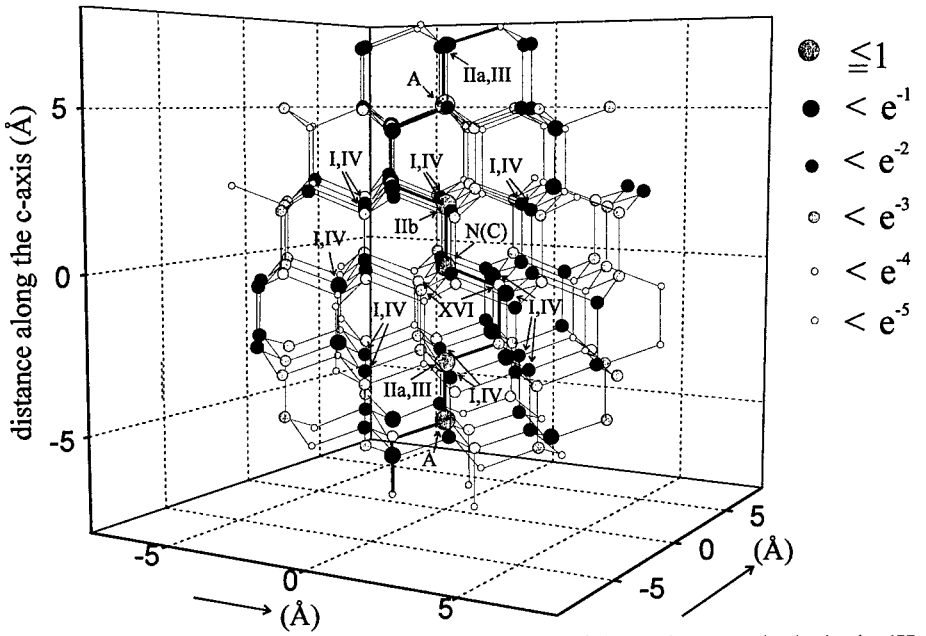


figure 3: The spatial distribution of the calculated isotropic hfi of the N donor at the k site in 4H-SiC. The black and shaded disks (numbers e^{-1} - e^{-5}) indicate the hfi on the Si and C relative to the N(C) which has density 1. No distinction was made between Si and C. The roman numbers indicate the nuclei to which ENDOR lines of fig. 2 have been assigned [13].

introduced by Kohn and Luttinger[14] to calculate the isotropic hf interaction of ^{13}C and ^{29}Si nuclei, in which the interference effect is explicitly taken into account. As an illustration we show in fig. 3 the results of our calculations for the distribution of the hf interaction around the *k* site in 4H-SiC together with a tentative assignment of the ^{29}Si and one ^{13}C ENDOR line to nuclei surrounding the N-donor.

A possible explanation for the difference in the electronic wave function of the N donor in 4H-SiC and 6H-SiC can be found in the large difference in the band structure of the two polytypes and in the position of the minima in the Brillouin Zone. As a result the linear combination of atomic orbitals describing the wave function of the donor electron is different. Thus the wave function might have a completely different symmetry and a different distribution of *s* and *p* character on the Si and C atoms. From band structure calculations it is not clear whether Si or C bands lie lowest in the minima in 4H-SiC and 6H-SiC. Our results are consistent with mainly Si-like conduction-band minima in 4H-SiC and C-like conduction-band minima in 6H-SiC.

Conclusion

From the hyperfine interaction of the unpaired electron spin of the N donor with the ^{13}C and ^{29}Si nuclei, the distribution of the electronic wave function of the N donor is determined. The main part of the spin density in 4H-SiC is located on the Si sublattice and the wave function contains a relatively large portion of Si *p*-character. For the three sites in 6H-SiC the main part of the spin density is located on the C sublattice and the wave function is built mostly of *s*-like C atomic orbitals. Comparing the three sites in 6H-SiC, the *h* site wave function has the largest delocalization and is most isotropic. In the k_2 site the wave function is most localised and least isotropic. The difference in the behaviour of the wave function in the 4H and 6H polytypes seems to be due to the difference in their conduction-band structure. They suggest mainly Si-like conduction-band minima in 4H-SiC and C-like conduction-band minima in 6H-SiC.

References

[1] G. Feher, Phys. Rev. **114** (1959), p. 1219.
[2] R.C. Fletcher, W.A. Wagner, G.L. Pearson, A.N. Holden, W.T. Read, and F.R. Merritt, Phys. Rev **94** (1954), p. 1392; R.C. Fletcher, W.A. Yager, G.L. Pearson, and F.R. Merritt, Phys. Rev **95** (1954), p. 844.
[3] J.L. Ivey and R.L. Mieher, Phys. Rev. B **11** (1975), p. 849, and references therein.
[4] A. v. Duijn-Arnold, J. Mol, R. Verberk, J. Schmidt, E.N. Mokhov, and P.G. Baranov, Phys. Rev. B **60** (1999), p. 15829.
[5] W.J. Choyke and L. Patrick, Phys. Rev. **127** (1962), p. 1868; W.J. Choyke, D.R. Hamilton, and L. Patrick, Phys. Rev. **133** (1964), p. A1163.
[6] P.J. Colwell and M.V. Klein, Phys. Rev. B **6** (1972), p. 498.
[7] H.H. Woodbury and G.W. Ludwig, Phys. Rev. **124** (1961), p. 1083; G.W. Ludwig and H.H. Woodbury, Solid State Phys. **13** (1962), p. 223.
[8] G.E.G. Hardeman and G.B. Gerritsen, Phys. Rev. Lett. **20** (1966), p. 623.
[9] L. Patrick, Phys. Rev. B **5** (1972), p. 2198; L. Patrick, Phys. Rev. **138** (1965), p. A1477.
[10] E.N. Kalabukhova, N.N. Kabdin, and S.N. Lukin, Sov. Phys. Solid State **29** (1987), p. 8.
[11] S. Greulich-Weber, M. Feege, J.-M. Spaeth, E.N. Kalabukhova, S.N. Lukin, and E.N. Mokhov, Solid State Communications **93** (1995), p. 393.
[12] S. Greulich-Weber, phys. stat. sol. (a) **162** (1997), p. 95.
[13] A. v. Duijn-Arnold, R. Zondervan, P.G. Baranov, E.N. Mokhov and J. Schmidt, Phys. Rev. B (submitted for publication).
[14] W. Kohn and J.M. Luttinger, Phys. Rev. **97** (1995), p.1721; W. Kohn, *Solid State Physics*, edited by F. Seitz and D. Turnbull (Academic Press Inc., New York, 1957) **5**, 257.

Materials Science Forum Vols. 353-356 (2001) pp. 529-532
© 2001 Trans Tech Publications, Switzerland

Identification of Iron and Nickel in 6H-SiC by Electron Paramagnetic Resonance

P.G. Baranov, I.V. Ilyin, E.N. Mokhov and V.A. Khramtsov

A.F.Ioffe Physico-Technical Institute, Russian Academy of Sciences,
Polytechnicheskaya 26, RU-194021 St.Petersburg, Russia

Keywords: Electron Paramagnetic Resonance, Iron, Nickel, Semi-Insulating Layers

Abstract. We report on the first observation of electron paramagnetic resonance of iron and photo-EPR of nickel impurities in 6H-SiC crystals. Iron exists in Fe^{3+} ($3d^5$) charge state with electron spin $S = 5/2$. Nickel exists in Ni^{3+} ($3d^7$) charge state with electron spin $S = 3/2$. Both impurities seem to occupy silicon sites in the 6H-SiC lattice. Possibility of using iron doping to obtain semi-insulating SiC crystals is discussed.

1. Introduction

Silicon carbide (SiC) is a wide-bandgap semiconductor that attracts great interest because of possible applications in high-power or high-frequency devices. Transition metals have been successfully used as a deep compensating centers to produce semi-insulating materials urgently needed for applications. Vanadium is used in SiC to produce semi-insulating layers [1,2] but since the compensating effect in originally *n*-type material is not sufficient at high temperatures, a search for other impurities with suitable deep levels is desirable [3]

Electron paramagnetic resonance (EPR) has proven to be an extremely powerful tool for the study of defects in semiconductors. Most of the available information about the transition metals arises from EPR experiments. By now 3*d*- (Sc, Ti, V, Cr) and 4*d*-group (Mo) transition ions were investigated in SiC using EPR, see reviews [5, 6]

We report here on the first observation of the 3*d* transition group ions Fe^{3+} and Ni^{3+} in 6H-SiC crystal.

2. Experimental procedure

In this work we investigated iron-doped 6H-SiC bulk crystals grown by the sublimation sandwich method [7,8]. The growth process was carried out in Ar atmosphere at temperature 2500°C. Growth rate was about 0.2 mm/hour. Doping with iron was performed during growth process. Crystals were of *n*-type conductivity due to presence of N-donors with concentration $N_d = 10^{17}cm^{-3}$. The samples have the shape of 4x8mm platelet and were oriented for rotation in the $\{11\bar{2}0\}$ plane. The EPR spectra were studied on a conventional JEOL X-band (9.25 GHz) EPR spectrometer in the temperature range 4 - 300 K.

3. Fe^{3+} in 6H-SiC

In Fig.1 we show the EPR spectra observed in orientations $B \parallel c$ and $B \perp c$ in 6H-SiC:Fe. One can see that spectra consist of a number of EPR lines. Experimentally measured angular dependence of the signals which we ascribe to Fe^{3+} are shown as circles in the Fig.1. The observed angular dependence is characteristic for a center with $S = 5/2$ in strong axial crystalline field. Since crystal

which we have studied was doped with iron it is natural to ascribe these signals to Fe^{3+} ($^6S_{5/2}$, $3d^5$) impurity centre with $S = 5/2$.

Angular dependence of Fe^{3+} (S = 5/2, $3d^5$) ion in axial (C_{3v}) crystalline field can be described by the spin Hamiltonian of the form [9]:

$$H = g\mu_B \boldsymbol{H}\cdot\boldsymbol{S} + \frac{1}{6}a\{S_\xi^4 + S_\eta^4 + S_\zeta^4 - \frac{707}{16}\} D\{S_z^2 - \frac{35}{12}\} + \frac{7F}{36}\{S_z^4 - \frac{95}{14}S_z^2 + \frac{81}{16}\}. \quad (1)$$

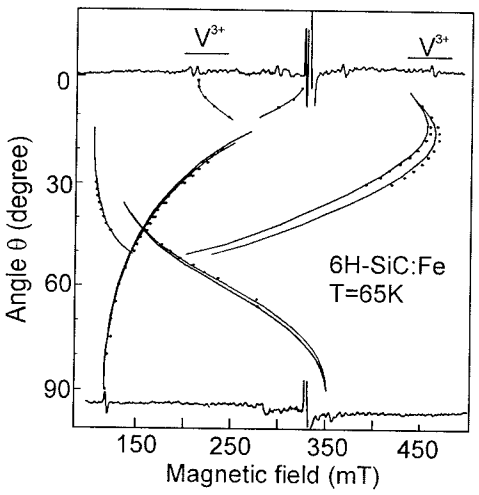


Fig. 1 The EPR spectra in 6H-SiC:Fe for $B \parallel c$ and $B \perp c$ orientations. Circles and lines show experimental and calculated angular dependence of Fe^{3+} EPR signals.

A system of coordinates, $\xi\eta\zeta$, arises from three perpendicular cubic crystal-field axes of the fourth order with the center at the Si site of the SiC crystal. The z-axis is parallel to the hexagonal c-axis of the crystal (the same as the <111> axis of the $\xi\eta\zeta$ system) while x-axis lies in one of the $\{11\bar{2}0\}$ planes and y-axis is perpendicular to both x- and z-axes. Parameters D, F and a characterize the axial and cubic crystal fields.

An investigation of the angular dependence of the Fe^{3+} EPR spectrum allowed us to find spin Hamiltonian parameters for Fe^{3+} signal The following parameters were found: $g \approx 1.99$, axial crystal field splitting $|D| = 0.25$ cm^{-1} and cubic field splitting $|a| = 0.016$ cm^{-1}. The calculated angular dependence of fine-structure line positions of Fe^{3+} ions is plotted as lines in the Fig. 1 and is in good agreement with experimental one.

In principle spin Hamiltonian (1) for iron should include a term which describe hyperfine interaction of unpaired electron with nuclear spin I = 1/2 of ^{57}Fe isotope. However we have not observed hyperfine splitting of Fe^{3+} lines because ^{57}Fe isotope have low natural abundance of 2.15% and hyperfine structure could not be found in non-enriched samples.

Some signals in Fig. 1 arise due to the presence of V^{3+} (S = 1) impurity [4,9]. Positions of the two groups of lines which belong to V^{3+} impurity in one quasi-cubic lattice site are marked for $B \parallel c$ orientation in Fig. 1. Hyperfine splitting within groups caused by ^{51}V I = 7/2 nuclear spin is difficult to observe on such small-scale figure.

The EPR signals of Fe^{3+} could be observed at temperatures from 4K up to room temperature with maximum intensity at about 100K.

Here we summarize the main features of Fe^{3+} in 6H-SiC. Iron exists in Fe^{3+} charge state, electronic configuration $3d^5$, $^6S_{5/2}$. The g-factor is nearly isotropic and it's value is close to 2 in accordance with $^6S_{5/2}$ ground state. Parameter of the axial crystalline field D is strong and much greater than cubic field parameter a. Small cubic crystalline field produce only weak influence on the position of the signals in the spectrum. In particular it causes splitting of lines in angular dependence of the EPR spectra, see Fig. 1. From EPR spectra observed in X-band at 65K it is only possible to find relative signs of crystal field parameters. We have found that D, a-F and a have the same sign.

One of the most important points is simultaneous presence of Fe^{3+} and V^{3+} signals in the EPR spectra of 6H-SiC. This implies that positions of energy levels of these ions in 6H-SiC

bandgap are rather close. It is known that energy level position of V^{3+} in 6H-SiC bandgap is 0.6eV below the conduction band [5]. So one may expect that Fe^{3+} produces energy level which also lies deep in the 6H-SiC bandgap. Furthermore, energy level of vanadium in V^{4+} charge state lies near the middle of the bandgap [5] and V^{4+} is used to produce semi-insulating SiC layers. Thus we can expect that if Fe^{4+} charge state is stable then it can also produce energy level in the middle of the 6H-SiC bandgap. This will allow to use Fe^{4+} impurity to obtain semi-insulating 6H-SiC layers instead of vanadium.

In 6H-SiC there are three non-equivalent lattice sites: two quasi-cubic and one hexagonal one. However EPR of Fe^{3+} is observed for only one lattice site. This may imply that iron energy levels within the bandgap could depend significantly on the lattice site occupied. Similar situation was observed for Mo^{3+} and Mo^{4+} ions in 6H-SIC [10]. For the reasons mentioned in the above paragraph it is important to find EPR of iron in another charge state Fe^{4+} with $S = 2$.

We suppose that Fe^{3+} ions occupy silicon sites in 6H-SiC lattice. From intensities of iron EPR signals we have estimated concentration of iron impurity in the sample to be approximately $10^{17}cm^{-3}$.

4. Nickel in 6H-SiC

In the sample, where EPR signal of Fe^{3+} were found, other signals could be observed if the sample is illuminated with visible or infrared light. In Fig. 2 we show EPR spectra observed in 6H-SiC:Fe crystal at 12K in different orientations of the crystal with respect to external magnetic field under rotation in $\{11\bar{2}0\}$ plane. The two strongly anisotropic EPR lines could be seen. The inset in Fig.2 shows EPR spectra on expanded scale at angles close to $B \parallel c$. Two lines is clearly seen in such large-scale figure.

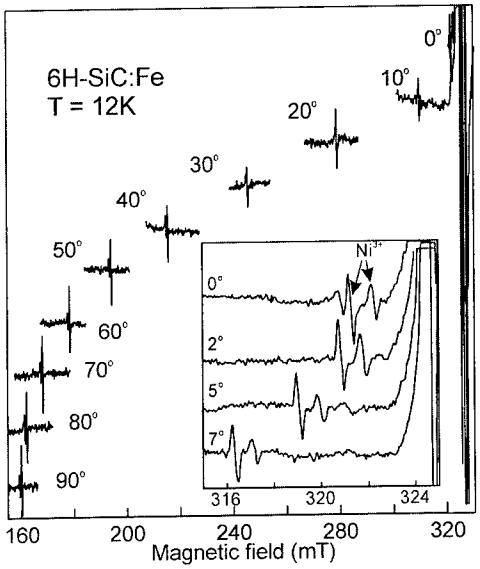


Fig. 2 Angular dependence of the EPR spectra of Ni^{3+} in 6H-SiC. Inset shows part of the dependence on the expanded scale.

The observed EPR spectra could be described in terms of effective spin $S' = 1/2$ with a spin Hamiltonian

$$H = g_{\parallel}'\mu_B B_z S_z' + g_{\perp}'\mu_B(B_x S_x' + B_y S_y'), \quad (2)$$

where g' is the effective g-factor and S' is an effective spin $S' = 1/2$. From experimental data we can obtain the following values of effective g-factors: $g_{\parallel}'(1)=2.032$, $g_{\parallel}'(2)=2.026$ $g_{\perp}'(1)=4.10$, $g_{\perp}'(2)=4.08$.

Anisotropy of the EPR spectra is characteristic for an $S = 3/2$ system in a strong axial crystalline field and positive g shift is consistent with the electron configuration d^7 .In terms of real spin $S = 3/2$ EPR spectrum can be described by a spin Hamiltonian of the form

$$H = g_{\parallel}\mu_B B_z S_z + g_{\perp}\mu_B(B_x S_x + B_y S_y) + D[S_z^2 - 1/3S(S+1)] \quad (3)$$

with $S = 3/2$, z denotes the c-axis of the crystal (principal axis of the centre); D is the axial fine structure parameter. Investigation of angular dependence of new signal allowed us to find a best-fit

parameters for spin Hamiltonian of Eq. 2: $g_{\|} = 2.032; 2.026$, $g_{\perp} = 2.05; 2.06$, $|D| > 1.5$ cm^{-1}

It is possible to use effective spin approximation since the magnitude of the zero-field splitting $2D$ is much larger than the microwave energy at the X-band (the strong zero-field limit). Thus only transitions within the M_S=±1/2 Kramers doublet can be detected. Practically, it is impossible at the X-band to determine parameter D of the spin Hamiltonian of Eq. 3 for a real magnetic field in the strong zero-field limit. Our analysis has shown that $D \geq 1.5$ cm^{-1}.

The signal could be observed at the temperatures from 4K up to 55K with maximum intensity at 12-20K.

The question arises about the nature of the center. It should be an ion in d^7 electronic configuration with small natural abundance of odd isotopes, since no hyperfine structure was observed. Two candidates are possible: Fe^+ and Ni^{3+}. On the one hand, the crystal studied was doped with iron and Fe^{3+} EPR signal have been found in it. Incident light may cause recharging of iron ions. On the other hand, no change in Fe^{3+} EPR intensity was observed when the light is turned on. Moreover, Fe^+ charge state is not very probable for substitutional Fe ion, rather for interstitial one. No direct EPR evidence about interstitial transition ions in SiC is available up to now. At last, we have found this signal in the 4H-SiC crystal, heavily doped with Al where no trace of Fe^{3+} signal could be found. Thus we believe that this new signal belongs to Ni^{3+} ions. Nickel has one stable odd isotope ^{61}Ni (I = 3/2) with low natural abundance of 1.1%. So there is no surprise that no hyperfine interaction have been observed. We believe that two lines that were observed belong to Ni^{3+} impurity in two crystallographicaly non-equivalent lattice sites.

The most interesting feature of Ni^{3+} EPR signal is its photosensitivity. It has very low (nearly zero) intensity before illumination, only irradiation with visible or near-IR light make it possible to detect EPR. After the signal appeared, its intensity does not change after the light is turned off at low temperatures. Heating of the sample up to the temperatures >100K is needed to destroy the EPR signal. Investigation of dependence of EPR spectra intensity on wavelength could give information about position of Ni^{3+} energy level in 6H-SIC bandgap. Now it is only possible to state that the Ni^{3+} signal have maximum intensity when exciting with 1000-1500 nm light.

This work was partially supported by Russian Foundation for Basic Research under Grant No. 98-02-18241.

References

[1] McD H. Hobgood, R.C.Glass, G.Augustine, R.H.Hopkins, J.Jenny, M.Skowronski, W.C.Mitchel, M.Roth, Appl.Phys.Lett. **66** (1995), p.1364

[2] T.Kimoto, T.Nakajiama,H.Matsunami, T.Nakata, M.Inoue, Appl.Phys.Lett. **69** (1996), p.1113

[3] N.Achtziger, W.Witthuhn, Phys.Rev.B **57** (1998-I), p. 12181

[4] J.Schneider, H.D.Mueller, K.Maier, W.Wilkening, F.Fuchs, A.Dornen, S.Leibenzeder, R.Stein, Appl.Phys.Lett. **56** (1990), p. 1185

[5] J.Baur, M.Kunzer, J.Schneider, Phys.Stat.Sol. (a) **162** (1997), p. 153 and references therein

[6] P.G.Baranov, Phys. of the Solid State **41** (1999), p.789 [Fiz.Tverdogo Tela **41** (1999), p. 789]

[7] Yu.A.Vodakov, E.N.Mokhov, A.D.Roenkov, D.T.Saidbekov, Phys.Stat.Sol. A**51** (1979), p. 209

[8] Yu.A.Vodakov, M.I.Karklina, E.N.Mokhov, A.D.Roenkov, Inorganic Mater. **17** (1980), p. 537

[9] A.Abragam and B.Bleaney, 1970 *Electron Paramagnetic Resonance of transition ions* (Oxford: Clarendon Press) v 1 ch 7

[10] K.F.Dombrovski, M.Kunzer, U.Kaufmann, J.Schneider, P.G.Baranov, E.N.Mokhov, Phys.Rev.B **54** (1996), p. 7323

Materials Science Forum Vols. 353-356 (2001) pp. 533-536
© 2001 Trans Tech Publications, Switzerland

Calculated Positron Annihilation Parameters for Defects in SiC

T.E.M. Staab[1], L.M. Torpo[1,2], M.J. Puska[1] and R.M. Nieminen[1]

[1] Laboratory of Physics, Helsinki University of Technology, P.O.Box 1100, FI-02015 Hut, Finland

[2] IFM, Linköping University, SE-581 83 Linköping, Sweden

Keywords: Divacancies, Irradiation, Monovacancies, Positron Annihilation Parameters

Abstract We calculate positron annihilation parameters (lifetime and high momentum part of the Doppler broadening of the annihilation radiation) for different native defects in 4H-SiC. To figure out the influence of lattice relaxations, we consider atomic coordinates in the ideal lattice as well as those determined as minimum energy structures from *ab-initio* calculations. We then compare the calculated annihilation parameters to experimental data on irradiated bulk SiC, where vacancies in different sublattices can be identified. If we qualitatively take into account the influence of the trapped positron on the relaxation pattern, we find good agreement with experimental data.

1 Introduction and Methods

Silicon Carbide (SiC) is a very promising material for semiconductor devices under extreme conditions. However, the application of SiC has been problematic due to its growth properties: it has turned out to be difficult to control the incorporation of defects (*e.g.* micropipes) or retain the same polytype. SiC exhibits polymorhism, which means that the order of stacking may be different – resulting in different electronic structures: for example the value of the indirect bandgap may vary more than 1 eV for different polytypes [1]. The most important polytypes are 3C, 2H, 4H, and 6H, characterized by their different degree of hexagonality. Important properties of semi-conductor materials such as SiC are often determined by vacancies or vacancy-related defects (*cf. e.g.* [2]). Vacancies mediate diffusion (dopants) or may reduce the density of free carriers. Since the growth procedure has been improved a few years ago, it has become important to identify defects after irradiation damage. Different methods (EPR, ODMR, ENDOR, DLTS, PL, ...) have been applied. Nevertheless, the identification many of the optical centers is still an outstanding problem, since the detailed microscopic identification of vacancies and vacancy complexes in SiC has turned out to be difficult. While also carbon vacancies have been detected experimentally, theoretical calculations as well as EPR studies indicate that Si vacancies in neutral or negative charge state dominate in n-doped SiC [3, 4, 5, 6].

Positron annihilation, however, is a method directly sensitive to vacancies. Positron lifetime spectroscopy indeed showed, in conjunction with EPR experiments, the existence of negatively charged native vacancies in n-type SiC [7]. Nevertheless, positron lifetime measurements alone, which probe mainly the electron density at the trapping site, are able to identify defects on different sublattices in compound semiconductors only if the size difference of the two atomic species is large [8, 9]. For a more conclusive identification or to detect vacancy-impurity complexes, one can make use of the positron annihilation momentum distribution. The chemical surrounding of the annihilation site can be identified using the high momentum part of this distribution [8, 10, 11, 12], since the main contribution is arising from annihilation of the positron with tightly bound core electrons possessing high momenta. If measurements are correlated to calculations of lifetime and momentum distribution, an identification of these defects is possible [8, 10]. Experimentally, the coincident detection of both 511-keV γ quanta from single annihilation events allows the observation of the high momentum part of the annihilation distribution due to a strong reduction of the disturbing background [8, 10, 11, 12].

In this work, we utilize the structures calculated for the different defects in SiC using first-principles methods [3]. Using these structures, theoretical calculations of the annihilation parameters are then performed employing free atomic wave functions using the method introduced in refs. [8, 10]. The momentum distribution is obtained by summing up the contributions from each core electron state weighted with its partial annihilation rate. The partial annihilation rate is calculated within the generalized gradient approximation (GGA) of electron-positron correlation [13]. From the theoretically calculated momentum distribution, the W parameter is determined in the range $20 - 25 \times 10^{-3}\, m_0 c$. Positron lifetimes calculated using the local-density approximation (LDA) scheme employing Boronski-Nieminen enhancement [14, 15] (high-frequency dielectric constant: $\varepsilon_\infty = 6.7$) give similar results as in ref. [9]. We use the GGA scheme [10] in a supercell of 128 atoms in order to compare the result to relaxed coordinates from plane wave pseudo potential (PWPP) calculations [3, 16].

Vacancies on different sublattices in SiC have been recently identified employing a combination of positron lifetime and coincidence Doppler broadening [17, 18]. The results are given in Table 1.

Due to large outward breathing mode relaxations of the carbon atoms surrounding the silicon monovacancy [3], Si monovacancies may actually lead to longer positron lifetimes than estimated by previous calculations using unrelaxed coordinates ($\approx 195\,\mathrm{ps}$) [9].

Table 1: 6H-SiC: Irradiated with different energies of electrons $E(e^-)$. This leads for low energy ($\approx 0.4\,\mathrm{MeV}$) to atoms exclusively displaced from the carbon sublattice. High energy electron irradiation ($\approx 2.5\,\mathrm{MeV}$) leads to atomic displacement mainly on the silicon sublattice.

sample	$E(e^-)$[MeV]	Lifetime τ[ps]	scaled to τ_{bulk}	identified defect
6H-SiC [17]	bulk	146 ± 1	1.000	—
6H-SiC [17]	0.35	160 ± 5	1.096	V_{C}
6H-SiC [17]	2.50	210 ± 5	1.438	V_{Si}

2 Results and Discussion

Provided that bulk samples are available, a simultaneous measurement of the positron lifetime spectrum and the annihilation momentum distribution is possible, and this provides the basis for an accurate way to check for the agreement between theory and experiment. Then the experimental annihilation momentum distribution can, in principle, be directly compared with the theoretical result. For this purpose, the annihilation momentum distribution f_{vac} of the vacancy has to be extracted from the measured momentum distribution f_{exp}, since $f_{\mathrm{exp}} = (1-\eta) f_{\mathrm{bulk}} + \eta f_{\mathrm{vac}}$ is the superposition of the momentum distributions in the defect-free SiC lattice (f_{bulk}) and in the vacancy (f_{vac}). While f_{bulk} is known from the SiC reference sample, the fraction η of positrons trapped at vacancies can be determined from the positron lifetime results.

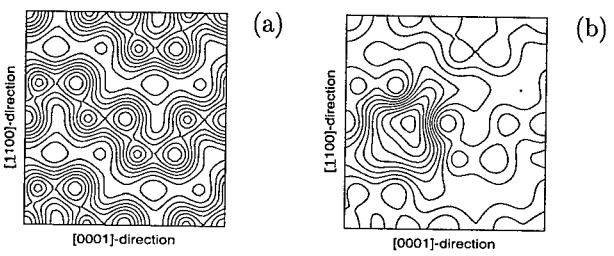


Figure 1: Unrelaxed atomic positions in the {0010}-plane in 4H-SiC: Density of the positron wave function (left: bulk, right: $V_{\mathrm{C}}^{\mathrm{cub}}$): The different cubic and hexagonal sites in the bulk are clearly seen since the positron is repelled from the ionic cores (a). The positron localizes only weakly at the missing carbon site (b). The contour spacing is 1/8 of the maximum value for (a), and 1/10 for (b).

The density of the delocalized positron in bulk 4H-SiC is shown in Fig. 1 (a), while in Fig. 1 (b) the density of the positron trapped to a vacancy in cubic site on the carbon sublattice ($V_{\mathrm{C}}^{\mathrm{cub}}$) is presented. Fig. 2 (a) and (b) show the positron localized in a vacancy in the cubic site on the silicon sublattice ($V_{\mathrm{Si}}^{\mathrm{cub}}$) and in a divacancy ($V_{\mathrm{Si}}^{\mathrm{cub}}\, V_{\mathrm{C}}^{\mathrm{cub}}$). Since there are only minor differences between vacancies on

Table 2: 4H-SiC in 128 atom supercell: Calculations are done using the GGA scheme for unrelaxed coordinates and those taken from PWPP calculations, employing the LDA lattice constant in the latter case. E_{bind} is the binding energy of the positron to the vacancy.

Configs.	E_{bind}[eV]		Lifetime τ[ps]		scaled to τ_{bulk}		rel. W-param.		core contrib.	
	unrel	PWPP	unrel	PWPP	unrel	PWPP	unrel	PWPP	unrel	PWPP
bulk	0.00	0.00	134.4	130.7	1.000	1.000	1.00	1.00	0.0233	0.0239
$V_{\text{C}}^{\text{cub}}$	-0.04	+0.09	144.2	136.7	1.072	1.046	0.98	0.99	0.0226	0.0234
$V_{\text{C}}^{\text{hex}}$	-0.06	+0.06	144.8	137.6	1.078	1.052	0.98	0.99	0.0225	0.0235
$V_{\text{Si}}^{\text{cub}}$	-1.48	-2.07	180.3	195.1	1.342	1.492	0.43	0.38	0.0105	0.0093
$V_{\text{Si}}^{\text{hex}}$	-1.50	-2.01	181.3	193.4	1.350	1.479	0.43	0.38	0.0104	0.0093
$V_{\text{Si}}^{\text{cub}}\ V_{\text{C}}^{\text{cub}}$	-2.25	—	208.6	—	1.553	—	0.44	—	0.0103	—
$V_{\text{Si}}^{\text{cub}}\ V_{\text{C}}^{\text{hex}}$	-2.25	-2.66	208.5	215.7	1.552	1.649	0.44	0.40	0.0104	0.0096
$V_{\text{Si}}^{\text{hex}}\ V_{\text{C}}^{\text{cub}}$	-2.26	—	208.9	—	1.555	—	0.44	—	0.0104	—
$V_{\text{Si}}^{\text{hex}}\ V_{\text{C}}^{\text{hex}}$	-2.27	-2.59	209.7	213.5	1.561	1.633	0.44	0.40	0.0103	0.0098

cubic and hexagonal sites, we omitted the hexagonal ones. Note the weak localization of the positron in the case of the carbon vacancy. Whereas there seems to be not such a significant difference in localization for the positron between the silicon monovacancy and the divacancy. This is also reflected in the calculated positron lifetimes (*cf.* Table 2).

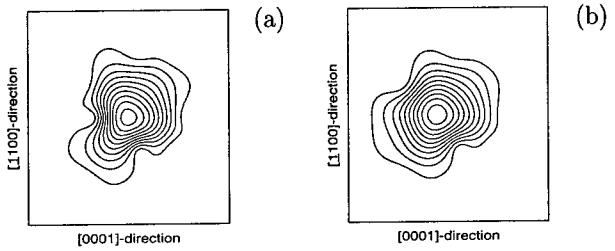


Figure 2: Unrelaxed atomic positions in the {0010}-plane in 4H-SiC: Density of the positron wave function (left: $V_{\text{Si}}^{\text{cub}}$, right: divacancy $V_{\text{Si}}^{\text{cub}}\ V_{\text{C}}^{\text{cub}}$): The positron localizes much better in the monovacancy on the silicon sublattice than on the carbon sublattice (a). But the difference towards the divacancy is small (b). The contour spacing is 1/10 of the maximum value for (a) and (b).

Comparing the unrelaxed to relaxed PWPP coordinates, we find for V_{C} that the scaled positron lifetime decreases slightly while no binding of the positron is observed anymore. Employing Hellmann-Feynman forces induced by the trapped positron, they slightly over compensate the electronically induced forces pointing inwards, and, hence, would result in longer positron lifetimes. In the case of V_{Si} the PWPP calculations indicate a strong outward breathing mode relaxation of surrounding C-atoms [3, 4], and, hence, the scaled lifetimes increase by roughly 12...15 ps. For the divacancies a similar effect is found resulting in an increase of 4...7 ps. Including positron induced forces the lifetimes may increase even further.

The calculated high-momentum part of the annihilation momentum distribution coincides well with the experimentally determined for momenta $p_z > 20 \times 10^{-3}\, m_0 c$ as given in Fig. 3 (a). Remarkable are the large differences in the ratio to bulk between vacancies on different sublattices given in Fig. 3 (b). Due to the relaxation only the intensity but not the shape of the ratio curves is shifted.

3 Conclusions

In this work, we have demonstrated a practical way how to identify vacancies on different sublattices in SiC by a comparison of theoretically calculated annihilation parameters with experiments. Indispensable is to employ a combination of positron lifetime spectroscopy and measurement of the core annihilation momentum distribution by coincidence Doppler broadening spectroscopy.

Defect-related positron lifetimes as well as the intensity and shape of the annihilation momentum

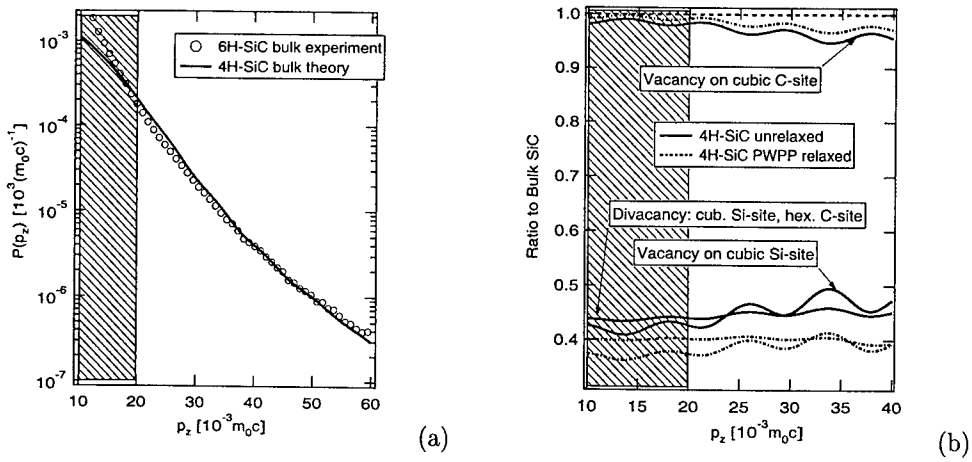


Figure 3: Comparison between experimental data for 6H-SiC and theoretical data for 4H-SiC (a). In the right panel (b) the calculated ratio to bulk is given for unrelaxed and PWPP-relaxed coordinates. The shaded areas indicate the momentum range to be excluded in a comparison between experiment and theory.

distribution are different for Si and C vacancies. From Fig. 3 the ratio between the annihilation momentum distribution for divacancies and bulk is nearly constant for high momenta, while vacancies on the carbon and silicon sublattice exhibit an opposite slope. Comparing to annealing experiments after irradiation [19], the positron lifetime component of ≈ 230 ps detected after annealing up to 900°C may be due to divacancies, which are found to be very stable [16].

References

[1] F. Bechstedt *et al.*. *phys. stat. sol.* (b)202 (1997) p. 35

[2] H. Itoh *et al.*. *phys. stat. sol.* (b)202 (1997), p. 173

[3] L. Torpo, M. Marlo, T.E.M. Staab, and R.M. Nieminen. Submitted to *Phys. Rev.* B, October 2000.

[4] A. Zywietz, J. Furthmüller, and F. Bechstedt. *Phys. Rev.* B59(23) (1999), p. 15166

[5] N.T. Son *et al.*. *J. Appl. Phys.* 79(7) (1996), p. 3784

[6] E. Sörman *et al.*. *Phys. Rev.* B61(4) (2000), p. 2613

[7] A. Kawasuso *et al.*. *Appl. Phys.* A67 (1998), p. 209

[8] M. Alatalo *et al.*. *Phys. Rev.* B51(7) (1995), p. 4176

[9] G. Brauer *et al.*. *Phys. Rev.* B54(4) (1996), p. 2512

[10] M. Alatalo *et al.*. *Phys. Rev.* B54(4) (1996), p. 2397

[11] P. Asoka-Kumar *et al.*. *Phys. Rev. Lett.* 77(10) (1997), p. 2097

[12] U. Myler and P.J. Simpson. *Phys. Rev.* B56(22) (1997), p. 14303

[13] B. Barbiellini M. Hakala M.J. Puska and R.M. Nieminen. *Phys. Rev.* B56(12) (1997), p. 7136.

[14] M.J. Puska, S. Mäkinen, M. Manninen, and R.M. Nieminen. *Phys. Rev.* B39(11) (1989), p. 7666

[15] M.J. Puska and R.M. Nieminen. *J. Phys. F: Metal Phys.* 13 (1983), p. 333

[16] L. Torpo, T.E.M. Staab, E. Janzén, and R.M. Nieminen. to be submitted to *Phys. Rev.* B, October 2000.

[17] A.A. Rempel *et al.*. Proc. of the ICPA-12 München August 2000 – to be published in Mater. Sci. Forum.

[18] S. Arpiainen, K. Saarinen, L. Henry, and M.-F. Barthe. To be published, 2000.

[19] C.C. Ling, C.D. Beling, and S. Fung. *Phys. Rev.* B62(12) (2000), p. 8016

Materials Science Forum Vols. 353-356 (2001) pp. 537-540
© 2001 Trans Tech Publications, Switzerland

Annealing Process of Defects in Epitaxial SiC Induced by He and Electron Irradiation: Positron Annihilation Study

A. Kawasuso[1,4], F. Redmann[1], R. Krause-Rehberg[1], P. Sperr[2], Th. Frank[3], M. Weidner[3], G. Pensl[3] and H. Itoh[4]

[1] Martin-Luther-Universität, Friedemann-Bach-Platz 6, DE-06108 Halle, Germany

[2] Universität der Bundeswehr München, DE-85577 Neubiberg, Germany

[3] Universität Erlangen-Nürnberg, Staudtstr. 7/A3, DE-91058 Erlangen, Germany

[4] Japan Atomic Energy Research Institute, 1233 Watanuki, Takasaki, Gunma 370-1292, Japan

Keywords: Annealing, Defect, Doppler Broadening, Epitaxial Layers, Positron Annihilation, Vacancy

Abstract

Annealing processes of vacancy-type defects in epitaxial 6H SiC after 2 MeV electron irradiation and multiple He implantation have been investigated using positron annihilation spectroscopy. Vacancy-type defects are found to disappear in two annealing stages: at 500-800°C and 1200-1500°C. Silicon vacancies are the major positron trapping centers after electron irradiation. Two annealing stages after electron irradiation are attributed to the disappearance of isolated silicon vacancies and complexes associated with silicon vacancies, respectively. In He-irradiated SiC, divacancies are also generated in addition to silicon vacancies.

Introduction

Radiation-induced defects in SiC are of great importance from both fundamental and technological viewpoints. In SiC device processing, ion implantation is indispensable for the selective doping because of small diffusion coefficients of dopants in this material. To enhance the electrical activity of implanted dopants, defects induced by implantation should be removed. Electron irradiation is also used for the control of minority carrier lifetime. Electrical devices based on SiC tend to be fabricated using high-quality epilayers. It is therefore important to identify defects in SiC epilayers induced by irradiation and to clarify their thermal stability.

In deep level transient spectroscopy (DLTS) measurements, several deep levels termed E_1/E_2(E_C-0.39~0.43 eV), RD_5(E_C-0.43~0.47 eV), Z_1/Z_2(E_C-0.65~0.72 eV) and R(E_C-1.17~1.27 eV) centers are commonly seen in 6H SiC epilayers after fast-particle irradiation [1-5]. These defects are significantly reduced by heat treatment up to 1700°C [1, 2]. The photoluminescence (PL) D_1 spectrum is also a main center observed after irradiation and subsequent heat treatment [6]. The complementary study using DLTS and PL [2] suggests that E_1/E_2 levels and D_1 centers are originating from the same defect species. The origins of these deep levels are however still open questions. Optically detected magnetic resonance (ODMR) studies show the generation of silicon vacancies after electron irradiation and their annealing at around 750°C [7].

Positron annihilation spectroscopy is a suitable method to investigate vacancy-type defects in semiconductors [8]. Using the positron beam technique, defects in thin films can also be detected. We performed annealing experiments for 6H SiC epilayers after He implantation and electron irradiation. In this report, we show the annealing characteristics of vacancy-type defects.

Experimental

Samples used in this study are cut from a high-quality 6H SiC epilayer (4.9 μm thick) doped with nitrogen (n-type: n=4x10^{15}cm^{-3}). As a reference, we also used p-type epitaxial SiC. They were subjected to 2 MeV electron irradiation with a dose of 3x10^{17}e$^-$/cm^2 and He implantation at room temperature. In the He implantation, an eight-fold implantation with energies from 30 to 950 keV

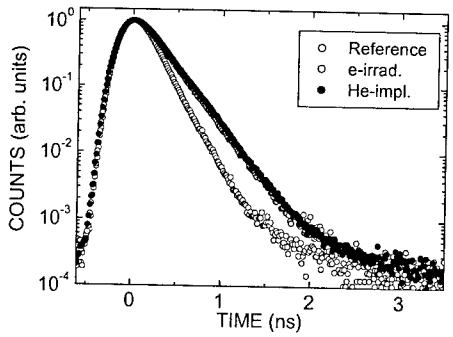


Fig. 1 Positron lifetime spectra obtained at E=17 keV. The reference spectrum is measured with unirradiated p-type specimen.

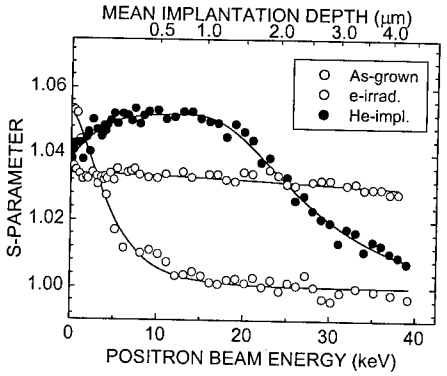


Fig. 2 S-parameters (normalized) as a function of positron beam energy. Solid lines are the results of VEPFIT analysis.

and doses from 8.0×10^{11} to 1.3×10^{12} He^+/cm^2 was carried out to form a box-shaped damage profile with a maximum depth at 2.4 μm. After irradiation, isochronal annealing was done from 100 to 1700°C for 30 minutes. Using a monoenergetic positron beam, Doppler broadening measurements were performed at room temperature after each annealing. Positron annihilation parameters called S and W, which are defined as peak and tail areas [8], respectively, of Doppler spectrum, were calculated. To see the change of dominant defect species during annealing, S-W correlation was also examined. Positron lifetime measurements were performed with a 17 keV positron beam. The average lifetime was determined.

Results and Analysis

Figure 1 shows positron lifetime spectra for the reference (unirradiated p-type) and irradiated samples. The average positron lifetime for the reference sample is 140 ps. This is in good agreement with the bulk lifetime reported so far. Positron lifetimes clearly increase after irradiation showing the presence of vacancy-type defects. The average lifetimes for the electron-irradiated and He-implanted samples are 197 ps and 212 ps, respectively. Figure 2 shows S-parameters as a function of positron beam energy E. Here, S-parameters are normalized to the bulk value. For the unirradiated sample (n-type), S-parameter is almost constant at E>15 keV. This shows that most positrons annihilate in perfect region. The increase in S-parameter in low energy region is due to surface effects. For the electron-irradiated sample, S-parameter is almost constant up to E=39 keV indicating the homogeneous vacancy distribution. For the He-implanted sample, S-parameter is greater than that of the unirradiated sample below 20 keV and decreases at higher energies. The VEPFIT [9] analyses were made with a uniform and a box-shaped defect distribution for the electron-irradiated and He-implanted samples, respectively. The results of fitting are also shown in Fig. 2. For the He-implanted sample, the layer boundary of defect region determined by the analysis agrees well with

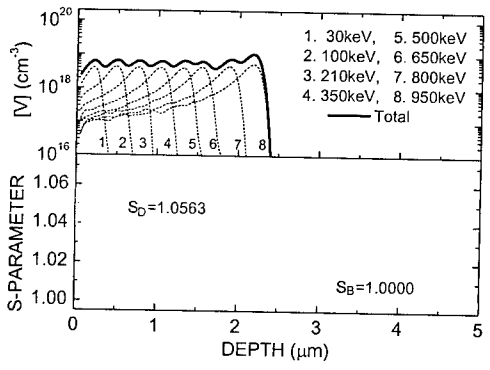


Fig. 3 Distributions of S-parameter for the He-implanted sample from VEPFIT analysis and vacancies from SRIM simulation [10].

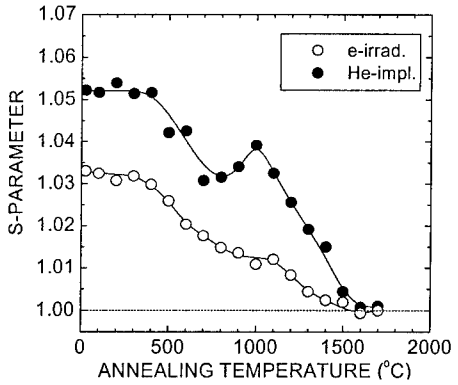


Fig. 4 Annealing behavior of *S*-parameters in defect region obtained from VEPFIT analysis.

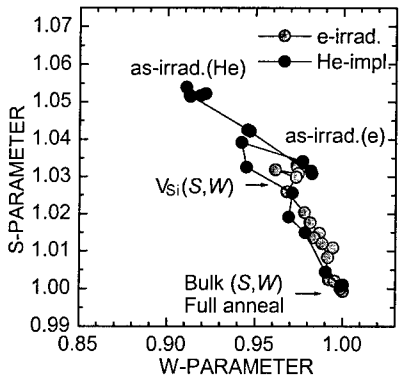


Fig. 5 *S-W* plot. Grey regions show (*S*,*W*) for silicon vacancies and bulk. (*S*, *W*) for bulk coincides with fully annealed state.

that obtained from the SRIM simulation [10] (Fig. 3). Annealing behavior of *S*-parameters is shown in Fig. 4. For both the electron-irradiated and He-implanted samples, two annealing stages appear at 500-800°C and 1200-1500°C. The *S*-parameter approaches the unirradiated state until 1700°C. For the He-implanted sample, *S*-parameter tends to increase from 800°C to 1000°C before the second annealing stage. The *S-W* correlation is also shown in Fig. 5. In this figure, *S* and *W* parameters for silicon vacancies determined previously [11,12] are also displayed.

Discussion

A. *Electron irradiation*

The lifetime of positron at a silicon vacancy was experimentally determined to be 188 ps for 3C SiC at room temperature [13]. Theoretical positron lifetimes for a carbon vacancy, a silicon vacancy and a divacancy are reported to be about 153 ps, 194 ps and 214 ps, respectively [14]. The average lifetime for the electron-irradiated sample (197 ps) is close to the positron lifetime for silicon vacancies. Thus, silicon vacancies are considered to be the major positron trapping centers. Divacancies may also be generated. Considering that the displacement energy for SiC is about 30 eV [15], the average primary knock-on atom energy for 2 MeV electron irradiation is 70-80 eV. The concentration of divacancies is therefore expected to be much smaller than that of silicon vacancies. Carbon vacancies are also primary defects and stable at room temperature [16]. However, since the positron lifetime for a carbon vacancy is fairly close to the bulk lifetime, carbon vacancies may have a minor effect. As seen from the *S-W* plots (Fig. 5), before annealing *S* and *W* for the electron-irradiated sample is located in the region for silicon vacancies. In addition, almost one straight correlation is found until the full annealed state. These also indicate that silicon vacancies are the major defects and the concentration decreases upon annealing.

It is known that silicon vacancies in 3C SiC are mobile above 600°C [17]. Carbon vacancies disappear below 300°C [16]. It is also shown that the density of silicon vacancies in epitaxial 6H SiC drastically decreases after the annealing at 750°C by ODMR [7]. The first annealing stage at 500-800°C is consistently explained as the disappearance of isolated silicon vacancies. Above 1000°C, only one annealing stage appears suggesting one type of defects act as positron trapping centers. The annealing stage at 1200-1500°C is attributed to the disappearance of complexes associated with silicon vacancies, which have higher thermal stability than isolated silicon vacancies [12,18]. In electron-irradiated epitaxial 6H SiC, only E_1/E_2 levels are reported to remain after annealing at 1000°C and these levels drastically decrease above 1400°C [3]. Thus, it is possible to assign the E_1/E_2 levels to complexes related to silicon vacancies.

B. *He implantation*

For the He-implanted sample, the average lifetime is 212 ps. This is greater than the positron lifetime for silicon vacancies. The *S*-parameter for the He-implanted sample is also greater than that for silicon vacancies. Probably, in the He-implanted sample, divacancies are also important positron trapping centers in addition to silicon vacancies. The He-implanted sample also shows two annealing stages at 500-800°C and 1200-1500°C. From the *S-W* plots (Fig. 4), it is found that dominant defect species changes above 800°C. The *S-W* correlation above 1000°C approaches the line between silicon vacancies and bulk. Probably, divacancies and isolated silicon vacancies are annealed up to 800°C. Divacancies are considered to disappear due to the recombination with interstitials [17,18]. Above 800°C, complexes including silicon vacancies are major defects and they disappear up to 1700°C as well as the electron-irradiated sample. The increase of *S*-parameter at 800-1000°C indicates the formation of this defect due to annealing.

According to the DLTS experiments for He-implanted epitaxial 6H SiC, the annealing temperatures of RD_5 and R levels are reported to be 100-500°C and 500-1000°C, respectively [1]. The Z_1/Z_2 level disappears in rather broad range from 100°C to 1400°C [1,2]. The concentration of E_1/E_2 levels increases at around 700°C and drastically decreases at 1200-1400°C [2]. It seems that the decrease in the *S*-parameter until 800°C coincides with the annealing of RD_5 and R levels. The annealing characteristics of *S*-parameter above 800°C is similar to that of E_1/E_2 levels. Thus, the E_1/E_2 levels are possibly originating from vacancy-type defects.

Summary

In summary, we studied annealing processes of vacancy-type defects in epitaxial 6H SiC after electron irradiation and He implantation. Two major annealing stages at 500-800°C and 1200-1500°C related to vacancy-type defects are detected. It was found that silicon vacancies are the main positron trapping centers in the electron-irradiated SiC. In the He-implanted sample, divacancies are also comparable positron trapping centers to silicon vacancies. Vacancy-type defects were no longer detected after the annealing at 1700°C.

References

[1] T. Dalibor *et al.*, Phys. Stat. Sol. (a)**162** (1997), p.199.
[2] Th. Frank *et al.*, Mater. Sci. Forum **338-342** (2000), p. 753.
[3] M. Gon *et al.*, J. Appl. Phys. **85** (1999), p.7604.
[4] C. Hemmingsson *et al.*, J. Appl. Phys. **84** (1998), p. 704.
[5] V. S. Ballandovich and G. N. Violina, Cryst. Latt. Def. and Amorph. Mat., **13** (1987), p.189.
[6] W. J. Choyke, Inst. Phys. Conf. Ser. **31** (1977), p. 58.
[7] E. Sörman *et al.*, Phys. Rev. B**61** (2000), p. 2613.
[8] "Positron Annihilation in Semiconductors", vol. 127 of "Solid-State Sciences", R. Krause-Rehberg and H. S. Leipner (Springer-Verlag , Berlin 1999).
[9] A. van Veen *et al.*, Appl. Scurf. Sci. **85** (1995), p. 216.
[10] "The Stopping and Range of Ions in Solids", eds. J. F. Ziegler, J. P. Biersack and U. Littmark (Pergamon Press, New York, 1996).
[11] H. Itoh *et al.*, Mater. Sci. Forum **117-118** (1993), p. 501.
[12] A. Kawasuso *et al*, Mater. Sci. Forum **264-268** (1998), p. 611.
[13] A. Kawasuso *et al.*, Appl. Phys. A **67** (1998), p. 209.
[14] G. Brauer *et al.*, Phys. Rev. B **54** (1996), p. 2512.
[15] A. L. Barry *et al.*, IEEE Trans. Nucl. Sci. **38** (1991), p.1111.
[16] H. Itoh *et al.*, Inst. Phys. Conf. Ser. **137** (1993), p. 255.
[17] H. Itoh *et al.*, J. Appl. Phys. **66** (1989), p. 4529.
[18] A. Kawasuso *et al.*, J. Appl. Phys. **80** (1997), p. 5639.

Chapter 4:

Processing of SiC

Materials Science Forum Vols. 353-356 (2001) pp. 543-548
© 2001 Trans Tech Publications, Switzerland

Recent Progress in SiC Epitaxial Growth and Device Processing Technology

T. Kimoto, H. Yano, S. Tamura, N. Miyamoto, K. Fujihira, Y. Negoro and H. Matsunami

Department of Electronic Science and Engineering, Kyoto University, Yoshidahonmachi, Sakyo, Kyoto 606-8501, Japan

Keywords: SiC-(11$\bar{2}$0), Homoepitaxial Growth, Ion Implantation, MOSFET, Pin Diode

Abstract Recent progress in SiC epitaxial growth, ion implantation, and MOS technologies made in the authors' group are described. Thick (> 30 μm) SiC epilayers grown by improved cold-wall CVD show a background doping level of 1~5x10^{14} cm^{-3} with a low trap concentration of 3~4x10^{12} cm^{-3}. Specular SiC epilayers have been grown at a growth rate over 15 μm/h by a chimney-type CVD reactor at 1700℃. High-dose P^+ and Al^+ implantations have resulted in low sheet resistances of 105 Ω/□ and 3600 Ω/□, respectively. Successful MeV Al^+ and B^+ implantations are demonstrated. A high channel mobility of 96 cm^2/Vs for 4H-SiC(11$\bar{2}$0) MOSFET originates from the much lower interface state density near the conduction band edge.

1. Introduction

Breakthroughs in SiC boule and epitaxial growth technologies in the 1980's have been accelerating the development of various prototype SiC devices projected for high-power, high-frequency, and high-temperature electronics [1]. To meet the requirements for wide commercialization of SiC electronic devices, however, there still remain crucial issues in both growth and device processing. The size and structural defects including micropipes of SiC wafers, for example, have limited high-current handling capability of SiC devices. Fast epitaxy and further purification of epilayers will be also future challenges. Difficulty in activation of implanted p-type dopants, low inversion channel mobility in SiC MOSFETs, and oxide reliability at high temperatures are to be solved before the full potential of SiC is achieved in real electronic devices. This paper describes recent progress in SiC epitaxial growth, ion implantation, and MOS technologies made in the authors' group.

2. Epitaxial growth of thick and high-purity SiC

Epitaxial growth was performed by atmospheric-pressure chemical vapor deposition (CVD) in a cold-wall horizontal reactor [2]. Source gases were SiH_4 and C_3H_8 with a Pd-cell purified H_2 carrier gas. The authors have succeeded in epitaxial growth of thick and high-purity SiC by cold-wall CVD at 1500℃ with a growth rate of 3.2 μm/h. The improvements of susceptor design and growth process have enabled to grow 30~54 μm-thick SiC epilayers with a low net doping concentration of 1~5x10^{14} cm^{-3}. A prolonged growth run leads to the reduced donor concentration, owing to the "baking effect". Although macrostep bunching was more pronounced for thick epilayers grown with a higher C/Si ratio, a specular surface was obtained by keeping the C/Si ratio below 3. By optimizing the HCl etching condition prior to CVD and starting CVD with a slow growth rate of 1 μm/h, "triangular-defects" and "carrot-like grooves" could be eliminated, with a greatly reduced

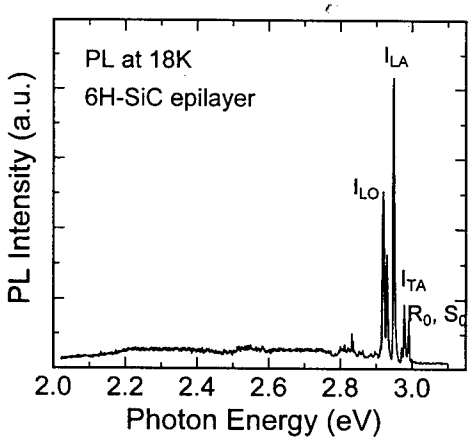


Fig.1 Photoluminescence spectrum at 18 K taken from a 32 μm-thick 6H-SiC epilayer.

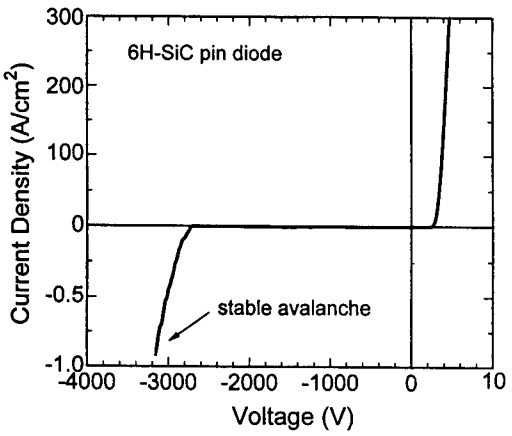


Fig.2 Current density-voltage characteristics of an epitaxially grown 6H-SiC *pin* diode with a 31 μm-thick *i*-layer.

surface defect density of 40~120 cm^{-2}. Surface-defect free area over 1x1 mm^2 could reproducibly be produced. Figure 1 represents the photoluminescence spectrum at 18 K taken from a 32 μm-thick 6H-SiC epilayer. The spectrum reveals that free exciton peaks denoted by the "I" series dominate, and very few signs of unwanted impurities such as Al, B, and Ti can be observed. From isothermal capacitance transient spectroscopy (ICTS) measurements, one deep trap located at E_C-0.67 eV for 4H-SiC and two traps closely located at E_C-0.35 and 0.41 eV for 6H-SiC epilayers were detected. However, the trap concentration was as low as 3~4x10^{12} cm^{-3}.

Figure 2 depicts the current density-voltage characteristics of an epitaxially grown 6H-SiC *pin* diode with a 31 μm-thick *i*-layer. At a reverse voltage of –3200V, the diode exhibited stable and reversible avalanche breakdown, and the diode withstood a relatively high current density of 1 A/cm^2. In the forward direction, a low on-resistance of 4.6 $m\Omega cm^2$ was achieved, indicating effective conductivity modulation of the *i*-layer. This value is lower than not only the theoretical limit of specific on-resistance for SiC unipolar devices but also the on-resistance of Si *pin* diodes in the similar blocking-voltage region. From the turn-off measurements of diodes, the minority carrier lifetimes were determined to be 0.45 μs for 4H-SiC and 0.64 μs for 6H-SiC. The diffusion length of minority carriers was estimated to be 10~12 μm, suggesting high material quality.

High-quality SiC epilayers with excellent surface morphology can be produced on "micropipe-free" SiC(11$\bar{2}$0) substrates. The (11$\bar{2}$0) epilayers showed very smooth morphology with a surface roughness of 0.18 nm. An X-ray diffraction analysis revealed that lattice-mismatch strain between n^--epilayers and n^+-substrates can be minimized by introducing n-type buffer layers [3]. The doping efficiency of both donor and acceptor impurities on (11$\bar{2}$0) is located in between (0001)Si and (000$\bar{1}$)C faces. The lowest donor concentration of unintentionally doped epilayers is 1x$10^{14}$$cm^{-3}$. Molten KOH etching experiments revealed a relatively high stacking fault density of 10^2 cm^{-1} for (11$\bar{2}$0) epilayers. Nevertheless, Ni/4H-SiC(11$\bar{2}$0) Schottky barrier diodes exhibited lower leakage current density than SiC(0001) diodes [3].

Recently, vertical hot-wall (chimney-type) CVD [4] has been investigated in the authors' group to increase the growth rate. With this up-flow configuration at a reduced pressure of 150~200 Torr, a very low H_2 carrier flow of 2~3 slm is sufficient to obtain large growth windows. At a high

growth temperature of 1700℃, however, the optimum C/Si ratio to obtain mirror-like surfaces is much lower, 0.4~0.7, than that at 1500℃(1.5~3), probably due to the considerably increased equilibrium pressure of Si-related species at the high temperature. Mirror-like surface has been obtained at a high growth rate over 15μm/h. The thickness and doping uniformities (at a $1x10^{15}cm^{-3}$ doping level) on a half two-inch wafer were 4% and 6%, respectively. The donor concentration of unintentionally doped SiC(0001) epilayers can be reduced down to $7x10^{14}$ cm^{-3} by increasing the C/Si ratio up to 0.7, following the site-competition concept [5]. The X-ray rocking curve (ω scan) measurements of 26 μm-thick 4H-SiC epilayers showed a small FWHM value of 12 arcsec.

3. High-dose/high-energy ion implantation

Phosphorous ion (P^+) implantation, instead of N^+ implantation, has attracted increasing attention to form selective n^+ region in SiC [6,7]. In this study, multiple P^+ implantation was performed into p-type 4H-SiC epilayers at either room temperature or 800℃ to create a 0.25 μm-deep box profile. The total implant dose was fixed at $4x10^{15}$ cm^{-2}. Typical data are summarized in Table 1. As is expected, P^+ implantation at elevated temperatures followed by high-temperature annealing at 1700℃ is effective to form heavily doped n^+ region with a sheet resistance as low as 105 Ω/□. The authors have found that a similar sheet resistance (110 Ω/□) can be achieved even by room-temperature P^+ implantation, when 4H-SiC(11$\bar{2}$0) epilayers were employed (not shown). Significantly better lattice recovery may be realized on 4H-SiC(11$\bar{2}$0) than (0001), owing to much faster recrystallization rate along the <11$\bar{2}$0> direction [8]. Thus, SiC(11$\bar{2}$0) may possess much potential to reduce implantation and annealing temperatures.

High-dose aluminum ion (Al^+) implantation for p^+ doping has been a major remaining issue in SiC processing technology, due to the difficulty of dopant activation as well as the large ionization energy of Al acceptors [9]. Although recent trials of hot Al^+ implantation at 500℃ followed by annealing at 1700℃ resulted in a reasonable sheet resistance of 3600 Ω/□, as shown in Table 1, further improvement is required, especially to reduce contact resistivity on p-type SiC.

Table 1 Typical results of high-dose P^+, N^+, and Al^+ implantation into 4H-SiC. The total implant dose is $4x10^{15}cm^{-2}$.

Implanted Ion	Implantation Temperature	Annealing Temperature	Sheet Resistance
P^+	20℃	1600℃	200 Ω/□
		1700℃	180 Ω/□
	800℃	1600℃	110 Ω/□
		1700℃	105 Ω/□
N^+	800℃	1600℃	420 Ω/□
Al^+	20℃	1600℃	150 kΩ/□
		1700℃	95 kΩ/□
	500℃	1600℃	12.5 kΩ/□
		1700℃	3.6 kΩ/□

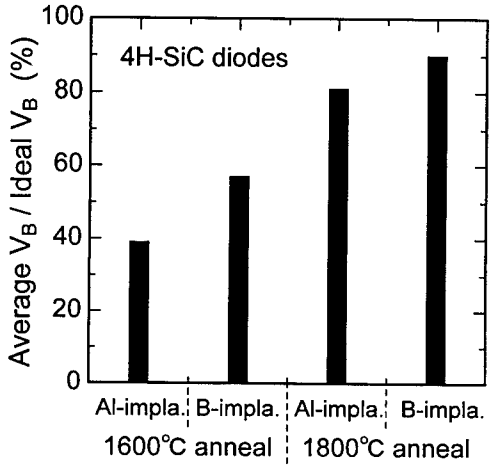


Fig.3 Ratio of average blocking voltage measured and ideal blocking voltage calculated from the diode structure for Al^+- or B^+-implanted SiC *pin* diodes annealed at two different temperatures.

High-energy (MeV) Al and B ion implantations into SiC have been investigated to form 3 μm-deep pn junction for future several kV-class DIMOSFET and IGBT fabrication. The 3 μm-deep box profiles were created by multiple Al^+ (50 keV~6.2 MeV) or B^+ (30 keV~3.4 MeV) implantations with a total dose of $3.0x10^{14}cm^{-2}$. After annealing at 1600°C, the electrical activation ratios, defined as the ratio of the acceptor concentration measured by C-V and the average implanted impurity concentration, remained low, 32% for Al^+ and 2% for B^+ implantations. Nearly perfect electrical activation (> 90%), with correcting the out-diffusion effect in the case of B^+ implantation, could be attained by annealing at 1800°C.

Reverse blocking performance of MeV-implanted diodes was investigated by fabricating 4H-SiC(0001) mesa *pin* diodes. High blocking voltages over 3000V and a low leakage current density of 10^{-8}~10^{-7} A/cm^2 at –1000 V could be achieved for 1800°C-annealed diodes with 15 μm-thick *i*-layers. Furthermore, these diodes could withstand high avalanche current density up to 2 A/cm^2 at a voltage of –3080V, indicating excellent robustness of SiC devices. Figure 3 represents the ratio of average blocking voltage measured and ideal blocking voltage calculated from the diode structure, for Al^+- or B^+-implanted 4H-SiC *pin* diodes annealed at two different temperatures. Annealing at 1800°C has significantly improved the blocking performance, and more than 80% of parallel-plane breakdown voltage has been realized. Recent deep level analyses revealed that the trap concentration near the junction interface for 1800°C-annealed diodes is lower than 1600°C-annealed diodes by two orders of magnitude [10].

4. High-channel mobility in SiC(11$\bar{2}$0) MOSFETs

Very high channel mobilities of 96 and 116 cm^2/Vs have been achieved for inversion-type 4H- and 6H-SiC MOSFETs fabricated on (11$\bar{2}$0), respectively [11]. In this section, the authors describe the temperature dependence of MOSFETs and the C-V curves of MOS capacitors to provide better understanding of SiC MOS interface.

N-channel planar MOSFETs were fabricated on boron-doped p-type 4H- and 6H-SiC (11$\bar{2}$0) and off-axis (0001) epilayers. The source and drain regions were formed by room-temperature N^+ implantation followed by annealing at 1550℃ for 30 min in Ar. Then, samples were cleaned by the RCA process prior to gate oxidation. The 40 nm-thick gate oxides were formed by wet oxidation at 1100℃ for 60 min on (11$\bar{2}$0) or at 1150℃ for 120 min on (0001), taking account of 3~5 times faster oxidation rate on (11$\bar{2}$0). The channel length and width were 30 and 200 μm, respectively.

When 4H-SiC(0001) and (11$\bar{2}$0) MOSFETs were tested at elevated temperatures, the channel mobility of the 4H-SiC(0001) MOSFET was thermally activated with increasing temperature. This abnormal dependence may be caused by the severe Coulomb scattering and/or the trapping of mobile electrons in the inversion layer at a high density of interface states. In contrast, the 4H-SiC MOSFET on (11$\bar{2}$0) exhibits high channel mobility at room temperature and decreases with increasing temperature above 200K, according to the $T^{-2.2}$ dependence, due to phonon scattering, demonstrating a superior MOS interface on (11$\bar{2}$0). The authors have suggested that negative charges near the MOS interface, which include immobile electrons trapped at interface states or oxide traps and fixed charges, may control the channel mobility [12]. Schörner et al. have proposed that the channel mobility is mainly affected by acceptor-like interface states near the conduction band edge [13]. One evidence for these speculations can be seen in the temperature dependence of threshold voltage shown in Fig.4. The threshold voltage of 4H-SiC(0001) MOSFET is very high, 7.8 V at room temperature, and it greatly decreases down to 2.7 V at 500K. This characteristic is

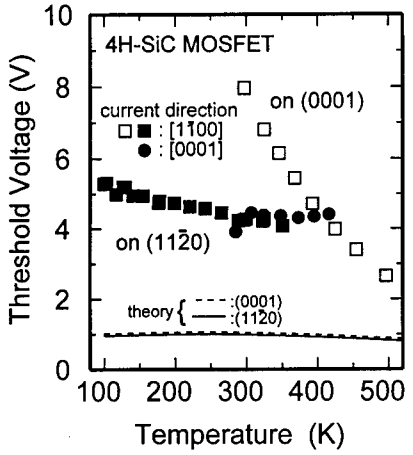


Fig.4 Temperature dependence of threshold voltage for 4H-SiC(0001) and (11$\bar{2}$0) MOSFETs.

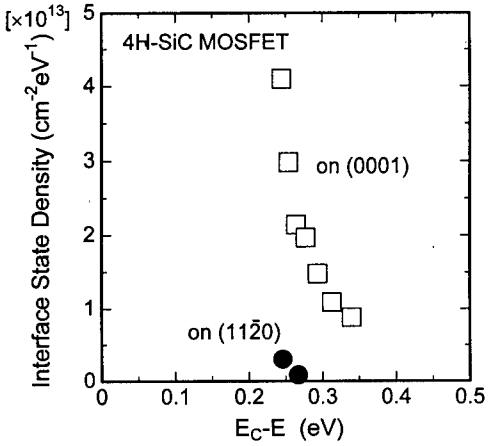


Fig.5 Distribution of interface state density for 4H-SiC(0001) and (11$\bar{2}$0) MOS structure calculated from the threshold voltage shift.

accompanied with the increase in channel mobility, indicating the reduced negative charges near the MOS interface at elevated temperatures. However, the threshold voltage of 4H-SiC(11$\bar{2}$0) MOSFET is lower, 4.0 V, and is insensitive to temperature (with the decrease in mobility at elevated temperatures).

Based on these data, the interface state density near the conduction band edge was estimated by assuming that the shift of threshold voltage as a function of temperature is mainly attributed to the emission (detrapping) of electrons from the MOS interface states. Figure 5 represents the distribution of interface state density for 4H-SiC(0001) and (11$\bar{2}$0) MOS structures calculated from the threshold voltage shift. The interface state density near the conduction band edge is much lower for (11$\bar{2}$0). Since the interface state density is in the 10^{12}~10^{13} cm^{-2} range, being the same order as the sheet charge density in an inversion layer induced by the gate bias, most of electrons in the inversion channel may be trapped at these interface states and become immobile [14]. Thus, the lower interface state density on (11$\bar{2}$0) leads to the higher concentration of mobile electrons in an inversion layer together with higher channel mobility. This may the reason why the dramatically improved MOSFET performance is realized on SiC(11$\bar{2}$0).

Recent C-V measurements on n-type 4H-SiC(0001) and (11$\bar{2}$0) MOS capacitors have revealed that (11$\bar{2}$0) MOS capacitors exhibit much smaller frequency dispersion in the accumulation [15]. The interface state density determined from C-V curves is also 2~3 times lower on (11$\bar{2}$0) than on (0001), as far as we focus on the interface states near the conduction band edge. The authors have also clarified that the high-quality (11$\bar{2}$0) MOS interface can be formed by wet oxidation and not by dry oxidation [15]. Further fundamental investigations are required to understand the chemical nature and generation mechanism of interface states or near interfacial traps [16] in SiC MOS structure.

5. Conclusions

Recent progress in SiC epitaxial growth, ion implantation, and MOS technologies made in the authors' group were discussed. Photoluminescence, ICTS, and high-voltage *pin* diode performance

have demonstrated high quality and high purity of thick (> 30 μm) SiC epilayers grown by improved cold-wall CVD. The (11$\bar{2}$0) epilayers showed very smooth morphology and the quality can be improved by introducing a buffer layer to minimize lattice-mismatch strain between n^--epilayers and n^+-substrates. Specular SiC epilayers have been grown at a growth rate over 15 μm/h by a chimney-type CVD reactor at 1700℃. Low sheet resistances of 105 Ω/□ and 3600 Ω/□ were obtained by high-dose P^+ and Al^+ implantations, respectively. MeV Al^+ and B^+ implantations followed by high-temperature annealing at 1800℃ resulted in nearly perfect activation and excellent blocking performance of *pin* diodes. 4H-SiC(11$\bar{2}$0) MOSFETs exhibited a high channel mobility of 96 cm^2/Vs, a negative temperature coefficient of channel mobility, and temperature-independent threshold voltage. These properties can be ascribed to the much lower interface state density near the conduction band edge on (11$\bar{2}$0).

Acknowledgments

The authors would like to thank Dr. Y.Chen, S.Nakamura, S.Nakazawa, and T.Hirao at the authors' group for their contribution to this work. They also express gratitude to Dr.N.Ohtani at Nippon Steel Corp. for supplying 4H-SiC(11$\bar{2}$0) substrates. Special thanks are due to Dr.M.Watanabe at Ion Engineering Research Institute for the use of ion implantation systems. This work was partially supported by a Grant-in-Aid for Specially Promoted Research, No.09102009, from the Ministry of Education, Science, Sports and Culture, Japan, and NEDO.

References

[1] *Silicon Carbide and Related Materials – 1999*, C.H.Carter, Jr., R.P.Devaty, and G.S.Rohrer, Eds. (Trans Tech Publication, Zuerich, 2000), part 2.

[2] H.Matsunami and T.Kimoto, Mat. Sci. & Eng. **R20**(1997), p.125.

[3] T.Kimoto, T.Yamamoto, Z.Y.Chen, H.Yano, and H.Matsunami, Mat. Sci. Forum **338-342**(2000), p.189.

[4] A.Ellison, J.Zhang, W.Magnusson, A.Henry, Q.Wahab, J.P.Bergman, C.Hemmingsson, N.T.Son, and E.Janzén, Mat. Sci. Forum **338-342**(2000), p.131.

[5] D.J.Larkin, P.G.Neudeck, J.A.Powell, and L.G.Matus, Appl. Phys. Lett. **65**(1994), p.1659.

[6] V.Khemka, , R.Patel, N.Ramungul, T.P.Chow, M.Ghezzo, and J.Kretchmer, J. Electron. Mat. **28**(1999), p.167.

[7] S.Imai, S.Kobayashi, T.Shinohe, K.Fukuda, Y.Tanaka, J.Senzaki, H.Tanoue, N.Kobayashi, and H.Okushi, Mat. Sci. Forum **338-342**(2000), p.861.

[8] M.Satoh, Y.Nakaike, K.Uchimura, and K.Kuriyama, Mat. Sci. Forum **338-342**(2000), p.905.

[9] J.W.Palmour, L.A.Lipkin, R.Singh, D.B.Slater, Jr., A.V.Suvorov, and C.H.Carter, Jr., Diamond and Related Mat. **6**(1997), p.1400.

[10] A.Schöner, N.Miyamoto, T.Kimoto, and H.Matsunami, *in this volume*.

[11] H.Yano, T.Hirao, T.Kimoto, H.Matsunami, K.Asano, and Y.Sugawara, IEEE Electron Device Lett. **20**(1999), p.611.

[12] H.Yano, F.Katafuchi, T.Kimoto, and H.Matsunami, IEEE Trans. Electron Devices **46**(1999), p.504.

[13] R.Schörner, P.Friedrichs, and D.Peters, IEEE Trans. Electron Devices **46**(1999), p.533.

[14] N.S.Saks, S.S.Mani, A.K.Agarwal, and V.S.Hegde, Mat. Sci. Forum **338-342**(2000), p.737.

[15] H.Yano, T.Kimoto, and H.Matsunami, *in this volume*.

[16] V.V.Afanasev, M.Bassler, G.Pensl, and M.Schulz, phys. stat. sol. (a) **162**(1997), p.321.

Materials Science Forum Vols. 353-356 (2001) pp. 549-554
© 2001 Trans Tech Publications, Switzerland

Doping of Silicon Carbide by Ion Implantation

B.G. Svensson[1,2], A. Hallén[1], M.K. Linnarsson[1], A.Yu. Kuznetsov[1], M.S. Janson[1], D. Åberg[1], J. Österman[1], P.O.Å. Persson[3], L. Hultman[3], L. Storasta[3], F.H.C. Carlsson[3], J.P. Bergman[3], C. Jagadish[4] and E. Morvan[5]

[1] Royal Institute of Technology, Solid State Electronics, Electrum 229, SE-16440 Kista-Stockholm, Sweden

[2] Oslo University, Physical Electronics, Department of Physics, P.B. 1048 Blindern, NO-0316 Oslo, Norway

[3] Department of Physics and Measurement Technology, Linköping University, SE-581 83 Linköping, Sweden

[4] The Australian National University, Electronic Materials Engineering, Canberra, ACT 0200, Australia

[5] Centro Nacional de Microelectrónica (CNM-CSIC), Campus UAB, ES-08193 Bellaterra, Spain

Keywords: Defect Recombination, Dopant Activation, Dopant Compensation, Interstitial Clusters, Ostwald Ripening, Transient Enhanced Diffusion

Abstract A brief survey is given of some recent results on doping of 4H- and 6H-SiC by ion implantation. The doses and energies used are between 10^9 and 10^{15} cm^{-2} and 100 keV and 5 MeV, respectively, and B and Al ions (p-type dopants) are predominantly studied. After low dose implantation ($\leq 10^{10}$ cm^{-2}) a strong compensation is observed in n-type samples and this holds irrespective of implantation temperature up to 600 °C. However, at higher doses (10^{14}-10^{15} Al/cm^2) the rate of defect recombination (annihilation) increases substantially during hot implants ($\geq$200 °C), and in these samples one type of structural defect dominates after post-implant annealing at 1700-2000 °C. The defect is identified as a dislocation loop composed of clustered interstitial atoms inserted on the basal plane in the hexagonal crystal structure. Finally, transient enhanced diffusion (TED) of ion-implanted boron in 4H-samples is discussed.

Introduction

One key issue when realizing SiC devices is doping to tailor the electrical properties. Controlled doping of bulk crystals and epitaxial layers can be performed in-situ during growth, and in particular, using vapour phase epitaxy (VPE) the concentration of dopants in epitaxial layers is accessible over a wide range[1]. However, for a genuine implementation of SiC devices a planar technology with selective area doping is required. One alternative is thermal diffusion but it is not considered as a viable concept in device processing because of the extremely high temperatures needed; to reach reasonable diffusivities ($\geq 10^{-13}$ cm^2/s) temperatures around or in excess of 2000 °C must be used for most elements.

In principle, ion implantation is ideally suited for selective area doping because of the possibility to accurately control the dopant concentration and the thickness of the implanted region without any chemical or thermodynamic constraints. However, a major drawback is the generation of damage destroying the crystalline structure of the semiconductor material. The damage can range from point defects caused by single collision cascades at low ion doses to complete amorphization at high enough doses. Post-implant annealing is required to restore the crystal structure and electrically activate the implanted dopants as shallow acceptors or donors.

For SiC, our knowledge about such annealing processes is severely limited, and to understand and control these annealing processes is, indeed, a major scientific challenge. In this contribution we give a brief overview of some recent results covering a wide dose and energy regime from 10^9

to 10^{15} cm^{-2} and 100 keV to 5 MeV, respectively. Predominantly, B and Al ions have been studied.

Experimental

The samples used were mainly low doped (~1-5x10^{15} cm^{-3}) high purity epitaxial layers of n-type grown by VPE on Cree substrate wafers. The layers were of polytype 4H or 6H and doped with nitrogen. More details about the sample growth can be found in Ref.2.

After growth, the wafers were cut into small samples with a typical size of 7x7 mm^2 and then implanted with ^4He, ^{11}B or ^{27}Al ions using energies in the range of 100 keV to 5 MeV. The implantation temperatures were between 25 °C and 800 °C, and the MeV energy implants were performed at the Uppsala tandem accelerator facilities[3] while the keV energy implants were carried out at the semiconductor laboratory in Kista-Stockholm.

For sample characterization different techniques like capacitance-voltage (CV) measurements, deep level transient spectroscopy (DLTS), atomic force microscopy (AFM), secondary ion mass spectrometry (SIMS), Rutherford backscattering spectrometry (RBS) and transmission electron microscopy (TEM) were applied. Details about sample preparation (cleaning, contact growth, etc) and measurement procedures can be found in Refs.4-6.

Results and Discussion

Fig. 1 compares the charge carrier concentration, as obtained by 1 MHz CV measurements, in 4H-SiC and Si samples implanted with 1.7 MeV He ions at room temperature (RT) to a dose of 2x10^9 cm^{-2}. Prior to implantation both samples had a free and uniform electron concentration of (0.9-1.0)x10^{15} cm^{-3}. According to simulations using the transport of ions in matter code (TRIM, version 96.01)[7] the projected range for 1.7 MeV He ions is ~3.8 μm and ~5.9 μm in SiC and Si, respectively. In the former sample strong compensation (~80 %) occurs at the implantation damage peak (~3.6 μm) while only a minor effect is observed at the peak position (~5.6 μm) in the silicon sample. The apparent increase in doping with a maximum at ~4.1 μm is a measurement artifact indicative of deep acceptor traps and is due to contributions from both the leading and trailing edges of the Debye tail to the measured capacitance[8]. Fig. 1 shows a maximum compensation of ~8x10^{14} cm^{-3} in the SiC sample and ~1x10^{14} cm^{-3} in the Si sample, i.e., the generation rate of compensating defects is about a factor of 5-10 times higher in SiC[9]. For Si, it is known that only a few percent of the implantation-induced vacancies and self- interstitials survive immediate recombination at RT and form stable defects at low doses[10]. Apparently, this is not true for SiC, and different explanations can be put forward. First, SiC is a compound semiconductor and antisite defects (Si on a C-site and vice versa) are likely to form during recombination between vacancies and self-interstitials. Second, the mobility of vacancies and self-

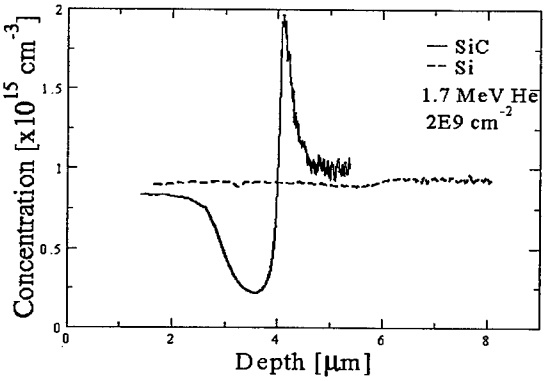


Fig.1 Comparison of the electrical carrier concentration profiles in n-type SiC and Si samples after implantation of He ions at RT.

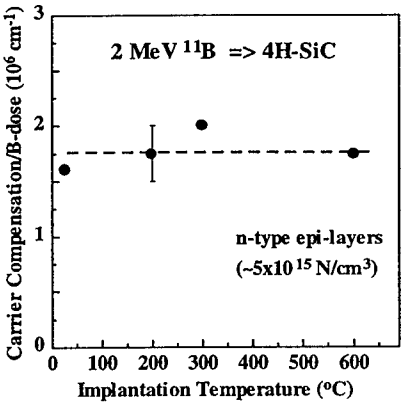


Fig.2 Carrier compensation per ion dose versus implantation temperature for n-type 4H epi-layers implanted with 2 MeV B ions.

interstitials is low in SiC reducing the probability for annihilation relative to that in Si.

DLTS measurements[4] reveal no deep-level defects of acceptor type with concentrations comparable to the compensation observed in Fig. 1. One possibility is, however, acceptors with levels very close to the middle or even in the lower part of the energy bandgap. Further, passivation (neutralization) of the nitrogen donors by implantation-induced defects can also contribute to the compensation. It is interesting to note that the compensation exhibits no dependence on implantation temperature between RT and 600 °C, as illustrated in Fig. 2. This suggests that the mobility of vacancies and self-interstitials, promoting defect recombination, has only a minor influence (if any) on the compensation effect.

On the other hand, for defect accumulation at higher doses the implantation temperature is known to play a vital role. Fig. 3(a) shows the concentration of disordered Si atoms as a function of depth in 4H epi-samples implanted with 100 keV Al ions to a dose of $5x10^{14}$ cm^{-2} at RT, 200 °C and 400 °C. The implants were performed at a tilt angle of 8° relative to the <0001> axis and RBS in the channeling mode (RBS/C, 2.4 MeV He+ ions) was employed for sample analysis. The concentration profiles in Fig. 3(a) were extracted from the measured RBS spectra by applying the formalism according to Eisen[11]. In addition to the main maximum at ~1000 Å a pronounced accumulation of defects is also observed in the near-surface region. A similar surface peak has been

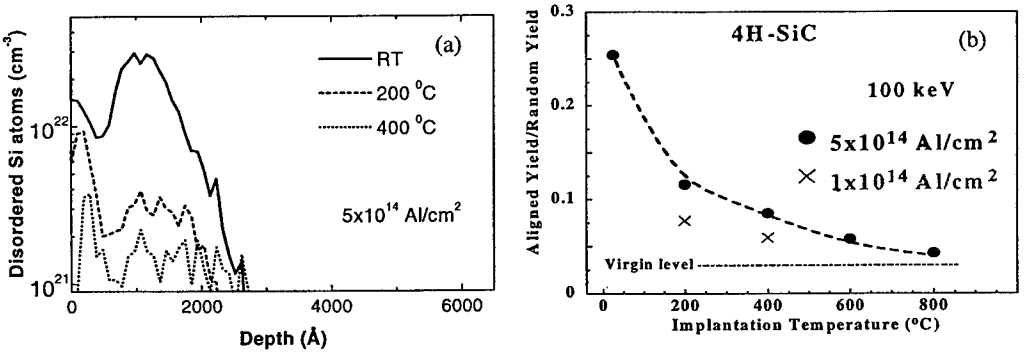


Fig.3 (a) Disordered Si atoms as a function of depth and (b) relative damage versus implantation temperature for 4H-SiC samples implanted with 100 keV Al ions, as determined by RBS/C.

reported in previous studies on Si, Ge, GaAs and GaN and attributed to an amorphous layer at the semiconductor surface, presumably formed due to trapping of migrating point defects by the surface[12]. For the implants at elevated temperatures a substantial reduction in the concentration of disordered Si atoms occurs, especially around the main peak. This shows an enhanced defect recombination during the hot implants, and as demonstrated in Fig. 3(b), where the ratio between the channeled and random RBS yields below the damaged layer is depicted as a function of the implantation temperature, the main decrease in defect production takes place already below 200 °C. Hence, the process controlling the defect recombination can be associated with a relatively low activation energy, and at 800 °C the damage level extracted from RBS/C is close to that in virgin samples.

In this context it should be emphasized that the layer in Fig. 3(a) is not rendered amorphous by $5x10^{14}$ Al/cm^2 even at RT. Actually, the dose required to form an amorphous layer in SiC at RT is comparable to that in silicon, as opposed to the results obtained at low doses, Fig. 1. This 'contradiction' shows that the damage buildup in SiC as a function of ion dose is different compared to Si. The former one appears to be more linear over a wide dose range, which is consistent with the small (if any) dependence on ion mass for amorphization of SiC at RT[13]. Here, the low mobilities of point defects in SiC, reducing defect annihilation, and the interplay with the ion dose rate are key factors.

A high resolution cross sectional TEM image of a 4H-sample implanted at 600 °C with 180 keV Al ions to a dose of $1.3x10^{14}$ cm^{-2} and subsequently annealed at 1700 °C for 30 min is shown in Fig. 4. In this kind of samples only one type of structural defect is observed, and detailed TEM studies have identified it as a dislocation loop composed of clustered interstitials inserted on the basal plane in the hexagonal structure[5]. As a result, the surrounding planes bend to accommodate the loop and a corresponding strain field is generated in the c-direction. It is interesting to note that the loops align in a staircase fashion with the edges located on top of each other, presumably due to a minimization of the elastic lattice energy. Assuming that the surface density of atoms in the loops equals that of SiC the density of interstitials stored in the loops is estimated to be ~$1.0x10^{14}$ cm^{-2} using plan-view micrographs. This value is close to the dose of implanted Al ions and indicates an efficient recombination process of the implantation-induced vacancies and self-interstitials leaving only one (or less) excess interstitial per implanted ion. The identity of the interstitial atoms stored in the loops is not fully established but it is tempting to suggest that they are Si self-interstitials. For the dose and annealing conditions used close to 100 % of the implanted Al ions are anticipated to be electrically activated as shallow acceptors [14], i.e., they occupy predominantly substitutional Si sites, and thus, a considerable concentration of excess Si self-interstitials can be expected.

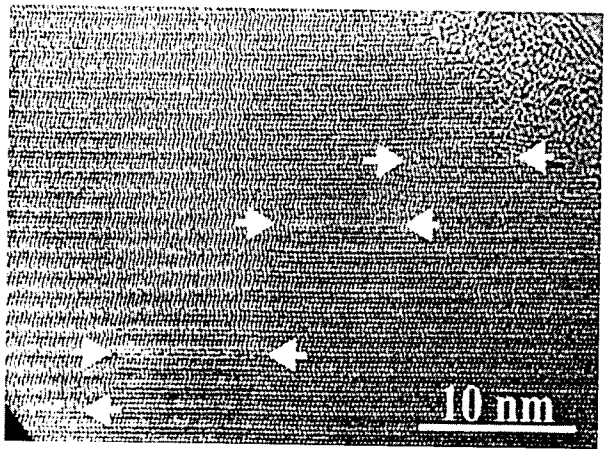


Fig.4 High resolution cross-sectional image of a sample implanted with Al ions (180 keV, $1.3x10^{14}$ cm^{-2}) showing alignment of dislocation loops in a stair-case fashion after annealing (1700 °C, 30 min). The arrows indicate the edges of each loop. The speckled area in the upper right corner is an amorphous edge caused by ion milling.

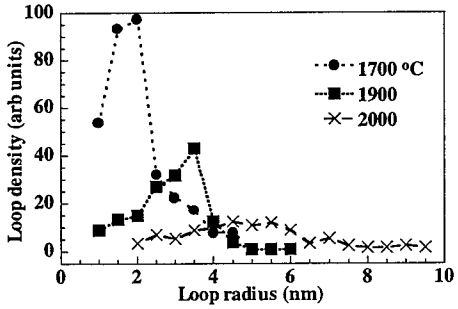


Fig.5 Loop density versus loop radius for Al-implanted and subsequently annealed (30 min) 4H-SiC samples.

Fig. 5 displays the density of loops versus loop radius in three samples annealed for 30 min at 1700, 1900 and 2000 °C, respectively. The mean radius of the loops increases with temperature from ~3.1 nm at 1700 °C to ~5.9 nm at 2000 °C. Concurrently, the density of loops decreases and the total number of interstitials stored in the loops remains constant. Thus, interstitials are exchanged between the different loops, and the evolution is characteristic of an Ostwald ripening process[15] where large defects grow on the expense of smaller ones. The driving force for this coarsening of the loops is a minimization of the interfacial (surface) and elastic energies.

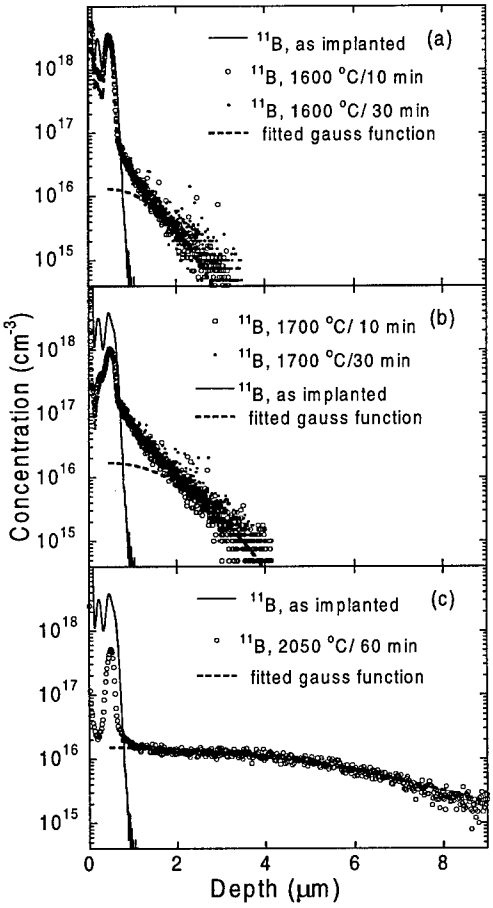


Fig.6 Boron concentration versus depth profiles in as-implanted and annealed 4H-SiC epi-layers.

The excess concentration of defects induced by ion implantation and the resulting non-equilibrium conditions during post-implant annealing can grossly affect the diffusion of dopants. Indeed, different groups have recently reported an anomalous diffusion of ion-implanted boron in SiC[16,17]. Fig. 6 shows SIMS-profiles of boron-implanted 4H-samples before and after annealing at 1600, 1700 and 2050 °C. A substantial out-diffusion occurs through the surface but here we will focus on the diffusion into the undamaged part of the samples, beyond the as-implanted distribution. At 1600 and 1700 °C almost exponential tails extending ≥3 μm into the samples are observed, and furthermore, the tails obtained after 10 and 30 minutes annealing are identical showing that the migration is due to a transient process. In contrast, after annealing at 2050 °C the B profile exhibits a concave shape, as expected for classical diffusion from a limited source in a (semi-)infinite medium[18]. The shape and evolution with time of the nearly exponential tails in Figs. 6(a) and 6(b) cannot be described by an ordinary, concentration independent Fickian diffusion process, i.e., Gaussian or erfc solutions. However, in order to obtain a quantitative measure of the observed diffusion Gaussian functions are fitted to the fast diffusing, low concentration part of the profiles. These are depicted as broken lines in Fig. 6 and using the extracted

values of the broadening, σ, an effective diffusion coefficient $D_{B_{eff}}$ can determined by applying the relation $D_{B_{eff}} = \sigma^2/2t$ [18]. For the sample annealed at 2050 °C the Gaussian fit is excellent over the entire diffusion tail suggesting that equilibrium conditions apply and $D_{B_{eff}}$(2050 °C), 2.5×10^{-11} cm^2/s, agrees closely with previous values reported in the literature[19]. On the other hand, $D_{B_{eff}}$ at 1600 and 1700 °C, $\geq 6.7 \times 10^{-12}$ and $\geq 1.3 \times 10^{-11}$ cm^2/s, are enhanced by at least a factor of 160 and 50, respectively, compared to the literature data. In fact, a similar transient enhanced diffusion (TED) is well-established in B-implanted crystalline silicon, and in this case, TED is attributed to interaction of the B atoms with implantation-induced excess Si self-interstitials through the interstitialcy or kick-out mechanism[20]. However, for SiC the amount of data is too scarce at this stage to identify the mechanism mediating TED and further work is being pursued.

Acknowledgements

Financial support from the Swedish Foundation for Strategic Research (SiCEP program) and the Swedish Foundation for International Cooperation in Research and Higher Education (STINT) is gratefully acknowledged. Fruitful discussions with Profs. U. Lindefelt, E. Janzén, G. Pensl and B. Breitholtz, and Drs. H. Bleichner, H. Lendenmann, A. Schöner, P. Skytt, B. Åstrand, and C. Ovrén are highly appreciated.

References

[1] H. Matsunami, K. Shibahara, N. Kuroda, W. Yoo and S. Nishino, in *Amorphous and Crystalline SiC* (eds. G.L. Harris and C.Y.-W. Yang, Springer Verlag, Berlin), Springer Proc. Phys. **34** (1989), p. 34; D.J. Larkin, S.G. Sridhara, R.P. Devaty and W.J. Choyke, J. Electr. Mater. **24** (1995), p. 289.

[2] O. Kordina, C. Hallin, A. Henry, J.P. Bergman, I. Ivanov, A. Ellison, N.T. Son and E. Janzén, Phys. Stat. Sol. B**202** (1997), p. 321.

[3] A. Hallén, P.A. Ingemarsson, P. Håkansson, B.U.R. Sundqvist and G. Possnert, Nucl. Instr. Meth. B**36** (1989), p. 345.

[4] D. Åberg, A. Hallén and B.G. Svensson, Physica B **273/274** (1999), p. 672.

[5] P.O.Å. Persson, L. Hultman, M.S. Janson and A. Hallén, to be published (2000).

[6] M.K. Linnarsson and B.G. Svensson, Phys. Rev. B**60** (1999), p. 14302; M.K. Linnarsson, M.S. Janson, S. Karlsson, A. Schöner, N. Nordell and B.G. Svensson, Mat. Sci. Eng. B**61-62** (1999), p. 275.

[7] J.P. Biersack and L.G. Haggmark, Nucl. Instrum. Meth. **174** (1980), p. 257.

[8] L.C. Kimerling, J. Appl. Phys. **45** (1974), p. 1839.

[9] A. Hallén, A. Henry, P. Pellegrino, B.G. Svensson and D. Åberg, Mater. Sci. Eng. B**61-62** (1999), p. 378.

[10] B.G. Svensson, C. Jagadish, A. Hallén and J. Lalita., Phys. Rev. B**55** (1997), p. 10498.

[11] F.H. Eisen, in *Channeling* (ed. D.V. Morgan, Wiley, London, 1973), p. 415.

[12] See for example, S.O. Kucheyev, J.S. Williams, C. Jagadish, J. Zou and G. Li, Phys. Rev. B**62** (2000), in press.

[13] V. Heera and W. Skorupa, Mat. Res. Soc. Symp. **438** (1997), p. 241.

[14] T. Kimoto, A. Itoh, N. Inoue, O. Takemura, T. Yamamoto, T. Nakajima and H. Matsunami, Mater. Sci. Forum **264-268** (1998), p. 675.

[15] W. Ostwald, Z. Phys. Chem. **34** (1900), p. 495.

[16] M. Laube, G. Pensl and A. Itoh, Appl. Phys. Lett. **74** (1999), p. 2292.

[17] M.S. Janson, M.K. Linnarsson, A. Hallén and B.G. Svensson, Appl. Phys. Lett. **76** (2000), p. 1434.

[18] J. Philibert in *Atom movements Diffusion and mass transport in solids* (les éditions de physique, Les Ulis, France 1991).

[19] E.N. Mokhov, E.E. Goncharov and G.G. Ryabova, Sov. Phys. Semicond. **18** (1984), p. 27.

[20] P.A. Stolk, H.-J. Grossman, D.J. Eaglesham, D.C. Jacobson, C.S. Rafferty, G.H. Gilmer, M. Jaraiz, J.M. Poate, H.S. Luftman and T.E. Haynes, J. Appl. Phys. **81** (1997), p. 6031.

Materials Science Forum Vols. 353-356 (2001) pp. 555-558
© 2001 Trans Tech Publications, Switzerland

Neutron Irradiation of 4H SiC

F.H.C. Carlsson[1], L. Storasta[1], B. Magnusson[1],
J.P. Bergman[1], K. Sköld[2] and E. Janzén[1]

[1] Department of Physics and Measurement Technology,
Linköping University, SE-581 83 Linköping, Sweden

[2] Institute for Neutron Research, Uppsala University, SE-61182 Nyköping, Sweden

Keywords: Donors, Intrinsic Defects, Isoelectronic Defects, Neutron Irradiation, Neutron Transmutation Doping, Phosphorus, Photoluminescence

Abstract. The effect of neutron irradiation on 4H SiC epitaxial layers are studied. Several different doses of both fast and thermal neutrons have been used and the samples have been annealed from 500 °C to 2000 °C. The defect concentration dependence on the fast neutron flux and on the annealing temperature is investigated. At temperatures from 900 °C to 1300 °C new lines between 3960 Å and 4270 Å appear. They are similar in behavior to the E_A and D1 spectra and are assumed to be related to excitons bound to isoelectronic centers. After annealing at 2000 °C another new line appears at 3809 Å. The similarity of this line with phosphorus in 6H makes us tentatively ascribe it to phosphorus.

Introduction

Neutron irradiation is a way to obtain a well controlled and homogenous n-type doping, in semiconductors like Si and SiC. This is very important for materials intended for high power devices, and the Neutron Transmutation Doping (NTD) is an established technique in Si technology. In NTD thermal neutrons, produced in a fission reactor, is absorbed by ^{30}Si transmutating it into ^{31}P creating a donor. The isotope ^{30}Si have a 3.12% natural abundance and is evenly distributed in SiC. With a NTD much higher than the original doping concentration the resulting n-type doping will be very homogenous. The reactor also produce fast neutrons with higher kinetic energy. These does not contribute to the NTD, but can damage the lattice by creating interstitials and vacancies. The fast neutrons create mostly intrinsic defects by direct interaction with Si and C. Nuclear reactions with impurities such as Al also occurs. They can create beta and alpha decays that cause more lattice damage and transform the impurities into new ones. The amount of intrinsic defects will be determined by the total dose of fast neutrons, which in turn depends on the desired doping and the ratio of fast to thermal neutrons. This can be useful for fundamental studies of intrinsic defects. The lattice damage can, at least in Si, be removed by high temperature annealing.

In 6H the transformation of p-type SiC to n-type SiC by NTD have been shown by several authors [1,2]. The phosphorus bound exciton (BE), first shown in doped CVD layers [3], appears after annealing at 2000 °C [1]. In 4H SiC no previous report on NTD have been published and the phosphorus BE have never been observed.

In this work we have done a series of irradiations of epitaxial 4H SiC, using different doses and different relations between fast and thermal neutrons. After irradiation and after annealings up to 2000 °C, the layers have been analyzed mainly with optical techniques but electrical techniques have also been used. The defect evolution with dose and annealing temperature have been studied.

Experimental

For all neutron irradiations hot wall epitaxial 4H CVD [4] material have been used with, an epi-layer thickness of 20 μm - 40 μm, a nitrogen doping of $2 \cdot 10^{14}$ cm^{-3} to $2 \cdot 10^{15}$ cm^{-3} and a low acceptor concentration. The neutron irradiations have been performed at the fission research reactor at Studsvik. The neutrons produced by a fission reactor have a wide range of energies. The energy distribution can to some extent be controlled and we have varied the ratio of fast to slow neutrons from 10 to 0.001. The dose of thermal neutrons were varied between $5 \cdot 10^{11}$ cm^{-2} and $3 \cdot 10^{18}$ cm^{-2}, where $3 \cdot 10^{18}$ cm^{-2} results in a phosphorus concentration of $5 \cdot 10^{14}$ cm^{-3}. The influence of fast and slow neutrons on SiC can be studied by varying their fluence ratio.

After the irradiation all samples were measured before any annealing. The following annealing temperatures ranged from 500 °C to 2000 °C. Several characterization techniques were used to study the effects of the neutron irradiation. Optical techniques like Photoluminescence (PL), Time Resolved PL (TR-PL) and Fourier Transform Infra-Red spectroscopy (FT-IR) were mainly used. Electrical measurements for characterization includes Deep Level Transient Spectroscopy (DLTS), Admittance Spectroscopy, IV, CV and Photo Induced Current Transient Spectroscopy (PICTS).

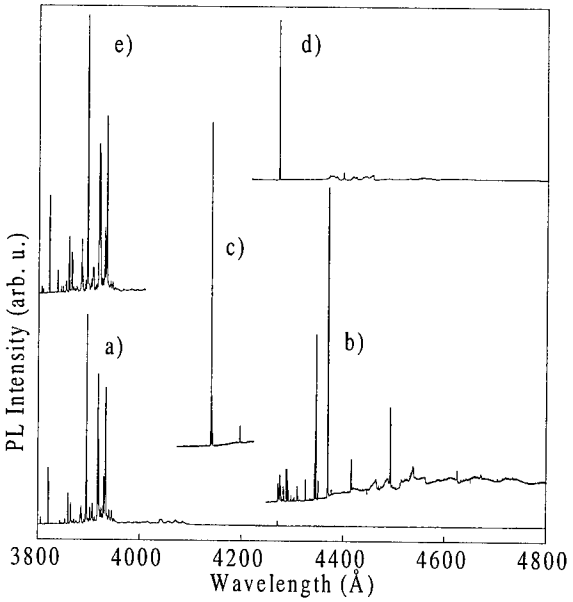


Figure 1. Photoluminescence spectra for a) as grown, b) as irradiated, c) annealed at 1200 °C, d) annealed at 1700 °C and e) annealed at 2000 °C. The spectra are shifted vertically and limited horizontally for clarity.

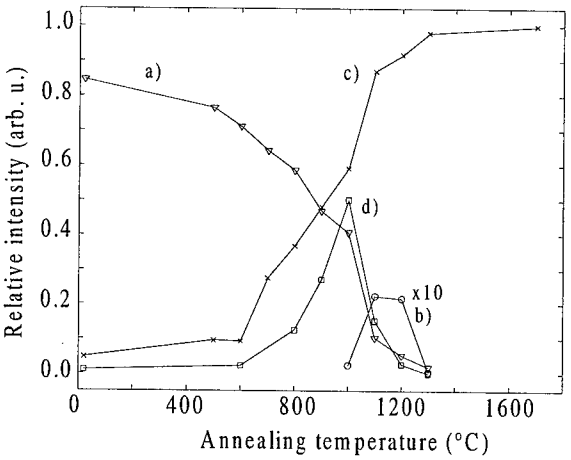


Figure 2. The effect of annealing on defects. The a) E_A spectra, b) new defect lines, c) D1 and d) IR lines. The IR lines are not normalized against the other.

Experimental Results

The low temperature photoluminescence spectra from as-grown 4H SiC epitaxial layers are completely dominated by the near bandgap emissions, including the recombination of bound excitons related to nitrogen and free exciton (FE), as can be seen in figure 1a. No other emission are normally observed with comparable intensities in the as grown samples. The PL measurements after irradiation does not show any changes for samples irradiated with a dose of fast neutrons of $3.9 \cdot 10^{12}$ cm^{-2}. An increase of fast neutrons will create lines in the region of 4260 Å – 4420 Å, this is the previously well investigated E_A spectra [5], as can be seen in figure 1. A further increase of the fast neutron dose leads to the decrease of the original band edge emissions from nitrogen BE's and the FE in PL as the E_A spectra grows stronger. The dose dependence between the nitrogen BE Q_0 and the E_A spectra can be seen in figure 3. The E_A spectra will increase in intensity

while the band edge emission disappears until a further increase of fast neutrons to around 10^{16} cm^{-3} quenches all luminescence. The effects of thermal neutrons on the intrinsic defects are small.

Annealing at temperatures from 500 °C to 800 °C results in an increase of the D1 line at the expense of the E_A spectra. Some of the E_A lines anneal out at 800 °C.

At annealing temperatures between 900 °C and 1400 °C the D1 line, see figure 1c, grows strongly and the E_A spectra disappears. New, and to our knowledge previously not reported, lines also appear in this temperature range. They are observed in the spectral range between 3960 Å and 4270 Å, as can be seen in figure 1c and figure 4. These lines shows a similar properties as the other intrinsic lines such as the E_A lines and the D1 [6]. They have long lifetimes (49 μs) and quenches at temperatures above 100K, which can be expected from an exciton bound to an isoelectronic defect [6]. In the infrared a set of four no phonon lines and their phonon replicas can be seen [7] with a maximum intensity after annealing at 1000 °C as can be seen in figure 2d.

After annealing at temperatures above 1500 °C, D1 is the dominating emission. The E_A and the new lines between 3960 Å and 4270 Å have now completely disappeared. For samples irradiated with high doses of fast neutrons the original nitrogen bound excitons and the free exciton returns but with very weak intensities.

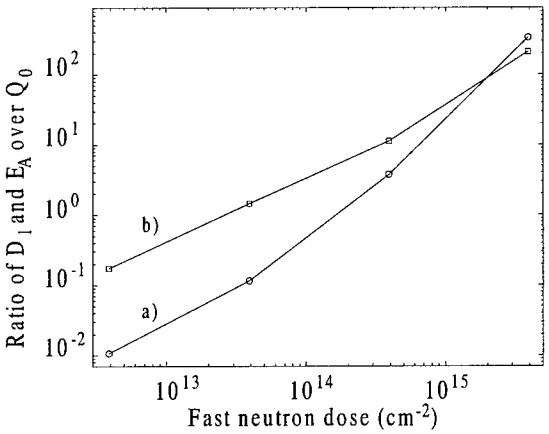


Figure 3. The dose dependence of as irradiated a) E_A and the 1700 °C annealed b) D_1 spectra.

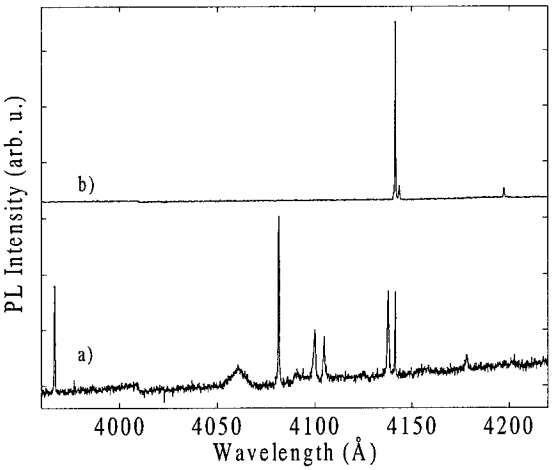


Figure 4. The new lines that appear after annealing at a) 1100 °C and b) 1200 °C. The spectra are shifted vertically for clarity.

Annealing at 2000 °C improves the crystal structure and more of the band edge emissions returns as can be seen in figure 1e, the emission from D1 is however still dominating. A new line at 3.255 eV (3809 Å) appears as can be seen in figure 5. The intensity of this line increases with an increase of the dose of thermal neutrons. This line have also been seen in phosphorus implanted material, but not in aluminum or boron implanted material, which indicates that it is not an intrinsic line. We attribute this, to our knowledge never previously reported, line to phosphorus.

Discussion

The effect of neutron irradiation of 4H SiC have been investigated. After annealing at 900 °C new lines appear. These lines anneal out at 1400 °C and are probably of limited interest for devices. They do however show the same characteristics as E_A and D1 and may be closely related to them. The study of these lines may provide an improved understanding of E_A and D1. The effect on PL on the dose of fast neutrons gives a strong indication to the dose of fast neutrons that can be acceptable for device fabrication on NTD material. This should be taken into consideration when

the desired doping and the fluence ratio between fast and slow neutrons are determined. A new PL line at 3.255 eV has been observed. The position of this line is between the two nitrogen bound excitons, which is the expected position of the phosphorus BE, based on the observation of phosphorus in 6H SiC [3]. In 6H SiC it has been shown that NTD and annealing at 2000 °C results in emission of the phosphorus BE [1]. The experimental evidence suggest that it is related to phosphorus. The emission is however weak and more experiments are needed verify the proposed assignment. The dominating defect observed optically after NTD and annealing is the D1. This defect is usually believed to be hole-attractive [8] and hence a minority carrier limiting deep defect. In order for NTD to be useful for doping SiC, irradiation without producing this defect or techniques that can anneal this defect has to be developed.

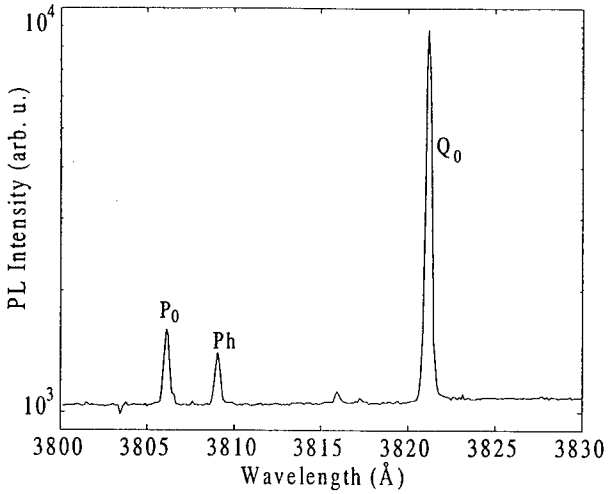


Figure 5. The low temperature PL spectra of neutron irradiated sampled annealed at 2000 °C. The new emission attributed to phosphorus has been labeled Ph.

Acknowledgements

The authors acknowledge the support from the SSF (Swedish Foundation for Strategic Research) Silicon Carbide Program, SiCEP.

References

[1] S. Tamura, T. Kimoto, H. Matsunami, M. Okada, S. Kanazawa and I. Kimura, Mater. Sci. Forum 338-342 (2000), p. 849.

[2] H. Heißenstein, C. Peppermüller and R. Helbig, J. Appl. Phys. 83 (1998), p. 7542.

[3] S.G. Sridhara, L.L. Clemen, D.G. Nizhner, R.P. Devaty, W.J. Choyke and D.J. Larkin, Mater. Sci. Forum 264-268 (1998), p. 465.

[4] O. Kordina, C. Hallin, A. Henry, J.P. Bergman, I. Ivanov, A. Ellison, N.T. Son and E. Janzén, phys. stat. sol. (b) 202 (1997), p. 321.

[5] T. Egilsson, A. Henry, I.G. Ivanov, J.L. Lindström and E. Janzén, Phys. Rev. B 59 (1999), p. 8008.

[6] T. Egilsson, J.P. Bergman, I.G. Ivanov, A. Henry and E. Janzén, Phys. Rev. B 59 (1999), p. 1956.

[7] B. Magnusson, A. Ellison, F.C.H. Carlsson, N.T. Son and E. Janzén, Mater. Sci. Forum 353-356 (2001), p. 365.

[8] T. Egilsson, I.G. Ivanov, A. Henry and E. Janzén, Mater. Sci. Forum 338-342 (2000), p. 647.

Materials Science Forum Vols. 353-356 (2001) pp. 559-562
© 2001 Trans Tech Publications, Switzerland

Techniques for Depth Profiling of Dopants in 4H-SiC

J. Österman[1], A. Hallén[1], S. Anand[1], M.K. Linnarsson[1],
H. Andersson[1], D. Åberg[1], D. Panknin[2] and W. Skorupa[2]

[1] Department of Electronics, Royal Institute of Technology,
P.O. Box Electrum 229, SE-16440 Kista-Stockholm, Sweden

[2] Institute of Ion Beam Physics and Material Research, Forschungszentrum Rossendorf,
P.O. Box 510119, DE-01314 Dresden, Germany

Keywords: Dopant Activation, Dopant Profile, Scanning Capacitance Microscopy (SCM), SEM, Spreading Resistance Profiling (SRP)

Abstract: Three different methods for measuring the depth distribution of dopants in 4H-SiC have been investigated: (1) Spreading Resistance profiling (SRP), (2) Scanning Capacitance Microscopy (SCM) and (3) Scanning Electron Microscopy (SEM). The investigated samples included p- and n-type epitaxial layers grown by vapor phase deposition with doping concentrations of 10^{16}-10^{20} cm^{-3}. Also p^+n implanted profiles using a combination of Al and B multi-energy implantations were studied. All techniques were able to provide doping profiles qualitatively corresponding to secondary ion mass spectrometry (SIMS) data. The SRP results suggest a lower limit of the p-doping concentration below which the ohmic contact between the probe tip and sample becomes more Schottky-like. The magnitude of the SCM signal corresponds well to the chemical doping profile except in the depleted region surrounding the metallurgical junction of the p^+n structure.

Introduction

A semiconductor device structure is defined by its distribution of free charge carriers. At present, there exists no established and well-understood method for profiling highly graded dopant distributions in SiC. For spreading resistance profile (SRP) measurements, both the wide bandgap and extreme hardness complicates the reproducible formation of stable ohmic contacts [1]. Other traditional methods for semiconductor doping profiling include repeated etching and subsequent measurements of the sheet resistance, i.e. stripping Hall measurements, but again SiC has been proven problematic, since no suitable wet-etch is available. Novel scanning probe techniques, such as scanning capacitance microscopy (SCM), have been shown to be in good qualitative agreement with SIMS. Problems still exist though; for example contrast reversal have been observed for p-type doping levels below 10^{17} cm^{-3}, probably related to poor surface oxide quality [2].

In this work we will evaluate and compare three techniques, SRP, SCM and scanning electron microscopy (SEM). Despite the various complications mentioned above, the investigated methods show potential usefulness and are able to provide qualitative agreement with SIMS for both n- and p-type 4H-SiC.

Experimental

The SRP measurements were carried out with a SENTECH SR-210 device using probes of sintered tungsten carbide. The tip bias was kept in the mV range, corresponding to a maximum resistance of 1 GΩ. Further details can be found in [1].

A Digital Instruments Dimension™ 3000 scanning probe microscopy (SPM) system operating in contact mode AFM was used for SCM profiling. The tips were commercial metal-coated silicon tips with radius ~30 nm. Both dC/dV and feedback bias modes were used. In the former, the magnitude of the dC/dV signal is inversely proportional to the carrier concentration, whereas in feedback bias mode, where instead the differential capacitance is kept constant by changing the applied voltage, a higher signal corresponds to a higher carrier concentration.

Secondary electron emission shows a dependence on doping concentration [3], an effect that can be used for semiconductor dopant imaging. The SEM images/profiles in this study were acquired in a JEOL 825-JSM scanning electron microscope using acceleration voltages of 0.3 to 30 keV and e-beam currents in the p- to nA-range.

The two investigated structures shown here consisted of a 4H-SiC epi layer grown by vapor phase epitaxy with five aluminum peaks with concentrations of 2×10^{19} to 2×10^{20} cm^{-3} and a background doping of 10^{16} cm^{-3}. In addition, boron and aluminum implanted samples with maximum doping concentration at the surface of 10^{20} cm^{-3} were used. The implantation was performed in n-type epi-layers with nitrogen concentration of roughly 10^{15} cm^{-3} followed by annealing at 1700°C for 10 min. The substrates were commercial Cree wafers doped with nitrogen to about 10^{18} cm^{-3}. The chemical profile had previously been determined by secondary ion mass spectrometry (SIMS) analysis, using a Cameca IMS 4f microanalyser. The SRP samples were prepared by beveling (using a 0.1 μm diamond emulsion) and Ar sputtering [1]. Cross-sections for SCM and SEM analysis were prepared by cleaving, since polishing was found to create topographic variations –valleys– where the doping was high. The observation is most likely related to a decreased hardness in these regions. After cleaving, a selection of samples were investigated before and after treatment in diluted (5 %) hydrofluoric- (HF) acid.

Results and Discussion

Figure 1 shows the SRP and the SIMS data of an Al and B implanted n-type epi-layer. For comparison, the SIMS data is presented here as the sum of implanted species, while the SRP is displayed as the inverse of the measured data (in order to correspond to the number of charge carriers). The Al ions have a range of <0.2 μm, and are thus the dominant species in the high dopant concentration observed close to the surface. The B implantation reaches deeper, about 0.5 μm, but is also implant anneal [4]. The SRP accordingly suggests a small but detectable increase in conductance both close to the surface and in the 0.5 μm region. Also below the B peak, the SRP data show a decreasing conductance in accordance with SIMS, until about 0.9 μm where the schottky-like behavior becomes dominating and the ohmic contact is lost. However, the low conductance in the Al dominated region scarcely reflects the number of charge carriers, although the reduction in both mobility and activation expected at such high implantation doses could partly account for the loss in dynamic range relative to the SIMS. In addition, it is not clear about the influence from the biased probe on the degree of activation in this region.

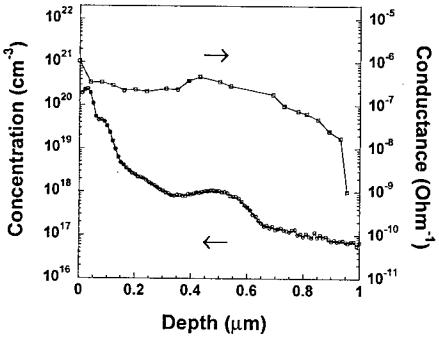


Figure 1. SRP (□) and SIMS (o) of an Al and B implantation in 4H-SiC

The SIMS profile of a 4H-SiC CVD grown epitaxial structure is shown in figure 2 a). The structure consists of five Al doped peaks in a low doped p-type background. Figure 2 b) shows a SCM image obtained in feedback bias mode of the same epi-layer. The five Al-peaks can be identified as the bright regions, with widths consistent with SIMS data. Changing the biasing conditions enables also the relative peak concentrations to be distinguished. This is shown in the SCM line scan superimposed on image 2b, although the peak nearest to the surface can not be resolved properly. This information can not be obtained from SEM data. The shape of the "tail" at the edge of each peak can also be observed to change; from left of the peak in the SIMS profile to right in the SCM. This phenomenon can not be eliminated by changing AC- or DC biasing conditions and is very likely related to the contrast reversal that has been observed for Al-doped SiC in this concentration range [2]. In Figure 2 c) the corresponding SEM image is depicted. The SEM-contrast is in qualitative agreement with theory; i.e. secondary electron-emission increases with increasing p-type doping [3]. Hence the Al-peaks can again be identified as the five bright stripes, although they are not as clearly defined as in fig. 2 b. At depths >10 μm a small part of the n-type substrate -the black stripe at the far right- is seen to have a very low yield of secondary electrons, which is also consistent with [3].

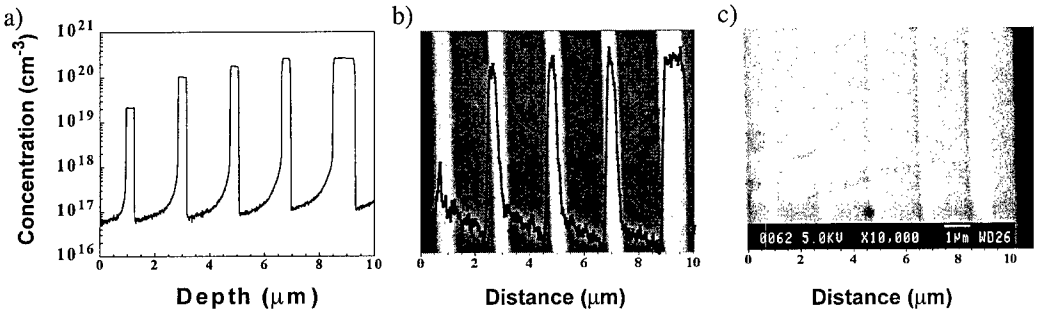


Figure 2. a) SIMS-, b) SCM- and c) SEM profile of an Al-doped epi-layer of 4H-SiC. The SCM measurements are performed in feedback bias mode (DC bias of 2V and 4 V for the image and the superimposed line scan, respectively). The SEM image is acquired at an acc. voltage of 5 keV. Due to variations in growth rate (<10%) over the wafer area, a small distortion of the total epi-layer thickness may be present in-between the images.

It appears however more difficult to reproduce SEM measurements than SCM. For instance, contrast reversal between Al-peak/background and memory effects have been observed in SEM, where areas previously subjected to beam exposure exhibit a general reduction of SE-emission, although much more pronounced at the Al-peak positions relative to the low-doped background. This observation is consistent with studies of GaAs/AlGaAs multilayers, showing the same behavior at the Al-rich layers upon exposure of the e-beam [5]. The effect may originate from preferential oxidation of the Al-rich regions, which would increase the work function and thus reduce the SE-emission [3]. For SiC the oxide thickness may also vary up to a factor of 5-6 depending on the exposed cleavage plane and if the surface is terminated by Si or C. The weak reproducibility of SEM data suggests the SE-emission to be even more sensitive to the surface conditions than SCM measurements, which is also further supported by the results from HF etching.

Figure 3 shows a SCM line scan measured in dC/dV mode for an Al and B implanted p^+nn^+ structure, with an about 30 μm thick n-region. The SIMS and SRP data are shown in Figure 1. Consistently, the high-doped substrate exhibits a lower dC/dV signal than the low doped epi-layer.

The dC/dV signal then reaches zero at the expected position of the pn-junction. The peak at about 9 μm is also a characteristic feature of the dC/dV signal at the edges of the depleted zones. Due to the topography close to the cross-section edge, the magnitude of the measurement points nearest to the surface show low reproducibility and do not represent reliable data. New p^+p-type implantation profiles and preparation techniques are currently being developed for this purpose.

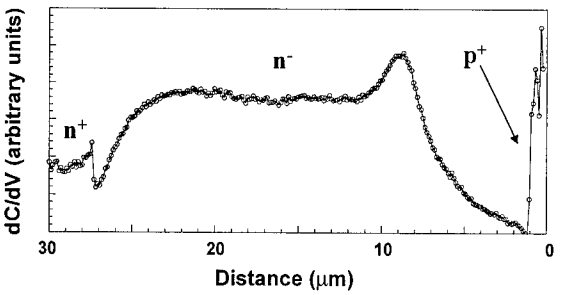


Fig 3. SCM line scan in dC/dV at AC and DC bias of 4 and 2 V

Conclusions

Spreading resistance, scanning capacitance microscopy, and scanning electron microscopy techniques have been applied to obtain depth concentration profiles of doping in implanted and epitaxial 4H SiC structures. SRP and SCM clearly show a potential usefulness for doping profiling, and a combination of the two methods may be especially suitable, since the techniques are complementary to each other. SRP suggest a lower detectable concentration limit of about 10^{17} cm^{-3} below which the ohmic probe-to-sample contact is lost. SCM exhibits a strong and reproducible doping contrast, although methods for sample preparation need to be improved. SEM shows a weaker and more complicated doping dependence, but may be used e.g. for identifying n-/p-type material and estimates of epi-thickness. The methods are at present only able to provide relative profiles, but with calibration samples of known constant doping, e.g. determined by CV-measurements, SRP and SCM data may be calibrated to obtain a fully quantitative characterization also of strong doping gradients in SiC.

Acknowledgements

Stefan Karlsson at ACREO and Henry Bleichner at ABB corporate research are gratefully acknowledged for providing the sample material used in this study. Financial support was given by the Swedish Foundation for Strategic Research within the SiCEP program.

References

[1] T. Gebel, D. Panknin, R.Riehn, S. Parascandola and W. Skorupa, Mat. Sci. Forum 338-342 (2000), p. 741.
[2] O. Bowallius, S. Anand, N. Nordell, G. Landgren and S. Karlsson, to appear in Mat. Sci. in Semcond. Proc. (2000)
[3] M. S. Jansson, M. K. Linnarsson, A. Hallén, and B. G. Svensson, Appl. Phys. Lett. 76 (2000), p. 1434
[4] D. D. Perovic, M. R. Castell, A. Howie, C. Lavoie, T. Tiedje, J.S.W. Cole, Ultramicroscopy 54 (1995), p. 104
[5] A. L. Bleloch, M. R. Castell, A. Howie and C. A. Walsh, Ultramicroscopy 54 (1994), p. 107

Materials Science Forum Vols. 353-356 (2001) pp. 563-566
© 2001 Trans Tech Publications, Switzerland

Growth of δ-Doped SiC Epitaxial Layers

S. Karlsson[1], C. Adås[2], A. Konstantinov[1] and M.K. Linnarsson[3]

[1] ACREO AB, Electrum 236, Isafjordsgatan 22, SE-164 40 Kista, Sweden

[2] Ericsson Microelectronics AB, Isafjordsgatan 20, SE-16440 Kista, Sweden

[3] Royal Institute of Technology, Solid State Electronics,
P.O. Box Electrum 229, SE-16440 Kista, Sweden

Keywords: Delta-Doping, Vapor Phase Epitaxy

Abstract N- and p-type δ-doped SiC epitaxial layers have been grown by vapour phase epitaxy and characterised by SIMS and CV measurements. Different techniques of achieving δ-doped layers are examined. Doping profiles with FWHM from 1 to 10nm have been obtained at different peak concentrations.

Introduction

Silicon Carbide device research is constantly making progress towards higher voltages, temperatures and frequencies. As a result of this development the degree in complexity of SiC device structures is increasing, which puts further demands on dopant and thickness control of both thick and very thin layers. δ-doping is a technique widely used in the epitaxial growth of III-V semiconductors in order to spatially confine dopants in a narrow region, ideally to one atomic layer. By using structures with δ-doping, the performance of advanced electronic and optoelectronic devices have been improved [1].

One possible application for δ-doping in SiC devices is FETs where a δ-layer potentially could be used as a barrier under the channel to suppress short channel effects (see Fig. 1), as was earlier shown for GaAs [2-3]. The δ-doping technique can also be used to confine avalanche multiplication in IMPATT devices. In this paper the first attempts in growing n- and p-type δ-doped SiC epitaxial layers by vapour phase epitaxy are presented.

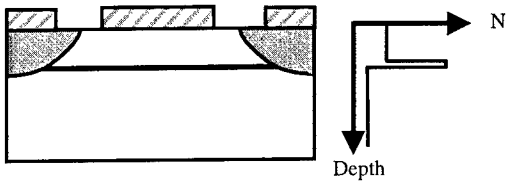


Figure 1. Schematic drawing of a FET device showing a δ-doped layer below the epitaxial channel.

Growth and characterisation

4H-SiC layers were grown by vapour phase epitaxy using a standard single wafer horizontal hot-wall reactor from Epigress AB. The epitaxial growth was performed on n- and p-type commercially available substrates using silane and propane as growth precursors, and nitrogen (100%) and trimethylaluminium (TMA) (18°C, 750mbar) as doping precursors to achieve n- and p-type conductivity, respectively. The material was grown at a temperature of 1600°C at 250mbar with a growth rate between 1.6 and 2.2μm/h using a C/Si ratio between 1 and 3.

Two basically different methods of achieving δ-doping have been tried. One is the straightforward method of a low growth rate and a limited time of dopant introduction (A). The second method is a version of a common MOCVD procedure including pre-δ-doping purge, δ-doping and post- δ-doping purge (B1-3). The pre-purge step removes residual growth precursors

and stops all growth before the δ-doping step, where only a dopant precursor is introduced to be adsorbed on the non-growing surface. To minimise doping memory effects when the growth is resumed a post-purge step is necessary. In the field of III-V epitaxy all three steps (method B2) have been used to successfully achieve δ-doping [1]. It has been shown for GaN [4] that higher doped layers are achieved using this δ-doping sequence without the post-δ-doping purge step (method B1). A third version (B3) has been tried including all steps described above but together with another doped growth step with a different C/Si-ratio located between the δ-doping step and the post purge step, see table 1.

Dopant	Method	Pre-growth	Pre-purge	δ-doping	δ-doping and growth	Post-purge	Post-growth
		SiH4+C3H8 +H2	H2	dopant +H2	SiH4+C3H8 +dopant+H2	H2	SiH4+C3H8 +H2
N	A (Std)	⇒	-	-	⇒	-	⇒
	B1	⇒	⇒	⇒	-	-	⇒
Al	A (Std)	⇒	-	-	⇒	-	⇒
	B2	⇒	⇒	⇒	-	⇒	⇒
	B3	⇒	⇒	⇒	⇒	⇒	⇒

Table 1. Overview of different δ-doping methods explored in this investigation.

The δ-doped layers were characterised by secondary ion mass spectrometry (SIMS) and capacitance-voltage (CV) measurements. To determine the thickness and the atomic concentration of the samples using SIMS a Cameca ims 4f instrument was used with an O_2^+ primary ion beam to detect aluminium ($^{27}Al^+$) and a Cs^+ primary beam to detect nitrogen ($^{13}C^{14}N^-$). The atomic concentrations were calibrated with implanted standards and the thicknesses determined from crater depth measurements using an Alphastep 200 surface stylus profilometer and assuming a constant sputter rate.

The net doping concentration was evaluated by CV measurements using evaporated Ti schottky and ohmic contacts. Both contacts were prepared on the epitaxially grown layer by lithography, metal deposition and lift-off to achieve well-defined contacts with a diameter of 400μm. The CV measurements were performed at room temperature with a HP4284A precision LCR meter at a frequency of 1 MHz for nitrogen doped samples and at 30 kHz for aluminium doped samples. All samples characterised by CV measurements were doped to the $1x10^{17}cm^{-3}$ range before and after the δ-layer.

Results and discussion

A low growth rate and a limited time of dopant introduction (method A) were found to be efficient when growing thin layers with full width half maximum (FWHM) of 8-9nm for Al and 16-17nm for N. These thicknesses were achieved using constant doping flows and a doping time between 4-32s resulting in concentrations from $7x10^{17}cm^{-3}$ to $3x10^{19}$ cm^{-3}, see fig.2. At 64s of doping both N and Al seem to approach vapour pressure equilibrium since peak concentrations are levelling out and the FWHM are doubled. It is possible that the lower FWHM limits can be fine-tuned by using extremely low growth rates but the basic parameters determining the final doping profiles are hardware-related. It is important to have a completely laminar flow all the way from source to wafer but even so there will always be a delay in the stabilisation of dopant precursor vapour pressures. A dopant has to be transported to the hot-zone, cracked, diffused through the boundary layer and then adsorbed on the surface before it can be incorporated. Other reasons for broadening are rough surfaces as well as thermal diffusion and segregation. After the doped growth step the desorption of dopants from surrounding walls causes the well-known memory effect and more broadening. The

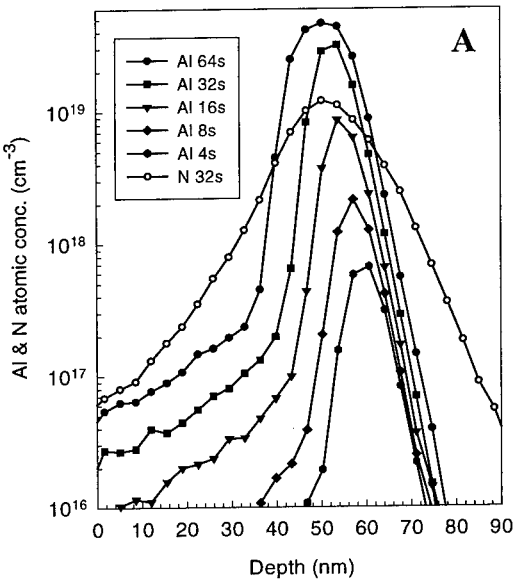


Figure 2. SIMS profiles of Al and N doped peaks grown using std doping technique (method A).

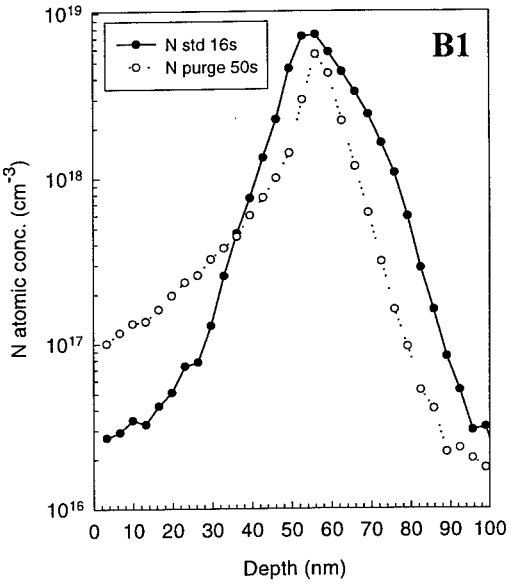


Figure 3. Comparison between SIMS profiles of N doped peaks grown using method A and B1.

reason why N gives twice the FWHM compared to Al for the same doping times can be explained by different doping efficiencies and therefore the need of almost a factor of ten higher flow of nitrogen than TMA.

The GaN method (B1) was tried using nitrogen with a pre-purge step and a δ-doping step (without growth) varied in length between 2 and 50 s. Delta layers grown using this method had smaller FWHM than the ones achieved using standard doping technique, as can be seen in fig.3. The length of the pre-purge step did not have any influence since almost the same result was achieved for both 2 and 50s. It seems as if residual growth precursors left in the system after they have been switched out are not contributing significantly to broadening of the δ-layers. The effect of longer dopant flushing times resulted in higher doped peaks up to $6x10^{18}$ cm^{-3} for 50s. Since the memory effect mechanism should be similar for method A and B1, it is not surprising to see that layers doped by flushing a long time have a more extensive broadening or memory effect than std delta-layers grown at shorter times, especially at lower concentrations.

The same doping technique except for an added post-purge step was used for aluminium (method B2). As expected the measured peak concentrations decreased with increasing post purge times. The aluminium desorption from the surface during 50s of purging resulted in one order of magnitude lower concentration than if the post-purge-step was only 2s. The FWHM of the δ-layers was similar (9nm) as for the std doping sequence in the $1x10^{18}cm^{-3}$ range but thicker for δ-layers in the $1x10^{17}cm^{-3}$ range. At this range there is an extensive memory effect broadening occurring in all Al δ-doped samples grown in this investigation and any effect from different step lengths is not seen. The results from using techniques B1 and B2 shows that peak broadening after dopant turn off can be substantial even though an interruption in the growth sequence is used.

A third method of δ-doping (B3) is a combination of the standard technique (A) and the III-V technique (B2). The idea is to use a growth step at elevated C/Si ratio between the δ-doping step

and the post-purge step in order to "lock" a high doping level but still use any advantages from the purge techniques. Fig.4 shows an Al doping profile calculated from CV measurements on a δ-layer "lock"-grown for 16s. The FWHM is around 1nm and the layer can be considered a "true" δ-layer. Similar layers did not show these kind of extreme dimensions when measured by SIMS. This can only be explained by either a limitation of the SIMS equipment or that the growth process used is unpredictable and not very reproducible. The latter explanation is most likely since the profile obtained with CV measurements was so thin that it in other samples might have been etched away during the post-purge step. On the other hand, sharp doping profiles measured with SIMS have a broadening on the trailing edge (when sputtering material from high to low concentration) due to ion cascade mixing. This broadening has been estimated to approximately 2nm at FWHM and could therefore explain why such peaks do not show up during SIMS measurements. There is also a potential problem in measuring non-uniform layers with the CV technique. What is actually measured is the effective majority carrier density and not the doping density. It has been shown that a step profile cannot be resolved accurately to less than about two to three Debye lengths [5]. The Debye length for 4H-SiC doped $1x10^{18}cm^{-3}$ is 3-4 nm which means that any delta layer thinner than about 10nm could not be correctly measured by the CV technique. Practically, this means that all layers are thinner than that indicated by CV measurements.

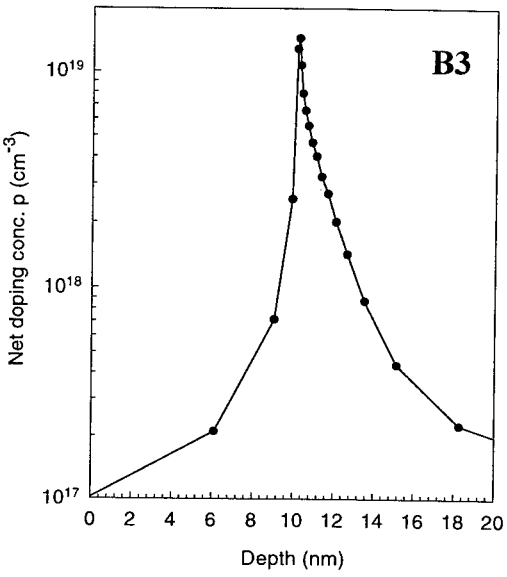


Figure 4. CV-profile of Al δ-doped SiC grown using method B3.

Conclusion

Reproducible δ-doped epitaxial layers with a FWHM thickness between 8 and 10nm has been grown using both Al- and N-doping at different concentration levels. In addition, a true Al delta doped layer with a FWHM of 1nm and a peak concentration of $1x10^{19}cm^{-3}$ has been grown indicating the possibility of beneficial 2DEG (two-dimensional electron gas) effects. The use of purge and doping steps in the doping sequence is not as successful for SiC as for III-V materials. The reason for this is the higher temperatures needed for growth causing desorption processes to be more dominant.

Acknowledgements

The work was supported in part by Office of Naval Research (ONR) contract N00014-99-1086.

References

[1] G. Li, C.Jagadish, Solid-State Electronics 41 (1997), p.1207.
[2] T.A.Winslow, R.J.Trew, P.Gilmore, C.T.Kelley, Cornell Conference on Advanced Concepts in High Speed Semiconductor Devices and Circuits, IEEE Proceedings (1991), p.188.
[3] A.Asenov, S.Saini, IEEE Transactions on Electron Devices (1999), p.1718.
[4] Jong-Hee Kim et al, MRS Internet J. Nitride Semicon. Res. 4S1, G3.49 (1999).
[5] D.K. Schroder, Semiconductor mat. and device char. John Wiley & Sons, (1998), p.68.

Materials Science Forum Vols. 353-356 (2001) pp. 567-570
© 2001 Trans Tech Publications, Switzerland

Effect of Residual Damage on Carrier Transport Properties in a 4H-SiC Double Implanted Bipolar Junction Transistor

S. Ortolland[1], N.G. Wright[1], C.M. Johnson[1], A.P. Knights[2], P.G. Coleman[3], C.P. Burrows[3] and A.J. Pidduck[4]

[1] Dept. of Electronic and Electrical Engineering, University of Newcastle, Newcastle NE1 7RU, UK

[2] Surrey Ion Beam Centre, University of Surrey, Guildford GU2 5XH, UK

[3] Department of Physics, University of Bath, Claverton Down, Bath BA2 7AY, UK

[4] Defence Evaluation and Research Agency, Great Malvern, Worcs WR14 3PS, UK

Keywords: AFM, Annealing, Bipolar Transistor, BJT, Implantation, PAS, Rutherford Backscattering Spectroscopy (RBS)

Abstract: Nitrogen implantation into a boron implanted layer is a potential technology for the fabrication of double-implanted n-p-n bipolar transistor. The effect of various implant and anneal schedules on two key device parameters is studied: 1) residual implant damage close to the emitter-base junction and 2) ohmic contact resistance of the highly doped implanted emitter. The effects of post-implant anneal conditions on the level of residual damage under the nitrogen implant after different anneal processes are investigated using the PAS and RBS techniques. The PAS data show clearly that after implantation there is a substantial defect concentration as far as 400nm - significantly below the range of the nitrogen implant (in this case 150nm). The surface morphology of the nitrogen implanted emitter after a high temperature annealing is investigated by AFM. Surface roughness increases significantly at higher annealing temperatures, taking the form of a periodic undulation at 1700C. Hall effect and contact resistivity measurements show that higher annealing temperatures result in decreased ohmic contact resistivity but poor surface mobility. Finally surface profiles show significant lattice swelling following highly doped nitrogen implant which can only partially be removed after annealing.

1. Introduction

Although the potential of bipolar technology in SiC has already been demonstrated using multilayer epitaxial wafers [1, 2], it is of interest to investigate alternative technology employing multiple implants since this reduces wafer costs and may offer a relatively easy route for commercialisation. To this end, double implanted bipolar transistors (BJT) (nitrogen implanted emitter into a Boron implanted base) have been fabricated which display high breakdown voltage (1600V) but a relatively low gain (~2) [3]. It is the purpose of this paper to study the effect of different annealing strategies on the transistor emitter region characteristics and hence on transistor gain. Bulk properties, both before and after high temperature (1300C to 1700C) annealing, are investigated by RBS and PAS. Then AFM is used to explain what kind of surface morphology modifications occur during the post-implantation annealing process. Finally, surface properties are correlated with electrical results obtained by Hall effect and contact resistivity measurements.

2. Experimental procedure

4H-SiC wafers, provided by Cree Research Inc. and diced into 5mm x 5mm square samples, were used in all our experiments. Multi-implants were performed at room temperature with the ion beam perpendicular to the surface to avoid channeling. Boron implants were performed at the following energies and doses: (20 keV, 50 keV, 100 keV, 160 keV) and (10^{13} cm^{-2}, 2×10^{13} cm^{-2}, 3×10^{13} cm^{-2}, 3×10^{13} cm^{-2}) respectively. In the case of nitrogen implants, the energies and doses were (20 keV, 40 keV, 60 keV) and (4×10^{14} cm^{-2}, 4×10^{14} cm^{-2}, 10^{15} cm^{-2}) respectively. These parameters were chosen

to give a shallow (0.15 μm-deep) highly doped (~ 10^{20} cm^{-3}) box profile suitable for a BJT emitter region. A J.I.P.ELEC SiC furnace System, specially developed for high temperature processing of silicon carbide, was used for post-implantation annealing. This RF induction furnace imposes a very fast temperature ramp (50C/s) under argon ambient pressure. To optimise emitter properties, a fixed annealing period of 20 min was chosen while the annealing temperatures were varied over the range 1300C to 1700C. The reactor vessel was composed of a graphite susceptor and cap, covered by silicon carbide, plus a cover plate of CVD silicon carbide. In these conditions, a silicon over-pressure is maintained to avoid silicon sublimation from the sample surface, which is known to occur for temperatures above 900C [4]. A full description of the BJT fabrication can be found in the literature [3].

3. Results and discussion

PAS and RBS techniques, both sensitive to crystalline damage, were used to monitor residual defects after implant and annealing. The RBS spectrum of a nitrogen implanted sample (see Fig.1) shows an amorphous layer in the as-implanted sample. The RBS signal decreases significantly after annealing at 1300C indicating that this temperature is sufficient to recrystallise the amorphous layer as has been shown previously [5]. Although the RBS draws near to the as-grown level for higher annealing temperature, it remains higher, indicating that all the lattice damage is not completely removed even after 1600C annealing. Figure 2 shows PAS results with both boron and nitrogen implants which indicate that damage induced by implantation produces a region containing both Si and C vacancies which is favorable for nitrogen substitution [6 ,7]. The high vacancy concentration close to the surface (corresponding to the range of the nitrogen implant) was not removed by low temperature annealing but is almost completely recovered by 1600C. However there are still defects within the boron base region even after annealing to 1600C (albeit at a much reduced level) and it is these defects which are believed to affect the gain of implanted base bipolar transistors.

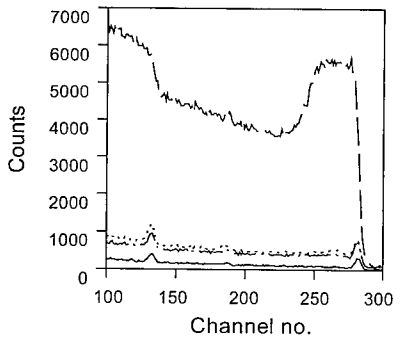


Fig:1: RBS-c data for nitrogen implanted 4H-SiC samples. Unimplanted (solid line), as-implanted (dashed line), annealed at 1300C (dotted line), at 1600C (dot-dash line).

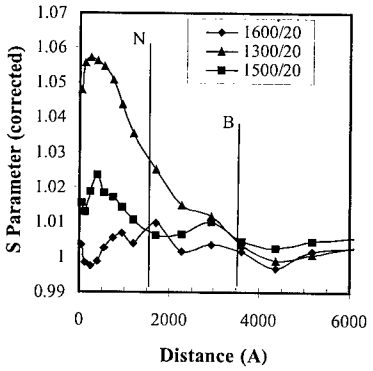


Fig.2: Positron S parameter versus distance (Å) for samples annealed for 20 min at 1300C (triangles), 1500C (squares), or 1600C (circles). The vertical lines are guides to the eye showing the approximate boundaries of the nitrogen and boron implants.

AFM was used to investigate nitrogen implanted surface in order to understand surface related mechanisms involved during the annealing process. The surface roughness of the as-implanted sample (r.m.s =3.1 nm) was found to be greater than that of the as-grown sample (r.m.s < 2 nm).

Some sub-micron features were observed and might be due to surface contamination or a consequence of the implantation process. After annealing, the surface roughness increased to give stochastic features, the r.m.s roughness in the middle range of annealing temperature (6 nm @ 1300 C, 40 nm @ 1500 C) being in good agreement with previous values [8].

The topography of the 1700 C annealed sample was, however, very different. Triangular profile undulations up to 100 nm high with a period of about 320 nm can be observed in such samples (see Fig.3). The sides are differently angled to the wafer surface at an average of 13° and 8° (see Fig.4). The latter angle is presumably the same as the angle at which the starting wafer was cut to the (0001) basal plane and it might, therefore, be assumed that the undulations are due to step bunching. However the step heights observed here (approx. 100nm) are much larger than those typical of step bunching found on an as-grown 4H-SiC epilayer surface (two to four bilayers or between 8.2nm and 16.4nm) [9]. As the features are not observed in as-implanted samples, it is probable that their formation is thermally activated. The undulations may be created by the desorption of silicon containing species (such as Si, SiC_2, Si_2C ...) from the exposed surface and subsequent regrowth during the high temperature annealing [10]. It is of interest to note that these large-scale regular undulations do not occur with other dopants. It seems that the particular combination of nitrogen and very high (>1600 C) annealing temperature provides the correct conditions for enhanced growth of undulations.

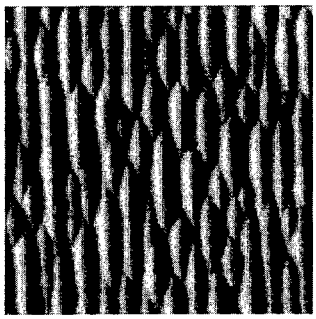


Fig3: 10μm x 10μm AFM picture of a nitrogen implanted 4H-SiC sample after 1700C anneal. The height of the undulations is approx 100nm.

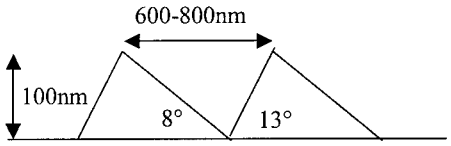


Fig 4: Cross-section of a nitrogen implanted 4H-SiC sample after 1700C anneal.

The sheet resistance measured by Hall effect measurements on a nitrogen implanted surface was found to increase by 7% and the mobility decreased by 38% as the annealing temperature was raised from 1300C to 1700C. This drop in mobility is likely to be related to the increased degree of surface roughness (noted in the AFM experiments) rather than a decrease in the bulk mobility. By way of contrast, the net carrier concentrations showed a significant increase, rising by 56% over the same range of annealing temperature. This indicates that the proportion of implanted ions on electrically active substitutional Carbon sites increases with annealing temperature. Indeed, following a 1700C anneal, an estimated 6.6 % of implanted N atoms are ionized at room temperature. If the average ionization energy for nitrogen is taken as 85meV this means that nearly 100% of implanted atoms are potentially electrically active. It is of interest to note that although a relatively low (1300C) anneal can yield almost complete bulk recrystallisation, it does not allow complete activation of the dopant. The reordering that occurs at higher anneal temperatures will include the migration of nitrogen atoms to the electrically active and energetically stable substitutional Carbon sites. The increases in active nitrogen dopant are thus evidence for reduced levels of lattice damage. In contrast to the mobility results, contact resistivity decreased monotonically from a value of $0.1\Omega cm^2$ at 1300C to 0.0057 Ωcm^2 at 1700C. It thus seems plausible that a very high roughness is advantageous for ohmic contacts because of increased effective surface area.

At high nitrogen implant doses, lattice swelling can occur. To investigate this effect further, nitrogen was implanted in a boron implanted P-well, (energies remained the same as before but all the doses were increased by a factor of 2). In this case, the nitrogen region becomes amorphous after the room temperature implantation and swelling is observed as shown in Fig.5. After 1300C annealing, the implanted patterns disappear completely. However, for higher annealing temperature (in the range of 1400 - 1700C), patterns re-appear and look darker, indicating that the surface is carbonised.

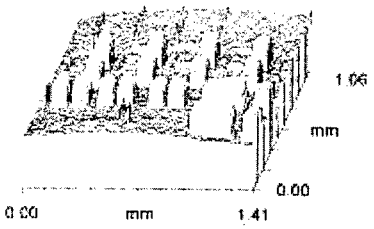


Fig.5: Profilometric picture of nitrogen implants into a boron p-well after a 1700 C anneal. The 50 nm-high steps correspond to nitrogen implanted areas

4. Conclusion

The effects of nitrogen implantation and subsequent high temperature (1300C to 1700C) annealing on the emitter region properties of 4H-SiC BJT have been studied. Bulk crystal properties were studied using RBS and PAS. The RBS spectra show almost complete recrystallisation is achieved after a 1300C anneal. However, there is evidence that some structural irregularities remain even after annealing at the highest temperatures. The PAS results show a high concentration of divacancies within the emitter which are can only be removed by high temperature annealing. The PAS spectra however clearly indicate that residual damage from the nitrogen implant is still present beyond the implant range (i.e. in the boron implanted base region) even after annealing at 1600C. AFM analyses show that the surface roughness increases progressively with annealing temperature. The degree of surface roughness has been correlated with significant reductions in the resistivity of ohmic contacts and reductions in the measured value of mobility. Finally significant lattice swelling can appear after a highly doped nitrogen implant which can only partially be removed after annealing.

References

[1] J. W. Palmour, J. A. Edmond, H. S. Kong and C. H. Carter, Jr. Physica B 185 (1993), p 461
[2] A. Agarwal, S.-H. Ryu, M. E. Levinshtein, P. A. Ivanov, S. L. Rymyantsev, R. Singh and J. Palmour, Proc. HiTEC, June 2000, Alberquerque, NM.
[3] N. G. Wright, C. M. Johnson, A. G. O'Neill, A. Horsfall, S. Ortolland, K. Adachi, A. P. Knights and P.G.Coleman Proc. of MRS , May 2000, San Francisco.
[4] K.W. Bryant, M.J. Bozack. Proc. ICSCRM'99, Mater. Sci Forum 238 (1999), p 335.
[5] T. Kimoto, N. Inoue, H. Matsunami. Phys. Stat. Sol. (a) 162 (1997), p 263.
[6] S. Seshadri, G.W. Eldridge, A.K. Agarwal. Appl. Phys. Lett. 72 (1998), p 2026.
[7] G. Brauer, W. Anwand, P.G. Coleman, J. Stormer, F. Plazaola, J.M. Campillo, Y. Pacaud, W. Skorupa. J. Phys. Condens. Matter. 10 (1998), p 1147.
[8] M. Treu, E.P. Burte, R. Schorner, P. Friedrichs, D. Stephani, H. Ryssel. J. Appl. Phys. 84 (1998), p 2943.
[9] T. Kimoto, A. Itoh, H. Matsunami, T. Okano. J. Appl. Phys. 81 (1997), p 3494.
[10] M.V. Rao, J.B. Tucker, M.C. Ridgway, O.W. Holland, N. Papanicolaou, J. Mittereder. J. Appl. Phys. 86 (1999), p 752.

Materials Science Forum Vols. 353-356 (2001) pp. 571-574
© 2001 Trans Tech Publications, Switzerland

High Electrical Activation of Aluminium and Nitrogen Implanted in 6H-SiC at Room Temperature by RF Annealing

M. Lazar[1], L. Ottaviani[1], M.L. Locatelli[1], C. Raynaud[1], D. Planson[1], E. Morvan[2], P. Godignon[2], W. Skorupa[3] and J.P. Chante[1]

[1] CEGELY (UMR CNRS n°5005), Bât. 401, INSA de Lyon, 20 avenue A. Einstein, FR-69621 Villeurbanne Cedex, France

[2] Centro Nacional de Microelectrónica (CSIC), Campus UAB, ES-08193 Bellaterra, Spain

[3] Forschungszentrum Rossendorf e.V., PO Box 510119, DE-01314 Dresden, Germany

Keywords: AFM, Annealing, Electrical Activation, Ion Implantation, Recrystallization, SIMS

Abstract. Al and N implantations were carried out in 6H-SiC n-type epitaxial layers at room temperature. RBS/C analysis confirms the presence of an amorphous layer up to the surface in the as-implanted samples. The samples rf-annealed at 1700°C during 30 mn with a preliminary 40°C per second heating slope are recrystallised in RBS/C analysis terms. SIMS measurements show no dopant loosing after the annealing and dopant profile distributions are in agreement with CNM Monte-Carlo simulation. A good surface stoichiometry is revealed by XPS after annealing but AFM surface measurements reveal a relatively high rms roughness (14 nm) on annealed samples. High electrical activation of dopants was found, 19 kΩ/□ sheet resistance, which corresponds to 50 % electrical dopant activation for Al implanted layer, and 6.7 kΩ/□ sheet resistance and 100% electrical activation for N-implanted layer.

Introduction

Ion implantation in SiC, an indispensable technique for the p-n junction creation, due to very weak dopant diffusion coefficients, generates an important density of defects which involve high temperature annealing and particular conditions on ramp temperatures and environment partial pressures. High temperature and/or high energy ion implantations were used to reduce the material damage [1-4], however, these implant conditions remain not interesting in an immediate perspective of industrial applications. In this paper we present room temperature (RT) aluminium (Al) and nitrogen (N) ion implanted and rf-annealed samples with viable physico-chemical and electrical properties.

Experiment

Aluminium implantations were performed at RT in 6H-SiC n-type epitaxial layer samples purchased from Cree Research ($3x10^{15}cm^{-3}$ epitaxial doping) with energies ranging from 25 up to 300 keV and 100 to 400 keV with a total dose of $1.75x10^{15}cm^{-2}$ and $1x10^{15}cm^{-2}$ respectively. A thin aluminium mask (1500 Å) was used for the second implant series to avoid the channeling of Al ions, a major effect in 6H-SiC. Nitrogen was implanted in similar SiC samples at RT with energies ranging from 30 to 190 keV and a $1x10^{13}$ cm^{-2} total dose, following an Al 350 keV high dose implantation in order to realise a n-p junction in surface.

All these samples were annealed at 1700°C during 30 mn with a preliminary heating slope of 40°C/s in argon atmosphere with a silicon carbide partial pressure, in a J.I.P.ELEC™ rf-induction heating furnace. The decreasing of the temperature at the end of the annealing is governed by thermal inertia.

SiC annealing in a rf induction furnace presents important advantages such as very high heating slope. This can allow the recrystallization of amorphised layers. Specially 4H and 6H-SiC samples need a very high heating slope in temperature to preserve the polytype from cubic inclusions, which may be generated during the solid phase epitaxy at too low temperature [5,6].

An inhomogeneous temperature in the heated wafer support is a drawback of the induction technique. Lateral and vertical thermal variations can induce SiC etching if appropriate

environments and configurations rich in silicon and carbon are not provided. Silicon volatilizes at temperatures above 1300°C at one atmosphere pressure [3].

Dopant distributions before and after annealing have been investigated by Secondary Ion Mass Spectroscopy (SIMS) measurements, and have been compared to CNM-Monte Carlo simulations [7] of Al implantations in 6H-SiC. Damage induced in materials and recrystallization have been analyzed by Rutherford Backscattering Spectrometry in the Channeling mode (RBS/C). Concerning the surface its stoichiometry has been examined by X-Ray Photoelectron Spectroscopy (XPS) and its roughness by Atomic Force Microscopy (AFM). Finally electrical activation of dopants, i.e. incorporation of Al and N in substitutional SiC lattice sites, has been evaluated by sheet resistance measurements with a four point probe technique at RT.

Results

SIMS measurements

In order to examine the dopant profile distribution, CNM Monte-Carlo simulations were carried out as well as SIMS analyses before and after rf-annealing (Figure 1). The CNM Monte-Carlo simulation of Al ions implanted in 6H-SiC allows us to quantify the point defect generation and their effects in impurities distribution after annealing. We remark a good agreement between simulation and SIMS before annealing measurements

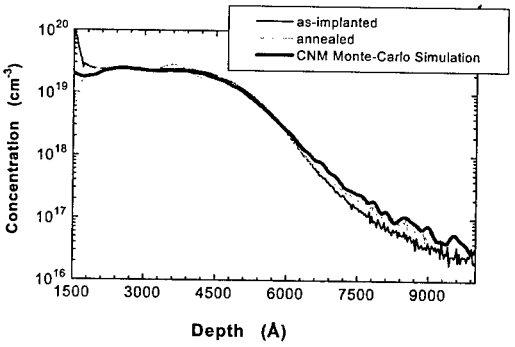


Fig1. *CNM Monte-Carlo simulation and SIMS analysis for the 100 to 400 keV Al-implanted layer*

SIMS profiles after annealing are not flat, Al dopant peaks are formed in high defect concentration zones due to an amorphous layer formation (Al peak at 3580 Å depth in Figure 1). We notice no dopant loosing after annealing.

RBS/Channeling measurements

Residual damage before and after annealing, SiC recrystallisation were evaluated by RBS/C technique. RBS spectra before and after annealing have been compared to a complete disoriented analyzed sample (amorphous) and a not implanted one (virgin). RBS/C analyses confirm the presence of an amorphous layer up to the surface in the implanted samples. Despite that, after a rf-annealing a satisfactory recrystallisation is found, the backscattering yield for the 1700°C/30 mn nearly coincides to the virgin one.

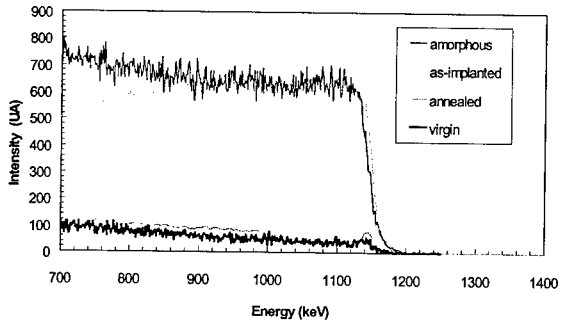


Fig2. *RBS/C measurements for the 25 to 300keV Al implanted samples before and after annealing*

To understand silicon carbide recrystallisation in RBS/C terms the heating slope during annealing was varied from 10°C per second to 40°C per second for samples implanted with the same dose or higher (18 times). RBS/C analyses showed that the layer remains amorphous in this

latter case, and there is no influence of the heating slope on recrystallisation rate. It is possible, that there are at least two amorphous states depending on the implantation dose. Above a given deposited nuclear energy threshold, the layer may loose all bulk crystallinity information, and epitaxial recrystallisation may then become impossible even in optimized annealing conditions.

Surface analyses

A good surface stoichiometry is obtained by XPS after annealing. In Table 1 are presented the atomic ratio [Si/C] in surface and after thin layers Ar^+ sputtering. The thickness values correspond to a silica reference material. Two samples have been analyzed. Sample (A) placed in the suscepteur during annealing and sample (B) at the periphery. We remark that the surface of the sample (B) shows a carbonic layer deposited probably due to a lateral temperature gradient evaluated to be about 50°C.

	Depth (Å)	% C	% O	% Si	Si/C
Sample A	*surface*	*44.4*	*16.0*	*39.6*	*0.89*
	10	*46.6*	*4.6*	*48.8*	*1.04*
	70	*48.3*	*2.1*	*49.6*	*1.03*
Sample B	*surface*	*84.3*	*3.6*	*12.1*	*0.14*
	10	*75.8*	*0.8*	*23.4*	*0.31*
	70	*56.2*	*1.6*	*42.2*	*0.75*
	200	*51.6*	*2.0*	*46.4*	*0.9*

Table 1 *Atomic ratio determined by XPS for two samples annealed in the center (A) and the periphery of the suscepteur (B).*

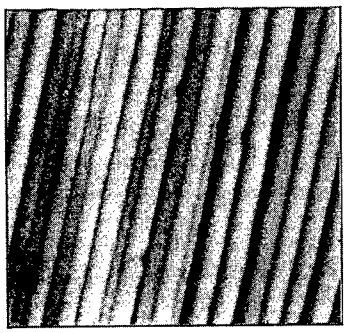
C_{1s} XPS energetic shifts are more related to a deposited layer rich in C-C/C-H bonds than a Si volatilization process. At 20 nm depth, sample B looks like sample A.

AFM surface measurements reveal a relatively high rms roughness (14nm) on annealed samples. Many samples have been analyzed to discern if either the recrystallization of the amorphized layer or either the rf-annealing is responsible for this roughness. For the virgin sample (Figure 3) a rms roughness of 0.31 nm before annealing denotes a good initial surface quality.

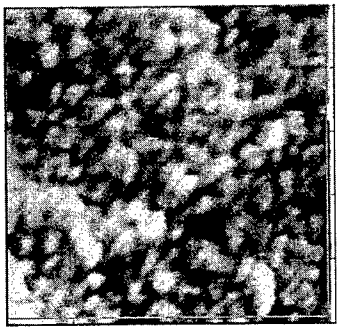
After annealing we found very close values: 13.5 nm rms roughness for the virgin annealed and 14.4 nm rms roughness for the 100 to 400 keV Al implanted and annealed sample. Surface morphologies are nearly similar, the annealed virgin sample presents furrows much more parallel which is normal seeing the initial surface before the annealing of the implanted sample. These results are completely different, compared to an anneal in a resistive heating furnace with very similar time



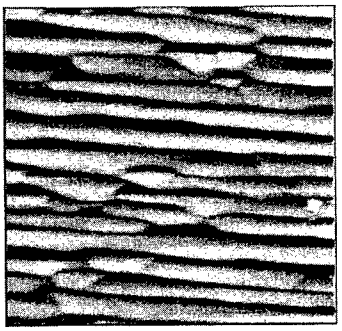
a



b



c



d

Fig3. *Atomic force micrographs of (a) a virgin sample, (b) a virgin sample 1700°C/30 mn rf-annealed, (c) Al as-implanted sample and (d) Al implanted and 1700°C/30 mn rf-annealed sample. Edge length of images correspond to 5μm for non annealed samples and 19μm for annealed ones.*

and temperature parameters (1700°C / 40 min) [8]. In these experiments indeed, the implantation step was responsible for an increase of the surface roughness.

Electrical measurements

Sheet resistance measurements by a RT four point probe technique on Al and N implanted and rf-annealed samples prove a high electrical dopant activation for RT implanted samples, in terms of Al and N incorporation in SiC lattice sites (Si and C respectively). For Al-implanted samples a 19 kΩ/□ sheet resistance at 300K has been found which corresponds to an electrical dopant activation of 50%. Better results are found for N-implanted samples (Figure 4): 6.7 kΩ/□ sheet resistance and 100% electrical dopant activation.

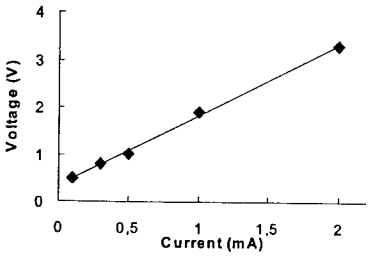


Fig4. *Sheet resistance measurements at 300K on a RT N-implanted layer*

Conclusion

Al and N room temperature implantations were realized in 6H-SiC. Rf-annealing at 1700°C during 30 mn in a special silicon and carbon rich configuration performs satisfactory physico-chemical properties. Amorphous layers are recrystalized, dopants are not loosed during the heating process. If a good stoichiometry are obtained in surface a relatively high roughness is created at 1700°C. Reasonable electrical properties are attained, 50% activation for Al implanted dopants and 100% for N.

Acknowledgements

We would like to thank Mr André Plantier from the Institut of Nuclear Physics of Lyon for ion implantations, Mr Yves Monteil from LMI of Univ. C. Bernard Lyon I for AFM surface analysis, Mr Bruno Canut from DPM of Univ. C. Bernard Lyon I and Mr. M. Voelskow from Forschungzentrum Rossendorf for RBS/C measurements, Ms Christiane Dubois from LPM of INSA de Lyon for SIMS analysis, CIME of Grenoble for technological means and four point probe measurements, GIRCEP, Schneider Electric and Infineon for their interest in our investigations.

References

[1] T. Troffer, M. Schadt, T. Frank, H. Itoh, G. Pensl, J. Heindl, H.P. Strunk, M. Maier, phys. stat. sol. (a) 162 (1997), p. 277.
[2] M. Lazar, L. Ottaviani, M.L. Locatelli, D. Planson, B. Canut and J.P. Chante, Mater. Sci. Forum 338-342 (1999), p. 921.
[3] M. Ghezzo, M. Brawn, E. Downey, J. Kretchmer, W. Hennessy, D.L. Polla and H. Bakhru, IEEE Electron Device Letters, 13 (1999), p. 639.
[4] O. Takemura, T. Kimoto. H. Matsunami, T. Nakata, M. Watanabe, M. Inoue, Mater. Sci. Forum 264-268 (1998), p. 701.
[5] J. Pezoldt, A.A. Kalnin, D.R. Moskwina and W.D. Savelyev, Nuclear Instruments and Methods in Physics Research B80/81 (1993), p. 943.
[6] Ye.N. Potapov and F. Neubert, Prikl. Vopr. Fiz. Tverd. Tela 1 (1987), p. 88.
[7] E. Morvan, P. Godignon, J. Montserrat, J. Fernandez, D. Flores, J. Milan and J.P. Chante, Mater. Sci. Eng. B46 (1997), p. 218.
[8] M.A. Capano, S. Ryu, M.R. Meloch, J.A. Cooper Jr., and M.R. Buss, J. Electron. Mater., 27 (1998), p. 370.

Materials Science Forum Vols. 353-356 (2001) pp. 575-578
© 2001 Trans Tech Publications, Switzerland

Enhancement of Electrical Activation of Aluminum Acceptors in 6H-SiC by Co-Implantation of Carbon Ions

T. Ohshima, H. Itoh and M. Yoshikawa

Japan Atomic Energy Research Institute, 1233 Watanuki, Takasaki, Gunma 370-1292, Japan

Keywords: Aluminium Acceptor, Carbon Co-Implantation, Electrical Activation, Ion Implantation

Abstract Carbon (C) ions were co-implanted with aluminum (Al) ions into hexagonal silicon carbide (6H-SiC). The hole concentration (p) in an Al-implanted layer increases by a co-implantation of C at a concentration range from $2x10^{17}$ to $5x10^{18}$ /cm^3. The maximum value of p is obtained at $1x10^{18}$ C/cm^3. The electrical activation of Al acceptors is much more enhanced by C co-implantation at 800 °C as compared with that at room temperature.

1. Introduction

Silicon carbide (SiC) is expected to be applied to high-power and high-frequency devices because of its excellent chemical and physical properties[1]. Besides, since SiC has a strong radiation resistance[2], it is also regarded as a candidate for electric devices used in ionizing radiation environments such as the space and nuclear reactors.

One of the key issues of applying SiC to electronic devices is the development of acceptor impurity doping technique. Recently, Itoh et al.[3] reported that the co-implantation of carbon (C) with acceptor impurities such as aluminum (Al) and boron (B) enhanced their electrical activation. However, the optimum condition of C co-implantation has not yet been obtained. In this study, we have carried out co-implantation of Al and C into 6H-SiC and investigated the electrical properties of co-implanted layers by Hall effect measurements. We report the dependence of the electrical activation of Al on implantation temperature, the co-implanted C concentration and the sequence of co-implantation.

2. Experimental

The samples used in this study were n-type 6H-SiC epitaxial films (N_D-N_A ~ $5x10^{15}$ /cm^3) grown on 6H-SiC substrates. Five-fold implantation of Al (20, 50, 110, 200 and 340 keV) was carried out to form a box profile (depth: 0.5 μm) with a mean Al concentration of $2x10^{18}$ or $2x10^{19}$ /cm^3. A box profile of C with a thickness of 0.5 μm was also formed in a mean C concentration range from $2x10^{17}$ to $3x10^{19}$ /cm^3 by five-fold C-implantation (20, 60, 120, 190 and 270 keV). The samples were annealed at 1650 °C for 30 min in argon (Ar) atmosphere after implantation. The Al electrodes deposited on the samples were alloyed at 900 °C for 3 minutes in Ar to form ohmic contacts. The carrier concentration was measured using van der Pauw arrangement between 150 and 550 K. The hole concentration, p, in Al-implanted layers was determined from the Hall coefficient, R_H, according to

$$p = \frac{r_H}{eR_H}, \qquad (1)$$

where r_H and e are the Hall scattering factor and electron charge, respectively. In our analysis, r_H is taken as unity because the precise r_H values for 6H-SiC are not known. The temperature dependence of p obtained experimentally was fitted by using the charge neutrality equation described below.

$$p = \frac{N_A(Al)}{1+\frac{gp}{N_V}\exp\left(\Delta E(Al)/kT\right)} - N_{comp}, \qquad (2)$$

where N_{comp}, g, k and T are the concentration of compensation centers, the spin degeneracy factor (g=4), Boltzmann constant and temperature, respectively. The value of N_{comp} was determined by the fitting. N_V is expressed as $2(2\pi m_{p,de}kT/h^2)^{3/2}$, where $m_{p,de}$ is the effective density of states mass of hole[4] and h is Planck's constant. From the fitting, we can obtain the acceptor concentration N_A(Al) and the ionization energy of Al acceptors ΔE(Al).

3. Results and discussion

Figure 1 shows the relationship between co-implantation of C ($1x10^{18}$ /cm^3) and p at RT for the samples implanted with Al at $2x10^{18}$ and $2x10^{19}$ /cm^3. The "C/Al" and "Al/C" mean the co-implantation sequence, i.e., implantation of C prior to Al and that of Al prior to C, respectively. These implantations were performed at RT or 800 °C. The Al concentration for each samples was confirmed by SIMS measurements. No significant difference of the depth profile of Al atoms was observed between only Al-implanted and C-co-implanted samples. This result indicates that C co-implantation has little effect on redistribution of Al atoms. All co-implanted samples have higher p than the one implanted with Al only. This result can be interpreted in terms of the site competition with Al and C atoms because Al atoms act as shallow acceptors at Si sub-lattice sites.

As for the C-implantation temperature dependence of p, the values of p in samples hot-implanted with C are higher than those in the RT-implanted ones. In contrast to this result, as for the Al-implantation temperature dependence of p, no significant difference of p is observed between RT- and 800°C-implantations of Al. It was reported that in low dose phosphorus (P) implantation into 6H-SiC, the electron concentration was independent of the implantation temperature after annealing at 1400 °C due to the fact that almost all vacancy type defects were annealed out[5]. Thus, the result that p did not depend on Al-implantation temperature can be interpreted in terms of the elimination of defects by 1650 °C-annealing. However, the increase of p due to C hot-implantation can not be attributed to the same scheme. It is, therefore, considered that this effect is particular to C co-implantation. Assuming that the migration of interstitial C atoms is enhanced by hot-implantation, the number of C atoms occupying C sub-lattice sites increases during hot-implantation. A decrease of C vacancies could enhance the introduction of Al atoms into Si sub-lattice sites. To clarify this point, further investigations are necessary. Concerning the relation of p to the sequence of co-implantation, no significant difference is observed between both sequences.

The co-implanted C concentration dependence of p at RT for the samples implanted with Al at $2x10^{18}$ and $2x10^{19}$ /cm^3 is shown in Fig. 2. The samples were implanted with C at 800 °C prior to Al at RT. The values of p in the samples implanted with Al only at RT (reference sample) are also shown as the broken lines for comparison. For both implantations of Al at $2x10^{18}$ and $2x10^{19}$ /cm^3, an increase of p due to C-implantation is observed in a concentration range from $2x10^{17}$ to $5x10^{18}$ C/cm^3. The maximum values of p are obtained at $1x10^{18}$ C/cm^3. These results show that C co-implantation enhances the electrical activation of Al acceptors, and that the optimum C concentration is $\approx 1x10^{18}$ /cm^3. At $1x10^{18}$ C/cm^3, the values of p in the samples implanted with Al at $2x10^{18}$ and $2x10^{19}$ /cm^3 are about 2.5 and 1.5 times higher than those in the reference samples, respectively. Thus, the influence of C co-implantation tends to be small when implanted Al concentration increases.

At a high concentration of co-implanted C ($3x10^{19}$ C/cm^3), the values of p are lower than those in the reference samples. It was reported that residual defects introduced in 6H-SiC by high dose implantation still remain after annealing at 1700 °C[6]. Since residual defects act as carrier traps and/or compensation centers[7], the obtained result can be explained as an increase of residual defects after annealing in such a high dose C-implantation.

Figure 3 shows the temperature dependence of p in the samples co-implanted at $2x10^{18}$ Al/cm^3 and $1x10^{18}$ C/cm^3 or $3x10^{19}$ C/cm^3. The result for the sample implanted with Al only is

also shown in the figure for comparison. The solid lines in the figure represent the fitting results obtained using Eq. 2. As a result of fitting for every sample, the ionization energy of Al acceptors is estimated to be 200 meV. This value is in good agreement with the value reported previously (199 meV) [8]. For the sample co-implanted with C at $1x10^{18}$ /cm^3, N_A and N_{comp} are estimated to be $2.0x10^{18}$ and $6.0x10^{16}$ /cm^3, respectively. The former value means that the activation ratio, which is defined as N_A/N_{impla} (where N_{impla} is the concentration of implanted Al atoms), is 100 %. Here, we should point out that the obtained activation ratio includes some uncertainty because r_H is assumed to be unity in this analysis. As for N_{comp}, the obtained value is the smallest of the three samples. This result indicates that the electrical activation of Al acceptors is enhanced as well as the compensation centers are reduced by the co-implantation of C at $1x10^{18}$ /cm^3. It was reported from the admittance spectroscopy measurements for 4H-SiC co-implanted with $1x10^{18}$ C/cm^3 and $1x10^{18}$ B/cm^3 that the peak height corresponding to the B shallow acceptor level increased and that the peak for B-related defect (D_1) disappeared[9]. Thus, it may be presumed that co-implantation of C is useful not only for the disposition of acceptor atoms at Si sub-lattice sites but also the elimination of compensation centers. On the other hand, N_A for the sample co-implanted at $3x10^{19}$ C/cm^3 is estimated to be $6.8x10^{17}$ /cm^3. This value is smaller than that for the sample implanted with Al^+ only. In addition, N_{comp} for the sample co-implanted at $3x10^{19}$ C/cm^3 shows the highest value of the three samples. That is, the co-implantation of C at $3x10^{19}$ /cm^3 reduces the electrical activation of Al acceptors and raises the concentration of compensation centers. It was reported that large vacancy clusters were formed by annealing in the case of high dose implantation[6]. Nakano et al. reported that the concentration of shallow B acceptors decreased and new defects were generated by high dose C co-implantation into B-implanted 4H-SiC[9]. Therefore,

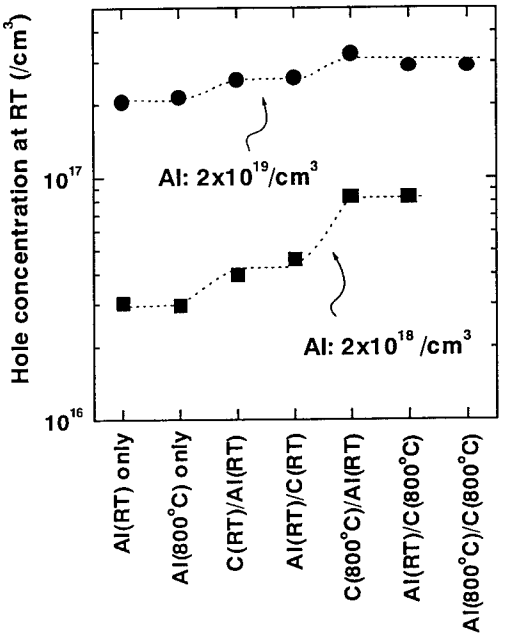


Fig. 1 Relationship between co-implantation of C ($1x10^{18}$/cm^3) and the hole concentration at RT for 6H-SiC implanted with Al. Squares and circles represent the results for samples implanted at $2x10^{18}$ and $2x10^{19}$ Al/cm^3, respectively. All these samples were annealed at 1650 °C after implantation.

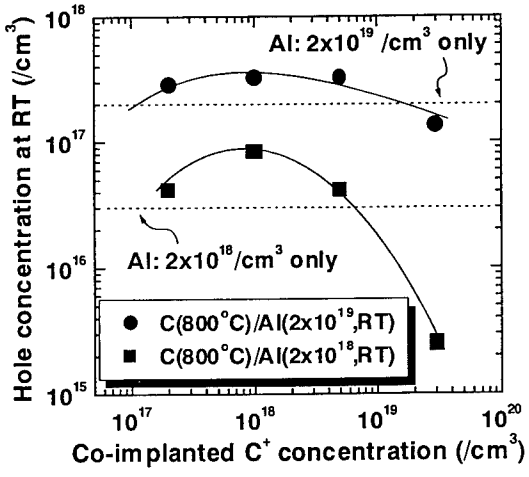


Fig. 2 Co-implanted C concentration dependence of the hole concentration at RT for 6H-SiC implanted with Al at $2x10^{18}$ (squares) and $2x10^{19}$ /cm^3 (circles) and subsequently annealed at 1650 °C. The samples were implanted with C at 800 °C prior to Al at RT. The broken lines represent the results for samples implanted with Al only.

the obtained result can be interpreted in terms that Al atoms in the samples co-implanted with such a high dose C combine with vacancy clusters during annealing, leading to a decrease in the activation ratio of implanted Al atoms and an increase in compensation centers.

4. Summary

Co-implantation of C and Al into 6H-SiC was performed in a C concentration range between $2x10^{17}$ and $3x10^{19}$ /cm^3 and in Al concentrations of $2x10^{18}$ and $2x10^{19}$ /cm^3 to find the optimum condition for improving the electrical activation of Al acceptors. The value of p in Al-implanted layers increases in a C concentration range from $2x10^{17}$ to $5x10^{18}$ /cm^3, and the maximum p value is obtained at $1x10^{18}$ C/cm^3. Hot-implantation of C at 800 °C is found to be quite useful for the improvement of the electrical activation of Al acceptors. As for implantation temperature of Al and the sequence of co-implantation, no significant improvement in p is observed.

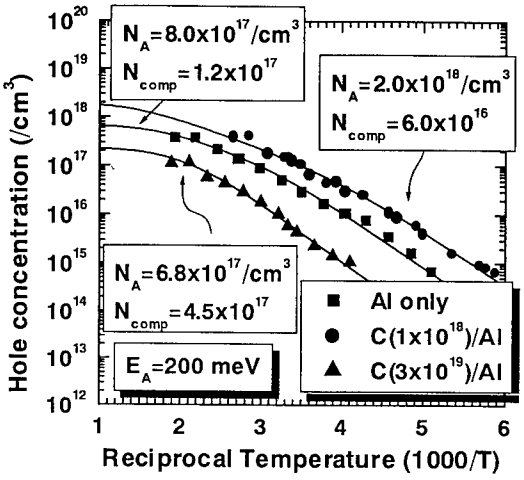


Fig. 3 Temperature dependence of the hole concentration in 6H-SiC co-implanted with Al at $2x10^{18}$ /cm^3 and C at $1x10^{18}$ (circles) or $3x10^{19}$ /cm^3 (triangles). The result for sample implanted with Al only is also shown in the figure (squares). The solid lines indicate the fitting results using Eq. 2.

Acknowledgments

Authors are very thankful to Prof. O. Eryu and Mr. K. Abe in Nagoya Institute of Technology for their help in SIMS measurements. One of the authors (T. O) would like to acknowledge the financial support by Murata Science Foundation.

References

[1] For example: *Fundamental Questions and Applications of SiC* (Guest Editors: W. J. Choyke, H. Matsunami, G. Pensl), Special Issue: phys. status solidi (a) **162** (1997) & phys. status solidi (b) **162** (1997).
[2] H. Itoh, M. Yoshikawa, I. Nashiyama, S. Misawa, H. Okumura, S. Yoshida, IEEE Trans. Nucl. Sci. **NS-37** (1990), p.1732.
[3] H. Itoh, T. Troffer, G. Pensl, Mater. Sci. Forum **264-268** (1998), p.685.
[4] G. Wellenhofer, U. Rossler, phys. status solidi (b) **202** (1997), p.107.
[5] T. Ohshima, A. Uedono, K. Abe, H. Itoh, Y. Aoki, M. Yoshikawa, S. Tanigawa, I. Nashiyama, Appl. Phys. A 67 (1998), p.407.
[6] T. Ohshima, A. Uedono, H. Itoh, M. Yoshikawa, K. Kojima, S. Okada, I. Nashiyama, K. Abe, S. Tanigawa, T. Frank, G. Pensl, Mater. Sci. Forum **338-32** (2000), p.857.
[7] G. C. Rybicki, J. Appl. Phys. **78** (1995), p.2996.
[8] G. Pensl, V.V. Afanas, M. Bassler, M. Schadt, T. Troffer, J. Heindl, H. P.Strunk, M. Maier, W. J. Choyke, Inst. Phys. Conf. Ser. **142** (1996), p.275.
[9] Y. Nakano, T. Kachi, H. Tadano, R. K. Malhan, J. Crystal Growth **210** (2000), p.283.

Materials Science Forum Vols. 353-356 (2001) pp. 579-582
© 2001 Trans Tech Publications, Switzerland

High Dose Implantation in 6H-SiC

V. Heera[1], W. Skorupa[1], J. Stoemenos[2] and B. Pécz[3]

[1] Forschungszentrum Rossendorf, PO Box 510119, DE-01314 Dresden, Germany

[2] Aristotle University of Thessaloniki, Physics Department, GR-54006 Thessaloniki, Greece

[3] Research Institute for Technical Physics and Materials Science, PO Box 49, HU-1525 Budapest, Hungary

Keywords: 6H-SiC, Aluminium, Al_4C_3, C, Diamond, High Dose Implantation, Phase Formation, TEM

Abstract: The phase formation in 6H-SiC due to high dose implantation was studied as function of temperature by means of transmission electron microscopy. Two examples demonstrate the feasibility of ion beam synthesis of crystalline phases in 6H-SiC which are epitaxially aligned with the surrounding matrix. In the first example Al^+ ions were implanted up to concentrations of 15 at% at temperatures between RT and 800°C. The precipitation of carbon phases due to high dose C^+ implantation in 6H-SiC at temperatures between 300°C and 900°C was investigated in the second example.

1. Introduction

Most of the studies devoted to implantation in SiC focus on doping [1] and radiation damage [2]. Typically, the impurity concentrations obtained were below 0.1 at% (10^{20} cm^{-3}). The goal of the present study is to investigate the effects of ion implantation in 6H-SiC with doses resulting in impurity concentrations above 1 at%. Such concentrations are much higher than the equilibrium solubilities of dopants in SiC and can even exceed the critical concentration for impurity incorporation under the dynamic conditions of ion irradiation. Therefore, precipitation and compound formation can be expected. Compared to high dose effects observed in Si the situation in SiC is much more complex due to the presence of two reactive elements in the matrix and the very dense lattice structure [3]. In order to avoid the amorphization of the 6H-SiC lattice the implantations must be performed at elevated temperatures. The phase formation in 6H-SiC due to high dose implantation of Al^+ and C^+ was studied as function of temperature by means of transmission electron microscopy.

2. Al implantation

In a previous experiment 350 keV Al^+ ions were implanted in 6H-SiC with doses of $1 \cdot 10^{17}$ cm^{-2} and $3 \cdot 10^{17}$ cm^{-2} at 500°C [4]. Below Al concentrations of 10 at% the SiC matrix remains stable and the Al atoms preferentially occupy Si sites in the 6H-SiC lattice. A detailed XTEM analysis revealed the formation of a narrow band of Al_4C_3 and Si precipitates with laminar shape in the depth region where the Al concentration exceeds the threshold of about 10 at%. It could be demonstrated that the precipitates are epitaxially aligned with the surrounding 6H-SiC lattice which is only weakly damaged. This is surprising when considering the huge volume expansion and the lattice misfit associated with the Si precipitation [4].

The influence of the implantation temperature on the phase formation in 6H-SiC implanted with 300 keV, $3 \cdot 10^{17}$ Al^+ cm^{-2} has been investigated in further experiments. Implantation at room temperature

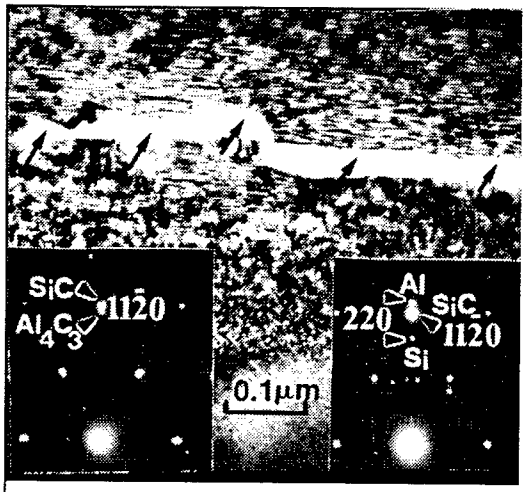


Fig. 1 XTEM micrograph showing the band of Al and Si precipitates due to Al implantation at 550°C. The corresponding plan view diffraction pattern is given in the right inset. Implantation at 500°C at low dose rate results in the formation of Al_4C_3 as shown for comparison in the left diffraction pattern.

led to complete amorphization of the surface layer. After an annealing at 700°C for 30 min this layer is transformed to heavily damaged 6H-SiC. It can be assumed that the recrystallization temperature of SiC [5] is lowered by the high Al content. No precipitates could be detected in the recrystallized layer. The same result was obtained after implantation at 400°C. In this case the temperature is high enough to avoid amorphization, but the radiation damage in the 6H-SiC lattice is still high. Therefore, it can be concluded that precipitation does not occur because the Al atoms are incorporated into the defect rich lattice. It is clear from the melting temperatures of the Al-Si eutecticum (577°C) and the metallic Al (660°C) that the temperature range between 500°C and 700°C is very critical. Indeed, there are strong differences in the phase formation at 500°C or 550°C. At the higher temperature precipitates of metallic Al and Si were observed, forming an almost continuous zone (Fig. 1). Plan view selected area diffraction pattern reveals that the precipitates are again epitaxially aligned with the SiC lattice (right inset in Fig. 1). No Al_4C_3 could be detected. Similar results were found at implantation temperatures of 600° and 700°C. The attempt to produce a closed, buried layer of Al in the SiC matrix by implantation of $1 \cdot 10^{18}$ Al^+ cm^{-2} at 800°C led to surface cracking and material outflow (Fig. 2). According to surface profile measurements the wall heights are between 0.5 and 2 μm.

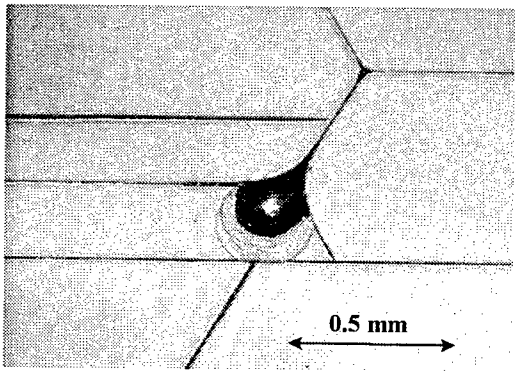


Fig. 2 Optical microscope image of the SiC surface after implantation of $1 \cdot 10^{18}$ Al^+ cm^{-2} at 800°C. Material outflow from surface cracks is visible.

Our results are partly in contradiction to the results of Yang et al. [6] who implanted 87 keV Al^+ to doses of $2.4 \cdot 10^{17}$ cm^{-2} at 800°C which results in the formation of Al_4C_3 precipitates. Si precipitates were not detected. Instead a C enrichment due to Si outdiffusion was obtained. According to Yang et al. [6] the C enrichment in SiC is a necessary condition for the Al_4C_3 formation. However, in our experiments C enrichment has never been observed, although sometimes the Si precipitates were absent. We found that the phase formation is determined by the dose rate - temperature regime. For example at 500°C only Al_4C_3 precipitates were formed at a dose rate of 2 $\mu A/cm^2$ as demonstrated in the left inset of Fig. 1. Additional Si precipitates were formed at a dose rate of 8 $\mu A/cm^2$. Yang et al [6] used in their experiments a much higher dose rate of 35 $\mu A/cm^2$. This and the shallower Al profile could explain the observed differences. It seems that radiation enhanced diffusion and segregation have a strong influence on the phase formation.

The presence of Al or Si precipitates is the main obstacle for the annealing of the radiation damage in the Al implanted SiC. Typically, temperatures higher than 1500°C are necessary [1,3] at which both Al and Si melts. The consequence of the high temperature annealing of SiC with high Al content is the

formation of cavities and large Al blocks [7].

3. C implantation

6H-SiC was implanted with 60 keV, $1 \cdot 10^{18}$ C^+/cm^2 at temperatures of 300°, 600° and 900°C. The composition of the compound is about $Si_{0.20}C_{0.80}$ in the carbon maximum at the depth of 130 nm. The temperature range was chosen because 300°C is the critical temperature necessary to avoid amorphization of SiC [3] whereas 900° is well above the temperature where graphitization of diamond is obtained by ion implantation [8]. The surface of the implanted SiC was inspected with an optical microscope. Neither cracks nor inhomogeneities were observed and the surface remains mirror like. This is in strong contrast to the results of Al implantation. Obviously, the smaller C atoms can occupy interstitial sites in the SiC lattice. Thus, only a minor volume swelling occurs.

The phase formation was investigated by XTEM and first results were published in Ref. 9. In the sample implanted at 300°C a buried amorphous phase is produced in the depth region between 75 and 210 nm which is followed by a small zone of highly defective crystalline 6H-SiC of about 45 nm width. A crystalline 6H-SiC near surface layer is left although the damage energy in this region is more than 200 times higher than the amorphization energy of SiC at room temperature [3]. This means that an effective self-annealing of radiation damage caused by the C ions takes place in SiC at 300°C. Because the damage energy in the amorphized zone is not substantially higher than in the near-surface region, it can be concluded that the amorphous phase is stabilized by the excess carbon atoms in this region.

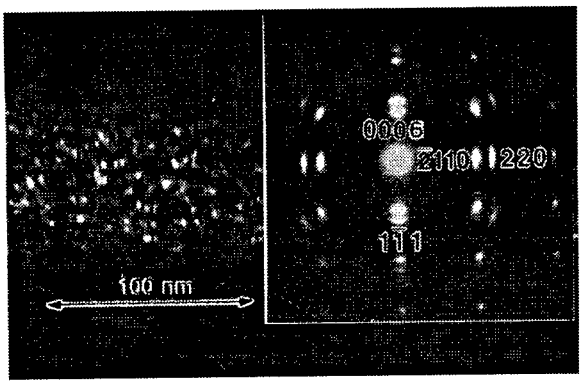


Fig. 3 Dark field XTEM image taken with the (220) diamond reflection demonstrating the distribution of diamond grains in the implanted zone. The selected area diffraction pattern is shown in the inset.

Substrate amorphization is completely prevented for C implantation at 600°C. The XTEM analysis reveals a top surface region, 55-60 nm thick, which is almost defect-free 6H-SiC. The adjacent 6H-SiC layer with a width of about 30 nm contains several lattice defects. The main zone is a 100 nm thick layer with crystalline precipitates which could be identified by selected area diffraction as graphite embedded in SiC [9]. Interestingly, the precipitates have a strong texture where the hexagonal axis of graphite is perpendicular to the 6H-SiC hexagonal axis. The formation of graphite precipitates by the excess carbon inside the SiC crystal is not surprising, because all Si-C bonds are saturated and graphite is the only equilibrium phase of carbon.

Quite different results were obtained for the carbon implantation at 900°C. Around the depth of 150 nm a buried zone with precipitates is found in the weakly damaged 6H-SiC matrix. The SAD pattern (inset Fig. 3) reveals the coexistence of SiC and diamond grains, which are in perfect epitaxial relation. The size of the diamond grains is between 2 and 5 nm as determined by dark field imaging with the (220) reflection of diamond (Fig. 3). The width of the diamond zone is about 100 nm. No graphitic inclusions were detected by the TEM analysis in the implanted layer.

The mechanism of the diamond formation by IBS in SiC is not quite clear. It can be assumed that the tetrahedrally coordinated SiC lattice, which is preserved during the high temperature implantation, acts as a template for the growth of diamond. This is in agreement with the model of diamond nucleation inside a SiC transition layer during CVD growth on Si [10]. In addition, local nonequilibrium conditions in the ion cascades (thermal spikes, shock waves) or temporary stress on interstitially incorporated carbon atoms by the surrounding SiC lattice could facilitate the diamond

nucleation. Weselowski et al. [11] demonstrated the transformation of graphitic carbon onions to diamond by ion irradiation in the temperature range between 700°C and 1100°C. They explained the transformation process by a compression of the carbon onions induced by knock-on displacements. Obviously, the target temperature plays a crucial role for the diamond formation. Occasionally formed diamond nuclei are destroyed by the implantation damage below temperatures of 700°C resulting in growing graphite or amorphous carbon at temperatures of 600°C or 300°C, respectively.

4. Conclusions

The feasibility of ion beam synthesis of crystalline, epitaxially aligned phases in 6H-SiC was demonstrated by two examples. High dose Al implantation at elevated temperatures leads to the formation of precipitates if a critical impurity concentration in the matrix is exceeded. It is about 10 at% for implantation at 500°C. This critical concentration is much higher than the equilibrium solubility for Al in SiC during crystal growth [1].

It is very difficult to control the phase formation in the Al-SiC system because to its high sensitivity to the dose rate / temperature regime. Al_4C_3 precipitates were formed at 500°C whereas at higher temperatures a clear tendency for Al precipitation was observed. The Si atoms released in the chemical reaction between Al and SiC seem to be mobile under the irradiation and form either precipitates or diffuse out. High temperature annealing results in a layer degradation because of local melting of Al or Si precipitates.

In the second example the evolution of the more simple, binary system C - SiC was studied as function of implantation temperature. An amorphous, carbon rich phase was produced at 300°C. Precipitates of graphite were obtained at 600°C, whereas at 900°C small diamond grains were produced. These grains are in perfect epitaxial relation with the surrounding SiC lattice. It can be assumed that the tetrahedrally coordinated SiC lattice, which is preserved during the high temperature implantation, acts as a template for the growth of diamond.

Acknowledgements: One of the authors (V.H.) would like to acknowledge financial support by Deutsche Forschungsgemeinschaft (Contract No. He 2604/2). B.P. acknowledges financial support from OTKA T 030447 project.

References

[1] T. Troffer, M. Schadt, T. Frank, H. Itoh, G. Pensl, J. Heindl, H.P. Strunk, M. Maier, phys. stat. sol. (a) 162 (1997), p. 277.
[2] E. Wendler, A. Heft, W. Wesch, Nucl.Instr.Meth. B 141 (1998), p. 105.
[3] V. Heera, W. Skorupa, Mater.Res.Soc.Symp.Proc.Vol 438 (1997), p. 241.
[4] V. Heera, H. Reuther, J. Stoemenos, B. Pécz, J.Appl.Phys. 87 (2000), p. 78.
[5] A. Höfgen, V. Heera, F. Eichhorn, W. Skorupa, J.Appl.Phys. 84 (1998), p. 4769.
[6] Z. Yang, H. Du, M. Libera, J.Mater.Res. 10 (1995), p. 1441.
[7] J. Stoemenos, B. Pécz, V. Heera, Mater. Sci. Forum 338-342 (2000), p. 881.
[8] R. Kalish, Appl.Surf.Sci. 117/118 (1997), p. 558.
[9] V. Heera, W. Skorupa, B. Pécz, L. Dobos, Appl. Phys.Lett. 76 (2000), p. 2847.
[10] R. Stöckl, M. Stammler, K. Janischowsky, L. Ley, M. Albrecht, H.P. Strunk, J.Appl.Phys, 83 (1998), p. 531.
[11] P. Weselowski, Y. Lyutovich, F. Banhart, H.D. Carstanjen, H. Kronmüller, Appl.Phys.Lett. 71 (1997), p. 1948.

Materials Science Forum Vols. 353-356 (2001) pp. 583-586
© 2001 Trans Tech Publications, Switzerland

Precipitate Formation in Heavily Al-Doped 4H-SiC Layers

M.K. Linnarsson[1], P.O.Å. Persson[2], H. Bleichner[3], M.S. Janson[1], U. Zimmermann[1], H. Andersson[1], S. Karlsson[4], R. Yakimova[2], L. Hultman[2] and B.G. Svensson[1,5]

[1] Royal Institute of Technology, Solid State Electronics, PO Box E229, SE-16440 Kista-Stockholm, Sweden

[2] Department of Physics and Measurement Technology, Linköping University, SE-581 83 Linköping, Sweden

[3] ABB Corporate Research, PO Box E215, SE-164 40 Kista-Stockholm, Sweden

[4] ACREO AB, P.O. Box E236, SE-164 40 Kista-Stockholm, Sweden

[5] Oslo University, Physical Electronics, Dept. of Physics, P.B. 1048 Blindern, NO-0316 Oslo, Norway

Keywords: Aluminium, Precipitate, SIMS, Solubility Limit, TEM

Abstract Epitaxially grown 4H-SiC structures with several heavily Al doped layers were used. The samples were annealed in Ar atmosphere in a RF-heated furnace between 1500 and 2000°C for 0.5 to 3h. Secondary ion mass spectrometry (SIMS) was used to measure the aluminum concentration versus depth as well as the lateral distribution (ion images). Transmission electron microscopy (TEM) was employed to study the crystallinity and determine phase composition after heat treatment. A solubility limit of $2x10^{20}$ Al/cm^3 at 2000°C is extracted. Ion images of the lateral Al distribution reveal a pronounced dependence on the Al content. Precipitate formation occurs after heat treatment at 1700 – 2000°C when the Al concentration exceeds $2x10^{20}$ cm^{-3} and energy-filtered TEM (EFTEM) shows that the precipitates contain Al.

Introduction

To form high quality p-type ohmic contacts on silicon carbide heavily aluminum doped material is of prime interest. Highly Al doped SiC layers can be prepared by ion implantation or during epitaxial growth taking advantage of site competition [1]. Dopant incorporation during epitaxial growth is kinetic-controlled and solubility limits may be exceeded. However, in subsequent annealing steps thermodynamic considerations have to be made. The thermal stability of heavily Al doped contact layers can be predicted from the ternary phase diagram Al-Si-C [2-5]. The three binary subsystems are well known with two intermediate phases, Al_4C_3 and SiC. Three ternary intermediate phases, Al_8SiC_7, Al_4SiC_4 and $Al_4Si_2C_5$ have been reported in the isopleth Al_4C_3-SiC. Inou et al. [6] observed the $Al_4Si_2C_5$ phase in 1980, but their results have not been confirmed in later studies [2]. The chemical interaction between pure aluminum metal and SiC is well documented over a broad temperature range (room temperature up to 1600 °C) [3,4], but unfortunately, the SiC rich side, which is the area of interest for highly doped SiC layers, is not known in detail.

In this contribution we have studied three-dimensional distributions of Al in epitaxially grown p-type 4H-SiC. A solubility limit of $2x10^{20}$ cm^{-3} (2000°C) is revealed and at higher aluminum concentrations precipitates may form. Secondary ion mass spectrometry (SIMS) has been utilized to obtain Al-concentration versus depth profiles as well as lateral distributions (ion images). Transmission electron microscopy (TEM) has been performed to investigate the crystal structure and determine phase compositions in the heavily doped SiC.

Experimental

4H-SiC epitaxial structures with Al doped layers separated by undoped material have been grown at 1500°C. The Al concentration was in the range $3x10^{19}$ to $5x10^{20}$ cm^{-3}. Subsequent heat treatments were carried out in Ar atmosphere in a RF-heated furnace between 1500 and 2000 °C for 0.5 to 3h.

Analysis of the aluminum depth distribution as well as lateral distributions (ion images) were performed via SIMS using a Cameca IMS 4f microanalyser. A sputtering beam of 8.2 keV $^{32}(O_2)^+$ ions was employed. In depth profiling the primary beam is rastered over an area of 200x200 μm^2 and the secondary ions of $^{27}Al^+$ were collected from the central part of this area (diameter of

analyzed area ~60 μm). The erosion rate was typically 30 Å/s. During ion image acquisition the primary beam (diameter ≤ 1 μm) was rastered over an area of 25x25 μm^2 and a typical erosion rate was 0.5 Å/s. HRTEM was done using a Philips CM20UT, equipped with a LaB_6 filament operated at 200 kV. Furthermore, energy-filtered TEM (EFTEM) was performed in a TECHNAI F30 ST FEG-TEM operated at 300 kV.

Results and discussion

Three SIMS spectra are displayed in Fig.1a showing the ^{27}Al depth distribution in an as grown sample and after heat treatment at 2000°C for 0.5 and 2 h, respectively. At 2000°C Al diffusion is detected in four of five of the Al structures. When the Al concentration decreases the diffusion decreases and no broadening was observed at the lowest doping level. This strong concentration dependence in Al diffusion is remarkable. The diffusion fronts are very steep with a shape diverging from a pure Fickian diffusion. In layer 5, Fig.1a, the out-diffusion starts at a level of $2x10^{20}$ cm^{-3} while a higher concentration, i.e., the as grown concentration, remains in the center of the layer. The same type of diffusion curves are obtained after heat-treatment at 1700, and 1900°C for 0.5 to 3h. Diffusion curves of this kind indicate that the solubility limit has been exceeded and precipitates may form. The level of out diffusion can be interpreted as a solubility limit, in this case $2x10^{20}$ Al/cm^3 (2000°C). No pronounced temperature dependence in the solubility limit is revealed between 1700 and 2000°C. The out diffusion is symmetric and no difference is observed between the [0001] and [000$\bar{1}$] directions. Solubility limits of $7x10^{20}$ ((0001), silicon face) and $9x10^{19}$ ((000$\bar{1}$) carbon face) Al/cm^3 in sublimation grown 6H-SiC has previously been reported by Vodakov et. al [7]. This anisotropy in impurity doping concentration is attributed to the kinetic nature of the incorporation process and the results will differ from the values obtained at thermodynamic equilibrium.

Ion images of the lateral Al distribution reveal a pronounced dependence on the Al content. In layers with high enough Al concentration the Al distribution is no longer homogenous after heat treatment at 1700°C or above, as seen by brighter regions in the SIMS images; Fig. 1b shows the lateral Al distribution recorded in a layer with a dopant level of $3x10^{20}$ cm^{-3}. A post-grown heat treatment at 2000°C during 2h has been performed. No lateral inhomogeneities in the Al concentration are resolved in layers with concentrations below $1x10^{20}$ cm^{-3} or without post-grown heat treatment. The lateral resolution is given by the diameter of the sputtering ion beam, typically ≤1 μm. Hence, the detected intensity is an average over an area with the size of the primary beam and frequent small structures, homogeneously distributed, may not be resolved.

HRTEM has been utilized to further investigate if any Al rich precipitates are present. Cross-sections were prepared from two of the samples, as grown and after heat treatment at 2000°C for 30 minutes, which were also used in the SIMS depth profiling in Fig.1a. In the as grown sample no

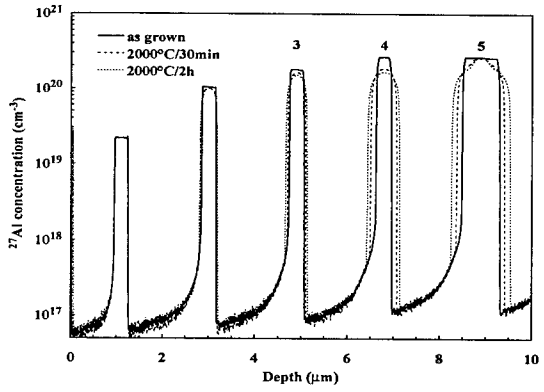


Fig.1a. SIMS profiles of the aluminum concentration versus depth for 4H-SiC samples. Three samples are analyzed, one as-grown and two annealed at 2000°C for 0.5 and 2 h, respectively.

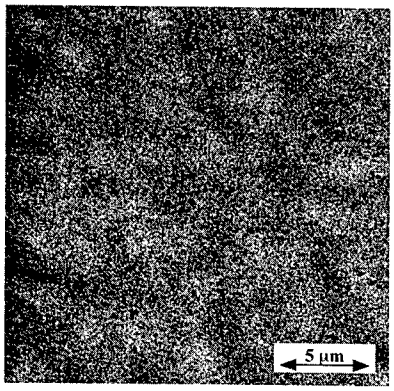


Fig.1b. Ion image of the Al distribution obtained by SIMS. The data is recorded in the middle of layer 5 in the sample heat treated at 2000°C for 2h shown in Fig.1a.

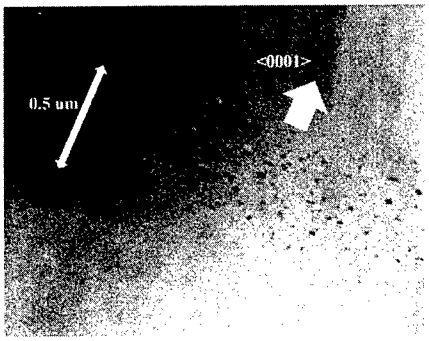


Fig.2a. Cross-sectional TEM image of heavily Al doped 4H-SiC after anneal at 2000°C for 30 minutes. A SIMS depth profile for the same sample is given in Fig. 1a. A track of defects is observed in the middle of the fifth Al layer.

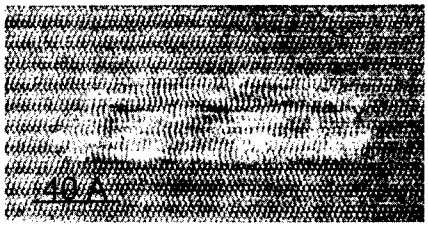


Fig.2b. Cross-sectional HRTEM of one of the defects in Fig.2a in the $(11\bar{2}0)$ plane.

precipitates were observed, but in layer five the lattice was slightly stressed. No disorder was detected in layer one to four after heat treatment. In layer five a 0.5 μm broad track of defects was observed (Fig.2a). These defects have the preferential orientation of the c-axes in SiC. In Fig. 2b a HRTEM image of one defect is displayed. The surrounding SiC lattice is not markedly influenced. A typical thickness of the structure is 40 Å and the extension perpendicular to the c-axis is in the range 30 to 300 Å. If $1x10^{20}$ Al atoms mixed with $5x10^{22}$ Si atoms form Al containing precipitates with a size of 300x300 Å there will be about 2 precipitates/μm^2. This is close to the detection limit in ion imaging by SIMS, since at higher precipitate densities, homogeneously distributed, the Al intensity will average out.

These results obtained by SIMS and HRTEM are further substantiated by EFTEM revealing that the precipitates are an Al containing phase. EFTEM suggests also a reduction in the Si concentration in the precipitates relative to the matrix and the most probable phase can be predicted from the ternary phase diagram Al-Si-C. Fig. 3a shows the Al-Si-C isothermal section at 2000°C and Fig. 3b the isopleth Al_4C_3-SiC, redrawn from Oden and McCune [2]. If Al is introduced by ion implantation the silicon to carbon ratio in SiC is conserved and the overall concentration varies along a line connecting Al with SiC (indicated with - - - in Fig.3a). This is not the case when the Al dopants atoms are introduced during growth. Al will be incorporated in the lattice on Si sites and below the solubility limit the amount of Si and Al atoms will add up to the C content (indicated by .... in Fig.3a). When the solubility limit is exceeded, the Si plus Al to C ratio may differ slightly from one and the composition may approach the isopleth Al_4C_3-SiC. According to the phase

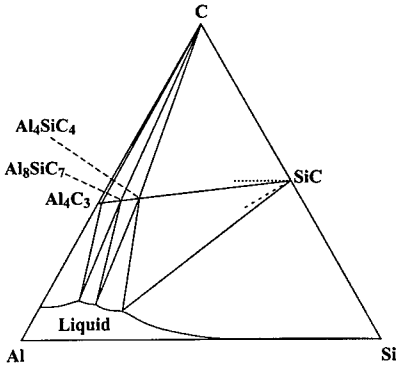


Fig.3a. Al-Si-C isothermal section at 2000°C. Redrawn from Oden et. al [2].

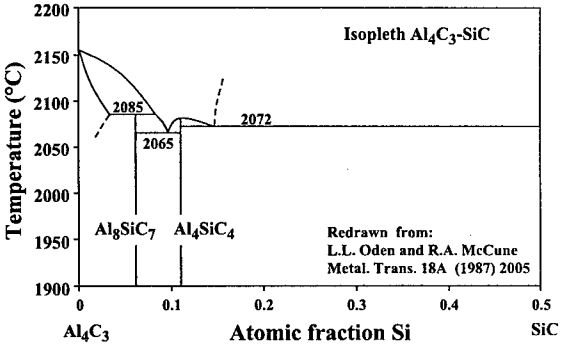


Fig.3b. Isopleth Al_4C_3-SiC. Redrawn from Oden et al. [2].

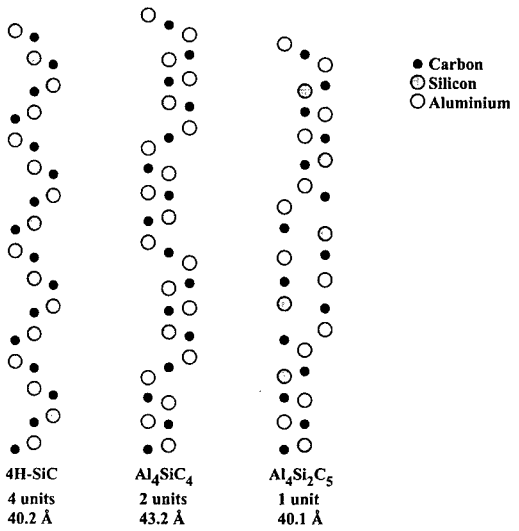


Fig.4. Stacking sequences in the $(11\bar{2}0)$ plane for 4H-SiC, Al_4SiC_4 and $Al_4Si_2C_5$

diagram, when the solubility limit of Al in SiC is exceeded Al_4SiC_4 will form. $Al_4Si_2C_5$ has also been identified as a possible candidate [6] but its stability is doubtful and the compound has therefore not been included in the phase diagram. Keeping in mind that if $Al_4Si_2C_5$ is stable, it will most likely form from a supersaturated solution of Al in SiC at thermodynamic equilibrium. Furthermore, the formation of Al_4C_3 during high dose ($3x10^{17}$ cm^{-2}, 350 keV) Al implantation at 500°C has also been reported [8].

A hexagonal lattice can describe Al_4C_3, Al_4SiC_4, $Al_4Si_2C_5$ as well as 4H-SiC and their space groups have been identified as $R\bar{3}m$, $P6_3mc$, $R\bar{3}m$ and $P6_3mc$, respectively [6]. The unit cell dimensions corresponding to a hexagonal lattice are a=3.3388 Å, c=24.996 Å (Al_3C_4), a=3.2771 Å, c=21.676 Å (Al_4SiC_4), a=3.2512 Å, c=40.1078 ($Al_4Si_2C_5$) and a=3.080 Å, c=10.050 Å (4H-SiC). According to the space groups there is a distinct possibility of aligning the c-axis of all the aluminum containing carbides with the 4H-SiC lattice in a phase mixture. The extension in the c direction of two unit cells of Al_4C_3 (50Å) coincides with five unit cells of 4H-SiC, and one unit cell of Al_4SiC_4 and $Al_4Si_2C_5$ coincide with two and four unit cells of 4H-SiC, respectively. The mismatch to 4H-SiC is negligible for Al_4C_3 and $Al_4Si_2C_5$ while a small mismatch is revealed for Al_4SiC_4 but it is not large enough to prevent epitaxial growth. A comparison between the thickness of matching units and the extension of 40 Å observed HRTEM (Fig.2b) indicates that the precipitates may consist of Al_4SiC_4 or $Al_4Si_2C_5$. In Fig.4 the stacking sequences in the $(11\bar{2}0)$ plane for 4H-SiC, Al_4SiC_4 and $Al_4Si_2C_5$ are shown. The unit cell of Al_4SiC_4 and $Al_4Si_2C_5$ contains "layers" of Si-C with the same structure as in 4H-SiC and appears as a natural cross over between an aluminum containing phase and SiC.

Summary

A solubility limit of $2x10^{20}$ cm^{-3} (2000°C) is extracted for Al in 4H-SiC. Anneals in the temperature range 1700-2000°C of super-saturated Al doped 4H-SiC results in inhomogeneous Al distribution and Al containing precipitate formation. The precipitates have the preferential orientation of the c-axis in SiC. According to the ternary Al-Si-C phase diagram and the lattice structures a probable composition of the precipitating phase is Al_4SiC_4 or $Al_4Si_2C_5$.

Acknowledgment

The authors are grateful to Prof. Eva Olsson (Ångström laboratory, Uppsala, Sweden) for her assistance in EFTEM. Financial support was partly received from Swedish foundation for Strategic Research (SSF) SiCEP program.

References

[1] D.J. Larkin, P.G. Neudeck, J.A. Powell and L.G. Matus, Appl. Phys. Lett. 65 (1994), p.1659.
[2] L.L. Oden and R.A. McCune, Metal. Trans. 18A (1987), p.2005.
[3] J.C. Viala, P. Fortier and J. Bouix, J. Mat. Sci. 25 (1990), p.1842.
[4] J.C. Viala, F. Bosselet, V. Laurent and Y. Lepetitcorps, J. Mat. Sci. 28 (1993), p.5301.
[5] J. Gröbner, H.L. Lukas and F. Aldinger, Calphad 20 (1996), p.247.
[6] Z. Inou, Y. Inomata, H. Tanaka and H. Kawabata, J. Mat. Sci. 15 (1980), p.575.
[7] Y.A. Vodakov, E.N. Mokhov, M.G. Ramm and A.D. Roenkov, Springer Proc. Phys. 56 (Editors: G.L. Harris, M.G. Spencer and C.Y. Yang, Springer-Verlag Berlin Heidelberg 1992), p.329.
[8] J. Stoemenos, B. Pécz and V. Heera, Appl. Phys. Lett. 74 (1999), p.2602.

Materials Science Forum Vols. 353-356 (2001) pp. 587-590
© 2001 Trans Tech Publications, Switzerland

Flash Lamp Annealing of Implantation Doped p- and n-Type 6H-SiC

D. Panknin[1], T. Gebel[1,2] and W. Skorupa[1,2]

[1] Institut für Ionenstrahlphysik und Materialforschung, Forschungszentrum Rossendorf, PO Box 510119, DE-01314 Dresden, Germany

[2] nanoparc GmbH i.G., Bautzener Landstr. 45, DE-01454 Dresden-Rossendorf, Germany

Keywords: Doping, Ion Implantation, Flash Lamp Annealing

Abstract

The electrical properties of Al, B, N implanted 6H-SiC after flash lamp annealing are discussed in comparison with furnace annealing. For high concentrations the electrical activity of Al is distinctly enhanced using flash lamp annealing. For B implanted layers an enhancement is observed for concentrations < $3x10^{20}$ cm^{-3} using flash lamp annealing. The dopant outdiffusion is strong reduced. N activates by a two-step process. There is an optimum temperature-time regime.

1. Introduction

One of the key problems of ion implantation doping of SiC is the electrical activation, particularly for high dopant concentrations. Furnace annealing is reasonable only up to temperatures of about 1800°C because of remarkable Si sublimation. Using short-time annealing techniques, temperatures higher than the sublimation temperature are possible.

The mainly investigated dopants in SiC are Al and B for p-doping and N for n-doping. Short-time annealing in SiC was applied by some groups. Pensl et al. [1] annealed nitrogen implanted 6H-SiC ($2x10^{19}$ cm^{-3}) using rapid isothermal annealing (RIA). The electrical activation is enhanced with increasing annealing temperature (1050°C and 1200°C) and annealing time (between 2 and 4 min), respectively. Compared to furnace annealing (1470°C, 7 min.) no enhancement of carrier concentration was measured after RIA. Hirano et al. [2] annealed high N-implanted 3C-SiC by rapid thermal annealing (RTA) at 1100°C, 10 s in nitrogen ambient. Compared to furnace annealing at 1200°C , they found a higher electrical activity (factor 2) after RTA. Wirth at al. [3] observed a distinct enhancement of the hole concentration in highly Al-implanted 6H-SiC after flash lamp annealing (about 2000°C, 20 ms) in Ar ambient compared to furnace annealing at 1700°C. Dzhibuti et al. [4] successfully applied short time annealing (RTA (10 s) as well as flash lamp annealing (10 ms)) for defect annealing of high dose B implanted layers. Ahmed et al. [5] used a 308 nm XeCl eximer laser (pulse duration of 27 ns) for annealing of Al- and N-implanted layers. They observed a distinct redistribution of the dopants towards the surface. An electrical activation of more than 100 % was deduced from Spreading Resistance measurements which points to problems in the interpretation of these measurements.

In this contribution the results of electrical activation are briefly reported concerning the implantation of Al, B and N into 6H-SiC in a wide concentration range followed by flash lamp annealing (about 2000°C, 20 ms) in comparison to furnace annealing.

2. Experimental

The Al-, B- and N-ions were implanted at 400°C [6] with different energies and doses into epitaxially grown 6H-SiC wafers in order to form a 500 nm thick, box-shaped doped layer. The plateau concentrations were varied between $1x10^{18}$ cm^{-3} and $5x10^{21}cm^{-3}$ (Al), $1x10^{18}$ cm^{-3} and $1.5x10^{20}$ cm^{-3} (B), and $5x10^{17}$ cm^{-3} and $5x10^{20}$ cm^{-3} (N), respectively. The wafer were annealed in Ar ambient between 1450 °C and 1700 °C for 10 min. using an inductively heated furnace. Flash lamp annealing was performed at about 2000 °C by light irradiation on the wafer back side using an array of xenon lamps with a flash duration of 20 ms.
The samples were characterized by temperature dependent resistivity and Hall effect measurements.

3. Results

3.1 Al-doped layers

In Fig.1 the hole concentration, measured at room temperature (RT), is shown in dependence on the Al plateau concentration. For Al concentrations higher than 10^{20} cm^{-3} a strong increase of the hole concentration is measured for both increasing Al concentration and annealing temperatures. For higher concentration a temperature dependent limit of the hole concentration is observed. Using flash lamp annealing with temperatures above the temperature of Si sublimation a further enhancement of the hole concentration is observed.

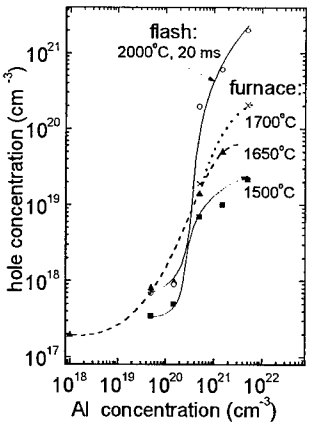


Fig.1: Hole concentration vs. implanted Al concentration after annealing at different temperatures and techniques

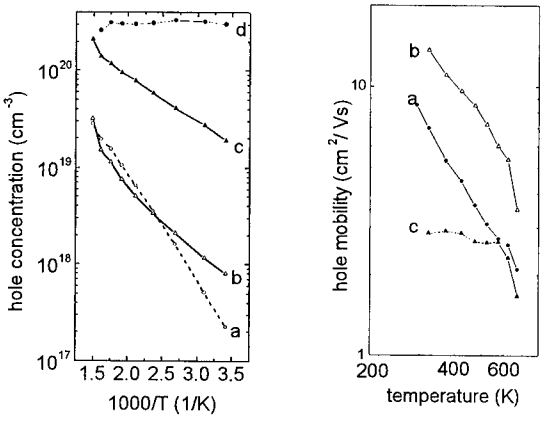


Fig. 2: Hole concentration and mobility vs. temperature
a,b: $5x10^{19}$ cm^{-3}: a- flash; b: furnace
c,d: $5x10^{20}$ cm^{-3}; d- flash; c- furnace

In Fig. 2 hole concentration and mobility are shown as a function of temperature for a low and a high Al concentration and both annealing techniques. For the low Al concentration, thermally induced conductivity is dominating independent of the annealing technology. For high Al concentration the temperature dependent hole concentration shows a smaller slope after furnace annealing, because the effective ionization energy of Al acceptors decreases as a result of interaction between the dopants. After flash lamp annealing the hole concentration is nearly independent of the temperature, indicating the transition towards metallic conductivity. The

temperature dependence of the mobility shows the typical behaviour for ionized impurity scattering in the low concentration case. For high concentration, additional scattering centres are effective due to the high Al concentration.

3.2 B-doped layers

In Fig. 3 the hole concentration and mobility, measured at RT, are shown as a function of the B content after furnace and flash lamp annealing, respectively. With increasing B concentration the hole concentration decreases and the mobility increases. For B content < $3x10^{20}$ cm^{-3} after flash

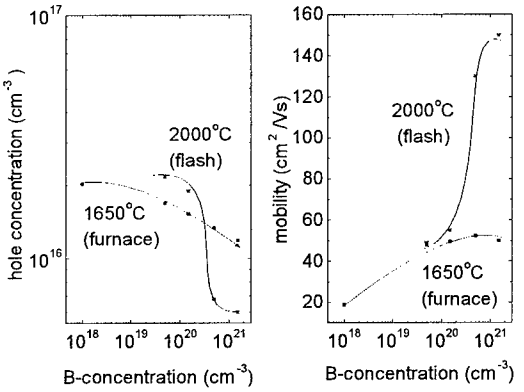


Fig. 3: Hole concentration and mobility vs. the implanted B concentration

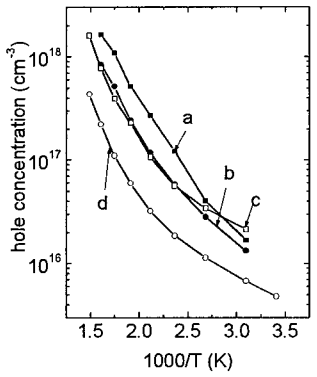


Fig. 4: hole concentration vs. temperature
a,b: $5x10^{19}$ cm^{-3}; c,d: $5x10^{20}$ cm^{-3}
a,c: furnace; b,d: flash

lamp annealing a higher hole concentration is measured. Measurements of the temperature dependence of hole concentration (Fig. 4) show comparable slopes for the different B contents and annealing technologies, indicating the same activation mechanism. This means that the effective dopant concentration decreases due to outdiffusion and segregation of B, supported by Ostwald ripening. Using flash lamp annealing segregation and Ostwald ripening are dominating [7].

3.3 N-doped layers

In Fig. 5 carrier concentration and mobility, measured at RT, are shown as a function of the implanted N concentration after both furnace and flash lamp annealing. With increasing N content the carrier concentration increases and the mobility decreases. Compared to furnace annealing, after flash lamp annealing (curve d) a lower carrier concentration was observed despite the higher annealing temperature. First measurements for high N concentration show that a two step process, flash lamp annealing and subsequent furnace annealing, leads to a somewhat higher electrical activation compared to furnace annealing (curve e).
In Fig. 6 the Arrhenius plot of the carrier concentration is presented after flash lamp and furnace annealing at 1650°C, respectively. The furnace annealed samples show the typical dependence for N doped layers with two energy levels corresponding the occupation of hexagonal and cubic lattice sites. The analysis of the Hall effect measurements by fit of the neutrality equation results in a levels of 79 meV (low temperature range) and 128 meV (high temperature region) assuming a concentration ratio of 1 : 2, which agrees with the ratio of inequivalent hexagonal to cubic lattice sites within the unit cell of the 6H-SiC [8]. After flash lamp annealing only one energy level of 81 meV can be deduced in Fig. 6 characterizing the occupation mainly of hexagonal lattice sites.

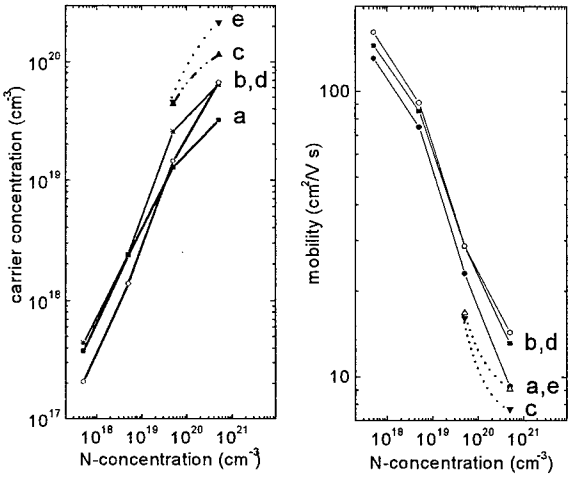


Fig. 5: Carrier concentration and mobility vs. N-conc. (furnace: a-1450°C; b-1550°C, c- 1650°C; d- flash lamp annealing; e-furnace + flash)

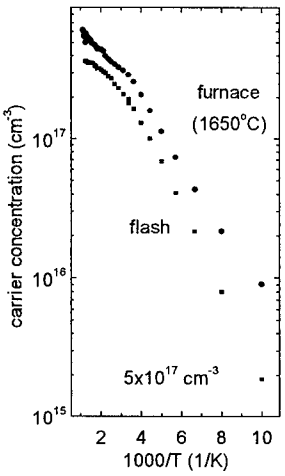


Fig. 6: Carrier concentration vs temperature

4. Discussion and conclusions

Al, B and N implanted 6H-SiC layers show after flash lamp annealing different electrical activation efficiency.

The electrical activation of Al increases with increasing annealing temperature. Flash lamp annealing at the temperature of about 2000°C leads to a higher solubility of dopants on the SiC lattice sites. These substitutional Al atoms are frozen-in during the radiative cooling down, because the diffusion of Al is negligible during the short annealing time of 20 ms.

For B doped layers the diffusion and segregation of B lead to a reduction of the electrically active dopants and therefore an increase of the mobility. Using flash lamp annealing a higher hole concentration is observed for B concentrations up to $3x10^{20}$ cm^{-3} due to the high cooling down rate [7]. The outdiffusion is negligible.

The electrical activation of N in 6H-SiC takes place in two steps. During the first step the low energetic hexagonal lattice sites are occupied realized successfully by flash lamp annealing. The occupation of the cubic lattice sites during the second step requires longer annealing time. Obviously, there is an optimum temperature-time regime for the second annealing step [2, 9].

5. References

[1] G. Pensl, W. Suttrop, H. Zhang, R. Helbig, P. Glasow, P. Lanig, G. Ziegler, Advances in Physics and Material (1989), p. 159
[2] Y. Hirano, T. Inada, J. Appl. Phys. 77 (1995), p. 1020
[3] H. Wirth, D. Panknin, W. Skorupa, E. Niemann; Appl. Phys. Lett. 74 (1999), p. 979
[4] Z. V. Dzhibuti, N. D. Dolidze, G. Sh. Narsiya, G. L. Eristavi, Tech. Phys. Lett. 23 (1997), p. 746
[5] S. Ahmed, C. J. Barbero, T. W. Sigmon, Appl. Phys. Lett. 66 (1995), p. 712
[6] D. Panknin, H. Wirth, A. Mücklich, W. Skorupa, Mat. Sci. Eng. B61-62 (1999), p. 363
[7] D. Panknin, H. Wirth, A. Mücklich, W. Skorupa, submitted at J. Appl. Phys.
[8] G. Pensl, W. J. Choyke, Physica B 185 (1993), p. 264
[9] J. N. Pan, J. A. Cooper, M. R. Melloch, J. Electr. Mat. 26 (1997), p. 208

Materials Science Forum Vols. 353-356 (2001) pp. 591-594
© 2001 Trans Tech Publications, Switzerland

Structural and Electrical Characterization of Ion Beam Synthesized and n-doped SiC Layers

C. Serre[1], D. Panknin[3], A. Pérez-Rodríguez[1], A. Romano-Rodríguez[1], J.R. Morante[1], R. Kögler[3], W. Skorupa[3], J. Esteve[2] and M.C. Acero[2]

[1] Electronic Materials and Engineering (EME), Dept. Electrònica, Universitat de Barcelona, Martí i Franquès 1, ES-08028 Barcelona, Spain

[2] Centre Nacional de Microelectrònica, CNM-CSIC, Campus UAB, ES-08193 Bellaterra, Spain

[3] Forschungszentrum Rossendorf, PO Box 510119, DE-01314 Dresden, Germany

Keywords: Doping, Ion Beam Synthesis, Ion Implantation, SiC on Si

Abstract. This work reports preliminary data on the ion beam synthesis of n-doped SiC layers. For this, two approaches have been studied: i) doping by ion implantation (with N^+) of ion beam synthesized SiC layers and ii) ion beam synthesis of SiC in previously doped (with P) Si wafers. In the first case, the electrical data show a p-type overcompensation of the SiC layer in the range of temperatures between –50° C and 125° C. The structural (XRD) and in-depth (SIMS, Spreading Resistance) analysis of the samples suggest this overcompensation to be induced by p-type active defects related to the N^+ ion implantation damage, and therefore the need for further optimization of their thermal processing. In contrast, the P-doped SiC layers always show n-type doping. This is also accompanied by a higher structural quality, being the spectral features of the layers similar to those from the not doped material. Electrical activation of P in the SiC lattice is about one order of magnitude lower than in Si. These data constitute, to our knowledge, the first results reported on the doping of ion beam synthesized SiC layers.

Introduction. Owing to its high stiffness and mechanical strength, extreme chemical inertness, together with its wide bandgap (allowing stable electronic properties at high temperatures and high radiation resistance), SiC is a very promising material for the development of Micro-Electro-Mechanical-Systems (MEMS) for harsh environment conditions, including chemically or physically aggressive ambient. However, the development of SiC based technologies is compromised by the availability of bulk single crystal wafers: although bulk single crystal wafers are already commercially available, they have a relatively poor structural quality and their price is still too high.

Epitaxial SiC layers can also be grown on Si substrates [1-3], but this requires the use of expensive dedicated Molecular Beam Epitaxy (MBE) or Chemical Vapour Deposition (CVD) Systems, and the quality still requires to be improved (voids, micropipes, density of dislocations...).

High temperature carbon ion implantation into Silicon has been proved as a suitable technique to produce high crystalline quality cubic SiC (β-SiC) layers with extremely low level of residual stress [4]. This has allowed the fabrication of micromechanical test structures such as beams and membranes [5], as well as complex multilayer structures as SiC on Insulator (SiCOI) [6].

On the other hand, local doping of SiC still remains a critical issue. Due to the extremely slow diffusion of the impurities in SiC, doping has to be performed by ion implantation, and very high annealing temperatures are usually required to achieve activation levels suitable for device application [7]. Moreover, annealing of radiation damage is much more difficult in SiC than in Si [8]. Therefore, reducing radiation damage caused by ion implantation is a key problem in SiC processing.

In this framework, this paper presents preliminary structural and electrical characterization results on n-doped Ion Beam Synthesized (IBS) SiC layers. These constitute, to our knowledge, the first data reported on the doping and electrical behavior of IBS SiC. The structures were obtained by high dose multiple carbon ion implantation into Si wafers, using the implantation and annealing conditions already reported for the synthesis of high structural quality layers [9]. Two doping approaches are explored: i) ion implantation doping of IBS SiC layers and ii) IBS of SiC in pre-doped Si wafers, and two different species are investigated: N and P. In a first stage, doping of the layers is studied by N^+ ion implantation, while P has been selected as dopant species for the pre-doped Si wafers.

Experimental. The IBS SiC layers were obtained by a four-step C^+ ion implantation into (100) p-type Si wafers (10-24 Ω.cm), with doses of 10^{18}, $4.7x10^{17}$, $3.3x10^{17}$ and $2.6x10^{17}$ cm^{-2}, and at energies of 195, 150, 120 and 100 keV respectively. These implantation conditions allow the formation of a buried layer with a flat carbon profile with stoichiometric SiC composition within the implanted layer (fig.1). The C implants were performed at 500°C in order to avoid amorphization, so that high crystalline quality cubic SiC (β-SiC) layers with extremely low level of residual stress are obtained after a final annealing at 1150°C during 6 hour in Ar ambient. These layers show n-type conductivity as determined by Hall effects measurements. In the first doping approach, these layers were subsequently N^+ implanted with a four-fold process to form a box-like doped region with plateau concentrations between $1.5x10^{19}cm^{-3}$ and $5x10^{20}cm^{-3}$. This process was performed at 400°C to reduce the implantation-induced damage level. A 10 minutes post implantation annealing was carried out in Ar ambient in the temperature range between 1000°C and 1300°C. In the second doping approach, the initial Si wafers were pre-doped with a single P^+ implantation (10^{14}, $5x10^{14}$ and 10^{15} cm^{-2}, at 120 keV) followed by an activation annealing (2h at 950°C). This leads to a n-doped buried layer that will be included within the subsequent C^+ implanted region. The structural characterization was carried out by in-depth SIMS analysis and X-ray diffraction measurements. The electrical properties were investigated by resistivity and Hall effect measurements as well as by Spreading Resistance measurements. The determination of dopant type by Hall measurements was done taking into account that the substrate is p-type.

Results and Discussion. Figure 1 shows typical results of the N^+ ion implantation into an IBS SiC layer. The in-depth chemical analysis (fig.1a) indicates a doping of the top half of the IBS SiC layer. The Spreading Resistance profile (fig.1b) exhibits a decrease of resistance in this region. The resistivity of this sample is plotted in Figure 2 as a function of temperature. Surprisingly, p-type conduction is observed in the temperature range ≈ -50° C to 125° C, while the expected n-type behavior is found at other temperatures.

These data reveal the existence of an overcompensation of the n-type impurities by unidentified acceptors. This behavior is similar to that previously reported by Reichert [10] on epitaxial β-SiC layers implanted with N^+ ions, and has been attributed to compensation of the electrons introduced by the dopants with holes from

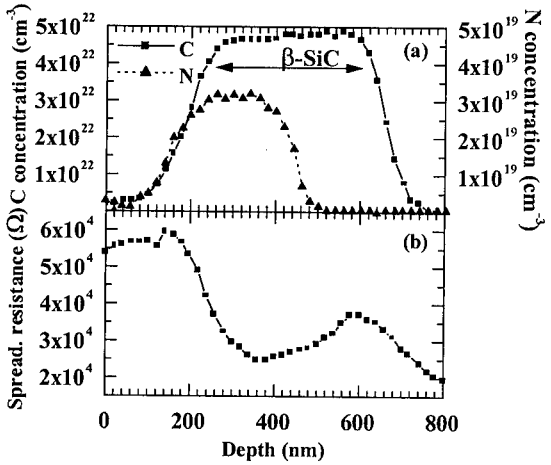


Fig.1. a) Typical in-depth concentration profiles from SIMS analysis of an N^+ implanted IBS SiC, and b) Spreading resistance profile of the same sample.

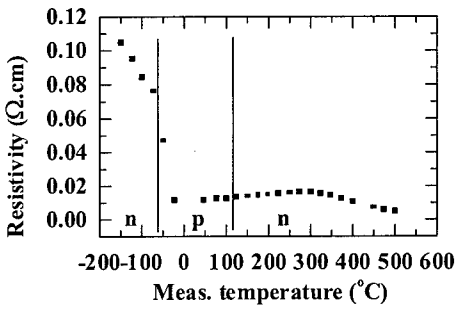


Fig.2. Resistivity vs temperature, measured from the same sample as in figure 1.

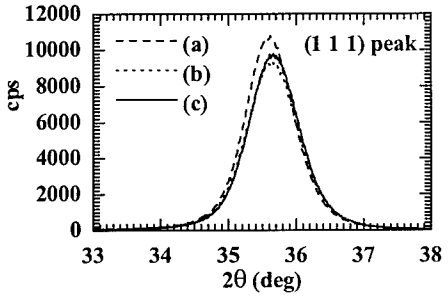


Fig.3. a) X-ray diffraction measurements of the sample shown in figure 1 and b) same sample without intermediate annealing. c) Undoped IBS reference SiC sample.

the initial p-type doping of the SiC layer. In our case, this could be due to unintentional p-doping of the IBS SiC layer, related to structural defects produced during the C^+ implantation, or to the presence of electrically active defects induced by the N^+ implantation. The SIMS and Spreading Resistance profiles suggests that the latter might be the source of this unexpected p-type doping.

The hypothesis of structural defects in the layers is corroborated by X-ray diffraction measurements, which show the presence of a significant residual strain in the N^+ implanted and annealed samples (fig.3a). This can be compared to samples implanted with N^+ ions without intermediate annealing and with a longer final annealing (1150° C, 6 h, fig.3b). In this case, the XRD spectra are similar to those from not doped reference IBS SiC samples, (fig.3c), and show a full lattice recovery. The lack of a fully strain recovery by the final anneal step supports the previous hypothesis of p-overcompensation related to implantation induced damage, and suggests the need to optimize the final anneal step. A further electrical analysis of these samples is under progress to clarify the correlation between residual strain and p-overcompensation.

On the other hand, IBS of SiC in P^+ pre-doped Si wafers has been studied. In this case, only n-type conduction is found in the whole range of measuring temperatures. At T> 400 K, leakage from Si substrate takes place. It has been found that the carrier content increases with the P content in the initial Si wafer (Table 1). According to these data, pre-doping of target Si wafers allows successful n-doping of IBS SiC layer, with medium mobility values. As shown in Table 1, electrical activation of the P atoms in the SiC lattice is about one order of magnitude lower than in the starting Si matrix. From the structural point of view, it is worth noticing that all X-ray diffraction spectra (not shown) are identical to those from undoped IBS SiC reference samples, which points out the absence of additional stress related to P-doping. SIMS measurements are under progress to assess the P distribution in the final structure, and check if the dopant remains confined to the SiC layer.

Implanted doses (cm^{-2})	10^{14}	$5x10^{14}$	10^{15}
Carrier concentration in Si (cm^{-3})	$1.2x10^{18}$	$6x10^{18}$	$1.5x10^{19}$
Carrier concentration in SiC (cm^{-3})	$1.3x10^{17}$	$2x10^{17}$	$6x10^{17}$
Mobility in SiC ($cm^2/V.s$)	150	800	600

Table 1: Electrical characterization of P^+ predoped samples

Conclusions. In summary, the first data on n-type doping and electrical behavior of ion beam synthesized SiC layers are reported. N^+ ion implantation into IBS SiC should allow n-doping. However, special care has to be taken to avoid p-type defects that cause p-overcompensation at room temperature. XRD and in-depth SIMS and Spreading Resistance measurements suggest these

defects to be related to N^+ ion implantation induced damage. Further optimization of the final thermal annealing step is proposed to solve this problem.

On the other hand, n-type doping of the IBS SiC layers has been successfully achieved by pre-doping of the Si wafer (before C^+ ion implantation) with P. This allows to avoid effects related to ion implantation damage in the SiC lattice. Preliminary data on the electrical analysis of these samples suggest an electrical activation of the P dopants about one order of magnitude lower than in the intitial Si matrix. In-depth (SIMS, spreading) analysis is in progress, to asses P redistribution during IBS process.

Acknowledgements The multiple C implantations were performed at the AIM-Center for Application of Ion Beams in Materials Research, in the Forschungzentrum Rossendorf, under the "Access to Large-Scale Facilities" program of the European Union. This work has been partially funded by the "Direcció General de Recerca" from "Generalitat de Catalunya" through the project ITT-CTP98-4 ("Programa de Projectes de Cooperació en Matèria d'Innovació i de Transferència Tecnològica- Comunitat de Treball dels Pirineus).

References:

[1] S. Nishino, J.A. Powell and H.A. Will, Appl. Phys. Lett., **42** (1983), p. 460.
[2] J.A. Powell, L.G. Matus and M.A. Kuczmarski, J. Electrochem. Soc., **134** (1987), p. 1558.
[3] I. Golecki, F. Reidinger and J. Marti, Proc. Mat. Res. Soc. Symp., **242**, (1992), p. 519.
[4] C. Serre, A. Pérez Rodríguez, A. Romano Rodríguez, J.R. Morante, R. Kögler and W. Skorupa, J. Appl. Phys. **77** (1995), p. 2978.
[5] C. Serre, A. Pérez-Rodríguez, A. Romano-Rodríguez, L. Calvo-Barrio, J.R. Morante, J. Esteve, M.C. Acero, W. Skorupa, R. Kögler, J. Electrochem. Soc. **144** (1997), p. 2211.
[6] C. Serre, A. Pérez-Rodríguez, A. Romano-Rodríguez, J.R. Morante, L. Fonseca, M.C. Acero, R. Kögler and W. Skorupa, Sensors & Actuators **A74** (1999), p. 169.
[7] K. Wongchotigul, in Properties of Silicon Carbide, G.L. Harris ed. (1995), p. 157.
[8] V. Heera and W. Skorupa, Mat. Res. Soc. Symp. Proc., **438** (1997), p. 241.
[9] C. Serre, A. Pérez-Rodríguez, A. Romano-Rodríguez, J.R. Morante, J. Esteve and M.C. Acero, J. Micromech. Microeng. **9** (1999) p.190.
[10] W. Reichert, Dissertation, Technical University Berlin (1998), p. 50.

Materials Science Forum Vols. 353-356 (2001) pp. 595-598
© 2001 Trans Tech Publications, Switzerland

Channeling Measurements of Ion Implantation Damage in 4H-SiC

A.Yu. Kuznetsov[1], M.S. Janson[1], A. Hallén[1], B.G. Svensson[1,2], C. Jagadish[3], H. Grünleitner[4] and G. Pensl[4]

[1] Department of Electronics, Royal Institute of Technology, Electrum 229, SE-16440 Kista-Stockholm, Sweden

[2] Oslo University, Physical Electronics, Department of Physics, P.B. 1048 Blindern, NO-0316 Oslo, Norway

[3] Department of Electronic Materials Engineering, Australian National University, Research School of Physics Sciences and Engineering, Canberra, ACT 0200, Australia

[4] Institute of Applied Physics, University of Erlangen-Nürnberg, Staudtstr. 7/A3, DE-91058 Erlangen, Germany

Keywords: Aluminium, Annealing, Displaced Silicon Atoms, Implantation Induced Defects, Interstitial, Vacancies

Abstract Rutherford backscattering spectrometry in the channelling mode using MeV He^+ ion beam is employed to measure 100 keV Al^+ and 450 keV Xe^+ ion implantation damage profiles in 4H-SiC as a function of implantation temperature and dose. The dechanneled fraction in the silicon sublattice has been evaluated and profiles of disordered silicon atoms are extracted from the measurements. Strong surface accumulation of disordered silicon atoms is observed. In addition it is found that the number of displaced silicon atoms normalized by the dose for $5x10^{14}$ and $1x10^{15}$ Al^+/cm^2 implants follows an Arrhenius dependence in the temperature range of 25-400 ^0C and a preliminary value for the activation energy is in the range of 0.1 eV.

Introduction

Acceptor dopant ion implantation into a n-type 4H-SiC epilayer is a key technology to fabricate p^+-doped emitter regions for power diode applications [1]. However, the implantation process produces radiation defects, which have to be removed during activation anneals. The understanding of radiation defect annealing mechanisms in SiC is not mature [2], in part due to the complexity of initial radiation damage that is a strong function of implantation parameters. For example, there is still no agreement on such basic parameters as recombination and migration properties of primarily point defects in SiC. In this work we (i) have measured profiles of disordered Si atoms after Xe^+ and Al^+ ion implants performed at different substrate temperatures and using different doses and (ii) discussed defect recombination phenomena that occur during these implants.

Experimental

The samples used are epitaxial layers, with a thickness of more than 10 μm, doped with nitrogen in the low 10^{15} cm^{-3} range grown on 4H n-type SiC wafers by chemical vapour deposition. One set of samples was implanted with 100 keV Al^+ ions at 25, 200, 400, 600, and 800 ^0C using two doses, $5x10^{14}$ and $1x10^{15}$ cm^{-2}. The other set of samples was implanted with 450 keV Xe^+ ions at 25 ^0C using two doses, $2x10^{13}$ and $2x10^{14}$ cm^{-2}. The ion flux was kept in the order of 10^{11}-10^{12} cm^{-2} s^{-1} during all implants. Rutherford backscattering spectrometry in the channelling mode along the <0001> direction (RBS/C) using 2.0 and 2.4 MeV He^+ ions with a scattering angle of 168° was employed to measure implantation damage profiles. In order to extract profiles of the displaced silicon atoms, the dechannelled fraction ($\chi_R(x)$) has been evaluated in all samples in accordance with the formalism suggested by Eisen *et al.* [3] which is discussed in further details elsewhere [4].

In short, $\chi_R(x)$, the fraction of dechanneled He^+ ions at a depth x that interacts with crystal atoms in both substitutional and interstitial positions, was calculated and the RBS/C data have been converted to defect concentration (N) versus depth profiles in accordance with $N=N_0[(\chi(x) - \chi_V(x))/(1 - \chi_V(x))]$ where N_0 and $\chi(x)$ are the silicon atomic density in 4H-SiC (4.82×10^{22} cm^{-3}) and normalized backscattering yield in the channeling direction [3,5].

Results and conclusions

Figure 1 shows the silicon portion of normalised RBS/C spectra of samples after 5×10^{14} Al/cm^2 implants. These signals are readily comparable with $\chi(x)$ after a channel-to-depth conversion using surface or mean energy approximation [5].

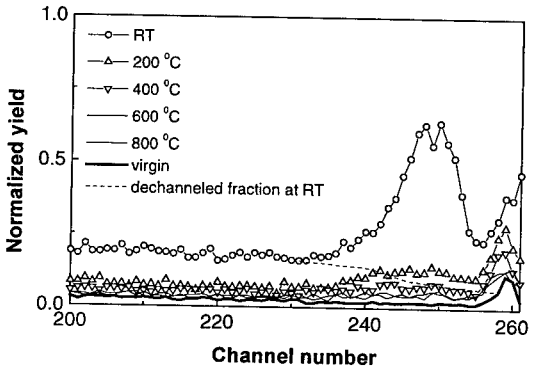


Figure 2. Disordered silicon atoms vs depth profiles in 4H-SiC after 5×10^{14} Al^+ ion at RT, 200, and 400 ^0C.

The thick line in Fig.1 represents the normalised RBS/C yield from unimplanted, virgin, sample. The accuracy of our measurement allows us to distinguish between the normalised yields from the samples implanted at room temperature (RT), 200 and 400 ^0C while after 600 and 800 ^0C implants the signal are almost indistinguishable, Fig. 1.

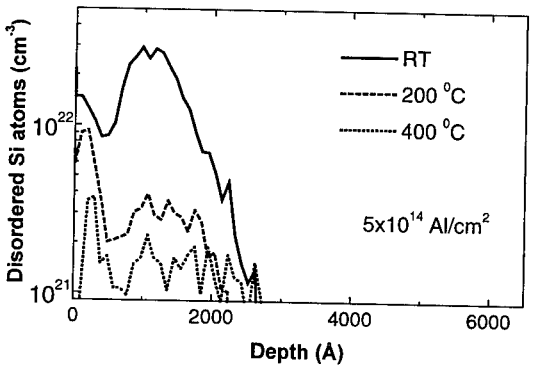


Figure 2. Disordered silicon atoms vs depth profiles in 4H-SiC after 5×10^{14} Al^+ ion at RT, 200, and 400 ^0C.

The same holds for samples implanted up to 1×10^{15} Al/cm^2 (not shown). The damage profiles after RT, 200, and 400 ^0C Al^+ implants have been chosen for the further analysis. Radiation damage after Xe^+ ion implants was also measured and the data are used in the discussion below. Figures 2 and 3 show the concentration versus depth profiles of disordered silicon atoms, N, calculated using the experimental data taken from the RBS/C measurements for Al^+ and Xe^+ implants, respectively.

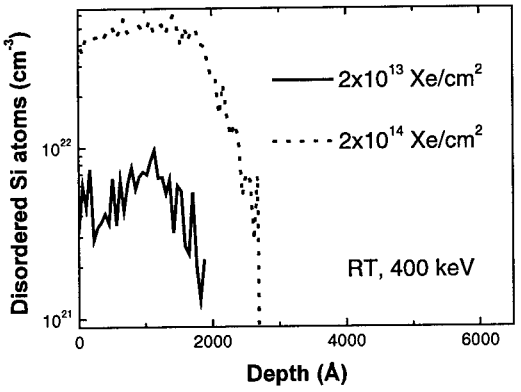


Figure 3. Silicon displaced atoms vs depth profiles in 4H-SiC after $2x10^{13}$ and $2x10^{14}$ Xe^+ ion implants at 25 ^{0}C.

Profiles of the disordered silicon atoms follow ion ranges but are found to be somewhat deeper comparing with the simulation of the vacancy profiles made using TRIM, Figure 4. The measurement of implanted impurity chemical profiles (not shown) indicates, however, that the channelling effect was negligible during at least Al^+ ion implants. Thus, a separation between experimentally measured Si self-interstitial and simulated Si vacancy profiles could be a manifestation of the momentum transfer to the displaced atoms during the development of a

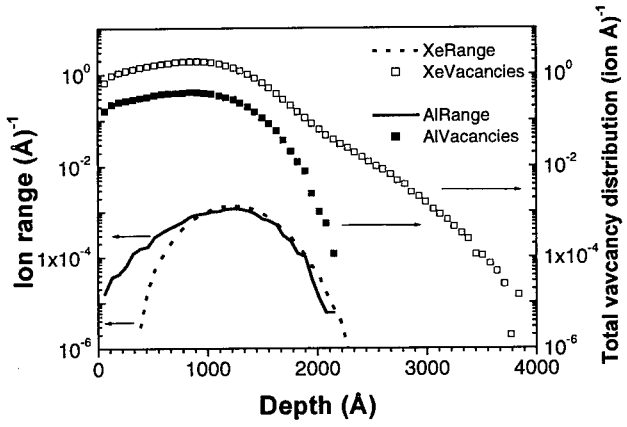


Figure 4. Range and vacancy versus depth distribution calculated using conventional TRIM software for Xe^+ and Al^+ ions using 3.21 g/cm^3, 20 eV, and 2eV for the density, displacement and binding energy in 4H-SiC, respectively.

collision cascade [6]. However, it must be pointed out that the depth conversion in Figs.2 and 3 did not account for a possible change of the material density after implants, which may result in an extra uncertainty for the comparison of the simulated and experimental profiles.

Another interesting result is a significant accumulation of the displaced defects in the near-surface regions in Fig.2 and 3 (in the late case in particular for the $2x10^{13}$ Xe/cm^2 implant). A similar surface peak has been reported in previous studies on Si, Ge, GaAs, and GaN and attributed to an amorphous layer at the semiconductor surface [7]. For the implants at elevated temperatures a substantial reduction in the concentration of disordered silicon atoms occurs, specifically for the "main peak" situated at the depth of the ion range. The fact that the relative importance of the near-surface peak become more pronounced after implantation at elevated temperatures may indicate substantial diffusion of radiation defects during and after the development of the cascade.

A tempting application of the profiles in Figs.2 and 3 may be to fit them to solutions of a diffusion equation, which includes generation, recombination and Fickian diffusion terms for silicon self-interstitials and vacancies in 4H-SiC. This is, however, a difficult exercise since diffusion, recombination, and even some defect generation parameters, e.g., displacement energy threshold, are not established and must be convoluted simultaneously. Instead of doing this analysis, a qualitative measure of the activation energy for the recombination process of silicon self-interstitials may be extracted from our data.

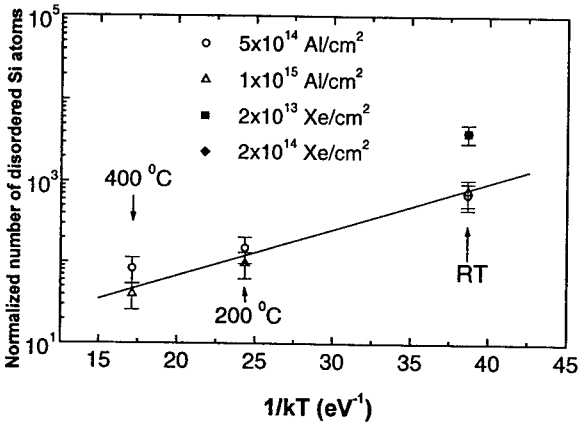


Figure 5. Number of displaced silicon atoms (interstitials) in 4H-SiC after implantations at different temperatures and normalised with the implantation dose.

Figure 5 is an Arrhenius plot for normalised numbers of disordered silicon atoms produced in 4H-SiC after Al^+ ion implantations at RT, 200, and 400 ^{0}C. In other words, the vertical axis represents the number of disordered silicon atoms (in the first approximation self-interstitials) per one incident Al^+ ion that survived recombination. Results of Xe^+ ion implants at RT are also included in Fig.5. At this stage the limited amount of data allows only to make a preliminary estimate of the activation energy for this recombination process that is found to be in the range of 0.1 eV.

Acknowledgements

Partial financial support for this work was received from the Swedish Foundation for Strategic Research (SSF), the Swedish Foundation for International Cooperation in Research and Higher Education (STINT).

References

1. T. Troffer, M. Schadt, T.Frank, H.Itoh, G. Pensl, J. Heindl, H.P. Strunk, and M. Maier, phys.stat.sol. A, **162** (1997) p. 277.
2. E.Wendler, A. Heft, W.Wesch, Nucl.Instrum.Method B, **141** (1998) p. 105.
3. F.H. Eisen, In *Channeling*. Eds. D.V. Morvan, (Wiley: New York, 1973.) p.326.
4. A.Yu. Kuznetsov, M.Janson, A. Hallén, B.G. Svensson, C. Jagadish, Proc. Of 2nd II International Workshop on Advanced Defect Engineering in Semiconductors, Kista, Sweden, 2000, p.218.
5. W.-K. Chu, J.W.Mayer, M.-A. Nicolet, *Backscattering Spectrometry* (Academic Press., 1978) p.384.
6. J.W. Mayer, L. Eriksson, and J.A. Davies, *Ion Implantation in Semiconductors*, (Academic Press., 1970) p.280
7. See, for example, S.O. Kucheyev, J.S. Williams, C. Jagadish, J. Zou, and G. Li, Phys. Rev. B, 62 (2000) in press.

Materials Science Forum Vols. 353-356 (2001) pp. 599-602
© 2001 Trans Tech Publications, Switzerland

The Monte Carlo Binary Collision Approximation Applied to the Simulation of the Ion Implantation Process in Single Crystal SiC: High Dose Effects

G. Lulli[1], E. Albertazzi[1], R. Nipoti[1], M. Bianconi[1] and A. Carnera[2]

[1] CNR-Istituto LAMEL, via Gobetti 101, IT-40129 Bologna, Italy

[2] Dipartimento di Fisica and INFM, Università degli Studi di Padova, via Marzolo 8, IT-35131 Padova, Italy

Keywords: Ion Implantation, Process Simulation, Swelling

Abstract In this work the Monte Carlo - Binary Collision Approximation is applied to the profile simulation of 500 keV Al^+ ions implanted at room temperature in 6H-SiC. A very large fluence range that goes from almost perfect to amorphous as-implanted crystals was simulated. For increasing ion fluence the code takes dynamically into account the reduction of channeling tails and the variation of SiC density, both due to the accumulation of crystal damage. The predicted shift of the projected range towards deeper depths and the saturation of channeling tails for increasing ion fluence are confirmed by the Secondary Ion Mass Spectrometry characterisation.

Introduction

In the framework of process simulation for electronic materials, the simulation of the ion implantation process in crystalline semiconductors is used for accurate prediction of the as-implanted doping distribution. In the case of SiC the modelling of the implantation process in crystalline substrates is quite recent and the number of published papers is increasing [1-5]. These works mainly differ for the physical approximation used for describing the atomic collision phenomena, the ion energy loss models and the crystal modification due to the ion damage build up. This paper presents the simulation and the experimental characterisation of the dynamic effects due to damage accumulation on as-implanted Al profiles, which lead to the reduction of the channeling tails and the shift of the as-implanted doping profile.

Experiment

Both on axis and off-axis <0001> 6H-SiC wafers were used for this work. 0.5 MeV Al^+ was implanted at RT and different fluence values in the range 1×10^{13} cm^{-2} ÷ 3×10^{15} cm^{-2}. The wafers were misaligned with respect to the beam direction in order to produce a random implant geometry [1]: the <0001> axis was tilted 8° while keeping the beam direction within the (10-10) plane and then the plane (0001) was twisted 22° around the <0001> axis.

The as-implanted samples were characterised by Secondary Ion Mass Spectrometry (SIMS). A Cameca IMS-4f spectrometer was used with 8 keV O_2^+ primary beam having 120 nA total current and swept over 125×125 μm^2 sputtering area. The secondary ion signal was collected from a central circular spot having a 60 μm diameter. In order to avoid changes in the spectrometer collection efficiency due to sample charging effects, which were detected in high-dose implanted SiC samples, a ±125 eV energy window was used. Such an energy window was more than enough to keep constant collection efficiency in all the experimental conditions, since the secondary beam energy shifts do not exceed 30 eV even in fully amorphised SiC layers.

These SIMS analyses require the solution of one of the main problems of the SIMS spectrometry, i.e. the precise calibration of the depth scale for samples having density and/or sputtering yield varying with depth. In fact, the linear relation between swelling and integral of disorder in as

implanted crystalline SiC [6] allows us to hypothesise the presence of a density variation versus depth proportional to the disorder profile. First of all the erosion speed of crystalline and ion amorphised SiC was determined by performing several sputtering experiments for different sputtering times on unimplanted and heavy damaged samples. The erosion speed, defined as the crater depth divided by the sputtering time, of the amorphous material was (12±1) % faster than the crystalline one. Taking into account that the estimated density difference between ion amorphised and crystalline SiC was 13.5 % [6] it turns out that the erosion speed is inversely proportional to the density of the eroded layer. Thus the depth scale seems determined only by the area density of atoms encountered by the eroding ion beam and not by their volume density. Neither a difference in the surface binding energy of the crystalline with respect to the ion amorphised SiC seems to be important. In fact, the total sputtering yield, that is defined as the total number of sputtered atoms per incident ion [7], remains constant and this is true as long as the surface binding energy, which determines the probability for an atom to escape from a solid, does not change.

The following procedure was established for computing the species profile for those samples with a buried heavily damaged layer. Several SIMS spectra were measured for each sample: one including the total profile, the others including only a part of it. Taking into account the damage profiles measured by Rutherford Back Scattering channeling (RBS-C) the sample depth was divided in sub layers for which, depending on the damage level, an erosion speed equal to the ion amorphised or the crystalline SiC was assumed. The depths of the crystalline to amorphous interfaces were chosen at about 90% of displaced atoms. The position of the crystalline to amorphous interfaces was fixed for the computation of every ensemble of profiles. The agreement between the total crater depth estimated by means of this procedure and the experimental values directly measured at the end of the sputtering time was always better than 1%. Moreover, if evaluated by such a procedure, the profiles of each ensemble fit one another, that it is not the case when the usual "average" constant erosion speed is assumed. We take this as a proof of the reliability of the calibration method proposed for the SIMS depth scale. Fig. 1 shows the result of such a procedure applied to the sample implanted with 3×10^{15} Al^+/cm^2. As the RBS-C profile of this sample showed an amorphous layer at the sample surface [6], the sample depth was divided in two layers: one amorphous and one crystalline. The amorphous/crystal interface depth corresponds to that measured by RBS-C. The influence of the swelling phenomenon on the RBS-C depth scale was taken into account as discussed in refs. [4,6].

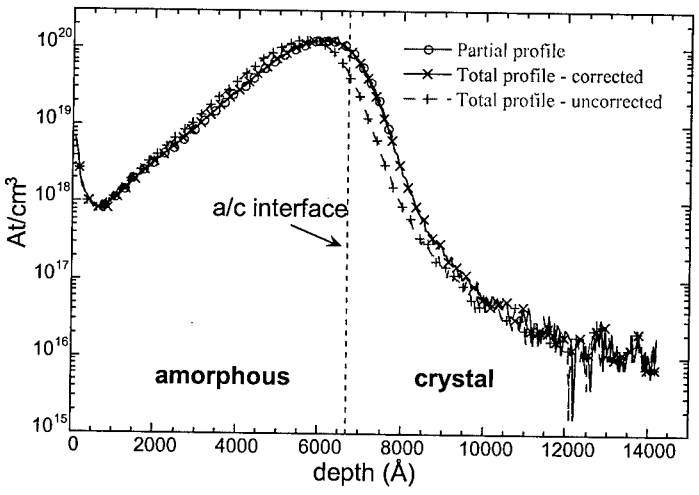


Fig. 1 SIMS profile of the sample 3×10^{15} Al/cm^2. The dashed line is the profile computed by using an "average" erosion speed constant for the whole profile. The continuous lines profiles were computed by the procedure described in the Experimental section.

Simulation

The ion-implantation process simulation was performed by the KING-IV program, which is based on a binary collision approximation (BCA) model. The most important features of the computer

code, already described in previous papers [1,4], are reviewed in the following. The parameters of the semi-empirical model of electronic stopping, which account for the dependence of energy loss on the path of Al ions through the lattice are empirically scaled in order to reproduce low-dose profiles implanted in the energy range 0.5-2 MeV [8]. For low fluence the effects of damage accumulation are negligible; long penetration tails are observed in the as-implanted profiles, even if the substrate is tilted in order to minimise channeling. This effect is due to ions which, as a consequence of elastic scattering with lattice atoms, are deflected towards axial and planar directions, and become channelled. Disorder accumulation at higher doses reduces such tails, since defects progressively obstruct open channels in the crystal. A further effect of damage accumulation in SiC is the large induced volume expansion (swelling) [6]. This will cause a density variation of the implanted region that reaches a maximum of about 13 % when the target is amorphised. Swelling will induce a dynamic change of the depth scale as measured from the surface of the target. In order to reproduce these features a correct evaluation of damage accumulation and associated swelling is required. The KING-IV program simulated the ion-induced damage by full recoil calculation, where effective threshold energies for atomic displacement in Si and C sub-lattices equal to 8 eV and 4 eV, respectively, were used. As shown previously [4] these values are those that better fit the damage growth versus dose measured by the RBS-C technique [6]. As concerns the model of swelling, the lattice deformation is assumed to occur only in the direction normal to the surface, since the constraint of the bulk material prevents any lateral expansion of the implanted region. The target thickness is divided into several layers, each one containing the same integer number of unit cells, up to a depth unreached by primary ions. According to the damage accumulated and the swelling model, the new density, cell parameter along the <0001> axis, and thickness of each layer are calculated. Being the deepest (unperturbed) layer fixed in the bulk, such a procedure causes a shift of the surface. The empirical swelling model included in the simulation comes from the observation of experimental data [4] and includes two contributions, one linearly correlated with the integral of damage accumulated prior to amorphisation, and the other accounting for the additional relaxation observed at the onset of the crystalline to amorphous transition [4,6]. As previously reported [4], the empirical parameters appearing in the model are adjusted to fit the experimental measurement of surface expansion versus dose [6]. It is worth mentioning that point defects in the SiC lattice are treated as atoms randomly displaced from a crystalline site and surrounded by undistorted lattice. This is the same approximation used when extracting experimental damage profiles from RBS-C spectra. This procedure ensures that the BCA damage parameters adjusted through the comparison with RBS-C

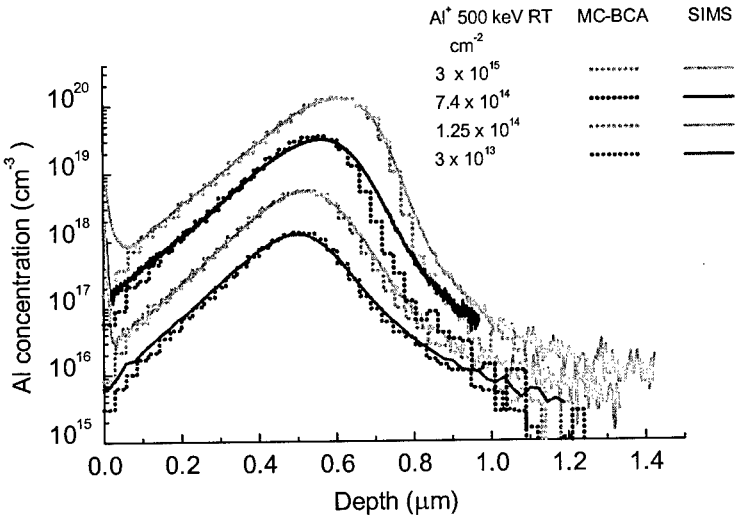


Fig. 2 Al profile versus ion fluence in as-implanted 6H-SiC: comparison between MC-BCA simulated and SIMS

results will give 'effective' defect profiles that account for the correct dechanneling effect of disorder.

Results and discussion

Fig. 2 shows the comparison between simulated and measured as-implanted Al profiles at different fluence. The agreement is very good at any fluence value for the profile shape at the front tail and around the peak of the distribution. While at larger depths the agreement is good for fluence up to 1.25×10^{14} cm^{-2} and becomes poor at the fluence of 7.5×10^{14} cm^{-2}, which corresponds to the onset of target amorphisation, as seen by RBS-C [6], and improves a little for the maximum fluence of 3×10^{15} cm^{-2}. The agreement at the front tail and around the projected range indicates that the swelling phenomenon and its effect on the profile shape are well described by the simulation. The reason of the discrepancy, which reaches the maximum at the threshold of target amorphisation, is not clear at the moment. The parameters of damage accumulation and swelling models used in the simulation give defect profiles and surface expansion that closely match experimental finding [4], so it seems unlikely that they are responsible of the problem. Possible explanations may be an unrealistic description of the heavily damaged crystal, or inaccuracies in the procedure of RBS-C calibration of damage model in the critical region before and above the onset of amorphisation.

Conclusion

Although the procedure proposed for an accurate calibration of the SIMS depth scale is complicated and always requires the knowledge of the damage profile, it can be considered highly reliable because it has no adjustable parameters and it is based on fundamental arguments regarding the sputtering process. The only possible weak point of the procedure is the assumption that the surface binding energy in an amorphous or in a crystalline material is the same. At the moment the perfect correspondence between the material density change and the change in the erosion speed seems to indicate that assumption is reasonable. As it concerns MC-BCA simulation, the profile shift and the reduction of channeling due to damage accumulation have been found in good agreement with SIMS results except for the description of the profile end tails at fluence equal and above the onset of crystalline-to-amorphous transition. The reason of that is still unclear.

Acknowlegment

The Italian Progetto Finalizzato MADESS-II funded this work.

References

[1] E. Albertazzi and G. Lulli, Nucl. Instr. and Meth. B 120 (1996) 147.
[2] M.V. Rao, J.A. Gardner, P.H. Chi, O.W. Holland, G. Kelner, J. Kretchmer, M. Ghezzo, J. Appl. Phys. 81 (1997) 6635.
[3] E. Morvan, P. Codignon, J. Montserrat, J.F. Fèrnandez, D. Flores, J. Millàn and J.P. Chante, Mat. Sci. Eng. B 46 (1997) 218.
[4] G. Lulli, E. Albertazzi, M. Bianconi, and R. Nipoti, Nucl. Instrum. and Meth. in Phys. Res. B 148 (1999) 573.
[5] E. Morvan, N. Mestres, F.J. Campos, J. Pascual, A. Hallén, M. Linnarson and A. Yu. Kuznetsov, Material Science Forum 338-342 (2000) 893.
[6] R. Nipoti, E. Albertazzi, M. Bianconi, R. Lotti, G. Lulli, Cervera, and A. Carnera, Appl. Phys. Lett. 70 (1997) 3425.
[7] A. Benninghoven, F.G. Rüdenauer and W. Werner "Secondary Ion Mass Spectrometry " Wiley Intersience 1987
[8] N. Mestres, M. Ben El Mekki, F. J. Campos, J. Pascual, E. Morvan, P. Godignon, J. Millan and G. Lulli, Mat. Sci. Forum 264/268 (1998) 733.

Materials Science Forum Vols. 353-356 (2001) pp. 603-606
© 2001 Trans Tech Publications, Switzerland

Formation of Large Area Al Contacts on 6H- and 4H-SiC Substrates

O. Korolkov and T. Rang

Department of Electronics, Tallinn Technical University,
Ehitajate tee 5, EE-19086 Tallinn, Estonia

Keywords: Bond Strength, Diffusion Welding (Bonding), Schottky Contacts, SiC Substrates, Specific Contact Resistance

Abstract The results of experimental investigations of diffusion welded (bonded) large area Al/SiC contacts are presented. The novel data on adhesion of Al to 4H- and 6H-SiC are proposed. The specific contact resistance is determined for Al-6H-SiC contacts. The V-I characteristics for Al-4H-SiC Schottky contacts are measured.

Introduction

To utilize all the wonderful properties of SiC semiconductors, formation of reliable, homogeneous, ohmic and/or rectifying contacts can be a critical issue, especially for such type of devices as Schottky diode. There are a lot of papers reporting very good results of metallization for different polytypes of SiC. But the dimensions of Me contacts are usually restricted by hundreds of microns diameter and some few microns thick. As far as we known no results have been reported on large area and acceptable for power devices thickness of Me contacts to the SiC structures. In this paper we report the combined results of our initial attempts [1, 2] and the later research in forming thick (50 ÷ 200 μm) and large area (tens of millimeters diameter) Al contact to 6H- and 4H-SiC using diffusion welding (**DW**) techniques.

Materials and Method

Diffusion welding is a solid state joining process, which can be utilized to bond "difficult to join" materials. In our experiments aluminum has been chosen for a contact material because of its low melting point (later in high power applications, other metals should be used due to the same reason), relative inertness to SiC in the solid state, and its importance as a matrix material in metal semiconductor composites. For the process the 0.05 and 0.2 mm thick 99.99% Al foil has been used.

The SiC, used in our experiment was 6H- and 4H-SiC substrates of USA CREE Research Inc. Company with the specification:

6H-SiC – wafers diameter 35.0 mm, thickness 0.33 mm, n-type conductivity, dopant nitrogen, net doping density (N_D-N_A), $3.6\cdot10^{18}$ cm^{-3} and $1.3\cdot10^{18}$ cm^{-3} surface treatment: C – face polished, Si – face ground.

4H-SiC – wafer diameter 35.0 mm., thickness 0.35 mm., n-type conductivity, dopant nitrogen, net doping density of substrate $8.5\cdot10^{18}$ cm^{-3}, with 5 μm thick epilayer concentration $2\cdot10^{17}$ cm^{-3}, surface treatment: Si- and C- faces polished as specified.

Prior the metallization the 4H- and 6H-SiC substrates and Al foil were given to chemical clean in special *solutions*.

The vacuum **DW** process was performed in specially designed, continuous-action, commercial type equipment UDS-6 with various combinations of temperature and pressure. Such scheme enables to form all the contacts to the C- and Si faces of the SiC substrates simultaneously.

Results

The Al/SiC contacts, under variety of **DW** conditions were first characterised by mechanical adhesion measurements

The adhesion of Al to 4H-SiC surface was examined by means of conventional techniques normally used for estimation of bond strength of copper to woven glass or other ceramic substrates in radio-electronics. The strips of Al foil in 0.2 mm thick and in 1÷2-mm width, under variety of pressure and temperature combinations were welded on the SiC surface. After welding the strips were pulled off from the surface by means of special device shown in Fig.1.

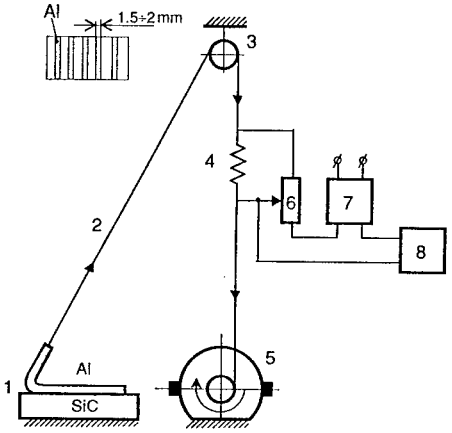


Fig. 1. Description of the adhesion proof experiment. 1-wafer with Al strips, 2-string, 3-pulley, 4-spring, 5-acting motor drive gear (2r.p.m.), 6-linear slide potentiometer, 7-power supply, 8-plotter.

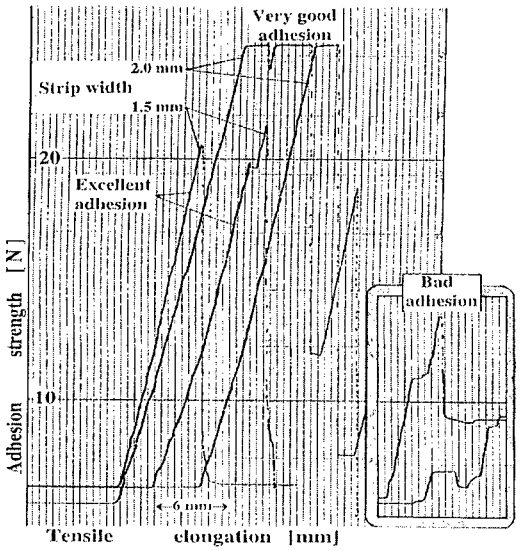


Fig. 2. Tension curves for the adhesion test.

The maximum tensile strength in N-s (Newton) divided by the width of the strip is defined as a bond strength. The way of detachment and the condition of the destruction regions determine the quality of the joint. The results of Al adhesion quality for Al-4H- and 6H-SiC contacts are shown in Table 1.

Fig. 2 shows the typical form of the tension curves obtained in the process of detach test and corresponding to the excellent", "very good", and "bad quality" of bonding.

Table 1

Temperature [°C]	Pressure [MPa]	Bond quality
500	20 - 50	None
550	20 - 50	Bad
600	20	Bad
600	30	Very good
600	50	Excellent

The lack of bond is qualified as "very weak joint" with no evidence of Al on the separated surface of SiC. In the case of "bad bond" after the strip detaching Al retains poor interrupted tracks on the

separated carbide surface. "Good bond" corresponds to the tensile strength close to the breaking strength of the annealed aluminium. On the separated surface of the SiC the dense thick track of aluminium is retained. In the case of "excellent bond" the tensile strength exceed the breaking strength of the annealed aluminium, and it's impossible to separate the aluminium strip from silicon carbide surface.

The specific contact resistance (ρ_c) measurement was carried out for 6H-SiC wafer with n-type conductivity and net concentration (N_D–N_A) equal to $3.6 \cdot 10^{18}$ cm^{-3}. Specific resistance ρ_c was determined by means of surface potential distribution measurement near the spot of metal contact (S.C. extrapolation method [3]). The block scheme of the equipment for measurement procedure is shown in Fig. 3.

Fig. 4. shows the measured specific contact resistance versus current for SiC wafers (*C-face* under different applied voltage polarities).

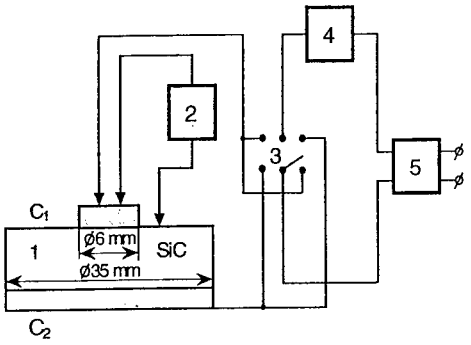


Fig. 3. Block scheme of contact resistance 1-SiC wafer with Al contacts measurement current (C_1 contact to be measured; C_2 back side contact), 2-voltmeter, 3-switch, 4-ampermeter, 5-power supply.

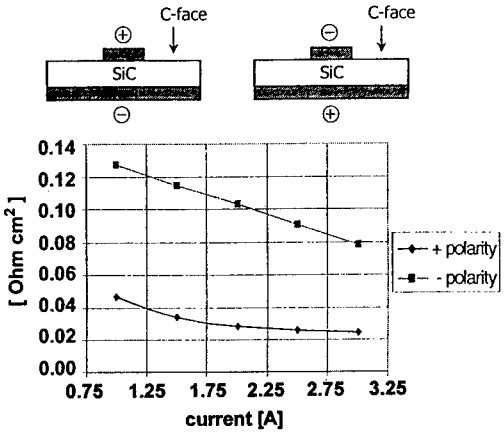


Fig. 4. Specific contact resistance versus measurement current.

For the *U-I* characteristics measurements the special structures were manufactured. The SiC wafers were cut into squire pieces with the 10×10-mm dimensions. Then, the *Si-face* was welded via aluminium foil to the tungsten electrode with 18-mm diameter and 1.2 mm thick. Simultaneously, aluminium contact in 8-mm diameter was formed to *C-face* of SiC.

The *U-I* characteristics for Al/SiC Schottky type structures were measured by specially designed tester with measurement range up to 3A and 30V at temperature interval between 20° and 600°C. Fig. 5 and Fig. 6 show the temperature influence on measured reverse and forward *U-I* characteristics for 4H-SiC Schottky structures.

Discussion and Conclusions

1. The diffusion welding techniques gives the possibility to perform reliable, homogeneous large area of Al/SiC contacts. Today, only the dimensions limit the area of metal contacts of provided SiC wafers. The bond strength of Al/SiC contact exceeds the breaking strength of annealed aluminium, irrespectively of SiC polytype. At the same time, from the point of view of mechanical strength the optimum welding interval is being large enough to control the electrical properties of Schottky contact.

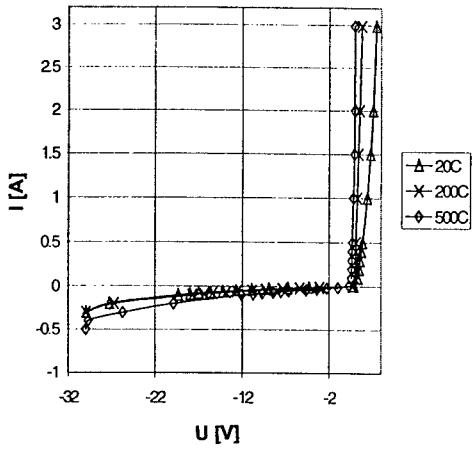


Fig. 5. Temperature dependence of *U-I* characteristic for Al/4H-SiC structure.

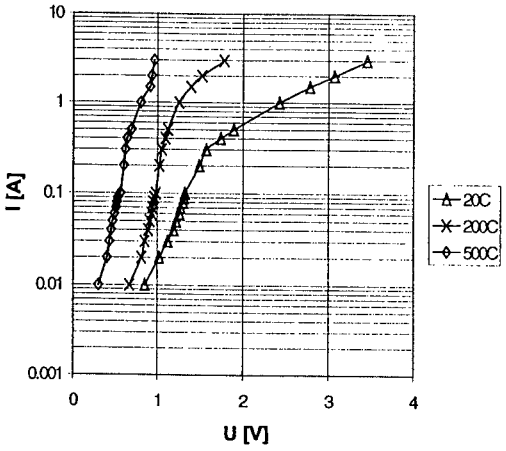


Fig. 6. Forward branch of the *U-I* characteristic

2. Unfortunately, the results carried out by ρ_c measurement are not the subject of direct comparison with the results offered in other papers because of the essential difference in conditions, techniques and materials. Nevertheless, when the conditions are close, (e.g. [4]), where the preliminary estimated $\rho_c \sim 10^{-3}$ Ωcm^2, the results for diffusion welded contacts of Al to n-type 6H-SiC may be considered as convenient.

3. *U-I* characteristics obtained for diffusion welded Al/SiC contacts have sheer non-linear and asymmetric form. But due to very high dopant concentration in epitaxial layer of 4H-SiC and absence of any special edge treatment or surface passivation activity, the value of the reverse breakdown voltage has been determined to be relatively low.

The results presented in this paper are first of all phenomenological and must be supplemented with new data and analytical treatment.

References

[1] O. Korolkov, T. Rang: Proc. 6th Baltic Electronics Conference (BEC'98), Tallinn, Estonia, Oct. 7-9, 1998, 251-252.

[2] T. Rang, O. Korolkov, R. Kurel, and M. Pikkov: In "Materials Mechanics Fracture Mechanics Micro Mechanics", Eds. T. Winkler, A. Schubert, Druckhaus Dresden GmbH, Germany, 1999, 574-579.

[3] H.H. Berger: J. Electrochem. Soc., vol 119, No 4, 1972, 507-514.

[4] G. Nakamara, H. Shimada and M. Satoh: Abstracts of International Conference on Silicon Carbide and Related Materials. (ICSCRM'99 Sheraton Imperial Center, Research Triangle Park, NC, 10-15 Oct. 1999), 44.

Materials Science Forum Vols. 353-356 (2001) pp. 607-610
© 2001 Trans Tech Publications, Switzerland

Ru Schottky Barrier Contacts to n- and p-type 6H-SiC

M.E. Samiji[1], E. van Wyk[1], L. Wu[1], A. Venter[2] and A.W.R. Leitch[1]

[1] Department of Physics, University of Port Elizabeth,
PO Box 1600, Port Elizabeth 6000, South Africa

[2] Department of Physics, Vista University, Private Bag X 613,
Port Elizabeth, South Africa

Keywords: Contacts, Hydrogen, Metallization, Ruthenium, Schottky Contacts

Abstract

We have investigated the formation of ruthenium Schottky contacts on both *n*- and *p*-type 6H-SiC wafers. It is found that Ru forms good quality rectifying contacts, with barrier heights of 0.67 eV and 1. 06 eV for *n*-type and *p*-type SiC, respectively and ideality factors in the range 1.4 – 1.6. Annealing experiments indicated that the Ru Schottky contacts remained stable up to 450 °C, above which a general deterioration in the quality of the contacts (as indicated by an increase in the measured idealities as well as an increase in the reverse bias leakage currents) was observed. It is also shown that the Ru Schottky contact to *p*-type SiC provides an excellent means through which to introduce hydrogen into the SiC using a hydrogen plasma.

Introduction

SiC is a wide band gap semiconductor with properties that make it well suited for high temperature, high power and high frequency device applications. The further development and commercialization of such devices however depends on the fabrication of reliable ohmic and rectifying contacts that have good adhesion properties and are stable at elevated temperatures. Good quality Schottky contacts are also essential for fundamental studies of the electrical properties of SiC. These electrical properties may be drastically altered, for example, by the unintentional introduction of electrically active impurities during either the growth of the material or subsequent device processing steps. A study of the possible passivation by hydrogen of these electrically active impurities also requires stable rectifying contacts.

There have been several studies in recent years that have dealt with various metal contacts to 6H-SiC [1]. To our knowledge, however, the ruthenium metal contact to SiC has not yet been reported. In this paper we report on an investigation into the electrical properties of ruthenium rectifying contacts to both *p*- and *n*-type 6H-SiC. Ruthenium is one of the Pt-group metals that in the past has been used to successfully form good quality Schottky contacts to both *n*-and *p*-type GaAs [2,3]. The thermal stability, chemical inertness and large work function of Ru make it an ideal metal to use as a rectifying contact to an *n*-type semiconductor. An added advantage of Ru is that it is permeable to hydrogen, in contrast to other metals more commonly used for rectifying contacts. Thus hydrogen can be intentionally introduced into the semiconductor *through* the metal, by exposing the metalised surface to a hydrogen plasma, with minimal accompanying surface damage that usually results from direct exposure.

In this paper we also discuss the thermal stability of the Ru-rectifying contacts to both *n*- and *p*-type SiC, and compare the results with the thermal stability of the more commonly used Al-contact to *p*-type SiC. We also show how hydrogen may be efficiently introduced into *p*-type SiC by exposing the Schottky contact to a hydrogen plasma.

Experimental

Al-doped (p = 1.5 x 10^{18} cm^{-3}) as well as N-doped (n = 1 x 10^{18} cm^{-3}) 6H-SiC material, obtained from Cree Research Inc, was used in this study. The material was cleaned in standard organic solvents and dipped in a dilute HF solution before being dried in a flow of N_2 and loaded in the vacuum chamber. Low resistance ohmic contacts were formed on *p*-type SiC by thermally evaporating Al (180 nm) and Ti (50 nm) on the back surfaces, after which the samples were annealed for 10 min at 600 °C, followed by a further 5 min at 900 °C. In the case of *n*-type SiC, ohmic contacts were formed by evaporating Ni (200 nm) and subsequently annealing at 950 °C for 5 min.

Schottky barrier diodes (SBDs) were fabricated by depositing (using electron beam evaporation) a Ru film through a metal shadow mask, to form 0.8 mm diameter dots on the polished top surface of the SiC. A Ru film thickness of typically 45 nm was found to be sufficient for forming a stable rectifying contact. The quality of each fabricated SBD was evaluated in terms of the measured ideality n and the barrier height φ_B using standard current-voltage (*I-V*) measurements in the dark at room temperature. The thermal stabilities of the Al and Ru SBDs were compared by sequentially annealing the samples up to a temperature of 500 °C. The anneals were performed for 15 min in a dried argon ambient.

Results

i) *n*-type 6H-SiC

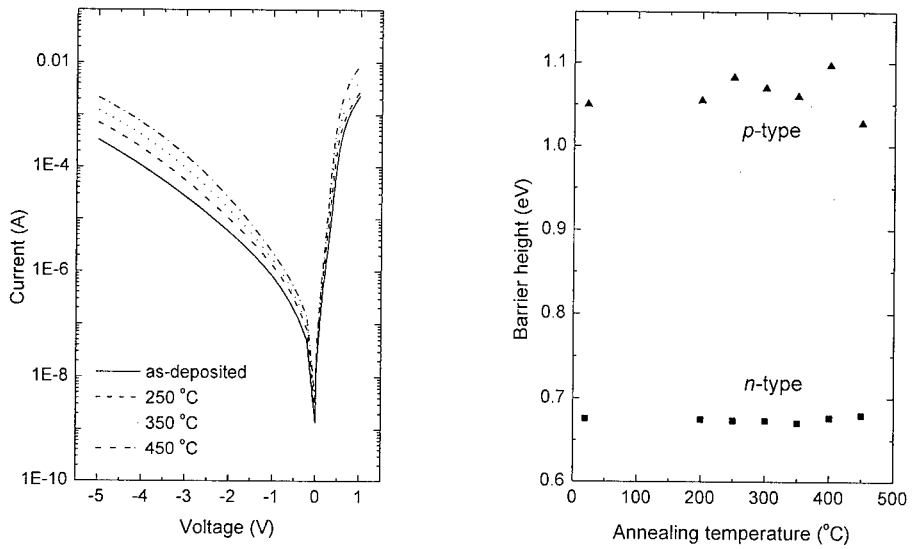


Fig. 1: (a) Forward and reverse *I-V* curves of as-deposited, as well as subsequently annealed, Ru Schottky contacts to *n*- 6H-SiC. (b) Measured Schottky barrier heights φ_B for both *n*- and *p*-type SiC after isochronal annealing up to 450 °C.

Fig. 1 (a) shows a series of forward and reverse biased *I-V* curves for a typical Ru Schottky contact to *n*-type 6H-SiC. The as-deposited SBD is clearly rectifying, although a fairly large leakage current of greater than 10^{-4} A flows when a reverse bias of 5 V is applied. This large current is attributed in part to the high carrier concentration of the samples (1 x 10^{18} cm^{-3}). The measured barrier height, averaged over several different Schottky contacts, was (0.67 ± 0.02) eV, while the ideality factor ranged between 1.4 and 1.6.

The thermal stability of the Ru Schottky contacts is also shown in Fig. 1 (a). It is seen that for annealing temperatures up to 450 °C, the SBDs remained relatively stable, with the leakage current deteriorating slightly. Fig 1 (b) shows that the barrier height φ_B remained constant at 0.67 eV, up to 450 °C. Beyond this temperature however, the reverse bias leakage current increased dramatically, indicating non-rectifying behaviour of the metal contact.

ii) *p*-type 6H-SiC

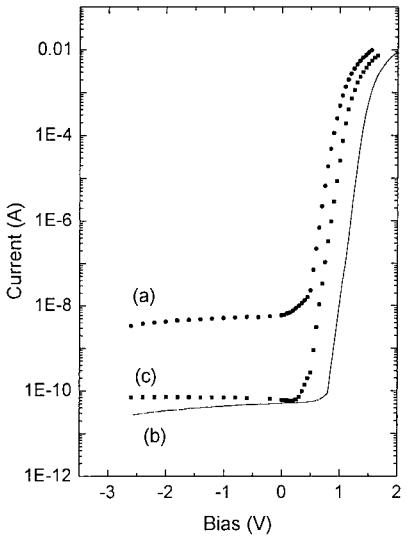


Fig. 2: Forward and reverse *I-V* curves for Ru Schottky contacts to *p*-type 6H-SiC. Curve (a): as-deposited. Curve (b): after exposure to a hydrogen plasma at 200 °C. Curve (c): after subsequent annealing at 300 °C for 25 hours.

Ru Schottky contacts to *p*-type SiC exhibited larger barrier heights of typically 1.1 eV, while idealities *n* of roughly 1.6 were obtained. Fig. 2 (curve (a)) shows a typical *I-V* curve for the Ru Schottky contact on *p*-type SiC. The reverse bias leakage current is clearly far lower than what was measured for *n*-type SiC. Isochronal annealing experiments indicated that the Ru Schottky contact to *p*-type SiC is also stable up to 450 °C. The barrier height φ_B remained constant at (1.06 ± 0.04) eV, as is seen in Fig. 1 (b). For temperatures of 500 °C and higher, however, the measured idealities and reverse bias leakage current deteriorated dramatically.

It is also seen in Fig. 1 (b) that the sum of the barrier heights for *n*- and *p*-type SiC does not yield the energy gap, as has been reported for several other metal – SiC systems [6]. This may be attributed to the fact that Ru is extremely difficult to deposit, even by means of electron beam evaporation. During the evaporation process it is likely that surface states are introduced from the electron irradiation of the SiC surface. These surface states will modify the barrier heights formed by the Ru on the SiC.

We also examined the effect of hydrogen plasma exposure and subsequent annealing on the stability of the Ru Schottky contact on *p*-type SiC. The Ru metal contact was exposed to a dc hydrogen plasma at a temperature of 200 °C for 30 min. Note that this temperature is lower than what is generally used for the introduction of hydrogen into SiC [4]. Fig. 2, curve (b) shows that the measured barrier height increased to 1.42 eV, with an accompanying reduction in the reverse bias leakage current. Capacitance-voltage (*C-V*) measurements indicated that the hydrogen efficiently passivated the free carriers up to 0.4 μm into the SiC, reducing the carrier concentration by more than an order of magnitude. It is therefore expected that the hydrogen will also passivate the surface states present, yielding an overall improved Schottky contact with an increased barrier height that approaches the theoretical value of 1.59 eV for *p*-type SiC. By comparison, no reduction in the free carrier concentration was measured for *n*-type SiC after exposure to a hydrogen plasma.

Fig. 2, curve (c) shows the *I-V* response of the hydrogen plasma treated Ru Schottky contact, after subsequent annealing at 300 °C for extended periods of time (in excess of 25 hours), to systematically remove the hydrogen from the SiC. In spite of the thermal treatment, the quality of the Schottky contact remained good. We were therefore in a position to examine the dissociation kinetics of the hydrogen-acceptor complex as well as to obtain its dissociation energy. These results will be presented elsewhere [5].

Finally, it is instructive to compare the *I-V* results for Ru Schottky contacts with those for Al-Schottky contacts, on *p*-type SiC. Aluminium is known to form a good rectifying contact to *p*-type 6H-SiC, with reported barrier heights ranging from 1.36 - 1.66 eV [1]. However, very little has been reported about its thermal stability [6,7]. In this study we routinely measured barrier heights of 1.39 eV for Al Schottky contacts to *p*-type SiC. However, isochronal annealing revealed that the Schottky contacts were only stable up to 250 °C. Above this temperature, the overall quality of the Schottky contact rapidly deteriorated.

Conclusions

It has been shown that Ru forms a good, stable Schottky contact to both *n*- and *p*-type 6H-SiC, with barrier heights of (0.67 ± 0.02) eV and (1.06 ± 0.04) eV, respectively and ideality factors in the range 1.4 – 1.6. In both cases the Schottky contacts are found to be stable up to 450 °C, with no degradation noticeable up to that temperature. By comparison, Al Schottky contacts to *p*-type SiC were measured to be stable only up to 250 °C. It has also been shown that it is possible to introduce hydrogen into *p*-type SiC by exposing the evaporated Ru film to a hydrogen plasma at 200 °C.

We thank M.C. Wagener for useful discussions. This work was supported by the South African National Research Foundation, under the Hungary - South Africa Bilateral Agreement. One of us (MES) acknowledges the Third World Organization for Women in Science for financial support.

References

[1] For a recent review, see L.M. Porter and R.F. Davis, Mater. Sci. and Eng. B34 (1995), p. 83.
[2] M.C. Wagener, J.R. Botha and A.W.R Leitch, Semicond.Sci.Technol. 14 (1999), p. 1080.
[3] G. Myburg and F.D. Auret, Appl. Phys. Lett. 60 (1992), p. 604.
[4] F. Ren, J.M.Grow, M. Baskaran, R.G. Wilsaon and S.J. Pearton, J. Electron. Mater. 25 (1997), p. 198.
[5] M.E. Samiji, A. Venter and A.W.R. Leitch, to be submitted to Appl. Phys. Lett (2000).
[6] J.R. Waldrop, J. Appl. Phys. 75 (1994), p. 4548.
[7] S.R. Smith, A.O. Evwaraye and W.C. Mitchel, J. Appl. Phys. 79 (1996), p. 301.

Materials Science Forum Vols. 353-356 (2001) pp. 611-614
© 2001 Trans Tech Publications, Switzerland

Stability of Molybdenum Schottky Contact to Silicon Carbide

Kouichi Nishikawa, Masaaki Shimizu, Brian Foster and Hiroaki Iwakuro

R&D Center, Shindengen Electric Mfg. Co., Ltd.,
10-13 Minami, Hannou, Saitama 357-8585, Japan

Keywords: Auger Electron Spectroscopy, Molybdenum, Refractory Metal, Reliability, Schottky Contacts, Stability

Abstract Molybdenum was investigated as a candidate material for a stable Schottky contact to silicon carbide. The Mo contact showed only a small change in Schottky properties after a heat treatment at 1173 K for 30 min. The specimens were investigated with X-ray diffraction and least linear square fitted Auger electron spectroscopy. These analyses showed the formation of Mo_2C at the Mo/SiC interface.

Introduction Since silicon carbide (SiC) itself is a very stable material, SiC devices have the potential to be operated at a higher temperature than silicon devices. In order to realize these devices, stable electrodes and insulators will also be required. However, when SiC devices are operated under high temperature for long time, reaction between SiC and the electrodes/insulators can not be avoided. Therefore research concerning a stable Schottky contact electrode is important for SiC based Schottky rectifier and MES-FET.

Refractory metals and their alloys are candidates for a stable Schottky electrode material since their melting points are high and they can form both silicides and carbides [1]. Some of the refractory metals have already been applied to Schottky rectifiers [1-5], but few were analyzed for their thermal stability [4-6]. The purpose of this paper is to show the stability of a refractory metal used for a Schottky contact. We chose to use Mo because it is easy to pattern by wet etching and it has high eutectic points to both carbides and silicides [7, 8].

Experimental As the substrate, (0001)Si face of n-type 4H-SiC from Cree Inc. was used. The SiC wafer had a 10-μm-thick n-type epilayer with doping concentration of 1×10^{16} cm^{-3} and a 0.35-mm-thick n-type substrate. The wafer was cleaned by a mixture of sulfuric acid and peroxide, rinsed in de-ionized water and etched in diluted HF(1:100) prior to Mo deposition. The Mo film was deposited by sputtering with a base pressure below 10^{-6} Torr. Argon (Ar) gas at 5.0 mTorr was used as a sputtering gas.

In order to examine the effect of heat treatment, two kinds of specimens were made: (a) as deposited and (b) annealed at 1173 K for 30min in Ar ambient. On the Schottky contact side (Mo) circular contacts of 0.40mm in diameter were developed using standard lithographic techniques and

wet etching solutions. The devices did not include a guard ring. Finaly, Ti was sputter deposited on the backside of the wafer for an Ohmic contact. During current-voltage measurements, the temperature of the rectifiers was kept at 295 K. X-ray diffraction (XRD) analysis was also made on both specimens using the Cu $K\alpha$ line. Additionaly, in order to investigate the interface between Mo and SiC, least linear square fitted analysis of Auger electron spectroscopy (LLS-AES) [9] was performed.

Results and discussions Fig.1 shows the current density-voltage characteristics of the Mo Schottky rectifiers. Electric properties calculated from the forward characteristics in Fig.1 are summarized in Table 1. Annealing lowered the Schottky barrier height by 0.07eV and brought the ideality factor 0.01 closer to 1. The forward drop at 100 Acm^{-2} was also lowered by 0.02 V. Despite that the barrier height is lowered by annealing, leakage current also looks to be lowered (Fig.1). Since no guard ring is used, the main part of the leakage current is not determined by Schottky barrier height but by the field concentration at the electrode edge or by crystal defects. When compared to Nickel, which can not form carbide and shows a high increase in leakage current after high temperature treatment [6], Mo shows a stable Schottky contact.

In order to understand the stability of the contact, XRD analysis was performed. Fig.2 shows the XRD pattern of both specimens. The as deposited specimen showed a strong texture for Mo{112} but a weak intensity for Mo{110} and Mo{130}. After annealing, diffraction peaks of Mo_2C appeared, which means that Mo carbide is formed by annealing. In order to investigate the formation of Mo_2C, concentration depth profile was measured by AES. Since the AES spectrum of C in Si carbide and that in Mo carbide is different (as shown in Fig.3), the compounds were divided as in Fig.4(c) and 4(d) using LLS method.

In both specimens, carbon is distributed in Mo at the concentration of about 5mol%. The origin of the C is expected not to originate from the substrate SiC but from ambient gas during sputtering, because there exists no excess Si proportional to C. Excess Si should exist if SiC and Mo react to form Mo carbide. At the Mo/SiC interface, C from Mo carbide shows a peak and the peak is broadened, but also reduced by annealing. Also the inclination of Si depth profile becomes shallower. This implies that Mo and SiC reacted and formed Mo_2C at interface. Though C exist in Mo film and at Mo/SiC interface before annealing, XRD showed no peaks from Mo_2C. This means that as deposited Mo contain super saturated C or have amorphous structutre and transformed into crystalline Mo_2C by annealing.

Even though the amount of Mo_2C is realativily small, other compounds, such as Mo silicide were not detected. This implies that even at an elevated temperature of 1173 K, there is very little reaction at the interface. As a result the main compounds at the interface are Mo, SiC and Mo_2C. SiC and Mo are both well known for their high thermal stability. Additionaly, the eutectic point of Mo carbide is also quite high (2478 K), therefore the interface is not subject to much change even at an elevated temperature such as 1173 K.

Conclusion The stability of a Mo Schottky contact with SiC was investigated by current-voltage measurement, XRD and AES. Heat treatment at 1173 K for 30 min showed no significant change in electric properties. However, it can be concluded that annealing causes Mo carbide present at the interface to transform into crystaline Mo_2C and diffuse slightly. Even though this small change occurs, the high eutectic point of Mo_2C, along with the high thermal stability of SiC and Mo, results in a stable contact. Thus Mo demonstrates good characteristics for use as a Schottky contact metal under high temperatures.

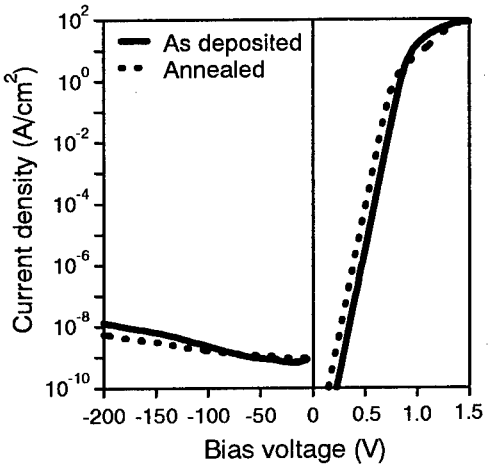


Table 1. Summary of forward properties

Specimen	V_F@100Acm^{-2}	ϕ_{Bn}	n
As deposited	1.53V	1.24eV	1.02
Annealed	1.51V	1.17eV	1.01

In calculation of ϕ_{Bn} and n, we assumed the effective Richardson constant to be 146 AK^{-2}cm^{-2} from ref. [10].

Figure 1 Current density-voltage properties of Mo SBD.

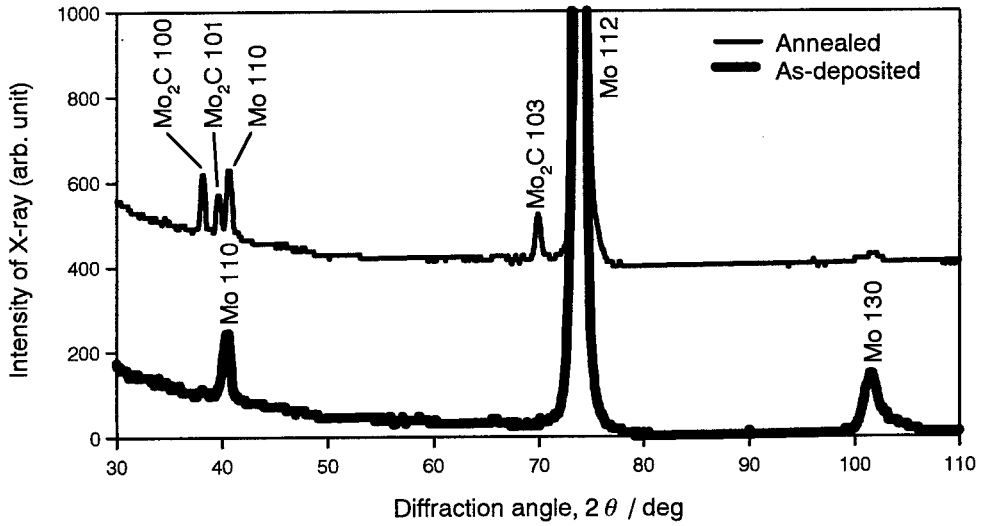


Figure 2 X-ray diffraction pattern of (a) as-deposited and (b) annealed specimens. Cu $K\alpha$ line is used. The as deposited specimen shows a strong presence of Mo{112}. After annealing, small amount of Mo_2C appears.

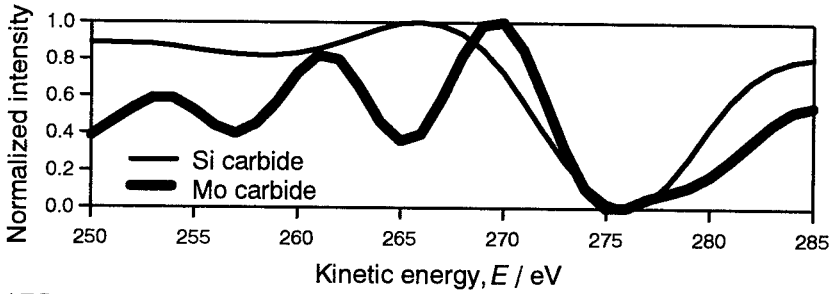


Figure 3 AES spectrum of carbon in Si carbide and carbon in Mo carbide.

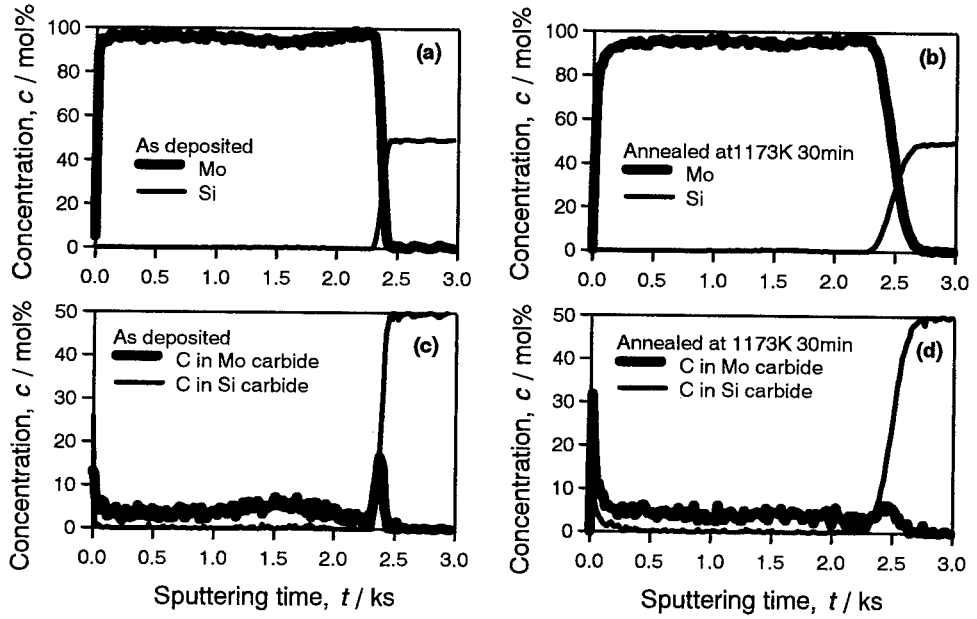


Figure 4 Concentration depth profile of (a) (c) as deposited and (b) (d) annealed specimens obtained by LLS-AES method. Carbon forming Mo carbide and carbon forming SiC are devided by LLS method. As deposited specimen shows sharp Mo carbide peak at the interface. After annealing, the interface carbon peak is broadened.

References

[1] J.B. Petit, P.G. Neudeck, C.S. Salupo, D.J. Larkin and J.A. Powell, Inst. Phys. Conf. Ser. 137 (1993), p.679.
[2] N. Lundberg, P. Tägström, U. Jansson and M. Östling, Inst. Phys. Conf. Ser. 142 (1996), p.677.
[3] A. Afanasjev, V. Il'in, V. Luchinin, A. Nikiforov and A. Petrov, *Abstract of the 5th International High Temperature Electronics Conference*, (New Mexico, USA, 2000) p.52.
[4] N. Lundberg, C.-M.Zettering and M. Östling, Appl. Surf. Sci. 73 (1993), p.316.
[5] S.-K. Lee, C.-M. Zetterling and M. Östling, J. Appl. Phys. 87 (2000), p.8039.
[6] J.N. Su and A.J. Steckl, Inst. Phys. Conf. Ser. 142 (1996), p.697.
[7] F.J.J. van Loo, F.M. Smet, G.D. Rieck and G. Verspui, High temperatures-High pressures 14 (1982), p.25.
[8] H. Nowotny, E. Parthé, R. Kieffer and F. Benesovsky, Monatshefte für Chemie 85 (1954), p.255.
[9] T. Morohashi, T. Hoshi, H. Nakaido and M. Kudo, J. Vac. Sci. Technol. A 16 (1998), p.2257.
[10] A. Itoh, T. Kimoto and H. Matsunami, *Proc. International Symp. on Power Semiconductor Devices & ICs* (1995), p.101.

Materials Science Forum Vols. 353-356 (2001) pp. 615-618
© 2001 Trans Tech Publications, Switzerland

Effects of Thermal Annealing on Cu/6H-SiC Schottky Properties

Tomoaki Hatayama, Takashi Suezaki, Kazuaki Kawahito,
Yukiharu Uraoka and Takashi Fuyuki

Graduate School of Materials Science, Nara Institute of Science and Technology,
Takayama 8916-5, Ikoma, Nara 630-0101, Japan

Keywords: Annealing, Barrier Height, Copper (Cu), On-Resistance, Schottky Rectifiers, Silicides

Abstract

Effects of thermal annealing for copper (Cu) contacts on 6H-SiC (0001) Si-face were analyzed in detail. Cu/6H-SiC structures had good Schottky electrical properties with the ideality factor below 1.1 even after thermal annealing at 500℃. The barrier height of 1.22V for an as-deposited Cu contact increased to 1.45V after annealing at 500℃. However, electrical properties were deteriorated after annealing over 500℃, which is caused by the formation of copper silicides at the Cu/6H-SiC interface.

Introduction

Successful results in high-quality homoepitaxial growth and large diameter wafer of SiC have inspired intensive research for high-performance SiC devices such as high blocking-voltage rectifiers and high-power transistors [1]. As an application to high-frequency power circuits, Schottky barrier diodes are very important rectifiers owing to low switching power dissipation and fast reverse-recovery characteristics. Schottky barrier height is affected for the power loss in operating devices. A suitable barrier height for the reduction of power loss is proposed at around 1.0～1.3V for 6H- and 4H-SiC rectifiers with blocking voltages above 1kV [2]. The barrier height of metal/SiC rectifiers using gold (Au), nickel (Ni), titanium (Ti), and aluminum (Al) has been analyzed by current-voltage (I-V), capacitance-voltage (C-V) characteristics, internal photoemission spectroscopy [3], and X-ray photoelectron spectroscopy [4]. The barrier height depends on a metal work function without strong pinning in metal/SiC rectifiers [3]. The control and stability of barrier height are important issues to realize high-performance SiC devices. Besides, it is also required to form a metallic contact showing stable performance at high operating temperatures. Copper (Cu) is one of the expecting metal because of its low resistivity ($1.673 \times 10^{-6}\,\Omega$cm at 300K) and high thermal conductivity (4.01W/cmK).

In this study, electrical properties of Cu/6H-SiC Schottky rectifiers are discussed in relation to the effects of thermal annealing.

Experiments

The substrates used were n-type 6H-SiC (0001) Si-face with a resistivity of $0.06\,\Omega$cm and $300\,\mu$m thickness. Thickness and donor concentration of epilayers were $10\,\mu$m and 1.4×10^{16}cm^{-3}, respectively. An ohmic contact on the back of substrate was employed by the deposition of Ni and alloyed by a rapid thermal annealing method in nitrogen (N_2) ambient at 1000℃. Before fabrication of Cu/6H-SiC structures, surfaces were cleaned by a 5% HF solution for 10 minutes to remove native oxide layers. Then, it was loaded into a sputter chamber with a base pressure below 5×10^{-7}Torr. Cu contacts on the epilayers were deposited by the RF magnetron sputtering method at room temperature and patterned by photolithography. Diameter and

thickness of Cu contacts were 200 μ m and 200nm, respectively. To analyze effects of thermal annealing on electrical properties, the as-deposited Cu contacts were treated in N_2 ambient at 300~700℃ for 5 minutes.

Results and Discussion

Cu/6H-SiC structures had good Schottky properties with a small ideality factor (n) below 1.1 even after annealing at 500℃. Figure 1 shows the forward current density-voltage (J-V) characteristics at room temperature for typical Cu/6H-SiC Schottky rectifiers. Solid and dashed curves correspond to as-deposited and 500℃ annealing Cu contacts, respectively. In the forward-bias condition, the characteristics followed the thermionic emission equation with the ideality factor below 1.06 at low current density ($<10^{-1}$A/cm^2). The barrier heights (ϕ) calculated from the forward characteristic of as-deposited and 500℃ annealing Cu/6H-SiC structures were 1.22 V and 1.47 V, respectively. The Richardson constant was calculated as about 65 AK^{-2}cm^{-2}. Specific on-resistances of Cu/6H-SiC rectifiers were not affected strongly with thermal annealing, which were about 12 mΩcm^2. The specific on-resistances for the present rectifiers were still high compared to a value (~8.6mΩcm^2) expected from the device structure, which could be explained by the non-optimized back-side ohmic contact.

In the reverse-bias condition, a leakage current density of mid 10^{-7}A/cm^2 at 200V was observed. The leakage current for thermally annealed Cu/6H-SiC rectifiers became lower in about 1/6 compared to that for an as-deposited rectifier. However, there was no difference in the distribution of breakdown voltages between Cu/6H-SiC rectifiers with and without thermal annealing. In the present rectifiers, breakdown occurred typically at 820V, which were about 48% of the ideal value estimated from the device structure. The increase of breakdown voltage can be expected by the formation of edge termination around the periphery of Cu Schottky contact.

The barrier height of as-deposited Cu contact on 6H-SiC was 1.41V examined by capacitance-voltage (C-V) measurement. On the other hand, a barrier height of 1.21V and the Richardson constant were calculated as about and 14AK^{-2}cm^{-2} from the temperature dependence of J-V characteristics in the range of -170~25℃. Barrier height obtained from I-V and C-V characteristics is affected by ideality factor, leakage current, series resistance, and interfacial layer [3]. To avoid the influences of above problems, the reliable barrier height of as-deposited Cu/6H-SiC rectifier was analyzed by internal photoemission spectroscopy [5] with irradiation of monochromatic light in the range of 1.4~3.1eV. The barrier height of Cu/6H-SiC (0001) Si-face was determined to be 1.26V. This value was in the middle between the barrier height from J-V and C-V characteristics. Since the barrier height (1.26V) of as-deposited Cu contact corresponds to a suitable value (1.0~1.3V) for the reduction of power dissipation [2], a low power-loss Schottky property is expected for the as-deposited Cu contact than Ni (1.37V) or Ti (0.64V) contacts.

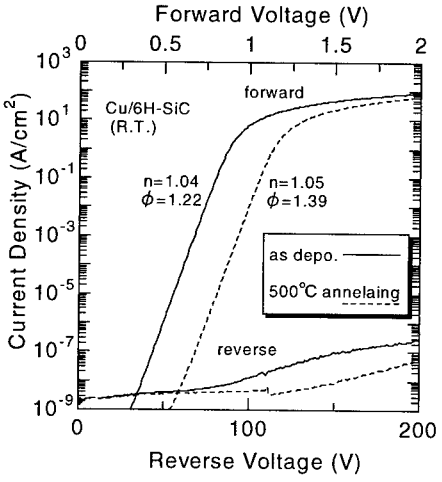


Fig. 1. Current density-voltage characteristics at room temperature for Cu/6H-SiC Schottky rectifiers. Solid and dashed curves correspond to Cu contacts as-deposited and annealed at 500 ℃ Cu contacts, respectively.

Recently, a barrier height of as-deposited Cu contacts

on the 4H-SiC (0001) Si-face has been analyzed, which was determined to be 1.61V.

To improve the reliability for a high-temperature operation, Cu contacts were covered by 200nm thick Al films. Figure 2 shows the temperature dependence of on-resistance for Cu/6H-SiC Schottky rectifiers between room temperature and 200℃ in air. Open and closed circles denote with and without Al covers on Cu contacts, respectively. On-resistance (R_{on}) increased monotonously with the increase of temperature (T), which was proportional to $T^{1.8}$. The relationship between on-resistance and temperature was close to $T^{2.0}$ of a Au/6H-SiC Schottky rectifier [6]. In the case of Cu/6H-SiC without Al covers, relationship of $T^{1.8}$ deviated over 125℃. It is considered that a Cu contact oxidized during the high-temperature operation in air, and then, the resistivity of Cu contact increased. On the other hand, in the case of Cu/6H-SiC with Al covers, relationship of $T^{1.8}$ was kept even at 200℃. Cu/6H-SiC Schottky rectifiers with Al covers are useful for high-temperature operations.

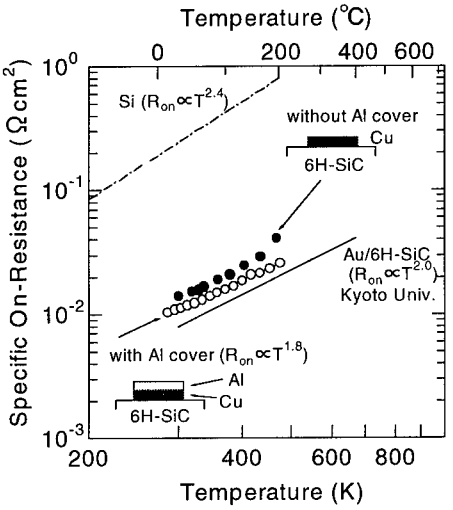


Fig. 2. Temperature dependence of on-resistance for Cu/SiC Schottky rectifiers. Open and closed circles show with and without Al cover on Cu Schottky contacts, respectively.

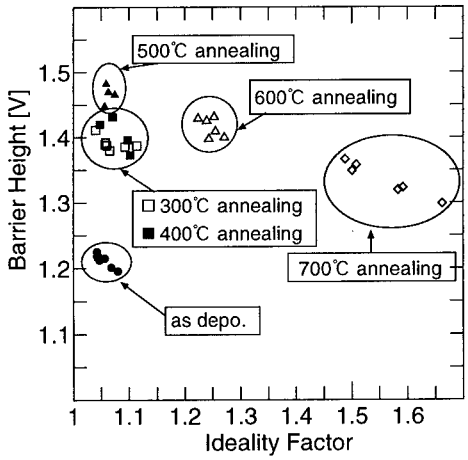


Fig. 3. Annealing temperature dependence of barrier height and ideality factor for Cu/6H-SiC Schottky rectifiers.

Figure 3 shows the annealing temperature dependence of barrier height and ideality factor for Cu/6H-SiC Schottky rectifiers measured at room temperature. Distributions of the ideality factor and the barrier height at each annealed condition might be caused by the nonhomogenous distribution of crystal defects in the 6H-SiC substrates. Barrier heights increased with the increase of annealing temperature up to 500℃ ; nevertheless, the ideality factor was kept below 1.1. The relationship between barrier height and ideality factor will be discussed elsewhere in detail [7].

With the increase of annealing temperature over 500℃, however, Cu/6H-SiC Schottky properties were deteriorated : Barrier heights decreased to about 1.3V, and ideality factors increased over 1.45 after the thermal annealing at 700℃. This result was caused by the reactions between Cu and 6H-SiC at the interface.

Interactions between Cu and 6H-SiC with thermal annealing were characterized by X-ray diffraction analysis. To avoid the influence of strong diffraction from the 6H-SiC substrate, a glancing angle of an X-ray beam was fixed at 0.5°, and an X-ray detector was scanned in the range of 40~80°. X-ray diffraction spectra of Cu/6H-SiC interfaces from (a) as-deposited and (b) 700℃ annealed Cu contacts are shown in Fig. 4. The spectra of as-deposited Cu contact showed three diffraction peaks of Cu (111), Cu (200), and Cu (220) at about 44°, 51°, and 74°, respectively. There was no difference in the diffraction spectra between as-deposited and annealed one below 500℃, nevertheless, the barrier heights of Cu/6H-SiC increased with the increase of annealing temperature. It will be

considered that chemical bond between Cu and 6H-SiC at the interface changed by the thermal annealing. After the annealing at 700℃, the diffraction peaks related Cu completely disappeared and two diffraction peaks were newly observed. Diffraction peaks at about 67° and 74° are corresponding to Cu_5Si (420) and Cu_5Si (422), respectively. It was revealed that the copper silicide of Cu_5Si was formed by the thermal annealing over 500℃, leading to the deterioration of Cu/6H-SiC Schottky properties.

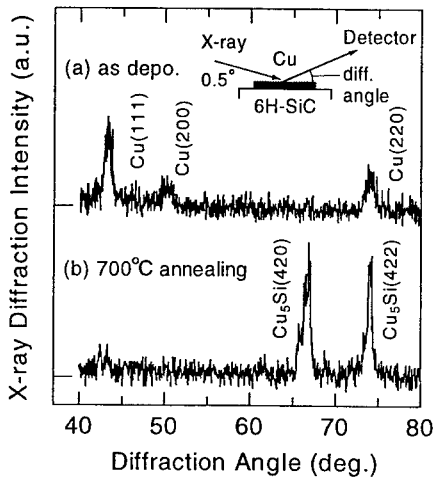


Fig. 4. X-ray diffraction spectra of Cu/6H-SiC structures from (a) as-deposited and (b) 700℃ annealing.

Thermal reaction between Cu and 6H-SiC(000$\bar{1}$) C-face has been reported by Auger electron spectroscopy [8]. Copper silicides were formed by 200℃ annealing for a Cu/6H-SiC(000$\bar{1}$) structure in ultrahigh vacuum for 20 minutes [8]. Since the chemical reactivity of (0001) Si-face is considered to be weaker than that of (000$\bar{1}$) C-face [1], the copper silicide of Cu_5Si was formed by the annealing temperature above 500℃ in our case. To clarify the relation between Schottky properties and thermal annealing, analysis of chemical bonds at the Cu/6H-SiC interface should be further investigated.

Summary

Cu/6H-SiC Schottky rectifiers were fabricated by an RF magnetron sputtering method and subsequent thermal annealing. The barrier height of as-deposited Cu contact on 6H-SiC(0001) Si-face was 1.26V measured by internal photoemission spectroscopy. A Cu contact covered with an Al film was found to be tolerant for oxidation, which leads to a thermally stable rectifier for high temperature operation. Cu/6H-SiC Schottky rectifiers had reliable electrical properties with the ideality factor below 1.1 after thermal annealing at 500℃. After annealing over 500℃, Schottky properties were deteriorated, which is caused by the formation of copper silicide of Cu_5Si at the interface.

Acknowledgment

This work was partly supported by Research Foundation of the Electrotechnology of Chubu.

References

[1] W. Choyke, H. Matsunami and G. Pensl, phys. stat. sol. (a) 162 + (b) 202 (1997)

[2] A. Itoh, T. Kimoto and H. Matsunami, IEEE Elect. Dev. Lett. 16 (1995), p. 280.

[3] A. Itoh and H. Matsunami, phys. stat. sol. (a) 162 (1997), p. 389.

[4] J.W. Waldrop and R.W. Grant, Appl. Phys. Lett. 62 (1993), p. 2685.

[5] R.H. Fowler, Phys. Rev. 38 (1931), p. 45.

[6] T. Kimoto, T. Urushidani, S. Kobayashi and H. Matsunami, IEEE Elect. Dev. Lett. 12 (1993), p. 548.

[7] T. Hatayama, Y. Uraoka and T. Fuyuki, submitted to Jpn. J. Appl. Phys.

[8] K. Nishimori, H. Tokutake, S. Nakanishi, S. Kishida and N. Ishihara, Jpn. J. Appl. Phys. 28 (1989), p. L1345.

Materials Science Forum Vols. 353-356 (2001) pp. 619-622
© 2001 Trans Tech Publications, Switzerland

Electrochemical Characterization of p-Type Hexagonal SiC

M. Kayambaki[1], K. Zekentes[1], K. Tsagaraki[1], E. Pernot[2] and R. Yakimova[3]

[1] Foundation for Research and Technology Hellas, Microelectronic Research Group, IESL, PO Box 1527, Vassilika Vouton, GR-71110 Heraklion/Crete, Greece

[2] Laboratoire de Materiaux et de Génie Physique, UMR CNRS/INPG 5628-ENSPG, BP 46, FR-38402 St. Martin d'Hères, France

[3] Department of Physics and Measurement Technology, Linköping University, SE-581 83 Linköping, Sweden

Keywords: C-V Characteristics, Doping Profile, Electrolytic Etching, Etch Pit

Abstract. Electrochemical etching experiments in combination with C-V measurements of 6H and 4*H*-SiC p-type material can be used to determine the doping profile and the evaluation of the types and distribution of crystal defects. Dislocation-related etch-pits appeared on the etched surfaces due to a preferential etching process. Doping profiles were obtained for etched depths down to 84 μm. The experiments were conducted in a simple commercial apparatus and the reproducibility of the method was demonstrated.

Introduction

Electrolytic dissolution of silicon carbide is the only wet etching process that may be carried out at room temperature. In a previous work, we have shown that it is possible to employ an Electrochemical Capacitance-Voltage (ECV) profiler for determining the epilayer doping level and the thickness of p-type 6H-SiC films[1]. Moreover, the same process can be used for evaluating the types and the distribution of crystal defects on both the Si and C faces of p-type 6H and 4H-SiC [2]. Several groups have previously investigated the electrochemical and photoelectrochemical properties of the SiC polytypes, but there were no studies concerning the use of electrochemical etching for evaluating the crystal quality of SiC epitaxial films and substrates and very few for determining the doping concentration profile [3, 4].
In this work, we extend our doping profiling results for 4H-SiC and we investigate crystal defects on p-type (4H- and 6H-) SiC material grown by various techniques. Concrete examples of investigated samples are given in order to show the possibilities of the method.

Experimental – Results

The investigated samples were commercially available epitaxial films and substrates, as well as films grown by sublimation epitaxy [5]. All 4H and 6H-SiC investigated wafers were 8° and 3.5° misoriented from (0001) orientation, respectively. The etching conditions were the same as that in ref. [1]. A BIORAD PN4200 system and an HF-based electrolyte (2% by volume in water) were used. A series of measurements and results like the linearity of Schottky-Mott plot, the low value of the cathodic dark current, the smoothness of the etched surface and the abruptness of the etch walls for each etching experiment permitted to control depth resolution and doping profile accuracy.

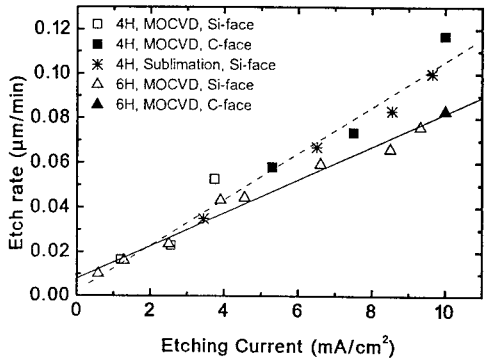


Fig. 1. Dependence of the etch rate on the etch current density for 6H and 4H polytypes and for both surface polarities (C-face: solid symbols)

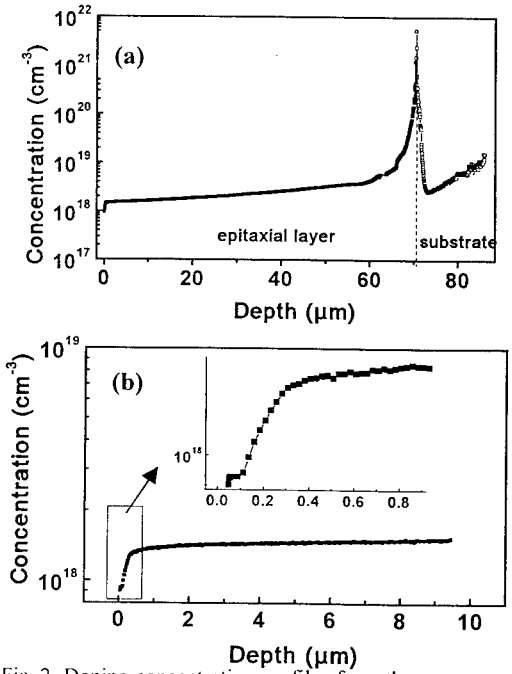


Fig. 2. Doping concentration profiles from the same sample etched down to (a) 84 and (b) 9.8 μm. The insert in (b) shows clearly the existence of a surface layer with lower doping.

The reproducibility of the measurements is also shown in Fig.1 where the dependence of the etch rate on the etching current density for different samples of both polytypes (4H and 6H) as well as for both surface polarities (Si and C-face) is reported. The linear dependence indicates electrolytic etching of the same material (Faraday law).

Fig. 2 shows doping profiles of an Al-doped 4H-SiC film grown by sublimation epitaxy [5] on the Si face of an n-type, 8° off substrate. Multiple etching experiments with different etching depths were performed on this sample. The profiles down to an etched depth of 26 μm have been obtained under similar experimental conditions in order to study the reproducibility of the measurements and the effect of the etched depth on the morphology of the etch pits (see discussion below). Note that in Fig. 2a the total etched depth is 84 μm and the n-type substrate has been reached. The measured doping concentration was $(1.45\pm 0.10)\times10^{18}cm^{-3}$ in all cases. Moreover, it is evident that a surface layer of 0.1μm thick with a lower acceptor concentration is present suggesting an Al depletion of the surface layer. This can be related to a thin surface layer grown during the cooling down stage with a lower Al incorporation. Indeed, according to cathodoluminescence (CL) experiments of other samples, the blue luminescence which is commonly related to Al-N centers shows an increase of its intensity from the surface of the layer, which can be induced either from surface morphology or from the difference in Al concentration near the surface. ECV experiments indicate that the latter is responsible for the CL intensity change.

The etched areas of the above sample were investigated by Nomarski and Atomic Force (AFM) microscopy, as well as by an A-step Tencor profilometer. A smooth surface, even for the etched depth of 84 μm, was observed and an etch pits density (EPD) of 10^5cm^{-2} was present. Fig. 3 shows AFM micrographs as well as characteristic tip traces indicated in the photo by a straight line. The etch pits are elliptical with a pointed bottom and the elongated direction of them all is parallel to one of the six {1-100} planes. Synchotron X-ray topography experiments have shown that basal plane dislocations are not present in these epitaxial layers and it was concluded that the etch pits originate from screw dislocations. Indeed, such images should be expected since

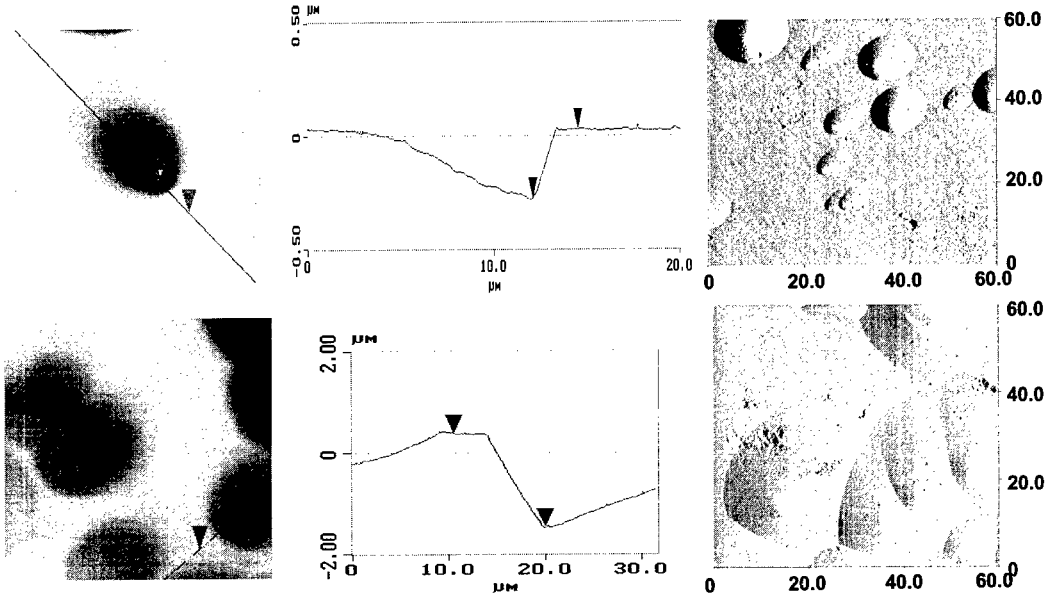


Fig. 3. AFM results of the etched area of the sample of figure 2 for an etched depth of 3.7 µm (top) and of 26 µm (bottom). From the left to the right are the topography mode micrographs, the corresponding tip trace and the deflection mode micrographs. The micrographs area is 15x15µm (top) and 60x60 µm (bottom).

the growth is performed on off-axis substrates and the threading screw dislocations are not normal to the surface. For all the etching depths the smallest angle of the triangle formed by the tip trace along the elongated direction of the etch pits was 2.2 degrees. The etch pits are related to dislocations as they maintain the shape of the pointed bottom and their distribution as the etching proceeds [6]. Indeed, the latter was confirmed by the constant EPD for different etched depths and the constant location of the etch pits in the case of overlapping etched areas corresponding to different etching experiments. In the case of deep etch (Fig. 3-bottom) the etch pits merge but the pointed bottoms which are characteristic of screw dislocations are always visible.

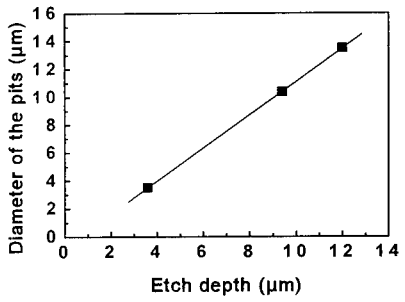


Fig. 4. Dependence of the etch pit mean diameter on the etched depth for the sample of Figs. 2-3 (points at 3.7 and 9.8 µm) and for a sample of the same origin (point at 12 µm) exhibiting the same type of defects.

The dependence of the etch-pit mean diameter on the etched depth is shown in Fig. 4. Since the defects merge for etching depths higher than ≈20 µm, the plot is limited to etched depths down to 12 µm. The linear behavior observed on different samples and etched depths shows that the etch pits originate from defects of the same type as the anisotropic etching rate is the same.

Fig. 5 shows two optical micrographs from the etched area of a commercial 6H-SiC p-type epitaxial layer. The doping profiles and details on the ECV measurements have been reported previously [1]. From Fig. 5b it is obvious that the etch pits are less elongated and the pointed bottom is near to their center. This results from the lower misorientation of the wafers (3.5 deg.). The etch pits can be grouped into two types: (a) the large (≥10 µm) and deep (≥100 nm) with a well resolved pointed bottom (see Fig. 5b) and, (b) the small (≈5µm) and shallow (≤ 40 nm). The first are similar to those

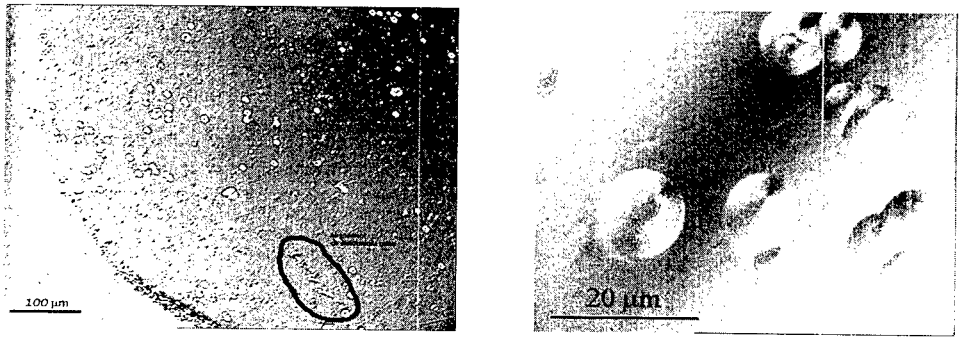


Fig. 5. Optical micrographs from the etched areas of a 6H-SiC sample. The arrow in the left image indicates the edge of the etched area and the ellipse indicates a row of etch pits.

of Fig. 3 and it was concluded that they are 1c screw dislocations. The latter are often grouped in rows aligned along [1-100] a typical feature of 1/3 [11-20] edge dislocations [6].

Summary

It was demonstrated that electrochemical etching in combination with C-V profiling is a powerful and necessary method for characterizing p-type hexagonal SiC material. The distribution and the type of dislocations existing in the material under investigation are determined by the etch pits appearing in the etched surfaces due to an anisotropic etching process. The results are similar to that obtained by preferential etching in molten KOH. However, the electrochemical etching is a much simpler process as it happens at room temperature and the used solutions are much less hazardous. In addition, the accuracy and reproducibility of the obtained doping profile indicate that this method can be used, not only for evaluating epitaxial material in an everyday basis, but also for dopant activation studies which are an open issue for p-type SiC.

Acknowledgements

This work was partly supported by NATO SfP 971879 grant. The authors would like to thank Dr. V. Cimalla for his help in the interpretation of AFM measurements.

References

[1] M. Kayambaki, K. Zekentes, Mat. Sci. Forum 338-342 (2000), p.1061.

[2] M. Kayambaki, K. Tsagaraki, V. Cimalla, K. Zekentes, and R. Yakimova, J. Electrochem. Soc. 147 (2000), p. 2744.

[3] J. S. Shor and A. D. Kurtz, J. Electrochem. Soc. 141 (1994), p. 778.

[4] C. E. Stutz, J. Electron. Mat. 27 (1998), p. L81.

[5] M. Syväjärvi, R. Yakimova, M. Tuominen, A. Kakanakova-Georgieva, M. F. MacMillan, A. Henry, Q. Wahab, E. Janzén, J. Cryst. Growth 197 (1999), p. 155.

[6] J. Takahashi, M. Kanaya and Y. Fujiwara, J. Cryst. Growth 135 (1994), p. 6

Materials Science Forum Vols. 353-356 (2001) pp. 623-626
© 2001 Trans Tech Publications, Switzerland

A Novel Technique for Shallow Angle Beveling of SiC to Prevent Surface Breakdown in Power Devices

J. Neil Merrett[1], David C. Sheridan[2], John R. Williams[1], Chin-Che Tin[1] and John D. Cressler[2]

[1] Department of Physics, Auburn University, Auburn AL 36849, USA

[2] Electrical and Computer Engineering Department, Auburn University, Auburn AL 36849, USA

Keywords: Beveling, Edge Termination, Etch Mask, Power Devices, Reactive Ion Etching

Abstract. In this paper, a process for shallow angle beveling of SiC is described in which photoresist is used as a mask in a reactive ion etcher using pure NF_3. Etch results are shown and power device applications are discussed.

1. Introduction

In order to utilize the potential of SiC in power devices, effective edge termination is necessary to prevent surface breakdown. For mesa isolated structures, beveling the sidewalls of the device is one method by which to reduce the electric field at the surface. For a positive bevel, one in which the higher doped side of the junction has a larger area, theory states that angles of 30 to 60° from horizontal are sufficient to insure bulk breakdown [1]. Bevel angles of 30 to 80° have been previously obtained on SiC by using a wet-etched SiO_2 layer as a plasma etch mask [2]. Similar angles have been achieved using Nano™ XP SU-8 based photoresist as an etch mask [3]. Positive bevels of around 45° have been successfully used on SiC diodes to prevent surface breakdown [4].

For the case of a negative bevel, however, the junction needs to be highly graded, and the bevel angle needs to be very small [1]. Also, the angle necessary for bulk breakdown is a function of the ratio of the depletion widths of the two sides of the junction [1]. An effective angle, ϕ, has been defined by the equation:

$$\phi = (0.04)*\theta*(W/d)^2 \qquad (1)$$

where θ is the actual bevel angle and W and d are the depletion layer widths of the lightly and heavily doped sides of the junction, respectively [1]. Numerical simulations show that an effective angle of around 5° is necessary to reduce the surface field strength enough to ensure bulk breakdown [1]. We have developed an etching technique in which very shallow angles can be achieved at junctions up to several microns deep. This technique can be applied to p-n diodes or to multiple layer structures such as thyristors where the critical junction might be much deeper.

2. Procedure

Our shallow angle technique involves applying two different photoresists to make the etch mask. First, SU-8 25 photoresist is spun on and patterned. SU-8 can be spun on at a wide variety of thicknesses from around 8 to over 100 μm, depending on the total etch depth desired. Next, a much thinner positive photoresist is spun onto the sample. STR® 1045 and AZ® 5214-E photoresists were both used and both gave good results. The surface tension of the thinner photoresist causes it to stick to the sides of the SU-8 pillars forming a concave beveled profile (Fig.1). The 5214 is thinner than the 1045 and therefore produces smaller angles for the same spin speed. The sample is then exposed with UV light through a mask which shields a circle of positive photoresist around the SU-8 with a radius about 70 μm larger than the SU-8 pillar. If the photoresist appears rough, the

sample can be baked for a few minutes on a hotplate (90°C for the 1045 and 115°C for the 5214) to smooth the surface.

During SiC etching, the photoresist mask is also gradually etched away. As the photoresist recedes, more SiC surface is exposed. The end result is a SiC mesa having a profile with curvature similar to that of the etch mask. Etching was performed in an RIE system using a 13.6 MHz RF power supply. Pure NF_3 was used as the etch gas at a pressure of around 65 to 70 mTorr. The NF_3 flow rate was 4.3 sccm. The RF power was set at 18 W, giving a power density of about 0.5 W/cm^2. The electrode was cooled with 10°C water. Lowering the cooling water temperature prolongs the life of the photoresist mask. The etch quality of was determined largely by the cleanliness of the sample surface prior to the start of the etching procedure. In addition to a thorough organic cleaning prior to lithography, very clean etches were obtained by exposing the sample to an oxygen plasma for about 1minute before the NF_3 etch. The oxygen plasma removes the residue left during the developing of the photoresist. Any SU-8 remaining after etching is removed with (2:1) H_2SO_4: H_2O_2. It is also recommended that a sacrificial oxide is thermally grown to remove surface states created by etch damage. Profiles of finished devices were made with a stylus profilometer capable of measuring angles from horizontal up to 60°.

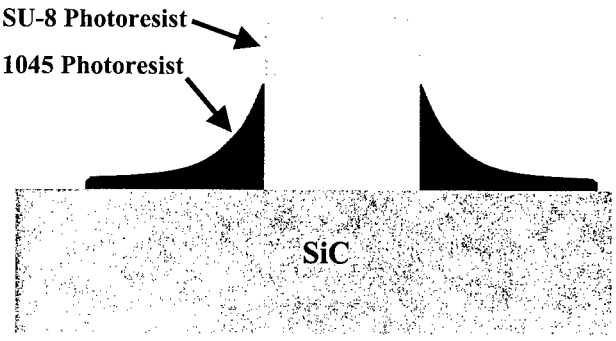


Fig. 1. Photoresist etch mask

3. Results

The above parameters produced etch rates averaging around 940 Å/min. with a variation of about four percent over the 5x5 mm wafers used. For devices not to close to the edge of the sample the bevel angle remained fairly consistent around the edge of each device and uniformity between devices was good. Close to the edge of the sample, however, uniformity became poor due to the tendency of photoresist to bead up along the edges of the sample. Uniformity would most likely be improved by using larger samples where the edge bead effect would not be as much a factor. The 5214 produced better uniformity than the 1045 in part, because the 1045 tends to flow more when

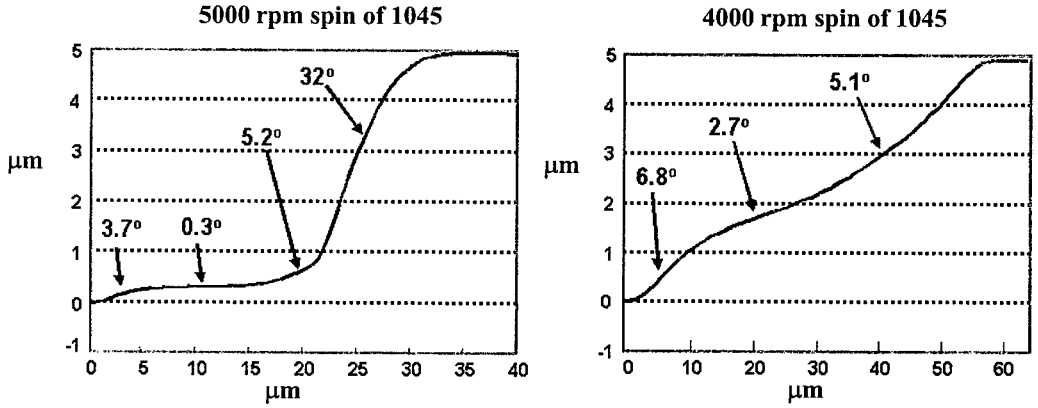


Fig. 2. SiC etch profiles. The angles indicated are the angles between the horizontal and lines drawn tangent to the profile curve at the position of the arrows.

baked, thus making the bevel angle more sensitive to variations in bake temperature. Varying the

spin speed of the 1045 or the 5214 photoresist achieved bevel angles ranging from less than a degree to around ten degrees. Profiles of two samples taken with a stylus profilometer are shown in Fig. 2. Once the thin photoresist is etched away, the thick SU-8 mask remains, allowing the shallow profile to be etched to necessary depth. The SU-8, used as a mask by itself, leaves bevel angles of around 30° that are sufficient for positive bevels. This result is thought to be due to horizontal etching of the SU-8 in the NF_3 plasma. The selectivity of all three types of photoresist used on 4-H SiC was around 0.3 to 0.4. Thus, a 100 μm SU-8 mask could be expected to last for etch depths of up to 30μm. Fig. 3 shows an SEM of a GTO structure made using this technique. Testing of this technique on actual devices is in progress.

4. Conclusion

A technique for clean, shallow angle beveling has been demonstrated for SiC device fabrication. The compound angle produced with this method (Fig. 2) allows shallow angles to be applied to deep junctions without the consumption of excessive amounts of die area around the edge of the device. Theory and preliminary results give promise that this technique could be useful in the termination and fabrication of SiC power devices.

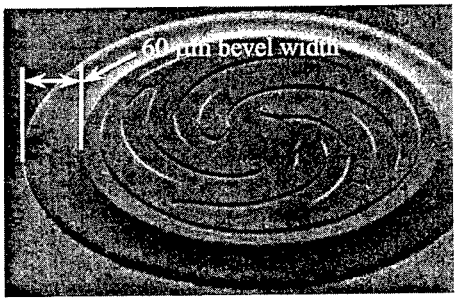


Fig. 3: SEM of beveled GTO structure. Etch depth is 5 μm.

References

[1] B. J. Baliga, *Power Semiconductor Devices*, PWS, Boston (1996), p. 103
[2] F. Lanois, P. Lassagne, D. Planson, and M.L. Locatelli, Appl. Phys. Lett. 69, (1996), p. 236
[3] D. C. Sheridan, J. B. Casady, C. E. Ellis, R. R. Siergiej, J. D. Cressler, R. M. Strong, W. M. Urban, W. F. Valek, C. J. Seiler, and H. Buhay, Mater. Sci. Forum 338-342 (1999), p. 1053
[4] A. O. Konstantinov, Q. Wahab, N. Nordell, and U. Lindefelt, Appl. Phys. Lett. 71, (1997), p. 90

Materials Science Forum Vols. 353-356 (2001) pp. 627-630
© 2001 Trans Tech Publications, Switzerland

Interface States of SiO_2/SiC on $(11\bar{2}0)$ and (0001) Si Faces

H. Yano, T. Kimoto and H. Matsunami

Department of Electronic Science and Engineering,
Kyoto University, Yoshidahonmachi, Sakyo, Kyoto 606-8501, Japan

Keywords: SiC-$(11\bar{2}0)$ Face, Acceptor-Like Interface States, MOS, Shallow Traps

Abstract Interface states of SiO_2/4H- and 6H-SiC on the $(11\bar{2}0)$ and (0001)Si faces were systematically characterized using high-frequency C-V measurements of n-MOS capacitors at 300K and 100K. The interface of SiO_2/4H-SiC$(11\bar{2}0)$ formed by wet oxidation has smaller interface state density near the conduction band edge than that of SiO_2/4H-SiC(0001)Si. The flatband voltage shift and hysteresis in C-V characteristics at 100K revealed different interface properties between the $(11\bar{2}0)$ and (0001)Si faces. The effects of dry oxidation on interface properties were also investigated.

1. Introduction

MOSFET performance is sensitive to a surface orientation, since higher channel mobility can be obtained on the $(11\bar{2}0)$ face compared to the (0001)Si face[1,2]. The higher channel mobility on the $(11\bar{2}0)$ face is due to reduced Coulombic scattering because of a smaller number of negative charges at the interface. The origin of negative charges is mainly given by electrons trapped at acceptor-like interface states, and their density increases toward the conduction band edge. Therefore, the channel mobility is easily affected by acceptor-like interface states near the conduction band edge. Only one paper related to the SiO_2/SiC$(11\bar{2}0)$ interface properties has been reported to date[3], which focused on interface states at deeper energies away from the conduction band edge. In this paper, we evaluate interface state densities near the conduction band edge on the $(11\bar{2}0)$ and (0001)Si faces for both 4H- and 6H-SiC. The effects of oxidation ambient are also discussed.

2. Experiments

MOS capacitors were fabricated on N-doped n-type epilayers grown on 4H- and 6H-SiC with surface orientations of $(11\bar{2}0)$-on and (0001)-off axis substrates. The epilayers have a variety of donor concentrations (N_d) from 6×10^{14} to 2×10^{17}cm^{-3} achieved by changing growth conditions. The samples were cleaned by an RCA cleaning prior to gate oxidation. Then, thermal oxidation was performed in wet or dry O_2 at 1100°C for 50min or 60min, respectively. The oxide thickness under these conditions was approximately 50nm for the $(11\bar{2}0)$ face and 13nm for the (0001)Si face samples. For (0001)Si face samples, also 40nm-thick oxides were grown by wet oxidation at 1150°C for 120min. After thermal oxidation, all samples were subjected to post oxidation annealing at the oxidation temperature for 30min in Ar. Al was used for both a gate electrode and a backside contact. High-frequency (1kHz, 1MHz) capacitance-voltage (C-V) characteristics were measured at both room temperature (300K) and low temperature (100K) with a bias sweep rate of 0.1V/s.

3. Results and Discussion

Figures 1(a) and 1(b) show C-V curves of 4H-SiC MOS capacitors fabricated on $(11\bar{2}0)$ and (0001)Si faces with wet oxides (N_d=1×10^{16}cm^{-3}). The measurements were done at 300K and the sweep direction was from accumulation (positive bias) to depletion (negative bias). Other 4H-SiC MOS capacitors showed similar positive flatband voltage shifts as observed in Fig. 1, meaning that effective negative charges exist at the interface. These charges include both fixed

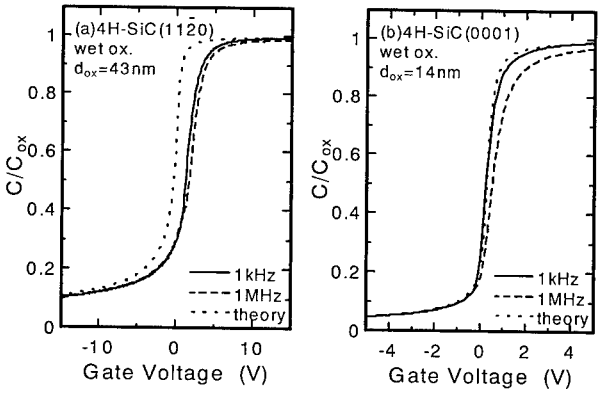


Fig.1: High-frequency C-V curves of 4H-SiC n-MOS capacitors with wet oxides on (a)(11$\bar{2}$0) and (b)(0001)Si (N_d=1×10^{16}cm^{-3}).

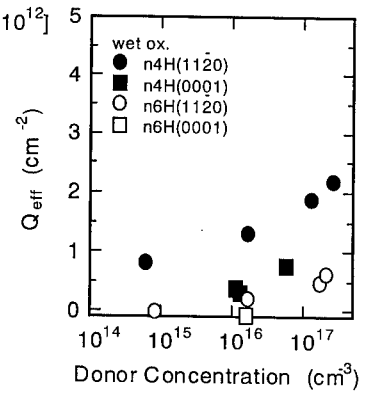


Fig.2: Effective negative charge density as a function of donor concentration.

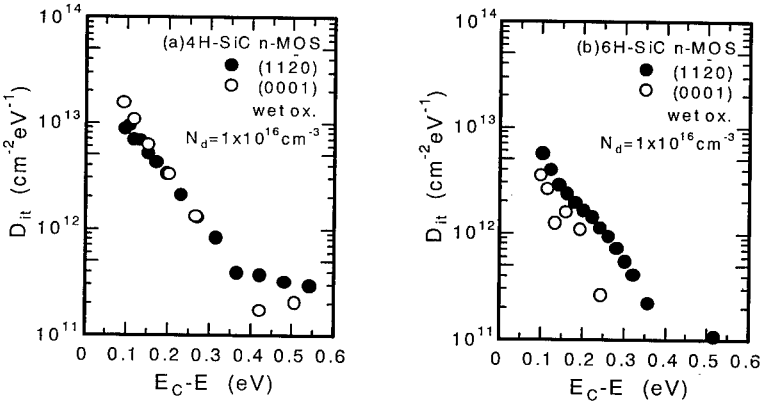


Fig.3: Interface state density of (a)4H-SiC and (b)6H-SiC n-MOS capacitors as a function of energy from conduction band edge.

charges and electrons trapped at acceptor-like interface states. The effective negative charge density (Q_{eff}) per unit area was calculated from the flatband voltage shift in C-V curves (1MHz) and the oxide capacitance. The results are shown in Fig. 2. The samples with higher donor concentrations showed higher Q_{eff} values. For higher donor concentrations, the Fermi level at the flatband condition moves to the conduction band edge. As a result, the number of electrons trapped at the acceptor-like interface states increases. 4H-SiC MOS capacitors show higher Q_{eff} than 6H-SiC regardless of the surface orientation. The fixed charge density is considered to be the same for 4H- and 6H-SiC because of the same atomic composition and simultaneous oxidation. Therefore, the higher Q_{eff} values in 4H-SiC indicate higher acceptor-like interface state density near the conduction band edge compared to 6H-SiC.

C-V curves measured at different frequencies are easily affected by interface states near the conduction band edge. Such shallow states may respond to the measurement frequency of 1kHz, but they may not respond to 1MHz. Hence, a high density of interface states near the conduction band edge leads to the large frequency dispersion shown in Fig. 1(b) for the 4H-SiC (0001)Si face sample. On the (11$\bar{2}$0) face, however, a smaller frequency dispersion was observed as in Fig. 1(a), suggesting a lower density of interface states near the conduction band edge compared to the (0001)Si face.

The interface state density (D_{it}) as a function of energy was estimated from the Terman

method using C-V curves at 1MHz measured at 300K, and the results are shown in Figs. 3(a) and 3(b) for 4H- and 6H-SiC MOS capacitors with a donor concentration of 1×10^{16}cm^{-3}. Similar distributions of D_{it} were obtained for samples with different donor concentrations. Comparing the (11$\bar{2}$0) and (0001)Si face samples of 4H-SiC oxidized in wet O_2, the (11$\bar{2}$0) face sample shows 2$\sim$3 times smaller D_{it} than the (0001)Si face near the conduction band edge. The lower D_{it} near the conduction band edge results in the smaller number of electrons trapped at the acceptor-like interface states, which should be the primary cause for higher channel mobility on the (11$\bar{2}$0) face. At deeper energies, higher D_{it} on (11$\bar{2}$0) leads to an injection-type hysteresis (not shown in Fig. 1(a), discussed later).

As shown in Fig. 3(b), the distributions of D_{it} in 6H-SiC MOS capacitors with wet oxides are different from that of 4H-SiC. 6H-SiC MOS capacitors on the (0001)Si face indicate smaller D_{it} than on the (11$\bar{2}$0) face over the whole energy range. As for the channel mobility, however, higher values were obtained on the (11$\bar{2}$0) face even in 6H-SiC[2]. Therefore, another factor such as reduced surface roughness of the epilayers[4] may cause higher channel mobility in 6H-SiC(11$\bar{2}$0).

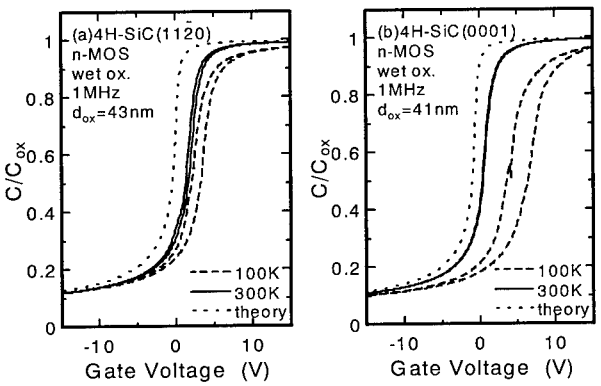


Fig.4: High-frequency (1MHz) C-V curves of 4H-SiC MOS capacitors on (a)(11$\bar{2}$0) and (b)(0001)Si measured at 300K and 100K.

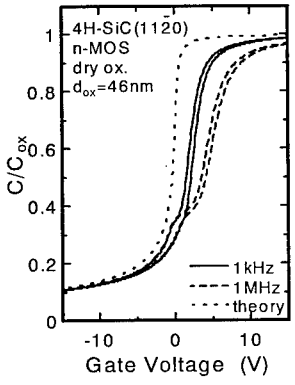


Fig.5: High-frequency C-V curves of 4H-SiC(11$\bar{2}$0) n-MOS capacitor with dry oxides.

In order to investigate the interface states near the conduction band edge, C-V measurements were performed at 100K. At lower temperatures, the Fermi level at the flatband condition shifts toward the conduction band edge. Furthermore, the time constant related with interface traps increases with decreasing temperature. Hence, a high density of interface states near the conduction band edge causes a large positive flatband voltage shift due to more electrons trapped at the interface states. In addition, at lower temperatures electrons trapped at interface states very close to the conduction band edge are gradually emitted to the conduction band during voltage sweep from accumulation to depletion and returning to accumulation, resulting in a large injection-type hysteresis. At room temperature, such quite shallow states do not contribute to both the flatband voltage shift and hysteresis because of fast trap time constant.

Figures 4(a) and 4(b) show C-V curves at 1MHz for 4H-SiC MOS capacitors on the (11$\bar{2}$0) and (0001)Si faces, respectively, measured at 300K and 100K. Both samples were oxidized in wet O_2, but at different oxidation temperatures and different times to obtain the similar oxide thickness of 40nm. The results of flatband voltage shift (ΔV_{FB}), hysteresis (ΔV_{hys}) and their corresponding charge densities (Q_{eff}, Q_{hys}) are listed in Table 1. On 4H-SiC(11$\bar{2}$0), a hysteresis of 0.4V is observed at 300K, and it increases to 0.9V at 100K. These hysteresis corresponds to an emitted electron density of mid-10^{11}cm^{-2}. However, their increase is not very significant, meaning that the interface state density does not increase rapidly toward the conduction band edge on 4H-SiC(11$\bar{2}$0). On the other hand, 4H-SiC(0001)Si MOS capacitors showed a quite large hysteresis of 2.4V at 100K in spite of a small hysteresis of 0.1V at 300K. The hysteresis of 2.4V corresponds to an emitted electron density of 1.3×10^{12}cm^{-2}. Besides the large positive

Table 1: Flatband voltage shift (ΔV_{FB}) and hysteresis (ΔV_{hys}) of MOS capacitors at 300K and 100K and corresponding charge density.

	surface	d_{ox}(nm)	Temp.(K)	ΔV_{FB}(V)	Q_{eff}(cm^{-2})	ΔV_{hys}(V)	Q_{hys}(cm^{-2})
4H-SiC	(11$\bar{2}$0)	43	300	2.59	1.29×10^{12}	0.42	2.09×10^{11}
			100	4.85	2.41×10^{12}	0.95	4.71×10^{11}
	(0001)	41	300	1.22	6.51×10^{11}	0.10	5.14×10^{10}
			100	8.01	4.28×10^{12}	2.40	1.29×10^{12}
6H-SiC	(11$\bar{2}$0)	43	300	0.45	2.22×10^{11}	0.11	5.31×10^{10}
			100	0.61	3.01×10^{11}	0.10	5.02×10^{10}
	(0001)	34	300	0.19	1.22×10^{11}	0.03	2.02×10^{10}
			100	0.29	1.86×10^{11}	0.08	5.26×10^{10}

flatband voltage shift was observed at 100K. These results for 4H-SiC(0001) indicate another evidence that the interface state density increases significantly toward the conduction band edge, as was described in ref.5. For 6H-SiC MOS capacitors, such a significant increase was not observed for both (11$\bar{2}$0) and (0001)Si faces.

The interface properties are sensitive to the oxidation ambient for the (11$\bar{2}$0) face. Both 4H- and 6H-SiC(11$\bar{2}$0) MOS capacitors indicated 4$\sim$5 times higher D_{it} and 2$\sim$3 times higher Q_{eff} at 300K when the samples were oxidized in dry O_2. A large frequency dispersion at the accumulation condition and a kink at the onset of deep depletion are observed in Fig. 5, due to a high density of interface states at shallow and deep energies. On the other hand, D_{it} of MOS capacitors with dry oxides on the (0001)Si face were insensitive to the oxidation ambient.

4. Conclusions

The interface states near the conduction band edge at SiO_2/4H- and 6H-SiC on the (11$\bar{2}$0) and (0001)Si faces were characterized by high-frequency C-V measurements at 300K and 100K. For 4H-SiC with wet oxides, the (11$\bar{2}$0) face sample showed smaller D_{it} near the conduction band edge than the (0001)Si face sample (determined by the Terman method). This result is separately confirmed by the C-V measurement at 100K, in which a small change in flatband voltage shift and hysteresis on 4H-SiC(11$\bar{2}$0) and a large change on 4H-SiC(0001)Si were observed. The smaller D_{it} near the conduction band edge should be the primary cause for the higher channel mobility on the 4H-SiC(11$\bar{2}$0) face. The effects of dry oxidation on interface properties were also examined.

Acknowledgement

This work was supported by a Grant-in-Aid for Specially Promoted Research, No. 09102009, from the Ministry of Education, Science, Sports and Culture of Japan. The authors express gratitude to Kyoto University Venture Business Laboratory for the partial support to this work. The authors gratefully acknowledge Nippon Steel Corporation for the supply of (11$\bar{2}$0) substrates.

References

[1] H. Yano, T. Hirao, T. Kimoto, H. Matsunami, K. Asano and Y. Sugawara, IEEE Electron Device Lett. 20 (1999), p.611.

[2] H. Yano, T. Hirao, T. Kimoto, H. Matsunami, K. Asano and Y. Sugawara, Mater. Sci, Forum 338-342 (2000), p.1105.

[3] J.N. Shenoy, M.K. Das, J.A. Cooper, Jr., M.R. Melloch and J.W. Palmour, J. Appl. Phys. 79 (1996), p.3042.

[4] Z.Y. Chen, T. Kimoto, H. Matsunami, Jpn. J. Appl. Phys. 38 (1999), p.L1375.

[5] M. Bassler, V. Afanas'ev, G. Pensl and M. Schulz, Mater. Sci. Forum 338-342 (2000), p.1065.

Materials Science Forum Vols. 353-356 (2001) pp. 631-634
© 2001 Trans Tech Publications, Switzerland

Interface Properties of MOS Structures Formed on 4H-SiC C(000$\bar{1}$) Face

K. Fukuda[1], S. Suzuki[2], J. Senzaki[1], W.J. Cho[1], T. Tanaka[2] and K. Arai[1]

[1] Ultra-Low-Loss Power Device Technology Research Body (UPR), Electrotechnical Laboratory, 1-1-4 Umezono, Tsukuba, Ibaraki 305-8568, Japan

[2] Ultra-Low-Loss Power Device Technology Research Body (UPR), R&D Association for Future Electron Devices (FED), c/o Eletrotechnical Laboratory, 1-1-4 Umezono, Tsukuba, Ibaraki 305-8568, Japan

Keywords: C(000-1) Face, C-V Characteristics, Interface State Density, Surface Morphology, TEM

Abstract. We have investigated the oxidation and post oxidation annealing (POA) effects on the capacitance-voltage (C-V) characteristics and the interface state density (D_{it}) of n-type SiC MOS structures formed on the C(000$\bar{1}$) face. In addition, we analyzed the SiC surface and the SiO_2/4H-SiC interface by atomic force microscopy (AFM) and transmission electron microscopy (TEM). Oxidation and a subsequent high-temperature hydrogen annealing reduced D_{it} near the conduction-band edge. However, the value of D_{it} at the energy level from the conduction band edge (E_c-E) ≈0.6eV is one order of magnitude higher than that of n-type MOS structures formed on the Si(0001) face. Moreover, AFM revealed that the surface roughness of C(000$\bar{1}$) face was comparable with that of Si(0001) face. TEM presented that the SiO_2/SiC interface on the 4H-SiC C(000$\bar{1}$) face was rougher than that on the 4H-SiC Si(0001) face.

Introduction

Silicon carbide (SiC) is an attractive material for higher-power, higher-temperature, and higher-frequency devices compared with Si-based devices. Recently, several researchers have carried out various studies on SiC MOSFETs[1,2]. Usually, SiC MOSFETs are fabricated on the Si(0001) face. The C(000$\bar{1}$) face has superior properties such as a faster oxidation[3]. The fabrication processes such as the field oxidation in MOSFETs or the edge termination in Schottky barrier diodes require thick oxide films (a few nm). Therefore, the oxidation processes would become simple if the C(000$\bar{1}$) face is used. However, the channel mobility of 4H-SiC MOSFETs formed on the C(000$\bar{1}$) face is very low compared with the Si(0001) face[4]. Therefore, it is necessary for the clarification of the low channel mobility for MOSFETs formed on the C(000$\bar{1}$) face to investigate the interface properties such as D_{it}, the effects of surface morphology of SiC and the interface structure of SiO_2/SiC.

In this paper, we report on the effect of oxidation and POA on the C-V characteristics and the D_{it} and we show the results for the surface morphology and the interface structure using AFM and TEM.

Experimental

8° off-angled n-type 4H-SiC C(000$\bar{1}$) face substrates with 4.9-μm-thick n-type epitaxial layers were purchased from Cree Research Inc. The effective carrier density was 2.5×10^{16} cm^{-3}. First of all, the RCA cleaning was carried out. Next, a sacrificial oxide of 10nm thickness was grown at 1200°C, and then it was removed with 5% HF solution. Then, AFM images of SiC surface were taken.

Gate oxide films were thermally grown at 1200°C for 22 min in dry O_2 (dry oxidation, samples (a) and (c)) and 6 min in water vapor atmosphere (wet oxidation, samples (b) and (d)). The ratio of the flow rates of O_2 and H_2 gases was 1.5 : 0.5. The thickness of the gate oxide films, estimated from the C-V characteristics, was 52 ± 5nm. After both oxidations, all samples were annealed in argon for 30 minutes at 1200°C, and then gradually cooled in argon. In addition, samples (c) and (d) were annealed in hydrogen at 800°C for 30 min and then gradually cooled in hydrogen. High-temperature hydrogen annealing was used, because it is effective for the reduction of the D_{it} in MOS structures formed on the Si(0001) face[5]. The ramp-down rate of the temperature after the oxidations and annealings was fixed to -5°C/min. Aluminum on the top of the oxide films and on the back of the samples was evaporated to make gate electrodes and ohmic contacts to MOS structures, respectively. C-V measurements and the D_{it} estimation were performed using a KI82 system. TEM images of SiO_2/SiC interface were observed for sample (d) and the sample formed on Si (0001) face using the dry oxidation and the hydrogen annealing.

Results and discussion

1. C-V characteristics

Figure 1 shows C-V characteristics of samples (a), (b), (c) and (d). The high-frequency characteristics (solid lines) were measured at the frequency (f) =100 kHz, and the quasi-static characteristics (dotted lines) were measured at the delay time (t_d) =10 seconds and step voltage (V_s)=50mV.

Figure 2 presents the D_{it} distributions of SiC MOS structures on the C(000$\bar{1}$) face, which were estimated from eq.(1) using the KI82 system.

$$D_{it}=q^{-1}[(C_q^{-1}-C_{ox}^{-1})^{-1}-(C_h^{-1}-C_{ox}^{-1})^{-1}], \quad (1)$$

where q is the electric charge, and C_h, C_q, and C_{ox} are the high-frequency, quasi-static, and oxide capacitance per unit area, respectively[6]. The D_{it} is underestimated at E_c-E above approximately 0.6eV, because the measurements are performed at room temperature [7]. The D_{it} of a sample with dry oxidation and hydrogen annealing at 1000℃ is also shown for comparison.

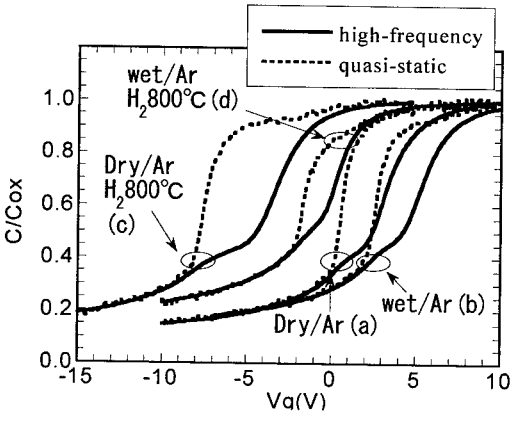


Fig. 1 Effect of oxidation and POA on C-V characteristics.

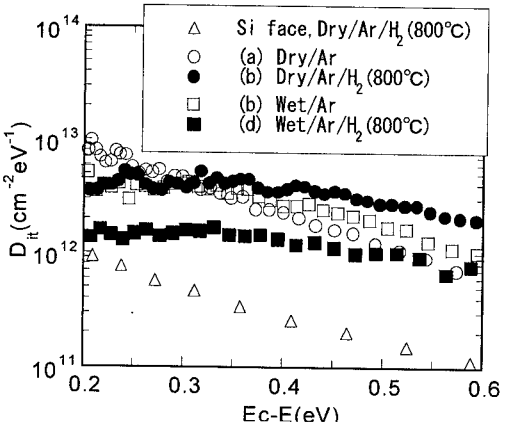


Fig. 2 Effect of oxidation method and POA on D_{it}.

Figures 1 and 2 reveal that the D_{it} near the conduction-band edge of sample (b) prepared by wet oxidation is lower than that of sample (a) prepared by dry oxidation although the ΔV_{fb} of sample (b) is larger than that of sample (a). Hydrogen annealing at 800°C decreases the D_{it} of MOS structures formed on the C(000$\bar{1}$) face by wet oxidation [sample(d)]. On the other hand, the D_{it} of MOS structures formed on the C(000$\bar{1}$) face by dry oxidations is increased by hydrogen annealing at 800°C [sample(c)]. However, in the case of the Si(0001) face, high-temperature hydrogen annealing reduces the D_{it} of n-type MOS structures regardless of the oxidation method (dry or wet oxidation)[5,8]. The effect of hydrogen annealing on the C-V characteristics and the D_{it} of MOS structures formed by dry oxidation is different for the Si(0001) and the C(000$\bar{1}$) faces although the reason for this is still unclear. The value of the D_{it} near E_c-E=0.2eV decreases considerably and is almost the same as that observed for the n-type SiC MOS structure on the Si(0001). On the other hand, the value of the D_{it} around E_c-E=0.6eV does not change at all, and is approximately one order of magnitude higher than the D_{it} for the n-type SiC MOS structures on the Si(0001) face, which indicates that a large amount of interface states exists at the deep level in n-type SiC MOS structures on the C(000$\bar{1}$) face. Therefore, the quality of the SiO_2/SiC interface formed on the C(000 $\bar{1}$) face is inferior to that of the Si(0001) face.

2. Surface morphology and SiO_2/SiC interface

Figures 3 and 4 show the AFM images of the Si(0001) face and the C(000$\bar{1}$) face, respectively. The average roughness (Ra) of the Si(0001) face and the C(000$\bar{1}$) face is 0.093nm and 0.118nm, respectively. The surface roughness of both faces reveals almost the same.

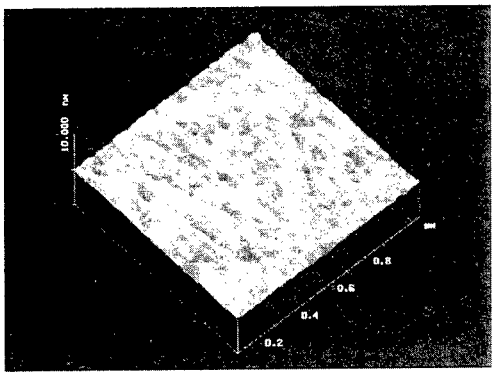


Fig. 3 3-D AFM image of the Si(0001) face. X: 0.2μm/division, Z: 10nm/division

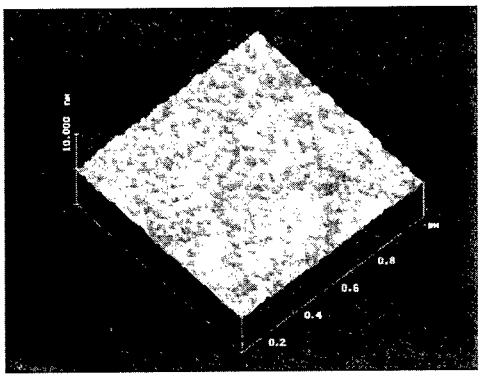


Fig. 4 3-D AFM image of the C(000$\bar{1}$) face. X: 0.2μm/division, Z: 10nm/division

Figures 5 and 6 show the TEM images of SiO_2/SiC interface formed on the Si(0001) face and the C(000$\bar{1}$) face, respectively. The oxidation method that achieves the low D_{it} is different between the Si(0001) face and the C(000$\bar{1}$) face as mentioned above. Therefore, the dry oxidation was performed for the Si(0001) face. On the other hand, the wet oxidation was performed for the C(000$\bar{1}$) face. The hydrogen annealing at 800°C for 30 min was performed after the oxidation. The SiO_2/SiC interface structure on the C(000$\bar{1}$) face is much rougher than that on the Si(0001) face although the surface roughness is almost the same before the oxidation. This might be due to the strong face orientation dependence of the oxidation ratio for the SiC substrate. This large roughness

in SiO_2/SiC interface on the C(000$\bar{1}$) face is considered to be one of reasons for the low channel mobility for SiC MOSFETs fabricated on the C(000$\bar{1}$) face.

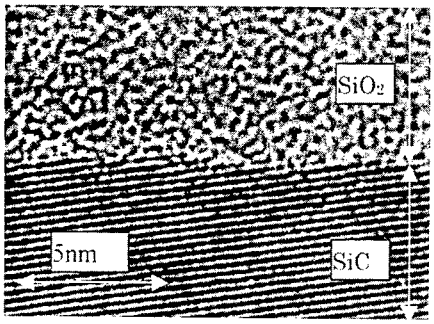


Fig. 5 Typical cross-sectional TEM image for SiO_2/SiC interface formed on the Si(0001) face.

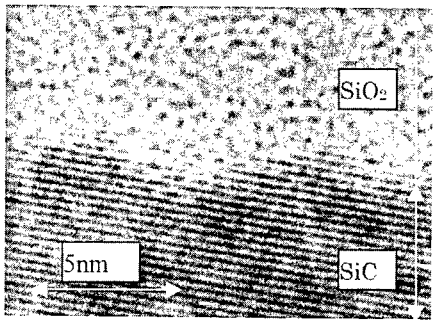


Fig. 6 Typical cross-sectional TEM image for SiO_2/SiC interface formed on the C(000$\bar{1}$) face.

4. Conclusion

We have investigated the oxidation and POA effect on the D_{it} of n-type SiC MOS structures formed on the C(000$\bar{1}$) face. Wet oxidation and hydrogen annealing reduce the D_{it} near the conduction-band edge of n-type 4H-SiC MOS structures on the C(000$\bar{1}$) face as well as on the Si(0001) face. However, there is no change in the D_{it} around E_c-E=0.6eV. Moreover, it was found that SiO_2/SiC interface structure on the C(000$\bar{1}$) face is much rougher than that on the Si(0001) face. It is considered to be necessary for a MOSFET with high channel mobility on the C(000$\bar{1}$) face to reduce the D_{it} at the deep level and the large roughness at SiO_2/SiC interface.

This work was performed under the management of FED as a part of the MITI New Sun Shine Program (R&D of Ultra-Low-Loss Power Device Technologies) supported by NEDO.

References

[1] N. S. Saks, S. S. Mani, A. K. Agarwal, and M.G. Ancona, IEEE Electron Device Lett. 20 (1999), p. 431.
[2] P. M. Shenoy and B. J. Baliga, IEEE Electron Device Lett. 18 (1997), p. 589.
[3] A. Gölz, G.Horstmann, E. Stein von Kamienski and H. Kurz, Inst.Phys. Conf. Ser. No. 142 (1996), p. 633.
[4] S.Ogino,T. Oikawa, and K. Ueno, Mater. Sci. Forum Vol.338-342 (2000),p.1101.
[5] K. Fukuda, S. Suzuki, T. Tanaka, and K. Arai, Appl. Phys. Lett. 76 (2000), p.1585.
[6] E. H. Nicollian, and J. R. Brew, MOS (Metal Oxide Semiconductor) physics and Technology (Wiley, New York.1982).p.332.
[7] J. A. Cooper jr., phys. stat. sol. (a) 162 (1997), p. 305.
[8] S. Suzuki, K. Fukuda, R. Kosugi, W. J. Cho, T. Tanaka and K. Arai, in Extended Abstract of the 1st International Workshop on Ultra-Low-Loss Power Device Technology (FED, Tokyo, 2000), p. 191.

Materials Science Forum Vols. 353-356 (2001) pp. 635-638
© 2001 Trans Tech Publications, Switzerland

Steam Annealing Effects on CV Characteristics of MOS Structures on (11$\bar{2}$0) Face of 4H-SiC

M. Yoshikawa[1], T. Ohshima[1], H. Itoh[1], K. Takahashi[2] and M. Kitabatake[2]

[1] Japan Atomic Energy Research Institute, 1233 Watanuki, Takasaki, Gunma 370-1292, Japan

[2] Advanced Technology Research Laboratories, Matsushita Electric Industrial Co. Ltd., Hikaridai 3-4, Seika-cho, Kyoto 619-0237, Japan

Keywords: SiC-(11$\bar{2}$0) Face, CV-Characteristics, Interface Trap, MOS, Oxide-Trapped Charges, Re-Oxidation, Steam Annealing

Abstract Epilayers grown on the (11-20) and (1-100) faces of n-type 4H-SiC substrates were oxidized pyrogenically at 1100°C for 1 hour to make oxide layers of about 50 nm in thickness and annealing in steam (re-oxidation) was successively performed at 800, 850 or 950°C for 3hours. After the re-oxidation process, gold was deposited to form metal-oxide-semiconductor (MOS) structures on the (11-20) and (1-100) faces. Capacitance-voltage characteristics were measured for these MOS structures to obtain the density of interface traps per unit area (D_{it}) near the conduction band edge and the total number of interface traps per unit area (N_{it}). It was found that D_{it} as well as N_{it} in oxide layers on the (11-20) face decrease by annealing in steam around 800°C.

1. Introduction

Hexagonal type silicon carbide (4H-SiC) has a large band gap (3.2 eV), excellent thermal and chemical stabilities, a large saturation drift velocity (about 10^7 cm/s), and high electron mobility (approximately 800 $cm^2/(Vs)$) comparable to that of cubic type SiC [1]. In addition, insulators are easily obtained with the similar oxidation process as used for the fabrication of silicon (Si) metal-oxide-semiconductor (MOS) devices. This is one of the most important characteristics of 4H-SiC for electronic applications. Many researchers have fabricated MOS capacitors and metal-oxide-semiconductor field-effect-transistors (MOSFETs) using the thermal oxide layers as gate insulators and examined the electrical characteristics such as capacitance-voltage (*CV*), conductance-voltage, and current-voltage characteristics. Many efforts have been made for improving these electrical characteristics, however, there remain many problems, including the relatively low electron mobility in an inversion layer at the SiO_2/4H-SiC interface [2]. Some researchers consider that some of the problems are linked to the high density of interface traps near the conduction band edge [3]. Recently, it has been reported that MOSFETs made on the (11-20) faces of 4H and 6H-SiC substrates have higher channel mobility compared to those made on the (0001) faces [4]. If the interface traps near the conduction band edge are related to the low electron mobility in an inversion layer near the SiO_2/4H-SiC interface on the (0001) face, the interface trap density near the conduction band edge on the (11-20) face is estimated to be less than that on the (0001) face. However, there is only a few reports regarding the energy profile of the interface trap density at the SiO_2/4H-SiC interface on the (11-20) faces.

In this paper, we fabricate MOS structures on the (11-20) and (1-100) faces of n-type 4H-SiC substrates, and measure their *CV* characteristics to obtain the energy profile of interface trap density per unit area (D_{it}) near the conduction band edge and the total number of interface traps per unit area (N_{it}). We also examine the influence of annealing in steam after oxidation on D_{it} and N_{it} in the oxide layer and discuss the influence of annealing in steam on the generation of interface traps in relation to the surface orientation.

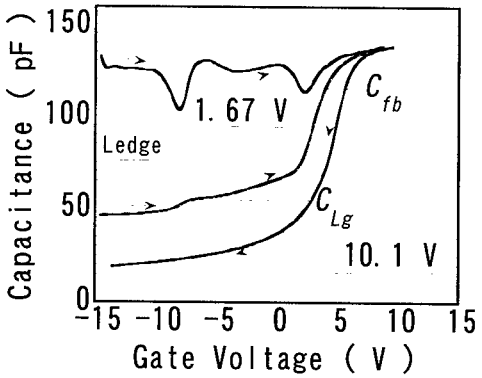


Fig.1. *CV* characteristics of a MOS structure formed on the (11-20) face with the oxide layer that is not annealed in steam.

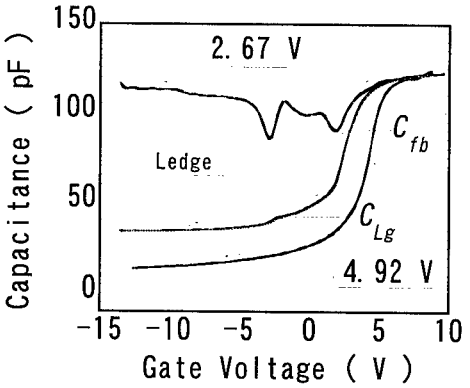


Fig.2. *CV* characteristics of a MOS structure formed on the (11-20) face with the oxide layer that is annealed in steam at 800°C for 3 hours.

2. Experiments

Substrates of n-type 4H-SiC were cut from (11-20) and (1-100) wafers purchased from Nippon Steel Co. Ltd.. The net donor concentration of the wafers was about 10^{18} cm^{-3}. Epilayers were grown on the substrates at 1600°C by chemical vapor deposition (CVD) method using SiH_4-C_3H_8-H_2 reaction gases. The flow rates of SiH_4 and C_3H_8 were 3 sccm both. The flow rate of H_2 was 2 slm and the growth pressure was 700 Torr. Details of the growth procedures have been reported elsewhere [5]. The resultant epilayers were about 4.5 μm in thickness and showed n-type conduction with the donor concentration of approximately $1.0x10^{16}$ cm^{-3}. After CVD growth, sacrificed oxidation for the epilayer surfaces was performed. Thereafter pyrogenic oxidation was carried out at 1100°C for 1 hour to make gate oxide layers of about 50 nm in thickness. At the final stage of oxidation, annealing in steam was performed at 800, 850, or 950 for 3 hours. After these processes, gold was deposited on the oxide layers to form gate electrodes of 0.50 mm in diameter. For fabricating an ohmic electrode, oxide layers grown on the back surface of the substrates were removed, and aluminum was evaporated on the bared surfaces of them. The simultaneous *CV* characteristics (S*CV*) were measured for the 4H-SiC MOS structures to obtain the gate voltage corresponding to flat-band condition (V_{fb}) and the energy profile of interface trap density (D_{it}) near the conduction band edge. The MOS structures were illuminated with a low-pressure mercury lamp to induce an inversion layer before sweeping the gate voltage. After the inversion layer was formed, the gate voltage was swept from negative to positive gate voltage side under dark condition at room temperature. The *CV* curve swept rapidly from positive to negative gate voltage side was also measured for the same sample before and after the S*CV* measurement to calculate N_{it} using a photo *CV* technique [6].

3. Results

Figure 1 shows the *CV* characteristics of a MOS structure formed on the (11-20) face, whose oxide layer is not annealed in steam. The notations C_{fb} and C_{Lg} indicate the capacitance values corresponding to the flat band condition and the ledge of the high-frequency *CV* curve swept from negative to positive gate voltage side, respectively. There is a split near the accumulation region between quasi-static and high-frequency *CV* curves which are swept from negative to positive gate voltage side. This indicates that fairly large amount of interface traps exists near the conduction band edge. The difference in gate voltages at C_{fb} and C_{Lg} levels between high-frequency *CV* curves is approximately 1.67 V and 10.1 V, respectively. Figure 2 shows the *CV* characteristics of a MOS structure formed on the (11-20) face with the oxide layer annealed in steam at 800°C for 3 hours. Though the split and the gate voltage difference at C_{fb} level still exist, the gate voltage difference at

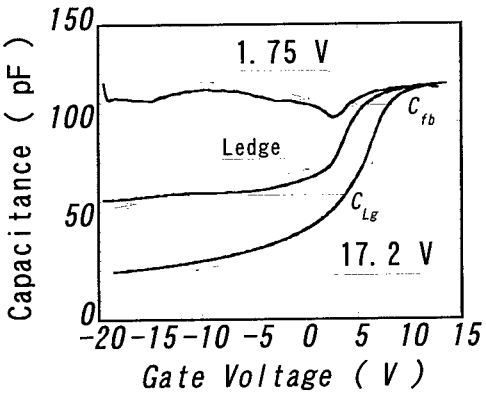


Fig.3 *CV* characteristics of a MOS structure formed on the (1-100) face, whose oxide layer

C_{Lg} level decreases by the annealing. The difference in gate voltages at C_{fb} and C_{Lg} is approximately 2.67 V and 4.92 V, respectively. The annealing in steam at 850 or 950°C was also carried out. Although the split near the accumulation region between quasi-static and high-frequency *CV* curves did not disappear, the difference in gate voltages at C_{fb} and C_{Lg} levels was about 3.33 V and 5.16 V for the annealing at 850°C, and 3.16 V and 8.07 V for the annealing at 950°C.

As for MOS structures on the (1-100) face, only the *CV* characteristics for samples with oxide layers annealed at 800 and 850°C was measured. For most of the samples, including the sample without the steam annealing, a large leakage current flowing through the oxide layer was detected. On the (1-100) surface, many defects that were seen like a line were observed after the epitaxial growth. It is considered that such a leakage current is responsible for the defects on the surface. Figure 3 shows the *CV* characteristics of a MOS structure formed on the (1-100) face, whose oxide layer is annealed in steam at 800°C. The split, whose origin is the same as that on the (11-20) face, is seen at the accumulation region. The difference in gate voltages at C_{fb} and C_{Lg} levels was about 1.75 V and 17.2 V for the annealing at 800°C, and 2.53 V and 9.42 V for the annealing at 850°C.

4. Discussion

A. (11-20) face

The value of D_{it} near the conduction band edge is given by the equation as follows:

$$D_{it} = \frac{1}{qS}\left[\left(\frac{1}{C_q}-\frac{1}{C_{ox}}\right)^{-1} - \left(\frac{1}{C_h}-\frac{1}{C_{ox}}\right)^{-1}\right], \qquad (1)$$

where C_q, C_h, C_{ox}, are quasi-static, high-frequency of 1 MHz and oxide capacitances, respectively, and q and S are the electronic charge and gate electrode area, respectively. Figure 4 shows the profiles of D_{it} near the conduction band edge of SiO_2/4H-SiC interface, that are extracted from *SCV* curves using Eq.(1), before and after the annealing in steam at 800, 850, or 950°C. Large amounts of D_{it} exist near the conduction band edge before the annealing. The value of D_{it} increases steeply around 0.3 eV below the conduction band edge (E_c-0.3 eV). By the annealing in steam, D_{it} near the conduction band edge is found to decrease by the annealing in steam. It is found that the annealing around 800°C has a significant influence on decreasing D_{it} near the conduction band edge.

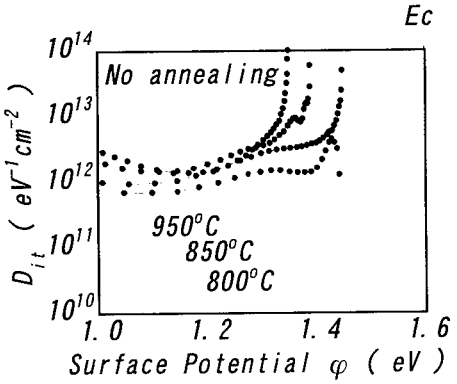


Fig.4 Change in the energy profiles of D_{it} near the conduction band edge for MOS structures on the (11-20) face of a 4H-SiC substrate.

The value of N_{it} , which involves the number of interface traps in the deep energy region, is also obtained by the photo-*CV* technique at room temperature [6] in order to understand the effects of annealing in steam on electrical characteristics of SiO_2/4H-SiC interface. Figure 5 shows N_{it} as a

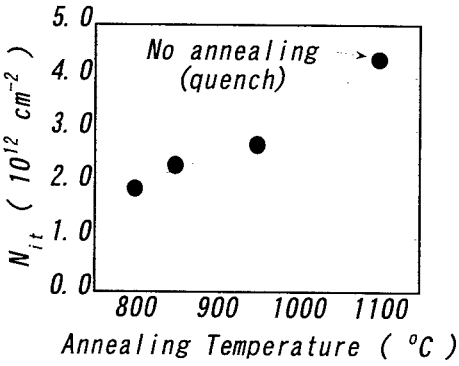


Fig.5 Steam annealing temperature dependence of N_{it} for MOS structures on the (11-20) face of a 4H-SiC substrate.

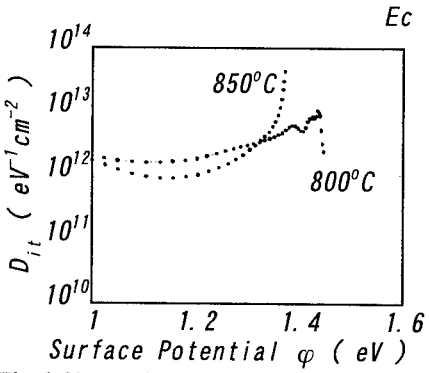


Fig.6 Change in the energy profiles of D_{it} near the conduction band edge for MOS structures on the (1-100) face of a 4H-SiC substrate.

function of annealing temperature for MOS structures on the (11-20) face of a 4H-SiC substrate. The value of N_{it} for MOS structures with oxide layers that is not annealed in steam is also plotted for comparison. The value of N_{it} decreases significantly with decreasing the annealing temperature. It is found that the steam annealing has significant influences on decreasing the interface traps at SiO_2/4H-SiC interface formed on the (11-20) face.

B. (1-100) face

Figure 6 shows the energy profiles of D_{it} near the conduction band edge after 800 and 850°C annealing. The value of D_{it} near the conduction band edge decreases slightly with comparing that for the annealing at 850°C. On the other hand, N_{it} for the sample annealed at 800 and 850°C is obtained to be 3.59×10^{12} and 9.77×10^{11} cm^{-2}, respectively. Significant decrease was found to observe for the 850°C annealing. Since the oxidation-rate for the (1-100) face is lower than that for the (11-20) face, the optimum annealing temperature is considered to be higher value. In order to reveal the steam annealing effects in detail, further study is needed for 4H-SiC (1-100) face.

5. Summary

We have investigated the effects of annealing in steam below 950°C after oxidation on the *CV* characteristics of MOS structures formed on the (11-20) and (1-100) faces of 4H-SiC substrates. The split near the accumulation region between quasi-static and high-frequency *CV* curves is observed on the (0001), (11-20) and (1-100) faces. This indicates that no surface orientation dependence on the generation of interface traps near the conduction band edge. Interface traps near the conduction band edge as well as those in the middle region of the band gap decrease significantly by the annealing in steam around 800°C. Though many interface traps exist near the interface of MOS structures on the (11-20) and (1-100) faces just after the oxidation, the traps on the (11-20) face are reduced significantly by annealing in steam around 800°C.

References

[1] W.E.Nelson and *et al.*, J.Appl.Phys. **37**(1966), p.333.
[2] W.J.Zhu and *et al.*, *Materials Science Forum*, **338-342**(2000), p.1311.
[3] M.Bassler and *et al.*, *Materials Science Forum*, **338-342**(2000), p.1065.
[4] H.Yano and *et al.*, *Materials Science Forum*, **338-342**(2000), p.1105.
[5] K.Takahashi and *et al.*, *Materials Science Forum*, **338-342**(2000), p.141.
[6] J.A.Cooper, Jr., Phys.stat.sol.(a), **162**(1997), p305.

Materials Science Forum Vols. 353-356 (2001) pp. 639-642
© 2001 Trans Tech Publications, Switzerland

Role of H_2 in Low Temperature Post-Oxidation Anneal for Gate Oxide on 6H-SiC

V. Raineri[1], S. Lombardo[1], P. Musumeci[2], A.M. Maktari[2] and L. Calcagno[2]

[1] CNR-IMETEM, Stradale Primosole 50, IT-95121 Catania, Italy

[2] INFM (Istituto Nazionale per la Fisica della Materia) and Dipartimento di Fisica, Corso Italia 57, IT-95129 Catania, Italy

Keywords: Gate Oxide, Interface State, Oxidation

Abstract. A significant improvement of the oxide characteristics grown on 6H-SiC n-type have been obtained after post-anneal treatments in hydrogen ambient. The role of hydrogen in the passivation of interface trap states is investigated by several analytical methods. The improvement is related to the amount of atomic hydrogen present during the post-annealing process.

Introduction

Oxidation of SiC produce SiO_2 layers with electrical properties sufficient for the fabrication of metal oxide semiconductor (MOS) transistors and circuits, but further reductions in both fixed charge and surface state density would have a dramatic impact on SiC MOS technology [1]. The interface trap densities obtained to date are around 10^{11} cm^{-2} eV^{-1} [2, 3]. Similar values are obtained when oxidising silicon for ULSI. However, in Si the number of interface traps is dramatically reduced by post-oxidation annealing in a hydrogen environment (down to 10^{10} cm^{-2} eV^{-1}) because of passivation of dangling bonds at the SiO_2/Si interface by hydrogen. Similar attempts, to hydrogen passivate the SiO_2/SiC interface, have not resulted in any reduction of the interface state density [4, 5]. In this work we have investigated carefully the role of hydrogen on the SiO_2/SiC interface by different treatments. As main result we obtained a significant improvement on the SiO_2 electrical properties for a particular hydrogen treatment.

Experimental details

6H-SiC n-n+ epitaxial wafers supplied by CREE were oxidised at 1100 °C in dry ambient with 1.5% per cent of HCl. Higher temperatures resulted in lower oxide quality while lower temperatures resulted in too slow growth rate. The interface trap density was minimised by choosing opportunely the cooling ramp as specified in the following. A low cooling rate ramp (10 °C per minute) has been adopted allowing to the volatile carbon-oxide compound formed during oxidation to escape from the oxide layer. Surface states and fixed charge densities can be also reduced by a correct surface preparation of SiC surface before oxidation [6]. In our work we adopted a standard cleaning procedure (RCA) on new and virgin epitaxial wafers after a surface treatment in H_2SO_4 H_2O_2 (3:1) for 10 min and a subsequent HF (10%) dip and water rinse.

Then, a metallic oxide semiconductor (MOS) device was fabricated with a metal (Ti) gate contact. Hydrogen treatments were performed on the MOS devices at temperature up to 200 °C in plasma hydrogen or up to 500 °C in horizontal ovens using forming gas. The interface chemical morphology was investigated by analytical x-ray transmission electron microscopy (EDX). The interface morphology was monitored by transmission electron microscopy (TEM).

C-V measurements were performed using the conductance method on the MOS at temperatures up to 200°C. This highest temperature has been chosen to probe a significant portion of the band-gap (E_c-E from 0.15 to 0.6 eV). The C-V characteristics were measured with test frequencies ranging

from 20 Hz to 1 MHz. The conductance of the MOS structure was measured simultaneously to obtain the information concerning the oxide/SiC interface. The C-V characteristics were determined before and after hydrogen treatments.

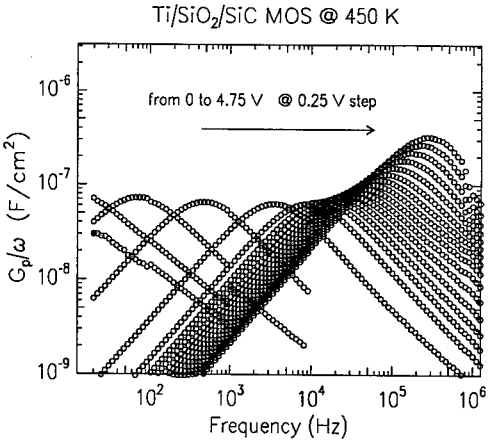


Fig. 1 - G_p/ω vs. frequecy Hz for a as grown oxide at 1100 °C in dry ambient.

Results and discussion

The capacitance measurements have been performed in the quasi-static mode. The conductance method (G_p/ω vs. frequency Hz) was adopted to extract information concerning the interface traps. This method provides a precise evaluation of interface trap density in the investigated energy band by checking the measurements at different voltage and temperatures. A typical measurement obtained on the as-grown oxide is shown in Fig. 1. The peak heights of the G_p/ω curves are proportional to the interface trap densities being $D_{it} \approx 2.5/q\{G_p/\omega\}_{max}$ where q is the elementary charge. An interface trap density of $D_{it}=5\times10^{11}$ cm^{-3} is obtained. So high values are obtained also when oxidising silicon and they are due to not saturated silicon bond at the interface, where a few monostrates of substechiometric oxide are present. Normally the interface trap density in silicon is decreased down to 10^{10} cm^{-3} saturating these dangling bonds by hydrogen or nitrogen treatments. However, the same effect has not been observed in SiC [1]. In more recent works the effect has been reported even if its intensity is not relevant [7]. The main reason is the chemical nature of the interface where the presence of C can induce an accumulation of carbon at the interface and dangling bonds can be avoided by the presence of C-O Si-C-O bonds. So that to improve the oxide quality by hydrogen treatments, C accumulation at the interface should be avoided.

We reduced C accumulation at the interface by slow cooling ramp after oxidation and optimising the oven conditions. In Fig. 2 is reported the EDX analyses in the SiC layer from bulk to the interface for the optimised oxidation. Clearly no accumulation of C is observed being the signal of carbon decreasing with no peak or spike.

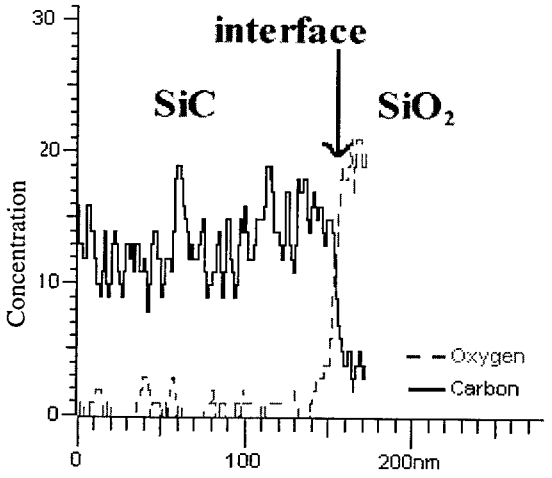


Fig. 2 - EDX spectrum for O and C at the SiC/SiO2 interface for an optimised as-grown oxide.

The sharp interface has been observed also in TEM analyses. In Fig. 3a the high-resolution transmission electron microscopy of the interface for an optimised as-grown oxide is shown. The atomic planes sharp finish at the interface where no cluster, precipitate or layer is observed.

The same structure is obtained after post - annealing in hydrogen independently on the treatment. As an example, in Fig. 3b the image of the interface after an annealing in forming gas at 450° for 20 minutes is also reported.

A more complete electrical characterisation of the oxide can be

achieved by the complete C-V plot. The measurements obtained on the as-grown oxide are reported in Fig. 4a. A hysteresis behaviour is observed, as previous reported for oxide grown on SiC [8, 9]. A low minority carrier generation and recombination rate is believed to be the basis for this hysteresis effect [1].
Moreover, a tail is present in the deep depletion region indicating the presence of surface states. We concluded that the low interface trap density is mainly related with dangling bonds present at the interface. So we tried to passivate these dangling bonds by hydrogen treatments.
Hydrogen treatments were performed by plasma immersion at several temperatures in the range between room temperature and 400°C changing the treatment pressure. Even changing the pressure from 10^{-7} to 10^{-4} torr plasma treatments are performed in vacuum, i.e. the presence of atomic H is low. A higher concentration of atomic H can be obtained by furnace annealing (atmospheric pressure) in forming gas or directly in H_2 gas flow. However, to break the H_2 molecule, since only atomic H is diffusing true the oxide and passivating dangling bonds, a temperature higher than 800 °C is necessary. Nevertheless, these thermal treatments are particularly dangerous. A method to obtain atomic H in furnace under a forming gas flow at lower temperatures (300 - 500°C) is just to have Al in the oven, since water in SiO_2, present even in dry oxides, reacts with the aluminium to form Al_2O_3 and atomic hydrogen (H). The H can diffuse to the SiC/SiO_2 interface, where it reacts chemically with traps, rendering them electrically inactive [7]. For comparison, we also performed furnace annealing in forming gas with no Al presence. Summarising, we could perform hydrogen treatments at the same temperature but changing the number of atomic H by several order of magnitudes.

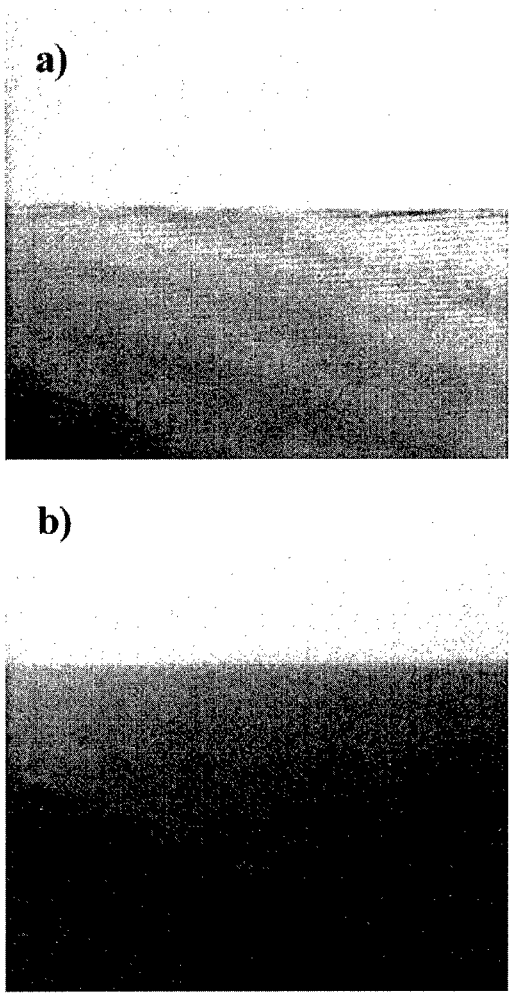


Fig. 3 - TEM analyses at the interface for a as grown sample (a) and the same sample after a post anneling in forming gas at 450 °C for 20 minutes (b).

No change in the electrical behaviour has been observed after plasma treatment independently on the temperature. Just a slightly improvement has been observed increasing a lot the hydrogen pressure inside the chamber. Instead, a significant improvement has been obtained for furnace annealing but only in presence of Al (see Fig.4 b).
The first relevant result was the disappearing of the hysteresis effect. Due to this result the hysteresis cannot be attributed to low minority carrier generation and recombination rate but rather to charge densities at the interface probably associated with dangling bonds. When they are saturated their electrical effect is suppressed. When an electric field is applied they are charged trapping carriers and they remain charged for a long time.

Furthermore, a clear disappearing of the tail in the deep depletion region is observed. This clearly indicates a decreasing of surface states and it is in agreement with the first main result. The comparison between Fig. 4 a) and Fig. 4 b) show also a large shift of the flat band voltage demonstrating a large fixed charge reduction at the SiC/SiO_2 interface.

All the effects remain after thermal stress up to 400 °C. The results obtained can be interpreted considering dangling bonds at the SiC/SiO_2 interface. If a high density of them is present they can produce all the phenomena observed. Furthermore, they can be passivated by hydrogen during post-annealing in hydrogen ambient.

However, obtaining a sharp interface with no C accumulation is fundamental to allow hydrogen to saturate dangling bonds. If a supersaturation of C remain at the interface the Si dangling bonds can be saturated with Si-C bonds. Indeed, when a fast cooling ramp was used no decrease in the interface trap density has been measured after post-oxidation treatments in atomic H.

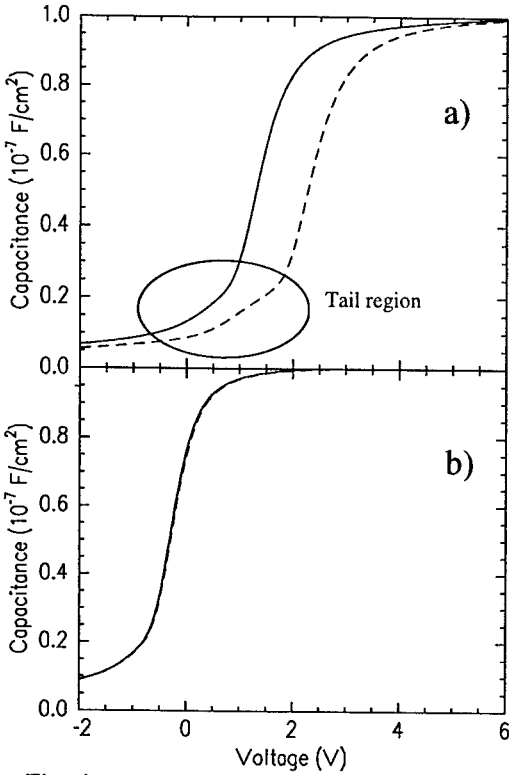


Fig. 4. - a) C-V characteristics of as-grown oxide. b) C-V characteristic of the same oxide after hydrogen treatement at 450°C for 20 min.

Summary

Oxidation of 6H-SiC has been performed in dry ambient using 1.5% of HCl. A significant improvement of the oxide electrical characteristics has been observed when post-oxidation thermal treatments were performed in atomic hydrogen ambient. The result has been related to the passivation of the interface states and it is linked to the hydrogen concentration during the post-oxidation treatments.

References

[1] M.R. Melloch and J.A. Cooper, MRS Bulletin 22 (1997), p. 42.
[2] J.N. Shenoy, J.A. Cooper, Jr., and M.R. Melloch, Appl. Phys. Lett. 68 (1996), p. 803.
[3] G.G. Jernigan, R.E. Stahlbush, M.K. das, J.A. Cooper, Jr., L.A. Lipkin, Appl. Phys. Lett. 74 (1999), p. 1448.
[4] E. Stein von Kamienski, A. Golz and H. Kulz, Mat. Sci. and Eng. B 29 (1995), p131.
[5] V.V. Afanas'ev, M. Bassler, G. Pensl and M. Schulz, phys. stat. sol. 162 (1997) p.321.
[6] J.N. Shenoy, G.L. Chindalore, M. R. Melloch, j. A. Cooper, Jr, J.W. Palmour, and K.G. Irvine, J. Electro. Mater. 24 (1995), p. 303.
[7] S. Wolf and R.N. Tauber, *Silicon processing* (Lattice Press, Sunset Beach, USA 1986) p. 220.
[8] C.M. Zetterling and M. Ostling, Physica Scripta T54 (1994), p. 291.
[9] S.M. Tang, W.B. Berry, R. Kwor, M.V. Zeller, and L.G. Matus, J. Electrochem. Soc. 137 (1990), p. 221.

Materials Science Forum Vols. 353-356 (2001) pp. 643-646
© 2001 Trans Tech Publications, Switzerland

Influence of the Post-Oxidation Process on the MOS Interface and MOSFETs Properties

S. Suzuki[1], W.J. Cho[2], R. Kosugi[2], J. Senzaki[2], S. Harada[2] and K. Fukuda[2]

[1] Ultra-Low-Loss Power Device Technology Research Body (UPR), R&D Association for Future Electron Devices (FED), c/o Electrotechnical Laboratory, 1204, 1-1-4 Umezono, Tsukuba, Ibaraki 305-8568, Japan

[2] Ultra-Low-Loss Power Device Technology Research Body (UPR), Electrotechnical Laboratory, 1-1-4 Umezono, Tsukuba, Ibaraki 305-8568, Japan

Keywords: Channel Mobility, Interface State Density, MOS Capacitor, MOSFET

Abstract We have investigated the influences of the gate-oxide preparation process on the properties of 4H-SiC MOS interface and MOSFETs. Quite different behaviors between n- and p-type SiC MOS interface properties were observed depending on the preparation process of the gate oxide. The results suggested that the interface state density D_{it} near the conduction band and valence band have a different origin. The lower D_{it} near the conduction band of the MOS interface resulted in the lower threshold voltage and higher channel mobility for the MOSFETs.

Introduction

A beneficial feature of SiC processing technology is that SiC can be thermally oxidized to form SiO_2 having superior dielectric properties for MOS applications. Improvement of the thermally grown SiO_2/SiC interface is a critical issue to realize MOSFETs and MOS related devices based on SiC. Wet re-oxidation annealing (wet ROA) was established for reducing the interface state density D_{it} for p-type SiC MOS capacitors [1,2]. We have reported that the post-oxidation annealing in hydrogen (H_2 POA) was very effective for the improvement of the n-type SiC MOS interface quality [3-5]. Recently, several groups pointed out that the inversion mobility of MOSFETs was suppressed owing to the high density of interface states near the conduction band edge [6-9]. POA in hydrogen is thought to be a useful method for the improvement of the inversion mobility. Here, we report on the relationships between MOS interface and the MOSFETs properties.

Experimental

N- and p-type 4H-SiC(0001) wafers with a 4.9μm-thick homoepitaxial layer, purchased from CREE Research Inc., were used in this study. Effective doping density (N_D-N_A or N_A -N_D) of the epitaxial layer was about $5x10^{15}$ cm^{-3}. The wafers were cleaned by conventional RCA cleaning and sacrificial oxidation.

(a) MOS capacitors

Because of the wide bandgap of SiC, capacitance–voltage (*C-V*) measurements of MOS capacitors give the energy distribution of interface state density D_{it} only in the majority carrier side in the bandgap. N- and p-type SiC substrates were used in order to obtain the D_{it} distribution in the upper and lower half of the bandgap, respectively. We assume that the difference of dopants and the quality of SiC epitaxial wafers do not affect the MOS interface quality.

A thermal oxide was grown in dry or wet O_2 at 1200°C resulting in a thickness of 47±2 nm. Wet oxidation was performed using the pyrogenic method. After oxidation, all the samples were *in-situ* annealed in Ar at the oxidation temperature for 30 min, then cooled down in Ar with the ramping rate of –5°C/min to 600°C. Some SiO_2/SiC samples were annealed in pure hydrogen at 800°C for 30 min or in wet oxidation ambient at 950°C for 180min [1]. Aluminum was used as the

gate and ohmic electrode. Hi-lo *C-V* measurements were performed using a simultaneous *C-V* system (Keithley KI-82 system). The high-frequency properties were measured at 100kHz with a small signal amplitude of 15mV. The step voltage and delay time was 50mV and 10sec, respectively.

(b) MOSFETs

N-channel lateral MOSFETs were fabricated on the p^+ substrate with a p-type 4H-SiC epitaxial layer. Source and drain regions were formed by phosphorous ion implantation at 500°C with the total dose of $7x10^{15}/cm^2$. Activation annealing for implanted impurities was performed at 1500°C for 5min in Ar. The gate oxide was grown by the method described above, and its thickness was 42 $\pm$2nm. Aluminum was used as both the gate metal and the contact metal for the source and drain. The typical designed length (L) and the width (W) of the gate electrode were 10 and 50μm, respectively. The channel mobility was determined by three methods; the field effect mobility μ_{fe} from the transconductance at V_D=0.1V, the saturation mobility μ_{sat} from the slope of $I_D^{1/2}$-V_G in the saturation region, the low-field mobility μ_0 from the slope of $I_D/g_m^{1/2}$-V_G plot (V_D=0.1V) [11]. The threshold voltage V_{th} was determined from the transfer characteristics at V_D=10V.

Results and Discussion

(a) MOS capacitors

Figure 1 shows the high frequency *C-V* curves of the MOS capacitors prepared by dry and wet oxidation. The dependences of the oxidation method on the flatband voltage shift ΔV_{fb} were almost similar with the ones reported by several groups. The ΔV_{fb} of the SiC MOS capacitor is influenced by not only the amount of the charge in the oxide but also the charged deep interface states. The large ΔV_{fb} of the dry-oxidized p-type MOS is caused by the large amount of deep states. Figure 2 shows the energy distribution of D_{it} near the (a) conduction (n-type MOS) and (b) valence band (p-type MOS) derived from the hi-lo *C-V* method. Lower D_{it} is

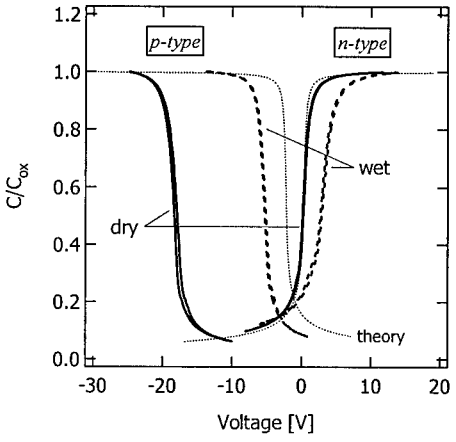


Fig.1 : The high frequency C-V curves for the MOS capacitors prepared by dry and wet oxidation.

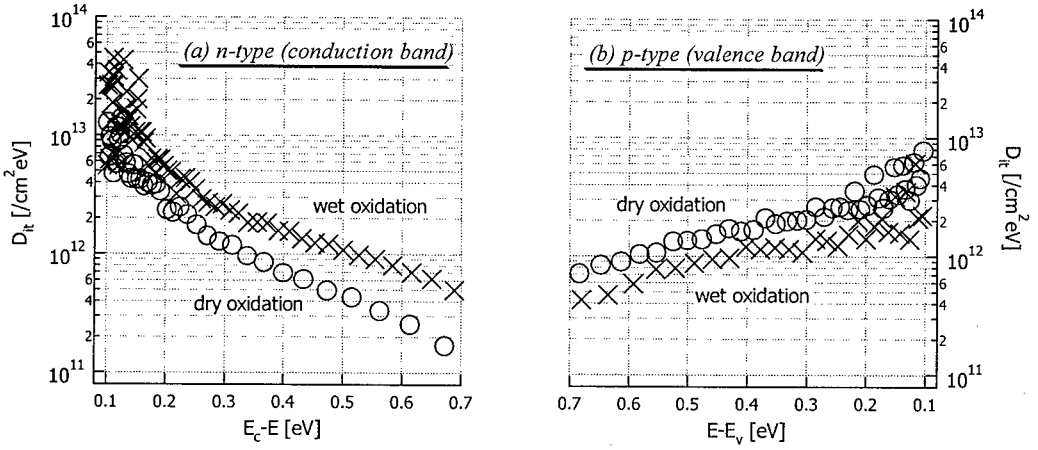


Fig.2 : Oxidation method dependence on energy distribution of D_{it} in the bandgap. N- and p-type MOS capacitors were used for measuring the D_{it} in the conduction and valence band side, respectively. E_c-E and E-E_v represent the energy from the conduction and valence band edge, respectively.

obtained by dry oxidation in the conduction band side, and by wet oxidation in the valence band side. This result is similar to the model proposed by Yano *et al.* [10]. The D_{it} dispersion near the conduction band edge E_c is more remarkable than that of the valence band edge E_v. Although D_{it} values are not correct quantitatively in the shallow level below ~0.2eV, it might be related to the existence of a high density of interface states near E_c.

We have investigated the influence of the post-oxidation process on the dry oxidized MOS interface. Figure 3 shows the high frequency *C-V* curves of the MOS capacitors prepared by dry oxidation with POA. The effect of H_2 POA is contrary to that of wet ROA. For n-type MOS, H_2 POA shifted the *C-V* curve to the negative bias voltage, while wet ROA shifted it to the positive bias voltage. For the p-type MOS, the change of ΔV_{fb} of the C-V curve by H_2 POA is very small (0.4V), in contrast, wet ROA shifted drastically to the positive bias voltage (16.6V) as shown in Fig.3. Figure 4 shows the D_{it} energy distribution near (a) E_c and (b) E_v for the MOS interface prepared by dry oxidation with POA. H_2 POA decreased the D_{it} near E_c effectively, however, it hardly affected the D_{it} near E_v. In contrast, wet ROA decreased the D_{it} near E_v, and increased the D_{it} near E_c, as reported by Chung *et al.* [11].

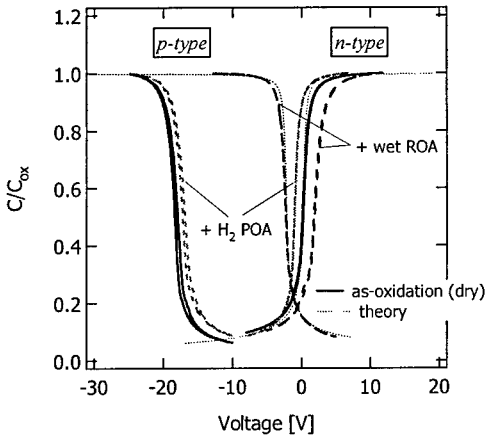


Fig.3 : The high frequency C-V curves for the MOS capacitors prepared by dry oxidation with POA.

These results suggested that the origin of the D_{it} near E_c and E_v in the 4H-SiC bandgap is quite different. Considering the influence of H_2 POA and wet ROA process on the D_{it}, we suppose that the D_{it} near E_c and E_v is originated in the dangling bond and the carbon related species at the interface, respectively. Not all the experimental results, however, can be explained sufficiently by this model, we need to study the matter further.

(b) MOSFETs

We have also investigated the relationship between MOS interface and MOSFET properties. Gate oxides of the MOSFETs prepared by wet oxidation, dry oxidation, and dry oxidation with H_2 POA were compared. The values of threshold voltage V_{th}, field-effect mobility μ_{fe}, saturation mobility μ_{sat} and low-field mobility μ_0 are summarized in Table 1. The low field mobility μ_0

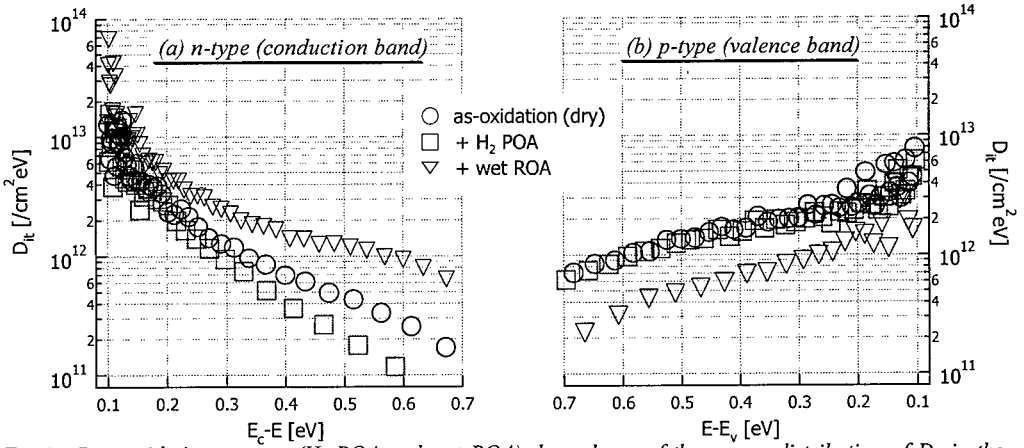


Fig.4 : Post oxidation process (H_2 POA and wet ROA) dependence of the energy distribution of D_{it} in the bandgap. Gate oxide was grown by dry oxidation.

Table1 The values of threshold voltage and channel mobility of the MOSFETs

oxidation	POA	V_{th} [V]	μ_{fe} [$cm^2/V{\cdot}s$]	μ_{sat} [$cm^2/V{\cdot}s$]	μ_0 [$cm^2/V{\cdot}s$]
wet	-	7.31	7.07	4.27	10.0
dry	-	3.78	6.35	3.70	11.2
dry	H_2 POA	1.45	7.63	4.55	19.4

is corrected for both source and drain resistance as well as the mobility reduction due to the transverse electric field [12]. The values of V_{th} and μ_0 seem to have a strong relation to the D_{it} distribution near E_c shown in Fig.4, as pointed out in the study of the MOSFETs using various SiC-polytypes. [6,10]. In strong inversion, electrons are trapped by the D_{it} near E_c, assumed to be an acceptor-type, and the D_{it} is negatively charged, resulting in forming a large amount of scattering centers for mobile electrons. Therefore, MOSFETs having lower D_{it} near E_c exhibited lower threshold voltage and higher channel mobility. H_2 POA reduced the D_{it} near E_c, and increased μ_0 by about twice (11.2→19.4$cm^2/V{\cdot}s$). The channel mobility, however, is still far from the value of the bulk mobility of 4H-SiC. The D_{it} dispersion near E_c seems to be unchanged even after H_2 POA (Fig.4). The inherent electron traps in SiO_2 (near interface traps [8]) may prevent the improvement of channel mobility.

Summary

The influences of the gate-oxide process on the MOS interface and MOSFET properties have been investigated. The D_{it} near E_c and E_v were decreased by H_2 POA and by wet ROA, respectively. The results suggested that the interface state density D_{it} near E_c and E_v have different origins. The lower D_{it} near E_c of the MOS interface resulted in the lower threshold voltage and higher channel mobility of the MOSFETs. The low-field mobility of 19.4$cm^2/V{\cdot}s$ was obtained for the MOSFET with a gate oxide processed using H_2 POA.

Acknowledgment

This work was performed under the management of FED as a part of the MITI New Sun Shine Program (R&D of Ultra-Low-Loss Power Device Technologies) supported by NEDO.

References

[1] L.A.Lipkin and J.A.Palmour, J. Electron. Mat. 25 (1996), p.909.
[2] M.K.Das, J.A.Cooper, JR. and M.R.Melloch, J. Electron. Mat. 27 (1998), p.353.
[3] S.Suzuki, K.Fukuda, H.Okushi, K.Nagai, T.Sekigawa, S.Yoshida, T.Tanaka and K.Arai, Mater. Sci. Forum 338-342 (2000), p.1073.
[4] K.Fukuda, S.Suzuki, T.Tanaka, and K.Arai, Appl Phys.Lett. 76 (2000), p.1585.
[5] W.J.Cho, R.Kosugi, S.Suzuki, K.Fukuda and K.Arai, to be published in Appl.Phys.Lett.
[6] R.Schörner, P.Friedlichs, D.Peters, and D.Stephani, IEEE Electron Device Lett. 20(1999), p.241.
[7] M.K.Das, B.S.Um and J.A.Cooper, Mater. Sci. Forum 338-342 (2000), p.1069.
[8] V.V.Afanas'ev, A.Steamans, M.Bassler, G.Pensl, and M.J.Schulz, Appl. Phys.Lett. 76 (2000), p.336.
[9] N.S.Saks, S.S.Mani, and A.K.Agarwal, Appl.Phys.Lett. 76 (2000), p.2250.
[10] H.Yano, T.Kimoto, H.Matsunami, M.Bassler, and G.Pensl, Mater. Sci. Forum 338-342 (2000), p.1109.
[11] G.Y.Chung, C.C.Tin, J.H.Won, and J.R.Williams, Mater. Sci. Forum 338-342 (2000), p.1097.
[12] G.Ghibaudo, Electron. Lett. 24 (1988), p.534.

Materials Science Forum Vols. 353-356 (2001) pp. 647-650
© 2001 Trans Tech Publications, Switzerland

Observation of SiO_2/SiC Interface with Different Off-Angle from Si(0001) Face Using Transmission Electron Microscopy

K. Fukuda[1], S. Suzuki[2], J. Senzaki[1], R. Kosugi[1], T. Tanaka[2] and K. Arai[1]

[1] Ultra-Low-Loss Power Device Technology Research Body (UPR), Electrotechnical Laboratory, 1-1-4 Umezono, Tsukuba, Ibaraki 305-8568, Japan

[2] Ultra-Low-Loss Power Device Technology Research Body (UPR), R&D Association for Future Electron Devices (FED), c/o Electrotechnical Laboratory, 1-1-4 Umezono, Tsukuba, Ibaraki 305-8568, Japan

Keywords: Channel Mobility, Off-Angle, Polytypism, SiO_2/SiC Interface, TEM

Abstract

We have observed the SiO_2/SiC interfaces formed on 3.5° and 8° off-angle 6H-SiC (0001) and 8° off-angle 4H-SiC (0001) substrates using transmission electron microscopy (TEM).
The step structures were observed even after the oxidation. It was found that the number of Si-C bilayer at the steps increased and the roughness of SiO_2/SiC interface became large as the off-angle increased. Therefore, it is considered that one of the reasons for lower channel mobility for 4H-SiC MOSFETs fabricated on 8°off-angle SiC substrate is due to rougher SiO_2/SiC interface compared to 6H-SiC MOSFETs fabricated on 3.5°off-angle SiC substrate.

1. Introduction

SiC is expected to be an attractive material for higher-power, higher-temperature, and higher-frequency devices compared with Si-based devices. Recently, several researchers have carried out various studies on SiC devices [1-3]. Power MOSFETs are one of promising candidates for switching devices because they are superior to bipolar transistors due to their fast switching speeds and low switching losses. Theoretical on-resistance (R_{on}) of SiC MOSFETs is predicted to be much lower than that of Si MOSFETs. A large part of R_{on} for power MOSFETs is dominated by channel resistance. Therefore, it is expected that the channel mobility of 4H-SiC MOSFETs is higher than that of 6H-SiC MOSFETs and the R_{on} of 4H-SiC MOSFETs is lower than that of 6H-SiC MOSFETs because the bulk mobility of 4H-SiC is higher than that of 6H-SiC. However, the experimental channel mobility of 4H-SiC MOSFETs fabricated on the Si(0001) face is approximately one order of magnitude lower than that of 6H-SiC MOSFETs. In Si MOSFETs, the channel mobility of Si MOSFETs depends on both the electric charge and the roughness at the SiO_2/Si interface. The channel mobility is reduced by Coulomb scattering originating from electrons trapped at interface states. Some groups have reported the interface state density (D_{it}) near the conduction band of 4H-SiC MOS structures is much higher than that of 6H-SiC[4-6]. Therefore, the channel mobility of 4H-SiC MOSFETs is lower than that of 6H-SiC MOSFETs. Moreover, the investigation of the SiO_2/SiC interface structure is very interesting because the

surface roughness lowers the channel mobility as mentioned above. Usually, the 6H- and 4H-SiC MOSFETs are fabricated on 3.5° and 8° off-angle SiC (0001) substrates, respectively. The off-angle might affect strongly SiO_2/SiC interface structures and the channel mobility.

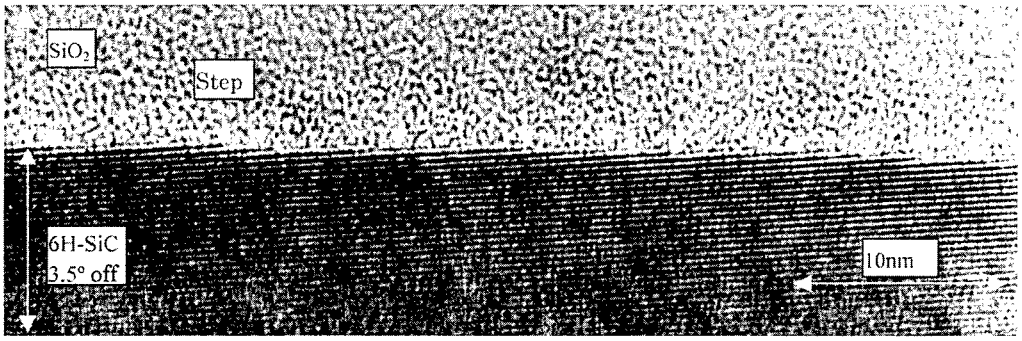
In this paper, we have investigated the SiO_2/SiC interface formed on 3.5° and 8° off-angle 6H-SiC (0001) and 8° off-angle 4H-SiC (0001) substrates using transmission electron microscopy (TEM).

2. Experimental

3.5° and 8° off-angle 6H-SiC (0001) and 8° off-angled 4H-SiC (0001) substrates with a 4.9μm thick n-type epitaxial layer were purchased from Cree Research. The samples were 3.5° or 8° off-angle from Si(0001) face toward to [11$\bar{2}$0]. After the standard RCA cleaning, a sacrificial oxidation was performed at 1200°C in dry O_2, and then sacrificial oxide films were removed by 5% HF solution. Gate oxide films were thermally grown at 1200°C for 2.5 hours in dry O_2. After oxidation, samples were cooled down gradually in Ar(1.1×10^5 Pa). Furthermore, samples were annealed in hydrogen (1.1×10^5 Pa) at 800°C for 30 min. The SiO_2/SiC interfaces were observed from [1$\bar{1}$00] direction using TEM.

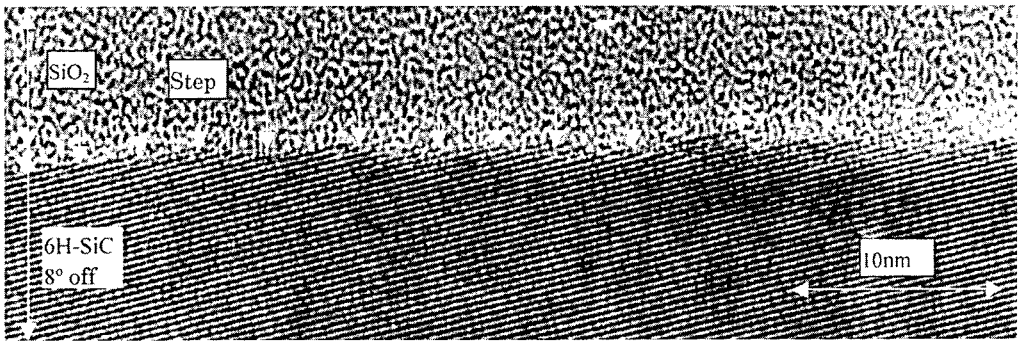
3. Results and discussion

Kimoto et al. have reported the step structures on the surface of SiC substrate. They found that there exist macrosteps with a terrace width of 220nm to 280nm and a step height of 3nm to 6nm on Si(0001) face[7]. Figures 1,2 and 3 show the typical cross-sectional TEM images of SiO_2/SiC interface formed on 3.5° and 8° off-angle 6H-SiC (0001) and 8° off-angle 4H-SiC (0001) substrates, respectively. The step structures exist even after the oxidation as shown in Figs 1,2 and 3. The steps are indicated by the white arrows in these figures. The average numbers of Si-C bilayer at steps and the terrace widths are summarized in Table 1. The average number of Si-C bilayers at steps are approximately 1 and 2 for the SiO_2/SiC interface formed on 3.5° and 8° off-angle SiC (0001) substrates, respectively. The average terrace widths at SiO_2/SiC interface formed on 3.5° and 8° off-angle SiC (0001) substrates are 5nm and 3nm, respectively. The average number of Si-C bilayer at the SiO_2/SiC interface increases and the average terrace width decreases with increasing the off-angle. The SiO_2/SiC interface formed on 3.5°off-angle 6H-SiC (0001) substrate is much smoother than those on 8°off-angle 4H-SiC (0001) substrate. Therefore, there is a possibility that lower channel mobility for 4H-SiC MOSFETs fabricated on 8°off-angle SiC substrate is due to rougher SiO_2/SiC interface compared to 6H-SiC MOSFETs fabricated on 3.5°off-angle SiC substrate.



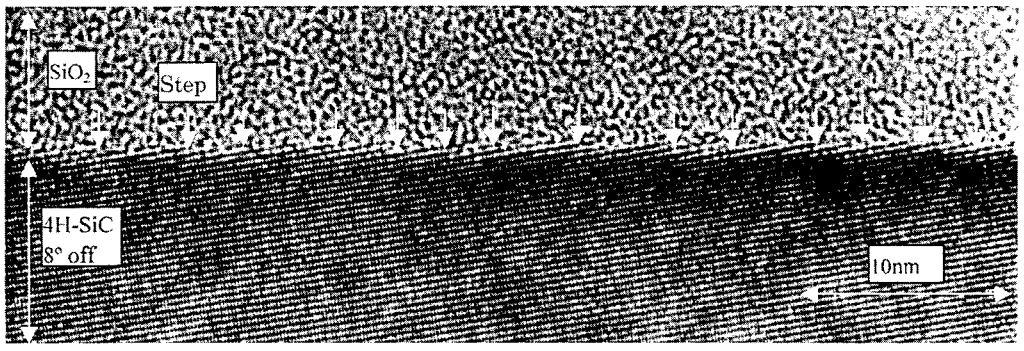
[0001]
↑
⊙ → [11$\bar{2}$0]
[1$\bar{1}$00]

Fig. 1 Typical cross-sectional TEM image for the SiO_2/SiC interface formed on 3.5° off-angle 6H-SiC (0001) substrate.



[0001]
↑
⊙ → [11$\bar{2}$0]
[1$\bar{1}$00]

Fig. 2 Typical cross-sectional TEM image for the SiO_2/SiC interface formed on 8° off-angle 6H-SiC (0001) substrate.



[0001]
↑
⊙ → [11$\bar{2}$0]
[1$\bar{1}$00]

Fig. 3 Typical cross-sectional TEM image for the SiO_2/SiC interface formed on 8° off-angle 4H-SiC (0001) substrate.

Table 1 Average number of Si-C bilayers at step and terrace width

	Average number of Si-C bilayer at step	Average terrace width
SiO_2/3.5°off-angle 6H-SiC interface	1	5 nm
SiO_2/8°off-angle 6H-SiC interface	~2	3 nm
SiO_2/8°off-angle 4H-SiC interface	~2	3 nm

4. Conclusion

We have investigated the SiO_2/SiC interfaces formed on 3.5° and 8° off-angle 6H-SiC (0001) and 8° off-angle 4H-SiC (0001) substrates using TEM. The step structures were observed even after the oxidation. The number of Si-C bilayers at the steps and the SiO_2/SiC interface roughness increased as the off-angle increased. The SiO_2/SiC interface roughness affects the channel mobility of SiC MOSFETs on the analogy of Si MOSFET. Therefore, it is very important to investigate the relationship between the off-angle and the channel mobility.

Acknowledgements

This work was performed under the management of FED as a part of the MITI New Sun Shine Program Technologies) supported by NEDO.

References

[1] N.S. Saks, S. S. Mani, A. K. Agarawal, and M. G. Ancona, IEEE Electron Device Lett. 20 (1999), p.431.

[2] J. Tan, J. A. Cooper, Jr., and M. R. Melloch, IEEE Electron Device Lett.19 (1998),p.487.

[3] P. M. Shenoy and B. J. Baliga, IEEE Electron Device Lett. 18 (1997), p.589.

[4] N.S. Saks, S. S. Mani, A. K. Agarawal, Appl.Phys.Lett.76(2000), p.2250.

[5] M.K. Das, B. S. Um and J. A. Cooper, Jr., Mater. Sci. Forum,Vol. 338-342(2000), p.1069.

[6] K. Fukuda, S. Suzuki, J. Senzaki, R. Kosugi, N.Nagai, T. Sekigawa, H. Okushi, S. Yoshida, T. Tanaka, and K. Arai, Mater. Sci. Forum Vol. 338-342 (2000), p.1283.

[7] T. Kimoto, A. Itoh, and H. Matsunami, in Silicon Carbide, edited by W. J. Choyke, H. Matsunami, and G. Pensl, Vol. II (Akademie, Berlin,1997), p.247.

Materials Science Forum Vols. 353-356 (2001) pp. 651-654
© 2001 Trans Tech Publications, Switzerland

Remote PECVD Oxide Utilized in U-MOS Structures and Different MOSFETs on SiC

S. Scharnholz, O. Hellmund, J. Stein, B. Spangenberg and H. Kurz

Institute of Semiconductor Electronics (IHT-II), University of Technology Aachen (RWTH), Sommerfeldstr. 24, DE-52074 Aachen, Germany

Keywords: MOSFET, Oxide, Recessed Channel, Remote PECVD, SiO_2, Stress, Trench, U-MOS

Abstract. This paper deals with the utilization of deposited oxides as gate dielectrics for MOSFETs on 4H- and 6H-SiC using the remote (R) PECVD technique. In a first step RPECVD oxides have been optimized by investigating planar MOS-diodes. Then the electric field strength of the optimized oxides has been analyzed in trench structures. A process for recessed-channel (RC) MOSFETs was developed, showing the general suitability of RPECVD oxide for trench gate structures on SiC. Finally, RPECVD oxides are compared to thermal oxides after supplying DC-stress to not self aligned (notSA) MOSFETs.

Introduction

Among the most promising properties of SiC, the possibility to oxidize this material to SiO_2 plays a central role from a technology point of view. On the way to a SiC-based MOS-technology the microscopic mechanism of oxidation has to be investigated thoroughly. Although the oxidation rate and interface quality is still quite poor compared to silicon, recently achieved progress opened the way to interesting technical solutions [1, 2]. Specifically, the problems of the low oxidation rates and the anisotropy encountered can been overcome using deposited oxide instead of thermally grown ones. The deposition technology is critical for the fabrication of U-MOSFETs or RC-MOSFETs on the Si-face of SiC wafers.

Remote PECVD oxide

It has already been found on MOS capacitors, that oxide deposited by the RPECVD technique exhibits a low density of SiC/SiO_2 interface states and fixed oxide charges after subsequent heat treatments in inert gas and/or hydrogen [3]. On the basis of these results our process was adapted to a commercial RPECVD reactor, suitable for the deposition of high quality gate oxide on silicon [4].

Table 1: Process sequence for the realization of high quality remote (R) PECVD oxide on SiC.

No.	*Process*	*Gas*	*Temp. [°C]*	*time [min]*	*Equipment*	*Purpose*
1	plasma pre-cleaning	H_2	250	10	RPECVD	Smoothening, reduction of C
2	plasma pre-oxidation	O_2	250	0.5	RPECVD	Definition of the interface
3	oxide deposition	SiH_4/ O_2	250	16	RPECVD	Deposition of the SiO_2-layer
4	post deposition annealing	Ar	1150	20	Furnace	Reorganization, CO_x out-diffusion
5	re-oxidation	O_2/ H_2O	950	60	Furnace	Compensation of oxygen deficits

In contrast to previous results [5] the post deposition treatment was finished by a re-oxidation (ReOx) instead of a post deposition annealing (PDA) in inert gas, resulting in less negative flat band voltages V_{fb} on p-type SiC (Fig. 2). In order to keep the post deposition treatment as short as necessary, a PDA time of 20 min and a re-oxidation duration of 60 min were chosen. Extensive investigations on MOS-capacitors indicate that for these times the major effect on the defect reduction has taken place. RPECVD oxide treated like this exhibits a total charge density of $N_f = 1\times10^{12}$ cm^{-2}, as calculated from the V_{fb} shift of MOS-diodes on p-type 4H- and 6H-SiC. If not indicated differently, RPECVD oxide, considered here, is fabricated in this way.

MOS-diodes fabricated with RPECVD oxide exhibit break down electric fields of 9.5 MV/cm, being a little inferior to those with thermal oxide (10 MV/cm). In the Fowler-Nordheim (FN) regime (1.27 10^{-6} A/cm^2, 8 MV/cm) and after an injected charge density of 1×10^{17}cm^{-2} the MOS-diodes show a degradation of ΔV_{fb} = -6 V and -4.5 V on 4H- and 6H-SiC, respectively. Thus the density of hole traps, responsible for the negative voltage shift is in the same order as for a wet thermal oxide without any subsequent annealing [6].

U-MOS structures

To develop a MOS-System for U-MOSFETs on the preferred Si-face, RPECVD oxide was investigated in trench structures on n-type 6H-SiC wafers etched by an ECR-RIE process. In the case of silicon the deposition technique used is suitable to obtain a good vertical coverage with a ratio of 55 % relative to the horizontal surface, in trenches being 100 nm wide and 200 nm deep [4]. On SiC trenches were investigated down to 2 µm width and 2.6 µm depth. An example of the oxide thickness profile is shown in Fig 1. The oxide thickness was estimated from a high resolution SEM image. The profile indicates a ratio of 66 % which is ideal for U-MOSFETs and besides superior to that of thermal oxide on the Si-face of SiC wafers.

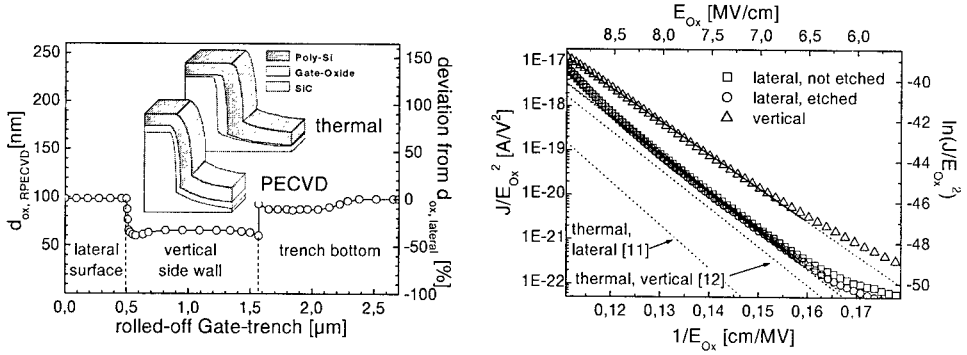


Fig. 1 left: Rolled-off gate-trench profile of Remote-PECVD oxide and *right:* FN-plot of MOS-capacitors on n-type 6H-SiC compared to [11, 12] giving an Φ_{eff} = 2.7 eV for lateral and 2.5 eV for vertical structures

In order to test the electric field strength of trench-MOS structures, IV-measurements have been performed on n-doped polysilicon MOS-diodes (5×10^{-4} cm^2) separately placed on the surface and the etched trench bottom as well as on completely covered trenches (vertical area: 1.9×10^{-4} cm^2). The lateral oxide thickness was 42 nm, as determined by HFCV-measurements. Lateral and vertical structures sustain electric fields between 9.2 and 9.5 MV/cm. The FN-plot data shown in Fig. 1 have been extracted through the formula

$$\Phi_{eff} = \left(\sqrt{(B_0 \cdot 3 \cdot \hbar)/4} \cdot (2 \cdot q \cdot m_{ox}^*)^{-1}\right)^{2/3} eV \approx 0{,}79944 \cdot 10^{-5} \cdot (B_0)^{2/3} eV \; . \qquad (1)$$

Φ_{eff} is the effective barrier height for electrons, $-B_0$ is the slope of the FN straight line, $\hbar$ is the Planck's constant, q is the electronic charge and m_{ox}^* is the effective electron mass in the oxide ($0.42\ m_0$). Lateral structures on the surface as well as on the bottom reveal Φ_{eff} = 2.7 eV, which is comparable to previously published results [12]. The vertical barrier height of 2.5 eV deviates from results published in [11], which is probably caused by the better electrical properties of thermal oxide used there.

Recessed-Channel (RC) MOSFETs

RC-MOSFETs [7] have been developed for two reasons: first to circumvent the problem arising with the implantation and activation of the source/drain-regions and second to test deposited oxide in trench gate structures. RC-MOSFETs were fabricated using the same mask set and almost the same process sequence as described for notSA-MOSFETs elsewhere [8]. In contrast to these transistors, the source and drain regions of the RC-MOSFETs were realized by etching (RIE) through the top, 700 nm thick, 1×10^{19} cm^{-3} n-doped epilayer, resulting in n$^+$ source and drain mesas on the 4.5×10^{16} cm^{-3} Al-doped second epitaxy grown on a

2.5×10^{18} cm^{-3} p-dopted 6H-SiC substrate.[1] The junction depth was estimated by SEM cross-section images and interference microscope to be d_j = -100 nm. The RIE mask consisted of deposited SiO_2, structured by AF-etch, resulting in smooth edge profiles, and thus avoiding problems with tearing-off metal contacts.

The two RC-MOSFET samples considered differ in the order of the post deposition treatment (PDA and ReOx) of the 30 nm thin, deposited gate oxide (Table 1, Fig. 2). Both devices have a reduced on-resistance $R_{DS(on)}$ compared to previously published results [8, 9]. A plot of $R_{DS(on)}$ versus L_{geo} for different V_{GS} gives a parasitic series resistance times gate width of $R_s \cdot W = 65\ \Omega\cdot mm$. The dominating part for small gate length devices is the shift layer resistance between source/drain and channel ($R_{sh} = 234\ \Omega/\square$), whereas contact and especially transition resistance play a minor role.

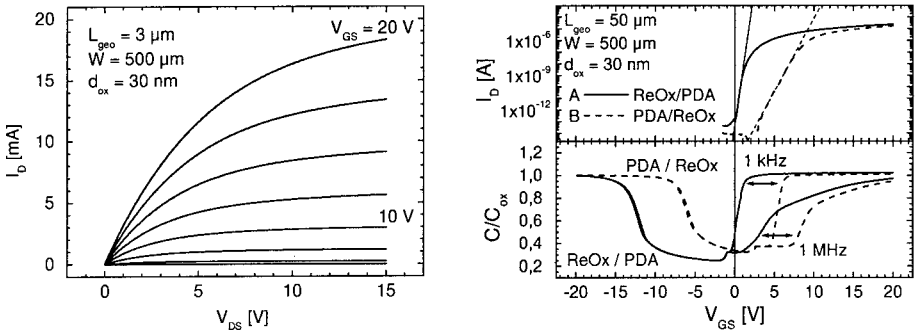


Fig. 2 left: Output- and *right:* Transfer-characteristic and gate-capacitance C/C_{ox} vs. gate-source voltage V_{GS} of RC-MOSFETs with different order of subsequent PDA and ReOx.

The transfer characteristic and gate capacitance (Fig. 2 right) of the two RC-MOSFETs give evidence for two gate oxide states analogous to [8]: a non passivated (with a final PDA) and a better passivated (with a final ReOx). The passivation of interface defects (mainly deep donor-like interface states) leads to flat band and threshold voltages being closer to the ideal value. Furthermore, for passivated RPECVD oxide the higher sub-threshold swing indicates a higher density of interface traps at the onset of week inversion. On the other hand, since the mobility is extracted above V_t [13], likewise in strong inversion, both mobility values do not differ a lot ($\mu_0 = 20\pm1\ cm^2/Vs$). Therefore it is obvious, that the carrier transport in the inversion layer is not affected by the passivation of donor-like interface traps. This is in agreement with the recently proposed asymmetrical D_{it} distribution [10]. As a result, on SiC n-channel MOSFETs are mainly affected by a very high density of acceptor like states in the upper half of the band gap. Additionally, taking into account the higher substrate doping [10] of the RC-MOSFETs, their mobility is not inferior to the one of notSA-MOSFETs with RPECVD oxide (N_A-$N_D = 7\times10^{15}\ cm^{-3}$, $\mu_0 = 25\ cm^2/Vs$) considered in the next paragraph. Consequently, the RC-MOSFETs indicate no additional such as etch induced interface defects.

DC-Stress in notSA-MOSFETs

The stress conditions were chosen so that an obvious degradation could be expected. The MOSFETs under investigation were not self aligned (notSA) with an oxide thickness between 36 and 39 nm and an effective gate length of 2.65 µm, as determined by a plot of $R_{DS(on)}$ versus the nominal gate length for different V_{GS}. The drain-source voltage was set to V_{DS} = 30 V, ensuring a high lateral electric field, while at the same time remaining well below the blocking voltage of V_b = 45 V. With the aim of degrading the device by hot carrier injection, V_{GS} was adjusted at the point of maximum substrate current $I_{sub} = 1 \pm 0.1\ \mu A$, resulting in values of $V_{GS} = 10 \pm 1$ V for the different devices. Fig. 3 shows the results of DC-stress experiments performed on notSA-MOSFETs. Plotted is the shift of two characteristic parameters, mobility μ_0 and threshold voltage

[1] Specifications of the 6H-SiC wafer given by Cree Research, Inc., Durham NC, USA.

versus the accumulated stress duration. The parameters were extracted from I_D-V_{GS} curves (V_D = 50 mV) [13], taken at the stress temperature after successively applying DC-stress for 0, 10, 50 and 520 min.

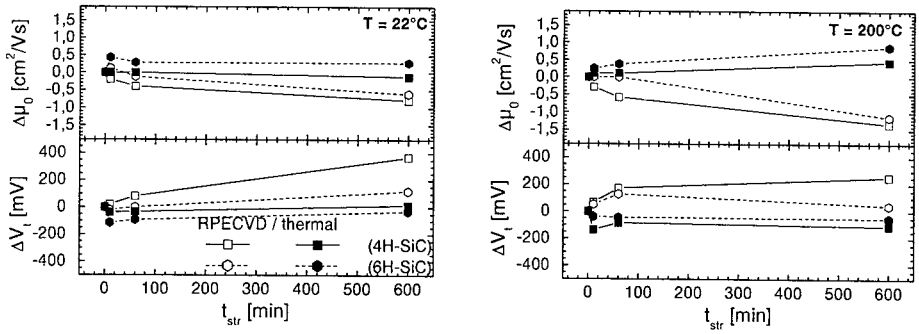


Fig. 3: Mobility μ_0 and Threshold V_t shift vs. duration of DC-stress t_{str} at 22°C (left) and 200°C (right) for notSA-MOSFETs with RPECVD (open) and thermal oxide (filled) on 4H- (square) and 6H-SiC (hexagon).

Independent of the stress temperature all measurements show qualitatively the same behavior, which is quantitatively more distinct for 200°C. Both mobility and threshold shift indicate a characteristic behavior which is continuously changing from thermal oxide on 6H-SiC to deposited oxide on 4H-SiC. For instance in MOSFETs with thermal oxide on 6H-SiC stressed at RT, two reactions can be distinguished: an initial mobility increase (threshold decrease) followed by a continuous mobility and threshold degradation. We believe these two competing processes to be present in all devices. While for MOSFETs with thermal oxide on 6H-SiC stressed at 200°C the first process is dominating, devices on 4H-SiC with RPECVD oxide show a continuous degradation right from the beginning. The physical reason for the first process is attributed to a decrease in states close to the interface, reducing the mobility by trapping and detrapping electrons. This assumption is supported by the observation that the threshold voltage is not changing, indicating an equal amount of fixed charges which reduces the mobility by Coulomb scattering. The second (degradation) process is attributed to the creation of interface traps and fixed charges affecting both mobility and threshold.

Conclusions

Remote PECVD oxide has been optimized on p-type 4H- and 6H-SiC resulting in a two step post deposition treatment: 10 min POA at 1150°C followed by 60 min ReOx at 950°C. This oxide was investigated in trenches, showing an almost ideal coverage, best suitable for the development of U-MOSFETs. The optimized RPECVD oxide sustains electric fields of up to 9.5 MV/cm on the initial lateral as well as on etched surfaces. Moreover, RC-MOSFETs have been designed, fabricated and tested, indicating no additional such as etched induced interface defects. Finally, DC stress was supplied to notSA-MOSFETs showing stable operation up to 200°C for thermal and a distinct degradation for RPECVD oxide, especially on 4H-SiC.

References

[1] H. Yano, T. Hirao, T. Kimoto, H. Matsunami, K. Asano, et al., Mat. Science Forum 338-342 (2000), p. 1109
[2] R. Schörner, P. Friedrichs, D. Peters and D. Stephani, IEEE Electron Dev. Let. 20 (1999), p. 1105.
[3] A. Gölz, S. Scharnholz, and H. Kurz, Microelectronic Engineering 36 (1997), p. 187.
[4] J. Stein, Ph.D. thesis RWTH Aachen, Shaker Verlag Aachen (1999).
[5] A. Gölz, S. Groß, E.G. Stein von Kamienski, and H. Kurz, Diamond and Rel. Mat. 6 (1997), p. 1420.
[6] E. Stein von Kamienski, F. Portheine, J. Stein, A. Gölz, and H. Kurz; J. Appl. Phys. 79 (1996), p. 2529.
[7] S.M. Sze, Physics of Semiconductor Devices, 2ed Edition, John Wiley & Sons, 40 (1981).
[8] E.G. Stein von Kamienski, C. Leonhard, S. Scharnholz et al., Diamond and Rel. Mat. 6 (1997), p. 1497.
[9] S. Scharnholz, E. Stein von Kamienski, A. Gölz, et al., Mat. Science Forum 493-496 (1998) p. 1001.
[10] R. Schörner, P. Friedrichs and D. Peters; IEEE Trans. Electr. Dev. 46 (1999), p. 533.
[11] P. Friedrichs, E.P. Burte, R. Schörner, Appl. Phys. Lett. 65 (1994), p. 1665.
[12] A.K. Agarval, S. Seshadri, and L.B. Rowland, IEEE Electr. Dev. Let. 18 (1997), p. 592.
[13] G. Ghibaudo, Electronics Letters 24 (1988), p. 543.

Materials Science Forum Vols. 353-356 (2001) pp. 655-658
© 2001 Trans Tech Publications, Switzerland

Indications for Nitrogen-Assisted Removal of Carbon from SiO_2-SiC Interface

P. Jamet, S. Dimitrijev and P. Tanner

School of Microelectronic Engineering, Griffith University,
Nathan, QLD 4111, Australia

Keywords: Growth Rate, Nitrided Oxide (NO and N_2O), Oxidation, SIMS, SiO_2-SiC Interface

Abstract

Nitrogen passivates SiO_2–Si interface by creating interfacial Si≡N bonds. While the same effect is observed in the case of SiC, there is a growing evidence that nitrogen plays an additional role at the SiO_2–SiC interface, which relates to more efficient removal of carbon from the interface. Indications for the existence of this effect evolved from earlier atomic-force microscope (AFM) and x-ray photoelectron spectroscopy (XPS) analyses. This paper adds new effects by comparing the rates of oxide growth in NO/N_2O and the associated secondary-ion-mass-spectroscopy (SIMS) profiles of nitrogen for the cases of Si and SiC substrates. The assumption that the nitrogen is involved in carbon removal from the interface can explain the experimentally observed differences in both nitrogen concentrations at the interfaces and relative growth rates.

Introduction

Thermal oxidation is the only process known to lead to MOSFET-quality dielectric–semiconductor interface. This fact and the unique electrical properties of SiO_2 are the main reasons for the long-lasting dominance of silicon over many other semiconductor materials, with apparently better bulk properties. Thermal oxidation of SiC also leads to creation of SiO_2 at the surface, and in addition to that, SiC is a wide energy-gap material with superior bulk parameters compared to silicon. However, the release of carbon during thermal oxidation of SiC appears as an inherent disadvantage. Presence of carbon at the interface has been identified as a reason for unfavourable electrical properties of the SiO_2–SiC interface [1].

Our recent investigation of electrical and physical properties of NO-nitrided SiO_2–SiC interface have indicated the possibility that carbon is more efficiently removed from the interface in the case of the nitrided samples [2,3]. However, there is a belief that nitrogen is unlikely to react with carbon to remove it from the interface. In this paper, we report two additional effects and systematize the growing indication that there is a nitrogen-assisted removal of carbon from nitrided SiO_2–SiC interfaces.

Experimental Details

Silicon faced, 8° off-axis, n-type 4H-SiC wafer, purchased from CREE research, was used in this experiment. The SiC substrate had a 2.0 μm epitaxial layer grown on a heavily doped substrate. The nitrogen doping concentration of the epilayer was $8x10^{15}$ cm^{-3}. The silicon wafer used in the present work was n-type, (100) oriented, with resistivity of 0.6-1.0 Ωcm. The Si and SiC wafers were first cleaned in a mixture of H_2SO_4 and H_2O_2 followed by an RCA clean, and immediately prior to oxidation, dipped in a 1% HF for 20 sec. Si and SiC samples were oxidized in a conventional tube

furnace at 1100°C for different times in O_2, NO, and N_2O ambient. Oxide thicknesses were determined from the high frequency capacitance in accumulation. Secondary ion mass spectroscopy (SIMS) analysis was also performed to obtain nitrogen, oxygen, silicon, and carbon profiles. To give high depth resolution and reduce matrix and knock-on effects, SIMS data were acquired using a low energy (.5 keV) Cs^+ ion bombardment while monitoring clustered secondary species of the form M^+Cs.

Results and Discussion

Table 1 lists the indications for nitrogen-assisted removal of carbon from the SiO_2–SiC interface. Let us first summarize the two already published effects. Tanner *et al* [2] presented SIMS profiles of carbon at the SiO_2–SiC interface in samples with post-oxidation annealing in either NO or Ar. The comparison revealed a significantly sharper carbon profile in the case of NO annealed (nitrided) samples. Associated atomic-force microscopy (AFM) images established that interface protrusions existed in the Ar-annealed samples, but they did not exist in the NO-annealed samples. Correlating these results with independent conclusions that carbon clusters could be formed at the interface [1], it was concluded that the AFM-observed protrusions and the SIMS-observed stretch out of the carbon profile were due to carbon clustering at the interface of Ar-annealed samples. The fact that identical samples did not have the carbon clustering when annealing in NO was performed indicated that either nitrogen or NO were involved in a process of carbon removal.

Table 1 Effects indicating nitrogen involvement in the process of carbon removal from SiO_2–SiC interface

Brief Description	Reference
• Atomic Force Microscopy reveals that NO nitridation removes carbon clusters from the SiO_2-SiC interface	[2]
• XPS binding-energy analysis indicates existence of C–N bonds near the SiO_2-SiC interface	[3]
• Normalization of the oxide-growth rates in nitrogen-rich environments (NO and N_2O) by the growth rate in dry O_2 shows a higher reaction-rate constant in SiC compared to Si, indicating existence of a carbon–nitrogen interaction	this paper
• Lower nitrogen concentration at the SiO_2-SiC interface (according to NRA [4], SIMS and XPS analyses) can be explained by the nitrogen involvement in carbon removal from the SiO_2-SiC interface	this paper

The second indication comes from X-ray photoelectron spectroscopy (XPS) analysis of NO and Ar annealed MOS structures on SiC [3]. It was demonstrated that a less complex SiO_2–SiC interface, free of oxide–carbon compounds, was achieved by NO annealing compared to the Ar-annealing process. Moreover, two-peak XPS spectrum of nitrogen at the interface of the NO-annealed samples was observed. It was established that one of the peaks corresponds to Si≡N bonds, whereas binding energy analysis led to assumption that the second peak is due to N–C bonds. Therefore, Li *et al* [3] speculated that NO nitridation is removing interface carbon, reducing the imperfections at the SiC–SiO_2 interface.

In this experiment, we analyse the growth rates and SIMS profiles of oxides grown in NO, N_2O, and O_2 on both Si and SiC. Table 2 presents the linear growth rates for all the samples. In addition to that, relative growth rates in NO and N_2O, with respect to the growth rates in dry O_2, are determined and also presented in Table 2. It can be seen that the relative growth rates are about three times as high for the case of SiC substrate compared to Si for either nitrogen-rich ambient: NO and N_2O.

Table 2 Absolute and relative linear-growth rates of oxide on Si and SiC at 1100°C for three different oxidizing ambient: O2, N_2O, and NO.

	Silicon	Silicon carbide
$(dx/dt)_{O2}$ [nm/min]	9.6 [5]	0.1
$(dx/dt)_{N2O}$ [nm/min]	0.77 [6]	0.022
$(dx/dt)_{NO}$ [nm/min]	0.6	0.01875
$\frac{(dx/dt)_{NO}}{(dx/dt)_{O2}}$	0.0625	0.1875
$\frac{(dx/dt)_{N2O}}{(dx/dt)_{O2}}$	0.0802	0.22

The extended Deal-Grove oxidation model, which includes so-called *growth sites*, can provide an insight into this effect. The extended equation for the linear-growth rate *(dx/dt=B/A)* is expressed as [5,6]:

$$\frac{dx}{dt} = \frac{B}{A} \equiv r\frac{Co}{Cox}Cgr \tag{1}$$

where *Co* and *Cox* are the concentrations of the oxidizing species at the interface and at the surface of the oxide, respectively, r is a reaction constant independent of the concentration of growth sites, and *Cgr* is the concentration of growth sites. The values of *Co* and *Cox* are the same for both cases (assuming identical oxide properties on both Si and SiC), and the initial growth-site concentration and the rate of nitrogen capture by the growth sites [5] should be approximately the same. Therefore, the most likely reason for the increased relative growth rate of oxide on SiC is a relative increase in the reaction constant *r* due to the existence of carbon. Note that the words "relative increase" and "increased relative growth" basically mean that less pronounced nitrogen-related growth retardation is observed in the case of SiC. Either description relates to existence of a nitrogen-related mechanism at the SiO_2–SiC interface, which has opposite effect to the single passivating mechanism (growth retardation) observed in silicon. The obvious difference between Si and SiC is the existence of carbon at the interface, so it can be assumed that carbon is involved in the additional nitrogen-related mechanism. Finally, SIMS depth profiles of oxygen and nitrogen are compared in Fig. 1 for the cases of oxides grown in NO on Si and SiC substrates. The interface regions for the Si and SiC samples were aligned using normalised oxygen profiles. The depth scale for the SIMS profile was established from the sputtering rate, converted to thickness based on the oxide thickness obtained from the accumulation capacitances and the point on the profiles where the oxygen and the carbon profiles intersect. The results show that there is no other difference in the nitrogen profiles but the intensity of the nitrogen peak. Recently published data obtained by nuclear reaction analysis (NRA), for the case of SiO_2–SiC interface annealed in NO at a pressure of 10 mbar for either 1 or 4 hr, indicate an order of magnitude lower atomic concentration of nitrogen compared to SiO_2–Si treated in identical way [4]. This is in a good correlation with the SIMS results shown in Fig. 1 and the earlier published XPS analyses [2,7]. It can be assumed that the initial concentration of growth sites *(Cgr)* is approximately the same for Si and SiC, as the density of surface silicon atoms is about the same. In addition to that, it is quite obvious that the concentration of the nitridizing species at the interface is the same in either case. However, the difference in the concentration of nitrogen incorporated at the SiO_2–Si and SiO_2–SiC interfaces shows a lower *effective* rate of growth-site neutralization by nitrogen.

Given that the growth sites should capture nitrogen at about the same rate at either interface, we can only conclude that there is an enhanced nitrogen release in the case of SiC. This can be explained

by the assumed nitrogen-carbon reaction, which removes both some nitrogen and carbon from the interface. Looking at possible mechanism between nitrogen and carbon, standard enthalpy of formation of complex oxygen/nitrogen/carbon compounds CO, HOCN, and HCN are –27.37 kcal/mol, -4.03 kcal/mol, and +30.59 kcal/mol respectively at 1100°C. It can be speculated here that HCN formation is most unlikely, however HOCN might be a possibility as it releases energy.

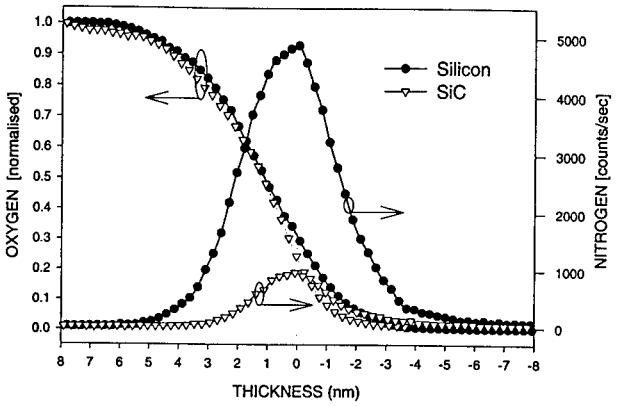


Figure 1. Normalised oxygen and nitrogen profiles at the oxide–semiconductor interface, for the cases of oxide grown on Si in NO at 1100°C for 20 min (solid circles) and oxide grown on SiC in NO at 1100°C for 1.5 h (open triangles)

Conclusion

In analogy with the effects of nitridation of gate oxides in Si technology, it was established that nitrogen provides passivating effects at the SiO_2–SiC interface. However, there is a growing evidence that the nitrogen plays an additional role in the case of SiC — assistance with the removal of carbon from the interface. As the exact mechanism remains unclear, it is important to present all the existing evidence, achieved by different and independent techniques. This paper adds some new effects and systematizes the existing indication for nitrogen-assisted removal of carbon from the SiO_2–SiC interface as follows: (1) NO nitridation can remove carbon clusters from the interface, (2) XPS indicates existence of C–N bonds, and (3) the concentration of growth sites neutralized by nitrogen is reduced, and the relative (nitrogen related) growth rate is increased in SiC.

Acknowledgments

The authors would like to acknowledge the financial supports of the Australian Research Council (large ARC grant) and Motorola (University Partnership in Research).

References:

[1] V.V. Afanas'ev, A. Stesmans and C.J. Harris, Mater. Sci. Forum 264-268 (1998), p.857.
[2] P. Tanner, S. Dimitrijev, H.F. Li, D. Sweatman, K.E. Prince and H.B. Harrison, J. Electron. Mater., 28, (1999), p.109.
[3] H.F. Li, S. Dimitrijev, D. Sweatman, H.B. Harrison and P. Tanner, J. Appl. Phys., 86, (1999), p.4316.
[4] K. McDonald, M.B. Huang, R.A. Weller and L.C. Fedman, Appl. Phys. Lett. 76, (2000), p.568.
[5] S. Dimitrijev, H.B. Harrison and D. Sweatman, IEEE Trans. Electron Dev., 43, (1996), p.267.
[6] S. Dimitrijev and H.B. Harrison, J. Appl. Phys., 80, (1996), p.2467.
[8] Z.Q. Yao, J. Appl. Phys. 78, (1995), p.2906.

Materials Science Forum Vols. 353-356 (2001) pp. 659-662
© 2001 Trans Tech Publications, Switzerland

Dissolution Mechanism of the Carbon Islands at the SiO_2/SiC Interface

O.H. Krafcsik, K.V. Josepovits and P. Deák

Technical University of Budapest, Budafoki út 8,
HU-1111 Budapest, Hungary

Keywords: Carbon Islands, Dissolution Mechanism, SiO_2-SiC Interface

Abstract

During oxidation of SiC small graphitic carbon islands are known to form at the SiO_2/SiC interface. The parameters influencing the stability of these islands are not known and due to the small size of the carbon islands it is extremely difficult to investigate this problem directly. Therefore we have deposited a graphitic amorphous carbon (a-C) layer onto high quality SiO_2 and investigated the indiffusion of carbon into SiO_2. We have found that if the oxygen contamination of the a-C layer is negligible, no carbon enters the oxide up to the highest temperature we investigated (1190°C). This means that in an oxygen-poor environment the carbon islands can not be dissolved at the usual temperature of SiC oxidation. We find however that if the a-C layer is prepared with oxygen contamination, carbon enters into SiO_2 already at 1140°C. The outdiffusion of carbonaceous species (probably CO) is very fast at this temperature. Therefore, the stability of the carbon islands at the SiO_2/SiC interface must be controlled by the availability of oxygen.

1. Introduction

One of the advantages of SiC as a base material for a future generation of power electronic devices that it has a passivating native oxide: SiO_2. The quality of the SiO_2/SiC interface is, however, far from that achieved in silicon technology. A main cause for electrically active interface states is the formation of carbon islands at the interface[1,2]. Oxygen reaching the SiC through the growing oxide reacts with silicon to form SiO_2, while carbon is removed. The way carbon leaves the interface is not well understood.[1-3] It is possible that carbon outdiffusion is hindered causing carbon excess at the interface. In a study of oxygen and carbon diffusion through the SiO_2 layer during thermal oxidation of SiC, it was found that at 1200 and 1450 °C no carbon gradient develops in the oxide. i.e., diffusion of carbonaceous species is fast in SiO_2.[4] The same study has shown that oxygen has a fast (low activation energy) and a slow (high activation energy) diffusion mechanism, probably connected to the motion of oxygen molecules and atoms, respectively. In recent computer simulation studies of diffusion in α-quartz[5] it was shown, that indeed, this is the case for oxygen but also for carbon. CO species diffuse very fast but the activation energy of atomic C diffusion is about 1.9 eV even in a perfect crystal (traps, like vacancies and dangling bonds may increase the activation energy above around 4 eV). Therefore, availability of oxygen may influence the diffusion characteristics of carbon in SiO_2 and in the oxygen-poor environment at the interface the formation of fast diffusing CO species may be retarded.

The direct study of the carbon islands at the SiO_2/SiC interface is very difficult due to their small size and sporadic occurrence. Therefore, as a model system, we have investigated the dissolution mechanism of carbon and its indiffusion into SiO_2 from an amorphous carbon layer deposited onto a high-quality thermally grown SiO_2. The deposition was carried out at low pressure and low temperature in order to preserve the quality of the oxide. The oxygen contamination of the carbon layers was checked to monitor the presence or lack of excess oxygen.

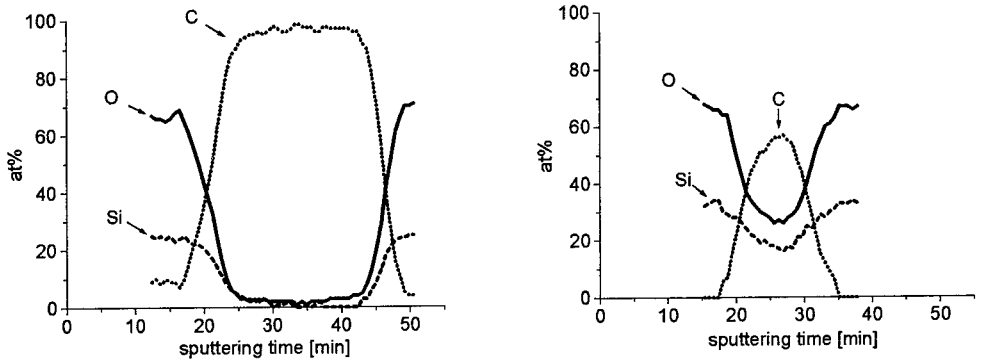
2. Experiment

High quality SiO_2 layers with a thickness of 100 nm were thermally grown (at 1050 °C in dry oxygen) on Si substrates cut from (100) oriented boron doped Wacker wafers (resistivity 5.1-6.9 Ω cm). Capacitance-Voltage measurements showed that the density of electrically active states was below 10^{11} cm^{-2} both at the interface and in the oxide. On top of this, amorphous carbon layers with thickness between ~20 and ~50 nm were deposited from CH_4 by RF-plasma assisted CVD at 8 Pa gas pressure and -500 V self-bias, without sample heating. The oxygen partial pressure was < 2 mPa and the substrate temperature during deposition was about 40°C. Onto the carbon layer a protective SiO_2 layer of 20 nm thickness was evaporated for the annealing experiments (to avoid the burning down of the carbon layer). Furnace annealing in an N_2 flow of 100 cm^3/min was carried out for 30 minutes at 6 different temperatures between 500-1190°C.

The chemical composition of the layers was determined by X-ray photoelectron spectroscopy (XPS) measurements. Concentration depth-profiles were taken by SIMS and Auger Electron Spectroscopy (AES). XPS and AES were carried out in the same analytical chamber, using the Mg K_α radiation (1253.6 eV) of a twin anode X-ray source without monochromatization in XPS and an electron gun in AES measurements. The background pressure was $5 \cdot 10^{-7}$ Pa. For AES and SIMS profiling an Ar^+ sputtering gun was used with ion energy of 3 keV and ion current of 1 μA. In SIMS profiling the diameter of the spot was 3 mm and the background pressure was $6 \cdot 10^{-7}$ Pa. The SIMS experiments were carried out by using the technique of reactive sputtering[6] with oxygen inlet amounting to a partial pressure of $3 \cdot 10^{-3}$ Pa. This technique has two advantages: it enhances the sensitivity and eliminates the effect of the changing oxygen concentration in the sample on the secondary ion yields of other elements. Under the above conditions the ion sputtering rate in SiO_2 was 1.7 nm/min.

3. Results

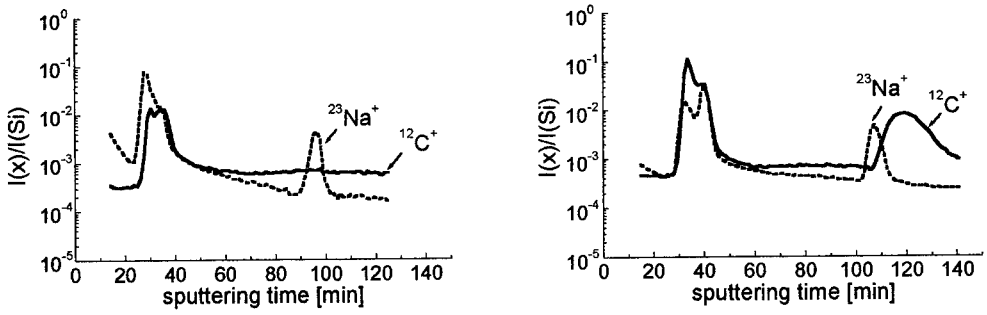
XPS spectra taken after each deposition step on the surface showed an oxygen to silicon ratio of 1.95 on the surface of both SiO_2 layers. The spectra on the surface of amorphous carbon showed 87 at% carbon and 13 at% oxygen. The latter is adsorbed oxygen on the surface of the rather porous carbon layer. Most of the carbon atoms, 65 at%, are in a graphitic environment. AES depth profiling were carried out on the carbon layers before heat treatment. Figure 1.a and 1.b show the C, O, and Si atomic concentrations vs. sputtering time on two samples with ~50 and ~20 nm carbon layer thickness, respectively. Approximate atomic concentrations were calculated using C KLL (272 eV), O KLL (503 eV) and Si LMM (76 eV) peak to peak intensities and relative sensitivity factors.[7] Since the shape of the Si Auger peak throughout the carbon layer shows only a slight difference from that in the stoichiometric SiO_2, O and Si sensitivity factors relevant to SiO_2 were used. For carbon, the sensitivity factor relevant to graphite was applied. As can be seen, in contrast to the ~50 nm thick carbon layer, the ~20 nm thick one contains significant amount of Si and O impurities. At this thickness the transition regions between the SiO_2 films below and over the carbon layer overlap. The O/Si ratio here is 1.6. The small change in the shape of the Si Auger peak indicates a decrease in the oxidation number of Si. Most probably $Si_{1-x}C_xO_y$ (y = 2) is present.



(a) (b)

Figure 1.: AES depth profiles of (a) sample with ~50 nm thick and (b) sample with ~20 nm thick carbon layer.

Depth profiling of the $C/SiO_2/Si$ system (excluding the evaporated SiO_2 protective layer) was carried out by SIMS. The $^{28}Si^+$, $^{23}Na^+$ and $^{12}C^+$ secondary ion yields were measured in cps against sputtering time. *On samples with a 50 nm carbon layer with negligible oxygen contamination no C diffusion into or segregation in the SiO_2/Si system was found up to our highest annealing temperature of 1190 °C.* For samples with an oxygen contaminated, 20 nm thick carbon layer this is only true up to 1100 °C. The SIMS depth profiles of $^{23}Na^+$ and $^{12}C^+$, normalized to the yield of $^{28}Si^+$, are shown before annealing in Figure 2.a, and after annealing at 1140°C in Figure 2.b. (Note, that the measurements before and after annealing were taken at different spots, and the carbon layer is somewhat inhomogeneous.)



(a) (b)

Figure 2.: SIMS depth profiles (a) before and (b) after annealing the sample with 20 nm carbon layer at 1140°C.

After about 30 minutes ion sputtering through the protecting SiO_2 layer, the carbon layer appears in the profiles. The alkaline ion impurities (Na, K) segregate at the SiO_2/Si interface so the $^{23}Na^+/^{28}Si^+$ ratio serves as a marker for the place of that interface. As can be seen in Figure 2.b, the $^{12}C^+/^{28}Si^+$ ratio in the SiO_2 layer is very similar to that in Figures 2.a, but at the SiO_2/Si interface, on the Si side (right behind the peak in the $^{23}Na^+/^{28}Si^+$ ratio) carbon accumulation appears. This means that at this temperature range all of a sudden carbon begins to diffuse very fast out of the oxygen-contaminated carbon layer, and all of the mobile carbon species reach the SiO_2/Si interface during the time of annealing. Carbon accumulation has not been observed in the SiO_2 layer. To make sure that the source of the carbon accumulation at the interface is the carbon layer and not the silicon substrate, annealing of a "bare" SiO_2/Si structure (without a carbon layer) was carried out at 1190°C for 30 minutes. No carbon segregation was found at the SiO_2/Si interface in this case.

Conclusion

Our results can be interpreted the following way. In lack of excess oxygen the activation energy of dissociation from the graphitic amorphous carbon phase is too high to obtain free carbon up to 1190 °C. In the presence of excess oxygen in the carbon layer, however, carbonaceous species (probably CO) are released already above 1100 °C. In agreement with earlier carbon diffusion experiments where oxygen was available for carbon,[4] the diffusion is very fast at this temperature, and all of the mobile carbon reaches the SiO_2/Si interface. These results on the model system have the consequence that the carbon islands at the SiO_2/SiC interface are stable at the usual oxidation temperature of SiC. Their dissolution depends on the availability of oxygen, which — above 1100 °C — can decompose them. Once CO species are formed, they can diffuse out easily through the oxide. Therefore, the quality of the SiO_2/SiC interface is controlled by the incoming oxygen flux.

Acknowledgments

The authors would like to thank I. Bársony (MTA-MFA) for supplying the thermally oxidized Si samples and for the CV measurements, as well as I. Pócsik (MTA-SZFOKI) for the deposition of the carbon layers. Valuable discussions with Ch. I. Harris (ACREO) and N. T. Son (U. Linköping), as well as Ch. Köhler and Z. Hajnal (U. Paderborn) are appreciated. This work was supported by the FKFP Grant No. 0289/1997, the German-Hungarian DFG-MTA Project Nr. 112, the Swedish-Hungarian IVA-MTA Project Nr.36, and the Research Foundation of the Hungarian Academy of Sciences under Project No. 98-30 2,2.

References

[1] V. V. Afanas'ev, A. Stesmans and Ch. I. Harris, ICSC III-N'97 Sweden p. 423.
[2] M. Bassler, G. Pensl and V. Afanas'ev, Diamond and Rel. Mat. **6** (10) (1997) p. 1472.
[3] J. Schmitt and R. Helbig, J. Electrochem. Soc. **141** (8) (1994) p. 2262.
[4] Z. Zheng, R. E. Tressler and K. E. Spear, J. Electrochem. Soc. **137** (3) (1990) p. 854.
[5] Ch. Köhler, Z. Hajnal, P. Deák, Th. Frauenheim, private communication
[6] J. Giber and V. K. Josepovits, in Proceedings of the 7th International Vacuum Congress and the 3rd International Conference on Solid Surfaces, Vienna (1977) p. 2585.
[7] L. E. Davis, N. C. MacDonald, P. W. Palmberg, G. E. Riach and R. E. Weber, Handbook of Auger Electron Spectroscopy, 2nd ed., Physical Electronics Industries Inc., Minnesota (1976)

Materials Science Forum Vols. 353-356 (2001) pp. 663-666
© 2001 Trans Tech Publications, Switzerland

Dependence of Wet Oxidation on the Defect Density in 3C-SiC

M. Eickhoff[1,3], N. Vouroutzis[2], A. Nielsen[1,3], G. Krötz[1] and J. Stoemenos[2]

[1] DaimlerChrysler AG, Department: FT2/M, Postfach 800465, DE-81663 München, Germany

[2] Physics Department, Aristotle University Thessaloniki, GR-54006 Thessaloniki, Greece

[3] Present address: Infineon Technologies AG, WS GS SNS D3, Otto-Hahn-Ring 6, DE-81739 München, Germany

Keywords: Antiphase Boundary, Cubic Silicon Carbide, Oxidation Rates, Oxide Roughness, Planar Defects, Wet Oxidation

Abstract The dependence of wet oxidation on the defect density in 3C-SiC films epitaxially grown on Si substrates was studied. Under wet atmosphere preferential oxidation at the antiphase boundaries (APBs) was observed, resulting in the formation of rough oxide surfaces. A semi-logarithmic relation between defect density and the oxidation rate was found.

1. Introduction

Oxidation of 3C-SiC is important for device development, as well as for realization of complex structures like 3C-SiC on Insulator (SICOIN) using the technique of wafer bonding. The presence of planar defects in 3C-SiC results in uneven wet oxidation [1,2] whereas dry oxidation exhibits smoother surfaces not affected by the presence of defects [2,3]. However, in the latter case the interface trap density is almost one order of magnitude higher than in oxides produced by wet oxidation [4,5]. Another disadvantage of dry oxidation is the low oxidation rate above 1000°C compared to wet oxidation [6]. In this work the influence of defect density on the wet-oxidation rate and the resulting oxide roughness in 3C-SiC is systematically studied.

2. Experimental procedure

3C-SiC films were deposited on (100) Si-wafers at 1200°C [7]. Wet oxidation was carried out at 1150°C in a horizontal hot-wall quartz tube furnace at atmospheric pressure O_2-atmosphere. Water vapour was added to the oxygen by passing the O_2-flow through a de-ionized water bubbler at 95°C. The oxidation time was 8h. Transmission Electron Microscopy (TEM) and Atomic Force Microscopy (AFM) were used for structural characterization of oxide and interface layers. In order to reduce the surface roughness all specimens were polished prior to oxidation, leading to a RMS roughness lower than 24nm, and subsequently oxidized. The main characteristics regarding the oxidation conditions are summarized in Table I.

3. Results and discussion

After oxidation hillocks were observed at the surface forming close loops, as shown in the AFM micrograph in Fig.1. The mean height of these hillocks was 250nm and the width 600nm, as the corresponding profile along line (a) reveals in the inset in Fig.1, suggesting preferential oxidation enhancement. Removing the oxide by dipping the specimen into HF, the hillocks appear as grooves, as shown in the lower part of the micrograph in Fig.1. A further proof is given by the AFM profile along line (b), shown in the inset of Fig.1. The morphology of the loops in the oxide and the grooves in the 3C-SiC suggest preferential oxidation at antiphase boundaries (APBs). In order to prove the direct relation of the APBs with the formation of hillocks during oxidation, the following experiment was performed. The specimen (1743-2) was thinned from the backside so that only the oxide and a thin layer from the uppermost part of the 3C-SiC film were left for Plane View TEM

(PVTEM) observations. Due to the thick amorphous oxide the diffraction contrast was very poor, attributed to absorption from the oxide thickness variations. Thus, the darker areas correspond to the thicker oxide, as shown in the PVTEM micrograph in Fig.2a, exhibiting similar morphology as the AFM micrograph in Fig.1. The letters A, B, and C in Fig2a denote some characteristic areas, subsequently the oxide was etched in HF, so that only the SiC-layer was left as shown in Fig.2b.

Specimen	Oxidation time [min]	Oxide thickness [nm]	Defect density at SiO_2/SiC-interface [cm^{-2}]	Surf.-roughn. RMS [nm] before Ox.	Surf.-roughn. RMS [nm] after Ox
1743-2	300	290	$9x10^9$	24	36
1742-2	300	360	$4x10^{10}$	14	43
1742-1	300	390	$7x10^{10}$	5	33
1919	480	780	$2x10^{11}$	11	37
1914	480	390	$6x10^9$	8	36
1913	480	400	$8x10^9$		
1908 (front)	480	430	$1x10^{10}$	13	43
1908 (back)	480	850	$1x10^{12}$	1	1

Table I: Wet oxidation of 3C-SiC at 1150°C

Now a strong diffraction contrast due to the crystalline 3C-SiC layer is observed in the same area. In that case two dominating kinds of defects can be identified: Stacking Faults (SFs) and APBs. It is evident that the preferentially oxidized areas in Fig.2a correspond only to the APBs shown in Fig.2b, whereas SFs show "normal" oxidation behavior. APBs and SFs in an oxidized and subsequently etched area are shown at higher magnification in Fig.2c. The APBs are delineated as bright in Fig.2c, due to preferential etching at the APBs during oxidation. The enhanced oxidation at the APBs can be attributed either to the weakness of strained -C-C- and -Si-Si- bonds at the APBs or to Si-migration from the substrate through the APBs, as silicon mass transport in 3C-SiC films through the existing defects has been reported before [8]. In order to get experimental evidence for the dominating mechnanism windows were opened in the substrate by anisotropic wet etching from the backside in specimen 1908, which was deposited under the standard conditions [7], leaving only a thin 3C-SiC diaphragm, so that also the SiC of the former SiC/Si interface was exposed for oxidation (Fig.3a). The oxidation rates were measured at the front side of the SiC-diaphragm, denoted by the letter A in Fig.3a, as well as in the areas where the Si-substrate remained. The oxidation rate at the uppermost part of the 3C-SiC film was not influenced by presence or absence of the Si-substrate. Therefore, enhanced oxidation at the APBs must be attributed solely to the strained -C-C- and -Si-Si- bonds.

The diaphragm-experiment has also monitored the influence of the defect density on the oxidation behavior of the film. The oxide at the former interface layer was very smooth, as shown in Fig.3b, with a roughness of less than 3nm. The measured oxide thickness of 850 nm was two times thicker than at the front side. This significant difference in the oxidation rate of the two sides of the SiC film is attributed to the difference in the density of existing defects. The SiC/SiO_2 interface at the backside is very rough, as shown in the inset in Fig.3b. This difference can be explained by considering that during the growth the defect density is reduced as the film thickness increases [1,9]. Therefore, as oxidation advances from the backside, significant fluctuations of the oxidation rate are caused by the strong decrease in defect density.To quantify this behaviour, a systematic study of the oxidation rate versus defect density was performed. In 3C-SiC the most common defects are SFs and APBs as shown in Fig.2c. Near the SiC/Si interface twins also exists, which are extended up to 100nm [1,10]. Close to the interface the defect density is very high and decreases fast as the thickness of the film increases. Above 3.5μm the reduction of the defect density is very slow [9]. Taking this behavior into account, specimens with different thickness were deposited and subsequently oxidized under the same conditions (specimens 1913, 1914, 1908-F and 1919). The measured characteristics of the polished specimens before and after oxidation are shown in Table I.

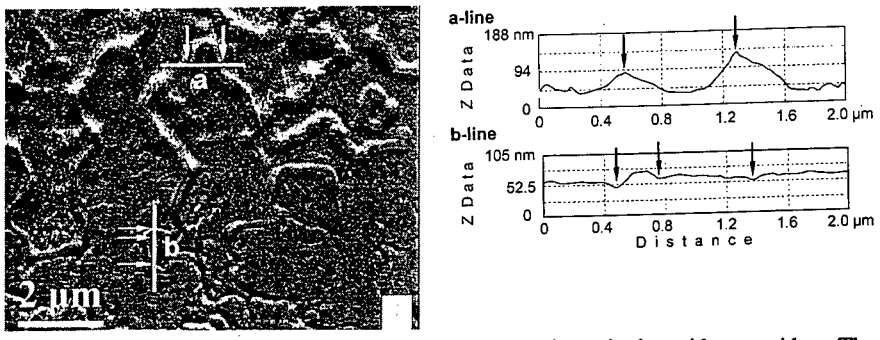


Fig.1 AFM micrograph after wet oxidation, bumps that form close loops in the oxide are evident. The profile of the bump along the line (a) is shown in the inset. In the lower part of the photograph the oxide was etched. Now the bumps appear as grooves. This is evident from the profile along the line (b) shown in the inset.

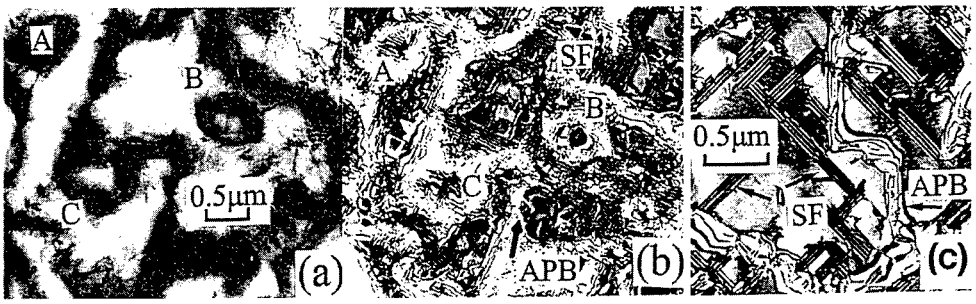


Fig.2: PVTEM micrographs from specimen 1743-2 after wet oxidation a) The 290nm thick oxide and the uppermost part of a 160nm thick 3C-SiC are superimposed. Close loops due to preferential oxidation at the APBs are evident, characteristic areas are denoted by the letters A, B and C. b) The same area after etching the oxide, now strong diffraction contrast due to crystalline 3C-SiC is evident. The APBs are clearly delineated corresponding to the bumps in figure (a). c) PVTEM micrograph at higher magnification after etching the oxide, APBs and SFs can be clearly seen.

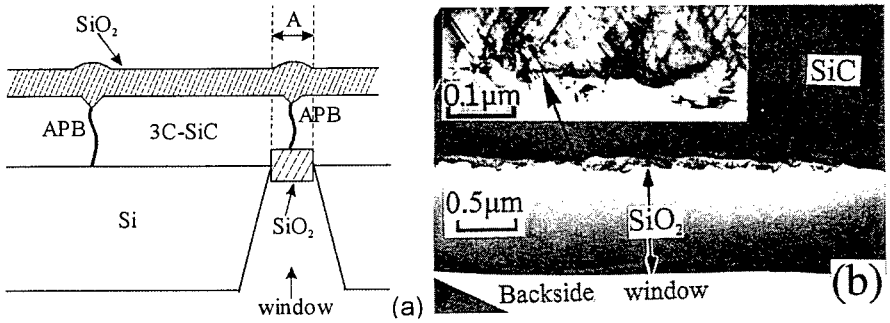


Fig.3: Wet oxidation experiment after opening windows in the Si-substrate, in specimen 1908 a) Schematic representation of the structure in the windows after oxidation. b) XTEM micrograph from the backside window, the oxide is very smooth and significantly thicker than at the front side. The SiC/SiO_2 interface is very rough, as shown in the inset

The increase of the oxidation rate with increasing defect density is quantitavely shown in Fig.4.

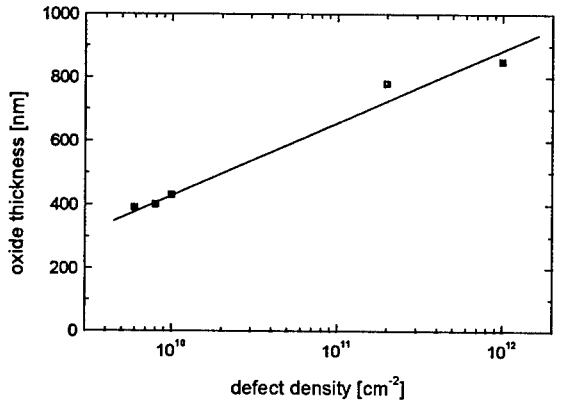


Fig.4: Oxide thickness versus defect density for 8h wet oxidation of 3C-SiC

The two limiting cases of this relation are governed by the oxidation rate of monocrystalline silicon carbide for low defect densities on the one hand and by the oxidation rate monitored by the height of the hillocks at crystal-defects after oxidation for high defect densities on the other hand. The slope on the increasing parte between these two assymptotic cases is determined by the geometrical shape of the hillocks as it mirrors overlapping between adjacent hillocks. This relation can be exactly reproduced if an adequate approximation for the shape of the hillocks is assumed as well as the dependence of surface roughness after oxidation on defect density can be understood [11]. To get a first estimate for the quantitative relationship between oxidation rate and defect density basing on the measurement results, the increasing part can be approximated by a semilogarithmic relation. Evaluation of this reveals:

$$R = 0.47 \cdot \log D - 3.8 \qquad (1)$$

where R is the oxidation rate in nm/min and D the defect density per cm^2.
The very fast oxidation rate, which was observed in the SiC/Si interface layer of epitaxially grown 3C-SiC, is also attributed to the slightly misoriented grains, which are formed during the carbonization process in the early stage of growth [1,2].

4. Conclusions

The relation of the oxidation behavior and defect density in 3C-SiC films was shown. The surface roughness of the oxide was attributed to the APBs as direct PVTEM observations revealed. At very high defect densities the surface roughness decreases due to homogeneous distribution of defects. Enhanced oxidation is observed near the SiC/Si interface in single crystalline 3C-SiC, where slightly misoriented SiC islands form low angle boundaries during coalescence.

Acknowledgements:
This work was supported by the EU, BRITE-EURAM project CT96-0261

References:

[1] C.H. Carter, Jr. and R.F. Davis, S.R. Nutt, J. Mater. Res.1 (1986), p. 811
[2] S.R. Nutt, J. Davis, H.J. Kim and R.F. Davis, Appl. Phys. Lett.50 (1987), p. 203
[3] J. Palmour, H. J. Kim and R.F. Davis, MRS proceedings, Vol.54 (1986), p. 285
[4] S. Zalma, K. Orioda, Y. Koide and Y. Yasuda, J. Appl. Phys. 68 (1990), p. 6304
[5] S.M. Tang, W.B. Berry, R. Kwor, M.V. Zeller and L.G. Matus, J. Electrochem. Soc. 137 (1990), p. 221
[6] S.C. Singhal, J. Mat. Sci. 11 (1976), p. 1246
[7] H. Möller, M Eickhoff, M.Rapp, H.W. Grueninger and G. Krötz, Appl. Phys. A68, (1999), p. 461
[8] Ph. Komninou, J. Stoemenos, G. Nouet, Th. Karakostas J. Crystal Growth 203, (1999), p. 103
[9] J. Stoemenos, C. Dezauzier, G. Arnaud, J. Camassel, J. Pascual, J.L. Robert, Mat. Scien. Eng. B29 (1995), p. 160
[10] P. Pirouz, C.R. Chorey, T.T. Cheng and J.A. Powell. Mat. Rec. Soc. Sym. Proc. Vol.91 (1987), p. 399
[11] M. Eickhoff, N. Vouroutzis, A. Nielsen, G. Krötz and J. Stoemenos, to be published

Chapter 5:

SiC Devices

Materials Science Forum Vols. 353-356 (2001) pp. 669-674
© 2001 Trans Tech Publications, Switzerland

SiC Microwave Power Devices

Erwan Morvan, Olivier Noblanc, Christian Dua and Christian Brylinski

Thomson-CSF, Laboratoire Central de Rechereches (LCB),
Domaine de Corbeville, FR-91404 Orsay Cedex, France

Keywords: Microwave Power, Semi-Insulating SiC, SiC MESFET, Trapping

Abstract: Mesfet power RF / Microwave transistors based on SiC substrates and epitaxy are now trying to emerge as commercial products. Impressive power emission results [1] have already been published. Initial predictions [2,3,4] about the higher voltage handling and output impedance level have now been experimentally confirmed. Moreover, linearity of SiC Mesfets seems good, at least as good as for silicon LD-MOS, which is crucial for any amplifier to be used in the next generations of telecommunications systems with complex modulation schemes.. Thermal management does not seem to be as simple as expected, due to: (1) the very high dissipated power density, (2) the non-linear thermal conductivity of SiC, and (3) the rapid decrease of electron mobility with temperature. Some device samples have already been delivered to a few selected potential customers, at least in USA and Europe. However, it seems that there are still technical issues to be solved before they can be established as "normal" products. One major issue is the stability of the device electrical characteristics [4,5]. A second one is the power density, still too low, lower than 2 W/mm for 30 W devices. Both seem to be strongly related to the substrate and epitaxy quality, and it is now clear that the requirements on the SiC semi-insulating substrates and the epitaxy used for making the SiC Mesfets are extremely severe. Some improvement can be obtained using adequate buffering structures, but it seems that the decisive step forward will come from the use of purer semi-insulating substrates. If those problems cannot be solved rapidly, there is a significant chance/risk that the availability of III-N/SiC HEMT can eliminate the interest for SiC Mesfet, as a consequence of the higher gain of III-N HEMT and due to the fact that III-N materials and technology experience rapid progress as a spin-off of the efforts devoted to III-N optoelectronics. However, III-N microwave and III-N optoelectronics technologies are not so similar; and there are still many problems to be solved before the III-N devices can meet the performance even of the imperfect SiC Mesfets demonstrated today

1 Microwave power market and target performance

1.1 Market driven requirements

SiC Mesfet transistors are presently being developed for the applications at frequencies in the range 1 – 5 GHz. At higher frequency, the general opinion today is that III-N semiconductors (GaN and related) based devices will perform better. We will come back to this opinion at the very end of this presentation. The main identified market for SiC transistors is the market of power amplifiers for the transmitters of the future base stations for the next generations of telecommunication and/or broadcast systems. The other known markets are small, although some of them appear as strategic for some professional electronics applications. Those small volume applications will try to get device supply from a larger volume technology, with rather minor modifications in order to adapt the products to the actual needs of each specific application.

As any new device, SiC based transistors can only find market if they bring additional performance as compared to the existing devices. At present, there are mainly three kinds of opportunities for new microwave power transistors: (1) Devices leading to better linearity, (2) Devices leading to lower equipment manufacturing cost, (3) Devices allowing sharing of one equipment by different customers.

1.2 Opportunities for SiC transistors

SiC based devices are trying to compete on each of these three kinds of opportunities.

1.2.1 Linearity:

The first available results from linearity measurements at Cree and at Thomson-CSF show linearity equal or slightly better as commercial LD-MOS or GaAs HBT for the same level of power, around 10 W@2GHz. So, today, linearity is neither a strong point for SiC nor a weakness. In recent presentations, Cree has expressed the opinion that SiC Mesfet can deliver significantly better linearity than Si LD-MOS.

1.2.2 Manufacturing cost:

By allowing to increase the bias voltage - today up to 50 V, tomorrow up to 100 V - the use of SiC transistors simplifies the impedance matching. Up to probably 3 GHz, no pre-matching will be necessary in the transistor package. In the long term, it means that many applications can be covered by exactly the same transistor. In the short term, it means that elimination of the in-package passive matching network will bring cost reduction which can partly compensate the increase of the device cost due to the high price of the SiC substrate and epitaxy. Outside the package, the easier impedance matching will reduce the need for many passive elements and for the matching adjustment labour required for manufacturing the amplifiers. Moreover, even if the thermal management of SiC transistors is not as simple as claimed initially, it will be possible in the future to raise the temperature difference between case and ambiance by 50 to 100%, which means that, for the same power level, the heat sink volume, weight and cost can be reduced by the same amount.

1.2.3 Equipment sharing:

Easier impedance matching paves the way to lower-cost large bandwidth amplifiers. High-linearity large bandwidth amplifiers may become manufacturable, while they are nowadays real nightmares even for experienced amplifier designers trying to use existing Si or GaAs devices. Transmitters based on wideband amplifiers will allow to transmit several telecommunication standards on the same equipment, a way to save infrastructure costs.

In conclusion, the commercial arena offers real opportunities to the SiC transistors in the short and long terms, provided competitive devices can be manufactured with the right level of performance and reliability. The market is there., but the SiC products are not ready yet, and the competing technologies make constant progress. The success depends on the progress SiC devices will make within the next coming two years.

2 Performance of SiC Mesfet transistors

2.1 Device structure

The situation governing the choice of SiC transistor structure for microwave power has not changed much for at least 5 years. MOS microwave devices do not exist because MOS interfaces on SiC still exhibit too low electron mobility. Even the enhanced values around 100 $cm^2V^{-1}s^{-1}$, recently obtained in US (oxide nitridation at Cree), Japan (a-axis face at Kyoto University) and Germany (15R polytype at Siemens) are not sufficient for high frequency devices. Minimum values around 400 $cm^2V^{-1}s^{-1}$ would be required.

On the other hand, SiC based bipolar structures have not received much attention recently. Although first encouraging DC results were published around 1994, we have not seen any publication on III-N / SiC HBT showing RF amplification capability yet. The only basic structures really explored today are based on the Schottky contact field effect current control.

Static Induction Transistor (SIT), a kind of vertical Mesfet or JFET, is explored by Northrop Grumann, following Westinghouse works. The impressive power results published around 1996 at frequency around 0.6 GHz (up to 350 W CW and 1,75 kW pulse mode) have been now extended into L-band up to 700W CW@1.5 GHz and to S-band up to 2.9 GHz, but in pulse mode only (200 W for a few microseconds). Northrop Grumann does not seem to have any intention to commercialise this kind of SiC devices. No other team has published on microwave power SiC SIT. The processing of SIT devices for microwaves is very difficult and there are also some limitations related to the conductive substrate used so far. On the other hand, SIT , as a vertical device, is less sensitive to surface and/or substrate charge trapping. This has been a real advantage so far, as will be discussed later.

All other groups identified as active in the area of SiC microwave power devices are working on the SiC Mesfet, with topology rather similar to GaAs Mesfet. Hereafter we will only discuss further about the results on SiC Mesfet

2.2 Bias voltage

Today, efficient 50 V operation of SiC Mesfet at 2 GHz is demonstrated at Cree and at Thomson-CSF, as compared to 28-33V for available silicon transistors working in the same frequency range. Silicon devices working at 40-50 V can be found in a few catalogues, and as prototype devices, but there still seems to be problems of power gain and reliability.Thomson-CSF has been able to operate some SiC Mesfets up to 100 V bias voltage under RF power load-pull conditions with good power gain and without breakdown, but no increase of the power density has been observed from 50 V up to 100V. It remained lower or around 2 W/mm, both under CW and pulse regimes. Since DC plots show strong degradation of drain resistance after high voltage stress, we tend to attribute the low power density obtained, to the influence of trapping effects enhanced at high drain voltage.

2.3 Output power

2.3.1 LOAD-PULL MEASUREMENTS

Load-pull conditions mean that the output load and input source impedances can be adjusted to get optimum behaviour of the device under test. Today, the 80 W CW and 120 W pulse output power levels published by Cree around 3 GHz are certainly the highest for this frequency for any solid state technology. Moreover, it has been obtained with only one chip at rather high supply voltage (40 - 50 V).

2.3.2 SIC 75 W CW @1.5 GHz COMPLETE AMPLIFIER

At Thomcast, the broadcast company of the Thomson-CSF group, a complete amplifier for operation at 1.5 GHz (DAB transmitter application) has been built with SiC Mesfet transistors in the frame of the EC "Esprit" TELSIC project. The amplifier conditions differ from the load-pull conditions by the fact that the amplifier includes the necessary matching networks in order for the amplifier input to look as 50 ohms resistive charge over the whole amplifier bandwidth, and for the output to give optimum performance with a charge looking as 50 ohms resistive load. This amplifier gave more than 75 W output power with power added efficiency over 40 %. This is probably the first published result on a complete amplifier based on SiC transistors with this level of power. In this amplifier, the substrate comes from Cree in the USA, the epitaxy from ACREO in Sweden, the chip design is a common work between Thomson-CSF and Ericsson, the device packages come from Japan, the processing of the SiC chips, the design, realisation and testing of the amplifier have been done at Thomson-CSF in France. The amplifier combines the power from two push-pull transistors, each of them made of two SiC chips with 21.6 mm periphery. This means more than 500 SiC elementary transistor fingers working together with good parallel association efficiency. There is no prematching inside the packages and a simple second order filter cell is sufficient to get very good matching both on the input and on the output side.

2.4 Output impedance

As predicted, the output impedance level of SiC transistors seems clearly much higher than that of silicon ones. As an example, with Thomson SiC Mesfet prototypes, 25 to 50 ohms optimum output impedance level is reproducibly obtained without any pre-matching inside the package for 30 W SiC Mesfet devices working

at 1.5 GHz with 50 V power supply voltage. It is about 5 times the level of impedance of silicon devices working at the same frequency with the same power level, which always require pre-matching networks inside the package.

2.5 Drain efficiency

Excellent drain efficiency has been obtained on SiC Mesfet in class AB regime, both at Cree and at Thomson-CSF. The values recorded correlate well with those obtained by Northrop Gruman using SIT device structure. At Thomson-CSF, at 0.6 GHz and around 50 V drain bias voltage, values over 50 % are reproducibly obtained for 30 W power level, while values over 60 % have been obtained with the best 20 W device samples. For higher frequency, the drain efficiency of Mesfets with one micrometer gate length decreases slowly down to typically 35 % at 2 GHz. It is rather easy to study the influence of the temperature using microwave power measurements under pulse conditions, for which there is no problem with heat sinking. We have obtained recently our first results under such regime (typically 100 microseconds pulse). We can obtain drain efficiency over 50 % at power level around 50 W at 1.4 GHz with drain voltage around 50 V from one single chip. So, it seems that the decrease of drain efficiency observed at high power level and especially at high frequency is essentially due to the thermal effects, probably in relation with the rapid decrease of the electron mobility with temperature.

2.6 Thermal management

Thermal management for wide bandgap devices is not as simple as was claimed in the early stage of the SiC research and development. Indeed the SiC material itself and the related technological surrounding materials seem to resist to higher temperature as compared to any previous microwave device technology. However, since the electron mobility in SiC is going down rapidly with temperature (as $T^{-2.2}$), both current density and access conductance for source and drain decrease very rapidly with the delivered power if the chip design is dense. This does not mean that SiC Mesfets cannot work at high temperature - RF operation over 300°C junction temperature is now demonstrated -, but it means that a compromise has to be found between the RF performance, the chip design density, and the temperature of operation. Using the classical chip cooling techniques (chip back-face brazed onto a plate mounted on a copper or aluminium heat sink), 20-30 W/mm^2 seems the maximum practical power density that can be obtained with SiC transistor chips. This power density is however 2-3 times over the maximum power density that can be efficiently evacuated with classical heat sinks, and special care will be necessary in any case.

2.7 Linearity

Linearity measurements are very difficult to perform, and the various published results, extremely difficult to compare. Measurements directly on devices are generally unreliable and the only kind of test which brings some confidence is testing a complete amplifier. Cree has published results showing better linearity for SiC Mesfets as compared to silicon LD-MOS. The first linearity tests on Thomson SiC Mesfets have been performed on amplifiers designed and realised in the frame of the European Community "Esprit" TELSIC project. They show linearity figures rather similar to silicon LD-MOS (-44 dB for excitation level -10 dB below 1dB compression point). This first set of results must be carefully interpreted because it means comparing results on SiC devices imperfect prototypes with those measured on commercial silicon devices from an established technology. "Imperfect prototypes" means that the SiC Mesfets available to us still suffer from trapping effects as will be detailed hereafter.

3 The substrate issue

In our opinion, the substrate issue is still the main factor controlling the entrance of the SiC microwave power device into the commercial area. 4H is the favoured polytype. Semi-insulating seems the favourite conduction type because it brings many advantages related to the on-chip circuitry including lines and pads which present highly reduced parasitic capacitance as compared to those made on conductive substrate. More generally, ideal substrate for microwave power applications is electrically insulating and thermally conductive. Indeed, semi-insulating SiC is one of the best possible, and probably the best available today. Maybe semi-insulating single crystal AlN could be equivalent. Probably only insulating diamond and a few very exotic other materials could be better.

3.1 SiC semi-insulating (S.I) substrates

Westinghouse was the first to publish on devices made on S.I SiC. Cree Research has started to commercialise 4H semi-insulating substrates around 1996-1997. Those substrates have opened the way to an improvement of the RF performances, as compared to the results obtained previously from devices made on conductive SiC substrates. The substrates and devices have been dramatically improved along the past years. The DC characteristics drifts observed on devices made with the first semi-insulating substrates have now disappeared in most cases. However, the devices we have obtained on those substrates today still do not perform close to the simple theoretical calculations and simulations. The main residual problem is an anomalous decrease of power density and efficiency at high voltage, typically over 50V.

The same kind of behaviour can be observed using epitaxy from 3 different sources, so we do not tend to suspect the epitaxy quality. Also, this phenomenon does not appear on devices made on conductive substrate with five micrometers p-type buffer for device-to-device P/N junction isolation. So we cannot suspect the passivation of the free surface, which is the same for the two kinds of devices. This is why we suspect the substrate. In our opinion, substrate purity has still to be improved together with crystal structural quality and price, before SiC Mesfets can become competitive industrial products.

One way to overcome the problem can be to get purer substrates. We now can start to explore this approach using the first HT-CVD S.I material samples. But during the past years, with only one source of substrates, we have had to try to live with the existing substrates, trying to isolate the channel layer from the substrate layer. During the EC Esprit "TELSIC" project (1998-2000), Thomson-CSF and ACREO have worked together to define more efficient buffering structures. ACREO has demonstrated by numerical simulation that electron injection can nearly be completely eliminated using special buffer structures. By realising such structures by epitaxy and characterising devices made on those structures, we have obtained devices with almost perfect DC characteristics even after 80 V drain bias stress.

3.2 Structural quality

State of the art semi-insulating (S.I) substrates already allow to make devices with periphery as large as 36 mm without too much decrease of process yield. The reason is that the sensitive area (recess zone) for the device is only < 5 micrometers wide , and so, even for a transistor considered as big nowadays, the sensitive total area is around 0.1 mm^2 and the killing defect critical density, around 1000 cm^{-2}.

4 SiC FETs vs III-N HEMT

For wide bandgap semiconductors, as for medium bandgap III-V materials, the use of heterojunction structures brings strong improvement of the devices performance. Today, at least on small periphery devices (typically 0.1 to 0.3 mm gate width), AlGaN/GaN HEMTs prototypes exhibit outstanding performance. Owing to the higher channel mobility. They offer much higher (roughly a factor 2) drain current, transconductance, and cut-off frequencies as compared to SiC Mesfets with same geometry and same voltage handling. Therefore, there is a great pressure towards unifying the microwave wide bandgap power transistors technology by adapting III-N HEMT to applications from DC to millimeter wavelength. Moreover, there is a pressure towards manufacturing the III-N on sapphire or semi-insulating GaAs substrates, instead of semi-insulating SiC, since GaAs or sapphire are available on the market at acceptable price, quality and diameter (up to 100 mm or more). Remaining obstacles against this very rationalistic approach are a few issues for which the answers are not known yet..

- While many reports can be found about small III-N HEMT devices, very few teams (HRL and Cree), have made large devices.
- Many III-N devices are still affected by strong trapping effects. The respective roles of surface passivation and material defects still need clarification. It will be easy to propose new options for passivation, but not easy to decrease dramatically defect density in III-N materials, all grown today by hetero-epitaxy on a highly mismatched substrate.
- High static voltage handling has been demonstrated for III-N FETs, at least up to 600 V for Mesfet devices.

- On the other hand, nearly all RF characterisation results have been performed at drain bias voltage lower than 50 V. It is not obvious yet whether III-N FETs will be able to work properly with drain bias voltage higher than 50 V.
- The very high density of defects in III-N layers brings also a question about the possible influence of those defects on the device reliability. If even a small proportion of the defects can become electrically charged or can move under high electric field, there is a risk that III-N FETs will not be both optimally performing and reliable. The good level of reliability of III-N LEDs brings no information on this aspect, since there is no high electric field in a LED at work.

It is the role of the III-N microwave power research and development world wide to answer those questions and we are quite confident that answers will become available by the next coming three years, at least to a limited number of happy few laboratories.

As an opinion, we think it is wise to keep working on SiC transistors and especially SiC Mesfets until III-N FETs can actually show similar power performance at the same frequency with the same reliability. Although still exotic today, the possible availability of polytype heterojunction in the future may change the situation by bringing the same level of performance as III-N FETs without the mismatch defects.

Acknowledgments

The SiC activity at Thomson-CSF is supported by the French DoD DGA / DSP / STTC, by European Community through Esprit "TELSIC"and Brite Euram "JESICA" projects, and by French Ministry of Research and Education through the "Saut Technologique SiC" and RNRT "Physic" projects.

References:

[1] S.T. Allen, W.L. Pribble, R.A. Sadler, T.S. Alcorn, Z. Ring, and J.W. Palmour (Cree), *Progress in High Power SiC Microwave Mesfets*, 1999 IEEE MTT-S Digest, pp 321.

[2] R.J. Trew, *The operation of Microwave Power Amplifiers Fabricated from Wide Bandgap Semiconductors*, 1997 IEEE MTT-S Digest, pp 45.

[3] C.E. Weitzel, Silicon Carbide High Frequency Devices, Mater. Sci. Forum 264-268 (1998), p. 907.

[4] M.Roschke, F. Schwierz, G. Paasch, and D. Schipanski, *Evaluating the Three Common SiC Polytypes for MESFET applications*, Mater. Sci. Forum 264-268 (1998) p. 965.

[5] O.Noblanc, C. Arnodo, E. Chartier, and C. Brylinski , *Characterization of Power Mesfets on 4H-SiC Conductive and Semi-Insulating Wafers,* Mater. Sci. Forum 949-952 (1998).

[6] O.Noblanc, C. Arnodo, C.Dua, E. Chartier, and C. Brylinski, *Progress in the use of 4H-SiC semi-insulating substrates for microwave of power MESFETs,* Materials Sci. and Eng. , B 61-62, (1999), p.339.

Materials Science Forum Vols. 353-356 (2001) pp. 675-678
© 2001 Trans Tech Publications, Switzerland

1700 V SiC Schottky Diodes Scaled to 25 A

D. Peters, K.O. Dohnke, C. Hecht and D. Stephani

SiCED Electronics Development Ltd.,
Paul-Gossen-Str. 100, DE-91052 Erlangen, Germany

Keywords: Freewheeling Diode, High Voltage, Schottky Diodes, Ultrafast Switching Device

Abstract This paper reports on a study of SiC Schottky diodes focused on high current rating and high blocking voltage: 25 A / 1200 V and 1700V, resp. With an active area of 10 mm^2 we successfully explored new ground for SiC devices. The device concept, fabrication process, yield aspects and measured results of static and dynamic characteristics as well as the temperature behavior are described. The reverse currents are very low (<500 µA) even at 125°C and their temperature dependence is lower than expected by thermionic emission since tunneling mechanisms through the Schottky barrier rule the current transport at high blocking voltages .

1. INTRODUCTION

A recently published study demonstrated the superior performance of 4H SiC Schottky diodes for ultrafast high voltage switching applications [1]. These diodes were designed for 600 V blocking voltage and exhibited a very low leakage current and a weak dependence of leakage current on temperature. They also proved a long term stability under high temperature reverse bias tests (150°C, -600 V, 1000 h) and thermal cycling up to 400 °C. Motivated by these encouraging results we used this technology in order to fabricate SiC Schottky diodes for a current / blocking voltage rating of 25 A / 1200V, respectively 1700 V. The active area was 10 mm^2 in both cases. This is a rather large area for SiC devices with respect to the defect density of today available SiC wafers.

2. DEVICE CONCEPT AND FABRICATION

In principal, the device is based on a concept using a planar junction termination extension (JTE) [1,2]. A schematic cross section of the fabricated diodes is sketched in Fig. 1. The diodes were processed on selected 35 mm wafers with low micropipe density ≤ 10 cm^{-2} purchased from Cree.

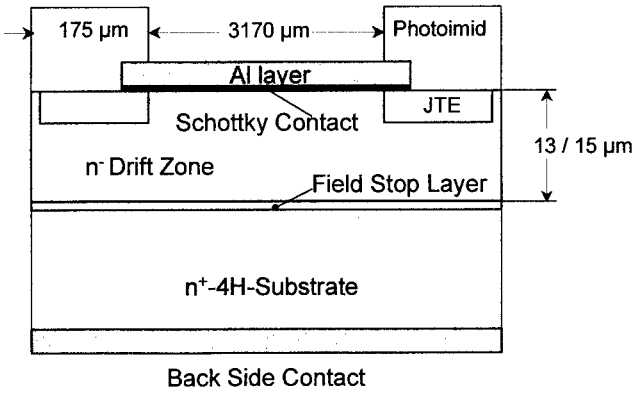


Fig. 1: Schematic cross section of the SiC Schottky

In case of a homogenous epi layer the optimum for the n type doping N_D and thickness d_{epi} of the drift zone leads to a trapezoidal field profile with values according to [3]

$$d_{epi} = \frac{3U_{max}}{2E_{max}} \quad and \quad N_D = \frac{4\varepsilon_S E_{max}^2}{9qU_{max}} \tag{1}$$

whereas q is the elementary charge and ε_S is the permittivity of 4H-SiC. The maximum field strength at the metal semiconductor interface E_{max} depends on the Schottky barrier used and the reverse leakage current which is acceptable under worst case conditions. In addition, process tolerances of the epi layer doping and thickness as well as Schottky barrier fluctuations across the wafer and from run to run have to be taken into account. For the epi layer layout a value of E_{max} = 1.5 MV/cm has been assumed which keeps leakage currents very low. The n^- epitaxial layers were grown in a multi wafer epi system described in [4]. The measured average values are listed in Table 1. These average values slightly differ from the calculation according to eq. (1) since process tolerances have been taken into account in order to ensure the field strength not exceeding 1.5 MV/cm. For details of the fabrication process please refer to [1].

The dies (3.52 mm x 3.52 mm) were mounted on a DCB substrate, bonded with 4 parallel bond wires of 250 µm diameter and insulated with a polymerized silicon rubber (Fig. 2).



Fig. 2: 1200V SiC Schottky diodes and IGBT mounted on a DCB substrate

3. Basic Device Characteristics

The static room temperature I-V-characteristics of a representative 1200 V sample and a 1700 V sample are shown in Fig. 3. The forward characteristics are measured in pulse mode such that intrinsic heat production is neglectable (duty cycle < 0.01). The forward voltages taken at the nominal forward currents are listed in Table 1.

Table 1: Key device data of the 4H SiC Schottky diodes

Maximum Reverse Voltage	*1200 V Type*	*1700 V Type*
Schottky contact area	10.0 mm^2	10.0 mm^2
Die area	12.4 mm^2	12.4 mm^2
n^-epi layer doping	5.0 x 10^{15} cm^{-3}	2.5 x 10^{15} cm^{-3}
n^-epi layer thickness	13 µm	15 µm
Forward voltage @ 25 °C	1.7 V @ 25 A	2.3 V @ 25 A
Forward voltage @ 125 °C	2.3 V @ 25 A	3.4 V @ 25 A
Reverse current @ 25 °C	4 µA @ 1200V	150 µA @ 1700 V
Reverse current @ 125 °C	12 µA @ 1200V	450 µA @ 1700 V
Space charge	100 nC	60 nC
R_{diff} @ 25 °C	30 mΩ	50 mΩ
R_{diff} @ 125 °C	60 mΩ	100 mΩ

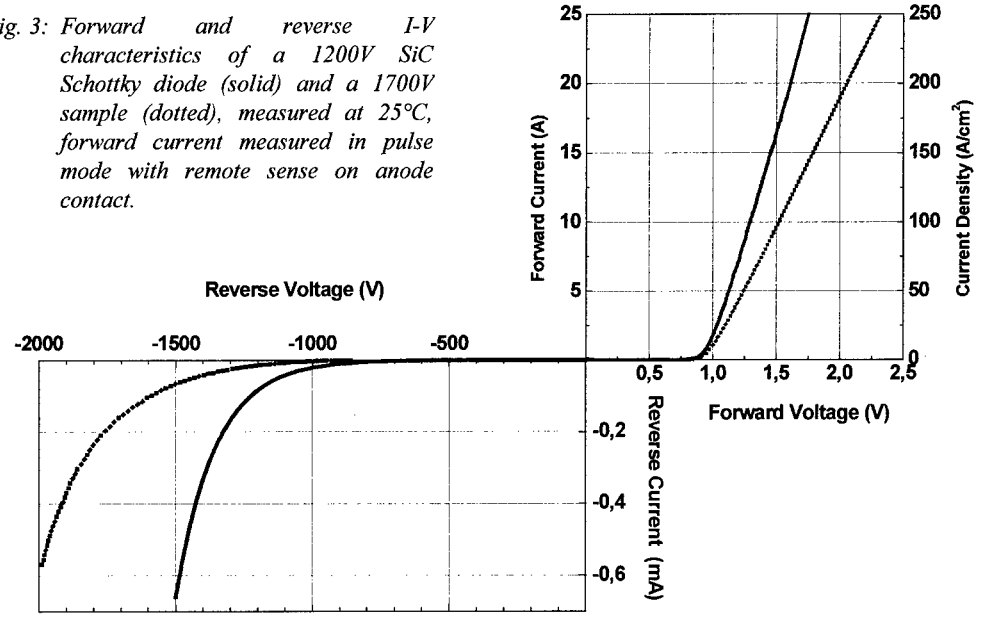


Fig. 3: Forward and reverse I-V characteristics of a 1200V SiC Schottky diode (solid) and a 1700V sample (dotted), measured at 25°C, forward current measured in pulse mode with remote sense on anode contact.

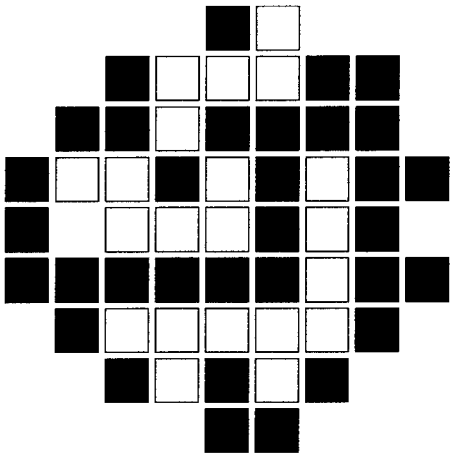


Fig. 4: Yield distribution on a 35 mm 4H-SiC wafer (MPD < 10 mm2). The 21 white squares indicate a reverse current < 100 µA @ 1000 V, the 33 dark marked dies are defective.

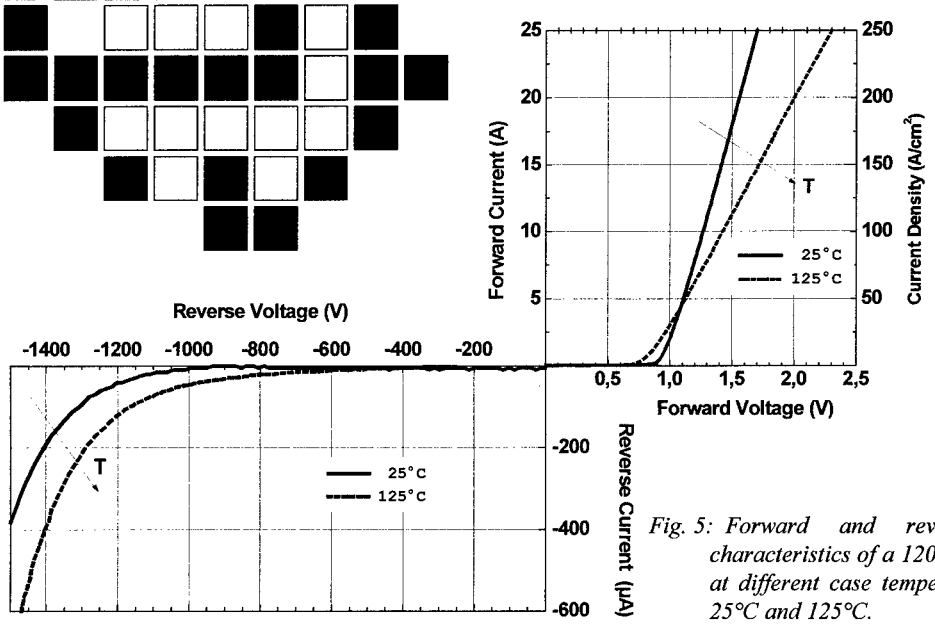


Fig. 5: Forward and reverse I-V characteristics of a 1200V sample at different case temperatures at 25°C and 125°C.

At maximum blocking voltage the leakage current is very low and the diode can be driven up to blocking voltages 300 V above the nominal value, with exponentially increasing current which is only limited by the cooling conditions of the case ambient.

Fig. 4 shows a yield mapping of a representative wafer. With respect to the yield criterion (leakage current at 1000 V less than 100 μA) 21 of 54 devices are working. This corresponds to a yield of 39%. However, this yield varies from wafer to wafer. The average value for all selected wafers was about 30%. This is in good agreement with a rough yield estimation which assumes the micropipe density MPD to be the yield dominating defect:

$$yield = \exp(-A \quad x \quad MPD) \tag{2}$$

(the chip area A is 12.4 mm^2, the MPD = 10 cm^{-2}.) However, this model neglects clustering of defects. Hence the actual yield values may be slightly better.

A comparison of the forward I-V characteristics for two different temperatures (25°C and 125°C) is shown in Fig. 5 in case of a 1200V sample. This behavior follows the simple Schottky theory. The ideality factor was determined to 1.05. The differential resistance at high current densities (see Table 1) is dominated by the drift zone resistance. Hence, if the junction temperature rises from 25°C to 125°C the decrease of the electron mobility leads to a doubling of the differential resistance according to the relation

$$\mu_{n^-} \propto (T/300K)^{-2.6}. \tag{3}$$

The temperature dependence of the leakage current is weaker than the simple Schottky theory suggests since at high blocking voltages the current is dominated by thermionic field emission through the barrier. The results are in good agreement with simulations [5].

We studied the switching behavior in a chopper circuit using a 1200 V IGBT (Fig. 2) with forward currents up to 40 A against 600 V DC link voltage with high dV/dt, di/dt gradients. As soon as the forward current becomes zero, the reverse voltage is immediately built up since there is no storage charge, neither from the Schottky barrier nor from the JTE. Only a small displacement current < 3 A flows in reverse direction due to the space charge which is independent of the temperature and the forward current (see Table 1). The order of dynamic switching losses dissipated in the diode can roughly be estimated by the product *space charge * blocking voltage * switching frequency.*

4. Conclusion

The aim of this study was to enlarge the active area of SiC Schottky diodes as much as possible with respect to the defect density of today available SiC wafers. For this purpose Schottky diodes capable to block 1200 and 1700 V have been fabricated with an active area of 10 mm^2. This attempt turned out to be successful resulting in an average yield of 30%. The diodes exhibit the temperature and switching behavior which has been expected and fits to results reported earlier, but now with significant higher forward current and higher blocking voltage.

References

[1] R. Rupp, M. Treu et al., Mater. Sci. Forum 338-342 (2000), p. 1167.
[2] H. Mitlehner, U. Weinert, W. Bartsch, K. Dohnke, D. Stephani, Proc. 9th EDPE 64-67 (1996).
[3] C. Hu, IEEE Power Electronics Specialists Conference Record (1979), p. 385.
[4] R. Rupp, A. Wiedenhofer, D. Stephani, Mater. Sci. Eng. B 61-62 (1999), p. 125.
[5] M. Treu, R. Rupp, H. Kapels, W. Bartsch, Mater. Sci. Forum 353-356 (2001), p. 679.

Materials Science Forum Vols. 353-356 (2001) pp. 679-682
© 2001 Trans Tech Publications, Switzerland

Temperature Dependence of Forward and Reverse Characteristics of Ti, W, Ta and Ni Schottky Diodes on 4H-SiC

M. Treu[1], R. Rupp[1], H. Kapels[1] and W. Bartsch[2]

[1] Infineon Technologies AG, AI IP DD SIC, PO Box 3220, DE-91050 Erlangen, Germany

[2] SiCED GmbH, PO Box 3220, DE-91050 Erlangen, Germany

Keywords: Field Emission, Schottky Diodes, Temperature Dependent C-V Characteristics

Abstract. In this study Ta, W, Ti, and Ni Schottky diodes are characterized under forward and reverse bias for temperatures between +21 °C and +200 °C. Additionally the Ti Diodes were characterized for temperatures between –168°C and +21°C. It will be shown that the reverse current is dominated by thermionic field emission for all metals, if the junction temperature is in the typical device operating temperature range. Furthermore we will show that non-ideal forward characteristics not necessarily have a negative influence on the reverse characteristics of the diodes. This will be explained by a model proposed by Tung, which considers the pinch off of the defects by the defect free areas around the defect.

Introduction

Schottky diodes on Silicon Carbide (SiC) are promising rectifiers for blocking voltages between 300 V and several kV mainly because of their fast switching capabilities. Although theoretical studies about the electrical behavior of Schottky contacts exist for some decades [1], the exact description of the forward and reverse characteristics is still an issue [2]. The leakage current of Schottky diodes on SiC is much higher than the leakage current predicted by the classical Schottky theory, which is typically used to describe Schottky diodes on silicon. For the design of SiC Schottky diodes it is crucial to be able to describe the reverse current by an adequate model, which will be presented in this work.

Experimental

The substrates used in this work were *n*-type 8° off-axis 4H-SiC supplied by Cree Research. A *n*-type 2.5 µm thick buffer layer and 8µm thick drift region were grown homoepitaxially on the substrates by a low pressure chemical vapor deposition process described elsewhere [3]. The net donor concentration of the drift region was between 5×10^{15} cm^{-3} and 9×10^{15} cm^{-3}. A 70 µm wide guard ring described by Mitlehner et al. [4] with an implanted Al concentration of 5.5×10^{17} cm^{-3} annealed at 1500 °C was used as an edge termination of the diodes. The Schottky metals with a thickness of 150 nm were deposited by sputtering. After defining the Schottky contact area of 1.54×10^{-2} cm^{-2} the diodes were annealed at 400°C for 4 hours. The electrical measurements above room temperature were done at wafer level and the measurements below room temperature were done with the diodes packaged in a TO220 case. With this punch-through design and a reverse bias of 600 V the maximum electrical field is only 3 % higher than in the non-punch-through (npt) case with the same drift layer doping concentration. Thus we assume that we have a npt design if we calculate the reverse current.

Results and Discussion

Forward characteristics. Ideally the forward characteristic of a Schottky diode is described by the equations

$$J = J_S \exp(V/nkT)(1-\exp(-V/kT)) \quad \text{with } J_S = AT^2\exp(-\phi/kT)) \qquad (1,2)$$

with the bias V between the anode and cathode, the ideality factor n, the Boltzman constant k, the absolute temperature T, and the saturation current density J_S with the Richardson constant A, the elementary charge q, and the Schottky barrier height ϕ [1]. The barrier height and the Richardson constant can be determined experimentally by measuring the forward characteristics with the temperature as a parameter and fitting the theoretical curves to the measured characteristics as shown in Fig.1. By this method we determined the values listed in Tab. 1 for the different Schottky metals. For W ranges are given because this metal behaves very unstable and varied its barrier while the temperature was changed for the measurements.

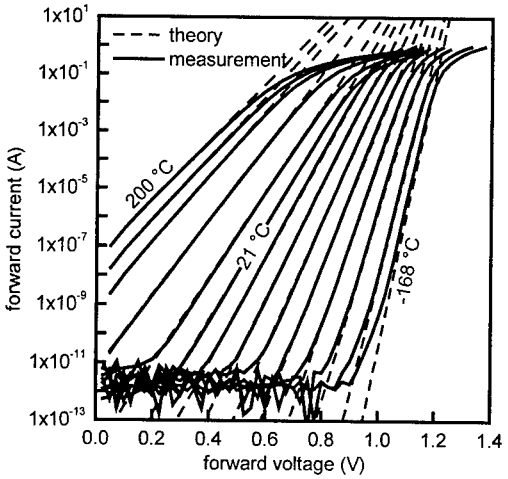


Fig. 1, Forward current of a Ti Schottky diode as a function of forward bias with the temperature as a parameter.

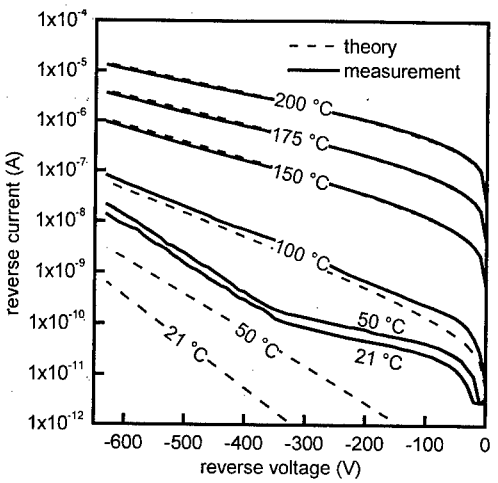


Fig. 2, Measured and calculated reverse characteristics of a Ti Schottky diode with the temperature as a parameter.

Modeling of the reverse current. The reverse current of Schottky diodes on silicon is normally described by the thermionic emission theory. This theory cannot explain the reverse behavior of Schottky diodes on SiC since the observed leakage current is much higher than the thermionic emission current. To describe the reverse current it has to be considered that the electrical field in a SiC device is much higher than in a comparable Silicon device. In our case the electrical field near the interface at 600 V reverse bias is around 1.35 MV/cm. At such high fields it seems likely that tunneling through the barrier has to be considered as dominating rather than thermionic emission.

Padovani and Stratton [5] proposed a model to describe the reverse current of Schottky diodes on highly doped, degenerated semiconductors considering field emission and thermionic field emission through the barrier. The thermionic field emission current can be expressed as

$$J = J_S \exp(V/E') \text{ with} \tag{3}$$

$$J_S = \frac{A\sqrt{\pi E_{00}}}{k}\sqrt{-V + \frac{\phi}{\cosh^2(E_{00}/kT)}}\exp(-V/E_0),\ E_0 = E_{00}\coth(E_{00}/kT), \tag{4a, 4b}$$

$$E_{00} = q\hbar\sqrt{N_d/(2\varepsilon)}\Big/\sqrt{2m^*}\text{, and } E' = E_{00}[(E_{00}/kT) - \tanh(E_{00}/kT)]^{-1}, \tag{5a, 5b}$$

if the following condition is fulfilled:

$$1 - c_1 kT < kT\sqrt{2f_1} \text{ with } c_1 = 2\sqrt{\phi_b/(\phi_b - V)}\Big/E_{00}\text{, and } f_1 = -\tfrac{1}{4}E_{00}V\,. \tag{6a, 6b, 6c}$$

m^* is the effective mass of an electron in the semiconductor, and ε is the dielectric constant of the semiconductor. If the temperature gets lower or the reverse bias gets higher this condition maybe not fulfilled and the current is dominated by pure field emission which can expressed as

$$J = \frac{AT\pi E_{00}\exp[-2\phi^{3/2}/3E_{00}(\phi - V)^{1/2}]}{k[\phi/(\phi - V)]^{1/2}\sin\{\pi kT[\phi/(\phi - V)]^{1/2}/E_{00}\}}. \tag{7}$$

With equation 6a it can be easily shown that field emission or thermionic field emission has to be considered for our diodes. Fig. 2 and Fig. 3 show the measured and calculated reverse current for the Ti and Ta Schottky diodes. The parameters used for the calculated currents are printed in Table 1. In the case of the Ti Diodes the measured and calculated thermionic field emission reverse current is nearly equal for temperatures of 100 °C and higher. For lower temperatures the model does not fit to the measurements and the reverse current is independent of the temperature as long as the thermionic field emission current is lower. Furthermore, we observed that the reverse current at room temperature varies within about two orders of magnitude and is also independent of the doping. This phenomenon is clear to see in Fig. 4 where the reverse current of 50 Ti diodes at –500 V is analyzed for two temperatures. At room temperature the reverse

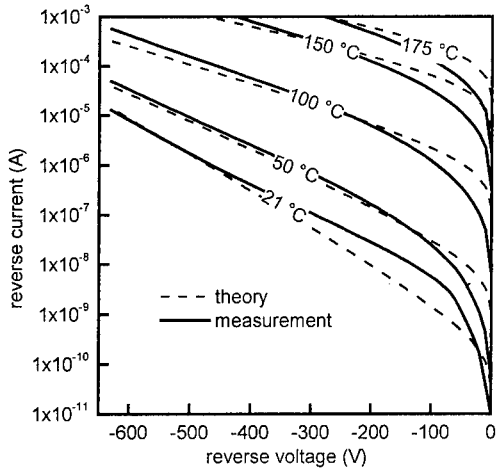


Fig. 3, Measured and calculated reverse characteristics of a Ta Schottky diode with the temperature as a parameter.

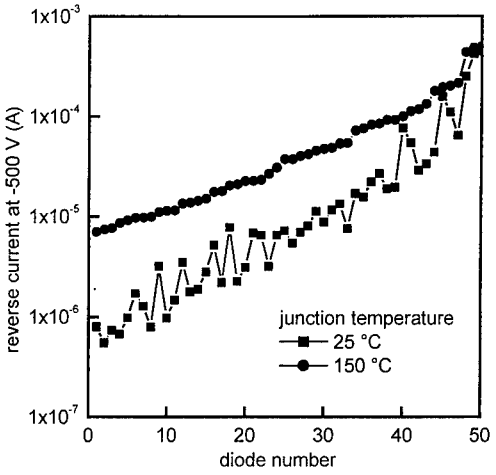


Fig. 4, Reverse current of 50 Ti diodes at -500 V with the temperature as a parameter. In this case the drift region was 4 µm thick with a doping concentration between 12 $\times 10^{15}$ cm^{-3} and 18 $\times 10^{15}$ cm^{-3}.

current varies about two orders of magnitude. At 150 °C the reverse current varies only about one order of magnitude which corresponds to the variation of the doping mentioned above. The origin of the reverse current at room temperature is not yet clear. But we can deduce from Fig. 2 that there are two mechanism leading to this current: one is dominating at moderate reverse voltages down from 0 V to –350 V (electrical fields below 1 MV/cm), the second one is dominating for higher reverse voltages.

In the case of the Ta diodes the calculated reverse current can be described by thermionic field emission for all considered temperatures since the reverse current is much higher due to the lower Schottky barrier. Similar results were also obtained for W. For the Ni diodes it was not possible to find reasonable parameters to describe the reverse current, which showed a very low temperature dependence. We think that the interface was not as perfect as for the other metals. This is indicated by the relatively high ideality factor of 1.10. To describe these measurements it may be necessary to introduce an interface layer. This will be subject of further work.

Metal	Forward Characteristics			Reverse Characteristics		
	ϕ [eV]	n	A [A/cm^{2}K^2]	ϕ [eV]	m*	A [A/cm^{2}K^2]
Ta	1.03	1.05	300	0.95	0.30	200
W	1.04 to 1.18	1.04	110 to 500	1.08 [1)]	0.19 [1)]	300 [1)]
Ti	1.27	1.05	400	1.27	0.22	200
Ni	1.40	1.10	150			

Table 1, Parameters extracted from the measurements of the forward and reverse characteristics at different temperatures. [1)] extracted only for one diode which had a stable Schottky barrier

Non-ideal forward characteristics and correlation with the reverse current? In contrast to the ideal forward characteristics it is also possible that the diodes show a non-ideal behavior as depicted in Fig. 5. This plot shows the measurements of diodes on a wafer which was intentionally processed in a way that produces a lot of defects, degenerating the forward characteristics. In the literature this behavior is described by local Schottky barrier height lowering e.g. caused by crystal defects or contamination enabling a higher current to flow over the barrier [2]. These areas with the lower barrier may also be preferred paths for the reverse current. To check this assumption we plotted the reverse current at 600 V as a function of the forward current at 0.3 V at room temperature in Fig. 6. In this plot all points right of the vertical line represent diodes that are affected by barrier height lowering down to 1 eV. The horizontal line represents the expected reverse thermionic field emission current for the same barrier height. In contrast to the first assumption the reverse currents of most of the diodes with a higher forward current (lower barrier) show nearly the same

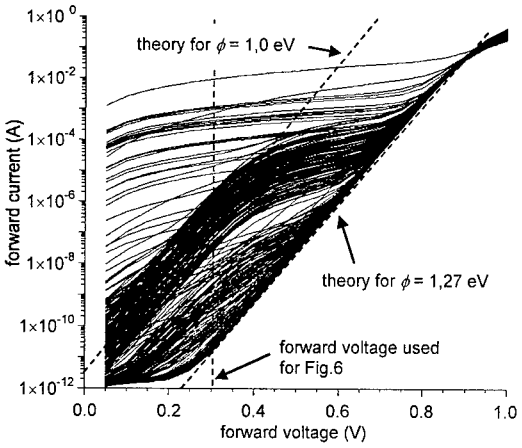


Fig. 5, Forward current as a function of forward bias with the temperature as a parameter for a Ti Schottky diode compared with the Schottky theory (dashed).

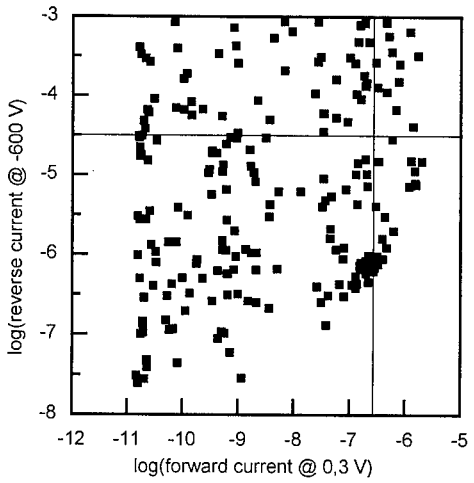


Fig. 6, Reverse current at –600 V as a function forward current at 0.3 V for Ti Schottky diodes on one wafer at room temperature. The lines are the theoretical values for a barrier of 1 eV.

reverse current as the diodes with an ideal forward characteristic. This behavior can be explained by a model proposed by Tung [6]. This model proposes that areas with a lower barrier which have smaller dimensions than the space charge region are effectively pinched off by the surrounding area with the higher barrier. This is comparable to the effect used in a merged pin Schottky rectifier where the area with the lower Schottky barrier is shielded by the area with the higher pn junction barrier [7]. Of course it is also possible that diodes with a relatively low forward current have a high reverse current, if the sum of the defective areas is relatively small but the size of the individual defects is to large to be shielded.

This leads to the conclusion that the reverse current cannot be described by a simple electrical equivalent circuit consisting of Schottky diodes with different barrier heights and areas in parallel. Such a model is only valid if the device quality is poor because of defects which are significantly larger than the space charge region. If the defects get smaller the modeling of the reverse current gets more complicated (see Tung [6]) or the reverse current is not affected significantly by such defects although the forward characteristics may be non-ideal.

Conclusion and Summary

It was shown that the reverse current of Schottky diodes on SiC can be described by the thermionic field emission theory in a wide temperature range and that the extracted barrier height is comparable to the barrier height extracted from the forward characteristics with the classical Schottky theory. The necessity of different values for the effective mass of the electrons is understandable because the effective mass at the interface may be different from the effective mass in the bulk of the semiconductor and furthermore may be influenced by the metal and its specific chemistry at the interface. It was also shown that defects at the interface which can be easily detected in the forward characteristic are not influencing the reverse current if they are small enough to be shielded by the defect free area around. This may be an explanation for the fact that it possible to produce Schottky diodes on SiC with a high yield although the density of crystal defects (e.g. stacking faults) is still very high in SiC substrates.

References

[1] E.H. Rhoderick, Clarendon Press, Oxford 1980
[2] D. Defives, O. Noblanc, C. Dua, C. Brylinski, M. Barthula, V. Aubry-Fortune, IEEE Trans. Electr. Dev. 46 (1999), p. 449
[3] R. Rupp, P. Lanig, J. Völkl, and D. Stephani, J. Crystal Growth 146 (1995), p. 37
[4] H. Mitlehner, U. Weinert, W. Bartsch, K. Dohnke, D. Stephani, 9th EDPE, Dubrovnik, Croatia (1996), p. 64
[5] F.A. Padovani, R. Stratton, Solid-State Electronics 9 (1966), p. 695
[6] R.T. Tung, Phys. Rev. B 45 (1992), p. 13509
[7] Baliga J.B., IEEE Transactions on Electron Devices 43 (1996), p. 1717

Materials Science Forum Vols. 353-356 (2001) pp. 683-686
© 2001 Trans Tech Publications, Switzerland

A High Performance JBS Rectifier - Design Considerations

F. Dahlquist[1,2], H. Lendenmann[1] and M. Östling[2]

[1] ABB Corporate Research, Electrum 215, SE-164 40 Kista-Stockholm, Sweden

[2] Department of Electronics, KTH, Electrum 229, SE-16440 Kista, Sweden

Keywords: JBS Rectifier, Junction Barrier Schottky (JBS), Power Rectifier, Punch-Through

Abstract

2.8 kV JBS diodes in 4H-SiC were fabricated with design variations in parameters controlling the trade-off in forward voltage drop and leakage current. The various components of the forward drop are analyzed, and a new optimization for the drift region resistance was found by choosing a "33%" punch through design. Moreover, for striped p+ grid designs, a grid spacing of 7-9 μm is optimal, with regard to minimum forward voltage and low leakage. This optimization takes also second order effects of high temperatures and current densities >100 A/cm^2 into account.

Introduction

The Junction Barrier Schottky (JBS) diode in silicon carbide is a promising rectifier for the medium voltage range (<3kV) since it combines the low forward voltage drop of a Schottky diode with blocking properties of a PiN diode. In comparison with a SiC PiN diode it is the unipolar low static losses that makes the JBS diode attractive in said voltage range. When compared to a Si PiN diode it is mainly the low-loss switching behavior which makes the JBS diode a competitor for high operating frequencies. Furthermore, the JBS diode has low leakage properties at blocking voltage also for elevated temperatures because of the pn-junction like leakage characteristics. When designing a JBS diode the design parameters have to be optimized with respect to operating current density, temperature and frequency. This paper presents experimental results on trade-offs in forward voltage drop versus leakage current as function of temperature and current density for different designs. The results are based on a 2.8kV JBS experiment earlier reported [1].

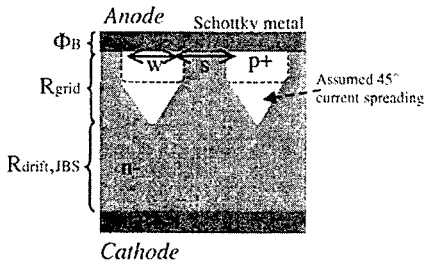


Figure 1 Part of JBS diode structure showing the main contributions to the on-resistance.

In a JBS diode the forward current flows unipolar between the anode and cathode in channels between the p+n junctions (see diode structure in Figure 1). The relationship between the forward voltage and current density is equal to that of a Schottky diode, except that the Schottky barrier current density needs to take the area taken up by the p+ regions in the structure into account. The modified current density across the Schottky barrier for a striped p+ grid design can be written as [2]:

$$J_{F,JBS} = \frac{s+w}{s-2d} J_F \qquad (1)$$

where w is the width of the p+ regions and s is the spacing in between, i.e., the active Schottky area region. d is the junction depletion width from the p+ regions. By using Schottky barrier theory

based upon thermionic emission the total forward voltage drop of a JBS diode at a defined current density can be written as:

$$V_{F,JBS} = \frac{nkT}{q}\ln\left(\frac{J_{F,JBS}}{A^{**}T^2}\right) + n\phi_B + R_{grid} * J_F + R_{drift,JBS} * J_F \quad (2)$$

where k is Boltzmann's constant, q is the electron charge, T is temperature and J_F is the forward current density at $V_{F,JBS}$. A** is the Richardson's constant. *Rgrid* is the sum of resistance from the p+ grid and current spreading below the grid.

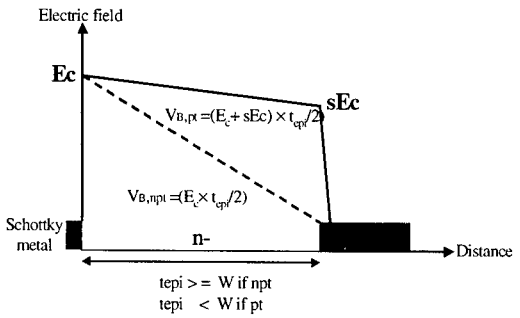


Figure 2 Definition of non punch-through (npt) and punch-through (pt) epi design. For the pt case, the epi thickness is made thinner and also doping is lower in order to reach a nearly rectangular field distribution.

From Equation 2 it is clear that the main parameters to optimize are the drift region resistance, the Schottky barrier height and the p+ grid design, controlling the trade-off in forward voltage drop and leakage current for a given voltage. Lowering of the leakage current, i.e., shielding of the Schottky barrier, without too much increase in on-resistance can be obtained if an optimized spacing and width of the p+ grid is used.

For a non punch-through design (compare with Figure 2), i.e., the depletion region at blocking voltage is not exceeding the epi thickness, the drift resistance increases quadratically with blocking voltage [1], see Equation 3. Since the drift resistance is a major part of the JBS on-resistance it is also important to consider an optimization of the drift region resistance, which is determined by the epi thickness and doping according to Equation 4.

$$R_{drift,npt} = \frac{4V_B^{\,2}}{\varepsilon\mu_n E_c^{\,3}} \quad [\Omega cm^2] \quad (3) \qquad R_{drift} = \frac{t_{epi}}{q\mu_n N_d} \quad [\Omega cm^2] \quad (4)$$

By introducing a punch-through factor s (see Figure 2), defined as the electric field at the substrate interface divided by the junction field, Equation 3 can be modified for a punch-through epi design:

$$R_{drift,pt} = \frac{4V_B^{\,2}}{\varepsilon\mu_n E_c^{\,3}} \cdot \frac{1}{(1-s^2)(1+s)} \quad [\Omega cm^2] \quad (5)$$

Minimizing this expression gives a minimum drift region resistance for s =1/3. This reduces the drift resistance by 16% compared to the non punch-through case for the appropriate epi doping and thickness combinations.

Design and experimental

High voltage JBS and reference Schottky-, PiN diodes were processed on the same 4H-SiC wafer [1]. A striped grid geometry for the JBS diodes was designed with a p^+ width of 3μm. The smallest spacing was 3μm and then increasing in steps of 3μm to a maximum spacing of 21μm. A punch-through design with 1/3 of the junction field at the substrate interface was used, giving an epi thickness of 27 μm and a doping of 3e15 cm^{-3}. If 100% electrical critical field strength is reached, according to reported breakdown field strengths [3], these epi parameters correspond to a blocking voltage of 4000V. If 80% critical field is reached, consistent with screw dislocation limitations [4], this epi should sustain 2500V. The JBS grid and PiN emitter were ion implanted with aluminum to

a profile depth of 0.6 μm. After that a two zone JTE was implanted with different masks and an implantation anneal was carried out at 1700 °C. For the frontside Schottky contact and combined Ohmic contact, titanium was chosen as metal. A 500 °C anneal in vacuum resulted in a barrier height of 1.4 eV and an ideality factor of 1.1. All results in this paper are from devices with a 200x200μm contact area.

Results and discussion

In Figure 3 the forward voltage drop at 100 A/cm^2 versus leakage current at -500V for different grid spacing is shown. Each data point is the average over 15 devices. By increasing the spacing from 3μm to 9μm the forward drop is reduced >0.1V while the leakage is not affected. Further increase in spacing gives almost no improvement in forward drop but the leakage starts to increase, indicating less effective shielding of the Schottky barrier. Figure 4 shows the linear forward characteristics for one single device with 9 μm spacing and p+ width=3 μm. The characteristic increase of on-resistance due to a decrease in electron mobility is shown for temperatures up to 225°C. A current density of 100 A/cm^2 in the graph (0.036 A), clarifies the importance to account for the operating temperature when choosing the optimal operating current density.

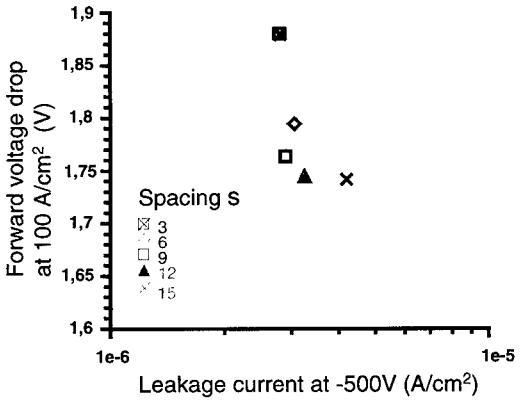


Figure 3 Forward voltage drop at 100 A/cm^2 versus leakage current at -500V for different grid spacings, p+ width=3μm. T=30 °C.

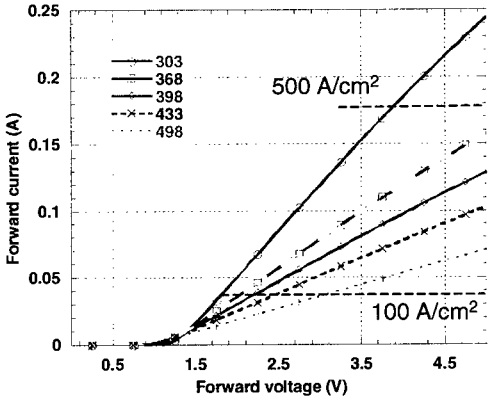


Figure 4 Forward characteristics for a single JBS device for different temperatures in Kelvins. Spacing is 9μm and p+ width =3μm.

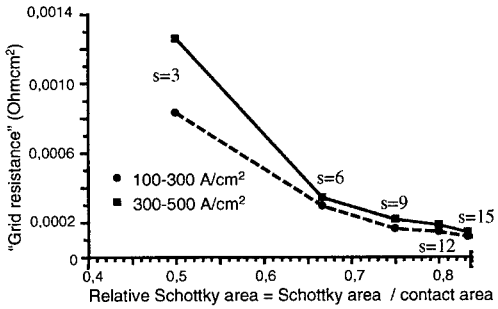


Figure 5 "Grid resistance" versus relative Schottky area for low (100-300 A/cm^2) and high (300-500 A/cm^2) current densities. T=30 °C.

In Figure 5 the same set of devices is measured up to 500 A/cm^2. The differential on-resistance is extracted at 100-300 A/cm^2 and 300-500 A/cm^2. The drift resistance is then subtracted to extract the grid resistance (see Figure 1), and then plotted versus relative Schottky area, with spacings from 3μm to 21μm. Since the drift resistance is very sensitive to the local epi doping and thickness a resistance Rd=4.5mOhmcm^2 was extracted from an adjacent Schottky diode. For the 3 μm spacing the grid resistance is higher than expected. Interesting to note is that the resistance is increasing with current density compared to the designs with wider

spacing. This confirms that a spacing close to 9 μm is optimal if high operating current densities are intended.

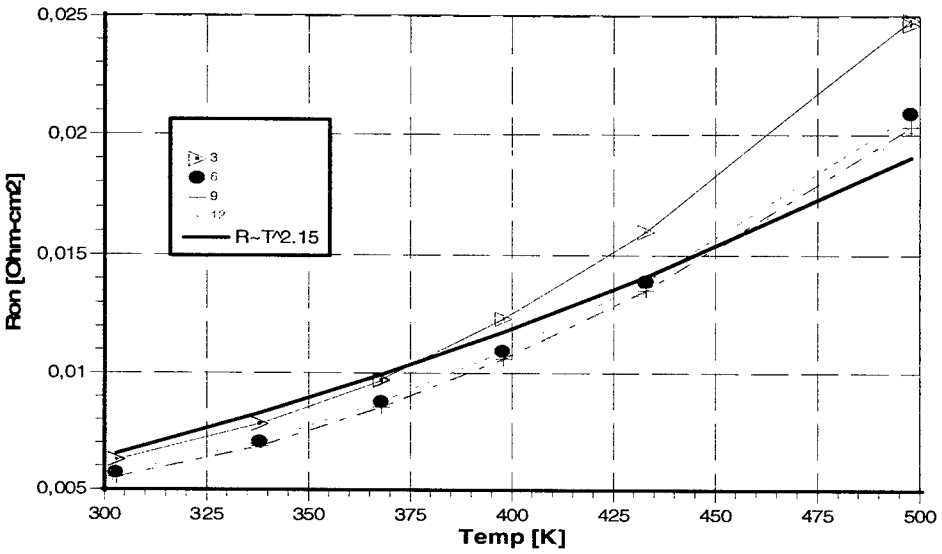


Figure 6 Differential on-resistance versus temperature for different grid spacings. Solid line without markers is the theoretical Ron(T) relationship.

In Figure 6 the on-resistance (between 33-100 A/cm^2) is measured for six temperatures, up to 500 °C. Plotted is also the theoretical temperature dependence with a mobility decrease of $T^{-2.15}$[5]. The smallest grid spacing 3 μm shows a much stronger temperature dependence than the wider spacing. This is most likely self-heating effects due to the high current density (2x) in the conducting channels, which decreases the mobility further.

Conclusions

Experimental results in grid spacing revealed trade-offs in forward voltage drop and leakage current for JBS diodes. It was found that small spacing (3-6μm) is non-attractive because the high grid resistance results in a increased temperature and high current density dependence of the on-state drop. When the grid spacing is increased to about 9μm-12μm the forward voltage is lowered while low leakage is maintained.

Acknowledgements

This work was done in cooperation with the Swedish SiCEP program.

References

[1] F. Dahlquist et. al., Mat. Sci. Forum 338-342 (1999), p.1179
[2] B.J. Baliga, Solid-State Electron. 28 (1985), p.1089
[3] A. O. Konstantinov, Appl. Phys. Lett. 71 (1997), p.90
[4] P. G. Neudeck, et. al., IEEE Trans.Electron Dev. March, 46 (1999), p.478
[5] W.J. Schaffer, G.H. Negley, K.G. Irvine, J.W. Palmour, Mat. Res. Soc. Symp. Proc. 339 (1994), p. 595

Materials Science Forum Vols. 353-356 (2001) pp. 687-690
© 2001 Trans Tech Publications, Switzerland

Design and Characterization of 2.5kV 4H-SiC JBS Rectifiers with Self-Aligned Guard Ring Termination

D.C. Sheridan[1], J.N. Merrett[2], J.D. Cressler[1], S.E. Saddow[3], J.R. Williams[2], C.E. Ellis[1] and G. Niu[1]

[1] Alabama Microelectronics Science & Technology Center, Electrical and Computer Engineering Department, 200 Broun Hall, Auburn University, Auburn AL 36849, USA

[2] Department of Physics, Auburn University, Auburn AL 36849, USA

[3] Emerging Materials Research Laboratory, Mississippi State University, Mississippi State MS 39762, USA

Keywords: Edge Termination, Guard Ring, Junction Barrier Schottky (JBS), Schottky Diodes, Simulation

Abstract. 4H-SiC JBS rectifiers were designed with multiple floating guard ring termination using numerical simulation methods, and were fabricated using a simplified self-aligned process sequence. Simulations were used to investigate forward voltage drop and reverse electric field shielding with respect to JBS spacing. Optimized devices were fabricated on 30μm lightly doped n-epitaxial layers. JBS diodes exhibited 2.5kV blocking capability with reverse leakage currents below $2x10^{-5}$ Acm^{-2} at 2kV, and a forward voltage drop of 2.95V at $100Acm^{-2}$.

1. Introduction

SiC Schottky rectifiers are superior to Si pn diodes for high voltage switching applications because of their fast switching speed and low reverse recovery currents. SiC Schottky diodes have been demonstrated with breakdown voltages near 5kV [1], with switching decreasing power losses over a factor of four smaller than comparable Si pin diodes [2]. Critical to successful SiC Schottky diode commercialization is the maximization of breakdown voltage and suppression of excess reverse leakage currents. Experimental results for SiC Schottky diodes, however, have shown extremely soft reverse breakdown and excess leakage currents greatly exceeding the theoretically expected values [3]. These leakage mechanisms in SiC Schottky diodes under strong reverse bias include image-force barrier lowering and significant tunneling currents. Since these mechanisms are driven by the peak electric field at the Schottky interface, device designs which can reduce the internal electric fields must be considered. The junction barrier Schottky (JBS) rectifier [4] shown in Fig.1 was proposed in order to alleviate the leakage currents in high voltage Schottky diodes with low barrier heights. The JBS structure is simply composed of a Schottky diode with closely spaced p^+ regions inside the active Schottky area. Under reverse bias the p^+ regions are designed to shield the Schottky interface by pinching off the narrow Schottky regions, reducing the peak electric field at the Schottky interface.

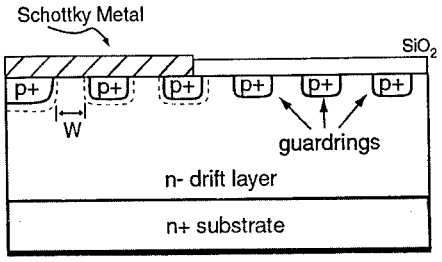


Fig. 1: Schematic cross section of a JBS diode with floating guard ring edge termination.

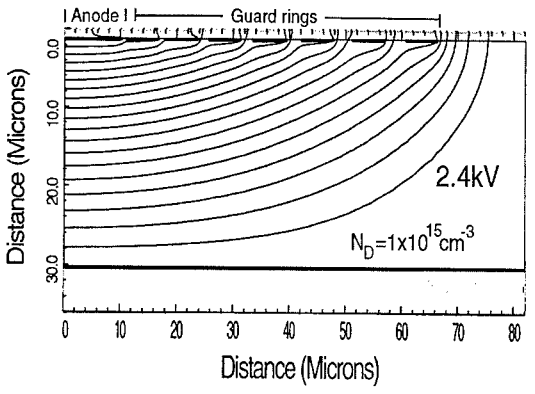


Fig. 2: Potential contours of an optimized 7 guard ring design at 2.4kV.

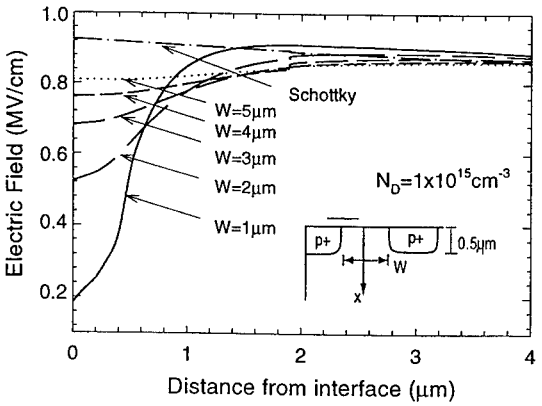


Fig. 3: Simulated decrease in interface electric field as a function of JBS p^+ spacing.

However, devices with poor edge termination can result in decreased breakdown voltages and device leakage mechanisms dominated by the currents generated at the device periphery, rendering the JBS properties useless. Various edge termination methods such as the junction termination extension (JTE), field plates, and floating guard rings, have been utilized to increase breakdown of Schottky diodes to near ideal parallel plane values [5-6]. While the JTE is more suitable for high voltage devices than the field plate, it requires additional processing steps as well as precise dopant activation, which is difficult in SiC. Alternatively, the floating guard ring method has been successfully used in SiC [7], and can be formed simultaneously with the active JBS region. This self-aligned simplifies processing by eliminating a mask layer and eases lithography constraints of exact guard ring placement.

2. Simulation

Multiple floating guard ring termination simulations were performed with MEDICI [8] using a previously calibrated method [7]. Designs for guard ring profiles up to 7 rings were simulated with a predicted maximum blocking voltage of 2.4kV for a diode with a 30μm epitaxial layer and a doping concentration of $1x10^{15}cm^{-3}$. Individual simulated guard rings were 5μm wide with a junction depth of 0.5μm, and a doping of $1x10^{19}cm^{-3}$. The large diode structure needed for breakdown simulations required a large number of nodes and precise grid generation for stable convergence. Fig. 2 shows the simulated diode structure with the electric field distribution at a reverse bias of 2.4kV, exhibiting an effective spreading of the depletion layer.

Under reverse bias, a portion of the increasing electric field is absorbed by the heavily doped p^+ regions in the active JBS area, reducing the peak field at the Schottky interface. The amount of shielding is predominantly dependent on the spacing between adjacent p^+ regions (W). In Fig. 3, the electric field in the center of two p^+ ($1x10^{19}cm^{-3}$) regions (W/2) is plotted versus vertical distance into the device. Compared to a pure Schottky diode, the peak interface field can be reduced by 43%, 26%, and 18% using a JBS spacing of 2μm, 3μm, and 4μm, respectively. Unfortunately, the JBS rectifier suffers from an increased forward resistance as a result of the current constriction between the p^+ regions. The simulated forward characteristics shows that the pinch resistance can add as much as 1V to the diode's forward voltage drop at $100Acm^{-2}$. Therefore, the desired JBS

structure must be optimized according to application requirement, for best tradeoffs between low forward voltage drop and reduced leakage currents.

3. Fabrication

Circular JBS diodes with diameters ranging from 100μm to 400μm were fabricated on 4H n^+ wafers with a 30μm 1-2.5x$10^{15}$$cm^{-3}$ n^- epitaxial layer. Using a thick Mo layer for implant masking, a single Al implanted box profile using energies ranging from 30keV to 300keV was used to form both the active JBS region and the guard ring edge termination. All implanted guard rings as well as p^+ implants used in forming the JBS active region were 5μm in width, and were fixed as the JBS spacing (W) varies. Al implants were annealed at 1600°C in a silane ambient as has been described in the literature [9]. A high quality thermal oxide followed by 1μm converted poly-Si layer was used for passivation. Ni was deposited for the backside Ohmic contacts and annealed at 1100°C for 2 minutes in vacuum, followed by evaporation of Ti and Au for decreased contact resistance. Schottky contact openings were formed by selective RIE followed by a BOE etch through the passivation and immediate loading into the metalization chamber for Ni Schottky contact evaporation. Schottky contacts were completed with Ti and Au overlayers.

4. Experimental Results

The forward current-voltage characteristics of the Ni JBS diodes are shown in Fig. 4. These devices closely follow the thermionic emission theory with an extracted ideality factor of 1.04. The extracted Barrier height of 1.80eV using the theoretical Richardson's constant for 4H-SiC of A*=146A$K^{-2}$$cm^{-2}$ introduced a moderate error in the modeled forward I-V curves when compared to the experimental data. Using temperature measurements from 23°C to 300°C, an experimental effective Richardson's constant of 0.0731A$K^{-2}$$cm^{-2}$ was extracted, corresponding to an experimental barrier height of 1.58eV that correctly fits the thermionic emission equation. The specific on-resistance for a pure Schottky diode fabricated on the same die was a low 17mΩcm^2 with a forward voltage drop of 2.73V at 100Acm^{-2}. The forward voltage drop at 100Acm^{-2} for the JBS diodes increased from 2.85V for W=5μm to 3.25V for W=2μm, as shown in Fig. 5.

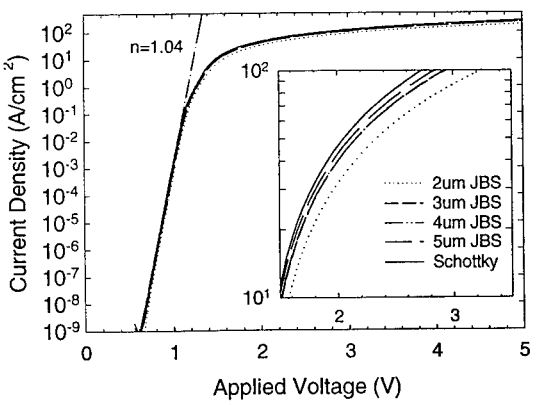


Fig. 5: Forward voltage drop versus JBS Schottky width.

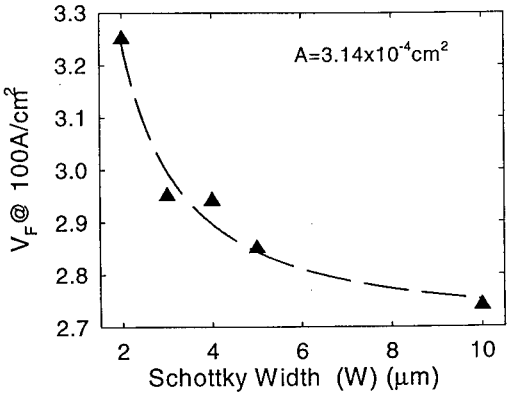


Fig. 4: Forward IV characteristics of 4H-SiC JBS rectifiers.

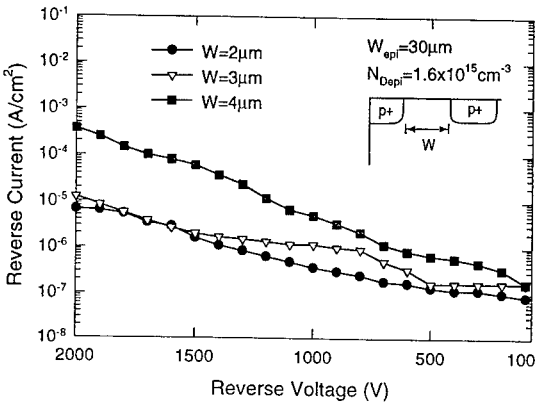


Fig. 6: Reverse bias I-V characteristics of several JBS rectifiers with A=1.26x10^{-3}cm^2.

In reverse blocking mode, the multiple guard ring termination proved effective with blocking voltages reaching 2.5kV, in excellent agreement with the predicted simulation values. A graph of the reverse leakage currents is shown in Fig. 6 for several 400μm JBS diodes with various p^+ spacing. As designed, the closely spaced p^+ regions had a positive effect on reducing the reverse leakage currents. At 2kV the leakage current for W=2μm and W=3μm devices is below 2x10^{-5}Acm^{-2}, and for W=4μm the current is ~4x10^{-4}Acm^{-2}. This reduction in reverse leakage currents is important in limiting the power dissipation when in reverse blocking mode.

4. Summary

A novel JBS structure with a self-aligned guard ring termination has been demonstrated to be effective in producing high voltage rectifiers with low leakage currents. The process sequence requires only a single implant and eliminates several processing steps from the more complicated JBS-JTE designs. We have shown that with a JBS spacing of 3μm-4μm, it is possible to reduce the peak interface fields and reduce the leakage currents by slightly trading off the forward voltage drop. We can expect to further improve on the JBS performance through the use of lower barrier height metals, where forward voltage drop could be significantly reduced.

Acknowledgements

This work was supported by the Center for Space Power and Advance Electronics, located at Auburn University, under NASA Contract #NCC5-459.

References

[1] H.M. McGlothlin, D.T. Morisette, J.A. Cooper, Jr. and M.R. Melloch, *Technical Digest of the IEEE Device Research Conf.*, Santa Barbara, CA, (June 28-30, 1999).

[2] G.M. Dolny, D.T. Morisette, P.M. Shenoy, M. Zafrani, J. Gladish, J.M. Woodall, J.A. Cooper, Jr. and M.R. Melloch, *IEEE Device Research Conf.*, Charlottesville, V.A, (June 22-24, 1998).

[3] K.J. Schoen, J.M. Woodall, J.A. Cooper, Jr., M.R. Melloch, *IEEE Electron Dev.* 45, No. 7, (1998), p.1595.

[4] Baliga BJ., *Power Semiconductor Devices.*, Boston: PWS Publishing Co., 1995.

[5] Y. Sugawara, K. Ansano, R. Singh and J.W. Palmour, *Mater. Sci Forum* 338-342 (1999), p. 1183.

[6] Q. Wahab, T. Kimoto, A. Ellison, C. Hallin, M. Tuominen, R. Yakimova, A. Henry, J.P. Bergman, E. Janzén, *Appl. Phys. Lett.* 72, No. 4, (1998), p.445.

[7] D.C. Sheridan, G. Niu, J.N. Merrett, J.D. Cressler, C. Ellis and C.C. Tin, *Solid-State Electron.* 44, No.8, (2000), p.1367.

[8] MEDICI 2-D semiconductor device simulator, ver. 4.3, Avant! Corp., Palo Alto, Ca, 1999.

[9] S.E. Saddow, M. Capano, J.A. Cooper, M.S. Mazzola, J. Williams and J.B. Casady, *Mater. Sci. Forum* 338-342 (1999), p.901.

Materials Science Forum Vols. 353-356 (2001) pp. 691-694
© 2001 Trans Tech Publications, Switzerland

Improvements in the Electrical Performance of High Voltage 4H-SiC Schottky Diodes by Hydrogen Annealing

Q. Wahab[1], E.B. Macák[1,2], J. Zhang[1], L.D. Madsen[1] and E. Janzén[1]

[1] Department of Physics and Measurement Technology, Linköping University, SE-581 83 Linköping, Sweden

[2] now at Materials Research Institute, Sheffield Hallam University, Howard Street, Sheffield S1 1WB, UK

Keywords: Dangling Bond, Hydrogen Annealing, Interface State Density, Power Devices, Schottky Diodes

Abstract. A significant improvement in all the important parameters of the diodes were observed by annealing in H_2 at 300 °C. The forward current increased from 55 mA to 100 mA at a bias voltage of 2.5 V. The reverse leakage current measured at -500 V was reduced from 3.5 x 10^{-9} to 4.8 x 10^{-10} Amps for a 0.5 mm diameter diode. The average value of the barrier height increased by at least 0.2 eV, measured by Capacitance-Voltage and Current-Voltage technique indicating the increase of both static and effective barrier heights. The average value of ideality factor also improved and a best value of 1.06 was obtained for the hot-wall CVD grown samples after H_2 annealing. Hydrogen atoms may passivate the dangling bonds at the metal-semiconductor interface and thus by saturating the dangling bonds reduce the interface state density.

Introduction

Schottky diodes in 4H-SiC have various advantages over Si based diodes in the market of high power electronics. Silicon carbide Schottky diodes can pave the way to improve the performance of power electronics in traction and auxiliary converters because of the voltage source since there performance is superior to other diodes in the breakdown voltage range of less than several kV. The power losses will drastically be reduced thus providing advantages in the designing of thermal systems due to less effort required for cooling. In this article we present the results of hydrogen annealing effects on the electrical performance of high-blocking voltage Ni/4H-SiC Schottky diodes. Hydrogen is known to passivate electrically active centers in various semiconductors.

Experimental

The 4H-SiC samples used for the study were grown either by hot-wall or chimney chemical vapor deposition (CVD) techniques on commercially available 4H-SiC substrates. The growth using hot-wall CVD technique was carried out at 1550 °C with the source gases SiH_4 and C_3H_8. The epilayer grown by this technique had a thickness of 35 μm. The growth of epi-layer by chimney CVD was performed at 1850 °C and the film thickness varied from 38 to 43 μm. The details of the hot-wall and chimney CVD systems are described elsewhere [1-2].

The diode processing technique utilizes the metal-overlap onto oxide layer as an edge termination for avoiding electric field crowding at the periphery of the diode. The SiO_2 layer was first thermally grown using dry oxidation method at 1200 °C for 4 hours, which resulted in about 2000 Å thick layer. A second SiO_2 layer of thickness ~2.2 μm was deposited using a plasma CVD technique. The total oxide thickness was 2.4 μm, which was believed to be sufficient to sustain high voltage in the reverse bias. For ohmic contacts Ni was thermally evaporated on the backside of the

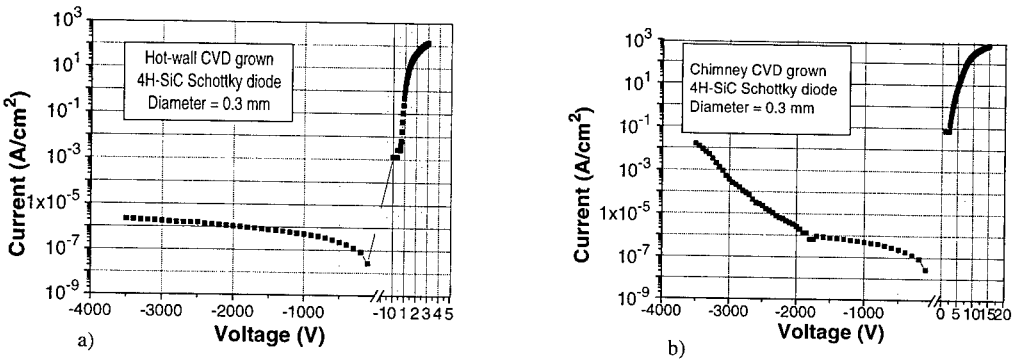


Fig. 1 Semilogrithmic current density *vs* Voltage plot measured to -3.5 kV of a) the diode processed on hot-wall CVD layer, b) the diode processed on Chimney CVD layer.

wafer and was subsequently annealed at 1000 °C to form the silicides for obtaining low ohmic contact resistance. The circular diode pattern was drawn using standard photolithography. Ni was deposited by thermal evaporation and was used as a Schottky contact. Finally a 200-nm thick Au layer was deposited as a cap layer. The details of the diode processing are defined elsewhere [3]. The hydrogen annealing was performed in Ar+2%H_2 ambient in a quartz tube at the temperatures of 200, 300 and 400 °C while the annealing time was 10 min for each annealing step.

The current-voltage (I-V) measurements were performed by a Keithley-237 source measurement unit together with a 5 kV Bertan power supply. The capacitance-voltage (C-V) measurements were performed by a HP-4284 LCR meter. For electrical measurements the samples were glued to a copper plate using conducting carbon cement. For high voltage I-V measurements the copper plate was immersed in a copper bath filled with high resistive fluorinated fluid in order to avoid sparking.

Results and Discussion

The doping concentration of the epi-layer grown by hot-wall CVD was measured by C-V to be ~2-3 x 10^{15} cm^{-3} and was found to be uniform along the substrate surface and also along the gas flow direction. By using the value of doping concentration and thickness of the epi-layer, the breakdown voltage for the parallel plane case was calculated to be ~4.2 kV. The doping concentration of the epitaxial layer grown by Chimney CVD was found to be in the range of 8 x 10^{14} to 1 x 10^{15} cm^{-3} and was found to be lower at the regions where its thickness was higher. The I-V characteristics shown in Figure 1a and 1b are the representative diodes processed on the sample grown by hot-wall and Chimney CVD respectively. Both diodes blocked more than 3.5 kV in the reverse bias conditions. The diode processed on hot-wall CVD sample showed a reverse leakage current density as low as 2.1 x 10^{-6} A cm^{-2} at 3.5 kV. In the forward direction the diode conducted a current density of 100 A cm^{-2} at a voltage drop of 3.3 V. The ideality factor of the diodes measured from the initial part of the curve was found to vary on the same chip from 1.06 to 1.8. The barrier height measured by the forward I-V characteristics was in the range of 1.0-1.4 eV while the static barrier height measured by C-V was 1.4 - 1.6 eV.

The diodes processed on a Chimney CVD sample also blocked more than 3.5 kV. The Chimney CVD technique is very attractive for power devices where thick epilayer (25-80 μm) can be grown at a rate of 20-50 μm h^{-1}, in the temperature range of 1800-2000 °C, while it take at least 8 hours to grow by conventional CVD since the growth rate is limited to 4 μm h^{-1}.

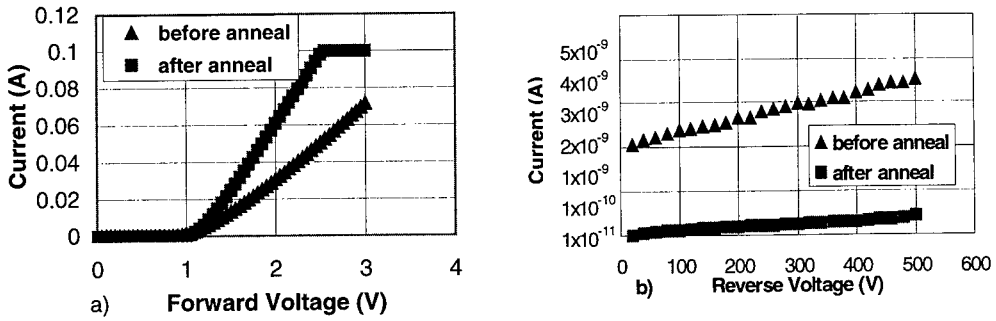


Fig. 2 is showing the effect of H2 annealing at 300°C on the performance of the diodes a) in the forward direction, b) in the backward direction.

The reverse leakage current density was quite low up to 1.8 kV and started to increase steeply compared to hot-wall CVD grown sample and at 3.5 kV was 0.01 A/cm^2. In the forward direction the voltage drop at a current density of 100 A cm^{-2} was 7.6 V, indicating a higher on resistance than the sample grown by hot-wall CVD. The ideality factor obtained from the initial part of the current was in the range of 1.2-1.9. The barrier height obtained by C-V technique was found to be 1.4-1.7 eV essentially in the same range as obtained on the samples grown by hot-wall CVD. The barrier height obtained by I-V technique was 0.9–1.2 eV, the difference is attributed to the static and effective barrier heights, which is related to the local defect density.

The diode characteristics measured after annealing at 200 °C in H_2 atmosphere showed a slight improvement both in the forward and reverse currents. A further annealing at 300 °C resulted in significant improvement in all the important parameters of the Schottky diode like forward and reverse current, barrier height and ideality factor. For the sample grown by hot-wall CVD, the forward current was increased from 55 mA to 100 mA at a constant bias of 2.5 V indicating a power gain of 22 W cm^{-2}, see Fig. 2a. The reverse leakage current of the diode was reduced from 3.5 x 10^{-9} to 4.8 x 10^{-10} Amps to a bias voltage of –500 V, see Fig. 2b. The reduction in the reverse leakage current is desired in the designing of high blocking voltage diode, where a slight increase in the leakage current results in a substantial increase of the dissipated power due to high voltage. Similar results were obtained for the diodes fabricated on the sample grown by Chimney CVD technique.

The barrier heights of the hot-wall CVD layer diodes measured from $1/C^2$ *vs* voltage plot were in the range of 1.18-1.39 eV before annealing and were increased to 1.39–1.6 eV and are shown in Fig. 3. The figure shows the barrier height values of 5 selected diodes of diameter 0.5 mm on the chip. Almost all the measured diodes on the chip showed an increase in the barrier height after annealing in H_2. No further improvement and/or degradation was observed by further annealing at 400 °C. It is interesting to note that this increase in the barrier height is not the same for all the diodes. Some diodes showed a larger increase than others and as can be seen in the Fig. 3 that the diode #2 showed an increase from 1.37 to 1.46 eV while the diode #5 showed an increase from 1.25 eV to 1.6 eV. This mechanism is not clearly understood at the moment. The barrier heights in the Schottky diodes depend on the interface state density between the metal and semiconductor. These results indicate that the interface state density in the SiC Schottky diode is primarily due to dangling bonds which were passivated by the hydrogen atoms during annealing and some of the interface states were released resulting in the increase of barrier height. The individual behavior of the diodes can also be related to the localized defect density under the active area of the diode reacting with the

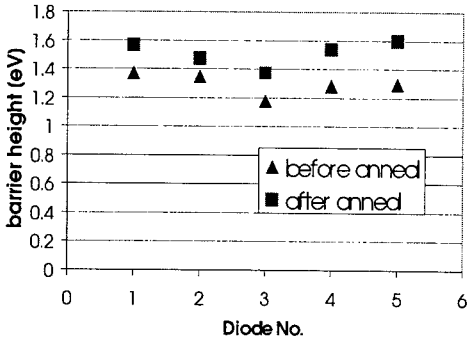


Fig. 3 Barrier height measured by C-V before and after annealing.

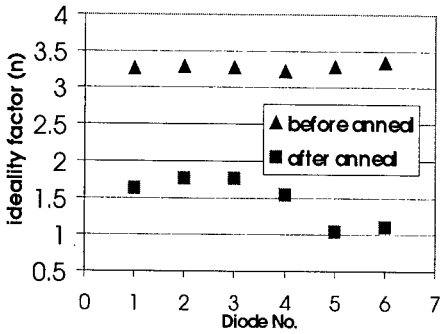


Fig. 4 Ideality factor of the diode measured before and after annealing

hydrogen atoms individually since the SiC crystal is containing a high density of screw dislocations which were randomly distributed over the wafer surface area [4]. Figure 4 shows the improvement in the ideality factor and a best value of 1.06 was obtained after annealing. Dislocations are also assumed to create additional states within the bandgap due to atomic strain and internal stress. In the MOS structure of 4H-SiC the reduction in the interface state density and its saturation at 800 °C by H_2 annealing is also reported recently where the density was reduced to as low as 1 x 10^{11} eV^{-1} cm^{-2} [5]. The interface states at SiO_2/4H-SiC are also thought to originate from the dangling bonds.. Hydrogen in the epilayer may also form stable H-impurity complex (like H-B), which may result in an increase of the effective doping near the interface region and thus increase the forward current of the diode. On the other hand if B and/or other deep level defects participate in the carrier generation, the formation of H-impurity complex may decrease the reverse current. The study performed on the hydrogen passivation of N in 6H-SiC indicated a less efficient N-H binding and is a greater prevalence in p-type because the Fermi level is close to the valence band increasing the H^+ fraction [6].

Summary

The H_2 annealing effectively improved all the important characteristics of the Ni/4H-SiC Schottky diode. The best value of the ideality factor was only achieved after H_2 annealing. This indicates that the interface state density in 4H-SiC Schottky diode is primarily due to dangling bonds.

References

[1] O. Kordina, A. Henry, C. Hallin, R. C. Glass, A. O. Konstantinov, C. Hemmingson, N. T. Son and E. Janzen, MRS Symp. Proc. 339 (1994), p. 405.

[2] A. Ellison, J. Zhang, J. Peterson, A. Henry, Q. Wahab, J. P. Bergman, Y. N. Markarov, A. Vorobev, A. Vehanen and E. Janzen, J. Mat. Sci. & Eng. B61-62 (1999), p. 113.

[3] Q. Wahab, T. Kimoto, A. Ellison, C. Hallin, M. Tuominen, R. Yakimova, A. Henry, J. P. Bergman and E. Janzen, Appl. Phys. Lett. **72** (1998), p. 445.

[4] A. Ellison, Ph.D thesis No. 599, Department of Physics, Linköping Univeristy, Sweden, 1999.

[5] K. Fukuda, S. Suzuki, T. Tanaka and K. Arai, Appl. Phys. Lett. 76 (2000), p. 1585.

[6] B. Theys, F. Gendron, C. Porte, E. Bringuier and C. Dolin, J. Appl. Phys. 82 (1997), p. 634.

Materials Science Forum Vols. 353-356 (2001) pp. 695-698
© 2001 Trans Tech Publications, Switzerland

Influence of the Buried p-Layer on the Blocking Behavior of Vertical JFETs in 4H-SiC

Peter Friedrichs[1], Heinz Mitlehner[1], Reinhold Schörner[1], Rainer Kaltschmidt[2], Karl-Otto Dohnke[1] and Dietrich Stephani[1]

[1] SiCED GmbH & Co. KG, a Siemens Company,
Paul-Gossen-Str. 100, DE-91052 Erlangen, Germany

[2] Siemens AG, MED SPE, Paul-Gossen-Str. 100, DE-91052 Erlangen, Germany

Keywords: Avalanche Breakdown, Buried Layers, Power Switching, Simulation

Abstract
For vertical JFETs in silicon carbide, the use of an buried gate with a lateral channel concept in order to achieve a high blocking gain was shown to result in promising device performance. However, due to field crowding at the edges of the buried p-layer, the breakdown voltage is reduced compared to fully planar devices which are able to use the bulk breakdown field of 4H-SiC. The following work presents a possibility how to further enhance the breakdown voltage of SiC JFETs with buried layers by implementing a buried layer with optimized shape and doping. Consequently, for a given blocking voltage, the specific on-resistance can be reduced, resulting in lower losses for the device.

Introduction
Generally, one of the most important key parameters characterizing a unipolar switching device is its specific on-resistance. For classical high voltage (>100V) solid state switching devices, this parameter is dominated by the resistance of the epilayer necessary for blocking the desired reverse bias. In the case of silicon carbide devices, this epilayer can be designed thinner and with an higher doping density compared to conventional Si-devices due to the high electric breakdown field of SiC, resulting in on-resistances two orders of magnitude below Si-MOSFETs, e.g [1]. Unfortunately, vertical 4H-SiC MOSFETs still suffer from a poor channel mobility [2,4]. However, vertical 4H-SiC JFETs exhibit promising electrical parameters for low loss, fast switching applications in the range above 1000V blocking voltage [3]. In order to demonstrate the advantages of these benefits in practical applications, we investigated VJFETs for different reverse bias classes. It was shown that the avalanche breakdown of such vertical JFETs in SiC can be controlled to start at the buried p-islands and is therefor non-destructive [3]. However, the electric field at the breakdown voltage reaches only up to 50% of the bulk breakdown field in SiC. Therefor, the devices exhibit a higher specific on-resistance compared to theoretical numbers like figures of merit, e.g , which base on the full breakdown field [1]. The stimulating challenge for the presented research was to look for a way how to increase the breakdown voltage for a given set of epi parameters (thickness, doping) and consequently further reduce the losses for a certain class of blocking voltage. In order to do this, extensive simulation work was performed and the results were tested by implementing them in the real device.

Device structure, simulation
Figure 1 (left) shows the basic structure of the VJFETs investigated in this work. Important features are the lateral channel and vertical current flow, the short circuit between the buried gate and the source and the use of two different epitaxial layers for controlling the device current and blocking the desired reverse voltage, resp. Technological details will be discussed in the next chapter. Compared to a more conventional SIT like structure of vertical JFETs, these concepts results in a much higher blocking gain. However, due to field crowding at the edges of the buried layer, e reduction in breakdown voltage compared to identically processed planar junctions can be expected.

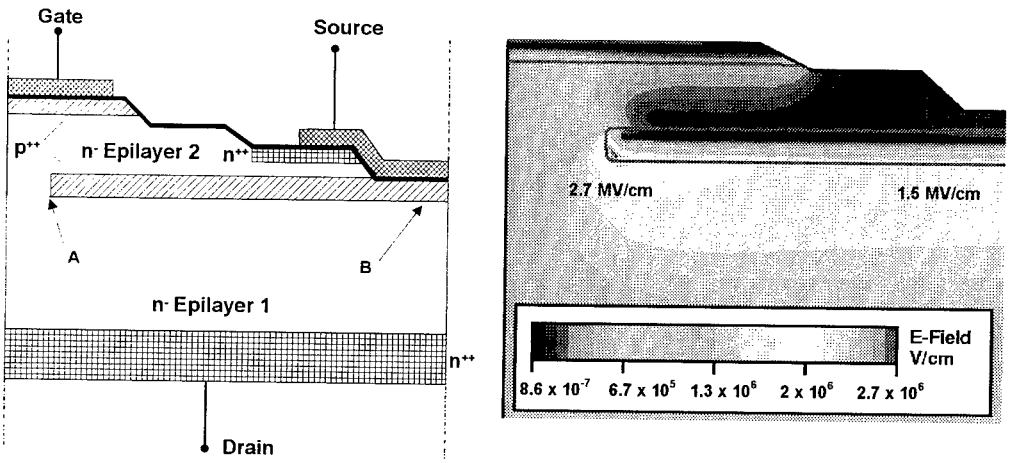


Fig. 1 : Cross section through the JFET investigated in this work together with the field distribution in the blocking mode (V_{GS} = -35V, V_{DS} =1200V)

Simulations of the blocking behavior reveal that the breakdown starts at the edge of the buried layer (see figure 1, point A, 2.7MV/cm). The ratio between the electric field under the planar part of the buried pn-junction (point B, 1.5MV/cm) and the critical point A gives an estimate for the full use of the possible breakdown voltage in SiC devices. Assuming a *classical* doping profile which can be realized by conventional ion implantation (E_{max} = 400keV) and using a single mask, it was possible to achieve a breakdown voltage corresponding to 50% of the bulk breakdown field of SiC.
Since the modeling showed that the breakdown behavior can be influenced by adjusting the doping and the shape of the buried layer at point A, two *modified* structures in detail :

1) extension of the buried layer into the depth by using a higher energy implantation while maintaining the overall implantation dose
2) introducing an additional lateral step in the buried layer (see figure 2a) and simultaneous extension into the depth

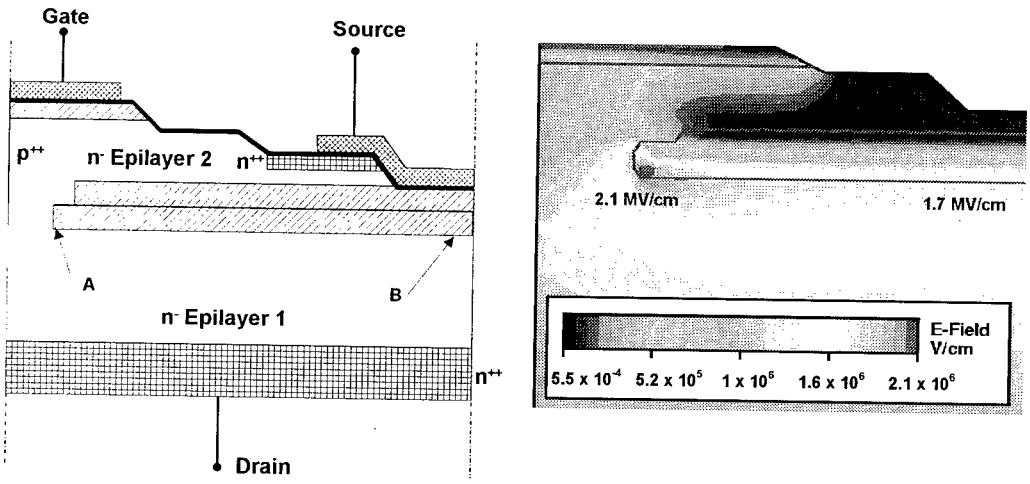


Fig. 2 : Cross section through the modified JFET together with the field distribution in the blocking mode (V_{GS} = -35V, V_{DS} = 1200V)

For both solutions, the simulation predicted an increase of the blocking voltage for a 1200V device (epi data see chapter technology) of approximately 200V. As can be seen from the field distribution, the ratio between the field at the edge and below the planar junction decreases from approximately 0.8 to 0.55 for the modified design. Additionally, for the same conditions, the absolute value of the electric field at the edge is well below the critical value (2.1MV/cm vs. 2.7MV/cm). The high field area is smeared out along the bottom of the buried layer and thus, the breakdown voltage increases. The simulation reveal further that for an aspect ration in the channel (channel length vs. channel height) of larger than 3, no influence on the blocking behavior can be seen. Generally, the here presented attempts represent only examples how to reduce the critical field at the edge of the buried layer in such vertical structures. Similar designs like triangle shaped edges e.g., which also result in a field reduction at the critical point, are conceivable.

Technology

In order to prove the results obtained by the above presented simulations, the modified structures (deep implantation and lateral step) were directly compared to the classical structure by processing them simultaneously on one wafer (left half *classical*, right half *modified*). The substrate material was n-type 4H-SiC from Cree with a specific resistivity between 16 and 20mΩcm. A first n-type epitaxial layer ($6x10^{15}cm^{-3}$, 15µm) was grown onto the substrate by LPCVD. For the deep profile version, the buried p-layer was implanted selectively into the first epitaxial layer at both halfs of the wafer. For the lateral step structure, the lower part of the buried p-layer was implanted into the first epilayer, then a second layer was grown (0,5µm, $6x10^{15}cm^{-3}$). Into this second layer, the upper part of the step profile (one half) and the classical profile were implanted. After completing this, a second/third layer of 2µm (doping $1,5x10^{16}cm^{-3}$) was grown forming the so-called head of the structure. At the top of the layer, the p-gate was implanted with aluminum. Several subsequent lithographic, dry etching and implantation steps for the source region and the electric connection of the buried layer defined the final layout. After annealing the implantations at around 1700°C, nickel based contacts were deposited at the top (gate and source areas) and at the bottom (drain contact) of the wafers. The contacts were annealed at about 1000°C. An insulating oxide layer of 400nm was deposited via PECVD and opened in the gate pad and source area. Subsequently, an aluminum metallization of 3µm serving as a bond area was evaporated and patterned. The complete device consists of 1452 parallel cells resulting in an active area of $2,3mm^2$.

Results

The simultaneous processing of the classical and the modified structure on one wafer allowed us to evaluate directly the influence of the design of the buried layer. For the profile extended into the depth (high energy implantation), no improvement in the blocking behavior was observed. However, the use of the step like structure resulted in a considerable increase of the blocking voltage. Figure 4 shows a distribution of the blocking voltage for one wafer with the conventional profile at the left side and the modified profile at the right side.

In can be clearly observed, that at the half of the wafer having the modified buried p-structure, an increase of the blocking voltage from approx. 1300V to 1800V occurs. The corresponding breakdown fields are 1.7MV/cm and 2.1 MV/cm, resp. The parallel plane breakdown field for this epilayer is approx. 2.3MV/cm [5]. Thus, using the modified profile, it is possible to exploit more than 80% of the bulk breakdown field of silicon carbide. The broader distribution of the breakdown voltage at the right sight is caused by technological tolerances which are induced by the complicated formation of the step structure. Obviously, three epilayers must be grown, in each of them must be an implantation aligned to the first layer with a tolerance of less than 1µm (especially important between the first and the second layer). The main benefit of the concept is the fact that the specific on-resistance for a given breakdown voltage decreases. Comparing the results from earlier works, it can be estimated that for the 1800V device, the on-resistance decreases by at least 20% [3].

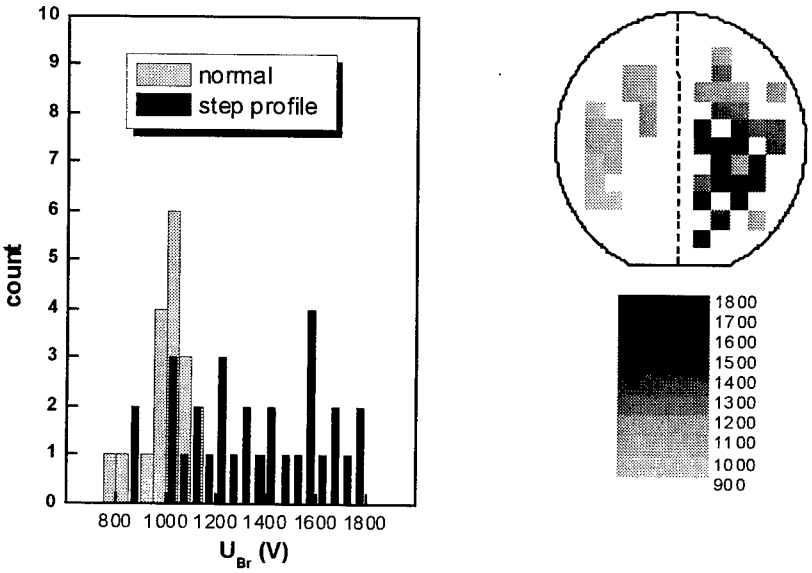


Fig. 2 : Distribution of the breakdown voltage across one wafer with the conventional profile at the left side and the step like structure at the right side

Additionally, the maximum current which can be driven through the channel without self pinch-off (saturation) can be increased since the effective channel length is reduced.

Summary

The presented work shows a possibility how to increase the blocking voltage of a vertical JFET structure with an buried gate by adjusting the shape and the doping of the buried layer. However, the method represents a technological challenge and introduces additional process steps. Further work should find straightforward methods how to reduce the specific on-resistance of SiC switching devices. Additionally, the concept presented here will be tested in a new JFET configuration [4]. This new approach gives also with the conventional buried profile on-resistances of approximately one half of the value obtainable with the here presented design.

References

[1] K.Shenai, R.S.Scott, B.J.Baliga, "Optimum Semiconductors for High-Power electronics", IEEE Trans.Electron Devices, **36**, 1989, p.1811

[2] M.K.Das, B.S.Um, J.A.Cooper, "Anomalously High Density Of Interface States Near the Conduction Band in SiO_2/4H-SiC MOS Devices", Mat. Sci. Forum, **338-342** (2000), p.1069

[3] P.Friedrichs, H.Mitlehner, W.Bartsch, K.O.Dohnke, R.Kaltschmidt, U.Weinert, B.Weis, D.Stephani, "Static and dynamic Characterisctics of 4H-SiC JFETs Designed for Different Blocking Categories" , Mat. Sci. Forum, **338-342** (2000), p.1243

[4] P.Friedrichs, H.Mitlehner, D.Peters, K.O.Dohnke, R.Schörner, U.Weinert, E.Baudelot, D.Stephani, "SiC power devices with low on-resistance for fast switching applications" , Proceedings of the ISPSD '99, Toulouse, May 22-24, 2000.

[5] German Patent DE 197 39 547 A1, Assignee: Nissan Motor Co., Inventor: Hoshi, Masakatsu, 9.9.1997.

Materials Science Forum Vols. 353-356 (2001) pp. 699-702
© 2001 Trans Tech Publications, Switzerland

A Comparison between Physical Simulations and Experimental Results in 4H-SiC MESFETs with Non-Constant Doping in the Channel and Buffer Layers

J. Eriksson[1], N. Rorsman[1], H. Zirath[1], R. Jonsson[2,3], Q. Wahab[2] and S. Rudner[2,3]

[1] Department of Microelectronics, Chalmers University of Technology, SE-412 96 Göteborg, Sweden

[2] Department of Physics and Measurement Technology, Linköping University, SE-581 83 Linköping, Sweden

[3] FOA Defence Research Establishment, PO Box 1165, SE-581 11 Linköping, Sweden

Keywords: Doping Profile, MESFET, Physical Simulations, SIMS

Abstract. The performance of SiC MESFETs, fabricated on a structure with non-constant doping-profiles in the channel and buffer layers have been studied. A good correspondence between experimental DC-characteristics and physical simulations was obtained, when using the doping profiles from SIMS measurements.

Introduction

Silicon carbide can offer major improvements in the output power of microwave transistors due to its physical properties. The performance of SiC MESFETs is however still affected by deficiencies in the material such as defects giving rise to lower mobility. Peaks in the doping profile also affect the performance of the devices in a drastic way. In this paper we present the results from a comparison between experiments and physical simulations of SiC MESFETs based on transistor structures with non-constant doping-profiles in the channel and buffer layers.

Experiment

The transistor structures consist of buffer, channel and contact layers epitaxially grown on semi-insulating 4H-SiC substrates. Five different layer structures were investigated of which two are described in this paper. Secondary ion mass spectroscopy (SIMS) was utilized to obtain the doping concentrations and layer thicknesses.

Transistor processing

The transistor processing consists of one electron beam lithography (EBL) and six optical steps. The process steps are: mesa and recess etching, thermal oxidation and dielectric deposition, ohmic contact formation, gate formation by EBL, passivation and pad deposition. The mesa and recess was obtained by dry etching using a CF_4/O_2 plasma mixture. Ohmic contacts were formed by annealing nickel at 1000°C in a RTA furnace. The gate contact consists of a multilayer metal structure of Au/Pt/Ti. The channel thickness under the gate of the component was about 0.20 μm. The gate-length, gate to source and gate to drain spacing, are 0.5 μm, 0.5 and 1.0 μm respectively.

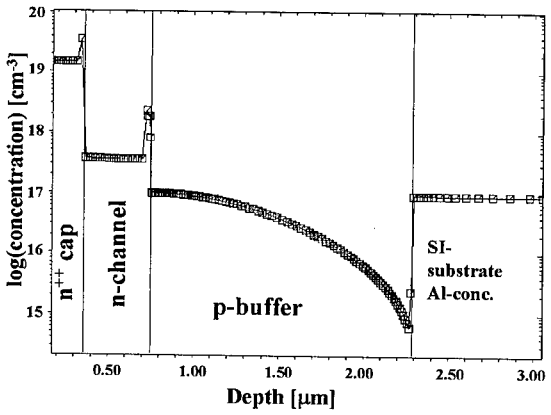
SIMS results

The doping profiles were calculated from the SIMS measurements. The doping concentrations in the cap and channel layers were between 1-2 x 10^{19} and 2-3 x 10^{17} cm^{-3} respectively. A peak of a highly doped thin layer in the cap and channel adjacent to the interfaces between cap-channel and channel-buffer were observed in all the samples and a typical example can be seen in fig. 1a. While the channel doping in this case was 2 x 10^{17} the peak concentration was 1.3 x 10^{18} cm^{-3}. The Al concentration in the buffer layer for this wafer was found to be decreasing continuously from 1 x 10^{17} down to 1 x 10^{15} cm^{-3} (fig. 1a). The Al concentration in the substrates was 1 x 10^{17} cm^{-3} while the V concentration was 9 x 10^{16} cm^{-3}. Since the N concentration was not measured, it could not be determined if the substrates are semi-insulating or slightly p- or n-type, but simulations indicate that they are p-type.

Device simulation and comparison to measured data

Numerical drift-diffusion simulations were performed using a commercial program; Medici from Avant Corporation [1]. The two materials examined have different buffers. SiC-3 has a thick high-doped buffer, which by itself is sufficient, to keep the electrons in the channel.

1a)



1b)

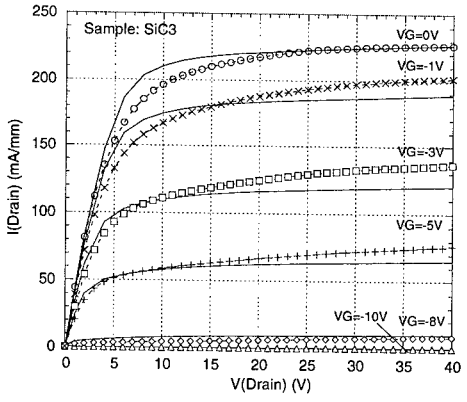
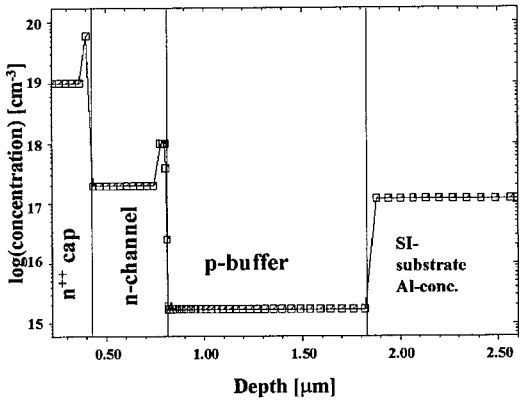


Fig. 1: The doping profile from SIMS measurements non-uniform buffer doping wafer. (a). Simulated and measured drain characteristics of the transistor with doping profile shown in fig. 1a. The solid lines show simulation while the symbols show measurements (b).

SiC- 5 has a thick low-doped buffer, where electrons travel into the buffer and the pn-junction is due to the substrate.

The simulated and measured drain characteristics shown in fig.1b correspond to the SiC-3 structure shown in Fig. 1a. The pinch-off voltage was –10 V. The measured saturation drain current as shown in Fig. 1b was 220 mA/mm and the breakdown voltage was 130 V. The SIMS-measurement, DC-simulation and -measurement for SiC-5 are shown in Fig. 2. Since the buffer is low doped (with an assumed N_D of 2 x 10^{15} cm^{-3}), the gate pinch-off voltage was as high as –28 V for a drain bias of 40 V. The maximum drain current was higher than 400 mA/mm.

2a)



2b)

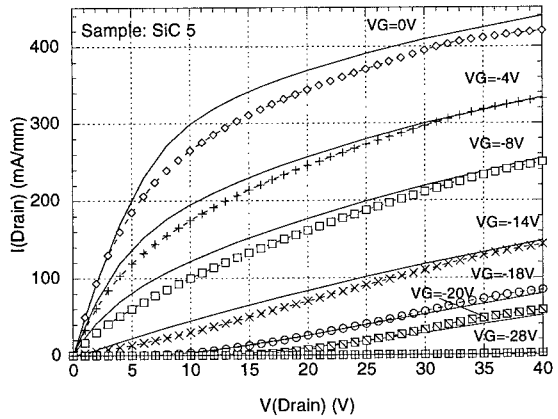


Fig. 2: The doping profile from SIMS measurements of a low buffer doping wafer. The nitrogen in the buffer layer is estimated, since it is below the detection limit (a). Simulated and measured drain characterstics of the transistor of the structure shown in fig. 2a. The solid lines show simulation while the symbols show measurements (b).

When the substrate is modelled as a p-type instead of a material with the Fermi-level in the mid-bandgap, simulations give results closer to the measured. These results and the SIMS measurements given above lead us to believe that it is highly resistive and p-type. Even better agreement between simulations and measurements for the saturated drain characteristic was observed for both materials when the electron mobility value in the simulations was reduced to about 77% ($\mu_{n,max}$=729 cm^2/Vs) of the Hall mobility measured by Schaffer et al [2]. The mobility value used in the simulations is based on the Arora model [3]. By using this model

the electron mobility value for the current channel doping is 370 cm^2/Vs, which was confirmed with Hall measurements on a similar structure grown on a semi-insulating SiC substrate [4]. The difference between our experimental values and the values reported earlier [2] can be attributed to the crystalline defects in the substrate that have propagated to the growing epitaxial layer. Lower mobility has also been used in MESFET simulations by others [5], and their value is close to ours, if their value is adjusted for incomplete ionization.
Incomplete ionization of donors was taken into account. All simulations were performed using field dependent, anisotropic mobility. The simulator uses Newton's method with Fermi-Dirac statistics.
Despite the complex profiles shown in figs 1a and 2a, the simulations accuratly describe the characteristics of the two MESFET structures. Our results indicate that the substrate by itself or with help of the buffer form the reversed biased pn-junction to the channel.

Summary

The comparison between simulations and DC-characteristics of microwave transistors are presented for two structures with non-constant doping profiles in the buffer and channel layers. Peaks in the transition between buffer and channel must be controlled, because the charge addition of these can give rise to more than double the current anticipated without them. The SI-substrate and/or the buffer give a desired reversed biased pn-junction towards the substrate. Both substrate and buffer must be taken into account in an accurate simulation, unless the substrate is totally screened by the buffer.
The Arora model is used to describe the mobility vs doping and temperature. The values from Schaffer[2] was used, except for the maximum electron mobility. This value (729 cm^2/Vs) is calculated from a Hall mobility measurement on a sample with known doping.

Acknowledgments

The author acknowledge financial support from: CHACH (Chalmers Centre for Highspeed Technology), EMW (Ericsson Microwave Electronics), FOA (Swedish Defense Research Establishment), FMV (Swedish Defense Material Administration), NUTEK (Swedish National Board for Industrial and Technical Development), Linköping University, Royal Institute of Technology, SaabTech Electronics, SSF (Swedish Foundation for Strategic Research), and TFR(Swedish Research Council for Engineering Sciences). The authors would also like to thank M.Linnarson (KTH) for making the SIMS measurements.

References

[1] Avant Corporation, 3400 W. Warren Avenue, Fremont, CA 9453 85425 USA.
[2] W.J. Schaffer, G.H. Negley, K.G. Irvine and J.W. Palmour, MRS Symposium Proc. 339 (1994), p. 595.
[3] N.D. Arora, J.R. Hauser and D.J. Rouulston, IEEE Trans Electron Devices ED-29 (1982), p. 292.
[4] To be published by the Dept. of Physics, Linköping University, S-581 83 Linköping, Sweden.
[5] M. Huang, N. Goldsman, C.H. Chang, I. Mayergoyz, J.M. McGarrity and D. Woolard, J. Appl. Phys. 84 (1998), p. 2065.

Materials Science Forum Vols. 353-356 (2001) pp. 703-706
© 2001 Trans Tech Publications, Switzerland

Noise Behavior of 4H-SiC MESFETs at Low Drain Voltage

C. Banc[1], A.S. Royet[1,2], T. Ouisse[1], E. Bano[1], O. Noblanc[3] and C. Brylinski[3]

[1] Laboratoire de Physique des Composants à Semiconducteurs (LPCS), UMR-CNRS 5531, ENSERG, 23 rue des Martyrs, BP 257, FR-38016 Grenoble Cedex 1, France

[2] LEMO (UMR CNRS 5530), ENSERG, 23 rue des Martyrs, BP 257, FR-38016 Grenoble Cedex 1, France

[3] Thomson-CSF, Laboratoire Central de Recherches, Domaine de Corbeville, FR-91401 Orsay Cedex, France

Keywords: 4H-SiC, Deep Level, Hooge Parameter, Low Frequency Noise, MESFET, Semi-Insulating Substrate, Trapping

Abstract We have investigated the influence of two different substrate types on the low field (low drain bias) noise characteristics of 4H-SiC power MESFETs in the range 1 Hz-100 kHz. All devices were fabricated on semi-insulating SiC substrates. A first series included a p-buffer layer between the active channel and the substrate whereas the other series had no buffer. We show that devices on buffered substrate exhibit volumic noise whereas devices without buffer are characterized by a constant noise level at all gate biasing conditions. These results are discussed in terms of trapping phenomena occurring inside the semi-insulating substrate.

Introduction

High transient phenomena have been reported to occur in 4H-SiC power MESFETs [1, 2, 3]. These transients can strongly reduce the drain current during operation of such devices and they are believed to be responsible for lower power densities than expected [1]. The exact origin of these transients is still not clear. Noblanc *et al.* [1, 2] ascribe them to trapping processes occurring inside the semi-insulating substrate. The filling of unoccupied states in the substrate creates a space charged region below the channel which in turn induces a depletion in the active channel, thus reducing the current level of the device. Hilton et al. [3], however, claim that the reduction in the drain current is due to charging of the SiC surface above the drain depletion region and suggest that appropriate surface treatment is a key element to reduce the effect. In this paper, we present low frequency (1 Hz-100 kHz), low field noise measurement results supporting the "substrate origin" of the transients.

1 Devices and experimental set-up

Two series of devices were investigated. For all devices, the 300 μm thick semi-insulating 4H-SiC substrate was purchased from Cree Research. For one series of devices, a 1 μm thick p-type buffer was epitaxially grown with a net doping level equal to 5.2×10^{16} cm^{-3}, followed by a 0.27 μm thick n-type layer (1.6×10^{17} cm^{-3}). For the second series, no buffer was grown, the n-type layer being directly grown on the semi-insulating substrate. The n^+ contact layers were 0.2 μm thick and had a doping level equal to 1.1×10^{19} cm^{-3}. The MESFETs which structures are shown in Fig. 1a and Fig. 1b were fabricated at Thomson-CSF/LCR. The recesses were formed by RIE etching, a metallic multi-layer (Ti/Pt/Au) was used for the gates, and source and drain contacts were done using nickel. For this study, 2 μm and 4 μm gate lengths were investigated, the source/gate and drain/gate spacing were respectively around 0.5 and 2.5 μm. Preliminary measurements showed that the unbuffered devices had strong transients comparable to those reported in [1, 2] whereas the buffered devices exhibited no transient. However, we carefully checked before and during the noise measurements that at low drain biases (typically 50 to 100 mV), both kind of devices were stable (a decaying drain current such as those occurring at higher voltages would induce erroneous spectra).

The noise measurements were performed at room temperature using a HP 35665A dynamic signal analyzer. The drain and gate voltages were kept constant by using Cd-Ni batteries and the drain current fluctuations were converted into voltage fluctuations by a low-noise pre-amplifier (EG&G 5182). The voltage fluctuations were then fed into the spectrum analyzer. The analysis was done for a low drain bias (50 mV).

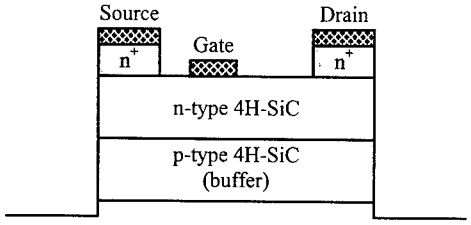


Fig. 1a: schematic cross-section of a buffered device (not on scale).

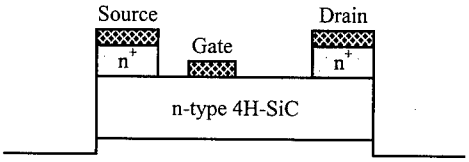


Fig. 1b: schematic cross-section of a non-buffered device (not on scale).

2 Noise spectra

In "open channel" conditions (very low $|V_G|$), the noise characteristics are similar for the two substrate types: 1/f noise followed by a plateau at high frequencies (Fig. 2). The noise levels around 100 Hz have the same magnitude for both types of devices. This can also be seen on the high current part of Fig. 4a. This 1/f shape of the spectra is common to most semiconductor devices where conductance fluctuations is the origin of the noise [4] and the plateau is due to the thermal noise (its level is proportional to the conductance of the device). As the devices are biased toward "pinch off" (Fig. 3), the behavior of the two substrates are different. For the buffered devices, the overall noise level decreases, following the decrease in the drain current. In the case of the devices without buffer, the 1/f part of the spectrum undergoes almost no change. Only the thermal noise contribution decreases and remains comparable to that of the buffered devices.

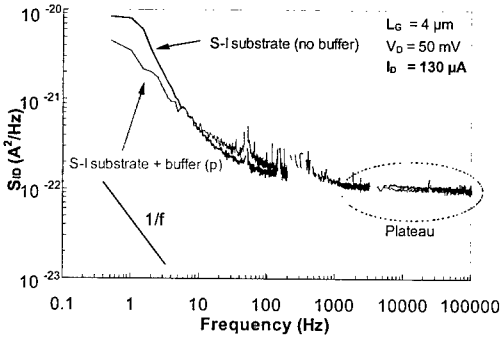


Fig. 2: Noise spectra in „open channel" condition.

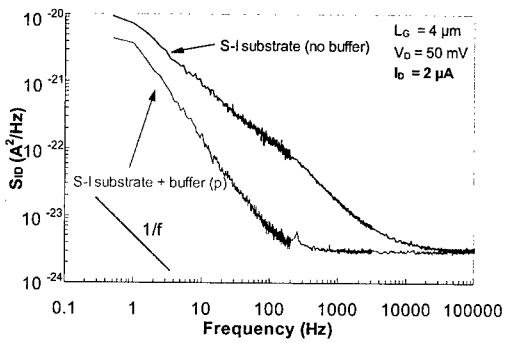


Fig. 3: Noise spectra near „pinch off".

3 Noise levels at 100 Hz

The study of the noise levels around 100 Hz gives us interesting hints about the processes affecting the carriers inside the channel. "Conventional" MESFETs operating at low fields are expected to exhibit 1/f type noise described by [4]:

$$\frac{S_{ID}}{I_D^2} = \frac{\alpha_H}{N_{eff} \times f}. \quad (1)$$

Where S_{ID} is the drain current noise power spectral density (A^2/Hz), I_D is the drain current (A), N_{eff} the effective number of carriers in the channel of the device, f the frequency of analysis (Hz), and α_H the Hooge parameter (dimensionless). Under linear operating conditions (low drain voltages), N_{eff} is given by:

$$N_{eff} = \frac{Lg^2}{q \times \mu_n \times \frac{V}{I_D}}, \quad (2)$$

where Lg is the gate length, μ_n the electron mobility in the channel, and V the applied voltage. In that case, N_{eff} is proportional to I_D and S_{ID} is then also proportional to the current. This means that the carriers are similarly affected by the processes at the origin of the noise for all the gate biasing conditions (from open channel to pinch-off).

The buffered devices strictly follow Eq. (1) with a Hooge parameter equal to 6×10^{-6} (Fig. 4a and 4b) but it is clearly not the case for the unbuffered devices. In contrast, these latter exhibit an almost constant noise level over the whole range of biasing conditions (Fig. 4a). This means that the carriers closer to the substrate are more affected than the carriers in the upper part of the channel and that the resulting noise dominates other sources. In that case, an attempt to plot α_H as a function of N_{eff} results in the $1/N_{eff}$ behavior shown on Fig. 4b. This kind of behavior has already been seen on GaAs MESFETs built on InP substrates and was attributed to trapping phenomena near the channel-buffer interface of the devices [5]. In our case, the trapping could be ascribed to the lack of buffer and related to the high drain current transients observed at high fields [1, 2].

It is also important to notice that under open channel condition (see right hand side of Fig. 4a) the two series of devices behave identically and their noise levels are the same. The dominating noise source is then common for all samples. And since most current contributing carriers are far from the substrate, the relative influence of the substrate on the noise level vanishes.

The Hooge parameter found for the buffered devices (6×10^{-6}) is comparable to the one previously reported by Levinshtein *et al.* [6] also in 4H polytype. They found α_H to be $2\text{-}4\times10^{-6}$ at 20 Hz and attributed this low value to a high degree of structural perfection of the material.

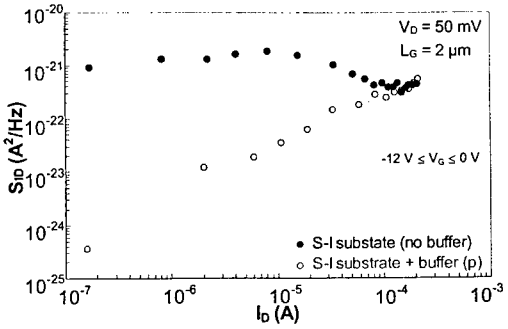


Fig. 4a: Noise level at 100 Hz.

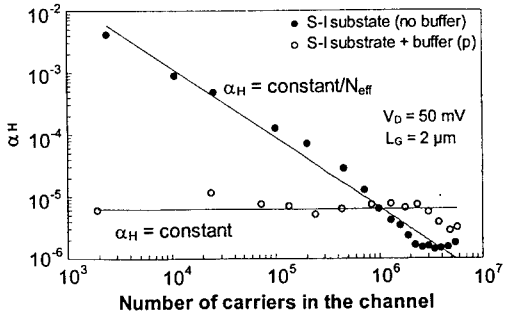


Fig. 4b: Hooge parameter at 100 Hz.

4 Discussion

The semi-insulating character of the substrate being achieved through compensation by deep levels (mean density: $1\text{-}3\times10^{17}$ cm^{-3}), a direct contact between the active channel and the substrate favors trapping into the unoccupied states of the substrate. We believe that the constant noise level measured for the unbuffered devices is the signature of this trapping. In that case the observed 1/f noise is mostly to be due to the carrier number fluctuations in the channel induced by the trapping [5]. In the buffered devices however, the carriers in the channel are prevented from interacting with these states by the p-type layer, hence the noise characteristics of such samples are more conventional.

Summary

We have investigated the low frequency noise characteristics of 4H-SiC power MESFETs under low field operation. Two types of devices were tested: a first series included a buffer layer between the active channel and the underlying semi-insulating substrate whereas a second series had no buffer to isolate the channel from the substrate. We have shown that the devices without buffer exhibited an almost constant noise level independent of the channel configuration (open or pinched off) whereas the buffered devices followed a more conventional behavior (the noise level scaled with the drain current). We attribute this constant noise level to trapping processes occurring in the semi-insulating substrate and we believe that this trapping is related to the strong drain current transients observed under high field conditions for the unbuffered devices.

References

[1] O. Noblanc, C. Arnodo, E. Chartier and C. Brylinski, Mater. Sci. Forum 264-268 (1998), p. 949.

[2] O. Noblanc, C. Arnodo, C. Dua, E. Chartier and C. Brylinski, Mat. Sci. Eng. B 61-62 (1999), p. 339.

[3] K.P. Hilton, M.J. Uren, D.G. Hayes, P.J. Wilding, H.K. Johnson, J.J. Guest and B.H. Smith, Mater. Sci. Forum 338-342 (2000), p. 1251.

[4] F.N. Hooge, T.G.M. Kleinpenning and L.K.J. Vandamme, Rep. Prog. Phys. 44 (1981), p. 480.

[5] M. Chertouk and A. Chovet, IEEE Trans. Electron. Devices 43 (1996), p. 123.

[6] M.E. Levinshtein, S.L. Rumyantsev, J.W. Palmour and D.B. Slater Jr., J. Appl. Phys. 81 (1997), p. 1758.

Materials Science Forum Vols. 353-356 (2001) pp. 707-710
© 2001 Trans Tech Publications, Switzerland

Double Implanted Power MESFET Technology in 4H-SiC

A.B. Horsfall[1], S. Ortolland[1], N.G. Wright[1], C.M. Johnson[1] and A.P. Knights[2]

[1] Dept. of Electrical and Electronic Engineering, University of Newcastle, Newcastle NE1 7RU, UK

[2] Surrey Ion Beam Centre, University of Surrey, Guildford, Surrey GU2 5XH, UK

Keywords: Annealing, Ion Implantation, MESFET, Roughness

Abstract A MESFET structure has been used to determine the preferred annealing strategy for depletion mode devices in SiC. Based on Boron and Nitrogen implantation the device removes the need for multi-epitaxial layer growth. It is shown that the annealing strategy for the implants has a strong influence on the electrical characteristics of the device, and the adopted two step anneal technique increases the current density of the device by increasing the mobility of the carriers by an order of magnitude. Further, the reduction in temperature of the channel anneal step has reduced the surface roughness of the device to that of the unimplanted wafer. This decrease in the surface roughness gives a lower leakage current through the gate contact of the device, allowing a higher gate bias to be used.

1 Introduction

Since the introduction of commercial wafers in the early 90's there has been a dramatic rise in the interest of SiC as a material for high power semiconductor electronics [1]. Due to the high electrical breakdown field, high thermal conductivity and large electron saturation velocity it has become attractive for high temperature high power applications. The technology required for the fabrication of simple devices such as Schottky diodes has been demonstrated previously [2], while work on switching devices is at present less developed. Due to problems with the oxide interface, MOSFET technology is still immature [3] and so other switching devices are being pursued. Currently devices have been demonstrated based around FET technology such as, JFET [4], MESFET [5] as well as npn bipolar structures [6]. Generally devices are fabricated using epitaxially grown conduction channels, which is expensive with multiple epitaxial layers required on each wafer. The work presented is based on MESFET devices fabricated by ion implantation and subsequent annealing. The effect of annealing conditions on the carrier mobility, surface roughness of the die and the leakage of Schottky barrier diodes is discussed with respect to the fabrication of MESFET devices.

2 Device Design

In a MES controlled device the channel implant dose requires adjusting to achieve the maximum channel saturation current without loss of gate control. Too low an implant dose will result in low saturation current, whilst a high dose will result in breakdown under the gate contact before pinch-off has occurred. Another limiting factor is the leakage current through the gate contact, which often limits the applied bias to low levels. The leakage current through the gate contact is

dependant on the surface quality of the channel implant, and measures have to be taken prevent increased roughness as a result of the high temperature anneals used to activate the implants.
Figure 1 shows the cross-sectional view of the device. The channel implant was determined from the requirement to have a pinch off voltage below –10V with a channel thickness of 0.1μm. The implantation dose of $1.5x10^{14}$ cm^{-2} gives a free carrier concentration of $1.5x10^{18}$ cm^{-3} in the channel which equates to a pinch off voltage of –6.9V. The built in potential of a nickel Schottky contact on 4H SiC is 1.49V [2] and so pinch off should be possible with an applied bias of –5.4V. The p-well is implanted with Boron ions to a depth of 0.4μm with a ion density of $2x10^{17}cm^{-3}$. This is designed to remain undepleted even at the pinch-off voltage required to modulate channel conduction. The device has been simulated using commercial Medici TCAD software from TMA to fine tune the parameters prior to fabrication.

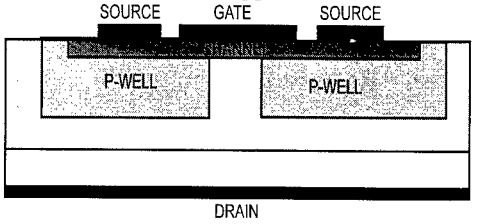


Figure 1 : Cross-section of the MESFET

3 Fabrication process

The devices in this work were fabricated using commercial n-type 4H-SiC material supplied by CREE Inc. The substrate is highly doped n-type ($N_D=1x10^{18}cm^{-3}$) with a lightly doped n-type epitaxial layer (10μm $N_D=3x10^{15}cm^{-3}$). Two sets of samples have been fabricated, one using a conventional implant and anneal process and the other with the 'two step' process. Both batches were patterned with photoresist and then implanted with Boron ions at energies and doses of 30KeV $1.8x10^{12}$ cm^{-2}, 60KeV $2.5x10^{12}$ cm^{-2}, 90KeV $6.3x10^{12}$ cm^{-2}, 130KeV $7.5x10^{12}cm^{-2}$ 180KeV $7.5x10^{12}cm^{-2}$. The first batch were then re-patterned with resist before being implanted with Nitrogen ions at the following energies and doses 25KeV $2.7x10^{12}$ cm^{-2}, 45KeV $3.6x10^{12}cm^{-2}$, 70KeV $8.4x10^{12}cm^{-2}$. The die were then annealed at 1700°C for 30 minutes under argon atmosphere in a JIPELEC RF induction furnace. This RF induction furnace has a very rapid ramp rate 50°C s^{-1}. The reactor chamber of the furnace comprises a graphite susceptor and cap, which is covered in SiC, with a SiC plate to maintain a silicon overpressure. This over pressure helps reduce silicon sublimation from the sample surface which occurs at temperatures over 900°C.
Batch two were annealed at 1600°C for 20 minutes under Argon as described previously after Boron implantation. The surface of the die were then recovered using low powered RIE with CHF_3:O_2 (90:5) plasma. The die were then patterned before Nitrogen implantation at the following energies and doses 25KeV $2.7x10^{13}$ cm^{-2}, 45KeV $3.6x10^{13}cm^{-2}$, 70KeV $8.4x10^{13}cm^{-2}$. The die were then annealed at 1300°C under argon as before.
Both batches of devices were then etched with RIE to recover the surface before further processing. Before each metalisation step the die is immersed in HF:H_2O (1:9) to remove the native oxide layer. Patterned Ni contacts were thermally evaporated on the upper surface (700Å Thickness) to act as source contacts and a 700Å blanket Ni contact on the rear of the substrate to form the drain. The contacts are then annealed at 1000°C under Ar atmosphere in a rapid annealing furnace to form low resistance ohmic contacts. The samples are chemically cleaned in H_2SO_4:H_2O_2 to remove contaminants prior to the gate Schottky contacts formed with 400Å of thermally evaporated nickel.

A dielectric layer of polyimide is spun onto the sample and patterned, before 500Å of gold is deposited as a pad metal to allow probing.

4 Results

The roughness of the implanted channel regions has been measured using optical interferometry. For the batch one devices the roughness of the nitrogen implanted regions is 10nm r.m.s. whilst the unimplanted sections of wafer has a roughness of 4nm. The roughness in the unimplanted regions is caused by the thermal cycling during annealing. The roughness in the implanted regions is lower than the values quoted in the literature [7] due to the low implantation dose. Leakage currents in excess of 12mA cm^{-2} were measured at a bias of –3V at the gate contacts. The resistance of the implanted channel has been measured using the TLM method. The contact resistance and sheet resistance of batch one were found to be in the region of 10Kohms. The doping profile of the channel has been determined with C-V profiling, giving a donor density of $1.2x10^{17}cm^{-3}$ and a channel depth of 0.08μm. This can be seen in figure 2. From this the mobility of the carriers in the channel of the device was determined to be $5cm^2V^{-1}s^{-1}$. Modulation of the drain current was achieved, although the current levels were very low. This is due to the mobility of the carriers in the channel, and can be seen in figure 3.

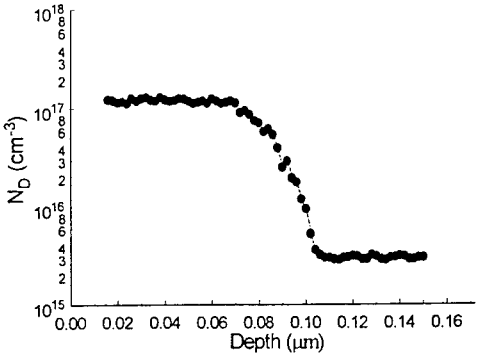


Figure 2 : C-V profiling of the channel implant on the Batch 1 devices

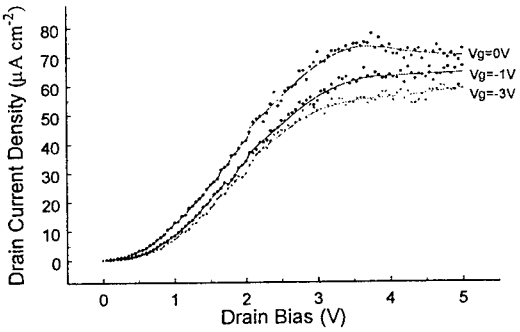


Figure 3 : Batch 1 characteristics

The two step annealing process used on the second batch of devices was designed to lower the surface roughness of the die and to increase the carrier mobility. It has been demonstrated previously [8] that the roughness of nitrogen implanted regions becomes more significant for annealing above 1600°C, where large undulations appear on the upper surface with heights close to 100nm. This is a severe problem in depletion mode devices where the channel is often thinner than 100nm. The reduction in temperature also gives an improvement in mobility of 38% when annealing at 1300°C compared to 1700°C. The increase in the implant dose is to counter the decrease in the electrical activation observed after lower temperature anneals.

The roughness of the batch two samples is 4nm, in both the implanted and unimplanted regions. Leakage currents of 10mA cm^{-2} at –6V bias were measured at the gate contacts. The mobility of the carriers in the batch two devices is $50cm^2V^{-1}s^{-1}$. The limited bias available at the gate contact has not proved to be sufficient to cause pinch off in the device, although a current modulation of approximately 20% has been observed.

	Batch 1	Batch 2
Annealing Conditions	1700°C 30 minutes	1600°C 20 minutes 1300°C 20 minutes
Surface Roughness	10nm	4nm
Schottky Leakage	12mA cm^{-2} at –3V	10mA cm^{-2} at –6V
Mobility	5 $cm^2V^{-1}s^{-1}$	50 $cm^2V^{-1}s^{-1}$

Table 1 : Results summary

5 Conclusions

The two step annealing process developed in this study has shown a reduction in the surface roughness of the annealed die. In contrast to the high temperature short-burst annealing favoured in high implant dose material ($1x10^{16}cm^{-2}$) it appears that conduction channel devices benefit from lower annealing temperature for a longer period. This may be linked to the implanted ions having to move further within the implanted region to form a homogenous doping. At high dose the ions may coalesce and form islands which will be detremental to electron transport behaviour when annealed for long periods.

The reduction in surface roughness has enabled a higher gate bias to be used on the device, which will enable a higher current modulation to be achieved. In order to increase the bias further, alternative surface recovery techniques will have to be employed. Previous work has shown the leakage current through a Schottky barrier diode is lowest for surfaces which have subject to sacrificial oxidation and strip [9], and it is planned to utilise this in further work on MESFET technology.

References

[1] Cassidy, JB, Johnson, RW, Solid State Electronics, **39/10**, (1996), p1409
[2] D J Morrison, N G Wright, A B Horsfall, C M Johnson, A G O'Neill, A P Knights, K P Hilton, M J Uren, Submitted to Solid State Electronics
[3] J Wang, B W Williams, IEEE T Electron Dev, **46/3**, (1999), p589
[4] C W Hatfield, G L Bilbro, S T Allen, et al, IEEE T Electron Dev, **45/9** (1998) p2072
[5] K Moore, M Bhatnagar, C Weitzel, et al, Mat. Sci. Forum, **264-2**, (1998) p957
[6] N G Wright, C M Johnson, A G O'Neill, A B Horsfall, S Ortolland, K Adachi, A P Knights, P.G.Coleman, Proceedings of the MRS, Spring 2000
[7] S Ortolland, C M Johnson, N G Wright, A P Knights, A J Kestle, Submitted to J. App. Phys.
[8] H Wirth, D Panknin, W Skorupa, E Niemann, App Phys Lett, vol. **74**, (1999), p979
[9] D J Morrison, A J Pidduck, V Moore, P J Wilding, K P Hilton, M J Uren, C M Johnson, Mat Sci Forum, **338-342** (2000) p1199

Materials Science Forum Vols. 353-356 (2001) pp. 711-714
© 2001 Trans Tech Publications, Switzerland

Source Resistance Analysis of SiC-MESFET

M. Arai[1], M. Ogata[1], H. Honda[2], H. Sawazaki[1],
A. Nakagawa[2] and M. Kitamura[3]

[1] Microwave Division, New Japan Radio Co., Ltd.,

[2] Advanced Technology Center, New Japan Radio Co., Ltd.,

[3] Synergic Business Research Center, New Japan Radio Co., Ltd.,

Keywords: MESFET, Ohmic Contacts, Rapid Thermal Annealing (RTA), Sheet Resistance, Silicides, Source Resistance

Abstract. We fabricated a 0.5μm gate MESFET with a combination of optical and electron-beam lithography technique. A cutoff frequency and a maximum oscillation frequency were 2.8GHz and 8.6GHz, respectively. And we measured the source resistance of MESFET and found that it was 76Ω. This value was about 4 times higher than that of 22.6Ω calculated by using TLM results, the specific contact resistance of ρ_c=2.2$\times$10^{-5}Ω $\cdot$ cm^2 and the sheet resistance of ρ_{sh}=657Ω/$\square$. This difference between measured 76Ω and calculated 22.6Ω was caused by the high value of ρ_{sh} under the contact, which could not be obtained from TLM measurements. Nickel ohmic contact reacts with SiC underneath and makes Ni-silicide which penetrates by 0.2μm into the n$^+$ contact layer and reduces its thickness. This Ni-silicide formation increased ρ_{sh} under the contact by a factor of ten compared to that of the initial contact layer.

Introduction

SiC is a promising material for high-power and high-frequency devices, due to the combination of its high breakdown electrical field, high electron saturation velocity, and high thermal conductivity. High frequency SiC devices will find application in power amplifier for base station transmitters for wireless telephone systems, High Definition Television (HDTV) transmitters, power modules for phased-array radars, and other applications. A. W. Morse et al. reported that a UHF Silicon Carbide module provide 400W average output power and can be used in HDTV Transmitter [1]. MESFET is a promising candidate for the first SiC commercial product, because its simple structure and small chip size make possible to produce FET even though some defects are present in the substrate. A cut-off frequency of ft=24GHz and maximum operation frequency of fmax=56GHz on MESFET has been reported [2], and an RF output power density of 4.3W/mm at 10GHz has been demonstrated [3].

In this paper, we study a source resistance of MESFET fabricated on semi-insulating substrate with epitaxial layers. Source resistance is one of the important technologies to improve the RF characteristics of high frequent FETs. Source resistance is measured as a function of gate source spacing, and it is separated into contact resistance element and bulk resistance element. These values are comparing to the expected source resistance calculated by using TLM data.

Fabrication process and electrical properties of FET

We used an 4H-SiC semi-insulating wafer with epitaxital layers produced by Cree. This epitaxial wafer produced by CREE consists of semi-insulating substrate and a 0.3μm n-channel layer having a doping density of 3.0$\times$10^{17}/cm^3, a 0.2μm n+ cap layer having a doping density of 1.0$\times$10^{19}/cm^3. At first, mesa structure and recess structure are formed by plasma etching. Then sacrificial oxidation layer is grown 10nm in thickness. Nickel metal is deposited by electron beam evapolation and forms ohmic contact by thermal annealing at 950°C for 2min in Argon atmosphere by Rapid Thermal Annealing apparatus. A specific contact resistivity of 2.2$\times$10^{-5}Ω $\cdot$ cm^2 and contact sheet resistance of 600Ω/$\square$ are obtained from Transmission Line Model (TLM) fabricated on the same wafer. Finally, Ti/Pt/Au

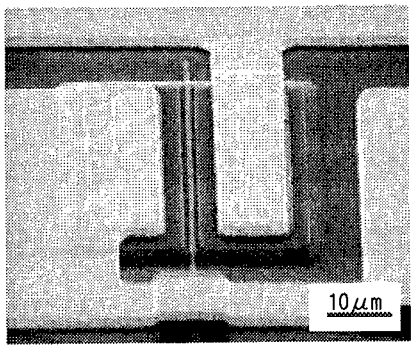


Fig.1 SEM photograph of a 0.5μm gate SiC-MESFET with a 50μm gate width.

gate metal is deposited by electron beam evapolation and formed by lift-off process. Fig.2 shows the enlarged microscope photography.

DC and small signal RF characteristics of the FET

Fig.2 shows a static electrical characteristic of a 0.5μm gate MESFET with the 50μm gate width. The gate-source and gate-drain spacings are 0.3μm and 0.7μm respectively. The saturation drain current (Idss) and transconductance (gm) are 256mA/mm and 12.5mS/mm respectively. Drain current is well pinched-off at –26V gate voltage. Fig.3 shows a small RF signal characteristic of the FET. A cut-off frequency of 2.8GHz and a maximum operation frequency of 8.6GHz are obtained. These results, lower than expected, seem to be caused by the immature fabrication process and the parasitic effects.

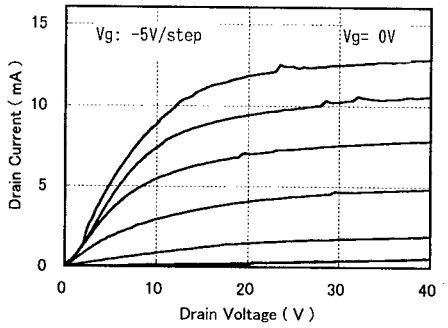


Fig.2 I-V characteristic of a 0.5μm gate MESFET with a 50μm gate width, gate to source spacing of 0.3 μm and gate to drain spacing of 0.7μm. A saturation draincurrent and a transconductance is 256mA/mm and the maximum transcondactance is 12.5mS/mm.

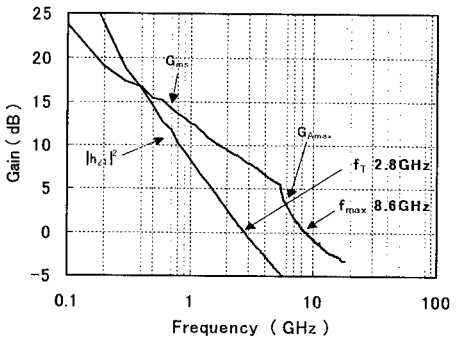


Fig.3 A small signal RF characteristics of the 0.5μm gate MESFET at gate voltage of –12V and drain voltage of 40V.

Source resistance of the MESFET

The source resistance reduction is one of the important features to improve the electrical properties of high frequency devices. The source resistance of a MESFET is obtained from the Igs-Vgs characteristics measurement by dividing the gate threshold voltage difference (ΔVgs) by the current increase (ΔIs) as the drain voltage is changed. Fig.4 shows the source resistance of the MESFET as a function of gate to source spacing (Lgs). Doted circles and a doted line are experimental data and an approximated experimental line has been obtained by a least squares method. SEM photographs were used to determine the gate to source spacing. The source contact resistance of 76Ω is obtained from the vertical intercept of approximated line and provides a major part of the total resistance. The source resistance of the MESFET consists of a bulk resistance in channel layer and a contact resistance of metal/SiC interface. The expected source resistance (R_s) is given by

$$R_s = \rho_{chan}\frac{L_{gs}}{W_g} + \frac{\sqrt{\rho_{con}\times\rho_c}}{W_g} \qquad (1)$$

where ρ_{chan} is the channel layer sheet resistance , Wg is the gate width, ρ_{con} is the sheet resistance of the contact layer, ρ_c is the specific contact resistance. In this study, Transmission Line Model (TLM) pattern and van der Pauw pattern are fabricated on the same plane of the FET to determine the sheet resistances and the specific contact resistance. Fig.6 shows TLM linear plot of the contact resistance as a function of Ni contact spacing, whose contact pad is 30μm long $\times$100μm wide, and the spacing between contact pads is 10μm, 20μm, 40μm, 80μm, 160μm. In the TLM method, the data is fitted to a straight line whose vertical intercept is proportional to the contact resistance (R_c) and whose slope is proportional to the contact layer sheet resistance. The horizontal intercept of fitted line is " transfer length", it will give the current distribution capability underneath the contact pad. In our TLM pattern, the contact spacing is so large that the measured resistance value is several hundred ohms, much larger than the R_c we

have to measure accurately, and pad area is too small to measure the contact resistance by Kelvin probe method with using four needles probe. Then our TLM data should include some measurement tolerances

In ideal case, the specific contact resistance obtained from the vertical axis intercept and the transfer length, and the contact layer sheet resistance obtained from the slope is $2.2\times10^{-5}\,\Omega\cdot cm^2$ and $657\,\Omega/\square$, respectively. The channel sheet resistance is obtained as $3060\,\Omega/\square$ from Van der Pauw method. When these measurement results and gate width are substituted into Eq.(1), the expected source resistance shown in Fig.4 can be calculated. Fig.4 indicates that the source contact resistance of $76\,\Omega$ is about 4 times higher than that of $22\,\Omega$ obtained by the vertical intercept of the expected line. In the following session we will discuss about the reason why the contact resistance is so different.

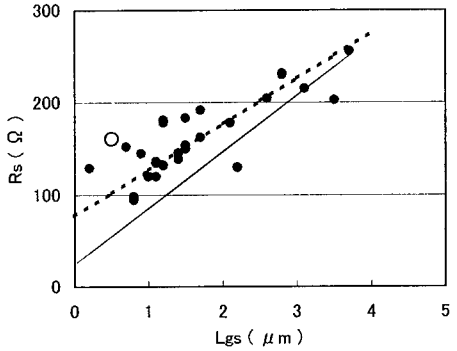


Fig.4 Source resistance of the MESFET as a function of gate to souce spacing (Lgs).

(●: Experimental data, -----: Experiment (method of least squares), ——: Expected line, ○: [4])

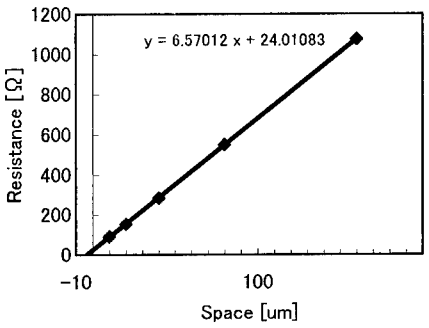


Fig.5 TLM linear plot of the contact resistance as a function of contact spacing for Ni metalization, which is fabricated on the same plane as the FET chip.

Discussion

As a result of source resistance measurement, the source contact resistance of $76\,\Omega$ is about 4 times higher than that of $22\,\Omega$ which is obtained from the vertical intercept of the expected line calculated from Eq.(1) using the results of TLM. An open circle in Fig.5 is a source resistance of the SiC-MESFET reported by N.Rorsman et al. [4]. Their source resistance shows a good agreement with our experimental results because their ohmic contact was formed by annealing nickel at 950°C with RTA furnace as same process as us.

C. Arnodo et al. reported that, after the nickel metal on SiC is annealed at 950°C Si is extracted from the substrate and a $NiSi_2$ layer is formed at the metal/SiC interface [5]. Fig.7 shows an Auger analysis result of the Ni contact samples annealed at 950°C for 2min in Ar ambience in our experiment, and indicates that the silicide reaction occurs at Ni/SiC interface. We believe that this silicide is responsible for the low contact resistivity. It is obvious, however, that the nickel silicide is formed by consuming silicon in SiC substrate, and thus, the composition of SiC at the Ni/SiC interface would sift towards a silicon-depleted direction and isolated graphite carbon atoms would be left behind. Fig.8 shows a schematic diagram of metal/SiC interface before high temperature annealing (a), and after the annealing (b). The nickel-silicide layer formation causes the reduction of the contact layer thickness, which results in the increasing of the sheet resistance underneath the contact metal. Eq. (1) shows that the contact resistance change in proportion to the root square of sheet resistance. Then the difference between the $76\,\Omega$ to the $22\,\Omega$ seems to be caused by the sheet resistance change underneath the contact. When we calculate the reduction of contact layer thickness from the change of source resistance from $22\,\Omega$ to $76\,\Omega$, then it suggests that the contact layer thickness have been reduced to one-tenth of its initial contact layer thickness. This silicide reaction and the reduction of contact layer lead to the significant contact resistance difference between the source contact of the FET and calculated contact resistance. T. Nakamura, et al. reported that $NiSi_2$ metal contact formed on SiC by electron beam evaporation realize ohmic characteristic without the consumption SiC substrate for annealing temperature from 800°C to 900°C[6]. Such ohmic contact formation process with controlled silicide process will be expected to improve the electrical characteristic of SiC-MESFET. When we calculate the specific contact resistivity in TLM method, the sheet resistance underneath the contact is assumed to be same value as the initial contact layer, and the horizontal intercept are obtained by the extrapolation of the solid line from the first quadrant of Fig.6. If the sheet resistance underneath the contact is larger than the initial sheet resistance, the slope of the line at the second quadrate become much steeper than that of the first

one. So, the specific contact resistivity is apt to be overestimated by normal TLM method. To measure the accurate specific contact resistivity, we have to take the accurate sheet resistance underneath the contact into consideration [7].

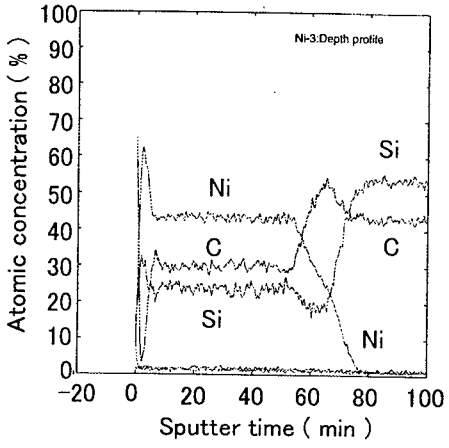


Fig.7 Auger profile on a Ni ohmic contact formed by RTA annealing at 950°C for 2 min in Ar ambiante.

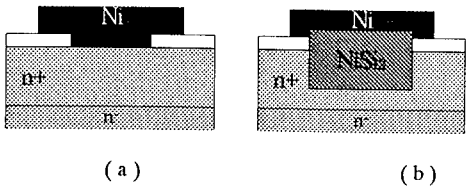


Fig.8 Schematic cross section picture of metal/SiC interface before high temperature annealing process (a), after high thermal annealing process (b).

Summary

We fabricated a sub-micron gate length SiC-MESFET with optical and electron-beam lithography apparatus. A cut-off frequency of 2.8GHz and maximum operation frequency of 8.6GHz was obtained from the 0.5μm gate MESFET with the gate width of 50μm. The source resistance of the FET is analyzed and is revealed that the source contact occupies the major part of the total resistance. The source contact resistance of 76Ω is about 4 times as high as that of 22Ω which is calculated by using the specific contact resistance and the sheet resistances measured from TLM and Van der Pauw pattern. Silicide reaction at the nickel and SiC interface causes the reduction of the contact layer thickness and increases the sheet resistance of cap layer. In order to reduce the source resistance of FET, development of process technique to form ohmic contact preventing from silicide reaction is needed.

Acknowledgement

The authors wish to thanks to Dr. C. Kimura and H. Tamai for their valuable technical discussions and encouragements..

This work is performed under the management of FED as a part of the MITI NSS Program(R&D of Ultra-Low-Loss Power Device Technologies) supported by NEDO.

References

[1] A. W. Morse, P. M. Esker, S. Sriram, J. J. Hawkins, L. S. Chen, J. A. Ostop, T. J. Smith, C. D. Davis, R. R. Barron, R. C. Clarke, R. R. Siergiej and C. D. Brandt: IEEE MTT-S Digest, (1997) , p.53.

[2] R. J. Trew: "Wide Bandgap Semiconductor Transistors for microwave power Amplifiers" microwave march 2000, p.46.

[3] S. T. AlLen, W. L. Pribble, T. S. Alcorn, Z. Ring, and J. W. Palmour : IEEE MTT-S Digest (1999), p. 321.

[4] N. Rorsman, J. Eriksson and H. Zirath: Material Science Forum Vols. 338-342, (2000), p.1259.

[5] C.Arnodo, S. Tyc, F. Wyczisk and C. Brylinski: Inst. Phys. Conf. Ser. No 14. chapter 3, (1995), p.577.

[6] T. Nakamura, H. Shimada and M. Sato: Material Science Forum Vols. 338-342 (2000), p.985.

[7] G. K. Reeves and H. B. Harrison: IEEE Electron Device Lett. Vol. EDL3, (1982), p.111.

Materials Science Forum Vols. 353-356 (2001) pp. 715-718
© 2001 Trans Tech Publications, Switzerland

Design and Implementation of RESURF MOSFETs in 4H-SiC

S. Banerjee, K. Chatty, T.P. Chow and R.J. Gutmann

Center for Integrated Electronics and Electronics Manufacturing,
Rensselaer Polytechnic Institute, Troy NY 12180-3590, USA

Keywords: MOSFET, RESURF

Abstract. High-voltage lateral RESURF MOSFETs in 4H-SiC have been designed and fabricated. The devices block 900 V and have a specific on-resistance of 0.5 Ω-cm^2. The optimum RESURF dose in 4H-SiC is almost an order of magnitude higher than that of silicon but this dose leads to gate oxide breakdown due to a very high electric field in the oxide. An alternate design, which helps to suppress high gate oxide field with two zones in the RESURF region, is discussed.

1 Introduction

Power MOSFETs in silicon carbide(SiC) have the potential of lower specific on-resistance, faster switching times and high-temperature operation due to superior material qualities of SiC (wide bandgap $\sim$ 3-3.2 eV, high breakdown field $\sim$ 2.5-3 MV/cm and large thermal conductivity $\sim$ 4-5 W/cm-K) [1]. SiC lateral power MOSFETs have been demonstrated in both 4H [2, 3] and 6H [4] polytypes. We have reported lateral RESURF MOSFETs in 4H-SiC that block above 900 V with a specific on-resistance of 0.5 Ω-cm^2 and showed that though the optimum dose in the RESURF layer of 4H-SiC is $\sim 10^{13}$ cm^{-2} [3]. However, such high dose has resulted in excessively high electric field in the gate oxide which leads to breakdown in the oxide [4, 5]. In this paper, we discuss in detail the fabrication process and design of the devices. We also show that by using two zones in the RESURF region, the oxide breakdown problem can be avoided and high breakdown voltage can be achieved.

2 Device Structure and Fabrication Process

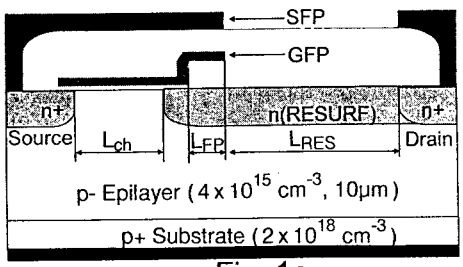


Fig. 1a

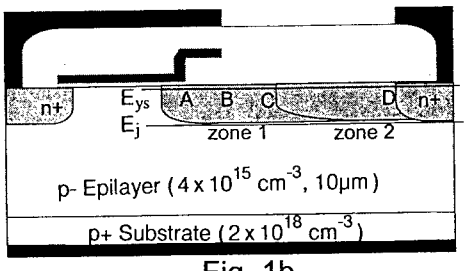


Fig. 1b

Fig. 1. a) Lateral RESURF MOSFET structure indicating the gate field plate(GFP) and source field plate(SFP). b) Two-zone RESURF MOSFET structure indicating the high field points as discussed in Sec. 4

Fig. 1a shows the schematic cross-section of a lateral RESURF MOSFET in SiC with a gate field plate and a source field plate. The gate field plate (GFP) is implemented by extendig the

polysilicon on the field oxide while the source field plate (SFP) is implemented by extending the source metal on the inter-level dielectric(ILD) between polysilicon gate and source metal. The field plates protect the gate corner from high electric field by spreading the depletion layer at that point and for a single-step field plate either one of them can be used. Fig. 1b shows the schematic cross-section of a RESURF MOSFET with two zones and indicates the positions of the peak electric field in the device which is dicussed in sec. 4.

Single-zone RESURF MOSFETs were fabricated on p/p+ 4H-SiC wafers with epitaxial thickness and doping of 10 μm and 4-6$\times 10^{15}$ cm^{-3} respectively. The devices have single-level field plating with either the gate field plate or the source field plate. 1.5 μm thick oxide was deposited and annealed to be used as a mask for the source/drain and RESURF region implants. Phosphorus (4×10^{15} cm^{-2}, $\sim$0.5 μm) was implanted in the source/drain regions; while a light dose (1×10^{13} cm^{-2}) and a heavy dose(5×10^{13} cm^{-2}) of nitrogen were used in the RESURF region in different wafers. The masking oxide was stripped and the implants were activated at 1200°C in argon for 1 hour which is expected to give about 10-20% activation. 600 nm high temperature oxidation (HTO) was deposited as field oxide, reoxidized in steam and patterned to expose the active area. Next, gate oxide (HTO) was deposited (100 nm or 200 nm) and then reoxidized in steam, first at 1100^{0}C for 3 hours, then at 950^{0}C for 1 hour and finally pulled out at 800^{0}C in steam ambient. Heavily doped polysilicon was used as gate and 1 μm thick oxide as the inter-level dielectric (ILD). Al/Ni/Al layers were used as contact and were annealed at 1000^{0}C for 2 minutes in argon.

3 Results and Discussion

Fig. 2a shows the blocking characteristics of the devices and the results for different variations of the RESURF dose, gate oxide thickness and field plate structures, which are summarized in Table 1. The gate field plate devices with light RESURF dose (1×10^{13} cm^{-2}) and thicker oxide (200 nm) block 900 V for 16 μm RESURF length while the devices break down at low voltage ($\sim$50-300 V) for thinner oxides (100 nm) or higher RESURF dose (5×10^{13} cm^{-2}). The low breakdown voltage of the devices is attributed to a high electric field at the gate corner and breakdown of the oxide [5]. The field oxide thickness (600 nm) is optimized for reducing the electric field at the gate edge while the ILD (1 μm) is thicker than the optimum and was chosen for sufficient isolation between the gate and the source/drain contacts. This explains the lower breakdwon voltage obtained from the source field plate structure.

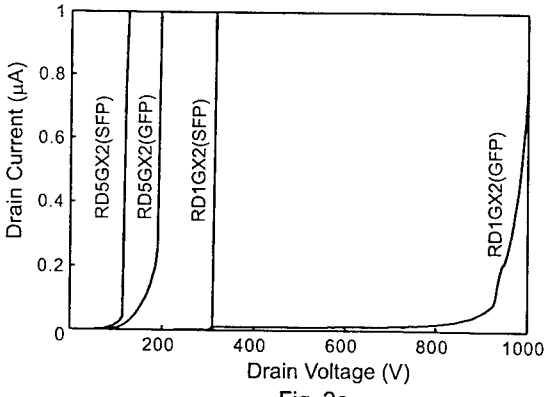


Fig. 2a

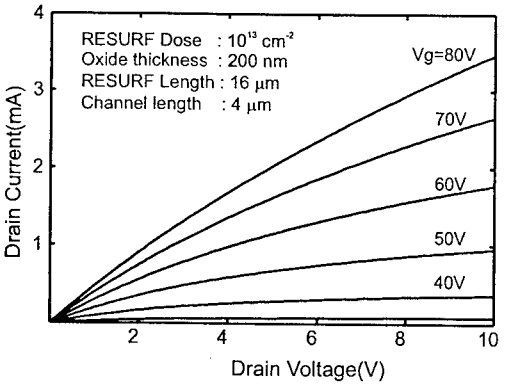


Fig. 2b

Fig. 2. Experimental results. a)Blocking characteristics of MOSFETs with different RESURF dose, gate oxide thickness and field plate structures. b)Forward I-V characteristics of MOSFET that block high voltage.

Table 1. Summary of experimental results obtained from various processing and design variations.

Sample	RESURF Dose(cm^{-2})	Gate oxide (nm)	RESURF sheet resistance(KΩ/sq.)	Breakdown Voltage(V)		
				GFP	SFP	Scaling with L_{RES}
RD5GX1	5×10^{13}	100	18-20	50-100	50-100	No
RD5GX2	5×10^{13}	200	18-20	100-200	50-200	No
RD1GX1	1×10^{13}	100	70-90	100-200	50-200	No
RD1GX2	1×10^{13}	200	70-90	800-900	300-500	50 V/μm (GFP)

The forward I-V characteristics of devices from sample RD1GX2 with 16 μm RESURF length and 4 μm channel length are shown in Fig. 2b. The effective channel width of the device is 610 μm and the specific on-resistance is $\sim$0.5 Ω-cm^2 (active area $\sim 2.9\times10^{-4}$ cm^2). The resistance contributions from different components are estimated from the inversion layer mobility(10-14 cm^2/V-s), RESURF region sheet resistance ($\sim$75 kΩ/sq.), source/drain sheet resistance($\sim$0.9 kΩ/sq.) and the contact resistance ($\sim$ 0.07 mΩ-cm^2) extracted from the test structures. The RESURF region contributes to 80% of the total resistance for the 16 μm RESURF length devices, while the channel region accounts for the other part; the source/drain region series resistance is negligible for these devices. The improvement in the on-resistance, compared to earlier devices [3] is mainly due to the improvement in inversion layer mobility(14 cm^2/V-s compared to 0.5 cm^2/V-s) achieved by an improved oxidation process [6]. The devices also demonstrate that phosphorus is the appropriate implant species for n^+ layers (source/drain region) and nitrogen for lightly or moderately doped n-type layers(RESURF region) as suggested earlier [3].

4 Two-zone RESURF MOSFET

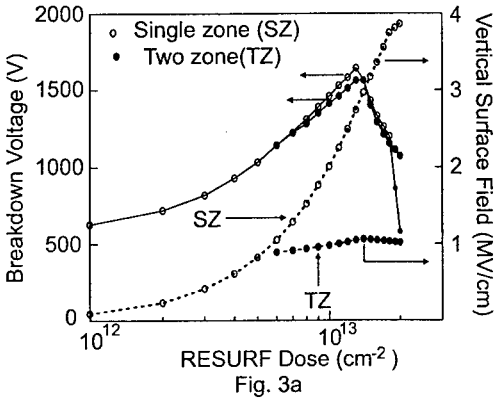


Fig. 3a

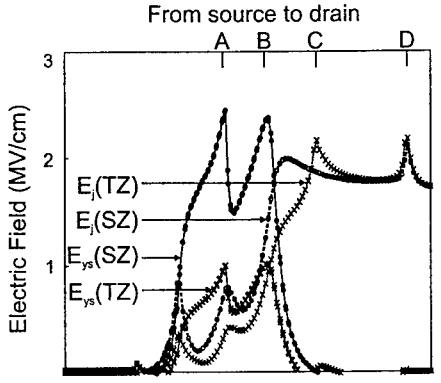


Fig. 3b

Fig. 3. Comparison between single-zone and two-zone RESURF MOSFETs; RESURF Length : 16 μm, gate oxide thickness : 200 nm, optimized field oxide thickness, dose below gate in two-zone : 5×10^{12} cm^{-2}; second zone : 4 μm from field plate. a)Simulated avalanching voltage and vertical component of surface electric field(E_{fs}). b)Field at junction(E_j) and vertical component of field at surface (E_{ys}) for dose = 10^{13} cm^{-2}. A : Gate edge, B : Field plate edge, C : Edge of second zone in two-zone RESURF, D : Drain edge (indicated in Fig. 1b)

The high breakdown field (2.5-3 MV/cm) of SiC leads to the problem of gate oxide breakdown before there is avalanching in the semiconductor and this will lead to instability in the device and permanent failure. One solution to avoid oxide breakdown is to have a lighter dose in the RESURF region, but this reduces the avalanching voltage and increases the specific on-resistance of the device. A graded doping in the RESURF region increasing from the gate edge

to the drain edge can be used to minimize the surface electric field. The specific on-resistance of the device for a particular avalanching voltage is also reduced in such a structure. The graded doping can be approximated by multiple zones of progressively higher dose, the simplest of which is a two-zone RESURF MOSFET with a lighter dose below the gate overlap and field plate and a heavier dose in the rest of the RESURF region. Fig. 3a shows the simulated avalanching voltage and vertical component of the electric field at surface(E_{ys}) for different RESURF doses in case of single zone and two zone RESURF MOSFETs.

For the maximum breakdown voltage, the RESURF dose has to be slightly above 10^{13} cm^{-2}. In that case, the field at the gate edge(point A in Fig. 1b) in the case of a single-zone device is above 2 MV/cm which translates to 5 MV/cm (field in oxide is multiplied by the ratio of dielectric constant of oxide and SiC; $\epsilon_{SiC} = 9.7$) in the oxide. Also, the field increases sharply with the dose; while in the device with two zone, the field at the gate edge is independent of the dose in the second zone and remains almost constant at a much lower value depending on the dose in the first zone. The breakdown voltage in the two cases is almost the same. Fig. 3b shows the field distribution at breakdown (~1400 V) for a particular RESURF dose (10^{13} cm^{-2}) in the two structures. The vertical component of the field at the SiC surface(E_{ys}) and the total field at the junction(E_j) are plotted (Fig. 3b), indicating the high field points in the device (Fig. 1b). The field distribution close to the drain is similar in both cases but the field below the gate in the single-zone device is considerably higher than that in the two-zone device. This demonstrates that with two zones, a high dose in the second zone does not affect the field below the gate. So, a lower surface field and similar avalanching voltage can be achieved in the two-zone device with shorter RESURF length and higher RESURF dose, compared to that in the single-zone device. Both the structures have been optimized by numerical simulation to achieve similar breakdown voltage(1400 V) and surface field(1.2 MV/cm); the device with two RESURF zones has about 30% lower specific on-resistance compared to the single-zone device.

5 Conclusions

High-voltage 4H-SiC lateral RESURF MOSFETs that block above 900 V with a specific on-resistance of 0.5 Ω-cm^2 have bee designed and fabricated. With a single RESURF zone in the MOSFET, the maximum RESURF dose is limited by oxide breakdown and not by avalanching in SiC. Simulation results demonstrate that the electric field below the gate is suppressed if two zones are used in the RESURF region with a lower dose below the gate and the field is not a strong function of the dose in the second zone.

Acknowledgement : The authors gratefully acknowledge the support of this work by DARPA under Contract # MDA972-98-C-0001, Philips Research, Briarcliff Manor, NY, the Office of Naval Research under MURI Contract # N00014-95-1-1302, and NSF Center for Power Electronics Systems under Award # EEC-9731677.

References

[1] C. E. Weitzel *et al.*, IEEE Trans. on Electron Devices 43(1996), p. 1732.

[2] J. Spitz, M. R. Melloch, J. A. Cooper, Jr., and M.A. Capano, IEEE Electron Device Lett. 19(1998), p. 100.

[3] K. Chatty, S. Banerjee, T. P. Chow, and R. J. Gutmann, IEEE Electron Device Lett. 21(2000), p. 356.

[4] A. K. Agarwal, N. S. Saks, S. S. Mani, V. S. Hegde and P. A. Sanger, Mater. Sci. Forum 338 – 342(2000), p. 1307.

[5] S. Banerjee, K. Chatty, T. P. Chow and R. J. Gutmann, Device Research Conf., Denver, USA, 2000.

[6] S. Banerjee, K. Chatty, T. P. Chow and R. J. Gutmann, Electronic Materials Conf., Denver, USA, 2000.

Materials Science Forum Vols. 353-356 (2001) pp. 719-722
© 2001 Trans Tech Publications, Switzerland

Comparison of Super-Junction Structures in 4H-SiC and Si for High Voltage Applications

K. Adachi[1,3], C.M. Johnson[3], H. Ohashi[4], T. Shinohe[1,4], K. Kinoshita[4] and K. Arai[1,2]

[1] UPR Ultra-Low-Loss Power Device Technology Research Body, 1-1-4 Umezono, Tsukuba, Ibaraki 305-8568, Japan

[2] Electrotechnical Laboratory, 1-1-4 Umezono, Tsukuba-shi, Ibaraki-ken, Tokyo 305-8568, Japan

[3] University of Newcastle, Newcastle upon Tyne NE1 7RU, UK

[4] Toshiba Corporation, 1 Komukai Tohisba-cho, Saiwai-ku, Kawasaki 210-8582, Japan

Keywords: High Voltage Devices, Simulation, Super Junction Structure (SJS)

Abstract In this paper super-junction structures (SJS), which realise very low on-resistance, R_{on}, for a given breakdown voltage, V_{br}, are studied and comparisons made between 4H-SiC and Si. Simplified expressions are derived which describe the electric field distribution in the SJS under conditions where a charge imbalance exists in the drift region. These expressions are employed in determining the structure parameters which minimise the on-resistance of the SJS for a given breakdown voltage. The results show that SiC has more than 140 times lower Ron and smaller effects of pillar charge imbalance than Si, for the same V_{br}. In addition, the design margin for the pillar doping is defined and derived. It is shown that SiC has a 3.3 times higher margin than Si and it is concluded that the SJS is well suited to wide-bad-gap semiconductor materials.

1. Introduction

The operation of SJS [1] (for example CoolMOS™ [2]) is based on the concept of charge compensation between heavily doped p-type and n-type pillars, which repeat across the width of the structure. Fig.1 shows a cross section of a half cell of the SJS used in this study. The p and n pillars, p+ source and n+ drain regions have net impurity concentraions of N_a, N_d, N_{as} and N_{dd} respectively. The half pillar width, w, is designed to be much smaller than the pillar depth, d. Upon application of drain voltage, V_d, the pillars become fully depleted by lateral extension of the depletion region from the p-pillar – n-pillar junction at low drain bias. Since the depleted pillars contain no net charge, further application of drain voltage is evenly supported throughout the pillar, rather like a capacitor with plate spacing d. A primary theory of SJS thus gives $V_{br}=E_c*d$ and $R_{on}=w*V_{br}/\mu\varepsilon E_c^2$, where E_c is the critical electric field, μ is the carrier mobility and ε is the dielectric constant [1, 3]. It is clear that for high voltage devices, R_{on} will be much lower than for conventional FET structures (where R_{on} varies roughly as $V_{br}^{2.5}$).

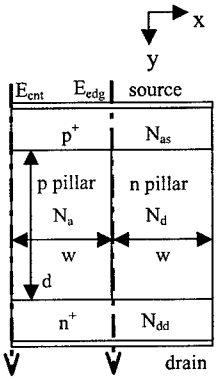


Fig.1 SJS for study

Such a simplified model ignores a number of important features: 1) the true electric field distribution in the pillars is non-uniform and is heavily influenced by pillar width and doping, 2) charge imbalance between the pillars affects the electric field distribution and reduces the breakdown voltage [3], 3) depletion caused by the built-in potential reduces the available conduction area, leading to an increase in on-resistance [4]. Optimisation of the structure, to obtain the minimum on-resistance for a given breakdown voltage, is thus a complex task. It is clearly possible to achieve this optimisation by using TCAD simulation over a large number of structural variants. This is, however, very time-consuming. The method adopted in this paper makes use of simplified analytical expressions, which are employed in an iterative optimisation routine. The program runs on a PC and allows rapid optimisation of SJS design.

2. Electric field distribution in pillars

The complex two-dimensional nature of the electric field distribution in the pillars is best illustrated using TCAD simulation. Fig.2 shows the electric field distribution in SJS in the case of perfect charge balance (a) and imbalance (b) between p and n pillars. Note that perfect balance produces a uniform y-directed electric field in the pillar, while imbalance creates a trapezoidal distribution. It is found that two ionisation paths dominate breakdown through impact generation. One is at the centre of the pillar (E_{cnt} in Fig. 1) and the other is at the pn pillar junction (E_{edg} in Fig, 1).

2.1 Simplified field distribution (perfect doping balance)

When V_d increases, the depletion region extends from the pn pillar junction in the x-direction. At a certain voltage, V_{df}, the depletion region reaches the centre of the pillar:

$$V_{df} = \frac{qN}{\varepsilon} w^2 - V_{bi} \qquad (1)$$

where $N=N_a=N_d$. The x component of the electric field at the pillar junction, E_{cnt_x}, increases with V_d up to $V_d=V_{df}$, but for higher V_d it saturates at:

$$E_{edg_x} = \frac{qN}{\varepsilon} w \qquad (2)$$

The y component of E_{edg}, E_{edg_y}, is derived by using a parallel plate capacitor approximation:

$$E_{edg_y} = V_d / d . \qquad (3)$$

Therefore the magnitude becomes

$$E_{edg_mag} = \sqrt{E_{edg_x}^{\ 2} + E_{edg_y}^{\ 2}} . \qquad (4)$$

Ecnt has no x component of electric field due to the symmetrical nature of the structure. The peak electric field, E_{cnt_junc}, appears at the pn junction at the end of the centre of the pillars. Its magnitude increases with increasing V_d and then saturates once $V_d=V_{df}$. E_{cnt_junc} is assumed to behave as a 1D pn junction and is given by:

$$E_{cnt_junc} = \alpha \frac{qN_{dd}}{\varepsilon} w \qquad (5)$$

where α is a value related to the ratio of N_a to N_{dd} and varies from 0.5 to $1/\sqrt{2}$. The electric field remote from the pillar ends, E_{cnt_flat}, starts to increase at $V_d>V_{df}$, and is given by:

$$E_{cnt_flat} = (V_d - V_{df}) / d . \qquad (6)$$

2.2 Simplified field distribution (unbalanced doping)

In practice, tolerances in the fabrication process will result in some residual net charge (an error charge) in the pillars. This alters the flat electric field distribution to a trapezoidal one. The doping error, err, is defined through $N_a=(1+e_{rr})*N_d$, and therefore the net charge is $Q_{net}=q(N_a-N_d)=q*e_{rr}*N_d$. The distribution of electric field with error is shown in Fig.3 (c) and (d) for E_{edg} and E_{cnt} respectively. E_{edg_s} and E_{edg_d} are values of E_{edg} at source and drain side, while E_{cnt_s} and E_{cnt_d} are the corresponding values for E_{edg}. In the case where $N_a>N_d$ the n pillar becomes fully depleted at $V_d=V_{df}$ (Eq. 1) while the p pillar still contains an undepleted charge. For $V_d>V_{df}$ the remaining charge in the p pillar is depleted creating a trapezoidal electric field distribution, similar to that found in a 1D punch-through structure. The slope of electric field within pillar with respect to y is well approximated by:

$$g_E = \frac{Q_{net} d}{2\varepsilon} = \frac{q e_{rr} N d}{2\varepsilon} . \qquad (7)$$

Therefore E_{edg_s} and E_{edg_d} are given by:

$$E_{edg_s} = \sqrt{\left(\frac{qN_d}{\varepsilon} w\right)^2 + \left(\frac{Vd}{d}\right)^2} \qquad (8)$$

and

$$E_{edg_d} = \sqrt{\left(\frac{qN_d}{\varepsilon} w\right)^2 + \left(g_E d + \frac{Vd}{d}\right)^2} \qquad (9)$$

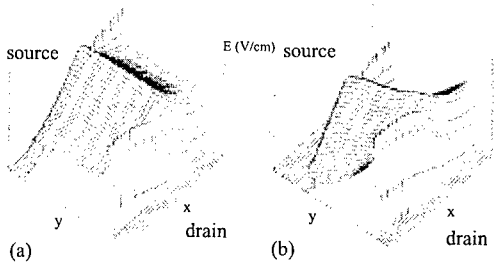


Fig.2 Electric field magnitude distribution for perfect charge balance (a) and imbalance (b) (arbitrary units)

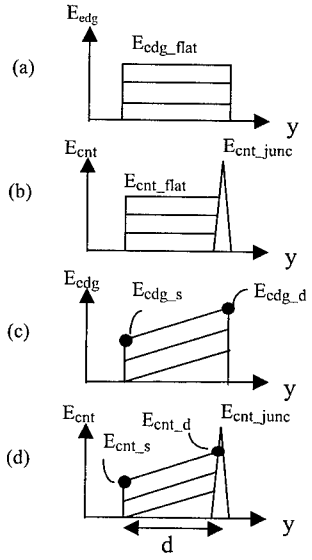


Fig.3 Simplified y-component of electric field distribution at the edge of p pillar (a)(c) and at the centre of p pillar (b)(d), with perfect balance (a)(b) and imbalance (c)(d).

The difference in applied voltage, V_{net}, between fully depleting the n pillar and depleting the p pillar is given by:

$$V_{net} = \frac{g_E d^2}{2}. \quad (10)$$

E_{cnt_junc} increases with increasing V_d until the p pillar is depleted, therefore Eq. 5 becomes:

$$E_{cnt_junc} = \alpha \frac{qN_d}{\varepsilon} w + g_E d \quad (11)$$

and, E_{cnt_s} and E_{cnt_d} are given by

$$E_{cnt_s} = \frac{V_d - V_{df} - V_{net}}{d} \text{ and} \quad (12)$$

$$E_{cnt_d} = E_{cnt_s} + g_E d. \quad (13)$$

3. On-resistance

The primary theory shows that R_{on} is perfectly proportional to w. However, for small values of pillar width R_{on} is increased by depletion of the conducting region as a result of the built-in potential [4]. The value of R_{on} (at $V_d = 0$) may be estimated:

$$R_{on} = \frac{2d}{\mu q n \left(1 - \frac{w_{d0}}{w}\right)} \quad (14)$$

where n is the electron carrier density in n pillar (n may be less than N_d because of incomplete ionisation). The factor of 2 in the numerator arises because current flows only in the n pillar. w_{d0} is the one-side depletion width in n pillar extending from the pn pillar junction, given by:

$$w_{d0} = \sqrt{\frac{2\varepsilon}{qN_d} \frac{(1+e_{rr})}{(2+e_{rr})} V_{bi}}. \quad (15)$$

4. Valid range of pillar doping for a given pillar width

It has been reported that for a given pillar width, V_{br} starts to fall above a certain pillar doping, N_{max}, and R_{on} starts to rise rapidly below a certain pillar doping, N_{min} [3]. The former is due to an increase in the peak electric field at the pillar junction (Eq.2) and the latter is due to restriction of the undepleted region resulting in reduction of current flow (Eq.15).

Values for N_{max} and N_{min} may be derived for the case of perfect doping balance from equations 2 and 15 respectively:

$$N_{max} = \frac{\varepsilon E_c}{qw} \quad (16)$$

$$N_{min} = \frac{\varepsilon V_{bi}}{qw^2} \quad (17)$$

The ratio of these two quantities may be used as a measure of the flexibility of the material with respect to the design of super-junction structures with a given half-pillar width:

$$N_{margin} = \frac{N_{max}}{N_{min}} = \frac{wE_c}{V_{bi}}. \quad (18)$$

Comparing 4H-SiC and Si using Equ.18 shows that 4H-SiC has 3.3 times higher margin than Si. Note that the minimum possible w, w_{min}, is defined when N_{margin}=1 and is given by:

$$w_{min} = \frac{V_{bi}}{E_c}. \quad (19)$$

w_{min} is about 0.015μm for 4H-SiC and 0.05μm for Si.

5. Ron vs. Vbr: a comparison of 4H-SiC with Si

For a specified breakdown voltage and pillar doping error, values for w, d and N are found that minimise the value of R_{on}. The breakdown voltage condition is imposed by solving the impact ionisation integral both along the edges (E_{edg}) and at the centre (E_{cnt}) of the pillars (see Fig. 1). Results for several values of pillar doping error are shown in Fig. 4 (a) for SiC and Fig. 4(b) for Si. MOSFET results are shown for comparison and assume that the device is dominated by the drift region resistance. The values of V_{br} and R_{on} obtained from the simplified equations show good agreement with TCAD simulation results.

For low levels of charge error, the SJS structure displays the expected proportional relationship between R_{on} and V_{br}. At higher levels of charge error the relationship becomes more like that exhibited by the MOSFET (i.e. $R_{on} \sim V_{br}^{2.5}$). This effect becomes more noticeable at high breakdown voltage and becomes more significant at higher V_{br}. It is clear that the effectiveness of the SJS structure is severly diminished by charge error levels of just a few percent.

With zero charge error, the on-resistance of the SiC SJS structure is some 140 times lower than the optimum Si SJS structure for the same breakdown voltage level. At lower voltage levels the on-resistance for the conventional MOSFET approaches that of the SJS with an intersection point at around 600V for SiC and 60V for Si.

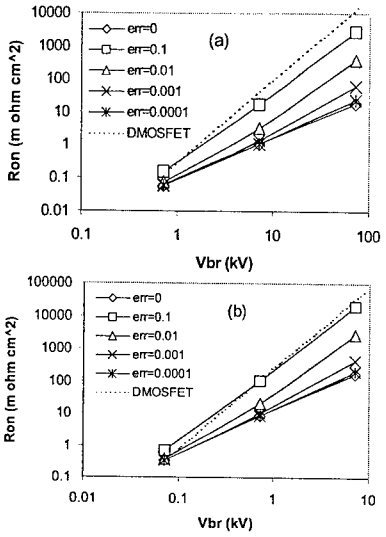


Fig.4 R_{on} vs. V_{br} for SiC (a) and Si (b)

6. Conclusion

Simplified expressions have been derived which describe the electric field distribution in super-junction structures under conditions where a charge imbalance exists in the drift region. These expressions have been employed in a PC based optimisation program in order to determine the structure parameters which minimise the on-resistance of the SJS for a given breakdown voltage. The minimum value of Ron is shown to increase with the level of charge imbalance, an effect that becomes more significant at higher Vbr. It has been shown that the on resistance of 4H-SiC SJS is about 140 times lower that the equivalent Si structure at perfect balance of doping. In addition, the 4H-SiC SJS is more tolerant of doping error and displays a 3.3 times wider design window for choice of pillar doping. This demonstrates that the SJS is potentially an effective sturucture for wide band-gap semiconductors. In the case of 4H-SiC, SJS structures are likely to be effective at voltage levels exceeding 2kV.

Acknowledgement

This work was performed under the management of FED as a part of the MITI NSS Program (Ultra-Low Loss Power Device Technology Project) supported by NEDO and was supported in part by the UK Engineering and Physical Sciences Research Council under research grant GR/L62320.

References

[1] T. Fujihara, Japan. J. Appl. Phys., 36 (1997), p. 6254.
[2] L. Lorenz, G. Deboy, A. Knapp, M. Maerz, IEEE International Symposium on Power Semiconductor Devices and ICs (ISPSD), (1999), p. 3.
[3] P.M. Shenoy, A. Bhalla, G.M. Dolny, IEEE International Symposium on Power Semiconductor Devices and ICs (ISPSD), (1999), p. 99.
[4] Y. Kawaguchi, K. Nakamura, A. Yahata, A. Nakagawa, IEEE International Symposium on Power Semiconductor Devices and ICs (ISPSD), (1999), p. 95.

Materials Science Forum Vols. 353-356 (2001) pp. 723-726
© 2001 Trans Tech Publications, Switzerland

SiC Junction Control, an Alternative to MOS Control High Voltage Switching Devices

A. Mihaila[1], F. Udrea[1], G. Brezeanu[2], R. Azar[1] and G. Amaratunga[1]

[1] Engineering Department, Cambridge University, Trumpington Street, Cambridge CB2 1PZ, UK

[2] Faculty of Electronics and Telecommunications, 'Polytehnica' University of Bucharest, 313 Splaiul Independentei, RO-77206 Bucharest, Romania

Keywords: SiC JFET, SiC Trench MOSFET

Abstract - This paper discusses for the first time the benefits of SiC junction control devices compared to MOS-type devices. Whereas MOS control silicon switching devices undoubtedly exhibit superior over-all performance compared to junction control devices due to reduced leakage, normally-off operation, high input impedance and improved SOA, this paper argues that SiC MOSFET devices have theoretical and practical disadvantages which may limit their operation and arguably bring back in light junction switching devices such as the JFET. In this study a numerical comparative view of two SiC devices, namely a trench MOSFET and a JFET, is provided. It is pointed out that the severe SiC MOSFET gate oxide limitations can be overcome by using a SiC JFET. To investigate the off-state behaviour of both devices, extensive numerical simulations using MEDICI and ISE TCAD have been carried out.

Introduction

In the recent years, among other wide band-gap materials, silicon carbide (SiC) has been granted with an enhanced attention [1-3]. SiC offers a very low intrinsic carrier concentration, a band-gap three times higher than that of silicon, a high avalanche breakdown electric field of $2\div4\times10^6$V/cm and high electron saturation velocity. All these properties make SiC one of the most attractive wide band-gap semiconductors for switching power devices.

This paper provides a comprehensive numerical comparison between a 4H-SiC 1.2kV SiC trench MOSFET and a JFET. Trench technology has been selected for the MOSFET, since it offers a high channel density and eliminates the parasitic JFET effect characteristic of DMOS structures. In spite of its advantages, such as MOS voltage control and low saturation currents, SiC trench MOSFET suffers from several major drawbacks such as relatively high threshold voltage and poor mobility in the channel, which adversely affects its on-resistance. Another severe drawback encountered in trench MOSFETs is the gate oxide breakdown, which can occur prior to semiconductor breakdown [4]. We here carried out a numerical analysis of the oxide/SiC trade-off breakdown and determine the design conditions to avoid the premature breakdown. The study also points out that the theoretical value of the drift doping, calculated from the avalanche condition, can lead to premature breakdown due to punch-through of the p well.

A viable alternative for the SiC trench MOSFET is the SiC JFET [5-7]. In this way, major drawbacks like gate oxide breakdown and low mobility in the channel are eliminated. A JFET structure characterised by buried gate regions and a buffer layer placed on the top of the drift region is proposed [8].

SiC MOS Control - MOSFET

As it was mentioned above, one of the strongest limitations in SiC trench MOSFET is that the dielectric breakdown can occur before the semiconductor body breaks down. Writing the Gauss law at the SiC/SiO_2 interface, $\varepsilon_{SiO2}E_{SiO2}=\varepsilon_{SiC}E_{SiC}$, and considering $E_{SiC_BR}=2.4\times10^6$V/cm, it is found that

the maximum allowable value of the electric field in the oxide (E_{oxide}) is 5.96×10^6V/cm. However, due to two-dimensional effect at the trench corner, the value of the electric field in the oxide can be higher than 6×10^6V/cm. This is close to the practical limit of the electric field strength in the oxide. This means that the oxide breakdown can take place before avalanche occurs in the actual semiconductor body. Hence in order to have a reliable device, the peak of the gate oxide electric field should be kept under its practical critical value of $\approx6\times10^6$V/cm.

As pointed out above, SiC trench MOSFET can suffer from premature breakdown due to punch-through of the p well. The punch-through can be avoided by increasing the p well doping and decreasing the drift region doping or by making the channel longer. The first sets a very strong limitation on the minimum threshold voltage for the trench MOSFET while the second and the third further degrades the on-resistance.

The cross section of a SiC 1.2kV MOSFET, 10μm width cell is shown in fig. 1(a). The gate oxide is 0.2μm thick. The p well has a Gaussian doping profile with a peak concentration of $N_A=9\times10^{17}cm^{-3}$ at the source contact, this relatively high value preventing the device from suffering premature breakdown due to p well punch-through.

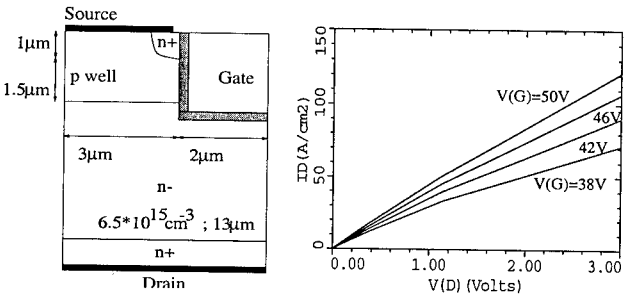


Fig. 1(a) - Cross section of half a cell for the trench MOSFET; (b) - MOSFET I-V characteristics for different gate voltages.

From off-state simulations it was found that at V_D=1260V, the value of the oxide electric field at the trench corner is 8.76×10^6V/cm. This practically means that at this voltage level oxide breakdown has already taken place.

Two methods have been used to address this problem. First, wider trenches have been used, in this way the curvature of potential lines at the trench corner being softened (field plate effect like). It is well known that trench structures with rectangular corners suffer from electric field crowding effect. Thus, the classical procedure of using rounded trench corners was the second method employed to alleviate further the tension on the gate oxide.

The values of the oxide electric field as a function of the trench width, for rectangular and rounded trench corners and t_{ox}=0.2μm, at a drain voltage of 1260V are summarised in table 1. For a trench width of 8μm, the value of the oxide electric field (7.02×10^6V/cm) was reduced with about 20% when compared to the one corresponding to a 4μm trench width. Moreover, using rounded trench corners, the oxide electric field underwent a further reduction, its value decreasing under the theoretical limit given by Gauss law. As a consequence, by using wide trenches in conjunction with rounded trench corners, the oxide electric field can be kept under its critical value theoretically calculated.

Table 1 Oxide electric field at the trench corner as a function of the trench width, for rectangular and rounded trench corners; t_{ox}=0.2μm and V_D=1260V.

Trench width(μm)	4	6	8
$E_{oxide}(\times10^6$V/cm) rectangular corner	8.76	8.45	7.02
$E_{oxide}(\times10^6$V/cm) rounded corner	6.5	6.3	5.4

Table 2 The dependence of the oxide electric field at the trench corner on the gate oxide thickness, atV_D=1260V, for different trench widths.

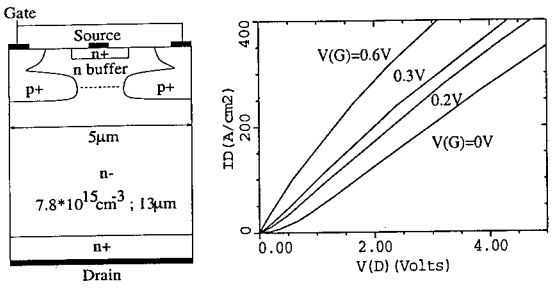
Oxide thickness(μm)	0.1	0.2	0.3
$E_{oxide}(\times10^6$V/cm) Trench width = 6μm	9.2	6.3	5.5
$E_{oxide}(\times10^6$V/cm) Trench width = 8μm	6.4	5.4	4.9

For the "rounded trench" MOSFET, off-state simulations have been carried out in order to investigate the influence of the gate oxide upon the oxide electric field. The values of the oxide electric field at V_D=1260V, for different oxide thickness and trench widths, are listed in table 2. The off-state simulations results show that for devices designed to have breakdown voltages higher that

1.2kV, the gate oxide thickness should be at least 0.2μm. Although the simulator does not take into account the oxide breakdown, it can be inferred that if the peak in the electric field exceeds 6.5×10^6V/cm the device breaks down due to tunnelling through the gate oxide.
The I-V characteristics of the SiC trench MOSFET obtained through numerical simulations are shown in fig. 1(b). The p well doping being quite high, this results in a relatively high threshold voltage of 22V. At a current density of 100A/cm^2 and for V_G=50V, the extracted on-state resistance is 23mΩcm^2.

SiC Junction Control - JFET

Using a SiC JFET one can eliminate two of the drawbacks encountered for SiC trench MOSFET, namely the gate oxide breakdown and the poor mobility in the channel. The cross section of a SiC 1.2kV JFET structure is shown in fig. 2(a). The JFET distinctive feature is a buffer layer placed on the top of the drift region having a doping concentration of $N_D=2.9\times10^{16}$cm^{-3}, higher than the doping of the drift layer. The depth of the buried gate region is 2μm and the channel length is 1μm. The JFET proposed here is normally-off.



(a) (b)

Fig. 2(a) - Cross section of the JFET structure; (b) - JFET I-V characteristics for different gate voltages.

However, in order to withstand a blocking voltage of 1.2kV, a negative voltage of about –20V should be applied to the gate. The 3D plot for the electric field in the JFET, for a negative gate voltage V_G=-17V and a breakdown voltage V_{BR}=1310V, is shown in fig. 3. It can be clearly seen that the breakdown occurs at the p$^+$buried gate/n$^-$drift/n buffer point. By further increasing (in modulus) the negative voltage gate, the breakdown will occur at the surface, for the two pin diodes formed between the gate/buffer/source and the buried gate/buffer/source. Still, by increasing the distance between the gate and the source the lateral diode breakdown can be easily avoided.

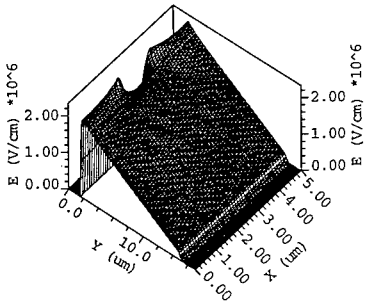


Fig. 3 - 3D shape of the electric field in the JFET, for a negative gate voltage V_G=-17V.

The JFET on-state characteristics for different gate voltages are shown in fig. 2(b). For V_G=0.6 V and at a current density of 100A/cm^2, the JFET on-resistance is 6mΩcm^2. When compared with the MOSFET, the JFET on-resistance is improved by a factor of 3 or 4, the difference resulting mainly from the very low electron mobility in the MOSFET channel.

Table 3 The dependence of the JFET breakdown voltage on the buffer layer doping; V_G=-17V.

$N_{buffer}(\times10^{16}cm^{-3})$	2	2.5	2.9	3	3.1
V_{BR}(V)	2120	1790	1310	1230	1160

The dependence of the breakdown voltage on the buffer doping, for V_G=-17V, is shown in table 3. As expected, the higher the buffer doping, the lower the blocking voltage. One can also observe that with the expense of a higher (in modulus) gate voltage, a higher blocking voltage can be achieved with a very low on-resistance.

Table 4 The dependence of the JFET breakdown voltage on the gate voltage; $N_{buffer}=2.9\times10^{16}$cm^{-3}.

Gate voltage(V)	-15	-17	-20	-40	-60	-80
V_{BR}(V)	960	1310	1615	2498	2503	2364

The influence of the gate voltage

upon the blocking voltage is shown in table 4. Comparing the values, it can be observed that there is a peak gate voltage (-60V) corresponding to the highest breakdown voltage (2503V). As long as the gate voltage is equal or higher than –60V, blocking voltages as high as 2.5kV can be achieved with a very low on-resistance. Increasing further the gate voltage, the blocking voltage will decrease and, as mentioned above, the breakdown point will move towards the surface and it will occur for the p^+buried gate/n buffer/n^+source parasitic PIN diode. In fact, for V_G=-100V, breakdown occurs for the vertical parasitic PIN diode even before applying a voltage to the drain.

Comparison between MOS and Junction Control

SiC main advantage of having a high breakdown electric field paradoxically turns facilitates the breakdown of the gate oxide. Thus, mainly under off-state conditions, the SiC trench MOSFET undergoes very severe problems in terms of gate oxide reliability. Although improved results can be obtained by using wide trenches and rounded corners, realising practically wide trenches and filling them is still a problematic task. All these problems disappear when using a SiC JFET. However, due to the fact that the current path is junction controlled, a negative voltage should be applied to the gate to withstand the voltage in the off-state. It is also worth noting that the JFET has two parasitic PIN diodes at the surface. However, with a careful design, their effect on the breakdown performance can be negligible. Using the junction control, two more MOS characteristic problems are eliminated: that is the low channel mobility, which adversely affects the on-resistance and the premature breakdown due to p well punch-through.

According to the above considerations, it can be inferred that SiC junction control is a strong alternative to MOS control for high voltage power devices. In addition, MOS-bipolar high voltage devices such as the Trench Insulated Gate Bipolar Transistors (TIGBT) which have been extremely successful in silicon technology [9] will be, in the authors opinion, of little use in the current SiC technology. This is because the SiC large band-gap results in a large anode junction built-in potential which leads to high on-state voltages and, consequently, unacceptably high power losses.

Conclusions

In summary, a SiC JFET is proposed as a viable alternative to the SiC trench MOSFET. In this way, MOSFET's major drawbacks, such as gate oxide breakdown, poor mobility in the channel and high threshold voltage can be overcome. Moreover, the on-resistance of the 1.2kV JFET is 3-4 times smaller than that of an equivalent SiC MOSFET. At the same time the JFET technology is easier than that of the MOSFET due to the elimination of trench gate formation. Nevertheless, the full blocking of the JFET can only be accomplished by applying a negative voltage to the gate. This may lead to a compromise in the complexity of the control circuitry.

Acknowledgement

A. Mihaila acknowledges the award of a research scholarship from Cambridge Overseas Trust. F. Udrea acknowledges the award of an advanced research fellowship (AF/100027) from the Engineering and Physical Sciences Research Council (EPSRC), UK.

References

1. M. Bhatnagar and B. J. Baliga, IEEE Trans. Electron Devices, vol. 40 (1993), p. 645
2. J. W. Palmour et al., Proc. ISPSD (1997), p. 25
3. M. Ruff et al., IEEE Trans. Electron Devices, vol. 41 (1994), p. 1040
4. A. K. Agarwal et al., Proc. of ISPSD (1996), p. 119
5. T. Iwasaki et al., Proc. ISPSD (1997), p.149
6. H. Mitlehner et al., Proc. ISPSD (1999), p.339
7. P. Friedrichs et al., Proc. ISPSD (2000), p. 213
8. A. Mihaila et al., Proc. Int. Semic. Conf., Sinaia (1999), p. 191
9. F. Udrea et al., IEEE Electron Devices Letters, vol. 20 (1999), p. 428

Materials Science Forum Vols. 353-356 (2001) pp. 727-730
© 2001 Trans Tech Publications, Switzerland

Long Term Operation of 4.5kV PiN and 2.5kV JBS Diodes

H. Lendenmann, F. Dahlquist, N. Johansson, R. Söderholm,
P.A. Nilsson, J.P. Bergman and P. Skytt

ABB Corporate Research, SE-721 78 Västerås, Sweden

Keywords: Forward Degradation of SiC Diodes, High Voltage, Large Area Diodes, Reliability

Abstract. Large area SiC diodes (20mm^2 and 40mm^2) for high power applications were manufactured on selected defect free areas of 4H Epi wafers. The forward and reverse characteristics of these 4.5kV PiN and 2.5kV JBS diodes are analyzed. Various device non-idealities are discussed and compared to known crystal imperfections. Large PiN diodes were parallel connected together with silicon IGBT switches using conventional press-pack technology. Dynamic switching up to 1250V and 400A nominal current is reported. Long term data for continuos switching revealed a new drift phenomena of the forward voltage drop of bipolar diodes. However, long term blocking tests confirmed reliable reverse characteristics.

Introduction

Many high power applications, such as motor drive systems and HVDC transmission systems use voltage source converters. SiC devices have the potential to impact this converter technology fundamentally. However, such systems are often in the MW or even >100MW range and require devices with a large active area. This paper focuses on the state of art of large area SiC PiN diodes and their properties under application condition and in reliability tests. Even with large SiC diodes, parallel connection of several chips is necessary to reach the >100A current level. At this point, the active device area with a sufficient yield as well as the long term device stability is still limited by material related deficiencies.

Fabrication of Devices

On 35mm 4H SiC wafers from CREE, a hot-wall CVD Epi layer of 35 – 45um thickness with n-type doping in the low 10^{15}cm^{-3} range is grown [1]. Depending on the assumed critical field strength for this low doping, a theoretical blocking voltage of about 4.5–6.0kV is expected. These wafers are then characterized with an optical microscope to locate all visible defects. Individual for each wafer, large area diode chips of 20mm^2 and 40mm^2 are then placed in the defect free areas. The remaining area is used for small (1-5mm^2) monitoring devices. The implanted anode uses a multi energy Al-B profile, annealed at 1700°C. The devices are terminated using an implanted multi-zone junction termination extension with an oxide surface passivation layer. The details of the design and the process were described previously [2]. For the JBS diodes mentioned for comparison, a process based on the same technology steps was used.

Static Characteristics of PiN and JBS diodes

Figure 1 shows the conduction characteristic of typical diodes. At 100A/cm^2 the forward voltage V_f is 3.4V for the 4.5kV PiN diode. No difference in on-state voltage is seen for smaller diodes down to about 1mm^2. This V_f shows a negative temperature coefficient of α_T~-1.1mV/K (at 100A/cm^2). In comparison, a 2.5kV JBS diode has only 2.0V forward voltage at a temperature coefficient of +4-5mV/K. However, for current densities above 150-250A/cm^2 or for higher blocking voltages, the

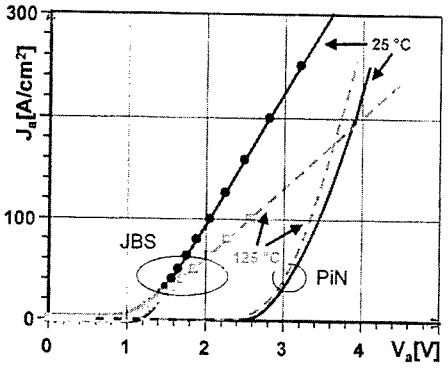


Figure 1 Linear forward characteristic of a 20mm^2 PiN (–) and a 0.1mm^2 JBS diode.

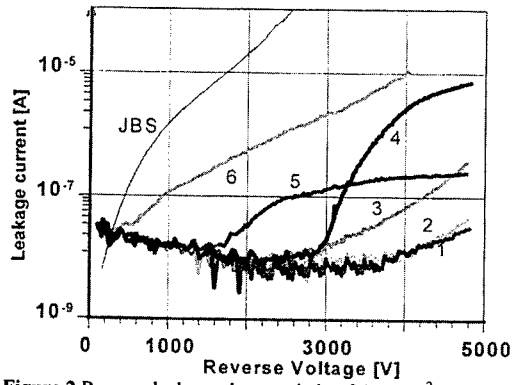


Figure 2 Reverse leakage characteristic of 6 20mm^2 PiN diodes at 25°C and a 0.1mm^2 JBS diode.

un-modulated JBS forward voltage starts exceeding the PiN diode.

For PiN diodes, several slight anomalies are observed in the forward IV curves. For example excess recombination current in the sub-threshold region or a strongly varying α_T over the wafer (up to -5mV/K was observed). Such effects are attributed to recombination centers in the n-base or at the junction, reducing locally the minority carrier lifetime (nominally 0.5µs–1µs) also seen in Figure 3. Substrate related crystal imperfections such as screw and edge dislocations, low angle grain boundaries and stacking faults or remaining impurities in the Epi and substrate are presumed to be the main sources of these electrically active defects (Table 1).

Figure 2 shows the reverse characteristic of six 20mm^2 diodes on the same wafer. These samples show good blocking (avalanche >5kV). However, while a few diodes have ideally low leakages (trace 1,2), others show current traces (4,5) similar to dislocation related conduction [7] or show an abnormal exponentially increasing leakage (trace 6). These devices (without visible defects) still contain several 100 to 1000 dislocations in the active area, which together with other

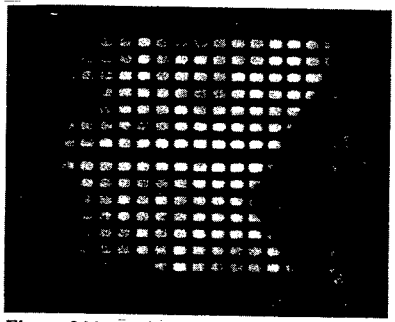


Figure 3 Non-uniform optical emission at 5A/cm^2 of test-structure diode with windows in anode metallization.

defect type	typical dens.	device effect
Micropipes	1-30cm^{-2}	<50 - 70% E_{cr}
Carrots	0.1-10cm^{-2}	E_{cr}, J_L, n
Major pits	1-100cm^{-2}	-, E_{cr}, J_L
Screw disloc.	10^3cm^{-2}	< 80% E_{cr}
Edge dislocations	10^4-10^5cm^{-2}	not known
Low angle grain boundaries	10^2-10^3cm^{-2}	τ-reduction, forward char.
threading dislocations	few cm^{-2}	not known
stacking faults	10^0-10^2cm^{-2}	τ-reduction

Table 1 Most common defects in 4H SiC, typical density, and effects on power device characteristics [4,5,6]

material imperfections are presumably responsible for these variations (see Table 1).

Dynamic module operation

For dynamic operation conventional press packaging technology is used to assemble four 2.5kV IGBTs ($4x1cm^2$) together with four $40mm^2$ SiC diodes chips. The measurement in Fig. 4 shows the SiC diode turn-off for 400A and 1250V at T_j=125°C. The reverse recovery charge for 400A is with 4µC about a factor of three higher than the expected depletion layer charge, indicating that carrier plasma is removed during the recovery. A module with silicon diodes for identical rating and switching conditions leads to 130mJ loss energy for this event, while the shown SiC module causes merely a loss of 4mJ. Compared to Silicon diodes for the same voltage class both the SiC-PiN reverse recovery charge and the diode transient loss are negligible (<3%).

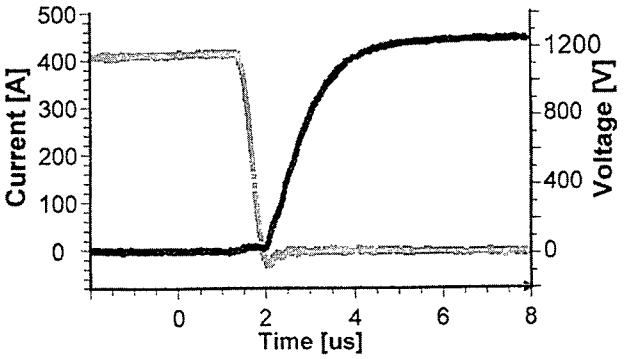


Figure 4 Transient turn-off operation of Si-SiC diode module. V-t and I-t curves for a diode turn-off at 1250V, 400A at Tj=125°C.

Long term properties of SiC Diodes

With diodes from the same process technology long-term reliability tests were carried out in statistically relevant quantities. Diodes with static blocking in the 3.2-4.0kV range were selected, packaged, and exposed to high temperature (125°C) while biased at 2250V reverse. The leakage currents over 500h are plotted in Fig. 5. Most diodes show a leakage in the 10^{-5} to $10^{-4}A/cm^2$ range. While the current of most diodes is not completely constant, generally no increasing trends are observed. A few diodes do show unexplained larger variations, however also diodes with high initial leakage current can remain stable over the entire testing period.

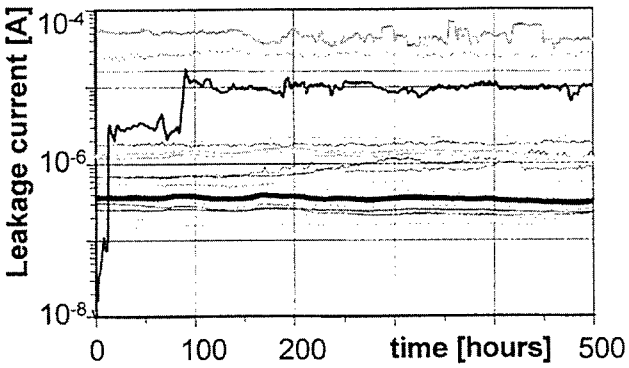


Figure 5 Long term leakage of 25 $1.3mm^2$ test diodes. The static break-down of these diodes is 3.2-4.0kV. Diode bias is at -2250V at 125°C.

Long term continuos operation was also tested. If the PiN diodes are characterized at intervals during operation, an increase of the static forward voltage is observed in some of these high voltage components (Fig. 6A). Typical traces over time are given in Fig. 6B. While some diodes can drift rather fast as in trace a), slow drifting diodes or non-drifting diodes are found on the same wafer. A higher temperature or current accelerates the phenomena. Investigations ruled out contact related degradations. However, concurrent with the increase of V_f, an increase of the shaded areas in Fig. 3 is observed. This indicates that the effective minority carrier lifetime in the material decreases during operation. This is independently confirmed by optical and electrical measurements.

It was found, that the substrate material can make marked differences in the occurrence of this phenomenon. The optical observed Epi defects mentioned earlier in the paper, however, do not explain the occurrence rate of this drift. Therefore process generated or from the substrate into the Epi replicated dislocations could act as nucleation sites for this behavior. Modifications in process steps and sequence can reduce or eliminate this drift substantially, while wafer areas with high defect densities remain drifting. Devices from the best wafer areas show no measurable drift over >1000h. In contrast to bipolar PiN diodes, the unipolar schottky or JBS type diodes have all a characteristic of trace c) in Fig 6B.

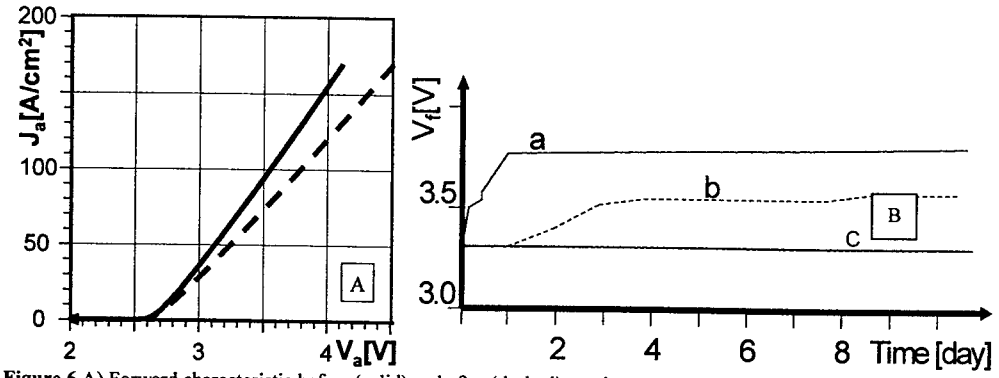


Figure 6 A) Forward characteristic before (solid) and after (dashed) continuos converter operation. B) Forward voltage at sample intervals during operation: a) fast, b) slower, c) non-drifting diodes.

Summary

20mm^2 4.5kV SiC diodes have been shown feasible. Using paralleling, switching at 400A leads to only 3% dynamic component loss compared to equivalent silicon diodes. However, crystal defects within the active region of large devices affect both forward and reverse characteristic adversely. The most severe limitation for ~1cm^2 chips is the large variation in leakage current. The detailed properties of the defects causing this leakage remain unknown and their elimination unsolved. Reliability tests have shown that SiC diodes have excellent long-term blocking stability. However, real converter operation causes the forward voltage of some diodes to drift. This phenomenon is believed to be related to defects in the substrate, Epi and junction layer, affecting the minority carrier lifetime adversely. Improvements in substrate material and uniform processing have already shown that this drift can largely be eliminated.

The authors acknowledge contributions from the entire ABB SCRIPT team, and A. Galeckas.

References

[1] O. Kordina, A. Henry, E. Janzen, C. H. Carter, Mat. Sci. Forum, 264-268, (1998), p. 97.
[2] K. Rottner, et. al, Mat. Sci. and Eng., B61-62, *(1999), p. 330.*
[3] A. Lebedev, "Deep level centers in SiC" *Semiconductors*, vol. 33, (1999), p. 107.
[4] P. G. Neudeck, et. al., *IEEE Trans.Electron Dev. (USA) March*, vol. 46, (1999), p. 478.
[5] A. Ellison, PhD Dissertation, Linköping University, (1999), p. 153.
[6] C. H. Carter, et. al., UPD2000, FED-171, Nara, Japan, (2000), p. 3.

Materials Science Forum Vols. 353-356 (2001) pp. 731-734
© 2001 Trans Tech Publications, Switzerland

Planar p-n Diodes Fabricated by MeV-Energy and High-Temperature Selective Implantation of Aluminum to 4H-SiC

H. Sugimoto, S. Kinouchi, Y. Tarui, M. Imaizumi,
K. Ohtsuka, T. Takami and T. Ozeki

Mitsubishi Electric Corporation, Advanced Technology R&D Center,
8-1-1 Tsukaguchi-Honmachi, Amagasaki City, Hyogo 661-8661, Japan

Keywords: Electrical Activation, Aluminium, Annealing, Diode Characteristics, Hall Effect, Implantation Damage, Leakage Current, Rutherford Backscattering Spectrometry (RBS), Selective Implantation

Abstract High-energy and high-temperature (1000℃) implantations are studied. Implanted p region with 3 μm thickness and $5x10^{18}/cm^3$ concentration are fabricated. RBS measurements show that high-temperature implantation reduces the damage of implantation before as well as after activation annealing. C-V measurements indicates that most of the implanted Al ions are activated to acceptors over 1500℃ annealing. Hall effect measurements show that Hall mobility increases with annealing temperature to $30cm^2/Vs$ and sheet resistance decreases to 5kΩ/□. Planar p-n diodes with 3 μm thick p regions are fabricated by selective implantation using masks of Mo. High-temperature implantation has effect to reduce reverse leakage currents. It is assumed that the high-temperature implantation dose not cause the severe damage, which may remain the origin of leakage currents after activation annealing.

Introduction

High-energy ion implantation techniques [1,2] are required for the fabrication of thick p-type regions, which is desirable for the designs of high breakdown voltage devices as well as for the structure reducing the electrical field at the oxides of MOSFET devices [3]. High-temperature ion implantation techniques are also necessary to form excellent p-n junctions by reducing implantation damages [4-7]. The research on high-energy and high-temperature ion implantation techniques [8] were scarcely reported. We report on implantation of Al at 1000℃ with the energy of 7.0MeV and the fabrication of planar p-n diodes with 3 μm thick p regions.

Experimental procedures of implantation

Epitaxial layers (n^-: $5x10^{15}/cm^3$) on 4H-SiC substrates were used for implantation experiments. Ions of Al with 7 step energies from 0.9 to 7MeV were implanted in order to form box profiles. The samples were implanted at room temperature (RT), 500℃, 750℃, and 1000℃. Ions with 6 step energies from 0.9 to 5.6MeV were implanted for the experiment of selective implantation. Masks of Mo with the thickness of 3 μm were used for selective implantation. The Mo masks were formed by sputtering deposition and were etched by wet etching, which induced the sloped edges of the masks. The samples were annealed for activation, at from 1300℃ to 1650℃ in an atmosphere of Ar for an hour. The annealed samples were etched by RIE of CF_4/O_2 gas in order to remove the surface layers with little Al density. Schottky metal electrode of Ti and ohmic contacts electrode of Al/Ti were formed for the C-V and Hall effect measurements, respectively.

The depth profiles of Al in implanted region and in masked region were measured with secondary ion mass spectrometry (SIMS). In order to characterize the implantation damage, channel spectra of Rutherford backscattering spectrometry (RBS) were measured using He ions of 2 MeV both before and after the annealing. Acceptor densities were measured by C-V method. Hole densities, sheet resistance, and mobility are measured by Hall effect measurements. Effects of temperatures at implantation ($T_{implant}$) and temperatures for the activation annealing (T_{anneal}) were studied. The real temperatures of sample surfaces during annealing are assumed to be higher than T_{anneal} measured in the experiments by about a hundred degrees.

Depth profile of implantation

The SIMS profile of the sample implanted selectively using the Mo mask at RT is shown in Fig. 1. The depth profile of Al in the implanted region shows the box profiles of 3 μm thickness and about $5x10^{18}/cm^3$ concentration [9]. The profile has 6 ripple peaks corresponding with the 6 steps of implantation energies and nearly coincides with the simulation of TRIM. In masked region, most of

implanted ions of Al stop in the Mo mask and a few percent ions reach through the SiC surface, which may be due to the effect of column structure of the sputtered Mo layer.

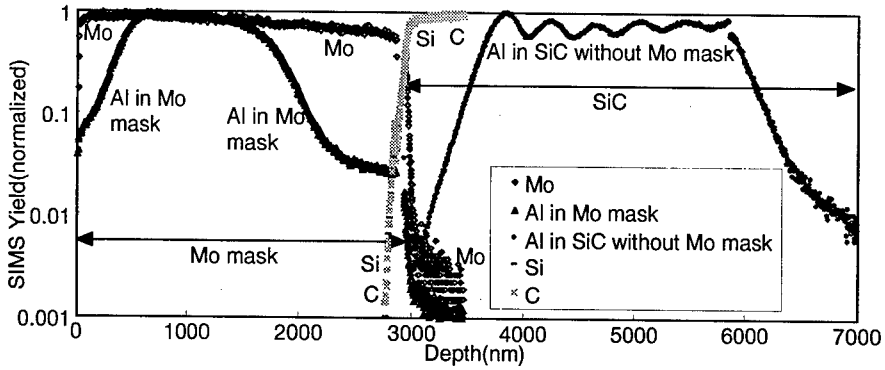


Fig. 1 SIMS profile of the selectively implanted sample (*Timplant*: RT)

Under the condition of *Timplant* lower than 750℃, no reaction of the Mo mask to the SiC surface are observed. SEM views of the sample at *Timplant* of 1000 ℃ reveals remarkable reaction of the Mo mask to the SiC surface. Fig.2 shows cross sectional and birds-eye SEM views of the implanted p region at 500 ℃ after the annealing and the Mo mask. The slope at the edge of the Mo mask formed by wet etching brings about sloped implantation profile. Depth of the p region is 4.1 μ m and accords with the depth including the tail of the Al distribution.

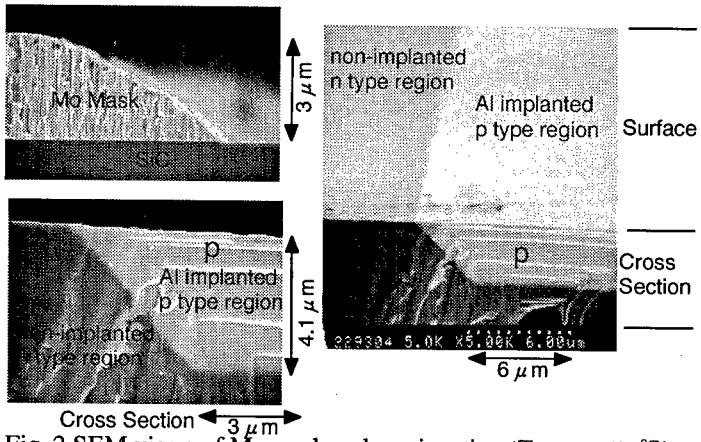


Fig. 2 SEM views of Mo mask and p-n junction (*Timplant*: 500℃)

Implantation damage measurement by RBS

Signal yields of RBS channel spectra were measured before and after the annealing of 1600℃[9]. The signal yields of the samples implanted at RT and 500℃ before annealing exceeded one half of the signal yields of random level, which showed that the serious crystal irregularity were induced by implantation damage at RT and 500℃. On the other hand, the signal yields of the samples implanted at 1000℃ before annealing was less than two times of that of the reference sample with no implantation. The result indicated the 1000 ℃ implantation dramatically reduced the implantation damage compared with RT. Troffer et al. [6] examined RBS spectra of low-energy (280keV) ion implanted samples and showed that 500℃ hot implantation can prevent remarkable crystal irregularity. It is assumed that high-energy implantation needs higher temperature in order to prevent serious damage than low-energy implantation.

As for the data after the annealing, the signal yields of the samples of all *Timplant* decreased and became close to that of the reference sample, but there remained the deviation of the signal yields of implanted sample from that of the reference sample. The deviation of 1000℃ was smaller than that of RT. The result shows that high-temperature implantation reduce the implantation damage before as well as after the annealing.

Electrical properties by C-V and Hall effect measurement

The dependence of sheet resistance on *Tanneal* is shown in Fig. 3 with *Timplant* as parameters. Sheet resistances of every *Timplant* decrease with *Tanneal* and approach to 5kΩ/□ above 1500℃. *Timplant* has effects on sheet resistance at the region where activation is insufficient below 1500℃. Acceptor

densities measured by C-V method are shown in Fig. 4. The acceptor densities increase with T_{anneal} and approach the concentration of Al measured by SIMS ($5x10^{18}/cm^3$). Most of the implanted Al atoms are activated to acceptors for T_{anneal} over 1500℃. At the dose level of the experiments, $T_{implant}$ has no significant effect on acceptor densities. Hole densities from Hall effect measurements show the same tendencies and reach $2.5x10^{17}/cm^3$ over 1500℃ as shown in Fig. 5. Hall mobility, as shown in Fig. 6, increases with T_{anneal} to $30cm^2/Vs$, which is comparable with the reported data of doped epitaxial layers. The data over 1600℃ is assumed to be affected by the slight diffusion of Al which is observed in SIMS profiles of the samples annealed over 1600℃. At the dose level employed, $T_{implant}$ has no apparent effect on electrical properties measured by C-V or Hall effect measurements. On the other hand, T_{anneal} has apparent effects. Studies on lower energy implantation [6,7] revealed the similar results, which showed that hot implantation has no apparent effect on electrical properties such as hole concentration or mobility.

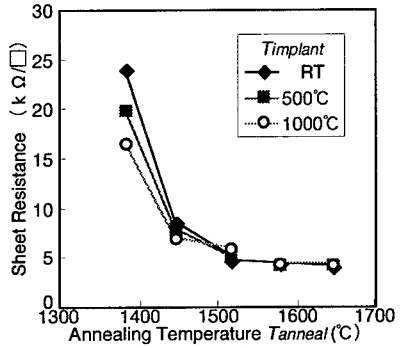


Fig. 3 Dependence of sheet resistance on T_{anneal}

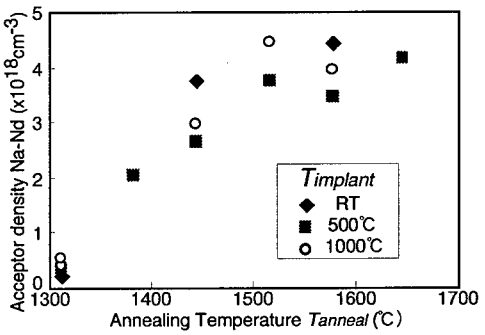


Fig. 4 Acceptor densities measured by C-V method

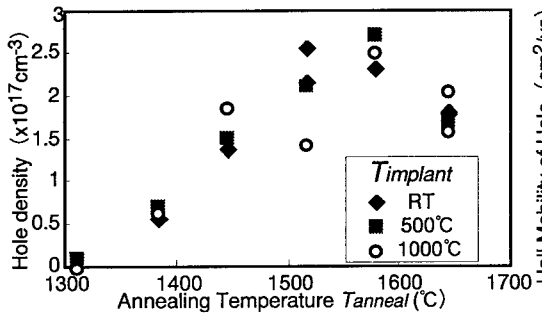


Fig. 5 Hole densities from Hall effect measurement

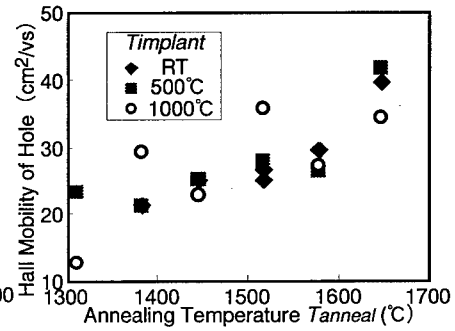


Fig. 6 Hall mobility of hole

Fabrication of planar diode

Planar p-n diodes were fabricated on epitaxial layers (n^-:$5x10^{15}/cm^3$) with the thickness of 10 μm by selective ion implantation with the masks of Mo as mentioned above. Ions of Al with 6 step energies from 0.9 to 5.6MeV were implanted. From the thickness of p layer shown in Fig. 2, drift layer thickness was estimated to be about 6 μm. The implanted samples were annealed at 1575℃ for 10 minutes, at 1575℃ for 60 minutes, and at 1650℃ for 10 minutes. The annealed samples were etched by RIE and 1 μm thick surface layer were removed. Ohmic contacts electrode of Al/Ti and Ni were formed on the surface and the backside, respectively. The diameters of the pn junction were from 100 μm to 500 μm. Effects of $T_{implant}$ and activation annealing condition were studied.

Characteristics of diodes

Typical reverse I-V characteristics of the p-n diodes with diameter of 500 μm are shown in Fig. 7. The figure shows the data of leakage currents of the diodes fabricated under several conditions of implantation and annealing to the reverse voltage of 100V. The leakage currents of the sample implanted at 500℃ are remarkably larger than that of 1000℃. The time of annealing also effects on the characteristics. Compared with the data of 10 minute, the leakage currents of 60 minutes are fairly small. The leakage current data of diodes with several diameters and several fabrication conditions are doted in Fig. 8. It reveals that on the average, leakage current of 1000℃ is about two

orders smaller than that of 500℃ and that the leakage current decrease with T_{anneal} and annealing time. Kawase et al. [7] examined the leakage currents of the lower-energy (180keV) and high-temperature implantation and reported the similar result of the decrease of leakage current at 1000℃.

Fig. 9 shows typical forward I-V characteristics. There are excess currents composed of at least two parts. One is the current in the region below 1.5V and the other is a part of shoulder from 1.5V to 2.5V. The forward characteristics have same tendency as the reverse one. Both the excess currents of the diodes implanted at 500℃ are remarkably larger than that of 1000℃. The excess currents of 60 minutes are also fairly smaller than that of 10 minute. It is assumed that the implantation damages induces the origins of the leakage and excess currents and that the high-temperature implantation at 1000℃ significantly reduce the damage, compared with implantation at 500℃. In the measurements of the characteristics of the diodes, excess currents with the time decays of several seconds are observed even for the devices implanted at 1000℃. It is supposed that the damages causing the origins of long lifetime remain even under our best fabrication condition.

Breakdown voltage is typically about 1kV and no distinct influence of $T_{implant}$ and T_{anneal} on breakdown voltage has been observed yet. Differential on-resistance is 6mΩcm^2 at 100A/cm^2.

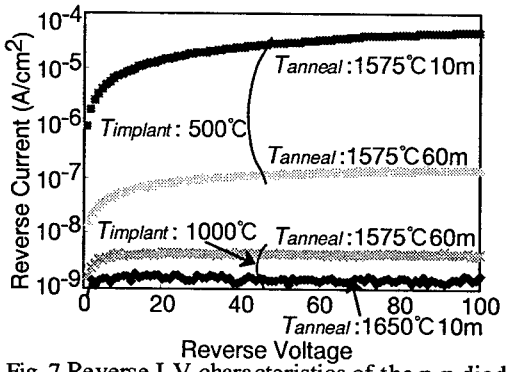


Fig. 7 Reverse I-V characteristics of the p-n diodes (Diameter: 500 μ m)

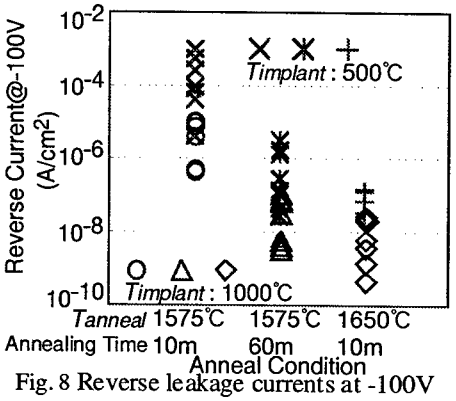


Fig. 8 Reverse leakage currents at -100V (Data of several diameters are doted.)

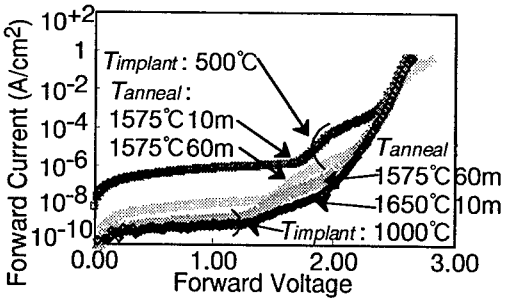


Fig. 9 Forward I-V characteristics of the pn diodes (Diameter: 500 μ m)

Summary

Under the experimental conditions of this report such as implantation dose and maximum annealing temperature, the high-temperature implantation of 1000℃ has effects of reducing the influence of implantation damages on pn junction characteristics and the data of RBS. On the other hand, electrical properties of C-V and Hall effect measurements are not apparently influenced by $T_{implant}$.

Acknowledgments: The authors would like to gratefully thank Mr. K. Sekine and Mr. H. Kawami in Ion Engineering Research Institute Corp. for the high-energy and high-temperature implantation.

References

[1] N. Miyamoto, A. Saitoh, T. Kimoto, and H. Matsunami et al., 1st International Workshop on Ultra-Low-Loss Power Device Technology Extended Abstracts, (2000), PSIII01, p.169.
[2] N. Mestres et al., Mater. Sci. Forum **264-268** (1998), p.733.
[3] M. Shenoy, B. J. Baliga, Mater. Sci. Forum **264-268** (1998), p.993.
[4] N. Ramungul et al., Inst. Phys. Conf. Ser. **No.142** (1996), p.713.
[5] N. Inoue et al., Inst. Phys. Conf. Ser. **No.142** (1996), p.525.
[6] T. Troffer et al., phys. stat. sol. (a) **162** (1997), p.277.
[7] D. Kawase, T. Ohno, T. Iwasaki and T. Yatsuo, Inst. Phys. Conf. Ser. **No.142** (1996), p.513.
[8] M. V. Rao et al., Apply. Phys. **77** (1995), p.2479.
[9] S. Kinouchi, H. Sugimoto et al., International Workshop on Hard Electronics'98 S2-08 (1998)

Materials Science Forum Vols. 353-356 (2001) pp. 735-738
© 2001 Trans Tech Publications, Switzerland

Silicon Carbide Zener Diodes

K. Vassilevski[1,2], K. Zekentes[1], E.V. Bogdanova[2], M. Lagadas[1] and A. Zorenko[3]

[1] Foundation for Research and Technology Hellas, Microelectronic Research Group, IESL, PO Box 1527, Vassilika Vouton, GR-71110 Heraklion/Crete, Greece

[2] A.F.Ioffe Physico-Technical Institute, Russian Academy of Sciences, Polytechnicheskaya, RU-194021 St.Petersburg, Russia

[3] State Scientific & Research Institute 'Orion', Kyiv 252057, Ukraine

Keywords: Avalanche Breakdown, Ohmic Contacts, p-n Junction, Zener Diode

Abstract. 4*H*-SiC p^+-n-n^+ Zener diodes having avalanche breakdown voltages of about 300 V and low dynamic impedance were fabricated and characterized at continuos and pulsed avalanche currents. The diodes were capable of operating at dc currents up to 60 mA corresponding to a power of 18 W. They exhibited a value of dynamic impedance of 170 Ω at a test current of 10 mA, a leakage current of 60 nA at 230 V and a positive temperature coefficient of breakdown voltage of $3 \cdot 10^{-4} K^{-1}$.

Introduction

Specially designed Zener diodes operating at reverse bias under avalanche or tunneling breakdown conditions [1] are widely used for voltage regulation and transient voltage suppression. Currently, Zener diodes with breakdown (or Zener) voltage (V_Z) from about 4 V to several hundred volts are commercially available [2]. The advantage of silicon carbide (SiC) as a semiconductor for use in Zener diodes is based on its fundamental properties. SiC remains semiconducting at temperatures up to 900°C and has an excellent thermal conductivity (of about 4 W/cm at room temperature). These properties of silicon carbide shall allow the fabrication of SiC Zener diodes handling higher current density and operating at higher temperatures in comparison with conventional diodes. Another advantage of SiC becomes obvious in the case of fabrication of Zener diodes with high V_Z values. Indeed, the specific dynamic impedance (R_Z) of these diodes at voltages higher than V_Z is defined mainly by the resistivity of the space charge region (SCR). Due to the higher breakdown field, SiC p-n junctions have lower thickness and higher doping level of SCR than silicon junctions with the same breakdown voltage. By this reason, SiC Zener diodes shall have lower dynamic (or Zener) impedance (Z_Z) than Si diodes with the same capacitance and V_Z values or lower capacitance and leakage current than Si diodes with the same V_Z and Z_Z values. For example, let us estimate the R_Z value and the capacitance of p^+-n structure having a $V_Z = 300$ V. Donor concentration in the diode base corresponding to this V_Z value is about $N_D = 10^{15} cm^{-3}$ for Si diode [3] and about $1.1 \cdot 10^{17} cm^{-3}$ for 4*H*-SiC diode [4]. For a rough estimation, the value of R_Z of such a structure may be written as [5]:

$$R_z = Z_z . A \approx \frac{V_z}{qN_D v_s} \qquad (1)$$

where v_S is the saturated drift velocity of the electrons and A the area of the diode. Substituting in this expression the values of $v_S \approx 0.9 \cdot 10^7$ cm/s for Si [3] and $v_S \approx 0.8 \cdot 10^7$ cm/s for 4*H*-SiC [5] gives the R_Z value of 0.2 Ω·cm^2 and 0.002 Ω·cm^2 for Si and 4*H*-SiC diodes respectively. The capacitance of the diode depends on the reverse voltage bias ($V = V_Z$) as:

$$C(V) = A\sqrt{\frac{\varepsilon\varepsilon_O qN_D}{2(V_{bi}+V)}} \approx \frac{1}{Z_Z}\sqrt{\frac{\varepsilon\varepsilon_O R_Z V_Z}{2(V_{bi}+V)v_S}} \qquad (2)$$

where V_{bi} is the built-in voltage of p-n junction and ε and ε_0 are the relative and vacuum permittivities. Substituting V_{bi}, ε and v_S in this equation gives:

$$\frac{C(0)|_{\mathrm{Si}}}{C(0)|_{4\mathrm{H-SiC}}} = 19.7 \quad \text{and} \quad \frac{C(V_Z)|_{\mathrm{Si}}}{C(V_Z)|_{4\mathrm{H-SiC}}} = 10.4 \qquad (3)$$

Hence, 4*H*-SiC Zener diodes may be designed to have 10 times lower dynamic impedance than Si diodes with the same values of capacitance and Zener voltage, or to have the 100 times smaller area and 10 times smaller capacitance at the same values of V_Z and Z_Z. The choice is defined by concrete diode applications when the low capacitance and leakage current (ultra high frequency and data transmission circuits) or low dynamic impedance and clamping voltage (the voltage at maximum surge current) are critical parameters.

SiC Zener diodes were fabricated with the use of 6*H*-SiC epitaxial layers grown by the sublimation sandwich method [6]. They exhibited a breakdown voltage of about 45 V and were capable to dissipate a dc power up to 5 W (corresponding to an avalanche current up to 100 mA) at an operating temperature up to 300°C. The dynamic impedance of these diodes was mainly defined by the resistivity of the substrate and of ohmic contacts and it was comparable with the Z_Z values of silicon diodes.

This paper reports on the fabrication and electrical characterization of 4*H*-SiC Zener diodes having avalanche breakdown voltages about 300 V and low dynamic impedance.

Experimental

Commercially available 4*H*-SiC p^+-n-n^+ epitaxial wafers with minimum available resistivity of the substrate (0.015-0.028 Ω·cm) were used to fabricate the diodes. The n layer had a donor concentration of $N_D = 1.1\cdot10^{17}\mathrm{cm}^{-3}$. The thickness of the n layer (2 μm) was chosen to be close to the thickness of the SCR at avalanche breakdown in an abrupt 4*H*-SiC p^+-n junction having this donor concentration. The acceptor concentration in the 1 μm thick p^+ layer was equal to $(6\text{-}8)\cdot10^{18}\mathrm{cm}^{-3}$. The thickness and the doping concentration in the layers and substrate were verified by Hg-probe C-V measurements, SIMS profiling of epitaxial structures, and C-V measurements of fabricated diodes.

Nickel of 200 nm thickness annealed at 950°C for 120 sec. was used as the back ohmic contact. The geometry of the contacts to p^+- type 4*H*-SiC epitaxial layer was defined by contact UV lithography. The metals were deposited in a single run in the following sequence: Al(50 nm)/ Ti(100 nm)/ Pt(25 nm)/ Ni(50 nm). After excess metal removal by lift-off, the anneal process was performed. The fabrication and the characterization of these contacts were described elsewhere [7, 8]. Gold overlays having 200 nm thickness were deposited on both sides of the sample. The geometry of the Au overlay deposited on the contact to p^+ epitaxial layer was defined by contact UV lithography and lift-off procedure. A commercial plasma system was used to form the mesa structures. An aluminum mask was used to define the mesa structures with different areas from $1.26\cdot10^{-5}$ to $3.14\cdot10^{-4}\mathrm{cm}^2$. The wafers to be etched were placed on the *RF* electrode and its temperature was kept at 20°C. The process was optimized to obtain contamination free, smooth surface of the side walls. The etch rate was approximately 100 nm/min at 200 W *RF* power, 20 sccm flow of SF_6, 20 sccm flow of argon and pressure of 30 mTorr. Uncovered SiC was etched away down to the n^+ epitaxial layer. Simultaneously, structures for controlling the resistivity of the contact to the p-type SiC layer, by the TLM method, were fabricated. After the SiC mesa etching,

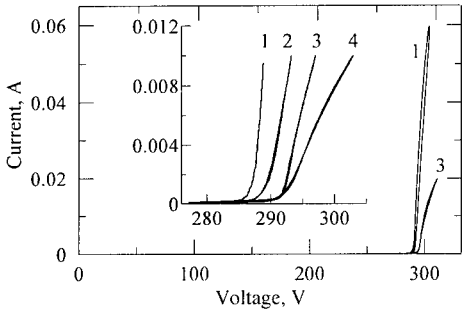


Fig 1. *I-V* characteristics of the 4*H*-SiC *p -n* diode at maximum dc avalanche current and at smaller test currents (shown in the insert) for various mesa structure diameters: 1 - 200 μm; 2 – 80 μm; 3 – 60 μm; 4 – 40 μm.

the Al mask was selectively removed. The side walls of mesa structures were not passivated. The fabricated diodes were characterized on-wafer in an air ambient.

Results

The diodes with diameter of mesa structure D= 40 μm had series resistance about 8 Ω defined mainly by the resistivity of ohmic contacts to p type layer (~$6 \cdot 10^{-5}$ Ω·cm^2) and the diodes with D= 200 μm had series resistance about 1.8 Ω. Capacities of the diodes were varying from 17 to 0.7 pF depending on the area of mesa structure. The diodes revealed stable operation at continuous avalanche current. Fig. 1 shows the *I-V* characteristics of 4*H*-SiC diodes having a breakdown voltage about 290 V at maximum continuous current obtained from a Tektronix 370 curve tracer. The maximum dc current of 60 mA was measured on the diodes with D=200 μm corresponding to a dissipated power of 18 W. The current increased exponentially with applied voltage in the initial part of the *I-V* characteristics until the diode self heating resulted in increasing values of Z_Z. It is clearly seen in the insert of Fig. 1 by the change of the curve's slope. Parameters of the diodes with different mesa structure diameters are given in Table 1. Parameters of two commercial silicon diodes are also given in Table 1 for comparison purposes. The test current I_{ZT}, at which V_Z and Z_Z were measured, was chosen at the minimum Z_Z value. The scattering of V_Z value through the wafer did not exceed 3%. The diodes with the highest capacitance of 17 pF had a dynamic impedance of 170 Ω at I_{ZT}=10 mA. The maximum dc current density passed through the diodes was 950 A/cm^2 for the diodes with D= 40 μm corresponding to the power density of 280 kW/cm^2. All the diodes revealed a positive temperature coefficient (β) of V_Z of about $3 \cdot 10^{-4}$K^{-1} measured at both dc current [9] and pulsed current conditions (see Fig. 2). This value of β is appreciably lower than 10^{-3}K^{-1} – the typical value for silicon *p-n* junctions with the same breakdown voltage [10]. The relatively low β value in 4*H*-SiC p^+-n junction shall lead to a higher thermal stability of SiC Zener diodes.

The minimum specific dynamic impedance of the diodes measured at dc current was much higher than the value calculated with Eq. (1). To avoid the influence of diode self heating and to reach the conditions of "ideal" avalanche breakdown when the value of Z_Z is defined by the resistivity of SCR only, some diodes were cut from the wafer and packaged for pulse measurements.

Mesa diameter, D [μm] or Si diode type	Capacitance at zero bias, C_0 [pF]	Zener voltage at I_{ZT}, V_Z [V]	Test current, I_{ZT} [mA]	Dynamic impedance, Z_Z(Ω) at 1mA	Dynamic impedance, Z_Z(Ω) at I_{ZT}	Maximum dc current, I_{ZM} [mA]	Leakage current at V_R=230V, I_R [nA]	Typical temperature coefficient of V_Z, β [%/°C]
40	0.7	295-304	3	1000	800	12	20	0.03
60	1.6	294-296	5	950	500	20	25	0.03
80	2.8	291-295	5	900	400	35	40	0.03
200	17	286-293	10	450	170	60	60	0.03
1N4993		300	5	2100	800	15.6	2000	0.120
1N5110		300	3		1900	10	1000	0.105

Table 1. Parameters of 4*H*-SiC diodes with different mesa structure diameters and of commercial silicon Zener diodes [2].

Current pulses having a duration of 100 ns were applied to the diodes with a duty factor 1:1000. *I-V* characteristics of the diode with D=200 μm measured in a pulse mode are shown in Fig. 2. The measured value of Z_Z = 6.3 Ω is in good agreement with Eq. (1) and thus it is defined by the resistivity of the SCR at avalanche breakdown.

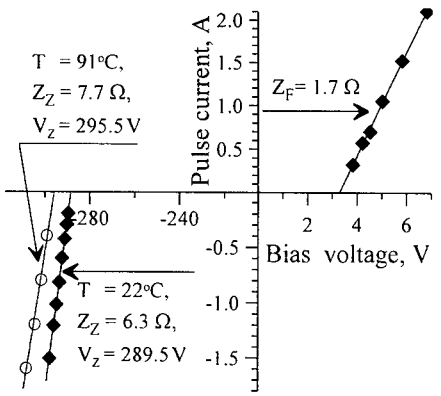


Fig 2. Pulsed *I-V* characteristics of the 4*H*-SiC *p -n* diode with a 200 μm diameter mesa.

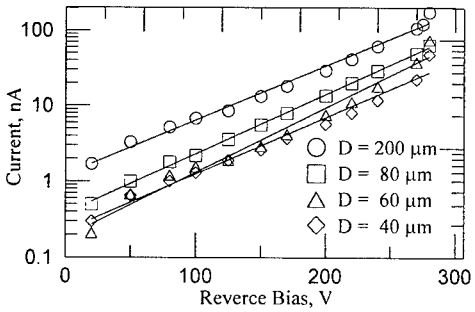


Fig 3. Leakage current of the 4*H*-SiC *p -n* diodes with different mesa structure diameters.

Although the side walls of the mesa structures were not passivated, the diodes revealed very low leakage current, comparing with conventional Si Zener diodes. It was directly proportional to the length of the diode mesa structure periphery and did not exceed 60 nA at a reverse voltage of 230 V (see Fig. 3.).

Summary

4*H*-SiC diodes having avalanche breakdown voltages of about 300 V and low dynamic impedance were processed and characterized in order to prove the advantage of SiC over silicon for fabricating high power and high voltage Zener diodes. They were capable to operate at continuous current up to 60 mA corresponding to a power of 18 W. These diodes had a dynamic impedance of 170 Ω at a test current of 10 mA, which is appreciably lower than the dynamic impedance of commercial Si Zener diodes with the same breakdown voltage. At the same time they had lower leakage currents and a lower temperature coefficient of breakdown voltage.

Acknowledgements

This work was supported by INTAS – CNES 97-1386 and NATO SfP 971879 grants.

References

[1] T.H. Beeforth, H.J. Goldsmid, Physics of Solid State Devices (Pion Limited, London, 1970)
[2] Microsemi Corporation Products Catalogue, http://www.microsemi.com
[3] S. M. Sze, *Physics of Semiconductor Devices*, Second Edition, (John Wiley & Sons, Inc, USA, 1981).
[4] A.O. Konstantinov, Q. Wahab, N. Nordell, U. Linderfelt, Mater. Sci. Forum 264-268 (1998), p.513.
[5] K. Vassilevski, K. Zekentes, A. Zorenko, L. Romanov, Mat. Res. Soc. Symp. 622 (2000), T1.8.1.
[6] A.M. Strelchuk, M.M. Anikin, A.N. Andreev, V.V. Zelenin, A.A. Lebedev, M.G. Rasstegaeva, N.S. Savkina, A.P. Syrkin, V.E. Chelnokov, L.N. Shestopalova, J. of Techn. Physics 40 (1995), p.801.
[7] K.V. Vassilevski, S.V. Rendakova, I.P. Nikitina, A.I. Babanin, A.N. Andreev, K. Zekentes, Semiconductors 33 (1999), p.206.
[8] K.V. Vassilevski, K. Zekentes, G. Constantinidis, N. Papanicolaou, I.P. Nikitina, A.I. Babanin, Mater. Sci. Forum 338-342 (2000), p.1017.
[9] K. Vassilevski, K. Zekentes, A. Zorenko, L. Romanov, IEEE Electron Dev. Lett. 21 (2000), p.485.
[10] P. Mars, Int. J. Electronics 32 (1971), p.23.

Materials Science Forum Vols. 353-356 (2001) pp. 739-742
© 2001 Trans Tech Publications, Switzerland

Characteristics of Epitaxial and Implanted N-Base 4H-SiC GTO Thyristors

J.B. Fedison and T.P. Chow

Center for Integrated Electronics and Electronics Manufacturing, Rensselaer Polytechnic Institute, 110 8th Street, Troy NY 12180, USA

Keywords: Bipolar Devices, GTO Thyristor, Ion Implantation, Power Devices

Abstract We report on the electrical characteristics of an implanted n-base GTO thyristor made from 4H-SiC. The fabricated GTO shows a forward blocking voltage of 250 V and an on-state voltage drop of 8-10 V at room temperature. An implanted n-base sheet resistance of between 40 and 50 kΩ/sq has also been measured. The doping profile of the implanted n-base layer determined from C-V measurements indicates only 5 percent of the implanted phosphorus was activated under the implant and anneal conditions used. The implanted n-base GTO also exhibits a current limitation of approximately 2 A/cm^2, above which the forward on-state voltage increases more rapidly. An epitaxial n-base GTO in 4H-SiC has also been fabricated and is compared with the implanted n-base GTO.

1. Introduction

There has been heightened interest in the reduction of dynamic and static power losses in today's power semiconductor devices and systems. For high-voltage switching applications the gate turn-off thyristor (GTO) represents a very good candidate due to its low on-state conduction losses and inherently high blocking voltage in the off-state. Silicon carbide presents the possibility of creating faster power switches that can operate at higher temperatures and higher voltages compared to silicon based devices. Its wide-bandgap energy (3.26 eV, 4H-SiC) and large critical electric field (2.5×10^6 V/cm) give it superior characteristics relative to silicon, especially in high-voltage and high-temperature applications.

SiC GTO thyristors have been demonstrated based on epitaxially grown layers where blocking voltages ranging from 700 to 3000 V have been reported [1-4]. A more flexible approach to device fabrication would be to implant either the p+ anode layer, the n-base layer or both layers. Implanted layers are also attractive due to the controllability and repeatability of the ion-implantation process. In this work, we report on the characteristics of the first implanted n-base GTO thyristor in silicon carbide. The device exhibits a blocking voltage of 250 V and an on-state voltage of 8.7 V at 1 A/cm^2.

2. Fabrication

The starting material for this device is shown in Fig. 1(a) where three p-type epitaxial layers are grown on n+ 4H-SiC substrates as shown. Unlike silicon-based thyristors, the n+ substrate is favored in silicon carbide due to the lower n+ substrate resistivity compared to the p+ substrate and the higher open-base breakdown voltage of the NPN transistor compared to the PNP. Multiple high-energy phosphorus implants (0.8 – 1.9 MeV) were carried out at 500°C to form a box profile between 0.5 and 1.5 μm below the surface at a concentration of 4×10^{17} cm^{-3} with a total dose of 3.2×10^{13} cm^{-2}. An n+ phosphorus implant was also performed in the gate contact regions to improve the n-contact resistance. These implants were activated using a 30 minute, 1200°C anneal in flowing

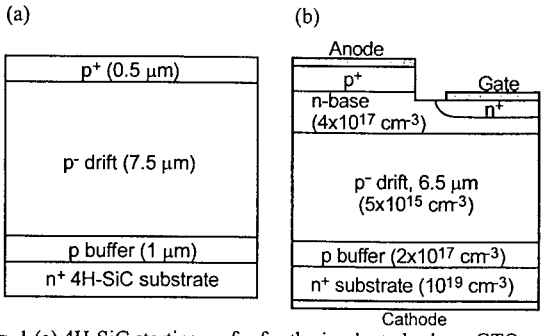


Fig. 1 (a) 4H-SiC starting wafer for the implanted n-base GTO thyristor (b) Device cross-section of implanted n-base GTO thyristor.

argon. Fig. 1(b) shows the cross-section of the fabricated implanted n-base GTO where RIE has been used to isolate the p+ anode/n-base junction. A three-step trench termination, also fabricated by RIE, is used for edge termination of these devices. The n-contact is deposited over the n+ implanted regions while the p-contact is deposited on the p+ anode as grown. The n-contact metallization consists of a Ti/Ni/Al tri-layer and the p-contact is an Al/Ni/Al tri-layer. These contacts were annealed simultaneously at 1050°C for 5 minutes in flowing argon.

3. Results and Discussion

Electrical characteristics of the fabricated GTOs were measured on a Tektronix 370A curve tracer and an HP4155A semiconductor parameter analyzer. Capacitance versus voltage (C-V) measurements were carried out on an HP4280A 1 MHz C-V meter.

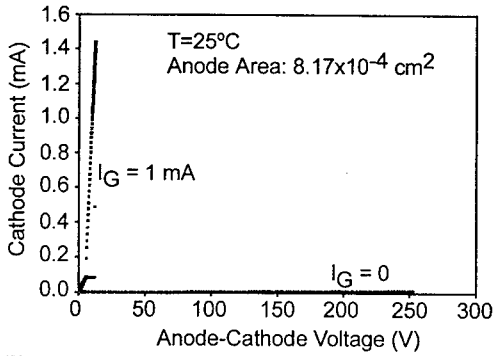


Fig. 2 Forward current-voltage characteristics of implanted n-base GTO thyristor.

The room temperature forward characteristics of the implanted n-base GTO are shown in Fig. 2 where a forward on-state voltage of 8.7 V is measured at 1 A/cm^2. With zero gate current, a forward blocking voltage of 250 V is measured. At higher current densities, the on-state voltage increases rapidly and may be the result of reduced carrier lifetime in the n-base due to implant damage. Current-voltage characteristics of the anode/n-base junction confirm an ideality factor of 2 at low and moderate bias indicating that the recombination current dominates over the entire current range. The large recombination in the n-base is attributed to defects introduced by the implant and indicates that the implant and activation anneal conditions require further optimization. A lower limit to the hole lifetime in the n-base can be estimated by considering how low the lifetime can be before the base transport factor decreases appreciably. When the hole diffusion length is equal to the n-base thickness (W) the base transport factor falls to 0.65 and the minority carrier lifetime in the n-base is related to the diffusion coefficient (D) by $\tau_p = W^2/D$. With an n-base thickness of 1 μm and an assumed hole mobility of 80 cm^2/Vs, a lower limit of 5 ns is calculated for the hole lifetime at room temperature. The hole lifetime appears to be on the order of 5 ns or less for the implanted n-base GTO. Table 1 summarizes the on-state voltage (at 1 A/cm^2) and gate trigger current at different temperatures for the implanted and epitaxial n-base GTOs. At higher temperatures, the on-state voltage and gate trigger current increases for the implanted

Table 1 GTO on-state characteristics versus temperature.

	Implanted N-Base		Epitaxial N-Base	
T (°C)	V_{ON} (V)	I_{GT} (mA)	V_{ON} (V)	I_{GT} (mA)
25	8.7	1.0	3.60	110
50	8.8	4.5	3.53	60
75	9.3	10	3.41	34

n-base GTO in contrast to what we observe in the epitaxial n-base GTO[2]. These unexpected characteristics of the implanted n-base devices are attributed to implant related defects in the n-base.

Specific contact resistance has been measured at room temperature using a four-terminal Kelvin contact resistance test structure. The specific n-contact resistance is measured to be $2.28\times10^{-4} \pm 0.57\times10^{-4}$ $\Omega\cdot cm^2$ and the specific p-contact resistance is $1.82\times10^{-2} \pm 0.42\times10^{-2}$ $\Omega\cdot cm^2$. From the simulated n+ implant, the surface concentration below the n-contact is approximately 10^{20} cm^{-3} while a surface concentration of 10^{19} cm^{-3} exists at the p+ anode. A higher p+ anode surface concentration is needed to further reduce the p-contact resistance.

The implanted n-base was characterized using four-terminal van der Pauw sheet resistance and two-terminal junction capacitance measurements. The sheet resistance of the implanted n-base decreases with temperature as shown in Fig. 3. The epitaxial n-base sheet resistance, also shown in Fig. 3, indicates the opposite trend in which falling mobility with temperature causes the n-base sheet resistance to increase at elevated temperatures. This epitaxial n-base has a doping concentration of 6×10^{16} cm^{-3} (nitrogen) and a thickness of 2.5 μm. For the implanted n-base, if all of the implanted phosphorus were activated, an n-base sheet resistance of 4 kΩ/sq would be expected. The actual sheet resistance of 42 kΩ/sq at room temperature is an order of magnitude higher indicating incomplete physical activation of the implanted phosphorus as confirmed by C-V measurements below. The decrease of n-base sheet resistance with temperature is attributed to defects introduced by implant induced damage.

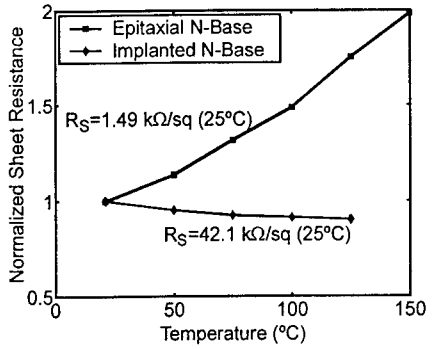


Fig. 3 Comparison of implanted and epitaxial grown n-base sheet resistance versus temperature.

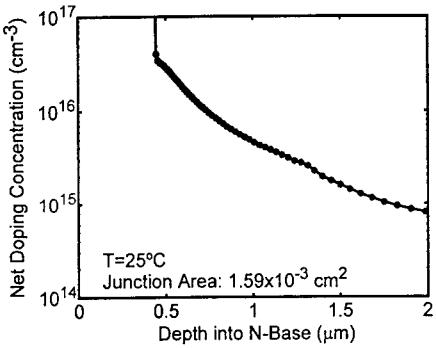


Fig. 4 Measured capacitance-voltage doping profile of implanted n-base from p+ anode/n-base junction.

Capacitance versus voltage measurements were performed to determine the net doping concentration $[N_D - N_A]$ in the implanted n-base. Because the p+ anode is heavily doped ($N_A \sim 10^{19}$ cm^{-3}) the depletion layer extends almost entirely into the n-base. At zero bias, the capacitance is 2×10^{-8} F/cm^2 indicating that 0.43 μm of the n-base is depleted due to the built in potential. Fig. 4 shows the net doping profile ($N_D - N_A$) versus depletion layer depth in the n-base from C-V measurements of the p+ anode/n-base junction. At a profile depth of 1 μm, a net concentration of 5×10^{15} cm^{-3} is extracted indicating a donor concentration of 1×10^{16} cm^{-3} (background $N_A=5\times10^{15}$ cm^{-3}). At 0.5 μm the donor concentration is 3.3×10^{16} cm^{-3}. These data indicate between 2.5 and 8 percent physical activation of the implanted phosphorus relative to the total implanted concentration of 4×10^{17} cm^{-3} and confirm that low physical activation of phosphorus contributes to the higher than expected sheet resistance. Also, the low donor concentration in the n-base results in the forward blocking voltage being limited by n-base punchthrough.

4. Conclusion

An implanted n-base GTO thyristor has been demonstrated in SiC for the first time. The device exhibits room temperature operation with a gate trigger current of 1 mA, an on-state voltage of 8-10 V, and a forward blocking voltage of 250 V, limited by n-base punchthrough. The

implanted n-base GTO also exhibits rapid increase of on-state voltage above 2 A/cm^2 indicating a hole lifetime in the n-base of 5 ns or less attributed to implant damage. C-V measurements indicate approximately 5 percent physical activation of phosphorus and the measured sheet resistance shows a decrease with temperature indicating the influence of implant related defects in the n-base. Further optimization of the n-base implant and anneal cycle are needed to improve physical activation and damage removal in this layer. The epitaxial n-base GTO thyristors showed more typical characteristics in which the n-base sheet resistance increased with temperature and the gate trigger current and on-state voltage decrease with temperature.

5. Acknowledgement

This work was supported by the Office of Naval Research (MURI Grant N0014-95-1-1302), DARPA (Contract MDA 972-98-C-0001), and the National Science Foundation (EEC-9731677). The authors also thank Dr. Mario Ghezzo of the GE Corporate Research and Development Center for helpful discussions.

6. References

[1] A. Agarwal, J. Casady, L. Rowland, S. Seshadri, R. Siergiej, W. Valek and C. Brandt, IEEE Elect. Dev. Lett. 18 (1997), p. 518.

[2] J. Fedison, T. Chow, M. Ghezzo, J. Kretchmer and M. Nielsen, Mater. Sci. Forum 338-342 (2000), p. 1391.

[3] A. Agarwal, S. Ryu, R. Singh and J. Palmour, Mater. Sci. Forum 338-342 (2000), p. 1387.

[4] J. Fedison, T. Chow, A. Agarwal, S. Ryu, R. Singh, O. Kordina, Proc. 58th Annual Device Research Conference, June 19-21 (2000), p. 135.

Materials Science Forum Vols. 353-356 (2001) pp. 743-746
© 2001 Trans Tech Publications, Switzerland

Turn-off Performance of a 2.6 kV 4H-SiC Asymmetrical GTO Thyristor

A.K. Agarwal[1], P.A. Ivanov[2], M.E. Levinshtein[2], J.W. Palmour[1], S.L. Rumyantsev[2], S.H. Ryu[1] and M.S. Shur[3]

[1] Cree, Inc., 4600 Silicon Drive, Durham NC 27703, USA

[2] A.F.Ioffe Physico-Technical Institute, Russian Academy of Sciences, Polytechnicheskaya, RU-194021 St.Petersburg, Russia

[3] Department of Electrical, Computer and Systems Engineering and Center for Integrated Electronics and Electronics Manufacturing, CII 9017, Rensselaer Polytechnic Institute, Troy NY 12180-3590, USA

Keywords: Carrier Lifetime, Gate Turn-Off Thyristor, Pulse Measurements

Abstract 4H-SiC asymmetrical gate turn-off thyristors (GTO's) with 2.6 kV breakover voltage have been tested with respect to gate turn-off performance. Transient characteristics of the GTO's and pulse regime of gate turn-off processes were studied in the temperature range from 293 to 500 K. Under cathode current density of 300 A/cm^2, turn-off current gain, K_G, of 12.5 was achieved at room temperature. The value of K_G is the highest reported for SiC GTO's. The temperature dependencies of turn-off time, pulse turned off gate current and holding current were studied.

Introduction

Silicon carbide has a tremendous potential for bipolar device applications such as inverters and switch-mode power supplies. Recently, remarkable progress has been made in this field including developments of 6H- and 4H-SiC based GTO thyristors [1-5].
In this paper, we report on quasi-static and pulse gate turn-off performance of 4H-SiC asymmetrical GTO thyristor with 2.6 kV breakover voltage, for temperatures ranging from 293 to 500 K.

Experimental details

The 4H-SiC GTO's were fabricated by Cree Inc. [5]. Five epilayers were grown on 380 μm 8° off-axis 4H-SiC n-type substrate with resistivity of 0.02 Ω·cm. The blocking p^--base layer was 50 μm thick, doped at about 7×10^{14} cm^{-3}. The underneath p-buffer layer of 2.5 μm doped to $(2–5)\times10^{17}$ cm^{-3} made the device asymmetrical. The 2.5 μm thick n-base layer was doped at $(2–5)\times10^{17}$ cm^{-3}. The other two layers were a 1.5 μm p^+-emitter layer doped at 2×10^{19} cm^{-3} and 1μm n^+-emitter layer doped at 5×10^{18} cm^{-3}. The blocking junction was terminated with a Junction Termination Extension. The GTOs of 1 mm × 1 mm in size are of interdigitized geometry with 19 anode fingers and 20 gate fingers. Each anode finger is 30 μm in width and 654 μm long thus the total anode area is 3.7×10^{-3} cm^2.
Switch-on and switch-off pulses with rise time of 100 ns were applied between grounded anode and gate pads with a frequency of 1 Hz to provide isothermal conditions.

Results and discussion

Figure 1 shows the main transient processes in GTO's. At $t = 0$, a negative pulse is applied to the gate, and after the delay time, the thyristor is turned on. The turn-on rise time decreases from ~ 600 ns to ~ 100 ns with temperature increase from 293 to 500 K (similar results were obtained earlier in [6] for 700 V thyristors). Cathode current in on-state, I_{Con} is governed by the load resistance R_l and the cathode bias V_b. At $t = t_1$ (t_1 = 2 μs in Fig. 1), a positive turn-off gate pulse is applied to the

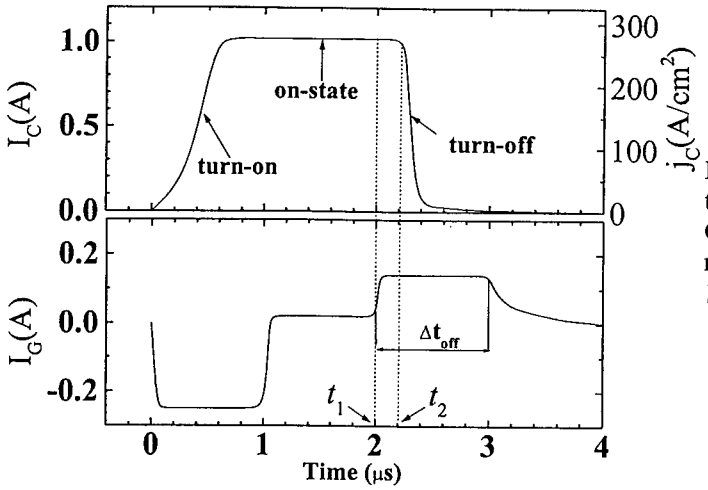


Fig. 1. Main stages of transient processes in GTO's. T = 300 K. Load resistance R_l = 25 Ohm, V_b= 30 V.

structure. After some delay ($t_2 - t_1$ in Fig. 1), the GTO is turned off. The turn-off time increases monotonically with a temperature increase.

At every temperature, there is a maximum value of I_{Con} which can be turned off by gate current. At room temperature, I_{Con} is equal to 3.3 A, which corresponds to the on-state current density j_{Con} = 1000 A/cm^2. The turn-off current gain K_G=I_C/I_G depends on temperature, gate turn-off pulse duration Δt_{off}, and the current density in the on-state. Fig.1 shows the turn-off process with K_G≈7. With Δt_{off} increase the current gain also increases and reaches its maximum K_G≈12.5 (at j_{Con}=300A/cm^2 and T=300K). At maximum current density j_{Con}=1000A/cm^2 which can be turned off at 300K the current gain K_G≈6.

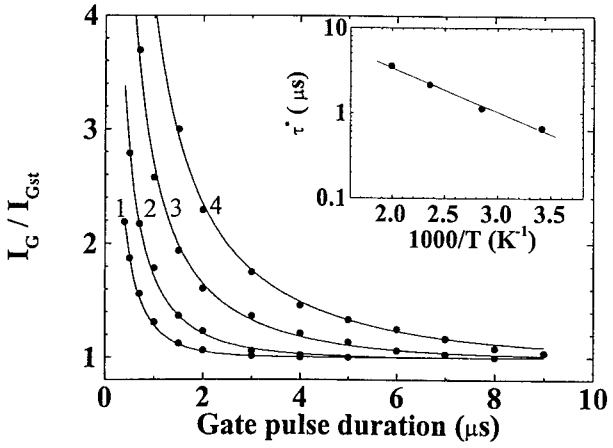


Fig. 2. The dependencies of normalized turned-off gate current I_G/I_{Gst} on gate pulse duration at different temperatures. Solid lines are plotted according to Eq. 1 with τ* as a fitting parameter. 1 – 293 K, 2 – 351 K, 3 – 424 K, 4 – 502 K. R_l = 25 Ohm. Inset shows the dependence of τ* versus 1000/T.

The amplitude of the turned off gate current pulse, I_G increases with a decrease in Δt_{off}. Figure 2 demonstrates the dependence of I_G/I_{Gst} versus Δt_{off} at different temperatures. Here I_{Gst} is the turned

off gate current in quasi-static regime. At given temperature T, the cathode current was chosen twice as high as the holding current. It is seen that at given I_G/I_{Gst} ratio, the turned off gate pulse duration increases with temperature growth. At $T = 293$ K (curve 1), the I_G is practically equal to I_{Gst} at $\Delta t_{off} \approx 2.5$ μs; at $T = 502$ K (curve 4), this time exceeds 10 μs. In paper [7], the following semiempirical formula was suggested for the dependence of I_G/I_{Gst} on Δt_{off}:

$$I_G / I_{Gst} = \frac{1}{1 - \exp(-\Delta t_{off} / \tau^*)}, \qquad (1)$$

where τ^* is a fitting parameter which can be considered as a rough estimate of the value of the carrier lifetime at high injection level in the blocking base.

It is seen that Eq. (1) describes the experimental dependences very well over the entire temperature range. Inset in Fig. 2 shows the temperature dependence of τ^*. The value of τ^* grows exponentially from 0.6 to 3.6 μs in the temperature interval from 293 to 502 K.

Figure 3 shows the transient turn-off GTO characteristics at different temperatures.

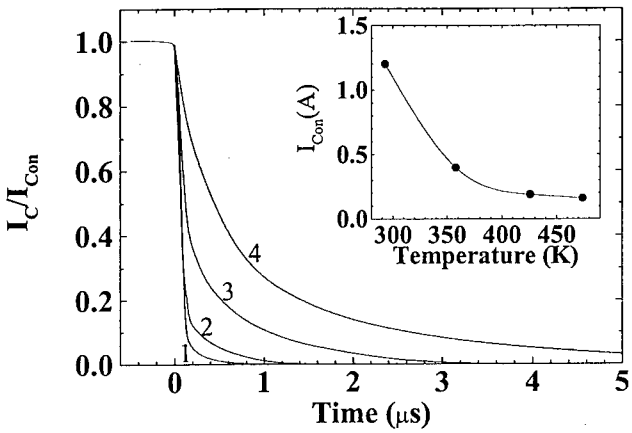


Fig. 3. The cathode current decay during the turn-off process at different temperatures. T(K): 1 – 293, 2 – 358, 3 – 426, 4 – 474. In all cases, very long (quasi-static) turn-off gate pulse of 100 mA is applied. Inset shows the temperature dependence of I_{Con}, which can be turned-off by a 100 mA gate pulse.

The time $t = 0$ in Fig. 3 corresponds to $t = t_2$ in Fig. 1, i.e. only the turn-off process is shown in Fig. 3. For every temperature, the cathode current $I_C(t)$ is normalized to the current I_{Con}, which can be turned off by 100 mA gate pulse (The inset shows the temperature dependence of this value of I_{Con}). One can see that the turn-off time increases monotonically with temperature increase. Furthermore, two steps can be observed in the turn-off process in the temperature interval 293 K < T < 420 K (curves 1–3 in Fig. 3). At 293 K, the cathode current falls down very sharply to $I_C \sim 0.1\ I_{Con}$. Then the current decay becomes smoother. At $T > 450$ K, only the slow step can be observed. Note that the duration of the slow step is very close to τ^* value at a given temperature. The total turn-off time at T=293K is of the same order of magnitude as was reported in [2] for 700V SiC thyristors.

Figure 4 shows the temperature dependence of the cathode holding current I_{Ch}. The value of I_{Ch} decreases from 0.54 A to 0.052 A with the increase in temperature from 293 to 502 K. One can assume that two effects are responsible for I_{ch} versus T dependence. First, the increase in the carrier lifetime in the blocking base layer increases the common-base current gain in the base. Second, the

injection efficiency of p^+n junction between the p^+-emitter and the n-base increases with temperature due to the enhanced thermal ionization of relatively deep Al acceptor level.

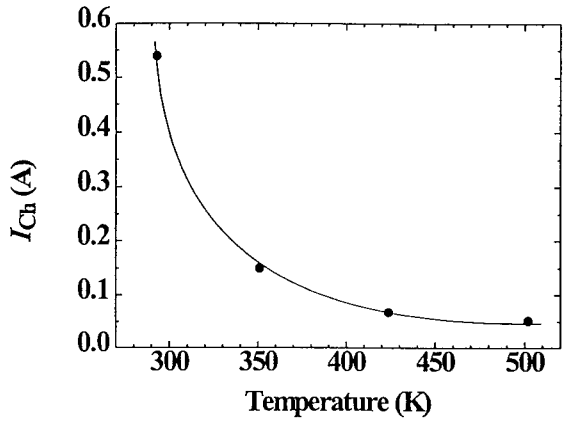


Fig. 4. The temperature dependence of cathode holding current I_{Ch}

Conclusions

The dependence of the turn-off current gain on turn-off gate pulse duration manifests a strong increase in carrier lifetime in the blocking base layer with temperature. The maximum cathode current, which can be turned off, decreases with increase in temperature. The turn-off time increases and the holding current decreases with temperature as expected [3,6]. The carrier lifetime estimated from turn-off transient characteristics is close to that measured for high-voltage diode structures [8].

Acknowledgement

This work was supported by the Office of Naval Research MURI program under Contract No N00014-95-1-1302, monitored by Dr. J. Zolper.

References

[1] K. Xie, J.H. Zhao, J.R. Flemish, T. Burke, W.R. Buchwald, G. Lorenzo, and H. Singh, *IEEE Electron Device Lett.* **17** (1996), p. 142.

[2] A.K. Agarwal, J.B. Casady, L.B. Rowland, S. Seshadri, R.R. Siergiej, W.F. Valek, and C.D. Brand, *IEEE Electron Device Lett.* **18** (1997), p. 518.

[3] B. Li, L. Cao, and J.H. Zhao, *IEEE Electron Device Lett.* **20** (1999), p. 219.

[4] J.B. Fedison, T.P. Chow, M. Ghezzo, J.W. Kretchmer, and M.C. Nielsen, Mater. Sci. Forum **338-342** (2000), p. 1391

[5] A.K. Agarwal, S.H. Ryu, R. Singh, O. Kordina, and J. Palmour, Mater. Sci. Forum **338-342** (2000), p. 1387

[6] N.V. Dyakonova, M.E. Levinshtein, J.W. Palmour, S.L. Rumyantsev, and R. Singh, *Semicond. Sci. Tecnol.*, **13** (1998), p. 241

[7] I.L. Kaganov and E.S. Malahov, in Reports of Scientific-Technical Conference of All-Union Electrotechnical Research Institute. Moscow, 1966 (in Russian).

[8] P. A. Ivanov, M. E. Levinshtein, K. G. Irvin, O. Kordina, J. W. Palmour, S.L. Rumyantsev and R. Singh, Electronics Letters, **35** (1999), p. 1382

Materials Science Forum Vols. 353-356 (2001) pp. 747-752
© 2001 Trans Tech Publications, Switzerland

SiC Based Gas Sensors and their Applications

S. Savage[1], H. Svenningstorp[2], L. Unéus[2], A. Kroutchinine[2], P. Tobias[2], L.-G. Ekedahl[2], I. Lundström[2], C. Harris[1] and A. Lloyd Spetz[2]

[1] ACREO AB, Electrum 236, Isafjordsgatan 22, SE-164 40 Kista, Sweden

[2] S-SENCE and Div. of Applied Physics, Linköping University, SE-581 83 Linköping, Sweden

Keywords: Car Exhausts, Electronic Nose, Flue Gases, Gas Sensors, MOSFET, Schottky Diodes

Abstract

The development and field-testing of hardy high-temperature sensors based on silicon carbide devices has to date shown promising results in several application areas. As the need to take care of the environment becomes more urgent, these small and relatively cheap sensors could be used to increase the monitoring of gases, or to replace or complement larger and more expensive sensor technologies used today. In this paper the development of Silicon Carbide MOSFET transistor sensors and Schottky diode sensors is described. The devices are tested in industrial applications such as monitoring of car exhausts and flue gases.

1. Introduction

As environmental issues become more widely debated and regulated, the requirement to detect and control unwanted emissions becomes more urgent. Gas sensors that can be used at high temperatures and in aggressive environments have the potential to improve our environment through the control of industrial and car emissions, and also provide the capability for in-line monitoring of production processes. Silicon carbide (SiC) is an ideal material from which to produce these sensors. Its wide bandgap permits its use at temperatures up to 1000°C [1]. Also, silicon carbide is very hard and chemically inert, which permits its use in aggressive atmospheres.

2. Sensor function

An electronic device based on silicon carbide can function as a sensor by the deposition of a catalytic metal on a thin insulating layer to its surface. The catalytic metal can be for example platinum, iridium, palladium, or combinations of these. Metal oxides can also be used as catalytic layers on devices where the gate material does not need to conduct large currents.

Thick, homogeneous catalytic metals can be used to directly detect hydrogen or hydrogen-containing molecules, such as hydrocarbons. The molecule dissociates on the surface of the metal, and the resulting hydrogen atoms diffuse through the metal in the order of nano- to microseconds to the insulator surface, see Fig.1. This creates a polarized layer on the surface of the insulating layer, which in its turn causes a change in the number of mobile carriers in the device, and hence a change in the device's electrical characteristic. For example, a change can be detected in the flat-band voltage of a capacitor or in the I-V characteristic of a Schottky diode. Figure 2 shows the measured I-V curves of a Schottky diode in two different atmospheres that contain propane and oxygen, respectively. It is seen that the curve is shifted to lower voltages in the case of the propane containing atmosphere. The gas response can thus be measured as a voltage shift at a constant current level.

Molecules such as O_2, NO and CO, when in the presence of hydrogen-containing molecules, can be indirectly detected by thick catalytic metals through their chemical reactions on the surface of the catalytic metal, which in turn influences the concentration of polarised species at the metal insulator

interface. Thin films or thick porous metal films can be used to directly detect non-hydrogen-containing molecules, as well as those that do contain hydrogen. Charged or polarised gas species on the oxide surface exposed in the metal cracks and holes cause a change in the number of mobile carriers in the device and so permit detection of the gas.

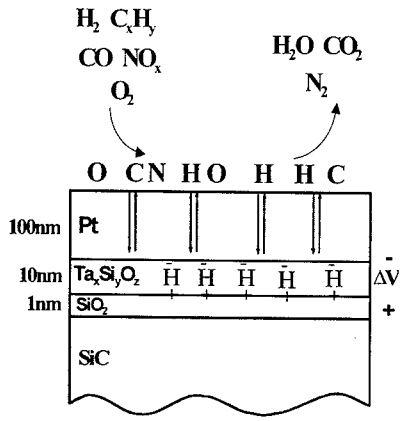


Fig. 1. Schematic picture of a MISiC sensor. Possible chemical reactions and adsorption of molecules are shown.

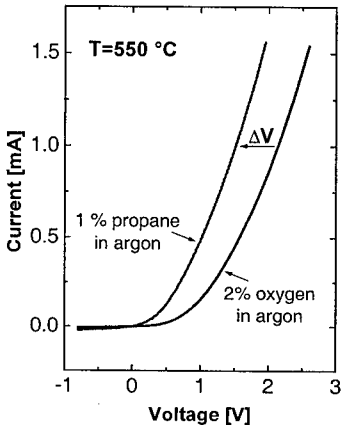


Fig. 2. I-V characteristics of a Schottky diode sensor in two different atmospheres.

3. Sensor devices

The simplest electronic devices are capacitors and Schottky diodes, and silicon carbide sensors based on these devices have been under development for several years [1-3]. The capacitor sensors have demonstrated gas-sensitivity up to a temperature of 1000°C, for a limited time. The SiC epitaxial layers required in the devices were grown at Linköping University in Sweden on substrates from Cree [1,4]. To date, most trials in a number of applications have been carried out on SiC Schottky diodes [2,5-8]. In early devices, which had an adhesion layer of Ta or $TaSi_x$ underneath the platinum layer, a strange behaviour in the sensor response was noted shortly before the devices failed. This was an abnormally large gas response, 2-3V in size but rather unstable, to a change between hydrogen and oxygen in the ambient. This was attributed to the formation of nanoparticles of Ta with an oxidic shell [9]. An ozone treatment (10 min at RT) of the HF etched SiC surface was introduced. It was found by spectroscopic ellipsometry analysis as well as photoelectron spectroscopy utilizing synchrotrone radiation, that an oxide of 1 nm, close to SiO_2 in composition, was formed by the ozone exposure [10, 11]. This thin oxide increased the stability of the Schottky diodes considerably. However, both capacitor devices and Schottky diodes have disadvantages. Capacitors require complicated surrounding circuitry in order to measure the gas response, and the extremely thin insulating layers under the catalytic metal required for Schottky diodes can lead to instabilities and degradation of the device characteristic at high temperatures and during long term operation.

During the past two years, a gas sensor based on a silicon carbide field-effect transistor (MISiCFET) has been under development in a co-operative effort between S-SENCE and ACREO. The silicon carbide FET was designed and processed by ACREO [12] for stability at the highest temperatures, and functioned as a gas sensor by the application of one of the catalytic metals previously developed by S-SENCE [13]. The device design is shown in Fig. 3. A voltage applied between the source and drain contacts (marked "S" and "D" in Fig. 3), causes a current to flow between these contacts through the channel region. The catalytic metal (marked "G" in the figure) is placed over the channel region. The presence of gas molecules in the atmosphere causes the concentration of mobile carriers in the channel to change in the manner described in section 2 of this article, which shifts the characteristic in a similar

way to that shown in Fig 2. Source and gate of the device are connected to create a convenient two terminal sensor device. In order to promote high-temperature stability, medium-doped extension regions to the source and drain regions were included in the design, as shown in Fig 3. This promotes an improvement in the quality of the gate passivation, which overlaps these regions and so improves the stability of the device.

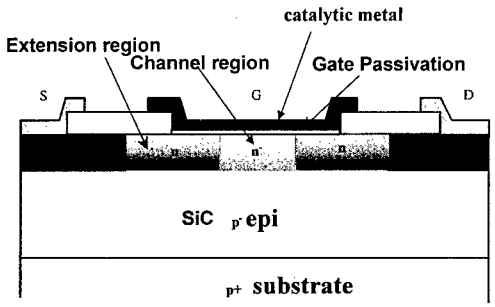


Fig. 3. Cross-section of silicon carbide FET (MISiCFET) sensor.

The first two batches of FETs have been completed. It was shown that the devices from batch number 1 were not entirely stable at temperatures over 500°C. Therefore, a second batch with an improved design was processed and shown to have greater stability. At 700°C the transistors can be operated as gas sensors for more than 44 hours and at 500°C for more than two weeks. Severe degradation of the metal surface was observed after failure at the highest temperatures, and it was concluded that catalytic etching by the hydrogen /oxygen atmosphere was the main failure mechanism at these temperatures. The MISiCFET devices from batch 2 have been used in several of the applications described in section 4.

For use in both laboratory and industrial applications, the sensor chip is mounted by gluing onto a ceramic heater, which is attached with an air gap to a 16 pin holder. This allows the sensor chip to be heated to 600°C, while the holder stays below 200°C. The sensor response is measured as the voltage at a constant current of 0.1 mA.

4. Sensor applications

The sensors produced by S-SENCE and ACREO have been tested in a variety of applications, both in simulated environments in the laboratory and in real environments in the field. One application for these sensors is cylinder-specific monitoring of hydrocarbons in the exhaust gases of automobile engines. In field tests, the silicon carbide sensor is placed in the exhaust system, at the point where the four outlet pipes from the cylinders join together, see Fig. 4 a. A typical measurement cycle is shown in Fig. 4 b, where one of the cylinders has been deliberately injected with excess fuel. The sensor is operated at a temperature of about 700°C in this situation, and the catalytic metal is 100 nm Pt with a 10 nm layer of $TaSi_x$ underneath. It is seen in Fig. 4 b that the sensor is sufficiently fast to show which

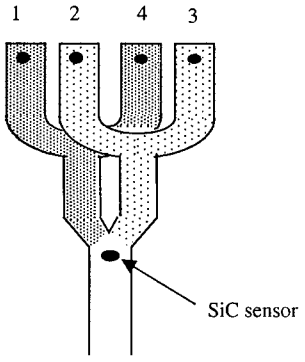


Fig. 4 a. Positioning of a MISiC sensor in the exhaust system of an automobile engine

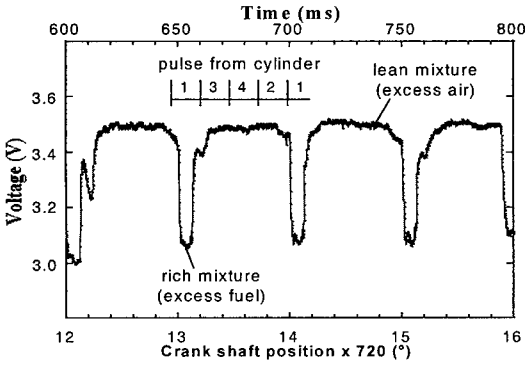


Fig. 4 b. Response of a MISiC sensor when one cylinder is injected with excess fuel.

of the four cylinders is misfiring. This has been demonstrated by both the Schottky diode sensor and the MISiCFET sensor [2,5]. The speed of response from these sensors provides the opportunity for cylinder-specific adjustments from the output of the one sensor, a feat which is not possible with the sensors used today.

Sensors with a thick platinum gate do not normally show any response to reducing gases in an excess of oxygen. MISiC sensors with thin porous platinum and iridium gates have been tested and shown to respond to reducing gases even in an excess of oxygen, for example in synthetic diesel exhausts and flue gases. The selectivity to different gases can be enhanced by modifying the gate metal and by the choice of operation temperature. In Fig. 5 a the signal from a MISiC sensor with a gate metal of 50 nm Pt + 8 nm Ir is shown during exposure to propene in a staircase function in a background of gases simulating petrol engine exhausts (CO_2 9%, CO 0.455 %, O_2 0.088-1.65 % / 1.15 %, H_2 0.1015 %, NO_x 0.16 %, H_2O 2 %) [8]. The sensor signal shows no response to variations of the HC concentration in this ambient at an operation temperature of 300°C. The reason for this is probably of reaction kinetic nature, due to a combination of the low temperature and the low oxygen concentration even at $\lambda > 1$. However, at 500°C, where the chemical reactions are faster, this sensor responds to a change between 200 and 400 ppm of HC, and this is especially clear for the lean conditions, lambda = 1.05, where there is a constant small excess of oxygen. The behaviour at rich conditions, lambda = 0.99, where there is a small constant excess of HC, is more complex, but at a constant oxygen concentration it is again clear that the response of this sensor saturates at a rather low concentration, here at the step between 200 and 700 ppm of HC. The chosen steps in HC concentration are apparently too large to show the dynamics of the response to HC for this sensor.

Figure 5 b shows the signal of a MISiC sensor with 100 nm Ir as the gate metal, again with a background of synthetic gases, see above. This sensor follows the HC variation nicely when there is an excess of oxygen, even at an operation temperature of 300°C. The reactivity of HC seems to be higher on the Ir surface, than on the surface of the layered structure of Pt + Ir. The signal is noisy when HC is in excess, but follows even the larger concentrations of HC nicely, when the oxygen concentration is kept constant. If the 100 nm Ir film is a porous film this could explain the higher dynamic range of this sensor compared to the sensor with the thinner metal gate in Fig. 5 a. More gas molecules are consumed by the thicker film, without giving rise to detectable species. A similar difference in dynamic range was also observed for thin and thick porous Pt films for the detection of ammonia [7]. This indicates the possibility to tailor-make sensors by the choice of structure and thickness of the catalytic metal, for a certain concentration range.

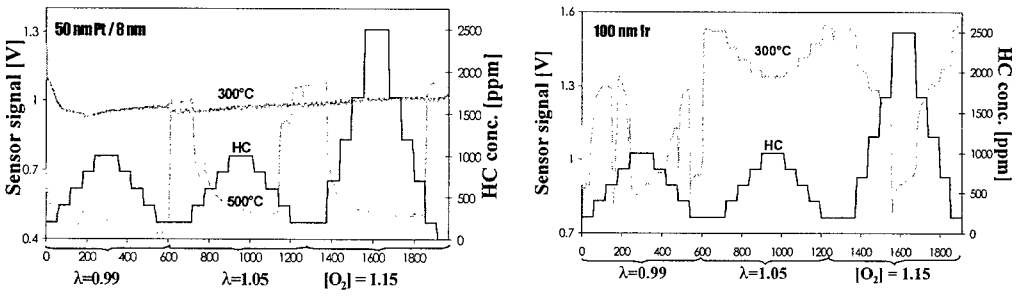


Fig. 5. *Sensor signal from a MISiC sensor with a. 50 nm Pt + 8 nm Ir and b. 100 nm Ir as the gate metal during exposure to different HC, propene (C_3H_6), concentrations varied in a staircase function in a back ground of synthetic exhausts. The oxygen concentration is varied to keep a constant lambda value or kept constant at 1.15 %.*

Another application area for these sensors is the monitoring of gases such as carbon monoxide (CO) in flue gases from small power plants, boilers. These can currently be detected by optical techniques such as fourier transform infrared (FTIR) instruments, but this is too expensive and complex for use in boilers. Field tests of on-line monitoring by silicon carbide sensors containing platinum (Pt) or iridium (Ir) catalytic metals have been carried out. Also commercially available Metal Oxide Sensors (MOS) and a linear lambda sensor were used. Flue gas from a 500 kW pellets fuelled boiler, used for heating apartment blocks, has been used to feed the sensors and the experimental set-up of reference instruments. Data was collected over several weeks. Data from the first day was used to build a PLS (partial least square) model of the CO concentration. Predictions from the model were compared with experimental data collected during day 5, and the results are shown in Fig 7. Even NO could be modelled to some extent. Long-term tests have now been carried out and the results will be treated with drift compensation algorithms [14], which is expected to extend the time for relevant prediction considerably.

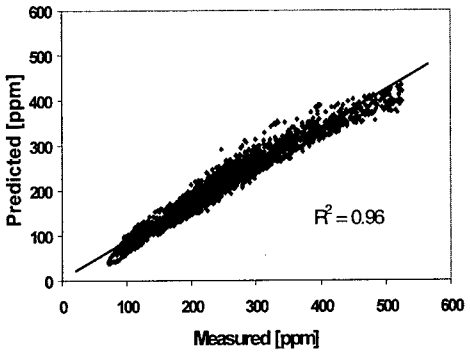


Fig. 6. Prediction of the CO concentration in flue gases after 5 days by the use of a PLS model on data from the first day of measurements.

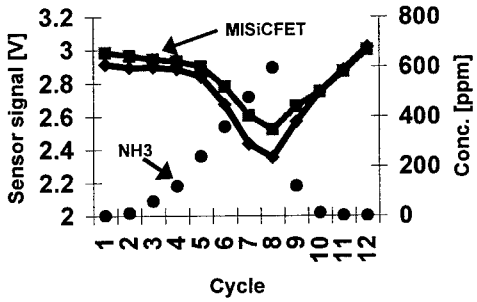


Fig. 7. The signal from two MISiCFET sensors, both with a porous Pt gate and operated at 300°C, responding to stepwise changes in the NH3 conc. in the exhaust after a diesel engine.

The selective catalytic reduction of NO in diesel exhausts is carried out by the injection of ammonia or urea. Therefore, the presence of an ammonia sensor in the system is highly desirable. Figure 7 shows the signal of two MISiCFET sensors responding to stepwise changes in the NH_3 concentration in the exhaust of a diesel engine. The results showed that a thick porous Pt film and a thin Pt film have different dynamic ranges for the ammonia response [7].

5. Summary

Results from tests of silicon carbide based sensors point towards the possibility to use arrays of sensors with different catalytic metals, different metal structures (for example, porous or non-porous) and different operation temperatures in a high temperature electronic nose to identify several components in, for example, flue gases, car exhausts, and for in-line production monitoring. The development of silicon carbide technology will in the future permit smart sensor systems for high temperature monitoring with sensors and electronics integrated on the same chip.

Acknowledgement

The measurements were performed at Mecel AB, Sweden, Volvo Technological Development, Sweden and Vattenfall TU, Sweden. The research on high temperature chemical sensors based on silicon and silicon carbide is supported by grants from the Swedish National Board for Industrial and Technical Development and Swedish Industry through the center of excellence, Swedish Sensor Center, S-SENCE. The research is also supported by grants from the Swedish Research Council for Engineering Sciences and from the SSF-SiCEP program.

References

[1] A. Lloyd Spetz, A. Baranzahi, P.Tobias, and I. Lundström, Physica Status Solidi (a) 162 (1997) p. 493.

[2] A.Baranzahi, P. Tobias, A. Lloyd Spetz, I Lundström, P. Mårtensson, M. Glavmo, A. Göras, J. Nytomt, P. Salomonsson, and H. Larsson, SAE Techn. Paper Series 972940 (SP-1300) (1997) p. 231.

[3] G. W. Hunter, L.Y. Chen, P. G. Neudeck, D. Knight, C. C. Liu, Q. H. Wu, H. J. Zhou, D. Makel, M. Liu, W. A. Rauch, NASA / TM-1998-208504.

[4] Cree Research Inc, 4600 Silicon Drive, Durham, NC 27703, USA.

[5] P.Tobias, P. Rask, A. Göras, I. Lundström, P.Salomonsson, and A.Lloyd Spetz, Sensoren und Messysteme 2000, VDI Berichte 1530, VDI Verlag, Düsseldorf, March 13-14, (2000) p. 179.

[6] L. Unéus, M. Mattsson, P. Ljung, R. Wigren, P. Mårtenssson, L-G. Ekedahl, I. Lundström, and A. Lloyd Spetz, conf. Proc. ISOEN´2000, Brighton, England, July 24-26, 2000, p. 15.

[7] H. Svenningstorp, P. Tobias, A. Kroutchinine, P. Salomonsson, B. Häggendal, I. Lundström, L. – G. Ekedahl, and A. Lloyd Spetz, Eurosensors XIV, Copenhagen, Denmark, August 28-30, 2000, acc.

[8] H. Svenningstorp, B. Widén, P. Salomonsson, L. –G. Ekedahl, I. Lundström, P. Tobias, and A. Lloyd Spetz, Proc. 8 IMCS2000, Basel, Switzerland. July 2-5, 2000, submitted.

[9] D. Schmeisser, O. Böhme, A. Yfantis, T. Heller, D. R. Batchelor, I. Lundström, and A. Lloyd Spetz, Phys. Rev. Lett. 83, 2 (1999) p. 380. O. Böhme, A. Lloyd Spetz, I Lundström, and D. Schmeisser, submitted.

[10] S. Zangooie, H. Arwin, P. Tobias, I. Lundström and A. Lloyd Spetz, Proc. of ICSCRM´99, Research Triangle Park, NC, USA, October 10-15, 1999, Material Science Forum 338-342 (2000) p. 1085.

[11] R. P. Mikalo, P. Hoffman, D. R. Batchelor, A. Lloyd Spetz, I. Lundström, and D. Schmeisser, this conference proceeding, submitted.

[12] S. M. Savage, A. Konstantinov, A. M. Saroukan, C. Harris, Proc. of ICSCRM´99, Research Triangle Park, NC, USA, October 10-15, 1999, Material Science Forum 338-342 (2000) p. 1431.

[13] H. Svenningstorp, P. Tobias, P. Salomonsson, I. Lundström, P. Mårtensson, and A. Lloyd Spetz, Proc. of ICSCRM´99, Research Triangle Park, NC, USA, October 10-15, 1999, Material Science Forum 338-342 (2000) p. 1435.

[14] T. Artursson, T. Eklöv, I. Lundström, P. Mårtensson, M. Sjöström, M. Holmberg, Journal of Chemometrics, Proc. SSC6, accepted.

Materials Science Forum Vols. 353-356 (2001) pp. 753-756
© 2001 Trans Tech Publications, Switzerland

High Temperature 10 Bar Pressure Sensor Based on 3C-SiC/SOI for Turbine Control Applications

S. Zappe[1], J. Franklin[1], E. Obermeier[1], M. Eickhoff[2,5], H. Möller[2,6], G. Krötz[2], C. Rougeot[3], O. Lefort[3] and J. Stoemenos[4]

[1] Technical University of Berlin, DE-13355 Berlin, Germany

[2] DaimlerChrysler Research and Technology, DE-81663 München, Germany

[3] Sextant Avionique, Valence, France

[4] Aristotle University Thessaloniki, GR-54006 Thessaloniki, Greece

[5] now at: Infineon Technologies, München, Germany

[6] now at: Deutsche Bahn Research, München, Germany

Keywords: 3C-SiC/SOI, High Temperature, Pressure Sensor

Abstract The FE (Finite Element) simulation, fabrication and characterization of a membrane-type piezoresistive pressure sensor with piezoresistors consisting of 3C-SiC is presented. The nominal pressure of the device is P_{nom} = 10 bar, the maximum operating temperature is T_{max} > 400 °C. The sensitivity at RT is S = 0.5 mV/V bar. The device is suitable for turbine control applications.
The membrane of the sensor was defined by ICP etching of a UNIBOND SOI wafer. Due to the vertical sidewalls produced by the etching process, the desired pressure range of the device can simply be adjusted by controlling the etch depth/membrane thickness.
An overload protection was realized by choosing a centerboss membrane structure. For a nominal pressure range of P_{nom} = 10 bar a membrane thickness, an inner membrane diameter and an outer membrane diameter of 60 µm, 500 µm and 2 mm, respectively, were chosen.
The sensors are absolute pressure sensors with a closed cavity which was realized by bonding the structured UNIBOND wafer to a silicon wafer. A 2.2 µm thick SiC layer was deposited onto the SOL of the UNIBOND wafer on top of the sensor cell at 1220 °C during an LPCVD process using methylsilane. In situ doping was achieved by adding NH_3 to the process gas. The 3C-SiC piezoresistors were structured by RIE. The resistors were connected in a Wheatstone Bridge configuration. The high temperature stable metallization system TiWN/Au was used.

Introduction

The development of piezoresistive pressure sensors based on 3C-SiC epitaxially grown on Silicon On Insulator (SOI) is very attractive because the 3C-SiC-on-SOI system combines high temperature capabilities with well established micromachining processing. Furthermore, the use of the material system 3C-SiC-on-SOI is a low cost alternative to sensors fabricated using 6H-SiC or 4H-SiC bulk substrates.
A very good 3C-SiC crystal quality and hence a high gauge factor were already demonstrated in the past [1], [2]. The high quality 3C-SiC films used for this work were deposited using a low temperature LPCVD growth process [3].
The fabrication of sensors operating up to T = 400 °C e.g. in order to control combustion engines or for oil well logging applications is possible [4], [5].
The sensor presented here is suitable for turbine control applications (nominal pressure P_{nom} = 10 bar, operating temperature T_{op} > 400 °C).
It was possible to realize absolute pressure sensors by applying a silicon fusion bonding process. As no connection to a reference pressure line is needed, packaging of the sensors is facilitated. The influence of different thermal expansion coefficients of sensor and packaging materials and their impact on sensor signal stability and drift can be significantly reduced.

FE Simulation of the Sensor

The sensor concept is shown in Fig. 1. The FE (Finite Element) ANSYS model of a quarter of the membrane part of a pressure sensor as shown in Fig. 2 was used for design optimization.



Fig. 1: Cross section of the sensor cell. A UNIBOND SOI wafer is structured by ICP etching in an STS machine. The etched wafer is bonded to a silicon substrate and the 3C-SiC layer is deposited onto the UNIBOND wafer. The piezoresistors are structured by RIE (Reactive Ion Etching) in an SF_6/O_2 plasma.

For a nominal pressure of 10 bar, a membrane thickness of 60 µm was chosen. At an applied pressure of 10 bar, the deflection of the centerboss in z-direction is $\delta_z = -3.8$ µm. Maximum tensile and compressive stresses in the 3C-SiC top layer are about $\sigma = \pm 280$ MPa. (Fig. 2) This corresponds to maximum strain values around $\varepsilon = \pm 0.9$ E-3. Based on the simulation results, the relative change of resistance $\Delta R/R_0$ was calculated for a transverse and a longitudinal oriented resistor and optimized positions of the piezoresistors were determined (Fig. 3).

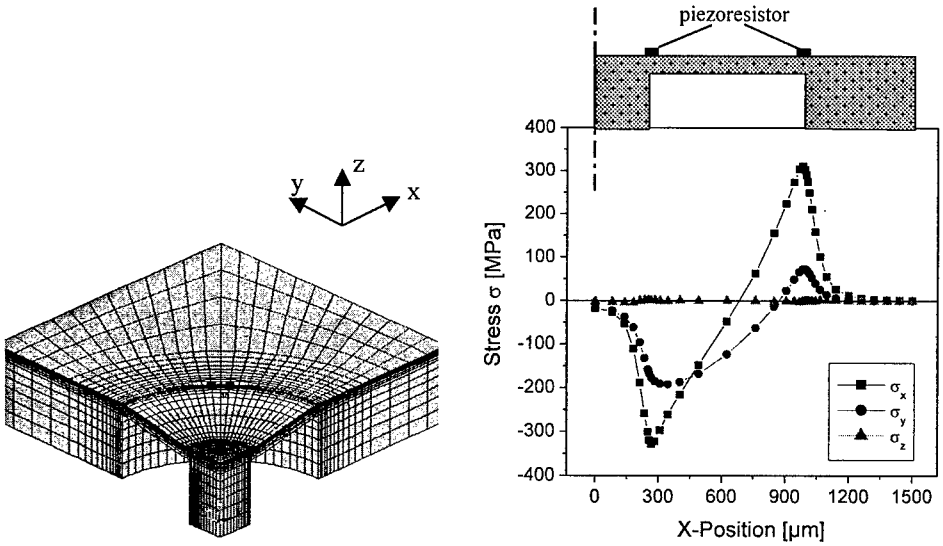


Fig. 2: Left: FE model (ANSYS) of a quarter of the membrane part of a pressure sensor. Chip Size is 3 x 3 mm^2, wafer thickness is 300 µm, membrane thickness is 60 µm, inner and outer membrane diameter are 500 µm and 2 mm, respectively. Right: Radial stress σ_x and tangential stress σ_y on top of the membrane in the 3C-SiC film along the (100) direction. The deflection of the centerboss in z-direction is–3.8 µm (applied pressure: P = 10 bar).

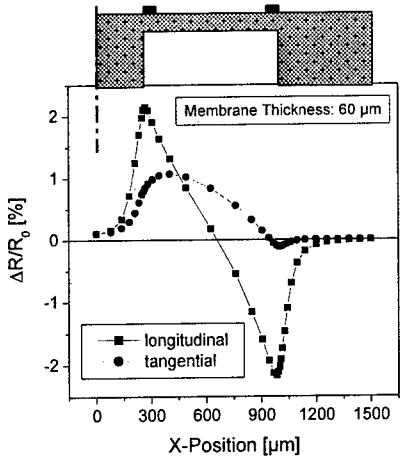


Fig. 3: Relative change of resistance at 10 bar of a longitudinal and a transversal stressed piezoresistor in dependence on the position of the resistor. Values are based on the simulation results (Fig. 2).

Fabrication of the Sensor Devices

A cross section of a complete sensor device is given in Fig. 1. A UNIBOND SOI wafer with a buried oxide (BOX) thickness of 400 nm and a silicon overlayer (SOL) thickness of 200 nm was used for the realization of the membrane structures. The gap of about 4.5 µm between centerboss and silicon substrate was defined in a first Reactive Ion Etching (RIE) process. The membrane structure was defined by anisotropic ICP-etching in an STS machine using a thick photoresist mask. The UNIBOND membrane wafer and the silicon substrate were joined together by applying a Silicon Fusion Bonding process under vacuum with a subsequent bond annealing step at 1000 °C for 3 hours. The rest gas pressure at room temperature inside the cavities is approx. P_{rest} = 50 mbar. A nominally 2.2 µm thick 3C-SiC film was deposited onto the wafer stack during an LPCVD process at 1200 °C for 30 minutes. The 3C-SiC layer and the SOL were etched (RIE, with an aluminum mask) in order to define the piezoresistors. A silicon oxide passivation layer was formed afterwards by dry thermal oxidation at 1100 °C for 3 hours. Contact holes were opened using buffered HF and the metallization system (TiWN/Au) was sputtered. A 2 µm thick gold layer was grown at the bondpad regions using a galvanic process and finally the metallization system was structured by wet chemical etching. A photograph of a sensor chip is shown in Fig. 4.

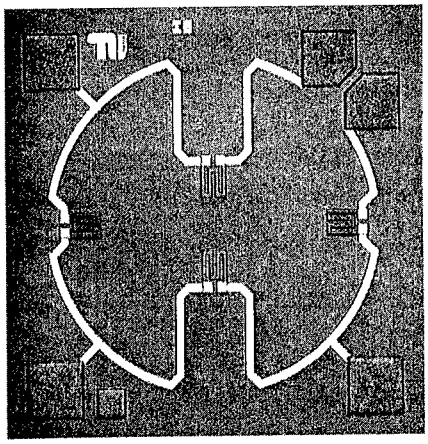


Fig. 4: Photograph of the sensor.

Measurement Results

The sensors were mounted on a TO-8 header and first pressure measurements were carried out using a climate control system with a maximum operating temperature of 170 °C.

The temperature dependent output characteristics of a sensor are shown in Fig. 5. At 10 bar, the centerboss touches the ground. The sensitivity is decreased in the overload range (P > 10 bar) from the nominal sensitivity of S = 0.5 mV/V bar to the reduced value of S = 0.03 mV/V bar. The decrease of the sensitivity from T = 25 °C to T = 165 °C is 8 %. The drift of the offset voltage within the same temperature range is about 20 mV.

High temperature measurements (up to T = 400 °C) with a different measurement setup are currently in progress.

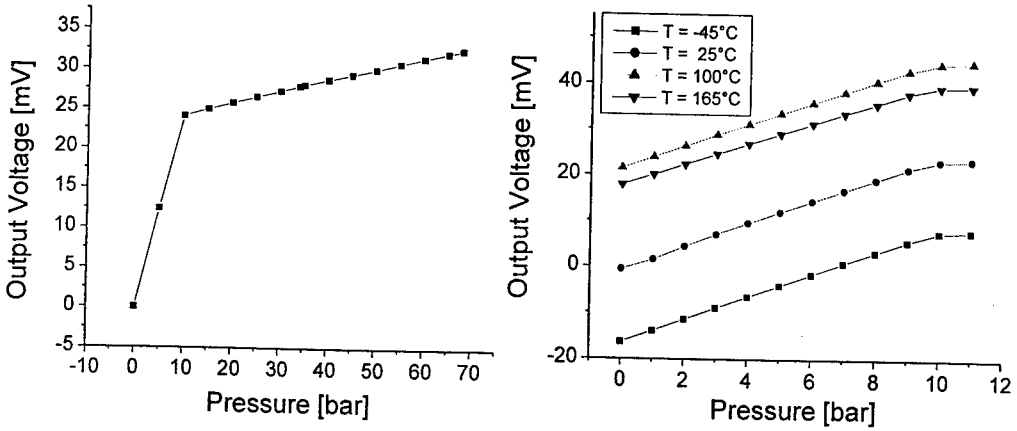


Fig. 5: Left: Output characteristic at room temperature. At a pressure of 10 bar, the centerboss touches the ground. Right: Output charcteristics at various temperatures. High temperature measurements (up to 400 °C) are currently in progress. (Supply voltage during measurements: 5 V. The offset voltage at room temperature V_{off} = -179 mV was substracted from all graphs).

Acknowledgement

Financial support through the European Community (project no. BRPR CT96 0261) is gratefully acknowledged.

References

[1] W. Reichert, M. Gonzáles Sirgo, J. von Berg, E. Obermeier, (1996), Trans. of the 3rd Int. High Temp. El. Conf., Albuquerque, New Mexico, USA, Vol. 2, p. 137.

[2] J.S. Shor, D. Goldstein, A.D. Kurz, (1993), IEEE Trans. Electron Dev., 40, p.1093.

[3] H. Möller, M. Eickhoff, M. Rapp, H.W. Grüninger, G. Krötz, J. Appl. Phys. A 68, (1999), p. 461.

[4] J. von Berg, R. Ziermann, W. Reichert, E. Obermeier, M. Eickhoff, G. Krötz, U. Thoma, C. Cavalloni, J.P. Nendza, (1998), Proc. of the HITEC '98, Albuquerque, New Mexico, USA, p. 245.

[5] S. Zappe, E. Obermeier, M. Eickhoff, H. Möller, G. Krötz, E. Bonnotte, Y. Barriol, J.L. Decorps, C. Rougeot, O. Lefort, J. Stoemenos, Proc. HITEC 2000 Conf., Albuquerque, New Mexico, USA, 2000.

Materials Science Forum Vols. 353-356 (2001) pp. 757-762
© 2001 Trans Tech Publications, Switzerland

Charged Particle Detection Properties of Epitaxial 4H-SiC Schottky Diodes

F. Nava[1], P. Vanni[1], G. Verzellesi[2], A. Castaldini[3], A. Cavallini[3], L. Polenta[3], R. Nipoti[4] and C. Donolato[4]

[1] INFN and Physics Department, University of Modena and Reggio Emilia, via Campi 213/A, IT-41100 Modena, Italy

[2] INFM and DSI, University of Modena and Reggio Emilia, via Campi 213/B, IT-41100 Modena, Italy

[3] INFM and Physics Department, University of Bologna, v. le Berti Pichat 6/2, IT-40100 Bologna, Italy

[4] CNR-Istituto LAMEL, via Gobetti 101, IT-40129 Bologna, Italy

Keywords: Minority Carrier Lifetime, Recombination and Trapping Centers, Solid State Detectors

Abstract This work presents measurements of the charge-collection properties of 4H-SiC Schottky diodes under alpha radiation and investigates the influence of native and alpha induced defects on the detector performance. The contribution of the diffusion of minority carriers to the charge collection efficiency is pointed out. Values of 500 ns and 95 μs are inferred for the hole and electron lifetime, respectively.

1. Introduction

The recent development of silicon carbide (SiC) material has demonstrated the outstanding potential of this wide band gap semiconductor for ionising radiation detection [1,2]. As the atomic displacement energy is higher for SiC than for other semiconductor crystals [3], it is expected that SiC detectors will be radiation harder than Si or GaAs detectors. In addition, impurities and defects, which may act as trapping centers in SiC, are expected to be less effective in SiC detectors because of the very high value of the critical electric field in this material.

In the aim of a full exploitation of SiC as a material for radiation detectors, further research concerning the SiC behavior when irradiated by ionizing particles is required. This work presents measurements of the charge-collection properties of 4H-SiC Schottky diodes under alpha-particle radiation and investigates the influence of native and alpha induced defects on the detector performance.

2. Experimental

A commercial, <0001> oriented, Si-face, n-type, Nitrogen doped, 8° off-axis 4H-SiC epitaxial wafer was used as a substrate for the realisation of Schottky diodes. Starting from the surface, the wafer structure was a lightly doped (2.2×10^{15} cm^{-3}) 30 μm thick epitaxial layer, a heavily doped (1×10^{18} cm^{-3}) 1 μm thick buffer layer, and a heavily doped (3×10^{18} cm^{-3}) 320 μm thick substrate. Schottky Au and ohmic Ti contacts were realised at the front and back wafer surfaces, respectively, as described in [2]. No heat treatment was performed after the e-beam metal deposition. The lightly doped layer under the Au contact is the detector active layer.

Alpha-particles of 5.48 MeV and 2.00 MeV from a ^{241}Am source were used to measure the charge collection efficiency (CCE) of the Schottky diodes as a function of the diode reverse bias (V_{rev}) at room temperature. The lower energy was obtained by decelerating in air the 5.48 MeV α-particle. The energy needed to produce an electron-hole pair in SiC was taken equal to 8.40 eV, while the α-particle ionising energy loss (Bragg ionisation curve) in crystalline 4H-SiC was approximated by that in amorphous SiC and was computed by the code TRIM [4]. The SiC CCE data are normalised to those of a Si surface barrier detector measured with the same experimental set-up.

The semiconductor-device drift-diffusion analysis program DESSIS [5] was used to numerically simulate the Au/SiC junction dynamic response to an impinging α-particle. The diode CCE was

simulated as the ratio between the integral of the current pulse and that of the injected charge. Material and transport related parameters were customised to 4H-SiC using the values in Ref. [6].
The Electron Beam Induced Current (EBIC) technique [7] was employed to image unirradiated and irradiated diodes. The contrast of these images is a qualitative characterisation of the recombination of injected carriers in the semiconductor under the metal contact. The EBIC technique was also employed to quantitatively evaluate the minority carrier diffusion length by the measurement of the charge collection efficiency versus the electron beam energy [8].
The diodes were analysed by Deep Level Transient Spectroscopy (DLTS) and Isothermal Capacitance Transient Spectroscopy (ICTS) up to the maximum temperature of 400 K. By comparing DLTS and ICTS findings the characterisation of the trap levels results very accurate and also shallow levels, not detectable by DLTS, can be reliably investigated.

3. Results and discussion

Figure 1(a,b) shows the experimental and simulated CCE versus V_{rev} curves for 5.48 MeV and 2 MeV α-particles. The analytical computation of CCE versus V_{rev} assuming only drift in the depleted region is also shown for comparison.

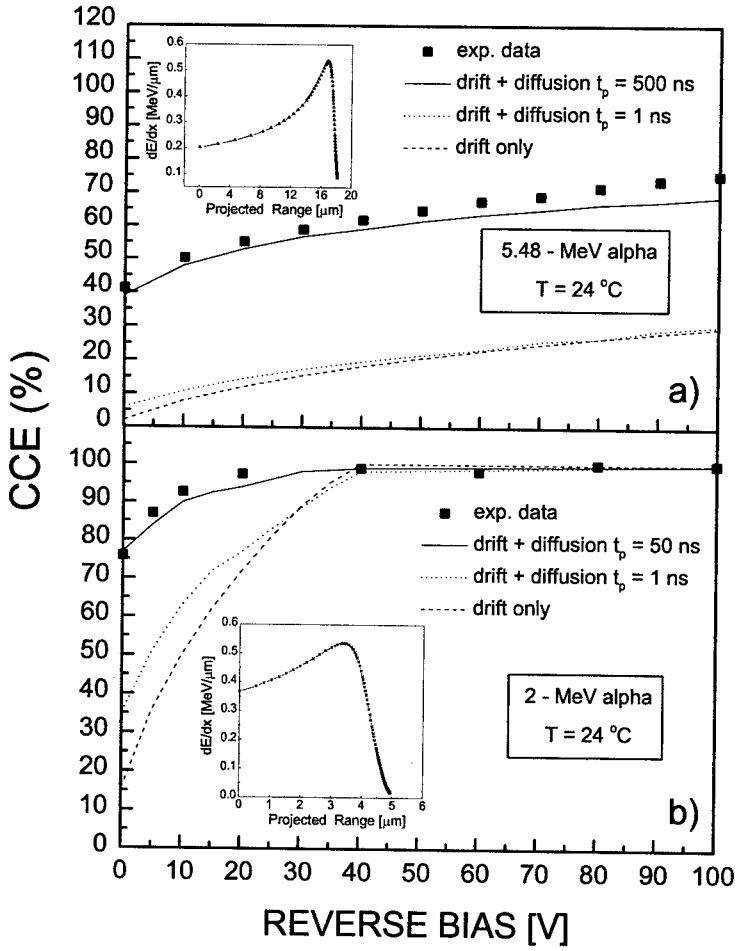


Fig. 1 Experimental and theoretical Charge Collection Efficiency (CCE) values for 5.48 MeV (a) and for 2.00 MeV (b) α-particles. The corresponding Bragg ionization curves are shown in the insets.

The Bragg ionization curves computed by TRIM simulations are reported in the insets. The experimental CCE curves always increase for increasing V_{rev} and reach the 100% value for 2 MeV α-particles at $V_{rev} > 40V$. In fact, above this voltage the depleted region becomes thicker than 4.7 μm and entirely contains the 2 MeV α-particle generation track. The drift-only CCE curves are much lower than the experimental data; this demonstrates that an important contribution to CCE arises from the carriers generated in the neutral region and diffusing to the junction. The DESSIS code accounts for this contribution and from the code outputs shown in Fig. 1(a, b) we can see that a very short hole lifetime t_p (= 1 ns) must be assumed to reproduce the drift-only CCE curve. Much longer t_p values must be assumed to describe the 5.48 MeV and 2 MeV α-particles experimental data, 500 ns and 50 ns, respectively. As the 2 MeV measurements were performed on previously 5.48 MeV irradiated diodes, they must be affected by the previous radiation damage.

Figure 2 shows the EBIC contrast of a diode partially irradiated by a few MeV He^+ per unit area. The existence of 10 μm wide area darker than the surrounding in the unirradiated area indicates regions of reduced current collection efficiency. The irradiated area appears darker because of the recombination centers introduced by the ion damage. This phenomenon is evident even if the number of ions per unit area is quite low (a few). This agrees with the different t_p values necessary to fit the experimental data of Fig. 1(a,b).

Figure 3(a) shows the measured collection efficiency of electron-injected carriers as a function of electron beam energy in the range 15-40 kV. This measure was done in an area almost 100 μm wide and free of extended defects (area A) of Fig. 3(b). In the range 25-40 kV this plot is linear and from its slope it is possible to evaluate the minority carrier diffusion length L_p [9] which was found to be 18 μm. The average L_p value for the diode of Fig. 3(b) is 12.5 μm. This value is consistent with the 500 ns hole lifetime, obtained from the DESSIS simulation of the CCE for 5.48 MeV α-particles (Fig.1a), which corresponds to an $L_p = 13$ μm.

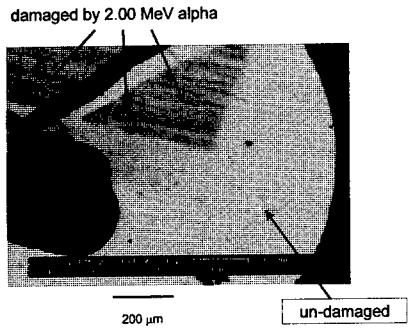


Fig. 2 30 keV Electron Beam Induced Current image of a Au/SiC n-type diode partially irradiated by MeV He^+ ions.

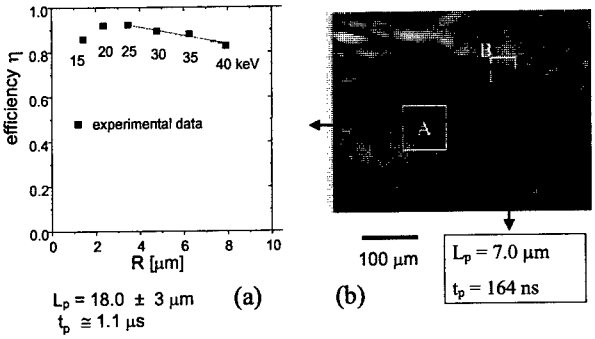


Fig. 3 (a) EBIC collection efficiency η versus the electron range measured in the region A of (b); the slope of the linear part yields $L_p = 18$ μm. The estimated value of L_p in region B is 7 μm.

Figure 4 shows the Arrhenius plot of the DLTS and ICTS measurements: the squared temperature T(K) relevant to the capacitance peaks divided by the emission rate en (sec^{-1}) is plotted versus the inverse of the temperature. Six electron traps were detected: the energy level, density and possible identification of which are reported in Table 1. The mean detrapping time t_D, and the mean free drift time before trapping t_e associated with the deepest electron trap, i.e. that at 0.91 eV, were computed to be of the order of 10^6 sec and about equal to 95 μs, respectively, by using the equations: $t_D = [1/(N_c \sigma v_{th})] \times \exp(E/kT)$ and $t_e = 1/(N_{s3} \sigma v_{th})$ [10], where N_c and v_{th} are the density of states at the bottom of the conduction band and the electron thermal velocity of SiC, respectively, while σ was measured to be equal to 2.4×10^{-17} cm^2 (Fig.5). In spite of the fact that the mean detrapping time

associated with a given level can reach very high values, the deeper bulk trapping levels do not play a main role in limiting the detector performance at room temperature [10,11]. In fact, electrons and holes require about $2.2x10^{-11}$s and $4x10^{-10}$s, respectively, to drift the SiC detector depleted region (these values where obtained by dividing the depletion width at 40V by the mean carrier drift velocity). As both these values are much shorter than the electron and hole lifetime evaluated by deep level spectroscopy (t_e) or by the DESSIS simulations (t_p), the absence of trapping events within the depleted region can be hypothesized. This also gives a reasonable explanation for the measured full charge collection efficiency.

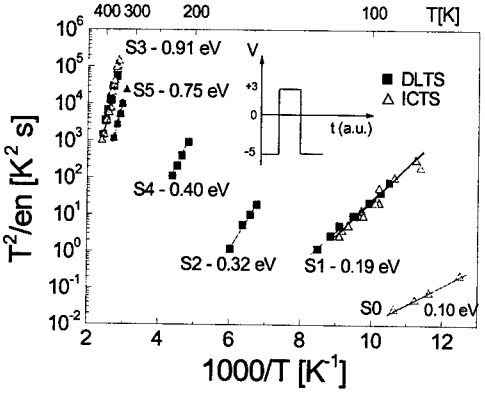


Fig. 4 Arrhenius plot of the DLTS and ICTS measurements. The inset shows the filling pulse conditions to detect traps S4 and S5.

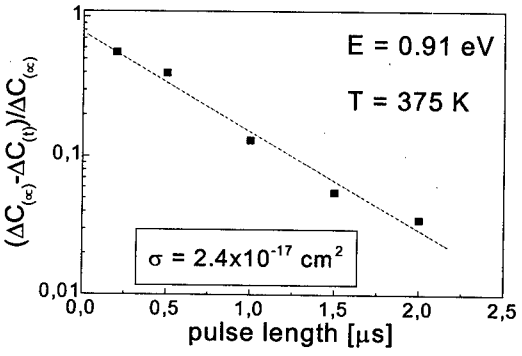


Fig. 5 Determination of the capture cross section for trap S3.

Table 1. Energy level, density and related impurity for the trapping centres detected by DLTS and ICTS.

	S0	S1	S2	S3	S4	S5
E (eV)	0.10	0.19	0.32	0.91	0.40*	0.75*
N_T (cm^{-3})	2×10^{11}	8.9×10^{12}	6×10^{11}	2.2×10^{13}	4.5×10^{12}	1.4×10^{13}
related impurity	nitrogen	chromium		vanadium		

(*) at the Au/epitaxial SiC interface.

4. Conclusions

This work shows the good performance of very lightly doped 4H-SiC as an active material for the realization of "fully depleted" α-particle solid state detectors with collection efficiency near unity. Moreover, the electron and hole lifetimes in this material were evaluated by spectroscopic measurements and simulation of the detector performance in condition of partial depletion. The last approach also allowed us to estimate the hole lifetime reduction due to the α-particle damage.

Acknowledgments: This work was partially supported by Istituto Nazionale di Fisica Nucleare, Italy and by Progetto Finalizzato MADESS-II: SiC for microelectronics applications. We would like to thank Dr. C.Lanzieri of Alenia Marconi Systems in Roma, Italy for the diode realization, Prof. C.Manfredotti and Dr. E.Vittone of Torino University for useful discussions and Dr. C. Frigeri of the CNR-MASPEC of Parma, Italy for help with some EBIC measurements.

References

[1] F.H. Ruddy, A.R. Dullo, J.G. Seidel, S. Seshadri, IEEE Trans. on Nucl. Sci. 45 (1998), p. 536.
[2] F. Nava, P. Vanni, C. Lanzieri, C. Canali, Nucl.Instr.&Meth. A437 (1999), p. 354.
[3] A.L. Barry, B. Lehmann, D. Fritsch, D.Braunig, IEEE Trasn. Nucl. Sci. 38 (1991), p. 1111.
[4] J.F. Ziegler, J.P. Biersack, IBM-Research, Yorktown Heights, New York, USA (1996).
[5] DESSIS-6.0 Reference Manual, ISE Integrated Systems Engineering AG., Zurich (Switzerland).
[6] C.E. Weitzel, J.W. Palmour, C.H. Carter Jr., K. Moore, K.J. Nordquist, S.Allen, C. Thero, M. Bhatnagar, IEEE Trans. on Electron Devices 43 (1996), p. 1732.
[7] H.J. Leamy, J. Appl. Phys. 53 (1982) R51.
[8] C.J. Wu, D.B. Wittry, J. Appl. Phys. 49 (1978), p. 2827.
[9] C. Donolato, Solid State Electron. 28 (1985), p. 1143.
[10] M. Martini, J. W.Mayer, K. Zanio, Applied Solid State Science (Ed. Wolfe), Vol.3, Academic Press, New York (1972).
[11] F. Nava, M. Alietti, C. Canali, A. Cavallini, C. Chiossi, C. del Papa, V. Re, C.Lanzieri, IEEE Trans. Nucl. Sci. 43 (1996), p. 1130.

Materials Science Forum Vols. 353-356 (2001) pp. 763-766
© 2001 Trans Tech Publications, Switzerland

Thin Heavily Compensated 6H-SiC Epilayers as Nuclear Particle Detectors

A.A. Lebedev[1], N.B. Strokan[1], A.M. Ivanov[1], D.V. Davydov[1] and V.V. Kozlovskii[2]

[1] A.F.Ioffe Physico-Technical Institute, Russian Academy of Sciences, Polytechnicheskaya st. 26, RU-194021 St.Petersburg, Russia

[2] St. Petersburg State Technical University, Polytechnicheskaya 29, RU-194251 St.Petersburg, Russia

Keywords: Alpha Particle Detection, Compensation, Epitaxy, Radiation Hardness

Abstract P^+-n-n^+ structures based on 6H-SiC films grown by CVD on n^+ substrate were used. The initial concentration of uncompensated donors in the n-type layer was $N^+_D - N^-_A = 4.5*10^{16}$ cm^{-3} at layer thickness of several μm. The structures were exposed to a dose of $8*10^{15}$ cm^{-2} with 8 MeV protons and the effect of irradiation was studied by means of precise α-spectrometry. Results obtained in two modes were compared: (i) through-penetration of a particle across the structure and (ii) complete deceleration of a particle. It is shown that at (i)-mode and forward bias the signal is formed by the mechanism of "through conducting channel" (TCC). The practical possibility is demonstrated of detecting ions by 6H-SiC films upon proton dose of ~ 10^{16}cm^{-2}. The product of electron mobility by lifetime retains values sufficient for effective electron transport, including signal amplification in the TCC mode. The positive charge $N^+_D - N^-_A$ is in fact determined by the concentration of initial uncompensated donors.

Introduction Application of SiC as a detector media of nuclear radiation arises from its wide energy bandgap and high radiation hardness. As a consequence detectors capable for working at high temperatures and radiation fields [1,2]. One of the perspectives of SiC detectors is spectroscopy of charge particles. As shown in [3], the sublimation technique gives 6H-SiC layers with concentration of uncompensated impurities N^+_D-$N^-_A \approx 10^{15}$ cm^{-3} and hole diffusion length 2-3 μm. The high fields of electric breakdown allow creating a space-charge region up to tens of μm. The low concentration of nonradiative recombination centers ensures carrier lifetimes sufficiently high for effective transport [4].

Experimental The work is concerned with the ability of SiC films to detect alpha particles under the conditions when the carrier transport is hindered by the high content of structural defects. The initial (CVD-grown) films had effective donor concentration N_D^+-$N_A^- = 4.5*10^{16}$ cm^{-3}. Then p^+-n-n^+ structures on their base were irradiated with 8 MeV protons at a dose of $8*10^{15}$ cm^{-2}. This led to a strong compensation with the resistivity $\rho = 5*10^9$ ohm cm.

Irradiation with protons at doses of up to ~$3*10^{14}$ cm^{-2} has been studied previously [5]. It was found that irradiation leads to formation of both donor N_D and acceptor N_A deep centers, with $N_D > N_A$. As a result, on the one hand, the N_D^+-N_A^- value increases, and, on the other, the base conductivity at room temperature decreases because of electron capture to deeper centers.

In this work the proton doses were an order of magnitude higher. As in [5], annealing at T = 450^0 C for 10 min was used to stabilize the material. At $\rho \approx 5*10^9$ ohm cm, C-V characteristics are difficult to measure. For this reason, the transport of non-equilibrium charge in pulsed ionization by alpha particles emitted by ^{244}Cm was studied using the amplitude analysis technique. The setup comprised

a charge-sensitive preamplifier, amplifier with RC-shaped bandwidth, and amplitude analyzer. The analyzer scale was calibrated using a Si detector.
The following regimes were used: with particle flight through p^+-n layers or with a particle slowing-down completely in the n-base of the detector. Reverse (U_{rev}) and forward (U_{for}) biases were applied. All measurements were done at room temperature.

Results

Particle passes through the detector structure.

1. In the regime with U_{rev}, the compensation can be disturbed (see [6]) through thermal emission of carriers from deep centers. For example, electrons arriving from deep levels in the conduction band drift toward the n^+ electrode, leaving uncompensated positive charge in the bulk. The applied U_{rev} turns out to be insufficient for complete depletion, and a region of neutral high-resistivity base appears.
If the Maxwell relaxation time in the base exceeds the RC constant, the carrier transport within the electrode space of width d will be limited to w and the signal will decrease by a factor of w/d. Under these conditions, we have for the detected charge

$$Q \sim (dE_\alpha / dx)*w*(w/d) \sim w^2 \sim U_{rev}, \qquad (1)$$

where (dE_α / dx) is the specific loss of particle energy in SiC and $w \sim (U_{rev})^{1/2}$. However, measurements (Fig. 1) give $Q \sim w \sim (U_{rev} + 1.5)^{1/2}$. This should be attributed to the accelerated relaxation in the base owing to the high non-equilibrium conductance within the particle track.

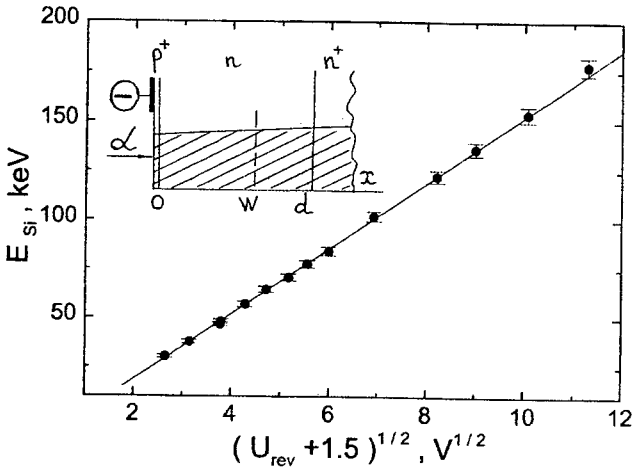


Fig. 1. Signal of detector N 4d vs. the reverse bias. The signal is expressed in energy units and is proportional to the charge induced at the detector's electrodes. Insert: detector design. The specific energy loss by alpha particle is shaded.

Evaluation of N_D^+-N_A^- value from $w(U_{rev})$ dependence showed that N_D^+-N_A^- in the semi-insulating film is close to its initial value (see Table 1).

2. In the regime with U_{for}, account should be taken of the arrival of carriers from the external circuit. An analysis [7, 8] has shown that in particle passage through a semi-insulating film there appears a "through conducting channel" with electron circulation through the sample. The amount of transferred charge exceeds that created by ionization, q, by a factor ($\mu F \tau$ / d):

$$Q = q*(\mu F \tau / d) \qquad (2)$$

where μ and τ are the mobility and lifetime of electrons, and F is the electric field strength. The experimental dependence of the signal on U_{for} (Fig. 2) were linear in accordance with formula (2) and corresponded to $\mu\tau = 7*10^{-9}$ cm^2/ V and amplification factor $\mu F \tau$ / d of 1.7. At mobility $\mu \approx 30$ cm^2/ (V s) we have for the electron lifetime $\tau \approx 2*10^{-10}$ s. Values of $\mu\tau$ obtained on different diodes are listed in the Table 1.

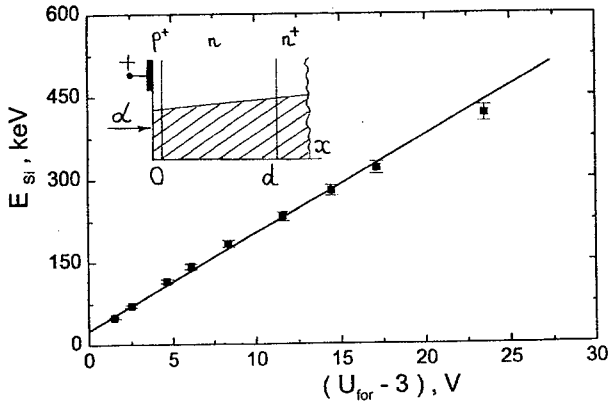


Fig. 2. Signal of detector N 4d vs. forward bias. The specific energy loss by alpha particle is shaded.

Table 1. Film parameters obtained from the signal dependence in Fig. 1 and 2. The N_D^+-N_A^- and $\mu\tau$ values are determined for reverse- and forvard-biased structures, respectevely.

Sample no.	$\mu\tau*10^9$, cm^2/V	$(N_d^+ - N_a^-)*10^{-16}$, cm^{-3}
4d	7.0	2.3
4c	6.0	4.0
4b	6.0	2.45
3c	-	2.2

Particle slows-down in the detector.
The case of complete slowing-down of alpha particles in the SiC film reveals a difference between the U_{for} and U_{rev} regimes. For example, under U_{for}, the charge starts to decrease earlier (at higher energies) and this decrease is more abrupt.

1. As soon as a region with unmodulated conductivity appears in SiC with decreasing particle energy, the TCC regime is broken. The high resistance of the d - R layer (R is the particle range in SiC) limits the through current and no charge amplification can be achieved. Further, for high-resistivity sample the path traveled by a carrier in the d space is still important for the signal. Therefore, the signal decay becomes stronger (Fig. 3, curve 1) because of the growing contribution to the carriers transport from holes having small $\mu\tau$.

2. On the other hand, under U_{rev}, the appearance of a d - R layer is less critical for the signal. With the base modulated to a depth R, the signal is given by $Q=q_0*(R / d)$, where q_0 is the charge introduced into the space charge region. It can be seen from Fig. 3 (curve 2) that up to $\Delta \approx 40$ mm the signal decay at a rate of R/d is compensated by the passage through the space charge region of the peak of the Bragg ionization curve. Further, the signal decreases mainly because of the ionization diminishing, since the R/d factor cannot be less than w/d value.

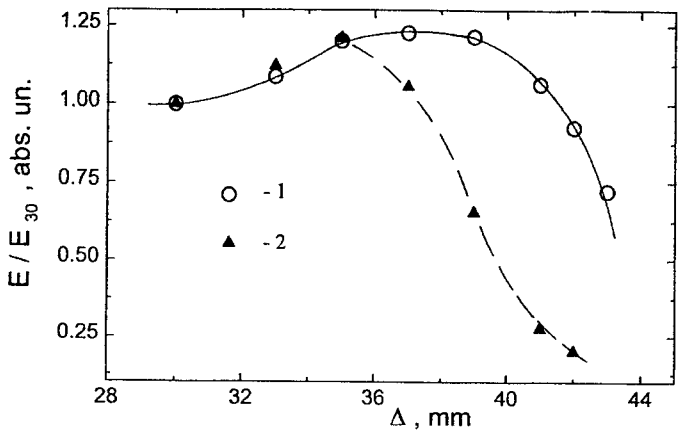


Fig. 3. Signal of detector N 4c on reducing the alpha-particle energy for forward bias U_{for} = 20 V (curve 1) and reverse bias U_{rev} = 100 V (curve 2). Δ-sample-source distance.

Discussion and conclusions

The results obtained demonstrate the high radiation hardness of the structures studied. The originally doped films with high amount of introduced radiation-induced centers (total defects concentration ~10^{17} cm^{-3}) can detect fast ions. The problem associated with p^+-n detectors based on films of this kind is in all probability related to increasing of the value N_D^+-N_A^- rather than to carrier transport.

The nontrivial combination of film characteristics allowed using of four detection regimes. The observed specific features of the signal are of interest for understanding the general principles of detector operation. It is shown that the unconventional forward biasing of the structures leads to signal amplification in the TCC regime. A new result is that the signal is formed under conditions of accelerated relaxation of the semi-insulating base of the detector. This is ensured by the high non-equilibrium conductivity within the ion track.

References

[1] R.V Babcock, H.C. Chang, Neutron dosimetry, vol.1, Vienna (1963), p. 613.
[2] P.C. Canepa, P.Malinaric, R.B. Campbell, J.Ostroski, IEEE Trans., NS-11 (1964), p.262.
[3] N.S.Savkina, A.A.Lebedev, D.V.Davydov, A.M.Strelchuk, A.S.Tregubova, M.A.Yagodkina, Mat. Science and Eng., B. 61-62 (1999), p.165.
[4] A.A.Lebedev, N.S.Savkina, A. M. Ivanov, N.B. Strokan, D.V.Davydov, Semiconductors, V. 34 (2000), p. 243.
[5] A.A.Lebedev, A.I.Veinger, D.V.Davydov, V.V.Kozlovski, N.S.Savkina, A.M.Strelchuk, Semiconductors, V. 34 (2000), N. 8, p. 897.
[6] V.K.Eremin, N.B.Strokan, N.I.Tisnek, FTP, Vol. 8 (1974), p. 1157.
[7] S.M.Ryvkin, JTF, XXXVI (1956), p. 2667.
[8] N.A.Vitovskiy, P.I.Maleev, S.M.Ryvkin, JTF, XXVIII (1958), p. 460.

Chapter 6:

III-Nitrides and Related Materials

Materials Science Forum Vols. 353-356 (2001) pp. 769-778
© 2001 Trans Tech Publications, Switzerland

The Role of Threading Dislocations in the Physical Properties of GaN and its Alloys

J.S. Speck

Materials Department, University of California, Santa Barbara CA 93106, USA

Keywords: Carrier Scattering, Deep Levels, Extended Defects, Gallium Nitride, Leakage, Non-Radiative Recombination, Threading Dislocations, Traps

Abstract

In this paper, we review progress on understanding the role of threading dislocations (TDs) in the physical properties of GaN and its alloys. A growing body of work provides compelling evidence that TDs in the group-III nitrides behave as non-radiative recombination centers, have energy levels in the otherwise forbidden energy gap, act as charged scattering centers in doped materials, and provide a leakage current pathway. In comparison with conventional III-V semiconductors, the relatively small minority carrier diffusion length L_d (~50 nm) in the III-nitrides, combined with favorable TD geometries, minimize dislocation-related degradation. The small value of L_d also allows for appreciable optical emission in materials with TD densities as high as 10^{10} cm^{-2}.

Introduction

The 1990s have been a time of remarkable progress in wide bandgap semiconductors, particularly in the group III-nitride system. The 'nitride revolution' was motivated by the early pioneering work of Pankove [1]. The two singular achievements which have enabled current nitride technology were the development of two-step growth by Akasaki and co-workers at Nagoya University which lead to high structural quality GaN films on sapphire substrates [2, 3], and the subsequent developments of an efficient route to *p*-type doping by Nakamura and co-workers at the Nichia Chemical company [4]. These two results were followed by the development by Nakamura of InGaN quantum well structures and the demonstration of bright nitride-based blue LEDs [5]. The realization and early commercialization of Nichia LEDs catalyzed most of the recent work on nitride semiconductors.

Currently, there are still no widely available lattice-matched substrates for the growth of wurtzitic GaN. As a result, most materials today still have high threading dislocation (TD) densities. Transmission electron microscopy (TEM) studies on early Nichia LEDs showed that the material had TD densities in excess of 10^{10} cm^{-2} passing through the active region, which is approximately four to six orders of magnitude higher than TD densities in conventional III-V optoelectronic devices [6]. The remarkably high TD densities in the III-nitrides lead to speculation that TDs were benign in the nitrides or perhaps even beneficial for the optoelectronic properties. However, there is a continually increasing body of work that shows TDs are indeed deleterious for the physical properties of the nitrides.

Here, we summarize the key work elucidating the role of extended defects in the physical properties of the nitrides. We begin by briefly reviewing current state-of-the-art microstructures for GaN on sapphire and SiC substrates, followed by a brief discussion of the role of TDs in the morphology of growing nitride surface, and then we review key papers which focus on the physical

properties of TDs in the nitrides. We concentrate on III-nitride films grown by metal-organic chemical vapor deposition (MOCVD) either on (0001) sapphire or SiC substrates.

Background on Extended Defects in the Nitrides

During the past ~5 years there has been extensive work on understanding the extended defect structure in the nitrides. The commonly observed extended defects in (0001) oriented GaN grown on sapphire substrates include (0001) stacking faults and stacking disorder and related Shockley and Frank partial dislocations, inversion domains, and TDs [7]. In high quality MOCVD-grown GaN films, the stacking disorder and partial dislocations usually only occur in the region in immediate adjacency to the substrate and are associated with the growth of a disordered low temperature nucleation layer (NL) [8]. Inversion domains are normally associated with nitrogen polar domains that have grown either through to the free surface of an otherwise Ga-polar film (which is the usual polarity for high quality MOCVD films) or are overgrown by Ga-polar material. The TDs have typical total densities in the range 10^8 – 10^{10} cm^{-2}. There are two different predominantly observed TDs: pure edge, with Burgers vectors in the family $\frac{1}{3}\langle\bar{2}110\rangle$ and [0001] line directions; and mixed character, with Burgers vectors in the family $\frac{1}{3}\langle\bar{2}113\rangle$ and line directions inclined ~10° from [0001] towards the Burgers vector. Pure screw TDs (b = [0001] and line direction [0001]) are represent a small fraction (~0.1 – 1%) of the total density of TDs [7].

In previous work, we have shown that for MOCVD growth of GaN on sapphire, the TDs form as a consequence of the coalescence of slightly misoriented GaN high temperature islands (this work is reviewed in detail in ref. [9]). The microstructure of GaN grown on a more closely lattice matched substrate, namely SiC, shows very similar characteristics. Thus, TDs are the most important extended defect to study in the context of understanding the physical properties of GaN thin films grown on Al_2O_3 substrates.

The Role of Threading Dislocations in Growth

Before reviewing the effects of TDs on the physical properties, we briefly review the important role of TDs in the growth of nitrides, namely the formation of 'V-defects' [10]. Many nitride-based device heterostructures require reduced growth temperature. For example, InGaN layers are typically grown at ~750 – 800°C in MOCVD, which is ~300°C lower than optimal MOCVD growth conditions for GaN – the lower temperature is necessary because of the high volatility of indium. Similarly, the growth temperature for AlGaN is generally limited by reactor or heater considerations. The low growth temperatures facilitate the formation of 'V-defects' which consist of six $\{10\bar{1}1\}$ family planes and form an inverted hexagonal pyramid. The V-defects always form at TDs, with a higher propensity for formation at mixed character TDs, but they also form at pure edge TDs.

Wu *et al.* attributed the formation of V-defects to a kinetically-limited growth process in which the surface depression associated with a TD (as predicted by Frank [11]) assists in the formation of $\{10\bar{1}1\}$ facets [10]. Under kinetically-limited growth conditions, the surface morphology will be dominated by the slowest growing planes, and thus in this scenario the $\{10\bar{1}1\}$ planes have a slower growth rate in the [0001] direction. Subsequent high temperature growth of GaN will cause the V-defects to be filled and there will be no surface morphological evidence for their presence. More recently, Northrup *et al.* have performed first principle calculations of the energies of the (0001) and the {1011} planes for GaN and InGaN. Northrup has shown that V-defects at energically favorable for InGaN growth and their formation is driven by a balance of

surface energy increase (due to the increased total surface area of the six $\{10\bar{1}1\}$ planes of the V-defect relative to the area of the (0001) plane) and strain energy reduction due to the open defect volume which would otherwise have a TD [12].

V-defects are deleterious for the growth of both optoelectronic and electronic device heterostructures. For InGaN/GaN quantum well structures, the V-defects cause the wells to be non-planar and may also lead to changes in the indium composition through a series of wells. As will be discussed later, V-defects are important sources of reverse leakage in diodes, and have been correlated to the very poor electro-static discharge (ESD) in these structures. For laser structures, the V-defects will be light scattering centers. Nitride-based high electron mobility transistor (HEMT) structures consist of AlGaN/GaN layers. It is quite common for V-defects to form during the growth of the AlGaN cap layer. In the case of HEMT structures, there is no further nitride growth after the AlGaN layer and thus the V-defects can concentrate electric fields both at ohmic source/drain contacts and more importantly at the Schottky gate contact.

Key Work on the Role of Threading Dislocations in the Physical Properties of the Group III Nitrides

Table 1 provides a summary of the key studies that have focused on the role of TDs in the physical properties of the group III-nitrides. In this section, we summarize this work.

Non-Radiative Recombination Centers

Cathodoluminescence (CL) Studies

In 1997 Rosner *et al.* reported on a CL study on MOCVD grown *n*-type GaN on sapphire substrates [13]. This study involved correlated atomic force microscopy (AFM) and CL studies, in which the investigators used a combination of fiducial marks on their samples and a registered specimen stage to ensure imaging of exactly the same region by both techniques. It had been demonstrated in other studies that TDs affect the surface morphology of GaN, namely that mixed character TDs and sometimes edge TDs give rise to surface depressions (again, as predicted by Frank and recently discussed by Heying *et al.* [14]). Rosner *et al.* found that the 'pit' features in the AFM images were strongly correlated with dark regions in the CL images. Rosner *et al.* were able to generate maps of the pit locations, corresponding to the intersection of the TDs with the film free surface, and then calculate CL images based on known solutions for the minority carrier concentration from a dislocation, which was assumed to be a line of non-radiative (NR) recombination centers. In this study the fits were done visually and it was found that the best agreement between the calculated and observed CL images was realized for a minority carrier diffusion length of 250 nm. This study used bulk GaN samples and 10 kV primary electrons which broaden into a bulb-like volume with a radius of ~250 nm, which then provides an upper bound on the diffusion length.

The concepts developed by Rosner *et al.* were further advanced in a coupled plan-view TEM and CL study reported by Sugahara *et al.* on *n*-type MOCVD-grown GaN [15]. In this study, CL images were recorded on TEM foils *prior* to TEM investigation (apparently, there is sufficient radiation damage to the samples such that no CL was observable if the TEM studies were performed on the foils before CL studies). The authors found a one-to-one correspondence between the position of dark spots in the CL images and TDs in the plan-view TEM. The authors estimated a hole diffusion length of 50 nm based on the width of the dark regions in the CL maps. The lower minority diffusion length in these studies, in comparison with those reported by Rosner *et al.*, is primarily due to the minimal probe broadening in a thin TEM foil.

In a more recent study, Rosner *et al.* used CL mapping to study the dislocation structure in GaN grown by lateral epitaxial overgrowth (LEO) [16]. Full details of the LEO process can be

found elsewhere [17], but in summary, this technique involves first growing a GaN layer, then masking this layer with SiO_2 or a similar material while leaving openings into which the GaN can grown, and subsequently regrowing material through the window opening and then laterally over the mask. When the orientation of window openings and growth conditions are optimized, it is possible to grow material with a TD density of ~10^4–10^6 cm^{-2} in the window region. Rosner *et al.* demonstrated the possibility of imaging individual TDs which propagate laterally into the overgrown region. This work included studies of InGaN single quantum wells which were grown on LEO stripes. It was found that there was a correspondence between dark regions, associated with vertically propagating TDs, in the GaN luminescence at 365 nm and the $In_{0.15}Ga_{0.85}N$ at 421 nm, thus demonstrating that TDs also behave as NR centers in InGaN. The image widths for the dark regions was comparable for the GaN and InGaN luminescence and an upper bound of 200 nm was determined for the minority carrier diffusion length for both GaN and InGaN. In the overgrown regions, where there were few, if any TDs propagating to the growth surface for this sample set, the InGaN luminescence was homogeneous, demonstrating that the InGaN any heterogeneity in the InGaN was limited to a length smaller than 200 nm.

It is additionally important to note that in conventional III-V technology, devices can be fabricated with dislocations (dark line defects) present and still achieve reasonable quantum efficiencies. However, since diffusion lengths are typically greater than 1 μm and defects often have glide habits (in the case of strained layer cubic materials) that put the line parallel to the surface of the film, the tolerable density is several orders of magnitude lower than in the III-nitride technology. More importantly, in the conventional III-V systems, these defects move and multiply under a combination of applied stress and current injection, and this process causes rapid degradation of the devices. This often requires extremely small numbers of defects to be present initially to guarantee reasonable lifetimes for the devices. In (0001) oriented wurtzitic group III-nitride films, the TDs experience no shear stress because the lie on vertical planes, so dislocation multiplication and motion is not a contributor to device degradation. It appears that the differences between conventional III-V and III-nitride technologies do not require new physics as suggested by early reports, but rather can be accounted for by these two properties, the very short diffusion lengths and the relative immobility of the defect structures.

Photoelectrochemical (PEC) Etching Studies

Photoelectrochemical wet etching is a technique in which a semiconductor is illuminated with above gap radiation to generate minority carriers at the semiconductor surface [18]. The photogenerated minority carriers facilitate the etching by weakening near-surface bonds and allowing surface atoms to dissolve into the electrolyte. In two important papers, Youtsey *et al.* described PEC etching studies of *n*-type GaN films (prepared either by MOCVD or by hydride vapor phase epitaxy) [19, 20]. They found under certain conditions, GaN 'whiskers' formed with a density on the order of 10^9 cm^{-2}. The whiskers had diameters between 10 and 50 nm and lengths up to 1 μm. Subsequent TEM studies on the whiskers showed that that each whisker contained a TD. The authors speculated that the TDs could either behave as NR centers, thus inhibiting minority carriers (holes) from reaching the sample surface near TDs, or behave as charged lines which repel minority carriers.

Traps/Deep Levels

The work describe above, which has provided a strong basis that TDs do behave as NR centers in GaN, implies that the TDs have deep acceptor levels for *n*-type material and presumably donor levels for *p*-type material (indeed CL images on *p*-type material also show dark regions

associated with TDs [21]). We now address the studies which have provided further insight on whether there are indeed deep levels associated with the nitrides.

Electronic Structure Calculations

Currently, there are two different views that have resulted from electronic structure calculations of TDs and GaN. Elsner *et al.* presented the first electronic structure calculations for pure screw and for pure edge TDs in GaN [22]. These studies used both *ab initio* local-density functional (LDF) methods and density functional tight binding methods. For closed core pure screw TDs, the authors found deep states with energies 0.9 to 1.6 eV above the valence band maximum and states 0.2 eV below the conduction band minimum. The authors then addressed open core screw TDs, in which the inner most 1 – 2 unit cells of material was removed. This core structure was found to yield only shallow states which were related to the high local shear strains from the dislocation displacement field. Calculations of the energies of pure edge TDs showed no deep levels and the energetically favorable structure had a closed core. In a subsequent paper, Elsner *et al.* considered oxygen impurities, gallium vacancies, and clusters of these two species in the vicinity of edge TDs in GaN [23]. It was found that gallium vacancy-oxygen complexes are favorably trapped at the dislocation core and that these complexes do give rise to deep acceptor levels. The authors concluded that these acceptor levels may be responsible for yellow luminescence in the nitrides.

In a separate set of papers, Wright and co-workers calculated the formation energies and energy levels for pure edge TDs in AlN and GaN using density functional theory [24, 25]. For both AlN and GaN, Wright *et al.* considered full core, open core, group III-vacancy core, and N-vacancy core structures. All calculations were performed for Fermi levels ranging from the valence band maximum to the conduction band minimum for both nitrogen-rich and gallium-rich growth conditions. For both AlN and GaN, the edge dislocation was found to have levels in the forbidden energy gap for all core structures that were studied. Subsequently, Leung *et al.* calculated the formation energies for the four different core structures as a function of donor (assuming Si dopants) and acceptor (assuming Mg dopants) concentrations for both gallium-rich and nitrogen-rich growth conditions [26]. The TDs had both acceptor and donor energy levels. In this work, Coulomb interactions were explicitly considered, namely, charge could transfer between dopants and TDs. The line charges per site were then calculated for TD densities of 10^8 cm^{-2}, 10^9 cm^{-2}, and 10^{10} cm^{-2} as a function of dopant concentration for both *n*-type and *p*-type material for the two most favorable core structures. The transition from uncharged to fully charged TDs occurred at a dopant density corresponding to the bulk density of dislocation-related sites (assuming one site per unit cell), *e.g.*, a TD density of 10^9 cm^{-2} corresponds to $2x10^{16}$ cm^{-3} TD-related defect sites - this is the approximate transition from uncharged to charged dislocations shown in Leung *et al.*'s work for 10^9 cm^{-2} TD density material. Leung *et al.* noted that for low *n*-type dopant densities, the number of defect sites will be much larger than the number of donors, and thus all carriers are transferred to dislocation-defect levels. In this case, the Fermi energy will be pinned near the defect level and there will be no free carriers – this is consistent with semi-insulating behavior in high TD density GaN. At large donor densities, the TDs are fully charged, but there are excess free carriers which cause the Fermi level to rise toward the donor level.

Transport Studies and Transport Modeling

The concept of carrier scattering by charged dislocation lines can be found in textbooks on semiconductor physics [27]. Weimann *et al.* used the formalism first developed by Bonch-Bruevich and Kogan [28] and later by Pödor [29] to obtain a transverse carrier mobility [30]. In this work, Weimann first calculated the trap occupation, apparently by assuming a dislocation trap level 2.2 eV below the conduction band minimum. Then the scattering amplitude was calculated for the charged

line which then was used to determine the transverse mobility. The overall transverse mobility was calculated using Matthiesen's rule. In this model, the mobility first increases with increasing free carrier concentration, which is attributed to screening of the dislocation charge, and then decreases due to ionized impurity scattering. Weimann *et al.*, and Ng *et al.* in related study [31], verified the predicted trends on a series of GaN samples grown by molecular beam epitaxy (MBE) with varying TD density and free carrier concentrations.

More recently, Look and Sizelove have rigorously developed the transverse mobility in material with charged TD lines [32]. Then, the theory was applied to the temperature dependent mobility and carrier concentration data for two sets of samples with well characterized microstructures. Look and Sizelove were able to obtain excellent fits for both the temperature dependence of the carrier concentration and mobility for both samples with no arbitrary fitting parameters – the only adjustable fitting parameters were the donor concentration and energy and the TD density, all of which are known within reasonable bounds. The fitted TD density for the first sample ('sample A') was in the range 4–8x10^8 cm^{-2}, depending on details for the screening, whereas the measured TD density was 4x10^8 cm^{-2}. For the second sample, the fitted TD density was in the range 2 – 3.5x10^{10} cm^{-2}, whereas the experimentally observed TD density was 2x10^{10} cm^{-2} (note that the TD densities were determined by plan-view TEM). The rigor of Look and Sizelove's work and the ability to accurately predict experimentally observed TD densities is remarkable. It is important to emphasize that Look and Sizelove modeled the TD as having one acceptor state per unit translation (c-axis translation) along the TD, in accordance with the model of Wright *et al.* Look and Sizelove noted that V_{Ga}-O_N complex could also give rise to the acceptor state. However, it seems unlikely that each TD line would be fully decorated with oxygen for the range of TD densities and growth techniques. Rather, it seems that Look and Sizelove's work supports the ideas of Wright *et al.* – namely, TDs, independent of impurities or kink sites, have deep levels in the forbidden gap.

Scanning Capacitance Microscopy (SCM)

SCM is a scanning probe microscope technique closely related to AFM. In this technique, a low frequency (5 – 100 kHz) ac field with amplitude of ~1 – 5 V is applied between a metallized AFM tip and a semiconductor sample (which presumably has a native oxide) at a defined dc offset bias. At the same time, the capacitance is measured at high frequency (915 MHz) with a small superimposed voltage swing [33, 34]. The SCM images then are typically displayed as changes in capacitance dC in response to the low frequency ac voltage swing dV. Concurrent dC/dV maps and contact mode AFM images were recorded. The surface morphology of high quality MOCVD-grown GaN films shows Ga-N bilayer steps. Terminations of pairs of steps correspond to the intersection of screw-component TDs with the surface. Hansen *et al.* carried out SCM and local C-V studies of unintentionally doped *n*-type GaN (n ~5x10^{16} cm^{-3}) [35]. In these studies there was a a strong correlation with the SCM (dC/dV) contrast and positions of TD intersections with the film surface. Local C-V curves recorded from regions near TDs in comparison to those away from TDs were consistent with a flatband shift due to negative charge accumulation at the TDs.

Leakage Paths

Several studies are now appearing in the literature that demonstrate that TDs behave as current leakage pathways in GaN. The development of LEO for the nitrides has lead to clear demonstrations of the dramatic contrast in leakage currents between normal GaN with TD densities on the order of 10^9 cm^{-2} and LEO material with TD densities in the range 10^4–10^6 cm^{-2}.

Ballistic Electron Emission Microscopy (BEEM)

Brazel *et al.* reported on BEEM studies of unintentionally-doped *n*-type GaN films (n ~$5x10^{16}$ cm^{-3}) in which the Schottky barrier was formed by depositing at 7 nm Au layer on the GaN [36]. Surprisingly, the Au layer had pit features with a density and distribution similar to the mixed character TD density, and thus it was inferred that the pits in the Au layer corresponded to the position of screw-component TDs in the underlying GaN layer. Simultaneously recorded collector current images and STM images showed high collector current density regions associated with the pit features for both negative (electron) and positive (hole) tunneling bias. The threshold bias varied from 0.3 to 0.95 V for electron injection and from 0.3 to 1.3 eV for hole injection. The authors attributed the high current densities and reduced Schottky barrier heights to acceptor and donor-like traps in the vicinity of screw-component TDs.

Reverse Bias Diodes on LEO GaN

Kozodoy *et al.* used the high contrast in TD density in LEO structures to study the effect of TDs on reverse bias leakage currents in *p-n* junctions [37]. In this study, *p-n* junctions were formed on uncoalesced GaN LEO stripes, where the junctions were placed either over the wing region (TD density <10^6 cm^{-2}) or over the window region (TD density ~10^9 cm^{-2}) on the same LEO stripe. Under reverse bias, the leakage current densities were at least three orders of magnitude higher for the window regions in comparison with the wing region. In a similar study, Parish *et al.* fabricated AlGaN-based *p-i-n* UV solar detectors on LEO GaN [38]. The diodes on the wing regions typically had six to eight orders of magnitude lower reverse bias leakage current than for diodes grown on conventional ('dislocated') GaN. Additionally, the LEO-based diodes had sharper current cutoffs and much more sharply defined spectral response curves in comparison with diodes produced on conventional GaN.

Summary

The body of work described above provides a picture in which the TDs in the group III-nitrides are electrically active and clearly deleterious for transport, emission, and detection properties. The CL, PEC etching, and transport studies are all consistent with dislocation-related deep acceptor levels for *n*-type GaN. In this case of optical-related properties, these levels appear to act as NR centers. For low doping densities, the TD-related deep levels can fully deplete the material of free carriers, rendering it semi-insulating. For high doping densities, the TD-related traps act as a charged line scattering centers. Dislocation-related deep levels may also play a role in leakage. It remains unclear whether the TD-related traps are an intrinsic feature of dislocations in the nitrides or if they are cause by impurity segregation. Continued progress in high purity growth techniques, such as MBE, may eventually resolve this issue.

The prospects appear to be excellent for achieving GaN single crystal 'pseudo-substrates' using techniques such as LEO, thick hydride vapor phase epitaxy, and laser-assisted substrate removal and combinations of these techniques. The economic advantages are minimal for developing single crystal GaN substrates for high volume commodity devices such as LEDs. However, for low volume, technology-enabling devices, such as laser diodes and possibly high performance transistors, the performance improvement on low TD density material appears to merit the use of single crystal substrates. Although Nakamura realized cw emission in GaN-based laser diodes in normal dislocated material, his realization of 10,000 hour cw nitride-based laser operation was facilitated through the use of thick GaN on LEO substrates [39]. Fortuitously, the technological drive for single crystal GaN substrates will provide material with sufficiently low TD densities that many of the properties will unambiguously fall within the 'point-defect' limited regime. This exciting possibility should provide a wide variety of opportunities for the defect science community.

Acknowledgements

The authors thank all of the members of the nitride groups at UCSB and HP Laboratory. Financial support for the work at UCSB was provided by ONR (Colin Wood and John Zolper, contract monitors) and by Hewlett-Packard Laboratories.

References

1. J.I. Pankove, E.A. Miller, and J.E. Berkeyheiser, *J. Lumine.* **5**, 84 (1972).
2. Y. Koide, N. Itoh, K. Itoh, N. Sawaki, and i. Akasaki, *Jpn. J. Appl. Phys.* **27**, 1156 (1988).
3. I. Akasaki, H. Amano, Y. Koide, K. Hiramatsu, and N. Sawaki, *J. Cryst. Growth* **98**, 209 (1989).
4. S. Nakamura, T. Mukai, M. Senoh, and N. Iwasa, *Japn. J. Appl. Phys.* **31**, L139 (1992).
5. S. Nakamura, T. Mukai, and M. Senoh, *Appl. Phys. Lett.* **64**, 1687 (1994).
6. S.D. Lester, F.A. Ponce, M.G. Craford, and D.A. Steigerwald, *Appl. Phys. Lett.* **66**, 1249 (1995).
7. X.H. Wu, L.M. Brown, D. Kapolnek, S. Keller, B. Keller, S.P. DenBaars, and J.S. Speck, *J. Appl. Phys.* **80**, 3228 (1996).
8. X.H. Wu, D. Kapolnek, E.J. Tarsa, B. Heying, S. Keller, B.P. Keller, U.K. Mishra, S.P. DenBaars, and J.S. Speck, *Appl. Phys. Lett.* **68**, 1371 (1996).
9. X.H. Wu, P. Fini, E.J. Tarsa, B. Heying, S. Keller, U.K. Mishra, S.P. DenBaars, and J.S. Speck, *J. Cryst. Growth* **189-190**, 232 (1998).
10. X.H. Wu, C.R. Elsass, A. Abare, M. Mack, S. Keller, P.M. Petroff, J.S. Speck, and S.J. Rosner, *Appl. Phys. Lett.* **72**, 692 (1998).
11. F.C. Frank, *Acta. Cryst.* **4**, 497 (1951).
12. J.E. Northrup, L.T. Romano, and J. Neugebauer, *Appl. Phys. Lett.* **74**, 2319 (1999).
13. S.J. Rosner, E.C. Carr, M.J. Ludowise, G. Girolami, and H.I. Erikson, *Appl. Phys. Lett.* **70**, 420 (1997).
14. B. Heying, E.J. Tarsa, C.R. Elsass, P. Fini, S.P. DenBaars, and J.S. Speck, *J. Appl. Phys.* **85**, 6470 (1999).
15. T. Sugahara, H. Sato, M. Hao, Y. Naoi, S. Kurai, S. Tottori, K. Yamashita, K. Nishino, L.T. Romano, and S. Sakai, *Japn. J. Appl. Phys. (Part 2)* **37**, L398 (1998).
16. S.J. Rosner, G. Girolami, H. Marchand, P.T. Fini, J.P. Ibbetson, L. Zhao, S. Keller, U.K. Mishra, S.P. DenBaars, and J.S. Speck, *Appl. Phys. Lett.* **74**, 2035 (1999).
17. H. Marchand, J.P. Ibbetson, P.T. Fini, S. Keller, S.P. DenBaars, J.S. Speck, and U.K. Mishra, *J. Cryst. Growth* **195**, 328 (1998).
18. M.S. Minsky, A.M. White, and E.L. Hu, *Appl. Phys. Lett* **68**, 1531 (1996).
19. C. Youtsey, L.T. Romano, and I. Adesida, *Appl. Phys. Lett.* **73**, 797 (1998).
20. C. Youtsey, L.T. Romano, R.J. Molnar, and I. Adesida, *Appl. Phys. Lett.* **74**, 3537 (1999).
21. S.J. Rosner and J.S. Speck, *unpublished* .
22. J. Elsner, R. Jones, P.K. Sitch, V.D. Porezag, M. Elstner, T. Frauenheim, M.I. Heggie, S. Oberg, and P.R. Briddon, *Phys. Rev. Lett.* **79**, 3672 (1997).
23. J. Elsner, R. Jones, M.I. Heggie, P.K. Sitch, M. Haugk, T. Frauenheim, S. Oberg, and P.R. Briddon, *Phys. Rev. B* **58**, 12571 (1998).
24. A.F. Wright, and J. Furthmuller, *Appl. Phys. Lett.* **72**, 3467 (1998).
25. A.F. Wright, and U. Grossner, *Appl. Phys. Lett.* **73**, 2751 (1998).
26. K. Leung, A.F. Wright, and E.B. Stechel, *Appl. Phys. Lett.* **74**, 2495 (1999).
27. K. Seeger, *Semiconductor Physics, 4th Edition.* (Springer, New York, 1989).
28. V.L. Bonch-Bruevich and S.M. Kogan, *Sov. Phys. - Solid State* **1**, 1118 (1959).
29. B. Pödör, *Phys. Stat. Solidi* **16**, K167 (1966).

30. N.S. Weimann, L.F. Eastman, D. Doppalapudi, H.M. Ng, and T.D. Moustakas, *J. Appl. Phys.* **83**, 3656 (1998).
31. H.M. Ng, D. Doppalapudi, T.D. Moustakas, N.G. Weimann, and L.F. Eastman, *Appl. Phys. Lett.* **73**, 821 (1998).
32. D.C. Look, and J.R. Sizelove, *Phys. Rev. Lett.* **82**, 1237 (1999).
33. C.C. Williams, J. slinkman, W.P. Hough, and H.K. Wickramasinghe, *Appl. Phys. Lett.* **55**, 1662 (1989).
34. Y. Huang, and C.C. Williams, *J. Vac. Sci. Tech. B* **13**, 369 (1994).
35. P.J. Hansen, Y.E. Strausser, A.N. Erickson, E.J. Tarsa, P. Kozodoy, E.G. Brazel, J.P. Ibbetson, U. Mishra, V. Narayanamurti, S.P. DenBaars, and J.S. Speck, *Appl. Phys. Lett.* **72**, 2247 (1998).
36. E.G. Brazel, M.A. Chin, and V. Narayanamurti, *Appl. Phys. Lett.* **74**, 23672369 (1999).
37. P. Kozodoy, J.P. Ibbetson, H. Marchand, P.T. Fini, S. Keller, J.S. Speck, S.P. DenBaars, and U.K. Mishra, *Appl. Phys. Lett.* **73**, 975 (1998).
38. G. Parish, S. Keller, P. Kozodoy, J.P. Ibbetson, H. Marchand, P.T. Fini, S.B. Fleischer, S.P. DenBaars, and U.K. Mishra, *Appl. Phys. Lett.* **75**, 247 (1999).
39. S. Nakamura, *MRS Bulletin* **23**, 37 (1998).

Table 1 List of key references on the physical properties of threading dislocations in GaN and its alloys

Topic	Reference
Modification of minority carrier concentrations	
Cathodoluminescence Studies:	
S.J. Rosner *et al.*, *Appl. Phys. Lett.*, **70**, 420 (1997).	[13]
T. Sugahara *et al.*, *Japn. J. Appl. Phys.*, L398 (1998).	[15]
S.J. Rosner *et al.*, *Appl. Phys. Lett.*, **74**, 2035 (1999).	[16]
Photo-Electro-Chemical Etching (PEC):	
C. Youtsey, L.T. Romano, I. Adesida, *Appl. Phys. Lett.*, **73**, 797 (1998).	[19]
C. Youtsey *et al.*, *Appl. Phys. Lett.*, **74**, 3537 (1999).	[20]
Traps/Deep Levels	
Electronic Structure Calculations:	
'No states in the gap'	
J. Elsner *et al.*, *Phys. Rev. Lett.*, **79**, 3672 (1997).	[22]
J. Elsner *et al.*, *Phys. Rev. B.*, **58**, 12571 (1998).	[23]
'States in the gap'	
A.F. Wright and Ulrike Grossner, *Appl. Phys. Lett.*, **73**, 2751 (1998).	[25]
K. Leung, A.F. Wright, E.B. Stechel, *Appl. Phys. Lett.*, **74**, 2495 (1999).	[26]
Transport Studies & Transport Modeling:	
Nils G. Weimann *et al.*, *J. Appl. Phys.*, **83**, 3656 (1998).	[30]
H.M. Ng *et al.*, *Appl. Phys. Lett.*, **73**, 821 (1998).	[31]
D.C. Look and J.R. Sizelove, *Phys. Rev. Lett.*, **82**, 1237 (1999).	[32]
Scanning Capacitance Microscopy:	
P.J. Hansen *et al.*, *Appl. Phys. Lett.*, **72**, 2247 (1998).	[35]
Leakage Paths	
Ballistic Electron Emission Microscopy (BEEM):	
E.G. Brazel *et al.*, *Appl. Phys. Lett.*, **74**, 2367 (1999).	[36]
Reverse bias diodes on LEO vs. normal GaN:	
P. Kozodoy *et al.*, *Appl. Phys. Lett.*, **73**, 975 (1998).	[37]
G. Parish *et al.*, *Appl. Phys. Lett.*, **75**, 247 (1999).	[38]
Shuji Nakamura, *MRS Bulletin*, May 1998, 37.	[39]
Degradation	
Long life laser diodes on LEO GaN:	
Shuji Nakamura, *MRS Bulletin*, May 1998, 37.	[39]

Materials Science Forum Vols. 353-356 (2001) pp. 779-782
© 2001 Trans Tech Publications, Switzerland

AlN Crystal Growth by Sublimation Technique

S.Yu. Karpov[1], A.V. Kulik[1], M.S. Ramm[2], E.N. Mokhov[2], A.D. Roenkov[2], Yu.A. Vodakov[2] and Yu.N. Makarov[3]

[1] Soft-Impact Ltd., PO Box 33, RU-194156 St.Petersburg, Russia

[2] A.F.Ioffe Physico-Technical Institute, Russian Academy of Sciences, Polytechnicheskaya st. 26, RU-194021 St.Petersburg, Russia

[3] Lehrstuhl für Strömungsmechanik, Universität Erlangen-Nürnberg, Cauerstr. 4, DE-91058 Erlangen, Germany

Keywords: Critical Pressure, Growth Rate, Material Source, Sublimation

Abstract. Sublimation growth of AlN crystals in a sandwich system is studied both theoretically and experimentally. Two types of Al sources are examined – AlN powder and liquid Al. Two-dimensional modeling is employed to understand the nature of the growth failure at a pressure lower than the critical one, predicted in a recent paper [A.S.Segal et al, J.Cryst.Growth 211 (2000) 68]. A relationship between the temperature and pressure is found providing maximum AlN growth rates.

Introduction

Aluminum nitride is one of the most promising material to fabricate insulating substrates for Group III nitride microelectronic devices. Mostly, a sublimation technique employed first by Slack and co-workers [1,2] is used for AlN bulk crystal growth. The growth occurs from the gaseous Al and N_2 normally supplied by evaporation of an AlN powder charge in a hot zone of a crucible. Due to simplicity of chemical reactions involving Al and N_2 , modeling is believed to be an effective and powerful tool for growth process optimization. In particular, an important role of N_2 adsorption kinetics in the growth rate control has been recognized theoretically [3,4]. This factor is found to affect significantly the temperature and pressure providing a maximum growth rate [5]. Another prediction to be discussed is that AlN growth fails when the pressure becomes lower than a critical value generally dependent on temperature [4]. This effect requires more detailed examination and experimental verification.

In this paper we report on further theoretical and experimental study of AlN crystal growth in a sandwich system. Two types of Al source are examined – AlN powder and liquid aluminum. Growth conditions providing maximum growth rates are found using parametric simulations. For better understanding of the growth process near the critical pressure, two-dimensional modeling is applied.

Experiment

Growth of AlN layers was carried out in a nitrogen atmosphere at 1000 mbar (N-rich conditions) as described elsewhere [3,4]. We used either AlN powder or liquid Al (l-Al) as a material source and 6H/4H-SiC(0001) wafers of 10-12 mm in diameter as a seed. The clearance between the source and the seed was 2-3 mm. Growth temperature T was varied in the range of 1900-2300°C. Temperature difference between the source and the seed ΔT was maintained between 5°C and 20°C.

We have compared sublimation rates of both l-Al and AlN-powder sources. Contrary to expectations, we found no noticeable difference between the sublimation rates at T = 1900-2150°C. This was attributed to an AlN peel formation on the surface of the l-Al source retarding evaporation of liquid Al. A higher temperature resulted in a dramatic increase in the l-Al source sublimation rate. The effect was caused by explosion of the AlN peel due to high Al vapor pressure. The

sublimation rate obtained with the l-Al source was at least by order of magnitude higher than that of the AlN powder. However, explosive character of the l-Al source operation made difficult an accurate control and stabilization of the growth conditions.

Results

The model of AlN growth by using AlN-powder source has been described in detail elsewhere [4]. It is based on modeling the reactive species transport coupled with heterogeneous reactions on the source and seed surfaces. The l-Al source is simulated assuming the partial Al pressure at the source surface to be equal to the saturated vapor pressure over the liquid phase.

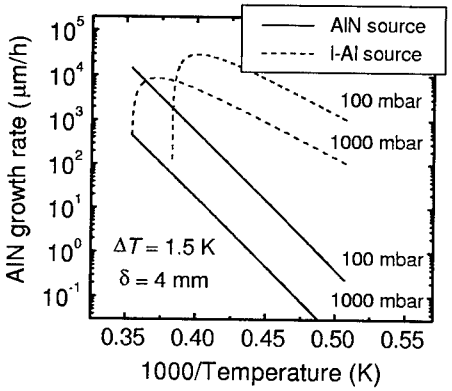


Fig.1. Comparison of computed AlN growth rates obtained with the l-Al and AlN-powder sources.

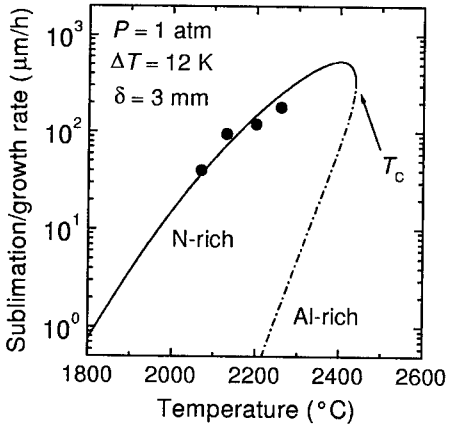


Fig.2. Sublimation/growth rate of AlN vs temperature. Lines are the computational results, circles are the experimental data of this work.

Fig.1 compares the AlN growth rates obtained with AlN-powder and l-Al sources. One can see that for $T < 2350$°C at $P = 100$ mbar and for $T < 2550$°C at $P = 1000$ mbar the l-Al source provides much higher growth rates than the AlN-powder source. In this case the Al partial pressure at the source surface is by several orders in magnitude higher than that at the seed. Moreover, the Al vapor is supersaturated with respect to AlN formation from the gaseous Al and N_2. As a result, an AlN peel appears on the liquid Al surface in accordance with our experimental observations. At a higher temperature, the Al partial pressure at the seed becomes greater than the saturated vapor pressure over liquid Al. Under these conditions, the l-Al source no longer works effectively that results in a drastic drop of the AlN growth rate. So, despite the high sublimation rate attractive for practice, the l-Al source has some drawbacks making this source difficult to operate during the long-term AlN growth.

Sublimation/growth rate of AlN obtained with the AlN-powder source is shown in Fig.2 as a function of temperature. It is seen that experimental points lie close to theoretical predictions. Growth rates up to ~200 μm/h are achieved for T and ΔT employed in the experiments. All the experimental data get in the temperature range below the critical point T_c. At $T = T_c$ the vapor phase is stoichiometric ($P_{Al} \cong 2P_{N_2}$) and the total pressure in the growth cell becomes equal to the critical pressure corresponding to the failure of sublimation growth predicted in [4]. Fig.2 shows that the maximum growth rate achievable for $P = 1000$ mbar and for chosen clearance between the source and seed surfaces is ~600 μm/h.

The large difference in the growth rate under N-rich and Al-rich conditions seen in Fig.2 is attributed to extremely low N_2 sticking probability onto the AlN surface [4]. Indeed, under Al-rich conditions nitrogen is the species limiting AlN growth while under N-rich conditions the growth rate is controlled by Al possessing no kinetic limitation for the incorporation into the solid. The difference in the sticking probabilities of Al and N_2 results also in

the fact that maximum growth rate can be reached under a nitrogen excess rather than in a stoichiometric vapor as assumed in [6]. To find the conditions providing maximum growth rates, we varied pressure and temperature in a wide range and calculated the corresponding growth rates of the crystal. Results of the computations are summarized in Fig.3. One can see that the growth rate increases with temperature, and that a higher pressure is necessary to reach the maximum growth rate at a higher temperature. Fig.3 shows that low pressures are not favorable for achieving high AlN growth rates. This is because the temperature range employed for AlN growth is limited from the top by the critical temperature T_c which decreases with pressure. The relationship between the temperature and the pressure providing maximum growth rate is plotted in Fig.4. It is seen that at $T > 2300$°C the optimum pressure lies in the range of 1000-2000 mbar.

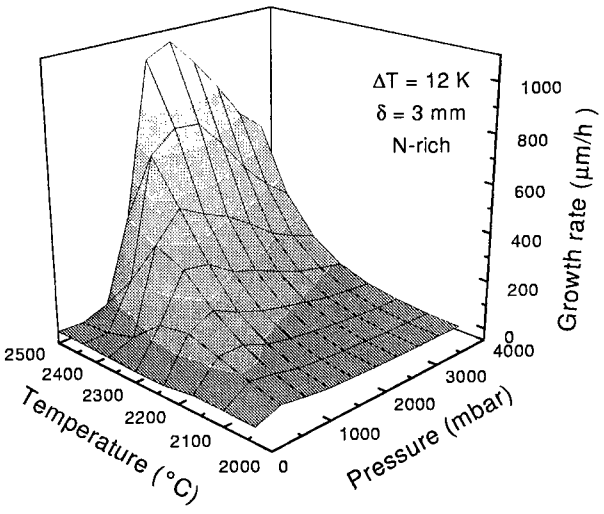


Fig.3. Computed AlN growth rate as a function of temperature and pressure.

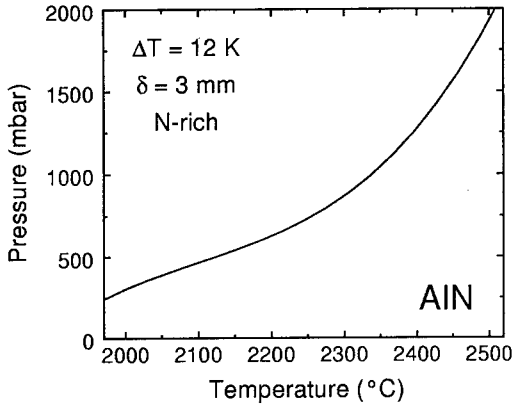


Fig.4. Relationship between the temperature and pressure providing maximum AlN growth rate.

The above consideration shows the critical pressure resulting in the growth failure to be an important factor for the sublimation technique. The existence of the critical pressure P_c has been predicted within the one-dimensional approach suggested in [4]. At $P < P_c$ the approach is no longer valid. To understand better the processes occurring in the growth system near the critical pressure we carried out two-dimensional simulation of the AlN growth in the sandwich system. For the simulation, we additionally assumed that the walls of the growth cell were chemically inert.

The geometry of the sandwich cell is shown schematically in Fig.5. AlN powder is placed at the bottom of the cell whereas the seed is on the top. The openings providing species exchange between the cell and ambience are located near the seed surface.

Fig.5 displays the gas flow streamlines and the Al concentration in the growth cell at a pressure greater (a) and lower (b) than the critical one. At $P > P_c$ the flow is directed from the source to the seed and has a nearly one-dimensional character. A similar behavior exhibits the gradient of Al concentration. This supports the one-dimensional approach [4] based on the assumption that the reactive species transport in the cell occurs predominantly from the source surface to the seed. In contrast, at $P < P_c$ the gas flow pattern is essentially two-dimensional. One can see that both the powder source and the seed sublime and the gas mixture goes out of the cell through the openings. In this case Al becomes uniformly distributed over the sandwich cell and transport of the reactive

species occurs via convection. The origin of the critical effect is that the sum of Al and N_2 partial pressures at the seed and source surfaces becomes higher than the total pressure controlled by ambience. Under these conditions the gas mixture has to flow out of the growth cell.

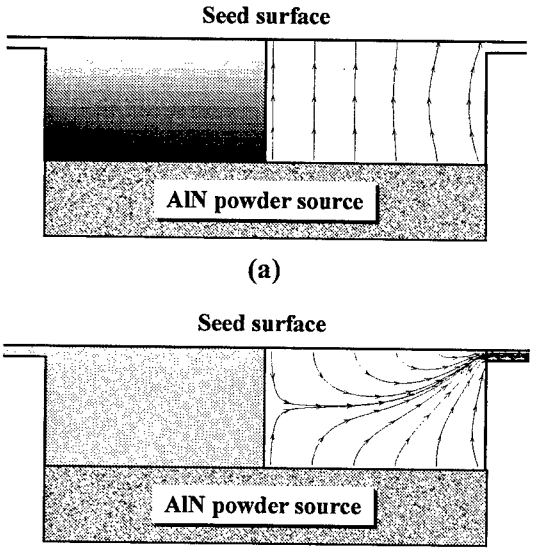


Fig.5. Gas flow streamlines (right) and Al concentration (left) computed (a) for 0.2 atm ($P > P_c$) and (b) for 0.1 atm ($P < P_c$) at 2200°C, $\Delta T = 4$ K and c = 3 mm . The color gradation from white to black corresponds to the increase of concentration.

The computations show that transition from the AlN growth to sublimation on the seed occurs drastically in a narrow range of pressure variation near the critical value P_c . At $P > P_c$ the results obtained by the one-dimensional and by the two-dimensional approaches are found to agree well with each other.

Summary

In this work, sublimation growth of AlN crystals in a sandwich system is studied both theoretically and experimentally. The study was focused on optimization of the growth condition to achieve maximum growth rates. At $T < 2300$°C an optimal pressure providing maximum growth rate lies in the range of 500-100 mbar. The growth rates ~ 1 mm/h can be obtained at $T > 2300$°C and at the pressure varied between 1000 and 2000 mbar.

We have shown that allowable variation of the growth parameters (temperature and pressure) is limited by the existence of a critical pressure below which the AlN growth fails. This effect includes a drastic transformation of the gas flow pattern from nearly one-dimensional to essentially two-dimensional, accompanied by the transition from AlN growth to sublimation on the seed.

From comparison of the one-dimensional and two-dimensional approaches we have found that they agree well with each other at $P > P_c$. This allows one to use the simple one-dimensional model [4] for quantitative analysis of the AlN growth by sublimation technique.

References

[1] G.A. Slack, T.F. McNelly, J. Cryst. Growth 34 (1976), p. 263.

[2] L.J Schowalter, J.C Rojo, N. Yakolev, Y. Shusterman, K. Dovidenko, R. Wang, I. Bhat, G.A Slack, MRS Internet J.Nitride Semicond.Res. 5S1 (2000), W6.7.

[3] S.Yu. Karpov, D.V. Zimina, Yu.N. Makarov, E.N. Mokhov, A.D. Roenkov, M.G. Ramm, Yu.A. Vodakov, Phys.Stat.Sol. (a) 176 (1999), p. 435.

[4] A.S. Segal, S.Yu. Karpov, Yu.N. Makarov, E.N. Mokhov, A.D. Roenkov, M.G. Ramm, Yu.A. Vodakov, J.Cryst.Growth 211 (2000), p. 68.

[5] A.S. Segal, M.S.Ramm, A.V.Kulik, S.Yu. Karpov, Yu.N. Makarov, M. Spencer, T. Hossain, to be published in J.Cryst.Growth

[6] P.M. Dryburgh, J.Cryst.Growth 125 (1992), p. 65.

Materials Science Forum Vols. 353-356 (2001) pp. 783-786
© 2001 Trans Tech Publications, Switzerland

Investigation of the Structure of 2H-AlN Films on Si(001) Substrates

J. Jinschek, U. Kaiser, V. Lebedev and W. Richter

Institut für Festkörperphysik, Friedrich-Schiller-Universität Jena,
Max-Wien-Platz 1, DE-07743 Jena, Germany

Keywords: ALN, Domain Film Structure, Off-Axis Substrate, TEM

Abstract. By conventional transmission electron microscopy (CTEM) investigations on 2H-AlN films grown by plasma-assisted molecular beam epitaxy (MBE) on Si(001) the influence of the off-axis angle of the substrate surface on the film structure was studied. Three types of Si(001) substrates were used: on-axis, ~1°, and ~5° off-axis Si(001) substrates. The AlN layer on an exact oriented Si(001) substrates consists of 3 AlN film domains: two main film domains, AlN_1 and AlN_2, and a small domain AlN_3 at substrate surface defects. Their c-axis orientations are parallel to the c-axis of the substrate: $[0001]AlN_{1,2,3} \parallel [001]Si$. The a-axes of AlN_1 and AlN_2 rotated by 30° to each other: $[11\bar{2}0]AlN_1 \parallel [01\bar{1}0]AlN_2 \parallel [1\bar{1}0]Si$ [3]. The a-axis orientation of AlN_3 is $[01\bar{1}0]AlN_3 \parallel [100]Si$. In 2H-AlN films grown on off-axis Si(001) substrates (~1° and ~5°) the ratio between the AlN_1 and AlN_2 film domains changes dramatically as far as a single domain film structure consisting of only AlN_1 is reached. The AlN c-axes of all domains on the off-axis substrates are not parallel to the Si c-axis but tilted by the off-axis angle of the Si(001) substrate (~1° respectively ~5°), i.e. [0001]AlN is parallel to the Si(001) substrate surface orientation.

Introduction

Aluminium nitride (AlN) is a promising material as a wide band-gap, high temperature, radiant resistant semiconductor. It exists in the thermodynamically stable wurtzite phase (basal plane lattice parameter a = 0.3112nm [1]) but also in the zincblende polytype [2]. Wurtzite AlN (2H-AlN) deposited on commonly used silicon (Si) (001) substrates (lattice parameter a = 0.54307nm) is a good solution as a template substrate for III-nitride electronic and optoelectronic devices. The successful AlN film epitaxy on Si(001) would allow to integrate the group III-nitride technology into the mature silicon technology. Especially the growth of single domain AlN films on Si (001) is a challenging task for heteroepitaxy due to the mismatch in the lattice parameters and the different crystallographic symmetry of the hexagonal closed-packed (0001)AlN lattice plane (six-fold symmetry) and the (001)Si substrate surface plane (four-fold symmetry).

Experimental

AlN films were grown in a home-made plasma-assisted molecular-beam epitaxy (PAMBE) system equipped with a radio-frequency plasma source for activated nitrogen supply and using thermally evaporated aluminium. Three different Si(001) substrate surfaces were prepared: A) on-axis (±0.5°) (for details [3]), and off-axis substrates with B) about 1° (±0.5°) , and C) about 5° (±0.5°) tilt of the substrate surface orientation towards [110]Si (for details [4]). Thin plan-view (pv) and cross-sectional (xs) foils for conventional transmission electron microscopy (CTEM) investigations were prepared using standard techniques. For the CTEM studies a JEOL JEM 3010 at 300kV was used. Plan-view specimen of the 2H-AlN/Si(001) heterosystem were examined in [0001]AlN zone axis and the cross-section specimen in $[1\bar{1}0]Si$ zone axis orientation.

2H-AlN on on-axis Si (001) substrate

Fig.1 shows CTEM images of a AlN film grown on an exact (±0.5°) oriented Si(001) substrate in plan-view (pv) orientation. In the diffraction pattern (DP) inserted in the upper right corner of the bright-field (BF) image (Fig.1a) the reflexes indicate an unusual 12-fold symmetry. The dark-field (DF) images in Fig.1b and 1c, where 1b was taken with the reflection marked by a square, and 1c with the reflection marked by a cycle, explain this phenomenon as two usual 6-fold symmetrical reflex systems of hexagonal 2H-AlN in c-axis viewing direction. Therefore the AlN film consists of two main film domains with a 30° rotation of their a-axes orientations to each other. The ratio of these domains in the entire film is approximately 1:1. At some areas of the film (see DF image in Fig.1d) the DP shows a third weak 6-fold symmetrical spot system in addition (marked by a triangle in the inserted DP in Fig.1d). The a-axes of the third 2H-AlN domain have a 15° rotation in respect to the two main domains. In cross-sectional (xs) view (Fig.2) we can determine the crystallographic orientation between the AlN film and the Si(001) substrate. The xs-CTEM images were taken in the [1 $\bar{1}$ 0]Si zone axis. Additionally to the Si reflections, the DP in Fig.2b shows the [11 $\bar{2}$ 0]AlN_1 and the [01 $\bar{1}$ 0]AlN_2 zone axis orientation at the same time, which confirmed the existence of two main domains. This can be explained by two completely identical symmetry fittings of the 6-fold (0001)AlN lattice plane on the 4-fold (001)Si plane. The reflections (0002)AlN and (002)Si are in one row (see Fig.2b). That means, the c-axes of AlN_1 and AlN_2 are parallel to the Si (001) surface orientation, i.e. in case of this on-axis substrate: [0001]AlN ‖ [001]Si. In Fig.2c the DF image was taken by a reflection of the AlN_1 domain (marked by a square) and the DF image in Fig.2d by a reflection (encycled) of the AlN_2 domain. This corresponds to the pv DF images in Fig.1b and 1c. Figs.2c and 2d are also nearly complementary except small AlN crystals in the film at the film substrate interface which can be seen in Fig.2e. This DF image was taken after a 15° tilt of the TEM specimen along the interface. That corresponds equal to a third domain (AlN_3) with an a-axis orientation of [01 $\bar{1}$ 0]AlN_3 ‖ [100]Si where the AlN_3 c-axis is parallel to the Si substrate c-axis as was the case for AlN_1 and AlN_2. The existence of the AlN_3 film domain is caused by irregularities at the Si substrate surface (arrowed in the BF image, Fig.2a) which are likely to be

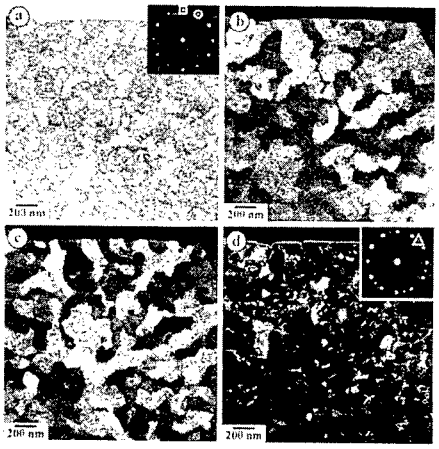


Figure 1 pv-CTEM images of the AlN film grown on on-axis Si(001) substrate. **(a)** BF image with the inserted DP. **(b)-(d)** DF images taken with the reflexes marked by a square (b), by a cycle (c), and by a triangle(d)

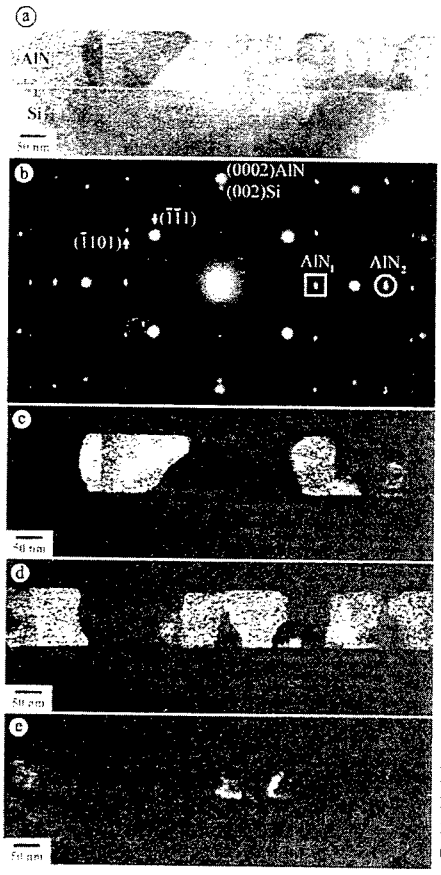


Figure 2 xs CTEM images in [1 $\bar{1}$ 0]Si viewing direction of the AlN film grown on on-axis Si(001). **(a)** BF image, **(b)** DP, **(c),(d)** DF images taken with the reflexes marked by a square (c) and by a cycle (d), (e) DF image after a 15° tilt along the film substrate interface.

caused by Si diffusion on the substrate surface.

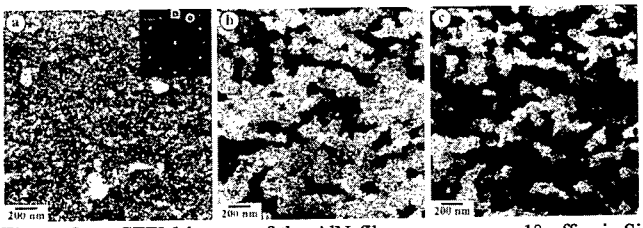


Figure 3 pv-CTEM images of the AlN film grown on a ~1° off-axis Si (001) substrate. **(a)** BF image (inserted DP), **(b),(c)** DF images taken with the reflections marked by a square (b) and by a cycle (c)

2H-AlN on ~1° off-axis Si(001)

Fig.3 shows the pv CTEM images of a AlN film grown on a ~1° (±0.5°, tilted towards [110]Si) off-axis Si(001) substrate surface. The DP inserted in the BF image in Fig.3a indicates two reflex systems with 6-fold symmetries but with different spot intensities. The DF image in Fig.3b was taken with the reflex of the more intensive system marked by a square in the DP, and Fig.3c taken with a weak reflex marked by the cycle. The AlN film consists of the same two film domains like in the on-axis case, but the ratio is approximately 2:1.

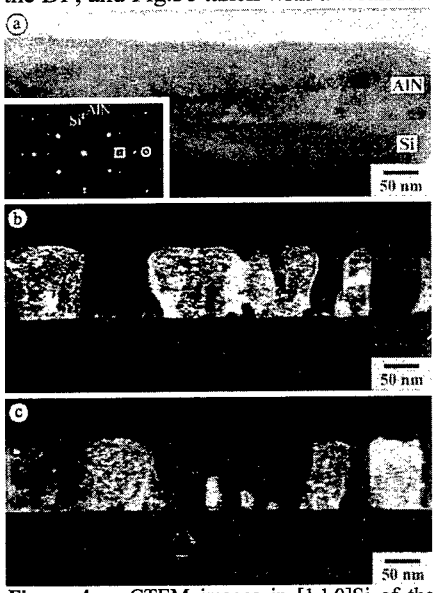


Figure 4 xs CTEM images in [1 1 0]Si of the AlN film grown on a ~1° off-axis Si (001) substrate. **(a)** BF image with inserted DP, **(b),(c)** DF images of the two AlN film domains

Fig.4 shows the corresponding xs-CTEM images in the $[1\,\bar{1}\,0]$Si zone axis orientation. In the DP (inserted in the BF image, Fig.4a) again the $[11\bar{2}0]AlN_1$ and the $[01\bar{1}0]AlN_2$ zone axis orientation can be indicated. The c-axes orientation (marked with "AlN" and "Si" in the DP in Fig.4a) are tilted towards each other by the off-axis angle (~1°) of the Si(001) substrate, i.e. the film c-axis is parallel to the substrate surface orientation. In Fig.4b the DF image was taken by a reflection of the AlN_1 domain (marked by a square in the DP) and the DF image in Fig.4c by a reflex of the AlN_2 domain (encycled). Fig.4b and 4c as well as Fig.3b and 3c are complementary. No AlN_3 orientation were revealed.

2H-AlN on ~5° off-axis Si(001)

The pv CTEM images in Fig.5 show an almost single domain structure of the AlN film grown on an off-axis Si(001) substrate surface, which has a surface orientation tilted ~5° (±0.5°) towards [110]Si. The DP inserted in the BF image in Fig. 5a indicates a single 6-fold symmetry of the AlN film. The DF image in Fig.5b was taken with the AlN reflex marked by a square in the DP. This AlN domain contributes to the entire film by approximately 95%. The other film parts have a 30° a-axis rotation which can be seen in the DP inserted in Fig.5c. This DF image was taken by the reflection marked by the a cycle in the DP in Fig.5c.

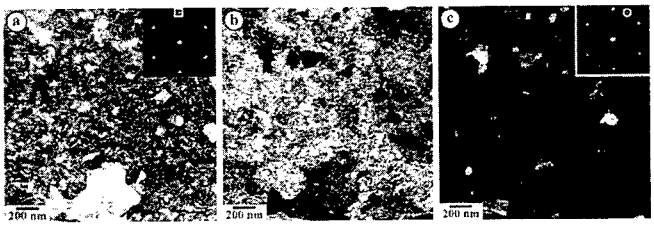


Figure 5 pv-CTEM images of the AlN film grown on a 5° (towards [110]Si) tilted Si (001) substrate surface. **(a)** BF image with the inserted DP, **(b)** DF image taken with the reflection marked by a square, **(c)** DF image taken with the encycled reflection in the inserted DP

The xs CTEM images in Fig.6 determine the crystallographic orientation of the main film domain in respect to the substrate. The BF image in Fig.6a and the DP in Fig.6b prove the existence of one main AlN_1 film domain with an a-axis orientation of $[11\bar{2}0]AlN_1 \parallel [1\,\bar{1}\,0]$Si. The AlN

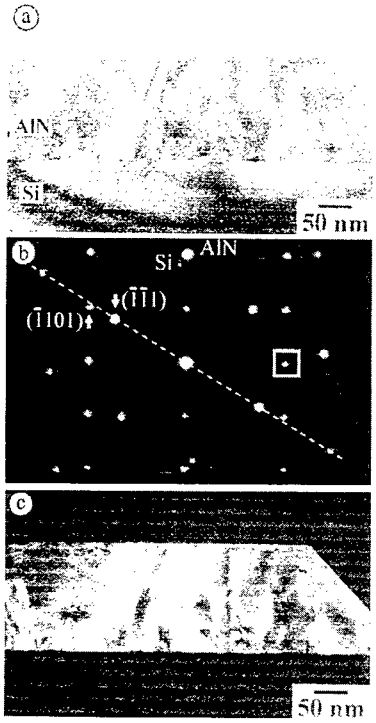


Figure 6 xs CTEM images in [1 $\bar{1}$ 0]Si of the AlN film grown on a ~5° off-axis Si (001) substrate. **(a)** BF image, **(b)** DP, **(c)** DF image taken with an AlN reflection (marked by a square)

c-axis (marked with "AlN" in the DP) shows a ~5° tilted to Si c-axis (marked by "Si) which is equal to the off-axis angle of the substrate. The AlN film c-axis is again parallel to the substrate surface orientation. The DF image in Fig.6c, which was taken by a AlN_1 reflection marked by a square, confirms the single domain structure of the 2H-AlN film.

The preferred appearance of the AlN_1 domain over AlN_2 may be explained crystallographically in the following way. The tilt of the Si(001) substrate surface towards the [110]Si direction leads to a better fit of the film domain with the [11 $\bar{2}$ 0]AlN_1 ∥ [1 $\bar{1}$ 0]Si orientation. The substrate surface lattice vector in [110] projection (cosine of the off-axis angle) is shortened compared to the on-axis case. While increasing the off-axis angle the resulting lattice mismatch between the AlN_1 domain and the Si in [110] direction is being decreased in contrast to the AlN_2 domain, where the similar mismatch in [1 $\bar{1}$ 0] projection remains unchanged. By comparison of the DP of the on-axis case in Fig.2b and the DP in Fig.6b it is possible to see that in the off-axis case the ($\bar{1}$ 101)AlN reflection (arrowed) is aligned with the ($\bar{1}$ $\bar{1}$ 1)Si reflection (arrowed) which may now caused a less strained state of the film. It is suggested that an off-axis angle of 6.64° leads to a complete single domain 2H-AlN film structure as that is the value at which the ($\bar{1}$ 101)AlN and the ($\bar{1}$ $\bar{1}$ 1)Si reflections are aligned along a symmetry line as marked.

Summary

The influence of the off-axis angle of the Si(001) substrate surface on the heteroepitaxial 2H-AlN film structure were studied by CTEM techniques. On on-axis substrate surfaces three AlN film domains were found: AlN_1 and AlN_2 with [11 $\bar{2}$ 0]AlN_1 ∥ [01 $\bar{1}$ 0]AlN_2 ∥ [1 $\bar{1}$ 0]Si, and AlN_3 with [01 $\bar{1}$ 0]AlN_3 ∥ [100]Si. The c-axis orientation of all 3 film domains are parallel to the c-axis of the substrate: [0001]$AlN_{1,2,3}$ ∥ [001]Si. Using off-axis Si(001) substrates slightly tilted by about 1°, it has been shown only one of the three film domain orientation (AlN_1) is preferred. Using off-axis Si(001) substrates tilted as far as about 5° towards [110]Si, the 2H-AlN films show an almost single domain (AlN_1) film structure.

This work was supported by the DFG (contract No. RI 650/5-1) and by HSP III (contract No. H 1-916/57/1).

References

[1] G.A. Jeffrey, G.S. Parry, J.Chem.Phys. Vol. 23 (1953), p. 406.
[2] S. Strite, H. Morkoc, J.Vac.Sci.Technol.B Vol. 10 (1992), p. 1237.
[3] V. Lebedev, J. Jinschek, U. Kaiser, B. Schröter, W. Richter, Appl.Phys.Let. Vol. 76 (2000), p. 2029.
[4] V. Lebedev, J. Jinschek, J. Kräußlich, U. Kaiser, B. Schröter, W. Richter, J.Crystal Growth, submitted.

Materials Science Forum Vols. 353-356 (2001) pp. 787-790
© 2001 Trans Tech Publications, Switzerland

Formation and Electronic Transport of 2D Electron and Hole Gases in AlGaN/GaN Heterostructures

A. Link[1], O. Ambacher[1], I.P. Smorchkova[2], U.K. Mishra[2], J.S. Speck[2] and M. Stutzmann[1]

[1] Walter Schottky Institute, Technische Universität München, Am Coulombwall, DE- 85748 Garching, Germany

[2] Electrical and Computer Engineering, University of California, Santa Barbara CA 93106, USA

Keywords: AlGaN/GaN Heterostructures, Polarization, Two Dimensional Carrier Gases

Abstract

Two dimensional hole (2DHG) and electron gases (2DEG) in wurtzite $GaN/Al_xGa_{1-x}N/GaN$ heterostructures are induced by piezoelectric and spontaneous polarization. The sheet carrier concentration and the electronic transport properties of the two dimensional carrier gases located close to one of the AlGaN/GaN interfaces are therefore sensitive to a high number of different physical properties such as polarity, alloy composition, strain, and barrier thickness. In this paper, the transport properties of 2DEGs and 2DHGs with sheet carrier concentrations between $2x10^{12}$ and 10^{13} cm^{-2} are evaluated by a combination of C-V profiling, Hall effect and Shubnikov-de-Haas measurements. By comparison of theoretical and experimental results we demonstrate that the formation as well as the transport properties of two dimensional carrier gases in GaN/AlGaN/GaN heterostructures are dominated by polarization induced interface charges.

Introduction

Recent investigations of undoped AlGaN/GaN heterostructures have shown that two- dimensional electron gases with high sheet carrier concentration forming the device channel of high electron mobility transistors are generated by positive polarization induced interface charges [1]. Kozodoy et al. observed an enhancement of the hole concentration by over five orders of magnitude in Mg-doped AlGaN/GaN superlattices compared to bulk Mg:GaN films. The high sheet hole concentration of the superlattices demonstrates the pivotal role of polarization induced interface charges in determining the band structure of p-type AlGaN/GaN heterostructure and the accumulation of holes with high concentration in the GaN wells [2].

In this paper we will discuss additional aspects of the formation and electronic transport properties of two dimensional electron and hole gases in GaN/AlGaN/GaN heterostructures grown by metalorganic chemical vapor deposition and/or plasma induced molecular beam epitaxy [1, 3]. Conduction and valence band profiles are calculated in order to determine the carrier distribution and the formation of two dimensional carrier gases at interfaces of heterostructures with N- and Ga-face polarity, taking polarization-induced interface charges into account. The theoretical predictions for $Al_xGa_{1-x}N/GaN$ based structures with different alloy composition of the barriers are compared to experimental results achieved by a combination of C-V profiling, Hall effect and Shubnikov-de Haas measurements.

Formation of 2DEGs and DHGs

Bernardini et al. have predicted that spontaneous polarization, P_{SP}, is present in wurtzite group III nitride crystals [4]. The calculated values of spontaneous polarization are large and increase from GaN to AlN. The piezoelectric constants also increase from GaN to AlN, leading to a larger piezoelectric polarization, P_{PE}, of AlN compared to GaN for the same amount of strain. To discuss the carrier confinement in group III nitride based heterostructures, we will restrict ourselves to

GaN/AlGaN heterostructures grown pseudomorphically on top of thick relaxed GaN buffer layers. In this particular case $Al_xGa_{1-x}N$ barrier layers are under tensile strain and the piezoelectric as well as the spontaneous polarization are pointing in the same direction. Since the value of the negative spontaneous polarization and the tensile strain of the barrier both become larger with increasing Al concentration, an increase of total polarization, $P = P_{SP} + P_{PE}$, has to be expected. To calculate the spontaneous and piezoelectric polarization of AlGaN alloys, we are using a linear interpolation between the spontaneous polarization, piezoelectric and elastic constants of the binary compounds discussed in more detail in Ref. [1, 4, 5]. As a consequence of the higher value of polarization of AlGaN compared to GaN, at an abrupt AlGaN/GaN interface the gradient in polarization causes a bound polarization interface charge:

$$\sigma(AlGaN/GaN) = P(GaN) - P(AlGaN) = P_{SP}(GaN) - \{P_{SP}(AlGaN) + P_{PE}(AlGaN)\} = -\sigma(GaN/AlGaN) \quad (1)$$

The value of the polarization induced sheet charge, σ/e, versus Al-concentration of the barrier , x, can be approximated by

$$\frac{\sigma}{e}(x) = (6.41 \cdot 10^{13} cm^{-2})x - (1.17 \cdot 10^{13} cm^{-2}) \cdot (1 - x). \quad (2)$$

The sign of the bound interface charge in AlGaN/GaN heterostructures is determined by the polarity. For crystals with Ga(Al)-face polarity, one bilayer consists of a Ga(Al) layer above the N layer. As a consequence, the total polarization of AlGaN and GaN is pointing from the surface towards the sapphire substrate, the gradient in polarization at the interface becomes negative and the bound charge density positive. If the polarity is flipped to N-face, one bilayer consists of a nitrogen monolayer which is located above a metal monolayer. Therefore, the orientation of polarization, the sign of the polarization gradient, and of the interface charge are inverted.

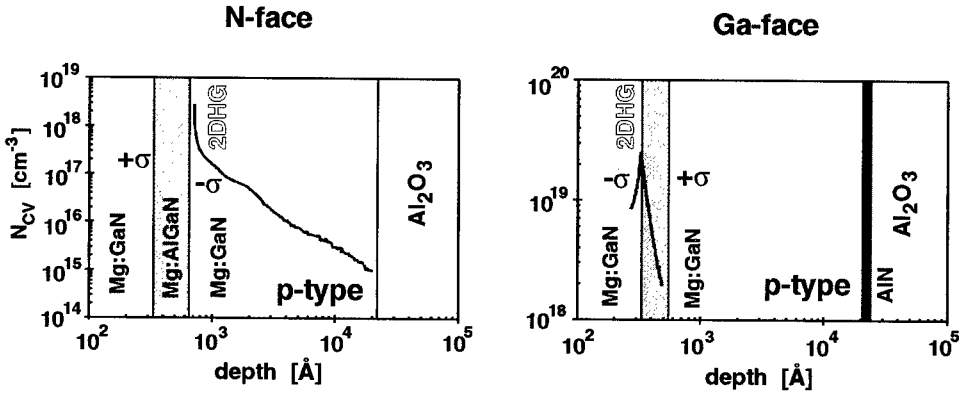


Figure 1. Hole concentration versus depth determined by C-V profiling in GaN/AlGaN/GaN heterostructures with N- or Ga-face polarity.

The positive polarization induced interface charge can be compensated by electrons leading to the formation of 2DEGs. In n-type Ga-face (N-face) GaN/AlGaN/GaN heterostructures, this 2DEG is located at the lower (upper) AlGaN/GaN (GaN/AlGaN) interface. In analogy, 2DHGs in p-type Ga-face (N-face) GaN/AlGaN/GaN heterostructures are located at the upper (lower) GaN/AlGaN (AlGaN/GaN) interface. To provide experimental evidence for these theoretical predictions we have deposited n- and p-type doped GaN/AlGaN/GaN heterostructures by plasma induced molecular beam epitaxy (PIMBE) [1]. Hole accumulation located at the lower (upper) interface of Ga- (N-)face heterostructures with sheet carrier concentrations of 0.4×10^{13} (2.0×10^{13} cm^{-2}) were observed in agreement with our predictions.

Based on the present theoretical understanding of the polarization induced charge we now wish to determine quantitatively the sheet carrier concentration of two-dimensional carrier gases and its

dependence on alloy composition. To enable the determination of the sheet carrier concentration and carrier distribution profile in AlGaN/GaN structures, including spontaneous and piezoelectric polarization induced bound sheet charges as well as the splitting of the valence band maximum due to crystal field and spin orbit coupling, we have used a modified one dimensional Schrödinger-Poisson solver [6].

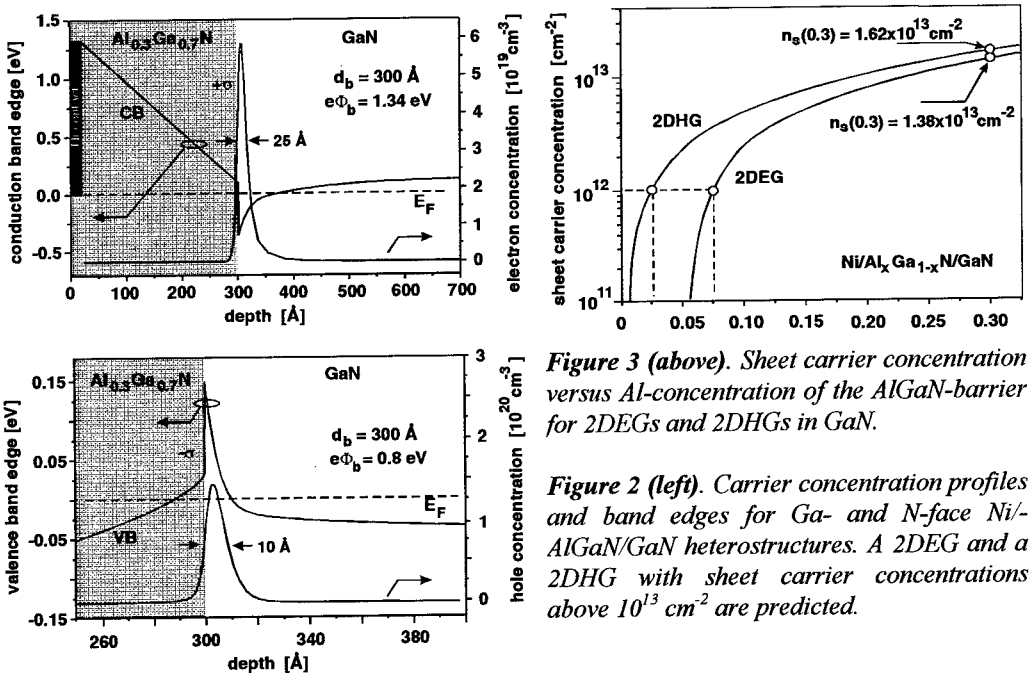


Figure 3 (above). *Sheet carrier concentration versus Al-concentration of the AlGaN-barrier for 2DEGs and 2DHGs in GaN.*

Figure 2 (left). *Carrier concentration profiles and band edges for Ga- and N-face Ni/-AlGaN/GaN heterostructures. A 2DEG and a 2DHG with sheet carrier concentrations above 10^{13} cm^{-2} are predicted.*

In Fig.2, the band edge profiles and carrier distribution profiles are shown for Ga-face and N-face $Ni/Al_{0.3}Ga_{0.7}N/GaN$ (50/30/2000 nm) heterostructure. A 2DEG is obtained close to the interface with a sheet carrier concentration of $1.4x10^{13}$ cm^{-2}, in good agreement with the experimental observations. To allow hole confinement close to the AlGaN/GaN interface the polarity of sample has to be N-face. Using a p-doped barrier ([Mg] = $5x10^{19}$ cm^{-3}) a 2DHG with a sheet carrier concentration of $1.6x10^{13}$ cm^{-2} should result. In both cases the formation of hole and electron gases is dominated by the polarization induced interface charge of $\sigma/e(x = 0.3) = 1.68x10^{13}$ cm^{-2}. In Fig.3 the calculated sheet carrier concentrations of 2DEGs and 2DHGs are shown, demonstrating the opportunity to change the sheet carrier concentrations of two dimensional carrier gases in AlGaN/GaN heterostructures by the alloy composition of the barrier.

Electronic transport properties

Because of the strong attraction between the bound interface charges and the free carriers, the average distance between the carriers and the AlGaN/GaN interface decreases with increasing Al-concentration and increasing sheet carrier concentration dropping below 20 Å for x > 0.25. As a consequence, the drift mobility should be much more affected by interface roughness scattering in AlGaN/GaN heterostructures in comparison to AlGaAs/GaAs heterostructures, where polarization induced interface charges are absent. To evaluate the transport properties of 2DEGs with different sheet carrier concentrations, we have performed temperature dependent Hall-measurements and Shubnikov-de-Haas experiments in tilted magnetic fields (Fig.4 and 5). For sheet carrier concentrations of $2.1x10^{12}$ cm^{-2}, a maximum mobility of 28000 cm^2/Vs is obtained below 10 K. At room temperature 2DEG mobilities between 1320 and 1610 cm^2/Vs are observed, increasing

proportional to $1/T^3$ with decreasing temperature. For temperatures below 100 K, a further decrease in temperature results in no or only a small enhancement of the mobility, which in AlGaAs/GaAs heterostructures is explained by significant scattering of electrons due to ionized impurities. Note that contrary to AlGaAs/GaAs heterostructures [6], a decrease of the low temperature mobility, μ_{2DEG}, is observed with increasing sheet carrier concentration, n_s ($\mu_{2DEG} \propto n_s^{(-1.1\pm0.2)}$), so the limiting scattering mechanism in AlGaN/GaN heterostructures must be different. In addition to the Hall effect measurements, we performed low temperature (430 mK) Shubnikov-de-Haas (SdH) experiments. The quantum scattering time, τ_q, was measured to be 0.23 ps at magnetic fields, that were tilted with respect to the 2DEG plane normal, and compared with the transport scattering time τ_t. The ratio τ_t/τ_q = 10 indicates that the scattering of electrons is dominated by small angle scattering mechanisms.

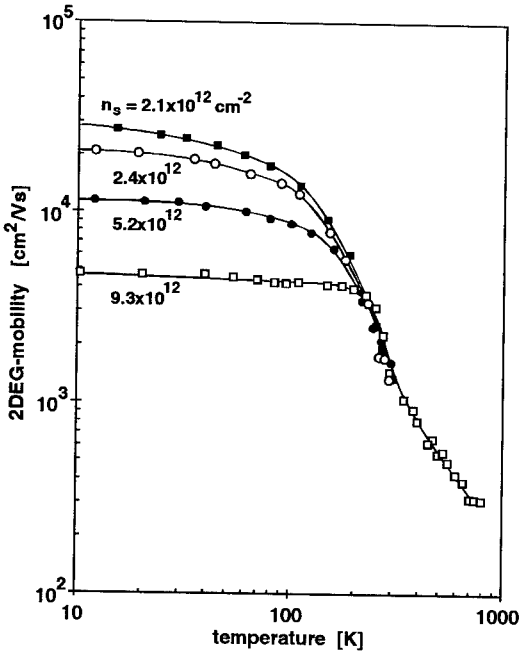


Figure 4. 2DEG-mobility versus temperature for AlGaN/GaN heterostructures with different sheet carrier concentrations.

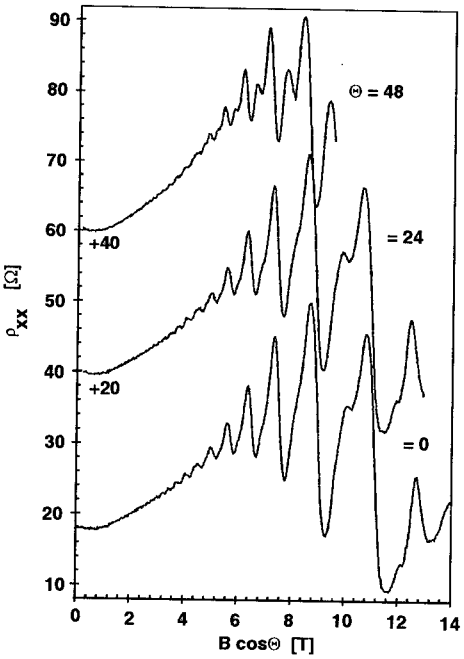


Figure 5. SdH-measurements at tilted magnetic fields. The sheet carrier concentration of the 2DEG is 2.4x10^{12} cm^{-2}.

The reduction of mobility with increasing sheet carrier concentration indicates a significant contribution of interface roughness scattering to the scattering mechanism of electrons as predicted by Oberhuber et al. [7]. Beside the scattering due to impurities, scattering caused by interface roughness is limiting the mobility at low temperatures. Interface roughness becomes important because of the low average distance of the carriers towards the AlGaN/GaN interface due to the presence of polarization induced interface charges.

[1] O. Ambacher et al., J. Appl. Phys. 85 (1999), p. 3222.
[2] P. Kozodoy et al., Appl. Phys. Lett. 75 (1999), p. 2444.
[3] I.P. Smorchkova et al. J. Appl. Phys. 86 (1999), p. 4520.
[4] F. Bernardini, V. Fiorentini and D. Vanderbilt, Phys. Rev. B 56 (1997), p. R10024.
[5] O. Ambacher et al., J. Appl. Phys. 87 (2000), p. 334.
[6] L. Pfeiffer et al., Appl. Phys. Lett. 55 (1989), p. 1888
[7] R. Oberhuber, G. Zandler, and P. Vogl, Appl. Phys. Lett. 73 (1998), p. 818.

Materials Science Forum Vols. 353-356 (2001) pp. 791-794
© 2001 Trans Tech Publications, Switzerland

Luminescence of InGaN/GaN Multiple Quantum Wells Grown by Mass-Transport

G. Pozina[1], J.P. Bergman[1], B. Monemar[1], M. Iwaya[2], S. Nitta[2], H. Amano[2] and I. Akasaki[2]

[1] Department of Physics and Measurement Technology, Linköping University, SE-581 83 Linköping, Sweden

[2] Department of Electrical Engineering and Electronics and High-Tech Research Center, Meijo University, 1-501 Shiogamaguchi, Tempaku-ku, Nagoya 468-8502, Japan

Keywords: Luminescence, Piezoelectric Field, Quantum Wells, Time-Resolved Photoluminescence

Abstract. We present an optical study of an $In_{0.12}Ga_{0.88}N$/GaN structure containing three quantum wells (QW) grown by metalorganic vapor phase epitaxy using mass transport. The mass-transport regions demonstrate a high structural quality with a threading dislocation density less than 10^7 cm^{-2}. The photoluminescence (PL) spectrum is dominated by a 40 meV - narrow line centered at 2.97 eV at 2 K. This emission has a typical PL decay time about 5 ns at 2 K within the PL contour. An additional line with longer decay time (about 200 ns) is observed at an energy of ~2.85 eV. The position of this line shifts towards higher energies with increasing excitation power. The data are explained in terms of a model, where the PL originates from two nonequivalent quantum wells, which could be realized due to a potential gradient across the layers.

Introduction

InGaN/GaN heterostructures are presently of high interest due to their successful application for fabrication of highly efficient blue and green light emitting diodes and violet laser diodes [1, 2]. Further device development demands, however, a higher structural quality of the material. It is also important to understand the recombination mechanisms in such structures. However, the physics of InGaN/GaN MQWs is still far from a complete understanding. The previous studies have revealed a variety of optical properties as well as different interpretations. In this work we report on the optical properties of a high quality InGaN/GaN MQW structure grown by metalorganic vapor phase epitaxy (MOVPE) utilizing the mass transport overgrowth technique [3, 4].

Experimental

A nominally undoped GaN layer of thickness 7 μm was grown by MOVPE on a (0001) sapphire substrate with an AlN buffer layer [4]. Micrometer-sized structures (lines) on the GaN surface were etched and after that the structure was annealed at 1100 °C in ammonia, which results in mass transport and lateral overgrowth of the etched areas. Finally, three InGaN quantum wells of width 35 Å separated by 105 Å thick GaN barriers were grown on top of such a GaN layer. In the following we will refer to overgrown areas as mass-transport regions, and others - non-transport.

On the same wafer three different areas with different line-spacing were fabricated: 3x3 μm, 5x5 μm and 10x10 μm. The GaN barriers were doped with Si to a concentration about 10^{18} cm^{-3}. Cathodoluminescence (CL) was measured using a standard Leo 1500 Gemini scanning electron microscope (SEM) with a MonoCL2 system. The third harmonic (λ_{exc} = 266 nm) from a Ti:sapphire fs laser with a pulse frequency of 250 kHz has been used for optical excitation in the time-resolved PL measurements. The photoluminescence signal was detected by a time-correlated photon counting system with time resolution better than 200 ps.

Results and discussion

The sample surface is flat, without pit defects, as demonstrated by SEM (Fig. 1(a)). However, we have found from cathodoluminescence measurements (Fig 1(b, c)) that the mass-transport regions have much higher structural and optical quality compared to the non-transport regions. We have

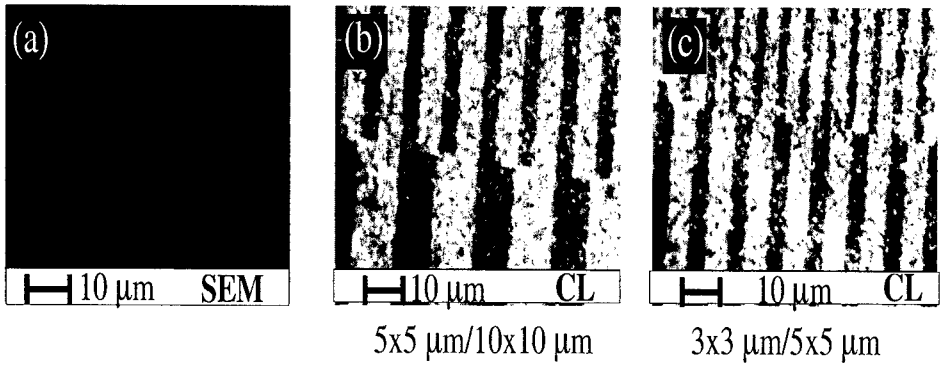


Fig. 1. (a) SEM image of the sample surface; (b) and (c) panchromatic CL images taken at T= 5 K at the border between areas with line/spacing width 5x5 μm and 10x10 μm, respectively (b) and 3x3 μm and 5x5 μm, respectively (c). Bright areas has higher emission intensity, and corresponds to mass-transport region.

estimated from CL patterns that the average threading dislocation density is about 10^8 cm^{-2} for non-transport and about 10^7 cm^{-2} for mass-transport regions, respectively. These values correlate with data obtained from transmission electron microscopy observations [4]. Thus, the structural improvement is significant for the mass-transport regions. The optical and structural properties are similar for the three areas with different line/spacing, thus in the following we will not mention which area is studied.

The photoluminescence (PL) spectra measured at low temperature and at low excitation power are dominated by a PL line X1 centered at 2.967 eV with full width at half maximum (FWHM) of 40 meV at low excitation density (see Fig. 2(a), solid line). This peak is most likely connected with the fundamental two-dimensional (2D) exciton localized in one of the QWs. However, besides this QW exciton transition the PL spectrum demonstrates an additional line X2 with position at ~2.85 eV and FWHM of 70 meV. This second line is accompanied by two LO phonon replicas. The position of X2 moves to higher energies (the shift is about 50 meV) with increasing excitation power and its intensity becomes comparable with the intensity of the main line X1, which, in contrast, does not move with the excitation power (see Fig 2(a), dashed line). The X1 line is also accompanied by a LO phonon replica, however, its position is very close to the X2 peak, and thus

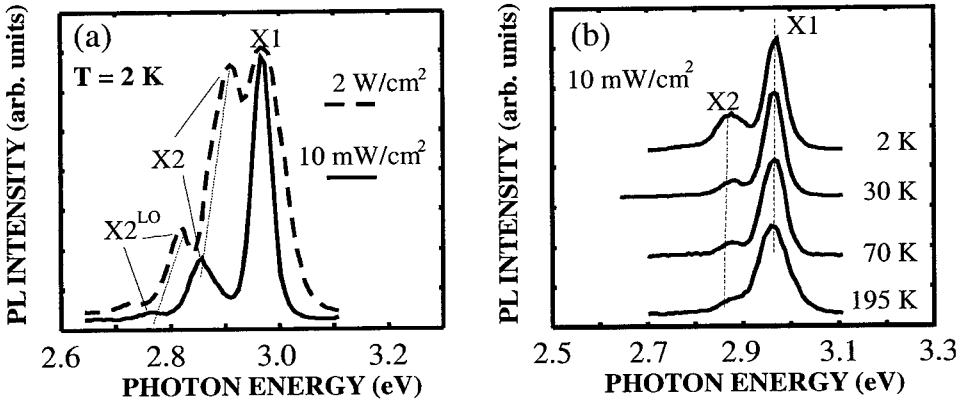


Fig. 2. (a) PL spectra of the InGaN/GaN MQW measured at low excitation density (solid line) and at high excitation density (dashed line), (b) Temperature dependent PL spectra measured at low excitation density.

not resolved. The peak energies of both lines are temperature independent and the X2 transition can not be detected at temperatures higher than 70 K (Fig. 2(b)).

Time-resolved spectra measured at 2 K, 70 K, and at 250 K are shown in Fig. 3. As we can see in Fig. 3(a) the temporal behavior at low temperature is quite different between the X1 line and the lower energy emissions X2. The X1 line demonstrates a near exponential PL decay with recombination times about 5 - 8 ns within the PL contour (for the lower energy spectral side the emission shows slightly slower decay). Within the X2 line two recombination processes with drastically different decay times of 5 ns and 200 ns, respectively, have been clearly observed. The PL decay curves measured at low temperature for two different photon energies corresponding to the X1 and X2 lines, respectively, are shown in Fig. 4(a). At temperatures higher than 70 K the recombination dynamics became similar within the whole PL spectrum and only the process with shorter decay time can be detected as shown in Fig. 3(b) and Fig. 3(c). An example of the PL decay curve measured at 250 K is shown in the inset in Fig. 4(a). The recombination time within the PL spectrum is about 3 ns at this temperature. The dependence of the recombination time on temperature for the both PL lines is shown in Fig. 4(b). For the X1 line the PL decay time decreases slightly from 5 ns down to 3 ns with increasing temperature up to room temperature. For the X2 line position the PL decay time decreases rapidly from 220 ns to 6 ns when the temperature

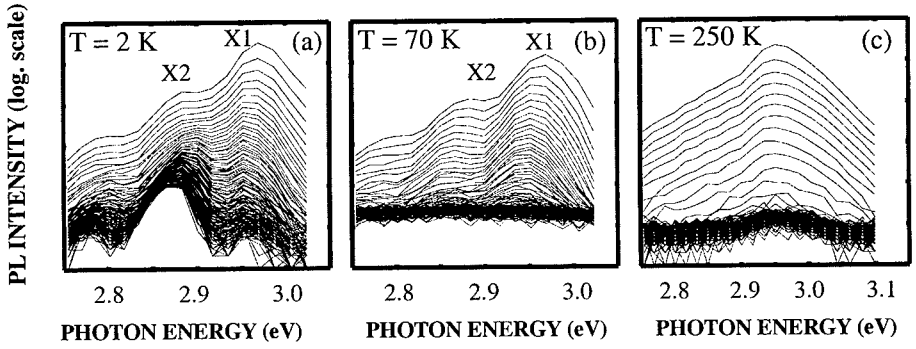


Fig. 3. Time-resolved spectra measured at different temperature: (a)-2 K, (b) – 70 K and (c) – 250 K. The time interval between each time-resolved spectrum is $\Delta t = 1.9$ ns.

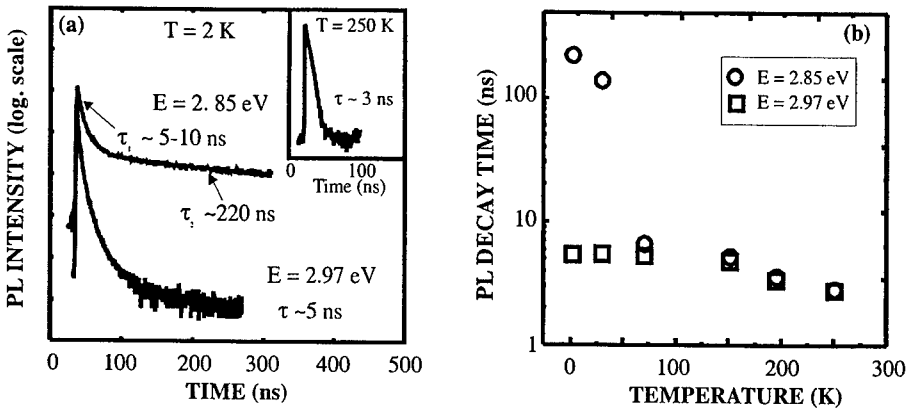


Fig. 4. (a) PL decay curves measured for two photon energies E = 2.97 eV and E = 2.85 eV, corresponding to the X1 and X2 lines, respectively, are shown for low temperature 2 K. The inset shows the PL decay curves measured for the photon energy of 2.98 eV at higher temperature (250 K). (b) The PL decay times measured for the X1 line (E= 2.97 eV) and the X2 line position (E=2.85 eV) are shown as a function of temperature.

increases up to ~ 40-50 K and at T = 70 K the values of the recombination times are similar for both lines.

We have clearly demonstrated from time-resolved PL, temperature dependent and power excitation dependent PL measurements, that X2 can not be a phonon replica of the MQW exciton. Most probably two (or three) nonequivalent quantum wells are realized in the studied sample. Theoretical modeling suggests a strong potential gradient close to the surface of the MQW structure, explaining the different spectra observed for the different QWs. The X1 line is associated with an exciton (or free carrier) recombination from the quantum wells which has a higher carrier filling, and hence a weaker piezoelectric field [5]. Such a quantum well should have a more flat potential profile, which explains the very small shift with excitation intensity for this line. The lower energy X2 peak shifts much more with excitation, and should then correspond to a quantum well with much smaller carrier filling, i. e. a larger piezoelectric field [5]. Thus, the X2 line is probably connected with the middle QW, which has a smaller screening of the piezoelectric field, and hence a smaller oscillator strength for the exciton. This is consistent with the longer PL decay times within the X2 line. No PL line corresponding to the QW closest to the surface is seen. The thermal quenching of the slower X2 recombination process at 70 K might be understood in terms of thermal activation of the carrier transport across the barriers in the potential gradient.

References

[1] S. Nakamura, M. Senoh, N. Iwasa and S. Nagahama, Japan. J. Appl.Phys. 34 (1995), p. L797.
[2] T. Mukai, T. Yamada and S. Nakamura, Japan. J. Appl.Phys. 38 (1999), p. 3976.
[3] M. Iwaya, T. Takeuchi, S. Yamaguchi, C. Wetzel, H. Amano and I. Akasaki, Japan. J. Appl. Phys. 37 (1998), p. L316.
[4] S. Nitta, T. Kashima, M. Kariya, Y. Yukawa, S. Yamaguchi, H. Amano and I. Akaski, Mater. Res. Soc. Internet J. Nitride Semicond. Res. 5S1 (2000), p. W2.8.
[5] V. Fiorentini, F. Bernardini, F. Della Sala, A. Di Carlo and Lugli, Phys. Rev. B 60 (1999), p. 8849.

Materials Science Forum Vols. 353-356 (2001) pp. 795-798
© 2001 Trans Tech Publications, Switzerland

From Relaxed to Highly Tensily Strained GaN Grown on 6H-SiC and Si(111): Optical Characterization

M. Leroux, H. Lahrèche, F. Semond, M. Laügt, E. Feltin,
N. Schnell, B. Beaumont, P. Gibart and J. Massies

Centre de Recherche sur l'Hétéro-Epitaxie et ses Applications-CNRS,
Rue Bernard Grégory, FR-06560 Valbonne, France

Keywords: Biaxial Strain, Luminescence, Nitride Heteroepitaxy, Reflectivity

Abstract We report on the optical properties of GaN grown on 6H-SiC and (111) Si and exhibiting tensile biaxial strains varying from nearly 0 up to $4.5x10^{-3}$. The layers have been assessed by X-ray diffractometry (strain measurements), reflectivity and photoluminescence (PL) as a function of temperature. Excitonic GaN gaps as low as 3.42 eV at 10 K are reported. For strains higher than $\sim 1.5x10^{-3}$, the low temperature PL is dominated by B-related donor bound excitons, though the B free exciton is not observed in σ geometry, as expected from selection rules. Our results also point to a similar behavior for A and B related excitonic luminescence as a function of temperature.

Introduction In spite of the steady progresses achieved in bulk GaN crystal growth and homoepitaxy [1], nitrides devices are still heteroepitaxially grown on various substrates, the most widely used being sapphire and SiC [2,3]. Due to size, quality, availability and cost reasons, nitride epitaxy on (111) Si substrates is also rapidly developing [4]. Heteroepitaxy is accompagnied by strain, due to the lattice parameter mismatch (which is always partially relaxed), and to the thermal dilatation mismatch between films and substrates [3,5]. GaN on sapphire is generally under compression [5], while the growth of GaN on 6H-SiC using an AlN buffer layer results in films under very slight tension or compression [3,6]. As such, the optical properties of GaN under high tension are still poorly known. Recently, a method was proposed for the direct growth by metalorganics chemical vapor deposition (MOCVD) of bidimentionnal GaN layers on 6H-SiC [6]. These layers exhibited a tensile strain that could be varied up to $4.5x10^{-3}$. In the present work, the photoluminescence (PL) and reflectivity of such layers are investigated. We also use our results to discuss the optical properties of GaN grown on (111) Si either by MOCVD or molecular beam epitaxy (MBE). Details of the MOCVD and MBE growth of the samples investigated are given in references [6] and [4] respectively. The PL and reflectivity set-up is described in reference [7].

Strain and optical properties The strain in our layers has been assessed by measuring the a and c parameters by X-ray diffraction. The results are shown in figure 1 that displays the out-of-plane deformation ε_{zz} as a function of the in-plane one ε_{xx}. Layers grown on 6H-SiC and (111) Si are reported. The error bars correspond to both the uncertainty in our lattice parameter measurements (most samples are only a few hundred nm thick), and to the remaining uncertainties of their values in *relaxed* GaN [6]. Dashed lines show reported values of $2C_{13}/C_{33}$, ratio of the elastic constants of GaN, that range between 0.60 and 0.46 [6,8,9]. Most of our data, including those corresponding to the highest strain, have $\varepsilon_{zz}/\varepsilon_{xx} \sim -0.5$. Hereafter, our samples will be assumed to be under a biaxial (0001) strain and we shall use $2C_{13}/C_{33}=0.53$ [8].
Some typical 10 K band-edge reflectivity and luminescence spectra of GaN grown on SiC are displayed in figure 2. The spectra corresponding to the sample grown using an AlN buffer (I, $\varepsilon_{xx}\sim 6x10^{-4}$) are typical of such samples [3,6]. The main PL features are due to donor bound excitons recombinations (I_2), and A free excitons recombinations. The I_2-A separation is ~ 6 meV,

which is typical in that kind of samples, and also in GaN/sapphire samples [7]. The reflectivity spectrum displays A, B and C polaritonic features. The B one is very faint and only a shoulder near the A one.

Turning now to the sample directly grown on SiC (II, ε_{xx}~$3.6x10^{-3}$), its PL spectrum is also dominated by two bands, though strongly broadened due to a large density of structural defects (typically 10^{10} dislocations/cm^2 in such samples, relative to 10^9 for the previous one). The high energy transition is due to A free excitons recombinations, as shows the comparison with the reflectivity spectrum. But the main line, also labeled I_2 (see below), is now 15 meV lower in energy than the A line. On the reflectivity spectrum, also broadened, only A and C excitonic features are resolved.

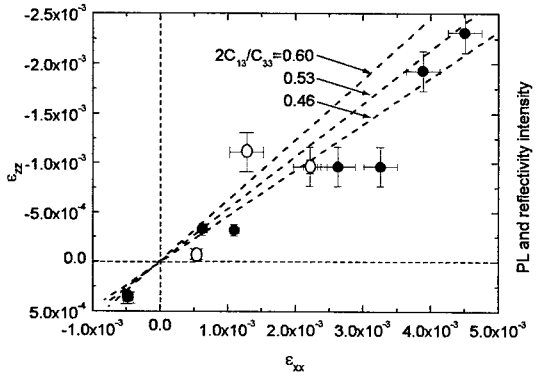


Figure 1: out-of-plane deformation as a function of in-plane deformation in tensily strained GaN. Closed symbols are samples grown on SiC, open ones on (111) Si.

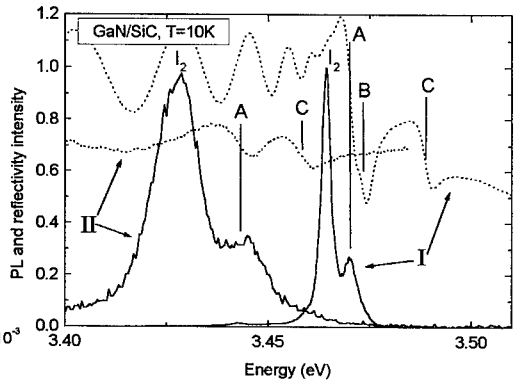


Figure 2: reflectivity (dotted lines) and normalized luminescence (solid line) spectra of two GaN samples grown on SiC with (I) or without (II) an AlN buffer.

To proceed further, we shall examine the strain dependence of the excitonic features recorded through PL and reflectivity. Figure 3 displays A, B and C excitonic energies in our samples as a function of ε_{xx}. Literature data for GaN on sapphire [10,11] and for homoepitaxial GaN [1] are also given. The strain ranges from $-2x10^{-3}$ compressive to $4.5x10^{-3}$ tensile. As expected, the A exciton energy varies linearly with strain, while B and C ones show an anticrossing. The strain coefficient of the A energy is $\partial E_A/\partial\varepsilon_{xx}$ = 9.5±1 eV, in very good agreement with references [5] and [12]. We mention however that figure 3 should be regarded with caution. Indeed, strain is measured at room temperature, and reflectivity at 10 K. The different variations of strain between 300 and 10 K for different substrates manifest through different variations of the energy of A. The A band gap typically increases of 70±2 meV when cooling from 300 to 10 K for GaN on sapphire [7], but only of 62±2 meV for GaN on SiC (and ~ 60 meV for GaN on Si). It can be concluded that there is a ~ $8x10^{-4}$ increase of strain when cooling samples grown on SiC (*relative* to those grown on sapphire). Taking this into account changes $\partial E_A/\partial\varepsilon_{xx}$ to ~ 8.5 eV. The curves in figure 3 are calculated using the parameters from [12], with a rigid shift of $+7x10^{-4}$ in ε_{xx}.

Since the A exciton energy is varying linearly with biaxial strain, a convenient and useful way to illustrate the strain dependence of the GaN band structure is to plot A, B and C transition energies as a function of that of A [5,12]. This also eliminates the scatter due to the strain uncertainties, as observed in figure 3. Such a plot is given in figure 4 for our GaN on SiC and GaN on Si samples. For the completeness and beauty of the figure, data corresponding to GaN on sapphire samples grown in our laboratory have been added. The solid lines are still calculated using [12]. The dashed lines labeled I_2(A) and I_2(B) are 6 meV lower in energy than the curves corresponding to A and B excitons. It is the expected position of donor bound excitons, whether the hole involved originates from the Γ_{9v} or the Γ_{7v}^u valence band. Since A and B Rydbergs are very similar [1], the localization

energy of A- and B-type donor bound excitons is expected to be the same. Figure 4 shows that the main PL line in the low temperature PL spectra of our samples are located either on the I_2(A) or I_2(B) line, depending on strain, allowing to identify them as donor bound excitons. This gives a natural explanation of the strong increase of the splitting between the main PL line and the A exciton when the strain exceeds ~$1.5x10^{-3}$, as reported in figure 2 [6].

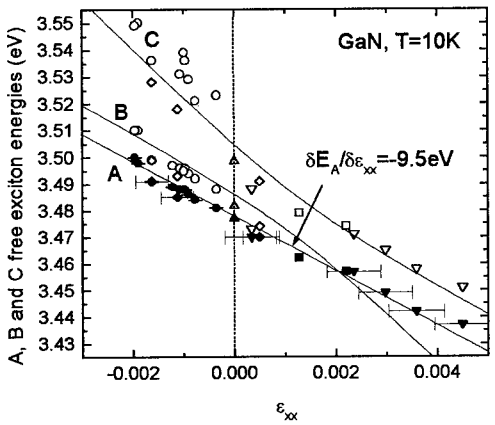


Figure 3: free A (solid symbols), B and C (open symbols) energies as a function of in-plane strain. GaN/Al_2O_3: diamonds [10] and circles [11]; homoepitaxial GaN: upwards triangles [1]; GaN on SiC: downward triangles; GaN on (111) Si: squares.

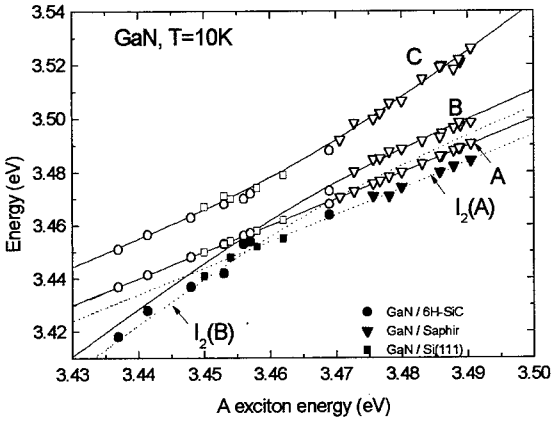


Figure 4 : free excitons (open symbols) and donor bound excitons (closed symbols) energies as a function of the A energy in GaN. Circles, squares and triangles correspond to GaN grown on 6H-SiC, (111) Si and sapphire, respectively.

Figure 2 also shows that in a weakly tensily strained sample (sample I) the B exciton is hardly seen, and that in a highly strained one (sample II), only A and C related features can be observed in the reflectivity spectrum [6]. This is to be expected from the wurtzite phase optical selection rules [13]. When the crystal field term in the Hamiltonian strongly increases positively or negatively, B and C excitons exchange their σ and π oscillator strengths. In highly compressively strained samples, C excitons disappear to the profit of B ones in σ geometry [13]. The reverse happens for highly tensily strained samples, as figure 2 shows.

Luminescence as a function of temperature The temperature dependence of the luminescence of our samples grown on either SiC or Si has been studied, for a comparison with samples grown on sapphire [7]. Figure 5 shows temperature dependent PL spectra near the band-edge of a GaN on Si sample. The low temperature PL spectrum is dominated by a broad band (fwhm=10.9 meV), and comparison with the reflectivity spectrum (upper spectrum in figure 5) shows that this band consists of unresolved free and donor bound excitons recombinations (I_2,A). This is confirmed by the slight blue shift (~3 meV) measured when heating the sample to about 50 K. The contribution of C free excitons increases with rising temperature. The temperature dependence of the intensity of the I_2,A main PL band displays two activation energies (7.5 and 30 meV). This is an intermediate behavior between bound and free exciton lines [7], which confirms our previous interpretation. The sample in figure 5 has an A excitonic energy of 3.462 eV. From figure 4, this is a situation where the A gap is the lower. It is interesting to look at a more highly tensily strained sample, where the B gap is the lower. Figure 6 displays the temperature dependence of the PL intensities of bound (I_2) and free (A and C) exciton lines in such a sample (sample II in figure 2). The temperature behavior of both I_2 and A lines are similar to that reported for GaN on sapphire samples [7]. The I_2 line quenching shows two successive activation energies, one corresponding to

the binding energy to donors (thermal freeing), and the second one to the sum of the previous one and of the Rydberg [7]. The A line shows only one activation energy of 27 meV, *i.e.* of the order of the A Rydberg. Since in such a strain configuration, the Γ_{7c}-Γ_{7v}^{u} continuum is lower than the Γ_{7c}-Γ_{9v} one, this suggests that the thermal dissociation of free excitons in GaN happens principally towards the respective band edges, not necessarily towards the lowest one.

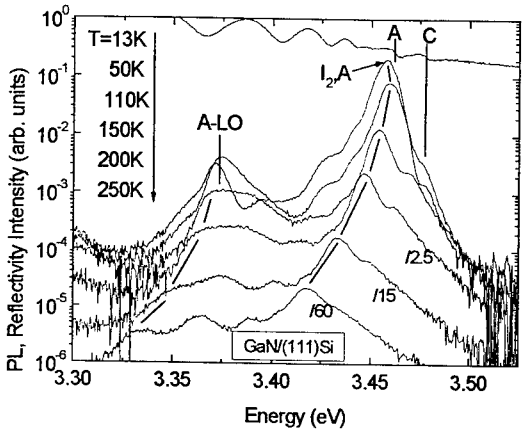


Figure 5: low temperature reflectivity and PL spectra as a function of temperature of GaN grown on (111) Si.

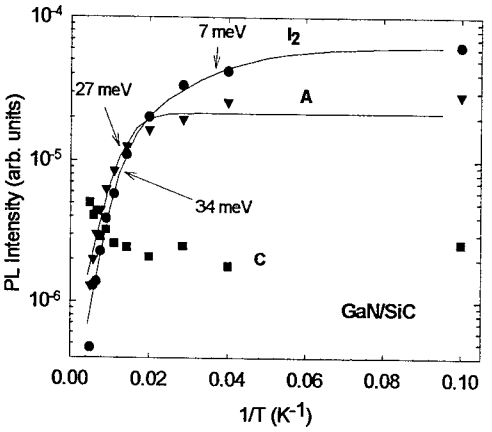


Figure 6: temperature dependence of the PL intensities of free and donor bound excitons in a highly tensily strained GaN/SiC sample.

References

[1] K. Kornitzer, T. Ebner, K. Thonke, R. Sauer, C. Kirchner, V. Schwegler, M. Kamp, M. Leszczynski, I. Grzegory and S. Porowski, Phys. Rev. B 60 (1999), p. 1471.

[2] S. Nakamura and G. Fasol, *The blue diode laser* (Springer, Berlin, 1997).

[3] W.G. Perry, T. Zheleva, M.D. Bremser, R.F. Davis, W. Shan and J.J. Song, J. Electron Mater. 26 (1997), p. 224.

[4] F. Semond, B. Damilano, S. Vézian, N. Grandjean, M. Leroux and J. Massies, J. Appl. Phys. 75 (1999), p. 82.

[5] M. Tchounkeu, O. Briot, B. Gil, J.P. Alexis and R.L. Aulombard, J. Appl. Phys. 80 (1996), p. 5352.

[6] H. Lahrèche, M. Leroux, M. Laügt, M. Vaille, B. Beaumont and P. Gibart, J. Appl. Phys. 87 (2000), p. 557.

[7] M. Leroux, N. Grandjean, B. Beaumont, G. Nataf, F. Semond, J. Massies and P. Gibart, J. Appl. Phys. 86 (1999), p. 3721.

[8] A. Polian, M. Grimsditch and I. Grzegory, J. Appl. Phys. 79 (1996), p. 3343.

[9] K. Funato, S. Hashimoto, K. Yanashima, F. Nakamura and M. Ikeda, Appl. Phys. Lett. 75 (1999), p. 1137.

[10] W. Shan, R.J. Hauenstein, A. J. Fisher, J.J. Song, W.G. Perry, M.D. Bremser, R.F. Davies and B. Goldenberg, Phys. Rev. B 54 (1996), p. 13460.

[11] A. Shikanai, T. Azuhata, T. Sota, S. Chichibu, A. Kuramata, K. Horino and S. Nakamura, J. Appl. Phys. 81 (1997), p. 417.

[12] B. Gil, in GaN (II), edited by J. Pankove and T. Moustakas, Semiconductors and Semimetals Vol. 57 (Academic, New York, 1999), p. 209.

[13] B. Gil and O. Briot, Phys. Rev. B 22 (1997), p. 2530.

Materials Science Forum Vols. 353-356 (2001) pp. 799-802
© 2001 Trans Tech Publications, Switzerland

Electron Traps in Undoped GaN Layers Subjected to Gamma-Irradiation and Annealing

D.V. Davydov, V.V. Emtsev, A.A. Lebedev, W.V. Lundin, D.S. Poloskin, N.M. Shmidt, A.S. Usikov and E.E. Zavarin

A.F.Ioffe Physico-Technical Institute, Russian Academy of Sciences, Polytechnicheskaya, RU-194021 St.Petersburg, Russia

Keywords: Annealing, Epitaxial Layers, Irradiation, Point Defects

Abstract Electrical properties of undoped epi-layers of n-GaN subjected to gamma-irradiation and annealing are investigated by means of Hall effect measurements and DLTS spectroscopy. Despite slight changes in the concentration of charge carriers in the studied materials, the behavior of the electron mobility points to the presence of radiation-induced defects in appreciable concentrations. DLTS spectra revealed three electron traps E_C-E_1 ≈0.25 eV, E_C-E_2 ≈0.58 eV, and E_C-E_3 =0.81 eV in the initial layers and two major traps E_C-E_4 ≈0.15 eV and E_C-E_5 =0.95 eV in the irradiated n-GaN. The parameters of there traps were determined. Both radiation-induced traps were annealed out at T=450°C. In addition the traps E_C-E_1 and E_C-E_2 changed in concentrations upon annealing, as well.

Introduction

Several electron traps with activation energies of E_C-E_{TRAP} 0.13 eV to 0.95 eV are introduced in GaN subjected to irradiation with fast electrons [1], protons [2], and He^+ ions [3] as well as in the course of Au sputtering [4]. Some of the above mentioned traps are believed to be associated with native defects. Up to now the identification of traps has been a matter of controversy. In the present paper the properties of deep centers in gamma-irradiated and annealed GaN layers were studied in some detail.

Experimental

Nominally undoped GaN layers were grown on sapphire substrates by the MOCVD technique at reduced pressure [5] and were n-type. The electron concentration and mobility were in the range of $2\cdot10^{17}$ cm^{-3} to $7\cdot10^{16}$ cm^{-3} and 600 $cm^2/V\cdot s$ to 700 $cm^2/V\cdot s$, respectively. Irradiation was performed at a ^{60}Co gamma-ray facility at room temperature. The irradiation dose was $1.2\cdot10^{19}$ cm^{-2}. The isochronal annealing of irradiated samples was carried out from T=300°C to T=750°C. The electron concentration and mobility versus temperature, $n(T)$ and $\mu(T)$, were measured by means of the Van der Pauw technique. DLTS measurements were taken using Ni/Au Schottky contacts of a diameter of 1100 μm. The surface morphology of these layers was studied with the help of scanning electron microscopy prior to and after irradiation as well as at each annealing step.

Results and Discussion

By way of example, several $n(T)$ and $\mu(T)$ curves for one of the samples studied are shown in Fig. 1 and Fig. 2. In the initial layers the electron conductivity at 100 K ≤ T ≤ 300 K is determined by shallow donor centers at ≈E_C –(20±3) meV and donor centers at ≈E_C–(70±10) meV in comparable concentrations. Our study of DLTS spectra for the initial material revealed three electron traps *E1*, *E2*, and *E3* whose concentrations were estimated to be less than the total concentration of centers responsible for the electron conductivity by three orders-of-magnitude (see Fig. 3 and Table 1). The traps *E1* and *E2* seem to be the same as those labeled D and B in [1] or *EO2* and *EO5* in [2-4].

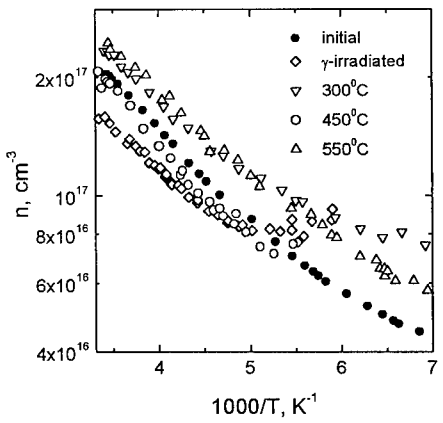


Fig.1 Temperature dependence of the electron concentration in the n-GaN layer in the initial state and after γ-irradiation with subsequent annealing at different temperatures.

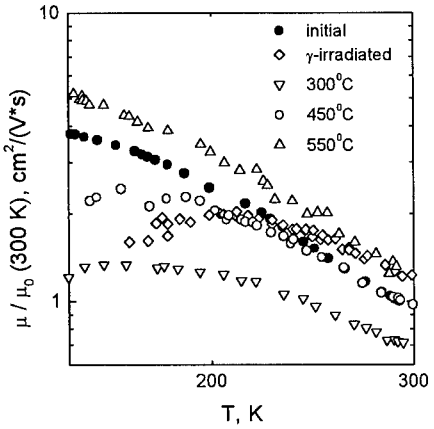


Fig. 2 Temperature dependence of the electron mobility in the same n-GaN layer as in Fig. 1. The reference point μ_0 (300 K) is the electron mobility in the initial n-GaN at T=300 K.

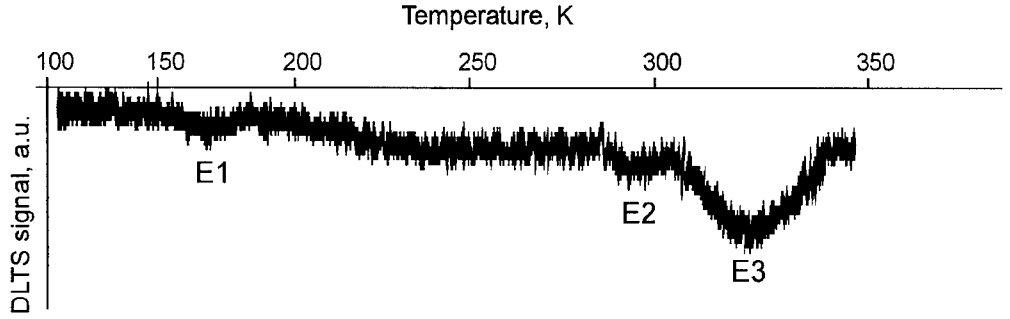


Fig.3 DLTS spectrum of the initial n-GaN. Rate window is 139 s^{-1}.

Table 1 Parameters of measured deep centers in the n-GaN

Deep center	E_C-E_0 eV	$\sigma_n, 10^{-15}$ cm^2	Concentration, 10^{13} cm^{-3}						
			initial	γ-irr.	After annealing to T				
					300°C	450°C	550°C	650°C	750°C
E1	≈0.25	1	2.5			200	86	110	70
E2	≈0.58	3	2.5	43	43	43	100	120	45
E3	0.81	60	15						
E4	≈0.15	0.2		1000	500				
E5	0.95	30		400	400				

- Below detection limit

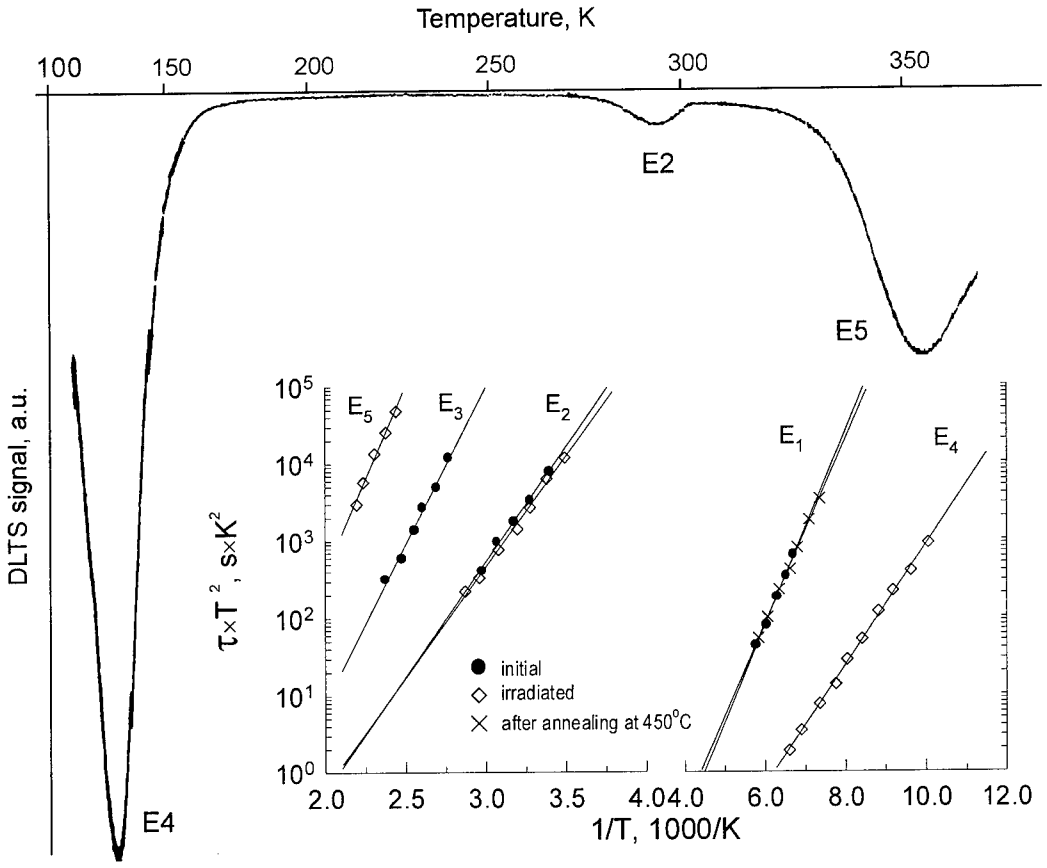


Fig. 4 DLTS spectrum of the irradiated n-GaN. Rate window is 139 s^{-1}. Arrhenius plots are given in the inset.

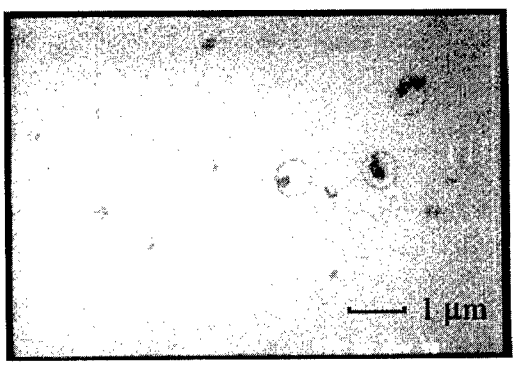


Fig. 5 Small dark dots and rings seen on the GaN surface after gamma-irradiation and annealing to T=300°C

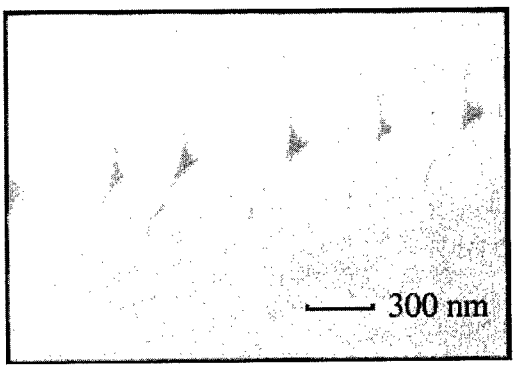


Fig. 6 Extended defects formed in the n-GaN after gamma-irradiation and annealing to T=650°C

As a result of gamma-irradiation the electron concentration at $T \geq 150$ K decreases only slightly; (see Fig. 1). It is difficult to give a plausible explanation for this relatively small reduction because of the complex nature of native defects. Much more pronounced changes are observed for the deep centers. Two electron traps *E4* and *E5* are produced by gamma-rays at dose high rates, up to 10^{-3} cm^{-1}; (see Fig. 4 and Table 1). In their properties the trap *E4* is similar to those of the trap *ER1* [2]. The same is true for the trap *E5* in the present work and *ER5* for He^{+} implanted GaN in [3]. However, it is impossible to attribute the *E5* traps to radiation-induced line or extended defects like what was done for the ER5 case in [3], since in the case of ^{60}Co gamma-irradiation of GaN only point defects can be produced.

The dominant electron traps *E4* were found to be annealed out at T=450°C; (see Table 1). Strikingly, the annealing process of these defects in the range of T=300°C to 450°C appear to be accompanied with strong changes in the mobility of charge carriers; (see Fig. 2). As the *E4* trap concentration decreases, the presence of other deep traps in the annealed n-GaN is seen in DLTS spectra; (see Table 1). At the last annealing step at T=750°C the concentration and mobility of charge carriers in n-GaN subjected to gamma-irradiation are practically restored to the initial values.

The surface morphology of n-GaN is also changed in the course of irradiation and annealing. Just after gamma-irradiation the shapes of nano- and micropipes are modified. Annealing to T=300°C leads to the appearance of small dark dots and rings; (see Fig. 5). These processes are thought to be associated with mobile Ga atoms, since similar defects can also be seen on the surface of GaN layers grown in the presence of excess Ga. The surface modification of irradiated n-GaN due to extended defects like those shown in Fig. 6 will be discussed in detail in a separate publication.

Conclusions

The behavior of Si-doped and nominally undoped n-GaN subjected to gamma-irradiation and annealing is different; cf [6] and present work. In contrast to Si-doped GaN, there are little changes in the concentration of charge carriers in undoped n-GaN at 100 K $\leq T \leq$ 300 K after irradiation and annealing. However, the behavior of the mobility of charge carriers in both materials upon annealing, especially at T= 300°C to 450°C, is similar and, hence, radiation-induced self-compensation processes cannot be excluded. There are two major traps *E4* (0.15 eV) and *E5* (0.95 eV) introduced in n-GaN by gamma-irradiation. The *E4* traps are most likely associated with native defects. They were found to be unstable at T= 300°C.

Acknowledgments

The work was partly supported by The Russian Foundation of Basic Research (grant 99-02-18318).

References

[1] Z.-Q. Fang, J.W. Hemsky, D. Look, M.P. Mack, Appl. Phys. Lett. 72 (1998), p. 448.
[2] F.D. Auret, S.A. Goodman, F.K. Koschnik, J.-M. Spaeth, B. Beaumont, P. Gibart, Appl. Phys. Lett. 74 (1999), p. 407.
[3] F.D. Auret, S.A. Goodman, F.K. Koschnik, J.-M. Spaeth, B. Beaumont, P. Gibart, Appl. Phys. Lett. 73 (1998), p. 3745.
[4] F.D. Auret, S.A. Goodman, F.K. Koschnik, J.-M. Spaeth, B. Beaumont, P. Gibart, Appl. Phys. Lett. 74 (1999), p. 2173.
[5] A.V. Sakharov, W.V. Lundin, A.S. Usikov, Yu.A. Kudryavtsev, A.V. Lunev, Yu.M. Sherniakov, N.N. Ledentsov, MRS Internet J. Nitride Semicond. Res. 3 (1998), p. 28.
[6] V.V. Emtsev, V.Yu. Davydov, V.V. Kozlovskii, V.V. Lundin, D.S. Poloskin, A.N. Smirnov, N.M. Shmidt, A.S. Usikov, J. Aderhold, H. Klausing, D. Mistele, J. Stemmer, O. Semchinova, J. Graul, Semicond. Sci. Technol. 15 (2000), p. 73.

Materials Science Forum Vols. 353-356 (2001) pp. 803-806
© 2001 Trans Tech Publications, Switzerland

Characterization of GaAlN/GaN Superlattice Heterostructures

Zs. Makkai[1], B. Pécz[1], M.A. di Forte-Poisson[2] and F. Huet[2]

[1] Research Institute for Technical Physics and Material Science of the Hungarian Academy of Sciences, PO Box 49, HU-1525 Budapest, Hungary

[2] Thomson CSF, Laboratoire Central de Recherches, Domaine de Corbeville, FR-91401 Orsay Cedex, France

Keywords: Inversion Domains, Segregation, Superlattice, Surface Pits

Abstract. GaAlN/GaN superlattices are grown onto GaN by MOCVD. Cross sectional transmission electron microscopy is used for the characterisation of the layers. V-shaped surface pits are observed on the surface of the layers. Inversion domains are found consequently in the middle of the V pits. Segregation of aluminium occurs in the inverted hexagonal pyramids.

Introduction

Superlattices of GaAlN/GaN are promising candidates for the preparation of HEMT transistors [1], which might be used in high temperature, high power devices. GaAlN/GaN as well as InGaN superlattices and thick layers are extensively investigated in these days for high power and for optoelectronic applications. There exists a special surface defect in InGaN which is called V-shape defect (also called inverted hexagonal pyramid) [2, 3]. These defects are formed when the indium concentration is high and explained by the segregation of indium to the sidewalls of the pits [3]. The inverted hexagonal pyramids are always connected to a dislocation in GaInN layers [4]. We have observed similar defects in thick GaAlN layers as well as in GaAlN/GaN superlattices. In this paper we will show that inversion domains play an important role in the formation of V-shaped defects in GaAlN.

Inversion domains are generally present in GaN layers [5-8] grown on sapphire beside other common defects like dislocations or stacking faults. The polarity of GaN is changed in those domains [9]. Usually the inversion domains appear as long and relatively narrow regions traversing through the whole GaN layer from the GaN/sapphire interface to the top surface. Inversion domains play a fundamental role in the formation of large pyramids grown out from the surface of GaN. By now it is clear that each of those pyramids contains an inversion domain in the middle of the pyramid [10].

The analysis of the surface pits formed in GaAlN thick layers as well as in GaAlN/GaN superlattices is the subject of the present paper. The role of inversion domains is investigated as well.

Experimental

Thick GaAlN layers as well as superlattices of GaAlN/GaN have been grown onto thick GaN layers (grown on sapphire) at 1150°C by metalorganic chemical vapor deposition (MOCVD), respectively. (0001) exactly oriented sapphire was used in all of the cases as substrate. Nitridation process of the sapphire substrate was not applied. At first a thin GaN buffer layer was deposited at 500°C followed by the growth of thick GaN layer at elevated temperature according to the two step growth method [11,12]. Layers have been grown with 6 and 8 at% of

aluminum as well. GaAlN/GaN superlattices were grown with the periodicity of 9, 20 and 30 nm.

Microstructure of the layers was investigated by transmission electron microscopy (TEM) in cross section. Cross sectional samples for TEM analysis have been prepared by cutting small pieces and embedding them in face to face position into a special Ti grid of a diameter of 3 mm [13]. The embedded samples have been ground by diamond paste to the thickness of 50 μm. Then the samples were placed into an ion miller and were bombarded by Ar^+ ions at 10 keV until perforation. Grazing angle of incidence was applied during thinning to get a large transparent region. Some of the specimens were bombarded further at 200 eV using a special, low energy ion gun to minimise the ion beam damage of the thinning [14]. Conventional microscopy was carried out in a Philips CM 20 TEM operating at 200 kV, while high resolution images were taken in a JEOL 4000EX microscope at 400 kV.

Results and discussion

Fig. 1. shows the top region of a thick GaAlN layer in cross section. The aluminium content of this layer is 8 at%. The total thickness of the ternary layer is about 1.2 μm. Although the surface of the sample is far from rough, pits are found at some places (Fig. 1.). About 8% of the surface area is covered by pits. The surface of the layer is flat among the regular shaped pits.

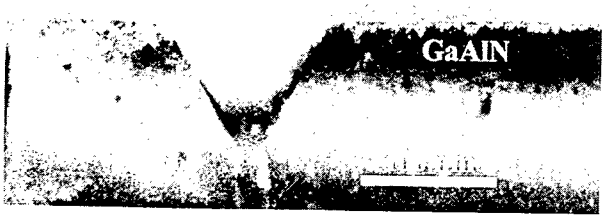


Fig. 1. Top surface region of a thick GaAlN layer grown on GaN.

Fig. 2. shows the cross section of a sample in which a GaAlN/GaN superlattice (marked by SL in Fig. 2) is grown with the periodicity of 9 nm onto GaN. The total thickness of the superlattice is about 1 μm, the aluminium content of the GaAlN layers is 6 at%. Fig. 3. shows the superlattice at high magnification. The GaAlN thin layers are marked by arrows. Note that dislocations are present in the SL region as well. One of the threading dislocations (left side in Fig. 3) clearly traversed into the SL region from the thick GaN layer. The GaAlN/GaN interfaces are sharp and parallel to the surface in the majority of the sample. However, the SEM image (Fig. 4) of the surface shows a network of pits.

Those pits were investigated in cross section as well. Bright field images have shown that the individual layers of the superlattice follow the direction of the sidewalls of the pit. High resolution images (Fig. 5) show that there is an inversion domain in the middle of the pit. This configuration was observed consequently in many pits and also characteristic for the thick layers (see the inversion domain below the pit in Fig. 1). This is a major difference to the case of InGaN, where the pits are connected to threading dislocations. However, the main mechanism of pit formation can be the same, i.e. segregation of aluminium in this case. EELS (Electron Energy Loss Spectroscopy) mapping of the sample proved the segregation of aluminium into the pits. The details of the segregation mechanism are not clear, but sidewalls of the inversion domain might act as diffusion path for aluminium.

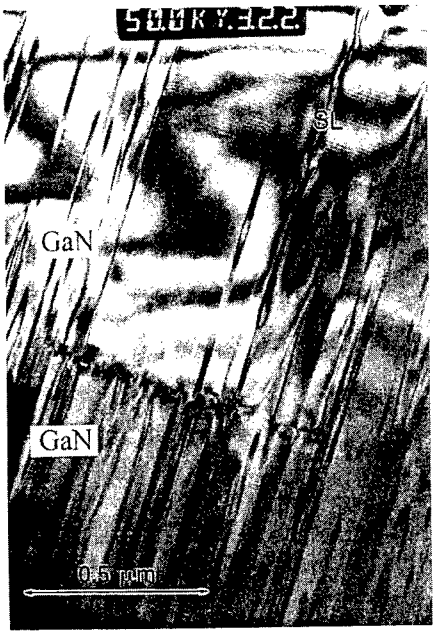


Fig. 2. Cross section of the sample with a superlattice in the top region.

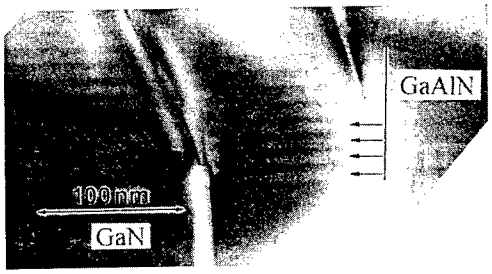


Fig. 3. High magnification image of GaAlN/GaN superlattices grown onto GaN.

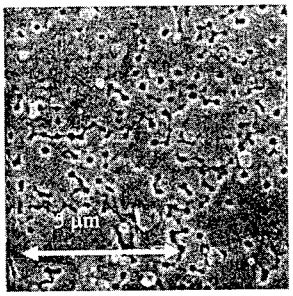


Fig. 4. SEM image of the same sample.

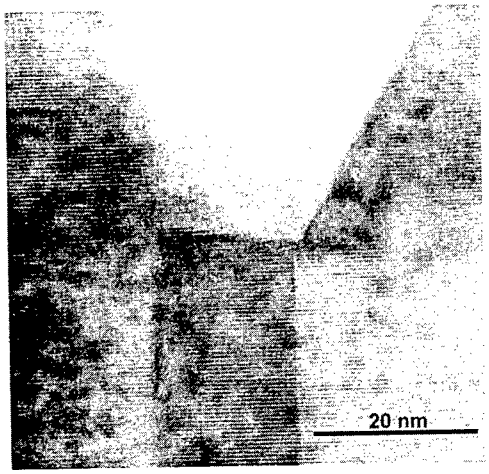


Fig. 5. High resolution image of a pit formed on the surface of GaAlN/GaN superlattice.



Fig. 6. Low magnification image showing the whole layer structure in cross section.

The inversion domains originated in the low temperature grown buffer GaN layer (on the top of sapphire) and traversed through the whole sample through the SL region emerging at the top surface in the middle of a pit (see the two inversion doamins in the middle of Fig. 6). It is essential to decrease the defect density in these layers. When superlattices are grown onto thick GaN, the above task means the improvement of the quality of thick GaN layer.

Conclusion

We have shown that pits are formed on the surface of thick GaAlN layers. Surface pits were also observed in GaAlN/GaN layers, altough in the majority of the samples sharp interfaces are observed in the superlattice. The pits have a regular shape. Aluminium is segregated into the pits during the growth of the layers. Each of the pits is connected to an inversion domain. Suppression of inversion domains promises improved surface quality in GaAlN layers and GaAlN/GaN superlattices.

Acknowledgement

Financial support of OTKA Contract No. T 030447 is acknowledged. A. L. Tóth is acknowledged for the SEM image. B.P. acknowledges Department of Materials, Oxford University for the access to the JEOL 4000 EX microscope.

References

[1] I. Akasaki, S. Kamiyama, T. Detchprohm, T. Takeuchi, H. Amano, MRS Internet J. Nitride Semicond. Res. 5S1 (2000), W6.8.
[2] P. Li, Soo-jin Chua, M. Hao, W. Wang, X. Zhang, T. Sugahara, S. Sakai, MRS Internet J. Nitride Semicond. Res. 5S1 (2000), W11.31.
[3] J. E. Northrup, L. T. Romano, J. Neugebauer, Appl. Phys. Lett. 74 (1999), p. 2319.
[4] X. H. Wu, C. R. Elsass, A. Abare, M. Mack, S. Keller, P. M. Petroff, S. P. DenBaars, J. S. Speck, and S. J. Rosner, Appl. Phys. Lett. 72 (1998), p. 692.
[5] L.T. Romano and J.E. Northrup, Mat. Res. Soc. Symp. Proc. 449 (1997), p. 423.
[6] B. Pécz, M.A. di Forte-Poisson, F. Huet, G. Radnóczi, L. Tóth, V. Papaioannou and J. Stoemenos, J. Appl. Phys. 86 (1999), p. 6059.
[7] W. Qian, M. Skowronski and G. S. Rohrer, Mat. Res. Soc. Symp. Proc. 423 (1996), p. 475.
[8] J-L. Rouviére, M. Arlery, A. Bourret, R. Niebuhr and K. Bachem, Inst. Phys. Conf. Ser. 146 (1995), p. 285.
[9] K. Dovidenko, S. Oktyabrsky, J. Narayan, M. Razeghi, MRS Internet J. Nitride Semicond. Res. 4S1 (1999), G6.46.
[10] J.L. Weyher, P.D. Brown, ARA. Zauner, S. Müller, C.B. Boothroyd, D.T. Foord, P.R. Hageman, C.J. Humphreys, P.K. Larsen, I. Grzegory and S. Porowski: Journal of Crystal Growth 204 (1999), p. 419.
[11] H. Amano, N. Sawaki, I. Akasaki and Y. Toyoda, Appl. Phys. Lett. 48, (1986) 353
[12] S. Nakamura, Jap. J. of Appl. Phys. 30 (1991), p. L1705.
[13] Á. Barna, G. Radnóczi and B. Pécz: in Handbook of Microscopy, (eds. S. Amelinckx, D. van Dyck, J. van Landuyt, G. van Tendelo) VCH Verlag, Vol. 3 (1997), p. 751
[14] A. Barna, B. Pécz and M. Menyhard: Ultramicroscopy 70 (1998), p. 161.

Materials Science Forum Vols. 353-356 (2001) pp. 807-814
© 2001 Trans Tech Publications, Switzerland

III-Nitride Power Devices - Good Results and Great Expectations

Michael Shur[1], Remis Gaska[2] and Asif Khan[3]

[1] Center for Integrated Electronics and Electronics Manufacturing & ECSE, Rensselaer Polytechnic Institute, 110-8th St., Troy NY 12180-3590, USA

[2] SET, Inc., 21 Cavalier Way, Latham NY 12110, USA

[3] Department of ECE, University of South Carolina, USA

Keywords: Gallium Nitride, Microwave Power, MOSHFET, SiC Substrates, Strain Energy Band Engineering

Abstract

High electron mobility, high current carrying capabilities, a relatively high thermal conductivity, high temperature operation, and a high breakdown field are the established key materials properties of GaN-based materials that make them competitive for high power applications. GaN-based devices have demonstrated high-temperature operation with little or no degradation up to 300 °C. The most spectacular results have been obtained for AlGaN/GaN microwave power High Electron Mobility Transistors (HEMTs) that yielded close to 10 W/mm power at 10 GHz. The maximum density of the two-dimensional electron gas at the GaN/AlGaN heterointerface or in GaN/AlGaN quantum well structures can exceed $2x10^{13}$ cm^{-2}, which is an order of magnitude higher than for traditional GaAs/AlGaAs heterostructures. Recently proposed Strain Energy Band Engineering technique should allow us to independently control of strain and lattice mismatch by using AlInGaN/GaN heterostructures and should find important applications in power devices. The prospects of GaN-based power device technology are also enhanced by a recent demonstration of high quality of GaN/SiO_2 interface. SiO_2/AlGaInN/GaN Metal Oxide Semiconductor Field Effect Transistors have exhibited performance comparable or superior to that of conventional AlGaN/GaN devices and hold promise for power applications.

Introduction.

The key materials parameters that are important for power device applications are current carrying capability, breakdown voltage, and thermal conductivity. Equally important are the availability and high quality of device building blocks, such as ohmic contacts, doped layers (n-type, and, if possible, p-type), Schottky contacts, insulator-semiconductor interfaces, device manufacturability and yield. As we discuss in this paper, GaN-based materials have met many of these criteria and have a good chance of competing for power applications not only with traditional semiconductors, such as silicon or gallium arsenide but also with different silicon carbide polytypes. In this paper, we first consider nitrides materials properties that make them suitable for power applications. We then discuss problems that need to be solved in order to make these applications a reality and the new physics of GaN-based devices that makes them different from more conventional

semiconductor materials. Finally, we review the existing results obtained for GaN-based power microwave devices and for prototype GaN power Schottky diodes. [1]

Nitrides materials properties

Nitride semiconductors have unique and excellent materials properties that make them very attractive for many important applications, such as applications for red, blue, green, white light emitters, solid state lighting, displays, visible-blind and solar-blind photodetectors, wireless communications, high temperature electronics, non volatile memories, high power microwave sources, and high power devices. High mobility, high saturation velocity, high sheet carrier concentration in AlN/GaN/InN heterostructures lead to a high current carrying capability. Their wide band gaps and high optical phonon energies result in a high breakdown voltage. A relatively decent thermal conductivity of GaN (reaching 2 W/cm-K at room temperature according to some recent reports) and a possibility of growing these devices on SiC substrates with a very high thermal conductivity ensure a good heat removal capability. Chemical inertness of these compounds, demonstrated good quality ohmic contacts, and the absence of micropipes promise high reliability. Finally, recent demonstration of novel insulated gate devices – MOSHFETs with extremely low gate leakage shows promise for the implementation of many power devices that use an insulated gate.

The measured mobility of the two-dimensional electron gas in AlGaN/GaN heterostructures exceeded 2,000 $cm^2/V\text{-}s$ [2] and 60,000 $cm^2/V\text{-}s$. [3] As shown in Fig. 1, the electron velocity in GaN exceeds that in GaAs by a large margin, especially at elevated temperatures.

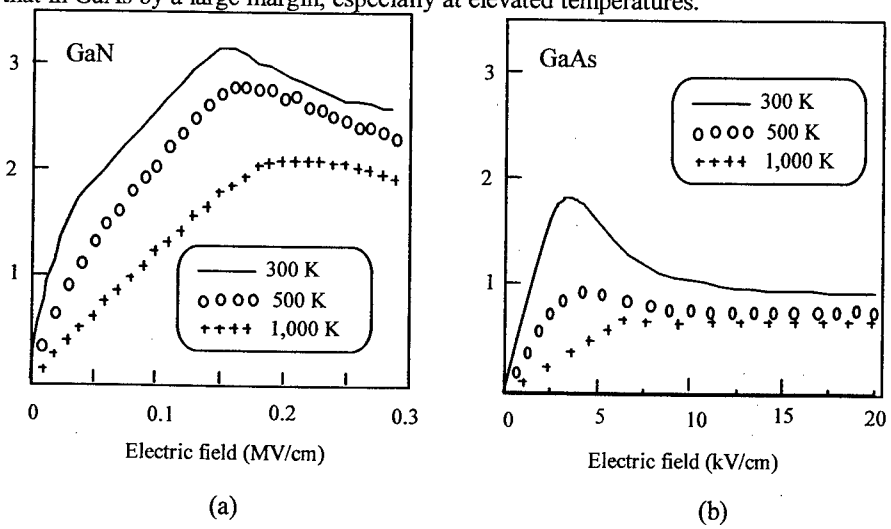


Fig. 1. Velocity-field characteristics of GaN (a) and GaAs (b) at room temperature and elevated temperatures. [4,5]Moreover, recent Monte-Carlo simulations show that overshoot and ballistic effects might be more pronounced in GaN and related materials owing to their capability to withstand very high electric fields in deep submicron devices. [6]

Microwave power transistors use two-dimensional electron gas. The measure value of the maximum sheet electron concentration in GaN-based Heterostructure Field Effect Transistors (HFETs) is as high as 1.5×10^{13} cm^2, which is almost an order of magnitude higher than for the GaAs/AlGaAs materials system. The use of quaternary AlGaInN-based heterostructures might further increase this value (see Fig. 2). The mobility-sheet carrier concentration product for GaN-based two-dimensional systems might also exceed that for GaAs/AlGaAs heterostructures and can be further enhanced by doping the conducting channels.

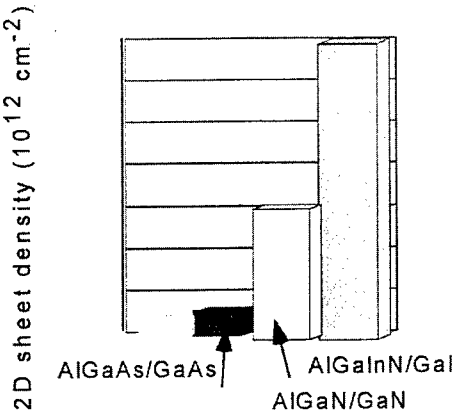


Fig. 2. Comparison of sheet electron density in different heterostructure systems.

All of this translates into a high current carrying capabilities, and the on-current in GaN-based HFETs as high as 1.7 A/mm has been reported. [7]

Figures 3 and 4 compare the breakdown field and thermal conductivity of GaN with those of other semiconductor materials. The data for nitrides in both figures are quite conservative. The breakdown field value is based on the measurement results reported in References [8,9].

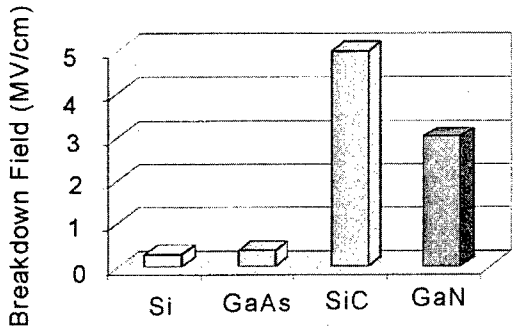


Fig. 3. Breakdown field for different semiconductors.

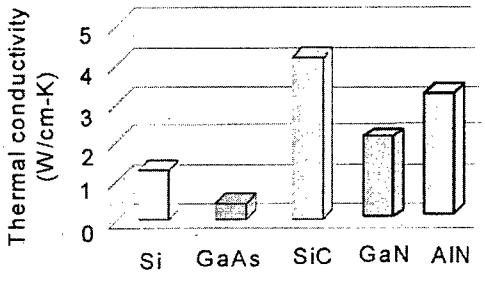


Fig. 4. Thermal conductivity for different semiconductors.

AlGaN/GaN HEMTs on insulating SiC substrates combine superior transport properties of GaN with a high thermal conductivity of SiC. Such an approach combines the best features of both GaN and SiC technologies; and GaN/SiC-based semiconductors and heterostructures should find numerous applications in power electronics. Fig. 5 compares the device characteristics of GaN-based HFETs grown and fabricated under identical conditions on SiC, bulk GaN, and sapphire substrates. As can be seen in the figure, the devices on SiC are superior to even homoepitaxial transistors.

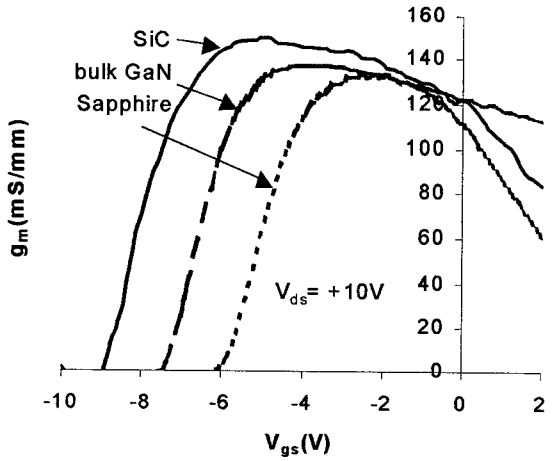


Fig. 5. Device characteristics of GaN-based HFETs grown and fabricated under identical conditions on SiC, bulk GaN, and sapphire substrates. [10]

The large lattice mismatch between GaN, AlN and InN and the strong piezoelectric effects in these materials significantly impact the electrical and optical properties of III-N heterojunction devices. Strain produces piezoelectric doping with about $1x10^{13}$ cm^{-2} sheet carriers. On the other hand, strain might be responsible for the long-term instabilities that several groups observed in their AlGaN/GaN HEMTs.

Problems be solved

The properties of nitrides discussed above hold promise for superior power devices. However, several problems have to be solved in order to make this dream a reality. The first and most urgent problem is that of a reliable, large-area (4 inch and, if possible, even 6 inch substrate). SiC seems to be one of the best candidates fro this role but the cost remains very high and substrate surface quality in many cases inadequate. At the moment, the cost of a GaN-based heterostructure wafer is close to \$5 per mm^2. This should be compared to the cost of a CMOS wafer, which is on the order of $\$10^{-4}$ per mm^2, just about the same as the cost of the New York City real estate.

Other problems are related to reproducibility and yield, as well as to aging effects, which are present at least in some GaN-based devices. As an example, Fig. 6 shows how one, fairly typical GaN-based HFET aged over the period of two years. We speculate that this aging effect is linked to the surface processes. Fig. 7 presents data that might collaborate this hypothesis. This figure shows the effect of the surface plasma treatment of GaN-based heterostructures, and, as can be seen, this treatment completely destroys the two-dimensional electron gas at the heterointerface.

It is also important to account for the new device physics specific to wurtzite semiconductors in general and to GaN-based materials in particular. These new effects include pyroelectric and piezoelectric effects that induce large sheet charge densities at devices surfaces and at the heterointerfaces. [11] The charges at the heterointerfaces might be screened by either 2D electron gas or even by the 2D hole gas yielding very high carrier sheet densities even without doping (see Figure 8).

Having an insulated gate is an important advantage fro power field effect transistors. Recently developed GaN-based Metal Oxide Semiconductor Heterostructure Field Effect Transistors

(MOSHFETs) demonstrated a good quality SiO_2/AlGaN interface and had many important device characteristics better than those for conventional AlGaN/GaN HFETs, including a six orders of magnitude smaller gate leakage, a higher drain current, a smaller low frequency noise and a better linearity. [12]

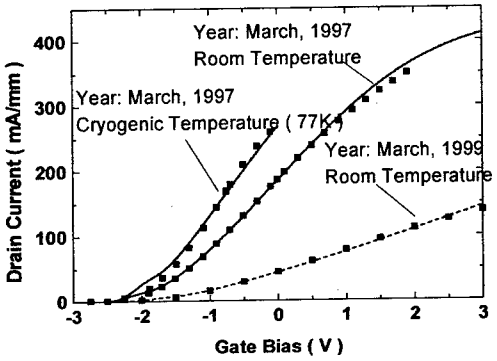


Fig. 6. Aging effects in GaN-based HFET. [13]

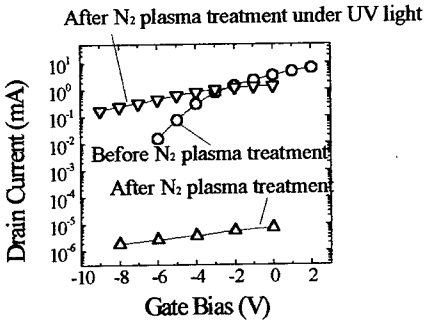


Fig. 7. Drain current in GaN-based HFET before and after N_2 plasma treatment.

Another important emerging trend is to use AlGaInN/GaN and AlGaInN/InGaN heterostructures. Since an Al atom is smaller than a Ga atom, whereas an In atom is larger, an addition of indium compensates the lattice mismatch and allows us to adjust strain and energy band discontinuities at the heterointerface (see Fig. 9).

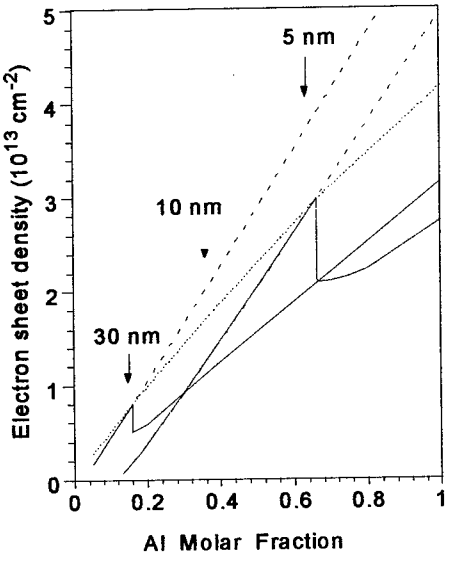


Fig. 8. Polarization induced electron sheet density in GaN-based HFET.

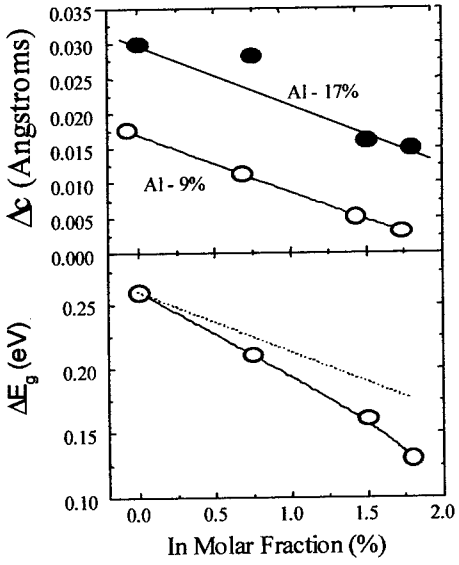


Fig. 9. Lattice mismatch and energy gap discontinuity in AlGaInN/GaN heterostructures. [14]

It also appears that an addition of indium improves the materials quality. This approach (called Strain Energy Band Engineering) is expected to be a powerful tool in design and optimization of GaN-based power devices.

GaN-based power devices

GaN-based power devices can be divided into two categories: microwave power devices and more traditional power devices for applications such as power supplies, surge suppressors, electrical motor controls, power conditioning for electric vehicles, electronic actuators, lamp ballasts, transportation, and heating and cooling systems. Most successes so far are in the area of power microwave GaN-based devices. Several groups demonstrated very high power operation at microwave frequencies, [15],[16],[17] including a record-breaking result of 9.8 W/mm demonstrated by UCSB/NITRES, Inc. group. At the Biennial IEEE Cornell University Conference Cree, Inc. reported on a 10 GHz radio frequency (RF) power performance from a GaN HEMT. The GaN HEMT transistor was incorporated into a hybrid amplifier that achieved 40 Watts of pulsed RF output power at 10 GHz. Cree also reported on the first MMIC in GaN, grown on a semi- insulating SiC substrate. This GaN MMIC achieved 20 Watts of pulsed RF output power at 9 GHz, well exceeding the highest RF output power gallium arsenide (GaAs) MMICs available for this frequency range.

The MOSHFET device mentioned above also showed state-of-the-art microwave performance that can be scaled up by using a multi finger design (see Fig. 9). [18]

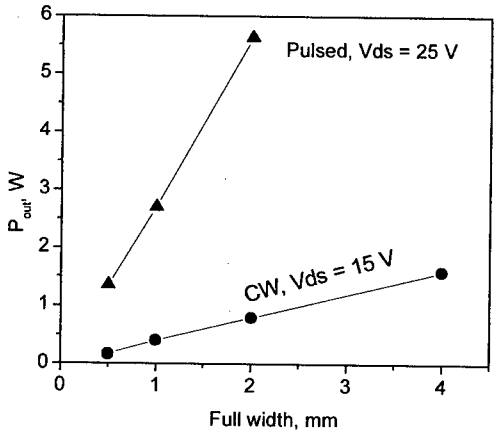


Fig. 9. Output powe of MOSHFET devices at 2 GHz. [18]

The University of Florida group is developing high-voltage GaN switching diodes. Tjey have demonstrated devices with breakdown voltages approaching 3000 V.[19] These results hold promise for developing conventional power devices based on GaN-based semiconductors.

Conclusion.

We discussed materials parameters and emerging designs of unipolar GaN power devices. This discussion and the review of recent device results shows that GaN-based power devices should be able to compete with or even outperform more developed SiC based power devices. Very

promising results have already been achieved for microwave power devices. Research on more conventional nitride-based power devices is still in the very beginning.

References

[1] G. T. Dang, A. P. Zhang, F. Ren, X. A. Cao, S. J. Pearton, H. Cho, J. Han, J.-I. Chyi, C.-M. Lee, C.-C. Chuo, S.N. G. Chu, and R. G. Wilson, IEEE Trans. Electron Dev. 47 (2000) p. 692

[2] R. Gaska, J. W. Yang, A. Osinsky, Q. Chen, M. Asif Khan, A. O. Orlov, G. L. Snider, M. S. Shur, Appl. Phys. Lett. 72 (1998) p. 707

[3] E. Frayssinet, W. Knap, P. Lorenzini, N. Grandjean, J. Massies, C. Skierbiszewski, T. Suski, I. Grzegory, S. Porowski, G. Simin, X. Hu, M. A. Khap, M. S. Shur, R. Gaska, and D. Maude, Appl. Phys. Lett. October 16 (2000)

[4] U. V. Bhapkar, and M. S. Shur, J. Appl. Phys. 82 (1997) p. 1649

[5] M. S. Shur and M. A. Khan, GaN and AlGaN Devices: Field Effect Transistors and Photodetectors, Gordon and Breach Science Publishers, Series Optoelectronic Properties of Semiconductors and Superlattices, Vol. 7 GaN and Related Materials II, pp. 47-86, S. Pearton, Editor (1999)

[6] B. E. Foutz, S. K. O'Leary, M. S. Shur, and L. F. Eastman, J. Appl. Phys. 85 (1999) p. 7727

[7] R. Gaska, M. S. Shur, and A. Khan, GaN-based HEMTs, Gordon & Breach Science Publishers, O. Manasreh an Ed Yu, Editors, to be published

[8] N. V. Dyakonova, A. Dickens, M. S. Shur, R. Gaska, J. W. Yang, Temperature dependence of impact ionization in AlGaN-GaN Heterostructure Field Effect Transistors, Applied Physics Letters. 72 (1998) p. 2562

[9] N. V. Dyakonova, A. Dickens, M. S. Shur, R. Gaska, J. W. Yang, Impact ionization in AlGaN-GaN Heterostructure Field Effect Transistors on Sapphire Substrates, Electronics Letters. 34 (1998) p. 1699

[10] M. A. Khan, J. W. Yang, W. Knap, E. Frayssinet, X. Hu and G. Simin, P. Prystawko, M. Leszczynski, I. Grzegory, S. Porowski, R. Gaska, M. S. Shur, B. Beaumont, M. Teisseire, and G. Neu Appl. Phys. Lett. 76(2000) p. 3807

[11] M. S. Shur, A. D. Bykhovski, R. Gaska, and A. Khan, GaN-based Pyroelectronics and Piezoelectronics, in Semiconductor Homo- and Hetero-Device Structures. Colin Wood, Editor, Academic press, 2000, to be published

[12] M. Asif Khan, X. Hu, G. Simin, A. Lunev, and J. Yang, R. Gaska and M. S. Shur. IEEE Electron Device Letters. 21, pp.63-65, (2000)

[13] J. Deng, R. Gaska, A. Khan, M. S. Shur, private communication

[14] M. A. Khan, J. W. Yang, G. Simin, R. Gaska and M. S. Shur, Hans zur Loye, G. Tamulaitis, A. Zukauskas, D. Smith, and R. Bicknell-Tassius, Appl. Phys. Lett. 76 (2000) p. 1161

[15] S. T. Sheppard, W. L. Pribble, D.T.Emerson, Z. Ring, R. P. Smith, S. T. Allen, and J. W. Palmour, Device Research Conference Digest (2000) p. 37

[16] N.X. Nguyen, M. Micovic, W.-S. Wong, P. Hashimoto, L.-M. McCray, P. Janke and C. Nguyen, Electron. Lett. 36 (2000) p. 468

[17] Y.-F.Wu, B.P. Keller, P. Fini, J. Pusl, M. Le, N. X. Nguyen, C. Nguyen, D. Widman, S. Keller, S. P. Denbaars, and U. K. Mishra, Electron. Lett. 33 (1997) p. 1742

[18] G. Simin, X. Hu, N. Ilinskaya, J. Zhang, A. Tarakji, A. Kumar, M. Asif Khan,R. Gaska and M. S. Shur, Large Periphery High-Power AlGaN/GaN Metal-Oxide-Semiconductor Heterostructure Field Effect Transistors on SiC With Oxide-Bridging, to be published

[19] S. J. Pearton et al, Interface, 9 (2000) p. 34

Materials Science Forum Vols. 353-356 (2001) pp. 815-818
© 2001 Trans Tech Publications, Switzerland

High-Performance Surface-Channel Diamond Field-Effect Transistors

Hitoshi Umezawa[1,3], Hirotada Taniuchi[1,3], Takuya Arima[1,3], Minoru Tachiki[1,3], Hideyo Okushi[2,3] and Hiroshi Kawarada[1,3]

[1] School of Science and Engineering, Waseda University, Okubo 3-4-1, Shinjyuku, Tokyo 169-8555, Japan

[2] Electrotechnical Laboratory, 1-1-4 Umezono, Tsukuba, Ibaraki 305-8568, Japan

[3] CREST, JST (Japan Science and Technology Corporation), Yonban 5-3, Chiyoda, Tokyo 102-0081, Japan

Keywords: Cut-Off Frequency, Field-Effect Transistor, Hydrogen-Terminated Surface Conductive Layer

Abstract

High transconductance and high channel mobility diamond field-effect transistors (FETs) utilizing self-aligned gate FET fabrication process have been operated. The 2 μm gate metal-semiconductor (MES) FET shows the high frequency operation for the first time. The obtained cut off frequency f_T and maximum frequency of oscillation f_{max} are 2.2 and 7 GHz, respectively. It is expected that the diamond MESFET with 0.5 μm gate length fabricated by self-aligned gate process shows 8 GHz of f_T and 30 GHz of f_{max}.

Introduction

Semiconducting diamond has a lot of advantages as a material for future electron devices. The figure of merit of diamond in the field of high power and high frequency devices are extremely high due to its high breakdown voltage (10^7 V/cm), highest thermal conductivity in materials (20 W/cmK), high carrier mobility (1800 cm^2/Vs (hole)) and low dielectric constant (5.7).

A thin p-type conductive layer emerges on the hydrogen-terminated diamond surface prepared by chemical vapor deposition (CVD) without doping impurities [1]. This surface channel possesses suitable properties for electric device application. The carrier sheet density is as high as 10^{13} /cm^2 [2]. The acceptors are fully activated at room temperature because of their low activation energy (less than 50 meV). The hydrogen-termination of dangling bonds lowers the density of surface states. Thus, the Schottky barrier heights between metal and diamond strongly depend on the electronegativity of metal [3]. Metals having low electronegativity such as gold or platinum show the low contact resistance advantageous for ohmic contact [3]. Due to these advantages of hydrogen-terminated surface channel, the merits of diamond can be quite utilized by fabricating the field-effect transistors on the hydrogen-terminated surface conductive layer [4].

In order to fabricate the high performance diamond FET, a high-precision self-aligned gate FET fabrication process has been developed. Utilizing the self-aligned gate FET fabrication process,

high transconductance and high channel mobility FETs and high frequency diamond MESFETs have been realized for the first time.

Self-aligned gate MESFET and MISFET

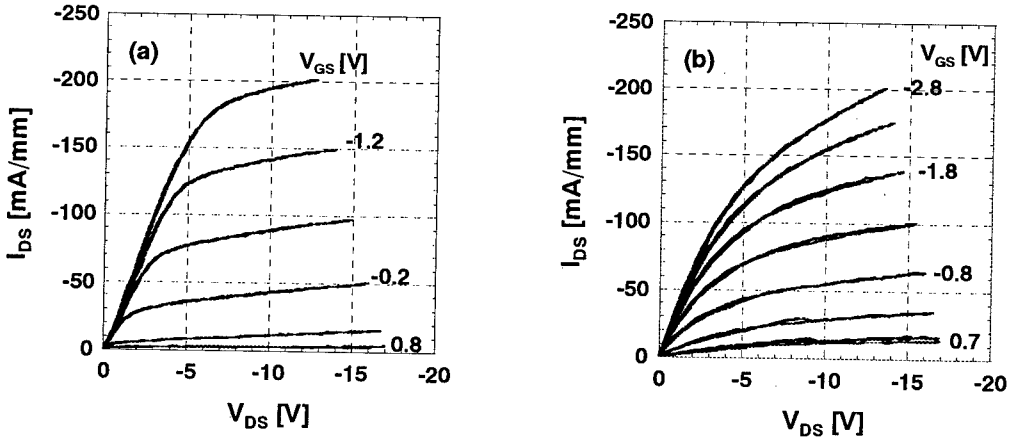
To improve the performance of diamond FET, it is required to minimize the parasitic resistance such as source resistance or drain resistance as well as the reduction of the gate length. In hydrogen-terminated diamond FET, the parasitic resistance is basically determined by the distance of metal contacts to diamond, because of the low contact resistance in ohmic contacts and the relatively high resistivity of the surface p-type layer between metal contacts. Application of the self-aligned gate process is effective to minimize the parasitic resistance.

Utilizing the self-aligned gate process, Cu gate MESFETs with 1 μm gate length have been fabricated [5]. The source to gate and the gate to drain distances and the gate width are 0.2 μm, 0.2μm and 26 μm, respectively. This short distance of source to gate electrode has been realized by improving the adhesion of electron beam resist and preventing the Au electrode from over etching by chemical etchant. Figure 1(a) shows the I_{DS}-V_{DS} characteristics of the Cu gate MESFET. The FET exhibits the normally-on operation, which is a feature of Cu gate MESFETs on a hydrogen-terminated diamond surface. The maximum transconductance, obtained at V_{GS} = -1.5 V is 110 mS/mm. This value is the highest value in the diamond FETs.

High performance surface-channel diamond metal-insulator semiconductor (MIS) FETs using calcium fluoride as gate insulator have been also fabricated by the self-aligned gate FET fabrication process. Figure 1(b) shows the I_{DS}-V_{DS} characteristics of the MISFET with 1.2 μm gate length. The maximum transconductance is 75 mS/mm. The channel mobility can be estimated by the following relationship in the slope S of the linear region in the g_D-V_{GS} characteristics,

$$S = \frac{\partial g_D}{\partial V_{GS}} = \mu_p C_i \frac{W_G}{L_G} \qquad (1)$$

where g_D, μ_p, C_i, W_G and L_G are the drain conductance in the linear region, the channel mobility, the



CaF_2 capacitance per unit area, the gate width, and the gate length, respectively. The channel mobility of the MISFET with 1.2 μm gate length shows 280 cm^2/Vs. This value is several times higher than the channel mobility of SiC MOSFET at present indicating the better quality of CaF_2 /diamond interface structure.

High frequency diamond MESFET

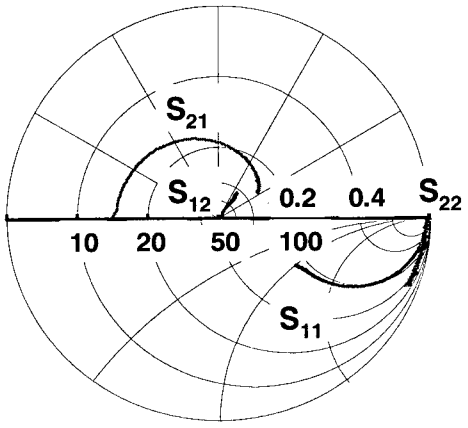
In spite of high expectation for the high frequency and high power application, the RF measurement had not been carried out in the diamond FETs. Then, the S-parameters of diamond FET have been measured to confirm the high frequency operation. This is the first study of small signal RF measurement for diamond FETs.

The Cu gate diamond MESFETs of 2 μm gate length are specially fabricated for the RF measurement. In order to reduce the parasitic resistances such as source or drain resistance, the self-aligned gate FET fabrication process has been also applied. The gate width and source to gate or gate to drain distance of each FET are 50, 0.1 μm respectively. For the accurate RF measurement, each electrode pad is electroplated by gold in order to reduce the contact resistance between each electrode pad and RF measurement probe.

The 2 μm gate MESFET shows high transconductance g_m of 70 mS/mm. This value is 50 % higher than the average value of Cu gate MESFET with 2 μm gate length reported before [5]. Owing to the electroplating of gold on the source, the gate and the drain electrode pads, the resistance between electrode pads and DC measurement probe has been reduced. Thus, high transconductance and drain conductance of intrinsic diamond FET are observed.

Small-signal RF measurement for the diamond MESFET has been carried out for the first time. In this study, S-parameters were measured in the frequency range from 50 MHz to 20 GHz using HP 8720 ES network analyzer and Cascade wafer prober applied for on-wafer measurement

Figure 2 shows the measured S-parameters of diamond MESFET with 2 μm gate length under the bias condition of V_{GS} = -1.5 V and V_{DS} = -5 V. S_{21} shows forward gain of this FET. In order to improve the forward gain, the increase of transconductance by reducing the gate length associated with the minimization of the parasitic resistance is required. The S_{22} shows high impedance, in spite of the high frequency as 20 GHz due to the low dielectric constant of diamond. S_{11} indicates the existence of resistance of approximately 100 Ω between gate to source electrode. This resistance consists of intrinsic channel resistance, source resistance and gate resistance. The source resistance mainly originates from the source and drain distance of 0.1 μm. The



sheet resistivity of this region is the same as bare hydrogen-terminated diamond surface conductive layer of 30-40 kΩ/sq. Then, the source resistance 60-80 Ω exists. In order to reduce the parasitic resistance, more fine fabrication process that can reduce the distance between the source and the gate is required.

Figure 3 shows the small signal RF gain of diamond MESFET with 2 μm gate length induced from the S-parameters. Maximum oscillation frequency (f_{max}) obtained from maximum stable gain and maximum available gain (MSG/MAG) is 7 GHz. The cut-off frequency (f_T) calculated from current gain (h_{21}) is 2.2 GHz. The transconductance and cut-off frequency as a function of gate length in the Cu gate diamond MESFETs are shown in Fig. 4. This figure indicates that the transconductance and the f_T are highly improved by the reduction of gate length. This tendency of transconductance is similar to the result reported before [5]. If carrier velocity saturation does not occur in the 1 μm gate length, the f_T is expected to be 8 GHz. With 0.5 μm gate length, the f_T will exceed 10 GHz despite of velocity saturation.

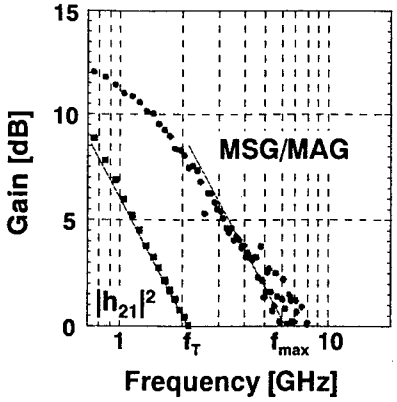


Fig. 3 Small signal RF gain of diamond MESFET with 2 μm gate length.

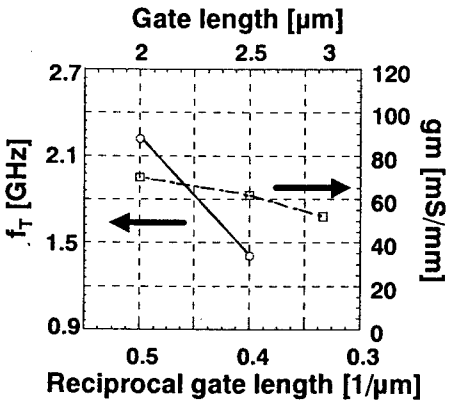


Fig. 4 The gate length dependence of the transconductance and f_T.

References

[1] T. Maki, S. Shikama, M. Komori, Y. Sakaguchi, K. Sakuta and T. Kobayashi, Jpn. J. Appl. Phys. 31 (1992), p. L1446

[2] K. Hayashi, S. Yamanaka, H. Okushi and K. Kajimura, Appl. Phys. Lett. 68 (1996), p. 376.

[3] H. Kawarada, Surf. Sci. Rept. 26 (1996), p. 205.

[4] H. Kawarada, M. Aoki and M. Itoh, Appl. Phys. Lett. 65 (1994), p. 1563.

[5] H. Umezawa, K. Tsugawa, S. Yamanaka, D. Takeuchi, H. Okushi and H. Kawarada, Jpn. J. Appl. Phys. 38 (1999), p. L1222

Author Index

A

Abe, Y. 81
Åberg, D. 431, 443, 549, 559
Acero, M.C. 591
Achtziger, N. 331, 471, 475
Adachi, K. 719
Adås, C. 563
Agarwal, A.K. 743
Akasaki, I. 791
Albertazzi, E. 599
Amano, H. 791
Amaratunga, G. 723
Ambacher, O. 787
Amy, F. 215
Anand, S. 559
Andersson, H. 559, 583
Anikin, M. 7, 21, 283
Aradi, B. 421, 455
Arai, K. 135, 295, 631, 647, 719
Arai, M. 711
Arima, T. 815
Aristov, V.Yu. 235
Atanasova, G. 251
Aulombard, R.L. 159
Avramenko, S.F. 41
Azar, R. 723

B

Bai, S. 115, 357
Bakin, A.S. 163
Banc, C. 703
Banerjee, S. 715
Bano, E. 703
Baranov, P.G. 509, 521, 525, 529
Barbier, D. 155
Barna, Á. 199
Bartsch, W. 679
Basset, A. 7
Basset, G. 7
Batchelor, D.R. 219
Battistig, G. 271
Bauer, A. 319
Beaumont, B. 795
Bechstedt, F. 211, 413
Berenguer, M. 393
Bereznjakova, L.A. 239
Bergman, J.P. 299, 377, 431, 549, 555, 727, 791
Bernard, C. 21, 61
Bianconi, M. 599
Bickermann, M. 25, 49, 397
Bikbajevas, V. 491
Billon, T. 7, 21
Birch, J. 291
Blanquet, E. 61, 111
Bleichner, H. 389, 583
Bluet, J.M. 385, 393
Bockstedte, M. 323, 447
Bogdanov, M.V. 57, 107
Bogdanova, E.V. 735
Bord, O.V. 37, 57, 107
Bracht, H. 327
Brady, M. 3
Bratus', V.Ya. 517
Breitholtz, Bo 389
Brezeanu, G. 723
Briddon, P.R. 349
Brink, D.J. 275
Brylinski, Ch. 215, 669, 703
Burrows, C.P. 567

C

Calcagno, L. 255, 639
Camassel, J. 275, 335, 385
Cantin, J.L. 349, 509, 513
Carlsson, F.H.C. 365, 377, 431, 549, 555
Carnera, A. 279, 599
Carosella, F. 381
Carter Jr., C.H. 3
Castaldini, A. 757
Cauwet, F. 85
Cavallini, A. 757
Chaix-Pluchery, O. 283
Chante, J.P. 571
Chassagne, T. 155
Chatty, K. 715
Chaussende, D. 85
Chen, C.Q. 361
Chen, Y. 495
Cheng, L.L. 191
Cheung, W.Y. 191
Cho, W.J. 631, 643

Chow, T.P. 715, 739
Choyke, W.J. 115, 357, 463
Chua, S.J. 345
Chung, J. 167, 171
Chuvilin, A. 259
Cimalla, V. 179, 187
Cloitre, T. 159
Coleman, P.G. 567
Contreras, S. 483
Cressler, J.D. 623, 687

D

Dahlquist, F. 683, 727
Danielsson, Ö. 91, 99
Danks, L. R. 381
Dauelsberg, M. 103
Davydov, D.V. 763, 799
Deák, P. 421, 435, 455, 463, 659
Dedulle, J.-M. 61
Derycke, V. 235
Devaty, R.P. 115, 357
Di Cioccio, L. 385, 483
Di Forte-Poisson, M.A. 803
Dimitrijev, S. 655
Dmitriev, V. 115
Doerschel, J. 29
Dohnke, K.O. 675, 695
Dolle, J. 29, 243, 263
Donolato, C. 757
Dua, Ch. 669
Durst, F. 65

E

Eckstein, R. 15
Egilsson, T. 405
Eickhoff, M. 151, 175, 663, 753
Ekedahl, L.-G. 747
Ellis, C. 687
Ellison, A. 91, 365, 373, 405
Emtsev, V.V. 799
Enriquez, H. 235
Epelbaum, B.M. 307
Eriksson, J. 699
Esteve, J. 591
Evans, G.A. 345, 381

F

Falk, F. 195
Falkovsky, L.A. 275, 335
Fall, C. J. 349
Faure, Ch. 7, 21
Fedison, J.B. 739
Feltin, E. 795
Feng, Z.C. 345
Ferro, G. 85, 155
Fissel, A. 211, 227, 409
Fontaine, F. 199
Fonteneau, P. 235
Forsberg, U. 99
Foster, B. 611
Frank, T. 401, 439, 537
Franklin, J. 753
Frauenheim, Th. 435, 455, 463
Friedrichs, P. 695
Fujihira, K. 543
Fujisawa, H. 131
Fukuda, K. 631, 643, 647
Furthmüller, J. 211, 413
Furusho, T. 73
Fuyuki, T. 615

G

Gajowski, J. 45
Galeckas, A. 389
Gali, A. 421, 435, 455, 463
Galyukov, A.O. 57
Gaska, R. 807
Gebel, T. 587
Gendron, F. 349
Gibart, P. 795
Girard, P. 393
Glass, R. 3
Glazer, A.M. 283
Godignon, P. 571
Goetz, K. 319
Goldhahn, R. 179
Gourbeyre, C. 155
Greulich-Weber, S. 505
Grillenberger, J. 471, 475
Grivickas, P. 353, 491
Grivickas, V. 353, 491
Grosse, P. 7
Grossner, U. 211
Grünleitner, H. 595
Guillot, G. 393
Gutmann, R.J. 715
Gyulai, J. 271

H
Hai, P.N. 499
Hajnal, Z. 435, 463
Hallén, A. 427, 431, 443, 549, 559, 595
Harada, S. 643
Harris, C.I. 747
Hatayama, T. 615
Hauser, T. 275
Hecht, Ch. 675
Hecht, U. 307
Heera, V. 151, 199, 579
Heissenstein, H. 287, 369
Helbig, R. 287, 361, 369, 401
Hellmund, O. 651
Henry, A. 91, 99, 373, 377
Henshall, D. 3
Heringer, D. 463
Herold, J. 331
Heß, G. 247
Heuken, M. 103
Hilton, K.P. 303
Hitzel, F. 163
Hobgood, D. 3, 357
Hoffmann, P. 219
Hofmann, D. 11, 25, 49, 65, 307, 397
Honda, H. 711
Hong, M.-H. 167, 171
Horsfall, A.B. 707
Horváth, Z.E. 271
Huet, F. 803
Hülsen, C. 331
Hultman, L. 315, 549, 583
Hunderi, O. 417
Hundhausen, M. 341
Hwu, Y.-K. 215

I
Ilyin, I.V. 521, 529
Imaizumi, M. 731
Irmscher, K. 95
Ishida, Y. 135
Ismail, M.M. 381
Itoh, H. 439, 537, 575, 635
Ivanov, A.A. 163
Ivanov, A.M. 763
Ivanov, I.G. 405
Ivanov, P.A. 743
Ivanov-Omskii, V.I. 239
Iwakuro, H. 611
Iwaya, M. 791
Izumi, K. 131, 311

J
Jacob, C. 123, 127, 139
Jacobsson, H. 143, 291
Jacquier, C. 85
Jagadish, C. 549, 595
Jamet, P. 655
Janson, M.S. 427, 549, 583, 595
Janzén, E. 91, 99, 143, 291, 365, 373, 377, 405, 431, 499, 555, 691
Jikimoto, T. 131, 311
Jinschek, J. 783
Johansson, N. 727
Johnson, C.M. 303, 567, 707, 719
Jones, R. 349
Jonsson, R. 699
Josepovits, K.V. 659
Jürgensen, H. 103

K
Kadinski, L. 11, 15, 65
Kaiser, U. 247, 259, 783
Kakanakov, R. 251
Kaltschmidt, R. 695
Kamata, I. 131, 311
Kapels, H. 679
Karlsson, S. 427, 563, 583
Karpov, D.S. 37
Karpov, S.Yu. 37, 57, 107, 779
Kassamakov, I. 251
Kassamakova, L. 251
Kato, T. 295
Kawahito, K. 615
Kawarada, H. 815
Kawasuso, A. 537
Kayambaki, M. 619
Keir, A. 303
Khan, A. 807
Khánh, N.Q. 271
Khramtsov, V.A. 529
Kildemo, M. 417
Kimoto, T. 451, 459, 543, 627
Kinoshita, K. 719
Kinouchi, S. 731
Kipshidze, G. 247
Kiselev, V.S. 41
Kitabatake, M. 635
Kitamura, M. 711

Klettke, O. 459
Knights, A.P. 567, 707
Kochuguev, S.K. 57
Kögler, R. 591
Kojima, K. 135
Kölbl, M. 15
Komissarov, A.E. 57, 107
Komlev, K. 247
Konstantinov, A. 563
Korolkov, O. 603
Koshka, Y. 115
Kosugi, R. 643, 647
Kótai, E. 271
Kozlovskii, V.V. 763
Krafcsik, O.H. 659
Krause-Rehberg, R. 537
Kräußlich, J. 319
Kreisel, J. 283
Krieger, M. 467
Krötz, G. 151, 175, 663, 753
Kroutchinine, A. 747
Kulik, A.V. 57, 779
Kunert, H.W. 275
Kurz, H. 651
Kushibe, M. 135
Kuznetsov, A.Yu. 549, 595

L

La Via, F. 255
Lagadas, M. 735
Lahrèche, H. 795
Larkin, D.J. 357
Larsson, K. 231
Laube, M. 45, 327, 401, 467
Laügt, M. 795
Lazar, M. 571
Le Berre, M. 155
Lebedev, A.A. 119, 763, 799
Lebedev, V. 227, 783
Lefort, O. 753
Lei, Y.M. 191
Leitch, A.W.R. 607
Lendenmann, H. 299, 683, 727
Leroux, M. 795
Levinshtein, M.E. 743
Ley, L. 223, 341
Lin, L. 191
Lin, S. 191
Lindefelt, U. 299, 353, 487
Lingner, Th. 505
Link, A. 787
Linnarsson, M.K. 373, 427, 549, 559, 563, 583
Linnros, J. 353, 389
Lloyd Spetz, A. 219, 747
Locatelli, M.-L. 571
Lohner, T. 271
Lombardo, S. 639
Lovtsus, A.A. 107
Lulli, G. 599
Lundin, W.V. 799
Lundström, I. 219, 747
Luo, E.Z. 191
Lysenko, V.S. 479

M

Macák, E.B. 691
Madar, R. 7, 21, 61, 283
Madsen, L.D. 691
Magaud, L. 111
Magerl, A. 287
Magnusson, B. 365, 373, 555
Makarov, Yu.N. 37, 57, 103, 107, 779
Makeeva, I.N. 517
Makkai, Zs. 803
Maktari, A.M. 639
Malherbe, J.B. 275
Malta, D. 3
Mantel, B.F. 223
Martinez, A. 353, 487
Masahara, K. 135
Masarotto, L. 393
Masri, P. 183
Massies, J. 795
Masuda, Y. 123, 139, 495
Matsunami, H. 451, 459, 543, 627
Matsuura, H. 495
Mattausch, A. 323, 447
Maurice, T.P. 275
Mehregany, M. 167, 171
Melnychuck, G. 115
Mermoux, M. 283
Merrett, J.N. 623, 687
Mihaila, A. 723
Mikalo, R.P. 219
Mikulskas, I. 353
Mishra, U.K. 787
Mitlehner, H. 695
Miyamoto, N. 451, 543
Mokhov, E.N. 147, 509, 521, 525, 529, 779

Möller, H. 753
Monemar, B. 791
Monteil, Y. 85, 155
Morante, J.R. 591
Moreaud, N. 159
Morrison, D.J. 303
Morvan, E. 549, 571, 669
Moulin, C. 7, 21
Müller, S. 3
Musumeci, P. 255, 639
Mynbaeva, M. 115

N
Nakagawa, A. 711
Nava, F. 757
Negoro, Y. 543
Neyret, E. 483
Nielsen, A. 175, 663
Nieminen, R.M. 533
Nilsson, H.-E. 487
Nilsson, P.A. 299, 727
Nipoti, R. 279, 599, 757
Nishiguchi, T. 69, 77
Nishikawa, K. 611
Nishino, S. 69, 73, 77, 123, 127, 139, 267, 495
Nishizawa, S.-i. 295
Nitta, S. 791
Niu, G. 687
Noblanc, O. 669, 703
Nordell, N. 427

O
Obermeier, E. 175, 753
Obyden, S.K. 147
Oestling, M. 683
Ofengeim, D.Kh. 57
Ogata, M. 711
Ogino, S. 131
Ohashi, H. 719
Ohno, H. 135
Ohshima, S. 73, 77, 123, 139
Ohshima, T. 575, 635
Ohtsuka, K. 731
Okulov, S.M. 517
Okushi, H. 815
Ólafsson, H.Ö. 479
Olander, J. 231
Ortolland, S. 567, 707
Oshima, S. 69
Osiyuk, I.P. 479
Österman, J. 549, 559
Ottaviani, L. 571
Ouisse, T. 703
Oyanagi, N. 295
Ozeki, T. 731

P
Pajot, B. 349
Palmour, J.W. 743
Panknin, D. 151, 559, 587, 591
Pankratov, O. 323, 447
Pasold, G. 471, 475
Passero, A. 7
Pasturel, A. 111
Pécz, B. 199, 579, 803
Pelissier, B. 7, 21, 283
Pensl, G. 45, 327, 341, 401, 439, 459, 467, 537, 595
Pérez-Rodríguez, A. 591
Pernot, E. 7, 21, 283, 619
Pernot, J. 385, 483
Pernot-Rejmánková, P. 7, 283
Persson, P.O.Å. 315, 549, 583
Peters, D. 675
Petrenko, T.L. 517
Petrenko, T.T. 517
Pezoldt, J. 179, 183, 187
Pidduck, A.J. 567
Piester, D. 163
Pirouz, P. 127, 167, 171
Pisch, A. 7, 21, 61
Pitt, G.D. 345
Planson, D. 571
Polenta, L. 757
Poloskin, D.S. 799
Pons, M. 7, 21, 61, 111
Potemski, M. 361
Powell, A. 3
Pozina, G. 791
Preston, I.H. 303
Prinsloo, L.C. 275
Puska, M.J. 533

R
Raffy, C. 111
Raineri, V. 639
Ramm, M.S. 37, 57, 779
Rang, T. 603
Rasp, M. 15, 49, 397

Rastegaev, V.P. 53
Ratnikov, V.V. 119
Rauls, E. 435, 455
Raynaud, C. 571
Redmann, F. 537
Ren, C.X. 191
Reshanov, S.A. 53
Richter, W. 211, 227, 247, 409, 783
Riedl, T. 163
Ristein, J. 223
Robert, J.L. 483
Roccaforte, F. 255
Roenkov, A.D. 147, 779
Rohmfeld, S. 341
Romano-Rodríguez, A. 591
Romanus, H. 179
Rorsman, N. 699
Rost, H.-J. 29, 243, 263
Rougeot, C. 753
Royet, A.S. 703
Rudenko, T.E. 479
Rudner, S. 699
Rumyantsev, S.L. 743
Rupp, R. 679
Ryu, S.-H. 743

S

Saddow, S.E. 115, 687
Sadowski, H. 401
Sadowski, M.L. 159
Saitoh, K. 259
Samiji, M.E. 607
Saparin, G.V. 147
Sasaki, M. 69, 77, 267
Savage, S.M. 747
Savkina, N.S. 119
Sawazaki, H. 711
Schaefer, J.A. 183
Scharmann, F. 187
Scharnholz, S. 651
Schlachetzki, A. 163
Schmeißer, D. 219
Schmidt, J. 525
Schmitt, E. 15
Schnell, N. 795
Schöner, A. 451
Schörner, R. 695
Schröter, B. 179, 227, 247
Schulz, D. 29, 243, 263
Schulze, N. 45, 341, 401
Seitz, C. 287
Selder, M. 11, 15, 65
Semennikov, A.K. 103
Semmelroth, K. 45
Semond, F. 795
Senzaki, J. 631, 643, 647
Serkov, A.M. 57
Serre, C. 591
Seyller, Th. 223
Shchukarev, A.V. 239
Sheridan, D.C. 623, 687
Shimizu, M. 611
Shimizu, T. 69, 77
Shinohe, T. 719
Shiomi, H. 267
Shmidt, N.M. 799
Shuman, V.B. 119
Shur, M.S. 743, 807
Siche, D. 29, 243, 263
Sieber, N. 223
Sielemann, R. 475
Sköld, K. 555
Skorupa, W. 151, 199, 559, 571, 579, 587, 591
Skytt, P. 299, 727
Smorchkova, I.P. 787
Söderholm, R. 727
Son, N.T. 365, 455, 499
Soukiassian, P. 215, 235
Spaeth, J.-M. 505
Spangenberg, B. 651
Speck, J.S. 769, 787
Sperr, P. 537
Spieß, L. 179
Sridhara, S.G. 377, 431
Staab, T.E.M. 533
Starke, U. 205
Stauden, Th. 179, 183, 187
Steeds, J. W. 345, 381
Stein, J. 651
Stephani, D. 675, 695
Stoemenos, J. 151, 175, 579, 663, 753
Stolwijk, N.A. 327
Stölzer, M. 491
Storasta, L. 431, 443, 549, 555
Straubinger, T.L. 11, 25, 33, 49, 65, 397
Strokan, N.B. 763
Stutzmann, M. 787
Suezaki, T. 615
Sugimoto, H. 731

Sundaraval, B. ... 191
Suzuki, S. ... 631, 643, 647
Suzuki, T. ... 135
Sveinbjörnsson, E.Ö. ... 479
Svenningstorp, H. ... 747
Svensson, B.G. ... 427, 443, 549, 583, 595
Syväjärvi, M. ... 143, 291, 373, 491
Szilágyi, E. ... 271

T
Tachiki, M. ... 815
Tairov, Yu.M. ... 53
Takahashi, K. ... 635
Takahashi, T. ... 135
Takami, T. ... 731
Tamura, S. ... 543
Tanaka, T. ... 135, 631, 647
Taniuchi, H. ... 815
Tanner, P. ... 655
Tarui, Y. ... 731
Tin, Chin-Che ... 623
Tobias, P. ... 747
Tomašiunas, R. ... 353
Torpo, L.M. ... 533
Treu, M. ... 679
Tsagaraki, K. ... 187, 251, 619
Tsiryulnikov, A.V. ... 57
Tsuchida, H. ... 131, 311
Tsuji, T. ... 131
Tsvetkov, V. ... 3
Tuomi, T. ... 291
Tyagulski, I.P. ... 479

U
Udal, A. ... 491
Udrea, F. ... 723
Umezawa, H. ... 815
Unéus, L. ... 747
Uraoka, Y. ... 615
Urban, S. ... 195
Uren, M.J. ... 303
Usikov, A.S. ... 799

V
Valakh, M.Ya. ... 41
van Duijn-Arnold, A. ... 525
van Wyk, E. ... 607
Vanni, P. ... 757
Vassilevski, K. ... 735
Velmre, E. ... 491
Venter, A. ... 607
Verzellesi, G. ... 757
Viala, J.C. ... 85
Vicente, P. ... 159, 335
Vodakov, Yu.A. ... 147, 779
Voegeli, W. ... 381
von Bardeleben, H.J. ... 349, 509, 513, 517
Vorob'ev, A.N. ... 103, 107
Vouroutzis, N. ... 151, 175, 663

W
Wagner, G. ... 95
Wahab, Q. ... 691, 699
Weber, A.-D. ... 15
Wehmann, H.-H. ... 163
Weidner, M. ... 439, 467, 537
Weingärtner, R. ... 25, 49, 397
Weissker, H.-C. ... 413
Wellmann, P.J. ... 11, 25, 33, 49, 65, 397
Williams, J.R. ... 623, 687
Williams, K.P.J. ... 345
Wilson, I.H. ... 191
Winkelmann, A. ... 227
Winkler, R. ... 361
Winnacker, A. ... 11, 25, 33, 49, 307, 397
Wischmeyer, F. ... 103
Witthuhn, W. ... 331, 471, 475
Wöhner, T. ... 183
Wollweber, J. ... 29, 243, 263
Wong, S.P. ... 191
Wood, C.E.C. ... 115
Wright, N.G. ... 567, 707
Wu, C.-H. ... 167, 171
Wu, L. ... 607
Wunderlich, B. ... 319
Wysmolek, A. ... 361

X
Xu, J.B. ... 191

Y
Yakimova, R. ... 143, 291, 373, 491, 583, 619
Yamaguchi, H. ... 295
Yano, H. ... 543, 627
Yoshida, S. ... 135
Yoshikawa, M. ... 575, 635
Yu, Y.H. ... 191
Yukhimchuk, V.A. ... 41

Z

Zappe, S. 175, 753
Zavarin, E.E. 799
Zawadzki, W. 483
Zekentes, K 187, 251, 619, 735
Zhang, J. 91, 405, 691
Zhmakin, A.I. 37, 57, 103
Zhmakin, I.A. 57
Zimmermann, U. 583
Zirath, H. 699
Zolnai, Z. 271
Zondervan, R. 525
Zorenko, A. 735
Zorman, C.A. 167, 171
Zou, S.C. 191

Keyword Index

^{13}C Isotope 341, 401

1
15R-SiC 69, 349

3
3C-SiC 143, 167, 171, 205
3C-SiC/Si Interface 151
3C-SiC/SOI 753

4
4H-SiC 25, 205, 291, 311, 361, 385, 389, 417, 483, 703
4H-SiC Sublimation Growth 21
4H-SiC(0001) 215

6
6H-SiC 205, 243, 275, 345, 349, 579
6H-SiC(0001) 215

A
Ab Initio Defect-Energetics 323, 447
Absorption 357, 505
Absorption Band 397
Absorption Mapping 397
Abstraction 231
Acceptor 45, 331, 467
Acceptor-Like Interface States 627
Acoustical Phonons 349
Admittance Spectroscopy 459
Adsorption 231
AES 191
AFM 139, 251, 567, 571
ALN 783
Al_4C_3 579
AlGaN/GaN Heterostructures 787
Alpha Particle Detection 763
Aluminium 45, 53, 385, 521, 579, 583, 595, 731
Aluminium Acceptor 575
Aluminium Doping 49
Aluminium Melt 85
Anisotropic Dielectric Function 417
Annealing 69, 275, 365, 385, 505, 537, 567, 571, 595, 615, 707, 731,799
Antiphase Boundary 663
Antisite 435, 499, 505
APCVD 167, 171
Auger Electron Spectroscopy 205, 611
Avalanche Breakdown 695, 735

B
Band Bending 223
Band Offset 475
Band Structure 357
Band-Gap Narrowing 353
Barrier Height 615
Beryllium 467
Beveling 623
Biaxial Strain 795
Bipolar Devices 739
Bipolar Transistor 567
Birefringence 283, 417
BJT 567
Bond Stacking 211
Bond Strength 603
Boron 327, 373, 455, 521
Boron Doping 49
Boron Migration 447
Boron-Related Defects 447
Brewster Angle 417
Buffer Layers 115
Bulk Growth 49, 61, 65, 143
Buried Layers 695

C
C 579
C(000$\bar{1}$) Face 631
C/Si Ratio 107
C_3H_8 Etching 123, 139
Car Exhausts 747
Carbon Co-Implantation 451, 575
Carbon Displacement Threshold 381
Carbon Islands 659
Carbon Particles 29
Carbon Sublattice 271
Carbonization 167, 179, 187
Carrier Lifetime 743
Carrier Recombination 389
Carrier Scattering 769

C-Face 205
Channel Mobility 643, 647
Channeling 279
Chemical Bonding 239
Chromium 471
Compensation 421, 763
Contacts 607
Copper 615
Core Level Photoemission 215
Coupled Thermodynamics-Mass Transfer Modeling 61
Crack Healing 77
Cracking 21
Critical Pressure 779
Cross Polarizer 267
Crystal Defects 287, 303
Crystal Field Splitting 357
Crystal Growth 69, 111
Crystal Shape 21, 41
C-Terminated Face 243
Cubic Silicon Carbide 663
Cut-Off Frequency 815
C-V Characteristics 45, 95, 619, 631, 635
CVD 91, 95, 99, 155, 159, 163

D

D_I Bound Exciton 361
D_{II} 377
Dangling Bond 691
Deep Acceptors 521
Deep Levels 365, 443, 471, 475, 703, 769
Defect Complexes 323
Defect Distribution 263
Defect Elimination 307
Defect Formation 259, 505
Defect Recombination 549
Defects 7, 15, 21, 295, 315, 369, 505, 509, 513, 517, 537
Degenerated Statistics 353
Delta-Doping 563
Density Functional Theory 111
Denuded Zones 393
Deposits 57
Device Stability 299
Diamond 199, 579
Dielectric Function 413
Diffusion 327, 331, 381, 467
Diffusion Length 389
Diffusion Welding (Bonding) 603
Diode Characteristics 731
Dislocation 299, 393
Displaced Silicon Atoms 595
Displacement Anisotropy 381
Dissociation 331
Dissolution Mechanism 659
Distribution of Carbon Inclusions 29
Divacancies 533
DLTS 131, 431, 439, 443, 459, 471, 475
Domain Film Structure 783
Donor Density 495
Donor Energy Level 495
Donors 555
Dopant Activation 549, 559
Dopant Compensation 549
Dopant Homogeneity 49
Dopant Profile 559
Doping 33, 53, 587, 591
Doping by Implantation 467
Doping Level Determination 397
Doping Levels 479
Doping Profile 619, 699
Doppler Broadening 537

E

Edge Termination 623, 687
Effective Pore Diameter 119
Electrical Activation 571, 575, 731
Electrical Properties 53
Electroluminescence 389
Electrolysis 303
Electrolytic Etching 619
Electron Channeling 227
Electron Irradiation 499, 509, 517
Electron Microscopy 199, 315
Electron Paramagnetic Resonance 499, 505, 513, 517, 521, 529
Electronic Bandgap 405
Electronic Nose 747
Electronic Wave Function 525
Elementary Screw Dislocation 311
Ellipsometry 183
EMT 191
Epitaxial Growth 99, 103, 115, 131, 311
Epitaxial Layers 291, 537, 799
Epitaxy 119, 763
Etch Mask 623
Etch Pits 3, 619
Etching 239
Evaporation Coefficient 61
Evolution 37

Exciton Recombination 405
Excitonic Bandgap 405
Extended Defects 769
Extrinsic Photocurrent 405

F
Field-Effect Transistor (FET) 219, 815
Field Emission 679
Flash Lamp Annealing 151, 587
Flow Orientation 91
Flue Gases 747
Formation 435
Forward Degradation of SiC Diodes 727
Free Carrier Concentration Spectroscopy (FCCS) 495
Freewheeling Diode 675
Frenkel Pairs 509
FTIR 369

G
Gallium Nitride 769, 807
Gas Phase Nucleation 103, 107
Gas Sensors 219, 747
Gate Oxide 639
Gate Turn-Off Thyristor 743
GA-XRD 191
Germanium 183, 187, 247
Gettering 393
Global Heat and Mass Transfer 65
Graphical Peak Analysis 495
Graphitization 37
Growth 53
Growth Parameter 29
Growth Process 91
Growth Rate 37, 107, 655, 779
GTO Thyristor 739
Guard Ring 687

H
Hall Concentration 483
Hall Effect 45, 369, 495, 731
Hall Mobility 483
Hall Scattering Factor 45
HCDS 127
HCI Etching 123, 139
Heat Transfer Simulation 7
Hemispherical Substrate 123
Heteroepitaxy 155, 159, 179, 183, 187
Heteropolytypic Structure 211
Heterostructures 205
Hexagonal Surfaces 205
Hexamethyldisilane 495
High Dose Implantation 579
High Field Transport 487
High Temperature 753
High Voltage 675, 727
High Voltage Devices 719
High-Resolution X-Ray Diffraction 291
HMDS 127
Hole Traps 431
Hollow Defects 307
Homoepitaxial Growth 123, 139, 211, 543
Hooge Parameter 703
Hot-Wall Reactor 91, 95
Hydrogen 331, 373, 427, 607
Hydrogen Annealing 691
Hydrogen Concentration 421
Hydrogen Implantation 275
Hydrogen Termination 223
Hydrogen-Terminated Surface Conductive Layer 815

I
Imaging Spectroscopy 389
Implantation Damage 335, 385, 513, 731
Implantation-Induced Defects 439, 451, 595
Implanted pn-Junction 451
Inclusions 29, 33, 263
Infrared Absorption 349
Infrared Reflectivity 385
Infrared Spectroscopy 223
In-Situ Observation 295
Interface 215, 255
Interface State Density 631, 643, 691
Interface States 479, 639
Interface Trap 635
Interstitial 595
Interstitial Clusters 549
Interstitial H 421
Intrinsic Defects 431, 435, 439, 455, 555
Intrinsic Photocurrent 405
Inversion Domains 803
Ion Beam Analysis 279
Ion Beam Synthesis 591
Ion Implantation 199, 255, 259, 271, 315, 327, 365, 443, 543, 567, 571, 575, 587, 591, 599, 707, 739
IR Reflectance 191
Iron 529
Irradiation 365, 533, 799

Isoelectronic Defects 555
Isothermal Capacitance Transient Spectroscopy 451

J
JBS Rectifier 683
Junction Barrier Schottky (JBS) 683, 687

K
k•p Approximation 487
Kick-Out Mechanism 327

L
Large Area Diodes 727
Laser Crystallization 195
Lateral Overgrowth 127
Lattice Parameter 319
Layer-by-Layer Analysis 239
Leakage 769
Leakage Current 731
LETI-Method 53
Level Splitting 475
Line Broadening 341
Liquid Phase Epitaxy 85, 307
Local Vibrational Modes 349
Low Frequency Noise 703
Low Off-Angled Substrate 135
Low Temperature 85, 401
Low-Energy Electron Diffraction 205
Luminescence 505, 791, 795

M
Macrostrains 119
Material Source 779
MCDA 505
Melting 195
MESFET 699, 703, 707, 711
Metallization 607
Micropipe 3, 303, 307, 311
Micropipe Closing 33, 311
Micropipe Filling 73
Micro-Raman Spectroscopy 335
Microscope 345
Microwave Power 669, 807
Minority Carrier Lifetime 757
Minority Carrier Transient Spectroscopy 431
Modified Lely Method 295, 401
Modified-PVT 33
Moissanite 3
Molecular Beam Epitaxy (MBE) 179, 183, 187, 227,247, 259, 409
Molybdenum 611
Monovacancies 533
Monte Carlo Simulation 487
MOS 627, 635
MOS Capacitor 643
MOSFET 543, 643, 651, 715, 747
MOSHFET 807
MOVPE 163
Multi-Substrate Arrangement 77
Multi-Substrates 77
Multi-Wafer Hot-Wall Reactor 103

N
N Donor 525
Nanocrystal 413
Nanostructures 247
Neutron Irradiation 287, 555
Neutron Transmutation Doping 555
Neutrons 369
Nickel 529
Nickel Silicide 255
Nitride Heteroepitaxy 795
Nitrided Oxide (NO and N_2O) 655
Nitrogen 369
Nitrogen Level 483
Nitrogen Plasma 239
Non-Destructive Depth Profiling 219
Non-Radiative Recombination 769
n-Type Doping 345
Nuclear Resonance 271
Numerical Modeling 11, 65
Numerical Simulation 15

O
Occupancy Level 455, 463
Off-Angle 647
Off-Axis Substrate 783
Off-Orientation 123, 139
Ohmic Contacts 251, 711, 735
On-Resistance 615
Optical Properties 409, 413
Ostwald Ripening 315, 549
Oxidation 215, 639, 655
Oxidation Rates 663
Oxide 651
Oxide Roughness 663
Oxide-Trapped Charges 635
Oxygen 459, 463

Ozone 219

P

PAS 567
Passivation 331, 421, 427
Persistent Defects 377
Phase Formation 199, 579
Phonon-Drag Effect 491
Phosphorus 369, 555
Photoconductivity 53
Photoelectron Diffraction 227
Photoelectron Spectroscopy 223
Photoemission Spectroscopy 235
Photoluminescence 115, 131, 345, 365, 373, 377, 393, 401, 409, 555
Physical Simulations 699
Physical Vapor Transport 3, 11, 65
Piezoelectric Field 791
PiN Diode 543
Planar Defects 663
p-n Junction 735
Point Defects 323, 447, 799
Polarity 227
Polarization 787
Polytype Dependence 475
Polytype Transformation 147
Polytypism .. 25, 111, 205, 211, 227, 397, 647
Porosity 37, 119
Porous SiC 115
Positron Annihilation 537
Positron Annihilation Parameters 533
Post Implantation Anneal 451
Powder Charge 37
Power Devices 623, 691, 739
Power Rectifier 683
Power Switching 695
Precipitate 583
Pre-Growth Etching 135
Pressure Sensor 753
Process Simulation 599
Propane 127
Proton Irradiation 431
p-Type 4H-SiC 467
p-Type 6H-SiC 45
Pulse Measurements 743
Punch-Through 683
PVT Growth 25, 41

Q

Quantum Dots 247, 413
Quantum Mechanical Calculations 231
Quantum Wells 791

R

Radiation Damage 271
Radiation Defect 505
Radiation Hardness 763
Radiotracer 475
Raman Scattering 345
Raman Spectroscopy 275, 341
Raman Spectroscopy Imaging 283
Rapid Thermal Annealing (RTA) 711
Reactive DC Sputtering 191
Reactive Ion Etching 623
Recessed Channel 651
Recombination 331
Recombination and Trapping Centers 757
Reconstruction 205
Recrystallization 571
Reflectivity 795
Refractory Metal 611
Reliability 611, 727
Remote PECVD 651
Re-Oxidation 479, 635
Residual Stress 41
RESURF 715
RHEED 179, 183, 187
Roughness 707
Ruthenium 607
Rutherford Backscattering Spectrometry (RBS) 567, 731

S

Scanning Tunneling Microscopy 205, 235, 247
Scanning Capacitance Microscopy (SCM) 559
Schottky Contacts 603, 607, 611
Schottky Diodes 131, 219, 675, 679, 687, 691, 747
Schottky Rectifiers 615
Secondary Phase Formation 107
Seebeck Coefficient 491
Segregation 803
Selective Epitaxy 127, 171, 175
Selective Implantation 731
Selective Method for a Vapor Growth of Crystals 81
Self-Diffusion 323
SEM 559

Semi-Insulating SiC 53, 669
Semi-Insulating Layers 529
Semi-Insulating Substrate 703
Shallow Traps 627
Sheet Resistance 711
Si Substrates 167
Si_3N_4 171
SiC Bulk Growth 29, 263
SiC Epilayers 459
SiC Growth 163
SiC JFET 723
SiC MESFET 669
SiC on Si 163, 591
SiC Sublimation Growth 7
SiC Substrates 603, 807
SiC Surfaces 215
SiC Trench MOSFET 723
SiC(0001) 205
SiC(000$\bar{1}$) 205
SiC-(11$\bar{2}$0) 543
SiC-(11$\bar{2}$0) Face 627, 635
SiC-(1120) Plane 69
SiC_xN_{1-x} 239
Si-Face 205
Silicides 615, 711
Silicon Displacement Threshold 381
Silicon Vacancy 509
SIMS 45, 95, 327, 373, 427, 571, 583, 655, 699
Simulation 99, 687, 695, 719
Singular Surface 147
SiO_2 ..... 171, 651
SiO_2-SiC Interface 647, 655, 659
S-Level 443
Solid State Detectors 757
Solubility Limit 583
Source Composition 263
Source Material 11
Source Resistance 711
Specific Contact Resistance 603
Spectral Mapping 393
Spectroscopic Ellipsometry 417
Spin Distribution 463
Spin Orbit Splitting 357
Spontaneous Growth 85
Spreading Resistance Profiling (SRP) 559
Stability 111, 611
Stacking Fault 69, 299
Stacking Sequence 205
Steam Annealing 635
Step Height 139
Step Structure 111
Strain 259
Strain and Stress Components 319
Strain Energy Band Engineering 807
Stress 119, 155, 651
Structural Correlation Length 287
Structural Transformation 311
Sub-Grain Boundary 267
Sublimation 3, 57, 267, 779
Sublimation Close Space Technique 73
Sublimation Epitaxy 73
Sublimation Growth 45, 77, 143, 147, 243
Sublimation Method 69, 73
Substrate Type 69
Subsurface Damage 335
Super Junction Structure (SJS) 719
Superlattice 803
Supersaturation 15
Surface influence 211
Surface Morphology 123, 135, 139, 239, 243, 631
Surface Pits 803
Surface Polarity 179
Surface Reconstruction 235
Surface Roughness 139
Surface Structure 205, 247
Swelling 599
Synchrotron Topography 291, 299

T

T5 Center 421
Tantalum 475
TEM 151,175, 259, 315, 579, 583, 631, 647, 783
Temperature Dependent C-V Characteristics 679
Temperature Dependence of Majority-Carrier Concentration 495
Temperature Distribution 99
Temperature Oscillation Method 81
Temperature Stable Defects 443
Thermal Gradients 15
Thermal Stability 251
Thermally Stimulated Current Spectroscopy 479
Thermoelastic Stress Distribution 65
Thermopower 491
Thickness Mapping 95
Thin Film 319

Thin Oxide 219
Threading Dislocations 769
Time-Resolved Photoluminescence . 377, 791
Time Resolved Reflectivity (TRR) 195
Transient Enhanced Diffusion 549
Transient Grating 353
Transition Metal 471
Transmission Line Model (TLM) 251
Trapping 669, 703
Traps 769
Trench 651
Tungsten 475
Tunneling 487
Two Dimensional Carrier Gases 787
Two Photon Absorption 381

U
Ultrafast Switching Device 675
U-MOS 651
Uniaxial Material 417

V
Vacancies 499, 505, 537, 595
Vacancy Defect 513
Vacancy-Hydrogen Complex 421
Valence Bands 357
Valley Orbit 483
Vanadium 53, 471
Vapor Phase Epitaxy 563
Virtual Reactor 57

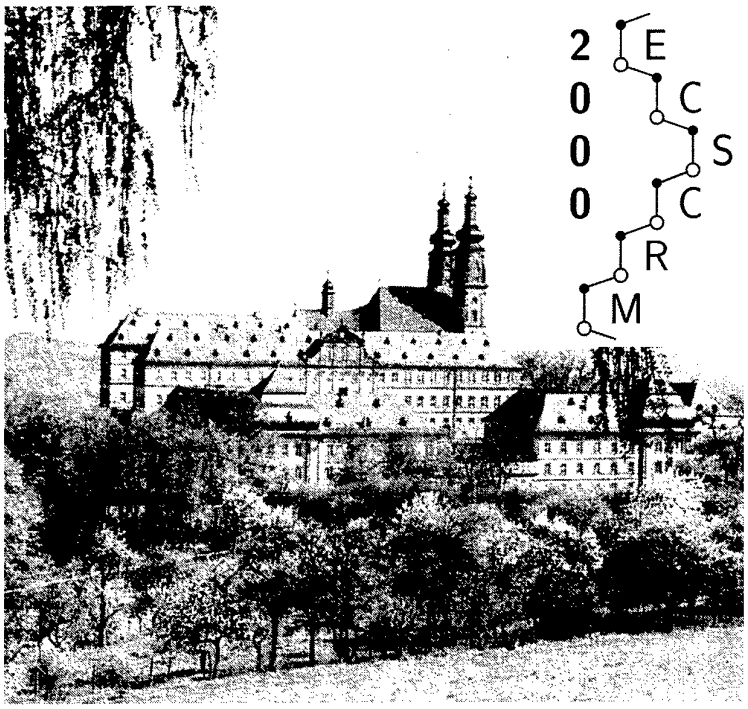
W
Wafering 335
Wet Oxidation 663

X
XPS 239, 251
X-Ray Diffraction 267, 287, 319
X-Ray Imaging 11
X-Ray Photoelectron Diffraction 179
X-Ray Topography 283, 295

Z
Zeeman Effect 361, 365
Zener Diode 735

Third European Conference on Silicon Carbide and Related Materials

ECSCRM2000



Kloster Banz, Germany
Sept. 3–7, 2000

Organized by
Friedrich–Alexander Universität
Erlangen–Nürnberg

20010502 133

Abstracts

R+D 9028-EE-02
N68171-00-M-6100
Dr PENSL

Session Index

Mo1	**Plenary 1**	**5-6**
Mo2	**Defects**	**7-11**
Mo3	**Structural Characterization**	**12-16**
MoP	**Poster I**	**17-97**
	Defects	17-33
	Measurement Techniques	34-36
	Characterization	37-57
	Bulk Growth	58-66
	Epitaxy	67-77
	Surfaces/Interfaces	78-83
	Processing	84-89
	Devices	90-97
Tu1	**Bulk Growth**	**99-104**
Tu2	**Epitaxy**	**105-110**
Tu3	**Industrial**	**111-112**
We1	**Surfaces**	**113-117**
We2	**Processing + Fabrication**	**118-122**
We3	**Electrical + Optical Characterization**	**123-127**
WeP	**Poster II**	**129-208**
	Characterization	129-149
	Bulk Growth	150-158
	Epitaxy	159-171
	Surfaces/Interfaces	172-181
	Processing	182-196
	Devices	197-208
Th1	**Devices**	**209-214**
Th2	**Plenary 2**	**215-216**
Th3	**Plenary 3**	**217-219**
Author Index		**221-228**

SiC Power Devices: From R&D to the market

R. Ploss, R. Rupp, I. Zverev
Infineon Technologies AG, Dep. AI IP, P.O. Box 80 09 49, D-81609 Munich, Germany

Since the last ECSCRM conference a lot of progress occurred concerning SiC device and material development. Among these good news there have been a demonstration of 4 inch SiC wafers and a >10kV SiC pn diode, a world record for a single solid state device. Nevertheless a mood of stagnation can be recognized in a huge part of the SiC community, because even with these exciting news there is still worldwide no money earned with SiC devices if one takes apart the optoelectronics business. A successful introduction of SiC devices requires an application which fulfills the following criteria:

1. Potential device market size of several Mio. $/year
2. Low current (small chips) to achieve reasonable yield values
3. System cost reduction which compensates the high SiC device costs at least

Especially the last point is a serious obstacle, because one has to convince the system manufacturer to spend a lot of design efforts in rebuilding his application around the SiC device based only on the unproved promises of a device manufacturer. To get out of this dead lock situation and to really do the step from R&D to the market, we developed application demonstrators to proof the benefit of SiC devices.

As pilot application we have chosen the power factor correction (PFC) stage (Fig. 1) used in switched mode power supplies between 100W to 2 kW, where we demonstrate the cost/performance benefit of a SiC Schottky diode. With this application we meet the first two of the success criteria mentioned above. A specific feature of this PFC subsystem is, that the switching frequency is pretty high (50 – 150 kHz at a voltage level of about 400 V) and therefore there is a serious need for a diode with low switching losses. All the reverse current generated by the diode (D1) will go straight through the FET switch (T1) and generate huge losses there. Having a zero reverse current device like the SiC Schottky diode at this place will allow the customers to use a significantly smaller FET and to reduce the switching losses. Due to ideal switching behavior the effort for the snubber circuit and other components can be reduced too. This compensates at least the higher cost of the SiC diode while providing better performance.

In this paper we will explain this benefits in more detail and also we will show, that in conjunction with compensation FETs like the CoolMOS™ the customers will be able to produce a new generation of power supplies with significantly improved power handling density.

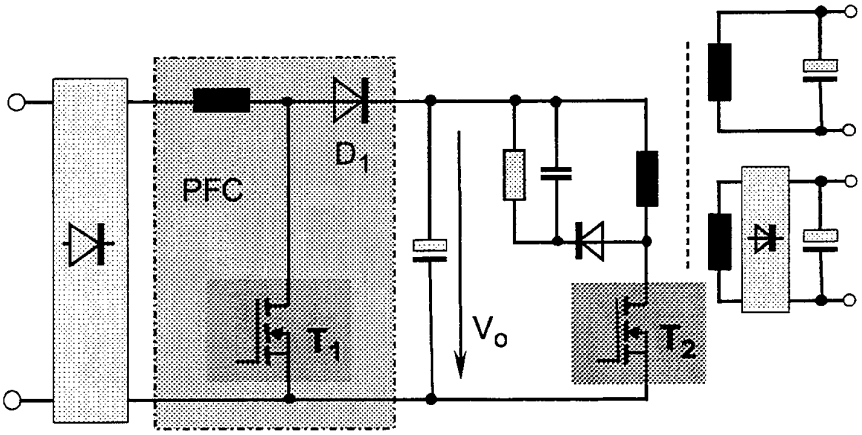


Fig. 1: Schematic of a power supply circuitry. The diode D1 is the target application for the SiC Schottky diode.

Mo1-2
(Invited)

Prospect of R&D of Ultra-Low-Loss Power Device Technologies in Japan

Kazuo ARAI

Electrotechnical Laboratory, Tsukuba-shi Ibaraki 305-8568 Japan
karai@etl.go.jp, Tel.:+81-298-61-5243, Fax:+81-298-61-5403

R&D of Ultra-Low-Loss Power Device Technologies was started in Oct. 1998 with a term of 5 years (FY1998-2002) under the "New Sunshine Project" of MITI after the leading research of "Hard electronics"(FY1996-1997). Hard electronics research showed that wide band gap semiconductors such as SiC, GaN and diamond have the potential to exceed the limits of Si power devices in low power loss, high frequency and operation under severe conditions. The main target of the project is to establish fundamental technologies for SiC power devices in response to the rapid progress of SiC device research in the world. The project involves all technologies needed for SiC power devices to overcome difficult problems between device performance and material issues. The project consists of two parts: (1) basic research on the development of innovative technologies required to realize practical use of SiC devices (bulk crystal growth technology, device processing technologies and device characterization), and (2) fundamental device technologies for the development of pn junction FET, MOSFET and MESFET. Tentative goals of the device performance are about 1/10 the on-resistance and 10 times the power density of Si devices. The basic research is being conducted by concentrating the activities of eight companies and ETL in ETL, in cooperation with nine universities. The fundamental device technology is being developed by three companies (distributed).

To understand fundamental material issues and reflect it in real device processing is a key approach in the project. An instrument was developed for real-time observation of X-ray topography during the sublimation growth of SiC. The in situ topographs demonstrated the movement of the micropipes and the monitoring of the growth rate during the crystal growth. Systematic study of the interface-state density (D_{it}) on ozone cleaning, post annealing , off-angle and orientation of crystal surface in relation to the channel mobility of SiC MOS are conducting, along with evaluation of gate oxide long-term reliability of MOS. D_{it} of 4H-SiC MOS structure was considerably reduced using hydrogen annealing above 800C. Ohmic contact resistances as low as 4.6×10^{-6} ohm cm^2 (without annealing) and 8.6×10^{-7} (with annealing) for n-4H-SiC, has been attained by elaborate surface processing along with proper ion implantation which is being transferred to MESFET fabrication. The fundamental devices have been designed, simulated and fabricated as the first trial. The process optimization is now under way through cooperation in the project.

THEORY OF HYDROGEN IN SILICON CARBIDE

Peter Deák*, Adam Gali, Balint Aradi

Department of Atomic Physics, Technical University Budapest
Budafoki út 8., H-1111 Budapest, Hungary
phone: [36]-(1)-463-1393; fax: [36]-(1)-463-4357

Hydrogen has profound and very versatile influence on the electronic characteristics of semiconductors by passivation of electrically active centers and sometimes by formation of active complexes. It is one of the most common impurities in electronic materials, introduced – among others – by both wet and dry etching. In SiC hydrogen is of special importance: graphite parts used in bulk growth may release substantial amounts of H, and in CVD growth H_2 is often used as carrier gas and H is always part of the precursor molecules. The presence of H in as grown SiC may, therefore, be expected but is only proven in p-type epitaxial layers. H-implantation or H-plasma treatments show passivation of only p-type samples as well. H remains rather elusive for spectroscopy, too: apart from sidebands of PL related to C-H vibrations of V_C + H complexes (V_C: vacancy at the C site), no signature of hydrogen has been found either in DLTS or in magnetic resonance spectroscopy. (It should be noted, however, that far more "vacancy-type" centers have been reported than one could possibly account for by simple combinations of V_C and V_{Si}.)

Modern methods of atomistic simulation are capable of making predictions about the stable form, energetics and spectroscopically observable properties of defects complexes by solving the Schrödinger equation for an assembly of relevant atoms. Except for fortunately simple cases, the accuracy of quantitative predictions cannot reach that of the experimental methods but qualitative estimates about the relative abundance of a defect and of its main effect on the electronic properties may be given, as well as the range can be pinpointed where spectral features of a defect should be looked for. In the present study the interaction of one or two hydrogen atoms is considered with the "perfect" SiC lattice and with an isolated vacancy (both at the C and the Si site) in SiC, using ab initio Local Density Approximation within Density Functional Theory to calculate total energies. A defective crystal is constructed by repeating supercells (of 32, 64 and 128 host atoms in case of 3C-SiC and of 96 host atoms in case of 4H-SiC) containing a single defect.

Interstitial hydrogen may act as a donor or as an electron trap in SiC. We predict high concentration of mobile, compensating H^+ centers in p-type material, whereas in n-type SiC — except for heavy doping and high temperature— the stable form of the hydrogen interstitial is H_2, and both solubility and mobility is predicted to be low. Interstitial hydrogen will more readily form complexes with V_{Si} and shallow acceptors than with V_C and shallow donors. The capture of subsequent hydrogens makes both the donor V_C and the acceptor V_{Si} gradually shallower — both acting as compensating centers. The latter can eventually be passivated with 4 H atoms, the former — holding only 2 hydrogens — cannot. While the formation energy of V_C is substantially lower than that of V_{Si}, hydrogenation decreases the formation energy of the latter below that of the former. If a supply of atomic hydrogen is available during growth, heavily n-type SiC may have a high concentration of acceptor type V_{Si} + nH defects.

The occupation levels, characteristic vibrations, and spin distribution in the paramagnetic state has been calculated for hydrogen in interstitial position and when captured in a vacancy. It is shown, that $[V_{Si} + H]^{q-1}$ and $V_{Si}^{\ q}$ for $q \le 0$, as well as $(V_C + H)^q$ and $V_C^{\ q-1}$ for $q \ge 0$ have similar properties. We propose that the T5 center [1] arises from a V_C + H defect, rather than from V_C.

* p.deak@eik.bme.hu

Mo2-2

Presence of hydrogen in SiC

A.Henry[1*], B. Magnusson[1], M.J. Linnarsson[2], and E. Janzén[1]
[1]Department of Physics and Measurement Technology
Linköping University, S-581 83 Linköping, Sweden
[2]Solid State Electronics, Royal Institute of Technology, S-164 40 Kista, Sweden
*Phone: +46 13 282414, Fax: +46 13 142337, E-mail: ahy@ifm.liu.se

In the early seventies, Choyke and Patrick (Ref. 1) reported strong bound exciton (BE) photoluminescence (PL) spectra in SiC implanted with the hydrogen isotopes, H (^{1}H) and D (^{2}H). The PL spectra in the case of H and D implantation are very similar apart from the energy positions of some prominent lines in the phonon assisted sidebands. The energy displacement of these lines from the no-phonon lines, approximately 369 meV in H-implanted, and 274 meV in D-implanted SiC, corresponds to the energies of C-H and C-D bond-stretching vibrational modes respectively. This confirmed the involvement of the implanted species (H or D) in the centers. The defect was proposed to consist of an H or D atom bonded to one of the four C atoms neighboring a Si vacancy. From as-grown epitaxial layer the H-related PL has also been observed only when special growth conditions were used which do not correspond to the standard epitaxial conditions (Ref. 2).

We will in this work show experimental evidence of the presence of hydrogen in 4H-SiC trapped at impurities, although the hydrogen/impurity complex is not observed. Low-temperature photoluminescence (PL) spectra reveal after secondary ion mass spectrometry (SIMS) the presence of both boron and hydrogen related lines which were not observed before the SIMS measurement (see fig.1) of the same sample. It is likely that the high-energy ions used in SIMS analysis break the B-H bonds. Hydrogen is then trapped by existing vacancies to form the known H-vacancy center, giving rise to the PL spectrum. This phenomenon is observable, only for certain impurity concentrations. The competition of various recombination channels during the PL experiments will also influence on the emission. This behavior has not been observed for higher-doped n-type ($n > 5 \times 10^{16}$ cm^{-3}) samples or compensated material showing donor-acceptor N-Al pair in the PL spectrum. The change of the PL spectrum is observable only in samples with enough boron concentration ($> 2 \times 10^{15}$ cm^{-3}, as determined by SIMS). This behavior has been observed from layers grown by chemical vapor deposition when hydrogen is used as a carrier gas. It has also been observed for material grown with the high temperature CVD technique where the carrier gas is not hydrogen but helium, however the precursor gases contain hydrogen. An interesting fact is that phenomenon is also observed from samples grown with a "hydrogen-free" technique such as the close-space sublimation, where hydrogen can be incorporated in the polycrystalline SiC material used as a source. Our results show that hydrogen trapped at impurities probably always is present in SiC.

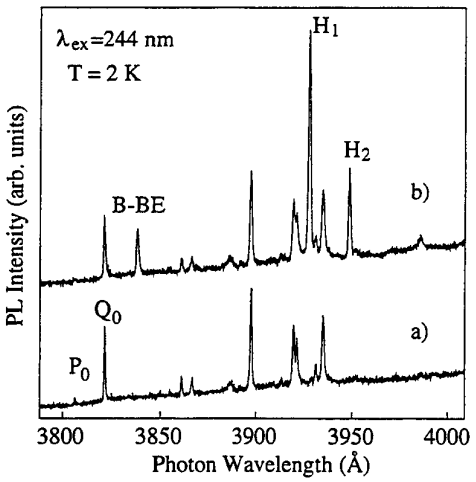


Fig. 1. The change in the PL spectrum for a 4H sample is shown in (b) after SIMS measurement compared to (a) before. As observed three new sharp lines appear and these are the B-BE and the two hydrogen related lines (H_1 and H_2).

[1] W.J.Choyke, and R.P.Devaty, Phys. Rev. B **9**, 3214 (1974).
[2] D.J.Larkin, S.G.Sridhara, R.P.Devaty, and W.J.Choyke, J. Electron. Mater. **24**, 289 (1995).

Low-frequency vibrational spectroscopy in SiC polytypes

B. Pajot[1], J. L. Cantin[1], H. J. von Bardeleben[1] and F. Gendron[2]

[1] Groupe de Physique des Solides, UMR 7588 du CNRS, Université Denis Diderot, 2 place Jussieu, 75251 Paris cedex 05, France

[2] LMDH, UMR 7603 du CNRS, UPMC, 4 place Jussieu, 75252 Paris cedex 05, France

An infrared absorption study of different p- and n-type (mainly 6*H*) SiC samples has been performed near 6 K below the one-phonon band using spectral resolutions down to 0.025 cm^{-1}. In this spectral region, absorption by local vibrational modes (LVMs) coexists with that of acoustical phonon modes with wave vectors k/k_{max} corresponding to special points of the phonon dispersion curves of SiC polytypes in the large zone scheme [1,2]. In all the 6*H* samples, a pair of sharp lines at 235 and 240 cm^{-1} correlates with another line at 506 cm^{-1}. These lines are due to longitudinal and axial phonons with wave vectors $k/k_{max} = 0.67$. In another sample, a doublet (255.23 and 256.82 cm^{-1}) whose components exhibit a full width at half maximum of 0.05 cm^{-1} correlates with a mode at 570 cm^{-1}. These latter lines are characteristic of acoustical phonons at $k/k_{max} = 0.8$ in the 15*R* polytype.
A LVM near 625 cm^{-1} is observed, in all the samples investigated. It has been attributed to residual ^{14}N in 4*H* SiC [3]. In a B-doped material grown by the Lely method, two LVMs related to $^{10}B_{Si}$ and $^{11}B_{Si}$ are observed and correlated to the B EPR signature. Their vibrational nature of the IR lines is inferred from a small upward shift of their frequencies between room and liquid helium temperatures.
In Al-doped samples, where the EPR signature of Al is detected, LVMs are observed between 684 and 691 cm^{-1}, whose intensity increases with electron irradiation dose, that could be due to Al-related local modes.

[1] D. W. Feldman, J. H. Parker, Jr., W. J. Choyke, and L. Patrick, Phys. Rev. **173**, 787 (1968).
[2] G. D. Dubrovskii and E. I. Radovanova, Sov. Phys. Solid State **14**, 2127 (1973).
[3] W. Götz, A. Schöner, W. Suttrop, W. M. Choyke, R. A. Stein, and S. Leibenzeder, Mater. Sci. Forum **143-147**, 69 (1994).

Boron in SiC: structure and kinetics

Michel Bockstedte, Alexander Mattausch and Oleg Pankratov
Lst. theor. Festkörperphysik, Universität Erlangen-Nürnberg,
Staudtstr. 7B2, D-91058 Erlangen, Germany

Boron as an acceptor-center in SiC has recently attracted much attention. New experiments have been focused on the electronic structure of boron-related centers [1], the electrical activation of the acceptor [2] and the properties of boron diffusion [3]. To date two different boron-related centers have been observed: a shallow acceptor and a deep center below mid-gap [1]. While the shallow center has been identified as a substitutional boron at a silicon site (B_{Si}), a boron-vacancy-complex (boron on a silicon-site with a neighbouring carbon vacancy) is currently proposed as a model for the deep center. Other configurations, especially boron on the carbon sublattice (B_C), have not been found. This might be related to the thermal stability. It was found that kinetic aspects play an important role. Implantation experiments [2,3] indicate that intrinsic point defects, most likely interstitials, affect the boron activation and, at the same time, are the driving power of boron diffusion. The aim of the present work is to develop an *ab initio* microscopic picture of boron-related defects in cubic SiC and their kinetic properties. Our calculations provide the microscopic structure as well as the energetics of the defect formation, defect reactions and migration.

For the substitutional centres, in agreement with earlier calculations [4], we do not find a distinct preference for boron incorporation on either the silicon or the carbon sublattice. However, by including charge state corrections we find the acceptor level of B_{Si} in significantly better agreement with the experimental value. Our investigation rules out a possible metastability of B_C and B_{Si} due to the formation of boron-interstitial-vacancy pairs. Thus, in equilibrium both B_C and B_{Si} should be present in similar concentration. Moreover the calculated position of the acceptor level of B_C coincides with the deep level observed experimentally. Our detailed analysis shows that the proposed boron-vacancy-complex [1,5] has deep levels close to the conduction band instead. This questions the correlation of this level with the model from ESR- and ENDOR-data. Comparing the formation energies of boron-related defects we have found that boron-interstitials and boron-vacancy-complexes are as favourable as substitutional boron under p-type conditions, leading to a reduced boron activation. We find the substitutional boron acceptor to be metastable against reactions with vacancies and intrinsic interstitials. Hence, beyond equilibrium the annealing kinetics should affect the boron activation in SiC. Boron-interstitials can migrate between carbon coordinated sites (which are energetically preferred) via silicon coordinated sites or split-interstitials (a boron and a silicon atom share a silicon site). The latter path may also lead to a kick-in reaction creating a B_{Si} while releasing a silicon-interstitial. We find that the defect relevant for a vacancy mediated boron diffusion consists of B_C and a neighbouring carbon vacancy. It migrates by second nearest neighbour hops. We discuss the energy barriers for these migration paths under various doping conditions.

[1] van Duijn-Arnold *et al.* , Phys. Rev. B **60**, 15829 (1999) and references therein.
[2] Itoh *et al.*, Appl. Phys. Lett. **73**,1427 (1998).
[3] Laube *et al*, Appl. Phys. Lett. **74**, 2292 (1999)
[4] Fukumoto, Phys. Rev. B **53**, 4458 (1996)
[5] Gali *et al.*, Phys. Rev. B **60**, 10620 (1999).

RADIATION-INDUCED PAIR DEFECTS IN 6H-SILICON CARBIDE STUDIED BY OPTICALLY DETECTED MAGNETIC RESONANCE

Th. Lingner, S. Greulich-Weber and J.-M. Spaeth

Department of Physics, University of Paderborn, 33095 Paderborn, Germany
e-mail: lingner@physik.uni-paderborn.de tel.: +49 5251 602749 fax: +49 5251 603247

We used the magnetic circular dichroism of the absorption (MCDA) and MCDA-detected electron paramagnetic resonance (MCDA-EPR) to study radiation-induced point defects in neutron and electron irradiated and subsequentially annealed 6H-silicon carbide. We found MCDA-lines at photon energies of 1075, 1049 and 1011meV (fig. 1) to be associated with EPR spectra for S=1 with axial symmetry along the c-axis of the hexagonal crystal and fine structure constants of 455, 446 and $429 \cdot 10^{-4} cm^{-1}$, respectively (fig. 2). These three MCDA lines and the corresponding MCDA-EPR spectra are attributed to the spin triplet state of a radiation-induced point defect at the three inequivalent lattice sites in 6H-SiC.

Two of these three EPR spectra have been observed previously by photoluminescence detected EPR (PL-EPR) [1]. However, corresponding opical transitions to these centers were not found. The PL-EPR spectra were associated with an efficient non-radiative recombination channel via a nearest-neighbour pair defect, i. e. associated with a shunt process.

We found that the optical transitions can be observed with the MCDA-technique as well as with PL. The PL signals can be detected upon excitation with above or below band gap light.

In a double-beam-experiment we excited the sample with the blue-green light of an Ar-ion-laser while simultaniously detecting the MCDA-EPR-signal. Under these conditions a nonthermal occupation of the Zeeman-levels of the S=1 systems was achieved, leading to the inversion of the high field MCDA-EPR-lines and a reduction of the relaxation times of the spin population. The latter made it possible to resolve the superhyperfine structure of the MCDA-EPR lines, which turned out to be similar to that of silicon-vacancy related defects reported in [3] (12 Silicon next nearest neighbours).

We discuss the model of a C_{Si}-V_C vacancy-antisite-pair which is a possible annealing product of the isolated silicon vacancy [2].

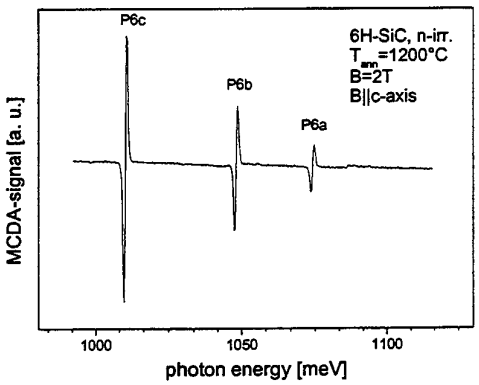


Fig. 1: The P6 MCDA-spectrum

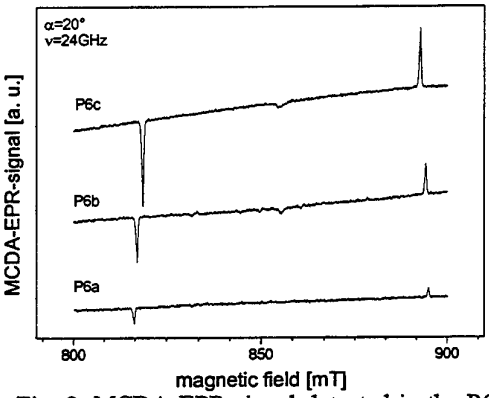


Fig. 2: MCDA-EPR-signal detected in the P6a b and c MCDA-lines under additional excitatio with visible light.

References:

[1] N. T. Son et al, Semicond. Sci. Technol. 14, 1141 (1999)
[2] E. Rauls et al, Phys. Stat. Sol. (b), 217/2, R1 (2000)
[3] E. Sörman et al, Phys. Rev. B 61 (4), 2613 (2000)

Mo3-1
(Invited)

Intrinsic defects in silicon carbide polytypes

N.T. Son, P.N. Hai[1], and E. Janzén
Department of Physics and Measurement Technology, Linköping University
S-581 83 Linköping, Sweden
Tel: 46-13-282531, Fax: 46-13-142337, e-mail: son@ifm.liu.se
[1]Permanent address: Department of Physics, University of Hanoi, 90 Nguyen Trai, Hanoi, Vietnam

Intrinsic defects are known to introduce deep level centers in semiconductors and to have strong influence on the electrical and optical properties of the material. In a compound semiconductor such as SiC, intrinsic defects can be vacancies, interstitials and anti-sites. In SiC, the single vacancies are stable well above room temperature. The anti-sites are expected to be even more stable. At high temperatures, these primary defects will interact with each other or impurities to form various associated complexes. Many of these secondary defects have been reported in SiC, but little is known about primary defects. Until now, only a few has been identified: the negatively charged silicon vacancy in 3C, 4H and 6H SiC, the positively charged carbon vacancy in 3C SiC, and the negatively charged carbon vacancy in 4H and 6H SiC. No experimental observation of interstitials or anti-sites in SiC has been reported so far. In this work, we report the latest results of our Electron Paramagnetic Resonance (EPR) studies of primary intrinsic defects in electron-irradiated SiC: the identification and electronic structure of the positively charged carbon vacancy and the silicon anti-site in 4H and 6H SiC.

The carbon vacancy in the positive-charge state has been identified based on the hyperfine structures due to the interactions with the four nearest Si neighbours and with twelve C atoms in the next nearest neighbour. The center has trigonal symmetry (C_{3V}) and an electron spin S=1/2. The electronic structure of the center will be presented in comparison with that of the positively charged carbon vacancy in 3C SiC.

Anti-sites have so far been studied only by theories in 3C SiC. In this work, we report our observation of the positively charged Si anti-site in 4H and 6H SiC. The defect was identified based on the ^{29}Si self-hyperfine of the anti-site and the hyperfine structure of the nearest Si neighbouring atoms. The defect has also trigonal symmetry (C_{3V}) and an electron spin S=1/2. Replacing a C atom by a bigger Si atom creates a considerable outward relaxation. A strong temperature dependence of this distortion has been observed. The microscopic structure of the defect and its dependence on the temperature will be presented.

The thermal stability of the carbon vacancy and Si anti-site will also be discussed.

Analysis of strain and defect formation of low-dimensional structures within a SiC matrix

U. Kaiser, K. Saitoh[1], A. Chuvilin[2]
Friedrich-Schiller Universität Jena, IFK, 07743 Jena, Germany,
kaiser@pinet.uni-jena.de, Tel.: 03641-947445, Fax: 03641-947442
[1]Research Institute for Scientific Measurements, Tohoku University Sendai 980-8577, Japan
[2]Institute for Catalysis, Novosibirsk, 90630090 Russia

SiC as a polytypic material has the advantage over most other semiconductors that quantum film devices in principle can be produced from one and the same chemical compound only using a combination of the cubic and hexagonal polytype. By incorporation of Si or Ge quantum dots, SiC as a wide band-gap material can show a large conduction band discontinuity that favours possible optical devices as they can be integrated in more highly developed Si technology. Defects on the atomic scale and unstrained nanocrystals can prevent the functioning of such devices. Therefore in this paper emphasis is placed on strain and defect characterization.

Three kinds of specimens have been studied: a) free-standing Si- and Ge-nanocrystals on cubic and hexagonal SiC grown in the "Stranski-Krastanow" growth mode by molecular beam epitaxy (MBE); b) embedded Ge-containing and Si nanocrystals inside the SiC matrix created after Ge^{++}-ion implantation and subsequent annealing; and c) quantum films of 3C-SiC inside hexagonal SiC grown by the layer-by-layer growth mode by MBE[1]. For comparison, results of thick cubic SiC films on Si and SiC substrates will be considered. A combination of various advanced transmission electron microscopy techniques, such as convergent-beam electron diffraction (CBED), high-resolution (HR) transmission electron microscopy, atom location by channeling enhanced microanalysis (ALCHEMI) and high-angle annular dark-field (HAADF) microscopy have been applied. Parts of the experiments have been accompanied by image simulations based on the multislice method or by Bloch wave calculation.

It was found that Si nanocrystals from about 5nm to 20nm in size grow by MBE on cubic SiC in two different orientations, however larger crystals appeared in one orientation only which may be explained by the different misfit between the nanocrystals and the substrate.. Local strain in the dot and the adjacent matrix has been determined directly from HRTEM images or CBED patterns. Lattice defects in the Si dots such as extrinsic stacking faults (SFs) have been identified. Their shift vector has been determined and the efficiency of strain relaxation either due to the defect or due to a wetting layer has been demonstrated. These defects are mostly originated at steps at the SiC surface which are often caused by SF spreading through the whole 3C matrix. For Si nanocrystals inside the 6H-SiC matrix produced by implantation was surprisingly found that SFs parallel (0001) planes of the hexagonal matrix are constrained follow the structure of the matrix. Ge-containing nanocrystals in cubic SiC created after implantation and subsequent annealing have been imaged in HR and HAADF, however further complementary information is required before a precise assignment of their strain state may be given. Prevailing defects in the cubic matrix are point defects and SFs on all {111} planes, as cubic SiC is formed after undergoing a phase transformation from hexagonal over the atomically disordered structure. As this results in a volume decrease, the hexagonal substrate is highly strained and a 6H-3C polytype transformation[3] was observed leading to thin 3C-SiC layers inside a hexagonal matrix. By CBED, the lattice parameter of these thin 3C layers and of the 3C quantum films grown by MBE have been determined and it is interesting to note that only the cubic MBE layer shows a rhombohedral distortion. Bloch wave calculation in combination with the ALCHEMI experiments, HR imaging and HR simulation revealed that the Ge atoms are clustered and located on interstitial positions in the case when no Ge-containing phase is crystallized. The resulting strong diffraction contrast and HR contrast differs strongly from the known lattice image contrast of the hexagonal SiC structure[3]. Very similar strain contrast was found at interfaces and occasionally inside layers grown by MBE that are expected to arise from impurities on interstitial positions.

The authors acknowledge the financial support of this research by the Sonderforschungsbereich 196.

[1] A. Fissel, B. Schröter, W. Richter, Festkörperprobleme (1998)
[2] P. Pirouz, J. W. Yang, Ultramicroscopy, 51 (1993) 189
[3] U. Kaiser, A. Chuvilin, W. Richter, Ultramicroscopy, 76 (1999) 21

Mo3-3

X-ray Diffraction, Micro-Raman and Birefringence Imaging of Silicon Carbide

E. Pernot[1], M. Mermoux[2], J. Kreisel[3], O. Chaix-Pluchery[1], P. Pernot-Rejmánková[1,4], M. Anikin[1], B. Pelissier[1], A.M. Glazer[3], R. Madar[1]

1 LMGP, UMR 5628 INPG/CNRS, BP 46, F-38402 St Martin D'Heres, France
Etienne.Pernot@inpg.fr; Tel: 33 (0)4 76 82 63 15; Fax: 33 (0)4 76 82 63 94
2 LEPMI, UMR 5631 CNRS/INPG, BP 75, F-38402 St Martin D'Heres, France
3 Clarendon Laboratory, University of Oxford, Parks Road, Oxford OX1 3PU, United Kingdom
4 ESRF, BP220, F-38043 Grenoble, France

Despite the significant progress in crystal growth, the industrial applications of silicon carbide crystals have up to now been severely limited by the insufficient quality and size of the commercially available substrates. Typical defects found in SiC are misoriented domains, inclusions, macrodefects, dislocations, micropipes and doping striations. Among the techniques of crystal characterization, X-ray diffraction imaging, polarized light microscopy and Raman spectroscopy imaging have proved of value as powerful tools for studying the defects in SiC.
This paper is devoted to the characterization and comparison of 4H- and 6H-SiC wafers by these three techniques. Stress analysis in SiC crystals can be performed by all of them, however, the physical phenomena involved in the creation of a recorded image are different.
X-ray diffraction imaging (topography) has been performed on the ID19 beam-line at the ESRF. White beam section and projection topographs in transmission have been recorded to study structural defects within the slices. White beam reflection topography has been performed using a low energy beam in order to observe the defects near the sample surfaces (~ tens of microns). Micropipes and dislocations can be easily observed by this method [1].
Micro-Raman spectroscopy imaging was applied also for the characterization of microscopic inclusions, polytype conversion, doping concentration and stress, with lateral resolution of about one micron [2].
4H- and 6H-SiC are materials with optical birefringence. Defects in SiC crystals result in local stress which modifies the orientation and the form of its optical indicatrix. We used a new birefringence imaging technique, which creates false-coloured images representing the light transmission I_0, the orientation of the indicatrix ϕ, and $|\sin\delta|$, a function of the retardation resulting from birefringence (and a measure of the magnitude of optical anisotropy) [3].
Figure 1 shows images of the same area of a 4H-SiC slice by using X-ray diffraction in transmission (1a), birefringence- (1b) and Raman-imaging (1c), respectively. The differences between the images and the information obtained from them is discussed in detail.

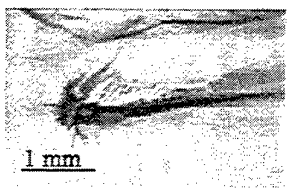


Fig 1a



Fig 1b

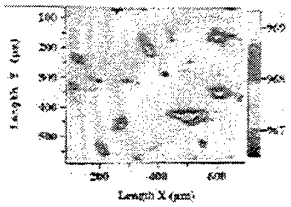


Fig 1c

[1] M. Dudley, S. Wang, W. Huang, C.H. Carter Jr, V.F. Tsvetkov, C. Fazi, J. Phys. D28 (1995) A63-68.
[2] E. Martin, J. Jimenez, M. Chafai, Solid State Electronic, Vol 42, 12 (1998) 2309-2314.
[3] M. Geday, J. Kreisel, A.M. Glazer, K. Roleder, J. Appl. Cryst. (2000) in print.

Crystal defects as source of anomalous forward voltage increase of 4H SiC diodes.

J. P. Bergman, H. Lendenmann, P. Å. Nilsson
ABB Corporate Research, 721 78 Västerås, Sweden
Tel: +46-13-282382, Fax: +46-13-142337, e-mail:peder.bergman@secrc.abb.se

One of the main applications for SiC devices is in high power systems such as voltage source converters, for example in motor drives or HVDC transmission systems. These applications have very high demand on the device regarding high blocking voltage, low switching losses and high current levels. This makes properties such as reliability and long term stability important.

Detailed results regarding performance and reliability of high power SiC diodes have recently been presented [1]. It was reported that some devices exposed to long term operation exhibit an increase of the static forward voltage drop after the testing. In this study we present a material investigation of diodes showing this behavior.

The investigated diodes were made on 35 mm 4H SiC wafers from CREE, cut with an 8 degrees off axis angle. An approximately 30μm thick epi-layer was grown using the hot wall CVD technique with a doping in the low 3 10^{15} cm^{-3}. Using a standard diode process [2] devices were fabricated. However, to ease the X-ray characterization in this work, the anode consisted of a simple p-type epilayer. These diodes were then stress tested in a controlled way reflecting continuos converter operation. The forward voltage drop at 100A/cm^2 was originally in the order of 3.4 V. Some of these diodes showed an increase of the voltage drop in the range of 50-100 mV after testing. The top metal layer was removed on selected diodes and the remaining epitaxial material was studied using synchrotron white beam x-ray topography (SWBXT), cathode luminescence (CL), low temperature photoluminescence (PL) and by optically measuring room temperature minority carrier lifetimes.

The SWBXT showed that crystal defects were created in the epitaxial material on tested diodes. These crystal defects are observed as triangular features and interpreted as stacking faults in the (0001) plane starting at the substrate/epilayer interface and propagating in the $<11\bar{2}0>$ direction towards the surface. Dislocations in the $<01\bar{1}0>$ and $<10\bar{1}0>$ directions bound the stacking faults. These defects are directly correlated to similar optical features observed in cathode luminescence at low temperatures, showing dark triangular shaped regions with reduced emission efficiency, in the area of the stressed diodes that did show increased forward voltage.

Optical measurements of the minority carrier lifetime revealed a local reduction, from about 400ns to below 200ns, in the regions of stressed diodes. Spatially high-resolution measurements showed further a correlation between the measured lifetime and the triangular shaped features observed in CL or SWBXT mapping measurements. This indicates that the created crystals defects, or defects connected to these, are electrically and optically active. The electrically observed increase in forward voltage drop in these diodes can be related to the reduction of minority carrier lifetime.

1) H. Lendenmann, F. Dahlquist, N. Johansson, J.P. Bergman, H. Bleichner, and C. Ovren, Invited Talk at 1st int. Workshop on Ultra-low-Loss Power Device technology, Nara Japan, 31 May - 2 June, 2000.

2) K. Rottner, et. al, "SiC power devices for high voltage applications," *ECSCRM (1998).*

Mo3-5

Micropipe closing via thick 4H-SiC epitaxial growth involving structural transformation of screw dislocations

I. Kamata, H. Tsuchida, T. Jikimoto and K. Izumi
Yokosuka Research Laboratory, Central Research Institute of Electric Power Industry
2-6-1 Nagasaka, Yokosuka, Kanagawa 240-0196, Japan. Phone: +81 468 56 2121, Fax:+81468 56 3540

The micropipe is a type of screw dislocation with a hollow core which penetrates a SiC (0001) substrate from the front to back surface along the [0001] axis. If screw dislocations including micropipes exist in substrate, they will propagate to the epitaxially grown surface. Current commercial 4H-SiC wafers contain micropipes in density in the order of 10^1 to 10^2 cm^{-2}. This high micropipe density restricts device area enlargement, because the device will suffer destructive damage if a single micropipe is present in the device area.

Micropipe closing through LPE has been reported recently [1, 2], however, it is not yet clearly understood how micropipe closing takes place. In this paper, we report on micropipe closing involving structural transformation of screw dislocations.

Molten KOH treatment was carried out on epilayers and substrates for defect etching, at temperature and duration of 480°C and 1 minute, respectively. Epitaxial growth was carried out on 8° off 4H-SiC (0001) substrates in a radiant-heating reactor [3].

Fig.1 shows the grown surface after KOH treatment. Seven hexagonal etch pits round in shape were observed aligned along the [11$\bar{2}$0] direction. Due to their similarity in size to other etch pits on the surface, they were identified as elementary screw dislocations. Fig.2 shows a KOH treated surface after the entire epilayer has been completely removed by abrading. The micrograph was taken from the same place as in Fig.1, and the dark hexagonal etch pit in Fig.2 indicates that a micropipe existed in the substrate at that location. This suggests that the micropipe was closed in the epilayer, with seven elementary screw dislocations appearing on the epilayer surface.

A screw component of the micropipe has Burgers vectors $b \geq 3c$ for 4H-SiC, where c is the lattice parameter along the [0001] axis. On the other hand, an elementary screw dislocation has $b = 1c$ with no hollow core. Thus our KOH analysis suggested that the micropipe was transformed into seven of the elementary screw dislocations during epitaxial growth, where the magnitude of Burgers vectors of the micropipe was divided into several $1c$ of the elementary screw dislocations.

To understand when micropipe closing takes place, repetition of cycle; abrading of a certain thickness, KOH treatment and pit evaluation were carried out as a depth analysis. From this analysis, a relationship were confirmed between the ratio of closing micropipes and layer thickness. It may be note that the ratio significantly increased from the interface to a few μm in thickness, whereas above a few μm to the surface of the 37 μm-thick-layer, it showed no marked increase. It appeared that the majority of micropipe closing took place near the interface. This suggested that most of the structural transformations occurred at the early stage of epitaxial growth.

We investigated over 150 micropipes in this experiment. Approximately 1/3 of the micropipes were closed via epitaxial growth.

[1] R. Yakimova *et .al.* Inst. Phys. Conf. Ser. **142** (1996) 101
[2] S. Rendakova *et .al.* J. Electron Mater. **27** (1998) 292
[3] H. Tsuchida *et .al. in Proc. Int. Conf. Silicon Carbide and Related Materials, NC, USA, Oct. 10-15,* 1999

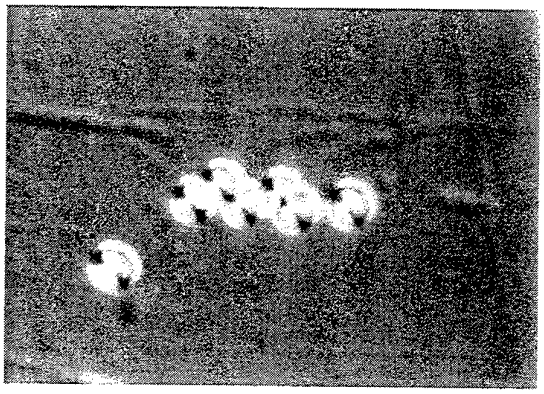


Fig.1. Micrograph of a grown surface after a KOH treatment.

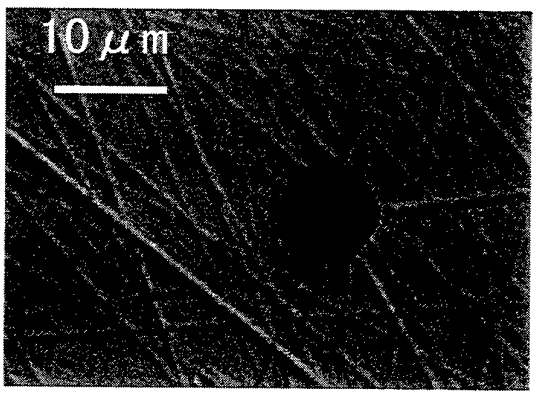


Fig.2. Micrograph of a KOH treated surface after the epilayer has been completely removed.

Self diffusion in SiC: the role of intrinsic point defects

Alexander Mattausch, Michel Bockstedte, and Oleg Pankratov
Lst. theor. Festkörperphysik, Universität Erlangen-Nürnberg,
Staudtstr. 7B2, D-91058 Erlangen, Germany

In recent experiments [1,2] evidence for transient enhanced diffusion of boron and aluminium impurities in SiC was found. It is known that mobile intrinsic defects such as interstitials and vacancies play a pivotal role in the diffusion of dopant atoms. At the same time they are responsible for self diffusion. The development of a microscopic picture of mobile intrinsic point defects and their migration mechanisms is a key to understanding both self diffusion as well as dopant diffusion. The aim of the present work is to develop such a picture for 3C-SiC from first principles theory. In a first step we employed first principles calculations based on density functional theory to investigate the energetics of the defect formation and defect reactions [4]. Here we present results of the second step, which is the analysis of the defect migration.

We show that carbon vacancies [3] and silicon interstitials [4] in both p-type and intrinsic material are the most abundant mobile defects. Silicon interstitials can migrate between tetrahedral carbon-coordinated sites (which are energetically preferred) via split-interstitials (two Si atoms sharing a lattice site) or via silicon-coordinated sites as intermediate configurations. For a carbon vacancy we exclude a migration via nearest neighbour hops, since the first intermediate state of the ring mechanism, the silicon vacancy-antisite complex, has been found unstable in all possible charge states. Hence we propose a vacancy migration mechanism based on second nearest-neighbour hops. It proceeds only on the carbon sublattice, in p-type and intrinsic material with an energy barrier of 5 eV. We have also analysed the migration of carbon atoms between split interstitial sites with (100)-orientation. For the migration of carbon interstitials these are the relevant and energetically lowest configurations, which consist of a carbon and a lattice atom forming a dumb bell oriented in the (100)-direction. The silicon vacancy can transform into a carbon-antisite-vacancy complex by a hop of a carbon neighbour. In p-type and intrinsic material this process has a small barrier ($\sim$ 1.6 eV) and is accompanied by a large energy gain. This behaviour is explained by the large difference of the formation energies for carbon and silicon vacancies. For n-type material, however, the energy difference between the silicon vacancy and the carbon-antisite-vacancy-complex becomes negligible and the barrier for the transformation increases above the barrier for the second nearest neighbour hop. Our calculation suggests that silicon self diffusion is dominantly based on an interstitial mechanism in p-type and intrinsic material and on vacancy migration in n-type material. We discuss the relevant mechanisms and the Fermi-level dependence of self diffusion.

[1] M. Laube *et al*, Appl. Phys. Lett. **74**, 2292 (1999)
[2] I. O. Usov *et al*, J. Appl. Phys. **86**, 6039 (1999).
[3] A. Zywietz *et al.*, Phys. Rev. B **59**, 15166 (1999).
[4] M. Bockstedte and O. Pankratov, Mater. Sci. Forum, in print

MoP-2

Intrinsic defect complexes in α-SiC

E. Rauls[1], Z. Hajnal[1,2], P. Deák[3], Th. Frauenheim[1]

[1] *Universität Paderborn, Fachbereich Physik, Theoretische Physik, Warburger Str. 100, 33100 Paderborn, Germany*

phone: +49-5251-602378, fax: +49-5251-603435, e-mail: rauls@phys.upb.de

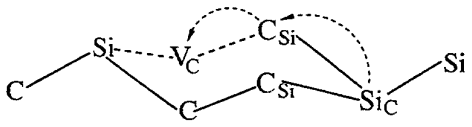
[2] *MTA Research Institute for Technical Physics and Materials Science,P.O.B. 49, H-1525 Budapest, Hungary*

[3] *Dept. of Atomic Physics, TU Budapest,Budafoki út 8, H-1111 Budapest, Hungary*

Properties of isolated intrinsic defects in SiC are widely studied and their atomic and electronic structure is already known. Although further experimental evidence shows the presence of defect complexes, only a few of them could be clearly identified up to now. In binary semiconductors antisite pairs play a special role. Although in SiC this is expected to be a defect with high formation energy, it is likely to be created during irradiation, or non–equilibrium growth. The properties and role of these defects in diffusion, in growth as well as their interaction with other defects deserves consideration. Therefore, we describe now the atomic structure and properties of selected vacancy–antisite complexes calculated within a selfconsistent charge density functional based tight binding scheme (*SCC-DFTB*).

We have investigated the formation of antisites in the perfect lattice first. The concerted exchange mechanism which is the lowest energy path for self diffusion in elemental semiconductors has too high a barrier for formation in a thermally activated process, and we have not yet been able to find any other path with lower energy. The net formation energy of the antisite pair is 5 eV. On the other hand the formation energy can be substantially lowered in the presence of other intrinsic defects.

According to our former results [*E. Rauls et al., phys. stat. sol. (b), 217/2, R1 (2000)*] the silicon vacancy diffuses with a low energy barrier into the more stable V_C-C_{Si} complex. Thus, we next examined this complex in combination with an antisite pair: V_C-C_{Si} + Si_C-C_{Si}. This structure (see figure) is stoichiometrically equivalent to a single V_{Si}, but it does not reconstruct spontaneously into it.



We find that by a simultaneous movement of the Si_C-C_{Si} pair (marked in the figure with the dashed arrows) ≈2.7 eV are necessary to activate the reaction V_C-C_{Si} + Si_C-C_{Si} ⟶ V_C-C_{Si} *(1)* and 3.5 eV to activate V_C-C_{Si} ⟶ V_{Si} *(2)* (the latter is also an endothermic reaction by 1.7 eV). The reverse of reaction *(1)* on the same route requires an activation energy of 4.8 eV. This means that the formation energy is a lot less than in the perfect lattice. However the activation energy for formation is still too high for the usual heat treatment processes (further work to check other routes is still in progress), so is the activation energy for recombination.

We have also found that the total energy of a V_C-C_{Si} + Si_C-C_{Si} complex is 3 eV less than that of V_C-C_{Si} and Si_C-C_{Si} far apart from each other. This means, that if antisite pairs are created, e.g. by irradiation, they will aggregate to V_C-C_{Si} defects. The properties of these defects, as well as the segregation of antisites is under study.

Intrinsic Defects in 6H-SiC generated by Electron Irradiation at the Silicon Displacement Threshold

H.J.von Bardeleben, J.L.Cantin, P.Baranov*, E.N. Mokhov *
Groupe de Physique des Solides, Universités Paris 6&7, 2 place Jussieu, 75005Paris
***A.F.Ioffe Physico-Technical Institute, St.Petersburg, Russia**

e-mail : vonbarde@gps.jussieu.fr

Electron irradiation in the MeV energy range allows to generate primary Frenkel pairs in the carbon and silicon sublattices as well as divacancy centres, which can be studied by the electron paramagnetic resosnce (EPR) technique. The stability of the primary defects will depend on various parameters such as the irradiation temperature and conditions, annealing steps and the initial doping of the crystals. The previously published EPR results[1-6] for high energy electron irradiations –typically 2MeV- have revealed a complex situation, which seems to indicate defect interactions.

We have focussed our interest on the vacancy defects generated by low energy electron irradiation: assuming an identical displacement energy of ~23eV for carbon and silicon atoms the minimum electron energies for the displacement of a carbon or silicon atom are ~100keV and ~300keV respectively. We have irradiated a series of n- and p-type doped 6H-SiC monocrystals with electrons of 300keV. At this energy carbon vacancies and interstitials and silicon close Frenkel pairs are the expected primary defects. The defects have been analysed by X-band electron paramagnetic resonace spectroscopy.

In p-type Al doped samples we observe two dominant EPR spectra after typical electron doses of $1x10^{18}cm^{-2}$. The first spectrum can be attributed from its spin Hamiltoian parameters to the positively charged carbon vacancy ; this defect has been already reported before[5,6]. The spectrum can be observed in the whole temperature range from 4K to 300K. The second spectrum is characterised by the following spin Hamiltonian parameters S=3/2, $g_{//}$=2.0032,g=2.0028,D=$68.7x10^{-4}cm^{-1}$; it shows superhyperfine interaction with 4 nonequivalent NN carbon and 12 nonequivalent NNN silicon atoms. The hyperfine structure demonstrates that the defect is a silicon vacancy related complex. We tentatively attribute this centre in agreemnt with the special irradiation conditions required to a negatively charged V_{Si}-Si Frenkel pair defect oriented parallel to the c axis.

In n-type N doped samples we donot observe the previous two vacancy defects. Instead we observe one dominant and different EPR spectrum with axial symmetry S=1/2, g values of $g_{//}$=2.00026, $g_{\perp}$=2.0029. The particularity of this spectrum is the absence of a central NN hyperfine spectrum and the only observation of Si SHF interaction doublets. To further investigate the defect model additonal information obtained from electron irradiated ^{13}C enriched samples will be presented.

1.L.A.Balona et al, J.Phys.C : Sol.State Phys.3,2344(1970)
2.T.Wimbauer et al, Phys.Rev.B56,7384(1997)
3.N.T.Son et al, Physica B273,655(1999)
4.E.Sörman et al , Phys.RevB, to be published (2000)
5.N.T.Son et al, Mat.Science Eng.B61,202(1999)
6.D.Cha et al , Mat.Sci.Forum 264-268,615(1998)

MoP-4

EPR Study of Proton Implantation Induced Intrinsic Defects in 6H- and 4H-SiC

H.J.von Bardeleben, J.L.Cantin,
Groupe de Physique des Solides,
Universités Paris 6&7,
2 place Jussieu, 75005Paris

e-mail : vonbarde@gps.jussieu.fr

Ion implantation and in particular proton implantation are important subjects for SiC based microelectronic applications. The implantation process will in addition to the doping introduce lattice defects due to elastic collisions between the high energy ions and the lattice atoms. The nature of the implantation related lattice defects and their annealing behaviour have been studied for many years but a definite picture of their microscopic structure has not yet been achieved[1].

One major difficulty in the analysis of the ion implanatation induced defects is their inhomogenous distribution over the ion track. Whereas in the first part the implanted ions will loose most of their energy by electronic excitations the energy loss in the end of range is due to collisions with lattice atoms. Thus the nature and concentration of defect will be different in the two ranges, called the trace region and end of range.

We have focussed our interest in this study on the defects introduced in the trace region. To do so we have used high energy (12MeV) proton implantation with a projected range of ~700μm, such that the protons will completely cross the 300μm thick samples. The samples were purchased from Cree Research. The defects have been analysed by X-band electron paramagnetic resonance spectroscopy.

In n-type nitrogen doped samples we observe under thermal equilibrium conditions three dominant EPR spectra, which have been reported previously. They can be attributed from their Spin Hamiltonian parameters to the negatively charged isolated Si monovacancy[4] and the neutral Si vacancy on the hexagonal and quasicubic lattice sites[5]. For proton irradiation doses between $1x10^{16}cm^{-2}$ and $8x10^{16}cm^{-2}$ the concentration of both defects increases linearly with proton dose. Their total introduction rate is $19cm^{-1}$; this rate is only 4% of what is expected from SRIM calculations. Such a low value indicates room temperature Si vacancy annihilation processes. No carbon vacancy related defect is observed. We will show, that the low thermal stability of the Si vacancy in irradiated SiC is not incompatible with the properties iof the Z1/Z2 centre[1], and we tentatively attribute this centre to the neutral Si monovacancy.

Additional results obtained in p-type Al doped material will be reported.

Acknowledgments : we thank L.Henry and M.F.Barthe from CERI (Orléans) for the proton irradiations

1.T.Dalibor et al, Inst.Phys.Conf.Ser.142,517(1996)
2.V.Heera et al, Mat.Res.Soc.Symp.Proc.438,241(1997)
3. A.Hallen et al, Mat.Science and Eng.B61,378(1999)
4. T.Wimbauer et al, Phys.Rev.B56,7384(1997)
5. N.T.Son et al, Phys.Rev.B to be published (2000)

Zeeman effect of D_1 bound exciton in 4H-SiC and 3C-SiC

C. Q. Chen[1], R. Helbig[1], R. Winkler[2], A. Wysmolek[3], M. Potemski[3]

[1] Institute of Applied Physics, University of Erlangen-Nürnberg, Staudtstrasse 7, 91058 Erlangen, Germany
[2] Institute of Technical Physics III, University of Erlangen-Nürnberg, Staudtstrasse 7, 91058 Erlangen, Germany
[3] High Magnetic Field Laboratory, CNRS/MPI-FKF, BP 166, 38042 Grenoble Cedex 9, France

The D_1 defect is the best known persistent defect in SiC which can not be removed by thermal annealing process even up to 1700°C. It has been observed in 3C, 4H, 6H and 15R SiC polytypes after ion implantation or after irradiation with high energy electrons or neutrons. It can be expected that the D_1 defect is an intrinsic defect since it does not depend on any specific impurities. The D_1 bound exciton exhibits an extremely effective recombination luminescence, which dominates the low temperature photoluminescence (PL) spectrum. In 4H-SiC, there is one no-phonon D_1 PL line L at low temperature although there exists two inequivalent substitution lattice sites. If the temperature is raised, two higher energy no-phonon lines M and H appear. At sufficiently high temperatures the D_1 PL lines are quenched. The large exciton binding energy E_{BX} and the existence of different forms of PL lines for low and high temperatures suggest that these lines are due to an exciton bound to an isoelectronic center by short-range forces.

In this work, an extensive experimental study of the Zeeman effect of the D_1 bound exciton in 4H-SiC was performed in magnetic fields of B up to 23 T. The measurements were carried out in four different configurations at different temperatures. Based on thermalization behavior, we deduce that the Zeeman splitting of the D_1 PL lines originates from the initial states of the luminescence process. There is no magnetic splitting in the final states in all four configurations. This supports that the D_1 defect is an isoelectronic center. Furthermore, the electronic fine structure of the D_1 bound exciton is obtained from magnetic splitting. Besides the L, M and H levels, there exists also three exciton L_H, L_L and N levels. The L_H and L_L levels result from the zero-field splitting of the L level with an energy interval of $\pm$ 0.35 meV. The N level is approximately 0.5 meV above the M level. The M and H levels remain unsplit in the magnetic field. The Zeeman splitting of the others four levels are strongly anisotropic and polarization dependent. In addition, the Zeeman effect of the D_1 bound exciton in 3C-SiC has also been measured. Similar to 4H-SiC, the L, M and H lines in 3C-SiC dominate at different temperatures. In the magnetic field, the H line remains unsplit while the M and L lines exhibit a very complicated splitting behavior. The energies of the Zeeman components are found to be independent of the direction of B, however, their intensity distributions are anisotropic. We will interpret our experimental results by means of a detailed symmetry analysis for the D_1 bound exciton.

MoP-6

Neutron Irradiation of 4H SiC

F. H. C. Carlsson[1], L. Storasta[1], J. P. Bergman[1], K. Sköld[2] and E. Janzén[1]

[1]Dept. of Physics and Measurement Technology, Linköping University,
S-581 83 Linköping, Sweden, Tel. +46 13 28 57 16, Fax +46 13 14 23 37, e-mail: freca@ifm.liu.se

[2]Inst. for Neutron Research, Uppsala University,
S-611 82 Nyköping, Sweden, Tel. +46 155 22 18 49, Fax +46 155 26 30 01

Neutron irradiation is of interest for different reasons. The irradiation produces intrinsic defects which are useful for fundamental studies. It is also a way to obtain homogenous doping, which is important in materials intended for high power devices, such as SiC. The Neutron Transmutation Doping (NTD) is an established technique in Si technology. In NTD thermal neutrons, produced in a fission reactor, is absorbed by ^{30}Si which is transmutated into ^{31}P creating a donor. The reactor also produce fast neutrons which have higher energy. The fast neutrons are believed to cause most of the damage.

In this work we have studied the effects of neutron irradiation on 4H SiC. The irradiation were performed at the research reactor in Studsvik where different fluences and ratios of fast and thermal neutrons were produced. After the neutron irradiation annealing were performed at temperatures from 500 °C to 2000 °C. Samples were characterized by the use of optical methods such as Photoluminescence (PL), Time Resolved PL (TR-PL) and Fourier Transform Infra-Red spectroscopy (FT-IR). Electrical measurements for characterization includes Deep Level Transient Spectroscopy (DLTS), Admittance Spectroscopy, IV, CV and Photo Induced Current Transient Spectroscopy (PICTS).

4H SiC samples were irradiated at Studsvik to create phosphorus doping from $5 \cdot 10^{14}$ cm^{-3} to $5 \cdot 10^{15}$ cm^{-3}. After irradiation the originally dominating emission from nitrogen bound excitons and the free exciton in PL disappears completely. In samples where the fluence of fast neutrons has been minimized, several previously well investigated lines from 4260 Å - 4420 Å, the E_A spectra [1], related to intrinsic defects may be seen.

When the samples are annealed in the temperature range of 1000 °C to 1400 °C, new and to our knowledge previously not reported lines in the 3960 Å - 4270 Å range appear in the spectrum. These lines shows similar behavior to intrinsic lines such as D_1 [2] and the previously mentioned E_A lines. The lifetimes are long as can be expected for an exciton bound to an isoelectronic defect [2]. The lines quenches at temperatures above 100 K. After high temperature annealing, above 1500 °C, all PL spectra is dominated by the intrinsic defect D_1. The bandedge luminescence from nitrogen bound excitons and free exciton returns but is much weaker than originally.

After high temperature annealing and under some irradiation conditions a weak PL emission at 3.256 eV that we attribute to phosphorus is observed. To our knowledge there has been no previous report of PL emission related to phosphorus in 4H-SiC. This emission is not seen in as-grown material or in material implanted with Al or B and annealed at the same temperatures. We can however se the same emission in phosphorus implanted material after annealing. The position of this line is between the two nitrogen bound excitons, which is similar to the observation of phosphorus in 6H SiC.

[1] T. Egilsson, A. Henry, I.G. Ivanov, J.L. Lindström and E. Janzén, Phys. Rev. B **59**, 8008 (1999)
[2] T. Egilsson, J.P. Bergman, I.G. Ivanov, A. Henry and E. Janzén, Phys. Rev. B **59**, 1956 (1999)

EPR study of carbon vacancy-related defects in electron-irradiated 6H-SiC

V.Ya.Bratus'[1], I.N.Makeeva[1], S.M.Okulov[1], T.L.Petrenko[1], T.T.Petrenko[1], H.J. von Bardeleben[2]
[1]Institute of Semiconductor Physics, National Academy of Sciences of Ukraine, Prospect Nauky 45, Kyiv 03028 Ukraine
Tel.: 38 044 265 8560 Fax : 38 044 265 8342 E-mail : endor@div51.semicond.kiev.ua
[2]Groupe de Physique des Solids, Universite Paris 6&7, Unite associee au CNRS 2, place Jussieu, F-75251 Paris Cedex 05 France
Tel.: 44 27 4685 Fax : 43 54 2878 E-mail : vonbarde@gps.jussieu.fr

During the past decade much information has been gathered with EPR, ENDOR and optically detected EPR about negatively charged silicon vacancy (V_{Si}^{-}) and related defects in different polytypes of SiC. The nature of the other simplest intrinsic defects has not been as intensively studied. Some EPR spectra have been assigned to a single carbon vacancy (V_C) and V_C-related defects in 3C-SiC [1] and recently in 4H- and 6H-SiC [2,3]. The observation of new EPR spectra on electron-irradiated *p*-type 6H-SiC samples is presented in this report. The spectra are tentatively identified as arising from a neutral boron-carbon vacancy (B_{Si}-V_C) complex and V_C^{+}.

The high quality *p*-type Lely-grown crystals of 6H-SiC with boron content about $4\cdot10^{17}$ cm^{-3} have been irradiated with 2.0 MeV electrons up to dose of $1\cdot10^{18}$ cm^{-2}. Most of the EPR measurements have been performed at 77K at X- and K-band in $(11\bar{2}0)$ and $(1\bar{1}00)$ planes of the crystals.

Apart from an intense central group of lines in a g-value range of 2.0015 – 2.0050 several hyperfine (hf) satellites are observed with the strongest splitting of about 150 G at $B \| c$ and 77K. The spectra can be described as arising from two defects in various inequivalent lattice sites, with spin S=1/2 and close principal values of g-tensor. For example, a spectrum assigned to hexagonal site of (B_{Si}-V_C) complex is axially symmetric with $g_{\|}$=2.0030, $g_{\perp}$=2.0047 and hf coupling parameters a=108.8·10^{-4} cm^{-1} and b=14.2·10^{-4} cm^{-1}, the symmetry axes of g-tensor and hf-tensor coincide with *c*-axis of a crystal. The intensity of hf satellites relative to the central part of this spectrum is about 4%, giving evidence that it arises from an isolated vacancy or vacancy-related defect at a carbon site.

Thermally activated reorientation from one inequivalent site to another causes broadening and narrowing effects on the EPR spectra in the temperature range 77 – 300K. A reduction of hf splittings up to 12% is observed in this range for both centers.

Detailed models for the defects are analyzed based on the results of *ab initio* calculations of the structure and hf coupling parameters for carbon vacancy in various charge states and (B_{Si}-V_C) complex. The resemblance of the defect features with those of the appropriate silicon vacancies in Si is discussed.

This work was partially supported by INTAS 97-2141 grant.

1. H.Itoh, M.Yosikawa et al. J. Electr. Mater. **21** (1992) 707.
2. D.Cha, H.Itoh et al. Mater. Sci. Forum **264-268** (1998) 615.
3. N.T.Son, W.M.Chen et al. Mater. Sci. Engin. **B61-62** (1999) 202.

MoP-8

Proton irradiation induced defects in 4H-SiC

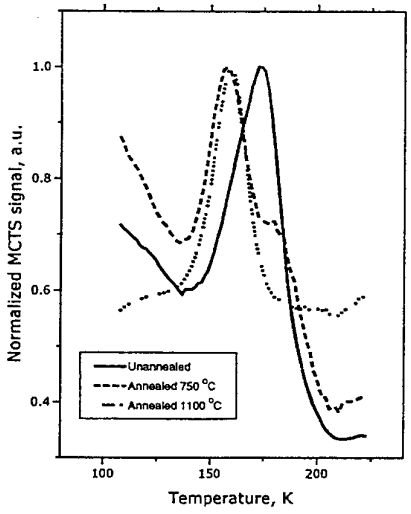
L.Storasta[1], F.H.C.Carlsson[1], S.G.Sridhara[1], D.Åberg[2], J.P.Bergman[1], A.Hallén[2], E.Janzén[1]

[1]Dept. of Physics and Measurement Technology, Linköping University
S-581 83 Linköping, Sweden, Tel. +46 13 288968, Fax +46 13 142337, e-mail: liutauras.storasta@ifm.liu.se

[2]Royal Institute of Technology, Department of Electronics, Solid State Electronics
Electrum 229, S-164 40 Kista – Stockholm, Sweden, Tel. +46 8 752 1125, Fax +46 8 752 7782

Proton irradiation is a convenient way to create intrinsic defects, because of good control of defects created and possible modelling. In this study proton irradiation with different doses was performed, and samples were characterised using electrical measurement techniques – I-V, C-V, Deep Level Transient Spectroscopy (DLTS) and Minority Carrier Transient Spectroscopy (MCTS), as well as optically by Photoluminescence (PL). Annealing behaviour of the introduced defects was studied by annealing the samples at 750 °C and 1100 °C.

4H-SiC 20 μm thick epilayer grown by hot wall CVD technique was irradiated by 2.9 MeV protons at room temperature with doses ranging from $1 \cdot 10^{11}$ to $3 \cdot 10^{13}$ cm^{-2}. Damage profile was flat with a peak located at 60 μm, therefore vacancies were distributed uniformly in the whole epilayer (20 μm thick). The calculated vacancy concentration (TRIM) in the epilayer was from $2 \cdot 10^{14}$ to $6 \cdot 10^{16}$ cm^{-3}. The nitrogen doping, $3 \cdot 10^{15}$ cm^{-3}, as measured by C-V did not change after irradiation for lightly irradiated samples, while nitrogen donors were partially compensated by the generated intrinsic defects in samples with higher irradiation dose, reducing the effective doping. DLTS and MCTS spectra were recorded in the temperature range of 80-750 K. Due to the low transparency of the Schottky contact metal in the UV range, the MCTS signal only comes from the edge of the contact. This fact makes it difficult to estimate the probed volume, and quantitative values of the defect concentration could not be calculated.



The MCTS spectra of minority carrier traps show peaks at $E_V + 0.35$ and $E_V + 0.44$ eV. The latter peak reduces and disappears with increasing annealing temperature, while the first one increases (see figure). The peak at $E_V + 0.35$ is probably related to the same defect as HH1 trap previously seen in electron irradiated material [1]. A new peak, corresponding to a trap located at $E_V + 0.75$ eV appears in the samples with higher implantation dose after annealing at 1100 °C. DLTS spectra, that show majority carrier traps have strong Z1 peak, which broadens on the low temperature side for unannealed samples, indicating the existence of several closely spaced levels, which are not possible to resolve. Annealing at 1100 °C reduces these and makes the Z1 peak more narrow. Other defect levels located at $E_C - 0.73$, 0.90, 1.1 eV are also observed in DLTS, and their dependence on implantation dose and annealing will be presented. These levels are similar to previously reported peaks in irradiated material[1,2].

1 C. Hemmingsson, N. T. Son, O. Kordina, J. P. Bergman, E. Janzen, J. L. Lindstrom, S. Savage, and N. Nordell, Journal of Applied Physics **81**, 6155-9 (1997).

2 T. Dalibor, G. Pensl, T. Kimoto, H. Matsunami, S. Sridhara, R. P. Devaty, and W. J. Choyke, Diamond and Related Materials **6**, 1333-7 (1997).

Generation and Annihilation of Intrinsic-Related Defect Centers in 4H/6H-SiC

Thomas Frank, Michael Weidner and Gerhard Pensl
Institute of Applied Physics, University of Erlangen-Nürnberg, Staudtstraße 7, D-91058 Erlangen, Germany

Hisayoshi Itoh
Japan Atomic Energy Research Institute, 1233 Watanuki, Takasaki, Gunma 370-1292, Japan

Intrinsic-related defect centers have been generated in n-type 4H/6H-SiC by bombardment with different particles like high-energy electrons (2 MeV), hydrogen (H), helium (He) or ions of heavier masses like neon (Ne) or argon (Ar).

DLTS spectra taken on 4H-SiC subsequent to e^-- irradiation (without annealing) reveal the Z_1/Z_2(4H)-center (energy level: $E(Z_1/Z_2)_{4H} = E_C$-630meV) at a concentration of $2.7 \times 10^{14} cm^{-3}$. Its annihilation process has been studied by isochronal anneals. For that purpose a number of samples has been annealed at a particular temperature T_A (T_A=600°C to 2000°C) for $t_{A,1}$=30min (Fig. 1, solid curve). The decrease of $[Z_1/Z_2]_{4H}$ starts at T_A=1400°C. After a second anneal of the identical samples at identical temperatures T_A for another 60min ($t_{A,2}$=90min) the annihilation process already starts at T_A=900°C (Fig. 1, dashed curve). Assuming first order kinetics, the activation energy ΔE_A for the annihilation process of the Z_1/Z_2(4H)-center is determined from the slope of the curves in Fig.1; it results in ΔE_A=2.1eV.

In 6H-SiC subsequent to the implantation of different ion species, annealing steps have been conducted at 700°C, 800°C, 1000°C, 1400°C and 1700°C. DLTS measurements taken on these samples reveal three prevailing intrinsic defects: E_1/E_2, Z_1/Z_2(6H), and the R-center. In Fig. 2, the annealing behavior of these defects is shown for a He-implanted sample. All three defects appear after anneals between 700°C and 1000°C with their respective concentration maximum at 800°C. Defect center E_1/E_2 survives annealing steps up to at least 1700°C; its concentration decreases with increasing annealing temperature. Z_1/Z_2(6H) appears also at 700°C, however, it disappears already at temperatures around 1400°C. The R-center is formed at annealing temperatures around 700°C, it disappears at elevated temperatures between 800°C and 1000°C. We also systematically conducted annealing steps with samples implanted with heavier ion masses. Anneals at 800°C result in a varying number of DLTS peaks; their generation depends on the particular ion mass. Subsequent to anneals at 1400°C, we again observe that the E_1/E_2-peak is the dominating feature in the DLTS spectra.

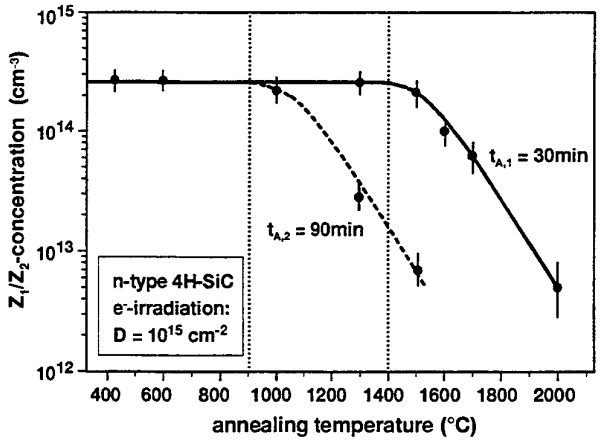


Fig.1: Concentration of Z_1/Z_2(4H) centers $[Z_1/Z_2]_{4H}$ determined in n-type 4H-SiC samples subsequent to isochronal anneals (t_A=30min and 90min).

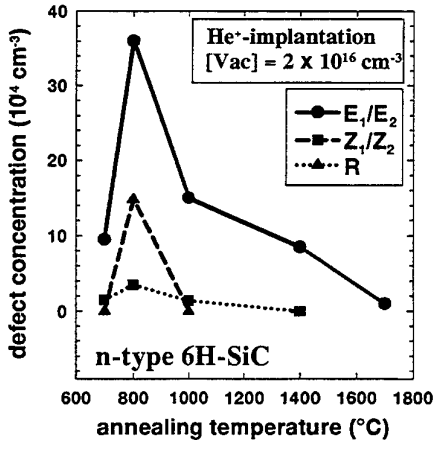


Fig.2: Defect concentration of the prevailing intrinsic-related defects in 6H-SiC as a function of the annealing temperature.

MoP-10

Annealing process of defects in epitaxial SiC induced by He and electron irradiation: Positron annihilation study

A. Kawasuso[A], F. Redmann[A], R. Krause-Rehberg[A], J. Gebauer[A], H. Itho[B], P. Sperr[C], G. Kögel[C], W. Triftshäuser[C], M. Weidner[D], T. Frank[D], G. Pensl[D]

[A]*Fachbereich Physik, Martin-Luther Universität Halle-00Wittenberg, D-06099 Halle, GERMANY*

[B]*Japan Atomic Energy Research Institute, 1233, Watanuki, Takasaki, Gunma 370-1292, JAPAN*

[C]*Universität der Bundeswehr Munchen, D-85577 Neubiberg, GERMANY*

[D]*Institut für Angewandte Universität Erlangen-Nürnberg, Staudstr. 7, D-91058, Erlangen GERMANY*

Ion implantation is an indispensable technique in SiC device process. Thus, it is very important to study properties of defects induced by irradiation. Deep levels in epitaxial SiC induced by fast particle irradiation has been studied with several methods, such as DLTS and photoluminescence (PL). Recently, the relationship between DLTS centers and PL lines in He-implanted 4H and 6H SiC was studied in detail through their annealing behavior [T. Dalibor *et al.* Inst. Phys. Conf. Ser. 142(1996)517, T. Frank *et al.*, to be published]. Optically-detected magnetic resonance (ODMR) measurements was also employed to identify atomic structure of radiation-induced defects [Sörman et al. PRB 61(2000)2613.]. However, species of defects induced by irradiation and their annealing temperature, chemical nature of electronic energy levels in DLTS and PL spectra, are still great open question. In this study, to characterize annealing kinetics of vacancy-type defects in 6H and 4H epitaxial SiC introduced by He and electron irradiation, we performed positron annihilation measurements.

Specimens used in this study were commercially supplied 4H and 6H SiC epilayers with net carrier concentration of 5×10^{15} cm^{-3}. These were subjected to He implantation and 2MeV electron irradiation. In the case He implantation, the implantation was done with several energies from 30 to 950 keV to form box-shaped damage profile. Isochronal annealing was taken place from 100 to 1700°C. Both positron lifetime and Doppler broadening measurements were performed. It was found that concentration of vacancy-type defects drastically decreases up to 1400°C. This result is very similar to that obtained for electron-irradiated bulk SiC[A. Kawasuso, JAP, 80(1996)5639]. We will report detailed annealing process of vacancy type-defects and also correlation with DLTS centers in the conference.

Optical transitions of native and irradiation-induced vacancy defects in 6H-SiC

K. Saarinen, S. Arpiainen, and P. Hautojärvi
Laboratory of Physics, Helsinki University of Technology, 02015 HUT, Finland,
tel. +358 9 451 3111, fax. +358 9 451 3116, e-mail : ksa@fyslab.hut.fi

L. Henry , M.-F. Barthe and C. Corbel
Centre d'Etudes et de Recherches par Irradiation, Centre National de la Recherche Scientifique, 3 rue de la Férollerie Orléans, France

H. J. von Bardeleben and J.L. Cantin
Groupe de Physique des Solides, Universités Paris 6&7, 2 place Jussieu,
75251 Paris Cedex 05, FRANCE

Positron annihilation spectroscopy can be used to identify vacancy defects in bulk semiconductor crystals and epitaxial layers. It yields quantitative information on vacancy concentrations in the range 10^{15} - 10^{20} cm^{-3}. Positron spectroscopy under monochromatic illumination is an efficient method to investigate optical transitions of vacancies in semiconductors [1]. We have now applied this technique to study native and irradiation-induced vacancies in silicon carbide bulk crystals.

Two different optical transitions are observed in both as-grown and irradiated SiC. At photon energies $h\nu > 0.6$ eV average positron lifetime τ_{av} decreases indicating that electrons are ionized from vacancies. At $h\nu > 2.0$ eV τ_{av} increases implying that vacancies convert into a more negative charge state. The concentration of the optically active vacancy increases in electron and proton irradiations. By combining the results of positron lifetime and two-detector Doppler spectroscopy we can associate both optical transitions to Si vacancy or a defect complex involving V_{Si}. The illumination threshold energies suggest that the vacancy defect has ionization levels at about 0.3 - 0.6 eV below the conduction band and 2.0(3) eV above the valence band.

[1] K. Saarinen et al., Phys. Rev. Lett. **70**, 2794 (1993).

MoP-12

Positron annihilation at vacancy type defects in 12 MeV proton implanted 6H-SiC

L. Henry, M.-F. Barthe, C Corbel, P. Desgardin, G. Blondiaux
Centre d'Etudes et de Recherches par Irradiation, Centre National de la Recherche Scientifique, 3A rue
de la Férollerie 45071 Orléans, France
L. Liszkay
KFKI Research Institute for Nuclear and Particle Physics, H-1525 Budapest 114, P.O. Box 49, Hungary
S. Arpiainen, K. Saarinen, P. Hautojärvi
Laboratory of Physics, Helsinki University of Technology, 02150 Espoo, Finland

Proton implantation is used in the Smart Cut* process to fracture a thin semi-conductor layer. In SiC, defects created along the track region of the ions change the electrical properties of the fractured layer. The nature of these defects is still unknown. Positron annihilation is a non destructive technique which can be used to identify vacancy type defects and investigate their charge state in semiconductors.

We use here positron annihilation to study the defects induced by 12 MeV proton implantation (Rp = 650 μm) in bulk nitrogen doped (n_D-n_A= $1.9x10^{17}$ cm^{-3}) Cree 6H-SiC. The proton implantations are performed with the cyclotron of CERI (Orléans-France), at room temperature for different fluences from $4x10^{14}$ up to $8x10^{16}$ cm^{-2}. Positron lifetime and electron momentum distribution (Doppler broadening spectrometry) have been measured with a ^{22}NaCl source as a function of temperature between 10 and 300 K. The lifetime results show the presence of negative ions and vacancy type defects in samples before and after proton implantation. The decomposition of the lifetime spectra shows that the lifetime corresponding to negatively charged vacancy type defects increases slightly with the proton fluence from about 210 ± 10 ps in the as-received state to 225 ± 5 ps for the highest fluences. These values are comparable to those which have been already reported by A. Polity *et al.* [1] for electron irradiated 6H-SiC and which have been associated to the Si-C divacancy. We can conclude that vacancy defects induced along the 12 MeV proton track region appear to have the same nature as those produced by 2 MeV electron irradiation and their concentration increases with proton fluence.

[1] *Defect characterization in electron-irradiated 6H-SiC by positron annihilation*, A. Polity, S. Huth and M. Lausmann, Phys. Rev. B59, 16 (1999), p 10603.

ADVANTAGES OF USING MAGNETO-OPTICAL DETECTION OF EPR TO IDENTIFY RADIATION-INDUCED DEFECTS IN SIC

Th. Lingner, S. Greulich-Weber and J.-M. Spaeth

Department of Physics, University of Paderborn, 33095 Paderborn, Germany
e-mail: lingner@physik.uni-paderborn.de tel.: +49 5251 602749 fax: +49 5251 603247

SiC samples irradiated with neutrons or electrons exhibit a large number of different photoluminescence (PL) and electron paramagnetic resonance (EPR) spectra, but so far only few correlations beween optical and EPR spectra are known. In some cases, as for the neutral silicon vacancy [1], the corresponding PL band has been identified by PL detected EPR. The PL-EPR method though is often limited by intensity problems, as it detects the EPR via a change in the radiative recombination rate and, especially in irradiated samples, numerous competing recombination channels can weaken the PL signal.

Even when the PL is too weak, magnetic circular dichroism of the absorption (MCDA) lines can often be measured at the same energetic position as the PL lines. EPR signals can be detected very sensitively via the MCDA, which directly probes the spin polarization of the ground state [2]. A radiation-induced pair defect (spectra P6a, P6b and P6c) has tentatively been identified by this method to be a C_{Si}-V_C pair at the three inequivalent lattice sites [3].

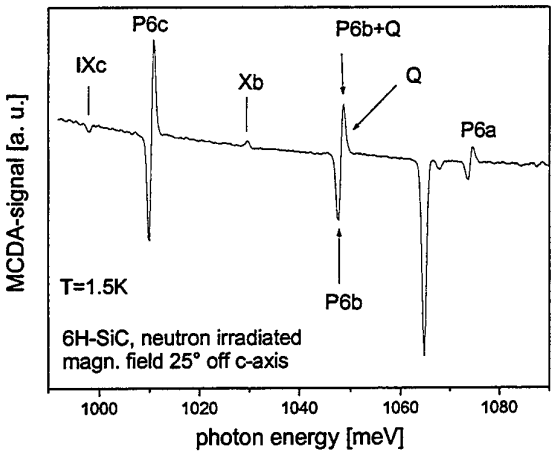


Fig.1: MCDA-spectrum of neutron-irradiated 6H-SiC under additional excitation with visible light.

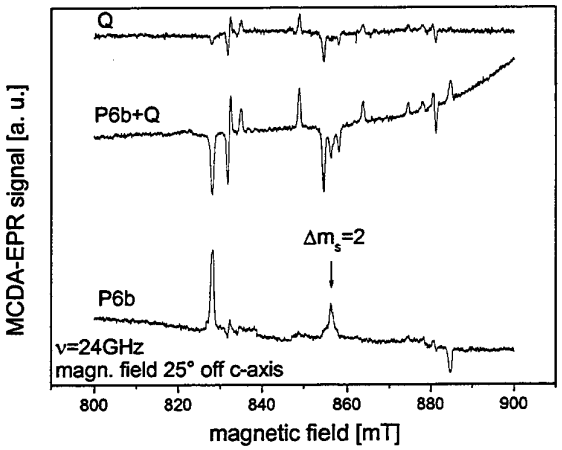


Fig.2: MCDA-EPR spectra measured in different parts of the P6b MCDA-line (indicated by arrows in fig. 1) prove: The P6b line is superimposed by another MCDA line associated with spectrum Q.

Another example for the potential of MCDA-EPR is given in fig. 1. Apart from the P6 spectrum [3], other MCDA-lines are seen in which MCDA-EPR signals were measured. The P6b MCDA line, e. g., is superimposed by another line not resolved in the MCDA-spectrum (fig. 1): MCDA-EPR measurements (fig. 2) show that the P6b EPR-spectrum and an EPR-spectrum labelled Q can be measured separately at different energetic positions within the line.

Recent results from MCDA-EPR measurements are compared with corresponding published EPR and PL spectra in order to correlate EPR and optical data.

References:

[1] E. Sörman et al, Phys. Rev. B 61 (4), 2613 (2000)

[2] J.- M. Spaeth, J. R. Niklas, R. H. Bartram, Structural Analysis of Point Defects in Solids, Springer Heidelberg (1992)

[3] Th. Lingner, S. Greulich-Weber, J.- M. Spaeth, these proceedings

Boron centers in 4H-SiC

B. Aradi[1], A. Gali[1], P. Deák[1], E. Rauls[2], Z. Hajnal[2], Th. Frauenheim[2], and W. J. Choyke[3]

[1]Department of Atomic Physics, Technical Unversity of Budapest, Budafoki út 8, H-1111, Hungary
tel.: [36]-(1)-463 1393, fax: [36]-(1)-463 4357
email: ab007@hszk.bme.hu

[2]Department of Physics, Theoretical Physics, University GH Paderborn, D-33098 Paderborn, Germany

[3]Department of Physics and Astronomy, University of Pittsburgh, Pittsburgh, PA 15260, USA

Abstract The origin of the deep boron center in SiC is subject of lot of controversy. A former ab initio LDA *molecular cluster* calculation showed (A. Gali et al, PRB **60**, 10620 (1999)) that the boron substituted in Si site next to a carbon vacancy complex ($B_{Si} + V_C$), found in ENDOR (A. Duijn-Arnold et al, PRB **57**, 1607 (1998)) is an acceptor and the charge on this acceptor is localized at the carbon site, in accord with PL measurements (H. Kuwabara et al, Phys. Status Solidi A **30**, 739 (1975)).

Now, ab initio LDA *supercell* calculations have been carried out for boron-related complexes to calculate the occupation levels in 4H silicon carbide. It has been found that the 0/- level for the $B_{Si} + V_C$ complex is much higher than E_V+0.63 eV, measured for the deep boron center (S.G. Sridhara et al, J. Appl. Phys. **83**, 7909 (1998)). This results indicates that the $B_{Si} + V_C$ complex can be disregarded as a possible candidate for the microscopic model for the deep boron center. Other feasible boron-related complexes have also been investigated to identify the origin of the deep boron center.

MoP-15

Dissociation energy of the passivating hydrogen-aluminum complex in 4H silicon carbide

M.S. Janson, A. Hallén, M.K. Linnarsson, N. Nordell *, S. Karlsson *, and B.G. Svensson

Royal Institute of Technology, Department of Electronics, P.O. Box E229, S-164 40 Kista-Stockholm, Sweden. Phone: +46 8 752 11 20, Fax: +46 8 752 77 82

* Royal Institute of Technology, Semiconductor laboratory, P.O. Box E229, S-164 40 Kista, Sweden.

It is a well known fact that hydrogen (H) has the capability to electrically passivate doping atoms as well as deeper impurities in silicon and other semiconductors. This feature has recently also been demonstrated in SiC for boron and aluminum (Al)[1,2], but no quantitative data has so far been presented. In this contribution we focus on the formation and thermal stability of the hydrogen-Al complex in Al-doped epitaxial 4H-SiC.

An epitaxial 4H-SiC film with a buried moderately doped Al-layer was implanted in the low-doped, near surface region, with 10 keV $^2H^+$ ions to a dose of 1×10^{15} cm^{-2}. The sample was then annealed at 300 °C for 30 min during which a small amount of the implanted ^2H migrated into the buried layer forming a well defined peak of ^2H-Al complexes in the buried layer (FIG.1). The surface layer, including the originally implanted ^2H, was then etched away and the sample was cut into smaller pieces. The smaller samples were then annealed at temperatures and times ranging from 280 to 410 °C, and 15 min to 72 h, respectively. Finally, the redistribution of the ^2H in the Al-layer was registered using secondary ion mass spectrometry (SIMS). ^2H was used instead of ^1H due to the higher sensitivity in the SIMS measurement. Following the kinetics of trap-limited diffusion, the ^2H-profiles are Gaussian shaped (FIG.2) and assuming a one-to-one ^2H-Al complex, the fitted Gaussians provide the dissociation frequency of the complex. The extracted frequencies cover three orders of magnitude and yield a close to perfect fit to an Arrhenius equation with the extracted ^2H-Al complex dissociation energy equal to 1.66 (±0.05) eV.

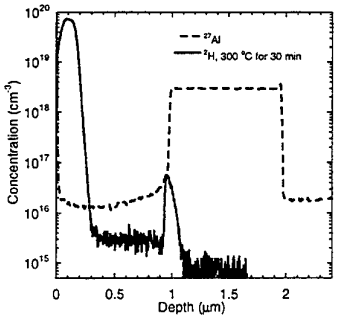


FIG.1. SIMS depth profiles of the ^2H implanted sample annealed at 300 °C for 30 min.

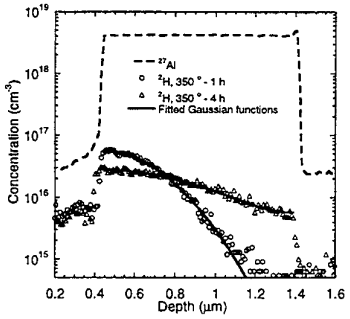


FIG.2. SIMS depth profiles of the sample in FIG.1. after a 0.5 μm etch followed by an anneal at 350 °C for 1 and 4 h, respectively. Gaussian functions are fitted to the profiles within Al layer.

[1]M. K. Linnarsson, M. Janson, A. Schöner, N. Nordell, S. Karlsson, and B. G. Svensson, *International conference on Silicon Carbide, III-nitrides and related materials-1997* (1997).

[2]N. Achtziger, J. Grillenberger, W. Witthuhn, M. K. Linnarsson, M. Janson, and B. G. Svensson, *Appl. Phys. Lett.* **73**, 945-947 (1998).

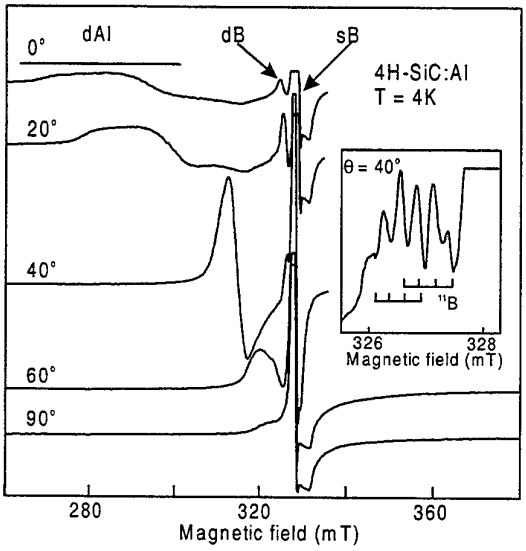
MoP-16

EPR of deep Al and deep B in heavily Al-doped as grown 4H-SiC

I.V. Ilyin, E.N. Mokhov and P.G. Baranov

A.F. Ioffe Physico-Technical Institute, Polytechnicheskaya 26, 194021 St.Petersburg, Russia
phone: +7-812-2479320, fax: +7-812-247-10-17, e-mail: Ivan.Ilyin@pop.ioffe.rssi.ru

We report on the electron paramagnetic resonance (EPR) observation of deep Al in 4H-SiC and the first EPR observation of deep B in as-grown SiC. The group-III acceptor impurities can form deep and shallow levels in SiC bandgap. Up to now deep B in 6H-, 4H- and 3C-SiC as well as deep Al and deep Ga in 6H-SiC were investigated by EPR [1,2]. The EPR of deep B could only be observed in SiC after B diffusion and was not observed in as grown SiC crystals. We have investigated *p*-type 4H-SiC crystals heavily doped with Al ($N_{Al} \approx 10^{19}cm^{-3}$).



The figure shows EPR spectra recorded for several orientations in 4H-SiC:Al crystal at 4K under rotation in $\{11\bar{2}0\}$ plane. In orientation $B \parallel c$ (0°) one can see three distinct EPR signals. One is marked as dAl (deep Al). It has angular dependence very close to that observed for deep Al centers in 6H-SIC [1]. Symmetry of this center is almost axial along the *c*-axis and the signal can be characterized with electron spin $S = 1/2$ and the following *g*-factors, which are strongly temperature dependent: $g_{\parallel}$=2.35; 2.23±0.05 at 4K; 2.11±0.02 at 9K, 2.09±0.02 at 20K and 2.06±0.02 at 45K; $g_{\perp} \approx 2$ for all temperatures. In $B \parallel c$ two lines could be seen for dAl signal at 4K. They appear due to the presence of Al impurity in two crystallographically non-equivalent *h* and *k* lattice sites. Temperature dependence of this signal is qualitatively the same as for deep Al in 6H-SIC. When the temperature is raised, the signal shifts to higher magnetic fields (*g*-factor lowers) and its intensity decreases. But while deep Al in 6H-SiC almost disappears at 9K, in 4H-SIC it can be observed up to 70K. Since the *g*-factors, angular and temperature dependence of this signal are very close to that of deep Al in 6H-SIC, we ascribe it to deep Al acceptor centers in 4H-SIC.

The line marked as sB arises due shallow B centers. B is a common trace impurity in *p*-type SiC. The signal named in figure as dB (deep B) can be seen at the left of shallow boron (sB) EPR line. It's angular and temperature dependence is completely the same as of deep B signals that was found earlier in 4H-SIC after B diffusion [2]. The inset in the figure shows this signal for orientation θ = 40° in which the characteristic hyperfine structure due to ^{11}B nuclear spin ($I = 3/2$) is well resolved. Thus we can conclude that this signal belongs to deep B centers. We believe that deep Al has the same structure as other deep acceptor centers in SiC [2]: a complex of an impurity in Si site next to carbon vacancy. The center is oriented along *c*-axis for all crystallographical positions.

1. P.G. Baranov, I.V. Ilyin and E.N. Mokhov. Solid. St. Comm., **100**, 6, 371-376 (1996).
2. P.G. Baranov, I.V. Ilyin and E.N. Mokhov. Phys. Solid State, **39**, 1, 52-57 (1997).

Quantitative modeling of hydrogen diffusion and reactivation of H-passivated Al-acceptors in SiC

C. Hülsen, N. Achtziger, J.Herold, W. Witthuhn

Institut für Festkörperphysik, Universität Jena, Max-Wien-Platz 1, 07743 Jena Germany
(phone: ++49-3641-947337, fax. ++49-3641-947302, e-mail: huelsen@pinet.uni-jena.de)

Abstract: The thermal stability of the hydrogen passivation of aluminum acceptors in p-type silicon carbid is investigated by annealing experiments. The passivation is done by low energy ion implantation (300eV per atom) to avoid the trapping of hydrogen at implantation defects. Annealing is done under the influence of the electrical field in a reverse biased Schottky diode. The influence of temperature, p-type doping level, and hydrogen isotope (^{1}H or ^{2}H) on the depth profile of passivated acceptors is investigated.

At temperatures around 500K, Al acceptors become reactivated. In the electrical field, released hydrogen is moving as a positive ion to greater depth and is able to passivate further acceptors. Without electrical field, the effect is reversible [1]. In a recent publication, we determined the thermal activation energy of the reactivation process to be about 1.8eV [2]. Regarding diffusion, only effective, i. e. trapped limited diffusion constants are known [3] or data from much higher temperatures [4]. Experimental data for the free diffusion of hydrogen in SiC at temperatures around 500K are not yet reported in the literature.

The reactivation process consists of some independent single processes: the dissociation of the Al-H complex, the free diffusion of hydrogen, the ion drift in the electrical field, and the recombination of free hydrogen with Al acceptors. To get a quantitative description for the whole process, a mathematical model is developed. It consists of two partial differential equations, which describe the time evolution of hydrogen and acceptor concentrations. The numerical solution successfully simulates the experimental data and provides quantitative results for the free diffusion constant and the dissociation rate. By studying their dependence on temperature, both the diffusion energy and the dissociation energy will be derived.

This work, for the fist time, provides quantitative diffusion data on free hydrogen in SiC at rather low temperatures around 500K. The mathematical model describes the reactivation of H-passivated Al-acceptors quantitatively and enables detailed predictions of the influence of temperature and electrical field on the process.

[1] N. Achtziger, C. Hülsen, W. Witthuhn, M. K. Linnarsson, M. Janson, B. G. Svensson: phys. stat. sol. (b) 210, p. 395 (1998)
[2] C. Hülsen, N. Achtziger, U. Reislöhner, W. Witthuhn: ICSCRM 1999
[3] M. K. Linnarsson, J. P. Doyle, B. G. Svensson: Mat. Res. Soc. Symp. Proc., Vol. 423, p. 625 (1996)
[4] M. Janson, M. K. Linnarsson, A. Hallén, B. G. Svensson: Mat. Res. Soc. Symp. Proc., Vol. 513, p. 439 (1998)

MoP-18

Investigation of spectroscopic Brewster angle ellipsometry for determination of below band gap uniaxial dielectric function

M. Kildemo and O. Hunderi
Applied Optics/Surface Physics ;
Departement of Physics ; NTNU; 7034 Trondheim ;Norway
Corresponding author : Morten.Kildemo@phys.NTNU.no
Tel. 00 47 73 59 50 91, Fax. 00 47 73 59 34 20

This paper investigates a novel approach for accurate refinement and direct determination of dielectric properties of uniaxial wide band gap materials available in form of a thick transparent double side polished wafer. In particular, the standard Brewster angle condition defined by the p-polarised reflection coefficient $r_{pp}=0$, is reformulated for a uniaxial material, to be a function of both the ordinary component and the difference in dielectric function between ordinary and extra ordinary component $\Delta\varepsilon$. The dielectric difference is determined from the oscillations arising in the ellipsometric recorded intensity from a thick semi transparent wafer. Figure 1 shows the ellipsometric measurements of the Brewster angle, defined by the zero crossing of the measured intensity proportional to $Re(r_{ss}r_{pp}^*)$. The difference in the dielectric function is determined at an incidence angle different from the Brewster angle. The method also requires an approximate knowledge of the oxide overlayer thickness, which we estimate directly from a spectroscopic fit, or from the deviation of the ellipsometric intensity $Im(r_{ss}r_{pp}^*)$ from zero. However, the Brewster angle method appears less sensitive to the overlayer than the spectroscopic fit. The results are thus compared to the spectroscopic fit using an Anisotropic Incoherent Reflection Model in combination with an anisotropic Sellmeier model. A combination of the spectroscopic fit and the Brewster angle method makes it possible to increase the measurement accuracy of the dielectric function of uniaxial wide band gap materials.

The optical crystallography problem related to ellipsometric measurements of off-axis wide band gap uniaxial material wafers, is also briefly discussed.

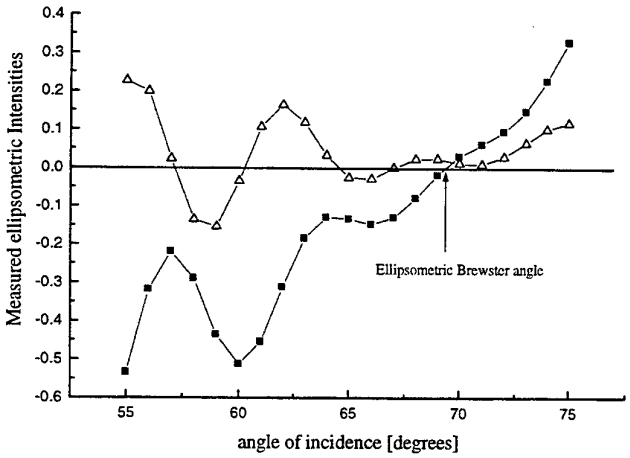


Figure 1. Ellipsometric intensities recorded from a semi-insulating on-axis double polished 4H-SiC, as measured by a phase modulated variable incidence angle spectroscopic ellipsometer. The above measurement corresponds to a photon energy of 2.0 eV.

4H- and 6H-SiC polytype finger print in the Rutherford Back-Scattering spectrometry

R. Nipoti
CNR-Istituto LAMEL, via Gobetti 101, I-40129 Bologna, Italy
phone +39 051 6399147 fax +39 051 6399216

The application of a structural diagnostic technique to the qualitative and quantitative characterisation of processed crystals requires the knowledge of the spectral characteristic figures of the unprocessed material. To our knowledge few are the works that give such figures for the Rutherford Back-Scattering Channeling (RBS-C) spectrometry applied to SiC and all of them concern the 6H-SiC polytype [1-3]. This work gives the characteristic figures for the principal 4H-SiC RBS-C spectra and angular dips, furthermore, a comparison with the 6H-SiC[2] is presented.
Fig. 1 shows the experimental angular dips for the 6H- and the 4H-SiC polytype: they are the transitions from the <0001> axis to the (10-10) and (11-20) planes and the transition from the (10-10) and (11-20) planes to the random alignment. A 2 MeV He^{+} beam at 170° back-scattering angle was used. The 4H- and 6H-SiC polytype have almost equal values for axial minimum yield and planar half-width, they have similar (11-20) minimum yield but quite different (10-10) minimum yield, finally they have individual shoulder shape. In particular, the <0001> to (11-20) transition shows a double peck structure for the 4H-SiC against a single peck structure for the 6H polytype. Taking into account that the dip shape depends on the variation of the ion close encounter probability within a crystal these results help us in understanding the ion channeling penetration within the different 4H- and 6H- SiC crystalline structure.

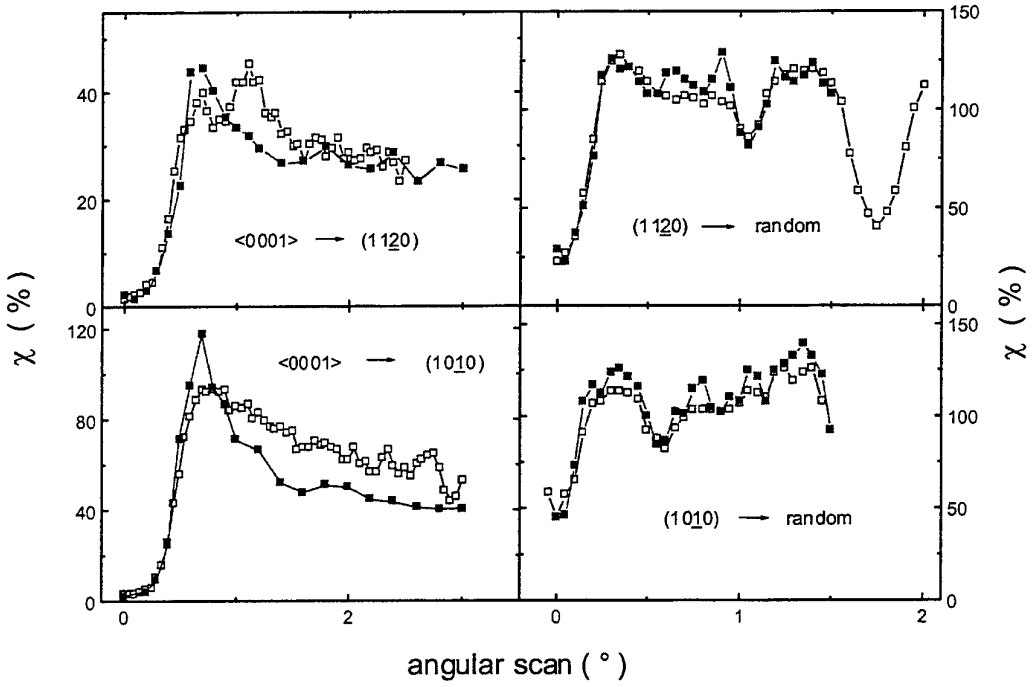


Fig. 1

[1] M. Satoh, K. Okamoto, Y. Iwata, K. Kuriyama, M. Kanaya and N. Othani, Material Science Forum Vols. 264-268 (1998) p.441-444.
[2] M. Bianconi, E. Albertazzi, A. Carnera, G. Lulli, R. Nipoti, A. Sambo, Nucl. Instrum. and Meth. B136-138 (1998) 1267.
[3] R. Nipoti, G. Lulli, M. Bianconi, E. Albertazzi, A. carnera and A. Sambo, 9th CIMTEC – World Forum on New Materials, Symposium II – Surface and Near –Surface Analysis of Materials, P. Vincenzini and S. Valeri Ed.s, Techna Srl (1999), p. 107-114.

A Simple Non-Destructive Technique to Detect Micropipes in Silicon Carbide

D.J. Morrison[1], A. Keir[2], I. H. Preston[2], K.P.Hilton[2], M. J. Uren[2], C. M. Johnson[1], N. G. Wright[1]
[1] Dept. of Electrical and Electronic Engineering, Newcastle University, Newcastle NE1 7RU, UK
Tel:+44 191 222 7345 Fax:+44 191 222 8180
[2] DERA, Great Malvern, Worcestershire, WR14 3PS, UK

The micropipe is recognised as the most detrimental defect in terms of silicon carbides device operation [1]. If a micropipe is present in the active device area, the blocking capability of the device will be severely impaired. Although micropipe densities of less than $0.1cm^{-2}$ have been achieved on research grade material [2], commercially available "standard micropipe density" wafers, still have micropipe densities up to $100cm^{-2}$ [2]. Often these micropipes are not evenly distributed across the wafers, but occur in clusters [3]. When developing a fabrication process, it is obviously useful to know which areas and how much of the wafer are relatively micropipe free before fabricating devices. Previously synchrotron white beam x-ray topography (SWXT) has been used to detect micropipes [4, 5]. Whilst this method has proved to be an effective tool in determining the location of micropipes it is an expensive method and therefore not suitable for day to day wafer quality assessment. Etching SiC in molten KOH is also commonly used to reveal micropipes, but this is a destructive process and so renders the wafer useless for device fabrication.

In this paper we describe a simple, inexpensive and totally non-destructive method to detect the quantity and the distribution of micropipes in SiC wafers. In this technique, a water electrolytic cell is set up and the SiC wafer is attached to the anode [Fig 1]. When a current is passed through the cell, bubbles of H_2 and O_2 gas are released. These bubbles propagate through the micropipe and rise to the waters surface in streams [Fig 2]. This visual effect allows the observer to ascertain the quantity and distribution of micropipes on the wafer. We present photographic evidence of this effect and the distribution of micropipes is verified using optical microscopy and x-ray topography. This technique is ideal for initial macroscopic wafer assessment, before fabrication.

REFERENCES

[1] P.G. Neudeck and J.A. Powell " Performance Limiting Micropipe Defects in SiC Wafers" IEEE Electron Device Letters, Vol. 15, No.2, **1994**, p63
[2] Cree Research Inc, Raleigh Durham, North Carolina, USA
[3] R. Yakimova, T. Yakimov, L. Hitova, E. Janzen "Defect Mapping in 4H-SiC Wafers" Materials Science and Engineering B46 (1997) p287
[4] C. M. Schnabel , M. Tabib-Azar, P.G. Neudeck, S. G. Bailey, H.B. Su, M.Dudley "Correlation of EBIC and SWBXT Imaged Defects and Epilayer Growth Pits in 6H-SiC Schottky Diodes" To be published in Proceedings of International Conference on Silicon Carbide and Related Materials, ICSCRM'99, Research Triangle Park, North Carolina, October **1999**, Abstract No. 224
[5] M. Dudley "Characterisation of SiC Using Synchrotron White Beam X-ray Topography" To be published in Proceedings of International Conference on Silicon Carbide and Related Materials, ICSCRM'99, Research Triangle Park, North Carolina, October **1999*b***, Abstract No. 108

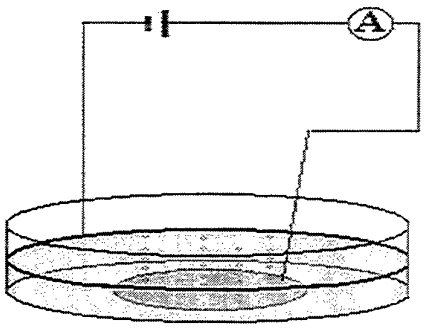


Fig 1: Schematic Diagram of Electrolytic Cell used to Detect Micropipes in SiC wafers

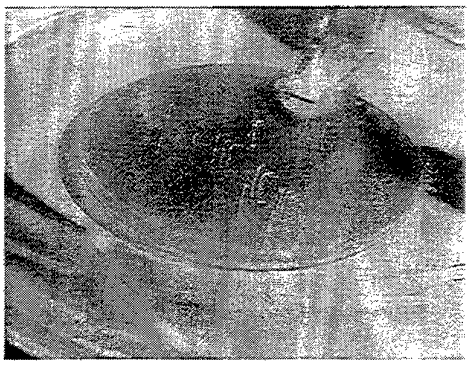


Fig 2: Optical micrograph of p-type 4H-SiC wafer during electrolysis

IMPROVED QUALITY OF MLM – SUBSTRATES BY CVD

J. Dolle, W. Eiserbeck, H.-J. Rost, D. Schulz, D. Siche, G. Wagner, J. Wollweber

Institute of Crystal Growth, Max-Born-Straße 2, D-12489 Berlin, Germany

Phone: +49 30 6392 2846 Fax: +49 30 6392 3003 e-mail: wagner@ikz-berlin.de

It is known, that low temperature growth methods like Liquid Phase Epitaxy may reduce micropipe density [1] for device application. CVD at lower temperature was used to improve the substrate for high temperature CVD [2].

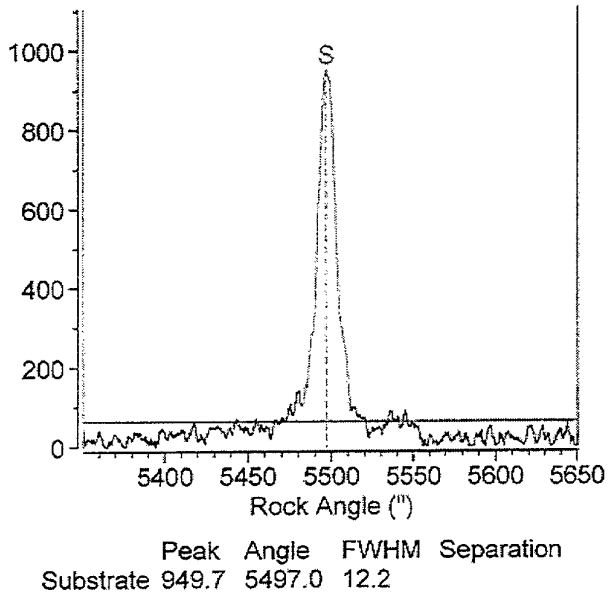


Fig. 1
Typical rocking curve of a
6H-SiC – wafer, ready for CVD

In this work bulk 6H-SiC substrate wafer have been investigated by microscopy in polarized light and rocking curve mapping on a double – crystal diffractometer (see Fig. 1) to characterize micropipes and domains. The location and density of micropipes as well as the domain areas were evaluated after wafer polishing and oxidation. Hot wall CVD was used to seal the defect areas before using the wafer as substrate for bulk growth by the Modified Lely Method. The influence of elevated temperatures on these sealed defects, especially on their propagation from the seed to the crystal will be discussed. Additionally, in CVD layers was an improvement concerning the domain structure observed. It was investigated, if this effect is stable at higher MLM growth temperature.

References

[1] S.E. Saddow, M.S. Mazzola, S.V. Rendakova, V.A. Dmitriev
Mater. Sci. Eng. B61-62 (1999) 158

[2] Suzuki, et.al.
US Patent 4,623,425, Nov. 18, 1986

MoP-22

The dislocation population and strains in GaN thin layers grown by HVPE directly on different 6H-SiC substrates

Irina P.Nikitina*, Galina N. Mosina*, Denis V. Tsvetkov**, Andrey E. Nikolaev*,
Yuriy V.Melnik**, Michail P. Sheglov*
*- Ioffe Institute, 26, Politechnicheskaya Str., St. Petersburg, 194021, Russia
Tel.: +7 812 2479314
Fax: +7 812 2476425
**- TDI, Inc., 8660 Dakota Dr., Gaithersburg, MD 20877, USA

We report on study of residual strains and dislocations structure in thin (~500 nm) GaN layers, grown by HVPE directly on SiC substrates. Structural properties were investigated by transmission electron microscopy (TEM) and XRD measurements using triple-crystal diffractometer. Residual strains were determined by measurements of lattice constants using a triple-crystal modification of Bond method.

Two different types of thin GaN layers grown by HVPE technique on different kinds of SiC substrates without buffer layer were studied. GaN deposition was performed on Si face of on-axis 6H-SiC grown by Lely method (first type film) and on Si face of on-axis 6H-SiC grown by modified Lely method (second type film). The GaN deposition was carried out in the same growth run at the growth temperature 1020^{0}C and growth rate 0.2 μm/min. The thickness of GaN films was 0.5 μm.

The comparison of structural properties of both GaN films was carried out. The difference in absolute values of residual strains and special features of the shapes, broadening of X-ray rocking curves, measured on symmetric and asymmetric reflections from both types of thin films was observed. These features were shown to be defined by the structure of initial highly defected layer and dislocation population in every type of GaN films. It was also shown that the nucleation stage and the type of threading dislocations in the layer depend on the kind of the SiC substrate. The formation of small gomogeneous grains in the initial stage of growth during the GaN deposition on the surface of SiC substrate grown by modified Lely method causes the predominance of pure edge threading dislocations in the GaN structure and the abrupt interface between the initial layer and the top part of the layer. The residual strains in these GaN layers are higher than those in GaN layers grown on the first type SiC substrate. This leads to more early cracking of thin GaN layers deposited on SiC substrates grown by modified Lely method.

We believe that the results of this study may be useful for understanding of cracks formation in GaN layers grown on SiC substrates.

Defect analysis of SiC sublimation growth by the *in-situ* x-ray topography

T. Kato[1], N. Oyanagi[2], H. Yamaguchi[1], S. Nishizawa[1], and K. Arai[1]
[1] Ultra-Low-Loss Power Device Technology Research Body (UPR),
Electrotechnical Laboratory,
[2] UPR, R&D Association for Future Electron Devices,
1-1-4 Umezono, Tsukuba, Ibaraki 305-8568, Japan
TEL : +81-298-61-5397, FAX : +81-298-61-3397, E-MAIL : ktomo@etl.go.jp

We report defects analysis of 6H-SiC bulk single crystal growth by in-situ x-ray topography. Occurrence and dynamics of the defects during SiC crystal growth were observed in a real time display. The experiments for the growth of 6H-SiC crystals by the modified Lely method were performed in an RF induction furnace combined with an x-ray topography. The crystal growth was performed at 2200°C and 10~400 Torr chamber pressure of the high purity Ar gas. A molybdenum rotating-anode was used as a source to generate the x-rays with maximum output of 18kW. The diffraction selected from $(10\bar{1}1)$ plane of the growing crystal was directly scanned as topographic images using a CCD camera. Fig.1 introduces the results of the *in-situ* x-ray topography measurement of the crystal grown on a (0001)6H-SiC Lely seed crystal. The topograph shows appearance of the domain boundary and micropipes. The topograph was taken from the region near an edge of the seed crystal. The initial seed crystal used for the growth contained defects and dislocations with relatively low density. However soon after the starts of the growth, the appearance of the topograph starts gradually changing to light and dark contrasts. These images are interpreted as occurrence of defects and dislocations in the grown portions. The crystal domains and their edges are captured clearly and are designated by Region A and white arrows in Fig.1(a) respectively. As the growth proceeds and progresses, domain edges make boundary at the center of the crystal, several micropipes are generated newly and captured as spot like images in Region B as shown in Fig.1(b). The appearance of other defects for example macro-defects, polycrystal, polytypes, etc. will be discussed at the conference. This study was performed under the management of FED as a part of the MITI NSS (R&D Ultra-Low-Loss Power Device Technologies) supported by NEDO of Japan.

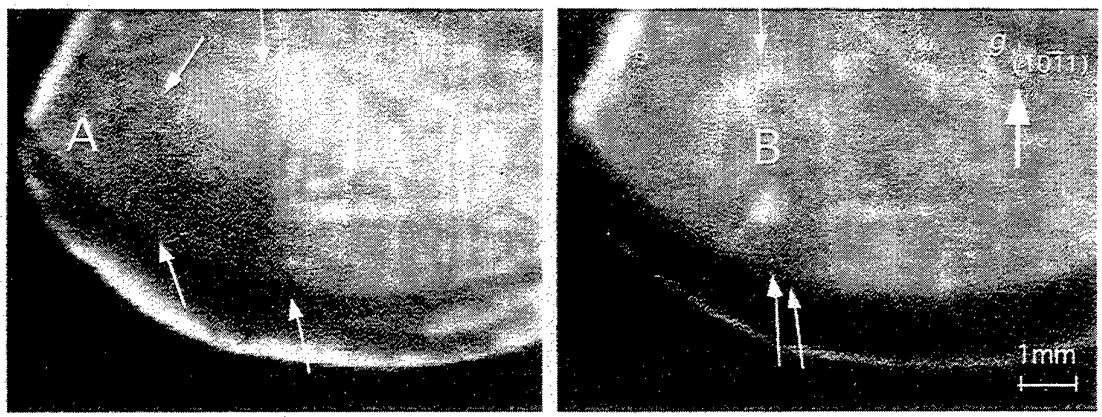


Fig.1 *In-situ* x-ray topographs for a SiC crystal. (a) Soon after the starts of the growth, the appearance of the topograph changes gradually to the light and dark contrasts, because of occurrence of defects and dislocations. Region A and white arrows are crystal domains and their edges, respectively. (b) As the growth proceeds, edges make domain boundary at the center of the crystal, micropipes are generated and captured as spot like images in Region B.

MoP-24

Lattice parameter measurements of 3C-SiC thin films grown on 6H-SiC substrate crystals

J. Kräußlich, A. Bauer, B Wunderlich, K. Goetz

Friedrich-Schiller-Universität Jena
Institut für Optik und Quantenelektronik
Max-Wien-Platz 1, 07743 Jena, Germany
Tel.: +49 (0)3641 947254 E-Mail: kraeusslich@ioq.physik.uni-jena.de

Silicon Carbide (SiC) occurs in many polytypes which differ in the periodic stacking sequences of hexagonal and tetragonal Si-C double layers. The SiC lattice parameters differ only slightly from polytype to polytype. Using X-ray diffraction methods the lattice parameters of **4H- and 6H-SiC single crystals** [1] as well as of **epitaxial 3C-SiC thin films** have been determined precisely.
The 3C-SiC thin films (thickness ≈ 1.2μm) were grown by solid-source molecular beam epitaxy on (0001)-oriented on-axis 6*H*-SiC crystal wafers at deposition temperatures between 780°C to 950°C and with growth rates between 30 nm/h to 120 nm/h [2].
Although the lattice parameters differ only slightly, well separated so-called family reflections of the 3C-SiC thin film and 6H-SiC substrate appeared, however at close neighbourhood. In this way, the thin film reflections were determined with respect to the well known 6H-SiC bulk crystal values and high precision thin film lattice parameters were obtained.

Results of the 3C-SiC thin film measuerements (here, a and c are given in adequate hexagonal terms although 3C-SiC is cubic):

- $c_{3C\text{-}SiC}/3 < c_{6H\text{-}SiC}/6$ → $\mathbf{c_{3C\text{-}SiC}/3 = 0.251\ 78\ nm \pm 3 \cdot 10^{-5}\ nm}$
- pseudomorphous growth → $\mathbf{a_{3C\text{-}SiC} = 0.308\ 13\ nm \pm 10^{-5}\ nm}$
  with respect to $c_{6H\text{-}SiC}/6 = 0.251\ 996\ 0\ nm \pm 0.3 \cdot 10^{-6}\ nm$
  $a_{6H\text{-}SiC} = 0.308\ 129\ nm \pm 4 \cdot 10^{-6}\ nm$
- $\mathbf{(c/(3a))_{3C\text{-}SiC} = 0.817\ 116} > 0.816\ 497 = \sqrt{(2/3)}$

The measured c/(3a)-relation of the 3C-SiC thin film is greater than the numerical value of $\sqrt{(2/3)}$ for the ideal non-deformed Si-C tetrahedron. That means that the SiC-tetrahedra that build up the 3C-SiC thin film are stretched in the **c**-direction (parallel to the surface normal) and compressed in the **a**-direction (perpendicular to the surface normal) compared to an ideal SiC tetrahedron.

Thence, the inherent **strain** and **stress components** of the epitaxial 3C-SiC thin film could be calculated by using the generalized Hook´s law:
$\mathbf{\varepsilon_3 = -\ 0.589\varepsilon_1}$
$\mathbf{\varepsilon_1 = \varepsilon_2 = \Delta a/a = -\ 4.77\ 10^{-4}}$ **and** $\mathbf{\varepsilon_3 = \Delta c/c = 2.81\ 10^{-4}}$
$\mathbf{\sigma_1 = \sigma_2 = 2.26 \cdot 10^8 N/m^2}$ for the in-plane stress components

[1] CREE Research Inc.
[2] A. Fissel, K. Pfennighaus, U. Kaiser, B. Schröter, W. Richter; Diamond and Related Materials 6 (1997) 1316

This work was financially supported by the Deutsche Forschungsgemeinschaft.

High-Resolution XRD evaluation of thick 4H-SiC epitaxial layers

H. Jacobsson, M. Syväjärvi, R. Yakimova, J. Birch, T. Tuomi and E. Janzén

Dept. Physics and Measurement Technology, Linköping University, S-581 83 Linköping, Sweden

Phone: +46 13 282476; Fax: +46 13 142337; E-mail: henja@ifm.liu.se

At present, several kinds of crystallographic imperfections exist in SiC wafers. In this work sublimation grown epitaxial layers on 4H-SiC commercial wafers have been studied concerning crystalline structure. The surfaces were off-oriented 8° towards $<11\bar{2}0>$ and the layer thicknesses were 100μm. The wafers and grown epitaxial layers have been separately investigated by high-resolution X-ray diffraction (HRXRD) and synchrotron topography. The result shows that the structural quality was improved in the epitaxial layers in the step-flow direction $<11\bar{2}0>$, concerning domain distribution, domain misorientation, mosaicity, and strain, compared with the commercial substrate wafers. As a demonstration of the crystalline improvement, a synchrotron topography image of a cross-section of the substrate and the epilayer is shown in Fig. 1. The darker areas in Fig.1 correspond to areas with higher density of crystalline imperfections. The difference in contrast in Fig.1 are due to strainfields caused by complex interference effects from crystallographic imperfections. The High-Resolution X-ray diffraction measurements show rocking curves from substrate with features characteristic of several domains located at almost the same omega value, but tilted with respect to each other in the omega direction. Rocking curves recorded from the epilayer show that the domain formation from the substrate has been reduced in the epilayer, Fig.2. The conditions for the observed structural improvement are discussed.

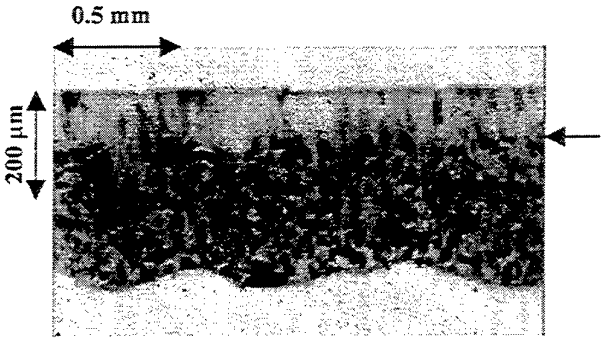


Fig.1. Synchrotron section topograph showing cross-section of the substrate and epilayer. The wavy lower edge is due to backside evaporation of the substrate during growth of the epilayer. The arrow marks the layer-substrate interface.

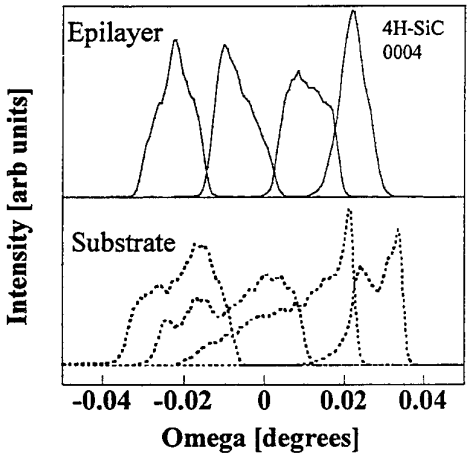


Fig.2 Rocking curves recorded at different positions translated along $<\bar{1}100>$ on substrate and epilayer. Spotsize is 1*9 mm

MoP-26

Modes of Plastic Deformation in Growing Silicon Carbide Ingot: Theory and Experiment

Lebedev A.O.[2], Avrov D.D.[1], Dorozhkin S.I.[1], Tairov Yu.M.[1]

[1]St.-Petersburg Electrotechnical University
Prof.Popov str.5, 197376 St.-Petersburg, RUSSIA
Phone/Fax: +7-(812) 234-3164, E-mail: SiC.ME@eltech.ru

[2]Physical-Technical Ioffe Institute
Politechnicheskaya str. 26, 194021, St.Petersburg, RUSSIA
Phone: +7-(812) 515-9292, Fax: +7-(812) 234-3164
Email: aswan@aport.ru

Silicon carbide ingots grown by LETI method is of great importance as a material for hard environment electronics. However, commercial use of the material is limited by not enough quality of ingots.

Modes of plastic deformation in growing SiC boule have been investigated in detail and systematized both theoretically and experimentally including X-ray diffractometry, Laue pattern method, Berg-Barrett and Land X-ray topography, cathodo- and photoluminescence measurements and comparative chemical etching.

Use of silicon carbide substrates of elevated diameter (2-3") in relatively small growth chamber, non-optimized thermal field in this chamber as a rule lead to non-uniform heating of the substrates so that the last is subjected to increasing stress. However, an exact stress relief analysis is complicated by the fact that the non-uniform and unstable relation between axial and lateral thermal gradients ad well as the "history" of the substrate, its spatial arrangement and method of fixing in the chamber may alter to a great extent the stress distribution. An accumulation of elastic energy during the growth necessarily causes plastic deformation of several predominant mechanisms.

When the stress are fairly small those may result in non-uniform network of dislocations and bending front of crystallization. The greater stress level usually cause relaxation in the form of the kink bands in the most stressed parts of the growing ingot when the dislocation slip on parallel planes is confined to small region, the lattice inside those rotates relative to the exterior matrix. In particular, numerous peripheral kinking bands have been described earlier [1] as slightly misoriented (less than 1 degree) radial segments in silicon carbide boules. Moreover, kinking occurs also for interior parts of ingot as an inclusion of small well-developed misoriented domains. Additional mechanisms of relaxation on a microscopic scale connected with the stress concentrations at a dislocation pile-ups produce microcracks and micropipes. Finally, exceeding the ultimate strength may lead to large-scale damage of ingot (brittle fracture of material).

The possible techniques that can be used for optimization of the defect structure of the ingots including enlargement of the growth chamber, minimization of lateral gradients, macropatterning and microprofiling, minimization of the growth temperature and the growth rate have been also considered.

References

1. Bakin A.S., Dorozhkin S.I. 6H and 4H – Silicon carbide For Device Applications 1998 4th International High Temperature Electronics Conference, IEEE 98EX145, p.253-256.

Effects of hydrogen implantation and annealing on the vibrationnal properties of n-type and p-type 6H-SiC.

H. W. Kunert[1], T. P.Maurice[1,3], T. Hauser[1], J. B. Malherbe[1], L.C. Prinsloo[2], D. J. Brink[1], L.A Falkovsky[3,4] and J.Camassel[3]

[1]*Department of Physics, University of Pretoria, 0002 Pretoria, South Africa*
[2]*Department of Chemistry, University of Pretoria, 0002 Pretoria, South Africa*
[3]*GES, UM2-CNRS, cc074, 34095, Montpellier cedex 05, France.*
[4]*Permanent address: Landau Institute, Moscow, Russia.*
Tel : +33 4 67 14 37 73, fax : + 33 4 67 14 37 60, e-mail: camas@ges.univ-montp2.fr

Hydrogen implantation in SiC is very important for SiCOI (SiC On Insulator) formation technology [1]. In this work, nitrogen (n-type) and aluminum (p-type) doped 6H-SiC was implanted with hydrogen at a total dose of $1x10^{17}$ cm^{-2} H^+ atom/cm^2 using a 1.0 MeV proton beam with a 90 mA current. The implantation-induced changes in vibration modes was investigated by means of backscattering Raman spectroscopy.

In the highly doped ($1x10^{19}$ cm^{-3}) as-grown samples, our Raman spectra exhibit all prominent first-order modes previously reported [2]. However, in the n-type doped sample we observe an additional feature at 682.5 cm^{-1}, and in the p-type doped at 640 cm^{-1}. The H^+-ion implantation anneals almost completely several first-order modes, like the transverse E_1 and A_1 frequencies at 794.4 and 965 cm^{-1} , respectively, or the Folded Transverse Acoustic (FTA) modes E_2 at 143.7 and 240 cm^{-1} or E_1 at 234 cm^{-1}, the folded Longitudinal ones (FLA) A_1 at 513 cm^{-1}, or the FTO E_2 at 765 cm^{-1}. The remaining modes, FTA E_2 at 149.6 cm^{-1}, FTO E_2 at 787.3 cm^{-1}, FLA A_1 at 512.9 cm^{-1} are mainly reduced in intensity and sometimes shifted to lower frequency. Finally, in the region 170 to 700 cm^{-1}, we find a pronounced effect of hydrogen implantation induced vibration bands at 185 and 526 cm^{-1} and a sharp defect mode at 658 cm-1 in the gap of the phonon DOS of as-grown SiC.

Concerning the second order Raman process, for high purity undoped 6H-SiC samples one should observe 12 (weak) modes labeled "a to l" in the region 1000 to 1850 cm^{-1} [2]. Our as-grown n-doped sample exhibits only 8 modes from "e to l". After hydrogen implantation, these features vanish due to amorphisation and a new mode centered at 1455 cm^{-1} appears. The p-doped sample is much less affected by implantation. In the region 1000 to 1850 cm^{-1}, it shows all high frequency modes from "a to l" (as-grown) and the implantation affects only the Gaussian bands a to d. While band "a" (~ 1100 cm^{-1}) splits into two sharp peaks, band d (1420 cm^{-1}) becomes sharper and exhibits new structures.

Annealing the n-type implanted sample at 700C (1 hr) causes reappearance of most of the initially existing modes (with weak intensity). However, the hydrogen implantation induced bands at 185, 526, and 658 cm^{-1} are still present. Annealing the p-type sample generates several new modes at 1067, 1084, and 1160 cm^{-1} and, in both samples, annealing at 950C (1 hr) causes even more drastic changes.

These results will be discussed in the light of a recent theory of defect interaction with optical phonons [4]. To facilitate the identification of the origin of the new bands, further annealing and polarized Raman spectra will be also presented.

[1] L.DiCioccio et al., Mat. Science Forum **264-268**, 765 (1998).
[2] S.Nakashima et al., Phys. Stat. Sol. (a), **162**, 39 1997
[3] A.Perez-Rodriguez et al., J. of. Elect. Mat., **25**, (1996).
[4] L.Falkovsky et al., Phys. Rev.B.**57**, 11283 (1998).

Withdrawn

As-grown and process-induced, intrinsic, deep-level luminescence in 4H SiC

B. Magnusson, A. Ellison, F.H.C. Carlsson, N.T. Son, and E. Janzén
Department of Physics and Measurement Technology
Linköping University, S-581 83 Linköping, Sweden
Phone: +46 13 282476, Fax: +46 13 142337, E-mail: bjmag@ifm.liu.se

In semi-insulating 4H SiC - not intentionally doped with vanadium - grown with the HTCVD technique [1] several deep levels appear, which have not been reported before. In this work we investigate the luminescence from one of these defect levels. The defect can also be induced during ion implantation or irradiation with electrons, protons or neutrons. A similar defect has earlier briefly been reported in the 6H polytype [2].

In figure 1 the PL spectrum of the center is showed. It consists of four no phonon-lines ranging from 1.09 to 1.15 eV, which are followed by a broad phonon-assisted replica (not shown in figure 1). The line width is about 0.4 meV and does not increase drastically with temperature during the PL experiment. It is also worth noting that it has not been possible to excite the center with below bandgap excitation. The annealing behavior of the defect is presented in figure 2. Even if the luminescence is observable in as-irradiated material it will increase in intensity with annealing up to 1000°C, and then vanish completely at 1300°C.

The fact that the defect can be induced with irradiation implies that it is a intrinsic defect even if it can be observed in some as-grown samples. The silicon vacancy starts to anneal out [3] at the same time as this deep level luminescence gain in intensity, therefore we assume that the complex involves the silicon vacancy. This will be more thoroughly discussed together with Zeeman measurement of the center.

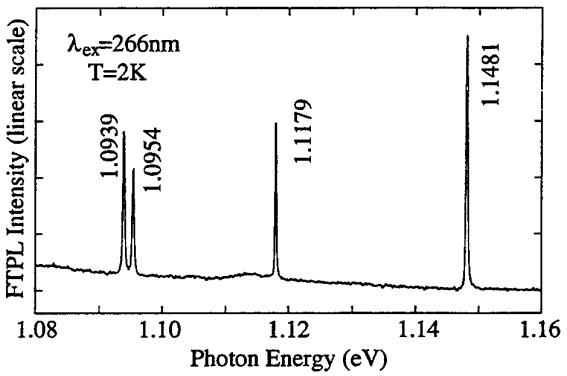


Fig. 1. FTPL spectrum of a neutron irradiated 4H SiC low-doped, epilayer (annealed at 1000°C).

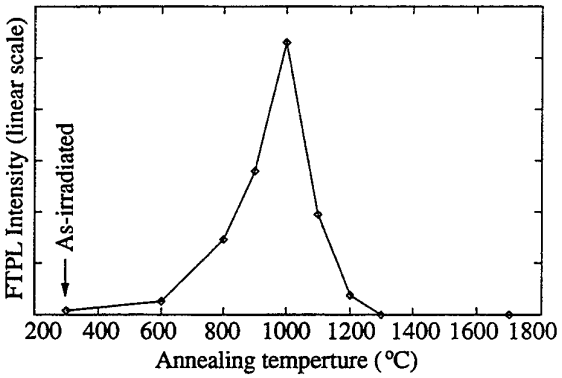


Fig. 2. Annealing behavior of the defect monitored at the 1.148 eV no phonon-line in figure 1.

[1] Ellison *et al*, Mater. Sci. Eng. B, **61-62**, 113 (1999).
[2] N.T.Son *et al*, Diam. Relat. Mater. **6**, 1378 (1997).
[3] H.Itoh *et al*, J.Appl.Phys. **66**,4529 (1989).

MoP-30

Investigation of an ion-implantation induced high temperature persistent intrinsic defect in SiC

S.G. Sridhara, F.H.C. Carlsson, J.P. Bergman, A. Henry and E. Janzén
Department of Physics and Measurement Technology, Linköping University
S-581 83 Linköping, Sweden. Tel: +46 013 282427, FAX: +46 013 142337

Among the various defect related luminescence lines seen after ion-implantation, only the D_I and D_{II} defect spectra are known to persist even after a 1700°C anneal, making them important defects from a device point of view. We report an indepth study of the D_{II} intrinsic defect spectrum in SiC, using time-resolved, PLE, magneto-optical and variable temperature PL spectroscopies. In 6H SiC, the D_{II}^{6H} spectrum at 2K, comprises at least four no-phonon lines [1]. The relative intensities of these no-phonon lines vary between different epilayers and also between different spots on the same epilayer which may indicate a stress sensitivity of the center responsible for these lines. A qualitative idea of the behaviour of these lines under stress can be derived by comparing PL spectra of an epilayer when it is fixed to the sample holder with an adhesive and when it is mounted in a stress-free fashion. As illustrated in Figure 1, a significant difference in the total intensity as well as a shift in the wavelengths of some of the lines in the spectra, is observed under the two conditions. At 20K the line d^4 is quenched, while the remaining lines persist upto about 80K, when the entire spectrum disappears. The luminescence decay of the no-phonon lines was investigated as a function of temperature and is shown in Figure 2. The long decay time at low temperatures of these lines is indicative of excitons bound at isoelectronic centers [2]. The long lifetime of the d^4 line in conjunction with its behaviour at higher temperatures suggests that it is a forbidden transition. We propose this line to be a transition from the ground state of the bound exciton. The lifetimes of the lines d^1 and d^2 approach each other at higher temperature indicating thermalization between the two states responsible for these lines, at these temperatures. We propose these lines to be related to excited states of the bound exciton (see inset, Figure 1). The fact that excited states can be seen even at 2K indicates that they are not thermalized at low temperatures. Inequivalency can be ruled out as the origin of these lines in the D_{II}^{6H} spectrum. Results in other polytypes will also be presented.

[1] S.G. Sridhara, D.G. Nizhner, R.P. Devaty, W.J. Choyke, T. Dalibor, G. Pensl and T. Kimoto, Materials Science Forum **264-268**, 493(1998).

[2] T. Egilsson, J.P. Bergman, I.G. Ivanov, A. Henry and E. Janzén, Phys. Rev. B **59**, 1956(1999).

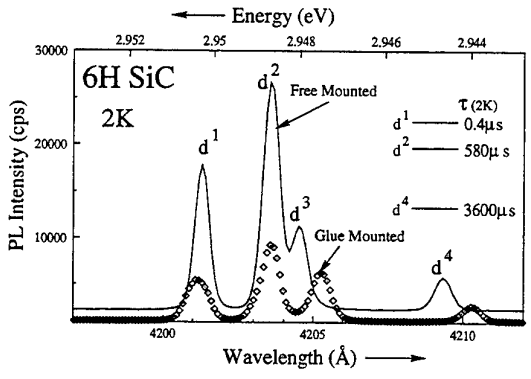


Figure 1: 2K PL spectrum illustrating the sensitivity of the D_{II}^{6H} no-phonon lines to stress in the epilayer.

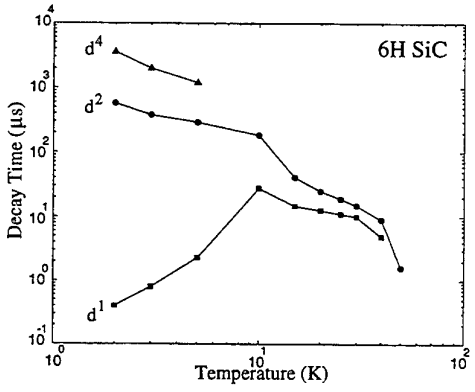


Figure 2: Variation of the decay time of three of the no-phonon lines in the D_{II}^{6H} spectrum, as a function of temperature.

Differentiation between C and Si related damage centres in 4H and 6H silicon carbide by the use of 90-300 kV electron irradiation followed by low temperature photoluminescence microscopy

J. W. Steeds, F.Carosella, G. A. Evans, M. M. Ismail and W.Voegeli
Department of Physics, University of Bristol, Bristol BS8 1TL, United Kingdom
Tel: +44 117 928 8730, Fax: +44 117 925 5624

Radiation damage of SiC is an important topic in view of the need to achieve local doping by ion implantation. However, the multiplicity of possible defects in implanted SiC has made difficult the interpretation of results obtained by different characterization techniques. In this work we have been able to distinguish between the results of Si and C displacement by carrying out near-threshold electron irradiation experiments using an ion-free transmission electron microscope with continuous control of its operating voltage. Because of the large difference in mass between C and Si atoms, two high energy electron displacement thresholds exist, one at about 90kV for C displacement and another at about 175kV for Si displacements. After irradiation the samples have been studied by photoluminescence (PL) microscopy at liquid helium temperatures using Renishaw micro-Raman spectrometers with 325 nm and 488 nm laser sources. A rich variety of spectra is revealed, one subset of which can be related to C displacements the other to Si displacements. Moreover, by carrying out the electron bombardment along [0001] and [000$\bar{1}$] directions, a major anisotropy of behaviour has been discovered near the C displacement threshold.

Results will be present for electron irradiation of n and p type 4H and 6H SiC samples at a variety of near-threshold electron energies. Comparison will be made with PL results already published in the literature and with related results obtained by other characterization techniques. Preliminary results of low and high temperature electron irradiation will also be presented. Discussion of the results will include the [0001]/[000$\bar{1}$] asymmetry and the evidence of diffusion of point defects out of the irradiated areas.

MoP-32

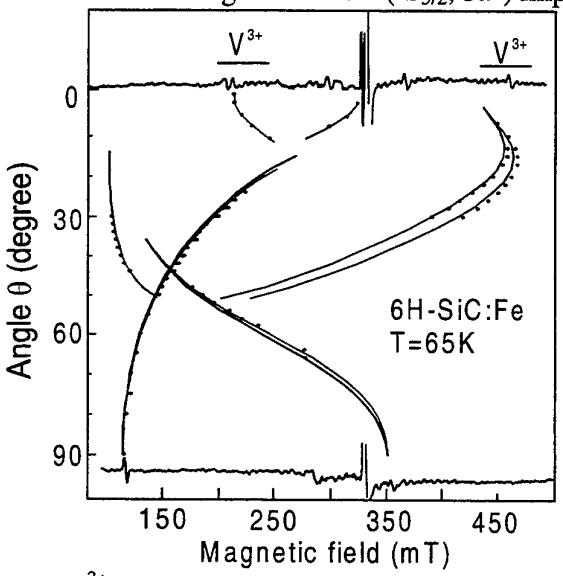
Identification of iron in 6H-SiC crystal by electron paramagnetic resonance

P.G. Baranov, I.V. Ilyin, E.N. Mokhov and V.A. Khramtsov

A.F. Ioffe Physico-Technical Institute, Polytechnicheskaya 26, 194021 St.Petersburg, Russia
phone: +7-812-2479320, fax: +7-812-247-10-17, e-mail: Pavel.Baranov@pop.ioffe.rssi.ru

We report on the first observation of electron paramagnetic resonance (EPR) of iron impurity in SiC:Fe crystals. We have investigated iron-doped 6H-SiC bulk crystals grown by the sublimation sandwich method.

Experimentally measured angular dependence of the signals which we ascribe to Fe^{3+} are shown as circles in the figure. The spectra observed in B||c and B⊥c are also shown in the figure. The observed angular dependence is characteristic for a center with S = 5/2 in strong axial crystalline field. Since crystal which we have studied was doped with iron it is natural to ascribe these signals to Fe^{3+} ($^6S_{5/2}$, $3d^5$) impurity centre with $S = 5/2$.



An investigation of the angular dependence of the Fe^{3+} EPR spectrum allowed us to find spin Hamiltonian parameters for Fe^{3+} signal The following parameters were found: $g \approx 1.99$, axial crystal field splitting $|D| = 0.25$ cm^{-1} and cubic field splitting $|a| = 0.016$ cm^{-1}. The calculated angular dependence of fine-structure line positions of Fe^{3+} ions is plotted as lines in the figure. No hyperfine structure of Fe^{3+} signals was observed due to low natural abundance of odd ^{57}Fe isotope. The EPR signals of Fe^{3+} could be observed at temperatures from 4K up to room temperature with maximum intensity at about 100K. The EPR of Fe^{3+} for only one lattice site could be observed. We suppose that Fe^{3+} ions occupy silicon sites in 6H-SiC lattice. From intensities of iron EPR signals we have estimated concentration of iron impurity in the sample to be approximately 10^{17}cm^{-3}.

Very important point is simultaneous presence of Fe^{3+} and V^{3+} signals in the EPR spectra of 6H-SiC. Positions of the two group of lines that belong to V^{3+} (S = 1) are shown in the figure for B || c. This implies that positions of energy levels of these ions in 6H-SiC bandgap are rather close. Since energy level position of V^{3+} in 6H-SiC bandgap is 0.6eV below the conduction band, one may expect that Fe^{3+} produce energy level, which also lies deep in the 6H-SiC bandgap. Furthermore, energy level of vanadium in V^{4+} charge state lies near the middle of the bandgap and V^{4+} is used to produce semi-insulating SiC layers. Thus we can expect that if Fe^{4+} charge state is stable then it can also produce energy level in the middle of the 6H-SiC bandgap and this would allow using Fe^{4+} impurity to obtain semi-insulating 6H-SiC layers.

Besides iron and vanadium EPR lines a great number of other EPR signals have been observed in the SiC:Fe crystals. These signals appear at angles larger than 15^0 on both sides of N donors signal and may arise due to complexes of iron ions with other defects.

The electronic structure of the N donor center in 4H-SiC and 6H-SiC.

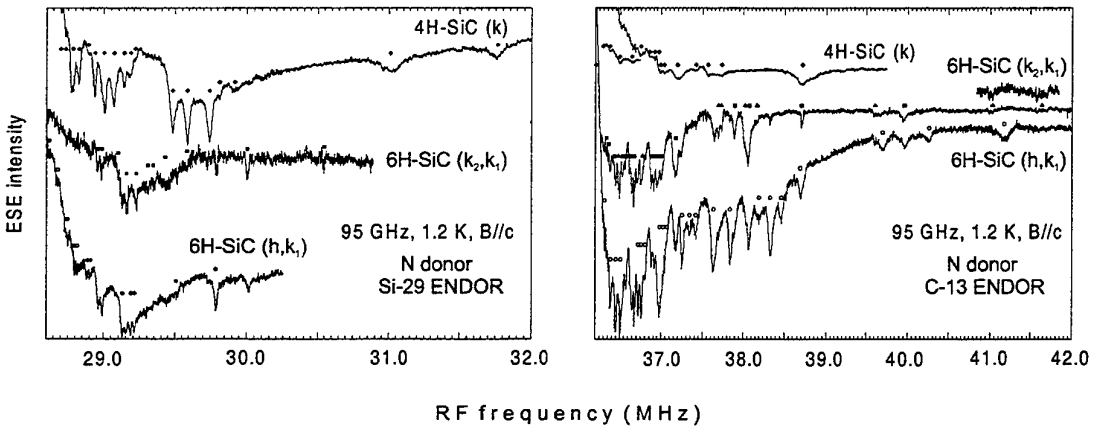
A. v. Duijn-Arnold, R. Zondervan and J. Schmidt

Huygens Laboratory, Leiden University, P.O. Box 9504, 2300 RA Leiden, The Netherlands
phone: +31-71-5275910, fax: +31-71-5275819, e-mail: mat@molphys.leidenuniv.nl

P.G. Baranov and E.N. Mokhov

A.F. Ioffe Physico-Technical Institute, Polytechnicheskaya 26, 194021 St.Petersburg, Russia

We present high-frequency (95 GHz) pulsed electron paramagnetic resonance (EPR) and electron-nuclear-double-resonance (ENDOR) measurements on the nitrogen (N) donor in 4H-SiC (k site) and 6H-SiC (h, k_1 and k_2 sites according to the accepted classification). From the isotropic (a) and anisotropic (b) hyperfine interaction (hfi) of the unpaired electron spin of the donor with the ^{13}C (35% ^{13}C-enriched samples were used) and ^{29}Si nuclei, the distribution of the electronic wave function of the N donor is determined. It is found that the electronic wave function (WF) of the N donor is quite different in the two polytypes. The figure shows the comparison between the different sites in 4H- and 6H-SiC for the ^{29}Si (left) and ^{13}C (right) ENDOR spectra (only the spectra on the high-frequency side of the ^{29}Si and ^{13}C Zeeman frequencies are shown) with the magnetic field B parallel to the c axis. It is clear that the spin density distribution of the N donor electron over the ^{13}C and ^{29}Si nuclei differs between 4H- and 6H polytypes. The same conclusion was made from EPR line broadening of N donor in ^{13}C-enriched 4H- and 6H-SiC compared with non-enriched crystals.



A main part of the spin density in 4H-SiC is located on the Si sublattice (the highest hfi for ^{29}Si: a=6.54 and b=1.26 MHz; for ^{13}C: a=5.02, $b\leq$0.01 MHz) and the WF contains a relatively large portion of Si p-character (anisotropic). For the three sites in 6H-SiC a main part of the spin density is located on the C sublattice (the highest k_2-site hfi for ^{13}C: a=10.75, b=0.065 MHz; ^{29}Si: a=3.86 and $b\leq$0.01 MHz) and the WF is built mostly of s-like C atomic orbitals (isotropic). Comparing the three sites in 6H-SiC, the h-site WF has the largest delocalization and is most isotropic. The k_2 site WF is most localised and less isotropic. The larger part of the spin density is located far into the crystal. The difference in the WF behaviour in 4H and 6H polytypes seems to be due to the difference in their conduction-band structure. The position of the N atom in SiC is also under discussion.

MoP-34

ESR Detection of Ni^{3+} as Residual Impurity in GaN Bulk Crystals.

E. Kalabukhova, S. Lukin, I. Krygin,
Institute of Semiconductor Physics, National Academy of Science of Ukraine,
Kiev, Pr. Nauki, 45, Ukraine, E-mail: katia@physic.kiev.ua
V. Dmitriev
A. Ioffe Physico-Technical Institute National Academy of Science of Russia, St-Petersburg

Two batches of undoped GaN samples grown by hydride vapor phase epitaxy (HVPE) and by sublimation sandwich method have been studied by EPR in Q-band at T = 300K.

A few samples of two batches of GaN samples revealed one single ESR line of different intensity with isotropic width (ΔH = 20 Gs). Angular dependence of g-factor of single line was displayed in Fig 1. The noticeable characteristic of the observed ESR line, is that rotation of magnetic field from perpendicular to parallel orientation with respect to the **c**-axis gives minimum of g-value at $\varphi = 40^0$.

The observed angular variation of g-factor of single line is typical for $3d^n$ paramagnetic ions of spin S = 3/2 in the case of strong magnetic field (when $h\nu > D$) and could be attributed to the resonance transition within the $|\pm 1/2>$ doublet. Since the ESR spectrum is observed at room temperature the ground state of $3d^n$ paramagnetic ion should be the orbital singlet. Taking into account the relatively small width of the line and the lack of hyperfine structure (the linewidth is isotropic) one would conclude that the one strongest candidate among $3d^n$ paramagnetic ions could be Ni^{3+} with $3d^7$ electronic configuration.

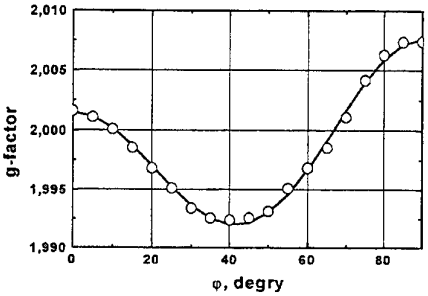


Fig. 1. Angular dependence of the ESR spectrum of undoped GaN. Open circles are experimental points, the solid line have been calculated using the parameters obtained by numerical diagonalization of spin-Hamiltonian (1).

Ground term of free Ni^{3+} ion is ^4F, electron spin is S = 3/2; nuclear spin I = 3/2 has only ^{61}Ni with natural abundance 1.13%. The ^4F term of free ion in tetrahedral crystal field splits into the ground - state orbital singlet $^4A_2$ and two upper lying triplets $^4T_2$, $^4T_1$. The $^4A_2$ splits into two spin doublets $|\pm 1/2>$ and $|\pm 3/2>$ caused by trigonal component of crystal field.
The spin-Hamiltonian appropriate for Ni^{3+} ignoring nuclear spin has the form:

$$H = g_{\|}\beta H_z S_z + g_{\perp}\beta(H_x S_x + H_y S_y) + D[S^2_z - 1/3\ S(S+1)] \qquad (1).$$

The parameters of spin-Hamiltonian were extracted by numerical diagonalization of the spin-Hamiltonian (1) taking into account the features of fine structure line position in magnetic field, see Fig. 1. Using the parameters obtained D = 0.225 cm^{-1}; $g_{\|}$ = 2.0015; $g_{\perp}$ = 2.002 the calculated angular dependence of the fine structure line was shown in Fig. 1. A good agreement with the experimental points is seen to exist.

As was seen from parameters obtained the zero-field splitting D is small compare to Zeeman energy $\Delta W = h\nu$ = 1.23 cm^{-1} (for ν = 37 GHz). In the case of $D < g_{eff}\beta H$ one expects to observe all fine structure transitions $|3/2> \rightarrow |1/2>$, $|1/2> \rightarrow |-1/2>$, $|-1/2> \rightarrow |-3/2>$ in ESR spectrum of paramagnetic ion with S = 3/2.

Our failure to observe the outer fine structure lines could be explained by smaller their intensities compare to the central $|1/2> \rightarrow |-1/2>$ line and broadening of the linewidth due to existence of residual lattice strain typical for thin GaN layers. The linewidth of $|3/2> \rightarrow |1/2>$, $|-1/2> \rightarrow |-3/2>$ transitions is also could influenced random crystal field while the central fine structure transition remains unaffected.

Donor Densities and Donor Levels in 3C-SiC Determined by a New Method Based on Hall-Effect Measurements

Hideharu Matsuura, Yasuichi Masuda[1], Yi Chen[1] and Shigehiro Nishino[1]
Osaka Electro-Communication University, 18-8 Hatsu-cho, Neyagawa, Osaka 572-8530, Japan
E-mail: matsuura@isc.osakac.ac.jp TEL/FAX: +81-72-820-9031
[1] Kyoto Institute of Technology, Matsugasaki, Sakyo, Kyoto 606-8585, Japan

Silicon carbide (SiC) has been regarded as a promising semiconductor for power electronic applications owing its excellent physical properties. In order to use SiC wafers or epilayers for electronic devices, an accurate evaluation of densities and energy levels of dopants in SiC is essential. One of the authors has proposed and experimentally tested a graphical method for determining those of several dopants using the temperature dependence $n(T)$ of the majority-carrier concentration obtained by Hall-effect measurements.[1-4] We apply this method to determine donor densities (N_D) and donor levels (ΔE_D) in undoped 3C-SiC grown on silicon by chemical vapor deposition using $Si_2(CH_3)_6$ that is called HMDS.

In the proposed method, the function $H(T, E_{ref})$ to be evaluated is defined by

$$H(T, E_{ref}) \equiv \frac{n(T)^2}{(kT)^{2.5}} \exp\left(\frac{E_{ref}}{kT}\right)$$

where k is the Boltzmann constant, T is the absolute temperature and E_{ref} is a parameter that can shift the peak temperature (T_{peak}) of $H(T, E_{ref})$ within the measurement temperature range. Since T_{peak} corresponds to one ΔE_D, from each peak temperature and peak value, ΔE_D and N_D of the corresponding dopant can be accurately determined.

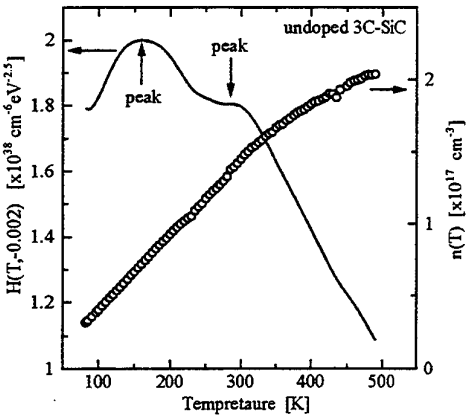


Fig.1 n(T) and H(T,-0.002)

Figure 1 shows $n(T)$ denoted by open circles and $H(T,-0.002)$ denoted by the solid line in 32 μ m thick 3C-SiC. Since two peaks appeared in the figure, at least two types of donors existed in the 3C-SiC. From the detailed analysis, three types of donors were found to exist. Their ΔE_D and N_D were determined to be 14 meV and $4.7\text{x}10^{16}$ cm^{-3}, 54 meV and $8.1\text{x}10^{16}$ cm^{-3}, and 120 meV and $1.0\text{x}10^{17}$ cm^{-3}, respectively. The acceptor density (N_A) was determined to be $5.7\text{x}10^{15}$ cm^{-3}. Figure 2 shows the experimental $n(T)$ and the $n(T)$ simulated with the obtained values. Since the simulated $n(T)$ is quantitatively in agreement with the experimental $n(T)$, the obtained values are considered to be reliable.

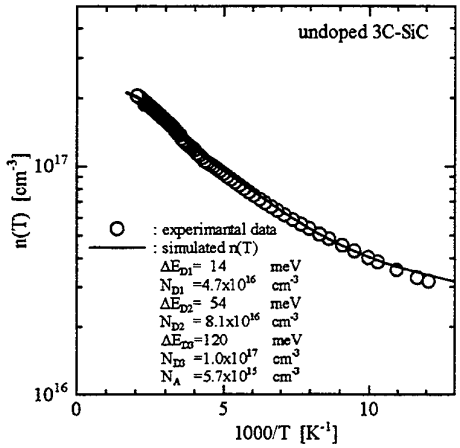


Fig. 2 Experiemtal and simulated n(T)

We investigated three kinds of 3C-SiC thicknesses (8 μ m, 16 μ m and 32 μ m). The values of N_D for 14 meV and 54 meV donors decreased with an increase in 3C-SiC thickness, while N_D for 120 meV was independent of its thickness.

References 1) H. Matsuura: Jpn. J. Appl. Phys. 36(1997)3541. 2) H. Matsuura et al.: Jpn. J. Appl. Phys. 37(1998)6034. 3) H. Matsuura et al.: Jpn. J. Appl. Phys. 38(1999)4013. 4) H. Matsuura et al.: Appl. Phys. Lett. 76(2000) 2092.

MoP-36

Tantalum and tungsten in silicon carbide: identification and polytype dependence of deep levels

J. Grillenberger[1], N. Achtziger[1], G. Pasold[1], R.Sielemann[2], and W. Witthuhn[1]

[1]Institut für Festkörperphysik, Universität Jena, Max-Wien Platz 1, D-07743 Jena, Germany (phone: ++49-3641-947337, fax: ++49-3641-947302, email: jojo@pinet.uni-jena.de)
[2]Hahn-Meitner-Institut Berlin, Glienicker Str. 100, D-14109 Berlin, Germany

To improve the quality of SiC bulk crystals, tantalum (Ta) is used in the growth containment during sublimation growth [1, 2, 3]. For epitaxial growth of SiC, TaC is used as a coating of the graphite susceptor [4]. In both cases, tantalum is present in the growth chamber and its incorporation in the growing crystal or layer is to be expected. Due to its extreme thermal stability, tungsten (W) may play a similar role in the future. In order to understand the electronic properties of these impurities in SiC, we are investigating band gap states of Ta and W in three different polytypes ($4H$, $6H$, $15R$). To establish a definite correlation between a band gap state detected by Deep Level Transient Spectroscopy (DLTS) and a certain element, we are using the concept of radioactive transmutation. The characteristic concentration change of radioactive isotopes serves as a unique fingerprint which is detected by sequential DLTS measurements during the elemental transmutation.

All measurements were done on n-type epilayers with a net donor concentration in the mid 10^{15} cm^{-3} range. Doping with the radioactive isotopes ^{177}Ta or ^{178}W was done by recoil implantation. Both isotopes transmute to stable Hf with a half-life of 56.6 h or 22 d respectively. In addition, conventional doping with stable isotopes was done by ion implantation with multiple energies between 1 and 6.2 MeV in order to create a rectangular depth profile with a mean concentration of 2×10^{14} cm^{-3}. Performing these experiments, we could definetly identify one donor like Ta-related level in the upper part of the band gap in each polytype [5]. The level energies exhibit a clearly resolved splitting due to inequivalent lattice sites. For W, one deep level in all polytypes and an additional level close to the conduction band in $4H$ were identified. The levels are each due to defects involving or are identical to exactly one W atom. Our experiments exclude Hf-related deep states in the part of the band gap investigated.

The data may be used to predict the consequences of a Ta or W incorporation on electrical properties of SiC. Furthermore, the polytype dependence of the energy level position follows the empirical rule of Langer-Heinrich and confirms our earlier prediction of the conduction band offset (0.22 eV between $4H$ and $6H$ [6]).

[1] E.N.Mokhov, M.G. Ramm, A.D.Roenkv, Yu.A.Vodakov, J.Cryst.Growth **181**, 254–258 (1997)
[2] Yu.A. Vodakov, A.D. Roenkov, M.G. Ramm, E.N. Mokhov, Yu.N. Makarov phys.stat.sol. (b) **202**, 177 (1997)
[3] D. Hoffmann, S.Yu. Karpov, Yu.N. Makarov, E.N. Mokhov, M.G. Ramm, M.S. Ramm, A.D. Roenkov, Yu.A. Vodakov, Inst.Phys.Conf.Ser. No.**142**, 29 (1996)
[4] L.B. Rowland, G.T. Dunne, Mat.Sci.For. **338-342**(2000), *at press*
[5] Radiotracer identification of a Ta-related deep level in $4H$-SiC, J. Grillenberger et al. (*subnmitted to Appl.Phys.Lett.*)
[6] N. Achtziger, J. Grillenberger, W. Witthuhn, Mat.Sci.For. **264-268**(1997)

Ion implantation induced deep levels in SiC-4H epilayer

D. Åberg[1*], L. Storasta[2], A. Hallén[1] and B. G. Svensson[1]

[1] Royal Institute of Technology, Solid State Electronics, P.O. Box E-229, S-164 40 Kista-Stockholm, Sweden

[2] Linköping University, Dep. Physics and Measurement Technology, S-581 83, Linköping, Sweden

* Phone:+46 8 752 1411 Fax:+46 8 752 7782 Email: denny@ele.kth.se

Abstract

4H SiC samples were boron implanted with a dose of 1×10^8 cm^{-3} at 1.96 MeV which gives a projected range of 2 μm. The low dose was selected to produce negligible electrical compensating damage, thereby eliminating difficulties during capacitance-voltage analysis and the normally necessary post-implantation anneals are thus eliminated. The material used was thick epi-layer (10 μm) 4H-SiC grown on Cree wafer by chemical vapor deposition (CVD) at Linköping university. The epi-material was nitrogen doped in the range 4 to 8×10^{15} cm^{-3}. The implantations were made at room temperature (RT), 300 and 600 °C. The point defects related electrically active traps were characterized using deep level transient spectroscopy (DLTS) and capacitance voltage (CV) measurements. Three distinct levels were found in the upper half of the band-gap having activation energies of E_C-0.40±0.04, E_C-0.69±0.03 and E_C-1.60±0.07 eV. In Fig. 1 is shown the spectra directly after implantation up to 400 K with the two most shallow levels clearly visible. Capture cross section measurement of the levels were performed using 20 ns to 50 ms pulse lengths. The E_C-0.69 level, known as the Z-level, was found to grow linearly with dose. Further, the Z-level peak was very broad after RT implantation, and the signal reduced drastically and sharpen after a mild heat treatment of 70 K above RT. The E_C-0.40 level was only seen in 300 °C implanted sample, but was seen to form after isochronal annealing of the RT implanted sample. Poole-Frenkel effect was seen for the E_C-0.40 level as it displayed electric field dependent emmision rates, strongly suggesting a 0/+ transition during ionization.

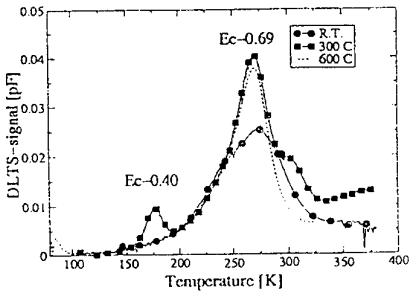


Figure 1: DLTS spectra directly after implantation during R.T, 300 °C and 600 °C. The Z-level is seen to grow with implantation temperature, while the E_C-0.4 level is only seen in the 300 °C implanted sample.

MoP-38

TWO-DIMENSIONAL CARRIER GASES INDUCED BY SPONTANEOUS AND PIEZOELECTRIC POLARIZATION IN AlGaN/GaN HETEROSTRUCTURES

Angela Link , Mike Murphy, Oliver Ambacher, Martin Stutzmann, Walter Schottky Institute, TU-Munich, GERMANY; Yulia Smorchkova, College of Engineering, Santa Barbara, California 93106

Two dimensional electron gases in GaN/$Al_xGa_{1-x}N$/GaN heterostructures suitable for high electron mobility transistors (HEMT´s) are induced by strong polarization effects. The sheet carrier concentration and the confinement of the two dimensional electron gases located close to one of the AlGaN/GaN interfaces are sensitive to a large number of different physical properties such as polarity, alloy composition, strain, thickness and doping of the AlGaN barrier. We have investigated the structural quality, the carrier concentration profiles and electrical transport properties of transistor structures by a combination of high resolution X-ray diffraction, Hall effect, C-V profiling and Shubnikov-de Haas measurements. The investigated heterostructures with N- and Ga-face polarity were grown by metalorganic vapor phase (MOCVD) or plasma-induced molecular beam epitaxy (PIMBE) covering a broad range of alloy compositions ($0.09<x<0.3$) and barrier thicknesses between 90 and 500 Å. High electron mobilities of 930 and 11200 cm^2/Vs were observed for sheet carrier concentrations of $5x10^{12}$ cm^{-2} at room temperature and He temperature, respectively.

By comparison of theoretical and experimental results we demonstrate that the formation of two dimensional electron gases in unintentionally doped AlGaN/GaN structures rely on the difference of both, piezoelectric and spontaneous polarization between the AlGaN and the GaN layer.

In addition the structural and transport properties of Mg-doped AlGaN/GaN heterostructures will be discussed. The presence of two dimensional hole gases is demonstrated by CV- and temperature dependent Hall-experiments, and the properties of electron and hole gases will be compared.

Presenting and Contact Author:
Angela Link
Walter Schottky Institute
Am Coulombwall
D-85748 Garching
Germany
Phone: +49 89 2891 2769
Fax: +49 89 2891 2737
E-mail: link@wsi.tu-muenchen.de

CALCULATED POSITRON ANNIHILATION PARAMETERS FOR DEFECTS IN 4H-SiC

T.E.M. Staab[a], L.M. Torpo[a,b], M.J. Puska[a], and R.M. Nieminen[a]

[a] Helsinki University of Technology, Laboratory of Physics, P.O. Box 1100, FIN-02015 HUT, Finland
[b] Linköping University, IFM, S-58183 Linköping, Sweden

email tst@fyslab.hut.fi

We calculate positron annihilation parameters (lifetime and high momentum part of the Doppler broadening lineshape) for different native defects in SiC. To figure out the influence of lattice relaxations we consider ideal lattice coordinates as well as those determined as minimum energy structures with a plane wave pseudopotential *ab-initio* code [1, 2]. We then compare the calculated annihilation parameters to experimental positron annihilation data in irradiated bulk SiC, where vacancies in different sublattices can be identified [4]. We find good agreement with experimental data [4] if the influence of the trapped positron on the relaxation features is taken qualitatively into account.

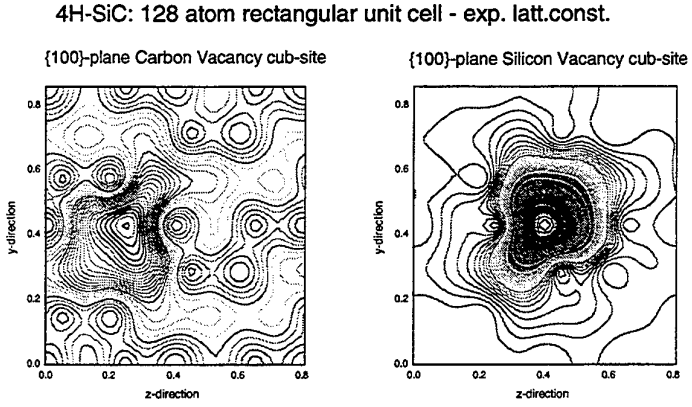


Figure 1: Positron densities in vacancies on different sublattices in 4H-SiC.

[1] L.M. Torpo, R.M. Nieminen, K.E. Laasonen, S. Pöykkö, Appl. Phys. Lett. **74** (2) (1999) 221

[2] L.M. Torpo, M. Marlo, and R.M. Nieminen, Computational study of monovacancies and antisite defects in SiC polytypes, to be published

[3] L.M. Torpo, E. Janzén, and R.M. Nieminen, Divacancies in 3C- and 4H-SiC, to be published

[4] S. Arpiainen, K. Saarinen, L. Henry, and M.-F. Barthe, this conference.

MoP-40

A study of band to band tunneling with application to high-field transport in hexagonal SiC polytypes

A. Martinez[1], H-E. Nilsson[2], and U. Lindefelt[1,3]

1) Solid State Electronics, Dept. of Electronics, Royal Institute of Technology (KTH), Electrum 229, S-164 40 Kista, Sweden, Electronic mail: antonio@ele.kth.se, phone: +46 8 752 1153
2) Mid-Sweden University, S-851 70 Sundsvall, Sweden
3) ABB Corporate Research, S-721 78 Västerås, Sweden

The band structure of hexagonal SiC has regions in k-space where two or more energy bands are very close to each other. Tunneling of electrons (or holes) between bands due to a high electric field is one of the processes that may allow the electron to jump between energy bands, which are separated by small energy gaps. It is important to consider this effect in order to understand high-field transport in these polytypes.

Recently, Krieger and Iafrate (KI) [1] have been able to write a system of ordinary differential equations in order to describe the time evolution of the probability amplitude for band tunneling. This time-dependent formulation allows implementation into the ensemble Monte Carlo (MC) simulation framework, which is the dominant method used to study high-field transport properties of semiconductor materials.

In this work we are using the two-band k·p method to calculate the time-dependent tunneling probability for electron transitions between two bands using the approach by KI. Energy gaps in the range 0.01-1.0 eV and electric field strengths between 0.1-5 MV/cm have been used to study the effect of tunneling. Drift times in the order of 10 fs have been considered, which is representative for the time between scattering events.

We have applied the k·p method for different points in the Brillouin zone of 4H-SiC and proved that there is considerable tunneling between bands under realistic electric field strengths and scattering times. The importance of having an accurate model for band-to-band tunneling to calculate high-field transport in hexagonal SiC polytypes has also been demonstrated in [2], in which another approximate model was used.

[1] J. B. Krieger and G. J. Iafrate, Phys. Rev. B 33, 5494 (1986)
[2] E. Bellotti et al., J. App. Phys. 87, 3864 (2000)

Free Carrier Diffusion in 4H-SiC

P. Grivickas[a], A. Martinez[a], I. Mikulskas[b], V. Grivickas[b], J. Linnros[a], U. Lindefelt[c] and R. Tomašiūnas[b]

[a] Department of Solid State Electronics, Royal Institute of Technology, Electrum 229, S-16440 Kista-Stockholm, Sweden, tel. +46 8 752 1345, fax. +46 8 752 7782, e-mail: paulius@ele.kth.se
[b] Institute of Material Research and Applied Sciences, Vilnius University, Sauletekio 10, 2054 Vilnius, Lithuania
[c] ABB Corporate Research, S-721 78 Västerås, Sweden

During recent years the quality of Silicon Carbide (SiC) material has gradually increased with following successful achievements in practical applications. However, still there are only few basic investigations performed on the electrical properties of SiC. One of the poorly explored ones is the free carrier diffusivity, which is a key parameter governing plasma behavior in the devices. Usually, it is indirectly evaluated from mobility data. In this work we present direct measurements of the free carrier diffusion coefficient over a large carrier injection range with particular emphasis to a high injections and high temperatures. These are the conditions of particular importance for high-power SiC devices. We utilize two optical Transient Grating (TG) techniques based on free-carrier induced effects: i) absorption [1] and ii) refraction index change [2]. We investigate 4H-SiC samples grown by two different methods: CVD ($6{\cdot}10^{14}$ cm^{-3}; 32 μm thick) and hot wall (HW) CVD ($1{\cdot}10^{15}$ cm^{-3}; 80 μm thick). From the main data indicated in Fig. 1 we extract the ambipolar and minority holes diffusion coefficients for 4H-SiC: D_a = (4.2±0.4) cm^2/s and D_h= (2.3±0.3) cm^2/s, respectively. At high injections an appreciable reduction of the ambipolar diffusivity is observed with the consequent fast increase at injections > 10^{18} cm^{-3}. These experimental results are simulated theoretically: the ordinary ambipolar diffusion equation is extended to include Fermi-Dirac statistics and a band gap narrowing (BGN) effect in the material. Two considered models for BGN calculations are compared: the inverse dielectric constant approximation by i) a single plasmon pole [3] and ii) the more precise random-phase one [4]. These theoretical results explain ~50% of the observed ambipolar diffusion reduction at room temperature. Theoretical calculations are also extended to higher temperatures with our experimentally determined diffusion versus temperature dependence $D \sim T^{1.3}$, showing good agreement with the experiment.

[1] J. Linnros and V. Grivickas, Phys. Rev. B, Vol. 50, No. 23, (1994) 16943.
[2] H. J. Eichler, P. Gunter, and C. W. Pohl, *Laser-induced Dynamic Gratings* (Springer Series in Optical Sciences), vol. 50, Berlin, 1986).
[3] J. F. Young and H. M. van Driel, Physical Review B, Vol. 26, No. 4, (1982) 2147.
[4] C. Persson, U. Lindefelt and B. E. Sernelius, submitted to Solid-State Electron. (1999).

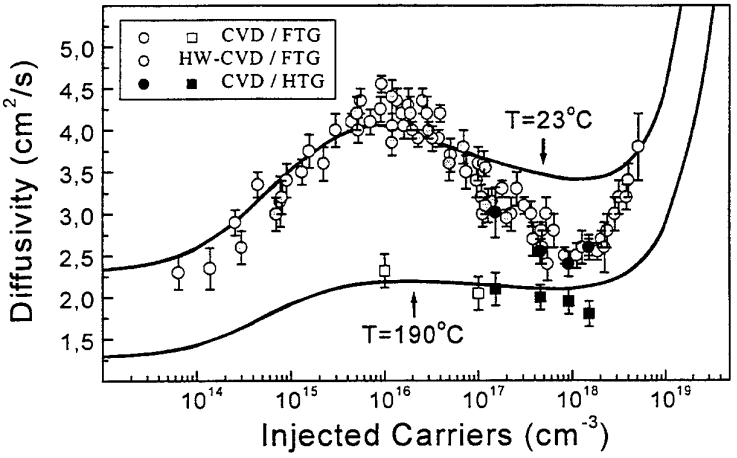


Fig. 1. Fee carrier diffusivity versus the injected carrier density at two temperatures. Measurements are done with two different techniques: absorptive (Fourier) or refractive (Holographic) TG. Material is grown by two methods (CVD, HWCVD). Continuous curves represent theoretical calculations of ambipolar diffusion coefficient dependence including Fermi-Dirac statistics and the bang gap narrowing effect.

MoP-42

SOURCE MATERIAL RELATED DISTRIBUTION OF DEFECTS IN 6H-SiC SINGLE CRYSTALS

H.-J.Rost, D.Siche, J.Dolle, D.Schulz, J.Wollweber

Institut für Kristallzüchtung, Max-Born-Straße 2, D-12489 Berlin, Germany

Phone: +49 30 6392 2847 Fax:+49 30 6392 3003 e-mail: rost@ikz-berlin.de

The quality of large diameter 6H-SiC single crystals is influenced by the composition of the vapour phase and the thermal conditions inside the growth chamber. Both are also effected by the composition of the SiC-source and its change during the growth. This seems to have an important influence on the formation of defects and their distribution in the crystal, too [1].

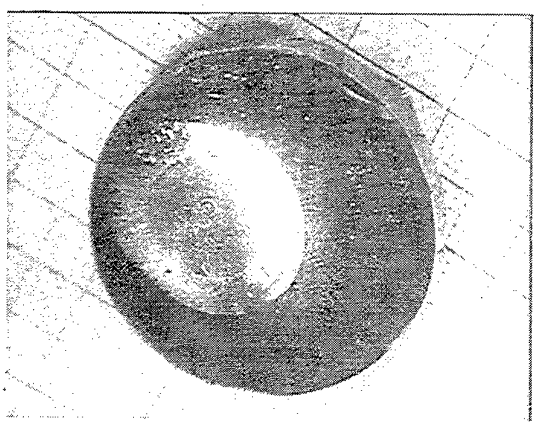


Fig 1 crystal grown from a SiC-powder source

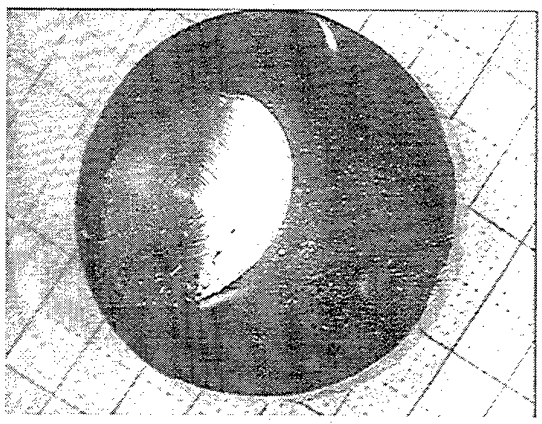


Fig 2 crystal grown from a sintered source

To investigate the distribution of defects like micropipes and inclusions, which has been identified as C-particles [2], a special series of crystals up to 30 mm diameter were grown by the Modified Lely Method on the silicon face of a seed. The growth conditions were kept constant (time, diameter, the temperature range between 2100°C-2400°C and the Ar-pressure between 5-50 hPa). Only the composition of the source material was varied. Starting with a SiC-powder source containing 1% silicon excess, in the following run the sublimated material was replaced by SiC-powder after removal of the graphite layer. Finally, a growth run was started with the pure sintered solid SiC-source. Seeds prepared from the same crystal were used to exclude the influence of different seed defect densities. Crystals were cut and polished parallel to the <0001> growth direction. The distribution of the defects along the growth direction and on the crystal surface was investigated by Optical Microscopy (Fig.1+2).

It was found that the number of defects detected at the crystal surface was indirectly proportional to the silicon content in the source in the investigated range. The same dependence was registered for the average growth velocity although an increase was found at the beginning of the growth run with increasing silicon content in the source [3]. Furthermore, the growth kinetic, especially the structure of the growth steps at the facet, was different. The distribution of the defects and the reason for their behaviour will be discussed.

[1] St.G.Müller, R.Eckstein, D.Hofmann, L.Kadinski, P.Kaufmann, M.Kölbl, E.Schmitt
Mater. Science Forum Vols 264-268 (1998) pp57-60

[2] H.-J.Rost, J.Dolle, J.Doerschel, D.Siche, D.Schulz, J.Wollweber
to be published

[3] H.-J.Rost, D.Siche, J.Dolle, W.Eiserbeck, T.Müller, D.Schulz, G.Wagner, J.Wollweber
Mater. Sci. Eng. B 61-62 (1999) 68-72

STABILITY CRITERIA OF 4H-SiC BULK GROWTH

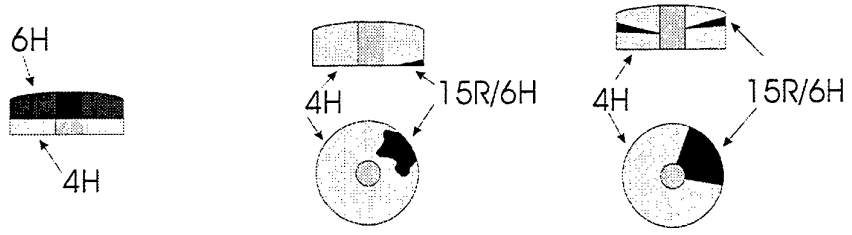
T.L. Straubinger, M. Bickermann, D. Hofmann, R. Weingärtner, P.J. Wellmann and A.Winnacker

Department of Materials Science 6, University of Erlangen, Martens Str. 7, 91058 Erlangen, Germany. Phone: +49-9131-85-27730; Fax: +49-9131-85-28495
Email: thomas.straubinger@ww.uni-erlangen.de

Currently 4H- and 6H-SiC are both commercially available in high crystal quality. However, while the 6H-polytype is known to be stable for a wide range of process conditions, 4H is stable only in a narrow range of growth parameters. Therefore it is of particular interest to better understand the origin of 4H to 6H/15R polytype transformations in order to improve the stability of the crystal growth process.
Our work will focus on PVT/4H/C-side experiments by discussing three types of polytype instabilities during crystal growth (Fig.1):

i. Complete conversion from 4H to 6H growth generated on the facet.
ii. Island growth of other polytypes during initial stage.
iii. Circular ring sector inclusions generated at the edge of the facet.

Concerning the complete conversion (Fig.1i.) it is stated in Literature [1] that a upper T^{Max}-value for stable 4H region exists. In this work we investigated the dependence of this temperature on other parameters like inert gas pressure (p^{Argon}) and axial temperature gradients (ΔT^{Ax}).
Therefore we performed more than 20 PVT growth experiments (d=35mm) with different T, ΔT^{Ax} and p^{Argon} and characterized the polytype evolution inside the crystals. No dependence of 4H stability on the argon pressure was visible but we detected a linear dependence of T^{Max} on the axial temperature gradient. For low axial T-gradients the critical temperature decreased.
In the 4H region two types of polytype inclusions (6H/15R) were observed which were not stable and were overgrown by 4H.
In the initial stage of growth several growth spirals of 15R and 6H polytype (Fig.1ii.) appeared on the 4H seed. These were found to be not critical for the main part of crystal growth because they were overgrown by the 4H growth spiral in the middle of the seed crystal. Furthermore they could be avoided by a seeding procedure with low saturation.
During further growth sector like polytype inclusions (Fig.1iii.), mainly 15R and only sometimes 6H, appeared on the edge of the facet and were overgrown again by the 4H facet. No dependence on pressure or axial temperature gradient was observed for this polytype generation mechanism.



i. ii. iii.

Figure 1: Three types of polytype instabilities observed during the 4H-SiC PVT process:
i. Complete conversion (axial cut) ii. Island Growth and iii. Circular ring sector inclusions (both axial cut and wafer)

Literature :

[1] G. Augustine et al., «PVT Growth and Properties of SiC Monocrystals of 4H Polytype », phys. Stat. Sol. (b) 202, 137 (1997).

MoP-44

AlN crystal growth by sublimation technique

Yu.A. Vodakov [1], S.Yu. Karpov [2], M.S. Ramm [1], E.N. Mokhov [1],
A.D. Roenkov [1], , Yu.N. Makarov [3]

[1)] A.F.Ioffe Physical-Technical Institute, Polytechnicheskaya 26, 194021 St.Petersburg, Russia, Phone +7 (812) 247-9145, Fax +7 (812) 326-6194

[2)] Soft-Impact Ltd, P.O.Box 33, 194156 St.Petersburg, Russia, Phone +7 (812) 554-4570, Fax +7 (812) 326-6194

[3)] Fluid Mechanics Department, University of Erlangen-Nuernberg, Cauerstrasse 4, D-91058 Erlangen, Germany, +49 (9131) 76-1248, +49 (9131) 76-1275

Aluminum nitride is commonly considered as a promising material to fabricate insulating substrates for group-III nitride technology. The most suitable method of AlN bulk crystal growth is the sublimation-recondensation technique introduced by Slack and co-workers [1,2]. In spite of intensive studies, general transport and growth mechanisms are still far from complete understanding mainly due to specific kinetics of nitrogen interaction with AlN surface.

In this paper we report new results of both experimental and theoretical study of AlN crystal growth in a sandwich system. Growth has been carried out in N_2 at atmospheric pressure in the temperature range of 2000-2300°C. Both AlN powder and liquid Al were used as the source of Al vapor. The SiC Lely crystals have been employed as seeds for AlN growth. Modeling is used to understand better mechanisms of sublimation growth of AlN and to optimize reactor design and growth process. A model proposed in [3] is used for analysis.Kinetics of N_2 adsorption on AlN surface plays crucial role in the growth process. This effect has been accounted for by a temperature dependent sticking coefficient derived in [4] from the data on Langmuir evaporation of AlN.

Comparison of liquid Al and AlN sources shows that the former is more efficient at low temperatures while the latter provides greater growth rates at high temperatures. The use of the liquid Al source results in parasitic AlN nucleation on the source surface. In contrast, the AlN powder source provides much more stable operation and, at sufficiently high temperatures, growth rate ~0.3-0.5 mm/h. In the paper, modeling results are compared with the measured AlN growth rate as a function of temperature and temperature difference between the surface and the seed. In particular, it is found that directional reactive species transportation from the source to the seed is possible only if the pressure P exceeds a critical value P_c depending on temperature. At $P < P_c$ the character of gas flow in the growth cell changes from one-dimensional to two-dimensional (the gas flows toward the openings of the growth cell), and the seed etching is predicted instead of AlN growth.

AlN growth on SiC seed occurs at high temperatures leading both to evaporation of SiC and to its chemical interaction with Al and N_2 . As a result, complex gaseous compounds containing Al, N, C and Si atoms are formed in the gas phase. In the paper we report on thermodynamic analysis of the species produced to understand better the composition of the vapor taking part in AlN growth. One more peculiarity is that growth of AlN on SiC does not occur until a certain temperature difference between the source and the seed is approached. This fact can be explained by strain in the AlN film on SiC substrate resulting in a shift of gas-solid equilibrium on the growth surface.

It is well known that oxygen can considerably interfere AlN crystal growth due to high Al reactivity. We estimate the gaseous N_2 purity required to avoid formation of parasitic Al_2O_3 phase inclusions in AlN crystal. The critical O_2 concentration in found to be a function both of temperature and pressure.

In the report we also discuss results of characterization of the grown AlN crystals.

References

[1] G.A. Slack, T.F. McNelly, J.Cryst. Growth 34 (1976) 263.

[2] G.A. Slack, T.F. McNelly, J.Cryst. Growth 42 (1977) 560.

[3] A.S. Segal, S.Yu. Karpov, Yu.N. Makarov, E.N. Mokhov, A.D. Roenkov, M.G. Ramm, Yu.A. Vodakov, J.Cryst.Growth 211 (2000) 68.

[4] M.V. Averyanova, I.N. Przhevalsky, S.Yu. Karpov, Yu.N. Makarov, M.S. Ramm, R.A. Talalaev, Mat.Sci.Engineer.B 43 (1997) 167.

Chemical Vapor Deposition of SiC by the Temperature Oscillation Method

Yutaka Abe
Hokkaido Automotive Engineering College,
Toyohira-Ku, Nakanoshima 2-6, Sapporo, 062-0922, JAPAN
Tel. +81+11+821-0171 Fax. +81+11-821-7300

I have explored a new type of the crystal growth method which has possibility of obtaining a crystal of much smaller amount of defects compared with one by the physical vapor deposition. Here, I adopted the method which is known as " temperature oscillation method". This method was initially developed by Schools and coworkers [1], consists of a periodic reversal of the temperature gradient between the source and the crystal. As a results of the alternation of temperature, intervals of crystal growth alternate with intervals of etching, making the crystal growth highly selective. The growth apparatus consists of independent two heaters in order to alternate the temperature gradient between the source and the crystal, which becomes more complex structure compared with the PVD apparatus. Moreover, an optimal controlling parameters, such as the time interval of growth and etching must be determined by a large amount of sequential experiments. When the alternation of temperature gradient turns off, a large number of small crystallite is observed on the surface of a substrate and the wall of quartz tube. (Temperature of the source is kept at 1600° C). Various temperature setting and the results are shown in the following table.

typical trials	Source temperature	Growth intervals (min.)	Etching intervals (min.)	Grown crystal
No.1	1600	30	10	a few small crystal.
No.2	1400	30	14	a few irregular-size crystal.
No.3	1600	initial stage 20 steady state 30	7 10	relatively large-size crystals.

X-ray investigations on the crystals indicate that the grown crystals are almost uniform phase, but several crystals involves twin boundaries. The size of the cristal is still very small even the growth time is over 300 hours. However, the density of the micropipe is extremely small, which indicates the present method strongly suppress the multi-nucleation of the crystals.

This work was supported by Hokkaido Foundation for the promotion of scientific and industrial technology, contract number you-020.

[1] H. Scholz, Acta Elektron, 17 (1974) 49, H. Scholz and R. Kluckpw, in: Crystal Growth, Ed, H. S. Peiser (Pergamon, Oxford, 1967) , 475-482.

Some aspects of sublimation growth of SiC ingots

S.F. Avramenko[1)], V.S. Kiselev[1)], M.Ya.Valakh[2)], V.A. Yukhimchuk[2)]

[1)]Special Design-and-Engineering Bureau with a pilot production of the Institute of Semiconductor Physics, NAS of Ukraine, Lisogorskaya St. 4, Kyiv, 03028, Ukraine, Fax: 380(44) 265-19-57, E-mail: kisvs@usa.net

[2)]Institute of Semiconductor Physics, NAS of Ukraine, 45 Prospekt Nauki, Kyiv, 03028,Ukraine, Fax: 380(44) 265-83-42, E-mail: valakh@isp-div6.kiev.ua

Silicon carbide SiC is a promising material for high temperature and power electronic devices. However, the deficiency of good quality large area substrates with low defect densities is a major drawback for further development. One of the outstanding issues is the relationship between crystal growth conditions as well as structural quality and polytype structure of bulk crystals. The aim of the present work is to analyze some parameters of the crystals: shape, surface morphology and quality.

The shape of the crystals depend on the construction of growth cavity. Change of geometry allowed to grow crystals with convex, concave or flat growth front. We have tested some internal assembles of a crucible and used different materials for thermal insulation: rigid carbon foam, graphite foil and graphite tissue. It let us to control the temperaturedistribution in a growth cavity in order to determine the shape of growth front and crystal shape.

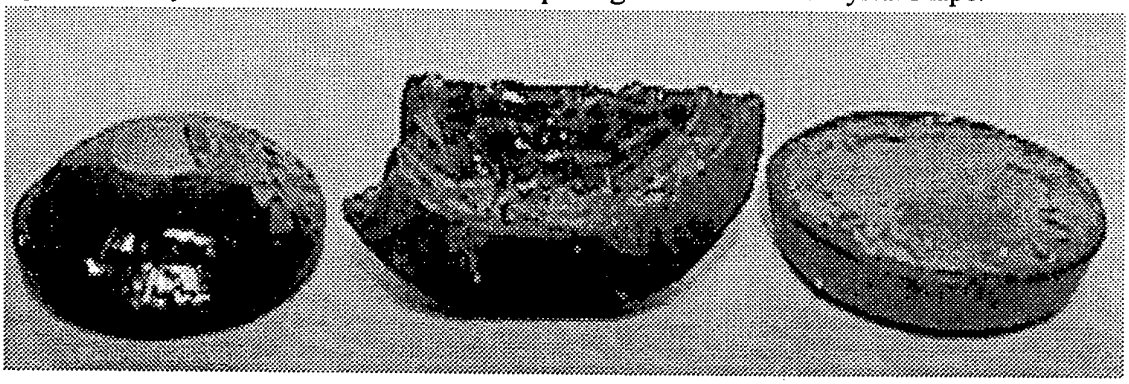


Fig.1. Photo of the crystals with convex, concave or flat growth front.

Using thermal field with symmetry like spherical let us to grow crystals in **a** and **c** directions [1]. The lateral growth of seed crystal lead to enlargement of ingots, but it is limited by polycrystals grown simultaneously. In that case the radial and axial temperature gradients imposed on growing crystal create stresses in the crystals. The concave growth front bring to downsizing of monocrystal part of ingots. The flat growth front seems to be the better one from commercial point of view [2]. The polytype homogeneity of substrates was examined by Raman measurements. High sensitivity of the method and the possibility to register even the smallest inclusion of different polytype are demonstrated. Raman line widths for the crystals obtained in this work do not exceed the minimum values mentioned in literature.

[1] S.F.Avramenko, V.S.Kiselev, M.Ya.Valakh, V.G.Visotski. Semiconductors Physics, Quantum Electronics & Optoelectronics, .2(11), 76-79 (1999).

[2] M.Anikin, M.Pons, K.Chourou, O.Chaix, J.M.Bluet, V.Lauer, and R.Madar, Materials Science Forum 45,264-268 (1998).

Characterization of 2 inch SiC wafer made by sublimation method

M.Sasaki, H.Shiomi and S.Nishino
Kyoto Institute of Technology, Matsugasaki, Sakyo, Kyoto 606-8585, Japan
Tel: +81-75-724-7415, Fax: +81-75-724-7400
E-mail: sasaki1m@djedu.kit.ac.jp, nishino@ipc.kit.ac.jp

From the device fabrication point of view, large size SiC wafers are needed. But to make large diameter bulk crystal, there are some problems such as homogeneity of the substrate temperature. Due to large temperature differences in the substrate, the grown crystal is inhomogeneously stressed. We evaluated 2 inch wafers cut from bulk crystals and discuss stress induced defects, etc. .

These wafers under cross polarized dark field condition. In this condition, if the wafer is not distorted, the image should be homogeneously dark. However, dark and white regions are mixed together as shown in Fig.1. This wafer was obtained from near the top surface of bulk crystal and it is clear that a lot of distortion exists in the wafer. These distortions appear as stripes in the cross polarized image. We believe there are two types of distortions in this wafer. One is the distortion near the edge of wafer (point A) and another is the distortion of the center area (point B). The distortion of point A was probably influenced by the graphite crucible, while the that of the point B was influenced by the shape of bulk surface. The bulk surface was convex for every growth and this may have generated the distortion at the center of wafer. The shape of the top surface is related to the growth rate of the bulk. In our experiment, central area became convex, which means the growth rate in this region is higher than the peripheral region. This different growth rate seems to be related to the distortion of the wafer and defect formation.

Figure.2 shows the photoluminescence spectrum spectrum of wafer at liquid N_2 temperature. Both the D-A pair spectrums of Al - N and B - N are the highest at the peripheral region of the wafer. In this wafer, there was dark area at the center and the peripheral region was transparent. However, the differences between these regions can not be understood from the PL results. The relation between doping concentration and stress distribution needs to be understood and will be discussed.

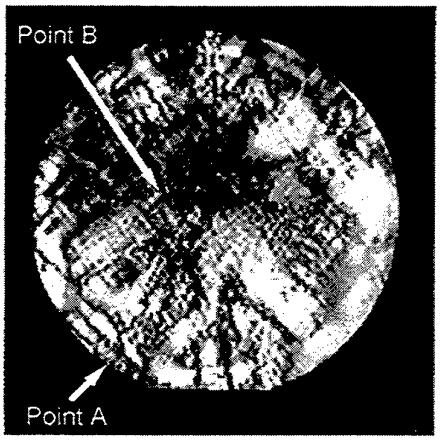


Fig.1 The cross-polarized image

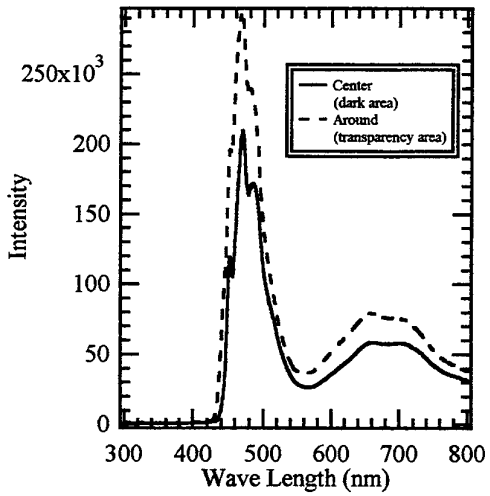


Fig.2 PL Spectrum

MoP-48

Growth of highly aluminum-doped p-type 6H-SiC single crystals by the modified Lely method

Norbert Schulze, Jürgen Gajowski, Gerhard Pensl
Institute of Applied Physics, University of Erlangen-Nürnberg
Staudtstr. 7/A3, 91058 Erlangen, Germany,
Phone: +49 (9131) 85-28434, Fax: -28423
E-Mail: Norbert.Schulze@rzmail.uni-erlangen.de

Low resistive (highly doped) p-type substrate material is desired for the production of especially vertical electronic devices. Common acceptors in SiC are aluminum (Al) or boron (B). The simple attempt to mix Al or B containing compounds among the SiC source powder fails because of the high partial pressure of Al and B for all the suitable compounds. Employing the modified Lely technique we have, therefore, put Al_4C_3 powder in a separate container which serves as Al source. The separate container was kept at temperatures significantly below the temperature of the SiC source (T_{source} = 2150°C-2180°C). Its exact temperature will be determined with an arrangement of several W/Re-thermocouples. We succeeded in growing p-type 6H-SiC boules on the Si-face of a n-type 6H-SiC seed crystal up to a length of about 1 cm.

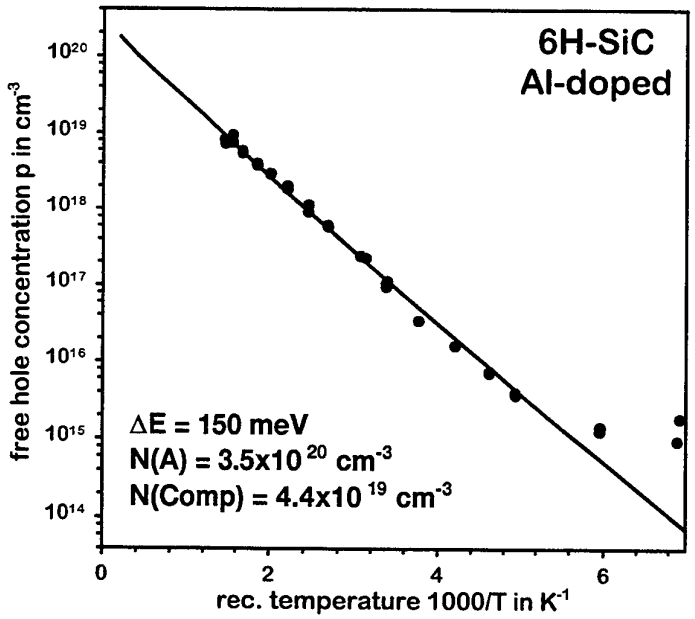


Fig.1. Free hole concentration p as a function of reciprocal temperature. The experimental data (circles) are obtained from a Hall-effect measurement. The solid line corresponds to a least-squares-fit of the neutrality equation to the experimental data. The fit parameters are given in the inset. ΔE, N(A) and N(Comp) denote the ionization energy, the total acceptor concentration and the concentration of the compensation, respectively.

The incorporation of Al has been investigated by Hall effect, C-V and SIMS measurements. The resistivity (at room temperature) is 3.4 Ωcm measured on a wafer, which is prepared from a region close to the seed crystal. Fig.1 shows the temperature dependence of the free hole concentration p (circles) taken on the same sample. A fit of the neutrality equation to the experimental data (solid line) results in an acceptor concentration N(A) of 3.5×10^{20} cm^{-3}. In contrast, SIMS and C-V measurements conducted on of the same sample lead to about 1×10^{19} cm^{-3} for the Al concentration and the net doping level, respectively. We attribute this contradiction to a wrong assumption used for the Hall effect evaluation. Because of the lack of experimental data for the Hall scattering factor r_H it is assumed that r_H is temperature independent and equal to one. We suppose that r_H is temperature dependent and is smaller than one at high temperatures which leads to smaller values of p in Fig.1. The temperature dependence of r_H will be estimated by comparison of the Hall effect data with the C-V and SIMS data obtained from identical 6H-SiC samples.

Coupled thermodynamic - mass transfer modeling of the SiC boule growth by the PVT method

A. Pisch[1], E. Blanquet[1], M. Pons[1], C. Bernard[1], J.M. Dedulle[2], R. Madar[2]

[1]Laboratoire de Thermodynamique et de Physico-Chimie Métallurgiques
UMR 5614 (CNRS/INPG/UJF), Domaine Universitaire, B.P.75,
F-38402 St. Martin d'Hères Cedex, France

[2]Laboratoire des Matériaux et du Génie Physique
UMR 5628 (CNRS/INPG), Domaine Universitaire, B.P. 46,
F-38402 St. Martin d'Hères Cedex, France

Phone: ++33 4 76826536, Fax ++33 4 76826767, E-mail: apisch@ltpcm.inpg.fr

Abstract

In order to relate the macroscopic growth features, as for example the growth rate and the shape of the growing single crystal as well as the Si/C ratio at the seed surface to the experimental parameters (temperature distribution and geometry of the growth cavity, reactive species pressure and overall pressure) a coupled thermodynamic/mass transfer simulation approach is necessary. Especially the initial conditions at the SiC powder surface are important, because the radial temperature distribution determines the pressure and the Si/C ratio of the reactive species. Experimental results show that the shape of the single crystal growth surface (flat, convex or concave) strongly depends on the overall pressure in the cavity. We have shown recently [1] that the evaporation of SiC is not congruent and kinetically hindered, leading to lower vapour pressures than predicted by thermodynamic equilibrium calculations. The real pressures can be described by introducing evaporation coefficients α, which relate the two pressures by $P_{real} = \alpha P_{theo}$. We have measured these coefficients by high temperature mass spectrometry for $Si_1(g)$, $Si_2(g)$, $Si_2C(g)$ and $SiC_2(g)$. In this contribution, we report on the results when employing these coefficients in the simulation and compare the calculated values to the experimental data.

[1] A. Pisch[1], A. M. Ferraria[1], C. Chatillon[1], E. Blanquet[1], M. Pons[1], C. Bernard[1], M. Anikin[2] and R. Madar[2], ICSCRM'99, Triangle Park, USA, oct. 1999

MoP-50

Progress in 4H-SiC crystal growth

M.Anikin [1], E.Pernot [1], B.Pelissier [1], M.Pons [2], A.Pisch [2], C.Bernard [2], C. Moulin [3], C. Faure [3], Th. Billion [3] and R.Madar [1]

[1] LMGP, UMR 5628 INPG/CNRS, BP 46, F-38402 St Martin d'Heres,France

[2] LTPCM, UMR 5614 CNRS/INPG/UJF, BP 75, F-38402 St Martin d'Heres, France

[3] LETI-CEA, F-38054 Grenoble cedex 9,France

4H crystals with diameters up to 35 mm have been grown by the Modified Lely Method with " in situ " sublimation etching. [1, 4]. An experimental set up with RF heating and graphite crucible was used. The crucible was wrapped by graphite felt for thermal insulation and the whole assembly was placed inside a water cooled quartz reactor. The growth temperature (measured on the top of graphite lid) was about 2200°C and the argon pressure was about 2 Torr. Under these experimental conditions we obtained 4H single crystals with thickness about 10 mm. The growth rate was between (1- 1.3) mm/h.

Both on-axis and 8° off-axis wafers were used as seeds. The growth took place on the (0001)C face after in situ etching at 1800°C at low argon pressure. Shape of the as-grown crystal surface was convex, concave or flat, depending on the growth cell geometry and the growth conditions. The optimal shape is flat because it allows to obtain the crystals with homogeneous doping and minimum low grain boundaries. However some cracking of the crystals with the flat surface was often observed when the diameter was larger than 25 mm.

It is worth noting that the growth took place in conjunction with poly -6H-SiC. The ratio between the growth rate of poly- and monocrystal was very important because the surface shape results from both the flux of SiC from the source and poly SiC position. The crystals with convex surface were more stable : the microcracking was observed only at the periphery of the crystal.

As-grown surface of the crystals grown on off-axis seed has the facet at the periphery of the crystal. The facet for a crystal grown on on -axis seed is located in the middle of the crystal . Therefore the crystals grown on the on axis seeds were more symmetric than those grown on off-axis seeds and the strain field was more homogeneous in these crystals. However 4H-SiC growth was more stable on the off-axis seed. The transformation 4H-SiC in 6H-SiC was more often observed during the growth on on-axis seed.

Moreover micropipes density was less in the crystals grown on the off-axis seeds. This can be explained by step-flow growth mechanism on the off-axis seed. Average pinholes density in our crystals was less than 50 cm^{-2}. This was determined by optical observation after etching in molten KOH and confirmed by synchrotron white beam X-ray topography (SWBXT).

References

[1] M.M.Anikin, R.Madar, A.Rouault, I.Garçon, L. Di Cioccio, J.L.Robert, J.Camassel and J.M.Bluet, Inst. Phys.Conf.Ser.N 142, Chapter 1, presented ISCRM-95, Kyoto, Japan, IOP Publishing Ltd (1996), 33.

[2] M.Anikin, R.Madar, Mat.Sci.and Eng.B46(1997)278.

[3] R.Madar, M.Anikin, K.Chourou, M.Labeau, M.Pons, E.Blanquet, J.M.Dedulle, C.Bernard, S.Milita. J.Baruchel, Diam. Rel. Mat. 6(1997)1249.

[4] M.Anikin, K.Chourou. R.Madar et al., Mat. Sci. Eng. B61(1999)73.

A comparison of SiO_2 and Si_3N_4 masks for selective epitaxial growth of 3C-SiC films on Si

C.-H. Wu, J. Chung, M.H. Hong, *C. A. Zorman, and *M. Mehregany
Department of Materials Science and Engineering
**Department of Electrical Engineering and Computer Science*
Case Western Reserve University, Cleveland, Ohio 44106, U. S. A.
Tel: (216) 368-3051, Fax: (216) 368-2668, e-mail: cxw36@po.cwru.edu

For electronic device applications, the use of 3C-SiC films grown on Si device is hampered by the high defect densities in the 3C-SiC films. One method currently under development to improve the quality of 3C-SiC films is selective epitaxial growth in conjunction with epitaxial lateral overgrowth. Selective epitaxial growth of SiC requires that the masking material must have good adhesion to the Si substrate, be mechanically stable at high-temperatures (~1300°C), be able to suppress nucleation and growth of polycrystalline SiC, and be chemically stable in a hydrogen atmosphere. In most cases, SiO_2 is used as the masking material. To improve selectivity, HCl is sometimes added to the carrier gas [1], but relatively thick SiO_2 masks are required (500 nm) to compensate for additional oxide etching. Si_3N_4 has also been used as a masking material for SiC selective epitaxial growth, but details regarding the crystal quality of the 3C-SiC layer, as well as selectivity to the nitride mask were not presented [2]. This paper presents the results of a systematic study to investigate the effects of masking material and mask geometry on the microstructure of 3C-SiC films selectively grown using a HCl-free growth process.

The masks used for selective epitaxial growth were fabricated from 200 nm-thick, thermally-growth SiO_2 and 100 nm-thick, LPCVD Si_3N_4 films deposited on 100 mm-diameter Si (100) wafers. The SiO_2 masks were fabricated by conventional photolithography followed by wet chemical etching in a buffered HF solution, while the Si_3N_4 masks were defined by photolithography and patterned by reactive ion etching using a SF_6-based plasma. The masks consisted of 2 to 20 μm-wide, 1 cm-long lines spaced 2 to 20 μm apart. 3C-SiC films were grown on the patterned substrates in an APCVD reactor using a two-step heteroepitaxial process. In this process, silane and propane were used as source gases, and hydrogen was used as the carrier gas. The exposed Si surfaces were carbonized by heating the substrates from below 500°C to 1280°C, and maintaining the temperature for 90 s in a propane/hydrogen ambient. Film growth was performed at 1280°C in a silane/propane/hydrogen ambient for growth periods of 3, 10, and 60 min.

SEM and TEM were used to characterize the as-grown films in the window areas and on top of the masks. SEM micrographs indicate that selective SiC growth can be achieved using the 2-μm-wide SiO_2 masks, but not using the Si_3N_4 masks (Fig.1). Despite the poor selectivity of the Si_3N_4 masks, the surface morphology of the 3C-SiC films in the window areas is smooth and the films are single crystalline, as confirmed by TEM. As for mask stability, delamination of the SiO_2 masks from the Si substrates was observed by cross-sectional TEM, while the Si_3N_4 masks showed no evidence of delamination.

The extended paper will detail the critical features of the masks, describe the effects of mask fabrication on the heteroepitaxial growth process, and present TEM and SEM data showing the effects of SiO_2 and Si_3N_4 masks on selectivity, surface morphology, and microstructure of the 3C-SiC films.

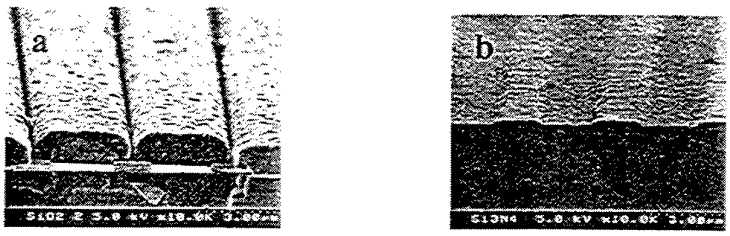


Fig. 1. SEM micrographs of selective epitaxy and lateral overgrowth of 3C-SiC on (a) SiO_2 and (b) Si_3N_4 masks.

[1] S. Nishino, H. Tanaka, K. Takahashi, and J. Saraie, Amorphous and Crystalline Silicon Carbide IV, 411, 1992.
[2] S.E. Saddow, G. Carter, G. Melnychuck, M.E. Okhuysen, M.S. Mazzola, Haibin Su, Li Jin, M. Dudley, B. Geil, T. Zheleva, K. Jones, Abstracts Inter. Conf. on SiC and Rel. Mat., Research Triangle Park, NC, U.S.A., Oct. 10-15. 1999, No. 231.

MoP-52

How to grow unstrained 3C-SiC heteroepitaxial layers on Si (100) substrates

T. Chassagne, G. Ferro, C. Gourbeyre[1], M. Le Berre[1], Y. Monteil, D. Barbier[1] and J. Bouix

Laboratoire des Multimatériaux et Interfaces, Université Claude Bernard Lyon 1
43 Bd du 11 Novembre 1918, 69622 Villeurbanne (France) / Tel: +33 4 72 43 13 92; Fax: +33 4 72 44 06 18

[1] Laboratoire de Physique de la Matière, Institut National des Sciences Appliquées Lyon1
20 Av. Albert Einstein, Bât. 502, 69621 Villeurbanne (France) / Tel: +33 4 72 43 89 98; Fax: +33 4 72 43 60 82

There are mainly two reasons which prevent the development of SiC large scale integration on silicon substrates : (1) the rather poor crystallinity of the 3C-SiC heteroepitaxial layers and (2) the important strain in the layers which bends the substrate or even makes cracks in the layers. For some applications such as pressure, temperature or gas sensors in which a high crystalline quality is not required, the latter problem becomes of main importance. The strain measured after cooling down of the sample is mainly due to the thermal mismatch between SiC and Si. Simple calculations taking only into account the thermal coefficients show that SiC should be in tensile stress at room temperature after the usual high temperature growth [1]. Although this tensile stress has been experimentally measured by many researchers [2-3], we report here the achievement of compression strained 3C-SiC heteroepitaxial layers on Si (100) substrates.

The growth experiments were carried out in a conventional vertical CVD reactor working at atmospheric pressure. The growth procedure involves the formation of a carburization buffer layer at 1150°C under a mixture of H_2 and C_3H_8. The propane is introduced in the reaction chamber before the ramp up to 1150°C as explained in our earlier work [4]. The subsequent epitaxial growth is performed at 1350°C by adding SiH_4. With that standard process, 3 µm thick SiC layers show a compression strain of about -500 MPa as measured by light deflection technique. These layers are equivalent to the state of the art in terms of crystalline quality, morphology and electrical properties.

As the tensile strain is most commonly found in 3C-SiC heteroepitaxial films on Si, we should be able to obtain tensile strained layers. Since the strain in the layers originates from the thermal mismatch with the substrate, we believe that the early stage of growth is very important as it sets the way it is hitched to the substrate. To confirm that hypothesis, we changed the conditions of carburization and measured the resulting strain after standard epitaxial growth. It was found that a tensile strain of about 500 MPa could be reproducibly obtained for some specific conditions of buffer layer formation. We are thus the first to demonstrate the possibility to achieve 3C-SiC layers with tensile or compression strain. By finely tuning the conditions of carburization, we observed a significant decrease in the strain. Work is under progress to understand the phenomenon and to achieve unstrained 3C-SiC heteroepitaxial layers. This would pave the way to large scale integration of SiC on Si substrates.

[1] H.P. Liaw and R.F. Davis, J. Electrochem. Soc. **131** (1984) 3014.
[2] S. Veprek, Th. Kunstman, D. Volm and B.K. Meyer, J. Vac. Sci. Technol. **A 15**(1) (1997) 10.
[3] C. Jacob and P. Pirouz, proceeding of the 10th conference on semiconducting and insulating materials, IEEE (1998) 275.
[4] G. Ferro, Y. Monteil, V. Thevenot, H. Vincent, F. Cauwet, Tran Min Duc and J. Bouix, J. Appl. Phys. **80**(8) (1996) 4691-4702

Growth of 3C-SiC using off-oriented 6H-SiC substrates

M. Syväjärvi, R. Yakimova, H. Jacobsson, and E. Janzén

Dept. Physics and Measurement Technology, Linköping University, S-581 83 Linköping, Sweden
E-mail: msy@ifm.liu.se; Tel. +46 13 285708; Fax: +46 13 142337

Development in epitaxial growth of the cubic polytype 3C-SiC has been held back due to lack of 3C-SiC substrates. Commonly, epitaxy on off-oriented 6H-SiC substrates results in homoepitaxial growth, i.e. replication by the epilayer of the substrate polytype. Growth conditions for avoiding inclusions of 3C-SiC within the layers have been studied extensively. We have studied formation of 3C-SiC grown on 6H-SiC substrates off-oriented 2.8° and 3.5° from (0001) in the [11$\bar{2}$0] direction. The 3C-SiC layer thicknesses reach hundreds of μm. The growth technique used is sublimation epitaxy and the growth rates range from 0.1 to 1 mm/h at 1800 to 1950°C. The (0001) face of 6H-SiC may be suitable as a substrate for 3C-SiC since the surface atomic structure of the (0001) face is similar to the atomic structure of the 3C-SiC(111) surface.

Our earlier studies of sublimation grown 3C have shown good quality material by low-temperature PL studies and well-ordered 3C-SiC(111) surfaces by LEED and Laue measurements [1].

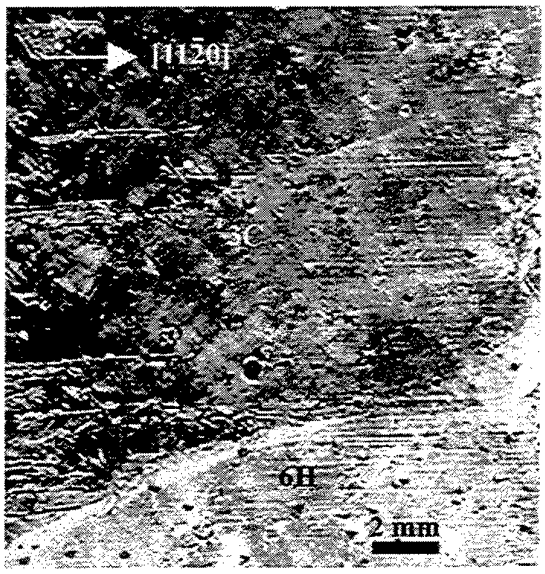


Fig. 1. Crossed-polarizer image of grown 3C-SiC on a 2.8° off-oriented 6H-SiC substrate.

In this study we present development in the growth of 3C-SiC for further understanding of necessary growth conditions for the polytype formation and growth mechanism. The grown 3C-SiC has been characterized using optical microscopy, crossed-polarizers, cross-sectional cleavages and high-resolution XRD measurements. Fig. 1 demonstrates an image taken with crossed-polarizers of 3C-SiC grown on an off-oriented 6H-SiC substrate. The lattice matching is demonstrated by 2θ/ω HRXRD measurements. The FWHM is less than 20 arcsec which shows that the 3C crystal growth on 6H-SiC has not resulted in severe crystal deformation of the 3C-SiC lattice. The development of the 3C-SiC crystal quality will be compared to our results for structural improvement in growth of 4H-SiC epilayers by sublimation epitaxy [2].

The important factors for growth of 3C-SiC will be presented. A model for the 3C-SiC growth using off-oriented 6H-SiC substrates will be given. The model is based on initial two-dimensional growth and 3C-SiC area enlargement by step-flow growth.

[1] M. Syväjärvi, R. Yakimova, P.-A. Glans, A. Henry, M.F. MacMillan, L.I. Johansson, and E. Janzén, J. Crystal Growth 198/199 (1999) 1019.
[2] M. Syväjärvi, R. Yakimova, H. Jacobsson, and E. Janzén, J. Appl. Phys., to be published (Aug 2000).

MoP-54

In situ RHEED studies on the influence of Ge on the early stages of SiC on Si (111) and (100) surfaces

V. Cimalla[1], K. Zekentes[1], K. Tsagaraki[1], Th. Stauden[2], F. Scharmann[2], J. Pezoldt[2]

[1]Foundation for Research and Technology Hellas, (FORTH), PO.BOX 1524, 71110 Heraklion, Greece
Phone: ++ 0 81 39 4134, Fax: ++ 0 81 39 4101, e-mail: cimalla@physics.uoc.gr
[2]TU Ilmenau, Institut für Festkörperelektronik, Postfach 100565, D-98684 Ilmenau, Germany

In the heteroepitaxial growth of SiC on silicon substrates the lowering of the growth temperature is still an important issue due to the large thermal mismatch between layer and substrate. The well developed CVD techniques generally require temperatures above 1000°C. The growth of SiC at the lowest temperatures is achievable by solid-source molecular beam epitaxy (SSMBE) due to the high reactivity of elemental sources. However, this causes several problems like the formation of a distinct grain structure and the deposition of additional phases. As for the CVD case, the nucleation is the most critical step and the initial layer, should be closed and block Si out-diffusion to the growing surface. Several approaches have been already presented to improve the initial growth like application of a defined heating cycle [1] as well as the use of Ge as surfactant or for lattice matching [2]. In this report we present a systematic study of the combination of these methods.

The SiC layers were grown in two different SSMBE configurations with a cross check of the reproducibility of the results for representative process conditions. The influence of Ge on the initial stages was investigated by depositing a thin 2D Ge layer on silicon immediately prior to the exposure to C. The growth processes were observed in situ by RHEED, while the final morphology was additionally analyzed by AFM, AES, and SEM.

Without the pre-deposition of Ge the nucleation proceeds through the formation of the known C-induced reconstructions, namely (4x4) and (2x2) for (001)Si and $\sqrt{3}x\sqrt{3}$ for (111)Si, which are only weakly dependent on the temperature with activation energies around 0.1-0.2 eV. The nucleation of SiC sets in either parallel or after the disappearance of the C induced reconstructions at high or low temperatures, respectively, with a cross-over temperature around 650°C. During the parallel nucleation the islands remain separated for a longer time resulting in a strong erosion of the silicon substrate and the growth of polycrystalline SiC. On such initial layers the deposition of single crystalline SiC is impossible.

The C induced reconstructions were not found on the Ge covered surface due to the high aversion between C and Ge atoms. Instead, during the nucleation of SiC the initial reconstructions transform to a disordered (1x1). Most striking is the evolution of the SiC lattice constant, which on pure Si immediately adopts the bulk value as expected for the large lattice mismatch of around 20%. In contrast, after the pre-deposition of Ge the initial SiC nuclei can have the lattice constant increased up to 5% for submonolayer growth. The final structure is comparable to the normal case. However, due to generally larger grains the process conditions for obtaining a closed initial layer are more critical

In most of the cases it was not possible to grow single crystalline SiC under isothermal nucleation conditions. Another approach is to stimulate an intermixing of C and Si to an alloy around 600°C prior to the SiC nucleation. Therefore two methods were applied after the Ge pre-deposition: (i) either the C was exposed during a well defined heating rate around 1-5 K/s depending on the applied C flux or (ii) 1-2 monolayers C were deposited prior to the heating. These methods improved the SiC structure drastically.

Finally, the investigations have shown, that the Ge introduced into the system as described acts as a surfactant, but the preferred growth at steps or step bands reveals, that it mainly passivates terraces and not steps.

[1] Cimalla, V.; Stauden, Th.; Eichhorn, G.; Pezoldt, J., Mater. Sci. Eng. B61-B62 (1999) 553.
[2] Zekentes, K.; Tsagaraki, K., Mater. Sci. Eng. B61-B62 (1999) 559.

Selective deposition of 3C-SiC epitaxially grown on SOI substrates

M. Eickhoff, S. Zappe[1], A.Nielsen, G. Krötz, E. Obermeier[1], N.Vouroutzis[2], J.Stoemenos[2]

DaimlerChrysler Research and Technology, Munich, Germany
[1]Technical University of Berlin, Secr. TIB 3.1, Gustav-Meyer-Allee 25, 13355 Berlin, Germany
[2]Aristotle University of Thessaloniki, Physics Department, 54006 Thessaloniki, Greece
Tel. +30-31-998191, FAX +30-31-214276

The epitaxial growth of 3C-SiC on Si-substrates imposes strain in the Si wafer due to the significant difference in the thermal expansion coefficients of SiC and Si. The strain increases with the thickness of the overgrown 3C-SiC and results in bending of the substrate or rupture of the 3C-SiC film at the interface. However, thick 3C-SiC films are preferable as they have lower defect densities. Nevertheless for the realization of devices most of the deposited 3C-SiC is etched off, demonstrating that depositition of 3C-SiC on the complete wafer surface layer leads to an unnecessary shrink in applicability. Therefore the selective deposition on prestructured Si-substrates has two main advantages in comparison to standard deposition processes: It reduces the area of the substrate, which is covered by the 3C-SiC, decreasing the mean strain imposed in the substrate, also simplifies device fabrication by dispensing the etching of the 3C-SiC. In this paper the structural characteristics of the selective deposition of 3C-SiC on prestructured Si-On-Insulator (SOI) substrates, applied for microsensor development is investigated using transmission electron microscopy (TEM).

The prestructured 200nm thick Si-overlayer (SOL) of a SOI wafer was wet oxidized at 1000°C. A 3C-SiC epitaxial layer with a nominal thickness of 2.2 μm was deposited on the patterned Si-overlayer by LPCVD process at 1220 °C using methylsilane. The piezoresistive 3C-SiC elements of the microsensors were studied by cross-section TEM. The general view of the structure at the edges of the SiC is shown in Fig.1. The buried oxide layer (BOX) is 400nm thick and the oxide mask has a thickness of 785nm. The quality of the 3C-SiC islands is comparable with the standard quality material, as shown in the high magnification micrograph in the inset in Fig.1. Cavities are observed in the SOL denoted by the letter C without the distraction of the BOX as shown in Fig.1. Lateral growth at the edge of the 3C-SiC film is observed, which is comparable with the thickness of the SiC film. The SOL was overetched at the edges of the patterned SiC, denoted by the letter E in Fig.1. The overetched area is extended inside the BOX not touching the Si substrate as shown in Fig.2. No rupture at the SiC/Si interface was observed. No traces of 3C-SiC islands on the oxide were found revealing that selective epitaxy at 1200°C or above is very successful.

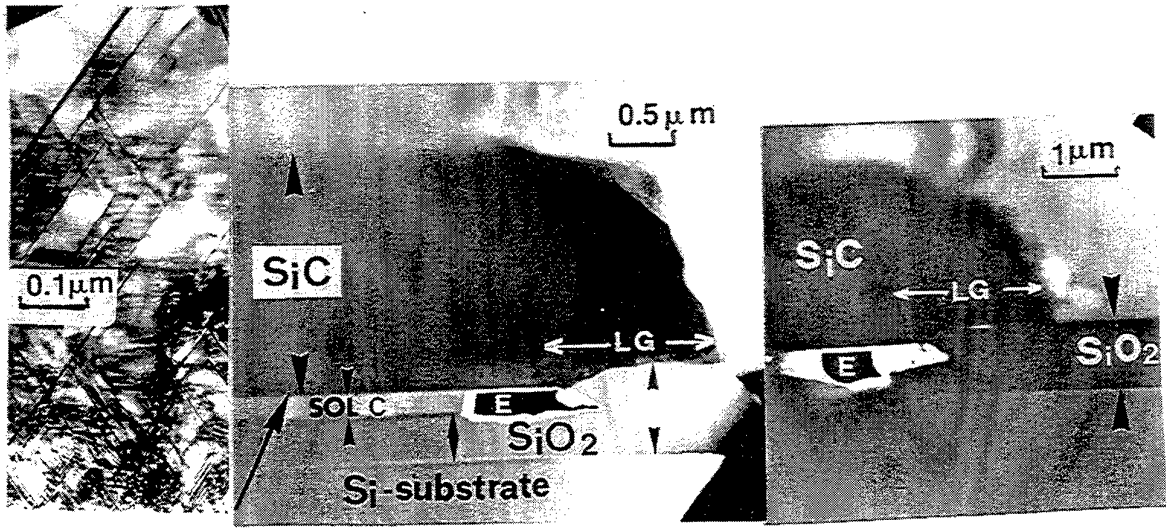


Fig.1

Fig.2

MoP-56

Abstract for the ECSCRM2000, Sept. 3-7, 2000, Kloster Banz, Germany

Comparison of various epitaxial growth processes on porous SiC substrates

M. Mynbaeva[a], *S.E. Saddow*[,b], *G. Melnychuk*,[b] *A. Syrkin*[c], *D. Bauman*[d], *N. Kuznetsov*[a], *I. Nikitina*[a] *A. Sitnikova*[a], *M. Scheglov*[a], *V. Solov'ev*[a] *and V. Dmitriev*[a,c]

[a] Ioffe Physico-Technical Institute, 194021 St. Petersburg, Russia,
Phone: 7(812)2479337, Fax: 7(812)2471017

[b] Emerging Materials Research Laboratory, Dept. of ECE, Mississippi State, MS 39762 USA
[c] TDI, Inc., Gaithersburg, MD 20877
[d] Crystal Growth Research Center, 194021 St. Petersburg, Russia.

We report on significant improvement of defect structure of SiC epitaxial layers grown on porous SiC substrates. Porous SiC substrates were fabricated from commercial 6H-SiC and 4H-SiC wafers. The properties of porous SiC were studied in terms of surface characteristics (SEM, AFM, RHEED) and crystal structure (x-ray diffraction, TEM). Epitaxial layers were grown simultaneously on porous and standard SiC substrates using three epitaxial methods: chemical vapor deposition, liquid phase epitaxy, and sublimation epitaxy. The defect structure of the layers was investigated by chemical etching, x-ray diffraction, and TEM. Electrically active defects in the epitaxial layers were studied by DLTS (Fig. 1). The minority carrier diffusion length measured by EBIC method for SiC layers grown on porous substrate was larger than that for SiC grown on standard substrate. Experimental results clearly indicate superior quality of SiC layers grown on porous substrates as compared to epitaxial layers grown on standard SiC wafers. These results include lower concentration of extended defects (dislocations) and point defects (shallow and deep-level centers) in SiC layers grown on porous substrates. The trend is clearly seen for all three epitaxy techniques. The role of porous substrate in the epitaxial growth of high-quality SiC layers will be discussed. Properties of porous SiC substrates and results of investigation of defects in SiC epitaxial layers grown by different techniques on porous SiC substrates will be presented.

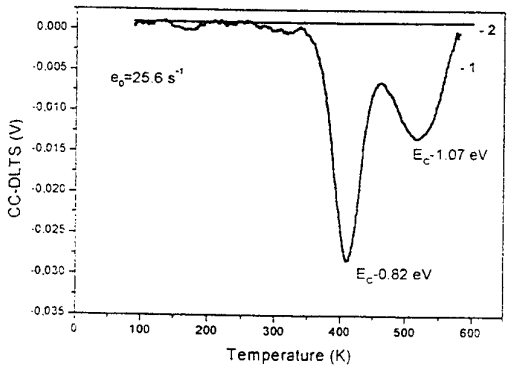


Figure 1. DLTS spectra for SiC layer grown on standard (1) and porous (2) substrates in the same epitaxial run. Two deep levels are detected in the layer grown on standard substrate.

Work at TDI is supported by the Office of Naval Research (contract monitor Colin Wood).

Effect of Sublimation Growth on the Structure of Porous Silicon Carbide: SEM and X-ray Diffraction Investigations.

N.S.Savkina, V.V.Ratnikov, V.B.Shuman, A.A.Lebedev.

Ioffe Phys.-Technical Institute, Russian Academy of Sciences, St.-Petersburg, Russia.
Fax: +7 (812) 2476425, Phone: +7 (812) 2479930, E-mail: nata.sav@.pop.ioffe.rssi.ru.

In a series of papers it has been demonstrated photoluminescence properties of porous silicon carbide (PSC). Previously [1], the possibility of obtaining high-quality 6H-SiC films on PSC has been demonstrated. The aim of the present work was to perform a comparative study by X-ray diffraction and scanning electron microscopy (SEM) of PSC before and after high-temperature growth of epitaxial 6H-SiC layers by sublimation.

The experiments were carried out on polished (0001)Si face of a commercial 6H-SiC 3.5° off wafer (CREE). The samples were anodized in a HF : H_2O : C_2H_5OH = 1:1:2 electrolyte with UV illumination at current densities equal 20, 60, and 100 mA/cm^2. The etching time was 15, 5, and 3 min, respectively.

The epitaxial growth of thin 6H-SiC layers on PSC was performed by vacuum sublimation at 2000°C in a vertical water-cooled quartz reactor. The thickness and morphology of PSC were determined by SEM images of cleaved surface before and after the high-temperature sublimation growth.

X-ray measurements were done on double-crystal (DCD) and triple-crystal (TCD) diffractometers in $CuK_{\alpha 1}$ radiation. The sample porosity was evaluated by absorption porometry (with accuracy of ± 5%), and macrostrains were determined from sample curvature radii R measured on DCD. The structural perfection of the layers was monitored by the behavior of the full width at half maximum (FWHM) of a symmetric Bragg's reflection (0006). In measurements on TCD θ- and (θ-2θ)-scanning modes were used.

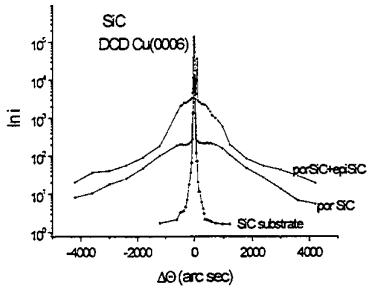


Fig.1. DCD rocing curves.

DCD rocking curves have the same shape for all PSC samples on SiC (Fig. 1), each containing a narrow peak on a broad diffuse "hump." The hump associated with diffuse scattering (DS) on a porous structure. The subsequent growth of an epitaxial layer on PSC is accompanied by a decrease in FWHM of both the narrow and the diffuse peaks. The pronounced (2-3 times) narrowing of the diffuse peak points to a structural transformation of the PSC. The integral FWHM of the dynamic peak suggests that the diffraction characteristics of the epitaxial layer are as good as those of the substrate. However, in contrast to the substrate, the epitaxial layer shows good uniformity of properties over the sample area.

The dramatic reduction of biaxial stresses in epitaxial SiC layers grown on PSC and the good uniformity of the diffraction characteristics of the layers over their area suggest that the given direction of research is rather promising.

[1]. M.Mynbaeva, N. Savkina, A.Zubrilov, N.Kuznetsov, A.Lebedev, I.Kotousova, V.Dmitriev, Book of Abstr. MRS Fall 1999 Meeting, Nov.29-Dec.3, Boston, Massachusets, SYMPOSIUM O 8.6, 251 (1999).

Prediction of optical properties of Si and Ge dots in SiC

H.-C. Weissker, J. Furthmüller, and F. Bechstedt

Friedrich-Schiller-Universität, Max-Wien-Platz 1, 07743 Jena, Germany
Tel.: ++49-(0)3641-947163, Fax: ++49-(0)3641-947152, E-mail: hcw@ifto.physik.uni-jena.de

Nanometer-sized Si and Ge structures give rise to an efficient photoluminescence at visible and even blue wavelengths. This observation has prompted many studies, both exploring technological applications and investigating fundamental properties. Such nanostructures have been fabricated by ion implantation in amorphous SiO_2 matrices, by electrochemical etching or by Stranski-Krastanov growth using molecular-beam epitaxy (MBE). Unfortunately, electroluminescence from the nanocrystals is limited by the insulating character or the too small energy gap of the matrix material. To overcome these limitations, embedding the nanoparticles in a wide-gap semiconductor, e.g. α-SiC, seems to be promising. Recent MBE deposition of Si and Ge dots on SiC in fact offers a realistic possibility for preparation of such embedded dots.

In this paper we present parameter-free calculations of the electronic structure and the frequency-dependent dielectric function in order to understand the optical properties of Si and Ge nanoparticles in a SiC matrix in dependence on their size and the surroundings. The calculations are based upon density-functional theory (DFT) in the local-density approximation (LDA). Ultrasoft pseudopotentials allow the *ab initio* treatment of supercells with up to 512 atoms. Each supercell contains one cluster with a varying number of Si or Ge atoms. The maximum number of 239 atoms corresponds to a dot diameter of about 1 nm. To simulate the influence of matrix material and strain, two different situations are studied. Fully strained dots are considered in a matrix of cubic SiC. A hydrogen termination of completely unstrained nanocrystals is used to simulate in particular the effect of a wide energy gap of the matrix material, as it occurs for instance in the case of hexagonal SiC.

The optical calculations are performed within the independent-particle picture. We make use of a partial cancellation of self-energy and excitonic effects. Matrix elements are calculated using all-electron wave functions. The tetrahedron method and a Gaussian-broadening histogram scheme are applied to the k-space integration. The influence of many-body effects is also discussed. Quasiparticle shifts are estimated using a simplified screening in the GW expression. Coulomb integrals give estimates for the electron-hole interaction.

We discuss the dependence of the resulting optical spectra on dot size, in particular that of the optical absorption, the dielectric constant, the lowest transition energies and their oscillator strengths. We find dot-matrix interface effects to be significant. This holds especially for the embedding in cubic SiC which seems to result in a type-II heterostructure. Several absorption peaks, among them the one developing into the bulk E_2 structure, are found with varying position and strength. The calculated spectra are compared with recent results for Ge nanostructures embedded in the "wide-gap" system sapphire.

Si- and Ge-Nanocrystals on SiC(0001)

G. Heß, A. Bauer, B. Wunderlich, J. Kräußlich, K. Goetz
Friedrich-Schiller-Universität Jena, Institut für Optik und Quantenelektronik,
Max-Wien-Platz 1, D-07743 Jena, Germany
Tel: +49 (0)3641 947253 Fax: +49 (0)3641 947202 Email: ghess@ioq.physik.uni-jena.de

A. Fissel, U. Kaiser, B. Schröter, W. Richter
Friedrich-Schiller-Universität Jena, Institut für Festkörperphysik, Max-Wien-Platz 1, D-07743 Jena, Germany

N. Schell, W. Matz
Forschungszentrum Rossendorf, Postfach 510119, D-01314 Dresden, Germany

The development of fast optoelectronic SiC devices requires detailed knowledge about the structural properties of low-dimensional structures epitaxially grown on SiC(0001)-surfaces. In our recent work, we investigated the growth and structure of Column IV nanocrystals using high resolution x-ray diffraction (HXRD), transmission electron microscopy (TEM) and atomic force microscopy (AFM). The reciprocal space maps could be obtained using the high intensity new material research goniometer of the ROBL beamline at the European Synchrotron Radiation Facility in Grenoble.
The Si- and Ge-nanocrystals were grown by molecular beam epitaxy on SiC(0001)-substrates using the Stranski-Krastanov growth mode. The number density, shape, size and size distribution, as determined by AFM and TEM, varies according to the specific process parameters. Furthermore, by changing the process parameters (flux, temperature), we were able to grow nanocrystals with different sizes (lateral dimensions 40-200 nm, vertical dimensions 5-50 nm) on different samples, but with a narrow size distribution of the nanocrystals on each sample. Reciprocal space maps around Si- and Ge-reflections revealed that the Si- and Ge-nanocrystals grow preferentially in two different orientations <111> and <110> with respect to the surface normal. However, by choosing specific growth conditions (low flux, high temperatures), we were able to grow (111)-nanocrystals selectively. Interestingly, for Ge-nanocrystals grown on Si-rich SiC-surfaces, our HXRD- and TEM-results show that the Ge-reflections are shifted towards the angular position of the corresponding Si-reflection. Such a peak shift can be explained by the change in the lattice constant due to the formation of a Si/Ge solid solution. Using vegard's law, it is possible to calculate the average composition of the nanocrystals from the peak shift. A quantitative analysis of the HXRD-data results in the average dimensions of the nanocrystalline regions and the stress and strain within the nanocrystals. The lateral orientation of the (111)- and (110)-nanocrystals was investigated by comparison of the azimuthal ϕ-scans of a nanocrystal-reflection (220-reflection for (111)-nanocrystals and 111-reflection for (110)-nanocrystals) with an appropriate substrate-reflection. This comparison revealed that the (111)-nanocrystals as well as the (110)-nanocrystals grow coherently with respect to the substrate. The 6-fold symmetry of the ϕ-scans shows clearly the existence of rotation twins. Since the FWHM of the ϕ-scan reflects the degree of coherence between nanocrystals and substrate, our data show that the correlation between the Si-nanocrystals (FWHM $\phi < 1°$) and SiC is much better than the correlation between Ge-nanocrystals (FWHM $\phi > 5°$) and SiC. The shape and the size of the nanocrystals were determined using TEM and AFM. Using this information as an input, a detailed analysis of the reciprocal space maps reveals that the amount of stress and strain is less in the Ge-nanocrystals compared with the Si-nanocrystals. Obviously, the Ge-crystals avoid the stress and strain due to the lattice mismatch by a poor alignment to the substrate. It is possible to improve this alignment by increasing the amount of Si within the Ge-nanocrystal.

MoP-60

Carbonization induced change of polarity for MBE grown 3C-SiC/Si(111)

J. Pezoldt[1], B. Schröter[2], V. Cimalla[1,3], Th. Stauden[1], R. Goldhahn[4], L. Spieß[5]

[1]TU Ilmenau, Institut für Festkörperelektronik, Postfach 100565, 98684 Ilmenau, Germany
[2]FSU Jena, Institut für Festkörperphysik, Max-Wien-Platz 1, 07743 Jena, Germany
[3]FORTH, Microelectronic Research Group, PO Box 1527, 71110 Heraklion/Crete, Greece
[4]TU Ilmenau, Institut für Physik, Postfach 100565, 98684 Ilmenau, Germany
[5]TU Ilmenau, Institut für Werkstofftechnik, Postfach 100565, 98684 Ilmenau, Germany

The lack of large, high-quality 3C-SiC bulk crystals has stimulated several groups to investigate systemically thin film growth on Si substrates. Beside the fundamental aspects of heteroepitaxy in a material system with large lattice mismatch, 3C-SiC/Si layered structures offer some attractive applications. The first is in the field of robust sensors operating at high temperatures and in harsh environments. At second, they can be successfully used as pseudo-substrates for the cubic nitride epitaxy [1]. The common technique to grow SiC on Si is a two step process consisting of a carbonization process, e.g. under CVD or MBE conditions, followed by epitaxial growth. The influence of the carbonized layer on the subsequent epitaxial process was studied mostly in the context of structural perfection of the film and how this quantity influences the structural perfection of the grown active layer. However in most studies, only one method was applied for the conversion of the silicon surface into silicon carbide. In this work we present a comparative study of the crystalline quality, surface morphology, and polarity for solid source MBE grown single phase 3C-SiC active layers if different carbonization processes are applied.

The first method (RTCVD) is based on the carbonization process in a propane hydrogen atmosphere in a rapid thermal processing reactor described in detail in [2]. The second one is a MBE based process consisting of the following process steps: (1) deposition of carbon on a (7x7) reconstructed Si surface at 325 °C, (2) heating up the Si wafer to 660 °C within 3 minutes, (3) gradually increase of the substrate temperature in steps of 50 degree up to the final growth temperature for SiC epitaxy. On both carbonized substrate types, 120 nm thick 3C-SiC epitaxial layers were grown at 1000 °C with a rate of 1nm/min. under Si rich conditions and continuously operating Si and C sources. The stability of the deposition conditions was controlled by reflection high energy electron diffraction (RHEED) monitoring the (3x3)-Si (111)SiC surface reconstruction. In addition, the growth process was monitored by *in-situ* real-time spectroscopic ellipsometry (SE). *Ex-situ* characterization of the films was performed by atomic force microscopy (AFM), X-ray diffraction (XRD), X-ray photoelectron diffraction (XPD), and SE.

The results emphasize that both substrate types lead to epitaxial layers characterized by a single domain 3C-SiC structure. The films grown on RTCVD carbonized substrates exhibit a smoother interface between SiC and Si, but a larger surface roughness compared to the layers grown MBE carbonized wafers. Furthermore, the full width of the half maximum of the (111)SiC XRD peak is found smaller in case of RTCVD material indicating a lower residual stress. Detailed XPD measurement revealed that the epitaxial layer grown on RTCVD material shows C-face surface polarity, whereas the material grown on MBE material is characterized by a Si-face polarity.

[1]D.J. As, T. Frey, D. Schikora, K. Lischka, V. Cimalla, J. Pezoldt, R. Goldhahn, S. Kaiser, W. Gebhardt, Appl. Phys. Lett., **76** 1686 (2000).
[2]V. Cimalla, K.V. Karagodina, J. Pezoldt, G. Eichhorn, Mater. Sci. Eng., **B29** 170 (1995).

SiC polytype transformation on the growth surface

E.N.Mokhov, S.K.Obyden*, A.D.Roenkov, G.V.Saparin*, Yu.A.Vodakov

A.F.Ioffe Physical-Technical Institute, Russian Academy of Sciences,
194021, St.Petersburg, Russia, Phone +7 (812) 515-9273, Fax: +7 (812) 515-6747
* Department of Physics, Moscow State University, 119899, Moscow,
Russia, Phone: +7 (095) 939-4829, Fax: +7 (095) 939-4829

Silicon carbide is wide known as a polytypic material. Different SiC polytypes are characterized specific semiconductor properties. But, still control of growth of SiC of a certain polytype is a complicated issue. Insufficient control of growth of SiC bulk crystals and epitaxial layers often results in polytype non-uniformity that decreases drastically quality of the semiconductor devices based on SiC.

In this work the polytype transformation in the SiC epitaxial layers has been investigated in dependence on growth conditions and structure of the growing surface. The layers were grown by sublimation sandwich method on the (0001)Si and (0001)C SiC seeds. Deposition of epitaxial layers was carried out in vacuum or in inert gas atmosphere in the temperature range 1700 - 2500°C. Temperature gradients varied from 10 to 90 °C /cm.

SiC crystals of 4H, 6H, 8H, 15R and 21R polytypes grown by Lely method were used as seed. The growth was performed on vicinal and singular surfaces. A method of artificial surface singularization was used for investigation of the growth mechanisms and polytype transformation. In this case the substrate has an artificial ly made profiled surface covered by projected areas with a linear size varying from 0,1 to 1mm.

Scanning electron microscopy technique in color cathodoluminescence mode was proposed for two-dimensional and three-dimensional studies of polytype structures. It allowed us to perform layer by layer structure analysis of a polytype on depths up to 2.5 μm with high resolution. The polytype structures have been studied by real color cathodoluminescence (CL) mode in scanning electron microscopy technique using true color contrast (CCL-SEM). Beam energy varied from 2 to 20 keV and the depth of electron penetration was changed from 0.1 up to 2.6 μm

High polytype stability of the growing SiC was revealed in case of vacuum condensation in the molecular kinetic mode, when normal growth mechanism was dominant and vicinal type of the growing surface remained. As a result the thick epitaxial layers (up to 1mm) and bulk crystals of different SiC polytypes (including rare polytypes such as 27R and 8H) may be grown simultaneously at the same growth conditions.

Presence of the impurities or insufficient preliminary cleaning of substrate surface promoted formation on substrate surface a separate non-coherent three dimensional nuclei which have caused the polytype syntaxy.

The layer- by- layer growth mechanism of SiC was usually prevailed under diffusion growth mode. The height of growth steps as a rule reached to macroscopic values (more than 0.1 μm) owing to step bunching processes. The dependence of the growth steps density and polytype structure on the substrate surface orientation was observed. It was shown that the polytype transformation during the growth process occurs mainly on the singular parts of the surface. We discovered the origin of separate nucleating centers at the edges and inside of singular parts of the growing surface.

The effect of polytype instability during the SiC epitaxial layer growth on the elevated parts of the singular (0001) surface is revealed. Polytype transformation probability is shown to be very high both on (0001)Si and (0001)C faces even at very low supersaturations.. As a results grown layer contains usually a set of the sublayers of different SiC polytypes with the thickness less than 1μm. The reasons of polytype instability are discussed. In particular, the surface clusters appearance is caused by interactions of matrix and impurity atoms with native point defects on the substrate surface may work as centers of new polytype nucleation during growth process. This conclusion is supported by specific dependence of the SiC growth rate on supersaturation observed in the case of singular surface

Increase of density of the structural and morphological defects on the substrate surface is shown to promote polytype stabilization. We observed reduction of polytype transformation probability in the epitaxial layers grown on the substrates with high dislocations density. The same effect is reached by the artificial damages of the substrate surface planarity. Polytype transformation is shown to be a less possible on the rough or stepped surface.

The tangential velocity of the macrosteps is shown to depend on the type of the surface and polytype. For example, the 4H thick macrostepped layers extend over the substrate surface on the great distances with the highest rate than other polytypes. They may cross wide (up to 1 mm and more) grooves and cracks. In result the 4H- SiC polytype layers are often covered by layers of other SiC polytypes.

MoP-62

Imaging the 3C-SiC(100) c(4x2) Surface Reconstruction by Empty and Filled Electronic States Scanning Tunneling Microscopy

V. Derycke, P. Fonteneau and P. Soukiassian
Commissariat à l'Energie Atomique, DSM-DRECAM-SIMA, Centre d'Études de Saclay, Bât. 462, 91191 Gif sur Yvette Cedex, France
and Département de Physique, Université de Paris-Sud, 91405 Orsay Cedex, France

Phone: *33 (0)1 69 08 70 11* Fax: *33 (0)1 69 08 35 92* E-Mail: *derycke@drecam.cea.fr*

We investigate the 3C-SiC(100) c(4x2) surface reconstruction [1] by atom-resolved filled and empty electronic states scanning tunneling microscopy (STM). Using a dual scan mode allowing to probe both filled and empty electronic state topographs of the same area of the surface, we are able to identify both up- and down dimers of the c(4x2) surface reconstruction. The down-dimer is identified by STM imaging when tunneling into the empty electronic states and could still be detected in the filled states topographs through intensity plots. In contrast, the up-dimer is seen when tunneling into the filled electronic states only. This behavior indicates that up-and down-dimers have very different electronic status. This investigation is in excellent agreement with recent core level photoemission spectroscopy experiments [2] and further supports the AUDD (alternately up- and down-dimer) model.

References

1-P. Soukiassian, F. Semond, L. Douillard, A. Mayne, G. Dujardin, L. Pizzagalli and C. Joachim, Physical Review Letters 78, 907 (1997).
2-V. Yu. Aristov, H. Enriquez, V. Derycke, P. Soukiassian, G. Le Lay, C. Grupp and A. Taleb-Ibrahimi, Physical Review B 60, 16553 (1999).

INVESTIGATION OF SIC SURFACE AFTER NITRAGEN PLASMA TREATMENT.

Bereznjakova L.A.[1)], *Shchukarev A.V.*[2)], *Ivanov-Omskii V.I.*[3)]
[1)] *Dept.of Microelectronics, St.-Petersburg State Electrotechnical university, Prof. Popov str.5, 197376, StPetersburg, Russia*
[2)] *Mechanobr-Analit, St. Petersburg, Russia*
[3)] *A. F. Ioffe Physical Technical Institute, St. Petersburg, Russia.*
Phone+7 812 234 30 64, Fax+7 812 234 31 64, E-mail: SiC.ME@eltech.ru

The current interest in silicon carbon nitride comes from the recent theoretical prediction about the existence of the superhard phase in the system Si-C-N [1]. Up to now, as far as we know only few experiments have been reported on such ternary systems, using various deposition techniques [2,3]. The stoichiometry of these ternary compound was found to be close to SiCN. The SiCN films were demonstrated to have amorphous structure. The wide band gap was observed in this compound [2].

The possibility of silicon carbon nitride formation by surface SiC treatment with the nitrogen plasma was examined in the present work. The processing was carried out in the high frequency plasma discharge. The samples were placed on the target. 6H-SiC Lely substrates with (0001)Si and (0001)C surface orientation and 3C-SiC epitaxial layers grown on the Si substrate were used as a samples.

As-grown films have been studied by the X-ray photoelectron spectroscopy (XPS) techniques. To study the composition and chemical bonding in the depth of films layer-by-layer analysis was applied. A deconvolution of photoelectron lines of each element was performed. It was shown that the formation of film consisting of three elemehts: Si, C, and N was occurred. XPS study reveals the existence of various chemical bonds such as Si-N, C-Si, C-N. A preliminary structure of the new compound was suggested using the chemical bonding data. The stoichiometry of the grown films was found to be close to SiC_xN_{1-x} where x is variable in depth of the films. Thickness of SiC_xN_{1-x} films was about 15-20nm. The Si-C chemical bonds typical for SiC are revealed at greater depth. There were no essentially differences between film thickness formed on the Si- and C- faces of 6H-SiC substrate. Besides the film thickness does not depend on the time of treatment in nitrogen plasma (from 5 min to 1 hour). However, thickness of SiC_xN_{1-x} film formed on the 3C-SiC depends on the treatment time strongly (increasing of the processing time as a factor 1.5 enlarges the thickness of SiC_xN_{1-x} layer as factor about 5)

Structure and surface morphology was investigated by electron diffraction technique and optical microscopy together with profile measurement technique. Layers was demonstrated to have amorphous structure. The undeteriorate quality of surface was observed for samples with different times of treatment in the nitrogenous plasma. Etching rate was about 0.7-0.8 μm/h and 1-1.3 μm/h for Si- and C-face of 6H-SiC respectively.

References

1. J.E. Lowther. Superharrd Materials. Phys. stat. sol. (b) 217, 533 (2000)
2.. L.C. Chen, C.K. Chen, S.L. Wei at al. Crystalline silicon carbon nitride: A wide band gap semiconductor. J. Appl. Phys. Lett., V. 72 2463-2465 (1998).
3.X. Xiao, Y.Li, L.Song at. al., Applied Surface Science 156 (2000).

Germanium on SiC(0001): surface structure and nanocrystals

B. Schröter[1], K. Komlev[1], U. Kaiser[1], G. Heß[2], G. Kipshidze[3], W. Richter[1]

[1] Institut für Festkörperphysik, [2] Institut für Optik und Quantenelektronik, Friedrich-Schiller-Universität, Max-Wien-Platz 1, D-07743 JENA, Germany, Phone: 0049-3641-947463, Fax: 0049-3641-947442
[3] Ioffe Physical-Technical Institute, St. Petersburg 194021, Russia

Germanium nanocrystals as potential candidates for a future optoelectronics have been grown on SiC(0001). A Stranski-Krastanov-like growth mode is observed due to the huge lattice mismatch of some 30% between silicon carbide and germanium.

The 4H and 6H on-axis and (high miscut) off-axis SiC(0001) surfaces were prepared ex situ either by plasma etching, subsequent oxidation and HF dip or by hydrogen etching and in situ by heating in a Si flux to get definite superstructures of 3x3, $\sqrt{3}x\sqrt{3}$-R30° or $6\sqrt{3}$ x $6\sqrt{3}$ observed by electron diffraction (LEED). Germanium was deposited from effusion cells with evaporation rates of 0.1 to 1.5 nm/min at substrate temperatures of 450 to 550°C. Additionally, several samples were deposited with germanium at room temperature and heated up to that temperature to form nanocrystals.

The surface composition before and after Ge evaporation was measured by x-ray photoelectron spectroscopy (XPS). Surface structure and morphology as well as size, geometry, density and distribution of nanocrystals were determined in situ by scanning tunneling microscopy (STM) and ex situ by atomic force microscopy (AFM), high-resolution X-ray diffraction and transmission electron microscopy.

A wetting layer was formed by Ge deposition at a low rate and a substrate temperature of 450 to 550°C depending on surface preparation. Usually, this wetting layer was atomically flat and, depending on the substrate surface, showed terraces with 1 or 2 ML high steps. Depending on Ge coverage different superstructures were observed in LEED and STM. Most of the samples showed a 1x1 LEED pattern after more than 2ML Ge deposition. In this temperature range the large lattice mismatch causes a transition from 2-dimensional to 3-dimensional (islands) growth of Ge on SiC at a coverage near 2 ML.

The samples grown at lower temperature and high rate show a narrow size distribution of the germanium nanocrystals. The average diameter was betweeen 50 and 150 nm and the average height between 4 and 30 nm for most of the samples. Depending on growth conditions also much smaller nanocrystals of only 2nm height and a high density were observed in a bimodal distribution of island sizes. Usually, the density of the medium-size nanocrystals was measured to 10^{10} cm^2. No nucleation at step edges were observed as well as no obvious difference between on axis and off axis substrates. Especially, large crystals showed a regular shape, like pyramides, with facets or with flat top, whereas, many samples showed an irregular shape of the islands.

Large nanocrystals were observed after heating a Ge film deposited at room temperature on SiC(0001) up to 500°C. These islands with facets and pyramids had a lateral size between 200 to 800 nm on different samples. Nanocrystals grown on silicon-rich (3x3) SiC surface showed Ge-Si alloying.

Interface properties of MOS structures formed on 4H-SiC C(000$\bar{1}$) face

K. Fukuda [1,3], S. Suzuki[1,2], J.Senzaki[1,2], W.J.Cho [1,3], T.Tanaka[1,2] and K.Arai[1,3]
Ultra-Low-Loss Power Device Technology Research Body[1], R&D Association for Future Electron Devices[2], Electrotechnical Laboratory[3], 1-1-4 Umezono, Tsukuba, Ibaraki 305-8563, Japan
TEL:+81-298-61-3320, FAX:+81-298-61-3397, E-mail:kfukuda@etl.go.jp

The C(000$\bar{1}$) surface has superior properties such as larger oxidation rate and smaller surface roughness as compared with the Si(0001) surface. Therefore, the oxidation process become easy and the channel mobility might increase if SiC MOSFETs can be fabricated on the C(000$\bar{1}$) surface. We have investigated the systematical oxidation method and post-oxidation annealing (POA) influence on electrical characteristics of SiC MOS structures formed on 4H-SiC C(000$\bar{1}$) surface.

8° off-angled n-type 4H-SiC C(000$\bar{1}$) face substrates with 4.9-μm-thick n-type epitaxial layers were purchased from Cree Research Inc. Nitrogen was used as the n-type dopant. The effective carrier density (N_d-N_a) of C(000$\bar{1}$) face substrates was 2.5×10^{16} cm^{-3}. A sacrificial oxidation of 10nm thickness followed by the standard RCA cleaning process was performed at 1200°C, and then removed with 5% HF solution. Gate-oxide films were thermally grown at 1200°C for 22 min in dry O_2 (dry oxidation, samples (a) and (c)) and 6 min in water vapor atmosphere (pyrogenic oxidation, samples (b) and (d)). The ratio of the flow rates of O_2 and H_2 gases was 1.5 : 0.5. The thickness of the gate-oxide films was 52 ± 5nm. After both oxidations, all samples were annealed in argon for 30 min at 1200°C, and then cooled in argon. In addition, samples (c) and (d) were annealed in hydrogen at 800°C for 30 min and cooled in hydrogen. Aluminum on the top of the oxide films and on the back of the samples was evaporated to make gate electrodes and ohmic contacts to MOS structures, respectively.

Figure 1 shows *C-V* characteristics of samples (a), (b), (c) and (d). The high-frequency characteristics (solid lines) were measured at the frequency (f) =100 kHz, and the quasi-static characteristics (dotted lines) were measured at the delay time (t_d) =10 seconds and step voltage (V_s)=50mV. The observed flat-band voltage shifts (ΔV_{fb}) of samples (a), (b), (c), and (d) are 4.6V, 6.8V, -1.7V and 1.7V, respectively. Figure 2 presents the D_{it} distributions of SiC MOS structures on the C(000$\bar{1}$) face.

Figures 1 and 2 reveal that the D_{it} near the conduction-band edge of sample (b) prepared by pyrogenic oxidation is lower than that of sample (a) prepared by dry oxidation although the ΔV_{fb} of sample (b) is larger than that of sample (a). Hydrogen annealing at 800°C decreases the D_{it} of MOS structures formed on the C(000$\bar{1}$) face by pyrogenic oxidation [sample(d)]. On the other hand, the D_{it} of MOS structures formed on the C(000$\bar{1}$) face by dry oxidations is increased by hydrogen annealing at 800°C [sample(c)]. It is considered that hydrogen annealing terminates the dangling bonds of Si and C atoms; a high temperature such as 800°C is necessary for the termination of dangling bonds of C atoms because the binding energy of C-H is larger than that of Si-H. The D_{it} near E_c-E=0.2eV decreases considerably and becomes almost the same as that observed for the n-type SiC MOS structure on the Si(0001) face by the hydrogen annealing. On the other hand, the value of the D_{it} around E_c-E=0.6eV does not change at all, and is approximately one order of magnitude higher than that of the n-type SiC MOS structures on the Si(0001) face, which indicate that a large amount of interface state exists at the deep level in n-type SiC MOS structures on the C(000$\bar{1}$) face. Therefore, the quality of the SiO_2/SiC interface formed on the C(000$\bar{1}$) face is inferior to that of the Si(0001) face.

This work was performed under the management of FED as a part of the MITI New Sun Shine Program (R&D of Ultra-Low-Loss Power Device Technologies) supported by NEDO.

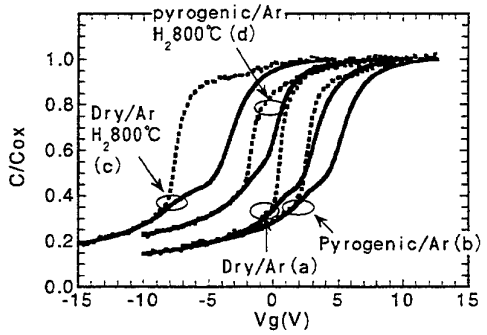


Fig.1 C-V characteristics

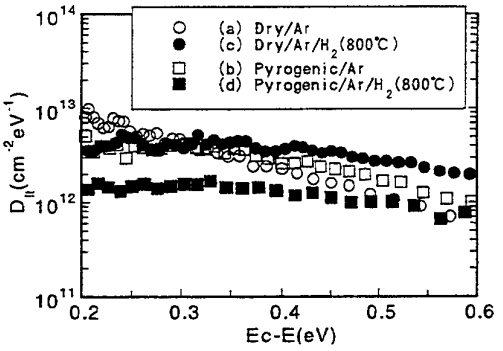


Fig.2 D_{it} distribution estimated from Fig.1.

MoP-66

Steam annealing effects on *CV* characteristics of MOS structures on (11-20) face of 4H-SiC

Masahito Yoshikawa, Takeshi Ohshima, and Hisayoshi Itoh
Japan Atomic Energy Research Institute, 1233 Watanuki, Takasaki, Gunma 370-1292, Japan
Phone:+81-27-346-9323, FAX:+81-27-346-9687, e-mail:htyskwm@taka.jaeri.go.jp
Kunimasa Takahashi and Makoto Kitabatake.
Advanced Technology Research Laboratories, Matsushita Electric Industrial Co.Ltd.
Hikaridai 3-4, Seika-cho, Kyoto 619-0237, Japan

Recently it has been reported that metal-oxide-semiconductor field-effect-transistors (MOS-FETs) fabricated on the (11-20) faces of 4H and 6H-SiC substrates have higher channel mobilities compared to those on the (0001) faces [1]. However, little is known about the physical and electrical properties of oxide layers grown on the (11-20) faces. In this study, we have fabricated MOS structures on the (11-20) and (1-100) faces of n-type 4H-SiC substrates, and measured their capacitance-voltage (*CV*) characteristics to obtain the number of interface traps per unit area (N_{it}). We have also examined the influence of steam annealing after oxidation on the number of interface traps near the interface region of the oxide layer.

Substrates of n-type 4H-SiC were cut from (11-20) and (1-100) wafers purchased from Nippon Steel Co. Ltd.. Epilayers were grown on the substrates at 1600°C by a chemical vapor deposition (CVD) method [2]. After CVD growth, pyrogenic oxidation was carried out at 1100°C for 1 hour to make gate oxide layers of about 50 nm in thickness. At the final stage of oxidation, steam annealing was performed at 850°C for 3 hours. After these processes, gold electrodes of 0.50 mm in diameter were formed to make MOS structures. The simultaneous *CV* characteristics (*SCV*) were measured for the 4H-SiC MOS structures to obtain the gate voltage corresponding to flat band condition (V_{fb}) and the energy profile of interface trap density (D_{it}) near the conduction band edge. The *CV* curve swept rapidly from positive to negative gate voltage side was also measured for the same sample before and after *SCV* measurement to calculate N_{it}.

Figure 1 shows the *CV* characteristics of a MOS structure formed on the (11-20) face with the oxide layer annealed in steam at 850°C for 3 hours. The notations C_{fb} and C_{Lg} indicate the capacitance values corresponding to the flat band condition and the ledge of the high-frequency *CV* curve swept from negative to positive gate voltage side, respectively. There is a split near the accumulation region between quasi-static and high-frequency *CV* curves. This indicates that fairly large amount of interface traps exists near the conduction band edge. The difference in gate voltage at C_{Lg} level is 5.33 V. The value before the steam annealing was 10.1 V. On account of the difference before and after the steam annealing, interface traps with deep energy levels can be concluded to disappear significantly by the steam annealing.

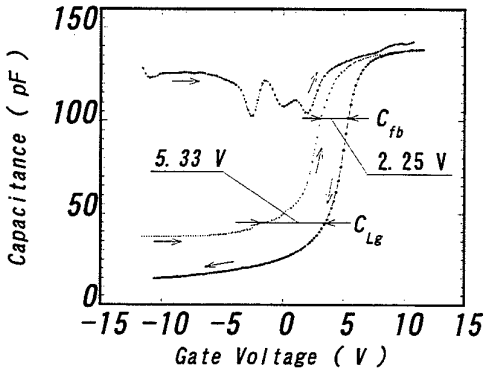


Fig.1. *CV* characteristics of a MOS structure formed on the (11-20) face with the oxide layer annealed in steam at 850°C for 3 hours.

[1]H.Yano, T.Hirao, T.Kimoto, H.Matsunami, K.Asano, and Y.Sugawara, *International Conference on Silicon Carbide and Related Materials 1999,* (Abstract, p311.)
[2]K.Takahashi, M.Uchida, M.Kitabatake, and T.Uenoyama, to be published in the proceedings of *International Conference on Silicon Carbide and Related Materials 1999.*

Shallow Dopant and Surface Levels in 6H-SiC MOS Structures Studied by Thermally Stimulated Current Technique

V. Lysenko[1], I. Osiyuk[1], T. Rudenko[1], I. Tyagulski[1], E.Ö. Sveinbjörnsson[2], H.Ö. Olafsson[2]

[1]Institute of Semiconductor Physics NASU, 252028 Kiev, Ukraine
Tel. +380 (44) 265 70 22, Fax +380 (44) 265 61 77, E-mail: tamara@lab15.kiev.ua
[2]Department of Microelectronics ED, Chalmers University of Technology, S-412 96 Göteborg, Sweden

In this work, the shallow traps in 6-H SiC MOS structures are studied using thermally stimulated current (TSC) measurements. A TSC method, which is based on dc measurements, is not adversely affected by increased series resistance due to the carrier freeze-out. This makes it suitable for the investigation of trap levels in the near-bandgap edge region. We observed TSC peaks associated with shallow dopants and a part of the spectrum associated with interface traps. Radically different features were revealed for interface states near the conduction band edge in the n-type SiC and the valence band edge in the p-type SiC.

MOS capacitors were fabricated on commercially available Al-doped and N-doped 6H-SiC epitaxial layers grown on the Si-face of SiC substrates. Thermal oxidation was performed at temperatures 1100^{0}C and 1150^{0}C in dry O_2 or in a pyrogenic steam. TSC measurements were performed with a linear heating rate of 0.2 K/s in the temperature range 8-100 K. Volume and surface components of the TSC spectrum were identified by measurements with various charging and discharging voltages. In addition to the TSC measurements, the MOS structures were characterized using the displacement current versus gate voltage measurements with a linear voltage ramp at different temperatures.

TSC measurements of the n-type samples shown in Fig1(a) reveal two clearly defined peaks and tooth-shaped plateau, which arises from the low-temperature edge of the spectrum as the charging voltage increases. The spectrum reached "saturation", when the charging voltage corresponds to sufficiently strong accumulation at the surface. When the charging voltage corresponds to flatband or depletion conditions at the surface, only two TSC peaks are observed (Fig1b). We suggest that the tooth-shaped plateau in the n-type samples is due to interface states near the conduction band edge, whereas the above peaks are associated with volume traps, in particular, with nitrogen in the hexagonal lattice site (h) and cubic (k_1 , k_2) sites. The systematic shift of both TSC peaks to lower temperatures was observed with increasing discharging (detrapping) voltage indicating that the emission rate from both centers is enhanced by the electric field. The activation energies obtained with taking into account the Poole-Frenkel effect were 83 meV and 126 meV, which is in a good agreement with reported ionization energies for nitrogen in 6H-SiC in the (h) Si-site and (k_1k_2) C-sites

Measurements on the p-type samples revealed a large TSC peak at temperature about 70 K, and a smooth hump at lower temperatures observed only when the SiC surface was in accumulation during cooling. If the SiC surface was depleted during both cooling and measurement, only one TSC peak was observed indicating that this peak is caused by volume traps. The energy activation obtained from the initial rise of the peak by taking into account of the Pool-Frenkel effect was 190 meV, that is in a reasonable agreement with values reported in the literature for Al in 6-H SiC. We find that a smooth hump, which is observed in TSC spectra below the Al-related peak for accumulation charging voltages, is caused by interface states.

An additional interesting result of this work is the radically different surface-related TSC spectrum, observed at temperatures below dopant-related peaks, namely, the tooth-shaped spectrum in n-type samples, and smooth, structureless spectrum in p-type samples, variously changing with charging and discharging voltages. This suggests essentially different interface trap distributions near the majority carrier band edges in n- and p-type SiC.

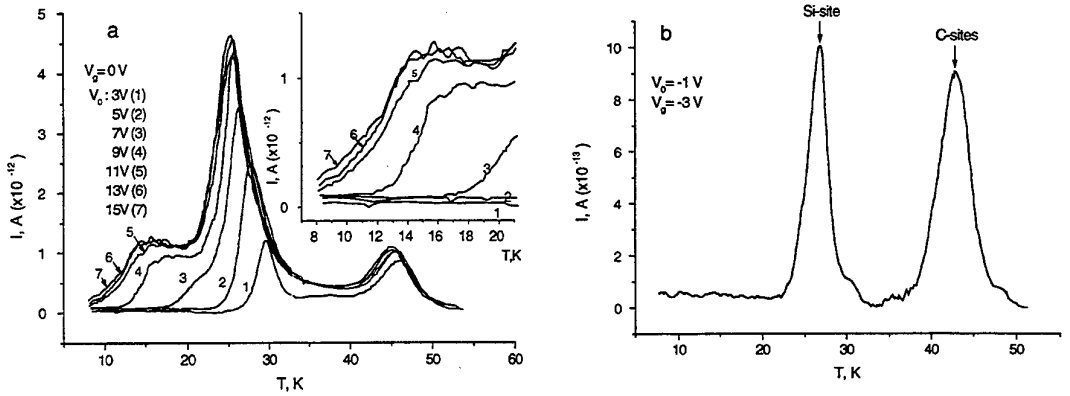


Fig.1. A TSC spectrum of the n-type sample measured (a) for various charging voltages, (b) when charging voltage corresponds to depletion. The insert shows the surface-related part of the spectrum.

MoP-68

Hydrogen diffusion in n-type 4H-SiC

M.K. Linnarsson[1]*, A. Lloyd-Spetz[2], M.S. Janson[1], D. Åberg[1], U. Forsberg[3], and B.G. Svensson[1]

[1]Royal Institute of Technology, Solid State Electronics, P.O. Box E229, SE-164 40 Kista-Stockholm, SWEDEN,
[2]Linköping University, S-SENCE and Div. of Applied Physics, SE-581 83 Linköping, SWEDEN
[3]Linköping University, Department of Physics and Measurement Technology, SE-581 83 Linköping, SWEDEN
* Phone:+46 8 752 1412 Fax: +46 8 752 7782 Email: marga@ele.kth.se

Hydrogen is a fast diffusing species in semiconductors and it may be mobile even at room temperature in SiC. However, hydrogen will readily form complexes with acceptor and donor impurities as well as deep level defects. Hence, the formation and dissociation temperature of these complexes are crucial for the effective hydrogen mobility. Since hydrogen is extensively used in device processing the stability of hydrogen-impurity complexes and the hydrogen mobility are of great concern for the reliability of SiC devices.

In this contribution we have studied diffusion and trapping of deuterium in nitrogen doped 4H-SiC. Epitaxially grown layers are used and hydrogen is introduced into these layers from a gas ambient in combination with a catalytic metal (Pt) coating [1]. Secondary ion mass spectrometry (SIMS) is used to determine concentration versus depth profiles. Deuterium (^{2}H) is employed instead of ordinary hydrogen (^{1}H) to increase the sensitivity of SIMS measurements. The electrical activity of shallow dopants is obtained from capacitance-voltage (CV) measurements. The samples are heat treated at temperatures between 400 and 700°C for 4 to 64 h.

Fig.1 shows deuterium concentration versus depth profiles in a layer doped with $5x10^{15}$ N/cm^3. A substantial incorporation of deuterium is revealed where the nitrogen dopants may act as trapping centers. The shape of the curves can be explained in terms of formation and dissociation of a hydrogen - impurity complex. Comparison will be made with numerical and analytical calculations of the reaction kinetics assuming a single trap model.

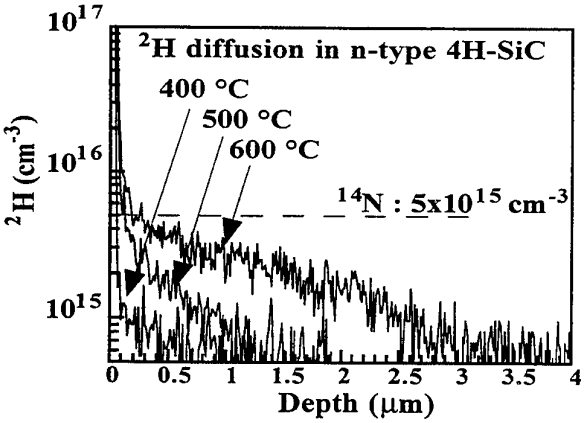


Fig. 1. SIMS measurements of the deuterium concentration versus depth in n-type ($5x10^{15}$ cm^{-3}) 4H-SiC. The samples were annealed in a deuterium and nitrogen ambient during 14 h at 400, 500 and 600 °C, respectively. All samples were coated with 200 Å Pt.

[1] M.K. Linnarsson, A. Lloyd-Spetz, M.S. Janson et. al., ICSCRM'99.

The Monte Carlo-Binary Collision Approximation applied to the simulation of the ion implantation process in single crystal SiC: high dose effects.

G. Lulli[§], E. Albertazzi[§], R. Nipoti[§] and A. Carnera*
[§] CNR-Istituto LAMEL, via Gobetti 101, I-40129 Bologna, Italy
* Dipartimento di Fisica and INFM, Università degli Studi di Padova, via Marzolo 8, I- 35131 Padova, Italy
phone + 39 051 6399145 fax +39 051 6399216

The Binary Collision Approximation (BCA) [1] has been successfully applied to the simulation of the ion implantation process in several crystalline materials that include also the SiC polytype since the 1996. The first [2] Monte Carlo BCA (MC-BCA) computation applied to SiC simulated the doping profiles in 6H-SiC implanted at low ion fluence. In that work the deep doping tails measured in the crystalline substrates were simulated as due to the channeling phenomena dependent on the tilt and twist implantation angles. In 1997 and 1999 the MC-BCA computation was applied for the simulation of damage accumulation in SiC versus ion fluence: experimental data concerning the absolute number of displaced atoms as well as the density variation of the damaged crystal were reproduced for 6H-SiC [3,4].
This work presents the use of the MC-BCA computation for the simulation of the doping profiles versus increasing ion fluence values in a range that goes from very low damage level to the production of an amorphous layer. The simulation accounts for both the projected range shift and the channeling tail reduction as far as the damage increases. Fig. 1(a, b) show the damage and doping simulated profiles overlapped to the corresponding experimental ones that were measured, respectively, by Rutherford Back-Scattering in channeling geometry and Secondary Ion Mass spectrometry. The data reported in Fig. 1 referee to 0.5 MeV Al^+ implanted in <0001> on-axis 6H-SiC wafers at RT with the <0001> axis 8° tilted within the (10-10) plane and with the (10-10) plane 22° twisted around the <0001> axis.

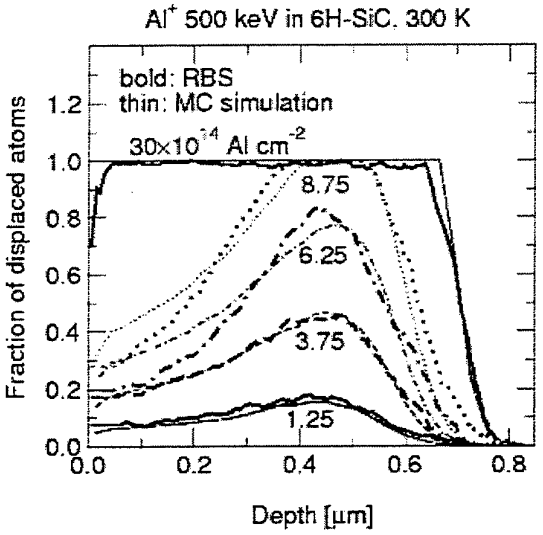


Fig. 1(a)

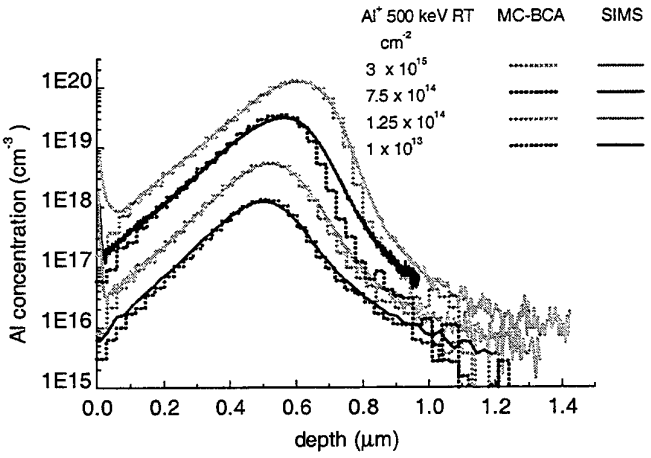


Fig. 1(b)

[1] M.T. Robinson and I.M. Torrens, Phys. Rev. B 9 (1974) 5008.
[2] E. Albertazzi and G. Lulli, Nucl. Instr. and Method. in Phys. Res. B120 (1996) 147.
[3] R. Nipoti, E. Albertazzi, M. Bianconi, R. Lotti, G. Lulli, M. Cervera and A. Carnera, Appl. Phys. Lett. 70 (1997) 3425.
[4] G. Lulli, E. Albertazzi, M. Bianconi and R. Nipoti, Nucl. Instr. and Method. in Phys. Res. B 148 (1999) 573.

MoP-70

High dose implantation in 6H-SiC

V. Heera[a)] and W. Skorupa
Forschungszentrum Rossendorf, P.O.B. 510119, D-01314 Dresden
J. Stoemenos
Aristotle University of Thessaloniki, Physics Department, 54006 Thessaloniki, Greece
B. Pécz
Research Institute for Technical Physics and Materials Science, H-1525, Budapest, P.O.B. 49, Hungary

[a)]Tel: ++49 351 260 3343, Fax: ++49 351 260 3411, e-mail: heera@fz-rossendorf.de

There are two major reasons to study the effects of high dose implantation in SiC. First, the production of low-resistivity, p-type layers requires high acceptor concentrations which are far above the equilibrium solubility. It is essential to know the critical acceptor concentration for thermally stable, homogeneously doped SiC. On the other hand, there is a lack of information about the precipitation of new phases in SiC, their properties and influence on the SiC matrix. Such information is needed for the assessment whether insulating or conductive layers with device quality can be formed in SiC by ion beam synthesis. Two examples of high dose implantation in 6H-SiC are presented.

In the first example high doses of 350 keV Al^+ ions were implanted in 6H-SiC single crystals at temperatures between 400°C and 800°C in order to preserve the crystallinity of the SiC matrix. The phase formation was studied by TEM, SIMS and AES. A critical Al concentration of about 10 at% was found below that the 6H-SiC structure remains stable during implantation at 500°C. The Al atoms occupy preferentially Si sites in the SiC lattice. At higher Al concentrations the SiC matrix is decomposed and precipitates of Si and Al_4C_3 are formed. It was found that the Al_4C_3 precipitates have a perfect epitaxial orientation to the SiC matrix. The phase transformation is accompanied by atomic redistribution and strong volume swelling. The observed atomic depth profiles can be accounted for by a a simple chemical reaction model. Implantation at 800°C leads to the formation of Si and Al precipitates accompanied by a dramatic volume swelling which results in surface cracking and material outflow. Post-implantation annealing above 1500°C severely deteriorates the SiC matrix by local melting of Al and Si precipitates.

In the second example the evolution of the binary system C → SiC was studied as function of implantation temperature. $1 \cdot 10^{18}$ cm^{-2}, 60 keV carbon ions were implanted into single crystalline 6H silicon carbide (SiC) at elevated temperatures. The formation of carbon phases in the crystalline SiC lattice was investigated by cross sectional transmission electron microscopy. An amorphous, carbon rich phase was produced at 300°C. Precipitates of graphite were obtained at 600°C, whereas at 900°C small diamond grains were produced. These grains are in perfect epitaxial relation with the surrounding SiC lattice. The mechanism of ion beam synthesis of diamond in SiC is not quite clear. It can be assumed that the tetrahedrally coordinated SiC lattice, which is preserved during the high temperature implantation, acts as a template for the growth of diamond. In addition, local nonequilibrium conditions in the ion cascades (thermal spikes, shock waves) or temporary stress on interstitially incorporated carbon atoms by the surrounding SiC lattice could contribute to diamond nucleation.

Diffusion of implanted beryllium in silicon carbide: a SIMS study

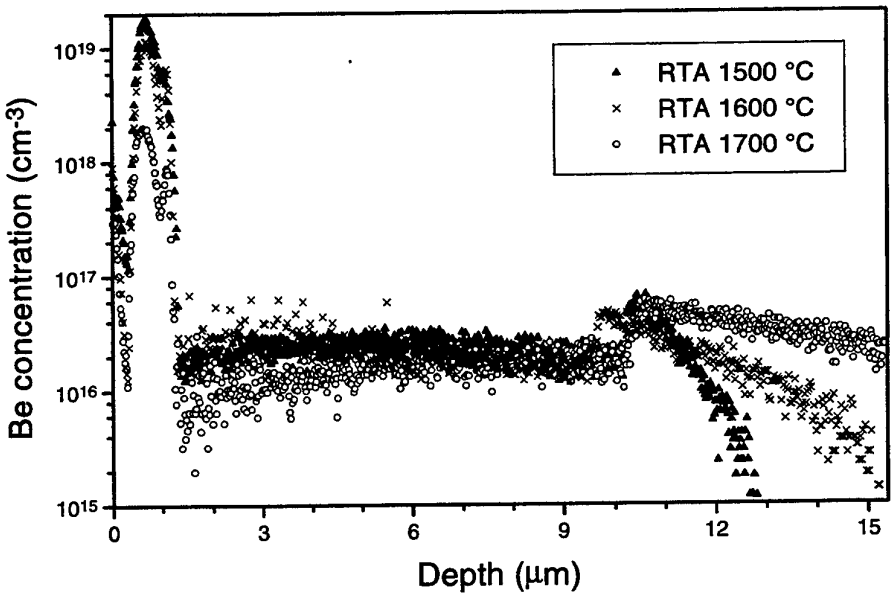
T. Henkel[1], N. Kobayashi[1], Y. Tanaka[1], H. Tanoue[1], and S. Hishita[2]

1) Quantum Radiation Division, Electrotechnical Laboratory, 1-1-4 Umezono, Tsukuba, Ibaraki 305-8568, Japan
Tel: +81-298-61-5690, Fax: +81-298-61-5683, Email: nkobayas@etl.go.jp
2) National Institute for Research in Inorganic Materials, 1-1 Namiki, Tsukuba, Ibaraki 305-0044, Japan

Silicon carbide (SiC) is currently being explored as a promising material for high-temperature and high-power device applications. For p-type doping, beryllium (Be) implantation in SiC has advantages such as high ion ranges and low damage accumulation in the crystal. However, there have been few studies on Be doped SiC. Recently, we reported on structural and electrical properties of Be implanted SiC [1,2]. In this work, diffusion of Be in SiC is investigated by secondary ion mass spectrometry (SIMS).

To obtain a box-shaped profile, multiple energy $^{9}Be^{+}$ implantation was performed in 6H-SiC epitaxial layers from Cree Research at room temperature. Post-implantation rapid thermal annealing was conducted in flowing Ar gas at temperatures up to 1700 °C. Be depth profiles were analyzed by SIMS using a CAMECA-ims-4f instrument.

Strong Be redistributions were found after annealing at temperatures above 1300 °C. In particular, the heat treatment caused out-diffusion into the annealing ambient. In-diffusion into the bulk of the material and trapping at defects were also observed (see Fig.). Effective diffusion coefficients were determined in bulk crystals applying a simple model. Considering further results obtained from C/Be and Si/Be co-implanted material, respectively, an interstitial-mediated diffusion model is proposed.



1. T. Henkel, Y. Tanaka, N. Kobayashi, H. Tanoue, M. Gong, X.D. Chen, S. Fung, and C.D. Beling, Mat. Res. Soc. Symp. Proc. **572**, 117 (1999).
2. T. Henkel, Y. Tanaka, N. Kobayashi, S. Nishizawa, and S. Hishita, Proc. 11th Internat. Conf. on Silicon Carbide and Related Materials (ICSCRM'99), 1999, NC (in print).

High Electrical Activation of Aluminium and Nitrogen Implanted in 6H-SiC at Room Temperature, by RF Annealing

M. LAZAR, M.L. LOCATELLI, C. RAYNAUD, D. PLANSON, L. OTTAVIANI, E. MORVAN*, P. GODIGNON*, J.P. CHANTE
CEGELY (UMR CNRS n°5005), Bât. 401, INSA de Lyon, 20, Av. A. Einstein, F-69621 Villeurbanne Cedex FRANCE
Fax: (33) (0)4 72 43 85 30, Tel: (33) (0)4 72 43 82 38, E-mail: lazar@cegely.insa-lyon.fr
*Centro Nacional de Microelectrónica (CSIC) Campus UAB, 08193 Bellaterra, SPAIN

Ion implantation in SiC, an indispensable technique for the p-n junction creation, due to very weak dopant diffusion coefficients, generates an important density of defects which involve high temperature annealing and particular conditions of ramp temperature and environment partial pressure. High temperature and energy ion implantations, were used to reduce the material damage, however these implant conditions remain not interesting in an immediate perspective of industrial applications. We present room temperature (RT) aluminium (Al) and nitrogen (N) ion implanted and rf-annealed samples with viable physico-chemical and electrical properties.

Al RT implantations were carried out in 6H-SiC Cree Research n-type epitaxial layers ($3x10^{15}cm^{-2}$) with energies ranging from 25 to 300 keV and 100 to 400 keV with a total dose of $1.75x10^{15}cm^{-2}$ and $1x10^{15}cm^{-2}$ respectively. A thin aluminium mask (1500Å) was used for the second implant series to avoid the channelling of Al ions, a major effect in 6H-SiC. Nitrogen was implanted with energies ranging from 30 to 190 keV and a $1x10^{13}$ cm^{-2} total dose, following an Al 350 keV high dose implantation to realise a n-p junction in surface. The samples were annealed at 1700°C during 30 mn in argon atmosphere and silicon carbide partial pressure, in a rf-heating furnace.

To understand the dopant profile distribution, CNM Monte-Carlo simulations were carried out as well as SIMS (Secondary Ion Mass Spectroscopy) analyses before and after rf-annealing (Fig.1). We remark a good agreement between simulation and the SIMS before annealing. Moreover the CNM Monte-Carlo simulation allows us to quantify the point defects generation, their effects in impurity distribution after annealing.

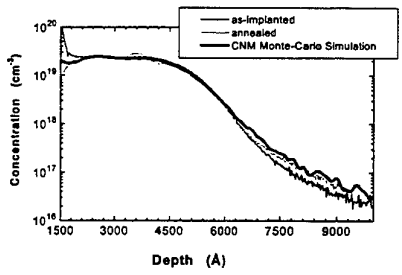


Fig1. *CNM Monte-Carlo simulation and SIMS analysis for the 100 to 400 keV Al-implanted layer*

SIMS profiles after annealing are not flat, Al dopant peaks are formed in high defect concentration zones due to the formation of an amorphous layer. We notice a lack of dopant loosing after annealing.

Residual damage before and after annealing, SiC recrystallisation were evaluated by RBS/C (Rutherford Backscattering Spectrometry in the Channelling mode) technique. RBS/C analyses confirm the presence of an amorphous layer up to the surface in the implanted samples, despite that, after rf-annealing a satisfactory recrystallisation is found. A good surface stoichiometry is obtained by XPS (X-Ray Photoelectron Spectroscopy) after annealing but AFM (Atomic Force Microscope) surface measurements reveal a relatively high rms roughness (14 nm) on annealed samples (Fig.2).

Sheet resistance measurements by a four point probe technique on Al and N implanted and rf-annealed samples prove a high electrical dopant activation for RT implanted samples, in terms of Al and N incorporation in SiC lattice sites (Si and C respectively). For Al-implanted samples a 19 kΩ/□ sheet resistance at 300K was found which corresponds to 50% electrical dopant activation. Better results are found for N-implanted samples: 6.7 kΩ/□ sheet resistance and 100% electrical dopant activation (Fig.3).

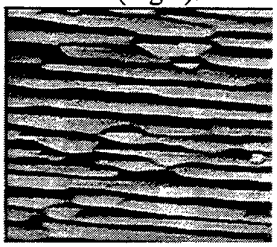


Fig2. *AFM measurements on a RT Al-implanted and 1700°C 30 mn rf-annealed sample. Edge length of image correspond to19 μm.*

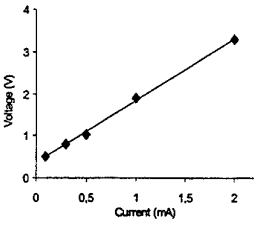


Fig3. *Sheet resistance measurements at 300K on a RT N-implanted layer*

STRUCTURAL AND ELECTRICAL CHARACTERIZATION OF ION BEAM SYNTHESYSED AND N DOPED SIC LAYERS

C. Serre*, A. Pérez-Rodríguez*, A. Romano-Rodríguez*, J.R. Morante*, J. Esteve**, M.C. Acero**, D. Panknin***, R. Kögler*** and W. Skorupa***.

* Electronic Materials and Engineering (EME), Dept. Electrònica, Universitat de Barcelona, Martí i Franquès 1, 08028 Barcelona, Spain. (Tel: +34 93 4021147. Fax: +34 93 4021148)

** Centre Nacional de Microelectrònica, CNM-CSIC, Campus UAB, 08193 Bellaterra, Spain.

*** Forschungszentrum Rossendorf, P.F. 510119, D-01314 Dresden, Germany.

Owing to its high stiffness and mechanical strength, extreme chemical inertness, together with its wide bandgap (allowing stable electronic properties at high temperatures and high radiation resistance), SiC is a very promising material for the development of Micro-Electro-Mechanical-Systems (MEMS) for harsh environment conditions, including chemically or physically aggressive ambient. However, the development of SiC based technologies is compromised by the availability of bulk single crystal wafers: although bulk single crystal wafers are already commercially available, they have a relatively poor structural quality and their price is still too high. Epitaxial SiC layers can also be grown on Si substrates, but this requires the use of expensive dedicated Molecular Beam Epitaxy (MBE) or Chemical Vapour Deposition (CVD) Systems, and the quality still strongly requires to be improved (voids, micropipes, density of dislocations...). High temperature carbon ion implantation into Silicon has been proved as a suitable technique to produce high crystalline quality cubic SiC (β-SiC) layers with extremely low level of residual stress. On the other hand, local doping of SiC still remains a critical issue. Due to the extremely slow diffusion of the impurities in SiC, doping has to be performed by ion implantation, and very high annealing temperatures are usually required to achieve activation levels suitable for device application. Moreover, annealing of radiation damage is much more difficult in SiC than in Si. Therefore, reducing radiation damage caused by ion implantation is a key problem in SiC processing,

According to this, this work will present structural and electrical characterisation results of ion beam synthesised SiC layers, n-doped by N ion implantation. The SiC structures were obtained by high dose multiple carbon ion implantation. The implantation conditions were selected to obtain a flat carbon profile with stoichiometric SiC composition within the implanted layer. The C implants were performed at 500°C in order to avoid amorphization. These layers were then n-doped by fourfold N implantation to form a box-like doped region with plateau concentrations between $5x10^{19}cm^{-3}$ and $5x10^{20}cm^{-3}$, and performed at 400°C to reduce the implantation-induced damage level. The N implantation is carried out either into the as-C-implanted layer or into the C-implanted layer after intermediate annealing at 1100°C, 6h. The post implantation annealing was carried out in Ar ambient in the first case at 1100°C, 6h and in the second case in the temperature range between 1000°C and 1200°C, 10min.

The depth distribution of C and N were measured by SIMS. The microstructure was analysed by XTEM, XRD, and FTIR. The electrical properties were investigated by resistivity and Hall effect measurements as well as by Spreading Resistance measurements

ACKNOWLEDGEMENTS

The multiple C implantations were performed at the AIM-Center for Application of Ion Beams in Materials Research, in the Forschungzentrum Rossendorf, under the "Access to Large-Scale Facilities" programme of the European Union. This work has been partially funded by the "Direcció General de Recerca" from "Generalitat de Catalunya" through the project ITT-CTP98-4 ("Programa de Projectes de Cooperació en Matèria d'Innovació i de Transferència Tecnològica- Comunitat de Treball dels Pirineus).

MoP-74

Abstract for ECSCRM2000, Sept. 3-7, 2000, Kloster Banz, Germany

Structural, electrical and optical properties of high dose 4H-SiC Al ion implanted p-n junctions.

E. Kalinina, G. Kholujanov, V. Solov'ev, A. Strel'chuk, A. Zubrilov, *Ioffe Institute, St. Petersburg, 194021 Russia. Fax/Tel: +7(812) 247-6425, e-mail: EVK@pop.ioffe.rssi.ru;* V. Kossov, R. Yafaev, *Electron Optronic, St. Petersburg, 194223, Russia;* A. Kovarskii, A. Shchukarev, *" Mekhanobr-Analyt" Centre, St. Petersburg, 199026, Russia;* A. Hallén, *Royal Inst. of Techn., Dept. of Electronics, Electrum 229, SE 164 40 Kista, Sweden;* A. Konstantinov, S. Karlsson, *Acreo, Electrum 233, SE 164 40 Kista, Sweden;* S. Rendakova, V. Dmitriev, *TDI, Inc., Gaithersburg, 20877 MD.*

In order to realize full benefits of SiC material for high-power applications, reduction of defect densities in SiC epitaxial materials is required. Another problem for SiC device fabrication is the high resistivity of the p-material since the acceptor concentration is limited by the solubility in SiC. However nonequilibrium doping by ion implantation (ID) with subsequent thermal anneal allows one to produce low-resistive p-layers. We report here on electrical and optical characteristics of p^+-n-n^+ structures formed by aluminum ID of 4H-SiC epitaxial layers.

Initial substrates were 4H-SiC 8° off-axis commercial wafers with Si face polished, concentration N_d-N_a=10^{19} cm^{-3} and the micropipe density less than 100 cm^{-2}. A micropipe filling process was performed on one wafer, reducing the micropipe density down to 5 cm^{-2}. Epitaxial layers, 25 μm thick, with concentration N_d-N_a = (3-5)×10^{15} cm^{-3} were grown on both wafers in the same epitaxial run by chemical vapor deposition method (CVD). Ion doping with Al was performed at ion energy of 150 keV and a dose of 5×10^{16} cm^{-2} followed by rapid thermal anneal at 1700°C. Ohmic contacts to n- and p-SiC were produced by vacuum thermal evaporation of Cr and Al, respectively. Mesa diodes were formed by reactive ion etching.

Structural perfection of the ID layers before and after anneal was investigated by reflection high energy electron diffraction and x-ray diffraction methods. Al distribution profiles across the n-layers after ID and anneal runs were measured using secondary ion mass spectrometry. Thickness of the CVD epitaxial layers and position of the ID p^+-n junctions in the structures were determined by scanning electron microscopy using electron beam induced current (EBIC) and back scattered electron modes. Diffusion length of minority carriers, L_p, in the epitaxial n-layers near the p^+-n junctions were determined using standard processing of the EBIC signal. Capacitance-voltage characteristics were measured at a frequency of 10 kHz. Forward current-voltage characteristics were measured in a temperature range 290-780 K under dc conditions at current densities up to 150 A cm^{-2} and with the use of 8 μs pulses at higher currents. Electroluminescence distribution over the p^+-n junction area and spectra at various excitation levels were studied.

It has been shown that rapid thermal anneal improves structural perfection of the CVD layers. It is also produces a low-resistive monocrystalline p^+-layers after Al ion doping. The high dose ID made it possible to obtain both (1) low-resistive contacts and (2) built-in potential U_c of the pn junction close to the theoretical values. The micropipe filling process leads to reproducible and repeatable electrical characteristics of the formed pn junction. ID p^+-n junctions with dynamic resistance of 3×10^{-3} Ω cm^{-2} at room temperature and forward current density of 3×10^3 A cm^{-2} at 12 V were obtained.

This work was supported by INTAS project № 97 – 2141. Work at TDI, Inc. was supported by BMDO and managed by ONR.

Comparison of super-junction structures in 4H-SiC and Si for high voltage applications

K. Adachi[*1*3], C.M. Johnson[*3], H. Ohashi[*4], T. Shinohe[*1*4], K. Kinoshita[*4], K. Arai[*1*2]
[*1]Ultra-Low Loss Power Device Technology Research Body,
[*2]Electrotechnical Laboratory, 1-1-4 Umezono, Tsukuba-shi, Ibaraki-ken, Tokyo 305-8568, Japan
[*3]University of Newcastle, Newcastle upon Tyne, UK, NE1 7RU U.K.
Tel. +44 191 222 7345, Fax. +44 191 222 8180, email kazuhiro.adachi@ncl.ac.uk
[*4]Toshiba Corp., 1 Komukai Toshiba-cho, Saiwai-ku, Kawasaki 212-8582, Japan

In this paper Super-junction structures (SJS) [1], which realise very low Ron for a given Vbr (for example CoolMOS™ [2]) are studied and comparisons made between 4H-SiC and Si. A primary theory of on-resistance (Ron) of SJS shows that it is proportional to pillar width (w)[1, 3]. However, Ron saturates at narrow w due to depletion (width (wd0)) caused by the built-in potential (Vbi) [4].

Since wide band-gap semiconductors like 4H-SiC have larger Vbi than Si, it is expected that Ron will deviate from the primary theory more than Si. In this paper equations of the breakdown voltage(Vbr) (Equ.1) and Ron (Equ.2) are derived as functions of pillar depth (d), w, pillar doping concentration (N), charge imbalance error (e) between n- and p-pillar, critical electric field (Ec), permitivity (ε_s), Vbi and α a parameter which varies from 1 to $\sqrt{2}$ depending on device structure. These simplified equations are shown to agree with TCAD simulation results.

$$Vbr = \left(Ec - (1 - \frac{w}{d}) \left(\frac{qNw}{\varepsilon_s} \right) - (\alpha - 1 + \frac{2w}{d}) \sqrt{\frac{qNVbi}{\varepsilon_s} - \frac{qeNd}{2\varepsilon_s}} \right) d + Vbi \qquad \text{(Equ.1)}$$

$$Ron = \frac{d}{\mu qN} \frac{1}{1 - \sqrt{\frac{\varepsilon_s Vbi}{qNw^2}}} \qquad \text{(Equ.2)}$$

Based on Equ.1 and Equ.2 the relationship between Ron and Vbr is obtained. Fig.1 and Fig.2 show, for 4H-SiC and Si respectively, that Ron increases with higher charge imbalance and becomes more significant at higher Vbr, and Ron of SiC is affected less than Si. One of the material characteristics of wide band-gap semiconductors is the incomplete ionisation of dopants (INC) due to high activation energy. It is found that INC does not affect Vbr, since the dopants are fully ionised in the space charge region, but it does affect Ron due to reduced carrier density.

For a given w there are critical maximum and minimum pillar doping concentrations. The ratio of these gives a design margin for pillar doping concentration, as represented by Equ.3.

$$Nmargin = \frac{Nmax}{Nmin} = \frac{wEc}{Vbi} \qquad \text{(Equ.3)}$$

Comparing 4H-SiC and Si using Equ.3 shows that 4H-SiC has 3.3 times higher margin than Si. It is therefore clear that SiC is well suited to SJS based devices in the voltage range 2kV to 10kV.

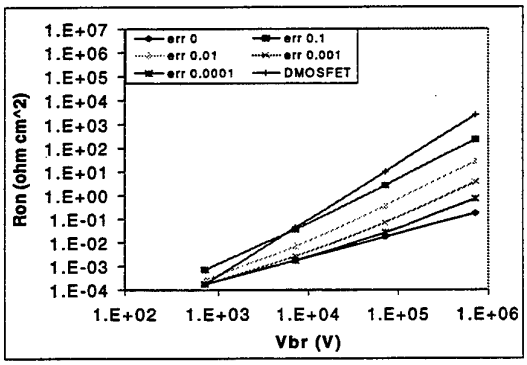


Fig.1 Ron vs. Vbr, at 300K (4H-SiC)

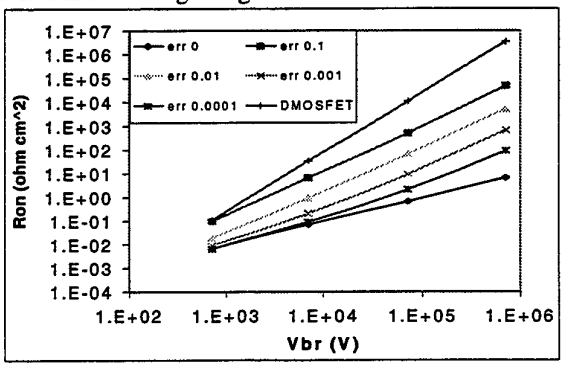


Fig.2 Ron vs. Vbr, at 300K (Si)

This work was performed under the manegement of FED as a part of the MITI NSS Program (Ultra-Low Loss Power Device Technology Project) supported by NEDO.

References

[1] 'Theory of Semiconductor Superjunction Devices' T.Fujihara, J.Appl.Phys. Vol.36(1997) pp.6254-6262
[2] 'COOLMOS™ - a new milestone in high voltage Power MOS' L.Lorenz, IEEE ISPSD 1999
[3] 'Analysis of the Effect of Charge Imbalance on the Static and Dynamic Characteristics of the Super Junction MOSFET' P.M.Shenoy, IEEE ISPSD 1999
[4] 'Predicted Electrical Characteristics of 4500V Super Multi-Resurf MOSFETs' Y.Kawaguchi, IEEE ISPSD 1999

Improvements in the electrical performance of high-voltage (3.85 kV) 4H-SiC Ni-Schottky diodes by Hydrogen annealing

Q. Wahab, E. Duranova, J. Zhang, L. D. Madsen and E. Janzén
Department of Physics and Measurement Technology, Linköping University, S-581 83 Linköping, Sweden. E-mail: quamar@ifm.liu.se, Tel: 46-13-288936, Fax: 46-13-137568

The effects of H_2 annealing on the electrical performance of high breakdown voltage Ni/4H-SiC Schottky diodes were studied. The low doped epitaxial layers were obtained by two different techniques, the hot wall chemical vapor deposition (Hot wall-CVD) and high temperature chemical vapor deposition (Chimney-CVD). The layer thickness and doping were 35 μm and 2 x 10^{15} cm^{-3} for hot-wall CVD grown layer and 43 μm with 3-7 x 10^{14} cm^{-3} for Chimney CVD. The breakdown voltage measured on the Schottky diode fabricated using hot-wall CVD layer was 3.56 kV, while it was 3.85 kV for the chimney CVD. The diodes were then annealed in Ar+2%H_2 at 300 and 400 °C for 10 minutes each. The effects on the electrical performance were studied before and after each annealing step.

The measurements performed on Hot-wall CVD grown sample showed an increase in the forward current from 55 mA to 100 mA at a constant bias of 2.5 V, this can be seen in Fig.1a. This increase in the current was observed after the first annealing at 300 °C, while no further improvement was observed after annealing at 400 °C. In the reverse direction the leakage current at -500 V before annealing was 3.5 x 10^{-9} A, while after annealing at 300 °C the leakage current was reduced to 4.8 x 10^{-10} A for the same bias voltage and this is shown in Fig.1b. No further improvement was observed for further annealing at 400 °C. The barrier heights as measured by capacitance-voltage technique were increased for all the diodes by at least 0.2 eV. Similar results were obtained for Chimney CVD sample. The physical mechanism accounting for this improvement could be that the H-atoms penetrate during the annealing to the metal-semiconductor interface and saturate the dangling bonds and thus occupy the interface states. This indicates that the interface state density in the Schottky diode is primarily due to dangling bonds and is not like the metal oxide semiconductor (MOS) structure where the interface state density reduction was not observed due to H annealing. Hydrogen in the epilayer may also form stable H-impurity complex (like H-B), which may result in an increase of the effective doping near the interface region and thus increase in the forward current. If B or other deep level defects participate in the carrier generation the formation of H-impurity complex may decrease the reverse current as well.

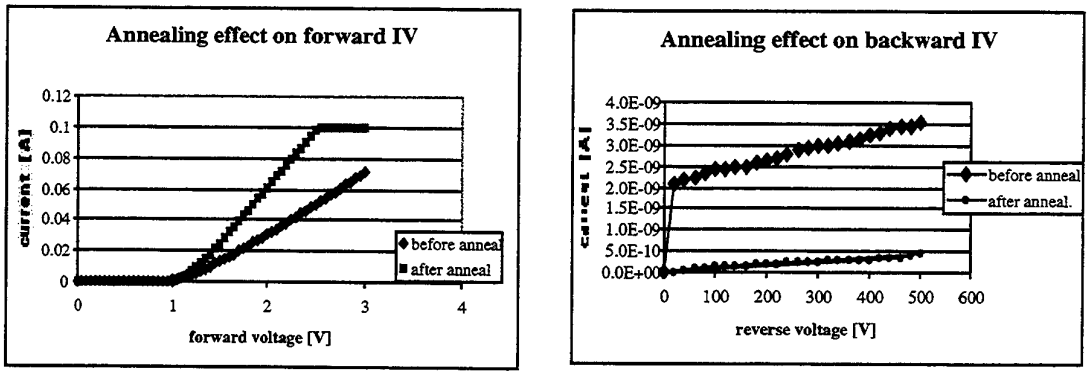


Fig. 1 Current-Voltage plot of Ni/4H-SiC Schottky diodes showing effects of H_2 annealing on (a) forward characteristics, (b) in reverse direction

Silicon Carbide Zener Diodes

K. Vassilevski[1], K. Zekentes[1], E. Bogdanova[2], M. Lagadas[1], A. Zorenko[3]
[1] *MRG, IESL, FOundation for Research and Technology-Hellas, P.O. Box 1527, Vassilika Vouton, 711 10 Heraklion, Greece, Tel: +30-81-394105, Fax: +30-81-394106, e-mail: kostya@physics.uoc.gr*
[2] *Ioffe Institute, St.Petersburg, 194021,Russian Federation*
[3] *State Scientific & Research Institute "Orion", Kyiv, 252057, Ukraine*

Specially designed Zener diodes operating in reverse bias under avalanche or tunneling breakdown conditions [1] are widely used for voltage regulation and transient voltage suppression. Currently, Zener diodes with breakdown voltages from about 4 volts to several hundred volts are commercially available [2]. The advantage of silicon carbide (SiC) as a semiconductor for use in Zener diodes is based on its fundamental properties. Due to the higher breakdown field, SiC Zener diodes shall have lower dynamic impedance and lower leakage current comparing with silicon diodes designed for the same Zener voltage and pulse power. The capability to operate at elevated temperature and excellent thermal conductivity of SiC shall allow to fabricate SiC Zener diodes handling higher current density and thus working at higher pulsed power or having smaller area and capacitance values comparing with conventional diodes.

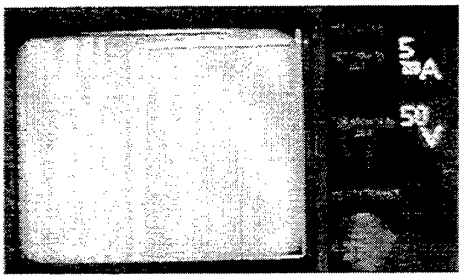


Fig. 1. I-V characteristics of 4H-SiC p -n-n diode with mesa structure area of 7.9×10^{-5} cm^2.

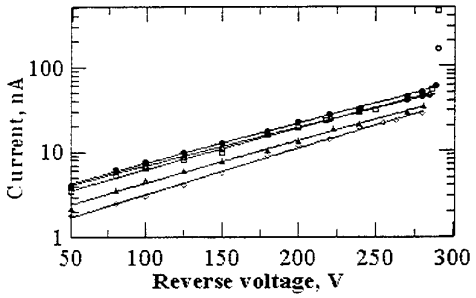


Fig. 2. Leakage currents of 4H-SiC p -n-n diode with different areas of mesa structure.

This paper reports on the fabrication and electrical characterization of 4*H*-SiC Zener diodes having avalanche breakdown voltages in the range of 260-295 V.

4*H*-SiC *p -n-n* epitaxial wafers purchased from Cree, Inc. were used to fabricate the diodes with different mesa structure areas from 1.26×10^{-5} to 3.14×10^{-4}cm^2. The diodes had series resistance lower than 4 Ω and capacities varying from 16 to 1.5 pF depending on the area of mesa structure. They revealed stable operation under avalanche breakdown conditions. Figure 1 shows the *I-V* characteristics of the 4*H*-SiC diode having breakdown voltage 270 V and operating at current 30 mA, corresponding to a power value of 8 W. The diodes with highest capacitance of 16 pF had a dynamic impedance value of 170 Ω at avalanche test current of 2 mA. The leakage current of the diodes was directly proportional to the length of diode mesa structure periphery. Moreover, it did not exceed 50 nA at reverse voltage of 250 V (see Figure 2.). The temperature coefficient of avalanche breakdown voltage (β) was measured for these diodes. It was found equal to about 3×10^{-4}K^{-1} appreciably lower than 10×10^{-4}K^{-1} – the typical value for silicon *pn* junctions with the same breakdown voltage [3]. The relatively low β value in 4*H*-SiC *p -n* junction shall lead to higher thermal stability of SiC Zener diodes. Capability of these diodes to operate under pulsed power was investigated also. They were found to be capable to operate at 300 W power conditions for 100 ns pulse duration. These investigations are under way. Detailed description of diode processing and measurement techniques as well as discussion of the results of electrical characterization will be given in the report.

This work was supported by INTAS – CNES 97-1386 and NATO SfP 971879 grants.

References

1. T.H. Beeforth, H.J. Goldsmid, Physics of Solid State Devices, Pion Limited, London, 1970, SBN 85086013, p.39.
2. Microsemi Corporation Products Catalogue, http://www.microsemi.com
3. P. Mars, Temperature dependence of avalanche breakdown voltage in *p-n* junctions, Int. J. Electronics, **32**, 23 (1971)

Design and Implementation of RESURF MOSFETS in 4H-SiC

S.Banerjee, K. Chatty, T. P. Chow and R. J. Gutmann
Center for Integrated Electronics and Electronics Manufacturing
Rensselaer Polytechnic Institute, Troy, NY-12180, USA
Tel: 518-276-6044, Fax: 518-276-8761, e-mail: baners3@rpi.edu

High voltage switches suitable for integration with low-voltage logic gates form a basic building block for power integrated circuits. In order to achieve a high blocking voltage with low on-resistance, RESURF(REduced SURface Field) technique is widely used in designing lateral devices in silicon. We have reported lateral RESURF MOSFETs[1,2] in 4H-SiC that can block 900V-1200V with a specific on-resistance ranging from 0.5Ω-cm^2-4Ω-cm^2. In this work, we show simulation and experimental results which confirm that the oxide below the gate is stressed under high voltage conditions and the maximum RESURF dose is limited by the oxide breakdown and not the breakdown in the semiconductor. We also suggest a possible solution that reduces the peak surface electric field and allows higher doping in the RESURF region.

The schematic cross-section of the device is shown in Fig.1. The RESURF region was implanted with nitrogen having a dose of 1e13 cm^{-2} and 5e13 cm^{-2} . Since the annealing is done at 1200^{0}C, the implant activation in these devices is expected to be low (~10-20%). Devices with low RESURF dose, thin gate oxides(200nm) or high RESURF dose, thick gate oxides(900nm) blocked high voltages(900-1200V) but all devices with thin gate oxides and high RESURF dose had problems of gate rupturing at very low voltage(100-200V). The electric field profile simulated for different RESURF doses, oxide thickness and field plate structures indicate that breakdown voltages above 1000V can be achieved with thin gate oxides only if a lighter doping is used in the RESURF region. This increases the on-resistance of the device because of the high RESURF region resistance, especially if the breakdown voltage is scaled to higher values. This can be overcome by having two RESURF regions with a lightly doped region below the gate and heavily doped region adjacent to the drain region. Fig2 shows the simulated breakdown voltage and peak surface field for two cases. For reasonable surface electric field (<1.5MV/cm) in the

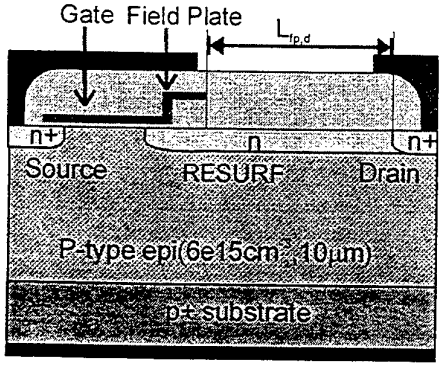


Fig.1 : Cross-section of lateral RESURF MOSFET

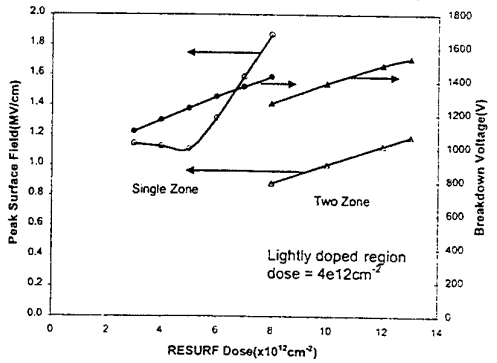


Fig.2 : Breakdown Voltage and peak surface field in the device for single zone and two-zone

semiconductor, the RESURF dose in the single zone device can not exceed 6-7e12 cm^{-2} while if two zones are used, the second zone can have a dose as high as 1.2-1.3e13 cm^{-2} without having the problem of high surface field. Detailed analysis of the two-zone device along with experimental results of the single-zone device will be presented at the conference.

Acknowledgment: The authors gratefully acknowledge the support of this work by DARPA under Contract # MDA972-98-C-0001, Philips Research, Briarcliff Manor, NY, the Office of Naval Research under MURI Contract # M00014-95-1-1302, and NSF Center for Power Electronics Systems under contract # EEC-9731677.

References:

1. K. Chatty, S. Banerjee, T. P. Chow, R.J. Gutmann and M. Hoshi; presented at DRC '99

3. S. Banerjee, K. Chatty, T. P. Chow and R. J. Gutmann; to be presented in DRC '00

Charged particle detection properties of epitaxial 4H-SiC Schottky diodes.

G. Verzellesi[♠], P. Vanni[♠], F. Nava[♠], E. Vittone[♦], C. Manfredotti[♦], A. Lo Giudice[♦], A. Castaldini[♥], A. Cavallini[♥], L. Polenta[♥], R. Nipoti[§] and C. Donolato[§]

[♠] INFM and DSI, University of Modena and Reggio Emilia, Via Campi 213/B, I-41100 Modena, Italy.
[♦] INFN and Physics Department, University of Torino, Via Giuria 1, I-10125 Torino, Italy.
[♥] INFM and Physics Department, University of Bologna, V.le Berti Pichat 6/2, I-40100 Bologna, Italy.
[♠] INFN and Physics Department, University of Modena and Reggio Emilia, Via Campi 213/A, I-41100 Modena, Italy, Tel. +39-059-2055260, Fax. +39-059-367488.
[§] CNR-Istituto LAMEL, via Gobetti 101, I-40129 Bologna, Italy

Silicon carbide is recently earning interest as a material for ionizing radiation detection because of high operating temperature capability and radiation damage resistance [1]. This work is aimed at investigating the charge collection properties and the effect of the intrinsic defects in Schottky detectors fabricated on 4H-SiC epitaxial layers. A description of the device fabrication process can be found in [2].

The charge collection efficiency (CCE) of such detectors has been measured at and above (80.°C) room temperature as a function of the applied reverse bias V_b in the range 0-100 V, for 5.48 MeV α and 2 MeV He^+ particles. CCE reaches 100% when the depleted region entirely contains the particle generation track, as happens in the He^+ case already at V_b = 40V, and is lower than 100% when the generation track reaches higher depths (80% at V_b=100 Volt for α particles). For both particles, the CCE values largely exceed those predicted by assuming full collection of generated carriers within the depleted region and zero collection probability outside. To asses the origin of such enhanced CCE, two-dimensional device simulations have been carried out using a drift-diffusion simulator (DESSIS) [3]. The code allows the dynamic response of the detector to impinging particle to be analysed. Simulations provide CCE values in good agreement with measured results, reproducing the voltage excess CCE observed experimentally.

To measure the effect of the grown-in defects in 4H-SiC epi-layer, which act as charge carrier trapping centres, on the SiC detector performance Deep Level Transient Spectroscopy and Isothermal Capacitance Transient Spectroscopy measurements were performed. The capture cross section of the deepest centre found (0.91 eV), which more likely will play a key role in limiting the detector performance, was carefully determined and an electron carrier lifetime, τ , was estimated in excess of 540 μs. The low concentration ($\cong 10^{12}$ cm^{-3}) of the trapping centres and the high value of τ indicate the high quality of the epitaxial layer and justify the full collection of the charge carriers generated by the ionising radiation when measured for depleted region wider than R_p.

Finally the Ion Beam Induced Charge (IBIC) and the Electron Beam Induced Current (EBIC) collection techniques were used to map the collection properties of the detector Shottky area. Electron and ion beam probes had, respectively, 3.5μm and 0.2μm large diameters. The IBIC experiment showed a CCE with 2.2% homogeneity and an energy resolution equal to 46 keV for 2 MeV He^+ particles and V_b > 40 V. EBIC images for V_b = 0 V and different electron penetration depths showed the presence of localised defects which reduce the collection efficiency by about -10%. These results show that the detectors can approach 100% CCE in spite of the presence of electrically active native defects, possible because of reduced recombination in the presence of the depletion field.

References

1 F.H.Ruddy et al., "*Development of a Silicon Carbide Detector*", IEEE Trans on Nucl. Science **NS-45** (1998),536.
2 F.Nava et al., "*Epitaxial silicon carbide charge particle detectors*", Nucl. Instr. and Meth. **A437** (1999),354.
3 DESSIS 6.0 Reference Manual, ISE AG, Zurich (Switzerland).

MoP-80

Thin Heavy Compensated 6H-SiC Epilayers as Nuclear Particle Detectors.

A.A.Lebedev, N.B.Strokan, A.M.Ivanov, D.V.Davydov, V.V.Kozlovski*

Ioffe Physicotechnical Institute, Russian Academy of Sciences, Politekhnicheskaya 26, 194021, St. Petersburg, Russia, Phone: +7 (812) 2479930, Fax:+7 (812) 2476425, E-mail: shura.lebe@pop.ioffe.rssi.ru

*) St. Petersburg State Technical University, Politekhnicheskaya 29, 194251, St. Petersburg, Russia, E-mail: kozlovski@tuexph.stu.neva.ru

P^+-n-n^+ structures based on 6H-SiC films grown by CVD on n+ substrate were used. The initial concentration of uncompensated donors in the n-type layer was $N^+_D - N^-_A = 4.5*10^{16}$ cm^{-3} at layer thickness of several μm. The structures were exposed to a dose of $8*10^{15}$ cm^{-2} of 8-MeV protons. The material was stabilized by annealing at T = 450^0 C for 10 min. The resulting film resistivity was $\rho = 5*10^9$ ohm cm.

It has been shown previously that proton creates a system of deep levels of both acceptor and donor nature [1]. This leads to a significant increase in ρ through electron capture by deep traps. However, C-V measurements at T = 700 K (when even the deepest levels have the emission times < 10 μs) gave a concentration $N^+_D - N^-_A = 9.1*10^{16}$ cm^{-3}, which is twice the value before irradiation. At the same time, $N^+_D - N^-_A$ decreased steadily at T = 300 K up to a dose of $4*10^{14}$ cm^{-2}. In the present work, the effect of much higher proton dose was studied by means of precision α-spectrometry [2].

Alpha particles ^{244}Cm (with energy of 5.77 MeV) were detected under both reverse and forward bias. It was found, under reverse bias the n-type base of the detector comprised a layer with ionized donors $N^+_D - N^-_A \approx 3*10^{16}$ cm^{-3} and a neutral high-resistivity region.

The range of α-particles ^{244}Cm (R ≈ 20 μm) exceeded the thickness d of the p^+-n-structure. Results obtained in two modes were compared: (i) through-penetration of a particle across the structure (R > d) and (ii) complete deceleration of a particle (R < d). The second mode was enforced by lowering the particle energy via deceleration in air. It is shown that at R > d and forward bias the signal is formed by the mechanism of "through conducting channel" [3]. This permit to determine the product of electron mobility by lifetime μτ.

Decrease in R (up to R<d) leads to varied behavior of the signal under the above biases. For example, the signal under forward bias decreases more sharply and at longer R values.

To conclude, the practical possibility is demonstrated of detecting fast ions by 6H-SiC films upon proton irradiation with doses of ~ 10^{16} cm^2. The parameter μτ retains values sufficient for effective electron transport, including signal amplification in the through-conducting-channel mode. It is also established that the positive charge $N^+_D - N^-_A$ is in fact determined by the concentration of initial uncompensated donors.

[1]. A.A.Lebedev, A.I.Veinger, D.V.Davydov, V.V.Kozlovski, N.S.Savkina, A.M.Strelchuk. To be published in Semiconductors, 2000.

[2]. A.A.Lebedev, N.S.Savkina, A. M. Ivanov, N.B. Strokan, D.V.Davydov. Semiconductors, Vol 34, N 2, 2000, pp. 243-249.

[3]. N.A.Vitovski, P.I.Maleev, S.M.Ryvkin. JTF, XXVIII (3), 460-469 (1958).

Silicon Carbide Schottky Junctions for X-Ray Spectroscopy

G. Bertuccio [1], R. Casiraghi [1], F. Nava [2]

[1] Politecnico di Milano, Department of Electronics Engineering and Information Science,

P.za L. da Vinci 32, 20133 Milano, Italy, Tel. +39.02.2399.6094, Fax.+39.02.2367604,

e-mail:Giuseppe.Bertuccio@polimi.it

[2] Università di Modena, Physics Department, via Campi 213/A, 41100 Modena, Italy

ABSTRACT

The nuclear radiation properties of silicon carbide radiation detectors have been already demonstrated for charged particles, neutrons and for dosimetry of high energy gamma radiation. These detectors are very interesting due to their capability to operate at high temperature and their high radiation hardness. No data are reported in literature on the behavior of SiC junctions as X-ray detectors. This work addresses the response of a Schottky junction on epitaxial 4H-SiC to X-ray photons from 14 keV to 60 keV, presenting the first experimental results and their analysis. The potentiality of SiC X-ray detectors stays in their low intrinsic noise due to the extremely low reverse current, almost two order of magnitude lower than for other semiconductor junctions. The tested devices have a junction area of 3 mm^2 on n-type epitaxial 4H-SiC layer 30 μm thick with a dopant concentration of $1.8x10^{15}$ cm^{-3}. At room temperature the reverse current density of the best device is 39 pA/cm^2 up to electric field of 10^5 V/cm. The devices have been tested with X-γ ray from ^{241}Am. Figure 1 shows the voltage pulses at the output of the shaper amplifier; the highest signal corresponds to the charge released by a 59 keV photon completely absorbed in the Silicon Carbide epitaxial layer. Figure 2 shows the first ^{241}Am spectrum acquired at room temperature with the SiC detector biased at 500 Volts. The main Np L X-ray lines at 13.9 keV, 17.8 keV and the ^{241}Am photons at 26.3 keV and 59.5 keV are clearly detected. The measured energy resolution is 2.7 keV FWHM, limited by the electronic noise due to the high junction capacitance, determined by the high area/thickness ratio of the depletion region. The design of advanced SiC detector structure, on low doped high purity SiC, able to achieve high energy resolution in X-ray spectroscopy is under way and will be presented.

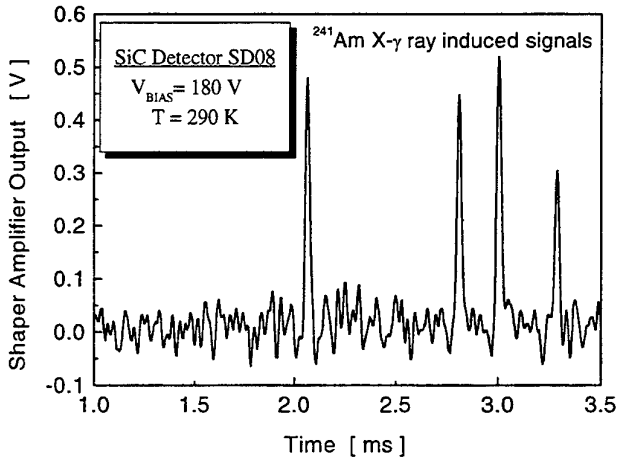


Fig. 1 *Signals at the output of the shaping amplifier when the SiC detector is irradiated with a ^{241}Am source. The highest peak corresponds to the full absorption of the 59 keV photon.*

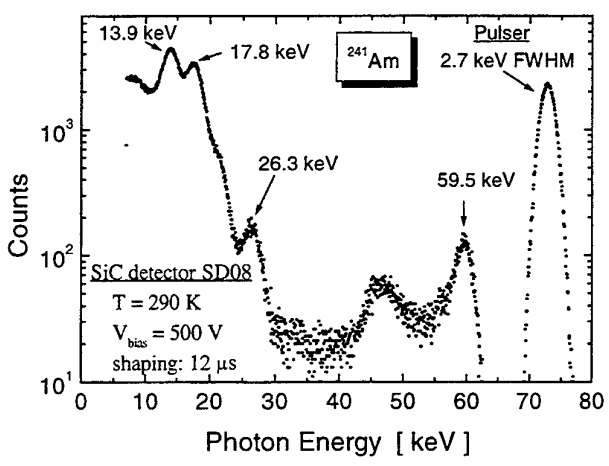


Fig. 2 *^{241}Am X-γ-ray spectrum acquired at room temperature with the silicon carbide detector. An energy resolution of 2.7 keV FWHM is measured.*

LARGE DIAMETER, LOW DEFECT SILICON CARBIDE BOULE GROWTH

C.H. Carter, Jr., R. Glass, M. Brady, D. Malta, D. Henshall, S. Muller, V. Tsvetkov, D. Hobgood and A. Powell

Cree, Inc., 4600 Silicon Drive, Durham, NC 27703
Ph: (919) 313-5300; FAX: (919) 313-5454

Realization of the full potential of semiconductor SiC for electronic and optical applications is critically dependent on the production of large diameter SiC single-crystals of high crystalline quality and controlled impurity content. In this presentation, recent empirical results reflecting the current state of the art of SiC bulk growth are presented. Recent progress in monocrystalline SiC bulk crystal growth is characterized by the attainment of: substrate diameters up to 100-mm; residual impurities in the 10^{15} cm^{-3} range; thermal conductivity approaching 5.0 W/cmK; near colorless 6H-SiC at crystal diameters up to 75-mm; and micropipe densities as low as 1.1 cm^{-2} over an entire 50-mm diameter 4H-SiC wafer and 8 cm^{-2} for 75-mm diameter 6H-SiC. The implication of these results for silicon carbide electronic devices operating at high power densities will be discussed. Additionally, the recent interest in SiC for the production of a unique near colorless gemstone material, moissanite, increases the demand for high quality SiC bulk material.

Tu1-2

DEFECT REDUCTION IN SUBLIMATION GROWN SILICON CARBIDE CRYSTALS BY ADJUSTMENT OF THERMAL BOUNDARY CONDITIONS

E. Schmitt, M. Rasp, A.-D. Weber, M. Kölbl, R. Eckstein

SiCrystal AG, Heinrich-Hertz-Platz 2, 92275 Eschenfelden, GERMANY
Phone: ++49 9665 913761 ; Fax: ++49 9665 913790 ; email : erwin.schmitt@sicrystal.de

L. Kadinski, M. Selder

Institute of Fluid Mechanics, University Erlangen-Nürnberg, Cauerstraße 4, 91058 Erlangen, GERMANY

In the past years an immense evolution of the semiconductor silicon carbide has taken place, concerning substrate size and quality, epitaxial deposition techniques and device processing. In many fields of semiconductor electronics this has lead to the demonstration of devices with excellent performance. But for the mass production of high quality devices, there is still a strong demand for an ongoing improvement of quality and homogeneity of silicon carbide substrates grown from the vapour. To meet these requirements the knowledge of the thermal boundary conditions and their influence on the defect structure of the growing crystal has to be further improved.

In this work we have carried out growth experiments using an simplified geometry for sublimation growth, where a variation of process conditions could be established better and more reproducible. During numerous growth experiments different thermal boundary conditions have been applied by varying the power supply, the relative position of crucible in respect to the induction coil and the reactor geometry.

The effects of these alternating conditions have been examined in two ways:

First of all, the temperature distribution inside the growth chamber was by two-dimensional numerical modelling. With these data a precise quantitative comparison of the different conditions could be carried out in respect to temperature and temperature gradients in the source material, the gaseous spacing and the growing crystal. In case of the bulk crystal we calculated axial temperature gradients in the range of 5...40 K/cm and radial temperature gradients in the range of 0,5..15 K/cm.

Secondly, several characterisation methods had been applied to the grown crystals and wafers, in order to obtain a comprehensive testimony of the crystal quality. With incidental and transmission optical microscopy we focussed our studies on the occurrence of micropipes, inclusions of secondary phases, planar defects and etch pits (revealed after etching in molten KOH). On as-grown surfaces disturbances were revealed by using differential interference contrast additionally. To verify the results we received from inspection with the optical microscope the scanning electron microscope was used. With stress birefringence of wafers an imaging of the axial and radial variation of stress contrast in crystals was done. Together with results obtained from XRD-measurements and etch patterns, information about the macroscopic crystalline quality was collected.

The results of our studies show clearly, that there is strong dependence of growth rate and defect generation on the thermal field. In subsequent growth runs, where the axial temperature gradient was increased by an factor of 3, we also observed an increase in the growth rate by the factor of 3. In regard to the defect generation we found out, that the occurrence and increase of some defects can be directly addressed to improper thermal boundary conditions, caused by high axial and/or radial temperature gradients imposed to the crystals in our simplified geometry. In the case of an transition of single crystalline to polycrystalline growth, we were able to determine a limit for the axial gradient.

With this elementary knowledge we were able to improve our process conditions for growth systems designed for growth of crystals with diameters of 50.8 mm and larger. Besides this we could demonstrate a decreased defect density and improved homogeneity in these crystals.

SiC SINGLE CRYSTAL GROWTH BY SUBLIMATION : EXPERIMENTAL AND NUMERICAL RESULTS

Cécile Moulin[1], Michel Pons[2], Alexander Pisch[2], Philippe Grosse[1], Christian Faure[1], Alain Basset[1], Gérard Basset[1], Antoine Passero[1], Thierry Billon[1], Bernard Pelissier[3], Michail Anikin[3], Etienne Pernot[3], Petra Pernot[3], Roland Madar[3]

[1]CEA-LETI, 17 rue des martyrs, 38054 Grenoble Cedex 9, France
[2]LTPCM- UMR 5614 (CNRS/INPG/UJF), F-38402 St. Martin d'Hères Cedex, France
[3]LMGP - UMR 5628 (CNRS/INPG), F-38402 St. Martin d'Hères Cedex, France
Corresponding author : C. Moulin, Phone ++33 4 76889954, Fax ++33 4 76885499, E-mail Cecile.moulin@cea.fr

4H ingots with diameter up to 30mm are grown by the Modified Lely Method [1]. A combined approach of this sublimation technique, involving numerical process modelling and experimental results is presented. Different geometric modifications of the reactor and process parameter are studied. Their relation with defect occurrence, polytype change are presented.

In our experimental set-up, the growth occurs in a closed graphite crucible heated by electromagnetic induction . The SiC powder is sublimated at temperature range of 2200-2600°C, and low pressure (2-10 torr). The modelling includes thermodynamic calculations, heat transfer and mass transport calculations [2]. The heat transfer analysis gives the feature of the thermal field inside the deposition chamber. By linking these thermal calculations with mass transport modelling and thermodynamic equilibrium, one can describe the macroscopic growth of SiC (deposition rate, crystal shape..). Combining this process modelling, fabrication and characterisation allows to quantify the impact of design and process parameters modifications on the material quality.

A first geometric modification is performed on the graphite foam. The graphite foam is always used around our crucible to ensure a good thermal insulation. Two kind of graphite foam have been tested. Processes that have been carried out with one of them have led to crystals with polytype mixing. The effect of these insulating materials on the temperature distribution in the cavity has been simulated. Simulation predicts an increase of 30% of the radial temperature difference along the seed for the unstabilized process. The results also indicate that a small increase of the radial temperature difference along the seed (in comparison with the working temperature) is sufficient to strongly deteriorate the quality of the material. Two hypothesis are given to explain how an increase of the radial temperature difference can lead to growth with polytype mixing.

A second geometric modification consists in varying the hole diameter in the graphite foam at the top of the crucible. This hole is known to have a strong influence on the axial temperature difference. A relationship between this hole's diameter modification and the defect occurrence in terms of secondary inclusions is established. Once again, it shows that temperature variations of about 1% compared to the working temperature can significantly influence the inclusions density (graphite particles and droplets). Some explanations are given to clarify the links between graphite particles and silicon droplets occurrence and the axial temperature difference. An investigation on these defects occurrence is also presented in Ref.[3].

Then, a third modification consists in conducting growth with two different argon pressure, the other parameters being the same. The resulting crystals shape are completely different : a first one is slightly concave whereas the second one is strongly convex. It shows that only thermal calculations are not sufficient to predict the crystal's shape. It is also controlled by mass transport from the source to the crystal. A comparison between experimental and modelling results is presented.

References

[1] Yu.M.Tairov and V.F. Tsvetkov, J. Cryst.Growth, 43 (1978) 209
[2] M. Pons, E. Blanquet, J.M. Dedulle, I. Garcon, R. Madar, C. Bernard, J. Electrochemical. Soc, 143 (1996), p. 3727-3735.
[3] D. Hofmann, E. Schmitt, M. Bickermann, M. Kolbl, P.J. Welmann, A. Winnacker, Materials Science and Engineering, B61-62, (1999), 48.

Tu1-4

IMPACT OF SiC SOURCE MATERIAL ON TEMPERATURE FIELD AND VAPOR TRANSPORT DURING SiC PVT CRYSTAL GROWTH PROCESS

P.J. Wellmann[1], D. Hofmann[1], L. Kadinski[2], M. Selder[2], T.L. Straubinger[1] and A. Winnacker[1]
[1]*Department of Materials Science 6, University of Erlangen, Martens Street 7, 91058 Erlangen, GERMANY.*
Tel.: +49-9131-85-27683, Fax: +49-9131-85-28495, Email: peter.wellmann@ww.uni-erlangen.de
[2]*Institute of Fluid Mechanics, University of Erlangen, Cauer Street 4, 91058 Erlangen, GERMANY.*

Physical vapor transport (PVT) growth is currently the most feasible technique for the preparation of silicon carbide (SiC) bulk crystals and wafers for commercial applications. Usually the growth is carried out in an inductively heated graphite crucible. The crystal quality (i.e. low defect density, homogenous doping, etc.) is known to depend sensitively on the temperature field inside the growth cell. In this paper we will investigate the impact of the SiC source material and its morphological changes during growth on the temperature field and vapor transport.

We have studied three different SiC sources. Source A was a fine SiC powder with a grain size <5μm and source B contained SiC powder with grains of 10μm...50μm in size. Source C was built out of macroscopic SiC pieces with a size in the range of 5mm...20mm. All sources were synthesized from elemental high purity Si and C in our lab. Digital x-ray imaging (Wellmann et al. Mat.Res.Soc.Symp.Proc.Vol.572) was carried out in order to study the consumption and morphological changes of the SiC sources. Numerical modeling of the temperature field inside the growth cell and numerical modeling of the vapor transport of Si- and C-containing gas species from the SiC source to the seed were performed to quantify the impact of changes inside the SiC source on the global growth process. Fig. 1 shows a x-ray image of the growth cell containing source C (macroscopic SiC pieces) after 15 hours of growth. Fig. 2 shows corresponding to Fig. 1 the temperature field and the SiC vapor flow evaluated from numerical modeling; the consumption and morphological changes (impact on heat conductivity) of the SiC source were taken into account by introducing separate blocks for the disk-like structure, the SiC core part and the graphitization area.

Due to the different morphologies of the initial SiC sources and the fundamental transitions during growth (i.e. evolution from powder to compressed SiC block) one would expect a strong non-stationary growth process. However, in contrary to this the experiments carried out indicate that the growth process is much more stable than would be concluded from the considerations above. In all cases (source A, B and C) the consumption of SiC started next to the hot side walls and bottom of the graphite crucible and proceeded to the center of the SiC source. Independent from the initial morphology of the SiC source (microscopic SiC powder source A and B, macroscopic SiC pieces source C) the formation of a disc-like structure of condensed SiC is observed at the top of the SiC source which improves the homogeneity of the temperature and the sublimation of SiC containing gas species. Numerical modeling confirmed the stabilizing impact of the disc-like structure on top of the SiC source on the global growth process.

We will show several series of x-ray images which illustrate the morphological evolution of the three SiC sources used in our experiments and we will present numerical calculations as a base for a detailed discussion of the underlying global crystal growth process.

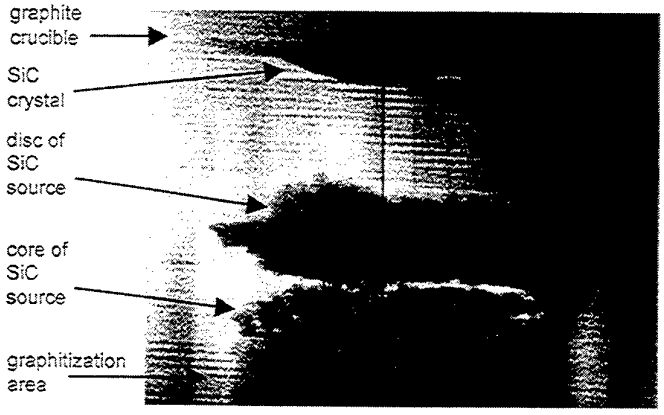


Fig.1. x-ray image of growth cell containing microscopic SiC powder (source A, initial size <5μm) after 16 hours of growth.

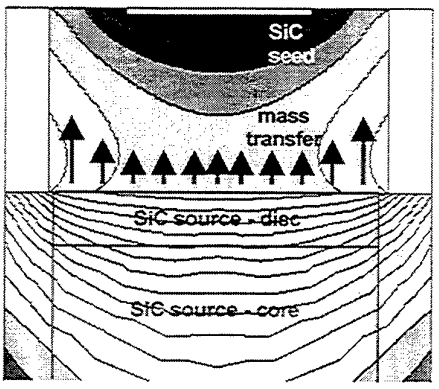


Fig.2. Numerical modeling of temperature field and the SiC vapor flow.

RECRYSTALLIZATION OF SiC BOULES BY MOTION OF HEXAGONAL VOIDS AND FORMATION OF MICROPIPES

T. A. Kuhr[1*], M. Skowronski[1], W. M. Vetter[2], and M. Dudley[2]

[1]Dept. of Materials Science and Engineering, Carnegie Mellon University, Pittsburgh, PA 15213
phone: (412) 268-2710, fax: (412) 268-3113

[2]Dept. of Materials Science and Eng., State University of New York, Stony Brook, NY 11794

The hexagonal voids observed in SiC boules grown by Physical Vapor Transport were investigated by optical microscopy, Atomic Force Microscopy , KOH etching, and White Beam Synchrotron Radiation Topography. Voids typically have irregular hexagonal platelet shape with the lateral size between 0.5 mm and 2 mm and thickness along the c-axis between 1 and 50 micrometers. Both, top and bottom facets of the voids are atomically flat with well defined growth steps. AFM investigation of top facets (facing the end of the boule) revealed etch pits due to screw dislocations and the step morphology consistent with evaporation. Bottom facet morphology (facing seed) resembled typical SiC growth surfaces and indicated deposition. The growth occurs in the step flow mode with steps typically nucleating at one of the edges of the void. Both observations indicate that voids travel through the SiC boule during growth moving from cold seed toward hot tail of the crystal.

On the bottom facet, the side of the void opposite the nucleation point usually shows a deep trench with depth of tens or hundreds of microns. The trench depth increases close to the corners of the voids. The depressions narrow down toward the seed and can extend for up to 1 mm. Synchrotron white beam x-ray topography and KOH etching of the areas above the voids show random distribution of screw and edge dislocations intersecting the void surfaces. Below the voids, both techniques show absence of screw dislocations over the void area with super-screw dislocations located at void corners. In addition, threading edge dislocations frequently line up along the edges opposite nucleation site and corresponding to trench location. The distribution of defects will be discussed and interpreted as due to the image force and void morphology. The void formation and motion appears to be the dominant mechanism responsible for formation of open core superscrew dislocations (micropipes) in silicon carbide boules.

Tu1-6

Virtual reactor: a new tool for analysis and optimization of sublimation growth of bulk SiC crystals

M.V. Bogdanov[1)], A.O.Galyukov[1)], S.Yu.Karpov[1)], A.V.Kulik[1)], S.K.Kochuguev[1)], D.Kh.Ofengeim[1)], A.V.Tsiryulnikov[1)], I.A.Zhmakin[1)],A.E.Komissarov[2)], O.V.Bord[3)], M.S.Ramm[3)], A.I.Zhmakin[3)], Yu.N.Makarov[4)]

[1)] Soft-Impact Ltd, P.O.Box 33, 194156 St.Petersburg, Russia, Phone +7 (812) 554-4570, Fax +7 (812) 326-6194
[2)] Institute for Fine Mechanics and Optics, 196117 St.Petersburg, Russia
[3)] A.F.Ioffe Physical-Technical Institute, Polytechnicheskaya 26, 194021 St.Petersburg, Russia, Phone +7 (812) 247-9145, Fax +7 (812) 326-6194
[4)] Fluid Mechanics Department, University of Erlangen-Nuernberg, Cauerstrasse 4, D-91058 Erlangen, Germany, +49 (9131) 76-1248, +49 (9131) 76-1275

Sublimation growth is extensively used for production of large-size SiC bulk crystals. It is known that the growth process occurs under unsteady conditions due to several factors, in particular, the crystal enlargement, movement of RF coil, variation of process parameters during the growth, degradation of the SiC powder, etc. In this paper we suggest an innovative approach for analysis and optimization of the reactor design and sublimation growth process. The approach utilizes the so-called "Virtual Reality" technology. The idea is to perform a whole growth process first in computer and to perform pre-analysis of effects of changes of geometry of the system and process conditions. Use of this approach allows significant reduction of time and cost of development of new reactors and growth processes.

The approach is based on modeling of processes which occur in the whole growth system during the growth process. Within the approach, duration of the growth process is divided into a number of stages. At every stage the process is assumed to be steady-state. After finishing computation for each stage, the crystal shape and the powder charge profile are calculated from the growth rate obtained, the inductor coil is shifted according to the settings predefined by crystal grower, and the system geometry is updated automatically. The growth modeling at each stage includes analysis of heat transfer and the reactive species transport [1]. Heat transfer in the powder charge is simulated using the effective heat conductivity calculated using SiC powder properties such as porosity and mean granule size. Etching of graphite crucible plays improtant role in supply of C to the growing crystal. An advanced surface chemistry model proposed in [2] predicts various deposits to be formed on the crucible walls. The SiC deposition is known to occur on the wall near the seed and to affect significantly the SiC growth at the seed and etching of the crucible wall. A special criterion is introduced to perform analysis of what kind of deposits can be formed at certain area of the crucible, and corresponding automatic modification of boundary conditions for the mass transport equations [3] is performed. The criterion considers all types of heterogeneous equilibrium available in the Si-C system and selects a solid phase thermodynamically favorable to be formed on the surface of the crucible. Being applied to the growth surface, the criterion predicts formation of secondary phase inclusions, e.g. graphite or silicon droplets, in the growing crystal.

SiC growth in the Virtual Reactor is supplemented by a special tool analyzing thermoelastic stress and dislocation density evolution in the crystal during the whole growth run. Anisotropic thermoelastic stress is computed using a two-dimensional approach allowed by SiC crystal symmetry. Dislocation density distribution is calculated using the Alexander-Haasen theory [4] and compared with that obtained assuming a full stress relaxation due to plastic deformation and crystal hardening [5]. In contrast to the latter model, the former one accounts for a memory effect in dislocation evolution.

The computations performed using the Virtual Reactor show good agreement with experimental data. The tool is used presently for optimization of crystal growth in Ta and graphite crucibles.

1. M.S.Ramm, E.N.Mokhov, S.E.Demina, M.G.Ramm, S.Yu.Karpov, A.D Roenkov, Yu.A.Vodakov, A.S.Segal, A.N.Vorob'ev, A.V.Kulik, Yu.N.Makarov, *Mat.Sci.Engin.* **B61-62**, 107 (1999).
2. A.S.Segal, A.N.Vorob'ev, S.Yu.Karpov, Yu.N.Makarov, E.N.Mokhov, M.G. Ramm, M.S.Ramm, A.D.Roenkov, Yu.A. Vodakov, A.I.Zhmakin, *Mat.Sci.Engin.* **B61-62**, 40 (1999).
3. M.S. Ramm, A.V. Kulik, I.A. Zhmakin, S.Yu. Karpov, O.V. Bord, S.E. Demina, Yu.N. Makarov, *MRS Spring Meeting*, 2000.
4. H.Alexander and P.Haasen, *Solid State Physics*, **21** (1968).
5. S. Yu. Karpov, A. V. Kulik, I. A. Zhmakin, Yu. N. Makarov, E. N. Mokhov, M. G. Ramm, M. S. Ramm, A. D. Roenkov, Yu. A. Vodakov, *J.Cryst. Gr.* **211**, 347 (2000).

Epitaxial growth of 4H SiC in a vertical hot-wall CVD reactor: Comparison between up- and down-flow orientations

J. Zhang, A. Ellison*, Ö. Danielsson, A. Henry and E. Janzén
Department of Physics and Measurement Technology, Linköping University, 58183 Linköping, SWEDEN
* Okmetic AB, Hans Meijers väg 2, 583 30 Linköping, SWEDEN
Phone: +46 13 28 57 16 Fax: +46 13 14 23 37 E-mail: jizha@ifm.liu.se

Introduction Epitaxial growth of 4H SiC with high growth rates and low residual doping has previously been reported in a vertical, hot-wall CVD reactor with up-flow orientation (also called chimney reactor) [1]. In the present study, growth experiments were performed in the same reactor operated in the down-flow orientation (inverted chimney) with the purpose to obtain a better understanding of the hot-wall growth process and the influence of the buoyancy effect on growth rate and N-doping behaviour. The similarity of the inverted chimney with a hot-wall barrel reactor geometry further motivates this investigation.

Experimental The growth experiments were performed in the inverted chimney reactor with the precursor gases of SiH_4 and C_2H_4 diluted in Pd purified H_2 carrier gas flowing from the top inlet down-wards through the hot-wall susceptor. The growth temperature ranged from 1750 to 1900 °C and the total pressure varied between 115 and 350 mbar. High N-doped epilayers with stair-case structure produced by varying only one growth parameter during the run were grown for SIMS measurement to determine both the growth rate and the N-doping. In addition low N-doped epilayers with thickness of 20 – 40 μm were also grown for the systematic study. The thickness of the low doped epilayers was measured with Fourier Transformed Infrared spectrometer.

Results and discussion The inverted chimney also produced epilayers with high growth rates and low residual doping comparable with those previously reported in the chimney process. The growth rate increases with increasing temperature with an activation energy of 27 kcal/mol, slightly lower than that in the chimney process (Fig. 1). While the growth rate in the chimney starts to decrease at temperatures higher than ~1800 °C, a continuous increase of growth rate with temperature is observed in the inverted chimney until temperatures as high as 1900 °C. A comparison of the pressure influence on the growth behaviour in the two orientations is expected to illustrate the buoyancy effect on the flow dynamics and the growth process. Our data showed a similar growth rate dependence on pressure in both orientations (Fig. 2). The growth rate increases with decreasing pressure until a critical value, below which it starts to decrease drastically with further reduced pressure. The insensitivity of the pressure effect to the reactor orientation indicates that the flow characteristics during the growth process are not dominated by free convection within the low pressure range investigated here [2]. The influence of the other growth parameters such as C/Si ratio and H_2 carrier flow has also been studied and the results have been compared with the chimney process. The observed difference between these two vertical orientations can be explained by the different flow and temperature distribution, especially at the inlet region, thereby different gas phase chemistry at this region.

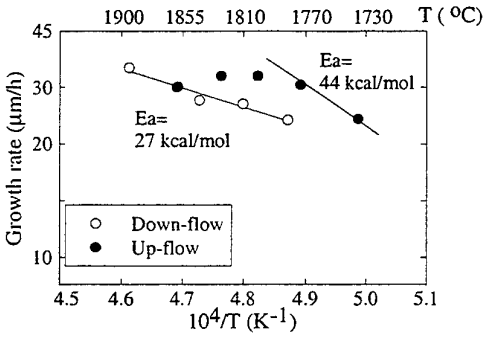


Fig.1 Growth rate dependence on temperature for both orientations, P=180 mbar and H_2 flow=3.2 L/min.

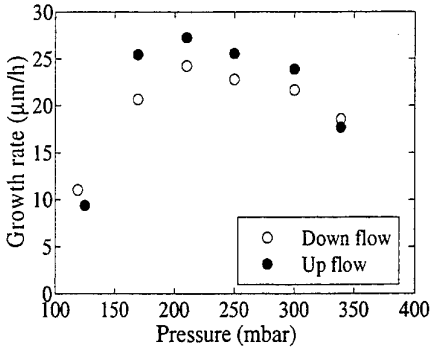


Fig.2 Growth rate dependence on pressure for both orientations, T=1770 °C and H_2 flow=3.2 L/min.

References

[1] A. Ellison, J. Zhang, A. Henry and E. Janzén, manuscript submitted to *J. Cryst. Growth* (2000)
[2] W. L. Holstein and J. L. Fitzjohn, *J. Cryst. Growth* 94 (1989), pp. 145 - 158

SiC Defect Density Reduction by Epitaxy on Porous Surfaces

S. E. Saddow,[1] M. Mynbaeva,[2] W. J. Choyke,[3] R. P. Devaty,[3] Song Bai,[3] G. Melnychuck,[1] Y. Koshka,[1] V. Dmitriev,[4] and C. E. C. Wood[5]

[1] Emerging Materials Research Laboratory, Dept. of ECE, Mississippi State, MS 39762 USA
[2] Ioffe Institute and Crystal Growth Research Center, St. Petersburg, 194021 Russia
[3] Department of Physics and Astronomy, University of Pittsburgh, Pittsburgh, PA 15260 USA
[4] TDI, Inc., Gaithersburg, MD, 20877 USA
[5] Office of Naval Research, 800 N. Quincy St., Arlington, VA 22217 USA

The presence of micropipes and dislocations in SiC wafers used as substrates for SiC epitaxial growth may cause formation of lattice defects in the epi-layers. In this research a chemical vapor deposition (CVD) process on porous SiC was developed to reduce structural defect concentrations in SiC epi-layers. We have previously reported on the growth and crystal quality of CVD epitaxial films on porous SiC (PSC) substrates.[1] Results of X-ray diffraction, RHEED, SEM and AFM characterization demonstrated good surface quality of these films grown on PSC substrates compared with conventional (control) substrates. For this study, the porous substrate surface was fabricated by surface anodization on half of a commercial 4H-SiC (0001) Si-face off-axis wafers. The other half of the wafer was protected by wax during this process and served as a control substrate. A 4H-SiC epilayer was then grown on the processed substrate by atmospheric pressure CVD at 1580°C with a Si to C ratio of 0.3. LTPL data taken at 2K (Fig 1) shows virtually no evidence of the L1 line for the film grown on PSC while the line is clearly evident in the spectra from films grown on the control substrate ('Clear Part' in fig.1). The L1 line appears in rapid CVD growth and is related to intrinsic defects in films grown too quickly.[2] In this paper we will present characterization data comparing epi grown on PSC and standard substrates.

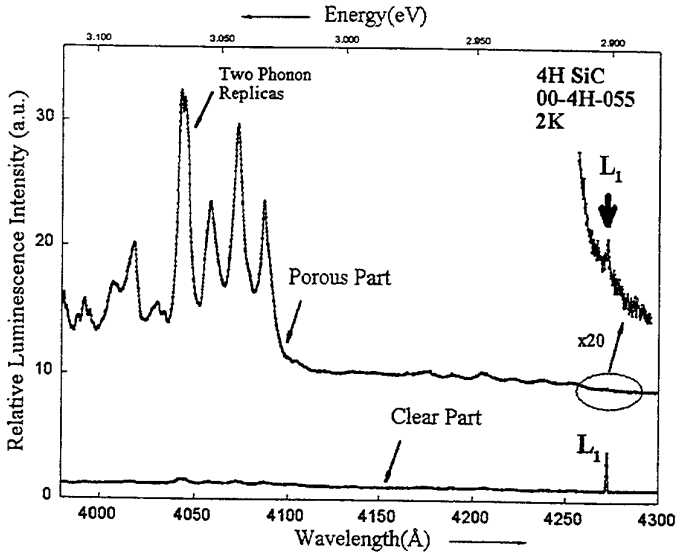


Figure 1 LTPL (2K) data comparing epi grown on PSC (top curve) to that on standard substrate (bottom curve). Note reduction in L1 and enhanced two-phonon replicas present in epi grown on PSC, indicating superior epi quality.

Acknowledgements

The authors acknowledge the assistance of I. Nikitina, A. Zubrilov, N. Kuznetsov, Ioffe Institute, and I. Kotousova, N. Seredova, Crystal Growth Research Center for material characterization.

References

[1] G. Melnychuk, S.E. Saddow, M. Mynbaeva, S. Rendakova, and V. Dmitriev, Materials Research Society, T4.2, San Fransisco, CA, April 2000.

[2] T. Frank, G. Pensl, S. Bai, R. P. Deavaty, and W. J. Choyke, ICSCRM'99 Material Science Forum, Vol. 338-342, p 753 (2000).

Gaseous Etching Effects on Homoepitaxial Growth of SiC on Hemispherical Substrates using CVD

Shigehiro Nishino, Yasuichi Masuda, Satoru Ohshima, and Chacko Jacob
Kyoto Institute of Technology, Matsugasaki, Sakyo, Kyoto 606-8585, Japan
TEL : +81-75-724-7415, FAX : +81-75-724-7400
e-mail : nishino@ipc.kit.ac.jp

keywords: Homoepitaxial growth, CVD, Etching, Surface Morphology, Off-orientation

Introduction

Orientation of the substrate is a key factor in determining the quality of SiC epitaxial layers grown by CVD. We already reported the orientation dependencies of surface morphology of epitaxial layer on 6H-SiC hemispherical substrate[1]. Recently we found that the gaseous etching before the growth is also an important parameter for surface morphology. This work investigates the effect of gaseous etching (H_2+HCl and H_2+C_3H_8) for surface morphology of the epitaxial layer on the hemispherical substrates. We show how the growth surface develops after the each etch procedure. Growth mechanism for each crysatl directions is discussed.

Experiment and Results

Hemispherical substrates were made on commercial 6H, 4H-SiC off-axis substrates inclined 3.5° or 8° from (0001) toward <11$\bar{2}$0>, and on Lely substrates (on-axis). Diameter of the hemisphere was 15 mm, and those hemisphere made angles were 0 degree to 15 degree axis from the basal plane, (0001) Si-face and (000$\bar{1}$) C-face. By using those substrates, morphological stability of the epilayer in various direction, <hkil>, could be investigated. The etching purpose, flow rates of a carrier H_2 gas, HCl (10% in H_2) and C_3H_8 (5% in H_2) were 1slm, 1sccm and 4sccm, respectively. The etching time was between 5 and 30min. The SiC epilayers were grown by atmospheric CVD using Si_2Cl_6 (hexachlorodisilane) as Si source and C_3H_8 as C source[2]. Growth rate on conventional flat substrates was 1.5μm/h and optimized for smooth surface of epilayer using 3.5 degree off-axis substrate (Si-face).

Figure 1 shows the surface morphology of the hemispherical epilayer after H_2+HCl etching on C-face of 6H-SiC observed by optical microscopy. The dark and rough regions, which 3D growth of 3C-SiC occurred, extend along <11$\bar{2}$0>[1]. Figure 2 shows the surface morphology of the hemispherical epilayer after H_2+C_3H_8 etching on C-face of 6H-SiC observed. In Fig. 2, 3D growth of 3C-SiC did not occurr along <11$\bar{2}$0>, and slightly rough regions were observed at the boundary between <11$\bar{2}$0> and <1$\bar{1}$00>. On Si-face, the surface morphology was not so dependent on the different etching procedures. A detailed analysis of the observations and growth mechanism will be presented.

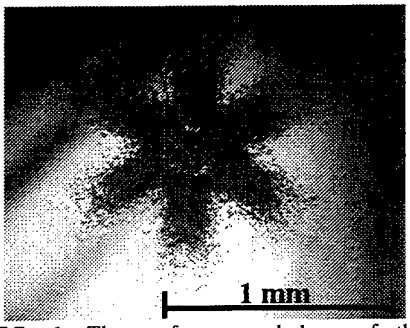


FIG. 1. The surface morphology of the hemispherical epilayer after H_2+HCl etching on C-face of 6H-SiC observed

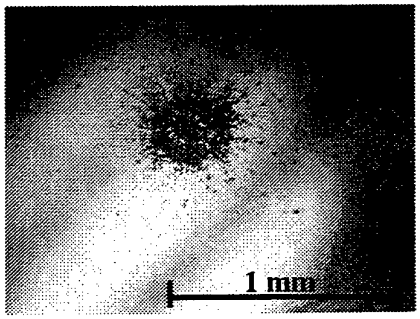


FIG. 2. The surface morphology of the hemispherical epilayer after H_2+C_3H_8 etching on C-face of 6H-SiC observed.

[1] S.Nishino, Y.Nishio, Y.Masuda, Y.Chen, and Chacko Jacob, Extended Abstracts of International Conference on Silicon Carbide and Related Materials, North Carolina, U.S.A. (1999) abs. No 280.

[2] S.Nishino, T.Miyanagi, Y.Nishio, Materials Science Forum vol.264-268 (1998) pp.139-142. (Trans Tech Publications, Switzerland)

Enlarging the usable growth area in a hot-wall silicon carbide CVD reactor by using simulation

Ö. Danielsson, U. Forsberg, A. Henry, E. Janzén

Department of Physics and Measurement Technology
Linköping University, S – 581 83 Linköping, Sweden
phone: +46 13 28 2532 fax: +46 13 14 2337
e-mail:orjda@ifm.liu.se

For the growth of epitaxial silicon carbide in a CVD reactor, it is important to have as large area as possible with homogeneous temperature distribution. This work will show that by changing the design of the CVD reactor we can enlarge this area in the reactor by at least 200%. By using a simulation tool, in this case CFD-ACE+ from CFD Research Corporation, we can try out the best new design in the computer before testing it in the lab. This software is designed to allow for specially written subroutines implemented by the user. This feature is used for dividing the simulation problem into two parts; one induction part and one heat transfer part.

The hot-wall CVD reactor used for validating the simulations in our work consists of an inductively heated graphite susceptor inside a quartz tube. We have simulated the inductive heating and the heat transfer in the reactor for a 2-dimensional axisymmetric case. To be able to compare the simulations with measurements a "2-dimensional" graphite tube has been used as susceptor in the experimental CVD reactor. The temperature distribution at the wall of the susceptor was measured by melting silicon pieces and by using a pyrometer measuring the temperature in a drilled hole (approx. black body radiating) from the back of the susceptor, with a depth corresponding to half of the susceptor length. The agreement between simulations and measurements was very good.

The temperature distribution of the standard reactor design was first simulated and then measured by melting silicon pieces. The result showed a parabolic shaped distribution, with the highest temperature approximately in the middle of the susceptor. By simulating various changes of the design of the reactor, we could achieve a more homogeneous temperature distribution over a larger area of the susceptor. The final design was then tested experimentally. The improved reactor design gives a more flat distribution with a variation in temperature of maximum 20 degrees over 80% of the length of the susceptor, while the previous design had the same variation over 24% of the total length. The length which has a temperature variation of less than 5 degrees increased from 12% to 68% of the whole susceptor. Moreover, the power input needed to reach the same maximum temperature as in the original reactor design was reduced by 15%. Fig. 1 shows the measured and simulated temperatures.

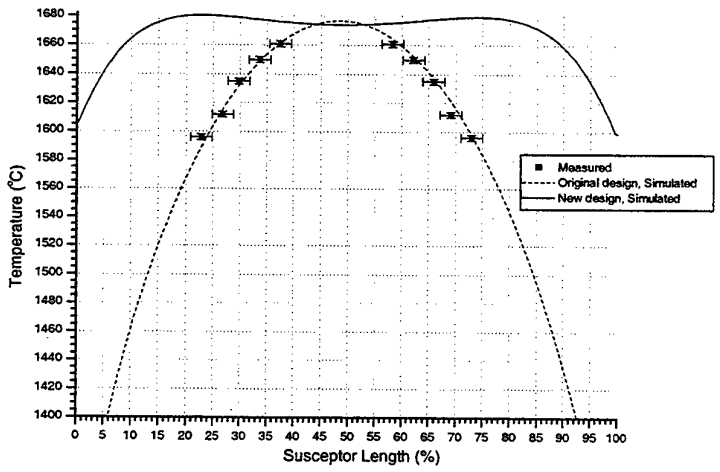


Fig. 1 Temperature distribution along the susceptor wall in a 2D graphite susceptor, measured and simulated values.

Although this investigation was made for a 2D axisymmetric case, we believe that the changes we have made for the 2D reactor also should improve the real 3D reactor towards a more homogeneous temperature distribution and thereby increasing the area of good growth conditions in the CVD reactor. By using the simulation tool when designing new reactors one can not only increase the yield of good material, but also decrease the energy costs of running the reactor.

Low Temperature Selective and Lateral Epitaxial Growth of Silicon Carbide on Patterned Silicon Substrates

Chacko Jacob, Pirouz Pirouz[1] and Shigehiro Nishino
Dept. of Electronics and Information Science, Kyoto Institute of Technology, Matsugasaki, Sakyo-ku, Kyoto 606 Japan
Tel. (+81) 75 724 7438 Fax. (+81) 75 724 7400 E-mail. chacko@dj.kit.ac.jp
[1]Dept. of Materials Science and Engineering, Case Western Reserve University, 10900 Euclid Ave., Cleveland, OH USA 44106

Selective epitaxial growth was performed in a conventional atmospheric pressure chemical vapor deposition (APCVD) system. Two different source species have been studied. In one instance, the sources were hexachlorodisilane (HCDS) and propane (two-source system). In the second case, the source was hexamethyldisilane (HMDS) (one source system). Hydrogen was used as the carrier gas and small amounts of hydrogen chloride (HCl) were added to improve the selectivity. Si(001) wafers, with a patterned oxide layer (~ 600 nm thick) as a mask, were used as substrates.

Selective growth was demonstrated in films grown at 1350°C and below utilizing the two-source system. However, the oxide mask was damaged at the growth temperatures [1]. Addition of trimethylaluminium (TMA) reduced the temperature of epitaxial growth to 1250°C but resulted in the formation of unwanted phases at the interface as well as promoted gas phase nucleation. Therefore, in order to reduce the epitaxial growth temperature, HMDS was used as the source. Selective epitaxial growth of SiC on Si was demonstrated at temperatures as low as 1150°C [2]. Utilizing the results of the above work, the growth using the two-source system has been further optimized. The present paper reports the selective epitaxy and lateral overgrowth of SiC on masked Si at 1150°C. Smooth and highly selective growth has been demonstrated (Figure1). Lateral overgrowth may be observed in this figure by comparing the stripe widths of the mask and window before and after growth. At this temperature, the oxide remains undamaged for growths up to an hour. Longer time growth runs are being investigated to study coalescence of the overgrown layers. Void formation in the substrate was suppressed in smaller windows suggesting that some sort of 'loading' effect was being observed.

[1] C. Jacob, M-H. Hong, J. Chung, P. Pirouz and S. Nishino, International Conference on Silicon Carbide and Related Materials, North Carolina (USA) October 10-15, 1999
[2] C. Jacob, J. Chung, M-H. Hong, P. Pirouz and S. Nishino, Mat. Res. Soc. Symp. Proc. Vol. 622, (MRS: Boston) (2000)

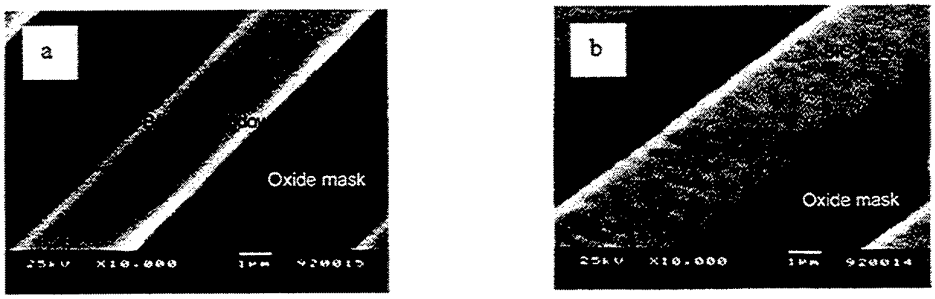


Figure 1. Epitaxial Lateral Overgrowth of SiC on Si (001) substrate a) before growth; b) after growth.

Tu2-6

Laser Crystallization of Amorphous SiC

S. Urban[a], F. Falk[a], H. Hobert[b], H. Stafast[a]

[a] Institut für Physikalische Hochtechnologie e.V., Fröbelstieg 3, D-07743 Jena, Germany, Phone: 03641/ 302 640, Fax: 03641/ 302 603, E-Mail: urban@ipht-jena.de
[b] Institute of Physical Chemistry, University of Jena, Lessingstrasse 10, D-07743 Jena, Germany

Silicon carbide is an ideal material for high-power, high-frequency and high-temperature electronic devices. For these applications nanocrystalline, polycrystalline, or single-crystalline SiC films are required. Usually, crystalline SiC films are produced by CVD either at high substrate temperature or followed by a high temperature annealing step in which amorphous SiC is crystallized. These processing technologies have the disadvantage that large area and low cost materials such as glass cannot be used as substrates. High temperature annealing can be avoided by pulsed laser irradiation of amorphous material.
Amorphous SiC films 100-400 nm thick were produced on glass (Corning 7059) by pulsed laser deposition from a stochiometric, polycrystalline SiC target. The ablation was carried out using a pulsed KrF excimer laser (248 nm, 25 ns) at a repetition rate of 50 pulses per second, a pulse energy of 250 mJ, a laser fluence of approximately 2 J/cm² on the target surface, and at approximately 200 °C substrate temperature.
The films were crystallized by single shots of the KrF laser at a fluence less than 1 J/cm². The crystallization process was studied by time resolved reflection and transmission (TRRT) measurements during laser annealing. A 10 mW cw He-Ne laser (633 nm) was used to probe the sample transmissivity and reflectivity. The He-Ne laser beam power was measured with a fast photodiode (2 ns time resolution) and registered by an oscilloscope. Since the transmissivity and reflectivity of liquid SiC is expected remarkably to differ from that of solid SiC, this method appears suitable to detect the liquid phase on the sample surface.
Before and after irradiation the samples were characterized by optical microscopy, Raman measurements, and transmission electron microscopy. Laser irradiation evidently led to polycrystalline SiC with a grain size of several hundred nanometers. The crystallites result from a SiC melt of approximately 50 ns according to the TRRT measurements. These findings are unexpected because they are in contradiction to the equilibrium phase diagram of SiC in which no liquid phase occurs at ambient pressure.

First 5x3"/7x2" Hot-Wall Planetary Reactor® for the CVD Growth of Large Area SiC

Frank Wischmeyer[1], Johannes Käppeler[2], Rune Berge[1], Jan-Olov Fornell[1], Martin Dauelsberg[2], Michael Heuken[2], Holger Jürgensen[2]

[1] EPIGRESS AB, Ideon Science & Technology Park, SE-22370 Lund, SWEDEN
Telephone: +46 46 286 89 47, Fax: +46 46 286 89 89, E-mail: frank.wischmeyer@epigress.se

[2] AIXTRON AG, Kackertstr. 15-17, D-52072 Aachen, GERMANY
Telephone: +49 241 8909 314, Fax: +49 241 8909 40, E-mail: wis@aixtron.com

The emerging market of SiC electronic devices requires mass production Chemical Vapor Deposition (CVD) systems for the growth of the electrically active SiC layers. Excellent uniformity and reproducibility of layer properties together with low costs per epi-layer are main specifications of such a production tool. Due to the high temperatures which have to be applied for the CVD growth of SiC (typically 1600°C) the design of the reactor has to ensure laminar flow conditions and a controlled depletion of the reactants inside the reactor. The careful choice of the employed materials and high components lifetimes are essential to maintain a low background impurity doping level at the high process temperatures.

In this contribution, we are presenting the novel Hot-Wall Multiwafer Planetary Reactor® VP2000. The reactor is based on the AIXTRON AIX 2000HT Planetary Reactor® which had been already successfully employed for CVD growth of high quality SiC. This system comprises a RF heated susceptor with planetary rotation of the substrates in a configuration of 7x2" wafers, or with an increased wafer capacity of 5x3". The double rotation feature effectively levels out any temperature non-uniformity and the depletion of reactants along the susceptor. For large area SiC epitaxy employing the 5x3" susceptor configuration this benefit becomes even more prominent.

For the Hot-Wall design of the reaction chamber, detailed computational simulations of the thermal management, gas flow dynamics and gas phase reactions have been performed. The result is a reactor ceiling which is actively heated, temperature controlled. The temperature uniformity or gradient in this wall can be adjusted very precisely. At the same time, this hot wall defines the reaction chamber height and the radial symmetric gas flow pattern. This feature allows a fast and independent heating of the reaction chamber ceiling and susceptor to the desired high temperatures. The reaction gases, which are utilized for the growth of SiC (e.g. SiH_4, C_3H_8 and H_2), are introduced into the chamber while keeping the temperature at the gas inlet at a low level. The thermal management of the reactor entrance is considered to be essential for the suppression of gas phase nucleation of Si and the desired high growth rates. For the first time essential experimental data on the reactor performance will be presented.

An Overview of SiC Power Device Development at Cree

John Palmour
Cree, Inc.,4600 Silicon Dr., Durham NC 27703.
Ph: 919-313-5646; Fax: 919-313-5696; E-mail: John_Palmour@cree.com.

This paper provides an overview of the SiC power device development effort ongoing at Cree. The detailed design, fabrication and high temperature characterization of 8.6 kV, 4H-SiC PiN diodes will be presented. The newly developed 100 μm 4H-SiC epitaxial layers utilized for the fabrication of these diodes result in a relatively uniform blocking and on-state characteristics across the entire wafer. The measured differential on-state resistance at 100 A/cm^2 was approximately 20 mΩ-cm^2, which is >30X smaller than the ohmic resistance of 625 mΩ-cm^2 of the epitaxial layer used for the fabrication of these diodes. High temperature (up to 300°C) reverse bias measurements are reported for the first time. The leakage current at 5 kV increases by an order of magnitude from room temperature to 300°C. The temperature dependence of switching characteristics show an approximately 50% increase in the peak reverse recovery current and a 100% increase in total reverse recovery charge from 300 K to 350 K (277°C).

High voltage power DiMOSFETs (Double implanted MOSFETs) in silicon carbide (SiC) are very attractive because they have the potential to match silicon IGBTs in on-state drop, but offer superior switching speed and higher operating temperatures. In SiC power DiMOSFETs, the peak electric field in the blocking region is designed to be approximately 10X higher than that of a Si device with equivalent blocking voltage. This can be detrimental to gate oxide if adequate shielding of the electric field is not provided. In this paper, SiC DiMOSFETs with JFET gaps ranging from 1 μm to 6 μm have been studied using a 2D device simulator, so that the optimal compromises between gate oxide protection and JFET resistance are found for 1200V (6H) and 2000V (4H) devices. Measurement data from DiMOSFETs with JFET gaps ranging from 1 μm to 6 μm fabricated in both 6H- and 4H- SiC are presented to compare with the simulation results. Another important issue for SiC DiMOSFETs is extremely low surface channel mobility, especially in 4H-SiC. Several methods, such as channel implantations and different anneals for gate dielectric have been suggested to improve MOS channel mobility. These methods were successful for simple devices built in lightly doped p-type epilayers. However, high channel mobilities on an implanted p-well, which is more practical for power MOSFETs, have yet to be demonstrated. In this paper, MOSFET results for several different channel implantation doses and gate oxide anneals are obtained for devices in implanted p-wells, and characteristics of power DiMOSFETs fabricated using these techniques are presented.

The first high voltage NPN bipolar junction transistors in 4H-SiC are demonstrated. The BJTs were able to block 1800V and showed an on-resistance of 10.8 mΩ-cm^2 at room temperature (I_C = 2.7A @ V_{CE} = 2V for a 1 mm x 1.4 mm active area), which outperforms all SiC power switching devices ever reported. Temperature-stable current gain was observed for these devices. This is due to higher percent ionization of the deep level acceptor atoms in the base region at elevated temperatures, which cancels effects of increased minority carrier lifetime at high temperatures. These transistors show positive temperature coefficient in the on-resistance characteristics, which enables easy paralleling of the devices.

A 2-mm x 2-mm, 4H-SiC, asymmetrical npnp Gate Turn-Off (GTO) thyristor with a blocking voltage of 3100 V and a current turn-off capability of 20 A is reported. This is the highest reported power handling capability of 62 kW for a single device in SiC. The 5-epilayer structure utilized a blocking layer that was 50 μm thick, p-type, doped at about 7-9x10^{14} cm^{-3}. The devices were terminated with a single zone Junction Termination Extension (JTE) region formed by ion-implantation of nitrogen at 650°C. The device was able to reliably turn-on and turn-off 20 A (500 A/cm^2) of anode current with a turn-on gain ($I_K/I_{G,on}$) of 20 and a turn-off gain ($I_K/I_{G,off}$) of 3.3.

We1-1
(Invited)

SiC Surfaces: Atomic Structure and Potential Application for Oxidation, Stacking and Growth

U. Starke

Lehrstuhl für Festkörperphysik, Universität Erlangen-Nürnberg
Staudtstr. 7, D-91058 Erlangen, Germany
phone: +49-9131-8528405, fax: +49-9131-8528400
email: ustarke@fkp.physik.uni-erlangen.de

The properties of SiC surfaces have been found to be of importance in connection with growth of SiC material as well as specific processing steps in the manufacturing of devices. SiC applications commonly involve the hexagonal surfaces, i.e. the silicon or carbon terminated bilayer truncation planes perpendicular to the c-axis. In this paper the stable surface phases and their reconstruction geometries are reviewed for both SiC(0001) and SiC(000$\bar{1}$), the orientations nominally terminated by silicon and carbon, respectively. The immediate relevance of the atomic surface structure for technological applications is demonstrated for examples related to oxidation, stacking and single crystal growth.

The different phases were prepared by either *ex situ* hydrogen treatment or by Si deposition and annealing in vacuum [1,2]. Their structure was analyzed using Scanning Tunneling Microscopy (STM), Auger Electron Diffraction (AES), X-Ray Photoelectron Spectroscopy (XPS) and Low-Energy Electron Diffraction (LEED) crystallography. The SiC(0001)-(3×3) phase consists of a *twisted* Si adlayer with all Si atoms four-fold coordinated terminated by a single Si adatom per unit cell. The extremely efficient dangling bond saturation of this phase allows step flow growth for monocrystalline homoepitaxial layers [3]. In the $(\sqrt{3}\times\sqrt{3})$R30° phase on this surface the unit cell is characterized by a single silicon adatom in the so-called T4 position, i.e. coordinated to three Si atoms and one carbon atom of the topmost bilayer. A switch to cubic layer stacking can be induced on hexagonal SiC(0001) samples when this phase is prepared under silicon rich conditions [4]. In contrast, on the SiC(000$\bar{1}$) surface a (2×2) reconstruction which also contains one Si adatom per unit cell leads to preferential hexagonal stracking termination of the surface [5]. This behaviour might be utilized as seed for polytype heterostructures. Finally, an epitaxially well matching silicon oxide monolayer with $(\sqrt{3}\times\sqrt{3})$R30° periodicity can be prepared on both SiC(0001) and SiC(000$\bar{1}$) by using a hydrogen etching or plasma treatment [6]. This initial layer promises to facilitate low defect oxide films for MOS devices.

This work was supported by Deutsche Forschungsgemeinschaft (DFG) through SFB 292.

[1] U. Starke, J. Schardt and M. Franke, Appl. Phys. A **65**, 578 (1997).

[2] J. Bernhardt, M. Nerding, U. Starke and K. Heinz, Mat. Sci. Eng. B **61-62**, 206 (1999).

[3] U. Starke, J. Schardt, J. Bernhardt, M. Franke, K. Reuter, H. Wedler, K. Heinz, J. Furthmüller, P. Käckell and F. Bechstedt, *Phys. Rev. Lett.* **82**, 2107 (1998).

[4] U. Starke, J. Schardt, J. Bernhardt, M. Franke and K. Heinz, *Phys. Rev. Lett.* **82**, 2107 (1999).

[5] A. Seubert, J. Bernhardt, M. Nerding, U. Starke and K. Heinz, *Surf. Sci.* **454-456**, 45 (2000).

[6] J. Bernhardt, J. Schardt, U. Starke and K. Heinz, *Appl. Phys. Lett.* **74**, 1084 (1999).

Interplay of surface structure, bond stacking and heteropolytypic growth of SiC

Ulrike Grossner, A. Fissel, J. Furthmüller, W. Richter, and F. Bechstedt

Friedrich-Schiller-Universität, Max-Wien-Platz 1, 07743 Jena, Germany
Tel.: ++49-(0)3641-947166, Fax: ++49-(0)3641-947152, E-mail: ulrike@ifto.physik.uni-jena.de

The growth of heteropolytypic structures based on SiC allows the fabrication of heterostructure devices using a single semiconductor material with varying stacking of the Si-C bilayers in [0001] direction. The molecular beam epitaxy (MBE) is a suitable method to grow such heteropolytypic systems. However, the conditions of a controlled layer-by-layer MBE growth of different polytypes need a deeper understanding.

In this contribution, a combination of total-energy (TE) studies of SiC surface structures with MBE growth experiments monitored by reflection high-energy electron diffraction (RHEED) is used to contribute to such an understanding. The TE and electronic-structure calculations are based on the *ab initio* pseudopotential-plane-wave code VASP. A supersoftening of the nonnormconserving pseudopotentials allows the accurate treatment of slabs with 12 Si-C bilayers and a corresponding amount of vacuum. The bottom layer is saturated by hydrogen. $\sqrt{3}\times\sqrt{3}$ and 3×3 reconstructions are considered to model different stoichiometries of the Si-terminated surfaces. Boron is used to study the adsorbate influence. The SiC films were grown between 900° and 1350°C in a RIBER-EVA 32 MBE system. The source flux of the materials Si and C is controlled by mass-spectrometer based flux meter. High-quality nominal on-axis SiC(0001) wafers are used. The surfaces are prepared by *in situ* sublimation etching in a Si flux.

The calculations show that stacking faults generated in different layers beneath the surface of a cubic 3C crystal are energetically unfavourable in contrast to the bulk situation. In general, a surface stabilizes the cubic stacking in the uppermost atomic layers. However, the degree of stabilization depends on the surface reconstruction. This is in agreement with observations of the MBE growth of SiC heterostructures under near equilibrium conditions. The cubic polytype occurs preferentially under Si-rich conditions (i.e. below 1300°C), where at lower temperatures the Si-rich 3×3 superstructure appears. The hexagonal polytypes grow under less Si-rich conditions (i.e. about 1300°C) corresponding to the $\sqrt{3}\times\sqrt{3}$ surface.

The TE studies of additional (pseudomorphically grown) cubic bilayers on top of 4H- and 6H-SiC with a $\sqrt{3}\times\sqrt{3}$ surface indicate a global minimum of the TE at four equally stacked (i.e. cubic) Si-C bilayers. This fact suggests a sensitive balance of surface and bulk effects for the growth of cubic or hexagonal polytypes on a hexagonal substrate. For the $\sqrt{3}\times\sqrt{3}$ reconstruction the uppermost layers grow with cubic stacking. After a certain number of layers a strain-induced solid phase transition cubic $\rightarrow$ hexagonal should occur. The most Si-rich surface showing a 3×3 reconstruction stabilizes an in-plane lattice constant closer to the cubic value. In this way a strain-induced phase transition is prevented.

Initial Oxidation of the 4H-SiC(0001) and 6H-SiC(0001) Surfaces

F. Amy and P. Soukiassian
Commissariat à l'Energie Atomique, DSM-DRECAM-SIMA, Centre d'Études de Saclay, Bât. 462, 91191 Gif sur Yvette Cedex, France
and Département de Physique, Université de Paris-Sud, 91405 Orsay Cedex, France

Yeu-kuang Hwu
Academia Sinica, Nankang, Taipei , Taiwan

C. Brylinski
Thomson-CSF, Laboratoire Central de Recherches, Domaine de Corbeville, B.P. 10, 91401 Orsay Cedex, France

Phone: *33 (0)1 69 08 23 45* Fax: *33 (0)1 69 08 35 92* E-Mail: *famy@drecam.cea.fr*

Surface passivation is a central issue in successful SiC device applications. The initial oxidation of 4H-SiC(0001) 3x3 and 6H-SiC(0001) 3x3 surfaces are investigated by valence band and core level photoemission spectroscopy using the Si 2p and C 1s core levels. The oxidation is performed at various oxygen exposures for room and elevated surface temperatures (from 25°C to 500°C). Unlike silicon surfaces, the oxidation is taking place at very low oxygen exposures with SiO_2 formation already at room temperature. The oxidation rate is significantly enhanced at increasing surface temperatures, with formation of SiO_2 as the dominant oxidation product with Si^{3+}, Si^{2+} and Si^{+} oxidation states present at the interface. The C 1s results also indicate the existence of oxygen atoms bonded to both Si and C species. Most significantly, the oxidation process appears to be significantly less efficient on the 4H-SiC(0001) 3x3 surface with smaller amount of oxidation products and presence of carbon species in the oxide layer. This finding is relevant in view of the higher interface state densities generally observed for oxide/4H-SiC(0001) interfaces.

Interestingly, the oxidation of Si overlayer pre-deposited onto the surface result in the formation of carbon free SiO_2 with abrupt interface formation [1].

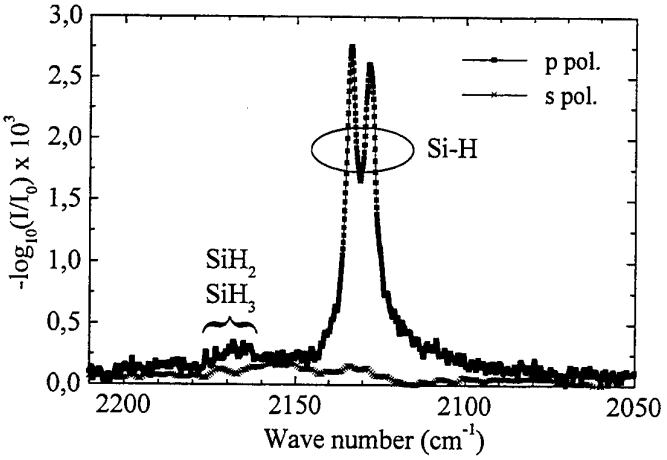
Reference

1-F. Amy, P. Soukiassian, Y.-K. Hwu and C. Brylinski, Applied Physics Letters 75, 3360 (1999).

Preparation and characterization of hydrogen terminated 6H-SiC

N. Sieber, B. Mantel, Th. Seyller, L. Ley
University Erlangen-Nürnberg, Institute of Technical Physics II,
Erwin-Rommel-Str. 1, D-91058 Erlangen, Germany
Tel.: ++49 911 8528882, Fax: ++49 911 8527889

Hydrogenation provides an ideal termination of silicon and diamond (111) surfaces in that it ties up all dangling bonds without the necessity for surface reconstruction. We have succeeded in saturating the hexagonal (0001) surface of 6H-SiC with a monolayer of hydrogen as well by exposing the SiC crystal to pure hydrogen at elevated temperatures. The photoemission spectra show only bulk related Si and C components and give no indication of adsorbates even after prolonged exposure to atmosphere. The Si-H bonds have been identified through their characteristic stretching modes at around 2130 1/cm using fourier transformed infrared spectroscopy (FTIR) (see Figure). The necessary sensitivity to detect a monolayer of Si-H bonds was achieved utilizing the attenuated total reflection (ATR) technique. The fact that the Si-H stretching bands are only observed in p-polarization and not in s-polarization demonstrates that the Si-H bonds are oriented perpendicular to the surface.



Low energy electron diffraction (LEED) was employed to monitor the transition from an unreconstructed to a reconstructed surface as hydrogen was desorbed at temperatures of 800°C in ultrahigh vacuum. The resulting ($\sqrt{3}$x$\sqrt{3}$) LEED pattern corresponds to the known reconstruction with Si adatoms in a T4 position. The C1s core level spectra indicate that the Si adatoms come from regions of the surface which graphitize as a consequence of Si depletion. Thus, the formation of the ($\sqrt{3}$x$\sqrt{3}$) reconstruction is the result of a dissociation of the stoichiometric SiC surface into Si-rich and Si-poor regions.

Polytype and polarity of silicon carbide and aluminium nitride films growing by MBE: A nondestructive identification

B. Schröter, A. Winkelmann, A. Fissel, V. Lebedev, W. Richter

Institut für Festkörperphysik, Friedrich-Schiller-Universität, Max-Wien-Platz 1
D-07743 JENA, Germany, Phone: 0049-3641-947463, Fax: 0049-3641-947442

The growth of heterostructures of SiC polytypes demands definite nucleation and growth conditions for each polytype. Up to now a controlled and reproducible deposition of high-quality heterostructures of various polytypes is an unsolved problem. Using solid-source molecular beam epitaxy, it is possible to control and vary the growth conditions of the cubic and hexagonal SiC polytypes. Furthermore, aluminium nitride films on SiC or Si may grow as a cubic or hexagonal polytype and show different polar faces. The polarity of III-nitride films is crucial for the growth and the properties of heterostructures.

The determination or monitoring of the growing polytype or of the stacking in a thickness range from a double layer up to a few nanometers, i.e., a few unit cells of the most common polytypes, requires suitable characterization techniques. Surface analysis methods such as LEED or RHEED are sensitive to a few bilayers only. We use these techniques for characterizing the surface structure during growth but an unambiguous determination of the polytype structure is limited due to their high surface sensitivity. Photoluminescence as well as X-ray diffraction and Raman scattering are capable to identify the polytype of thick films. By high-resolution transmission electron microscopy a thin-film polytype identification is possible but it is destructive, expensive and limited to local analyses.

For a nondestructive determination of the polytype and polarity we use the diffraction of electrons with medium kinetic energy of one or a few keV because their interaction length is in the nanometer range appropriate to polytype unit cells.

In X-ray photoelectron diffraction (XPD), chemically resolved diffraction patterns can be measured for each element separately. The information depth varies with energy and emission angle of the photoelectrons. Thus, XPD is useful to get information on the surface structure as well as on the polytype defined by a unit cell with a few nanometers thickness. Actually, we have found that an XPD pattern of medium-energy photoelectrons at common emission angles up to 70° is hardly influenced by surface structure or contamination but is sensitive to the polytype structure and the stacking sequence of more than 10 double layers. The patterns can be well described by a single-scattering cluster (SSC) theory. We have measured and calculated the diffraction patterns of the most common polytypes and their polar faces. These patterns can be used as fingerprints for the characterization of thin film structures. Furthermore, a simulation of the patterns of other polytypes, of heterostructures or of any stacking sequence is possible by SSC calculations. This is important for monitoring epitaxial growth and has been applied to in situ grown heterostructures of SiC polytypes.

XPD is also useful to identify the polar faces of various polar crystals in a nondestructive way. Especially, the determination of Si (0001) and C (000-1) face of the common SiC polytypes is easy because of the very different scattering of the photoelectrons in normal direction to the surface.

A quick identification of a thin film polytype is also possible by the technique of electron channeling pattern (ECP). In contrast to XPD, it utilizes the scattering of the incident beam in a scanning electron microscope and is not element specific. As the electron energy can be easily changed within a wide range, the information depth can be varied to identify the polytype in thicker films, too.

This work is supported by the Deutsche Forschungsgemeinschaft (SFB 196).

We2-1
(Invited)

SiC-BASED GAS SENSORS AND THEIR APPLICATIONS

Anita Lloyd Spetz
S-SENCE and Div. of Applied Physics, Linköping University, SE-581 83 Linköping, Sweden
Phone: +46 13 281710 Fax: +46 13 288969 e-mail: asz@ifm.liu.se

Field effect sensors based on silicon carbide have been demonstrated for different industrial applications including rough environments like high temperatures and corrosive gases [1]. Metal insulator silicon carbide, MISiC, Schottky diode devices as well as FET transistor devices that can be operated up to 700°C [2,3] have been used. Some device design considerations will be given.

For operation temperatures above 600°C the MISiC sensors respond within milliseconds to a change between an oxidizing and reducing atmosphere, and cylinder specific monitoring of a combustion engine has been demonstrated [4]. Changing the temperature in the range between 200 - 500°C and changing the type and structure of the gate metal give sensors with diverse response patterns to different components in e.g. exhaust gases and flue gases.

Urea or ammonia is used for Selective Catalytic Reduction (SCR) of nitric oxides in diesel exhausts. Sensor devices operating at 300°C in diesel exhausts show high selectivity to ammonia molecules [5]. At a higher temperature, about 500°C, some selectivity to HC is found in synthetic petrol exhausts. Boilers of the size 0.5 – 5 MW constitute a potential market for combustion monitoring sensors. MISiC devices used for monitoring of flue gases showed high selectivity to changes in the carbon monoxide concentration [6].

From aging of milk hexanal is produced, just like from aging of many other kind of foodstuff. MISiC sensors responded to the headspace of milk samples to which different concentrations of hexanal was added.

References:

1. A. Lloyd Spetz, M. Eriksson, L.-G. Ekedahl, and I. Lundström, Si and SiC-based field effect devices, 7:th International Symposium on Trends and Applications of Thin Films (TATF´2000), Nancy, France, March 27-30, 2000, pp. 72-81.
2. S. M. Savage, A. Konstantinov, A. M. Saroukan, C. Harris, Proc. of ICSCRM´99, Research Triangle Park, NC, USA, October 10-15, 1999, accepted.
3. H. Svenningstorp, P. Tobias, P. Salomonsson, I. Lundström, P. Mårtensson, and A. Lloyd Spetz, High temperature gas sensors based on catalytic metal field effect transistors, Proc. of ICSCRM´99, Research Triangle Park, NC, USA, October 10-15, 1999, accepted.
4. P.Tobias, P. Rask, A. Göras, I. Lundström, P.Salomonsson, and A.Lloyd Spetz, Platinum – Insulator – Silicon Carbide Structures as Small and Fast Sensors for Exhaust Gases, Sensoren und Messysteme 2000, VDI Berichte 1530, ISBN 3-18-091530-7, VDI Verlag, Düsseldorf, March 13-14, 2000, pp. 179-190.
5. H. Svenningstorp, P. Tobias, P. Salomonsson, B. Häggendal, I. Lundström, L.-G. Ekedahl, and A. Lloyd Spetz, MISiC Schottky Diodes and Transistors as NH_3 Sensors in Diesel Exhausts to Control SCR, Eurosensors XIV, Copenhagen, Denmark, August 27-30, 2000, accepted.
6. L. Unéus, P. Ljung, M. Mattsson, P. Mårtenssson, R. Wigren, P. Tobias, I. Lundström, L-G. Ekedahl and A. Lloyd Spetz, Measurements with MISiC and MOS sensors in flue gases, Proc. Eurosensors XIII, The Hague, The Netherlands, September 12-15, 1999, pp. 521-524.

Hot Al and C Co-Implants in 4-H SiC Annealed with AlN/C Caps

K.A. Jones*[1], P.B. Shah[1], M.A. Derenge[1] R.D. Vispute[2], T. Venkatesan[2], O.W. Holland[3]
[1]U.S. Army Research Lab - SEDD, 2800 Powder Mill Road, Adelphi, MD 20783 USA
[2]Physics Dept., University of Maryland, College Park, MD 20742 USA
[3]Oak Ridge National Laboratory, Oak Ridge, TN 37831 USA
(* P: (301) 394-2005, F: (301) 394-4562, KAJones@arl.mil)

Itoh *et al* have shown that co-implanting C with Al increases the hole carrier concentration, and Zhao *et al*, have shown that this reduces the sheet resistance and ohmic contact resistance. Because co-implanting Si with Al lowers the carrier concentration, it has been suggested that implanting with C encourages the Al to occupy Si sites. This cannot be the whole story as increasing the C concentration beyond the optimum C/Al ratio of 1:5 causes the carrier concentration to decrease when the implanted Al concentration was 5×10^{18} cm^{-3}. In addition, Al naturally prefers Si sites because Al and Si atoms are similar in size and Al-C bonds are energetically favored. Also, at the temperatures used to activate the implanted Al (>1600 °C) the preferential evaporation rate of the Si is large enough to create a significant number of Si vacancies. The reason it is so difficult to ascertain what is actually occurring is that a number of effects occur simultaneously, and, in all likelihood, are synergistic. They include annealing out the implant damage, activating the implant, and creating additional point defects through the preferential evaporation of Si. One cannot easily separate the latter two effects as they begin to occur at detectable rates at about the same temperature, but this problem to some extent can be overcome by using an AlN/C cap.

We have attempted to sort out the effects of co-implantation by examining box implants of Al or Al and an equal amount of C that were used to create an approximately uniform doping level of 1×10^{20} cm^{-3} to a depth of 0.3 μm that were capped and annealed at various temperatures for 30 min. For the samples that were implanted only with Al and annealed at 1400 °C, the sheet resistance, $R_\square > 10^6$ Ω/□ It decreased as the measurement temperature, T_m, increased, and it was more than an order of magnitude less when T_m = 150 °C. This suggests that there are some defect acceptor states that can be thermally accessed at the higher measuring temperatures. The effects of these states, if in fact they still exist after a 1500 °C anneal, are dominated by what we presume to be Al acceptor states for now $R_\square$= 80 Ω/□and it rises to 90 Ω/□at 150 °C. Presumably, the lower $R_\square$= 8.5 Ω/□after a 1600 °C anneal can be attributed to an increase in the number of Al implants that have been activated. The results for the co-implanted samples are quite different in that $R_\square$= 70 Ω/□after the 1400 °C anneal, is 12 Ω/□after the 1500°C anneal, but is 35 Ω/□after the 1600 °C anneal. This suggests that initially C implants facilitate the activation of Al implants, but, as they approach their equilibrium positions, they create states that in some way compensate the Al acceptors. That this occurs is further established by the fact that samples annealed with a C cap have much larger $R_\square$ (17,000 Ω/□for samples annealed at 1500 °C and 11,000 Ω/□for samples annealed at 1600 °C) that decrease substantially as T_m increases. To try to better understand what is occurring, we are currently looking at the samples with EPR and PL as well as samples annealed at 1700°C.

Effect of residual damage on carrier transport properties in a 4H-SiC double implanted bipolar junction transistor

[1]S. Ortolland, [1]N.G. Wright, [1]C.M. Johnson, [2]A. Knights, [3]P.G. Coleman
[1]Department of Electronic and Electrical Engineering, Merz Court, University of Newcastle, NE1 7RU Newcastle upon Tyne, UK. Tel : +44 (0) 191 222 7597, Fax : +44 (0) 191 222 8180, email : sylvie.ortolland@ncl.ac.uk
[2]School of Electronic, Engineering, Information, Technology and Mathematics, University of Surrey, Guildford GU2 5XH, UK
[3]Department of Physics, University of Bath, Claverton Down, Bath BA2 7AY, UK.

Abstract
Nitrogen implantation into a boron implanted layer is performed in order to make a double-implanted bipolar transistor. The effect of various implant and anneal schedules on two key device parameters is studied : 1) ohmic contact resistance of the highly doped implanted emitter and 2) electron transport properties in the boron implanted base. The effects of post-implant anneal conditions on the level of residual damage under the nitrogen implant after different anneal processes is investigated using the PAS and RBS techniques. The PAS data (Fig.2) show clearly that after implantation there is a substantial defect concentration as far as 500nm - significantly below the range of the implant (in this case 150nm). However such damage is almost completely recovered after anneal in contrast with the damage close to the implant range point. Such damage lies well within the emitter region of the device and may thus not significantly affect electron transport in the base. The RBS channeling data (Fig.3) again show that the majority of the damage is recovered by the anneal process. On the other hand, we note that a swelling damage occur after nitrogen implantation into the boron p-well (Fig.4) but can be partially removed after annealing. The electrical characteristics of simple BJT transistors with breakdown voltages in excess of 1000V and common-emitter gains of ~2 are described and related to the level of residual damage.

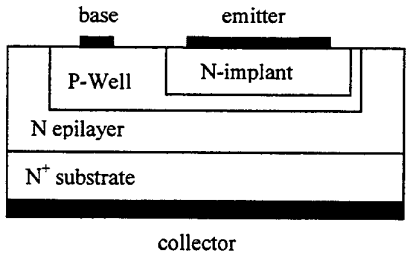


Fig.1: Basic bipolar transistor used in this paper as a test structure for physicochemical analyses and electrical measurements.

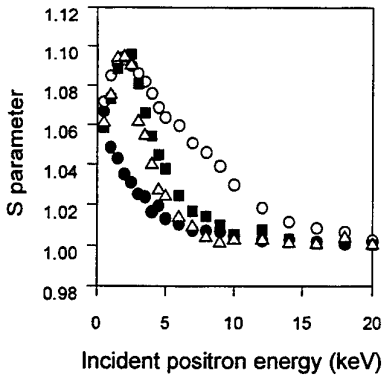


Fig.2: Positron S parameter versus positron for As-grown (solid circles) and as-implanted samples (open circles), annealed for 30 min at 1300°C (squares) or 1600°C (triangles).

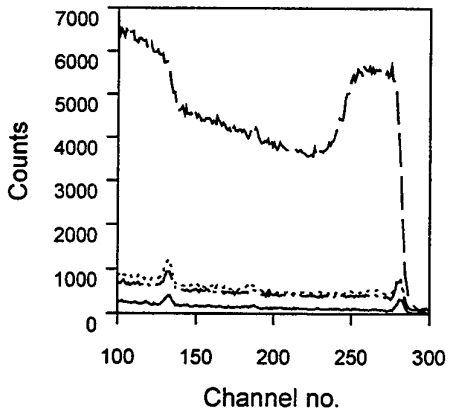


Fig:3: RBS-c data for nitrogen implanted 4H-SiC samples. Unimplanted (solid line), as-implanted (dashed line), annealed at 1300°C (dotted line), annealed at 1600°C (dot-dash line).

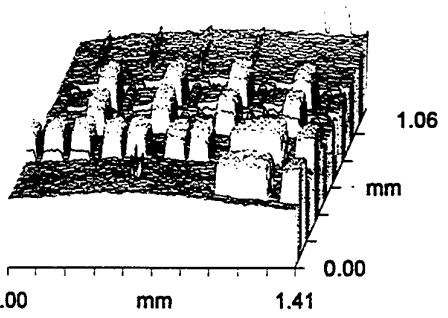


Fig.4: Profilometric picture of a double implanted (nitrogen into p-well) 4H-SiC surface after a 1700 C anneal. The 50 nm-high steps correspond to nitrogen implanted areas.

DEEP LEVEL INVESTIGATION OF PN-JUNCTIONS FORMED BY MeV ALUMINUM AND BORON IMPLANTATION INTO 4H-SIC

A. Schöner[1], N. Miyamoto[2], T. Kimoto[2], H. Matsunami[2]

[1] *ACREO AB, Electrum 236, Isafjordsgatan 22, S - 164 40 Kista - Stockholm, Sweden*
[2] *Department of Electronic Science and Engineering, Kyoto University, Yoshidahonmanchi, Sakyo, Kyoto 606-8501, Japan*
Phone: +46 8 632 7809 *Fax: +46 8 750 54 30* *E-mail: adolf.schoner @ acreo.se*

Electronic devices made from silicon carbide (SiC) are on the edge to be commercialized. To fabricate SiC devices, the formation of pn-junctions has become a critical issue, especially for power devices such as MOSFETs and IGBTs operating at voltages in the kV range. Because of the possibility to selectively dope through masking techniques, ion implantation is a key technology for the fabrication of pn-junctions in SiC, as diffusion is not applicable due to low diffusion coefficients of commonly used acceptor and donor dopants. In this study, we investigated pn-junction diodes implanted with MeV acceptor ions using isothermal capacitance transient spectroscopy (ICTS).

N-type 4H-SiC epilayers with a donor concentration of $1\text{-}2\cdot10^{15}$ cm^{-3} have been implanted at room temperature with aluminum (Al) and boron (B) ions. The total implanted Al and B fluence was adjusted to form a 3 µm box profile with an atomic acceptor concentration of around $1\cdot10^{18}$ cm^{-3}. Post implantation anneal was performed at temperatures of 1600 °C and 1800 °C for 30 min in argon atmosphere. In addition, the effect of carbon co-implantation as a possible way to enhance the electrical activation of the implanted acceptor species was investigated.

ICTS measurements at temperatures in the range of 120 K to 400 K were performed with various biasing conditions to determine the concentration and ionization energy of deep centers in the vicinity of the pn-junction. Compared with conventional deep level transient spectroscopy (DLTS), ICTS is not limited by trap concentrations higher or close to the doping concentration. This allows the acquisition of ICTS-spectra under forward bias and pulse conditions. The intention was to limit the extension of the depletion region close to the vicinity of the actual pn-junction in order to electrically probe the transition area between the layer damaged by the ion implantation and the virgin epilayer.

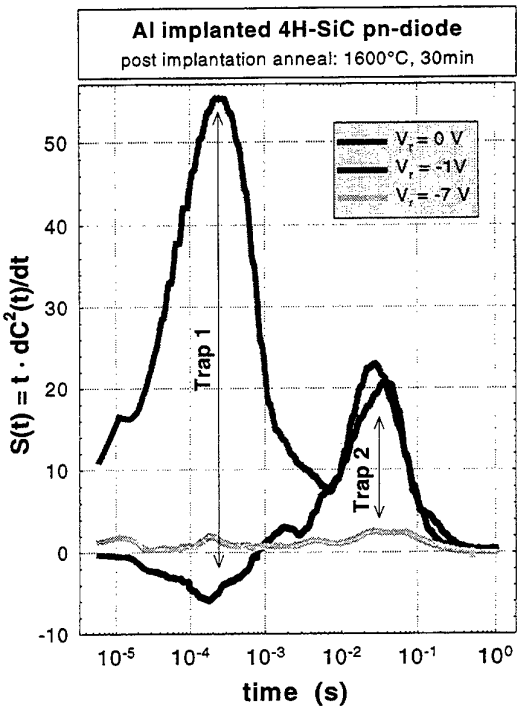


Fig.1 ICTS-spectra at room temperature for an Al-implanted pn-diode obtained at different reverse bias V_r with 1 V pulse voltage.

Depending on the bias conditions, the ICTS-measurements resulted in a variety of negative and positive transients, corresponding to dips and peaks in the ICTS-spectra (fig. 1). It was found that some dips and peaks are appearing at similar time position, indicating that they are related of the same trap (e.g. trap 1 in fig.1). In general, we observed two groups of traps. An Arrhenius analysis of the trap energies revealed that one group can be related to the shallow dopants such as nitrogen, aluminum, and boron. The second group consists of deep centers with an ionization energy of 500 meV to 700 meV. These deep centers could be attributed to remaining implantation damage (e.g. Z_1-center) or the deep boron center (D-center). The concentration of the deep centers were reduced by up to a factor of 10 in the diodes annealed at 1800 °C, indicating that higher post implantation annealing temperatures are required for better device performance due to a reduced concentration of possible recombination centers limiting the carrier lifetime.

High Temperature 10 Bar Pressure Sensor based on 3C-SiC/SOI for Turbine Control Applications

S. Zappe[1], J. Franklin[1], E. Obermeier[1], M. Eickhoff[2*], H. Möller[2+], G. Krötz[2], C. Rougeot[3], O. Lefort[3], J. Stoemenos[4]

[1]Technical University of Berlin, Germany
Secr. TIB 3.1, Gustav-Meyer-Allee 25, 13355 Berlin, Germany
phone: +49 30 314-72843, fax: +49 30 314-72603, email: zappe@mat.ee.tu-berlin.de
[2]DaimlerChrysler Research and Technology, Munich, Germany
[3]Sextant Avionique, Valence, France
[4]Aristotle University of Thessaloniki, Greece
*now at: Infineon Technologies, Munich ; +now at Deutsche Bahn Research, Munich

The FE simulation, fabrication and characterization of a membrane-type piezoresistive pressure sensor with piezoresistors consisting of 3C-SiC will be presented. The nominal pressure of the device is P_{nom} = 10 bar, the maximum operating temperature is T > 400 °C. The sensitivity at RT is S = 0.5 mV/V bar. The device is suitable for turbine control applications.

The membrane of the device was defined by ICP etching of a UNIBOND SOI wafer (Figure 1). Due to the vertical sidewalls of the etching process, the desired pressure range of the device can simply be adjusted by controlling the etch depth/membrane thickness.

An absolute pressure sensor with a closed cavity was realized by bonding the structured UNIBOND wafer to a silicon wafer. A 2.5 µm thick SiC layer was deposited onto the SOL of the UNIBOND wafer on top of the sensor cell at 1220 °C using methylsilane. In situ doping was achieved by adding NH_3 to the process gas. The 3C-SiC piezoresistors were structured by RIE. The resistors were connected in a Wheatstone bridge configuration.

An overload protection was realized by choosing a centerboss structure. The temperature dependent output characteristics of a sensor with a 60 µm thick membrane are shown in Figure 2. At 10 bar, the centerboss touches the ground. The sensitivity is decreased in the overload range (P > 10 bar) from the nominal sensitivity of S = 0.5 mV/V bar to the reduced value of S = 0.03 mV/V bar. High temperature measurements (up to T = 400 °C) are currently in progress and will also be presented.

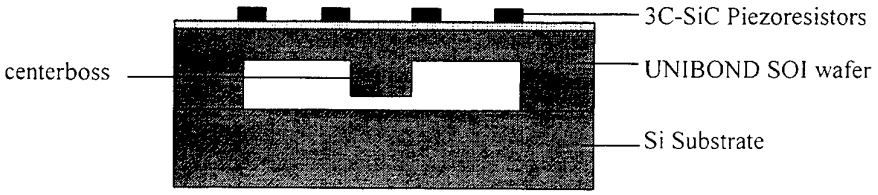


Fig. 1: Cross-section of the sensor cell. A UNIBOND SOI wafer is structured by ICP etching in an STS machine. The etched wafer is bonded to a silicon substrate and the 3C-SiC layer is deposited onto the UNIBOND wafer. The piezoresistors are structured by RIE (reactive ion etching) in an SF_6/O_2 plasma.

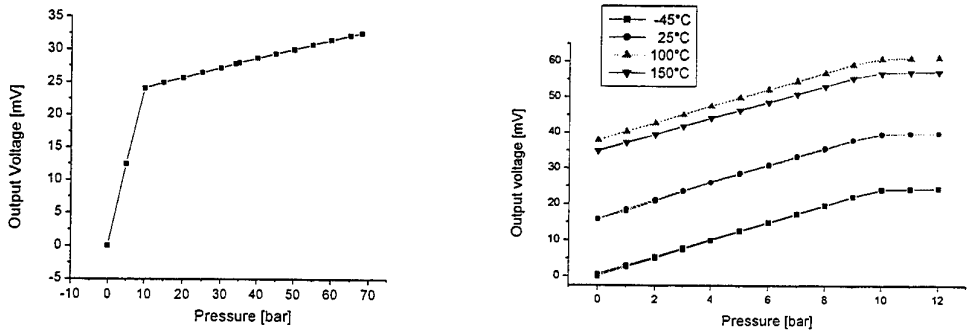


Fig. 2: Left: Output characteristic at room temperature. At a pressure of 10 bar, the centerboss touches the ground. Right: Output charcteristics at various temperatures. High temperature measurements (up to 400 °C) are currently in progress. (Supply voltage during measurements: 5 V).

Characterization of SiC materials: bulk, epitaxial and implanted layers

J. Camassel[1], P. Vicente[2] and L. Falkovski[1,3]

[1]*GES, UM2 "Sciences et Techniques" and-CNRS, cc074, 34095- Montpellier cedex 05, France.*
[2]*NOVASiC, Pomblières, 73600 Moûtiers, France.*
[3]*Permanent address: Landau Institute, Moscow,Russia.*
Tel : +33 4 67 14 37 73, fax : + 33 4 67 14 37 60, e-mail: camas@ges.univ-montp2.fr

The residual defects, which are present in all forms of SiC materials, play an important role in current technology. To achieve a better yield for processing devices, they have to be mastered and, as far as possible, eliminated. This makes rapid and non destructive optical characterization methods more and more. In the case of 4H and 6H-SiC wafers, for instance, absorption measurements have been shown to allow fast, non-contact and non-destructive on-line measurements of the spatial doping homogeneity [1]. However, in many cases, such simple optical methods suffer from intrinsic limitations due to the wide (indirect) band gap nature of the material [2]. This makes light scattering techniques, like micro-Raman, increasingly appealing. Moreover, provided it is used in a non standard (transverse) configuration, micro-Raman spectroscopy allows to probe in-depth perturbation effects. Since the optical phonons are sensitive to strain fluctuations and dislocations, one finds specific (additional) contributions to the linewidth and shift. In this work, we will consider the interaction of optical phonons with carriers and random imperfections of different natures.

Concerning preparation of bulk SiC wafers, for instance, we will show that micro-Raman spectroscopy constitute a very interesting tool to evaluate the extent of subsurface damage in n-type 4H and 6H-SiC. Because one can probe the LO-phonon–plasmon-coupled modes at various distance from the polished surface, and because subsurface damage influences dramatically the carrier concentration, the coupled mode frequency shifts. Then, from a line-shape analysis [3,4] the plasmon frequency and carrier concentration can be obtained.

Concerning implantation effects, we have performed SiC investigations using both micro-Raman and infra-red reflectivity techniques. Results on implantation damage in bulk SiC after 1 MeV proton implantation [5] and implantation damage annealing after 200 keV aluminum implantation in 4H epitaxial layers [6, 7] will be discussed.

[1] R.Weingartner, M.Bickermann, S.Buchevoy, D.Hofmann, M.Rasp, T.L.Straubinger, P.J.Wellmann and A.Winnacker, Proc. EXMATEC 2000, Heraklion (Crete, Greece) in press.
[2] A.Henry, I.G.Ivanov, A.Ellison and E.Jantzen, Mat. Science and Eng. **B61-62**, 234 (1999).
[3] H. Harima,S. Nakashima and T. Uemura, J. Appl. Phys. **78**,.1996 (1995).
[4] P.Vicente, D.David and J.Camassel, Proc. EXMATEC 2000, Heraklion (Crete, Greece) in press.
[5] H.W.Kunert, T.P.Maurice, T.Hauser, J.B.Malherbe, L.C.Prinsloo, D.J.Brink, L.Falkovsky and J.Camassel, this conference.
[6] J. Pernot, J. Camassel, S. Contreras, J.L. Robert, J.M. Bluet, J.F. Michaud and T. Billon, Proc. EXMATEC 2000, Heraklion (Crete, Greece) in press.
[7] J.Pernot, J.M. Bluet, J.Camassel and L. DiCioccio, this conference.

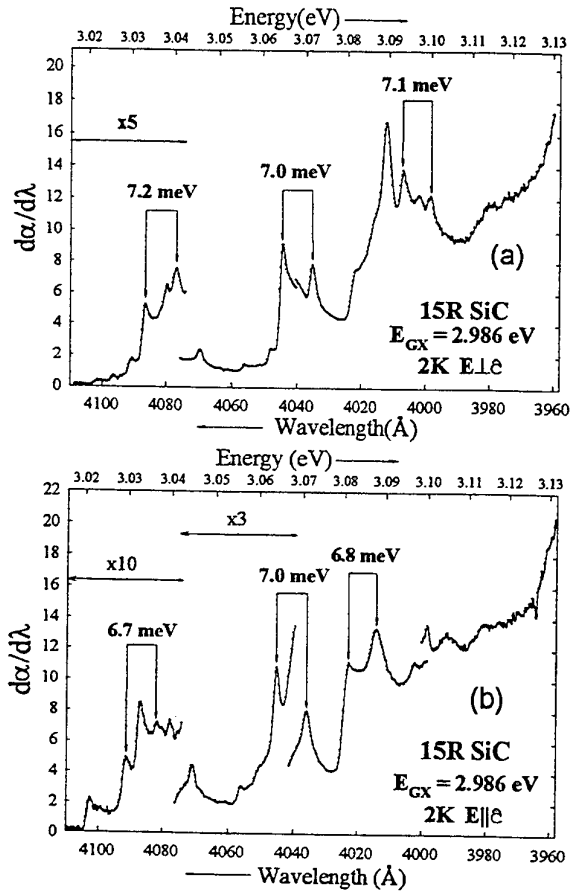
We3-2

Valence Band Splittings of 15R SiC Measured using Wavelength Modulated Absorption Spectroscopy

R.P. Devaty[1], S. Bai, W.J. Choyke[1], D. Hobgood[2] and D.J. Larkin[3]

[1]Dept. of Physics and Astronomy, University of Pittsburgh, Pittsburgh, PA 15260, USA
Tel: (412) 624-9009, FAX: (412) 624 –1479, E-Mail: devaty@imap.pitt.edu
[2]Cree, Inc., 4600 Silicon Dr., Durham, NC 27703, USA
[3]NASA Glenn Research Center, M.S. 77-1, 21000 Brookpark Road, Cleveland, OH 44135, USA

15R SiC has important advantages over 4H and 6H SiC for certain device applications. We will present our measurements of the spin orbit and crystal field splittings of the valence bands of 15R SiC. The samples are 0.2 cm thick slices of high quality boule material cut parallel to the $(1\bar{1}00)$ face and polished. The wavelength derivative of the absorption coefficient $d\alpha/d\lambda$ was measured at 2K using modulation spectroscopy.



The figure shows spectra measured with polarizations (a) $\mathbf{E} \perp \hat{c}$ and (b) $\mathbf{E} \parallel \hat{c}$. To assist the interpretation, we have also measured the 2K photoluminescence (LTPL) spectrum of a 15R SiC homoepitaxial film with very low background doping. The $\mathbf{E} \perp \hat{c}$ LTPL spectrum shows ten intrinsic lines associated with momentum conserving phonon assisted recombination of free excitons. The peak at 3.065 eV in the $\mathbf{E} \perp \hat{c}$ modulated absorption spectrum (a) is identified as the 77 meV phonon replica in the LTPL spectrum. For the $\mathbf{E} \perp \hat{c}$ spectrum we observe features corresponding to all ten phonon energies measured in the LTPL spectrum. Features assigned to the same phonon for the spin orbit split valence bands are indicated in both parts of the figure. The spin orbit splitting is $\Delta_{SO} = 7.0 \pm 0.3$ meV, which agrees with the much less accurate value obtained by Humphreys et al. [1]. Preliminary analysis indicates a value of about $\Delta_{CF} = 50$ meV for the crystal field splitting. This value is consistent with our previous results for 6H [2] and 4H SiC [3], based on the calculated linear dependence of Δ_{CF} on hexagonality [4].

[1] R.G. Humphreys, D. Bimberg and W.J. Choyke, Solid State Commun. **39**, 163 (1981).
[2] W.J. Choyke, R.P. Devaty and S.G. Sridhara, Phyica Scripta **T79**, 9 (1999).
[3] S.G. Sridhara, S. Bai, O. Shigiltchoff, R.P. Devaty and W.J. Choyke, Mater. Sci. Forum **338-342**, 567 (2000).
[4] W.R.L. Lambrecht, S. Limpijumnong, S.N. Rashkeev and B. Segall, Phys. Stat. Sol. (b) **202**, 5 (1997).

Intrinsic photoconductivity of 6H-SiC and the free-exciton binding energy

I.G. Ivanov, T. Egilsson, J.Zhang, A.Ellison and E. Janzén

Department of Physics and Measurement Technology, Linköping University, S-581 83 Linköping, Sweden

Phone: +46 13 - 28 25 32 Fax: +46 13 - 14 23 37 E-Mail: iiv@ifm.liu.se

The excitonic bandgap, i.e. the lowest energy of an intrinsic free exciton (FE), is known for many SiC polytypes. However, there are no reliable values for the binding energy of FE in none of the polytypes (see Ref.1 for a review). Consequently, the energy position of the conduction band remains unknown.

In this study, the photoconductivity (PC) spectra of 6H-SiC are measured at low temperature, aiming at the determination of the binding energy of FEs. In a perfect crystal, one would expect in general that the FEs, being electrically neutral, would not contribute to the photocurrent, unless they are excited in the continuum of non-bound states (above the edge of the conduction band). In this latter case, there exists a probability that the electron and hole excited by light will be separated away in externally applied electric field before they relax to a lower exciton bound state, or recombine. They will thus contribute to the photocurrent. The conduction band edge (the exciton continuum) would be indicated by a sharp increase in the photocurrent, as soon as the energy of the exciting light minus the lowest energy of a lattice phonon needed to conserve the momentum is enough to reach the bottom of the exciton continuum.

However, in a real crystal, FEs are very efficiently (=rapidly) captured to shallow impurities, where the fastest recombination mechanism is by Auger process, which produces free carriers (electrons in the case of binding to donors, or holes in the case of acceptors). Thus they contribute to the photocurrent, which is very well illustrated in the spectra taken from highly or moderately doped samples, where the sharp increase in the photocurrent occurs at the excitonic bandgap plus the lowest energy of a suitable phonon, known as absorption edge. Since at this energy also the onset of the fundamental absorption occurs [Ref.2], the PC-spectrum resembles an absorption spectrum in this case.

In very low-doped samples (N_D-$N_A \approx 10^{13}$ cm^{-3}), we have observed saturation of the photocurrent related to recombination of free excitons via the mechanism mentioned above: capturing to impurity -> Auger recombination. As the incident light energy increases above the fundamental absorption edge, more and more excitons are created per unit time until the capturing impurities are saturated. Further increase of the exciting photon energy does not increase the photocurrent. Actually, a decrease is observed, due to the decreasing penetration depth of the incident light. At energy of the incident light such that free carriers are created (in the exciton continuum), the photocurrent starts increasing again, and exibits the well known from the absorption "step-like" features [2]. Similar to absorption, the steps in the PC-spectrum, are due to the involvment of various phonons in the process of indirect generation of carriers via absorption of photon and emission of momentum-conserving phonon at low temperature. This enables us to determine the energy position of the bottom of the conduction band (the exciton continuum) at about 60 ± 5 meV above the excitonic bandgap (3023 meV in 6H-SiC), which determines also the binding energy of free excitons. Thus, the only reported value for the binding energy in 6H-SiC of 78 meV (Ref.3, see also Ref.1) seems to be overestimated. Some preliminary measurements on 4H-SiC will also be presented. The results are compared with a theoretical estimation based on the isotropic hydrogenic model.

References:

1. R.P. Devaty and W.J. Choyke, phys. stat. sol. (a) **162**, 5 (1997).
2. W.J. Choyke and L. Patrick, Phys Rev. **127**, 1868 (1962).
3. V.I. Sankin, Soviet Phys. - Solid State **17**, 1191 (1975).

Investigation of Electroluminescence across 4H-SiC $p^+/n^-/n^+$ Structures using Optical Emission Microscopy

A. Galeckas[1], J. Linnros[1], B. Breitholtz[1,2] and H. Bleichner[2]

[1] Department of Electronics, Royal Institute of Technology, Electrum 229, SE-16440 Stockholm, Sweden

[2] ABB Corporate Research, SE-72178 Västerås, Sweden

Phone: +46 8 7521290 Fax: +46 8 7527782 E-mail: galeckas@ele.kth.se

Studies have been conducted on the carrier recombination radiation properties across operating 4H-SiC $p^+/n^-/n^+$ structures. Evaluation-type diodes with Al/B-implanted p^+ anodes and 30 μm-thick low-doped n^- base regions epitaxially grown by CVD on commercial n^+ substrates were investigated. The utilized experimental method is based on spectrally resolved imaging of electroluminescence (EL) emitted from the cross-sectional plane of forward biased diodes. An optical emission microscopy setup equipped with a LN-cooled CCD camera and an imaging spectrometer was employed to obtain the in-depth mappings of EL in a temperature range of 100-400K. The spectral content of the luminescence across the active region was analyzed as a function of injection. The results show that with rising forward bias, the prevailing at low currents deep-boron related recombination within the *p-n* junction depletion region ("green") is gradually taken over by emission from the injection regions via shallow-dopant transitions ("blue"). Interestingly, this band-edge EL component is found to extend deep into the substrate, apparently resulting from excess carrier diffusion and recombination. The effective diffusion length (L_{eff}) of minority carriers was directly estimated from the profiles of EL penetration into the 4H-SiC substrate. A considerable dissimilarity of light emission from different $p^+/n^-/n^+$ structures was observed, yielding L_{eff} values for holes in the range from 15 to 30 μm at room temperature. The observed differences in L_{eff} are discussed taking into account doping inhomogeneity, carrier trapping, self-heating effects and also processing-induced changes in material properties.

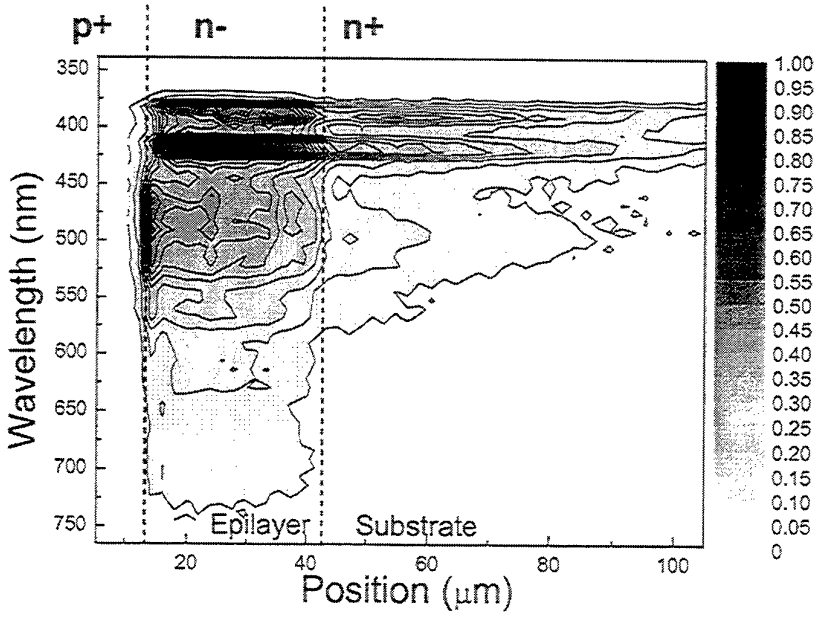


Fig. 1. Spectral content of EL emission across the 4H-SiC p+/n-/n+ structure at room temperature (100 A/cm^2).

Characterization of SiC prepared by nuclear transmutation due to neutrons.

Hans Heissenstein, Horst Sadowski, Christian Peppermueller, Reinhard Helbig
Institute of Applied Physics, University of Erlangen-Nuernberg, Staudstr.7/A3, D - 91058 Erlangen, Germany
Telephone 0049-9131-8528434, Fax 0049-9131-8528423
E – Mail : Hans.P.Heissenstein@physik.stud.uni-erlangen.de

Nowadays the method of nuclear transmutation doping (NTD) of silicon using the reaction $^{30}Si + n$ (thermal) -> $^{31}P + \beta^-$ is a standard technique. Thus extraordinary homogeneous doped n-type Si is produced for high power device technology (1). That NTD is also a useful doping technique for SiC was shown in (2, 3). But the doping concentrations to be achieved due to concentrations of background impurities are orders of magnitudes higher in SiC as in Si.

Therefore one has to apply higher fluences of neutrons for getting a homogeneous doping level in SiC which is dominated by phosphorous. The higher energetic part of a moderated neutron reactor spectrum (fast neutrons) is responsible for the lattice damage in the volume of SiC to a high extend. In order to prove the practical value of this method the mechanisms of damage production and the behaviour at thermal annealing of generated defects have to be studied.

We characterized the annealing behaviour of SiC samples after applying neutron fluences with different energy distributions. Epitaxial 4H and 6H layers of p- and n-type on substrates of the same kind were irradiated in different reactor positions with an applied fluence of thermal neutrons of 10^{19} cm^{-2} to 6.3 x 10^{20} cm^{-2} with achieved concentrations of phosphorous between 3 x 10^{15} cm^{-3} and 1 x 10^{17} cm^{-3} whereas the applied fluence of fast neutrons variied by a factor of approx. 10^5. Thus the p-type layers become n-type after annealing at high temperatures.

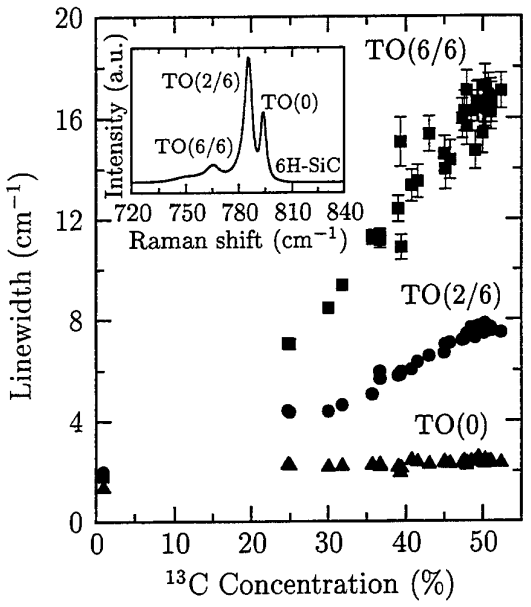
After irradiation the samples were subsequently annealed at temperatures between 600°C and 2000°C for half an hour in different atmospheres. The Number of radiation defects decreases with increasing annealing temperature, which is leading to well known residual defect structures in most cases. Because of the homogeneous distribution of radiation defects generated by fast neutrons the defect structures can be characterized by Low Temperature PhotoLuminescence (LTPL), Fourier Transform InfraRed spectroscopy (FTIR), I-V and C-V measurements.

Further these measurement techniques show that the fast neutrons are reasonable causing lattice damages in the tested range of fluences. The phosphorous impurity was additionally characterized by Halleffect and FTIR measurements.

(1) E.V. Haas and M. S. Schnöller, IEEE Trans. Electron Devices ED-23, 803 (1976)
(2) H. Heissenstein, C. Peppermueller and R. Helbig, Journal of appl. Phys., 83, 12, 7542 (1998)
(3) H. Heissenstein, H. Sadowski, C. Peppermueller and R. Helbig, Mater. Sci. Forum, to be published

Line broadening of phonons in the Raman spectra of isotopically disordered SiC

S. Rohmfeld, M. Hundhausen, and L. Ley
Institut für Technische Physik, Friedrich-Alexander Universität Erlangen-Nürnberg
Erwin-Rommel-Straße 1, D-91058 Erlangen, Germany
Phone: (49) 9131 8527259, FAX: (49) 9131 8527889
e-mail: Stefan.Rohmfeld@physik.uni-erlangen.de
N. Schulze and G. Pensl
Institut für Angewandte Physik, Friedrich-Alexander Universität Erlangen-Nürnberg
Staudtstraße 7 / A3, D-91058 Erlangen, Germany



The frequencies of vibrational modes in a solid depend on the interatomic force constants and the atomic masses. Changing the mass of one kind of atoms by isotopic substitution in a binary compound such as silicon carbide (SiC) results in a change of the frequencies of modes in a small but characteristic way that can be monitored by Raman spectroscopy [1].

We have grown 6H-SiC using a modified Lely technique (physical vapor transport (PVT)) [2] with a source material obtained by sintering a stoichiometric mixture of 99% pure ^{13}C and silicon powder with natural isotope composition. Due to the incorporation of ^{12}C from the crucible we obtain crystals with a concentration of ^{13}C up to 60 %. In this work, the influence of isotopic disorder in these samples is investigated. As can be seen in the figure, the phonon linewidth increases with increasing ^{13}C concentration. Moreover, the zone-center TO(0) mode is only weakly broadened, whereas larger broadening occurs for the TO(2/6) mode and particulary for the TO(6/6) mode. We explain these effects in the framework of the elastic scattering theory of Tamura, where the scattering rate is determined both by the mass variance and by the phonon density of states [3]. Our results are in agreement with this theory. The mass variance is responsible for the line broadening with increasing ^{13}C concentration, whereas the variation of the linewidth of the different modes can be ascribed to the variation of the phonon density of states at the corresponding mode frequencies.

[1] F. Widulle, T. Ruf, O. Buresch, A. Debernardi, and M. Cardona, Phys. Rev. Lett. **82**, 3089 (1999).
[2] N. Schulze, D. L. Barrett, and G. Pensl, Appl. Phys. Lett. **72**, 1632 (1998).
[3] S. Tamura, Phys. Rev. B **27**, 858 (1983).

For 2000 3rd Europ Conference on SiC, 3-7 Sept. 2000, Kloster Banz, Germany {www.ECSCRM2000.uni-erlangen.de}
E3. Characterization of material properties: electrical & optical properties of SiC

Micro-Raman and Photoluminescence Study on n-type 6H-SiC

Z.C. Feng[1], S.J. Chua[1,2], G.A. Evans[3], J.W. Steeds[3], K.P.J. Williams[4] and G.D. Pitt[4]

[1] Institute of Materials Research & Engineering, 3 Research Link, 117602 Singapore; tel: (65) 874-8366, fax: (65) 872-0785; E-Mail: zc-feng@imre.org.sg
[2] Centre for Optoelectronics, Department of Electrical Engineering, National University of Singapore, 119260 Singapore; tel: (65) 874-4452, fax: (65) 872-0785
[3] H. H. Wills Physics Laboratory, University of Bristol, Bristol BS8 1TL, UK; tel: (44) 1 117 928 8750, fax: (44) 1 117 925 5624
[4] Renishaw plc, Old Town, Wotton-under-Edge, Gloucestershire, GL12 7DW, UK; tel: (44) 1 453 844 302, fax: (44) 1 453 844 236

Research and development of SiC materials, devices and applications have gained much attention in recent years. The demand for good quality SiC wafers is increasing. A convenient technique of characterisation is needed to promote these demands, in particular for industrial production. This technique should be non-destructive, performed at room temperature (RT), easily operated, efficient to provide more information, and fast for quality control. Here we present a method to characterise the SiC wafer materials by the combined UV Raman and photoluminescence (PL) measurement via a Renishaw microscopic system. A series of N-doped n-type 6H-SiC bulk wafers are studied.

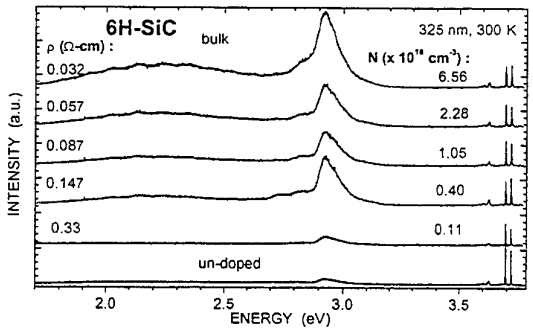


Figure 1. Combined PL-Raman spectra of bulk 6H-SiC, one un-doped and five N-doped with different doping levels or resistivity values, listed in the figure. Spectra were measured at RT and under excitation of 325 nm.

Figure 1 shows a series of combined UV Raman-PL spectra from one un-doped 6H-SiC as a comparison, and five n-type 6H-SiC commercial wafers with resistivities of 0.032, 0.057, 0.087, 0.147 and 0.33 Ω-cm, corresponding to N-doping levels of 6.56, 2.28, 1.05, 0.40 and 0.11 x10^{18} cm^{-3}, respectively. Each spectrum consists of sharp lines beyond 3.5 eV which are 6H-SiC characteristic Raman lines excited from 325 nm, a band with a peak at 2.92 eV which is the RT band edge luminescence from 6H-SiC and its phonon replica at 2.83 eV as the shoulder in the low energy side, and a broad band centred at 2.2 eV in the range of 1.7-2.7 eV, which is related to defects in 6H-SiC.

Correlations between the 6H-SiC material properties and these Raman-PL spectral features can be established through further spectral analyses and ratio comparison among them. For example, it is found that the intensity ratios between the 2.2-eV defects-related band and the 2.9-eV PL band, and between the 2.9-eV edge band and the first order strongest transverse optical (TO) and longitudinal optical (LO) phone modes, are varied with N-doping levels. These can also be used as merits of SiC material quality. Their mapping distributions further manifest the quality variations over the whole wafer. This method provides a good tool for the quality control of SiC production.

LOW TEMPERATURE PHOTOLUMINESCENCE PROCESSES OF ^{13}C ENRICHED 6H- AND 15R-SiC CRYSTALS GROWN BY THE MODIFIED LELY METHOD

Horst Sadowski, Norbert Schulze, Thomas Frank, Michael Laube, Gerhard Pensl, and Reinhard Helbig
Institute of Applied Physics, University of Erlangen-Nürnberg
Staudtstr. 7 A3, D-91058 Erlangen, Germany
Phone +49 9131 85 2 84 34, Fax +49 9131 85 2 84 23
e-mail: mpap12@rzmail.uni-erlangen.de

Atomic masses strongly influence the electronic and vibrational properties of semiconductors. In order to investigate this dependence in SiC, we enriched 6H- and 15R-SiC crystals with ^{13}C during the modified Lely sublimation growth[1]. We used ^{13}C in favor of ^{29}Si because of the higher relative mass difference. In this paper, we report the isotopic effect on the momentum-conserving phonon lines of the exciton recombination as well as on the zero-phonon exciton recombination lines.

Low temperature photoluminescence (LTPL) measurements were conducted at 2K using a He-Cd laser (325 nm) and a SHG-laser (257 nm) as excitation source.

The investigated 6H- and 15R-SiC samples are nitrogen-doped; Fig. 1 shows a LTPL spectrum of a 15R-SiC ^{13}C enriched compared with the reference spectrum of a 15R-SiC sample with natural carbon isotopic abundance. The energy shift to higher energies of the zero-phonon lines of nitrogen bound exciton lines (P_0, Q_0, R_0, S_0) and their acoustic phonon replica (TA, LA) is 1.5 meV. The shift of the optical phonon replica (TO, LO) is 4.0 meV.

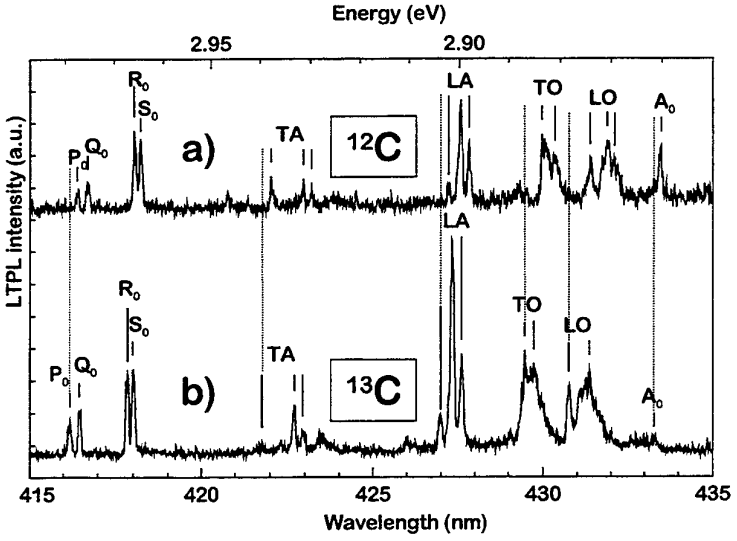


Fig. 1: LTPL spectra of 15R-SiC samples: a) natural carbon isotope concentration, b) enriched with ^{13}C

Another impurity is titanium (see e.g. line A_0 in Fig. 1). The shift to higher energies of the Ti-related line A_0 is smaller than for nitrogen-related zero phonon lines. In Fig. 1, the energy shift for A_0 is 0.85 meV.

A box-shaped profile of 1 μm in depth and of a mean vacancy concentration equal to $2x10^{17}$ cm^{-3} (calculated after TRIM_C) is generated by helium implantation into 6H-SiC to produce the D_I-defect (L-lines in LTPL spectra). The shift to higher energies of the corresponding L-lines is 0.8 meV. For a 6H-SiC crystal with pure ^{13}C, we estimate an energy shift to higher energies of the zero-phonon bound exciton lines of 2.19 meV for nitrogen and of 0.85 meV for titanium in comparison with a sample containing a natural C isotopic abundance.

[1] N. Schulze, D.L. Barrett, and G. Pensl, Appl. Phys. Lett., 72, 1632 (1998)

ABSORPTION MAPPING OF n- AND p-TYPE DOPED 4H-SiC and 6H-SiC

R. Weingärtner, M. Bickermann, D. Hofmann, M. Rasp, T.L. Straubinger, P.J. Wellmann and A. Winnacker
Materials Department 6, University of Erlangen, Martens Street 7, 91058 Erlangen, GERMANY.
Tel.: +49-9131-85-27730, Fax: +49-9131-85-28495, Email: roland.weingaertner@ww.uni-erlangen.de

The evaluation of the doping level distribution of n- and p-type doped 4H- and 6H-SiC substrate wafers is of particular interest due to its impact on the electrical properties of SiC based power devices and GaN based optoelectronic devices. We have developed a non-destructive and fast characterization method based on spectral absorption measurements and absorption mapping to determine doping type (n- or p-type), doping level (N_D-N_A) and doping level distribution. Numerical calculations as well as electrical Hall measurements have been used in order to quantify the experimental absorption data.

Fig. 1 shows the fundamental absorption bands of n-type 4H-SiC, n-type 6H-SiC and p-type 6H-SiC at T=300K. The numbers (1), (2) and (3) indicate three characteristic features. (1) is the band edge related valence band to conduction band absorption band, (2) indicates the valence band to donor (acceptor to conduction band) absorption in n-type (p-type) SiC and (3) represents free electron absorption into higher conduction bands in the case of n-type SiC. While the absorption bands (1) to (3) and their physical properties have been studied by several groups [1][2][3][4] we have applied numerical modeling to determine the band edge related absorption band (1) which is function of the doping level. Due to effects like band filling, band tailing (Coulomb interaction of free carriers with ionized impurities), band shrinkage (exchange interaction of free carriers) the band edge related absorption is modified by n-type or p-type doping [5]. Taking into account the latter effects we have calculated absorption band (1) for various n-type and p-type doping concentrations and we have compared these date with experimental absorption and electrical Hall measurements.

Absorption mapping of band (1) in 6H-SiC and band (3) in 4H-SiC was carried out in order to determine doping level and doping level distribution as well as inclusions of other polytypes. Mapping was carried out by illuminating the samples homogeneously with monochromatic light using a so-called Ulbrichtkugel and interference filters. The transmitted light was captured by a CCD camera and digitized by a computer.

Fig. 2 shows an absorption mapping of a 35mm n-type 4H-SiC wafer which has been grown by the PVT (physical vapor transport) method in our lab. The measurement was carried out at 460nm. At this wavelength electrons from the donor level are excited into the conduction band. The absolute values of the doping level were determined by using calibration data from the calculated absorption data in conjunction with electrical Hall data. In Fig. 2 the higher donor incorporation in the facetted area of the SiC crystal is demonstrated. A lateral variation of carrier concentration of < 2% was evaluated (mean carrier concentration $2.8 \cdot 10^{19}$ cm^{-3}).

We will present the numerical model for the near band edge related absorption. The calculated data will be compared with experimental data. Several doping level mappings of n-type and p-type SiC wafers will be presented and discussed.

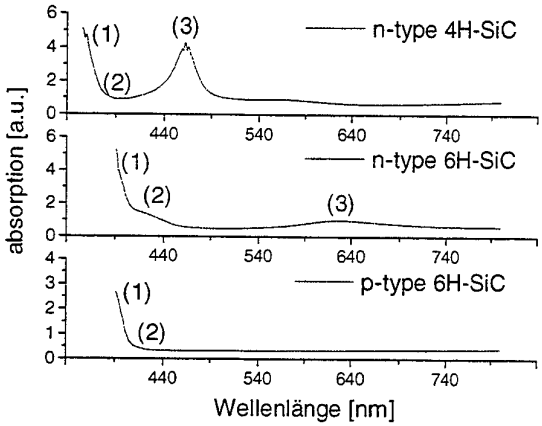


Figure 1: Absorption spectra of n-type 4H-SiC, n-type 6H-SiC and p-type 6H-SiC at 300K

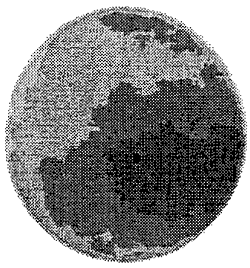


Figure 2: Absorption mapping of a 1.35" 4H-SiC wafer: n= $2.8 \cdot 10^{19} cm^{-3}$, $\Delta n/n$ (lateral) < 2%

[1] Biedermann, Solid State Comm. vol.3, p.343, 1965.
[2] Choyke and Patrick, Phys.Rev. vol.172(3), p.172, 1968.
[3] Dubrowskii, Lepneva and Radovanova, Phys.Stat.Sol.(b) Vol.57, p.423, 1973.
[4] Lindefelt, J.Appl.Phys. Vol.84(5), p.2628, 1998.

Defects Characterization in SiC by Scanning Photoluminescence Spectroscopy

L. Masarotto, J.M. Bluet, M. Berenguer, P. Girard and G.Guillot

Laboratoire de Physique de la Matière (UMR CNRS 5511), Institut National des Sciences Appliquées de Lyon, 20 avenue Albert Einstein, 69621 Villeurbanne cedex, France.

During the last several years, tremendous progress in SiC bulk growth and epitaxy have been realised. Nevertheless, the non uniformity of impurity and defect distribution in SiC wafers (particularly in semi-insulating one) and the doping inhomogeneities of the epitaxial layers still act as show-stopper for high performance and high reliability devices development. This is why a spatially resolved, non destructive and few time consuming characterization tool is strongly needed for a tight quality control of the wafers.

Toward this end, we have adapted a scanning photoluminescence (PL) apparatus previously developed for III-V compound characterization [1]. Indeed, the first results reported [2] indicate that PL imaging is a very promising tool for SiC material characterization. In our equipment, the PL mapping is obtained by scanning the sample, fixed to an x-y stage with 1 µm minimal step, under a doubled Ar^+ laser beam (244 nm) focused by a microscope objective (x52). For this excitation the spot diameter is less than 2 µm, and the penetration depth is about 1 µm for 4H-SiC. The PL signal can be either directly detected, giving integrated PL intensity, either dispersed using a monochromator, giving spectrally resolved PL (1 nm resolution). The signal is amplified and filtered by a lock-in amplifier and detected by a photomultiplier. Measurement can be realized at room temperature for near band edge studies or at low temperature (100 K) for deep defects investigation.

An example of integrated PL mapping with a 2 µm spatial resolution is given in figure 1, for a n-type ($1.6\ 10^{16}$ cm^{-3}) 6H epitaxial layer, 3 µm thick. We can clearly observe intense PL spot with diameter ranging from 10 to 30 µm approximately. A rough estimation of these spot density from a larger scanning area gives a concentration of about 10^4 cm^{-2} which roughly corresponds to typical dislocation density in SiC. Contrary to one can think, these bright spots could so be due to dislocations. Indeed, a zone in the vicinity of the dislocation can be stripped off from non radiative centres by a gettering effect leading then to a local exhaust of the PL intensity around the dislocation. Spectral measurements performed in order to analyse the PL origin and to confirm this hypothesis will be presented.

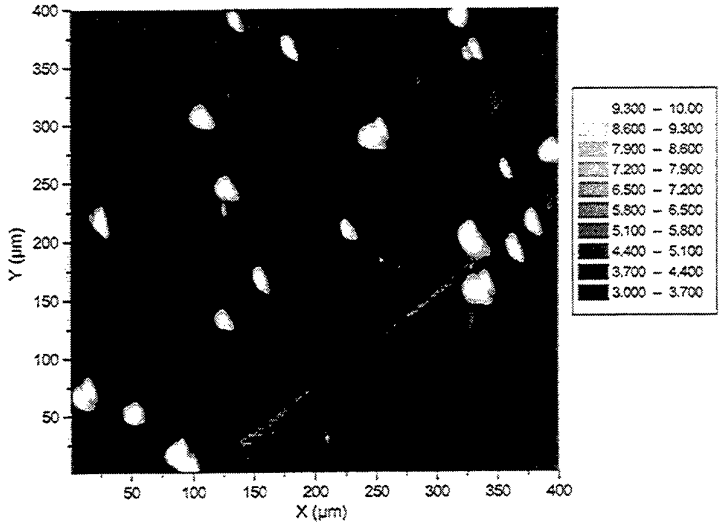


Figure 1: Integrated photoluminescence image with 2 µm spatial resolution. The image is taken on a 400*400 μm^2 area of a 6H-SiC n-type epitaxy.

[1] S.K. Krawczyk, Encyclopaedia of Advanced Materials, Pergamon Press Oxford (1994), p 2318-2336.
[2] M. Tajima, T. Nakane, T. Nakata and M. Watanabe, Jpn. J. Appl. Phys. Lett., Vol **38**, N° 4B (1999).

Luminescence of InGaN/GaN multiple quantum wells grown by mass-transport

J. P. Bergman, G Pozina and B. Monemar
Department of Physics and Measurement Technology, Linköping University, S-581 83 Linköping, Sweden
M. Iwaya, S. Nitta, H. Amano and I. Akasaki
Department of Electrical Engineering and Electronics and High-Tech Research Center, Meijo University, 1-501 Shiogamaguchi, Tempaku-ku, Nagoya 468, Japan
Tel: +46-13-282382, Fax: +46-13-142337, e-mail:peder.bergman@ifm.liu.se

InGaN/GaN heterostructures are presently of high interest due to their successful application for fabrication of blue and green light emitting diodes and violet laser diodes. In this work we report on the properties of a high quality $In_{0.12}Ga_{0.88}N$/GaN MQW structure grown by MOVPE utilizing mass transport. Micrometer-sized structures (lines) on the GaN surface were etched and after that the structure was annealed in ammonia, which results in overgrowth of the etched areas. Finally, three InGaN quantum wells of width 35 Å separated by 105 Å thick GaN barriers were grown on top of such a GaN layer. In the following we will refer to overgrown areas as mass-transport regions, and other - non-transport. On the same wafer three different areas with different line-spacing were fabricated: 3x3 μm, 5x5 μm and 10x10 μm.

We have found from cathodoluminescence (CL) measurements that the mass-transport regions have much higher structural and optical quality compared to the non-transport regions. CL images show clearly the intensity contrast between mass-transport and non-transport regions: the CL intensity measured in the mass-transport region is much higher than that for the non-transport region. We have estimated from CL patterns that the average dislocation density is about 10^8 cm^{-2} for non-transport and about 10^7 cm^{-2} for mass-transport regions, respectively. Thus, the structural improvement is significant for the mass-transport regions.

The photoluminescence (PL) spectra measured at low temperature and at low excitation power are dominated by a PL line X1 centered at 2.967 eV with full width at half maximum (FWHM) of 40 meV, which to our knowledge is the narrowest FWHM published for InGaN/GaN MQW structures. This peak is most likely connected with the fundamental 2D exciton localized in one of the QWs. However, besides this QW exciton transition the PL spectrum demonstrates an additional line X2 with position 2.85 eV and FWHM of 70 meV. This second line is accompanied by two LO phonon replicas. We have clearly demonstrated from time-resolved PL, temperature dependence and power excitation dependence PL measurements, that X2 can not be a phonon replica of the MQW exciton. The following characteristics are observed for the X2 process: the PL decay time for this line is about 200 ns which is 40 times longer than time decay for the X1 exciton (5 ns). The position of X2 moves to higher energies (the shift is about 50 meV) with increasing excitation power. The X2 transition can not be detected at temperatures higher than 70 K. Our explanation is that it is probably connected with the middle QW, which has a smaller screening of the piezoelectric field, and hence a smaller oscillator strength for the exciton. No PL line corresponding to the QW closest to the surface is seen. Theoretical modeling suggests a strong potential gradient close to the surface of the MQW structure, explaining the different spectra observed for the different QWs.

FROM RELAXED TO HIGHLY TENSILY STRAINED GaN GROWN ON 6H-SiC AND Si (111) : OPTICAL CHARACTERIZATION.

M.Leroux, H.Lahrèche, F.Semond, M.Laügt, E.Feltin, N.Schnell, B.Beaumont, P.Gibart and J.Massies

Centre de Recherche sur l' Hétéro-Epitaxie et ses Applications-CNRS
Rue Bernard Grégory, 06560 Valbonne, France
Tel : (33) 04 93 95 42 16 Fax : (33) 04 93 95 83 61 ml@crhea.cnrs.fr

It is known that the standard growth of GaN on 6H-SiC using AlN buffers results in layers under weak tensile or compressive strain [1]. We have recently shown that GaN can be directly grown by metalorganics chemical vapor deposition (MOCVD) on SiC. The in-plane tensile strain of such layers depends on growth conditions and can be as high as $4.5x10^{-3}$ as measured through X-ray diffractometry [2]. The optical properties of these layers have been assessed by reflectivity and photoluminescence (PL) as a function of temperature. Reflectivity allows to follow free A and C excitons as a function of strain, while the B one is not observed in the more strained samples (σ geometry), though their low temperature PL is ascribed to donor bound excitons originating from the Γ_7^n valence band (figure 1). Excitonic GaN gaps as low as 3.43 eV at 10 K are reported. The quenching of various PL transitions as a function of temperature is studied and compared to that reported for compressively strained GaN on sapphire [3]. Our results point to a similar behaviour for A and B excitonic luminescence as a function of T.

This first study is then used to interpret the optical properties (reflectivity and PL) of GaN grown on Si (111) either by MOCVD or molecular beam epitaxy. Such layers can be either relaxed or under tensile strain. We finally use our results and those on GaN grown on sapphire to discuss the question of deformation potentials in GaN.

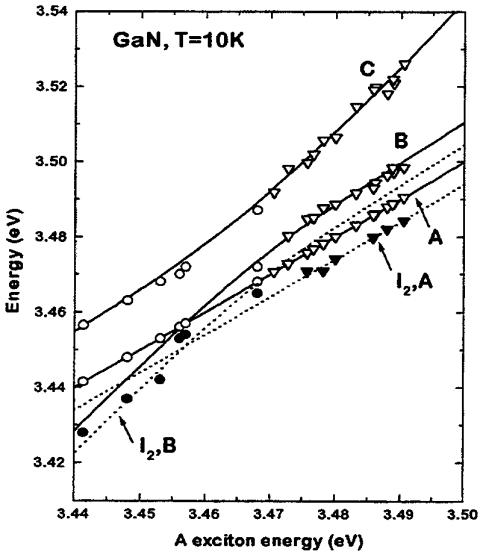


Figure 1 : free excitons (open symbols) and donor bound excitons (closed symbols) energies as a function of the A energy in GaN as measured through reflectivity and luminescence. Circles and triangles correspond to GaN grown on 6H-SiC and sapphire, respectively.

[1] W.G.Perry, T.Zheleva, M.D.Bremser, R.F.Davis, W.Shan and J.J.Song, J. Electron. Mater. **26**, 224 (1997).

[2] H.Lahrèche, M.Leroux, M.Laügt, M.Vaille, B.Beaumont and P.Gibart, J. Appl. Phys. **87**, 577 (2000).

[3] M.Leroux, N.Grandjean, B.Beaumont, G.Nataf, F.Semond, J.Massies and P.Gibart, J. Appl. Phys. **86**, 3721 (1999).

Infrared investigation of implantation damage and implantation damage annealing in 4H-SiC

J. Pernot[1], J.M. Bluet[2*], J. Camassel[1] and L. Di Cioccio[2]

[1]*GES, UM2 "Sciences et Techniques" and-CNRS, cc074, 34095- Montpellier cedex 05, France.*
[2]*CEA-LETI-DMITEC, 17 rue des Martyrs, 38054-Grenoble cedex 09, France.*
[*]*Present address: LPM, INSA-Lyon, 20 av. A. Einstein, 69621-Villeurbanne cedex, France.*
Tel : +33 4 67 14 39 73, fax : + 33 4 67 14 37

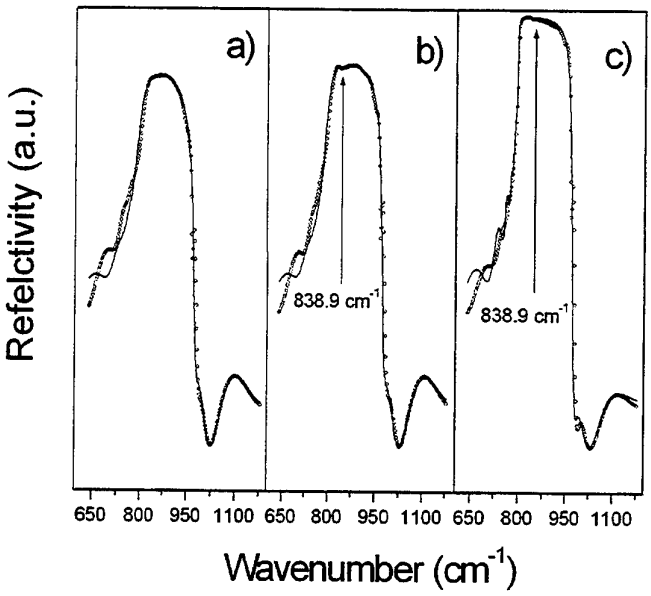
We have performed an infrared investigation of the effect of implantation damage, and implantation damage annealing, on the reststrahlen band of the 4H-SiC crystals. As prototype material, we have used a series of 4H epitaxial layers from Cree Research, implanted with Al ions to produce square like profiles. Implantation energy ranged from 20 to 200 keV. Targeted concentrations ranged from 10^{20} to 10^{21} cm^{-3} [1].

After implantation, infrared reflectivity spectra were collected at room temperature in the middle infrared range (500 - 4000 cm^{-1}). We used a Bio-Rad Fourier Transformed Spectrophotometer equipped with a microscope and a MCT detector. Near normal incidence was used. All measurements were repeated after post-implantation anneals.

Before annealing we observed a decrease and broadening of the topmost reflectivity structure versus implantation dose. This is shown in Figs.1-a and 1-b for targeted concentrations 10^{20} and 10^{21} cm^{-3}, respectively. After annealing, on the opposite, all spectra appeared identical. A typical example is shown in Fig.1-c. Provided on focuses on the reststrahl band, this shows that infrared spectra are very sensitive tools to probe a thin surface layer.

Having established IR reflectivity as a tool of implantation damage, we want to make it quantitative. Toward this hand, we have modelled our IR spectra using a transfer matrix method [2] and product oscillators [3].

Before annealing, the difference in experimental spectra correspond with different series of phonon damping parameters in i) the implanted zone and ii) the epitaxial layers. After annealing, all differences reduce but, still, weak additional broadening can be found with respect to bulk SiC. This is specially sensitive for the folded modes which resolve weakly between the main TO and LO phonons frequencies [4,5].



[1] for more details, see : J.M. Bluet, J. Pernot, J.Camassel et al., J. Appl. Phys. (15/08/2000 issue)
[2] O.S. Heavens, *Optical Properties of Thin Solid Films*, Dover, N.Y. (1965)
[3] F. Gervais and B. Piriou, Phys. Rev. B **10**, 1642 (1974)
[4] D.W. Feldman, J.H. Parker, W.J. Choyke and L. Patrick, Phys. Rev. **173**, 787 (1968)
[5] S. Nakashima and H. Harima, Phys. Stat. Sol (a) **162**, 39 (1997)

Temperature dependence of the band structure of 3C-, 2H - and 4H - SiC

S.M.Zubkova, L.N.Rusina, E.V.Smelyansky
I.N.Frantsevich Institute for Problems of Materials Science of the National Academy of Ukraine
3, Krzhyzhanovsky str., 03142, Kyiv, Ukraine
(36044) 444-1540/ 444-213, dep.4@ ipms.kiev.ua

Temperature dependences of some actual energy extrema and of the principal interband transitions in 3C -, 2H - and 4H -SiC have been calculated by the empirical pseudopotential method. For the finite - temperature calculation pseudopotential form factors were replaced by the temperature-dependent form factors using the Debye-Waller factors. A lattice effect has been taken into account using the temperature dependence of the linear expansion coefficient. The peculiarities of the temperature dependences of low conduction and top valence levels and interband transitions are discussed in details.

The obtained results are in a good agreement with our experimental data. For example, the temperature coefficient of the $X_1 - X_3$ - transition in the conduction band, which determines the narrow violet band in the breakdown electroluinescence spectrum in the 3C - SiC - p-n-structure being powered in reverse, appeared to be by an order of magnitude lower than temperature coefficients of all other interband transitions. It agrees well with the experimental curve of the temperature coefficient of the spectral density of the breakdown electroluminescence quantum yield. This curve has a minimum in this spectrum range.

Band gap states of Cr in the lower part of the SiC band gap

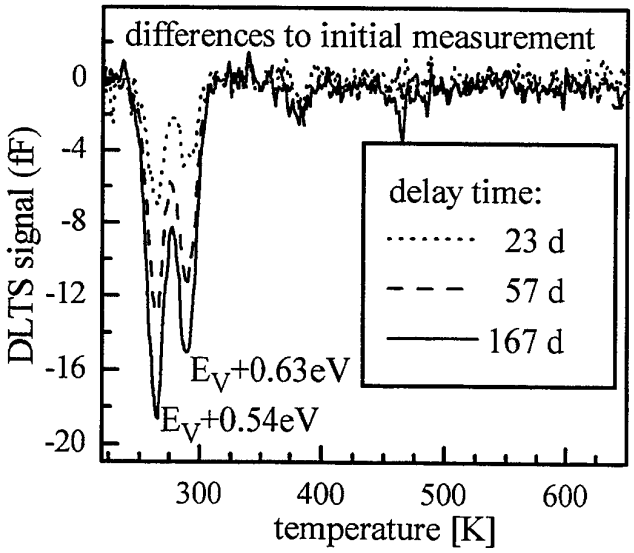
G. Pasold, N. Achtziger, J. Grillenberger, W. Witthuhn

Institut für Festkörperphysik, Universität Jena, Max- Wien- Platz 1, 07743 Jena Germany
(phone: ++49-03641-947337, fax: ++49-03641-947302, e-mail: pasold@pinet.uni-jena.de)

Similar to other transition metals [1,2], chromium is known to form electrically active band gap states in SiC. In the polytype 4H, an acceptor state at 0.74eV below the conduction band edge has definitely been identified by radiotracer DLTS [3]. A corresponding state also exists in the polytypes 6H [4] and 15R [5]. All these experiments were done by Deep Level Transient Spectroscopy (DLTS) on n-type SiC, being sensitive to the upper part of the band gap only. By performing DLTS on p-type SiC, we now provide information on chromium and vanadium-related band gap states in the lower part of the band gap for the first time.

Samples (p-type epitaxial layers, 4H) were doped with stable chromium (^{52}Cr) by multiple implantation (1...3 MeV) or with the radioactive isotope ^{51}Cr by recoil implantation [3], and subsequent annealing (1600 K, 4h). The ^{51}Cr isotope is used as a radiotracer (decay to V, half-life 27.7 d) to establish a definite chemical identification: deep levels of Cr or V will be uniquely marked by a time dependent concentration in the course of subsequent DLTS measurements during the transmutation Cr→V.

For both doping techniques, several implantation-induced peaks are observed. For the radiotracer samples, the Cr signals are singled out by forming differences: in the figure, the initially measured spectrum is subtracted from the spectra, i.e. time-independent peaks are eliminated. The negative peaks indicate a decreasing concentration, i.e. both peaks are due to Cr. There is no signal increasing, i.e. no deep level of vanadium exists in the accessible part of the band gap. The energy difference of the Cr levels is ascribed to inequivalent sites in the 4H polytype.



The right one of the two Cr peaks fully overlaps with a background peak present in all samples (D-center [6]). Hence, it is not possible to identify and to analyze the Cr peaks reliably in samples doped with stable Cr. The radiotracer concept, however, allows a clear distinction between the Cr related deep levels and the D-center.

[1] T. Dalibor, G. Pensl, H. Matsunami, T. Kimoto, W. J. Choyke, A. Schöner, N. Nordell, phys. stat. sol. (a) **162,** 199 (1997)
[2] J. Baur, M. Kunzer, J. Schneider, phys. stat. sol. (a) **162**, 153 (1997)
[3] N. Achtziger, W. Witthuhn, Phys. Rev. B **57**(19), 12181 (1998)
[4] N. Achtziger, J. Grillenberger, W. Witthuhn, Mat. Sci. For. **264-268**, 541 (1998)
[5] J. Grillenberger, thesis, University Jena, 2000
[6] A. A. Lebedev, Semiconductors **33**(2), 107 (1999)

Oxygen-related defect centers observed in 4H/6H-SiC epitaxial layers grown under CO_2 ambient

Oliver Klettke, Gerhard Pensl
Institute of Applied Physics, University of Erlangen-Nürnberg, Staudtstraße 7, D-91058 Erlangen, Germany

Tsunenobu Kimoto, Hiroyuki Matsunami
Department of Electronic Science and Engineering, Kyoto University, Kyoto 606-8501, Japan

Nitrogen (N)-doped 4H/6H-SiC epitaxial layers have been grown by the Chemical Vapor Deposition (CVD) technique on SiC substrates of the same polytype under additional CO_2 flow. CVD growth was performed in a SiH_4-C_3H_8-H_2 system at 1500°C. 4H and 6H-SiC substrates were placed side by side on an SiC-coated susceptor. Typical growth rate and the epilayer thickness were 3µm/h and 10µm, respectively. Growth runs with three different CO_2 flow rates have been conducted (see Table 1).

DLTS spectra of these 4H/6H-SiC epilayers reveal three energetically deep traps; their ionization energies and electrical capture cross-sections are identical with the corresponding parameters of defect centers O_{III}, O_{IV} and O_V observed in oxygen (O)-implanted 4H/6H-SiC samples [1, 2]. The determined defect concentrations range from $5x10^{12}cm^{-3}$ to $3x10^{13}cm^{-3}$.

Admittance spectroscopy investigations taken on the same epilayers result in the nitrogen donors (N(h), N(k1,k2)) and two further energetically shallow defects; for the 6H-SiC polytype, conductance spectra of epilayers #1 and #2 are displayed in Fig.1. The double peak O_I/O_{II} is also observed in O-implanted samples; it is caused by two O-related, energetically shallow donors [1, 2].

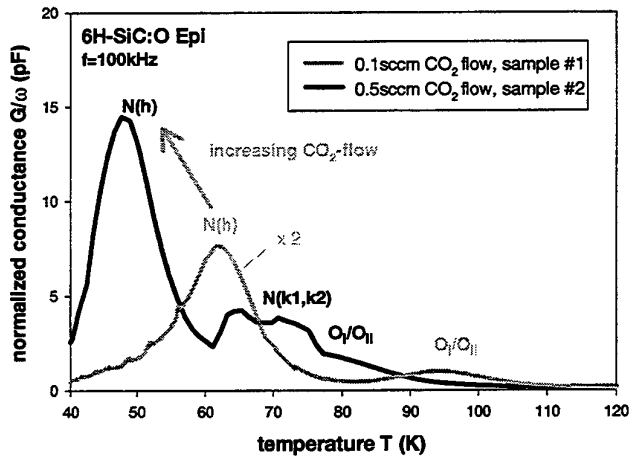


Fig.1: Normalized conductance G/ω as a function of temperature. The spectra are taken on 6H-SiC epilayer #1 and #2, respectively.

With increasing CO_2 flow, the concentration of O_I/O_{II} donors increases; however, this increase cannot explain the strong increase of the net donor concentration (N_D-N_A) determined by C-V measurements. For 6H-SiC epilayers, this increase results in more than three orders of magnitude (see Table 1). SIMS analyses confirm that this increase of donors is due to an increase in the N concentration although the basic growth conditions during all the CVD runs were kept constant (with exception of the CO_2 flow). Identical results are obtained for the 4H-SiC polytype. We suggest that the incorporation of nitrogen atoms during the CVD growth depends on the presence of oxygen.

Table 1: Net donor concentration of 6H-SiC epilayers grown under various CO_2 flow rates.

6H-SiC epilayer	CO_2 flow (sccm)	N_D-N_A (cm^{-3})
#1	0.1	$1x10^{15}$
#2	0.5	$2x10^{15}$
#3	1	$4x10^{18}$

References

[1] T. Dalibor, H. Trageser, G. Pensl, T. Kimoto, H. Matsunami, D.G. Nizhner, O. Shigiltchoff, W.J. Choyke. Mater. Sci. & Eng. **B61-62** (1999) 454.

[2] T. Dalibor, G. Pensl, T. Yamamoto, T. Kimoto, H. Matsunami, SG. Sridhara, D. Nizhner, R.P. Devaty and W.J. Choyke. Mater. Sci. For. Vols. **264-268** (1998) 553.

Electrical Activity of the Isolated Oxygen Defects in SiC

A. Gali[1], D. Heringer[1], P. Deák[1], Z. Hajnal[2], Th. Frauenheim[2], and W. J. Choyke[3]

[1]Department of Atomic Physics, Technical Unversity of Budapest, Budafoki út 8, H-1111, Hungary
tel.: [36]-(1)-463 1393, fax: [36]-(1)-463 4357
email: agali@eik.bme.hu

[2]Department of Physics, Theoretical Physics, University GH Paderborn, D-33098 Paderborn, Germany

[3]Department of Physics and Astronomy, University of Pittsburgh, Pittsburgh, PA 15260, USA

Abstract Ab initio LDA calculations have been carried out for oxygen-related complexes in 3C(cubic) and 4H(hexagonal) silicon carbide. Cluster models with localized basis functions were used to calculate vibrational frequencies and spin distributions while supercell calculations are used to determine the relative stabilities and occupancy levels.

The substitutional oxygen has been studied in the 2+/+/0/-/2- charge states on both the C and Si site. It has been found that the oxygen at the carbon site (O_C) is the most stable defect and it is an on-center double donor in 3C-SiC. The characteristic vibration frequencies and the hyperfine data for the paramagnetic state will be given. The O_{Si} defect is an amphoteric defect, it could be an hyper deep double donor in the lower half of the band gap as well as a hyper deep acceptor in the upper half of the band gap. The O_i defect is also electrically active defect with complicated bonds. The behavior of the isolated oxygen defects have also been investigated in 4H-SiC and compared to the outcome in 3C-SiC. The results are compared to the experimental data of Th. Dalibor et al, Mater. Sci. Forum **264-268** 553 (1998).

Beryllium-Related Defect Centers in 4H-SiC

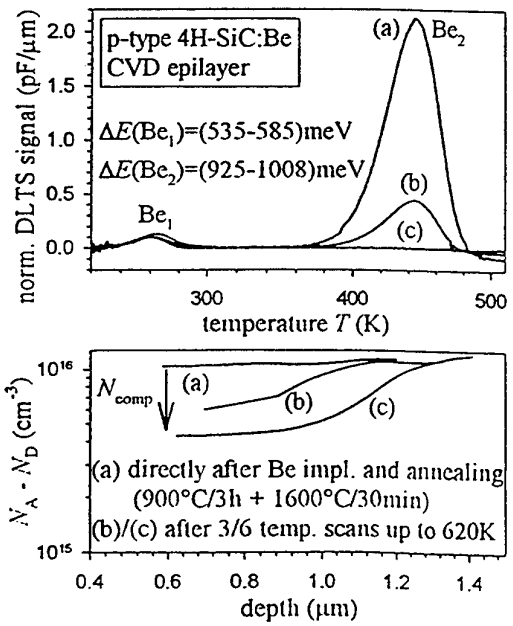
Michael Krieger, Michael Laube, Michael Weidner and Gerhard Pensl
Institute of Applied Physics, University of Erlangen-Nürnberg,
Staudtstr. 7, 91058 Erlangen, Germany
phone: +49 9131 85-28427, Fax: -28423, E-mail: michael.krieger@physik.uni-erlangen.de

Beryllium (Be), located in the second column of the periodic table, is a possible candidate for a double acceptor in SiC assuming that it resides at lattice sites. On the other hand, Be atoms which are of small size could also act as donors, if they occupy an interstitial lattice site. Up to now only a few data are published on the electrical properties of Be-related centers in SiC [1, 2] and the questions addressed above are not yet clarified.

A box-shaped Be profile (depth = 1.8μm, mean Be concentration = ($1x10^{16}$ to $1x10^{19}$) cm^{-3}) has been generated in n/p-type 4H-SiC epilayers by multiple Be implantation. SIMS analyses on Be-implanted and annealed (T_A = (1400 to 1700) °C, t_A = (0.5 to 3) h) samples reveal that Be is like boron a fast diffusing species in SiC.

DLTS spectra taken during a temperature scan between 200K and 620K on Be-implanted and subsequently annealed p-type 4H-SiC epilayers display two pronounced, Be-related peaks termed Be1 and Be2 (see Fig.1, upper plot). An Arrhenius evaluation assuming $\sigma = T^0/\sigma \propto T^{-2}$ results in energy levels at E(Be1) = E_V + (535/585) meV and E(Be2) = (E_V + (925/1008) meV. It turns out that level Be1 is stable during the temperature scan of the DLTS measurement, while the peak height of Be2 strongly decreases with increasing number of DLTS scans that is by repeated exposure to heat treatments up to 620K. Double-correlated DLTS investigations identify defect Be2 as an acceptor. The differing peak heights of Be1 and Be2 (see Fig.1, upper plot) and their extremely different thermal stability indicate that the two peaks are not caused by a double acceptor representing the two different charge states.

C-V profiles of the Al doping concentration determined in identical epilayers as used for the DLTS investigations reveal a decrease of the net Al acceptor concentration with increasing number of DLTS scans to a depth of about 1.2 μm (see Fig.1, lower plot).



The decrease of the electrically active Al acceptor concentration N_A-N_D (or increase of compensation N_{comp}= N_D) corresponds approx. to the decrease of concentration of Be2 centers. One possible mechanism which could explain the observed experimental data is the transformation of Be2 centers into a Be-related donor species.

Fig.1. DLTS spectra of a Be-implanted p-type 4H-SiC epilayer; curves (a), (b) and (c) are taken subsequent to a different number of DLTS scans up to 620K (upper plot) and corresponding net Al acceptor profiles taken by the C-V method (lower plot).

[1] Yu. P. Maslakovets et al., Sov. Phys.-Solid State **10** (1968) 634.
[2] N. Ramungul et al., IEEE Trans. Electron. Dev. **46** (1999) 465.

WeP-14

Intrinsic mobility of conduction electrons in 4H-SiC

J. Pernot[1], S. Contreras[1], E. Neyret[1,2], L. Di Cioccio[2], W. Zawadzki[1*] and J.L. Robert[1]

[1] *Groupe d'Etude des Semiconducteurs, UM2-CNRS, CC074, 34095 Montpellier cedex 5, (France)*
[2] *LETI-CEA, Département de Microtechnologie, 17 rue des Martyrs, 38054 Grenoble cedex 09, (France)*
**Permanent address : Institute of Physics, Polish Academy of Sciences, 02668 Warszawa, (Poland).*
Tel : +33 4 67 14 32 24, fax : + 33 4 67 14 37 60, e-mail: contre@ges.univ-montp2.fr

We study the Hall density and the Hall mobility of conduction electrons in 4H-SiC samples fabricated in a cold-wall CVD reactor at LETI (CEA). Temperature dependence of mobility was studied in the range of $20 < T < 850$ K. The sample having $n = 3.6 \times 10^{15}$ cm $^{-3}$ at room temperature exhibits the maximum mobility of $\mu = 12400$ cm^2/Vs at 50 K (cf figure), which is to our knowledge the highest value in 4H-SiC measured by the transport method (Meyer et al. [1] measured a maximum mobility of $\mu = 3 \times 10^5$ cm^2/Vs at 9 K using the cyclotron resonance on a 4H-SiC sample with not well known impurity density. Recently, Rutsch et al. reported a maximum Hall mobility of about 7000 cm^2/Vs, corresponding to a doping concentration of 1.6×10^{16} cm $^{-3}$ and a compensation of 6.4×10^{14} cm $^{-3}$ [2]). The solid line shows our theoretical calculation. The theory for mobility is based on a two-level impurity model, which is necessary to account for the corresponding temperature variation of electron density. We take into account the anisotropy of the effective mass and of the Hall factor [3]. Since the conduction band of 4H-SiC has the multi-valley character, intervalley phonon scattering processes are taken into account. Scattering by ionised and neutral impurities is also included. The neutral impurity mode is known to be important for SiC.

The density dependence of mobility at room temperature in the range of $10^{15} < n < 10^{20}$ cm^{-3} was also studied using different samples. The measured mobilities are well described by the theory. A comparison of our mobility values with those published by other authors [4-6] shows that our samples possess state-of-the-art quality.

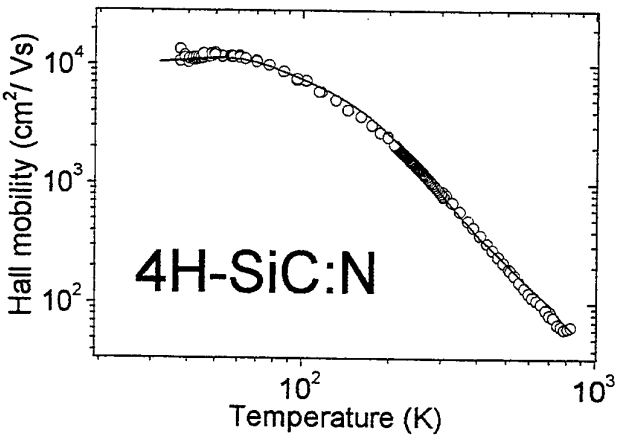


Figure: Hall mobility of weakly nitrogen-doped 4H-SiC versus temperature (open circles). Solid line: theoretical calculations.

[1] B.K. Meyer, D.M. Hofmann, D. Volm, W.M. Chen, N.T. Son and E. Janzén, Phys. Rev. B **61**, 1 (2000)
[2] G. Rutsch, R.P. Devaty, W.J. Choyke, D. W. Langer, L.B. Rowland, E. Niemann and F. Wischmeyer, Proceedings of ICSCRM99 (in press)
[3] T. Kinoshita et al., Mat. Sci. Forum **264-268**, 295 (1998)
[4] A.A. Burk et al., Sol Stat Elect. **43**, 1459 (1999)
[5] W.J. Schaffer et al., Mater. Res. Soc Symp Proc, Pittsburgh, p.595 (1994)
[6] A. Itoh, H. Akita, T. Kimoto, H. Matsunami, App. Phys. Lett. **65**, 1400 (1994)

Active Doping Profile Measurements of 4H-SiC

J. Österman[1], A. Hallén[1], S. Anand[1], M. Linnarsson[1], H. Andersson[1], D. Åberg[1], W. Skorupa[2] and D. Panknin[2]

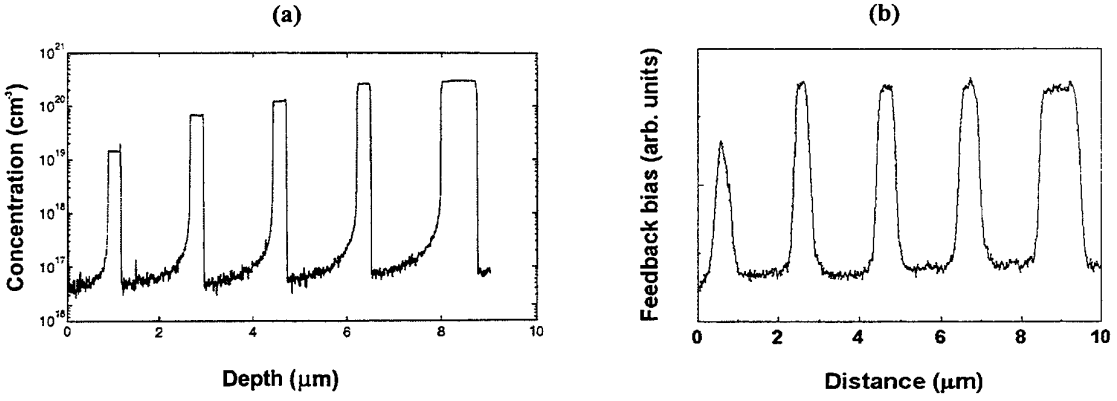
[1]*Department of Electronics, Royal Institute of Technology, P.O. Box Electrum 229, 164 40 Kista, SWEDEN*
Tel: +46 8 752 1246, Fax: +46 8 752 7782, email: john@ele.kth.se

[2]*Forschungszentrum Rossendorf, Institute of Ion Beam Physics and Material Research P.O. Box 510119, 01314 Dresden, GERMANY*

Information of the charge carrier distribution in a semiconductor device is crucial. For the case of profiling high doping gradients in silicon, especially spreading resistance (SRP) has proven to be a valuable tool. For SiC however, SRP measurements are difficult due to the wide bandgap and the extreme hardness, which complicates the establishment of an ohmic contact. Recent development of SRP [1] and also two-dimensional dopant imaging techniques, in particular the scanning capacitance microscopy (SCM) [2], but also the scanning electron microscopy (SEM) [3] may therefore be of special importance for SiC.

In this study, the different techniques for measuring active doping profiles in 4H-SiC are evaluated. Both aluminum doped epi-layers (10^{16}-10^{21} cm^{-3}) and aluminum and/or boron implanted n-type epi-layers are investigated. SCM data is collected at various DC-biasing conditions, and, in the SEM measurements, the emission of secondary electrons is studied as a function of the e-beam acceleration voltage and current. The SCM and SEM results are compared with SRP measurements of the same samples.

By comparing these profile measurements with secondary ion mass spectrometry (SIMS) profiles, which provide the chemical depth distribution of the dopants, an estimate of the degree of activation can be obtained. As an example we show in Figs (a) and (b) a 10 μm Al-doped epitaxal layer measured by (a) SIMS and (b) SCM on a cleaved cross-section (zero DC-bias). The SCM signal can reproducibly detect the varying widths of the Al-rich layers, both before and after anneal (the left peak nearest to the cross-sectioned edge is not clearly resolved though).



References:

[1] T. Gebel, D. Panknin, R. Riehn, S. Parascandola and W. Skorupa, Proceedings from ICSCRM, North Carolina, Oct. 1999.

[2] C. J. Kang, C. K. Kim, J. D. Lera Y. Kuk, K. M. Mang, J. G. Lee, K. S. Suh, C. C. Williams, Appl. Phys. Lett. 71 (11), 15 Sept. 1997.

[3] S. L. Elliot, R. F. Broom, C. J. Humphreys, E. J. Thrush, L. Considine, D. B. Thomson, W. B. de Boer, Inst. Phys. Conf. Ser. No 164, p. 727-729, 1999.

Thermopower measurements in 4H–SiC and theoretical calculations considering the phonon drag effect

V. Grivickas[1], M. Stölzer[2], E. Velmre[3], A. Udal[3], P. Grivickas[4], M. Syväjärvi[5], R. Yakimova[5] and V. Bikbajevas[1]

[1] *Institute of Materials Science and Applied Research, Vilnius University, Sauletekio 10, 2054 Vilnius, Lithuania, tel. +370 2 76 95 03, fax: + 370 2 76 73 13*
[2] *FB Physik, Martin Luther University, 06099 Halle, Germany*
[3] *Institute of Electronics, Tallinn Technical University, Ehitajate tee 5, 19086 Tallinn, Estonia*
[4] *Solid State Physics, Royal Institute of Technology, Electrum 229, SE-164 40 Kista-Stockholm, Sweden*
[5] *Department of Physics and Measurement Technology, Linköping University, SE-581 83 Linköping, Sweden*

The direct conversion of thermal into electrical energy depends to a large extend on the Seebeck effect. The Seebeck coefficient governs the efficiency of the process and appears as a factor in the equation term describing any nonisotermal part of SiC devices. The Seebeck effect was widely investigated in sixties and seventies. At that time it was observed that the Seebeck coefficient in α-SiC exceeds the ones in Si and Ge. It was believed that the reason for that phenomenon is a strong phonon-electron coupling – the so-called phonon drag effect. However, in those early investigations the polytypes and transport parameters of the samples were not specified accurately enough.

In this work, a new Seebeck coefficient study in 4H-SiC is presented. A 300-μm thick epilayer of *n*-4H-SiC ($N_d = 3 \cdot 10^{18}$ cm^{-3}) was grown on the substrate by sublimation technique. Then the substrate was carefully polishing away and ohmic contacts were deposited on the SiC. The measurements of the Hall effect and IR absorption have been used to determine the electron concentrations and their mobility in the temperature range of 80-400 K. Copper-Constantan thermocouples served as voltage probes and temperature sensors at the same time. A special heating technique employed positive or negative temperature gradient between the ends of the sample. The nearly perfect compensation of spurious voltages and variable small temperature difference ΔT along the sample are the major advantages of this technique (see Fig. 1). The comparison between experimentally obtained and theoretically calculated temperature dependencies of the electron Seebeck coefficient, *S*, in the direction perpendicular to the **c**-axis is presented in Fig. 2. In the present calculations, the phonon drag term has been used in the form obtained in [1] for the zero-order approximation to the variational solution of the coupled Boltzmann transport equations for electrons and phonons. The long wavelength phonon mean free path, a key parameter of the phonon drag term, has been estimated using an approximation to the measured thermal conductivity in high-purity SiC samples [2] The theoretical temperature dependence without taking into account the electron-phonon coupling is also shown in Fig. 2. As one can see, the phonon drag has a dramatic effect on the value of the Seebeck coefficient. In the full presentation a few other possible approaches to the phonon drag modelling will be discussed.

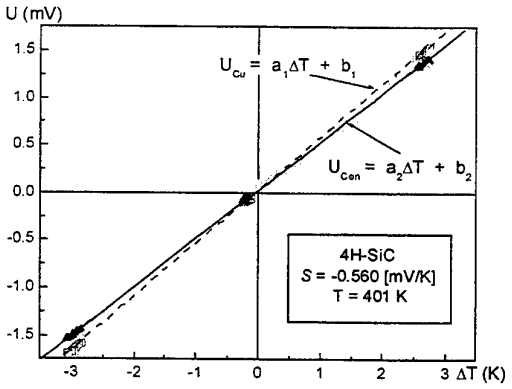


Fig. 1 Example of thermopower voltages versus ΔT. Copper or Constantan is used as contacts to SiC.

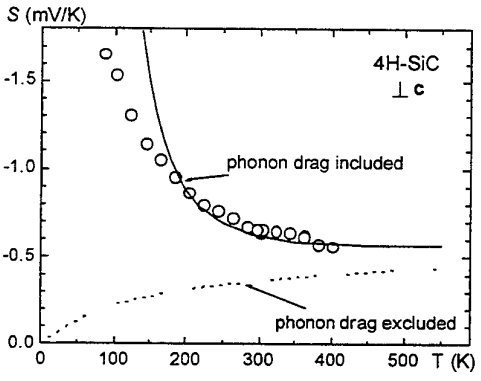


Fig. 2 Experimental and theoretical temperature dependencies of the Seebeck coefficient.

1. D. Dorn, *Z. Naturforschung*, **12a**, 739 (1957)
2. G. A. Slack, *Phys.Rev.*, **35**, 3460 (1964)

Growth Evolution of Dislocation Loops in Implanted 4H SiC

P.O.Å. Persson, L. Hultman
Thin Film Physics Division, Linköping University, S-58183 Linköping, Sweden
perpe@ifm.liu.se, Phone: +46 13 281248, Fax: +46 13 137568

For the purpose of producing SiC planar devices, selective area doping is necessary. Due to negligible diffusion coefficients in SiC of candidate dopant elements, the choice of technique today is mainly ion implantation. This technique has benefits in the sense that it can offer tailored dopant profiles. The implantation process on the other hand damages the crystal by inducing vacancies and interstitials from collisions between the implanted ion and the lattice. By heating the sample during implantation, it has been found that the lattice damage is less pronounced.[1] The as implanted ions predominantly occupy interstitial lattice sites where they are electrically inactive.[2] To electrically activate the implanted ions and to restore the damage induced in the implantation process, the sample is subject to a thermal annealing process.

TEM studies show that annealed SiC samples, irradiated by a dose of ions slightly lower than the amorphisation threshold contain crystal structural defects. These have been determined to be interstitial type dislocation loops, typically 1-10 nm wide.[3] It is the intention of this paper to present results on studies of the evolution of these defects after high temperature annealing.

In the present study samples were prepared by implanting 4H SiC with Al, C and Si respectively at energies ranging from 100-200 keV. A few samples were implanted at varying implantation temperatures. Most samples were subject to annealing studies in which the annealing time and temperature was varied. The annealed samples were then studied by EELS, Cross sectional TEM and Plan view TEM.

At low temperature implantations the entire volume affected by the implantation contains dislocation loops. However, after implantation at elevated temperatures only the volume in which the dopant concentration is highest contain loops. It was concluded that the dislocation loops contain self-interstitials. These originate from a supersaturation of excess atoms which are created in the process when the implanted ion occupy a substitutional site, thereby kicking out an excess atom, according to the +1 model. It is shown that when an implanted sample is annealed the excess interstitials start to cluster. As soon as equilibrium between point defects and nucleated loops has been established coarsening of defects occur according to the Ostwald ripening theory for planar precipitates, in which large defects grow on the expense of smaller. The limiting factor for loop growth is suggested to be diffusion of the excess interstitials. During the steady state loop growth an activation energy has been measured.[4]

1. E.Wendler, A.Heft and W.Wesch, Nucl. Instrum. and Methods B 141 (1998) 105.
2. M.V.Rao, P.Griffiths, O.W.Holland, G.Kelner, J.A.Freitas, D.S.Simons, P.H.Chi and M.Ghezzo, J. Appl. Phys. 77 (1995) 2479.
3. P.O.Å.Persson, Q.Wahab, L.Hultman, N.Nordell, A.Schöner, K.Rottner, E.Olsson and M.K.Linnarson, Mater. Sci. Forum 264-268 (1998) 413.
4. P.O.Å.Persson, Linköping Studies in Science and Technology Lic. Thesis no. 813, ISBN: 91-7219-685-8.

Micropipe-related screw dislocations with extremely large Burgers vectors in 4H-SiC evidenced by X-ray "magnifying" imaging

Jürgen Härtwig[1], Harald Kuhn[2], Xian-Rong Huang[3] and Michael Dudley[3]

[1]European Synchrotron Radiation Facility, BP 220, 38043 Grenoble, France, [2] SiCrystal AG, Heinrich-Hertz-Platz 2, D-92275 Eschenfelden, Germany, and [3]Department of Materials Sciences and Engineering, State University of New York at Stony Brook, Stony Brook, New York 11794, USA.

The performance and reliability of SiC-based devices are very sensitive to the presence of crystalline defects. Among the defects usually present in SiC, the most critical ones are the "micropipes," which have been shown to be giant dislocations with large Burgers vectors. How large these Burgers vectors can be? In this presentation, we will demonstrate that they can surprisingly be hundreds to thousands of nanometers. Compared with dislocations in silicon that have Burgers vectors around 0.4 nm, these micropipes are, indeed, *huge* dislocations. Their frequent presence in SiC crystals is thus a serious and persistent problem, which prevents crystal growers from growing high-quality crystals and heterostructures.

One very effective possibility to study such kind of lattice defects in large crystals is the utilisation of X-ray diffraction topography (diffraction imaging). Already long ago it was demonstrated, that the Burgers vectors of giant screw dislocations in ZnS polytype crystals can be easily measured using such techniques [1]. In a series of papers (for references see [2]) Dudley and his co-workers recently demonstrated the application of modern X-ray topographical techniques (white-beam synchrotron radiation) to clearly reveal and map micropipes in SiC crystals.

We used the same techniques, but at a third generation synchrotron radiation source. A distinct advantage of this source is that the large source-to-sample distance (145 m) and the extremely small source size (50 – 120 μm) make the synchrotron beam highly collimated. Consequently, it is possible to use large sample-to-detector distances (up to meters) without degrading the topographical images. The large imaging distance makes it possible to record significantly "magnified" defect images, which may be two or three orders of magnitude larger than the actual defect. Therefore, the third generation synchrotron radiation source provides an excellent tool to detect and to characterise in an efficient and very detailed way the micropipes in SiC wafers. As an example, we will report results of the investigation of micropipe-related screw dislocations with extremely large Burgers vectors detected in 4H-SiC. Micropipes with about 6 μm diameter showed images half a millimetre wide (recording the image 1.5 m from the sample) and evidenced Burgers vectors several hundred nanometers long. From this investigation the magnifying function of large-imaging-distance synchrotron topography is clearly demonstrated. The detailed mechanisms underlying the imaging process show that this technique is not restricted to large Burgers vectors, but also allows to easily and non-destructively detect 'small' pipes or normal screw dislocations, invisible by optical microscopy.

[1] S. Mardix, A. R. Lang & I. Blech, *Phil. Mag.* **24**,683 (1971)
[2] X. R. Wang, M. Dudley, W. M. Vetter, W. Huang, W. Si & C. H. Carter Jr., *J. Appl. Cryst.* **32**, 516 (1999)

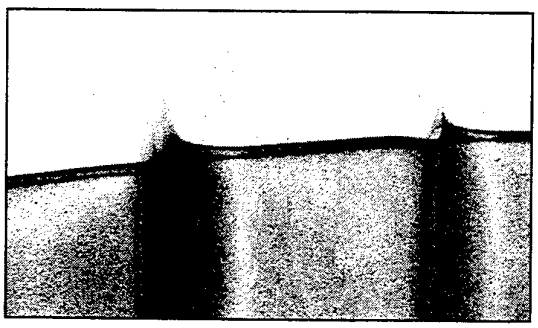


Figure 1: White beam transmission topography showing the images of micro-pipes in a 4H-SiC sample, cut parallel to [0001]. Bragg angle $\Theta_B \approx 7°$, sample to film distance 10 cm.

X-ray diffraction line profile analysis of neutron irradiated 6H-SiC

C. Seitz[1], A. Magerl[1], H. Heißenstein[2], R. Helbig[2]

[1] Lehrstuhl für Kristallographie und Strukturphysik, Universität Erlangen-Nürnberg. Bismarckstr. 10, D-91054 Erlangen, Germany. Tel: 0049-9131/85-22119 Fax: 0049-9131/85-22733

[2] Lehrstuhl für Angewandte Physik, Universität Erlangen-Nürnberg Staudtstraße 7/A3, D-91058 Erlangen, Germany.

Email: christoph.seitz@krist.uni-erlangen.de

Similar to a well established technique for Si, nuclear transmutation by neutron irradiation can also be applied to dope SiC. This method is useful to achieve a homogeneous doping in large crystal volumes. As a disadvantage, however, radiation induced defects occur, mainly by high energy neutrons. We have investigated the line broadening of Bragg peaks in irradiated 6H-SiC samples by high resolution x-ray diffraction. The effects of different neutron fluences, neutron spectra and annealing treatments have been studied. The data demonstrate a clear correlation of the defect densities of second kind with the neutron fluences and the annealing procedures. We were able to determine quantitatively the defect densities and to elucidate a change of the character of the defects upon annealing.

ION BOMBARDMENT INDUCED DAMAGE IN SILICON CARBIDE STUDIED BY ION BEAM ANALYTICAL METHODS

Z. Zolnai[1], E. Kótai[2], N.Q. Khánh[1], E. Szilágyi[2], Z.E. Horváth[1], T. Lohner[1], and J. Gyulai[1]

[1]Research Institute for Technical Physics and Materials Science
H-1121 Budapest, Konkoly Thege út 29-33, Hungary
Phone 36-1-392 2695
Fax: 36-1-392-2226
e-mail: lohner@mfa.kfki.hu

[2]Research Institute for Particle and Nuclear Physics
H-1121 Budapest, Konkoly Thege út 29-33, Hungary

Damage created by implantation of Al^+ ions into 4H-SiC and into Si (100) is characterized using Backscattering Spectrometry in combination with channeling. To create disorder, Al^+ ions with energy of 200 keV were implanted at room temperature. Considerable less damage was found in silicon than in 4H-SiC in the case of identical ion irradiation. As an independent cross-checking method, cross-sectional transmission electron microscopy was used to study the damage structure in irradiated 4H-SiC. Earlier observations were considered to minimize the damaging effect of the analyzing $^4He^+$ beam in 4H-SiC [1, 2].

Nuclear reaction or non-Rutherford elastic scattering are suitable methods to obtain concentration of low atomic number constituent in a compound sample. Nashiyama et al. applied the $^{12}C(d,p)^{13}C$ nuclear reaction and deuteron Rutherford backscattering in combination with channeling for investigation both carbon and silicon atom displacements in virgin and proton irradiated 3C-SiC [3]. Another appropriate method is the $^{12}C(^4He^+,^4He^+)^{12}C$ resonance at the resonance energy of 4260 keV, an enhancement factor of over hundred for ^{12}C can be reached. This resonance was utilized to investigate the ion bombardment induced disorder in the carbon sublattice of 4H-SiC. The disorder was created by implantation of 200 keV and 350 keV Al^+ ions at room temperature. The depth resolution of the method is discussed.

References

[1] W. Fukarek, R.A. Yankov, W. Anwand, and V. Heera, Nuclear Instruments and Methods in Physics Research B142 (1988) 561.
[2] N.Q. Khánh, Z. Zolnai, T. Lohner, L. Tóth, L. Dobos, and J. Gyulai, Nuclear Instruments and Methods in Physics Research B161-163 (2000) 424.
[3] I. Nashiyama, T. Nishijima, E. Sakuma, and S. Yoshida, Nuclear Instruments and Methods in Physics Research B33 (1988) 599.

POLARITY OF GaN EPITAXIC LAYERS BY KOSSEL EFFECT TECHNIQUE

Andrew N. Efimov, Andrew O. Lebedev & Alexander M. Tsaregorodtsev

Physical-Technical Ioffe Institute Politechnicheskaya str. 26, 194021, St.Petersburg, RUSSIA
Phone: +7-(812) 515-9292, Fax: +7-(812) 234-3164 Email: Aswan@aport.ru

III-V nitrides usually crystallize in the noncentrosymmetric wurtzite structure (point group 6mm) with a polar c axis. Determination of a direction of a polar sixfold axis for epitaxic GaN layers on a substrate by a traditional technique (comparative chemical etching) is very difficult because another layer side hidden under the substrate is not available.

For determination of polarity of GaN epitaxic layers grown on sapphire substrates by chloride transport process technique in the system Ga – HCl – NH_3 - Ar, we employed simple method of the Kossel effect stimulation by an electron beam in scanning electron microscopy. Experimental results, obtained by us as well as those published earlier by other authors for GaN (AlN) epitaxic layers grown on the high reticular density cuts of sapphire and also for comparison on other substrates are summarized in Table. The fine structures of the Kossel lines on the patterns produced from the various regions of the same sample are identical to each other, proving that the epitaxic layers grown by our technique are free from twinning with an inversion of the polar axis.

Substrate:	Orientation relationship	Polarity of external face
Sapphire		
(0001),[11-20]	(0001),[10-10] (GaN)	A/(0001)Ga/
(11-20),[0001]	(0001),[1-100] (GaN)	A
(10-14)	(0001) (GaN)	A
(01-12),[0-111]	(11-20),[0001] (GaN)	[01-1-1]Al2O3//[0001]Ga
Sapphire		
(0001),[11-20]	(0001),[10-10] (GaN)	A
Sapphire		
(01-12),[0-111]	(11-20),[0001] (AlN)	A
$MgAl_2O_4$		
(111),[1-21]	(0001),[1-100] (GaN0	A
SiC-6H		
(0001) Si,[11-20]	(0001),[11-20] (GaN)	B /(0001)N/
(0001) C,[11-20]	(0001),[11-20] (GaN)	A /(0001)Ga/

Mass transport and powder source evolution in sublimation growth of SiC bulk crystals

M.S. Ramm [a], D. S. Karpov [b], O. V. Bord [b], S. Yu. Karpov [b], A. I. Zhmakin [a], Yu. N. Makarov [c]

[a] A.F.Ioffe Physical-Technical Institute, Numerical Simulation Department, St.Petersburg, 194021, Russia, Phone +7 (812) 247-9145, Fax +7 (812) 326-6194

[b] Soft-Impact Ltd., P.O.Box 33, 194156, St.Petersburg, Russia, Phone +7 (812) 554-4570, Fax +7 (812) 326-6194

[c] Fluid Mechanics Institute, University of Erlangen-Nürnberg, Cauerstr. 4, D-91058 Erlangen, Germany, +49 (9131) 76-1248, +49 (9131) 76-1275

Silicon carbide powder is commonly used as a source of reactive species for growth of SiC bulk crystals by sublimation technique. In this paper we suggest a coupled model of species mass transport through the SiC powder charge and in the clearance between the powder and the seed. The proposed approach includes a set of mass transport equations accounting for heterogeneous chemical reactions at the surface of SiC granules. Phase state of a granule surface (pure SiC, graphitized SiC or SiC enriched by silicon) is found in every point of the powder using a thermodynamic criterion of extra phase formation [1]. The phase state controls the mechanism of chemical interaction between the granule surface and the vapor. We use the model to predict the effects of powder parameters (porosity and granule size) and growth conditions on SiC growth rate and seed graphitization during growth.

Evolution of the powder properties and of its phase state is simulated by using a quasi-steady-state concept based on the assumption that the transient time of all processes (response of the sublimation rate and of the granule phase state to changes in the local vapor composition) is much less than the growth duration. This permits one to replace an unsteady process of powder sublimation by a set of steady-state processes taking into account variation in the granule size, porosity and in the powder phase state from step to step.

The results predict existence of several zones in the powder source with different character of interaction between the multicomponent vapor and the granule surface. Our computations show that the temperature profile in the powder charge is crucial for location and size of the graphitization and recrystallization zones (the latter are formed due to crystallization of the supersaturated vapor species coming from the hot zones of the powder). The computations allow us to predict SiC growth rate evolution as a function of the initial powder granularity and to reveal the growth conditions resulting in the seed graphitization. Correlation between the powder and the seed graphitization is discussed. Specific features of the process like substitution of the inert gas by the reactive species, and the densification of SiC powder due to recrystallization are studied. Efficiency of the source utilization is discussed in context of the obtained results. The computational results are compared with the available experimental data. The model is used for analysis of degradation of the SiC powder during growth of bulk SiC crystals in sublimation sandwich system.

[1] M.S. Ramm, A.V. Kulik, I.A. Zhmakin, S.Yu. Karpov, O.V. Bord, S.E. Demina, Yu.N. Makarov, Presented on MRS Spring Meeting (2000).

MORPHOLOGY OF SUBLIMATION GROWN 6H-SIC-(000$\bar{1}$) SURFACES

D. Schulz, J. Dolle, H.-J. Rost, D. Siche, J. Wollweber

Institut für Kristallzüchtung, Max-Born-Str. 2, D-12489 Berlin, GERMANY

Phone: +49 30 6392 2844 Fax: +49 30 6392 3003 e-mail: dschulz@ikz-berlin.de

Seed polarity and orientation have a strong influence on sublimation grown SiC crystals. For physical vapor transport methods growth on the C-terminated face of 6H-SiC seeds has been rarely reported. Because of the observed polytype change from 6H to 4H during growth on a (000$\bar{1}$) face, Si-terminated seeds are prefered for crystal growth of the 6H polytype [1].
Sublimation grown epitaxial layers as well as crystals have been investigated by optical microscopy, atomic force microscopy and photoluminescence. Crystal growth was performed on the C-terminated surface of 6H seeds of 30 mm diameter. In addition seeds with an off-orientation a few degrees towards <11$\bar{2}$0> were used. The growth sequence was described elsewhere [2]. In case of epitaxial layers the growth has been interrupted by increasing the pressure and reducing the temperature simultaneously.
Even on off-oriented seeds step flow growth can only be maintained using source material with Si excess (Fig. 1). This was already found for growth on (0001)-6H seeds [2]. Step bunching is more pronounced when using a stoichiometric source. Furthermore, with decreasing temperature growth no longer proceeds via step flow. Step trains are transformed into meandering macrosteps.

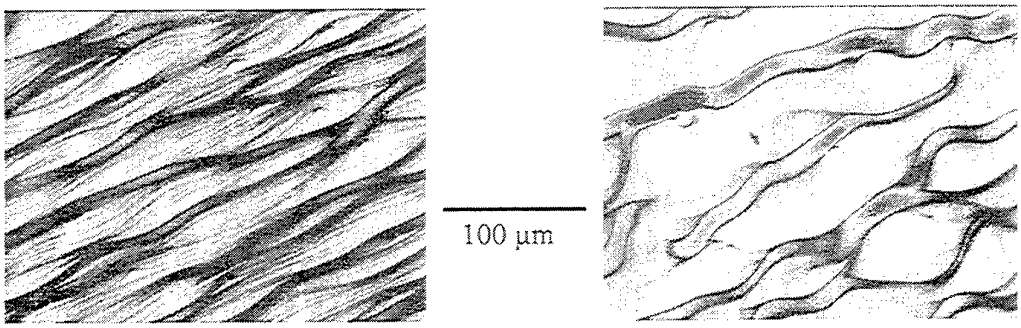


Fig. 1. Optical micrographs of layers grown by sublimation on (000$\bar{1}$)-6H seeds (left: Si excess in source material, right: stoichiometric source)

In contrast to off-oriented layers the on-axis grown material always exhibited a coalescence of individual islands. Growth spirals often seen on the Si-terminated face could not be observed on (000$\bar{1}$) faces [3]. This was independent of the supersaturation. The influence of selected growth parameters on polytype stability has been studied and a surprisingly low transformation probability from 6H to 4H was revealed. The results will be related to the observed step bunching and surface kinetics.

[1] R.A. Stein, P. Lanig, S. Leibenzeder, Mat. Sci. Engineer. B11 (1992) 69
[2] D. Schulz, G. Wagner, J. Doerschel, J. Dolle, W. Eiserbeck, T. Müller, H.-J. Rost, D. Siche, J. Wollweber, Mat. Sci. Engineer. B61-62 (1999) 86
[3] N. Ohtani, M. Katsuno, T. Aigo, T. Fujimoto, H. Tsuge, H. Yashiro, M. Kanaya, J. Crystal Growth 210 (2000) 613

FEATURES OF SEMI-INSULATING SiC SINGLE-CRYSTALS GROWTH BY PHYSICAL VAPOR TRANSPORT

S.A. Reshanov, V.P. Rastegaev, Yu.M. Tairov
Dept. of Microelectronics, St.-Petersburg State Electrotechnical university,
Prof. Popov str.5, 197376, St.-Petersburg, Russia
Phone +7 812 234 30 64, Fax +7 812 234 31 64, E-mail: SiC.ME@eltech.ru

The semi-insulating silicon carbide is required for many electronic devices on the basis of silicon carbide and nitrides. The present study is devoted to the problems of obtaining of insulating properties of SiC single-crystals at physical vapor transport (PVT) growth.

It is necessary to mark out two basic stages in obtaining semi-insulating properties of a SiC material:

1) obtaining a high-resistivity material by lowering the impurity concentration and compensation;
2) overcompensation of the residual impurities by deep impurity centres.

The analysis of parameters of known impurity centres in silicon carbide has shown that the most appropriate of them for obtaining insulating properties is vanadium. Being an electrically amphoteric impurity, vanadium forms both deep donor D^0/D^+ ($V_{Si}^{4+}(3d^1)/V_{Si}^{5+}(3d^0)$) and acceptor levels A^0/A^- ($V_{Si}^{3+}(3d^2)/V_{Si}^{4+}(3d^1)$) located accordingly at 1.35...1.47 and 0.68...0.97 eV below the conduction band bottom in 6H and 4H. The usage of vanadium donor levels is the most preferable, especially in 4H polytype.

The physico-chemical features of polytypes impose certain requirements on growth conditions, which in turn determines the level of doping and overcompensation. The growth in vacuum of 4H-SiC single-crystals on the (0001)C facet from aluminium containing source allows to obtain high-resistivity crystals with a low difference concentration of residual impurities. Doping of such crystals by vanadium at growth allows to compensate the dominant residual impurities (aluminium and nitrogen) completely and to obtain a semi-insulating material. Its electrical properties in a wide temperature range would only be determined by activation energy of vanadium.

The physico-chemical phenomena accompanying doping process of SiC single-crystals by vanadium and aluminium are considered proceeding from thermodynamic analysis of the vapor phase composition of SiC-C-V, Al system.

The influence of the seed orientation on vanadium doping level would be discussed. It is possible to control the concentration level by variation of growth temperature and composition of growth source mixture. The concentration level and crystal polytype structure are interdependent.

It is shown, that the single-crystals of silicon carbide possessing semi-insulating properties can be grown by physical vapor transport under the following conditions:

1) growth environment – vacuum (pressure range $10^{-3}...10^{-5}$ Torr);
2) growth cell material – dense graphite (15% porosity);
3) growth source composition – previously sintered silicon carbide powder doped specially by vanadium and aluminium;
4) growth plane orientation – (0001) C

The electrophysical and optical characteristics of PVT grown semi-insulating 4H-SiC:V single-crystals would be presented. For the first time is shown, that the miscibility of vanadium can achieve up to $1 \cdot 10^{19} cm^{-3}$.

The obtained results prove the viability of application of semi-insulating 4H-SiC:V as a substrate material.

GROWTH RELATED DISTRIBUTION OF SECONDARY PHASE INCLUSIONS IN 6H-SiC SINGLE CRYSTALS

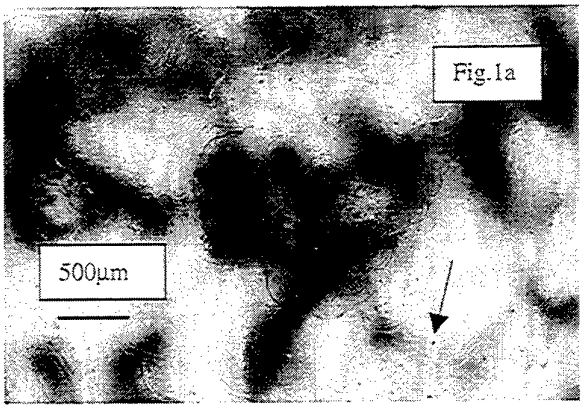
H.-J.Rost, J.Dolle, J.Doerschel, D.Siche, D.Schulz, J.Wollweber

Institut für Kristallzüchtung, Max-Born-Straße 2, D-12489 Berlin, Germany

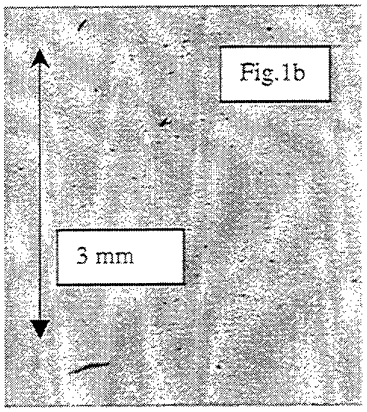
Phone: +49 30 6392 2847 Fax:+49 30 6392 3003 e-mail: rost@ikz-berlin.de

The quality of large diameter 6H-SiC single crystals is strongly influenced by the composition of the vapour phase and the thermal conditions inside the growth chamber. Beside the seed quality the grown in defects like misoriented regions and micropipes determine the yield [1]. Their formation is correlated with second phase inclusions, such as silicon droplets or carbon particles [2]-[4].

Inclusions



a) below the crystal surface (top view) (large black areas are graphite residues on the rear of the seed)



b) in a cut parallel to the <0001> growth direction

Crystals up to 35mm diameter grown on the silicon face by the Modified Lely Method in a temperature range between 2100°C-2400°C and an Ar-pressure from 5-50 hPa have been investigated. Inclusions could be identified as carbon particles by SEM and EELS. Their distribution along the growth direction and at the phase boundary were investigated by Optical Microscopy (Fig.1a; 1b). It was found that their density varies in axial as well as radial direction. The dependence of the carbon particle concentration on growth parameters such as seed temperature, time, pressure and the distance between source and seed is shown. To explain the behaviour a so called concentration model will be discussed. Therefore any change of the vapour phase composition characterised by the loss of silicon and caused by changing of a growth parameter may result in a drastic local increase of the carbon particle concentration. If a critical value is exceeded they can act as a nucleation centre for micropipes or misoriented regions. Measures to lower the second phase inclusions will be discussed.

[1] R.C.Glass, D.Henshall, V.F.Tsvetkov, C.H.Carter, Jr.
Phys. Stat. Sol. (b) 202,149 (1997)
[2] M.Dudley et al., A.Powell and S.Wang, P.Neudeck, M.Skowronski
Appl. Phys. Lett., Vol.75, No.6, 784 (1999)
[3] M.Tuominen, R.Yakimova, A.Vehanen, E.Janzen
Mater. Sci. Eng. B57 228 (1999)
[4] D.Hofmann, M.Bickermann, R.Eckstein, M.Kölbl, St.G.Müller, E.Schmitt, A.Weber, A.Winnacker
J. Crystal Growth, 198/199 (1999) 1005-1010

Micropipe Filling by Sublimation Close Space Technique

T.Furusho, S.Ohshima and S.Nishino
Kyoto Institute of Technology
Sakyo-ku, Kyoto, 606-8585 Japan
Tel: +81-75-724-7438 Fax: +81-75-724-7400
E-mail: furush5t@djedu.kit.ac.jp, nishino@ipc.dj.kit.ac.jp

The advantage of CST is that crystal growth is carried out in quasi-equilibrium [12]. The growth rate of CST is about 50 μm/h and is higher than that of CVD system. Therefore, it is advantageous for power device applications that need thick epitaxial layers. Micropipes in the substrate continue to propagate into the epitaxial layer. We demonstrate here using CST, micropipes in the substrate were filled during epitaxial layer growth.

Polycrystalline 3C-SiC plate was used as the source and 6H-SiC was used as the substrate. The growth temperature was 1800℃ and the growth pressure was about 2.0 $\times 10^{-3}$ Torr. The distance between the source and the substrate was 1.0 mm. The growth rate was about 50 μm/h under these conditions. Epitaxial layers were characterized by KOH etching, etc.

Depth profiles of the micropipes were easily observed under the optical microscope by focusing at different depths. The relationship between the film thickness of the epitaxial layer and the average diameter of micropipes is shown in Fig.1. The average diameter of micropipes decreases as the thickness of the epitaxial layer increases. The probability that micropipes under 20 μm diameter disappeared completely was about 86%. The reason for micropipe filling is that the epitaxial growth is carried out in the high vacuum level. In the conventional sublimation method, the pressure during the growth is about 50 Torr, but it is about 2.0×10^{-3} Torr in the CST system. In high vacuum condition, the surface diffusion length of chemical species is longer than in a low vacuum level. Therefore, chemical species can reach inside of the micropipes, whereby crystal growth occurs in the micropipes and consequently micropipes are completely filled. This approach can be applied to the conventional sublimation method and micropipes can be reduced in the SiC bulk crystal. In this report, a mechanism of micropipes reduction and characterization of epitaxial layers will be discussed.

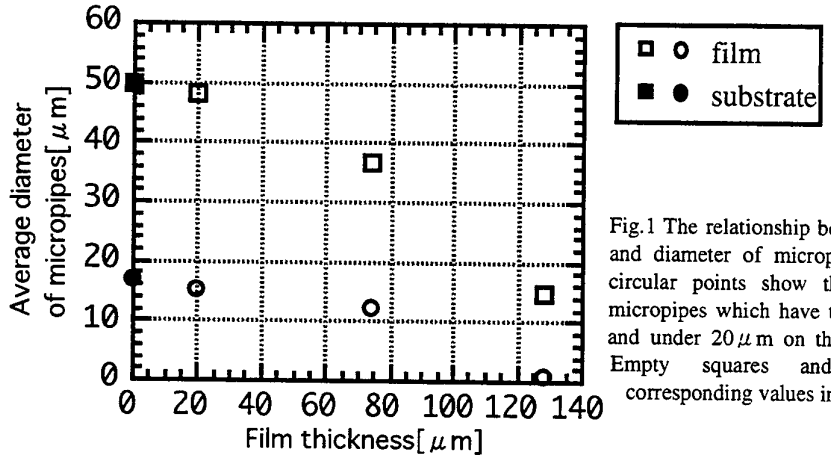


Fig.1 The relationship between the film thickness and diameter of micropipes. Square points and circular points show the average diameter of micropipes which have the diameter over 20 μm and under 20 μm on the substrate, respectively. Empty squares and circles show the corresponding values in the epitaxial layers.

[1]S.K.Lilov, Journal of Crystal Growth 46, pp.269～273, 1979
[2]Yu.M.Tairov, V.F.Tsvetkov, S.K.Lilov and G.K.Safarakiev, Journal of Crystal Growth 36, pp.147～151, 1976

Mechanism for Damage Healing of Cracked 6H-SiC Substrates by Sublimation Method

T. Shimizu, T. Nishiguchi, M. Sasaki, S. Ohshima and S.Nishino
Department of Electronics and Information Science, Kyoto Institute of Technology, Matsugasaki, Sakyo-ku, Kyoto 606-8585, Japan.
TEL:+81-75-724-7415 FAX:+81-75-724-7400 e-mail:nishino@ipc.kit.ac.jp

Introduction

Recently, the production of high-quality and large diameter bulk SiC crystals has been the most important problem. In general, large size bulk crystals are made by enlarging gradually from small size substrate crystals. However by this method, a very long time is needed to make large diameter bulk crystal. In our previous growth experiments, when we grew on cracked substrates, the crack disappeared on the surface after several growth runs [1]. Based on those experiments, an alternative way of enlarging the size of the crystals is suggested. This method consists of placing a number of small substrates on the graphite cap near each other and allowing the cracks or grooves of substrates to be healed. Implementing this idea, we placed two substrates, together confirmed transition from bi-crystal to mono-crystal. The mechanism of damage healing will be discussed.

Experiment and Result

A 1 inch 6H-SiC wafer, polished on both sides, was used as the starting substrate. This wafer was divided into two parts, and then these divided parts were set on the graphite cap. Crystal growth was achieved in a quartz tube reactor with a water-cooled jacket under argon atmosphere at 50 Torr. The source material was abrasive SiC powder. The crucible was heated externally by RF induction with a frequency of 300 kHz. The temperatures at the top (Ts) and the bottom (Tb) of the crucible were measured by an optical pyrometer. Ts and Tb were approximately 2050~2150 ℃ and 2250~2350 ℃, respectively. Bulk crystal was grown by recharging the source SiC three times material (total 11 hours). The thickness of the bulk was approximately 4.4 mm.

The facet appeared at the edge of grown surface over crack. Figure 1 and 2 show the surfaces of the first and third runs, respectively. After the first run, the crack still lingers on the facet (arrow in Fig. 1). However, after the third run, the crack disappeared on the surface as shown in Fig. 2. The surface was investigated in detail by KOH etching. However crack propagation into the newly grown layer was not observed. This suggests that crack between two substrates was healed, and that the substrates became mono-crystalline. At off-axis orientations, the crack was disappeared partially. It was confirmed that the crack was healed suddenly under the faceting plane, while the healing was gradual under off-axis orientations. From the above, we believe that the crack will be completely healed with increasing thickness of the grown layer. This idea is being investigated for large scale bulk growth.

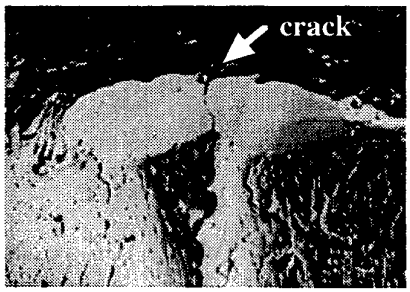


Fig.1. Facet of first grown surface

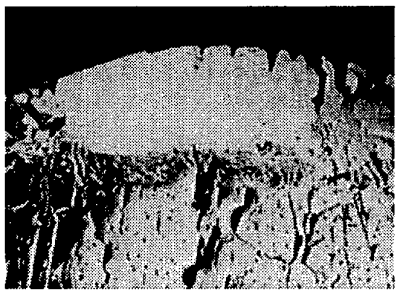


Fig.2. Facet of third grown surface

[1] S. Okada, T. Nishiguchi, T. Shimizu, M. Sasaki, S. Ohshima and S. Nishino, Abstracts of ICSCRM '99 (North Carolina), No. 465

Numerical Simulation of Process Conditions and Thermoelastic Stress Distribution During PVT Growth of SiC Bulk Crystals

M. Selder[a], L. Kadinski[a], F. Durst[a], T. Straubinger[b], P. Wellmann[b], D. Hofmann[b]

[a]Institute of Fluid Mechanics, University of Erlangen-Nürnberg,
Cauerstr. 4, D–91058 Erlangen, Germany
Phone: +49-9131-761244, Fax: +49-9131-761275, E-mail: selder@lstm.uni-erlangen.de

[b]Materials Science Department 6, University of Erlangen–Nürnberg,
Martensstr. 7, D–91058 Erlangen, Germany

To use SiC wafers as substrate material for electronic and optoelectronic devices in industrial scale, the production of high quality large diameter SiC single crystals at low cost has to be realized. At the moment, the standard technique to prepare SiC bulk single crystals is physical vapour transport (PVT) growth by the modified Lely method. The quality of the crystals is depending very sensitively on the thermal field inside the growth cell. Temperature inhomogeneities inside the crystal cause thermal stress. This is considered to be a main reason for a variety of crystal defects (e.g. micropipes, dislocations).

In this work, we will analyze the thermoelastic stress distribution in the growing SiC single crystal. The stress calculations are based on a global simulation of the SiC bulk crystal growth process. Analyzing the main heat and mass transfer processes, we determine the thermal field inside the growth cell and the temporal evolution of the growing crystal [1] and calculate the stress distribution at fixed points in time for the actual temperature field. We will present calculations of the thermoelastic stress distribution at different stages of the growth process. Comparisons of model predictions and experimental data will be given.

As an example, the calculated temperature isolines in a SiC crystal after some hours of growth are presented in Fig. 1a. The von Mises stress distribution resulting from this temperature field is shown in Fig. 1b indicating that the higher stress levels are at the periphery of the crystal. The experimentally observed stress patterns (bright areas indicate high stress levels) of an 1,4″-SiC-wafer determined by stress birefringency is presented in Fig. 1c showing a good qualitative agreement with theoretical predictions.

To get an estimate concerning the dislocation formation caused by thermoelastic stress, we evaluate the dislocation density according to Jordan et al. [2] and discuss the applicability of this model.

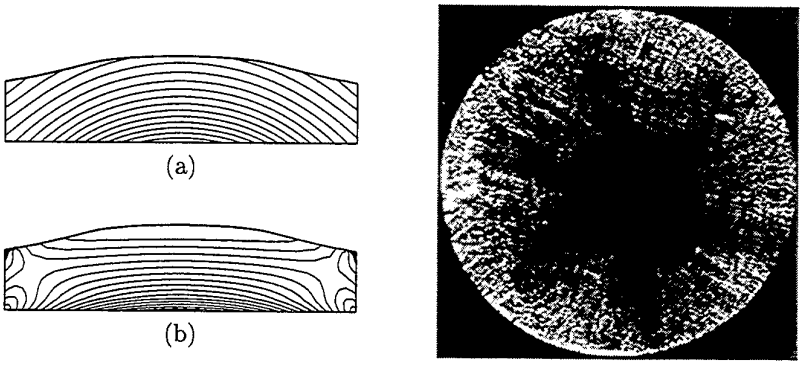


Figure 1: Calculated distribution of temperature (a) and stress (b) and experimentally observed stress patterns in an 1,4″-SiC-wafer (c). The calculated stress variation (b) and the bright contrast (c), respectively, indicate regions with higher stress levels at the periphery of the crystal.

[1] M. Selder, L. Kadinski, Y. Makarov, F. Durst, P. Wellmannn, T. Straubinger, D. Hofmann, S. Karpov, M. Ramm, *Journal of Crystal Growth* 211 (2000) 333–338.

[2] A. S. Jordan, R. Caruso, A. R. Von Neida, *The Bell System Technical Journal* 59:4 (1980), 593–637.

INVESTIGATION OF A PVT SIC-GROWTH SET-UP MODIFIED BY AN ADDITIONAL GAS FLOW

T.L. Straubinger, P.J. Wellmann and A.Winnacker

Department of Materials Science 6, University of Erlangen, Martens Str. 7, 91058 Erlangen, Germany.
Phone: +49-9131-85-27730; Fax: +49-9131-85-28495
Email: thomas.straubinger@ww.uni-erlangen.de

As the doping of PVT grown SiC crystals is often inhomogeneous because of changing surface temperatures during growth or source depletion it would be advantageous to supply dopant gases directly to the growing crystal (Figure 1). This would allow a better control of the concentration in front of the crystal surface.
Since an additional gas flow inside the growth cell could cause severe distortions of the vapor flow we have performed basic investigations. The influence of an inner Argon gas stream on the structural properties of the growing crystal was studied.
Through 2-dim heat transfer simulations we developed a geometry with the possibility of gas inlet and a thermal field between powder and seed which was comparable to that of the conventional PVT Process.
After we adjusted the gas flow so that it did not interrupt the thermal field we were able to grow crystals inside this setup which were comparable in size to those grown with normal PVT.
The structural properties of crystals grown with inner gas flow were different as compared to those grown without inner gas flow (parameters T, T-gradients and p were kept the same). (see Fig. 2)

i. No C-Inclusions were observed (Figure 2, dark part). Compare with the inclusions in the PVT grown seed (Figure 2, bright part).
ii. In the initial stage of growth a tendency for lateral pipe overgrowth was observed. One pipe is growing from the seed into the growing crystal while the others end at the seed-crystal interface.

The doping concentration in n-type material was rather high because nitrogen was added to the inner gas flow.

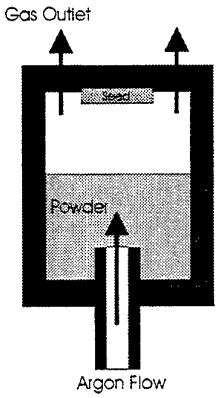


Figure 1: Crucible with tube for gas inlet and outlet

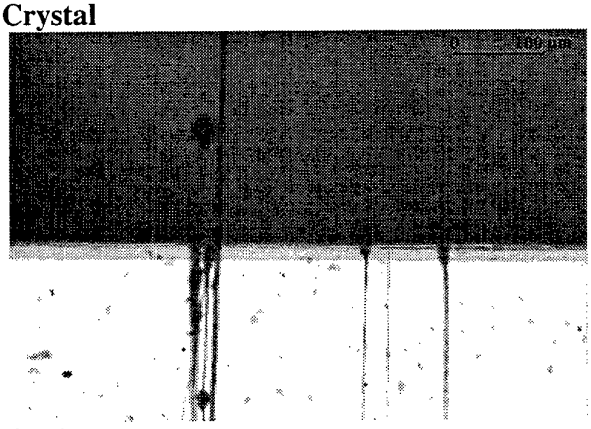


Figure 2: Interface seed-crystal: C-Inclusions and several MP in seed (brighter part); No Inclusions and only one MP in Crystal (darker part)

STUDY OF DOPANT (Al, B) INCORPORATION DURING PVT GROWTH OF p-TYPE SiC CRYSTALS

M. Bickermann, D. Hofmann, M. Rasp, T.L. Straubinger, R. Weingärtner, P.J. Wellmann, A. Winnacker

Department of Materials Science 6, University of Erlangen-Nürnberg,
Martensstr. 7, D-91058 Erlangen, Germany,
phone.: +49-(0)9131-85-27730, fax: +49-(0)9131-85-27472
e-mail: Matthias.Bickermann@ww.uni-erlangen.de

The availability of p-type highly conductive SiC bulk crystals with low defect densities is an important issue for the further development of SiC power electronics. Furthermore, defined p-doping at very low levels is a prerequisite for the preparation of semi-insulating, highly resistive SiC substrates for high frequency applications, where vanadium acts as deep donor for the compensation of residual acceptor levels. P-conduction is commonly established by Al or B doping. For the achievement of homogeneously doped p-type SiC Crystals in lateral and longitudinal directions a thorough understanding of the dopant incorporation both at low and high concentrations is necessary.

Difficulties in p-type doping arise on one side from the lack of an suited gas source, which, if constantly applied, will provide in principle homogeneously doped bulk crystals, as can be seen in n-type doping, where N_2 as a gas source is commonly used. On the other side, the amount of incorporated species and related electrical activity of p-dopants under PVT conditions is not clear. In this paper, p-type doping is performed by applying solid sources. Here several aspects are critical: First, the depletion of the dopant source has to be avoided. Second, segregation phenomena can provide local accumulation of dopants species resulting in inclusions or polycrystalline growth conditions. Third, as the temperature field at the growth interface changes with growth time, also the conditions of dopant incorporation can change. All of these aspects can lead to inhomogeneous doping up to the order of several magnitudes. Finally, temperature field and applied source strongly influence the overall doping level, which has also to be taken into account.

In our investigation several SiC bulk crystals were grown by the physical vapor transport (PVT) technique. The dopant was provided either by adding solid compounds as B_4C or Al_4C_3 to the undoped SiC source material or by doping the SiC powder during synthesis with varying amounts of B or Al, respectively. For reference purposes also some nominally undoped crystals were grown to take into account the residual impurities of the growth system. Wafers as well as longitudinal cuts were prepared from the crystals. Characterization was performed by doping level mapping via absorption measurements. Further investigation was performed by Hall measurements, GDMS and SIMS analysis. Also, a detailed study of the samples by optical microscopy was performed to analyze crystal quality and doping-induced defects like inclusions or grain boundaries.

We will present results on p-type SiC samples, doped with Al or B, with charge carrier concentration in the range from 10^{15} cm^{-3} to $5 \cdot 10^{18}$ cm^{-3} as measured by absorption and Hall effect. Several correlations in respect to growth parameters are revealed: The dopant incorporation of Al or B, respectively, is several times higher during crystallization on the silicon face with respect to the carbon face. At very high doping levels polycrystalline growth can occur on either face. For highly doped growth, the generation of voids and mesoscopic pipes and, in the case of B doping, inclusions of probably eutectic B-Si-C compounds, were observed. Doping inhomogeneities up to the order of one magnitude can arise from the variation of growth temperature and the structural evolution of the source during growth. Inhomogeneous doping is shown to be distinctive at low doping levels, especially for Al doped growth. For B doped growth, the range of dopant incorporation in dependence of growth conditions will be presented. Finally, implications of this study for PVT growth conditions with reduced dopant non-uniformities are discussed.

Characterization of 4H-SiC epilayers grown at a high deposition rate

H. Tsuchida*, T. Tsuji**, S. Ogino**, I. Kamata*, T. Jikimoto*, and K. Izumi*
*Central Research Institute of Electric Power Industry, 2-6-1 Nagasaka, Yokosuka, Kanagawa 240-0196 Japan, Tel: +81-468-56-2121, Fax: +81-468-56-3540
**Fuji Electric Corporate Research and Development, Ltd.

Improvement in growth rate, maintaining a high quality, is one of the current technical issues in SiC epitaxy. In this paper, we report on the results of optical and electrical characterization of 4H-SiC epilayers grown at a high deposition rate up to 16μm/h.

Epitaxial 4H-SiC layers were grown in a vertical radiant-heating reactor [1]. In this reactor, a susceptor is heated by radiation from a hot-wall. Epitaxial growth is performed under a reduced pressure (~50 torr) with upward SiH_4+C_3H_8+H_2 flow. The growth temperature is 1550-1600℃ (at the susceptor top), and a typical growth rate is 12-16 μm/h.

Photoluminescence (PL) and deep level transient spectroscopy (DLTS) were performed to check the quality of epilayers. Figure 1 shows PL spectra taken from a sample doped to low 10^{15} cm^{-3}. The spectrum shows strong free excitons and nitrogen bound excitons indicating a good purity. The purity of the epilayer is also shown by the weakness of the aluminum-, boron-, and titanium-related lines. Since defect-related L_1-line is clearly seen in the PL spectrum, we checked an intrinsic defect (Z_1 center) by DLTS measurement. Our DLTS measurement revealed that the Z_1 trap concentration of epilayers is generally $3x10^{13}$ cm^{-3}.

Schottky barrier diodes (SBD) were processed on epilayers. We employed nickel for Schottky contacts. Edge termination was achieved by a guard ring structure processed thorough boron implantation. A 10 μm-thick epilayer doped to high 10^{15} cm^{-3} was used in the first lot, and a 27 μm-thick epilayer doped to low 10^{15} cm^{-3} was used in the second lot. The process parameters were rather changed in the second lot. The best breakdown voltages for 1mmø SBD in the first and second lots are 1.2 kV and 2.3 kV, respectively. Figure 2 shows a distribution of leakage current at -600V for 1mmø SBD. Some of 1mmø SBD in the second lot could block -600V with a small leakage current density less than 1 μA/cm^2, although the average leakage current density was rather high probably due to both process and defect issues. The percentages of tolerable ones, that could block -600V within a critical leakage current less than 1mA, were over 85% for 1mmø SBD and 20% for 4mmø SBD.

We collated simply the I-V characteristics of SBD with morphological defects on epilayers. Large defect free areas over 10 mm^2, where no observable defects were existing except wavy-pits, were confirmed in microscope observation. This can be associated with the high yield of 1mm ø SBD and the production of 4mmø SBD within the critical leakage current. On the other hand, we recognized morphological defects that originated from micropipes in substrates and inclusions during epitaxial growth. To understand the poor yield of 4 mmø SBD, the total concentration of 10^1 cm^{-2} range for both types of defects is reasonable.

[1] H. Tsuchida et al., *in Proc. Int. Conf. Silicon Carbide and Related Materials, NC, Oct. 10-15*, 1999.

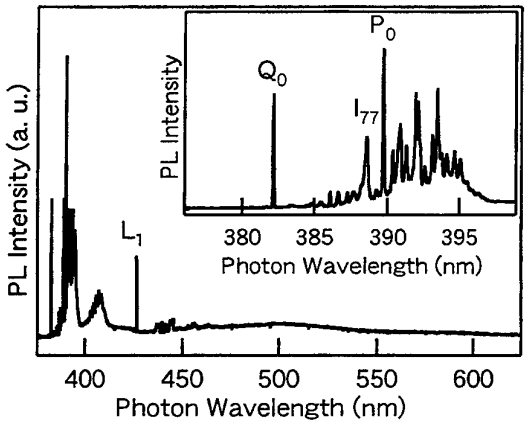


Fig. 1. PL spectrum from a epilayer.

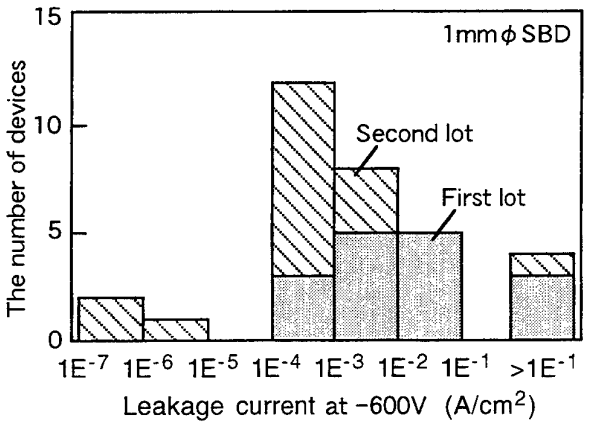


Fig. 2. Leakage current at -600V for 1mmø SBDs.

INFLUENCE OF THE GROWTH CONDITIONS ON THE LAYER PARAMETERS OF 4H-SiC EPILAYERS GROWN IN A HOT-WALL REACTOR

G.Wagner[1], B. Thomas[2], J. Dolle[1], K. Irmscher[1],

[1] Institut für Kristallzüchtung, Max-Born-Straße 2, D-12489 Berlin
[2] SiCED Electronics Development GmbH & Co. KG, Paul-Gossen-Str. 100, 91052 Erlangen

Phone: +49 30 6392 2846 Fax: +49 30 63923003 e-mail: wagner@ikz-berlin.de

This paper focuses on growth and characterisation of epitaxial layers for power device application. The hot-wall CVD process provides substantial advantages in terms of obtaining low doping and good morphology for thick layers [1].

The relation between the growth regime like total flow, system pressure, C/Si ratio and growth temperature and the characteristic of nominally undoped epilayers, such as surface morphology, thickness uniformity and background doping concentration have been investigated.

Thick SiC layers with growth rates up to 10 µm/h have been grown in a horizontal low pressure hot-wall CVD reactor on commercial 35 mm and 50 mm SiC wafers using the silane-propane-hydrogen system. The temperature range was between 1500 to 1600 °C. Layers up to 40 µm in thickness with a variation of about ± 4 % have been obtained.

Structural properties of the layers in comparison to the substrates have been characterised by X-ray diffraction. Rocking curve maps taken on substrates and epilayers show a clear reduction of the FWHM from about 40 to 10 arc sec .

The influence of the C/Si ratio, growth temperature and reactor pressure on the background net doping concentration was studied using C-V measurements. Epilayers with residual n-type doping levels in the low 10^{14} cm^{-3} ranges have been obtained on Si faces. SIMS measurements have shown that the impurity concentration of acceptors like B and Al is below 2×10^{14} cm^{-3}.

[1] O. Kordina, C. Hallin, A. Henry, J.P. Bergmann, I. Ivanov, E. Ellison, T. Son and E. Janzen
phys. stat. sol. (b) 202 (1997) 321

Influence of silicon gas-to-particle conversion on SiC CVD in a vertical cold-wall rotating-disc reactor

A.N.Vorob'ev [1], M.V.Bogdanov [1], A.E.Komissarov [1], S.Yu.Karpov [1], O.V.Bord [1], A.A.Lovtsus [1], Yu.N.Makarov [2]

[1] Soft-Impact Ltd, P.O.Box 33, 194156 St.Petersburg, Russia; van@unitel.spb.ru
[2] University of Erlangen-Nürnberg, Cauerstrasse 4, D-91058 Erlangen, Germany

Chemical vapor deposition (CVD) is widely used for growth of SiC epitaxial layers. In spite of considerable progress in this technique achieved in recent years, the complex species transport and growth mechanisms are still far from complete understanding. This makes difficult to find optimal CVD conditions providing high growth rate and required quality of the grown epilayers.

This paper reports on the numerical study of SiC growth in a cold-wall rotating-disk vertical CVD reactor using the model accounting for Si clustering in the vapor [1]. The model predicts reasonably well dependence of the growth rate on SiH_4 and C_3H_8 flow rates [1]. Growth rate and C/Si ratio at the growth surface have been computed as a function of SiH_4 and C_3H_8 inlet flow rates varied in a wide range (Fig.1). The predicted non-monotonic behavior of the growth rate with SiH_4 flow rate is related to nucleation of Si clusters in the vapor. The clusters can not reach the growth surface due to thermophoresis and, therefore, are transported away from the susceptor by the gas flow instead of contribution to the crystal growth. The effect of Si clustering makes impossible increasing of SiC growth rate above a definite value by only SiH_4 and C_3H_8 flow rate variation (see Fig.1). This prediction is not yet supported by experiments and, therefore, requires a special verification.

Many properties of the grown crystal are known to depend on C/Si ratio in the vapor established at the growth surface during CVD. The C/Si ratio is found to deviate significantly on that at the reactor inlet and is strongly affected by Si gas-phase nucleation. A special analysis of secondary phase (graphite and condensed silicon) formation has been carried out resulting in a phase diagram shown in Fig.2. The computations predict considerable changes in the width and location of SiC growth window due to Si gas-to-particle conversion. We have found a close correlation between the zones in the phase diagram and surface morphology observed experimentally on CVD grown SiC epilayers [2].

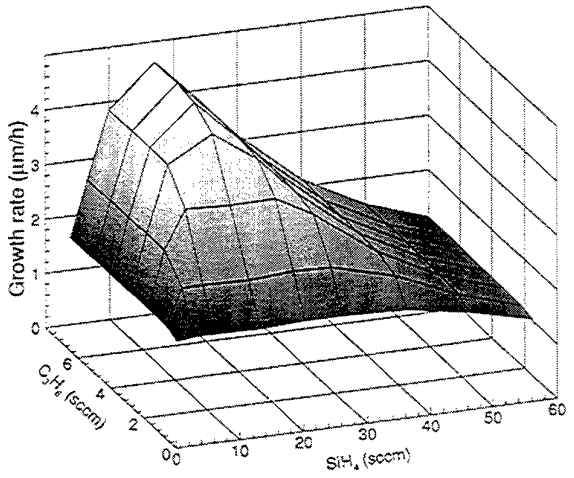


Fig.1. Growth rate vs C_3H_8 and SiH_4 flow rates at 1450°C.

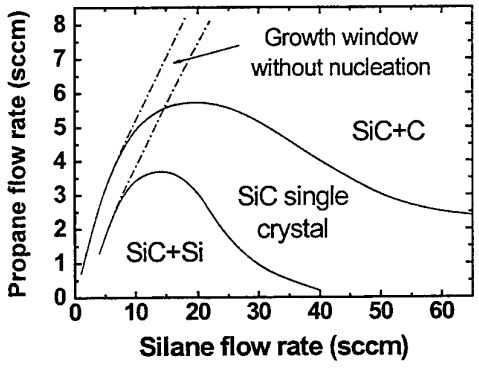


Fig.2. Secondary phase diagram.

[1] A.N.Vorob'ev, Yu.E.Egorov, Yu.N.Makarov, et al, Mat.Sci.Engineer.B 61/62 (1999) 172.
[2] R.Rupp et al, J.Cryst.Growth 146 (1995) 37.

Hexagonal AlN on cubic Si

J. Kräußlich[1], G. Heß[1], V. Lebedev[2], J. Jinschek[2], W. Richter[2]

Friedrich-Schiller-Universität Jena
[1] Institut für Optik und Quantenelektronik
[2] Institut für Festkörperphysik
Max-Wien-Platz 1, 07743 Jena, Germany
Tel.: +49 (0)3641 947254 E-Mail: kraeusslich@ioq.physik.uni-jena.de

In spite of the crystallographic difference, AlN thin films, grown by MBE technique on Si(001) wafer, exhibit an distinctly epitaxial growth.
X-ray diffraction and TEM investigations reveal, that the ***c***-axis of the hexagonal AlN lattice aligns with the surface normal of the wafer (i.e. parallel to the [001]-direction of the cubic Si). The three basal ***a***-axis of the hexagonal AlN align nearly parallel with the four <110>-directions of the cubic Si lattice, i.e they form an angle of 15° with the [100] and [010] axis of Si, respectively

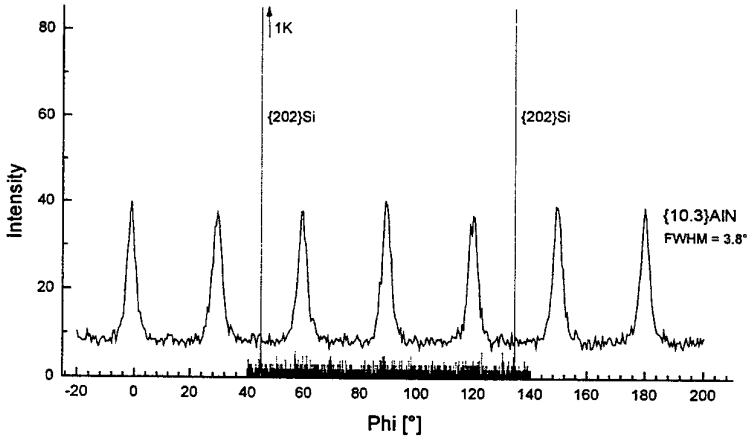


Fig. 1: Phi-scan x-ray diffraction pattern recorded with the inclined 10.3-reflection of AlN obtained by rotation around the surface normal oft the Si(001) wafer

The 12-fold rotation symmetry of inclined AlN reflections shown in fig. 1 demonstrates the growth of 30°-rotation twins of the hexagonal AlN on the 4-fold Si(001) surface. In the presented case the lateral arrangement of the 30°-rotation twins is nearly equal distributed with respect to the lateral a-axis of the Si substrate. However, the formation of rotation twins could be suppressed by using of an off-axis Si(001) substrate.
The coherent heteroepitactical nucleation of AlN on Si(001) will be explained by using an atomic surface steps model.

This work was supported by the Deutsche Forschungsgemeinschaft.

Pulsed low-energy ion-assisted reactive DC magnetron sputter deposition of high quality epitaxial AlN/6H-SiC

S. Tungasmita, P. O. Å. Persson, L. Hultman and J. Birch
Thin Film Physics Division, Department of Physics, Linköping University,
SE-581 83, Linköping, Sweden.
(E-mail: jeed@ifm.liu.se, Telephone: +46-13-288978, Fax: +46-13-288918)

Abstract

The wide-bandgap (6.2 eV at RT) semiconductor aluminum nitride (AlN) has become an important material for many electronic device technologies. We have recently demonstrated that the use of low-energy (17-27 eV) ion irradiation, during the growth of AlN by reactive UHV magnetron sputter deposition, greatly enhances the quality of the film.[1] However, since the ions are attracted towards the substrate by a negative DC substrate bias, the insulating properties of high quality AlN causes a positive charge build-up on the surface, effectively screening the bias potential and thus inhibiting the ion-assisted growth as the film reaches a thickness of ~100 nm. In this work, we show that *pulsed* low-energy ion-assisted DC magnetron sputter deposition under UHV conditions overcomes this limitation. AlN films have been grown on 6H-SiC substrates by using DC magnetron sputtering while the SiC substrates were biased with a pulsed voltage (< ±20 V), with a square waveform, to neutralize the charging effect. Pulse frequencies in the range 1 - 35 kHz have been used. High-resolution transmission electron microscopy, show that epitaxial AlN thin films with large domain width can be obtained, up to thicknesses of >400 nm. This is demonstrated in the cross-sectional TEM micrographs of figure 1. Furthermore, the AlN growth rate also increased by a factor of ~4 using pulsed substrate bias, indicating that the reactivity of nitrogen is increased at the growing AlN film surface.

Low-temperature (4K) cathodoluminescence (CL) measurements show near-band edge exciton emission at 206 nm (6.02 eV) and 212 nm (5.84 eV) as shown in figure 2, which an indicator of high quality material.

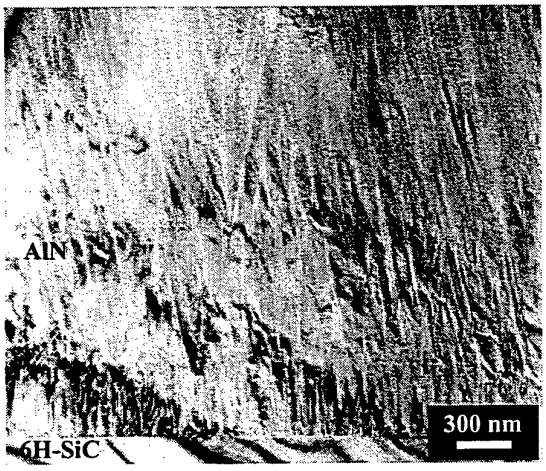


Figure 1 Cross-sectional TEM micrographs showing the microstructural evolution of AlN film grown with ±20 V pulsed-substrate bias

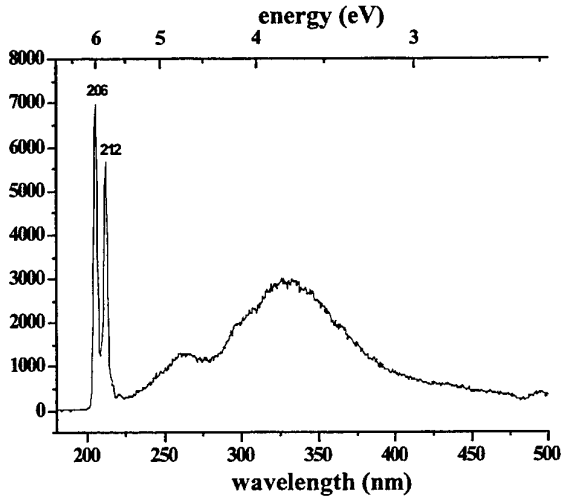


Figure 2 CL spectrum at 4K from AlN thin film grown with ±20 V pulsed-substrate bias

[1] S. Tungasmita, J. Birch, P. O. Å. Persson, K. Järrendahl and L. Hultman, Appl. Phys. Lett. **76**, 2 (2000), p.170-172

Investigation of the structure of 2H-AlN films on Si(001) substrates

J. Jinschek, U. Kaiser, V. Lebedev, J. Kräußlich, W. Richter

Institut für Festkörperphysik, Friedrich-Schiller-Universität Jena, Max-Wien-Platz 1, D-07743 Jena, Germany
Joerg.Jinschek@uni-jena.de Phone:++49-3641-947443 Fax:++49-3641-947442

Aluminium nitride (AlN) is a wide band-gap, high temperature, radiant resistant semiconductor material and exists in the thermodynamically stable wurtzite phase (basal plane lattice parameter, a = 0.3112nm [1]) but also in the zincblende polytype [2]. Wurtzite AlN deposited on commonly used silicon (Si) (001) substrates (lattice parameter, a = 0.54307nm) is a good solution as a template substrate for III-nitride electronic and optoelectronic devices. The successful AlN film epitaxy on Si(001) would allow to integrate the group III-nitride technology into the mature silicon technology.

The growth of wurtzite AlN thin films on Si (001) is a challenging task for heteroepitaxy due to the mismatch in the lattice parameters and in the crystallography of the (0001) AlN plane (six-fold symmetry) with the (001) Si plane (four-fold symmetry). AlN films were grown in a home-made plasma-assisted molecular-beam epitaxy (PAMBE) system equipped with a radio-frequency plasma source for activated nitrogen supply and using thermally evaporated aluminium. Thin cross-sectional foils for transmission electron microscopy (TEM) were prepared using standard techniques. A JEOL JEM 3010 microscope with a LaB_6 filament and an accelerating voltage of 300kV was used for TEM observation. The high-resolution (HR) image simulation has been carried out by the commercial software program MacTempas.

The results of the examination of 2H-AlN films which were grown on Si(001) substrate with different off-axis angles will be discussed.

Conventional TEM and X-ray diffraction (XRD) studies of the AlN layer, which was grown on a nominal Si(001) substrate, reveal a two-domain film structure (AlN^1 and AlN^2) with a 30° rotation between neighboring domain a-axes orientations and an epitaxial orientation relationship of [0001]AlN || [001]Si and [11-20]AlN^1 || [01-10]AlN^2 || [1-10]Si [3].

The same studies show in a AlN film, which was grown on an off-axis Si(001) substrate (~4.5° tilted towards [110]Si), a nearly single-domain structure with the main domain orientation of [11-20]AlN || [1-10]Si. The c-axis orientation ([0001]) of the AlN film is parallel to the substrate surface normal orientation (i.e. angle of 4.5° to [001]Si).

Using these results obtained in combination with high-resolution transmission electron microscopy (HRTEM) at the [1-10] zone axis of the Si substrate coupled with image simulation, the interface structure of the AlN films and the Si (001) substrate has been revealed.

This work was supported by the DFG (contract No. RI 650/5-1) and by HSP III (contract No. H 1-916/57/1).

[1] G.A. Jeffrey, G.S. Parry, J.Chem.Phys. 23 (1953) 406
[2] S. Strite, H. Morkoc, J.Vac.Sci.Technol. B10 (1992) 1237
[3] V. Lebedev, J. Jinschek, U. Kaiser, B. Schröter, W. Richter, Appl.Phys.Let. 76 (2000) 2029

Structural and Optical Properties of SiC Films Deposited on Si by DC Magnetron Sputtering

Y. M. Lei *, Y. H. Yu *,**, B. Sundaravel **, E. Z. Luo **, S. Lin **, C. X. Ren *, W. Y. Cheung **, S. P. Wong **, J. B. Xu **, S.C. Zou* and I. H. Wilson **.

*Ion Beam Laboratory, Shanghai Institute of Metallurgy, Chinese Academy of Sciences, Shanghai, China.

**Chinese University of Hong Kong, Hong Kong, China.

Tel: 86-21-62511070-8303 Fax: 86-21-62513510 E-mail: yhyu@itsvr.sim.ac.cn

Silicon Carbide has attracted intensive research efforts since its excellent physical properties for application in high temperature, high power, high frequency, high erosive and high irradiative conditions. In this paper, we studied the SiC films deposited on silicon and SOI substrates by reactive DC magnetron sputtering. A four-inches silicon target was sputtered in a Ar/CH_4 mixed atmosphere to deposit films onto a substrate of two inches heated to temperatures up to 900°C. AES studies show that under appropriate conditions, the prepared SiC films are stoichiometric with uniform compositional distribution throughout the film thickness. Magnified AES peaks of C KVV and Si LVV also show similar peak shapes as those of SiC reported in literature, indicating the formation of Si-C bond. The results of Non-Rutherford Backscattering (NBS) were quite close to those of AES studies, agreeing on that the films were uniform in composition and that stoichiometric SiC films were successfully prepared.

The crystalline structure of the deposited films was characterized using XRD, GA-XRD, cross sectional TEM, and planar TEM. XRD patterns show only one SiC peak near 35.6°, corresponding to 3C-SiC(111) crystalline plane diffraction. Glancing angle XRD revealed more 3C-SiC peaks in the diffraction patterns. In these patterns one can find 3C-SiC (111) (220) (311) peaks, indicating the crystalline phase in the films were composed of 3C-SiC, not any other polytypes of SiC. XRD studies also lead to the conclusion that higher temperature (900°C vs. 850°C) could result in better crystalline qualities (larger crystallites).

Infrared reflectance spectra in the range of $400cm^{-1}$~$4000cm^{-1}$ were employed to investigate the crystalline structure, structural dimension, structural defects of the SiC/Si and SiCOI structures, with the help of effective medium approaches and routine transfer matrix method. The IRRS of SiC were featured by a restsrahlen peak around $800cm^{-1}$~$1000cm^{-1}$. The experimental spectra can be best fitted by adjusting the structural parameters and the volume fraction of crystalline phases. The results show that IRRS is a suitable method for detection of the quality of the SiC/Si and SiCOI materials systems.

TEM investigation of Si implanted natural diamond

B. Pécz and Á. Barna
Research Institute for Technical Physics and Materials Science, H-1525, Budapest, P.O.B. 49, Hungary. Phone: 36-1-392 2587, fax: 36-1- 36-1-275-4996.
V. Heera, F. Fontaine and W. Skorupa
Forschungszentrum Rossendorf, P.O.B. 510119, D-01314 Dresden, Germany

Both, diamond and silicon carbide (SiC) are wide band gap semiconductors with excellent electronic properties. The ion beam synthesis of layered, diamond/SiC structures is a challenging task. For that purpose natural IIa diamond was implanted by Si at 150 keV to $3*10^{17}$ ions/cm^2 at a temperature of 900°C. The structure of the implanted diamond region was investigated by transmission electron microscopy (TEM).

Cross sectional samples for TEM analysis have been prepared by cutting the diamond pieces and embedding them in face to face position into a special Ti grid with a diameter of 3 mm. The embedded samples have been ground by diamond paste to the thickness of 100 μm. Then the samples were placed into an IV3/H/L ion miller for further thinning and were bombarded by Ar^+ ions at 10 keV until the perforation of the TEM sample. Grazing angle of incidence was applied during thinning to get large transparent region around the perforation. The perforated specimen was bombarded further at 200 eV using a special low energy ion gun to minimise the ion beam damage of the thinning. Amorphization, what is generally observed at the edges of the TEM samples, and graphitization of diamond, what is a characteristic artefact of ion beam thinned diamond specimens, were minimised in this way at low energy bombardment. The cross sectional TEM specimens were investigated in a Philips CM 20 electron microscope operating at 200 kV, while high resolution work was carried out in a JEOL 4000 EX microscope operating at 400 kV.

TEM analysis and selected area diffraction patterns (Fig.1.) revealed the formation of cubic SiC domains in a weakly damaged diamond matrix. All of the 3C-SiC domains are in epitaxial configuration to diamond. SiC domains are formed in stripes inside the diamond, instead of random distribution.

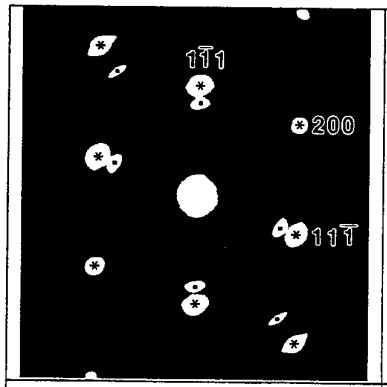


Fig. 1.



Fig. 2.

One of the 3C-SiC domains is shown inside the diamond matrix in Fig.2. Diamond regions are marked by letter D, while the misfit dislocations formed between the SiC domain and the diamond matrix are marked by arrows. The two lattices are matched according the criteria of: 4*(111)SiC=5*(111)diamond=1.0 nm and results in periodic array of misfit dislocations.

Growth of δ-doped SiC epitaxial layers

S. Karlsson, C. Adås, A. Konstantinov and M. Linnarsson
ACREO AB, Electrum 236, Isafjordsgatan 22, S-16440 Kista, Sweden
Phone: +46 8 6327790 Fax: +46 8 750 5430 Email: stefan.karlsson@acreo.se

Silicon Carbide device research is constantly making progress towards higher voltages, temperatures and frequencies. As a result of this development the degree in complexity of SiC device structures is increasing, which puts further demands on dopant and thickness control of both thick and very thin layers.

δ-doping is a technique widely used in the epitaxial growth of III-V semiconductors in order to spatially confine dopants in a narrow region, ideally to one atomic layer. By using structures with δ-doping, the performance of advanced electronic and optoelectronic devices have been improved [1].

One possible application for δ-doping in SiC devices is FETs where a δ-layer potentially could be used as a barrier under the channel to suppress short channel effects, as was earlier shown for GaAs [2-3]. The δ-doping technique can also be used to confine avalanche multiplication in IMPATT devices.

In this paper the first attempts in growing n- and p-type δ-doped SiC epitaxial layers by vapour phase epitaxy is presented. The layers were grown using a standard single wafer horizontal hot-wall reactor from Epigress AB. Two basically different methods of achieving δ-doping have been tried. One is the straightforward method of a low growth rate and a limited time of dopant introduction (A). The second method is a version of a common MOCVD procedure including pre-δ-doping purge, δ-doping and post- δ-doping purge (B). The grown layers were characterised by SIMS and CV measurements.

Fig. 1 shows a CV profile of the top part of a 0.73μm thick nitrogen doped 4H SiC layer. The sample was grown with a growth rate of 1.6μm/h for 27.5 minutes of which the nitrogen flow was increased a factor of 6.6 during 1 minute. This moderate increase in dopant flow resulted in a peak with FWHM of 26 nm and a maximum concentration of 1.3×10^{18} cm^{-3}. δ-doped p-type layers have also been grown using aluminium doping.

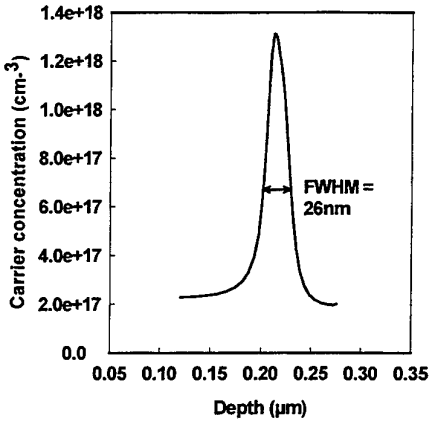


Figure 1. C-V measurement of a nitrogen doped δ-layer utilising method A.

[1] G. Li, C.Jagadish, Solid-State Electronics 41 (1997) 1207
[2] T.A.Winslow, R.J.Trew, P.Gilmore, C.T.Kelley, Cornell Conference on Advanced Concepts in High Speed Semiconductor Devices and Circuits, IEEE Proceedings (1991) 188
[3] A.Asenov, S.Saini, IEEE Transactions On Electron Devices (1999) 1718

Epitaxial growth and properties of SiC layers grown on α-SiC(0001) by solid-source MBE: A photoluminescence study

A. Fissel* and W.Richter

Friedrich-Schiller-Universität Jena, Institut für Festkörperphysik, Max-Wien-Platz 1, D-07743 Jena, Germany

A report will be given about growth experiments of SiC on hexagonal (or α)-SiC(0001). The experiments were performed by means of solid-source MBE at T_{SUB} between 1150-1300 °C. The epitaxial layers of about 1 μm thickness were characterized by low temperature photoluminescence spectroscopy at 4.2 K (liquid helium) (LTPL). The excitation was done with a 2 mW He-Cd laser operating at a wavelength of 325 nm. Homoepitaxial SiC layers of high quality have been grown via step-flow growth mode on 4H- and 6H-SiC(0001) without significant step-bunching. As revealed by photoluminescence spectroscopy, the layer properties were found to be different from those usually obtained for epitaxial layers grown by CVD. The LTPL-spectra show strong luminescence lines related to the D_1–"defect" center regularly found only after implantation and subsequent annealing. The intensity of the D_1 center luminescence was found to be increased with an improvement of layer quality and for samples intentionally doped with boron. No influence regarding the intensity of the D_1-centre luminescence was found by changing the chemical potential from Si-rich to more C-rich conditions. Spectra of B-doped samples grown under more C-rich conditions exhibit additional lines related to a four particle (bound exciton) complex associated with the neutral shallow boron acceptor.

3C-SiC layers were grown pseudomorphic on on-axis α-SiC substrates by an alternating supply of carbon at 1150 °C, where the size of double-position boundaries was in the range of 100 μm. Also spectra of these layers showed lines related to the D_1–center. However, the intensity was much lower compared to 4H- or 6H-SiC epilayers, which could be due to a lower perfection or the lower growth temperature, however, could be also result from the intrinsic stress due to the pseudomorphic growth. This is supported by a lower intensity observed for layers exhibiting a read-shift of the D_1-center line of about 4 meV.

Furthermore, no other peaks related to any kind of impurities were found in the LTPL spectra indicating a high purity of the grown layers.

The authors like to acknowledge the support of this work by the Sonderforschungsbereich of the Deutsche Forschungsgemeinschaft (SFB 196, project A03).

* *Corresponding author:* E-mail: p5anfi@rz.uni-jena.de

Modeling analysis of gas phase nucleation during SiC CVD in the Planetary Reactor®

Yu. N. Makarov[1], A. N. Vorob'ev[2], A. I. Zhmakin[3], M. Dauelsberg[4], F. Wischmeyer[5], M. Heuken[4] and H. Jürgensen[4]

[1]Fluid Mechanics Institute, University of Erlangen-Nürnberg, Cauerstrasse 4, D-91058 Erlangen, Germany
[2]Institute for Fine Mechanics and Optics, Sablinskaya 14, 197101 St.Petersburg, Russia
[3]A.F.Ioffe Physical-Technical Institute, St.Petersburg 194021, Russia
[4]AIXTRON AG, Kackertstr. 15-17, D-52072, Aachen, Germany
[5] EPIGRESS AB, Ideon Science & Technology Park, SE-22370 Lund, SWEDEN

Significant progress in the understanding and realization of the SiC chemical vapor deposition (CVD) has been made in a few last years. For economic production of SiC-based devices it is necessary to obtain reasonably high growth rate of epitaxial layers, to achieve good surface morphology and to provide high uniformity and controlability of the layer thickness and doping. It has been found that the quality of the grown epilayers depends significantly on the Si/C ratio in the gas mixture supplied onto the growing surface. It has been found that formation of Si clusters in the gas phase could occur during CVD of SiC due to the supersaturation of Si atomic vapor formed by decomposition of SiH_4. The cluster formation can result in the loss of Si and change of Si/C ratio.

In the present paper numerical computations of flow dynamics, heat and species mass transfer are conducted for the AIXTRON Planetary Reactor®. The model of the SiC CVD process as proposed in [1] is used in the present study. An analysis of the chemical processes which occur during the CVD of SiC is performed with the goal to understand the mechanism of gas phase nucleation of Si and to optimize reactor and process design in order to avoid the negative impact of cluster formation, to control the Si/C ratio and to improve layer thickness uniformity. The effect of process parameters like pressure, flow rate of silane and carrier gas on the onset of gas phase nucleation and layer thickness uniformity is studied. The advantages of the Hot Wall concept for CVD of SiC in this respect are discussed. In Figure 1 the decomposition of silane in the Planetary Reactor® is shown for typical process conditions.

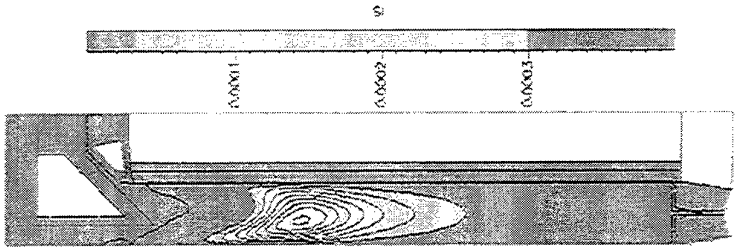


Fig. 1. Computed distribution of Si(g) mass fractions in the process chamber, as resulting from the decomposition of SiH_4

References

[1] A.N.Vorob'ev, Yu.E.Egorov, Yu.N.Makarov, A.I.Zhmakin, A.O.Galyukov, R.Rupp, Materials Science and Engineering, B61-62 (1999), 172-175.

Aluminium-Silicon as a melt for the low temperature growth of SiC crystals

D. Chaussende, C. Jacquier, G. Ferro, J.C. Viala, F. Cauwet, Y. Monteil and J. Bouix

Laboratoire des Multimatériaux et Interfaces, Université Claude Bernard Lyon 1
43 Bd du 11 Novembre 1918, 69622 Villeurbanne (France)
Tel : +33 4 72 43 13 92; Fax : +33 4 72 44 06 18

It is many decades since Liquid phase epitaxy (LPE) has been tentatively studied as an alternative for growing at a fast rate low cost SiC layers. Recently, it has proven to be the only technique which can "heal" the macro-defects of the commercially available hexagonal substrates [1]. However, LPE is difficult to operate because of the elevated temperatures required (higher than 1600°C) and the high reactivity and vapour pressure of silicon at these temperatures. The feasibility of SiC growth by LPE at low temperature has already been demonstrated in Al-Si based liquids to which Ga or Sn were added [2]. Growth rates of 0.1 to 1 µm/h were reported. However, such a procedure requires to master the quaternary systems Al-Si-Ga-C and Al-Si-Sn-C which are far to be well known. We report here the low temperature growth of SiC crystals in the simpler Al-Si-C ternary system for which detailed data on phase relations and phase equilibria are available [3, 4].

According to the Al-Si-C ternary phase diagram, two solid carbides can form at temperatures lower than 1400°C : SiC and Al_4C_3. This diagram also shows that silicon rich alloys are needed to avoid the formation of aluminium carbide. As a preliminary study, we carried out isothermal experiments to determine the conditions under which SiC could grow. The Al-Si-C samples were prepared by cold-pressing Al, Si and C powders. Carbon was added in small quantity so that the initial Si content of the Al-Si alloy was not drastically changed by the formation of SiC. The temperature and the Si content were varied from 730 to 1200°C and from 10 to 40 at%, respectively. The experiment time was set to 48 hours to ensure an important conversion of carbon into carbides.

It has been found that SiC is the only carbide to form in a wide range of experimental conditions. However, the morphology and constitution of this phase largely depend on the temperature and Si content. In some cases, aggregates of SiC microcrystallites (1-2 µm in diameter) are formed (fig.1). More interestingly, in other cases well faceted SiC crystals grow spontaneously in the Al-Si solution (fig. 2). By X-ray Diffraction and micro-Raman spectroscopy, the cubic polytype has been identified as the only SiC phase forming. Under optimal conditions, 3C-SiC crystals up to 100 µm in diameter have been obtained. A model explaining the spontaneous growth of these SiC crystals from Al-Si solutions will be presented taking into account local deviation from equilibrium.



Figure 1



Figure 2

[1] R. Yakimova, M. Syväjärvi, E. Janzén, Materials Science Forum **264-268** (1998) 159.
[2] S. Rendakova, V. Ivantsov, V. Dmitriev, Materials Science Forum **264-268** (1998) 163.
[3] J.C. Viala, P. Fortier and J. Bouix, J. Mater. Sci. **25** (1990) 1842.
[4] LL. Oden and R.A. McCune, Metal. Trans. **18A** (1987) 2005.

Corresponding author : chaussen@univ-lyon1.fr

Micropipe and macrodefect healing in SiC crystals during liquid phase processing

B.M. Epelbaum, D. Hofmann, U. Hecht, A. Winnacker

Department of Material Science 6, University of Erlangen-Nurnberg, Martensstr. 7, D-91058 Erlangen, Germany
Fax: +49(0)9131-8528495, e-mail: boris.epelbaum@ww.uni-erlangen.de

Micropipes (MP) in SiC crystals grown by physical vapor transport (PVT) limit their application as substrate in high-power electronics. Therefore MP elimination is considered as an important issue in the further development of SiC device technology. It was demonstrated, see Refs. [1-2] and references within, that MP present in the PVT substrate can be closed ('healed') during subsequent LPE growth. However published information on MP healing is very limited and even contradictory (for instance in the very recent paper of the authors of [1] an example of MP propagating from the substrate into the epitaxial layer without closing is given as a typical one [3]). Filamentary voids present in PVT substrate can be of different configuration and dislocation content: (1) MP, nearly cylindrical (often faceted) voids that have diameters < 10 μm , are nearly parallel to the c-axis and associated with a hollow core dislocation structure; (2) macrodefects, larger voids up to 50 μm in size with irregular cross-section; (3) narrow elongated crack-like structures usually associated with low angle boundaries.

In the present study we apply different liquid phase growth techniques, namely vertical dipping and sessile drop methods to evaluate the development of these hollow defects during liquid phase treatment. Experiments were performed on (0001) 6H wafers grown in our laboratory. High pressure of argon (100-130 bar) was used in order to suppress silicon melt evaporation [2]. The important feature of our approach is the possibility to vary strongly supersaturation conditions (starting from a 'negative' supersaturation, i.e. SiC substrate dissolution in silicon melt) and treatment time (1-6 hours). LPE processing at a low supersaturations made possible to evaluate the early stage of MP closing. Long-time experiments were targeted to examine stability of MP transformation. Treated samples were investigated using optical microscopy, AFM and SEM.

Large hollow defects of second and third type are found to be unstable in silicon melt: they transform into groups of smaller voids already at supersaturations close to zero, when growth inside the cavities goes due to Gibbs- Thomson effect. These defect structures were closed completely during long-term epitaxial layer growth. Elimination of MP requires a stronger supersaturation, which can be produced by significant temperature difference between epitaxial surface and carbon source. During LPE growth MP are observed to decompose into individually acting non-hollow core dislocations. After decomposition the activity of growth center based on MP is reduced. As a result a new growth center may dominate the surface and make healed MP completely invisible.

In the report experimental facts of MP healing by dissociation into non hollow core dislocation structures will be presented, corresponding closing mechanisms will be discussed in detail.

[1] R. Yakimova, M Tuominen, A.S. Backin, J.O. Fornell, A Vehanen and E. Janzen, Proc. ICSCRM (1995), Inst. Phys. Conf. Ser. 142 (1996) 101
[2] D. Hofmann, M. Müller, A. Materials Science &Engineering B61-62 (1999) 29
[3] M. Syväjärvi, R. Yakimova, E. Janzen, J. of Crystal Growth 208 (2000) 409

The microstructure and surface morphology of thin 3C-SiC films grown on (100) Si substrates using an APCVD-based carbonization process

C.-H. Wu, J. Chung, M. H. Hong, *C. A. Zorman, and *M. Mehregany
Department of Materials Science and Engineering
**Department of Electrical Engineering and Computer Science*
Case Western Reserve University, Cleveland, Ohio 44106, U. S. A.
Tel: (216) 368-3051, Fax: (216) 368-2668, e-mail: cxw36@po.cwru.edu

Heteroepitaxial growth of 3C-SiC films on (100) Si substrates often depends on the initial conversion of the Si surface to 3C-SiC prior to single crystal film growth. The conversion process, commonly called carbonization, is usually performed at high temperature (~1300°C) in a hydrocarbon ambient and produces a crystalline 3C-SiC template on which 3C-SiC film growth can occur. Recently, carbonization has been used to produce thin (100) 3C-SiC transition layers suitable for cubic GaN growth on (100) Si wafers. In both cases, the quality of the epitaxial film is critically dependent on the quality of the carbonized underlayer. The purpose of this study was to find proper processing techniques for production of high quality carbonization layers on large area substrates.

For this study, the carbonization of 100 mm-diameter, on-axis (100) Si wafers was performed in an APCVD reactor using propane as the carbon source gas and hydrogen as the carrier gas. Prior to carbonization, each wafer was subjected to an *in-situ* etch in hydrogen for 5 min at 1000°C to remove the native oxide on the Si surface, after which the temperature was lowered to below 500°C. Carbonization was initiated by injecting propane into the hydrogen carrier gas and increasing the temperature to 1280°C. Upon reaching 1280°C, the temperature and gas flows were held constant for a predetermined period. In this study, carbonization periods ranging from 30 s to 30 min were used. After carbonization, the wafer was cooled down to the room temperature. Atmospheres of hydrogen and argon were used in the cool-down step to examine the effect of hydrogen etching on the surface morphology of the SiC layers.

SEM and TEM were used to characterize the surface morphology, microstructure and film/substrate interface of the carbonized layers. In general, the carbonization process produces films with few voids at the 3C-SiC/Si interface, and void-free interfaces were observed when the argon cool-down step is used. In terms of crystal quality, all carbonization layers are single crystalline. The SiC thicknesses range from 2.3 nm to 7.3 nm for carbonization times of 30 s and 30 min, respectively. The surface morphology of the carbonized layers produced with hydrogen in the cool-down step exhibit pitting on the SiC surface, presumably from hydrogen etching. In severe cases, the pits completely penetrate the carbonization layer, exposing the underlying Si. Etch pit formation was eliminated by substituting hydrogen with argon during the cool-down step, as shown in the micrographs in Fig. 1.

The extended paper will present details concerning the carbonization process, the growth rate of the 3C-SiC layers, the microstructure of the SiC films, the surface morphologies of carbonized layers grown using hydrogen- and argon-based cool-down steps, and implications for growth of 3C-SiC and cubic GaN films on large-area Si wafers.

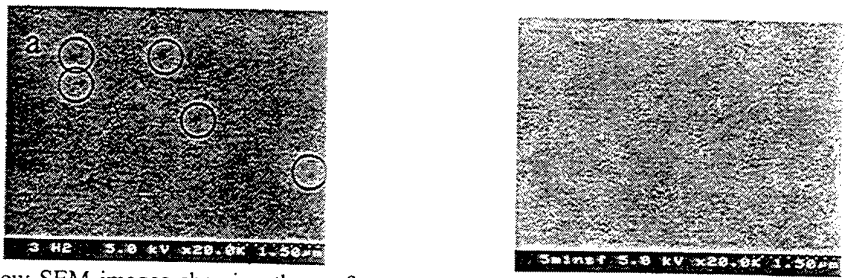


Fig. 1. Plan-view SEM images showing the surface morphology of carbonized layers (a) using a hydrogen cool-down step, and (b) an argon cool-down step. Etch pits produced by hydrogen etching are enclosed by circles.

Hydrogen Interaction with Silicon Terminated 3C-SiC(100) Surfaces

V. Derycke, N.P. Pham, P. Fonteneau and P. Soukiassian
Commissariat à l'Energie Atomique, DSM-DRECAM-SIMA, Centre d'Études de Saclay, Bât. 462, 91191 Gif sur Yvette Cedex, France
and Département de Physique, Université de Paris-Sud, 91405 Orsay Cedex, France

Phone: *33 (0)1 69 08 70 11* Fax: *33 (0)1 69 08 35 92* E-Mail: *derycke@drecam.cea.fr*

We use atom-resolved scanning tunneling microscopy and UV-photoemission spectroscopy to study the reaction of molecular and atomic hydrogen with the Si-rich and Si-terminated 3C-SiC(100) surface reconstructions. In the case of molecular hydrogen, we show that while the Si-rich 3x2 surface reconstruction is totally inert at room temperature, the Si-terminated c(4x2) surface reconstruction reacts very easily. This behavior of the 3C-SiC(100)-c(4x2) surface is very different from the one of the corresponding Si(100)-2x1 surface, which cannot decompose the H_2 molecules at room temperature except on very specific defect and step sites. The important difference in reactivity between the 3C-SiC(100)-3x2 and the 3C-SiC(100)-c(4x2) surface reconstructions allows us to prepare non-reacted silicon atomic lines on top of a hydrogenated and passivated surface. We also show that the interaction of atomic hydrogen on the 3C-SiC(100)-3x2 results in a well ordered 3x2 hydrogenated surface, with H atoms decorating the Si dangling bonds. This result, which is based on real-space surface imaging, strongly contrasts with the recently claim of a 3x2 to 3x1 transition as a result of atomic hydrogen exposure [1], and supports the so-called Yan-Semond model of the 3x2 surface reconstruction [2,3].

References

1-H.W.Yeom, I. Matsuda, Y.C. Chao, S. Hara and R.I.G. Uhrberg, Physical Review B 61, Rapid Communication, R2417 (2000).
2-H. Yan, A.P. Smith and H. Jónsson, Surface Science 330, 265 (1995).
3-F. Semond, P. Soukiassian, A. Mayne, G. Dujardin, L. Douillard and C. Jaussaud, Physical Review Letters 77, 2013 (1996).

Electronic structure of the 4H-SiC(0001)-($\sqrt{3}\times\sqrt{3}$)$R30°$ surface studied with two-photon photoemission spectroscopy

M. Wiets, M. Weinelt, I.L. Shumay, and Th. Fauster

Lehrstuhl für Festkörperphysik, Universität Erlangen-Nürnberg, Staudtstrasse 7, D-91058 Erlangen, Germany
Telephone: 0049-(0)9131-8528414, Facsimile: -8528400, email: wiets@fkp.physik.uni-erlangen.de

Among the large number of SiC polytypes and their surfaces, the 4H-SiC(0001)-($\sqrt{3}\times\sqrt{3}$)$R30°$ reconstruction has raised a lot of questions concerning its electronic structure. The energetically most reasonable configuration is given by one Si adatom per surface unit cell in the T_4 position on the surface, as found by quantitative LEED crystallography [1]. The Si adatoms saturate the three dangling-bond orbitals of the Si top layer atoms. These adatoms give rise to a new p_z-like dangling-bond orbital perpendicular to the surface which contains one unpaired electron per unit cell. In the single-particle picture, this one electron per unit cell leads to a half-filled surface band in the bulk band gap. Thus the surface should show a metallic behaviour [2], what is in clear contrast to experimental data. Photoemission spectroscopy shows one filled surface state which is about 1.2 eV below the experimental Fermi level [3]. At the Fermi level there is no density of states, so the surface is certainly not metallic. Furthermore, in inverse photoemission experiments an empty surface state at about 1.1 eV above the experimental Fermi level was observed [4]. It has been suggested that a Mott-Hubbard transition may occur at the surface which leads to a splitting of the originally half-filled surface band into two bands, the so-called "Hubbard bands". These bands are separated by a certain amount of energy, the on-site Coulomb interaction of the orbital, which is about 2 eV [5]. In a spin-polarized ab initio quasi-particle band-structure calculation within the GW approximation carried out for the ($\sqrt{3}\times\sqrt{3}$)$R30°$ reconstruction of 6H-SiC(0001) the resulting band structure shows one occupied and one empty surface band, separated by a direct band gap of 1.95 eV. There occurs an asymmetric splitting of the Hubbard bands, so the distance between the unoccupied state and the Fermi level is larger than the distance between the occupied state and the Fermi level [6].

We have investigated the ($\sqrt{3}\times\sqrt{3}$)$R30°$ reconstruction of the 4H-SiC(0001) surface with time-resolved bichromatic two-photon photoemission spectroscopy (2PPE). In 2PPE a photon from a pulsed laser excites an electron from a state below the Fermi level to an unoccupied state below the vacuum level. A second photon ionizes this intermediate state. The energy distribution of the photoelectrons yields information on the energetic position and the lifetime of the initial and the intermediate state. The advantage of 2PPE is on the one hand the high energy resolution of about 30 meV, compared to about 400 meV in IPES, and on the other hand given by the fact that both, occupied and empty states, could be observed simultaneously within the same experiment.

We used a Ti:sapphire laser system which produces laser pulses with a wavelength of 755-820 nm and a pulse-duration of about 20 fs at a repetition rate of 87 MHz. The pulses were frequency-tripled in a home-build tripler to yield laser pulses in the UV range (250-275 nm) and a duration of 45 fs. The laser light is focused onto the sample in the ultra-high vacuum chamber, which contains an electron energy analyser (Omicron EA 125 HR) and the usual equipment for surface preparation and characterisation. The surface was first prepared by heating the sample in a Si flux to a 3×3 reconstruction. Further heating leads to the ($\sqrt{3}\times\sqrt{3}$)$R30°$ reconstruction which shows an excellent LEED pattern. In UPS spectra we found an occupied surface state 1.05 eV below E_{Fermi} which is in good agreement with literature [3]. This state could be cleary detected in 2PPE. Furthermore an unoccupied state 1.27 eV above E_{Fermi} could be observed. These results confirm clearly the proposed asymmetric splitting of the two Hubbard bands around the Fermi level. The larger energetic distance (2.32 eV) between the two states compared to the 6H-polytype (1.95 eV) may occur due to the larger band gap. Moreover the so-called vacuum level can be cleary observed which can be used to determine the work function to about 4.67 eV.

Spectra taken from the (3×3) reconstruction indicate that this surface is semiconducting, meanwhile the ($6\sqrt{3}\times6\sqrt{3}$)$R30°$ reconstruction shows a metallic behaviour.

[1] Starke U. et al., Phys. Rev. Lett. **82**, 2107 (1999)
[2] Northrup J.E., Neugebauer J., Phys. Rev B **52**, R17001 (1995)
[3] Johansson L.I. et al., Surf. Sci. **360**, L478 (1996)
[4] Themlin J.-M. et al., Europhys. Lett. **39**, 61 (1997)
[5] Northrup J.E., Neugebauer J., Phys. Rev. B **57**, R4230 (1998)
[6] Rohlfing M., Pollmann J., Phys. Rev. Lett. **84**, 135 (2000)

The influence of Ge on the SiC nucleation on (111)Si surfaces

J. Pezoldt[1], T. Wöhner[1,2], Th. Stauden[1], J.A. Schaefer[2], P. Masri[3]

[1]TU Ilmenau, Institut für Festkörperelektronik, Postfach 100565, D-98684 Ilmenau, Germany, Phone: ++49 3677 693166, Fax: ++49 3677 693209, e-mail: pezoldt@e-technik.tu-ilmenau.de
[2]TU Ilmenau, Institut für Physik, Postfach 100565, D-98684 Ilmenau, Germany
[3]Groupe d'Etude des Semiconducteurs,CNRS-UMR5650,Université de Montpellier 2, 12 Place Eugène Bataillon, 34095 Montepellier CEDEX 5, France

In the heteroepitaxy of SiC on Si the common technique is the formation of a so called buffer layer by using a carbonization procedure. These layers act as a pseudosubstrate and as a diffusion barrier. This layers are not able to compensate the large lattice mismatch and the difference in thermal expansion. To improve the situation different methods were developed: (1) deposition on SOI substrates, (2) deposition on porous silicon, (3) the incorporation of Ge in the heterointerface between SiC and Si. All these methods lead to an improvement of the growth and residual stress in the heteroepitaxial system. For the last case, namely Ge addition into the growth process, a two fold influence of this element onto the epitaxial growth has to be expected. On the one hand side Ge incorporation may improve the lattice mismatch between silicon and silicon carbide. On the other hand Ge can act as a surfactant during the growth process. The aim of this study is the investigation of the influence of Ge on the SiC growth process on (111)Si. For this reason a high and a low temperature regime was chosen. In the low temperature regime (325°C) during the carbon deposition the SiC nucleation was suppressed and the SiC nucleation was initiated only with a step wise annealing procedure. In this regime the Ge was deposited before and after the carbon deposition. In the high temperature regime (750°C) SiC nucleates during the carbon deposition. Here the Ge deposition was carried out before and during the carbon deposition.

The layers were investigated by *in situ* spectroscopic ellipsometry, *ex situ* atomic force microscopy (AFM), X-ray photoelectron spectroscopy (XPS) and Fourier Transformed Infrared Spectroscopy (FTIR).

For all cases the Ge lead to an increase of the SiC grain size. Furthermore a smoothening of the SiC surface was observed. The only exception was the low temperature case with the C-Ge-sequence. This Ge deposition after the C deposition leads to a detoriation of the SiC formation and a disprovement of the crystallographic structure. The increase of the grain size and the improvement of the surface smoothness we attribute to the higher mobility of the C atoms on the partial Ge covered surface as well as the reduced stress.

For the high temperature case we observed a reduced silicon carbide growth rate if Ge was added. This might be due to the fact that on surface sites where Ge is located do not form carbidic bonds, i.e. Ge passivates the surface against SiC formation.

Furthermore from our investigations it follows that for a Ge incorporation into the SiC-Si heterointerface the Ge predeposition has to be preferred.

Abstraction of hydrogen by H radicals from hydrogen-terminated 4H-SiC(0001) surfaces at experimental temperatures

J. Olander and K. Larsson
Department of Inorganic Chemistry, Ångström Laboratory
Uppsala University, Box 538, S-751 21 Uppsala, Sweden
Telephone: +46-18-471 37 36, Telefax: +46-18-51 35 48

ABSTRACT

The thermodynamic probability of hydrogen abstraction by gaseous H radicals from H-terminated 4H-SiC(0001) surfaces, has been investigated theoretically using a first principal Density Functional Theory method. The long-term goal is to obtain a deeper knowledge of the 4H-SiC(0001) surfaces at experimental conditions. Car-Parinello-type molecular dynamic (MD) simulations and ordinary quantum mechanical calculations were performed, using experimental temperatures of either 1873 K or 2573 K.

In order to obtain high-quality films of materials like 4H-SiC (by using CVD methods) it is important to achieve a deeper understanding of the growth processes. It is then important to study the prerequisites of growth, such as the properties of the substrate surface and of the available gaseous precursors. For this reason, it is of interest to study the surface saturation, i.e. whether the growing surface is terminated (e.g., with H) or not. Hydrogen is capable of forming single bonds with the surface atoms in SiC, then sustaining their sp^3 configuration and thereby lowering the surface energy. However, it is not certain that hydrogen atoms stick to a SiC surface at the elevated temperatures commonly used during experimental deposition. It may be more favorable for them to desorb from the surface and subsequently form hydrogen gas molecules with free H radicals, i.e. to be abstracted.

Both the Si(0001) face and the C(000-1) face of 4H-SiC were included in the present investigation. The abstraction energies were calculated using the extreme energies obtained from the MD simulations, e.g. the energetically most favorable structure of the radical models and the energetically least favorable structure for the completely hydrogen terminated models. The abstraction energies were then calculated according to the following reaction:

$$E_{\text{surf-radical}} + E_{H2} \rightarrow E_{\text{surf}} + E_{\text{H-radical}}$$

where $E_{\text{surf-radical}}$ and E_{surf} are the total energies for the 4H-SiC surface with and without a radical surface site, respectively. E_{H2} and $E_{\text{H-radical}}$ denote the total energies for the gaseous H_2 molecule and H radical, respectively.

For both the Si(0001) surface and the C(000-1) surface, the abstraction energies obtained were exothermic. The reactions studied regarding a H abstraction of a surface hydrogen atom can therefore thermodynamically be regarded as probable to occur. As expected, the numerical values of the abstraction energies were larger at 2300 °C compared to 1600°C: For Si(0001), the values obtained are 310 kJ/mol and 450 kJ/mol for 1600 °C and 2300 °C, respectively. The corresponding values for C(000-1) are 350 kJ/mol and 490 kJ/mol, respectively.

Surface Morphology of 4H-SiC inclined towards <1$\bar{1}$00> and <11$\bar{2}$0> grown by APCVD using Si_2Cl_6+C_3H_8 system

Yasuichi Masuda, Satoru Ohshima, Chacko Jacob, and Shigehiro Nishino
Faculty of Engineering and Design, Kyoto Institute of Technology
Matsugasaki, Sakyo, Kyoto 606-8585, Japan
TEL : +81-75-724-7415, FAX : +81-75-724-7400
e-mail : masuda5y@djedu.kit.ac.jp, nishino@ipc.kit.ac.jp

In homoepitaxial growth of SiC, step-controlled epitaxy, in which a substrate cut several degrees from the (0001) face toward <11$\bar{2}$0> promotes high quality homoepitaxial growth, has been widely known[1]. Most of the work in SiC epitaxy has focused on substrates inclined toward <11$\bar{2}$0>. On the (0001) substrates inclined toward <1$\bar{1}$00>, stripe-like morphology appears and the incorporation of 3C-SiC occurs by long-time growth for 6H-SiC[2,3]. But, epitaxial growth on 4H-SiC (0001) inclined toward <1$\bar{1}$00> has been less studied. Recent work demonstrated that 4H-SiC epilayers with smooth morphologies could be grown on substrates inclined toward <1$\bar{1}$00> in a low pressure epitaxial growth system[4]. This work investigates the surface morphology of homoepitaxial films grown on 4H-SiC (0001) inclined toward <1$\bar{1}$00> and compares the results to films grown on 4H-SiC inclined toward <11$\bar{2}$0> by atmospheric pressure CVD using Si_2Cl_6+C_3H_8 system.

SiC epilayers were grown on 4H-SiC substrates inclined 8°±1° off from (0001) Si-face towards either <1$\bar{1}$00> or <11$\bar{2}$0>. The 4H-SiC films were grown by atmospheric pressure CVD using Si_2Cl_6 (hexachlorodisilane) as Si source and C_3H_8 (5% in H_2) as C source with H_2 as the carrier gas. Growth temperatures were in the range of 1400°C-1600°C. The specific growth parameters chosen for this work were those identified as optimal for growth on 4H-SiC (0001) inclined 8° off toward <11$\bar{2}$0>. No effort was made to optimize the growth parameters for epitaxial growth on 4H-SiC (0001) inclined 8° off toward <1$\bar{1}$00>.

The growth rate of epitaxial films for both the substrates inclined towards <1$\bar{1}$00> and <11$\bar{2}$0> was equal within experimental error, and was 1.9 μm/h. Figure 1 shows the surface morphology for epilayer thickness of 19 μm grown on the 4H-SiC inclined 8° off toward <1$\bar{1}$00>. By Raman scattering and low temperature Photoluminescence, only the peaks characteristic to 4H-SiC are observed in each spectrum for 19 μm films in both the off-directions. On the surfaces inclined in either direction, smooth epitaxial surface morphologies were obtained. Even though the film thickness was increased, the incorporation of 3C-SiC, large-scale step bunching, and rough 3D growth were not observed by Nomarski optical microscopy. AFM analysis revealed smooth surfaces particularly on epilayers inclined toward <1$\bar{1}$00>, the average RMS roughness of the epilayers was 0.16 nm for 2 μm thin film, 1.65 nm for 19 μm thick film (10x10 μm^2 scan area), respectively. The macrostep structure was obtained for epilayers in both off-directions. The macrosteps of epilayers inclined toward <1$\bar{1}$00> was observed more clearly than epilayers inclined toward <11$\bar{2}$0>. A detailed analysis of the observations, and growth mechanism will be presented.

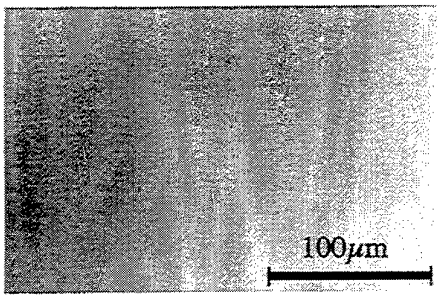


FIG. 1. The surface morphology for epilayer thickness of 19μm grown on the 4H-SiC inclined 8° off toward <1$\bar{1}$00>.

[1] N.Kuroda, K.Shibahara, W.S.Yoo, S.Nishino and H.Matsunami, Extended Abstracts of the 19th Conf. on Solid State Devices and Materials, Tokyo (1987) p.227
[2] T.Ueda, H.Nishino, and H.Matsunami, J. Crystal Growth, **104**, 695 (1990)
[3] H.S.Kong, J.T.Glass, and R.F.Davis, J. Appl. Phys. **64**, 2672 (1988)
[4] B.E.Landini and G.R.Brandes, Appl. Phys. Lett., **74**, 2632 (1999)

WeP-50

Ab initio study of silicon carbide : bulk and surface structures

C. RAFFY [1,2] ; L. MAGAUD [i] ; E. BLANQUET [2] ; A. PASTUREL [3]

[1] LEPES (Laboratoire d'Etudes des Propriétés Electroniques des Solides)
25, avenue des Martyrs – B.P. 166
38042 GRENOBLE Cedex 9 –FRANCE
tel. : 04 76 88 74 67 email : raffy@lepes.polycnrs-gre.fr
[2] LTPCM (Laboratoire de Thermodynamique et Physico-Chimie Métallurgiques)
[3] LPMMC (Laboratoire de Physique et Modélisation des Milieux Condensés)

In this work, we are interested in the modeling of silicon carbide growth from the vapor phase. Thin SiC films can be obtained by Chemical Vapor Deposition (CVD) from gaseous precursors, whereas bulk material is elaborated by sublimation of SiC powder (modified Lely method). The substrate is an off-oriented hexagonal SiC single crystal, which results in a step-flow growth.

Detailed studies of bulk and surface structures are needed to understand the growth mechanisms. The calculations are carried out within density-functional theory (DFT), in the local density approximation (with generalized gradient corrections). The code VASP uses wave functions expanded in terms of plane waves. Moreover, the electron-ion interaction is described by ultrasoft Vanderbilt pseudopotentials, which drastically reduce the size of the basis set and, then, allow the study of large cells (up to 200 atoms).

The geometries of hexagonal (2H, 4H, 6H) and cubic (3C) polytypes have been optimized. The total energies are discussed within the Axial Next-Nearest-Neighbour Ising model (ANNNI), for ideal and relaxed bulk structures. It appears that 4H and 6H are the most stable phases, which is in agreement with other calculations, but not with experiments that indicate a preference for the cubic form. The question of the origin of polytypism is raised : is it controlled by thermodynamics or growth conditions ? Thus we began an investigation of the surface of 4H SiC, which is the most interesting polytype regarding the electronic properties. After considering the flat (0001) surfaces, we studied the vicinal surfaces, since in a step-flow growth mechanism, the step morphology is of primary importance. We considered different misorientations from the directions [1-100] and [11-20], and the two polarities (C- or Si-terminated surfaces). In each case, we describe the geometry and discuss the stability of single steps versus step bunching.

Observation of SiO_2/SiC interface with different off-angle from Si (0001) face using transmission electron microscope

K. Fukuda[1),3)], S. Suzuki[1),2)], J. Senzaki[1),2)], R. Kosugi[1),3)], T. Tanaka[1),2)], and K. Arai[1),3)]
Ultra-Low-Loss Power Device Technology Research Body[1)], R&D Association for Future Electron Device[2)], and Electrotechnical Laboratory[3)], 1-1-4 Umezono, Tsukuba, Ibaraki 305-8568, Japan
TEL:+81-298-61-3320, FAX:+81-298-61-3397, E-mail:kfukuda@etl.go.jp

The channel mobility of 4H-SiC MOSFETs are reported to be lower than those of 6H-SiC MOSFETs although the mobility of 4H-SiC estimated from the Hall measurements is higher than that of 6H-SiC.[4,5] This is a large problem for practical use of 4H-SiC MOSFETs. Usually, the 6H- and 4H-SiC MOSFETs are fabricated on 3.5° and 8° off-angled SiC (0001) substrates, respectively. The off-angle is considered to affect largely SiO_2/SiC interface structures, resulting in the channel mobility. Therefore, we have investigated the SiO_2/SiC interface structures with different off-angle from Si(0001) face using transmission electron microscope(TEM).

3.5° and 8° off-angled 6H-SiC (0001) and 8° off-angled 4H-SiC (0001) substrates with n-type epitaxial layer were purchased from Cree Research Inc. After the standard RCA cleaning, sacrificial oxide films were grown in dry O_2, and then were removed by 5% HF solution. Finally, gate oxide films were thermally grown at 1200 °C in dry O_2. The SiO_2/SiC interface structures were observed using TEM.

Figures 1,2 and 3 show the typical cross-sectional TEM images of SiO_2/SiC interface formed on 3.5° and 8° off-angled 6H-SiC (0001) and 8° off-angled 4H-SiC (0001) substrates, respectively. These figures exhibits that the step structures exist even after the oxidation. The numbers of Si-C bilayer at steps is approximately 1 and 2 for 3.5°off-angled and 8°off-angled SiO_2/SiC interface, respectively. The terrace width of 3.5°off-angled and 8°off-angled SiO_2/SiC interface is also approximately 1.5nm and 3nm, respectively. The SiO_2/SiC interface on 3.5°off-angled 6H-SiC (0001) substrate is much smoother than those on 8°off-angled 4H-SiC (0001) substrate.

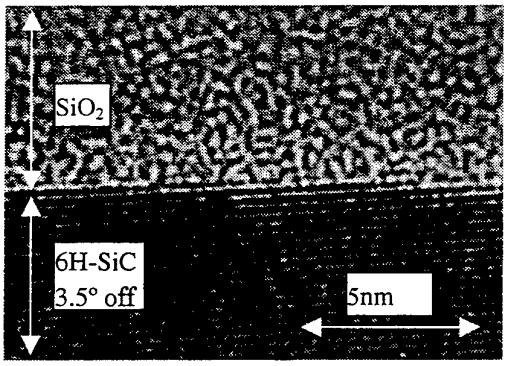


Fig. 1 TEM image of SiO_2/6H-SiC (3.5° off)

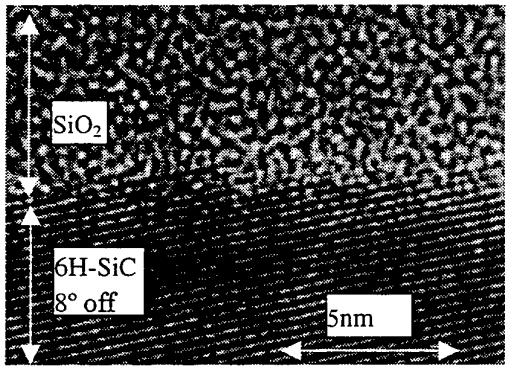


Fig. 2 TEM image of SiO_2/6H-SiC (8° off)

In Si-based MOSFETs, the channel mobility is reduced with increasing of the roughness of SiO_2/SiC interface. Therefore, it is considered that one of reasons of lower channel mobility of 4H-SiC MOSFETs fabricated on 8°off-angled SiC substrate is due to rougher SiO_2/SiC interface compared to 6H-SiC MOSFETs fabricated on 3.5°off-angled SiC substrate.

This work was performed under the management of FED as a part of the MITI New Sun Shine Program Technologies) supported by NEDO.

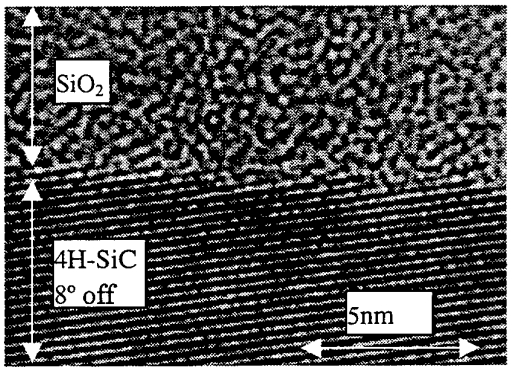


Fig. 3 TEM image of SiO_2/4H-SiC (8° off)

WeP-52

Dissolution Mechanism of the Carbon Islands at the SiO_2/SiC interface

O. H. Krafcsik, K. V. Josepovits, P. Deák

Department of Atomic Physics, Technical University of Budapest, H-1111 Budapest, Budafoki út 8. Hungary

Phone:[36]-(1)-463-1589
Fax: [36]-(1)-463-4357
E-Mail: krafcsik@goliat.eik.bme.hu

Abstract

During oxidation of SiC small graphitic carbon islands[1] are formed at the SiO_2/SiC interface. The parameters influencing the stability of these islands is not known. The limiting factor can be the activation energy for dissolution or the activation energy for carbon outdiffusion. Due to the small size of the carbon islands it is virtually impossible to investigate this problem directly. Therefore we have deposited a graphitic amorphous carbon (a-C) layer onto high quality SiO_2 and investigated the indiffusion of carbon by surface analytical methods. We have found that if the oxygen contamination of the a-C layer is negligible, no carbon enters the oxide up to the highest temperature we investigated (1190°C). This means that in an oxygen-poor environment the carbon islands can not be dissolved at the usual temperature of SiC oxidation. We find however that if the a-C layer is prepared with oxygen contamination, carbon enters into SiO_2 already at 1140°C. The outdiffusion of carbonaceous species (probably CO) is very fast at this temperature.

[1] V. V. Afanas'ev, A. Stesmans and C. Harris, ICSC III-N'97 Sweden p.423

Improvement of the 3C-SiC/Si interface by flash lamp annealing

D. Panknin, J. Stoemenos[1], M. Eickhoff[2], V. Heera, A. Nielsen[2], N. Vouroutzis[1], G. Krötz[2] and W. Skorupa
Forschungszentrum Rossendorf, P.O.B. 510119, D-01314 Dresden, Germany
[1]Aristotle University of Thessaloniki, Physics Department, 54006 Thessaloniki, Greece Tel.+30-31-998191, FAX +30-31-998191
[2]Daimler Chrysler AG, Department FT2/M, Postfach 800465,81663 München, Germany

The epitaxial growth of 3C-SiC on silicon substrate is possible in spite of the 21% misfit between the Si and 3C-SiC system. However due to the high misfit and the limitation of the process temperature to 1400°C, the density of the defects in the early stage of growth is very high, of the order 10^{12} cm^{-2}. Part of these defects is annihilated as the film grows. The remaining defects at the uppermost part of the 3C-SiC film are of the order of $10^{9}cm^{-2}$, which are responsible for the poor electrical characteristics of 3C-SiC films. In this paper we present results of a short time annealing of the 3C-SiC films by flash lamps. The specimens were irradiated in Argon ambient from an array of xenon lamps with a flash duration of 20ms. The maximum used energy density during the flash was about 120 J cm^{-2}.

The defect density of the as grown film at the 3C-SiC/Si interface is of the order $10^{12}cm^{-2}$, as shown in the cross-section micrograph in Fig.1a. The same film after flash lamp irradiation is shown in Fig.1b. A reduction of the defects by about one order of magnitude in the SiC at the interface is evident. In the non-irradiated specimens the diffraction patters appear as small arcs due to the mosaic structure of the film, as shown in Fig2a. After irradiation the same film exhibits very sharp diffraction spots as shown in Fig.2b. Although the 3C-SiC surface remains smooth after irradiation, the SiC/Si interface is very rough. 3C-SiC protrusions with trapezoidal shape bounded by (111) facets were formed inside the Si-substrate as shown in Fig.1b. This morphology reveals complete melting of the SiC and Si at the interface during the irradiation and subsequent redistribution during solidification reassembling liquid phase epitaxy. This explains the significant improvement of the 3C-SiC at the interface. The melting of the Si at the interface eliminates also the cavities, which are formed at the Si side during the carbonization process. Due to the transparency of the 3C-SiC, the irradiated energy is selectively absorbed at the SiC/Si interface where the most defective and consequently absorbing part of the 3C-SiC film is. The remaining intensity is absorbed by the Si at the interface. The uppermost part of the SiC film is not affected by the flash annealing. Therefore the flash lamp annealing can improve the quality of thin SiC films near the SiC/Si interface, which can be used as the seed for the growth of thicker 3C-SiC films.

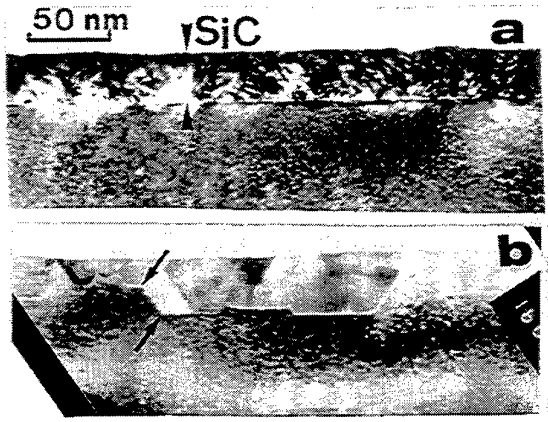


Fig.1

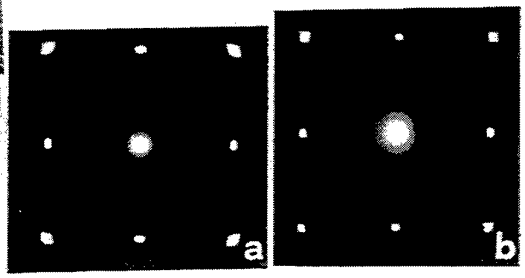


Fig.2

Enhancement of Electrical Activation of Aluminum Acceptors in 6H-SiC by Co-implantation of Carbon Ions

Takeshi Ohshima, Hisayoshi Itoh, and Masahito Yoshikawa
Japan Atomic Energy Research Institute, 1233 Watanuki, Takasaki, Gunma 370-1292, JAPAN
Phone: +81-27-346-9323, FAX: +81-27-346-9687, E-mail: ohshima@taka.jaeri.go.jp

One of the key issues of applying SiC to electronic devices is the development of acceptor impurity doping technique. Recently, Itoh et al.[1] reported that the co-implantation of carbon (C) with acceptor impurities such as aluminum (Al) and boron (B) enhanced their electrical activation. However, the optimum condition of C co-implantation has not yet been obtained. In this study, we have carried out co-implantation of Al and C into 6H-SiC and investigated the electrical properties of co-implanted layers by Hall effect measurement. We report the dependence of the electrical activation of Al on implantation temperature, C concentration and the sequence of co-implantation.

The samples used in this study were n-type 6H-SiC epitaxial films ($N_D \sim 5x10^{15}$ /cm^3) grown on 6H-SiC substrates. Five-fold implantation of Al^+ was carried out to form a box profile (depth: 0.5 μm) with a mean Al concentration of $1x10^{18}$ or $1x10^{19}$ /cm^3. A box profile of C with a thickness of 0.5 μm was also formed in mean C concentrations $2x10^{17}$ ~ $3x10^{19}$ /cm^3 by five-fold C^+-implantation. The samples were annealed at 1650 °C for 30 min in argon (Ar) atmosphere after implantation. The Al electrodes were alloyed at 900 °C for 3 minutes in Ar. The carrier concentration was measured using van der Pauw arrangement.

Figure 1 shows the co-implanted C^+ concentration dependence of hole concentration (p) at RT for the samples implanted with Al^+ at $1x10^{18}$ /cm^3 (triangles, upside-down triangles) and $1x10^{19}$ /cm^3 (squares). Closed and open symbols indicate the results for the samples implanted with C^+ prior to Al^+ and with Al^+ prior to C^+, respectively. C^+-implantation was carried out at 800 °C in every sample. The values of p in the samples implanted with Al^+ only (reference sample) are also shown as the broken lines for comparison. No significant difference between both sequence of co-implantation is observed. For the both samples implanted with Al^+ at $1x10^{18}$ and $1x10^{19}$ /cm^3, an increase of p due to C^+-implantation is observed in a C^+ concentration range from $2x10^{17}$ to $5x10^{18}$ /cm^3. The highest values of p are obtained at $1x10^{18}$ C^+/cm^3. At $3x10^{19}$ C^+/cm^3, the values of p are smaller than those in the reference samples. These results show that C^+ co-implantation enhances electrical activation of Al acceptors and that the optimum C concentration is ≈ $1x10^{18}$ /cm^3.

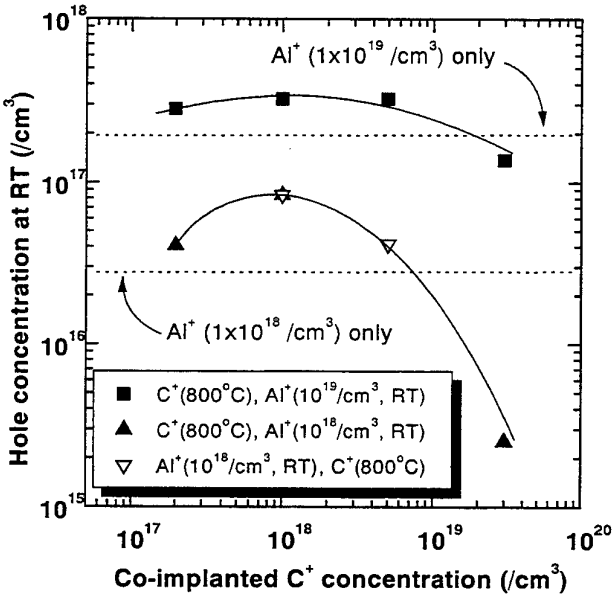


Fig. 1 Co-implanted C^+ concentration dependence of hole concentration (p) at RT for the samples implanted with Al^+ at $1x10^{18}$ and $1x10^{19}$ /cm^3 and subsequently annealed at 1650 °C. The broken lines in the figure represent the values of p in the sample with Al^+ only.

[1] H. Itoh et al.: Appl. Phys. Lett. **73**, 1427 (1998).

Cluster formation in heavily Al-doped 4H-SiC layers

M.K. Linnarsson[1]*, P.O. Persson[2], H. Bleichner[3], M.S. Janson[1], H. Andersson[1], S. Karlsson[4], R. Yakimova[2] and B.G. Svensson[1]

[1]Royal Institute of Technology, Solid State Electronics, P.O. Box E229, SE-164 40 Kista-Stockholm, SWEDEN
[2]Linköping University, Department of Physics and Measurement Technology, SE-581 83 Linköping, SWEDEN
[3]ABB Corporate Research, P.O. Box E215, SE-164 40 Kista-Stockholm, SWEDEN
[4]ACREO AB, P.O. Box E236, SE-164 40 Kista-Stockholm, SWEDEN
*Phone: +46 8 752 1412, Fax: +46 8 752 7782, E-mail: marga@ele.kth.se

The quality and thermal stability of heavily doped SiC layers, used in conjunction with ohmic contacts, are of great importance. In device production epitaxially grown layers as well as ion implantation are employed to form the contact layers. Key issues are solubility limit and precipitate formation of the dopant atoms.

In this work we have studied tree dimensional distributions of Al in epitaxially grown p-type 4H-SiC layers. Secondary ion mass spectrometry (SIMS) has been utilized to obtain Al-concentration versus depth profiles as well as lateral distributions (ion images). High-resolution transmission electron microscope (TEM) measurements have also been performed to study the crystal structure. Epitaxially grown SiC structures with several Al doped layers in the concentration range $3x10^{19}$ to $5x10^{20}$ cm^{-3} have been used. The samples were heat treated between 1500 and 2000 °C in Ar atmosphere in a RF-heated furnace for 0.5 to 3h.

Ion images of the lateral Al distribution reveal a pronounced dependence on the Al content. In layers with high enough Al concentration the Al distribution is no longer homogenous, as seen by the brighter regions in the SIMS images. In fig. 1, the lateral Al distribution is compared for two dopant levels, $3x10^{19}$ and $5x10^{20}$ cm^{-3}. A post-grown heat treatment at 1700°C during 60 minutes has been performed. No variation of the Al concentration over the surface is resolved in the $3x10^{19}$ cm^{-3} sample, while inhomogeneities are observed in the sample with $5x10^{20}$ Al/cm^3. These results can be explained in terms of solubility limits and cluster formation. Comparison will be made between SIMS and TEM results.

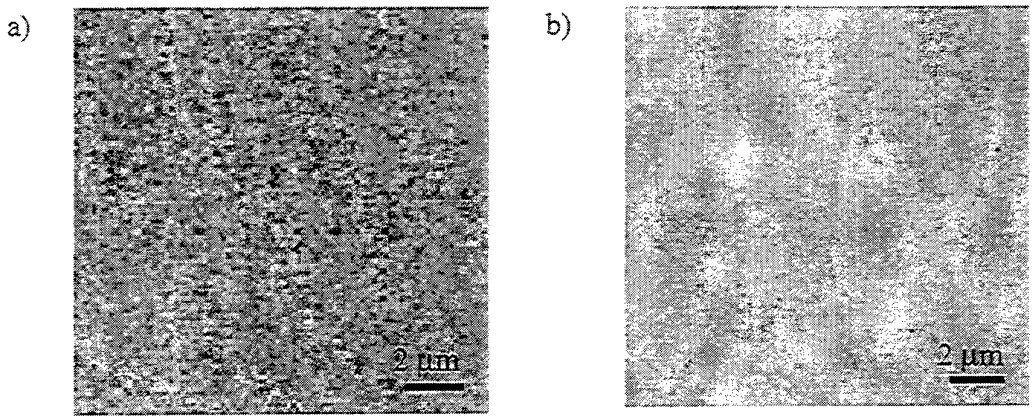


Fig.1. Ion images of Al distribution in SiC obtained by SIMS. The doping level is in a) $3x10^{19}$ and b) $5x10^{20}$ cm^{-3}. A linear scale is displayed and the maximum intensity is 35 and 350 counts/s in a) and b), respectively.

Channelling measurements of ion implantation damage in 4H-SiC

A.Yu. Kuznetsov, M. Janson, A. Hallén, and B.G. Svensson
Royal Institute of Technology, Department of Electronics, Electrum 229
SE-164 40, Kista-Stockholm, Sweden

H. Grünleitner, G. Pensl
University of Erlangen-Nürnberg, Institute of Applied Physics
Staudtstrasse 7, D-91058 Erlangen, Germany

Silicon carbide is a promising material for the fabrication of electronic and optoelectronic devices operating under extreme conditions (high electric power, temperature, etc). Al^+ ion implantation into an n-type 4H-SiC epilayer is considered to be an important technological step to produce a p^+-doped emitter region for power diode applications. However, the implantation process produces radiation defects, which have to be removed during Al-activation anneals. The understanding of radiation defect kinetics in SiC is not mature, in part due to the complexity of initial radiation damage, which is a strong function of implantation parameters. For example there is still no agreement on such basic parameters as the displacement energy and migration properties of vacancies and interstitials in SiC.

In the present work 100 keV Al^+ ion implantation damage profiles in low-doped 4H-SiC epitaxial layers have been measured by Rutherford backscattering spectrometry in the channelling mode (RBS-c) as a function of implantation dose (1×10^{13} to 1×10^{15} Al^+/cm^2) and implantation temperature (25-800°C). For the measurements 2.0 and 2.4 MeV He+ ions along <0001> direction was used. In addition, implantations have also been performed with ions of lower mass (protons) and higher mass (xenon) to study the effect of ion mass on the damage build-up. Damage profiles are estimated from the RBS-c measurements and, in particular, the effect of implantation temperature will be elucidated. Most of the quantitative measurements are obtained for the Si-sublattice and the results are furthermore compared to Monte-Carlo simulations.

Flash lamp annealing of implantation doped p- and n-6H-SiC

D. Panknin, W. Skorupa
Forschungszentrum Rossendorf, Institut für Ionenstrahlphysik und Materialforschung
PO Box 510 119, D-01314 Dresden,
Tel.: +49 351 260 3613; Fax: +49 351 260 3411

One of the key problems of ion implantation doping of SiC is the electrical activation particularly of high dopant concentrations. Furnace annealing is reasonable only up to temperatures of about 1800°C because of problems of Si sublimation. Using short time annealing techniques, like flash lamp annealing, higher temperatures up to 2000°C are available.
Al, B and N were implanted into 6H-SiC epitaxial layers at 400°C with different energies and doses in order to form a 500 nm thick box-shaped layer. The plateau concentration was varied for Al, B and N between $1x10^{18}cm^{-3}$ and $5x10^{21}cm^{-3}$, $5x10^{18}cm^{-3}$ and $1.5x10^{21}cm^{-3}$, and $5x10^{17}cm^{-3}$ and $5x10^{20}cm^{-3}$, respectively. The wafers were annealed in Ar by flash lamp irradiation at about 2000°C using an array of xenon lamps with a flash duration of 20 ms. For the purpose of comparison long time annealing was used in a temperature range between 1200°C and 1650°C, 10 min using an inductively heated furnace.
Al implanted wafers show a remarkably higher activation after flash lamp annealing for plateau concentrations $> 5x10^{20}cm^{-3}$ compared to furnace annealing. This effect is caused by freezing-in of the enhanced solubility of Al at the high temperature during the flash. For the highest Al concentration the layer is characterized by metallic-like conduction.
After boron implantation and annealing the hole concentration reaches a maximum value of about $2x10^{16}cm^{-3}$ for the plateau concentration close to $5x10^{18}cm^{-3}$. For higher boron concentrations a decrease of the hole concentration is observed. The maximum value of the hole concentration is caused by a competition of outdiffusion of the excess boron and formation of boron containing precipitates supported by Ostwald ripening.
Nitrogen implanted wafers show only a small activation after flash lamp annealing. Due to the short annealing time only the energetically lower hexagonal sites will be occupied. A combined flash lamp and furnace annealing leads to a slightly higher electrical efficiency compared to furnace annealing.

The role of titanium on the behaviour of Al/Si-based ohmic contacts to p-type LPE 4H-SiC

Liliana Kassamakova[1)], Roumen Kakanakov[1)], Ivan Kassamakov[1)],
Konstantinos Zekentes[2)]

1) Institute of Applied Physics, Bulgarian Academy of Sciences,
59 St. Petersburg Blvd., 4000 Plovdiv, Bulgaria,
Tel. +359 32 265 515, fax: +359 32 632 810, E-mail: ipfban@mbox.digsys.bg
2) Foundation for Research and Technology-Hellas, Institute of Electronic Structure and Laser, Microelectronics Research Group,
Vassilika Vouton, P.O. Box 1527, 711 10 Heraklion, Crete, Greece
Tel. +30 81 394108, fax: +30 81 394106, E-mail: trifili@physics.uch.gr

The thermal stability of ohmic contacts is one of the main factors limited the reliability of SiC devices. Usually the contact stability has been investigated at temperatures up to 500 °C. The recent progress in SiC device processing allows to fabricate devices operating at higher temperatures. For that reason, the improvement of the contact stability at temperatures above 500 °C is of great interest.

The study of Al/Si/SiC ohmic contacts showed their excellent thermal stability at 500 °C. However, they are not stable at operating temperature of 600 °C. In this paper the results of the investigation on the AlSi-based ohmic contacts with new composition, AlSi(2%)Ti(0.15%), is presented. The contacts were formed on p-type 4H-SiC layers grown by liquid phase epitaxy with a carrier concentration of (3-5)x10^{19} cm^{-3}. The metal film was deposited by electron-beam evaporation. The contact resistivity dependence on the annealing conditions in the interval 700 – 950 °C has been investigated. The new contacts showed good stability at operating temperature of 600 °C. The structure of the contact layer and the element distribution at the interface were studied by AFM, XPS and AES analyses. The results were discussed in respect to explain the improved contact stability at high operating temperature.

Acknowledgements

This work is supported financially by NATO project SfP-971879 for that the authors express their gratitude.

Corresponding author: R.Kakanakov

Ru Schottky barrier contacts to *n*- and *p*-type 6H-SiC

M.E. Samiji, E. van Wyk, L. Wu, A. Venter* and A.W.R. Leitch
Department of Physics, University of Port Elizabeth, PO Box 1600
Port Elizabeth 6000, South Africa
Tel: +27-41-504-2219; Fax: +27-41-504-2573
* Department of Physics, Vista University, Private Bag X613
Port Elizabeth, South Africa

Abstract:

Ruthenium is one of the Pt-group metals that in the past has been used to successfully form good quality Schottky contacts to both *n*-and *p*-type GaAs. Its thermal stability, chemical inertness and relatively high barrier heights make it an ideal metal for fundamental studies on SiC. To our knowledge, however, the Ru-metal contact to SiC has not yet been reported.

We have investigated the formation of ruthenium Schottky barrier diodes (SBDs) on both *n*- and *p*-type 6H-SiC wafers obtained from Cree Research, Inc. Ohmic contacts were first prepared by thermally evaporating and subsequently annealing either Ti/Al (for *p*-type) or Ni (for *n*-type) on the back surfaces of the SiC wafers. A Schottky barrier diode was then fabricated by depositing a Ru film (typical thickness 450 Å) on the polished and cleaned top surface by electron beam evaporation.

It is found that Ru forms good quality rectifying contacts to both *n*- and *p*-type SiC. From current-voltage (I-V) measurements the barrier heights of the Ru-SBDs were measured to be 0.85 eV and 1.1 eV for *n*-type and *p*-type SiC, respectively. The thermal stability of the Ru-SBDs was investigated in a series of isochronal anneals up to 550 °C. The barriers heights remained stable up to an annealing temperature of 400 °C. For higher temperatures however, a general deterioration in the quality of the barrier (as indicated by an increase in the measured idealities as well as an increase in the reverse bias leakage currents) was observed. These results will be discussed in the light of other metal Schottky barrier contacts to SiC.

Formation of Large Area Al Contacts on 6H- and 4H- SiC Substrates

O. Korolkov, T. Rang

Department of Electronics, TTU, Ehitajate tee 5, 19086 Tallinn, Estonia,
Phone: (+372) 6 202 155; Fax (+372) 6 202 151;
E-mail: oleg@va.ttu.ee

To utilize all the wonderful properties of SiC semiconductors, formation of reliable, homogeneous, ohmic and/or rectifying contacts can be a critical issue, especially for such type of devices as Schottky diodes. There are a lot of papers reporting very good results in formation of contacts for different polytypes of SiC. But the dimensions of metal SiC contacts are usually restricted by hundreds of microns in diameter and some few microns in thickness. In our best knowledge no results have been reported on large area and acceptable for power device thickness of metal contacts to the SiC structures. In this paper we report the combined results of our initial attempts [1, 2] and the later research in forming thick (50 ÷ 200 μm) and large area (tens of millimeters in diameter) Al contact to 6H- and 4H-SiC substrates using Diffusion Welding (**DW**) technique.

DW is a solid state joining process, which can be utilized to bond "difficult to join "materials. The process is performed on a specially designed, continuous-action, commercial type equipment UDS-6. The SiC used for experiments was 6H- and 4H-SiC, n-type $3.6 \cdot 10^{18}$ cm^{-3} and $8.5 \cdot 10^{18}$ cm^{-3} respectively provided by CREE Research Inc., (USA). For the contacts the 0.05 and 0.2 mm thick, 99.99 % Al foil has been used.

The Al/SiC contacts, under variety of **DW** conditions were first characterized by mechanical adhesion measurements. For this purpose the strips of aluminum foil were pulled of the SiC surface by special device. The maximum tensile strength in Newtons (N) divided by the width of the strip is formed as the bond strength. Fig. 1 shows the typical form of the tension curves obtained in the process of detach test and corresponding to the "exellent", "very good", and "bad" quality of the bonding. In the case of "excellent" bond the tensile strength exceed the breaking strength of annealed aluminum and it's impossible to separate the aluminum strip from a silicon carbide surface.

The specific contact resistance (ρ_c) measurement was carried out for 6H-SiC, n-type substrate with concentration $3.6 \cdot 10^{18}$ cm^{-3}, where ρ_c was determined by surface potential distribution measurement near by the spot of metal contact (S.C. extrapolation method [3]). Fig. 2 shows the dependence of specific contact resistance on measurement current.

The *U-I* characteristics for Al/SiC Schottky contacts were measured by tester with measurement intervals 0 ÷ 3 A and 0 ÷ 30 V. at temperature interval between 20°÷600 °C. The temperature influence on forward *U-I* measurements for 4H-SiC are given in Fig. 3.

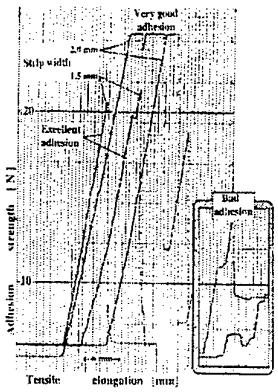


Fig. 1. Adhesion curves

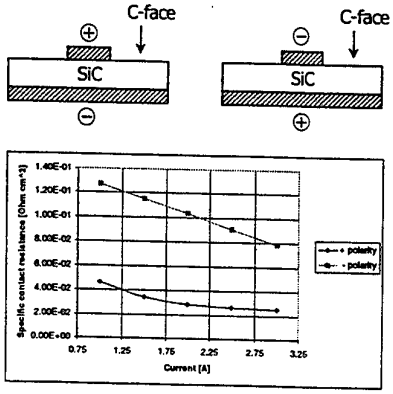


Fig. 2. Specific resistance

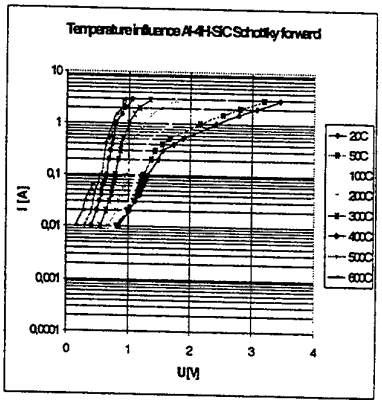


Fig. 3. Forward *U-I* characteristics

References

[1] O. Korolkov, T. Rang: "Diffusion welding technology for 6H-SiC substrates. In Proc. 6-th Baltic Electronics Conference (BEC'98), Tallinn, Estonia, Oct. 7-9, 1998, 251-252.

[2] T. Rang, O. Korolkov, R. Kurel and M. Pikkov: Large area high quality interface to SiC substrates-technology and modeling. In "Materials Mechanics Fracture Mechanics Micro Mechanics", Eds. T. Winkler, A. Schubert, Druckhaus Dresden GmbH, Germany, 1999, 574-579.

[3] H. H. Berger: Contact Resistance and Contact Resistivity. J. Electrochem. Soc., vol 119, N°4, 1972, 507-514.

Stability of Molybdenum Schottky Contact to Silicon Carbide

Kouichi Nishikawa, Masaaki Shimizu, Brian Foster and Hiroaki Iwakuro

R&D center, Shindengen Electric Mfg. Co., Ltd.

10-13 Minami, Hannou, Saitama 357-8585, Japan

Phone: +81-429-71-1084, fax.: +81-429-71-1458, e-mail: k_nishikawa@shindengen.co.jp

Introduction

Since silicon carbide itself is a very stable material, SiC devices have the potential to be operated at high temperature. In order to realize these devices, stable electrodes and insulators are also required. However, when SiC devices are operated under high temperature for long time, the reactions between SiC and electrodes/insulators can not be avoided. Therefore research of stable Schottky contact electrode is important for SiC based Schottky rectifier and MES-FET. Since molybdenum is a refractory metal and forms both silicide and carbide, Mo is a candidate for stable Schottky contact electrode. The purpose of this paper is to show the stability of Mo Schottky electrode.

Experimental

As the substrate, (0001)Si face of n-type 4H-SiC from Cree Inc. was used. The SiC wafer had a 10-μm-thick n-type epilayer with doping concentration of 1×10^{16} cm^{-3} and a 0.35-mm-thick n-type substrate. No guard ring was employed. The wafer was cleaned by SPM, rinsed in de-ionized water and etched in diluted HF(1:100) prior to Mo deposition. Mo film was deposited by sputtering with a base pressure below 10^{-6} Torr. Ar at 5.0 mTorr was used as a sputtering gas.

In order to examine the effect of heat treatment, two kinds of specimens were made: (a) as-deposited and (b) annealed at 1173K for 30min in Ar ambient. After the heat treatment, Ti was sputter deposited on the backside of the wafer for Ohmic contact. Circular contacts of 0.40mm in diameter were patterned using standard lithographic techniques and wet etching solutions. During current-voltage measurements, the temperature of the rectifiers were kept at 295K. X-ray diffraction (XRD) analysis was also made on both specimens.

Results

XRD analysis showed that the as-deposited film had a Mo(110) texture, and the annealed film had a Mo(110) texture with a small amount of Mo_2C. Figure 1 shows the current-voltage characteristics of the Mo-Schottky rectifiers. Electric properties obtained from forward characteristics are summarized in Table 1. The change in forward voltage drop and reverse leakage current is small. The same kind of experiments for Nickel showed high increase in leakage current. As the result we obtained a stable Schottky contact with Mo.

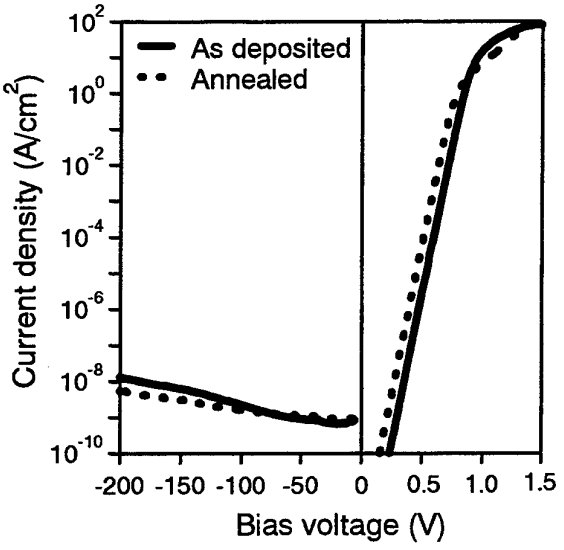


Figure 1. Current-voltage characteristics of Mo-Schottky rectifiers.

Table 1. Summary of forward properties

Specimen	V_F@100Acm^{-2}	ϕ_{Bn}	n
As deposited	1.53V	1.24eV	1.02
Annealed	1.51V	1.17eV	1.01

Effects of Thermal Annealing in Cu/6H-SiC Schottky Properties

Tomoaki HATAYAMA, Takashi SUEZAKI, Kazuaki KAWAHITO, Yukiharu URAOKA, and Takashi FUYUKI
Graduate School of Materials Science, Nara Institute of Science and Technology
Takayama 8916-5, Ikoma, Nara 630-0101, Japan Phone/Fax : +81-743-72-6072/-6078

Copper (Cu)/6H-SiC Schottky rectifiers with reliable electrical properties could be formed for the first time by sputtering method and subsequent thermal annealing. To obtain a high-power and high-temperature operating SiC devices, it is important to form a high-performance metal contact with a low resistivity and a high thermal conductivity. In this paper, electrical properties of Cu/6H-SiC junctions are discussed in relation to the effects of thermal annealing.

An n-type 6H-SiC epilayer with a 10 μ m thick and a donor concentration of 1.4×10^{16}cm^{-3} grown on a (0001) Si-face substrate was used. An ohmic contact on the back of substrate was employed by the deposition of nickel and annealed in N_2 ambient at 1000°C. Cu contacts were deposited by the RF sputtering method at room temperature. Diameter and thickness of Cu contacts were 200 μ m and 200nm, respectively. To analyze effects of thermal annealing, an as-deposited Cu/6H-SiC junction was treated in N_2 ambient at 300 ~700°C for 5 minutes. Electrical properties of Cu/6H-SiC junctions were measured at room temperature.

An as-deposited Cu/6H-SiC contact had a good Schottky property, which showed a relatively high current density of 100A/cm^2 at 2V and a low leakage current density of mid -10^{-8}A/cm^2 at −300V. Under the forward bias condition, small ideality factor (n) about 1.05 and barrier height about 1.2V were obtained (Fig.1). The Schottky barrier height of the as-deposited Cu/6H-SiC contact was also analyzed by internal photoemission spectroscopy, which was determined to be 1.26V.

As shown in Fig.1, annealing under 500°C was found to be improved the Schottky barrier height, *i.e.* the barrier height increased up to about 1.45V, and the ideality factor was kept below 1.1. The annealed Cu/6H-SiC interface was considered to be chemically reacted, leading to the thermally stable Schottky junction under high-temperature operations.

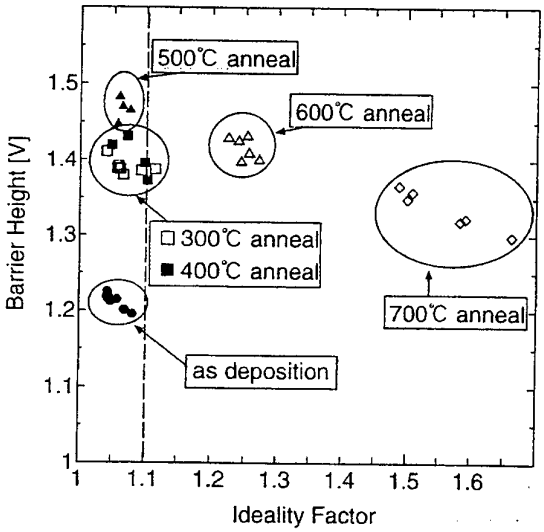


Fig. 1 Distribution of ideality factor and barrier height as a function of annealing temperature.

With the increase of annealing temperature over 500°C, however, Cu/6H-SiC Schottky properties became poor : Barrier heights decreased to about 1.3V, and ideality factors increased over 1.45 with the annealing at 700 °C. From X-ray diffraction analysis, degradation of Schottky properties is caused by the formation of Cu_5Si at the Cu/6H-SiC junction.

A Novel Technique for Shallow Angle Beveling of SiC to Prevent Surface Breakdown in Power Devices

J. Neil Merrett, David C. Sheridan[a], John R. Williams, Chin-Che Tin, John D. Cressler[a]

Department of Physics, Auburn University, Auburn, AL 36849 USA
Ph. 334-844-4795 Fax. 334-844-4613
[a]Electrical and Computer Engineering Department, Auburn University, AL 36849 USA

In order to realize the full potential of SiC power devices, it is necessary to prevent premature breakdown at the surface of the device. Theory shows that beveling the sidewalls of the mesa on which a device is constructed can reduce the surface electric field and ensure that breakdown occurs in the bulk material. Angles as large as 45° are sufficient to ensure bulk breakdown for a positive bevel. However, for negative bevels, much smaller angles are required [1]. We have developed an etching technique in which angles as low as a few degrees (Fig. 1) can be achieved at junctions up to several microns deep. This technique involves applying a very tall pillar of Nano™ XP SU-8 photoresist and then spinning on a layer of much thinner Microposit® STR 1045 photoresist. The surface tension of the 1045 pulls it up the sides of the SU-8 pillar forming an etch mask with parabolic edges. This technique has been applied to 4-H SiC thyristors (Fig. 2), and results will be presented comparing bevel angle and maximum forward breakover voltage. To date, a forward breakover voltage of around 1200 volts has been achieved for a blocking layer thickness of around eleven microns doped at $1x10^{16}cm^{-3}$.

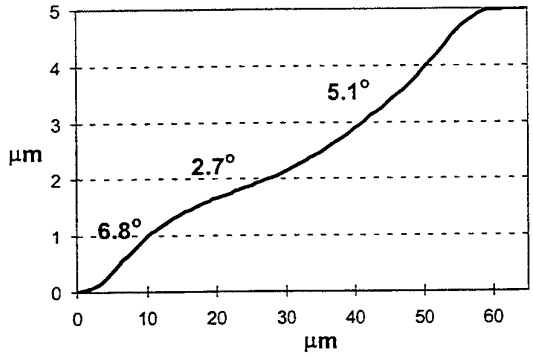


Fig. 1: Profile of a beveled mesa.



Fig. 2: SEM of GTO thyristor structure.

[1] B. J. Baliga, *Power Semiconductor Devices*, PWS, Boston,1996, pp. 103-105

Electrochemical characterization of p-type SiC

M. Kayambaki[1], K. Zekentes[1], K. Tsagaraki[1], E. Pernot[2] and R. Yakimova[3]
[1] *MRG, IESL, FOundation for Research and Technology-Hellas, P.O. Box 1527, Vassilika Vouton, 711 10 Heraklion, Greece, Tel: +30-81-394105, Fax: +30-81-394106, e-mail: trifili@physics.uoc.gr*
[2] *Laboratoire de Materiaux et de Génie Physique, UMR CNRS/INPG 5628-ENSPG, BP 46, 38402 Saint Martin D'Heres, France*
[3] *Department of Physics and Measurement Technology, Linköping University, 58183 Linköping, Sweden*

Electrolytic dissolution of silicon carbide is the only etching process that may be carried out at room temperature. In a previous work, we have shown that it is possible to employ an Electrochemical Capacitance-Voltage (ECV) profiler for the determination of the epilayer doping level and the thickness of p-type 6H-SiC films[1]. In this work, we present our results for 4H-SiC and we show that the ECV profiler can be used for evaluating the types and the distribution of crystal defects on both the Si and C faces of p-type 6H and 4H-SiC. In this way, both the doping profile and the crystal quality can be determined with only one measurement. Thus, electrochemical C-V profiling becomes a powerful characterization method for epitaxial and implanted SiC films.

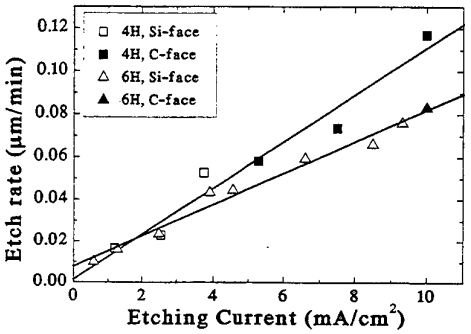


Fig. 1. Dependence of the etch rate on the etch current density for 6H and 4H polytypes and for both surface polarities.

The investigated samples were either commercially available (CREE Inc.) or grown by liquid phase and sublimation epitaxy [2]. The etching conditions were the same with that in ref. [1]. A series of measurements and results like the linearity of Schottky-Mott plot, the low value of the cathodic dark current, the smoothness of the etched surface and the abruptness of the etch walls for each etching experiment allowed us to control depth resolution and doping profile accuracy.

A clear linear dependence of the etch rate on the etching current without any saturation etching is obvious from the Fig. 1 as expected for electrochemical etching of the same material. Doping and thickness uniformity studies along the same sample demonstrated the usefulness of the method for optimizing growth conditions.

Doping profiles on 4H-SiC films grown by sublimation epitaxy showed a surface layer of 0.1μm thick with a lower acceptor concentration suggesting an Al depletion of the surface layer. This can be related to a thin surface layer growth during the cooling down stage with a lower Al incorporation.

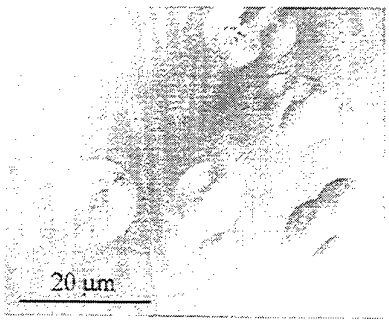


Fig. 2. Optical microscope image showing the etch-pit appearance following electrochemical etching of 6H-SiC epitaxial film.

Optical (Fig. 2.), Scanning Electron and Atomic Force microscopy images showed the appearance of etch pits on the etched surfaces. The similarities with surfaces obtained following anisotropic etching in molten salts are obvious. The round pits of Fig. 2 relate to dislocations as they maintain both the shape of pointed bottom as well as their distribution as etching proceeds [3].

This work was partly supported by the NATO SfP 971879 grant.

References

1. M. Kayambaki, K. Zekentes, to be published in *Proc. ICSCRM'99*, Oct. 1999, Raleigh, NC.
2. M. Syväjärvi, R. Yakimova, M. Tuominen, A. Kakanakova-Georgieva, M. F. MacMillan, A. Henry, Q. Wahab, E. Janzén, J. Cryst. Growth 197 (1999) 155
3. J. Takahashi, M. Kanaya and Y. Fujiwara, J. Cryst. Growth, 135(1994), 6

Indications for Nitrogen-Assisted Removal of Carbon from SiO_2–SiC Interface

P. Jamet, S. Dimitrijev, and P. Tanner

School of Microelectronic Engineering, Griffith University, Nathan Qld. 4111, Australia
(Ph: +61-7-3875 3625, Fax: +61-7-3875 5198)

ABSTRACT

Thermal oxidation is the only process known to lead to MOSFET-quality dielectric–semiconductor interface. This fact and the unique electrical properties of SiO_2 are the main reasons for the long-lasting dominance of silicon over many other semiconductor materials, with apparently better bulk properties. Thermal oxidation of SiC also leads to creation of SiO_2 at the surface, and in addition to that, SiC is a wide energy-gap material with superior bulk parameters compared to silicon. However, the release of carbon during thermal oxidation of SiC appears as an inherent disadvantage. Presence of carbon at the interface has been identified as a reason for unfavorable electrical properties of the SiO_2-SiC interface [1].

Our investigation of electrical and physical properties of NO-nitrided SiO_2-SiC interface have indicated the possibility that carbon is more efficiently removed from the interface in the case of the nitrided samples [2,3]. However, there is a belief that nitrogen is unlikely to react with carbon to remove it from the interface. In this paper, we will report and analyze two additional effects that are in a direct correlation with the hypothesis of nitrogen-assisted removal of carbon from the SiO_2-SiC interface (Table 1).

Table 1 Effects indicating nitrogen involvement in the process of carbon removal from SiO_2-SiC interface

Brief Description	Reference
• Atomic Force Microscopy reveals that NO nitridation removes carbon clusters from the SiO_2-SiC interface	[2]
• XPS binding-energy analysis indicates existence of C–N bonds near the SiO_2-SiC interface	[3]
• Oxide growth rates in NO and N_2O ambient indicate increased growth-site densities, possibly created by removal of carbon by NO and N_2O	this paper
• Lower nitrogen concentration at the SiO_2-SiC interface (according to NRA [4], XPS and SIMS analyses) could be related to the nitrogen involvement in carbon removal from the SiO_2-SiC interface	this paper

References:

[1] V.V. Afanas'ev, A, Stesmans and C.I. Harris, proc. 7th Intl. Conf. SiC, III-nitrides and related materials, Pt. 2, Stockholm, p.857, (1997).

[2] P.Tanner, S. Dimitrijev, H.F. Li, D. Sweatman, K.E. Prince, and H.B. Harrison, J. Electron. Mater., 28,n° 2 p.109 (1999).

[3] H. F. Li, S. Dimitrijev, D. Sweatman, H.B. Harrison, and P. Tanner, J. of Appl. Phys., vol. 86, n° 8, p. 4316 (1999).

[4] K. McDonald, M. B. Huang, R.A. Weller, and L.C. Fedman, Appl. Phys. Lett. 76, p. 568 (2000).

Influence of post-oxidation process on the MOS interface and MOSFETs properties

S.Suzuki[1], W.J.Cho[2], R.Kosugi[2], J.Senzaki[2], S.Harada[2], K.Fukuda[2]
[1]Ultra-Low-Loss Power Device Technology Research Body (UPR) / R&D Association for Future Electron Devices (FED)
c/o Electrotechnical Laboratory, 1204, 1-1-4 Umezono, Tsukuba, Ibaraki, 305-8568, JAPAN
Phone: +81-298-61-3320, Fax: +81-298-61-3397, E-mail: seiji@etl.go.jp
[2]UPR / Electrotechnical Laboratory; 1-1-4 Umezono, Tsukuba, Ibaraki, 305-8568, JAPAN

Improvement of the thermally grown SiO_2/SiC interface is a critical issue to realize SiC MOSFETs and MOS related devices. Here, we report on the influence of the post-oxidation process on the properties of MOS interface and MOSFETs, especially on the difference between high-temperature post-oxidation annealing (POA) in H_2 [1] and re-oxidation annealing (ROA) in the wet O_2 ambient [2]. 4H-SiC(0001) wafers with a lightly doped homoepitaxial layer were cleaned by the standard RCA cleaning and sacrificial oxidation. They were oxidized in dry O_2 at 1200°C resulting in 45±2nm-thick oxide. After oxidation, a 30min *in-situ* Ar annealing was performed at 1200°C, then cooled down in Ar with the ramping rate of –5°C /min to 600°C. Some oxidized samples were post-annealed in pure H_2 or wet O_2 ambient. H_2 POA and wet ROA was performed at 800°C for 30min and at 950°C for 3hours, respectively. Aluminum was evaporated as the gate and backside electrodes. Simultaneous capacitance-voltage measurements were performed using KI-82 system to analyze the energy distribution of the interface trap density D_{it}.

Fig.1 shows energy distribution of D_{it} for the (a) *n*- and (b) *p*-type SiC MOS capacitors. High temperature H_2 POA reduced D_{it} in the *n*-type 4H-SiC MOS interface [1], no change was observed in the *p*-type MOS. In contrast with the results of H_2 POA, wet ROA reduced the D_{it} in the *p*-type MOS interface as ever reported [2], however, it increased the D_{it} in the *n*-type MOS. These results suggested that the D_{it} near the conduction band and the valence band have the quite different origin. The relationship between the MOS interface and the MOSFETs properties are now being studied.

This work was performed under the management of FED as a part of the MITI NSS Program (R&D of Ultra-Low-Loss Power Device Technologies) supported by NEDO.

[1] K.Fukuda et al., Appl. Phys. Lett. 76, 1585 (2000), [2] L.A.Lipkin et. al., J. Electron. Mat. 25, 909(1996)

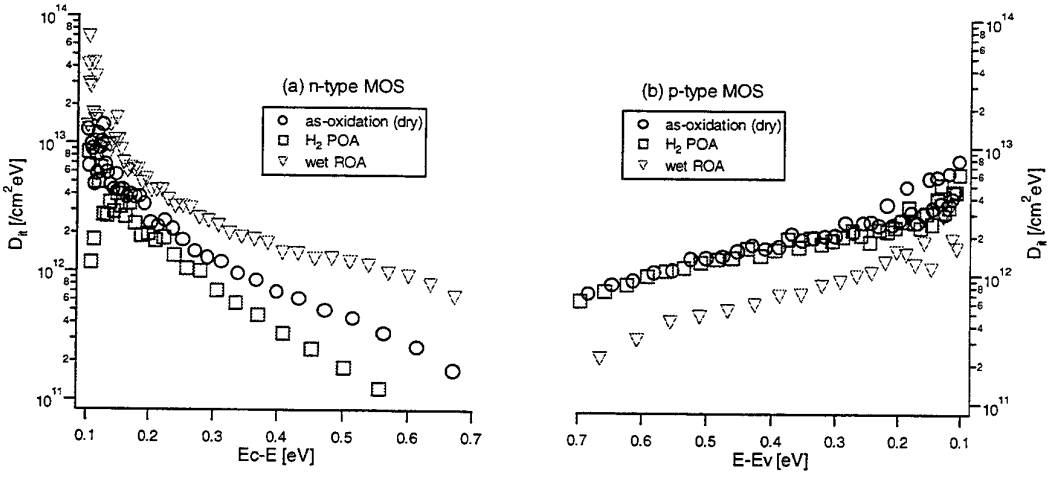


Fig1. Energy distribution of D_{it} for the (a) *n*-type and (b) *p*-type 4H-SiC MOS capacitors.

Remote PECVD oxide utilized in U-MOS structures and different MOSFETs on SiC

S. Scharnholz, O. Hellmund, J. Stein, B. Spangenberg, and H. Kurz
[a] Institut für Halbleitertechnik der RWTH Aachen, Sommerfeldstraße 24, D-52074 Aachen, Germany,
Tel.: +49 241 80 7894, Fax.: +49 241 8888 246

Among the most promising properties of SiC, the possibility to oxidize this material to SiO_2 playes a central role from the technology point of view. On the way to a SiC-based MOS-technology the mircoscopic mechanism of oxidation has to be investigated thoroughly. Although, the oxidation rate and interface quality is still quite poor compared to Si, there has been a lot of progress made recently. Especially the problems of the low oxidation rate and the anisotropy encountered have been overcome using deposited oxides instead of thermally grown ones. This deposition technology is critical for the fabrication of U-MOSFETs or *recessed channel* (*RC*) MOSFETs on the Si face of SiC wafers.

It has already been found on MOS capacitors, that oxide deposited by the *remote* (*R*) PECVD process, exhibits a low density of SiC/SiO_2 interface states and fixed oxide charges after subsequent heat treatments in inert gas and/or hydrogen.[1] In this contribution we report investigations on MOSFET parameters, especially on channel mobility, affected by the different process steps within the RPECVD-technique. The process sequence of oxide formation, as shown in Tab. 1, starts with two pre-deposition processes.

Tab. 1 Process sequence for the realization of high quality remote (R) PECVD oxide.

No.	Process	Gas	Temperature	Equipment	Purpose
1	plasma pre-cleaning	H_2	250°C	RPECVD	Smoothening, reduction of C
2	plasma pre-oxidation	O_2	250°C	RPECVD	Definition of the interface
3	oxide deposition	SiH_4/ O_2	250°C	RPECVD	Deposition of the SiO_2-layer
4	post oxidation anneal	Ar	1150°C	Furnace	Reorganization, out-diffusion of CO_x
5	re-oxidation	O_2/ H_2O	950°C	Furnace	Compensation of oxygen deficits

The performance of RPECVD oxide is tested in both, planar structures (MOS-capacitors and *not self aligned (notSA)* MOSFETs) as well as vertical, grooved structures (RC-MOSFETs and U-MOS capacitors). In contrast to transistors previously discussed in the literature [2], the source and drain of the actual *notSA*-devices were implanted with higher doses and energies at the FZR[3], leading to a lower sheet resistance and therefore to a better on-state behavior.

The results on RC-MOSFETs and grooved MOS structures encourage the use of RPECVD oxides in U-MOSFETs on SiC. The channel mobility of RC-MOSFETs indicates no additional, etch induced interface defects. I-V-measurements on MOS-diodes (with and without U-grooves) demonstrate an overall stability of RPECVD oxides with a maximum electric breakdown field of 9 MV/cm. In order to assess the quality of the oxide deposited, results from stress experiments will be presented, performed on MOS-diodes and MOSFETs with RPECVD and thermal oxides on 4H and 6H-SiC.

---

[1] A. Gölz, G. Lucovsky, K. Koh, D. Wolfe, H. Niimi, and H. Kurz: Plasma-assisted formation of low defect density silicon carbide-silicon dioxide, $SiC-SiO_2$, interfaces; Microelectronic Engineering 36; 1997.
[2] S. Scharnholz, E. Stein von Kamienski, A. Gölz, C. Leonhard, and H. Kurz; Dependence of channel layer mobility on the surface step orientation in planar 6H-SiC MOSFETs; Materials Science Forum 164-268; 1998.
[3] D. Panknin and W. Skorupa, Forschungszentrum Rossendorf (FZR), Institut für Ionenstrahlphysik und Materialforschung, Postfach 510119, D-01314 Dresden, Germany.

Dependence of wet oxidation on the defect density in 3C-SiC

M. Eickhoff*, N. Vouroutzis[1], A. Nielsen, G. Krötz and J. Stoemenos[1]

Daimler Chrysler AG, Department FT2/M, Postfach 800465, 81663 München, Germany
[1]Aristotle University of Thessaloniki, Physics Department, 54006 Thessaloniki, Greece

The oxidation of 3C-SiC films epitaxially grown on Si substrates is important for device fabrication, as well as for realization of complex structures, like 3C-SiC On Insulator (SICON), using the technique of wafer bonding. The presence of planar defects in results in an inhomegeneous wet oxidation, whereas dry oxidation exhibits smoother surfaces, not affected by the presence of the defects. However, the interface trap density in thermal oxides obtained by dry oxidation is almost one order of magnitude higher than in the case of wet oxidation. Thus, wet oxidation is superior to the because of the lower density of the fixed oxide charges, interface states and deep traps. Another disadvantage of dry oxidation processes is the very low oxidation rate, which is not compatible with the device fabrication processes. In the present work the dependence of oxidation rate and the structural characteristics of thermal oxide obtained by wet oxidation on the defect density in 3C-SiC films was studied.

3C-SiC films were deposited on (100) Si wafers in a low pressure CVD reactor at 1200°C using methysilane. After deposition a polishing step was performed to ensure equivalent surface roughness before oxidation. Then thermal oxidation was carried out at 1150°C in a horizontal hot-wall quartz tube furnace at atmospheric pressure O_2-atmosphere. Water vapour was added to the oxygen by passing the O_2-flow through a de-ionized water bubbler at 95°C. Transmission electron microscopy (TEM) and atomic force microscopy (AFM) were used to characterize the resulting oxide layers.

After oxidation hillocks were observed at the surface forming close loops, as AFM observations reveal. After removing the oxide by dipping the specimen in HF the hillocks appear as grooves. These hillocks were attributed to the preferential oxidation at the antiphase boundaries (APBs), which are related with weak C-C and Si-Si bonds, resulting in rough oxide surface. In order to have a direct proof on the relation of the APBs with the hillock the following experiment was performed. An oxidized specimen was thinned from the backside so that only the oxide and a thin layer from the uppermost part of the 3C-SiC film were left for plane view TEM (PVTEM) observations. Due to the thick amorphous oxide the diffraction contrast was very poor, attributed mainly to oxide thickness variations, exhibiting similar morphology as the AFM observations reveal. Subsequently the oxide was etched from this PVTEM specimen, so that only the SiC was left. Now strong diffraction contrast due to the crystalline 3C-SiC is observed in the same area. The easily recognized APBs follow the same close loops already observed before oxide removal.

The 3C-SiC films contain a high density of defects, which is reduced as the film thickness increases. The influence of the defect density in oxidation rate was systematically studied by performing oxidation on films with different thickness and determining the defect density by TEM observations. In order to study the oxidation rate of the 3C-SiC close to the SiC/Si interface a freestanding 3C-SiC diaphragm was prepared which allowed simultaneous oxidation of the silicon carbide surface as well as the former interface layer. Significant difference was found in the oxidation rate in the two sides. The oxidation rate increases with the defect density, exhibiting a semi-logarithmic relation.

* Corresponding author, present adress: Infineon Technologies, Dep. WS GS SNS D3, Otto-Hahn-Ring 6, 81739 Munich, Germany, Phone: (++49) 89-234 42890, Fax: (++49) 89-234 49687 e-mail: Martin.Eickhoff@infineon.com

Design and Characterization of 2.5kV 4H-SiC JBS Rectifiers with Self-aligned Guard Ring Termination

David C. Sheridan, J. Neil Merrett[1], John D. Cressler, Stephen E. Saddow[2], John Williams[1], Charles Ellis, and Guofu Niu

Alabama Microelectronics Science and Technology Center, 200 Broun Hall,
Auburn University, Auburn, AL 36849 USA Ph. (334) 844-1894 Fax. (334) 844-1888
[1]Department of Physics, Auburn University, Auburn, AL 36849 USA
[2]Emerging Materials Research Laboratory, Mississippi State University, MS 39762 USA

2.5kV JBS rectifiers were optimized with numerical simulations and fabricated with a innovative self-aligned guard ring edge termination design. This simple structure is advantageous because it allows the active area and edge termination implantation to be fabricated simultaneously, thereby simplifying processing by easing lithography tolerances and eliminating the precise dopant activation needed with junction termination extensions (JTE). With the optimized structure, the extracted specific on-resistance of 17mΩcm^2 is the lowest reported for Ni JBS diodes with breakdown voltages over 2kV [1]. Breakdown voltages (Fig.1) of 2.3-2.5kV (~60% ideal) correlated well with the simulated breakdown voltage of 2.4kV with 7 guard rings.

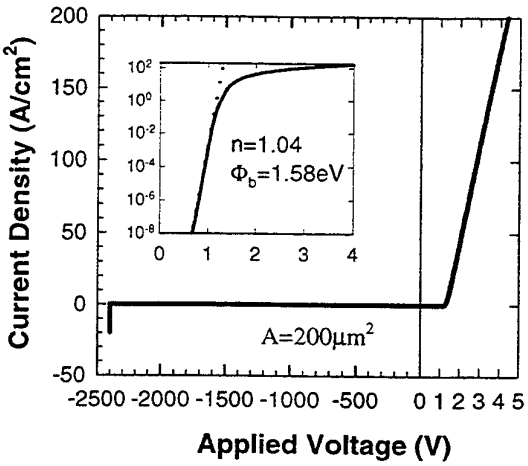


Fig. 1: IV characteristics of an optimized 200μm JBS diode with a Schottky width W=5μm.

JBS diodes were fabricated on 4H n$^+$ wafers with a 30μm 1-2.5x10^{15}cm^{-3} n$^-$ epitaxial layer. A single Al implanted box profile was used to form both the active JBS region and the guard ring edge termination. Al implants were annealed at 1600 °C in a silane ambient as has been described in the literature [2]. Ni was used for both backside ohmic and frontside Schottky contacts. Reverse current densities for the JBS structures (<1mA/cm^2 at 2000V) were at least an order of magnitude lower than comparable Schottky structures due to the reduced interface fields. High temperature characterization was performed up to 500°C. A barrier height of 1.58eV was calculated using an extracted A* of 0.0731AK^{-2}cm^{-2} from high temperature measurements. The measured forward voltage drop versus active Schottky width (W) is shown in Fig. 2, with the p$^+$ width held constant at 5μm.

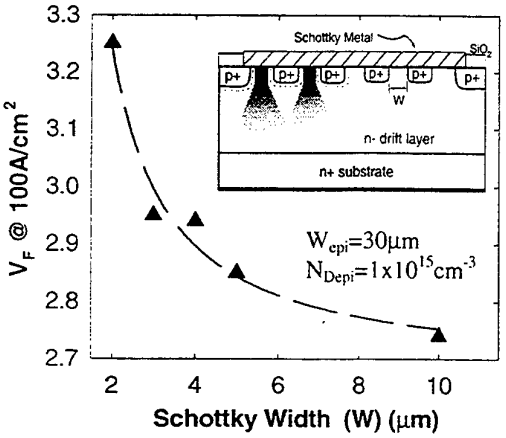


Fig. 2: Effect of active Schottky width (W) on forward voltage drop V_F.

[1] Y. Sugawara et al. ICSCRM'99, Raleigh, NC
[2] S. E. Saddow et al. ICSCRM'99, Raleigh, NC

SiC junction control, an alternative to MOS control high voltage switching devices

A. Mihaila[1], F. Udrea[1], G. Brezeanu[2], R. Azar[1] and G. Amaratunga[1]
1. Engineering Department, Cambridge University, Trumpington Street, Cambridge CB2 1PZ, UK
2. University "Politehnica" of Bucharest, Romania

This paper discusses for the first time the benefits of SiC junction control devices compared to MOS-type devices. Whereas MOS control silicon switching devices undoubtedly exhibit superior over-all performance compared to junction control devices due to reduced leakage, normally-off operation, high input impedance and improved SOA, this paper argues that SiC MOSFET devices have theoretical and practical disadvantages which may limit their operation and arguably bring back in light junction switching devices such as the JFET and SIT. In addition MOS-bipolar high voltage devices such as the Trench Insulated Gate Bipolar Transistors (IGBT) which have been extremely successful in silicon technology [1] will be in the authors opinion of very little use in SiC technology. This is because the SiC large band-gap also results in a large anode junction built-in potential which leads to high on-state voltages and, consequently, unacceptably high power losses.

This paper provides a comprehensive numerical comparison between 4H-SiC polytype 1.2kV SiC trench MOSFET and JFET. Trench technology has been selected for the MOSFET, since it offers the highest channel density and eliminates the parasitic JFET effect characteristic of DMOS structures. The cross section of a half a cell of the trench MOSFET is shown in fig.1 (a). In spite of its advantages, such as MOS voltage control and low saturation currents, SiC trench MOSFET suffers from several major drawbacks such as very high threshold voltage and poor mobility in the channel which adversely affects the on-resistance. Another severe drawback of the trench MOSFET is the gate oxide breakdown, which can occur in off-state, under high electric field condition [2]. We here carried out a numerical analysis of the oxide/SiC trade-off breakdown and determine the design conditions to avoid the premature breakdown. The study also points out that the theoretical value of the drift doping, calculated from the avalanche condition, can lead to premature breakdown due to punch-through of the p well [3]. The punch-through can be avoided by increasing the p well doping and decreasing the drift region doping or by making the channel longer. The first sets a very strong limitation on the minimum threshold voltage for a SiC trench MOSFET while the second and the third further degrades the on-resistance. The drawbacks encountered for SiC trench MOSFET, like gate oxide breakdown and poor mobility in the channel, can be eliminated by using a SiC JFET. A cross section of the JFET structure is shown in fig. 1 (b). Its distinctive feature is a buffer layer grown on the top of the drift region. In order to withstand a blocking voltage of 1.2kV, a negative voltage of about –20V should be applied to the gate. We have optimised the characteristics of the JFET to improve its on-resistance and avoid surface parasitic PIN diode breakdown The on-state characteristic of the JFET for different gate voltages is shown in fig. 2.

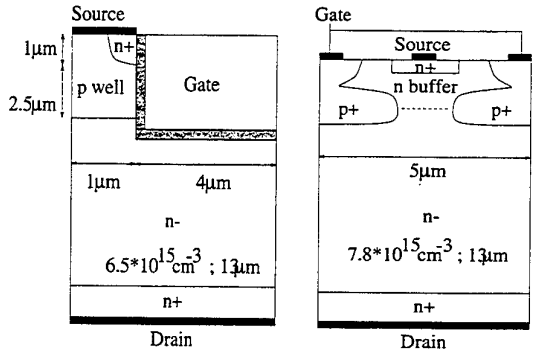


Fig. 1 (a) – Cross section of half of cell for the trench MOSFET; (b) – cross section of the JFET structure

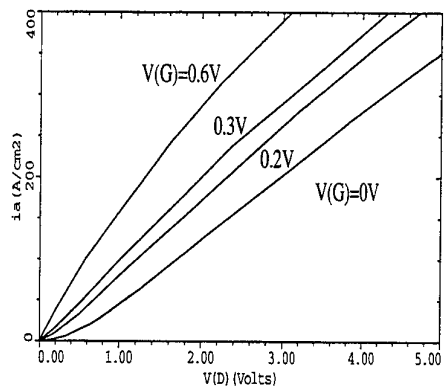


Fig.2 The on-state characteristics of the 1.2kV SiC JFET.

In summary, a SiC JFET is proposed as a viable alternative to the SiC trench MOSFET. In this way, MOSFET's major drawbacks, such as gate oxide breakdown, poor mobility in the channel and high threshold voltage can be overcome. Moreover, the on-resistance of the 1.2kV JFET is 2-3 times smaller than that of an equivalent SiC MOSFET. At the same time the JFET technology is easier than that of the MOSFET due to the elimination of trench gate formation. Nevertheless, the blocking of the JFET can only be accomplished by applying a negative voltage to the gate. This may lead to a compromise in the complexity of the control circuitry.

1. F. Udrea and al., IEEE Electron Devices Letters., vol. 20, No 8, pp 428-430, August 1999
2. A. K. Agarwal et al., Proc. of ISPSD '96, p. 119-122, 1996
3. R. Azar and F. Udrea, private communication

Characterisation of GaAlN/GaN superlattice heterostructures

Zs. Makkai, B. Pécz, M.A. di Forte-Poisson* and F. Huet*
Research Institute for Technical Physics and Material Science of the Hungarian Academy of Sciences, H-1525, Budapest, P.O.B. 49, Hungary. Phone: 36-1-392 2222 /1907
E-Mail: makkai@mfa.kfki.hu
*Thomson CSF, Laboratorie Central de Recherches, Domaine de Corbeville, 91404 Orsay, Cedex, France

Superlattices of GaAlN/GaN are promising candidates for the preparation of HEMT transistors, which might be used in high temperature, high power devices. GaAlN/GaN superlattices are extensively investigated in these days for the above reason. There is a special defect in GaAlN as well as in the above superlattices which is called V-shape defect (inverted hexagonal pits). The analysis of the above defect is the subject of the present paper.

Superlattices of $Ga_{0,94}Al_{0,06}N$/GaN have been grown onto thick GaN layers as well as onto sapphire directly at 1150°C by metalorganic chemical vapor deposition (MOCVD). Microstructure of the superlattices is investigated by transmission electron microscopy (TEM) in cross section, while the surface of the sample is investigated by scanning electron microscopy (SEM).

Fig. 1. shows the surface of a sample in which GaAlN/GaN superlattices are grown with the periodicity of 9 nm. The total thickness of the superlattice layers is about 1 μm. Fig. 1. shows the network of the V-shape defects formed on the surface.

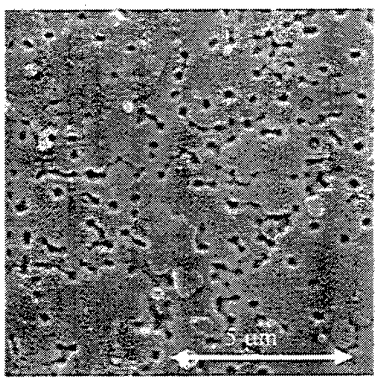


Fig.1.

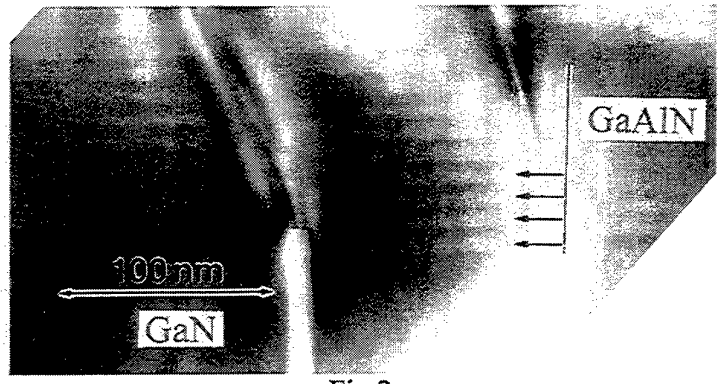


Fig.2.

Fig. 2. is a cross sectional TEM micrograph of the above sample, which shows that despite of the presence of V-shaped pits homogeneous superlattices are grown in the majority of the layer with sharp interfaces. V-pits are formed due to the segregation of aluminium to the side walls of the inverted hexagonal pyramid by the same mechanism as indium does in InGaN layers above a certain indium concentration. Each of the V-pits are connected to a dislocation in the layer. Therefore it is essential to decrease the defect density in these layers. When the superlattices are grown onto thick GaN, the above task means the improvement of the quality of thick GaN layer.

Injection Characteristics of p-n Structures Grown By Sublimation Heteroepitaxy of 3C-SiC on 6H-SiC

A.M.Strel'chuk, N.S.Savkina, A.N.Kuznetsov, A.A.Lebedev

Ioffe Physico-Technical Institute of the Russian Academy of Sciences, Politechnicheskaya 26, St. Petersburg, 194021, Russia
Phone: (812) 2479930, Fax: (812) 2476425,
E-mail: Anatoly.Strelchuk@pop.ioffe.rssi.ru

Cubic silicon carbide is in itself of considerable interest for semiconductor electronics having, in particular, the highest charge carrier mobility of all SiC polytypes. However, it is also known that β-SiC is sometimes found in the form of inclusions in epitaxial films of wider bandgap polytypes of α-SiC, in particular, in 6H- and 4H-SiC. Such inclusions of β-SiC (alongside with other inclusions, e.g., silicon and carbon, and crystal imperfections) undoubtedly affect the maximum parameters of devices (e.g., power devices) based on α-SiC. Therefore, studies of β-SiC and identification of the effects caused by the presence of β-SiC in α-SiC are of unquestionable interest.

In this work the results of a study of forward current–voltage (I-V) characteristics and injection electroluminescence (IE) of pn structures grown by sublimation heteroepitaxy are presented. Investigations by X-ray spectroscopy methods have shown that the epitaxial n-type film grown on a 6H-SiC (Lely) substrate over half of its area is a 3C-SiC film of rather high quality (the rest being a 6H-SiC film). The subsequently grown p-type layer consisted entirely of 3C-SiC (detailed characterization of the epitaxial layers by different methods will be presented in this conference in a paper [1]).

I-V characteristics of the grown structures were measured and these data were used to select structures having typical barrier properties, in particular, the exponential dependence of forward current on voltage of the form $I = I_0 \exp(qV/nkT)$. At low currents (10^{-7}- 10^{-3}A/cm^2) the minimum value of the ideality factor n were in the range of 2-3. Structures with such characteristics fell into two distinct groups with voltage values differing by about 0.7 V (with forward voltage drop 1.3-1.4 V and about 2.1 V at current density 10^{-5} A/cm^2 respectively). As the temperature was raised, the ideality factor diminished approaching the value of 2. Under forward current the structures luminescence emission was observed in the visible range. In different structures the IE color varied from red to blue. Besides, in many structures the IE emission was non-uniform in color over the structure area. Correspondence between IE features and parameters of I-V characteristics has been discussed. Interpretation of the forward currents was carried out by comparing parameters of the structures with thermal injection mechanisms in 3C-SiC pn structures (first identified and studied in pn structures prepared on the base of bulk 3C-SiC and presented by us at the previous European Conference on SiC [2]) as well as in 6H-SiC pn structures. Measured I-V characteristics were compared with typical excess currents in α-SiC based pn structures.

References

1. D.V.Davydov, A.A.Lebedev, N.S.Savkina, A.S.Tregubova, I.P.Nikitina, A.N.Kuznetsov, E.V.Bogdanova. 3C-SiC Epitaxial p-n Junction Produced by Sublimation Epitaxy on a 6H-SiC Substrate (this conference).
2. A.M.Strel'chuk, V.S.Kiselev, S.F.Avramenko. Thermal injection current in 3C-SiC pn structures. Materials Science and Engineering B61-62 (1999) 437-440.

Electron and Hole Transport in Amorphous SiC/ Crystalline Si Heterostructures

A.Nazarov, Ja.Vovk, V.Turchanikov and V.Krasnov
Institute of Semiconductor Physics, NASU, Prospekt Nauki 45, 03028 Kyiv, Ukraine
(E-mail: nazarov@lab15.kiev.ua, FAX: 380-44-265-6177)

SiC-Si heterostructures are of considerable interest in realizing wide-bandgap emitters or window regions in bipolar transistors, photodetectors and electroluminescence devices. The use of an amorphous a-SiC layer in these applications offers the prospect of decreasing significantly the deposition temperature, while retaining largely the important material properties such as band gap, thermal conductivity and chemical reactivity In this paper the mechanisms of charge transport in a-SiC/p-Si heterostructures (that display very high breakdown voltages) have been studied over a wide temperature range.

The SiC films, 1.0 μm thick, were deposited on <100> p-type silicon wafers at 1000°C by low-pressure CVD technique, with methyl-chlorosilane as source gas. Al contacts were then deposited on the SiC layer.

Electrical transport processes were studied by I-V and I-T characteristics, evaluated in the temperature range 80K – 473 K. The built-in potential was obtained from high-frequency (1MHz) C-V measurements in the same temperature range. Carrier trapping in the a-SiC/p-Si structure was studied by capacitance relaxation method.

At room temperature, the I-V characteristic of the Al/a-SiC/p-Si heterostructure represents a rectification ratio of 10^3 (at ±0.5V), and a hard breakdown at as high as 230V reverse bias. Forward I-V plots evaluated over a wide temperature range reveal three distinct regions of charge transport (Fig.1). In region **A** the current has a power law dependence on voltage [linear *log*(I) vs. *log*(V)]. Temperature dependence of the conduction is linear in this region, if plotted as $log(\sigma T^{1/2})$ vs. $T^{-1/4}$. Such dependence should be expected in the case of *electron* variable-range hopping (VRH) conductivity at Fermi level. From the slope of this dependence a density of state at Fermi level $N(E_F) = 2x10^{17}$ $cm^{-3}eV^{-1}$ has been estimated.

In region **B,** the *log*I-V plots have temperature-independent slopes. Such behaviour is characteristic of tunneling processes in the heterostructure. However, the temperature dependence of the current itself shows thermal activation, resulting in an expression for I_B of the form $I_B = I_{Bo} \exp(-E_a / kT)\exp(V / V_o)$, where E_a is the activation energy. E_a is found to decreases from 0.58 eV to 0.22 eV when the forward bias increases from 0.10 to 0.55 V. This I-V-T dependence has been ascribed to a multistep-tunnelling *hole* capture-emission process. In order to check the assumption about changing of carrier type when the A process changes the B one, a capacitance transient experiment for different forward biases have been performed. It is seen (Fig.2), that changing the (forward) filling voltage from 0.2V to 0.8V leads to changes in capacitance relaxation. At 0.2V, this relaxation corresponds to electron trapping and at 0.8V it corresponds to hole trapping in the a-SiC. Thus, we can conclude that at low temperatures increase of forward voltage leads to a change of type of charge carriers, which determine the electrical transport in the heterostructure.

In region **C**, we observe a current saturation that is caused by the bulk resistance of the a-SiC layer. In this region the I-V characteristics are described by a power law: $I_C=CV^N$, where N changes from 5 to 2 when the measurement temperature changes from 100K to 373K. Such dependence corresponds to space-charge-limited (SCL) current, which is possibly associated with hole transport limited by an exponential distribution of traps in the SiC film.

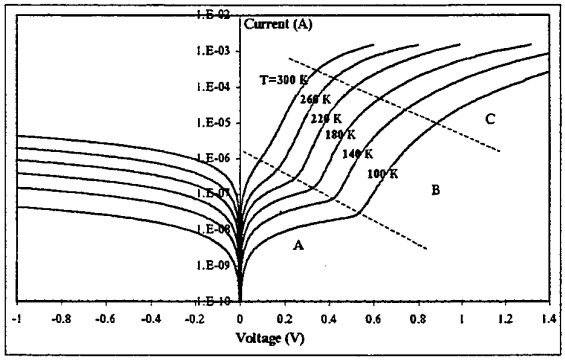


Fig.1.

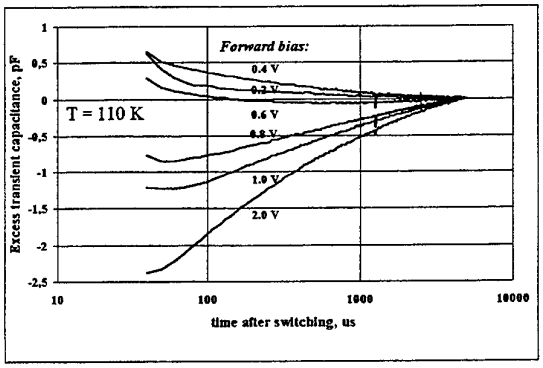


Fig.2.

Thus, main mechanisms of current transport in (a)SiC/p-Si heterostructure have been determined and the defect parameters relating to these processes have been estimated. Hole participation in the transport process is proved.

Noise behavior of 4H-SiC MESFETs at low drain voltages

C. Banc[1], A. S. Royet[1,2], T. Ouisse[1], O. Noblanc[3], and C. Brylinski[3]

[1] LPCS (UMR-CNRS 5531), ENSERG, 23 rue des Martyrs, BP 257, F-38016 Grenoble cedex 1, France
[2] LEMO (UMR-CNRS 5530), ENSERG, 23 rue des Martyrs, BP 257, F-38016 Grenoble cedex 1, France
[3] Thomson-CSF, Laboratoire Central de Recherches, Domaine de Corbeville, F-91404 Orsay cedex, France
correspondence: banc@enserg.fr

We have investigated the influence of two different substrate types on the low field (low drain bias) noise characteristics of 4H-SiC power MESFETs in the range 1 Hz-100 kHz. All devices were fabricated on semi-insulating SiC substrates. A first series included a p-buffer layer between the active channel and the substrate whereas the other series had no buffer. The first results obtained so far can be summarized as follows:

In "open channel" conditions, the noise characteristics are similar for the two substrate types: 1/f noise followed by a plateau at high frequencies (figure 1a). The noise levels around 100 Hz have the same magnitude for both types of devices. This can be seen on the high current part of figure 2.

As the devices are biased toward "pinch off" (figure 1b), the behaviors of the two substrates are radically different. Devices on buffered substrates exhibit volumic noise characterized by a linear relation between the drain current noise spectral density (S_{ID}) and the drain current (I_D) (figure 2). In such a case, the relative noise intensity is simply given in the form $S_{ID}/I_D^2 = \alpha_H/(N_{eff} \times f)$ [1], where N_{eff} is the total number of carriers in the active part of the device (proportionnal to I_D) and α_H is the Hooge parameter. This, in turn, leads to a constant α_H of about 8×10^{-6} (figure 3). In contrast, devices on non-buffered substrates show an almost constant noise level for all the biasing conditions (figure 2). In that case, an attempt to plot the Hooge parameter as a function of N_{eff} results in the $1/N_{eff}$ behavior shown on figure 3. This kind of behavior has already been seen on GaAs MESFETs built on InP substrates and was attributed to trapping phenomena near the channel-buffer interface of the devices [2]. In our case, the trapping could be ascribed to the lack of buffer and related to the high drain current transients observed at high fields [3]. The semi-insulating character of the substrate being achieved through compensation by deep levels, a direct contact between the active channel and the substrate favours trapping into the unoccupied states of the substrate.

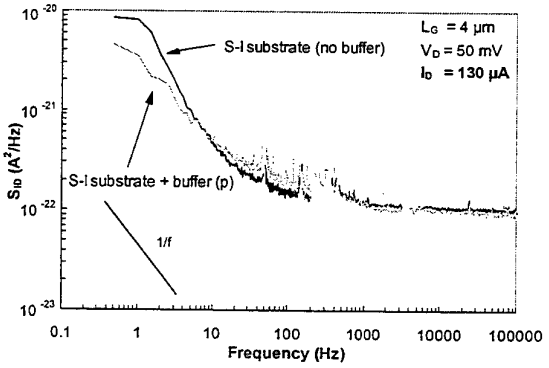


Figure 1a: Noise spectrum in "open channel" condition.

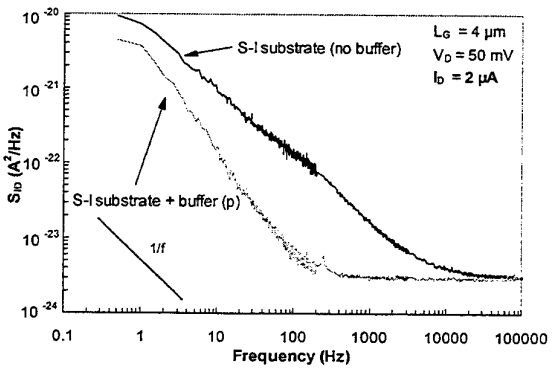


Figure 1b: Noise spectrum near "pinch off".

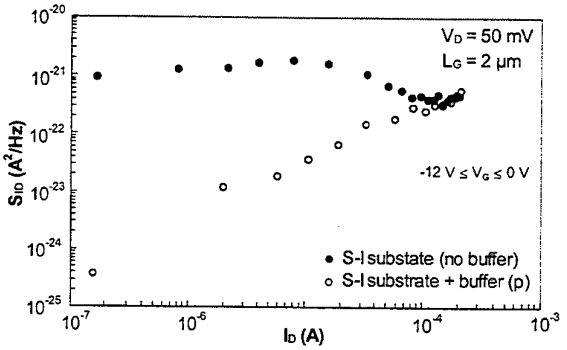


Figure 2: Noise level at 100 Hz.

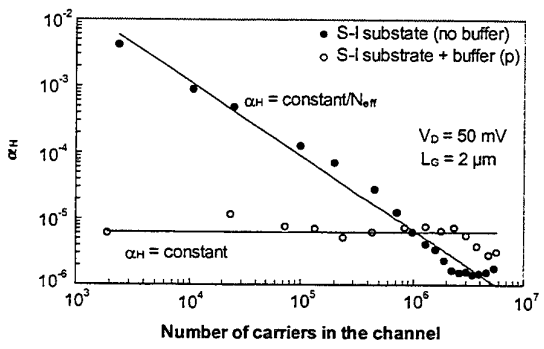


Figure 3: Hooge parameter at 100 Hz.

[1] F. N. Hooge, T. G. M. Kleinpenning and L. K. J. Vandamme, Rep. Prog. Phys. vol. 44, pp. 480-532, 1981
[2] Mourad Chertouk and Alain Chovet, IEEE Trans. Electron. Devices vol. 43 no. 1, pp. 123-28, 1996
[3] O. Noblanc, C. Arnodo, E. Chartier, and C. Brylinski, Mat. Sc. For. vol. 264-268, pp. 949-52, 1998

Short-channel effects in silicon carbide microwave MESFETs

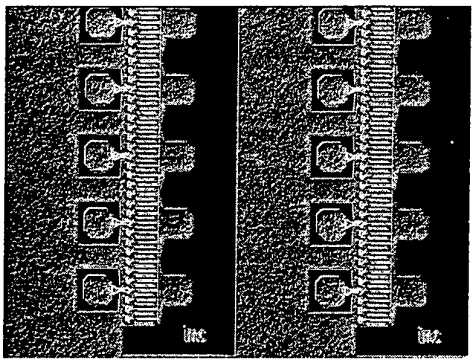
A.O. Konstantinov, A.-M. Saroukhan, J.-O. Svedberg, S. Karlsson, C. Adås, S.Tiensuu, C.I. Harris and A. Litwin*.

ACREO AB, Electrum-233, S-164 40 Kista-Stockholm, Sweden.
Fax: +46 8 750 5430; tel. +46 8 632 7792, e-mail andrey@acreo.se
*Ericsson Microelectronics AB, S-164 81 Kista-Stockholm, Sweden.

Silicon carbide is a promising material for microwave power device applications. Silicon carbide has a high breakdown field and a high saturation drift velocity, which can potentially increase the operation voltage by a factor of 20 as compared to silicon or GaAs. However, the performance of today's silicon carbide power microwave components does not meet theoretical expectations.

In the report we demonstrate that the operation voltage of silicon carbide microwave MESFETs is more commonly limited by short-channel rather than by avalanche breakdown. The high electric field at the drain side of the gate penetrates underneath the active channel region and modulates the channel length. This results in depletion of the buffer layer or the substrate underneath the gate. As the depleted region reaches the source a source-to-drain punch through occurs. The MESFET can no longer block the drain current in spite of the blocking voltage applied to the gate.

A theoretical study of short-channel effects has been performed with the use of tools for 2-dimensional semiconductor device simulation. Efficient means of short-channel effect suppression have been found, which employ non-uniform doping profile for the p-type buffer layer. An additional p-type layer with elevated p-doping was shown to considerably increase the punchthrough voltage.



Semiconductor structures for power silicon carbide MESFETs have been grown onto conductive substrates by depositing a 15-25 μm thick buffer layer, an active layer and an n+ contact layer using the hot-wall CVD technique. The active region was formed by mesa etching through the contact layer, and 0.9 μm Schottky gates were formed using the lift-off photolithography technique. High power devices had up to 140 parallel gates. Device paralleling was achieved using the airbridge technique. Image of completed airbridged MESFETs is shown in the figure.

Investigation of device characteristics has demonstrated a good agreement between model predictions and actual device parameters. In the report we will compare the characteristics of the MESFETs fabricated at ACREO with literature data and with those for the devices available from a commercial vendor.

Planar p-n diodes fabricated by MeV-energy and high-temperature selective implantation of aluminum to 4H-SiC

H. Sugimoto, S. Kinouchi, Y. Tarui, M. Imaizumi, K. Ohtsuka, T. Takami, T. Ozeki
Mitsubishi Electric Corp. Advanced Technology R&D Center
8-1-1, Tsukaguchi-Honmachi, Amagasaki City, Hyogo 661-8661
Tel.:+81-6-6497-7086, Fax.:+81-6-6497-7295, e-mail: sugimoto@qua.crl.melco.co.jp

High-energy ion implantation techniques are required for the fabrication of thick p-type regions, which is desirable for the designs of high breakdown voltage devices. High-temperature ion implantation techniques are also necessary to form excellent p-n junctions by reducing implantation damages. We report on Al implantation at 1000℃ with the energy of 7.0MeV and the fabrication of planar p-n diodes with 3 μ m thick p regions.

Epitaxial layers (n^-:$5x10^{15}/cm^3$) on 4H-SiC substrates were used for implantation experiments. Box profiles were formed by 7 implantation steps with energies from 0.9 to 7MeV. The depth profile by SIMS showed 3 μ m thickness and about $5x10^{18}/cm^3$ concentration[1]. Effects of temperatures at implantation (*Timplant*) and temperatures for activation annealing (*Tanneal*) were studied. Samples implanted at RT, 500℃ and 1000℃ were annealed at from 1300℃ to 1650℃ in Ar for an hour and characterized by CV and RT Hall effect measurements.

At the dose level employed, *Timplant* has no apparent effect on elctorical properties measured by CV or Hall effect measurements. On the other hand, *Tanneal* has apparent effects. Acceptor densities increase with *Tanneal* and approach the Al concentration measured by SIMS ($5x10^{18}/cm^3$). Most of the implanted Al ions are activated to acceptors for *Tanneal* over 1500℃. Hole density shows the same tendency and reaches $2.5x10^{17}/cm^3$ over 1500℃. Hall mobility also increases with *Tanneal* to $30cm^2/Vs$, which is comparable with the reported data of doped epitaxial layers. Sheet resistance decreases with *Tanneal* to 5kΩ/□.

Planar p-n diodes were fabricated on n^- epitaxial layers with the thickness of 10 μ m by selective ion implantation with the masks of Mo under the conditions mentioned above. Fig.1 shows the cross sectional SEM view of Mo mask and implanted and annealed p region. Slopes at Mo edge formed by wet etching bring about sloped implantation profile. The depth of p region (4.1 μ m) accords with the depth including the tails of the Al distribution.

Fig. 2 shows the typical I-V characteristics of the p-n diodes. Breakdown voltage is about 1kV and differential on-resistance is $6m\Omega cm^2$ at $100A/cm^2$. Influence of *Timplant* and *Tanneal* on diode characteristics will be discussed.

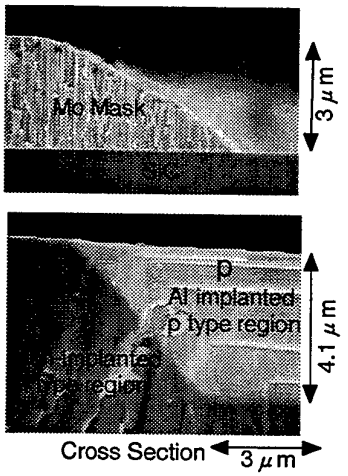


Fig. 1 SEM view of Mo mask and p-n junction.
(*Timplant*:500℃)

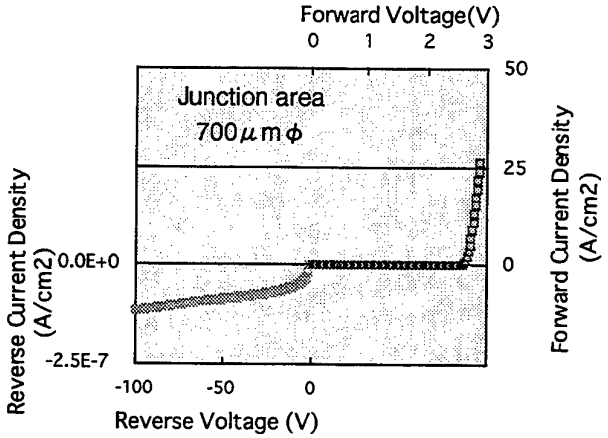


Fig. 2 p-n diode characteristic.
(*Timplant*:1000℃)

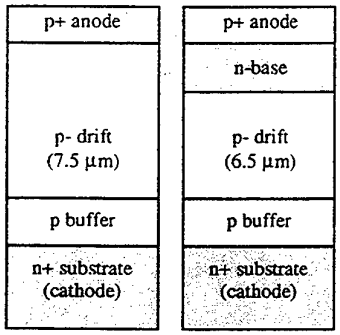
(Ion energy: 0.9-5.6MeV, *Tanneal*:1575℃)

[1]S.Kinouchi, H.Sugimoto et al., International Workshop on Hard Electronics'98 S2-08 (1998)

Characteristics of Epitaxial and Implanted N-Base 4H-SiC GTO Thyristors

Jeffrey B. Fedison and T. Paul Chow
Center for Integrated Electronics and Electronics Manufacturing
Rensselaer Polytechnic Institute, Troy, NY 12180, U.S.A.
Tel: (518) 276-6044, Fax: (518) 276-8761, e-mail: fedisj@rpi.edu

We report on the electrical characteristics of 4H-SiC GTO thyristors made with epitaxial and implanted n-base layers. An implanted n-base approach allows greater flexibility in the n-base doping profile compared to the epitaxial approach. In this work we have implanted the n-base with phosphorus donors using high energy ion-implantation to achieve a 1 μm thick n-type layer with a doping concentration of $4x10^{17}$ cm^{-3}. In effect this converts the first 1 micron of the lightly doped p-type drift layer ($5x10^{15}$ cm^{-3}) into an n-type layer as shown in Figs.1a and b. This is the first report of an implanted n-base GTO thyristor in silicon carbide to date. The implant profile was first simulated using TMA Suprem-III to achieve a box profile and the actual implantation was carried out at 500°C and then annealed at 1200°C in argon.



1(a) 1(b)

Forward characteristics of the implanted n-base GTO are shown in Fig. 2 in which the blocking voltage is 250V at room temperature and the on-state voltage is 8.7 V at 0.8 mA (1A/cm^2). The on-state voltage increases slightly with temperature (V_{AK}=9.2 V at 75°C). The gate trigger current is 1 mA at room temperature and increases to 10 mA at 75°C. Electrical test structures were fabricated on the same wafer to monitor the specific contact resistance and the n-base sheet resistance. Contact resistance measurements yielded ρ_c values of $1.5x10^{-4}$ and $1.3x10^{-2}$ Ω·cm^2 respectively for the n- and p-contacts. The n-base sheet resistance is shown in Fig. 3 as a function of temperature at two different locations on the wafer where a higher than expected sheet resistance is found, possibly due to implant damage or incomplete substitutional incorporation of phosphorus. At 25°C, the expected sheet resistance is 1.2 kΩ/Sq. assuming an electron mobility of 350 cm^2/Vs and 50 percent donor ionization whereas measured values are about 40 times higher in the range of 40-50 kΩ/Sq. at room temperature. Characterization at higher temperatures is in progress and will be reported at a later time.

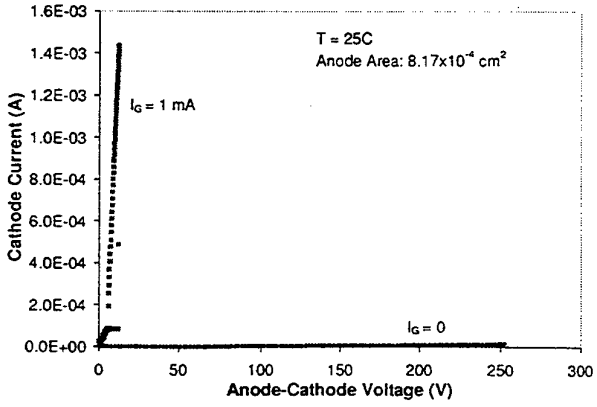


Fig. 2. Forward on-state and blocking characteristics of implanted n-base GTO thyristor

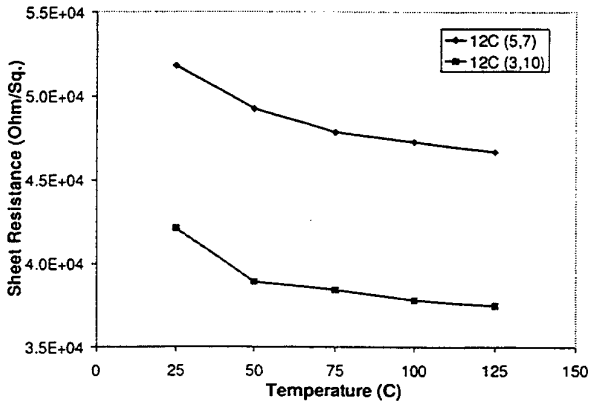


Fig. 3. Sheet resistance of implanted n-base versus temperature.

Acknowledgement: The authors gratefully acknowledge the support of the Office of Naval Research under MURI Grant #N0014-95-1-1302, monitored by Dr. John Zolper.

A high performance JBS rectifier - design considerations

F. Dahlquist[1,2], H. Lendenmann[1], M. Östling[2]

[1]ABB Corporate Research, Electrum 215, SE-164 40 Kista, Sweden
Phone: +46-8-7521040, Fax: +46-8-7521098, email: fanny.dahlqvist@secrc.abb.se
[2]Department of Electronics, KTH, Electrum 229, SE-164 40 Kista, Sweden

The Junction Barrier Schottky (JBS) diode in silicon carbide is a promising rectifier for the low voltage range (<3kV) since it combines the low forward voltage drop of a Schottky diode with blocking properties of a PiN diode. In comparison with a SiC PiN diode it is the unipolar low static losses that makes the JBS diode attractive in said voltage range. When compared to a Si PiN diode it is mainly the low-loss switching behavior which makes the JBS diode a competitor for high operating frequencies. Furthermore, the JBS diode has low leakage properties at blocking voltage also for elevated temperatures.

Since the drift region resistance is always the same for a given blocking voltage the main parameters are the Schottky barrier height and the p+ grid design, controlling the trade-off in forward voltage drop and leakage current for a given voltage. The p+ grid parameters are the spacing between p+ regions, grid geometry, shape of p+ profiles and the resulting total Schottky area. Lowering of the leakage current without too much increase in on-resistance can be obtained if an optimized p+ grid design is used.

High voltage Schottky-, JBS- and PiN diodes were processed on the same 4H-SiC wafer [1]. Forward voltage drops of less than 2V at 100A/cm^2 were obtained on JBS devices which blocked 2.5-2.8 kV. These blocking voltages correspond to the same expected theoretical breakdown field strengths for the used epi as for the PiN diodes. The devices show also a low leakage current (10^{-5} A/cm^2 at 225 °C and -500 V) at higher temperatures and operate well up to the tested temperature of 225 °C.

From experiment splits in grid dimensions it was found that a reduction in p+ grid spacing reduces the leakage by over a decade while not increasing the on-state. Further design controlled reduction of the leakage current leads to a moderate increase of the forward voltage. However, the minimum spacing is restricted when high current characteristics are taken into account since the characteristics change with grid dimensions. Thereby the suitable operating current density versus low forward voltage drop becomes a trade-off. These experimental results are corroborated with device simulations.

Furthermore, experiment splits in the implanted p+ grid profiles revealed a trade-off in forward voltage drop/leakage current depending of dopant (boron or aluminum). Current-voltage measurements of the on-state characteristics showed higher forward voltage drop for JBS diodes with boron implanted grid compared to the aluminum-implanted diodes. This can be well explained by lateral boron diffusion decreasing the current conducting area in the boron-implanted grids. The lateral diffusion length was estimated to be in the same order of magnitude as reported vertical diffusion [2,3]. Thus, the designed p+ grid area versus Schottky area is strongly affected by this diffusion.

This contribution will in detail discuss the influence of all mentioned JBS design parameters on the measured device properties.

[1] F. Dahlquist, et. al "A 2.8kV, 2V forward drop JBS diode with low leakage", ICSCRM (1999), in print.
[2] F. Dahlquist, et. al."Demonstration of lateral boron diffusion in 4H-SiC using the JBS device as test structure", Int. Workshop on Ultra-low-Loss Power Device technology, Nara Japan, (2000), accepted
[3] M.S. Janson, et. al "Transient enhanced diffusion of implanted boron in 4H-silicon carbide", Appl. Phys: Lett. 76. 1434 (2000)

DOUBLE IMPLANTED POWER MESFET TECHNOLOGY IN 4H SiC

A.B. Horsfall, S. Ortolland, N.G. Wright, C.M. Johnson, A.P. Knights*

Department of Electrical and Electronic Engineering, University of Newcastle, Newcastle, NE1 7RU, UK Tel +44 (0)191 222 7595 Fax +44 (0)191 222 8180
* Surrey Ion Beam Centre, University of Surrey, Guildford, GU2 5XH, UK
Tel +44 (0)1483 879831 Fax +44 (0)1483 534139

An ion implanted MESFET structure is presented. The device is fabricated in an n-type $3x10^{15}$ epitaxial layer that is 10μm thick grown on n-type substrate. The fabrication of the device is by implantation of boron ions at $2.5x10^{13}$ cm^{-2} for the p-well and nitrogen ions at $1x10^{15}$ cm^{-2} for the channel. After each of the implantations the die is annealed (1700C for boron and 1300C for nitrogen) under argon in an RF furnace. After annealing the surface damage is removed using low power reactive ion etching. The resulting structure for a vertical power MESFET is shown in figure 1. The channel is 0.15μm thick with a p-well of 0.4μm. Channel quality and homogeneity is dependent on implantation and anneal conditions as well as the method of surface reconstruction. Details of this will be presented in the paper. Electrical characteristics taken between 300 and 600K will also be presented. These show the effect on electron transport of deep levels from the ion implantation.
Simulation studies of the device have been performed using commercial TCAD software to determine the electronic characteristics of the device. Results consistent with measured characteristics have been obtained using reduced mobility models in the implanted regions. The results from the simulations are shown in figure 2 where the device is operating in depletion mode. The upper line shows a gate voltage of 0V and each subsequent line decreases the gate by 1V.

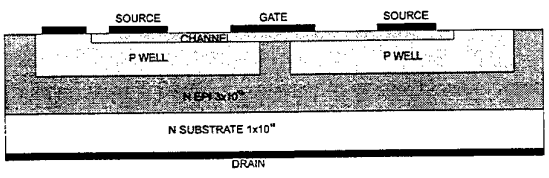


Figure 1 : Structure of Implanted Vertical Power MESFET

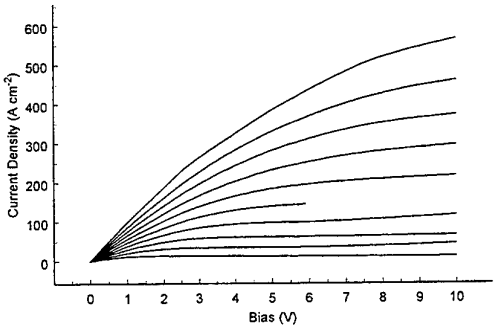


Figure 2 : Simulated Characteristics for Implanted Vertical Power MESFET

WeP-80

Influence of the buried p-layer on the blocking behavior of vertical JFETs in 4H-SiC

Peter Friedrichs, Heinz Mitlehner, Reinhold Schörner, Rainer Kaltschmidt*, Karl-Otto Dohnke, and Dietrich Stephani

SiCED GmbH & Co KG, a Siemens Company, and *Siemens AG, MED SPE
Paul-Gossen-Str. 100, D-91052 Erlangen
Tel.49-9131-734894, E-mail: peter.friedrichs@erls.siemens.de

Vertical JFETs fabricated in 4H-SiC exhibit promising electrical parameters for low loss, fast switching applications in the range above 1000V blocking voltage /1/. One of the most important key parameters characterizing a switching device is the specific on-resistance. For high voltage solid state switching devices this parameter is dominated by the resistance of the epilayer necessary for blocking the desired reverse bias. This epilayer can be designed thinner and with an higher doping density compared to conventional Si-devices due to the high electric breakdown field of SiC, resulting in on-resistances two orders of magnitude below Si-MOSFETs, e.g /2/.

In order to demonstrate the advantages of these benefits in existing applications, we fabricated VJFETs for different reverse bias classes. The breakdown of such vertical JFETs in SiC was shown to be avalanche-like and therefor non-destructive /1/. Numerical simulations showed that the value of the breakdown voltage for a given doping density and thickness of the epitaxial layer strongly depends on the shape and doping of the buried p-layer. The breakdown starts at the edge of the buried layer (see Fig.1) and expands laterally under the pn-junction. Using a traditional box like profile with a projected range of about 0,7µm, approximately 50% of the breakdown voltage of a planar pn-junction can be achieved. This value, however, can be increased by using a modified profile with a lateral step for the buried p-layer implanted to a depth of 1,2µm (see Fig.2).

In order to confirm these simulation results, VJFETs with a modified buried p-layer were fabricated and compared to conventionally processed devices. This work presents the results of the experiment compared to the simulation. It will be shown that e.g. for an epilayer with a doping density of approximately $6x10^{15}cm^{-3}$ and a thickness of 15µm an increase of the blocking voltage from 1200V for the conventional profile up to 1700V with the modified design can be achieved. Additional benefits will be discussed in detail.

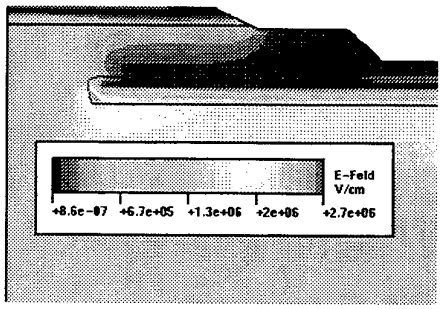


Fig. 1 : Distribution of the electric field for a conventional box profile as buried gate, the maximum is at 2,7MV/cm and located at the edge

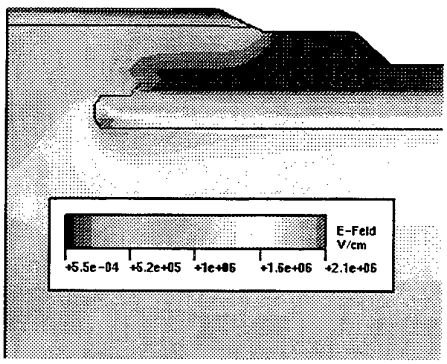


Fig. 2 : Field distribution for the modified design at 1200V, the maximum is at 2,1MV/cm and is smeared out along the pn-junction

/1/ P.Friedrichs, H.Mitlehner, W.Bartsch, K.O.Dohnke, R.Kaltschmidt, U.Weinert, B.Weis, D.Stephani, "Static and Characterictics of 4H-SiC JFETs Designed for Different Blocking Categories" , presented at ICSCRM'99, to be published

/2/ B.J.Baliga, *Power Semiconductors Devices*, PWS Publishing Company, 1996

1700 V SiC Schottky Diodes scaled to 25 A

Dethard Peters, Karl O. Dohnke, Christian Hecht, D. Stephani

SiCED Electronics Development Ltd.
Paul Gossen-Str. 100, D-91052 Erlangen
Phone ++49-9131-731529, e-mail: dethard.peters@erls.siemens.de

A recently published study demonstrated the superior performance of 4 H SiC Schottky diodes /1/. These Schottky diodes, designed for 600 V blocking voltage, exhibited a very low leakage current and a weak dependence of leakage current on temperature. They also proved a long term stability under high temperature reverse bias tests (150 °C, -600 V, 1000 h) and thermal cycling up to 400 °C.

Motivated by these encouraging results and on the need for fast switching devices, especially at higher current levels and blocking voltages, we fabricated SiC Schottky diodes for a current up to 25 A and a blocking voltage of 1700 V. The active area of these devices was 10 mm^2. This is a rather large area for SiC devices with respect to the present day state of defect density for SiC wafers. These diodes were processed on selected wafers with a low micropipe density purchased from Cree. As an example, Fig. 1 shows the static room temperature I-V-characteristics of a 1700 V diode, mounted on a DCB substrate with a heat sink. At a nominal current of 25 A the forward voltage drop amounts to 1.7 V, while at a blocking voltage of –1700 V the leakage current is 150 µA. The leakage current increases by approximately one order of magnitude if the diode is operated at 125°C junction temperature.

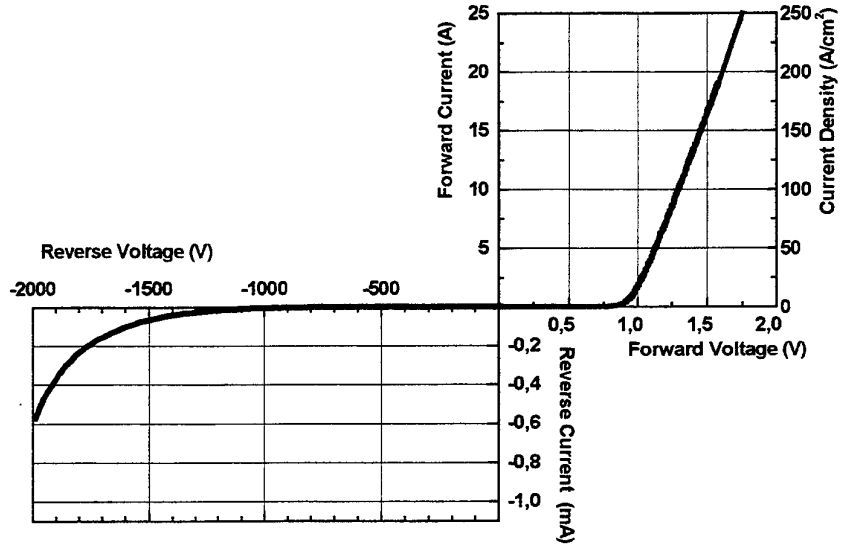


Fig. 1: Static I-V characteristics of a 25 A / 1700 V SiC Schottky diode at room temperature.

/1/ R. Rupp, M. Treu et al., ICSCRM'99, Oct. 99, North Carolina, USA.

A comparison between physical simulations and experimental results on 4H-SiC MESFETs with non-uniform doping in the channel and buffer layers

J. Eriksson, N. Rorsman and H. Zirath
Microwave Electronics, Department of Microelectronics, Chalmers University of Technology, 412 96 Göteborg, Sweden
R Jonsson[1,2], Q. Wahab[1] and S. Rudner[1,2]
[1]Department of Physics and Measurement Technology, Linköping University, SE-581 83 Linköping, Sweden.
[2] FOA Defence Research Establishment, P.O. Box 1165, SE-581 11 Linköping,

We present results on fabrication, characterisation, and numerical drift-diffusion simulations of high-frequency 4H-SiC MESFET on semi-insulating substrates.
The performance of SiC MESFETs is strongly dependent of the detailed doping profiles of the channel and buffer layers. The actual doping profile of commercial transistor materials may differ from the specifications (fig.1). It is therefore important to measure the doping profile to have the correct input data to the physical simulation. The parameters for physical simulations can then be correctly calibrated, and the simulations can be used to optimise the MESFET and understand the experimental results.
The processing sequence is mesa, recess, thermal oxidation, dielectric deposition, ohmic contact and gate formation, pad deposition, passivation and airbridge. The mesa and recess steps use reactive ion etching with a CF_4/O_2 gas mixture. Ohmic contacts were formed by annealing of nickel with a rapid thermal anneal furnace. The gate length is 0.5 um and the gate metalization is Au/Pt/Ti.
Five different layer structures have been processed, characterised and simulated. As can be seen in fig. 2 simulations based on measured material properties correspond well to the experimental results. In the final paper we will present results on several structures.
The transconductance is 25-30 mS/mm and the saturation current is 200-300 mA/mm. The maximum frequency of oscillation, f_{max}, is 40 GHz and the extrinsic transit frequency, f_T, is 6-7 GHz for a 100 μm MESFET.

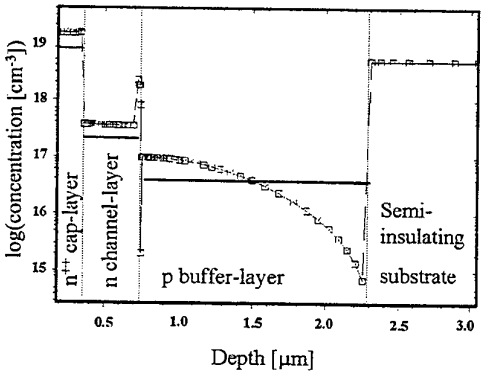


Fig. 1 Doping profile calculated from SIMS data.

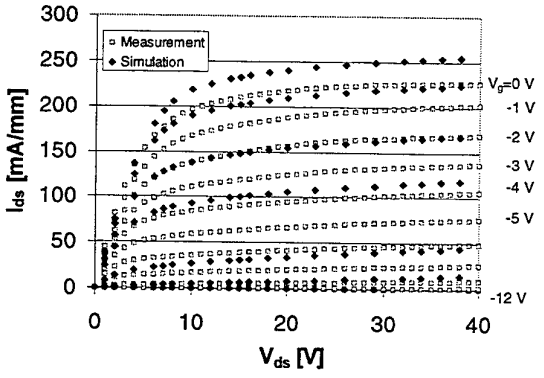


Fig. 2 Simulated and measured drain characteristics of the 4H-SiC MESFET.

Temperature Dependence of Forward and Reverse Characteristics of Ti, W, and Ta Schottky Diodes on 4H-Silicon Carbide

M. Treu*, R. Rupp, H. Kapels
Infineon Technologies AG, AI IP DD SIC, P.O. Box 3220, D-91050 Erlangen, Germany
W. Bartsch
SiCED GmbH, P.O. Box 3220, D-91050 Erlangen, Germany

Schottky diodes on Silicon Carbide are promising rectifiers for blocking voltages between 300 V and several kV. Although theoretical studies about the electrical behavior of Schottky contacts exist for some decades, the exact description of the forward and reverse characteristics is still an issue. The leakage current of Schottky diodes on SiC is much higher than the leakage current predicted by the classical Schottky theory, which is typically used to describe Schottky diodes on silicon. It will be shown that the high electric fields under reverse bias at the interface of SiC Schottky diodes lead to a different behavior.

In this study Ti, W, and Ta Schottky diodes are characterized under forward and reverse bias for temperatures between 21 °C and +200 °C. Additionally the Ti Diodes were characterized for temperatures between –168°C and 21°C. It was observed that part of the diodes show a nearly ideal behavior under forward bias (ideality $n \leq 1.05$) for the whole temperature range and others show a non-ideal as compared in Fig. 1. The results of this work obtained from a large amount of diodes will show clearly that this non-ideal behavior has not necessarily a negative influence on the reverse characteristics of the diodes. This will be explained by a model proposed by Tung [2], which considers the pinch off of the defects by the defect free areas around the defect. It will be shown that the reverse current of the diodes can be described by two mechanisms. The current induced by the first mechanism is nearly independent of the temperature up to a certain temperature T'. Thus we assign this current to trap assisted tunneling. Above the temperature T' the reverse current is dominated by thermionic field emission as proposed by Padovani and Stratton [3] (see Fig. 2). The value of T' depends on the trap density. If the trap density is high T' is also high because the field emission current has to reach a high level to dominate the whole current. It will be shown that the leakage current is dominated by thermionic field emission for Ti,, W, and Ta Schottky diodes at operation temperatures ≥ 100 °C.

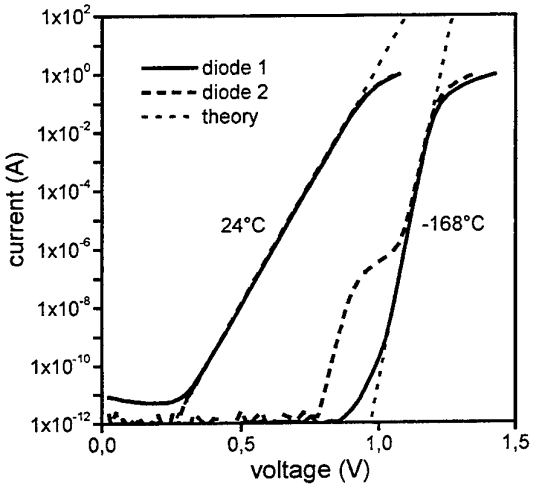


Fig. 1, Forward current as a function of forward bias of two Ti Schottky diodes compared with the Schottky theory with the temperature as a parameter.

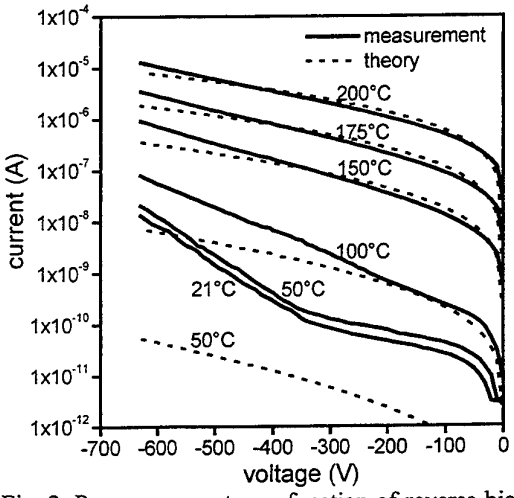


Fig. 2, Reverse current as a function of reverse bias of a Ti Schottky diode compared with the thermionic field emission theory with the temperature as a parameter.

[1] D.Defives, O.Noblanc, C.Dua, C.Brylinski, M.Barthula, V.Aubry-Fortune, IEEE Trans. Electron Devices, **46** (3), 449--455 (1999).
[2] R.T. Tung, Phys. Rev. B, **45** (23), 13509 (1992)
[3] E.H. Rhoderick, Clarendon Press, Oxford 1980, pp. 113

* phone: +49 9131 7 32072, e-mail: michael.treu@infineon.com

Long term operation of 4.5kV PiN and 2.5kV JBS diodes

H. Lendenmann, F. Dahlquist, N. Johansson, J. P. Bergman

ABB Corporate Research, Västerås, SE-721 78, Sweden

SiC devices with 10-fold breakdown strength compared to Si are currently considered to improve power electronic systems such as motor drives and HVDC transmission significantly. Recently, we reported good basic device properties such as forward voltage, low leakage currents and high current switching for large area ($20mm^2$ and $40mm^2$) PiN diodes for the 2.5kV range as well as near theoretical performance for $1mm^2$ 2.0-2.8kV JBS diodes [1,2,3].

These diodes were fabricated on 4H SiC wafers, with low $10^{15}cm^{-3}$ n-type doped hot-wall CVD Epi layers of 30 – 40um thickness. The implanted anode (or p+-stripes in case of the JBS) uses either a Al- or Al-B profile, annealed at 1700°C. The devices are terminated using an implanted multi-zone junction termination extension with an oxide surface passivation layer.

The state of art properties of our PiN and JBS SiC diodes is briefly summarized, which includes high power switching characteristics at 400A and 1250V with a switching loss of only 4 mJ (competitive silicon diodes cause 130mJ under identical conditions). Moreover, we report the successful scaling of the large area PiN diodes to a blocking voltage of 4.5kV.

Long term, high-temperature, blocking testing of these diodes was carried out in statistically relevant quantities. The observed leakage currents in 500h and 1000h tests at 2250V and 125°C are in the range of 10^{-5} to $10^{-4}A/cm^2$, which is consistent with the static leakage. The large variation maybe explained by in terms of the local substrate quality causing Epi defects with high leakage areas. However, after some initial transients, most diodes show an almost stable leakage current over the entire testing time.

Long-term converter operation was carried out with these diodes as well. Thereby, a new drift phenomenon of the forward voltage drop was discovered. For drifting diodes the increase in V_f may range from ~0mV to a few 100mV. In rare instances or under very severe conditions, also higher forward voltage drifts can be observed. Diodes with a rather fast drift (hours-days), coexist with slow- and non-drifting diodes (>2000h) on the same wafer with the identical process. The increase in forward voltage is accompanied by a reduction in the electrical measured minority carrier lifetime and by regions within the active area with reduced photoluminescence. These areas are also related to changes in the crystal matrix [4]. It was found, that the substrate material as well as process uniformity can make marked differences in the occurrence of this phenomenon. In contrast to bipolar PiN diodes, the JBS type diodes do not exhibit this phenomenon.

References

[1] H. Lendenmann et.al "Operation of a 2500V/150A Si-IGBT/SiC diode module", ICSCRM (1999), in print

[2] F. Dahlquist, et. al "A 2.8kV, 2V forward drop JBS diode with low leakage, "ICSCRM (1999), in print.

[3] H. Lendenmann, et. al."Performance and reliability of power diodes", Int. Workshop on Ultra-low-Loss Power Device technology, Nara Japan, (2000), accepted

[4] J.P. Bergman et. al. "Crystal defects as source of anomalous forward voltage increase of 4H SiC diodes", submitted to ESCSRM 2000

Turn-off Performance of a 2.6 kV 4H-SiC Asymmetrical GTO Thyristor

A. K. Agarwal [1], P.A. Ivanov [2], M.E. Levinshtein [2], J.W. Palmour [1], S. L. Rumyantsev [2,3], and M.S. Shur [3]

[1] Cree Inc., 4600 Silicon Drive, Durham, NC 27703, USA
[2] The Ioffe Institute of Russian Acad. of Sci., Politekhnicheskaya 26, 194021 St-Petersburg, Russia
[3] Rensselaer Polytechnic Institute, CII, 9015, Troy NY 12180-3590, telephone: (518)-276-2908, fax: (518)-276-2990, e-mail: roumis2@rpi.edu

Recently, 4H-SiC gate turn-off (GTO) thyristors with 2.6 kV forward blocking capability and up to 12 A of forward current have been demonstrated [1].

We report on the gate turn-off performance of a 4H-SiC asymmetrical GTO thyristor with 2.6 kV breakover voltage, for temperatures ranging from 293 K to 500 K. Both quasi-static and pulse regimes of the gate turn-off operation were studied. The temperature dependencies of the turn-off time and cathode holding current were investigated.

The maximum value of cathode current $I_{Con\ max}$, which can be turned off by the gate current depends on temperature. At room temperature, $I_{Con\ max}$ is equal to 3.3 A, which corresponds to the current density $j_C \approx 1000$ A/cm^2. The turn-off current gain, $K_G = I_C/I_G$, depends on temperature, on the gate pulse duration Δt_G, and on the current density in the on-state. K_G is the largest for a quasi-static turn-off by the current I_{Gst} (i.e. for large values of Δt_G). At $j_C = 1000$ A/cm^2, the maximum value of K_G is equal to 6. K_G increases with a j_C decrease, and at $j_C = 300$ A/cm^2, $K_G = 12.5$. To our knowledge the above value of K_G is the highest ever reported for SiC GTO's.

The turn-off gate current I_G increases with a decrease in Δt_G. A semiempirical formula suggested in [2] describes the experimental I_G/I_{Gst} dependencies on Δt_G over the entire temperature range:

$$I_G / I_{Gst} = \frac{1}{1 - \exp(-\Delta t_G / \tau^*)},$$

where τ^* is a fitting parameter which can be considered as a rough estimate of the carrier lifetime in the blocking base. τ^* is found to grow exponentially from 0.6 to 3.6 μs in the temperature interval from 293 to 502 K.

The cathode holding current I_{Ch} decreases from 0.54 A to 0.052 A with an increase in temperature from 293 K to 502 K. Two mechanisms are responsible for this effect. First, an increase in the carrier lifetime in the blocking base leads to an increase in the common-base current gain. Second, the injection efficiency of p^+n junction between the emitter and the n-base increases with temperature due to the enhanced thermal ionization of a relatively deep Al acceptor level.

These results confirm that 4H-SiC tu GTO thyristors show a high potential for bipolar device applications such as inverters and switch-mode power supplies.

This work was supported by the Office of Naval Research MURI program under Contract No N00014-95-1-1302, monitored by Dr. J. Zolper.

References

[1] A.K. Agarwal, S.H. Ryu, R. Singh, and J. Palmour, in *Abstracts of ICSCRM'99*, Research Triangle Park, NC, October 10-15, 1999, Abstract (474).

[2] I. L. Kaganov and E.S. Malahov, in Reports of Scientific-Technical Conference of All-Union Electrotechnical Research Institute. Moscow, 1966.

High-Performance Surface-Channel Diamond Field-Effect Transistors

H.Umezawa [a), c)], H.Taniuchi [a), c)], T.Arima [a), c)], M.Tachiki [a), c)], K.Tsugawa [a), c)], S.Yamanaka [b), c)], D.Takeuchi [b), c)], H.Okushi [b), c)] and H.Kawarada [a), c)]

[a)] *School of Science and Engineering, Waseda University, Okubo 3-4-1, Shinjyuku-ku, Tokyo, 169-8555, Japan*
[b)] *ETL (Electrotechnical Laboratory), Umezono 1-1-4, Tsukuba, Ibaraki, 305-8568, Japan*
[c)] *CREST, JST (Japan Science and Technology Corporation)*
TEL&FAX: +81-3-5286-3391
e-mail: umezawa@kaw.comm.waseda.ac.jp

High-performance diamond metal-semiconductor (MES) or metal-insulator-semiconductor (MIS) field-effect transistors (FETs) have been realized on hydrogen-terminated surface conductive layer of diamond. The p-type semiconductive layer of diamond surfaces displays desirable properties for the channel of FETs, such as low density of pining states (less than 10^{11} cm^{-2}), high carrier concentration (10^{13} cm^{-2}) and shallow depth (~10 nm). Recently, utilizing this layer as the channel, a Cu gate MESFET with 1 μm gate length has been fabricated by the self-aligned gate fabrication process, which minimizes effectively series resistance that degrades FET performance. Figure 1 shows the *Ids vs. Vds* characteristics of the MESFET. The transconductance of the MESFET is 110 mS/mm [(1)]. This value is the highest in diamond FETs and exceeds that of Si-nMOSFET in the same gate length. The 1 μm gate Cu/CaF_2/Diamond MISFET is also fabricated by the same FET fabrication process. The maximum transconductance of the MISFET is 86 mS/mm and the effective carrier mobility of the MISFET exceeds 250 cm^2/Vs. We have carried out small signal analysis by device simulation on the MISFETs of the average performance (40 mS/mm). The cutoff frequency (f_T) and the maximum frequency of oscillation (f_{max}) are 8 GHz and 60 GHz, respectively under 100 V drain bias condition.

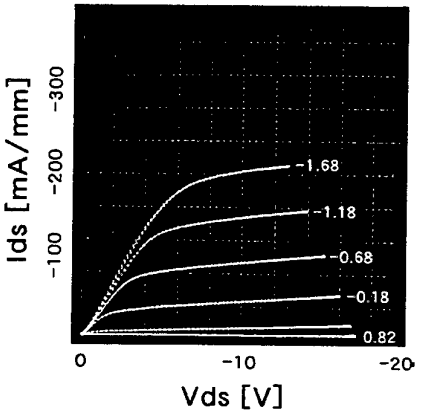


Fig.1 I-V Characteristics of homoepitaxial diamond MESFET with 1 μm gate

At the present, the MESFETs with the gate length of less than 0.5 μm have been fabricated. And, the new FET fabrication processes minimizing the parasitic resistance effect from source-gate or gate-drain distance are also developed. Using these advanced techniques the drastic improvement on DC and high-frequency characteristics of the diamond FET is expected.

(1) H.Umezawa et al.; Jpn. Appl. Phys. Vol.38 (1999) pp. L1222

Epitaxial Growth and Related Defects in III-Nitrides

Jim Speck
Materials Department, University of California, Santa Barbara, CA 93106, USA

In this talk, we review progress on understanding the role of threading dislocations (TDs) in the physical properties of GaN and its alloys. A growing body of work provides compelling evidence that TDs in the group III-nitrides behave as non-radiative recombination centers, have energy levels in the otherwise forbidden energy gap, act as charged scattering centers in doped materials, and provide a leakage current pathway. In comparison with conventional III-V semiconductors, the relatively small minority carrier diffusion length, ~50 nm in the III-nitrides, combined with favorable TD geometries, minimize dislocation-related degradation. The small value of the minority carrier diffusion length also allows for appreciable optical emission in materials with TD densities as high as 10^{10} cm^{-2}.

Th2-2
(Invited)

III-Nitride Power Devices - Good Results and Great Expectations

Michael Shur *, Remis Gaska **, Asif Khan ***

* CIEEM & ECSE, Rensselaer Polytechnic Institute, 110-8th St., Troy, 12180 3590USA

** SET, Inc, 21 Cavalier Way, Latham, NY 12110, USA

*** Department of ECE, University of South Carolina, USA

High electron mobility, high current carrying capabilities, a relatively high thermal conductivity, high temperature operation, and a high breakdown field are the established key materials properties of GaN-based materials that make them competitive for high power applications. GaN-based devices have demonstrated high-temperature operation with little or no degradation up to 300 °C. The most spectacular results have been obtained for AlGaN/GaN microwave power High Electron Mobility Transistors (HEMTs) that yielded close to 10 W/mm power at 10 GHz. The maximum density of the two-dimensional electron gas at the GaN/AlGaN heterointerface or in GaN/AlGaN quantum well structures can exceed $2x10^{13}$ cm^{-2}, which is an order of magnitude higher than for traditional GaAs/AlGaAs heterostructures. The mobility-sheet carrier concentration product for GaN-based two-dimensional systems might also exceed that for GaAs/AlGaAs heterostructures and can be further enhanced by doping the conducting channels. AlGaN/GaN HEMTs on insulating SiC substrates combine superior transport properties of GaN with a high thermal conductivity of SiC. Such an approach combines the best features of both GaN and SiC technologies; and GaN/SiC-based semiconductors and heterostructures should find numerous applications in power electronics.

The large lattice mismatch between GaN, AlN and InN and the strong piezoelectric effects in these materials significantly impact the electrical and optical properties of III-N heterojunction devices. Strain produces piezoelectric doping with about $1x10^{13}$ cm^{-2} sheet carriers. On the other hand, strain might be responsible for the long-term instabilities that several groups observed in their AlGaN/GaN HEMTs. Recently proposed Strain Energy Band Engineering technique should allow us to independently control of strain and lattice mismatch by using AlInGaN/GaN heterostructures and should find important applications in power devices.

The prospects of GaN-based power device technology are enhanced by a recent demonstration of high quality of GaN/SiO_2 interface. SiO_2/AlGaInN/GaN Metal Oxide Semiconductor Field Effect Transistors have exhibited performance comparable or superior to that of conventional AlGaN/GaN devices and hold promise for power applications.

Th3-1
(Invited)

Recent Progress in SiC Epitaxial Growth and Device Processing Technology

T. Kimoto, H. Yano, S. Tamura, N. Miyamoto, K. Fujihira, Y. Negoro, and H. Matsunami

Dept. of Electronic Sci. & Eng., Kyoto University Sakyo, Kyoto 606-8501, Japan
Phone: +81-75-753-5341 Fax: +81-75-753-5342 E-mail: kimoto@kuee.kyoto-u.ac.jp

Breakthroughs in SiC boule and epitaxial growth technology in the 1980's have been accelerating the development of various prototype SiC devices projected for high-power, high-frequency, and high-temperature electronics. To meet the requirements for wide commercialization of SiC electronic devices, however, there still remain crucial issues in both growth and device processing. This paper describes recent progress in SiC epitaxial growth, ion implantation, and MOS technologies made at the authors' group.

We have succeeded in epitaxial growth of thick and high-purity SiC by cold-wall chemical vapor deposition (CVD) at 1500℃. The improvements of susceptor design and growth process enabled to grow 30~50 μm-thick SiC epilayers with a low surface defect density of 50~100 cm^{-2}. Strong free exciton peaks in photoluminescence and a low net doping concentration of $1\sim3\times10^{14}$ cm^{-3} elucidate high purity of the SiC epilayers. Epitaxially grown pin diodes with a 31 μm-thick *i*-layer exhibited a 4200 V breakdown voltage with a low on-resistance of 4.6 $m\Omega cm^2$. High-quality SiC epilayers with excellent surface morphology can also be produced on "micropipe-free" SiC(11$\bar{2}$0) substrates. Recently, vertical hot-wall (chimney-type) CVD [1] has been investigated to increase the growth rate. A high growth rate over 15 μm/h has been achieved at 1700℃. The thickness and doping uniformities on a half two inch wafer were 4% and 6% (at a 1×10^{15} cm^{-3} doping level), respectively.

Phosphorous ion implantation at elevated temperature is effective to form heavily doped n^+ region with a sheet resistance as low as 100 Ω/□. High-dose aluminum ion implantation for p^+ doping has still resulted in a relatively high sheet resistance of 6300 Ω/□, being a future challenge. High-energy (MeV) aluminum and boron ion implantations have also been investigated to form 3 μm-deep pn junction. Very high-temperature annealing at 1800℃ significantly improves the pn junction characteristics and reduces the deep trap concentration near the junction [2]. High blocking voltages of 2500~3100 V with stable and reversible avalanche up to 2 A/cm^2 have been obtained for pn diodes with 15 μm-thick n^- layers.

Very high channel mobilities of 96 and 116 cm^2/Vs have been achieved for inversion-type 4H- and 6H-SiC MOSFETs fabricated on (11$\bar{2}$0), respectively [3]. The channel mobility of 4H-SiC(11$\bar{2}$0) MOSFET decreased according to the $T^{-2.2}$ dependence above 200 K, whereas the mobility on (0001) increased at elevated temperature, demonstrating superior MOS interface quality on (11$\bar{2}$0) face. The threshold voltage of 4H-SiC(0001) MOSFET is very high, 7.8 V at room temperature, and it greatly decreases down to 2.7 V at 500 K, which is accompanied with the increased channel mobility. In contrast, the threshold voltage of 4H-SiC(11$\bar{2}$0) MOSFET is lower, 4.0 V, and is insensitive to temperature. Recent study demonstrates much lower interface state density near the conduction band edge on (11$\bar{2}$0).

[1] A. Ellison et al., *presented at ICSCRM'99, TuB10.*
[2] A. Schöner et al., *to be presented at this conference.*
[3] H.Yano et al., IEEE Electron Device Lett. **20**(1999), p.611.

Th3-2
(Invited)

Doping of Silicon Carbide by Ion Implantation

by

B.G. Svensson[1,2], A. Hallén[1], M.K. Linnarsson[1], A.Yu. Kuznetsov[1],
M.S. Janson[1], D. Åberg[1], P.O. Persson[3], L. Hultman[3], L. Storasta[3],
F.C.H. Carlsson[3], J.P. Bergman[3], C. Jagadish[4] and E. Morvan[5]

[1]Royal Institute of Technology, Solid State Electronics, Electrum 229, SE-164 40 Kista-Stockholm, Sweden
[2]Oslo University, Physical Electronics, Department of Physics, P.B. 1048 Blindern, N-0316 Oslo, Norway
[3]Linköping University, Department of Physics and Measurement Technology, SE-581 83 Linköping, Sweden
[4]The Australian National University, Electronic Materials Engineering, Canberra, ACT 0200, Australia
[5]Centro Nacional de Microelectronica, CNM-CSIC, Campus UAB, 08193 Bellaterra, Spain

Abstract

One key issue when realizing SiC devices is doping to tailor the electrical properties. Controlled doping of bulk crystals and epitaxial layers can be performed in-situ during growth, and for instance, using chemical vapour deposition (CVD) dopant concentrations over a wide range are accessible. However, for a genuine implementation of SiC devices a planar technology with selective area doping is required; in principle, ion implantation is ideally suited for this because of the possibility to accurately control the dopant concentration in three dimensions without chemical or thermodynamic constraints. A major drawback is, however, the generation of damage destroying the crystalline structure of the implanted layer. The damage can vary from point defects caused by single collision cascades at low ion doses to amorphization at high enough doses, and post-implant annealing is required to restore the crystal structure and electrically activate the implanted dopants as shallow acceptors or donors.
For SiC, our knowledge and understanding of the damage build-up during implantation is severely limited and the same holds for the subsequent post-implant annealing processes. In this contribution a survey is given of the current status, and issues like ion ranges and channeling, implantation temperature, defect evolution as a function of dose, co-implantation and electrical activation of dopants, surface morphology, post-implant annealing and transient enhanced dopant diffusion are addresses. In addition, recent results on dopant compensation, dose rate (flux) effects, evolution of structural defects during annealing, cluster formation in heavily doped layers, and epitaxial regrowth of amorphous layers will be discussed.

SiC High Frequency Power Devices

Olivier Noblanc, Erwan Morvan, Christian Dua, and Christian Brylinski,
THOMSON CSF Corporate Research Laboratory (LCR),
Domaine de Corbeville F-91404 ORSAY Cedex (France), tel : + 33 1 69 33 94 21, fax : + 33 1 69 33 08 66,
email: christian.brylinski@lcr.thomson-csf.com

SiC Power RF / Microwave transistors are now trying to emerge as commercial products for the near future with some samples already delivered to strictly selected potential customers. However, few teams in the world are really active in this area and even fewer are publishing results. So, a very restricted number of people has to face all the initial problems always associated with the use of any new material. As some of the pioneers are already competing against each other, the progress is slower than financial markets observers would like it to be.

However, in our present view, the first microwave results on SiC-based prototype devices and amplifiers are now available and they justify the initial hopes and promises formulated long time ago on the use of this material. The main obvious advantages over existing technologies, forecasted long time ago, are now observed experimentally: Higher bias voltage (up to more than 50 V for over 2 GHz operation), higher output impedance: around 25 ohms for 50 W and 50 V bias at 1.5 GHz, and easier large bandwidth operation (over one octave seems quite easy around 1 – 2 GHz). Linearity behaviour also seems quite good on the preliminary tests, which is of prime importance for the future markets of telecommunications.

Mesfet is still the favoured structure. During the past two years, a few more teams have started to work on this kind of devices. No intention to commercialise SITs have been recorded yet from any side. The progress on the SiC MOS, though significant, is still slow and the published values for channel mobilities still appear too low for making good microwave devices.

The state of the art of crystal extended defects in semi-insulating (S.I) substrates allows to make devices with periphery as large as 36 mm without significant decrease of process yield, as compared to smaller devices. The reason is that the sensitive area for the device is only < 5 micrometers wide so that, even for a transistor considered as big nowadays, the sensitive total area is around 0.1 mm^2. All the S.I SiC wafers we have seen yet contain defective zones representing at least 20 % of the total surface, but it is generally possible to make working transistors with good „DC" process yield inside the other zones of the wafer. Only the results of the reliability studies, started recently, will tell whether devices made on very imperfect substrates can be considered as really usable by demanding customers.

On the performance side, the main real problem associated with the commercial S.I substrates available today on the market seems to be the deep centres density, still in the 1E16 – 1E17 cm^{-3} range. We have more and more clues to make us believe that those deep centres are responsible for the strong trapping effects still observed presently in most SiC Mesfet transistors at high drain voltage. Together with other partners, we are actively exploring two ways to come over those parasitic effects: one is the use of optimised buffer layers, and the second is the use of better substrates. The first track has already given improvement in the device DC stability and RF performance of the SiC Mesfets devices

Author Index

A

Abe, Y. MoP-45
Åberg, D. MoP-37, MoP-68, MoP-08, WeP-15, Th3-2
Acero, M. C. MoP-73
Achtziger, N. WeP-10, MoP-17, MoP-36
Adachi, K. MoP-75
Adås, C. WeP-39, WeP-75
Agarwal, A. K. Th1-5
Akasaki, I. WeP-06
Albertazzi, E. MoP-69
Amano, H. WeP-06
Amaratunga, G. WeP-70
Ambacher, O. MoP-38
Amy, F. We1-3
Anand, S. WeP-15
Andersson, H. WeP-55, WeP-15
Anikin, M. MoP-50, Mo3-3, Tu1-3
Aradi, B. MoP-14, Mo2-1
Arai, K. Mo1-2, MoP-23, MoP-65, MoP-75, WeP-51
Arima, T. Th1-6
Arpiainen, S. MoP-11, MoP-12
Avramenko, S. F. MoP-46
Avrov, D. D. MoP-26
Azar, R. WeP-70

B

Bai, S. We3-2, MoP-28, Tu2-2
Banc, C. WeP-74
Banerjee, S. MoP-78
Baranov, P. G. MoP-32, MoP-03, MoP-16, MoP-33
Barbier, D. MoP-52
Barna, Á. WeP-38
Barthe, M.-F. MoP-12, MoP-11
Bartsch, W. Th1-3
Basset, A. Tu1-3
Basset, G. Tu1-3
Bauer, A. MoP-24, MoP-59
Bauman, D. MoP-56
Beaumont, B. WeP-07
Bechstedt, F. MoP-58, We1-2
Berenguer, M. WeP-05
Bereznjakova, L. A. MoP-63
Berge, R. Tu3-1
Bergman, J. P. WeP-06, Mo3-4, MoP-06, MoP-30, Th1-4, MoP-08, Th3-2
Bernard, C. MoP-49, MoP-50
Bertuccio, G. MoP-81
Bickermann, M. WeP-30, WeP-04, MoP-43
Bikbajevas, V. WeP-16
Billion, T. Tu1-3, MoP-50
Birch, J. WeP-35, MoP-25
Blanquet, E. MoP-49, WeP-50
Bleichner, H. WeP-55, We3-4
Blondiaux, G. MoP-12
Bluet, J. M. WeP-05, WeP-08
Bockstedte, M. Mo2-4, MoP-01
Bogdanov, M. V. Tu1-6, WeP-33
Bogdanova, E. MoP-77
Bord, O. V. WeP-22, WeP-33, Tu1-6
Bouix, J. MoP-52, WeP-42
Brady, M. Tu1-1
Bratus, V. Ya. MoP-07
Breitholtz, B. We3-4
Brezeanu, G. WeP-70
Brink, D. J. MoP-27
Brylinski, C. We1-3, Th3-3, WeP-74

C

Camassel, J. We3-1, WeP-08, MoP-27
Cantin, J. L. MoP-04, Mo2-3, MoP-11, MoP-03
Carlsson, F. H. C. MoP-06, MoP-08, MoP-29, Th3-2, MoP-30
Carnera, A. MoP-69
Carosella, F. MoP-31
Carter Jr., C. H. Tu1-1
Casiraghi, R. MoP-81
Castaldini, A. MoP-79
Cauwet, F. WeP-42
Cavallini, A. MoP-79
Chaix-Pluchery, O. Mo3-3
Chante, J. P. MoP-72
Chassagne, T. MoP-52
Chatty, K. MoP-78
Chaussende, D. WeP-42
Chen, C. Q. MoP-05
Chen, Yi MoP-35
Cheung, W. Y. WeP-37
Cho, W. J. WeP-66, MoP-65
Chow, T. P. WeP-77, MoP-78
Choyke, W. J. We3-2, Tu2-2, MoP-28, WeP-12, MoP-14
Chua, S. J. WeP-02
Chung, J. MoP-51, WeP-44
Chuvilin, A. Mo3-2
Cimalla, V. MoP-54, MoP-60
Coleman, P. G. We2-3
Contreras, S. WeP-14
Corbel, C. MoP-12, MoP-11
Cressler, J. D. WeP-69, WeP-63

D

Dahlquist, F. WeP-78, Th1-4
Danielsson, Ö. Tu2-4, Tu2-1
Dauelsberg, M. WeP-41, Tu3-1
Davydov, D. V. MoP-80
Deák, P. Mo2-1, WeP-52, WeP-12, MoP-14, MoP-02
Dedulle, J. M. MoP-49
Derenge, M. A. We2-2
Derycke, V. WeP-45, MoP-62
Desgardin, P. MoP-12
Devaty, R. P. We3-2, Tu2-2, MoP-28
Di Cioccio, L. WeP-14, WeP-08
di Forte-Poisson, M. A. WeP-71
Dimitrijev, S. WeP-65
Dmitriev, V. MoP-34, Tu2-2, MoP-56, MoP-74
Doerschel, J. WeP-25
Dohnke, K. O. Th1-1, WeP-80
Dolle, J. MoP-21, WeP-25, WeP-23, MoP-42, WeP-32
Donolato, C. MoP-79
Dorozhkin, S. I. MoP-26
Dua, C. Th3-3
Dudley, M. WeP-18, Tu1-5
Duranova, E. MoP-76
Durst, F. WeP-28

E

Eckstein, R. Tu1-2
Efimov, A. N. WeP-21
Egilsson, T. We3-3
Eickhoff, M. WeP-68, MoP-55, WeP-53, We2-5
Eiserbeck, W. MoP-21
Ellis, C. WeP-69
Ellison, A. MoP-29, Tu2-1, We3-3
Epelbaum, B. M. WeP-43
Eriksson, J. Th1-2
Esteve, J. MoP-73
Evans, G. A. WeP-02, MoP-31

F

Falk, F. Tu2-6
Falkovski, L. We3-1, MoP-27
Faure, C. Tu1-3, MoP-50
Fauster, Th. WeP-46
Fedison, J. B. WeP-77
Feltin, E. WeP-07
Feng, Z. C. WeP-02
Ferro, G. MoP-52, WeP-42
Fissel, A. WeP-40, We1-2, We1-5, MoP-59
Fontaine, F. WeP-38
Fonteneau, P. MoP-62, WeP-45
Fornell, J.-O. Tu3-1
Forsberg, U. Tu2-4, MoP-68
Foster, B. WeP-61
Frank, Th. MoP-09, WeP-03, MoP-10
Franklin, J. We2-5
Frauenheim, Th. MoP-02, WeP-12, MoP-14
Friedrichs, P. WeP-80
Fujihira, K. Th3-1
Fukuda, K. WeP-51, MoP-65, WeP-66
Furthmüller, J. MoP-58, We1-2
Furusho, T. WeP-26
Fuyuki, T. WeP-62

G

Gajowski, J. MoP-48
Galeckas, A. We3-4
Gali, A. WeP-12, MoP-14, Mo2-1
Galyukov, A. O. Tu1-6
Gaska, R. Th2-2
Gebauer, J. MoP-10
Gendron, F. Mo2-3
Gibart, P. WeP-07
Girard, P. WeP-05
Glass, R. Tu1-1
Glazer, A. M. Mo3-3
Godignon, P. MoP-72
Goetz, K. MoP-24, MoP-59
Goldhahn, R. MoP-60
Gourbeyre, C. MoP-52
Greulich-Weber, S. Mo2-5, MoP-13
Grillenberger, J. MoP-36, WeP-10
Grivickas, P. MoP-41, WeP-16, WeP-16, MoP-41
Grosse, P. Tu1-3
Grossner, U. We1-2
Grünleitner, H. WeP-56
Guillot, G. WeP-05
Gutmann, R. J. MoP-78
Gyulai, J. WeP-20

H

Hai, P. N. Mo3-1
Hajnal, Z. MoP-02, WeP-12, MoP-14
Hallén, A. MoP-15, WeP-15, Th3-2, MoP-37, WeP-56, MoP-08, MoP-74
Harada, S. WeP-66
Harris, C. I. WeP-75
Härtwig, J. WeP-18
Hatayama, T. WeP-62
Hauser, T. MoP-27
Hautojärvi, P. MoP-11, MoP-12

Hecht, C. Th1-1
Hecht, U. WeP-43
Heera, V. MoP-70, WeP-38, WeP-53
Heissenstein, H. We3-5, WeP-19
Helbig, R. MoP-05, We3-5, WeP-19, WeP-03
Hellmund, O. WeP-67
Henkel, T. MoP-71
Henry, A. Mo2-2, Tu2-4, MoP-30, Tu2-1
Henry, L. MoP-12, MoP-11
Henshall, D. Tu1-1
Heringer, D. WeP-12
Herold, J. MoP-17
Heß, G. MoP-59, WeP-34, MoP-64
Heuken, M. Tu3-1, WeP-41
Hilton, K. P. MoP-20
Hishita, S. MoP-71
Hobert, H. Tu2-6
Hobgood, D. We3-2, Tu1-1
Hofmann, D. WeP-30, WeP-43, Tu1-4, WeP-04, MoP-43, WeP-28
Holland, O. W. We2-2
Hong, M. H. WeP-44, MoP-51
Horsfall, A. B. WeP-79
Horváth, Z. E. WeP-20
Huang, X.-R. WeP-18
Huet, F. WeP-71
Hülsen, C. MoP-17
Hultman, L. WeP-17, WeP-35, Th3-2
Hunderi, O. MoP-18
Hundhausen, M. WeP-01
Hwu, Y. We1-3

I

Ilyin, I. V. MoP-16, MoP-32
Imaizumi, M. WeP-76
Irmscher, K. WeP-32
Ismail, M. M. MoP-31
Itoh, H. WeP-54, MoP-66, MoP-09, MoP-10
Ivanov, A. M. MoP-80
Ivanov, I. G. We3-3
Ivanov, P. A. Th1-5
Ivanov-Omskii, V. I. MoP-63
Iwakuro, H. WeP-61
Iwaya, M. WeP-06
Izumi, K. Mo3-5, WeP-31

J

Jacob, Ch. Tu2-5, WeP-49, Tu2-3
Jacobsson, H. MoP-25, MoP-53
Jacquier, C. WeP-42
Jagadish, C. Th3-2
Jamet, P. WeP-65
Janson, M. S. MoP-15, WeP-56, MoP-68, WeP-55, Th3-2
Janzén, E. Mo3-1, Mo2-2, MoP-53, Tu2-4, MoP-30, MoP-29, We3-3, Tu2-1, MoP-76, MoP-06, MoP-25, MoP-08
Jikimoto, T. Mo3-5, WeP-31
Jinschek, J. WeP-36, WeP-34
Johansson, N. Th1-4
Johnson, C. M. MoP-75, We2-3, WeP-79, MoP-20
Jones, K. A. We2-2
Jonsson, R. Th1-2
Josepovits, K. V. WeP-52
Jürgensen, H. WeP-41, Tu3-1

K

Kadinski, L. WeP-28, Tu1-4, Tu1-2
Kaiser, U. Mo3-2, WeP-36, MoP-64, MoP-59
Kakanakov, R. WeP-58
Kalabukhova, E. MoP-34
Kalinina, E. MoP-74
Kaltschmidt, R. WeP-80
Kamata, I. Mo3-5, WeP-31
Kapels, H. Th1-3
Käppeler, J. Tu3-1
Karlsson, S. WeP-39, WeP-75, MoP-15, WeP-55, MoP-74
Karpov, D. S. WeP-22
Karpov, S. Yu. MoP-44, Tu1-6, WeP-22, WeP-33
Kassamakov, I. WeP-58
Kassamakova, L. WeP-58
Kato, T. MoP-23
Kawahito, K. WeP-62
Kawarada, H. Th1-6
Kawasuso, A. MoP-10
Kayambaki, M. WeP-64
Keir, A. MoP-20
Khan, A. Th2-2
Khánh, N. Q. WeP-20
Kholujanov, G. MoP-74
Khramtsov, V. A. MoP-32
Kildemo, M. MoP-18
Kimoto, T. Th3-1, We2-4, WeP-11
Kinoshita, K. MoP-75
Kinouchi, S. WeP-76
Kipshidze, G. MoP-64
Kiselev, V. S. MoP-46
Kitabatake, M. MoP-66
Klettke, O. WeP-11
Knights, A. We2-3, WeP-79
Kobayashi, N. MoP-71

Kochuguev, S. K. Tu1-6
Kögel, G. MoP-10
Kögler, R. MoP-73
Kölbl, M. Tu1-2
Komissarov, A. E. WeP-33, Tu1-6
Komlev, K. MoP-64
Konstantinov, A. WeP-39, MoP-74, WeP-75
Korolkov, O. WeP-60
Koshka, Y. Tu2-2
Kossov, V. MoP-74
Kosugi, R. WeP-66, WeP-51
Kótai, E. WeP-20
Kovarskii, A. MoP-74
Kozlovski, V. V. MoP-80
Krafcsik, O. H. WeP-52
Krasnow, V. WeP-73
Krause-Rehberg, R. MoP-10
Kräußlich, J. MoP-24, WeP-34, WeP-36, MoP-59
Kreisel, J. Mo3-3
Krieger, M. WeP-13
Krötz, G. MoP-55, WeP-68, We2-5, WeP-53
Krygin, L. MoP-34
Kuhn, H. WeP-18
Kuhr, T. A. Tu1-5
Kulik, A. V. Tu1-6
Kunert, H. W. MoP-27
Kurz, H. WeP-67
Kuznetsov, A. N. WeP-72, MoP-56
Kuznetsov, A. Yu. WeP-56, Th3-2

L

Lagadas, M. MoP-77
Lahrèche, H. WeP-07
Larkin, D. J. MoP-28, We3-2
Larsson, K. WeP-48
Laube, M. WeP-13, WeP-03
Laügt, M. WeP-07
Lazar, M. MoP-72
Le Berre, M. MoP-52
Lebedev, A. A. MoP-80, MoP-57, WeP-72
Lebedev, A. O. MoP-26, WeP-21
Lebedev, V. WeP-34, WeP-36, We1-5
Lefort, O. We2-5
Lei, Y. M. WeP-37
Leitch, A. W. R. WeP-59
Lendenmann, H. Th1-4, WeP-78, Mo3-4
Leroux, M. WeP-07
Levinshtein, M. E. Th1-5
Ley, L. WeP-01, We1-4
Lin, S. WeP-37
Lindefelt, U. MoP-40, MoP-41
Lingner, Th. MoP-13, Mo2-5
Link, A. MoP-38
Linnarsson, M. J. Mo2-2
Linnarsson, M. K. WeP-39, MoP-68, WeP-55, Th3-2, MoP-15, WeP-15
Linnros, J. We3-4, MoP-41
Liszkay, L. MoP-12
Litwin, A. WeP-75
Lloyd-Spetz, A. We2-1, MoP-68
Lo Giudice, A. MoP-79
Locatelli, M. L. MoP-72
Lohner, T. WeP-20
Lovtsus, A. A. WeP-33
Lukin, S. MoP-34
Lulli, G. MoP-69
Luo, E. Z. WeP-37
Lysenko, V. MoP-67

M

Madar, R. MoP-49, Mo3-3, MoP-50, Tu1-3
Madsen, L. D. MoP-76
Magaud, L. WeP-50
Magerl, A. WeP-19
Magnusson, B. MoP-29, Mo2-2
Makarov, Yu. N. WeP-41, MoP-44, WeP-22, WeP-33, Tu1-6
Makeeva, I. N. MoP-07
Makkai, Zs. WeP-71
Malherbe, J. B. MoP-27
Malta, D. Tu1-1
Manfredotti, C. MoP-79
Mantel, B. We1-4
Martinez, A. MoP-40, MoP-41
Masarotto, L. WeP-05
Masri, P. WeP-47
Massies, J. WeP-07
Masuda, Y. WeP-49, Tu2-3, MoP-35
Matsunami, H. WeP-11, We2-4, Th3-1
Matsuura, H. MoP-35
Mattausch, A. MoP-01, Mo2-4
Matz, W. MoP-59
Maurice, T. P. MoP-27
Mehregany, M. WeP-44, MoP-51
Melnik, Y. V. MoP-22
Melnychuk, G. Tu2-2, MoP-56
Mermoux, M. Mo3-3
Merrett, J. N. WeP-63, WeP-69
Mihaila, A. WeP-70
Mikulskas, I. MoP-41
Mitlehner, H. WeP-80
Miyamoto, N. We2-4, Th3-1
Mokhov, E. N. MoP-61, MoP-16, MoP-32, MoP-03, MoP-44, MoP-33
Möller, H. We2-5

Monemar, B. WeP-06
Monteil, Y. MoP-52, WeP-42
Morante, J. R. MoP-73
Morrison, D. J. MoP-20
Morvan, E. Th3-3, MoP-72, Th3-2
Mosina, G. N. MoP-22
Moulin, C. Tu1-3, MoP-50
Muller, S. Tu1-1
Murphy, M. MoP-38
Mynbaeva, M. MoP-56, Tu2-2

N

Nava, F. MoP-81, MoP-79
Nazarov, A. WeP-73
Negoro, Y. Th3-1
Neyret, E. WeP-14
Nielsen, A. WeP-68, MoP-55, WeP-53
Nieminen, R. M. MoP-39
Nikitina, I. P. MoP-22, MoP-56
Nikolaev, A. E. MoP-22
Nilsson, H.-E. MoP-40
Nilsson, P. Å. Mo3-4
Nipoti, R. MoP-19, MoP-69, MoP-79
Nishiguchi, T. WeP-27
Nishikawa, K. WeP-61
Nishino, S. Tu2-3, Tu2-5, WeP-26, MoP-47, WeP-49, MoP-35, WeP-27
Nishizawa, S. MoP-23
Nitta, S. WeP-06
Niu, G. WeP-69
Noblanc, O. Th3-3, WeP-74
Nordell, N. MoP-15

O

Obermeier, E. We2-5, MoP-55
Obyden, S. K. MoP-61
Ofengeim, D. Kh. Tu1-6
Ogino, S. WeP-31
Ohashi, H. MoP-75
Ohshima, S. WeP-26, WeP-49, Tu2-3, WeP-27
Ohshima, T. WeP-54, MoP-66
Ohtsuka, K. WeP-76
Okulov, S. M. MoP-07
Okushi, H. Th1-6
Olafsson, H. Ö. MoP-67
Olander, J. WeP-48
Ortolland, S. We2-3, WeP-79
Osiyuk, I. MoP-67
Österman, J. WeP-15
Östling, M. WeP-78
Ottaviani, L. MoP-72
Ouisse, T. WeP-74
Oyanagi, N. MoP-23
Ozeki, T. WeP-76

P

Pajot, B. Mo2-3
Palmour, J. Tu3-2, Th1-5
Panknin, D. WeP-57, WeP-53, MoP-73, WeP-15
Pankratov, O. MoP-01, Mo2-4
Pasold, G. WeP-10, MoP-36
Passero, A. Tu1-3
Pasturel, A. WeP-50
Pécz, B. WeP-38, WeP-71, MoP-70
Pelissier, B. MoP-50, Mo3-3, Tu1-3
Pensl, G. WeP-11, MoP-09, MoP-48, WeP-13, WeP-01, WeP-03, WeP-56, MoP-10
Peppermüller, C. We3-5
Pérez-Rodríguez, A. MoP-73
Pernot, E. Mo3-3, MoP-50, WeP-64, Tu1-3
Pernot, J. WeP-14, WeP-08
Pernot-Rejmánková, P. Mo3-3, Tu1-3
Persson, P. O. WeP-55, Th3-2
Persson, P. O. Å. WeP-17, WeP-35
Peters, D. Th1-1
Petrenko, T. L. MoP-07
Petrenko, T. T. MoP-07
Pezoldt, J. WeP-47, MoP-60, MoP-54
Pham, N. P. WeP-45
Pirouz, P. Tu2-5
Pisch, A. MoP-49, Tu1-3, MoP-50
Pitt, G. D. WeP-02
Planson, D. MoP-72
Ploß, R. Mo1-1
Polenta, L. MoP-79
Pons, M. Tu1-3, MoP-49, MoP-50
Potemski, M. MoP-05
Powell, A. Tu1-1
Pozina, G. WeP-06
Preston, I. H. MoP-20
Prinsloo, L. C. MoP-27
Puska, M. J. MoP-39

R

Raffy, C. WeP-50
Ramm, M. S. WeP-22, MoP-44, Tu1-6
Rang, T. WeP-60
Rasp, M. Tu1-2, WeP-30, WeP-04
Rastegaev, V. P. WeP-24
Ratnikov, V. V. MoP-57
Rauls, E. MoP-02, MoP-14
Raynaud, C. MoP-72

Redmann, F. MoP-10
Ren, C. X. WeP-37
Rendakova, S. MoP-74
Reshanov, S. A. WeP-24
Richter, W. WeP-40, We1-2, WeP-36, We1-5, WeP-34, MoP-64, MoP-59
Robert, J. L. WeP-14
Roenkov, A. D. MoP-61, MoP-44
Rohmfeld, S. WeP-01
Romano-Rodríguez, A. MoP-73
Rorsman, N. Th1-2
Rost, H.-J. WeP-25, MoP-42, WeP-23, MoP-21
Rougeot, C. We2-5
Royet, A. S. WeP-74
Rudenko, T. MoP-67
Rudner, S. Th1-2
Rumyantsev, S. L. Th1-5
Rupp, R. Mo1-1, Th1-3
Rusina, L. N. WeP-09

S

Saarinen, K. MoP-11, MoP-12
Saddow, S. E. Tu2-2, MoP-56, WeP-69
Sadowski, H. WeP-03, We3-5
Saitoh, K. Mo3-2
Samiji, M. E. WeP-59
Saparin, G. V. MoP-61
Saroukhan, A.-M. WeP-75
Sasaki, M. MoP-47, WeP-27
Savkina, N. S. MoP-57, WeP-72
Schaefer, J. A. WeP-47
Scharmann, F. MoP-54
Scharnholz, S. WeP-67
Scheglov, M. MoP-56
Schell, N. MoP-59
Schmidt, J. MoP-33
Schmitt, E. Tu1-2
Schnell, N. WeP-07
Schöner, A. We2-4
Schörner, R. WeP-80
Schröter, B. MoP-64, We1-5, MoP-60, MoP-59
Schulz, D. WeP-23, MoP-21, MoP-42, WeP-25
Schulze, N. MoP-48, WeP-03, WeP-01
Seitz, C. WeP-19
Selder, M. WeP-28, Tu1-4, Tu1-2
Semond, F. WeP-07
Senzaki, J. MoP-65, WeP-51, WeP-66
Serre, C. MoP-73
Seyller, Th. We1-4
Shah, P. B. We2-2
Shchukarev, A. MoP-63, MoP-74
Sheglov, M. P. MoP-22
Sheridan, D. C. WeP-69, WeP-63
Shimizu, M. WeP-61
Shimizu, T. WeP-27
Shinohe, T. MoP-75
Shiomi, H. MoP-47
Shuman, V. B. MoP-57
Shumay, I. L. WeP-46
Shur, M. Th2-2, Th1-5
Siche, D. MoP-42, WeP-25, WeP-23, MoP-21
Sieber, N. We1-4
Sielemann, R. MoP-36
Sitnikova, A. MoP-56
Sköld, K. MoP-06
Skorupa, W. MoP-70, WeP-57, WeP-38, WeP-15, WeP-53, MoP-73
Skowronski, M. Tu1-5
Smelyansky, E. V. WeP-09
Smorchkova, Y. MoP-38
Solov'ev, V. MoP-74, MoP-56
Son, N. T. Mo3-1, MoP-29
Soukiassian, P. We1-3, MoP-62, WeP-45
Spaeth, J.-M. Mo2-5, MoP-13
Spangenberg, B. WeP-67
Speck, J. Th2-1
Sperr, P. MoP-10
Spieß, L. MoP-60
Sridhara, S. G. MoP-30, MoP-08
Staab, T.E.M. MoP-39
Stafast, H. Tu2-6
Starke, U. We1-1
Stauden, Th. WeP-47, MoP-60, MoP-54
Steeds, J. W. MoP-31, WeP-02
Stein, J. WeP-67
Stephani, D. Th1-1, WeP-80
Stoemenos, J. WeP-53, MoP-70, WeP-68, MoP-55, We2-5
Stölzer, M. WeP-16
Storasta, L. MoP-08, MoP-37, MoP-06, Th3-2
Straubinger, T. L. WeP-29, MoP-43, WeP-28, WeP-30, Tu1-4, WeP-04
Strel'chuk, A. M. WeP-72, MoP-74
Strokan, N. B. MoP-80
Stutzmann, M. MoP-38
Suezaki, T. WeP-62
Sugimoto, H. WeP-76
Sundaravel, B. WeP-37
Suzuki, S. WeP-66, WeP-51, MoP-65
Svedberg, J.-O. WeP-75
Sveinbjörnsson, E. MoP-67

Svensson, B. G. Th3-2, MoP-37, WeP-56, MoP-15, MoP-68, WeP-55
Syrkin, A. MoP-56
Syväjärvi, M. MoP-53, MoP-25, WeP-16
Szilágyi, E. WeP-20

T

Tachiki, M. Th1-6
Tairov, Yu. M. WeP-24, MoP-26
Takahashi, K. MoP-66
Takami, T. WeP-76
Takeuchi, D. Th1-6
Tamura, S. Th3-1
Tanaka, T. MoP-65, WeP-51
Tanaka, Y. MoP-71
Taniuchi, H. Th1-6
Tanner, P. WeP-65
Tanoue, H. MoP-71
Tarui, Y. WeP-76
Thomas, B. WeP-32
Tiensuu, S. WeP-75
Tin, C.-C. WeP-63
Tomasiunas, R. MoP-41
Torpo, L.M. MoP-39
Treu, M. Th1-3
Triftshäuser, W. MoP-10
Tsagaraki, K. WeP-64, MoP-54
Tsaregorodtsev, A. M. WeP-21
Tsiryulnikov, A. V. Tu1-6
Tsuchida, H. WeP-31, Mo3-5
Tsugawa, K. Th1-6
Tsuji, T. WeP-31
Tsvetkov, D. V. MoP-22
Tsvetkov, V. Tu1-1
Tungasmita, S. WeP-35
Tuomi, T. MoP-25
Turchanikov, V. WeP-73
Tyagulski, I. MoP-67

U

Udal, A. WeP-16
Udrea, F. WeP-70
Umezawa, H. Th1-6
Uraoka, Y. WeP-62
Urban, S. Tu2-6
Uren, M. J. MoP-20

V

v. Duijn-Arnold, A. MoP-33
Valakh, M. Ya. MoP-46
van Wyk, E. WeP-59
Vanni, P. MoP-79
Vassilevski, K. MoP-77
Velmre, E. WeP-16
Venkatesan, T. We2-2
Venter, A. WeP-59
Verzellesi, G. MoP-79
Vetter, W. M. Tu1-5
Viala, J. C. WeP-42
Vicente, P. We3-1
Vispute, R. D. We2-2
Vittone, E. MoP-79
Vodakov, Yu. A. MoP-44, MoP-61
Voegeli, W. MoP-31
von Bardeleben, H. J. MoP-04, MoP-03, Mo2-3, MoP-07, MoP-11
Vorob'ev, A. N. WeP-33, WeP-41
Vouroutzis, N. WeP-68, WeP-53, MoP-55
Vovk, Ja. WeP-73

W

Wagner, G. WeP-32, MoP-21
Wahab, Q. MoP-76, Th1-2
Weber, A.-D. Tu1-2
Weidner, M. MoP-09, WeP-13, MoP-10
Weinelt, M. WeP-46
Weingärtner, R. WeP-04, MoP-43, WeP-30
Weissker, H.-C. MoP-58
Wellmann, P. J. Tu1-4, WeP-29, WeP-28, MoP-43, WeP-04, WeP-30
Wiets, M. WeP-46
Williams, J. R. WeP-63, WeP-69
Williams, K. P. J. WeP-02
Wilson, I. H. WeP-37
Winkelmann, A. We1-5
Winkler, R. MoP-05
Winnacker, A. WeP-29, WeP-43, Tu1-4, MoP-43, WeP-30, WeP-04
Wischmeyer, F. Tu3-1, WeP-41
Witthuhn, W. WeP-10, MoP-17, MoP-36
Wöhner, T. WeP-47
Wollweber, J. WeP-23, MoP-42, WeP-25, MoP-21
Wong, S. P. WeP-37
Wood, C. E. C. Tu2-2
Wright, N. G. We2-3, WeP-79, MoP-20
Wu, C.-H. MoP-51, WeP-44
Wu, L. WeP-59
Wunderlich, B. MoP-59, MoP-24
Wysmolek, A. MoP-05

X, Y

Xu, J. B. WeP-37
Yafaev, R. MoP-74
Yakimova, R. MoP-53, MoP-25, WeP-64, WeP-55, WeP-16

Yamaguchi, H. MoP-23
Yamanaka, S. Th1-6
Yano, H. Th3-1
Yoshikawa, M. MoP-66, WeP-54
Yu, Y. H. WeP-37
Yukhimchuk, V. A. MoP-46

Z

Zappe, S. We2-5, MoP-55
Zawadzki, W. WeP-14
Zekentes, K. MoP-77, WeP-64, MoP-54, WeP-58
Zhang, J. Tu2-1, MoP-76, We3-3
Zhmakin, A. I. WeP-41, WeP-22, Tu1-6
Zhmakin, I. A. Tu1-6
Zirath, H. Th1-2
Zolnai, Z. WeP-20
Zondervan, R. MoP-33
Zorenko, A. MoP-77
Zorman, C. A. MoP-51, WeP-44
Zou, S. C. WeP-37
Zubkova, S. M. WeP-09
Zubrilov, A. MoP-74
Zverev, I. Mo1-1